Twentieth Symposium on
NAVAL HYDRODYNAMICS

Ships in a Seaway
Propeller Cavitation Performance
Ship Motions Under Way; Wave Resistance
Oscillating Propulsors
Ship Motions—Nonlinear
Cavitation
Propeller Noise
Ships in Shallow Water
Cavitation Inception; Supercavitating Flows
Diffraction; Nonlinear Drift
Wave Breaking
Near-surface Turbulence
Ship-generated Vortices
Hydrodynamic Impact
Bubble Flows
Waves
Turbulent Ship Flows
Ship Viscous Flows
Forced Wave Motion
Computation of Viscous Propulsor Flows

DTIC QUALITY INSPECTED 4

DISTRIBUTION STATEMENT A
Approved for public release;
Distribution Unlimited

19970924 051



Attendees at the Twentieth Symposium on Naval Hydrodynamics, Santa Barbara, California, August 21-26, 1994.

Twentieth Symposium on
NAVAL HYDRODYNAMICS

Ships in a Seaway
Propeller Cavitation Performance
Ship Motions Under Way; Wave Resistance
Oscillating Propulsors
Ship Motions—Nonlinear
Cavitation
Propeller Noise
Ships in Shallow Water
Cavitation Inception; Supercavitating Flows
Diffraction; Nonlinear Drift
Wave Breaking
Near-surface Turbulence
Ship-generated Vortices
Hydrodynamic Impact
Bubble Flows
Waves
Turbulent Ship Flows
Ship Viscous Flows
Forced Wave Motion
Computation of Viscous Propulsor Flows

Sponsored Jointly by

Office of Naval Research

University of California, Santa Barbara

Naval Studies Board
Commission on Physical Sciences, Mathematics,
and Applications
National Research Council

NATIONAL ACADEMY PRESS
Washington, D.C. 1996

The National Research Council serves as an independent advisor to the federal government on scientific and technical questions of national importance. Established in 1916 under the congressional charter of the private, nonprofit National Academy of Sciences, the Research Council brings the resources of the entire scientific and technical community to bear on national problems through its volunteer advisory committees. Today the Research Council stands as the principal operating agency of both the National Academy of Sciences and the National Academy of Engineering and is administered jointly by the two academies and the Institute of Medicine. The National Academy of Engineering and the Institute of Medicine were established in 1964 and 1970, respectively, under the charter of the National Academy of Sciences.

The National Research Council has numerous operating units. One of these is the Naval Studies Board, which is charged with conducting and reporting on surveys and studies in the field of scientific research and development applicable to the operation and function of the Navy.

A portion of the work done to prepare this document was performed under Department of Navy Contract N00014-87-C-0018 issued by the Office of Naval Research under contract authority NR 201-124. However, the content does not necessarily reflect the position or the policy of the Department of the Navy or the government, and no official endorsement should be inferred.

The United States Government has at least a royalty-free, nonexclusive, and irrevocable license throughout the world for government purposes to publish, translate, reproduce, deliver, perform, and dispose of all or any of this work, and to authorize others so to do.

Printed in the United States of America

NAVAL STUDIES BOARD

David R. Heebner, Science Applications International Corporation (retired), *Chair*
George M. Whitesides, Harvard University, *Vice Chair*
Albert J. Baciocco, Jr., The Baciocco Group, Inc.
Alan Berman, Center for Naval Analyses
Norman E. Betaque, Logistics Management Institute
Norval L. Broome, Mitre Corporation
Gerald A. Cann, Rockville, Maryland
Seymour J. Deitchman, Chevy Chase, Maryland, *Special Advisor*
Anthony J. DeMaria, DeMaria ElectroOptics Systems, Inc.
John F. Egan, Lockheed Martin Corporation
Robert Hummel, Hummel Enterprises, Inc.
David W. McCall, Far Hills, New Jersey
Robert J. Murray, Center for Naval Analyses
Robert B. Oakley, National Defense University
William J. Phillips, Northstar Associates, Inc.
Mara G. Prentiss, Jefferson Laboratory, Harvard University
Herbert Rabin, University of Maryland
Julie JCH Ryan, Booz, Allen and Hamilton
Harrison Shull, Monterey, California
Keith A. Smith, Vienna, Virginia
Robert C. Spindel, Applied Physics Laboratory, University of Washington
David L. Stanford, Science Applications International Corporation
H. Gregory Tornatore, Applied Physics Laboratory, Johns Hopkins University
J. Pace VanDevender, Prosperity Institute
Vincent Vitto, Lincoln Laboratory, Massachusetts Institute of Technology
Bruce Wald, Arlington Education Consultants

Navy Liaison Representatives
Paul G. Blatch, Office of the Chief of Naval Operations (N911T1)
Ronald N. Kostoff, Office of Naval Research

Ronald D. Taylor, Director (as of October 2, 1995)
Associate Director (July 1, 1994, through September 29, 1995)
Lee M. Hunt, Director (through September 29, 1995)

COMMISSION ON PHYSICAL SCIENCES, MATHEMATICS, AND APPLICATIONS

Robert J. Hermann, United Technologies Corporation, *Chair*
Stephen L. Adler, Institute for Advanced Study
Peter M. Banks, Environmental Research Institute of Michigan
Sylvia T. Ceyer, Massachusetts Institute of Technology
L. Louis Hegedus, W.R. Grace and Co.
John E. Hopcroft, Cornell University
Rhonda J. Hughes, Bryn Mawr College
Shirley A. Jackson, U.S. Nuclear Regulatory Commission
Kenneth I. Kellermann, National Radio Astronomy Observatory
Ken Kennedy, Rice University
Thomas A. Prince, California Institute of Technology
Jerome Sacks, National Institute of Statistical Sciences
L.E. Scriven, University of Minnesota
Leon T. Silver, California Institute of Technology
Charles P. Slichter, University of Illinois at Urbana-Champaign
Alvin W. Trivelpiece, Oak Ridge National Laboratory
Shmuel Winograd, IBM T.J. Watson Research Center
Charles A. Zraket, Mitre Corporation (retired)

Norman Metzger, Executive Director

FOREWORD

The Twentieth Symposium on Naval Hydrodynamics was held in Santa Barbara, California, from August 21-26, 1994. This international symposium was organized jointly by the Office of Naval Research (Mechanics and Energy Conversion S&T Division), the National Research Council (Naval Studies Board), and the University of California, Santa Barbara. In addition to promoting the exchange of naval technical research developments of common interest to all the countries of the world, this biennial symposium encourages both formal and informal discussion of the presented papers, and the occasion provides an opportunity for direct communication among international peers.

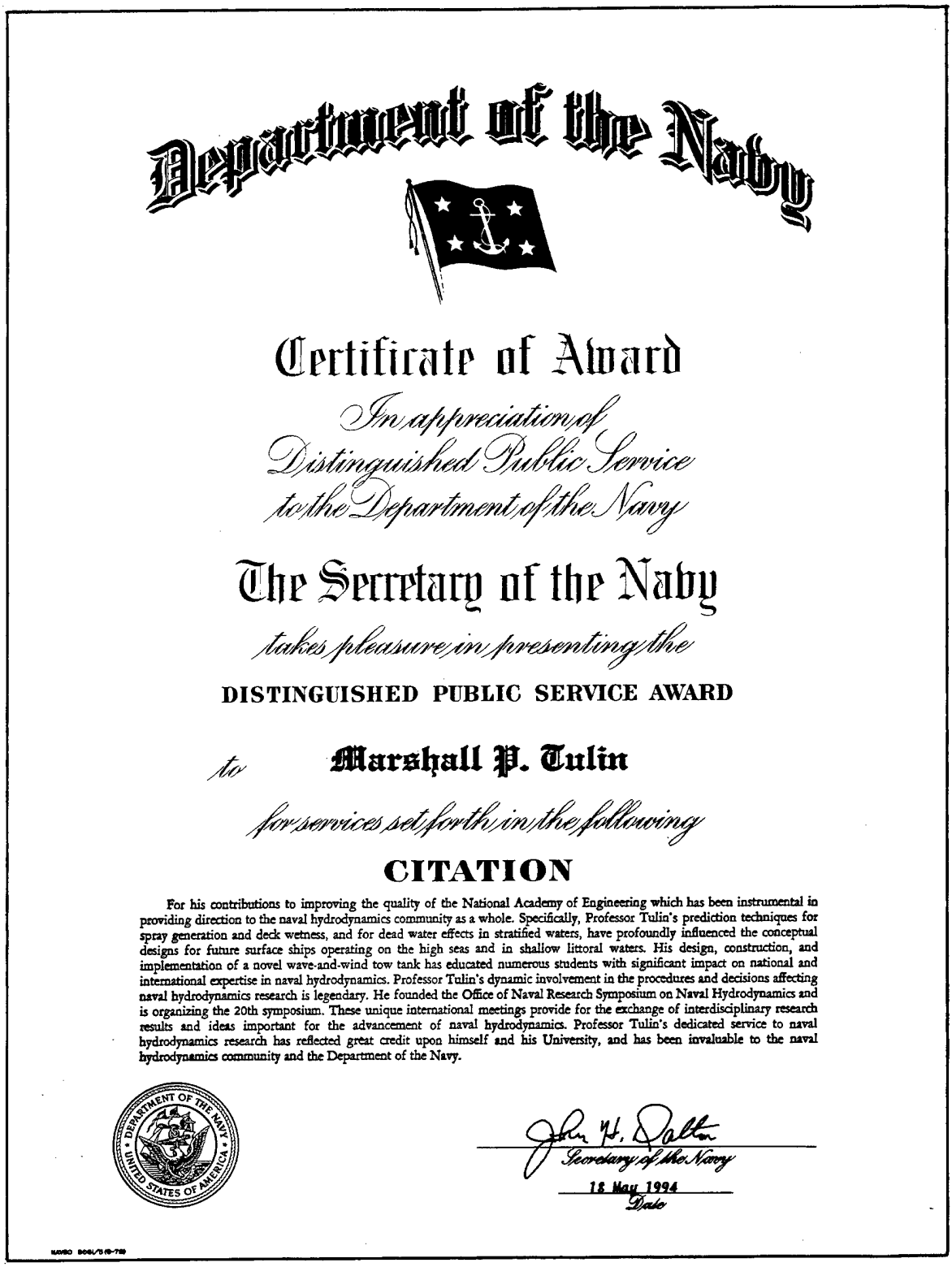
More than 130 participants from 13 countries attended the symposium. The attendees represented a mix of experiences and expertise: some were newly graduated students and others were of established international repute. Sixty-six papers were presented in twenty topical areas, including ships in a seaway; propeller cavitation performance; ship motions under way and wave resistance; oscillating propulsors; ship motions—nonlinear; cavitation; propeller noise; ships in shallow water; cavitation inception and supercavitating flows; diffraction and nonlinear drift; wave breaking; near-surface turbulence; ship-generated vortices; hydrodynamic impact; bubble flows; waves; turbulent ship flows; ship viscous flows; forced wave motion; and computation of viscous propulsor flows. These topical areas were chosen because of the recent significant advances made in them. Examples of such advances presented in the papers include nonlinear motions for ships in seaways, the effect of irregular waves on extreme ship motions, the effect of three-dimensional propeller geometry on cavitation, acoustic radiation produced by unsteady propeller cavitation, shallow water ship hydrodynamics, numerical experiments for breaking waves, direct simulations of free-surface turbulent flows, computations of bubble interactions with turbulent flows, computations of unsteady viscous three-dimensional propeller flows, and near-field numerical prediction of turbulent nonlinear free-surface flows around ships.

This brief list illustrates the quality and timeliness of the symposium for naval hydrodynamics. This occasion for the symposium marked its twentieth anniversary.

During the opening ceremony, the prestigious Distinguished Public Service Award was presented to Marshall Tulin by RADM Marc Pelaez, USN, Chief of Naval Research, on behalf of John Dalton, Secretary of the Navy, for a distinguished career and achievements that include the founding of this symposium series.

The success of this symposium was the result of hard work on the part of many people. The Organizing and Paper Selection Committee consisted of myself, Dr. Patrick Purtell, and Mr. James Fein (Office of Naval Research), Mr. Lee Hunt (National Research Council), Prof. Marshall Tulin (University of California, Santa Barbara), and Dr. William Morgan and Dr. Justin McCarthy (David Taylor Model Basin). The contribution of this committee was certainly the cornerstone for the success of the symposium. However, the administrative preparation and execution would not have been possible without the support of Mrs. Susan Campbell, Mrs. Mary G. Gordon, and the staff of the Naval Studies Board of the National Research Council.

Edwin P. Rood
Office of Naval Research



Department of the Navy

Certificate of Award

In appreciation of
Distinguished Public Service
to the Department of the Navy

The Secretary of the Navy

takes pleasure in presenting the

DISTINGUISHED PUBLIC SERVICE AWARD

to **Marshall P. Tulin**

for services set forth in the following

CITATION

For his contributions to improving the quality of the National Academy of Engineering which has been instrumental in providing direction to the naval hydrodynamics community as a whole. Specifically, Professor Tulin's prediction techniques for spray generation and deck wetness, and for dead water effects in stratified waters, have profoundly influenced the conceptual designs for future surface ships operating on the high seas and in shallow littoral waters. His design, construction, and implementation of a novel wave-and-wind tow tank has educated numerous students with significant impact on national and international expertise in naval hydrodynamics. Professor Tulin's dynamic involvement in the procedures and decisions affecting naval hydrodynamics research is legendary. He founded the Office of Naval Research Symposium on Naval Hydrodynamics and is organizing the 20th symposium. These unique international meetings provide for the exchange of interdisciplinary research results and ideas important for the advancement of naval hydrodynamics. Professor Tulin's dedicated service to naval hydrodynamics research has reflected great credit upon himself and his University, and has been invaluable to the naval hydrodynamics community and the Department of the Navy.

DEPARTMENT OF THE NAVY · UNITED STATES OF AMERICA

John H. Dalton
Secretary of the Navy

18 May 1994
Date

The prestigious Distinguished Public Service Award presented to Professor Marshall P. Tulin, Director, Ocean Engineering Laboratory, University of California–Santa Barbara, by RADM Marc Pelaez, USN, Chief of Naval Research, on behalf of John Dalton, Secretary of the Navy, for a distinguished career and achievements that include the founding of this symposium series.



Professor Marshall P. Tulin, Director, Ocean Engineering Laboratory
University of California–Santa Barbara.

CONTENTS

OPENING REMARKS

Rear Admiral Marc Pelaez, USN
Chief of Naval Research 3

TECHNICAL SESSIONS

Invited Lecture

Wave Loadings and Motions of Ships and High-Speed Marine Vehicles 9
O. Faltinsen (Norwegian Institute of Technology, Norway)

Ships in a Seaway

Prediction of the Seakeeping Characteristics of Ships 27
H. Bingham, F. Korsmeyer, J. Newman (Massachusetts Institute of Technology, USA)

Irregular Waves and Their Influence on Extreme Ship Motions 48
J. De Kat (Maritime Research Institute, The Netherlands)

Nonlinear Analysis of Bow Wave Breaking and Deck Wetness of a High-Speed Ship by the Parabolic Approximation 68
H. Maruo, W. Song (Yokohama National University, Japan)

Propeller Cavitation Performance

Effects of Skew and Rake on Cavitation Inception for Propeller Blades with Thick Blade Sections 83
G. Kuiper (Maritime Research Institute, The Netherlands)

Cavitation Performance Evaluation of Naval Surface Ship Propellers with Standard and Advanced Blade Sections 101
S. Jessup, W. Berberich, K. Remmers (David Taylor Model Basin, USA)

A Surface Vortex Lattice Method for Calculating Performances of Non- or Super-Cavitating Propellers 117
H. Yamasaki, M. Ikehata (Yokohama National University, Japan)

Ship Motions Under Way; Wave Resistance

Time-Domain Theory of Wave Diffraction for Ship Motions with Forward Speed 136
Z. Zhou (China Ship Scientific Research Center, China),
Z. Liang, D. Yishan (Harbin Shipbuilding Engineering Institute, China)

Free Surface Flows without Waves; Applications to Fast Ships with Low-Wave Resistance 157
M. Tulin, O. Oshri (University of California–Santa Barbara, USA)

Oscillating Propulsors

Hydrodynamic Design of Thrust Generators Based on Oscillating Wings 170
K. Rozhdestvensky, V. Ryzhov (St. Petersburg Marine Technical University, Russia),
A. Kurapov (Cambridge University, United Kingdom)

Boundary Layer Formation on an Oscillating Hydrofoil 187
D. Hart (Massachusetts Institute of Technology, USA)

Ship Motions—Nonlinear

Energy-Stable Model Equations for Water Waves and Ship Motions 199
E. van Daalen (Twente University of Technology, The Netherlands)

Large-Amplitude Motions and Wave Loads for Ship Design 205
W.-M. Lin, M. Meinhold, N. Salvesen (Science Applications International Corp., USA),
D. Yue (Massachusetts Institute of Technology, USA)

Nonlinear Ship Motion Computations Using the Desingularized Method 227
R. Beck, Y. Cao, S. Scorpio, W. Schultz (University of Michigan, USA)

Invited Lecture

Observations of Cavitating Flows 247
C. Brennen (California Institute of Technology, USA)

Cavitation

Viscous Effects in Tip Vortex Cavitation and Nucleation 268
R. Arndt, B. Maines (University of Minnesota, USA)

Bubble Dynamics and Cavitation Inception in Non-Uniform Flow Fields 290
G. Chahine (Dynaflow, Inc., USA)

Free Oscillation of a Nonspherical Bubble in a Quiescent Fluid 311
N. McDougald, G. Leal (University of California–Santa Barbara, USA)

Cloud Cavitation on an Oscillating Hydrofoil 328
G. Reisman, E. McKenney, C. Brennen (California Institute of Technology, USA)

Propeller Noise

An Experimental Investigation of the Mechanism and the Pressure of Counter-Rotating Vortices on a CPP at the Off-Design Condition 341
N. Okamura, R. Fujino, T. Tanaka (Ishikawajima-Harima Heavy Industries Co., Ltd., Japan)

Pressure Field Analysis of a Propeller with Unsteady Loading and Sheet Cavitation 355
W. van Gent (Maritime Research Institute, The Netherlands)

Ships in Shallow Water

Hydrodynamics of a Body Moving over a Mud Layer 368
G. Zilman, T. Miloh (Tel-Aviv University, Israel)

Nonlinear Theory of Asymmetric Motion of a Slender Ship in a Shallow Channel 386
X. Chen (University of Stuttgart, Germany), S. Sharma (Mercator University, Germany)

Linear and Nonlinear Calculations of the Free Surface Potential Flow Around Ships in Shallow Water 408
K. Kim, Y. Choi (Daewoo Shipbuilding and Heavy Machinery, Ltd., Korea),
C. Jansson (Chalmers University of Technology, Sweden),
L. Larsson (Flowtech International AB, Sweden)

Cavitation Inception; Supercavitating Flows

Observations of the Influence of Nuclei Content on the Inception and Form of Attached Cavitation 427
C. Li, S. Ceccio (University of Michigan, USA)

Nonlinear Analysis of Viscous Flow Around Cavitating Hydrofoils 446
S. Kinnas, S. Mishima, W. Brewer (Massachusetts Institute of Technology, USA)

Artificial Variation Problems Method for Three-Dimensional Lifting Cavity Flows 466
A. Achkinadze, G. Fridman (Marine Technical University of St. Petersburg, Russia)

Diffraction; Nonlinear Drift

Three-Dimensional Nonlinear Diffraction Around a Fixed Structure 477
A. DiMascio, M. Landrini, F. Lalli, U. Bulgarelli
(Istituto Nazionale per Studi ed Esperienze di Architettura Navale, Italy)

Wave-Drift Forces on Ships in Cross-Flow Conditions 487
R. Huijsmans (Maritime Research Institute, The Netherlands),
L. Sierevogel (Delft University of Technology, The Netherlands)

Time-Domain Calculations of the Second-Order Drift Force on a Tanker in Current and Waves 501
H. Prins, A. Hermans (Delft University of Technology, The Netherlands)

Invited Lecture

The Structure of Extreme Ocean Waves 513
O. Phillips (Johns Hopkins University, USA)

Wave Breaking

The Transition to Turbulence in a Spilling Breaker 521
J. Duncan, V. Philomin, H. Qiao (University of Maryland, USA)

The Vortical Structure of a Near-Breaking Gravity-Capillary Wave 530
D. Dommermuth, R. Mui (Science Applications International Corp., USA)

Wave Groups, Wave-Wake Interaction, and Wave Breaking: Results of Numerical Experiments 551
Y. Yao, P. Wang, M. Tulin (University of California–Santa Barbara, USA)

Kinematic and Dynamic Evolution of Deep Water Breaking Waves 568
O. Griffin, R. Peltzer, H. Wang (Naval Research Laboratory, USA),
W. Schultz (University of Michigan, USA)

Invited Lecture

Physical Processes of the Local Air-Sea Interactions—Current Understanding and Outstanding Questions 588
Y. Toba (Tohoku University, Japan)

Near-surface Turbulence

Attached Vortices in Free-Surface Turbulence 598
S. Kumar, R. Gupta, S. Banerjee (University of California–Santa Barbara, USA)

Dynamics of a Turbulent Jet Interacting with a Free Surface 618
N. Mangiavacchi, R. Gundlapalli, R. Akhavan (University of Michigan, USA)

Direct Numerical Simulation of Free-Surface Wave Generated by Turbulent Shear Flow 633
M. Zhu, H. Miyata (University of Tokyo, Japan),
T. Hino (Ship Research Institute, Japan)

Flow Structure Around a Surface-Piercing Blunt Body 650
E. Pogozelski, J. Katz (Johns Hopkins University, USA),
T. Huang (David Taylor Model Basin, USA)

Ship-generated Vortices

Numerical Prediction of the Effect of Forward Speed on Roll Damping 657
Y. Al-Hukail, P. Bearman, M. Downie (University of Newcastle upon Tyne, United Kingdom), J. Graham, Y. Zhao (Imperial College, United Kingdom)

The Influence of Vorticity upon Estimation of Manoeuvring Derivatives 669
G. Hearn, D. Clarke (University of Newcastle upon Tyne, United Kingdom),
H. Chan, A. Incecik, K. Varyani (University of Glasgow, United Kingdom)

Turbulence in Trailing Vortex Pairs 682
W. Devenport, J. Zsoldos, C. Vogel (Virginia Polytechnic Institute and State University, USA)

Hydrodynamic Impact

Hydroelastic Analysis of a Flexible Bag Structure 702
T. Ulstein, O. Faltinsen (The Norwegian Institute of Technology, Norway)

Blunt-Body Penetration into a Slightly Compressible Liquid 722
A. Korobkin (Lavrentyev Institute of Hydrodynamics, Russia)

Application of the Flux-Vector Splitting Method to Capture Shock Waves and Calculate Pressure in Ship Slamming 730
X. Wang, Z. Huang, C. Hsiung (Technical University of Nova Scotia, Canada)

Bubble Flows

Interaction of Bubbles with Turbulent Flow: Particle Tracking and Flow Field Characterization 742
A. Kolaini, S. Sinha, V. Rajendran (University of Mississippi, USA)

Direct Simulations of Bubbly Flows 753
P.-W. Yu, A. Esmaaeli, S. Ceccio, G. Tryggvason (University of Michigan, USA)

Experimental Study of a Bubbly, Turbulent, Free Shear Layer 766
P. Rightley, J. Lasheras (University of California–San Diego, USA)

Waves

Effects of Regular Waves on the Body Submerged in a Stratified Fluid 776
E. Ermanyuk, I. Sturova (Lavrentyev Institute of Hydrodynamics, Russia)

A Method for Simulation of Viscous, Nonlinear, Free-Surface Flows 791
B. Hodges, R. Street, Y. Zang (Stanford University, USA)

A Panel Method for Lifting Potential Flows Around Three-Dimensional Surface-Piercing Bodies 810
Z. Zou, H. Söding (Universität Hamburg, Germany)

Steady and Unsteady Ship Waves by a Higher-Order Boundary Element Method 822
S. Hong (Korea Research Institute of Ships & Ocean Engineering, Korea),
H. Choi (Seoul National University, Korea)

Invited Paper

A Review of Reynolds Stress Models for Turbulent Shear Flows 835
C. Speziale (Boston University, USA)

Turbulent Ship Flows

Numerical Simulation of the Drift Motion of a Ship 856
E. Campana, P. Esposito, R. Penna
(Istituto Nazionale per Studi ed Esperienze di Architettura Navale, Italy)

Prediction of Incompressible Tip Vortex Flows 871
L. Eça, J. Falcão de Campos (Instituto Superior Técnico, Portugal),
M. Hoekstra (Maritime Research Institute, The Netherlands)

Near-Field Flow Prediction for Ship Design 887
K. Weems, R. Korpus, W.-M. Lin, M. Fritts (Science Applications International
Corp., USA), H.-C. Chen (Texas A&M University, USA)

Calculation of Boundary Layer Considering Free-Surface Effect Around Ship Hulls 906
Y. Wang, Q. Wang (Dalian University of Technology, China)

Ship Viscous Flows

Three-Dimensional Flow Around a Surface-Piercing Body 913
R. Yeung, X. Yu (University of California–Berkeley, USA)

On the Intersection Flow Near a Fine Ship Bow 934
P. Sclavounos (Massachusetts Institute of Technology, USA)

Numerical Simulation of a Wave-Viscous Flow about a Ship Including Propeller Effects 946
O. Watanabe, A. Masuko, Y. Shiorose
(Isikawajima-Harima Heavy Industries Co., Ltd., Japan)

Forced Wave Motion

Comparison of Calculated and Measured Loads on a Flared Body Oscillating in a Free Surface 959
B. Maskew (Analytical Methods, Inc., USA),
M.-L. Wang, A. Troesch (University of Michigan, USA)

Computation of Viscous Propulsor Flows

Computation of Viscous Marine Propulsor Blade and Wake Flow 980
F. Stern, D. Zhang, B. Chen, H. Kim (University of Iowa, USA),
S. Jessup (David Taylor Model Basin, USA)

Three-Dimensional Navier-Stokes Solutions for a One-Stage Axial-Flow Pump 1001
Y.T. Lee (David Taylor Model Basin, USA),
C. Hah, J. Loellbach (NASA Lewis Research Center, USA)

An Integrated Method for Computing the Internal and External Viscous Flow Field Around the Ducted Propulsor Behind an Axisymmetric Body 1011
L. Zhou, F. Zhao (China Ship Scientific Research Center, China)

Computation of Unsteady Viscous Marine Propulsor Blade and Wake Flow 1021
B. Chen, F. Stern, W. Kim (University of Iowa, USA)

APPENDIX—LIST OF PARTICIPANTS 1043

Twentieth Symposium on

NAVAL HYDRODYNAMICS

Opening Remarks

Rear Admiral Marc Pelaez, USN
Chief of Naval Research

Chancellor [Henry T.] Yang, thank you for your wonderful introduction. There are few things that I would fly across country to kick off when I have to immediately then fly back, which unfortunately I have to do this morning. But the subject of this meeting is near and dear to my heart. I feel very strongly that this meeting concerns such an important area for all of us, all the countries of the world, that I wanted to personally give you a few thoughts. Not that they will necessarily be as insightful as all the papers that will be presented, but I didn't want to miss the opportunity, particularly on the occasion of this 20th Symposium.

As the Chief of Naval Research I have a broad interest in science and technology across all disciplines. As a naval officer, I have a particularly warm place in my heart for the field of naval hydrodynamics, which I feel deserves particular attention. This symposium is unique in the world and, as Chancellor Yang mentioned, it has a rich history. The technical content and the professionalism of the papers presented at this symposium are well recognized. In fact, so are the proceedings, as they are used throughout our world's educational systems in teaching hydrodynamics, and in naval architecture and related fields. I think it is appropriate to give a real tip of my hat to Marshall Tulin, whose vision provided for this whole symposium.

Now I will tell you that it's you, the attendees, who make this gathering either what it should be or what it could be, or else Santa Barbara is just a wonderful place to visit and not much would be accomplished. I think it will be the former based on the people I have seen here.

I looked over the program yesterday and am particularly pleased with the breadth of papers that will be presented. But I will contrast that fact with a couple of visions, and I will try not to be too controversial, although most of my people know that they cannot predict what I am going to say when I come up to speak. I wrote these notes this morning.

I will contrast the depth and quality of the papers with some discussions I have had with a number of professionals in the field who, to varying degrees, communicated their views on naval hydrodynamics to me prior to my coming to this conference. I will give you a few quotations:

"The last several decades have produced few if any CFD [computational fluid dynamics] design tools of demonstrated usefulness to the ship design process, and this absence particularly in the propulsion area has resulted in numerous design oversights."

Naval hydrodynamics is "old and venerable, naval architecture being about the most conservative of the conservative engineering fields."

"Even though it is well known that the results of hull-propeller interaction are of great significance for both maneuvering and propulsion performance predictions, cultures dictate that they be treated separately."

I think that these are rather condemning statements when they are taken together. But that's the sort of input I received!

At the reception I had a very interesting discussion with Chancellor Yang. We exchanged views on a number of science and technology issues, and I believe he captured my thoughts rather succinctly when he noted that a danger for many researchers is that they become a mile deep and a micron wide in their field. In reality they need to be a mile deep *and* a mile wide, and certainly not a mile deep and a micron wide. How to achieve that is a very basic issue.

You are here to discuss the state of hydrodynamics research a mile deep. I am not going to attempt to provide great technical insight in these brief opening remarks, particularly in light of the fact that Marshall Tulin is up here! I am going to refrain from that so that I will not be subject to having to defend my views—so that I can speak on a different level, if you do not mind. I would like to relate some of my views on science and technology, and on the community in general, and to do so from the perspective of my position.

Just prior to assuming my current job as the Chief of Naval Research I received numerous briefings on a broad range of disciplines. The one great thing about the office that I have the fortune of being in charge of is that it is truly multidisciplinary. It covers everything from basic research through

technology demonstration, and so the potential is enormous.

The thing that struck me about the briefs that I received as I was talking to my technical people was how narrowly focused everyone was. Very few people were able to relate their narrow science or technology piece in the broader context of its implications to, in our case, the Office of Naval Research, and its implications for the future of the Navy. But that is exactly what we all need to be able to do. We need to be able to be a mile deep and a mile wide.

I found also that the customers for the science were not well understood. People were very content to sit in their research area, deal in that narrow area, and in many cases not relate to their customers. And probably they could not say who their customers are. The fact of the matter is that they do not speak the same language as their customers. In general when you are dealing in scientific terms and get into the world of the people who have to use what you have developed in the long term, you have to somehow make the translation so that you both speak the same language, so that you can understand common goals and objectives.

Marshall Tulin has been in the business world, and he knows that if you do not understand and communicate with your customer, you go out of business. We in the scientific research communities tend to feel that we are somewhat immune from that. Some of the recent attacks in this country on the research budgets may well be symptomatic of concern about this very issue.

I think that the tendency of researchers is to be narrow, to go to the tenth decimal place without necessarily a clear articulation of the need to get to the tenth decimal place. There are times when that is entirely appropriate, and there are other times when it is not. We need something we can use practically to design new concepts in ships.

When the first symposium took place in 1956, 400 to 500 people attended. We have 130 people today. So you wonder what has changed in the world. Well, I will tell you that in the United States Navy in the 1950s, we were making enormous changes and experimenting with new concepts. In the broadest scale of things, whole new ship concepts, whole new ship designs (the Albacore hull, for instance) were developed for submarines in the 1950s, and in my own area of nuclear propulsion, considerable changes in experimentation took place. That is not what you see happening today.

So the questions now are, How do we make the links, how do we involve the broader technical community, how do we engage with the users of our science so that we can really make the sorts of strides that are necessary? I believe that it is extremely important to develop a corporate view of where we are headed.

One of the problems I see is that the rate of change of technology is so great that none of us is in a position to really pick the winners. We can pick some, but it is very difficult for us to determine what is really going to make the difference in the future.

There is a tendency as resources draw down to narrow the scope of that with which we have to deal. In this country—and I do not know if it is true internationally, but it probably is, because the trend is that way—the bureaucrats tend to develop lists of critical technologies to be pursued.

I am diametrically opposed to that. If we circulate a piece of paper in this room and ask each person to list the top 10 critical areas in science and technology, I guarantee you that the lists will be different. My list will not be the same as your list, and neither list will be right.

If I were to ask for a list of critical technologies, I think that most people would place "information technologies" somewhere on that list. If you were not at the Office of Naval Research, your chance of finding someone who would list "naval hydrodynamics," or even know how to spell it, would be very slim. So there is a real danger to us in others taking the approach of looking at critical technologies, and that is why I am so opposed to it. But we do need to develop some common corporate view to guide investments.

I personally believe in a broad science and technology base from which to draw. But how does one characterize that common view? The thing that I have pushed in my organization is the need to concentrate on the capability one is trying to achieve.

What I like to draw on is a little bit of history, to challenge my organization. I asked what we are working on that is really at the 10 dB level of change in, for instance, naval warfare: What is going to change the shape, the scope, of the Navy of the future by 10 dB? This is a technical way of phrasing a question that people can understand. Who really believes that they are working on something of that magnitude? I got no raised hands in response, because that is a very difficult concept to discuss.

If you look back to the mid-1940s, just to put this in context, when nuclear issues were all coming to a head, there was a vision for nuclear power for submarines. I am a nuclear submariner, so I can relate to this very well. In the mid-1940s someone had a vision that this science, this technology, could

change the way submarines operated. They combined that vision with numerous other things, such as Albacore and new hull designs from a systems view, and developed nuclear submarine technology which in fact did change the face of the Navy. I would say that that was definitely at least a 10 dB change. But it took a vision to bring that all together.

That vision actually drove a whole range of science and technology issues. The fact that submarines could stay submerged for months at a time forced us to deal with how to control the atmosphere in a submarine, and how to do a lot of the other things. How do you environmentally seal people up for many months in a small vessel like that and not have any bad effects?

That sort of vision, wherever it came from, however it evolved, became a corporate vision that drove whole fields of science and technology. And they were not just limited to naval hydrodynamics, and they were not just limited to nuclear propulsion.

My question is, What are we doing to set the standard for where we are going in the future? What is seen on the horizon that is really going to challenge this community that will change things for the future? There are a lot of pressures that are new today that weren't there 20 years ago, that weren't there when this conference started 40 years ago, such as environmental pressures, energy resources, and many other issues on which the naval hydrodynamics community can really have an impact—for example, the whole design of ships, both military and commercial platforms, that are efficient, that we can afford to operate into the next century, that we can afford to procure. All of those are issues that your community can significantly influence. Besides all the mile-deep discussion, there ought to be some discussion that can put this technology and this science into some sort of common perspective. The one thing I encourage you to do, and this is my challenge to you, is to think the broader thoughts in your field. You are going to find that there are whole other disciplines that will contribute to your field, to the advancement of your science and technology.

Last night, I discussed with a young PhD student from Caltech the fact that bioengineering was having an impact on naval hydrodynamics. It's doing so in some very subtle and interesting ways. Tommy Huang from David Taylor is currently undertaking a new project using a neural net chip that was developed by my office. It was developed in connection with research in the biological sciences, from modeling of the olfactory system, in conjunction with the microelectronics community. We in the Navy have applied that chip to signal processing. Tommy and the people at David Taylor under Dr. Bill Morgan are working to use this capability, this new technology, to address some of the interesting issues of naval hydrodynamics.

And so you may find yourselves depending on somebody who is doing work in a different field and helping to develop new approaches to computation and thinking. The challenge is not to try to understand all those pieces of science. The challenge is to think the broader thoughts in your field and be able to articulate what the grand challenges are, what the capabilities are that we think, if we achieved them, would be truly useful in changing the way business is conducted. I contend that is what you need to do as well as going a mile deep.

Do whatever you can do to encourage that broad thinking, to have that open discussion. I do not think that I have to encourage you in this group to speak out, because I think that technically all of you will do that. From everything I have heard, that is a real attribute of this conference.

Speak out about these other issues, at least over lunch or while you are sitting on the beach at that wonderful barbecue the organizers have planned. Talk about some of these issues, because I think that's really where it's at—that's where, as we say in this country, the rubber hits the road. It's about how you are going to take technology from the research area to the applications area and make a difference.

Twentieth Symposium on

NAVAL HYDRODYNAMICS

Technical Sessions

Wave Loadings and Motions of Ships and High-Speed Marine Vehicles

O. Faltinsen (Norwegian Institute of Technology, Norway)

1. ABSTRACT

The present understanding of wave induced motions and loads on mono- and multihulls, surface effect ships and foilcatamarans are presented. Special attention is given to slamming, added resistance in waves and finite amplitude ship motions and sea loads predictions. Future challenges are addressed.

2. INTRODUCTION

The Froude number (Fn) is a simplistic way to categorize ships and advanced marine vehicles hydrodynamically. For instance a hull is in the semi-displacement mode if $0.4<Fn<1.1$ and is planing if $Fn>1.1$. Displacement vessels correspond to $Fn<0.4$. By high-speed vessels we mean that $Fn>0.4$. Here $Fn=U(Lg)^{-1/2}$, where U is the ship speed, L is the ship length and g is the acceleration of gravity. The Froude numbers associated with semi-displacement and planing vessels are approximate values and other values of Froude numbers are used in the literature to define displacement and high-speed vessels. High-speed vessels can be put into categories like multihulls, monohulls, hydrofoils and air cushion supported vehicles. We will in particular discuss monohulls, catamarans, foilcatamarans and surface effect ships (SES). High-speed catamarans and SES used for passenger transportation have semi-displacement hulls. Their maximum speeds are typically 35 knots for the catamaran and 45 knots for the SES. A common ship length is about 30-40 m, but there exist longer vessels like the 74 m long "Sea-Cat" wave-piercing catamaran. Stena Line has designed a 120 m long catamaran for car and passenger transport. Not all types of advanced marine vehicles will be specifically mentioned in the main text. One example is the TSL-F, which is a combination of a submerged body of revolution equipped with hydrofoils and surface piercing struts carrying a monohull (Yamanaka et al. [1]). Considerable research and development is devoted in Japan to TSL-F, foilcatamarans and SES. Research and development in Norway is concentrated on catamarans, foilcatamarans and SES. The SWATH concept is a popular concept in some countries, but can often not be categorized as a high-speed vessel.

Vertical accelerations and relative vertical motions between the ship and the waves are important seakeeping variables. Accelerations determine loads on cargo and equipment and are an important reason for seasickness. The relative vertical motions can be used to evaluate the possibility and damage due to slamming and water on deck.

Rolling may be a problem from an operational point of view of fishing vessels, crane vessels, passenger ships and naval vessels. For smaller ships, rolling in combination with either wind, water on deck or motion of the cargo can cause the ship to capsize. Another important reason for capsizing of smaller ships is breaking waves. Following sea can cause different critical capsizing situations. If the wave profile is stationary relative to the ship, the ship may be statically unstable in roll relative to the waterline defined by the wave profile. The ship may also lose its directional stability in following waves. This can happen when the frequency of encounter between the ship and the waves is small. The result is an altered course relative to the waves. This situation is called "broaching" and is most critical with respect to capsizing of ships with small static stability.

The dynamic stability of high-speed vessels both in calm water and in waves is in general poorly understood. Cohen and Blount [2] have classified phenomena that can happen for monohulls as a function of speed. The hydrostatic pressure gets smaller importance relative to hydrodynamic pressure with increasing ship speed. The rudder, cavitation and ventilation phenomena will influence the dynamic stability of high-speed vessels.

Liquid sloshing in tanks may be a problem for bulkships, combination ships oil-bulk-ore (OBO), liquid natural gas (LNG) carriers and tankers loading at offshore terminals. Liquid sloshing can cause high local pressures as well as large total forces. Both

effects may be important in design.

For larger ships, wave-induced bending moments, shear forces and torsional moments are important. A general problem area for all high-speed vessels is the conflict between small weight and sufficient strength. Slamming is of concern in local structural design for all high-speed vessels. Global wave loads are considered important for high-speed catamarans, monohulls and SES when the vessel length is larger than 50 m. More specific problems are whipping and springing. Whipping is transient elastic vibrations of the ship hull girder caused for instance by slamming. Springing is steady-state elastic global ship vibrations caused by the waves. Both linear and nonlinear wave effects can affect springing.

Ship motions and sea loads can influence the ship speed significantly due to voluntary and involuntary speed reduction. Voluntary speed reduction means that the ship master reduces the speed due to heavy slamming, water on deck or large accelerations. Involuntary speed reduction is the result of added resistance of the ship due to waves and wind and changes in the propeller efficiency due to waves. Seakeeping criteria are normally related to slamming, deck wetness, roll RMS values and RMS values for vertical accelerations. They can be used to determine voluntary speed loss and operability of vessels in different sea areas. Faltinsen and Svensen [3] have pointed out the relatively large variations in published criteria. This may lead to quite different predictions of voluntary speed reduction. For high-speed marine vehicles other criteria are also needed. One example is operational limits due to the propulsion and engine system in a seaway. The seasickness criterion according to ISO 2631/3 is common to use for assessment of passenger comfort of high-speed vessels. It was recommended by the 20th ITTC (International Towing Tank Conference 1993) to be used by its members.

In the main text we will discuss linear theory for wave induced motions and loads on SES, foilcatamarans and high-speed semidisplacement monohulls and catamarans. Slamming is extensively discussed and challenges in the development of rational methods for nonlinear predictions of wave induced motions and loads on displacement vessels are pointed out. We will not concentrate on linear theory for displacement vessels. The load committee of the 12th ISSC (International Ship and Offshore Structures Congress 1994) conclude that "linear strip methods are the workhorse for the prediction of hydrodynamic loads for ship structures". By ships they mean displacement vessels.

The 12th ISSC committee on loads gives a good review of the progress in solving three-dimensional linear problems for wave loads on ships. This is a necessary step towards rational numerical prediction tools of wave induced motions and loads on ships. However I am not convinced that a three-dimensional theory always represents an important improvement of linear ship motion and load predictions. It would have been interesting to know more about how good three-dimensional theories are in following and quartering sea conditions, where strip theories are not satisfactory. Since three-dimensional theories may be more sensitive than strip theories to complicated geometrical hull geometries, it is important to study a broad class of realistic hull forms.

ITTC has strongly advocated that verification, validation and uncertainty analysis should be associated with all numerical work. This is not so common to do. One reason is obviously the difficulty in doing so. An attempt was made by Faltinsen and Svensen [3]. They presented an uncertainty analysis of strip theory programs for calculations of wave induced motions of ships operating at moderate speed. Due to lack of relevant theoretical and experimental work, it was difficult to assess the errors due to viscous and nonlinear effects.

3. SURFACE EFFECT SHIPS

The surface effect ship (SES) is an air cushion supported catamaran (see Fig. 1). The air cushion is limited by flexible seal systems at bow and stern and

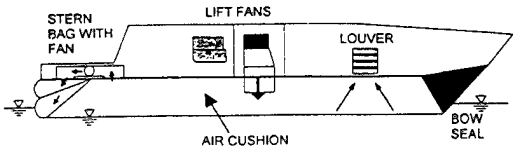


Fig. 1 Surface effect ship (SES)

by catamaran hulls. The aft seal is usually a flexible bag, consisting of a loop of flexible material open against the side hulls with one or two internal webs restraining the aft face of the loop into a two- or three-loop configuration. The bow seal is usually a finger seal, consisting of a row of vertical loops of flexible material. There is a fan system that provides the excess pressure in the air cushion and lift the

vessel and thereby reduces the water resistance. Typically the air cushion carries 80% of the weight of a high-speed SES. A SES has lower resistance than a similar sized catamaran, can achieve a higher speed with less power and have better seakeeping characteristics in high sea states. A major deficiency with the SES concept is the "cobblestone" effect that occurs in small sea states. Significant vertical accelerations can occur. This can be illustrated by a power spectrum of vertical accelerations of a SES obtained from full scale measurements (see Fig. 2).

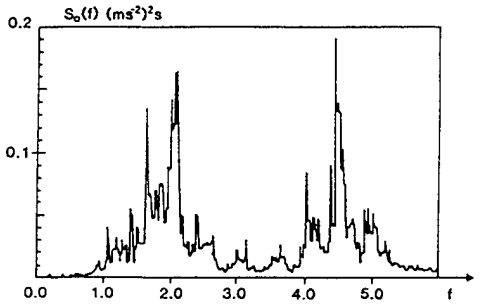


Fig. 2 Power spectrum $S_a(f)$ of vertical accelerations in the fore part of a SES of length 35 m operating at 44 knots in head sea waves with significant wave height 0.1 m (f = frequency in Hz).

The length of the vessel is 35 m, the speed is 44 knots, the significant wave height is 0.1 m and the wave heading is head sea. The measurements are taken in the bow part of the ship. We note two important frequency ranges. One is around 2 Hz and the other one is slightly below 5 Hz. The 2 Hz frequency is the resonance frequency described by Kaplan et al. [4]. According to their analysis the dynamic part of the excess pressure in the cushion is oscillating with the same amplitude all over the cushion. It is caused by compressibility effects of the air and excited because the waves change the enclosed air cushion volume. Historically most attention has been focused on this resonance phenomena and ride control systems have been designed to increase the damping of those resonance oscillations. However, from the figure it is seen that the frequencies around 5 Hz can be just as important as the frequencies around 2 Hz. An important contribution to the resonance behaviour around 5 Hz is a one-dimensional longitudinal standing acoustic pressure with nodes approximately midships. This pressure distribution causes a pitch moment on the vessel. This excites pitch accelerations of the vessel. This is consistent with the full scale measurements that showed smallest effect of the frequencies around 5 Hz at the center of gravity of the vessel and largest effect at the bow and stern part of the vessel.

The acoustic resonance phenomena has been studied by Steen and Faltinsen [5] by using a quasi-linear frequency domain-solution. The acoustic resonances are excited because the waves change the enclosed air cushion volume. There is an important interaction between the air flow in the cushion and inside the bag. The deformation of the bag will have a similar effect on the air cushion as a moving piston at the end of a long tube. This have a noticeable effect on the resonance frequencies. For instance if the SES described in connection with Fig. 2 had a rigid planing aft seal, the lowest acoustic resonance frequency would be about 6 Hz.

Important damping mechanisms of the cobblestone effects are due to the air flow into the air cushion through the fans and the air leakage underneath the seals and through louvers that are part of a ride control system. The damping level is low.

In reality one would use a ride control system to damp out some of the "cobblestone" effect. This is done by controlling the air flow out from the cushion in such a way that it effectively acts as a damping on the system. In order to do that properly one needs a simplified but rational mathematical method that accounts for the dynamic pressure variations in the air cushion in combination with the global heave and pitch accelerations of the vessel. We will illustrate a possible ride control system proposed by Sørensen [6] (see Fig. 3). He used a

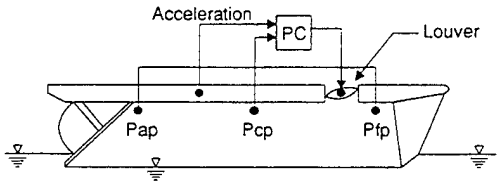


Fig. 3 Ride control system of a SES (Sørensen [6]).

louver system consisting of two vent valves in the front of the air cushion. The opening and closing of

the vent valves control the air flow from the air cushion so that one gets a damping effect on the system. There were used three pressure sensors in the air cushion and one accelerometer on the vessel as part of the ride control system. By properly filtering the signals from the measurement units and using a mathematical model for the system behaviour, the control system can give the correct signals to the louver system. The placement of the louver system is essential. For instance if the louver system is placed midships, it will have a negligible effect on the acoustic resonance mentioned above. The reason is simply that the acoustic pressure component has a small amplitude midships, while it has large absolute value at the ends of the cushion.

The mathematical model for the "cobble-stone" oscillations described by Steen and Faltinsen [5] needs to be validated. Comparisons with full scale measurements where the wave spectra have been properly measured, are necessary. This include effects of directional wave spreading. Qualitative comparisons with full scale experiments indicate that the predicted response is of the correct order of magnitude with well predicted resonance frequencies. Comparisons with model tests are difficult since resonance periods are approximately proportional to the ship length. This implies that model tests based on Froude scaling will not describe this resonance phenomenon properly.

Steen and Faltinsen [5] found that the wave and motion induced leakage area variations under the seals are important for the determination of the response magnitude. The deformation of the bag was analyzed quasi-statically. An hydroelastic analyses of a flexible bag structure bouncing on the free surface has been presented by Ulstein and Faltinsen [7]. The predicted time derivatives of the volume change of the air cushion due to the bag, indicate that the analyses of Steen and Faltinsen [5] can be improved. A time domain solution is then needed.

Steen and Faltinsen assumed that the incident waves pass undisturbed through the air cushion. The influence of the change in air cushion volume and leakage area due to diffraction of the incoming wave system by the presence of side hulls, cushion pressure, and bow seal should be studied.

Steen and Faltinsen used a quasi-steady analysis of the fans. Sullivan et al [8] report that dynamic fan effects may significantly reduce the spatially uniform pressure response in the air cushion.

Another deficiency with the SES concept is connected with the machinery and propulsion loading and response in a seaway. Meek-Hansen [9,10] presented service experience with a 37 m long SES equipped with diesel engines and waterjet propulsion. An example with significant wave height around 2 m, head sea and 35 knots speed showed significant engine load fluctuations at intervals of 3 to 5 seconds (see Fig. 4). These fluctuations result in increased thermal loads in a certain time period, caused by a very high fuel/air ratio. These high thermal loads combined with high-rated engines and reduced engine condition between major overhauls may lead to engine breakdowns.

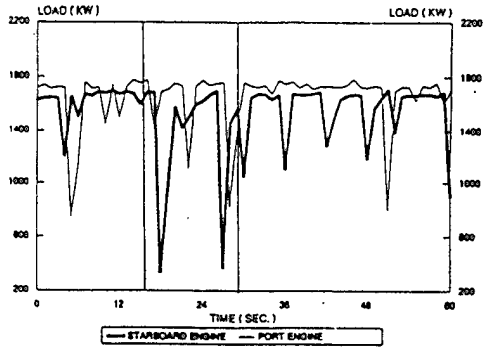


Fig. 4 Engine load during SES operation. $H_{1/3}$ = 2 m. 100% Engine Load. Water jet Propulsion (Meek-Hansen [9,10]).

Possible reasons for the engine load fluctuations are believed to be

* Exposure of the waterjet inlet to the free air
* Flow separation in front of and inside the inlet
* Ventilation and penetration of air from the free surface or from entrained air in the boundary layer

The phenomena mentioned above are often coupled in a complicated way. As an example, separation may be one of the requirements for onset of ventilation. Cavitation occurs in connection with separation. Under given conditions a cavity will be penetrated and filled with air. Separation and cavitation are first of all dependent on the pressure distribution in and near the waterjet inlet. For a given shape this distribution depends mainly on speed and thrust (resistance) of the ship.

Exposure of the waterjet inlet to free air is a result of the relative vertical motions of the craft. An

operational limit will be related to the probability of the relative motion amplitude between the vessel and the waves at the waterjet inlet exceeding a certain limit. For a SES equipped with flush inlets exposure to free air starts to represent a problem for small sea states. The reason is the small distance between the inlet and the calm water surface inside the cushion.

4. SEMIDISPLACEMENT MONO- AND MULTIHULLS

Details about a theoretical and numerical method used to analyze the steady and linear unsteady flow about high-speed non-planing mono- and multihulls in calm water and waves have been described by Faltinsen and Zhao [11,12]. It is assumed that the hulls are hydrodynamically independent of each other. This is a reasonable assumption at high speed as long as the hulls are not too close and the waves from one hull do not propagate to the other hull. The consequence of this is that one can concentrate on the study of monohulls. The method is applicable for Froude numbers higher than approximately 0.4. A reason is that the method neglects the effect of the transverse wave systems generated by the ship. It accounts only for the divergent wave systems. This can be shown theoretically (Ohkusu and Faltinsen [13]). It has also been demonstrated numerically by Hoff [14] that the method by Faltinsen and Zhao represents a good approximation. Hoff used a three-dimensional thin ship theory for both the steady flow problem and the forced heave and pitch problems.

For sway, roll and yaw motion there are not created any transverse wave systems. This implies that the method is also applicable for lower Froude numbers in the case of lateral motions. If the hulls ends in a trailing edge, it is important for the sway, roll and yaw problems to assume a vortex sheet leaving from the trailing edge in the downstream direction and to consider the ship to be a low aspect-ratio lifting surface.

The problem is formulated in terms of potential flow theory. The unsteady motions of the ship and the fluid are assumed to be small so that the unsteady body boundary and free surface conditions can be linearized. The boundary value problem is simplified by introducing the slenderness parameter ε. This expresses the order of magnitude of the beam or the draught to the ship length. The three-dimensional Laplace equation for the velocity potential is approximated by a two-dimensional Laplace equation in the cross-sectional plane. The Froude number based on the ship length is assumed to be 0(1). Non-dimensionalized frequency of encounter with respect to the ship length is assumed to be $0(\varepsilon^{-1/2})$. The form of the body boundary and free surface conditions depend on the order of magnitude of the longitudinal component n_1 of the unit normal vector **n** to the wetted part of the ship surface.

If $n_1 = 0(\varepsilon)$, which is normal to assume in slender body theory, it leads to the classical linearized free-surface conditions with forward speed. It means that there are no interactions between the unsteady flow and the local steady flow. In the case of $n_1 = 0(\varepsilon)$ the approach by Faltinsen and Zhao is a generalization of Chapmans' [15] method. If $n_1 = 0(\varepsilon^{1/2})$, it leads to nonlinear free-surface conditions in the steady flow part. In the unsteady free-surface and body boundary conditions there are interactions with the local steady flow. This involves calculating second derivatives of the local steady flow velocity potential ϕ_s. This cause problems at sharp corners on the body surface and at the intersection between a non-wall sided body surface and the free surface. In the body boundary conditions the interaction terms with the local steady flow occur because the steady flow satisfies the body boundary conditions on the mean oscillatory position and not the instantaneous position of the ship. Faltinsen and Zhao [11] have presented a procedure to avoid the numerical problems in evaluating the second derivatives of ϕ_s in the body boundary conditions near sharp corners. However, the treatment of the intersection between the free surface and a non-wall sided body surface needs improvement. It may actually have been better to also handle the unsteady free surface conditions in a non-linear manner. This means one cannot operate in the frequency domain.

Both when $n_1 = 0(\varepsilon)$ and $n_1 = 0(\varepsilon^{1/2})$ a numerical solution for the flow is found by starting at the bow. The free surface conditions are used to step the solution in the longitudinal direction of the hull. The velocity potential for each cross-section is found by a two-dimensional analysis. Transom stern-effects are accounted for by assuming that the flow leaves the transom stern tangentially in the downstream direction so that there is atmospheric pressure at the transom stern and the transom stern is dry. In a close vicinity upstream of the transom stern the prediction method will be in error. The reason is that the solution has no information that the pressure should change to atmospheric pressure at the transom stern. The error in the close vicinity of the transom stern, will in particular influence pitch moments and the prediction of pitch and steady trim angle. A solution satisfying the three-dimensional Laplace equation at the transom stern

and matches the upstream solution is needed.

Details about the validation of steady wave elevation, wave resistance, added mass and damping coefficients for high-speed monohulls are given by Faltinsen and Zhao [11]. The numerical results are generally in good agreement with experimental results. Even if the theory based on $n_1 = 0(\varepsilon^{1/2})$ may show better agreement with experiments, it is not recommended for routine calculations. One reason is numerical difficulties with calculating second derivatives of the steady flow velocity potential at the intersection between the free surface and a non-wall sided body surface. In the further discussion of numerical results it is assumed that $n_1 = 0(\varepsilon)$. Faltinsen and Zhao [12] showed that this gave good predictions of heave, pitch and vertical accelerations of a high-speed monohull in regular head-sea waves. The generalization of the method to multihulls is straightforward since the hulls are assumed hydrodynamically independent of each other. Ohkusu and Faltinsen [13] have used this method for high-speed catamarans and shown reasonable agreement with experimental values for heave and pitch added mass and damping coefficients.

Faltinsen et al [16] present numerical and experimental results of global wave loads on a catamaran at Fn = 0.49. The numerical method is a further development of the high-speed theory presented by Faltinsen and Zhao [11,12]. "Steady state" response is assumed. The global loads are the vertical bending moments, vertical shear forces and pitch connecting moments on the half part of the catamaran obtained by intersecting along the centre plane. The agreement between theory and experiments is generally satisfactory except for vertical shear forces. Motions were also compared. The agreement was satisfactory for the heave and pitch motion, but not for roll. Roll influences in particular vertical shear force and pitch connecting moment. However possible experimental sources should also be kept in mind. The experiments were carried out with a free running model of lenght 3.8 m in a basin of 80 m length and 50 m breadth. Regular incident waves of different wave headings were used. Examples of experimental error sources are:

* non-constant wave amplitude along the track of the model
* difficulties in accurate heading control
* insufficient number of response oscillations and transient effects in beam, quartering and following seas
* non-linear effects.

Small deviations in heading may have a noticeable influence on the global loads. The effect of the autopilot system and the rudder-propulsion system on the global loads and sway, yaw and roll are not investigated systematically. There is need for good numerical modelling of these effects to scale the results properly to full scale conditions without autopilot system.

The numerical method by Faltinsen and Zhao cannot satisfactorily predict the socalled "deck-diving". This occur for instance with a semi-displacement catamaran in following regular waves at small frequency of encounter. The catamaran can come in a position relative to the waves so that the fore part of the vessel dives into a wave crest (see Fig. 5). If there is not sufficient buoyancy in the fore part of the vessel, a critical situation may occur. A non-linear quasi-steady theory is needed to predict this phenomena.

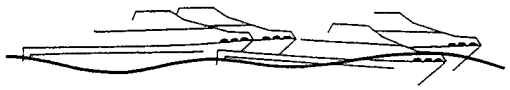


Fig. 5 Illustration of "deck-diving" of a high-speed catamaran in following waves (Werenskiold [17]).

5. FOILCATAMARANS

Successful building and operation of foilcatamarans have been reported from Norway and Japan. With a speed of approximately 50 knots "Foilcat 2900" (Svenneby and Minsaas, [18]) has a couple of fully submerged inverted T-foils forward and a full width foil at the stern. Speed Z propeller drives are incorporated in the struts of the rear foil. "Super Shuttle 400 (Rainbow)" represents a Japanese foilcatamaran. It has full width fully submerged foils, both at the bow and the stern and it is equipped with waterjet propulsion. Both vehicles are run by diesel engines and the catamaran hulls are lifted out of the water completely, at operating speeds.

The "Foilcat 2900" has a length over all = 29.25 m, total breadth = 8.36 m, draft = 3.7 m, maximum draft reduction when lifting = 1.9 m, span of rear foil = 7.79 m, span of front foil 2.50 m, weight = 112-120 tons, main engines output = 2 · 2000 kW, propeller diameter = 1.25 m, number of passengers = 160. Details about the foil system are shown in Fig. 6. The rear foil carries about 60% of

the weight in foilborne condition. The strut of the front foils act as rudders and can be turned +/- 25

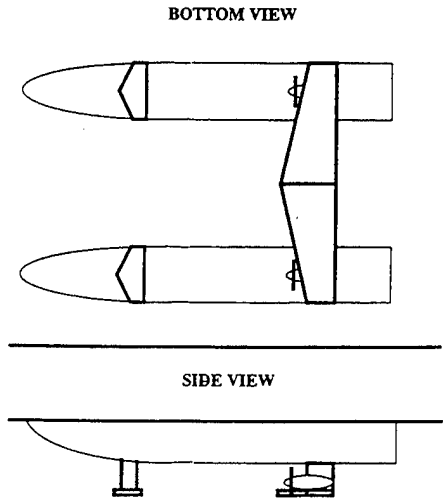


Fig. 6 Foil configuration on the "Foilcat 2900" (Svenneby and Minsaas [18]).

degrees. Each front foil is equipped with a flap and the rear foil with three flaps. Due to the high speed it is important to avoid cavitation on the foils and the propellers. The tip vortices from the front foils can locally cause a large angle of attack of the flow on the rear foils. This must be avoided. Otherwise cavitation occurs. This has consequences for the design of the rear foils. The front foils were equipped with winglets. This has both positive effect on the lift-drag ratio of the front foils and weakens the strength of the tip vortices from the front foil. The foils of the foilcatamaran are designed so that the catamaran hulls are out of the water at high speed in both calm water and small sea states. A consequence of this is that a foilcatamaran has a much lower resistance than a similar sized catamaran at the same speed. When the hulls of the foilcatamaran are out of the water, the vessel can easily roll over to one side. The reason is a small restoring roll moment. To counteract this undesired behaviour a ride control system is used. By continuously measuring the position of the vessel an automatic control system changes the flap angles on the foils. In this way sufficient restoring roll moment is created. The control system is also used to keep a nearly constant vertical position of the center of gravity and to control the trim angle of the vessel. The foils have a very positive effect on the vertical accelerations and motions of the vessel. The vertical acceleration level is much lower than for similar sized catamarans without foils.

In the design of the foils it is important to avoid cavitation and ventilation on the foils. If this occurs, an obvious consequence is a significant reduction of the lift capacity of the foils. It can also create undesired roll and pitch moments on the vessel.

The horizontal wave induced loads on the struts are important for structural design. Ultimate strength and fatigue of the struts are of concern (Moan et al. [19]).

Falch [20] has presented a numerical method that calculates the linear wave induced motions and loads on a foilcatamaran. No effects of cavitation and ventilation are accounted for. The dynamic loads on the foils are found by a linear unsteady lifting line approach. The frequency dependency of the liftforces is accounted for and is of importance. The free surface effect is included by a biplane-mirroring. There is no hydrodynamic interaction between foils and hull if the hulls are submerged. The interaction between struts and foils on one foil-strut system is accounted for. The hydrodynamics loads on the hulls are evaluated by the procedure outlined in the section on mono- and multihulls. However, this cause problems when the hull bottom is close to the mean free surface so that parts of the hull are in and out of the water. A linear theory is then no longer applicable to describe the wave induced loads on the hulls. A time-domain non-linear analysis is then needed.

The numerical method described by Falch [20] needs to be validated against model test results. Mørch and Minsaas [21] pointed out the importance of accounting for the roll up of a free vortex sheet behind a front foil in the numerical study of the behaviour of the rear foil. This a nonlinear effect which is not considered in the theory by Falch [20]. Generation of free surface waves by the foil system may also matter. A biplane-mirroring about the free surface may be sufficient for the analysis of the front foils, but are questionable for the rear foil. Since the front foils presented in Fig. 6 have small aspect ratios, one may question the applicability of a lifting line approach.

6. SLAMMING

A proper description of water entry of structures is needed in studies of slamming and nonlinear ship motions and loads. Physical phenomena that can effect slamming pressures are compressibility of the water, formation of airpockets and bubbles at the interphase between the water and the structure, cavitation, flow separation and hydroelasticity. The magnitude of the pressure may be sensitive to the

structural form, the impact velocity, the ship accelerations, the forward speed of the ship and the relative orientation between the structure and the water surface. When the relative angle between the water surface and the body is small, high pressures with rapid variations in space and time can occur.

A common procedure is that hydrodynamicists study slamming pressures and structural engineers use the slamming pressures in their structural analysis. A much stronger interaction between hydrodynamics and structural mechanics should be encouraged. It is prediction of stresses that is needed in the structural design. Too strong emphasize on very high local slamming pressures can be misleading from a structure's point of view. It may lead to unrealistic structural dimensions, if peak pressures obtained from experiments where the relative angle between the water surface and body is small, are used as spatially uniform static loads in local structural design.

When high slamming pressures are extremely localized in space and time, large variations in measured maximum pressures can occur in equal deterministic sea conditions. Possible reasons are small disturbances of the water surface and variations in where the water initially hits the structure. It has therefore been suggested that slamming should not be handled deterministically even in deterministic environmental conditions. However, if maximum strains are measured instead of pressure, it is likely that the variations are small in equal deterministic sea conditions. A reason for this is that large pressures that are highly localized in space and time, do not significantly influence the maximum stresses in the structure. This will be further discussed later in the text.

Slamming is often characterized as bottom slamming, bow flare slamming and wetdeck slamming. By wetdeck is meant the structural part connecting two side hulls of a multihull vessel (see Fig. 7). We will first discuss water entry of ship

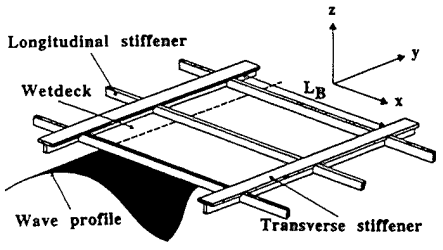


Fig. 7 A detail of the wetdeck structure of a multihull vessel.

cross-sections and consider slamming loads on a bow flare section, which have been experimentally examined by Yamamoto et al [22]. The bow flare section was inclined at a constant angle during the drop tests to account for, in an approximate way, the rolling of the corresponding vessel. This section has been numerically studied by Arai and Matsunaga [23] and Faltinsen [24]. Arai and Matsunaga [23] used the "volume of fluid" method by Nichols and Hirt [25]. The method solves the time dependent Euler equations by the finite difference method. Faltinsen [24] used the boundary element method by Zhao and Faltinsen [26]. Incompressible fluid and irrotational flow were assumed. They represented the velocity potential of the flow by using Green's second identity over an instantaneous fluid domain Ω that contains parts of the jet flow at the intersections between the water surface and the body surface. The surface S enclosing Ω consists of AB, CD, S_B, S_F and S_∞. S_∞ is a control surface far away from the body. AB is shown in Fig. 8. The angle between the body surface and AB is 90 deg., while

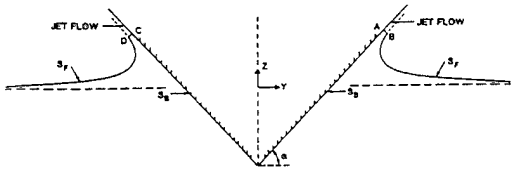


Fig. 8 Definitions of control surfaces used in numerical solution of water entry of a wedge by a boundary element method. α = deadrise angle. (Zhao and Faltinsen [26])

the angle between AB and the free surface is close to 90 deg. The line AB is in an area where the jet starts and where the pressure can be approximated by atmospheric pressure. CD is symmetric with AB about the z-axis. S_B is the wetted body surface between the points A and C. S_F is the free surface outside the points B and D and inside S_∞. A one-dimensional flow is assumed at AB and CD. The nonlinear free-surface conditions without gravity are used at S_F, AB, and CD. The effect of gravity is neglected compared with the large fluid accelerations. (However, including gravity would not cause difficulties). The pressure is set equal to a constant atmospheric pressure on the free surface. Zhao and Faltinsen concluded that the free surface

shape has to be described by at least quadratic piecewise functions in areas with high curvature. This is needed to satisfactorily satisfy continuity of mass.

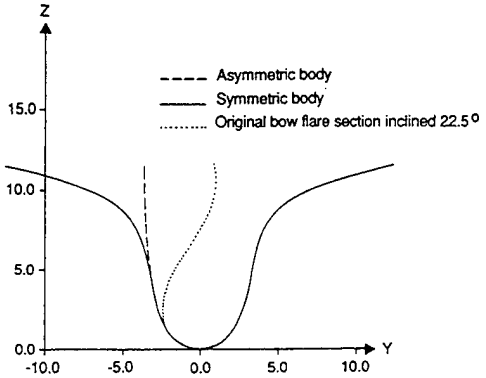


Fig. 9 Cross-section of model used by Yamamoto et al. (1985) in their drop tests together with two models used in numerical solution (Faltinsen [24]).

Fig. 9 shows the tested bowflare section by Yamamoto et al. [22] as well as two sections used in the numerical studies. These two sections will be referred to as the symmetric and the asymmetric section. Only the half-part of the model where the pressure was recorded was correctly numerically modelled. The reason is that the boundary element method with the jet flow approximation cannot handle cases where the local deadrise angle is larger than 90 deg. Flow separation may then occur. Viscous effects have to be included to predict flow separation from continuously curved surfaces.

Fig. 10 presents comparisons between experimental and numerical values of the pressure for the pressure gauges P-2, P-3 and P-4 as a function of the time. The asymmetric section in Fig. 9 is used in the numerical calculations. The vertical velocity during the experiments and in the numerical simulations are shown in Fig. 10. The difference in the numerical and experimental velocity in the first part of the time record is of no importance. The large retardation (about 3 g) that occurs later on is of importance. Since the boundary element method by Zhao and Faltinsen is presently not able to predict flow separation from the knuckles, the numerical simulations are limited in time relative to the experiments. We note from Fig. 10 that the numerical method predicts well when the pressure starts to deviate from atmospheric pressure

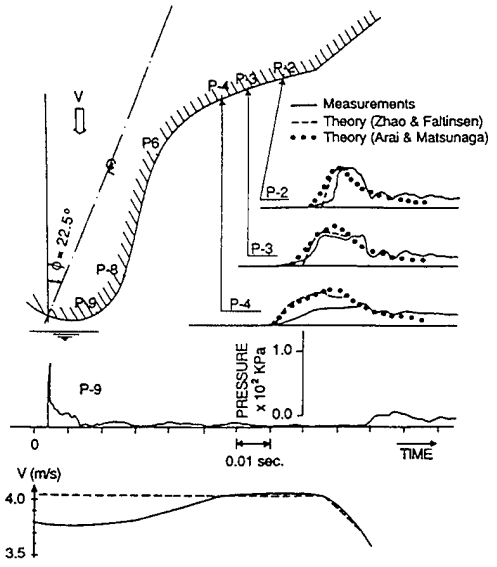


Fig. 10 Comparisons between numerical and experimental pressure measurements on bow flare section. Experiments are drop test results by Yamamoto et al. (1985). The sections are presented in Figure 9 (Faltinsen [24]).

at P-2, P-3 and P-4. In calculating the time, we have accounted for the varying velocity and the difference in starting time of the experiments and the numerical simulations. The magnitude of the pressure is well predicted for P-2 and P-3, while the numerical predictions are too large for P-4. An error source is that the complete cross-section was not correctly modelled, but this is not significant (see Faltinsen [24]). Arai and Matsunaga [23] have also made numerical comparisons with the Yamamoto et al. [22] drop test experiments. Their results are also presented in Fig. 10 and show good agreement with the results by Zhao and Faltinsen. The effect of gravity as well as separation from the knuckle was incorporated. Due to the satisfactory agreement between the numerical and experimental pressures at P-2 and P-3 and the theoretical basis of the numerical method, it is reasonable to assume that

compressibility of the water, creation of air pockets and hydroelasticity are not important in this particular case. However, these effects may not be negligible when the local angle between the body surface and the free surface is small. For instance an airpocket is entrapped when a wedge with knuckles and deadrise angle less than 2-3 degrees is entering the free surface (Koehler and Kettleborough [27]). This is associated with the air flow between the bottom of the structure and the water when the air gap is very small. It is believed that large pressure gradients in the air flow near the knuckles of the wedge is important. The water is raised near the knuckles and traps an airpocket. Three-dimensional and forward speed effects are likely to influence entrapment of air pockets.

Beukelman [28] presented experimental results for three-dimensional models. He showed that forward speed has a strong influence on the pressure level when the deadrise angle was lower than ~2 deg.. This forward speed dependence will not be taken care of if one uses a strip theory approach to evaluate the pressure distribution. It may be that the strong speed dependence is associated with three-dimensional effects due to the air flow between the keel and the water surface. This should be further investigated.

Hayman et al [29] presented results from drop tests of a two-dimensional model. One model was made of GRP sandwich and had a deadrise angle of 30 deg. and the other one was an aluminium model with deadrise angle 28.8 deg.. An important finding in Hayman et al.'s experiments is that the results for the maximum pressure are not very dependent on the flexibility of the model. The influence of hydroelasticity is expected to be important for structural configurations where the initial impact loads are large.

Wetdeck slamming is a case when the local deadrise angle is small and where hydroelasticity is important. Acoustic effects in the water matter in a small initial phase of the impact. Air pockets can be entrapped if the wetdeck between stiffeners (see Fig. 7) is initially buckled due to fabrication or permanent deformations due to previous extreme wetdeck slamming. Cavitation can also occur after an initial impact phase. The physical mechanism causing air pockets during water entry of a wedge with knuckles may not apply to a perfectly flat wetdeck when the slamming occurs away from the ends of the wetdeck.

Graham [30] presented experimental pressures for wetdeck slamming of a SWATH model. The experimental maximum impact pressures are presented in Fig. 11 as a function of measured impact velocity. Only one pressure gauge was used

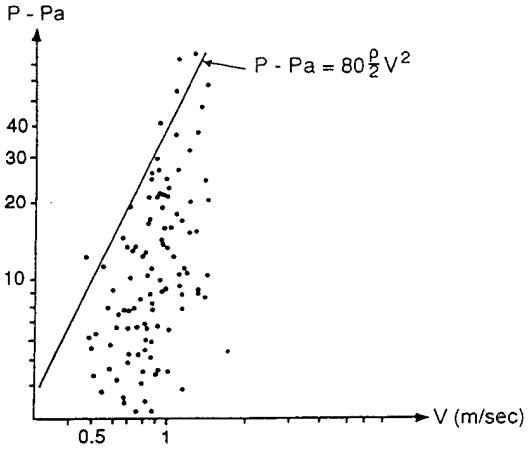


Fig. 11 Wetdeck peak pressures p measured on a SWATH model as a function of the measured impact velocity V. p_a = atmospheric pressure (Based on Graham [30]).

in the experiments. The pressures show a major variation for constant impact velocity. This could be expected since the large impact pressures are very localized in space and time and depend on where the waves initially hit the structure. The results in Fig. 11 may discourage any deterministic analyses. It is tempting to start out with stochastic models and not rely on any deterministic model as a part of the statistical analysis in different sea states. I have a different philosophy when it comes to impact problems where large pressures are highly localized in space and time. I do not think that these very high pressures normally influence the design stresses in the structure. The reason is that they last too short and are too concentrated in space to cause any significant force impulse locally to the structure. This was evident in a study by Kvålsvold and Faltinsen [31]. They examined wetdeck slamming numerically and analytically by including the effect of local hydroelasticity. Their method is a further development of the work by Meyerhoff [32] who examined hydroelastic effects during water entry of wedges. Kvålsvold and Faltinsen divided the wetdeck slamming problem into three time phases. In the initial phase, which lasted very briefly, compressibility effects in the water mattered. The maximum pressure was the one-dimensional acoustic pressure. This is very high but highly localized in space. The second time phase lasts a fraction of the

time it takes for the wetdeck between two transverse stiffeners to be wetted. The magnitude of the very high pressures occurring at the spray root of the jet flow at the intersection between the water surface and the wetdeck is not important. It is the hydrodynamic force as a function of time that matters. This accelerates the local structural mass of the wetdeck elastically and can cause the total relative velocity between the wetdeck and the waves to be close to zero. This means that the local average velocity in space due to elastic deformations is opposite and close to the rigid body impact velocity. In the third time phase the integrated added mass loads due to local elastic deformations tend to balance the bending stiffness loads. This time phase lasts longest and the maximum stresses in the wetdeck occur during this time phase.

Kvålsvold and Faltinsen [31] approximated the wetdeck locally by a Timoshenko beam model. The non-dimensionalized time describing the third time phase is $t(EI/\rho L_B^5)^{1/2}$. Here t is the time, E = Youngs modulus, I = area moment of inertia of the beam cross-section divided by the distance between two longitudinal stiffeners, L_B = length between two transverse stiffeners, ρ = mass density of water. A proper scaling of the maximum stresses σ_{max} was found to be $\sigma_{max} = K_0|V|(\rho L_B^3 E/I)^{1/2}$ where V is the rigid body impact velocity. K_0 is mainly dependent on z_{na}/L_B, where z_{na} is the distance in the beam cross-sectional area from the neutral axis to the point where the maximum bending stress occurs. If V is small, the curvature of the waves at the initial impact matters.

The study by Kvålsvold and Faltinsen [31] shows that the slamming pressure measured by one pressure gauge does not say anything quantitatively about the local maximum stresses in the wetdeck. One should instead measure strains in combination with rigid body impact velocities. We also have to know how to scale model test results of maximum stresses due to slamming. If the beam model used by Kvålsvold and Faltinsen [31] is sufficient, their study gives us necessary information on scaling.

Kvålsvold and Faltinsen [31] show that σ_{max} has approximately a linear dependence on the rigid body impact velocity V as long as V is not too small. The position where the waves initially hit, is not of significant importance for σ_{max}. This indicates an easy way to find the extreme values of σ_{max} in a short and long term statistical model. However, there is a need to further continue the work by Kvålsvold and Faltinsen to include a more complete structural model of the wetdeck and to experimentally validate the results. Preliminary experimental results by Aarsnes [33] of droptests of a flat horizontal elastic plate on waves of different steepnesses are encouraging. Both the magnitude and scaling of the stresses and time are qualitatively in agreement with the method by Kvålsvold and Faltinsen. However, experimental studies with elastic ship models at different Froude numbers are also needed for validation.

The study by Kvålsvold and Faltinsen [31] assumes that the forward speed U of the ship only influences the global ship motions. If the vertical impact velocity V is the same, the slamming response is not changed. When U is high, this is questionable. The studies by Ulstein and Faltinsen [7] are relevant in this connection. They studied water entry of a flexible bag. Small V/U-values were assumed. The bag behaves hydrodynamically as a two-dimensional unsteady planing surface at high Froude number. A Kutta condition is needed at the trailing edge. A solution is found by combining the solution for an unsteady lifting surface in infinite fluid with an integral equation for the wetted length. The same solution technique can be used for wetdeck slamming at high Froude number. A difficulty is to know where to apply the Kutta condition. However Kvålsvold and Faltinsen indicated that the wetted length can be approximated by the geometrical intersection between the rigid wetdeck and the undisturbed wave. Fig. 12 illustrates the differences in the boundary value problems solved by Kvålsvold and Faltinsen for large V/U-values and by Ulstein and Faltinsen for small V/U-values. In both cases the body boundary conditions and the free surface conditions are transferred to a horizontal line. When V/U is large, the velocity potential $\phi=0$ on the free surface. When V/U is small, $\phi=0$ upstream on the free surface ($x>c(t)$) and downstream on the free surface for $x<-Ut$, where t is time. $t=0$ is the initial time of impact. When $-Ut<x<0$, the free surface condition is $\partial\phi/\partial t - U\partial\phi/\partial x=0$ and ϕ is varying with x. No Kutta condition is used when V/U is large. When V/U is large the wetted length is found from the vertical fluid velocities at the free surface on both sides of the submerged body. When V/U is small, a separation point is fixed at the trailing edge $x=0$, where a Kutta condition is used. The upstream wetted part is found from both the horizontal velocity U and the vertical fluid velocity. The wetted length follows in both cases from a nonlinear integral equation which is a generalization of what Wagner did for slamming. It is not obvious how to combine the solutions for small and large V/U-values.

Since an irregular sea is described stochastically, the slamming response in irregular sea must also be described stochastically. We have already referred to the work by Kvålsvold and

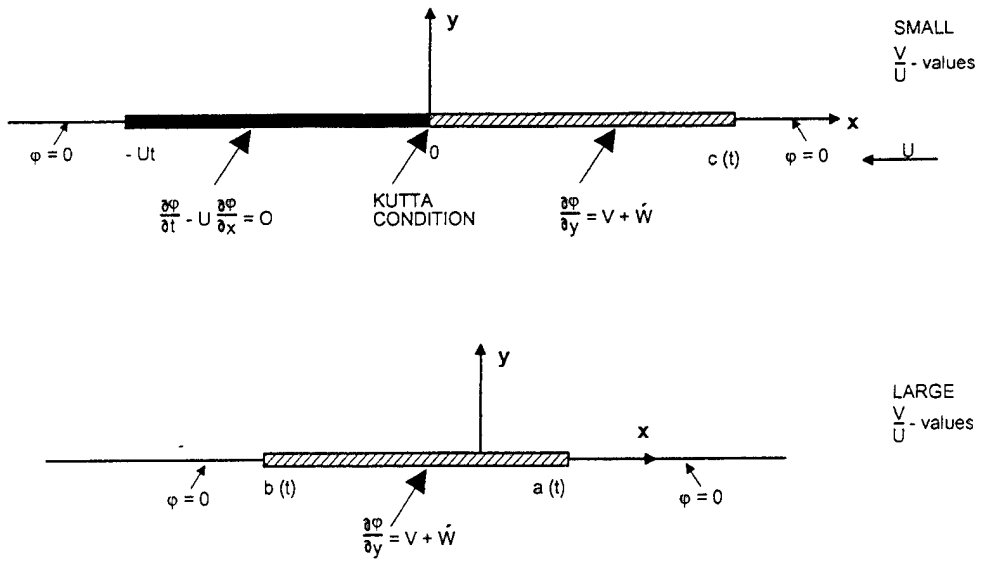


Fig. 12 Boundary value problems for two dimensional water impact at small and large values of V/U. Locally small deadrise angles assumed. V = vertical rigid body impact velocity. $\dot{w}$ = vertical velocity due to elastic deformations. U = forward speed of the section. ϕ = velocity potential due to the body. Instantaneous body shape located between 0 and c(t) for small V/U-values and between b(t) and a(t) for large V/U-values. t = time variable.

Faltinsen, which indicates an easy way to find extreme values for maximum stresses σ_{max} during wetdeck slamming. This is based on that σ_{max} is linearly dependent on V and that the statistical distribution of V in a short term sea state can be approximated by a Rayleigh distribution.

The conventional way to describe the extreme values of slamming pressure on a monohull is to assume that the magnitude of the impact pressure p can be written as

$$p - p_a = \frac{1}{2} \rho k |V_R|^2$$

where p_a is atmospheric pressure and k depends on the sectional form. $|V_R|$ is the amplitude of the relative normal velocity to the cross-section and is a function of heave, pitch and the undisturbed vertical wave velocity. By using that $|V_R|$ is Rayleigh distributed in a short term sea state and combining this with the probability for the ship cross-section to be out of the water, the statistical distribution follows easily (Faltinsen [34]). This procedure does not account for that the relative orientation of the section to the wave surface is influenced by roll and that the impact pressure can be very sensitive to the relative orientation of the section. When the slamming pressure is large and highly concentrated in space and time, one should not use the maximum pressure (see Zhao and Faltinsen [26], that presents pressure distribution for wedges with deadrise angles between 4° and 81°). The average pressure over plate panels on the hull is believed to be a more relevant quantity from a structural stress point of view. However, this should be further studied by studying the structural response due to slamming loads.

There is also a need to study the occurrence of slamming. Number of slams is important for assessing voluntary speed reduction. The normal way to find number of slams involves definition of a threshold velocity V_{cr}. Ochi's [35] formula for V_{cr} does not distinguish sufficiently between different hull forms. Many high-speed vessels have very slender forebodies. Applying the conventional criteria for slamming and voluntary speed reduction could mean that slamming was predicted to be a problem, while it was not in reality. The criteria should relate to slamming loads that cause plastic deformation over plate panels of the hull.

To assess the voluntary speed reduction due to slamming means to study the vessel in moderate sea conditions, where slamming is a rarely occurring event. The Seakeeping Committees of the 18th and 19th ITTC have pointed out that number of slamming events can be too few in model tests and lead to wrong conclusions on slamming occurrence.

7. NONLINEAR SHIP MOTIONS AND LOADS

The committee on loads of the 12th ISSC has given a recent state of art review on prediction methods for nonlinear ship motions and loads of displacement vessels. The simplest type of method is a direct extension of strip theory. It assumes that vertical nonlinear hydrodynamic loads on a cross-section can be extracted from the sum of $d(A_{33}V_R)/dt$ and an integration of hydrostatic pressure and incident wave (Froude-Kriloff) pressure over the instantaneous wetted surface defined by the ship motions and the incident wave elevation. Here A_{33} is the infinite frequency two-dimensional added mass in heave of the cross-section as a function of the submergence of the cross-section. V_R is the relative vertical velocity between the ship and the undisturbed waves. The problem is solved in the time domain by combining linear strip theory with the nonlinear loads described above. Irregular waves are described as a superposition of regular waves and frequency dependent added mass and damping coefficients are made frequency independent. Different versions of a such a method exist in practical use. The procedure can give qualitatively correct trends and seems practical in terms of simulation time, but it is not rational.

A more rational procedure would be to use a perturbation method with the motion response and the incident wave amplitude as small parameters. The problem can then be solved in the frequency domain. It is obvious that a perturbation method must have limited validity when ship cross-sections are out of the water or when green water on deck occurs. To properly include higher order terms beyond second order seems cumbersome. However, since added resistance or involuntary speed is of most interest in moderate sea conditions, a second order theory is useful in this context. Gerritsma and Beukelman formula [36] seems to be the most popular method for predicting added resistance of displacement vessels. The formula is simple and can be evaluated based on linear strip theory. The method seems reliable in the frequency range where ship motions influence added resistance, but the results may depend on what strip theory is used. In small wave lengths where ship motions are small, asymptotic formula presented by Faltinsen et al. [37], Sakamoto and Baba [38], Naito et al. [39] give better predictions of added resistance of blunt ship forms. Faltinsen [40] showed that theoretical predictions of added resistance of a fine ship form at low wave lengths and Froude numbers up to 0.3 need to be improved.

Faltinsen et al [41] have presented a theoretical method to predict added resistance in waves of high-speed semidisplacement mono- and multihulls. It is partly based on a direct pressure integration method using expressions from a linear unsteady flow analysis in regular waves. The problem is solved to second order in wave amplitude. The regular wave expressions can be combined with a sea spectrum in the normal way to obtain mean wave forces or added resistance in a sea state (e.g. Faltinsen [34]). Transom stern effects are included in the expressions and are of importance. The interaction with the local steady flow is accounted for in an approximate way. It is demonstrated by Faltinsen et al. [41] that the latter effect is important for hulls with non-vertical sides at the waterline in the bow region. In general, comparisons with model tests show satisfactory results. The linear theory used in the expressions for added resistance does not include interactions between the unsteady and the local steady flow. This is not consistent with saying that interactions with the local steady flow are important in calculating added resistance in waves. However, if this should have been done consistently, it is likely to lead to numerical problems with higher order derivatives of the local steady flow velocity potential. The interaction with the local steady flow is therefore evaluated by a quasisteady approach where the steady longitudinal force on the vessel is calculated in different oscillatory positions of the ship. The expressions are then time-averaged. The difficulties in consistently handling the interaction between the local steady flow and the unsteady flow, imply that one should investigate the possibility of using a time domain solution. An obvious drawback will be the required CPU-time relative to a frequency domain solution.

The air leakage from the cushion in waves has an important effect on the added resistance of a SES in waves. The air leakage causes the SES to sink and the still water resistance components to change. For instance, the altered excess pressure in the cushion changes the wave resistance due to the air cushion. Further, the increased wetted surface area of the hulls changes the frictional and wavemaking resistance due to the hulls. In addition, there is a contribution to the added resistance in a

similar way as described previously for mono- and multihulls. This is due to second order nonlinear interaction between the dynamic vessel oscillations and the incident waves. The air resistance of a SES due to wind and the vessel's own speed is also important. This is not so much the case for a catamaran. Reasons for this are the presence of the skirt on a SES and a lower hull resistance on a SES relative to a catamaran. A method to predict the added resistance in waves of a SES is presented by Faltinsen et al. [41]. This is based on finding the mean air leakage in waves. The expected value for the drop in pressure in the cushion is found by using the characteristics for the cushion fans in combination with an expression for the expected value of the dynamic change of the leakage area. The fan characteristics gives a relation between the excess pressure and the volume flow for constant fan speed. When the pressure drop in the cushion has been found, an estimate of the sinkage is found by balancing the weight of the SES with the vertical forces due to the excess pressure in the cushion and the buoyancy forces on the hulls. Due to the increased sinkage of the SES, a change in the still water resistance on the hulls occurs. The change in the excess pressure in the cushion also changes the still water wave resistance due to the cushion pressure. The results will, for instance, depend on the condition of the skirts and how fan speed is controlled.

Faltinsen et al. [41] presented numerical results that showed that the involuntary speed loss of a SES would be more severe than for a similar sized high-speed catamaran. There exist full scale data of qualitative nature confirming that a SES may suffer a heavy speed loss in a seaway and that the theoretical predictions are realistic. However, quantitative agreement based on controlled experimental data is needed.

Even if perturbation methods are useful in describing added resistance, they have limited applicability in describing wave induced motions and loads in severe sea conditions. A rational time domain solution is then needed. As a step towards this goal the socalled "weak scatter" hypothesis may be useful (Pawlowski and Bass [42], Lin and Yue [43]). The incident waves are assumed large. The waves generated by the ship are assumed small relative to the incident waves. The exact body boundary conditions below the instantaneous wetted surface due to the motions and the incident waves are satisfied while the free surface conditions are linearized about the incident wave elevation.

Satisfaction of nonlinear free surface conditions is necessary in a rational large amplitude theory for ship motions and sea loads. However, this is not trivial due to numerical and physical problems at the intersection between the free surface and the body surface. It is recommended to start out with a two-dimensional analysis of the problem in order to have sufficient numerical control and get physical insight. A von Karman type of approach where the local run-up of water at the body surface is neglected, is not generally recommended except for cases where the relative angle between the body surface and the undisturbed free surface is large. The local run-up of water was crucial in the study of the bow flare section presented in Fig. 10. The method by Zhao and Faltinsen [20] is encouraging for the water entry phase. Important features of the method are the description of the free surface shapes in areas with high curvature and the jet flow approximation at the intersections between the free surface and the body surface. Special care has to be shown at the impact stage. It is not straightforward to handle entrapment of air and breakdown into bubbles. However due to the short duration of this flow phase, it is possible that the effect on global ship motions and loads can be neglected. If air entrapment is not occurring and a blunt ship cross-section hits the free surface, very short time steps are needed in the numerical method. This may be impractical in a time domain ship motions program. A far more simpler and still rational method for blunt ship forms with low penetration into the water is to use the asymptotic method by Cointe [44]. This is a further development of Wagner's method [45]. It is believed that Cointe's method can represent a starting solution for the method by Zhao and Faltinsen. It is also necessary to include possible separation from knuckles and green water effects. However, longitudinal flow effects are likely to be important for green water on deck. Grochowalski [46] has demonstrated experimentally significant effects on ship motions and loads when water rushes onto the weather deck and the water is shed again.

The water exit problem needs to be more extensively studied. Greenhow [47] presented experimental flow visualizations and numerical studies of the water exit of a submerged two-dimensional circular section. The method by Vinje and Brevig [48] was used. This is a time-domain potential flow method where the exact body and free surface conditions are satisfied. Thin layers of fluid on the upper part of the cylinder and draw-down of the free surface at the cylinder were demonstrated numerically and experimentally. The sudden breaking of the free surface at the lower part of cylinder was not possible to simulate.

All the nonlinear methods mentioned above are based on non-separated potential flow. It is well

known that viscous effects due to flow separation are important in predicting rolling of ships at resonance. Faltinsen [24] suggested that viscous effects due to flow separation may also be significant for large amplitude vertical motions, in particular for ships with sharp corners like bilge keels. He used a two-dimensional vortex tracking method. The vorticity was assumed to be concentrated in thin boundary layers and free shear layers shed from sharp corners. This method has the advantage that it represents a straightforward generalization of potential flow boundary element methods and is able to accurately describe necessary fine details of the flow at a sharp corner. However, there are problems with long time simulations since the method only convects vorticity and neglects diffusion effects. After some time in oscillatory ambient flow there will be a complicated picture of free vortex sheets close to the body. They become numerically timeconsuming to follow. A vortex-in-cell method or full Navier-Stokes solvers will solve some of these problems and are necessary in describing flow separation from continuously curved surfaces. At a certain stage towards a complete numerical prediction of wave induced motions and loads on ships one has to incorporate rational methods for viscous flow predictions. A natural first step is to do that in combination with a strip theory formulation and include the combined effect of wave radiation and flow separation. However, three-dimensional effects and ship speed will certainly have an influence on the viscous effects. For instance lift from the hull, appendages and the rudder are important for roll damping at high speed.

The generation of large amplitude stochastic waves in a numerical model represents also a challenge. If a wave maker is used in the numerical model, intersection problems between the free surface and the wave maker occur. If plunging breaking waves are generated, the numerical solution may break down after the simulation of the breaker. Air will be physically mixed with water during this phase.

Nonlinear effects due to wetdeck slamming and sloshing in tanks can in some cases be combined with a linear description of the exterior hydrodynamic loads on the hulls. Zhao and Faltinsen [49] used a method like that for wetdeck slamming of high-speed catamarans. They showed that wetdeck slamming influences the global vertical accelerations of the vessel. A rigid wetdeck was used. Introduction of local hydroelastic effects will reduce the effect on global accelerations of the catamaran.

The load committee of the 12th ISSC has reported that some progress in numerical solutions of sloshing loads have been made. But knowing that the fluid motion can be very violent during resonant conditions, extreme care has to be shown in the numerical analysis. I think this is a good case where verification and validation of numerical methods are important. This includes listing of benchmark experimental results that numerical methods can be compared with. One should encourage numerical results to contain error estimates. This is actually of special importance for all types of nonlinear predictions.

Since a time-domain solution is time consuming, it is necessary to address how long simulation time is needed to get good statistical estimates of different response variables in a short-term sea state. Nonlinear responses may in some cases require substantially longer simulation time than simulation of linear response variables. For instance the nonlinear slow-drift behaviour of a turret-moored ship in irregular waves have been thoroughly experimentally studied and documented through extensive, long-duration model tests within the Norwegian FPS2000 research programme (Stansberg [50]). The model tests reported by Stansberg [50] showed that 18 hours testing duration (full scale) in irregular waves was satisfactory for proper estimation of the extreme-value behaviour of the actual non-Gaussian slow-drift system. This corresponds to approximately 700 slow-drift oscillations. With only 100 - 200 oscillations, corresponding typically to about 3 hours,a proper extreme value estimation is more uncertain, although rough estimation of a possible non-Gaussian nature of the signal may still be done. This may be concluded on basis of the experimental statistical distributions combined with the study of random variability in Stansberg [51], where the extreme value variability of nonlinear slow-drift motions is shown to be 2 - 3 times larger than for linear motions.

It is not difficult to show that a complete nonlinear three-dimensional numerical method with viscous effects, will lead to unrealistic CPU-time estimates. The challenge must be to simplify the important non-linear effect in a rational manner.

8. CONCLUSIONS

Wave induced motions and loads on Surface Effect Ships (SES), semidisplacement mono- and multihulls and foilcatamarans are discussed.

Acoustic effects in the air cushion of a SES are important for vertical "cobblestone" accelerations

of a SES. Future work on "cobblestone" oscillations should concentrate on the influence of diffraction of incident waves by the vessel, the dynamic fan characteristics and the interaction between the free surface and the elastic behaviour of the aft bag seal.

The behaviour of the machinery/propulsion system of a SES in a seaway needs better understanding.

Better and simplified modelling of transom stern effects is needed in approximate high-speed theories.

The wake from front foils of a foilcatamaran can cause cavitation of rear foils. The steady and unsteady interaction between foil systems and the free surface should be studied.

Slamming analysis should concentrate more on structural stresses. Too strong emphasize on very high local slamming pressures can be misleading from a structure's point of view. Very high local slamming pressures are much more sensitive to small variations in the environmental description and structural configuration than maximum stresses.

Hydroelasticity is important for wetdeck slamming. Wetdeck slamming at high ship speed and low impact velocity should be further studied.

Numerical methods satisfying exact free surface and body boundary conditions can give satisfactory predictions of bow flare slamming loads.

Prediction methods for added resistance of displacement vessels in waves can often give satisfactory results except for fine ship forms at low wave lengths. The interaction between the unsteady and local steady flow can be significant for added resistance of high-speed vessels and needs to be further studied. Speed loss of a SES in a seaway can be large. Prediction methods need to be validated by experiments.

Strip theory is still the workhorse for linear motion and sea loads predictions for displacement vessels. Practical and rational numerical methods for large amplitude motions and loads seem to be lacking. It is recommended to focus more on a two-dimensional analysis of the problem and include important effects of flow separation. The flow at the intersection between the free surface and the body surface needs to be further studied. Progress in analyzing the water entry problem is reported. The water exit problem needs more attention.

Since a rational time domain solution of nonlinear ship motions and sea loads is time consuming, it is necessary to address how long simulation time is needed to get good statistical estimates of different response variables in a seaway. Some nonlinear responses may require substantially longer simulation time than simulation of linear response variables.

REFERENCES

1. Yamanaka, N., Yamamoto, O., Satoh, R., Nagatsuka, T., Arii, T., Fuwa, T., 1991, "A submerged Hull and Foil Hybrid Super-High Speed Liner", Proceedings, FAST'91, K.O. Holden et al., ed., Tapir Publishers, Trondheim, Norway, Vol. 1, pp. 163-178.
2. Cohen, S., Blount, D., 1986, "Research Plan for the Investigation of Dynamic Instability of Small High-Speed Craft", Transactions of SNAME, Vol. 94, pp. 197-214.
3. Faltinsen, O., Svensen, T., 1990, "Incorporation of Seakeeping Theories in CAD", Proceedings, International Symposium on CDF and CAD in Ship Design, G. van Oortmerssen, ed., Elsevier Science Publishers B.V., Wageningen, Netherlands, pp. 147-164.
4. Kaplan, R., Benton, J., Davies, S., 1981, "Dynamics and Hydrodynamics of Surface Effect Ships", Transactions of SNAME, Vol. 89, pp. 211-248.
5. Steen, S., Faltinsen, O., 1994, "Cobblestone Oscillations of a SES with Flexible Bag aft Seal", Submitted to Journal of Ship Research (see also Steen, S., 1993, Cobblestone Effect on SES, Dr.ing.Thesis, Division of Marine Hydrodynamics, The Norwegian Institute of Technology).
6. Sørensen, A.J., 1993, "Modelling and Control of SES in the Vertical Plane", Dr.ing.thesis, Dept. of Eng. Cybernetics, The Norwegian Institute of Technology. (see also Sørensen, A.J., Steen, S., Faltinsen, O., 1993, SES Dynamics in the Vertical Plane, Schiffstecknik Bd 40, pp. 71-84).
7. Ulstein, T., Faltinsen, O., 1994, "Hydroelastic analysis of a flexible Bag-Structure", 20th Symposium on Naval Hydrodynamics, University of California, Santa Barbara.
8. Sullivan, P.A., Gosselin, F., Hinchey, M.J., 1992, "Dynamic Response of an Air-Cushion Lift Fan", Proceedings, HPMV'92, Conference and Exhibits, ASNE, Flagship Section, Arlington, VA, pp. ACV39-ACV47.
9. Meek-Hansen, B., 1990, "Damage Investigation on Diesel Engines in High Speed Vehicles" Proceedings, Fifth International Congress on Marine Technology Athens'90, Hellenic Institute of Marine

Technology, Athens, Greece.

10. Meek-Hansen, B., 1991, "Engine Running Conditions during High Speed Marine Craft Operation", Proceedings, FAST'91, K.O. Holden et al. ed., Tapir Publishers, Trondheim, Norway, Vol. 2, pp. 861-876.

11. Faltinsen, O., Zhao, R., 1991a. "Numerical Predictions of Ship Motions at High Forward Speed", Phil. Trans. Royal Society, Series A, Vol. 334, pp. 241-252.

12. Faltinsen, O., Zhao, R., 1991b, "Flow Prediction around High-Speed Ships in Waves", Mathematical Approaches in Hydrodynamics, SIAM, T. Miloh, ed., pp. 265-288.

13. Ohkusu, M., Faltinsen, O., 1990, "Prediction of Radiation Forces on a Catamaran at High Froude Number", Proceedings, 18th Symposium on Naval Hydrodynamics, University of Michigan, Ann Arbor, National Academy Press, Washington, DC, pp. 5-19.

14. Hoff, J.R., 1990, "Three-Dimensional Green Function of a Vessel with Forward Speed in Waves", Dr.ing.Thesis 1990-25, Division of Marine Hydrodynamics, Norwegian Insitute of Technology, Trondheim, MTA-Report 1990:71.

15. Chapman, R.B., 1975, "Free Surface Effects fo Hydrodynamic Forces on a Surface-Piercing Plate oscillating in Yaw and Sway", Proceedings, 1st International Conference on Numerical Ship Hydrodynamics, David W. Taylor Naval Ship R & D Center, Bethesda, MD, pp. 33-50.

16. Faltinsen, O.M., Hoff., J.R., Kvålsvold, J., Zhao, R., 1992, "Global Wave Loads on High-Speed Catamarans", Proceedings, PRADS'92, J.B. Caldwell & G. Ward, ed., Elsevier Applied Science, London and New York, Vol. 1, pp. 1.360-1.375.

17. Werenskiold, P., Private Communication.

18. Svenneby, E.J., Minsaas, K.J., 1992, "Foilcat 2900, Design and Performance", 3rd Conference on High-Speed Marine Craft, Norwegian Society of Chartered Engineers, Kristiansand, Norway.

19. Moan, T. Skallerud, B., Skjåstad, O., 1991, "Structural analysis and design of hydrofoils and struts", Proceedings, FAST'91, K.O. Holden et al., ed., Tapir Publishers, Trondheim, Norway, Vol. 2, pp. 743-764.

20. Falch, S., 1991, "Seakeeping of Foilcatamarans", Proceedings, FAST'91, K.O.Holden et al., ed., Tapir Publishers, Trondheim, Norway, Vol. 1, pp. 209-221.

21. Mørch, H.J.B., Minsaas, K.J., 1991, "Aspects of Hydrofoil Design; with Emphasis on Hydrofoil Interaction in Calm Water", Proceedings, FAST'91, K.O.Holden et al., ed., Tapir Publishers, Trondheim, Norway, Vol. 1, pp. 143-161.

22. Yamamoto, Y., Iida, K., Fukusawa, T., Murakami, T., Arai, M., Ando, M., 1985, "Structural Damage Analysis of a Fast Ship due to Bow Flare Salmming", Intern. Shipbuilding Progr., Vol. 32, No. 369, pp. 124-136.

23. Arai, M., and Matsunaga, K., 1989, "A Numerical and Experimental Study of Bow Flare Slamming (in Japanese)", Journal of SNAJ, Vol. 166, pp. 343-353.

24. Faltinsen, O., 1993, "On Seakeeping of Conventional and High-Speed Vessels", 15th Georg Weinblum Lecture, Journal of Ship Research, 37, 2, pp. 87-101.

25. Nichols, B.D. Hirt, C.W., 1982, "Volume of Fluid Method (VOF) for Dynamic Free Boundaries", Journal of Computational Physics, No. 39.

26. Zhao, R., Faltinsen, O., 1993, "Water Entry of Two-Dimensional Bodies", Journal of Fluid Mechanics, Vol. 246, pp. 593-612.

27. Koehler, B.R., Kettleborough, C.F., 1977, "Hydrodynamic Impeact of a Falling Body upon a Viscous Incompressible Fluid". Journal of Ship Research, 21, 3, pp. 165-181.

28. Beukelman, W., 1992, "Slamming on Forced Oscillating Wedges at Forward Speed, Part I: Test Results", Report No. 888, Delft University of Technology, Netherlands.

29. Hayman, B., Haug, B., Valsgård, S., 1991, "Response of Fast Craft Hull Structures to Slamming Loads", Proceedings, FAST'91, K.O. Holden et al., ed., Tapir Publishers, Trondheim, Norway, Vol. 1, pp. 381-398.

30. Graham, R., 1988, "Slamming Experiments with a Radio-Controlled SWATH Model", RINA Int.Conf. SWATH Ships and Adv. Multi-Hulled Vessels II, London.

31. Kvålsvold J., Faltinsen, O., 1994, "Hydroelastic Modelling of Wetdeck Slamming on Multihull Vessels", Submitted to Journal of Ship Research (see also Kvålsvold, J., 1994, Dr.Ing.Thesis, Divison of Marine Hydrodynamics, The Norwegian Institute of Technology).

32. Meyerhoff, W.K., 1965, "Die Berechnung Hydroelasticher Stösse", Schiffstechnik, 12, 60.

33. Aarsnes, J.V., 1994, "An Experimental Investigation of the Effect of Structural Elasticity on Slamming Loads and Structural Response", Technical report number A94-0094, 602119.00.01.

34. Faltinsen, O., 1990, "Sea Loads on Ships and Offshore Structures", Cambridge University Press.

35. Ochi, M.K., 1964, "Prediction of Occurrence and Severity of Ship Slamming at Sea". Proceedings Fifth Symp. on Naval Hydrodynamics, pp. 545-596. Washington D.C. Office of Naval Research - Department of the Navy.

36. Gerritsma, J., Beukelman, W., 1972, "Analysis of the Resistance in Waves of Fast Cargo

Ship", Intern Shipbuilding Progr. 19, 217, pp. 285-293.

37. Faltinsen, O., Minsaas, K., Liapis, N., Skjørdal, S.O., 1980, "Prediction of Resistance and Propulsion of a Ship in a Seaway", Proceedings Thirteenth Symp. on Naval Hydrodynamics, ed. T. Inui, pp. 505-30, Tokyo: The Shipbuilding Research Association of Japan.

38. Sakamoto, T., Baba, E., 1986, "Minimization of Resistance of Slowly Moving Full Hull Forms in Short Waves", Proceedings Sixteenth Symp. on Naval Hydrodynamics, ed. W.C. Webster. pp. 598-613, Washington D.C. Office of Naval Research.

39. Naito, S., Nakamura, S., Nishiguichi, A., 1987, "Added Resistance in Regular Head Waves of a Ship with Blunt Bow", PRADS'87, The Norwegian Institute of Technology, Trondheim, Norway.

40. Faltinsen, O., 1983, "Bow Flow and Added Resistance of Slender Ships at High Froude Number and Low Wave Lenghts", Journal of Ship Research, Vol. 27, Sept. pp. 160-171.

41. Faltinsen, O., Helmers, J.B., Minsaas, K., Zhao, R., 1991, "Speed Loss and Operability of Catamarans and SES in a Seaway", Proceedings, FAST'91, K.O. Holden et al., ed., Tapir Publishers, Trondheim, Norway, Vol.2 pp. 709-725.

42. Pawlowski, J.S., Bass, P.W., 1991, "A Theoretical and Numerical Model of Ship Motions in Heavy Seas", Tr. SNAME 99, p. 319.

43. Lin,W.M., Yue, D.K.P., 1993, "Time-Domain Analysis for Floating Bodies in Mild-Slope Waves of Large Amplitudes", The Eighth International Workshop on Water Waves and Floating Bodies, St. John's, Newfoundland.

44. Cointe, R., 1991, "Free Surface Flows close to a Surface-Piercing Body", Mathematical Approaches in Hydrodynamics, SIAM, T. Miloh, ed., pp. 319-333.

45. Wagner, H., 1932, "Über Stoss- und Gleitvorgänge an der Oberfläche von Flüssigkeiten", Zeitschrift für Angewandte Matematik and Mechanic, Band 12, Heft 4, pp. 194-235.

46. Grochowalski, S., 1988, "Investigation into the Physics of Ship Capsizing by Combined Capture and Free-Running Model Tests", Tr. SNAME'97, p. 169.

47. Greenhow, M., 1988, "Water-entry and -exit of a Horizontal Circular Cylinder", Applied Ocean Research, Vol. 10, No.4. pp. 191-198.

48. Vinje, T. Brevig, P., 1981, "Nonlinear Two-Dimensional Ship Motions", Proceedings 3rd Int. Conf. Num. Ship Hydro, Paris, June, pp. 257-266.

49. Zhao, R., Faltinsen, O., 1992, "Slamming Loads on High-Speed Vessels", Proceedings 19th Symposium on Naval Hydrodynamics, Seoul, Korea.

50. Stansberg, C.T., 1992, "Model Scale Experiments on Extreme Slow-drift Motion in Irregular Waves", Proceedings, BOSS'92 Conference, London, UK, Vol. 2, pp. 1207-1222.

51. Stansberg, C.T., 1992, "Basic Statistical Uncertainties in Predicting Extreme 2nd Order Slow-Drift Motion", Proceedings 2nd ISOPE Conference, San Fransisco, California, Vol. 3, pp. 526-531.

Prediction of the Seakeeping Characteristics of Ships

H. Bingham, F. Korsmeyer, J. Newman
(Massachusetts Institute of Technology, USA)

Abstract

This paper summarizes the development of a three-dimensional time-domain program for predicting the seakeeping characteristics of ships. The program is based on the panel method, using distributions on the ship hull of singularities which satisfy the linear free-surface condition. The solution is performed in the time domain, using convolution to account for the memory effects associated with the free surface. The results are presented in terms of impulse-response functions, which can be used directly to predict the time histories of unsteady motions in prescribed regular or pseudo-random incident waves, or indirectly via Fourier transformation to evaluate the response of the ship in the frequency domain. The method is also useful to determine calm-water characteristics such as wave resistance, sinkage, and trim, by analyzing the large-time limit of problems where the ship is accelerated from rest to a constant forward velocity.

This program, known as TiMIT, is intended for general use by naval architects and hydrodynamicists. Typical applications are described for a Series 60 hull and for a submarine hull.

Nomenclature

The computed and measured quantities shown in the figures are nondimensionalized, as indicated in the respective captions, in terms of the gravitational acceleration g, fluid density ρ, incident wave amplitude A, ship length L, displaced volume ∇, wetted surface area S, and velocity U. All other quantities are defined when they are introduced.

1 Introduction

At the First Symposium on Naval Hydrodynamics, in 1956, Georg Weinblum presented a seminal lecture on the "Contribution of Ship Theory to the Seaworthiness Problem." In the published record of that lecture [1] a comprehensive list of practical problems was enumerated, and various theoretical approaches were outlined. The importance of understanding and predicting the behavior of ships in a seaway was self-evident, but the extent to which theory and computations could be used to address these problems was not so obvious. Weinblum's lecture served as a stimulus and guide for much of the subsequent work in this field, which evolved as one of the most active research areas in naval hydrodynamics.

The practical fallout from these activities commenced only after several years of theoretical research, and with the expanding role of digital computers. Within a period of 10-15 years reliable strip theories were in common use throughout the world, serving a valuable role to supplement or replace experiments. Strip theory has filled an important niche in ship hydrodynamics. It is able to provide useful estimates of the vertical motions of conventional ships, with relatively simple computer programs which can be used routinely by practicing naval architects. However, the assumption of two-dimensional flow in transverse planes restricts the validity and applicability of strip theories, and the practical limits of this approach are not well understood.

The development and utilization of fully three-dimensional theories and computer programs did not enjoy such an early and universal success, although much effort has been devoted to analytical and numerical treatments of the three-dimensional ship-motion problem [2]. Various three-dimensional approaches have been used in

recent years to study seakeeping, involving different numerical procedures and assumptions. Many of these approaches have been developed to the level of research codes capable of performing useful analyses for practical seakeeping problems. However their complexity is a deterrent to everyday use by nonspecialists.

The state of this field contrasts with that of offshore platforms, where three-dimensional programs are used routinely to analyze the interactions of ocean waves with platforms of any practical configuration. The usual approach is to assume a Fourier decomposition of the problem, so that a sequence of regular-wave problems is solved in the frequency domain, with the complex time dependence $e^{i\omega t}$. Most programs used for this purpose are based on the boundary-integral method where sources and normal dipoles are distributed on the submerged surface of the structure, and an integral equation for the strength of these singularities is derived from the corresponding boundary conditions. Free-surface Green functions are used to ensure that the solution will satisfy the boundary condition on the free surface.

The principal difficulty in extending this approach to the seakeeping problem for ships is the much more complicated expression for a singularity which is moving with a constant horizontal velocity beneath the free surface. This problem can be circumvented by using instead the transient Green function in the time domain, and advancing each singularity at successive time-steps, in much the same manner as was first used by Kelvin to predict the classical ship-wave pattern.

Other advantages of performing the computations in the time domain are the facts that the equations are real, rather than complex, and that (in the approach used here) only the right-hand side of the linear system depends on time.

In addition to these features, which relate primarily to numerical and computational aspects, performing the seakeeping analysis in the time domain offers a wide variety of possible extensions and applications which are not readily accommodated in the frequency domain. These include large-amplitude motions in the horizontal plane, as in ship maneuvering; using the large-time limit to determine the steady-state wave resistance, sinkage, and trim; consideration of nonlinear hydrostatic effects and semi-empirical nonlinear roll damping; and coupling with nonlinear structural analysis programs to analyze wave-induced hydroelastic problems.

In this paper we describe the development of the time-domain panel code TiMIT for analyzing seakeeping problems in three dimensions. Our objective in this work is to refine and extend the numerical methodology and associated computer program so that important practical problems can be analyzed by naval architects, in much the same manner as for the parallel design process in offshore engineering. In this effort we have benefited from our experience in the latter field [3], and from parallel research reported by our colleagues [4, 5, 6]. The authors also note that the present work could not have been completed without long-term financial support from the Office of Naval Research, and this Twentieth Symposium on Naval Hydrodynamics is an appropriate opportunity to report on our progress.

Our approach is based on the assumption of potential flow, with linearization of both the equations of motion and the velocity potential. Brief summaries of the theory and numerical techniques are given in Sections 2 and 3; more details can be found in [7] and [8]. In Section 4, illustrative examples are presented showing computations of conventional seakeeping parameters for the Series 60 hull. In Section 5, results are shown for the important hydrodynamic parameters affecting a submarine which is moving with low velocity near the free surface, both in calm water and in waves. Possible future extensions and applications are discussed in the concluding Section 6.

2 Theory

We employ Cartesian coordinates (x, y, z) which move with the steady forward velocity U of the ship, in the $+x$-direction. The origin is in the plane of the free surface, and z is positive upwards. Six degrees of unsteady motion are defined by the corresponding displacements $x_k(t)$, where $k = 1, 2, ..., 6$ for surge, sway, heave, roll, pitch, and yaw, respectively.

Assuming the ship is a stable linear system, the equations of motion may be written in the form [9]

$$\sum_{k=1}^{6}(M_{jk} + a_{jk})\ddot{x}_k + b_{jk}\dot{x}_k + (C_{jk} + c_{jk})x_k + \int_{-\infty}^{t} d\tau\, K_{jk}(t-\tau)\dot{x}_k(\tau) = X_j(t) \qquad j = 1, ..., 6, \quad (1)$$

where an overdot indicates differentiation with respect to time.

The terms X_j on the right side of (1) are the components of the exciting force and moment due to the incident wave elevation $\zeta(t)$, defined at a prescribed reference point in the ship-fixed coordinate system. ('Force' is understood hereafter in the generalized sense to include the moment, for $j = 4, 5, 6$.) Following [4], the exciting-force components are expressed by means of convolution integrals in the form

$$X_j(t) = \int_{-\infty}^{\infty} d\tau \; K_{jD}(t-\tau;\beta)\zeta(\tau). \qquad (2)$$

Here the kernel, $K_{jD}(t;\beta)$, is the diffraction impulse-response function: the force on the ship in the j^{th} direction due to a uni-directional impulsive wave elevation with a heading angle of β.

The impulsive incident wave is two-dimensional (long-crested) and contains all frequencies. (A more complete discussion of this function, along with an illustration, can be found in [12], Section 3.5.) For $U > 0$ and heading angles $-\frac{\pi}{2} < \beta < \frac{\pi}{2}$ (following seas) care must be taken in the solution of the diffraction problem since the ship is necessarily in the half of the free surface with non-zero wave elevation regardless of how large a negative time is chosen for the start of the diffraction solution. Moreover the ambiguity of the frequency of encounter requires three separate problems to be solved, each forced by a different range of wavelengths.

The hydrodynamic coefficients and the kernel of the convolution on the left-hand side of (1) comprise the radiation impulse-response function: the force on the ship in the j^{th} direction due to an impulsive velocity in the k^{th} direction, with the coefficients a_{jk}, b_{jk}, c_{jk}, accounting for the instantaneous forces proportional to the acceleration, velocity, and displacement, respectively, and the memory function $K_{jk}(t)$ accounting for the free-surface effects which persist after the motion occurs. For the radiation problem we use the term 'memory function' to distinguish this portion of the impulse-response function from the instantaneous force components on the first line of (1). For the diffraction problem, the memory function is equal to the impulse-response function.

The convolution on the left-hand side of (1) could be expressed alternatively in terms of the displacements x_k or accelerations $\ddot{x}_k$. With the latter choice, (1) is replaced by

$$\sum_{k=1}^{6}(M_{jk}+a_{jk})\ddot{x}_k + b_{jk}\dot{x}_k + (C_{jk}+c_{jk})x_k + \int_{-\infty}^{t} d\tau \; L_{jk}(t-\tau)\ddot{x}_k(\tau) = X_j(t) \qquad j = 1, ..., 6, \quad (3)$$

The kernels in (1) and (3) are related to each other by differentiation [8], specifically:

$$K_{jk}(t) = \frac{\partial}{\partial t} L_{jk}(t) \qquad (4)$$

The ship's inertia matrix is M_{jk}, and the first-order hydrostatic restoring-force coefficients are given by C_{jk}.

With the assumptions of linearized potential flow, the velocity potential can be expressed in the form

$$\Phi = -Ux + \bar{\phi} + \sum_{k=1}^{6}\phi_k + \phi_I + \phi_S, \qquad (5)$$

where each term in (5) is a solution of the Laplace equation in the fluid domain. In this decomposition the first two terms on the right side represent the steady velocity potential due to the streaming flow, with velocity $-U$ in the x-direction, and the steady perturbation of this flow by the ship hull with the potential $\bar{\phi}$. The remaining terms in (5) represent the unsteady motion, including six radiation potentials ϕ_k, each corresponding to one rigid-body mode of motion, and the diffraction potential $\phi_I + \phi_S$ corresponding to the incident wave (I) and the scattered disturbance (S) when the ship is fixed in its mean position.

To derive appropriate boundary conditions we adopt the Neumann-Kelvin linearization, where the assumption is made that each of the potentials ϕ in (5) is a small perturbation of the base flow (represented by the potential $-Ux$). It follows that each of the unsteady potentials in (5) satisfies the free-surface boundary condition

$$\left(\frac{\partial}{\partial t} - U\frac{\partial}{\partial x}\right)^2 \phi + g\frac{\partial \phi}{\partial z} = 0, \qquad \text{on } z = 0. \quad (6)$$

In this equation ϕ is used to represent any of the perturbation potentials. On the mean position of the body surface, $\bar{S}_b$, the following boundary conditions are applied:

$$\begin{aligned} \vec{n}\cdot\nabla\bar{\phi} &= U\,n_1 \qquad (7)\\ \vec{n}\cdot\nabla(\phi_I+\phi_S) &= 0\\ \vec{n}\cdot\nabla\phi_k &= n_k\dot{x}_k + m_k x_k. \end{aligned}$$

The generalized unit normal n_k is defined by

$$\begin{aligned} (n_1, n_2, n_3) &= \vec{n} \qquad (8)\\ (n_4, n_5, n_6) &= \vec{r}\times\vec{n}. \end{aligned}$$

The steady and the unsteady potentials are coupled through the presence of the m-terms in the body boundary condition, which are

$$m_k = (0, 0, 0, 0, Un_3, -Un_2),$$

for the Neumann-Kelvin linearization.

Since the memory functions for different impulsive motions are related by differentiation, as in (4), the specification of the canonical radiation problems is somewhat arbitrary. Here we define $x_k(t)$ to be an impulsive acceleration, *i.e.* $\ddot{x}_k = \delta(t)$, $\dot{x}_k = H(t)$, and $x_k = r(t)$, where $\delta(t)$ is the Dirac function, $H(t)$ is the Heaviside function, and $r(t)$ is the ramp function. With this choice the last line of (7) becomes

$$\vec{n} \cdot \nabla\phi_k = n_k H(t) + m_k r(t). \qquad (9)$$

Appropriate initial conditions must be applied on the free surface. For the radiation problems these are

$$\phi_k = \phi_{kt} = 0 \quad \text{on } z = 0 \quad \text{for } t \to 0, \qquad (10)$$

and for the diffraction problem

$$\phi_S \to 0 \quad \text{on } z = 0 \quad \text{for } t \to -\infty. \qquad (11)$$

The linearized pressure associated with each of these perturbation potentials is given by

$$p = -\rho\left(\phi_t - U\,\phi_x\right). \qquad (12)$$

We apply Green's theorem to ϕ_t, and integrate in time, to obtain an integral equation for the unknown potential on the mean position of the submerged body surface, $\bar{S}_b$:

$$\begin{aligned} 2\pi\phi \;&+ \int\!\!\int_{\bar{S}_b} dS\,\left(\phi G_n^{(0)} - G^{(0)}\phi_n\right) \qquad (13)\\ &- \int_{-\infty}^{t} d\tau \int\!\!\int_{\bar{S}_b} dS\,\left(\phi G_{\tau n} - G_\tau \phi_n\right)\\ &- \frac{U}{g}\int_{-\infty}^{t} d\tau \int_{\bar{\Gamma}} dl\, n_1 \left(\phi\left(G_{\tau\tau} - UG_{\tau\xi}\right)\right.\\ &\qquad \left. - G_\tau\left(\phi_\tau - U\phi_\xi\right)\right) = 0. \end{aligned}$$

Here $\bar{\Gamma}$ is the waterline contour and the Green function is $G(\vec{x};\vec{\xi},t) = G^{(0)} + G^{(f)}$, where

$$G^{(0)} = \left(\frac{1}{r} - \frac{1}{r'}\right),$$

$$G^{(f)} = 2\int_0^\infty dk\,\left[1 - \cos(\sqrt{gk}\,t)\right] e^{kZ}\, J_0(kR)$$

$$\left.\begin{matrix} r \\ r' \end{matrix}\right\} = \sqrt{(x-\xi)^2 + (y-\eta)^2 + (z \mp \zeta)^2}$$

$$Z = (z + \zeta)$$

$$R = \sqrt{(x - \xi + U\,t)^2 + (y-\eta)^2},$$

and J_0 is the Bessel function of order zero. The arguments of the functions appearing in equation (13) have been omitted for brevity, but note that the temporal argument of the Green function in the convolution integrals is retarded [*i.e.* $G_\tau = G_\tau(\vec{x};\vec{\xi},t-\tau)$]. Equation (13) is valid for any point $\vec{x}$ on the body surface, and the spatial integrations are performed in the dummy variable $\vec{\xi}$.

The radiation and diffraction potentials are solutions of (13) with the appropriate body boundary conditions applied. The steady potential $\bar{\phi}$ is usually thought of in the context of a separate steady-state solution, but here it is convenient to consider this potential as the steady-state limit of the radiation problem for an impulsive surge acceleration.

Integrating the pressures (12) due to the canonical radiation and diffraction potentials over the hull surface gives the thirty-six radiation impulse-response functions, and the six diffraction impulse-response functions. These completely characterize the hydrodynamic response of the ship, translating at a given forward velocity, in a uni-directional sea. (Additional diffraction impulse-response functions are needed in following and/or multi-directional seas.) Once these canonical problems have been solved, evaluation of a design in numerous operating environments is straightforward and of relatively small computational burden.

3 Numerical Solution

The integral equation (13) is discretized spatially by subdividing the surface $\bar{S}_b$ into N planar quadrilateral (or triangular) panels, on which the potential is assumed to be constant. A system of N linear equations is generated by collocation, satisfying the discretized form of (13) at the panel centroids. The integrals over each panel involving $G^{(0)}$ and its normal derivative are performed using the algorithms in [10], and the remaining integrals are evaluated by the mid-point rule. The time-dependent function $G^{(f)}$ and its derivatives are evaluated for each pair of panel centroids using the algorithms described in [11].

The solution of the diffraction problem for $\frac{\pi}{2} < \beta < \frac{3\pi}{2}$ (head seas) is initiated smoothly at an appropriate negative time, before there is significant wave amplitude in the vicinity of the ship. The computation is terminated at a similarly appropriate positive time. For $-\frac{\pi}{2} < \beta < \frac{\pi}{2}$ (following seas) the situation is more complicated, as noted in Section 2. The exciting force $X_j(t)$ depends on the sum of the solution ϕ_S and the known ϕ_I. Details of numerical aspects of the diffraction problem are provided in [12].

The solution of the radiation problem is facilitated by decomposition into three parts [8]. Two time-independent potentials, $\mathcal{N}_k(\vec{x})$ and $\mathcal{M}_k(\vec{x})$, correspond to the n_k and m_k portions of the body boundary condition, respectively, and are solutions to (13) for $t = 0$. This leaves a third, time-dependent, potential $\psi_k(t)$, which is a solution to the complete equation (13) starting from $t = 0$. The hydrodynamic coefficients a_{jk}, b_{jk}, and c_{jk}, depend only on $\mathcal{M}_k$ and $\mathcal{N}_k$, while L_{jk} depends only on ψ_k.

The solution for either $\phi_S(t)$ or $\psi_k(t)$ is carried out at a sequence of equal time-steps Δt. The convolution integrals are evaluated using the trapezoidal rule, with the same Δt. Since $G_t(0) = 0$, there is no contribution to the convolution on the second line of (13) at the upper limit of integration ($\tau = t$). Thus this convolution only involves the values of the potential at preceding time-steps, which can be placed on the right-hand side of the linear system as known quantities. However there is a contribution to the left-hand side from the convolution of the waterline integral on the third and fourth lines, since $G_{tt}(0) \neq 0$. Thus there are two left-hand-side matrices, one for $t = 0$ and the other for $t > 0$, but since these are independent of time they only need to be evaluated and factored once.

The dominant computational burden is the evaluation of the convolution integrals at each time-step. Since the time-steps are equal and the coordinate system is fixed to the translating ship, values of $G^{(f)}$ (and its derivatives) can be saved to avoid redundant computation, but the large number of such values (proportional to the product of N^2 and the number of time-steps) usually requires disk storage with relatively slow access time for retrieval. If the storage required exceeds the available disk space, the values of $G^{(f)}$ must be re-computed at each time-step.

For conventional ships with port-starboard symmetry, the potentials can be decomposed into symmetric and antisymmetric components to reduce the number of unknowns by a factor of two. The left-hand side work and storage is then reduced by a factor of four, and the burden of evaluating the right-hand-side convolution integrals is reduced by a factor of two. Since the latter is dominant, the overall reduction in computational cost is effectively one-half.

Once the potentials resulting from the impulsive forcing are known, impulse-response functions for the radiation and diffraction forces are computed by integration of the pressure (12) over the ship surface using the same discretization as above. Impulse-response functions for local quantities such as the velocity and pressure on the ship surface, or in the fluid, may be defined as well.

The impulse-response functions provide the complete hydrodynamic characterization of the ship hull and are the basis for subsequent time-domain simulation or frequency-domain analysis. Further computations made using the impulse-response functions entail computational burdens which are relatively small.

The temporal integration of the equations of motion (1) is carried out by a fourth-order Runge-Kutta scheme. Fourier transforms of the impulse-response functions are evaluated by Filon quadrature. This method is suitable for global quantities such as the transformations for added-mass, damping, and exciting-force coefficients. If a large number of local-quantity impulse-response functions for velocity and pressure are needed, the FFT could be used to accelerate the computation.

3.1 Asymptotic Continuation

The potential $\psi_k(t)$ may exhibit large-time behavior which complicates the use of the memory function $L_{jk}(t)$ in convolutions and Fourier transforms. Depending on the mode of motion, $L_{jk}(t)$ tends to a constant or a linear function of time as $t \to \infty$. This behavior is reduced by one order in time by numerical differentiation, to yield $K_{jk}(t)$, as in (4). In the case of modes where $L_{jk}(t)$ tends to a linear function of time, the constant which remains in $K_{jk}(t)$ at large time is evaluated and subtracted off. This constant is added to c_{jk}.

Computational efficiency dictates that the hydrodynamic problems should be solved over as short a time range as possible. However due to forward speed, the memory functions display a slowly decaying oscillation in time at the non-dimensional critical frequency $\omega_c = (4F_n)^{-1}$ where $F_n = U/\sqrt{gL}$ is the Froude number. Our approach is to truncate the computations as soon

as there is sufficient information in each memory function to accurately estimate this large-time behavior. We assume, based on the Green function, that the large-time oscillation of the memory function is of the form

$$K_{jk}(t) \sim a_0 + \frac{1}{t}[a_1 \cos(\omega_e t) + a_2 \sin(\omega_e t)], \quad (14)$$

as $t \rightarrow \infty$. The constants in equation (14) can be determined by a least squares fit, so that integrations involving K_{jk} may be divided into two ranges: one which terminates at the end of the computed time-history, and one which continues with the asymptotic form (14). A more precise form for the solution, as $t \rightarrow \infty$, is given [13] by

$$\phi \sim C_0 + \Re(C_1 \frac{e^{-\alpha t}}{t} + C_2 \frac{1}{t^2}) e^{i\omega_e t}, \quad (15)$$

in which C_i and α are parameters depending upon the ship geometry and the forward speed. However this distinction is unimportant at realistic ship speeds [8].

3.2 Fourier Transform

If the ship motion and the incident wave elevation are assumed to be time harmonic at the frequency of encounter ω ($x_k(t) = \Re \tilde{x}_k e^{i\omega t}$, $\zeta(t) = \Re \tilde{\zeta} e^{i\omega t}$), then as $t \rightarrow \infty$ the equations of motion can be written

$$\sum_{k=1}^{6} \Big\{ -\omega^2 [M_{jk} + A_{jk}(\omega)] + i\omega B_{jk}(\omega) + C_{jk} + c_{jk} \Big\} \tilde{x}_k(\omega) = \tilde{X}_j(\omega). \quad (16)$$

The frequency-dependent coefficients in equation (16) are related to the impulse-response functions through the Fourier transforms

$$A_{jk}(\omega) = a_{jk} + \Re \frac{-i}{\omega} \int_0^\infty dt\, K_{jk}(t) e^{-i\omega t},$$

$$B_{jk}(\omega) = b_{jk} + \Im\, i \int_0^\infty dt\, K_{jk}(t) e^{-i\omega t},$$

$$\tilde{X}_j(\omega) = \int_{-\infty}^{\infty} dt\, K_{jD}(t) e^{-i\omega t}. \quad (17)$$

These integrals are treated as suggested above. If the memory function tends to a constant at large time, this is subtracted off and added to c_{ij}. Then, the contributions to (17) from the computed range of the memory functions are evaluated numerically by Filon quadrature. The remaining contributions, associated with the oscillatory terms in (14), are expressed in terms of the sine and cosine integrals [8].

3.3 Irregular Behavior of Solutions

For surface ships, discrete numerical solutions of the transient integral equation (13) will contain non-physical oscillations. At zero forward speed these oscillations persist indefinitely in time. The Fourier transforms of these solutions display a behavior in the vicinity of the irregular frequencies which is nearly identical to what is observed in solutions to the corresponding time-harmonic integral equation.

In [8] and [14] arguments are presented to show that the continuous transient integral equation is free from any irregular behavior, because its solutions are unique and coincide with the unique solutions to the corresponding initial-boundary-value problem. These works also put forward the conjecture that discretization of the integral equation relaxes the satisfaction of the initial conditions, and consequently is responsible for allowing the time harmonic (at the irregular frequencies) solutions to co-exist with the transient ones.

Figure 1 illustrates the oscillations in the heave-heave memory function calculated for a Wigley hull at $U = 0.0$ with 144 panels used to describe half of the hull. Note the small oscillations which appear to persist indefinitely. In Figure 2, which shows the heave-heave damping coefficient computed from this function, the irregular behavior is more distinct in the frequency domain. Also shown in Figure 2 is the same damping coefficient calculated in the frequency domain using the computer program WAMIT [3] with identical geometrical input. It is remarkable that the erroneous results are practically identical in the frequency domain based on these two complimentary methods. The small differences are probably due to the truncation of the memory function prior to the numerical Fourier transform.

At non-zero forward speed, the irregular oscillations in the solution are of finite duration. After a time t_1, these oscillations are absent from the solution. The time t_1 is very close to the time needed for the ship to travel one ship length after the initial impulse. If time is non-dimensionalized by the ship length L and the gravitational acceleration g, t_1 is approximately the inverse of the Froude number. Figures 3 and 4 demonstrate this behavior in the surge-surge memory function as the speed is increased to $F_n = 0.2$ and $F_n = 0.3$. The value of t_1 is indicated on each plot and can be identified as approximately the point of transition between the irregular frequency contaminated region of the calculation and the large-time behavior which is dominated by the critical fre-

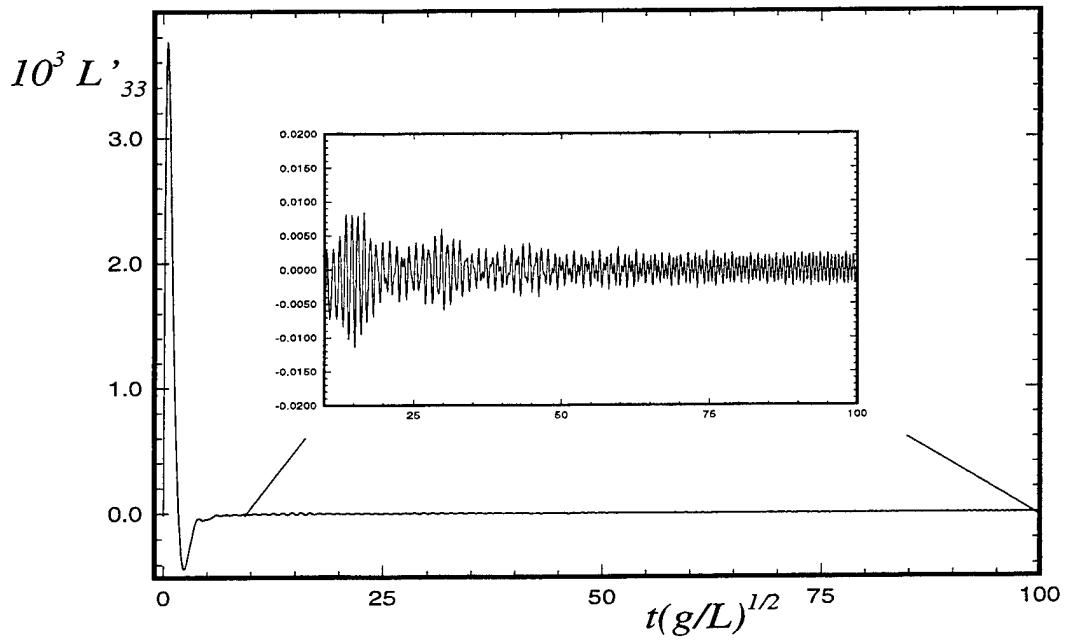


Figure 1: Impulsive acceleration heave-heave memory function for a Wigley hull at $F_n = 0.0$, showing the irregular behavior in the time domain. $L'_{33} = L_{33}/\rho L^3 (g/L)^{\frac{1}{2}}$.

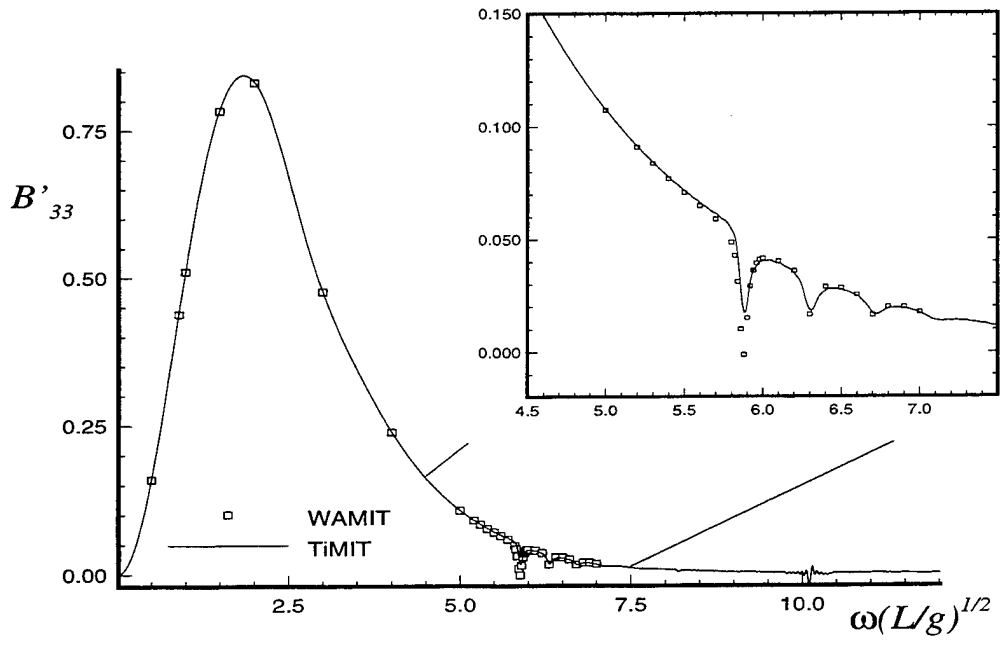


Figure 2: Heave-heave damping coefficients for a Wigley hull at $F_n = 0.0$, showing irregular behavior in the frequency domain. $B'_{33} = B_{33}/\rho \nabla \omega$

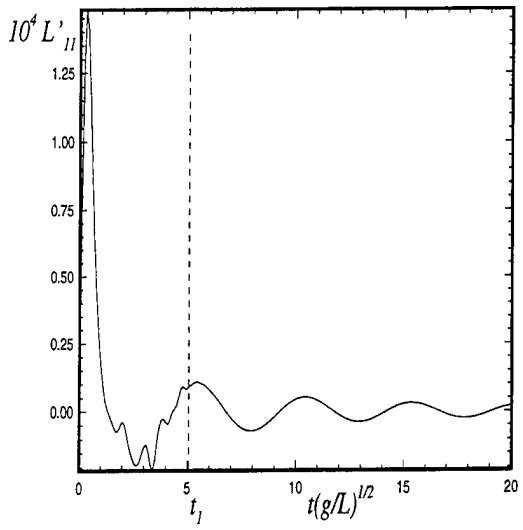


Figure 3: Impulsive acceleration surge-surge memory function for a Wigley hull at $F_n = 0.2$, $L'_{11} = L_{11}/\rho L^3 (g/L)^{\frac{1}{2}}$.

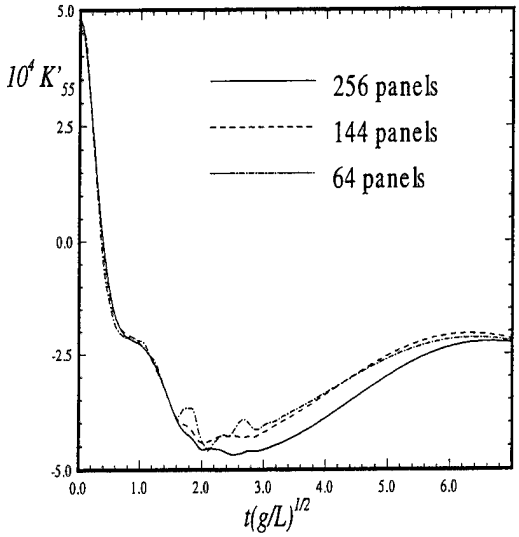


Figure 5: Impulsive velocity pitch-pitch memory function for a Wigley hull at $F_n = 0.3$. The irregular behavior in the time domain is reduced with discretization refinement. $K'_{55} = K_{55}/\rho L^5 (g/L)$.

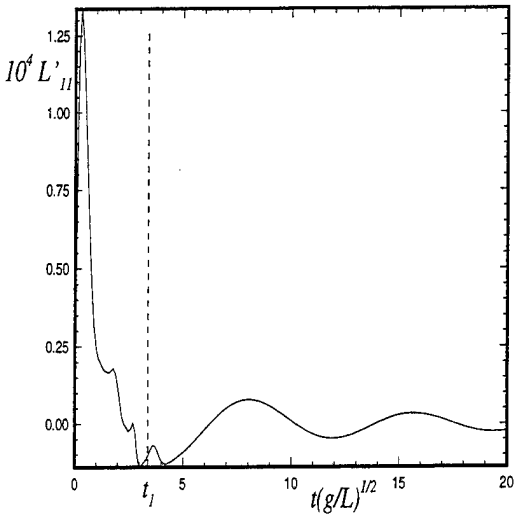


Figure 4: Impulsive acceleration surge-surge memory function for a Wigley hull at $F_n = 0.3$, $L'_{11} = L_{11}/\rho L^3 (g/L)^{\frac{1}{2}}$.

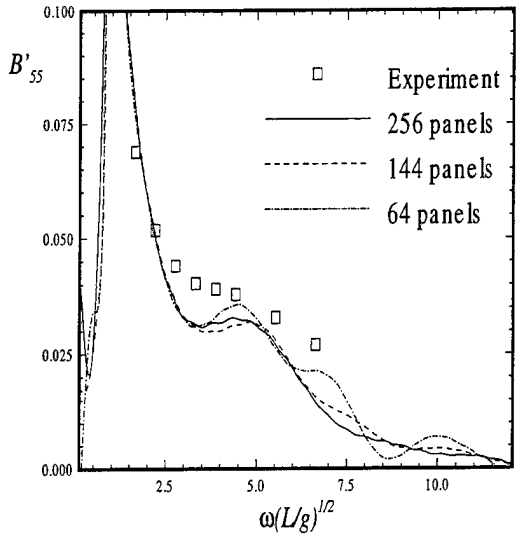


Figure 6: Pitch-pitch damping coefficients for a Wigley hull at $F_n = 0.3$, showing corresponding reduction of irregular behavior in the frequency domain. $B'_{55} = B_{55}/\rho \nabla L^2 (g/L)^{\frac{1}{2}}$.

quency oscillations discussed in Section 3.1. This compression in time of the oscillation leads to a corresponding expansion in the frequency content.

The irregular behavior can be reduced by refining the discretization. Figures 5 and 6 show the effect of increasing the numbers of panels used to discretize the hull in both the time and frequency domains (these results are all converged with respect to the temporal discretization).

To conclude the discussion of numerical issues we draw attention to Figure 7. This figure shows the surge-surge memory function for a Wigley hull at $F_n = 0.1$, calculated using 144 panels on half of the ship and a non-dimensional time-step $\Delta t = 0.1$. The gross features of this function differ very little from the zero speed response, and at this low speed, truncation at $t \approx 20$ would be appropriate. If we examine this solution closely however, four distinct regions are observed (see the expanded view inserted into the same figure). In the interval from $0 < t < 5$ the greatest magnitudes of the transient response occur. For $5 < t < 10$ ($t = 10$ being the time required to travel one ship length), the irregular oscillation can be observed in combination with the oscillations at the critical period. In this case $T_c = 2.513$, and the lowest irregular wave period $T_i \approx 1.1$ can be clearly identified. For $t > 10$ the solution can be described by the asymptotic form (15) with $C_0 = 0$. This region initially displays the exponential decay of the dominant second term ($10 < t < 25$). Subsequently the third term becomes dominant ($t > 30$). (This plot is convenient for illustration, but at higher, more practical, Froude numbers, the point of transition between the dominance of the two asymptotic terms is at very large time.)

4 The Series 60 Hull

This Section presents typical calculations which can be performed with TiMIT for a surface ship. The Series 60, $C_b = .7$, hull is used for this purpose since it has been extensively studied analytically and experimentally. The computations are presented for a range of Froude numbers.

4.1 First-Order Wave Effects

Our analysis begins with the motions of the ship in waves at zero forward speed. Figures 8 and 9 show two typical memory functions computed using 256 panels on half of the ship and a non-dimensional time step $\Delta t = 0.05$. The Fourier transform of these functions gives the added-mass and damping coefficients shown in Figures 10 and 11. These quantities are compared to results computed in the frequency domain with WAMIT [3].

The response amplitude operator (RAO), which is the ratio of the ship motion amplitude to the incident wave amplitude, can be calculated by two alternative methods. In the first method (identified as "TiMIT$_1$" in the figures) the Fourier transforms (17) are used to evaluate the added mass, damping, and exiting-force in the frequency domain, and the equations of motion (16) are solved to obtain the RAO's. In the second method (identified as "TiMIT$_2$") a time-domain simulation is performed using a pseudo-random spectrum of incident waves, and the RAO is computed as the Fourier transform of the motion history, divided by the Fourier transform of the incident wave elevation.

Figures 12 through 15 show the motions of the ship, free to heave and pitch in head seas, calculated using TiMIT and compared to the same quantities computed using WAMIT. In Figure 12 the RAO's computed using both methods are compared, and the results are practically identical, except at very low frequencies where the finite length of the simulation affects the computations.

Next we investigate the effects of forward speed on the ship's motions. Figures 16 and 17 show the heave-heave memory function and the heave-pitch added-mass coefficient for Froude numbers between 0.0 to 0.25. Figures 18 and 19 show the effects of increasing speed on the magnitude of the RAO in heave and pitch in head seas.

4.2 Forces in Calm Water

The steady wave resistance, sinkage force and trim moment acting on the ship in otherwise calm water can be computed from the steady-state limit after an impulsive acceleration in surge to a forward speed U. Figure 20 shows a sample time history of the wave resistance coefficient after an impulsive acceleration to a Froude number of 0.2. Figures 21 through 23 show the steady limits of the wave resistance, sinkage, and trim at several Froude numbers.

5 The Submarine

An axisymmetric submarine hull can be described by the following formula [15] for the local radius of

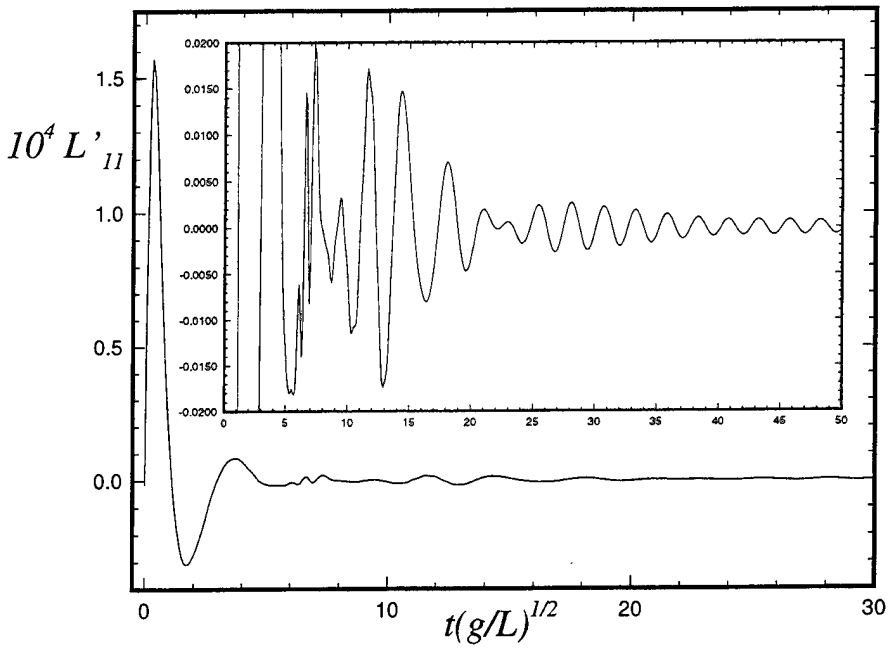


Figure 7: Impulsive acceleration surge-surge memory function for a Wigley hull at $F_n = 0.1$, showing transition to large-time behavior. $L'_{11} = L_{11}/\rho L^3 (g/L)^{\frac{1}{2}}$. Insert vertical scale is magnified and horizontal scale is extended.

a body of revolution as a function of position forward (r_f) and aft (r_a) of a parallel middle body:

$$r_f = R\left[1 - \left(\frac{x_f}{L_f}\right)^2\right]^{1/2}$$
$$r_a = R\left[1 - \left(\frac{x_a}{L_a}\right)^3\right]. \qquad (18)$$

Here R is the radius of the parallel middle body, $L_{f,a}$ are the lengths of the hull forward or aft of the parallel middle body, and $x_{f,a}$ is a local coordinate which runs from zero at the parallel middle body up to L_f or L_a. For the results presented here, the overall length of the submarine is taken as unity, with the following values used for the parameters in (18): $L_f = 0.167$, $L_a = 0.389$, and $R = 0.046$.

A paneled representation of this hull is shown in Figure 24. The solutions of the canonical potential problems is carried out in the manner described in Section 3. Note that the waterline integral in equation (13) vanishes, and there is no irregular behavior (as described in Section 3.3) in these solutions because the ship is not surface-piercing.

A single condition has been investigated for this hull: $F_n = 0.1$, head seas, with the depth of submergence of the hull centerline equal to the diameter at the parallel middle body. Three discretizations have been used with 64, 144, and 324 panels on half of the hull. In all cases, results presented for a certain spatial discretization are believed to be converged in the temporal discretization.

5.1 Forces in Calm Water

Figures 25 and 26 present the calm-water vertical force and trim moment respectively. The convergence of the computations as the number of panels is increased confirms that the discretization with 324 unknowns is adequate for these forces. The vertical force is a suction force towards the free surface, while the trim moment about midships is negative (bow up). The center of buoyancy of this hull is forward of midships, and the trim moment about this point is positive, tending to rotate the hull bow-down.

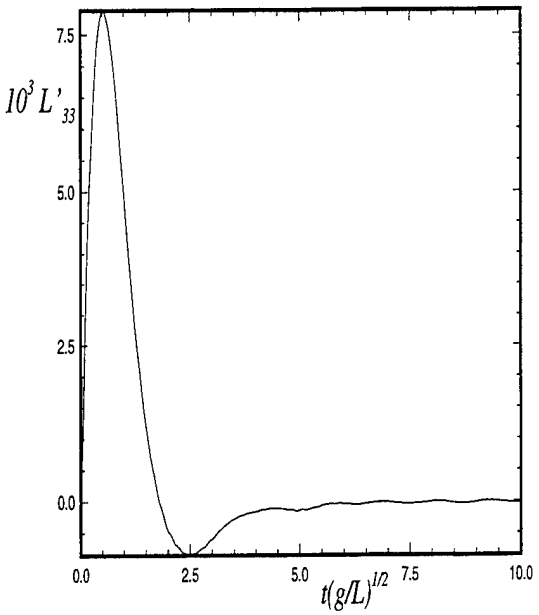


Figure 8: Impulsive acceleration heave-heave memory function for the Series 60 hull at $F_n = 0.0$, $L'_{33} = L_{33}/\rho L^3(g/L)^{\frac{1}{2}}$.

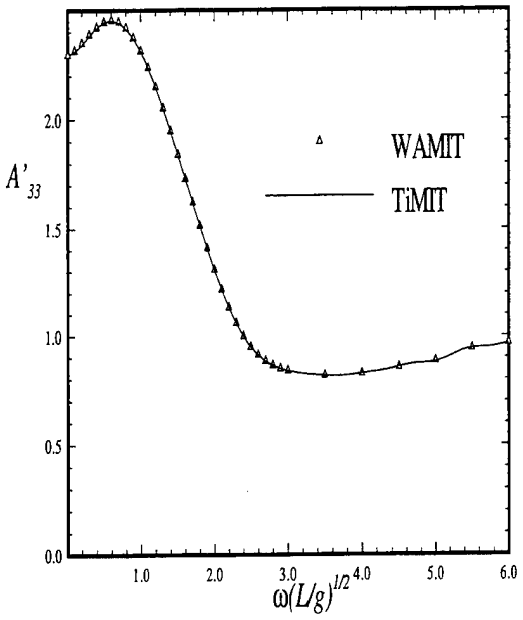


Figure 10: Heave-heave added-mass coefficients for the Series 60 hull at $F_n = 0.0$, $A'_{33} = A_{33}/\rho\nabla$.

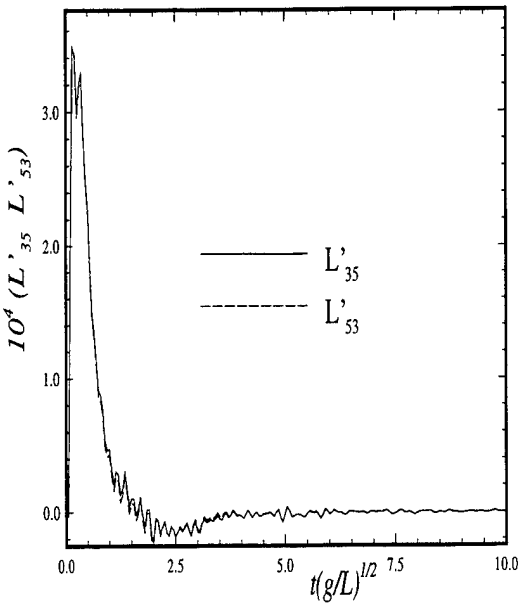


Figure 9: Impulsive acceleration cross-coupling memory functions heave-pitch for the Series 60 hull at $F_n = 0.0$, $L'_{ij} = L_{ij}/\rho L^4(g/L)^{\frac{1}{2}}$.

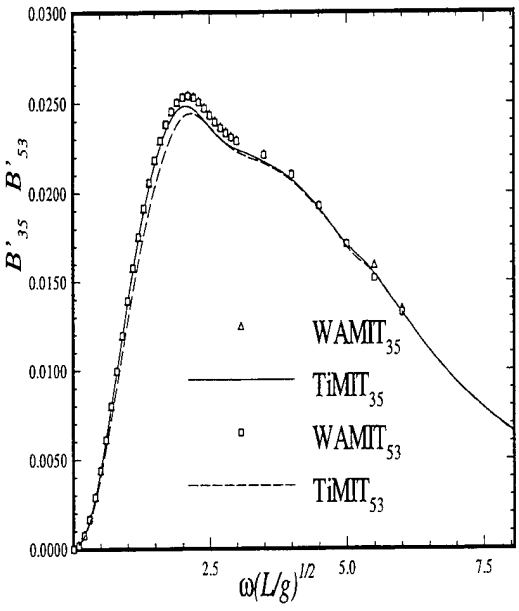


Figure 11: Heave-pitch cross-coupling damping coefficients for the Series 60 hull at $F_n = 0.0$, $B'_{35} = B_{35}/\rho\nabla L\omega$.

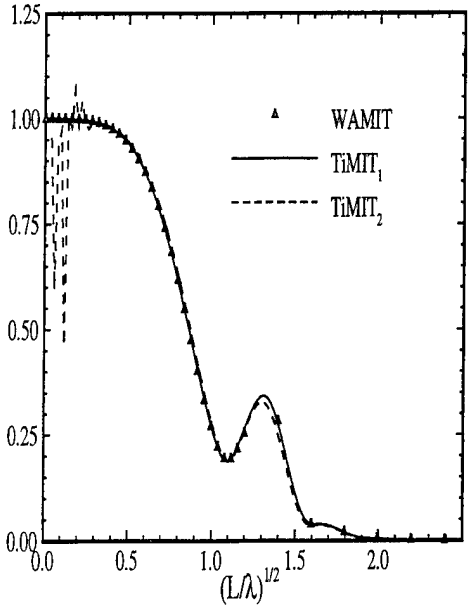


Figure 12: Magnitude of the heave RAO for the Series 60 hull at $F_n = 0.0$

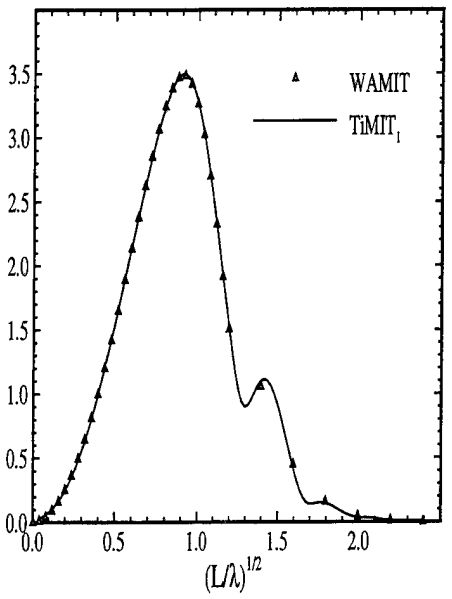


Figure 14: Magnitude of the pitch RAO for the Series 60 hull at $F_n = 0.0$

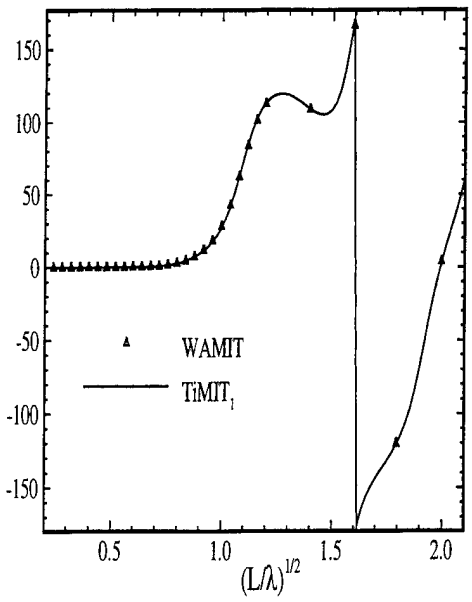


Figure 13: Phase angle of the heave RAO for the Series 60 hull at $F_n = 0.0$

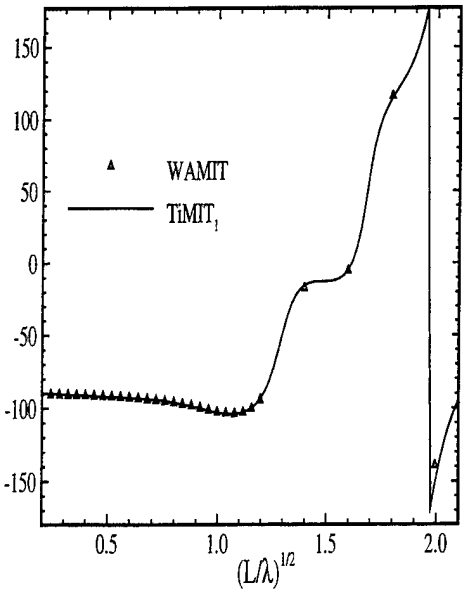


Figure 15: Phase angle of the pitch RAO for the Series 60 hull at $F_n = 0.0$

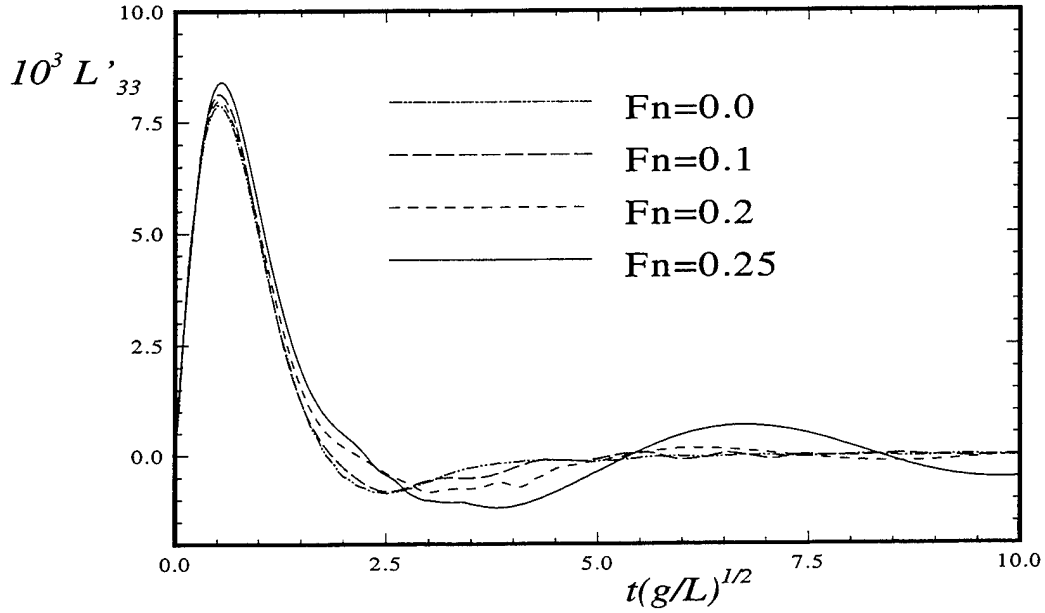


Figure 16: Impulsive acceleration heave-heave memory function for the Series 60 hull at various Froude numbers, $L'_{33} = L_{33}/\rho L^3 (g/L)^{\frac{1}{2}}$.

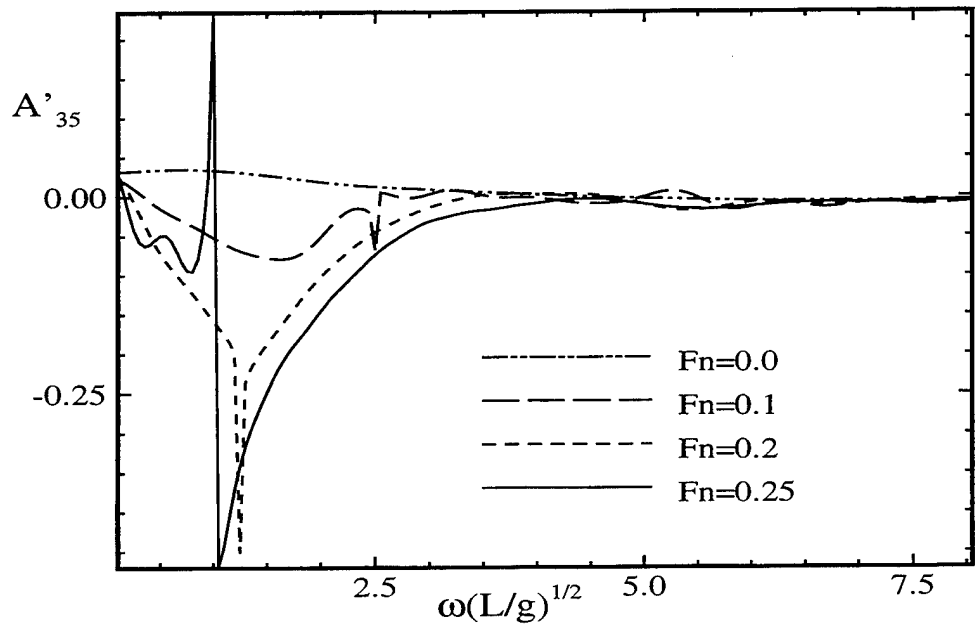


Figure 17: Heave-pitch added-mass coefficients for the Series 60 hull at various Froude numbers, $A'_{35} = A_{35}/\rho\nabla L$.

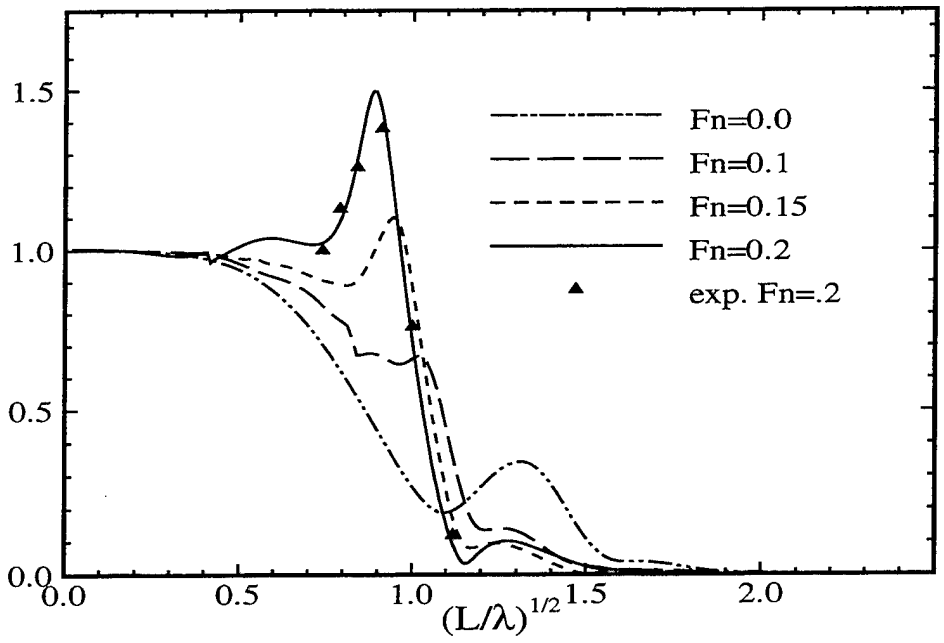


Figure 18: Magnitude of the heave RAO for the Series 60 hull at various Froude numbers.

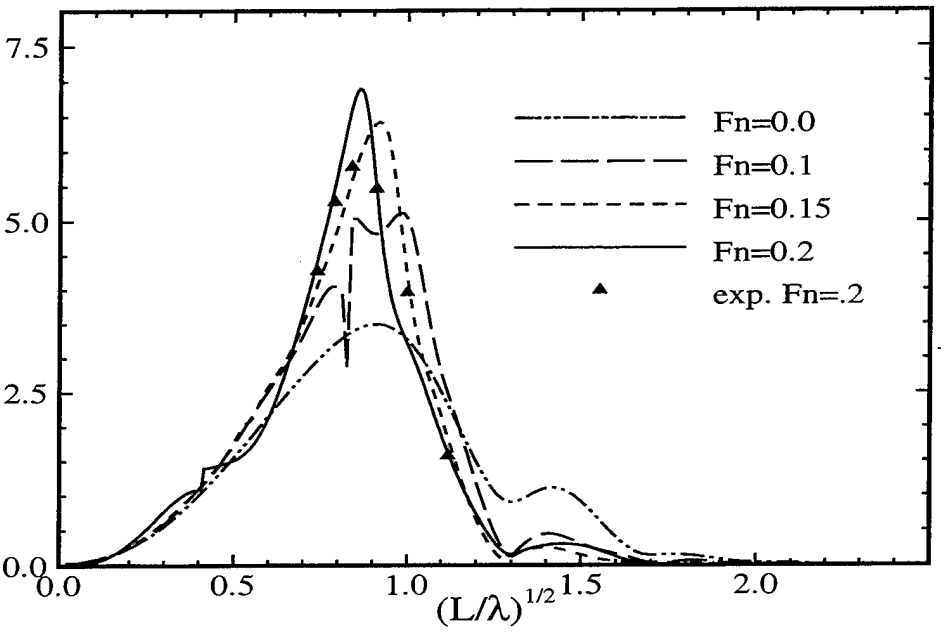


Figure 19: Magnitude of the pitch RAO for the Series 60 hull at various Froude numbers.

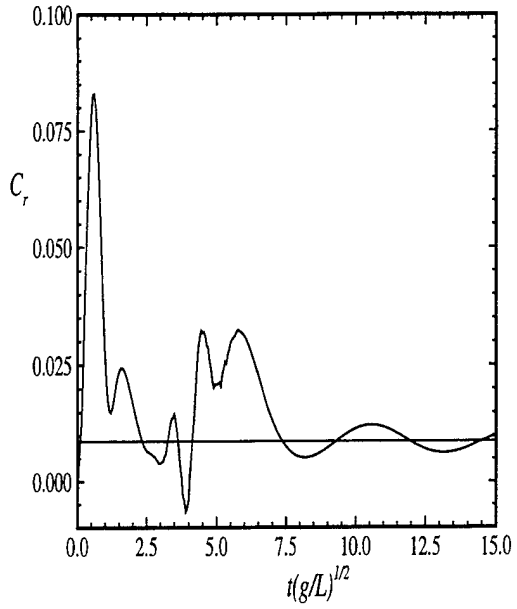


Figure 20: Time history of the unsteady wave resistance for the Series 60 hull at $F_n = 0.2$, $C_r = -F_x/\frac{1}{2}\rho U^2 S$.

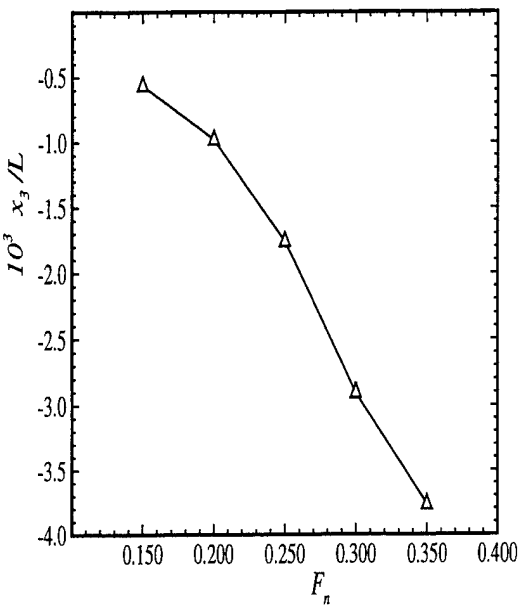


Figure 22: Non-dimensional sinkage vs. Froude number for the Series 60 hull.

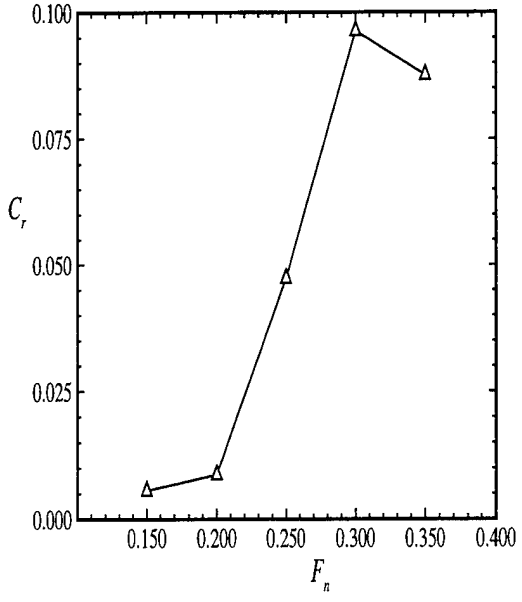


Figure 21: The steady wave resistance coefficient for the Series 60 hull at various Froude numbers, $C_r = -F_x/\frac{1}{2}\rho U^2 S$.

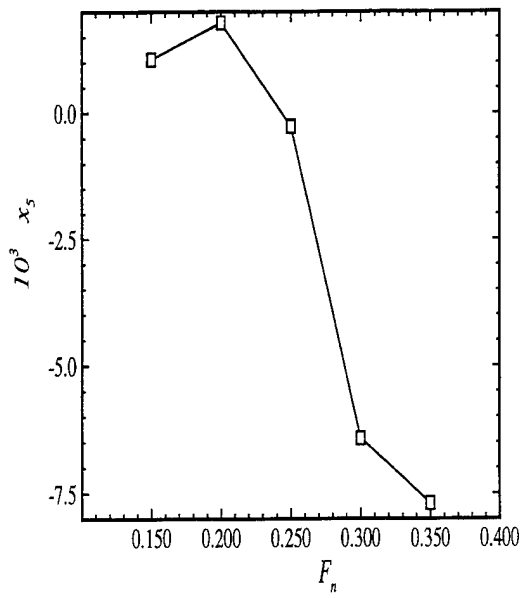


Figure 23: Non-dimensional trim vs. Froude number for the Series 60 hull.

5.2 First-Order Wave Effects

Figure 27 is included to demonstrate the convergence of the memory functions. The heave-pitch memory function L_{35} is presented since the off-diagonal responses converge most slowly. Figures 28 and 29 present the heave and pitch RAO's for head seas, respectively.

5.3 Mean Forces in Waves

The mean second-order forces acting on a submarine or surface ship are due entirely to time-averaged products of first-order quantities at each separate frequency of monochromatic wave encounter. In general these mean forces involve quadratic products of the radiation and diffraction solutions. For simplicity we only consider the latter, corresponding to the case where the submarine's unsteady motions are neglected. In this case, since the wetted surface is fixed, the only contribution is from the quadratic term in the Bernoulli equation, and the mean second-order force is

$$\bar{F}_i(\omega) = \overline{\frac{-\rho}{2} \int\int_S dS \; n_i \vec{\nabla}(\phi_I + \phi_S) \cdot \vec{\nabla}(\phi_I + \phi_S)}. \tag{19}$$

Here the diffraction potential $(\phi_I + \phi_S)$ is for a steady-state (regular wave) solution, at a specified frequency of encounter, the overbar denotes the time average over one period, and n_i is the generalized normal as defined in (8).

Note that the quadratic nature of the integrand in (19) precludes direct analysis in the time domain using an impulsive input, and it is necessary in this case to solve the first-order problem separately for each frequency of interest. Thus the input is a monochromatic incident wave system, and the analysis must be continued in time until a steady state is achieved. A more efficient, hybrid approach, which combines the time- and frequency-domain analyses, allows the use of the impulsive inputs (see Section 6).

Figure 30 shows the second-order vertical force and moment defined in (19), *before* the time average is taken, for an incident wave of $\lambda/L = 0.80$, a Froude number of $F_n = 0.1$, and for three discretizations of the submarine. Note that the pitch moment has converged to graphical accuracy while the heave force requires a computation at a finer discretization before such a conclusion may be drawn. The mean vertical force is positive, corresponding to a suction force attracting the submarine towards the free surface. The mean moment computed about midships is negative, but about the center of buoyancy this moment is positive, tending to rotate the hull bow-down. The normalization of the mean forces is not the same as that for the calm-water forces, so a direct comparison is not meaningful; however at this low Froude number and in moderate sea states, the orders of magnitude of the coefficients suggest that the mean second-order forces are more important than the calm-water steady forces.

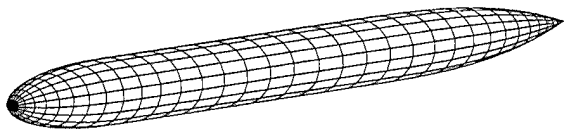


Figure 24: The submarine with 648 panels on the entire hull.

6 Conclusions and Recommendations

In this paper we have described the development of a three-dimensional panel code, intended to analyze transient (or steady-state) motions of ships and submarines in the presence of a free surface, and to be suitable for widespread use by naval architects and hydrodynamicists. This code permits the analysis of seakeeping problems, and also of problems involving steady motion in calm water. The hydrodynamic theory is consistently linearized, but nonlinear forces which are readily described can be included directly in the simulation, as in the cases of nonlinear hydrostatics and empirical estimates of viscous roll damping.

An important advantage of this linear analysis, both for computational efficiency and for usefulness to the ship designer, is that the hydrodynamic analysis can be carried out for appropriate velocity potentials associated with separate components of the overall problem, and for canonical inputs defined in terms of impulsive motions and impulsive incident waves. The solution for

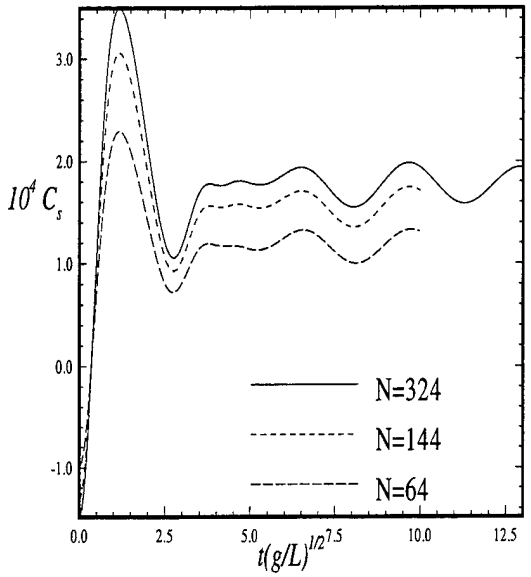


Figure 25: Convergence of the steady calm-water suction force on the submarine at $F_n = 0.1$, $C_s = F_z/\frac{1}{2}\rho U^2 S$.

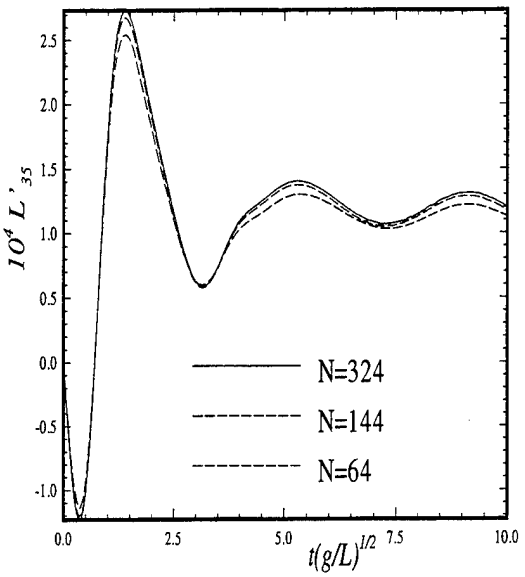


Figure 27: Convergence of the impulsive acceleration heave-pitch memory function for the submarine at $F_n = 0.1$, $L'_{35} = L_{35}/\rho L^4 (g/L)^{\frac{1}{2}}$.

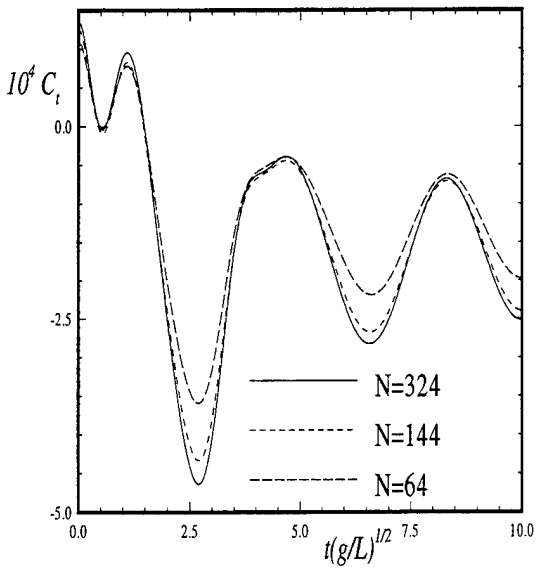


Figure 26: Convergence of the steady calm-water trim moment on the submarine at $F_n = 0.1$, $C_t = M_y/\frac{1}{2}\rho U^2 L S$.

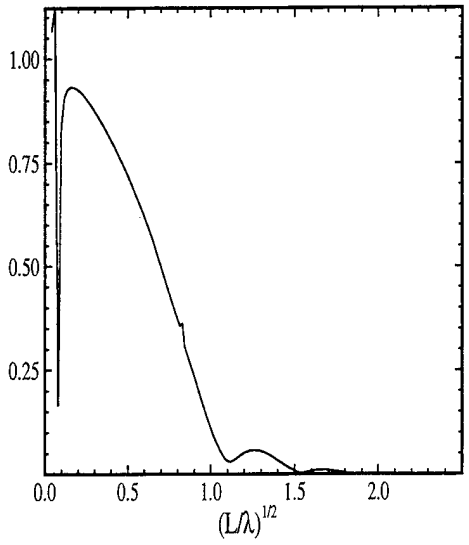


Figure 28: Magnitude of the heave RAO for the submarine at $F_n = 0.1$.

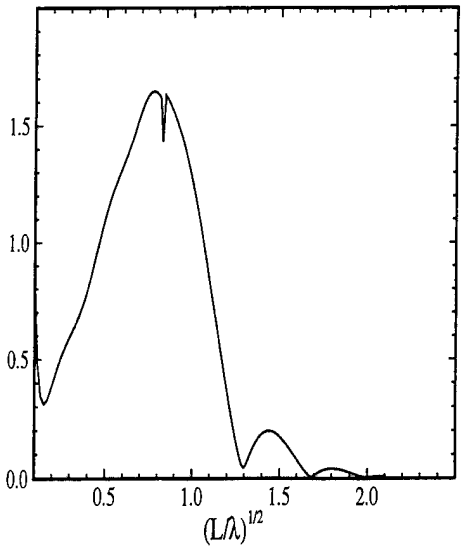


Figure 29: Magnitude of the pitch RAO for the submarine at $F_n = 0.1$.

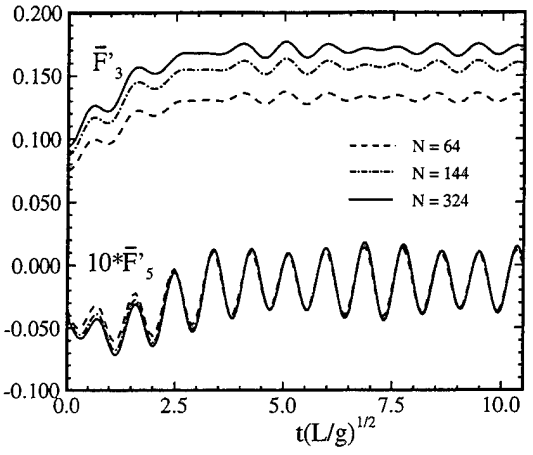


Figure 30: The mean second-order vertical force and moment on the submarine. $F'_i = F_i/\rho g A^2 L^k$, $k = 1$ for $i = 3$, $k = 2$ for $i = 5$.

each of the potentials, which is the dominant computational burden, can be performed once for a given hull form and stored for subsequent post-processing. Quantities of physical interest can then be computed, with relatively little effort, including the impulse-response functions of global forces, local pressures, or any other first-order hydrodynamic quantity of interest. This information may be used repeatedly in different time-domain simulations, or it may be transformed and used for analysis in the frequency domain.

The decoupling of the potential problem from the specific tasks of seakeeping analysis has allowed our efforts to be focused on the former, to produce an efficient implementation of the transient, forward-speed theory. The subsequent processing tasks of Fourier transformation, computation of the RAO, and simulation have been implemented in the TiMIT suite of programs for convenience. Since we cannot foresee all of the broad range of specific applications and simulations to which this methodology can be applied, the intent is to develop the code in a form where it can be readily adapted to a variety of applications by different users.

At present the code is capable of performing simulations by solving the equations of motion in their standard linear form (1). Left for future work is the inclusion of nonlinear effects, particularly nonlinear hydrostatics and roll damping. We anticipate that the former will be accomplished by updating the exact hull position in the simulation and computing the hydrostatic forces, while the hydrodynamic forces are computed from the first-order impulse-response functions. The latter effect may be included using a nonlinear roll coefficient, based on empirical data or estimates. Another important topic for future development is the inclusion of radiation modes corresponding to structural deflections and their coupling with the structural analysis of the ship hull in the time-domain.

Numerous extensions of the basic solution can be envisaged, involving finite-depth effects, ship-to-ship interactions, complete second-order mean forces in waves, and large-amplitude motions.

The extension to a fluid of constant finite depth is straightforward in principle, but further work is required to develop effective algorithms and subroutines for the finite-depth Green function [11]; significant progress on this problem has been reported in [16].

The extension to consider certain types of ship-to-ship interactions has been reported in [17] in

the relatively simple context of low-Froude number operations, where free-surface effects are weak and bank or bottom topography may be a more important factor.

We have given one example of how mean second-order forces can be computed using the present code, through time-averaging of the periodic response in monochromatic waves. A more efficient approach may be to use the impulsive incident wave to compute impulse-response functions for all three components of velocity on each panel in the time domain, and then Fourier transform these to evaluate the mean second-order force integral in the frequency domain.

The consideration of large-amplitude motions, in conjunction with a linearized free-surface condition, the *body-exact* problem, requires a similar program architecture to the described first-order approach. However the computational burden is increased in two important ways: (1) the Green function evaluations are not re-usable and must be recomputed for all previous time at every time-step, and (2) simulations must be conducted with the complete hydrodynamic problem solved at every time-step. The former burden is of some concern, but the latter is a serious drawback and one must be convinced that this analysis is appropriate before conducting it. For this reason, the body-exact formulation should be considered a useful addition to, rather than a substitute for, the first-order analysis.

The development of this program has been motivated by the need to supplement, if not replace, the much simpler strip theory. In comparing the two approaches from a practical standpoint, two important issues should be recognized, concerning (1) the limitations of the strip theory itself, and (2) the relatively greater computational and human costs of applying the three-dimensional panel method.

The role of strip theory and its limitations is a subjective issue, but it may be appropriate to state that while a large number of important seakeeping problems can be adequately analyzed using strip theory, many other problems require a fully three-dimensional approach. These include, among others, unconventional ships (*e.g.* SWATH), low-frequency motions (*e.g.* following waves), structural loads, problems such as added-resistance where the diffraction solution itself is important, and the analogous problem of predicting second-order forces on submarines. In all of these cases the availability of an off-the-shelf three-dimensional panel program is an important addition to the tool-kit of ship designers and hydrodynamicists.

With respect to computer time, it is practical to use the three-dimensional panel method described here with medium performance workstations. The benchmark results presented in Section 4 for the Series 60 hull with 256 unknowns (512 panels on the complete hull), carried out for 300 time-steps, required 22 cpu hours on the entry-level SGI Indigo (MIPS 3000 processor). A lesser number of time-steps is actually required for engineering work, and so on a medium performance workstation we estimate 1 to 2 cpu hours for the analysis of a candidate design. It is important to re-emphasize that the canonical potentials provide the complete hydrodynamic characterization of a ship hull and so once computed, the computationally intensive part of a design evaluation is over. Neither Fourier transformation to obtain frequency-domain results nor the simulation of hull performance in pseudo-random seas are computationally burdensome. Time-domain simulations may be computed at a rate which is much faster than real time.

If the Green function evaluations are computed once for the entire time range and stored, then substantial disk space is required. For the Series 60 run specified above, the storage of the Green function values requires 350 Mbytes. Alternatively, if disk space is not available, the Green function may be evaluated as it is needed which will increase the computation time by a factor between two and seven, depending on the machine.

We must note the added human costs of implementing these more complete and sophisticated methods. Like all three-dimensional approaches this one requires the effort of producing a geometric description of the ship hull. Then, to conduct an analysis with TiMIT, there are decisions which must be made for the run-time parameters, such as time-step size and range; and for the operating conditions, such as speed and wave heading. The documentation and the organization of input is intended to mitigate these human costs, but the increased analytic capability represented by a computer code like TiMIT does not come without greater demands on the user.

The availability of a more complicated theory and associated program may seem a daunting prospect for users of the relatively simple strip theories. Many who heard Weinblum's lecture [1] thirty-eight years ago must have had a similar reaction to using *any* theory to predict the seakeeping characteristics of ships. A period of time

may be required for users to gain experience and confidence in the three-dimensional methodology, but this effort will be rewarded both in terms of greater confidence in the validity of the results, and in the broader range of problems to which this methodology can be applied.

Acknowledgment

This research was sponsored by the Office of Naval Research, Contract Number N00014-90-J-1160. Additional support was provided under a Joint Industry Project sponsored by the Chevron Oil Field Research Company, Conoco Norway, Exxon Production Research, Mobil Oil Company, the National Research Council of Canada, Norsk Hydro, Offshore Technology Research Center, Petrobrás, Saga Petroleum, the Shell Development Company, Statoil, and Det Norske Veritas. We are indebted to Lt. Cdr. G. R. Thomas for assistance with the submarine analysis.

References

[1] Weinblum, G. P. Contribution of ship theory to the seaworthiness problem. In *1st Symp. on Naval Hydrodynamics*, 61–107, Washington D.C., 1956.

[2] Newman, J. N. The quest for a three-dimensional theory of ship-wave interactions. *Phil. Trans. of the Royal Society*, **A**, 334, 27–41, 1991.

[3] Newman, J. N. and Lee, C. -H. Sensitivity of wave loads to the discretization of bodies. In *8th Int. Conf. on the Behavior of Offshore Structures*, London, 1992.

[4] King, B. W., Beck, R. F., and Magee, A. R. Seakeeping calculations with forward speed using time domain analysis. In *17th Symp. on Naval Hydrodynamics*, The Hague, Netherlands, 1988.

[5] Liapis, S. J. Time domain analysis of ship motions. Technical Report 302, The Department of Naval Architecture and Marine Engineering, The University of Michigan, Ann Arbor, 1986.

[6] Lin, W. M. and Yue, D. K. P. Numerical solutions for large-amplitude ship motions in the time domain. In *18th Symp. on Naval Hydrodynamics*, Ann Arbor, 1990.

[7] Korsmeyer, F. T. *The first- and second-order transient free-surface wave radiation problems.* PhD thesis, Massachusetts Institute of Technology, Cambridge, 1988.

[8] Bingham, H. B. *Simulating ship motions in the time domain.* PhD thesis, Massachusetts Institute of Technology, Cambridge, 1994.

[9] Cummins, W. E. The impulse response function and ship motions. *Schiffstecknik*, **9**, 101–109, 1962.

[10] Newman, J. N. Distribution of sources and normal dipoles over a quadrilateral panel. *J. of Engineering Mathematics.*, 20:113–126, 1986.

[11] Newman, J. N. The approximation of free-surface Green functions. In *Wave Asymptotics*, P. A. Martin and G. R. Wickham, editors, 107–135. Cambridge University Press, 1992.

[12] Bingham, H. B., Korsmeyer, F. T., Newman, J. N., and Osborne, G. E. The simulation of ship motions. In *6th Int. Conf. on Numerical Ship Hydrodynamics*, Iowa City, 1993.

[13] Liu, Y. and Yue, D. K. P. On the solution near the critical frequency for an oscillating and translating body in or near a free surface. *J. of Fluid Mechanics*, **254**, 251–266, 1993.

[14] Bingham, H. B. and Korsmeyer, F. T. The role of irregular frequencies in the transient Neumann-Kelvin problem. In *9th Int. Workshop on Water Waves and Floating Bodies*, Kyushu, 1994.

[15] Jackson, H. A. *Submarine Design Trends.* Course Notes. MIT Department of Ocean Engineering, Cambridge, 1991.

[16] Clarisse, J. -M., Newman, J. N. and Ursell, F. Asymptotic expansion of the Cauchy-Poisson problem in a fluid of finite depth. In *9th Int. Workshop on Water Waves and Floating Bodies*, Kyushu, 1994.

[17] Korsmeyer, F. T., Lee, C. -H. and Newman, J. N. The computation of ship interaction forces in restricted waters. *J. of Ship Research*, **37**, 4, 298–306, 1993.

DISCUSSION

L. Doctors
University of New South Wales, Australia

About ten years ago, when I was experimenting with the steady-state Neumann-Kelvin problem from a surface ship myself, Prof. John Wehausen (who is the chairperson at this session) asked me whether I had any proof that a solution to this problem really exists. Your presentation today describes the numerical solution of the time-domain (unsteady) Neumann-Kelvin problem. Would you care to comment on the existence of solution?

My second question relates to the apparently much better convergence rate, as the mesh is refined, of the moment on the submarine in Figure 30, in contrast to the poorer convergence rate for the heave forces. Are there any reasons for this?

AUTHORS' REPLY

Although it has not been proven, we expect a unique solution to exist for the initial-value Neumann-Kelvin problem. For the steady-state problem it is not so clear because of the lack of initial conditions, but we feel that we can avoid this issue by computing steady-state quantities as limits of corresponding transient ones.

The apparently better convergence rate of the second-order steady moment compared to the force is a plotting artifact. The mean value of the second-order steady moment is an order of magnitude less than that of the force, but we have plotted them on the same axes.

Irregular Waves and Their Influence on Extreme Ship Motions

J. De Kat (Maritime Research Institute, The Netherlands)

ABSTRACT

This paper examines random waves in relation to capsizing and broaching of a steered, intact ship. Particular attention is paid to the validity of the random Gaussian wave model when simulating motions in severe, long-crested seas.

Wave characteristics investigated are those thought to be relevant for extreme ship motions: joint distributions of individual wave properties such as wavelength and steepness, spatial properties, deviations from Gaussianity, and group speed effects in astern seas. Where possible, comparisons are made between numerical simulations, model tests and full scale observations.

A brief description is given of a numerical model to simulate extreme ship motions. With this model, a number of capsize and broaching modes have been predicted; analysis of these extreme events provides details on the physical mechanisms involved and on critical wave conditions.

1. INTRODUCTION

Intact ships can be considered safe with respect to capsizing under most conditions. In survival conditions, however, the combination of severe waves, loading condition, ship speed and heading angle may lead to dangerous situations. When an intact ship does capsize, the process can take place in a very short time period; particularly in the case of high ship speeds this may happen without any forewarning, as the randomness of the waves can cause the sudden appearance of a critical wave or wave group endangering the vessel.

Twenty years ago Oakley *et al.* [1] presented the first comprehensive paper on the identification and simulation of three capsize modes that may occur in severe, astern seas. De Kat and Paulling [2] presented an extended time domain simulation model capable of predicting these and some other capsize modes for intact ships. Although ships satisfying standard stability criteria will be safe from a capsize point of view, little is known about their actual margin of safety. This applies especially to modern hull forms that have a significantly different hull shape compared with traditional hulls. Current stability criteria were developed decades ago, when ships current at that time provided the physical and statistical reference material, i.e., these criteria will not necessarily result in the same level of safety for modern hull forms as for conventional ships.

In 1990, a 4-year joint effort was launched by five navies (from Australia, Canada, the Netherlands, United Kingdom and United States) and MARIN to investigate wave-induced capsizing of intact frigates. One of the final objectives of the project was to arrive at new criteria that reflect the dynamic ship behavior in extreme wave conditions, while making extensive use of numerical simulations. To achieve these goals, activities consisted of:

- validation and updating of ship motion simulator
- modeling of wave climate
- identification of capsize modes and mechanisms
- development of stability design and operational guidelines
- capsize risk analysis

This paper focuses on some physical considerations of this Dynamic Stability project: comparisons between measured and simulated wave environment, and some capsize modes that can occur in irregular seas. Important properties of irregular seaways include limiting significant wave height as a function of peak period, joint distributions of wavelength and wave steepness, and encountered wave group properties. With the help of the simulation model developed and available model test data, a large number of potential capsize modes have been identified. The majority of capsize modes may

occur for an intact ship traveling in astern (i.e. following to stern quartering) seas, where the risk of capsizing increases with increasing speed. The project methodology and route toward criteria have been presented by De Kat [3] and De Kat *et al.* [4].

2. MODELING OF EXTREME SEA STATES

One of the key questions of interest is whether and to what extent a severe sea state can be considered as "Gaussian". The surface elevation of such a seaway would follow the Gaussian distribution; measurements in low to moderate sea states suggest this is indeed the case. This is particularly relevant from a theoretical and computational point of view, as the common representation of the surface by the linear superposition of sinusoids with random phases is very convenient. For high sea states the situation is less clear: even in deep water appreciable crest steepening effects will occur, which undoubtedly will result in deviations from Gaussianity.

To investigate the appropriateness of using the linear (Gaussian) wave model with random phases in ship motion analysis, joint distributions of wave surface properties are analyzed for a variety of sea states. Only long-crested seas are considered in this work.

2.1. Some extreme sea state properties

Characteristic steepness

As has been aptly described by for example Pierson [5], storm waves can have an extremely nonlinear character. Nonlinearities will become more prevalent for sea states with increasing characteristic steepness, s_{char}, defined as the ratio of significant wave height to wavelength associated with the spectral peak period, T_p. Ocean wave measurements suggest that the characteristic steepness of a seaway tends to be bounded as follows (Le Méhauté and Hanes, [6]):

$$0.02 < \frac{H_s}{\lambda_p} < 0.05 \qquad (1)$$

Therefore, the maximum steepness is typically less than 0.05, and the steepest possible sea state occurs when the significant wave height in deep water is:

$$H_{s,max} = 0.05 \frac{g T_p^2}{2\pi} \qquad (2)$$

The above maximum wave height is in agreement with the survivability envelope for storm waves with periods less than 15 s proposed by Buckley [7]. For worst annual storms in the North Atlantic, the mean and standard deviation of characteristic steepness are 0.035 and 0.0037, respectively; the Weibull distribution provides an excellent fit of wave steepness (De Kat *et al.*, [4]). In an absolute sense, the highest H_s measured in the Northern Hemisphere is around 17 m, associated with a peak period of 18 s.

Spectral shape

For fully developed seas, the Bretschneider spectrum is traditionally accepted, which is the same as the JONSWAP formulation with a peak parameter γ equal to 1. Recent analysis of extreme North Sea wind seas suggests that JONSWAP spectra with $\gamma = 1.9$ apply (Torsethaugen, [8]), while Buckley [7] suggests $\gamma = 1.3$ based on NOAA buoy data for extreme sea states with peak periods exceeding 13 s.

2.2. Measured and computed joint distributions

Physical observations and simulations suggest that extreme ship motions and capsizing are sensitive to both wavelength and wave steepness. Under certain conditions, encountered wave group properties also can be important. The joint distributions of relevant wave parameters will provide useful information in this respect. Before proceeding, a number of wave parameters are defined below.

Time domain analysis at a fixed point

Usually wave data are available at a fixed point only. Following the convention proposed by Myrhaug and Kjeldsen [9], properties of individual waves are defined as shown in Fig. 1, based on zero-crossing analysis in the time domain.

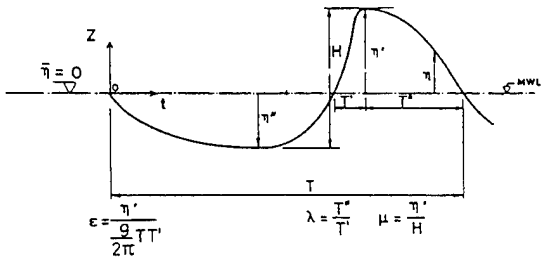


Fig. 1. *Definition of individual wave parameters (from Myrhaug and Kjeldsen, 1987)*

In this figure, the parameter ε represents the crest front steepness, μ is a measure of the crest

elevation with respect to the wave height H, and λ indicates the crest front versus back asymmetry (not to be confused with wavelength used further on in this paper).

Dahle and Myrhaug [10] make use of the joint distributions of crest steepness and wave period in capsize risk analysis of small fishing vessels, for which wave breaking in steep beam seas is cited as the most likely cause of capsizing; here the parameter ε seems to be suitable for describing critical wave conditions. For larger intact ships, astern sea conditions tend to be the most onerous from the viewpoint of capsizing. The analysis of related capsize mechanisms suggests that the onset of capsizing may be governed by the wave as a whole (crest-to-trough height and spatial wavelength). Therefore, overall wave steepness is considered as an additional parameter of interest:

$$s = \frac{H}{\lambda_z} \tag{3}$$

where H is the crest-to-trough height and λ_z is the associated wavelength based on the zero-crossing period T_z:

$$\lambda_z = \frac{g T_z^2}{2\pi} \tag{4}$$

Spatial analysis in the time domain

The motions of a ship will be governed by the time-dependent *spatial* wave surface characteristics. Wave profile data can yield parameters that are similar to the ones defined above. Based on either spatial measurements or calculations evaluated over a finite spatial distance equal to a characteristic wavelength, the following parameters are introduced: H_{spat} - crest-to-trough wave height, λ_{spat} - wavelength defined by either crest-to-crest length or 2 x crest-to-trough length (in the absence of two crests), s_{spat} - wave steepness defined by H_{spat}/λ_{spat}, ε_{spat} and μ_{spat} - same as ε and μ from above but based on equivalent spatial properties. The wave slope was evaluated numerically, but will not be treated here.

Joint probability density functions

Tank tests and simulations have been carried out to model a variety of sea states by increasing the significant wave height for a fixed peak period. Here we will focus on a fairly steep seaway scaled to: H_s = 14.5 m, T_p = 14.7 s, JONSWAP with γ = 2 (s_{char} = 0.043). The tests were carried out at scale 1 to 50 with 3-hour full scale duration; basin dimensions are 200 x 4 x 3.7 m. Wave elevations were measured and computed at 8 equidistant locations over a distance associated with the spectral mean wave period, along the centerline of the basin (200 m full sacle). The mean period is defined by $T_1 = 2\pi/\bar{\omega} = 2\pi m_0/m_1$, where m_0 and m_1 are the zero and first order spectral moments. The simulations are based on Fourier analysis, where a large number of superimposed sinusoidal components with uniformly distributed phase angles define the seaway.

To illustrate some results, we will focus on the joint probability density functions (joint pdf's) of several of the above parameters. If p(x,y) is the joint pdf of two continuous variables x and y, integrating this function with respect to those two parameters will yield unity. The marginal pdf can also be of interest; the marginal pdf of x is given by:

$$p(x) = \int_0^\infty p(x,y)\, dy \tag{5}$$

The joint pdf's obtained for the above case are shown for the following wave parameters: T_z and H in Fig. 2, ε and H in Fig. 3, μ and H in Fig. 4, and λ_z and s in Fig. 5. The contours in these figures show the (dimensional) joint pdf values. The outer contour is an indicator of extreme (and rare) events. The contour data are obtained by dividing the number of samples per bin (of width Δx and height Δy) by the total number of observations multiplied by $\Delta x \Delta y$, where the contours are fitted through the discrete set of bins. The upper graph of the figures represents the marginal pdf of the wave parameter on the horizontal axis of the joint pdf plot. Fig. 2 shows that both in the test and simulation the period associated with the highest waves corresponds to approximately the mean period, T_1. The correspondence between the joint distributions of the physical and simulated waves is quite good. In contrast, Fig. 3 shows that the simulation model underpredicts the crest front steepness of extreme waves (as might be expected). Examination of Fig. 4 suggests that the distribution of the measured crest-wave height ratios is almost symmetric. For the highest waves, computed crest and trough height are approximately the same ($\mu \approx 0.5$), while there is a tendency toward higher crests than troughs in the physical tests - this agrees with Fig. 3. Fig. 5 shows reasonable correspondence between tests and simulations as regards wavelength and overall steepness; waves having a length between 100 to 200 m tend to be the steepest in this sea state.

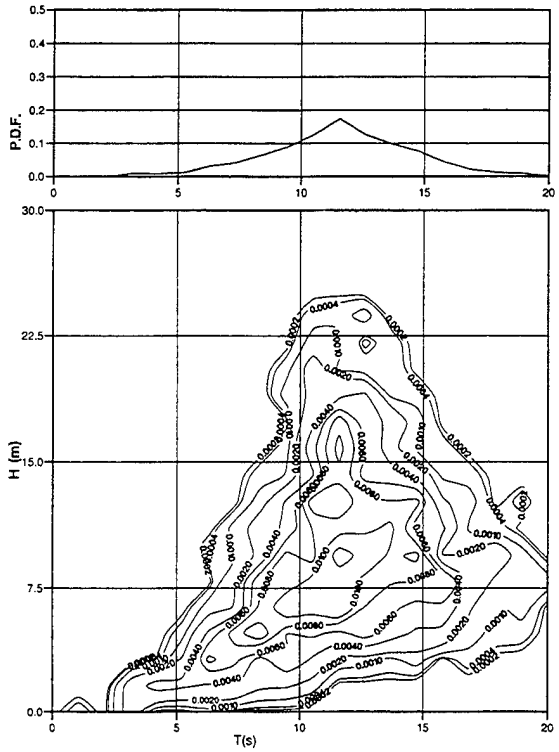


Fig. 2a. *Joint pdf of zero-crossing wave period and height (model test, $H_s = 14.5$ m, $T_p = 14.7$ s). Upper graph represents marginal pdf of T_z.*

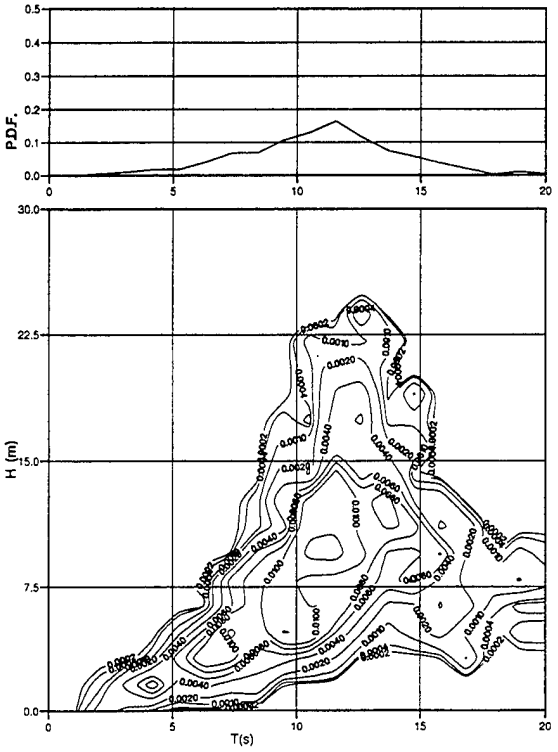


Fig. 2b. *Joint pdf of zero-crossing wave period and height (simulation, $H_s = 14.5$ m, $T_p = 14.7$ s). Upper graph represents marginal pdf of T_z.*

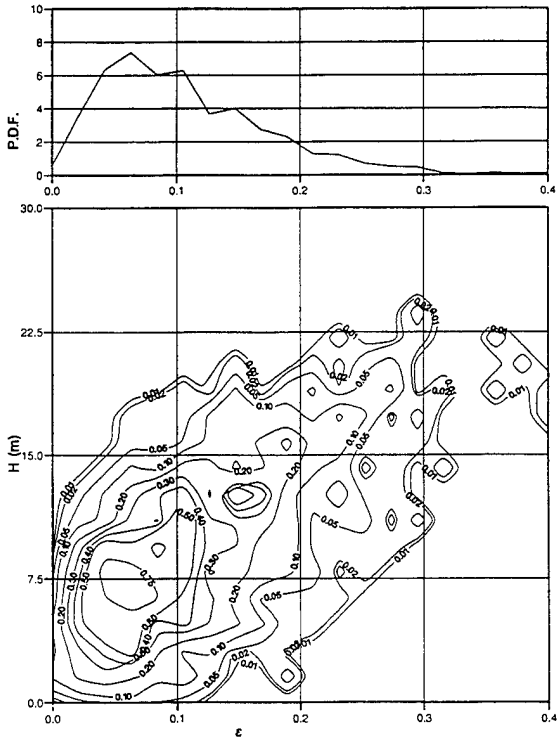


Fig. 3a. *Joint pdf of crest front steepness and wave height (model test, $H_s = 14.5$ m, $T_p = 14.7$ s). Upper graph represents marginal pdf of* ε.

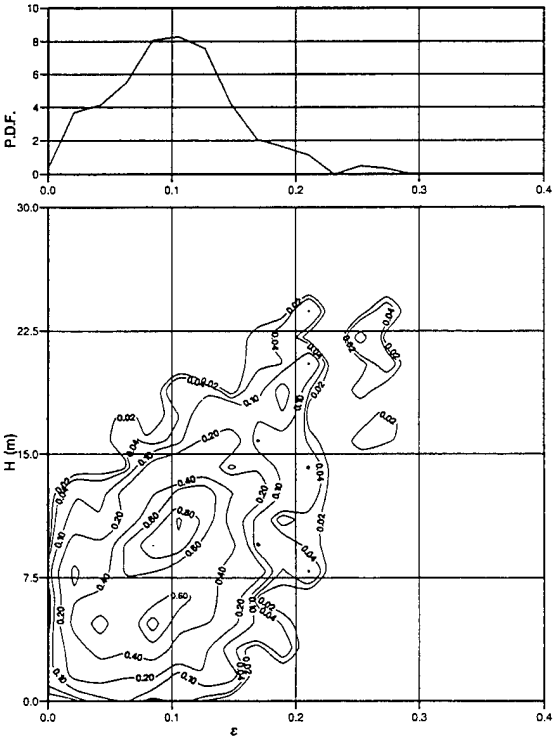


Fig. 3b. *Joint pdf of crest front steepness and wave height (simulation, $H_s = 14.5$ m, $T_p = 14.7$ s). Upper graph represents marginal pdf of* ε.

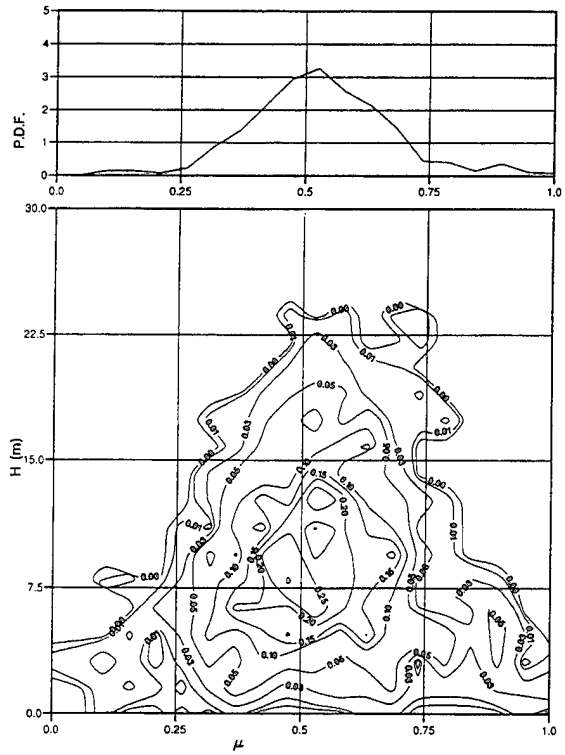


Fig. 4a. *Joint pdf of crest height-wave height ratio and wave height (model test, H_s = 14.5 m, T_p = 14.7 s). Upper graph represents marginal pdf of* μ.

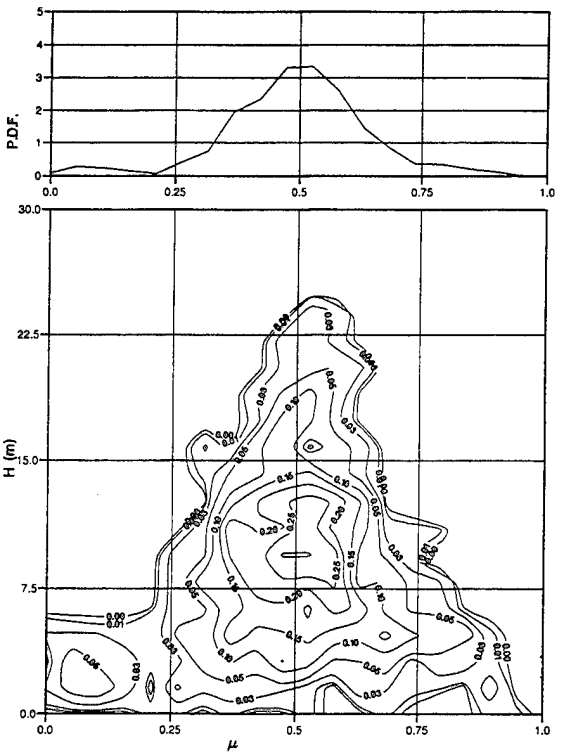


Fig. 4b. *Joint pdf of crest height-wave height ratio and wave height (simulation, H_s = 14.5 m, T_p = 14.7 s). Upper graph represents marginal pdf of* μ.

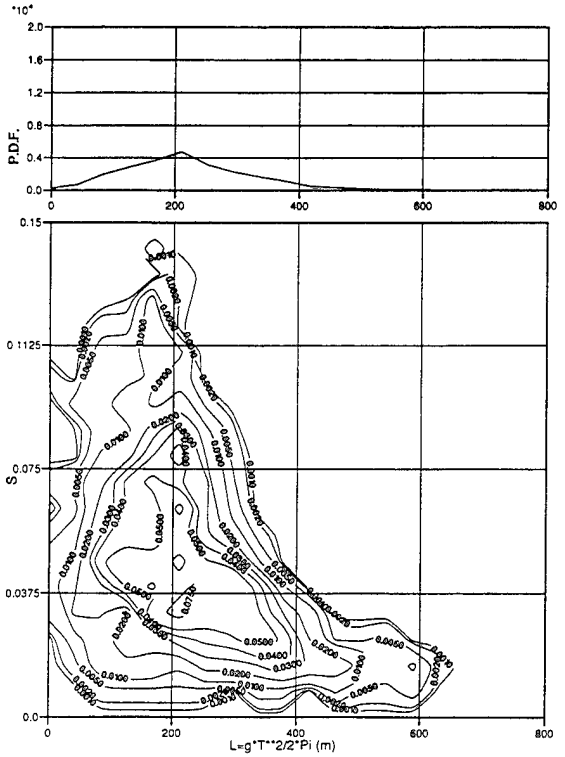


Fig. 5a. *Joint pdf of wavelength and steepness (model test, H_s = 14.5 m, T_p = 14.7 s). Upper graph represents marginal pdf of wavelength.*

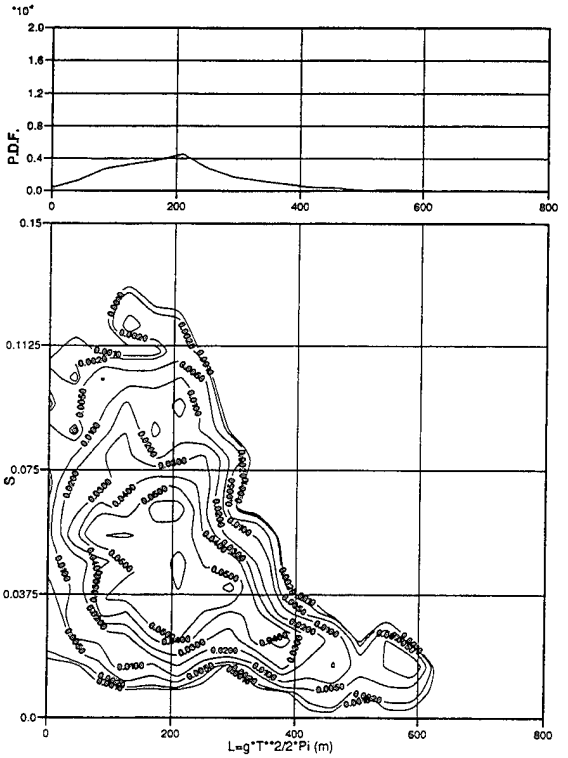


Fig. 5b. *Joint pdf of wavelength and steepness (simulation, H_s = 14.5 m, T_p = 14.7 s). Upper graph represents marginal pdf of wavelength.*

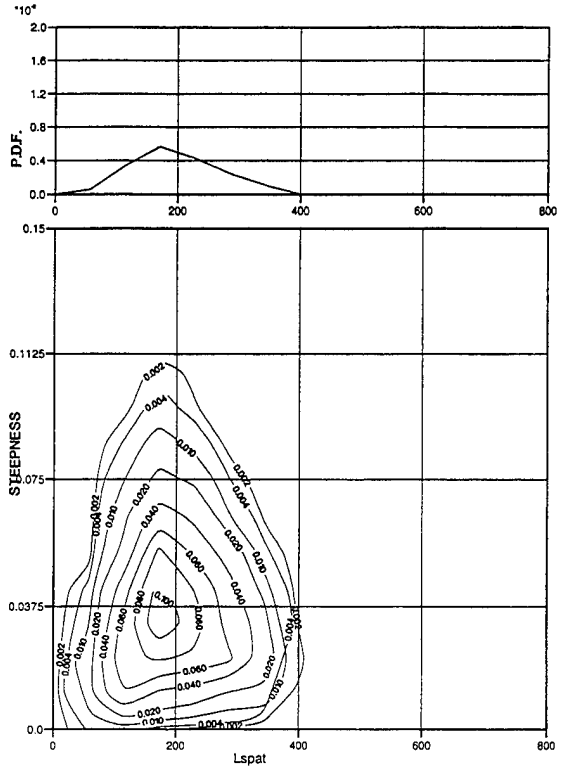


Fig. 6a. *Joint pdf of spatial wavelength and steepness (model test, H_s = 14.5 m, T_p = 14.7 s). Upper graph represents marginal pdf of wavelength.*

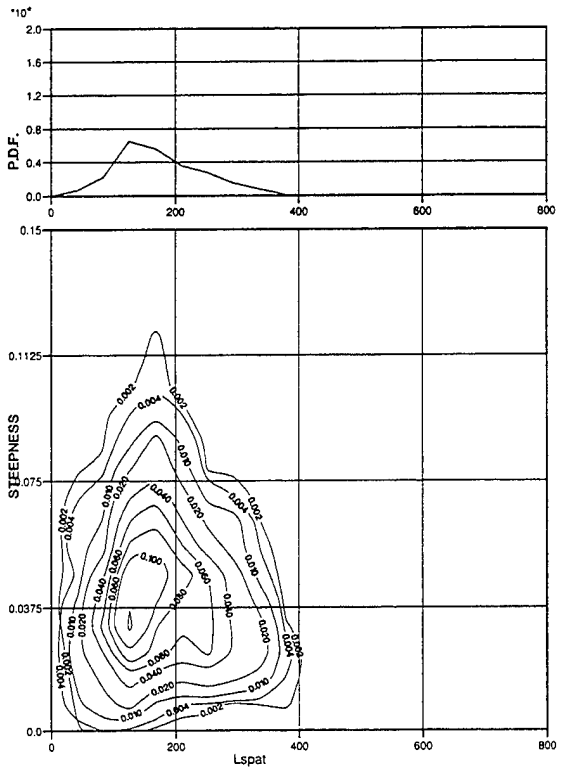


Fig. 6b. *Joint pdf of spatial wavelength and steepness (simulation, H_s = 14.5 m, T_p = 14.7 s). Upper graph represents marginal pdf of wavelength.*

Although the time-dependent spatial characteristics of a wave are not necessarily the same as those at a fixed point, their statistical distribution properties tend to be quite similar. As an example, Fig. 6 shows the measured and computed joint distribution of λ_{spat} and s_{spat}. Due to the finite distance covered by the wave gauges (200 m), it is not possible to predict wavelengths accurately exceeding twice that distance. For wavelengths under 400 m, the same general trends apply for temporal and spatial analysis, but there are some local differences concerning e.g. maximum steepness (this may be due partly to the relatively coarse resolution in the spatial analysis). There is good correspondence between the spatial properties of measured and simulated waves.

One major conclusion is that the joint distributions of overall wave properties are reasonably well predicted using the Gaussian random wave model. Similar observations apply even to the steepest sea state considered in the experiments (same peak period as in the test case above, but with s_{char} = 0.048). For sea states of moderate steepness, with $s_{char} \leq 0.03$, predicted and measured distributions of local crest effects, e.g. ε and H, are rather close also.

Miles and Mansard [11] found that wave parameters derived from zero-crossing time domain analysis at a point were not the same as those derived from spatial analysis; furthermore, for random waves with $s_{char} < 0.03$, spatial wave profiles were predicted well using the linear, Gaussian wave model when compared with wave flume data, while for a steeper sea state local differences were observed in the crests.

Crest asymmetry effects

The analysis from above suggests that for steep sea states the Gaussian random wave model results in wave crests that are not as asymmetric as observed in model tests, particularly for higher waves. Fig. 7 illustrates the asymmetry of the measured wave profile during the passage of a high wave (from the test example above); the crest is preceded by a shallow trough and followed by a relatively deep trough. Surface elevation skewness provides some measure of crest asymmetry; it is defined by the third order moment:

$$\alpha = \frac{E[(\zeta - E[\zeta])^3]}{\sigma_\zeta^3} \qquad (6)$$

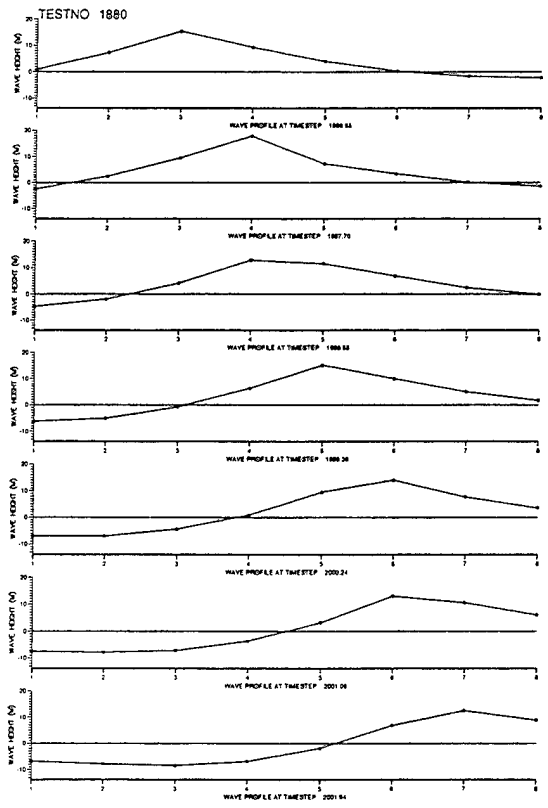


Fig. 7. *Measured successive spatial wave profiles during passage of a high wave (model test, H_s = 14.5 m, T_p = 14.7 s, horizontal distance is 200 m).*

where E[ζ] is the expected value and σ_ζ is the standard deviation of the wave elevation. The skewness for all simulated wave elevations is zero, as one would expect for a Gaussian process. The skewness of the wave elevation of the above basin test is 0.14, indicating the presence of asymmetric waves.

Crest-trough asymmetry can for a large part be attributed to second order effects, where waves can be regarded as 'weakly nonlinear'. Second order, irregular waves have been the subject of recent research, particularly in conjunction with offshore design applications, where absolute crest height can be critical.

Marthinsen and Winterstein [12] developed a mathematical model to estimate skewness and kurtosis taking into account both sum frequency and difference frequency terms; Stansberg [13] estimated skewness and kurtosis as a function of characteristic steepness using numerical simulations with sum frequency effects in deep water; Taylor [14] investigated crest asymmetry using a second order model. Pierson [5] takes a step toward stochastic nonlinear waves by considering irregular waves as the superposition of several higher (third) order Stokes-like waves, thereby introducing the dependence of phase speed on wave amplitude.

From the point of view of simulating ship motions, the question is to what extent asymmetry effects are important. Individual crest properties are sensitive to wave steepening effects and tend to have a more nonlinear character than overall wave height properties. While the shape of the wave profile is critical for loads, including slamming, it is not so critical for ship motions. One could argue that so long as the overall shape of the wave is approximately the same, the absolute crest height is not a critical parameter. Besides the ε-parameter, the crest period parameter λ (defined in Fig. 1) provides another measure of the shape of the crest. Fig. 8 shows the marginal pdf of measured and computed period parameter λ, which suggests that the difference between crest front length and length of its trailing side are predicted well using the random Gaussian model. Also the joint pdf's of λ from the simulation and test are much more alike than is the case for ε.

Field observations

Full scale wave measurements provide useful data for comparison with laboratory experiments. To derive statistically reliable joint distributions on the basis of ocean wave measurements, long duration measurements are needed. More often than not one is faced with the problem of nonstationarity of the wave process: within 1 hour or less, both peak period and significant wave height may vary appreciably.

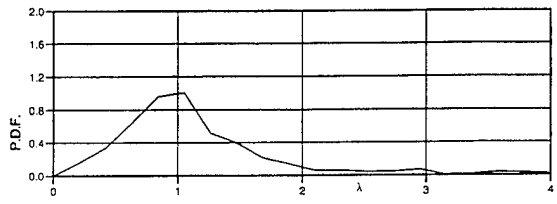


Fig. 8a. *Marginal pdf of crest period parameter λ (model test, H_s = 14.5 m, T_p = 14.7 s).*

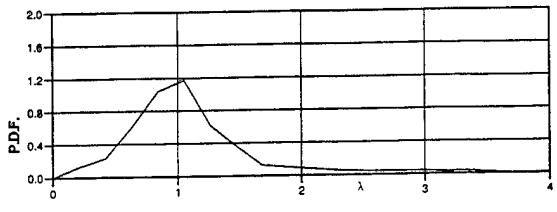


Fig. 8b. *Marginal pdf of crest period parameter λ (simulation, H_s = 14.5 m, T_p = 14.7 s).*

Long records of stationary data can only be obtained in controlled circumstances. One solution is to combine many short measurements to derive long-term statistics, or for example during the duration of a storm to scale the measured wave elevations to a common significant wave height.

In the present work an attempt is made to estimate joint distributions from single 30 minute measurements in 85 m water depth. The following steep sea state serves as an example: H_s = 6.6 m, T_p = 9.7 s, s_{char} = 0.045. The power spectrum is shown in Fig. 9. The measured joint distribution of T_z and H are shown in Fig. 10, Fig. 11 shows ε and H, Fig. 12 shows μ and H, and Fig. 13 shows λ_z and s. Albeit the short duration, the same general trends show up as in the tank tests and simulations.

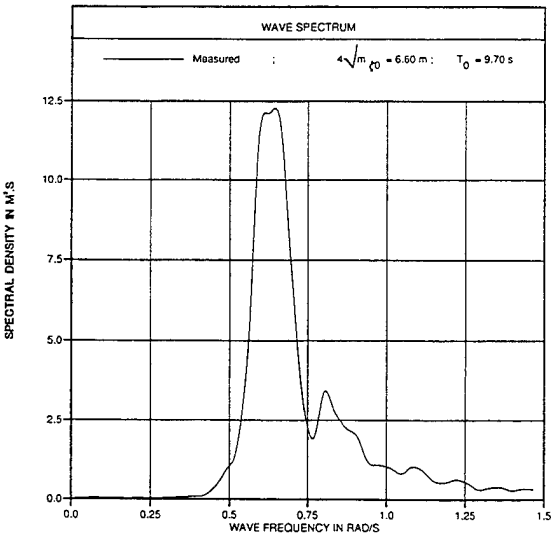


Fig. 9. *Power spectral density and distribution of measured wave elevation in 85 m water depth (H_s = 6.6 m, T_p = 9.7 s)*

This paper does not lay claim to the final answer concerning the range of validity of the linear, random wave model. Based on the observations made thus far, there is at least evidence to state that the overall joint wave properties are modeled surprisingly well by the Gaussian wave model even for steep sea states. Discrepancies appear as regards local crest properties; if we disregard wave breaking effects, the random wave model may provide a reasonable input for modeling ship motions in a severe sea state. If extreme ship motion behavior is more sensitive to overall wave steepness than to individual crest steepness, linear random wave theory may be acceptable for simulating extreme ship motions even in relatively steep random seas.

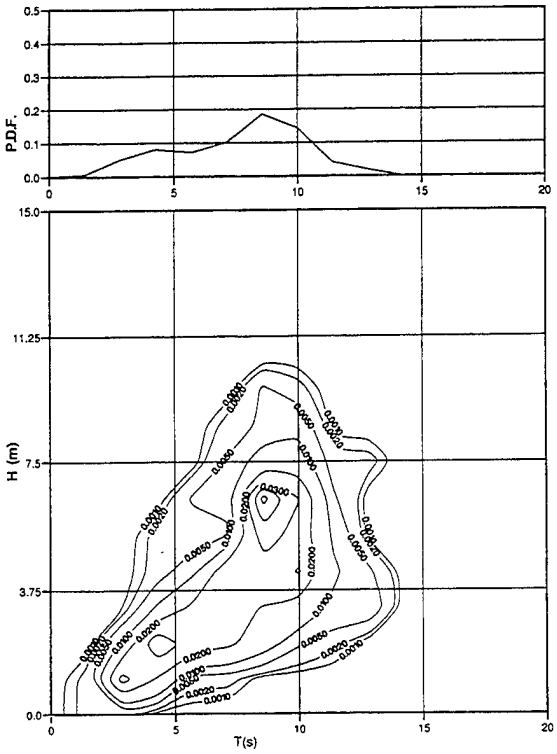


Fig. 10. *Joint pdf of zero-crossing wave period and height (85 m water depth, H_s = 6.6 m, T_p = 9.7 s)*

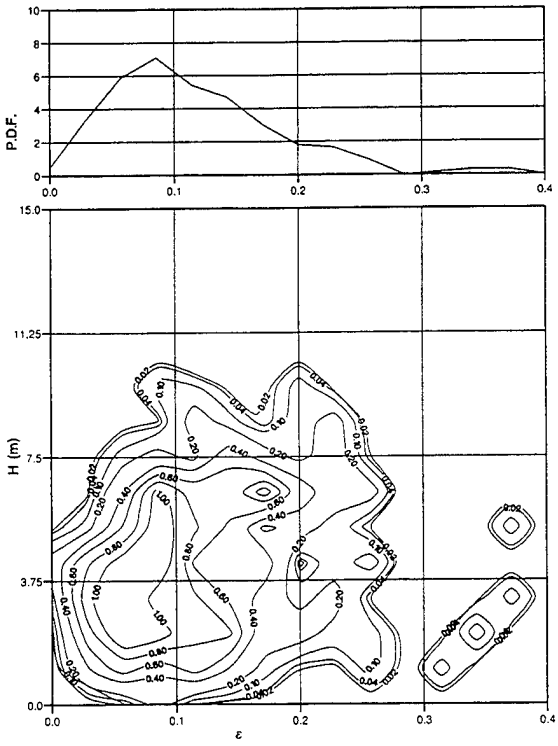


Fig. 11. *Joint pdf of crest front steepness and wave height (85 m water depth, H_s = 6.6 m, T_p = 9.7 s)*

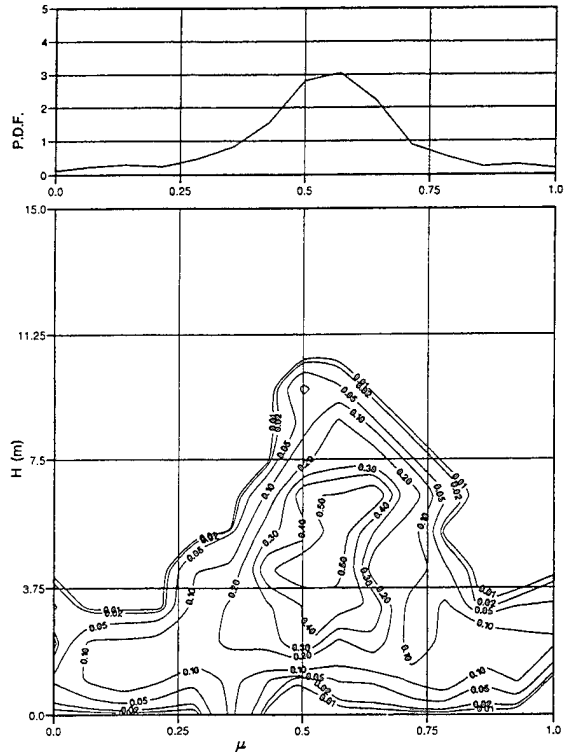


Fig. 12. *Joint pdf of crest height-wave height ratio and wave height (85 m water depth, H_s = 6.6 m, T_p = 9.7 s)*

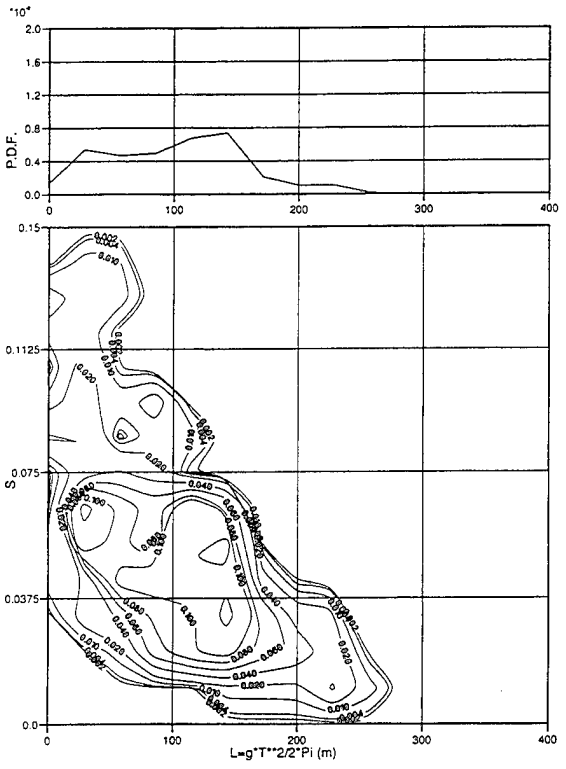


Fig. 13. *Joint pdf of wavelength and steepness (85 m water depth, H_s = 6.6 m, T_p = 9.7 s)*

This hypothesis may not apply to hull girder loads, slamming, or green water effects on deck, which tend to be more sensitive to local wave characteristics.

Joint distributions of zero-crossing period and height of storm waves analyzed by Sobey [15] show similar properties as those derived above from tank tests and simulations. Other studies on the validity of the Gaussian wave model have concentrated on distributions of single parameters, such as wave height. Osborne [16], for example, concludes that the Gaussian model works reasonably well in predicting wave height distributions, while it underpredicts probability densities of crest heights; again this is attributed to crests behaving in a more nonlinear fashion than wave height.

The occurrence of observed extreme wave heights tends to be overpredicted when using the Gaussian wave model (i.e., by the Rayleigh distribution), see for example Osborne [16] and Tayfun [17]. On the other hand, based on a large number of ocean wave measurements, Takeda *et al.* [18] state that while the Rayleigh model predicts the standard deviation of surface elevation correctly, not only the highest 1/100 observed wave crest heights are underpredicted but also the 1/100 highest overall wave heights can be underpredicted considerably for relatively low sea states (mean wave heights of 2 m or less); on the average, the Rayleigh model tends to overpredict maximum wave height. It should be noted that waves of maximum height are not necessarily the most critical for extreme ship motions.

2.3. Probability of occurrence of critical waves

Knowing the joint probability density functions of wave period and height from simulations or measurements, we can estimate the probability of occurrence of waves having a critical wavelength and steepness as a function of significant wave height and peak period:

$$P[(\lambda_{min} \le \lambda \le \lambda_{max}) \cap (s \ge s_{crit}) \mid H_s, T_p] = \int_{\lambda_{min}}^{\lambda_{max}} \int_{s_{crit}}^{s_{max}} p(\lambda, s)\, ds\, d\lambda \qquad (7)$$

If this conditional probability is determined for a number of sea states, it could subsequently be used to estimate the probability of capsizing in a given operating area with known statistical distributions of H_s and T_p, thereby neglecting any wave grouping effects. A significant amount of

information is available on theoretical and measured joint distributions for wave height and period, see for example Longuet-Higgins [19], Skrokosz and Challenor [20], Tayfun [16]. Rather than using theoretical distributions, which tend to be based on narrow-bandedness assumptions and neglect spectral shape, Sobey [15] advocates the use of long-duration simulations employing the linear Gaussian model as used above for the sea surface to derive joint distributions. Myrhaug and Kjeldsen [9] derived fitted joint distributions of crest front steepness and wave height based on Weibull parameters; Myrhaug and Rue [21] proposed joint distributions for two successive waves.

3. IRREGULAR ASTERN SEAS

Here we will consider the critical influence of group speed in astern seas. Astern (following and quartering) seas tend to be most critical with respect to capsizing of large ships. The perceived characteristics of the irregular seaway change drastically for such headings with forward speed; the effect on the encounter spectrum is discussed by Oakley et al. [1] and De Kat [22], among others. For a range of speeds the encounter spectrum collapses, i.e., it becomes very narrow-banded and average wave group lengths increase; the same applies to ship excitation forces and response. Tikka and Paulling [23] discuss the influence of forward speed on encountered wave group properties and the effect on capsizing.

The group speed is defined as:

$$C_{g,p} = \frac{g}{2\omega_p} = \frac{g\,T_p}{4\pi} \qquad (8)$$

which is the speed at which the main energy of the seaway travels. For ship speeds in the neighborhood of the group speed, substantial roll excitation of extended duration can occur. According to Tikka and Paulling [23] the longest encountered wave group lengths occur with the highest probability for the group speed associated with the mean zero-crossing period T_2, which is $C_{g,2} = g/(2\omega_2)$.

3.1. Excitation in astern seas

The effect of forward speed on measured encounter spectra of wave elevation and roll moment excitation in following seas is discussed by De Kat [3]. The following serves as an illustration of the time-dependent characteristics of hydrodynamic excitation in these conditions. Model tests have been conducted at scale 1 to 50 with a heeled container ship in following seas (ϕ = 15°, L_{pp} = 125 m). The ship model was partly captive and allowed to heave and pitch; the surge force and roll moment were measured. Here we will consider two sea states represented by Bretschneider spectra: (1) H_S = 4 m, and T_p = 9 s, and (2) H_s = 8 m, T_p = 11.3 s. For sea state (1), $C_{g,p}$ = 7 m/s (13.7 kn), and $C_{g,2}$ = 5 m/s (9.7 kn). For the case with both zero forward speed and V = $C_{g,2}$, Figs. 14 and 15 show part of the measured time series of the roll exciting moment and the surge force.

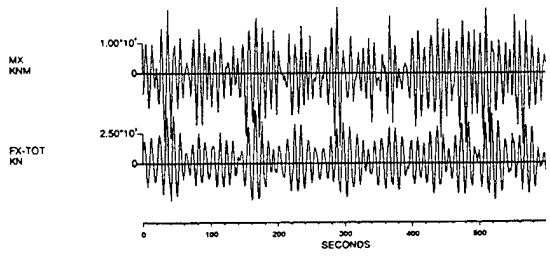


Fig. 14. *Measurements with heeled ship model in following seas (MX is the roll excitation moment, FX-TOT is the surge excitation moment, zero speed)*

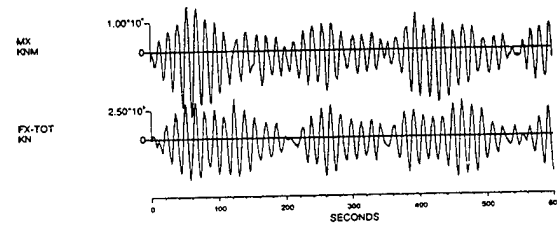


Fig. 15. *Measurements with heeled ship model in following seas (MX is the roll excitation moment, FX-TOT is the surge excitation moment, V = $C_{g,2}$ = 5 m/s)*

These measurements indicate that in irregular following seas the total wave excitation forces follow the same trend as the encountered wave characteristics at one location, i.e., the roll excitation can be of a regular nature during the passage of a wave group, despite the inherent spatial wave irregularities.

When a ship is subjected to narrow-banded, large amplitude roll excitation moments for extended time periods related to the length of the encountered wave groups, dynamic loss of transverse stability or parametric (low cycle) resonance, for example, could be the result. A range of operating speeds resulting in narrow-banded wave energy would be approximately:

$$0.7C_{g,p} \leq V.\cos\psi \leq 1.3C_{g,p} \quad (9)$$

where ψ is the heading angle with respect to the direction of wave travel (0° = following seas).

3.2. Wave grouping and temporal correlation of irregular wave surface

The question remains why the roll excitation (and other modes also) can have a regular character in spatially irregular and random waves, since the wave elevation behavior at one location of the ship is not indicative of the encountered time-dependent irregular wave profile.

Closer analysis of wave surface measurements carried out at forward speed in following seas provides the answer. The model tests mentioned above were also carried out without the presence of a model to focus purely on wave characteristics. Along the length of the imaginary ship (i.e., over a distance of 125 m full scale), 9 equidistant wave gauges were located to measure the instantaneous wave profile. To illustrate encountered wave characteristics, we will consider sea state (2) encountered at a speed of $C_{g,2}$ = 6.29 m/s = 12 kn in following seas.

Fig. 16 shows the regular character of the measured undisturbed wave elevation at three locations (signal WAVE9 corresponds to the aft perpendicular, WAVE5 to amidships, and WAVE1 to the forward perpendicular position).

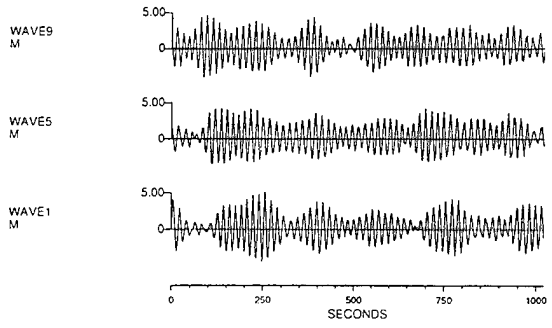


Fig. 16. *Measured wave elevation in following seas (model test, H_s = 8.0 m, T_p = 11.3 s; no model, WAVE9 corresponds to APP, WAVE5 to amidship and WAVE1 to FPP location, L = 125 m, V = $C_{g,2}$ = 6.3 m/s)*

Let us consider the wave profiles encountered during the period where a long wave group slowly overtakes the imaginary ship; for example between t = 135 s and 275 s, all locations of the vessel would be subjected to a relatively regular wave elevation of the same order of magnitude. Figs. 17a through 17d show successively encountered wave profiles during four wave encounters from t = 150 to 215 s (from left to right in the plots corresponds to aft to forward). The striking feature of these figures is the repeating nature of the irregular wave surface during each wave encounter. In fact, the wave profiles repeat themselves, with some modulation, during the complete passage of the encountered group. The same has been observed at speed V = $C_{g,p}$. Encountered wave profiles obtained by simulations with the linear random wave model show the same features.

Thus, when the wave elevation character at a moving point is regular over some finite distance and for an extended period of time, the irregular surface characteristics (wave profiles) can repeat themselves every wave encounter during the duration of the group. So although the spatial character is irregular and changes during the passage of an overtaking wave system, there is a strong temporal correlation between successively encountered wave profiles at the encounter period during the encountered wave group duration. Therefore, if an encountered wave group has only a few waves of regular appearance at some ship-fixed location, the correlation of successive spatial profiles will be low; for long duration wave groups, the correlation can be high, which will result in a regularly repeating irregular wave surface and hence in regular excitation forces.

3.3. Theory for encountered wave surface

In accordance with the linear random wave model used above, let us assume that the irregular wave surface, seen in a stationary reference frame, can be represented by the Fourier sum of sinusoids:

$$\eta(x,t) = \sum_{i=1}^{\infty} a_i \cos(\omega_i t - k_i x + \varepsilon_i) \quad (10)$$

where $\omega_n = 2\pi n/T$ (T is the total time duration) and ε_i are uniformly distributed phase angles. Deep water is considered, so that $k_i = \omega_i^2/g$. In terms of the complex amplitude function (see e.g. Longuet-Higgins, [24]), the surface elevation is:

$$\eta(x,t) = \mathrm{Re}\, A(x,t) e^{i\bar{\omega} t} \quad (11)$$

where $\bar{\omega}$ is the mean frequency defined by m_1/m_0; m_0 and m_1 are the zero and first order spectral moment, respectively. Then:

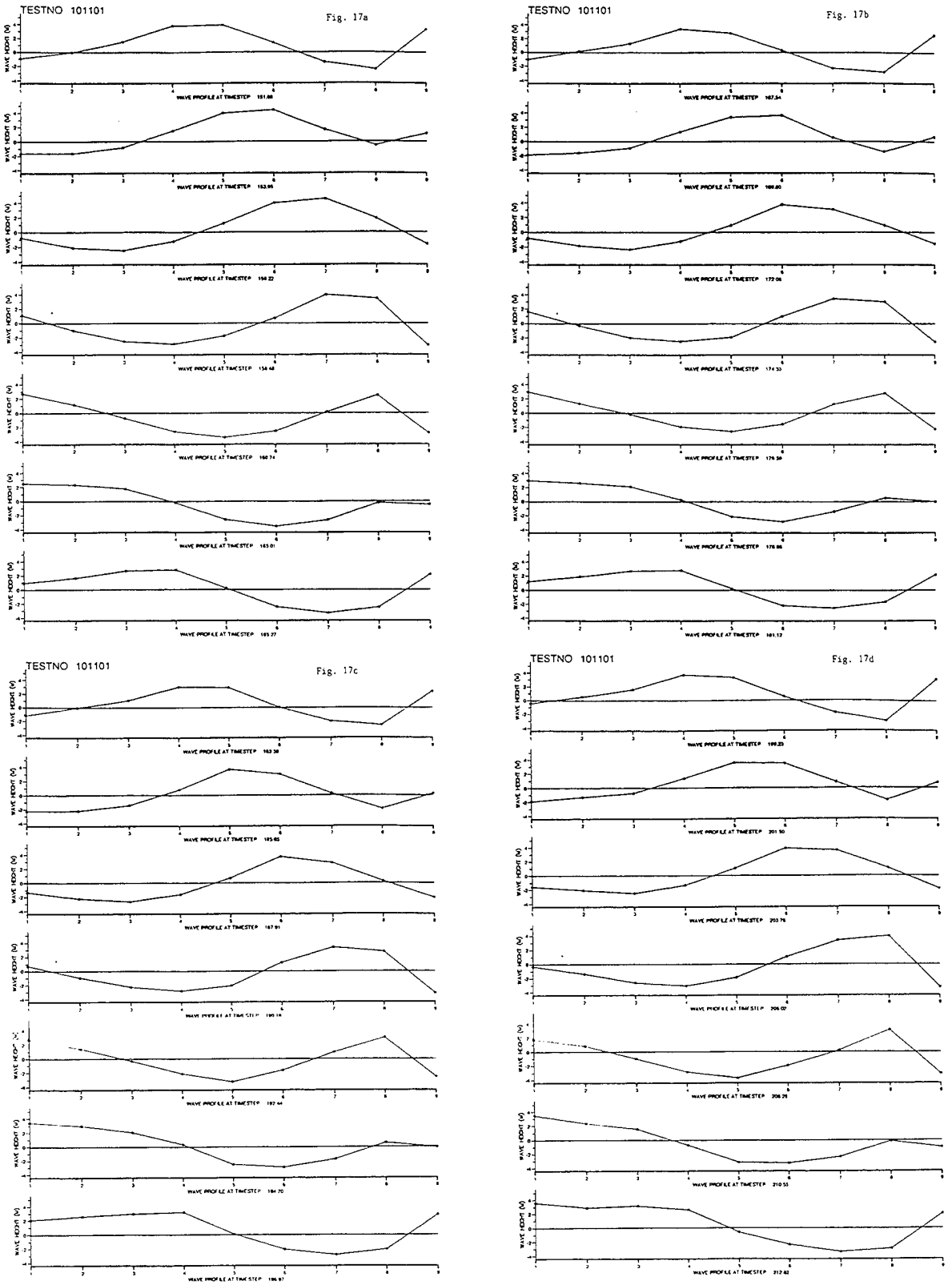


Fig. 17a-d. *Measured wave surface profiles in following seas for same conditions as for Fig. 16 during four wave encounters (point no. 1 corresponds to APP, no. 9 to FPP, L = 125 m); from t = 135 s to 213 s*

$$A(x,t) = \sum_i a_i e^{i[(\omega_i - \bar{\omega})t - k_i x + \varepsilon_i]} \quad (12)$$

which can be written in terms of the real envelope function ρ as follows:

$$A(x,t) = \rho(x,t) e^{i\phi(x,t)} \quad (13)$$

so that the real and imaginary parts of A(x,t) are:

$$\begin{aligned} \rho_c &= \rho\cos\phi = \sum_i a_i \cos[(\omega_i - \bar{\omega})t - k_i x + \varepsilon_i] \\ \rho_s &= \rho\cos\phi = \sum_i a_i \sin[(\omega_i - \bar{\omega})t - k_i x + \varepsilon_i] \end{aligned} \quad (14)$$

and

$$\rho(x,t) = \sqrt{\rho_c^2 + \rho_s^2} \quad (15)$$

We are interested in the encountered wave properties at nonzero forward speed. Let us consider the case of a moving reference frame, which translates steadily at speed V along a fixed heading ψ. Here we will focus on following seas ($\psi = 0$), but the approach applies to any heading. x' is the distance from the origin in the moving reference frame along the earth-fixed x-axis. The wave envelope at a fixed location is given as follows.

The wave surface encountered in the moving reference frame is given by:

$$\eta_e(x',t) = \sum_i a_i \cos(\omega_{e,i} t - k_i x' + \varepsilon_i) \quad (16)$$

where the encounter frequency for wave component i is defined by:

$$\omega_{e,i} = \omega_i - k_i V \cos\psi \quad (17)$$

In terms of the encountered group envelope, the wave surface elevation can be written as:

$$\eta_e(x',t) = \mathrm{Re}\, A_e(x',t) e^{i\bar{\omega}_e t} \quad (18)$$

where $\bar{\omega}_e$ is the mean encounter frequency defined by the spectral moments obtained at a point in the moving reference frame:

$$\bar{\omega}_e = \frac{m_1^e}{m_0^e} \quad (19)$$

The encountered complex envelope function is then:

$$A_e(x',t) = \sum_i a_i e^{i[(\omega_{e,i} - \bar{\omega}_e)t - k_i x' + \varepsilon_i]} \quad (20)$$

It should be noted that in the case of astern seas the wave elevation given by Eq. (16) is not a regular Fourier series, because of the non-unique frequency mapping from ω_i to $\omega_{e,i}$ for:

$$\omega_i \le \frac{(1+\sqrt{2})g}{2V\cos\psi} \quad (21)$$

If the encounter frequencies with the individual wave components lie close to the mean encounter frequency, Eq. (20) shows that encountered wave groups observed at a moving point can have long group periods. Group spectra of the wave envelope encountered at a point in a moving reference frame become significantly narrower than at a stationary point, when the speed lies in the range of the group speed.

If $\bar{\omega}_d$ is the dominant encounter frequency during the passage of a wave group, the wave surface profile would repeat itself after one wave encounter when:

$$\eta_e(x',t) = \eta_e(x', t + \frac{2\pi}{\bar{\omega}_d}) \quad (22)$$

According to Eq. (16),

$$\eta_e(x', t + \frac{2\pi}{\bar{\omega}_d}) = \sum_i a_i \cos(\omega_{e,i} t - k_i x' + \varepsilon_i + \frac{2\pi\,\omega_{e,i}}{\bar{\omega}_d}) \quad (23)$$

Hence if conditions were such that $\omega_{e,i} = \bar{\omega}_d$ for all frequencies, the same irregular wave profile would appear one wave encounter later. Usually this condition is not satisfied. In following seas, however, and particularly when V lies in the range of the group speed, encounter frequencies map to a narrow range, so that Eq. (22) may be satisfied approximately. In general, if the speed is equal to the group speed of a given wave component N, i.e. $V = g/(2\omega_N)$, in following seas, then the maximum encounter frequency is $\omega_{e,max} = \frac{1}{2}\omega_N$. This is illustrated by the case from Fig. 17 - sea state (2) encountered at a speed of $V = C_{g,2} = 6.29$ m/s. Fig. 18 shows the measured wave spectrum and the computed encounter frequency at speed V = 6.29 m/s, as well as for $V = C_{g,p} = 8.83$ m/s.

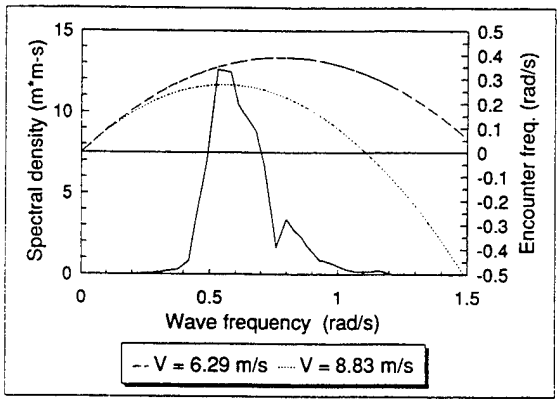


Fig. 18. *Measured spectral density at fixed location (model test, $H_s = 8.0$ m, $T_p = 11.3$ s), and encounter frequencies at two speeds ($V = G_{g,2} = 6.29$ m/s and $V = C_{g,p} = 8.83$ m/s)*

Fig. 18 shows that in the case of V = 6.29 m/s, all wave energy maps to frequencies lying between $\omega_e = 0.30$ and 0.39 rad/s. For V = 8.83 m/s, the energy of the spectral peak lies between approximately 0.26 and 0.28 rad/s, while for $\omega > 0.8$ rad/s there are wave components that cannot be part of dual component, overtaking wave groups with regular encounter appearance (all pairs of wave components having symmetrical frequency spacing with respect to a given ω_N can be considered as two-component wave groups traveling at the group speed $g/(2\omega_N)$, where both components overtake the moving reference frame while resulting in a single sinusoidal wave elevation encountered at a point in that frame moving with speed $V = g/(2\omega_N)$; the encounter frequency $\omega_{e,i}$ will differ slightly between the various two-component groups).

Defining the encounter frequency difference as $\delta\omega_{e,i} = \omega_{e,i} - \overline{\omega}_d$, we can write:

$$\frac{\omega_{e,i}}{\overline{\omega}_d} = 1 + \frac{\delta\omega_{e,i}}{\overline{\omega}_d} \tag{24}$$

Assuming that $\delta\omega_{e,i}$ is small for a range of frequencies (as it is in the above case), expressions like $\cos(\Phi+\alpha)$ where $\alpha << 1$ can be approximated by:

$$\cos(\Phi+\alpha) \approx \cos\Phi - \alpha\sin\Phi \tag{25}$$

Then Eq. (23) becomes:

$$\eta_e(x',t+\frac{2\pi}{\overline{\omega}_d}) = \eta_e(x',t) + -\sum_{i=1}^{\infty} a_i \frac{\delta\omega_{e,i}}{\overline{\omega}_d}\sin(\omega_{e,i}t - k_i x' + \varepsilon_i) \tag{26}$$

The above shows that when $\delta\omega_{e,i} << \overline{\omega}_d$ for components with significant wave energy, the wave profile will repeat itself approximately every wave encounter, whilst subject to group modulation and dispersion effects. When located in the speed range indicated by Eq. (9), a ship could experience a critical, steep overtaking wave repeatedly, which under certain conditions could pose an operational hazard.

It is noteworthy that also here the Gaussian random wave model seems adequate in predicting the observed temporal correlation of irregular wave profiles. Even in the event of steep waves that show overtopping, the same phenomenon applies: following an overtopping wave in a tank at its mean group speed, one will see the recurrence of that wave for several wave encounters. Similarly, in an adverse current the same wave will appear repeatedly after a wave encounter to a stationary observer, when the current speed equals the mean group speed of the waves running into the current.

3.4. Joint distribution encountered at forward speed

While wave properties encountered at a point in a moving reference frame can change drastically with forward speed, no information is available on the statistics of encountered spatial characteristics. Fig. 19 shows the joint probability density function of spatial wavelength and steepness based on a 3-hour duration simulation; the same sea state has been taken as in section 2.2 ($H_s = 14.5$ m, $T_p = 14.7$ s), and a forward speed at zero heading angle of $V = C_{g,2} = 8.6$ m/s. The encountered joint pdf is very similar to the one obtained at a fixed location (Figs. 5 and 6), so that Eq. (7) may be appropriate in estimating the probability of occurrence of critical waves based on zero-speed joint pdf's. Obviously, the joint pdf of two successive waves in a moving reference frame would be different from the joint pdf at zero forward speed.

4. NUMERICAL MODEL FOR EXTREME SHIP MOTIONS

A time domain ship motion simulation tool forms an essential part in understanding capsize physics. This simulator is frequently checked against model test results and the underlying physics are subjected to continuous examination. The program is foremost a practical engineering tool, which runs fast even on a PC; this is a prerequisite in the present derivation methodology for design guidelines, the development of which requires an extensive number of simulations.

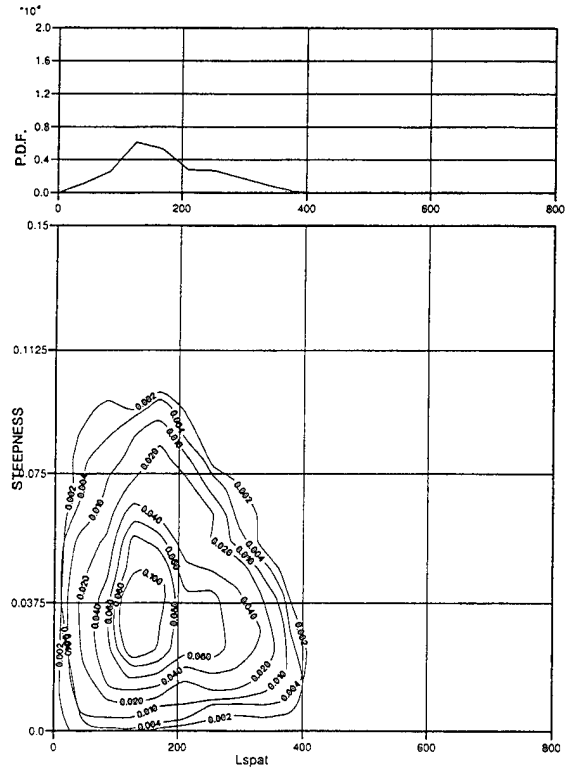


Fig. 19. *Joint pdf of spatial wavelength and steepness (simulation, H_s = 14.5 m, T_p = 14.7 s) encountered at V = $C_{g,2}$ = 8.6 m/s*

In the present investigations, use is made of extended, nonlinear strip theory embodied in the computer program FREDYN. Time domain simulations can be carried out for a steered ship in regular or long-crested irregular waves, and with or without the presence of (gusting) wind. In essence, the approach consists of superimposing all physically relevant force contributions in the coupled equations of motion:

$$\mathbf{M}\,\ddot{\mathbf{x}} = \sum_i F_i(t) \tag{27}$$

where **M** is the 6 x 6 mass matrix including added mass and inertia terms (at infinite frequency). The right hand side consists of the various force components:

- Froude-Krylov (static and dynamic wave pressure)
- diffraction
- convolution integrals of radiation forces
- viscous forces
- hull resistance
- propeller thust
- rudder lift
- wind

Because of the nature of the problem, the motions are solved in the time domain for six degrees of freedom. The setup is similar to the model presented by Hooft and Pieffers [25] and De Kat and Paulling [2]. The Froude-Krylov forces are evaluated up to the instantaneous free surface at each time instant and include hydrostatic effects. Linear theory is used in the time domain to estimate the diffraction and radiation contributions, where a correction is made to the convolution integrals to account for large amplitude motions. Viscous effects comprise roll damping due to hull and bilge keels, wave-induced drag due to orbital velocities, and maneuvering forces.

To illustrate the basic formulation of one component, we consider viscous hull forces associated with a drift angle at forward speed and wave orbital velocities. The resulting sway force is composed of a linear and nonlinear part:

$$Y_H = Y_{H,L} + Y_{H,NL} \tag{28}$$

where

$$Y_{H,L} = Y_{H,L}(u,v,\dot{\psi},\tau) \tag{29}$$

and

$$Y_{H,NL} = \int_{-\frac{L}{2}}^{\frac{L}{2}} Y_{NL}(x,t)\,dx \tag{30}$$

u, v and ψ' are the surge, sway and yaw velocities, respectively; τ is the instantaneous trim angle. The local transverse force is

$$Y_{NL}(x,t) = -\frac{1}{2}\rho\, C_D(x,\beta(t))\, T(x,t)\, v_r |v_r| \tag{31}$$

where T(x,t) is the local draft, v_r is the local relative velocity and $C_D(x,\beta(t))$ is the local drag coefficient estimated from experimental data, depending on section shape and drift angle β:

$$\beta = \arctan\left(\frac{v_r}{u}\right) \tag{32}$$

$$v_r = v + \dot{\psi}x - \dot{\eta}(x) \tag{33}$$

where $\dot{\eta}(x)$ is the local transverse wave orbital velocity, averaged over the cross-section. Taking moments and integrating $Y_{NL}(x,t)$ along the ship length will yield the associated roll and yaw moment. This yaw moment can become significant while running in astern seas, when the wave crest is

at the stern and the bow is in the trough region - the wave orbital velocities will contribute to a broaching moment.

Propeller and rudder interaction are also modeled, including the effect of orbital velocities. An autopilot or human navigator keeps the ship on course; alternatively, specific maneuvers such as a zig-zag test can be simulated. The model is in principle applicable to any type of ship; only the part related to the linear and nonlinear maneuvering forces in FREDYN has been adjusted specifically for frigate-type ships.

The advantage of this partially heuristic technique is the ease of adding physical phenomena to the model and the ease of computations. A major disadvantage is the lack of knowledge and control concerning the errors involved. The only way to instill confidence in this approach is to validate the method with a variety of model test results and full scale data. The present numerical model has been validated extensively by means of captive and free running model tests, as well as some full scale measurements. The model tests with various ship types comprised a large range of moderate and severe waves, including capsize conditions. Besides frigates, tests and simulations were also carried out with containership models to study parametric rolling.

5. CAPSIZING OF INTACT SHIPS

5.1. Identification of capsize modes

Based on the analysis of (few) full scale accounts, model tests and numerical simulations, two main categories of wave-induced capsizes are distinguished:

- *single* capsize modes in astern to beam seas
- *combined* capsize modes in astern seas

In principle, capsizing can occur at heading angles other than astern to beam seas. Parametric resonance in head seas has for instance been observed experimentally as a cause of capsizing. The risk of such events occurring is, however, viewed as too small for practical concern. A single capsize mode is applicable when one particular phenomenon is clearly the cause of the capsize. In many cases, capsizing cannot be attributed to one phenomenon only, but is often the result of a sequence of different events.

The "conventional" wave-induced capsize modes observed for large vessels in astern wave conditions comprise: pure loss of stability, low cycle resonance (due to parametric excitation), and broaching due to successive waves. These modes were first classified as such by Oakley *et al.* [1]; these and other modes were simulated by De Kat and Paulling [2]. The last two items are distinct physical (motion) phenomena that may or may not lead to capsizing. Other modes of broaching can occur at higher ship speeds. Another capsize mode, classified as "period bifurcation", has been observed experimentally by Kan *et al.* [26] for a containership model in stern quartering sea conditions.

Capsizing in beam seas can occur because of (1) steep, breaking waves, resulting in transverse impact loads and/or piling of green water on the side of the deck, (2) synchronized roll resonance, or (3) conditions resulting in an excessive wave-induced roll moment. It should be noted that capsizing due to resonance in beam seas has been studied in many instances to test theoretical models, but most ships will not capsize in such conditions. Small ships, such as fishing trawlers, are known to have capsized in steep beam sea conditions.

Water on deck and bulwark submergence can have a significant influence on capsizing, both in astern and beam seas. These effects can occur in conjunction with the modes discussed above; experimental and theoretical observations are presented by Grochowalski [27].

A ship can capsize in a multitude of conditions, where several distinct phenomena can finally lead to capsizing. For example, a vessel in stern quartering seas may first surfride, then broach and roll heavily, followed by deck submergence and loss of stability in the wave crest after getting back on course. Also, a ship may yaw violently, inducing large roll motions, followed by dynamic loss of stability. Invariably, a ship will in the end capsize in the absence of sufficient restoring moment, which may be quasi static (loss of righting arm) or dynamic (loss of restoring energy). Before capsize occurs, the ship should be viewed as a complete six degrees of freedom object with some steering mechanism. An overview of potential wave-induced capsize modes has been presented in [3] and [4].

To determine irregular wave conditions leading to capsizing, the following approach is used. For a given loading condition (with low initial GM), calm water speed and heading angle, simulations are carried out in many realizations of a selected severe sea state: 25 runs of 20 minutes full scale duration were performed with randomly selected seeds. This process is repeated for various Froude numbers up to Fn = 0.4 at some critical heading angles. The analysis consists of identifying capsize modes and the conditions leading to capsizing and determining the influence of the random nature of waves and to

what extent these random events can be related to more deterministic capsize behavior in regular waves. Once sufficient information is available on critical waves as a function of speed, heading angle, etc., their probability of occurrence may be estimated using Eq. (7), for example.

5.2. Some capsize mechanisms

A few capsize aspects are discussed below for an example frigate with transom stern, L = 125 m and low GM (GM/B = 0.05) at a 15 degree heading angle in different realizations of the following sea state: H_s = 12.8 m, T_p = 14 s. Analysis of the runs where capsizing occurs suggests that the mode of capsize depends strongly on the ship speed. For example, Fn = 0.4 results in broaching and capsizing, while Fn = 0.3 typically results in loss of stability in the wave crest. At Fn = 0.2, those few capsize events that do occur are associated with dynamic rolling in a critical wave group; here the ship speed is close to the group speed, and the ship rolls at the encounter frequency with increasing amplitudes until after 3 or 4 cycles capsize occurs (the phasing is such that during each cycle a wave crest is amidships when the largest roll angle is reached). The other two capsize modes are described in more detail below.

Broaching at Fn = 0.4

Many of the simulated broaches look rather alike in appearance when judged by overall motion behavior, yet closer scrutiny of the time series data and wave profiles reveals some fundamental differences in the physics involved. Although it is not possible to define one 'standard' critical wave that causes a given broach and capsize, we can identify the following 'classes' of broaching for this case.

Mode (1) - Broach due to bow trim: the wavelength λ is of the order of 1 to 1.5 times the ship length when the ship is running down its front slope and the spatial wave steepness H/λ_{spat} exceeds 0.06; while the crest is at the stern, gradually the ship speed increases to approximately the wave's phase speed; at the same time, the bow is located in the trough region, which leads to a yaw (broaching) moment caused by cross-flow drag forces (as in Eq. (31)) combined with a yaw moment associated with the wave-induced pressure (Froude-Krylov). Especially in a relatively short and steep wave the bow can be partially buried in the backslope of the preceding wave, resulting in decreased directional stability. Even though the rudder is hard over, the ship is forced broadside to the wave while experiencing a roll moment to the lee side because of inertia effects and the wave slope (Froude-Krylov) moment. The amount of rudder lift that is lost in the wave crest will depend on benefits from propeller outflow effects.

Mode (2) - Broach in steep, long wave: this mode is similar to mode (1), but occurs in a longer wave ($\lambda \approx$ 2L to 2.5L); there is no bow submergence effect in the trough. As the large steepness remains unchanged while the wave overtakes the ship and the yaw angle keeps increasing, the inertia and wave slope moment force the ship to roll to its lee side.

Mode (3) - Broach in wave of increasing steepness: similar to modes (1) and (2) - it starts as in (2), but after the onset of the broach the wavelength decreases rapidly while the wave height stays approximately the same, so that steepness increases drastically and while turning broadside, the ship is faced with a steep wave front.

Mode (4) - Broach followed by stern emergence: a steep wave causes the onset of a broach; as the ship starts to broach, the wave quickly loses its steepness; the roll angle is around 45 degrees, at which point the restoring moment is positive but not very large; while the ship slowly rightens, a steep trough suddenly develops under the stern; around 20% of the stern is out of the water, but as the ship in question has a wide transom (the aft body contributes significantly to the overall righting moment) the ship capsizes due to loss of stability.

Capsizing due to loss of stability at Fn = 0.3

The way in which the ship capsizes under these conditions is remarkably different from the above broaching cases. The majority of the capsizes occur with the wave crest amidships. This mode is usually preceded by moderate roll motions and can occur suddenly when the encountered wavelength is between 0.8L (with H/λ_{spat} exceeding 0.07) and 2L (with H/λ_{spat} exceeding 0.04). Loss of stability in irregular waves can be attributed to several mechanisms: (1) dynamic rolling during one cycle resulting in a capsize with the wave crest amidship, where the crest slowly overtakes the ship resulting in the reductionof righting capability over an extended period of time, (2) the sudden formation of a steep wave trough at the stern, which for a ship with a wide aft body results in the sudden loss of buoyancy and righting capabilities. Before capsizing the ship will roll at the dominant wave encounter period, which can be significantly longer than the natural roll period. In the present case, the actual roll period was about twice the natural roll period for small angles.

5.3. Determination of critical wave conditions

For each capsize case, the time-dependent spatial wave conditions immediatley prior to capsize were examined. The onset of capsizing was found to occur in a critical range of wavelengths above a certain associated spatial wave steepness. As an example, the time series of a Mode (1) broach are shown in Fig. 20a; the sequence of the spatial wave profiles as of the onset of the final broach is shown in Figs. 20b and 20c (the profiles are shown over a distance spanning three ship lengths in the direction of wave travel, where position No. 16 corresponds to the location of midship section at each time instant).

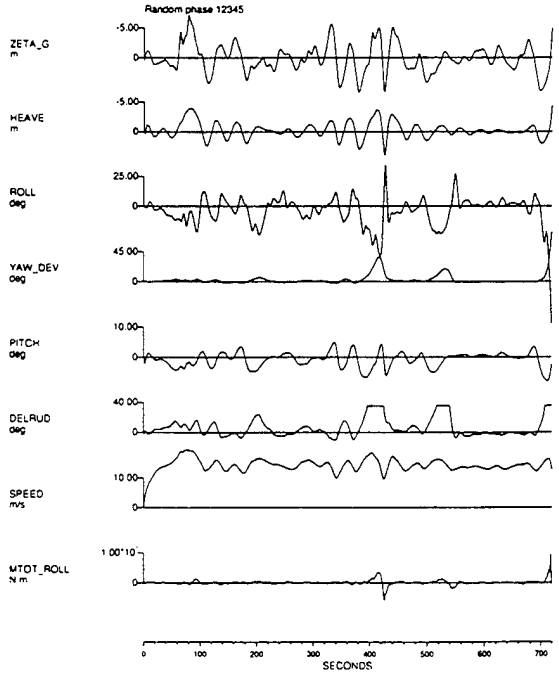


Fig. 20a. *Time series of simulated capsize due to broach with bow trim (ζ_G is the wave height at the center of gravity, δ_{RUD} denotes rudder angle). Test conditions: Fn = 0.4, ψ = 15°, GM/B = 0.05, H_s = 12.8 m, T_p = 13.4 s, JONSWAP with γ = 2.*

The onset of broaching and loss of stability in irregular waves is shown for the above example in Fig. 21 for different wave realizations, indicating the critical spatial wavelength and steepness. An important conclusion here is that for a given sea state a large range of waves with different spatial properties can lead to capsizing; the overall capsize mode is not sensitive to the wave realization process.

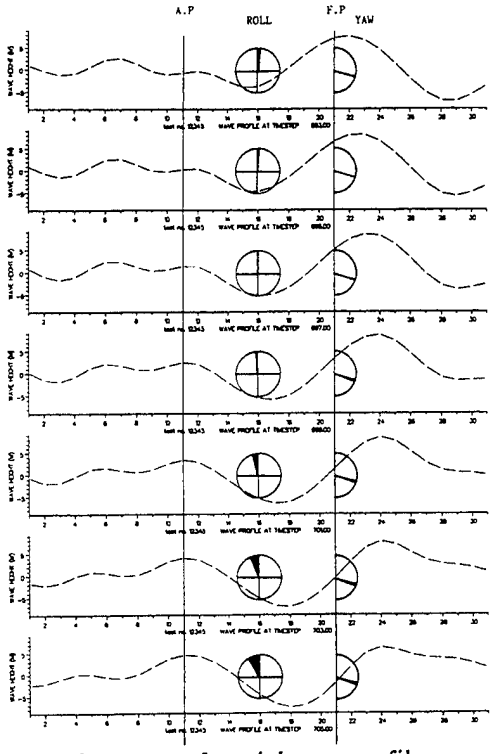


Fig. 20b. *Sequence of spatial wave profiles spanning 3 ship lengths (L = 125 m) along direction of wave travel; first profile corresponds to the onset of the broach.*

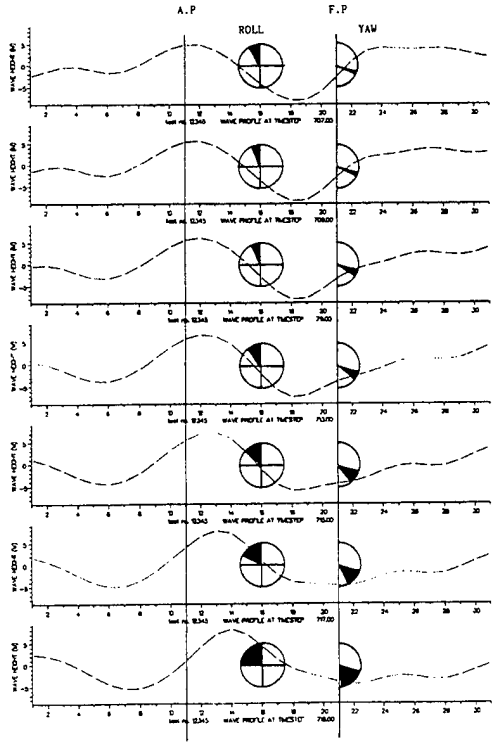


Fig. 20c. *Sequence of spatial wave profiles spanning 3 ship lengths (L = 125 m) along direction of wave travel; last profile corresponds to actual capsize.*

Comparison with the behavior in regular waves suggests that if the spatial wave characteristics (height and length) leading to capsize in irregular waves were used to generate a regular wave, the ship will typically also capsize; the physics involved can be different. By performing the same analysis for different sea states, an assessment can be made of the critical conditions leading to capsize as a function of loading condition, speed, heading angle and sea state. Combined with the joint distribution of wavelength and steepness, the probability of encountering critical conditions can be estimated.

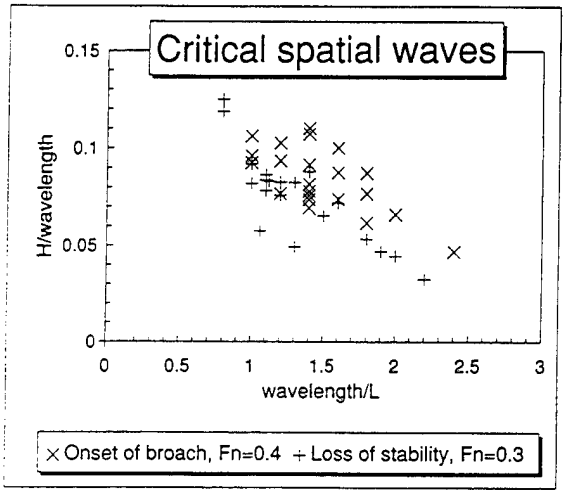


Fig. 21. *Critical spatial wavelength and steepness combinations leading to onset of capsize due to broaching and due to loss of stability in irregular sea state at 15 degrees heading angle. (L = 125 m, H_s = 12.8 m, T_p = 13.4 s)*

6. CONCLUSIONS

This paper presents some physical aspects of random waves in relation to capsizing and broaching of a steered, intact ship. Particular attention is paid to the validity of the random Gaussian wave model when simulating motions in severe, long-crested seas.

Wave characteristics investigated are those thought to be relevant for extreme ship motions: joint distributions of individual wave properties, spatial properties, deviations from Gaussianity, and group speed effects in astern seas. The results suggest that the joint distribution of overall wave parameters (such as crest-trough steepness and wavelength) is predicted quite well by the Gaussian wave model even for steep sea states, when compared with measured data. When sailing in astern seas at a speed close to the mean group speed, wave group lengths increase; it is shown that during the duration of an overtaking wave group the same, spatially irregular, wave will repeat itself every wave encounter - this can lead to large amplitude excitation of a regular nature.

A brief description is given of a numerical model to simulate extreme ship motions. With this model, a number of capsize and broaching modes have been predicted; analysis of these extreme events provides details on the physical mechanisms involved and on critical wave conditions. Critical (spatial) wave conditions leading to a capsize are found to be sensitive to the realization of a given sea state.

Work on the above topics continues as part of the second phase of the Dynamic Stability project.

ACKNOWLEDGEMENTS

The author would like to express his thanks to all members of the Cooperative Research Navies Dynamic Stability group for their permission to publish this paper.

REFERENCES

1. Oakley, O.H., Paulling, J.R. and Wood, P., "Ship Motions and Capsizing in Astern Seas," Proc. 10th Symposium on Naval Hydrodynamics, Cambridge, June 1974, pp. 297-350

2. De Kat, J.O. and Paulling, J.R., "The Simulation of Ship Motions and Capsizing in Severe Seas," Trans. SNAME, Vol. 97, 1989, pp. 139-168

3. De Kat, J.O., "The Development of Survivability Criteria Using Numerical Simulations," Proc. U.S. Coast Guard Vessel Stability Symposium 93, New London, March, 1993

4. De Kat, J.O., Brouwer, R., McTaggart, K.A. and Thomas, W.L., "Intact Ship Survivability in Extreme Waves: New Criteria from a Research and Navy Perspective," Proc. International Conference on Stability of Ships and Ocean Vehicles STAB '94 (to be presented), Melbourne, Florida, Nov. 1994

5. Pierson, W.J., "Ship Stability in Heavy Weather: the Real Situation and Models thereof", Proc. U.S. Coast Guard Vessel Stability Symposium, Groton, March, 1993

6. Le Méhauté, B. and Hanes, D.M.), Eds., The Sea, Ocean Engineering Science, Vol. 9, 1990, Part A, Wiley & Sons

7. Buckley, W.H., "Matching Vehicle Characteristics to Seaway Environments," Proc. Intersociety High Performance Marine Vehicle Conference, HPMV '92, June 1992, Arlington

8. Torsethaugen, K., "A two peak wave spectrum model", Proc. Offshore Mechanics and Arctic Engineering OMAE '93 Symposium, Vol. 2, Glasgow, June 1993, pp. 175-180

9. Myrhaug, D. and Kjeldsen, S.P., "Prediction of Occurrences of Steep and High Waves in Deep Water," J. Waterway, Port, Coastal, and Ocean Engineering, Vol. 113, No. 2, March 1987, pp. 122-138

10. Dahle, E.Aa. and Myrhaug, D., "Risk Analysis Applied to Capsize of Smaller Vessels in Breaking Waves", Trans. Royal Institution of Naval Architects, Vol. 135, 1993, pp. 237-252

11. Miles, M.D. and Mansard, E.P.D.), "Comparison of Wave Steepness Based on Spatial and Temporal Distributions,"Journal of Hydraulic Research, Vol. 29, No. 6, 1991, pp. 771-788

12. Marthinsen, T. and Winterstein, S.R., "On the Skewness of Random Surface Waves," Proc. Second (1992) International Offshore and Polar Engineering Conference, San Francisco, June 1992, Vol. III, pp. 472-478

13. Stansberg, C.T., "Second-Order Numerical Reconstruction of Laboratory Generated Random Waves," Proc. Offshore Mechanics and Arctic Engineering Conference OMAE 1993, Glasgow, May 1993, Vol.II, pp. 143-151

14. Taylor, P.H., "On the Kinematics of Large Ocean Waves," Proc. BOSS '92 Conference, Vol. I, 1992, pp. 134-145

15. Sobey, R.J., "The Distribution of Zero-Crossing Wave Heights and Periods in a Stationary Sea State," Ocean Engineering, Vol. 19, No. 2, 1992, pp. 101-118

16. Osborne, A.R., "The Simulation and Measurement of Random Ocean Wave Statistics," , Topics in Ocean Physics, Osborne & Rizzoli, Eds., North Holland, 1982, pp. 515-550

17. Tayfun, A. , "Joint Distribution of Large Wave Heights and Associated Periods", J. Waterway, Port, Coastal and Ocean Engineering, Vol. 119, No. 3, May/June 1993, pp. 261-273

18. Takeda, S., Satoh, K. and Kobayashi, K., "Statistical Analysis of Ship Encounter Waves - Application of Rayleigh Distribution to the Measured Wave Height," The Journal of Japan Institute of Navigation, Vol. 89, Sept. 1993, pp. 51-61

19. Longuet-Higgins, M.S., "On the Joint Distribution of Wave Periods and Amplitudes in a Random Wave Field," Proc. Royal Soc. London, Vol A 389, 1993, pp. 241-258

20. Srokosz, M.A. and Challenor, P.G., "Joint Distributions of Wave Height and Period: a Critical Comparison", Ocean Engineering, 1987, Vol. 14, No. 4, pp. 295-311

21. Myrhaug, D. and Rue, H., "Joint Distribution of Successive Wave Steepness Parameters," J. Offshore Mechanics and Arctic Engineering, Vol. 115, August 1993, pp. 191-195

22. De Kat, J.O. , "The Modeling of Ship Motions and Capsizing in Severe Seas," J. Ship Research, Vol. 34, No. 4, Dec. 1990, pp. 289-301

23. Tikka, K.K. and Paulling, J.R., "Prediction of Critical Wave Conditions for Extreme Vessel Response in Random Seas," Proc. Fourth International Conference on Stability of Ships and Ocean Vehicles STAB '90, Naples, Sept. 24-28 1990, pp. 386-394

24. Longuet-Higgins, M.S., "Statistical Properties of Wave Groups in a Random Sea State," Phil. Trans. Royal Soc. London, Vol. A 312, 1984, pp. 219-250

25. Hooft, J.P. and Pieffers, J.B.M., "Maneuverability of Frigates in Waves," Marine Technology, Vol. 25, No. 4, 1988, pp. 262-271

26. Kan, M., Saruta, T., Taguchi, H., Yasuno, M. and Takaishi, Y., "Model Tests on Capsizing of a Ship in Quartering Waves," Proc. Fourth International Conference on Stability of Ships and Ocean Vehicles STAB '90, Naples, Sept. 24-28 1990, pp. 109-116

27. Grochowalski, S., "Effect of Bulwark and Deck Edge Submergence in Dynamics of Ship Capsize," Proc. U.S. Coast Guard Vessel Stability Symposium 93, New London, March 1993

Nonlinear Analysis of Bow Wave Breaking and Deck Wetness of a High-Speed Ship by the Parabolic Approximation

H. Maruo, W. Song
(Yokohama National University, Japan)

ABSTRACT

Nonlinear computations of the free surface elevation at the bow region of a frigate model in the steady forward motion as well as in heaving and pitching oscillations in an incident sinusoidal wave are carried out under the slender body approximation, which reduces the fluid motion to the parabolic type in the longitudinal direction, and the boundary value problem becomes two dimensional in the cross flow plane fixed in space. The boundary integral equation method is employed to find the solution.

The computation for the steady forward motion well simulates the generation of spray and the breaking of bow waves. The computation for the oscillating ship at forward speed of Froude number 0.30 shows the effect of the incident wave height. The computation shows that deck wetness begins at the wave height of $H/\lambda = 0.02$, and the result is in good agreement with the experimental observation.

As a conclusion, the method proposed here serves as a useful tool for a prediction of deck wetness at large amplitude motion of a ship in rough seas.

1 INTRODUCTION

Among various problems of seakeeping qualities of ships, deck wetness or shipping of water becomes important especially in high speed operation in rough seas. It is a governing factor for determination of freeboard and the design of flare at the bow in ship design practice. The existing method of theoretical prediction of seakeeping qualities depends on the linearized theory of the fluid motion around the hull. In practice, hydrodynamic forces on the hull are predicted by means of the strip theory. It is generally accepted that the ship motion determined from the linear equation of the motion with hydrodynamic coefficients, derived from the linearized theory in two dimensions, shows a fairly good prediction for the ship behavior among waves, unless in very severe conditions. However it is known that some of the prediction by means of the linearized theory is not necessarily satisfactory in several problems of seakeeping characteristics including deck wetness and slamming impact. Deck wetness, which is the problem of the present interest, is determined by the relative height of the deck above the disturbed sea surface. The simplest approximation by the existing practice is that the wave surface is taken as if it were undisturbed by the existence of the ship hull [1]. It is clear that this is a too coarse assumption, because elevation of the sea surface changes due the disturbance by the hull to a considerable extent, so that the interaction between the hull and the free surface should be taken into account by the prediction of free surface elevation. The heave of the sea surface due to the disturbance by the hull is called the dynamic swell. The existing practice employs the strip theory with the linearized theory in two dimensions [2] applied to each cross section of the hull. Takaishi et al [3] calculated the relative height of the deck above the disturbed wave surface of a container ship by the above method. Fairly good agreement was observed between computation and experiment. Since this is the case of large container ship at forward speed of moderate Froude number, the ship motion is comparatively mild, and the linearized theory seems to work well. However the condition is different when the ship is operating at high speed in rough seas. Nonlinearity becomes remarkable in the fluid motion around the hull, and breaking wave or spray is observed at the bow, which is likely to have a consider-

able effect on shipping water. These phenomena are quite nonlinear and there has been no reliable method so far to predict deck wetness in such a severe condition.

As the analytical solution is not applicable to the nonlinear boundary value problem, which appears in the present case, the analysis depends on the numerical method in general. Although recent development of the computational fluid dynamics enables the numerical solution of the fully three-dimensional nonlinear free surface flow problem, the three-dimensional computation in the present problem does not seem practical because of large computer time and insufficient accuracy. The strip theory is the simplest approximation in which nonlinear effects can be considered. However the strip theory is unable to describe the effect of forward speed to the fluid motion in rational way. Application of the slender body technique to the ship moving through ambient ocean waves provides a rational approach. The existing theory of this kind is based on a series expansion of the solution with respect to two small parameters which are mutually independent [4]. The slenderness ratio of the hull and the ratio of wave height to the ship's length are taken as the perturbation parameters in general. Then the first order solution is determined from a set of linear boundary value problems in two dimensions in the plane perpendicular to the longitudinal axis of the hull. Thus the slender ship theory formulated in this way belongs originally to the linearized approximation. An implication of the two parameter expansion is the condition that the amplitude of the vertical motion of the hull as well as the free surface elevation is small as compared with the dimension of the cross section of the hull, i.e. breadth and draft. However the motion amplitude is not necessarily small in comparison with the draft, even though the amplitude of oscillation and wave height are both small in comparison with the ship's length, which is taken as the reference length in the perturbation scheme. This contradiction is the consequence of the assumption that the slenderness ratio and the amplitude ratio are mutually independent. As a matter of fact, these parameters are of the same order, and the separation of two variables is not applicable to the present analysis. Since the slenderness ratio and the amplitude ratio are of the same order, it is more ratioal that they are expressed by a common parameter. The perturbation expansion with respect to a single parameter leads to another set of boundary value problems, which is different from the existing slender ship theory based on the two parameter expansion. A great advantage of this scheme is that the first order solution allows the large amplitude motion in the local scale, even if a small amplitude is assumed in the global scale based on the ship's length. Different from the existing slender ship theory, the boundary value problem becomes nonlinear in the new approach. This may bring some complication in the solution technique. However the remarkable progress of the computational fluid dynamics in recent years has enabled the solution of fully nonlinear boundary value problem of the free surface flow to be tractable at least in two dimensions.

As far as the ship has no forward speed, the principal idea of the solution is similar to the nonlinear strip theory, by which the fluid motion at each transverse plane is purely two-dimensional and independent each other. When the finite forward speed is introduced, however, the fluid motion in a transverse plane at one cross section is subject to the effect of the fluid motion at other cross sections. Then the fluid motion around the hull becomes substantially three-dimensional. A great advantage of the slender body technique is that the three-dimensional fluid motion is determined by the solution of the two-dimensional boundary value problem at each cross section even though the fluid motion is three-dimensional. Then the numerical solution for the nonlinear free surface flow is much simplified from the fully three-dimensional solution. The numerical method for the solution of fully nonlinear free surface problem in two dimensions, which has been developed recently [5][6], is available in the solution of the three-dimensional problem in this manner.

In order to examine deck wetness, one must determine

1. Vertical movement of the deck,
2. Height of the free surface at the hull surface.

The vertical movement of the deck is determined from the equation of motion of the hull. Since the fluid motion around the hull is nonlinear, the hydrodynamic forces and moments are nonlinear functions of the ship and the incident wave. According to experimental data however, the nonlinearity of the hydrodynamic forces and moments acting on the hull as a whole is not remarkable except in such extreme conditions that bottom slamming takes place. It is generally accepted that the solution of linear equations of motion predicts the ship motion fairly well, if the hy-

drodynamic coefficients in the equations are suitably chosen. Correction may be applied to the hydrodynamic coefficients determined by the linear strip theory in order to illustrate the nonlinear effect. The nonlinear slender ship theory enables the nonlinear computation of hydrodynamic forces and moments. Then the ship motion may be determined by integration of the nonlinear equation of motion, but the numerical work will become enormous. In the present work, the ship motion is assumed to be given by a simple equation. Then the boundary condition on the hull surface is given by known functions, and the fluid motion around the hull is determined under given boundary conditions both on the hull surface and on the free surface.

Several problems are encountered in the development of a reliable computation scheme. The numerical solution shows instability sometimes. Another problem of difficulty is treatment of the intersection of the hull surface and the free surface, when the boundary condition takes different form on two boundaries of different kinds. Since the level of the point of intersection is the measure of deck wetness, determination of it is very important in the present problem. Wave breaking and spray are likely to appear on the bow region. The computation scheme should be able to handle the fluid motion accompanied by wave breaking and spray generation.

In the present work, effort is made to overcome the above difficulties in order to find out a method of determining the free surface elevation at the bow, which governs deck wetness, when wave breaking or spray generation is present. The aim of this work is to develop a method of predicting deck wetness, which is more accurate than the existing mothed based on the linearized strip theory.

2 OUTLINE OF THE MATHEMATICAL FORMULATION

Take the cartesian coordinates x, y, z fixed in space with the origin in the still water plane, with x and $y-$axes taken horizontally and $z-$axis taken vertically upwards.

The fluid is assumed as inviscid and incompressible. Then the fluid motion started from rest is irrotational and is specified by the velocity potential Φ which satisfies the Laplace equation in the space occupied by the fluid.

$$[L] \qquad \Phi_{xx} + \Phi_{yy} + \Phi_{zz} = 0 \qquad (1)$$

where subscripts mean the partial derivatives. The boundary condition for Φ consists of two parts. One is the boundary condition on the hull surface and the other is on the free surface.

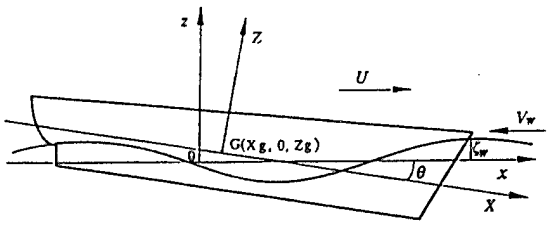


Fig. 1 Coordinate system.

As shown in Fig. 1, consider a ship moving through a regular train of waves with average forward speed U in the direction of positive $x-$axis. Take another coordinate system (X, Y, Z) fixed to the ship, with $X-$axis along the longitudinal axis of the ship, $Y-$axis athwart ships and $Z-$axis in the upward direction. The incident wave is taken to propagate in the $x-$direction with the profile expressed by the equation

$$z = \zeta_w = A\sin(kx + \omega t + \epsilon_0) \qquad (2)$$

where $k = 2\pi/\lambda = \omega^2/g$, λ is the wave length and ω is the circular frequency. The ship makes oscillations with three degrees of freedom, i.e. surge, heave and pitch. The motion of the ship is expressed by coordinates of the center of gravity $(x_g, 0, z_g)$ in terms of the $x, y, z-$axes, and the pitching angle θ, positive in the bow down rotation. The following transformation is valid between the coordinate system (x, y, z) and (X, Y, Z).

$$\begin{aligned} X &= (x - x_g)\cos\theta - (z - z_g)\sin\theta \\ Y &= y \\ Z &= (x - x_g)\sin\theta + (z - z_g)\cos\theta \end{aligned} \qquad (3)$$

The geometry of the hull surface is expressed by the equation

$$Y = F(X, Z) = f(x, z, t) \qquad (4)$$

The body boundary condition at the hull surface S_H is

$$[H] \quad f_t + \Phi_x f_x + \Phi_z f_z - \Phi_y = 0 \quad \text{on } S_H \qquad (5)$$

Writing

$$F_X = \partial F/\partial X, \quad F_Z = \partial F/\partial Z$$

one can express (5) in the form

$$\begin{aligned} &(-\dot{x}_g\cos\theta + \dot{z}_g\sin\theta - Z\dot{\theta})F_X \\ &+(-\dot{x}_g\sin\theta - \dot{z}_g\cos\theta + X\dot{\theta})F_Z \\ &+\Phi_x f_x + \Phi_z f_z - \Phi_y = 0 \end{aligned} \qquad (6)$$

where dots mean time derivatives.

The free surface condition consists of the kinematic and the dynamic conditions. If the free surface is expressed by $z = \zeta$, the kinematic condition is

$$[K] \quad \zeta_t + \Phi_x\zeta_x + \Phi_y\zeta_y - \Phi_z = 0 \quad \text{at } z=\zeta \qquad (7)$$

The dynamic condition that the pressure is constant on the free surface is

$$[D] \quad \Phi_t + \frac{1}{2}\left(\Phi_x^2+\Phi_y^2+\Phi_z^2\right)+g\zeta=0 \quad \text{at } z=\zeta \qquad (8)$$

The velocity potential is the sum of the incident wave potential ϕ_w and the disturbance potential ϕ, such as $\Phi = \phi_w + \phi$. We have the condition at infinity $\Phi = \phi_w$ at $\sqrt{x^2+y^2} \to \infty$. If the depth of water is infinite, we have the condition $\phi_z = 0$ at $z \to -\infty$. However these conditions for water of infinite stretch may not be convenient for numerical solution. Then the width and the depth of water are assumed finite in the actual computation.

The solution of the boundary value problem defined above is simplified to a great extent by application of the slender body theory. The fundamental assumption is that the breadth B and the draft d of the ship are both much smaller than the length L, $B/L \ll 1, d/L \ll 1$. Now let us define the slenderness ratio as $\varepsilon = d/L$, and assume $B/d = O(1)$. The slender body theory is based on a singular perturbation in the near field.

The formation is efficiently induced by the coordinate stretching technique. The governing equation is transformed to a system of stretched coordinate x', y', z' such as $x = x', y = \varepsilon y', z = \varepsilon z'$. The solution is expanded in ascending powers of ε, the governing equation is reduced to the Laplace equation in two dimensions in the transverse $y, z-$plane,

$$\Phi_{yy} + \Phi_{zz} = 0 \qquad (9)$$

In applying similar techniques to the boundary conditions, we assume the following,

$$\zeta/L = O(\varepsilon), \quad z_g/L = O(\varepsilon), \quad \theta = O(\varepsilon)$$

Then the hull surface condition is transformed to

$$\frac{\partial\Phi}{\partial n}=-\left[UF_X+\left(U\theta+\dot{z}_g-\overline{X}\dot{\theta}\right)F_Z\right]\left[1+F_Z^2\right]^{-1/2} \qquad (10)$$

where n is the outward normal of the hull contour and we can put $\overline{X} = x - x_g$. The kinematic and dynamic free surface conditions become

$$\zeta_t + \Phi_y\zeta_y - \Phi_z = 0 \quad \text{at } z=\zeta \qquad (11)$$

$$\Phi_t + \frac{1}{2}\left(\Phi_y^2 + \Phi_z^2\right) + g\zeta = 0 \quad \text{at } z=\zeta \qquad (12)$$

In the derivation of the above equations, we have assumed $\omega_1\sqrt{d/g} = O(1)$, where ω_1 is the circular frequency of encounter, $\omega_1 = \omega + kU$, otherwise the free surface condition becomes a trivial form.

Since the velocity potential is decomposed as

$$\Phi = \phi_w + \phi \qquad (13)$$

The boundary condition for the disturbance potential ϕ becomes

$$\frac{\partial\phi}{\partial n} = -\left[UF_X + \left(U\theta + \dot{z}_g - \overline{X}\dot{\theta}\right)F_Z\right] \times \left[1+F_Z^2\right]^{-1/2} - \frac{\partial\phi_w}{\partial n} \qquad (14)$$

If the incident wave is not steep, one can write

$$\frac{\partial\phi_w}{\partial z} = \frac{\partial\zeta_w}{\partial t} = \dot{\zeta}_w \qquad (15)$$

Putting

$$V = U\theta + \dot{z}_g - \overline{X}\dot{\theta} - \dot{\zeta}_w \qquad (16)$$

the hull surface condition is written as

$$\frac{\partial\phi}{\partial n} = -\left(UF_X + VF_X\right)\left(1+F_Z^2\right)^{-1/2} \qquad (17)$$

The free surface elevation due to the disturbance is

$$\zeta_1 = \zeta - \zeta_w \qquad (18)$$

Then the kinematic free surface condition can be written as

$$\zeta_{1t} + \phi_y\zeta_{1y} - \phi_z = 0 \quad \text{at } z=\zeta \qquad (19)$$

The dynamic condition becomes on the other hand

$$\phi_t + \frac{1}{2}\left(\phi_y^2+\phi_z^2\right)+\phi_z\dot{\zeta}_w+g\zeta_1=0 \quad \text{at } z=\zeta \qquad (20)$$

ζ_1 and ϕ at the free surface are determined by integration of (19) and (20) with time with a suitable initial condition. It is more convenient to employ the Lagrangian time derivative in order to integrate the above equations with time [7]. The Lagrangian derivative or the material derivative in the two-dimensional $y, z-$plane is defined by

$$\frac{d}{dt} = \frac{\partial}{\partial t} + \phi_y\frac{\partial}{\partial y} + \phi_z\frac{\partial}{\partial z} \qquad (21)$$

Then the kinematic condition is written as

$$\frac{d\zeta_1}{dt} = \phi_z \qquad \text{on } z=\zeta \qquad (22)$$

while the dynamic condition is written as

$$\frac{d\phi}{dt} = \frac{1}{2}(\phi_y^2 + \phi_z^2) - \phi_z\dot{\zeta}_w - g\zeta_1 \quad \text{at } z=\zeta \quad (23)$$

Thus the free surface from $z = \zeta$ and the value of ϕ on the free surface are determined from (22) and (23) respectively, but we must know the values of ϕ_y and ϕ_z on the free surface before integrating the above equations. The fluid velocities ϕ_y, ϕ_z are determined by the solution of the two-dimensional Laplace equation

$$\phi_{yy} + \phi_{zz} = 0 \quad (24)$$

which satisfies both the hull surface condition (17) and the free surface conditions (22) (23).

It should be noted that the condition at infinity, $\phi \to 0$ as $y \to \pm\infty$, is not applied, because the solution is valid only in the near field. The solution of (24) is generally expressed in the form $\phi_1 + g(x)$, where ϕ_1 satisfies the boundary condition and vanishes at infinity and $g(x)$ is an arbitrary function of x only, which gives some indeterminateness to the solution. In order to make the solution definite, one has to determine $g(x)$ by matching with the far field solution which may be obtained in another way. According to the linearized slender ship theory however, it is proved that $g(x)$ becomes negligible under the condition $\omega\sqrt{d/g} = O(1)$. Therefore the condition at infinity holds in the present case. The solution indicates that the disturbance propagates in the direction of negative X only in reference to the coordinate system moving with the hull, so that the boundary value problem is of the parabolic type along the X-axis. Thus the solution is the parabolic approximation of the originally elliptic problem.

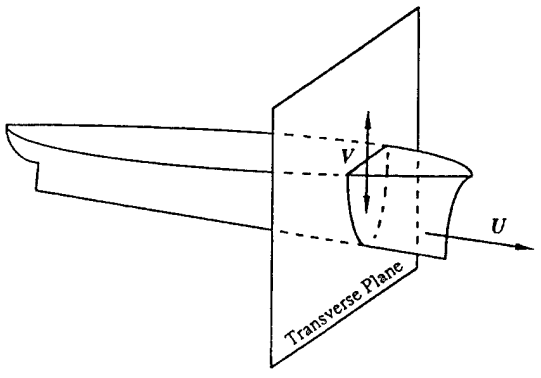


Fig. 2 A transverse plane fixed in space.

3 SOLUTION PROCEDURE

The slender body technique reduces the problem to the two-dimensional boundary value problem in the plane perpendicular to the longitudinal axis of the ship as explained in the previous section. One must remember that the problem is formulated in the coordinate system fixed in space rather than the coordinate system moving with the ship. Therefore the solution is found in the transverse plane fixed in space, and the hull is moving relatively to this plane as shown in Fig. 2. The cross section of the hull in the plane of solution at one instant is different from the cross section in the same plane at another instant.

Take a transverse plane at a certain position $x = x_1$ as the plane of solution. The domain in this plane occupied by the fluid is bounded by the hull cross section Γ_H and the intersection of the free surface Γ_F. The boundary value problem is to seek the solution of the two-dimensional Laplace equation (24), which satisfies the hull surface condition (17) on Γ_H together with the free surface conditions (22) (23) on Γ_F. The solution is obtained at each instant on planes at various positions $x = x_1, x_2, x_3, \cdots$. Then the three-dimensional flow field is determined.

The boundary value problem described above is solved through two steps.

[Step 1]

Assume that the value of ϕ on Γ_F is known at a certain instant $t = t_1$. The normal velocity ϕ_n on Γ_H is given by (17) if the motion of the hull is known. Now let us take a closed domain circumscribed by Γ_H, Γ_F and a contour Γ_∞ taken at a great distance surrounding the fluid domain, and apply Green's theorem in the domain Ω inside this boundary contour. Take a field point P inside Ω and a source point Q on the boundary contour $\Gamma = \Gamma_H + \Gamma_F + \Gamma_\infty$. Then Green's theorem gives

$$\phi_P = \frac{1}{4\pi}\int_\Gamma \left(\frac{\partial\phi}{\partial n} - \phi\frac{\partial}{\partial n}\right)_Q \ln\left[(y_P-y_Q)^2+(z_P-z_Q)^2\right] ds \quad (25)$$

where n is the normal to Γ in the inward direction to Ω, and subscripts P, Q mean the values at P and Q respectively. If P is a point on Γ, the integral is taken in the sense of the Cauchy principal value, and the equation becomes

$$\phi_P = \frac{1}{2\theta}\int_\Gamma \left(\frac{\partial\phi}{\partial n} - \phi\frac{\partial}{\partial n}\right)_Q \ln\left[(y_P-y_Q)^2+(z_P-z_Q)^2\right] ds \quad (26)$$

where $\theta = \pi$ when the contour has a continuous tangent. The normal velocity $\phi_n = \partial\phi/\partial n$

is given on Γ_H by the hull surface condition (17) while ϕ is assumed to be known on Γ_F. If the contour Γ_∞ is taken at an infinite distance, the condition at infinity is valid and the integral along Γ_∞ has no contribution. However it is found that Γ_∞ taken at a finite distance is more conveninet for numerical solution. Here we take Γ_∞ composed of two vertial lines on both sides of the hull and a horizontal line representing the water bottom of finite depth, and impose the condition $\phi_n = 0$ on this boundary. The value of ϕ on Γ_H and Γ_∞ is unknown, while ϕ_n on Γ_F is unknown. Then a set of simultaneous integral equations for these unknowns is derived from (26). The integral equation is solved by a numerical method.

[Step 2]

The solution of the integral equation obtained in Step 1 gives the normal velocity ϕ_n on Γ_F. Since the velocity potential ϕ is assumed to be known on Γ_F, the tangential velocity on Γ_F is obtained by differentiation of ϕ along Γ_F, $\phi_s = \partial\phi/\partial s$. The y and z components of the fluid velocity on the free surface are determined by

$$\phi_y = (\phi_s + \phi_n \zeta_{1y}) / (1 + \zeta_{1y}^2)^{1/2} \quad (27)$$

$$\phi_z = (\phi_s \zeta_{1y} - \phi_n) / (1 + \zeta_{1y}^2)^{1/2} \quad (28)$$

The free surface elevation and the velocity potential on the free surface at subsequent instants are determined by the evolution equations (22)(23) respectively. Applying the values of (27) and (28) to (22)(23), the increment of ζ_1 and ϕ in a short interval Δt is given by

$$\Delta\zeta_1 = \Delta t \, d\zeta_1/dt \quad (29)$$

$$\Delta\phi = \Delta t \, d\phi/dt \quad (30)$$

These values are calculated with respect to a definite fluid particle. The position of the particle is determined by

$$\frac{dy}{dt} = \phi_y, \quad \frac{dz}{dt} = \phi_z + \dot{\zeta}_w \quad (31)$$

Thus the free surface elevation $\zeta = \zeta_w + \zeta_1$ and the velocity potential on the free surface at the instant $t_2 = t_1 + \Delta t$ are determined, and the boundary value problem in Step 1 at the time $t = t_2$ is fully defined. The step by step, time marching procedure of Step 1 through Step 2 determines the evolution of the flow field in a control plane at a definite position $x = x_1$, say. Since this is an initial value problem, the initial condition at an initial point must be defined. The initial point is at the intersection of the stem of bow with the free surface, and the computation starts at the instant when the initial point reaches the control plane. The simplest idea for the initial condition is that $\phi = 0$ on the undisturbed free surface, while the normal velocity on the hull surface is given by the hull surface condition. However it is found after some trial computation that difficulty appears in the numerical solution of Step 1 by this type of initial condition because of the singularity at the intersection of the hull surface and the free surface. The initial condition employed here is as follows. In the first time interval after the initial point, the scale of the hull cross section in the control plane is very small, that means large Froude number of local fluid motion and the effect of gravity does not contribute to the fluid motion much. If the ship has a raked stem, the motion of the hull contour in the control plane is similar to the vertical motion of a sharp wedge, for which there is an analytical solution if gravity is not present. Here we employ Mackie's solution [8] for the entry of a sharp wedge into a free surface as the initial condition. According to this theory, the velocity potential and the free surface elevation, when a wedge of apex angle α enters the free surface at the velocity V, are given by

$$\phi = \frac{\alpha}{2\pi} \int_0^1 \ln \frac{y^2 + (z + z')^2}{y^2 + (z - z')^2} \, dz' \quad (32)$$

$$z = \frac{\alpha}{\pi} \left[\ln\left(1 + \frac{1}{y^2}\right) + 2y \tan^{-1}\left(\frac{1}{y}\right) - 2 \right] \quad (33)$$

where y and z are normalized by Vt and ϕ is normalized by $V^2 t$.

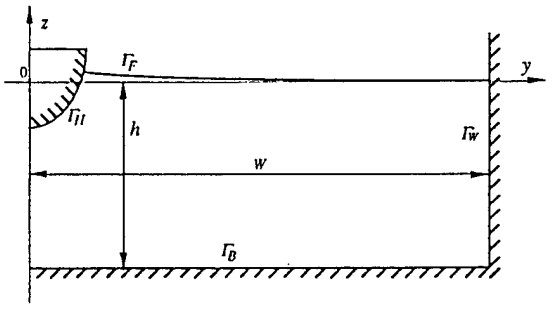


Fig. 3 Computational boundary.

4 NUMERICAL METHOD

The integral equation in Step 1 is solved by a numerical method. The boundary integral equation is written in the form

$$\theta\phi_P = \int_{\Gamma_H + \Gamma_F + \Gamma_\infty} \left(\frac{\partial\phi}{\partial n_Q} G(P,Q) - \phi \frac{\partial G(P,Q)}{\partial n_Q} \right) ds_Q \quad (34)$$

where

$$G(P,Q)=\frac{1}{2}\ln\left[\left(y_P-y_Q\right)^2+\left(z_P-z_Q\right)^2\right] \quad (35)$$

The numerical boundary is taken as that in Fig. 3. On the hull surface contour Γ_H, ϕ_n is given by the boundary condition, and on the free surface contour Γ_F, ϕ is given by the result of computation in Step 2. On the outer boundary, we set $\phi_n=0$. The outer boundary is divided into the side wall Γ_W and the water bottom Γ_B. The condition of the horizontal water bottom is satisfied by taking the image with respect to the bottom line at $z=-h$. Hereafter we define Γ_H and Γ_F by including their image contours.

The integral equation (34) is written for a point P on Γ_H or Γ_W in the form like

$$\theta\phi_P+\int_{\Gamma_H+\Gamma_W}\phi G_n ds-\int_{\Gamma_F}\phi_n G ds=\int_{\Gamma_H}\phi_n G ds-\int_{\Gamma_F}\phi G_n ds \quad (36)$$

where $G=G(P,Q), G_n=\partial G(P,Q)/\partial n_Q$ for brevity. If the point P is on Γ_F, the integral equation is written in the from

$$\int_{\Gamma_H+\Gamma_W}\phi G_n ds-\int_{\Gamma_F}\phi_n G ds=-\theta\phi_P+\int_{\Gamma_H}\phi_n G ds-\int_{\Gamma_F}\phi G_n ds \quad (37)$$

The right hand sides of the above equations are known quantities. The contour is divided by discrete points with small intervals by straight line segments connecting each adjacent point. The values of ϕ and ϕ_n are defined at these points, and the linear variation of ϕ and ϕ_n is assumed along each segment. The integral equation is then replaced by a set of simultaneous linear algebraic equations. The value of θ in the integral equation in this time is the angle interior to the domain Ω between each contiguous segment.

The simultaneous algebraic equations can be written in the matrix form

$$\begin{bmatrix}[A_1][D_1]\\ [A_2][D_2]\end{bmatrix}\begin{Bmatrix}\{\phi\}\\ \{\Phi\}\end{Bmatrix}=\begin{bmatrix}[B_1][C_1]\\ [B_2][C_2]\end{bmatrix}\begin{Bmatrix}\{\phi_n\}\\ \{\Phi_n\}\end{Bmatrix} \quad (38)$$

where ϕ,ϕ_n mean values on Γ_H or Γ_W, and Φ,Φ_n on Γ_F. If we write the above equation in the simpler form

$$[A_{ij}]\{\phi_j\}=[B_{ij}]\{\phi_{n_j}\} \quad (39)$$

the elements of the matrices are given by

$$A_{ij}=\theta_i\delta_{ij}+\frac{1}{s_j-s_{j-1}}\int_{j-1}^{j}sG_n ds-\frac{s_{j-1}}{s_j-s_{j-1}}\int_{j-1}^{j}G_n ds+\frac{s_{j+1}}{s_{j+1}-s_j}\int_{j}^{j+1}G_n ds-\frac{1}{s_{j+1}-s_j}\int_{j}^{j+1}sG_n ds \quad (40)$$

$$B_{ij}=\frac{1}{s_j-s_{j-1}}\int_{j-1}^{j}sG ds-\frac{s_{j-1}}{s_j-s_{j-1}}\int_{j-1}^{j}G ds+\frac{s_{j+1}}{s_{j+1}-s_j}\int_{j}^{j+1}G ds-\frac{1}{s_{j+1}-s_j}\int_{j}^{j+1}sG ds \quad (41)$$

We have a system of linear algebraic equations with respect to ϕ_j on Γ_H and Γ_W and ϕ_{n_j} on Γ_F. The unknown values of ϕ on Γ_H and Γ_W and ϕ on Γ_F are determined simply by the matrix inversion using the computer. Thus the flow field in a certain transverse plane Σ at a certain instant $t=t_1$ is completely determined.

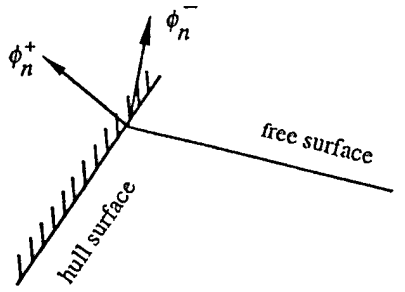


Fig. 4 Intersection point.

There are several points which need special treatment. Since a measure of deck wetness is relative height of the wave surface at the hull surface, and the point of intersection of the hull surface and free surface presents the top of the wetted region on the hull surface, it is obvious that cautious treatment of the intersection point is very important for the prediction of deck wetness. Several researchers have presented methods to treat this point, but some of their methods seem to be inaccurate, and some are not suitable in the present problem. The values of ϕ and ϕ_n are defined at nodal points connecting adjacent line segments which replace the boundary contour. Though the potential is unique at any nodal point, the normal velocity ϕ_n does not have a unique value at nodes where the normal to the boundary is not unique. In particular, the intersection point is a special node at which ϕ is continuous while ϕ_n is different on each side because of different boundary conditions as shown in Fig. 4. Write ϕ_n^+ for the normal velocity to the hull surface and ϕ_n^- to the free surface at the intersection point. Since ϕ_n^+ is known and ϕ_n^- unknown, (39) can be transformed to

$$[A_{ij}]\{\phi_j\}=[B_{ij}]\{\phi_{n_j}\}+[C_i]\{\phi_n^+\} \quad (42)$$

where $\phi_n^- \in \phi_{n_j}$. The unknown ϕ_n^- is determined from the above equation.

Another kind of nodal point which needs special treatment is the tip of the spray jet which sometimes occurs. The potential is given at this point, while the unknown normal velocity at the free surface has different values on both sides of the jet. Two unknowns at the same nodal point require another equation. The method to solve this problem involves discontinuous elements introduced by Brebbia and Dominguez [9] as shown in Fig. 5. Instead of the nodal point B connecting segments AB and BC, we take a point B′ on AB and B″ on BC. Then ϕ and ϕ_n are calculated at B′ and B″. The values of ϕ_n at B on both sides of the jet are obtained by extrapolation.

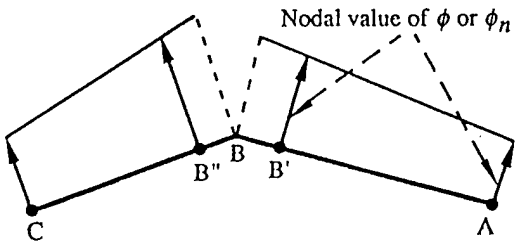


Fig. 5 Discontinuous elements.

The next time step is the determination of the free surface at the instant slightly later by a short time interval Δt. For each time step, the main computations described below are performed for the determination of the free surface.

1) Determination of unknowns ϕ, Φ_n: Equation (42) is rearranged in the form

$$[A]\{X\} = \{Y\} \tag{43}$$

$$[A] = \begin{bmatrix} [A_1][-C_1] \\ [A_2][-C_2] \end{bmatrix} \tag{44}$$

$$\{X\} = \begin{Bmatrix} \{\phi\} \\ \{\Phi_n\} \end{Bmatrix} \tag{45}$$

$$\{Y\} = \begin{bmatrix} [B_1][-D_1] \\ [B_2][-D_2] \end{bmatrix} \begin{Bmatrix} \{\phi_n\} \\ \{\Phi\} \end{Bmatrix} + \begin{bmatrix} [F_1] \\ [F_2] \end{bmatrix} \{\phi_n^+\} \tag{46}$$

where $[F_1]$ and $[F_2]$ are subvectors of $[C_i]$ in (42). The right hand side of (43) is a known vector, and $\{X\}$ is determined by the matrix inversion.

2) Time-stepping: The position of fluid particles and values of potential ϕ, on the free surface for the next time at $t = t_1 + \Delta t$, are determined by

$$y(t_1+\Delta t) = y(t_1) + \phi_y(t_1)\Delta t \tag{47}$$

$$z(t_1+\Delta t) = z(t_1) + \phi_z(t_1)\Delta t + \zeta_w(t_1+\Delta t) - \zeta_w(t_1) \tag{48}$$

$$\phi(t_1+\Delta t) = \phi(t_1) + \left[\frac{1}{2}(\phi_n^2+\phi_s^2) - \phi_z\dot{\zeta}_w - g\zeta_1\right]_{t_1}^{\Delta t} \tag{49}$$

The fluid velocity ϕ_y, ϕ_z is calculated by (27) (28), and the tangential velocity ϕ_s is expressed by a finite difference of ϕ using the three point Lagrange interpolation.

3) Smoothing: To depress a sawtooth instability of the wave profile, the five-point smoothing algorithem is used to filter the points which are not equally spaced on the free surface. s_i in the following formula is the distance between two nodal points.

For the first point (edge point):

$$\overline{f_0} = \frac{1}{2}\left\{\frac{1}{m-s_1}[m(f_0+f_1) - s_1(f_0+f_3)] + \frac{s_1 m}{n\ell(n-\ell)}[n(f_0-f_2) - \ell(f_0-f_4)]\right\} \tag{50}$$

For the second point:

$$\overline{f_0} = \frac{1}{2(m-s_1)}\left\{\frac{m}{s_{-1}+s_1}[s_1(f_0+f_{-1}) + s_{-1}(f_0+f_1)] - \frac{s_1}{s_{-1}+m}[m(f_0+f_{-1}) + s_{-1}(f_0+f_3)]\right\} \tag{51}$$

For the center point:

$$\overline{f_0} = \frac{1}{2}\left\{\frac{1}{s_{-1}+s_1}[s_1(f_0+f_{-1}) + s_{-1}(f_0+f_1)] + \frac{s_{-1}s_1}{\ell_{-2}\ell_2(\ell_{-2}+\ell_2)}[\ell_2(f_0-f_{-2}) + \ell_{-2}(f_0-f_2)]\right\} \tag{52}$$

where $\ell_{-2} = s_{-2} + s_{-1}, \ell = \ell_2 = s_1 + s_2, m = s_1 + s_2 + s_3, n = s_1 + s_2 + s_3 + s_4$.

4) Regriding: In some cases, node points on the free surface, especially near the hull, are either too close to or too far from each other, leading to numerical difficulties. The regriding technique is a useful way to keep the computation accurate. If the computed distance is less than d_{min} or greater than d_{max} which are the input control parameters, the points only near the hull are redistributed by cubic spline or linear interpolation.

Thus the computation at the next time step is repeated by the above procedure 1) through 4). Since the ship is moving with forward speed U, the hull section moves astern in each time interval, and reaches the stern at the time L/U after the beginning of the above procedure at the bow. Therefore the result of computation in one round dose not express the time evolution of the free surface at a definite section of the ship nor the free surface elevation in different sections at the same instant. In order to complete the computation to

obtain the result for every section throughout the length of the ship, the same computation procedures starting from the bow should be repeated by shifting the initial instant by the time interval $\Delta t = \Delta x/U$, where Δx is the interval of the section for which the result is required.

5 NUMERICAL EXAMPLES

A frigate model shown in Fig. 6 is employed for the numerical example. The computation of ship motion in regular waves by means of the strip method and results of towing tank experiment of this model have been published by O'dea and Walden [10].

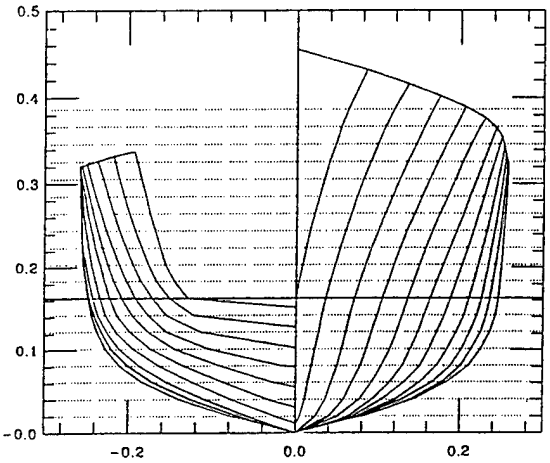


Fig. 6 Body plan of a frigate model (L=4.5m,B=0.496m,d=0.163m).

Numerical computations are carried out in two conditions. The first is the steady forward motion in still water. The Froude number varies from 0.10 to 0.60. We take $W = 60B$ and $h = 1.2L$ as the computationl domain. The number and intervals of the nodal points distributed on three boundaries Γ_H, Γ_W and Γ_F are as follows.

(1) On Γ_H: The number of nodes depends on the wetted depth of the hull contour, such as $\Delta s = d/20$ near the keel and $\Delta s = d/40$ near the point of intersection with Γ_F.

(2) On Γ_W: 15 points are distributed with an equal interval.

(3) On Γ_F: 150 points are distributed from the intersection with Γ_H in an equal interval $\Delta s = B/100$, and other 50 points are distributed along the remaining part of the boundary with arithmetic intervals.

The numerical results at the time interval Δt give the free surface profile in the transverse sections with intervals $\Delta x = U\Delta t$. The time step is chosen in such a way that the numerical results are obtained at the hull sections with the interval $\Delta x = L/800$. The reliability of the numerial results is comfirmed by changing the interval Δx and the grid density on the free surface.

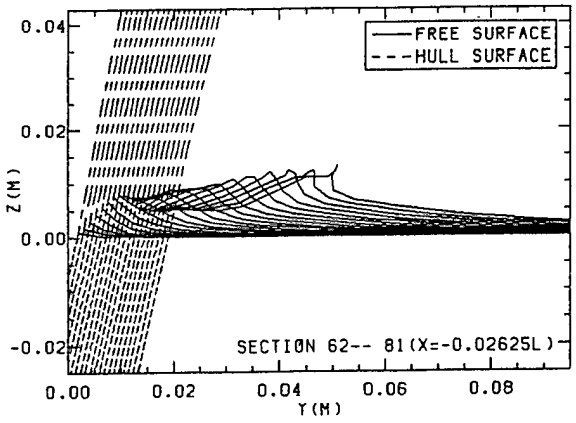


Fig. 7 Bow wave breaking for a fixed ship in still water at Fn=0.10, Δt=0.0085 s.

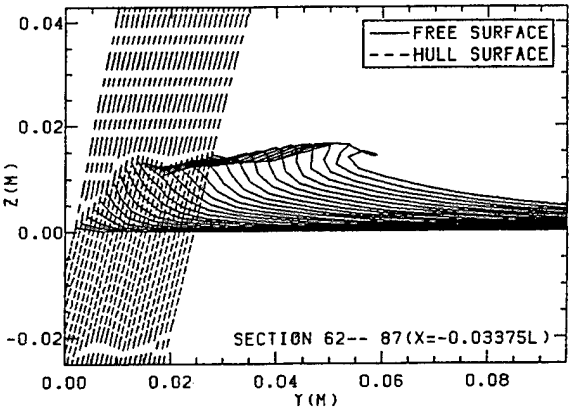


Fig. 8 Bow wave breaking for a fixed ship in still water at Fn=0.15, Δt=0.0056 s.

The results of computation are illustrated in Fig. 7 through Fig. 13. At low Froude numbers less than 0.2, generation of spray is not observed, but diverging waves generated at the bow are gradually steepened and eventually break at the pointed crest, suggesting the white cap. At Froude number 0.2, overturning of the wave crest is observed, but the spray is not developed yet. At Froude number 0.3, generation of spray by the overturning free surface is clearly observed. At Froude number 0.4, some instability appears on the free surface underneath the spray root, which may suggest the spilling type of wave breaking

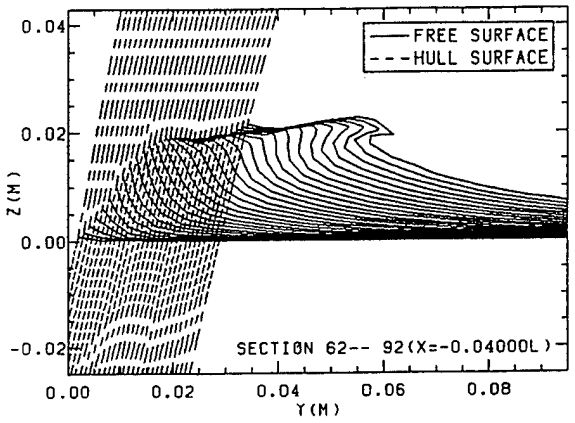


Fig. 9 Bow wave breaking for a fixed ship in still water at $Fn=0.20$, $\Delta t=0.0042\,s$.

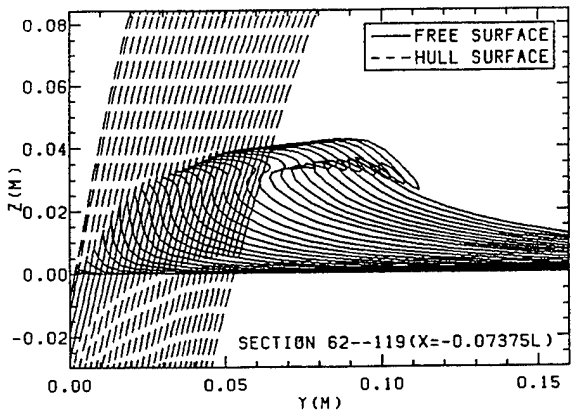


Fig. 10 Bow wave breaking for a fixed ship in still water at $Fn=0.30$, $\Delta t=0.0028\,s$, interval for plotting: 2 cross sections.

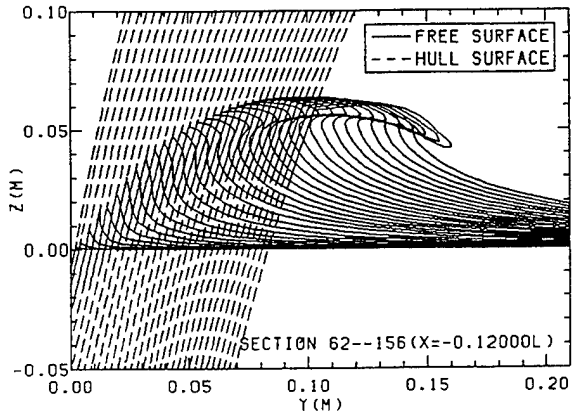


Fig. 11 Bow wave breaking for a fixed ship in still water at $Fn=0.40$, $\Delta t=0.0021\,s$, interval for plotting: 3 cross sections.

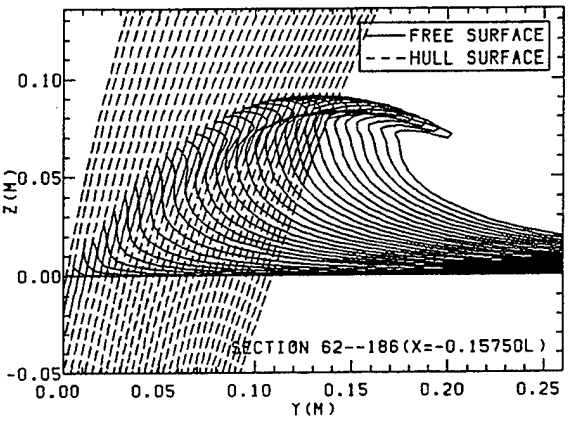


Fig. 12 Bow wave breaking for a fixed ship in still water at $Fn=0.50$, $\Delta t=0.0017\,s$, interval for plotting: 4 cross sections.

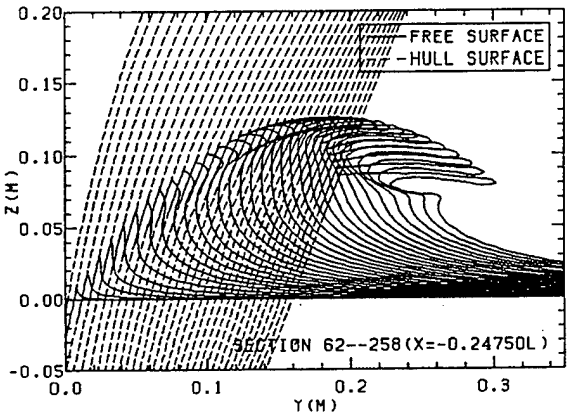


Fig. 13 Bow wave breaking for a fixed ship in still water at $Fn=0.60$, $\Delta t=0.0014s$, interval for plotting: 6 cross sections.

instead of the plunging type. At Froude number 0.5, some undulation appears on the free surface under the spray sheet, and this undulation grows up further at Froude number 0.6. This phenomenon suggests another type of wave breaking.

The second case is the same ship making heaving and pitching oscillation in sinusoidal head sea waves as expressed by Eq.(2) at uniform forward speed of Froude number 0.3. The length of the incident wave is so chosen as $\lambda/L = 1.2$, at which the maximum amplitude of the oscillations is observed in the experiment. The ship motion is given by

$$Z = Z_A \sin(\omega_1 t + kx_g + \varepsilon_0 + \varepsilon_1)$$
$$\theta = \theta_A \sin(\omega_1 t + kx_g + \varepsilon_0 + \varepsilon_2)$$

where $\omega_1 = \omega + kU$ and x_g is the $x-$coordinate of the center of gravity referred to the origin at F.P.. Values of Z_A, θ_A, ε_1 and ε_2 are taken from experimental data of O'dea et al [10].

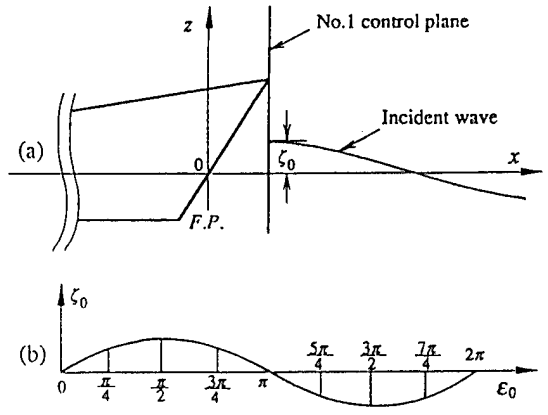


Fig. 14 The position of the No.1 control plane(a) and the expression of the initial phase of the incident wave(b).

The position of the control plane is defined by the phase angle of the incident wave on the control plane at the instant when the foremost point of the bow arrives at this control plane as shown in Fig. 14, and the numerical procedure starts at this instant. If the control plane fixed in space is arranged with the interval Δx_0, the phase difference between adjacent planes is $\Delta\varepsilon_0 = (\omega_1/U)\Delta x_0$. The numerical results for the free surface profile are obtained at hull sections with the interval $\Delta x = L/1000$, so the time interval of the computation is chosen as $\Delta t = 0.002256$ seconds. The reliability of the numerical results is checked by changing the interval Δx and the grid density as before.

Three kinds of the wave steepness (the ratio of wave height to wave length) i.e. $H/\lambda = 0.02$, 0.03 and 0.04 are chosen for the numerical examples. Computations are carried out at control planes at $\varepsilon_0 = 0.0$, $\pi/4$, $\pi/2$, $3\pi/4$, π and $7\pi/4$. However the preliminary computation has shown that there is no possibility of deck wetness at ε_0 greater than $\pi/2$, so that results with $\varepsilon_0 = 0.0$, $\pi/4$ and $\pi/2$ will be given here.

1) Results of H/λ =0.02

The evolution of the free surface profile in the bow region at the control plane $\varepsilon_0 = 0.0$ is shown in Fig. 15. At Section 133($X/L = -0.058$) of the hull, the level of the free surface exceeds the deck height, but water is pushed aside by the hull at the deck side. The overturning of the free surface results the sheet of spray jet directed outward, so that there is no shipping water on board as far as the vertical movement of the free surface relative to the deck is upward. At Section 201($X/L = -0.126$) however, the relative motion of the free surface turns to downward. Then water once lifted above the deck level is scooped up at the deck side, and a small amount of shipping water enters on deck as shown in Fig. 16.

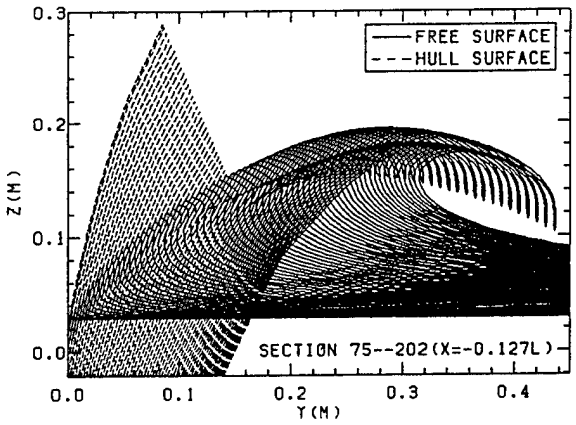


Fig. 15 Wave elevation for a ship with heaving and pitching oscillation in sinusoidal head sea waves (H/λ=0.02, ε_0=0.0), interval for plotting: 2 cross sections.

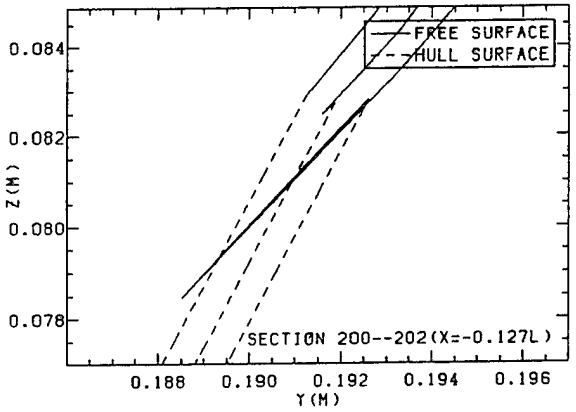


Fig. 16 The magnified portion of water entering on deck in Fig. 15.

The result at the control plane $\varepsilon_0 = \pi/4$ is shown in Fig. 17. The overturning free surface and the outward spray sheet are similar to the former case, but shipping water resulted by the relative movement of the free surface as shown in Fig. 16 in the former case does not take place in this case. Another difference is the appearance of

undulation of the free surface beneath the spray sheet, which may cause the breaking of free surface behind this position.

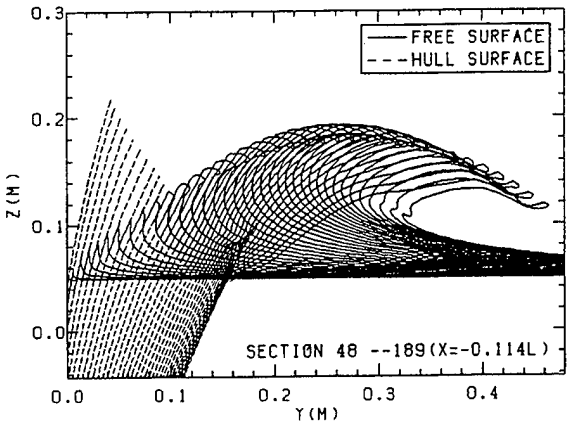


Fig. 17 Wave elevation for a ship with heaving and pitching oscillation in sinusoidal head sea waves (H/λ=0.02, $\varepsilon_0=\pi/4$), interval for plotting: 4 cross sections.

The result at the control plane $\varepsilon_0 = \pi/2$ is shown in Fig. 18. The behavior of the free surface is different from the former cases. As the heave of free surface exceeds the deck level at Section 58 much closer to the stem than in the former cases due to deep immergence of the bow, the spray appears at the tip of heaved water and turns inward over the deck due to outward movement of the deck side. Then shipping water on board is resulted.

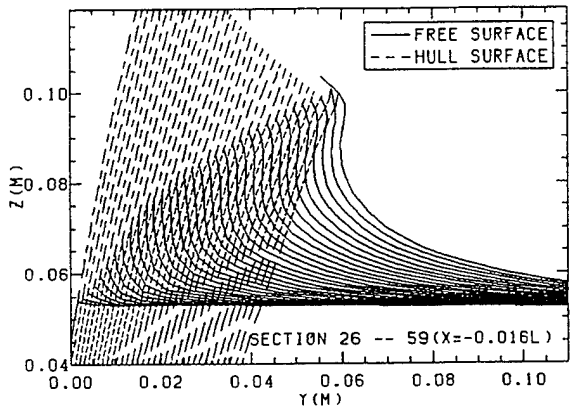


Fig. 18 Wave elevation for a ship with heaving and pitching oscillation in sinusoidal head sea waves (H/λ=0.02, $\varepsilon_0=\pi/2$).

Computations at the control plane $\varepsilon_0 = 3\pi/4$, π and $7\pi/4$ show no shipping water. As a consequence, one can conclude that deck wetness begins to take place in the wave height $H/\lambda = 0.02$ at $\varepsilon_0 = 0.0$ and $\pi/2$. This result is in agreement with experimental data.

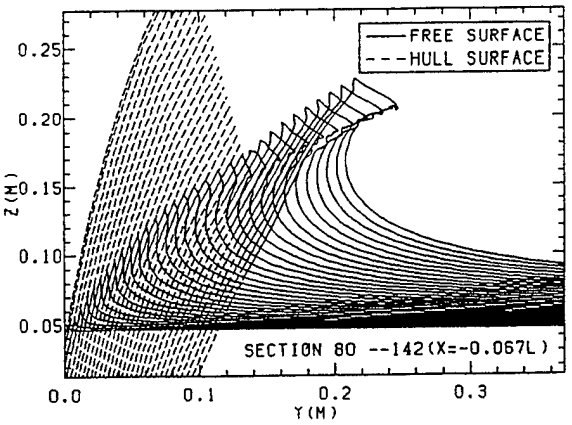


Fig. 19 Wave elevation for a ship with heaving and pitching oscillation in sinusoidal head sea waves (H/λ=0.03, ε_0=0.0), interval for plotting: 2 cross sections.

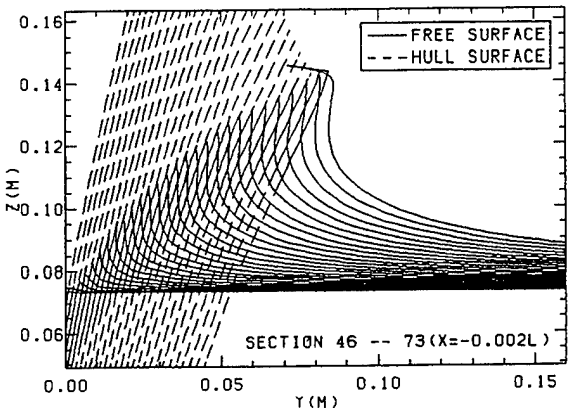


Fig. 20 Wave elevation for a ship with heaving and pitching oscillation in sinusoidal head sea waves (H/λ=0.03, $\varepsilon_0=\pi/4$).

2) Results of H/λ =0.03

The behavior of the free surface is quite different from the former case, because of the greater motion of the hull. Heavy deck wetness is reported in the experiment. The numerical result at $\varepsilon_0 = 0.0$ is shown in Fig. 19. As the bow plunges into the wave surface, a mass of water is raised up on both sides of the deck in thick spray like liquid walls. Water at the top of the wall spreads in both directions, forming spray sheets directing inward and outward to the hull. The inward

spray falls on deck, resulting heavy deck wetness. This phenomenon is similar to the collapse of a liquid column.

The result at $\epsilon_0 = \pi/4$ is shown in Fig. 20. After the heaving free surface exceeds the deck side, spray directing inward similar to the case of Fig. 18 appears at the tip, bringing shipping water. A similar behavior of the free surface is observed at the hull section closer to the stem at $\epsilon_0 = \pi/2$ as shown in Fig. 21.

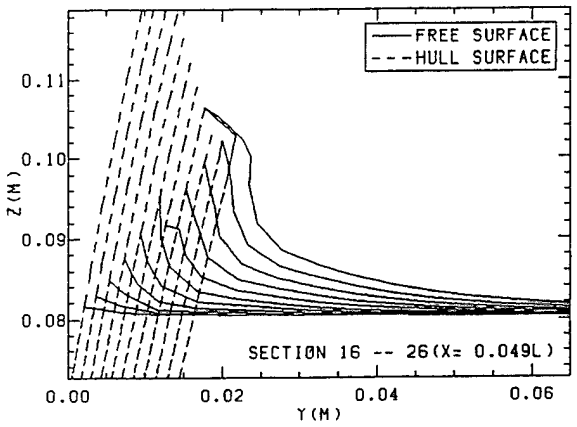


Fig. 21 Wave elevation for a ship with heaving and pitching oscillation in sinusoidal head sea waves (H/λ=0.03, $\epsilon_0=\pi/2$).

According to the experimental observation, the bow of the ship is lifted above the wave surface almost clear of water at the phase angle greater than $\epsilon_0 = \pi/2$. Then slamming is likely to take place at the bow region. The present computation scheme is not applicable to this situation.

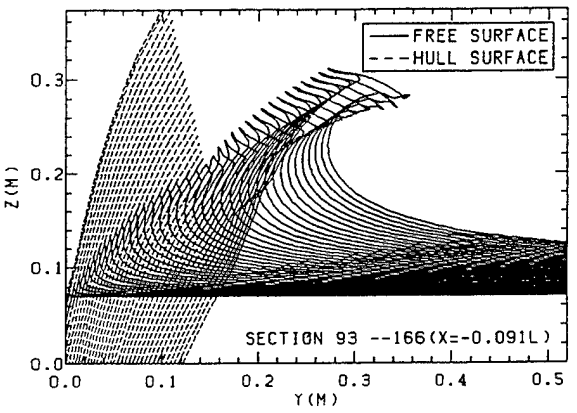


Fig. 22 Wave elevation for a ship with heaving and pitching oscillation in sinusoidal head sea waves (H/λ=0.04, ϵ_0=0.0), interval for plotting: 2 cross sections

3) Results of H/λ =0.04

The result at $\epsilon_0 = 0.0$ is shown in Fig. 22. The free surface phenomenon like the collapse of a liquid column is similar to that in Fig. 19, but in a much exaggerated form. The spray sheet at the top of lifted water is stronger, resulting heavy deck wetness.

Fig. 23 shows the result at $\epsilon_0 = \pi/4$. The heaved free surface turns inboard as exceeding the deck side and brings heavy shipping water in the bow region.

A similar phenomenon appears at the hull section closer to the stem at $\epsilon_0 = \pi/2$ as shown in Fig. 24.

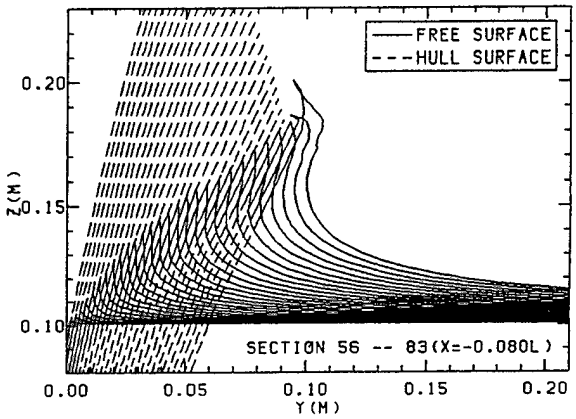


Fig. 23 Wave elevation for a ship with heaving and pitching oscillation in sinusoidal head sea waves (H/λ=0.04, $\epsilon_0=\pi/4$).

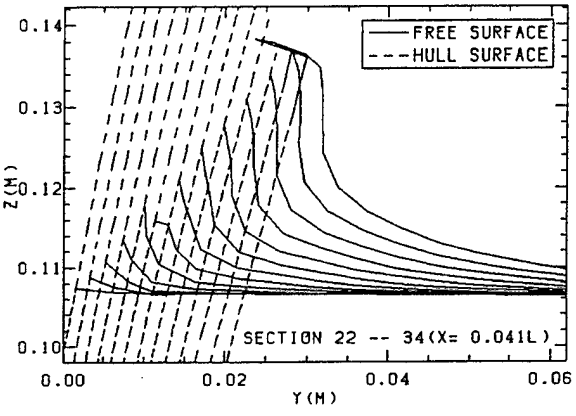


Fig. 24 Wave elevation for a ship with heaving and pitching oscillation in sinusoidal head sea waves (H/λ=0.04, $\epsilon_0=\pi/2$).

Programming of the numerical method and testing of the numerical examples were performed on an IBM Supercomputer (ES/9000-900). And

the final computations were run on a HP Workstation machine (Hp9000 Model 715/50). For the case of Fig. 15, the CPU time of the HP machine was about 9280 seconds. Approximately, 25% of the time corresponded to calculating the elements of the matrices Eqs.(40) (41), 67% to obtaining the solution of Eq.(43), and 8% to regriding and smoothing nodal points on the free surface, saving data into files and so forth.

6 CONCLUSIONS

Nonlinear computations of the free surface elevation at the bow region of a frigate model in the steady forward motion as well as in the heaving and pitching oscillations are carried out under the slender body approximation.

The computation for the steady forward motion well simulates the generation of spray and the breaking of bow waves. It is found that the pattern of breaking wave changes according to increase of forward speed.

The computation for the oscillating ship at forward speed of Froude number 0.30 shows the effect of the incident wave height. At the wave height of $H/\lambda = 0.02$, a mass of water is raised above the deck and pushed aside forming spray like the plunging breaker. However only a small amount of shipping water is observed. At greater wave height $H/\lambda = 0.03$ and 0.04, heavy deck wetness is resulted by falling water from the thick spray sheet at the lifted free surface over the deck. Deck wetness begins at the wave height $H/\lambda = 0.02$, and the result is in good agreement with the experimental observation.

Deck wetness does not necessarily take place even when the free surface heaves above the deck level, as water is pushed aside by the hull surface generating outward directing spray. It is found that the forward speed and the vertical motion of the hull relative to the heaving free surface have much influence to the water shipping on deck.

As a conclusion, the present method serves as a useful tool for a more accurate prediction of deck wetness at large amplitude motion of a ship in rough seas.

ACKNOWLEDGEMENTS

This work was supported by the Office of Naval Research Program in Nonlinear Ship Motions (Contract N00014-90-J-1245) organized by Mr.James Fein, to whom the authors wish to express their thanks for useful suggestions.

The main part of the work was carried out during the authors' stay at the Ocean Engineering Laboratory of University of California at Santa Barbara. The authors wish to express their deepest thanks to Prof. Marshall Tulin, who enabled the both authors to come to Santa Barbara CA and continuously took the responsibility for this research project, for his valuable suggestions and warm advice.

The authors also appreciate the Supercomputing Committee of UCSB and the Office of Academic Computing of UCLA, which provided free computer time on the IBM Supercomputer at UCLA.

The final part of the work was done at the Yokohama National University. The authors are extremely grateful to Prof. S. Kaguei for his kind suggestions and support to the research activities.

REFERENCES

1. Van Sluijs, M.P., "Vertical Ship Motions and Deck Wetness," Society of Naval Architects and Marine Engineers, 1969, Spring Meeting.

2. Tasai, F., "Wave Height at the Side of Two Dimensional Body Oscillating on the Surface of a Fluid," Report of Research Institute of Applied Mechanics, Kyushu Univ., Vol. 9, No. 35, 1961.

3. Takaishi, Y., Ganno, M., Yoshino, T., Matsumoto, N. and Saruta, T., "On the Relative Wave Elevations at the Ship's Side in Oblique Seas," Journal of the Society of Naval Architects of Japan, Vol. 132, 1972, pp. 147-158.

4. Maruo, H., "Evolution of the Theory of Slender Ships," Ship Technology Research, Vol. 36, No. 3, 1989, pp. 105-133.

5. Vinije, T. and Brevig, P., "Nonlinear, Two-dimensional Ship Motions," Norwegian Institute of Technology, Report R-112-81, 1981.

6. Cointe, R., "Nonlinear Simulation of Transient Free Surface Flows," Proceedings of Fifth International Conference on Numerical Ship Hydrodynamics, Hiroshima, Japan, 1989, pp. 239-250.

7. Longuet-Higgins, M.S. and Cokelet, E.D., "The Deformation of Steep Surface Waves on Water, II Growth of Nornal-Mode Instability," Proceedings of the Royal Society, London, A 364, 1978, pp. 1-28.

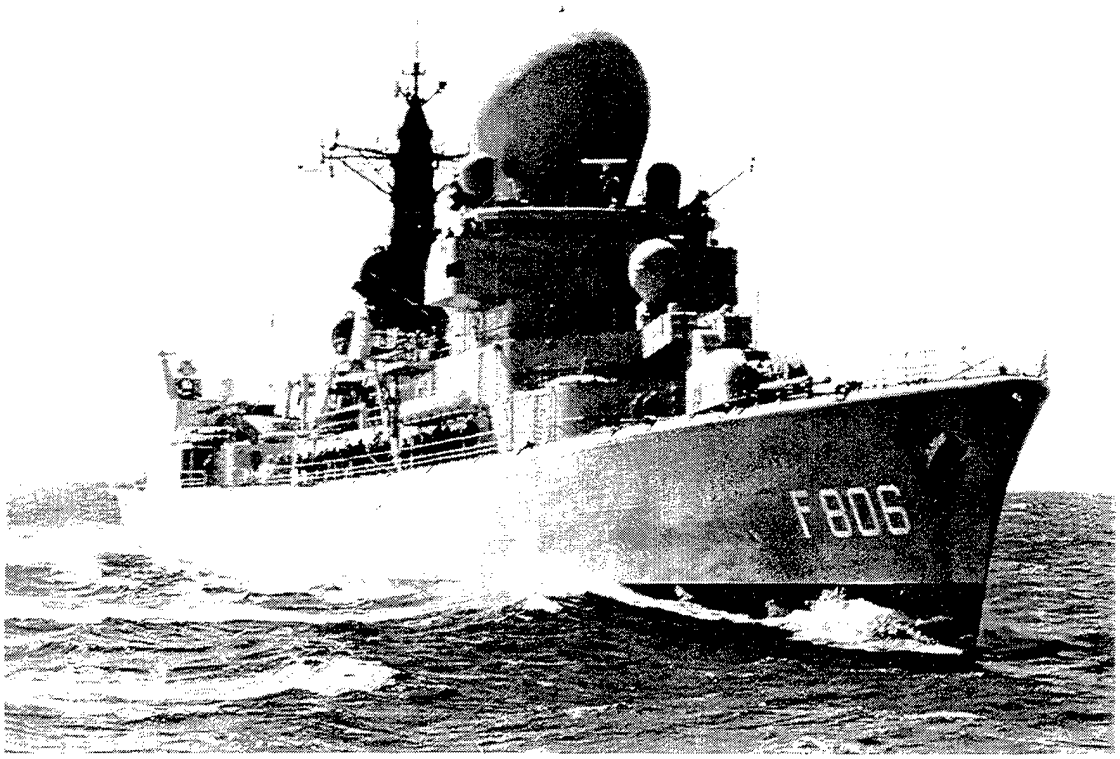
8. Mackie, A.G., "The Water Entry Problem," The Quarterly Journal of Mechanics and Applied Mathematics, Vol. 22, Part 1, Feb. 1969, pp. 1-17.

9. Brebbia, C.A., and Dominguez, J., "Boundary Elements, An Introductory Course," Computational Mechanics Publications, McGraw-Hill Company, 1989, pp. 70-74.

10. O'dea, J.F., and Walden, D.A., "The Effect of Bow Shape and Nonlinearities on the Prediction of Large Amplitude Motions and Deck Wetness," Proceedings of Fifteenth Symposium on Naval Hydrodynamics, Hamburg, Germany, 1984, pp. 163-176.

Effects of Skew and Rake on Cavitation Inception for Propeller Blades with Thick Blade Sections

G. Kuiper (Maritime Research Institute, The Netherlands)



The Guided Missile Frigate "De Ruyter" of the Royal Netherlands Navy

ABSTRACT

Using a design method for unsteady conditions the effects of skew and rake on cavitation inception are investigated. The type of cavitation at inception is tip vortex cavitation. The effect of a thick blade tip has been shown earlier. In this paper extreme rake is applied at the blade tip, which had a very favorable effect on tip vortex inception. This effect is additional to the effects of a thick blade tip. The effect of rake is greater and also different than that of skew. Full scale verification of a new propeller design with extreme rake and with a thick blade tip confirms the favorable behavior of cavitation inception on a raked propeller.

NOMENCLATURE

	description	unit
σ_n	$\frac{p_0 - p_v}{\rho n^2 D^2}$	-
D	Propeller Diameter	m
ρ	Specific Mass	kg/m^3
n	Propeller Rotation Rate	sec^{-1}
p_v	Vapor Pressure	N/m^2
p_0	Undisturbed Local Pressure	N/m^2
K_T	Thrust Coefficient $\frac{T}{\rho n^2 D^4}$	-
T	Propeller Thrust	N
J	Propeller Advance Ratio $\frac{V_s}{nD}$	-
V_s	Ship speed	m/sec
R	Propeller Radius (0.5 D)	m

INTRODUCTION

In a previous paper [1] a design method to maximize the inception speed of frigate propellers was described. In this method the blade sections were adapted to the inflow variations encountered in a wake behind the ship. The optimization of the blade sections is based on the minimum pressure at these blade sections and therefore takes only sheet and bubble cavitation into account.

The method was applied to improve the existing propeller of a Dutch guided misslile frigate Hr. Ms de Ruyter. One effect of the adaptation of the blade sections to the wake for this ship was a significant increase of the maximum thickness of the blade sections. The inception speed for sheet and bubble cavitation could easily be kept over 25 knots. However, the inception speed of a ship is nearly always determined by inception of tip vortex cavitation. The application of the thicker, new blade sections resulted also in a considerable increase of the inception speed for tip vortex cavitation. Although inception of tip vortex cavitation and its scaling problems were outside the scope of the design method, the effects of the new, thicker blade sections triggered some additional investigations on tip vortex inception. In this paper the design method as described in [1] is applied for alternative designs with extra skew and with an extreme rake distribution, to investigate the effect of skew and rake on such propellers. The final design with rake was manufactured at full scale and investigated behind the ship.

PROPELLER DESIGNS

In [1] the existing propeller of the frigate was improved using the same number of blades, blade contour and radial loading distribution.The existing propeller was optimized in a wake distribution, of which the axial velocity distribution at 0.7R is shown in Fig. 1. The resulting propeller with the blade section optimized at 0.8 R was designated propeller A. This nomenclature will be maintained in this paper. In [1] the radial loading distribution was varied to investigate the effect on the inception speed. In that context a loading distribution with unloaded tip and hub was used. The propeller with this loading distribution was designated propeller B. The unloading of the tip was found to be too extreme, so in the final design stage a third radial loading distribution was used, together with optimization of blade sections at two radii (0.6R and 0.8R). The resulting propeller was designated propeller D. The loading distributions of these propellers are shown in Fig. 2.

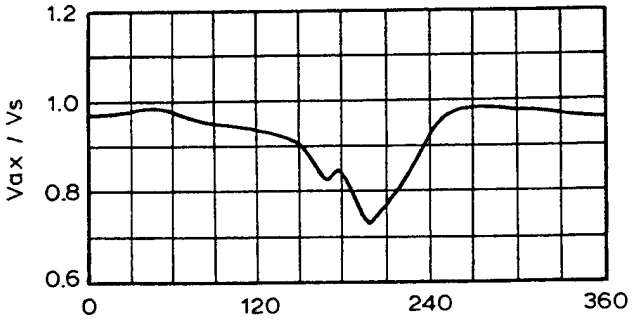


Figure 1: Axial Inflow Velocity at 0.7R

In this paper these propellers will be used to investigate the effect of skew and rake.

Propeller A was used a the reference propeller for the application of rake. The rake distribution of the existing propeller (Fig. 3), which had been maintained for propeller A with the new blade sections, was changed into a strongly varying rake at the outer radii, as shown in Fig. 4. The idea was to decrease the sensitivity of the blade tip to axial and tangential velocity variations. This results in a cusped blade, with the tip bend backwards (towards the propeller face). The design of propeller A was repeated with this rake distribution, while the radial loading distribution and the blade contour of propeller A were maintained.

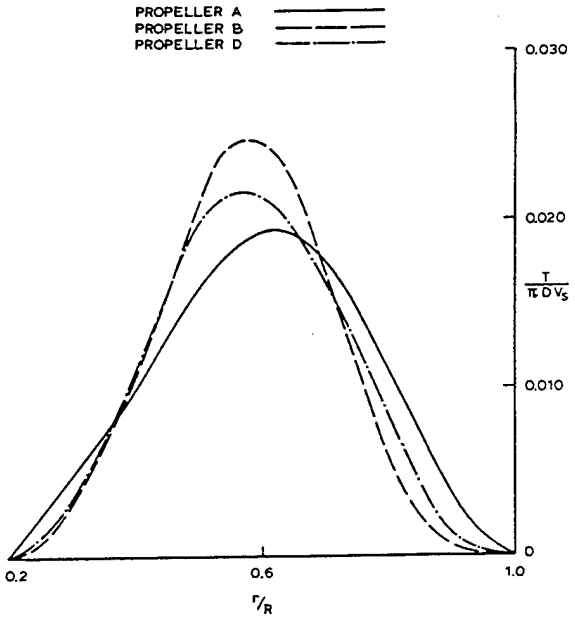


Figure 2: Radial Loading Distributions

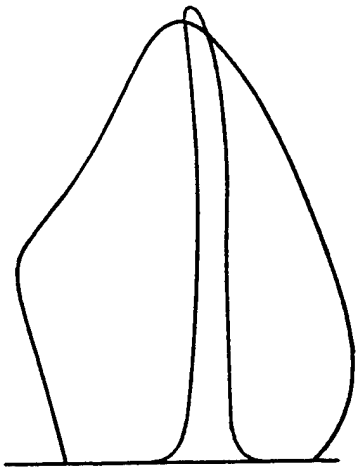


Figure 3: Existing Rake Distribution

This raked propeller is designated Propeller A-rake.

Propeller B was used a the reference propeller for the application of skew. The blade contour, as had been used for all other propellers (Fig. 5) had a moderate skew. The skew was doubled, resulting in the contour of Fig. 6. The propeller with skew is designated propeller B-skew. The effects of skew and rake on the operational curve was small, so for all propellers with modified blade

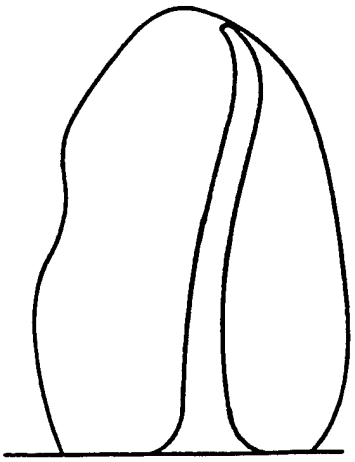


Figure 4: Rake Distribution of Propeller A-rake

sections the same thickness- and camber distribution was used. Only the pitch and the maximum camber was adapted to maintain the radial loading distribution.

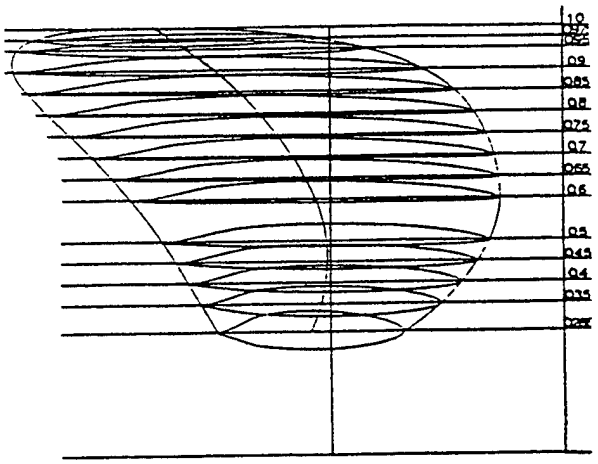


Figure 5: Existing Blade Contour

Based on the results with propellers A, B ,A-rake and B-skew two final designs were made. The design without rake was designated propeller D and this propeller had the radial loading distribution as given in Fig. 2. A variation on this design was the application of rake to this propeller. Based on experimental results of propeller A-rake a smoother rake distribution was chosen, as shown in fig. 7. The propeller with this rake distribution is designated propeller D-rake. This propeller was ultimately chosen for full scale verification.

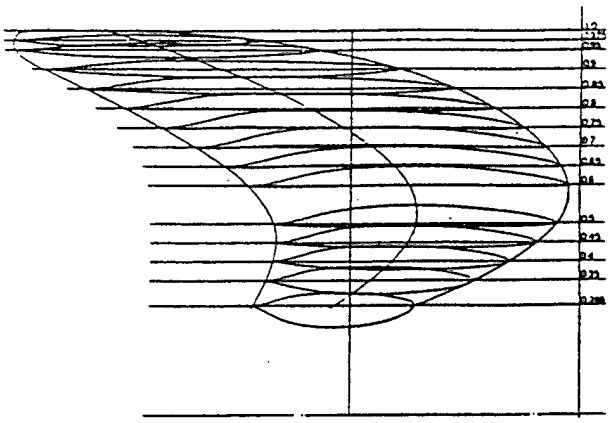


Figure 6: Contour of Propeller B-skew

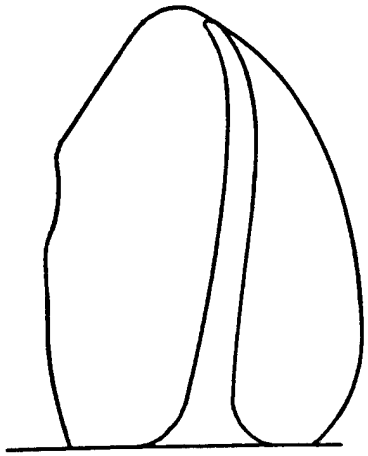


Figure 7: Rake Distribution of propeller D-rake

In summary: All propellers except the existing propeller on the ship had new blade sections. Propellers A,B,A-rake and B-skew had one section type at all radii, based on optimization in the wake at 0.8R, propellers D and D-rake had a variable section shape over the radius, based on optimum blade sections at 0.6R and 0.8R. An extension in the designation of the propeller indicates the design parameter that has been changed.

Radial Interpolation of New Blade Sections

When more than one blade section is applied in a propeller design a radial interpolation has to be applied to arrive at intermediate blade sections. In the case of propeller D the blade sections at 0.6R and 0.8 R are determined. The blade section at 0.6R has been maintained at radii below 0.6R and the blade section at 0.8R has been maintained outside 0.8R. In between of those radii a gradual transition has been made using a weight factor for both camber and thickness.

The Use of ANPRO and PBD10

When the blade sections have been determined using the program of Eppler and Somers, their chordwise loading distribution is used for the determination of the blade sections. The M.I.T. program PBD10 is applied for this purpose. However, this program calculates the sections for shock-free entrance in the mean wake. This is not necessarily so for the blade sections, certainly not when the wake peak is strong. In the case of frigates the difference was negligible, however.

Another complication was that during the analysis of the unsteady conditions the MARIN lifting surface code ANPRO was used. The positioning of the singularities and the wake model are slightly different from PBD10, which resulted in discrepancies in the calculated radial loading distribution. When propeller D was designed using PBD10 with a given radial loading distribution and ANPRO was used to determine the radial loading distribution of the design, the difference was as given in Fig. 8. No further corrections have been made to correct this difference.

The Open Water Inception Diagram

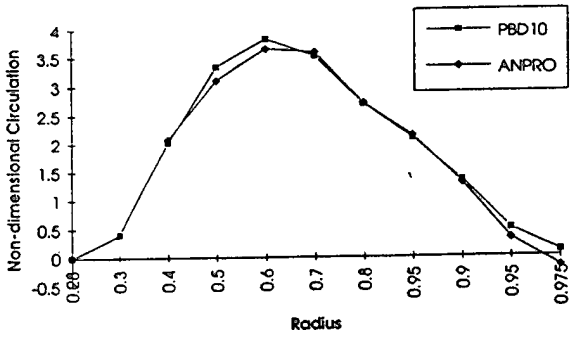


Figure 8: Difference in Calculated Loading between ANPRO and PBD10

Inception curves of all propellers were made both in open water condition and in behind con-

dition. The comparison can be used to judge the sensitivity of the propeller to inflow variations in a wake.

The inception curves in open water were made in the Cavitation Tunnel. These inception curves will not be given fully in this paper. Instead the width of the cavitation bucket at a certain cavitation index σ_n will be given, as illustrated in Fig. 9.

For a certain propeller the cavitation index is mainly determined by the rotation rate of the propeller. The corresponding value of K_T can be controlled by the propeller pitch. For limited variations of the pitch the cavitation index will not change significantly, so by adjusting the pitch the operating condition can be moved horizontally. At a certain value σ_n the width of the bucket w determines the range of the propeller loading at which cavitation free operation is possible.

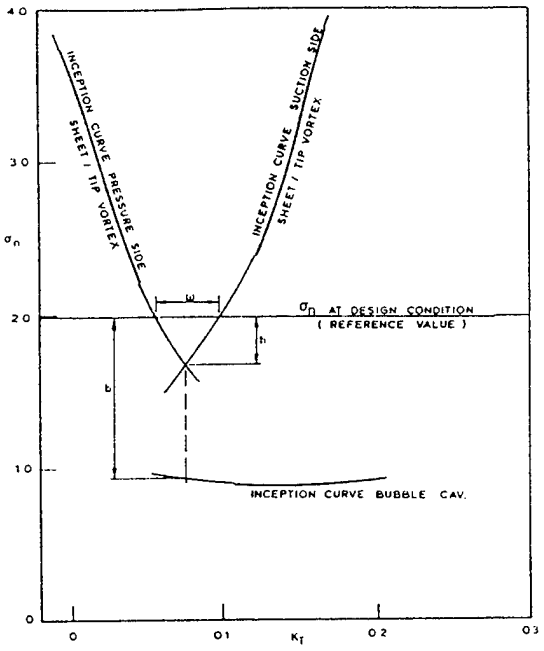


Figure 9: Margins in Open Water Inception Diagram

When the speed of the ship increases the K_T value does not increase very much, but the cavitation index decreases. So the distance h between the lowest point of the bucket and the operating condition indicates the speed range which is available for sheet or tip vortex cavitation. Similarly the distance b between the operating condition and the inception curve for bubble cavitation indicates the speed range available before bubble cavitation occurs.

For comparison with the inception diagram in behind condition the value of w from the open water diagram will only be given (as ΔK_T). This value will be given at a cavitation index σ_n=2. This value corresponds with a ship speed of approximately 23 knots.

EFFECTS OF SKEW

The inception curves in behind condition were made in the MARIN Depressurized Towing Tank at a model scale of 1:15. The inception curves from the model are extrapolated to full scale with a power of 0.35 for the Reynolds number ratio between ship and model, so

$$\sigma_i(ship) = [R_n(ship)/R_n(model)]^{0.35}\sigma_n(model)$$

The inception curve of propeller B is shown in Fig. 10, the inception diagram of propeller B-skew is shown in Fig. 11.

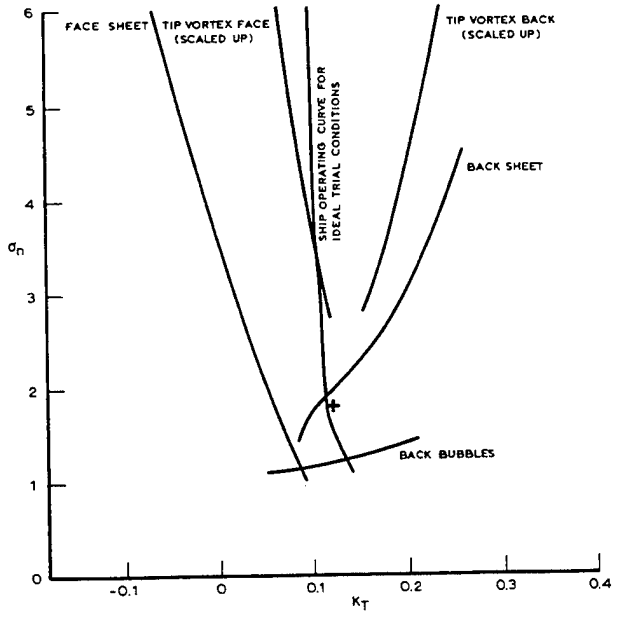


Figure 10: Inception Diagram of Propeller B

In both cases the design point, indicated by a

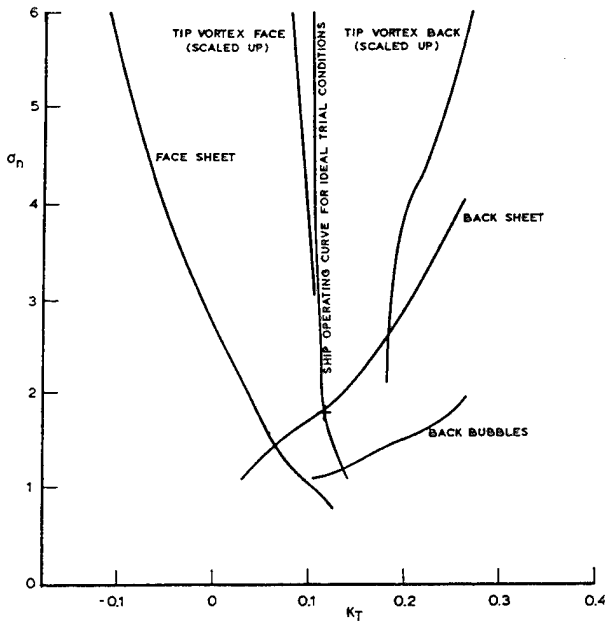


Figure 11: Inception Diagram of Propeller B-skew

	B	B-skew
tip vortex	0.2	0.21
sheet	0.095	0.13

Table 1: Width of the Inception Bucket in Open Water Condition

cross, is on the inception curve for back sheet cavitation. (For these propellers the blade section at 0.8R has been optimized only and this causes that the minimum of the bucket for sheet cavitation is not at the K_T value of the design point.) The effect of skew on tip vortex inception is significant, especially at low values of σ. There skew causes a widening of the inception bucket. This is a well known effect of skew. The bottom of the bucket cannot be determined, because in that case there is no cavitation at model scale. It should be kept in mind that both propellers B and B-skew have thick blade sections.

The bucket width w in terms of ΔK_T in open water conditions is given in Table 1. In open water conditions the effect of skew on tip vortex inception is smaller, so the change in behind condition is caused by the unsteady behavior in a wake.

The model cavitation pattern in behind condition at full power is shown in Figs 12 and 13. The sheet cavitation which was present at propeller B has been increased, but more important is that its maximum has shifted towards inner radii, which has a potential for erosion and damage. Still, in both cases the amount of sheet cavitation is very acceptable. The downgoing blade exhibits some bubble cavitation, which has a very fine structure due to the application of roughness at the leading edge. Although this is often considered harmfull, there are indications that this fear is exaggerated [2].

EFFECTS OF RAKE

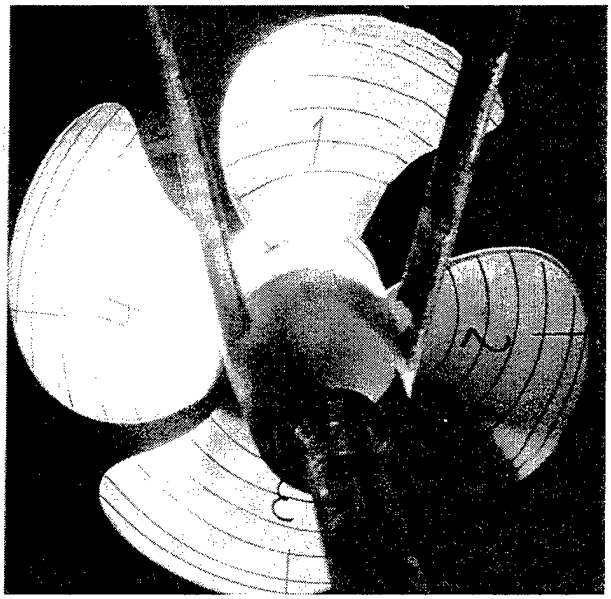


Figure 12: Cavitation Pattern on Propeller B

To improve the inception behavior of tip vortex cavitation further a new development has been investigated: the application of extreme rake at the tip. The intuitive reasoning behind it was that axial and tangential inflow variations would result in smaller loading variations at the tip. For this application propeller A was used as the reference propeller. The bucket of the tip vortex of propeller A is more narrow than that of Propeller B due to the heavier tip loading.

The inception diagram of propeller A in behind condition is given in Fig. 14. The inception diagram of Propeller A-rake is given in Fig 15. The effect of rake on inception of sheet and bubble cavitation is small, but the applied rake has a similar effect as the skew: it opens the inception bucket of the tip vortex. This effect was also

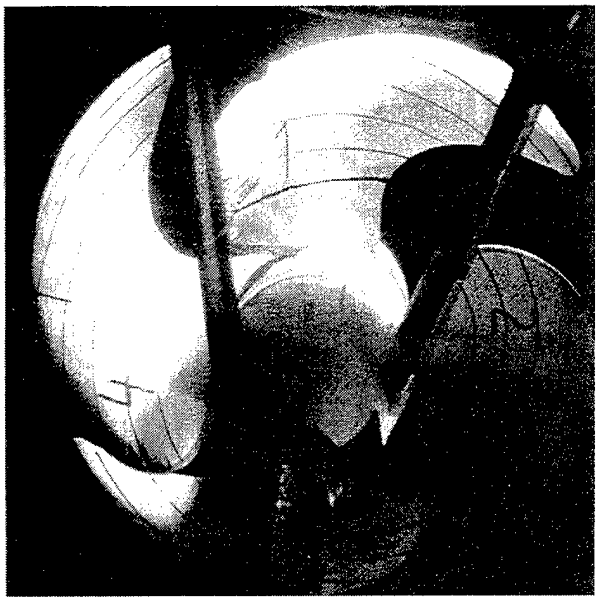


Figure 13: Cavitation Pattern on Propeller B-skew

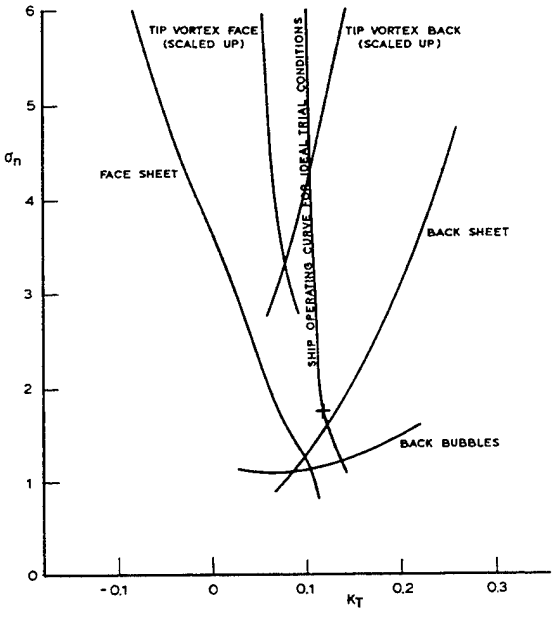


Figure 14: Inception Diagram of Propeller A

found in open water condition, as is shown in more detail in Fig. 16. In terms of the bucket width the effect of rake is given in Table 2.

The cavitation pattern at full power is given in Figs 17 and 18. A slight increase of sheet cavitation at inner radii is visible. It is not sure if the patch of sheet cavitation at inner radii in Fig. 18 is real. In any case the amount of cavitation is only minor.

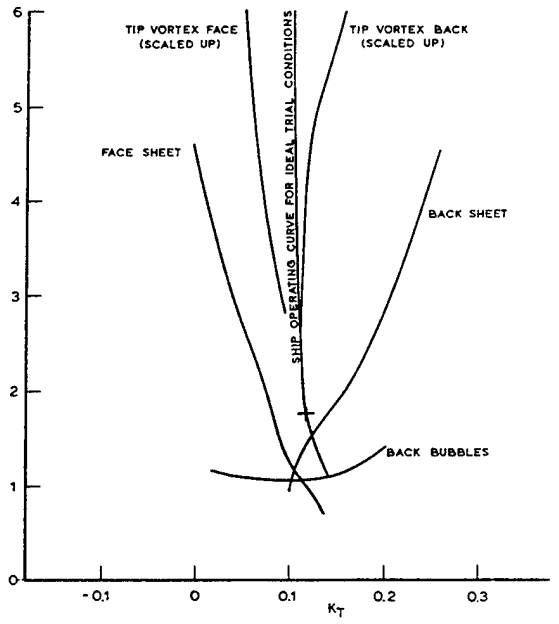


Figure 15: Inception Diagram of Propeller A-rake

	A	A-rake
tip vortex	0.14	0.15
sheet	0.11	0.10

Table 2: Width of the Inception Bucket in Open Water Condition

During the manufacturing of the model propellers it was recognized that the blade tips of the raked propeller were not thick at all. The definition of the thickness is in axial direction and the strong rake makes the blades with the same thickness in axial direction much thinner when measured perpendicular to the blade surface. Since the experience on propeller A was that the thick blade tip delayed inception of tip vortex cavitation, a further improvement might be possible when the blade thickness (in axial direction) was further increased, so that the thickness at the tip perpendicular to the blade with and without rake was comparable. This was applied in the final design.

CHOICE OF THE FINAL DESIGN

At this point the increase of inception speed based on model tests in the depressurized towing tank was as shown in Fig. 19. The reference is the

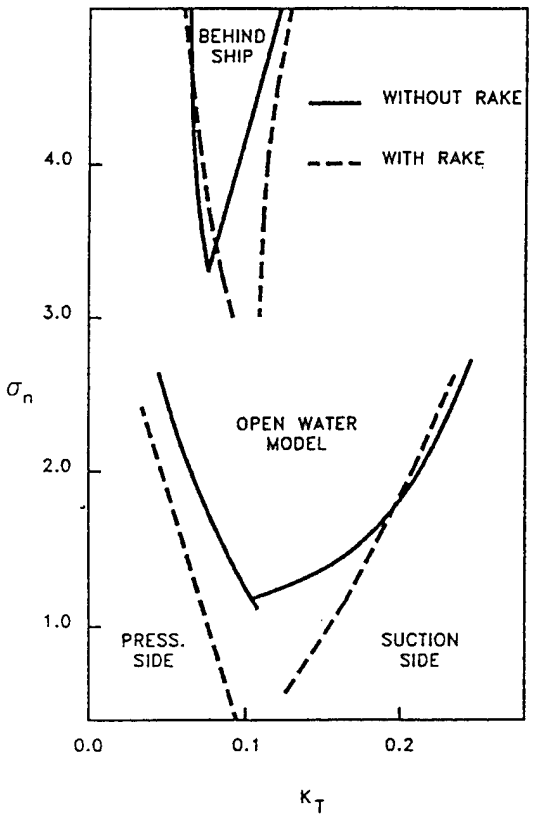


Figure 16: Inception Curves for Tip Vortex Cavitation with and without Rake

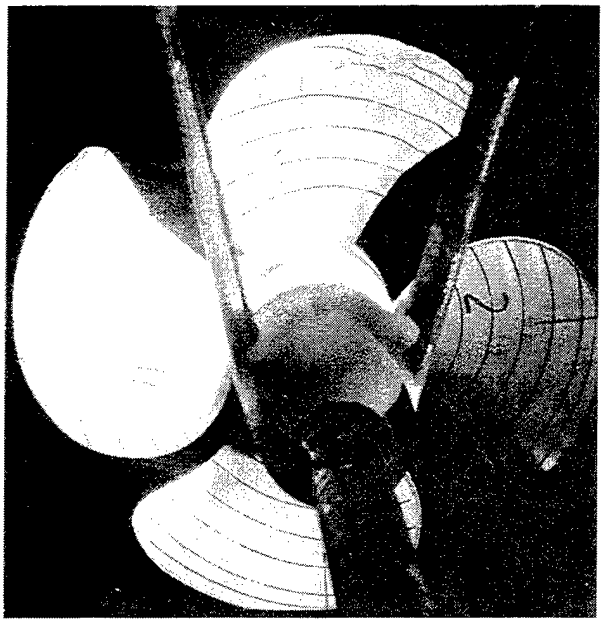


Figure 17: Cavitation Pattern on Propeller A

existing propeller. This improvement was not obtained without losses in performance. Based on model propulsion tests with a cavitating propeller

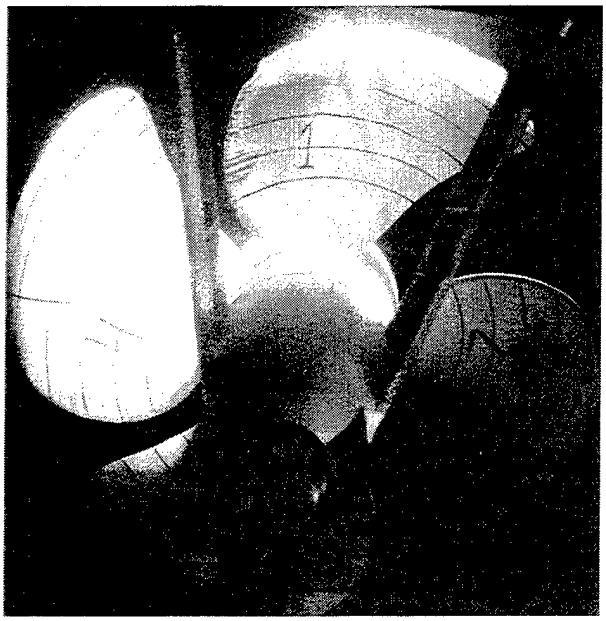


Figure 18: Cavitation Pattern on Propeller A-rake

the expected speed loss for the various propellers at maximum power is given in Fig. 20. This will be discussed below in more detail Again the

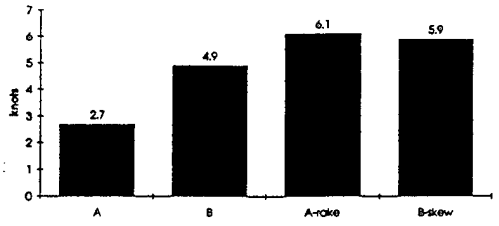


Figure 19: Increase of the Inception Speed

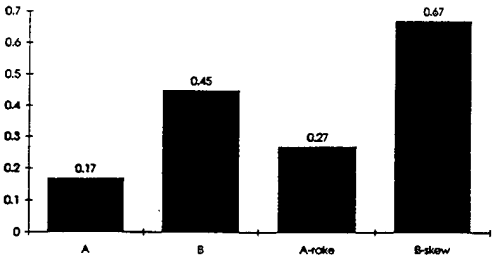


Figure 20: Speed Loss at Maximum Power

reference is the existing propeller. It was decided to make a final design and test it at full scale. Because the effects of rake were new and

unconfirmed, it was decided to design two final propellers, with the radial loading distribution as given in Fig. 2 for propeller D. These propellers were designed with optimized blade sections at 0.6R and 0.8R, so that the lowest point of the inception curve would coincide with the design point. One of the propellers was designed without rake and no skew and was designated propeller D. The other propeller was designed with a strong rake at the tip. To minimize the curvature at the tip the rake distribution was made more gradual at inner radii, as shown in Fig. 7. This propeller was designated propeller D-rake.

THE FINAL DESIGN

The inception diagrams of propeller D and propeller D-rakeis given in Fig. 21 and 22. The optimization of the blade sections at 0.6R and 0.8R proved to be sufficient to bring the lowest point of the bucket for sheet cavitation at the operating curve of the ship. This increased the margin against sheet cavitation. So in principle there is still room for further optimisation of the blade sections, by starting the design again with a higher estimated inception speed. This has not been done, however, because the effect of the tip vortex still determined the inception speed.

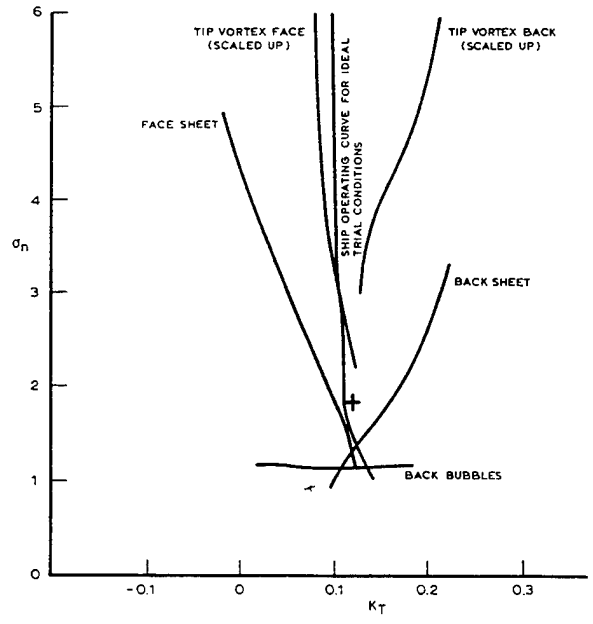


Figure 21: Inception Diagram of propeller D

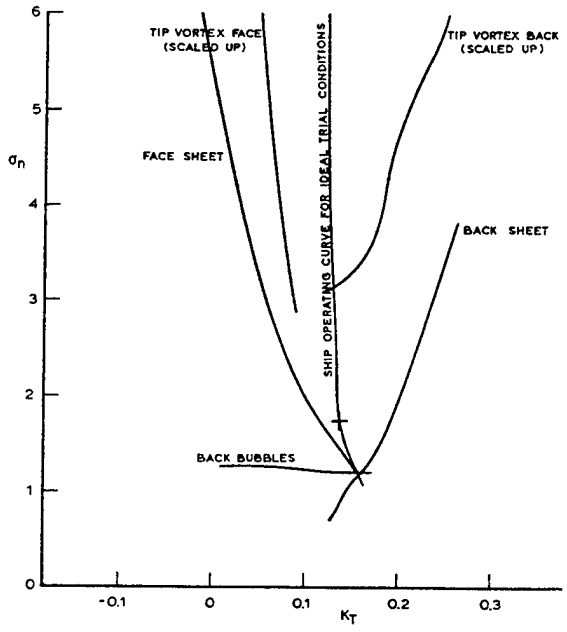


Figure 22: Inception Diagram of propeller D-rake

	D	D-rake
tip vortex	0.19	0.21
sheet	0.12	0.10

Table 3: Width of the Inception Bucket in Open Water Condition

The effect of the rake while maintaining the thickness perpendicular to the blade surface proved to be very effective for tip vortex inception. The additional thickness was only applied at radii larger than 0.9R. The depth of the inception curve of propeller D-rake is slightly higher than that of propeller D, but the width of the bucket is drastically increased (Fig. 22). The increase of the bucket width in open water conditions is given in Table 3. The open water conditions also showed an improvement of the bucket width of tip vortex cavitation. The improvement in behind condition is greater, however, so the main effect is due to a better response to the unsteady conditions. The raked tip can better handle inflow variations.

The cavitation patterns at full power for both final designs are given in Figs. 23 and 24. On propeller D the cavitation is mainly bubble cavitation on the downgoing blade, while there is some sheet cavitation behind the struts. On the raked

propeller D-rake there is slightly less bubble cavitation, but there is more sheet cavitation in the top position. This, however, is not an isolated sheet, which has its maximum extent at inner radii, but a sheet with its maximum extent at the tip. The exit of the sheet (see [2]) is therefore in the tip vortex or close to it and the risk of erosion is less.

EFFECTS ON PERFORMANCE

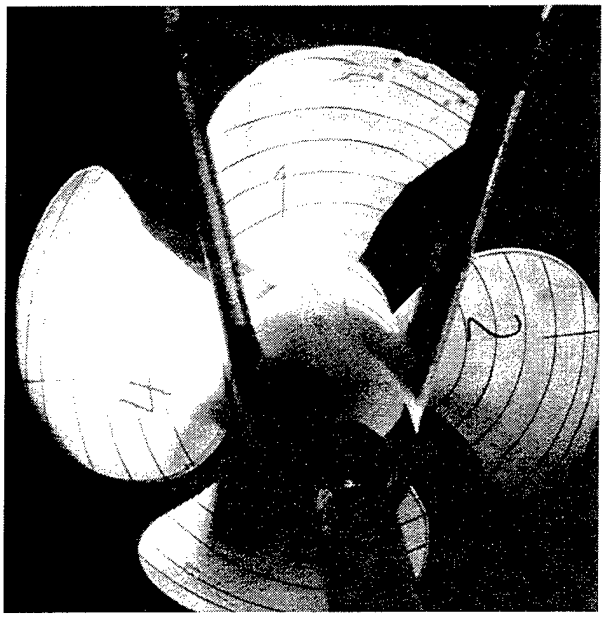


Figure 23: Cavitation Pattern on Propeller D

As has already been shown in Figs 19 and 20 the application of thicker blade sections has an effect on the propeller efficiency. This effect is difficult to measure at model scale because it is much smaller than the effects of laminar flow. The new blade sections have the minimum pressure at 80 percent of the chord and this strongly promotes laminar boundary layer flow. This effect has been countered by leading edge roughness. Due to the considerable amount of laminar flow on the propellers the effect of the leading edge roughness on the efficiency was also considerable. In Fig. 25 the effect of application of roughness on the efficiency in open water conditions is shown. At higher loadings ($J < 0.7$) the effect is negligible. At the design advance ratio of $J = 0.9$ the drop in efficiency can be as large as 7%. The effect of leading edge roughness increases rapidly when the propeller is unloaded further. Because of the strong gradient of the efficiency curve beyond the maximum efficiency these differences are not very

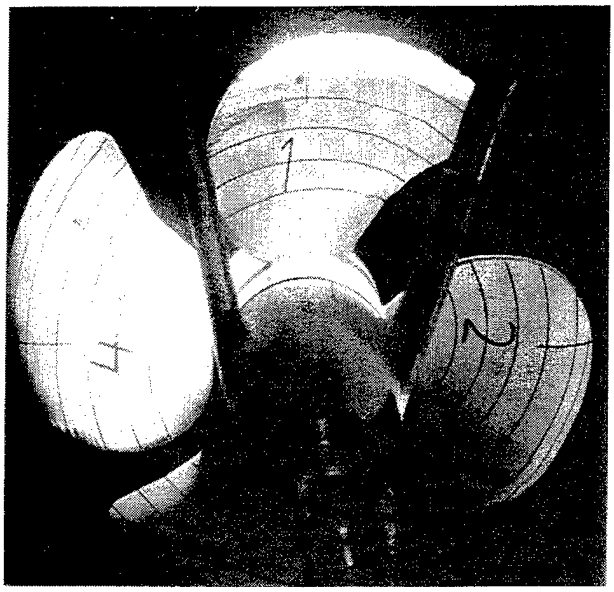


Figure 24: Cavitation Pattern on Propeller D-rake

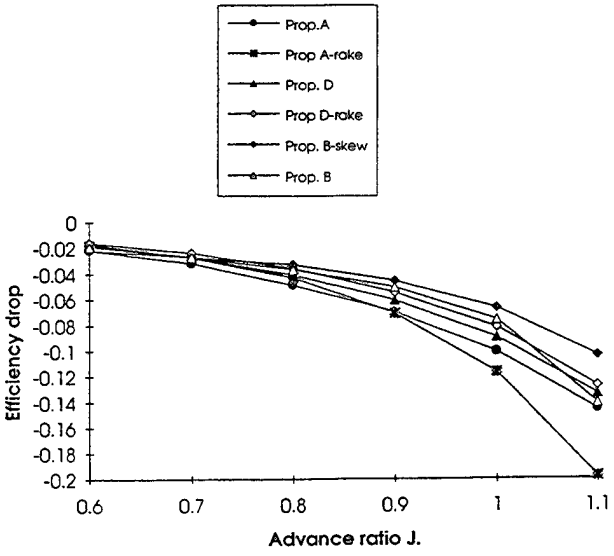


Figure 25: Drop in Open Water Efficiency due to Application of Leading Egde Roughness

accurate or relevant. In assessing the efficiency of the vrious designs the data with leading edge roughness have always been used.

The effect of skew on the open water efficiency is shown in Fig. 26 as $\eta(B_{skew}) - \eta(B)$. In this case with thick blade sections skew decreases the open water efficiency in the design condition (J=0.9) with 2.5(rough) to 3(smooth) percent.

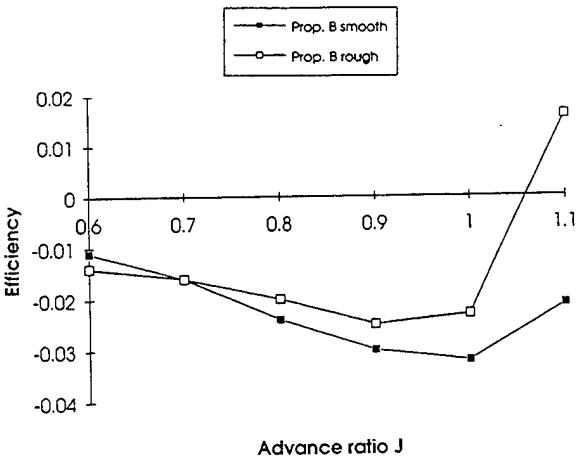


Figure 26: Increase of Open Water Efficiency Due to Skew

This is not uncommon for propellers with regular blade sections, so the blade sections do not change the effect of skew. Again the strong variation in efficiency above $J = 0.9$ has little meaning due to the strong gradient of the open water curve in that region.

The effect of rake on the open water efficiency is shown in Fig. 27. In the design condition the

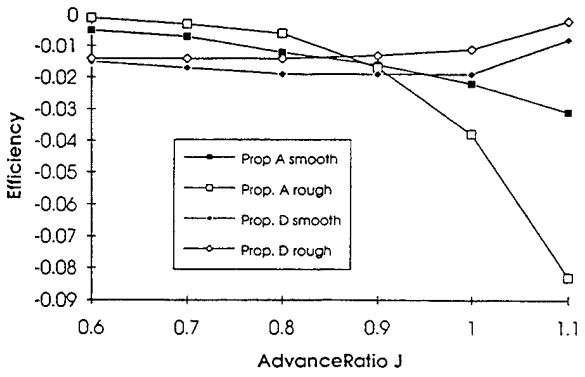


Figure 27: Increase of Open Water Efficiency Due to Rake

efficiency decreases approx. 1.5% due to the rake. This is the case for both the rough and the smooth propellers, so it has to do with the trailing vortex system and the losses of the wake. Propellers A and D show a different trend. The efficiency of propeller A decreases at higher loadings (lower J-values) due to the application of rake, while this effect is smaller or negligible for propeller D. The main difference between the two is the radial loading distribution. Propeller D has a slightly unloaded tip compared to propeller A. In this case the effect of rake on the efficiency increases with decreasing tip loading. If this is a general trend remains to be seen and the physical explanation is not yet clear either.

The effects on open water efficiency are also found in the propulsion test. A comparison of the maximum speed of the final designs together with the data of Fig. 20 is shown in Fig. 28. The

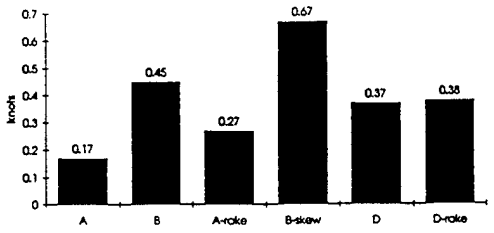


Figure 28: Speed Loss at Maximum Power

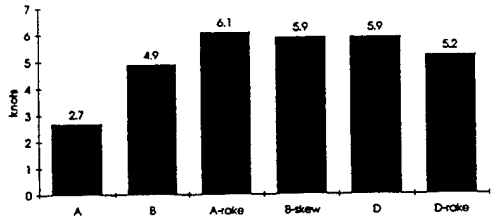


Figure 29: Increase of the Inception Speed

reference in this case is the existing propeller. So both final designs cause a decrease in maximum speed of 0.35 knots. The increase in inception speed, as shown in Fig. 29 is from 5.2 knots for propeller D-rake to 5.9 knots for propeller D. The latter number is rather sensitive to scaling effects and operational conditions, since the inception line of tip vortex face cavitation in Fig. 21 is almost parallel to the operating curve.

FULL SCALE VERIFICATION

Although the theoretical inception speed of Propeller D was higher than that of Propeller D-rake, it was decided to choose propeller D-rake for full scale verification. The difference in theoretical inception speed was considered to be less important than the increase in bucket width for

tip vortex cavitation, as found on propeller D-rake. So the blades according to propeller D-rake were manufactured and mounted on the existing hub, as shown in Fig. 30. Paint lines were drawn at 50, 70 and 90 percent of the radius and at 25,50 and 75 percent of the chord. Because the opening angle of the camera was small (15 degrees) each chord position and radial position was indicated with signs to facilitate orientation of the observations.

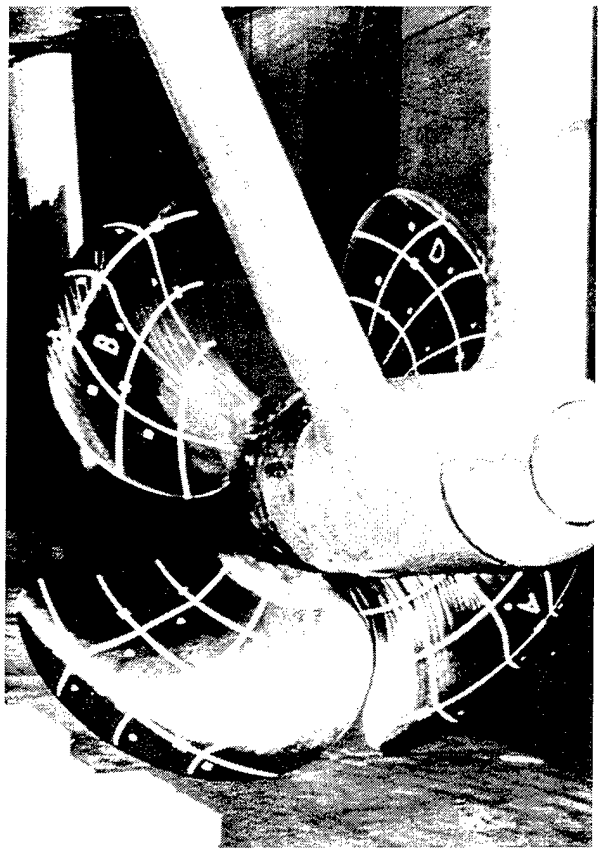


Figure 30: Propeller Blades according to Design D-rake mounted on the Ship

Trials were carried out to establish the effect on the maximum speed, while cavitation observations were made to determine the inception speed. The ship was also tested on the sound range, to determine the effect of the new propeller on the radiated noise level.

The cavitation observations were used to check also the pitch setting of the blades. This was done by observing a nonius on the hub of each blade. A discrepancy between the recorded pitch setting on board and the actual blade pitch was observed, which required a correction. The pitch setting was also checked by the measured power/rpm relation. Even when the pitch measurement, which is done by measuring the position of the yoke in the hub, is accurate, differences between the blades may occur. Although these differences are smaller than half a degree, their effect on the inception speed is not negligible. This seems to be a major source of inaccuracy for inception.

The Maximum Speed

The maximum speed with the new propeller at the measured mile was half a knot lower than predicted from the model tests. The main reason was that the draft of the ship was 0.25m larger than the design draft. In the same conditions the speed penalty of the new propeller was 0.5 knot, in agreement with the prediction from model tests.

Inception

Cavitation inception was observed using a camera with 300 times light amplification. This made it possible to use a moderate amount of stroboscopic light. The camera was mounted in a ball bearing, as shown in Fig. 31.The ball bearing was mounted directly in the hull. The bearing can be mounted by a diver using a dome, which can be bolted to the hull from outside. Illumination of the propeller was done with stroboscopic light, which was brought to similar ball bearing as used for the camera through fibers.

Detailed observations were made of inception. The type of cavitation occurring at inception is shown in Fig. 32. An idea of the size of the cavity streak can be obtained from the thickness of the paint line on the blade in this figure, which is 4 cm. The paint line indicates the 50 percent chordline at the tip.

It is important to note that inception took place at the blade surface. Although the location is in the expected tip vortex, the cavity has the appearance of a streak originating from the blade surface.

The measured inception speed could be compared to that of the existing propeller before modification. The prediction was that the new propeller would increase the inception speed with 5.2 knots (Fig. 29). The actual increase was between 4.5 and 5 knots, except for one blade. From the

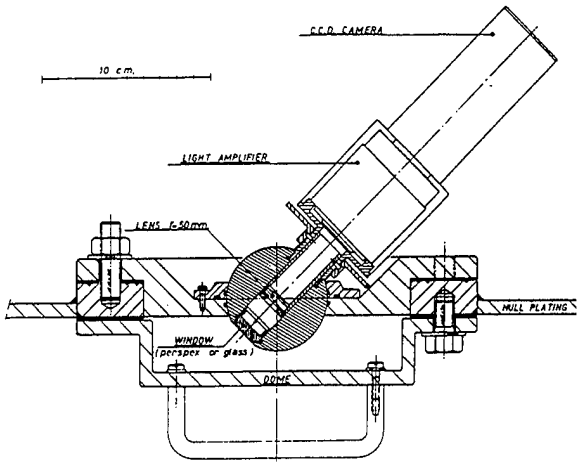


Figure 31: Camera in Ball Bearing



Figure 32: Inception of Cavitation at the Blade Tip

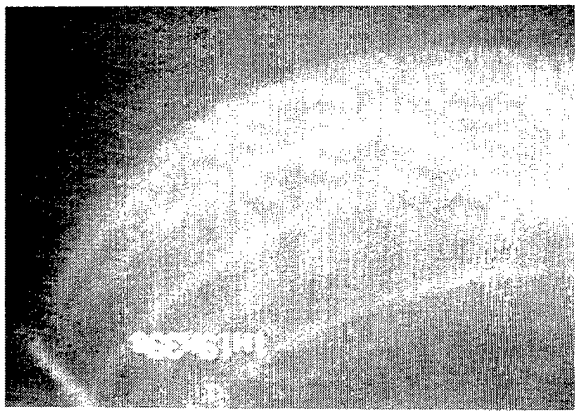


Figure 33: Observation of Sheet Cavitation

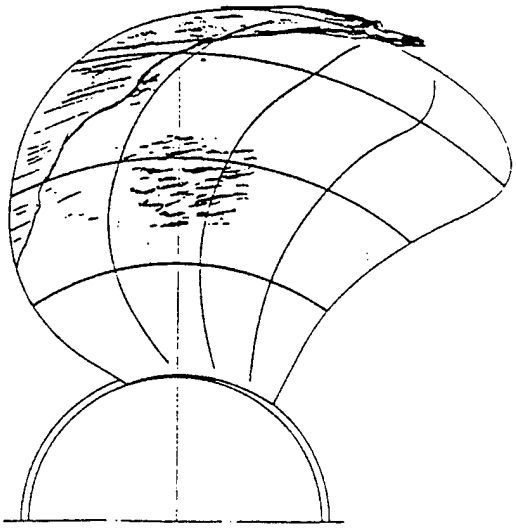


Figure 34: Composition of Full Scale Cavitation at 90 percent of the Maximum Speed

nonius on the hub it could be observed that this deviation was due to a difference in pitch setting.

Developed Cavitation

Observations of cavitation at full power were also made. An example of an observation of the inner side of the sheet cavity is shown in Fig. 33. Since the camera had only a small opening angle the cavitation picture had to be composed from a number of these observations. In general the observed cavitation was more extensive than indicated by Fig. 24. The cavitation extent as found at 90 percent of the maximum speed is shown in Fig. 34. The radial extent of the sheet was larger than at model scale, while distinct bubble cavitation occurred at midchord. During the growth and collaps of the cavity the cavitation was very unstable, resulting in rapid variations of the chordwise extent of the sheet.

The allowance of bubble cavitation at high speed increases the risk of erosion when the traditional criteria are maintained. However,after three months of operation, including some periods with high speed operations, no trace of erosion could yet be discovered. This period is too short, however, to draw conclusions.

Noise Radiation

The radiation of noise has been measured at

the same sound range for the existing propeller and for the new design. The gain in radiated noise by the new propeller is shown in Fig. 35. There was also a significant gain at lower speeds due to the fact that on the new design no pressure side cavitation occurred. This was especially advantageous when using a towed array. The high resistance of the thicker profiles against variations in angle of attack was advantageous in those conditions. The cavitation on the new design was less noisy than on the existing propeller, which may be an indication that the erosiveness is not excessive either.



Figure 35: Decrease of Noise Level (octave bands) of Propeller D relative to the Existing Propeller

CONCLUSIONS

The investigation described in this paper is highly experimental. That illustrates the lack of control of tip vortex cavitation in the design stage. Even the physical parameters involved are unclear: the cavitation at inception had the appearance of surface spots, which require no special scaling rules for extrapolation, but for the extrapolation from model to full scale a highly empirical correction method for inception of vortex cavitation was used. Either the type of inception at model scale is different from full scale or the minimum pressure on the blade surface has something to do with the tip vortex and its viscous scale effects. So although the correlation between prediction and full scale was good, this does not mean that the physical phenomena are properly understood.

The experience that a thicker blade tip increases the inception speed is confirmed when rake is applied. The cavitation bucket of the thicker blade tip of propeller D-rake was considerably wider than that of the thinner tip of propeller A-rake. The U-shape of the cavitation bucket of propeller D-rake may be related with the fact that the minimum pressure occurs on the blade surface and not in the core of a trailing vortex.

Skew also had a favorable effect on cavitation inception and this effect was similar to the effect of skew on a blade with conventional sections. It should be mentioned that due to the strongly reduced pitch at the tip the increase of the skew caused a skew induced rake at the tip. The blade tips of the skewed propeller were therefore raked forward behind the generator line. This was countered again by the application of extreme rake at the tip.The effects of skew were smaller than the effects of rake.

The application of extreme rake at the propeller tip is the main new element in this study, and the effects were surprising. Even when the blade thickness (perpendicular to the blade) was reduced, the effect of rake on inception was still favorable. This effect was also found in open water conditions. The explanation is still lacking. Preliminary calculations of the trailing vortex system have shown that extreme rake delays the roll-up of the tip vortex. If this can explain the increase of the inception speed in open water conditions remains to be investigated. Since inception occurs on the blade surface, viscous effects may also play a role, but these effects, in relation with the type of cavitation, also remain to be investigated.In a wake the effect of rake was larger than in open water, so part of the improvement of a raked tip is in the smaller sensitivity to inflow variations. A strongly raked tip can be seen as a faired tip plate, which is sometimes used to distribute the trailing vorticity at higly loaded tips. Such an effect may also occur at the raked tip.

When rake is applied in combination with thick blade tips the result was very favorable and this favorable behavior was confirmed at full scale. The design objective of maximum inception speed resulted in an increase of the inception speed of approx. 5 knots, with the penalty of a decrease of the maximum speed of 0.5 knots.

ACKNOWLEDGEMENTS

The project was carried out at Marin. Many design calculations were done by Dr. J.A.C. Fal-

cao de Campos, Mr. B.R.I. Luttmer and by Mr. J. auf dem Keller. The Royal Netherlands Navy, represented by Mr. Keizer, made available "Hr. Ms. de Ruyter" for full scale testing. The project was carried out as part of the NL/US Partial Agreement AFDEASR between the US Navy and Marin. The support of DTRC by Dr. Morgan and Mr. S.Hawkins was very important. Direct technical support was given by Dr. S.Jessup of DTRC. The progress of the three year project was monitored by Dr.E.N.Comstock and Captain W.R.Wheeler of Naval Sea Systems Command.

References

[1] G.Kuiper, S.Jessup, " A Propeller Design Method for Unsteady Conditions", SNAME Annual Meeting, New York, November 1993.

[2] G.Kuiper, 1994, "Cavitation and New Blade Sections", ASME Sympsium on Cavitation and Gas Liquid Flows in Machinery, Lake Tahoe, Nevada,USA, June 1994.

DISCUSSION

R. Arndt
St. Anthony Falls Hydraulic Laboratory, USA

I am curious about the relative amount of tip vortex and surface cavitation between model and full scale tests. Our work in a water tunnel indicates the relative amount of tip and surface cavitation is very sensitive to nuclei content.

AUTHOR'S REPLY

The critical condition of the full-scale propeller is the inception condition. In this condition only tip vortex inception is present, although the shape of the incipient cavitation is a cavity spot. Surface cavitation begins at a much higher speed.

The amount of surface cavitation was larger than found at model scale. No sharp distinction between sheet and bubble cavitation could be made, however, and at midchord indications are that the cavity was mainly bubble cavitation. Bubble cavitation is sensitive to the nuclei content, and it may be concluded that there were abundant nuclei present at full scale, as was expected. Apparently the nuclei content of the model test was (relatively) lower, although both electrolysis in front of the propeller and leading edge roughness at both sides of the tip were applied. However, inception of the tip vortex, scaled with the simple Reynolds power of 0.35, gave a reasonably accurate prediction of the full-scale performance. Since inception of tip vortex cavitation is sensitive to the nuclei content, it is suspected that this exponent contains an element of nuclei content.

DISCUSSION

W. Day
David Taylor Model Basin, USA

This paper presents a valuable comparison of design calculation, towing tank/cavitation tunnel experiments and full-scale trial observations. Could the author please comment on the following points:

1. Was any consideration given to the scaling of the inflow or wake to the propeller? Was there any conclusion from the full-scale trial performance concerning the necessity for such scaling?

2. Could the author comment on the success or failure of the scaling of tip vortex inception from the model to the full-scale particularly considering the very high slope of the inception curves. (see for example figures 11, 15, and 21)

3. Were any observations made of the change in flow patterns over the raked and the skewed blades? Could the author comment on any comparison between model and full-scale flows over these more complex blade surfaces?

The author has made a clear exposition of a systematic investigation through full-scale performance measurement and for his effort is to be congratulated.

AUTHOR'S REPLY

The propeller inflow used for the design of the propellers was the nominal inflow distribution. No efforts were made to scale the wake distribution. The good inception characteristics of the new designs indicate that the most important characteristics of the wake distribution are properly taken into account.

The mean wake fraction for the design was derived from the extrapolated full-scale thrust, so scale effects on the mean wake are taken into account in the design. In the extrapolation of the propulsion test data from model to full scale, the standard ITTC method for the extrapolation of the open water thrust and torque to full scale (dKt and dKq) could not be applied due to the presence of the leading edge roughness. On the smooth propellers the standard ITTC method could not be applied either due to excessive regions of laminar flow on the blades. New corrections for the open water thrust and torque coefficients were applied, based on earlier correlation with full scale. This topic needs further investigation.

The success of the scaling method applied for tip vortex inception can only be measured by the increase of the inception speed at full scale. The prediction of the inception speed with the simple power of the Reynolds number works remarkably well. The determination of the inception speed remains very sensitive, however, both at model and full scale. The steep slope of the inception lines is one of the reasons for that problem. The inception speed of propeller A (Fig. 15) can be very high, but the bucket is very narrow. In practice the inception speed will therefore be much lower, due to slight disturbances such as rudder actions, variations in draft, etc. The steepness

of the inception curves is no problem when the bucket is wide, as in the case with the final design (Propeller D-rake, Fig. 22). The bottom of the tip vortex bucket seems to be caused by surface cavitation on the thicker tip. The scaling law for vortices still has to be applied, however. So the structure of the flow field near the tip needs further clarification.

This applies also to the last question of Dr. Day. Observations of the flow pattern on the model propeller were made using the well known paint tests. However, these observations may reveal something about the boundary layer or about separation, but they do not show the structure of the flow field in a highly vortical region. At full scale only visual observations were made. Investigations of the effect of extreme rake on the position of the trailing vortices are presently being carried out. The most promising way to investigate the effects of rake and blade thickness on the tip flow seems application "Computational Fluid Dynamics." In that case Navier Stokes solvers have to be used. Even when the flow structure cannot yet be calculated realistically due to, e.g., the turbulence model, trends may be derived from such calculations, which can be verified experimentally.

DISCUSSION

W. Morgan
David Taylor Model Basin, USA

This is a very interesting paper and clearly shows the advantage of the advanced design methods. I have three questions.

1. Was the decrease in efficiency due more to the change in load distribution (decrease in load distribution toward the blade tip) than the change in rake and skew?

2. The improvements in cavitation and noise performance were significant compared to the initial propeller. Was the initial propeller (the propeller originally designed for the ship) considered a good propeller?

3. Explain some of the problems of using the "new" blade sections.

AUTHOR'S REPLY

The propellers A and A-rake had the same radial loading distribution. the reduction of the maximum speed with 0.1 knot, and thus the loss in efficiency (Fig. 28 of the paper), can thus be attributed to the rake. This is also the case for propellers D and D-rake, where the speed loss was insignificant. So the loss of efficiency due to rake was not consistent. Propeller D had a slightly reduced tip loading compared to propeller A, so the effect of rake may increase with increasing tip loading.

The speed loss due to skew between propellers B and B-skew was 0.22 knots. Again, the radial loading distributions are the same in both cases, so the effect is due to skew.

The radial loading distribution was input for the program PBD10, which calculated the propeller geometry. When these propeller geometries were calculated with a lifting surface code (ANPRO), the effects of skew and rake on the propeller efficiency were negligible. So the effect is not fully taken into account in the programs. Consequently it is not sure if the radial loading distribution was really the same with and without rake or skew. The effect of rake on efficiency may still be due to variations in radial loading distribution. The programs may also fail to account for the increased viscous sectional drag of the blade sections due to the increased blade area when rake is applied. This remains to be investigated.

The effect of rake and skew can be compared with the effect of a change in radial loading distribution by comparing propellers A, B, and D. Those are propellers without rake or skew, but with different radial loading distributions. The tip loading was decreased from propeller A to propeller D to propeller B. The unloading of the tip of Propeller B is extreme. A more common variation is that between propeller A and B. So the decrease of efficiency due to tip unloading in this case (0.21 knots) is comparable to the effect of skew and larger than the effect of rake. It is, however, dangerous to generalize these findings. The variations in the effects of rake illustrate this.

The existing propeller on the frigate, which was used as a reference, was not the first propeller on this ship. The first propeller was a propeller with traditional NACA type blade sections. The existing propeller is the second design, made ten years later, and it had blade sections based on YS920 profiles. These profiles have been designed for maximum bucket width using

the same Eppler code as used in this program. The existing propeller therefore was a good propeller, reflecting the state of the art of propeller design. This emphasizes the fact that application of new blade sections itself does not necessarily lead to large improvements. The existing propeller already had "new" blade sections, but these were not adapted to the incoming wake distribution. This is the essence of the new design method.

The main problem for the new blade sections was that at full power bubble cavitation was present. Since the rule of thumb is that this type of cavitation is erosive, this was a risk. Although no erosion was found yet at full scale, the time was too short to be sure that the cavitation was not erosive. There are, however, many indications that the reputation of bubble cavitation as being erosive is not fully justified. This remains to be investigated.

A new aspect of the new blade sections is the sensitivity of the cavity length to variations in inflow. The flat pressure distribution at inception causes an incipient cavity which is a thin long sheet over the whole chord. Small variations in inflow can create large variations in cavity length. This was indeed observed at full scale in specific conditions, where just beyond inception the variations in cavity length between subsequent revolutions were large. This is a variation per revolution, however, and not an unsteadiness during one blade passage. So this does not necessarily lead to cloud cavitation and erosion. the fact that the new propeller was more silent at all speeds indicates that no serious problems occur.

DISCUSSION

S. Kinnas
Massachusetts Institute of Technology, USA

A likely explanation of the delay of cavitation in the case of skewed or raked propeller (for the same thickness distribution) may be the increase in leading edge radius (normal to the leading edge line). It is a well known fact than leading edge radius delays and or reduces sheet cavitation. What are the author's comments on this?

AUTHOR'S REPLY

Skew increases the leading edge radius of the blade sections, when measured perpendicular to the leading edge. This may cause an additional delay of cavitation inception. This is generally not taken into account in programs, but it is also not clear if the leading edge radius should be measured perpendicular to the flow. The major effect of skew seems to be the formation of a leading edge vortex and a subsequent change in chordwise loading of the blade sections. This is not taken into account in lifting surface programs, in which the flow is assumed to remain attached to the propeller surface. Also the effect of skew on the wake structure remains to be investigated.

Contrary to skew, application of rake while maintaining the thickness in the traditional sense (in a cylindrical cross section of the blade) *decreases* the thickness perpendicular to the blade. So the increase of the inception speed due to rake cannot be due to a virtual increase of the leading edge thickness. Again the wake structure may be changed. But a plausible hypothesis is that the radial velocities in the tip region play a role. These velocities are neglected in linear theory.

Cavitation Performance Evaluation of Naval Surface Ship Propellers with Standard and Advanced Blade Sections

S. Jessup, W. Berberich, K. Remmers
(David Taylor Model Basin, USA)

ABSTRACT

Model and large scale cavitation performance evaluations have been performed for two propellers designed for a modern naval surface ship. The first propeller incorporated traditional blade sections, while the second incorporated new blade sections designed to increase cavitation inception speed. Model scale cavitation tests were conducted at the David Taylor Model Basin's, (CDNSWC), 36" Water Tunnel (36"WT) and Large Cavitation Channel (LCC). Large scale cavitation viewing tests were also performed. Cavitation inception and extent were compared to calculated predictions for the various types of cavitation: blade surface, root and tip vortex.

NOMENCLATURE

C	Chord length
C_p	Blade surface pressure coefficient $(p-p_0)/(1/2\rho V^2)$
C_{pmin}	minimum pressure coefficient
C_L	Blade section lift coefficient $L/(1/2\rho V_R^2 C)$
D	Propeller diameter
F	Maximum blade section camber
f	Local blade section camber
J	Advance coefficient $V/(nD)$
K_T	thrust coefficient, $T/\rho n^2 D^4$
p	fluid static pressure
p_V	fluid vapor pressure
R	Propeller tip radius
r	Propeller local radius
R_n	Propeller blade Reynolds number $V_R C/\nu$ @ 0.7R
T	blade section maximum thickness
V	Effective volume mean average axial velocity at propeller plane
V_R	section inflow velocity $(V^2+(2\pi nr)^2)^{1/2}$
$V_{R,1}$	First harmonic amplitude of radial velocity
$V_{T,1}$	First harmonic amplitude of tangential velocity
X	Distance from section leading edge along chordline
ΔC_p	C_p difference between upper and lower surface of blade section
Γ	blade section circulation
η	propeller efficiency
ρ	fluid density
σ	cavitation number $(p-p_V)/(1/2)\rho V^2$
σ_i	cavitation number at inception
σ_s	blade section cavitation index $(p-p_V)/(1/2)\rho V_R^2$
ν	Kinematic viscosity

INTRODUCTION

In recent years, numerous propeller design organizations have developed procedures to incorporate customized propeller blade sections to optimize propeller cavitation performance. Much of this work has been developed out of two-dimensional foil design procedures, such as work by Shen and Eppler (1). A process of adapting the two-dimensional foil geometry to the propeller geometry has been developed and experimentally evaluated by Bailar, Jessup, and Shen (2). Bailar et al. demonstrated cavitation inception gains using the new blade section design procedure for a limited experimental evaluation in the DTMB 36 inch Water Tunnel.

In this paper, a more complete evaluation of a standard and new blade section propeller geometry will be presented. The propeller design procedure will be summarized, and compared for the two designs. Model test evaluation will be presented utilizing the 36" Water Tunnel (36"WT) and the Navy's new Large Cavitation Channel (LCC). The quality of the propeller wake inflow simulation is critical in predicting the full-scale cavitation performance. The LCC provided the capability to install the entire wetted hull model within the 3.05 meter by 3.05 meter by 12.4 meter test section as discussed by Etter and Wilson (3). This potentially provides the best propeller inflow simulation.

The configuration evaluated is a twin screw surface ship with open shafting and shaft support struts. Figure 1 shows starboard side and stern profiles of the hull configuration.

In the LCC, an entire 11 meter long hull model was installed into the flat upper surface of the tunnel at the approximate water line. In the 36" WT the flow was simulated with inclined shafting with shaft barrel and support struts properly modeled. Propellers of 404 mm (15.9") diameter tested.

Evaluations discussed will include cavitation inception, and extent. Performance is compared between the two propellers for typical cavitation forms: root, blade surface, and tip vortex cavitation. Large scale trial data has been obtained for both standard and new section propellers. Both model and large scale results are compared with calculated predictions utilizing potential based panel methods.

DESCRIPTION OF PROPELLERS

The Controllable, Reversible Pitch (CRP) propellers are characterized by relatively large hubs (0.3R), and blade chord limits due to the requirement of blade passage during pitch reversal for backing. Also, balanced skew is incorporated to maintain a favorable blade spindle axis moment. The blade outlines for the two propellers tested are shown in Figure 2.

Two Dimensional Blade Section Design

Traditionally, marine propellers have been designed incorporating blade section shapes from standard families, for example the NACA 66 and 16 thickness forms and the a=0.8 meanline camber form. The section thickness and camber are scaled appropriately using modern lifting line and lifting surface design procedures. This approach is somewhat restrictive since the blade pressure distribution will generally retain similarity to the original two dimensional profile.

In recent years procedures have been developed to design blade section shapes for arbitrary specified blade pressure distributions (2) from custom designed two dimensional foil sections using the procedure of Shen and Eppler (1). In the present study, these procedures were used to design an alternative propeller to a standard propeller design utilizing NACA 66 (DTMB mod.) thickness and a=0.8 meanline forms.

The design procedure starts with the calculation of the blade section operating conditions in the specified propeller inflow wake field, section loading and propeller submergence depth. This is compared against the cavitation bucket diagram for a particular 2-D foil geometry, as shown in Figure 3. The section lift coefficient, C_L, and section cavitation index, σ_S, are calculated for various positions around the propeller disk (4), in this case for cruise and maximum speed. The propulsion characteristics for this hull result in a significant increase in blade section loading (section angle of attack) with increasing speed from cruise to full power conditions.

New foil sections were designed to improve the cavitation bucket for the standard section propeller; to increase the noncavitating region inside the bucket about the specified operating range of the blade sections. Shown in Figure 3 is the standard propeller bucket and a bucket for a newly designed section using the Shen and Eppler approach. The new foil section incorporated reduced thickness, significant aft section loading, and leading edge unloading relative to the standard section. Figure 4 shows the two dimensional foil shapes for comparison. The new section foil has significant

comparison. The new section foil has significant camber near the trailing edge which shows a characteristic hook or cupping. Figure 5 shows the calculated pressure distribution at the design lift coefficient at cruise speed. Clearly seen is the leading edge unloading and the trailing edge loading of the new section relative to the standard. This characteristic results in an avoidance of an upper surface suction peak as the angle of attack increases with increasing speed.

Incorporation of Two Dimensional Sections into Propeller Geometry

The new designed section shapes are incorporated in propeller geometry using propeller lifting surface design procedures. For this case, nine sections were independently designed for various radii across the blade span. From the two-dimensional pressure distributions calculated at the design lift coefficients, the chordwise loading is calculated, as the Cp difference between the upper and lower surface. A sample loading distribution is shown in Figure 6 for various propeller radii. Also shown is a standard 0.8 meanline loading distribution. The loading distribution provides input to the lifting surface design procedure, PBD-10 of Greeley and Kerwin (5). The two dimensional thickness distribution of the various radial sections is input into PBD-10, and is incorporated directly into the propeller geometry. PBD-10 calculates the blade pitch and camber distribution to produce the specified input loading distribution. The final three-dimensional camber distributions vary significantly from the two-dimensional camber, as shown in Figure 7.

A verification of the design process can be made by comparing the two-dimensional blade section pressure distributions with those calculated for the actual propeller geometry at the design condition using a potential-based panel method (6,7). Figure 8 shows this comparison for the new section propeller at 0.5R. Generally, correlation is best mid-span on the blade, and is not as good at the root and tip region due to three dimensional effects.

CHARACTER OF THE WAKE

The propeller inflow nonuniformity is due primarily to the wake of the shaft and struts and the flow inclination relative to the shaft axis. A wake survey was conducted on a 23 foot hull model in the DTMB tow tank run at 5.6 knots using five hole pitot tubes positioned at the propeller disk (without the propeller). Figure 9 shows the cross plane vectors and the axial velocity contours relative the the propeller shaft axis. The dominant upwash due to the inclination of the flow relative to the propeller axis can be seen. Also, the upwash near the hub is augmented by the transverse flow around the propeller hub. The axial velocity contours show the wake due to the shaft and shaft barrel and the struts. The outboard strut wake is visible while the inboard strut is masked by the shaft wake. The hull boundary layer is only slightly visible at the propeller tip. The majority of the propeller disk is in undisturbed flow. Complications associated with propeller-hull interaction, wake scaling, and blade operation in viscous regions is minimal compared to propeller operation in a typical merchant ship hull wake.

MODEL TEST EVALUATIONS

In the Large Cavitation Channel (LCC) 11 meter hull model was mounted into the tunnel test section top. A flat ground board was fit around the hull model flush with the test section ceiling, positioning the hull at the cruise speed trim and pitch. Stern view of the installation is shown in Figure 10A. Pitot tube wake surveys were conducted at the propeller plane for a number of conditions, and compared to the tow tank surveys. As reported by Jessup et al. (9) the wake surveys conducted in the LCC configuration were closer to the tow tank results when the hull bilge keels were removed. Also surveys showed some improvement in the wake simulation over the idealized configuration simulating the shaft inclination, shaft barrel and struts in DTMB's 36"WT shown in Figure 10B.

Cavitation performance was measured and compared for the two propellers. The types of cavitation observed were root, tip vortex and blade surface. Most forms of cavitation incepted within a range of cavitation numbers, $\sigma = 1$ to $\sigma = 2$ corresponding to medium, cruise speed. To simulate the propeller operating conditions, the tunnel pressure and velocity were set to establish the specified cavitation index, σ, where

$$\sigma = (p - p_V) / (1/2)\, \rho\, V^2$$

p = pressure at propeller shaft
V = velocity at the propeller plane
p_V = vapor pressure
ρ = fluid density

Also, the propeller loading was simulated by setting the propeller rotation speed, n, to match the specified thrust loading, at the advance coefficient,

$$J = V/(nD).$$

where, D = propeller diameter
n = rotation rate, rps

Inception was determined visually by varying rotational speed (J at constant σ) and observing the inception of the various types of cavitation. Inception was called when cavitation was observed on a three of the five blades. Tests were performed at a Reynolds number around $R_n = 4 \times 10^6$, based on blade inflow velocity and chord at 0.7 radius. Observations of cavitation extent were performed by setting the specified σ and J for various hull speeds.

LARGE SCALE EVALUATIONS

Large scale tests were conducted with both the standard blade section and new section propellers. Propeller operation was viewed through ports installed in the hull above the port side propeller. Video was used to record observations using strobe illumination at night and available light during the day. Inception observations were made visually with increasing hull speed, called when cavitation was observed on any of the five blades. The large scale propeller Reynolds number was approximately 5×10^7.

A remote camera was also used providing a wide field of view outside the hull. The camera housing with a hemispherical viewing window was extended about 150mm below the hull. Pan and tilt control of the lens head permitted viewing along the hull at the starboard propeller, struts and rudders.

The overall uncertainty in the observed cavitation inception and extent was significantly larger that was typical from model tests. The primary factors were test condition variability and the limited viewing of the entire propeller disk. Only the upper half of the propeller disk was observable. View of the lower half of the disk was blocked by the propeller hub, the nearby blades and the lack of illumination. Therefore cavitation inception was biased by observations that could be made only within the upper part of the propeller disk. These limitations were the same for both propeller evaluations, such that relative comparisons were more accurate than the absolute inception indices. Some observations could be made of the starboard propeller during daylight viewing.

Variability in trial conditions produced precision and bias errors also influencing the comparisons of the two propellers. The sea conditions for the standard propeller were ideal with calm seas and no wind, while the new section propeller tests were conducted in a sea state 2 with 30 knot winds at a 4% heavier displacement. Only the effect of displacement was quantifiable.

Finally, the cavitation inception precision was dependent on the number of the incrementally increasing speed runs performed. At best, 1 knot increments were typical.

PREDICTION OF CAVITATION INCEPTION AND EXTENT USING PANEL METHOD

Cavitation inception predictions were performed using potential based panel methods. A quasi-steady simulation of the unsteady flow was performed using the steady panel method, PSF10 of Kerwin et. al. (6). A fully unsteady panel calculation was performed using PUF10 developed by Kinnas and Hsin (7). For both calculations, blades were paneled with a 25 cosine spaced chordwise by 30 uniformly spaced spanwise distribution for each side of the blade. The hub was approximated as cylindrical with a parabolic shaped fairwater represented by 64 panels. The cavitation inception index, σ_i, was determined from C_{pmin}, the minimum pressure at various specified regions of the blade. Thus assuming cavitation occurs when vapor pressure, p_v, is reached, so that,

$$\sigma_i = -C_{pmin}$$

The quasi-steady calculations were performed by inputting, from wake survey data, circumferential average tangential inflow equivalent to the first harmonic amplitude of the tangential velocity as shown in Figure 11. To simulate the maximum loading condition, tangential velocity opposite to the direction of propeller rotation was used. To simulate the minimum loading condition, tangential velocity in the direction of prop rotation was input. The unsteady calculation was performed by inputting the measured tow tank wake. The quasi-steady approach was used during the propeller design phase to optimize the spanwise variation in cavitation performance and demonstrate the relative performance difference between the standard and new section propellers.

An initial comparison of the calculated pressure distributions for the unsteady and quasi-steady methods were described by Jessup (8). Inception of suction side midspan cavitation correlated well with the two methods. At the minimum loading condition, the two methods show significant differences at the leading edge. This discrepancy was thought to be due to the more accurate representation of the wake in the unsteady method. The quasi-steady approach considers only the wake due to the shaft inclination. No attempt is made to represent the strut wake, therefore, the quasi-steady approach can not accurately predict inception that occurs behind the struts. Because of the long computation times of the unsteady method, and previous extensive use of the quasisteady method all calculations shown in this paper were performed with the quasi-steady method.

Investigations of tip and outer span cavitation performance have demonstrated possible inaccuracies with the panel method. Calculated average spanwise circulation distributions for the two propellers, when compared to the original design circulations, showed a large underprediction at the outer span of the standard propeller as shown in Figure 12. Figure 13 shows comparisons of the 2-D section pressure distributions and the calculated distributions using the panel method. At the inner radius, 0.5R, the distributions are similar with some decrease in pressure around 0.7C that has been attributed to the CRP blade shape and hub effects by Yang (9). At 0.8R the distributions deviate significantly at the trailing edge. The negative loading is believed to be due to effects of the skewed shape of the blade panels at the trailing edge. The panel shape is controlled by the sweep of the trailing edge which is most pronounced with the standard propeller as shown in Figure 2. Table 1 shows a comparison of the calculated and measured open water load performance for the two propellers. The standard propeller shows a consistent underprediction in propeller thrust.

PROP	K_T MEAS.	K_T CALC.	η MEAS	η CALC
STD.	0.231	0.216	0.734	0.711
NEW	0.233	0.227	0.738	0.711

TABLE 1 OPEN WATER PERFORMANCE, J=1.27

Surface representations of the blade pressure distributions are shown in Figure 14. The suction side pressure surface is shown at the maximum loading condition for the standard and new propellers at J=1.210 and J=1.225. The standard propeller produces a relatively smooth pressure surface, because of its incorporation of one section shape. The new propeller surface appears "lumpy" because of difficulties fairing the blade geometry produced from the nine individually designed sections.

The standard propeller has extreme suction peaks at the leading and trailing edge at the tip. These are believed to be unrepresentative of the real flow and may be due to the more extreme tip geometry of the standard propeller and related to the trailing edge flow problems discussed in the previous section. The standard propeller has a midspan suction peak along the leading edge, which, near the tip, becomes very extreme. The new section propeller also has a suction peak at the tip, but it is located midchord, and is less extreme.

Also it has been well recognized that the panel methods are presently unable to accurately calculate the flow in the tip region. Work by Kinnas (10) and Hsin (11) has begun to more accurately address the tip flow, but present blade paneling methods appear to fail outboard of the 0.95 to 0.98 radius. The most accurate region for panel calculations appears to be from the hub to 0.95 radius or where the blade sweep is not too extreme.

From these observations it is assumed that there is some uncertainty in the panel method prediction techniques. Although the trailing edge flow is not directly relevant to minimum pressures associated with cavitation inception, the trailing edge flow has some effect on the leading edge stagnation flow and possibly the magnitude of calculated leading edge suction peaks.

Accuracy at the root is somewhat dependent on the proper representation of the hub. An idealized cylindrical hub model was used to represent the hub shown in Figure 2. The effect of this idealization along with the effect of structural fillets is assumed small. Complete paneling of the exact geometry would help quantify their importance.

BLADE SURFACE CAVITATION INCEPTION

The most significant gain in cavitation performance of the new section propeller over the standard propeller was in the inception of blade surface suction side leading edge (SSLE) cavitation. This was expected from the new section design approach described earlier. Figure 15 shows the inception results for SSLE cavitation. The operating

curve of the propellers are represented by relating σ, the cavitation index, with propeller advance coefficient, J. The inception of suction side leading edge cavitation occurs for both propellers in the wake of the outboard strut around 0.6 radius. The SSLE cavitation on the new section propeller incepts at a significantly lower σ_i than the standard propeller at both model and large scale. The large scale inception of blade surface leading edge cavitation for the standard propeller occurred at σ_i somewhat lower that the model test results, again, occurring behind the outboard strut. This could imply that the large scale strut wake deficit is less due to increased Reynolds number.

For each large scale propeller evaluation, the two spots shown indicate, at the higher σ_i, the condition where cavitation was not observed, while the lower value corresponds to the next test condition where cavitation was visible. This represents an estimate of the upper and lower bounds inception, which qualitatively includes effects of hindered visibility at large scale.

Also compared are predictions of leading edge cavitation using the quasi-steady panel method at the maximum load condition. For both propellers the calculated slopes of the inception curves match the model result well. For both propellers, the panel method predicts SSLE cavitation at a σ_i about 0.1 lower than model scale results. Both model results and predictions fall within the upper and lower bounds of the full scale results, except for the model scale standard propeller result. Also shown is the predicted inception of midchord cavitation on the new section propeller at around 0.75 radius.

Pressure side cavitation, in all cases, occurred well outside the operating range of the propellers and was not observed at large scale. Figure 16 shows pressure side leading edge (PSLE) cavitation inception. The new section propeller is closer to the operating curve at lower cavitation numbers, as would be expected, since some sacrifice in pressure side performance was allowed as shown in Figure 3. Pressure side cavitation occurred near the blade tip when passing between the inboard strut and the top of the disk. The panel method at the minimum loading condition predicts PSLE inception index consistently higher than model results and thus would provide a conservative estimate of pressure side performance.

ROOT CAVITATION INCEPTION

From model test results, root cavitation inception performance for the two propellers was similar. The new section design only slightly improved the root performance, which is primarily controlled by blade thickness and propeller planform near the root. Figure 17 shows the comparison of the suction side root cavitation (SSRT) performance. The model test results were very similar for the two propellers and are shown as one curve. The panel method predictions also showed similar results, but the large scale results were quite different.

It is thought that the standard propeller's large scale performance was controlled by modifications that were made to the leading edge root area. The new propeller may have performed better at large scale than predicted because of the unloading of the root section due to a significant gap between the root trailing edge and the hub. This tendency was demonstrated by calculating the maximum load condition with no hub modeled. The SSRT minimum pressure was improved similarly to large scale. Modeling the as-built blade root gap accurately is beyond present capability.

Figure 18 shows the pressure side root cavitation performance comparison with mixed correlation. The two propellers performed similarly, but the model and large scale results were quite different. The two propellers were predicted to perform differently. The pressure side cavitation generally initiated at the leading edge of the root section, and was therefore sensitive to variations in leading edge root details and the root loading effected by the root-hub gap on the new propeller. This region of the blade is very difficult to numerically model and manufacture and may also explain the variation seen in the comparison.

TIP VORTEX CAVITATION INCEPTION

Model scale, suction side tip vortex (SSTV) cavitation was improved with the new section propeller. Improvements were attributed to tip and near tip new blade section geometry and tip pitch. Reynolds Number scaling was performed using the method of McCormick (12). A Reynolds Number scaling exponent of 0.4 was used with results shown in Figure 19. large scale results showed less improvement and higher σ for both propellers.

A number of factors may help to explain these results. Large scale determination of inception was performed acoustically detecting initially one blade

and later multiple blades. Uncertainty was increased with two propellers operating and the possibility of other cavitation sources being heard. It is believed that acoustic detection results in an upper bound on the actual σ_i.

Model scale determination of inception unfortunately had to be observed visually. This was because of the existence of other cavitation forms. At model scale, the procedure is to call inception when it is observed on a majority of blades. This may result in a σ_i closer to a lower bound of the actual value. A proper correlation between the two methods has not yet been developed.

In both the 36" WT and the LCC the tip vortex incepted at the bottom of the disk. This location does not seem reasonable, since the maximum blade loading occurs when the blade is at the outboard side of the disk advancing downward. As seen in Figure 9, there is no apparent wake perturbation at the bottom of the disk that would cause increased blade loading resulting in SSTV cavitation.

Until the most recent large scale tests with the new propeller, large scale visual observations of tip vortex inception occurred at much lower σ near the top of the propeller disk. That implied very little or no scaling required and was contrary to model tests. During the last trials conducted, careful observations of the starboard propeller with the remote camera revealed tip vortex at the bottom of the disk at relatively high σ_i, which correlated approximately with acoustic detection.

Using the prediction tools, some attempt was made to explain the inception index and its location at the bottom of the disk. From the panel method calculations C_{pmin} at the tip was correlated with the model and full scale test results. For the standard propeller the leading edge peaks shown in Figure 14A produced C_{pmin} values greater than ten with an unreasonable variation with J. The midchord suction peaks shown for the new propeller in Figure 14B were plotted verses J in Figure 20. The three conditions shown are the maximum loading condition, where the positive distribution of tangential velocity was included with the axial inflow, the average condition, where, V_T=0, and a condition simulating the lower part of the disk flow where the radial inward velocity distribution shown in Figure 21 was included with the axial inflow. The results show very reasonable trends, matching the slope of the model test result. The maximum loading condition shows the largest σ, followed by the radial and uniform inflow cases. For the new propeller, the seemingly unreasonable pressure at the tip may have significance for predicting inception, perhaps at least for relative comparisons. The poor correlation with the standard propeller appears related to its specific tip geometry producing extreme leading and trailing edge pressures.

CAVITATION EXTENT

Qualitative comparisons of cavitation extent were made for the two propellers at high speed when cavitation was more fully developed. Figure 22 shows the panel method computations for the maximum loading condition of the two propellers. The horizontal axis of the surface plots is set to the operating σ of 1.32 so that any surface pressure above the axis would expect to produce cavitation.

Figure 23 shows the model and large scale comparison of the standard propeller at σ= 1.32. Extensive cavitation from the 0.6 radius to the root is shown to be similar model and large scale. The panel method calculation shows a similar area where cavitation is estimated to occur. The outboard leading edge suction peak from the panel calculation does not occur either at model or at large scale, implicating further a breakdown of the computation method in this region on the standard section propeller.

The new propeller, shown in Figure 24, at model scale shows no cavitation except at the root and tip. The panel calculation in Figure 22, shows a slight extent of leading edge cavitation which is also observed full scale. But also, at large scale, some midchord bubble cavitation can be seen.

At a slightly lower σ= 1.21, Figure 25 shows the model and large scale cavitation extent. At model scale, blade surface cavitation can be seen as long streaks of cavitation which appear very thin at the leading edge. This is consistent with the flat pressure distribution intended in the design . The extent of the cavity is similar to the large scale shown in Figure 25B, but a distinct leading edge sheet is observed which appears to lap over the bubble cavitation occurring downstream of the leading edge. At large scale, as σ was reduced further, the leading edge sheet became longer, eventually extending to the trailing edge, but always remaining narrow in spanwise extent at the cavity trailing edge. There appears to be scaling effects controlling the formation of leading edge cavitation on the new propeller. The chordwise pressure gradients are very small, but at large scale, if even a slight suction peak occurs, then a typical sheet cavity is formed, which appears as streak cavitation at model scale. The

dynamics of large scale cavities may be influencing cavity development.

The panel method calculation shown in Figure 26 begins to also show the occurrence of midchord cavitation starting at 0.7 radius which is consistent with its initiation at large scale, but starting at σ lower than large scale observations by 0.15.

THRUST BREAKDOWN

Thrust breakdown experiments were performed during model scale tests to determine performance lost due to cavitation. The propellers were run up through the operating range to full power, initially at high tunnel pressure to suppress cavitation, noting the measured thrust, torque and tunnel velocity. The conditions were repeated at the specified ambient pressure, noting again the measured thrust and torque with cavitation. Finally the propeller rotation speed was increased to regain the thrust lost under cavitating conditions. From these results, the loss in maximum speed could be determined.

	Thrust lost @ max. power	model scale max speed	large scale max speed
Standard	10%	----	----
new	4%	+0.5 kts	+0.25kts

TABLE 2 THRUST BREAKDOWN RESULTS

Table 2 shows the thrust lost under cavitating conditions for the standard and new section propellers at maximum power. The reduction in cavitation extent at high speed reduced the amount of thrust lost for the new section propeller. The model scale improvement in thrust breakdown with the new section propeller resulted in a 0.5 knot increase in maximum speed over the standard propeller. At large scale, the gain in maximum speed with the new propeller was 0.25 knots. This improvement is believed to be a lower bound due to the adverse trial conditions for the new section propeller.

CONCLUSIONS

Incorporation of new blade sections into Naval surface ship propellers can significantly improve cavitation free operation and reduce thrust breakdown. The suppression of root cavitation on CRP propellers is limited due to the severe geometric restrictions at the root area.

Potential based panel methods have demonstrated usefulness in predicting propeller cavitation inception. Accuracy is sufficient for comparative calculations. The prediction of tip vortex cavitation inception has shown promise, but accuracy appears geometry dependent.

The discrepancies in model and large scale tip vortex cavitation inception are believed to be due to visual versus audible detection processes. A recalibration of McCormick's scaling law could simply be adopted. Further understanding of the inception occurrence at the bottom of the disk may lead to a more rational approach to the scaling issue.

ACKNOWLEDGMENTS

This work was sponsored by the Chief of Naval Operations (OP-035), with management participation by the Office of Naval Research (ONR) and the Naval Sea Systems Command (Code 03X7). The authors would like to thank Mr. James Bailar and Ms. Han-Ch'ing Wang for performing the numerous panel method calculations incorporated in this paper.

REFERENCES

1. Shen, Y.T. and Eppler, R., "Wing Sections for Hydrofoils - Part II: Nonsymmetrical Profiles, Journal of Ship Research, Vol. 25, No.3, 1981.

2. Bailar, J. , Jessup, S. and Shen, Y., "Improvement of Surface Ship Propeller Cavitation Performance Using Advanced Blade Sections," 23rd ATTC Conference, New Orleans, LA, 1992.

3. Etter, R. and Wilson, M., "The Large Cavitation Channel," 23rd ATTC Conference, New Orleans, LA, 1992.

4. Rader, H.P., "Cavitation Phenomena in Non-uniform Flows," Appendix II of the Cavitation Committee Report, Proceedings, 12th ITTC Conference, 1969.

5. Greeley, D.S. and Kerwin, J.E., "Numerical Methods for Propeller Design and Analysis in Steady Flow,"Transactions SNAME, Vol. 90, 1982.

6. Kerwin, J.E., et. al.," A Surface Panel Method for the Hydrodynamic Analysis of Ducted Propellers," Transactions SNAME, Vol 95, 1987.

7. Kinnas, S.A. and Hsin, C.-Y., "Boundary Element Method for the Analysis of the Unsteady Flow

Around Extreme Propeller Geometries," AIAA Journal, Vol. 30, No. 3, 1992.

8. Jessup, S.D., Remmers, K.D. and Berberich, W.G., "Comparative Cavitation Evaluation of a Naval Surface Ship Propeller," ASME International Symposium on Cavitation Inception, FED-Vol. 17710, 1993.

9. Yang, C.I. and S.D. Jessup," Benchmark Analysis of a Series of Propellers with a Panel Method," 1988 SNAME Propeller Symposium, Virginia Beach, Virginia, 1988.

10. Kinnas, S.A., Pyo, S., Hsin, C.-Y. and Kerwin, J.E. , "Numerical Modeling of Propeller Tip FLows," Sixth International Conference on Numerical Ship Hydrodynamics, Iowa City, Iowa, 1993.

11. Hsin, C-Y., Kerwin, J.E. and S.A. Kinnas, "A Panel Method for the Analysis of the flow Around Highly Skewed Propellers," Propeller/Shafting '91 Symposium, Virginia Beach, Virginia, 1991.

12. McCormick, B.W., "On Cavitation Produced By a Vortex Trailing From a Lifting Surface, " ASME Journal of Basic Engineering, 1962.

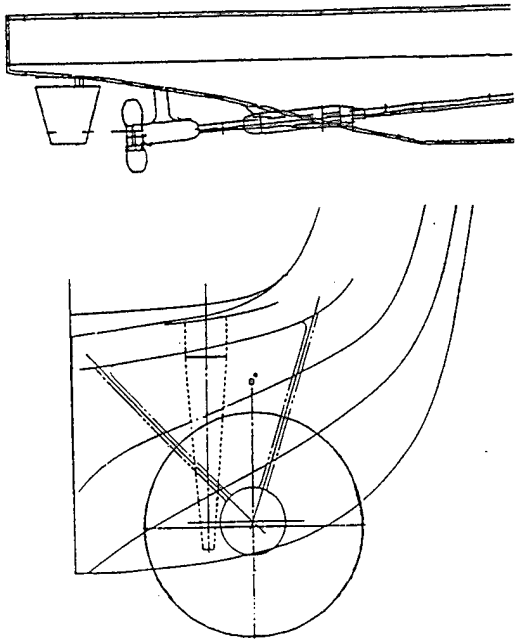


FIG. 1 HULL CONFIGURATION

FIG. 2 BLADE OUTLINES OF THE STANDARD AND NEW BLADE SECTION PROPELLERS

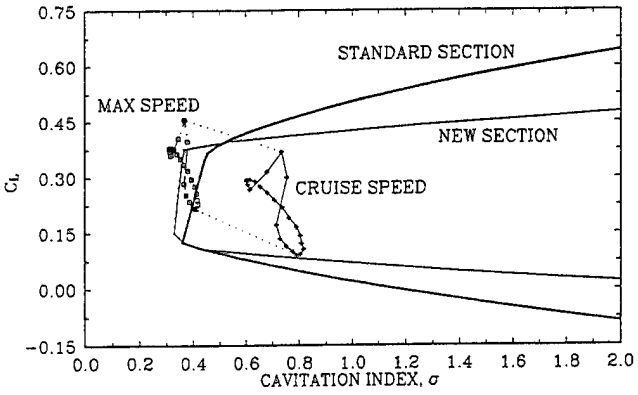


FIG. 3 BLADE SECTION OPERATING POINTS AND CAVITATION BUCKETS

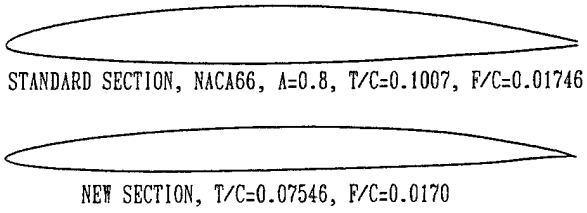


FIG. 4 TWO DIMENSIONAL FOIL SECTIONS

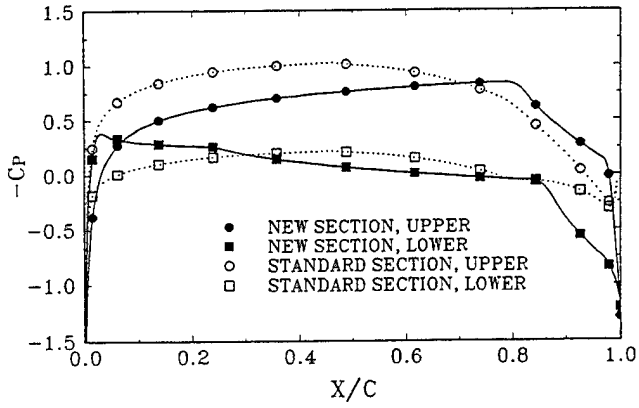


FIG. 5 TWO DIMENSIONAL SECTION PRESSURE DISTRIBUTIONS

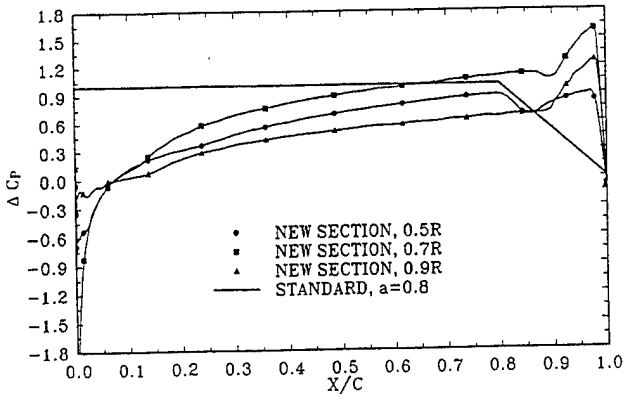


FIG. 6 CHORDWISE LOADING DISTRIBUTIONS

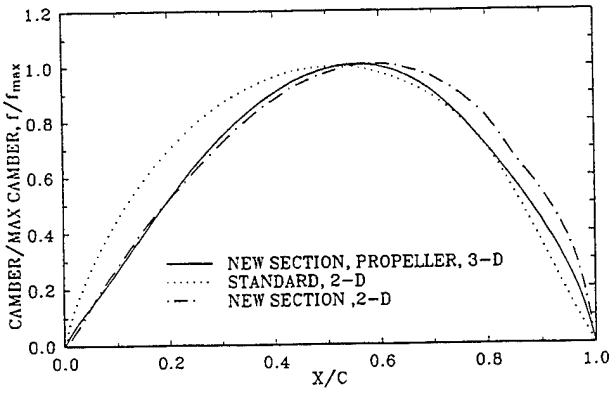


FIG. 7 CAMBER DISTRIBUTIONS

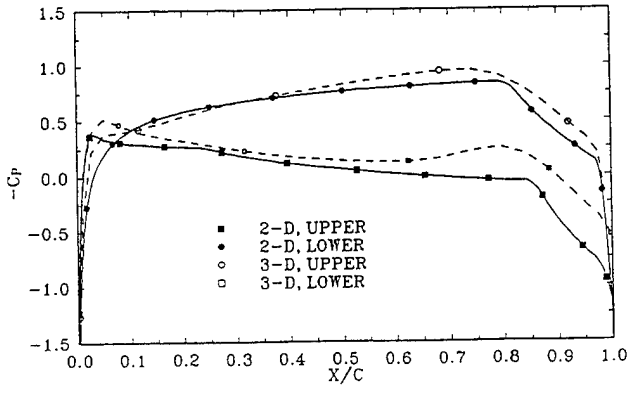


FIG. 8 2-D FOIL AND 3-D PROPELLER SECTION PRESSURE DISTRIBUTIONS

FIG. 9 NOMINAL WAKE SURVEY MEASURED IN TOW TANK

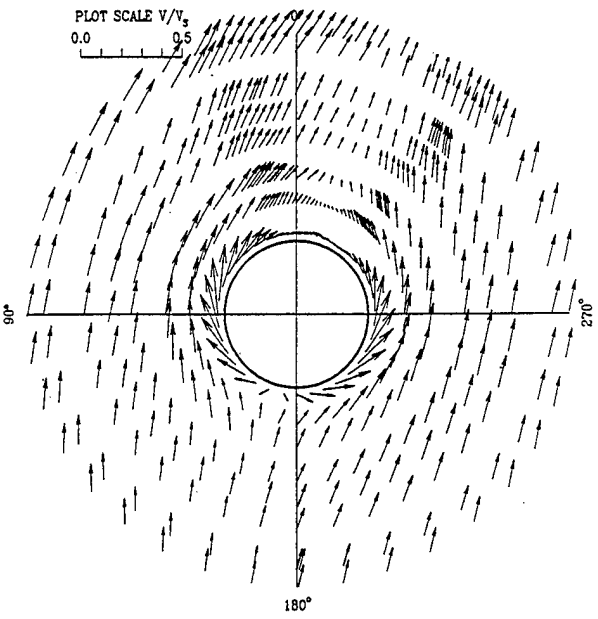


FIG. 9A. CROSS PLANE VECTORS

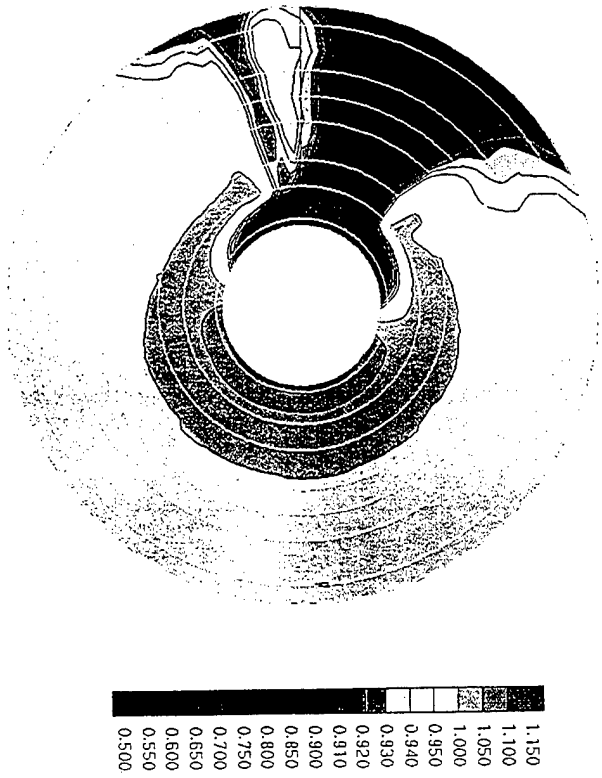


FIG. 9B. AXIAL VELOCITY CONTOURS

FIG. 10 MODEL TEST CONFIGURATIONS

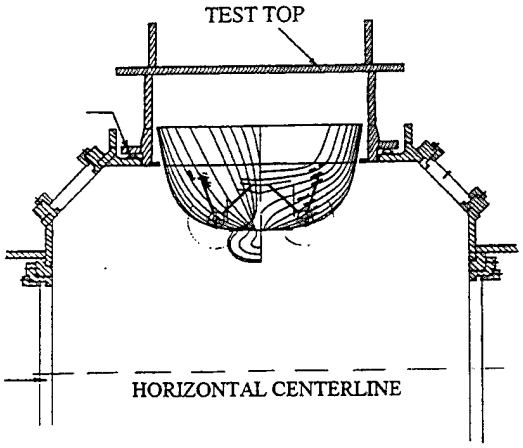


FIG. 10A. LARGE CAVITATION CHANNEL

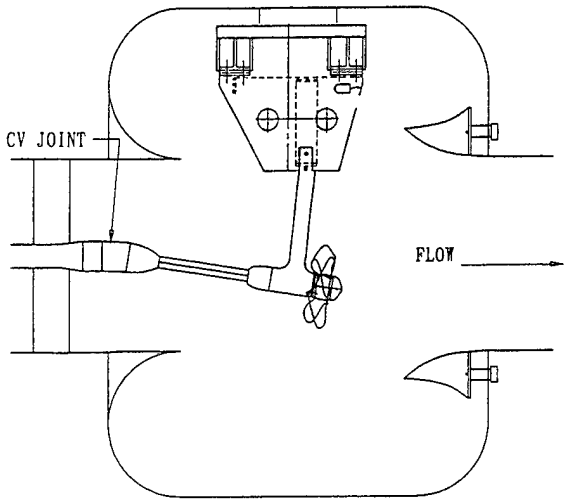


FIG. 10B. 36" WATER TUNNEL

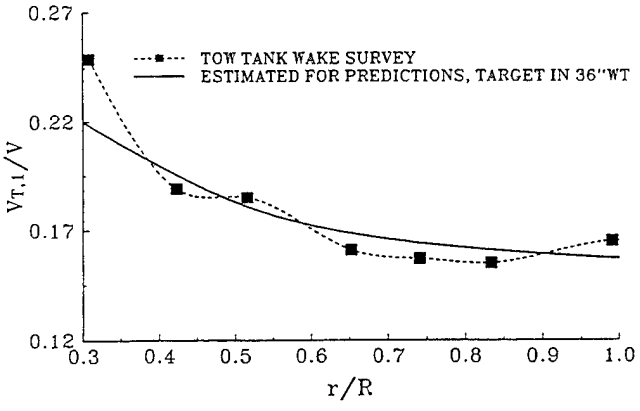


FIG. 11 AMPLITUDE OF FIRST SHAFT RATE HARMONIC OF TANGENTIAL VELOCITY

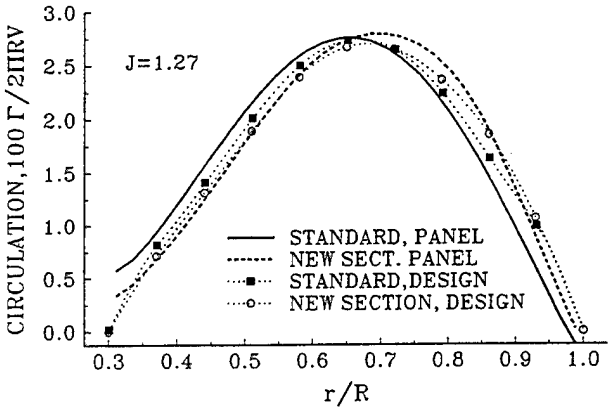


FIG. 12 PROPELLER SPANWISE CIRCULATION DISTRIBUTIONS

FIG. 13 2-D FOIL AND 3-D PROPELLER SECTION PRESSURE DISTRIBUTIONS FOR STANDARD PROPELLER

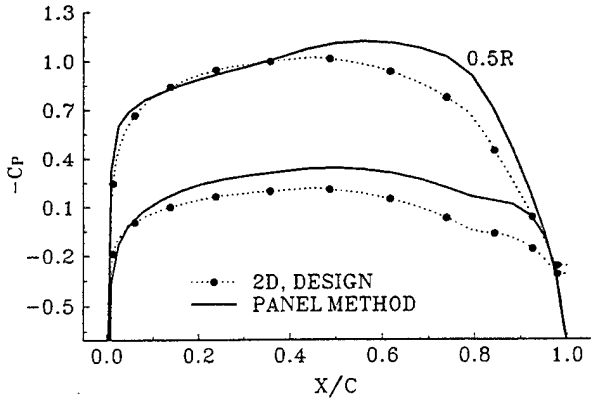


FIG. 13A. 0.5 RADIUS

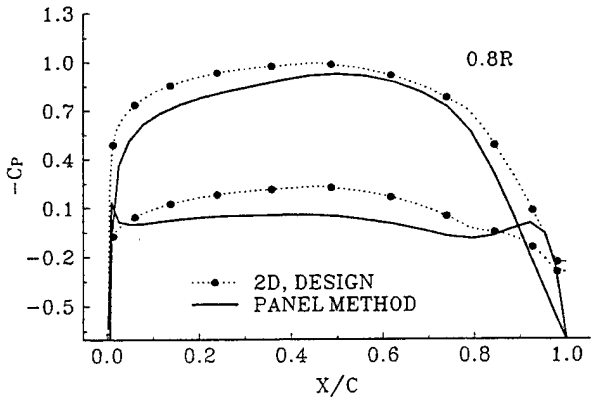


FIG. 13B. 0.8 RADIUS

FIG. 14 SURFACE REPRESENTATION OF BLADE SUCTION SIDE AT MAXIMUM LOADING CONDITION USING PANEL METHOD

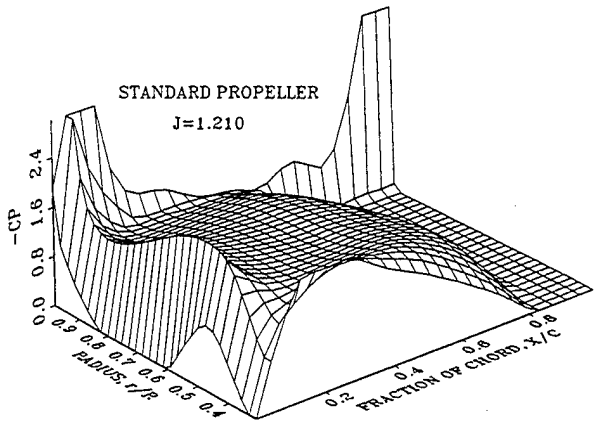


FIG. 14A. STANDARD PROPELLER, J=1.210

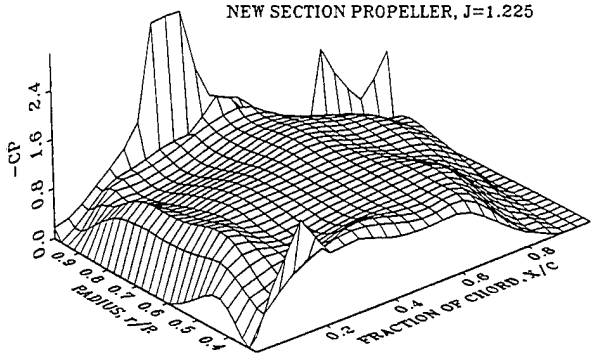


FIG. 14B. NEW SECTION PROPELLER, J=1.225

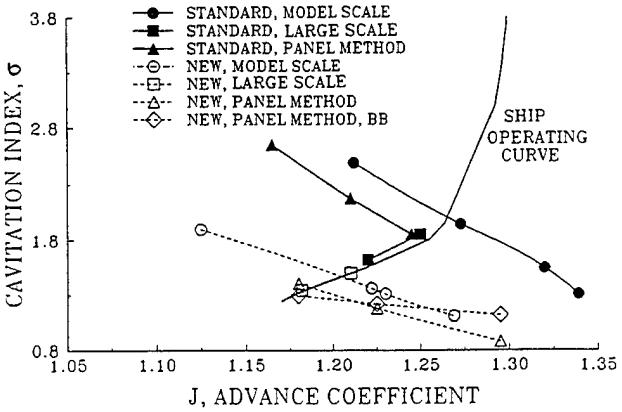


FIG. 15 SUCTION SIDE BLADE SURFACE CAVITATION INCEPTION

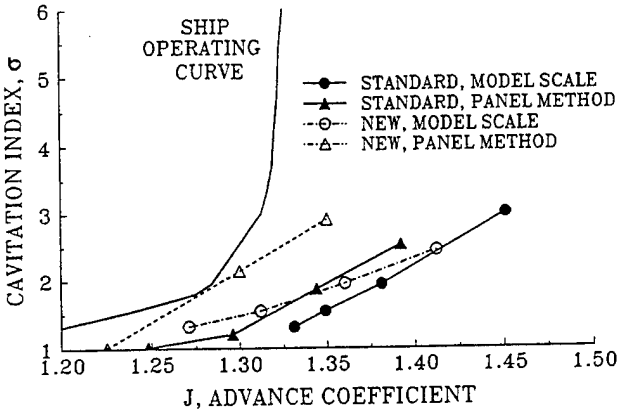


FIG.16 PRESSURE SIDE LEADING EDGE CAVITATION INCEPTION

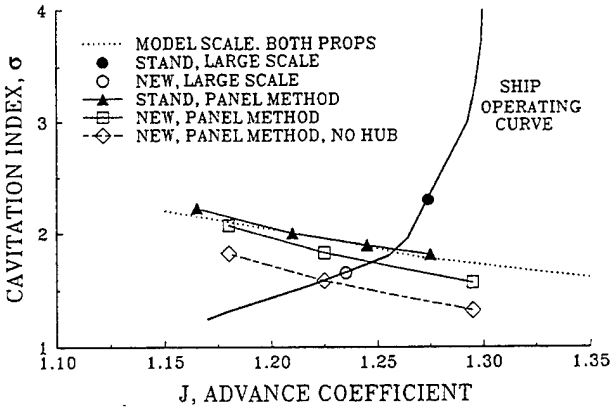


FIG. 17 SUCTION SIDE ROOT CAVITATION INCEPTION

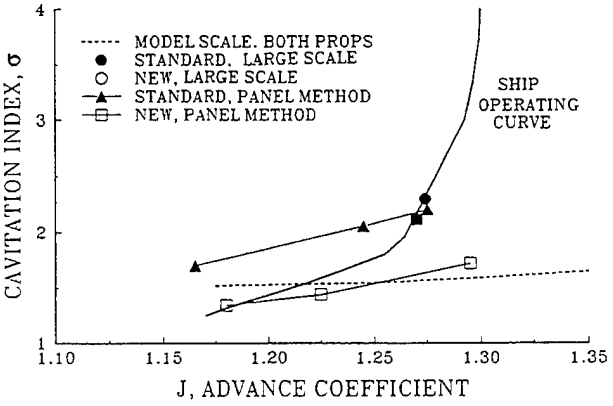


FIG. 18 PRESSURE SIDE ROOT CAVITATION INCEPTION

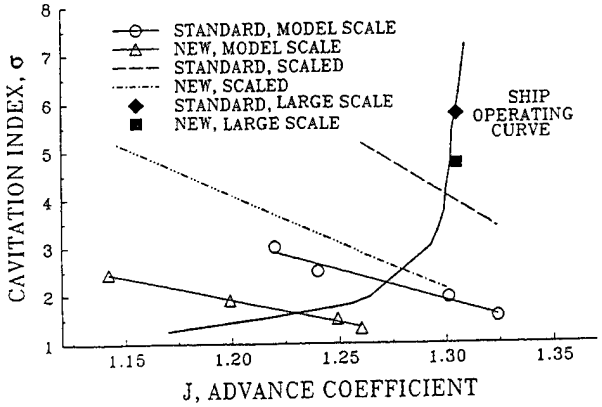


FIG. 19 TIP VORTEX CAVITATION INCEPTION

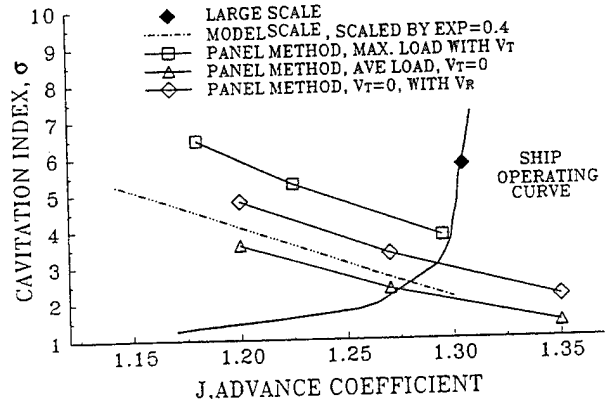


FIG. 20 PREDICTION OF TIP VORTEX CAVITATION

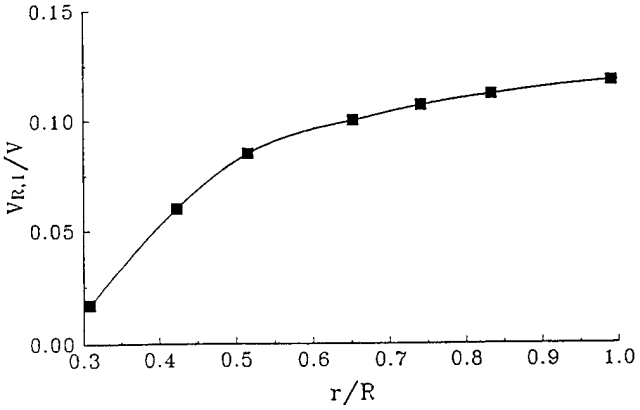


FIG. 21 AMPLITUDE OF FIRST HARMONIC OF SHAFT RATE OF RADIAL VELOCITY

FIG. 22 ESTIMATION OF CAVITATION EXTENT USING PANEL METHOD

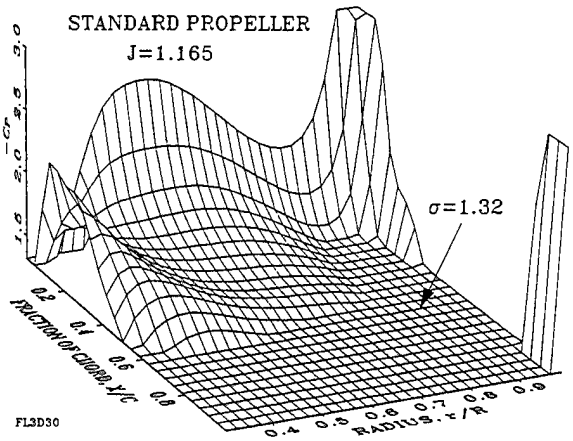


FIG. 22A. STANDARD PROPELLER

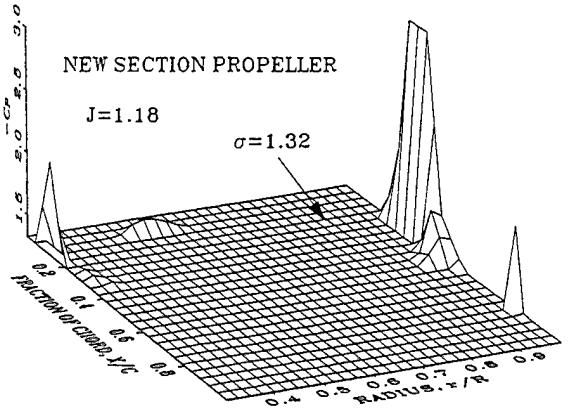
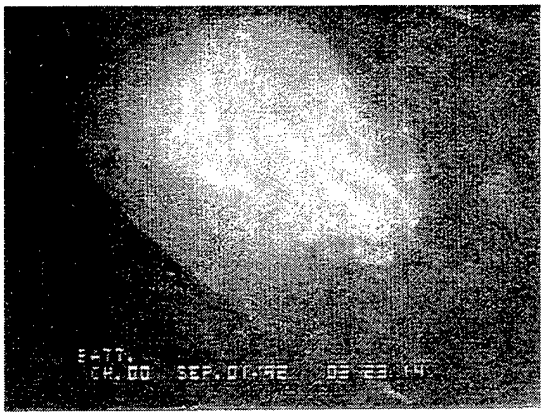


FIG. 22B. NEW SECTION PROPELLER

FIG. 23 CAVITATION ON STANDARD PROPELLER AT HIGH SPEED



FIG. 23A. MODEL SCALE



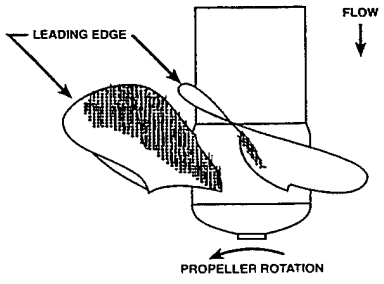


FIG. 23B. LARGE SCALE

FIG. 24 CAVITATION ON NEW SECTION PROPELLER AT HIGH SPEED

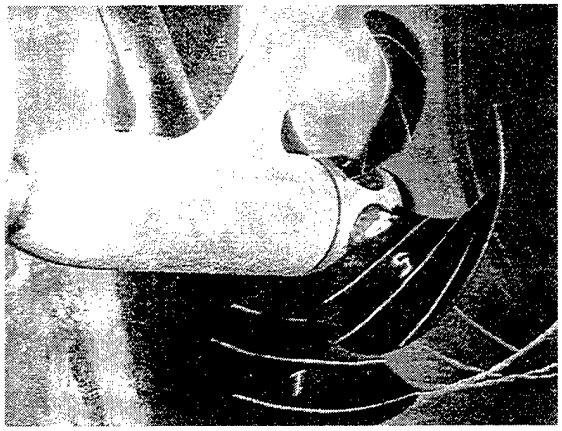


FIG. 24A. MODEL SCALE



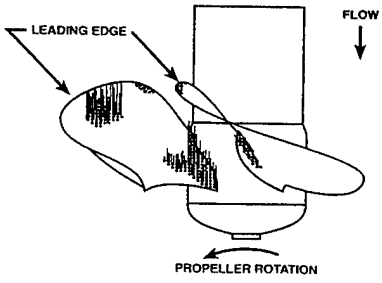


FIG. 24B. LARGE SCALE

FIG. 25 CAVITATION ON NEW SECTION PROPELLER AT HIGHER SPEED

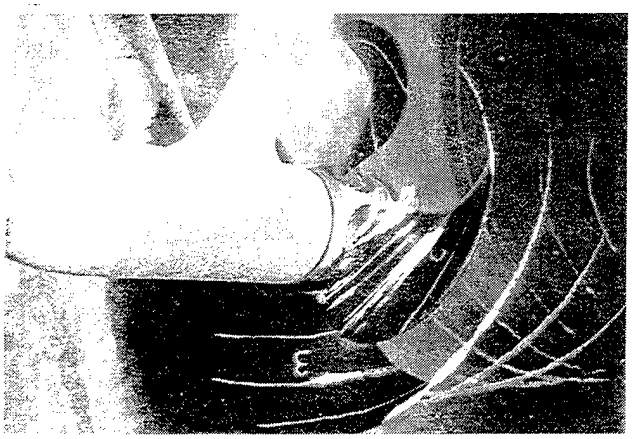


FIG. 25A. MODEL SCALE



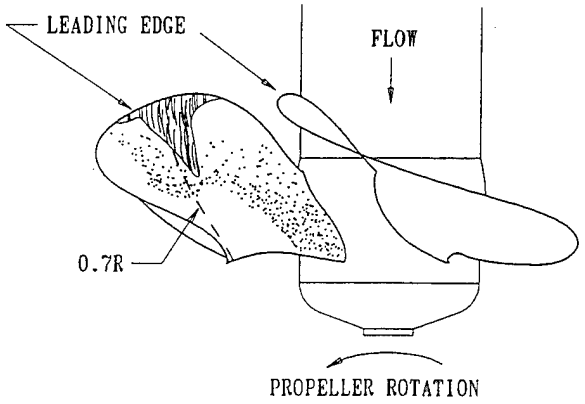


FIGURE 25B. LARGE SCALE

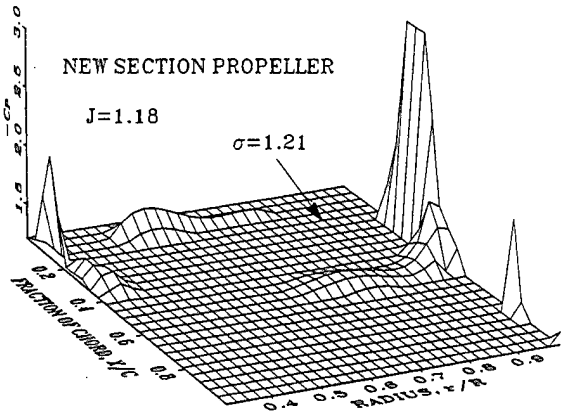


FIG. 26 ESTIMATION OF CAVITATION EXTENT USING PANEL METHOD

A Surface Vortex Lattice Method for Calculating Performances of Non- or Super-Cavitating Propellers

H. Yamasaki, M. Ikehata
(Yokohama National University, Japan)

ABSTRACT

In this paper, the applications of a panel method based on the velocity for the marine propellers in non or super - cavitating condition are presented. The panel method is called surface vortex lattice method and uses the conception of the vortex latttice method in the lifting surface theory.

The surface vortex lattice method is possible to simulate a lifting body including thickness or volume effects of propeller blades by distributing sources and horse - shoe vortices on the surface of the body. The propeller open characteristics and pressure distribution on the blade concerning to the marine propellers in non- or super-cavitating condition and the expansion of the cavity of three super-cavitating propllers have been calculated by the present method. The results of these calculations are in good agreements with experiment and other theoretical calculation results.

NOMENCLATURE

C_P	:	pressure coefficient
h	:	thickness of cavity
K	:	number of propeller blades
M	:	number of chordwise panels
N	:	number of spanwise vortices
N_W	:	number of dividing trailing vortices in the propeller wake
n	:	propeller rotational speed
$\boldsymbol{n}$	:	normal vector to surface
Q	:	strength of source
Q_n	:	strength of n-th interporated source
Q'	:	strength of source meaning cavity
r	:	radial distance from the origin
s	:	chordwise coordinate from leading edge
u	:	normal component of velocity induced by unit vortex
V_i	:	inflow velocity at each control point
β_T	:	pitch angle of propeller wake
δs	:	spanwise length of a panel
Γ	:	circulation of spanwise vortex
$\boldsymbol{\Gamma}$	:	circulation vector of spanwise vortex
γ	:	density of circulation distribution
σ_V	:	cavitation number

Subscripts and Superscripts

B	:	back side index
C	:	cavitation index
c	:	chordwise tangential index
F	:	face side index
G	:	vortices relating the propeller
h	:	hub index
i	:	control point index
m	:	spanwise index
n	:	chordwise index
Q	:	source relating the propeller and cavity

INTRODUCTION

For last several years, the applications of the vortex lattice method to the marine propeller have been reported by many researchers and they can be reaching to not only the steady and the unsteady condition, but also the interaction and the cavitation problem now.

On the other hand, it is necessary to get more accurate results of the simulation by numerical method because of the requirements of the high skew and cavitation reduction, etc. of the marine propeller recently. As a result, many panel methods based on the lifting body theory instead of the vortex lattice method done on lifting surface theory has been used widely.

The best point of this method is the fact that it is possible to arrange the panels faithfully on the body configuration and to calculate the pressure on the blade more accurately. Many application examples of various panel methods to the marine propeller have been reported by many researchers. Ryo(1) used the direct method of the boundary element method, Koyama(2) solved the integral equation concerning to only the doublet distribution based on the velocity field and Hoshino(3), Kerwin(4) made use of Morino method(5) developed in aerodynamic field.

These methods were very powerful tools to the complex configuration body but they had a weak point to limitation of the wake geometry behind the propeller blade. In the marine propeller, the estimation of the wake geometry is a very important point. Ishii(6) reported that not only the pressure distribution on the blade but also the open characteristics are affected by the wake geometry.

For getting more correct simulation of the wake geometry, it is very easy to express it by vortex lattices and it'll be able to coincide with our physical consideration. Consequently, in case of the simulation of the lifting body like the marine propeller, making the vortices to distribute on the body will be suit to the actual phenomena.

The methods can be found out in the aerodynamic field. Woodward(7), Maskew(8) and Miranda(9) had used the vortex distribution on the wing surfaces and they had gotten the excellent results. However, any report concerning to the marine propller by use of the methods have never seen because it would be difficult to apply to the three dimensional complex configuration like the marine propller.

In this paper, the applicability of the surface vortex lattice methods is discussed. The new method based on the concept that the abundant technics made in lifting surface theory can be used widely and it is easy to extend the vortex lattice method to the surface vortex lattice method. The differences between the VLM and the SVLM are the arrangement of the vortices and the treatment of the source distribution. Accordingly, in even case of the cavitating condition, the same manner using in the VLM can be applied in the SVLM.

MATHEMATICAL MODELING AND DISCRETIZATION

General Discussion

When a propeller rotates in steady condition, there are generated spanwise and chordwise vortices on the real blade surface and trailing vortices in wake.

By applying Kerwin's formula(10) based on the principle of conservation of circulation, we can replace chordwise vortex and trailing vortex in terms with only discrete spanwise vortices.

In the vortex lattice method, the lifting surface on the mean camber surface of each blade is represented by horse-shoe vortices and the effects of thickness are done by sources. The strength of sources is determined by thin thickness assumption.

Now, in this paper, two kinds of the surface vortex lattice methods can be considered. Concerning to one of them, only the vortex lattices are placed just on the blade surface. In another method, not only the vortex lattices are distributed but also the sources are done on the blade surface.

Both of the analytical expressions are derived for the perturbation velocity field induced by each horse- shoe vortex (vortex lattice). These are deduced to calculate the coefficients of a system of linear equations relating the magnitude of the normal velocity at each control point on the blade surface to the unknown spanwise vortex strength. So as to satisfy the boundary condition at the control points the spanwise vortex strengths are determined by solving this system of equations by an iterative procedure.

Numerical Computing Procedure In Non - Cavitation Condition

The boundary condition in non - cavitation condition is given by the equation.

$$\boldsymbol{V}_i \cdot \boldsymbol{n}_i = 0 \qquad (1)$$

,where $\boldsymbol{V}_i$ is the resultant velocity vector and $\boldsymbol{n}_i$ is the normal vector to the blade surface at the i-th control point. The resultant velocity $\boldsymbol{V}_i$ at the i-th control point is summation of induced velocities by the singularities elements and undisturbed inflow velocity.

There are two kinds of the surface vortex lattice methods by the differences of selection of singularities. In this paper, the vortex only and

the combination of the vortex and the source distribution as the singularities are selected. In case of only the vortex distribution, the resultant velocity $\boldsymbol{V}_i$ is summation of induced velocities by the vortex lattices and undisturbed inflow velocity.
Specifically,

$$\boldsymbol{V}_i = \boldsymbol{V}_{iG} + \boldsymbol{V}_{iu} \tag{2}$$

,where $\boldsymbol{V}_{iG}$ is the velocity induced by the votrices relating to the propeller and $\boldsymbol{V}_{iu}$ is the undisturbed inflow at i-th control point.

On the other hand, in case of taking the combination of the vortex and the source distribution, resultant velocity $\boldsymbol{V}_i$ is summmation of $\boldsymbol{V}_{iG}$, $\boldsymbol{V}_{iu}$ and induced velocities by source distribution.

$$\boldsymbol{V}_i = \boldsymbol{V}_{iG} + \boldsymbol{V}_{iu} + \boldsymbol{V}_{iQ} \tag{3}$$

,where $\boldsymbol{V}_{iQ}$ is the velocity induced by the source distribution. Considering equation (2) and (3), equation (1) becomes the following two equations respectively for such two kinds of singularities.

$$\boldsymbol{V}_{iG}\cdot\boldsymbol{n}_i = -\boldsymbol{n}_i\cdot\boldsymbol{V}_{iu} \tag{4}$$

$$\boldsymbol{V}_{iG}\cdot\boldsymbol{n}_i = -\boldsymbol{n}_i\cdot(\boldsymbol{V}_{iu} + \boldsymbol{V}_{iQ}) \tag{5}$$

We can transform equation (4) with respect to the strengths of spanwise vortices as unknown variables.

$$\sum_{k=1}^{K}\left[\sum_{m=1}^{M}\sum_{n=1}^{N}\Gamma_{nm}^{B}\cdot\left\{u_{inm}^{B\square}(k)+\sum_{n_w=2}^{N_w}u_{inm}^{Bw}(k)\right\}\right.$$

$$\left.+\sum_{m=1}^{M}\sum_{n=1}^{N}\Gamma_{nm}^{F}\cdot\left\{u_{inm}^{F\square}(k)+\sum_{n_w=2}^{N_w}u_{inm}^{Fw}(k)\right\}\right] = d_i \tag{6}$$

,where

$$d_i = -\boldsymbol{n}_i\cdot\boldsymbol{V}_{iu} \tag{7}$$

K : number of propeller blades
M : number of spanwise vortex elements of a propeller blade
N : number of chordwise vortex elements of a propeller blade
N_w : number of trailing vortex elements of propeller wake
Γ_{nm} : strength of spanwise vortex at (n,m)
$u_i^{\square}$: normal component of the velocity at the i-th control point induced by unit ring vortex
u_i^{w} : normal component of the velocity at i-th control point induced by unit trailing vortex in wake
B, F : index of back side or face side of blade

The $u_{inm}^{B\square}$ in the equation (6) means normal induced velocity at the i-th control point by a ring vortex at n-th chordwise and m-th spanwise on the back side surface having unit strength.
The velocity induced by a ring vortex can be calculated by Biot - Savart law.

Although there are including two kinds of singularities in equation (5), in this paper only the vortex strengths are set to unknown variables and the source strengths Q are fixed on a value as known calculated by the equation (8).

$$Q_i = -\boldsymbol{n}_i\cdot\boldsymbol{V}_i \tag{8}$$

Accordingly, the equation (6) and equation (9) are used in the condition.

$$d_i = -\boldsymbol{n}_i\cdot(\boldsymbol{V}_{iu} + \boldsymbol{V}_{iQ}) \tag{9}$$

Numerical Computing Procedure in Super-Cavitation Condition

The surface vortex lattice method in the super - cavitating condition is considered as the extension of the SVLM in the non - cavitating condition.

In the method, the former concept is used to a part of the propeller blade and the wake without cavitation and new concept is done to parts of them with cavitation. However, to make easy calculation the following assumptions are made concerning to the occurence of the cavitation.

1. Cavitation occures on the back surface only.
2. Cavitation occures from the leading edge on the back side and do not occure on the way to chordwise direction.
3. Cavitation in the wake behind the body closes itself at the crossing point of two trailing vortices from the back side and from the face side.

The governing equation in the super - cavitating condition is represented by equation (5). The differences of concept between non- and super- cavitating condition are the boundary conditions and selection of singularity elements. The boundary conditions are set to two parts.

1. Boundary condition on the blade surface(without cavitation)
   On the boundary surface without cavitation, the condition is represented by the equation

$$\boldsymbol{V}_i \cdot \boldsymbol{n}_i = 0 \tag{10}$$

   The unknown variables are only the vortex strengths and the source strength Q is given by the equation (11).

$$Q = -\boldsymbol{n}_i \cdot \boldsymbol{V}_{iu} \tag{11}$$

2. Boundary condition on the cavitation surface
   On the surface where the cavitation are occuring, the boundary conditions are divided into two parts. One of them is that flow does not across the surface and the other condition is that the pressure coefficients on the body are equal to cavitation number.
   Accordingly,

$$\boldsymbol{n}_c \cdot \boldsymbol{V}_i = 0 \tag{12}$$

$$|\boldsymbol{V}_C| = |\boldsymbol{V}_{iu}|\sqrt{1+\sigma_V} \tag{13}$$

   ,where $\boldsymbol{n}_c$ means a unit normal vector on the cavity surface and $|\boldsymbol{V}_C|$ is a chordwise tangential velocity. The vortices and the sources as two unknown variables are distributed on the cavity surface.

By using these two kinds of boundary conditions, the strengths of the vortices and the sources distributed on the body or cavitation surface can be gotten by solving the simultaneous equations. However, it is very difficult to solve a problem of cavitation because the region of the cavity is not defined.

In this paper, the cavitation occurence on the surface of the blade and the wake is simulated by the following iterative calculation.

The iterative procedures are made by two parts. The cavity extension is obtained as a first approximate estimate at the first step, after that, the cavity thickness is done at the second step.

First step: Determination of the cavity extension

(a). It is assumed that the cavity occures on the whole back side surface of the wing or blade, and the vortices and the sorces as unknown variables are distributed on the cavity surface. By using the boundary conditions as mentioned above, the simultaneous equations are solved and the strengths Q of the source are obtained.

(b). The strengths of the sources on the back side surface without cavitation are calculated by the equation.

$$Q^t = -\boldsymbol{n}_i \cdot \boldsymbol{V}_i \tag{14}$$

(c).We can consider that Q obtained at (a) is summation of Q^t representing blade thickness and Q' meaning the cavity thickness and the following equation is satisfied.

$$Q' = Q - Q^t \tag{15}$$

(d).The cavity thickness h is obtained by the equations (14) and (16).

$$\frac{dh}{dc} = \frac{Q'}{|\boldsymbol{V}_i|} \tag{16}$$

(e).Concerning to h, when the thickness at the trailing edge of the cavity is a positive value, the calculation is moved behind the trailing edge and in case of a negative value, the region of the cavity is shortened to the direction of the leading edge.

After that, the iterative procedure from (a) to (d) is repeated many times until the convergence of the cavity end.

Second step: Determination of the cavity thickness

After the determination of the cavity extension by the iterative procedure (a) to (e), more accurate cavity thickness can be obtained by the following procedure. At the first step, we have gotten the first approximate cavity thickness by use of Q' and equation (16).

(f).The n-th approximate cavity thickness h_n is added to the boundary surface and the new boundary surface is rearranged as the boundary surface including the cavity.

After calculating the n-th source strength ${Q^t}_n$ meaning the boundary thickness, the source

strength Q_n can be obtained by solving the simultaneous equations.

(g).From $Q^t{}_n$ and Q_n at (f), Q'_{n+1} showing the (n+1)-th cavity thickness can be calculated by use of the equation(17).

$$Q'_{n+1} = Q_n - Q^t_n \tag{17}$$

And (n+1)-th approximate thickness of the cavity h_{n+1} can be made by Q'_{n+1}.

By repeating the procedures (f) and (g), and calculating until $Q'_n$is close to zero and $h_1, h_2, h_3, ...$ can be obtained.

Accordingly, we can have the most accurate cavity thickness after subtracting the blade thickness from the convergent boundary surface [the cavity thickness$(h_1 + h_2 + h_3 +, ..., h_n)$+the blade surface].

PANEL DIVISION OF PROPELLER BLADE AND WAKE MODEL

Propeller Blade

The continuous vortex distribution representing the blade is replaced with discrete one. There are three kinds of arrangements related to singularities in three conditions.

One of them is that the discrete vortices are placed at the front of the small panel and the control point is taken at the center of the panel of chordwise direction. In this arragement, two vortices on the back and face surfaces which are the closest to the leading edge are placed at a distance of $\alpha \cdot C$ from the leading edge as shown Fig.1. The C is a chord length and α is 0.01 in this calculation. This arrangement is used in the case of utilization of only the vortex system.

Second one is that the discrete vortices are placed at the line of a quarter chord of the small panel and the control point is taken at the point of three-quarter chord like the vortex lattice method. This arrangement is used in case of the combination of the vortex and source system.

The last one is that the discrete vortices are placed at the same position to the second arrangement and surface distributed constant sources are arranged in each small panel like Hess & Smith method. This arrangement is used in super - cavitating condition.

We experienced the fact that the singularity between vortices on the surfaces close to the tip as propeller blade is too strong to get good accuracy solutions.

In the present method, to avoid this problem the real surface panels satisfying the following expression are replaced by lifting surface panels.

$$\frac{b}{a} < \beta \tag{18}$$

In equation (18) a means distance from spanwise vortex to control point on the back side and b is distance from spanwise vortex on the opposite face side to control point on the back side, β is taken 1.025.

The back and face surface of a propeller blade are divided into $N \times M$ panels.
In the chordwise spacing, same spacing is selected and in the spanwise spacing, cosine spacing used by Hoshino(3) is adopted.

$$r_m = \frac{1}{2}(r_t + r_h) - \frac{1}{2}(r_t - r_h)cos\alpha_m \tag{19}$$

$$\alpha_m = \begin{cases} 0 & for \quad m = 1 \\ \frac{(2m-1)\pi}{2(M+1)} & for \quad m = 2, .., M+1 \end{cases} \tag{20}$$

,where r_m are radial positions of the corner points of each panels and r_h is the radius of the boss, the r_t are radial distances represented by following expression.

$$r_t = \frac{(r - r_h)(4M+1)}{4M+2} \tag{21}$$

Propeller Wake Model

Fig.2 shows the flow chart for the simulation of the geometry of the propeller wake by iterative procedure.
In the first step, we calculate the strengths of the vortices in the whole system including classical wake whose pitch distribution is equal to propeller's with no consideration of any contraction and compute the induced velocity at each end of the segments of the discrete propeller wake, in order to meve them to new position by using following expressions.

$$P_W^{(N+1)} = P_W^N + \boldsymbol{V}_W \cdot \Delta t \tag{22}$$

$$\boldsymbol{V}_W = (V_a + V_x, V_r, 2\pi nr + V_\theta) \tag{23}$$

,where $P_W^{(N)}$ are the coordinates of the ends of the discrete wake segments at the N-th time step and V_x, V_r, V_θ are each components of the axial, radial and circumferential induced velocity by vortex distribution respectively.

Moreover, the Δt in the expression (22) is determined by the following expression

$$\Delta t = \frac{1}{n \cdot N_W} \tag{24}$$

,where n means the number of propeller revolution. After the second step, simulations are continued by the process as mentioned above untill the thrust coefficient at each time step converges.

Calculation of the Density of Circulation Distribution and the Pressure Distribution on the Blade

We have obtained the density of circulation distribution on i-th control point

$$\begin{aligned} \gamma_i &= \frac{1}{2} \cdot (\boldsymbol{\Gamma}^b_{nm} \times \boldsymbol{n}_{nm}/|\boldsymbol{L}_{nm}| \\ &+ \boldsymbol{\Gamma}^b_{n+1,m} \times \boldsymbol{n}_{n+1,m}/|\boldsymbol{L}_{n+1,m}|) \end{aligned} \tag{25}$$

,where γ_i is the density of circulation distribution, $\boldsymbol{\Gamma}^b_{nm}$ is the bound vortex vector at (n,m)-th panel, δs is the spanwise length of the panel and $\boldsymbol{L}$ means spanwise vortex segment vector.
According to Yuasa(11), the pressure at i-th control point has been calculated by using Bernoulli's equation.

$$C_{PB} = 1 - \frac{{V_i^B}^2}{V_{iu}^2} \tag{26}$$

$$C_{PF} = 1 - \frac{{V_i^F}^2}{V_{iu}^2} \tag{27}$$

$$V_i^B = | \boldsymbol{V}_i^B | + \frac{\gamma_i^B}{2} \tag{28}$$

$$V_i^F = | \boldsymbol{V}_i^F | + \frac{\gamma_i^F}{2} \tag{29}$$

Calculation of Hydrodynamic Forces, Thrust and Torque

The hydrodynamic force acting on each discrete element has been composed of the following terms.

1. Pressure acting on a panel on the surface.
2. Viscous drag at each blade element.

We can get the viscous drag working at each blade element by following equation

$$C_F = \left(1 + \frac{t_{max}}{C}\right) \cdot \frac{0.455}{(\log_{10} R_e)^{2.58}} \tag{30}$$

,where t_{max} is maximum thickness of the each blade section and R_e is the Reynolds number.

The thrust and the torque of the propeller have been calculated by the summation of each components of the above terms.

RESULTS AND DISCUSSION

We have some test calculation to make sure that the correct results can be gotten in simple configuration body like three dimensional wing by use of the present method. In case of the non - cavitation condition, it is a three dimensional rectangular wing whose results made by use of various panel methods were reported by Johnson(12). In case of the super - cavitation condition, we select two kinds of section wing which called Newton - Rader and Johnson 5 terms wing. Concerning to the marine propeller, three type propellers are selected in non - cavitation and two propellers are done in super - cavitation condition.

Non - Cavitation Condition

Three dimensional rectangular wing

The wing are divided into 12(chordwise)× 8(spanwise) panels and the pressure distribution on the both surfaces are calculated.

Fig.3 shows the pressure coefficients obtained by three methods which are Morino method, SVLM used the vortex only and used the vortex and source. The results of SVLM represented the wing surface by the vortex only have not a little difference in comparison with other two methods near the leading edge. Another SVLM added the source distribution gives results in closer to Morino method. These results are reasonable because the displacement thickness effect is taken to account by source distribution. We can not find diffrence between two SVLM in the region from midchord to the trailing edge, but the improvement can be found in the results of SVLM with vortex and source in the vicinity of the leading edge. Accordingly, the method used the arrangement of the combination of the vortex and source is better than the vortex

only.

Conventional and highly skewed propeller

We have three type propellers for calculation by the present method. One of them is a conventional propeller(CP), second one is a highly skewed propeller(HSP) and the last one is DTRC4119. The principle particulars of these propellers are tabulated as Table 1. The arrangements of vortex lattice system of the each three propellers are described in Fig.4,Fig.5 and Fig.6. All propellers are divided into the same number panels which is 12 chordwise and is 10 the spanwise. Propeller bosses are not yet included.

Fig.7 to Fig.9 show the pressure distribution on the blade of CP at r/R=0.3,0.7 and 0.8. Fig.10 and Fig.11 show that of HSP at r/R=0.7 and 0.8. These advance coefficients J are set to 0.66. The results of the direct method of the boundary element method made by Ryo are put in these figures for the comparison.

Concerning to the pressure distribution at r/R=0.3 of CP shown in Fig.7, it can be concluded that the two SVLM are different from BEM at the whole chordwise positions. The difference must be caused by the effect of the hub which is included in the results made by Ryo(1) but not done in the present method. The results of the method using the vortex only have large difference among other methods in the region near the leading edge for the same reason in the case of the rectangular wing.

In Fig.8 and Fig.9 showing the pressure distribution of CP at 0.7 and 0.8 radius, SVLM using the vortex and source can be in good agreement with the experiment and BEM. But SVLM using the vortex only is smaller than other results near the leading edge.

Fig.10 and Fig.11 show the pressure coefficients of HSP at r/R=0.7 and r/R=0.8. The pressure coefficients obtained by the two SVLM are higher than BEM at the whole position, but SVLM by vortex and source has improved near the leading edge.

The simulation results of the wake geometry of CP are shown in Fig.12. The calculated results by the present method are compared with experiment results done by Ishii(13). The variable shown in this figure β_T means pitch angle of the wake geometry and it can be obtained by following equation defined in the reference(13).

$$\beta_T = arctan\left(\frac{V_a + V_x}{2\pi nr + V_\theta}\right) \qquad (31)$$

As the measuring positions in experiment are X/R=0.4 and 1.0, it is best to suit to them. But induced velocity is calculated by using only interpolation of axial direction and not radius direction. As shown in this figure, calculations are little different from experiments, so that the calculations can simulate the actual phenomena of the wake behind propeller faithfully. The pitch of wake geometry calculated are greater than geometric pitch of blade at radius position which are between 0.3R and 0.7R. And they are smaller at positions which are near 0.2R and greater than 0.7R. These distributions mean that the effect of the wake vortices occuring from the root and the tip of the propeller are so strong as to make their own geometry to be deformed.

Fig.13 and Fig.14 show open water characteristics of CP and HSP, respectively. Calculation results agree with experiment results on both CP and HSP. But torque coefficients are smaller than experiments at high load condition in case of two propellers. In order to avoid this it will be necessary to consider separated vortex model of tip vortex reported by Ishii(6).

DTRC4119

We have selected DTRC4119 for calculation as high pitch propeller. As Jessup(14) mesured many items concerning to this propeller by use of LDV, the results can be compared with the present results. Figs.15,16 and 17 show pressure distribution on blade of DTRC4119 at 0.3,0.7 and 0.9 radius respectively in working at J=0.833.

Fig.15 shows that the calculations are a little smaller than the experimental results on the whole chord because the effect of the hub is not considered as mentioned above, and the pressure coefficient near the leading edge in case of the vortex only are much smaller than other results.

Concerning to pressure distribution at 0.7 radius shown in Fig.16, the calculation of the combination of the vortex and source agrees very well with to the experiment in the whole chord but about at 0.9 radius shown in Fig.17, we cannot obtain so good results and they are strange distribution. We think that the unreality of this distribution were induced by the singularlity of the close vortices on opposite sides.

Fig.18 shows comparison between experiments and calculations of open water characteristics. The thrust coefficients of the calculations are in good agreement with the experimental results, but the torque coefficient shows the larger

differences at the lower advance coefficient. They are caused by shortage of frictional resistance which are calculated by the expression using that of flat plate and by no consideration of separation of the tip vortex.

Fig.19 shows pitch distribution of the propeller wake calculated by the present iterative procedure. The distances from the center line are 0.328 and 0.95 radius. Both of the calculated distributions are similar to the experimental results but they are not in good agreement. We think that the strength of the tip vortex is not calculated correctly or it might be necessary to make convergence of not only the open water characteristics but also wake geometry.

Super - Cavitation Condition

We select two super - cavitation wings and two super - cavitation propellers whose experiments are given. Although these numerical calculations are made by the method as mentioned before, in case of the marine propellers, classical wake is used and the assumed region where the cavity occurs at initial step is not set to the whole back side surface but to the experiment data for reduction of CPU time. The wing and blade sections are shown in Fig.20. The wings are Newton - Rader wing and Johnson 5 terms wing, and propeller blade sections are SSPA and SRIJ-II. The condition of the wings for experiments and calculations are tabulated in Table 2 and principle particulars of the propllers are in Table 3. The number of panel division on the surfaces in the present calculation is as follows.

1. Super - cavitation wing
   (a) chordwise×spanwise:12×12
   (b) length of wake :6×chord
2. Super - cavitation propeller
   (a) chordwise×spanwise:15×20(SSPA), 12×10(SRIJ-II)
   (b) wake(one cycle) :60
   (c) length of wake :two cycles

The panels of wake are arranged to the direction of uniform flow with respect to the super - cavitation wing and are set to classical wake about super- cavitation propeller in the initial stage. In case of the wing having a thickness at the trailing edge like Johnson 5 terms wing, wakes are made of two layers generating from the back and the face surfaces but vortex surface on the cavity are distributed above the back side of the body surface and it is duplicated on the face side wake at the end point of the cavity.

Super - cavitation wing

Calculation results are represented by hydrodynamic forces, cavity extension and shape. Lift coefficients, drag coefficients and cavity extension versus change of σ_V are shown in Fig.21 to Fig.23 and experiment results of Ship Research Institute of Japan and Tokyo University are put in figures for comparison.

As shown Fig.21a, lift coefficients of N-R wing calculated by the present method are close to the experimental results of SRI and they change linearly to σ_V which are less than 0.6. Although the experiments take a maximum value at σ_V=0.6 and after that, they are decreasing radically, calculations have no peak. At $\sigma_V = 0.6$, N-R wing is in super - cavitation condition in experiment but as mentioned above, the present method cannot correspond to this change of the condition.

The same discussion as the lift coefficients can be done about drag coefficients shown in Fig.21b. As the experimental data have scattering, we cannot make quantity discussion. But it may be correct that partial cavitation suddenly changes to super cavitation. Such change cannot appear in the calculation.

The cavity extension are shown in Fig.23a. Although the experimental data are given at $\sigma_V < 0.3$, considering the change of the hydrodynamic forces mentioned above, it is expected that the cavity extensions will become less than 1.0 near σ_V=0.6. Comparison between the present method and experiments shows good agreemwnt in the range of $\sigma_V < 0.3$(super - cavitation condition).

Fig.22a shows lift coefficients of Johnson 5 terms wing.
The lift coefficients are good agreement with experiments at the cavitation number less than 0.4, and so we can partially confirm accuracy of the present method. But calculations cannot simulate correctly the phenomena of experiments which the lift coefficients suddenly drop at $\sigma_V > 0.4$. It will be one of future works to simulate correctly the transition condition which shift from partial cavitation to super - cavitation condition.

Fig.22b shows drag coefficients of Johnson 5 terms wing.

We cannot do exact discussions for scuttering of experimental data similar to N-R wing. The calculated drag coefficient increases proportionally to σ_V and the gradient of the curve of C_D changes at σ_V=0.4 where super - cavitation condition changes to partial cavitation condition.

Fig.23b shows extension of cavity with respect to Johnson 5 terms wing. The calculations are a little longer than experiments at the cavity numbers less than 0.3. Some problem might happen in the case that the wing section is cut off having a thickness at the trailing edge.

Super - cavitation propeller

Results concerning to the two super - cavitation propellers are represented by pressure distribution at 0.71 radius, open water characteristics, and extension of cavity.

Calculations of pressure distribution on the blade at 0.71 radius of SSPA are shown in Fig.24. The calculation is made at only design point which σ_V is equal to 0.4 and advance coefficient J is equal to 1.1. The pressure coefficients calculated on the back surface coincide with cavity number because boundary surface of back side are in the cavity. The pressure coefficients of the face side go up near the leading edge keep a constant near the mid-chord and go down near the trailing edge. The fluctuation behind the leading edge will be improved by using smaller panels.

The open water characteristics of SSPA propeller are shown in Fig.25. Both of thrust and torque coefficient of the calculation are lower than experiment, especialy diffrence between them of torque is larger. This is because strengths of the vortices cannot be solved correctly. Since the wing sections at 0.7 radius to tip of SSPA propeller are very thin and back and face surfaces are parallel, it is difficult to get more accurate vortex distribution on the blade by the present method. For making application of the present method to the propellers having sections whose thickness is very thin near the leading edge and a surface is parallel to another surface, it is necessary to arrange smaller panels or use surface vortex distribution instead of discrete vortex lattice.

Fig.26 and Fig.27 show extension and thickness of cavity.
As shown in Fig.26, the cavity is extending linearly from boss to 0.8 radius and contracting from 0.8 radius to tip. The cavity thickness distribution along the chord of SSPA propeller shown in Fig.27 increases straightly from the leading edge to 0.8 chord, takes a maximum value in rear of the trailing edge, after that suddenly happens to decrease near 1.4 chord and close at 1.6 chord.

Results of pressure distribution of SRIJ-II are shown in Fig.28. Here are including calculation results by SC-VLM in SRI. Although a great fluctuation can be seen in the calculations of SC-VLM on the face side surface, that of the present method is less. But we may suppose that integrations of the pressure difference between back and face surfaces equal to each other.

Fig.29 shows open water characteristics of SRIJ-II propeller. The experimental data are given by SRI like SSPA propeller. Conditions of calculations are that cavitation number is 0.4 and advance coefficients are 0.9, 1.1 and 1.3 among which the design point becomes the center of the three points. As shown in this figure, both of the thrust and torque are a little smaller than the experiments. About these differences, it is possible to eliminate the differences by considering of iterative deformation of the wake.

Extension and thickness of cavity are shown in Fig.30 and Fig.31 respectively.
The experimental data(extension of cavity) made by SRI are put in Fig.30 and results(cavity thickness) calculated by using SC-VLM in SRI are shown in Fig.31. With respect to the extension of the cavity shown in Fig.30, calculations are longer than experiments from hub to 0.45 radius and they are shorter than experiments from 0.45 radius to the tip. About the cavity thickness shown in Fig.31, the calculations by the present method are more than SC-VLM at the trailing edge and they are closing smoothly at 1.5 chord. As this phenomena is caused by a assumption that bottom surface of cavity concerning to wake is forced to coincide with classical wake generating from face side surface, we would get better results if an actual wake geometry which were made by iterative procedure.

CONCLUSIONS

The surface vortex lattice methods have been applied to the wings and the marine propllers in non- or super- cavitation conditon. As results, we have found the following conclusion about these methods.

1. Although the surface vortex lattice method with the vortex only distribution has an important discrepancy near the leading edge, the improved surface vortex lattice method

with combination of the vortex and source distributions can be applied to even the marine propeller having three dimensional complex configuration in non - cavitation condition.

2. The improved surface vortex lattice method can be used to the marine propeller working in super - cavitation condition and calculated results are in good agreement with experimental results concernong to lift coefficients. But it is necessary to investigate more detail by comparing with some experimental data about components of drag.

3. Good results concerning to extension of cavity can be obtained to both of super - cavitation wings and propellers. As we cannot discuss detail of cavity thickness for lack of experimental data, we shall have to research experimentally as well as theoretically in the future.

4. In the super - cavitation condition, accurate results can be gotten by use of the surface vortex lattice method but as future work, we would like to investigate the following items.

   (a) Improvement for wing having thin and parallel surface section

   (b) Geometry of the wake with consideration of deformation by iterative procedure in super - cavitation condition

   (c) Simulation of partial cavitation

ACKNOWLEDGMENTS

The present research was carried out as the co - operative research, Project No.SR214, of the Japan Ship Research Association.

The authors are grateful to Prof. H. Kato, the chairman of SR214, and to other all members of SR214 for their good discussions and the kind permission of presentation to this Symposium.

And the authors thank Mr. H., Hosoi, master student in Yokohama National University for his help.

REFERENCES

1. Ryo, S., Sasaki, Y., and late Takahashi, M.,"Analysis of Three Dimensional Flow around Marine Propeller by Direct Formulation of Boundary Element Method," Proceedings of the International Symposium on Propeller and Cavitation, Aug. 1992

2. Koyama, K., Kakugawa, A. and Okamoto, M.,"Experimental Investigation of Flow around a Marine Propeller and Application of Panel Method to the Propeller Theory," 16th Symposium on Naval Hydrodynamics, 1986

3. Hoshino, T.,"Hydrodynamic Analysis of Propellers in Steady Flow Using a Sureface Panel Method," Journal of the Society of Naval Architects of Japan, Vol.165, 1989 pp.55-70

4. Kerwin, J.E. Kinnas, S. A., Lee, J. T. and Shih W. Z.,"Asurface panel method for the hydrodynamic analysis of ducted propellers," Trans. SNAME, 95, 1987

5. Morino, L., Chen, L.,T. and Sciu,E.O.,"Steady and Oscillatory Subsonic and Supersonic Aerodynamics around Complex Confugurations," AIAA Journal, Vol.13, March 1975

6. Ishii, N.,"The influence of tip vortex on propeller performances,"Journal of the Society of Naval Architects of Japan, Vol.168, Dec. 1990, pp.77-88

7. Woodward, F.A.,"An Improved Method for the Aerodynamic Analysis of Wing-Body-Tail Configurations in Subsonic and Supersonic Flow, Part 1 Theory and Application,"NASA CR-2228 May, 1973

8. Maskew, B.,"Numerical Lifting Surface Methods for Calculating the Potential Flow about Wings and Wing-Bodies of Arbitrary Geometry," Ph.D. Thesis, Department of Transport Technology, Loughborough University of Technology, Lecis, England, 1972

9. Miranda, L.R.,"Extended Applications of the Vortex Lattice Method, Vortex Lattice Utilization," NASA SP-405, May, 1976

10. Kerwin, J.E. Lee, C. S.,"Prediction of Steady and Unsteady Marine Propeller Performance by Numerical Lifting-Surface Theory," SNAME, Vol.86, 1978, pp.218-253

11. Yuasa, H.,"Application of Numerical Lifting-Surface Theory on Steady Performance of Propeller/Duct System", Journal of the Society of Naval Architects of Japan, Vol.147, 1980 pp.53-70

12. Johnson, F.T.,"A General Panel Method for the Analysis and Design of Arbitrary Configurations in Incompressible flows", NASA CR-3079, May, 1980

13. Ishii, N., Ide, T.,"A study on the predictionof propeller slipstream and the numerical analysis of lifting surface," Journal of the Society of Naval Architects of Japan, Vol.160, Dec. 1986 pp.54-65

14. Jessup, S., D.,"An Experimental Investigation of Viscous Aspects of Propeller Blade Inflow," The Catholic University of America , Desertation for PHD, 1989

15. Matsuda, N., Kurobe, Y., Okamoto, M., and Ukon, Y."Propeller Open Water Test Using Four Kinds of Dynamometer", Papers of Ship Research Institute, Japan, 1992

Table 1 Principal Particulars of Propellers

Propeller Type	CP	HSP	DTRC4119
Diameter (m)	0.300	0.300	0.3048
Boss ratio	0.2133	0.2133	0.200
Pitch ratio	0.95(const)	0.944(0.7R)	1.084(0.7R)
Exp. Area ratio	0.65	0.70	
Angle of rake	6.00	-3.03	0.00(const.)
B-T ratio	0.0442	0.04961	
Number of blades	5	5	3
Blade section	MAU	SRI-B(mod.)	NACA66a=.8

Table 2 Experiments and calculation condition

	wing type	velocity(m/s)	Reynolds number
SRI (exp.)	N-R	8.0	1.0×10^6
	Johnson	8.0	1.0×10^6
UT (exp.)	N-R	8.0	1.5×10^6
	Johnson	6.0	1.1×10^6
YNU (cal.)	N-R	8.0	1.0×10^6
	Johnson	8.0	1.0×10^6

Table 3 Principal Particulars of Propellers

Propeller Type	SSPA	SRIJ-II
Diameter (m)	0.2000	0.2000
Boss ratio	0.1900	0.1900
Pitch ratio	1.60(0.7R)	1.4695(0.7R)
Exp.area ratio	0.500	0.641
Angle of rake	10.0(const.)	10.0(const.)
Number of blades	3	3
Blade section	SSPA	SRJN

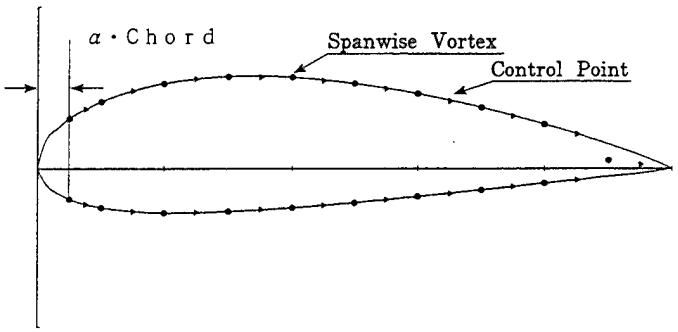


Fig.1 Arrangement of Surface Vortex Lattice Model

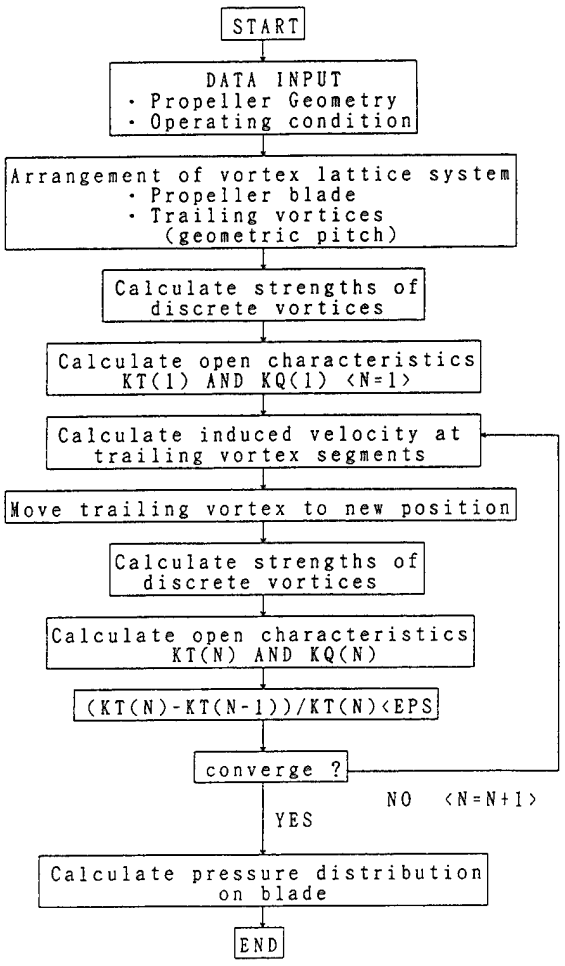


Fig.2 Flow Chart of Present Calculation

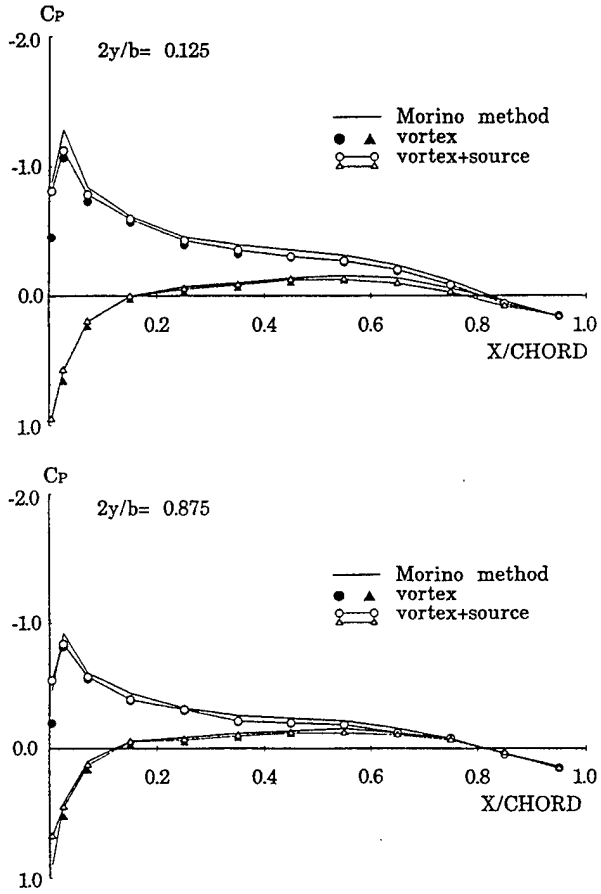


Fig.3 Pressure Coefficients of B-TR17
(Attack Angle 5.73 deg. Asp.Ratio: 2.00)

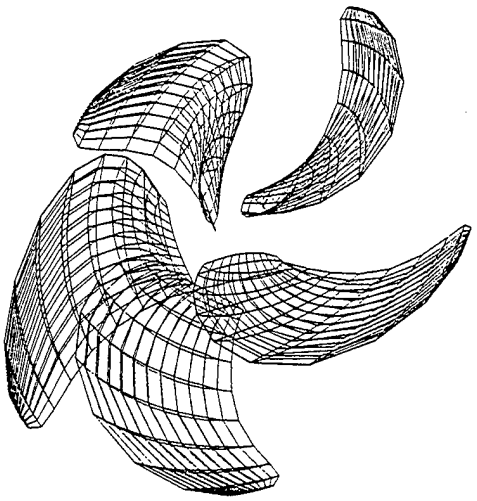


Fig.5 Arrangement of Surface Vortex
Lattice System of HSP

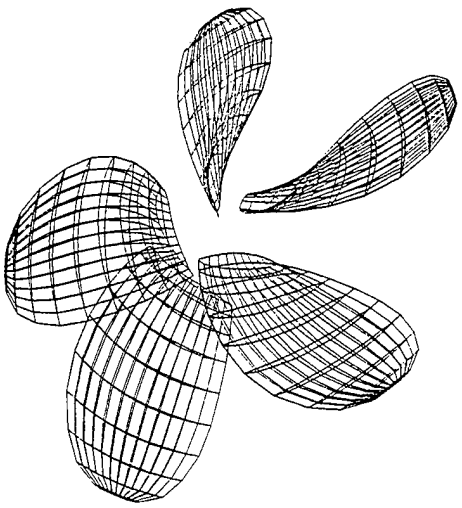


Fig.4 Arrangement of Surface Vortex
Lattice System of CP

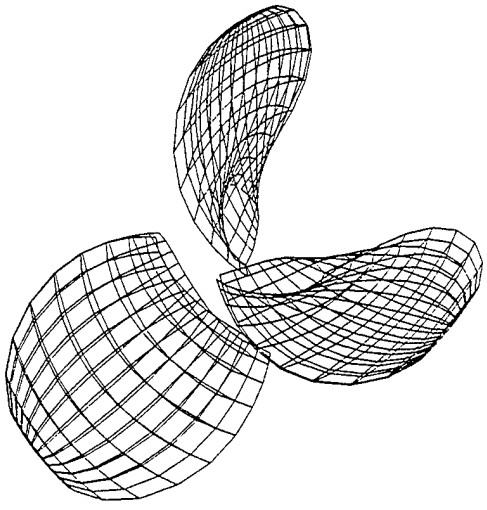


Fig.6 Arrangement of Surface Vortex
Lattice System of DTRC4119

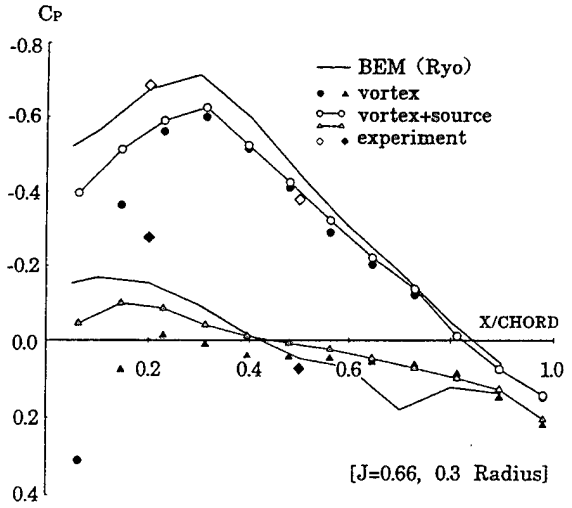


Fig.7 Pressure distribution of CP

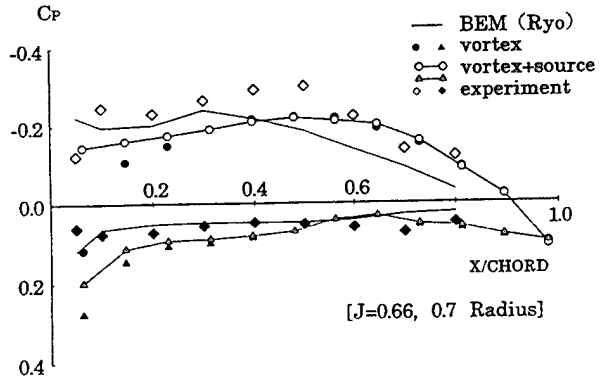


Fig.8 Pressure distribution of CP

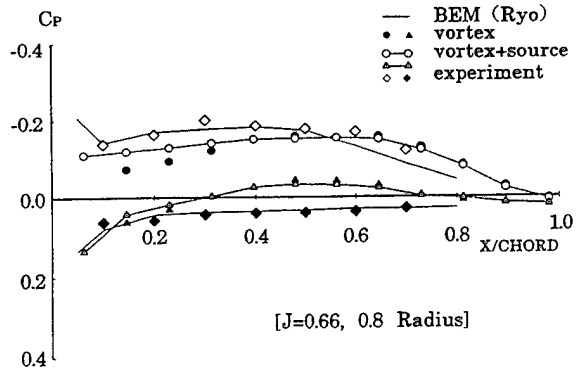


Fig.9 Pressure distribution of CP

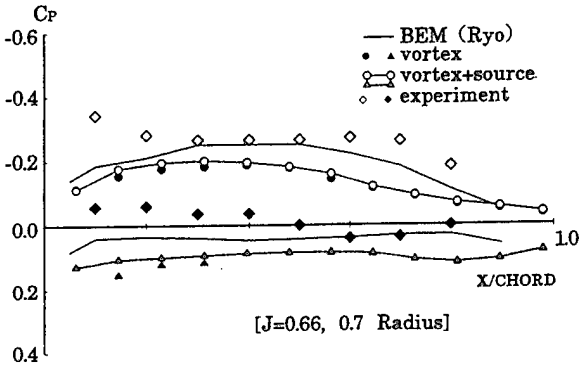


Fig.10 Pressure distribution of HSP

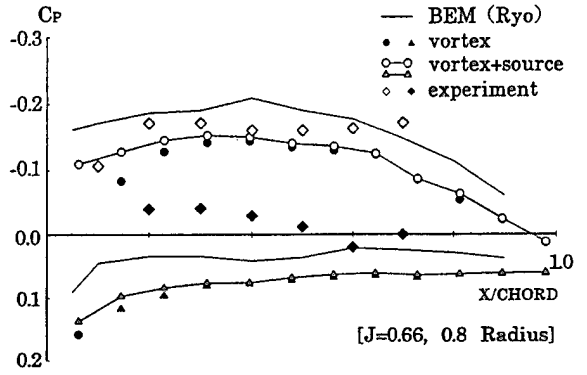


Fig.11 Pressure distribution of HSP

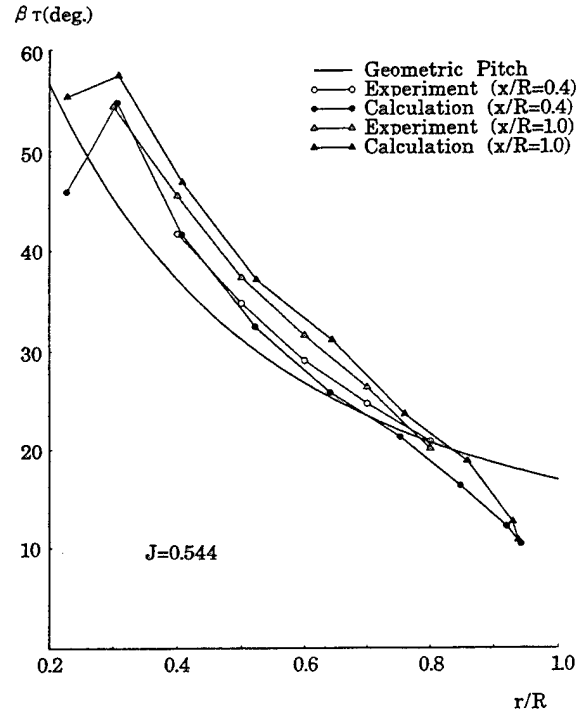


Fig.12 Wake Pitch Angle of CP

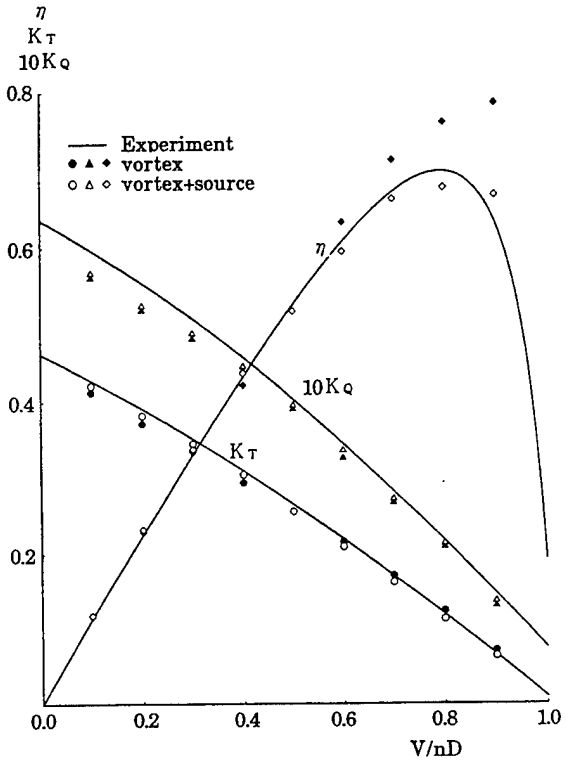


Fig.13 Open Water Characteristics of CP

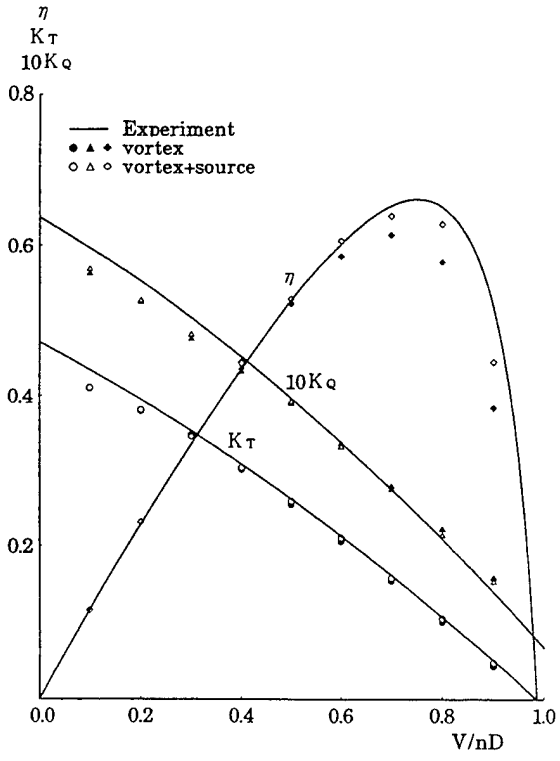


Fig.14 Open Water Characteristics of HSP

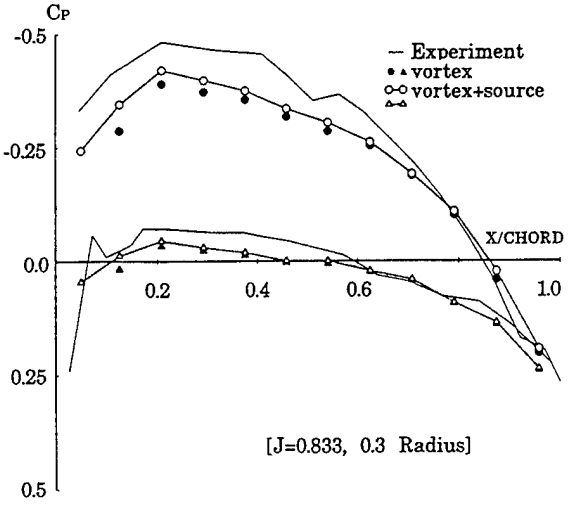


Fig.15 Pressure distribution of DTRC4119

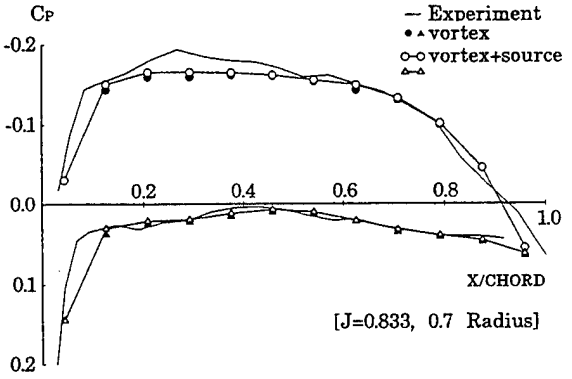


Fig.16 Pressure distribution of DTRC4119

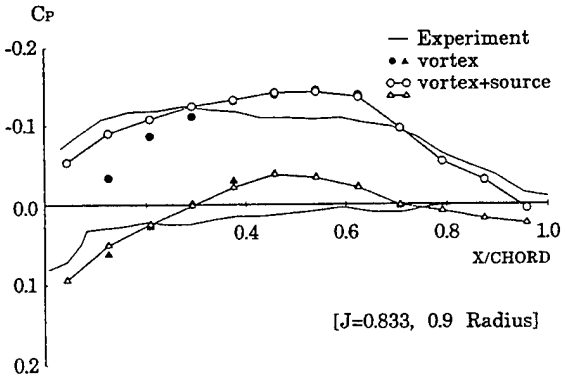


Fig.17 Pressure distribution of DTRC4119

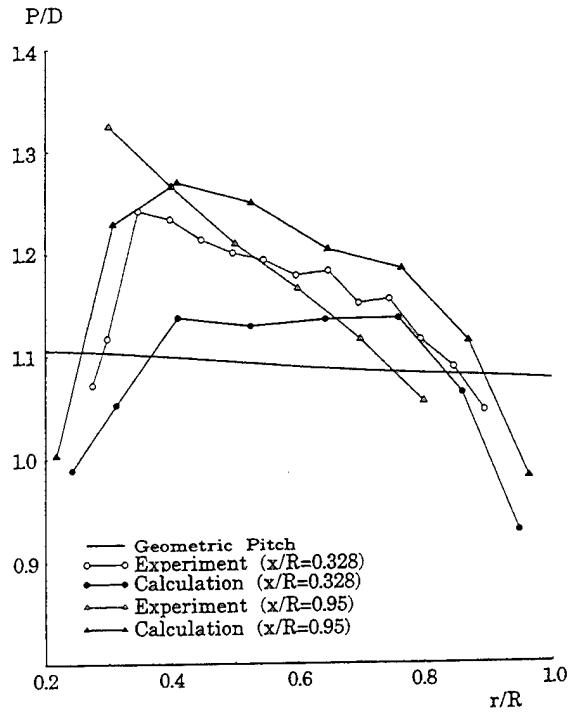


Fig.18 Wake Pitch of DTRC4119

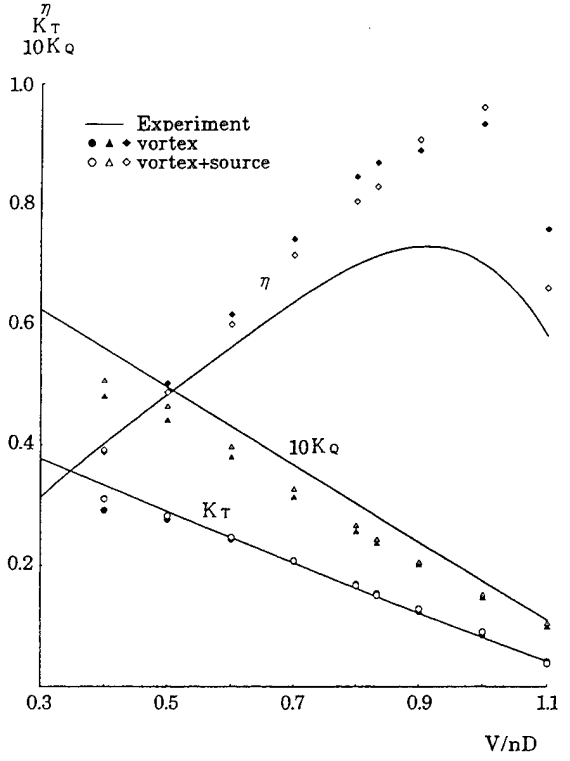


Fig.19 Open Water Characteristics of DTRC4119

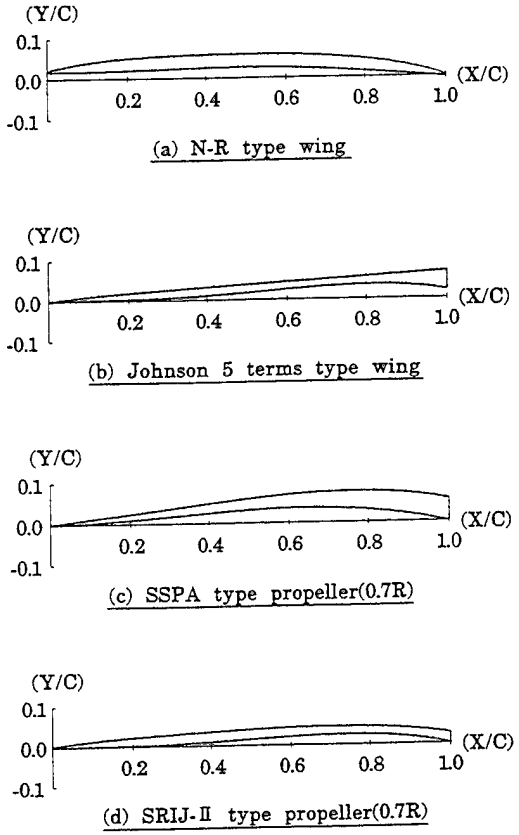
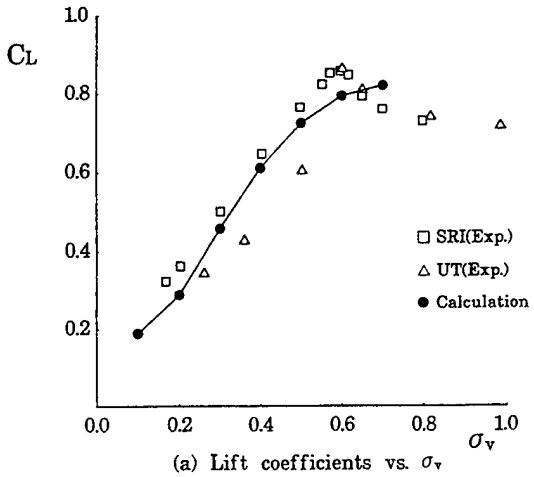
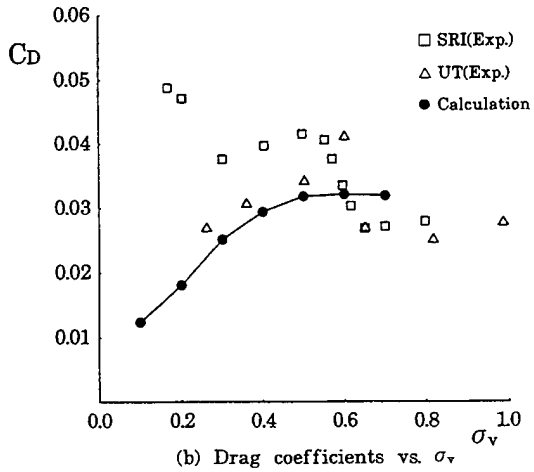


Fig.20 Sections of Wing or Propeller Blade

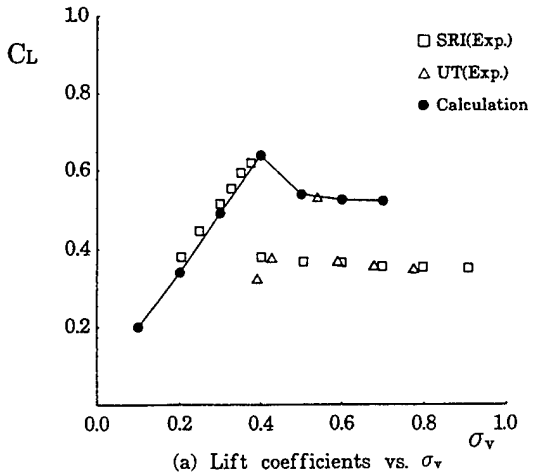


(a) Lift coefficients vs. σ_v

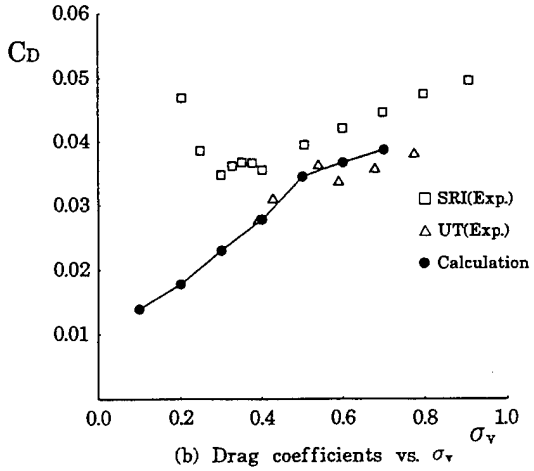


(b) Drag coefficients vs. σ_v

Fig.21 Comparison between experiments and calculation
(N-R wing, attack angle= 3.0 deg.)

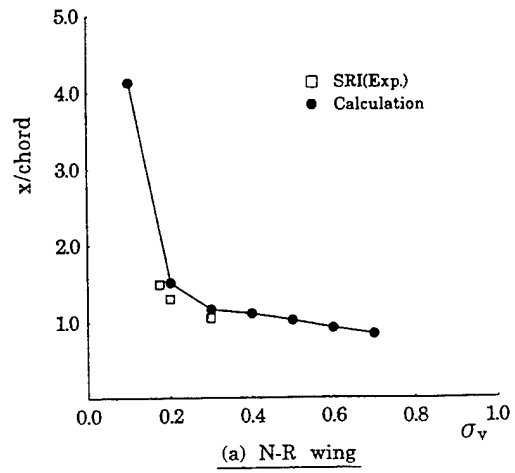


(a) Lift coefficients vs. σ_v

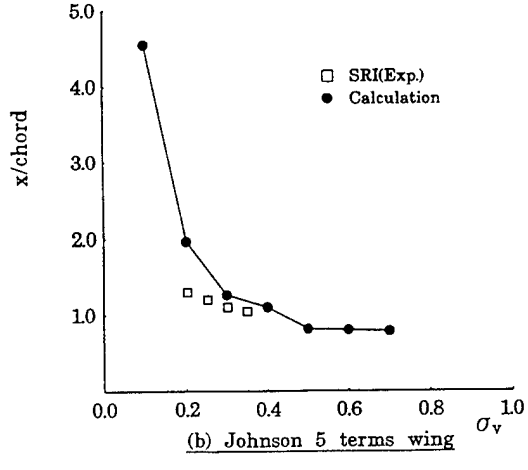


(b) Drag coefficients vs. σ_v

Fig.22 Comparison between experiments and calculation
(Johnson 5 terms wing,
attack angle= 3.0 deg.)



(a) N-R wing



(b) Johnson 5 terms wing

Fig.23 Comparison between experimental and calculated extension of cavity

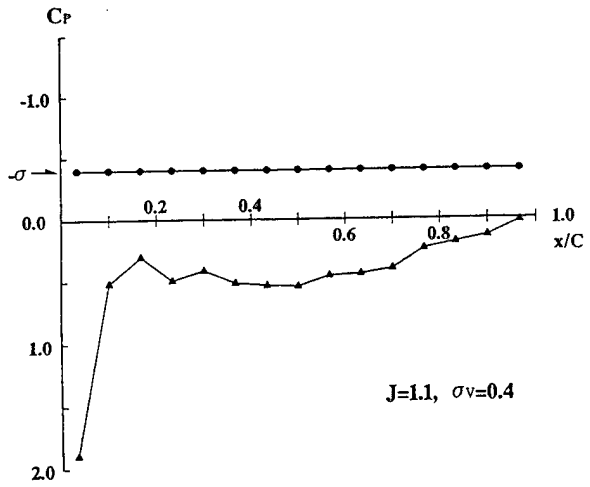


Fig.24 Pressure distribution of SSPA at 0.71R

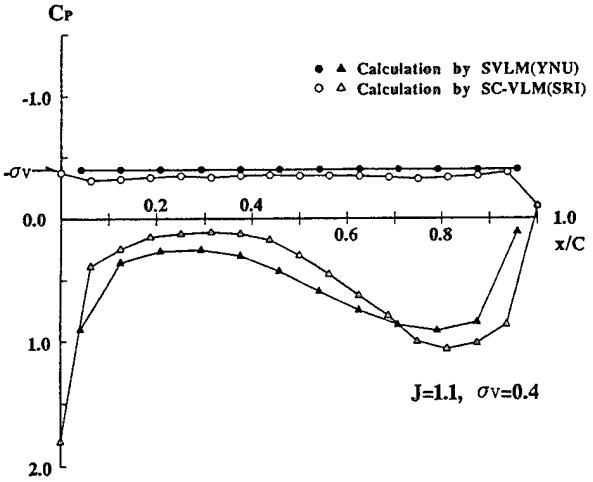


Fig.28 Pressure distribution of SRIJ-Ⅱ at 0.71R

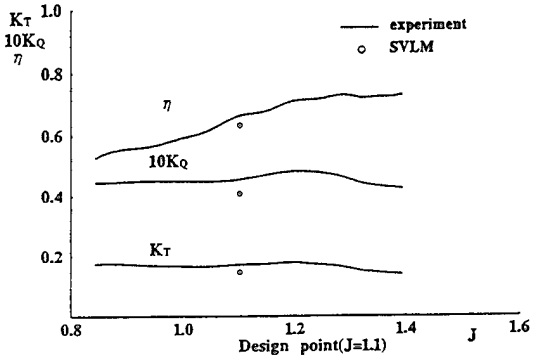


Fig.25 Cavity Extension of SSPA (J=1.1,σ_V=0.4)

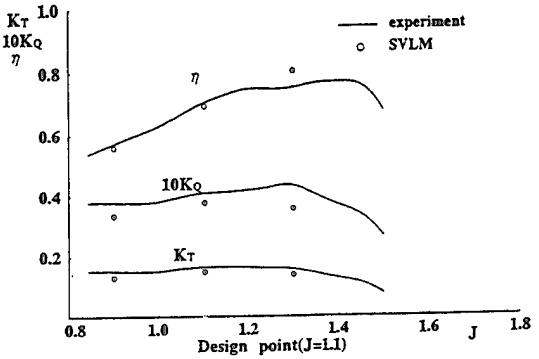


Fig.29 Cavity Extension of SRIJ-Ⅱ (J=1.1,σ_V=0.4)

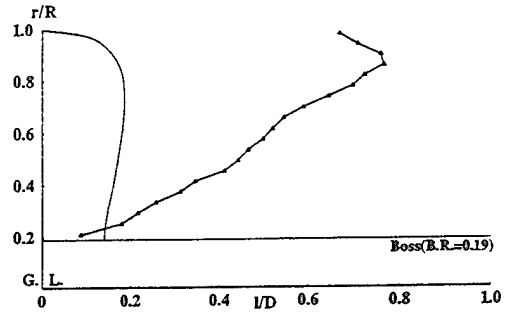


Fig.26 Open Water Characteristics of SSPA (σ_V=0.4)

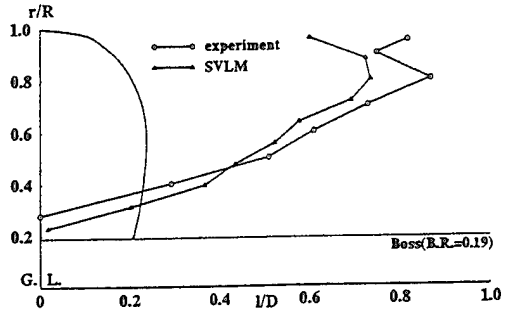


Fig.30 Open Water Characteristics of SRIJ-Ⅱ (σ_V=0.4)

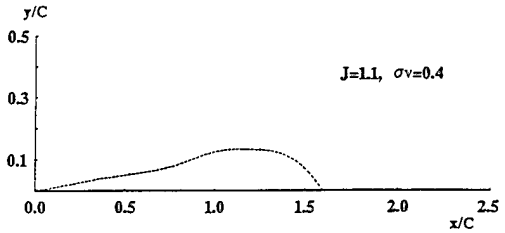


Fig.27 Cavity Thickness of SSPA at 0.7R

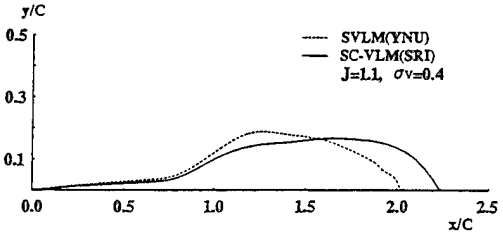


Fig.31 Cavity Thickness of SRIJ-Ⅱ at 0.71R

DISCUSSION

S. Kinnas
Massachusetts Institute of Technology, USA

It would be nice if the authors provide convergence tests (both with chordwise and spanwise number of panels) of their method (in *non-cavitating* and *cavitating* flow) as applied to propellers. Despite the good comparison of their method with experiments, it is *important* to establish the convergence of their method.

AUTHORS' REPLY

Professor Kinnas has asked for the convergence test on Surface Vortex Lattice Method. We provide the convergence test that the chordwise and spanwise number of panels are changed in non-cavitation condition.

Fig. A shows the results of the thrust and torque convergence tests by Surface Vortex Lattice Method. As shown in this figure, we could get good results of convergence tests for the spanwise and chordwise number.

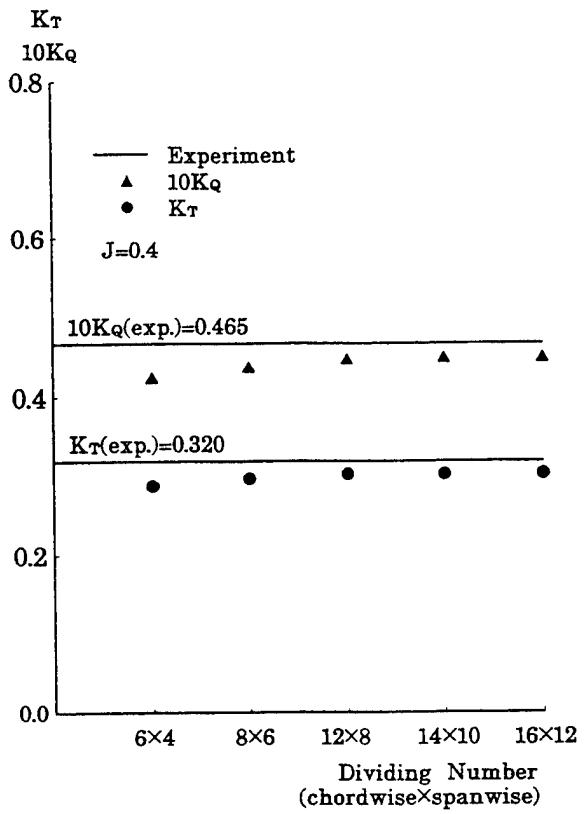


Fig.A Convergence of Open Water Characteristics (Conventional Propeller)

Time-Domain Theory of Wave Diffraction for Ship Motions with Forward Speed

Z. Zhou (China Ship Scientific Research Center, China),
Z. Liang, D. Yishan (Harbin Shipbuilding Engineering Institute, China)

ABSTRACT

A diffraction problem for a surface ship traveling at a constant forward speed in waves is studied by time domain analysis. A new formulation is proposed for computing wave exciting forces, in which diffraction forces are described according to the incident wave potential and the auxiliary-radiation potential corresponding to the motion in the opposite direction, therefore the exciting forces in time-domain can be given without computing the diffraction potential itself, the resulting integral equations of the auxiliary-radiation potentials need to be solved only once for all incident wave frequencies, which saves CPU time greatly and results in the time-domain theory can be used in ship engineering for practical purpose.

This paper also proves mathematically that for an arbitrary floating body, the terms of the waterline integral in the formula for computing diffraction forces will vanish, assuming the fluid disturbance due to steady forward motion is not small in free-surface condition. Physically the terms of waterline integral are the result of interaction between the steady forward motion and the unsteady motion.

Comparisons are made between the results of the time-domain computations, the conventional frequency-domain calculations and that of experiments. They validated the accuracy of the proposed formulation and demonstrated the efficiency of the method.

It is hoped that the present method may be a major step forward in the development of prediction tools for ship motions and loads with forward speed.

Keywords: wave forces, diffraction, time-domain theory

1. INTRODUCTION

The accurate prediction of ship motions and wave loads for ship design is a major purpose of seakeeping study. Although the flow field and resulting motions of a ship (3-D body) advancing in waves is a nonlinear, three-dimensional boundary value problem, for design purpose, the traditional engineering solution is to use a strip theory, in which the frequency is assumed to be large and the geometry of the body to be long and slender so that a solution can be approximated by a series of two-dimensional problems in the cross-flow plane. Strip theory gives rather accurate predictions for slender ships and ships moving at low speed, however, since in strip theory, the three-dimensionality of the flow field is neglected and the forward speed effects are accounted only in a simplistic manner (c.f. Zhou,et al,1991), therefore for high speed ships

or for ships and ocean structures of complex geometries, the strip theory is not theoretically correct for prediction purposes.

In order to account for the three dimensionality of the ship hull geometry, the three-dimensional frequency-domain panel method has been obtained a widespread development. By assuming motions to be small and harmonic, the resulting boundary-value problem is solved using a singularity distribution method on the mean body boundary thus reducing the complex 3-D boundary problem to the solving of a set of Fredholm integral equations of the second kind on the body surface. For zero speed problems, this approach is quite successful and has become a standard tool for the design of large offshore structures. In the presence of forward speed, especially at high speeds, the corresponding Neumann-Kelvin problem is significantly more difficult to attack due primarily to the difficulty and complexity of computing the corresponding Green functions. Thus, despite that a number of methods have been developed by a number of workers(e.g., Chang, 1977; Inglis and Price, 1981; Guevel and Bougis, 1982; Sun, et al, 1991; Zhou, et al, 1991), a truly satisfactory numerical solution is not yet available.

An alternative approach to the frequency-domain method is the time-domain analysis, in which the solution of the initial-value problem is formulated by time-domain approach. Cummins(1962) and Ogilvie(1964) first discussed the use of time-domain analysis to solve unsteady ship motion problems. In the case of linearized motions (small amplitude) with zero or a constant forward speed, the time-domain solutions are formally related to the frequency-domain results via Fourier transforms. Recently there appears a development of the time-domain method because the derived time-dependent Green function retains the same relatively simple form regardless of the body's velocity. It is much more simple than the corresponding Green function in the frequency domain, yet it is capable of describing arbitrary (large-amplitude) motions of ships or floating bodies when the proper free-surface memory effects are included. Beck and Liapis(1987) used linear time-domain analysis to solve the radiation problem for arbitrary bodies at zero forward speed. Liapis and Beck(1985) also gave results for the linearized radiation problem with constant forward speed. King, Beck and Magee(1988) studied the general linearized problem with constant forward speed. Lin and Yue(1990) extended the time-domain approach to arbitrary large-amplitude motions (with a linearized free-surface condition) of a surface piercing body in a seaway. They gave numerical results for linearized radiation and diffraction problems, for large-amplitude forced motions and free motions of a floating body with and without forward speed, and for calm water resistance and added wave resistance problems. Ferrant(1990), and Beck & Magee(1990) also investigated the large-amplitude motions.

However most of the above time-domain methods probably may not become a practical tool for prediction and ship design, because those time-domain methods are time consuming, requiring a large powerful high-speed computer. As we willsee it, a new time-domain method that saves computer time to even less than the frequency-domain method may be developed. One possible way is to separate the effects of ship hull geometry and ship speed from the effects of incident wave and ship transient motions in the integral equations. For radiation, it is possible to separate the effect of ship hull geometry from that of ship (time-dependant) motions (Liapis and Beck 1985). Thus when solving for hydrodynamic coefficients (added mass and damping coefficients), the integral equations of radiation potentials need to be solved only once and for all, independent of ship transient velocities. But, for diffraction problems at a constant forward speed, it is different and becomes very difficult to separate the effect of ship hull geometry from that of incident waves. Therefore the integrals of potentials contain incident waves. The process of solving the inte-

grals of diffraction potential is repeated every time when there is a change of incident wave frequency. Therefore, the computation is time consuming.

The above difficulty points to the requirement of developing the new mathematical model to deal with diffraction problem. In this paper, a new mathematical model of diffraction for a surface ship with forward speed will be presented, the proposed formulae for computing wave exciting forces and diffraction forces are derived. According to the new method, the effect of ship hull geometry willbe separated from the effect of incident waves, which will result in a new time-domain theory which can save a lot of CPU time.

2. THEORETICAL FORMULATION

Assuming that a ship advances with a constant speed u in waves and undergoes arbitrary six-degree-of-freedom motion in water of infinite depth. The coordinate system shown in Figure 1 is fixed to the mean position of the ship at midship with the z-axis positive upwards and x positive to the bow. The x-y plane is coincident with the calm water level.

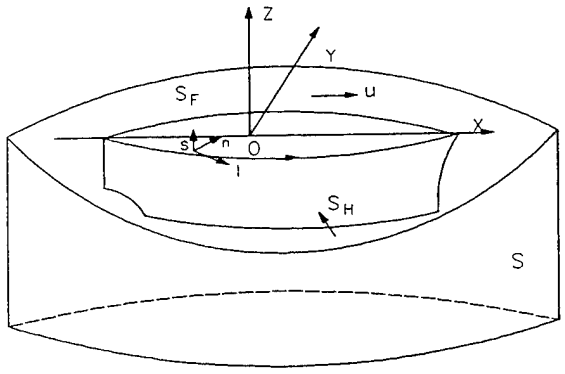


Fig. 1 Definition sketch

It is assumed that the fluid is incompressible, inviscid and the flow irrotational. To set up a linearized problem it is assumed that the fluid disturbances due to the steady forward motion and the unsteady oscillations are small and can be separated. In this case, the total velocity potential can be written as:

$$\Phi_T(x,y,z,t) = (-ux + \phi_0) + \phi_I + \phi_D + \phi_R \tag{1}$$

Where the term $-ux + \phi_0(x,y,z)$ is the potential due to the steady translation of the ship and ϕ_I, ϕ_D, ϕ_R represent all the unsteady effects, in which, ϕ_I is the incident wave potential, ϕ_D the diffracted wave potential, ϕ_R the radiation potential due to the ship's transient motions.

The boundary conditions on the diffraction potential are:

$$\nabla^2\phi_D(x,y,z,t) = 0 \qquad \text{in} \quad V$$

$$\left(\frac{\partial}{\partial t} - u\frac{\partial}{\partial x}\right)^2 \phi_D + g\frac{\partial \phi_D}{\partial z} = 0 \qquad on \quad z = 0$$

$$\frac{\partial \phi_D}{\partial n} = -\frac{\partial \phi_I}{\partial n} \qquad on \quad S_H$$

$$\nabla\phi_D \to 0 \qquad as \quad z \to -\infty \tag{2}$$

Where S_H represents the mean underwater hull surface, S_∞ represents the enclosing surface at infinity, and the calm water surface being denoted by $S_F(z=0)$.

Since an initial value problem is being treated and the disturbances generating the unsteady potentials originate in the neighborhood of the origin, the gradient of the diffraction potential must vanish at infinity for finite time.

$$\nabla\phi_D \to 0$$

$$\frac{\partial \phi_D}{\partial t} \to 0 \qquad on \quad S_\infty, \quad t > 0$$

The initial condition for the diffraction potential is :

$$\phi_D|_{t=0} = 0$$

$$\frac{\partial \phi_D}{\partial t}|_{t=0} = 0 \qquad on \quad S_F$$

The unsteady pressure of diffraction in the fluid is given by the linearized Bernoulli equation:

$$p = -\rho \frac{\partial \phi_D}{\partial t} - \rho \vec{w} \cdot \nabla \phi_D$$

where $\vec{w}$ is the velocity vector due to the steady translation. The wave diffraction forces acting on the body are found by integrating the pressure on the instantaneous underwater hull surface, which is given by

$$F_{Dk}(t) = -\rho \int\int_{S_H} \frac{\partial \phi_D}{\partial t} n_k ds - \rho \int\int_{S_H} (\vec{w} \cdot \nabla \phi_D) n_k ds \qquad k = 1, 2, \ldots, 6 \qquad (3)$$

The second term of Eq.(3) involves derivatives of the potential ϕ_D, a quantity which is difficult to evaluate. This gradient of the potential may be eliminated using the theorem presented in Ogilvie and Tuck(1969).

$$F_{Dk}(t) = -\rho \int\int_{S_H} \frac{\partial \phi_D}{\partial t} n_k ds + \rho \int\int_{S_H} \phi_D m_k ds - \rho \oint_\Gamma \phi_D n_k (\vec{l} \times \vec{n}) \cdot \vec{w} dl \qquad k = 1, 2, \ldots, 6 \qquad (4)$$

where

$\vec{l}$ is the unit vector in the tangential direction along the waterline; n_k are components of generalized unit normal, out of fluid domain.

$$(n_1, n_2, n_3) = \vec{n}$$

$$(n_4, n_5, n_6) = \vec{r} \times \vec{n}$$

$$\vec{r} = (x, y, z)$$

m_k are gradients of the steady velocities in the normal direction.

$$(m_1, m_2, m_3) = -(\vec{n} \cdot \nabla)\vec{w}$$

$$(m_4, m_5, m_6) = -(\vec{n} \cdot \nabla)(\vec{r} \times \vec{w})$$

and $\vec{w} = \nabla(-ux + \phi_0)$.

It should be noted that for most ship-like forms $(\vec{l} \times \vec{n})$ is almost perpendicular to $\vec{w}$ and thus the line integral is of higher order and may be neglected. Therefore :

$$F_{Dk}(t) = -\rho \int\int_{S_H} \frac{\partial \phi_D}{\partial t} n_k ds + \rho \int\int_{S_H} \phi_D m_k ds \qquad k = 1, 2, \ldots, 6 \qquad (5)$$

In order to separate the effect of incident wave from that of the ship hull geometry, we consider radiation potentials ψ_{1k}, ψ_{2k} and the auxiliary potentials $\chi_k^{(-)}$ corresponding to the motion in the opposite direction, these potential satisfy:

$$\nabla^2 \psi_{1k}(p) = 0 \qquad k = 1, 2, \ldots, 6 \quad \text{in} \quad V$$

$$\psi_{1k}(p) = 0 \qquad on \quad z = 0$$

$$\frac{\partial \psi_{1k}}{\partial n} = n_k \qquad on \quad S_H$$

$$\nabla \psi_{1k}(p) \to 0 \qquad at \quad S_\infty \qquad (6)$$

For ψ_{2k}, it satisfies:

$$\nabla^2 \psi_{2k}(p) = 0 \qquad k = 1, 2, \ldots, 6 \quad \text{in} \quad V$$

$$\psi_{2k}(p) = 0 \qquad on \quad z = 0$$

$$\frac{\partial \psi_{2k}}{\partial n} = m_k \qquad on \quad S_H$$

$$\nabla \psi_{2k}(p) \to 0 \qquad at \quad S_\infty \qquad (7)$$

For auxiliary radiation potentials corresponding to a translation in the opposite direction, we set:

$$\nabla^2 \chi_k^{(-)}(p,t) = 0 \qquad k = 1,2,\ldots,6 \quad \text{in} \quad V$$

$$\left[\left(\frac{\partial}{\partial t} + u\frac{\partial}{\partial x}\right)^2 + g\frac{\partial}{\partial z}\right][\chi_k^{(-)}(p,t) - \psi_{2k}(p)] = 0 \qquad \text{on} \quad z = 0$$

$$\frac{\partial \chi_k^{(-)}}{\partial n} = 0 \qquad \text{on} \quad S_H$$

$$\chi_k^{(-)}|_{t=0} = 0$$

$$\frac{\partial \chi_k^{(-)}}{\partial t}|_{t=0} = -g\frac{\partial \psi_{1k}}{\partial z} \quad (z = 0) \tag{8}$$

The $\psi_{1k}(p)$ describes the instantaneous effect of fluid due to a unit ship displacement, in which, the ship moves instantaneously from 0 to 1 in the k^{th} mode at t=0. This jump is impulsive, so that the velocity is a delta function, $\delta(t)$.

The $\psi_{2k}(p)$ and $\chi_k^{(-)}$ represent the motion of the fluid subsequent to the initial step motion. They may be considered as composed of two components: The first results from a change in body orientation due to the step function, after which the body will have a unit displacement in the k^{th} mode. This in turn, in the presence of a steady velocity of translation of the ship, results in changes of fluid velocities on the body surface. In order for the body boundary conditions remain to be satisfied these changes must be compensated out. Therefore, $\frac{\partial \psi_{2k}}{\partial n}$ is required to have the value m_k on the body surface for all t>0; as m_k is the gradient of the steady velocity. The second component is the result of the impulsive velocity (the ψ_{1k} problem) inducing a disturbance into the flow field which in the subsequent time willpropagate as a wave motion away from the body. Consequently, $\chi_k^{(-)}$ willhave to satisfy (for t>0) the free surface condition, and the fixed body surface condition. $\chi_k^{(-)}$ will also have to satisfy (at t=0) the initial wave elevation condition. $\chi_k^{(-)}$ gives the memory effect of the fluid. It is different from the usual radiation potential in that the u and ψ_{2k} in the free-surface condition change from positive to negative signs; i.e. as ifsolving a radiation problem in which the ship moves in the opposite direction.

In order to change the form of diffraction forces in Eq.(5), we rewrite the first term of Eq.(5) using the body surface condition of ψ_{1k} and ϕ_D as following:

$$\int\int_{S_H} \frac{\partial \phi_D}{\partial t} n_k ds = \int\int_{S_H} \frac{\partial \phi_D}{\partial t}\frac{\partial \psi_{1k}}{\partial n} ds = A_k - \int\int_{S_H} \psi_{1k}\frac{\partial^2 \phi_I}{\partial n \partial t} ds \tag{9}$$

Where

$$A_k = \int\int_{S_H}\left(\frac{\partial \phi_D}{\partial t}\frac{\partial \psi_{1k}}{\partial n} - \psi_{1k}\frac{\partial^2 \phi_D}{\partial n \partial t}\right) ds \tag{10}$$

By applying Green's identity to Eq.(10) and considering the free-surface condition of ψ_{1k} we obtain:

$$A_k = -\int\int_{S_F}\left(\frac{\partial \phi_D}{\partial t}\frac{\partial \psi_{1k}}{\partial z} - \psi_{1k}\frac{\partial^2 \phi_D}{\partial z \partial t}\right) ds = -\int\int_{S_F} \frac{\partial \phi_D}{\partial t}\frac{\partial \psi_{1k}}{\partial z} ds \tag{11}$$

where S_F is the surface of xoy plane with the surface of the ship's waterplane deducted. Rewriting Eq.(11) according to the boundary conditions of ψ_{1k} and ϕ_D:

$$-\frac{\partial \phi_D}{\partial t}\frac{\partial \psi_{1k}}{\partial z} = \frac{1}{g}\frac{\partial \phi_D(p,t)}{\partial t}\cdot\left[\frac{\partial \chi_k^{(-)}(p,t)}{\partial t}\right]|_{t=0}$$

$$= -\frac{1}{g}\int_0^t \frac{\partial}{\partial \tau}\left[\frac{\partial \phi_D(p,\tau)}{\partial \tau}\cdot\frac{\partial \chi_k^{(-)}(p,t-\tau)}{\partial \tau}\right] d\tau$$

$$= -\frac{1}{g}\int_0^t \left[\frac{\partial^2 \phi_D(p,\tau)}{\partial \tau^2}\cdot\frac{\partial \chi_k^{(-)}(p,t-\tau)}{\partial \tau} + \frac{\partial \phi_D(p,\tau)}{\partial \tau}\cdot\frac{\partial^2 \chi_k^{(-)}(p,t-\tau)}{\partial \tau^2}\right] d\tau$$

$$= \frac{1}{g}\int_0^t [(-2u\frac{\partial^2\phi_D}{\partial x\partial\tau} + u^2\frac{\partial^2\phi_D}{\partial x^2}$$

$$+ g\frac{\partial\phi_D}{\partial z})\frac{\partial\chi_k^{(-)}(p,t-\tau)}{\partial\tau}$$

$$+(2u\frac{\partial^2\chi_k^{(-)}(p,t-\tau)}{\partial x\partial t} + u^2\frac{\partial^2\chi_k^{(-)}}{\partial x^2}$$

$$+ g\frac{\partial\chi_k^{(-)}}{\partial z} - g\frac{\partial\psi_{2k}}{\partial z})\frac{\partial\phi_D}{\partial\tau}]d\tau$$

Changing the form of following terms :

$$\frac{2u}{g}\left(-\frac{\partial^2\phi_D}{\partial x\partial\tau}\frac{\partial\chi_k^{(-)}}{\partial\tau} + \frac{\partial^2\chi_k^{(-)}}{\partial x\partial t}\frac{\partial\phi_D}{\partial\tau}\right) = -\frac{2u}{g}\frac{\partial}{\partial x}\left(\frac{\partial\phi_D}{\partial\tau}\frac{\partial\chi_k^{(-)}}{\partial\tau}\right)$$

$$\frac{u^2}{g}\left(\frac{\partial^2\phi_D}{\partial x^2}\frac{\partial\chi_k^{(-)}}{\partial\tau} + \frac{\partial^2\chi_k^{(-)}}{\partial x^2}\frac{\partial\phi_D}{\partial\tau}\right)$$

$$= \frac{u^2}{g}\left[\frac{\partial}{\partial x}\left(\frac{\partial\phi_D}{\partial x}\frac{\partial\chi_k^{(-)}}{\partial\tau} + \frac{\partial\chi_k^{(-)}}{\partial x}\frac{\partial\phi_D}{\partial\tau}\right) - \frac{\partial}{\partial\tau}\left(\frac{\partial\phi_D}{\partial x}\frac{\partial\chi_k^{(-)}}{\partial x}\right)\right]$$

$$\int_0^t \frac{\partial\phi_D}{\partial z}\frac{\partial\chi_k^{(-)}(p,t-\tau)}{\partial\tau}d\tau = -\int_0^t \chi_k^{(-)}\frac{\partial^2\phi_D}{\partial z\partial\tau}d\tau$$

$$-\int_0^t \frac{\partial\psi_{2k}(p)}{\partial z}\frac{\partial\phi_D}{\partial\tau}d\tau = -\frac{\partial\psi_{2k}}{\partial z}\cdot\phi_D(p,t)$$

This gives

$$A_k = \int_0^t d\tau\int\int_{S_F}\left[\frac{\partial\chi_k^{(-)}}{\partial z}\frac{\partial\phi_D}{\partial\tau} - \chi_k^{(-)}(p,t-\tau)\cdot\frac{\partial^2\phi_D}{\partial z\partial\tau}\right]ds$$

$$-\int\int_{S_F}\frac{\partial\psi_{2k}}{\partial z}\cdot\phi_D(p,t)ds$$

$$-\frac{u^2}{g}\int\int_{S_F}ds\int_0^t\frac{\partial}{\partial\tau}\left(\frac{\partial\phi_D}{\partial x}\frac{\partial\chi_k^{(-)}(p,t-\tau)}{\partial x}\right)d\tau$$

$$-2\frac{u}{g}\int_0^t d\tau\int\int_{S_F}\frac{\partial}{\partial x}\left(\frac{\partial\phi_D}{\partial\tau}\frac{\partial\chi_k^{(-)}}{\partial\tau}\right)ds$$

$$+\frac{u^2}{g}\int_0^t d\tau\int\int_{S_F}\frac{\partial}{\partial x}\left(\frac{\partial\phi_D}{\partial x}\frac{\partial\chi_k^{(-)}}{\partial\tau} + \frac{\partial\chi_k^{(-)}}{\partial x}\frac{\partial\phi_D}{\partial\tau}\right)ds$$

(12)

The third term of Eq.(12) vanishes due to the initial conditions of $\phi_D(p,t)$ and $\chi_k^{(-)}(p,t)$. For the first and second terms of Eq.(12), it can be transformed into a new expression by Green's identity.

$$\int_0^t d\tau\int\int_{S_F}\left[\frac{\partial\chi_k^{(-)}}{\partial z}\frac{\partial\phi_D}{\partial\tau} - \chi_k^{(-)}(p,t-\tau)\cdot\frac{\partial^2\phi_D}{\partial z\partial\tau}\right]ds$$

$$-\int\int_{S_F}\frac{\partial\psi_{2k}}{\partial z}\cdot\phi_D(p,t)ds$$

$$= -\int_0^t d\tau\int\int_{S_H}\left[\frac{\partial\chi_k^{(-)}}{\partial n}\frac{\partial\phi_D}{\partial\tau} - \chi_k^{(-)}\frac{\partial^2\phi_D}{\partial n\partial\tau}\right]ds$$

$$+\int\int_{S_H}\left(\phi_D\frac{\partial\psi_{2k}}{\partial n} - \psi_{2k}\frac{\partial\phi_D}{\partial n}\right)ds$$

$$-\int\int_{S_H}\psi_{2k}\frac{\partial\phi_I}{\partial n}ds + \int\int_{S_H}m_k\phi_D ds$$

$$-\int_0^t d\tau\int\int_{S_H}\chi_k^{(-)}\frac{\partial^2\phi_I}{\partial n\partial\tau}ds$$

(13)

Applying Stokes' theorem to the fourth and fifth terms of Eq.(12) yields:

$$-2\frac{u}{g}\int_0^t d\tau\int\int_{S_F}\frac{\partial}{\partial x}\left(\frac{\partial\phi_D}{\partial\tau}\frac{\partial\chi_k^{(-)}}{\partial\tau}\right)ds$$

$$+\frac{u^2}{g}\int_0^t d\tau\int\int_{S_F}\frac{\partial}{\partial x}\left(\frac{\partial\phi_D}{\partial x}\frac{\partial\chi_k^{(-)}}{\partial\tau} + \frac{\partial\chi_k^{(-)}}{\partial x}\frac{\partial\phi_D}{\partial\tau}\right)ds$$

$$= 2\frac{u}{g}\int_0^t d\tau\oint_\Gamma\frac{\partial\phi_D}{\partial\tau}\frac{\partial\chi_k^{(-)}}{\partial\tau}dy$$

$$-\frac{u^2}{g}\int_0^t d\tau\oint_\Gamma\left(\frac{\partial\phi_D}{\partial x}\frac{\partial\chi_k^{(-)}}{\partial\tau} + \frac{\partial\chi_k^{(-)}}{\partial x}\frac{\partial\phi_D}{\partial\tau}\right)dy$$

(14)

Where Γ = intersection of the mean hull surface and the plane z=0. The positive sense of the line integral is in the counterclockwise direction.

The final result for diffraction forces of a surface ship in time-domain is :

$$F_{Dk}(t) = \rho\int\int_{S_H}\psi_{1k}\frac{\partial^2\phi_I}{\partial n\partial t}ds - \rho\int\int_{S_H}\psi_{2k}\frac{\partial\phi_I}{\partial n}ds$$

$$+\rho\int_0^t d\tau\int\int_{S_H}\chi_k^{(-)}(p,t-\tau)\cdot\frac{\partial^2\phi_I(p,\tau)}{\partial n\partial\tau}ds$$

$$-\frac{2u\rho}{g}\int_0^t d\tau\oint_\Gamma\frac{\partial\phi_D}{\partial\tau}\frac{\partial\chi_k^{(-)}}{\partial\tau}dy$$

$$+\frac{\rho u^2}{g}\int_0^t d\tau\oint_\Gamma\left(\frac{\partial\phi_D}{\partial x}\frac{\partial\chi_k^{(-)}}{\partial\tau} + \frac{\partial\chi_k^{(-)}}{\partial x}\frac{\partial\phi_D}{\partial\tau}\right)dy$$

(15)

Eq.(15) is the formula of wave diffraction forces for a surface ship (an arbitrary 3-D body). In the case of a submerged body, Eq.(15) also gives its wave diffraction forces while the water line integrals vanish. Therefore, the formula of wave diffraction forces for a submerged body traveling near free-surface becomes a special case of Eq.(15).

For surface ships which may be considered as slender bodies, the water line integral terms may also be neglected. Since $dy = dl \cdot \sin\theta$, and θ is the angle that $\vec{dl}$ subtends with ox axis, a small quantity of $o(\epsilon)$, where $\epsilon = B/L$ (B is the ship width, and L is the ship length), therefore dy is of $o(\epsilon)$, and the integrals round the water line become quantities of higher order than ϵ^2. In the case of a slender body, the wave diffraction forces of Eq.(15) are given by the following expression.

$$F_{Dk}(t) = \rho \int\int_{S_H} \psi_{1k} \frac{\partial^2 \phi_I}{\partial n \partial t} ds - \rho \int\int_{S_H} \psi_{2k} \frac{\partial \phi_I}{\partial n} ds$$

$$+ \rho \int_0^t d\tau \int\int_{S_H} \chi_k^{(-)}(p, t-\tau) \cdot \frac{\partial^2 \phi_I(p,\tau)}{\partial n \partial \tau} ds$$

$$k = 1, 2, \ldots, 6 \quad (16)$$

In fact, the results of numerical experiment show that the line integral term indeed is of high order.

The exciting forces acting on the slender ship due to incident waves are determined as following.

Expressing Froude-Krylov forces as:

$$F_{Ik}(t) = -\rho \int\int_{S_H} \frac{\partial \phi_I}{\partial t} n_k ds + \rho \int\int_{S_H} \phi_I m_k ds$$

$$k = 1, 2, \ldots, 6 \quad (17)$$

The total exciting forces are the sum of Froude-Krylov force and the diffraction force, thus, the exciting forces acting on the slender ship are given by

$$F_k(t) = \rho \int\int_{S_H} \left(\psi_{1k} \frac{\partial^2 \phi_I}{\partial n \partial t} - \frac{\partial \phi_I}{\partial t} n_k \right) ds$$

$$- \rho \int\int_{S_H} \left(\psi_{2k} \frac{\partial \phi_I}{\partial n} - \phi_I m_k \right) ds$$

$$+ \rho \int_0^t d\tau \int\int_{S_H} \chi_k^{(-)}(p, t-\tau) \frac{\partial^2 \phi_I(p,\tau)}{\partial n \partial \tau} ds$$

Substituting Eq.(6) and (7) into the above equation yield a new time-domain expression (18) of wave exciting force, which shall be referred to as the Dai-Zhou-Zhang expression in our present and later papers.

$$F_k(t) = \rho \int\int_{S_H} (\psi_{1k} \frac{\partial}{\partial n} \left(\frac{\partial \phi_I}{\partial t} \right) - \frac{\partial \phi_I}{\partial t} \frac{\partial \psi_{1k}}{\partial n}) ds$$

$$- \rho \int\int_{S_H} \left(\psi_{2k} \frac{\partial \phi_I}{\partial n} - \phi_I \frac{\partial \psi_{2k}}{\partial n} \right) ds$$

$$+ \rho \int_0^t d\tau \int\int_{S_H} \chi_k^{(-)}(p, t-\tau) \frac{\partial^2 \phi_I(p,\tau)}{\partial n \partial \tau} ds$$

$$k = 1, 2, \ldots, 6 \quad (18)$$

Expression (18) shows that wave exciting forces of a slender ship traveling at a forward speed can be calculated only according to the incident wave potential, the radiation potentials and the auxiliary radiation potentials, without solving the diffraction potential problem. It is similar to the Haskind relation at zero speed in frequency-domain. From (18), the effect of ship hull geometry may be separated from the effect of the unsteady incident wave history, which enable us to solve the integral equations of ψ_{1k}, ψ_{2k}, $\chi_k^{(-)}$, independent of incident wave frequencies, and only once, then for any arbitrary incident wave frequency, the wave exciting forces can be obtained by the convolution integral. It saves CPU time greatly. The numerical results in this paper are obtained through the use of the Dai-Zhou-Zhang expression.

For an arbitrary floating and advancing vessel in general, its wave diffraction forces are expressed by Eq.(15) which include water line integrals. It may be proved mathematically that

for an arbitrary floating body, the water-line integral terms in Eq.(15) vanish, if the fluid disturbance due to steady forward motion is not small in the free surface condition. Physically, the water-line integral terms are the result of interactions between the steady forward motion and the unsteady ship motions. This conclusion may be proved by solving the wave diffraction problem of a fixed body when swept past by waves and current, as follows.

Assume an arbitrary body (zero speed) to be fixed in space and under the action of oncoming waves and current. An earth-fixed Cartesian coordinate system is chosen with $x_0 - y_0$ plane coincident with the quiescent free surface, and z_0 positive upward.

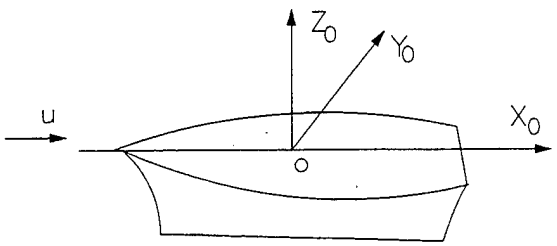


Fig.23 Definition sketch

The fluid motions under this condition may be described by a velocity potential

$$\Phi_T = u\phi_s + (\phi_I + \phi_D) = u\phi_s + \tilde{\Phi} \qquad (19)$$

Where ϕ_s is the steady state potential, $\phi_s \sim x$ at infinity (S_∞), $\tilde{\phi}$ is the unsteady potential. Assuming $\phi_s = O(1)$, $\phi_I = \phi_D = o(\epsilon)$, we shall retain the terms $O(u)$ and $O(\epsilon)$ in the equations, and neglect high order terms such as $O(u^2)$, $O(\epsilon^2)$, ...

We impose the nonlinear condition on the free surface:

$$\frac{\partial^2 \Phi_T}{\partial t^2} + g\frac{\partial \Phi_T}{\partial z_0} + 2\nabla\Phi_T \cdot \nabla\left(\frac{\partial \Phi_T}{\partial t}\right)$$

$$+\frac{1}{2}\nabla\Phi_T \cdot \nabla(\nabla\Phi_T \cdot \nabla\Phi_T) = 0$$

$$on \quad z_0 = \eta \qquad (20)$$

By the above assumption, the wave elevation is :

$$\eta = -\frac{1}{g}\left(\frac{\partial \tilde{\Phi}}{\partial t} + u\nabla\phi_s \cdot \nabla\tilde{\Phi}\right) \qquad (21)$$

Expanding Eq.(20) on the mean free-surface ($z_0 = 0$), and comparing the order of every term, the approximation for the free-surface condition of $\phi_I + \phi_D$ becomes

$$\frac{\partial^2(\phi_I + \phi_D)}{\partial t^2} + 2u\nabla\phi_s \cdot \nabla\frac{\partial(\phi_I + \phi_D)}{\partial t}$$

$$+u\left(\frac{\partial^2\phi_s}{\partial x_0^2} + \frac{\partial^2\phi_s}{\partial y_0^2}\right)\frac{\partial(\phi_I + \phi_D)}{\partial t} + g\frac{\partial(\phi_I + \phi_D)}{\partial z_0} = 0$$

$$(z_0 = 0) \qquad (22)$$

Since for the incoming wave, its free-surface condition is already known as

$$\frac{\partial^2\phi_I}{\partial t^2} + 2u\frac{\partial^2\phi_I}{\partial x_0 \partial t} + u^2\frac{\partial^2\phi_I}{\partial x_0^2} + g\frac{\partial\phi_I}{\partial z_0} = 0$$

$$(z_0 = 0) \qquad (23)$$

Thus the free-surface condition of ϕ_D is

$$\frac{\partial^2\phi_D}{\partial t^2} + 2u\nabla\phi_s \cdot \nabla\frac{\partial\phi_D}{\partial t}$$

$$+u\left(\frac{\partial^2\phi_s}{\partial x_0^2} + \frac{\partial^2\phi_s}{\partial y_0^2}\right)\frac{\partial\phi_D}{\partial t} + g\frac{\partial\phi_D}{\partial z_0} = P(\phi_I)$$

$$(z_0 = 0) \qquad (24)$$

where $P(\phi_I)$ is a function of incident wave ϕ_I only,

$$P(\phi_I) = 2u\left(\frac{\partial^2\phi_I}{\partial x_0 \partial t} - \nabla\phi_s \cdot \nabla\frac{\partial\phi_I}{\partial t}\right)$$

$$-u\left(\frac{\partial^2\phi_s}{\partial x_0^2} + \frac{\partial^2\phi_s}{\partial y_0^2}\right)\frac{\partial\phi_I}{\partial t} + u^2\frac{\partial^2\phi_I}{\partial x_0^2}$$

we express diffraction forces as :

$$F_{Dj}(t) = -\rho \int\int_{S_H} \frac{\partial \phi_D}{\partial t} n_j ds + \rho u \int\int_{S_H} \phi_D m_j ds$$

$$j = 1, 2, \ldots, 6 \qquad (25)$$

Here m_j is as before, but $\vec{w} = \nabla \phi_s$. Defining radiation potentials $\psi_{1j}, \psi_{2j}, \chi_j$ as follows:

$$\nabla^2 \psi_{1j}(p) = \nabla^2 \psi_{2j}(p) = 0 \quad j = 1, 2, \ldots, 6 \quad \text{in} \quad V$$

$$\psi_{1j}(p) = \psi_{2j}(p) = 0 \quad on \quad z = 0$$

$$\frac{\partial \psi_{1j}}{\partial n} = n_j, \quad \frac{\partial \psi_{2j}}{\partial n} = u m_j \quad on \quad S_H$$

$$\nabla \psi_{1j}(p) = \nabla \psi_{2j}(p) \to 0 \quad at \quad S_\infty$$

(26)

and

$$\nabla^2 \chi_j(p,t) = 0 \qquad j = 1, 2, \ldots, 6 \quad \text{in} \quad V$$

$$\frac{\partial^2 \chi_j}{\partial t^2} - 2u \nabla \phi_s \cdot \nabla \frac{\partial \chi_j}{\partial t} - u \left(\frac{\partial^2 \phi_s}{\partial x_0^2} + \frac{\partial^2 \phi_s}{\partial y_0^2} \right) \frac{\partial \chi_j}{\partial t}$$

$$+ g \frac{\partial \chi_j}{\partial z_0} = g \frac{\partial \psi_{2j}}{\partial z_0} \qquad (z_0 = 0)$$

$$\frac{\partial \chi_j}{\partial n} = 0 \qquad on \quad S_H$$

$$\chi_j|_{t=0} = 0$$

$$\frac{\partial \chi_j}{\partial t}|_{t=0} = -g \frac{\partial \psi_{1j}}{\partial z_0} \quad (on \quad S_F)$$

(27)

The process of derivation is the same as that of Eq.(15), but noting that $\frac{\partial \phi_s}{\partial n} = 0$, we obtain the diffraction forces in this case finally as:

$$F_{Dj}(t) = \rho \int\int_{S_H} \psi_{1j} \frac{\partial^2 \phi_I}{\partial n \partial t} ds - \rho \int\int_{S_H} \psi_{2j} \frac{\partial \phi_I}{\partial n} ds$$

$$+ \rho \int_0^t d\tau \int\int_{S_H} \chi_j(p, t-\tau) \cdot \frac{\partial^2 \phi_I(p,\tau)}{\partial n \partial \tau} ds + f(\phi_I)$$

$$j = 1, 2, \ldots, 6 \qquad (28)$$

Where $f(\phi_I)$ is the term determined by ϕ_I only. In the above equation, we see that water-line integrals vanish, which validates our original assumption.

In order to compute the exciting forces expressed by Eq.(18), the integral equations of $\psi_{1k}, \psi_{2k}, \chi_k^{(-)}$ should be given. First of all, we introduce a transient free-surface Green function for an impulsive source below free-surface:

$$G(p,t;q,\tau) = \left(\frac{1}{r_{pq}} - \frac{1}{r_{pq'}} \right) \delta(t-\tau)$$

$$+ H(t-\tau) \tilde{G}(p,t;q,\tau)$$

(29)

where $\tilde{G}$ is the memory part of the wave-making on the free surface,

$$\tilde{G}(p,t;q,\tau)$$

$$= 2 \int_0^\infty \sqrt{kg}\, e^{k(z+\zeta)} J_0(kR) \sin(\sqrt{kg}(t-\tau)) dk$$

$$z \le 0, \quad \zeta \le 0 \qquad (30)$$

Where

$$p = (x, y, z)$$

$$q = (\xi, \eta, \zeta)$$

$$r_{pq}^2 = (x-\xi)^2 + (y-\eta)^2 + (z-\zeta)^2$$

$$r_{pq'}^2 = (x-\xi)^2 + (y-\eta)^2 + (z+\zeta)^2$$

$$R^2 = [(x-\xi) - u(t-\tau)]^2 + (y-\eta)^2$$

$\delta(t-\tau)$ is the delta function; $H(t-\tau)$ is unit step function, $H(t-\tau) = 0, \quad if \quad t<0; \quad 1, \quad if \quad t \ge 0.$

The Green function represents the potential at the field point p and at a time t due to an impulsive source (at the point q) suddenly created and annihilated at a time τ. This source acts like an underwater disturbance which generates a wave system as represented by the $\tilde{G}(p,t;q,\tau)$ term, $G_0 = \left(\frac{1}{r} - \frac{1}{r'} \right)$ is the Rankine part of the Green functions. Fixing the field point p while moving the source point q, it is easy to show that the Green function satisfies the following initial boundary value problem:

$$\nabla_q^2 \tilde{G} = 0 \qquad (\tau < t)$$

$$\left(\frac{\partial}{\partial \tau} + u\frac{\partial}{\partial \xi}\right)^2 \tilde{G} + g\frac{\partial \tilde{G}}{\partial \zeta} = 0 \qquad (on \quad S_F)$$

$$\tilde{G}, \quad \frac{\partial \tilde{G}}{\partial \tau} = o\left(\frac{1}{R^3}\right) \qquad (R \to \infty)$$

$$\tilde{G}|_{t-\tau} = 0 \qquad (31)$$

$$\frac{\partial \tilde{G}}{\partial \tau}|_{t-\tau,\xi-0} = g\frac{\partial}{\partial \xi}\left(\frac{1}{r_{pq}} - \frac{1}{r_{pq'}}\right)|_{\zeta-0}$$

To obtain a boundary integral formulation for $\psi_{1k}(p)$, we apply Green's identity to $\psi_{1k}(q)$ and $G_0 = \left(\frac{1}{r_{pq}} - \frac{1}{r_{pq'}}\right)$, in a fluid domain $V(\tau)$ bounded by $S = S_H + S_F + S_\infty + S_p$. A small surface S_p is built up to exclude the point p. Now, consider boundary integral equation at the wetted surface of the body. This gives:

$$\psi_{1k}(p) + \frac{1}{2\pi}\int\int_{S_H} \psi_{1k}(q)\frac{\partial}{\partial n_q}\left(\frac{1}{r_{pq}} - \frac{1}{r_{pq'}}\right)ds_q$$

$$= \frac{1}{2\pi}\int\int_{S_H}\left(\frac{1}{r_{pq}} - \frac{1}{r_{pq'}}\right)n_k(q)ds_q \qquad (32)$$

The integral equation for $\psi_{2k}(p)$ is found in the same way as:

$$\psi_{2k}(p) + \frac{1}{2\pi}\int\int_{S_H} \psi_{2k}(q)\frac{\partial}{\partial n_q}\left(\frac{1}{r_{pq}} - \frac{1}{r_{pq'}}\right)ds_q$$

$$= \frac{1}{2\pi}\int\int_{S_H}\left(\frac{1}{r_{pq}} - \frac{1}{r_{pq'}}\right)m_k(q)ds_q \qquad (33)$$

The integral equation for determining $\chi_k^{(-)}(p,t)$, the auxiliary-radiation potential in the opposite direction, is found by applying Green's identity to $(\chi_k^{(-)}(q,\tau) - \psi_{2k}(q))$ and $\tilde{G}(p,t;q,\tau)$. Integrating the resulting equation with respect to τ, we obtain

$$\int_0^t d\tau \int\int_{S_F+S_H}[(\chi_k^{(-)} - \psi_{2k})\frac{\partial \tilde{G}}{\partial n_q} - \tilde{G}\frac{\partial}{\partial n_q}(\chi_k^{(-)} - \psi_{2k})]ds_q = 0 \qquad (34)$$

According to the boundary and initial conditions of $\chi_k^{(-)}, \psi_{1k}, \psi_{2k}$, the integral over the free-surface is

$$\int_0^t d\tau \int\int_{S_F}[(\chi_k^{(-)} - \psi_{2k})\frac{\partial \tilde{G}}{\partial n_q} - \tilde{G}\frac{\partial}{\partial n_q}(\chi_k^{(-)} - \psi_{2k})]ds_q$$

$$= -\int\int_{S_F}\chi_k^{(-)}(q,t)\cdot\frac{\partial}{\partial n_q}\left(\frac{1}{r_{pq}} - \frac{1}{r_{pq'}}\right)|_{\zeta=0}\,ds_q$$

$$+\int\int_{S_F}\frac{\partial \psi_{1k}}{\partial n}\tilde{G}(p,t;q,0)ds_q$$

$$+2\frac{u}{g}\int_0^t d\tau \oint_\Gamma \chi_k^{(-)}\frac{\partial \tilde{G}}{\partial \tau}d\eta$$

$$+\frac{u^2}{g}\int_0^t d\tau \oint_\Gamma\left(\chi_k^{(-)}\frac{\partial \tilde{G}}{\partial \xi} - \tilde{G}\frac{\partial \chi_k^{(-)}}{\partial \xi}\right)d\eta \qquad (35)$$

To eliminate the integral over S_F, we apply the Green's identity to $\chi_k^{(-)}(q,t)$ and $G_0 = \left(\frac{1}{r_{pq}} - \frac{1}{r_{pq'}}\right)$,

$$-\int\int_{S_F}[\chi_k^{(-)}\frac{\partial}{\partial n_q}\left(\frac{1}{r_{pq}} - \frac{1}{r_{pq'}}\right)ds_q$$

$$= 2\pi\chi_k^{(-)}(p,t) + \int\int_{S_H}\chi_k^{(-)}(q,t)\frac{\partial}{\partial n_q}\left(\frac{1}{r_{pq}} - \frac{1}{r_{pq'}}\right)ds_q \qquad (36)$$

Again we apply the Green's identity to $\psi_{1k}(q)$ and $\tilde{G}(p,t;q,\tau)|_{\tau=0}$, thus

$$\int\int_{S_F} \tilde{G}(p,t;q,0)\frac{\partial \psi_{1k}}{\partial n}ds_q$$

$$= \int\int_{S_H} \psi_{1k}(q)\frac{\partial \tilde{G}(p,t;q,0)}{\partial n_q}ds_q$$

$$- \int\int_{S_H} n_k(q)\tilde{G}(p,t;q,0)ds_q$$

(37)

Substituting Eq.(35)-(37) into Eq.(34) yields

$$\chi_k^{(-)}(p,t) + \frac{1}{2\pi}\int\int_{S_H} \chi_k^{(-)}(q,t)\frac{\partial}{\partial n_q}\left(\frac{1}{r_{pq}} - \frac{1}{r_{pq'}}\right)ds_q$$

$$+ \frac{1}{2\pi}\int_0^t d\tau \int\int_{S_H} \chi_k^{(-)}(q,\tau)\frac{\partial \tilde{G}(p,t;q,\tau)}{\partial n_q}ds_q$$

$$+ \frac{u^2}{2\pi g}\int_0^t d\tau \oint_\Gamma [\chi_k^{(-)}(q,\tau)\frac{\partial \tilde{G}(p,t;q,\tau)}{\partial \xi}$$

$$- \tilde{G}(p,t;q,\tau)\frac{\partial \chi_k^{(-)}(q,\tau)}{\partial \xi}]d\eta$$

$$+ \frac{u}{\pi g}\int_0^t d\tau \oint_\Gamma \chi_k^{(-)}(q,\tau)\frac{\partial \tilde{G}(p,t;q,\tau)}{\partial \tau}d\eta$$

$$= \frac{1}{2\pi}\int\int_{S_H} n_k(q)\tilde{G}(p,t;q,0)ds_q$$

$$- \frac{1}{2\pi}\int_0^t d\tau \int\int_{S_H} m_k(q)\tilde{G}(p,t;q,\tau)ds_q$$

$$- \frac{1}{2\pi}\int\int_{S_H} \psi_{1k}(q)\frac{\partial \tilde{G}(p,t;q,0)}{\partial n_q}ds_q$$

$$+ \frac{1}{2\pi}\int_0^t d\tau \int\int_{S_H} \psi_{2k}(q)\frac{\partial \tilde{G}(p,t;q,\tau)}{\partial n_q}ds_q$$

$$p \in S_H \qquad (38)$$

Eq.(38) is also correct for a submerged body by eliminating the line integral terms in the equation.

3. NUMERICAL METHOD

3.1 Discretization of Integral Equations

The integral equations of potentials $\psi_{1k}(p), \psi_{2k}(p)$ and $\chi_k^{(-)}(p,t)$, are solved numerically using the panel method. The ship hull surface S_H is divided into M quadrilateral elements over which the source strength is assumed constant. This discretization reduces the continuous singularity distribution to a finite number of unknown potential strengths. The integral equations are satisfied at collocation points $p_i \quad (i = 1,2,\ldots,M)$ corresponding to the null points of each panel. This gives a system of algebraic equations which is solved for the unknown potential strengths.

In general, most ships are symmetrical about xoz plane. For a symmetrical ship, the equations can be solved using only half the number of panels. It is easy to prove that $\psi_{1k}(p), \psi_{2k}(p)$ and $\chi_k^{(-)}(p,t)$ (k=1,3,5) are symmetrical about xoz plane for a symmetrical ship.

$$\psi_{lk}(p) = \psi_{lk}(p^-) \qquad l = 1,2; \quad k = 1,3,5$$

$$\chi_k^{(-)}(p,t) = \chi_k^{(-)}(p^-,t) \qquad (39)$$

Where $p = (x,y,z), \quad p^- = (x,-y,z)$

Equations (32) and (33) may be discretized for a symmetrical ship as:

$$\sum_{j=1}^{M/2} A_{ij}(\psi_{lk})_j = (B_{lk})_i$$

$$i = 1,2,\ldots,M/2; \quad l = 1,2; \quad k = 1,3,5 \quad (40)$$

where M is the number of quadrilateral elements,

$$A_{ij} = \vec{n}_j \cdot \int\int_{S_j} \nabla_{p_i}\left(\frac{1}{r_{ij}} - \frac{1}{r_{i'j}} + \frac{1}{r_{i''j}} - \frac{1}{r_{i'''j}}\right)ds \quad j \neq i$$

$$= 2\pi + \vec{n}_j \cdot \int\int_{S_j} \nabla_{p_i}\left(-\frac{1}{r_{i'j}} + \frac{1}{r_{i''j}} - \frac{1}{r_{i'''j}}\right)ds \quad j = i$$

$$(B_{lk})_i = \sum_{j=1}^{M/2} n_{lk}(p_j)\int\int_{S_j}\left(\frac{1}{r_{ij}} - \frac{1}{r_{i'j}} + \frac{1}{r_{i''j}} - \frac{1}{r_{i'''j}}\right)ds$$

(41)

$$n_{lk} = n_k, \quad if \quad l=1$$

$$= m_k, \quad if \quad l=2$$

$$r_{ij}^2 = (x-\xi)^2 + (y-\eta)^2 + (z+\zeta)^2$$

$$r_{i^-j}^2 = (x-\xi)^2 + (y+\eta)^2 + (z-\zeta)^2$$

$$r_{i^-j}^2 = (x-\xi)^2 + (y+\eta)^2 + (z+\zeta)^2$$

The solution of Eq.(40) involves integrals of potentials of the type $\frac{1}{r}$ and of their local derivatives over each panel for the coefficients A_{ij} and $(B_{lk})_i$. They are evaluated by the method presented by Hess and Smith(1964).

The integral equation of $\chi_k^{(-)}(p,t)$ in Eq.(38) contains memory terms. The solution of $\chi_k^{(-)}(p,t)$ is obtained by a time stepping method. Assuming that $\chi_k^{(-)}(p,t)$ satisfies the linear distribution in every time interval, a trapezoidal rule is used to evaluate the convolution integrals in Eq.(38). At each time step, equation (38) is solved employing the same panel discretization that is used to solve $\psi_{1k}(p), \psi_{2k}(p)$. The system of equations which must be solved at each time step has the form:

$$\sum_{j=1}^{M/2} a_{ij}\chi_k^{(-)}(p_j,t_N) = b_k(p_i,t_N)$$

$$i=1,2,..,M/2; \quad k=1,3,5 \qquad (42)$$

where

$$a_{ij} = A_{ij}$$

$$b_k(p_i,t_N) = -\sum_{j=1}^{M/2}(s_1+s_2+s_3\Delta t)$$

$$(43)$$

$$S_1 = -\left[n_k(p_j) - \frac{\Delta t}{2}m_k(p_j)\right]G_A$$

$$S_2 = \left[\psi_{1k}(p_j) - \frac{\Delta t}{2}\psi_{2k}(p_j)\right]G_n$$

$$S_3 = \sum_{n=1}^{N-1}[(-\psi_{2k}(p_j) + \chi_k^{(-)}(p_j,t_n))G_{n\tau}$$

$$+ m_k(p_j)G_\tau]$$

$$G_A = \int\int_{s_j}\left[\tilde{G}(p_i,p_j,t_N) + \tilde{G}(p_i^-,p_j,t_N)\right]ds$$

$$G_n = \int\int_{s_j}\frac{\partial}{\partial n_j}\left[\tilde{G}(p_i,p_j,t_N) + \tilde{G}(p_i^-,p_j,t_N)\right]ds$$

$$G_\tau = \int\int_{s_j}[\tilde{G}(p_i,p_j,t_N-t_n)$$

$$+ \tilde{G}(p_i^-,p_j,t_N-t_n)]ds$$

$$G_{n\tau} = \int\int_{s_j}\frac{\partial}{\partial n_j}[\tilde{G}(p_i,p_j,t_N-t_n)$$

$$+ \tilde{G}(p_i^-,p_j,t_N-t_n)]ds$$

$$(44)$$

A very important property of the coefficient matrix A_{ij} in Eq.(42) is that it is independent of time. As a result it needs to be inverted only once at the beginning of the time stepping. For a sufficiently large number of panels this property results in a significant computational advantage over the frequency domain algorithm.

The right-hand side term $b_k(p_i,t_N)$ involves integrals of the Green function and its derivatives over each quadrilateral. They are evaluated by using coordinate mapping and Gauss quadrature. The arbitrary quadrilateral is first mapped into a square. A product Gauss rule is then used to evaluate the integral. Over most of the panels a 4*4 Gauss rule is sufficiently accurate.

In the case of k=2,4,6, its numerical model is given by Zhou(1992).

3.2 Evaluation of the Free-surface Transient Green Function

The numerically more time consuming task is the evaluation of the memory term $\tilde{G}$ and its derivatives which, because of the convolution integrals, must be evaluated at a large number of times. There has been much effort in recent years (e.g. Newman(1990),Beck, et al(1987) and Ferrant(1990)) to develop efficient and accurate numerical methods for calculating $\tilde{G}$ and its derivatives. A considerable speed-up was obtained by using a tabulation interpolation procedure. The numerical evaluation of the Green function used in this paper follows the development given by Newman(1990) and D.B. Huang(1991).

The memory part $\tilde{G}$ of the Green function can be easily put under the following form:

$$\tilde{G} = 2\sqrt{g}\, r_1^{-3/2} Im\{F(\cos\theta, \tau)\}$$

$$F(\cos\theta, \tau) = \int_0^\infty k^{1/2} e^{(i\sqrt{k}\tau - k\cos\theta)} J_0(k\sin\theta)\, dk \qquad (45)$$

with $\cos\theta = -(z+\zeta)/r_1$ and $\tau = t\sqrt{g/r_1}$.

Thus, the only non-trivial term to be evaluated during the computation of the convolution integrals is reduced to the function F and its first derivatives.

A method of tabulation interpolation is exploited. The 2-D domain described by $\cos\theta$ and τ is truncated at a large value of τ_{max}, and the remaining bounded domain is mapped by a discrete set of unequal-spaced points for which F and its derivatives are computed by numerical schemes described by Newman(1990). This computations are performed once for all, and the results are stored on permanent disk files. When a simulation has to be performed, the evaluations of the memory part of the Green function are based on linear bivariate interpolations of the stored data. Note that the content of the file is read once for all at the beginning of the simulation, so that no disk access is necessary during the time-stepping procedure. The tabulated part of the $(\cos\theta, \tau)$ domain is sufficiently extended to allow the use of simple large-time asymptotic expressions when $\tau > \tau_{max}$. τ_{max} is taken as 30 in this paper. In a very thin layer near $\cos\theta = 0$ where the function presents large oscillations, the precision of the interpolation may be insufficient and we employ a simple algorithm to maintain both precision and low Cpu time in this portion of the computational domain. For example, defining $G_1 = Im\{F(\cos\theta, \tau)\}$, when τ is large,

$$G_1 = -\frac{4}{\tau^3} + \sqrt{\frac{2}{\sin\theta}}\left(\frac{\tau}{2}\right) e^{-\frac{1}{4}\tau^2\cos\theta} \sin\left[\frac{\tau^2}{4}\sin\theta - \frac{3}{2}\theta + \frac{3}{4}\pi\right] \qquad (46)$$

Again defining G_1^* as the approximation of oscillation term for G_1 when $\cos\theta = 0$,

$$G_1^* = \frac{\tau}{\sqrt{2}} e^{-\frac{1}{4}\tau^2\cos\theta} \sin\left(\frac{\tau^2}{4}\right) \qquad (47)$$

The numerical results of $G_1(\cos\theta, \tau)$ and $G_1^*(\cos\theta, \tau)$ are close to each other, so that the difference $\overline{G_1} = G_1 - G_1^*$ varies smoothly making it suitable for interpolation. Thus we use $\overline{G_1}$ obtained from tabulation interpolation adding the $G_1^*(\cos\theta, \tau)$ given by Eq.(47) to obtain the Green function in the layer near $\cos\theta = 0$.

In the layer of $0.99 < \cos\theta < 1.$, we return back to the original numerical schemes since the calculation in this region is not time consuming.

The grid in this paper is composed of about 200×1200 points in the rectangular domain defined by $0 \le \cos\theta \le 1$. and $0 \le \tau \le 30$. For the Green function and its gradients, 3 tables have to be stored, resulting in about 3 Mbytes on a 32 bit computer.

4. NUMERICAL RESULTS

Numerical computations have been performed for diffraction problems with forward speeds. For simplicity we limitourselves to surge,

heave and pitch modes in head seas, although the present code is capable of dealing fully the six-degrees-of-freedom modes. The hull form chosen in this calculation is a Wigley-type hull used by Gerritsma in his seakeeping experiments. This is designated as the "W_{sk}" hull hereafter. This hull form was chosen because experimental results are available. The hull has a beam-to-length ratio $2b/L = 0.1$, and draft-to-length ratio H/L=0.0625. The half beam y is given by:

$$\frac{y}{b} = (1-X)(1-Z)(1+0.2X) + Z(1-Z^4)(1-X)^4 \qquad (48)$$

where $X = (2x/L)^2$, $Z = (z/H)^2$.

Before presenting the numerical results, two simplifications have been made. The first is the steady flow approximation. From the conclusion of Zhang, et al(1992), for a submerged body travelling at constant speed near and bellow the free-surface, the contribution of the steady perturbation potential ϕ_0 to the wave exciting forces may be neglected in head seas (and in following seas for high or low frequency regions), but the contribution should be taken into account in following seas in the frequency region $L/\lambda = 0.8 \sim 1.8$. The results presented here are in head seas, therefore the free stream approximation is used. Thus, $\vec{w} = (-u, 0, 0)$ and the corresponding values of m_j are $m_j = (0, 0, 0, un_3, -un_2)$.

The elimination of the steady perturbation velocities greatly eases the computational burden but it does not affect the time-domain analysis procedure.

The second simplifying assumption is to neglect the evaluation of the line integral terms in Eq.(38), because of their higher orders of smallness and because of their numerical uncertainties in computation.

For convenience, all quantities in force are nondimensionalized by fluid density ρ, gravitational acceleration g, and ship length L, wave amplitude A, displacement volume ∇. The panel numbers, N, indicated are always for half of the body. The time step size, Δt, is shown in the nondimensional form defined as $\Delta t^* = \Delta t\sqrt{g/L}$. In this paper, N=96, Δt=0.25, the number of time steps $N_T = 100$.

Figures 2-7 show the amplitude and phase of the wave exciting forces on the Wigley hull moving at a forward speed of $F_n = 0.2$ in head seas. The present computational results are referred to as Zhou, and numerical results from the linearized time-domain method developed at the University of Michigan are included and denoted as "Michigan". The comparisons to the time-domain results of Michigan, strip theory and experiments are generally satisfactory. The results of Michigan ,strip theory and experiments are taken from Lin and Yue(1990). In these figures, our results are very close to Michigan's results and both 3-D time-domain calculations show much better correlations to the experiments than the strip theory. Comparing with strip theory, the proposed Dai-Zhou-Zhang expression may be applied to high speed ships or ships with complex geometries. Comparing with the method of Univ. of Michigan, the Dai-Zhou-Zhang formula may separate the effect of ship hull geometry from that of unsteady motions of incident waves, thus the diffraction forces are evaluated without recourse to computing the diffraction potential itself. The resulting integral equations need to be solved only once for any incident wave of arbitrary frequency. This saves the Cpu time greatly. The resulting code is very fast: about 5-8 minutes are sufficient for evaluating the wave exciting forces(k=1,3,5) of 60 to 80 frequencies (N=96, $N_T = 100$) on an ALLIANTFX/40 computer.

In the older days, only Froude-Krylov forces are taken into account in the prediction of ship motions. This is because they lack efficient methods to compute the effect of diffraction. Figures 8-10 give the Froude-Krylov, diffraction and exciting force components for W_{sk} ship. As can be seen that although the Froude-Krylov force is the dominant part in $L/\lambda \leq 1.5$, the order of diffraction forces is still enough to affect considerably the predictions of the total exciting force. When $L/\lambda > 1.5$ the Froude-Krylov and diffraction force components are almost of the same order, which is a notable property for engineers in dealing with "springing" of large vessels in the relatively short wave domain. In the case of about $L/\lambda = 1.0$, the diffraction component is still considerably large, which may be interesting to ship designers.

Figures 11-16 show the time history calculated from the different components of wave forces on the Wigley hull for a forward speed of $F_n = 0.2$. The time is defined in nondimensional form $t^* = t\sqrt{g/L}$ The same tendency as in Figures 8-10 is seen. The diffraction component is about one-fourth or one-third of the corresponding Froude-Krylov force when L/λ is small, but it is of considerable order when L/λ is high. The difference in phase is about 180°. Therefore the component of diffraction must be included when computing exciting forces.

Figures 17-22 show the memory function $\chi_k^{(-)}(p, t-\tau)$ on the ship hull as a function of time. Figures 17,19 and 21 are the memory functions on the part forward amidships, and Figures 18,20 and 22 are those on the aft part. Noting when the position of the panel is near the free-surface, the memory function $\chi_k^{(-)}(p, t-\tau)$ does not simply steeply decrease to zero, but vibrates. The memory function decays steeply to zero as increasing water depths. The slight high frequency oscillation appearing on the memory function curve near the free surface may be due to insufficiency of panel numbers. Presumably a further increase in the number of panels and a decrease in the step size may reduce them further. Furthermore, the memory function on the aft part decays more slowly than that on the forward part. Itappears that the memory function $\chi_k^{(-)}(p, t-\tau)$ is sensible to longitudinal positions and draft. In Figures 21 and 22, the memory function $\chi_k^{(-)}(p, t-\tau)$ decays to a constant value which is not zero. This is because the actual impulse response function is $\chi_k(p, t-\tau) = \chi_k^{(-)}(p, t-\tau) - \psi_{2k}(p)H(t-\tau)$, which decays to zero, but $\chi_k^{(-)}(p, t-\tau)$ does not.

The effects of panel numbers, time step size Δt and the numbers of time steps N_T have been investigated. Setting the panel number (half of the body) N=96,120,192 respectively, the results of Froude-Krylov force show that the changes in panel numbers have little influence on wave forces, the difference is only about 3%. Since Froude-Krylov force is a dominant part of the wave exciting force, so a conclusion may be reached that the wave exciting force is not sensible to the numbers of panels. An order of 200 panels for a body should be enough to get essential accuracy in engineering.

Although increasing the number of time steps N_T may result in a more steady time history of wave forces, it increases the storage on disk and Cpu time. So, a suitable N_T should be determined. The numerical results show that $N_T = 80 \sim 100$ is enough for computing wave forces. Increasing the number of time steps N_T does not increase the accuracy of the computation. Maybe the main contribution of the memory function $\chi_k^{(-)}(p, t-\tau)$ has already been included when $N_T = 80 \sim 100$.

The requirement for time step size Δt is different in lower and higher frequency domains. In the lower frequency region, the time history period of wave force is large, which requires a suitably large time step Δt when in the case of fixed N_T to get enough numbers of periods of wave forces for determining the force amplitude and phase. In the higher frequency region, the time history period of wave force is short, which

requires a suitably small time step Δt when in the case of fixed N_T to get enough numbers of numerical results in one period in order to avoid missing the maximum point during the determining force amplitude and phase. We also investigated the effect of varying Δt. Setting Δt=0.1,0.15,0.2,0.25, the results show only slight differences of wave force in amplitude and phase.

5 CONCLUSION

1. A diffraction problem for a surface ship traveling at a constant forward speed in waves is studied by a time domain method. The basic conclusion from this work is that the proposed Dai-Zhou-Zhang expression seems to be a good method for computing wave exciting forces with forward speed. It appears to be faster and easier than the equivalent frequency-domain calculation and than the other time-domain methods. The diffraction forces are given in terms of the incident wave potential and of the auxiliary-radiation potentials. Therefore the exciting forces in the time-domain may be calculated without computing the diffraction potential itself. The resulting integral equations of the auxiliary-radiation potentials need to be solved only once for all incident wave frequencies, which saves CPU time greatly. In comparisons with experiments, strip theory, and other prediction methods, the results show that the accuracy and efficiency of the proposed Dai-Zhou-Zhang expression is also good.

2. This paper also showed mathematically that for an arbitrary floating body, the waterline integral terms in the formula for computing diffraction forces may vanish, if the fluid disturbance due to steady forward motion is not small on the free-surface condition. Physically these waterline integral terms are the result of interaction between the steady forward motion and the unsteady wave motion.

3. The numerical results show that the method using a tabulation interpolation procedure for the computing the time-domain Green function is efficient. It saves Cpu time and retains the numerical accuracy.

4. The diffraction force is of a certain amount in each frequency that we are interested in. This amount is enough to considerably affect the predictions of the total exciting force. Thus, it can not be neglected.

Variation of panel numbers and time step size Δt, do affect the results of calculation of wave forces, but the influence is slight. Proper selection of the two depend on different requirements in applications. By chosing a suitable number of time steps N_T, the tail of memory function $\chi_k^{(-)}(p, t-\tau)$ may be truncated suitably. Numerical results show that $N_T = 80 \sim 100$ and $\Delta t = 0.25$ is a good figure for solving wave forces, because the main contribution of the memory function $\chi_k^{(-)}(p, t-\tau)$ has been included.

REFERENCES

1. Beck, R.F. And Liapis, S.J.(1987), "Transient motions of floating bodies at zero forward speed". Journal of Ship Research, Vol.31, N0.3, pp. 164-176.

2. Beck, R.F. And Magee, A.R.(1990), "Time-domain analysis for predicting ship motions", Proceedings IUTAM Symposium on Dynamics of Marine Vehicles & Structures in Waves, London.

3. Chang,M.S.(1977), "Computation of three-dimensional ship-motions with forward speed", Proceedings 2nd International Conference on Numerical Ship Hydrodynamics, University of California, Berkeley, pp. 124-135.

4. Cummins,W.E.(1962), "The impulse response function and ship motions", Schiffstechnik, Vol.9, pp. 101-109.

5. Ferrant, P.(1990), "A coupled time and frequency approach for nonlinear wave radiation", Proceedings 18th Symposium on Naval Hydrodynamics, ONR, The University of Michigan, Ann Arbor.

6. Guevel,P. And Bougis,J.(1982), "Ship motions with forward speed in infinite depth", International Shipbuilding Progress, Vol.29, No.332, pp. 105-117.

7. Huang,D.B.(1992), "Numerical calculation of time-domain Green function and its derivatives", Journal of Shipbuliding of China, in press.

8. Inglis,R.B. And Price,W.G.(1982), "A three-dimensional ship motion theory-comparison between theoretical prediction and experimental data of the hydrodynamic coefficients with forward speed", Transactions Royal Institution of Naval Architects, Vol.124, pp. 141-157.

9. King,B.K.,Beck,R.F. And Magee,A.R.(1988), "Seakeeping calculations with forward speed using time-domain analysis", Proceedings 17th Symposium on Naval Hydrodynamics, ONR, The Hague, Netherlands.

10. Liapis, S.J. And Beck, R.F.(1985), "Seakeeping computations using time-domain analysis", Proceedings of the 4th International Symposium on Numerical Hydrodynamics, National Academy of Sciences, Washington, D.C.,pp. 34-54.

11. Lin,W.-M.and Yue, D.K.P.(1990), "Numerical solution for large amplitude ship motions in the time domain", Proceedings 18th Symposium on Naval Hydrodynamics, ONR, The University of Michigan, Ann Arbor.

12. Newman, J.N.(1990), "The approximation of free-surface Green functions", F.Ursell Retirement Meeting, March 20-30.

13. Ogilvie, T.F.(1964), "Recent progress toward the understanding and prediction of ship motions". Proceedings 5th Symposium on Naval Hydrodynamics, ONR, Washington, D.C., pp. 3-128.

14. Ogilvie, T.F.And Tuck, E.O.(1969), "Arational strip theory of ship motion: Part 1", Report No. 13, Dep. of Naval Architecture and Marine Engineering, The University of Michigan, Ann Arbor.

15. Sun,B.Q., Dong,S.Y. And Gu,M.X.(1991), "The computation of the response, wave loads and added resistance of an arbitry 3-D body with low forward speed", Proceeding of the 5th National Symposium on Seakeeping, China.

16. Zhou, Z.Q., Miao,G.P., Liu,Y.Z. And Gao,H.Q.(1991), "The theoretical prediction of ship motions", Journal of Shipbuliding of China, Vol. 114.

17. Zhou,Z.Q., Gu,M.X., Sun,B.Q. And Dong,S.Y.(1991), "The prediction of relative motion for a ship in waves", Proceeding of the 5th National Symposium on Seakeeping, China.

18. Zhou,Z.Q. (1991), "Time-domain theory of ship motions with forward speed: Part 1, diffraction problem", Report of China Ship Scientific Research Center.

19. Zhang, L. And Dai, Y.S. (1992), "A time-domain simulation of diffraction for a body near free surface at forward speed", Journal of Shipbuliding of China, in press.

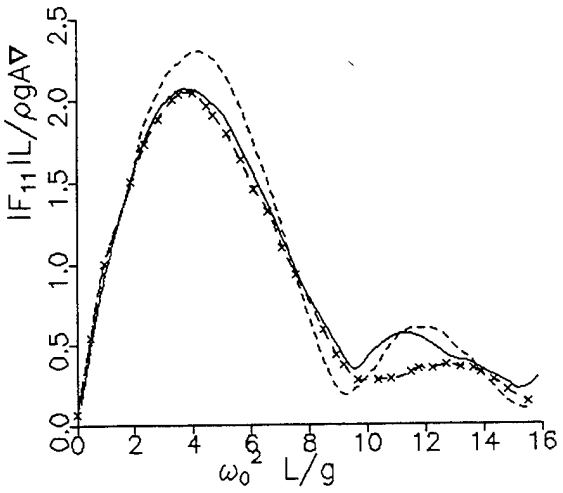


Fig.2

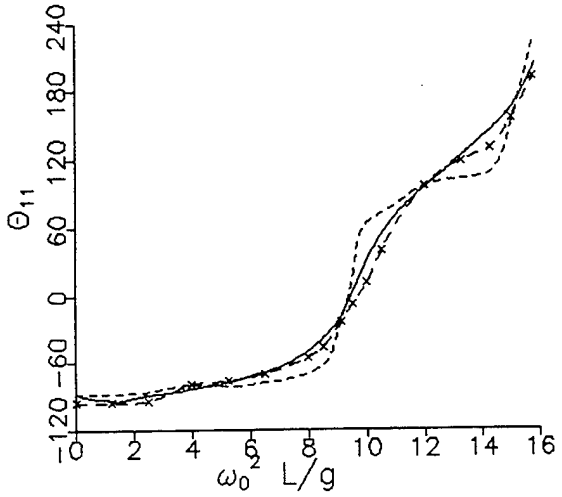


Fig.3

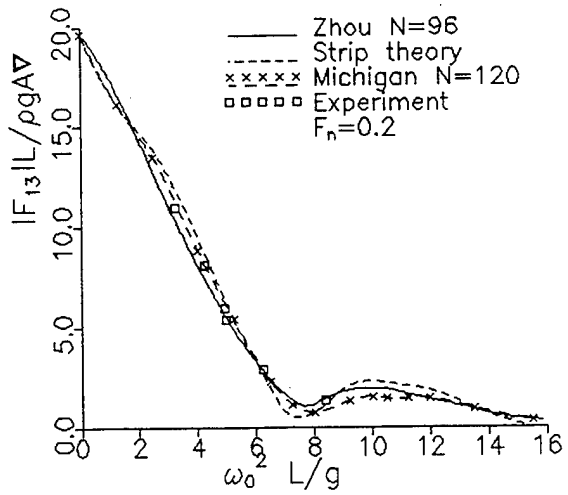


Fig. 4

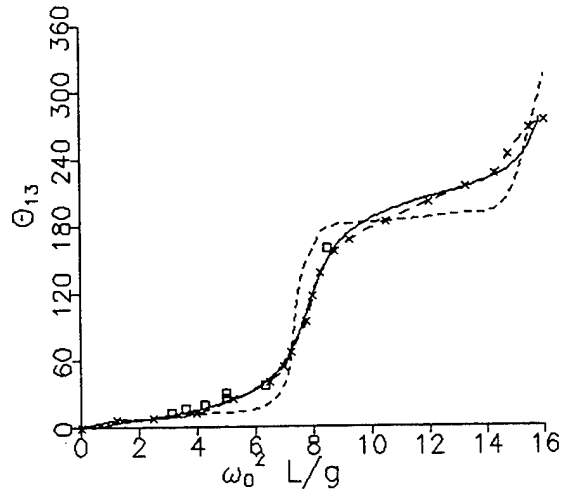


Fig. 5

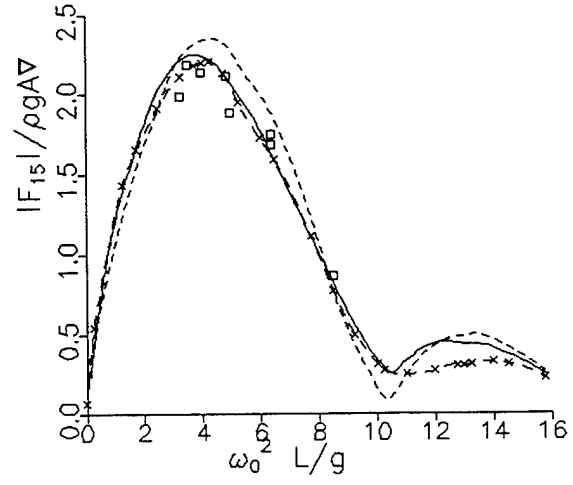


Fig. 6

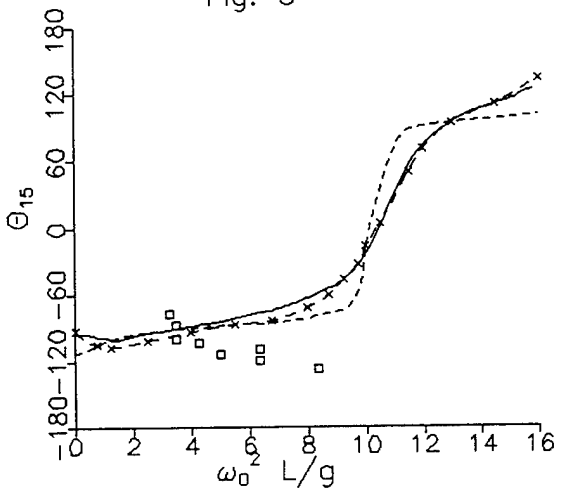


Fig. 7

Magnitude and phase of the wave exciting forces on a W_{sk} hull

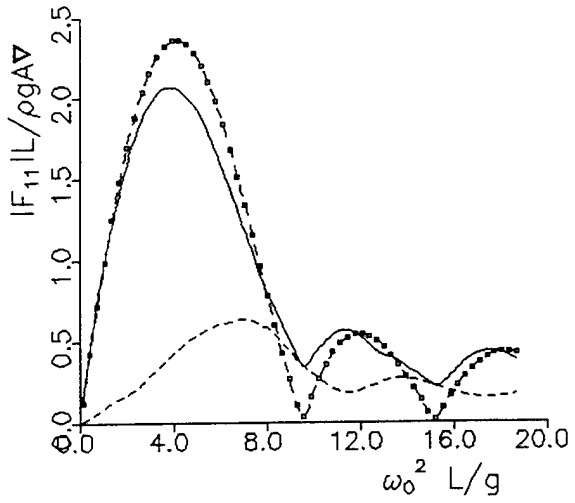


Fig. 8

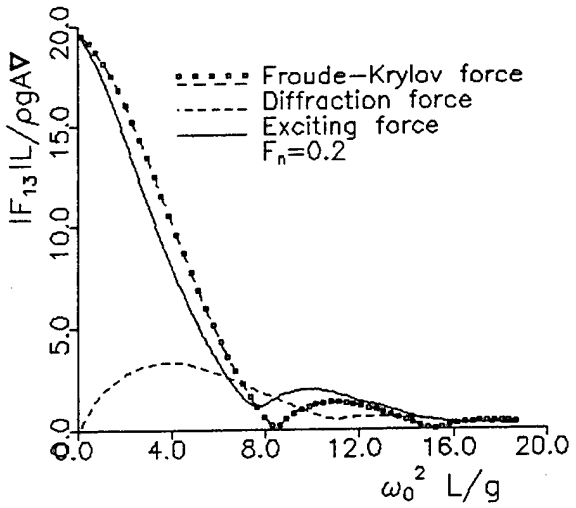


Fig. 9

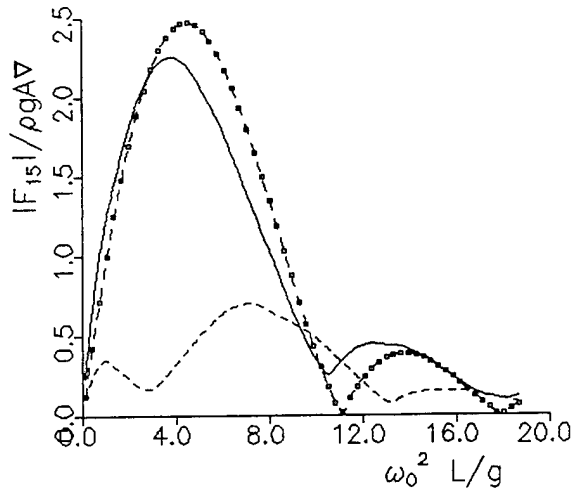


Fig. 10

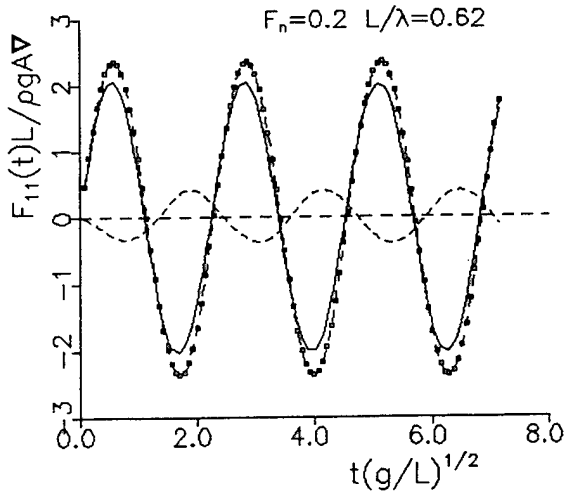


Fig. 11

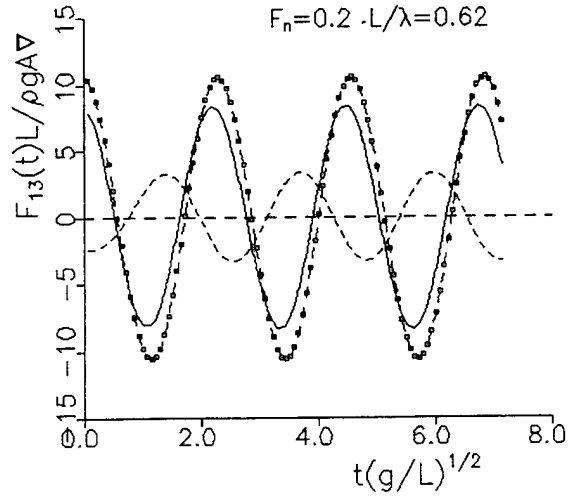


Fig. 12

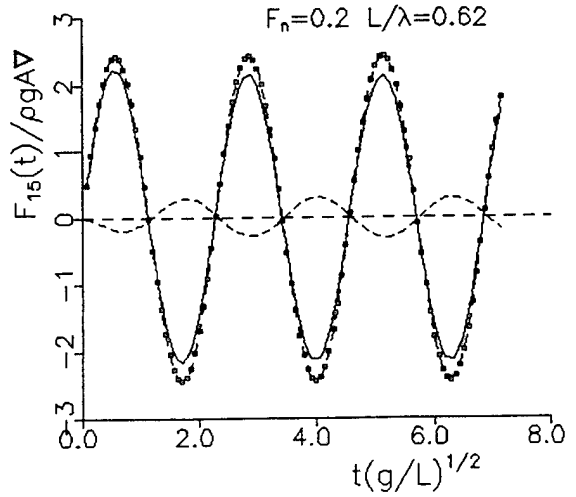


Fig. 13

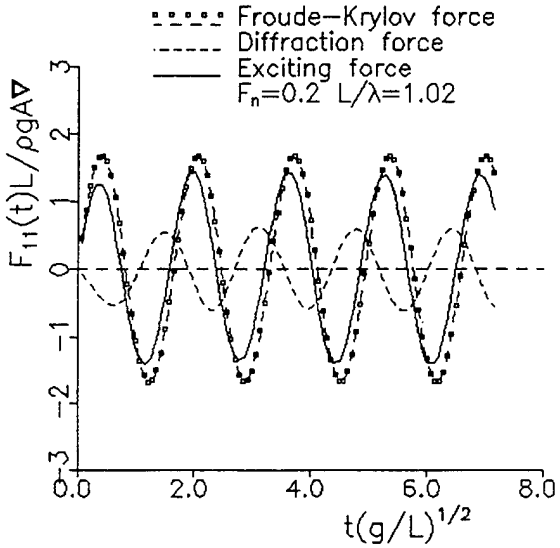


Fig. 14

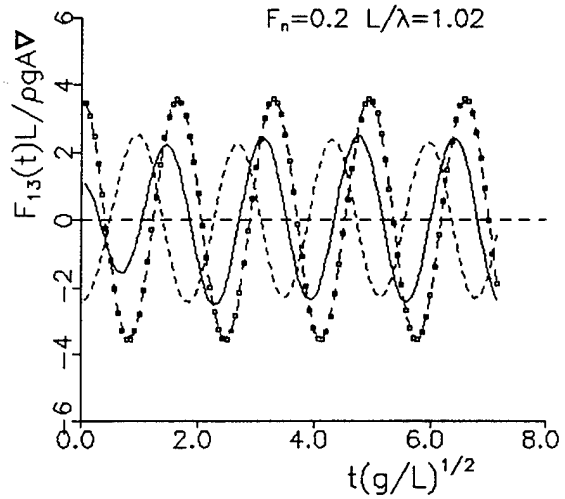


Fig. 15

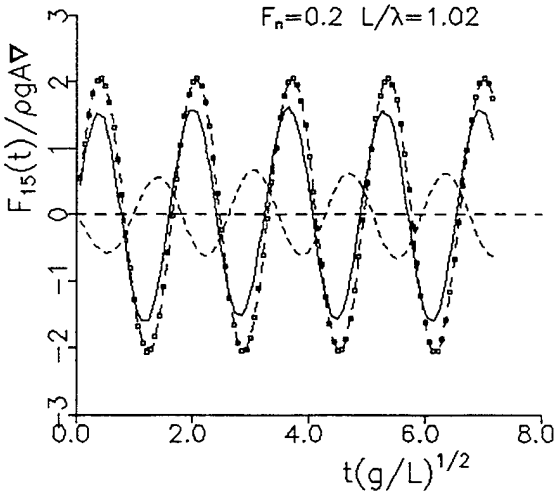


Fig. 16

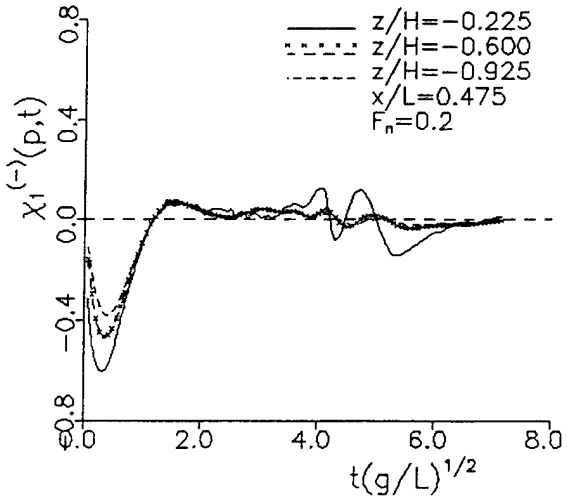


Fig. 17

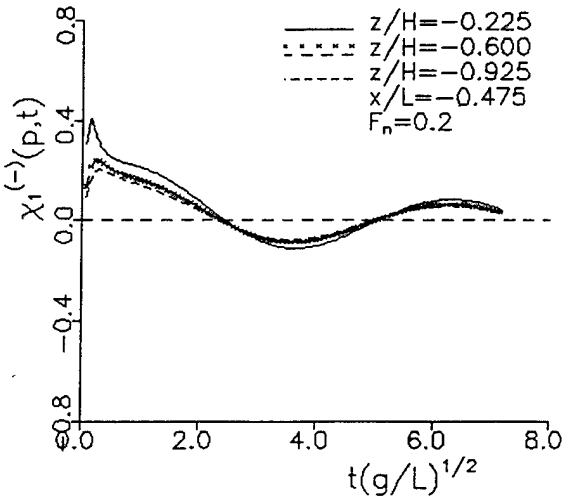


Fig. 18

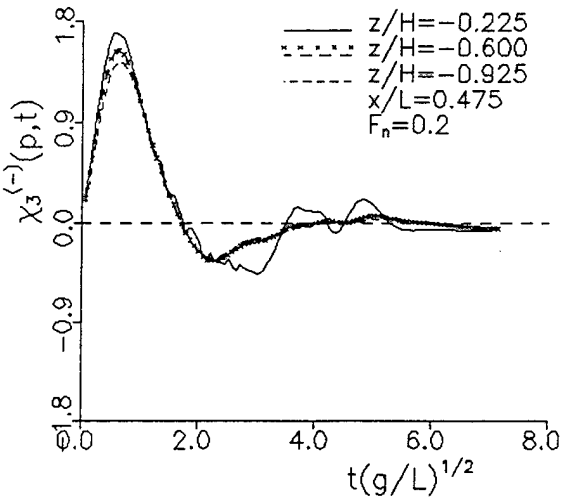


Fig. 19

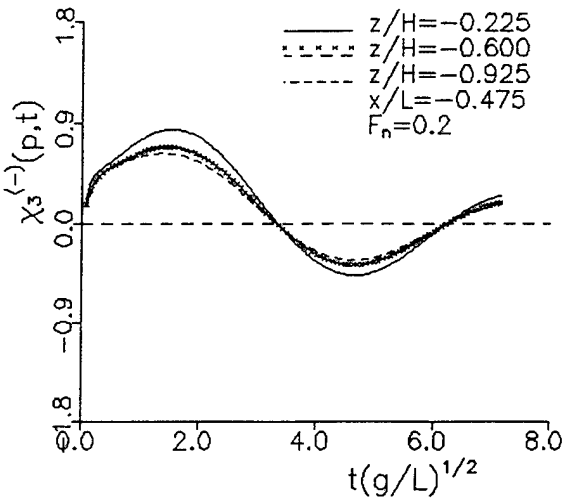


Fig. 20

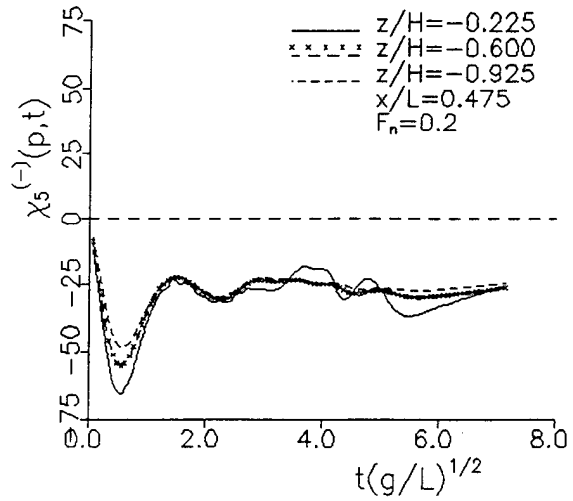


Fig. 21

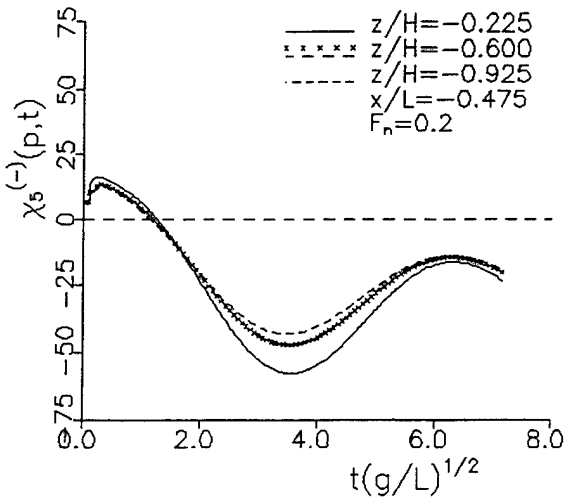


Fig. 22

Free Surface Flows without Waves; Applications to Fast Ships with Low-Wave Resistance

M. Tulin, O. Oshri
(University of California-Santa Barbara, USA)

ABSTRACT

The ideas & theory of Tulin (1976, 1982) are utilized here to demonstrate how combining vertical force distribution (vertical dipole) & cross section squashing (transverse quadrupoles) together with buoyancy (sources) provides means for substantially reducing the wave resistance of both near surface submerged & Wigley type hulls over a wide range of Froude numbers.

The basic tool is a 3D compound singularity composed of the above elements in proportions optimized at each non-dimensional depth. The lifting capacity of the hull is hardly changed by the vertical lift distribution which has an essentially zero sum.

Application are made to submerged hulls & modified Wigley hulls. The resistance of the submerged body, which is very close to the surface, is reduced by an order of magnitude over the speed range & for the Wigley hull by a factor of 0.2 at F=0.35 and 0.3 at F=0.5.

INTRODUCTION

Here we extend and use certain theoretical results which are about twenty years old, Tulin (1976 and 1982), in order to design shapes of either zero (two dimensions) or small (three dimensions) wave resistance. We utilize the linearized free surface condition & distributions of compound singularities; the latter define bodies which may be found by streamline tracing. Our purpose is to gain further understanding of wave-making phenomena & hopefully to reveal important principles which may be applied in design. The results seem highly encouraging.

In the past, going back to Froude, constructive interference between parts of the ship hull, notably the bow & stern, has been the main tool for resistance minimization. The fundamental technique, limited in 2D to $F<\sqrt{1/2\pi}$, or 0.399, is illustrated in Figure 1. To this may be added the constructive interference between a bow bulb & the main hull, extensively investigated by Inui (1960).

In virtually all theoretical studies of wave resistance up to the 60's, the ship was envisioned as a distribution of volume forming singularities, either horizontal dipoles or their equivalent sources. An exception is to be found in the interesting work by Yim (1962, 1963 & 1966) who actually described a wave free ship (of infinite draught) in terms of a horizontal distribution of sources and sinks along the length of the ship, and two vertical distributions of dipoles descending to infinite depths from bow and stern. He also described, Yim (1963), a wave free singularity of zero volume : a vertical dipole and a horizontal quadrupole, of strength depending on the Froude number.

The senior author undertook a general theory of wave free compound singularities beginning in the late 60's. Starting with two dimensional flows he utilized analytic functions & the method of images. Recognizing that the free surface conditions in their analytic function form required both hard and soft image systems, he was able to show that at each Froude number two separate wave free compound singularities exist which are volume forming, see Figures 2 & 3. He was then able to extend his method to three dimensions where he found the same result, Figure 4. Notice that the compound singularities, located beneath the free surface, include an appropriate

FIGURE 1 - WAVE FREE BODIES; CRITICAL SPACING, PLANAR FLOW

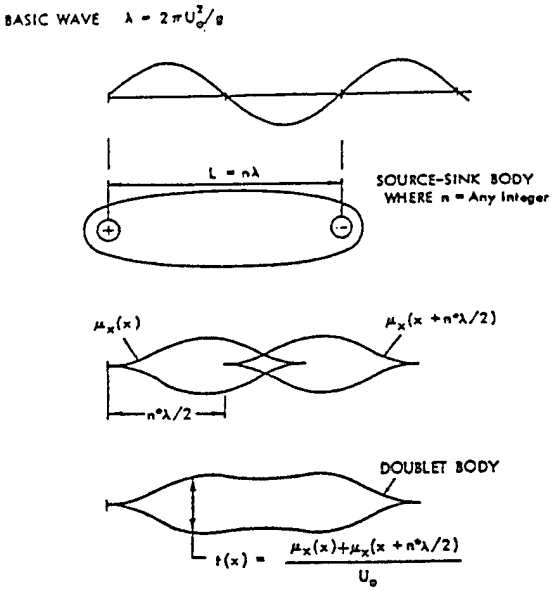


FIGURE 2 - WAVE FREE FLOWS OF TYPE I

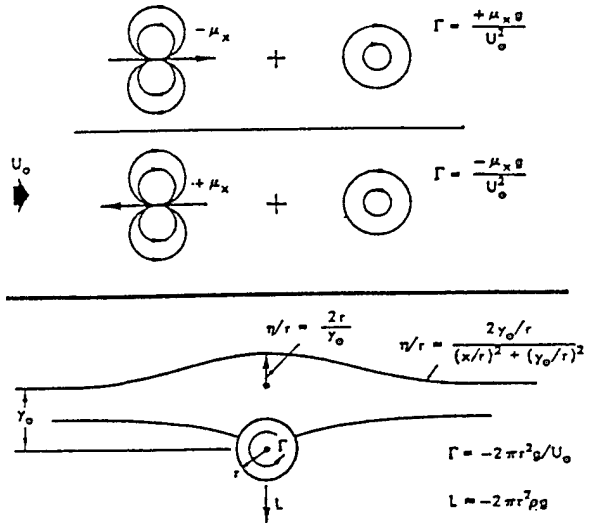


FIGURE 3 - WAVE FREE FLOWS OF TYPE II

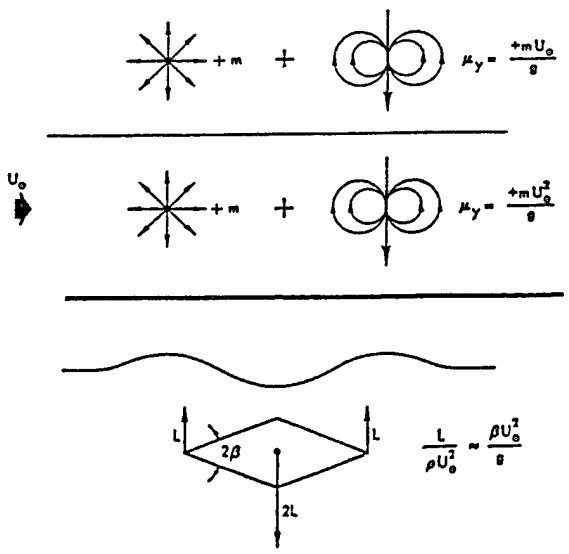


FIGURE 4 - TYPE II SINGULARITIES IN 3-DIMENSIONS.

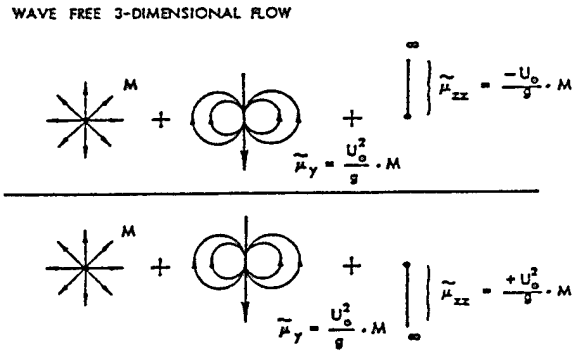


image singularity.

A compound singularity consists of a combination of basic singularities (source, dipole, quadrupole) centered about a fixed point (or, sometimes, a line) in space. Providing that the compound singularity contains a source or horizontal dipole it is volume forming, as in all cases demonstrated by Tulin. In this case it may be used to construct real-bodies. Of course, streamline tracing must be carried out in order to verify that a physically real system has been produced.

The mechanism of wave free compound singularities may be looked at in two different ways: i) taken as a whole it satisfies the free surface condition without producing waves (this is how Tulin originally produced them), or , ii) taken separately, each singularity produces waves in the far field which cancel when the singularities are combined (we use this technique in the present paper).

A great advantage would arise through the use of volume forming, wave free, compound singularities in the construction of ship shapes, since their use does not depend on constructive interference. The latter technique, for example, can only be used for Froude numbers smaller than the last hollow in the resistance curve, $F \approx 0.35$, whereas the present technique can be used successfully at high speeds, even at the last large hump in resistance, $F \approx 0.5$.

Tulin (1974, 1982) denoted his two separate wave free systems as Type I and II. In each case a vertical force is associated with volume forming; these vertical forces arise through vertical dipoles (2 & 3D) or vortices (2D). Therefore, the generation of particular vertical force distributions by the ship hull is the central theme of this work. Another theme which emerges (Type II - 3D) is volume element deformation or squashing, which arise through transverse quadrupoles.

In the case of bodies comprised of Type I wave free singularities, bodies require a negative total lift. In the case of slender bodies, this negative total lift is to first order equal to the buoyancy of the body. The ship of Type I therefore lacks ability to carry weight, and would seem useless. The type I flows are interesting, however, as they include cavity flows beneath a free surface, which are therefore wave free, a property earlier noted by Fruman (1965). An even earlier antecedent of these flows is to be found in the circulatory flow about a circular cylinder; Vladimirov (1955) had noted that a particular circulation, depending on the Froude number, resulted in zero wave resistance.

Tulin's Type I singularity was later rediscovered by Tuck (1989), Tuck & Tulin (1990). Based on his results, Mori (1993) has tested a submerged body with a hydrofoil wing lifting downwards & has reported a net reduction in the resistance.

Tulin's Type II wave free singularity requires a vertical force distribution on the hull related to the rate of change of the hull area, see Figures 3 & 4, involving no net lift on the hull (to first order). The net moment due to this dynamic lift distribution is also zero for symmetric hulls. In addition, the relative changes in hull shape required to generate the wave-reducing vertical hull forces are proportional to F^2 and are therefore not extreme for practical ships speeds. Type I singularities, on the other hand, require relative changes in hull shape proportional to F^{-2}.

In two dimensions, Type II singularities can generate wave free bodies; the shapes can be rather remarkable. Examples are given here, see Figures 6, 9, 10 and 11.

The generation of vertical forces is represented in singularity theory by vertical dipoles, while quadrupoles represent deformation or squashing of volume elements. In three dimensions, Tulin's Type II wave free singularity involves a vertical distribution of transverse quadrupoles extending from the volume forming singularity to infinite depth. It is only in a such a way that the prohibition on wave free finite hulls in 3D, Krein (1968), can be avoided.

In the present work, we replace the line of quadrupoles by a single quadrupole at the position of the source and dipole. We then optimize the dipole and quadrupole strengths, depending on depth and F, and study the effectiveness of these compound singularities, Type IIA, in generating ship forms of small wave resistance, especially for higher speeds. Using the above Type IIA singularities, we show that the resistance of a near surface submerged body may be virtually eliminated at all speeds up to $F=0.4$, & reduced by an order of magnitude up to $F=0.5$, see Figures 17 & 18. The optimization is, however, not effective immediately at the water line, for a normal ship shape. Nevertheless, a Wigley shape is modified to produce an optimized resistance reduced by factors of ≈ 0.2 at $F=0.35$ and ≈ 0.3 at $F=0.5$. Further progress may be achieved through better knowledge of the divergent wave system & its prediction, since the optimized singularity is limited by divergent wave production.

EXACT 2D BODIES WITH ZERO WAVE RESISTANCE

We know that wave free bodies result from general distributions of Type II singularities along a line between x=±*l*/2 located both beneath & above the free surface. These can be expressed in analytic function form.

In the particular case where the source distribution, m(x), decreases linearly along a horizontal line located at depth h with source density ±m at x=±*l*/2, the complex potential for the wave free flow is found to be:

$$\Psi(z) = \varphi + i\psi = \sum_{y_0=\pm h} \left\{ \frac{1}{2} Fz - A\left[\left(\frac{z^2-1}{2} \right) - z + i2F^2 z \ln\left(\frac{z+1}{z-1} \right) \right] \right\} \tag{1}$$

where

$$\Psi = \frac{\Psi'}{\sqrt{gll}}; \qquad A = \frac{m}{2\sqrt{gl}};$$

$$z = \frac{x + i(y - y_0)}{l/2}; \qquad F = \frac{U}{\sqrt{gl}};$$

The body corresponding to (1) corresponds to $\psi(x,y) = 0$. The velocity field, may be found from $\Psi'(z) = 0$; the stagnation points correspond to $|\Psi'(z)| = 0$. The body shape is found by first finding the stagnation points and then the locus of $\psi = 0$. The case of F=0.35, h/l=1/8, diam./l=1/8 has been computed. The body corresponding to the source distribution & its positive image alone is shown in figure 5, and the wave free body in Figure 6, together with the shape of the free surface, Figure 7.

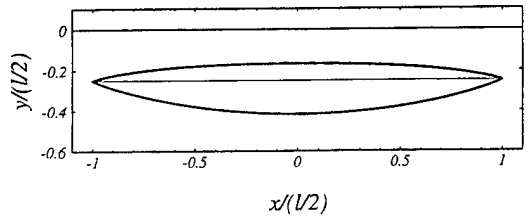


Figure 5 - 2D Body produced by a linear source distribution

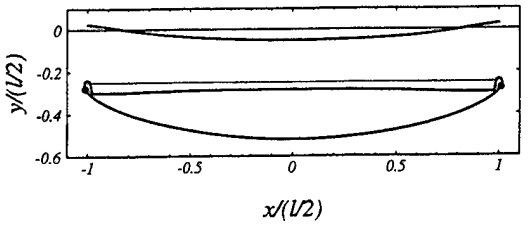


Figure 6 - 2D wave Free Body; F=0.35. The dots are stagnation points.

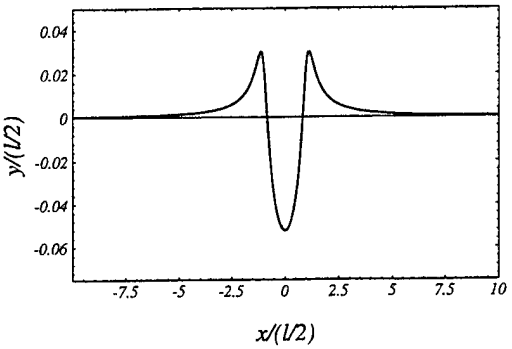


Figure 7 - The free surface above the body in Figure 6

The "horns" at x=±*l*/2 produce the concentrated vertical force required by this system, see Figure 3. The negative camber on the remainder of the body produces a distributed force of approximately constant density, as required (the force density is proportional to the gradient in the source density distribution). This negative body force is to first order canceled by the vertical concentrated force on the horns at the bow and stern.

Viscous separation would, of course, prevent the utilization of the horns. They might be replaced, however, by small foils with the required amount of positive lift, see Figure 8, which is schematic.

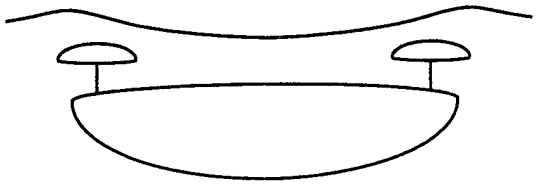


Figure 8 - Schematic of a wave free 2D body

The example above, for F=0.35, lies within the range where constructive interference may be used for elimination of wave resistance, i.e. F<0.399. We have attempted to find a wave free flow outside this range at a Froude number near the peak of the resistance curve, F≈0.5. A horned body as above, fails at F=0.55 due to crossing of the streamlines near the base of the horn, see Figure 9.

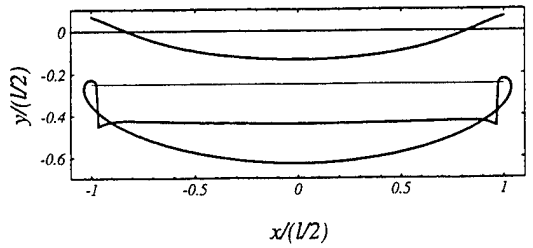


Figure 9 - 2D Wave Free body; F=0.55

For the sake of diversity we have taken a different source distribution with finite gradients in the source density at the bow and stern :

$$m(x)=\left(x^2-l^2\right)x \qquad (2)$$

The corresponding wave free complex potential, found by integration, is :

$$\Psi(z)=\ \varphi+i\psi= \qquad (3)$$

$$\sum_{y_0=\pm h}\left\{\frac{1}{2}Fz-A\left[3\left(z^2-1\right)^2\ln\left(\frac{z+1}{z-1}\right)+10z-6z^3+i8F^2\left[3\left(z^2-1\right)^2 z\ln\left(\frac{z+1}{z-1}\right)-6z\right]\right]\right\}$$

where $A=m/24\sqrt{gl}$

We have calculated, by streamline tracing, two shapes at different Froude numbers. Notice that the source distribution used, eq (2), has resulted in elimination of the "horns".

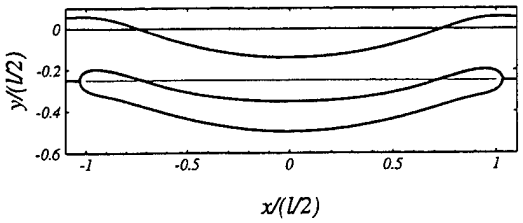


Figure 10 - 2D Wave Free Body at F=0.35

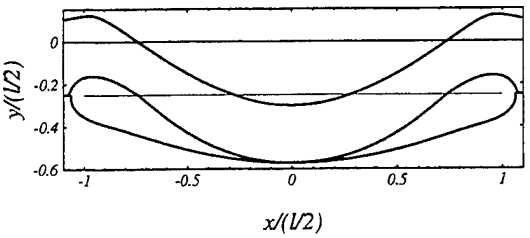


Figure 11 - 2D Wave Free Body at F=0.49

The curious example shown in Figure 11 is wave free at a significantly higher Froude number than is possible utilizing constructive interference.

The specific examples shown here demonstrate the diversity of 2D wave free body shapes which may be produced utilizing the present method. It would be worthwhile to demonstrate the existence of these wave free bodies experimentally.

3D FLOWS - OPTIMIZED SINGULARITIES

The 3D Compound Singularity (Concentrated)

Our purpose is first to find a practical compound singularity of minimum wave resistance, and then to construct practical hulls. Toward this end we replace the infinite line of quadrupoles in the wave free singularity by a single quadrupole at the location of the source & vertical dipole. Then we minimize the wave resistance of the combination through appropriate choice of the dipole & quadrupole strengths.

Far Field Formulation

In order to minimize we use the far field amplitude function & the Havelock (1934a, b) formulation of the resistance :

$$R = \frac{\pi\rho U}{2}\int_{-\frac{\pi}{2}}^{\frac{\pi}{2}} |A(\theta)|^2 \cos^3(\theta)\,d\theta \tag{4}$$

where $A(\theta)$ is the usual amplitude function defined through the far field representation of the displacement, η, in terms of a spectrum of stationary waves :

$$\eta(x,z) = \int_{-\frac{\pi}{2}}^{\frac{\pi}{2}} A(\theta)\exp\left[iK_o \sec^2(\theta) \times \left[(x-x_0)\cos(\theta)+(z-z_0)\sin(\theta)\right]\right]d\theta \tag{5}$$

where $K_0 = g/U^2$ and θ is the angle between a component wave vector & and the ships's direction. The corresponding potential is :

$$\phi(x,y,z) = \int_{-\frac{\pi}{2}}^{\frac{\pi}{2}} \frac{iU}{\sec(\theta)} A(\theta) \times \exp\left[yK_o \sec^2(\theta)\right]\exp\left[iK_o \sec^2(\theta) \times \left[(x-x_0)\cos(\theta)+(z-z_0)\sin(\theta)\right]\right]d\theta \tag{6}$$

The source singularity of strength M, located at depth h possesses the amplitude function :

$$A_s(\theta) = \frac{iK_0 M}{\pi U}\sec^3(\theta)\exp\left[-K_o h \sec^2(\theta)\right] \tag{7}$$

and the corresponding dipole & quadrupole singularities can be found by differentiation :

$$\phi_d = -(\phi_s)_h; \qquad \phi_q = (\phi_s)_{zz} \tag{8}$$

with the result in terms of the corresponding amplitude functions :

$$A_d(\theta) = \frac{iK_0^2 \mu_d}{\pi U}\sec^5(\theta)\exp\left[-K_o h \sec^2(\theta)\right] \tag{9}$$

and,

$$A_q(\theta) = \frac{iK_0^3 \mu_q}{\pi U}\sec^7(\theta)\sin^2(\theta) \times \exp\left[-K_o h \sec^2(\theta)\right] \tag{10}$$

The total amplitude function, A_T, is the sum of (7), (9), & (10) :

$$A_T(\theta) = \frac{i\alpha_s}{\pi}\left[\cos^2(\theta)+\beta_{ds}-\beta_{qs}\tan^2(\theta)\right] \times \sec^5(\theta)\exp\left[-K_o h \sec^2(\theta)\right] \tag{11}$$

where $\alpha_s = K_0^2 \frac{M}{U}$; $\beta_{ds} = K_0 \frac{\mu_d}{M}$; $\beta_{qs} = K_0^2 \frac{\mu_q}{M}$

Optimized Strengths & Amplitude Functions

It can been seen from (11) that the dipole term, β_{ds}, may be used to cancel the longest transverse waves $\theta \to 0$, exactly as it does in 2D. This will, however, result in strong dipole generated divergent waves. These in turn may be offset in part by an appropriate quadrupole singularity. The quadrupole is eventually too successful in generating divergent waves. It is clear that an appropriate balance must be found between dipole & quadrupole strengths.

The resistance is minimized for each compound singularity by finding the β's so that (using (4) & (11)) :

$$\frac{\partial R}{\partial \beta_{ds}} = \frac{\partial R}{\partial \beta_{qs}} = 0 \tag{12}$$

This very lengthy process involves expressing the β's in terms of Whittaker functions of the second kind & using appropriate computer programs. The minimizing values of each β are a function of $K_o h$. The final results are shown in Figures 12 & 13.

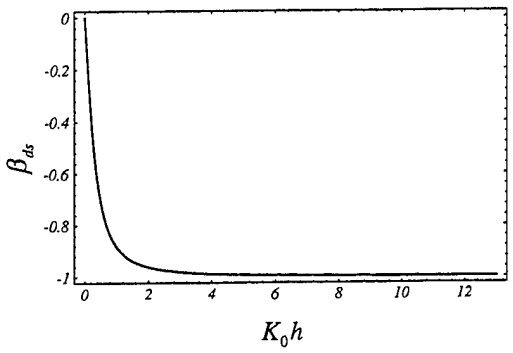


Figure 12 - Optimized strength of dipole

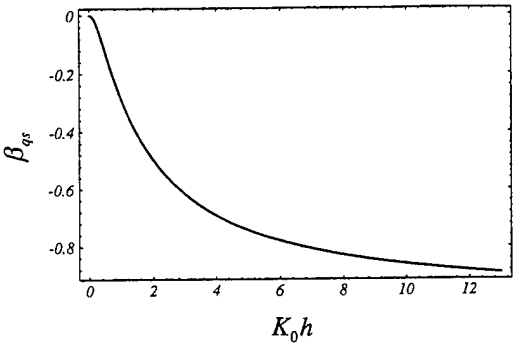


Figure 13 - Optimized strength of quadrupole

It can be seen that the optimized system approaches a source at the water line, and that the strengths of the dipole & quadrupole approach that of the source at large depths.

An example of the resulting amplitude function is shown in Figure 14 for K_oh=0.20. The optimization has traded a reduction in transverse waves for a large increase in short divergent waves. These waves almost certainly do not exist in practice as they are too steep & would in practice break. The question exists whether they nevertheless represent a real wave resistance. This deserves careful study. In the present work, we simply assume that they do. If they do not, then the resistance estimates of optimized hulls given here are certainly conservative. The difference will be heightened near the free surface.

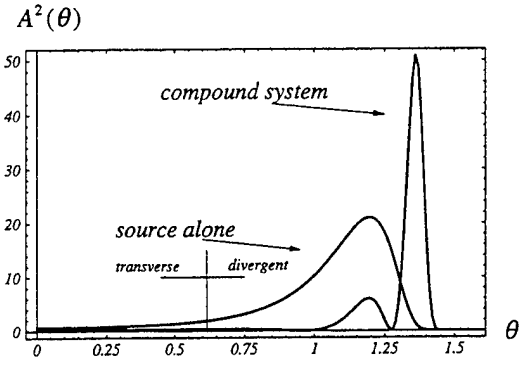


Figure 14 - Amplitude function for a source and compound system
K_0h=0.20

The Wave Resistance of Optimized Compound Singularities

We expressed the singularity wave resistance, R, in dimensionless form, $\hat{R}_c$:

$$\hat{R}_c = R / \frac{\rho}{2}\left(\frac{U}{K_0}\right)^2 \qquad (13)$$

This resistance is shown in Figure 15.

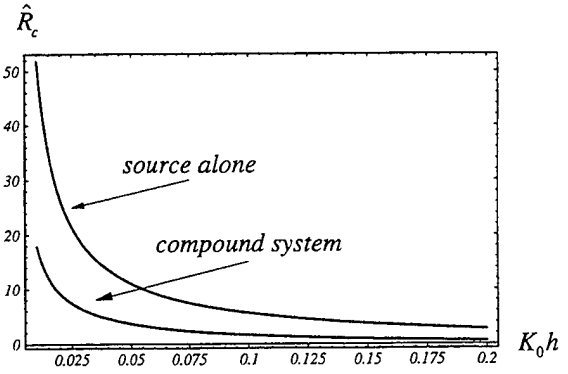


Figure 15 - Wave resistance for a source and the compound system

With increase in depth the reduction over the source resistance is considerable, see Figure 16.

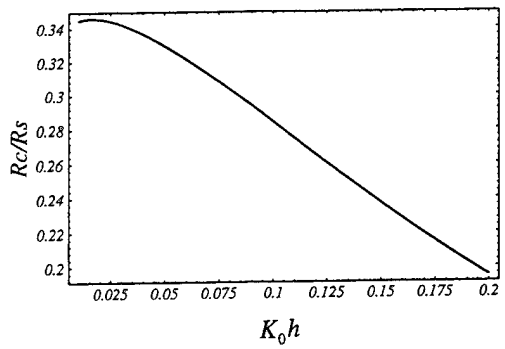


Figure 16 - The ratio of the compound wave resistance to the source wave resistance

Unfortunately, the contributions of the hull near the waterline play a great role in determining the resistance. As shown subsequently, the use of optimized compound singularities can very successfully reduce, even nearly eliminate, the resistance of submerged hulls, & less so for normal hulls. Nevertheless, even in the latter case, substantial reductions may be obtained.

SUBMERGED NEAR SURFACE HULLS

Singularity Distribution

We shall create hulls by distributing compound singularities along a horizontal line of length l at depth, H. The sources alone represent a submerged body of revolution; the dipoles will produce a downward camber of the body of revolution, symmetrical about midsection & greatest there; the quadrupoles will result in squashing of the circular body cross section into a shape flattened in the vertical plane. The source distribution may be varied, but here we use the ellipsoid distribution, varying linearly in the horizontal direction.

Perhaps these optimized hulls will be of importance in connection with the design of semi-submerged catamaran hulls like the Swath ship.

Resistance

The non-dimensionalized wave resistance of the hull is :

$$\hat{R}_H = R / \frac{\rho}{2} l^2 U^2 \qquad (14)$$

(15)

$$\hat{R}_H = \frac{8}{\pi}\alpha_s^2 \int_0^{\frac{\pi}{2}} \sec(\theta)\gamma\left(\theta, \frac{\delta}{F^2}\right)^2 \times \exp\left[-2\frac{\delta}{F^2}\sec^2(\theta)\right] \times \left[\cos\left[\frac{\sec(\theta)}{2F^2}\right] - 2F^2\cos(\theta)\sin\left[\frac{\sec(\theta)}{2F^2}\right]\right]^2 d\theta$$

where $\delta = H/l$ and

$$\gamma = 1 + \beta_{ds}\sec^2(\theta) - \beta_{qs}\sec^4(\theta)\sin^2(\theta)$$

The strength of the source distribution determines α_s and the fineness ratio of the equivalent body of revolution, D/l, where D is the equivalent diameter. The relation between α_s and D/l is based on the ellipsoid in an infinite domain.

The particular case, δ=1/10, and D/l=1/8 (α_s = 0.0165) has been calculated as an example & the estimated resistance using the appropriate compound singularities at each Froude number is shown in Figure 17.

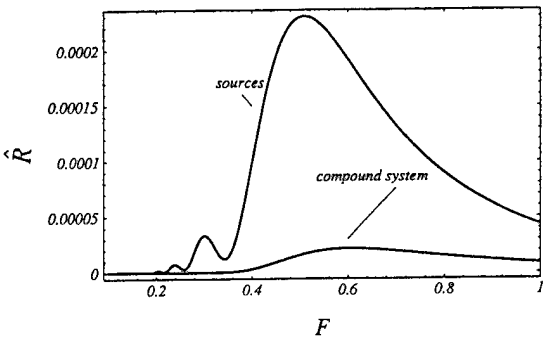


Figure 17 - Submerged Hulls - wave resistance. Optimized at h/l=0.1; D/l=0.125

Similarly, the resistance curves based on compound singularities which, once determined, do not vary with Froude number, are shown in Figure 18.

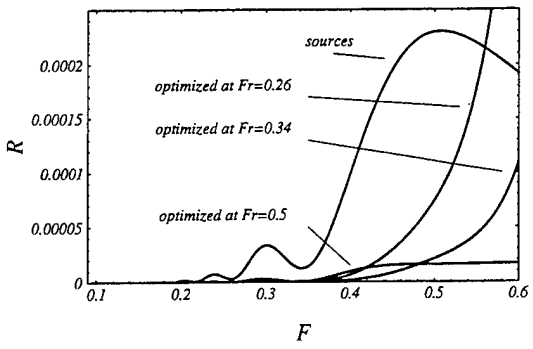


Figure 18 - Submerged hull - wave resistance. Optimized hulls, variation with F
h/l=0.1; d/l=0.125

It is evident that the optimization process has been highly successful in reducing the wave resistance of the original body of revolution (sources). In fact, the resistance is virtually eliminated at Froude numbers up to 0.4, & much reduced even at much higher speeds.

Body Shape

We have obtained a cut of the body intersection with the vertical plane using streamline tracing based on the compound singularity and its appropriate images; therefore we have neglected the effect of wave creating images as these are small. The appropriate images are : positive for the source and the dipole, negative for the transverse quadrupole.

Calculation have been made for F=0.25, 0.35, and 0.50, & the shapes are shown in Figures 19-21.

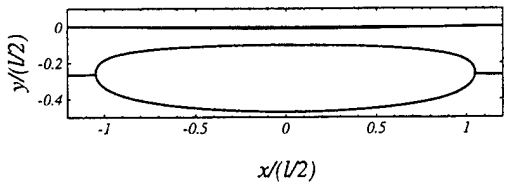


Figure 19 - Submerged hull - cross section in the vertical plane. F=0.25. h/l=0.1; D/l=0.125

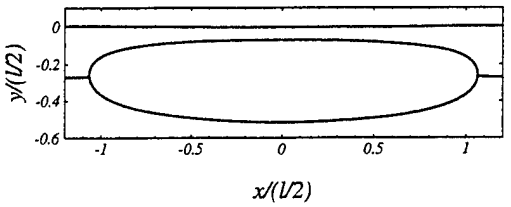


Figure 20- Submerged hull - cross section in the vertical plane. F=0.35. h/l=0.1; D/l=0.125

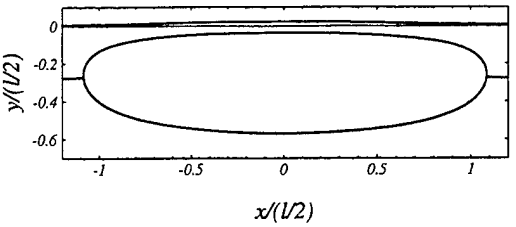


Figure 21- Submerged hull - cross section in the vertical plane. F=0.5. h/l=0.1; D/l=0.125

It is seen that both the negative camber (dipole effect) & squashing (quadrupole effect) increase markedly with F in this range. The top of the body increasingly approaches the free surface, but remains completely submerged, even at the highest speed.

The vertical flattening of the body (reduction in transverse width) which must accompany the enlargement of the cross sections shown will result in reduction in wave loads, as well as wave resistance. The actual cross section shapes have not yet been calculated.

SHIP FORMS; THE OPTIMIZED WIGLEY HULL

The Wigley Hull

In order to study the potential of compound singularities for the construction of real ship hulls; we begin with the Wigley hull. It is apparent that Type IIA singularities have the advantage that the source distribution may be prescribed in advance & the effect of the optimizing dipoles and quadrupoles determined thereafter. The vertical ordinate of the normal Wigley hull is :

$$\eta = (1-\zeta^2)(1-\xi^2) \qquad (16)$$

where : $\xi = 2x/l;\ \eta = 2y/B;\ \zeta = z/D$ and where B and D are the beam and draft, respectively. The corresponding density distribution, $\sigma(x,y)$, is according to Michell theory :

$$\sigma = -\frac{1}{2\pi}\left(\frac{B}{l}\right)\frac{\partial \eta}{\partial \xi} = \frac{1}{\pi}\left(\frac{B}{l}\right)\xi\left(1-\zeta^2\right) \tag{17}$$

and the solution for the wave resistance is well known, Lunde (1951), Figure 7.

The Optimized Resistance

Upon distributing the compound singularities according to eq (17), the resultant amplitude function for the optimized Wigley hull may be found :

$$\begin{aligned} K_0 A(\theta) = -\frac{2}{\pi} F^{-2} \frac{BD}{l^2} \sec^2(\theta) \\ \left[\cos\left(\frac{\sec(\theta)}{2F^2}\right) - 2F^2\cos(\theta)\right. \\ \left.\times \sin\left(\frac{\sec(\theta)}{2F^2}\right)\right] \\ \times \int_{-1}^{0}\left(1-\zeta^2\right)\gamma\left(\theta, \frac{D/l}{F^2}\zeta\right) \\ \times \exp\left[-\frac{D/l}{F^2}\zeta\sec^2(\theta)\right]d\zeta \end{aligned} \tag{18}$$

where :

$$\begin{aligned} \gamma\left(\theta, \frac{D/l}{F^2}\zeta\right) = 1 + \beta_{ds}\left(\theta, \frac{D/l}{F^2}\zeta\right)\sec^2(\theta) \\ -\beta_{qs}\left(\theta, \frac{D/l}{F^2}\zeta\right)\sec^2(\theta)\tan^2(\theta) \end{aligned}$$

and the β's are given as in Figures 12 & 13. The corresponding non-dimensional resistance is :

$$\begin{aligned} \hat{R} = \frac{8}{\pi}\left(\frac{B}{l}\right)^2\left(\frac{D}{l}\right)^2 \int_0^{\frac{\pi}{2}} \sec(\theta) \\ \times \left[\cos\left(\frac{\sec(\theta)}{2F^2}\right) - 2F^2\cos(\theta)\right. \\ \left.\times \sin\left(\frac{\sec(\theta)}{2F^2}\right)\right]^2 \left[\int_{-1}^{0}\left(1-\zeta^2\right)\gamma\left(\theta, \frac{D/l}{F^2}\zeta\right)\right. \\ \left.\times \exp\left[-\frac{D/l}{F^2}\zeta\sec^2(\theta)\right]d\zeta\right]^2 d\theta \end{aligned} \tag{19}$$

As is well known, for a given draft ratio, the resistance varies as $\left(B/l\right)^2$, while the variation in draft is more complicated. In the present example we choose the specific beam & draft ratios chosen by Lunde (1951). The optimized non-dimensional resistance is compared with the basic Michell resistance in Figure 22, and their ratios in Figure 23. The optimized hull will itself change with F.

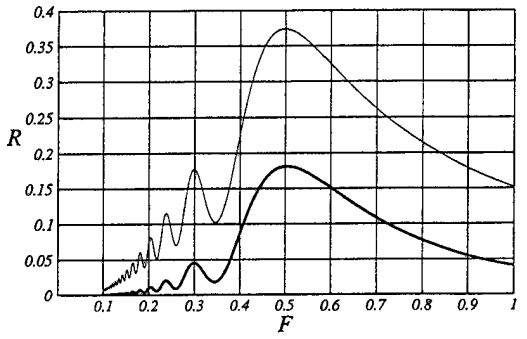


Figure 22 - Wave resistance, Wigley hull. Thin line-Michell. D/l=1/16, B/l=.094. Thick line-optimized Wigley hull. Type IIA singularities

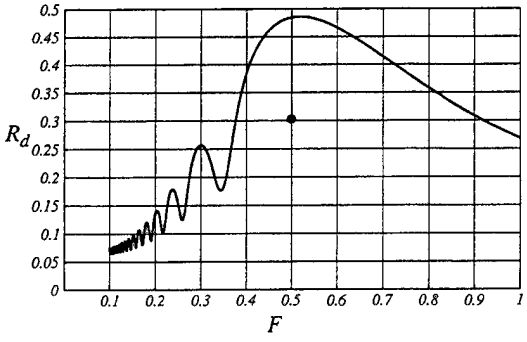


Figure 23 - R_d : The ratio of the optimized to Michell wave resistance. The dot represents a further optimization

It can be seen that the use of IIA compound singularities almost eliminates the wave resistance up to F≈0.2 and reduces it very substantially up to F≈0.35, the last hollow. The resistance contribution of the transverse & divergent waves separately is shown in Figures 24 and 25, and it appears that the reduction in the divergent wave resistance is substantially larger than for the transverse resistance, except for the lowest speeds where the reduction is almost complete for each wave system.

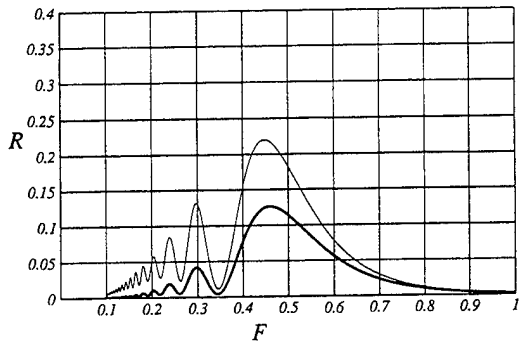


Figure 24 - Wave resistance, Wigley hull. Transverse waves. Thin line - Michell. Thick line - compound system

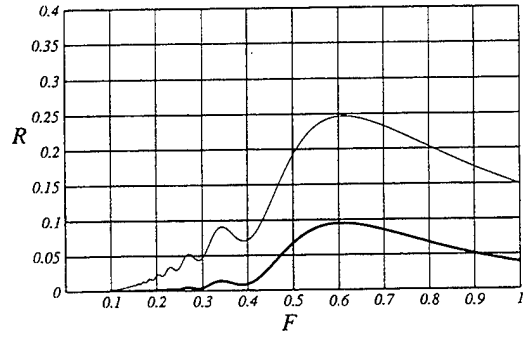


Figure 25- Wave resistance, Wigley hull. Divergent waves. Thin line - Michell. Thick line - compound system

These curves suggest that the optimization of the compound singularities may be further improved through consideration of constructive interference as an additional factor.

This last suggestion is borne out by calculations of wave resistance vs F for three fixed bodies, each optimized at a different F (0.27, 0,35, 0.5). As can be seen in Figure 26, the resistance of the body (F=0.35) is substantially less than that of the body (F=0.5) at F=0.5.

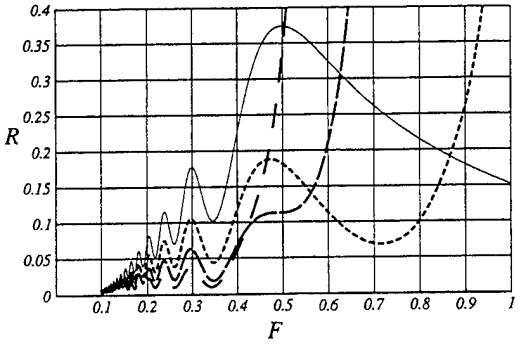


Figure 26- Wave resistance, Wigley hull. Optimized bodies.

——— *sources*

— — *F=0.27*

— — - *F=0.35*

- - - - - *F=0.5*

In fact, this curve suggests that in every case, the optimized body excels at Froude numbers in excess of the design value : Body (F=0.27) excels to about F=0.41; and body (F=0.35) to about F=0.57. Therefore, the optimized resistance shown in Figure 22 can clearly be improved upon; as an example, the dot in Figure 23 shows the resistance ratio at F=0.5 using the F=0.35 singularities.

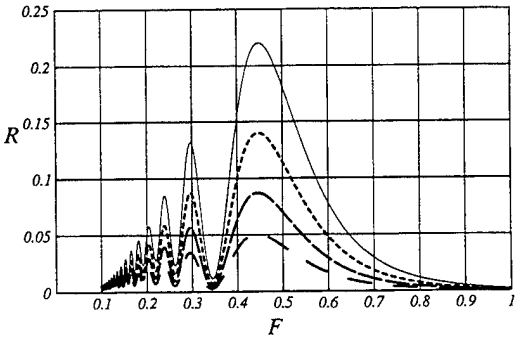


Figure 27- Wave resistance, Wigley hull. Transverse waves. Optimized bodies.

——— *sources*

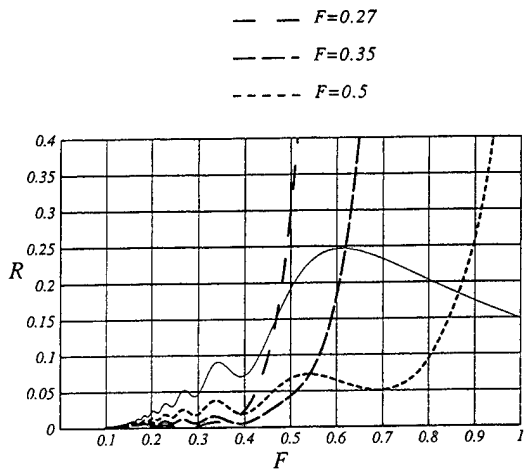


Figure 28- Wave resistance, Wigley hull. Transvrese waves. Optimized bodies.

——— *sources*
— — *F=0.27*
— — - *F=0.35*
- - - - - *F=0.5*

Divergent Waves

The division of the wave resistance for the fixed optimized bodies is shown in Figures 27 & 28. These figures make clear the importance of the divergent wave resistance in optimization, especially in the hump region. This importance arises from the fact that the dipoles we have used to cancel the transverse waves produce divergent waves, which cannot be completely eliminated by the quadrupoles, and which cause increasing resistance at higher speeds. At the same time we know that linear theory must fail to predict the divergent waves accurately. According to ray theory, short waves are only produced at the waterline by singularities in the hull shape, and notably at the corners represented by the bow & the stern. Beyond this clue, a good physical understanding of divergent wave origin is lacking and is badly needed. For example, is it possible that the divergent waves partially originate at the splash which is highly visible at the bow of most fine ships ? If so, non-linear calculations may be required for their analysis. It is clearly an important subject especially for the reduction of high speed wave resistance, as the present work makes clear.

Concluding Remarks

It has been successfully demonstrated that the generation of particular vertical lift distributions (vertical dipole) and body squashing (transverse quadrupoles) can together result in substantial reductions in the wave resistance of both near-surface submerged and Wigley type hulls. It is especially important that these reductions are achieved at high speeds, in the vicinity of the hump speed.

It has to be recognized that the present studies are incomplete in certain respects. In particular, the shape of the modified hulls has not yet been determined. However, the proposed technique, using compound singularities to create hull shapes, offers versatile possibilities for creating practical, if unusual, hulls. For example, these singularities need not be confined to a line in space, as in the case of the submerged hull, nor the vertical plane, as in the case of the modified Wigley hull.

Another factor, vital to the optimization, is the transverse thinning due to the transverse quadrupoles. It is not yet clear how much of the reduction in the resistance is due to the reduction in body width, accompanied by an increase in draft, & how much is due to the vertical lift effect due to the dipoles. The importance of the quadrupoles again depends on the divergent waves, about which we do not yet know enough in reality.

Nevertheless, the theory & calculations presented here would seem to offer a new dimension for the study of ship wave resistance and for the design of hulls of reduced resistance, especially at higher speeds around the hump.

ACKNOWLEDGEMENT

The authors are grateful for support from the Office of Naval Research, Ocean Technology Program, directed by Dr. Thomas Swean.

REFERENCES

Fruman, D., "Problems de Profils Sub et Supercavitating Pres de la Surface Libre, Resolutions Rheoelectriques," These, A la Faculte des Science de l'Universite de Paris, 1965.

Havelock, T.H., "Wave Pattern and Wave Resistance," T.I.N.A., Vol. 76, 1934a, pp. 430-443.

Havelock, T.H., "The Calculation of Wave Resistance," Proc. Roy. Soc. A 144, 1934b, pp.

514-521.

Inui, T., Takahei, T., and Kumano, M., "Wave Profile Measurements on the Wave-Making Characteristics of the Bulbous Bow," Society of Naval Architecture of Japan, 1960.

Kostchukov, A.A., Theory of Ship Waves and The Wave Resistance, State Union Publishing House for the Shipbuilding Industry, Leningrad, 1959 (Available in English Translation by Max Oppenheimer, Jr., E.C.I., Iowa City, 1968).

Krein, M.G., Doklady Akademi Nauk SSSR, Vol. 100, No. 3, 1955.

Lunde, J.K., "On the linearized theory of wave resistance for displacement ships in steady and accelerated motion," Trans. Soc. Naval. Arch. Marine Engrs., Vol 59, 1951, pp. 24-76, discussion, pp. 76-85.

Nagaya, S., and Mori, K., "Wave-Making Resistance of a Submerged Body with Wing which Produces Downward Lifting Force," 2nd Symposium on Nonlinear and Free-Surface Flows, Hiroshima University, 1993.

Tulin, M.P., "Free Surface Flows Without Waves," Abstract and Lacture, 13th IUTAM Congress (Delft), 1976.

Tulin, M.P., "Free Surface Flows Without Waves," HYDRONAUTICS, Incorporated Technical Report 8035-2, 1982.

Tuck, E.O., "A Submerged Body with Zero Wave Resistance" Journal of Ship Research, Vol 33, No. 2, June 1989, pp. 81-83.

Tuck, E.O., and Tulin, M.P., "Submerged Bodies That Do Not Generate Waves," Proc. of 7th International Workshop on Water Waves and Floating Bodies, val de Reuil, France, 1992.

Vladimirov, A.N.," Approximate Hydrodynamic Design of Finite Span Hydrofoils," NACA Memorandum, 1341, 1955.

Wigley, W.C.S., "The Theory of the Bulbous Bow and its Practical Application," Trans. N.E.C.I.E.S., Vol. LIII, 1936, pp. 65-88.

Yim, B., "On Ships with Zero Wave Resistance," HYDRONAUTICS, Incorporated Technical Report 117-2, 1962c.

Yim, B., "On Ships with Zero and small Wave Resistance," Proceedings of the International Symposium on Wave Resistance, Ann Arbor, 1963, pp. 1033-1082.

Yim, B., "Analyses on Bow waves and Stern Waves and Some Small-Wave-Ship Singularity Systems," Proceedings, Sixth Symposium on Naval Hydrodynamics, Office of Naval Research 1966.

Hydrodynamic Design of Thrust Generators Based on Oscillating Wings

K. Rozhdestvensky, V. Ryzhov (St. Petersburg Marine Technical University, Russia), A. Kurapov (Cambridge University, United Kingdom)

Abstract

The paper discusses some problems of hydrodynamic design of different devices, incorporating oscillating wing elements. Unconventional propulsors and energy extracting devices are described by means of appropriate mathematical models, utilizing numerical and asymptotic methods. A review is given of the approaches enabling to account for the influence of different physical factors upon performance of such systems. Results obtained by the present authors are compared with available theoretical and experimental data.

Introduction

The idea of utilization of the thrust generated by an oscillating wing has been known long ago from the observations of the surrounding nature. As far back as the end of the last century many qualitative investigations had been conducted of the flapping flight. However, it took quite a while to pass from the first notions to a scientific formulation of the problem. By the forties of our century two main concepts had been established of the hydrodynamic interaction of a lifting body in unsteady motion with the fluid.

One of the hypothesis set forth by V.V. Golubev [1] was based upon an assumption that in the process of oscillations of the wing (at its extreme positions) there takes place a discrete vortex shedding resulting in formation of the Karman double vortex street, [2]. Application of the momentum conservation theorem with respect to the flow with such a vortex structure indicates the existence of a thrust force.

In accordance to another hypothesis the mechanism of thrust generation of the oscillating wing is analyzed within the assumptions of the ideal fluid flow model and on the basis of the unsteady wing theory. The approaches advocated by A.I. Nekrasov [3], M.D. Khaskind [4] and L.I. Sedov [4] employ the principle of substitution of the wing and its wake by various "continuous" vortex systems. The thrust generation in these schemes is ascribed largely to the so called *suction force*, caused by considerable suctions at the leading edge of the wing.

Although the above approaches treated the two-dimensional flow case, they and the subsequent works of M. Lighthill [5] and T. Wu [6, 7] lay the foundation of the theory of the flapping flight. Further on this basic model was extended to account for different physical factors.

At the present time the motivation for development of relevant mathematical models is connected with several possible practical applications of flapping wings: use of these wings as propulsors [8, 9, 10]; devices of transformation of the unsteady flow energy into a useful work and , in particular, as the means of transformation of the energy of ship rolling into its translatory motion [11, 12]; as the working element of pumps of special types, *etc.* One of characteristic features of such devices is the capacity to synthesize different functions, for example to serve as the propulsor and a control device at the same time. As such they can be used as a system of dynamic positioning for offshore structures, or as a generator of additional thrust and a ship-roll damping device, [13, 14].

The interest of researchers as regards wing propulsors is also connected with the wish to thoroughly study effective mechanisms of swimming of aquatic animals, [15, 16, 17]. Data from observations of the natural environment can also be used in development of imitating technical devices which incorporate some essential characteristic features of live objects , such as fish and birds.

These features have to be reflected in corresponding mathematical models.

Numerical and asymptotic methods of the wing theory - from the lifting line [18] to the lifting surface [19, 20] approaches enabled effective determination of propulsive characteristics of the wing of arbitrary planform and aspect ratio in the wide range of relative frequencies of oscillations and in presence of the flow boundaries, [21]. An appropriate model of the thrust generation in extreme ground effect, i.e. in close proximity of rigid boundaries, was developed with utilization of the matched expansions techniques, [22].A certain progress had been achieved in the theory of the optimal flapping wing, which resulted in recommendations as to the choice of geometry and kinematics, resulting in a maximum thrust or efficiency, [7, 18, 23]. Several publications are dedicated to determination of propulsive characteristics of a wing in a wavy stream , [24, 25, 26]. The influence of the free surface gravitational effects was considered in [27]. Some simplified approaches are known to have been developed to predict cavitation and leading edge separation of a wing in unsteady flow, [20, 28]. Some results are reported of mathematical modelling of the influence of elasticity upon characteristics of oscillating wings including matters of rational distribution of inertial properties and rigidity, [29, 30, 31, 32].

Research works referred to above have been done mostly within assumptions of linear theory. It should be mentioned that there already exist nonlinear approaches to mathematical modelling of performance of devices based on oscillating wing, [33, 34, 35, 36]. The author abstain from their review and analysis and leave this for the future.

In parallel with theoretical methods there exist some established experimental techniques, available experimental data confirming adequacy of developed mathematical models, [17, 25, 37, 38]. The measurements of thrust on oscillating wings are known to be rather complicated. That is why the number of these is limited. Nonetheless, they provide a good basis for direct analysis of factors influencing propulsive characteristics of the wing type thrust generators as well as for establishment of the range of validity of relevant mathematical models.

There exist some full-size implementations of the oscillating wing thrust generators. Such systems are installed on surface ships and launches, [8, 11] and on small submersibles [9] as the main (active) or/and passive propulsors.It can be mentioned that the authors of the present paper participated in hydrodynamic design and development of the rudder-propulsor system for a small human powered submarine of Saint-Petersburg Marine Technical University (MTU), [10].

The goal of the present paper is to give an outline of research work on the wing-type thrust generators carried out at MTU and to discuss some mathematical models enabling prediction of performance of such devices.

General mathematical model of the flapping wing propulsor

Consider a lifting and propulsive system, consisting of a finite number of flat thin wing of finite aspect ratio and arbitrary planform, in a bounded flow of ideal incompressible fluid, Fig. 1.

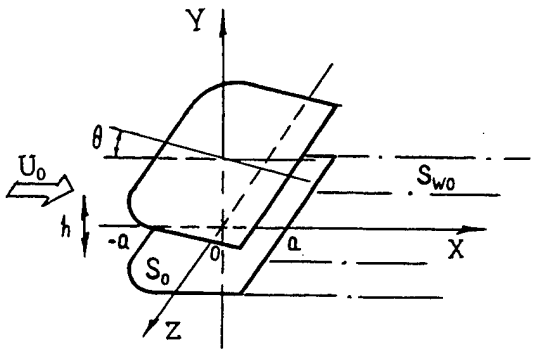


Figure 1: Wing system and coordinates

Let fluid density be ρ the oncoming flow velocity U_0. The boundary can be represented by a rigid flat plane or a free surface, these two cases corresponding to limiting Froude numbers 0, ∞. The wing elements can perform harmonic oscillations or be subject to given deformations with frequency ω around equilibrium. Adopt assumption of small perturbations induced by the system, justifying use of a linear unsteady theory of lifting surface, [20]. The problem of the flow past a propulsor represented by a system of oscillating wings is reduced to solving of a Laplace equation for a perturbed flow potential with linearized boundary conditions of the flow tangency on wings' surfaces; dynamic and kinematic conditions on a free vortex sheet and a free surface;

condition of decay of perturbations at infinity and a Zhukovsky condition at sharp trailing edges.

The formulated boundary problem can be reduced to solution of a singular integral equation, relating nondimensional complex amplitudes of the pressure jump $[p_j(\xi,\zeta)]$ and the downwash $\alpha(x,z)$ upon a lifting surface with a number j

$$\frac{1}{4\pi}\int_{S_{oj}}[p_j(\xi,\zeta)]K_j(x-\xi,z-\zeta)\,d\xi d\zeta=\alpha(x,z) \tag{1}$$

In linear case the generalized downwash $\alpha(x,z)$ is a sum of the downwash, induced by the wing proper $\alpha_j(x,z)$ and downwash $\alpha_{ji}(x,z)$, induced by other wing of the system. One can write

$$\alpha_j(x,z)=iky_c(x,z)+\frac{\partial y_c(x,z)}{\partial x}, \tag{2}$$

where $y_c(x,z)$ - form of the wing oscillations; $k=\frac{\omega a}{U_0}$ - a relative frequency of oscillations (Strouhal number); a - semichord of the wing.

In case when the propulsor consists of one oscillating wing $\alpha_{ji}(x,z)=0$.

Concrete form of the singular kernel $K_j(x-\xi,z-\zeta)$ depends on whether the boundary is a rigid plane or a free surface. Singular integrals entering the kernel are calculated with the help of special interpolation quadrature formula, [20].

The equation (1) can be solved by means of a collocation method. Representing the amplitude of the pressure jump in new angular variables (μ,φ) as the modified Birnbaum-Prandtl series

$$[p(\mu,\varphi)]=\frac{S_0}{la(\varphi)}\sum_m\sum_n a_{mn}\omega_m(\mu)\sin(n\varphi) \tag{3}$$

we can reduce the integral equation (1) to a system of linear algebraic equations with respect to unknown coefficients a_{mn} of the series. The following wing notations have been introduced in equation (3): $\omega_0=(1-\cos\mu)/\sin\mu;\omega_m=\sin m\mu,\ m>1;l$—span of the wing; $a(\varphi)$—current semichord of the wing, S_0 — area of the wing. As seen from (3), coefficients a_{mn} determine the loading distribution across the wing and, consequently its lifting and propulsive characteristics. The lift Y, hydrodynamic moment M, power P spent to support the wing oscillations in the fluid can be calculated by means of the formulae

$$Y=\rho U_0^2\int_{S_0}Re[p]e^{ikt}\,ds,$$

$$M=-\rho U_o^2 a\int_{S_0}Re\Big([p]e^{ikt}(x-x_0)\Big)\,ds, \tag{4}$$

$$P=-\rho U_0^3\int_{S_0}Re([p]e^{ikt})Re\frac{\partial}{\partial t}(y_ce^{ikt})\,ds.$$

The thrust force T is determined as a sum of the suction force S and the projection of the resultant X of normal hydrodynamic loads upon the direction of the wing motion

$$S=\rho U_o^2\frac{2\pi}{S_0}\int_{l_1}A^2\cos(\nu_n,x)\,dl,$$

$$X=\rho U_0^2\int_{S_0}Re([p]e^{ikt})Re(\frac{\partial y_c}{\partial x}e^{ikt})\,ds, \tag{5}$$

where A is the strength of a square root singularity of the loading at the leading edge l_1 of the wing. It can be shown by appropriate stretching of coordinates the in immediate vicinity of the leading edge the flow is close to a two-dimensional one in the plane normal to the wing planform contour, and the component of the perturbed velocity lying in this plane dominates. Evaluation of behavior of the series (3) near the leading edge permitted to find both to find corresponding asymptotics of the loading $[p]$ and the strength of singularity A, which can be expressed in terms of coefficients a_{mn} found as a result of numerical solution of equation (1). Coefficients of hydrodynamic forces and moments can be expressed through coefficients of hydrodynamic derivatives

$$C_Y=\sum_j\Big(C_Y^{q_j}q_j+C_Y^{\dot q_j}\dot q_j\Big),$$

$$C_M=\sum_j\Big(C_M^{q_j}q_j+C_M^{\dot q_j}\dot q_j\Big), \tag{6}$$

$$C_S=\sum_j\sum_i\Big(C_S^{q_iq_j}q_iq_j+C_S^{q_i\dot q_j}q_i\dot q_j+C_S^{\dot q_i\dot q_j}\dot q_i\dot q_j\Big),$$

where q_j independent kinematic parameters, a dot corresponds to a derivative with respect to time. In case, when a rigid wing participates in both heave h and pitch θ oscillatory motions, the kinematic parameters q_j can be written as

$$h=h_0e^{i(kt+\varphi_h)};\quad \theta=\theta_0e^{i(kt+\varphi_\theta)}, \tag{7}$$

where $\varphi_h,\varphi_\theta,h_0,\theta_0$ - phase angle shift and oscillations amplitudes.

For the purpose of evaluation and analysis of propulsive characteristics of the propulsor it is convenient to introduce coefficients averaged over the period of oscillations

$$\left\{c_T, c_S, c_X, c_P\right\} = \frac{k}{2\pi}\int_0^{2\pi/k} \{C_T, C_S, C_X, C_P\}\, dt \tag{8}$$

The efficiency of the oscillating wing propulsor can be determined as in [7]

$$\eta_i = \frac{c_T}{c_P}. \tag{9}$$

Some results of calculations of propulsive characteristics versus principal parameters of the problem are presented in Fig. 2.

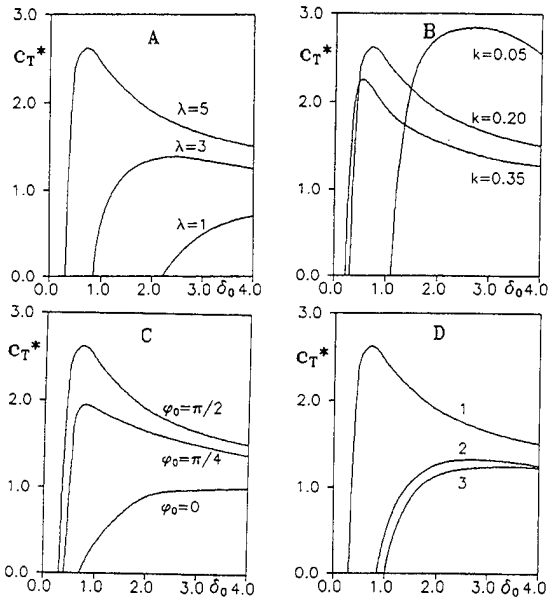


Figure 2: Relative average thrust coefficient for heave and pitch of a rectangular wing : A–versus aspect ratio ($k = 0.2; \varphi_0 = \pi/2; x_0 = 0; h_b = 0.1$; rigid wall); B– versus Strouhal number ($\lambda = 5; \varphi_0 = \pi/2; x_0 = 0; h_b = 0.1$; rigid wall); C–versus shift of phase angle ($\lambda = 5; k = 0.2; x_0 = 0; h_b = 0.1$; rigid wall); D– versus distance from the boundary ($\lambda = 5; \varphi_0 = \pi/2; k = 0.2; x_0 = 0$; 1– rigid wall, $h_b = 0.1$; 2–infinite fluid; 3–free surface, $h_b = 0.1$)

Some conclusions can be drawn from analysis of these results.

- Increase of the wing aspect ratio and Strouhal number leads to augmentation of the averaged thrust for purely heave or pitch oscillations and for combined (heave and pitch) oscillations as well.

- In case of combined oscillations within a certain range of the amplitudes ratio $\delta_0 = h_0/\theta_0$ and phase shift angles $\varphi_0 = \varphi_\theta - \varphi_h$ it is possible to gain in thrust as compared with purely heave oscillations ($c_T^* = c_{Th\theta}/c_{Th} \geqslant 1$). It should be mentioned that there exists such an amplitudes ratio for which this gain achieves a maximum. Relative gain grows with increase of aspect ratio and decrease of Strouhal number. There exists an optimal angle of phase shift between heave and pitch, which tends to $\pi/2$ for $k \to 0$.

- In the case of combined oscillations the closer is the wing to a rigid boundary the larger is the averaged thrust. When the wing oscillates near a free surface the thrust is somewhat less as compared to an infinite fluid case.

The results discussed above were obtained within assumption of vanishing thickness. In the frame of linear theory incorporation of the thickness effects can be carried out by means of distribution of sources upon projection of the wing surface on (x, z) plane with strength proportional to the x–derivative of the wing thickness distribution. The presence of boundaries (rigid or free surface) is accounted for by means of the mirror image techniques. The contribution of the sources distributed on the wing itself to induced downwash is zero. Therefore, the downwash on the wing due to its thickness is fully determined by that of the sources of the "mirror" image of the wing. Consideration of some computed results obtained by present authors show that when the wing approaches a rigid boundary there occurs an increment of averaged thrust, the magnitude of which depends on the square of relative thickness, geometry of the lifting surface and the clearance with respect to the boundary. As shown by calculations, this increment is very small and can be neglected. Obviously, within assumptions of the linear theory, thickness effects have zero contribution to the thrust for the infinite fluid case.

On the whole, the results calculated for rigid wings correlate well with the known experimental data, [37, 38]. See Fig. 3 , 4.

It is practical to consider the propulsive characteristics of oscillating wing systems . Qualitatively, these characteristics behave similarly to those of oscillating wings. However, an investigation of some practical configurations, for example: biplane, tandem, "cross", "box" (see Fig. 5) facilitates the process of design of a propulsor with improved performance parameters.

In particular, it can be concluded:

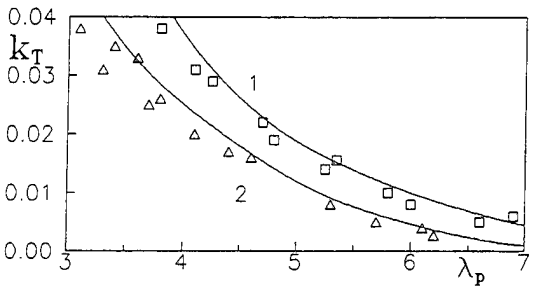


Figure 3: Comparison of calculated and experimental [37] results for average thrust coefficient (alternative form) $k_T = 2\bar{T}/\rho(U_0^2 + (\omega h_0)^2)^{1/2} S_0$ as a function of parameter $\lambda_p = 1/2kh_0$. Heave of a rectangular wing ($\lambda = 4$, NACA–0015, $h_0 = 0.18$): 1– rigid wall,$h_b = 0.3$; 2– free surface,$h_b = 0.27$

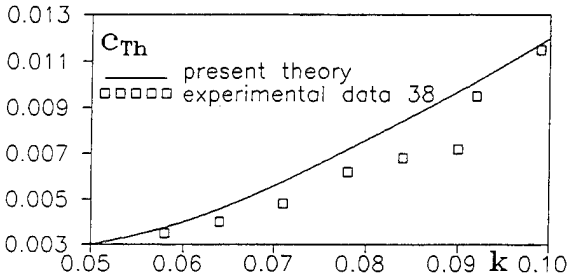


Figure 4: Comparison of calculated and experimental [38] results for average thrust coefficient at heave of a rectangular wing in infinite fluid ($\lambda = 4$, NACA–0015, $h_0 = 0.63$)

- A biplane scheme with wing elements, oscillating in the counter-phase regime (a case analogous to that of a single wing oscillating near the ground), provides better propulsive performance than a single wing i infinite fluid and enables to compensate the "side" force.
- A tandem scheme with correctly chosen geometry and kinematics is characterized by a minimal energy drop into the wake, and therefore is rather promising as a possible device configuration for extraction of energy of waves. Calculations show that the tandem system can become still more effective with increase of the number of elements.

The analysis of instantaneous characteristics of oscillating wing systems allows to make a conclusion that with increase of the number of elements

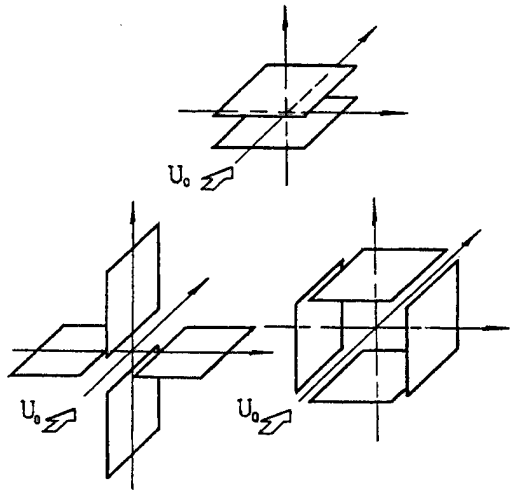


Figure 5: Some practical configurations of a wing-propulsor

in considered configurations it is possible to essentially diminish pulsations of thrust during the period, thus enhancing stability of the propulsive system.

Asymptotic model of the flow past a wing oscillating near a wall or between parallel walls

As indicated in the previous section, the thrust of the oscillating wing propulsor increases near a rigid boundary. This fact is confirmed in numerical study in [39] made on the basis of the method of discrete vortices and in the experiments of [40] carried out in the towing tank. The later author also investigated the case of the wing oscillating near parallel walls and found out that in this case the increment of thrust due to the ground effect becomes still larger. The general conclusion stated in [40] was that in presence of rigid boundaries both thrust and the efficiency of the oscillating wing propulsor increase in comparison with the infinite fluid case. The most interesting situation when the average distance from the rigid flat boundary is small can be readily studied through application of the method of matched asymptotics expansions [41]. In case of small relative clearances h the flow in highly constrained region between the wing and rigid boundary becomes "almost" two-dimensional in the plane parallel to the boundary. Within linear theory the 3D Laplace equation degenerates into

a 2D Poisson equation, so that the problem is governed by the following relationships

$$h_b\Big(\frac{\partial^2\Gamma}{\partial x^2}+\frac{\partial^2\Gamma}{\partial z^2}\Big)=\frac{\partial y_c}{\partial x}-\frac{\partial y_c}{\partial t},\quad (x,z)\in S_0, \tag{10}$$

$$\Gamma=0 \quad \text{at the leading and side edges,} \tag{11}$$

$$\frac{\partial\Gamma}{\partial x}-\frac{\partial\Gamma}{\partial t}=0 \quad \text{at the leading edge,} \tag{12}$$

where Γ is a jump of velocity potential across the wing, $y_c(x,y,z)$ is a function, describing instantaneous position of the wing with respect to the wall; S_0- a projection of the wing upon the boundary plane. In many practical cases the problem (10)–(12) can be solved analytically. For the sake of saving place we shall confine ourselves to writing down the simplest formulae for the averaged thrust coefficient c_T and ideal efficiency coefficient η_i of a heaving flat plate of infinite aspect ratio

$$c_T=\frac{h_0^2k^2[(2+k^2)^2+k^2]}{8h_b(1+k^2)^2},$$

$$\eta_i=\frac{1}{2}\Big(\frac{2+k^2}{1+k^2}\Big)\Big[1+\frac{k^2}{(2+k^2)^2}\Big], \tag{13}$$

where h_0 is the amplitude of heave oscillations. Some results of calculations are given in Fig. 6, 7. Fig. 6 illustrates behavior of the averaged thrust coefficient versus Strouhal number k for different aspect ratios λ of a rectangular wing performing heave oscillations.

In Fig. 7 a comparison is presented of the ideal efficiency of the flat plate wing of infinite aspect ratio versus Strouhal number for the cases of oscillations in close proximity to the rigid boundary $h_b << 1$,see formula (11), and oscillations in unbounded fluid, [3].

Note that in case of pitch oscillations the axis of rotation is located at the distance of one quarter of chord from the leading edge of the foil. It is easy to extend the same approach to the case of a wing-boundary system with lateral curvature. As an example some results are presented in Fig. 8. illustrating dependence of the averaged thrust of a heaving circular wing, surrounding the cylinder, as function of Strouhal number for different radia of the cylinder.

In case of a wing in oscillations in a narrow channel of width H with possible lateral curvature it can be shown that the above results for a wing near one wall should be corrected in the following way.

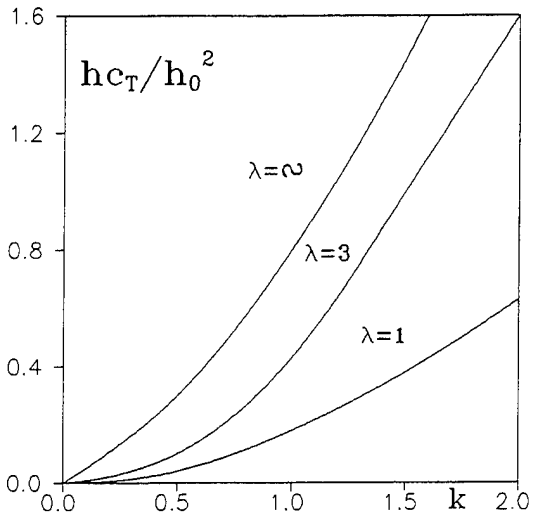


Figure 6: Average thrust coefficient of a rectangular wing at heave versus Strouhal number, $h_b << 1$

$$c_{TH}=c_T\frac{H}{H-h_b},\quad c_{PH}=c_P\frac{H}{H-h_b},$$

$$\eta_H=\eta. \tag{14}$$

Thus, if a wing propulsor functions in a narrow channel both its thrust and required power increase by a factor of $H/(H-h_b)$ as compared to the one wall case, and the ideal efficiency coefficient retains its value.

Note, that applications of wing propulsors oscillating near walls, between parallel walls and in narrow tubes include propulsive devices for flat bottomed vehicles moving in water, pumps, *etc.*

Influence of elasticity upon hydrodynamic characteristics of oscillating wings

Account of the influence of elasticity in design of unconventional propulsor is necessitated with solution of some practical problems.

The first of such problems is connected with a fact that in real technical systems the rigid wing elements can be connected to one another and to the drives of control mechanisms by means of elastic ties,having a finite number of degrees of freedom.

The second problem, which follows from analysis of performance of propulsors of aquatic animals ,is the necessity of account for a proper elasticity of oscillating wing elements. A rational

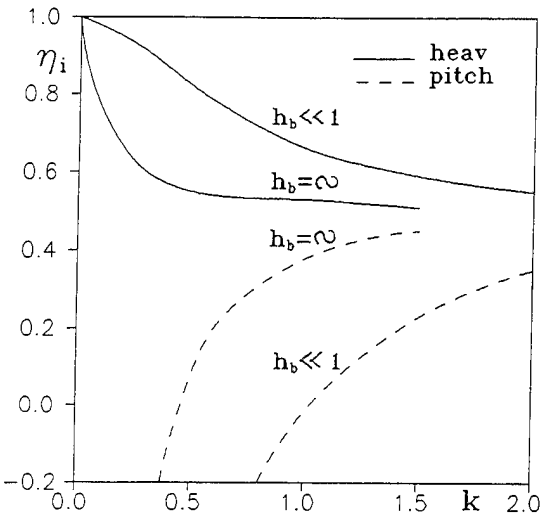


Figure 7: Comparison of magnitudes of ideal efficiency for a foil at very small distances from the rigid boundary ($h_b << 1$) and in infinite fluid,[3]

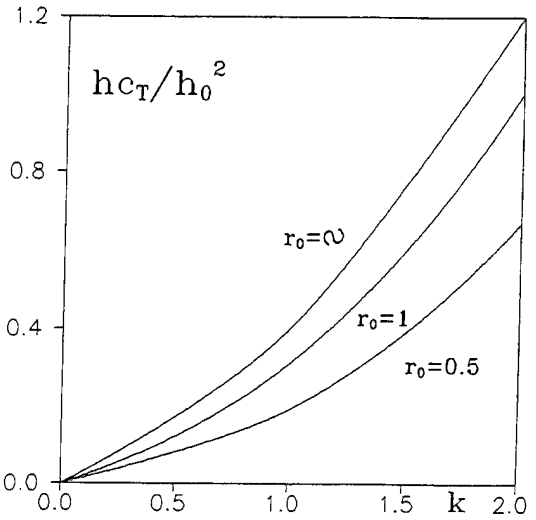


Figure 8: Influence of Strouhal number and radius of the infinite length cylinder upon average thrust coefficient of a circular wing in pitch, $h_b << 1$

choice of inertial and elastic properties of the wing can serve to enhance the efficiency of the propulsor.

A certain practical interest exists in consideration of the thrust generation in the parameter range close to the hydrodynamic resonance (flutter). Let us consider a simplified mathematical model of the flow past a wing with elastic ties, providing two degrees of freedom, [26]. Adopting assumptions of the linear unsteady lifting surface theory, consider a rigid wing, the heave and pitch oscillations of which are excited through two elastic ties (see Fig. 9).

As a result of hydroelastic interaction of the wing with the fluid,the law of oscillations (h, θ) of the lifting surface will differ from the initial law of kinematic excitation $(\tilde{h}, \tilde{\theta})$.

In this case the system of equation of equations, describing elastic oscillations of a rigid wing, will have the form

$$m\ddot{h} + K_h(h - \tilde{h}) + m(x_0 - x_c)\ddot{\theta} = Y,$$

$$J\ddot{\theta} + K_\theta(\theta - \tilde{\theta}) + m(x_0 - x_c)\ddot{h} = M, \qquad (15)$$

where m, J are respectively a mass and the mass moment of inertia of the wing with respect to the axis of rotation; K_h, K_θ– stiffness coefficients of elastic ties with respect to heave and pitch; x_0 and x_c–abscissa of the axis of rotation and abscissa of the center of gravity of the wing.

Confining the analysis to that of the nonhomogeneous solution of the system of equations (15),

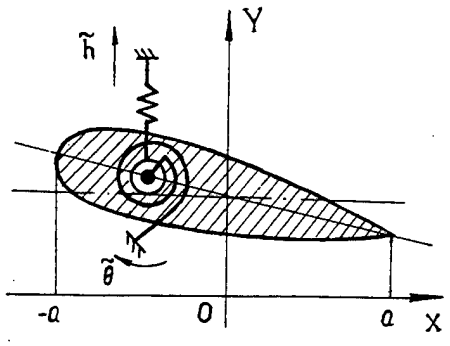


Figure 9: Rigid wing with two elastic ties

we can obtain such parameters of resulting (forced) oscillations as amplitudes (h_0, θ_0) and phase angle shifts $(\varphi_h, \varphi_\theta)$, which are expressed by means coefficients of hydrodynamic derivatives, entering the expansions of the lift Y and the moment M in kinematic parameters, (see (6)).

As a result of oscillations taking place due to kinematic excitation of the system there is realized a thrust force, which can be calculated with use of the formulae (5).

In this way we can analyze the influence of main parameters of the problem: relative frequency k, elasticity parameters $w_h = \omega/\omega_h$, $w_\theta = \omega/\omega_\theta$ (where $\omega_h = \sqrt{K_h/m}, \omega_\theta = \sqrt{K_\theta/J}$); shifts of phase angles and the amplitudes' ratio upon propulsive characteristics of the system.

Some of calculated results, obtained on the basis of the above stated model, are presented in Fig. 10– 13.

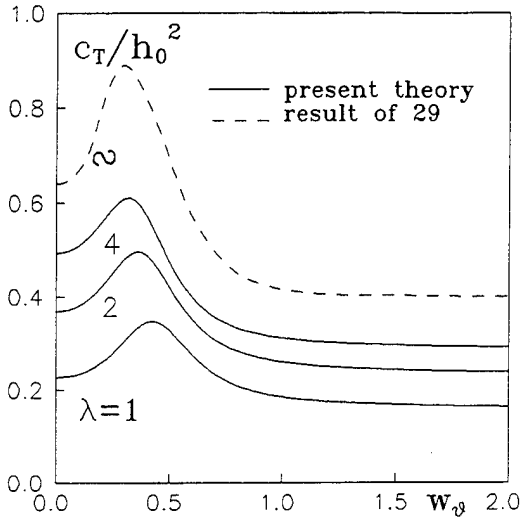


Figure 10: Comparison of the present theory with calculated results of [29] for a given heave; $k = 0.8, \beta^* = \rho a^3 l^3/2J\lambda = 6.36; \beta^{**} = ma^2/J = 0; x_0 = x_c = -0.5; \omega/\omega_h = 0; \tilde{\theta}_0 = 0$

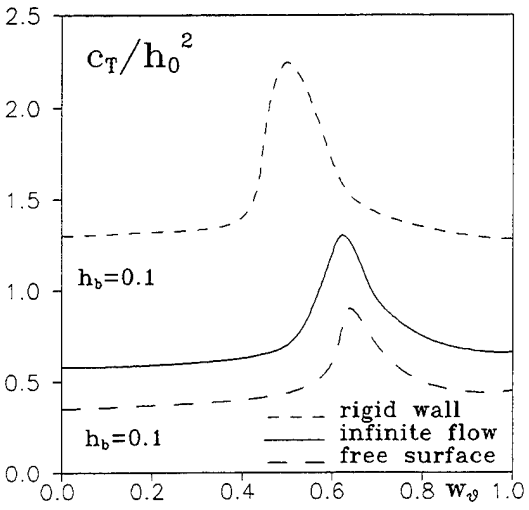


Figure 11: Influence of a rigid wall upon average thrust coefficient at heave; λ=3, k=1.5, x_0=x_c=0

Analysis of the calculated curves shows that for relatively large Strouhal numbers there take place resonant maxima of the thrust. The magnitudes of these maxima increase when the wing approaches to the rigid boundary and somewhat decrease near the free surface.

If elastic ties are sufficiently pliable, then with variation of Strouhal number the two resonance zones can be observed.Each of the elastic ties has its own characteristic resonance zone. In Fig. 12 the left zone corresponds to the resonance in heave whereas the right zone corresponds to the resonance in pitch.

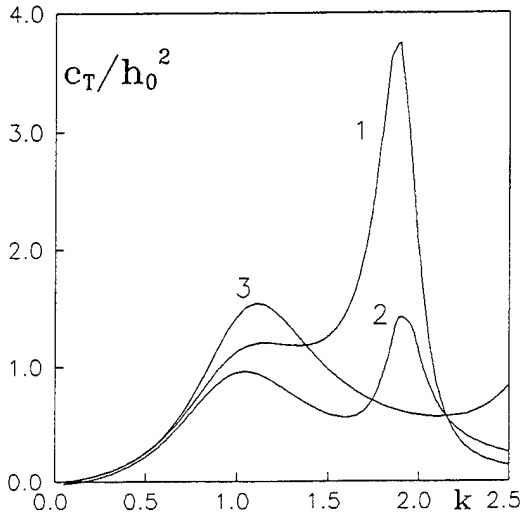


Figure 12: Resonance zones for a rigid wing with two elastic ties ($k_{0h} = 2; \beta^* = 2; \delta^* = \rho a l^2/2m\lambda = 1; x_0 = x_c = -0.5$). 1 - $k_{0\theta} = 2, \tilde{\theta}_0 = 0$; 2 - $k_{0\theta} = 2, \tilde{\theta}_0/\tilde{h}_0 = 0.2, \varphi_0 = \pi$; 3 - $k_{0\theta} = 3, \tilde{\theta}_0 = 0$

With increase of $k_{0h} = \omega_h a/U_0$ and $k_{0\theta} = \omega_\theta a/U_0$ these zones shift to the region of higher magnitudes of k. The coefficient of the averaged power, required to support oscillations of the wing , varies according to a similar law. Considering the components of the thrust coefficient, i.e.c_S and c_X at resonance regime,it is worthwhile to mention that the resonance in heave takes place with a noticeable increase of the suction force, so that the thrust is provided mainly due to the suction component.

Practically there exists a necessity in reduction of the ratio c_S/c_T with an overall increase of the thrust. This is related to the fact that the modes with large magnitudes of this ratio often fail to be realized due to the leading edge stall. The calculations show that it is possible to achieve a decrement of the suction force relative contribution c_S/c_T for a wing near a resonance in pitch.

Fig. 13 show some typical curves of propulsive characteristics near resonance for a wing with two elastic ties, which is subject to excitation in heave.

As can be seen from the Figure, the resonance for the components c_S and c_X of the suction force

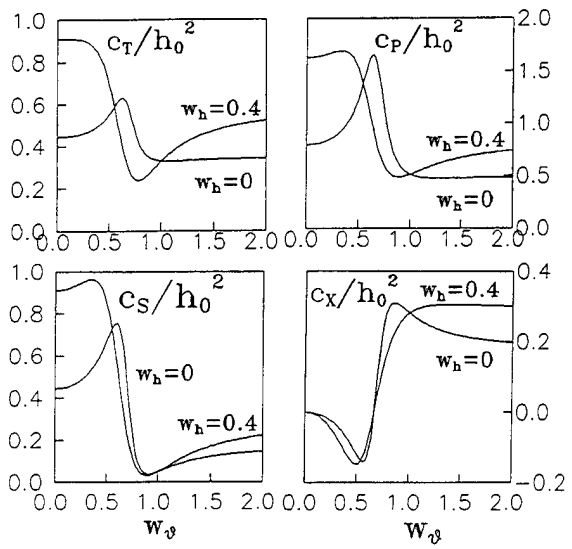


Figure 13: Main propulsion coefficients versus elasticity parameter ω/ω_θ for a given heave. Rectangular wing $\lambda = 3; k = 0.8; \beta^* = 2; \delta^* = 1; x_0 = x_c = -0.2; \tilde{\theta}_0 = 0$

takes place in different ranges (a maximum of c_S is reached for $\omega/\omega_\theta = 0.5 - 0.7$, a maximum of c_X occurs at $\omega/\omega_\theta = 0.8 \div 0.9$) The spent power coefficient has a maximum in the zone of maximum of the suction force. Then it drops in magnitude and ,eventually, becomes smaller than a corresponding coefficient c_P for a wing without elastic ties.

Thus, as a wing reaches a (resonant) maximum in suction force there takes place an increase in the spent power. So, supposedly, this performance mode is unfavorable (or not realizable due to the leading edge separation effects). The second state of resonance (in c_X) for which the spent power decreases,i.e. the propulsor efficiency increases,can be characterized as quite plausible. This phenomenon is confirmed by available results of observations of aquatic animal propulsion,[16].

Now, let us pass over to a more general mathematical model of an elastic wing, represented by a thin isotropic plate of variable thickness $\tau(x,z)$ with a known density ρ_S, the Young module E and the Poisson coefficient ν.

The wing leading edge can be subject to given kinematic excitations (heave and pitch). In this case the points of the wing will displace in response to hydroelastic interaction with the fluid according to the law

$$y_c(x,z,t) = [y_0 + y_1(a+x) + y_e(x,z)]e^{ikt}, \quad (16)$$

where y_e is the form of induced elastic oscillations.

When considering the oscillating wing the problem of the unsteady lifting surface theory (1) should be complemented by the equation of dynamic bending with corresponding boundary conditions (given oscillations at the rigidly fixed leading , conditions at other edges with no forces applied)

$$\Delta(D\Delta y_c) - (1-\nu)\Big(\frac{\partial^2 D}{\partial x^2}\frac{\partial^2 y_c}{\partial z^2} - 2\frac{\partial^2 D}{\partial x\,\partial z}\frac{\partial^2 y_c}{\partial x\,\partial z} + \frac{\partial^2 D}{\partial z^2}\frac{\partial^2 y_c}{\partial x^2}\Big) + m_S\frac{\partial^2 y_c}{\partial t^2} = l[p(x,z,t)], \quad (17)$$

where $D = E\tau^3/12(1-\nu^2)$ is cylindrical stiffness and $m_S = \rho_S\tau$ is a surface distribution of mass.

The solution is carried out by way of representation of the unknown wing ordinates y as a double series in terms of a system of fundamental functions, satisfying kinematic boundary conditions at the leading edge, with subsequent application of the generalized Bubnov-Galerkin technique.

In view of a large number of the significant parameters of the general problem,complicating the analysis of results, we consider a particular case of the above stated problem, namely –elastic oscillations of a wing of infinite aspect ratio. This simplified model would facilitate qualitative analysis of behavior of the system. Within the two-dimensional theory a complementing equation of dynamic bending of the beam-strip will acquire much simpler form

$$\frac{\partial^2}{\partial x^2}\Big[D(x)\frac{\partial^2 y_c}{\partial t^2}\Big] + m_S(x)\frac{\partial^2 y_c}{\partial t^2} = l[p(x,t)], \quad (18)$$

where $D(x)$ - bending stiffness; $m_S(x)$ - distribution of mass chordwise.

The equation (18) is complemented by the boundary conditions at the leading edge for which parameters of heave and pitch are prescribed and at the trailing edge which is free from loading.

A distributed loading upon the wing is calculated with utilization of the solution given by T. Wu,[7]. For the case of an elastic foil with the bending stiffness and mass uniformly distributed chordwise the form of elastic oscillations $y(x)$ is represented by means of expansion in terms of orthogonal functions $Y_n(x)$ based on the forms of the bending oscillations of a prismatic beam-strip in vacuum

$$y_e(x) = \sum_n^{\infty} c_n Y_n(x) \qquad (19)$$

As mentioned previously, the solution of the problem is carried out by Bubnov–Galerkin technique, which permits passage from the system of linear differential relationships to the system of linear algebraic equations with respect to the unknown series coefficients c_n. The later system with infinite number of unknowns can be solved by the reduction method.

Some calculated results for propulsive characteristics of an elastic foil are presented in Fig. 14, 15.

Results of calculations reveal that with variation of the elasticity parameter $B = \rho U_0^2 a^3 l / D_0$ (where D_0 is a bending stiffness at the point of application of exciting force and moment) there are observed some resonant modes (see Fig. 14).

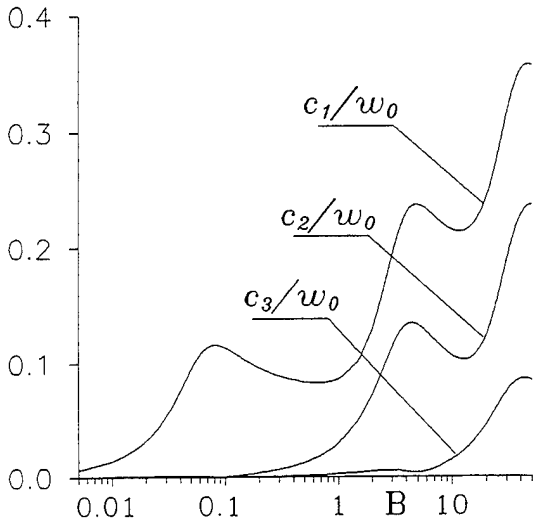


Figure 14: Resonant character of the increase of absolute magnitudes of forms of elastic oscillations($h_0 = 0; \theta_0 = 0; k_w = 2; \gamma = m/al\rho = 0.05$)

These maxima of thrust occurs at sufficiently high magnitudes of Strouhal number. In the state of resonance of a completely elastic wing the trends of variation of the thrust components c_S and c_X are different which is similar to the case of a rigid wing with two elastic ties. The suction force coefficient c_S decreases and c_X coefficient increases. This may imply that in the state of resonance the predicted propulsive characteristics are likely to be realized (see Fig. 15)

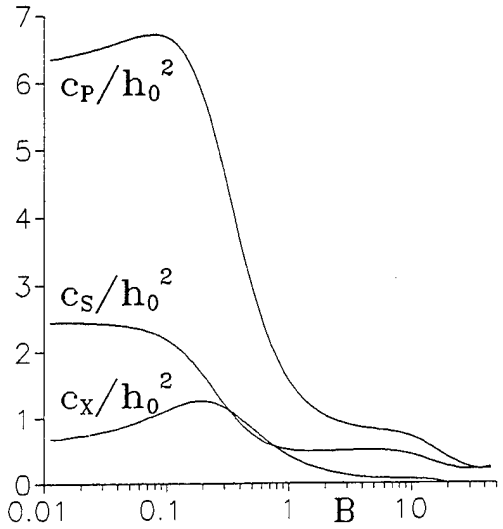


Figure 15: Main propulsive coefficients versus elasticity parameter B ($k = 2; k_w = .64; \gamma = 0.2; \theta_0/h_0 = 0.5; \varphi_0 = \pi$)

Oscillating wing in wave flow

To account for the influence of the wave flow upon propulsive characteristics of oscillating wing, we consider a two–dimensional regular wave of small amplitude A_w, propagating along the x-axis.

Following T.Wu, assume that the propulsor is located far enough from the free surface to be able to neglect a reverse influence of the wing on parameters of fluid motion near a free surface. This assumption can hold if the wing oscillates at distances from the free surface not exceeding the length of two chords.

Beside, it is assumed that the apparent frequency of the wave and the frequency of wing oscillations coincide. Ratio of the orbital motion velocity amplitude to the velocity of the oncoming flow is assumed to be small.

The expression for the form of the oncoming wave can be written down as follows

$$y_w = h_b + Re\left[A_w e^{i(\omega_0 y + k_w x)}\right], \qquad (20)$$

where $k_w = 2\pi/\lambda_w$ is a wave number; λ_w–wave length; ω_0– apparent frequency of the wave, related to frequency of the wave by equation $\omega_0 = \omega_w + k_w U_0, \omega_w = \sqrt{g k_w \tanh(g H_*)}$, H_*- the depth of fluid.

The vertical component of velocity of fluid particles in the wave, determining contribution of perturbed velocities to the downwash in (x, z) plane can be written down as follows

$$V_{y_w} = iw_0 e^{i(\omega_0 t - k_w x)}, \qquad (21)$$

where w_0 is the amplitude of the vertical component of orbital motion of fluid particles in the wave, evaluated at the depth of submergence of the wing.

Thus, the influence of fluid particles in the wave upon the wing is accounted for only through contribution of the induced velocities to a total downwash $\alpha(x, z)$, entering the right-hand side of the integral equation (1). The further analysis of the problem is specified depending on whether the wing is rigid, on elastic ties or completely elastic. Corresponding models of previous sections are utilized.

Let us briefly analyze some specifics of determination of propulsive characteristics of oscillating wing in a wave stream.It is known, that the power required to sustain the wing oscillation in fluid, is equal to the work of the thrust force plus kinetic energy E, transmitted by the wing to the fluid per unit time.This relationship for characteristics averaged for the duration of the period of oscillations has the form

$$c_P = c_T + c_E. \qquad (22)$$

One of three possible regimes can be realized in the wave stream for a wing which provides a positive thrust

$$0 < \eta < 1, \quad c_P > 0, \quad c_E > 0, \qquad (23)$$

$$\eta > 1, \quad c_P > 0, \quad c_E < 0, \qquad (24)$$

$$\eta < 0, \quad c_P < 0, \quad c_E < 0. \qquad (25)$$

Omitting the well known regime (23), note that two remaining regimes are characterized by the energy extraction from the stream. The regime (25) is more efficient because to sustain given oscillations the energy has even to be taken away from the wing.

The wing system with elastic ties, placed into a wave stream, can initiate the oscillation process without energy supply through control devices. Such a system, which ,on one hand, provides "depression" of the wave, and, one another hand, serves to extract energy from the flow, can be called a propulsor of passive type. For all that all extracted energy is completely utilized for thrust generation, i.e. $c_T = -c_E, c_P = 0$.

It is convenient to characterize the efficiency of the above device by means of a special parameter, representing the ratio of the work performed by the thrust per unit time to the power of the oncoming wave

$$\eta_w = \frac{\bar{T}U_0}{P_w l}, \qquad (26)$$

where P_w is the power of the oncoming wave per unit length of the wave front, $\bar{T}$–average thrust.

As an example confirming workability of the mathematical model of a wing in wave stream a comparison is presented of some calculated results with the experimental data[25]. Note that in[25] a wing with elastic ties was mounted on a carriage of the towing tank . Waves ,generated in the tank, excited oscillatory motions of the wing. As a result a thrust force was generated which was sufficient to induce motion of both the wing and the carriage in direction opposite to that of the wave front. For comparisons the calculations were carried out for a wing of relatively high aspect ratio in order to account for conditions of the experiment which aimed at providing a two-dimensional flow. In spite of a somewhat conditional character of the comparison, theoretical magnitudes of speed of motion and amplitude of oscillations agree with those obtained in the tests both qualitatively and quantitatively. In particular, it became possible, to predict (with satisfactory accuracy) the optimal length of the wave for which there occurs a resonance in thrust (speed) and amplitudes of oscillations (Fig. 16).

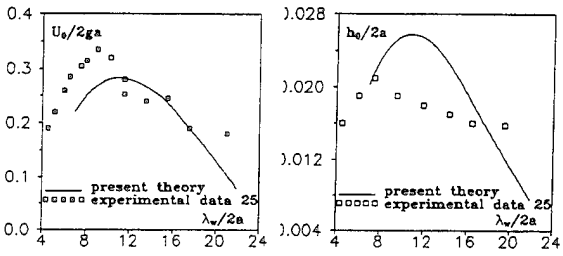


Figure 16: Comparison of results of the present theory with experimental data,[25]

Optimal characteristics of a propulsor based on oscillating wings

As follows from both experiments and calculations characteristics of the oscillating wing propulsor are closely related to kinematic parameters, namely: amplitude, phase angles of heave and pitch oscillations. Therefore tone of the important problems consists in determination of an

optimal law of the wing oscillations, providing maximum attainable efficiency.

This conditional optimization problem may be formulated in the following way: within a certain given class of functions $y_c(x,z)$ find the one, minimizing the power required to generate a prescribed thrust

$$c_P \to \min,$$
$$c_T = c_{T0}. \qquad (27)$$

There may also be formulated an inverse optimization problem

$$c_T \to \max,$$
$$c_P = c_{P0}. \qquad (28)$$

Parameters c_{T0} and c_{P0} in equations (27) and (28) define isoperimetric conditions imposed upon the coefficients of the averaged thrust and power.

The conditional optimization problem for an isolated rigid wing is considered with respect to the unknowns: amplitudes of oscillations h_0, θ_0 and phase angles φ_h, φ_θ. In case of a system comprising several wings the number of design parameters of the problem increases in proportion to the number of wing in the system.

The optimization problem may be simplified by means of introduction of new independent variables ψ , representing parameters completely describing wing's kinematics. Due to this the form of expressions for propulsive coefficients become more simple and convenient, and there is no need to impose any restrictions upon the new parameters.

In view of the fact that each of the considered propulsive coefficients can be written down as a corresponding quadrature form with respect to parameters of motion ψ, the problems (27),(28) can be written in the following general form

$$\psi^T A^{(2)}\psi + A^{(1)}\psi + A^{(0)} \to \text{extr},$$
$$\psi^T B^{(2)}\psi + B^{(1)}\psi + B^{(0)} = 0, \qquad (29)$$

where $(A^{(2)}, B^{(2)}), (A^{(1)}, B^{(1)}), (A^{(0)}, B^{(0)})$ are quadratic, linear and constant terms of corresponding quadrature forms, $\psi = (\psi_1, \ldots, \psi_n)$ is the vector of the unknown kinematic parameters of the problem.

The algorithm of optimization is based upon classical method of Lagrange multipliers, reducing (29) to a system of nonlinear equations of the second order with respect to the vector of unknown kinematic parameters ψ and Lagrange multiplier λ^*.

Using a special linear transformation of coordinates the above mentioned system can be reduced to one nonlinear algebraic equation with respect to λ^*. All stationary solutions of this equation can be found through calculation of roots of this equation. An additional verification of whether the conditions of extremum are fulfilled enables to obtain a final set of optimal solutions. Numerical analysis show that, as a rule, there are left two optimal solutions, one of which corresponds to a maximum and the other – to the minimum.

Fig. 17– 20 represent results of calculations of optimal characteristics for an isolated rigid wing.

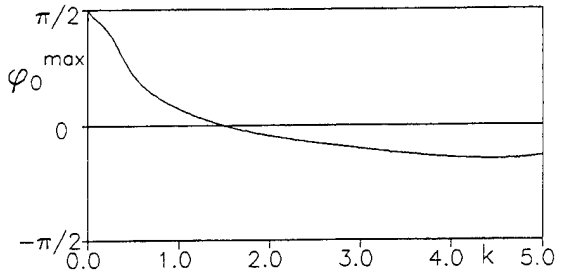


Figure 17: Optimal shift of phase angle for heave–pitch oscillations of a rectangular wing versus Strouhal number ($\lambda = 2; x_0 = 0$)

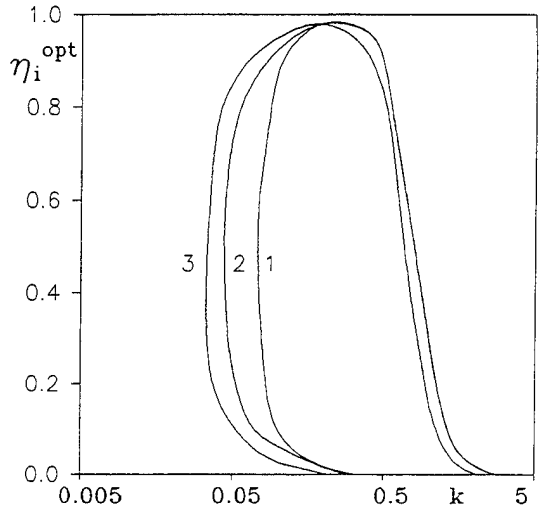


Figure 18: Optimal ideal efficiency η_i^{opt} versus Strouhal number and the wing planform for $c_{T0} = 0.01$(1– rectangular, $\lambda = 2$; 2– elliptic, $\lambda = 3.25$; 3–triangular, $\lambda = 4, \chi = 45$)

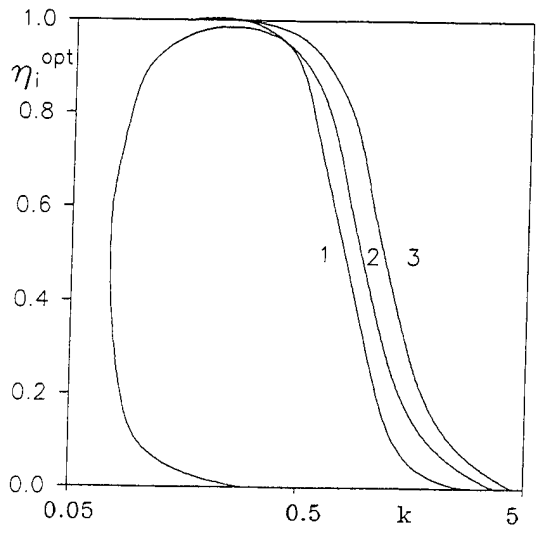


Figure 19: Optimal ideal efficiency η_i^{opt} versus Strouhal number for different number of rectangular wing elements ($\lambda = 2$) of the propulsive system for $c_{T0} = 0.01$(1– isolated wing; 2– biplane; 3– "box" type wing system)

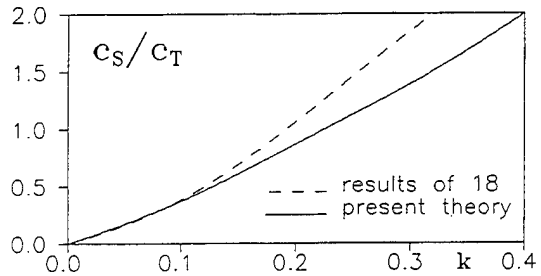


Figure 20: Comparison of the present theory with calculated results of [18] for an elliptic wing of the aspect ratio $\lambda = 8$

An approach to prediction of cavitation and laminar separation occurrence at the leading edge of the oscillating wing thrust generator

Theoretically predicted optimal oscillations of the wing can be performed with relatively large contribution of the suction force to the total thrust c_S/c_T. As indicated earlier, in practice such regimes may not be realized due to the leading edge stall. Therefore, trying to obtain an optimal performance of the wing for a given thrust coefficient c_T it is necessary to minimize the ratio c_S/c_T. In this connection it is reasonable to introduce a certain upper bound for this ratio, i.e. to require $c_S/c_T \leqslant c_0$. Choice of the constant c_0 for a concrete regime of the flow can be carried out on the basis of some additional limiting factors such as separation and cavitation occurrence at the leading edge, [20, 41, 42, 43]. As shown in the above cited references, it is possible to relate the limiting value of the suction force coefficient with cavitation number and/or separation criteria. Using the matched asymptotic techniques in case of oscillating thin wings one can obtain simple analytical formulae for flow velocity components near the leading edge of a wing, namely

$$V_n^i = \sqrt{\frac{X_n}{X_n + \bar{\rho}_n/2}}\left(U_1 \pm \frac{U_2}{\sqrt{X_n}}\right),$$
$$V_\tau^i = -U_0 \sin\chi, \qquad (30)$$
$$p^i = 1 - (V_n^i)^2 - (V_\tau^i)^2,$$

where V_n, V_τ - local (inner) velocity components in directions normal and tangential to the leading edge planform contour;X_n -the inner stretched abscissa measured along the normal to the leading edge planform contour; $\bar{\rho}_n = \rho_n/\delta^2$- stretched radius of curvature of the leading edge;δ - relative thickness of the wing section; χ- local sweep angle; U_1 and U_2 -parameters, characterizing the local oncoming flow velocity and circulatory flow around the rounded edge respectively. Parameters U_1 and U_2 are determined by means of asymptotic matching of solutions in the inner and outer regions of the flow. Through these quantities the far-field characteristics (geometry of the wing , law and parameters of oscillations, distance from boundaries and distance from them, *etc.*) exhibit themselves near the leading edge. Roughly, the cavitation inception can be predicted by means of the minimum pressures buckets (diagrams). In general case the bucket consists from its "profile"part and its "edge"branches. The "profile "part can be obtained through utilization of a linear theory of lifting surface. To obtain "edge" branches it is convenient to use the local solutions describing the flow near the rounded leading edge, presented by the formulae above. In particular, it is easy to deduce the following analytical expression for the minimum of pressure coefficient on the leading edge

$$p^i_{min} = cos^2\chi - U_1^2 - \frac{2(U_2^{max})^2}{\rho_n}. \qquad (31)$$

Assuming that cavitation inception takes place at a point of the pressure minimum ($\sigma = -p_{min}$) and accounting for the fact that the local suction force coefficient can be expressed through the

strength of the leading edge square root velocity singularity, it is not difficult to relate cavitation number σ with a maximum of instantaneous suction force coefficient C_S. For example, in a simple case of the two-dimensional flow the following formula can obtained

$$C_S^{max} = \frac{\pi\rho_n}{4}(U_1^2 - 1 - \sigma). \qquad (32)$$

For an elliptic foil one can derive from (32) $C_S^{max} \approx \pi\delta^2\sigma/4$, for the foil NACA–66012 the corresponding coefficient is $C_S^{max} \approx 0.22\pi\delta^2\sigma$, where δ as above is a relative thickness of the foil.

In Fig. 21 a characteristic minimum pressure bucket is shown for the case of heave oscillations of a rectangular wing, [43]. In this Figure c_Y stands for the wing pressure coefficient, solid line corresponds to calculation of the pressure minimum with utilization of uniformly valid expressions for the pressure coefficient obtained by the matched asymptotics techniques, dotted line corresponds to results predicted by formula (31).

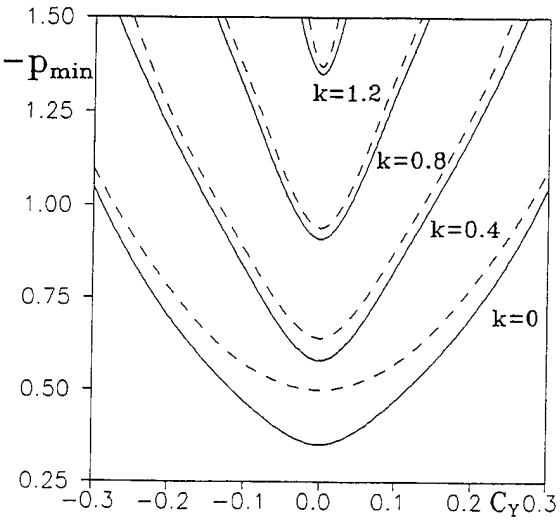


Figure 21: Minimum pressure buckets for heave oscillations of a rectangular wing $\lambda = 3$ with symmetric cross-section profile NACA–0012, $h_0 = 0.12$.

Analyzing results for different laws of oscillations one can conclude that:

- For heave oscillations the leading edge pressure drops (the suction force augments) with increase of Strouhal numbers, which may lead to earlier cavitation inception.
- For pitch oscillations, increasing Strouhal number up to a certain magnitude, which depends on the wing aspect ratio and location of the rotation axis, it is possible to postpone cavitation inception. In other words, for pitch oscillations it is possible to reduce the suction force contribution to the thrust, thus simultaneously reducing the possibility of occurrence of cavitation.

As far as relationship between suction force coefficient and occurrence of separation , it is evident from physical viewpoint that the more intensive is the circulatory motion of the flow across the leading edge the more probable becomes separation of the viscous fluid flow from the edge. An approach to estimate the required relationship quantitatively can be worked out on the basis of the research results, published in [28, 42]. By means of straightforward integration of the laminary boundary layer equations on an osculating parabola, which approximates a rounded leading edge it is found in these works, that laminar separation occurs when the aforementioned parameters U_2 and U_1 of the leading edge flow are related to each other in the following way

$$U_2 = k_0\sqrt{\rho_n}U_1, \qquad (33)$$

where separation parameter k_0 was determined by integration of the momentum thickness equation of the laminar boundary layer as 0.921. Using more accurate procedure of numerical integration of the differential equations of laminar boundary layer along the osculating parabola the separation parameter is known to be 1.1556 (see [44] and [45]). In a two-dimensional example, introducing the instantaneous suction force coefficient as $C_S = 2\pi\delta^2U_2^2$, one can easily obtain an upper boundary of the suction force coefficient as

$$C_S^{max} = 2\pi k_0^2\rho_n U_1^2. \qquad (34)$$

It is easy to see from this formula that the maximum admissible magnitude of the suction force coefficient for which no separation occurs is linearly proportional to the radius of curvature of the edge.

Note that similar estimates can be obtained for average values of the suction force coefficient.

Conclusion

The present authors have made an attempt to give an outline of some research work carried out at Saint-Petersburg Marine Technical University

with utilization of numerical and asymptotic methods with the goal to provide a tool for hydrodynamic design of the propulsive and lifting systems comprising oscillating wings. Some perspective of the developments is seen in utilization of nonlinear approaches. One of these approaches, providing account of the influence of the side edge local vortex roll-up on thrust is currently being developed.

References

[1] Golubev,V.V., "The Mechanism of Generation of Thrust by the Flapping Wing", Trudy nauchno-tekhicheskoi konferentsii VVIA imeny professora N.E. Zhukovskogo, Moskva, T.3, 1947, ss.7–19.

[2] Karman, T. Von, Burgess, J.M., "General Aerodynamic Theory: Perfect Fluids", Aerodynamic Theory, ed. Durand,W.F., Springer-Verlag, Leipcig, 1935.

[3] Nekrasov, A.I., " Theory of a Wing in Unsteady Flow", Izdanye AN SSSR, Moskva-Leningrad, 1947.

[4] Sedov, L.I., "Two-Dimensional Problem of Hydromechanics and Aerodynamics", Gostekhizdat, Moskva, 1950.

[5] Lighthill, M.J., "Hydromechanics of Aquatic Animal Propulsion", Annual Review of Fluid Mechanics, Vol.1, 1969, pp.413–446.

[6] Wu, T.Y., "Swimming of a Waving Plate", Journal of Fluid Mechanics, Vol.10, 1961, pp.321-344.

[7] Wu, T.Y., "Hydrodynamics of Swimming Propulsion", Journal of Fluid Mechanics, Vol. 46, 1971, part 1, pp. 337-355, part 2, pp.521-568.

[8] Isshiki, N. *et al.*, "The Study on a Propulsion System by Fin Stroke", Bulletin of Marine Engineering Society of Japan, Vol. 81, 1980, pp.71-79.

[9] Skidmore, J.K., Lueschen, J.D., Renzo, J.A. and Landrum, J.A., "Design of a Human Powered Wet Submersible for Competition", Proceedings of the International Conference "Ocean'89"addressing methods for understanding The Global Ocean, Seattle, Washington, Vol.6, 1989, pp. 30-37.

[10] Rozhdestvensky, K.V., Ryzhov, V.A., Kurapov, A.L., "Hydrodynamic Design of Propulsion Systems Based on Oscillating Wings",INEC 94: Cost Effective Defence (to be published).

[11] Bulletin of the Society of Naval Architects of Japan, N 719, 1989, pp.18-26.

[12] Kulikov, S.V., Kovalevsky, F.V., Shapovalova, N.A., "Application of a Hydrofoil System as a Passive Energy Saving Means for a Ship Advancing in Seas", Proceedings of the Scientific and Methodological Seminar on Ship Hydromechanics, Varna, 1988, pp. 1–6.

[13] Pavlenko, G.E., "Utilization of Energy of Rolling in Waves for Ship Propulsion", Sudostroenie, Leningrad, N 6, 1936, pp.394-401.

[14] Bessho, M., Kuozuka, Y., "On the Ship Motion Reduction by Anti-Pitching Fins in Head Seas", 15th Symposium on Naval Hydrodynamics, Session 2: Seakeeping Problems, 1984.

[15] Swimming and Flying in Nature, Eds. Wu, T., Brokaw, Ch., Brenner, Ch., Plenum Press, New-York, 1975.

[16] Pershin, S.V., "Basics of Hydrobionics", Sudostroenie, Leningrad, 1988.

[17] Triantafyllou, M.S. *et al.*, "Wake Mechanics for Thrust Generation in Oscillating Foils", Physics of Fluids, A3 (12), 1991, pp. 2835-2837.

[18] Ahmadi, R.A., Widnall, S.E., "Energetics and Optimum Motion of Oscillating Lifting Surface", AIAA Paper, N 1710, 1983, p.18.

[19] Belotserkovsky, S.M., Skripach, B.K., "Aerodynamic Derivatives of an Aircraft and a Wing Moving with Subsonic Speeds",Nauka, Moskva, 1975.

[20] Rozhdestvensky, K.V., Ryzhov, V.A., "Mathematical Models in the Theory of Oscillating Wing", Leningrad Shipbuilding Institute, 1985.

[21] Rozhdestvensky, K.V., Ryzhov, V.A., "Investigation of the Influence of Boudaries upon Thrust and Efficiency of a Wing of Finite Aspect Ratio Performing Oscillations in the Wide Range of Strouhal Numbers",

Methods of perturbations in mechanics, AN SSSR, Irkutsk, 1984, pp.59-64.

[22] Rozhdestvensky, K.V., "Method of Matched Asymptotic Expansions in Hydrodynamics of Wings", Sudostroenie, Leningrad, 1979.

[23] Potze, W., Sparenberg, J.A., "On the Efficiency of Optimum Finite Amplitude Sculling Propulsion", International Shipbuilding Progress, Vol. 30, N 351, 1983, pp. 238–244.

[24] Wu, T.Y., "Extraction of Energy from Wind and Ocean Current", 13th Symposium of Naval hydrodynamics, Tokyo, 1980, pp. 132–144.

[25] Isshiki, H. *et al.*, " A Theory of Wave Devouring Propulsion", 1st, 2nd, 3d, 4th Reports, Journal of the Society of Naval Architects of Japan, 1st Report: Vol. 151, 1882, pp. 54–64; 2d Report: Vol. 152, 1982, pp. 89–100; 3d report: Vol. 154, 1983, pp. 125–135; 4th Report: Vol. 156, 1984, pp. 102–104.

[26] Rozhdestvensky, K.V., Ryzhov, V.A., Kurapov, A.L., "Analysis of Hydrodynamic Characteristic of an Energy Saving Wing System", Proceedings of the Central Scientific research Institute of Marine Fleet, St. Petersburg, 1992, pp. 71–79.

[27] Grue, J., Mo, A., Palm, E., "Propulsion of a Foil Moving in Wather Waves", Journal of Fluid Mechanics, Vol. 186, 1988, pp. 393–417.

[28] Rozhdestvensky, K.V., Mishkevich, V.G., "On an Equation of the Parametric Boundary for the Nonseparated Flow Past a Lifting Surface", Proceedings of Krylov Scientific Society, Vol. 8, 1984, pp. 60–65.

[29] Gorelov, D.N., " Flapping Flight at High Frequency of Wing's Oscillation", Izvestia AN SSSR, seria: Mekhanika Zhidkosti i Gaza, N 2, 1984, pp. 32-41.

[30] Kudo, T.*et al.*, "Study on Propulsion by Partially Elastic Oscillating Foil", 1st, 2d Report, Journal of the Society of Naval Architects of Japan, Vol. 156, 1984, pp. 82–101.

[31] Rostovtsev, D.M., Rozhdestvensky, K.V., "A Mathematical Model of Oscillating Wing on an Elastic Tie", Trudy Leningradskogo korablestroitelnogo instituta: Systemy avtomatizirovannogo proektirovania v sudostroenii, 1987, pp. 39–46.

[32] Kurapov, A.L., Rozhdestvensky, K.V., Ryzhov, V.A., "Hydrodynamics of Elastic Wing. Optimal Characteristics", Proceedings of the 5th All-Russia summer school "Hydrodynamics of high speeds", Cheboksary, 1994, pp.38–46.

[33] Zervos, A., Coulmy, G., "Unsteady Periodic Motion of a Flexible Thin Propulsor Using the Boundary Element Method", Notes in Numerical Fluid Mechanics, Vol. 7, 1984, pp. 378–385.

[34] Ward-Smith, A.J., "Analysis of the Aerodynamic Performance of Birds During Bounding Flight", Math. Biosci., Vol. 68, N1, 1984, pp 137–150.

[35] Algazin, V.A., "Theoretical Investigation of Thrust of Oscillating Wing of Finite Aspect Ratio", Bionika, N 18, 1984, ss. 52–57.

[36] Zaitsev, A.A., Fedotov, A.A., "Flow of Ideal Incompressible Fluid Past a Thin Wing Oscillating With Large Amplitude", Izvestia AN SSSR, seria: Mekhanika Zhidkosti i Gaza, N 5, 1986, ss. 75–82.

[37] Grebeshov, E.P., Sagoyan, O.A., "Hydrodynamic Characteristics of a Lifting Wing as a Lifting Surface and a Propulsor", Trudy Tsentralnogo Aerogidrodynamicheskogo Instituta imeni Zhukovskogo, Moskva, N 1725, 1976, pp. 3–30.

[38] De Laurier, J.D., Harris, J.M., "Experimental Study of Oscillating Wing Propulsion", Journal of Aircraft, Vol. 19, N 5, 1982, pp. 368–373.

[39] Algazin, V.A., Gorelov, D.N., Piner, A.V., "An Investigation of Thrust Generated by Oscillating Wing", Trudy 4 Kongressa po Teoreticheskoi i Prikladnoi Mekhanike, Varna, 1981, ss. 60–65.

[40] Grebeshov, E.P., Kovrizhennykh, L.D., "Propulsive Characteristics of a Wing-Propulsor, Working Near Screening Surfaces", Trudy Tsentralnogo Aero- Hydrodynamicheskogo Instituta, Moscva, N 2211, 1983, ss. 42–54.

[41] Rozhdestvensky K.V., "Asymptotic Theory of a Wing-Propulsor, Oscillating Near a Wall or Between Parallel Walls",Trudy Gorkovskogo Politehnicheskogo Instituta: Gidrodinamika i Optimalnoye Proektirovanie Transportnykh Sredstv, Gorky, 1985, pp.39–50.

[42] Mishkevich, V.G., Rozhdestvensky, K.V., Bubentsov, V.P., "Unsteady Flows Near Leading Edges of Lifting Surfaces: Pressures, Flow Separation, Cavities", Proceedings of the 4th International Symposium on Bubble Noise and Cavitation Erosion in Fluid Systems, New Orleans, Louisiana, 1993, pp. 9–91.

[43] Rozhdestvensky, K.V., Bubentsov, V.P., "Prediction of Minimum Pressures on the Surface of Hydrofoils in Steady and Unsteady Motion Using Asymptotic Approach", Transactions of the Chinese Society of Naval Architecture and Marine Engineering, Vol.4, N 2, 1986, pp.10-21.

[44] Werle, M.D., Davis, R.T., "Separation Point of an Incompressible Boundary Layer on Parabola at an Angle of Incidence", Journal of Applied Mechanics, N 1, 1951, pp.312-322.

[45] Ruban, A.I., " A Singular Solution of the Boundary Layer Equations Continuously Extendable Across the Point of Zero Surface Friction", Izvestia AN SSSR, seria: Mekhanika Zhidkosti i Gaza, N 6, 1981, ss.63-71.

Boundary Layer Formation on an Oscillating Hydrofoil

D. Hart (Massachusetts Institute of Technology, USA)

Abstract

Propulsors and control surfaces invariably operate in unsteady flow conditions due to asymmetries in the inflow or erratic motions of the system. These unsteady flows result in a loss of lift, an increase in drag and give rise to the early onset of surface and trailing vortex cavitation. The reasons for this can be observed in the changes in the boundary layer profile of the flow around the lifting surface as it operates in unsteady conditions. This paper presents a quantitative experimental investigation of one of the fundamental unsteady flow induced effects, the periodic change in angle of attack of a lifting surface. Details of the change in the boundary layer profile on the suction and pressure side of a two-dimensional and a three-dimensional hydrofoil are presented as a function of the reduced frequency and phase of the foil oscillation.

Nomenclature

δ = Boundary layer thickness, *m*

σ = Cavitation number = $(p - p_v)/(\frac{1}{2}\rho U_\infty^2)$

σ_i = Cavitation inception index = $(p_i - p_v)/(\frac{1}{2}\rho U_\infty^2)$

Γ = Circulation = $\oint_c \bar{u} \cdot d\bar{y}$, *m²/s*

μ = Dynamic viscosity, *kg/ms*

ρ = Fluid density, *kg/m³*

α = Hydrofoil angle of attack, *degrees*

ω = Hydrofoil excitation frequency, *rad/s*

ϕ = Hydrofoil phase angle, *degrees*

γ = Vorticity = $\nabla \times \bar{u}$, *rad/s*

$\Delta\alpha$ = Hydrofoil oscillation amplitude, *degrees*

α_m = Hydrofoil mean angle of attack, *degrees*

A = Hydrofoil surface area, *m²*

AR = Aspect ratio = 2s/c

c = Hydrofoil chord length, 0.152*m* (6*in*)

C(k) = Theodorsen's lift deficiency factor

DAC = Dissolved air content, *ppm*

$d\Gamma/dy$ = Rate of change of bound circulation, *m/s*

f = Excitation frequency, *Hz*

Hz = Hertz, s^{-1}

k = Reduced frequency = $\omega c/2U_\infty$

LDV = Laser Doppler Velocimetry

LTWT= Low Turbulence Water Tunnel

PDA = Particle Diameter Analyzer

p_0 = LTWT test section pressure, *kPa*

ppm = Parts-per-million

p_V = Water vapor pressure, *kPa*

Re = Reynolds number = $\rho U_\infty c/\mu$

s = Semispan of foil, *m*

t = Time, *s*

u = Flow velocity in streamwise direction, *m/s*

U_∞ = LTWT test section velocity, *m/s*

v = Flow velocity in spanwise direction, *m/s*

w = Flow velocity perpendicular to foil, *m/s*

x = Downstream distance from leading edge, *m*

y = Spanwise distance from foil root, *m*

z = Distance orthogonal to x-y plane, *m*

1 Introduction

Boundary layer phenomena has been a prominent area of research in both hydrodynamics and aerodynamics since Prandtl in the early part of this century. It is key to our present understanding of lift and drag. For this reason, it is an important aspect in our understanding of unsteady flow phenomena.

The level to which the boundary layer is disturbed by unsteady flow depends on the "depth" of the flow interrupted by a propeller or control surface. A dimensionless *reduced* frequency is often used as a reference to characterize the relative unsteady effects. For a propeller, the reduced frequency is the shaft speed times the chord divided by the radius and is typically in the range of 0.05 to 0.2.

In pump applications and in applications where flutter can occur, such as control surfaces and appendages, these frequencies can reach much higher values; on the order of 5 to 10.

Unsteady flows are prevalent in most fluid applications. It is, therefore, not surprising that the study of its effects on the performance of fluid machinery has become a subject of much interest. It is, however, not a new area of interest. The first investigations were made in the 1930's. Among the best known and more perceptive analyses are those by Theodorsen [1935] and von Kàrmàn and Sears [1938], who studied the periodic oscillation of a two-dimensional flat plate. Their analyses, although based on an inviscid model, has proven to be quite accurate at predicting unsteady lift and drag behavior. This is not always sufficient, however, to characterize the performance of lifting surfaces in hydrodynamic applications. In these applications, the local or small scale behavior of the fluid such as wake rollup and boundary layer separation is critical because of its effect on the inception of cavitation leading to increased noise and erosion as well as loss in lift

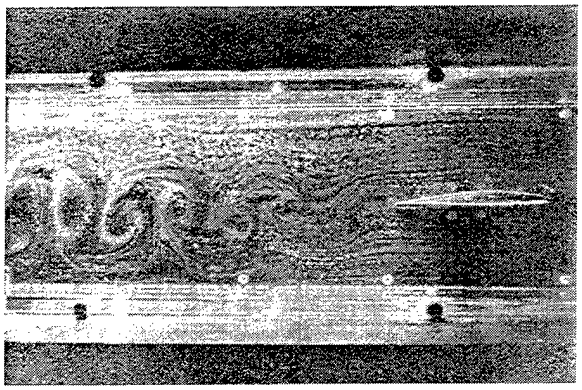


Figure 1. Wake Formation of a Two Dimensional Hydrofoil

At these very high reduced frequency, the spanwise vortex formation are clearly visible in the wake of this two-dimensional hydrofoil as it oscillates in pitch. (α_m=7°, $\Delta\alpha$=±2°, k=7).

Numerous experimental and numerical studies on oscillating airfoils and hydrofoils have characterized some of these small scale flow behaviors [McCroskey 1982]. Experimental studies of two-dimensional and three-dimensional, harmonically pitching hydrofoils show the formation of complex trailing vortex patterns in the wake which develop due to the changing circulation about the foil during a period of oscillation, Figure 1 [Abramson, Chu, Irick 1967; DeLaurier, Harris 1981; Hart, Acosta, and Leonard 1990; Katz 1981; Koochesfahani 1989; Satyanarayana 1978]. Because these oscillations occur about some mean flow condition, the net circulation about the lifting surface remains unchanged. The result is a series of vortices that form in the wake with strength equal but opposite to the change in circulation relative to the mean circulation about the lifting surface. In this way, vorticity is conserved within the flow. Experimental studies of the wake of a finite aspect lifting surface show that the trailing vortices link to each other through the tip vortex region and that in these three-dimensional flows, there are two vortices which form and wrap on one another creating a spanwise vortex pattern similar to that formed by oscillating two-dimensional foils, Figure 2 [Hart, Acosta, and Leonard 1990]. Numerical studies such as those by Mook and Dong [1994], Chen and Sheu [1989], and Spalart and Leonard [1981] have explored the transient behavior of the flow near the surface as well as the wake rollup behavior of oscillating two-dimensional foils. These studies have characterized the vortex rollup phenomena as a process initiating near the leading edge of the foil which then sheds to form the vortex patterns observed in the wake of the experimental studies.

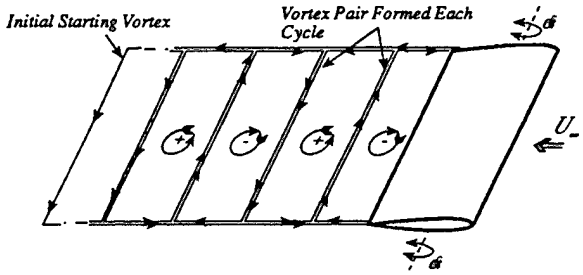


Figure 2. Vortex Structure Schematic

This schematic shows a simplified model of the trailing vortex structure in the wake of a finite aspect ratio oscillating hydrofoil. During each oscillation cycle a pair of spanwise vortices are formed. The net circulation around the pair is zero, corresponding to a zero net change in circulation about the hydrofoil. These spanwise vortices link to each other by wrapping around the tip vortex, which produces periodic changes in the circulation of the tip vortex structure.

The significance these vortex formations have on cavitation is not fully understood. It is, however, known that unsteady flows, in general, have a

strong influence on the inception and formation of cavitation on the surface and in the wake of both two- and three-dimensional foils [Franc, Michael 1988; Shen, Gowing 1986; Shen, Peterson 1978, 1980; Hart, Brennen, and Acosta 1990]. Studies of the wake of three-dimensional oscillating hydrofoils have shown that cavitation first appears in a region where the spanwise vortices in the wake interact with the tip vortex formation. Numerical vortex studies by Zabusky and Melander [1989] indicate that vortices that behave in this manner may develop regions of low pressure. It is speculated that these regions may be the areas where cavitation first initiates.

Despite these studies, however, there is still little known about the behavior of boundary layer formations on hydrofoils in unsteady conditions. These unsteady boundary layer formations may have a strong influence on the inception of surface and wake cavitation. Because of this and because of the importance of boundary layer phenomena to our present understanding of the performance of lifting surfaces in steady flow conditions, it is important to understand these formations in unsteady conditions if we are to fully understand how unsteady flows effect the performance of lifting hydrodynamic surfaces. Presented in this paper is an experimental investigation of the unsteady boundary layer formation near the trailing edge of a two-dimensional and a three-dimensional hydrofoil oscillating in pitch. While this work is far from being an exhaustive study of the subject, it does provide a glimpse at the complexities and intricacies of this important flow phenomena.

2 Experimental Approach

2.1 Facility

The experiments presented in this paper were conducted in the Caltech Low Turbulence Water Tunnel (LTWT). The LTWT, described in detail by Gates [1977], is a closed-circuit facility with a 16:1 contraction ratio. It is driven by a $14kW$ ($30hp$) DC motor at velocities up to $10m/s$. The tunnel has a $30cm \times 30cm \times 250cm$ rectangular test section which is enclosed by ground, polished glass side windows and two top and two bottom transparent Plexiglas removable windows. The test section diverges slightly along the top and bottom, compensating for the increase in boundary layer thickness from the inlet to the exit. A low turbulence level (<0.04%) is maintained over the full tunnel velocity range through use of vaned turning elbows and a settling chamber containing two honeycombs and three turbulence damping screens. A $4kW$ ($5hp$) vacuum pump controls the tunnel pressure from $120kPa$ down to $15kPa$.

Water quality is maintained by filtration and deaeration systems. The tunnel is equipped with two filtration systems which can be run independently or in series: A diatomaceous earth system removes particles down to $20\mu m$ at a rate of approximately $8.0m^3$ per hour. A filtration bag system removes particles down to $5\mu m$ at a rate of approximately $5.0m^3$ per hour. The dissolved air content of the water (measured by a van Slyke Blood Gas Analyzer) is controlled by spraying tunnel water inside a vacuum chamber. This deaeration system can reduce the dissolved air content of the water from $15ppm$ (saturation) down to $6ppm$ in about two hours and down to $3ppm$ in about 6 hours. Deaeration and filtration of the tunnel water are done between experiments. No noticeable change in water quality occurs during a typical experiment.

Velocity and pressure measurements are made either with mercury-water manometers or with absolute and differential pressure transducers. A Zenith Intel-8086 based computer continually monitors the tunnel operating parameters during tests including the cavitation number. The accuracy of these measurements is within 0.5%.

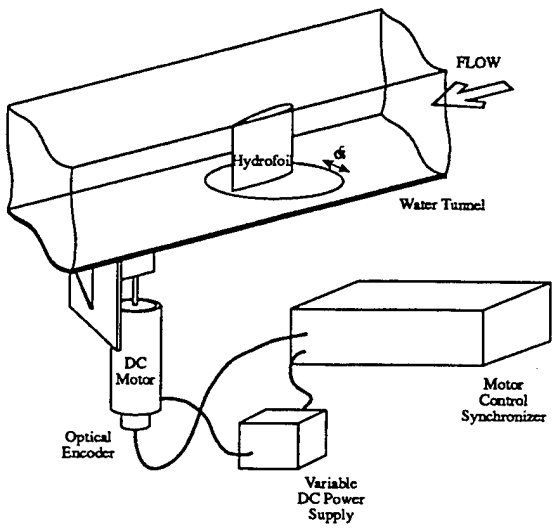


Figure 3. Oscillating Hydrofoil Setup
A 750 watt DC motor connected by a four bar linkage oscillates the hydrofoil in pitch in a sinusoidal fashion about the 0.38 chord position. An optical shaft encoder connected to the DC motor allows instrumentation to be synchronized to the phase of the foil.

The experiments presented in this paper were conducted using a stainless steel hydrofoil with an NACA 64A309 asymmetric foil section and rounded tip. The hydrofoil has a rectangular planform, with an 15.2*cm* (6*in*) chord length, and a span of 17.5*cm* (7*in*). It was reflection plane mounted to the floor of the LTWT test section giving it an effective aspect ratio of 2.3.

The hydrofoil is connected to a 750 watt DC motor by a four-bar linkage such that it oscillates nearly sinusoidally in pitch about a point near the center of pressure, x/c=0.38, Figure 3. Mounting the foil near the center of pressure reduced the torsional loading on the drive mechanism, allowing the foil to be oscillated at frequencies up to 50*Hz*. A collet connecting the oscillation linkage to a coupling shaft allows adjustment of the mean angle of attack of the foil. In addition, by changing the pivot point of the oscillation linkage connection to the motor spindle, adjustments of oscillation amplitudes ranging from ±1° to ±5° can be made. The oscillation rate of the hydrofoil can be adjusted by a Sabina DC motor control unit operating under open loop control. An optical shaft encoder mounted to the DC motor provides a digital signal (1024 pulses/revolution), used to synchronize flow measurements with the phase of the foil.

Two-dimensional hydrofoil investigations were accomplished by removing the tip section of the foil and mounting a Plexiglas panel over the top of it. The panel was held in place by two Plexiglas struts bolted to the top window. Nylon bushings were used to adjust the clearance of the panel relative to the foil tip. Tip clearance was maintained at a distance less than 1*mm*.

2.2 Measurement of Trailing Edge Flow Velocities

A Dantec Particle Dynamics Analyzer (PDA) was configured as a Laser Doppler Velocimeter (LDV) to measure velocities at the trailing edge of the foil. The Dantec system was used as a single axis 500*mW* LDV with separate receiver and transmitter. A manual traversing system was built to position the LDV to collect data along the span of the foil and across the trailing edge. The LDV measurements were taken as close as possible to the trailing edge of the foil at reduced frequencies of k=0.48, 0.96, and 1.92. In each case, the mean geometric angle of attack was 5.3° and the oscillation amplitude was ±5°. The freestream velocity was held constant at 5*m/s*. Four different locations along the span of the finite aspect ratio foil were measured: 20% span (just above the test section floor boundary layer), 50% span, 80% span (just below the tip vortex region), and at the foil tip. At each spanwise location and for each frequency, streamwise and spanwise velocity data were collected at seven different stations across the wake of the foil (perpendicular to the freestream – see Figure 4). Plots of the velocity data vs. phase at each station, such as the one in Figure 5, show a clear drop in the freestream velocity each time the foil boundary layer sweeps by that location.

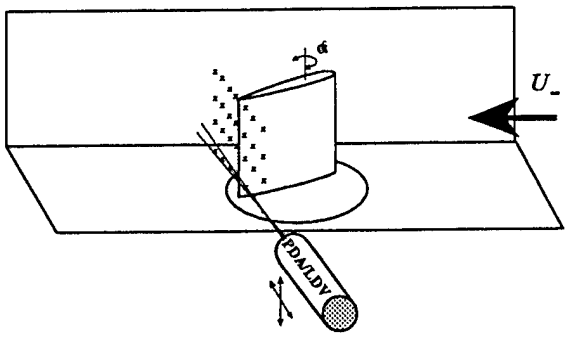


Figure 4. Oscillating Hydrofoil LDV Setup
The location of the LDV transmitting optics is shown, as well as the 28 data stations at the trailing edge of the foil where the LDV velocity measurements were taken.

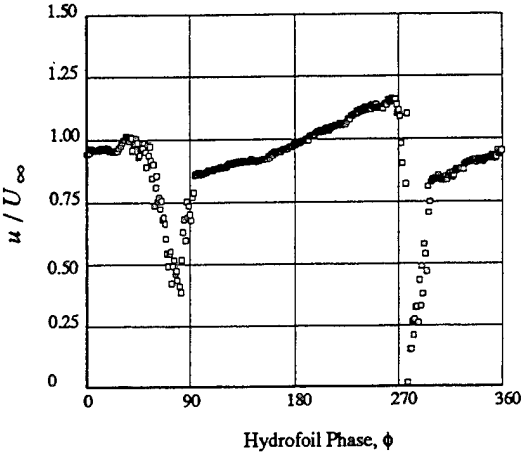


Figure 5. Phase Averaged Measurements of the Trailing Edge Flow
Data collected over several hundred oscillations. The sudden drops in velocity are the locations where the boundary layer of the oscillating hydrofoil passes through the location at which these measurements were taken. The angle of attack of the hydrofoil is decreasing as the trailing edge passes through the data location at a phase of 90° and it is increasing as it passes through the data location at a phase of 180°, accounting for the difference in the two velocity drops (Re=1.2×10^5, Δ α =± 5°, k=1.92).

3 Data Reduction

3.1 Determining The Wake Velocity Profile

The LDV measurements were encoded with the phase position of the foil and collected into a file. The data were ensemble-averaged and transposed into the coordinate frame of the oscillating hydrofoil based on the sinusoidal oscillation motion. Because the data was ensemble-averaged over hundreds of oscillation cycles, it was periodic relative to the phase when transposed into the coordinate frame of the trailing edge. It could, therefore, be accurately fit to a harmonic function in time. In this manner, an analytic smooth function was generated to replace the discrete data locations thus allowing details of the wake flow to be analyzed. It should be observed that the data was fit only in time and not in space. Thus, the characteristics of the boundary layer thickness was preserved. The resulting fit outside the boundary layer of the foil using a first harmonic function was within 0.5% of the original data. Near the core of the boundary layer formation, the scatter in the data was greater and an error as great as 20% was observed between the harmonic function and the LDV measurements. This was, however, still well within the standard deviation of the experimental measurements and did not effect the determination of the boundary layer thickness nor did it effect measurements of the change in bound circulation.

3.2 Estimating Unsteady Bound Circulation

The structure of the wake, the lift, the drag, and the unsteady boundary layer formation of an oscillating hydrofoil are all functions of the bound circulation around the foil and the shed Vorticity. Because of the added mass component of the fluid-foil interaction it is not possible to simply measure the force on the foil and extract the circulation from the equation $L/s = \rho U \Gamma$ as is done in the steady-state case. To directly measure the circulation experimentally requires taking many simultaneous measurements of velocity around the foil. This method is impractical because of the enormous amounts of data that would have to be collected simultaneous with respect to the phase of the foil oscillation to accurately resolve the unsteady circulation. It is considerably easier to determine the *change* in circulation due to the oscillation of the foil.

We begin with the definition of circulation,

$$\Gamma = \oint_C \bar{u} \cdot d\bar{y}$$

which by Stokes's theorem can be written

$$\Gamma = \int_A \bar{\omega} \cdot d\bar{A}.$$

The Lagrangian time derivative of this equation, by the Reynolds Transport Theorem, is

$$\frac{D\Gamma}{Dt} = \frac{d}{dt}\int_A \bar{\omega} \cdot d\bar{A} = \int_A \frac{d\bar{\omega}}{dt} \cdot d\bar{A} + \int_{x_i} \omega_i u_j \cdot dx_i$$

but, by Kelvin's theorem,

$$\frac{D\Gamma}{Dt} = 0$$

so that

$$\int_A \frac{d\bar{\omega}}{dt} \cdot d\bar{A} = -\int_{x_i} \omega_i u_j \cdot dx_i .$$

However, the Eulerian time derivative of the circulation is

$$\frac{d\Gamma}{dt} = \int_A \frac{d\bar{\omega}}{dt} \cdot d\bar{A}.$$

Therefore,

$$\frac{d\Gamma}{dt} = -\int_{x_i} \omega_i u_j \cdot dx_i .$$

Because the flow is essentially irrotational outside the boundary layer of the hydrofoil, the limits of integration can be taken from the boundary layer edges. Thus, the rate of change in circulation around the hydrofoil in the spanwise direction can be written as

$$\frac{\partial \Gamma_{sp}}{\partial t} = \int_{\delta_s}^{\delta_p} u\, \omega_{sp}\, dy \approx \frac{u_p^2 - u_s^2}{2}$$

(where δ_p is the thickness of the boundary layer on the pressure side of the foil, and δ_s the thickness on the suction side of the foil), since $\omega_{sp} = \frac{dw}{dx} - \frac{du}{dy} \approx -\frac{du}{dy}$ assuming the flow is nearly parallel at the trailing edge of the hydrofoil. This equation can be non-dimensionlized with respect to the freestream velocity of oscillation by writing it as;

$$\frac{d\Gamma_{sp}^*}{dt} \equiv \frac{1}{U_\infty^2}\frac{d\Gamma_{sp}}{dt} = \frac{1}{U_\infty^2}\int_{\delta_p}^{\delta_s} u\gamma dy \approx \frac{u_p^2 - u_s^2}{2U_\infty^2} \quad (1)$$

Similarly, the change in streamwise circulation along the span of the foil at the trailing edge can be expressed, from the fundamental definition of a vortex sheet, as

$$\frac{d\Gamma_s^*}{ds} \equiv \frac{1}{U_\infty}\frac{d\Gamma_s}{ds} = (v_r - v_s)/U_\infty \qquad (2)$$

Thus, the change in circulation about an unsteady hydrofoil can be determined by measuring the instantaneous velocities at the trailing edge.

Since the identification of the trailing edge velocities depends upon accurately locating the boundary layer edge, there is an uncertainty which can result in a slight error in calculating the circulation in this manner. The velocity profiles outside the boundary layer, however, were noted to taper off gradually with distance from the foil making this a relatively small error (<10%). In order to improve the accuracy of the estimated velocity jump, for each value of phase ϕ, the shape of the velocity profile outside the boundary layer on each side of the foil was fit to a straight line. The velocity jump was then extrapolated through the boundary layer to the trailing edge.

3.3 Comparison Between 2-D Theoretical Predictions and Experimental Measurements

An expression for the rate of change of circulation of a two-dimensional foil can be derived from the theoretical analyses of Theodorsen [1935] and Garrick [1936]. This expression,

$$\frac{d\Gamma_{sp}^*}{dt} \equiv \frac{1}{U_\infty^2}\frac{d\Gamma_{sp}}{dt} = k2\pi C_o \Delta\alpha \cos(\omega t + \theta) \qquad (3)$$

where

$$C_o = \frac{2}{\pi k}\sqrt{A_o^2 + B_o^2}$$

and

$$\theta = -\left[\tan^{-1}(A_o/B_o) + k\right]$$

characterizes the relative effects of the reduced frequency k on circulation. Here,

$$A_o = J - Mk(\tfrac{1}{2} - a),$$

and

$$B_o = M + Jk(\tfrac{1}{2} - a).$$

where

$$J = \frac{J_1 + Y_0}{D},\ M = \frac{Y_1 - J_0}{D},$$

and

$$D = (J_1 + Y_0)^2 + (Y_1 - J_0)^2.$$

Y_0, Y_1, and J_0, J_1 are solutions to the Bessel functions and $-1 \le a \le 1$ is the pitching axis relative to the center of the foil where a=-1 is at the leading edge and a=1 is at the trailing edge..

C_o and θ are plotted in Figures 6 and 7 respectively. As can be seen in Figure 8, this theoretical prediction is quite accurate at predicting the rate of change of circulation of the pitching two-dimensional hydrofoil.

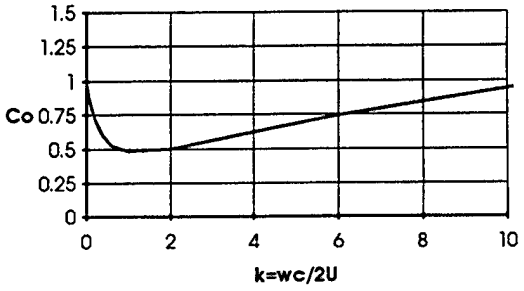


Figure 6. Circulation Rate of Change Coefficient

Graphic description of the magnitude of the circulation rate of change for a two-dimensional foil oscillating in pitch about the 38% chord position. The loading at first decreases as the reduced frequency increases and then increases.

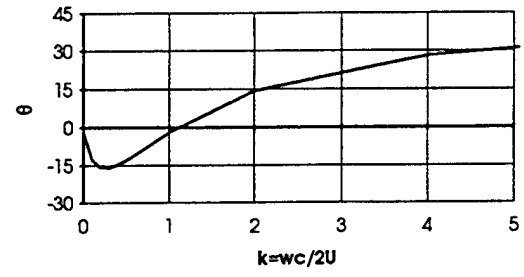


Figure 7. Phase Shift in Circulation Rate of Change.

Phase shift due to oscillation of a two-dimensional foil about the 38% chord position. The phase shift lags the foil motion and then leads approaching 45 degrees as the reduced frequency increases. This is due to a shift from a predominantly circulatory change in loading of the foil to a predominately non-circulatory loading (added mass loading) of the foil at high reduced frequencies.

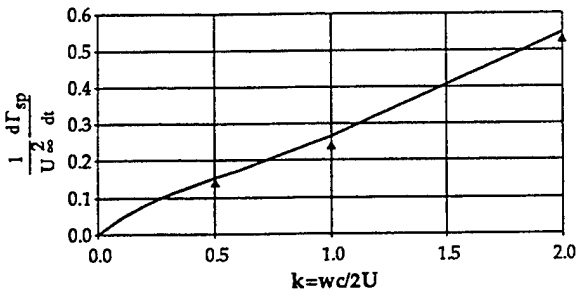


Figure 8. Comparison Between Experimental Measurements of Change in Circulation with Theoretical Prediction.

Theoretical prediction, based on Theodorsen's analysis, of the time rate of change of circulation around a two-dimensional foil matches closely with experimental measured time rate of change of circulation.

4 Results

The multi-dimensionality of the data in space and time makes it difficult to present in a fashion which can be easily interpreted in two-dimensions. For the visualization of the boundary layer formation, it is, perhaps, easiest to interpret the data from a gray-scaled plot such as shown in Figures 9, 11, 12 and 14-16. In these figures, the streamwise velocity near the trailing edge of the oscillating hydrofoil is displayed relative to the freestream velocity using shading. Black in these figures represents a zero velocity ratio and white represents a velocity ratio of 1.25. The velocity data is plotted in this manner showing its position relative to the hydrofoil trailing edge (The distance from the trailing edge perpendicular to the freestream flow.) and the phase of the hydrofoil at which the velocity was measured. The boundary layer appears as a dark region located near the center of the plots. The pressure side of the foil is shown as negative values of distance from the trailing edge relative to the chord length and the suction side as positive values. The hydrofoil is at a maximum angle of 10° at the 0° phase position, its angle of attack decreases to 0° at the 180° phase position and then increases back to 10° at the 360° phase position. Thus, these figures illustrate the relative streamwise velocity in both time and space near the trailing edge of the foil.

4.1 Unsteady 2-D Wake

Figure 9 shows the streamwise wake velocity of a two-dimensional hydrofoil oscillating at a reduced frequency of k=1.0. A large velocity difference can be observed between the pressure side and the suction side of the foil at phase angles of roughly 90° and 270°. These phase angles are the angles at which the greatest rate of angular change occurs in the foil's oscillation cycle. Thus, as one would expect, the greatest rate of change of circulation about the foil occurs in this region of the foil's cycle, Figure 10. At the 90° phase position, the velocity on the suction side of the foil outside the boundary layer is much greater than the velocity outside the boundary layer on the pressure side of the foil. This corresponds to a large decreasing rate of change of circulation. In turn, the velocity on the pressure side of the foil at a phase angle of 270° is much lower than the velocity on the suction side corresponding to a large increasing rate of change of circulation. The net change in circulation over the entire 360° oscillation is zero as expected since the mean angle of attack of the foil is unchanged. The reduced velocity region in the wake is apparent in this plot as a dark region near the trailing edge. This region is, on the average, much larger on the suction side of the foil than it is on the pressure side. Note that this region grows significantly on the suction side of the foil as the angle of attack of the foil increases. Some growth in this region is also apparent on the pressure side of the foil as the angle of attack of the foil decreases. This growth is small relative to the growth on the suction side during an increasing angle of attack. Proportional to the mean thickness of this region, however, the increase on the pressure side during decreasing angle of attack is roughly the same as the increase on the suction side during an increasing angle of attack. The average width of the reduced velocity region is about 1% of the chord length (15mm) on the suction side and 0.1% on the pressure side (1.5mm).

At a lower reduced frequency of k=0.5, Figure 11, the average thickness of this reduced velocity region grows significantly on the suction side of the foil almost doubling to 2% of the chord length. This region is relatively unchanged in width except between a phase angle of 180 and 300 where it drops back to about 1% of the chord length. This is the region in which the angle of attack of the hydrofoil is increasing in its oscillation cycle.

At a higher reduced frequency of k=2.0, Figure 12, the average thickness of the wake velocity region increases also. This region, however, thins to almost zero thickness near the 130 phase position and then grows to roughly 4.5% of the chord length by the 270 phase position as the hydrofoil is increasing in angle of attack.

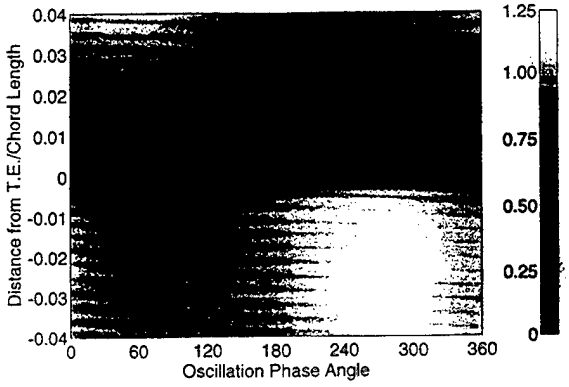


Figure 9. Streamwise Velocity at the Trailing Edge of a 2-D Hydrofoil Pitching at k=1.0.

Gray scale plot of the streamwise velocity relative to the freestream velocity at the trailing edge of a 2-D pitching hydrofoil. The Y axis of this plot shows distances from the trailing edge perpendicular to the freestream flow. The pressure side of the foil is shown as negative values and the suction side as positive values. The hydrofoil is pitching ±5° about the 38% chord position at a mean angle of attack of 5°. The hydrofoil is at its maximum angle of attack of 10° at the 0° and 360° phase position and at its minimum angle of attack at the 180° phase position. Note the change in the low velocity region on the suction side of the foil as the pitch of the foil changes.

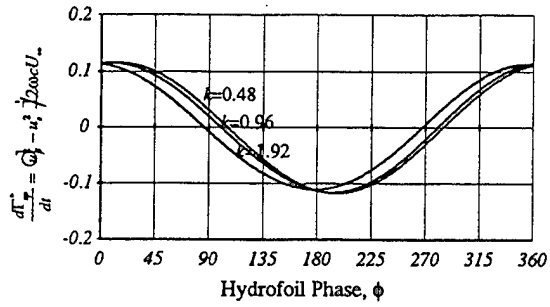


Figure 10. Change in Spanwise Circulation.

The change in spanwise circulation is shown non-dimensionalized with the free stream velocity for reduced frequencies of k=0.48, 0.96, and 1.92. The hydrofoil is oscillating ± 5° about a mean angle of attack of 5°. The hydrofoil is at its maximum angle of attack of 10° at the 90° phase position and at the minimum angle of attack, 0°, at the 270° phase position. The peak change in circulation increases linearly with reduced frequency. Note also that the phase of the loading of the hydrofoil shifts with increasing reduced frequency.

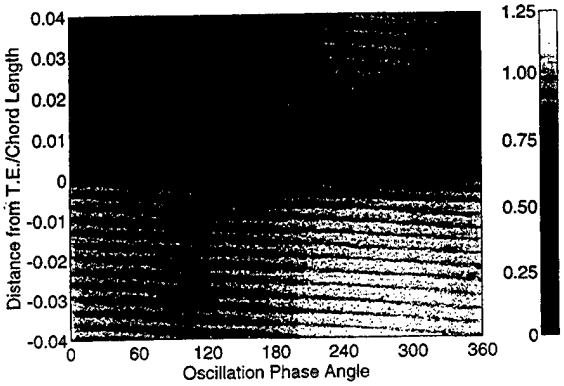


Figure 11. Streamwise Velocity at the Trailing Edge of a 2-D Hydrofoil Pitching at k=0.5.

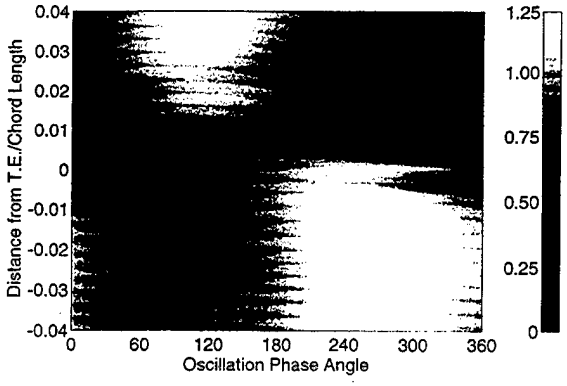


Figure 12. Streamwise Velocity at the Trailing Edge of a 2-D Hydrofoil Pitching at k=2.0.

4.2 Unsteady 3-D Wake

The thickness of the wake profile at the trailing edge of the finite aspect hydrofoil was found to be considerably smaller than that of the two-dimensional hydrofoil at the same reduced frequency, Figures 14-16. The finite aspect ratio hydrofoil generates a streamwise vorticity component as well as a spanwise vorticity component. The change in this vorticity was found to change significantly in both amplitude and phase as a function of span, Figure 13. This change in amplitude and phase was also evident in the wake profiles. Figure 14 shows the wake velocity profile near the root of the foil, 20% span. The wake region is almost symmetrical about the trailing edge

relative to the phase of oscillation. At the mid-span of the foil, Figure 15, an increase in the thickness of the wake region occurs on the suction side at a phase of roughly 180°, just after the angle of attack begins to increase. The wake region on the pressure side of the foil is almost non-existent at this phase. Near the tip of the foil, Figure 16, the wake region on the suction side of the foil is larger and is located near the 240° phase position. Again, the wake region on the pressure side is very small.

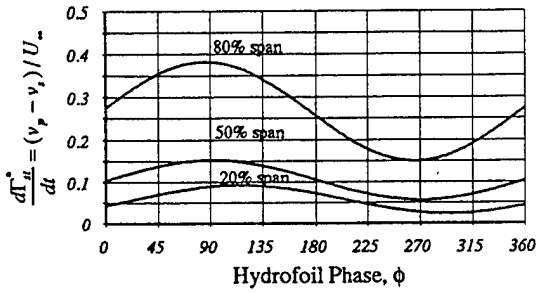


Figure 13. Change in Streamwise Circulation.

The change in streamwise circulation is shown, non-dimensionalized by the freestream velocity, for span locations of 20% (near the base of the foil), 50%, and 80% (near the tip of the foil). The hydrofoil is oscillating ± 5° about a mean angle of attack of 5° at a reduced frequency of 1.92. The hydrofoil is at its maximum angle of attack of 10° at the 90° phase position and at the minimum angle of attack, 0°, at the 270° phase position. The majority of change in streamwise circulation occurs within the last 30% of the span of the foil.

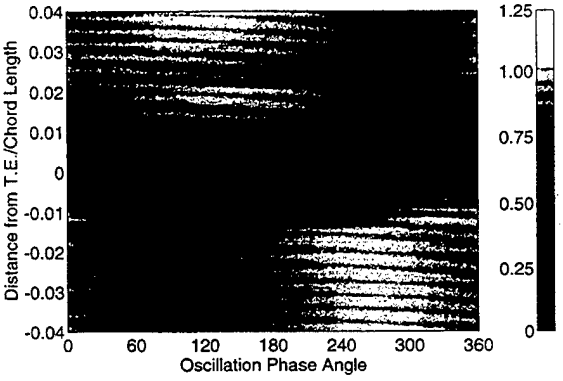


Figure 14. Streamwise Velocity at the 20% Span of a 3-D Hydrofoil Pitching at k=1.0.

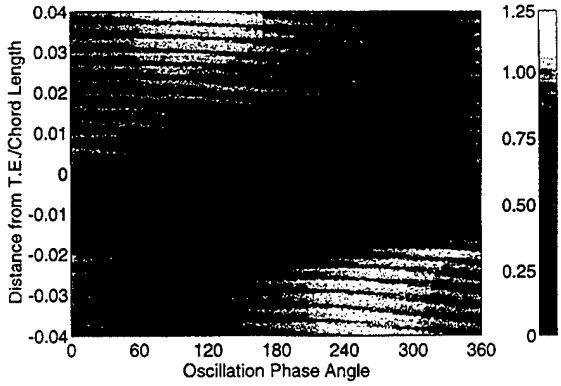


Figure 15. Streamwise Velocity at the 50% Span of a 3-D Hydrofoil Pitching at k=1.0.

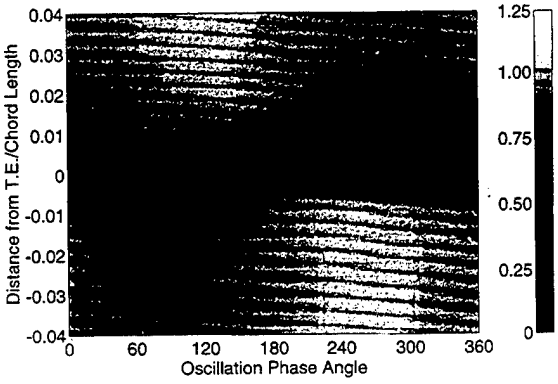


Figure 16. Streamwise Velocity at the 80% Span of a 3-D Hydrofoil Pitching at k=2.0.

5 Discussion

The technique of ensemble averaging the LDV data and utilizing knowledge of temporal periodicity to improve spatial resolution allows details of the flow to be observed with minimal amounts of data compared with more conventional LDV scanning techniques. Even so, the data sets required to make these measurements are in the megabytes. As in the more conventional LDV scanning techniques, the accurate placement of the LDV collection point is critical to resolving the wake velocity profile. This technique, however, utilizes the angular resolution of the hydrofoil phase input which is generally far greater than the resolution that can be obtained by the positioning system of a scanning LDV. In

general, there is a tradeoff between the number of positions at which LDV data is collected and the resolution of the ensemble-averaged data in time. In the present study, seven data locations were selected. This value was chosen because of the difficulty of accurately positioning the LDV system relative to the hydrofoil trailing edge. No attempt was made to optimize this value for the particular application. Spatial resolutions greater than that used are not possible with the present system due to the difficulties involved in positioning the laser head. The placement at each of the seven data locations, however, was accurate to within about 0.5mm. In practice, the limiting factor for data collection locations is the collection volume of the LDV and the stability of the LDV relative to the hydrofoil. In most unsteady hydrodynamic applications, the flow rates are relatively low compared to the internal clock resolutions of the LDV system. Therefore, improvements in the spatial resolution can most often be accomplished using this technique.

In applications allowing greater number of data collection locations which overlap with one another when transformed into the moving coordinate frame, the data can be fit to higher harmonic functions allowing higher periodicity events to be observed. Like all LDV measurements of this type, however, we are limited to analyzing the time averaged phenomena. Transient events or semi-periodic events can not be resolved.

The burst in the boundary layer profile observed on the suction side of the foil is expected. As the angle of attack of the foil increases, an increase in circulation occurs. This increase is driven by an increased pressure difference from the suction side of the foil to the pressure side. The flow across the suction side of the foil must, therefore, recover from a greater pressure drop. The, the boundary layer acts against an increased pressure gradient and separation is likely. The data, however, is inconclusive as to whether the observed increase in wake thickness is due to separation of the boundary layer, vortical flow formations transitioning across the surface, or simply an increase in the boundary layer thickness. Except for the tests conducted at a reduced frequency of 2.0, the flow near the trailing edge was never observed to reverse directions relative to the mean flow. This, however, only indicates the condition of the flow at the trailing edge and does not negate the possibility that the flow separates from the foil a short distance upstream.

It is likely that the increase in the wake region on the suction side is not due to the passing of a vortical rollup formation since the observed growth on the pressure side is minimal in comparison. If this region were due to a vortical formation forming at the leading edge as the foil oscillated, we would expect to see a similar formation on the pressure side. A slight increase is observed on the pressure side. This increase, however, is only a fraction of the size of the formation observed on the suction side. Because the data is ensemble-averaged, it is possible that a vortical formation forming at the leading edge might be lost in the measurements if its occurrence was not consistent from cycle to cycle of the foil oscillation. Observations of the wake, however, indicate that this is not the case. If the spanwise vertical formations in the wake are in fact initiated at the leading edge as observed in many of the numerical models of this flow, then they should be very consistent relative to the hydrofoil oscillation phase as observed in the experiments. The present data is not conclusive in establishing the existence or non-existence of this type of structure. Details of the velocity profile near the surface of the foil might shed light on this matter but have not been made at this time.

6 Conclusions

Measurements of the boundary layer near the trailing edge of a two-dimensional and finite aspect ratio pitching hydrofoil have been made. The unique phase ensemble averaged LDV technique used to make these measurements allowed details of the boundary layer structure to be analyzed relative to the phase of the foil oscillation. Comparisons between the change in circulation about a two-dimensional hydrofoil calculated from these measurements show good agreement with theoretical predictions.

The boundary layer was observed to be strongly dependent on both the reduced frequency of the hydrofoil oscillation and the phase of the motion. As the reduced frequency was increased, an increase was observed in the unsteadiness of the boundary layer formation. In addition, a change in phase was observed between the foil motion and the boundary layer thickness. The phase shift that occurred on the two-dimensional hydrofoil was consistent with the phase shift in circulation predicted by unsteady inviscid flow calculations. A rapid growth in the

boundary layer thickness was observed on the suction side of both the two-dimensional and finite aspect ratio hydrofoil as the angle of attack of the hydrofoil increased. This growth became very prominent as the reduced frequency of oscillation was increased. A similar trend was observed on the pressure side of the hydrofoil as the angle of attack of the hydrofoil decreased. The growth on the pressure side, however, was observed to be only a fraction of that observed on the suction side. The boundary layer on the finite aspect hydrofoil was observed to be smaller than the boundary layer on the two-dimensional foil. The effects of pitching oscillation on boundary layer thickness were also less prominent on the finite aspect foil. In addition, a phase shift in the growth and collapse of the boundary layer relative to the motion of the foil was observed along the span of the finite aspect hydrofoil. There was no clear indication of the passing of a vortical rollup structure along the surface of the pressure and suction sides of the hydrofoil as predicted in many unsteady numerical solutions of this flow. This may, however, be the result of the ensemble averaging technique used to make the measurements. More detailed measurements are needed along the chord of the foil to resolve these formation which may emanate from the leading edge during an oscillation cycle to form the classic wake structure observed in flows of these types. It is also not apparent from the measurements presented in this paper whether or not the flow separates from the foil during a pitching cycle. Under all test conditions, the flow was never observed to reverse directions in both the instantaneous measurements made at the trailing edge and the ensemble averaged measurements. This does not, however, negate the possibility that the flow separates upstream of the trailing edge. It is believed that the formation of vortical structures near the leading edge of the foil and separation of the boundary layer due to foil oscillation may be significant in the inception and formation of surface cavitation in unsteady conditions. Further numerical and experimental work is needed to understand the significance of these unsteady flow effects.

Acknowledgments

The experimental measurements presented in this paper were made at the California Institute of Technology in Pasadena, CA. The author is grateful for the support of the Office of Naval Research under grant number N00167-85-K-0165, Technical Monitor J. Fein. In addition, the author would like to thank Professor Allan J. Acosta of the Mechanical Engineering Department at Caltech for his advice and considerations.

References

Abbott, I. H., von Doenhoff, A. E., 1959. *Theory of Wing Sections.* Dover Publications, Inc., New York.

Abramson, H. N., Chu, Wen-Hwa, Irick, J. T., 1967. "Hydroelasticity with Special Reference to Hydrofoil Craft." Naval Ship Research and Development Center, Report 2557.

Acosta, A. J., Delong, R. K., 1971. "Experimental Investigations of Non-Steady Forces on Hydrofoils Oscillating in Heave." Non-Steady Flow of Water at High Speeds, Proceedings of the IUTAM Symposium, Leningrad, June 22-23, pp. 95-104.

Basu, B. C., Hancock, G. J., 1978. "The Unsteady Motion of a Two-Dimensional Aerofoil in Incompressible Inviscid Flow." *J. Fluid Mech.*, Vol. 87, pp. 159-178.

Chen, D. R., Sheu, M. J., 1989. "Numerical Solutions for Oscillatory Aerofoil at High Reduced Frequency." *Computer Methods in Applied Mechanics and Engineering*, Vol. 74, pp. 55-68.

Commerford, G. L., Carta, F. O., 1974. "Unsteady Aerodynamic Response of a Two-Dimensional Airfoil at High Reduced Frequency." *AIAA Journal*, Vol. 12, No. 1, pp. 43-48.

DeLaurier, J. D., Harris, J. M., 1981. "Experimental Study of Oscillating-Wing Propulsion." *J. Aircraft*, Vol. 19, No. 5, pp. 368-373.

Dengler, M. A., Goland, M., 1952. "The Subsonic Calculation of Circulatory Spanwise Loadings for Oscillating Airfoils by Lifting-Line Techniques." *Journal of Aeronautical Sciences*, November, pp. 751-759.

Faler, J. H., Leibovich, S., 1977. "Disrupted States of Vortex Flow and Vortex Breakdown." *The Physics of Fluids*, Vol. 20, No. 9, pp. 1385-1400.

Fleeter, S., 1980. "Trailing Edge Conditions for Unsteady Flows at High Reduced Frequency." *AIAA Journal*, Vol. 18, No. 5, pp. 497-503.

Franc, J. P., Michel, J. M., 1988. "Unsteady Attached Cavitation on an Oscillating Hydrofoil." *J. Fluid Mech.*, Vol. 193, pp. 171-189.

Fujita, H., Kovasznay, L. S. G., 1974. "Unsteady Lift and Radiated Sound from a Wake Cutting Airfoil." *AIAA Journal*, Vol. 12, No. 9, pp. 1216-1221.

Garrick, I. E., 1936. "Propulsion of a Flapping and Oscillating Airfoil." *NACA T.R.* No. 567.

Gates, E. M., 1977. "The Influence of Freestream Turbulence, Freestream Nuclei Populations, and Drag-Reducing Polymer on Cavitation Inception on Two Ansymmetric Bodies." Calif. Inst. of Tech., Div. of Eng. and Appl. Sci., Report No. E182-2.

Giesing, J. P., 1969. "Vorticity and Kutta Condition for Unsteady Multienergy Flows." *ASME J. Appl. Mech.*, Vol. 19, pp. 608-613.

Giesing, J. P., 1968. "Nonlinear Two-Dimensional Unsteady Potential Flow with Lift." *J. Aircraft*, Vol. 5, No. 2, pp. 135-143.

Green, S. I., 1988. "Tip Vortices - Single Phase and Cavitating Flow Phenomena." Ph.D. Thesis, Calif. Inst. of Tech., Div. of Eng. and Appl. Sci., Report No. 183-17.

Gustafson, K. E., Sethian, J. A., 1991. *Vortex Methods and Vortex Motion*. Society for Industrial and Applied Mathematics, Philadelphia, Pennsylvania.

Hart, D. P., 1991. "Cavitation Inception in the Tip Vortex Region of an Oscillating Hydrofoil." Proceedings of the ASME Cavitation and Multiphase Flow Forum, pp. 35-41.

Hart, D. P., Acosta, A., Leonard, A., 1992. "Observations of Cavitation and Wake Structure of Unsteady Tip Vortex Flows." International STG Symposium on Propulsors and Cavitation, June 22-24, Hamburg, Germany.

Hart, D. P., Brennen, C. E., Acosta, A. J. 1990. "Observations of Cavitation on a Three-Dimensional Oscillating Hydrofoil." Proceedings of the ASME Cavitation and Multiphase Flow Forum, Toronto, pp. 49-52.

Johnson, W., 1980. *Helicopter Theory*. Princeton University Press, Princeton, New Jersey, pp. 471-498.

Johnston, R. T., Sullivan, J. P., 1991. "The Vortex Interactions in a Propeller/Stator Flow Field." Proceedings of the AIAA 22nd Fluid Dynamics, Plasma Dynamics & Lasers Conference, June 24-26, Honolulu, Hawaii.

Jones, R. T., 1990. *Wing Theory*. Princeton University Press, Princeton, New Jersey.

Jones, R. T., 1938. "The Unsteady Lift of a Finite Wing." N.A.C.A. T.R. No. 682.

Kàrmàn, T. V., Sears, W. R., 1938. "Airfoil Theory for Non-Uniform Motion." J. of the Aeronautical Sciences, Vol. 5, No. 10.

Katz, J., 1981. "Cavitation Inception In Separated Flows." Ph.D. Thesis, California Institute of Technology, Report No. 183-5.

Katz, J., 1984. "Cavitation Phenomena Within Regions of Flow Separation." *J. Fluid Mechanics*, 140, pp. 397-436.

Katz, J., Plotkin, A., 1991. *Low-Speed Aerodynamics From Wing Theory to Panel Methods*. McGraw-Hill Series in Aeronautical and Aerospace Engineering, pp. 421-495.

Katz, J., Weihs, D., 1981. "Wake Rollup and the Kutta Condition for Airfoils Oscillating at High Frequency." *AIAA Journal*, Vol 19, No. 12, pp. 861-863.

Katz, J., Weihs, D., 1978. "Behavior of Vortex Wakes from Oscillating Airfoils." *J. Aircraft*, December, pp. 861-863.

Koochesfahani, M. M., 1989. "Vortical Patterns in the Wake of an Oscillating Airfoil." *AIAA Journal*, Vol. 27, No. 9, pp. 1200-1205.

Lawrence, H. R., Gerber, E. H., 1952. "The Aerodynamic Forces on Low Aspect Ratio Wings Oscillating in an Incompressible Flow." *Journal of Aeronautical Sciences*, November, pp. 769-781.

Lorber, P. F., Covert, E. E., 1982. "Unsteady Airfoil Pressures Produced by Periodic Aerodynamic Interferences." *AIAA Journal*, Vol. 20, No. 9, pp. 1153-1159.

Lugt, H. J., 1983. *Vortex Flow in Nature and Technology*. John Wiley & Sons, New York.

McCroskey, W. J., 1982. "Unsteady Airfoils." *Annual Review of Fluid Mechanics*, Vol. 14, pp. 285-311.

McKenney, E. A., Hart, D. P. 1993. "Quantification of Unsteady Bound Vorticity of a Finite Oscillating Hydrofoil." Proceedings of the ASME Cavitation and Multiphase Flow Forum, Washington, pp. 87-92.

Mook, D.T., Dong, B. 1994. "Perspective: Numerical Simulations of Wakes and Blade Vortex Interaction." *J. of Fluids Engineering*, March, Vol. 116, pp. 5-21.

Postel, E. E., Leppert, E. L., Jr., 1948. "Theoretical Pressure Distributions for a Thin Airfoil Oscillating in Incompressible Flow." *J. of the Aeronautical Sciences*, August, pp. 486-492.

Ravindra, K., 1989. "Experimental Investigation of the Behavior of Cavities Behind a Wedge Oscillating in Pitch." International Conference on Mechanics of Two-Phase Flows, June, Taipei, Taiwan.

Satyanarayana, B., Davis, S., 1978. "Experimental Studies of Unsteady Trailing-Edge Conditions." *AIAA Journal*, Vol. 16, No. 2, pp. 125-129.

Sclavounos, P. D., 1987. "An Unsteady Lifting-Line Theory." *J. of Eng. Mathematics*, Vol. 21, pp. 201-226.

Sears, W. R., "Some Aspects of Non-Stationary Airfoil Theory and Its Practical Applications." *J. of the Aeronautical Sciences*.

Shen, Y. T., Peterson, F. B.,1978. "Unsteady Cavitation on an Oscillating Hydrofoil." Proceedings of the 12th Symposium on Naval Hydrodynamics, June, Washington, D.C..

Shen, Y. T., Peterson, F. B.,1980. "The Influence of Hydrofoil Oscillation on Boundary Layer Transition and Cavitation Noise." Proceedings of the 13th Symposium on Naval Hydrodynamics, October 6-10, Tokyo, pp. 221-241.

Shen, Y, Gowing S., 1986. "Pressure Measurements on an Oscillating Foil in Fully Wetted and Cavitating Conditions." International Symposium on Cavitation, April, Sendai, Japan, pp. 95-102.

Spalart, P. R., 1985. "Simulation of Rotating Stall by the Vortex Method." J. of Propulsion and Power 1, p. 235.

Spalart, P. R., and Leonard, A., 1981. "Computation of Separated Flows by a Vortex-Tracing Algorithm." AIAA-81-1246

Theodorsen, T., 1935. "General Theory of Aerodynamic Instability and the Mechanism of Flutter." NACA T.R. No. 496.

von Karman, T., Sears, W. R. 1938. "Airfoil Theory for Nonuniform Motion." *J. Aeronautical Sciences*, Vol. 5, pp. 379-390.

Weihs, D., 1972. "Semi-Infinite Vortex Trails, and Their Relation to Oscillating Airfoils." *J. Fluid Mech.*, Vol. 54, part 4, pp. 679-690.

Zabusky, N. J., Melander, M. V., 1989. "Three-Dimensional Vortex Tube Reconnection: Morphology for Orthogonally-Offset Tubes." *Physica D*, Vol. 37, pp. 555-562.

Energy-Stable Model Equations for Water Waves and Ship Motions

E. van Daalen (Twente University of Technology, The Netherlands)

ABSTRACT

Our primary aim here is to show that the Hamiltonian formulation for nonlinear wave-body interactions, as presented by van Daalen (1993), can be exploited to obtain *approximative* equations describing water waves and ship motions. Such equations are then stable in the sense that they retain the Hamiltonian structure of the *exact* nonlinear equations, thus conserving the total energy of the wave-body system.

NOMENCLATURE

Symbol	Description
A	wave amplitude
B	bottom
F	free surface
g	gravitational acceleration
G	center of gravity
$\mathcal{H}$	Hamiltonian
$\vec{I}$	body inertia
$\mathcal{J}$	action integral
$\mathcal{K}$	kinetic energy
$\mathcal{L}$	Lagrangian
M	body mass
$\mathcal{M}$	generalized mass matrix
$\vec{n}$	normal vector
p	Bernoulli pressure
$\mathcal{P}$	potential energy
$\vec{r}$	position vector relative to G
R	free surface arclength factor
S	wetted body surface
t	time
x	horizontal coordinate
$\vec{x}_G$	body position
$\vec{x}_S$	point on S
y	horizontal coordinate
z	vertical coordinate
η	free surface elevation
$\vec{\theta}_G$	body orientation
∇	gradient operator
$\vec{\nu}$	generalized normal vector
$\vec{\xi}$	generalized body coordinates
π	canonically conjugate momentum
Σ	cylindrical vertical surface
ϕ	velocity potential
Φ	free surface potential
Ω	fluid domain

INTRODUCTION

For all we know, the first description of the evolution of water waves in terms of a Hamiltonian density and generalized variables was made by Zakharov (1968), who presented the canonical equations of motion for an infinite-depth free surface potential flow in a homogeneous gravity field. Few years later, Broer (1974) independently showed that — for a fluid of *arbitrary* depth — the kinematic and dynamic free surface conditions constitute an infinite-dimensional Hamiltonian system, with the elevation and the free surface potential as the canonical variables and the total energy as the Hamiltonian density. Other valuable contributions in this field are due to Miles (1977, 1981).

The first optimal variation principle for water waves is due to Luke (1967), who showed that the *full* set of governing equations for the classical water-wave problem can be obtained from a *single* variation principle. The integrated Bernoulli pressure plays the role of the Lagrangian density, and the velocity potential and the free surface elevation are the independent variables. Miloh (1984) extended Luke's principle to water waves interacting with multiple floating bodies oscillating at a common frequency.

For many dynamical systems the transition from a Lagrangian principle to a Hamiltonian formulation can easily be made by means of the *Legendre transformation*. The essence is the definition of 'canonical' momenta which are conjugate to the chosen 'canonical' coordinates. The possibility of this transition to a Hamiltonian description of the fully nonlinear wave-body problem was demonstrated by van Daalen, van Groesen and Zandbergen (1993).

As stated in the abstract, our main goal is to exploit this special Hamiltonian structure to obtain approximative 'energy-stable' equations for wave-body interactions. In sections 1 and 2 the variational formulation and the corresponding Hamiltonian description are presented. As a simple example, we show in section 3 that the linearized versions of the free surface conditions and the hydrodynamic equations of motion for the ship describe a Hamiltonian system. Further applications to ship-wave interactions will be presented at the symposium.

1. VARIATION PRINCIPLE

The system under consideration consists of a fluid, bounded by the impermeable bottom B (which is not necessarily even), the free surface F, and the wetted surface S of a rigid body, see Figure 1. In the horizontal directions x and y, the fluid domain is cut off by a cylindrical vertical surface Σ of infinite radius; Σ extends from the bottom to the free surface.

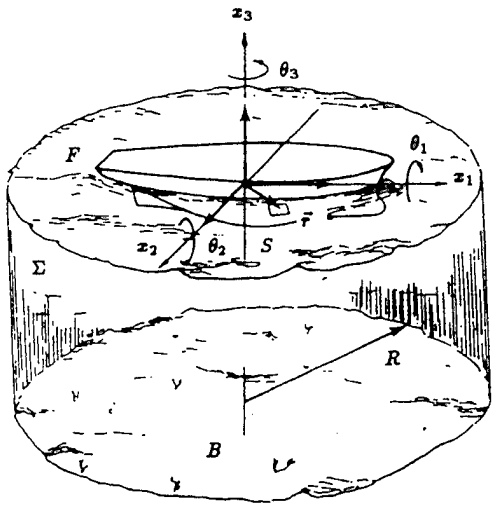


Figure 1: Definition of fluid domain and floating body.

The body mass and moments about its principal axes of inertia are denoted by M and $\vec{I} = (I_1, I_2, I_3)^T$ respectively. The position of the body is specified by the centre of gravity

$$\vec{x}_G = (x_1, x_2, x_3)^T \tag{1}$$

corresponding to surge, sway and heave motion, and the body orientation by the 'roll-pitch-yaw vector'

$$\vec{\theta}_G = (\theta_1, \theta_2, \theta_3)^T \tag{2}$$

Gravity is acting in negative z-direction.

To facilitate notation, the body 'coordinate' $\vec{\xi}$, the 'normal' $\vec{\nu}$ and the 'mass' matrix $\mathcal{M}$ are defined as

$$\vec{\xi} \equiv \begin{bmatrix} \vec{x}_G \\ \vec{\theta}_G \end{bmatrix} \tag{3}$$

and

$$\vec{\nu} \equiv \begin{bmatrix} \vec{n} \\ \vec{r} \times \vec{n} \end{bmatrix} \tag{4}$$

and

$$\mathrm{diag}\,(\mathcal{M}) \equiv [M, M, M, I_1, I_2, I_3]^T \tag{5}$$

where

$$\vec{r} = \vec{x}_S - \vec{x}_G \tag{6}$$

denotes the position of a point on S relative to G, see Figure 1.

Following Luke, the Lagrangian for the fluid is given by

$$\mathcal{L}_f \equiv \iiint_{\Omega(t)} p \, d\Omega = -\iiint_{\Omega(t)} \left(\phi_t + \frac{1}{2} \nabla\phi \cdot \nabla\phi + gz \right) d\Omega \tag{7}$$

i.e. the Bernoulli pressure p integrated over the transient fluid domain $\Omega(t)$; the fluid density is taken as unity.

The Lagrangian for the body is taken as kinetic minus potential energy, i.e.

$$\mathcal{L}_b \equiv \mathcal{K}_b - \mathcal{P}_b \tag{8}$$

where

$$\mathcal{K}_b = \frac{1}{2} \mathcal{M} \dot{\vec{\xi}} \cdot \dot{\vec{\xi}} \tag{9}$$

and

$$\mathcal{P}_b = \mathcal{M} g \vec{e}_3 \cdot \vec{\xi} \tag{10}$$

The Lagrangian for the *total* system is defined as the sum of the two Lagrangians, i.e.

$$\mathcal{L}_s \equiv \mathcal{L}_f + \mathcal{L}_b \tag{11}$$

The proposed variation principle reads

$$\delta J = 0 \quad \text{with} \quad J \equiv \int_{t_1}^{t_2} \mathcal{L}_s \, dt \tag{12}$$

for all variations in the free surface elevation η, the velocity potential ϕ, and the body coordinate $\vec{\xi}$. These variations are subject to the restrictions that they vanish at times $t = t_1$ and $t = t_2$; moreover, the variations in η and ϕ must equal zero on Σ.

Then, following the standard procedure in the calculus of variations, (7-12) yields

$$\begin{aligned}
\delta J \;=\; & \\
& - \int_{t_1}^{t_2} \left\{ \iiint_{\Omega(t)} \left(\delta\phi_t + \nabla\phi \cdot \nabla\delta\phi\right) d\Omega \right\} dt \\
& + \int_{t_1}^{t_2} \left\{ \iint_{F} p\, \delta\eta\, R^{-1} dS \right\} dt \\
& + \int_{t_1}^{t_2} \left\{ \iint_{S} p \left(\delta\vec{x}_S \cdot \vec{n}\right) dS \right\} dt \\
& + \int_{t_1}^{t_2} \left\{ M\ddot{\vec{x}}_G \cdot \delta\dot{\vec{x}}_G - Mg\vec{e}_3 \cdot \delta\vec{x}_G \right\} dt \\
& + \int_{t_1}^{t_2} \left\{ \left(\vec{I} \otimes \ddot{\vec{\theta}}_G\right) \cdot \delta\dot{\vec{\theta}}_G \right\} dt \\
& = 0
\end{aligned} \tag{13}$$

where $\otimes$ defines a component-wise vector-vector product (the outcome is also a vector), $\vec{n}$ is the unit normal vector along $\partial\Omega \supset S$, and

$$R(\eta) \equiv \left(1 + \eta_x^2 + \eta_y^2\right)^{1/2} \tag{14}$$

giving

$$dS = R\, dx\, dy \tag{15}$$

In (13) $\vec{x}_S$ denotes the position of a point on the wetted body surface S; the change in $\vec{x}_S$ due to the variations in $\vec{x}_G$ and $\vec{\theta}_G$ is given by

$$\delta\vec{x}_S = \delta\vec{x}_G + \delta\vec{\theta}_G \times \vec{r} \tag{16}$$

Taking into account the motion of $\Omega(t)$, we may write

$$\begin{aligned}
\iiint_{\Omega(t)} \delta\phi_t d\Omega \;=\; & \frac{\partial}{\partial t} \iiint_{\Omega(t)} \delta\phi \, d\Omega \\
& - \iint_{F} \eta_t \delta\phi \, R^{-1} dS \\
& - \iint_{S} \left(\dot{\vec{x}}_S \cdot \vec{n}\right) \delta\phi \, dS
\end{aligned} \tag{17}$$

The first term on the right-hand side of (17) vanishes due to the restriction $\delta\phi = 0$ at times $t = t_1$ and $t = t_2$.

With Green's first identity we obtain:

$$\begin{aligned}
\iiint_{\Omega(t)} \nabla\phi \cdot \nabla\delta\phi \, d\Omega \;=\; & \iint_{\partial\Omega} \phi_n \delta\phi \, dS \\
& - \iiint_{\Omega(t)} \nabla^2\phi \, \delta\phi \, d\Omega
\end{aligned} \tag{18}$$

Due to the restriction $\delta\phi = 0$ on $\Sigma \subset \partial\Omega$, the corresponding contribution on the right-hand side of (18) vanishes.

Integration by parts, and using the restrictions $\delta\vec{x}_G = \vec{0}$ and $\delta\vec{\theta}_G = \vec{0}$ at times $t = t_1$ and $t = t_2$, gives

$$\begin{aligned}
\int_{t_1}^{t_2} M\dot{\vec{x}}_G \cdot \delta\dot{\vec{x}}_G \, dt = & \\
& - \int_{t_1}^{t_2} M\ddot{\vec{x}}_G \cdot \delta\vec{x}_G \, dt
\end{aligned} \tag{19}$$

and

$$\begin{aligned}
\int_{t_1}^{t_2} \left(\vec{I} \otimes \ddot{\vec{\theta}}_G\right) \cdot \delta\dot{\vec{\theta}}_G \, dt = & \\
& - \int_{t_1}^{t_2} \left(\vec{I} \otimes \dddot{\vec{\theta}}_G\right) \cdot \delta\vec{\theta}_G \, dt
\end{aligned} \tag{20}$$

With (13-20) the proposed variation principle reads

$$\delta J = \int_{t_1}^{t_2} \left\{ \iint_{F} p\, \delta\eta\, R^{-1} dS + \iiint_{\Omega(t)} \nabla^2\phi \, \delta\phi \, d\Omega \right\} dt$$

$$
\begin{aligned}
&- \int_{t_1}^{t_2} \left\{ \iint_F \left(R\phi_n - \eta_t \right) R^{-1} \delta\phi \, dS \right\} dt \\
&- \int_{t_1}^{t_2} \left\{ \iint_S \left(\phi_n - \dot{\vec{x}}_S \cdot \vec{n} \right) \delta\phi \, dS \right\} dt \\
&- \int_{t_1}^{t_2} \left\{ \iint_B \phi_n \delta\phi \, dS \right\} dt \\
&+ \int_{t_1}^{t_2} \left\{ \left(\iint_S p\,\vec{n}\, dS - Mg\vec{e}_3 - M\ddot{\vec{x}}_G \right) \cdot \delta\vec{x}_G \right\} dt \\
&+ \int_{t_1}^{t_2} \left\{ \left(\iint_S p\,(\vec{r} \times \vec{n})\, dS - \vec{I} \otimes \ddot{\vec{\theta}}_G \right) \cdot \delta\vec{\theta}_G \right\} dt \\
&= 0 \qquad (21)
\end{aligned}
$$

From this it is clear that invariance of J with respect to a variation in the free surface elevation η yields the dynamic free surface condition:

$$
\begin{aligned}
p &= -\left(\phi_t + \frac{1}{2} (\nabla\phi \cdot \nabla\phi) + gz \right) \\
&= 0 \quad \text{on} \quad F \qquad (22)
\end{aligned}
$$

Similarly, invariance of J with respect to a variation in the velocity potential ϕ yields the field equation:

$$
\nabla^2 \phi = 0 \quad \text{in} \quad \Omega(t) \qquad (23)
$$

the kinematic free surface condition:

$$
\eta_t + \eta_x \phi_x + \eta_y \phi_y = \phi_z \quad \text{on} \quad F \qquad (24)
$$

the 'contact' condition on the wetted body surface:

$$
\phi_n = \dot{\vec{x}}_S \cdot \vec{n} \quad \text{on} \quad S \qquad (25)
$$

and the impermeability condition on the bottom:

$$
\phi_n = 0 \quad \text{on} \quad B \qquad (26)
$$

Finally, invariance of J with respect to variations in the body position $\vec{x}_G$ and orientation $\vec{\theta}_G$ yields the equations of motion for the body:

$$
\begin{aligned}
\iint_S p\,\vec{n}\, dS - Mg\vec{e}_3 &= M\ddot{\vec{x}}_G \qquad (27) \\
\iint_S p\,(\vec{r} \times \vec{n})\, dS &= \vec{I} \otimes \ddot{\vec{\theta}}_G \qquad (28)
\end{aligned}
$$

Hence, (12) is a proper variational principle for nonlinear water waves in hydrodynamic interaction with a freely floating body.

3. HAMILTONIAN FORMULATION

Taking into account the evolution of the fluid domain and integrating by parts, we may write formally — see van Daalen et al (1993) —

$$
\mathcal{L}_s \left(\eta_s, \dot{\eta}_s \right) = \pi_s \dot{\eta}_s - \mathcal{H}_s \left(\eta_s, \pi_s \right) \qquad (29)
$$

with the following choices for the canonical coordinates and conjugate momenta:

$$
\begin{aligned}
\eta_s &= (\eta_f, \vec{\eta}_b) \equiv \left(\eta, \vec{\xi} \right) \qquad (30) \\
\pi_s &= (\pi_f, \vec{\pi}_b) \\
&\equiv \left(\Phi, \mathcal{M}\dot{\vec{\xi}} + \iint_S \phi\, \vec{\nu}\, dS \right) \qquad (31)
\end{aligned}
$$

where Φ is the restriction of ϕ to the free surface:

$$
\Phi(x, y; t) \equiv \phi(x, y, z = \eta; t) \qquad (32)
$$

In (31) the integral over S is the well-known 'Kelvin impulse' contribution of the velocity potential.

The Hamiltonian is the total energy:

$$
\begin{aligned}
\mathcal{H}_s &= \iiint_{\Omega(t)} \left(\frac{1}{2} \nabla\phi \cdot \nabla\phi + gz \right) d\Omega \\
&+ \frac{1}{2} \mathcal{M}\dot{\vec{\xi}} \cdot \dot{\vec{\xi}} + \mathcal{M} g \vec{e}_3 \cdot \vec{\xi} \qquad (33)
\end{aligned}
$$

Then, with ϕ satisfying the boundary value problem (23, 25, 26, 32), we can prove — see also van Daalen (1993) — the following theorem:

Theorem: *The equations of motion for gravity driven water waves interacting with a body floating freely in or below the free surface describe an infinite-dimensional Hamiltonian system in the canonically conjugate variables π_s and η_s and with the total energy $\mathcal{H}_s$ as Hamiltonian: the canonical equations*

$$
\partial_t \begin{pmatrix} \pi_s \\ \eta_s \end{pmatrix} = \begin{pmatrix} 0 & -1 \\ 1 & 0 \end{pmatrix} \begin{pmatrix} \delta\mathcal{H}_s/\delta\pi_s \\ \delta\mathcal{H}_s/\delta\eta_s \end{pmatrix} \qquad (34)
$$

are equivalent with the nonlinear free surface conditions (22-24) and the hydrodynamic equations of motion (27-28) for the body.

The proof of this theorem follows directly from the next lemma:

Lemma: *The variational derivatives of the kinetic fluid energy*

$$\mathcal{K}_f(\Phi,\eta) = \iiint_{\Omega(t)} \frac{1}{2}(\nabla\phi\cdot\nabla\phi)\,d\Omega \tag{35}$$

are given by:

$$\delta_\Phi \mathcal{K}_f = R(\eta)\left(\frac{\partial\phi}{\partial n}\right)_{z=\eta} \tag{36}$$

$$\delta_\eta \mathcal{K}_f = \frac{1}{2}(\nabla\phi\cdot\nabla\phi)_{z=\eta} - \delta_\Phi\mathcal{K}_f\left(\frac{\partial\phi}{\partial z}\right)_{z=\eta} \tag{37}$$

Proof of (36): Keep η and $\vec{\xi}$ fixed and let ϕ vary such that its variation $\delta\phi$ corresponds to a change $\delta\Phi$. Then the first variation in $\mathcal{K}_f(\Phi,\eta)$ reads

$$\begin{aligned}\delta\mathcal{K}_f(\delta\Phi) &= \iiint_{\Omega(t)} \nabla\phi\cdot\nabla\delta\phi\,d\Omega \\ &= \iiint_{\Omega(t)} \nabla\cdot(\nabla\phi\,\delta\phi)\,d\Omega \\ &\quad - \iiint_{\Omega(t)} \nabla^2\phi\,\delta\phi\,d\Omega\end{aligned} \tag{38}$$

With Gauss' divergence theorem and (23, 25, 26, 32) we obtain

$$\delta\mathcal{K}_f(\delta\Phi) = [(\nabla\phi\cdot\vec{n})\,dS]_{z=\eta}\,\delta\Phi \tag{39}$$

Using $dS = R\,dx\,dy$, the proof is completed.

Proof of (37): Now, vary η and assume that the solution ϕ of the BVP is correspondingly modified for the varied fluid domain. At the modified free surface we have to lowest order:

$$\begin{aligned}\phi(\eta+\delta\eta) &= \phi(\eta) + \delta\eta\left(\frac{\partial\phi}{\partial z}\right)_{z=\eta} \\ &\equiv \Phi + \delta_\eta\Phi\end{aligned} \tag{40}$$

With the above result the total effect of a variation $\delta\eta$ in $\mathcal{K}_f$ is found to be

$$\delta\mathcal{K}_f(\delta\eta) + \delta\mathcal{K}_f(\delta_\eta\Phi) = \delta\eta\left\{\frac{1}{2}(\nabla\phi\cdot\nabla\phi)_{z=\eta}\right\} \tag{41}$$

and hence, to lowest order

$$\delta_\eta\mathcal{K}_f + \delta_\Phi\mathcal{K}_f\left(\frac{\partial\phi}{\partial z}\right)_{z=\eta} = \frac{1}{2}(\nabla\phi\cdot\nabla\phi)_{z=\eta} \tag{42}$$

from which the second part of the lemma follows.

3. LINEARIZED SHIP-WAVE INTERACTIONS

The exact contribution to the kinetic energy due to the fluid motion is given by

$$\mathcal{K}_f = \iiint_{\Omega(t)} \frac{1}{2}\nabla\phi\cdot\nabla\phi\,d\Omega \tag{43}$$

which, using Gauss' theorem, the continuity equation (23) and the Neumann conditions (25-26) is re-written as

$$\mathcal{K}_f = \iint_F \frac{1}{2}\phi\,\phi_n\,dS + \iint_S \frac{1}{2}\phi\left(\dot{\vec{\xi}}\cdot\vec{\nu}\right)dS \tag{44}$$

At the free surface we have

$$\vec{n} = \frac{(-\eta_x,-\eta_y,1)^T}{R(\eta)} \tag{45}$$

and

$$dS = R(\eta)\,dx\,dy \tag{46}$$

Here we consider waves with small amplitude A compared to the wavelength and the mean water depth. Then, retaining terms up to second order (in A) only, we find

$$\begin{aligned}\mathcal{K}_f \approx \tilde{\mathcal{K}}_f &= \iint_{\bar{F}} \frac{1}{2}\Phi\,D(\Phi)\,dx\,dy \\ &\quad + \iint_S \frac{1}{2}\phi\left(\dot{\vec{\xi}}\cdot\vec{\nu}\right)dS\end{aligned} \tag{47}$$

where $\bar{F}$ is the mean waterplane corresponding to $z=0$ and $D(\Phi)\equiv(\phi_z)_{\bar{F}}$. Since D is self-adjoint, i.e. $D = D^*$, it follows that

$$\delta_\Phi\tilde{\mathcal{K}}_f = D(\Phi) = (\phi_z)_{z=0} \tag{48}$$

The same holds for the (nonlinear) operator expressing ϕ_n on S in terms of the generalized body velocity $\dot{\vec{\xi}}$.

With these results we can easily prove that (34), with $\mathcal{K}_f$ replaced by $\tilde{\mathcal{K}}_f$, is equivalent with the linearized free surface conditions

$$\phi_t = -g\eta \quad\text{and}\quad \eta_t = \phi_z \quad\text{on}\quad z=0 \tag{49}$$

and the linearized hydrodynamic equations of motion for the ship:

$$\iint_S p_L\vec{\nu}\,dS - \mathcal{M}g\vec{e}_3 = \mathcal{M}\ddot{\vec{\xi}} \tag{50}$$

where the linearized Bernoulli pressure p_L is defined as

$$p_L = -(\phi_t + gz) \tag{51}$$

Next, suppose that ϕ can be expressed in terms of the so-called radiation potentials ϕ^k, each corresponding to a unit amplitude mode of motion of the ship, i.e. put

$$\phi = \dot{\xi}_k \phi^k \tag{52}$$

Equation (50) can then be re-written to

$$(\mathcal{M} + \mathcal{A})\ddot{\vec{\xi}} + \mathcal{B}\dot{\vec{\xi}} + \mathcal{C}\vec{\xi} = 0 \tag{53}$$

where $\mathcal{A} = (a^{kl})$, etc., with

$$a^{kl} = \iint_S \phi^k \nu^l dS \tag{54}$$

and

$$b^{kl} = \iint_S \phi_t^k \nu^l dS \tag{55}$$

and

$$c^{kl} = \iint_S gz\, \nu^l dS \tag{56}$$

Clearly, $\mathcal{A}$ is the hydrodynamic mass matrix and $\mathcal{C}$ contains the hydrostatic restoring coefficients. The role of the remaining matrix $\mathcal{B}$ can be understood by noting that

$$b^{kl} = \partial_t a^{kl} \tag{57}$$

Hence, equation (53) can be put in its simplest (canonical) form:

$$\partial/\partial t \left[(\mathcal{M} + \mathcal{A})\dot{\vec{\xi}}\right] = -\partial/\partial\vec{\xi}\left[\frac{1}{2}\mathcal{C}\vec{\xi}\cdot\vec{\xi}\right] \tag{58}$$

CONCLUSIONS AND FUTURE RESEARCH

In this paper we have demonstrated the possibility of deriving stable model equations for ship-wave interactions from a Hamiltonian formulation. With an approximation of the kinetic fluid energy, we obtained energy-stable equations which, indeed, respect the Hamiltonian structure.

In the near future, we intend to include the following effects in our formulations:

- diffraction
- forward speed effects
- ship wavemaking and wave resistance

Further progress will be reported at the symposium.

ACKNOWLEDGEMENTS

Financial support from the Royal Dutch Academy of Sciences (KNAW) made this research possible. The author wishes to thank professor P.J. Zandbergen, professor E. van Groesen (Faculty of Applied Mathematics, University of Twente) and professor T. Miloh (Department of Fluid Mechanics, Tel-Aviv University) for their support and encouragement.

REFERENCES

Broer, L.J.F., "On the Hamiltonian theory of surface waves", Applied Scientific Research, Vol. 29, 1974, pp. 430-446.

Daalen, E.F.G. van, Numerical and Theoretical Studies of Water Waves and Floating Bodies, 1993, Ph.D. thesis, University of Twente, Enschede, The Netherlands.

Daalen, E.F.G. van, Groesen, E. van, and Zandbergen, P.J., "A Hamiltonian formulation for nonlinear wave-body interactions", 1993, Abstracts of the Eight International Workshop on Water Waves and Floating Bodies, St. John's, Newfoundland.

Luke, J.C., "A variational principle for a fluid with a free surface", Journal of Fluid Mechanics, Vol. 27, No. 2, 1967, pp. 395-397.

Miles, J.W., "On Hamilton's principle for surface waves", Journal of Fluid Mechanics, Vol. 83, 1977, pp. 153-158.

Miles, J.W., "Hamiltonian formulations for surface waves", Applied Scientific Research, Vol. 37, 1981, pp. 103-110.

Miloh, T., "Hamilton's principle, Lagrange's method and ship motion theory", Journal of Ship Research, Vol. 28, No. 4, 1984, pp. 229-237.

Zakharov, V.E., "Stability of periodic waves of finite amplitude on the surface of a deep fluid", Journal of Applied Mechanics and Technical Physics (translated from Russian), Vol. 2, 1968, pp. 190-194.

Large-Amplitude Motions and Wave Loads for Ship Design

W.-M. Lin, M. Meinhold, N. Salvesen
(Science Applications International Corp., USA),
D. Yue (Massachusetts Institute of Technology, USA)

ABSTRACT

A new three-dimensional time domain approach for the assessment of the large-amplitude motions and wave loads of a ship in a seaway is presented. In this approach, the body boundary condition is satisfied on the instantaneous wetted surface of the moving body below the *incident* wave surface, while the free surface boundary conditions are linearized about the incident wave.

Results for four ships with different geometry features are presented using the new approach, as well as simplified versions derived from the new approach. The results include linear and nonlinear motion and load responses of ships advancing in regular and irregular seas. The results clearly demonstrate the importance and the magnitude of nonlinear effects in ship motions and wave loads.

The ongoing development of a fully integrated computational system for design assessment of not only the ship motions and wave loads but also the structural responses is discussed. The necessary steps to fulfill the difficult requirements for a practical and complete design support system are also presented.

INTRODUCTION

The accurate prediction of large amplitude nonlinear wave-induced motions, hydrodynamic loads, and resulting structural responses is of crucial importance in ship design. In addition to compromising efficiency and comfort, severe motions can limit operability and affect safety, while extreme loads may lead to structural failure. Furthermore, the importance of accurate predictions of ship motions, loads, and responses in design and safety assessment is increasing with the advent of new ship types, innovative designs and more demanding operational requirements.

Naval Ship Needs

The urgent need for an improved motion and load assessment capability within the U.S. Navy is demonstrated by the following examples.

- *Innovative Ship Design* – When the SWATH was first proposed it represented a radically new idea in ship design. At that time its benefits in terms of improved seakeeping were known (Salvesen, 1973). Yet the SWATH has taken more than twenty years to work its way through the design cycle, in large part due to an inability to accurately predict hydrodynamic loads.

- *Extrapolations from Current Designs* – Current ship design is performed primarily through interpolation from known hull forms. Extrapolation beyond the historical database is risky. The design of the catamaran U.S.S. Hayes was an example of an extrapolation from known hulls. She experienced severe damage from slamming in rough seas in the North Sea.

- *Modifications to Existing Ships* – The modifications to the carrier U.S.S. Midway included the addition of blisters to gain buoyancy. This resulted in such a severe degradation in seakeeping that aircraft landings had to be curtailed.

- *Safety* – Although during the serviceable lifetime of a ship only a few encounters with highly nonlinear extreme seas are experienced, it is precisely those encounters that dictate safety margins. Recent structural damage on several ships of the CG47 and CG52 classes have demonstrated the lack of an adequate design capability.

Commercial Ship Needs

The same need for predictive capability exists outside the naval community.

- *Catastrophic Structural Damages* – Between January 1990 and September 1991 thirty-six bulk carriers suffered severe structural damages causing the loss of twenty-one ships and two hundred and fifty lives (Grove *et al*, 1992). In most of these cases, structural failure due to hydrodynamic loads imposed by the seaway was the primary cause of casualty.
- *Capsizing of Fishing and Pleasure Craft* – In the Fastnet Race of 1979 seventy-seven boats were capsized and fifteen sailors died in what is considered to be the greatest disaster in the history of the sport of yachting. Stephens, *et al*, (1981) pointed out that the current design practice measured stability by static criteria and compensated for dynamic effects through safety margins. Their investigation revealed that because of the fundamental difference between static and dynamic stability "... certain factors which result in favorable static stability characteristics may actually present greater danger when considered in light of a dynamic analysis". The same considerations apply to powered pleasure craft and fishing vessels.
- *Load Line Assessment* – At the January 1993 International Maritime Organization (IMO) Meeting of the Sub-Committee on Stability, Load Lines and Fishing Vessel Safety - 37th Session (SLF37) an entirely new approach for the future Load Line Convention was adopted. Two separate paths will be allowed in determining the load line. Path one utilizes the well established Freeboard Table. Path two is a new Equivalent Level of Safety Assessment using accurate computational methods for predicting ship responses in extreme sea conditions to assess conformance to safety performance criteria.

System Requirements

As can be seen from the previous examples, there is a pressing need to expand current ship design assessment capabilities for both naval and commercial ships. Additional expertise is needed in a wide range of disciplines - for example, in structures, hydrodynamics, computational methods, and electronic database management. It also seems clear that to be effective in design practice this new capability must evolve into a tightly integrated system so that design assessments and optimizations can include all factors which significantly effect any aspect of the ship's performance.

This paper is organized into two main sections. The first addresses the core requirement for accurate predictions of ship motions and loads in moderate and severe seas. A general overview of computational methods for motion and loads predictions is immediately followed by an introduction to the Large Amplitude Motion Program (LAMP) system of codes which have been developed by the authors for calculations of motion and loads in large amplitude waves. A detailed discussion of both the accuracy and efficiency of the existing codes follows, together with plans for code improvements.

The second section addresses the development of an integrated design assessment system and its use in practical design environments and applications. The first part of this discussion focuses on the progress made thus far in developing the Interactive Design Evaluation and Analysis System (IDEAS) and presents examples of design assessments which are currently performed with it. The second part of the discussion centers on extensions to the system both in terms of added capability for structural responses to impulse loads such as slamming as well as improvements in utility for design. The concluding remarks of the paper provide the broad overview of future requirements for such systems if they are to truly impact the practice of ship design.

MOTIONS AND LOADS PREDICTIONS

Fortunately, advances in computational ship hydrodynamics over the past decade have resulted in increasingly capable and accurate computer codes for the prediction of ship motions and loads. The application of these codes has been accelerated over the past few years by the ever-increasing power of modern computers, so that some of these advanced numerical calculations may now be done within design time scales. As a result of these advances, a new level of computational capability is now emerging for the prediction of the nonlinear ship motions and wave loads for severe sea conditions.

Linear Methods

Traditionally, the ship motion problem is formulated in the frequency domain, and lin-

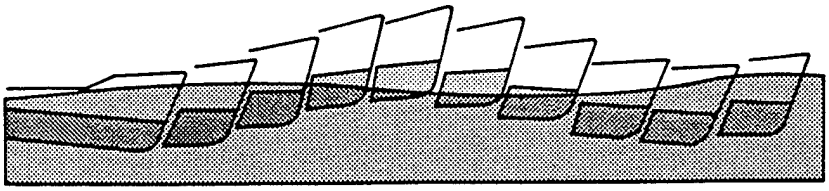


Figure 1: Destroyer Hull in Sinusoidal Wave, $\lambda = 1.20L$ and $H/\lambda = 0.013$. (From Salvesen, 1978)

earized by assuming that the magnitude of the motions and the incident waves are small relative to the draft of the ship. The most commonly used linear tools presently available are based on the strip-theory originated by Korvin-Kroukovsky (1955). These tools were brought to the present state of development by a number of researchers in the United States, Europe and Japan during the mid-1960s. The U.S. Navy standard ship motion program, SMP is a typical code in common use by designers today. The later development of fully three-dimensional linear methods has also resulted in several useful codes. The most promising ones provide solutions using either the transient free-surface Green function (*e.g.*: Beck & Magee (1991), Lin & Yue (1990), Bingham, *et al*, (1993)) or the Rankine source methods (*e.g.*, Nakos & Sclavounos (1990)).

Linear frequency-domain methods have been very successful in many respects; for example, in determining sea state operability limitations for weapon systems on naval vessels (Kennel, *et al*, 1985). Such methods have also been useful in estimating the wave induced loads for large ships (Liu, *et al*, 1992). However, the linearity assumption of small motions relative to the draft is violated by the bow motions of most ships even in moderate head waves. Consider, for example, a typical destroyer hull. The relative bow displacement can be as much as four times the wave amplitude at $Fn = 0.35$ (Frank & Salvesen, 1970). Therefore the bow will exit the surface in moderate waves. Figure 1 illustrates the bow motions for a destroyer hull in sinusoidal wave with $\lambda = 1.20L$ and $H/\lambda = 0.013$.

Since it can be expected that a large percentage of the waves are much steeper than $H/\lambda = 0.013$, the assumption of small displacements at the bow will often be violated. Much steeper waves can occur when waves receive energy from currents or reflections. For example, Smith (1976) points out that off the southeast coast of South Africa the rapid Agulhas Current can result in waves with $H/\lambda = 0.10$. Buckley (1994) has reported that "the most nonlinear waves" in the hurricane Camille wave data had "a height to length ratio of about 1/7" ($H/\lambda = 0.14$). Note that for non-breaking waves the maximum theoretical value of H/λ is 0.14.

Nonlinear Methods

Due to the severe limitations of the linear ship motion theories, several investigators have extended the frequency-domain strip-theory approach to large-amplitude time-domain strip-theory approaches. In these large-amplitude approaches, the nonlinear hydrostatic restoring forces and the Froude Krylov forces are calculated accurately whereas the hydrodynamic restoring and diffraction forces are calculated by some approximate extensions of the strip-theories.

In the United States, such an approach has been applied by de Kat and Paulling (1989) to predict capsizing with quite some success. In particular, for low-frequency following seas their method showed very promising results. Outside the United States, such methods have had noticeable success in calculating the nonlinear global loads (bending moments and shear forces) (see for example, Fujino and Yoon, 1986). Approximate methods of this type can be very useful if they are applied carefully and with full understanding of their limitations.

The more recent research efforts in the United States have been focused on the development of nonlinear methods. These methods may be divided into two categories: fully nonlinear methods and approximate nonlinear methods. Typically, fully nonlinear methods address the exact free surface condition as well as the exact nonlinear body boundary conditions, whereas approximate nonlinear methods apply certain approximations to the nonlinear free surface conditions. Most of the theories in either category are formulated within classical potential flow theory. Good examples of the fully nonlinear approach are the work of Korsmeyer, *et al*, (1992), Maskew (1991), Cao, *et al*, (1992), and Yue (1994). The

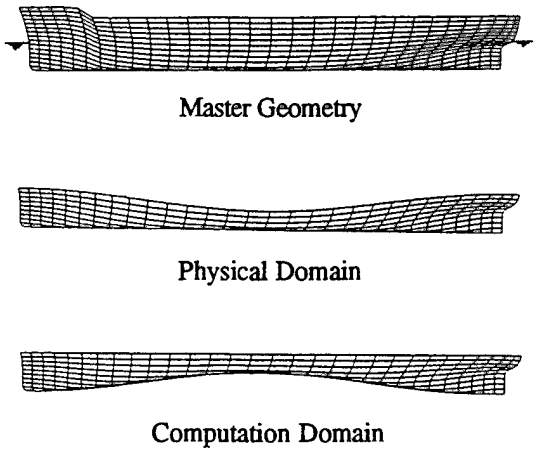


Figure 2: Master Geometry and Panel Distribution in both Physical and Computation Domains.

approximate method of Lin & Yue (1990), and Beck & Magee (1991) solve the body-exact problem in which the free-surface condition is linearized. The work of Pawlowski and Bass (1991) is another example of an approximate nonlinear method. Tulin and Maruo (1992) address the nonlinear deck wetness problem with promising approximate method based on a 2-1/2-D formulation.

It is believed that the approximate nonlinear approaches will result in practical and validated computational tools which can be run on modern advanced workstations within the near future. The fully nonlinear methods will require advanced supercomputers and for the near future will remain research codes serving as validation tools of the more approximate methods.

LARGE AMPLITUDE METHOD

In 1990, Lin & Yue presented a three-dimensional time-domain method to study large-amplitude motions and loads of floating bodies in waves. In their so-called "body-exact" approach, the free-surface boundary conditions are linearized and the body boundary condition is satisfied exactly on the portion of the instantaneous wetted surface which lies below the undisturbed free surface. The problem is solved using a transient free-surface Green function singularity distribution. The validity and practical utility of this method have been demonstrated by several studies including predictions of large-amplitude motion coefficients, motion history of a ship advancing in an irregular seaway, as well as the effect of bow flare on wave loads (see Lin & Yue 1990, 1992; Lin *et al*, 1991, 1992).

This method was employed for the prediction of motions and loads of a cruiser hull, CG47, in waves (Lin & Meinhold, 1991; Lin & Yue, 1993). The results were satisfactory for moderate seas but difficulties were encountered in severe seas. The difficulties arise from the fact that the body-exact approach models only that portion of the hull below the *undisturbed* free surface. When the wave amplitude is large compared to the ship draft, this representation becomes inadequate, especially near the transom stern.

New Formulation

In order to improve the Lin & Yue (1990) method and extend its applicability to more severe wave conditions, a new large-amplitude method has been developed in which both the *body motions* and the *incident waves* can be large (Lin & Yue, 1993). In this new Large-Amplitude Motion Program, LAMP, the body boundary condition is satisfied on the instantaneous wetted surface below the *incident* wave profile with the assumption that the diffracted waves are small compared to the incident wave and that the incident wave slopes are small. At each time step, local incident free surface elevations are used to transform the body geometry into a computational domain with a deformed body and a flat free surface. By linearizing the free surface boundary conditions about this incident wave surface, the problem can be solved in the computational domain using linearized free-surface transient Green functions.

Figure 2 shows a typical master geometry and panel distributions in both physical and computation domains. The solution procedures used for the problem in the computational domain are very similar to those used in the physical domain (Lin & Yue, 1993). Both the source formulation and potential formulation can be used. The two main features of this new large-amplitude approach are: (i) true hydrodynamic effects for the wetted portion of the ship under the incident wave surface; and (ii) automatic inclusion of the correct hydrostatic and Froude-Krylov forces.

In oblique or beam seas, forces due to viscous and lift effects will have a significant effect on the motions and loads. LAMP includes an option to approximate these effects in the time-domain. The viscous and lift effects approximated are as shown in Table 1. For each effect, the table

Table 1: Viscous and Lift Effects

Effect	Reference	Linearity
Hull Lift	Low Aspect Ratio Lifting Theory	Linear
Skeg, Bilge Keel and Foil Lift	High Aspect Ratio Lifting Theory	Linear
Hull Eddymaking	Tanaka (1960) and Ikeda et al. (1978)	Non-Linear
Bilge Keel Eddymaking	Kato (1966)	Non-Linear
Skeg and Foil Eddymaking	Hoerner (1958) and Ikeda et al. (1978)	Non-Linear
Hull Skin Friction	Kato (1958)	Non-Linear

presents a reference for the calculation method and whether it is a linear or non-linear effect. These components are determined in a manner very similar to that used in the U.S. Navy's SMP code (Meyers *et al*, 1981). However, in the SMP code, the forces are calculated in the frequency domain, assuming certain *averaged* magnitudes of roll displacement and roll velocity.

Such an *averaged* roll damping approach is not satisfactory for time domain calculations where a primary objective is the accurate calculations of the extreme response events. The new calculation method uses the formulae from the references in Table 1, but uses the current magnitude of roll displacement and roll velocity rather than an averaged value. At every time step, the time history of roll displacement and roll velocity is examined for a peak value, positive or negative. These peak values generate parameters for the viscous forces until a new peak is found. At any given time step, the actual forces depend on these parameters and the instantaneous value of roll displacement and roll velocity.

In the present version of LAMP the incident wave can be represented by a superposition of any number of harmonic wave components at any direction relative to the ships heading. Given a wave spectrum, the program will generate automatically an irregular wave representation with random phases and a pre-specified spreading function. Irregular wave representations for multiple spectra can also be generated. The wave field may also be represented by higher-order Stokes waves.

For any given wave representation, LAMP will calculate the time-domain six-degree-of-freedom coupled motions and the time-domain wave-induced global loads, that is the bending and torsional moments and shear forces at any cross-section along the length of the ship. The program also calculates at each time step the hydrodynamic pressure distribution over the instantaneous wetted hull surface below the incident wave surface. Furthermore, the added resistance in waves as well as the wave resistance can be calculated. Typically the program is run with the ship advancing at a given heading angle and constant forward speed; however, any path and/or speed may be specified.

The Multi-Level Code System

A complete computational capability for the assessment of ship motions and wave loads must be based on a multi-level approach. Such a system integrates methods which are based not just on one single code or one single level of sophistication, but rather on a system of codes with different levels of sophistication. As a general rule, the physics underlying the ship/wave interactions is best understood using comparisons generated by incremental increases in complexity - a procedure which also moderates computer usage. Analysis tools at the lower levels may employ several approximations to attain a short enough turnaround time for use in early stages of the evaluation process. Examination of results obtained by the lower level code guides the engineer in choosing areas where more accurate theories must be used. In other words, the lower level codes should be used as a filtering mechanism for the selection of more accurate but more complicated and computationally intensive codes.

A multi-level system can also effectively tie the probabilistic and deterministic approaches together providing the missing ingredient of probabilistic prediction. Statistical data of ship motion in given random seas can be obtained by using lower level evaluation codes to efficiently compute the ships responses to a very wide range of deterministic excitations. The severe ship responses can be selected from these, to be examined with the higher level nonlinear simulations. Conversely, nonlinear dynamic simulations of ships in episodic wave events can be used to

Table 2: Computation Methods and Hardware Requirements for the LAMP Code. ($Z = 0$ and $\mathcal{F}(t)$ are Still Water Surface and Incident Wave Surface Respectively)

Method	Hydrodynamic, Restoring and Froude-Krylov Forces	Hardware
LAMP-4	Free Surface Boundary Conditions on $\mathcal{F}(t)$ 3-D Large-Amplitude Hydrodynamics Nonlinear Restoring and Froude-Krylov Forces	Supercomputer
LAMP-3	Free Surface Boundary Conditions on $\mathcal{F}(t)$ 2-1/2-D Large-Amplitude Hydrodynamics Nonlinear Restoring and Froude-Krylov Forces	Workstation
LAMP-2	Free Surface Boundary Conditions on $Z = 0$ 3-D Linear Hydrodynamics Nonlinear Restoring and Froude-Krylov Forces	Workstation
LAMP-1	Free Surface Boundary Conditions on $Z = 0$ 3-D Linear Hydrodynamics Linear Restoring and Froude-Krylov Forces	Workstation

understand the actual physical mechanisms underlying the ship responses to these events, such as capsizing, and to identify dominant factors of vessel stability, which can be used in the statistical screening process using the lower level codes.

Recognizing the need for a fully integrated multi-level code system, we have developed the Interactive Design, Evaluation and Analysis System (IDEAS) consisting of a total of five computational methods of different levels of sophistication.

- LAMP-4: The large-amplitude 3-D nonlinear method
- LAMP-3: The large-amplitude 2-1/2-D nonlinear method
- LAMP-2: The approximate large-amplitude 3-D nonlinear method
- LAMP-1: The linearized 3-D time-domain method
- SMP: The U.S. Navy linear strip-theory Ship Motion Program

The total capability is labeled the IDEAS Ship Motion and Wave Load System. The most advanced code is the Large Amplitude Motion Program, LAMP-4 discussed in the previous section. Three simplified versions of the LAMP-4 code have also been developed. The lowest level code uses the linear strip theory.

The LAMP-4 method is the complete large-amplitude method where the 3-D potential is computed with the linearized free-surface condition satisfied on the surface of the incident wave. Both the hydrodynamic and hydrostatic pressure are computed over the instantaneous hull surface below the incident wave surface. Large computer resources are required for this method.

The LAMP-3 method is presently under development as part of the Cooperative Norwegian/USA High-Speed Craft Project. The method, which includes impact forces, is intended originally for planing craft, but is being extended to include displacement hull forms. The hydrodynamic forces are computed by a 2-1/2-D slender-body approximation which includes all of the most important nonlinear hydrodynamic effects for moderate and high-speed displacement hulls.

In the LAMP-2 method, the linear 3-D approach is used to compute the hydrodynamic part of the pressure forces. An option is available to approximate large-amplitude effects by stretching the hydrodynamic pressure. However, the hydrostatic restoring and Froude-Krylov forces are calculated with the same accuracy as in LAMP-4. The reason for developing this simplified method is that it drastically reduces the requirements for computer resources.

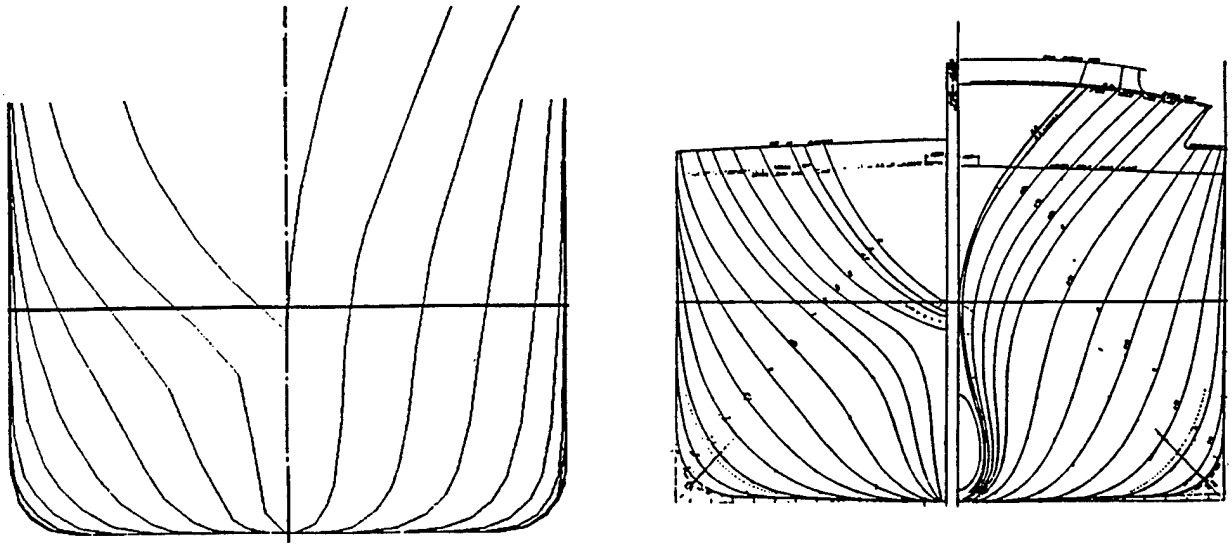
The LAMP-1 method is the linearized version of the LAMP-4 method. This 3-D time-domain method includes a routine for automatic generation of the frequency domain results.

The SMP is the linear strip-theory code presently used by the U.S. Navy. It is based on the theory developed by Salvesen, Tuck and Faltinsen (1970).

Table 2 shows how the hydrostatic restoring and Froude-Krylov forces and the hydrodynamic (added mass, damping and diffraction) forces are calculated for the four different LAMP methods. The hardware requirements for the four

Table 3: General Dimensions

	LBP	B/L	D/L	C_B	F_n	R_g/L
Series 60	N/A	0.143	0.057	0.700	0.200	0.25
S175	175.0	0.146	0.054	0.572	0.275	0.24



Series 60, C_B = 0.70 S175 Containership

Figure 3: Body Plans for Series 60, $C_B = 0.70$ Hull Form and S175 Containership.

methods are also shown in the Table. Note that all of the nonlinear methods, LAMP-2, LAMP-3 and LAMP-4 are based on the approach that both the motions and the waves may have large amplitudes. For all of these three nonlinear methods, the restoring and Froude-Krylov forces are calculated exactly over the instantaneous wetted surface below the incoming wave surface.

VALIDATION

An extensive validation study of the LAMP code system is presently ongoing. We will here present some sample results for two ship cases in order to demonstrate that the results obtained by the new nonlinear motion and load capability are generally in good agreement with experimental and other theoretical data. The result should also serve to demonstrate the importance of the nonlinear effects. In particular, it is hoped that they will assist in forming a better understanding of the relationship between ship hull geometry and the nonlinearity of the responses.

Result are presented in this section for two hull forms, the Series 60, $C_B = 0.7$ parent hull and the S175 Containership. The general dimensions and body plans for these two ships are given in Table 3 and Figure 3, respectively. The Series 60 hull has mostly wall-sided bow sections with small bow flare and a typical old fashioned cruiser stern. This ship has very small nonlinear geometry features. The S175 Containership has a moderate U/V-shaped bow with considerable flare and a small bulb. The stern is a typical cruiser stern quite similar to the Series 60.

The Series 60, $C_B = 0.7$ Parent Hull

All of the results presented for the Series 60 hull are for regular head waves at $F_n = 0.20$. Figure 4 shows the comparisons between linear theories (SMP and LAMP-1) and experimental results (Vossers, *et al*, 1961) for pitch and heave displacements and phases. For this particular case a reasonably good agreement between strip theory (SMP) and experimental results was established more than twenty years ago (Frank and Salvesen, 1970). The SMP results are included here so that comparisons with a well established existing design tool can be made. It is seen in

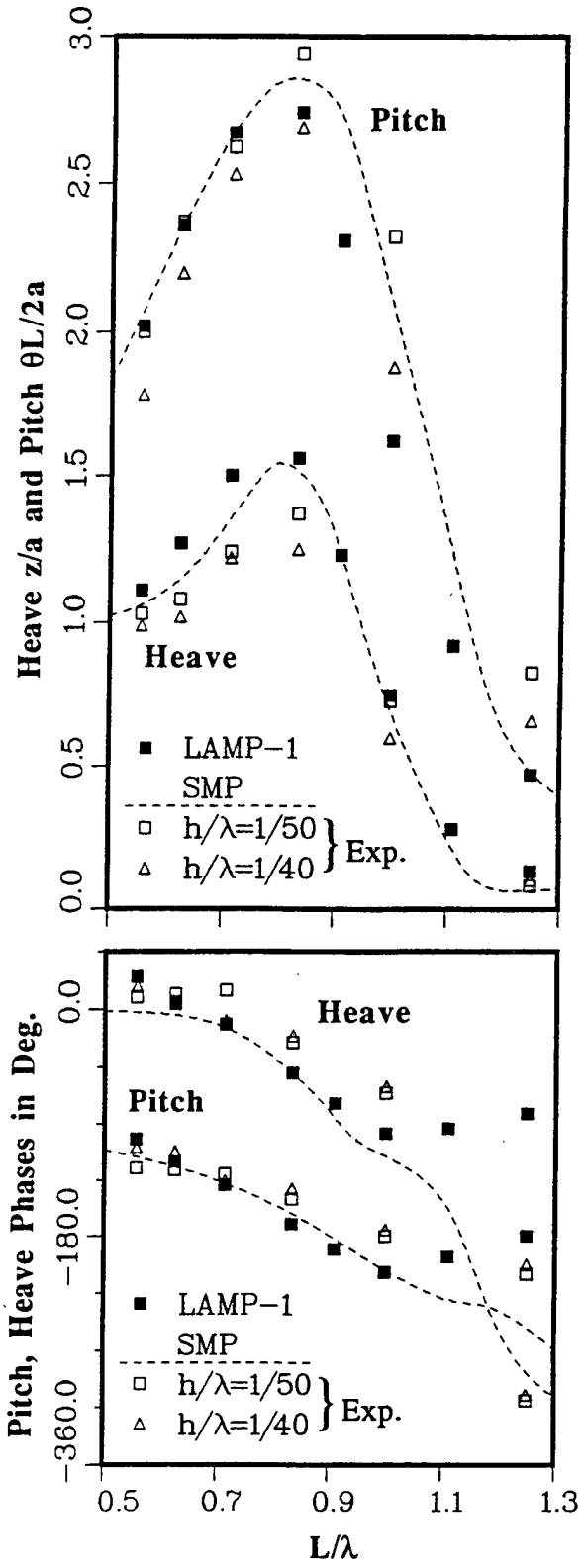


Figure 4: Heave and Pitch Displacements and Phases in Regular Waves for Series 60, $C_B = 0.7$ Hull at $F_n = 0.20$. Comparison of Linear Theories and Experiments.

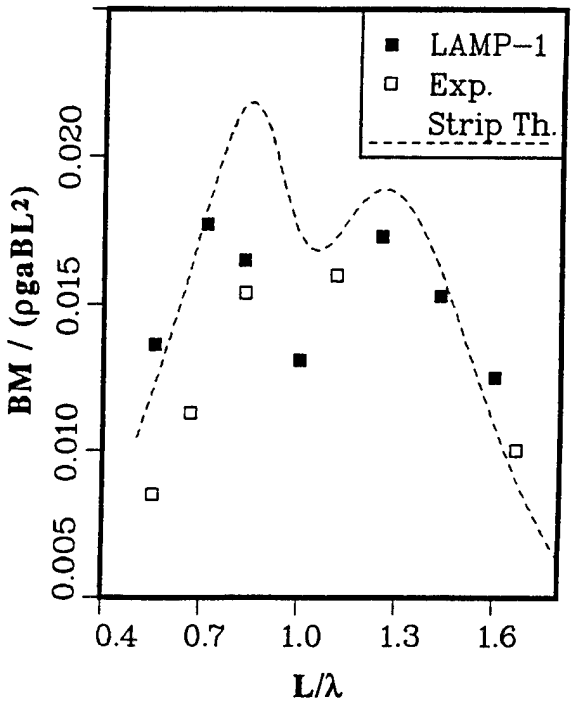


Figure 5: Vertical Midship Bending Moment in Regular Waves for Series 60, $C_B = 0.7$ Hull at $F_n = 0.20$. Comparison of Linear Theories and Experiments.

Figure 4 that the three-dimensional linear theory (LAMP-1) also agrees well with the experiments in general. Other comparisons between LAMP-1 and strip theory have also shown close agreement for slender hull forms at moderate speeds (Lin & Meinhold, 1991).

Figure 5 shows a similar comparison between linear theories and experimental results for the vertical midship bending moments. There are some noticeable differences between the strip-theory results and the LAMP-1 results. However, both predict two peaks which in this case do not seems to be present in the experimental results. Experimental results for other ship cases have demonstrated the existence of such double peaks (Wahab, 1967). The first peak occurs near the frequency where the heave and pitch motions are close to maximum. At this frequency, the bending moments are dominated by inertia loads. The second peak occurs when the motions are very small and therefore seems to be dominated by the hydrodynamic wave excitations.

A sample comparison between bending

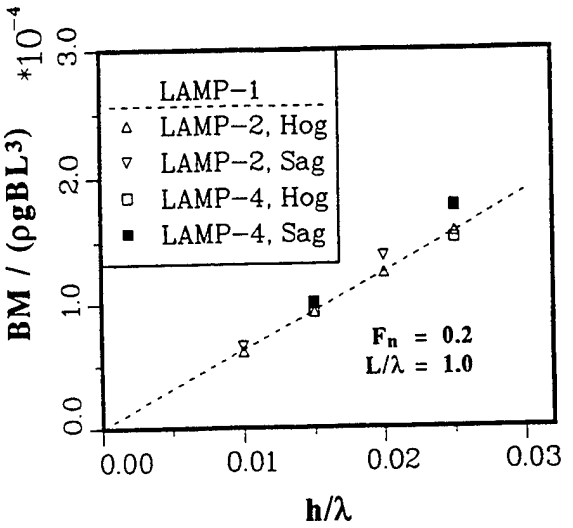


Figure 6: Vertical Midship Bending Moment in Regular Waves with $L/\lambda = 1.00$ as s Function of Wave Height for Series 60, $C_B = 0.7$ Hull at $F_n = 0.20$. Comparison of Linear Theories (LAMP-1) and Nonlinear Theories (LAMP-2 and LAMP-4).

moment results from linear and nonlinear theories are shown in Figure 6 for $\lambda/L = 1.0$. The results show small nonlinear effects as would have been expected for a hull form with relatively small nonlinear geometry features. For the steepest wave case, $h/\lambda = 0.025$, the nonlinear calculations (both LAMP-2 and LAMP-4) show about 14% increase in the sagging bending moment relative to the LAMP-1 calculations. It is seen in the figure that the hogging bending moments predicted by linear and nonlinear theories are in good agreement in this case. It is important to note here that for this ship LAMP-2 and LAMP-4 results are very close.

The S175 Containership

The S175 is one of the few hull forms for which there exists substantial experimental information about the nonlinear effects. In particular, the experimental data include heave and pitch data in regular head waves with increasing wave steepness (O'Dea, *et al*, 1992). Figure 7 shows comparison between nonlinear calculations (LAMP-2 and LAMP-4) and the experimental heave and pitch data for three wavelengths, $\lambda/L = 1.0, 1.2$, and 1.4. It is encouraging to note that the LAMP-4 results shows very much the same nonlinear trend as found in the experiments. However, the pitch predictions seem to be lower than the experimental values. Similar underpredictions were observed near this wave

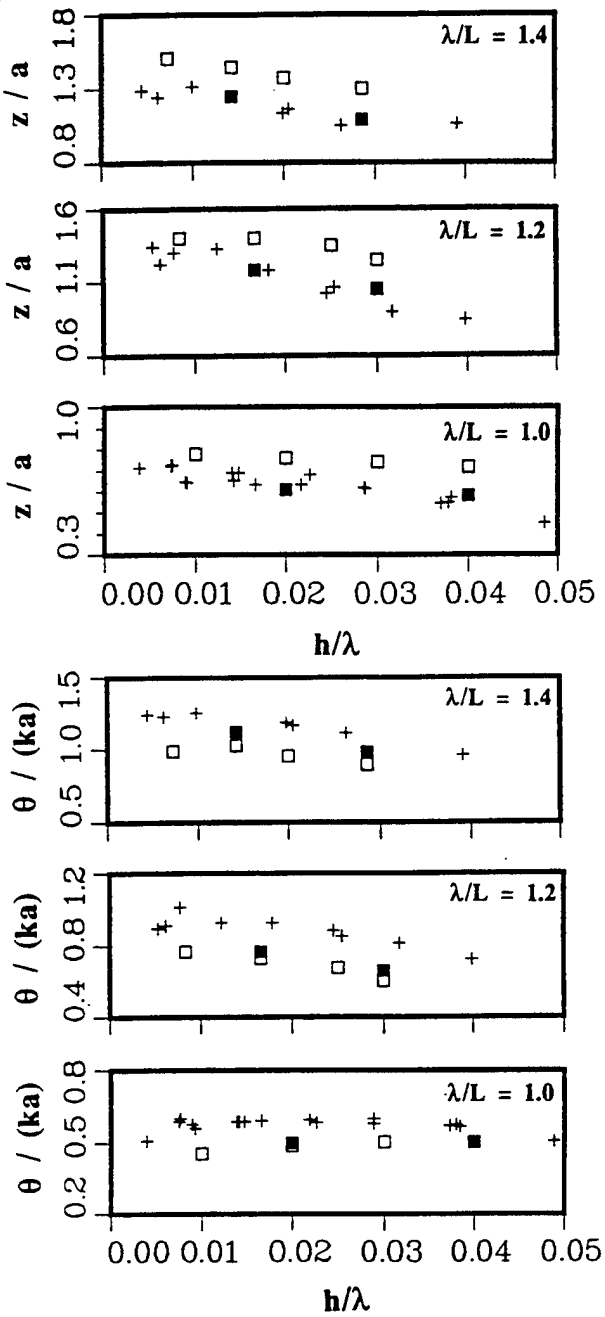


Figure 7: Heave (upper half) and Pitch (lower half) Displacements as a Function of Wave Height for S175 Containership at $F_n = 0.275$ in Three Regular Wave Conditions. Comparison of Nonlinear Theories(LAMP-2, □, and LAMP-4, ■) and Experiments (+).

length range for the Series 60, $C_B = 0.7$ hull form. Further investigation is required on this aspect.

Results predicted by LAMP-2 and LAMP-4 seem to agree well for pitch motion, whereas the

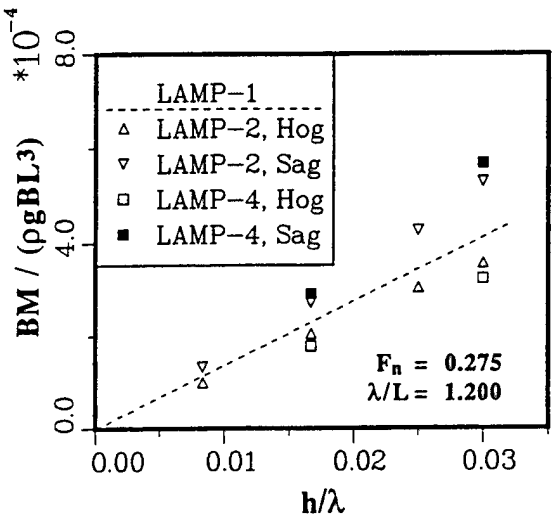


Figure 8: Vertical Midship Bending Moment in Regular Waves with $\lambda/L = 1.20$ as s Function of Wave Height for S175 Containership at $F_n = 0.275$. Comparison of Linear Theories (LAMP-1) and Nonlinear Theories (LAMP-2 and LAMP-4).

heave motions are overpredicted by LAMP-2. A careful assessment has shown that the heave results are sensitive to the implementation of the so called "m-term" effects associated with forward speed (Ogilvie & Tuck, 1969). In LAMP-4, the body boundary condition is satisfied on the instantaneous location of the wetted hull boundary under the incident wave surface. Therefore, the "m-term" effects are automatically and exactly included. In LAMP-2, only simple forward speed terms are included. We intend to introduce an improved m-term approximation method in the LAMP-1 and LAMP-2 code.

Linear and nonlinear vertical midship bending moment results as a function of wave height for $\lambda/L = 1.2$ are presented in Figure 8. The calculations show relatively large nonlinear effects both for the sagging and hogging moments. For the steepest wave case with $h/\lambda = 0.03$, the sagging and hogging moment predicted by LAMP-4 are 35% larger and 21% smaller, respectively, than that predicted by LAMP-1. This clearly shows that the nonlinear wave-load effects are substantial and that they must be included in design assessment. Furthermore, the results in Figure 8 show that the nonlinear effect predicted by LAMP-2 is somewhat smaller than those predicted by LAMP-4, but the trend is very much the same.

Table 4: CPU Time Requirement for Different Motion and Load Methods on a Workstation and a Supercomputer (LAMP-3 is under development)

	IBM RS6000/550 Workstation	CRAY-YMP Supercomputer
SMP	2.5 seconds	0.5 seconds
LAMP-1	5.0 minutes	1.0 minutes
LAMP-2	6.0 minute	1.2 minute
LAMP-3	–	–
LAMP-4	4.0 hours	0.8 hours

LAMP EFFICIENCY

Effective use of computer tools such as LAMP code depends a great deal on computation speed. Table 4 shows the CPU time required for a typical one minute real-time ship motion simulation on a high-end workstation and on a supercomputer. With ever increasing simulation capabilities and demands on hydrodynamic codes such as LAMP, the overall efficiency and robustness become crucial factors in the overall success and impact of these codes. Recent research has made appreciable strides in these respects. We highlight two of the more significant developments which can both be incorporated into the LAMP system.

High-Order Boundary-Element Method

Programs such as LAMP use the traditional constant-panel method (CPM) approximation wherein the boundary geometry is discretized into piecewise linear elements within which singularity strengths are assumed to be constant. CPM is in some sense the simplest boundary-element discretization possible and leads to simplifications in terms of geometry, analyses and code structure. It is now known, however, that CPM is not computationally optimal and often require far too many panels for a given accuracy than is suggested from geometric considerations. Figure 9 shows typical performance of CPM as compared to the quadratic (both geometry and singularity distribution) boundary-element method (QBM) of Xü & Yue (1992). The problem considered is the time-domain calculation of the (linear) impulse-response function of a heaving sphere using transient free-surface Green functions. The number of unknowns, N, required for a given ac-

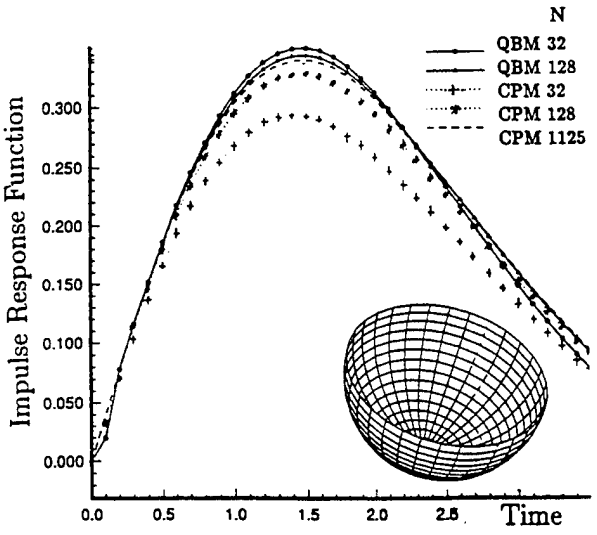


Figure 9: QBM vs. CPM for Computing the Impulse Response Function of a Heaving Hemisphere

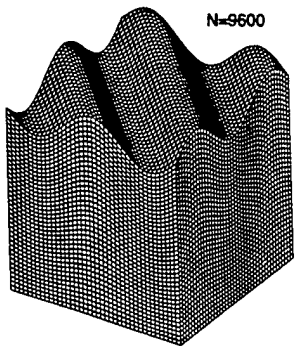
curacy is $O(10 \sim 20)$ times greater for the CPM. Even factoring in the increased operation count per N for QBM, the overall savings in computational time for comparably optimized code can be a factor of $O(10^2)$ or more, depending on the required accuracy.

Another important and possibly paramount consideration is the loss of robustness of CPM at edges and corners of the boundary, for example near the body waterline. In this case, it is known that CPM may in fact fail to converge in terms of the maximum local error (Xü & Yue 1992). Such non-uniform convergence is eliminated when QBM is used. The incorporation of high-order capabilities such as QBM into LAMP is now under way and is expected to significantly enhance its utility in routine design and analysis simulations.

Fast ($O(N)$) Multipole-Expansion Methods

Even with optimal boundary elements and efficient preconditioning and iterative solution of the resulting equations, the ultimate feasibility of boundary element methods for increasingly larger and more complex problems is limited by the $O(N^2)$ operation count where N is the total number of (spatial) unknowns. Recent development of fast multiple-expansion techniques for boundary-integral methods requiring only $O(N)$ computational effort (see, e.g., Korsmeyer, Yue, Nabors & White 1993) has removed such limitations for all practical purpose. Tables 5 and 6 illustrate the typical efficiency of an $O(N)$ scheme (using CPM) as compared to a direct ($O(N^2)$) method for two 3-D problems – wave sloshing in a tank and the Cauchy-Poisson development of an initial disturbance, respectively. The cross-over value for the number of unknowns is $N_C \sim O(10^2)$. The computational savings (by a factor of N/N_C) for large N (say up to $N \sim O(10^4 - 10^5)$) is profound. Another feature of these $O(N)$ schemes is their special suitability for massively-parallel computers. Our recent experience with such a code on the CM-5 suggests that an $O(1)$ time count for moderately large N may be feasible.

Table 5: CPU Time Comparison between an $O(N)$ Scheme and an $O(N^2)$ Method for Tank Sloshing Problem. CPU Times are in Seconds and CPU* is Normalized CPU.

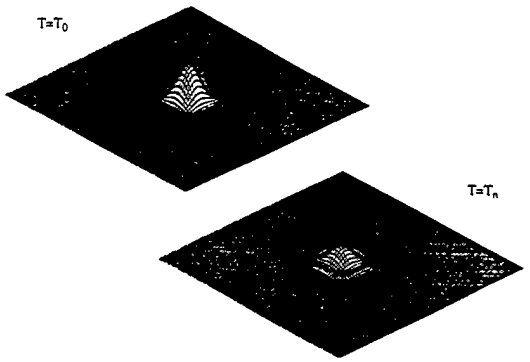


	O(N) Scheme		Direct Scheme	
N	CPU	$(CPU^*)/N$	CPU	$(CPU^*)/N^2$
600	7.23	1.0	10.8	1.0
1350	16.3	1.0	62.3	1.1
2400	31.7	1.1	321.4	1.8
3750	55.4	1.2	–	–
5400	71.9	1.1	–	–
7350	103.7	1.2	–	–
9600	143.8	1.2	–	–

SYSTEM DEVELOPMENT

As discussed in the Introduction, the ship design community is now at the threshold of acquiring a new generation of hydrodynamic design assessment tools of unparalleled accuracy and utility. The IDEAS for ship motions and wave loads is just one example of such emerging capabilities. The motivation for the IDEAS

Table 6: CPU Time Comparison between an $O(N)$ Scheme and an $O(N^2)$ Method for the Cauchy Poisson Problem. CPU Times are in Seconds and CPU* is Normalized CPU.



	O(N) Scheme		Direct Scheme	
N	CPU	$(CPU^*)/N$	CPU	$(CPU^*)/N^2$
400	3.2	1.0	7.3	1.0
3600	25.6	0.9	632.1	1.0
10000	79.7	1.0	–	–
14400	120.9	1.0	–	–

concept came from a need for rapid assessment of new designs and design changes aided by analysis of hydrodynamic performance characteristics. Although the computational capability for flow analysis had been markedly improving for decades in both the hydrodynamic and aerodynamic communities, no means existed for a rapid assessment of the effects of configuration changes on mission effectiveness in either area.

The term hydro-numeric design was coined at SAIC to characterize a new discipline which now integrates geometry manipulation, numerical hydrodynamic computation and design performance assessment (Salvesen, *et al*, 1985). The iterative nature of the design process would permit the use of complex, general purpose codes in a systematic manner. The proximate goal in motivating the IDEAS system happened to come from the need to support yacht design for the Americas Cup. However, once the methodology was formalized, it was obvious that the existence of such a system could have a large impact throughout the maritime industry. The design of the 12-meter yacht Stars & Stripes for the 1987 Americas Cup races was a textbook example of the successful use of direct analysis methods coupled to explicit performance criteria, in this case, the probability of winning the Cup (Oliver, *et al*, 1987). The primary lesson learned in that contest was that rapid analysis using state-of-the-art CFD codes was absolutely critical to support design decisions both in the building phase and for last minute design modifications.

The total IDEAS Ship Motion and Wave Load System has been constructed by integrating the hydrodynamic codes with geometry modeling, panelization, visualization and design criteria evaluation codes running on graphics engineering workstations. The primary objective with IDEAS has been to develop a fully integrated *hydro-numeric design* system with sufficient performance, accuracy, and ease of use to impact conceptual and preliminary ship design problems.

The IDEAS Motion and Load System as now configured is shown in Figure 10. This multilevel system allows us to build computational capability progressively. As new computational codes are developed, they can be integrated into the system and validated against existing ones. It must be kept in mind that codes used at each level are limited by different approximations. The confidence level at each level needs to be established through model testing and extensive computations.

The Geometry and Panelization capability within the motion and load system consists of several codes (see Figure 10). Presently the two primary codes are the FASTSHIP geometry generation code by Design Systems & Services, Inc. and the I3G interactive panelization code developed the U.S. Air Force. The two example codes included as part of the Design Evaluation and Assessment capability are the SEP Seakeeping Evaluation Program developed by the U.S. Navy and the ANIMATE code for visualization of time-domain ship motions, including the free-surface elevations.

As seen in Figure 10, the hydrodynamic codes are grouped within three levels of sophistication:

Level I	*Linear Methods*
	SMP (strip-theory)
	LAMP-1 (3-D theory)
Level II	*Approximate Large-Ampl. Methods*
	LAMP-2 (3-D approximate)
	LAMP-3 (2-1/2-D theory)
Level III	*Complete 3-D Large-Ampl. Method*
	LAMP-4

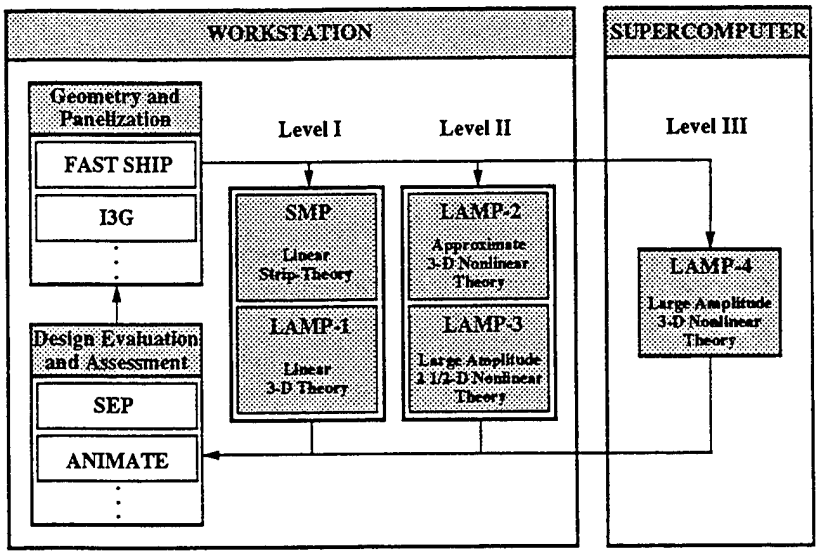


Figure 10: The Present IDEAS Ship Motion and Wave Load System

Consider the application of the Motion and Load System for tanker hull design. In this case, the SMP strip-theory code may be used as a Level I code and the approximate 3-D LAMP-2 code as a Level II code. On the other hand, for higher-speed naval ships where the inclusion of accurate prediction of trim and sinkage is important the 3-D LAMP-1 code which includes the wave-resistance potential would be used as a Level I code. The 2-1/2 D LAMP-3 code, which includes most of the important higher forward speed effects, would be recommended in this case as a Level II code.

Effective use of a computation system such as IDEAS for design depends a great deal on computation speed of different codes and how to use these codes. Table 4 shown previously clearly illustrates how computer resource limitations may affect the use of various methods in the IDEAS system. These numbers also show the need and advantages of using lower level codes as filters to determine the events for which the higher level code can most efficiently be used.

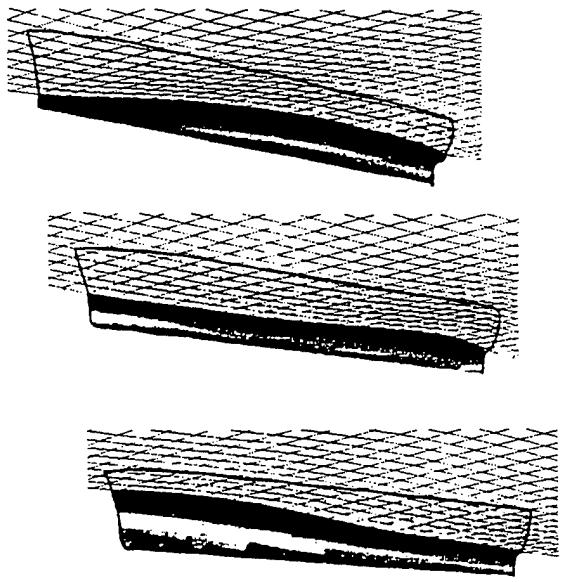


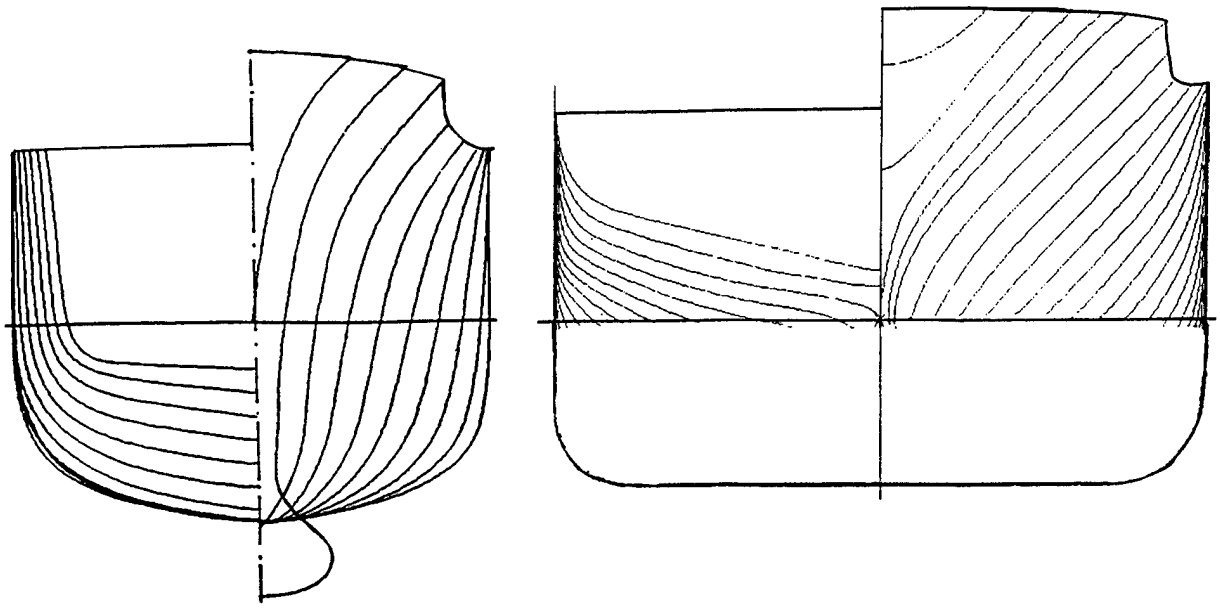
Figure 11: Instantaneous Pressure Distributions for Series 60, $C_B = 0.7$ Hull Form Advancing in Regular Waves

Coupling to Structural Models

Both the approximate large-amplitude code LAMP-2 and the complete large-amplitude code LAMP-4 calculate the hydrodynamic pressure distributions over the instantaneous wetted hull surface below the incident wave surface. Sample LAMP-2 pressure calculations for the Series 60, $C_B = 0.70$ hull advancing in regular head waves are shown in Figure 11. Interfaces between the hydrodynamic pressure data and three different finite-element codes have been made: the MAESTRO code (in collaboration with its developer Prof. O. Hughes of Va. Tech. (Frankline & Hughes, 1992)), the NASTRAN code (with the American Bureau of Shipping), and the STAGS

Table 7: General Dimensions

	LBP	B/L	D/L	C_B	F_n	R_c/L
CG47	162.3	0.103	0.042	0.510	0.260	0.25
APL	260.8	0.151	0.042	0.557	0.244	0.25



CG47 AEGIS Cruiser

APL Containership

Figure 12: Body Plans for CG47 AEGIS Cruiser and APL Containership

code (with the Lockheed Missiles and Space Company, Inc).

The integrated LAMP/STAGS system has been made an integral part of the ARPA Simulation Based Design demonstration system now under development by Lockheed, Newport News Shipbuilding and SAIC. This hydrodynamic and structural code system will serve as a demonstration of the use of multi-level, multi-disciplinary physics-based code systems within the Simulation Based Design approach.

Design Applications

To illustrate the application of the IDEAS Motion and Load System, two ships were selected. These two ships, CG47 AEGIS cruiser and a APL Containership, are typical modern hull forms in the existing naval and commericial fleets. The general dimensions and body plans for the two ships are given in Table 7 and Figure 12, respectively. It is seen in the figure that the CG47 cruiser has a very fine U-shaped bow with a sonar dome and considerable flare. It has a wide submerged transom stern. The APL Containership is an example of a modern containership. The hull shape below the 10 meter waterline is proprietary and is not shown here. Note that the design waterline is at 11 meters. The bow has large V-shaped flare. The stern has a wide transom which is above the calm water level. This ship has large nonlinear geometry features both at the bow and at the stern which are *not* captured in any linear ship motion theory. Also note that this modern containership has quite different bow and stern shapes than the much older S175 Containership shown in Figure 3.

The CG47 AEGIS Cruiser

We shall briefly discuss an earlier application of the motion and load system to the prediction of the responses of the U.S. Navy AEGIS Cruiser advancing at 10 knots in head seas (Lin and Meinhold, 1991). A thirty-minute linear wave record was generated using a sea spectrum representing Sea State 5.

To run the nonlinear LAMP-4 code for the

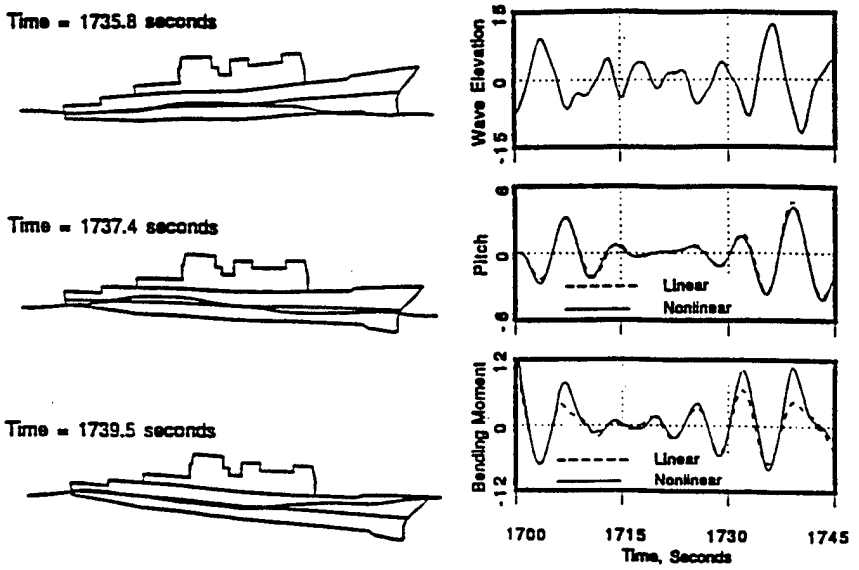


Figure 13: Profile of CG47 at 10 knots in Large-Amplitude Unidirectional Irregular Head Seas and Time Records of Wave Elevations (Ft), and Linear (LAMP-1) and nonlinear (LAMP-4) Predictions of Pitch (Deg.) and Vertical Midship Bending Moments (Ton*Ft*10^4)

entire thirty minute wave record was not practical. (Note that the 1991 version of the LAMP-4 code is somewhat different from the LAMP-4 code presented here.) The linear LAMP-1 code was run for the entire wave record to identify three short-term wave events where the midship bending moments were the largest. The nonlinear LAMP-4 code was then used to predict the nonlinear response for these three wave events.

Figure 13 shows the ship advancing in this wave field at three closely spaced time steps as predicted by LAMP-4. Also presented in the figure are the time records of the wave elevations for one of the three wave events as well as the linear and nonlinear pitch and bending moment responses as predicted by LAMP-1 and LAMP-4. The maximum wave height in this wave event is about 25 ft. As shown in the figure, the maximum bending moment predicted by the LAMP-4 code is substantially larger than that predicted by the LAMP-1 code. This difference is believe to be mainly due to the very large bow flare of this hull form which is reflected in the LAMP-4 calculations but cannot be included in the LAMP-1 calculations.

Furthermore, it is seen in Figure 13 that there is practically no difference in the pitch motions predicted by the linear and nonlinear codes. This is important, since it is usually believed that the good agreement between linear-theory heave and pitch motions and experiments is an indication that the bending moments are also quite linear. The example above indicates that the bending moment can be very nonlinear even though the motion seems to be linear.

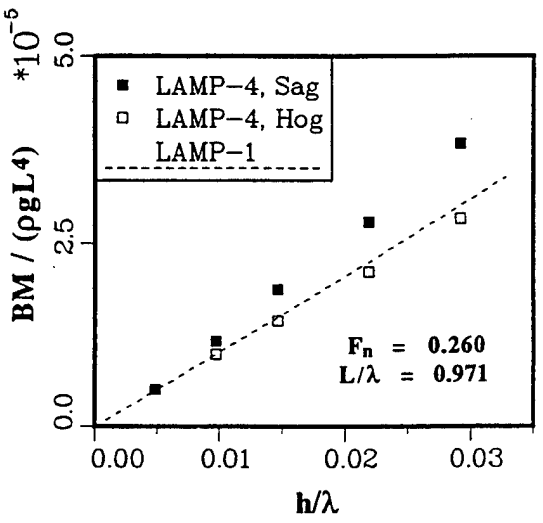


Figure 14: Vertical Midship Bending Moment in Regular Waves with $L/\lambda = 0.971$ as s Function of Wave Height for CG47 at $F_n = 0.260$. Comparison of Linear (LAMP-1) and Nonlinear (LAMP-4) Predictions.

The bending moment for CG47 in regular waves with $L/\lambda = 0.971$ as a function of wave steepness is presented in Figure 14. Both lin-

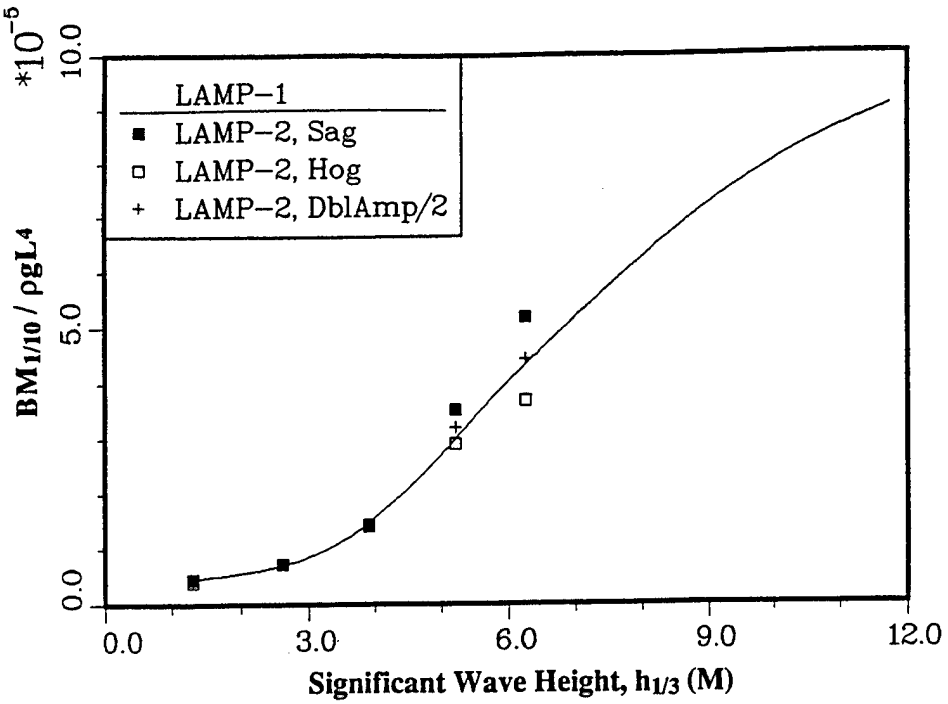


Figure 15: Average One-Tenth Highest Vertical Midship Bending Moments as a Function of Significant Wave Height for APL Containership at $F_n = 0.244$ in Unidirectional Irregular Head Seas. Comparison of Linear Theories (LAMP-1) and Nonlinear Theories (LAMP-2).

ear (LAMP-1) and nonlinear (LAMP-4) results are presented. It is seen that for the steepest wave condition ($h/\lambda = 0.029$), the sagging moment predicted by LAMP-4 is about 28% higher than that predicted by LAMP-1, whereas the nonlinear hogging moment is only about 6% less than the linear prediction. These computations seem to demonstrate that for such naval hull forms, the accuracy of extreme bending moment predictions based on linear superposition methods may be substantially less than required for design applications.

The APL Containership

We are presently in the initial phase of an investigation of the nonlinear aspects of the motions and loads for the APL Containership shown in Figure 12. We are primarily interested in an estimate of the magnitude of nonlinear contributions to the bending moment for operations in realistic irregular seas. The averaged one-tenth highest vertical midship bending moment ($BM_{1/10}$) as a function of significant wave height ($h_{1/3}$) are presented in Figure 15. The results are for unidirectional head seas generated from ITTC one-parameter spectrum. For this initial investigation, LAMP-2 has been used for the nonlinear predictions. However, it is recognized that the LAMP-4 code is required for more accurate predictions.

The results presented in Figure 15 show that for significant wave height, $h_{1/3} = 6.26$ meter (corresponding to the high range of Sea State 6), the sagging moment predicted by LAMP-2 is about 20% higher than that predicted by linear theory. The nonlinear hogging moment is about 15% lower than that predicted by linear theory. Also shown as a reference are the "double-amplitude" bending moment divided by 2 as predicted by LAMP-2. It is most convenient in model test to measure the "double amplitude" bending moment values; however, the results presented here clearly demonstrate that the doubl-amplitude approach has some severe limitations.

The actual time record of the wave elevations and the linear and nonlinear heave, pitch, and vertical midship bending moment predictions are shown in Figure 16, for the $h_{1/3} = 6.26$ meter case. Note that the length of the time record presented in the figure corresponds to 7.5 minutes in full scale. A substantially larger time sequence may be required for a more accurate estimation of the $BM_{1/10}$ values. This again demonstrates the importance of the multi-level approach. LAMP-2 may be used for the long time sequences and then LAMP-4 may only be required for short wave records. This procedure may be used to deter-

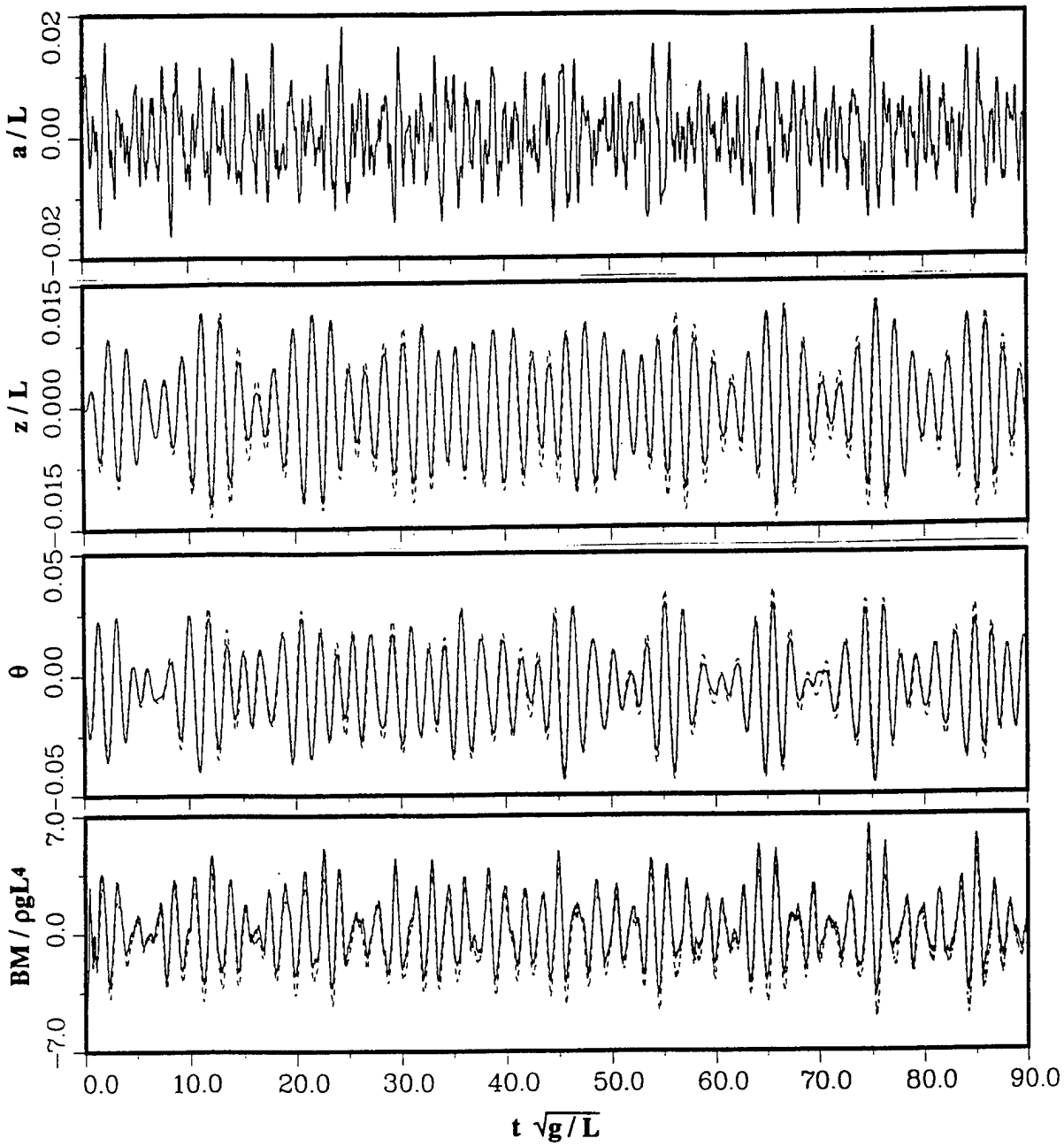


Figure 16: Time Record of wave Elevation and Linear (LAMP-1, - - - -) and Nonlinear (——) Predictions of heave, Pitch, and Bending Moment for APL Containership at $F_n = 0.244$ in Unidirectional Irregular Head Seas with $h_{1/3} = 6.261$ meter.

mine a correction factor which can be used with the statistical values obtained by the LAMP-2 code.

We have barely begun the investigation of the nonlinear aspects of this APL Containership responses. In addition to the wave induced loads, we intend to investigate the occurence of slamming and the nonlinear parametric roll excitation problem. In particular, a better understanding of the parametric roll problem is of critical importance to the shipping companies.

SYSTEM EXTENSIONS

The results presented here demonstrate that the IDEAS Ship Motion and Wave Load System has the potential to become a new revolu-

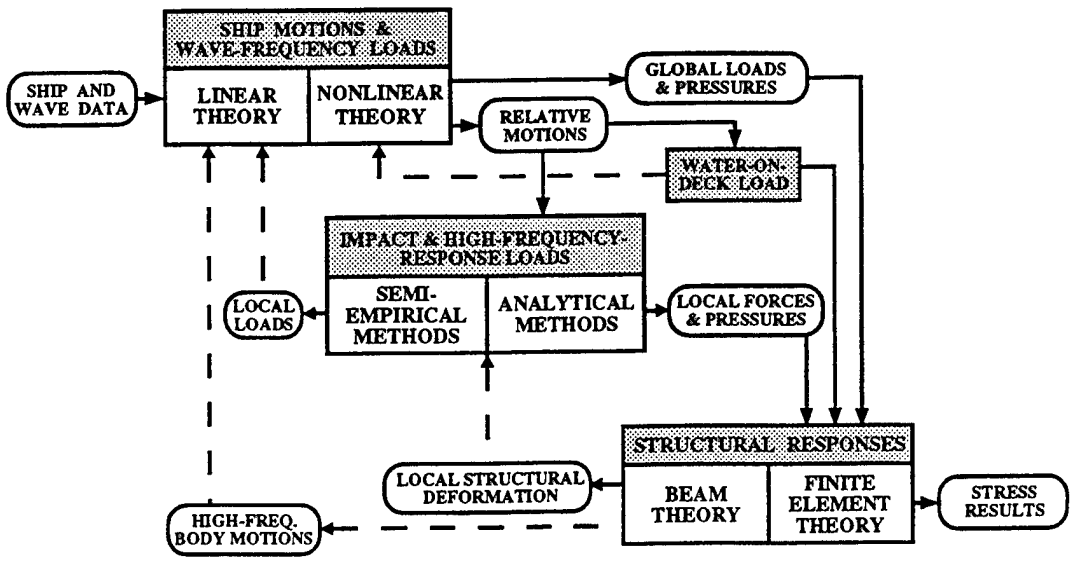


Figure 17: The Complete System for Ship Motion, Wave Load and Structural Response Predictions

tionary tool which will have a major impact on ship design; however, substantial additional work in several important areas is required before the system can meet all the expectations. We shall discuss here some of the most critical areas.

Wave Impact Loads

The inclusion of wave impact loads or slamming is by far the most important extension. Most traditional methods for analyzing slamming rely on semi-empirical force estimates rather than on accurate prediction of the actual slamming pressure distribution. Furthermore, the traditional methods address only head-sea cases with symmetric slamming. However, the CG47 Cruiser problem and several commercial ship problems have clearly demonstrated that some of the most severe structural failures have been caused by asymmetric slamming loads in oblique seas. It is important, therefore, that any attempt to resolve the total slamming problem must include not only the accurate time-domain simulation of the highly nonlinear motions in oblique seas, but also the prediction of the asymmetric slamming pressures.

The objective will be to develop advanced robust slamming prediction methods and to integrate these methods with both the present hydrodynamics and structural codes to produce a complete capability which includes all of the important components. Figure 17 shows the major components of the total system: (i) ship motions and wave-frequency loads; (ii) impact and high-frequency response loads; and (iii) structural responses. Each of these components will consist of a multi-level code system. Water-on-deck loads are also to be included. The capability will be used as a testbed to determine areas where improved physics modeling is most critically required for improving overall accuracy.

It is expected that the development of a new multi-level computational impact load capability will follow the following steps.

First the experience gained in the cooperative U.S./Norwegian High-Speed Craft project will be incorporated into the LAMP code system. Under the cooperative project, some aspects of the fully-nonlinear slamming load prediction method developed by Zhao and Faltinsen (1992) has been incorporated by Lin (1992) into a new method for motion and load SIMulation of PLANing hulls (SIMPLAN).

A nonlinear 2-D slamming simulation capability which provides the pressure distribution will be further developed into a robust code applicable to general naval and commercial ship shapes including asymmetric cases. This slamming pressure code will then be incorporated into the LAMP system and will become the first complete capability for assessing slamming problems for ships advancing in realistic head and oblique sea conditions. Even though the 2-D approach has its limitations, it is believed that it may be quite accurate for a large class of naval and commercial ship problems and at least far superior to

the existing semi-empirical force methods.

The next step will be to integrate into the LAMP system the more advanced 2-D and 3-D slamming pressure methods presently under development. This integration may require further developments to produce robust slamming codes applicable to general ship geometries. Some of the research issues that need to be addressed include the treatment of trapped air, hydroelasticity effects and water compressibility in certain cases. Again the total capability will be used as a testbed to determine the accuracy and applicability of the different slamming methods for ships operating in real sea environments.

We envisage the following multiple-level capability in the near future: (i) simple 2-D phenomenological/empirical models and database for global slamming loads; (ii) extended databases for local pressure distribution for geometrical and operational parameter regimes; (iii) a fully-nonlinear 2-D slamming simulation capability coupled directly into the 2-1/2-D (LAMP-3) and 3-D (LAMP-4) body-nonlinear time-domain computations; (iv) a limited database of 3-D fully-nonlinear slamming simulation for global and local loads; (v) incorporation of fully-nonlinear 3-D capabilities in the LAMP-4 code. This proposed system is based on the following key considerations: (a) the need for a multiple-level capability involving a full range of accuracy/reliability and accompanying computational demands applicable from preliminary to final design and prototyping; (b) the usefulness of simple models for a wide range of applications which however are limited in validity in specific situations; (c) slams are often temporally and spatially very much confined in terms of the entire simulation.

Other Important Improvements

There are other extensions to the LAMP system which are all important; however, here they will only be addressed briefly.

Improved Oblique Seas Calculations

Accurate oblique- and beam-sea calculations are essential for the prediction of, for example, the torsional moments, slamming, violent quartering sea motions and capsizing. It is believed that the first step is the development of an improved time-domain viscous roll damping approach. The present method relies on mostly 2-D frequency domain empirical data. Our intention is to develop an entirely new method based on unsteady 3-D RANS calculations.

Wave Environment Modeling

The application of the motion and load prediction system to design assessment will require a well defined approach for specifying the wave environment. Different wave-modeling approaches may be used for the estimation of the different responses. For example, in the estimation of comfort level, weapon operability and fatigue loads, the wave environment can in most cases be specified by a sea energy spectrum from which long term time-domain wave events can be generated by assuming linear super-position of the individual wave components. However, predictions of the extreme motion, as for example, capsizing and the most extreme structural loads will require a much better modeling and definition of extreme wave events. Also, we will need a method for estimating the probability of occurrence of the particular wave/vessel encounters which results in the most critical responses.

Accuracy and Uncertainty

The estimation of the accuracy and uncertainty is probably one of the most critical elements in the application of any prediction method in engineering. In particular, in the development of new design approaches which are to be based on advanced physics codes (e.g. Simulation Based Design), a knowledge of the accuracy and uncertainty is absolutely essential. All aspects of accuracy and uncertainty must be accounted for in estimating the total risk associated with building and operating a new construction.

This is a research topic which goes far beyond the more conventional approach to code validation. It will require the development of a new methodology for tracking all of the uncertainties throughout all of the stages in the design. Most importantly, the designer needs to know the sensitivity of the individual errors on the final risk factor for the overall design.

Fully Nonlinear 3-D Capabilities

Fully-nonlinear 3-D wave-body simulations are, in some sense, the ultimate capability in motion and load predictions in the context of free-surface potential flow. Such capabilities are now becoming available (see Xü & Yue, 1992, Yue 1994) at least for basic research applications. Figure 18 shows a typical simulation of

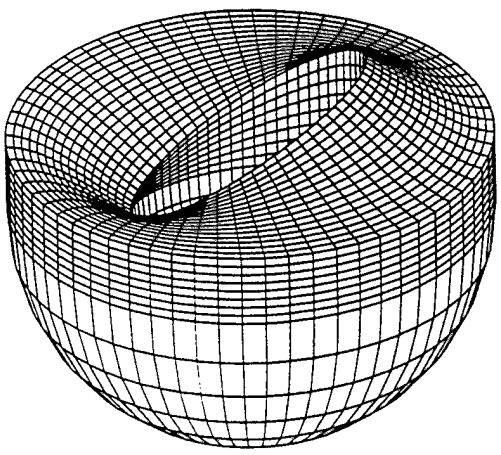


Figure 18: Numerical Simulation of Fully-Nonlinear Wave Diffraction by Floating Body

fully-nonlinear wave interactions with a ship-like floating body. The nonlinear Lagrangian inner computational domain (shown here with $O(2000)$ QBM nodes) is matched to a body-nonlinear outer wavefield via a QBM matching boundary (with $O(1000)$ nodes). Such a matching capability leads to a significant reduction in the total number of surface unknowns. More importantly, since "full" nonlinearity are typically well confined spatially and temporally, a combined approach involving LAMP-like body-nonlinear domains matched to limited dynamic/moving fully-nonlinear regions appears quite feasible. Thus, LAMP is a natural platform for these more advanced 3-D nonlinear tools as they become practically useful.

System Availability

The effort required to maintain the total Ship Motion and Wave Load and Structural Response System and to serve the entire design and regulatory community is quite similar to that required to operate an experimental seakeeping facility. It is our belief that in order to provide a successful national assessment capability, the final total system must be installed at a national center. A central location for this system is not only of primary interest to the U.S. Navy, but also to the U.S. Coast Guard and ABS as well as the research, the design, and the shipbuilding communities.

Presently, there does not exist a center which has a common focus for academia, industry, and government agencies within the U.S. maritime industry. The U.S. Navy Ship Technology Center located at the David Taylor Model Basin is a start in this direction. This Center was initiated by ARPA, but currently operating under the direction of NAVSEA. The complete Ship Motion and Wave Load System presented in this paper is to be installed at the Tech Center under an ONR contract. It is expected that the Tech Center will soon establish a procedure for serving the entire naval and maritime community.

CONCLUDING REMARKS

From the discussions presented in this paper it is becoming increasingly clear that the development of a motions, loads, and structural response prediction capability for ships is at a crossroads. On the one hand, hydrodynamics codes are now emerging which are capable of providing an unparalleled level of efficiency and accuracy in calculations for practical design assessment. On the other hand, the integration of these codes into robust, multidisciplinary tools to aid in design decisions is just beginning.

To be most effective, future development of the design tools must be tied to specific design application areas. As in IDEAS, current empirical and computational methods must be available as low level routines which will continue to quickly provide trusted results whenever the required level of accuracy is appropriate. Unless current design expertise is captured in a manner that permits flexible and user-friendly access, there will not exist a matrix of design knowledge within which we can embed the new computational capability. By far the best technique for ensuring that the relevant body of expertise has been included is to develop the system within a design environment, tied to a specific design development.

Once a fairly complete prototype design system exists, the system developers and designers will be in a position to evaluate collaboratively the true impact of additional improvements to the capability. It is anticipated that a design decision support system will permit error estimation and risk propagation as well as cost and performance. This information is exactly what is required to make rational decisions concerning expenditure of resources for additional fidelity, speed, or robustness in the computational codes.

The effort required to develop these systems should not be underestimated. The development of design tools has already begun, but it is still in its infancy. A much higher level of robust-

ness, efficiency, and integration will be necessary to begin to capture existing expertise in a system which can be extended to ongoing research results. The effort in code validation and accuracy estimation alone is daunting. In an era of reduced defense budgets, dissipating design expertise, and increasingly complex design requirements, there may not be a choice. Without such systems, the archiving of naval ship design knowledge and the competitive re-entry of the U.S. into commercial shipbuilding may be extremely difficult.

ACKNOWLEDGEMENT

This research has been sponsored by the Office of Naval Research, the U.S. Coast Guard, the Advanced Research Projects Agency, and the America Bureau od Shipping. We are grateful to Cray Research, Inc., for the use of their Cray supercomputer. We wish to thank APL for granting us permission to use their hull form and for allowing us to show the very interesting above waterline features of the bow and stern. We thank Dr. M. Fritts for his valuable advices and Mr. K. Weems for his technical and graphical help.

REFERENCES

Beck, R.F. and Magee, A. (1991), "Time-Domain Analysis for Predicting Ship Motions," *Developments in Marine Technology: 7: Dynamics of Marine Vehicles and Structures in Waves*, Elsevier Science Publishers B.V., Amsterdam.

Bingham, H.B., Korsmeyer, F.T., Newman, J.N., and Osbone, G.E. (1993), "The Simulation of Ship Motions," *Proc. of the 6th Intl. Conf. on Numerical Ship Hydro.*, Iowa City, Iowa.

Buckley, W.H. (1994), "Stability Criteria: Development of a First Principles Methodology," *Proceeding of The Fifth International Conference on Stability of Ships and Ocean Vehicles.*

Cao, Y., Lee, T. and Beck, R.F. (1992), "Computation of Nonlinear Waves Generated by Floating Bodies", *Proc. of the 7th Intl. Workshop on Water Waves and Floating Bodies*, Val de Reuil, France.

de Kat, J.O. and Paulling, J.R. (1989), "The Simulation of Ship Motions and Capsizing in Severe Seas", *Transactions of the Society of Naval Architects and Marine Engineers*, 97.

Frank, W. and Salvesen, N. (1970), *The Frank Close-Fit Ship Motion Computer Program*," DTNSRDC, Report 3289.

Franklin, P. and Hughes, O. (1992), "An Approach to Conducting Timely Structural Fatigue Analysis of Large Tankers," *Report VPI-AOE-192*, Aerospace and Ocean Engineering Dept. VPI

Fujino, M. and Yoon, B.S. (1986), "A Practical Method of Estimating Ship Motions and Wave Loads in Large Amplitude Waves," *International Shipbuilding Progress*, 33.

Grove, T.W., Rynn, P.G. and Ashe, G.M. (1992), *Bulk Carriers, A Cause for Concern*, Presented at the June 4, 1992 Meeting of the Great Lakes/Great Rivers Section of The Society of Naval Architects and Marine Engineers.

Hoerner, S.F. (1951), *Aerodynamic Drag*, published by the author.

Ikeda, Y., Himeno, Y., and Tanaka, N. (1978), "Components of Roll Damping of Ship at Forward Speed," *Journal of the Society of Naval Architects of Japan*, Vol. 143.

International Maritime Organization (IMO) (1993), Sub-Committee on *Stability and Load Lines and Fishing Vessel Safety - 37th Session (SLF 37) Working Group Interim Report*, Revision of Technical Regulations of the 1966 International Load Line Convention.

Kato, H. (1958), "On the Frictional Resistance to the Roll of Ships," *Journal of the Society of Naval Architects of Japan*, Vol. 102.

Kato, H. (1966), "Effect of Bilge Keels on the Rolling of Ships," *Memories of the Defense Academy*, Japan, Vol. 4.

Kennel, C., White, B. L. and Comstock, E. N. (1985), "Innovative Designs for North Atlantic Operations," *Transactions of the Society of Naval Architects and Marine Engineers*, 93.

Korsmeyer, F.T., Ma, C., Xü, H. and Yue, D.K.P. (1992), "The Fully Nonlinear Diffraction of Water Waves by a Surface Piercing Strut", *Proc. of the 19th Symp. on Naval Hydrodynamics*, Seoul, Korea.

Korsmeyer, F.T., Yue, D.K.P., Nabors, K. & White, J. (1993), "Multipole-accelerated preconditioned iterative methods for three-dimensional potential problems," *Proc. BEM XV.*

Korvin-Kroukovsky, B.V. (1955), "Investigation of Ship Motions in Regular Waves," *Trans. Soc. of Naval Architects and Marine Engineers*, 63.

Lin, W.M. and Yue, D.K.P. (1990), "Numerical Solutions for Large-Amplitude Ship Motions in the Time-Domain", *Proc. 18th Symp. Naval Hydro.*, The University of Michigan, Ann Arbor, MI, U.S.A.

Lin, W.M. and Meinhold, M. (1991), *Summary Technical Report of Hydrodynamics Loads Calculations for Advanced Marine Enterprises*, SAIC Report No. 91-1050 (revised).

Lin, W.M. and Yue, D.K.P. (1992), "Wave Forces on A Surface-Piercing Sphere Undergoing Large-Amplitude Motions", *Proc. of the Seventh International Workshop on Water Waves and Floating Bodies*, Val de Reuil, France.

Lin, W.M. (1992), *Simple and Advanced Theories for Planing Hulls*, Report presented at the Bi-Annual Review Meeting of the IDEAS System for High- Speed Craft, Washington D.C.

Lin, W.M., Meinhold, M. and Salvesen, N. (1992), *IDEAS System for Ship Motions and Wave Loads*,

SAIC Report No. 92-1187.
Lin, W.M. and Yue, D.K.P. (1993), "Time-Domain Analysis for Floating bodies in Mild-Slope Waves of Large Amplitude", *Proceedings of the Eighth International Workshop on Water Waves and Floating Bodies*, St. John's, Newfoundland, Canada.
Liu, D., Spencer, J., Itoh, T., Kawachi, S. and Shigematsu, K. (1992), Dy- namic Load Approach in Tanker Design, Transactions of the Society of Naval Architects and Marine Engineers, 100.
Maskew, B. (1991), "A Nonlinear Numerical Method for Transient Wave/ Hull Problems on Arbitrary Vessels', *Transactions of the Society of Naval Architects and Marine Engineers*, 99.
Meyers, W.G., Applebee, T.R. and Baitis, A.E. (1981),"Users Manual for the Standard Ship Motion Program, SMP," *DTNSRDC Report SPD-0936-01.*
Nakos, D.E. and Sclavounos, P.D. (1990), Ship Motions by a Three-Dimensional Rankine Panel Method, *Proceedings of the 18th Symposium on Naval Hydrodynamics*, Ann Arbor, Michigan.
Oliver, J.C., Letcher, J.S. Jr., and Salvesen, N. (1987), "Performance Predictions for Stars & Strips," *SNAME Transaction.*
O'Dea, J.F., Powers, E.J., and Zseleczky, J. (1992), "Experimental Determination of Nonlinearities in Vertical Plane Ship Motions," *Proc. of the 19th Symp. on Naval hydrodynamics*, Seoul, Korea.
Ogilvie, T.F., and Tuck, E.O. (1969), "A Rational Strip-Theory of Ship Motion: Part I," Dept. of Naval Architecture, U. of Michigan, Rept. No. 013.
Pawlowski, J.S. and Bass, D.W. (1991), "A Theoretical and Numerical Model of Ship Motions in Heavy Seas", *Transactions of the Society of Naval Architects and Marine Engineers*, 99.
Salvesen, N., Tuck, E.O. and Faltinsen, O. (1970), "Ship Motions and Sea Loads', *Transactions of the Society of Naval Architects and Marine Engineers*, 78.
Salvesen, N. (1973), "A Note on the Seakeeping Characteristics of Small-Waterplane-Area-Twin-Hull Ships," *Journal of Hydronautics*, Vol. 7, No. 1.
Salvesen, Nils (1978), "Ship Motions in Large Waves," *Proceedings of The Professor Timman Symposium on Applied Mathematics*, University of Technology Delft, The Netherlands.
Salvesen, N., von Kerczek, C.H., Scragg, C.V., Cressy, C.P., and Meinhold, M.J. (1985), "Hydro-Nmeric Design of SWATH Ships," *SNAME Transaction.*
Smith, R., (1976), "Giant Waves," *Journal of Fluid Mechanics*, Vol. 77, Part 3, pp. 417-431.
Stephens, O.J. II, Kirkman, K.L. and Peterson, R.S. (1981), "Sailing Yacht Capsizing", *Proc. of the Chesapeake Sailing Yacht Symp.*, Annapolis, Maryland.
Tanaka, N. (1957-1961), "A Study on the Bilge Keel," (Parts 1-4), *Journal of the Society of Naval Architects and Marine Engineers of Japan*, Vol. 101, 103, 105, and 109.
Tulin, M. and Mauro (1992), "Nonlinear Deck Wetness", Presentation at Office of Naval Research Program Review Meeting, M.I.T., Cambridge, Massachusetts, (unpublished).
Vossers, G., Swaan, W.A., and Rijken, H. (1961), "Vertical and Lateral Bending Moment Measurements on Series 60 Models," *International Shipbuilding Progress*, Vol. 8, No. 83.
Whahab, R (1967), "Amidships Forces and Moments on a $C_B = 0.80$ Series 60 Model in Waves from Various Directions," Netherlands Ship Research Center TNO Report No. 100S.
Xū, H. and Yue, D.K.P. (1992), "Computations of Fully-Nonlinear Three- Dimensional Water Waves," *Proceedings of the Nineteenth Symposium on Naval Hydrodynamics*, Seoul, Korea.
Yue, D.K.P. (1994), "Program for Fully-Nonlinear Wave-Body Interactions," Presented at *ONR Workshop on the Nonlinear Ship Motions* at DTRC.
Zhao, R. and Faltinsen, O. (1993), "Water Entry of Two-Dimensional Bodies," *Journal of Fluid Mechanics* vol. 246, pp. 593-612.

Nonlinear Ship Motion Computations Using the Desingularized Method

R. Beck, Y. Cao, S. Scorpio, W. Schultz
(University of Michigan, USA)

ABSTRACT

Fully nonlinear water wave problems are solved using Euler-Lagrange time stepping methods in conjunction with a desingularized approach to solve the mixed boundary value problem that arises at each time step. In the desingularized approach, the singularities generating the flow field are outside the fluid domain. This allows the singularity distribution to be replaced by isolated Rankine sources with the corresponding reduction in computational complexity and computer time.

Examples of the use of the method in two-dimensions are given for the exciting forces acting on a wedge and the free motions of a box barge. For three-dimensions, the added mass and damping of a modified Wigley hull in heave and pitch are presented. Comparisons with experimental results show good agreement.

INTRODUCTION

As computational power and numerical methods have improved, there has been more and more interest in solving fully nonlinear free surface problems. Most of this work has assumed that the fluid is incompressible and inviscid and that the resulting flow is irrotational. These assumptions lead to a boundary value problem that is significantly easier to solve than the fully nonlinear, viscous problem and is the bases for the research discussed in this paper.

Fully nonlinear free surface computations can be performed by many different methods. Longuet-Higgins and Cokelet (1976) first introduced the mixed Euler-Lagrange method for solving two-dimensional fully nonlinear water wave problems. This is a time stepping procedure that requires two major tasks at each time step: the linear field equation is solved in an Eulerian frame; then the fully nonlinear boundary conditions are used to track individual Lagrangian points on the free surface to update their position and potential values. Variations of this method have been applied to a wide variety of two- and three-dimensional problems. Two-dimensional problems have been investigated by Faltinsen (1977), Vinje and Brevig (1981), Baker et al. (1982) and more recently Grosenbaugh and Yeung (1988), Cointe et al. (1990), Saubestre (1990), and Sen (1993). In three dimensions, the computations become much more difficult because of the large number of unknowns that are required. Results have been obtained by a number of researchers, including Lin et al. (1984), Dommermuth and Yue (1987), Kang and Gong (1990), Zhou and Gu (1990), Cao (1991), Cao et al. (1990, 1991, 1992), Lee (1992) and Beck et al. (1993).

To successfully implement an Euler-Lagrange algorithm requires a stable time stepping scheme and a fast and accurate method to solve the mixed boundary value problem that results at each time step. In our research, the mixed boundary value problem is solved using a desingularized boundary integral method. The solution is constructed by integrating a distribution of fundamental singularities over a surface (the integration surface) outside the fluid domain. The integral equation for the unknown distribution is obtained by satisfying the boundary conditions on the surface (the control surface) surrounding the fluid domain. By distributing the singularities on a surface slightly removed from the control surface, the resulting kernel in the integral equation is nonsingular (or desingularized) and special care is not required to evaluate integrals over the panels. Simple numerical quadratures can be used to greatly reduce the computational effort, particularly by avoiding transcendental functions. In fact, we have found that for the source distribution method, the distributed sources may be replaced by simple isolated Rankine sources. Higher order singularities such as dipoles can easily be incorporated. Isolated Rankine sources also allow the direct computation of the induced velocities in the fluid and on its boundaries without further numerical integration or differentiation. The resulting code does not require any special logic and

is easily vectorized. At present, the method is $O(N^2)$, but by using multipole expansions it could be reduced to an $O(N)$ method.

A number of researchers have used the desingularized approach. Webster (1975) was probably the first to apply the technique to panel methods. He used triangular patches of linearly distributed sources "submerged" within the body surface to study the steady flow past an arbitrary three-dimensional body. Schultz and Hong (1989) showed the effectiveness and accuracy of the desingularized method for two-dimensional potential flow problems. Cao et al. (1991) investigated convergence rates and error limits for simple three-dimensional flows including a source-sink pair traveling below a free surface.

The desingularized method has been successfully applied to several free surface problems. The formation of solitons propagating ahead of a disturbance moving in shallow water near the critical Froude number have been studied by Cao et al. (1993). Bertram et al. (1991) compared the wave resistance, lift force and pitch moment acting on a submerged spheroid traveling beneath the free surface as computed by fully nonlinear methods and by linear theory. Using an iterative technique combined with the desingularized method, the wave resistance for steady forward motion was computed by Jensen et al. (1986, 1989) and Raven (1992). The desingularized method has been applied to ship motion problems by Bertram (1990) and Lee (1992). Beck et al. (1993) presents a variety of unsteady results with comparisons to other fully nonlinear calculations and to experiments.

In the next section, the desingularized approach using isolated Rankine sources to solve fully nonlinear marine hydrodynamic problems will be discussed. The solution is developed in the time domain starting from rest. To determine the hydrodynamic forces the time derivative of the potential on the body must be known. In contrast to the conventional approach of finding this derivative using backward differencing, a technique is presented to find directly the derivative at the current time step. The derivative is found by solving a boundary value problem that has the same kernel matrix as the boundary value problem for the potential itself and consequently does not require a substantially greater computational effort. Following the theoretical development, numerical methods and results are presented for two and three-dimensional problems. Comparisons with experimental results are shown for the Wigley hull form.

FULLY NONLINEAR PROBLEM FORMULATION

Boundary Value Problem

An ideal, incompressible fluid is assumed and surface tension is neglected. The problem is started from rest so that the flow remains irrotational. This implies the existence of a velocity potential such that the fluid velocity is given by its gradient and the governing equation in the fluid domain is the Laplace equation.

A coordinate system Oxyz translating in the negative x direction relative to a space fixed frame is used. The time dependent velocity of translation is given by $U_0(t)$. The Oxyz axis system is chosen such that the $z = 0$ plane corresponds to the calm water level and z is positive upwards. The x-z plane is coincident with the centerplane of the vessel. The total velocity potential of the flow can then be expressed as

$$\Phi = U_0(t)x + \phi(x,y,z,t) \tag{1}$$

where $\phi(x,y,z,t)$ is the perturbation potential. Both Φ and ϕ satisfy the Laplace equation

$$\nabla^2\Phi = 0 \tag{2}$$

Boundary conditions must be applied on all surfaces surrounding the fluid domain: the free surface (S_F), the body surface (S_H), the bottom (S_B) and the surrounding surface at infinity (S_∞). A kinematic body boundary condition is applied on the instantaneous position of the body wetted surface:

$$\frac{\partial\phi}{\partial n} = -U_0(t)n_1 + \mathbf{V}_H \cdot \mathbf{n} \quad \text{on} \quad S_H \tag{3}$$

where $\mathbf{n} = (n_1, n_2, n_3)$ is the unit normal vector into the surface (out of the fluid domain) and $\mathbf{V}_H$ is the velocity of a point on the body surface including rotational effects relative to the Oxyz coordinate system. The subscripts 1,2,3 refer to the x, y, and z axis directions respectively. The kinematic condition is also applied on the bottom:

$$\frac{\partial\phi}{\partial n} = -U_0(t)n_1 + \mathbf{V}_B \cdot \mathbf{n} \quad \text{on} \quad S_B \tag{4}$$

where $\mathbf{V}_B$ is the velocity of the bottom relative to the Oxyz system. For an infinitely deep ocean equation (4) reduces to

$$\nabla\phi \to 0 \quad \text{as} \quad z \to -\infty \tag{5}$$

Finite depth will increase the computational time because of the additional unknowns necessary to meet the bottom boundary condition but there is no increase in computational difficulty. In fact, the flatness of the bottom is immaterial. The only overhead relative to a flat bottom is an increase in the required number of nodes to represent the nonflat bottom.

On the instantaneous free surface both the kinematic and dynamic conditions must be satisfied. The kinematic condition is

$$\frac{\partial \eta}{\partial t} = -\nabla\phi \cdot \nabla\eta + \frac{\partial \phi}{\partial z} - U_o(t)\frac{\partial \eta}{\partial x} \quad \text{on } S_F \qquad (6)$$

where $z = \eta\,(x, y, t)$ is the free surface elevation. The dynamic condition requires that the pressure everywhere on the free surface equals the ambient pressure, P_a. The ambient pressure is assumed known and may be a function of space and time. Normally it would be set equal to zero. Using Bernoulli's equation, the dynamic condition becomes:

$$\frac{\partial \phi}{\partial t} = -g\eta - \frac{1}{2}\nabla\phi \cdot \nabla\phi - U_o(t)\cdot\frac{\partial \phi}{\partial x} - \frac{P_a}{\rho} \quad \text{on SF} \qquad (7)$$

where ρ is the fluid density and g the gravitational acceleration.

Because we are solving an initial value problem with no incident waves, the fluid disturbance must vanish at infinity :

$$\nabla\phi \to 0 \quad \text{as} \quad R \to \infty \qquad (8)$$

In addition, the initial values of the potential and free surface elevation must be specified such that

$$\phi = 0 \quad t \le 0 \quad \text{in fluid domain}$$
$$\eta = 0 \quad t \le 0 \qquad (9)$$

In the Euler-Lagrange method, a time stepping procedure is used in which a boundary value problem is solved at each time step. At each step, the value of the potential is given on the free surface and the value of the normal derivative of the potential is known on the body surface and bottom surface. After the mixed boundary value problem is solved, the free surface potential and elevation are updated by integrating with respect to time (or time marching) the free surface boundary conditions, equations (6) and (7). The body and bottom boundary conditions are prescribed for the forced motion problem. In the case of a freely floating body, the equations of motion must be integrated with respect to time in a manner similar to the free surface conditions.

On the free surface, the kinematic condition is used to time step the free surface elevation and the dynamic condition is used to update the potential. Many different approaches are possible to time march the free surface boundary conditions. The most common is the material node approach used by Longuet-Higgins and Cokelet (1976) in which the nodes or collocation points follow the individual fluid particles. Another technique is to prescribe the horizontal movement of the node but allow the node to follow the vertical displacement of the free surface. The prescribed movement may be zero such that the node locations remain fixed in the x-y plane. Depending on the problem, one of the techniques may be easier to apply than the others.

It is convenient to rewrite the free surface boundary conditions, equations (6) and (7), in terms of the time derivative of a point moving with a prescribed velocity $\mathbf{v}$ relative to the Oxyz coordinate system. By adding $\mathbf{v}\cdot\nabla\eta$ to both sides of (6) and $\mathbf{v}\cdot\nabla\phi$ to both sides of (7) and after some algebraic manipulation, the kinematic and dynamic conditions can be put in the form

$$\frac{\delta \eta}{\delta t} = \frac{\partial \phi}{\partial z} - (\nabla\phi - \mathbf{v})\cdot\nabla\eta - U_o(t)\frac{\partial \eta}{\partial x} \quad \text{on } S_F \qquad (10)$$

and

$$\frac{\delta \phi}{\delta t} = -g\eta - \frac{1}{2}\nabla\phi\cdot\nabla\phi + \mathbf{v}\cdot\nabla\phi - \frac{P_a}{\rho} - U_o(t)\frac{\partial \phi}{\partial x} \quad \text{on } S_F \qquad (11)$$

where

$$\frac{\delta}{\delta t} \equiv \frac{\partial}{\partial t} + \mathbf{v}\cdot\nabla \qquad (12)$$

is the time derivative following the moving node. $\frac{\delta}{\delta t}$ is similar to the usual material derivative of fluid mechanics except the velocity is the prescribed $\mathbf{v}$ rather than the fluid velocity.

If $\mathbf{v}$ is set equal to $\left(U(t), V(t), \frac{\delta \eta}{\delta t}\right)$ the node follows a prescribed path with velocity (U(t), V(t)) in the x-y plane and moves vertically with the free surface. Setting $\mathbf{v} = \left(0, 0, \frac{\partial \eta}{\partial t}\right)$ results in the x-y locations of the nodes remaining fixed in the Oxyz coordinate system. In the material node approach, the velocity $\mathbf{v}$ is set equal to the fluid velocity such that $\mathbf{v} = U_o(t)\mathbf{i} + \nabla\phi$.

The form of the free surface boundary conditions given by the above equations allows the value of the elevation and potential to be stepped

forward in time. The left hand sides of equations (10) and (11) are the derivatives with respect to time of the potential and wave elevation moving with the node. The quantities on the right hand side are all known at each time step. The spatial gradient of the potential can be determined analytically after solving the boundary value problem. The difficulty is the gradient of the free surface elevation ($\nabla\eta$ in equation (10)) that must be evaluated numerically and can lead to numerical inaccuracies. However, this term is only needed in the prescribed horizontal node movement approach. In the material node approach, no spatial derivatives of the free surface elevation need to be evaluated and this probably explains why this is the approach most often used. With material nodes one must always be concerned that the nodes do not penetrate the body surface between time steps since they are unconstrained. In zero forward speed problems, material nodes or fixed nodes seem to be the most appropriate. In problems with forward speed, the material node approach has difficulties near the body because nodes tend to pile up near the bow and stern stagnation regions. The prescribed horizontal node movement approach does not have this difficulty since the node movement is constrained. An appropriate choice of $\mathbf{v}$ is one which parallels the body waterline and is close to the fluid velocity. In this case, the contribution of the $\nabla\eta$ term to the right hand side of (10) will be small and numerical inaccuracies will be minimized. Consequently, fast, simple numerical derivatives can be used to evaluate the $\nabla\eta$ term.

At each time step a mixed boundary value problem must be solved: the potential is given on the free surface and the normal derivative of the potential is known on the body surface and the bottom. In terms of a desingularized source distribution, the potential at any point in the fluid domain is given by

$$\phi(\mathbf{x}) = \iint_{\Omega} \sigma(\mathbf{x}_S) G(\mathbf{x};\mathbf{x}_S)\, d\Omega \tag{13}$$

where $G(\mathbf{x};\mathbf{x}_S)$ is the Rankine source Green function and Ω is the integration surface outside the fluid domain.

Applying the boundary conditions, the integral equations that must be solved to determine the unknown source strengths $\sigma(\mathbf{x}_S)$ are

$$\iint_{\Omega} \sigma(\mathbf{x}_S) G(\mathbf{x}_C;\mathbf{x}_S)\, d\Omega = \phi_F(\mathbf{x}_C) \tag{14}$$

$$\mathbf{x}_C \in \Gamma_d$$

and

$$\iint_{\Omega} \sigma(\mathbf{x}_S) \frac{\partial}{\partial n} G(\mathbf{x}_C;\mathbf{x}_S)\, d\Omega = \chi(\mathbf{x}_C) \tag{15}$$

$$\mathbf{x}_C \in \Gamma_n$$

where $\mathbf{x}_S$ = a point on the integration surface, Ω
$\mathbf{x}_C$ = a point on the real boundary
ϕ_F = the given potential value on the free surface at $\mathbf{x}_C$
Γ_d = surface on which ϕ_F is known
χ = the given normal velocity on the solid boundaries at $\mathbf{x}_C$
Γ_n = surface on which χ is known

Hydrodynamic Forces

The hydrodynamic forces acting on the body are found by integrating the pressure over the instantaneous wetted surface. The generalized force acting on the body in the jth direction is thus given by:

$$\bar{F}_j = \iint_{S_H} P\bar{n}_j\, ds \tag{16}$$

where $\bar{n}_j$ is the generalized unit normal into the hull defined as

$$(\bar{n}_1, \bar{n}_2, \bar{n}_3) = \bar{\mathbf{n}} \tag{17}$$

$$(\bar{n}_4, \bar{n}_5, \bar{n}_6) = \mathbf{r} \times \bar{\mathbf{n}}$$

$\bar{\mathbf{n}}$ = unit normal to body surface (out of fluid) in body axis system
$\mathbf{r} = (\bar{x}, \bar{y}, \bar{z})$
$O\bar{x}\bar{y}\bar{z}$ = body axis system

and $j = 1,2,\ldots 6$ corresponds to the three directions and the three rotations about the $\bar{x}, \bar{y}, \bar{z}$ axes respectively. The generalized forces in the Oxyz system, F_j, can be easily determined from $\bar{F}_j$ by a simple transformation.

The pressure in the moving coordinate system is given by Bernoulli's equation:

$$\frac{P}{\rho} = -\frac{\partial\phi}{\partial t} - U_o(t)\frac{\partial\phi}{\partial x} - gz - \frac{1}{2}\nabla\phi\cdot\nabla\phi \tag{18a}$$

$$= -\frac{\delta\phi}{\delta t} - U_o(t)\frac{\partial\phi}{\partial x} - gz - \frac{1}{2}\nabla\phi\cdot\nabla\phi + \mathbf{v}\cdot\nabla\phi \tag{18b}$$

where $\frac{\delta\phi}{\delta t}$ is the time derivation of the potential following a moving node on the body and $\mathbf{v}$ is the velocity of the node relative to the Oxyz system.

Rigid Body Dynamics

The motions of a body freely floating on the free surface are governed by Euler's equations of motion that relate the body velocities and accelerations to the forces and moments acting on it. In six degrees of freedom there are three equations of translation and three equations of rotation yielding six nonlinear differential equations for the six unknowns: the translational velocities of surge, sway, heave and the angular velocities of roll, pitch and yaw. The six differential equations may be found in most elementary textbooks on dynamics. They are usually written in terms of the Euler angles and are highly nonlinear for large amplitudes of motion.

In the absence of towlines or mooring lines, the forces acting on the body are hydrostatic, hydrodynamic and gravitational. The gravitational forces depend only on the mass of the body and its orientation. The hydrostatic and hydrodynamic forces depend not only on the orientation but also the body velocity and acceleration. These fluid forces and moments must be solved simultaneously along with the equations of motion. To do this it is convenient to use the state variable representation of the complete system.

Hydrodynamic problem

$$\frac{d\mathbf{X_F}}{dt} = \mathbf{F_1}\left(\mathbf{X_F}, \phi_\mathbf{F}, \mathbf{X_G}, \mathbf{V_G}\right) \qquad (19a)$$

$$\frac{d\phi_\mathbf{F}}{dt} = \mathbf{F_2}\left(\mathbf{X_F}, \phi_\mathbf{F}, \mathbf{X_G}, \mathbf{V_G}\right) \qquad (19b)$$

Euler's equation of motion

$$\frac{d\mathbf{X_G}}{dt} = \mathbf{V_G} \qquad (20a)$$

$$\frac{d\mathbf{V_G}}{dt} = \mathbf{F_3}\left(\mathbf{X_F}, \phi_\mathbf{F}, \mathbf{X_G}, \mathbf{V_G}, \frac{d\mathbf{V_G}}{dt}\right) \qquad (20b)$$

where the state variables are defined by the generalized vectors:

$\mathbf{X_F}$ = location of free surface nodes
$\phi_\mathbf{F}$ = potential of free surface nodes
$\mathbf{X_G}$ = location of vessel center of gravity in 6-degrees of freedom
$\mathbf{V_G}$ = 6 components of body velocity at center of gravity

Equations (19a) through (20b) are a system of first-order ordinary differential equations with respect to time in the state variables $\mathbf{X_F}, \phi_\mathbf{F}, \mathbf{X_G}, \mathbf{V_G}$. They can be time stepped using conventional numerical techniques. For this paper, we use a fourth-order Runge-Kutta technique. The first two equations (19a, 19b) represent the hydrodynamic problem that must be solved at each time step to determine the potential and elevation of the free surface nodes. The equations of motion of the body are symbolized by equations (20a) and (20b). The functional relations on the right hand side indicate the variables upon which the time derivatives depend.

There are two difficulties associated with the time stepping illustrated by equations (19a) - (20b). The first is that the accurate evaluation of $\frac{\delta\phi}{\delta t}$ or $\frac{\partial\phi}{\partial t}$ that is critical to the computation of the hydrodynamic forces acting on the body at each time step. For forced motions in which the body velocity is prescribed, this is not difficult since the body motion does not depend on a knowledge of the hydrodynamic forces. Consequently, the hydrodynamic forces acting on the body can be post-processed and a simple central differencing is sufficient to determine $\frac{\delta\phi}{\delta t}$.

In free body motions, the body velocity and acceleration are a function of the hydrodynamic forces as related through the equations of motion (20a) - (20b). The body motions must be simultaneously computed along with the hydrodynamic forces. This requires that $\frac{\delta\phi}{\delta t}$ or $\frac{\partial\phi}{\partial t}$ be known at the present time step. A conventional technique is to compute $\frac{\delta\phi}{\delta t}$ using backward differencing, but this can lead to poor estimates of the derivative and possible instabilities. We have developed a technique to compute directly $\frac{\partial\phi}{\partial t}$ on the body at the present instant of time. Similar techniques have been used by other researchers such as Vinje and Brevig (1981), Yeung (1982), Kang and Gong (1990) and Cointe et al. (1990).

Since $\frac{\partial\phi}{\partial t}$ is harmonic in the fluid domain, it is the solution of an integral equation that has the same form as the integral equation that is solved to find ϕ and η. In fact, if the fundamental singularities are the same for both problems, then the influence matrix of the resulting system of linear equations is identical for both the ϕ problem and the $\frac{\partial\phi}{\partial t}$ problem. The only difference is that the right hand side of the system of equations is altered. Thus, to solve for $\frac{\partial\phi}{\partial t}$ directly does not require a

great deal of additional computational effort as long as the inverse of the influence matrix is known.

The dynamic free surface boundary condition (7) gives the value of $\frac{\partial \phi}{\partial t}$ on the free surface. Once the potential problem is solved, the required value of $\frac{\partial \phi}{\partial t}$ at each node on the free surface is easily calculated from (7).

The normal derivative of $\frac{\partial \phi}{\partial t}$ on the body can be shown to be:

$$\frac{\partial}{\partial n}\left(\frac{\partial \phi}{\partial t}\right) = \frac{\partial \mathbf{n}}{\partial t}\cdot\left(\mathbf{V}_H - \nabla\Phi\right) + \mathbf{n}\cdot\frac{\partial \mathbf{V}_H}{\partial t} - \frac{\partial U_0(t)}{\partial t} n_1 \tag{21}$$

where $\mathbf{V}_H$ and $\frac{\partial \mathbf{V}_H}{\partial t}$ are the velocity and acceleration, including rotational terms of the body surface at the nodes. Knowing the velocity and acceleration of the body fixed coordinates, $\frac{\partial}{\partial n}\left(\frac{\partial \phi}{\partial t}\right)$ can be calculated for each node on the body surface. Given the Dirichlet condition for $\frac{\partial \phi}{\partial t}$ on the free surface, the Neumann boundary condition for $\frac{\partial \phi}{\partial t}$ on the body surface, and a far-field condition of the same type as used in the potential problem, the mixed boundary value problem for $\frac{\partial \phi}{\partial t}$ can be solved in the same manner as the potential problem.

A second difficulty is that the time derivative of $\frac{d\mathbf{V_G}}{dt}$ in equation (20b) is not explicitly expressed in terms of the state variables. It is possible to develop a solution technique that factors out the $\frac{d\mathbf{V_G}}{dt}$ term from the functional form on the right hand side of (20b). This is the approach taken by Vinje and Brevig (1981), Kang and Gong (1990), and others. For the calculations presented in this paper, we use an iterative procedure in which an assumed value of $\frac{d\mathbf{V_G}}{dt}$ is used on the right hand side of equation (20b) and then iterated until convergence. The iterative procedure typically takes 5 to 10 iterations to converge at each time step. For six degrees of freedom this is less computational effort than would be necessary in the factorization method.

NUMERICAL TECHNIQUES

The details of the numerical techniques using the desingularized method to solve the boundary value problem at each time step are described by Beck et al. (1993).

Because of the desingularization isolated Rankine sources are used and the integrals in equations (14) and (15) are replaced by simple summation. There is a source associated with each node on the boundary. Each source is placed in the normal direction from the node at a distance proportional to the square root of the local node spacing. A domain-decomposition technique is often used because the node spacing on the free surface and the body surface can be very different which leads to ill-conditioning of the influence matrix. In this technique, the source strengths above the free surface and the source strengths in the body are determined separately using an iterative procedure. The equations to determine the source strengths can be solved using either a direct or an iterative solver. For the two-dimensional results presented in the next section, a LU decomposition solver is used. In three-dimensional problems, an iterative solver, GMRES, is used for the free surface sources and the direct solver is used for the body sources.

A fourth-order Runge-Kutta-Fehlberg scheme is used for the time stepping of the free surface nodes and the state variables in free motion problems. For the results presented in the next section, material nodes are used for the zero forward speed computation. For the Wigley hull calculations, we prescribe the path around the hull and use the computed fluid velocity in the x-direction to move the nodes along this path. As long as the prescribed paths are close to the actual streamlines, the "semi-material nodes" will not cross the body surface and will have characteristics close to the actual material nodes.

It should be noted that for all the results presented in the next section, no filtering or smoothing was used. For the forward speed calculation, the free surface nodes move along a prescribed path at each sub-time step and are re-gridded after each major time step. The body surface nodes are moved at each sub-time step in order to keep an even distribution of the nodes over the wetted surface of the hull.

The far field boundary conditions at the edge of the computational domain are always a problem. At zero forward speed, either the edge of the computational domain must be far enough away that there is no disturbance or appropriate wall conditions must be specified. If not, an indeterminacy can develop as encountered by Lee (1992). For most zero speed computations adsorbing beaches or wave makers are placed along the far field boundaries.

For problems with forward speed, upstream boundary conditions must be specified. In our computations, we impose zero perturbation potential and zero free surface slope. Downstream, we drop the nodes as they move out of the computational domain. On the side edge, we prescribe the nodes to move downstream along a straight path and do not impose any further condition. This saves computational effort, but can lead to wave reflection. The wave reflection can be numerically damped by ever increasing transverse spacing of the nodes near the side edges as was proposed by Lee (1992).

NUMERICAL RESULTS

In this section we present results for a variety of cases. Two-dimensional computations are shown for the exciting forces acting on a wedge in incident waves and the responses of a freely floating body in sinusoidal waves. Both steady and unsteady results are presented for the three-dimensional Wigley hull. The Wigley hull was chosen because its mathematical hull form allows the direct computation of node locations and unit normals. This is important because in fully nonlinear computations the nodes move on the hull surface at each time step and the mathematical definition avoids the need for complex hull surface programs. For further results using the desingularized method with comparisons to other calculations and experiments, reference may be made to Beck et al. (1993), Cao et al. (1992), or Lee (1992).

Exciting Forces on a Two-Dimensional Wedge

As illustrated in figure 1, the exciting forces acting on a two-dimensional wedge due to regular waves were computed. The wedge was in the middle of a 30 unit long tank with a pneumatic wave maker at one end. The wedge has a half-beam of 1, a depth of 3 and the incident wavelength is π.

Figure 2 shows the wave profiles near the wedge. The spray plume that develops and causes the computations to stop as the incident waves strike the wedge is clearly visible. Physically, this spray plume has very little effect on the total exciting forces since it is thin and at essentially atmospheric pressure. To avoid the difficulty, we have used a small spray damping region in the vicinity of the wedge. The damper is a pressure applied to the free surface at each node with the appropriate sign so that energy is continuously taken from the system. For figure 2, the damping is equal to $25\left(\frac{\partial\phi}{\partial n}\right)^3 \mu(x)$, where $\mu(x)$ is the spatial variation of the damping and quickly decays with distance from the body/free surface intersection. As can be seen, the spray damping causes no significant change in the wave profile until later times. At these times the spray plume is developing and the reflected waves are undoubtedly modified by the presence of the damping.

Figure 3 plots the total energy in the wave tank versus time. Two curves are shown: the first curve is the work input by the wave maker and the second is the wave energy in the tank. As can be seen, until the waves reach the spray damping region, the input energy and the energy in the system agree to within 0.1%. This indicates that there is very little numerical damping in the desingularized method. After the incident waves reach the spray damping region, the two curves diverge as expected.

Figure 4 shows the effect of the spray damping on the fully nonlinear exciting forces acting on the body. The solid line is for the case without damping and it increases without bound at around $t^*=50$ due to the numerical instability caused by the spray plume. The dash curve is the case with spray damping and it continues until the calculations cease at $t^*=70$. As can be seen, the damping region has very little effect on the exciting forces except at the peaks. It appears that the spray damping region is an effective means of eliminating the spray plume without significantly altering the exciting forces acting on the body.

Two-Dimensional Freely Floating Body in Waves

The motions of a freely floating two-dimensional box have been computed. The box has a beam (B) of 2, a draft (T) of 1, and a bilge radius of .25. The wave tank is 31 units long and 3 units deep with a piston type wave maker at one end and an adsorbing beach at the other. Two numerical schemes have been used for the calculations. In both, the desingularized method was used for the hydrodynamic calculations at each time step. The difference between the two schemes was the method used to compute the time derivative of the potential on the body. In the first scheme (scheme A), the technique presented in equations (7) and (21) was used to compute $\frac{\partial\phi}{\partial t}$ at each time step. The equations of motion, (20a, b), could then be integrated to determine the time history of the motion. As pointed out previously, the hydrodynamic forces also depend on the acceleration of the body. An iteration procedure was used in which the solution at each time step was determined using an assumed body acceleration. The assumed acceleration was checked against the computed acceleration, if it did not agree to within a prescribed error (ε), the iteration continued with the assumed

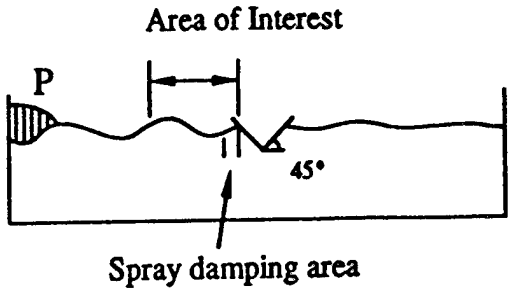


Figure 1: Exciting forces acting on a two - dimensional wedge due to regular waves

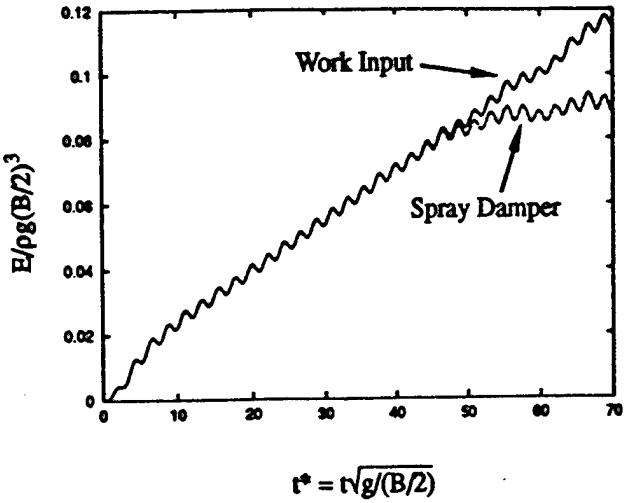


Figure 3: Total energy in the wave tank versus time

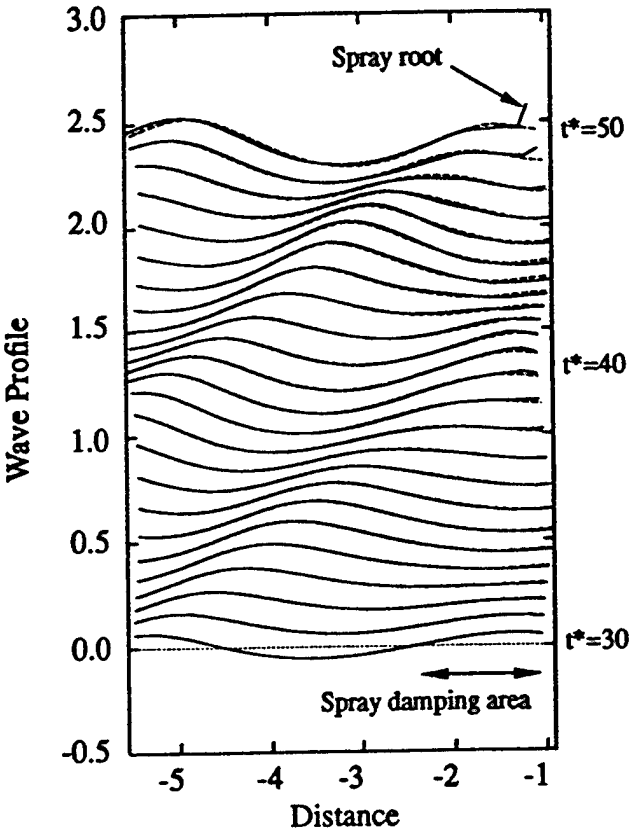


Figure 2: Wave profiles near the wedge

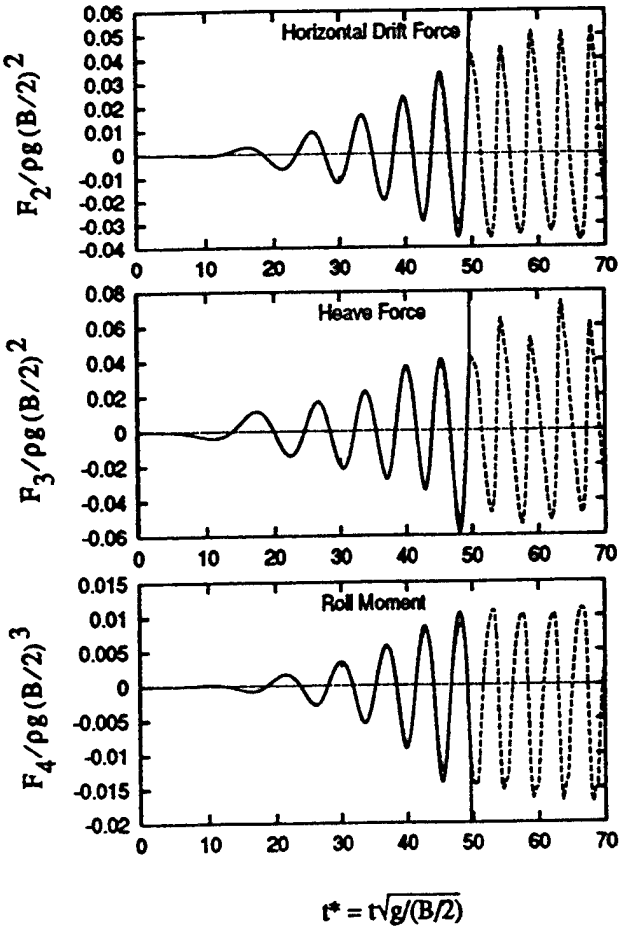


Figure 4: Effect of spray damping on fully nonlinear exciting forces acting on the body

$$\text{-------}\ 25\left(\frac{\partial\phi}{\partial n}\right)^3$$

——— Undamped

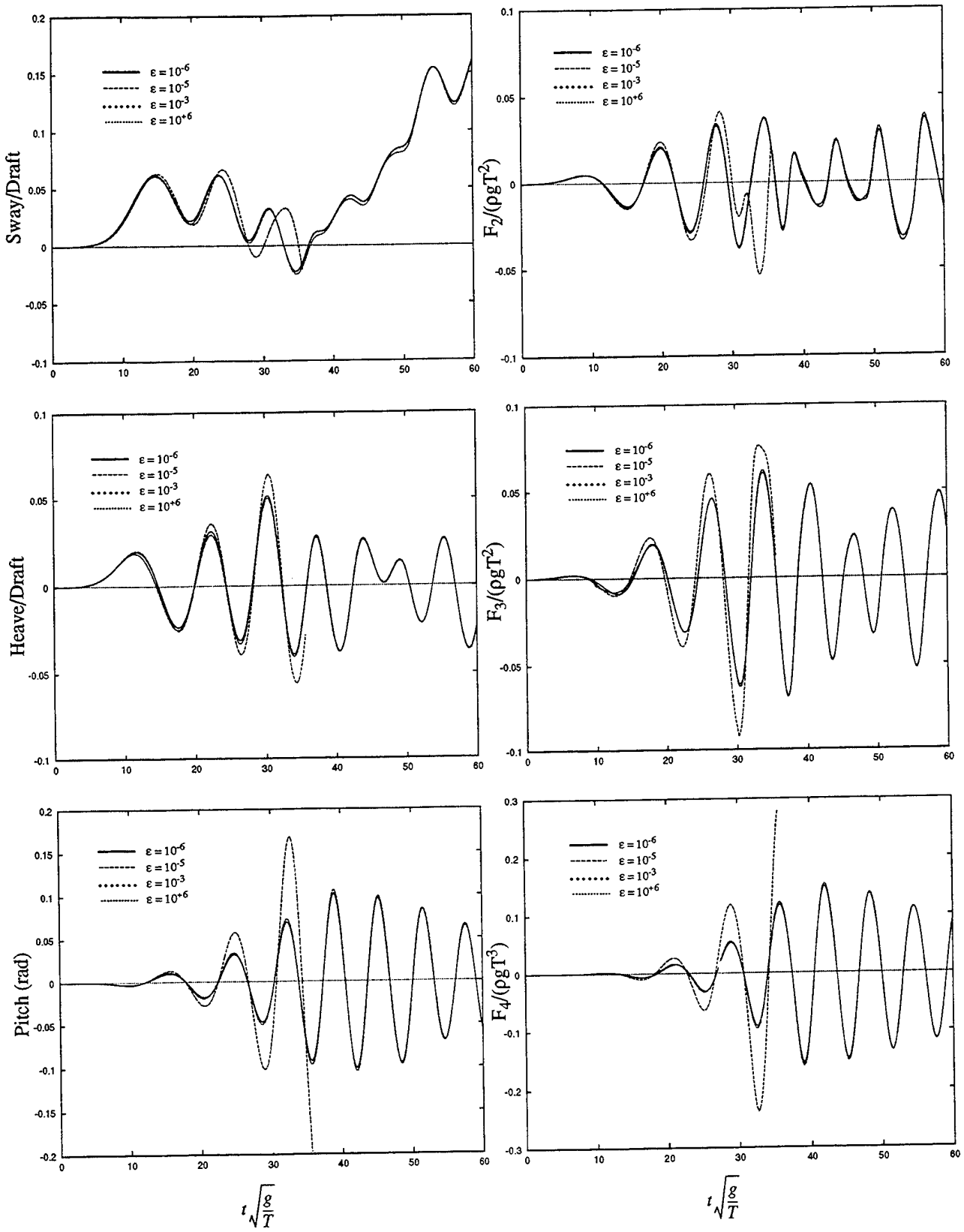


Figure 5: Effect of error tolerance on body motions and hydrodynamic forces ($dt^* = 0.2$)

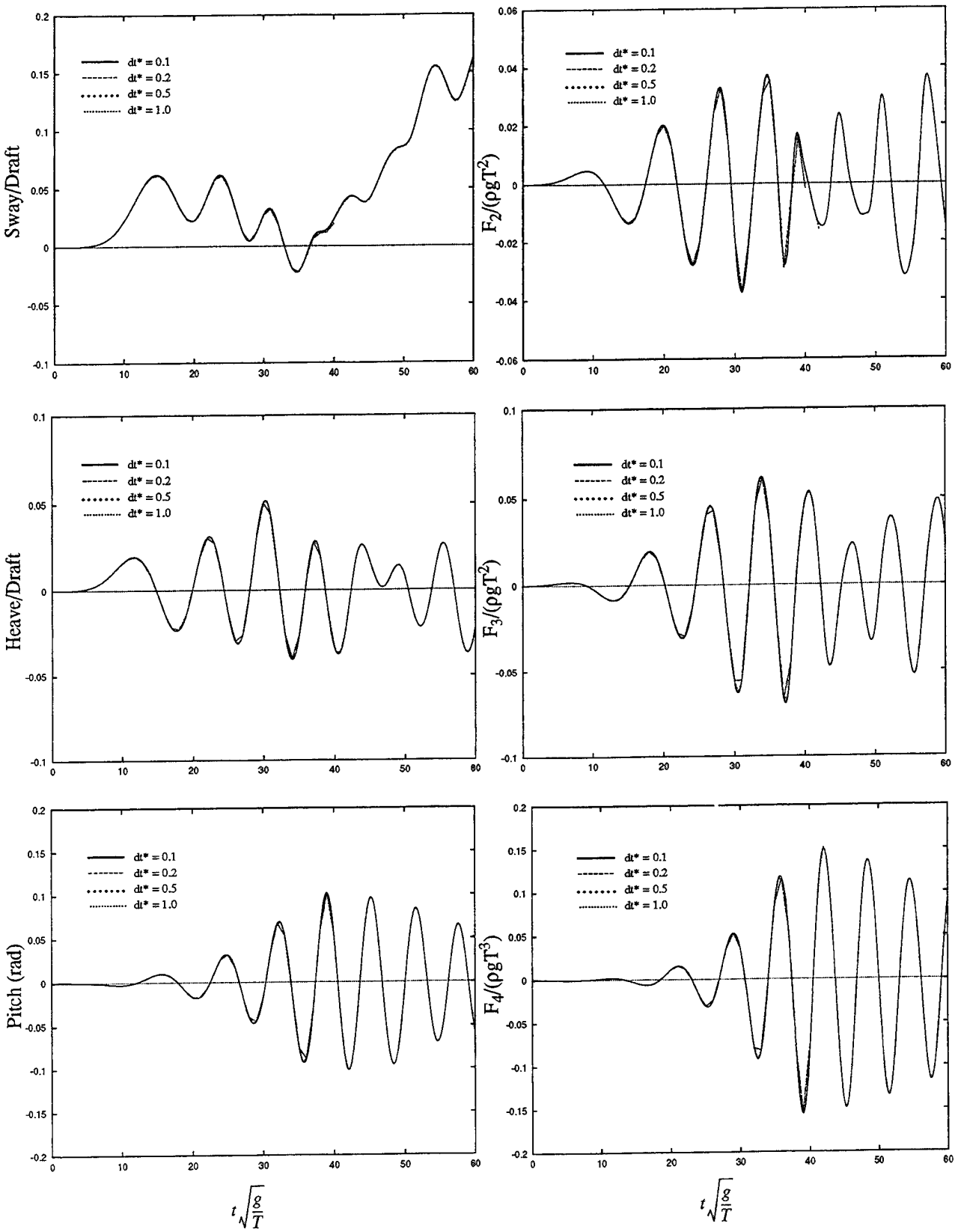


Figure 6: Effect of time step size on body motions and hydrodynamic forces ($\varepsilon = 10^{-6}$)

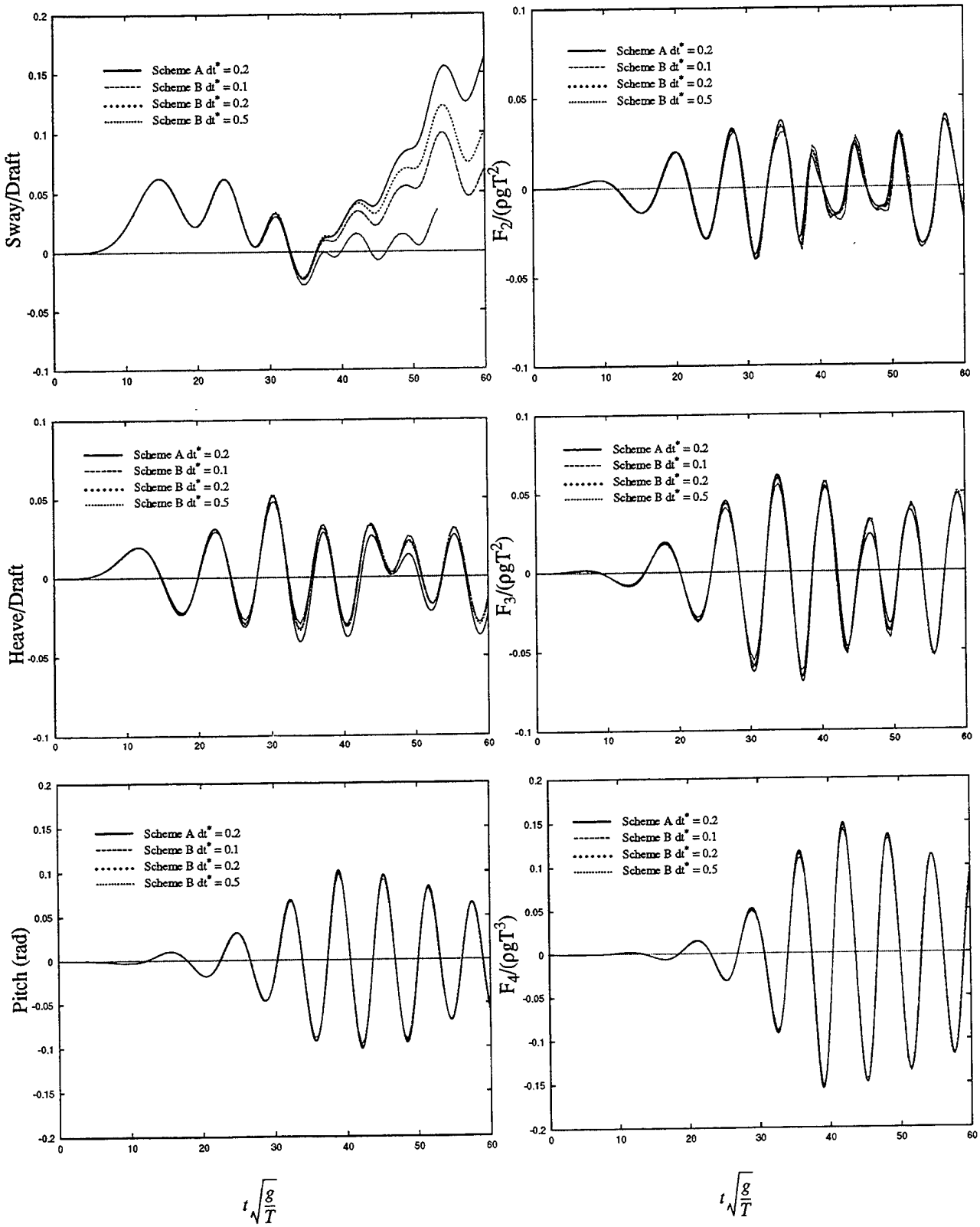


Figure 7: Comparisons of body motion and hydrodynamic force computed using the two schemes

value set equal to the average of the old and new values.

In the second scheme (scheme B), backward differencing was used to determine $\frac{\delta\phi}{\delta t}$. The iteration procedure was then used to determine the body accelerations and motions as with the first scheme.

Figure 5 shows the effects of the error tolerance in the iteration for body acceleration on the sway, heave, and roll motions and their respective hydrodynamic forces. As can be seen, an error tolerance of 10^6 (i.e. there is no iteration) does not converge at $t^*=35$ where $t^*=t\sqrt{g/T}$. A tolerance below 10^{-3} does not change the answers significantly. The second order drift of the body is clearly visible for the sway motion. The highly tuned roll motion is also evident by the very sinusoidal response.

The variation of the response with time step size is shown in figure 6. A time step size of $dt^*=1.0$ is too large since the results did not converge around $t^*=40$. The other three sizes all yield essentially the same results.

A comparison of the results computed by the first and second schemes is shown in figure 7. The solid line in the figure is the converged result computed by the first method with a time step size of .2 and an error tolerance of 10^{-6}. As can be seen, the backward-differencing results accumulate error. The computations using a $dt^*=.5$ diverge after $t^*=55$. The other results approach those of scheme A as the time step size is decreased. The sway motion is most critical, probably because there is no restoring force to prevent the motions from drifting.

Wigley hull

The wave resistance and radiation forces due to heave and pitch have been computed for a Wigley hull form. The Wigley hull is a mathematical form with the hull surface defined by the equation:

$$y(x,z)=\frac{B}{2}\left(1-\left(\frac{2x}{L}\right)^2\right)\left(1-\left(\frac{z}{T}\right)^2\right)\left(1+a_2\left(\frac{2x}{L}\right)^2\right) \qquad (22)$$

where L = model length
B = model full beam
T = model draft
a_2 = coefficient for bow fullness
= 0.0, standard hull
= .2 for modified Wigley hull III

For both the standard hull and the modified hull III, L/B=10 and B/T=1.6.

The standard hull has been extensively tested for calm water resistance characteristics at model tanks around the world. The experimental

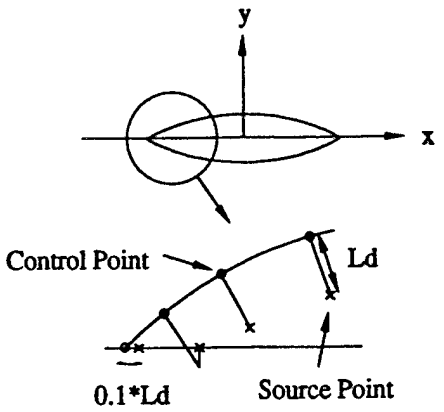


Figure 8: Desingularization near the leading edge of a Karman - Trefftz airfoil.

results presented in this paper are taken from Noblesse and McCarthy (1983). A series of four modified Wigley hulls were tested at Delft University of Technology by Gerritsma and Journée. Journée (1992) presents the complete heave and pitch results for the added mass and damping, exciting forces, and amplitudes and phase angles at a variety of Froude numbers and frequencies. For this paper comparisons were made with the modified Wigley hull III.

Because of the placement of the singularities inside the body, difficulties can arise in using the desingularized method for sharp leading edges, such as the bow of a ship. To investigate this problem, the desingularized method was applied to a two-dimensional Karman-Trefftz airfoil in an infinite fluid. The exact solution to this problem is known analytically. Figure 8 is a sketch of the Karman-Trefftz airfoil and the placement of the desingularized source points near the leading edge. The source points near the leading edge can cross the centerline, in which case they are moved back to the centerline without changing the x-coordinate. The source point corresponding to the leading edge node is placed a small distance behind the node; this distance is critical in order to obtain accurate results near the leading edge.

Figure 9 plots the tangential velocity on the surface of the foil for two different entrance angles. The solid line is the numerical results using 60 nodes with cosine spacing and the dots are the analytic results. As can be seen, the analytic and numerical results agree to within 0.1% as long as the source associated with the leading edge node is desingularized only a small amount. For the large entrance angle, the numerical results are accurate even for a large ($x=.5L_d$) placement of the leading edge source from the nose. However, for the sharp

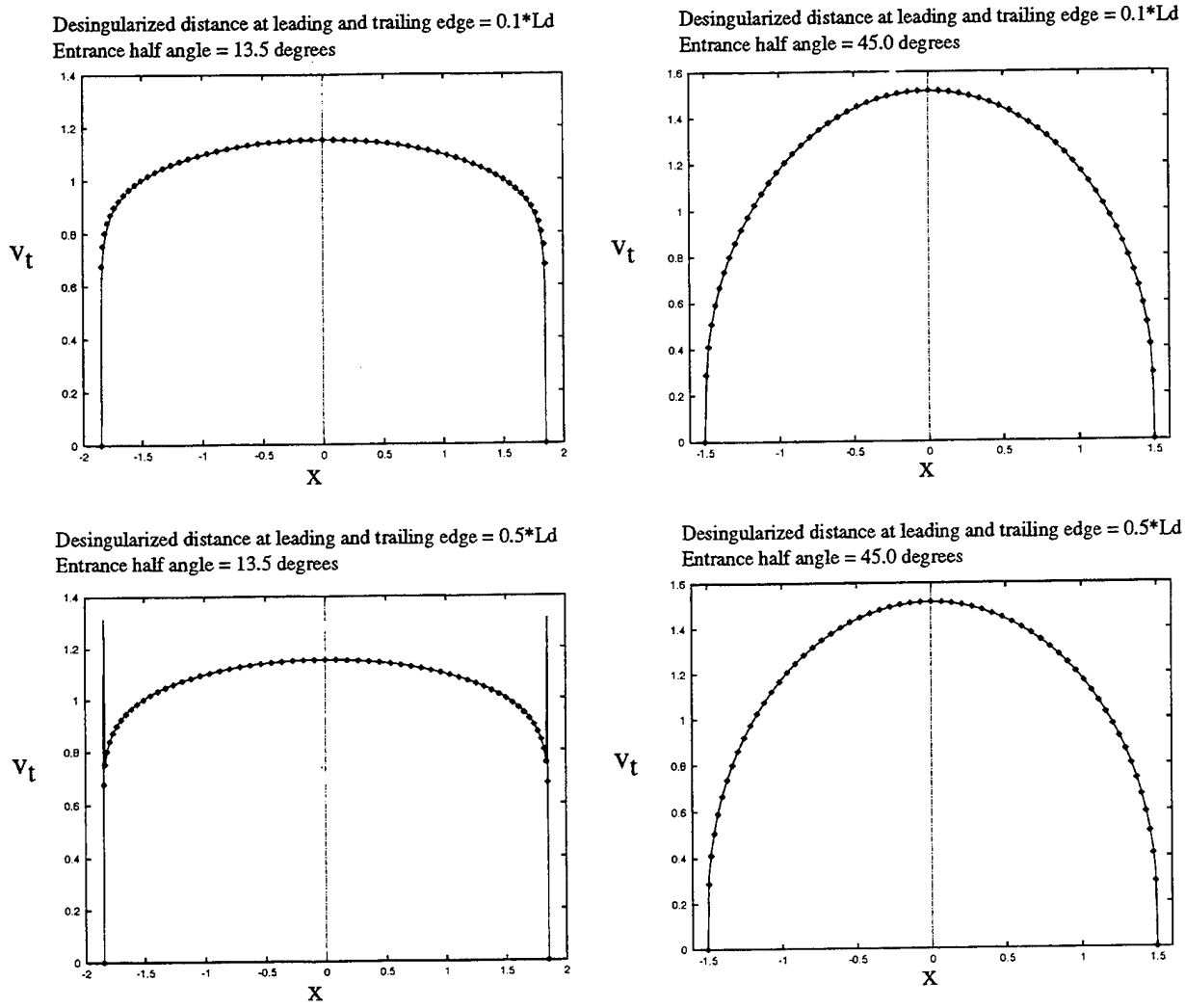


Figure 9: The effect of desingularized distance on surface tangential velocity (v_t) for a Karman-Trefftz airfoil

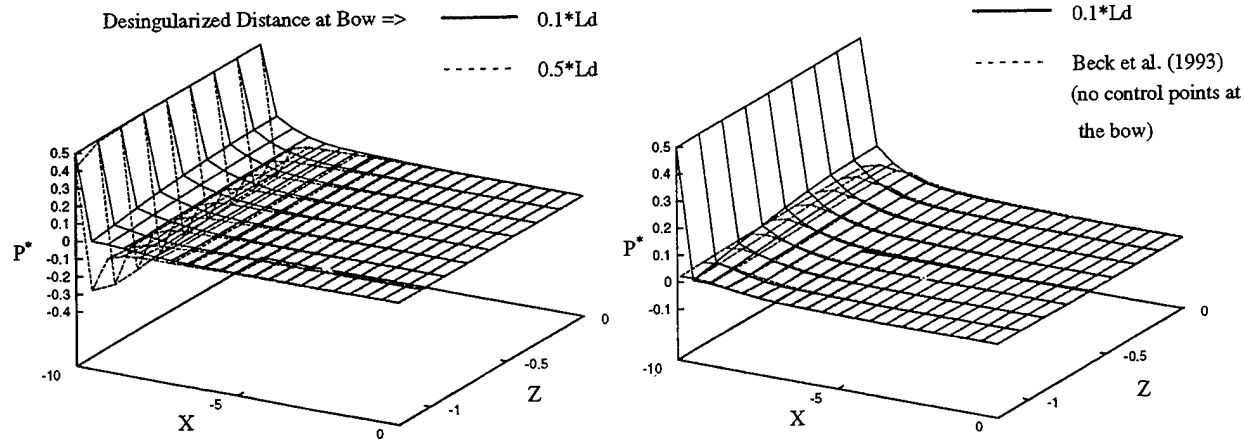


Figure 10: Wigley hull double body pressure on the forward half of the body

entrance angle, a spike develops as the distance of the leading edge source is moved back. The agreement over most of the foil is still good. The further away that the leading edge source is placed, the worse the solution. Also, the narrower the entrance angle, the sooner the spike develops. The cause of the spike is the strength of the leading edge source. This source must be strong enough to cancel the free stream velocity at the leading edge node which is also the stagnation point. The further back this source is placed, the larger its strength has to be. This large source strength in turn induces a large tangential velocity at the second node. As the leading edge source is moved forward, its induced tangential velocity at the second node is decreased and its required strength is also decreased. The net result is that the spike does not develop. The narrower the entrance angle, the greater the effect.

The same effect of poor definition of the flow near the leading edge can be seen in three-dimensions. Figure 10 is a plot of the pressure coefficient near the bow of a standard Wigley hull double body. The upper plot shows the change in pressure distribution due to a change in desingularization of the leading edge source from $.1*L_d$ to $.5*L_d$. Reducing the $.1*L_d$ further does not change the results. For the $.5*L_d$ case, the spike in tangential velocity appears as a dip in pressure coefficient. In the lower plot, the $.1*L_d$ result is compared to the node placement used by Beck et al. (1993) in which no node was put right at the bow. As can be seen, the deletion of the bow node eliminates the spike in velocity but the stagnation pressure peak is also lost.

The loss of stagnation pressure caused a large underprediction of the bow wave in the calculations with a free surface. Figure 11 is a plot of the wave amplitude along the side of the standard Wigley hull as measured at the University of Tokyo on a 2.5m model fixed in sinkage and trim (cf. Noblesse and McCarthy 1983). Also shown in the figure are the results of the numerical calculations using the desingularized method. As can be seen, the new node and source placement has made a significant improvement in the bow wave amplitude prediction. The amplitude is larger and the phase has been shifted forward more inline with the experimental results.

Due to the new node placement, the predicted wave resistance coefficient changed from Cw =.00085 found by Beck et al. (1993) to Cw=.001. The experiments show a range of values centering around .00081.

Computations have been done for the forced heave and pitch motions of the modified Wigley hull III. Figure 12 shows the nondimensional surge force, heave force and pitch moment as a function of time for a forced pitching amplitude of 1.5 degrees. The Froude number is .3 and the oscillation

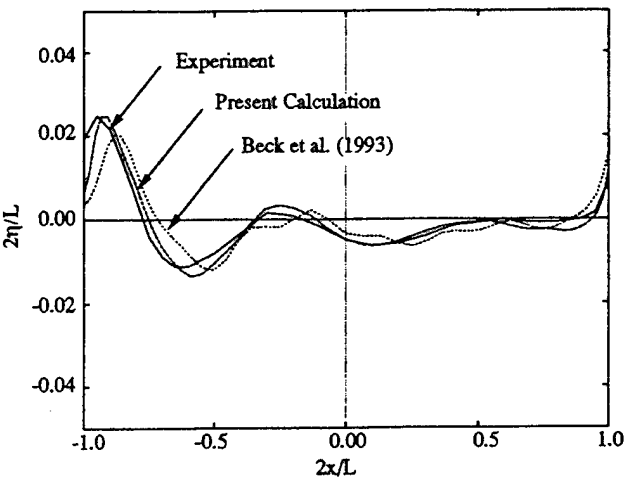


Figure 11: Wave profile along the standard Wigley hull (Fr = 0.25, fixed sinkage and trim)

frequency is $\omega\sqrt{(L/g)}=2.76642$. The number of nodes on the hull surface was 612 and there were 3267 nodes on the free surface. The model was started from rest and smoothly accelerated up to speed. At $t_o^* = t_o\sqrt{\frac{g}{L}} = 14$ the pitch motion was slowly increased to the final amplitude of 1.5 degrees. For both the speed and motion, the smooth increase was of the form:

$$f(t) = f_o(t)\left(1 - e^{-a(t-t_o)^2}\right)\cdot H(t-t_o)$$

where

a = adjustable constant
t_o = time at initial start of motion
H(t) = heaviside step function

In the figure, the total force along with its five separate components are plotted. The five components result from the five terms in the pressure equation (18b). The first component and largest during the initial start-up, is due to the time derivative of the potential following each individual node $(-\rho\frac{\delta\phi}{\delta t})$. The second term is the linear pressure due to the forward speed $\left(-\rho U_o(t)\frac{\partial\phi}{\partial x}\right)$. This is the usual linear pressure component in steady forward motion problems. It is the dominant component for the surge and heave forces. The third is the gravity term due to the change in the integration of $-\rho gz$ over the wetted surface. For steady forward speed this

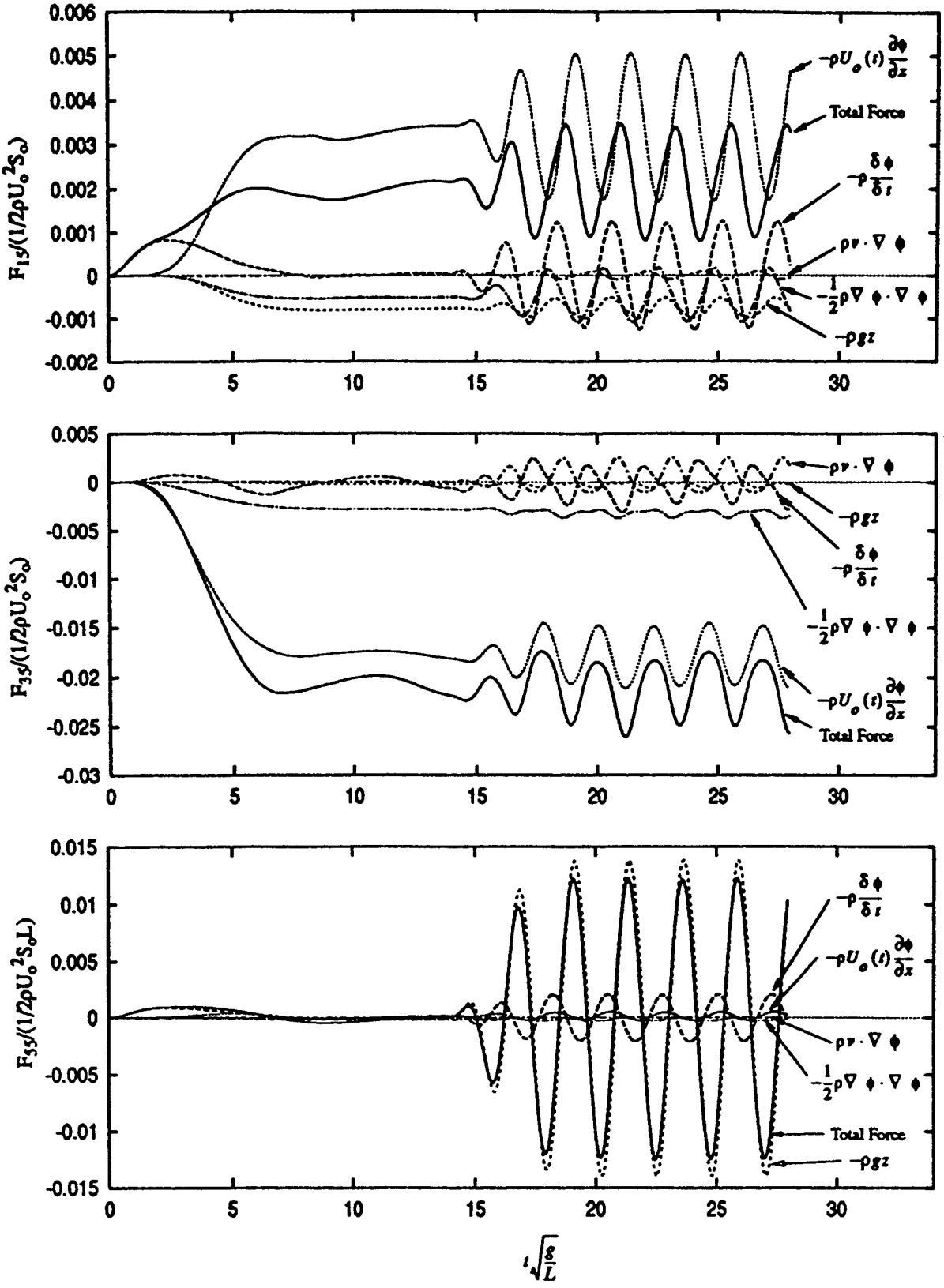


Figure 12: Modified Wigley hull III - force components due to pitch excitation
Fr = 0.3, pitch amplitude = 1.5°, $\omega/(g/L)^{1/2} = 2.76642$

term is proportional to the wave elevation squared and is small and negative. In unsteady motions, this term includes the hydrostatic restoring force and can be the largest component. The fourth component ($-1/2\rho\nabla\phi\cdot\nabla\phi$) is the velocity squared term which is also small and negative. The final component ($\rho v\cdot\nabla\phi$) is the correction for the moving nodes. The node movement is due to the changing wave elevation along the hull that results in the nodes being redistributed along the hull section. For typical computations this component is relatively small; for steady wave resistance this component will go to zero as the wave elevation becomes constant.

The starting sequence of first accelerating the model up to speed and then starting the unsteady motions has been found to minimize the transients compared to starting both the forward speed and the unsteady motions at t*=0. The acceleration to steady forward speed is run first. All the unsteady cases then use this as a starting point. Either way the computations have to be carried out to t*=28 However, the unsteady motion calculations need only be done from t*=14 to t*=28. If the calculations had been started from zero, each frequency would have to be run from t*=0 to t*=28.

Examining the start up phase of t*<14 in figure 12, several characteristics that are typical of the wave resistance problem can be seen. First, the surge force (positive out the stern) is equivalent to the wave resistance. Initially the $-\rho\frac{\delta\phi}{\delta t}$ term is the largest and then decays to zero as the model comes up to speed. As the model reaches steady speed, the linear term is, as expected, the largest component. The component due to the $-\rho gz$ term and the component due to $-1/2\rho\nabla\phi\cdot\nabla\phi$ are the same order of magnitude and both negative.

There is a fairly large sinkage (or negative heave) force acting on the model in steady forward motion. The trim (or pitch) moment starts off as bow up, reverses to bow down and then goes to approximately zero. This is consistent with experimental measurements on the standard hull that found almost no trim angle for a Froude number of .3. In the computations, the model could have been given the freedom to respond to the sinkage force and trim moment, but this is inconsistent with the experiments of Journée that were conducted fixed about the calm waterline. As with the surge force, the biggest component of the heave force is the $-\rho U_o(t)\frac{\partial\phi}{\partial x}$ term.

At t*=14 the forced pitch motion begins. As can be seen, the hydrodynamic forces acting on the model quickly build to steady state. For surge, the two largest components of the force are still the linear terms ($-\rho\frac{\delta\phi}{\delta t}$ and $-\rho U_o(t)\frac{\partial\phi}{\partial x}$). While not obvious because there is not enough time for the steady results to settle down completely, there is a mean shift between the steady portion (t*<14) and the unsteady portion of the curve. This mean shift is the added resistance due to pitch motion. One of the advantages of fully nonlinear calculations is that higher order quantities such as added drag are automatically accounted for.

The character of the heave force is similar to the surge in that the linear components are the most prominent and there is a significant mean shift. Again, the mean shift changes due to the unsteady motions. There also appears to be a low frequency component to the heave force that is a carry over from the original start-up.

As expected, the pitch moment is dominated by the $-\rho gz$ term. This component is a combination of the usual linear hydrostatic restoring moment and the nonlinear effect caused by the varying wetted surface. The other components of the force are all relatively small.

The time histories of the unsteady forces and moments, such as those plotted in figure 12, can be used to determine the equivalent linear added mass and damping coefficients. As shown in Journée (1992), the equivalent linear coefficients are found by equating the actual unsteady force time history to the linear representation of the force using the added mass and damping coefficients. Since the time histories are not perfectly linear, some care must be taken to ensure an equivalent linearization. We have found that Fourier series or least square fit of the data over several cycles yield the same results.

Figures 13 and 14 show the added mass and damping coefficients as a function of frequency for the modified Wigley hull III at a Froude number of .3. Figure 13 is for forced heave and figure 14 is for forced pitch. The experimental results and the other numerical calculations were taken from Journée (1992). Our coordinate system leads to cross coupling coefficients with the opposite sign of those presented in Journée (1992). In order to compare with Journée's and others' results, we have plotted in figures 13 and 14 the negative of our cross coupling coefficients. The strip theory results are computed using the modified strip theory coefficients of Salvesen et al. (1970) with a close fit method to compute the two-dimensional added mass and damping. The three-dimensional hybrid results were computed using the three-dimensional zero speed coefficients calculated by WAMIT and modified for forward speed by the Salvesen et al. (1970) forward speed corrections. In general, the two linearized computations are fairly close indicating that three-dimensional effects are not too important for this relatively slender model.

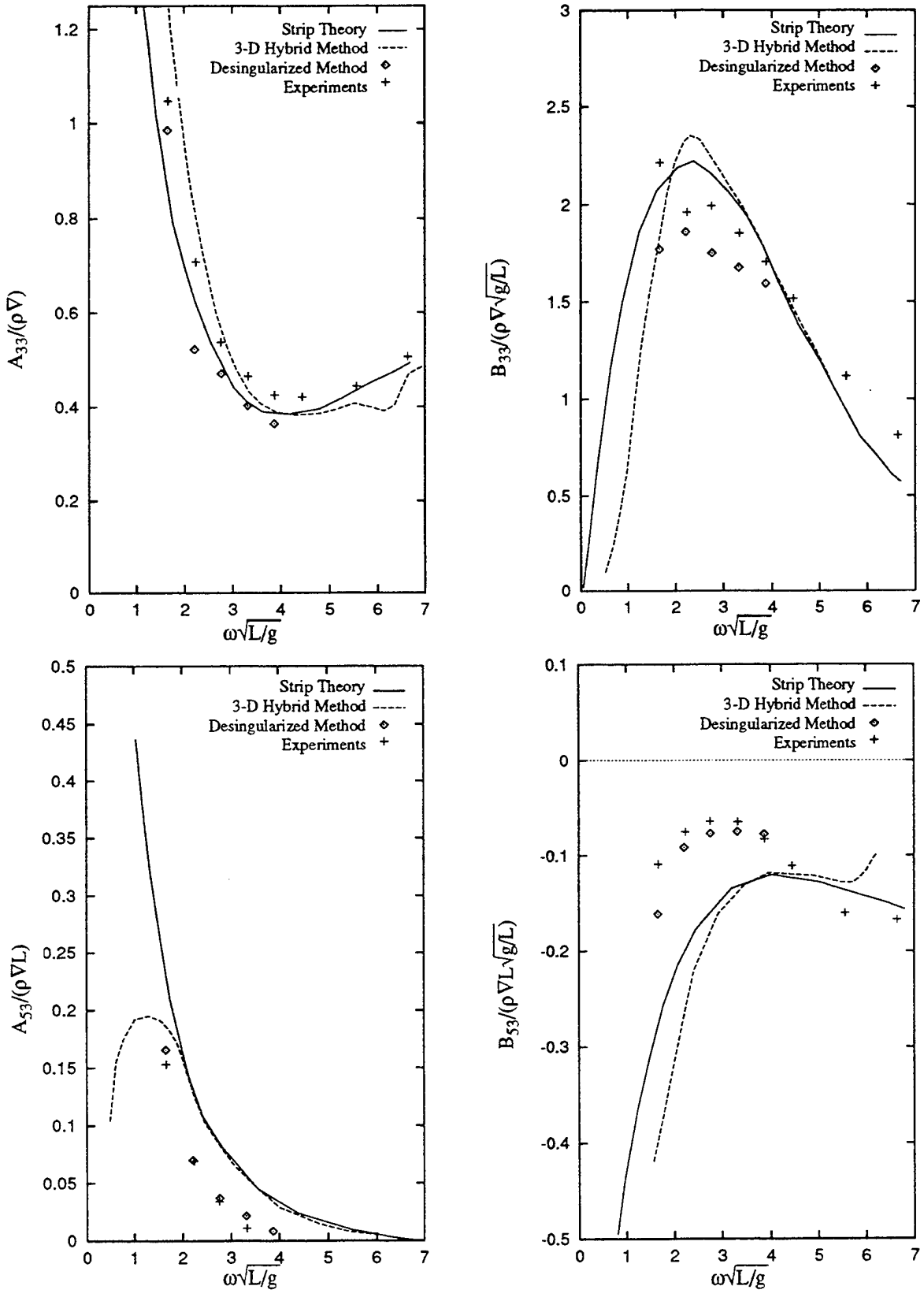


Figure 13: Comparisons of experimental and theoretical added mass and damping coefficients for forced heave (Wigley model III, Fr = 0.3, z_a/L= 0.00833)

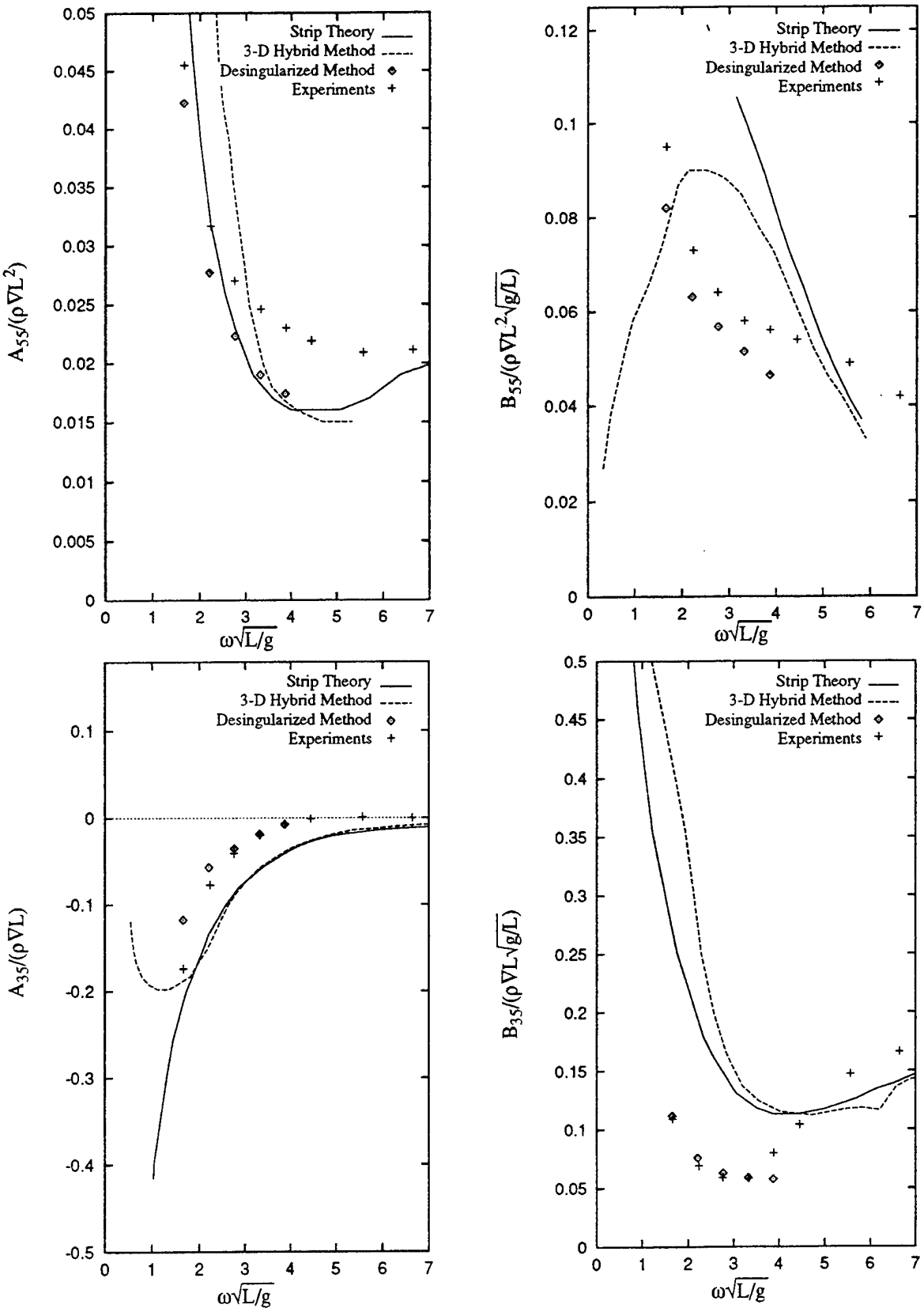


Figure 14: Comparisons of experimental and theoretical added mass and damping coefficients for forced pitch (Wigley model III, Fr = 0.3, pitch amplitude = 1.5°)

As can be seen, the fully nonlinear computations show much better agreement with experiments than either of the linearized computations. The added mass and damping due to heave (A_{33} and B_{33}) are both a little low but the trends of the curves agree with the trends shown by the experiments. The heave damping is over predicted by the linearized computations. The pitch moments due to heave (A_{53} and B_{53}) show excellent agreement in contrast to the linearized predictions that are poor.

As with the heave, the pitch added mass and damping (A_{55}, B_{55}) are underpredicted by the fully nonlinear computations relative to the experiments. However, for pitch damping the nonlinear computations agree with experiments much better than the linear theory predictions. For the pitch added mass, the nonlinear computations are approximately the same as the linear results. The reasons for the underpredictions are not known. It is expected that the damping predictions would be low because viscous effects are neglected.

The fully nonlinear pitch cross-coupling coefficients show very good agreement with experiments. It appears that the cross coupling coefficients are better predicted than the heave and pitch added mass and damping coefficients.

CONCLUSIONS

The desingularized method is a fast and accurate technique to solve fully nonlinear water wave problems. The desingularization allows the use of isolated Rankine sources rather than the more complex panel distributions. Unlike panel methods the free surface and body surface are not discretized with panels, thus avoiding the difficulties associated with compound curvature.

Computations for the Wigley hull have shown that the fully nonlinear calculations greatly improve the predictions of the added mass and damping coefficients relative to those of strip theory or a hybrid three-dimensional method. Further studies for convergence rates and more complex hull forms need to be done.

ACKNOWLEDGEMENTS

This research was funded by the Office of Naval Research Grant Number N-00014-70-J-1818 and the University of Michigan/Sea Grant/ Industry Consortium in Offshore Engineering. Computations were made in part using a CRAY Grant, University Research and Development Program at the San Diego Supercomputer Center.

REFERENCES

1. Baker, G.R., D.I. Meiron, and S.A. Orszag (1982), "Generalized Vortex Methods for Free-Surface Flow Problems," *J. Fluid Mech.*, 123, pp. 477-501.

2. Beck, R.F., Y. Cao and T.-H. Lee (1993), "Fully Nonlinear Water Wave Computations Using the Desingularized Method," *Proceedings* 6th International Conference on Numerical Ship Hydrodynamics, University of Iowa.

3. Bertram, V. (1990), "Ship Motions by Rankine Source Method," *Ship Technology Research*, Vol. 37, No. 4, pp. 143-152.

4. Bertram, V., W.W. Schultz, Y. Cao, and R.F. Beck (1991), "Nonlinear Computations for Wave Drag, Lift and Moment of a Submerged Spheroid," *Ship Technology Research*, Vol. 38, No. 1, pp. 3-5.

5. Cao, Y., W.W. Schultz and R.F. Beck (1990), "Three-Dimensional, Unsteady Computations of Nonlinear Waves Caused by Underwater Disturbances," *Proceedings* 18th Symposium on Naval Hydrodynamics, Ann Arbor, Michigan, pp. 417-427.

6. Cao, Y. (1991), "Computations of Nonlinear Gravity Waves by a Desingularized Boundary Integral Method," Ph.D. Thesis, Technical Report No. 91-3, Department of Naval Architecture and Marine Engineering, The University of Michigan, Ann Arbor, Michigan, USA.

7. Cao, Y., W.W. Schultz and R.F. Beck (1991), "A Three-Dimensional Desingularized Boundary Integral Method for Potential Problems," *International Journal of Numerical Methods in Fluids*, Vol. 11, pp. 785-803.

8. Cao, Y., T. Lee and R.F. Beck (1992), "Computation of Nonlinear Waves Generated by Floating Bodies," 7th International Workshop on Water Waves and Floating Bodies, Val de Reuil, France, pp. 47-52.

9. Cao, Y., R.F. Beck and W.W. Schultz (1993), "Numerical Computations of Two-Dimensional Solitary Waves Generated by Moving Disturbances," *International Journal for Numerical Methods in Fluids*, Vol. 17, pp. 905-920.

10. Cointe, R., P. Geyer, B. King, B. Molin, and M. Tramoni (1990), "Nonlinear and Linear Motions of a Rectangular Barge in a Perfect Fluid," *Proceedings* 18th Symposium on Naval Hydrodynamics, Ann Arbor, MI, pp. 85-99.

11. Dommermuth, D.G. and D.K.P. Yue (1987), "Numerical Simulations of Nonlinear Axisymmetric Flows With a Free Surface," *Journal of Fluid Mechanics*, Vol. 178, pp. 195-219.

12. Faltinsen, O.M. (1977), "Numerical Solution of Transient Nonlinear Free-Surface Motion Outside or Inside Moving Bodies, *Proceedings 2nd Conf. on Num. Ship. Hydro.*, U.C. Berkeley, (ed. J.V. Wehausen and N. Salvesen), pp. 347-357, University Extension Publications.

13. Jensen, G., H. Söding and Z.-X. Mi (1986), "Rankine Source Methods for Numerical Solution of the Steady Wave Resistance Problem," *Proceedings* 16th Symposium on Naval Hydrodynamics, University of California, Berkeley, pp. 575-582.

14. Jensen, G., V. Bertram and H. Söding (1989), "Ship Wave-Resistance Computations," *Proceedings* 5th International Conference on Numerical Ship Hydrodynamics, Hiroshima, Japan, pp. 593-606.

15. Journée, J.M.J. (1992), "Experiments and Calculations on Four Wigley Hull Forms," Report No. 909, Ship Hydromechanics Laboratory, Delft University of Technology, Delft, The Netherlands.

16. Kang, C.-G. and I.Y. Gong (1990), "A Numerical Solution Method for Three-Dimensional Nonlinear Free Surface Problems," *Proceedings* 18th Symposium on Naval Hydrodynamics, Ann Arbor, Michigan, pp. 427-438.

17. Lee, T.-H (1992), "Nonlinear Radiation Problems for a Surface-Piercing Body," Ph.D. Thesis, Report No. 323, Department of Naval Architecture and Marine Engineering, University of Michigan, Ann Arbor, Michigan.

18. Lin, W.M., J.M. Newman and D.K. Yue (1984), "Nonlinear Forced Motions of Floating Bodies," *Proceedings* 15th Symposium on Naval Hydrodynamics, Hamburg, pp. 33-49, Washington: National Academy Press.

19. Longuet-Higgins, M.S. and E.D. Cokelet (1976), "The Deformation of Steep Surface Waves on Water: I. A Numerical Method of Computation," *Proc. R. Soc. Lond.*, A350, pp. 1-26.

20. Noblesse, F. and J.H. McCarthy (1983), editors, "Ship Wave-Resistance Computations," *Proceedings* of the Second DTNSRDC Workshop.

21. Raven, H.C. (1992), "A Practical Nonlinear Method for Calculating Ship Wavemaking and Wave Resistance," *Proceedings* 19th Symposium on Naval Hydrodynamics, Seoul, Korea.

22. Salvesen, N., E. O. Tuck and O. Faltinsen (1970), "Ship Motions and Sea Loads," *Trans.* Soc. of Naval Arch. and Marine Engin., Vol. 78, pp. 250-287

23. Saubestre, V. (1990), "Numerical Simulation of Transient Nonlinear Free-Surface Flows with Body Interaction," Technical Report 90-52, Department of Mechanical and Environmental Engineering, University of California, Santa Barbara.

24. Schultz, W.W. and S.W. Hong (1989), "Solution of Potential Problems Using an Overdetermined Complex Boundary Integral Method," *J. Comput. Phys.*, No. 84, pp. 414-440.

25. Sen, D. (1993), "Numerical Simulation of Motions of Two-Dimensional Floating Bodies," *Journal of Ship Research*, Vol. 37, No. 4, pp. 307-330.

26. Vinje, T. and P. Brevig (1981), "Nonlinear Ship Motions," *Proceedings* 3rd International Symp. Num. Ship Hydro., Paris, pp. 257-268, Bassin d'Essais des Carenes, France.

27. Webster, W.C. (1975), "The Flow About Arbitrary, Three-Dimensional Smooth Bodies," *J. Ship Research,* No. 19, pp. 206-218.

28. Yeung, R.W. (1982), "The Transient Heaving Motion of Floating Cylinders," *Journal of Engineering Mathematics*, Vol. 16, pp. 97-119.

29. Zhou, Z. and M. Gu (1990), "A Numerical Research of Nonlinear Body-Wave Interactions," *Proceedings* 18th Symposium on Naval Hydrodynamics, Ann Arbor, MI., pp. 103-118.

DISCUSSION

Z. Zou
Universitat Hamburg, Germany

I think your desingularized method corresponds to a first-order panel method, or better to say a zero-order panel method. I wonder if your method can also be used to calculate the higher order derivatives of the velocity potential due to the simple isolated sources at nodes or collocation points on the body surface?

AUTHORS' REPLY

The desingularized method can be used to calculate higher order derivatives at any point on the body or in the fluid. Once the desingularized source strength is known, higher order derivatives can be computed analytically. Because of the desingularization all velocities and higher order derivatives are continuous everywhere on the body surface.

Observations of Cavitating Flows

C. Brennen
(California Institute of Technology, USA)

ABSTRACT

This paper will present a review of some of the recent advances in our understanding of the dynamics and acoustics of cavitating flows. We focus first on the individual events which evolve from a single travelling nucleus and describe observations of the intricate micro-fluid-mechanics which affect both the bubble shape and the subsequent emission of noise. These phenomena have important consequences in terms of their implications for the scaling of cavitation damage and noise. We also present calculations of the interaction between the individual traveling bubbles and the irrotational flow outside of the boundary layer of the headform. Comparisons of predicted and experimentally observed bubble shapes show qualitative agreement but further work is neccessary to understand the details of the interactions between the viscous boundary layer and the bubble.

To model the processes of cavitation inception, noise and damage it is neccessary to generate a model of the cavitation event rate which can then be coupled with the consequences of the individual events. In the second part of this paper we describe recent efforts to connect the observed event rates to the measured distributions of cavitation nuclei in the oncoming stream. Such studies neccessarily raise questions regarding the nuclei distributions in water tunnels and in the ocean and it would seem that we still know little of the nuclei population dynamics in either context. This is illustrated by a few observations of the population dynamics in a particular facility.

The third subject addressed in this paper is the question of the noise produced by an individual travelling cavitation event. It is shown that the distortions in the shape of cavitation bubbles leads to acoustic impulses which are about an order of magnitude smaller than those predicted by the spherical bubble dynamics of the Rayleigh-Plesset equation. However, at the higher cavitation numbers, the upper bound on the experimental impulses scales with speed and size much as one would expect from the spherical bubble analysis. Initially, as the cavitation number is decreased, the impulse increases as expected. But, beyond a certain critical cavitation number, the noise again decreases in contrast to the expected increase. This phenomenon is probably caused by two effects, namely the interaction between events at the higher event densities and the reduction in the impulse due to a change in the dominant type of cavitation event.

From the single event we then move to the larger scale structures and the interactions which occur when the density of the events becomes large and individual bubbles begin to interact. One of the more important interaction phenomena which occur results from the behaviour of a cloud of cavitation bubbles. Most previous theoretical studies of the dynamics of cavitating clouds have been linear or weakly non-linear analyses which have identified the natural frequencies and modes of cloud oscillation but have not, as yet, shown how a cloud would behave during the massively non-linear response in a cavitating flow. We present non-linear calculations which show the development of an inwardly propagating shock wave during the collapse phase of the motion. These observations confirm the earlier speculation of Mørch and his co-workers.

INTRODUCTION

Recent years have seen a significant advance of our understanding of the dynamics and acoustics of cavitating flows and the purpose of this paper will be to attempt to summarize some of the improvements in our knowledge of these hydrodynamic and acoustic phenomena.

We begin by describing the effect of the flow on a single cavitation "event", the term used to denote the processes which follow when an individual cavitating nucleus is convected into a region of low pressure. The pioneering observations of single

events which were made by Knapp (see, for example, Knapp and Hollander 1948) were followed by the analyses of Plesset (1949), Parkin (1952) and others who sought to model these observations of the growth and collapse of a travelling cavitation bubble using Rayleigh's equation for the dynamics of a spherical bubble (Rayleigh 1917). Parkin opined that the lack of agreement between the theory and his experimental observations was due to the neglect of the boundary layer. Rayleigh-Plesset models of travelling bubble cavitation which attempted to incorporate the effects of the boundary layer followed and included the work of Oshima (1961), Van der Walle (1962), Holl and Kornhauser (1970) and Johnson and Hsieh (1966). Like Plesset's and Parkin's original models these improved versions continued to make two assumptions, namely that the bubbles remain spherical (except in the later phase of collapse) and that bubbles or events do not interact with one another. Most of the present paper will focus on the departure from these assumptions which occur in real flows and the consequences of these departures in so far as damage potential and noise emission are concerned.

Observations of real flows demonstrate that even single cavitation bubbles are often far from spherical. Indeed, they may not even be single bubbles but rather a cloud of smaller bubbles. In recent years, it has become clear that departure from sphericity often occurs as a result of the interaction of the bubble with the pressure gradients and shear forces in the flow. We shall begin by examining some of these effects while still assuming that the events are sufficiently far apart in space and time that they do not interact with one another or modify the global liquid flow in any significant way.

Before describing some of the experimental observations of bubble/flow interactions, it is valuable to consider the relative sizes of the cavitation bubbles and the viscous boundary layer. In the flow of a uniform stream of velocity, U, around an object such as a hydrofoil with typical dimension, ℓ, the thickness of the laminar boundary layer near the minimum pressure point will be given qualitatively by $\delta \approx (\nu\ell/U)^{\frac{1}{2}}$ where ν is the kinematic viscosity of the liquid. Parenthetically we note that transition to turbulence usually occurs downstream of the point of minimum pressure and consequently the laminar boundary layer thickness is the appropriate dimension for limited cavitation confined to the immediate neighbourhood of the low pressure region. Moreover, the asymptotic growth rate of a bubble yields a typical maximum bubble radius, R_M, given by

$$R_M \approx 2\ell(-\sigma - C_{pmin}) \qquad (1)$$

where σ is the cavitation number defined as $2(p_\infty - p_v)/\rho U^2$ where p_∞ and p_v are respectively the upstream and vapor pressures and ρ is the liquid density. The coefficient of pressure, C_p, is defined as $2(p - p_\infty)/\rho U^2$ where p is the local pressure in the flow and C_{pmin} denotes the minimum pressure coefficient in the flow. It follows that the ratio of the boundary layer thickness to the maximum bubble radius, δ/R_M, is given approximately by

$$\frac{\delta}{R_M} = \frac{1}{2(-\sigma - C_{pmin})}\left\{\frac{\nu}{\ell U}\right\}^{\frac{1}{2}} \qquad (2)$$

Therefore, provided $(-\sigma - C_{pmin})$ is of the order of 0.1 or greater, it follows that for the high Reynolds numbers, $U\ell/\nu$, which are typical of most of the flows in which cavitation is a problem, the boundary layer is usually much thinner than the typical dimension of the bubble. This does not mean the boundary layer is unimportant. But we can anticipate that those parts of the cavitation bubble furthest from the solid surface will interact with the primarily inviscid flow outside the boundary layer, while those parts close to the solid surface will be affected by the boundary layer and the shear forces associated with it.

When the frequency of cavitation events increases in space or time such that they begin to interact with one another a whole new set of phenomena may be manifest. They may begin to interact hydrodynamically with important consequences for both the global flow and the dynamics and acoustics of the individual bubble. For example, clouds of cavitating bubbles are often shed from a cavitating foil and the coherent dynamics of the cloud can result in a collapse process which has much greater potential for noise production and damage than the individual bubbles would have acting independently (see, for example, Soyama *et al.* 1992).

INDIVIDUAL EVENTS

Some of the early (and classic) observations of individual travelling cavitation bubbles by Knapp and Hollander (1948), Parkin (1952) and Ellis (1952) make mention of the deformation of the bubbles by the flow. But the focus of attention soon shifted to the easier observations of the dynamics of individual bubbles in quiescent liquid

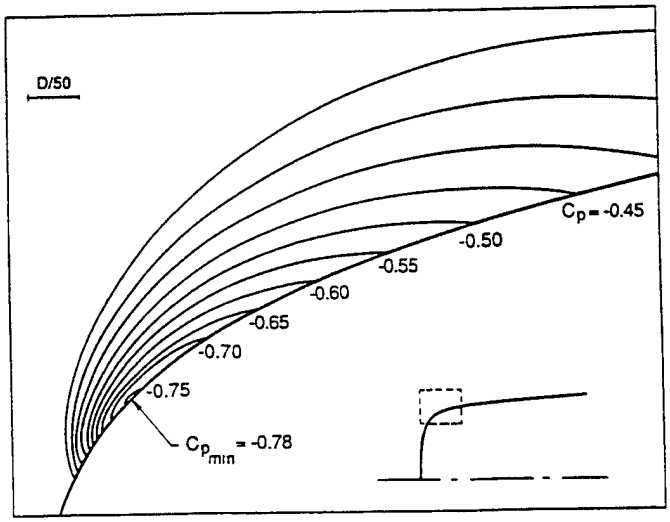


Figure 1: Isobars in the vicinity of the minimum pressure point on the axisymmetric Schiebe headform with values of the pressure coefficient, C_p, as indicated. The pressures were obtained from a potential flow calculation. The insert shows the headform shape and the area that has been enlarged in the main figure (dashed lines). From Schiebe (1972) and Kuhn de Chizelle *et al.* (1992).

and it is only recently that investigations of the deformation caused by the flow have resumed. Both Knapp and Hollander (1948) and Parkin (1952) observed that almost all cavitation bubbles are closer to hemispherical than spherical and that they appear to be separated from the solid surface by a thin film of liquid. Such bubbles are clearly evident in other photographs of travelling cavitation bubbles on a hydrofoil such as those of Blake *et al.* (1977) or Briançon-Marjollet *et al.* (1990).

A number of recent research efforts have focussed on these bubble/flow interactions including the work of van der Meulen and van Renesse (1989) and Briançon-Marjollet *et al.* (1990). Recently, Ceccio and Brennen (1991) and Kuhn de Chizelle *et al.* (1992) have made an extended series of observations of cavitation bubbles in the flow around axisymmetric bodies including studies of the scaling of the phenomena. Two axisymmetric body shapes were used, both of which have been employed in previous cavitation investigations. The first of these was a so-called "Schiebe body" (Schiebe 1972). One of the important characteristics of this shape is that the boundary layer does not separate in the region of low pressure within which cavitation bubbles occur. The second body had the ITTC headform shape which was originally used by Lindgren and Johnsson (1966) and exhibits laminar separation within the region in which the cavitation bubbles occur. For both headforms, the isobars in the neighbourhood of the minimum pressure point exhibit a large pressure gradient normal to the surface as illustrated by the isobars for the Schiebe body shown in figure 1. This pressure gradient is associated with the curvature of the body and therefore the streamlines in the vicinity of the minimum pressure point. Consequently, at a given cavitation number, σ, the region below the vapor pressure which is enclosed between the solid surface and the $C_p = -\sigma$ isobaric surface is long and thin compared with the size of the headform. Only nuclei which pass through this thin volume will cavitate.

The observations of Ceccio and Brennen (1991) at relatively low Reynolds numbers will be described first. Typical photographs of bubbles on the $5.08cm$ diameter Schiebe headform during the cycle of bubble growth and collapse are shown in figure 2. Simultaneous profile and plan views provide a more complete picture of the bubble geometry. In all cases the shape during the initial growth phase was that of a spherical cap, the bubble being separated from the headform surface by a thin layer of liquid of the same order of magnitude as the boundary layer thickness. Later developments depend on the geometry of the headform and the Reynolds number so we begin with the simplest case, namely the Schiebe body at relatively low Reynolds number. Typical photographs for this case are included in figure 2. As the bubble begins to enter the region of adverse pressure gradient the exterior frontal surface begins to be pushed inward

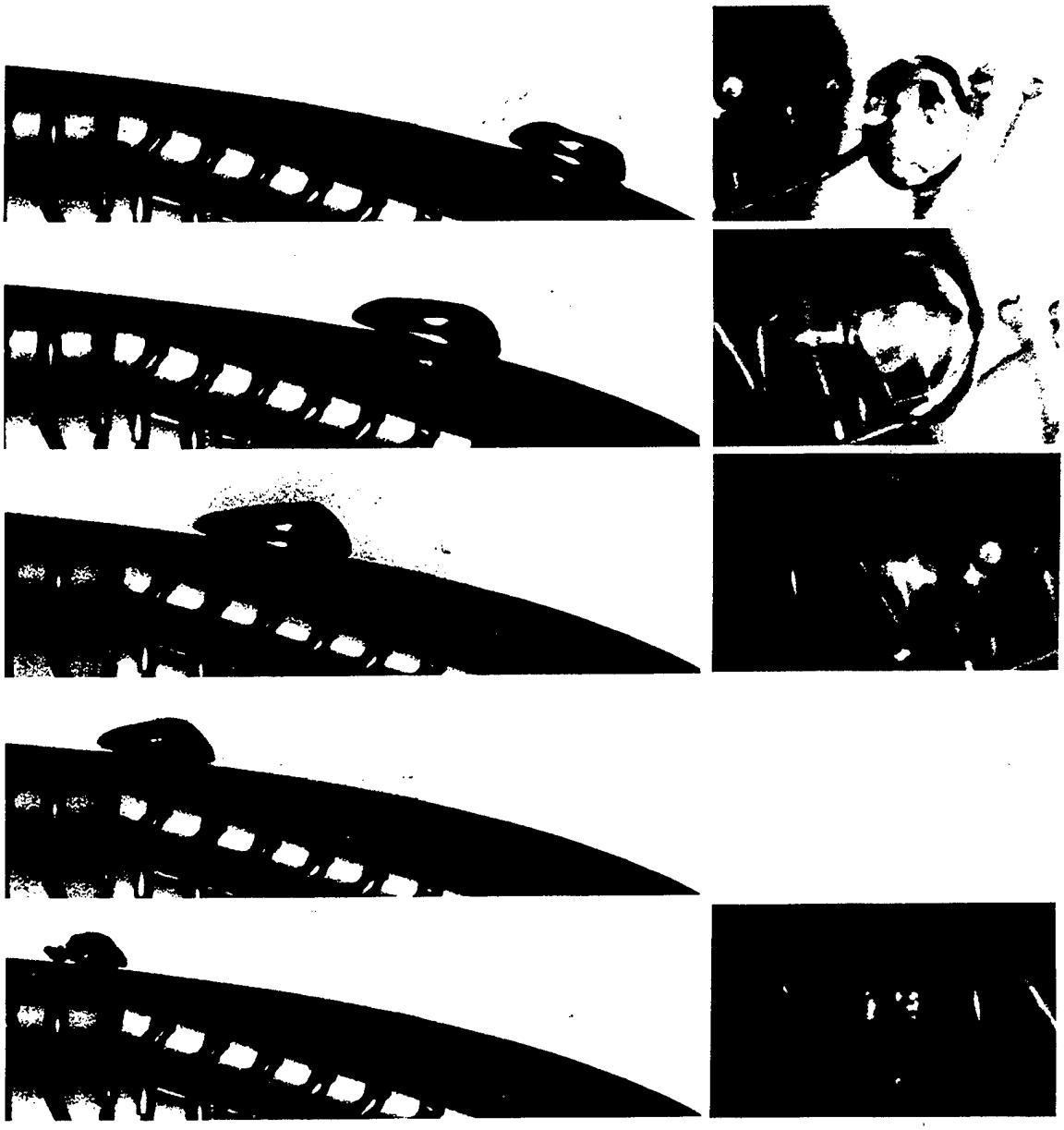


Figure 2: A series of photographs illustrating the growth and collapse of travelling cavitation bubbles in a flow around a 5.08cm diameter Schiebe headform at $\sigma = 0.45$ and a speed of 9 m/s. Simultaneous profile and plan views are presented but each row is, in fact, a different bubble. The flow is from right to left. The scale is 4.5 times lifesize. From Ceccio and Brennen (1991).

causing the profile of the bubble to appear wedge-like. Thus the collapse is initiated on the exterior frontal surface of the bubble and this often leads to the bubble fissioning into forward and aft bubbles as seen in figure 2.

But, two other processes are occuring at the same time. First, the streamwise thickness of the bubble decreases faster than its spanwise breadth (spanwise being defined as the direction parallel to the headform surface and normal to the oncoming stream) so that the largest dimension of the bubble is its spanwise breadth. Second, the bubble acquires significant spanwise vorticity through its interactions with the boundary layer during the growth phase. Consequently, as the collapse proceeds this vorticity is concentrated and the bubble

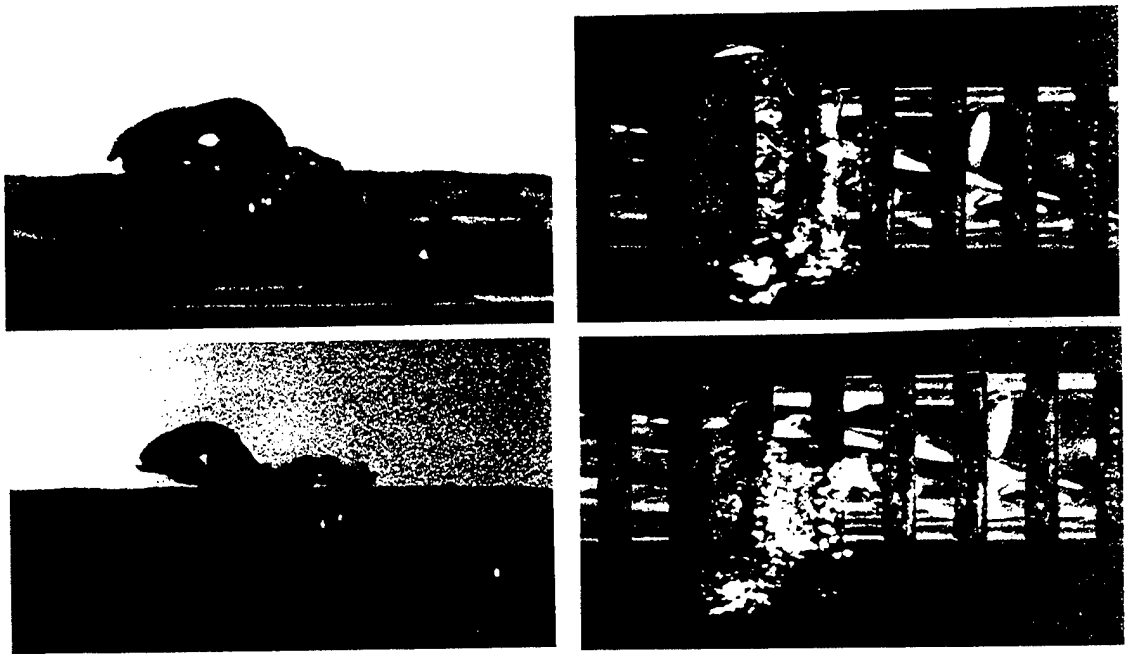


Figure 3: Examples from Ceccio and Brennen (1991) illustrating the instability of the liquid layer under a travelling cavitation bubble (for $\sigma = 0.45$ and a speed of 8.7 m/s). The photographs are 3.8 times lifesize.

evolves into one (or two or possibly more) cavitating vortices with spanwise axes. These vortex bubbles proceed to collapse and seem to rebound as a cloud of much smaller bubbles. Often a coherent second collapse of this cloud was observed when the bubbles were not too scattered by the flow. Ceccio and Brennen (1991) (see also Kumar and Brennen 1993b) conclude that the flow-induced fission prior to collapse can have a substantial effect on the noise impulse.

Two additional phenomena were observed on the headform which exhibited laminar separation, namely the ITTC headform. The first of these was the observation that the layer of liquid underneath the bubble would become disrupted by some instability. As seen in figure 3 this results in a bubbly layer of fluid which subsequently gets left behind the main bubble. Thus the instability of the liquid layer leads to another mechanism of bubble fission. Because of the physical separation, the bubbly layer would collapse after the main body of the bubble.

The second and perhaps more consequential phenomenon observed with the ITTC headform only occurs with the occasional bubble. Infrequently, when a bubble passes the point of laminar separation, it triggers the formation of local "attached cavitation" streaks at the lateral or spanwise extremities of the bubble as seen in figure 4. Then, as the main bubble proceeds downstream, these "streaks" or "tails" of attached cavitation are stretched out behind the main bubble, the trailing ends of the tails being attached to the solid surface. Subsequently, the main bubble collapses first leaving the "tails" to persist for a fraction longer as illustrated by the lower photograph in figure 4.

The importance of these occasional "events with tails" did not become clear until tests were conducted at much higher Reynolds numbers, with larger headforms (up to 50.5cm in diameter) and somewhat higher speeds (up to 15 m/s). These tests were part of an investigation of the scaling of the bubble dynamic phenomena described above (Kuhn de Chizelle *et al.* 1992) which was conducted in the Large Cavitation Channel (LCC, Morgan 1990). One notable observation was the presence of a "dimple" on the exterior surface of all the individual travelling bubbles; examples of this dimple are included in figure 5. They are not the precursor to a re-entrant jet for the dimple seems to be relatively stable during most of the collapse process. More importantly, it was observed that, at higher Reynolds number, "attached tails" occurred even on these Schiebe bodies which did not normally exhibit laminar separation. Moreover, the probability of occurence of attached tails

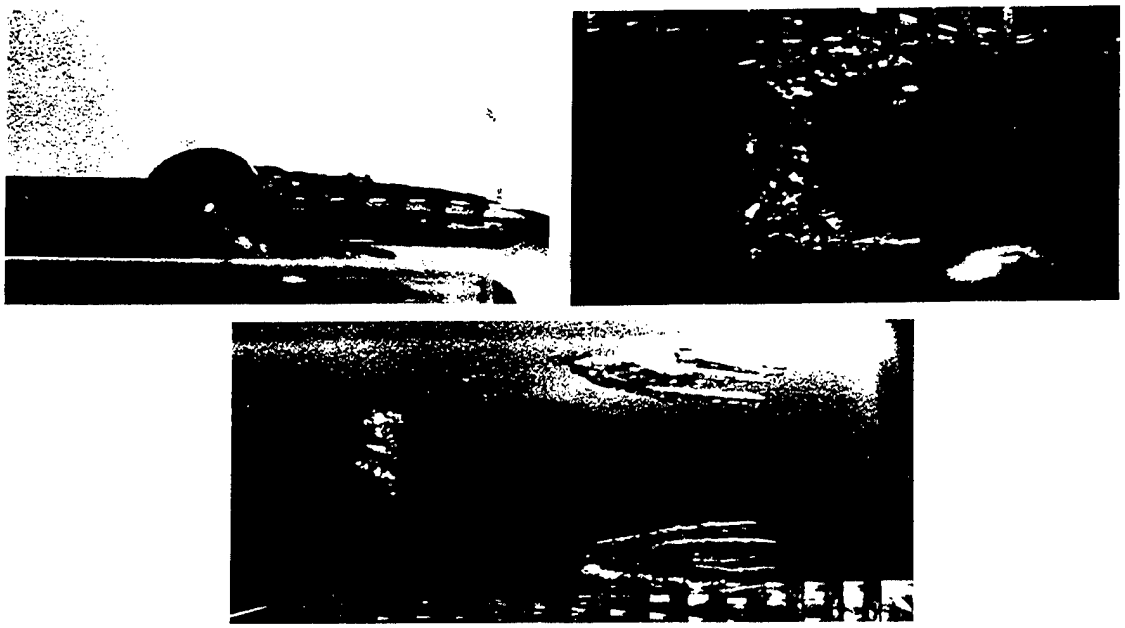


Figure 4: Examples from Ceccio and Brennen (1991) illustrating the attached tails formed behind a travelling cavitation bubble (for $\sigma = 0.42$ and a speed of 9 m/s). The top two are simultaneous profile and plan views. The bottom shows the persistence of the tails after the bubble has collapsed. The photographs are 3.8 times lifesize.

increased as the Reynolds number increased and the attached cavitation began to be more extensive. As the Reynolds number increased further, the bubbles would tend to trigger attached cavities over the entire wake of the bubble as seen in the lower two photographs in figure 5. Moreover the attached cavitation would tend to remain for a longer period after the main bubble had disappeared. Eventually, at the highest Reynolds numbers tested it appeared that the passage of a single bubble was sufficient to trigger a "patch" of attached cavitation (figure 5, bottom) which would persist for an extended period after the bubble had long disappeared. We note that Howison *et al.* (1993) have recently examined an inviscid model for such patch cavities.

This progression of events and the changes in the probabilities of the different kinds of events with Reynolds number imply a rich complexity in the micro-fluidmechanics of cavitation bubbles, much of which remains to be understood. Its importance lies in the fact that these different types of events cause differences in the collapse process which, in turn, alters the noise produced (see Kuhn de Chizelle *et al.* 1992) and, in all probability, the potential for cavitation damage. For example, the events with attached tails were found to produce significantly less noise than the events without tails. Due to the changes in the probabilities of occurence of these events with Reynolds number, this implies a scaling effect which had not been previously recognized. It also suggests some possible strategies for the reduction of cavitation noise and damage.

When examined in retrospect, one can identify many of these phenomena in earlier photographic observations, including the pioneering, high-speed movies taken by Knapp. As previously remarked, Knapp and Hollander (1948), Parkin (1952) and others noted the spherical-cap shape of most travelling cavitation bubbles. The ITTC experiments (Lindgren and Johnsson 1966) emphasized the diversity in the kinds of cavitation events which could occur on a given body and later authors attempted to identify, understand and classify this spectrum of events. For example, Holl and Carroll (1979) observed a variety of different types of cavitation events on axisymmetric bodies and remarked that both travelling and attached cavitation "patches" occurred and could be distinguished from travelling bubble cavitation. A similar study of the different types of cavitation events was reported by Huang (1979) whose "spots" are synonymous with "patches".

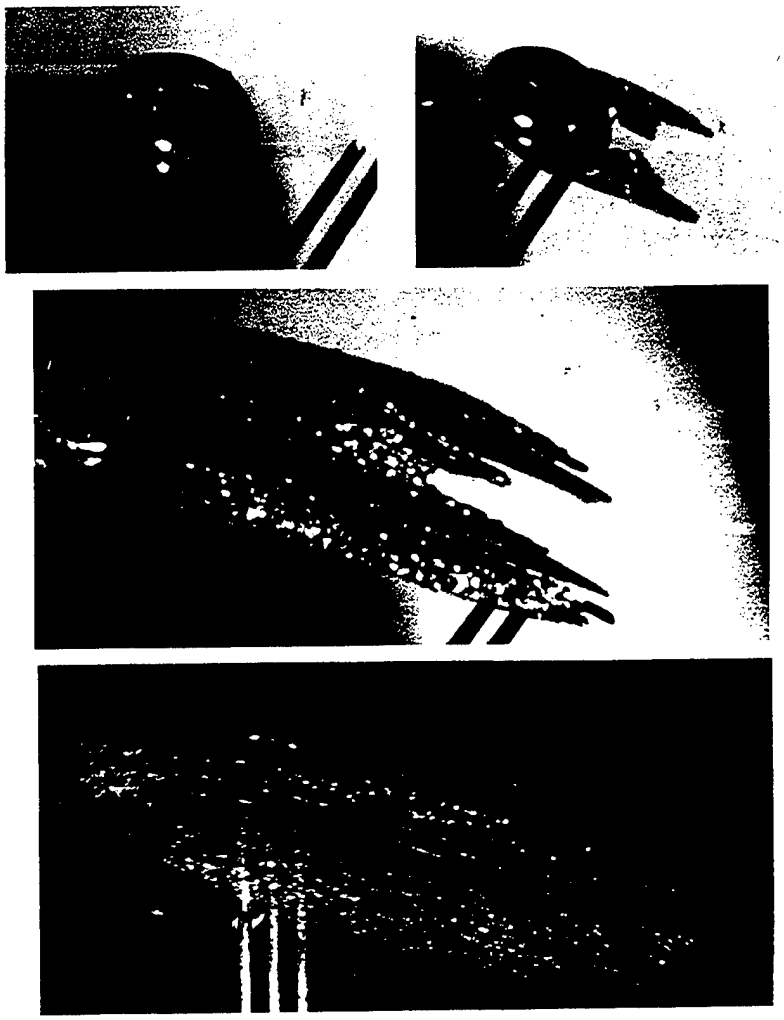


Figure 5: Typical cavitation events from the scaling experiments of Kuhn de Chizelle *et al.* (1992) showing an unattached bubble with "dimple"(upper left), a bubble with attached tails (upper right) and a transient bubble-induced patch (middle) all occuring on the $50.8cm$ diameter Schiebe headform at $\sigma = 0.605$ and a speed of 15 m/s. The bottom photograph shows a patch on the $25.4cm$ headform at $\sigma = 0.53$ and a speed of 15 m/s. The flow is from right to left. The top four are shown at 1.3 times lifesize and the bottom at 1.25 times lifesize.

MODELLING THE BUBBLE DYNAMICS

It is clear that the Rayleigh-Plesset analysis of a spherical bubble cannot reproduce many of the phenomena described in the preceding section. To study this further, Kuhn de Chizelle *et al.* (1994) developed an unsteady numerical code which models the bubbles using travelling sources and incorporates the distortion caused by the pressure gradients in the flow around the body. Only the irrotational flow outside of the boundary layer is addressed so the interaction of the bubble and the boundary layer is not treated by this method. The objective was to focus on the interaction of the bubble with the irrotational flow and the resulting shape of the exterior surface of the bubble. Different, viscous flow analyses would be needed to study the phenomena of the liquid layer instablity and the triggering of attached cavitation.

The basic, simplifying assumption behind the model is that the perturbations in the irrotational flow caused by the bubble can be fairly accurately modelled by a simple travelling source of adjustable intensity and position and that, once an image source is added to substantially satisfy the boundary condition on the headform surface, the remain-

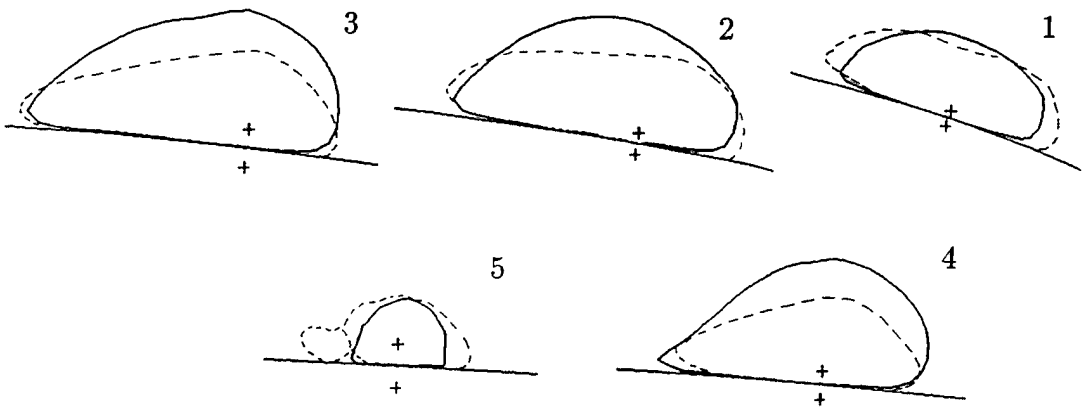


Figure 6: Comparison between the profiles of bubbles in figure 2 (dashed lines) and the profiles calculated by Kuhn de Chizelle *et al.* (1994) (solid lines) at five different moments during growth and collapse, consecutively numbered 1 through 5. The flow is from right to left. The locations of the source and the image source are shown by the crosses.

ing corrections which are required involve small modifications of the basic structure of the flow. It is, of course, possible to solve the inviscid, irrotational problem by using a boundary integral method in which the surface of the headform and the surface of the bubble are divided into boundary elements. Indeed, Chahine (1992) made some preliminary calculations of this kind. However, the travelling source method has the advantage of improved resolution of the bubble dynamics at much reduced computational time. The method could also be extended to allow studies involving more than one bubble so that interaction effects might be examined.

Typical results are presented in figure 6 where the bubble profiles from the photographs of figure 2 are compared with the profiles computed at the same five moments in time (labelled 1 to 5) during the bubble evolution. It can be seen that the overall size of the bubbles are in good agreement with the observations and that there is qualitative agreement in the general shape of the bubble as well as the way it changes with time. The program reproduces the spherical-cap shapes which are separated from the headform by a thin liquid layer. During the growth phase we note a minor depression in the top of the cap which is reminiscent of the dimples on the top of the bubbles observed by Kuhn de Chizelle *et al.* (1992) but is not as pronounced. Later the bubble assumes the wedge-like shape similar to the experiments. The computed bubbles are not, however, as elongated as those observed experimentally, particularly at the higher cavitation numbers; the probable reason for this is that the shape distortions which can be modelled by a single source are limited. Clearly, however, dipoles or higher order models for the bubble would allow more distorted bubble shapes.

One of the advantages of such a calculation is that it allows computation of the unsteady pressure field surrounding the bubble. This allows evaluation of potential interactions between bubbles. By examining the flow perturbations for different cavitation numbers, the potential for bubble/bubble interactions can be evaluated. Moreover, the present method could readily be extended to include a number of simultaneous cavitation events and therefore allow direct evaluation of these interactions.

CAVITATION EVENT RATES

In order to synthesize the cumulative effects of a stream of travelling cavitation bubbles it is neccessary to supplement the details of individual events with the rates at which these events occur. In this section we shift attention to this other aspect of the problem, namely the prediction of the event rate.

Many investigators have anticipated a relationship between the cavitation event rate and the concentration of cavitation nuclei in the oncoming stream (see, for example, Schiebe, 1972, Keller, 1972 and 1974, Keller and Weitendorf, 1976, Kuiper, 1978, Gates and Acosta, 1978). At first sight this seems like a straightforward problem of computing the flux of nuclei into the region for which $C_p < -\sigma$. However many complications

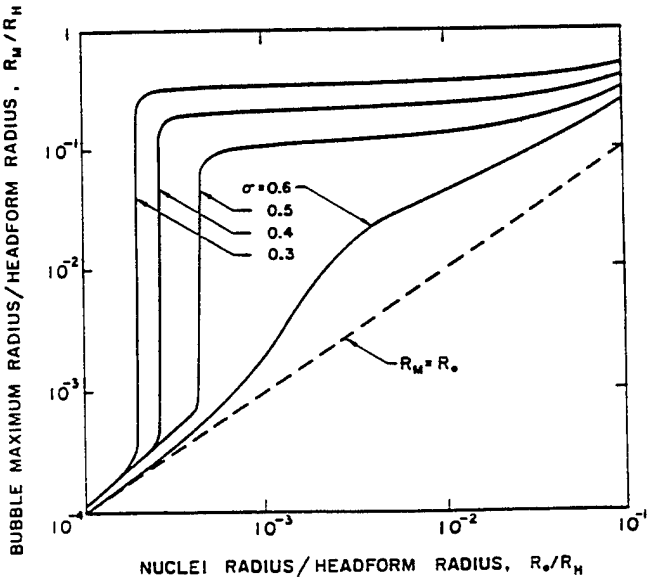


Figure 7: The maximum size, R_M, to which a cavitation bubble grows according to the Rayleigh-Plesset equation as a function of the original nucleus size, R_o, and the cavitation number, σ, in the flow around the Schiebe headform with Weber number, $\rho R_H U^2/S = 28000$.

arise which make this analysis more complex than might otherwise appear and we shall discuss some of the specific issues below. But these difficulties do not account for the lack of experimental research into the relationship. Rather, the difficulties involved in the accurate measurement of the incoming nuclei number distribution function, $N(R)$, have been responsible for the delay in any detailed, quantitative investigation of this component of the problem. By definition, $N(R)dR$ is the number of nuclei with size between R and $R + dR$ per unit volume. As Billet (1985) remarked in his review of nuclei measurement techniques, the only reliable method of obtaining $N(R)$ has been the extremely time consuming method of surveying a reconstruction of an *in situ* hologram of a small volume of tunnel water. However, the time and effort required to construct one $N(R)$ distribution by this method has seriously limited the scope of these investigations.

The recent development of light scattering instruments employing phase doppler techniques (Saffman *et al.* 1984, Tanger *et al.* 1992) has improved the situation. In our own laboratory we have attempted to validate and calibrate a Dantec Phase Doppler Anemometer (PDA) instrument by taking simultaneous measurements with the PDA and a holographic system (Liu *et al.* 1993a). The great advantage of the PDA system is the speed with which $N(R)$ can be measured. After validation, the PDA system could be used with confidence for investigations of the nuclei population dynamics in a water tunnel and of the aforementioned relation between $N(R)$ and the cavitation event rate.

The population dynamics within a facility are important because they determine the rate of change of $N(R)$ with run time and its dependence on tunnel velocity, pressure and air content. However, the dynamics probably vary considerably from one facility to another depending, for example, on whether the facility has a resorber or not. Liu *et al.* (1993a) showed that, in the Low Turbulence Water Tunnel at Caltech (which does not have a resorber), significant variations in $N(R)$ commonly occurred during run times of the order of several minutes though $N(R)$ would asymptote to some steady distribution after about 25 minutes. This "steady state" would not only depend, however, upon the tunnel pressure, velocity and air content but also on the object in the working section and whether or not it was cavitating. This recognition that the nuclei population adjusts to the conditions of the experiment, only serves to emphasize even more strongly the need to monitor $N(R)$ in any cavitation experiment. The role played by a cavitating body (mounted in the working section) in supplying nuclei to the tunnel was

further studied by Sato *et al.* (1993) who examined the distributions at various points in the wake behind a cavitating circular cylinder. In the case examined the nuclei population in the wake was several orders of magnitude larger than in the tunnel as a whole and the process of mixing and diffusion with distance downstream was readily apparent. Recently, Watanabe and Prosperetti (1994) have investigated some simple models for the nuclei created by cavitation and have compared their results with the observations of Sato *et al.*. Clearly, however, more study is required before there is any real understanding of the nuclei population dynamics either in water tunnel facilities or, for that matter, in the ocean (O'Hern *et al.* 1988).

If the nuclei number distribution is known or measured, then the important question is how that determines the cavitation event rate. If the nuclei were to follow the fluid motion without any slip and if the bubble was always spherical and always small relative to the important dimensions of the flow, the problem would be relatively simple. For each streamtube passing close to the body in which nuclei are likely to grow into macroscopic bubbles, one could input the pressure time history into the Rayleigh-Plesset equation and, for a range of initial nuclei sizes and cavitation numbers, calculate the resulting cavitation bubble size history. Such, of course, was the approach taken in the pioneering work of Plesset (1949), Parkin (1952) and others. An example of such a calculation (taken from Ceccio and Brennen, 1991) is shown in figure 7 which presents results from the integration of the Rayleigh-Plesset equation for bubbles in the flow around a Schiebe headform. The maximum size which the bubbles achieve is plotted as a function of the size of the original nucleus for a typical Weber number, $\rho R_H U^2/S$, where U and R_H are the free stream velocity and headform radius and S is the surface tension. Data are plotted for four different cavitation numbers, σ. Note that the curves for $\sigma < 0.5$ all have abrupt vertical sections at certain critical nuclei sizes which correspond to the appropriate Blake critical nuclei sizes (Blake 1949, Daily and Johnson 1956). Since this decreases with decreasing σ an increasing number of smaller nuclei are activated as σ is decreased. The calculations of figure 7 were carried out using the pressure distribution on the surface of the headform. It is clear from figure 1, that the pressure distributions on streamsurfaces further from the headform do not have such low pressures and therefore the Blake critical radius increases with distance from the surface until one reaches a streamline on which there are no nuclei large enough to be activated. Note also from figure 7 that, whatever their initial size, most unstable nuclei grow to roughly the same maximum size. This is because both the asymptotic growth rate and the time available for growth are relatively independent of the size of the original nucleus.

But there are other complications which occur in the actual flow and create more serious problems. First, the boundary layer on the headform surface will clearly have an effect on the volume flux through the low pressure region. Secondly, the relative motion between the nuclei and the liquid can be important. Johnson and Hsieh (1966) included relative motion in their analysis and identified an important phenomenon which occurs when the nuclei experience the large fluid accelerations in the vicinity of the stagnation point. Specifically the nuclei migrate outwards onto streamlines further from the stagnation streamline/body surface as a result of the large centripetal accelerations near the stagnation point. And the larger the nuclei, the larger this shift so that the flow acts as a screen or filter. The larger nuclei which are those most likely to cavitate may, in fact, be so displaced that they no longer experience tension in the low pressure region. Both the boundary layer effect and the screening effect are included in the more recent, numerical calculations of Meyer, Billet and Holl (1992). Liu *et al.* (1993b) have constructed an approximate analytical method of evaluating both of these effects.

Other problems arise because the growing bubble rapidly reaches a size which is comparable to important dimensions such as the height of the isobar, $C_p = -\sigma$, above the headform surface. As a result different parts of the bubble surface are exposed to different pressures and the bubble itself changes the local pressure distribution within the flow. Then it becomes neccessary to resort to a complex procedure such as that described in the preceding section in order to calculate the shape and growth of the bubble. Such analyses, which would take the place of the Rayleigh-Plesset calculations, are too complex for inclusion in the present event rate analyses at least initially. In place of this Liu *et al.* (1993b) have devised a somewhat heuristic treatment of these "finite bubble size" effects which involves an altered, effective trajectory for the bubbles.

Figure 8 presents some of the typical results of the Liu *et al.* analysis applied to a $5.08cm$ Schiebe

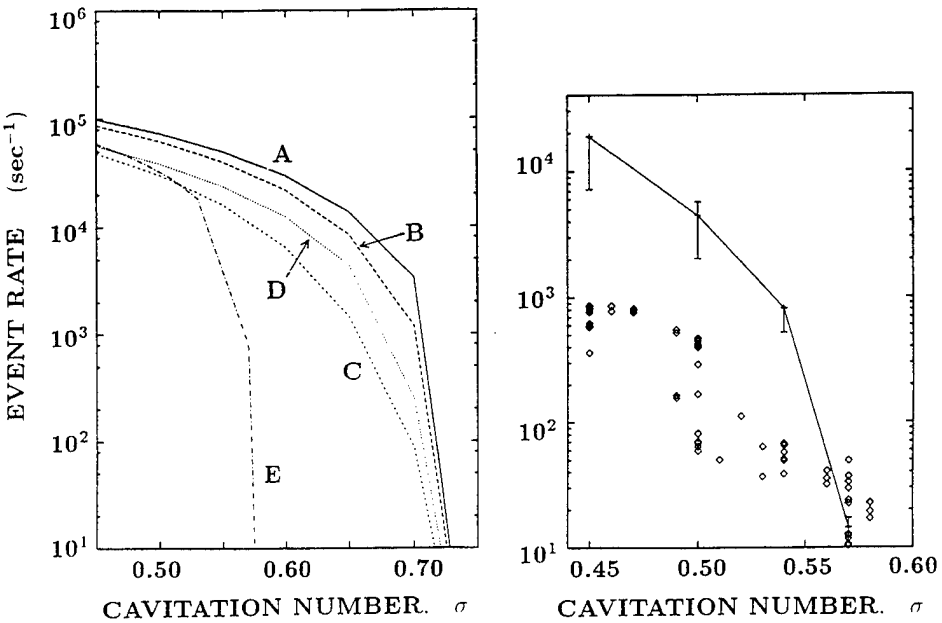


Figure 8: Left: Typical event rates calculated using an assumed but typical nuclei distribution by the method of Liu *et al.* (1993b) for flow around a 5.08cm Schiebe body at a velocity of 9 m/s. A: Basic method not including the additional effects included in other lines. B: As A but including the boundary layer flux effect. C: As A but including the bubble screening effect. D: As A but including the surface interference effect. D: As A but including only "observable" bubbles larger than 1mm in radius. Right: Comparison of observed cavitation event rates ($\diamond$) on a 5.08cm Schiebe body in the LTWT at a speed of 9 m/s with the anticipated event rate based on simultaneously measured nuclei distributions (from Liu and Brennen, 1994).

body at a tunnel speed of 9 m/s. This shows the individual changes in the event rate due to four separate effects, namely the boundary layer flux effect, the screening effect and the finite size effect in the low pressure zone. Also shown is the effect of assuming that the observer will only detect bubbles whose maximum radius is greater than 1mm. Note that all these effects produce significant alterations in the event rate. Also included in figure 8 is a comparison between experimentally measured event rates and the prediction of the Liu *et al.* method based on the simultaneously measured nuclei distribution. Note that the event rates are in rough agreement at the larger cavitation numbers but that a progressively increasing discrepancy develops as the cavitation number decreases and the event rate increases. At the lowest cavitation numbers this discrepancy is over one order of magnitude. Liu *et al.* surmise that this additional effect is caused by the interaction between nuclei at low cavitation numbers. More explicitly, that many of the smaller nuclei in the liquid surrounding a larger nuclei are not activated because the growth of the larger nuclei generates a sufficient increase in the pressure surrounding the smaller nuclei so that the latter never become unstable.

The scaling effects implicit in both the Meyer *et al.* (1992) and Liu *et al.* (1993b) models provide a qualitative explanation of some of the trends in the experimental observations such as those of Kuhn de Chizelle *et al.* (1994). This is illustrated in figure 9 where data from the LCC experiments of Kuhn de Chizelle *et al.* is presented. Shown on the right in figure 9 are results from the Liu *et al.* model for several speeds and headform sizes using an assumed but typical nuclei distribution function since Kuhn de Chizelle *et al.* were unable to measure the actual distributions in the LCC. Note that changes in the headform size are fairly well modelled whereas changes with tunnel speed are not. The probable explanation is that the changes in tunnel pressure needed to create the same cavitation number at different tunnel speeds result in major changes in the nuclei population in the facility.

Finally we observe that the prediction of the cavitation inception number is inextricably connected with a detailed understanding of the event rate

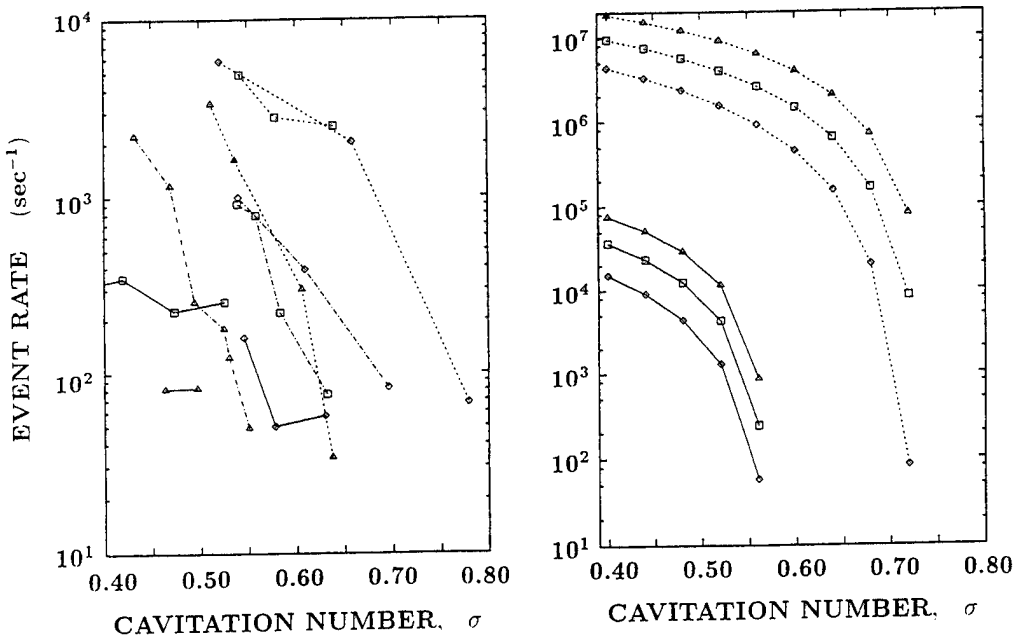


Figure 9: Left: Event rates measured during the scaling experiments of Kuhn de Chizelle *et al.* (1994) in the LCC. Data are shown for three headform diameters ($50.8cm$ = dotted line, $25.4cm$ = dash-dot line, $5.08cm$ = solid line) at three different tunnel velocities ($9m/s = \diamond$, $11.5m/s = \square$, $15m/s = \triangle$). Right: Typical event rates calculated using an assumed but typical nuclei distribution by the method of Liu *et al.* (1993b) for flow around Schiebe bodies of two different sizes ($50.8cm$ = dashed lines, $5.08cm$ = solid lines) for three different velocities ($9m/s = \diamond$, $11.5m/s = \square$, $15m/s = \triangle$). These calculations include the boundary layer flux effect and the screening effect but not the observable size effect.

(Billet and Holl 1979). In figures 10 we make a qualitative comparison between the inception number observed in the LCC experiments of Kuhn de Chizelle *et al.* (1994) and those calculated from the model of Liu *et al.* (1993b) using an assumed but typical nuclei distribution function. Both the observed and calculated σ_i are based on an arbitrarily chosen critical event rate of 50 events per second. In comparing the two graphs in figure 10 we note that the scaling with size is similar while the scaling with speed is quite different probably for the same reason given in the last paragraph.

In conclusion, it seems clear that an adequate model for the event rate is an essential prerequisite for an understanding of cavitation inception (as well as cavitation noise and damage rates).

SINGLE BUBBLE NOISE

With a better understanding of the dynamics of individual cavitation events we now turn to the measurements of the noise produced by those events. In doing so we recognize that noise evaluation provides not only valuable practical information but is also useful as a diagnostic.

The radiated acoustic pressure, p_a, at a large distance, $\mathcal{R}$, from the center of a bubble of volume, $V(t)$, will be given by (Blake 1986)

$$p_a = \frac{\rho}{4\pi\mathcal{R}} \frac{d^2V}{dt^2} \tag{3}$$

It is clear that the noise pulse generated at bubble collapse results from the very large and positive values of d^2V/dt^2 which occur when the bubble is close to its minimum size. A good measure of the magnitude of the collapse pulse is the acoustic impulse, I, defined as the area under the pulse or

$$I = \int_{t_1}^{t_2} p_a dt \tag{4}$$

where t_1 and t_2 are times before and after the pulse at which p_a is zero. It is also useful in the present context to define a dimensionless impulse, I^*, as

$$I^* = 16\pi I\mathcal{R}/\rho U D^2 \tag{5}$$

where $\mathcal{R}$ is now the distance from the cavitation event to the point of noise measurement and D

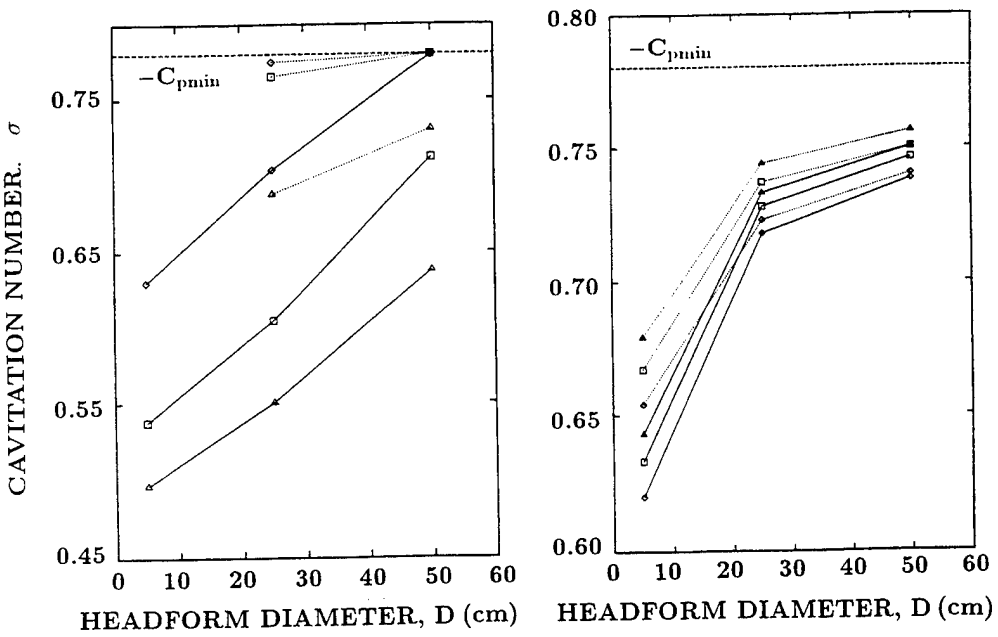


Figure 10: Left: Cavitation inception numbers observed in the scaling experiments of Kuhn de Chizelle *et al.* (1994). Data is shown for three different speeds ($9m/s = \diamond$, $11.5m/s = \square$, $15m/s = \triangle$) and two dissolved oxygen contents (30% = solid lines, 80% = dotted lines) based on a critical event rate of $50s^{-1}$. Right: Predicted cavitation inception numbers at three different speeds ($9m/s = \diamond$, $11.5m/s = \square$, $15m/s = \triangle$) based on a critical event rate of $50s^{-1}$, an assumed but typical nuclei distribution and two minimum observable bubble radii of $1mm$ (solid lines) and $0.5mm$ (dotted lines). From Liu *et al.* (1993b).

is the headform diameter ($D = 2R_H$). We shall compare the experimentally measured values of I^* from individual events on headforms of different size with those from numerical calculations of the growth and collapse of bubbles obtained from integration of the Rayleigh-Plesset equation. Details of these calculations are given in Ceccio and Brennen (1991) and Kuhn de Chizelle *et al.* (1992). For present purposes, we note that variations in the Weber number, Reynolds number and initial size of the nucleus had little effect on the computed impulses (within ±10%).

For a range of experimental cavitation numbers, both Ceccio and Brennen (1991) and Kuhn de Chizelle *et al.* (1994) were able to identify within the hydrophone output the signal produced by each cavitation event and to measure the acoustic impulses of these events. The average values of the largest impulses obtained in this way are plotted against cavitation number in figure 11. In viewing this data it must be emphasized that there is considerable variability in the magnitude of the impulses occurring at a particular operating condition. Consequently, the standard deviations corresponding to the averaged I^* values of figure 11 are usually between 25% and 80% of the average value. In both sets of experiments the collapse of an individual bubble (or event) seems to be characterized by a fairly well-defined maximum possible value of the impulse. However the same conditions can also produce impulses which are a fraction of this maximum.

Also shown in figure is a hatched area which encompasses the results from the Rayleigh-Plesset calculations using the pressure distribution on the *surface* of the headform. Note first that the upper envelope of the experimental data for all the headforms and velocities is roughly consistent. However, this envelope of maximum values is approximately one order of magnitude smaller than the impulses obtained from the Rayleigh-Plesset calculations. There are probably two reasons for this. First, the actual maximum volume of the bubbles is significantly smaller than the maximum volume of the Rayleigh-Plesset bubbles as was documented by Kuhn de Chizelle *et al.* (1994). Since the impulse is correlated with the maximum volume, this is clearly one reason for the discrepancy. This effect can be accounted for as will shortly be demonstrated. A more speculative, second reason for the

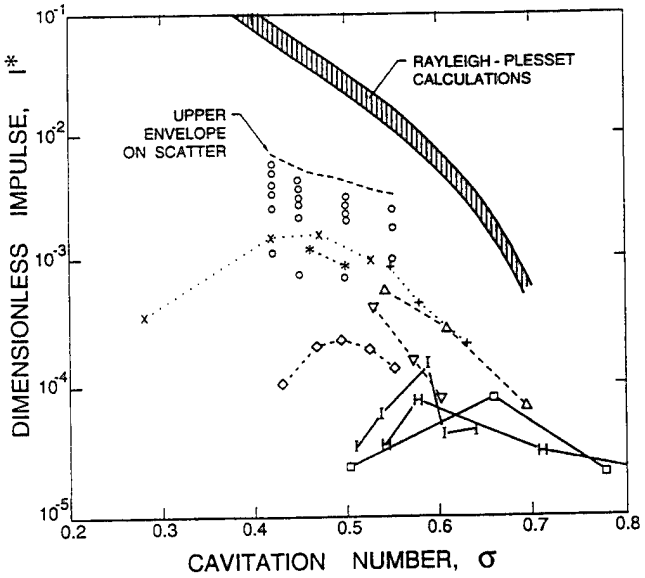


Figure 11: The dimensionless impulse, I^*, as a function of cavitation number, σ. All the calculations using the Rayleigh-Plesset equation lay within the hatched region. The experimental measurements of Ceccio and Brennen (1991) on a $5.08cm$ headform (o) are shown along with the upper envelope which was defined by that data. The results of Kuhn de Chizelle *et al.* (1994) are shown for three headform diameters ($50.8cm$ = thick solid line, $25.4cm$ = thin solid line, $5.08cm$ = dotted line) at three different tunnel velocities ($9m/s$ = +, $\triangle$, $\square$, $11.5m/s$ = $\times$, $\triangledown$, H, $15m/s$ = $*$, $\diamond$, I).

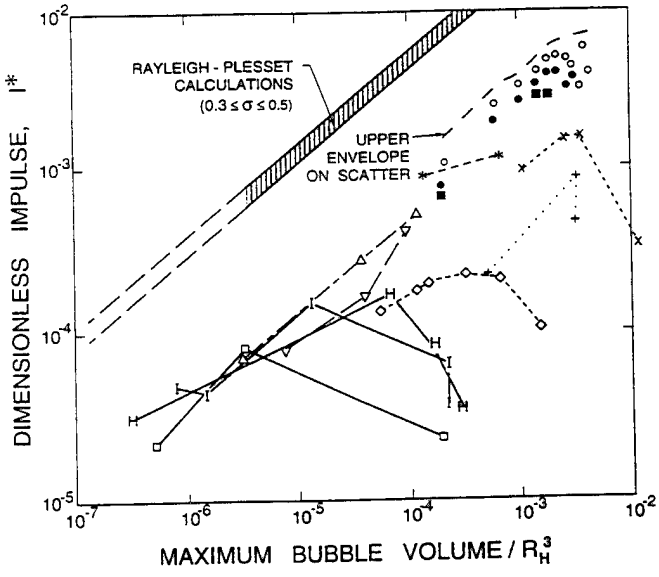


Figure 12: The dimensionless impulse, I^*, as a function of maximum volume of the bubble (divided by $D^3/8$). All the calculations using the Rayleigh-Plesset equation for $0.3 \leq \sigma \leq 0.5$ lie within the hatched region. The experimental measurements on a $5.08cm$ headform by Ceccio and Brennen (1991) are shown for $\sigma = 0.42$ ($\odot$), 0.45 ($\bullet$) and 0.50 (solid $\square$) along with the upper envelope which was defined by that data. The results of Kuhn de Chizelle *et al.* (1994) are coded as in figure 11.

discrepancy is that the more non-spherical the collapse, the less noise is produced since a spherical collapse produces the maximum focussing of the unsteady pressures. The interactions of the bubble with the pressure gradients and the boundary layer produce deformations in the shape which, in turn, alter the noise produced.

We speculated that the acoustic impulses would be better correlated with the maximum bubble volume than with the cavitation number. This correlation has been anticipated by many authors including Fitzpatrick and Strasberg (1956), Hamilton *et al.* (1982) and Vogel *et al.* (1989). For this reason Kuhn de Chizelle *et al.* (1994) replotted the impulse data against the maximum cavity volume as shown in figure 12. Note that the correspondence of the upper envelope of the data is improved over that of figure 11, confirming again that the upper bound on the impulse correlates strongly with the maximum bubble volume.

The upper envelope on the experimental data in figure 12 and of the Rayleigh-Plesset calculations are both consistent with a relation of the form

$$I^* \approx \beta \left(\frac{R_{max}}{D} \right)^{\frac{5}{2}} \tag{6}$$

where β is some proportionality constant. There is an explanation for the form of this relation which proceeds as follows. From the definitions given in equations 3, 4 and 5 one can obtain

$$I^* = \frac{4}{UD^2} \left[\left(\frac{dV}{dt} \right)_{t_2} - \left(\frac{dV}{dt} \right)_{t_1} \right] \tag{7}$$

If the typical bubble radius at times t_1 and t_2 is denoted by R_X and the typical pressure coefficient is denoted by C_{px} then it follows from the Rayleigh-Plesset equation (by setting $d^2V/dt^2 = 0$ and evaluating dV/dt) that

$$I^* \approx 32\pi \left(\frac{R_X}{D} \right)^2 (C_{px} - \sigma)^{\frac{1}{2}} \tag{8}$$

Numerical calculations of the Rayleigh-Plesset equation for a wide range of flows and conditions showed that $R_X/R_{max} \approx 0.62$. Moreover calculations with the Schiebe headform pressure distribution showed that $(C_{px} - \sigma) \propto R_{max}/D$. Substituting these two expressions into equation 8 yields the relation 6.

There is, however, another effect which is present in the data of figures 11 and 12. Virtually all of the data for a specific headform size and tunnel velocity tends first to increase as the cavitation number is reduced below the inception value. However, in almost all cases, this trend reaches a maximum at a particular cavitation number (or bubble volume) and begins to decrease with further reduction in σ. There are two effects which may contribute to this phenomenon. First, the noise or impulse may decrease due to the interactions between events as they become more numerous with decreasing σ. Second, the impulse may decrease due to a change in the dominant type of event as σ is decreased. Kuhn de Chizelle *et al.* (1994) showed that the impulses are maximum when the cavities cover about 20% of the surface area of the headform. This is in agreement with the observations of Arakeri and Shanmuganathan (1985) who reported that area void fractions larger than about 25% resulted in significant interactions between the bubbles and a reduction in the acoustic noise. In figure 11, the locations of the maxima appear to be shifted towards higher cavitation numbers at the lower velocities. This trend is consistent with that of Kuhn de Chizelle *et al.* (1994) who found an increase in the area void fraction with decreasing velocity at the same cavitation numbers.

There is, however, an additional effect which causes the observed decrease in the impulse below a certain σ. Kuhn de Chizelle *et al.* (1994) were able to demonstrate that events with tails are more likely to occur as the cavitation number is decreased and that such events produce much less noise, presumably because the tails cause further defocussing of the collapse.

In summary, we find that the micro-fluid-mechanics associated with individual events have an important effect on the noise produced by each event and that changes in the micro-fluid-mechanics with Reynolds number produce previously unrecognized scaling effects. However the overall trends are consistent with those predicted by the Rayleigh-Plesset or Fitzpatrick-Strasberg analysis though the maximum acoustic impulses are about an order of magnitude smaller than those of the spherical bubble analyses.

CLOUD CAVITATION

As a final topic we include a few observations on one of the most important bubble interaction effects. When the frequency of cavitation events increases in space or time such that they begin to interact with one another a whole new set of phenomena may be manifest. They may begin to interact hydrodynamically with important consequences for both the global flow and the dynamics

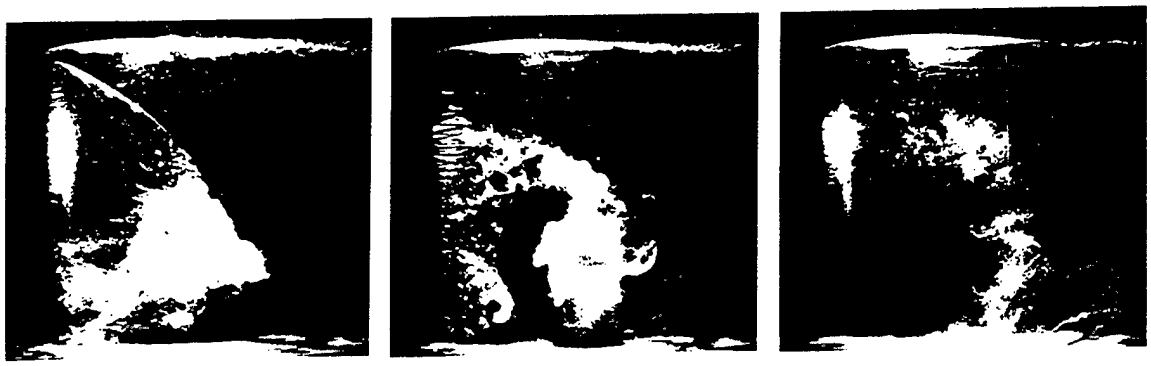


Figure 13: Three frames illustrating the formation, separation and collapse of a cavitation cloud on the suction surface of a hydrofoil ($0.152m$ chord) oscillating in pitch with a frequency of $5.8Hz$ and an amplitude of $\pm 5°$ about a mean incidence angle of 5°. The flow is from left to right, the tunnel velocity is 7.5 m/s and the mean cavitation number is 1.1. Photographs by E. McKenney.

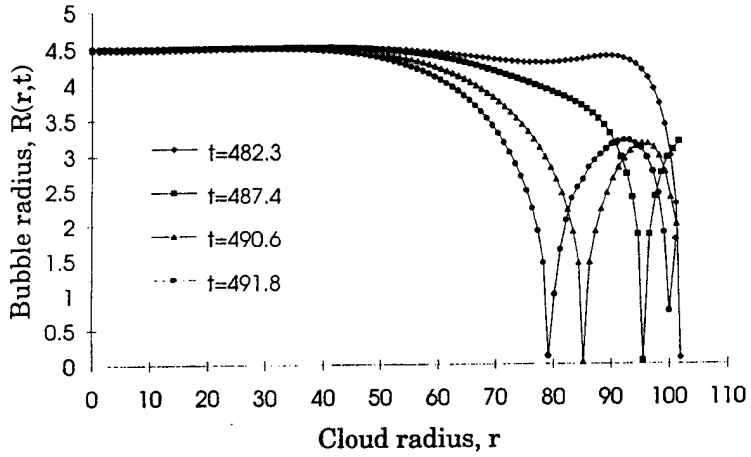


Figure 14: The dimensionless bubble size distribution in the cloud as a function of the dimensionless cloud radius at various times for $\sigma = 0.4$, $C_{pmin} = -0.5$, $\alpha_0 = 0.08\%$, $A_0 = 1cm$, $R_0 = 100\mu m$ and the dimensionless time, $t_G = 500$.

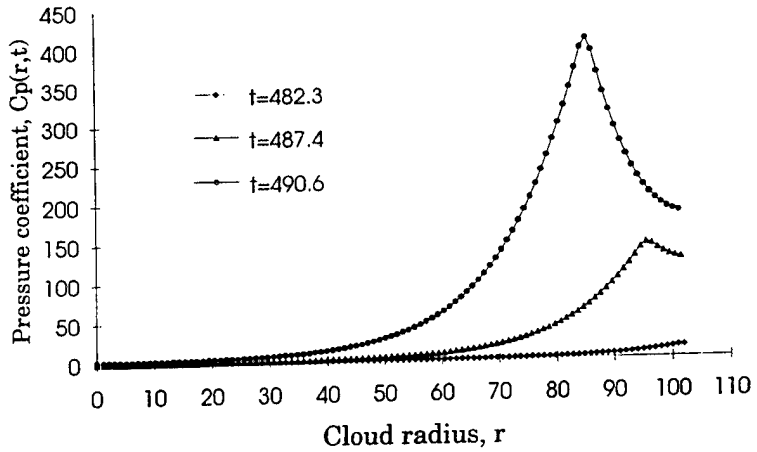


Figure 15: The pressure coefficient distribution in the cloud as a function of the dimensionless cloud radius at various times. Parameters as in figure 14.

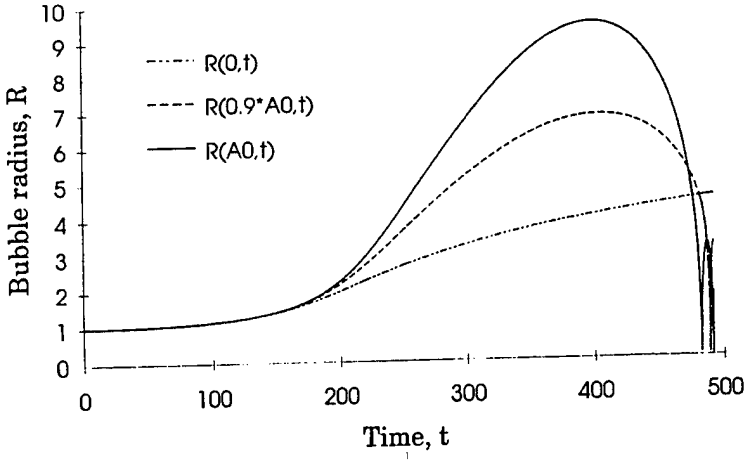


Figure 16: The time history of dimensionless bubble size at three different positions in the cloud, $r_0 = 0$, $r_0 = 0.9A0$ and $r_0 = A0$, where $A0$ is the radius of the cloud. Parameters as in figure 14.

and acoustics of the cavitation. In many flows of practical interest one observes the periodic formation and collapse of a "cloud" of cavitation bubbles. The temporal periodicity may occur naturally as a result of bubble-filled vortices or it may be the response to a periodic disturbance imposed on the flow. Common examples of imposed fluctuations are the interaction between rotor and stator blades in a pump or turbine and the interaction between a ship's propeller and the non-uniform wake created by the hull. In many of these cases the coherent collapse of the cloud of bubbles can cause more intense noise and more potential for damage than in a similar non-fluctuating flow. Bark and van Berlekom (1978), Shen and Peterson (1978), Bark (1985), Franc and Michel (1988) and Kubota *et al.* (1989, 1992) have studied the complicated flow patterns involved in the production and collapse of a cavitating cloud on an oscillating hydrofoil. These studies are exemplified by the photographs of figure 13 which show the formation, separation and collapse of a cavitation cloud on a hydrofoil oscillating in pitch. All of the above mentioned studies emphasize that a substantial bang occurs as a result of the collapse of the cloud; in figure 13 this occurred between the middle and right hand photographs.

Much recent interest has focused on the dynamics and acoustics of finite clouds of cavitation bubbles because of the very destructive effects which are observed to occur when such clouds form and collapse in a flow (see, for example, Bark and van Berlekom 1978, Soyama *et al.* 1992). Here we address the issue of the modelling of the dynamics of cavitation clouds, a subject whose origins can be traced to the work of van Wijngaarden (1964) who first attempted to model the behavior of a collapsing layer of bubbly fluid next to a solid wall. Later investigators explored numerical methods which incorporate the individual bubbles (Chahine 1982) and continuum models which, for example, analyze the behavior of shock waves in bubbly liquid (Noordzij and van Wijngaarden 1974) and identify the natural frequencies of spherical cloud of bubbles (d'Agostino and Brennen 1983). Indeed the literature on the linearized dynamics of clouds of bubbles is growing rapidly (see, for example, Omta 1987, d'Agostino *et al.* 1988 & 1989, Prosperetti 1988). However, apart from some weakly non-linear analyses (Kumar and Brennen 1991, 1992, 1993b) only a few papers have addressed the highly non-linear processes involved during the collapse of a cloud of bubbles. Chahine and Duraiswami (1992) have recently conducted numerical simulations using a number of discrete bubbles and demonstrated how the bubbles on the periphery of the cloud develop inwardly directed re-entrant jets. However, most clouds contain many thousands of bubbles and it therefore is advantageous to examine the non-linear behavior of continuum models.

Another perspective on the subject of collapsing clouds was that introduced by Mørch and his coworkers (Mørch 1980 & 1981, Hanson *et al.* 1981). They speculated that the collapse of a cloud of bubbles involves the formation and inward propagation of a shock wave and that the geometric focusing of this shock at the center of cloud creates the enhancement of the noise and damage potential associated with cloud collapse. Most recently Wang and Brennen (1994) have used the mixture models

employed earlier by d'Agostino *et al.* (1983, 1988, 1989) to study the non-linear growth and collapse of a spherical cloud of bubbles. A finite cloud of nuclei is subjected to a decrease in the ambient pressure which causes the cloud to cavitate and then to a pressure recovery which causes collapse. Of necessity, the solutions are numerical but they clearly confirm Mørch's vision of cloud collapse. Some typical numerical results are shown in figures 14, 15 and 16. Figures 14 and 15 illustrate the spatial distribution of bubble radius and pressure at several moments in time during the beginning of collapse. Note the formation and inward propagation of a shock wave. The structure of this shock is very similar to those in the bubbly flows investigated by Noordij and van Wijngaarden (1974); it develops a series of rebounds and secondary collapses which probably produce a ringing in the radiated sound. Note also from figure 15 how the pressure pulse increases in amplitude as the shock propagates inwards. Finally, figure 16 presents the time history of bubble size at several Lagrangian locations within the cloud and shows how the bubbles at the cloud surface ($R(A0,t)$) collapse first and shield the interior so that collapse of the interior bubbles is delayed.

Both experimental and analytical studies of this phenomenon are currently being pursued.

CONCLUDING COMMENTS

In this paper we have summarized some of the recent advances in our understanding of travelling bubble cavitation and cloud cavitation. We have demonstrated that it is possible to synthesize the cavitation from knowledge of the nuclei number distribution and the detailed flow field especially that in the neighbourhood of the minimum pressure point. The observations of the dynamics of individual bubbles or events clearly display a rich variety of fluid mechanical phenomena as the bubbles interact with the largely irrotational flow outside the boundary layer and with the boundary layer itself. Many of the observed phenomena remain to be understood, particularly the instability of the thin liquid layer underneath the bubble and the separation phenomena induced by the passage of the bubble. It has been demonstrated that these microfluidmechanical effects are important because they influence the coherence of the collapse and therefore the noise and damage potential which are produced.

We have, of course, omitted any discussion of vortex cavitation or attached cavitation, not because these are less important but rather because the modelling of these forms are less well understood in terms of their noise producing mechanisms and their damage potential. Recent evidence suggest that vortex cavitation and, perhaps, attached cavitation are also affected by the nuclei population and it seems clear that future research should explore that relationship.

ACKNOWLEDGEMENTS

In writing this review, I came to recognize, again, the debt I owe to a series of outstanding graduate students who contributed much of the work described herein. My profound thanks to Luca d'Agostino, Steven Ceccio, Douglas Hart, Sanjay Kumar, Yan Kuhn de Chizelle, Beth McKenney, Zhenhuan Liu, Yi-Chun Wang and Garrett Reisman. As always, my friend and colleague Allan Acosta provided valuable insights and inspiration. I am also deeply grateful for the support of the Office of Naval Research who sponsored much of the research and supported the preparation of this paper under Contract N00014-91-J-1295.

References

[1] Arakeri, V.H. and Shanmuganathan, V., "On the evidence for the effect of bubble interference on cavitation noise," *J. Fluid Mech.*, 1985, Vol. 159, pp. 131-150.

[2] Bark, G. and van Berlekom, W.B., "Experimental investigations of cavitation noise," *Proc. 12th ONR Symp. on Naval Hydrodynamics*, 1978, pp. 470–493.

[3] Bark, G., "Developments of distortions in sheet cavitation on hydrofoils," *Proc. ASME Int. Symp. on Jets and Cavities*, 1985, pp. 215–225.

[4] Billet, M.L. and Holl, J.W., "Scale effects on various types of limited cavitation," *ASME Int. Symp. on Cavitation Inception*, 1979, pp. 11-24.

[5] Billet, M.L., "Cavitation nuclei measurement - a review," *ASME Cavitation and Multiphase Flow Forum Booklet*, 1985, pp. 31–38.

[6] Blake, F.G., "The onset of cavitation in liquids: I," *Acoustics Res. Lab., Harvard Univ., Tech. Memo.*, 1949, No. 12.

[7] Blake, W. K., Wolpert, M. J. and Geib, F. E., "Cavitation noise and inception as influenced by

boundary-layer development on a hydrofoil," *J. Fluid Mech.*, 1977, Vol. 80, pp. 617–640.

[8] Blake, W.K., "Mechanics of flow-induced sound and vibration," Academic Press, 1986.

[9] Briançon-Marjollet, L., Franc, J.P. and Michel, J.M., "Transient bubbles interacting with an attached cavity and the boundary layer," *J. Fluid Mech.*, 1990, Vol. 218, pp. 355–376.

[10] Ceccio, S.L. and Brennen, C.E., "Observations of the dynamics and acoustics of travelling bubble cavitation," *J. Fluid Mech.*, 1991, Vol. 233, pp. 633–660.

[11] Chahine, G.L. Personal communication, 1992.

[12] Chahine, G.L. and Duraiswami, R., "Dynamical interactions in a multibubble cloud," *ASME J. Fluids Eng.*, 1992, Vol. 114, pp. 680-686.

[13] d'Agostino, L. and Brennen, C.E., "On the acoustical dynamics of bubble clouds," *ASME Cavitation and Multiphase Flow Forum*, 1983, pp. 72-75.

[14] d'Agostino, L. and Brennen, C.E., "Acoustical absorption and scattering cross-sections of spherical bubble clouds," *J. Acoust. Soc. of Amer.*, 1988, Vol. 84, No.6, pp. 2126–2134.

[15] d'Agostino, L. and Brennen, C.E., "Linearized dynamics of spherical bubble clouds," *J. Fluid Mech.*, 1989, Vol. 199, pp. 155-176.

[16] Daily, J.W. and Johnson, V.E., Jr., "Turbulence and boundary layer effects on cavitation inception from gas nuclei," *Trans. ASME*, 1956, Vol. 78, pp. 1695–1706.

[17] Ellis, A.T., "Observations on cavitation bubble collapse," *Calif. Inst. of Tech. Hydr. Lab. Rep.*, 1952, No. 21-12.

[18] Fitzpatrick, H.M. and Strasberg, M., "Hydrodynamic sources of sound," *Proc. First ONR Symp. on Naval Hydrodynamics*, 1956, pp. 241-280.

[19] Franc, J.P. and Michel, J.M., "Unsteady attached cavitation on an oscillating hydrofoil," *J. Fluid Mech.*, 1988, Vol. 193, pp. 171–189.

[20] Gates, E.M. and Acosta, A.J., "Some effects of several free-stream factors on cavitation inception on axisymmetric bodies," *Proc. 12th ONR Symp. on Naval Hydrodynamics*, 1978, pp. 86–108.

[21] Hamilton, M.F., Thompson, D.E. and Billet, M.L., "An experimental study of traveling bubble cavitation and noise," *Proc. ASME Int. Symp. on Cavitation Noise*, 1982, pp. 25-33.

[22] Hanson, I., Kedrinskii, V.K. and Mørch, K.A., "On the dynamics of cavity clusters," *J. Appl. Phys.*, 1981, Vol. 15, pp. 1725-1734.

[23] Holl, J.W. and Kornhauser, A.L., "Thermodynamic effects on desinent cavitation on hemispherical nosed bodies in water at temperatures from $80°F$ to $260°F$," *ASME J. Basic Eng.*, 1970, Vol. 92, pp. 44–58.

[24] Holl, J.W. and Carroll, J.A., "Observations of the various types of limited cavitation on axisymmetric bodies," *Proc. ASME Int. Symp. on Cavitation Inception*, 1979, pp. 87–99.

[25] Howison, S.D., Morgan, J.D. and Ockendon, J.R., "Patch cavitation in flow past a rigid body," *Proc. IUTAM Symp. on Bubble Dynamics and Interface Phenomena, Birmingham, England.*, 1993.

[26] Huang, T.T., "Cavitation inception observations on six axisymmetric headforms," *Proc. ASME Int. Symp. on Cavitation Inception*, 1979, pp. 51–61.

[27] Johnson, V.E., Jr., and Hsieh, T., "The influence of the trajectories of gas nuclei on cavitation inception," *Proc. 6th ONR Symp. on Naval Hydrodynamics*, 1966, pp. 163–182.

[28] Keller, A.P., "The influence of the cavitation nucleus spectrum on cavitation inception, investigated with a scattered light counting method," *ASME J. Basic Eng.*, 1972, pp. 917–925.

[29] Keller, A.P., "Investigations concerning scale effects of the inception of cavitation," *Proc. I.Mech.E. Conf. on Cavitation*, 1974, pp. 109–117.

[30] Keller, A.P. and Weitendorf, E.A., "Influence of undissolved air content on cavitation phenomena at the propeller blades and on induced hull pressure amplitudes," *Proc. IAHR Symp. on Two Phase Flow and Cavitation in Power Generation Systems*, 1976, pp. 65–76.

[31] Knapp, R.T. and Hollander, A., "Laboratory investigations of the mechanisms of cavitation," *Trans. ASME*, 1948, Vol. 70, p. 419.

[32] Kubota, A., Kato, H., Yamaguchi, H. and Maeda, M., "Unsteady structure measurement of cloud cavitation on a foil section using conditional sampling," *ASME J. Fluids Eng.*, 1989, Vol. 111, pp. 204–210.

[33] Kubota, A., Kato, H. and Yamaguchi, H., "A new modelling of cavitating flows - a numerical study of unsteady cavitation on a hydrofoil section" *J. Fluid Mech.*, 1992, Vol. 240, pp. 59–96.

[34] Kuhn de Chizelle, Y., Ceccio, S.L., Brennen, C.E. and Gowing, S., "Scaling experiments on the dynamics and acoustics of travelling bubble cavitation," *Proc. 3rd I.Mech.E. Int. Conf. on Cavitation, Cambridge, England*, 1992, pp. 165–170.

[35] Kuhn de Chizelle, Y., Ceccio, S.L., Brennen, C.E. and Shen, Y., "Cavitation scaling experiments with headforms: bubble acoustics," *Proc. 19th Symp. on Naval Hydrodynamics, Seoul, Korea*, 1992, pp. 72–84.

[36] Kuhn de Chizelle, Y., Ceccio, S.L. and Brennen, C.E., "Observations, scaling and modelling of travelling bubble cavitation", submitted for publication, 1994.

[37] Kuiper, G., "Scale effects on propeller cavitation inception," *Proc. 12th ONR Symp. on Naval Hydrodynamics*, 1978, pp. 400–429.

[38] Kumar, S. and Brennen, C.E., "Non-linear effects in the dynamics of clouds of bubbles," *J. Acoust. Soc. Am.*, 1991, Vol. 89, pp. 707-714.

[39] Kumar, S. and Brennen, C.E., "Harmonic cascading in bubble clouds," *Proc. Int. Symp. on Propulsors and Cavitation, Hamburg*, 1992, pp. 171-179.

[40] Kumar, S. and Brennen, C.E., "A study of pressure pulses generated by travelling bubble cavitation," *J. Fluid Mech.*, 1993a, Vol. 255, pp. 541–564.

[41] Kumar, S. and Brennen, C.E., "Some nonlinear interactive effects in bubbly cavitating clouds," *J. Fluid Mech.*, 1993b, Vol. 253, pp. 565-591.

[42] Lindgren, H. and Johnsson, C.A., "Cavitation inception on headforms. ITTC comparative experiments," *Proc. 11th Int. Towing Tank Conf.*, 1966, pp. 219-232.

[43] Liu, Z., Sato, K. and Brennen, C.E., "Cavitation nuclei population dynamics in a water tunnel," *ASME Cavitation and Multiphase Flow Forum*, 1993a, FED-Vol.153, pp. 119–125.

[44] Liu, Z., Kuhn de Chizelle, Y. and Brennen, C.E., "Cavitation event rates and nuclei distributions," *Proc. ASME Symp. on Cavitation Inception*, 1993b, FED-Vol.177, pp. 13–24.

[45] Liu, Z. and Brennen, C.E., "The relation between the nuclei population and the cavitation event rate for cavitation on a Schiebe body," *Proc. ASME Symp. on Cavitation and Gas Liquid Flows in Fluid Machinery*, 1994.

[46] Meyer, R.S., Billet, M.L. and Holl, J.W., "Freestream nuclei and traveling-bubble cavitation," *ASME J. Fluids Eng.*, 1989, Vol. 114, pp. 672–679.

[47] Mørch, K.A., "On the collapse of cavity cluster in flow cavitation," *Proc. First Int. Conf. on Cavitation and Inhomogenieties in Underwater Acoustics, Springer Series in Electrophysics*, 1980, Vol. 4, pp. 95-100.

[48] Mørch, K.A., "Cavity cluster dynamics and cavitation erosion," *Proc. ASME Cavitation and Polyphase Flow Forum*, 1981, pp. 1-10.

[49] Morgan, W.B., "David Taylor Research Center's Large Cavitation Channel," *Proc. Int. Towing Tank Conference, Madrid, Spain.*, 1990.

[50] Noordij, L. and van Wijngaarden, L., "Relaxation effects, caused by relative motion, on shock waves in gas-bubble/liquid mixtures," *J. Fluid Mech.*, 1974, Vol. 66, pp. 115-143.

[51] O'Hern, T., D'Agostino, L. and Acosta, A.J., "Comparison of holographic and counter measurements of cavitation nuclei in the ocean," *ASME J. Fluids Eng.*, 1988, Vol. 110, pp. 200-207.

[52] Omta, R., "Oscillations of a cloud of bubbles of small and not so small amplitude," *J. Acoust. Soc. Am.*, 1987, Vol. 82, pp. 1018-1033.

[53] Oshima, R., "Theory of scale effects on cavitation inception on axially symmetric bodies," *ASME J. Basic Eng.*, 1961, Vol. 83, pp. 379–398.

[54] Parkin, B.R., "Scale effects in cavitating flow," *Ph.D. Thesis, Calif. Inst. of Tech.*, 1952.

[55] Plesset, M.S., "The dynamics of cavitation bubbles," *ASME J. Appl. Mech.*, 1949, Vol. 16, pp. 228-231.

[56] Prosperetti, A., "Bubble-related ambient noise in the ocean," *J. Acoust. Soc. Am.*, 1988, Vol. 84, pp. 1042-1054.

[57] Rayleigh, Lord (Strutt, John William), "On the pressure developed in a liquid during the collapse of a spherical cavity," *Phil. Mag.*, 1917, Vol. 34, pp. 94–98.

[58] Saffman, M., Buchhave, P. and Tanger, H., "Simultaneous measurements of size, concentration and velocity of spherical particles by a laser doppler method," *Proc. 2nd Int. Symp. on Applications of Laser Anemometry to Fluid Mechanics, Lisbon*, 1984.

[59] Sato, K., Liu, Z. and Brennen, C.E., "The microbubble distribution in the wake of a cavitating circular cylinder," *ASME Cavitation and Multiphase Flow Forum*, 1993, FED-Vol.153, pp. 75–80.

[60] Schiebe, F.R., "Measurements of the cavitation susceptibility of water using standard bodies," *St. Anthony Falls Hydr. Lab., U. of Minnesota*, Rep. No. 118., 1972.

[61] Shen, Y. and Peterson, F.B., "Unsteady cavitation on an oscillating hydrofoil," *Proc. 12th ONR Symp. on Naval Hydrodynamics*, 1978, pp. 362–384.

[62] Soyama, H., Kato, H. and Oba, R., "Cavitation observations of severely erosive vortex cavitation arising in a centrifugal pump," *Proc. Third I.Mech.E. Int. Conf. on Cavitation*, 1992, pp. 103-110.

[63] Tanger, H. and Weitendorf, E.A., "Applicability tests for the phase doppler anemometer for cavitation nuclei measurements," *ASME J. Fluids Eng.*, 1992, Vol. 114, pp. 443–449.

[64] van der Meulen, J. H. J. and van Renesse, R. L., "The collapse of bubbles in a flow near a boundary," *Proc. 17th ONR Symp. on Naval Hydrodynamics, The Hague*, 1989, pp. 195–217.

[65] van der Walle, F., "On the growth of nuclei and related scaling factors in cavitation inception," *Proc. 4th ONR Symp. on Naval Hydrodynamics*, 1962.

[66] van Wijngaarden, L., "On the collective collapse of a large number of gas bubbles in water," *Proc. 11th Int. Conf. Appl. Mech.*, Springer-Verlag, Berlin, 1964, pp. 854-861.

[67] Vogel, A., Lauterborn, W. and Timm, R., "Optical and acoustic investigations of dynamics of the laser-produced cavitation bubbles near a solid boundary layer," *J. Fluid Mech.*, 1989, Vol. 206, pp. 299-338.

[68] Wang, Y.-C. and Brennen, C.E., "Shock wave development in the collapse of a cloud of bubbles," *ASME Cavitation and Multiphase Flow Forum*, 1994.

[69] Watanabe, M. and Prosperetti, A., "The effect of gas diffusion on the nuclei population downstream of a cavitation zone," *Proc. ASME Symp. on Cavitation and Gas Liquid Flows in Fluid Machinery*, 1994.

Viscous Effects in Tip Vortex Cavitation and Nucleation

R. Arndt, B. Maines
(University of Minnesota, USA)

ABSTRACT

This paper is concerned with the physics of cavitation in trailing vortices. The research was aimed at investigating the interrelated effects of vortex structure and bubble dynamics. The experimental phase utilizes a series of hydrofoils and includes lift and drag measurements, oil flow visualization of the boundary layer flow, and observation of both cavitation inception and desinence in strong and weak water. The complex bubble dynamics inherent in the inception process have been studied using an improved photographic technique. The bubble growth process is strongly dependent on the size and number of nuclei in the free stream and on the strength of the vortex. Numerical simulations indicate that the minimum pressure in the vortex is very close to the tip of the lifting surface, in agreement with the observation that the inception process also occurs very close to the tip under most conditions.

NOMENCLATURE

a	core radius
b	foil half span
c_g	dissolved gas content
C_L	lift coefficient
C_{p0},C_{pmin}	pressure coefficient
c_0	foil root chord
f	frequency (Hz)
K,K_1,K_2	constants
m	constant
p	pressure
p'	fluctuating pressure
p_a	acoustic pressure
p_c	critical pressure
p_v	vapor pressure
Re	Reynolds number
T	water tensile strength (N/m^2)
t	time
U,u	velocity
$\ddot{V}$	second time derivative of volume
r,θ,z	cylindrical coordinate system
x,y,z	cartesian coordinate system
α	angle of attack
α_0	angle of zero lift
β	Henry's constant
Γ,Γ_0	Circulation
ν	Kinematic viscosity
ρ	density
σ,σ_{iw},σ_{is}	cavitation number
ω	vorticity

INTRODUCTION

The focus of this paper is on tip vortex cavitation. The motivation for this study is discussed elsewhere (Arndt and Maines, 1994). This problem was first studied in detail by McCormick (1954, 1962). Subsequently, little further attention was given to this topic until recently, when there has been a resurgence of interest in the problem. Our understanding of the physics has been considerably enhanced in the past decade (1983-1993). The emphasis of this paper is on the details of the inception process. Both numerical and experimental results are discussed. In addition, a brief discussion of noise and developed cavitation is also given, followed by a few suggestions for future research.

BACKGROUND

Cavitation Inception

Following McCormick(1954,1962), Arndt and Keller(1992) and Maines and Arndt(1993b), the cavitation inception index is given by

$$\sigma_i = [\frac{K_1}{4\pi}]^2 C_{p_c} C_1^2 R_e^n + \frac{K_2\sqrt{\overline{p^2}}}{\frac{1}{2}\rho U^2} - \frac{T}{\frac{1}{2}\rho U^2} \quad (1)$$

where the second and third terms on the right hand side of Eq. 1 incorporate the effects of unsteadiness and bubble dynamics respectively. K_2 is a complex function of the pressure field statistics and the nuclei size and number (Arndt and Keller,1992, Arndt,1993). Arndt and Keller (1992) have pointed out that these terms can be estimated by comparing cavitation data obtained in water with an adequate supply of nuclei (σ_{iw}) with cavitation data obtained in degassed and pre-pressurized water (σ_{is}). Thus

$$\frac{T}{\frac{1}{2}\rho U^2} = \sigma_{iw} - \sigma_{is} \quad (2)$$

$$\frac{K_2\sqrt{\overline{p^2}}}{\frac{1}{2}\rho U^2} = \sigma_{iw} + C_{p_m} \quad (3)$$

The effect of flow unsteadiness is not understood at this time. A comparison between σ_{iw} and $-C_{pmin}$ inferred from velocity measurements by Arndt and Keller (1992) suggested the possibility that flow unsteadiness could be important, however Fruman et al(1994) note that flow unsteadiness is generally not an issue for analyzing the inception process. Laser doppler measurements of turbulence intensity do indicate significant levels in the core region, but as noted by Fruman et al (1994), the effect of vortex wandering is significant and must be taken into account. They concluded that, in fact, pressure reductions due to turbulence are insignificant close to the tip but can be more significant further downstream. As will be discussed subsequently, this could be important under certain circumstances.

Green and Acosta (1991) have measured pressure and velocity using holographic observation of small bubbles injected into the vortex core. Their observations are in qualitative agreement with the velocity data of Arndt and Keller(1992). Green (1991) was also able to use the same technique to estimate the magnitude of pressure fluctuations in the vortex. His data indicate that the core pressure is highly unsteady, $p'_m / \frac{1}{2}\rho U^2 \approx 1.8$. Unfortunately, these data correspond to distances greater than 1 chord length from the tip. This is significant. Fruman et al (1992) have made careful observations of incipient cavitation in vortices trailing from hydrofoils of elliptic planform. Their results indicate that the position of the lowest pressure in the vortex is located very close to the tip of the hydrofoil. This is also in agreement with recent numerical calculations made in this study by Song and Chen (1993). Thus, both experimental and numerical results indicate that the lowest pressure occurs in a region very close to the tip where the vortex is not completely wrapped up.

The basic issues in understanding the inception process are the viscous effects on vortex development, the minimum pressure in the flow and the details of the bubble dynamics. Further study is necessary to understand in sufficient detail the interrelated effects of vortex strength and viscosity on vortex structure. The fact that vortices are capable of supporting large values of tension is related to the issue of bubble dynamics in highly vortical flows. Velocity measurements made by Arndt et al (1991) indicate that rotational speeds as high as 220,000 rpm are possible in their experimental setup. This means that radial accelerations of the order 10^5 m/sec^2 occur in the core region. One objective of the current study is to observe the cavitation process in detail.

Other complex interactions between bubble dynamics and viscous effects may also be important. For example, Arndt et al (1991) also noted that under certain conditions, flow in a laminar separation bubble on the surface of a NACA 66_2 - 415, a = 0.8 hydrofoil could become supersaturated and provide additional nuclei to the flow. This results in a complex interrelationship between Reynolds number and gas content. Complexities of this type make it extremely difficult to infer prototype conditions from laboratory experiments.

Developed Cavitation

Developed cavitation in a trailing vortex has been studied by Souders and Platzer (1981), Arakeri, et al (1988) and Higuchi, et al (1989). Arndt et al (1991) found that the shape of the vortex trajectory does not change over a wide range

of sigma, gas content, lift coefficient and Reynolds number. The spanwise position of the vortex is observed to be asymptotic to the theoretical value of z/b = $\pi/4$. Arakeri, et al (1988) were able to calculate the core radius as a function of σ which correlates well with the measurements of Souders and Platzer(1981). Using a similar model, Arndt and Keller (1992) were able to show that the inception process is highly unstable since a fully cavitating vortex and a single phase vortex are equally likely when the cavitation number is just equal to σ_i. They suggested that this may explain the fact that the inception process is highly intermittent.

EXPERIMENTAL SET-UP

Four hydrofoils of elliptic planform with aspect ratio 3 but different cross sections were used for this study. The hydrofoil sections chosen were a NACA 66_2-415 a=0.8, a modified NACA 4215 (designated herein as NACA 4215M), a NACA 16-020 and a NACA 66-012. Two sets of each foil were constructed. The smaller set had a root chord c_0, of 81 mm and a half span, b, of 95 mm while for the larger set c_0 = 129.4 mm and b = 152.4 mm. The small set was utilized for cavitation testing, force measurements and observation of the bubble dynamics while the larger set was used for force measurements and oil flow visualizations. Only the small version of the NACA 66-012 was constructed. These complementary studies provide a comprehensive view of tip vortex cavitation inception.

Testing has been conducted in three water tunnels, two at SAFHL each having a 190 mm square cross section (Arndt, et al 1991) and the other at the Versuchsanstalt für Wasserbau in Obernach, Germany with a 300 mm square cross section (Arndt & Keller, 1992). Oil flow visualizations were obtained in two wind tunnels, one at the Department of Aerospace Engineering at the University of Minnesota (Higuchi et al, 1987) and the second at SAFHL (originally an air model of the HYKAT facility, Wetzel & Arndt, 1991).

Cavitation inception tests at SAFHL were performed by fixing the angle of attack and velocity and then slowly lowering the pressure until inception was detected visually. This procedure was repeated for a range of velocities at each angle of attack. Tests were performed in weak water (no tensile strength) for all four foils. A series of tests in strong water (rupture considerably below vapor pressure) were conducted using the 4215M to compare with similar data obtained in weak water.

Oil flow data were obtained using a spray of fine droplets of an oil and titanium-oxide mixture (Maines & Arndt, 1993b). The wind tunnel was run at the test velocity of 56 m/s (Re $\approx$ 485,000). This technique highlighted the details of the boundary layer flow especially in the tip region.

Observations of the bubble dynamics were obtained using an improved photographic technique. Data have been collected over a range of lift coefficients, velocities and water quality for two different hydrofoils.

NUMERICAL SIMULATIONS

Progress in understanding the details of the inception process has been hampered by a lack of sufficient knowledge about the structure of the tip vortex very close to the tip. The detailed investigation of Fruman, et al (1992) clearly indicated that inception generally occurs very close to the tip. This observation is supported by our own studies (Maines and Arndt, 1993a). In order to provide a framework for our experimental research, numerical simulation of the tip vortex flow was undertaken with a view toward providing guidance for the measurement program and to lay the ground work for a detailed numerical simulation of the bubble dynamics within the viscous vortex core.

The method relies on a large eddy simulation based on the weakly compressible hydrodynamic equations developed by Professor Song and his co-workers (Song and Chen, 1993). Simulation of the flow around the NACA 4215M was carried out at a calculated lift coefficient of 0.72 which is very close to the measured value of 0.73. Although the minimum pressure in the vortex cannot be accurately predicted at present, the model does provide useful insight into the overall problem.

Figure 1 is a plot of the calculated vorticity iso-contours obtained at a distance $x/c_0 = 0.6$ which is well downstream of the point of inception under most conditions. It is important to note that the vortex is still asymmetric and to also note the importance of the wake flow in the roll-up process. Using these numerically generated data, the circulation can be calculated as both a function of radial position from the center of the vortex and axial position. The results are shown in Figure 2. Here circulation, defined in the usual manner,

$$\Gamma = \oint \vec{u} \cdot d\vec{r} \qquad (4)$$

and normalized to the theoretical value of $\Gamma_o = \frac{1}{2}C_l U c_o$ is plotted as a function of radial distance, r/c_o for various axial positions. The vortex is apparently fully rolled up for $x/c_o > 0.6$ where $2\Gamma/C_l U c_o$ reaches a maximum value of 1.05[1]. Close to the tip this value is found to be only 0.75. This is also evident in plots of mean vorticity defined by

$$\overline{\omega}(r) \doteq \frac{\Gamma(r)}{2\pi r^2} \qquad (5)$$

as shown in Figure 3. The lowest pressure in the vortex is found to be very close to the tip as shown in Figure 4. This is in agreement with our cavitation inception observations to be subsequently described. It is also interesting to note that the growth in core radius is found to be very rapid in the development region close to the tip in agreement with measurements (Figure 5). In spite of the fact that the boundary layer flow on the foil surface is not accurately resolved, the tip vortex trajectory is accurately predicted as shown in Figure 6. Arndt, et al (1991) found that the tip vortex trajectory is relatively insensitive to Reynolds number and lift coefficient, apparently confirming the numerical result that the tip vortex trajectory is insensitive to the details of the boundary layer flow.

This simulation must be considered to be qualitative in nature, because of problems related to spatial resolution. However, this simulation of vortex flow does indicate that vortex development may be relatively insensitive to the details of the boundary layer flow. Viscous diffusion is apparently an important factor close to the tip. Unfortunately, the minimum pressure in the vortex cannot be accurately calculated. Therefore, it is still difficult to determine whether the effects of flow unsteadiness are important. It should also be pointed out that because of the apparent asymmetry in the flow, it is difficult to ascertain the accuracy of estimates of the minimum pressure that are based on velocity measurements made across a single radial in the flow (e.g. Arndt, et al, 1991, Fruman, et al 1992, Arndt and Keller, 1992). To date, only Fruman et al have made velocity measurements that are close enough to the tip to warrant comparison with inception measurements.

[1] The theoretical value is unity. The discrepancy could be due to wall effects which were included in the calculation. (The boundary conditions were identical to the experimental set-up.)

VISCOUS EFFECTS ON CAVITATION INCEPTION

Oil flow visualizations of the boundary layer were performed to characterize the differences and similarities between the hydrofoils. If McCormick's hypothesis concerning the relation between the boundary layer thickness and the core radius is correct, then comparison at equal lift, and thus equal vortex strength should provide insight to vortex roll-up. Details of the oil flow analysis were previously published in Maines & Arndt (1993b), and only the basic features will be summarized for clarity.

The lift and drag were measured for each foil over a range of Reynolds numbers at the SAFHL and Obernach facilities. Figure 7 shows the lift curves as a function of $(\alpha - \alpha_0)$ where α_0 is the angle of zero lift. Note that the 66_2-415 and the 4215M have similar lift curves but the 16-020 deviates quite dramatically. This unusual behavior can be qualitatively related to the separation characteristics on the suction side of the foil. These differences in boundary layer characteristics are clearly indicated in Figure 8 which is a plot of the position of the suction side separation line at $y/b = 0.8$ versus angle of attack. Both the 66_2-415 and the 16-020 have an aft separation line at low angles. The sudden forward translation of the separation line corresponds to the suction peak shifting to the leading edge. Little chordwise variation of the separation line is observed for the 4215M. Differences in the boundary layer characteristics are also seen on the pressure side as shown in Figure 9. The boundary layer on the 4215M separates near the leading edge at low angles of attack but shifts rearward for increasing angles. Only a slight rearward movement of the separation line is seen for the other two foils with increasing angle.

Although the overall boundary layer characteristics are quite dissimilar, some similarities of the vortex roll-up process near the tip exist. This is shown in Figure 10 which contains a series of four photographs that are composites of oil flow visualization in air and cavitation studies in the SAFHL water tunnel for the NACA 66_2-415 and NACA 4215M hydrofoils at comparable lift coefficient. Note that there are substantial

differences in the boundary layer flow on the suction side.

In contrast to the suction side, the boundary layer flow on the pressure side of each foil has similar characteristics as is shown in Figure 10b. The oil droplets clearly visualize the vortex roll-up process. Measurements of the flow angle at the trailing edge of the 66 series foil indicate that the flow field turning angle increases from near the tip to a maximum turning angle just downstream of the separation line at $x/c_o = 0.125$. At this angle of attack, the flow on the 4215M foil remains attached to the trailing edge. The maximum flow turning angle occurs at $x/c_o \approx 0.07$ and then decreases downstream of this position. The position of maximum turning angle on the 66_2-415 foil agrees with the observations of Maines and Arndt (1993a) which indicate that the maximum growth rate of bubbles occurs at $0.10 < x/c_o < 0.15$. These observations were made at a higher Reynolds number ($Re = 8.3 \times 10^5$) but the same lift coefficient. Similar results for the NACA 16-020 foil (see Maines and Arndt, 1993b) agree with the observations of Fruman, et al (1992) who have observed from velocity measurements near the tip of the same foil at the same Reynolds number and the same lift coefficient that the tangential velocity increases from $x/c_o = 0$ to a maximum at $x/c_o = 0.125$ and then decreases downstream. Hence, all three foils have qualitatively similar boundary layer characteristics on the pressure side, at least at moderate lift coefficients.

Recent tip vortex inception data (Arndt and Dugue, 1992) have shown that the inception process can be described by a universal relation as suggested by Equation 1 (the effects of flow unsteadiness are neglected and the effects of tension are absorbed into the definition of σ defined in terms of $p_c = p_v - T$.). Following Keller and Eichmann (1989), the critical pressure was determined by plotting test section pressure at inception, p_o, versus U^m for various angles. The exponent, $m = 2.4$ was chosen based on achieving the best linear correlation between p and U. Extrapolation to $U = 0$ defines p_c. Data were discarded if hysterisis was present. A typical extrapolation is shown in Figure 11. Cavitation data for the three foils already discussed as well as for the NACA 66-012 are shown in Figure 12. The data are restricted to $600{,}000 \le Re \le 1{,}300{,}000$ to avoid complexities related to water quality at lower velocities (mentioned in the next section). Also included in Figure 12 are data from the studies of Souders and Platzer (1981) with an elliptic hydrofoil of aspect ratio 2.55. At low lift coefficients, the linear range is closely fitted by

$$\sigma_i = KC_l^2 Re^{0.4} \qquad (6)$$

where $0.045 \le K \le 0.073$. It should be pointed out that there was almost no correlation between the NACA 16-020 and NACA 66_2-415, $a = 0.8$ data when comparisons were made on an equal angle of attack basis. Only K is variable in Equation 6. The Reynolds number exponent of 0.4 appears to be "universal". As pointed out by Maines and Arndt (1993b), the variations in K can be attributed to differences in the constant of proportionality between boundary layer thickness and a fractional power of Reynolds number. Clearly, the details of the boundary layer flow in the tip region must be understood more completely before improvements can be made in the scaling law.

WATER QUALITY EFFECTS

Inception

The data shown in Figure 12 were obtained using weak water with only minor differences between p_c and p_v (refer to the curve for weak water in Figure 11). Arndt and Keller (1992) found that significant levels of tension are sustainable when the number of nuclei are suppressed by pre-treatment of the water. An example of their results is shown in Figure 13 for the 66_2-415 foil. Similar results are found with the 4215M foil in the SAFHL tunnel as shown in Figure 14. Both sets of data indicate that the amount of tension, as deduced using Equation 2, appears to increase with increasing lift coefficient. Unfortunately the trends deduced at higher velocities were inconsistent. However, very consistent results were obtained using the extrapolation procedure shown in Figure 11. These data were normalized with respect to the measured tension using a venturi apparatus designed by Dr. Keller (Keller, 1987). Sample normalized data are shown in Figure 15. The trend shown appears to be very repeatable. Note that only at high values of lift coefficient is the apparent tension at inception in the vortex comparable to that measured by the venturi apparatus. Research on this point is still in progress.

Desinence

In reviewing the progress made in understanding the cavitation process, it became clear that the interrelated effects of bubble dynamics and viscous flow phenomena make it difficult to interpret cavitation data under varying conditions of water quality and with different Reynolds numbers. This point is underscored in Figure 16. This data set corresponds to "strong" water using the NACA 4215M hydrofoil, with varying lift coefficients. Arndt, et al (1991) pointed out that a significant factor in the substantial variation of σ_i with velocity is due to bubble dynamics. Unfortunately, σ_i is also a function of Reynolds number (Arndt and Dugue, 1992). Hence, a reliable method for measuring σ_i is of paramount importance in distinguishing between the interrelated effects of bubble dynamics and viscous flow phenomena.

Pauchet, et al (1993) have suggested that desinence, defined as the point of detachment of a fully cavitating vortex core from the hydrofoil tip gave the most consistent results. In order to verify this, four different procedures have been evaluated; a) inception in "weak" water, b) inception in "strong" water, c) desinence in "weak" water, and d) desinence in strong water.

The most consistent results were obtained with desinence in "strong" water. As shown in Figure 17 the extrapolation procedure always indicated that p_c was approximately equal to vapor pressure. When similar tests were carried out in weak water, p_c was found to be greater than p_v:

$$p_c \cong K\beta C_g \qquad (7)$$

where K was in the range $0.3 \leq K \leq 0.4$, and β is Henry's constant. This is in agreement with previous results (e.g. Holl et al, 1972). Thus desinence tests in water with high gas content introduce additional complexities, since nucleation can be influenced by gaseous diffusion.

Based on these studies, desinence in degassed water appears to give the most consistent results using σ based on p_c. This is illustrated in Figure 18. The desinence data shown here are compared with the strong water inception data shown in Figure 16. The strong water inception data are presented in the form of curves (dotted lines) that are the best fit to the data in Figure 16. As expected, the two sets of data are asymptotic to each other at high velocity.

There is apparently some mismatch in the data at high velocity that was first attributed to experimental inaccuracies. However, an alternate explanation is as follows. Careful observation of cavitation in strong water indicates that inception always occurs well downstream of the tip with fully developed cavitation progressing rapidly upstream after inception. Because the size and number of nuclei are considerably smaller than in weak water, it is much more likely that entrainment of nuclei occurs further downstream in a region where flow unsteadiness is more significant. Because of this the inception pressure could actually be lower than at the tip where inception normally occurs.

Fig. 18 does illustrate how the combined effects of bubble dynamics and Reynolds number scaling can be isolated using a specialized desinence procedure.

BUBBLE DYNAMICS

A study of the bubble dynamics during inception in the tip vortex is underway using a new technique based on the ideas of Keller (1972) and Ceccio and Brennen (1991). The high speed movie camera used in Maines & Arndt (1993a) imposed several limitations such as low resolution (16mm format), a limited maximum framing rate (6000 fps) and a variable elapsed time between each successive frame. Since the duration of each roll of film was only one second, the random nature of cavitation at inception made data collection expensive. The new system is activated by individual cavitation events with equivalent framing rates of up to 100,000/sec. Many samples at each stage of growth can then be collected and ensemble averaged to describe the bubble dynamics.

The system consists of a laser beam "trip wire", photodetector, a threshold/delay circuit, strobe lighting, a photodiode (for strobe light flash detection), absolute and differential pressure transducers, and a standard 35mm camera with extension bellows. As a nucleus or bubble enters the vortex core and cavitates, it passes through the laser beam, scattering light which is collected by the photodetector. When the signal of the photodetector is greater than a predetermined threshold value, the delay circuit is triggered. At the end of the delay, the strobe lights are flashed and pressure data are recorded. The photodiode detects the flash and enables the exact delay time to be determined. Each photo is digitized and measurements are taken to determine bubble position, size, velocity and growth rates. The

resolution of the digitized pictures has a minimum of 0.012 mm/pixel and a maximum of 0.022 mm/pixel corresponding to the magnification of the original photo. The estimated relative precision error in bubble length is ±0.37% and ±4.0% for the bubble diameter. The estimated precision in velocity is ± 0.86%.

Observations have indicated that the bubble growth in the tip vortex is non-spherical. Maines & Arndt (1993a), described tip vortex cavitation in terms of four different phases. A spherical nucleus is first drawn into the vortex core, apparently from the freestream, and then grows as a spheroidal bubble over the foil tip. As the bubble travels downstream, growth in the radial direction (perpendicular to the vortex axis), is arrested while the bubble continues to grow at an almost constant rate of change in its length as shown in Figure 19. These results are intuitively consistent with the strong radial pressure gradient and negligible axial pressure gradient found in the vortex. As time increases (t > 1.5 msec.), both the bubble length growth rate and bubble radius decrease.

A series of photographs depicting the later stages of inception is shown in Figure 20. This series was obtained using the laser trip wire technique and clearly shows the cylindrical bubble growth. Each photograph depicts the bubble which best describes the average at that particular time. The additional bubbles at the right hand side for times t = 0.631 msec and 0.673 msec are previous events which have not yet exited from the frame. Close examination of this series reveals a complex growth mechanism not visible in the photographs presented in Arndt & Maines (1994) or Maines & Arndt (1993a). These recent photographs have revealed that the bubble can split at any position down stream of the laser trip wire and then coalesce back into a single bubble. During the measurement of each photo, approximately 29% of the pictures were found to contain bubbles which had possibly split. Split bubbles were excluded from the average. The highest percentage of split bubbles occurred in the regions $0.110 \le x/c_0 \le 0.120$ (0.471 msec $\le t \le$ 0.512 msec), $0.136 \le x/c_0 \le 0.144$ (0.673 msec $\le t \le$ 0.707 msec), and finally between $0.228 \le x/c_0 \le 0.235$ (1.458 msec $\le t \le$ 1.499 msec). The origin, $x/c_0 = 0.0$, is at the foil tip. Possible examples of bubbles which have coalesced can be seen in Figure 20 at time delays of 0.391, 0.553, 0.631, 1.485 and 1.499 milliseconds. The bubble seen at t=0.707 msec. appears to be nearly split, however close-up examination shows that the bubble is still connected.

As the velocity is increased, some clear differences in the bubble growth are observed. Figure 21 contains a comparison between bubble growth at 6 m/s (Fig. 20), and 10 m/s. The series of photographs taken at 10 m/s are at a slightly lower cavitation number, i. e. σ = 4.4 compared to σ = 4.7 at 6 m/s. Note that both the length and diameter of the bubbles are much larger at 10 m/s than at 6 m/s at equal downstream positions. For the photographs at 10 m/s, the laser trip wire was inadvertently positioned so that bubbles which entered the vortex from the pressure side were responsible for triggering the flash. Notice that in all cases the bubble nose is hidden behind the foil tip. The bright spot seen at the nose of the bubble is actually laser light reflected from the foil surface. It is interesting to note that fewer bubbles were observed to split at 10 m/s than at 6 m/s.

Bubble splitting has been suggested as a mechanism for noise production. Chahine (1994) has shown through numerical calculations that bubbles grow cylindrically with a bulbous center which then collapses causing the bubble to split. Similar bubble shapes and bubble splitting have been observed experimentally. Previous work (Frizell et al, 1987), indicates that bubble splitting is a significant noise source. Even without splitting, bubble oscillations can be a significant source of sound. Higuchi et al (1989a) have published time histories of the pressure oscillations produced by tip vortex inception. The frequencies were found to vary between 2.5 KHz to 6 KHz depending on the test conditions. It was noted that these frequencies were too low to be associated with bubble collapse, but were comparable to the natural frequencies of spherical bubbles of equivalent volume at a partial pressure corresponding to the freestream gas content. However, no discernable relationship was found between frequency and gas content. It was also stated that the pressure amplitude far exceeded that expected from simple spherical bubble oscillations. The present observations indicate that the bubble grows cylindrically at almost a constant rate with a superimposed oscillation of the total volume.

In order to compare these older results with the present observations, preliminary calculations of the sound pressure produced by the ensemble averaged bubble growth oscillations shown in Figure 20 and Figure 21b are plotted in Figure 22 (Figure 21b contains additional points not presented). These calculations were made using the well known acoustical model for compact sources:

$$p_a = \frac{\rho \ddot{V}}{4\pi r} \qquad (8)$$

where $\ddot{V}$ is the second time derivative of bubble volume. As shown in Figure 22, the calculated frequency and amplitude using the measured bubble oscillation data are approximately 10 KHz to 14 KHz and 45 Pa at 6 m/s and 300 Pa at 10 m/s. The calculated pressure amplitude is approximately half (3 dB down) of Higuchi et al's measured value while at 10 m/s the amplitude is triple that of Higuchi's. The qualitative agreement between the calculated and measured noise appear to confirm the idea that bubble oscillations may be a significant noise source.

In order to determine whether the primary noise mechanism is splitting or simply due to bubble oscillations, preliminary noise measurements were made using the laser trip wire technique described above. A reference point was marked in the time histories when a cavitation event was initiated. As before, flash delay times could be adjusted to allow bubble shape observations at different locations within the vortex. Figure 23a contains three typical time histories of an acoustic event at a freestream velocity of 10 m/s. Time is referenced to the laser triggering. Included in the plots are the approximate downstream locations based on bubble velocities inferred from the photographic observations. Figure 24 is a typical noise trace over a much longer period of time to illustrate the random nature of acoustic events and confirm the validity of the laser trip wire technique. Although not shown, the amplitude of the sound at 6 m/s was greatly reduced in agreement with sound pressure calculations shown in Figure 22. The visual observations clearly indicate that a significant noise event is correlated with a bubble oscillation in the absence of splitting. These visual observations strongly suggest that bubble oscillations are a key noise mechanism. Additional research on this point is currently underway.

Additional studies were conducted using the NACA 66_2-415 hydrofoil in filtered and unfiltered water over a range of lift coefficients, freestream velocities, and dissolved air content. Figure 25 shows two photographs of the bubble at different lift coefficients. Figure 25a is at C_L = 0.58 while C_L = 0.67 for Figure 25b. The bubble centroids are at approximately equal downstream positions and thus at similar growth stages. Note the large change in bubble length. Figure 26 is a plot of the bubble length versus downstream position of the bubble centroid, x/c_0, for different lift coefficients. There is a clear trend of increasing bubble length with increasing lift coefficient. Although not shown, the bubble diameter follows a trend similar to that for length with increasing lift coefficient. The effects of water quality are seen in Figure 27 which compares unfiltered water with filtered water at equal dissolved gas contents, lift coefficients and freestream velocity. Apparently, the unfiltered water contains a larger supply of nuclei which reduces the level of tension under which cavitation occurs, effectively reducing the rate of bubble growth. Thus, preliminary observations indicate that there is a complex relationship between the bubble growth, vortex strength and water quality.

It is also possible to determine the axial velocity conditions in the vortex core during inception. It is assumed that the velocity of the bubble center should reflect the axial velocity conditions in the core. Figure 28 contains a plot of the velocity of the bubble centroid normalized with respect to the freestream velocity for different lift coefficients. An excess axial velocity exists in the vortex core which increases with angle of attack. These data agree well with unpublished data from Maines & Arndt (1993), using the same foil at equal conditions. Likewise, the variation of axial velocity with lift coefficient is asymptotic to non-dimensionalized LDV data collected further downstream (Arndt & Keller,1992). The large excess axial velocity noted for the second data set at C_L = 0.67, U = 10 m/s is not unexpected as Pauchet et al (1993), have observed core axial velocities as high as 2.4U near the tip for elliptic planform hydrofoils. Since the velocity is averaged from the time the bubble passes the laser trip to the photograph, one must also consider that the large axial elongation rates of the bubble may artificially accelerate the bubble centroid. However, Maines & Arndt (1993a), found that at C_L = 0.49, and U = 10 m/s, each end of the bubble appeared to expand with equal but opposite velocities which would tend to cause the bubble centroid to follow the local fluid velocity. Note also that data at 6 m/s in Figure 28, show a rapid change from a large axial velocity defect to an excess between $0.09 \le x/c_0 \le 0.30$. A plot of the bubble trajectory as shown in Figure 29 indicates that bubbles photographed for this series (see Figure 20), initially passed through the trip wire outside the vortex core. As the bubble spirals toward the vortex axis the velocity increases to match the core velocity. Downstream of x/c_0 =

0.30, the bubbles appear to match the trajectory of a fully cavitating core. Included in Figure 29 are the trajectory data from Maines & Arndt (1993a). Although there appears to be an offset, most of the bubbles travel directly down the vortex axis indicating that cavitation does not significantly affect the vortex trajectory.

FULLY DEVELOPED CAVITATION AND NOISE

Careful inspection of fully developed cavitation shows the evolution of complex structures which are not easily modeled analytically. Figures 30 and 31 are close-up photographs of fully developed cavitation for the NACA 4215M at C_L = 0.45 and Re = 4.8 x 10^5. In Figure 30, the cavitation number was lowered below that of inception until a fully cavitating core developed. Note the characteristic bulb at the leading edge of the cavity. The bulb is located in the region of minimum pressure. Further lowering of the cavitation index results in an attached cavity without a bulb. Figure 31 illustrates a wave-like structure at the tip as the cavitation number is lowered still further. This phenomenon has also been observed in photographs published in Arndt et al (1991), for the NACA 66_2-415 hydrofoil.

Under some conditions, these complex cavitating core structures seem to be correlated with a travelling wave that develops on the hollow core vortex and radiates a significant level of noise at a discrete tone, much like that of a "singing propeller", but due to an entirely different mechanism. This so-called "singing vortex" was first reported by Higuchi et al (1989) but only a cursory qualitative study was conducted describing the basic phenomenon. Higuchi et al's study was conducted with the NACA 66_2-415 hydrofoil. They reported that within a narrow range of angle of attack and cavitation number, a discrete tone was generated. Within that narrow range of cavitation number the frequency of the tone would vary with small changes in cavitation number. Limited data indicated that the frequency varied linearly with velocity. They reported that the phenomenon was associated with the braided structure of the fully developed cavitating core which pulsated and rotated in synchronism with the generated tone. Flow induced vibration was discounted since the tonal frequency varied continuously with cavitation number.

In the present study this phenomenon was more closely examined by varying the hydrofoil cross-section, water quality, angle of attack and cavitation number. Preliminary results agree with Higuchi et al, but it was found that the tone could occur over a much wider range of angle of attack and produce tones of higher frequency.

The phenomenon of the singing vortex can be most easily described as an area varying travelling wave. Figure 32 shows photographs of a cavitating vortex with and without singing. In Figure 32a, the cavitation number has been raised just enough to suppress the singing. In Figure 32b, sigma has been lowered so the vortex begins to sing. Note the thickening of the core just downstream of the hydrofoil tip. Apparently this wave travels downstream with the freestream velocity.

Singing was easily observed on the 66_2-415 but was not observed on the 4215M during a preliminary search over a few angles of attack and velocities. As previously noted, major differences in the boundary layer characteristics exist between the two hydrofoils. An aft separation bubble is present on the 66_2-415 suction side up to approximately (α - α_o) = 12 to 13 degrees. Above this angle, the zone of separation is at the leading edge. In contrast, separation on the 4215M always occurs around x/c_o = 0.20 for all angles. It is interesting to note that singing on the 66_2-415 could not be achieved above approximately (α - α_o) = 11 degrees. At this angle of attack, the separation bubble has begun shifting toward the leading edge. With this in mind, the remainder of the discussion pertains to the NACA 66_2-415 with an aft laminar separation bubble.

In general, higher frequencies occur at lower angles of attack when data were collected at cavitation numbers just above the onset of surface cavitation. It should be noted that for a given angle and freestream velocity, a small change in sigma around the test condition would vary the tonal frequency. A slight increase in sigma would raise the frequency while lowering sigma below the test point would further decrease the frequency until surface cavitation developed. Thus, the conditions of each test case were slightly subjective. Still photographs were taken for each condition with and without vortex singing to measure both the wave length of the disturbance and the hollow core diameter. The measured Strouhal number defined as

$$S = \frac{f\lambda}{U_\infty} \qquad (9)$$

where λ is the wave length of the disturbance, was measured to be S = 1, which suggests that the

disturbance is a simple travelling wave. When the relative amplitude of the signal at each condition is plotted versus frequency, there appears to be a "lock in" at frequencies that are roughly multiples of 300 Hz. The reason for this behavior is not clear. One assumption is that resonance occurs at frequencies corresponding to vibrational modes of the hydrofoil.

Further investigations are required to determine the mechanism of noise production. Several suggestions have been put forth which include lock in with structural natural frequencies, viscous dominated effects or surface tension. Consider first the lock in phenomenon. Although Higuchi et al (1989a) discounted this possibility, personal communications with C. C. S. Song indicate that a small flow disturbance can induce lock in at frequencies slightly higher than the structure's natural frequency.

Lundgren[2] (in private communication) has proposed a linearized travelling wave disturbance at the interface between the fluid and vapor filled core of a cavitating vortex. Using perturbation analysis, he found that a fully cavitating vortex core is receptive to travelling wave disturbances. The high wave number asymptote in his theory predicts a Strouhal number of unity as noted experimentally. Clearly, the relationship between theory and experiment needs to be explored further. An important issue is that this tone appears to be connected with specific viscous flow phenomena on the surface of the foil.

SUMMARY AND CONCLUSIONS

Cavitation inception has been studied with a series of elliptical planform hydrofoils differing only in cross section. Correlations were made with measured lift, boundary layer characteristics and the nuclei content in the water. Significantly different boundary layer characteristics were noted on the suction side. However, the process of vortex roll-up appeared to be similar, which was evident from inspection of the boundary layer flow characteristics on the pressure side of the foils. Cavitation data collected in weak water indicate that an almost universal law can be fitted to the data:

$$\sigma_i = KC_l^2 Re^{0.4} \qquad (10)$$

where $0.043 \leq K \leq 0.073$. The Reynolds number exponent appears to be "universal". It is suggested that the variability in K reflects small relative differences in boundary layer growth on the surface of each hydrofoil.

Cavitation data, even in weak water, were found to be more consistent when σ is defined in terms of p_c rather than p_v. In the weak water tests p_c was often found to be greater than p_v. Significant levels of tension can be sustained before inception in strong water. The amount of tension increases with lift coefficient approaching the value measured by a venturi cavitation susceptibility meter.

In comparing various experimental methods to define inception, it was noted that a special method of cavitation desinence in degassed water appears to give the most consistent results. Comparisons of different test techniques have only been made at this point with the NACA 4215M hydrofoil. Tests with other hydrofoil shapes must be made before a general conclusion can be made.

A new photographic system has been developed to investigate the details of the inception process. Preliminary results indicate that, in the latter stages of the inception process, cylindrical shaped bubbles are formed that achieve an equilibrium radius that appears to be less than the viscous core radius while continuing to grow in length at a constant rate. After reaching $x/c_0 \approx 0.25$ the growth rate of the bubble length appears to decrease. The velocity of the bubble's centroid roughly reflects that of the local fluid and can therefore be used to determine the axial velocity conditions in and around the core. Observations indicate that cavitation inception occurs both inside and outside the vortex core. Nuclei which cavitate just outside the core quickly spiral into the vortex axis. The presence of cavitation bubbles does not significantly affect the vortex trajectory. Preliminary results also indicate that larger bubbles are created when inception occurs in strong water. Larger bubbles are also noted at higher lift coefficients.

Recent experimental evidence indicates that bubble splitting is more prevalent than expected. Previous research (Frizell et al, 1987), indicates that bubble splitting is an important source of sound. Even in the absence of bubble splitting, bubble oscillations can radiate measurable levels of sound. Observations of fully developed cavitation indicate

[2] Professor of Aerospace Engineering and Mechanics at the University of Minnesota.

that there are some complex flow patterns close to the tip which may also have important implications for radiated sound. Preliminary results indicate that an additional important noise source is associated with a fully cavitating tip vortex. Inviscid wave theory appears to provide a basis for analysis. However, the noise can only be generated under certain viscous flow conditions.

Numerical calculations, utilizing a large eddy simulation technique (LES) have provided considerable qualitative information on the details of vortex formation. Clearly evident in the computations is the interaction between the viscous wake and the tip vortex. The vortex is clearly asymmetric, indicating that velocity measurements made with a single traverse through the vortex can be misleading. Clearly, particle image velocimetry (PIV) would be a significant aid in further understanding of the cavitation process. Unfortunately, the numerical model is unable to accurately predict the minimum pressure in the vortex, due to lack of sufficient spatial resolution with the grid currently used. However, the numerical model does predict the minimum pressure location to be very close to the tip in agreement with experimental evidence.

ACKNOWLEDGEMENTS

This paper was prepared under the sponsorship of the U.S. Office of Naval Research. Dr. Edwin Rood is the contract monitor. Mr. Dong Ma provided invaluable help in collecting data on the correlation between the level of tension in the vortex and the measured strength of the test water. The numerical simulations are the work of the co-principal investigator, Professor C.C.S Song and his student, Mr. C. Chen.

REFERENCES

Arakeri, V. H., Higuchi, H. and Arndt, R. E. A. (1988),"A Model for Predicting Tip Vortex Cavitation Characteristics," J. Fluids Eng., 110:190-193.

Arndt, R. E. A. (1993) "Cavitation in Vortical Flows," Proc. Intl. Symp. on Aerospace and Fluid Science, (in commemoration of the 50th anniversary of the Institute of Fluid Science) Sendai, Japan, Nov 11 - 16

Arndt, R. E. A., Arakeri, V. H. and Higuchi, H. (1991), "Some Observations of Tip Vortex Cavitation," J. Fluid Mech., 229:269-289.

Arndt, R. E. A. and Dugue, C. (1992), "Recent Advances in Tip Vortex Cavitation," Proc. Intl. Symp on Propulsors and Cavitation, Hamburg, Germany.

Arndt, R. E. A. and Keller, A. P. (1992), "Water Quality Effects on Cavitation Inception in a Trailing Vortex," J. Fluids Eng., 114, No. 3: 430-438.

Arndt, R. E. A., and Maines, B. H., (1994), "Further Studies of Tip Vortex Cavitation," 2nd Intl. Symposium on Cavitation, Tokyo, Japan.

Arndt, R.E.A., and Maines, B.H., (1994b), "Vortex Cavitation: A Progress Report," Symp. on Cavitation and Gas-Liquid Flow in Fluid Machinery and Devices, ASME, NY, June.

Ceccio, S. L., and Brennen, C. E., (1991) "Observations of the Dynamics and Acoustics of Travelling Bubble Cavitation" J. Fluid Mech., Vol 233, pp 633-660

Chahine, G. L. (1994), "Bubble Interaction with Vortices," Chapter 19 in Fluid Vortices, I. S. Green, ed. to appear.

Frizell, W. K., Cheng, J. and Arndt, R. E. A. (1987) "Characteristics of Bubble Splitting Noise", ASME Cavitation and Polyphase Flow Forum, June

Fruman, D. H., Dugue, C., Pauchet, A., Cerrutti, P. and Briancon-Marjolet, L. (1992), "Tip Vortex Roll-up and Cavitation," Proc. 19th Symp Naval Hydro., Seoul, Korea.

Fruman, D. H., Castro, F., Pauchet, A., and Pichon, T. (1994) "On Tip Vortex Turbulence, Wandering and Cavitation Occurence" Proc. The 2nd Intl. Symp. on Cavitation, Tokyo, Japan, April

Green, S. I. (1991), "Correlating Single Phase Flow Measurements with Observations of Trailing Vortex Cavitation," J. Fluids Eng., 113:125-129.

Green, S. I. and Acosta, A. J. (1991), "Unsteady Flow in Trailing Vortices," J. Fluid Mech., 227: 107-134.

Higuchi, H., Arndt, R. E. A., Arakeri, V. H., and Killen, J. M. (1989), "The Structure of Tip Vortices Over a Wide Range of Cavitation Number," Proc. Amer. Towing Tank Conf., St. Johns, New Foundland.

Higuchi, H., Arndt, R. E. A., and Rogers, M. F. (1989a), "Characteristics of Tip Vortex Noise", J. Fluids Eng., Dec.

Higuchi, H., Quadrelli, J. C. and Farell, C. (1987), "Vortex Roll-up for an Elliptically Loaded Wing at Moderate Reynolds Number", AIAA J., Vol. 25, pp. 1537-1542.

Holl, J. W., Arndt, R. E. A., and Billet, M.

L. (1972), "Limited Cavitation and the Related Scale Effects Problem," Proc. 2nd Intl. Symp. Fluid Mech. and Fluidics, pp. 303-314, JSME, Tokyo, Sept.

Keller, A. P. (1972), "The Influence of the Cavitation Nucleus Spectrum on Cavitation Inception, Investigated with a Scattered Light Counting Method," J. Basic Engrg., 94:917-925.

Keller, A.P. (1987), "A Vortex-Nozzle Cavitation Susceptibility Meter in Routine Application in Cavitation Inception Measurements" Proc. Euromech Colloquium 222 - Unsteady Cavitation and its Effects, Wageningen, The Netherlands

Keller, A. P. and Eichmann, G. (1989), "Velocity and Size Scale Effects for Incipient Cavitation of Axisymmetric Bodies in Water of Different Quality,", Pro. Intl. Symp. Cav. Inception, ASME, N.Y. 79-86.

Maines, B. H. and Arndt, R. E. A. (1993a),"Bubble Dynamics of Cavitation Inception in a Wing Tip Vortex," Proc. Cav. and Multiphase Flow Forum. ASME, N.Y., June

Maines, B. H. and Arndt, R. E. A. (1993b), "Viscous Effects on Tip Vortex Cavitation," Proc, 4th Intl. Symp Cav. Inception, ASME, N.Y., November

McCormick, B. W. (1954), "A Study of the Minimum Pressure in a Trailing Vortex System," Ph.D Thesis, Dept. Aerospace Engrg., Penn. State Univ., University Park, PA.

McCormick, B. W. (1962), "On Cavitation Produced by a Vortex Trailing from a Lifting Surface," J. Basic Eng. 84:369-379.

Pauchet, A., Briancon-Marsollet, L. and Fruman, D. H. (1993), "Recent Results on the Effect of Cross Section on Hydrofoil Tip Vortex Occurrence at High Reynolds Numbers", Cavitation and Multiphase Flow Forum, ASME FED - Vol. 153, June.

Song, C. C. S. and Chen, C. (1993), "Numerical Simulation of(Turbulent Flows Around a Hydrofoil," Proc. Sixth Intl. Conf. on Num. Ship Hydrodynamics, Iowa City, IA, Aug. 2-5.

Souders, W. G. and Platzer, G. P. (1981), "Tip Vortex Characteristics and Delay of Inception of a Three Dimensional Hydrofoil," DTNSRDC, Rpt. No. 81/007, David Taylor Res. Center, Bethesda, MD.

Wetzel, J. M. and Arndt, R. E. A. (1991), "Hydrodynamic Design Considerations for Hydroacoustic Facilities", Proc. Symp. on Hydroacoustic Facilities, Instrumentation and Exp. Techniques, ASME, Atlanta, GA., Dec.

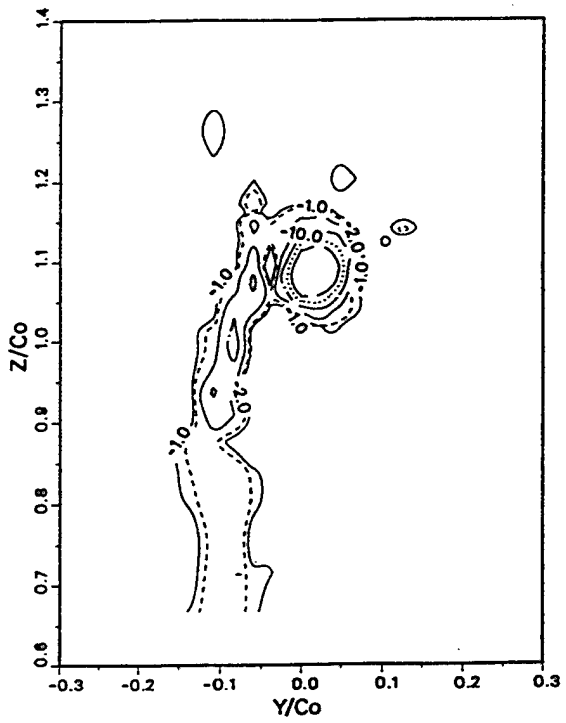


Figure 1 Computed vorticity contours at x/c_0 = 0.60 in the tip vortex formed by the NACA 4215M hydrofoil at C_L = 0.73. (Song and Chen, 1993)

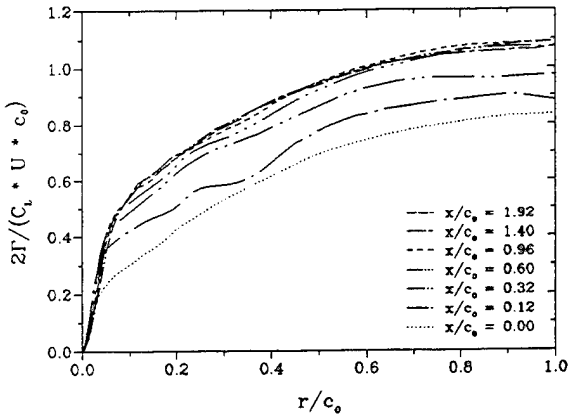


Figure 2 Computed circulation in the tip vortex for the NACA 4215M at the same conditions as Figure 1. (Song and Chen, 1993)

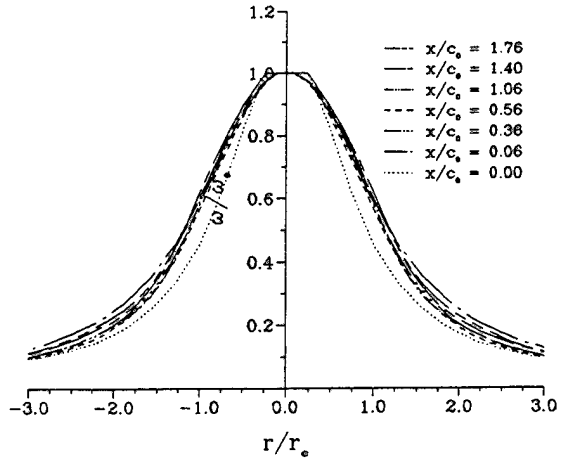


Figure 3 Computed mean vorticity for the NACA 4215. (Song and Chen, 1993)

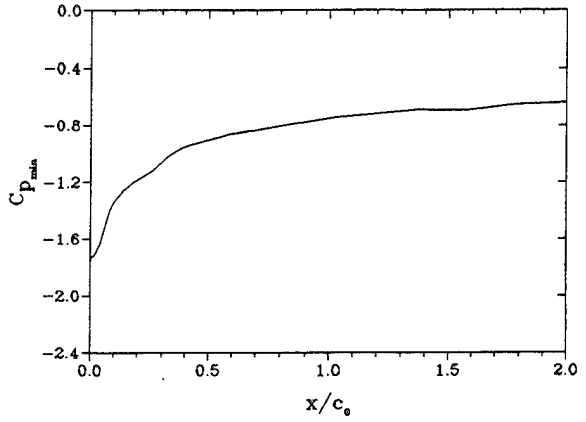


Figure 4 Computed minimum pressure in the tip vortex for the 4215M. (Song and Chen, 1993)

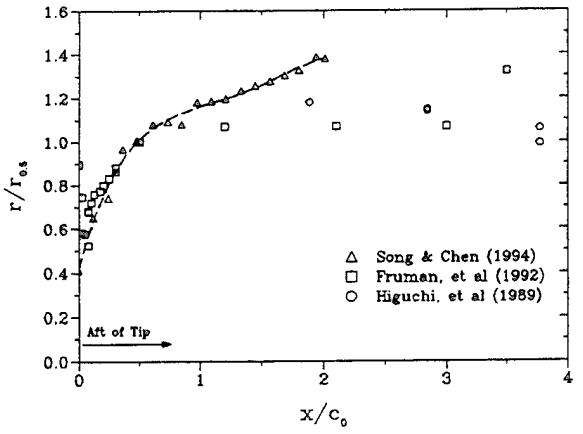


Figure 5 Computed core radius versus x/c_0 of the tip vortex for the 4215M. (Song and Chen, 1993)

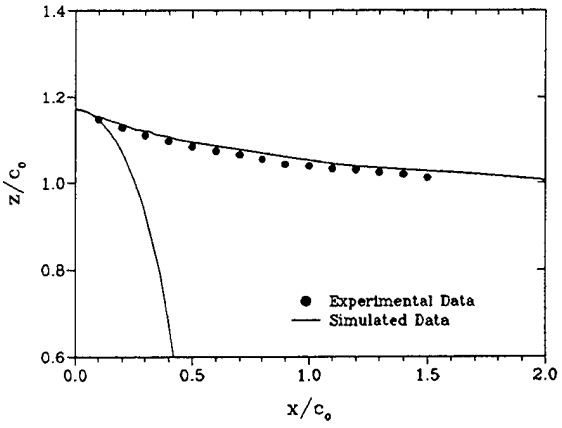


Figure 6 Computed core vortex trajectory for the 4215M. (Song and Chen, 1993)

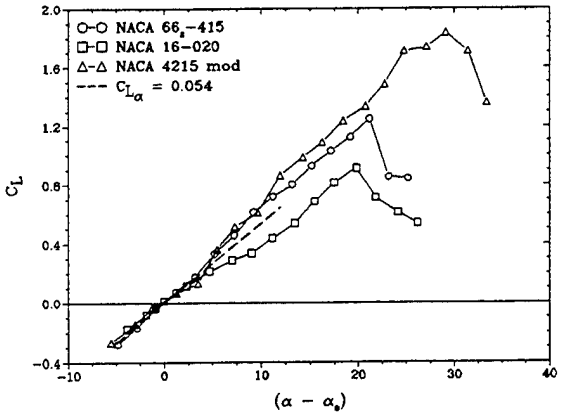


Figure 7 Measured lift for three foils at Re ≈ 6.5×10^5. (Obernach Facility, Maines & Arndt, 1993b)

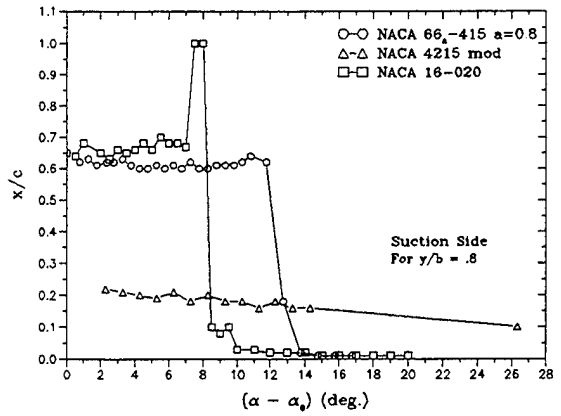


Figure 8 Suction side separation lines at Re ≈ 4.85×10^5. (Maines & Arndt, 1993b)

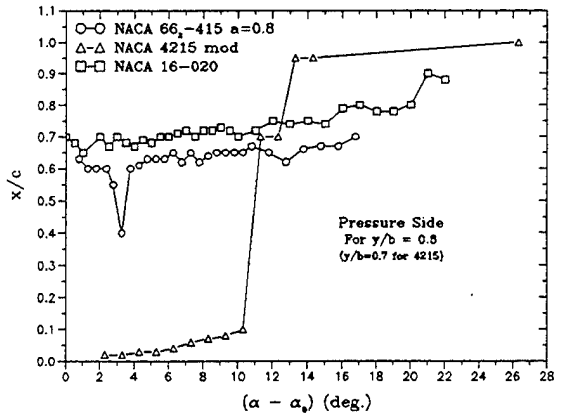


Figure 9 Pressure side separation lines at Re ≈ 4.85×10^5. (Arndt and Maines, 1994)

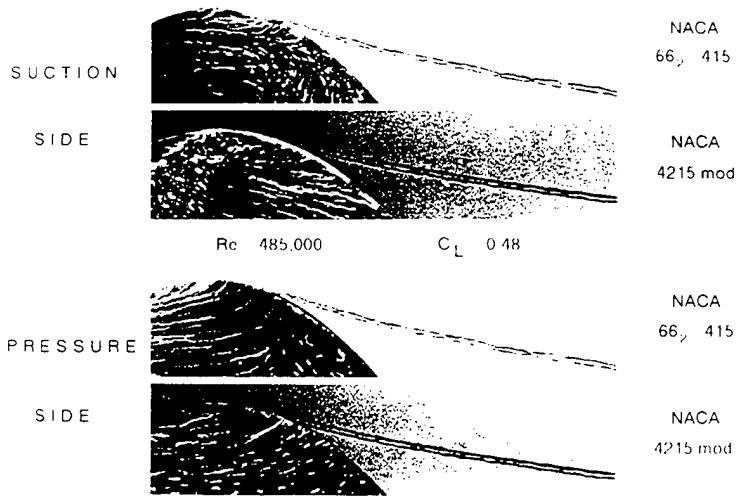


Figure 10 Superposition of oil flow and cavitation photographs. (Arndt and Maines, 1994)

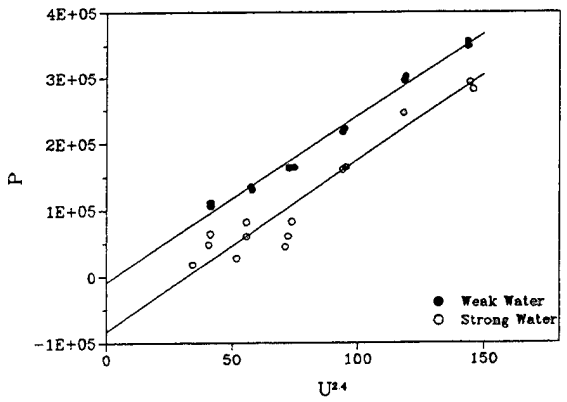


Figure 11 Extrapolation to determine the critical pressure at cavitation inception. (Arndt and Maines, 1994)

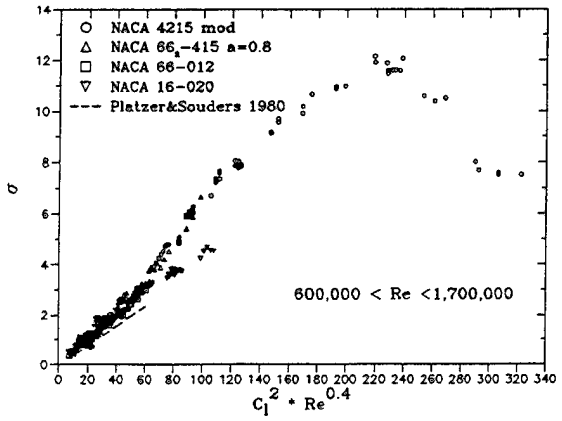


Figure 12 Correlation of cavitation data with measured lift for σ based on p_c (weak water). (Maines & Arndt, 1993b)

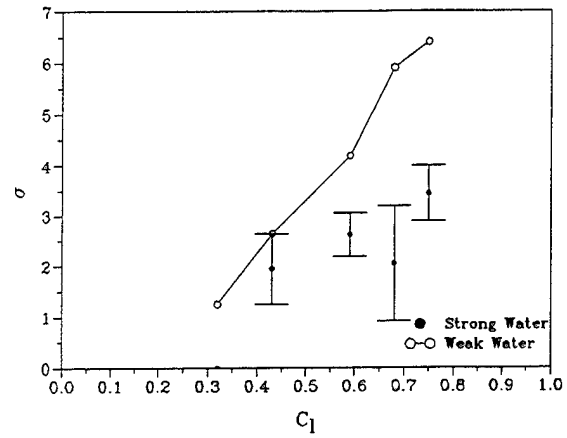


Figure 13 Comparison of σ for strong and weak water for the 66_2-415 at Re≈1.0x10^5. (Arndt & Keller, 1992)

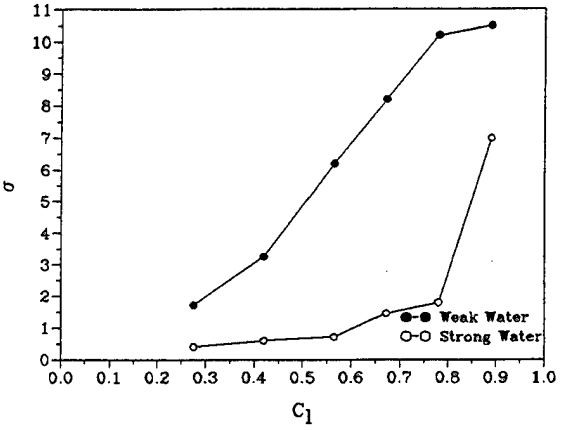


Figure 14 Comparison of σ for strong and weak water for the 4215M at Re ≈ 4.0x10^5. (Arndt and Maines, 1994)

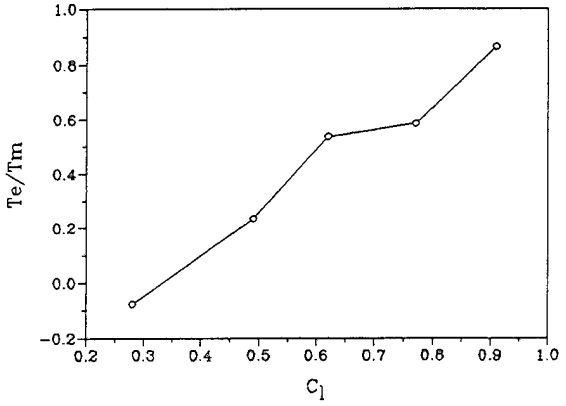


Figure 15 Apparent tension versus lift coefficient. (Arndt and Maines, 1994)

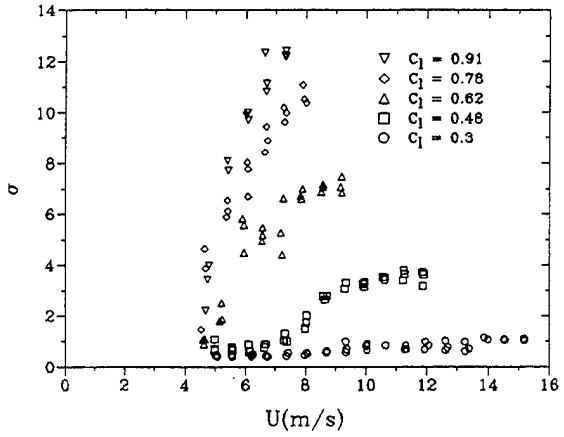


Figure 16 Cavitation inception data for strong water and varying lift coefficient (NACA 4215M). (Arndt & Maines, 1994b)

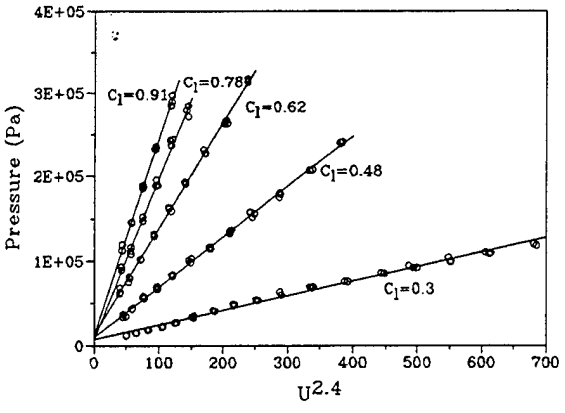


Figure 17 Extrapolation of strong water desinence data to determine p_c (NACA 4215M). (Arndt & Maines, 1994b)

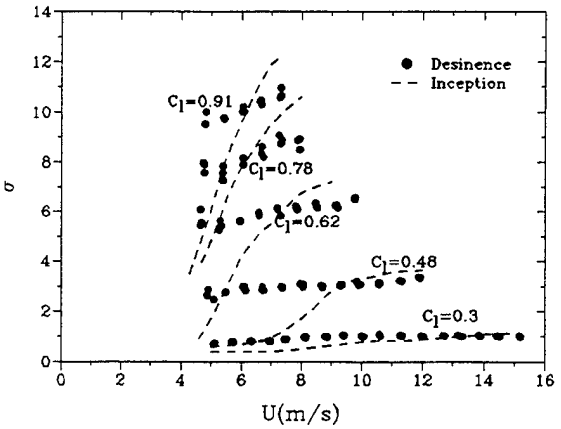


Figure 18 Comparison between desinence and inception in strong water. (NACA 4215M) (Arndt & Maines, 1994b)

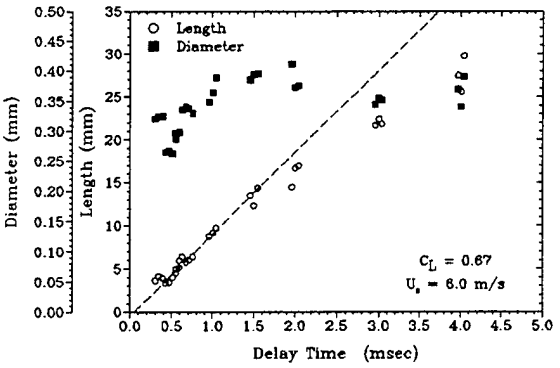


Figure 19 Bubble length and diameter plotted versus time (NACA 66_2-415, U_0=6 m/s, σ=4.7, C_L=0.67). (Arndt & Maines, 1994b)

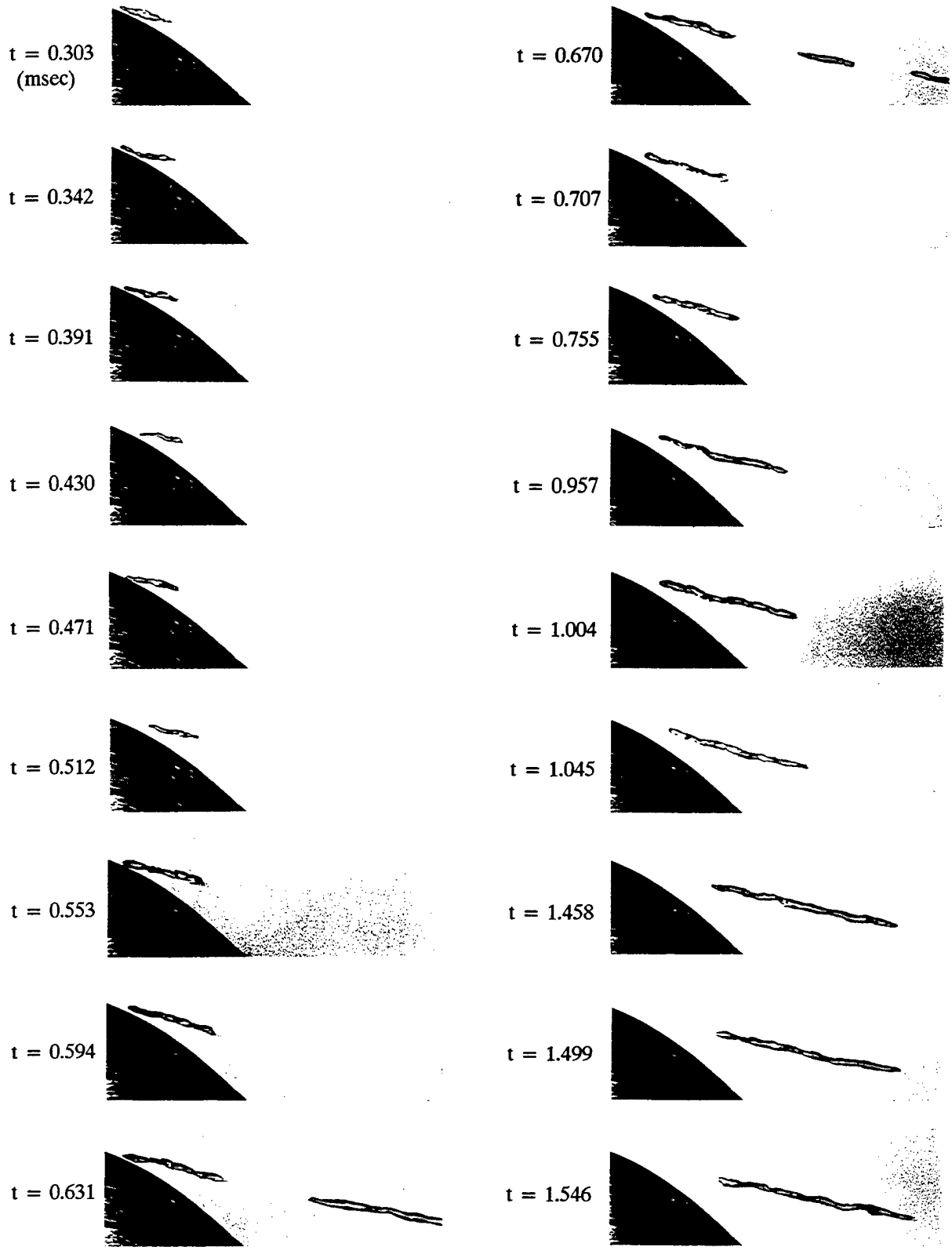


Figure 20 Cylindrical bubble growth during the later stages of inception (NACA 66_2-415, U_0=6 m/s, σ=4.7, C_L=0.67). (Arndt & Maines, 1994b)

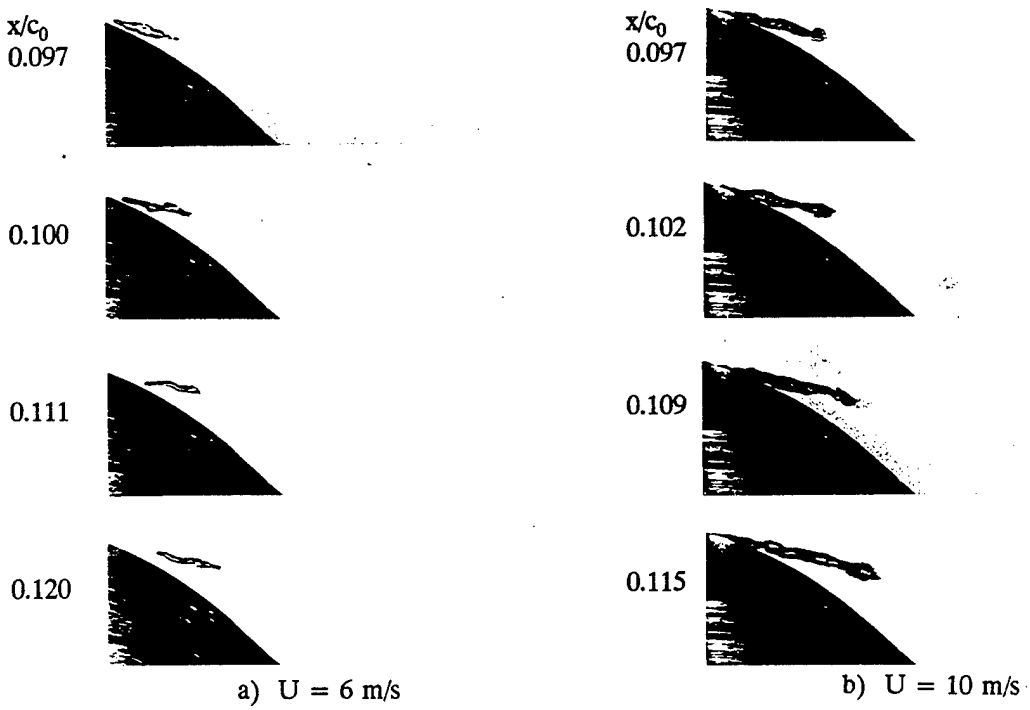


Figure 21 Comparison of bubble growth for different freestream velocities.

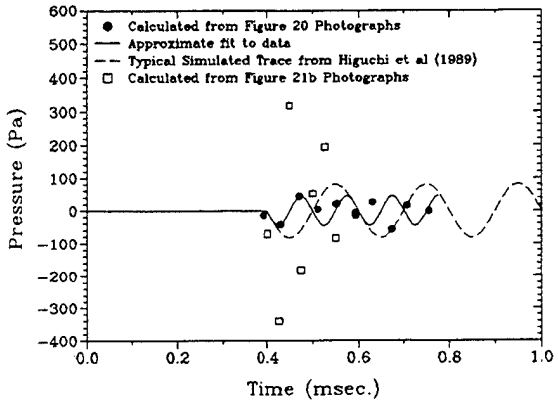


Figure 22 Comparison of measured and calculated acoustic pressure (NACA 66_2-415).

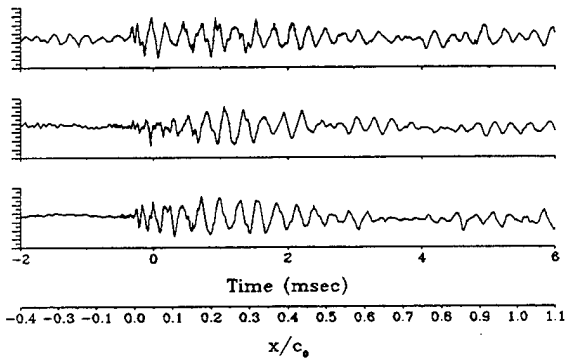


Figure 23 Measured sound of single cavitation events.

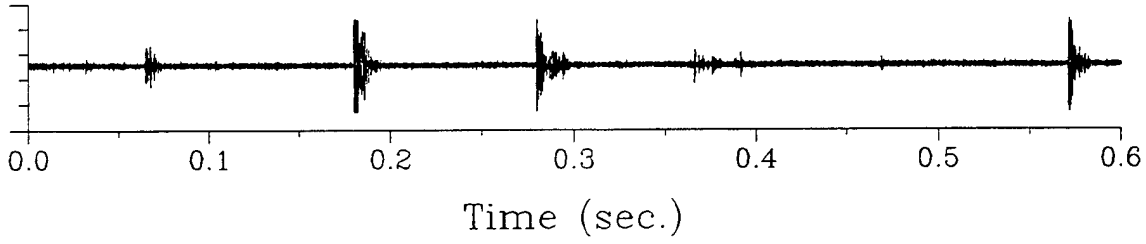
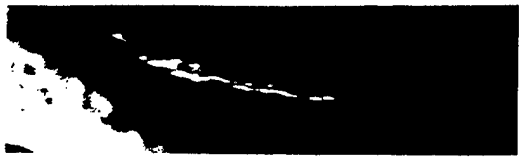


Figure 24 Typical measured sound trace of cavitation inception over a long duration.

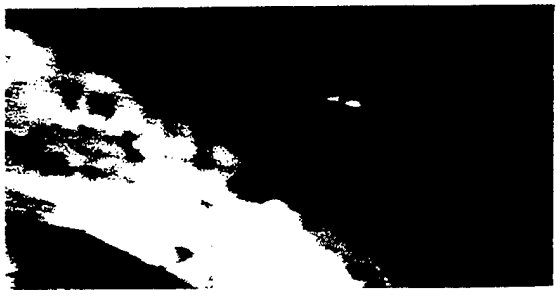


a) $C_L = 0.58$



b) $C_L = 0.67$

Figure 25 Effect of lift coefficient on bubble growth (NACA 66_2-415, U_0 = 10 m/s). (Arndt and Maines, 1994)



a) Unfiltered



b) Filtered

Figure 27 Effects of unfiltered and filtered water on bubble growth (NACA 66_2-415, U_0 = 10 m/s). (Maines and Arndt, 1994)

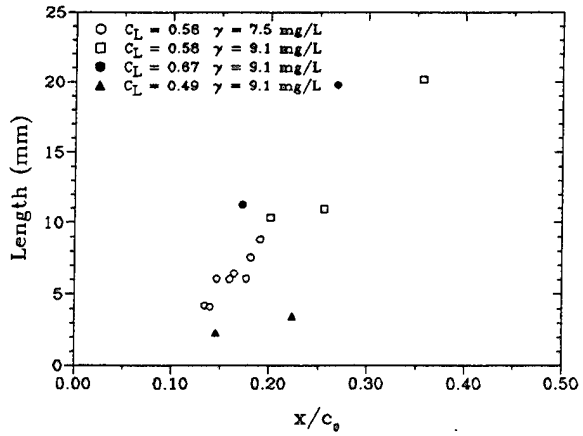


Figure 26 Plot of bubble length for various lift coefficients (NACA 66_2-415, U_0 = 10 m/s). (Arndt and Maines, 1994)

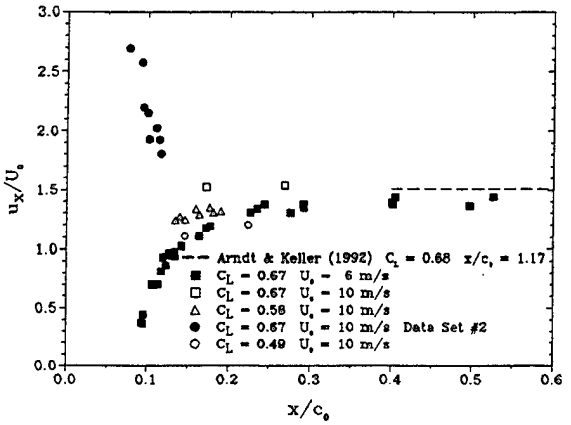


Figure 28 Vortex core axial velocity for various lift coefficients (NACA 66_2-415).

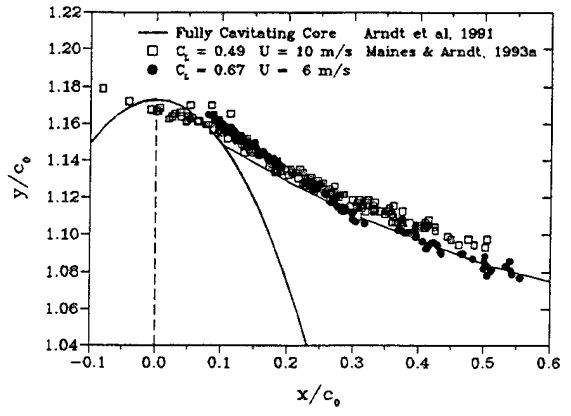


Figure 29 Comparison of bubble trajectories and the shape of a fully cavitating vortex. (NACA 66_2-415) (Arndt & Maines, 1994b)



Figure 30 Close-up photograph a continuous vortex core and characteristic bulb for the 4215M (Maines & Arndt, 1993a).

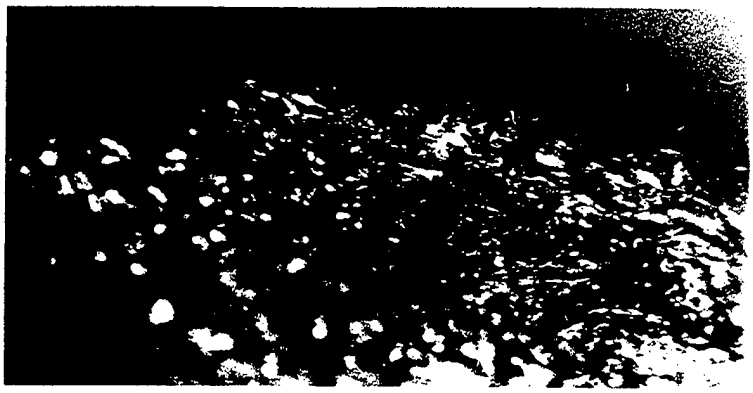


Figure 31 Enlargement of wavelike structure for sigma well below inception (NACA 4215M). (Arndt and Maines, 1994)



a) Sigma greater than test condition
No singing

b) Sigma at test condition
Singing Vortex

Figure 32 Photographs of Developed Tip Vortex Cavitation

DISCUSSION

J. Matusiak
Helsinki University of Technology, Finland

My question concerns your model of cloud cavitation. What is initial bubble size distribution in the cloud? Is it uniform, that is are the bubbles of the same size?

T. Huang
David Taylor Model Basin, USA

The bubble size distribution measurements shown in the figure are questionable, especially for diameters less than 5 Tm. Please give the detail of comparison between the two methods. What distribution did you use in your computation?

S. Banerjee
University of California, Santa Barbara, USA

I was struck by the similarity in shape between the cavitating bubbles that develop tails and vortex structures that one sees near walls—the tails being like the quasi-streamwise leg of "horseshoe" or "hockey-stick" vortices. Would you care to comment?

D. Fruman
ENSTA/GPI, France

How can you explain the change from traveling bubbles to attached patches with increasing Reynolds numbers?

AUTHORS' REPLY

I would like to thank Professor Matusiak, Dr. Huang, Professor Banerjee, and Dr. Fruman for the interest and their questions.

In response to Professor Matusiak's questions, the numerical calculations of the growth and collapse of a cloud of cavitating bubbles were carried out with an initially uniform distribution of bubbles, all of which had the same initial size. The method is not restricted to these simple choices; rather they seemed the obvious initial selections. Of course, as the cloud grows and collapses, the bubbles at different radial positions within the cloud have a different size.

Dr. Huang raises a very good point which I should, perhaps, have addressed at greater length. First, let me say that Dr. Huang is correct in doubting the validity of the nuclei size distribution measurement at the smallest diameter (about 5 μm), We were unable to validate the PDA for such small nuclei sizes and it may be that the PDA is underestimating the number of nuclei in the size range below 10 μm). It is possible that this is a factor which is contributing to the discrepancy between the calculated and observed event rates. However, it is important to recall that only nuclei larger than the Blake critical radius will become unstable and grow into macroscopically observable events. The Blake critical radius for the current experiments can be observed as the vertical portions of the curves in figure 7. Note that, at the typical σ of 0.5, the critical value of R_O/R_H is approximately 5×10^{-4}. Consequently, the critical radius for the 5.08 cm headform tests was approximately 25 μm. Under these circumstances, it would appear that any discrepancies in the nuclei number distribution below a radius of 25 μm would not contribute to the discrepancy highlighted in figure 8 (right). However, we are also aware that this is based on the spherical bubble analysis which could be inaccurate and that small errors could bring the Blake critical radius close to the region of uncertainty. Perhaps this illustrates, yet again, the need for further studies of the relation between the observed and anticipated event rates.

As always, Professor Banerjee's comments are most insightful. There is, indeed, a marked similarity between the "bubbles with tails" and the horseshoe vortices that occur in turbulent boundary layers. Of course, the scale of the present structure is much larger than the present boundary layer. But the vortex dynamics which underlie the two structures are very similar. As the bubble grows and collapses, it acquires circulation or vorticity about a transverse axis. As the bubble collapses, this circulation is focused and the "rotational" velocity of the bubble intensifies. Indeed, toward the end of the first collapse phase, the photographs clearly show that the bubble is very much like a short vortex (transverse axis parallel with the headform surface) with a vapor/gas core. However, the vortex lines proceed from the lateral extremities of the vortex-bubble down to a point on the headform surface. I would speculate further that, under some circumstances, perhaps, the strength of these "tail vortices" is inadequate for such a vapor/gas core to form. Hence, one can imagine a possible explanation for the tails. All of this is highly speculative, but is motivated by the analogy Professor Banerjee has remarked upon.

Dr. Fruman's question is an important one to which we do not have a complete answer. What we observed in the experiments was a change in the probability of occurrence of the various events. As we moved to the larger head forms, higher speed, and lower cavitation numbers, the bubble-induced attached cavitation was more likely to be spread over the entire wake of the bubble rather than to be confined to the bubble extremities. Thus, the traveling bubble induced a localized and transient "patch" of cavitation numbers; the traveling bubble could therefore cause the formation of a patch as it passed over the surface and this patch would often remain for some time after the initiating bubble had passed. In summary, we observed that there exists a continuous spectrum of events from traveling bubbles to attached patches and that there appeared to be a clear connection between the mechanics of formation of all these structures.

Bubble Dynamics and Cavitation Inception in Non-Uniform Flow Fields

G. Chahine (Dynaflow, Inc., USA)

ABSTRACT

The study of cavitation inception in non-uniform flow fields requires complex and sophisticated methods. These need to account for the interaction between the nuclei and the underlying flow, often in the neighborhood of walls, in shear layers, in separated regions, and in turbulent flow fields. This paper describes our contributions towards the development of techniques for the study of fully 3D bubble/bubble and bubble/flow interactions. With the advent of fast and affordable computers such techniques have become more and more practical, and can be effectively used as tools for the description of large scale bubble/vortical flow field interaction simulations.

INTRODUCTION

In order to achieve a cavitation free design of a submerged body such as a propeller, or to test a scale model in a laboratory environment, it is necessary to establish criteria for cavitation inception and to define scaling parameters between models and full scale. The traditional cavitation number based on the engineering definition of cavitation inception: *a liquid flow experiences cavitation if the local pressure drops below the liquid vapor pressure* is obviously not always adequate. A large number of studies over the years have aimed to replace this criterion with a more adequate one based on spherical bubble dynamics, following introduction of the concept of *critical pressure* to replace *vapor pressure*. In fact, cavitation very seldom occurs under the format of spherical bubble growth and collapse. Cavitation inception appears in several forms [1, 2], the most recognized being :

(a) Explosive growth of individual bubbles,

(b) Sudden appearance of transient cavities or "flashes" on boundaries,

(c) Sudden appearance of attached partial cavities, or sheet cavities,

(d) Explosive growth of bubble clouds behind attached cavities or a vibrating surface.

(e) Sudden appearance of rotating filaments, or vortex cavitation.

Upon further scrutiny, all of these forms can be related to the explosive growth of *pre-existing* nuclei in the liquid when subjected to pressure drops generated by various forms of local pressure disturbances. These are either acoustically imposed pressure variations, uniform pressure drops due to local liquid accelerations, or strongly non-uniform pressure fields due to streamwise or transverse large vortical structures. The presence of nuclei or *weak spots* in the liquid is therefore, essential for cavitation inception to occur. Indeed, a pure liquid free of nuclei can sustain very large tensions, in the hundreds of atmospheres, before a cavity can be generated through separation of the liquid molecules. Any fundamental analysis of cavitation inception has to start from the observation that, any real liquid contains nuclei which when subjected to variations in the local ambient pressure will respond dynamically by oscillating and eventually *growing explosively* (i.e. *cavitate*).

In most real flow conditions which involve non-uniform flow fields the conditions leading to cavitation inception involve subjection of the cavitation nuclei not only to significant pressure drops, but also to equally significant pressure and/or velocity gradients. The spherical model, despite all the help it has provided over the years, fails to address these conditions because it assumes that the bubble follows the flow, and that its size remains smaller than the length scales of the pressure and velocity fluctuations. However, detailed and precise observations of flow fields in even the most simplified flow conditions (hemispherical body, simple two-dimensional blades, linear tip vortices, vortex rings, submerged jets, etc.) show that the velocity and pressure fluctuations in these flow fields are on the scale of strong eddies of the same size as the microbubbles present in the liquid. These observations gain further importance

when one notices that all laboratory scale model experiments are inevitably done under conditions in which the eddies and the bubbles are not scaled in the same proportions (if bubbles are scaled at all). The study of bubble dynamics in non-uniform flow fields then stands out as being as fundamental and important as spherical bubbles have been for the past decades.

In this paper we describe our efforts towards the understanding of this problem and complement our contribution at the previous symposium [3]. To do so we consider three fundamental problems of relevance to real flow field configurations: 1. bubble dynamics in the boundary layer of a flat wall, 2. bubble dynamics in the boundary layer of a head-form, and 3. Bubble dynamics in a vortical flow field. This should enable one to deduce criteria for cavitation inception accounting for large bubble deformation and splitting. In addition, in the case of the bubble dynamics in a vortex flow, we present schemes to model flow modification by the bubble dynamics.

SOLUTION METHOD

One of the numerical methods that has proven to be very efficient in solving the types of free boundary problems associated with bubble dynamics is the Boundary Element Method. Several investigators [4, 5, 6, 7] used this method in the solution of axisymmetric problems of bubble growth and collapse near boundaries. This method was extended to three-dimensional bubble dynamics problems by Chahine *et al.* [8, 9]. We describe here the model, then apply it to various cases of bubbles in a vortical flow. More analytical methods such as those we presented at the previous ONR Symposium [3], give very good insight into the dynamics but are limited to small bubble/flow field interactions.

Statement of the problem

Let us consider the dynamics of bubbles oscillating in a non-uniform flow field ("*basic flow*") of velocity $\mathbf{V}_o$ that is known (or determined by the problem solution) and which satisfies the incompressible Navier Stokes equations:

$$\frac{\partial \mathbf{V}_o}{\partial t} + \mathbf{V}_o \cdot \nabla \mathbf{V}_o = -\frac{1}{\rho}\nabla P_o + \nu \nabla^2 \mathbf{V}_o \ . \quad (1)$$

Without any additional assumptions, in the presence of oscillating bubbles the resulting velocity field, given by $\mathbf{V}$, also satisfies the incompressible Navier Stokes equation:

$$\frac{\partial \mathbf{V}}{\partial t} + \mathbf{V} \cdot \nabla \mathbf{V} = -\frac{1}{\rho}\nabla P + \nu \nabla^2 \mathbf{V} \ . \quad (2)$$

Let us then define the *bubble flow* velocity and pressure variables, $\mathbf{V}_b$ and P_b, as follows:

$$\mathbf{V}_b = \mathbf{V} - \mathbf{V}_o, \qquad P_b = P - P_o. \quad (3)$$

We now consider the case where, because we are interested in cavitation bubbles with high but subsonic bubble wall velocities, the "*bubble flow*" field is potential.

$$\mathbf{V}_b = \nabla \Phi_b, \qquad \nabla^2 \Phi_b = 0, \quad (4)$$

We now subtract (1) from (2) accounting for (4) to obtain

$$\nabla \Psi = \mathbf{V}_b \times (\nabla \times \mathbf{V}_o), \quad (5)$$

$$\Psi = \frac{\partial \Phi_b}{\partial t} + \frac{1}{2} \mid \mathbf{V}_b \mid^2 + \mathbf{V}_o \cdot \mathbf{V}_b + \frac{P_b}{\rho}. \quad (6)$$

This equation, once integrated, is to replace the classical unsteady Bernoulli equation.

The assumption of potential "*bubble flow*" may imply that no new vorticity can be generated by the bubble behavior with the chosen model. However, if we allow the basic flow to interact with the bubble dynamics and be modified by it in a unrestricted and rotational manner, as done later below, we can recover generation and modification of vorticity by the presence and dynamics of the bubble.

For the particular cases considered in this paper, the following integrations can be made. In the case of a flat wall boundary layer flow such that all velocity vectors are parallel to the wall, and depend only on the distance to the wall, $\mathbf{V}_o = f(z).\mathbf{e}_x$, where $\mathbf{e}_x$ is the unit vector in the flow direction, and $\mathbf{e}_z$ is the unit vector in the direction perpendicular to the wall, Equation (6) becomes:

$$\Psi = \textit{constant in the } \mathbf{e}_y \textit{ direction}. \quad (7)$$

For the case where the basic flow field is composed of linear vortices of axis direction, $\mathbf{e}_z$, $\mathbf{V}_o = V_\theta.\mathbf{e}_\theta$, with V_θ the tangential velocity, Equation (6) becomes:

$$\Psi = \textit{constant in the } \mathbf{e}_z \textit{ direction} \ . \quad (8)$$

Bubble Flow Equations

As stated above, we consider the cases where the presence of bubbles in the flow has significant effects, that is cases where bubble volume variations are not negligible. This implies large but subsonic bubble wall velocities. Therefore, we consider a *bubble flow* that is potential.

The solution must satisfy initial conditions and boundary conditions at infinity, at the bubbles walls and at the boundaries of any nearby bodies. At all moving or fixed surfaces (such as a bubble surface or a nearby boundary) an identity between fluid velocities normal to the boundary and the normal velocity of the boundary itself is to be satisfied:

$$\nabla\Phi_b \cdot \mathbf{n} = \mathbf{V_S} \cdot \mathbf{n}, \tag{9}$$

where $\mathbf{n}$ is the local unit vector normal to the bubble surface and $\mathbf{V_S}$ is the local velocity vector of the moving surface.

The bubble is assumed to contain noncondensible gas of partial pressure, P_g, and vapor of the surrounding liquid of partial pressure, P_v. Vaporization of the liquid occurs at a fast enough rate so that the vapor pressure may be assumed to remain constant throughout the simulation and equal to the equilibrium vapor pressure at the liquid ambient temperature. In contrast, since time scales associated with gas diffusion are very large, the amount of noncondensible gas inside the bubbles remains constant and the gas pressure is assumed to satisfy the polytropic relation,

$$P_g \mathcal{V}^k = constant, \tag{10}$$

where $\mathcal{V}$ is the bubble volume and k the polytropic constant, with $k = 1$ for isothermal behavior and $k = c_p/c_v$ for adiabatic conditions.

The pressure in the liquid at the bubble surface, P_L, is obtained at any time from the following pressure balance equation:

$$P_L = P_v + P_{g_0}\left(\frac{\mathcal{V}_o}{\mathcal{V}}\right)^k - \mathcal{C}\gamma, \tag{11}$$

where P_{g_0} and $\mathcal{V}_o$ are the initial gas pressure and volume respectively, γ is the surface tension, $\mathcal{C}$ is the local curvature of the bubble, and $\mathcal{V}$ is the instantaneous value of the bubble volume. In the numerical procedure P_{g_0} and $\mathcal{V}_0$ are given quantities at $t = 0$.

3-D Boundary Integral Method

In order to render possible the simulation of single or multiple bubble behavior in complex geometry and flow configurations including the full non-linear boundary conditions, a three-dimensional Boundary Element Method was developed and implemented [8, 9, 10, 11]. This method was chosen because of its computational efficiency. By considering only the boundaries of the fluid domain it reduces the dimension of the problem by one. This method provides a solution of the Laplace equation (4) in terms of Green's equation, which provides Φ_b^P anywhere in the domain of the fluid (field points P) if the velocity potential, Φ_b , and its normal derivatives are known on the fluid boundaries (points M),

$$\int_s \left[\frac{-\partial\Phi_b}{\partial n}\frac{1}{|\mathbf{MP}|} + \Phi_b\frac{\partial}{\partial n}\frac{1}{|\mathbf{MP}|}\right] ds = \Omega\Phi_b^P, \tag{12}$$

where Ω is the solid angle under which P sees the fluid. $\Omega = 4\pi$ if P is a point in the fluid; $\Omega = 2\pi$ if P is a point on a smooth surface, and $\Omega < 4\pi$ if P is a point at a sharp corner of the surface.

If the field point is selected to be on the surface of any of the bubbles or on the surface of the nearby boundaries, then a closed set of equations can be obtained and used at each time step to solve for values of $\partial\Phi_b/\partial n$ (or Φ_b) assuming that all values of Φ_b (or $\partial\Phi_b/\partial n$) are known at the preceding step.

Discretization

To solve Equation (12) numerically, it is necessary to discretize each bubble into panels, perform the integration over each panel, and then sum up the contributions to complete the integration over the entire bubble surface. To do this, the initially spherical bubbles are discretized into geodesic shapes using flat, triangular panels. To evaluate the integrals over any particular panel, a linear variation of the potential and its normal derivative over this panel is assumed. In this manner, both Φ_b and $\partial\Phi_b/\partial n$ are continuous over the bubble surface, and are expressed as a function of the values at the three nodes which delimit a particular panel.

Equation (12) then becomes a set of N equations (N is the number of discretization nodes) of index i of the type:

$$\sum_{j=1}^{N} A_{ij}\frac{\partial\Phi_{b,j}}{\partial n} = \sum_{j=1}^{N} B_{ij}\Phi_{b,j} - \Omega\Phi_{b,i}, \tag{13}$$

where the matrices A_{ij} and B_{ij} are the discrete equivalent of the integrals in (12).

Curvature and tangential velocity computations

In order to proceed with the computation of the bubble dynamics several quantities appearing in the above boundary conditions need to be evaluated at each time step. The bubble volume presents no particular difficulty, while the unit normal vector, the local surface curvature, and the local tangential velocity at the bubble interface need further development. In order to compute the curvature of the bubble surface, a three-dimensional local bubble surface

fit, $f(x,y,z) = 0$, is first computed. The unit normal at a node can then be expressed as:

$$\mathbf{n} = \pm \frac{\nabla f}{|\nabla f|}, \tag{14}$$

with the appropriate sign chosen to insure that the normals are always directed towards the fluid. The local curvature is then computed using

$$\mathcal{C} = \nabla \cdot \mathbf{n}. \tag{15}$$

To obtain the total fluid velocity at any point on the surface of the bubble, the tangential velocity, $\mathbf{V}_t$, must be computed at each node in addition to the normal velocity, $\mathbf{V}_n = \partial\Phi_b/\partial n\ \mathbf{n}$. This is also done using a local surface fit to the velocity potential, $\Phi_l = h(x,y,z)$. Taking the gradient of this function at the considered node, and eliminating any normal component of velocity appearing in this gradient gives a good approximation for $\mathbf{V}_t$:

$$\mathbf{V}_t = \mathbf{n} \times (\nabla\Phi_l \times \mathbf{n}). \tag{16}$$

Time stepping

The basic procedure can then be summarized as follows. With the problem initialized and the velocity potential known over the surface of the bubble, an updated value of $\partial\Phi_b/\partial n$ can be obtained by performing the integrations in (12) and solving the corresponding matrix equation (13). $D\Phi_b/Dt$ is then computed using the "modified" Bernoulli equation (7) or (8). Using an appropriate time step all values of Φ_b on the bubble surface can then be updated using Φ_b at the preceding time step and,

$$\frac{D\Phi_b}{Dt} = \frac{\partial\Phi_b}{\partial t} + \left(\frac{\partial\Phi_b}{\partial n}\mathbf{n} + \mathbf{V_t}\right) \cdot \nabla\Phi_b. \tag{17}$$

In the results presented below the time step, dt, is based on the ratio between the length of the smallest panel side, l_{min} and the largest node velocity, V_{max}. This choice limits the motion of any node to a fraction of the smallest panel side. It has the great advantage of constantly adapting the time step, by refining it at the end of the collapse – where l_{min} becomes very small and V_{max} very large – and by increasing it during the slow bubble size variation period. New coordinate positions of the nodes are then obtained using the displacement:

$$d\mathbf{M} = \left(\frac{\partial\Phi_b}{\partial n}\mathbf{n} + V_t\mathbf{e}_t + \mathbf{V}_o\right) dt, \tag{18}$$

where $\mathbf{n}$ and $\mathbf{e}_t$ are the unit normal and tangential vectors. This time stepping procedure is repeated throughout the bubble growth and collapse, resulting in a shape history of the bubble.

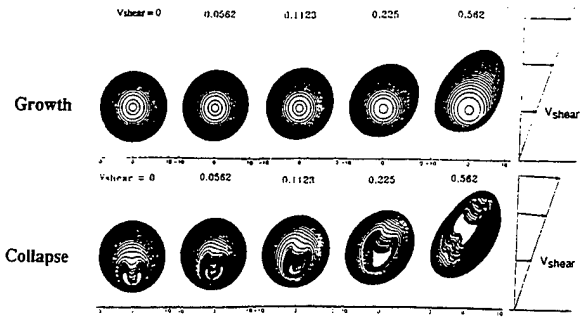


Figure 1: Influence of a linear shear velocity on the collapse of a bubble near a solid wall. V_{shear} is normalized with the Rayleigh velocity $\sqrt{(\Delta P/\rho)}$.

The developed code and method were validated using comparisons with known results in the literature for spherical or axisymmetric bubble configurations. Convergence of the 2-D and 3-D model were then established for cases of interest using increased numbers of grid points. Such detailed comparisons can be found in [12].

BUBBLE COLLAPSE NEAR A FLAT WALL IN A SHEAR FLOW

In most previously published studies of bubble dynamics near solid walls, the wall was considered rigid and infinite, and the liquid quiescent in the absence of the bubble. The only asymmetry in the problem is then due to the presence of the infinite wall, and the bubble behaves axisymetrically. In this case, the bubble forms a reentering jet perpendicular to the plate during the collapse phase. Such a model has been extensively used by many authors both for experimental and analytical/numerical studies mainly aimed at studying erosion due to cavitation bubbles, and was justified in the absence of more advanced techniques. It is however, obvious that this configuration is rarely encountered in practical cavitating flow fields.

Figure 1 shows the results obtained with a relatively simple model for the wall flow using our BEM code **3DynaFS**. The velocity is assumed to vary linearly from a value, V_{shear} at a distance R_{max} from the wall to zero at the wall. The *"basic"* pressure, P_{amb}, is assumed constant across the shear layer and is an input of the problem as is the initial gas

pressure inside the bubble, P_{g_0}. The bubble center is located at a distance L from the wall. The bubble behavior strongly depends on the parameter, $\epsilon = R_{max}/L$, characterizing wall proximity, and on a shear parameter, χ, ratio between the shear velocity, V_{shear} , and a characteristic bubble dynamics velocity: $\chi = V_{shear}/\sqrt{\Delta P/\rho}$.

Figure 1 shows selected bubble contours of the bubble during its growth and collapse. These are cross cuts of the 3-D bubble shapes obtained along the plane of symmetry (perpendicular to the wall and parallel to the flow direction). The presence of shear is clearly apparent during the bubble growth: downstream bubble points move away from the initial bubble center much faster than upstream points. This follows the simple intuitive reasoning that each point on the bubble surface moves with a velocity composed of the velocity it would have in absence of shear plus the local velocity of the *"basic flow"*. For instance the farthest upstream bubble points sees its undisturbed growth velocities increased by V_{shear} while the farthest downstream point has its velocity decreased by V_{shear}. The opposite is true during the collapse phase. As can be seen by comparing the various cases of increasing χ in Figure 1 "stretching" of the bubble in the flow direction increases with the shear intensity.

During the bubble collapse an even more significant effect of the presence of shear on the bubble dynamics can be seen. The formation and development of the reentering jet seems to be very dramatically modified. Even when the shear velocity is very small, the jet is very much delayed and weakened in comparison with the case of the absence of shear. Let us note that in the absence of a *"basic flow"* the jet is directed towards the wall, and that in the other extreme case, i.e. no wall and uniform flow, the reentering jet is directed upstream. For a finite value of χ one would expect a jet angled towards the wall and upstream.

For increased values of χ, the bubble deformation and elongation is enhanced during the growth. During collapse for small values of χ, the re-entering jet is deviated for increasing values of χ from the perpendicular to the plate. For larger values of χ, the re-entering jet formation is totally modified and the bubble tends to cut itself into two bubbles. In addition, an interesting lifting effect is observed. The bubble centroid is seen to move further and further away from the wall with increasing values of χ. This is probably due to an interaction between the wall shear flow and the bubble rotation.

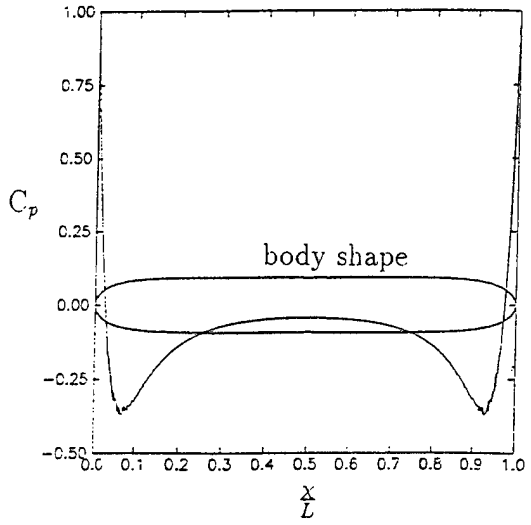


Figure 2: The hemispherical Rankine body shape used in the simulations and the corresponding pressure coefficient, c_p, distribution.

BUBBLE DYNAMICS NEAR A HEMISPHERICAL BODY

Cavitation on hemispherical bodies has been studied for a long time. The Schiebe body for instance has been used in various laboratories for studying cavitation scaling effects. More recently, an extensive program for the study of cavitation inception for various Schiebe body sizes was conducted at Caltech and in the Large Cavitation Tunnel (LCC) in Memphis [13, 14]. Very interesting observations of bubble behavior on these headforms were made. These observations indicated strong interaction between the bubbles and the boundary layer on the headform. Large deviations from spherical bubble shapes were observed, including bubble splitting and breakup, formation of a weak reentering jet during bubble growth, and formation of long 'secondary cavitation' or a trail behind the bubble. We present in this section a numerical simulation of these effects using the methods described above. The objective here is not to reproduce all the characteristics of the experimental studies, but to observe which characteristics can be captured by the present solution method.

To do so, the flow field around the Schiebe body was simulated using a very elongated Rankine oval closed body. Figure 2 shows the hemispherical body shape and the corresponding pressure distribution along the body. One can clearly observe the presence of a very sharp pressure drop at the upstream body at location $x/L = 0.05$, followed by a pressure rise which is maintained until the downstream location, $x/L = .95$, where a second symmetric pressure drop is present. The "*basic flow*" for the problem here is defined as that due to the superposition of

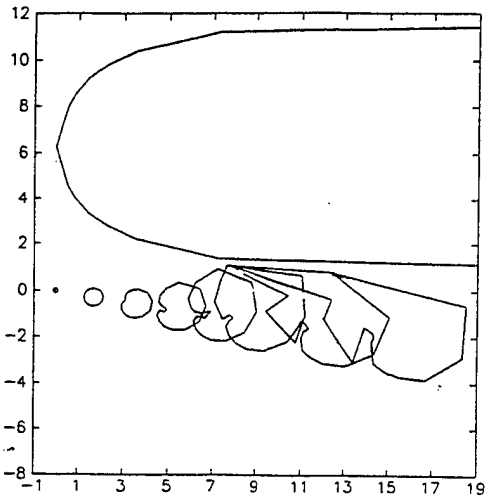


Figure 3: Simulation of the behavior of a bubble near a hemispherical Rankine body shape showing formation of indentation and trail.

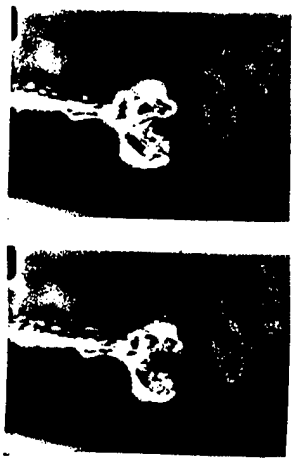


Figure 4: Bubble behavior in the boundary layer of a cambered lifting surface showing the formation of a long trail behind the bubble (from [15])

a uniform flow, V_∞, and two sources of intensity Q. To maintain the body shape for various values of the uniform flow velocity, the ratio V_∞/Q was maintained constant. In order to account for the presence of a boundary layer on the body, this inviscid flow field was modified arbitrarily in the neighborhood of the hemispherical body shape, in such a way that the velocity was decreased linearly to zero on the body.

In the following figures, the selected Rankine body had a radius of 4 inches, and a length of 55 inches. In the simulations we have conducted the bubble sizes were varied from 10 to 1000μm, and the flow velocities from 0 to 20 m/s. The cases presented here are selected because they reproduce many of the characteristics of the experimental observations in [13, 14]. Figure 3 shows bubble contours at various times, and illustrates clearly several key experimental observations: the formation of an indentation on the bubble top while the bubble is being convected downstream by the hemispherical body, the formation of a wedge shape on the downstream portion of the bubble, the lifting of this portion of the bubble from the wall, and the formation of a 'trail' behind the bubble during its motion.

The indentation appears due to the opposing effects on the upstream bubble portion of the basic flow and the bubble growth velocity. This bubble portion moves away the least from the initial bubble center. With time due to the presence of the shear, as in the flat wall case, this bubble region rolls away from the body into the flow direction and, then, encounters a pressure rise which enhances the motion of the indentation towards the body wall. On the other hand, the bubble points that penetrate the simulated 'boundary layer' of the body, find themselves quasi-trapped in that layer. As a result, these points lag behind the rest of the bubble and a bubble 'trail' appears. With the simple model used here, this trail differs from that in the experiments by the fact that it issues from the center part of the bubble and not from its side. This could also be a scaling effect, in the sense of differing ratios between the bubble and the body sizes. Figure 4 taken from observations on a lifting surface [15] shows a trail which resembles very much those obtained by the present numerical simulations.

Figure 5 shows the case of a bubble where the rolling motion of the bubble points is not strong enough for the reentering point to relocate itself above the wall. Instead, the indentation occurs early on in the downstream portion of the bubble leading to a fission of the bubble and the formation of a long trail.

Figure 6 shows the case where fission of the front of the bubble is very obvious. This case resembles very much to the experimental observations, and precedes bubble collapse and rebound.

BUBBLE /VORTEX INTERACTIONS

A fundamental aspect of cavitation in turbulent flows, and in boundary and shear layer flows concerns the interaction between bubbles and vortices. A simple example is that of a 'tip vortex' cavitation on propellers and three-dimensional airfoils. The interaction between bubbles and vortex flows is in fact of relevance to several fluid engineering problems involving submerged jets, flows behind constrictions and orifices, in wakes and in separated flow areas.

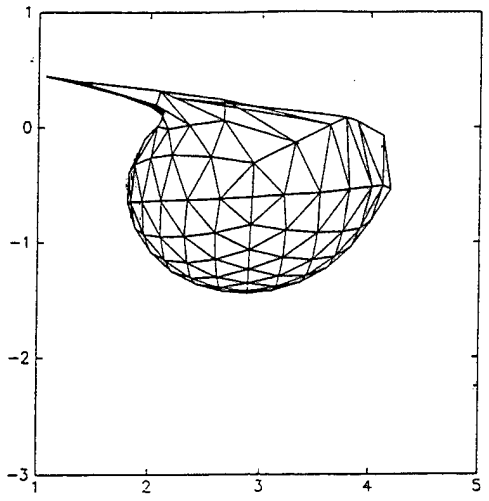


Figure 5: 3-D view of the bubble shape near a hemispherical Rankine body shape after formation of a trail.

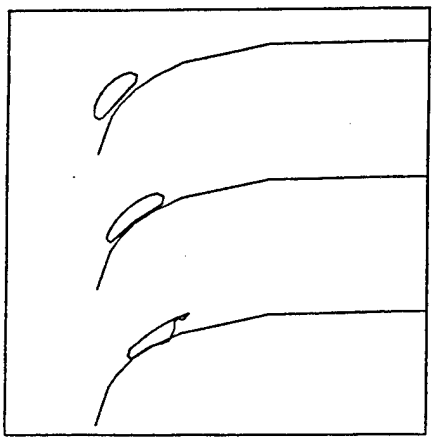


Figure 6: Bubble end splitting near a hemispherical Rankine body shape.

Mechanistic Description

When a bubble approaches a region of high vorticity in a liquid, it is accelerated towards the center of rotation due to the highly asymmetric pressure field. On its path the bubble experiences a decreasing ambient pressure which leads to an increase in its volume. Simultaneously, since the non uniformity of the pressure field increases with proximity to the vortex axis, bubble shape deformation increases.

Over the last decade several investigators have addressed the phenomenon of bubble capture by a vortex [16, 18, 19]. These studies made the simplifying assumption that the bubble, even though able to undergo volume changes, remains spherical. In addition, the type of interactions they considered was one-sided, since they did not consider vortex flow modification by the presence and behavior of the bubble. More recently we considered a broader approach where bubble deformation and motion were coupled while neglecting flow field modification by the bubble presence [10, 20]. This study showed that the pressure gradient across the bubble can lead to significant departure from bubble sphericity, and led to the suggestion that the deformation and later splitting of the bubble during its motion towards the vortex center is, in addition to its volume change, a main source of noise in tip vortex cavitation. This appears to explain the reason for the location of tip vortex noise at cavitation inception very close to the blade [22], and is in agreement with recent observations by [23] about bubble capture in tip vortex cavitation.

One can distinguish three phases in the interactive dynamics of bubbles and vortices: a) bubble capture by the vortex, b) interaction between the vortex and the bubble, c) dynamics of bubbles elongated only on the vortex axis. We consider these aspects below.

Order of magnitude considerations

In order to discuss the problem of bubble capture and behavior in a line vortex let us consider a Rankine vortex flow field. We define Γ as the vortex line circulation, and u_θ the only non-zero velocity component. For distances r smaller than R_c, the radius of the viscous core, the flow has a solid body rotation behavior while for distances r larger than R_c the flow behaves as an ideal inviscid irrotional vortex:

$$u_\theta = \frac{\Gamma r}{2\pi R_c^2}, \quad r \leq R_c; \quad u_\theta = \frac{\Gamma}{2\pi r}; \quad r \geq R_c. \quad (19)$$

For such a flow the pressure field, $p(r)$, is known. Its value and the corresponding pressure gradient are

given by the following normalized expressions.

$$\begin{aligned} \overline{p}(\overline{r}) &= 1-\Omega/\overline{r}^2; \quad \partial\overline{p}/\partial\overline{r} = 2\Omega/\overline{r}^3; \quad \overline{r} \geq 1, \\ \overline{p}(\overline{r}) &= 1-\Omega\left(2-\overline{r}^2\right); \quad \partial\overline{p}/\partial\overline{r} = 2\Omega\overline{r}; \quad \overline{r} \leq 1 \end{aligned} \tag{20}$$

with

$$\overline{r} = r/R_c; \quad \overline{p}(\overline{r}) = p(r)/p_\infty. \tag{21}$$

The parameter , Ω, defined as

$$\Omega = \frac{1}{2}\rho(\frac{\Gamma}{2\pi R_c})^2/p_\infty \ , \tag{22}$$

characterizes the intensity of the pressure drop due to the rotation relative to the ambient pressure, p_∞.

The pressure gradient steepens in the inviscid region when the viscous core is approached, achieves its maximum at $\overline{r} = 1$, and levels off in the viscous core close to the vortex axis. In this pressure field, the bubble experiences a higher pressure on its right side than on its left side, the difference being greater the larger the bubble is. Similarly, the bubble is 'sheared', since fluid particles on the bubble/liquid interface experience different velocities. The type of shearing action depends on the position of the bubble relative to the viscous core/inviscid fluid boundary, R_c. If the bubble is fully immersed in the inviscid region of the flow, fluid particles on its left side will experience larger velocities, while if it is fully immersed in the solid body rotation region of the flow, fluid particles on its right side will experience larger velocities. The most complex situation is when the bubble is partly in the viscous core and partly in the inviscid region.

The degree of bubble shape deviation from sphericity is a function of the relative orders of magnitude of the pressure gradient, the bubble wall acceleration due to volume change, and surface tension forces. An evaluation of the bubble wall acceleration can be obtained from a characteristic bubble radius, R_b, and from the Rayleigh time, τ_R, time needed for an empty bubble to collapse from its radius R_b to 0, under the influence of the pressure outside the bubble. If we take for characteristic outside local pressure the pressure at $r = R_c$, the characteristic bubble wall acceleration, γ_{growth}, is :

$$\gamma_{growth}|_{r=R_c} \simeq p_\infty(1-\Omega)/\rho R_b \tag{23}$$

This value is to be compared with the acceleration force $\gamma_{gradient}$ due to the pressure gradients expressed in (20):

$$\gamma_{gradient}|_{r=R_c} \simeq 2\Omega p_\infty/\rho R_c, \tag{24}$$

The ratio between these two accelerations is:

$$\left.\frac{\gamma_{gradient}}{\gamma_{growth}}\right|_{r=R_c} = \frac{2R_b}{R_c}\cdot\frac{\Omega}{1-\Omega} \tag{25}$$

This expression underlines the importance between the ratio of characteristic bubble size R_b, to viscous core size R_c . Keeping the surface tension parameter the same, the larger the ratio (25) is, the more important bubble deformation will be. *This remark has important implications concerning scale effects where R_b and R_c do not increase in the same proportion between model and full scale*, since in most practical cases bubble distributions and sizes are uncontrolled and typically cannot be scaled much, while sizes of the vortical regions depend on the selected geometry and velocity scales.

The ratio (25) is only an indication of the relative importance of bubble growth and slip forces at a given position. In fact the relative importance of these competing forces changes during the bubble capture process. For instance, the acceleration of the bubble toward the vortex axis increases with its proximity to the viscous core while the growth rate tends toward a constant value (decreasing pressure gradient). This indicates that strong deformation becomes predominant relative to volume change when either the bubble is very close to the axis or when Ω becomes large.

Another important physical factor which affects bubble shape is the surface tension. A normalized value of this pressure can be obtained as a ratio of the surface tension pressure and either the pressure difference between the inside and the outside of the bubble, or the amplitude of the variations of the local pressures (pressure gradients) around the bubble. The first number, W_{e_1}, is given by:

$$W_{e_1} = R_b\left[p_i - p_\infty(1-\Omega)\right]/\gamma, \tag{26}$$

where p_i is the pressure inside the bubble. The second number, W_{e_2}, is given by:

$$W_{e_2} = R_b\left(\partial p/\partial r\right)/\left(\gamma/R_b\right), \tag{27}$$

which can be written for $r = R_c$:

$$W_{e_2} = W_{e_1}\frac{2\Omega}{p_i/p_\infty - (1-\Omega)}\frac{R_b}{R_c}. \tag{28}$$

For small values of either of these two numbers, surface tension forces are predominant and prevent bubble distortion and deviation from sphericity. Expressions (28) shows that this is possible only if Ω is small and if R_b is much smaller than R_c. Therefore, as for the discussion on the acceleration forces, one should expect larger bubble deformations for strong vortex circulations and large bubbles.

Bubble capture by a vortex

Despite several significant contributions to the study of bubble capture by a vortex, to our knowledge no complete approach has yet been undertaken. The complexity of the full problem due to bubble deformation during its capture has led the various contributors to neglect one or several of the factors in play, and therefore to only investigate the influence of a limited set of parameters.

The order of magnitude of the bubble capture time by the vortex can be easily obtained [16, 17] if one considers, the case where the rate of change of the bubble volume is negligible relative to the other terms. In this case, the distance between the sphere center and the vortex center, $\zeta(t)$, is given by:

$$\bar{\zeta}(\bar{t}) \simeq \sqrt{1 + (\overline{v_{\theta o}}^2 - 3)\,\bar{t}^2} \leq \sqrt{1 - 3\bar{t}^2}, \qquad (29)$$

where ζ is normalized with the initial bubble position, ζ_o, time is normalized with $(2\pi\zeta_o^2/\Gamma)$, and $\bar{v}_{\theta o}$ is the initial bubble tangential velocity normalized by $(\Gamma/2\pi\zeta_o)$.

The capture time, T_c, for a bubble initially at rest in the fluid $(\overline{v_{\theta o}} = 0)$ is therefore of the order:

$$\bar{t}_c \simeq \sqrt{\frac{1}{3}}; \qquad or \qquad T_c \simeq \frac{2\pi\zeta_o^2}{\Gamma\sqrt{3}}. \qquad (30)$$

In fact, for a sphere, only viscous friction forces are responsible for bubble entrainment with the flow. The characteristic time of viscous effects, or the time needed by the bubble to be entrained by the flow is

$$T_\nu = a_o^2/\nu. \qquad (31)$$

The qualitative nature of the capture depends on the relative size between T_c and T_ν.

If $T_c \gg T_\nu$ the capture time is too long, viscous effects are predominant, and the bubble is entrained by the liquid and it swirls around the vortex while approaching the center very slowly.

If $T_c \ll T_\nu$ the opposite situation occurs. Viscous effects are very slow to take effect and the bubble is practically sucked into the vortex and moves towards its center almost in a purely radial fashion.

Finally, for $T_c \approx T_\nu$ entrainment by the liquid and attraction towards the center of the vortex occur on the same time scale. Therefore, the bubble approaches the axis in a spiral fashion.

The above reasoning allows one to define a "*violent capture radius*" around the vortex which is bubble radius dependent. A bubble of radius a_o will be sucked in by the vortex if it is within the radial distance $R_{capture}$:

$$R_{capture} = a_o \left(\frac{\Gamma\sqrt{3}}{2\pi\nu}\right)^{\frac{1}{2}}. \qquad (32)$$

This implies for a tip vortex flow field, for instance, that only nuclei present in a small 'window' are rapidly attracted by the vortex and strongly interact with it, which explains difficulty in observing with some precision tip vortex cavitation inception events.

Numerical Results: Large bubble growth rate, low surface tension

As expected from the discussion presented above numerical simulations using the fully three-dimensional numerical code **3DynaFS** reveal potential for strong bubble deformation during capture by a vortex. The numerical results indicate that this is the case for a very wide range of bubble sizes and initial values of the pressure difference between the inside and the outside of the bubble.

Figure 7 shows bubble behavior in the case where the ratio between the pressure inside the bubble and the ambient pressure is significantly large, $p_i/p_\infty \simeq 584$. This would be the case where the bubble in equilibrium in a high ambient pressure environment is suddenly subjected to the flow field of a vortex, as for instance when a propeller tip vortex suddenly captures a cavitation bubble [23, 24]. In a Cartesian system of coordinates, the bubble is initially centered at (0,0,0), and the line vortex is parallel to the Z axis, at $\overline{X} = X/R_{max} = 2R_{max}$ is the maximum size the bubble would have if allowed to grow under the same pressure difference in an infinite medium). The core size is $4R_{max}$. With this geometry the bubble center remains in the plane $Z = 0$.

Figure 7*a* gives a projected view of the bubble in the XOY plane at different instants. The observer is looking down on the XOY plane from very far on the Z axis. The bubble is seen spiraling around the vortex axis while approaching it. At the same time, due to the presence of the pressure gradient, the bubble strongly deforms and a reentering jet is formed directed towards the vortex axis, indicating the presence of a much larger dynamic pressure on the bubble side opposite to the vortex axis.

Figure 7*b* shows a projected view of the same bubble in the YOZ plane seen from the OX axis. Here some moderate elongation of the bubble is observed along the axis of the vortex as well as a very distinct side view of the re-entrant jet. *This result is totally contrary to the usually held belief that bubbles*

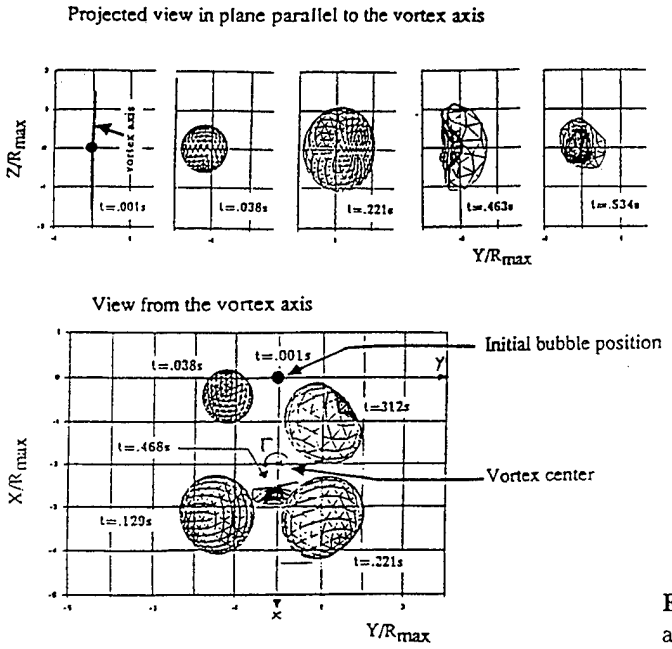


Figure 7: 3D bubble shapes at various times. Bubble initially at the origin of coordinate and vortex at $X = 2R_{max}$. $\Omega = 0.474$, $p_i/p_\infty = 584.3$, $R_c/R_{max} = 4$. Projected view a) in the XOY plane; b) in the XOZ plane.

constantly grow during their capture until they reach the axis and elongate along it.

Figure 8 shows in the XOY plane perpendicular to the vortex axis the motion of two particular points on the bubble, A and B, initially along OY. Also shown is the motion of the midpoint, C. While C seems to follows a path similar to the classical logarithmic spiral, A and B can follow more complicated paths, even moving away from the vortex axis at some point in time for case (b) where the vortex axis was initially at $X = 1$.

Small growth rate and surface tension

Figure 9 considers the influence of bubble size on bubble behavior during the capture process. In all three cases shown in the figure a ratio between the pressures inside and outside the bubble equal to one is considered, $p_i/p_\infty = 1$. In all cases, the viscous core radius is chosen to be $R_c = 2.2\ mm$, while the initial distance between the vortex center and the center of each bubble is chosen to be $\zeta_o \simeq 1.5R_c = 3.2\ mm$. The dimensions shown are normalized with the initial bubble radius for each case. The circulation in the vortex is chosen to correspond to a practical value for the case of a tip

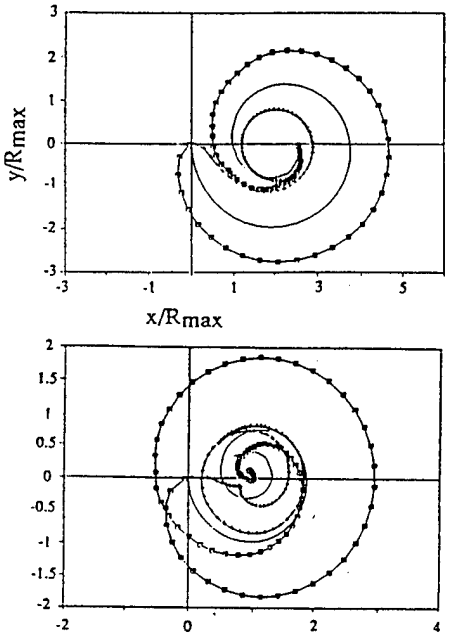


Figure 8: Motion of points A and B initially on axis OX, and mid point C, versus times. $\Omega = 0.474$, $p_i/p_\infty = 584.3$, $a_c/R_{max} = 4$. Vortex at a) $X = 2R_{max}$; b) $X = R_{max}$.

vortex behind a foil, such as in the experiments described in [23, 24], $\Gamma = 0.152\ m^2/s$. Three bubble sizes are considered: 10 μm, 100 μm and 1000 μm. As expected, bubble deformation increases with the bubble size. The deformation is small for a_o=10 μm, becomes very significant for a_o=100 μm, and is extremely important for a_o=1000 μm. In all cases, the bubbles, while remaining in the inviscid region, are seen to be sheared very strongly by the flow. The smaller bubbles appear to deform in the expected way in a shear flow. The larger bubble case (a_o=1000 μm) shows extreme bubble elongation and wrapping around the viscous core region.

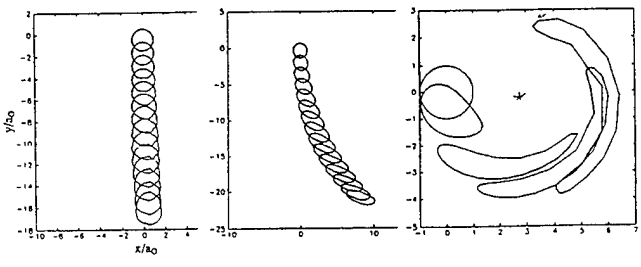


Figure 9: Bubble contours at various times. $\Gamma = 0.1527 m^2/s$, $p_i = p_\infty$, $a_c = 2.2mm$, vortex at $X = 3.2mm$, with a_o = a) $10\mu m$, b) $100\mu m$, c) $1000\mu m$.

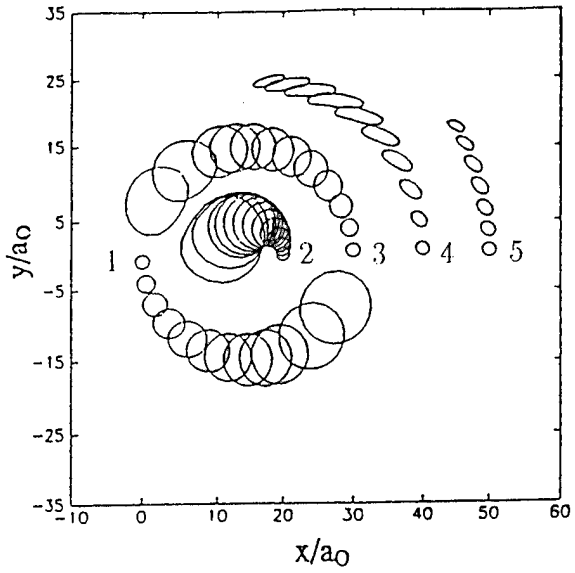


Figure 10: Behavior of 5 bubbles in a vortex line flow - Contour shapes at various times. The vortex line is perpendicular to the page and centered on $Y = 1.5mm$. $R_c = 2.2mm$, $\Gamma = 0.1573m^2/s$. $\Omega = 0.872$. All bubbles have $a_0 = 100\mu m$.

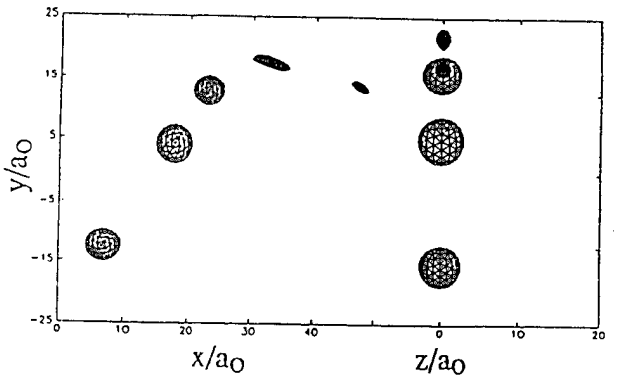


Figure 11: 3D bubble shapes in the vortex line flow field of Figure 8 before collapse of buble No. 1. View from a) OZ axis, b) OX axis.

Multiple Bubbles

One of the key question that one needs to address in the practical studies of bubble/vortical field interaction is how does a distribution of bubbles modify the flow field. In order to address such a problem the program **3DynaFS** is being modified for effective implementation on a supercomputer. Indeed one of the difficulties of such a study is the required large number of discretization points which prevents significant runs on typical memory and speed limited computers. Some preliminary multibubble interactions were considered in [27, 26]

Figure 10 shows the case of a 5-bubble configuration. This run has the advantage of including both vortex/bubble and bubble/bubble interactions. All five bubbles are chosen such that in absence of the vortex flow field, the pressures inside and outside each of them is the same and equal to 0.74 atm, $p_i/p_\infty = 1$. The viscous core radius and the circulation are again chosen to be in the same ranges as those in the experiments described in [23, 24]. The viscous core is chosen to be $R_c = 2.2mm$, while $\Gamma = 0.1573\ m^2/s$, $\Omega = 0.872$. The initial bubble centers are selected to be on OY axis at $Y = 0, 2, 3, 4$ and 5 mm. The vortex line is parallel to OX axis and is centered on $Y = 1.5\ mm$. As a result, bubbles No. 1, 2 and 3 are initially located in the viscous core, while bubbles No. 4 and 5 are located in the inviscid flow region. All five bubbles considered have an initial radius of 100 μm. Figure 10 shows contours of the bubbles as they rotate around the vortex axis at various times. This figure clearly shows the presence of a non-uniform flow field. Indeed, Bubble No. 3 which is the closer to the region of highest angular velocity of the *"basic flow"* is seen to swirl around the vortex center at the fastest rate, while Bubble No. 2, which is the closest to the vortex center is seen to practically rotate around itself. Similarly, the highest shear is seen to occur close to the viscous core edge where the pressure gradients and their variations are steeper.

Since all bubbles were chosen to have the same initial radius and internal pressure, the natural period of oscillation of each of the selected bubbles increases with the proximity to the vortex axis. As a result, the farthest bubble from the axis, Bubble No. 5, collapses first while stretching and deforming.

Figure 11 shows two thee-dimensional views of the bubbles before the collapse of bubble No. 1. These views enable one to have a better idea of the bubble shape deformation and elongation during the capture phenomenon. Similar experimented observations were seen in [24].

Bubble on vortex axis

Let us consider now the case where the bubble is captured by the vortex and placed at its axis. Such a problem was considered earlier in [21] for an elongated bubble. Unfortunately, that study neglected an essential element of vortex dynamics: i.e. the

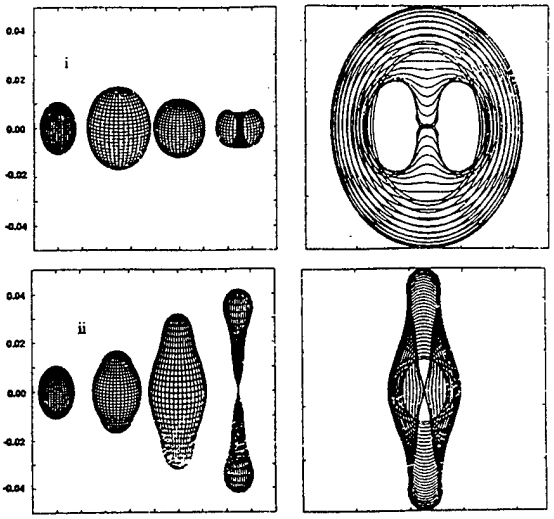


Figure 12: Comparison between the contours of an elongated bubble during its collapse in the absence and in the presence of swirl. Initial elongation ratio of 3. $p_\infty/p_i = 3.27$. a) No swirl. b) $\Omega = 0.56$. $R_c/R_{max} = 3$.

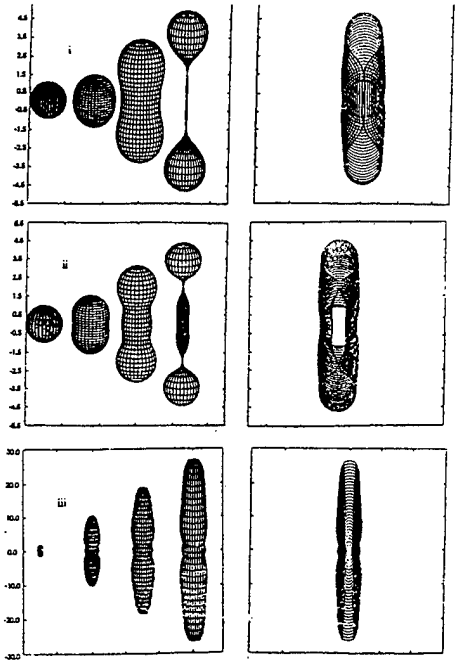


Figure 13: Bubble dynamics on the axis of a vortex line. Left side shows 3D shapes at selected times. Right side shows bubble contours at increasing times. $\Gamma = 0.005m^2/s$, $R_o = 100\mu m$. a)$p_i/p_\infty = 2$, $R_c/R_o = 1$, b) $p_i/p_\infty = 2$, $R_c/R_o = 1$, c) $p_i/p_\infty = 1$, $R_c/R_o = 0.57$.

presence of an azimuthal velocity, and a strong jet which initiated at both extreme points of the bubble along the axis of symmetry was obtained. As shown in Figure 12*a* such a behavior is reproduced using the program **2DynaFS** when the vortex flow field is neglected. However, the opposite effect is in general obtained when the rotation in the vortex flow is included. Figure 12*b* illustrates this for particular values of Ω and the normalized core radius, $\overline{R_c} = R_c/R_{max}$.

In both cases shown in Figures 12*a* and 12*b* the initial length to radius bubble elongation ratio was three. It is clear from the comparison that the swirl flow has a conclusive effect on the bubble dynamics. Bubble surface portions away from the vortex axis experience much higher pressures than bubble surface portions on and close to the vortex axis, and therefore move much faster during the collapse phase generating, instead of the sharp jets on the axis as in Figure 12*a*, a constriction in the mid-section of the bubble. This generates an hourglass shaped bubble which then separates into two tear-shaped bubbles.

In the following figure 13$a-c$, various configurations of initially spherical bubble dynamics are studied. The initial internal pressures inside the bubbles are taken to be larger than the pressure on the vortex axis, and the bubbles are left free to adapt to this pressure difference. The figures show that the bubble behavior depends significantly for a given value of the swirl parameter, Ω, on the normalized core radius $\overline{R_c}$, ratio of R_c to R_{max}. In all cases where R_{max} is larger than R_c it appears that the *bubble tends to adapt to the vortex tube of radius* R_c. This could lead to various bubble shapes as shown in the following figures ending up with a very elongated bubble with a wavy surface for large values of R_{max}/R_c.

Figures 13$a-c$ show bubble contours at various times during growth and collapse for increasing values of the core radius, R_c, and decreasing values of p_i/p_∞. Also shown are selected 3D shapes of the bubbles at various times. It is apparent from these figures, that during the initial phase of the bubble growth, radial velocities are large enough to overcome centrifugal forces and the bubble first grows almost spherically. Later on, the bubble shape starts to depart from spherical and to adapt to the pressure field. The bubble then elongates along the axis of rotation. Once the bubble has exceeded its equilibrium volume, bubble surface portions away from the axis – high pressure areas – start to collapse, or to return rapidly towards the vortex axis. To the contrary, points near the vortex axis do not experience rising pressures during their motion, are not forced back towards their initial position, and continue to elongate along the axis. As a result, a constriction appears in the mid-section of the bubble. The bub-

ble can then separate into two or more tear-shaped bubbles. It is conjectured that this splitting of the bubbles is a main contributor to cavitation inception noise. This behavior is very similar to that observed for bubble growth and collapse between two plates [15], which results in the formation of a vortex line!

Keeping Ω constant while reducing the core size R_c has the effect of steepening the radial pressure gradient along the bubble surface and increasing the rotation speed inside the viscous core. This enhances the deviation of the bubble shape from a sphere, and increases the centrifugal force on the fluid particles closer to the vortex axis. This has the consequence of increasing the elongation rate of the bubble and results in more and more complex dynamic shapes of the elongated bubbles. The bubble can then become subdivided into three, four or more satellite bubbles during the collapse. The elongated and wavy shapes obtained have been observed on cavitation on the axis of the vortex formed in a vortex tube [26].

Observation of the elongated bubble dimension variations with time are very revealing [10, 26]. Normalizing lengths by R_{max} and time by the Rayleigh time based on R_{max} and the pressure difference between P_{go} and the pressure on the vortex axis, one finds that the bubble length along the rotation axis strongly depends on Ω. However, the bubble cross-section radius closely follows the classical Rayleigh model and is very little dependent on Ω. Variations of Ω between 0.1 and 0.94 modify the normalized bubble period by less than 10 percent. One should notice, however, that bubble period is here defined as the time needed for the bubble to subdivide into two secondary bubbles.

More realistic vortex line model

While the Rankine model is very helpful to study the fundamentals of bubble/vortex interactions, it does not allow one to capture other features such as flow and bubble motion along the axis of rotation. In [28] we conducted a study where a Burgers vortex line flow field was considered.

$$u_r = -Cr, \quad u_z = Cz$$

$$u_\theta = \frac{\Gamma}{2\pi r}\left[1 - \exp\left(\frac{-r^2}{4\delta^2}\right)\right], \qquad (33)$$

where C is a constant, and δ is the viscous core radius. The pressure distribution can then be obtained by solving the momentum equation:

$$p(r,z,t) = p_\infty - 2\rho C^2 z^2 - 2\rho C^2 \delta^2 X^2 - B/2X^2 + B\left[\exp(-X^2) - \exp(-2X^2)/2\right]/X^2 + B\left[E_i(-X^2) - E_i(-2X^2)\right], \qquad (34)$$

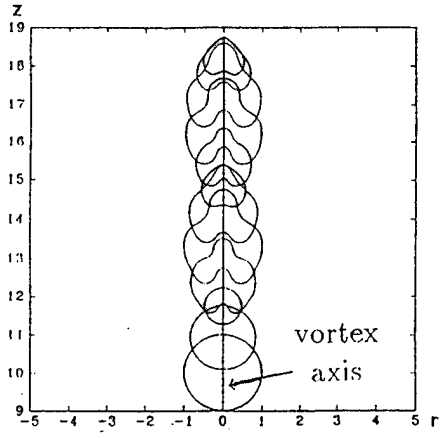


Figure 14: Bubble dynamics on the axis of a viscous line vortex. Contour shapes versus time. Basic field obtained using a viscous flow solver with viscous diffusion along x and r. Viscous core size $1mm$, initial bubble size $100\mu m$.

with $B = \rho\Gamma/2\pi\delta$ and $X = r/2\delta$. This flow and pressure field were used to study bubble dynamics on the vortex axis. When the bubble in initially centered at the origin of coordinates it has again a symmetric behavior. However, a much faster bubble elongation with time is then seen, but here again the bubble cross section does not exceed the core size.

Figure 14 show an example of bubble behavior in an even more realistic vortex line flow field. In this case the flow field of the vortex line is obtained by solving the viscous flow field due to an imposed Rankine vortex flow plus a uniform axial velocity at $z = 0$. This is to simulate the diffusion of a vortex line generated at the tip of a three-dimensional foil. The commercial Navier Stokes solver Fidap was then used at the Ecole Navale at Brest to obtain the diffusion of such a flow along the z axis, and included an axial flow at $x = 0$. The resulting flow field was then used as a basic flow to study 3-D bubble behavior using **3DynaFS**. In this case pressure gradients along the vortex axis are important enough to produce a reentering jet along the vortex axis while the bubble is entrained along the vortex line by the z component of the flow.

Experimental validation study

In order to validate the numerical studies on bubble vortex interactions, a fundamental experiment was conducted. This consisted of the controlled observation of the interaction between a vortex ring and a bubble. The results of the experiment were

then compared with those obtained with **3DynaFS** described above [25, 26]. The vortex ring was generated in a Plexiglas tank using a cylinder equipped with a 2.5 *cm* radius piston. The cylinder had a sharp lip exit to enhance the roll up of the fluid vortex generated at the lip. This results in a vortex ring with a diameter slightly larger than that of the cylinder. A spark generated bubble was produced where desired in the vortex ring flow field. The interaction between the generated ring and bubble was then observed using high speed photography. A triggering line allowed one to synchronize the departure of the piston and the triggering of the spark generator using pressure transducers to precisely detect the vortex ring motion.

Both the experimental observations and the numerical computations showed very similar behaviors. The results of these comparisons can be found in [25, 26]. Bubble shearing and splitting along the flow direction appears common. This can be qualitatively understood by considering the velocity and pressure fields around the bubble. The motion of each point on the surface of the bubble is the result of the combination of the underlying fluid velocity and of the velocity due to the bubble growth or collapse. The effect of the underlying fluid flow is usually small during initial bubble growth and later bubble collapse phases due to the large bubble wall velocity during these phases, but becomes most important at the end of the growth where bubble wall velocities reach a minimum. For a bubble in a uniform flow, the presence of the underlying flow reflects on the bubble shape during the growth by a larger extension of the bubble in the downstream direction and by a flattening of the bubble shape in the upstream direction. Later on due to inertia, the downstream bubble part that has extended further collapses faster forming a reentering jet directed upstream.

When the flow is not uniform, a similar phenomenon occurs but is stronger on one side of the bubble than on the other due to the typical asymmetry of a shear flow. In addition, the fact that the underlying shear flow becomes at some point during the bubble history stronger than the local bubble wall velocity creates the opportunity of a jet generated by the underlying flow, which can be opposite to the one described above and directed downstream. This leads to the formation of a constriction all around the bubble with a tendency for bubble splitting.

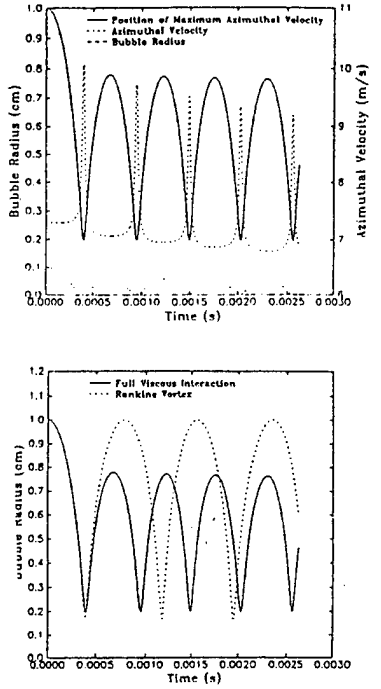


Figure 15: Dynamics of the interaction between a cylindrical bubble and a line vortex. $\Gamma = 0.5\ m^2/s$, P_{go} =$5\times10^3 Pa$, P_∞=$1.3\times10^5 Pa$. a) Bubble radius, value of maximum azimuthal velocity $u_{\theta\,\max}$, and position of $R_{\theta\,\max}$. b) Bubble radius versus time with and without viscous interaction.

FULL VISCOUS INTERACTION BETWEEN A CYLINDRICAL BUBBLE AND A LINE VORTEX

One weakness of the numerical approach presented above is the fact that, while the influence of the flow on the bubble was fully accounted for, the modification of the flow by the bubble presence and dynamics was restricted to the case where the "bubble flow" was potential. In the present section, we will remove this restriction in the simple case of the interaction between a cylindrical bubble and a line vortex. This corresponds to cases where the line vortex has the central part of its viscous core gaseous or vaporous. Such an analysis is important to determine criteria for unstable bubble growth (cavitation inception), and to describe how bubble dynamics affects the viscous flow itself. To do so, we consider the case where an axisymmetric elongated bubble of initial radius a_o is located on the axis of a fully viscous line vortex. For illustration, we consider the case where, at $t = 0$, the vortex line is a Rankine vortex. From there on, the vortex diffuses with time and interacts fully with the bubble. The generated flow satisfies the axisymmetric incompressible Navier-Stokes equations.

Denoting the radius of the bubble as $a(t)$, and its time derivative, $\dot{a}\ (t)$, the continuity equation leads to:

$$u_r = a(t)\,\dot{a}(t)/r. \tag{35}$$

Replacing u_r by its expression in the momentum equations one obtains:

$$\frac{1}{r}\left(a\,\ddot{a} + \dot{a}^2 - u_\theta^2\right) - \frac{a^2\,\dot{a}^2}{r^2} = -\frac{1}{\rho}\frac{\partial p}{\partial r}, \tag{36}$$

$$\frac{\partial u_\theta}{\partial t} + \frac{a\,\dot{a}}{r}\left(\frac{\partial u_\theta}{\partial r} + \frac{u_\theta}{r}\right) = \nu\frac{\partial}{\partial r}\left(\frac{1}{r}\frac{\partial}{\partial r}(r u_\theta)\right), \tag{37}$$

This set of coupled equations allows one to describe both the bubble dynamics and the flow field modification accounting for two-way interaction.

Method of Solution

In order to obtain a differential Equation for the bubble radius variations, similar to the Rayleigh Plesset Equation, Equation (36) is integrated between $r = a(t)$ and a very large radial distance, $r = R_{inf}$, beyond which the vortex flow is assumed to be inviscid (vortex line of circulation Γ). This leads to an integral term containing u_θ^2. In order to obtain this term, a space and time integration of Equation (37) is needed. This is obtained using a Crank-Nicholson finite difference integration scheme. To do so, the domain of integration is made time independent using the variable change,

$$s = r/a(t). \tag{38}$$

The integration region becomes for all times $[1; s_{\inf}]$, with $R_{inf}(t) = a(t)s_{inf}$. Equation 37 becomes:

$$\frac{D\overline{u_\theta}}{D\bar{t}} = -\frac{s}{\bar{a}}\frac{\dot{\bar{a}}}{\bar{a}}\frac{\partial\overline{u_\theta}}{\partial s} - \frac{\dot{\bar{a}}}{s\bar{a}}\frac{\partial\overline{u_\theta}}{\partial s} - \frac{\dot{\bar{a}}}{s^2\bar{a}}\overline{u_\theta} + \frac{1}{R_e}\frac{1}{\bar{a}^2}\left(\frac{\partial^2\overline{u_\theta}}{\partial s^2} + \frac{1}{s}\frac{\partial\overline{u_\theta}}{\partial s} - \frac{\overline{u_\theta}}{s^2}\right) \tag{39}$$

with

$$\bar{a} = \frac{a}{a_0}, \quad \bar{t} = \frac{t}{a_0}\sqrt{\frac{P_\infty}{\rho}}, \quad R_e = \frac{a_0}{\nu}\sqrt{\frac{P_\infty}{\rho}}. \tag{40}$$

Similarly, Equation (36) becomes:

$$\bar{a}\,\ddot{\bar{a}} + \dot{\bar{a}}^2 = \frac{\dot{\bar{a}}^2}{2\ln s_{\inf}}\left[\frac{-1}{s_{\inf}^2} + 1\right] + \frac{1}{\ln s_{\inf}}\int_1^{s_{\inf}}\frac{\overline{u_\theta}^2}{s}ds - \frac{1}{\ln s_{\inf}}\left[1 - \left(\frac{\overline{\Gamma}}{2\pi\bar{a}s_{\inf}}\right)^2 - \overline{p_v} + \overline{p_{go}}\left(\frac{1}{\bar{a}}\right)^{2k}\right] - \frac{1}{\ln s_{\inf}}\left[\frac{1}{W_e\bar{a}} - \frac{2\,\dot{\bar{a}}}{R_e\bar{a}}\right] \tag{41}$$

with

$$\overline{\Gamma} = \frac{\Gamma}{a_o}\sqrt{\frac{P_\infty}{\rho}}, \quad W_e = \frac{a_o P_\infty}{\sigma}. \tag{42}$$

Initial and Boundary Conditions

The initial conditions considered are as follows. For the bubble,

$$a(0) = a_o, \qquad \dot{a}(0) = 0. \tag{43}$$

For the line vortex, the equation at $t = 0$, is that of a Rankine vortex. In addition, the following boundary condition is imposed at the bubble interface:

$$P(a) = p_v + p_{g_o}\left(\frac{a_o}{a}\right)^{2k} - \frac{\sigma}{a} + 2\mu\frac{\partial u_r(a)}{\partial r}, \tag{44}$$

where μ is the dynamic viscosity, and the gas compression law is given by:

$$p_g = p_{g_o}\left(\frac{a_o}{a}\right)^{2k}. \tag{45}$$

To close the problem, the following condition is imposed on the pressure at the distance, R_{inf} :

$$P(R_{\inf}) = p_\infty - 2\rho\left(\frac{\Gamma}{2\pi s_{\inf}a(t)}\right)^2. \tag{46}$$

Some Preliminary Results

Figures 15*a* and 15*b* illustrate both the bubble/vortex flow field interaction and a case where there is a need to include this full interaction in the dynamics. In these two figures, the bubble has an initial radius of $1mm$, while the viscous core of the vortex has an initial radius of $1cm$. The initial circulation in the vortex is 0.5 m^2/s, and the initial pressure in the bubble is $5\times10^3 Pa$, while the ambient pressure is $1.3\times10^5 Pa$. Therefore, the bubble starts its dynamics by collapsing. Figure 15*a* shows simultaneously three characteristic quantities of the problem versus time. The first quantity is the bubble radius versus time, while the other two quantities are the radial position, $R_{\theta\,\max}$, of the maximum azimuthal velocity, $u_{\theta\,\max}$, and the value of this velocity. In the previous sections, these two last quantities remained constant with time. A very important first result very clearly shown in Figure 15*a* is that both the position of $R_{\theta\,\max}$, and the value of $u_{\theta\,\max}$, both directly depend on the variation of $a(t)$. The viscous core (of radius $R_{\theta\,\max}$) is seen to decrease with

the bubble radius during bubble collapse, and to increase with the bubble radius during bubble growth. This tendency of the viscous core to get displaced with the bubble wall, corresponds to intuition, but is proven numerically to our knowledge for the first time here and in [28].

Viscous effects appear more prominently when following the bubble dynamics over more than a single period of oscillation. Both maximum values of $R_{\theta\,\max}$ and $u_{\theta\,\max}$ are seen to decrease with time. Through conservation of momentum, the azimuthal velocity follows an tendency opposite to the core size. As the bubble wall moves inward the viscous core shrinks, simultaneously increasing the tangential velocity to a maximum when the bubble reaches maximum size. As the bubble grows again, the core expands and the tangential velocity decelerates to a minimum at the maximum bubble radius. When the fluid particles are pulled in towards the vortex axis they accelerate tangentially. This is similar to the phenomenon of vortex stretching .

Figure 15*b* shows the importance of the inclusion of full viscous flow / bubble interaction in the dynamics. The figure shows also the case where the underlying flow field is forced to remain that of a Rankine vortex. In that case, the bubble oscillations are repeatable with time, and no viscous decay of the amplitude of the oscillations are visible. To the contrary when the underlying flow is modified through viscous diffusion and interaction with the bubble, the bubble radius oscillations decays very much after the first collapse, and the flow field characteristics are modified as described in Figure 15*a*.

Figures 16*a* and 16*b* show, respectively, the influence on the problem dynamics of the initial gas pressure inside the bubble, P_{go}, and the ratio of initial core radius to initial bubble radius, R_c/a_o. For an initial pressure on the vortex axis of $7\times10^5 Pa$, Figure 16*a* shows the dynamics of the bubble and the viscous core size when the initial pressure in the bubble decreases from $5\times10^5 Pa$ to $1.5\times10^5 Pa$. For $P_{go} = 5\times10^5 Pa$ the bubble collapse is very weak, and the core radius is seen to follow the bubble wall oscillations. For all three other smaller values of P_{go} starting from $P_{go} = 4\times10^5 Pa$ the bubble collapse is strong enough to result in a full collapse of the viscous core which practically disappears (maximum azimuthal velocity at the bubble wall) during the later phases of the bubble collapse. This is followed by a much stronger rebound of the viscous core than the bubble rebound.

Figure 16*b* shows a behavior similar to the previous figure when the ratio, R_c/a_o, increases. Here again a strong core collapse and rebound is observed

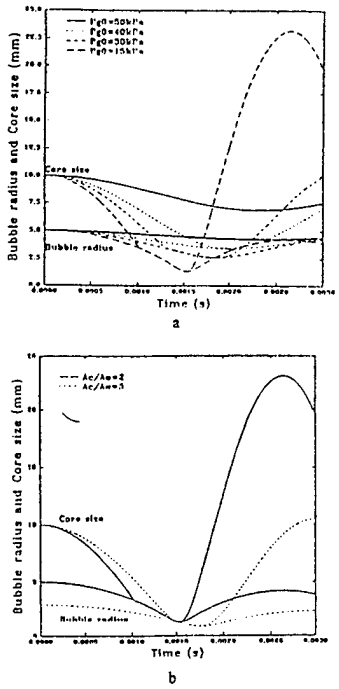


Figure 16: Dynamics of the interaction between a cylindrical bubble and a line vortex. $P_{axis} = 7\times10^5 Pa$. a) Influence of the initial bubble pressure, P_{go}, on bubble radius and position of $R_{\theta\,\max}$. $R_c/a_o = 2$. b)Influence of R_c/a_o on the bubble radius and position of $R_{\theta\,\max}$. $P_{go} = 1.5\times10^5 Pa$.

when the initial distance between the bubble wall and the core radius is decreased.

The case of initial bubble growth instead of collapse is not shown here because it presents the same character as observed in the rebound cases in the above figures.

INTERACTION BETWEEN A BUBBLE AND A VORTICAL FLOW

In order to extend the methods presented above to the more general case of the interaction between a bubble and a general rotational field, the BEM method was coupled to a vortex element method. With this approach the *basic vortical flow* is represented by a distribution of three-dimensional vortex elements, and if need be, by the addition of a potential component. The procedure then is to track in time both the bubble free surface motion and the vortex elements motion. By doing so, one is able to obtain not only the bubble motion and deformation, but also the vorticity distribution variation with time. Modification of the vortical field by the presence of the bubbles is thus an outcome of the interaction method.

The above is based on the basic principle that any arbitrary basic flow field may be decomposed

into a potential part, ϕ_o, and a rotational part, $\mathbf{A}$:

$$\mathbf{u} = \mathbf{u}_\phi + \mathbf{u}_\omega = \nabla\phi_o + \nabla \times \mathbf{A}. \qquad (47)$$

The rotational part of the velocity $\mathbf{u}_\omega$ derives from the vector potential $\mathbf{A}$ which satisfies

$$\nabla^2 \mathbf{A} = -\omega, \qquad (48)$$

where ω is the vorticity. The velocity is obtained by the Biot-Savart law:

$$\mathbf{u}_\omega(\mathbf{x}) = \frac{-1}{4\pi} \int \frac{(\mathbf{x}-\mathbf{y}) \times \omega(\mathbf{y})}{|\mathbf{x}-\mathbf{y}|^3}\, d\mathbf{y}. \qquad (49)$$

For numerical simulation, the vorticity field is discretized using a desingularized representation of vorticity [29, 30, 31].

$$\omega(\mathbf{x},0) = \sum_{i=0}^{N} \omega_i f_\delta(\mathbf{x} - \chi_i)\, dV_i \qquad (50)$$

where χ_i are the centers of the vortex elements,and f_δ is a spherical rapidly decaying core function or mollifier [29], which is chosen to be

$$f_\delta(r) = \frac{3}{4\pi\delta^3} e^{-\frac{r^3}{\delta^3}} \qquad (51)$$

following [31]. With the discretized vorticity distributed over vortex elements, we may also write $dV_i = dA_i \times d\chi_i$,and hence

$$\omega_i dV_i = \Gamma_i d\chi_i \qquad (52)$$

where Γ_i is the elementary circulation associated with the i-th line element. By virtue of Kelvin and Helmholtz theorems Γ_i remains invariant in time, and the elements follow the local velocity field enabling stretching and tilting of the elements. The change in the vorticity is represented by a change in the line element $d\chi_i$. The discretized velocity expression is:

$$\mathbf{u}_\omega(\mathbf{x}) = \sum_{i=0}^{N} \frac{1}{4\pi} \Gamma_i \frac{(\mathbf{x}-\chi_i) \times \mathbf{d}\chi_i}{|\mathbf{x}-\chi_i|^3} \kappa\left(\frac{\mathbf{x}-\chi_i}{\delta}\right),$$

$$\kappa = 1 - e^{-r^3}. \qquad (53)$$

The element positions are updated by the velocities at their end points

$$\chi_i(t+dt) = \chi_i(t) + \mathbf{u}(\chi_i, t)dt. \qquad (54)$$

The convergence of this vortex method was proven in [32]. The procedure is as follows. For a given vorticity distribution in the flow field of interest, a geometric distribution of three-dimensional vortex elements is selected. In the examples below a Gaussian distribution is selected. The inverse problem of (50) is then solved to obtain the values of the elementary circulations, Γ_i, associated with each finite line element. With the knowledge of this initial vortex element distribution, and the initial bubble discretization, one can proceed with the time stepping to solve the problem. The influence of all bubble panels and all vortex elements on the bubble and vortex nodes are computed. This allows determination of the new values of the velocity on all the bubble nodes. Knowing all values of Φ_b and $\partial\Phi_b/\partial n$ on the boundaries one can deduce the velocity anywhere, and in particular at all nodes of the vortex elements whose position can then be updated using (54).

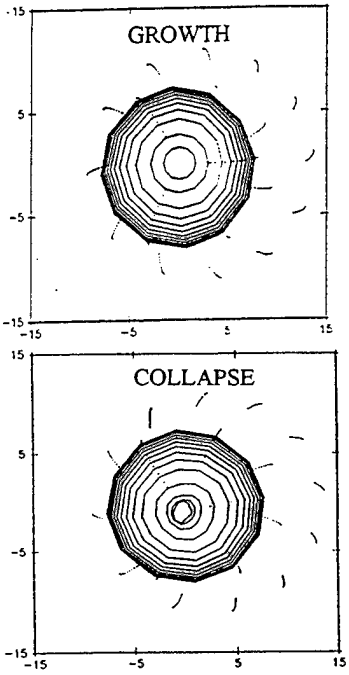


Figure 17: Interaction between a bubble and a finite thickness line vortex represented by 3D vortex elements. Crosscut in the plane of symmetry z=0. Note motion of the vortex line points close to the bubble deviate significantly from a pure circular motion as away from the bubble.

The case of a finite thickness line vortex was considered and represented with 18 vortex lines discretized into 3D elements. One can then obtain as shown in Figure 17 both the bubble and the vortex line deformations. Figure 17 shows the intersection at various times during bubble growth and collapse between the plane $z = 0$ and the bubble and the vortex elements. This shows both bubble and vortex elements motion with time. Note that the motion of the vortex line point close to the bubble deviate sig-

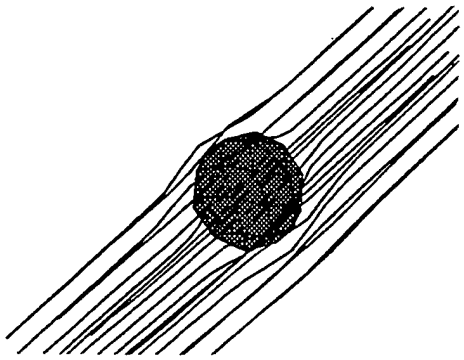


Figure 18: Interaction between a bubble and a finite thickness line vortex represented by 3D vortex elements. 3D view at maximum bubble size of the bubble and vortex line shapes

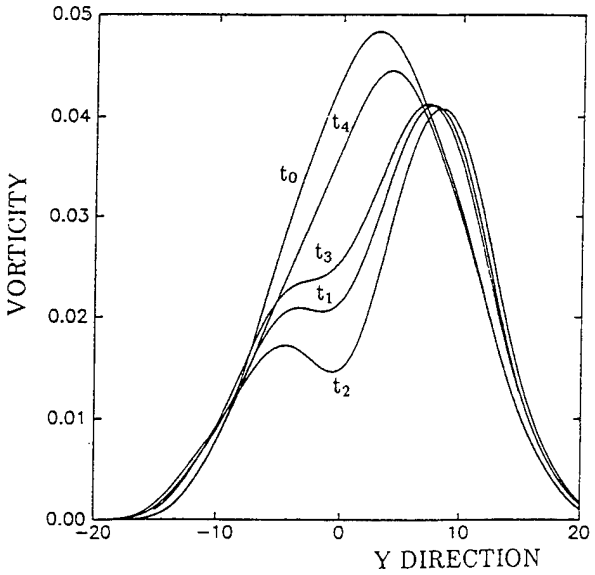


Figure 19: Vorticity distribution modification along the OY axis during bubble oscillation in a finite thickness line vortex represented by 3D vortex elements.

nificantly from a pure circular motion. Those away from it just rotate around the central point due their mutual interaction and to the symmetry of the distribution. Figure 18 shows a 3D snapshot of the bubble and vortex line shapes for the example of a bubble immersed in the vortical field. Figure 19 shows how the vorticity distribution along the OY axis has been modified by the dynamics and presence of the bubble. It is apparent in this case that very significant redistribution of the vortex field is possible during the bubble motion.

The above example is shown as an illustration of the method being developed. More detailed descriptions and a more extensive analysis are in preparation [33].

CONCLUSIONS

The study of bubble dynamics in non-uniform flow fields is complex but essential to any real attempt to study bubble dynamics in realistic flow conditions. Due to the difficulties involved in both experimental and analytical approaches, the trend is to address the problems by a two-pronged effort involving numerical and experimental simulations. This is made possible by the development of advanced high speed computers which render direct numerical simulations possible in reasonable amounts of time. The studies presented above addressed various aspects of the problem, namely bubble behavior in the vicinity of boundaries, bubble capture by a vortex and bubble dynamics in a vortical flow field. The most interesting development is the capability to study the influence of the bubble's presence on the vortical field itself. Our attempts in this direction were briefly presented and are presently very actively being pursued. It is hoped that a matching between a flow solver, at least in the vortical region, and a bubble dynamics solver such as **2DynaFS** or **3DynaFS** will enable one to describe with some acceptable accuracy the full interaction between the bubbles and the vortical flow field. This is of great importance since it would allow the user to understand the mechanics involved thus enabling one to manipulate the phenomena for technological advantage in applications such as, in ship wakes, bubble drag reduction, or cavitation inception delay.

ACKNOWLEDGMENTS

We are grateful for the support of the Office of Naval Research, under Contract N00014-89-C-0025 monitored by Dr. Edwin Rood. The author would like to acknowledge the contributions of colleagues at DYNAFLOW, INC. especially Drs. Kausik Sarkar,

Ramani Duraiswami and Kenneth Kalumuck. The author would also like to thank Drs. J.Y. Billard and P. Cerrutti from the Ecole Navale for providing the viscous flow vortex results and for the significant contribution of their students while at DYNAFLOW to several aspects of this study.

References

[1] Rood, E. P., 1991, "*Review - Mechanisms of Cavitation Inception,*" Journal of Fluids Engineering, Vol 113, June.

[2] Rood, E. P., 1992, "*Cavitation Inception Research - Focus and Direction*", Report on the Advisory Council on Cavitation Events, ONR meeting, Memphis, TN, May 20th, 1992.

[3] Chahine, G.L., Duraiswami, R., Rebut, M., 1992, "*Analytical and Numerical Study of Large Bubble/Bubble and Bubble/Flow Interactions,*" Proc. 19th ONR Symposium on Naval Hydrodynamics, Seoul, S. Korea.

[4] Guerri, L., Lucca, G., and Prosperetti, A., 1981, "*A Numerical Method for the Dynamics of Non-Spherical Cavitation Bubbles,*" Proc. 2nd Int. Coll. on Drops and Bubbles, JPL Publication 82-7, Monterey, CA.

[5] Blake, J. R., Taib, B.B. and Doherty, G., 1986, "*Transient Cavities Near Boundaries. Part I. Rigid Boundary,*" Journal of Fluid Mechanics, vol. 170, pp. 479-497.

[6] Blake, J. R, and Gibson, D. C., 1987, "*Cavitation Bubbles Near Boundaries,* " Annual Review Fluid Mechanics., Vol. 19, pp. 99-123.

[7] Wilkerson, S.,1989, "*Boundary Integral Technique for Explosion Bubble Collapse Analysis,*" ASME Energy Sources Technology Conference and Exhibition, Houston Tx.

[8] Chahine, G.L., Perdue, T.O., and Tucker, C.B., 1988, "*Interaction Between an Underwater Explosion and a Solid Submerged Structure,*" DYNAFLOW, INC. Technical Report 89001-1.

[9] G.L. Chahine and T.O. Perdue, 1989a, "*Simulation of the Three-Dimensional Behavior of an Unsteady Large Bubble Near a Structure,*" in "*Drops and Bubbles*" edited by T.G. Wang, A.I.P. Conference Proceedings, 197, 169-187.

[10] Chahine, G.L.,1990a, "*Nonspherical Bubble Dynamics in a Line Vortex,*" in Proceedings of the ASME Cavitation and Multiphase Flow Forum, Toronto, FED- Vol. 98, pp. 121-127.

[11] Chahine, G.L., 1990b, "*Numerical Modeling of the Dynamic Behavior of Bubbles in Nonuniform Flow Fields*" ASME Symposium on Numerical Methods for Multiphase Flows, Toronto, FED-Vol. 91, pp 57-65.

[12] Chahine, G.L., Duraiswami, R., 1993, "*Boundary Element Method for Calculating 2-D and 3-D Underwater Explosion Bubble Behavior in Free Water and Near Structures,*" Naval Surface Warfare Center, Dahlgren Division, White Oak Detachment, Report NSWCDD/TR-93/44.

[13] Ceccio, S.L., Brennen, C.E., 1991, "*Observation of the dynamics and acoustics of travelling bubble cavitation,*" Journal of Fluid Mechanics, vol., 233, 633-660.

[14] Dechizelle, Y.K., Ceccio, S.L., Brennen, C.E., Shen, Y., 1992 "*Cavitation Scaling Experiments with Headforms: Bubble Acoustics*", Proceedings Second Internatinoal Symposium on Propeller and Cavitation, Hangzhou, China.

[15] Chahine, G.L., 1979, "*Etude Locale du Phénomène de Cavitation -Analyse des Facteurs Regissant la Dynamique des Interfaces,*" Doctorat D'Etat Es-Sciences Thesis, Universite Pierre et Marie Curie.

[16] Bovis, A.G., 1980a, "*Asymptotic Study of Tip Vortex Cavitation*", ASME Cavitation and Polyphase Flow Forum, New Orleans, pp. 19-21.

[17] Bovis, A.G., 1980b, "*Etude Asymptotique du Phénomène de Cavitation. Cavités nonsphériques,*" Thèse de Docteur Ingénieur. Université Pierre et Marie CURIE, Paris.

[18] Latorre, R., 1982, "*TVC Noise Envelope - An approach to Tip Vortex Cavitation Noise Scaling*", Journal of Ship Research, Vol. 26, No. 1, pp. 65-75.

[19] Ligneul, P. and Latorre R., 1989, "*Study of the Capture and Noise of Spherical Nuclei in the Presence of the Tip Vortex of Hydrofoils and Propellers*", Acustica Vol. 68.

[20] Chahine, G.L., Duraiswami, R., 1992, "*Analytical Study of a Gas Bubble in the Flow Field of a Line Vortex,*" Proceedings, ASME Cavitation and Multiphase Flow Forum, Los Angeles.

[21] Crespo A., Castro F., Manuel, F., and Hernandez J., 1990, "*Dynamics of an Elongated Bubble*

During Collapse", Journal of Fluids Engineering, Vol 112, 232-237.

[22] Higuchi, H., Arndt, R.E.A. and Rogers, M.F., 1989, *"Characteristics of Tip Vortex Cavitation Noise"*, Journal of Fluids Engineering, Vol. 111, No 4, pp. 495-502.

[23] Maines, B.H., and Arndt, R.E.A., 1993, *"Bubble Dynamics of Cavitation Inception in a Wing Tip Vortex"*, ASME Cavitation and Multiphase Flow Forum, Washington D.C., FED-Vol. 153, pp. 93-99.

[24] Green, S.I., 1991, *"Correlating Single Phase Flow Measurements with Observations of Trailing Vortex Cavitation"*, Journal of Fluids Engineering, Vol. 113, No 1, pp. 125-130.

[25] Chahine, G.L., Delepoule, E., and Hauwaert, P., 1993a, *"Study of the Interaction Between a Bubble and a Vortical Structure*, "1993 ASME Cavitation and Multiphase Flow Forum, Washington D.C., FED-Vol. 153, pp. 39-47.

[26] Chahine, G.L., 1994, *"Bubble Interactions with Vortices,"* in *Fluid Vortices* Ed. Sheldon Green to be published by Kluwer Academic.

[27] Chahine, G.L., 1991, *"Dynamics of the Interaction of Non-Spherical Cavities," in "Mathematical Approaches in Hydrodynamics,"* ed. T. Miloh, SIAM, Philadelphia.

[28] Desgrees du Lou, G., Sarazin, T. and Chahine, G.L., 1993, *"Viscous Interaction Between Bubble and Line Vortex,"* DYNAFLOW, INC. Technical Report 6.002-15.

[29] Leonard, A., 1985, *"Computing Three- Dimensional Incompressible Flows with Vortex Elements,"* Ann. Rev. Fluid Mech., 17, 523-559.

[30] Sarpkaya, T., 1989, *"Computational Methods with Vortices— The 1988 Freeman Scholar Lecture,"* J. Fluids Engg., 111, 5-52.

[31] Knio, O. M., and Ghoniem, A. F., 1990, *"Numerical Study of a Three-Dimensional Vortex Method,"* J. Comp. Phys., 86, 75-106.

[32] Beal, J. T., and Majda, A., 1985, *"Higher Order Accurate Vortex Methods with Explicit Velocity Kernels,"* J. Comp. Phys., 58, 188-208.

[33] Sarkar, K., and Chahine, G.L., 1994, *"A Coupled Three-Dimensional Boundary Element-Vortex Method for Vortical Flows-Bubble Interactions"*, DYNAFLOW, INC. Technical Report 6.002-20 (in preparation).

DISCUSSION

T. Huang
David Taylor Model Basin, USA

Georges, you have selected a very important area of cavitation. Would you please analyze the frequency and the noise level of your computation for bubble dynamics in a vortex. Thank you very much for your excellent work and presentation.

AUTHOR'S REPLY

The author appreciates very much the comments of Dr. Huang. It is comforting to know that the fundamental work that we are conducting responds to some of the Navy researchers' questions. Even though we have not directly addressed yet the important questions of Dr. Huang, the results that we have presented in this paper and additional information in the referenced publications allow me to give a preliminary answer. The dynamics of "splitting" of the bubble entrapped in the vortex is controlled mostly by the bubble wall motion in the perpendicular plane to the vortex axis. The period of one "oscillation" or "collapse" in that direction scales well with the Rayleigh time based on the pressure on the vortex axis and on maximum size of the equivalent spherical bubble. As a result, the frequency of the emitted sound includes the same major frequencies as the equivalent spherical bubble defined above. However, since the achieved minimum volume is smaller, the amplitude is smaller. From computations of the pressure field (using post-processing and the Boundary Element Method), the emitted sound is more directive than in the spherical bubble case. Thank you again for your encouraging remarks.

Free Oscillation of a Nonspherical Bubble in a Quiescent Fluid

N. McDougald, G. Leal
(University of California-Santa Barbara, USA)

I. INTRODUCTION

Theoretical studies of the dynamics of gas and vapor bubbles in a liquid have recently undergone a strong resurgence of interest. From a physical point of view, this is a consequence of the realization that time-dependent changes in the bubble volume and shape are very often strongly coupled, with implications both in understanding bubbles as a source of sound, and in understanding possible mechanisms for bubble breakup. In fact, the initial impetus for much of the work on this topic over the past five years was the suggestion, due to Longuet-Higgins (1, 2), that a major source of the sound produced by breaking waves in the ocean could be the entrapment of nonspherical air bubbles, which become a strong acoustic source via a transfer of energy from the initial deformation of *shape* to a significant oscillation of the bubble volume. Further, though bubble *breakup* at high Reynolds number is generally assumed to result from deformation caused by velocity or pressure gradients, a bubble that oscillates in *volume* due to a *time*-dependent fluctuation of the ambient pressure may also reach the point of breakup due to the generation of large *shape* oscillations via a transfer of energy from the volume oscillations.

Motivated by these, and other, potential applications, a number of recent investigators have, in fact, tackled the problem of coupling between time-dependent changes in bubble shape and volume (1, 2, 3, 4, 5, 6, 7). These studies were all based upon *small amplitude* expansions, using a modal decomposition of the bubble shape in terms of spherical harmonics. In spite of their complexity, however, these analyses turn out to be incomplete (and even misleading) due to an unfortunate choice of a very special family of initial conditions (8).

In our group, we have followed two complimentary paths of investigation: the first, based again upon small amplitude perturbations of volume and shape (relative to equilibrium) but with an added advantage of modern tools and ideas from non-linear dynamics; and second, the application of numerical methods for the solution of free boundary problems to explore larger amplitude effects.

From our perspective, there are three classes of problem that provide a basis to understand situations of more direct technological significance: (1) The coupling between shape and volume oscillations in a quiescent fluid at constant ambient pressure; (2) The coupling between shape and volume oscillations in a quiescent fluid forced by time-dependent ambient pressure fields; and (3) The preceding problems in the presence of a mean flow (or other mechanism) that produces a nonspherical base state. Although the effects of boundaries, or of neighboring bubbles, can be very considerable in each of these processes, the work carried out in our group to date applies to a single bubble in an unbounded fluid.

In the present paper, we first summarize some aspects of our recent analytical studies. Following this, we introduce the numerical methods that have been developed for the solution of bubble dynamics problems involving large amplitude oscillations of shape and volume. Finally, we present numerical results showing our initial studies of bubble motions in an inviscid fluid. In the verbal version of this paper, we will expand upon these results to the extent allowed by our accomplishments during the next three months. This work is being carried out as part of the PhD dissertation research of one of us (9).

II. A SUMMARY OF RECENT ANALYTICAL STUDIES

Over the past several years, we have carried out a comprehensive analytic investigation of the coupling of small amplitude oscillations of a gas bubble in an incompressible, unbounded liquid. In this work, we neglect buoyancy effects and assume the Reynolds number associated with the bubble motions to be large so that viscous effects can either be neglected completely, or limited to weak boundary-layers confined to the immediate vicinity of the bubble surface. Further for simplicity, the bubble is assumed to be axisymmetric. Detailed descriptions of the work are reported in three recent publications (6, 8, 10). Here we limit ourselves to a brief synopsis of the results.

The primary tool for analysis is the familiar "domain perturbation" technique, pioneered by Joseph (11). The bubble shape is specified in terms of spherical harmonics. In general terms, for the small deformation limit, the coupled dynamics of the volume (P_0) and shape (P_n) modes correspond to a classic nonlinear oscillator system, whose behavior is determined largely by proximity to resonance conditions. If we denote the natural frequency for volume oscillations as ω_0,

$$\omega_0^2 \equiv \frac{\Gamma}{a^3\rho}\left[3\gamma\left(\frac{p_\infty}{\Gamma/a}+2\right)-2\right]$$

and the natural frequency of the n^{th} shape mode (P_n) as ω_n,

$$\omega_n^2 \equiv \frac{\Gamma}{a^3\rho}(n+1)(n-1)(n+2)$$

then exact resonance occurs generally for ω_0-$k\omega_n$=0, where k is an integer. [1]

If ω_0-$k\omega_n$ is *not* small, ω_0-$k\omega_n \geq 0(\varepsilon)$, where ε denotes the amplitude of shape or volume deformations (relative to equilibrium), coupling between the shape and volume modes occurs only at higher order (i.e. $0(\varepsilon^p)$ with p>1), and the domain perturbation analysis is well-behaved at all orders in ε.

On the other hand, for ω_0-$k\omega_n \leq 0(\varepsilon)$, the n^{th} shape mode and the volume mode are in a near-resonant (or exact resonant) state, and the coupling between these modes is stronger, occurring at $0(\varepsilon)$. In this case, the governing equations at the second-order contain secular terms, and the so-called *solvability conditions* required for bounded solutions yield dynamical equations for the slowly varying amplitudes of the P_0 and P_n modes at $0(\varepsilon)$. The details of resonant interactions depend upon k; on whether there is a *mean deformation* of shape via either a non-isotropic pressure distribution or a mean flow; and the nature of any time dependence of the ambient pressure.

We briefly summarize results for two cases that will later by studied at finite amplitude via numerical solution of the full nonlinear fluid mechanics problem.

a. Free Oscillations in a Quiescent Fluid

First, we consider the oscillation of a bubble in a quiescent inviscid fluid, in the presence of a *constant* ambient pressure. This is the problem originally studied by Longuet-Higgins (1, 2, 4), and eventually revisited by many other authors, including the earliest of our own studies, Yang et al (6).

It is a simple matter to show that there is a one-to-two internal resonance between oscillations in the bubble volume and the n^{th} shape mode whenever $\omega_0=2\omega_n$, and this has been recognized by all researchers beginning at least with Longuet-Higgins. However, all solutions up to the analysis of Feng and Leal (8) showed that the energy associated with an initial deformation of shape was always transferred completely at large times to oscillations of the bubble volume, thus suggesting that an initially nonspherical bubble would become a strong source of sound.

In contrast, however, the analysis of Feng and Leal (8) shows unequivocally that this inference is *incorrect, except for a very select set of initial conditions at exact resonance.* Feng and Leal considered the case of 1-2 ($\omega_0=2\omega_n$) resonance, but with allowance for a mismatch of $0(\varepsilon)$ from exact resonance, i.e.

$$\omega_0-2\omega_n=\beta_0\varepsilon$$

where β_0 is a so-called "detuning" constant of 0(1). In the notation of Feng and Leal, the bubble surface is at $r=1+\varepsilon f_1+0(\varepsilon^2)$ where

$$f_1=\frac{1}{2}\left(\alpha_{1,0}(\tau)e^{2i\omega_n t}+\alpha_{1,n}(\tau)e^{i\omega_n t}P_n(\eta)\right)+\text{c.c.}$$

and $\qquad \tau=\varepsilon^{-1}t.$

[1] Here, Γ is the interfacial tension, a the undeformed radius, ρ the liquid density, p_∞ the ambient pressure and γ is the ratio of specific heats (C_p/C_v).

In general, resonant coupling is found to lead to a *continuous interchange* of energy between the resonant shape and volume modes on a long time scale, $0(\omega_0\varepsilon)^{-1}$, which appears as a slow *modulation* of the oscillation *amplitudes* $\alpha_{1,0}(\tau)$ and $\alpha_{1,n}(\tau)$.

To visualize the predicted behavior, it is convenient to reproduce the phase diagram of Feng and Leal (8), and this is shown in Figure 1. Since the fluid is inviscid, total energy is conserved in the exchange of energy between volume and shape oscillations, and the solution trajectories for the slowly varying amplitude functions $\alpha_{1,0}$ and $\alpha_{1,n}$ can thus be drawn on the surface of a sphere, whose radius is proportional to the total energy. Specifically, in terms of spherical coordinates, the amplitude functions can be written in the form

$$\alpha_0 = r\cos\frac{\theta}{2}e^{i(\phi+\psi)} \qquad \text{(volume mode)}$$

$$\alpha_n = r\sin\frac{\theta}{2}e^{i\psi} \qquad (n^{th}\text{ shape mode})$$

where $\alpha_0 \equiv \left(\frac{4n-1}{4}\omega_n\right)\alpha_{1,0}$ and

$$\alpha_n \equiv \alpha_{1,n}\sqrt{(4n-1)^2\omega_n^2/64(n+1)(2n+1)}$$

A point at the north pole, where $\theta=0$, thus represents a purely radial oscillation, whereas a point at the south pole is a pure shape oscillation. The relative phase of the two resonant modes is determined by the azimuthal angle, ϕ.

Solution trajectories for 1-2 resonance conditions are sketched in Figure 1 for several values of the detuning parameter β_0. Generally, as indicated earlier, the trajectories trace *closed* paths on the sphere surface representing an *interchange* of energy as the point moves closer to, or further from the north and south poles. Fixed points in Figure 1 correspond to oscillations of volume and shape with no change in the amplitudes α_0 and α_n, and no change in the relative phase angle ϕ.

A key feature of the one-two resonance case is that the north pole N, representing purely radial oscillations, is *always a fixed point*. When the detuning parameter β_0 is large, there is only one other fixed point, but energy exchange is generally weak in any case, and the purely radial oscillation is stable. On the other hand, for $0\le\beta_0\le\beta c$, we see from Figure 1, that there are a total of *three* fixed points, and a *homoclinic orbit* that emanates from the purely radial fixed point at the north pole. This means that the purely radial mode is *unstable* to infinitesimal perturbations of shape for this range of β_0 values. The critical value of β_0 is

$$\beta_c = \frac{(4n-1)\omega_n}{2}\left[\alpha_{1,0}^2 + \frac{\alpha_{1,n}^2}{4(n+1)(2n+1)}\right]^{1/2}.$$

Although the individual amplitude functions depend on time, the term in square brackets is *constant*, and thus can be evaluated from the initial amplitudes of deformation.

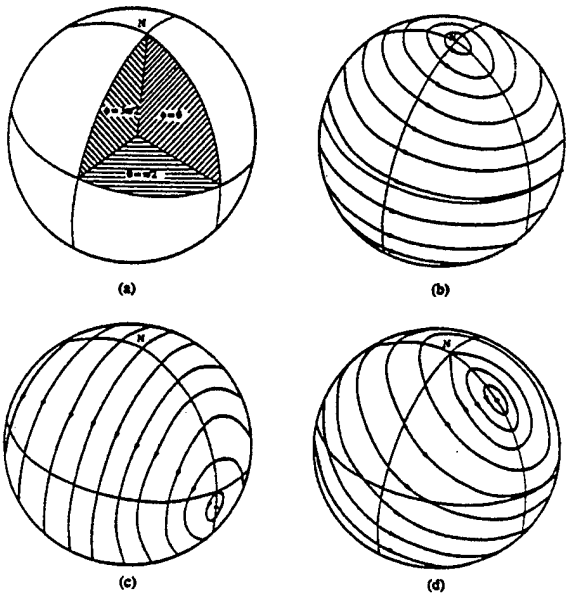


Figure 1: Phase diagrams for the one-two resonance case (a) coordinate orientation, (b) $\beta>2r$, i.e., large detuning, (c)$\beta=0$, i.e., no detuning, (d) $0<\beta<2r$.

A point of special interest is that the homoclinic orbit for exact resonance, $\beta_0=0$, becomes the great circle trajectory which passes directly through the south pole. Thus, any initial conditions which begin on this invariant manifold will end up at the north pole for $t\to\infty$. Ironically, the initial conditions considered by Longuet-Higgins (2), as well as the initial conditions of virtually all other investigators, can be shown to correspond to various points on the invariant great circle. It can be seen from Figure 1, however, that the behavior identified by these investigators is a very special case, limited to the specific set of initial conditions that happen to lie on the invariant great circle in the case of exact resonance, $\beta_0\equiv0$.

We may conclude from the results in this subsection, that *nonspherical* bubbles may be a significant source of sound, as suggested by previous investigators. Further, the *interchange* of energy that occurs between shape and volume modes whenever we are in the neighborhood of a resonant point is generally continuous in time. Clearly, the bubble response in these conditions (and the associated sound) *cannot* be predicted precisely from Rayleigh-Plessant theory. It may be noted, however, that there is a large amplification factor in going from a purely radial oscillation to a shape mode, while holding the total energy constant. Thus, even when the bubble undergoes rather large oscillations of shape at the expense of energy from the radial mode, the changes in the amplitude of the radial mode with time may remain quite modest. Finally, volume oscillations for conditions sufficiently close to resonance are unstable, and this may be a route to bubble breakup in the absence of gradients in either the ambient pressure, or the mean velocity of any external flow. We discuss the dynamics of a gas bubble with *larger* amplitude changes of volume or shape in Section IV, where we present some selected results of recent numerical studies.

b. The Effect of *Mean* Shape Deformation on Free Oscillations in a Quiescent Fluid

The second case studied in Section IV concerns the effects of a mean deformation of shape or volume on the bubble dynamics. There are, of course, a number of ways by which the shape of a bubble may be changed. The simplest is that a nonisotropic ambient pressure distribution may cause the bubble to deform. Another is that the bubble may be deformed by a mean flow of the suspending liquid. It is, perhaps, not surprising that these various routes to mean deformation can produce quite distinct results for the bubble dynamics.

The general case of a nonisotropic pressure distribution at the bubble surface was again treated by Feng and Leal (8), following the earlier work by Yang et al (6), which focused on exact resonance conditions. In this case, resonant interactions were found to occur both for $\omega_0=2\omega_n$ and $\omega_0=\omega_n$. Further, the mean deformation of shape is found to lead to a *shift* in the natural frequency of shape oscillations, with an increased frequency for *oblate* mean shapes and decreased frequency for *prolate* shapes. This frequency shift provides a *natural* mechanism for detuning from exact resonance.

In the case of 1-2 resonance, the predicted behavior is qualitatively similar to that described in the preceding subsection, but with the magnitude of detuning modified by the shift in frequencies that is caused by the mean deformation.

The phase diagram for 1-1 resonance is shown in Figure 2, *again* reproduced directly from Feng and Leal (8). Although the solution trajectories for various β values appear quite similar to those shown earlier for the 1-2 resonance case, there are a number of fundamental differences. The most important is that the north pole, N, is not a fixed point in this case for *any* value of β. Hence, there exists no region of β space where *purely* radial oscillations can be stable. Instead, an initial deformation of volume (from equilibrium) will *always* generate a corresponding shape oscillation. Two other features are worth mentioning here. First, the coupling coefficients between the shape and volume modes, which are *zero* in the absence of mean deformation, increase monotonically if there is an increase in the amplitude of the mean deformation—thus indicating stronger interactions with increased deformation. Second, these same coupling coefficients both contain the factor (n-3) in the numerator and are thus identically *zero* when the frequency match is between ω_0 and ω_3. This means that resonant coupling is not possible for the n=3 mode. Perhaps the most important consequence of the onset of 1-1 resonance, in addition to the 1-2 resonance identified earlier, is that the likelihood of

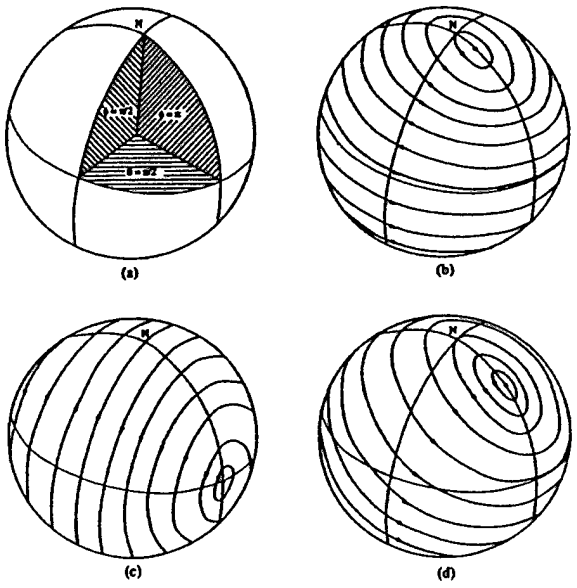


Figure 2: Phase diagrams for the one-one resonance case (a) Coordinate orientation, (b) β large, i.e., large detuning, (c) β-0, i.e., no detuning, (d) β intermediate.

coupling between shape and volume oscillations is *increased*, and hence too the range of conditions where we may expect departures from Rayleigh-Plesset predictions and/or the onset of conditions for bubble breakup.

It was noted earlier that changes in the mechanism for *mean* deformation will generally lead to changes in the characteristic dynamics of bubble shape and volume oscillations. Of particular consequence for applications is the influence of an external mean flow. We have, to date, considered only the single case of an axisymmetric extensional flow with a dimensionless rate of deformation of $0(\varepsilon^{1/2})$ (6). Although this is admittedly a special case, it shows that the coupling between shape and volume oscillations can be stronger in the presence of flow than would be true with the *same* mean shape but no flow. This implies that the interaction will occur on a much shorter time-scale than is possible in the absence of a mean flow. In particular, for the steady axisymmetric straining flow, when ω_0-$\omega_2=0(\varepsilon)$, resonant interaction between the volume and P_2 mode appears at $0(\varepsilon^{3/2})$ in the small amplitude expansions, and this translates to a time-scale, $0(\omega_0\varepsilon^{1/2})^{-1}$, rather than $0(\omega_0\varepsilon)^{-1}$ as in the case without flow. Furthermore, in this case, volume oscillations lead always to shape oscillations and vice versa (i.e. the bubble cannot undergo purely radial oscillations). The *mechanism* by which volume oscillations lead to shape oscillations is very simple—the bubble shape even at steady-state is a function of its size, and this is translated into changes of shape at the same frequency as the bubble undergoes a time-dependent change of volume.

c. Summary

The analyses summarized in this section were all based on the assumption of small amplitude changes in the bubble volume or shape relative to its equilibrium configuration. Thus, interactions are weak, even in the vicinity of resonant conditions, and the time-scale over which these interactions lead to changes in the bubble motion is correspondingly long. For an inviscid fluid, very long time-scale phenomena are possible because they are not damped by viscous dissipation. For bubbles in real liquids, however, the Reynolds number characteristic of bubble motions is often quite large, but viscous effects are never completely negligible, and it is likely that the predicted resonant interactions would not be observable at such small deformation amplitudes. When the amplitudes of shape or volume changes increase, however, the coupling between modes becomes stronger, and the time-scales become much shorter, thus reducing the importance of dissipative effects. In addition, of course, mode coupling will occur for conditions that are further from exact resonance, and will generally involve multiple shape modes.

To assess the practical significance of the phenomena identified in the small amplitude expansions, it is thus critical to study the effects of increased amplitude. This can be done, in principle, either experimentally, or theoretically by numerical solution of problems involving larger deformations using modern techniques for free-boundary problems. In the present work, and in the remainder of this paper, we pursue the latter alternative. It should be noted, however, that efforts are also under way to utilize levitation techniques developed in the microgravity research program at JPL-NASA, to carry out the type of controlled experimental studies that are required to obtain quantitative data.

In the next section, we briefly describe three numerical methods that have been used in our group for the solution of free-boundary problems. Following this, in the last section, we present some results focused upon the two classes of problem that were described in this section.

III. NUMERICAL METHODS

Three distinct numerical techniques have been developed for the solution of flow problems involving finite amplitude oscillations of volume and shape for a single bubble in an unbounded, incompressible liquid. These are: (1) a spectral code which utilizes a modal decomposition of the bubble shape in terms of spherical harmonics, and is suitable for purely inviscid flows; (2) a boundary-integral technique which is suitable for bubbles of arbitrary shape in either an inviscid fluid, or under circumstances (cf. Lundgren and Mansour (12)) where weak viscous effects are confined to a thin region at the bubble surface; and (3) a finite-difference code using boundary-fitted coordinates that is designed to solve free-boundary problems for the full Navier-Stokes equations. It can be used for Reynolds numbers up to 0(several hundred) at least.

a. The Spectral Method

The spectral method we employ is a slight variation of traditional spectral methods as discussed in Fletcher (13) and is based on the analytical work done for small amplitude oscillations (6, 8, 10). The algorithm is very efficient computationally for small amplitudes, but as the number of Legendre modes which must be retained for an accurate solution increases so does the computation time. The method we use assumes that the bubble surface can be

decomposed into a finite series of Legendre polynomials with time dependent coefficients, and that the potential function can likewise be represented by a series of "decaying" axisymmetric spherical harmonics based on Legendre polynomials. By doing this we automatically satisfy the governing equation for potential flow throughout the domain and are left with the time-dependent coefficients of the shape and potential functions to satisfy the boundary conditions. As with other spectral methods, we make use of the orthogonality of Legendre Polynomials and various recursion relations relating derivatives to lower order polynomials to generate ordinary differential equations for the time-dependent coefficients. The result of this technique is a system of 2N ordinary differential equations where N is the total number of modes kept in the Legendre series. These equations are advanced in time using a fourth order Runge-Kutta routine to give the evolution of the bubble shape and the external potential.

b. The Boundary Integral Method

The boundary integral method is well suited to the solution of free surface problems as it does not require the discretisation of the calculation domain. Instead, the solution of the problem is reduced to solving a set of equations on the boundary only which can be related to the entire domain through Green's functions thereby reducing the dimension of the system by one. In our treatment, we consider only axisymmetric shapes so our domain is two-dimensional and the boundary is represented by a one-dimensional curve. This is the main advantage of the boundary integral method over finite difference techniques. The boundary integral method is also computationally more efficient due partly to the reduction of the dimension of the problem, but also to the availability of efficient algorithms for the required matrix manipulations. The disadvantage of this approach is that it requires the velocity field to be expressed as a potential thereby preventing the inclusion of viscous effects explicitly. It is possible, however, to include weak viscous effects if the effect of vorticity is confined to a thin region near the surface (12). The boundary integral technique is analogous to representing the velocity potential as a distribution of point sources along the boundary. Our implementation of the scheme follows that of Brebbia (14) which treats the method as a special weighted residual method. The weighting functions are chosen to satisfy Laplace's equation and in fact are fundamental solutions corresponding to point sources on the boundary. The nature of the singularity occurring at each node is therefore known, allowing it to be integrated either analytically, if the boundary is discretized using simple linear elements, or by an appropriate numerical method for more complicated segmentation of the interface. In our case we use a 32-point Gaussian scheme to evaluate the nodal integrals and a five-point Gaussian scheme for other points along the interface as our elements are determined by a cubic spline interpolation between the nodes. The time advancement in the code is done using a fourth order Runge-Kutta routine to update the position of and the value of the potential at each node along the boundary.

c. Finite Difference Method

The finite difference scheme used for this study is essentially that described by Kang and Leal (15), but adapted to accommodate the finite compressibility of the bubble. This method uses a boundary-fitted coordinate transformation, updated at each time step, to discretize the domain. Since a detailed description is already available in the literature, no additional description will be given here. One point to note, however, is that we have found this technique to be moderately dissipative, and thus inaccurate at high Reynolds number (or in the inviscid flow limit) for free-oscillation problems (i.e. for problems *without* time-dependent forcing of the bubble volume or shape). With forcing, the numerical dissipation produces a modest phase-lag. but does not have much effect on the amplitudes of the bubble motion.

The results reported below represent the initial stages of what is intended to be an extensive study. In the work reported here, we consider only the *inviscid* limit, and thus utilize only the spectral and boundary integral codes. We have found that these produce virtually identical results in all cases. For convenience of presentation, we use generalized Fourier series decompositions to express the calculated shapes via the boundary integral technique in terms of Legendre components, P_2, P_4, etc.

IV. NUMERICAL RESULTS

The results in this section consider the problem of free oscillation in a quiescent fluid, and free oscillation in the presence of a nonspherical mean shape (due to an anisotropic mean pressure). They are preliminary, and incomplete in some respects.

a. Free Oscillation in a Quiescent Fluid

We have seen in section II that the small amplitude deformation theory predicts that there is a fundamental change in the solution structure at $\beta=2r$, i.e. at

$$(\varepsilon\beta_0)_c = \frac{(4n-1)\omega_n}{2}\left[\varepsilon^2\alpha_{1,0}^2 + \frac{\alpha_{1,n}^2\varepsilon^2}{4n^2(n+1)(2n+1)}\right]^{\frac{1}{2}}.$$

For deformation amplitudes such that the right hand side is smaller than $\varepsilon\beta_0$, the purely spherical solution is *unstable*. In the unstable regime, the interchange of energy will become stronger as $\varepsilon\beta_0$ becomes smaller and/or $\alpha_{1,0}$ and $\alpha_{1,n}$ become larger.

In the present brief study, we consider three cases with fixed values of $\alpha_{1,0}$ and $\alpha_{1,n}$ for n=2, and various β_0. The three cases are listed in Table 1

Case	$\varepsilon\alpha_{1,0}$	$\varepsilon\alpha_{1,2}$	$(\varepsilon\beta_0)_c$
A	-.005	0.01	0.063
B	-0.05	0.1	0.63
C	0.1	0.1	1.22

together with the critical value of $\varepsilon\beta_0$, calculated from the preceding equation.

The first case, A, has sufficiently small initial values of $\varepsilon\alpha_{1,0}$ and $\varepsilon\alpha_{1,2}$ to fall within the domain of validity of the small amplitude perturbation theory. The critical value of $\varepsilon\beta_0$ is 0.063. Calculations were carried out for $\varepsilon\beta_0 = 10^{-5}$, 10^{-2}, 0.1, 1.0 and 4.0, plus several values in the immediate vicinity of the critical value predicted from the small perturbation theory. Results for $\varepsilon\beta_0 = 10^{-5}$ and 0.1 are shown in Figures 3 and 4. In the first case, β_0 is very close to zero and although the initial conditions do not correspond to a point on the invariant great circle which passes from N to S in Figure 1c, the solution trajectory still passes very close to the south pole S, and there is almost a complete exchange of energy between the P_0 and P_2 modes. Note that the dimensionless period for one complete cycle of this resonant interaction is approximately 160. In Figure 4, on the other hand, the detuning parameter is $\varepsilon\beta_0$=0.1, which exceeds the critical value of 0.063, and there is very little exchange of energy, and a period that is shorter by approximately a factor of 2. In this case, the phase diagram is of the type 1b, and thus the trajectory starting to the left of the north pole (N) with $\phi=\pi$ travels a rather short path around the north pole with little energy exchange. The transition in behavior, in fact, occurs very near the value of $\varepsilon\beta_0$=0.063 predicted by the small amplitude theory. It is perhaps

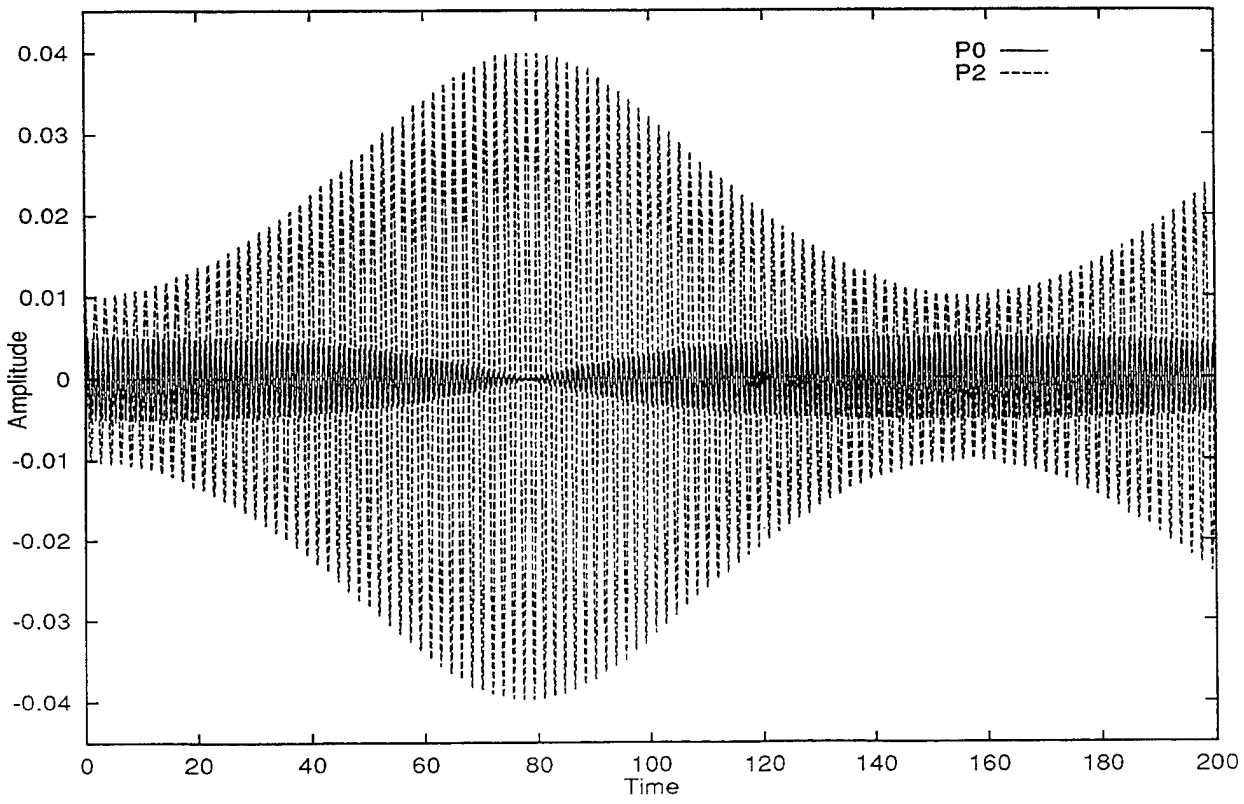


Figure 3: Amplitudes of the P_0 and P_2 modes for Case A (Table 1), with $\varepsilon\beta_0=10^{-5}$.

surprising that the transition in $\varepsilon\beta_0$ is as sharp as it is. With the initial conditions considered here, there is a sharp decrease in the degree of interaction at $\varepsilon\beta_0$=0.063 and almost no interaction beyond $\varepsilon\beta_0$=0.1.

The second case, corresponding to row B in Table 1, has the initial perturbation amplitudes increased by a factor of 10, which also increases the predicted critical value of $\varepsilon\beta_0$ by approximately ten times. Of course, since the amplitudes of deformation are now "finite," we should expect some deviation in the value of $\varepsilon\beta_0$ where the stability actually changes compared to the value predicted by the small deformation theory. We have considered a series of values from $\varepsilon\beta_0=10^{-5}$ to $\varepsilon\beta_0$=4. The predicted critical value is 0.63. We illustrate results for $\varepsilon\beta_0=10^{-5}$, 0.4, 0.5 and 0.6. For $\varepsilon\beta_0=10^{-5}$, shown in Figure 5, there is a strong exchange of energy as expected. However, in this case: (1) the period for energy exchange between modes is much shorter (~16 instead of 160, as expected qualitatively from the predicted scaling of the time εt, for resonant interactions at small amplitudes); (2) the exchange is never complete—i.e. the amplitude of the P_0 (or volume) mode always remains nonzero, and the corresponding increase in P_2 to a maximum of about 0.35 is smaller than the value 0.4 that one would expect via a linear scaling from the previous case; and (3) we see the intermittent appearance of the P_4 mode (there is also some P_6 and P_8 not visible in Figure 5). The results up to $\varepsilon\beta_0$=0.1 are virtually identical to those shown above. At $\varepsilon\beta_0$=0.4, we can begin to see the expected transition (corresponding to β=2r). The initial conditions considered lie outside the homoclinic orbit. Hence, initially, for $\beta_0\approx$0, where the homoclinic orbit coincides with the great circle between N and S, our solution trajectory begins to the left of the great circle at $\phi=\pi$ (see Figure 1) and remains there at all times, thus missing the south pole where the maximum amplitude shape mode occurs. As the homoclinic orbit retreats from the great circle that it occupies for $\beta_0\approx$0, and shrinks toward the fixed point at the north pole (Figure 1), the maximum amplitude of the shape mode in our solution will at first increase a little as the trajectory moves toward S and then decrease monotonically as the homoclinic orbit diminishes in size. We see this behavior in Figures 6, 7 and 8. At $\varepsilon\beta_0$=0.4, there is a slight increase in the maximum amplitude of the P_2 mode, but also a much longer period of interaction (~30). At $\varepsilon\beta_0$=0.5 there is a decrease in the maximum P_2, and very much less energy lost from the radial P_0 mode. The period is still longer, now ~50. Finally at $\varepsilon\beta_0$=0.6, there is almost no change in P_0, and the amplitude of P_2 decreases from the initial condition rather than increasing as in previous

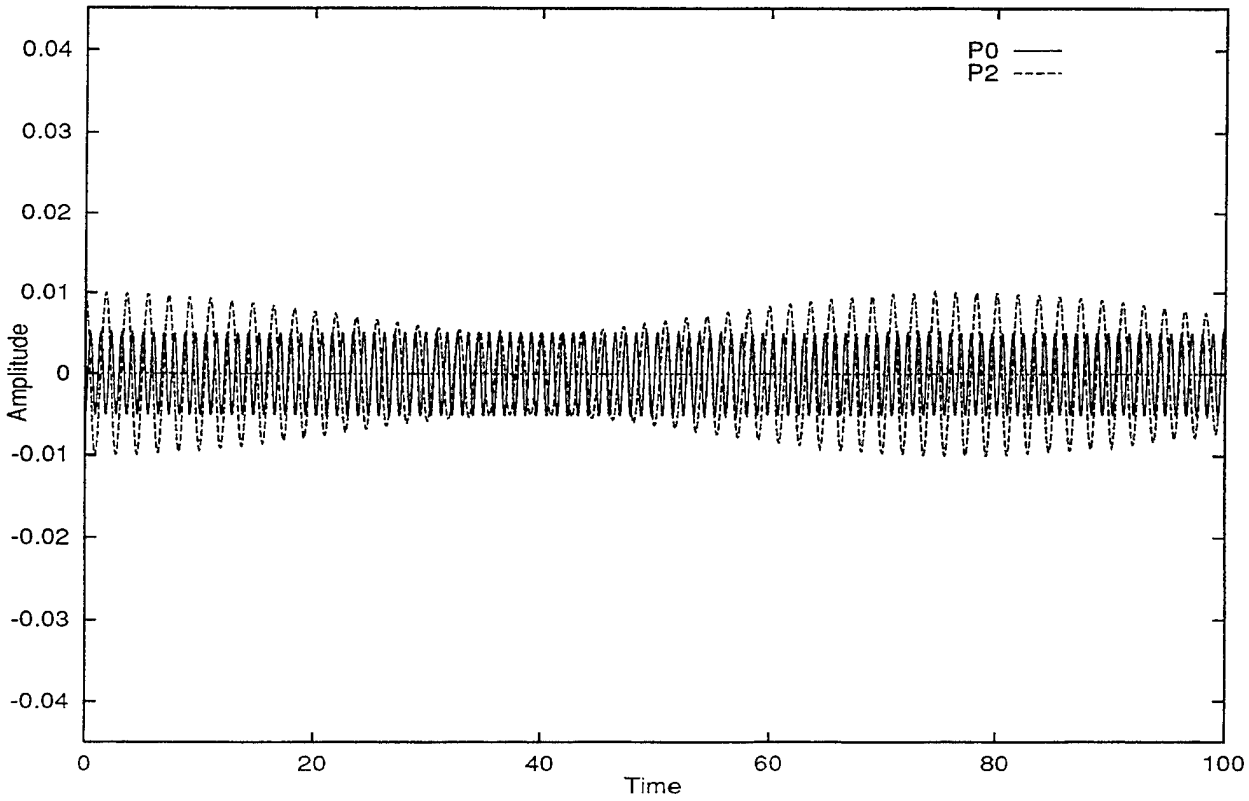


Figure 4: Amplitudes of the P_0 and P_2 modes for Case A (Table 1), with $\varepsilon\beta_0$=0.1.

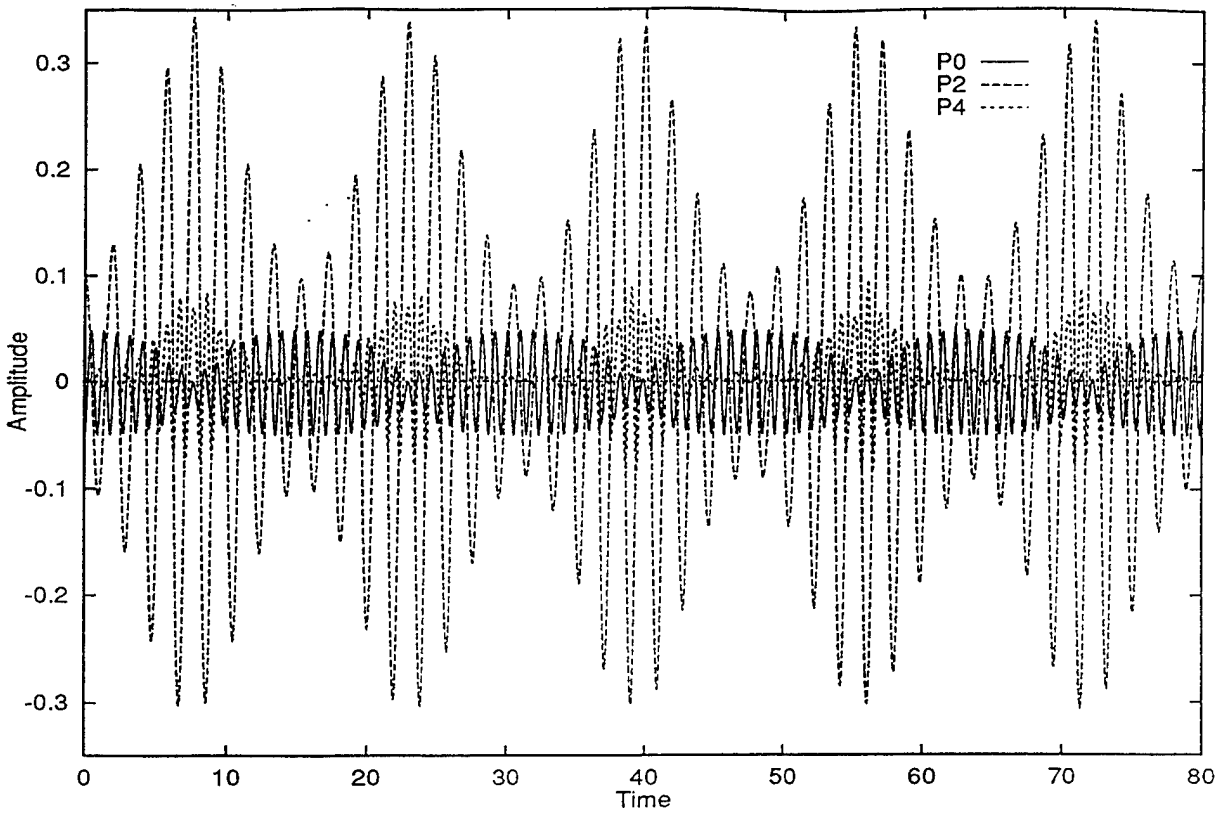


Figure 5: Amplitudes of the P_0, P_2 and P_4 modes for Case B (Table 1), with $\varepsilon\beta_0=10^{-5}$.

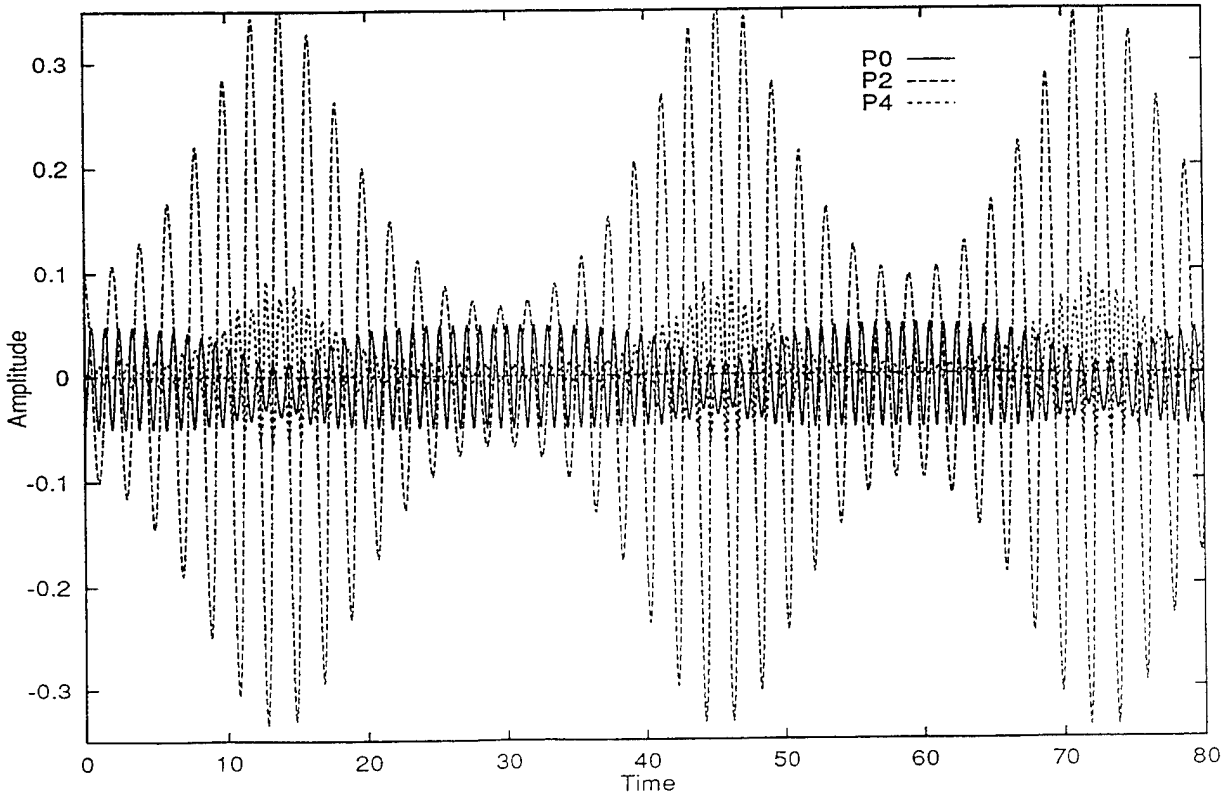


Figure 6: Amplitudes of the P_0, P_2 and P_4 modes for Case A (Table 1), with $\varepsilon\beta_0=0.4$.

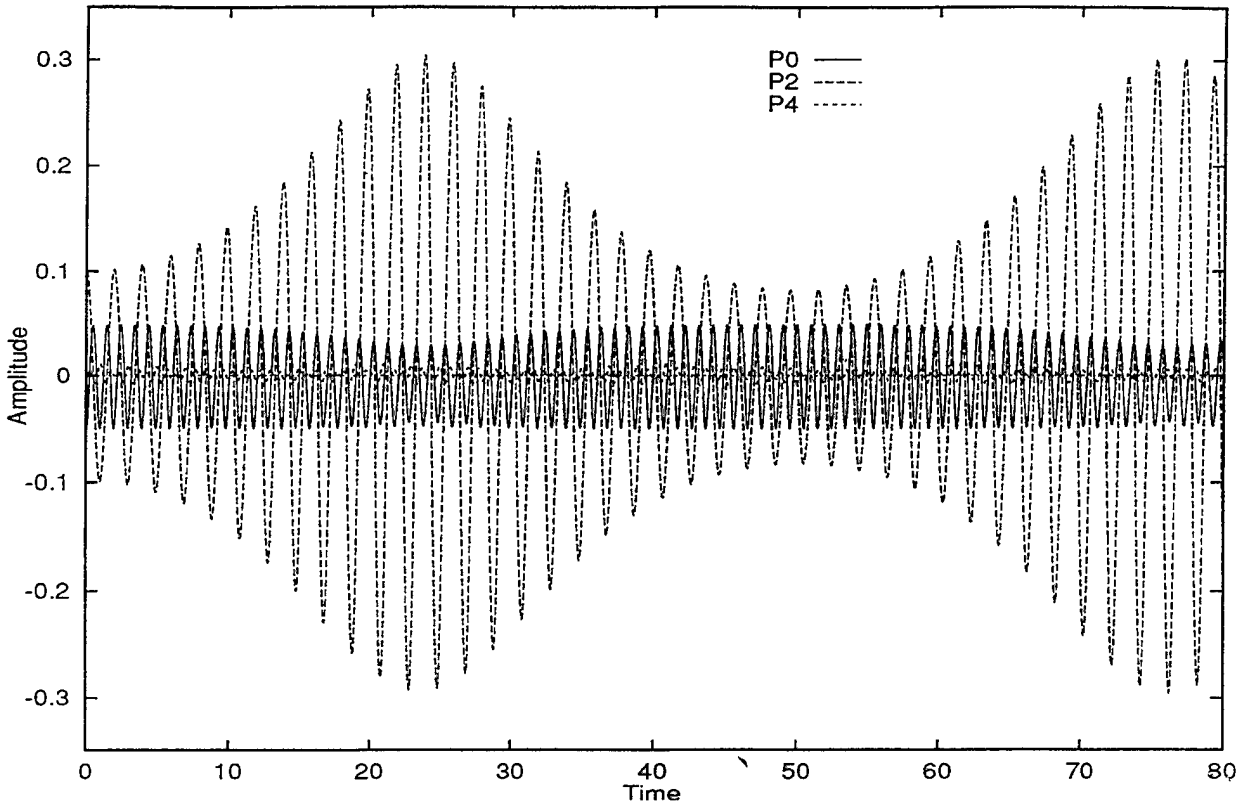


Figure 7: Amplitudes of the P_0, P_2 and P_4 modes for Case A (Table 1), with $\varepsilon\beta_0$=0.5.

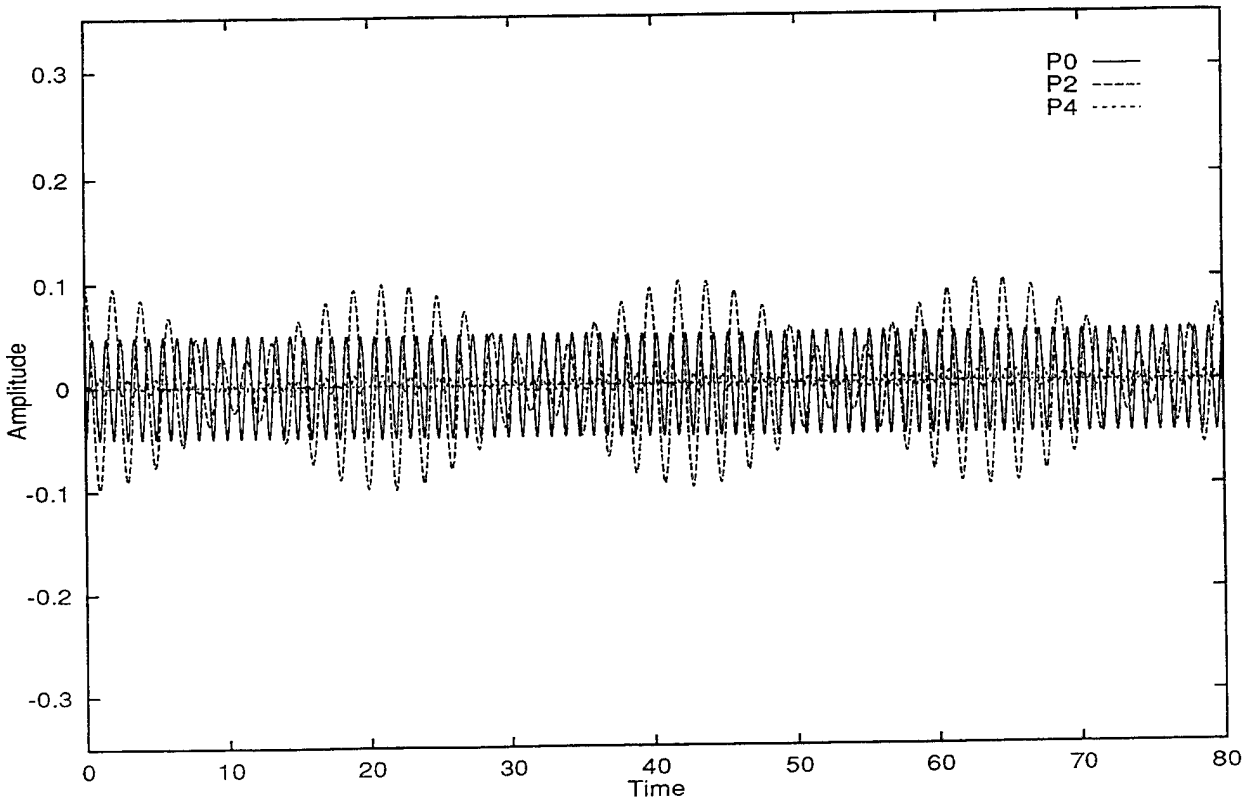


Figure 8: Amplitudes of the P_0, P_2 and P_4 modes for Case A (Table 1), with $\varepsilon\beta_0$=0.6.

cases. Our experience with many test cases, especially at small amplitudes, is that this initial decrease in P_2 is a signal of the transition in behavior corresponding to $\beta=2r$. We see, in this case, that the transition occurs for $\varepsilon\beta_0$ between 0.5 and 0.6. This is slightly smaller than the critical value of 0.63, predicted by the small deformation theory, presumably due to nonlinear effects.

Finally, two representative results are shown in Figures 9 and 10, for even larger perturbation amplitudes. As shown in row C of Table 1, the predicted critical point is $\varepsilon\beta_0=1.22$. We find that for $\varepsilon\beta_0=2.0$, there is little exchange of energy and the bubble oscillation is stable. For $\varepsilon\beta_0=1.0$, on the other hand, the exchange of energy is strong, and there is a rapid onset of higher order shape modes which leads to bubble breakup at t~19. It should be noted that the same result is obtained at t=19 by both the boundary integral and spectral cases, and we are convinced that the onset of breakup is real and not a numerical artifact.

One other set of calculations was done, holding $\varepsilon\beta_0=-1$ and $\varepsilon\alpha_{1,2}=0.01$, and then varying $\varepsilon\alpha_{1,0}$ to seek the condition for instability of the small nonspherical perturbation. The solution is stable for $\varepsilon\alpha_{1,0}=0.02$, 0.05 and 0.1, but for $\varepsilon\alpha_{1,0}=0.2$, there is a very rapid growth of P_2 (and higher modes) leading to breakup at t~8. The transition would be expected to occur at $\varepsilon\alpha_{1,0}\approx 0.08$ according to the perturbation theory.

b. Nonspherical Mean Shape

We have seen, in the summary of the analytical work, that a bubble with a nonspherical mean shape, exhibits both a 1-1 and a 1-2 resonance between oscillations of shape and volume, with the added feature that the frequency of the shape mode depends upon the degree of mean deformation. In the brief space available here, we concentrate on the 1-1 resonance for $\omega_0\approx\omega_2$. We consider only four cases, which are listed in Table 2

Case	$\varepsilon\beta_0^*$	$\varepsilon\alpha_{1,2}^{ss}$	$\varepsilon\alpha_{1,0}\big\vert_{t=0}$
D	-0.54	0.08	0.05
E	-0.54	0.04	0.05
F	0	0.16	0.05
G	0	0.08	0.05

where

$$\omega_0 - \omega_2 = \varepsilon\beta_0^*$$

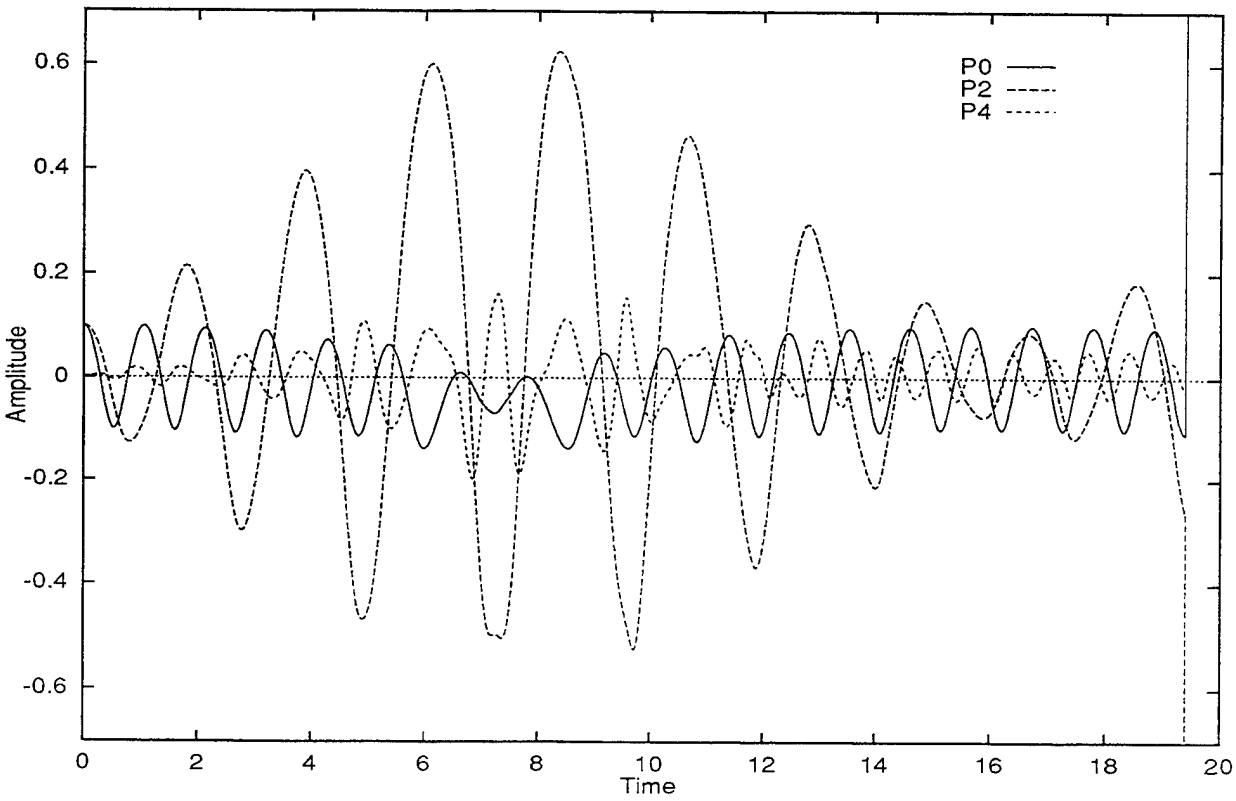


Figure 9: Amplitudes of the P_0, P_2 and P_4 modes for Case C (Table 1), with $\varepsilon\beta_0=1.0$.

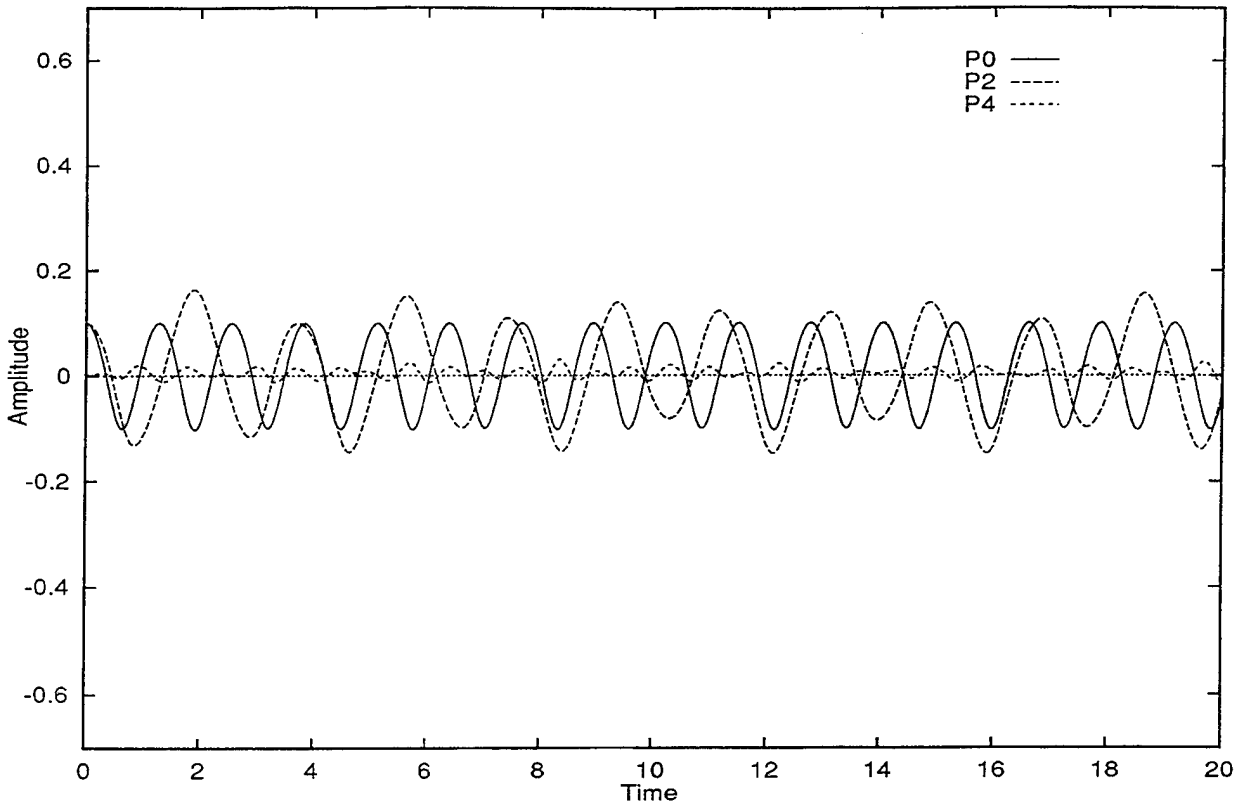


Figure 10: Amplitudes of the P_0, P_2 and P_4 modes for Case C (Table 1), with $\varepsilon\beta_0$=2.0.

In these cases the P_2 mode is started at its mean steady-state value, while the P_0 (volume) mode is initially given the same value $\varepsilon\alpha_{1,0}$=0.05 in all cases. The cases listed above were chosen to give an indication of the sensitivity to $\varepsilon\beta_0^*$ and to illustrate the effect of changes in the degree of steady-state deformation.

We begin with case D, shown in Figure 11. In this case, $\varepsilon\beta_0^*$=-0.54, which is a moderately large degree of detuning, yet the interaction between the P_0 and P_2 modes is surprisingly strong. The fact is, however, that the frequencies do not actually differ by as much as one would expect for the *specified* degree of detuning. We believe that this is due to the fact that the *frequency shift* associated with the mean deformation actually lessens the degree of detuning. Since the mean shape is prolate, the frequency of the P_2 mode is decreased relative to its value for oscillations about the spherical base state, and thus $\omega_0-\omega_2$ is closer to exact resonance than is indicated by the value of $\varepsilon\beta_0^*$.

The influence of the degree of mean deformation is illustrated by comparison of the cases D and E, shown in Figure 12, which both have $\varepsilon\beta_0^*$=-0.54, but with a mean deformation that differs by a factor of 2. It is evident that the amplitude of the P_2 oscillation, which exists only due to the coupling with P_0, is decreased with decrease in the mean deformation. According to the small deformation theory the amplitude of the P_2 oscillation should decrease in exact proportion to the amplitude of the mean deformation (i.e., by a factor of two in this case). However, careful comparison of Figures 11 and 12 shows that the amplitude for the smaller mean deformation is decreased by more than a factor of two. This is again a consequence of the frequency shift associated with mean deformation. The decrease in mean deformation means that the frequency shift is also reduced, and thus $\omega_0-\omega_2$ is actually larger for $\varepsilon\alpha_{1,2}^{ss}$ = 0.04 than for $\varepsilon\alpha_{1,2}^{ss}$ = 0.08, even though $\varepsilon\beta_0^*$ is the same in the two cases. Since we are farther from resonance in the small deformation case, this produces an additional decrease in the strength of

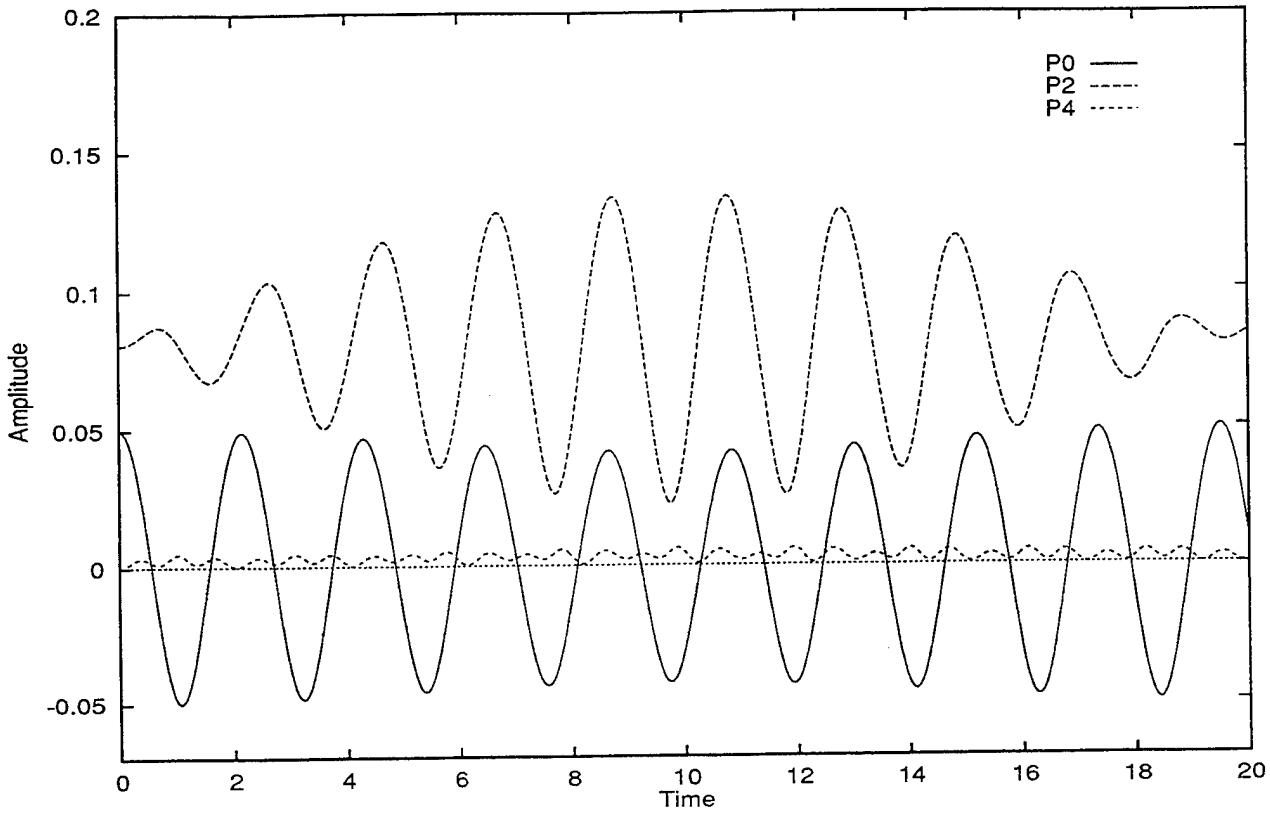


Figure 11: Amplitudes of the P_0, P_2 and P_4 modes for Case D (Table 2).

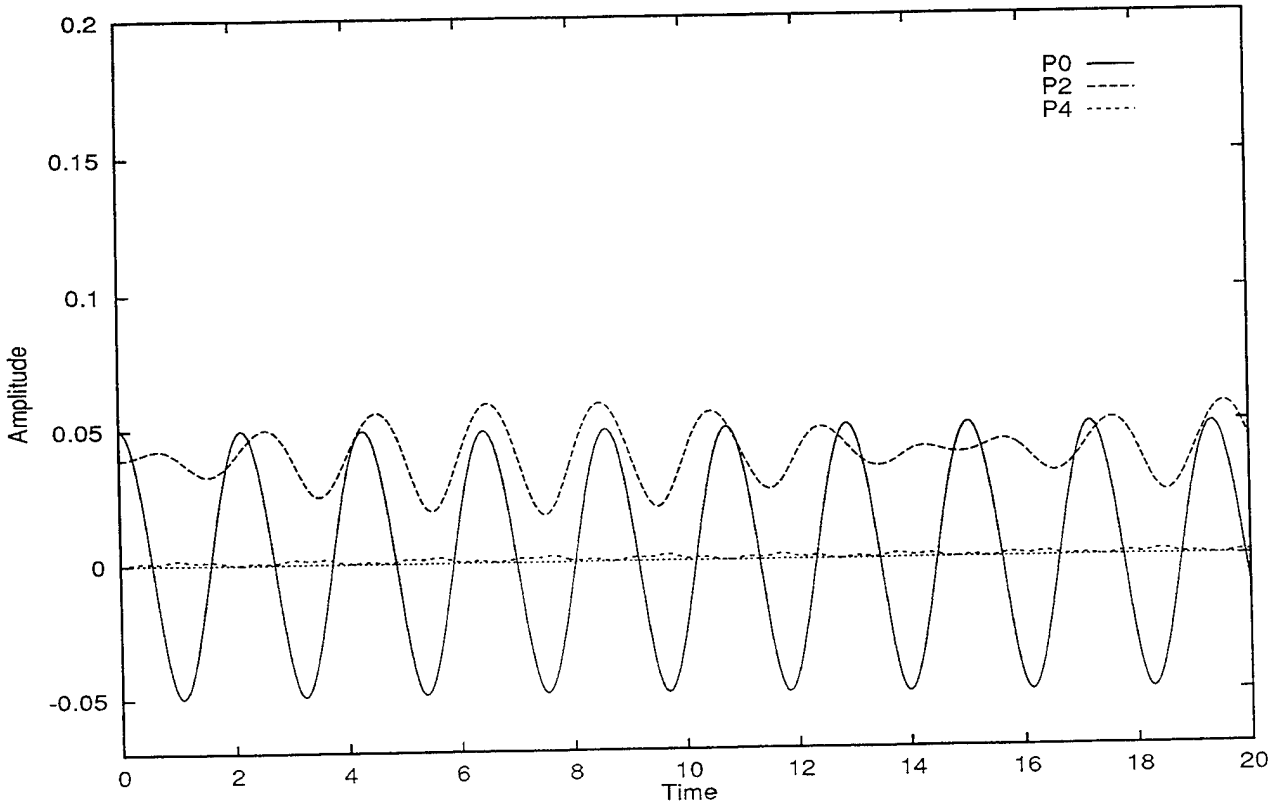


Figure 12: Amplitudes of the P_0, P_2 and P_4 modes for Case E (Table 2).

interaction, and thus also in the amplitude of the P_2 oscillation, beyond the "expected" factor of two.

Generally, without the deformation-induced frequency shift, we would expect the strength of interactions to *increase* when $\varepsilon\beta_0^*$ is increased from -0.54 to 0. However, if we compare the result for $\varepsilon\alpha_{1,2}^{ss} = 0.08$ and $\varepsilon\beta_0^* = 0$, shown in Figure 13, with the corresponding result for $\varepsilon\beta_0^* = -0.54$ in Figure 11, we see that there is actually a small *decrease* in the strength of the interaction for $\beta_0^* = 0$, as indicated by the amplitude of the P_2 mode oscillation. With the scaling used in these figures, the change from $\varepsilon\beta_0^*$ from -0.54 to 0 is reflected by an increase in the frequency of the P_0 mode. However, because of the deformation-induced frequency shift in the P_2 mode, this change in the frequency of the P_0 mode does not produce a match in frequencies as one would expect if the mean deformation were not present. Instead, the frequency of the P_2 mode which was originally slightly higher than that of P_0 (for $\varepsilon\beta_0^* = -0.54$), turns out to be slightly *lower* by almost the same amount for $\varepsilon\beta_0^* = 0$.

Finally, in case G, Figure 14, we consider a case with $\beta^* = 0$ and a steady deformation that is much larger, $\varepsilon\alpha_{1,2}^{ss} = 0.16$. Here, the effect of the deformation-induced frequency shift is even more obvious. Based upon the amplitude of the P_2 mode in case F, and the expectation from the small deformation theory that the strength of the interaction should double when we double $\varepsilon\alpha_{1,2}^{ss}$, we would expect the amplitude in case G to be about twice what actually occurs. However, in this case, the decrease in the frequency of the P2 mode is much larger, and the actual frequency mismatch $\omega_0-\omega_2$ is quite large in spite of the fact that $\beta^* = 0$.

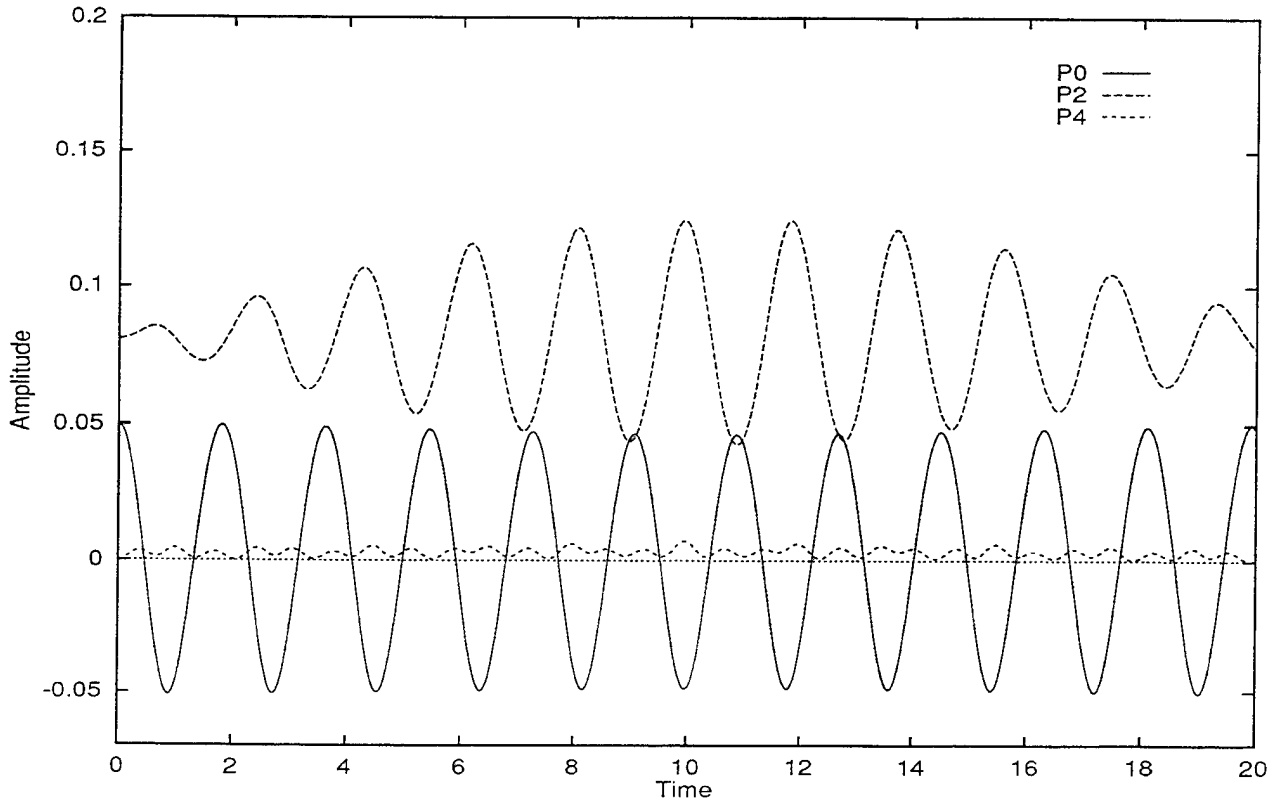


Figure 13: Amplitudes of the P_0, P_2 and P_4 modes for Case F (Table 2).

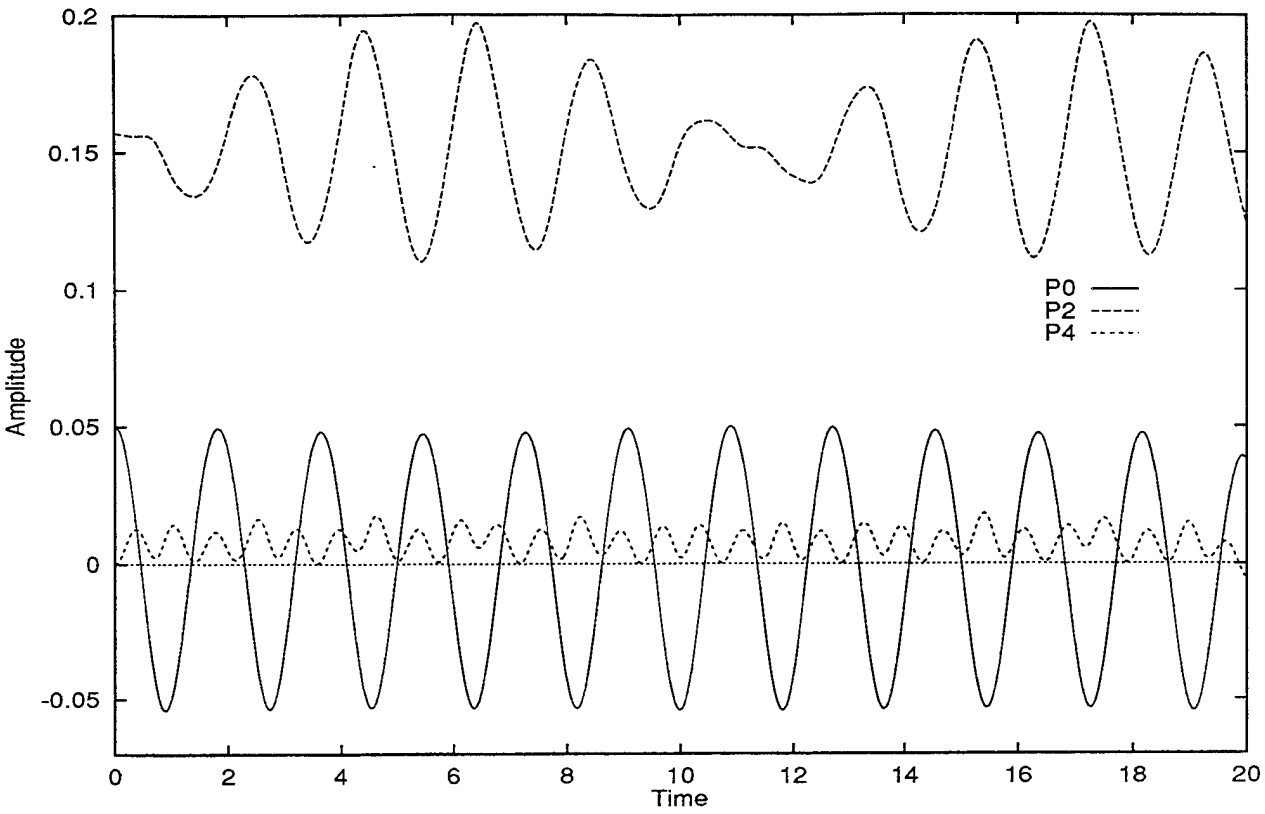


Figure 14: Amplitudes of the P_0, P_2 and P_4 modes for Case G (Table 2).

V. REFERENCES

(1) Longuet-Higgins, Michael S., "Monopole Emission of Sound by Asymmetric Bubble Oscillations. Part 1. Normal Modes" Journal of Fluid Mechanics, vol. 201, pp. 525-541, 1989.

(2) Longuet-Higgins, Michael S., "Monopole Emission of Sound by Asymmetric Bubble Oscillations. Part 2. An Initial-Value Problem" Journal of Fluid Mechanics, vol. 201, pp. 543-565, 1989.

(3) Ffowcs Williams, J. E. and Guo, Y. P., "On Resonant Nonlinear Bubble Oscillations" Journal of Fluid Mechanics, vol. 224, pp. 507-529, 1991.

(4) Longuet-Higgins, Michael S., "Resonance in Nonlinear Bubble Oscillations" Journal of Fluid Mechanics, vol. 224, pp. 531-549, 1991.

(5) Mei, C. C. and Zhow, X. C., "Parametric Resonance of a Spherical Bubble" Journal of Fluid Mechanics, vol. 229, pp. 29-50, 1991.

(6) Yang, S. M., Feng, Z. C. and Leal, L. G., "Nonlinear Effects in the Dynamics of Shape and Volume Oscilations for a Gas Bubble in an External Flow" Journal of Fluid Mechanics, vol. 247, pp. 417-454, 1993.

(7) Plesset, Milton S. and Prosperetti, Andrea, "Bubble Dynamics and Cavitation" Annual Reviews of Fluid Mechanics, vol. 9 pp. 145-85, 1977.

(8) Feng, Z. C. and Leal, L. G., "On Energy Transfer in Resonant Bubble Oscillations" Physics of Fluids A, vol. 5, pp. 826-836, 1993.

(9) McDougald, Neil. PhD Thesis (in preparation), UCSB, 1995.

(10) Feng, Z. C. and Leal, L. G., "Bifurcation and Chaos in Shape and Volume Oscillations of a Periodcally Driven Bubble with Two-to-One Internal Resonance" Journal of Fluid Mechanics, vol. 266, pp. 1-32, 1994.

(11) Joseph, D. D. "Domain perturbations: the higher order theory of infinitesimal water waver," Arch. Rat. Mech. Anal., vol. 51, pp. 295-303, 1973.

(12) Lundgren, T. S. and Mansour, N. N., "Oscillations of Drops in Zero Gravity with Weak Viscous Effects" Journal of Fluid Mechanics, vol. 194, pp. 479-510, 1988.

(13) Fletcher, C. A. J., Computational Techniques for Fluid Dynamics, volume 1. Springer-Verlag: New York, 1991.

(14) Brebbia, C. A., The Boundary Element Method for Engineers Halsted Press:New York, 1978.

(15) Kang, I. S. and Leal, L. G., "Numerical Solution of Axisymmetric, Unsteady Free-Boundary Problems at Finite Reynolds Number. I. Finite-Difference Scheme and its Application to the Deformation of a Bubble in Uniaxial Straining Flow" Physics of Fluids, vol. 30, pp. 1929-1940, 1987.

DISCUSSION

O. Phillips
The Johns Hopkins University, USA

Are there any conservation integrals for these coupled oscillations that would help in the interpretation of the time variations of the modes? Total energy, I presume. There may be at least one other. In wave interactions there are action partition integrals and I wondered if there is something analogous here, at least in the weakly non-linear cases.

AUTHORS' REPLY

The most important conserved quantity in our opinion is the total energy of the system. To understand the interaction between modes one should consider the analytical results of Feng and Leal (8) presented in figures 1 and 2 of the paper. The phase diagrams presented there show how energy is partitioned between the radial and shape modes for small amplitude oscillations for both 1-2 and 1-1 resonance conditions. In these figures the north pole corresponds to purely radial oscillations and the south pole to pure shape oscillation. As the trajectories trace closed paths around the sphere, the interchange of energy is seen as the trajectory draws closer to or further from the north and south poles. To see how the trajectories on the sphere relate to the amplitude versus time plots used to present the numerical results, consider the small amplitude result in figure 3. The conditions for this case are such that the results from the small amplitude theory can be used to predict the response of the bubble to an initial disturbance of shape and volume. The results in figure 3 correspond to a trajectory of the type shown in figure 1c which involve almost complete energy transfer between modes. At time $t > 0$, the trajectory is in the vicinity of the north pole. As time progresses the energy is transferred to oscillations of the shape mode, in this case P_2 , until around t=80 when the trajectory passes near the south pole and nearly all of the available energy resides in the shape oscillation. After t=80 the trajectory moves away from the south pole, transferring energy back to the volume mode, until approximately t=160 when the initial condition is revisited.

To understand the finite amplitude results we extend what we have learned from the small amplitude theory. One of the first effects we encounter is that more than one shape mode is involved in the near resonant cases. However, the general result that the oscillations of shape grow at the expense of radial oscillation remains valid. This indicates to us that energy transfer away from the radial mode due to resonant interaction with shape modes may present at least a partial explanation for the overprediction of the acoustic signal produced by oscillating bubbles by models which ignore variations in bubble shape.

Cloud Cavitation on an Oscillating Hydrofoil

G. Reisman, E. McKenney, C. Brennen
(California Institute of Technology, USA)

ABSTRACT

Cloud cavitation, often formed by the breakdown and collapse of a sheet or vortex cavity, is believed to be responsible for much of the noise and erosion damage that occurs under cavitating conditions. For this paper, cloud cavitation was produced through the periodic forcing of the flow by an oscillating hydrofoil. The present work examines the acoustic signal generated by the collapse of cloud cavitation, and compares the results to those obtained by studies of single travelling bubble cavitation. In addition, preliminary studies involving the use of air injection on the suction surface of the hydrofoil explore its mitigating effects on the cavitation noise.

NOMENCLATURE

c = Chord length of foil (m)
I = Acoustic impulse $(Pa \cdot s)$
I^* = Dimensionless acoustic impulse
k = Reduced frequency = $\omega c/2U$
p = Test section absolute pressure (Pa)
$\overline{p}$ = Time averaged pressure (Pa)
p_a = Radiated acoustic pressure (Pa)
p_A = Acoustic pressure intensity (Pa)
p_v = Vapor pressure of water (Pa)
q = Normalized air flow rate = Q/Ucs
Q = Volume flow rate of air at test section pressure and temperature (m^3/sec)
$\mathcal{R}$ = Distance between noise source and hydrophone (m)
s = Span of foil (m)
t = Time (s)
T = Period of foil oscillation (s)
U = Tunnel test section velocity (m/s)
V = Volume of cavitation bubble or cloud (m^3)
α = Instantaneous angle of attack of foil (deg)
$\overline{\alpha}$ = Mean angle of attack of foil (deg)
ρ = Fluid density (kg/m^3)
σ = Cavitation number = $(p - p_v)/\frac{1}{2}\rho U^2$
ω = Foil oscillation frequency (rad/s)

INTRODUCTION

In many flows of practical interest one observes the periodic formation and collapse of a "cloud" of cavitation bubbles. The cycle may occur naturally as a result of the shedding of bubble-filled vortices, or it may be the response to a periodic disturbance imposed on the flow. Common examples of imposed fluctuations are the interaction between rotor and stator blades in a pump or turbine and the interaction between a ship's propeller and the non-uniform wake created by the hull. In many of these cases the coherent collapse of the cloud of bubbles can cause more intense noise and more potential for damage than in a similar non-fluctuating flow. A number of investigators (Bark and van Berlekom [1], Shen and Peterson [2], Bark [3], Franc and Michel [4] and Kubota *et al.* [5, 6]) have studied the complicated flow patterns involved in the production and collapse of a cavitating cloud on a hydrofoil. The present paper represents a continuation of these studies.

Previous studies have shown that, as an attached cavity collapses and is shed into the wake, the breakup of the cavity often results in the occurrence of cloud cavitation. The structure of such clouds appears to contain strong vortices, perhaps formed by the shear layer at the surface of the collapsing cavity (see Kubota *et al.* [5], Maeda *et al.* [7]). These clouds then collapse with some violence, often causing severe erosion on the surface and generating significant amounts of noise (Bark and van Berlekom [1], Kato [8], Ye *et al.* [9]). Figure 1 shows two typical examples of cloud cavitation on the oscillating hydrofoil used in the current study.

One of the present goals was to relate the characteristics of the acoustic signature of a cavitating cloud to the dynamics of the associated collapse process. The details of the cavity growth and collapse and cloud formation are discussed by previous authors, including McKenney and Bren-

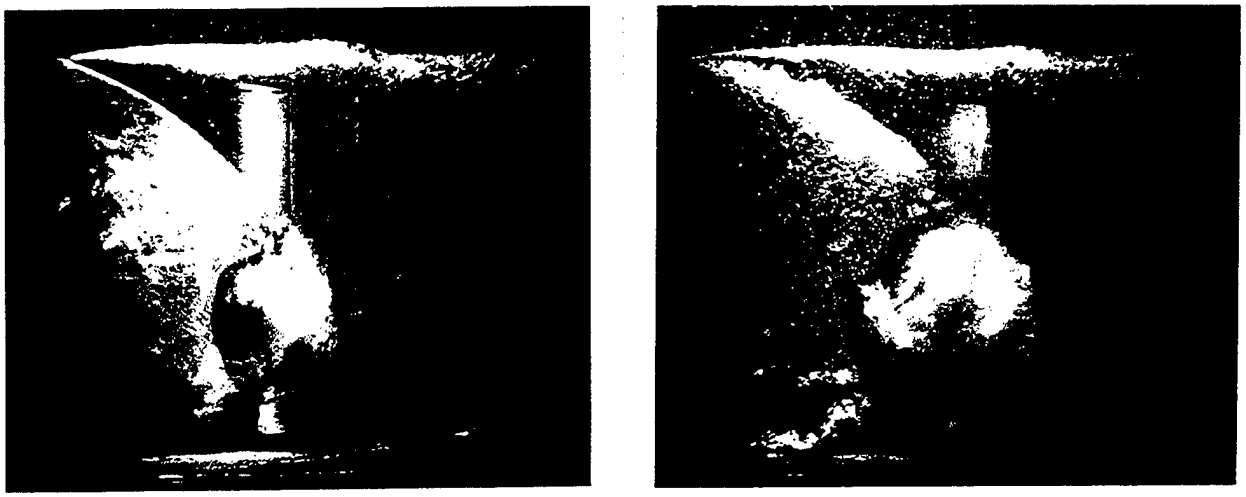


Figure 1: Cloud cavitation on an oscillating hydrofoil. The photograph on the left is without air injection, $\sigma = 1.2$, $k = 0.9$, $\alpha = 10.3°$ (α decreasing). The photograph on the right has a normalized air flow rate of $q = 2.2 \times 10^{-4}$, with $\sigma = 1.2$, $k = 0.8$, $\alpha = 7.4°$ (α decreasing).

nen [10]. Briefly, the cycle begins with the formation of travelling bubble cavitation near the leading edge of the foil as illustrated in figure 2. As the angle of attack increases, the bubbles grow and coalesce to form a single sheet cavity attached to the leading edge, as seen in figure 13. The downstream edge of this cavity is unstable and soon breaks down into a cloud of froth. In many cases a "sub-cloud" of the froth is ejected and travels downstream separately, with the main sheet cavity collapsing behind it. This sub-cloud is sometimes very coherent and may persist well after the remains of the sheet cavity have dispersed. The sub-cloud is believed to be the major source of the cavitation noise and its accompanying erosion.

As described by McKenney and Brennen [10], once the sub-cloud has travelled past the trailing edge of the foil there is a brief period in which there is no cavitation before the cycle begins again. A notable difference between those earlier experiments and the present work, however, is the hydrofoil mean angle of attack. In the previous work, the foil angle varied between 0° and 10°. Here, the angle of attack varies from 4° to 14°, so that even as the cloud from one cavitation cycle is dispersing a new sheet cavity has already begun to form at the leading edge. The photograph in figure 2 illustrates this overlap. Other than this, however, it appears that the sequence of events in the cavitation cycle



Figure 2: Between cavitation cycles: the cloud at the right is collapsing and beginning to disperse, while travelling bubble cavitation can already be seen near the leading edge just prior to forming a new sheet cavity. $\sigma = 1.0$, $k = 0.8$, $TAC = 4 - 5ppm$, $\alpha = 7.9°$ (α increasing).

is very similar in the current experiments to those described previously.

The present paper will focus on the noise generated by the collapse of cavitating clouds and its dependence on various parameters. These results

will then be related to the existing knowledge of the generation of noise by a single collapsing cavitation bubble. Our traditional understanding of single bubble noise stems from the work of Fitzpatrick and Strasberg [11] and others (see, for example, Blake [12]) and is based on the Rayleigh-Plesset analysis of the dynamics of a spherical bubble. The radiated acoustic pressure, p_a, at a large distance, $\mathcal{R}$, from the center of a bubble of volume $V(t)$ is given by Blake [12]

$$p_a = \frac{\rho}{4\pi\mathcal{R}} \frac{d^2V}{dt^2}$$

Clearly a large positive noise pulse will be generated at the bubble collapse, due to the very large and positive values of d^2V/dt^2 that occur when the bubble is close to its minimum size. A good measure of the magnitude of the collapse pulse is the *acoustic impulse*, I, defined as the area under the pulse or

$$I = \int_{t_1}^{t_2} p_a dt$$

where t_1 and t_2 are chosen in a systematic manner to identify the beginning and end of the pulse. It is also useful in the present context to define a dimensionless impulse, I^*, as

$$I^* = \frac{16\pi I\mathcal{R}}{\rho U L^2}$$

where $\mathcal{R}$ is now the distance from the cavitation event to the point of noise measurement and L is the typical dimension of the flow, taken in the present paper to be the chord of the foil.

Recently, both Ceccio and Brennen [13] and Kuhn de Chizelle *et al.* [14] were able to identify from within hydrophone data the acoustic signatures produced by the collapse of single travelling cavitation bubbles. They could thus measure the actual acoustic impulses of these events and compare them with the predictions of the Rayleigh-Plesset-Fitzpatrick-Strasberg theory for spherical bubbles. In general the measured values are about an order of magnitude smaller than the spherical bubble theory (see figure 8). The experiments also involved studies of the bubble shape distortions caused by the flow. Consequently it was possible to demonstrate that the reduction in the actual noise was correlated with the shape distortion. Crudely, one can visualize that a spherical collapse will be the most efficient noise-producing process since the collapse is focussed at a single point; thus any distortion in the sphericity of the bubble is likely to defocus the collapse and reduce the noise. In the present paper we shall compare the impulses resulting from cloud collapses with those of the above-mentioned measurements of single bubble impulses in an attempt to learn more about the dynamics and acoustics of clouds of bubbles.

A similar study was performed on acoustic signals generated by cloud cavitation (McKenney and Brennen [10]), where it was qualitatively shown that the major acoustic burst in each cycle seems to correspond to the collapse of the cloud cavitation. The long-term goal in all these acoustic studies is not only to gain an understanding of the flow mechanisms that produce the noise, but also to develop methods to reduce that noise and the erosive damage that generally accompanies it. It has been shown for the case of single bubble cavitation (Brennen [15]) that the presence of a contaminant gas reduces the rate of collapse and increases the minimum bubble volume. Thus one mitigation strategy is the deliberate injection of air to help "cushion" the collapse, thereby reducing the noise and damage potential. Several previous investigations have explored this strategy by ejecting air from ventilation holes in the suction surface of a hydrofoil. Ukon [16] used air injection from the leading edge of a stationary foil and found a consistent reduction in the noise in the frequency range 0.6 to $100kHz$. The maximum noise reduction achieved was of the order of $20dB$. There is some suggestion in his data that air flow rates above a certain optimal level no longer decrease the noise. Arndt *et al.* [17] performed similar air injection tests with a stationary foil and found some reduction in the mean square hydrophone signal in the 10 to $30Hz$ band. The reduction was a factor of approximately 3 to 5 for small air flow rates, but there was little additional effect at higher flow rates (see figure 11). In the present experiments we also explore the noise reduction due to air flow rate, normalized as $q = Q/Ucs$.

EXPERIMENTAL APPARATUS

The Caltech Low Turbulence Water Tunnel is a closed-circuit facility, with a $30.5cm \times 30.5cm \times 2.5m$ test section. It is capable of freestream velocities up to $10m/s$ and can support pressures down to $20kPa$. A complete description of this facility may be found in Gates [18]. The total air content (TAC) of the water in the tunnel was measured using a Van Slyke apparatus.

An NACA 64A309 hydrofoil was reflection-plane mounted in the test section, as shown in figure 3 and described in Hart *et al.* [19]. The hydrofoil

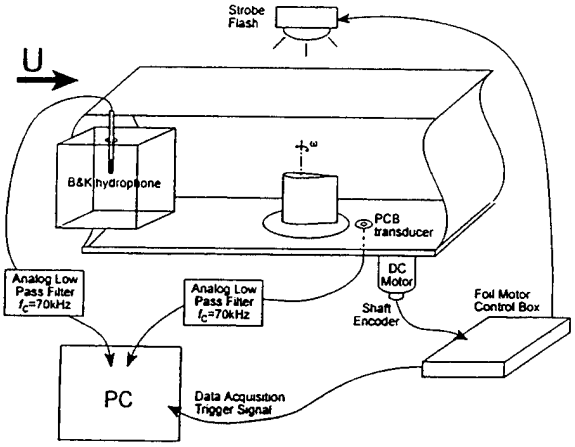


Figure 3: Oscillating hydrofoil in the water tunnel test section.

has a rectangular planform with a chord of $15.2cm$ and a span of $17.5cm$; it is made of stainless steel and polished to a smooth finish. It is connected to a 750 watt DC motor by a four-bar linkage such that it oscillates nearly sinusoidally in pitch about a point near the center of pressure, $0.38c$ from the leading edge. The mean angle of attack and the oscillation amplitude can be adjusted, and the oscillation frequency may be continuously varied from 0 to 50Hz. An optical shaft encoder mounted to the DC motor provides a digital signal (1024 pulses per revolution) which was used to synchronize acoustic measurements with the phase of the foil.

The sound generated by the cavitation on the hydrofoil was recorded using two transducers. A PCB model HS113A21 piezo-electric pressure transducer (bandwidth $100kHz$) was mounted flush with the floor of the test section, approximately $5cm$ downstream of the trailing edge of the foil. In addition, a B&K model 8103 hydrophone (bandwidth $100kHz$) was installed in a Lucite box filled with water and affixed tightly to the outside of the test section. As graphically demonstrated by Bark and van Berlekom [1], mounting a hydrophone externally in this way significantly degrades the signal. Analysis of the current data was used to compare results from these two transducers, with the following specific comments:

- The lucite box mounting approach is a simple way to obtain preliminary qualitative information. This method was used successfully by McKenney and Brennen [10] to correlate the cloud cavitation acoustics with high-speed motion pictures of the collapse.

- Acoustic pressure intensities calculated using the output from the hydrophone in the box were significantly smaller in magnitude than those derived from the flush-mounted transducer for the same event, generally by a factor of 2 or 3. This indicates that the presence of the walls of the test section and the lucite box has a severely attenuating effect on the measured signal.

- Although the PCB transducer lacks the omnidirectional capability of the B&K hydrophone, the transducer was mounted directly beneath the cloud collapse region and thus the radiated acoustic pressure impinges with normal incidence.

- The PCB transducer produced results with greater scatter, but better signal to noise ratio. The signal for the external hydrophone was significantly adulterated by resonances within the box.

These conclusions are very similar to those reached by Bark and van Berlekom [1], and led to the decision to focus on the results obtained with the PCB (flush-mounted) transducer.

The output signals from both transducers were low pass filtered prior to being recorded by a digital data acquisition system. Since the sampling rate was approximately $143kHz$, the filters were set to a cutoff frequency of $70kHz$, just below the Nyquist frequency. The data acquisition system also recorded timing information from the oscillation of the foil.

Still photographs were taken of various stages of the cavitation process by using the foil timing to trigger strobe lighting at the desired phase of the foil oscillation cycle.

For the air injection studies, four holes were drilled in the suction surface of the foil, located at the axis of rotation and equally spaced along the span. The air flow rate was measured to within a 12% error by using an orifice flow meter. For the current studies, the injection flow rate was kept constant at levels which preliminary tests showed would produce a finite effect.

EXPERIMENTAL PROCEDURES

Experiments were conducted in the following parameter ranges:

Mean angle of attack, $\overline{\alpha}$	9°
Oscillation amplitude, $\Delta\alpha$	±5°
Reduced frequency, k	0.55 to 0.93
Cavitation number, σ	0.9 to 1.5
Air content (ppm)	4 to 10
Normalized air injection, q	0 to 10^{-3}

Data for about 40 cycles were obtained at each condition and in selected cases still photographs were taken. Figure 4 shows a typical signal before high-pass filtering, along with a curve indicating the foil instantaneous angle of attack during one oscillation cycle. The origin of the time axis corresponds to $\alpha = 7.9°$ where α is increasing. The photograph in figure 2 was taken at the origin of the time axis in figure 4. Two clear pulses at about $\alpha = 10°$ represent the sound produced by the cloud collapse in this particular cycle. The multiple peaks seen in this signal are characteristic of many of the signals obtained in these experiments. The presence of multiple peaks may suggest the formation of more than one cloud during the collapse of the main cavity, or it may be the result of the rebound and recollapse of a single cloud.

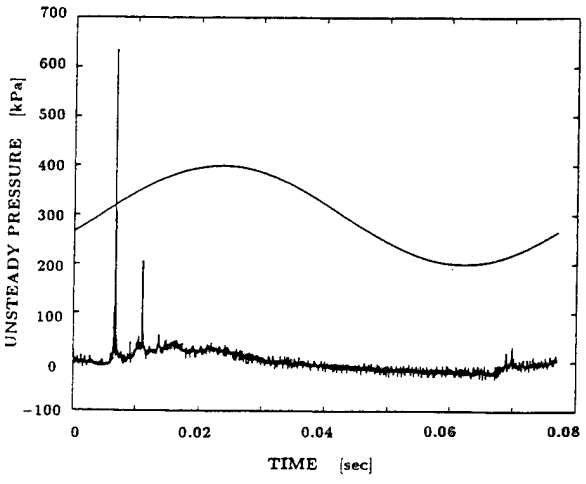


Figure 4: Typical output from the piezo-electric transducer. The signal from one oscillation cycle is shown together with a sinusoid qualitatively representing the instantaneous angle of attack of the foil. Data for $\sigma = 1.0$, $k = 0.8$, $TAC = 4 - 5ppm$.

The total air content was also measured before and after each run. For most of the experiments, the TAC was in the range of $8 - 10ppm$. Then the water was deaerated so that the TAC was in the range $4 - 5ppm$, and measurements were taken again at a few of the previous conditions.

We now turn to a discussion of the measurements of the noise generated by these flows. In the previous experiments, the sound level was evaluated by calculating the *acoustic pressure intensity*, which was measured over a whole oscillation cycle and nondimensionalized as follows:

$$p_A^* = \frac{p_A \mathcal{R}}{\frac{1}{2}U^2 c} \quad \text{where} \quad p_A = \left[\frac{1}{T}\int_0^T (p(t) - \overline{p})^2 dt\right]^{\frac{1}{2}}$$

This is related to the acoustic intensity defined in Coates [20] as $p_A^2/\rho c^*$, where c^* is the speed of sound in the fluid.

For the current experiments, in part to facilitate comparing our results with those of researchers studying single travelling bubble acoustics, we calculated the acoustic impulse by integrating only over the distinct peaks in the signal, thus neglecting low-frequency variations in pressure as well as high-frequency but low-amplitude noise. The digitized signal from a single foil oscillation cycle was first high-pass filtered in software with a cutoff frequency of $50Hz$ to remove the low frequency pressure changes due to the foil motion. Choosing the limits of integration for the impulse calculations proved to be a non-trivial procedure; results may depend heavily on irrelevant artifacts in the data if the limits are poorly chosen. The method used by Kumar [21] and Ceccio [22] was selected, both for its robustness and its similarity of application to the current data. The beginning of a peak was identified by the positive-going signal crossing a threshold value of $20kPa$. The end of the peak was defined as the moment when the signal crossed that same threshold value with a negative slope.

In addition, the spectra of the acoustic signals were compared under the different flow conditions. Average spectra from approximately 40 individual (unfiltered) cycles were acquired as follows: first the spectrum from each raw signal was normalized by the area under that spectrum following the method described in Kumar [21], then the normalized magnitudes at each frequency were averaged over all the cycles.

ACOUSTIC IMPULSE RESULTS

The experimental results depicted in figures 5, 6, and 7 illustrate the variation of the dimensionless impulse, I^*, with cavitation number, total air content, and reduced frequency. Each data point in these figures represents the average of approximately 40 cycles and the associated impulses. Within the parameter space, significant cycle-to-cycle variation was observed in both the physical attributes of the cavitation and the resulting impulse. A measure of this scatter is depicted in figure 5 and 6 by vertical bars which represent one standard deviation above and below the average impulse value. As demonstrated in these two figures, the standard deviation ranges from approximately 60% of the mean for dimensionless impulses greater than 0.4 to 120% of the mean for I^* less than 0.4. However it is important to observe that the repeatability of the mean value was approximately ± 0.1.

Figures 5 and 7 show the change in impulse with reduced frequency, k, for different cavitation numbers. As expected, the cavitation number, σ, and reduced frequency, k, have a significant effect on the measured impulse, but no simple relationship between either of these two parameters and the impulse is evident. The highest cavitation number, $\sigma = 1.5$, resulted in the lowest impulse for all but one value of k. With the same exception, the sound level produced at $\sigma = 1.2$ exceeded the level measured at $\sigma = 0.9$. This reduction in sound level was also readily detectable in the laboratory as the cavitation number was lowered from 1.2 to 0.9. Thus, in general, the noise appears to peak at some intermediate σ.

This non-monotonic effect with cavitation number differs from that found by McKenney and Brennen [10], perhaps because the present mean angle of attack, $\overline{\alpha}$, is larger. This seems to alter the cavitation number at which the noise peaks. In the present experiments, it was observed visually during the experiments that for $\sigma = 0.9$ the sheet cavity not only covered nearly the entire surface of the hydrofoil, but also extended past the trailing edge for a large part of the oscillation cycle. At the lower $\overline{\alpha}$ in the earlier work, however, the sheet cavity seldom covered more than about 60% of the foil surface.

Although the total air content (TAC) varied from $4ppm$ to $10ppm$ during the experiments, it appeared to have little effect on the noise, as shown in figure 6.

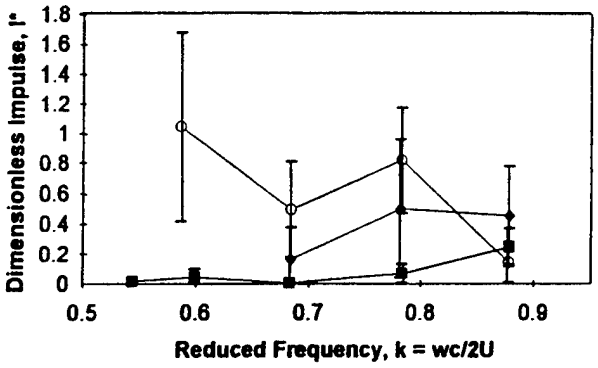


Figure 5: Effect of cavitation number, σ, on the dimensionless impulse, I^*. Data shown for $\sigma = 0.9$ (◆), $\sigma = 1.2$ (○), $\sigma = 1.5$ (■) with $TAC = 7 - 10ppm$.

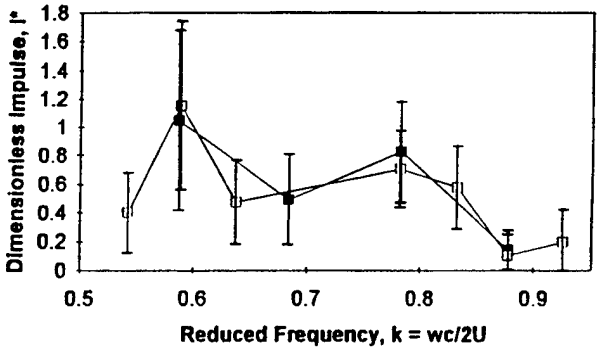


Figure 6: Effect of total air content (TAC) on dimensionless impulse, I^*. Data shown for $TAC = 4-5ppm$(□), $TAC = 8-10ppm$(■) with $\sigma = 1.2$.

Figure 7 presents a summary of the results for the averaged acoustic impulses and shows the variations with reduced frequency, cavitation number, and TAC. The results for the air injection experiments are also included in this figure and will be discussed in greater detail later.

It is interesting to compare the results for the acoustic impulse (depicted in figure 7) with previous results for single travelling bubbles. Figure 8 illustrates the approximate relations between the cloud cavitation impulses, the impulses observed by Kuhn de Chizelle *et al.* [14] for single travelling bubbles, and the impulse magnitudes predicted by the Rayleigh-Plesset equation for a spherical bubble. From this figure, it is evident that the noise generated by cloud cavitation is several orders of

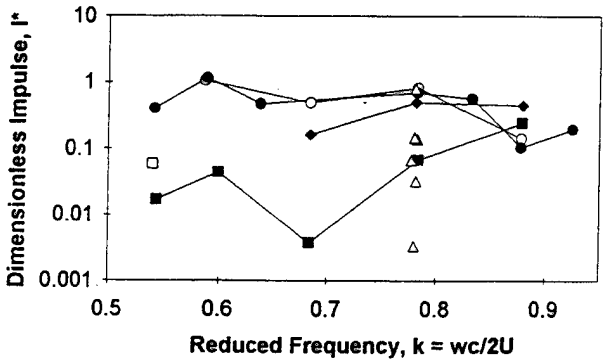


Figure 7: Summary of dimensionless impulse data for cloud cavitation. Data without air injection: $\sigma = 0.9$, $TAC = 7 - 8ppm$ (◆); $\sigma = 1.2$, $TAC = 4 - 5ppm$ (●); $\sigma = 1.2$, $TAC = 8 - 10ppm$ (○); $\sigma = 1.5$, $TAC = 4 - 5ppm$ (□); $\sigma = 1.5$, $TAC = 9 - 10ppm$ (■);. Data with air injection: $\sigma = 1.2$, $TAC = 4 - 10ppm$ (△).

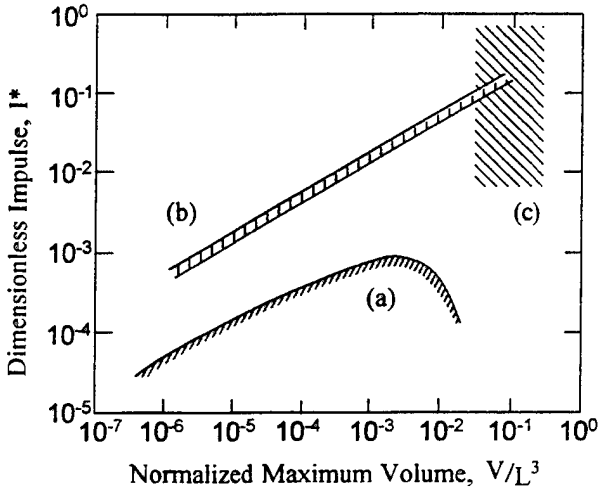


Figure 8: Acoustic impulse magnitude ranges as a function of the maximum bubble or cloud volume, for (a) single travelling bubble cavitation (Kuhn de Chizelle *et al.* [14]), (b) the Rayleigh-Plesset spherical bubble model for the conditions of the aforementioned experiments, and (c) cloud cavitation results from the present experiments.

magnitude larger than the sound level resulting from single travelling bubble cavitation. The impulses generated by some clouds are even greater than the theoretical prediction for a single spherical bubble of the same maximum volume. The figure suggests that clouds can be even more effective noise sources than single bubbles of the same volume. A possible explanation for this is the formation of an inwardly propagating shock wave within the collapsing cloud as originally suggested by Mørch [23] and recently demonstrated theoretically by Wang and Brennen [24].

SPECTRAL ANALYSIS

Further insight into cloud cavitation noise generation can be obtained by Fourier analysis of the radiated acoustic pressure. Figures 9 and 10 are two typical examples of cloud cavitation spectra. Each line in the figure corresponds to a single set of parameters and represents an average of approximately 40 Fourier transforms normalized using the method described above. The spectra obtained from the current experiments exhibit a characteristic behavior proportional to f^{-n} over the frequency range of $80 - 6000Hz$, where $0.7 > n > 0.8$. This compares reasonably well with the f^{-1} behavior of previous experimental results for single bubbles and for steady cavitating flows [15].

Figure 9 presents the averaged spectra for each of the three cavitation numbers. It is clear that there is a significant change in the spectrum with cavitation number particularly in the range from $100Hz$ to $5kHz$. Moreover, the changes in magnitude in this range correspond with previously described changes in the acoustic impulse with σ.

The large peak in the spectra at $9kHz$ appears for every data set in the entire parameter space. When the impulse response of the test section was measured, it indicated peaks at approximately 4, 32, and $64kHz$, but the response was flat in the frequency range near $9kHz$. Since the location and relative magnitude of the $9kHz$ peak shows no appreciable variation with the various flow parameters, cavitation noise is an unlikely explanation.

Another interesting feature of figure 9 is the presence of peaks at approximately $3kHz$. Unlike those at $9kHz$, these peaks vary somewhat with cavitation number. It is possible that these represent the frequency of the large radiated pressure pulses associated with cloud cavitation, such as those seen in figure 4. Figure 10 shows how the frequency content of the sound changes with variation in the reduced frequency. The spectra are similar, except for the three peaks between 2 and $4kHz$, whose frequency increases with decreasing reduced frequency. Average spectra were also examined for different air contents, but showed little change with

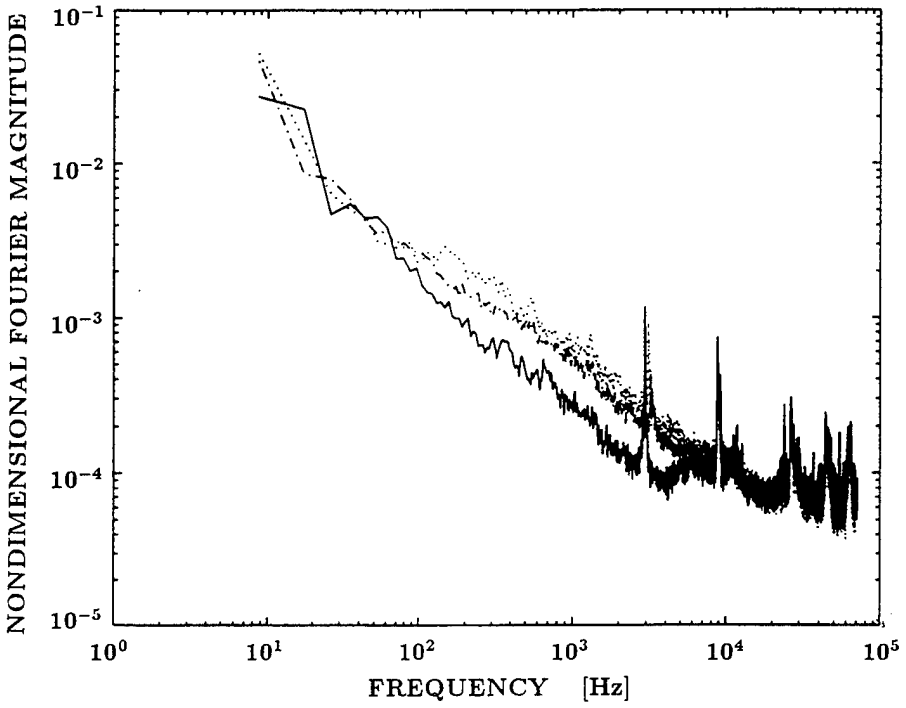


Figure 9: Comparison of the normalized spectra of unsteady pressures at three different cavitation numbers: $\sigma = 1.5$ (solid line), $\sigma = 1.2$ (dotted line), and $\sigma = 0.9$ (dash-dot line). Data for $k = 0.7$, $TAC = 7 - 10ppm$.

this parameter.

AIR INJECTION

Air injection resulted in a dramatic reduction in the sound level. At a sufficiently high air flow rate, the periodic "bangs" associated with cloud cavitation collapse could no longer be detected either by ear or by transducer. Figure 11 illustrates this noise reduction as a function of normalized air injection flow rate. Data from the current experiments are plotted along with results from work by Arndt, *et al.* [17] and Ukon [16]. The ordinates on this figure are the ratio of the sound pressure level at a given air flow rate to the sound pressure level without air injection. In this figure we have used the average impulses from the present experiments and the root mean squared acoustic pressure for the data from Arndt *et al.* and Ukon. We note that the present experimental data showed a very strong correlation between the impulse and the RMS acoustic pressure.

The experiments performed by Arndt *et al.* and Ukon utilized stationary hydrofoils. Although cavitation clouds can separate periodically from sheet cavitation on a stationary foil, the collapse usually lacks the intensity of cloud cavitation caused by an imposed periodicity. The resulting low ratio of cavitation noise to background noise could explain the relatively small noise reduction due to air flow which is apparent in the data of Arndt *et al.*.

In contrast, our observations indicate that the impulse could be reduced by a factor greater than 200 at an air flow rate, q, of approximately 0.001. At this flow rate, the periodic cloud cavitation noise was completely suppressed, and a further increase in the air flow rate had no discernible effect.

The spectral content of the cavitation noise also changed with air injection. Figure 12 shows the average normalized Fourier spectra for three different air flow rates. As the air injection flow rate is increased, the Fourier magnitudes in the frequency range between 100 Hz and 8 kHz decrease relative to the high and low frequency content.

Another effect of air injection was an increase in the average size of the sheet cavity. This phenomenon was previously noted by Ukon [16]. Al-

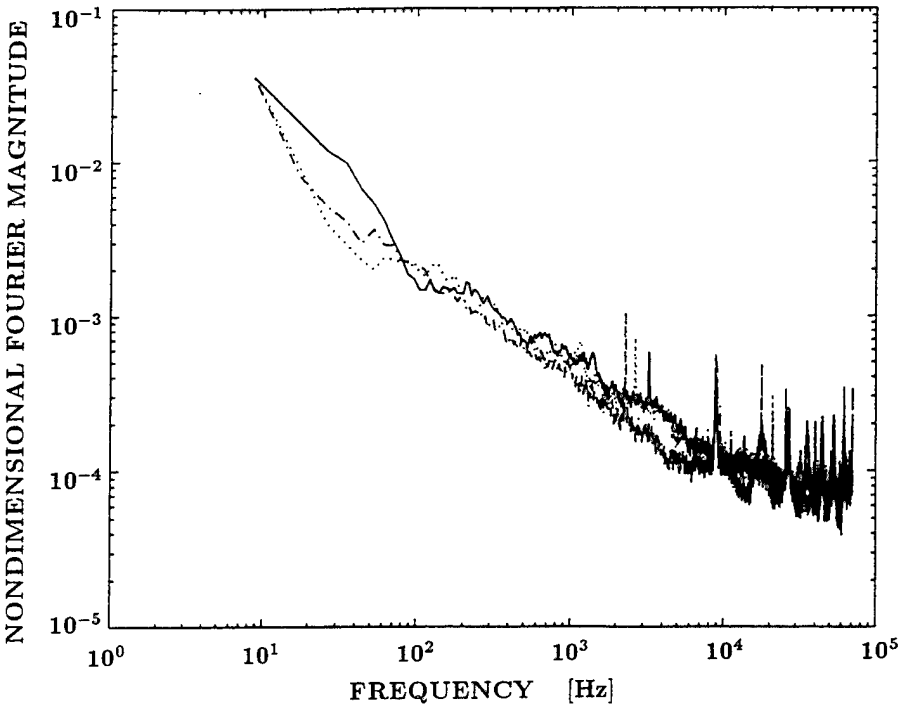


Figure 10: Comparison of the spectra of unsteady pressures at three different reduced frequencies: $k = 0.64$ (solid line), $k = 0.8$ (dotted line), and $k = 0.93$ (dash-dot line). Data for $\sigma = 1.2$, $TAC = 4 - 5ppm$.

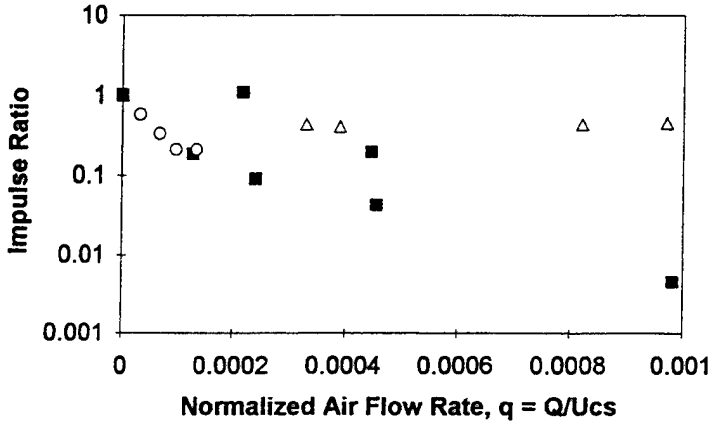


Figure 11: Effect of air flow rate on the radiated noise, normalized by the noise without air injection. Data for the current experiments at $\sigma = 1.2$, $k = 0.8$, $TAC = 5 - 10ppm$ are shown (■), and compared with data from Ukon [16] at $\sigma = 0.74$, $\alpha = 6.4°$, $U = 8m/s$ (○) and Arndt *et al.* [17] at $\sigma = 0.9$, $\alpha = 8°$, $U = 15$ and $7.5m/s$ (△).

though the two photographs in figure 13 were taken at identical cavitation numbers, reduced frequencies, and angles of attack, the cavity area is much larger in the air injection case. This effect is simply due to an increase in the mean pressure in the cavity and therefore a decrease in the effective cavitation number. Examination of the still photographs also shows that the added air also increases the size of the cloud generated when the sheet cavity collapses, as shown in figure 1. This rules out the possibility that the noise reduction is due to suppression of the cloud cavitation. Instead, it seems prob-

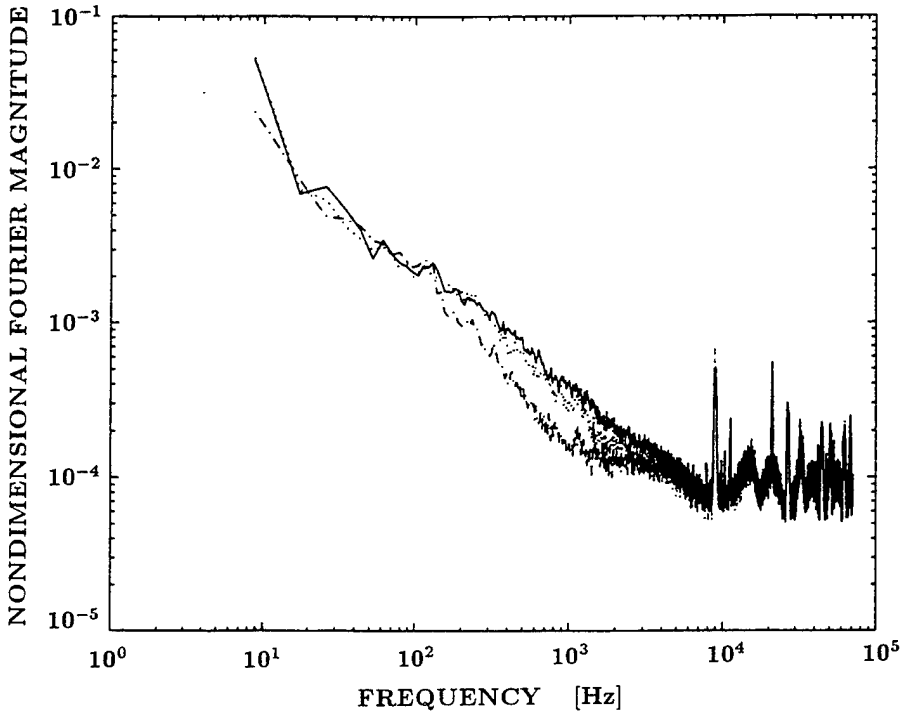


Figure 12: Effect of air injection on the spectral content of the noise for three normalized air flow rates: $q = 1.3 \times 10^{-4}$ (solid line), $q = 2.4 \times 10^{-4}$ (dotted line), $q = 9.8 \times 10^{-4}$ (dot-dash line). Data for $k = 0.8$, $TAC = 7 - 10ppm$.

able that the bubbles in the cloud contain more air, which cushions the collapse and reduces the overall sound produced.

CONCLUSIONS

This paper has examined the acoustic impulses produced by the collapse of clouds of cavitation bubbles. The clouds were generated by pitch oscillations of a finite aspect ratio hydrofoil in a water tunnel. The recorded noise was analyzed in several ways. First, large positive noise pulses were clearly present in the signal and corresponded to the collapse of clouds of bubbles shed by the foil. The acoustic impulses associated with these pulses were obtained by integration, and the variations with cavitation number, air content, and foil oscillation frequency were examined. The impulses appear to peak at the intermediate cavitation number studied and to be relatively independent of the air content. The variations with foil oscillation frequency are significant but not readily understood. We should also note that the impulses are consistent with, though somewhat larger than, what had been expected from the extrapolation of data on single bubbles. This suggests the existence of an additional mechanism in the cloud collapse that augments the noise, such as an inwardly propagating shock.

Spectra of the noise, averaged over more than 40 cycles, were also examined and exhibited a typical f^{-1} variation with frequency. Significant variations in the shape with cavitation number could be discerned, however air content and foil oscillation frequency produced no such discernible variation.

Air injection from the suction surface of the foil was investigated and produced major reduction in the noise similar to the reductions earlier observed by Arndt *et al.* [17] and Ukon [16], though we also observed much larger reductions (up to a factor of 200) in the acoustic impulses than the reduction in RMS noise measured by those previous authors. Indeed the large pulses seem to be eliminated, leaving only the incoherent bubble collapse noise. Comparison of the photographs of the cavitation suggests that the mechanism for the noise

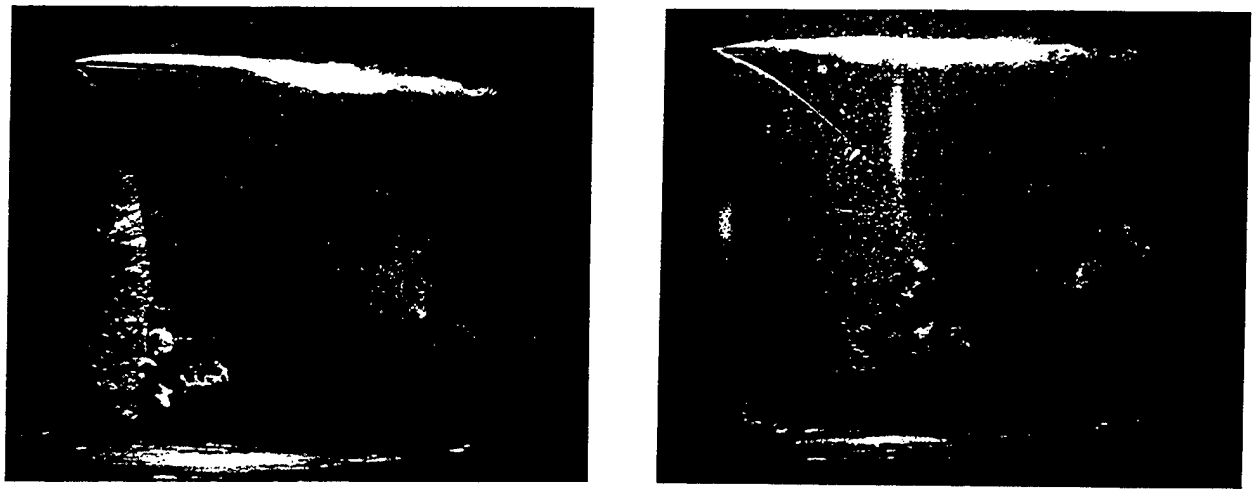


Figure 13: Effect of air injection on cavity size. The photograph on the left is without air injection, the photograph on the right has a normalized air flow rate of $q = 4.5 \times 10^{-4}$. Both photographs were taken at $\sigma = 1.2$, $k = 0.8$, $\alpha = 12.8°$.

reduction is an increase in the air contained in the bubbles which comprise the cloud. It also seems that air flow rates above a certain level produce no further reduction in the sound.

ACKNOWLEDGEMENTS

We wish to acknowledge our debt to Y.-C. Wang, J. Ando, F. d'Auria, T. Waniewski, R. and V. Zenit, and Z. Liu for help in conducting the experiments. Joe Fontana's machine shop assistance was greatly appreciated as well. The authors are grateful for the support of the Office of Naval Research under grant number N00014-91-J-1295.

References

[1] Bark, G. and van Berlekom, W. B. (1978). Experimental investigations of cavitation noise. *Proc. 12th ONR Symp. on Naval Hydrodynamics*, pp. 470–493.

[2] Shen, Y. and Peterson, F. B. (1978). Unsteady cavitation on an oscillating hydrofoil. *Proc. 12th ONR Symp. on Naval Hydrodynamics*, pp. 362–384.

[3] Bark, G. (1985). Developments of distortions in sheet cavitation on hydrofoils. *Proc. ASME Int. Symp. on Jets and Cavities*, pp. 215–225.

[4] Franc, J. P. and Michel, J. M. (1988). Unsteady attached cavitation on an oscillating hydrofoil. *J. Fluid Mech.*, Vol. 193, pp. 171–189.

[5] Kubota, A., Kato, H., Yamaguchi, H., and Maeda, M. (1989). Unsteady structure measurement of cloud cavitation on a foil section using conditional sampling. *J. Fluids Eng.*, Vol. 111, pp. 204–210.

[6] Kubota, A., Kato, H., and Yamaguchi, H. (1992). A new modelling of cavitating flows - a numerical study of unsteady cavitation on a hydrofoil section. *J. Fluid Mech.*, Vol. 240, pp. 59–96.

[7] Maeda, M., Yamaguchi, H., and Kato, H. (1991). Laser holography measurement of bubble population in cavitation cloud on a foil section. *Proc. ASME Symp. on Cavitation*, Vol. 116, pp. 67–75.

[8] Kato, H. (1985). On the structure of cavity: New insight into the cavity flow: A summary of the keynote speech. *Proc. of the ASME Int. Symp. on Jets and Cavities*, Vol. 31, pp. 13–19.

[9] Ye, Y. P., Kato, H., and Maeda, M. (1989). On correlation of cavitation erosion and noise on a foil section. *Int. Workshop on Cavitation*, pp. 68–75, Wuxi, Jiangsu, China.

[10] McKenney, E. A. and Brennen, C. E. (1994). On the dynamics and acoustics of cloud cavitation on an oscillating hydrofoil. *Proc. ASME Symp. on Cavitation and Gas-Liquid Flow in Fluid Machinery and Devices.*

[11] Fitzpatrick, H. M. and Strasberg, M. (1956). Hydrodynamic sources of sound. *Proc. First ONR Symp. on Naval Hydrodynamics*, pp. 241–280.

[12] Blake, W. K. (1986). *Mechanics of flow-induced sound and vibration.* Academic Press.

[13] Ceccio, S. L. and Brennen, C. E. (1991). Observations of the dynamics and acoustics of travelling bubble cavitation. *J. Fluid Mech.*, Vol. 233, pp. 633–660.

[14] Kuhn de Chizelle, Y., Ceccio, S. L., and Brennen, C. E. Observations, scaling and modelling of travelling bubble cavitation. Submitted for publication., 1994.

[15] Brennen, C. E. (1994). *Cavitation and Bubble Dynamics.* Oxford University Press.

[16] Ukon, Y. (1986). Cavitation characteristics of a finite swept wing and cavitation noise reduction due to air injection. *Proc. of the Int. Symp. on Propeller and Cavitation*, pp. 383–390.

[17] Arndt, R. E. A., Ellis, C. R., and Paul, S. (1993). Preliminary investigation of the use of air injection to mitigate cavitation erosion. *Proc. ASME Symp. on Bubble Noise and Cavitation Erosion in Fluid Systems*, Vol. 176, pp. 105–116.

[18] Gates, E. M. (1977). *The Influence of Freestream Turbulence, Freestream Nuclei Populations, and a Drag-Reducing Polymer on Cavitation Inception on Two Axisymmetric Bodies.* PhD thesis, Cal. Inst. of Tech.

[19] Hart, D. P., Brennen, C. E., and Acosta, A. J. (1990). Observations of cavitation on a three-dimensional oscillating hydrofoil. *ASME Cavitation and Multiphase Flow Forum*, Vol. 98, pp. 49–52.

[20] Coates, R. F. W. (1989). *Underwater Acoustic Systems.* John Wiley & Sons, Inc.

[21] Kumar, S. (1991). *Some Theoretical and Experimental Studies of Cavitation Noise.* PhD thesis, Cal. Inst. of Tech.

[22] Ceccio, S. L. (1990). *Observations of the Dynamics and Acoustics of Travelling Bubble Cavitation.* PhD thesis, Cal. Inst. of Tech.

[23] Mørch, K. A. (1980). On the collapse of cavity cluster in flow cavitation. *Proc. First Int. Conf. on Cavitation and Inhomogeneities in Underwater Acoustics*, Vol. 4, pp. 95–100. Springer Series in Electrophysics.

[24] Wang, Y.-C. and Brennen, C. E. (1994). Shock wave development in the collapse of a cloud of bubbles. *ASME Cavitation and Multiphase Flow Forum*, Vol. 153.

DISCUSSION

M. Su
Naval Research Laboratory, USA

Do you measure the bubble size spectra for the bubble cloud resulting from the break-up of the vortex sheet on an oscillating hydrofoil? Since you are interested in the sound generation from this process, the measurement of the bubble size distribution may help in physical interpretation of the spectra of the pressure fluctuation.

J. Matusiak
Helsinki University of Technology, Finland

Two years ago at the 19th SNH I presented a simple analytical method of evaluating cloud cavitation in relation to the unsteadiness of sheet cavitation, i.e., break-off. The structure of the cloud, that is bubbles, total volume, and size distribution is evaluated. Numerical simulation of their collapse yields broad-band pressure. Are you aware of this method? Have you experimental evidence on the form and size of the bubbles that you observed in your experiment?

AUTHORS' REPLY

We thank Dr. Su and Professor Matusiak for their interest in our work. In response to Dr. Su's question, the bubble size distribution was not measured in our experiments. As Dr. Su knows from his careful work on the bubbles produced by breaking waves, such measurements are not easily made even under the best of circumstances. Furthermore, when the distribution is a rapidly changing function of both time and position, as it is in the present case, it presents a difficult experimental challenge. We can only comment that such measurements would be very valuable in adding to our understanding of the phenomenon.

Professor Matusiak's analytical model of traveling bubbles shed from the trailing edge of an attached sheet cavity has resulted in a possible method of predicting the noise generated by this type of cavitation. However, our experiments have shown that in the more extreme case of cloud cavitation, several qualitative features of the bubble shedding and collapse process must be incorporated into any model of the dynamics.

The densely populated coherent cavitation clouds produced during our experiment resulted in acoustic impulses which were more than three orders of magnitude greater than the impulses generated by traveling bubble cavitation. Thus, we conclude that bubble interaction is an essential mechanism of the cloud cavitation noise generation process.

Furthermore, our high-speed movies indicate that the detachment of the bubble clouds from the sheet cavity occurs as the sheet cavity volume is increasing. The dynamics of this detachment process are highly complex and poorly understood.

Finally, as previously noted, the size distribution of the bubbles in our clouds is not known at the present time. Therefore, we can neither confirm nor deny the validity of the bubble size distribution function used by Dr. Matusiak.

An Experimental Investigation of the Mechanism and the Pressure of Counter-Rotating Vortices on a CPP at the Off-Design Condition

N. Okamura, R. Fujino, T. Tanaka
(Ishikawajima-Harima Heavy Industries Co., Ltd., Japan)

ABSTRACT

High frequency pressure fluctuations induced by propeller tip vortices caused a structural vibration problem on a new ship equipped with twin, highly skewed, controllable pitch propellers (CPPs). The vibration occurred at low ship speeds corresponding to an off-design condition. The acceleration spectrum of the vibration exhibited high broadband levels between the 4th and 10th harmonics of blade passing frequency.

A model propeller experiment result showed that a pair of counter-rotating vortices was generated on each blade and burst at the condition corresponding to the ship vibration. The bursting vortices cavitated and radiated intense fluctuating pressures of high frequencies(between 3rd and 11th harmonics of blade passing frequency). Flow visualization indicated that the counter-rotating vortices were generated by a long leading edge separation bubble rolled up on the blade.

From the experimental investigations and a vortex motion analysis based on a two-dimensional vortex theory, the pair vortex bursting was considered to be caused by vortex divergence from strong mutual vortex motions.

Air injection into the cavitating vortices was examined for reducing the pressures in the model experiment. The result showed that air reduced effectively the pressures on the model and on the ship.

NOMENCLATURE

C_T	Propeller tip clearance
D	Propeller diameter
G	Acceleration of gravity or Non-dimensional circulation
K_1, K_2	Strength of vortex
K_P	Pressure coefficient($P/\rho n^2 D^2$)
K_T	Thrust coefficient($T/\rho n^2 D^4$)
L	Distance between vortex centers
n	Propeller revolution
P	Single amplitude of pressure
P_S	Static pressure
P_V	Vapour pressure of water
R	Propeller radius
T	Propeller thrust
X	Distance of the vortex centroid from one of the vortices for a vortex pair
ρ	Density of water
σ_n	Cavitation number($(P_S-P_V)/\rho n^2 D^2$)
ω	Angular velocity

INTRODUCTION

High frequency vibration of the structure above propellers was experienced with a new ship equipped with twin, highly skewed, controllable pitch propellers(CPPs). This vibration occurred at low ship speeds corresponding to an off-design condition. The vibration acceleration showed a broadband type of spectrum with high levels at higher frequencies around 4th to 10th harmonic of the blade passing frequency. On the other hand, the ship hull vibrated mainly at the blade passing frequency at the high ship speeds of the design condition.

A detailed investigation into the cause of this high frequency vibration showed that the mechanical excitation from the main engines, the reduction gears, etc. were not the case but propeller induced pressures were very suspicious.

This kind of high frequency vibrations excited by highly skewed propellers were also reported with some other ships[1-3] but only one report[3] is related to the off-design conditions of CPP. Furthermore, the mechanism of such high frequency pressure generation has not been fully understood yet.

In order to clarify the cause of this high frequency vibration and establish countermeasures

for reducing the ship vibration, we have conducted experimental investigations with a model propeller at a cavitation tunnel and with the full scale ship together with propeller lifting surface calculations. Cavitation observations and pressure measurements were carried out at the model experiment along with flow visualizations of propeller vortices and blade surface streamlines. Structural vibration at an aft part of the ship was measured in the full scale experiment. By the experimental investigation and lifting surface calculation, it was found that the high frequency pressures were caused by the cavitation of a pair of bursting and counter-rotating vortices shed from each propeller blade. Also air injection into the vortices was found to be effective to reduce the pressure.

This paper presents the experimental data of the full scale ship and the model propeller. The generation mechanism of counter-rotating vortices and a hypothesis of bursting for a pair of vortices are described in this paper along with the air injection effect on the fluctuating pressure.

FULL SCALE EXPERIMENT

The particulars of the ship are as shown in Table 1. The ship was carefully designed to reduce the vibration by using elastic supports of the main engines, highly skewed propellers, etc. Although the ship vibration was very small at the design condition, the aft part of the ship vibrated at high frequencies at the off-design condition of low ship speeds. The maximum spectral components of the vibration acceleration against ship speeds were shown in Fig.1. Here the ship speed was controlled by changing the blade pitch angle with holding the propeller revolution constant except for the normal design condition. The vibration was measured at a 1st deck floor above the starboard propeller as shown in Fig.2.

Table 1. Main particulars of the ship

Length overall(m)	175
Breadth molded(m)	24.0
Draft design(m)	6.5
BHP(metric)	9420 x 2
Propeller	
Type x No.	CPP x 2sets
Diameter(m)	4.60
Expanded area ratio	0.572
Number of blades	4
Skew angle(deg.)	31

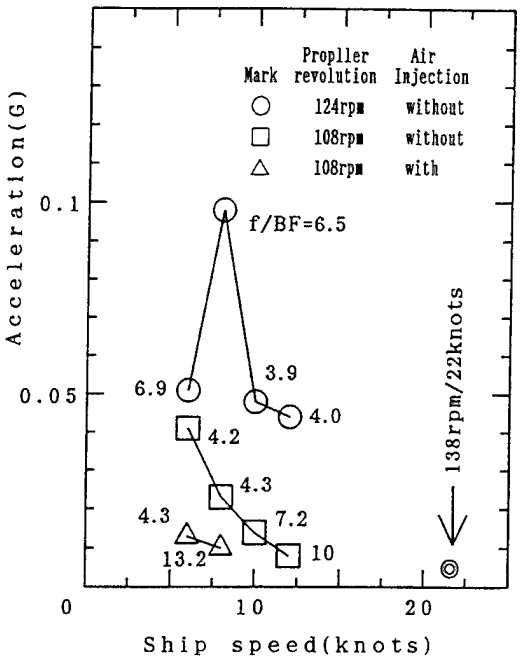


Fig.1 Vibration acceleration vs. ship speed

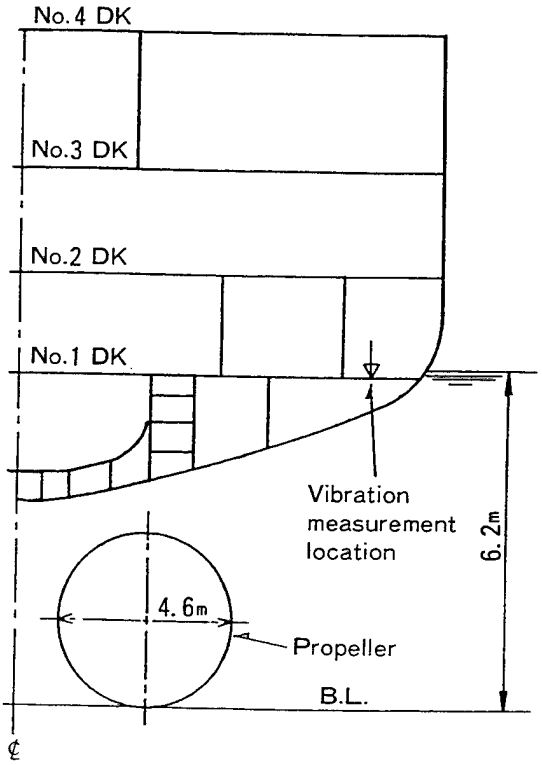


Fig.2 Measurement location of ship vibration

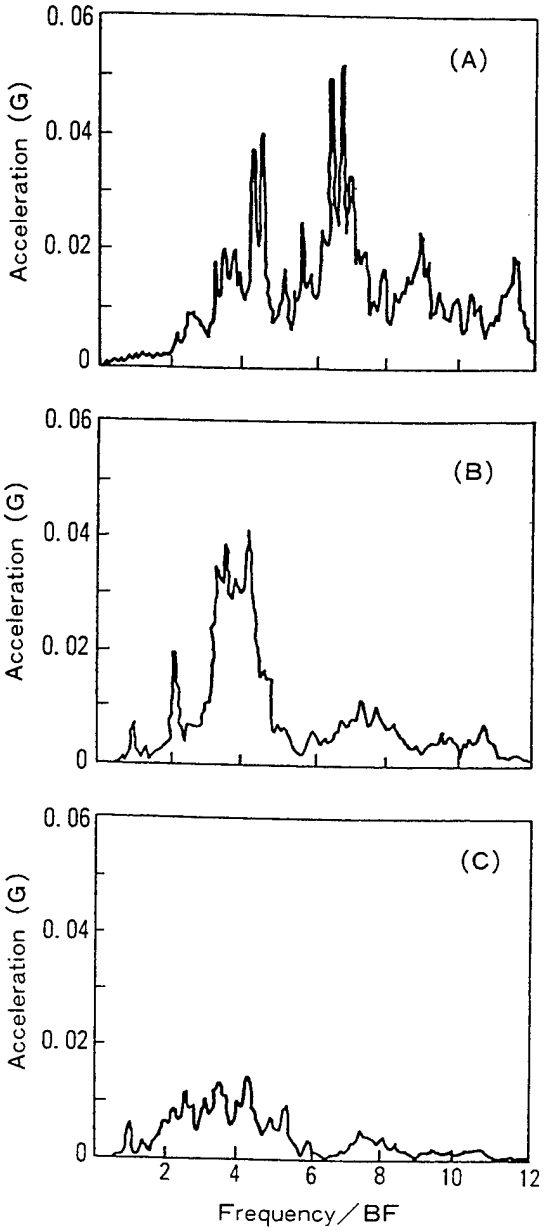


Fig.3 The spectra of ship vibration
(A) 124rpm/6knots without air
(B) 108rpm/6knots without air
(C) 108rpm/6knots with air,
BF:blade passing frequency

The upper curve in Fig.1 represents the vibrations at 124rpm of the propeller revolution, which had been a revolution number designed initially. Later we decreased this revolution to 108rpm for reducing the vibration. The results of this revolution decrease are shown in the middle curve in Fig.1 but the levels were still high. The lowest curve in Fig.1 shows the vibration after the introduction of air injection into the propeller tip region, indicating the usefulness of air. This air injection was applied to the ship based on the study by model experiment, which will be explained later in the section titled "Results of model experiment." The numbers at marks of each curve in Fig.1 show the frequencies divided by the blade passing frequency. These numbers indicate that the vibrations are dominated at high frequencies from about 4th to 10th harmonic of the blade passing frequency and the frequencies are distributed between the harmonics.

Fig.3 shows the vibration spectra at 124-rpm/6knots(propeller revolution/ship speed) and 108rpm/6knots. As seen in this figure, the spectra exhibit high broadband energy at higher frequencies. The spectra differ from the discrete spectrum usually observed at the design condition, where the blade passing frequency and a few higher harmonics are usually dominant. Also in this figure, there is a spectrum for the vibration at 108rpm/6knots after the introduction of air injection. This result shows the effectiveness of air injection.

Before starting the model experiments, a detailed investigation into the cause of the vibration was carried out from the mechanical excitation view point. The result showed that the mechanical excitation from the main engines, the reduction gears, etc. were not the case but propeller induced pressures were very suspicious and remained to be investigated.

MODEL PROPELLER EXPERIMENT

The purposes of model propeller experiment were to:

(1)attempt to reproduce the phenomena causing the high frequency propeller excitation,
(2)identify the cause of the vibration excitation, and
(3)evaluate countermeasures for vibration reduction.

Experimental techniques

Test facility and apparatus

The model propeller experiment was conducted in IHI cavitation tunnel[4] with 600mm square measuring section. The apparatus of the model experiment is as shown in Fig.4. A mesh screen simulated the model ship wake of starboard side that was measured in a towing tank. A flat plate representing the ship hull was set horizontally above the propeller keeping the propeller tip clearance ratio $C_T/D=0.260$(C_T:tip clearance, D: propeller diameter) same with the actual ship. Pressure gauges were mounted flush on that plate for recording the propeller induced pressures.

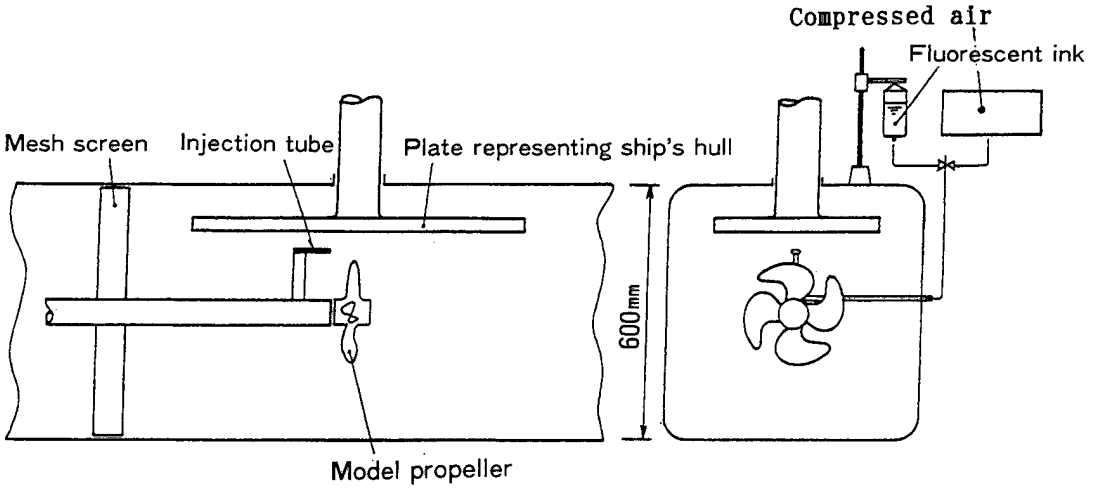


Fig.4 Apparatus of model propeller experiment

A small tube(outer diameter=1mm) upstream of the propeller was used for injecting fluorescent ink in order to visualize vortical flow around the propeller together with stroboscopic lighting. The tube was also used for injecting air into the propeller tip region in order to investigate the effect of air on propeller-induced pressure reduction.

Model propeller and test condition

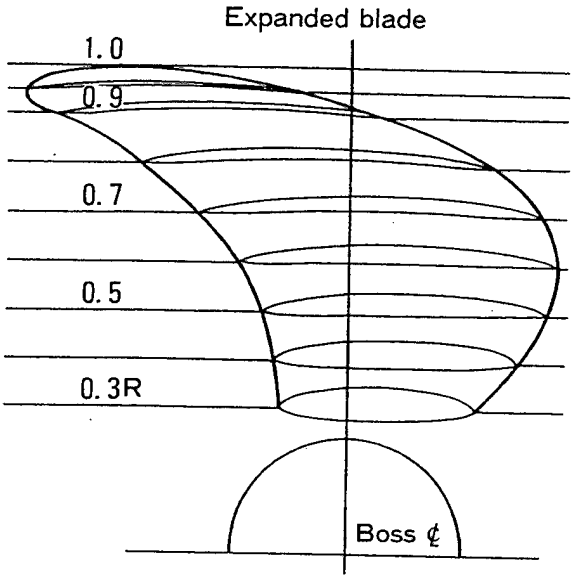
The particulars of the model propeller is described in Fig.5. The model propeller was operated in the simulated wake with identical thrust coefficient(K_T) and cavitation number(σ_n) of the full scale propeller. Here σ_n is defined by the static pressure at propeller shaft center. Table 2 shows the model propeller test conditions, which correspond to 124rpm/6knots of the off-design condition and 138rpm/22knots of the design condition of the actual ship.

Results of model experiments

Propeller cavitation

Figs.6 and 7 show the photographs and the sketches respectively of propeller cavitation at each condition. As seen in those figures, the cavities were unusual at 6knots, whereas they were typical at 22knots. The characteristic features of the cavities at 6knots are summarized as follows.

(1)A pair of cavitating vortices is shed from each propeller blade tip and forms a pair of helical trailing vortices in the down stream of propeller. The pattern of the pair vortex



Diameter(mm)	250.0
Pitch ratio(0.7R)	1.207
Expanded area ratio	0.572
Boss ratio	0.240
Number of blades	4
Skew angle(deg.)	31

Fig.5 Particulars of the model propeller

Table 2. Model propeller test condition

Case	Model propeller			Ship	
	K_T	σ_n	n (rps)	Vs (knots)	n (rpm)
1	0.016	3.01	17.0	6.0	124
2	0.180	2.35	19.7	22.0	138

K_T:Thrust coefficient
σ_n:Cavitation number
n :Propeller revolution
Vs:Ship speed

cavitation does not change so much with the propeller rotation angle.

(2)Each of the pair vortices appears to rotate in the opposite direction around each vortex center.

(3)Both pitches of the helical pair vortices are small.

(4)One of the pair vortex cavities starts from the face side leading edge of about 0.7R(R: propeller radius) and extends toward the blade tip along the leading edge, whereas the other appears first around the blade tip.

(5)The vortex cavities burst short after departing from the blade.

(6)After shedding from the tip, the pair vortices move a little outward apart from the propeller center.

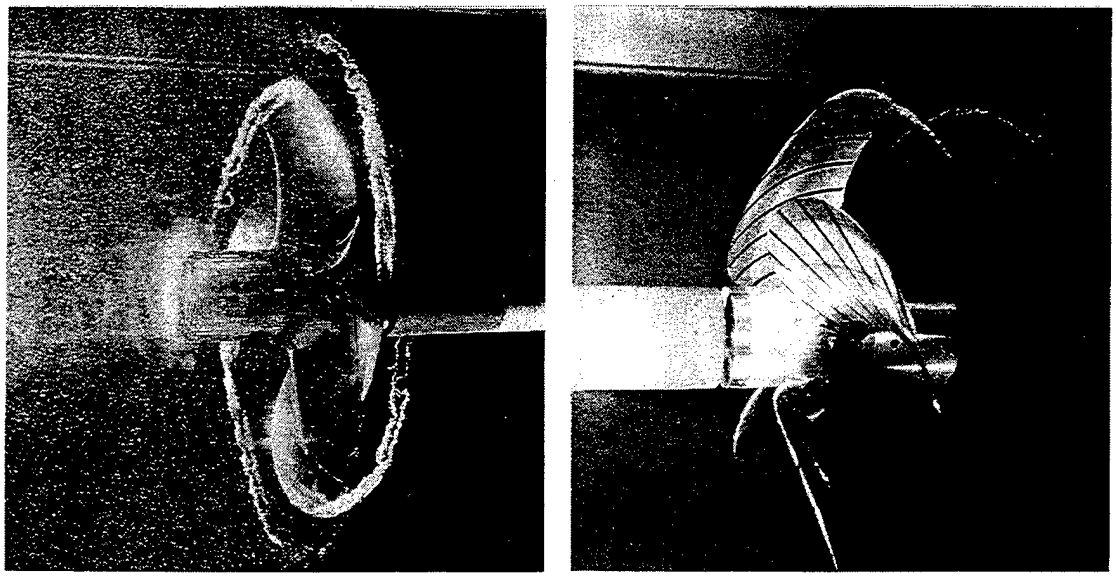
Propeller induced pressure fluctuation

The spectra of pressures measured on the plate just above the propeller were as shown in Fig.8. The spectrum at 22knots condition shows a typical pattern of propeller induced pressure where the blade passing frequency and a few higher harmonics are dominant. In contrast, the pressure at 6knots condition has a broadband type of spectrum having high levels at higher frequencies(between about 3rd and 11th harmonics), which resembles the corresponding ship vibration spectrum at 6knots (Fig.3(A)). These results tend to confirm that the high frequency ship vibration in question at the off-design condition may have been caused by the pair vortex cavitation.

Visualization of vortical flows

From the cavitation observations and pressure measurements, the high frequency vibration of concern at the off-design condition was found to be closely related with the special type of tip vortices. In order to investigate the vortex structure and the generation mechanism of such vortices, we conducted experiments of vortical flow visualization.

Fig.9 shows the photographs of the vortex flows visualized by injecting fluorescent ink from a small tube upstream of the propeller. Just the



(A) (B)

Fig.6 Photographs of model propeller cavitation
(A) 6knots condition / Face
(B) 22knots condition / Back

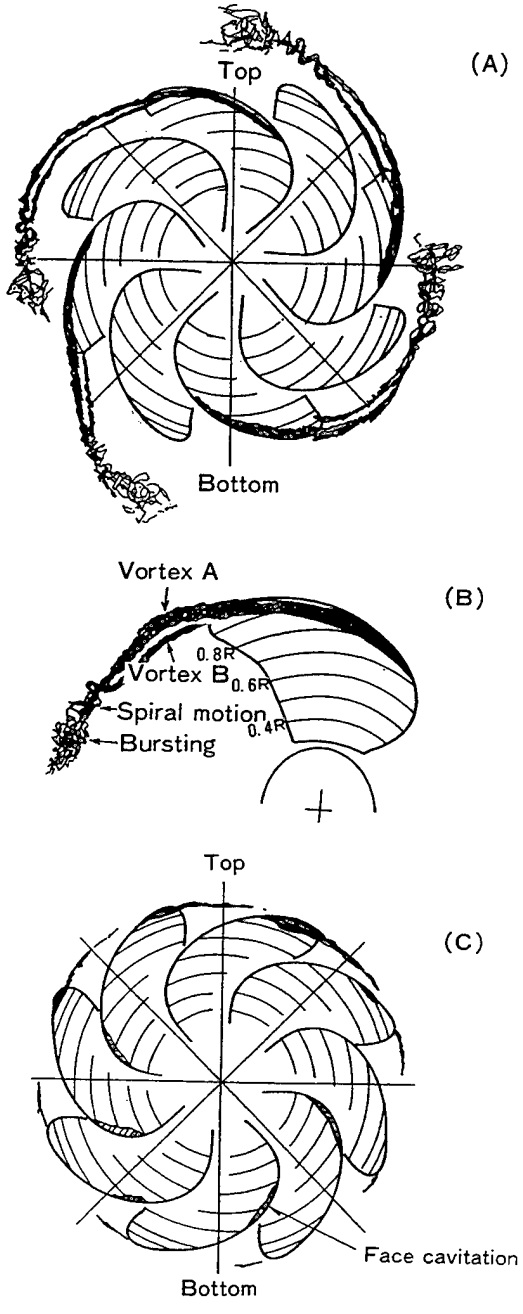


Fig.7 Sketches of model propeller cavitation
(A) 6knots condition / Face
(B) Typical cavitation pattern at 6knots
(C) 22knots condition / Back

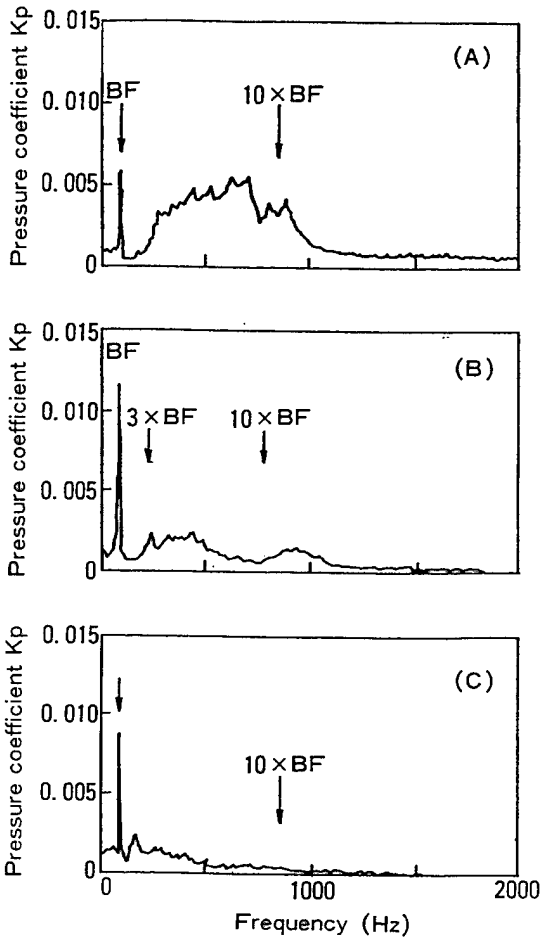
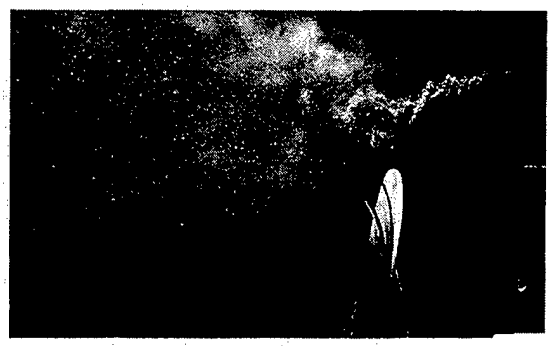
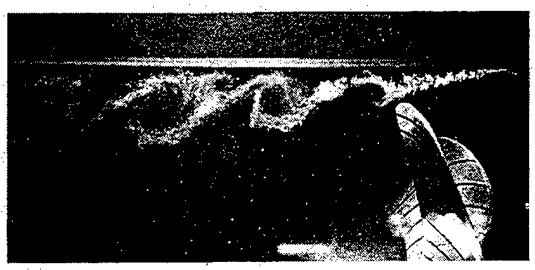


Fig.8 Pressure spectra of model propeller
(A) 6knots condition without air
(B) 22knots condition without air
(C) 6knots condition with air
BF:Blade passing frequency



(A)



(B)

Fig.9 Photographs of visualized vortical flows
(A) 6knots condition
(B) 22knots condition

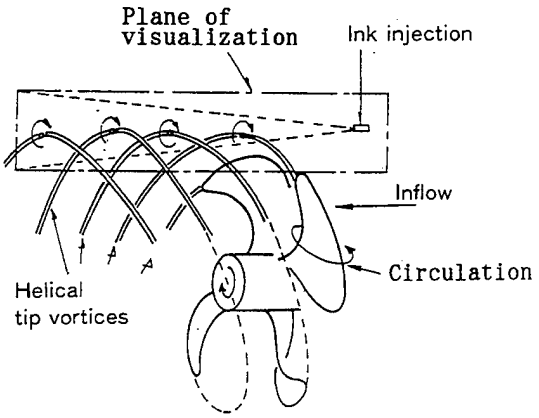


Fig.10 Schematic showing how to visualize vortical flows by fluorescent ink(22knots condition)

cavitation number in the cavitation simulation conditions was increased by increasing the tunnel static pressure at this visualization test. This pressure increase is to diminish the cavity and visualize just the vortical flows not affected by cavitation. As seen in these photographs, there is a pair of counter-rotating vortices around a blade tip at 6knots condition. On the other hand, four adjacent tip vortices of usual type with same rotational direction are observed at 22knots condition. Looking the downstream of the vortices at 6knots, there is a wide area where the injected ink was diffused and this diffused region is very similar to the bursting vortex cavitation region (Fig.6(A)). For understanding how to visualize by ink, a schematic explaining the tip vortex visualization at 22knots is depicted in Fig.10.

Fig.11 demonstrates the hard copies of successive video pictures showing the process of the pair vortex formation at 6knots. From a detailed analysis of the video pictures and as seen partly in Fig.11, it was found:

(1)one of the pair vortices(left one in Fig.11, hereafter called as "vortex A")rolled up around the outer leading edge on the face side,

(2)as the blade rotated, the second vortex (right one in Fig.11, hereafter called as "vortex B") appeared near the blade tip and then a pair of counter-rotating vortices drifted away into the propeller wake, and

(3)the pair vortices are counter-rotating (vortex A anticlockwise and vortex B clockwise in Fig.11).

To confirm that the visualized vortices are same with the cavitating vortices observed at the cavitation simulation test, the tunnel static pressure was decreased at the flow visualization test with keeping ink injection. This test showed that a pair of helical vortex cavities appeared and stretched through the visualized vortex centers as the static pressure decreased. This result means the visualized vortices by ink are the same ones observed at the cavitation simulation test.

Visualization of blade surface flows

From the vortex flow visualization, it is found that one of the pair vortices rolled up around face side leading edge of the blade. This kind of rolled-up vortex is usually closely related with leading edge flow separation as reported[5-6]. Therefore flow patters on the blade surfaces were visualized by using an oil film technique.

Fig.12 shows the sketches and the photographs of the oil flow patterns at 6knots condition. These flow patterns show the mean flow patterns for the whole propeller rotation angles because the oil film patters were obtained after running of the

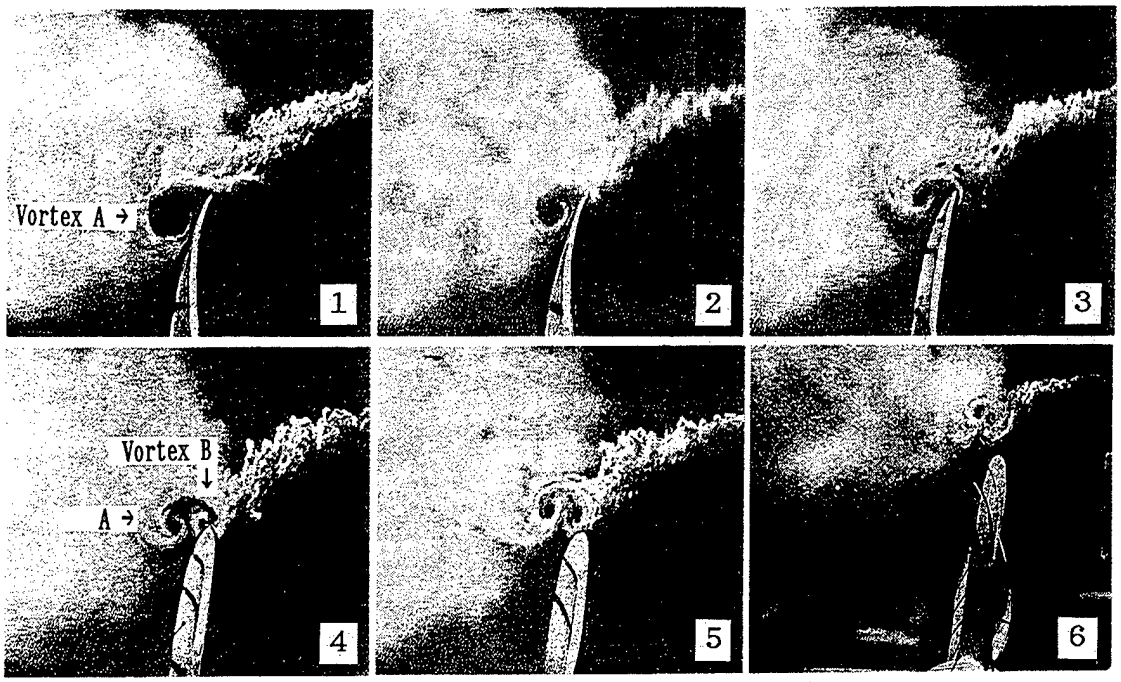


Fig.11 Video picture hard copies showing the process of counter-rotating pair vortex formation at 6knots condition. The numbers show the order of time process.

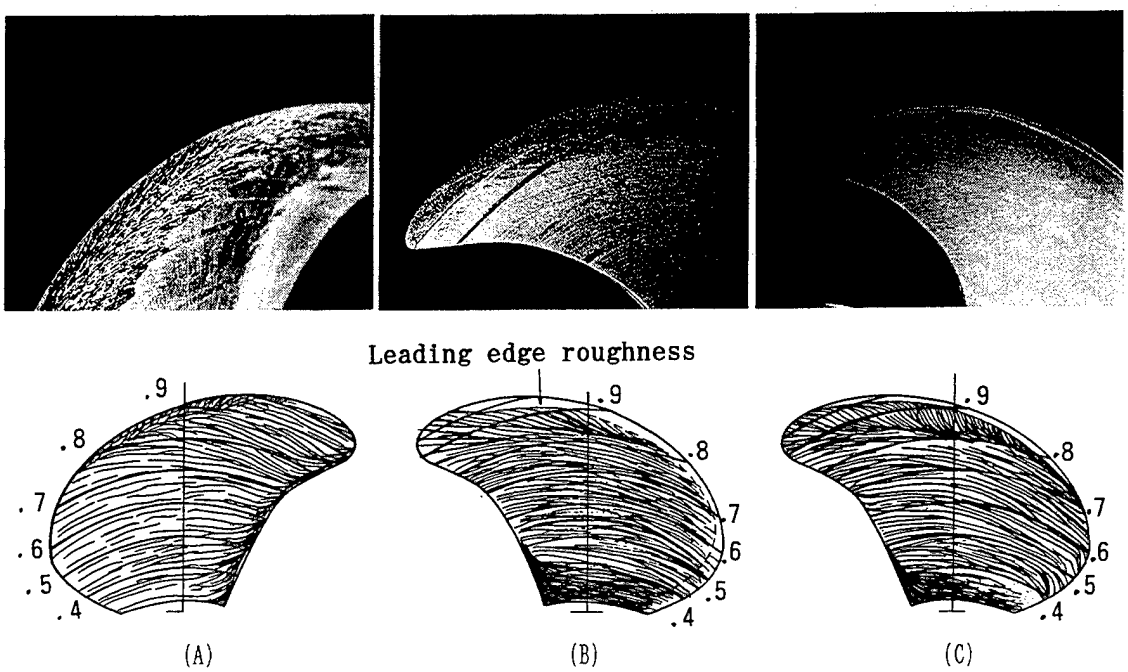


Fig.12 Photographs and sketches of oil flow patterns at 6knots condition
(A) Back side without leading edge roughness
(B) Face side with leading edge roughness
(C) Face side without leading edge roughness

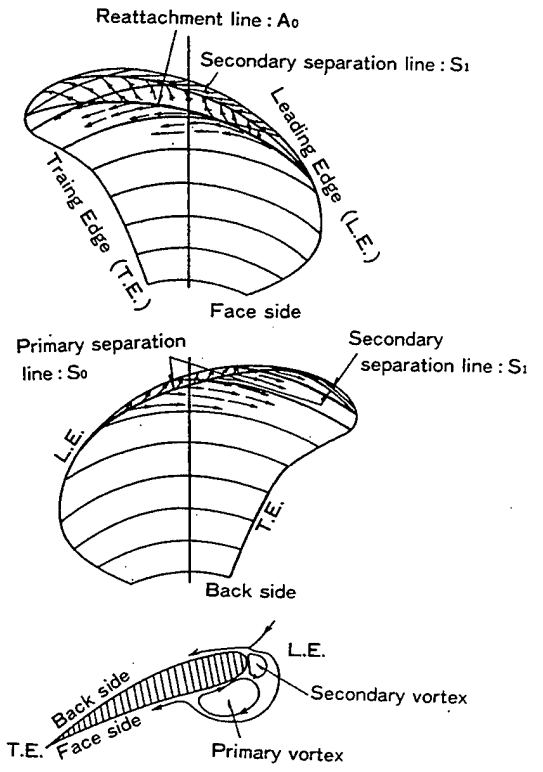


Fig.13 Schematic of the structure of leading edge separation at 6knots condition

propeller for 5 minutes or so. From these flow patterns it is recognized that there is a long leading edge separation in the outer radius region starting from around 0.7R. This leading edge separation tended to shrink a little but did not change so much by leading edge roughness introduced as a turbulent stimulator. Therefore the scale effect of this separation seemed to be little.

By repeating different kinds of oil painting at the oil film test such as point painting, line painting and different colour painting on each blade side, we could make out the structure of the leading edge separation as schematically illustrated in Fig.13. As seen in Fig.13, the flow on the blade separated at the back side leading edge(primary separation line S_0) and reattached on the face side apart from the leading edge (reattachment line A_0) forming a large separation bubble. Inside of this separation bubble, there was a secondary separation bubble the separation line of which is expressed as "secondary separation line S_1" in Fig.13.

Air injection

When bursting vortex type of tip cavitation occurred, a broadband type of pressure spectrum having high levels at higher frequencies was induced sometimes with highly skewed propellers if the propeller loading was high[1] or low[present paper]. This kind of high frequency pressure is considered to be induced by violent collapse of bursting vortex cavitation. In such cases, air injection into the bursting vortex region had been useful for reducing the high pressures at least in model experiment[2,12]. This pressure reduction was considered to be due to the cushioning effect of air.

We also examined the air injection to decrease the large amplitude pressures at high frequencies at 6knots condition in the model experiment. The result is shown in Fig.8 compared with the pressure without air injection. As seen, the pressures at high frequencies have been reduced much, whereas the blade rate component increased a little but was not an unacceptable one.

PROPELLER LIFTING SURFACE CALCULATION

The circulation distributions of the propeller in the wake and in the mean wake at the off-design condition were calculated by using an unsteady lifting surface program, PUF-3A developed by MIT. As a result, the circulations at 124rpm/6knots were found to be negative at outer radii and positive at inner radii as shown in Fig.14. In this figure, the circulation Γ is normalized as

$$G = \frac{\Gamma}{2\pi RW} \qquad (1)$$

where,

$$W = \sqrt{Vs^2+(0.7x2\pi nR)^2} \qquad (2)$$

and Vs is ship speed. The five curves in this figure show the circulations at 4 angular positions of the blade in the wake and at an angular position in the mean wake, respectively. It seems that the negative loading at outer radii(approximately $r \geq 0.75R$) is due to the excess low pitch at this condition along with the higher propeller revolution ,and responsible for the long leading edge separation.

DISCUSSION

From the results of model and full scale experiments along with propeller lifting surface calculations, the following facts have become clear regarding the high frequency vibration in question

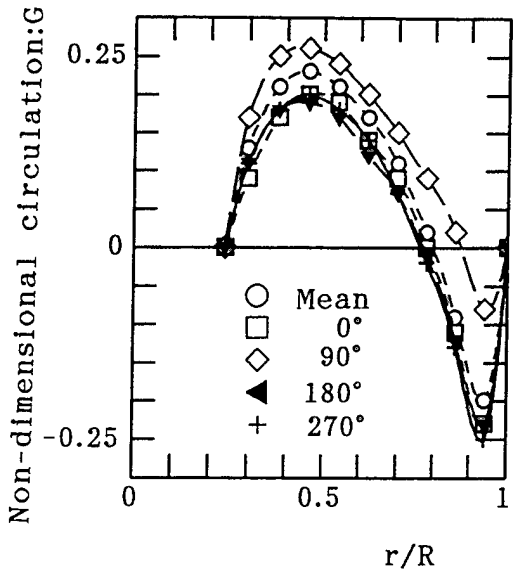


Fig.14 Radial distributions of circulation at 6knots condition calculated by PUF-3A

at the off-design condition.

(1)The mechanical excitation from the main engines and so on are not responsible for the vibration.

(2)The model propeller experiment at the off-design condition showed the existence of a pair of bursting vortices that was shed from each blade tip and cavitating.

(3)The spectrum of pressure induced by the model propeller at the off-design condition is of broadband type and similar in form to the ship vibration acceleration of concern.

(4)Air injection into the propeller tip region effectively reduced the propeller induced pressures at the model experiment and also decreased the ship vibration of concern.

(5)The pair vortices of the model propeller were counter-rotating with each other and one of them was observed to be formed by rolling up of a long leading edge separation on the blade face side.

(6)The circulation at the outer radii corresponding to the location of long leading edge separation had negative values according to the lifting surface calculation.

Based on the above facts, here we discussed the cause of the vibration, the generation mechanism of the counter-rotating pair vortices, a hypothesis of the bursting of counter-rotating vortices, etc.

The cause of the vibration

From the above facts (1) through (3), the vibration in question was considered to be caused by high frequency, high amplitude pressures induced by bursting cavitation of counter-rotating tip vortices from propellers. This consideration was confirmed by the above fact (4). This is because the air injection was confirmed by the model test to reduce effectively the exciting pressures and this air injection applied to the actual ship decreased sufficiently the ship vibration of concern.

The generation mechanism of counter-rotating tip vortices

From the above fact(5), one of the pair vortices(vortex A) was associated with rolling up of a long leading edge separation on the face side of blade. On the other hand, the origin of the second vortex(vortex B) was not obvious. But by comparing precisely the leading edge separation structure(Fig.13) with the vortex flow(Fig.11) and the vortex cavitation(Figs.6, 7), the followings are found:

(1)the vortical flow and the vortex cavitation of vortex B begin to appear at a location of the blade tip,

(2)this location corresponds to the shedding point of the secondary separation bubble if the secondary separation bubble rolled up,

From these findings, it is suggested that the secondary separation bubble rolled up and formed the vortex B. Also a schematic showing the counter-rotating vortex structure can be drawn as depicted in Fig.15.

Besides the vortices rolled up from long leading edge separation bubbles, there exists the other kind of vortices around a propeller — lifting surface vortices. For the radial circulation distribution having negative values at outer radii as already shown in Fig.14, the horseshoe vortex system can be expressed schematically as shown in Fig.16. In this horseshoe vortex system, the vortex a and d are the root vortex and the tip vortex respectively. Also the other two vortices(b,c) may be possible around the mid-span($r=r_1$ in Fig.15) because the circulation changes the value at $r=r_1$ from positive to negative. But the vortex b and c may not roll up as depicted in fig.5 because those vortices locate not at the tip nor the root but at the middle of the span.

From comparative investigations of the visualized vortices(Figs.11,13) and the horseshoe vortex system(Fig.16), it can be said the followings.

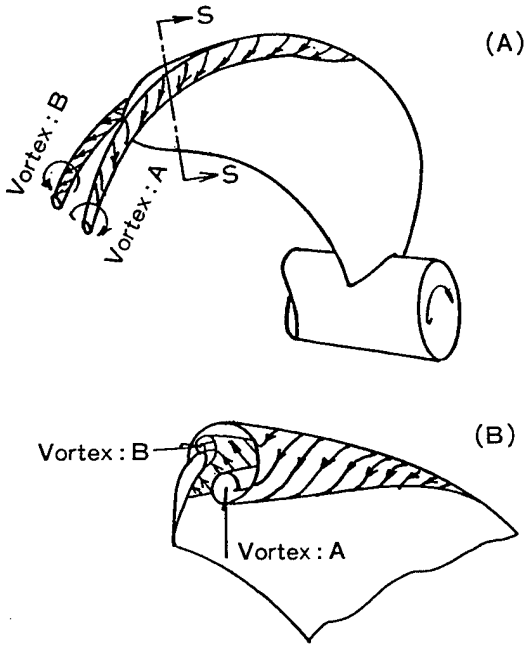


Fig.15 Schematic showing the structure of counter-rotating pair vortices
(A) General view
(B) Side view when cut at S-S

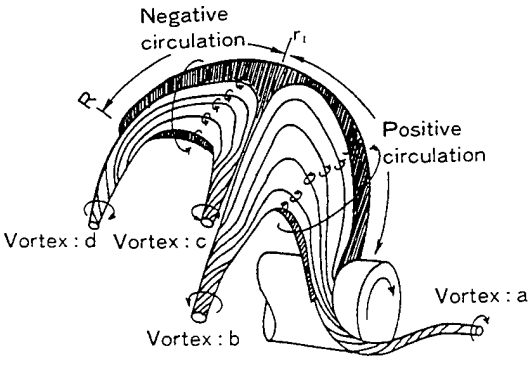


Fig.16 Horseshoe vortex system for 6knots condition

(1)The lifting surface tip vortex d is not the vortex B of the visualized counter-rotating vortices because of their opposite rotational directions. Therefore the vortex B must be the rolled-up vortex from the secondary separation bubble.
(2)The tip vortex d of lifting surface might be merged into the vortex A because the vortex d rotates in the same direction with the vortex A. But the bulk of the vortex A is considered to be composed of the rolled-up vortex from the primary separation bubble at the leading edge because the flow visualizations showed clearly that the vortex rolled up not at the blade tip but along the leading edge.

A hypothesis of counter-rotating vortex bursting

Our investigations showed that the counter-rotating pair vortices burst and cavitated radiating high frequency, high amplitude pressures. Also the pair vortices were associated with long leading edge separations.

Looking for other examples associated with the rolling-up vortices from leading edge separation, there are some reports with marine propellers [5,7,8], with airplane fans[6,9] and with delta wings[10,11]. The others to be referred are the reports regarding propeller tip vortex bursting [1,12] and regarding high frequency, high amplitude propeller induced pressures[1-3].

Reviewing the reference papers[5-11], it is known that the leading edge separation occurred at moderate to high angles of attack will roll up into a concentrated vortex if the leading edge was swept or skewed. Our case also corresponds to this condition because the propeller had a leading edge separation on each blade and was highly skewed, except that the separation of our case occurred on the face side at negative angles of attack.

As for the propeller induced pressures, Hadler et al.[1], Brubakk et al.[2] and English[12] showed examples of high frequency, high amplitude pressures induced by bursting tip vortex cavitation not at off-design conditions but at design conditions. The reasons of vortex bursting for those cases are not necessarily made clear.

As far as reading those reports, there is nothing showing the case of counter-rotating pair vortices as we experienced. Just the reference [3] shows some data and calculations of high frequency, high amplitude pressures at an off-design condition of a CPP. But there is nothing saying counter-rotating vortices nor tip vortex bursting. Seeing precisely the pictures of propeller cavitation in the paper[3], we can recognize a pair of trailing tip vortices on each blade, which seems very similar to the counter-rotating pair vortices we experienced. This

suggests that the high frequency pressures at the off-design condition of the CPP in the paper[3] would be generated by the same reason as in our case.

In considering the bursting of counter-rotating vortices, we investigated the mutual motion of a pair of counter-rotating vortices based on a two-dimensional vortex theory[13]. If two vortex filaments of strength k_1 and k_2 located in the fluid apart from each other's center by L(see Fig.17), the vortices rotate by the mutual induction with same angular velocity ω around the centroid of the vortices. The centroid is a point where the resultant induced velocity is zero, and locates on the line connecting the vortex centers apart from vortex k_1 by X as defined,

$$X = \frac{K_2 L}{K_1 + K_2} \qquad (3).$$

The angular velocity ω is expressed by,

$$\omega = \frac{K_1 + K_2}{L^2} \qquad (4).$$

If k_1 is positive, k_2 negative and $|K_1| > |K_2|$ as the case observed with the counter-rotating vortices we experienced, each vortex rotates around the centroid with a different rotation radius (Fig.17(A)). If such vortices were shed into a uniform flow, the vortex tracks will take the form as shown in Fig.17(B). These tracks are very similar to those of the cavities of counter-rotating pair vortices observed at the cavitation test(Figs.6, 7).

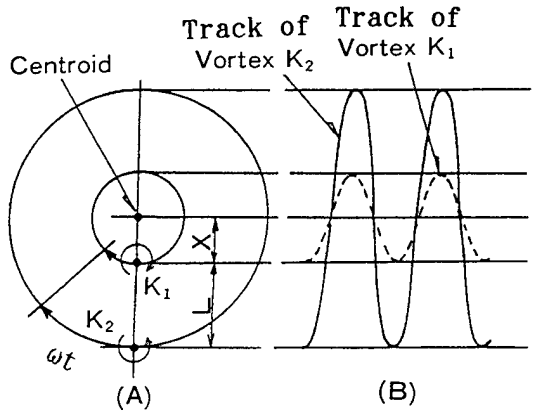


Fig.17 Tracks of two vortices shed into a uniform flow when K_1 is positive, K_2 negative and $|K_1| > |K_2|$
(A) Top view
(B) Side View

Once the distance between the vortex centers became very small by some fluctuations of propeller wake or so, the angular velocity increases very much as calculated by equation (4), which can give the vortices very strong disturbances. Looking precisely the video tapes, we could find that this kind of interacting, strong, spiral motions of vortices. Upon suffering such disturbances, the vortices can be diverged. This vortex divergence might be the reason of vortex bursting for the counter-rotating pair vortices. This reason — vortex divergence — corresponds to one of the three conditions of vortex bursting that Hadler suggested[1].

Seeing the equation (4), this kind of vortex bursting is possible also when the pair vortices are co-rotating. This suggests that the vortex bursting for highly skewed propellers at such high loading as when the leading edge separation occurs, might be the case. This is because at such a condition there could be a pair of co-rotating vortices. In this case, one of the co-rotating vortices should be the lifting surface tip vortex and the other the rolled-up vortex from a primary leading edge separation bubble. The co-rotation of these vortices can be understood if considered the vortex structure and the vortex system referring Fig.13 and Fig.16.

Zsoldos and Devenport[14] investigated experimentally interacting wing-tip vortex pairs, in which they showed the results of two cases i.e. co-rotating and counter-rotating vortex pairs with same strength of each component vortex. As for the co-rotating vortex pair, they indicated broadband flow turbulences were developed at the merging process of vortices, which supports above our hypothesis — vortex divergence caused by interacting vortex motions. In the case of counter-rotating vortex pair, as expected also from the vortex theory, each vortex moved together laterally without spiral motions and so there happened no vortex merging nor turbulence increase. If the vortex strengths had been unequal, vortex spiral motions and vortex divergences might have happened.

Issues associated with highly skewed propellers

The highly skewed propellers have a potential problem associated with leading edge separation as seen in this paper in spite of the advantages such as low vibration excitation, low noise radiation, etc. The issue is high frequency pressure induction due to vortex cavitation associated with leading edge separation. Also the rolled-up vortex from leading edge separation changes the pressure

distribution on propeller blade and the propeller performance[7,8].

Although the propellers with less skew may cause leading edge separations, the separations will not roll up because of the less sweep of the blade leading edges.

To design properly a highly skewed propeller, it is necessary to estimate the leading edge separation vortex.

CONCLUSION

High frequency ship vibration occurred on a new ship with twin CPPs at the off-design condition. Model propeller experiments and full scale vibration measurements revealed the cause of the vibration. From these experimental investigations, the following conclusions can be drawn.

1. The ship vibration spectrum was broadband in nature having high spectral levels at higher frequencies between about 4th and 10th harmonics of the blade passing frequency.

2. The vibration was caused by exciting pressures from cavitating tip vortices, which were counter-rotating pair vortices shed from each propeller blade tip.

3. The counter-rotating pair vortices were bursting and the cavitation of the bursting vortices was responsible for the higher frequency, high amplitude pressures.

4. At the off-design condition, a long leading edge separation on the face side occurred at outer radii of the propeller blade. The separation bubble (primary separation bubble) accompanied with a secondary separation bubble in it. It was observed that the two separation bubbles rolled up into two concentrated vortices forming the counter-rotating pair vortices. The skew or sweep of blade leading edge was considered to be responsible for the rolling-up of the leading edge separation bubbles.

5. The bursting of the counter-rotating vortices supposed to be caused by vortex divergence, which was induced by strong spiral motions of vortices due to mutual inductions.

6. Air injection into the bursting vortices was examined during the model experiment and successfully applied to the actual ship.

The use of highly skewed propellers may result in the type of vibration problems that we have encountered if not properly designed considering leading edge separation. It is needed a design method for highly skewed propellers considered properly the leading edge separation. The CFD technique may be useful for developing such a design method. Also it is necessary to verify the hypothesis regarding the bursting of counter-rotating vortices.

REFERENCES

1. Hadler, J.B., English, J.W. and Gupta, S.K., "Program to Minimize Propeller-Induced Vibration on Converted Maersk "E" Class Ships," SNAME Transactions, Vol. 92, 1984, pp.185-221.

2. Brubakk, E. and Smogeli, H., "QE2 from Turbine to Diesel - Consequences for Noise and Vibration," Proceedings of IMAS 88 - The Design and Development of Passenger Ships, May 1988, pp.169-176.

3. Oshima, A. and Hoshino, T., "Pressure Fluctuations Induced by Propeller Vortex Cavitation," Proceedings of the 7th Symposium on Cavitation, Science Council of Japan, Tokyo, Oct. 1992, pp.109-113.

4. Nishiyama, S., Okamura, N. and Sato, R., "Outline of the New IHI Cavitation Tunnel," IHI Engineering Review, Vol.13, No.2, 1980, pp.7-13

5. Greeley, D.S. and Kerwin, J.E., "Numerical Methods for Propeller Design and Analysis in Steady Flow," SNAME Transactions, Vol.90, 1982, pp.415-453

6. Vaczy, C.M. and McCormick, D.C., "A Study of the Leading Edge Vortex and Tip Vortex on Prop-Fan Blades," The Gas Turbine Conference and Exhibition, ASME, Anaheim, May 1987

7. Ukon, Y. and Yuasa, H., "Pressure Distribution and Blade Stress on a Highly Skewed Propeller," Proceedings of 19th ONR Symposium, Seoul, 1992

8. Yuasa, H. and Ishii, N., "Leading-Edge Separating Vortex and Pressure Distributions on Propeller Blades," Journal of the West Japan Society of Naval Architects of Japan, Vol.59, 1979, pp.151-162

9. Stefko, G.L., Rose, G.E. and Podboy, G.G., "Wind Tunnel Performance Results of an Aeroelastically Scaled 2/9 Model of the PTA Flight Test Prop-Fan," 23rd Joint Propulsion Conference, AIAA, AIAA-87-1893, San Diego, 1987

10. Chang, P.K., "Separation of Flow," Pergamon Press, New York, 1966, pp.460-464

11. Hoeijmakers, H.W.M. and Verhaagen, N.G., "Theoretical and Experimental Investigations into Vortex Flow," Netherlands Association of Aeronautical Engineerings(NVvL), PB88-165626, NRL MP 85085 U, Sep. 1982

12. English, J.W., "Cavitation Induced Hull

Surface Pressures - Measurements in a Water Tunnel," Symposium on Propeller Induced Ship Vibration, RINA, London, Dec. 1979, Paper No.5

13. Milne-Thomson, L.M., "Theoretical Hydrodynamics," 4th ed., Macmillan, London, 1962, pp.349-357

14. Zsoldos, J. and Devenport, W., "An Experimental Investigation of Interacting Wing-Tip Vortex Pairs," 19th ONR Symposium, Seoul, Aug. 1992, pp.17-35

Pressure Field Analysis of a Propeller with Unsteady Loading and Sheet Cavitation

W. van Gent (Maritime Research Institute, The Netherlands)

ABSTRACT

Hydrodynamic pressure fluctuations in the free space around a propeller are described theoretically from a consolidating point of view. The effects of propeller blade loading, thickness and dynamic sheet cavitation are formulated and their types as quadrupoles, dipoles and monopoles revealed.

A method to calculate the dynamic behaviour of sheet cavitation is presented. The choice of the method has been reasoned by the need to get insight in the relation between the non-uniform wake structure and the non-linear cavity volume variations; a most complete description of the cavity shape is not pursued.

Combination of unsteady lifting surface theory and the model for dynamic sheet cavitation leads to a system of differential equations for the cavity shape parameters under influence of the varying conditions on a propeller blade in a wake. Its solution gives the non-linear, dynamic behaviour of the sheet cavitation volume as a function of time, including volume velocity and acceleration as well as the time derivative of the velocity potential. The latter derivative gives the dominant contribution to propeller induced pressure fluctuations in the blade frequency range on the ship hull and to low frequency noise.

Typical calculation results of dynamic cavitation behaviour, part of a complete hydrodynamic propeller analysis are shown.

NOMENCLATURE

a = ellipse major axis divided by c,
b = ellipse minor axis divided by c,
c = chordlength of blade section,
D = diameter of propeller,
D_I = distance between field point and point of integration (on propeller),
D_I^{-1} = monopole spatial function,
$D_{I,s\text{-}I}$ = chordwise oriented dipole function,
$D_{I,n}^{-1}$ = normal oriented dipole function,
$D_{I,ss}^{-1}$ = chordwise oriented quadrupole function,
E = flow deformation tensor,
F_0 = collected non-linear, dynamic terms, n = 0,
F_2 = collected non-linear, dynamic terms, n = 2,
l = chordwise position of midcavity,
n = index for pressure requirement,
n = normal direction on surface or blade; on surface S into volume V, on blade from pressure to suction side,
N = rotation rate of propeller,
p = hydrodynamic pressure,
p_p = pressure side blade pressure,
p_s = suction side blade pressure,
p_i = field pressure contributions, i = 1,2,3,4,5,
p_D = Dynamic pressure term on cavity,
p_I = Interaction pressure term on cavity,
p_S = Static pressure term on cavity,
p_∞ = pressure of environment,
q = cavity cross-sectional area,
r = radial coordinate,
s = chordwise direction,
S = surface bounding volume,
t = time,
T = blade profile coordinate (thickness),
T_p = pressure side profile coordinate,
T_s = suction side profile coordinate,
v = velocity (vector),
V = volume,
V_{rel} = relative velocity of undisturbed fluid to propeller blade (in chordwise direction),
V_{res} = resultant velocity of fluid flow relative to blade,
w = vorticity (vector),
α = factor for 3-D effects in cylindrical cavity approximation,
γ = bound vorticity,
Γ = circulation,
η = elliptical coordinate,
κ = rake angle,
μ = fluid dynamic viscosity,

π = circle quadrature factor,
ρ = fluid mass density,
σ = dimensionless pressure term,
τ = cavity thickness,
ϕ = velocity potential.

INTRODUCTION

Cavity dynamics

Unsteadiness of cavitation often enhances propeller induced vibration to a level which is unacceptable from the comfort, structural and functional integrity points of view. Therefore understanding and quantification of the effects from cavitation are of interest for propeller design and hull vibration analysis. The first methods dealing with the unsteadiness of propeller cavitation in a ship wake field are quasi-steady approaches, in which a steady shape of cavitation is calculated for each blade position. From the sequence of steady shapes, found for a complete revolution, the cavity volume and the cavity growth velocity and acceleration are derived as functions of time. The unsteady pressure field is related to these functions. These methods can supply reasonable estimates for the lowest frequency of vibration excitation on the hull, viz. the blade passage frequency. For higher frequencies these methods suffer from the shortcoming that no dynamic feature of the cavity itself is involved; only the wake non-uniformity is transferred into a time dependent pressure field.

Advanced approaches, under development now, address the problem of the propeller with unsteady cavitation in a wake field with boundary elements methods. The velocity potential is used as a base and the kinematic and dynamic boundary conditions can be formulated 3-dimensional, nonlinear and time-dependent, see Fine and Kinnas (1)]. The cavity planform and shape have to be found by iteration. The cavity growth velocity forms part of the solution as this quantity is implied in the equations to be solved, Kinnas and Fine (2). The cavity growth acceleration, however, has to be obtained by numerical differentation of the final solution.

In between the first methods on one side and the advanced approaches on the other side, there is for practical reasons an option to address directly the cavity growth acceleration. One reason is the fact that this quantity dominates in the fluctuating pressure field and it is desirable to calculate it directly, i.e. avoiding numerical differentation. Another reason is that, especially at lower frequencies, there is no need to know all the details of the cavity geometry; mainly the volume and its time derivatives are of interest. The option can be realized by describing the cavity shape with only a few parameters. Then the boundary conditions on the cavity can be brought into an analytical form containing these parameters and also the environmental parameters of the propeller blade in the wake. This leads to a set of second order differential equations for the cavity shape parameters.

Such a method is dealt with in this paper; it is considered useful in investigating practically the effect of wake field structure on the frequencies of the pressure fluctuations around a propeller.

Pressure fluctuations

The phenomena leading to pressure fluctuations in the free space around a propeller comprise the thickness of the blades and the hydrodynamic loading as well as dynamic sheet cavitation on the rotating blades. The fluid flow is considered incompressible in the description; no acoustic effects will be revealed therefore. Propeller load variations and dynamic sheet cavitation are related to the presence of a wake field, however, here we will consider them as given quantities and leave the wake out of consideration. Direct effects of viscosity are disregarded, but the existence of a propeller trailing vortex system is observed. Potential flow theory then suffices to describe most of the flow phenomena. The presence of the ship hull is ignored, hence the main flow is simple (uniform and in axial direction), no boundary effects on the pressure field are considered. Therefore the calculated pressures are nominated as free space pressures.

As said already, the magnitude of the loading and the intensity of the dynamic cavitation are assumed to be known. They have to be obtained from additional and more detailed theoretical models like a lifting surface theory and a theoretical model for the cavitation. The present model for pressure fluctuations is a necessary supplement to such models as general models covering all the effects mentioned are not available or not yet practical.

As the various contributions to the pressure field are related to phenomena of different kinds, there is a need to approach them from the same point of view in order to obtain a correct composition. This is one of the objectives of the present study.

BASIC EQUATIONS

For scalar quantities, like the pressure, an important general relation holds, which is purely based on mathematical considerations. When such a quantity p/ρ has at least continuous spatial derivatives of order two, it follows from Green's representation theorem

that at a point in a volume V :

$$4\pi\frac{p}{\rho} = \iint dS\ \frac{p}{\rho}(\bar{n}\cdot\nabla\frac{1}{D_1}) - \iint dS\ \frac{1}{D_1}(\bar{n}\cdot\nabla\frac{p}{\rho}) = \iiint dV\ \frac{1}{D_1}(\nabla^2\frac{p}{\rho}) \quad (1)$$

D_1 is the magnitude of the position vector of the integration point relative to the point considered in the left hand side of (1). The left hand side of (1) stands for the instantaneous pressure in a point considered in free space away from the propeller. It does not matter whether this point moves or does not move. We choose for convenience's sake to consider a fixed point while the propeller translates in and rotates about the direction of its axis. Also the bounding surfaces move with the propeller.

In the three terms on the right hand side of (1) we need to consider the hydrodynamical and the geometrical aspects. First we deal with the hydrodynamic relationships which connect the pressure, or p/ρ, to the incompressible flow phenomena. Most general is the equation of motion which is written in the following convenient form (see Serrin (3):

$$\nabla(\frac{p}{\rho} + \frac{1}{2}v^2) = -\frac{\partial\bar{v}}{\partial t} + (\bar{v}\times\bar{w}) + \frac{\mu}{\rho}\nabla^2\bar{v} \quad (2)$$

From (2), which contains the first spatial derivative of the pressure, also the second derivative can be derived. Application of the divergence operator to (2) leads for incompressible flow to:

$$\nabla^2(\frac{p}{\rho} + \frac{1}{2}v^2) = \nabla\cdot(\bar{v}\times\bar{w}) \quad (3)$$

which can be transformed into:

$$\nabla^2(\frac{p}{\rho}) = \frac{1}{2}(\bar{w}\cdot\bar{w}) - (\bar{E}\cdot\bar{E}) \quad (4)$$

It is noted that in this relation the time derivative and the kinematic viscosity do not appear. Nevertheless it is generally valid for unsteady and for viscous flow.

A general relation that contains the pressure itself is not available, but the equation of Bernoulli can be used in potential flow regions where viscosity is negligible and without vorticity. This will be done in the next section for the flow around the propeller blades. It is advantageous to describe that flow in a reference system which rotates and translates with the propeller.

We conclude this section by noting that the above equations do not describe the pressure and velocity in the flow explicitly. A numerical solution of eq.(2) is required, satisfying kinematical and dynamical boundary conditions and covering for the potential flow the solution of the Laplace equation. Eq.(1) would then be satisfied identically by an exact solution and be of no further use. However, without a complete numerical solution of the equations, eq.(1) is very useful. This is because firstly the terms on the right hand side of eq.(1) can partly be determined from known boundary conditions, which govern the numerical solutions, hence there is no need to obtain these solutions. Secondly we can work with approximate representations of the flow phenomena like velocity potentials for propeller thickness and cavitation and like vortex distributions for propeller loading. In such a practical situation eq.(1) is a useful tool to investigate the composition of partial contributions and to indicate the omitted interactions.

Propeller Relative Flow

Now in case of a propeller the flow is an onset fluid motion relative to the blades, created by the propeller screw motion and a flow disturbance created by the fact that the blades have thickness, camber and pitch, deviating from helicoidal surfaces and cavitation. The disturbance flow is considered as potential flow. This flow usually is known, say the time and space derivatives of the potential, to an observer moving with the blades. We need to know, however, the time derivative to a not moving observer and therefore we have to find the relation between both.

For unsteady potential flow, which relates the pressure to the velocity field, this equation reads:

$$\frac{p}{\rho} + \frac{\partial\phi}{\partial t} + \frac{1}{2}v^2 = constant \quad (5)$$

which follows from (2) with the following definition of the fluid velocity field in relation to a potential:

$$\bar{v} = +\nabla\phi \quad (6)$$

The time derivative of the potential at a fixed point in space, as it occurs in (5), is related by:

$$\frac{\partial\phi}{\partial t} = \phi_{,t} + V_{rel}\phi_{,s} \quad (7)$$

The *constant* in (5) does not contribute to the first integral, which can be proved exactly. The effects of static height pressure from (2) and (5) in the first and second integrals exactly recover the static pressure at the point under consideration; there is no dynamic effect involved and therefore these terms are further left out of consideration.

For potential flow it follows then from equation (2) that:

$$(\bar{n}\cdot\nabla\frac{p}{\rho}) = -\frac{\partial}{\partial n}\left[\frac{\partial\phi}{\partial t} + \frac{1}{2}v^2\right] \quad (8)$$

Substitution of equations (4,5,6,7,8) into (1) finally

results into the following:

$$
\begin{aligned}
&4\pi\frac{p}{\rho} = \\
&-\iint dS\frac{\partial}{\partial n}\left(\frac{1}{D_1}\right)\left[\phi_{,t} + V_{rel}\phi_{,s} + \frac{1}{2}v^2\right] \\
&+\iint dS\,\frac{1}{D_1}\,\frac{\partial}{\partial n}\left[\phi_{,t} + V_{rel}\phi_{,s} + \frac{1}{2}v^2\right] \\
&-\iiint dV\;\frac{1}{D_1}\left[\frac{1}{2}(\bar{w}\cdot\bar{w}) - (\bar{E}\cdot\bar{E})\right]
\end{aligned}
\qquad (9)
$$

In the two surface integrals of (9) we distinguish impulsive and convective terms which are linear in the velocity potential derivatives and terms which are non-linear in the velocities. If the flow disturbance is small compared with the relative motion of the propeller we can linearize by disregarding the mentioned non-linear terms. For a further evaluation of the linear terms we have to investigate the behaviour of the integrands on the bounding surfaces, i.e. the flow boundary conditions. This is worked out in the next section; here we make some general remarks looking back to equation (1).

The hydrodynamic part of the integrand in the first integral of (1) is simply the pressure related to unsteady lift and equal to zero at the cavitation. It is practical experience that at the operational condition of propellers most often the steady thrust and hence the steady lift force on the blades is not influenced by cavitation. On this observation we base the assumption that the first integral of (1) is dominated by the lifting pressures and that the effect of cavitation is small. Therefore in the next section it is approximated by the case of the non-cavitating blade.

The integrand of the second integral in (1) and in (9) is related to the acceleration of the cavity surface. Here the effect of cavitation is dominating over the effect of the blade itself; this is further revealed in the next section where the kinematic boundary condition is considered.

The third integral in (1) and in (9) is non-linear in derivatives velocity viz. vorticity and deformation. The vorticity term is of special interest as it is a base to investigate contributions from the propeller trailing vortex system, from interaction between the vorticity in the ship wake field and the trailing vortex system and from the socalled propeller-hull vortex. These effects will not be investigated here, however, as formally the third integral can completely be disregarded in case of linearization.

In addition to linearization the practical and simplifying observation is made that the closed integration surfaces in the first and second integral are the surfaces of propeller blades with small thickness to chord ratios. The integration is built up of spanwise and chordwise directions. The normal vectors n on the pressure side and on the suction side will be approximated by the vector normal to the chord, pointing from pressure side to suction side. The positions relative to the point considered, D_1, are approximated by the chordwise position instead of the positions at both sides. These considerations finally result into the following expression for the pressure of one blade:

$$
\begin{aligned}
&4\pi\frac{p}{\rho} = \\
&-\int\frac{dr}{\cos\kappa}\int ds\frac{\partial}{\partial n}\left(\frac{1}{D_1}\right)\left[(\phi^s_{,t}-\phi^p_{,t}) + V_{rel}(\phi^s_{,s}-\phi^p_{,s})\right] \\
&+\int\frac{dr}{\cos\kappa}\int ds\,\frac{1}{D_1}\,\frac{\partial}{\partial n}\left[(\phi^s_{,t}-\phi^p_{,t}) + V_{rel}(\phi^s_{,s}-\phi^p_{,s})\right]
\end{aligned}
\qquad (10)
$$

where the superscripts p and s indicate pressure side and suction side values respectively. The difference in spanwise and radial directions for a raked propeller is accounted for by the cosine of the rake angle κ. Inspection of the terms of (10) reveals that far away from the propeller the linear pressure effects vanish.

In this section we have derived an expression for the pressure field in terms of properties of the velocity potential of the flow around the propeller blades. Typical for the derivation is that we do not start with the general assumption of potential flow for the whole field. Instead the starting point is a general expression for the pressure field in which the adequate properties of the flow field are introduced. Conclusions from this section are:

- the approximation of the pressure field around a cavitating propeller based on linear effects of the disturbance created by the propeller leads to contributions in terms of the velocity potential of the flow around the blades;
- contributions from the trailing vortex system are non-linear effects of the disturbance, hence in a linearized approach they can be ignored;
- through linearization with reference to the relative propeller velocity, the general pressure field expression is reduced to the surface integrals over the propeller blades. Apparently the structures of the flow in the wake and of the flow in the vicinity of the point of observation is irrelevant.

CONTRIBUTIONS TO THE PRESSURE FIELD

The various terms in (10) need further attention in order to relate them to the details of propeller geometry (thickness), loading (lift) and sheet cavitation.

Blade loading

This contribution comes from the first integral of (10),

which is worked out here for the non-cavitating case. In terms of pressure distribution this integral can be rewritten as:

$$\frac{p_5}{\rho} = \frac{1}{4\pi}\int \frac{dr}{\cos\kappa}\int ds \; \frac{p^s - p^p}{\rho} \; \frac{\partial}{\partial n}\left(\frac{1}{D_1}\right) \qquad (11)$$

where the pressure difference between suction side and pressure side is the lift distribution over the propeller blade. It is a distribution of dipoles with their axes in the opposite direction of the lift. Lifting surface models provide the lift distribution on the propeller in a wake. An alternative formulation is in terms of bound vorticity and circulation. The velocity potential terms in (10) can be rewritten as:

$$\left[(\phi^s_{,t} - \phi^p_{,t}) + V_{rel}(\phi^s_{,s} - \phi^p_{,s})\right] = \int_{l.e.}^{s} \gamma_{,t} \, ds + V_{rel} \, \gamma \qquad (12)$$

where γ = the local value of the bound vorticity on the blade and in which the integration is from the leading edge up to the chordwise point s. If we approximate the blade with a lifting line, we can take the local circulation Γ for the integrated vorticity and the lifting line at the midchord position. Then the pressure contribution from blade loading becomes:

$$\frac{p_5}{\rho} = -\frac{1}{4\pi}\int \frac{dr}{\cos\kappa}\left[\frac{c}{2}\,\Gamma_{,t} + V_{rel}\,\Gamma\right]\left[\frac{\partial}{\partial n}\left(\frac{1}{D_1}\right)\right]_{m.c.} \qquad (13)$$

The relative magnitude of the two terms in square brackets depends on the wake field. In many practical cases the second term will dominate.

Blade cavitation and displacement

These contributions come from the second integral of (10). The integrand can be transformed by using the kinematical boundary condition at the blade or cavity surface. This condition is in linearized form:

$$\phi_{,n} = \dot{\tau} + V_{res}\frac{d}{ds}[\tau + T] \qquad (14)$$

It is recalled that the superscripts p and s are used to indicate pressure side and suction side values respectively and that n indicates the direction from pressure side to suction side. Then, with the aid of expression (7) the partial derivatives of the velocity potential in (10) can be rewritten as:

$$\begin{aligned} \phi_{,nt} &= \ddot{\tau} + V_{res}\frac{d}{ds}\dot{\tau} \\ \phi_{,ns} &= \frac{d}{ds}\dot{\tau} + V_{res}\frac{d^2}{ds^2}[\tau + T] \end{aligned} \qquad (15)$$

from which we obtain:

$$\begin{aligned} \frac{\partial}{\partial n}\left[(\phi^s_{,t} - \phi^p_{,t}) + V_{rel}(\phi^s_{,s} - \phi^p_{,s})\right] &= [\ddot{\tau}^s + \ddot{\tau}^p] \\ &+ (V_{res} + V_{rel})\,\frac{d}{ds}[\dot{\tau}^s + \dot{\tau}^p] \\ &+ V_{res}\,V_{rel}\,\frac{d^2}{ds^2}[\tau^s + \tau^p + T^s + T^p] \end{aligned} \qquad (16)$$

In (16) we distinguish contributions from cavity growth acceleration, cavity growth velocity, cavity thickness and blade thickness, which are written out below in complete expressions. It is observed that the difference between V_{rel} and V_{res} can be ignored in view of the linearization and the former is used from here.

Cavity growth acceleration

This contribution comes from the first term in (16). In complete form (see (10)) it becomes:

$$\frac{p_4}{\rho} = \frac{1}{4\pi}\int \frac{dr}{\cos\kappa}\int ds \; \frac{\ddot{\tau}^s + \ddot{\tau}^p}{D_1} \qquad (17)$$

It behaves like a monopole and is the dominating contribution from cavitation.

Cavity growth velocity

This contribution comes from the second term in (16). The complete form (see (10)) becomes after partial integration:

$$\frac{p_3}{\rho} = -\frac{1}{4\pi}\int dr \frac{2V_{rel}}{\cos\kappa}\int ds \; [\dot{\tau}^s + \dot{\tau}^p] \; \frac{\partial}{\partial s}\left(\frac{1}{D_1}\right) \qquad (18)$$

This contribution behaves like a dipole with its axis in chordwise direction.

Cavity and blade thicknesses

As indicated already (16) also contains the displacement effects of cavity and blade thicknesses. Integrating twice partially in chordwise direction leads to the following contributions.The complete contribution from the cavity thickness is:

$$\frac{p_2}{\rho} = \frac{1}{4\pi}\int dr \frac{V_{rel}^2}{\cos\kappa}\int ds \; [\tau^s + \tau^p] \; \frac{\partial^2}{\partial s^2}\left(\frac{1}{D_1}\right) \qquad (19)$$

The complete contribution from the blade thickness is:

$$\frac{p_1}{\rho} = \frac{1}{4\pi}\int dr \frac{V_{rel}^2}{\cos\kappa}\int ds \; T \; \frac{\partial^2}{\partial s^2}\left(\frac{1}{D_1}\right) \qquad (20)$$

The various contributions to the pressure field are usually presented in dimensionless form:

$$K_p = \frac{p}{\rho \, N^2 \, D^2} \qquad (21)$$

We collect the various contributions now and rewrite

them in terms of dimensionless combinations of parameters:

$$K_p = \frac{p}{\rho N^2 D^2} = \frac{1}{8\pi} \int \frac{d(\frac{2r}{D})}{\cos\kappa} \left(\frac{V_{rel}}{ND}\right)^2 \int d(\frac{s}{c}) \sum_{i=1}^{5} k_i \qquad (22)$$

where:

$$\begin{aligned} k_1 + k_2 &= \left(\frac{c}{D}\right)^2 \left(\frac{T}{c} + \frac{\tau}{c}\right) D^3 D_{1,ss}^{-1} \\ k_3 &= -\frac{c}{D} \frac{\dot{\tau}}{V_{rel}} D^2 D_{1,s}^{-1} \\ k_4 &= +\frac{c}{V_{rel}^2} \ddot{\tau} D D_1^{-1} \\ k_5 &= +\frac{p^s - p^p}{\rho V_{rel}^2} D^2 D_{1,n}^{-1} \end{aligned} \qquad (23)$$

The various spatial derivatives of the distance D_1 between points on the hull and points on the propeller are indicated as follows:

monopoles

$$D_1^{-1} = \frac{1}{D_1} \qquad (24)$$

dipoles

$$D_{1,s}^{-1} = \frac{\partial}{\partial s}\left(\frac{1}{D_1}\right) \qquad D_{1,n}^{-1} = \frac{\partial}{\partial n}\left(\frac{1}{D_1}\right) \qquad (25)$$

quadrupoles

$$D_{1,ss}^{-1} = \frac{\partial^2}{\partial s^2}\left(\frac{1}{D_1}\right) \qquad (26)$$

These quantities can be worked out analytically in any coordinate system for the geometry and time dependent blade position; their numerical calculation does not offer any difficulty. In the Appendix the analytical expressions are given.

In this section we have demonstrated the derivation of various contributions to the propeller induced pressure field from one single master equation, viz. eq.(10). Such a derivation is not available in the literature; for a comparison of theoretical prediction methods it may be useful as a common reference. The choice made in the section "Basic Equations" to consider the pressure in a point fixed in space while the propeller motion is translational and rotational relative to the fluid, leads to simple expressions for the contributions. They can be compared with expressions found in the literature, see e.g. Breslin and Andersen (4). The simplicity is obtained by partial integration of the chordwise distributions of the cavity growth velocity and the cavity and blade thicknesses.

In summary the contributions are:
- monopoles for the cavity growth acceleration,
- chordwise directed dipoles for the cavity growth velocity,
- normal directed dipoles for the blade loading and
- chordwise directed quadrupoles for the cavity and blade thicknesses.

DYNAMICS OF SHEET CAVITATION

General model features

Global aspects of dynamic sheet cavitation are described theoretically. First aim is to obtain a robust model for the response of the cavity to the varying conditions on a propeller blade rotating in a wake field. Of subsequent importance is the accuracy of the shape of the cavity; it should be reasonably realistic. A principal feature of the method is that the cavity shape is described with a small number of parameters. Mutual relations between the parameters are fixed but their numerical values are free. In this paper a semi-elliptical shape is assumed for the chordwise cross-sections, following Stern and Vorus (5). This choice fixes the relation between the semi-axis, while their magnitude still has to be determined. Other choices can be made, however.

A second feature is that the velocity potential describing the fluid flow is separated in a dynamic part and a quasi-steady part (5). In the dynamic boundary condition at the cavity surface, i.e. the requirement of constant pressure, then terms for dynamic effects, quasi-steady effects and interaction between these can be distinguished. The restricted number of free parameters allow only an approximate satisfaction of this condition. Therefore an approach is taken to minimize the square of the deviation from constant pressure (5). This leads via the dynamic terms to a set of non-linear second-order ordinary differential equations with time as independent variable. Dependent dynamic variables are the cavity shape parameters, while the equations are controlled by the terms which depend on the quasi-steady conditions on the propeller blade. The quasi-steady terms can be obtained numerically by available means for flows with fixed boundaries.

Numerical solution of the set of equations directly produces the values of the dynamic parameters and their time derivatives, up to and including the required order, for the pressure field calculation. Therefore the method seems to be advantageous to meet the aim mentioned above.

Method equations

The method and elaborations of Stern and Vorus (5) are followed; an overview thereof is given also by Stern (5). Investigations of the method at

MARIN hitherto are reported by Salvati (7); giving special attention to the effects of viscosity and of surface tension. In this paper these effects are disregarded, while a modified version of the set of dynamic equations is used and different quasi-steady flow types are considered in the application. The description below is kept brief; derivations and details of the method are not repeated.

The velocity potential of the flow is composed of a dynamic and a static part

$$\phi = \phi_D + \phi_S \tag{27}$$

which is generally permitted provided that the boundary conditions can be satisfied. Of special interest is the pressure condition at the cavity surface. From the equation of Bernoulli, see (5) and (6), it follows that:

$$p = p_D + p_I + p_S = 0 \tag{28}$$

where we distinguish respectively the *D*ynamic pressure terms, the *I*nteraction pressure terms and the *S*tatic pressure terms:

$$\begin{aligned}
\frac{p_D}{\rho} &= \frac{p(\phi_D)}{\rho} &&= -\frac{\partial \phi_D}{\partial t} - \tfrac{1}{2}(\nabla\phi_D)\cdot(\nabla\phi_D) \\
\frac{p_I}{\rho} &= \frac{p(\phi_D,\phi_S)}{\rho} &&= -\frac{\partial \phi_S}{\partial t} - \tfrac{1}{2}(\nabla\phi_D)\cdot(\nabla\phi_S) \\
\frac{p_S}{\rho} &= \frac{p(\phi_S)}{\rho} &&= \frac{p_\infty}{\rho} - \tfrac{1}{2}(\nabla\phi_S)\cdot(\nabla\phi_S)
\end{aligned} \tag{29}$$

The approximation used by Stern and Vorus (5) to satisfy (28) is obtained by assuming that the cavity sheet has semi-elliptical chordwise cross-sections. This leads to the requirements that

$$\int_0^\pi (p_D + p_I + p_S)\cos(n\eta)\, d\eta = 0 \qquad n = 0,\ 1,\ 2 \tag{30}$$

where the integration variable is the elliptic coordinate in the range between the cavity leading and trailing edges.

The computational efforts for the solution of (28,29,30) are largely reduced by using slightly different environments for the semi-elliptical cavities under the dynamic conditions respectively the static conditions. This is depicted in Figure 1, where in the top picture the cavity is placed on a flat wall, while in the bottom picture the cavity is placed on a profile section. The situation with the cavity on a flat wall is used for an analytical calculation of the Dynamic pressure terms and the Interaction pressure terms of (29). The situation with the cavity on the profile section is used in a numerical calculation of the Static pressure terms of (29).The difference in flow situation means that the effect of the kinematical boundary conditions at the wetted surfaces is different. It is assumed that this is acceptable in connection with the aims of the modelling and with the assumption of an elliptic cavity.

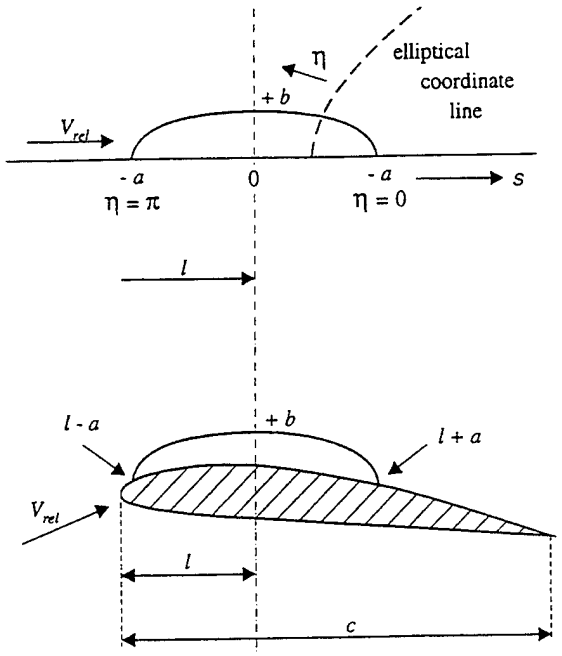


Figure 1 : Semi-elliptic cavity conditions.

In this way, as will be worked out in the following section, we find that the Dynamic pressure terms lead to second order time derivatives of the cavity volume and to non-linear terms in the first order time derivatives. The Interaction pressure terms lead to linear first order time derivatives and represent hydrodynamic damping. The Static pressure terms take fully into account the quasi-steady pressure distribution on the cavity shape on the profile section in a wake. Thus we obtain a non-linear system of equations in which the highest order time derivative, required for the calculation of the pressure field of a propeller, occurs.

Cavity model equations

The cavity volume on one blade is dealt with in chordwise strips, hence the chordwise cross-sectional areas are considered further for which hold:

$$\begin{aligned}
q &= \frac{\pi}{2} ab \\
\dot{q} &= \frac{\pi}{2}(b\dot{a}+a\dot{b}) \\
\ddot{q} &= \frac{\pi}{2}(b\ddot{a}+2\dot{a}\dot{b}+a\ddot{b})
\end{aligned} \tag{31}$$

The requirements (4) derived from the dynamic boundary condition in the previous section are rewritten in

dimensionless form. By defining for $n = 0,1,2$, while $m = 1$ for $n = 0$ and $m = 2$ for $n = 1,2$:

$$\sigma_D^{(n)} = \frac{m}{\pi}\int_0^{\pi} p_D \cos(n\eta)\, d\eta$$

$$\sigma_I^{(n)} = \frac{m}{\pi}\int_0^{\pi} p_I \cos(n\eta)\, d\eta \qquad (32)$$

$$\sigma_S^{(n)} = \frac{m}{\pi}\int_0^{\pi} p_S \cos(n\eta)\, d\eta$$

for the dynamic, interaction and static pressures terms we can write for the pressure requirements (30):

$$\sigma_D^{(n)} + \sigma_S^{(n)} + \sigma_I^{(n)} = 0 \qquad (33)$$

Dealing first with the dynamic pressure terms in the same way as in the literature (5) leads to:

$$\begin{aligned} \frac{1}{\alpha}(b\ddot{a} + 2\dot{a}\dot{b} + a\ddot{b}) &= -F_0 + \sigma_S^{(0)} + \sigma_I^{(0)} \\ -2b\ddot{l} &= 4\dot{b}\dot{l} + \sigma_S^{(1)} + \sigma_I^{(1)} \\ \tfrac{1}{2}(a\ddot{b} - b\ddot{a}) &= -F_2 + \sigma_S^{(2)} + \sigma_I^{(2)} \end{aligned} \qquad (34)$$

where non-linear terms on the right hand sides are collected in:

$$\begin{aligned} F_0 &= \frac{b\dot{a}^2 + a\dot{b}^2}{a+b} + \frac{b}{a}\dot{l}^2 \\ F_2 &= \frac{(\dot{a}-\dot{b})(a\dot{b}+b\dot{a})}{a+b} + 2\frac{b}{a}\dot{l}^2 \end{aligned} \qquad (35)$$

The factor α in the first equation of (34) has been introduced to account for the far field 3-D effects on the near field 2-D description of the (cylindrical) cavity. It is determined from:

$$\frac{1}{\alpha} = \ln\left[\frac{(a+b)/2}{ASPECT\ RATIO}\right] \qquad (36)$$

where the aspect ratio is taken for the practical case of the propeller blade. It yields a value for α between minus 1.0 and 0.0.

Next we deal with the interaction terms. The velocity potentials which are used in the interaction pressure terms, corresponding to the top picture in Fig.1 are for the static flow of an elliptic cylinder in uniform flow and for the dynamic flow of an expanding and moving elliptic cylinder in a fluid at rest. Both can be formulated analytically, see Milne-Thomson (8) and Stern and Vorus (5). The evaluation of the middle expression of (32) can be carried out straightforwardly and results into:

$$\begin{aligned} \sigma_I^{(0)} &= 2\frac{b}{a}\dot{a} \\ \sigma_I^{(1)} &= -2\left[(\dot{a}+\dot{b}) + \frac{a\dot{b} - b\dot{a}}{a+b}\right] \\ \sigma_I^{(2)} &= -2\frac{b\dot{a}}{a+b} \end{aligned} \qquad (37)$$

The left hand side of the first equation of (34) contains the second time derivative of the cavity cross-sectional area as given in (31). By addition and subtraction of the first and the third equation in (34) we can obtain separate equations for both the semi-axes of the cavity ellipse. The second equation of (34) for the chordwise position of the cavity is not used. Instead the condition is used that the leading edge of the cavity remains attached to the chordwise point where the pressure is minimum at inception. This reduces the number of degrees of freedom. The equations describing the dynamical system can finally be written in adequate form; the main equation governing the cross-sectional area is:

$$\ddot{q} = -\frac{\pi\alpha}{2}F_0 + \frac{\pi\alpha}{2}[\sigma_S^{(0)} + \sigma_I^{(0)}] \qquad (38)$$

which has to be used in combination with either:

$$b\ddot{a} = \frac{1}{\pi}\ddot{q} - \dot{a}\dot{b} - F_2 + [\sigma_S^{(2)} + \sigma_I^{(2)}] \qquad (39)$$

or:

$$a\ddot{b} = \frac{1}{\pi}\ddot{q} - \dot{a}\dot{b} + F_2 - [\sigma_S^{(2)} + \sigma_I^{(2)}] \qquad (40)$$

This set of equations demonstrate the dependency of the cavity parameters on the non-linear effects, the interaction effects and the static pressure distributions. In (38) it is seen that the cavity cross-sectional area depends on the pressure integrals of lowest order which is natural. In (39) and (40) the behaviour of the ellipse axes is seen. The first couple of terms on the right hand side of these equations let the axes follow the cross-section in equal proportions, i.e. the axes ratio remains constant. The remaining terms have opposite signs and will cause oscillations of the cavity cross-section at a constant area value.

Finally the calculation of the static pressure terms has to be considered. In this case the flow situation as shown in the bottom picture of Figure 1 is used. The elliptic cavity thickness distribution is added to the propeller blade section profile. The calculation of the static pressure distribution is carried out by a conformal mapping procedure, which is a part of the complete propeller analysis program.

PROPELLER ANALYSIS

The potential flow around the propeller blade with cavitation is built up from various parts. First the flow related to the (noncavitating) propeller blade loading in the wake field is calculated by means of unsteady lifting surface theory (9). The calculations are carried out in the frequency domain. The mean and periodic blade section loadings are obtained as chordwise distributions for a number of harmonics of the shaft rotation frequency. The number of harmonics is taken sufficiently to represent the effects of the non-uniform wake. The chordwise loading distributions for each section, which are composed of a number of base distributions, are transformed into effective two-dimensional angles of attack and camber lines of the blade section profiles (10). This section camber differs from the geometrical camber of the lifting surface and is called the effective camber. As a result of the lifting surface calculation the latter camber distribution is available for each radial position and each blade position, hence as a function of time.

Second the effective camber line is combined with local blade thickness to obtain a twodimensional (wetted) foil section. At any required instant of time a cavity shape is added to this section geometry; the static potential flow around this geometry is calculated by means of a conformal mapping method. This results in a pressure distribution on the foil section with a cavity shape. The pressure distribution includes the static and dynamic effects of the propeller blade thickness and loading in the wake, but excludes the dynamical behaviour of the cavitation. It is called the quasi-static cavity pressure.

Third the potential flow related to the dynamic behaviour of the sheet cavity is considered. For each blade section to be analyzed a solution, in the time domain, is obtained of the set of differential equations derived in the previous section. The coupling between the lifting surface model and the dynamic cavity model goes through the static pressure terms (third equation in (32)).

In this approach the problems of unsteady loading and unsteady cavitation are solved separately and coupled by the, quasi-steady, pressure distribution on the blade sections. The objectives are to obtain a method for prediction, in the low-frequency range, of the dynamic pressure field around a cavitating propeller including non-linear effects and without numerical differentation of the velocity potential and other quantities. A drawback may be that the description of the cavity shape is sectionwise and only with a few parameters per section.

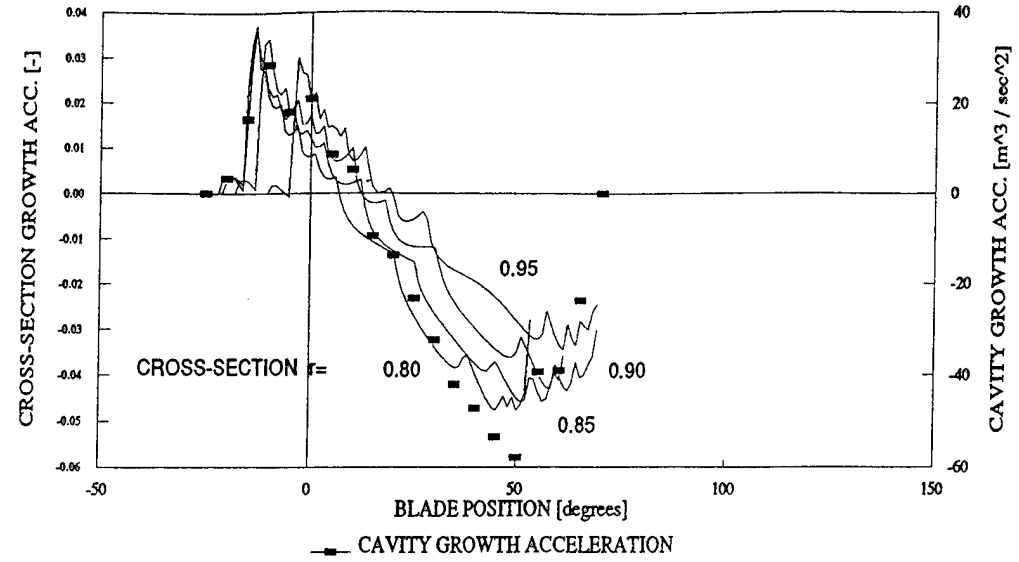
NUMERICAL RESULTS

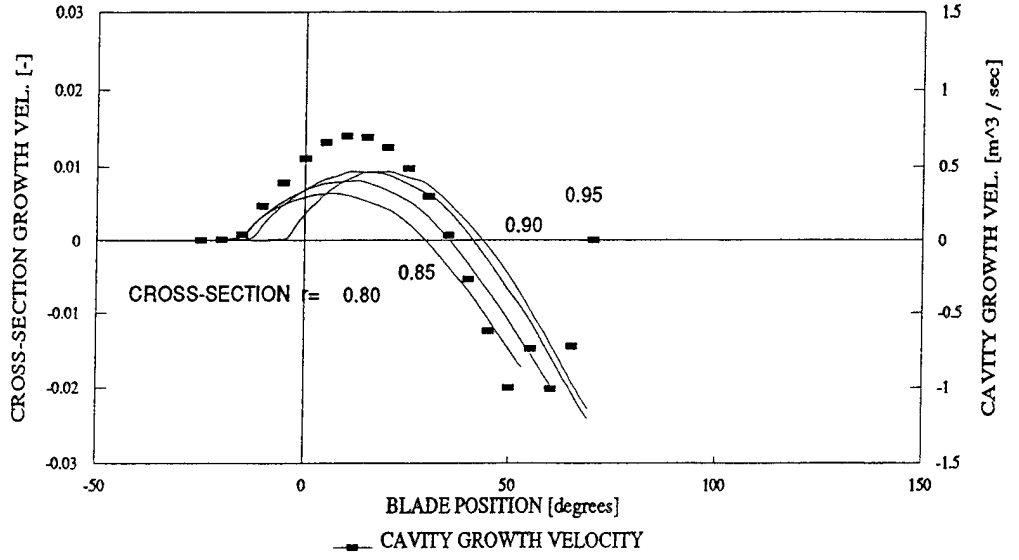
Typical results have been obtained from an analysis of a 4-bladed propeller, diameter = 6.0 m, of a container vessel. The wake field is dominated by a symmetric peak in the axial velocity distribution ranging from - 45 to + 45 degrees in the top region while the depth is half the ship speed. The effective angle of attack variations of the outer blade sections are about 1 degree.

In Figure 2 the acceleration and the velocity of the cavity growth and the cavity volume are shown in the top, middle and bottom pictures respectively. The four full lines in each picture correspond to four radial positions, as indicated, and show the cross-sectional properties. On the scale on the left hand side the quantities are give in non-dimensional form, where the chordlength is the length scale and the reduced frequency the inverse time scale. The rectangular dots give the cavity growth, acceleration and velocity, and the cavity volume for a complete blade. The scales on the right hand side give the physical values. So we can see in the bottom picture that the maximum volume is about 0.032 m^3 at a blade position of about 35 degrees through the top.

The acceleration curves in the top picture of Figure 2 are not smooth but exhibit small peaks. This is caused by the discretization of the blade section contour, described in a number of chordwise points, which are closely spaced near the leading edge and more widely towards the trailing edge of the profile. In the conformal mapping procedure for the calculation of the pressure distribution, the positions of the cavity endpoints are interpolated on the given set of chordwise points. Apparently a finer discretization of the blade section contour can improve the smoothness of the acceleration curves. The solution of the system of differential equations was obtained with time steps corresponding to 1 degree of the angular blade movement. The dots for the cavity volume per blade are given at intervals of 5 degrees, but intermediate values are also available.

The results in Figure 2 correspond to calculations for a fixed ratio of the elliptic cavity axes, viz. a : b = 40 : 2. Hence oscillations of the cavity axes' lengths at a constant cavity volume have been suppressed. The choice of the fixed ratio a : b is of influence on the volume variations, so in general this value has to be left free and is to be found from a solution of the complete set of differntial equations. The additional terms in these equations which control the constant volume oscillations make the solution much more sensitive to inaccuracies in the calculation of the pressure distribution and to the initial conditions. In some cases the cavitation becomes intermittent as desinence occurs





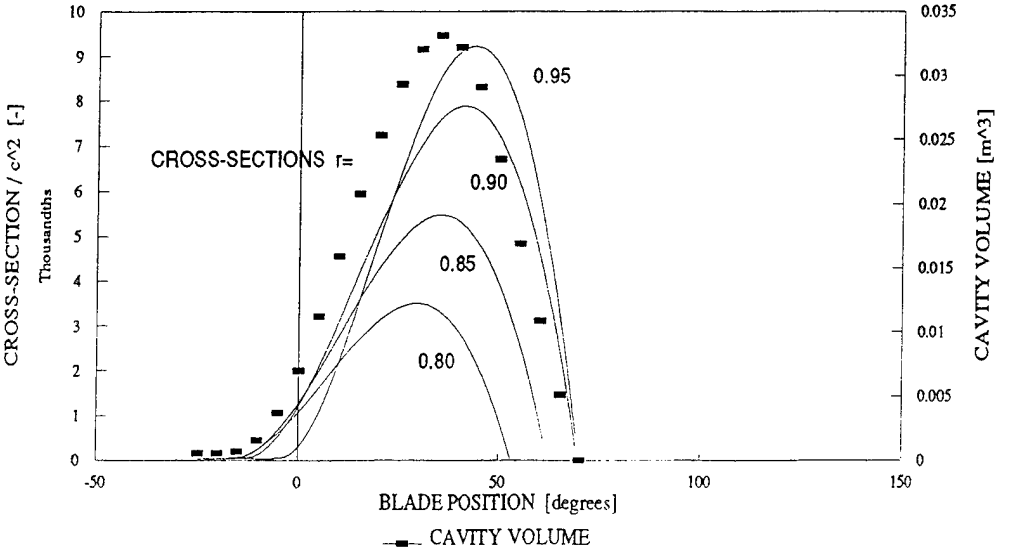


Figure 2 : Dynamic Cavitation Volume Properties for a : b = 40 : 2.

due to collaps of the cavity thickness. The effect of the cavity thickness ratio can be seen from a comparison of the results in Figure 3 with those of Figure 2. The conditions are identical, only the cavity is thinner in Figure 3, viz. a : b = 40 : 2. The overall difference is that cavitation occurs over a larger interval and that the cavity volume is larger. The maximum volume is about 0.11 m^3 at a blade position of 50 degrees.

At the radial positions r = 0.90 and 0.95 the cavity lengths become nearly equal to the chordlengths. As supercavitation is not covered by the theoretical model, an artificial measure is taken to control the occurrence of cavity length larger than 80 percent of the chord. For the part of the cavity beyond this percentage the pressure is taken equal to the stagnation pressure. This enhances the deceleration of the cavity growth as can be seen in the top picture of Figure 3, where for r = 0.90 and 0.95 strong negative values are shown.

CONCLUDING REMARKS

In this paper some aspects of the theoretical prediction of the time-dependent pressure field around a ship propeller are considered. Detailed conclusions are given in the various sections. Here we observe the main features.

- The derivation of the expression for the pressure field from basic flow equations demonstrates that the assumption of potential flow has only to be made for the flow in the vicinity of the propeller blades.
- In a linearized approach, where the propeller induced velocities are smaller than the blade motion velocities, there is no reason to compute contibutions to the pressure field from the trailing vortex system.
- The consolidated pressure field contributions, derived from one master equation, are monopoles, dipoles and quadrupoles.
- In the model for the dynamics of sheet cavitation along the lines set out by Stern and Vorus, it is considered essential that the relation between dynamic flow potential and cavity shape is maintained in analytical form. The solution of the system of equations of this model predicts directly the dominating contribution to the propeller pressure field, i.e. the second time derivative of the cavity volume.
- Numerical results for the propeller of a container vessel show qualitatively realistic values. Further parametric investigations are required to establish the method. In case the elliptic cavity shape is found to be insufficient realistic, other analytical shapes could be used but along the same method.

ACKNOWLEDGEMENT

The author wishes to express his gratitude to Dr G.A.Q. Salvati who at MARIN introduced, investigated and tested the method of Professor F. Stern referred to in this paper. Thanks also to Mr F. Assenberg who implemented the method in the propeller analysis program suit and advised on numerical procedures.

REFERENCES

1. Fine, N.E. and Kinnas, S.A., "The nonlinear numerical prediction of unsteady sheet cavitation for propellers of extreme geometry", 6th International Symposium on Numerical Ship Hydrodynamics, Iowa City, Aug.1993.

2. Kinnas, S.A. and Fine, N.E., "A nonlinear boundary element method for the analysis of unsteady propeller sheet cavitation", 19th Symposium on Naval Hydrodynamics, Seoul, Aug.1992.

3. Serrin, J., "Mathematical principles of classical fluid mechanics", Encyclopedia of Physics, (ed. S.Flügge), Vol.VIII/1, Fluid Dynamics I, Springer.

4. Breslin, J.P. and Andersen, P., "Hydrodynamics of Ship Propellers", 1994, ISBN 0 521 41360 5, Cambridge University Press.

5. Stern, F. and Vorus, W.S., "A nonlinear method for predicting unsteady sheet cavitation on marine propellers", Journal of Ship Research, Vol.27, No.1, Mar.1983, pp.56-74.

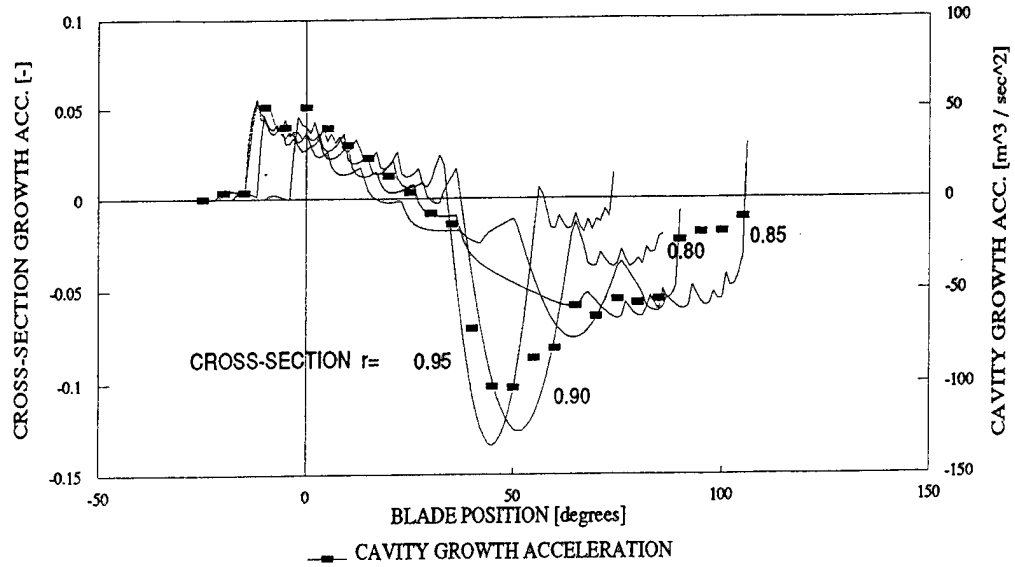
6. Stern, F., "Comparison of computational and experimental unsteady cavitation on a pitching foil", Journal of Fluid Engineering, Vol.111, Sept.1989, pp.290-299.

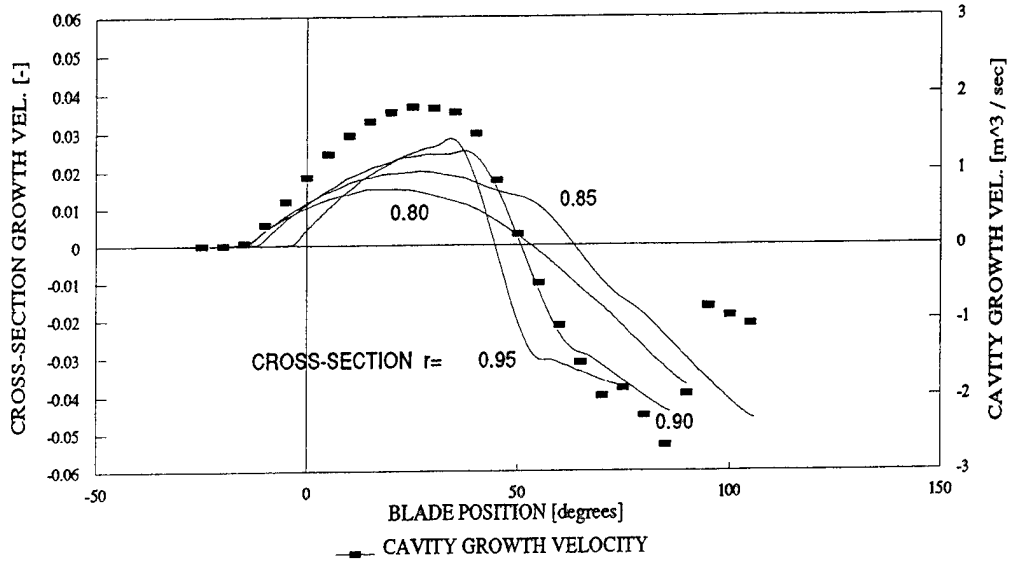
7. Salvati, G.A.Q., "Some physical and mathematical aspects related to the numerical prediction of unsteady sheet cavitation", Cavitation and Multiphase Flow Forum, Toronto, ASME-FED Vol.98, ed. O. Furuya, 1990, pp.93-99.

8. Milne-Thomson, L.M., "Theoretical Hydrodynamics", 5th revised Ed., 1968, MacMillan Press Ltd.

9. Van Gent, W., "Unsteady lifting-surface theory for ship screws: Derivation and numerical treatment of integral equation", Journal of Ship Research, Vol.19, No.4, Dec.1975, pp.243-253.

10. Van Gent, W., "Derivation of propeller blade section properties from lifting surface theory", International Shipbuilding Progress, Vol.27, No.314, 1980.





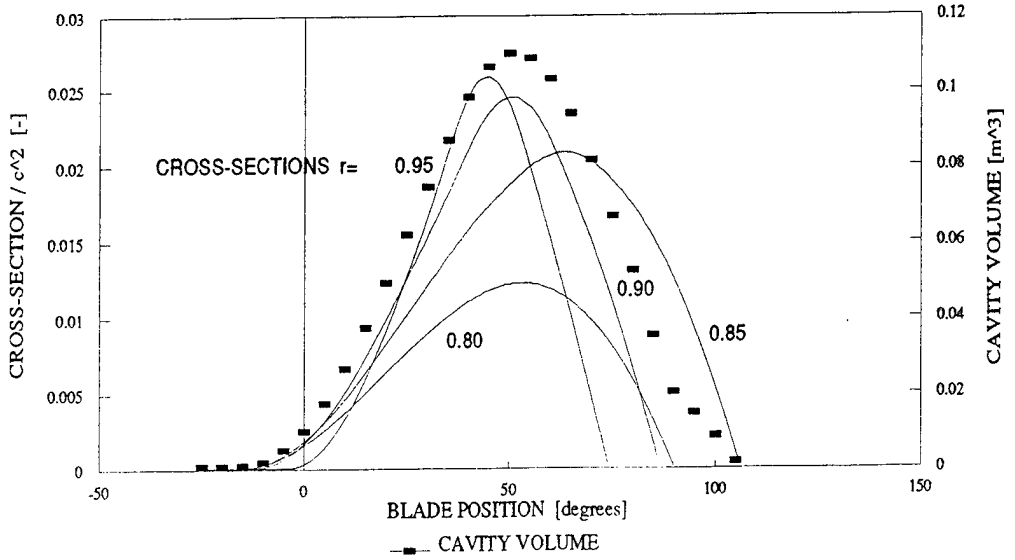


Figure 3 : Dynamic Cavitation Volume Properties for a : b = 40 : 3.

APPENDIX

Distance Related Quantities

In this Appendix the distance between points on the propeller and in the free field and the relevant spatial derivatives are worked out analytically. A Cartesian coordinate system is used with:
* x-axis in forward, propeller translation, direction;
* y-axis from starboard to port side of the ship hull;
* z-axis vertically upward.

Also a cylindrical system is used of which the x-axis is along the center of the propeller shaft forward and the angular position is measured from the z-axis in the direction of, right-handed, propeller rotation. In the Cartesian respectively the cylindrical system the following notations are used:

$$\text{Cartesian} \mid \text{cylindrical}$$
$$x_0,\ y_0,\ z_0, \ \mid \ x_0,\ 0\ ,\ 0\ ,$$

for the reference point on the shaft,

$$x\ ,\ y\ ,\ z\ , \ \mid \ x,\ r,\ \gamma\ ,$$

for a point on the propeller blade and

$$x_p,\ y_p,\ z_p, \ \mid \ x_p,\ R,\ \epsilon\ ,$$

for a point in the field or on the hull.

The relations between blade point and reference point are:

$$x = x_0 - r \sin\kappa - P\,\frac{\theta_m}{2\pi} - s \sin\beta$$

$$\gamma = \gamma_0 - \theta_m - \frac{s}{r}\cos\beta$$

$$\gamma_0 = 2\,\pi\,N\,t$$

where

- γ_0 = the angular blade position of the blade reference line, dependent of
- t = time and
- N = propeller rotation rate, while
- θ_m = midchord skew angle re blade reference line (positive back)
- κ = rake angle (positive back)
- P = local blade pitch
- β = local pitch angle
- s = chordwise distance re midchord (leading edge negative).

It is noted that the angular position of the field point is defined as:

$$\epsilon = \arctan\left(\frac{-y_p}{z_p}\right)$$

Unit vectors in chordwise direction and normal direction are defined as:

$$\bar{s} = (-\sin\beta,\ -\cos\beta)$$
$$\bar{n} = (+\cos\beta,\ -\sin\beta)$$

The distance between a blade point and a point in free space is:

$$D_1 = \sqrt{(x-x_p)^2 + R^2 + r^2 - 2Rr\cos(\gamma-\epsilon)}$$

and its spatial derivatives are:

$$\frac{\partial D_1}{\partial s} = \bar{s}\cdot\nabla D_1 = -\sin\beta\frac{\partial D_1}{\partial x} - \frac{\cos\beta}{r}\frac{\partial D_1}{\partial\gamma} = -\frac{D_2}{D_1}$$

$$\frac{\partial D_1}{\partial n} = \bar{n}\cdot\nabla D_1 = +\cos\beta\frac{\partial D_1}{\partial x} - \frac{\sin\beta}{r}\frac{\partial D_1}{\partial\gamma} = -\frac{D_3}{D_1}$$

where

$$D_2 = +(x-x_p)\sin\beta + R\cos\beta\,\sin(\gamma-\epsilon)$$

$$D_3 = -(x-x_p)\cos\beta + R\sin\beta\,\sin(\gamma-\epsilon)$$

The spatial first derivatives of the inverse distance then follow:

$$D_{1,s}^{-1} = \frac{\partial}{\partial s}\left(\frac{1}{D_1}\right) = -\frac{\bar{s}\cdot\nabla D_1}{D_1^2} = \frac{D_2}{D_1^3}$$

$$D_{1,n}^{-1} = \frac{\partial}{\partial n}\left(\frac{1}{D_1}\right) = -\frac{\bar{n}\cdot\nabla D_1}{D_1^2} = \frac{D_3}{D_1^3}$$

Finally the spatial second derivative of the inverse distance is considered:

$$D_{1,ss}^{-1} = \frac{\partial^2}{\partial s^2}\left(\frac{1}{D_1}\right) = \frac{\partial}{\partial s}\left(D_{1,s}^{-1}\right)$$
$$= \frac{1}{D_1^6}\left[D_1^3\frac{\partial D_2}{\partial s} - 3D_1^2D_2\frac{\partial D_1}{\partial s}\right]$$

which can be worked out with:

$$\frac{\partial D_2}{\partial s} = \bar{s}\cdot\nabla D_2 = -\sin\beta\frac{\partial D_2}{\partial x} - \frac{\cos\beta}{r}\frac{\partial D_2}{\partial\gamma} = D_4$$

$$D_4 = -(\sin\beta)^2 - \frac{R}{r}(\cos\beta)^2\cos(\gamma-\epsilon)$$

into:

$$D_{1,ss}^{-1} = D_4 / D_1^3 + 3D_2^2 / D_1^5$$

All these distance related quantities can be computed numerically for a given propeller blade geometry.

Hydrodynamics of a Body Moving over a Mud Layer

G. Zilman, T. Miloh
(Tel-Aviv University, Israel)

ABSTRACT

A ship is immersed in a layer of clean frictionless water overlaying a layer of fluid mud. The paper is centered on the following subjects:

- wave resistance of a ship moving with constant velocity;
- added masses and damping coefficients of a ship cross-section undergoing periodic oscillations with a prescribed frequency.

The Navier-Stokes equations, modeling the fluid mud, and the boundary conditions are linearized. The ship surface is replaced by wave sources, and the corresponding Green functions are derived. For evaluating the wave resistance (3-D problem) the mud layer is assumed to be shallow. In computing the added masses and damping coefficients (2-D problem) a mud layer of finite depth is considered.

Numerical results are presented for a parabolic strut, a body of revolution and a circular cylinder. It is demonstrated that the presence of a mud layer has a pronounced effect on the wave resistance, as well as on added masses and damping coefficient in a certain range of densimetric Froude numbers and frequencies of oscillation.

NOMENCLATURE

a_{kk}–added mass
b_{kk}–damping coefficient
B–beam of the ship
$\mathcal{D}_{1,2}$–fluid domain of the upper and lower layers
$F_{Rh_2} = U/\sqrt{\epsilon g h_2}$, $F_{R\overline{h}} = U/\sqrt{\epsilon g \overline{h}}$–densimetric Froude numbers
g–acceleration of gravity
$h_{1,2}$–depth of the upper and lower layers respectively
$\overline{h} = 1/(\gamma/h_1 + 1/h_2)$
$\mathbf{k}(k_x, k_y)$–wave number vector
L–length of the ship
$\mathbf{n}$–outward normal of the body surface into the fluid
$p_{1,2}$–dynamic pressure in the upper and lower layers
$\mathbf{r}(x, y)$–field point
$r_h = h_2/h_1$–depth ratio
R_w–wave resistance
S–body surface
T–draft of the ship
$\mathbf{U}(U_x, U_y, U_z)$–vector of ship linear velocity
$\mathbf{V}_2(u_2, v_2, w_2)$–vector of fluid velocity in the lower layer
$\gamma = \rho_1/\rho_2$–density ratio
ζ–interfacial wave elevation
$\epsilon = 1 - \gamma$
ν–kinematic viscosity of fluid mud
ρ_1–density of water
ρ_2–density of fluid mud
$\sigma(x, z)$–equation of ship surface
$\tau = \omega^2/g$
$\phi_{1,2}$–velocity potential in the upper and lower layers
Ω–angular velocity of ship's cross-section in roll motion
ω–frequency of oscillation

INTRODUCTION

In many applications of marine hydrodynamics and for practical purposes it is convenient and customary to define *water of finite-depth* as a water layer bounded by a free surface and a rigid bottom. It is well known that the presence of a rigid sea or river bottom may drastically affect the wave resistance, motion, maneuverability and squat of a ship. It can be said that the general

theoretical approach for evaluating the wave resistance of a ship navigating in finite-depth water has been outlined and summarized in several monographs such as Havelock [1], Kostyukov [2], Newman [3], Sretenskii [4], Wehausen [5], and in numerous papers, including, for instance Kirsh[6], Tuck [8], Lea and Feldman [9], and Mei [10].

We do not intend to discuss here the various theoretical methods for calculating the wave resistance in finite-depth water, as well as the agreement between the theoretical and experimental results. Neither we wish to enter into a lengthy discussion regarding fundamental questions such as the nonlinear phenomena of wave formation, the role of the viscous wake and even the precise definition of the wave resistance in a real fluid. The main goal of the present paper is to examine the effect of a non-rigid bed, since the rigidity of the sea bottom can not always be taken for granted. Very often the bottom of a harbor or the bed of a navigation channel are covered by *mud* or, in other words, by a thin layer of a dense mixture of water and particles of sand, clay, kaolinite, betonit, etc.

The effects of a silt-covered sea bed on the damping of sea waves are documented in a large body of theoretical and experimental works which, as a matter of fact, are related to certain coastal engineering problems, e.g., Dalrymple and Liu [11], Gade [12], Foda, Hunt and Chou [16], Hsiao and Shemdin [13], MacPherson [14] and Mei [15]. However, it is rather remarkable that the hydrodynamic forces acting on a body moving above a silt-covered bottom, to our best knowledge, have been considered only in the pioneering experimental work of Sellmeijer and Oortmerssen [17]. They gave a strong experimental evidence that the proximity of the ship bottom to the mud layer causes a pronounced effect on ship resistance and maneuvering characteristics. Such an effect is related to the *dead-water* phenomenon, which was investigated for a deep inviscid lower layer by Sretenskii [4], Miloh and Tulin [18], Sabuncu [19], Tulin and Miloh [20], and for inviscid lower layer of constant depth by Miloh, Tulin and Zilman [21], and Uspenskii [22].

The induced flow in the upper and lower layers involves a rich variety of physical phenomena of both viscous and inviscid nature. However, the influence of the rheological properties of the bottom material on the wave resistance have not been considered to date neither theoretically nor experimentally. We note that for a Newtonian mud flow the kinematic viscosity can be as large as 10^4 times that of pure water. For example, typical values of mud viscosity for the Rotterdam port range from 10^{-3} m^2/s to 10^{-2} m^2/s [17], while for the Mississippi River, [12] and [13] reported values as high as ν=(0.6–0.9) m^2/s. Thus, it can be expected, that the wave resistance attenuation due to the relatively large viscosity of the mud layer can be rather significant.

The maximum draught of large ships has been always limited by the bottom depth of a harbor or a dredged navigation channel [23]. In nautical practice, the requirements placed on the underkeel clearance are usually chosen with the view to prevent actual ship grounding. Thus, the resulting amplitudes of heave and pitch ship motion in shallow entrance channels are crucial parameters, frequently defining the minimal permissible clearance between the ship keel and the channel bottom.

The governing differential equations of ship motion incorporate added masses and damping coefficients which strongly depend on the water depth and the frequency of the body oscillations, as noted, for example, by Newman [3], Ursell [24], Haskind [26], Yu and Ursell [27], Kim [28], Sayer [29], Lewandowski [30], and Yeung and Vaidhyanathan [31]. In this context, the influence of the water viscosity on the inertial coefficients can be also essential, but only in the low-frequency range (Yeung and Ananthakrishnan [32], Yeung and Wu [33]). That is the reason why in the present investigation we consider the upper water layer as an inviscid fluid.

As already noted, except for [17], there are no theoretical and experimental works which consider the influence of the nonrigid bottom on ship hydrodynamic characteristics. According to [17], the added mass of a ship in sway motion depends mainly on the clearance between the ship bottom and the rigid bed, but not on the underlying mud depth and its features. It should be noted that this result relates to the horizontal oscillations of a body with a comparatively small frequency, which is typical for planar-motion mechanisms (PMM). Usually the frequencies in heave and pitch ship motion are considerable larger than the frequencies of sway and yaw provided by PMM. Thus, it is not clear whether the experimental conditions of [17] are actually relevant to the problem of ship motion in sway and heave with relatively high frequencies.

In the sequel we present:

- a theory of wave resistance for a ship moving over a mud covered bottom;

- a method for evaluating added masses and damping coefficients of a ship section oscillating over a movable bottom;
- numerical results displaying the influence of a mud covered bottom on the hydrodynamical forces acting on a ship.

1 WAVE RESISTANCE

1.1 General Assumptions

Herein two superposed fluid layers are defined by their corresponding depth, density and kinematic viscosity. Strictly speaking, one should note, that the mixing of such layers is inevitable, especially after disturbing the "mud-water" interface by a moving ship. However, in practical terms, the assumption of immiscibility of the layers is strongly supported by the results of field tests, conducted by Sellmeijer and Oortmerssen [17], who found that:

> "The density measurements showed that neither the density of the mud layer nor the density of the water on the top of the layer changed during the passage of the VLCC. After passage, the interface between mud and water was still intact; despite the small keel clearance, the mud was not disturbed."

To render the problem more tractable we also assume that the influence of viscosity of the upper layer on the wave formation is negligible. In the absence of viscous stresses, the fluid motion is irrotational and the velocity potential $\phi_1(x, y, z)$ is a harmonic function. Concerning the lower layer, it should be stressed that the rheological properties of a mud layer are still far from being understood [16] and, for instance, a variety of mud mathematical models, such as Newtonian fluid [11], [12], Bingham-plastic continuum [15], viscoelastic fluid [13], [14] have been suggested in the past.

Following [11], [12] we envisage the Newtonian viscous fluid as a sufficiently proper model for the intended purposes. Later in this paper we assume that the boundary layer on the ship bottom does not plough the interface, which allows us to consider the mud flow as laminar. Actually, under such circumstances the Reynolds number for the lower layer can be defined as follows: $Re_m = u_m h_2/\nu$, where u_m is the typical mud velocity, induced by ship motion. The criterion for transition from laminar to turbulent flow is $Re_m > 2000 - 3000$. The maximum characteristic speed U of a ship navigating in confined shallow water is usually less than 10 knots. In practice the depth of the mud layer does not exceed 2.0 to 4.0 m. Outside the ship boundary layer $u_m \ll U$, and so, due to the large mud viscosity one can presume that the mud motion remains laminar since the transition criteria is satisfied.

According to the experimental [17] and theoretical [21] data, the most pronounced effect of the mud layer on the wave drag, occurs at ship's speeds close to the critical velocity

$$U_c = \sqrt{\epsilon g \bar{h}} \quad (F_{R\bar{h}} = 1)$$

Obviously, for such comparatively low speeds (of the order of few knots), the conventional wave resistance induced by the free surface of the upper layer, is negligibly small. It allows us to consider the free surface as a horizontal rigid plate (the so-called *rigid-lid* approximation) which yields the sufficient for the intended purposes accuracy. Another important assumption, made in order to simplify the consequent analysis, is based on the fact that generally $h_2 << L$, which enables us to introduce the small parameter $\delta = (h_2/L)^2$. In turn, it allows us to employ a rational *shallow-water* approach by expanding the unknown values in asymptotic series in terms of δ.

Finally, it should be mentioned that the investigation, described below, is implemented within the realm of linear water-wave theory.

1.2 Mathematical Formulation

We select a Cartesian coordinate system attached to the moving body in such a manner that the x and y-axis are situated on the undisturbed interface and the z-axis is directed upward.

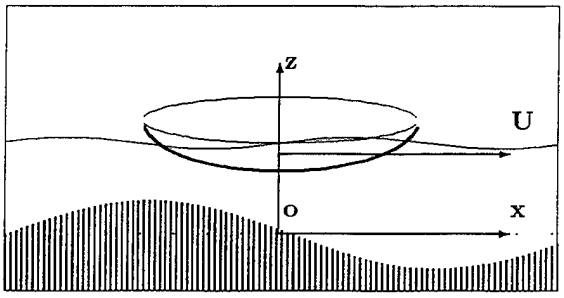


Fig. 1 Coordinate system

The ship moves with a constant velocity U in the direction of the positive x-axis so that its surface $y = \pm\sigma(x, z)$ does not intersect the interface "water-mud". For the sake of convenience,

we consider a correspondent unsteady problem in some inertial coordinate system which coincides with the moving system at some initial time, say at $t = 0$, and use the notation:

$$\frac{\partial}{\partial t} = -U\frac{\partial}{\partial x}.$$

The upper layer is considered to be inviscid, incompressible, homogeneous and irrotational, and, thus, the potential $\phi_1(x, y, z)$ is governed by the Laplace equation:

$$\Delta\phi_1(x, y, z) = 0 \qquad (\text{in } \mathcal{D}_1). \tag{1}$$

The flow in the lower layer is governed by the linearized Navier-Stokes equations:

$$\mathbf{V}_{2t} = -\frac{1}{\rho_2}\nabla p_2 - \mathbf{g} + \nu\Delta\mathbf{V}_2, \tag{2}$$

$$\nabla \cdot \mathbf{V}_2 = 0. \tag{3}$$

1.2.1 Boundary Conditions

The boundary condition on the free surface (the rigid-lid approximation) can be expressed as:

$$\phi_{1z} = 0 \qquad (\text{on } z = h_1). \tag{4}$$

The boundary condition of impermeability on the body surface is:

$$\frac{\partial\phi_1}{\partial n} = \mathbf{U} \cdot \mathbf{n} \qquad (\text{on } S)$$

Strictly speaking, for two inviscid layers the boundary conditions in $\mathcal{D}_1$ are not completed without additional requirements providing the uniqueness of the solution (1). The imposed conditions can be expressed in different mathematical forms. One of them is based on introducing artificial dissipative forces with an infinitesimal dissipative-coefficient $\mu_0 = +0$, which in some respect, relates to the actual infinitesimal fluid viscosity as $\mu_0 \sim \sqrt{\nu}$. That is why we do not impose additional restriction on the potential at infinity, since the fluid mud viscosity provides the dissipation of wave energy in the upper layer and the elimination of the so-called *free waves*.

Due to the assumed linearity of the problem, the following kinematic and dynamic boundary conditions can be applied on the undisturbed interface, at $z = 0$. The kinematic condition implies that a fluid particle initially on the interface will always remain there:

$$\phi_{1z} = \zeta_t \quad (\text{on } z = 0). \tag{5}$$

The vertical and horizontal velocities at the interface must also be continuous, but a discontinuity in the horizontal velocities is also acceptable because we have assumed the water to be a perfect fluid. Thus, only the continuity of the vertical velocities have to be enforced here:

$$w_2 = \phi_{1z} \quad (\text{on } z = 0). \tag{6}$$

At the interface between the water and the compliant bed the normal and tangential stress components must be also continuous. Since the upper layer is assumed to be inviscid, the shear stress in the lower layer just at the interface must be zero. This can be written as:

$$\rho_2\nu(u_{2z} + w_{2x}) = 0 \quad (\text{on } z = 0), \tag{7}$$

$$\rho_2\nu(v_{2z} + w_{2y}) = 0 \quad (\text{on } z = 0). \tag{8}$$

The normal stress is here expressed as

$$-p_1 = -p_2 + 2\rho_2\nu w_{2z} \quad (\text{on } z = \zeta), \tag{9}$$

where the pressure p_1 is determined by Bernoulli's relationship as:

$$p_1 = -\rho_1\phi_{1t} + g\rho_1(h_1 - z) \tag{10}$$

On the rigid bed at $z = -h_2$ the horizontal and vertical velocities must be zero:

$$\mathbf{V}_2 = 0 \quad (\text{on } z = -h_2). \tag{11}$$

1.2.2 Shallow Water Approximation For the Lower Layer

Let us next invoke the assumptions of the shallow-water theory with respect to the lower layer. It is equivalent to hypothesizing that the pressure p_2 is hydrostatic, the vertical component w and its derivatives with respect to (x, y) are small in comparison with the horizontal velocity components u, v and that

$$u_{2zz} \gg u_{2xx}; \quad u_{2zz} \gg u_{2yy}; \quad v_{2zz} \gg v_{2xx}.$$

Within the context of perturbation theory with respect to the small parameter $\delta = (h_2/L)^2$, the Navier-Stokes equations and the boundary conditions (7) and (8) can be reduced to:

$$u_{2t} = -\frac{1}{\rho_2}p_{2x} + \nu u_{2zz},$$

$$v_{2t} = -\frac{1}{\rho_2}p_{2y} + \nu v_{2zz},$$

$$p_{2z} = -\rho_2 g,$$

$$u_{2z} = v_{2z} = 0 \quad (\text{ on } z = 0), \tag{12}$$

$$u_2 = v_2 = 0 \quad (\text{ on } z = -h_2). \tag{13}$$

The above system of PDE's is not sufficient to render a unique solution, since we have only two equations for the three unknown functions u_2, v_2 and ζ. Accounting in the perturbation procedure terms for the first degree in δ, from (3) and (6) we can obtain the required additional relationship. Thus, by taking into account (9) and (10), we finally have:

$$u_{2t} = -\epsilon g \zeta_x + \gamma \phi^0_{1tx} + \nu u_{2zz}, \tag{14}$$

$$v_{2t} = -\epsilon g \zeta_y + \gamma \phi^0_{1ty} + \nu v_{2zz}, \tag{15}$$

$$\zeta_t = \phi^0_{1z} = -\int_{-h_2}^{0} (u_{2x} + v_{2y}) dz, \tag{16}$$

where $\phi^0_1 = \phi_1(x, y, 0)$ and $\phi^0_{1z} = \phi_{1z}(x, y, 0)$.

1.3 The Green Function For the Upper Layer

Applying the Fourier transform

$$FT[f(x,y)] = \hat{f}(k_x, k_y) = \int_{-\infty}^{\infty} f(x,y) e^{-i\mathbf{k}\cdot\mathbf{r}} dx dy,$$

to (14)–(16) and (5), we obtain a second-order ordinary differential equation for the unknown vector $\mathbf{s}(z) = [\hat{u}_2(z), \hat{v}_2(z)]$:

$$\mathbf{s}_{zz} + i \frac{k_x U}{\nu} \mathbf{s} = -\frac{U}{\nu} E \mathbf{k},$$

$$\mathbf{s}(-h_2) = 0; \quad \mathbf{s}_z(0) = 0,$$

where

$$E = \frac{\epsilon g}{k_x U^2} \hat{\phi}^0_{1z} + \gamma k_x \hat{\phi}^0_1.$$

The solution of this equation expresses the unknown functions $\hat{u}, \hat{v}$ in terms of the boundary values $\hat{\phi}^0_1$ and $\hat{\phi}^0_{1z}$ as follows:

$$\mathbf{s} = \frac{i}{k_x} (1 - \frac{\cosh \alpha z}{\cosh \alpha h_2}) E \mathbf{k}, \tag{17}$$

where

$$\alpha = [1 - \text{ sgn}(k_x)] \sqrt{\frac{|k_x| U}{2\nu}}.$$

To formulate the boundary-value problem for the potential ϕ_1 we use the Fourier transform of (16) which together with (17) yields the following relationship:

$$A \hat{\phi}_{1z} - B \hat{\phi}_1 = 0 \quad (\text{ on } z = 0), \tag{18}$$

where

$$A = 1 - \frac{\beta}{F^2_{Rh_2}} \cdot \frac{k^2}{k_x^2}; \quad B = \gamma k^2 h_2 \beta,$$

and

$$\beta = 1 - \frac{\tanh \alpha h_2}{\alpha h_2}.$$

Equation (18) together with the Fourier transform of (1)

$$\hat{\phi}_{1z} - k^2 \hat{\phi}_1 = 0 \quad (\text{ in } \mathcal{D}_1), \tag{19}$$

and the free-surface condition

$$\hat{\phi}_{1z} = 0 \quad (\text{ on } z = h_1), \tag{20}$$

completely define the boundary-value problem for the Fourier transform of the corresponding Green function.

Consider next the fundamental solution of (1) in the following form:

$$\mathcal{E}_3(x - x_0, y - y_0, z, z_0) = -\frac{1}{4\pi} [\frac{1}{r} + \frac{1}{r_1} + G], \tag{21}$$

where

$$r = \sqrt{\rho^2 + (z - z_0)^2}; \quad r_1 = \sqrt{\rho^2 + (z + z_0 - 2h_1)^2},$$

$$\rho^2 = (x - x_0)^2 + (y - y_0)^2$$

and G is a harmonic function satisfying the boundary condition on the interface and on the free surface. According to (20) we have,

$$\hat{G} = M \cosh k(z - h_1).$$

Recalling that

$$FT[\frac{1}{\sqrt{x^2 + y^2 + z^2}}] = \frac{2\pi}{k} e^{-k|z|},$$

and substituting the Fourier transform of (21) into (18), we obtain the formula for the Green function which, after invoking the inverse Fourier transform in polar coordinates, finally yields:

$$\mathcal{E}_3 = -\frac{1}{4\pi} (G_s + G_r), \tag{22}$$

where, for $z' = h - z$ and $z'_0 = h - z_0$, we define:

$$G_s = G^+_s + G^-_s, \tag{23}$$

$$G_s^+ = \sum_{n=-\infty}^{n=\infty} \frac{1}{\sqrt{\rho^2 + (z' + z_0' - 2nh_1)^2}},$$

$$G_s^- = \sum_{n=-\infty}^{n=\infty} \frac{1}{\sqrt{\rho^2 + (z' - z'_0 - 2nh_1)^2}},$$

$$G_r = -\frac{\gamma U^2}{\pi \epsilon g} \int_{-\pi}^{\pi} \cos^2\theta \, d\theta \int_0^{\infty} \frac{A(k)}{D(k,\theta)} e^{ik\chi} dk. \tag{24}$$

For the functions appearing in (24) the following notations are used:

$$A(k) = k{c_i}^2(k) \frac{\cosh kz' \cosh kz_0'}{\sinh^2 kh_1},$$

$$\chi = (x - x_0)\cos\theta + (y - y_0)\sin\theta,$$

$$D = \cos^2\theta - {c_i}^2(k)(1 - \mu),$$

where

$${c_i}^2(k) = \frac{1}{F_{Rh_2}^2} \cdot \frac{\tanh kh_1}{\tanh kh_1 + \gamma k h_2}, \tag{25}$$

$$\mu = F_{Rh_2}^2 \frac{1 - \beta}{\beta} \cos^2\theta,$$

For the particular cases ($\nu \to \infty$ and $h_2 \to 0$) the interface also turns into a rigid plate. Therefore, $G_r \to 0$ and, obviously, the potential is represented by the infinite sum (23). It is also worth mentioning that as $\nu \to +0$, formula (22) reduces to the limiting case of two inviscid layers [21].

1.4 Evaluation of Wave Resistance

The general formula for the velocity potential generated by the moving body is given by

$$\phi_1 = \int_S q(x_0, y_0, z_0) \mathcal{E}_3(x - x_0, y - y_0, z, z_0) dS \,, \tag{26}$$

where $q(x_0, y_0, z_0)$ denotes the source distribution on S. We express the wave resistance of a body moving in the upper layer in terms of the Krein-Kostyukov formula [2], i.e.:

$$R_w = -\rho_1 \int_S q(x, y, z) \frac{\partial K(x, y, z)}{\partial x} dS, \tag{27}$$

where

$$K = -\frac{1}{4\pi} \int_S q(x_0, y_0, z_0) G_r \, dS. \tag{28}$$

It should be noted that the term G_s does not contribute to (27) since

$$\frac{\partial}{\partial x} G_s(x, x_0; y, y_0; z, z_0) = -\frac{\partial}{\partial x} G_s(x_0, x; y_0, y; z_0, z)$$

and, consequently, the corresponding integration in (27) reduces to zero. The substitution of (24) into (27) yields the following formula for the wave resistance:

$$R_w = \frac{\gamma \rho_1 U^2}{\pi^2 \epsilon g} \int_0^{\pi/2} \cos^3\theta \int_0^{\infty} \frac{k^2 c_i^2 |H(k,\theta)|^2 \xi_2 \, dk \, d\theta}{(\cos^2\theta - c_i^2 + \xi_1)^2 + \xi_2^2}, \tag{29}$$

where $\xi_1 = \mathrm{Re}(\mu c_i^2)$, $\xi_2 = \mathrm{Im}(\mu c_i^2)$ and $H(k,\theta)$ denotes the Kochin function:

$$H(k,\theta) = \int_S q \frac{\cosh k(z - h_1)}{\sinh kh_1} e^{ik(x\cos\theta + y\sin\theta)} dS. \tag{30}$$

1.4.1 Inviscid Lower Layer

For zero viscosity $|\mu| \sim \sqrt{\nu} \to +0$ formula (29) can be transformed by employing the following formal relationship:

$$\lim_{|\xi_{1,2}| \to +0} \frac{\xi_2}{(\cos^2\theta - c_i^2 + \xi_1)^2 + \xi_2^2} = \pi \frac{\delta(k - k_0)}{|{c_{ik}}^2(k_0)|},$$

where $\delta(x)$ denotes the delta-function,

$${c_{ik}}^2(k_0) = \left. \frac{\partial {c_i}^2}{\partial k} \right|_{k=k_0},$$

and $k_0(\theta)$ is the root of the equation:

$$\cos^2\theta - {c_i}^2(k_0) = 0.$$

Thus, the inner integration of (29) is essential only for $k = k_0$. By changing the integration variable from θ to $\lambda = k_0(\theta)$, we have:

$$R_w = \frac{\gamma \rho_1 U^2}{2\pi \epsilon g} \int_{\lambda_0}^{\infty} c_i^4(\lambda) |H(\lambda)|^2 \frac{\lambda^2 d\lambda}{\sqrt{1 - {c_i}^2(\lambda)}}. \tag{31}$$

Here the Kochin function is the same as in (30), but with the following new notations:

$$\cos\theta = c_i; \quad \sin\theta = \sqrt{1 - {c_i}^2}.$$

The lower limit of the integral (31) is defined as follows:

$$\lambda_0 = \begin{cases} 0 & \text{if} \quad F_{R\bar{h}} > 1 \\ \text{root of } {c_i}^2(\lambda) - 1 = 0 & \text{if} \quad F_{R\bar{h}} < 1 \end{cases}$$

It should be noted that formula (31) is valid for both shallow and finite-depth lower layers . The only difference is that for a lower layer of finite depth the corresponding formula (25) should be written in the following form [21]:

$$c_i{}^2(k) = \frac{1}{F_{Rh_2}^2} \cdot \frac{\tanh kh_1 \tanh kh_2}{(\tanh kh_1 + \gamma \tanh kh_2)kh_2}. \tag{32}$$

1.4.2 Unbounded Upper Layer

Within the context of the present investigation it is instructive to verify the validity of the shallow-water approximation by using (31). The shallow-water assumption relates only to the lower layer, thus, it is expedient to neglect the influence of the free surface and to consider the limit $h_1 \to \infty$. Under such circumstances the wave resistance is a result of wave-making phenomena only on the interface. It should be noted in addition, that the hydrodynamics of a submersible moving near a silt-covered bottom, has an independent theoretical and practical interest. For an unbounded upper layer, the Kochin function is given by,

$$H(\lambda,\theta) = \int_S q(x,y,z)\mathrm{e}^{-\lambda z + i\lambda(x\cos\theta + y\sin\theta)}dS$$

In order to demonstrate the procedure for evaluating the wave resistance, let us consider a triaxial ellipsoid with semi-axes $a_e \geq b_e \geq c_e$ moving in such a manner that the distance between its longitudinal axis and the plane of the undisturbed interface is z_h. Following Kochin [34], we express the function H as:

$$H = (2\pi)^{3/2} a_e b_e c_e \frac{2iU\cos\theta}{2 - A_0} \frac{J_{3/2}(\lambda\varrho)}{\sqrt{\lambda}\varrho^{3/2}} e^{-\lambda z_h}, \tag{33}$$

where $J_{3/2}(x)$ is the Bessel function,

$$\varrho = \sqrt{a_e{}^2\cos\theta^2 + b_e{}^2\cos\theta^2 - c_e{}^2},$$

$$A_0 = a_e b_e c_e \int_0^\infty \frac{du}{u_a\sqrt{u_a u_b u_c}},$$

and $u_a = a_e{}^2 + u$, $u_b = b_e{}^2 + u$, $u_c = c_e{}^2 + u$. This yields the following expression for the wave resistance:

$$R_w = a_w \int_{\lambda_0}^\infty \lambda c_i^6(\lambda) \frac{J_{3/2}^2(\lambda\varrho)}{\varrho^3} \frac{d\lambda}{\sqrt{1 - c_i{}^2(\lambda)}}. \tag{34}$$

Here $\overline{\varrho} = \varrho/a_e$ and

$$a_w = \frac{16\pi^2\rho_1 U^2}{(2 - A_0)^2} \frac{b_e{}^2 c_e{}^2 h_2}{a_e}.$$

In addition, for a lower layer of finite depth

$$c_i{}^2(k) = \frac{1}{F_{Rh_2}^2} \cdot \frac{\tanh(kh_2)/kh_2}{1 + \gamma\tanh kh_2}, \tag{35}$$

whereas for a shallow lower layer

$$c_i{}^2(k) = \frac{1}{F_{Rh_2}^2} \cdot \frac{1}{1 + \gamma kh_2}. \tag{36}$$

1.4.3 Shallow Upper Layer

It can be rigorously shown that formulas (31) and (34) always yield bounded positive values for the wave resistance. As already mentioned, the shallow water approach is equivalent to approximating the integrand (31) in terms of an asymptotic series with respect to kh_2. The series is truncated after the first term of the expansion of $\tanh kh_2$. However, if we assume that the upper layer is also shallow and accordingly replace $\tanh kh_1$ by kh_1, then the formula for the wave resistance will be incorrect. Indeed, for this case (32) yields that

$$\lim_{\tanh kh_1 \to kh_1} c_i^2(k) = c_{i0}^2 = \frac{1}{F_{R\bar{h}}^2}$$

and

$$R_w = \frac{\gamma\rho_1 U^2}{2\pi\epsilon g h_1^2} \frac{c_{i0}^4}{\sqrt{1 - c_{i0}^2}} \int_0^\infty |H(\lambda)|^2 d\lambda.$$

Thus, at the critical densimetric Froude number $F_{R\bar{h}} = 1$, the wave-drag formula contains a square-root singularity. Certainly, it can be said, that the practical use of this result is very restricted. However, it clearly shows that at the vicinity of the critical Froude number the variation of the wave drag curve exhibits a very sharp peak and a fast decay for $F_{R\bar{h}} \gg 1$. The other important result is that the ultimate influence of the free surface on the wave resistance strongly depends not only on the ratio h_2/L but also on the ratio h_1/L.

1.5 Numerical Results

Herein we present some typical results of calculations for two particular bodies. The first is a triaxial ellipsoid,

$$y = \sigma(x,z) = \pm b_e\sqrt{1 - x^2/a_e^2 - z^2/c_e^2},$$

and the other is a parabolic strut:

$$\sigma(x,z) = \pm\frac{B}{2}(1-4x^2/L^2) \quad (\text{ for } -T < z < 0).$$

The dimensions of both forms are presented in Table 1.

Table 1. Particulars of ships

Body of revolution			
a_e	b_e	c_e	z_h
50 m	5 m	5 m	7 m
Parabolic strut			
L	B	T	h_1
220 m	33.8 m	13.5 m	16.8 m

Fig.2 shows the variation of the wave resistance coefficient

$$C_x = 2R_w/(\rho_1 U^2 S)$$

versus the densimeter Froude number for a body of revolution moving above an inviscid lower layer. The computation were done by employing formulas (35) (finite-depth) and (36) (shallow-water).

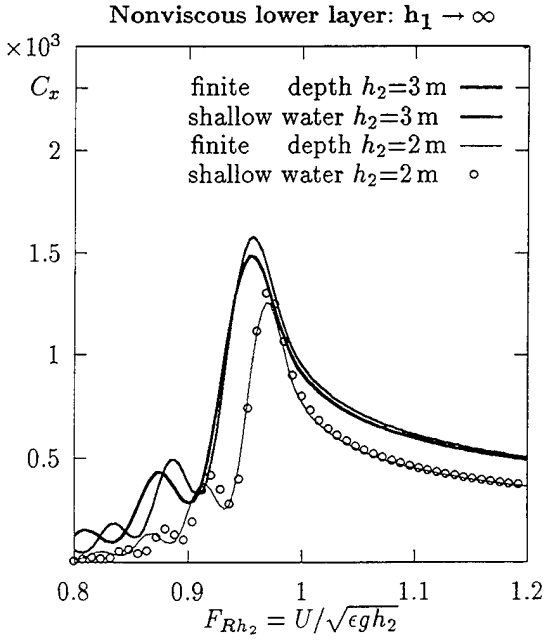


Fig. 2 Wave resistance coefficient of a body of revolution: γ=0.833

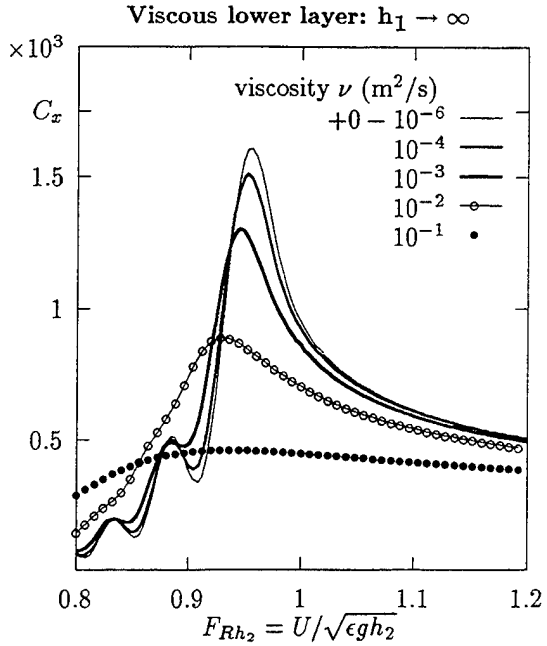


Fig. 3 Wave resistance coefficient of a body of revolution: h_2=3 m, γ=0.833

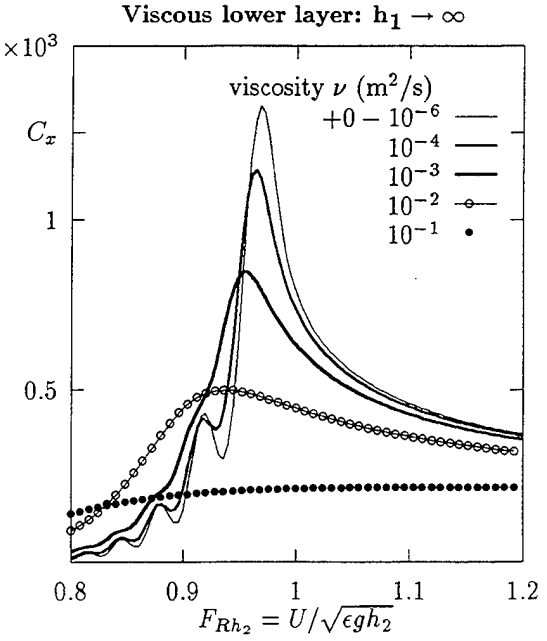


Fig. 4 Wave resistance coefficient of a body of revolution: h_2=2 m, γ=0.833

It can be seen that the corresponding agreement between these two approaches, is quite well at least as far as the wave resistance is concerned.

It is a clear indication that the shallow-water approach can also serve as a quite accurate approximation for analyzing the case of a viscous lower layer. Fig.3 and Fig.4 depict the wave resistance coefficient for the same body of revolution computed by using formula (29) and the Kochin function (33). They display a drastic influence of the mud viscosity on the wave resistance which results in a considerable reduction of the typical sharp peak at the vicinity of the critical Froude number $F_{R\bar{h}} \approx F_{Rh_2} \approx 1$.

The wave resistance of a parabolic ship was computed by invoking the Michell's thin-ship formula. Thus, the integration in the Kochin function was performed over the wetted area of the ship centerplane whereas the source distribution was determined by the formula $q = -2U\sigma_x(x,z)$. Fig. 5 illustrates the influence of the viscosity of the mud layer on the wave resistance coefficient for a parabolic strut. It can be seen, that the presence of the viscous lower layer significantly affects the wave resistance. These results are in full qualitative agreement with the experimental data reported in [17]. Thus, the influence of the mud viscosity on the wave resistance may be quite considerable.

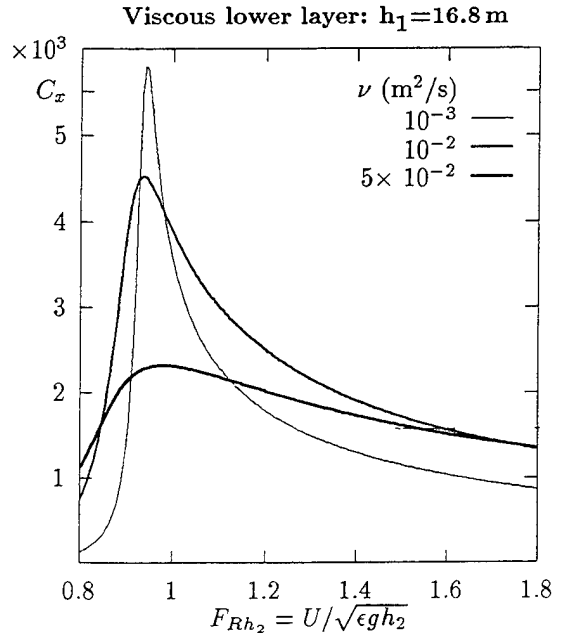


Fig. 5 Wave resistance coefficient of a parabolic strut: h_2=2.5 m, γ=0.7

2 THE ADDED MASSES AND DAMPING COEFFICIENTS

2.1 Mathematical Formulation

In present work we employ the geometric slenderness of a ship, which enables to invoke the strip theory and to consider the flow in each transverse ship section only in two dimensions and independently of the forward speed.

Thus, we study the problem of a ship cross-section which is partially immersed in a layer of water overlaying a viscous fluid of greater density and bounded below by a horizontal rigid plane. The body undergoes a forced periodic motion with a prescribed frequency ω.

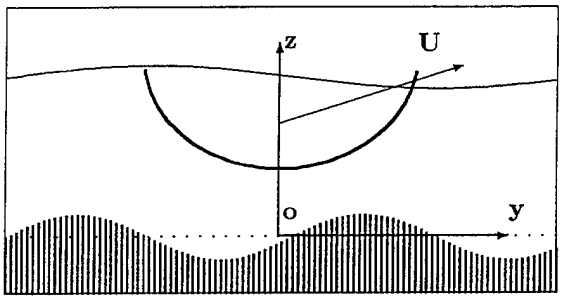


Fig. 6. Coordinate system.

The velocity potentials, velocities and all time-depending functions can be expressed as:

$$f(y,z,t) \equiv \mathrm{Re}[f(y,z)\mathrm{e}^{-i\omega t}].$$

For an inviscid upper layer the velocity field can be expressed as a gradient of a potential function $\phi_1(y,z,t)$ satisfying the two-dimensional Laplace equation:

$$\phi_{1yy} + \phi_{1zz} = 0.$$

For the lower layer we propose to model the mud as an incompressible viscous medium governed by the linearized Navier-Stokes equations and the continuity equation [35]:

$$\phi_{2yy} + \phi_{2zz} = 0,$$

$$\psi_{2t} = \nu(\psi_{2yy} + \psi_{2zz}),$$

$$v_{2y} + w_{2z} = 0,$$

where the components of field velocities v_2, w_2 are splited into a potential and rotational part as follows:

$$v_2 = \phi_{2y} + \psi_{2z}; \quad w_2 = \phi_{2z} - \psi_{2y}.$$

The pressure in both layers can be determined solely from the potential parts by using the relationships

$$p_j = -\rho_j \phi_{jt} - \rho_j g z \quad (j = 1, 2).$$

The potential ϕ_1 is subject to the linearized boundary condition on the free-surface according to:

$$\phi_{1tt} + g\phi_{1z} = 0 \quad (\text{on } z = h_1).$$

On the interface the shear-stress condition (8) becomes

$$2\phi_{2yz} + \psi_{2zz} - \psi_{2yy} = 0 \quad (\text{on } z = 0). \quad (37)$$

In terms of the velocity potential and the stream function the kinematic and dynamic boundary conditions on the interface (6) and (9) can be rewritten as:

$$\zeta_t = \phi_{2z} - \psi_{2y} = \phi_{1z} \quad (\text{on } z = 0), \quad (38)$$

$$\rho_2(\phi_{2t} + g\zeta) + 2\rho_2 \nu w_{2z} = \rho_1(\phi_{1t} + g\zeta) \quad (\text{on } z = 0) \quad (39)$$

On the rigid bed of finite depth $z = -h_2$, the no-slip boundary conditions (11) are:

$$v_2 = \phi_{2y} + \psi_{2z} = 0 \quad (\text{on } z = -h_2), \quad (40)$$

$$w_2 = \phi_{2z} - \psi_{2y} = 0 \quad (\text{on } z = -h_2). \quad (41)$$

The final condition to be applied on the contour of the body is:

$$\frac{\partial \phi_1(y, z, t)}{\partial n} = (U_2\Lambda_2 + U_3\Lambda_3 + U_4\Lambda_4)\mathrm{e}^{-i\omega t}, \quad (42)$$

where $U_2 \equiv U_y$, $U_3 \equiv U_z$, $U_4 \equiv \Omega$, $\Lambda_2 = \cos(n, y)$, $\Lambda_3 = \cos(n, z)$ and $\Lambda_4 = y\cos(n, z) - z\cos(n, y)$. The assumption of linearity allows us to represent the potential as a sum of three modes corresponding to ship motion in sway ($k = 2$), heave ($k = 3$) and roll ($k = 4$) respectively:

$$\phi_1(y, z, t) = \mathrm{e}^{-i\omega t} \sum_{k=2}^{4} U_k \phi_1^k(y, z).$$

Thus, the problem is reduced to three similar boundary-value problems for the Kirchhoff potentials,

$$\frac{\partial \phi_1^k(y, z)}{\partial n} = \Lambda_k. \quad (43)$$

If both layers are inviscid, in order to make the solution determinate the partial potentials have to satisfy an appropriate radiation condition. However, even an infinitesimal viscosity of the fluid mud $\nu = +0$ also provides the unique solution of the present boundary-value problem. Finally, the added masses and damping coefficients are defined by the well known formula [3], [26]:

$$a_{kk} - \frac{1}{i\omega} b_{kk} = -\rho_1 \int_{\partial D} \phi_1^k \Lambda_k ds(y, z) \quad k = 2, 3, 4, \quad (44)$$

where $ds(y, z)$ is the line element of ∂D which denotes the boundary of the submerged portion of the ship cross-section.

2.2 Boundary Integral Equation

Recalling that the considered method is applicable to all types of motion, it is convenient to drop tacitly the corresponding subscripts.

The body surface is represented by a layer of wave-sources distributed over ∂D

$$\phi_1(y, z, t) = \int_{\partial D} q(y_0, z_0) \mathcal{E}_2(y, y_0; z, z_0; t) ds(y_0, z_0), \quad (45)$$

where

$$\mathcal{E}_2 = \frac{\mathrm{e}^{-i\omega t}}{2\pi} \left[\frac{1}{2} \ln \frac{(y - y_0)^2 + (z - z_0)^2}{(y - y_0)^2 + (z + z_0)^2} + G \right]. \quad (46)$$

This representation together with the boundary condition (43), yield the following well known Fredholm integral equation of the second kind for the source density distribution;

$$\frac{q(y, z)}{2} + \int_{\partial D} q(y_0, z_0) \frac{\partial \mathcal{E}_2(y, y_0; z, z_0)}{\partial n} ds = \Lambda. \quad (47)$$

Discretization techniques of various degrees of sophistication may be used to solve this equation. Here we choose to approximate the section contour by a number of N straight segments, and to replace the contour integral by an appropriate quadrature. The integral equation then reduces to a complex system of linear algebraic equations in the form of

$$\{A^{ij}\}\{q^j\} = \{\Lambda^i\} \quad i, j = 1, 2, \cdots, N,$$

where i, j denote the specific segment. The corresponding elements of the complex $N \times N$ matrix $\{A\}$ are:

$$A^{ij} = l^j(1-\delta^{ij})\frac{\partial \mathcal{E}_2^{ij}}{\partial n} + \frac{\delta^{ij}}{2},$$

where l^j denotes the length of the jth linear segment and δ^{ij} is a Kronecker delta. It should be noted that for such a discretization the function $\mathcal{E}_2^{ij}$ and its derivatives have to be evaluated at the center of the jth segment. This requirement is imposed by the singular behavior of the kernel of the integral equation (47) and provides the correct limit of the quadrature to the principal-value integral as $N \to \infty$. Once the numerical solution of this equation is found, the added masses and damping coefficients can be directly computed by employing the corresponding quadratures in the right-hand side of (44) and (45).

2.3 The Green Function For a Pulsating Source

Let us next invoke the Fourier transform

$$\hat{f}(k) = \int_{-\infty}^{\infty} f(y)\mathrm{e}^{-iky}dy \qquad (48)$$

and look for a solution of the problem in terms of the potential $\phi_2(y,z)$ and the stream function $\psi_2(y,z)$ in the following form:

$$\hat{\phi}_2 = A\cosh kz + B\sinh kz,$$

$$\hat{\psi}_2 = C\cosh lz + D\sinh lz,$$

where $l = \sqrt{k^2 - i\omega/\nu}$. The boundary conditions (40) and (41) on the rigid bed, the shear-stress condition (37) and the kinematic conditions on the interface (38) allow to express the unknown constants A, B, C, D and, consequently, the functions $\hat{\phi}_2$, $\hat{\psi}_2$ and $\hat{\zeta}$ in terms of $\hat{\phi}_1^{\,0} = \hat{\phi}_1(y,0)$. By substituting them into (39) we obtain the following interfacial boundary condition:

$$a\hat{\phi}_{1z} + b\hat{\phi}_1 = 0 \quad (\text{on } z=0), \qquad (49)$$

where $b = i\omega\gamma$,

$$a = \frac{\epsilon g}{\omega^2} + \frac{i\nu^2}{\omega k}\cdot\frac{m_1 + m_2 + m_3 S_k^{(2)} S_l^{(2)}}{kC_k^{(2)}S_l^{(2)} - lC_l^{(2)}S_k^{(2)}},$$

$$m = (2k^2 - i\omega/\nu); \quad m_1 = 4k^2 lm;$$

$$m_2 = -l(4k^2+m^2); \quad m_3 = k(4k^2l^2+m^2),$$

and

$$S_k^{(j)} = \sinh kh_j; \quad C_k^{(j)} = \cosh kh_j, \quad (j=1,2)$$

$$S_l^{(2)} = \sinh lh_2; \quad C_l^{(2)} = \cosh lh_2.$$

The above interfacial condition, the boundary condition on the free surface

$$\hat{\phi}_{1z} - \tau\hat{\phi}_1 = 0 \quad (\text{on } z = h_1), \qquad (50)$$

and the governing equation

$$\hat{\phi}_{1zz} - k^2\hat{\phi}_1 = 0, \qquad (51)$$

enable us to define the corresponding Green function. Applying the Fourier transform (48) to the fundamental solution (46) we have:

$$\hat{\phi}_1(k,z) = \frac{\pi}{|k|}[\mathrm{e}^{-|k(z-z_0)|} - \mathrm{e}^{-|k(z+z_0)|}] + \hat{G}(k,z).$$

The substitution of this representation into (49) and (50) renders the following boundary conditions:

$$\hat{G}_z - \tau\hat{G} = 2\pi f_1 \quad (\text{on } z = h_1)$$

$$a\hat{G}_z + b\hat{G} = 2\pi f_2 \quad (\text{on } z = 0),$$

where

$$f_1 = \mathrm{e}^{-|k|h_1}(1 + \frac{\tau}{|k|})\sinh(|k|z_0)$$

and

$$f_2 = -a\mathrm{e}^{-z_0|k|}.$$

We seek a solution of (51) in the form:

$$\hat{G}(k,z) = M_1\cosh\, kz + M_2\sinh\, kz,$$

where the unknowns M_1 and M_2 can be determined from the boundary conditions on the free-surface and the interface. Thus, the expression for the Green function can be written as:

$$G(y,z) = \int_{-\infty}^{\infty}\frac{\alpha_1\cosh kz + \alpha_2\sinh kz}{D(k,\nu)}\mathrm{e}^{ik(y-y_0)}dk, \qquad (52)$$

where

$$\alpha_1 = akf_1 - [kC_k^{(1)} - \tau S_k^{(1)}]f_2,$$

$$\alpha_2 = -bf_1 + [kS_k^{(1)} - \tau C_k^{(1)}]f_2,$$

and

$$D(k,\nu) = ak[kS_k^{(1)} - \tau C_k^{(1)}] - b[kC_k^{(1)} - \tau S_k^{(1)}]. \qquad (53)$$

An alternative form of the potential $\phi_1(y,z)$ can be obtained by including the logarithmic term of (46) in the integral representation (52) for $(z-z_0)>0$, yielding:

$$\phi_1(y,z) = -\int_{-\infty}^{\infty} \frac{N(k,z,z_0)}{D(k,\nu)} \frac{\exp[ik(y-y_0)]}{k} dk, \tag{54}$$

where

$$N(k,z,z_0) = N_1(k,z)N_2(k,z_0),$$

$$N_1(k,z) = [k\cosh k(h_1-z) - \tau \sinh k(h_1-z)],$$

and

$$N_2(k,z_0) = [ak\cosh kz_0 - b\sinh kz_0].$$

For the case of an inviscid lower layer, the equation

$$D(k,+0) = 0 \tag{55}$$

reduces to the classical dispersion relation [35], which has two positive real roots and an infinite number of purely imaginary roots. If the lower layer viscosity is finite the dispersion relation yields a set of complex roots

$$r_n = r_{rn} + ir_{in} \quad n = 1,2,\cdots$$

in the complex upper half-plane $\tilde{k} = k + ik'$. The real part of $r_{1,2}$ represents the real wave number which is related to the far-field wave length and its positive imaginary component determines the spatial damping rate. The imaginary parts of the roots r_3, $r_4, \cdots$ define the near-field disturbances and their real parts determine the corresponding damping rate. Thus, the two roots $r_{1,2}$ and the infinite number of roots r_3, $r_4, \cdots$ are located in the upper half-plane as depicted in Fig.7.

For illustration, we show in Fig. 8 the imaginary part of the nondimensional wave number $\overline{r}_{i1} = r_{i1}\sqrt{gh_1}/\omega$, while Fig.9 displays the real part of the same wavenumber $\overline{r}_{r1} = r_{r1}\sqrt{gh_1}/\omega$.

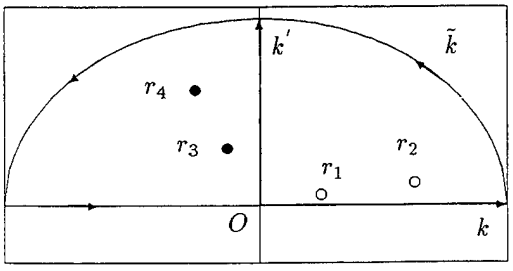


Fig. 7 Location of roots in the complex plane.

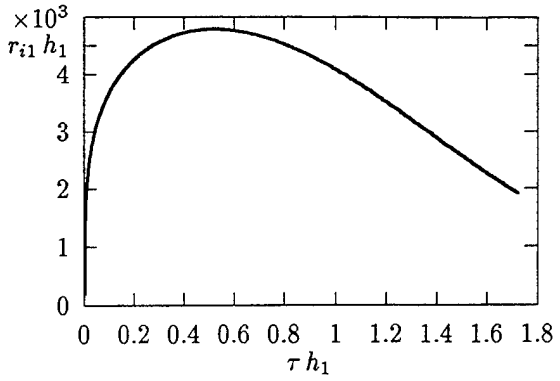


Fig. 8 Dimensionless imaginary part of the first root: γ=0.833, ν=1.0m^2/s, h_2/h_1=0.4

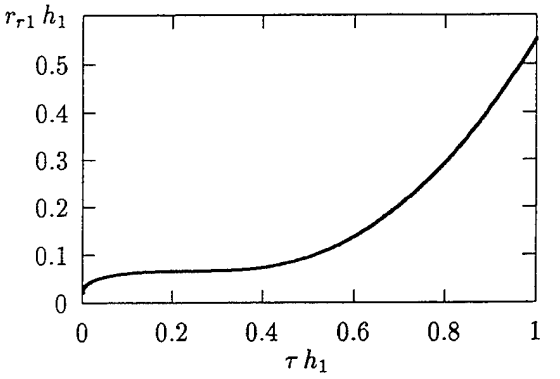


Fig. 9 Dimensionless real part of the first root: γ=0.833, ν=1.0m^2/s, h_2/h_1=0.4

We are now in a position to perform the integration path in (54) by taking it from $-\infty$ to ∞ along the real axis and an infinite semicircle located in the upper half-plane (Fig.7). The positive imaginary parts of complex roots provide an exponential decay of the integrand, and thus, the integral along the semicircle vanishes. Therefore, the integral (54) can be written as a sum of residues of the integrand as follows:

$$\phi_1(y,z) = 2\pi i \sum_{n=1}^{\infty} \frac{N(r_n,z,z_0)}{D_k(r_n,\nu)} e^{-r_{in}|y-y_0| + ir_{rn}|y-y_0|} \tag{56}$$

where

$$D_k(r_n,\nu) = \frac{\partial D(k,\nu)}{\partial k}|_{k=r_n}.$$

The resulting function is a regular potential function of $(y-y_0, z, z_0)$ except at the singular point $(y=y_0, z=z_0)$. Note that for $\nu > 0$ the terms of the series (56) decrease exponentially, and formula (56) can be used without the restrictive assumption of $(z-z_0) > 0$.

2.4 Numerical Results and Discussion

The computations were performed for a circular cylinder of radius $R = B/2 = T = 9\,\mathrm{m}$, for different ratios γ, r_h and kinematic viscosities of the fluid mud. In Fig.10 and Fig.11 we present a plot of the nondimensional parameter $\overline{\zeta} = -\mathrm{Re}[\phi_{1z}(y,z,0)/(i\omega\zeta_c)]$, where ζ_c is the amplitude of the cylinder heave motion. Thus, $\overline{\zeta}(y,h_1,0)$ represents the nondimensional wave elevation on the free-surface and $\overline{\zeta}(y,0,0)$ is the wave elevation on the interface at t=0. It is seen that the two wave systems propagate with the same period but with different wavelengths. The surface-wave mode corresponds to the smaller root r_{r1} and has a larger wavelength. It is worth mentioning, that the interfacial wave can be hardly observed or detected on the free surface. This effect is again closely related to the dead-water phenomena where an oscillating body generates waves on the interface, which are almost imperceptible on the free surface. Nevertheless, for some conditions, the resulting effect of the internal waves on the hydrodynamical forces acting on the body can be rather significant.

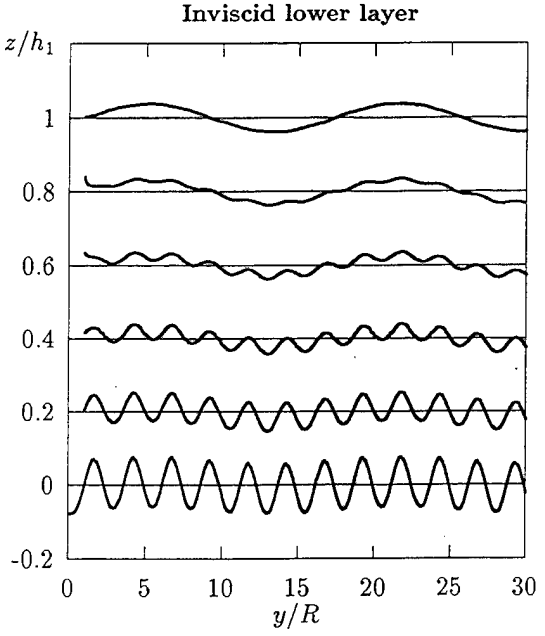


Fig. 10 Nondimensional vertical displacement of a fluid particle in the upper layer : R/h_1=0.9, h_2/h_1=0.4, τR=0.2

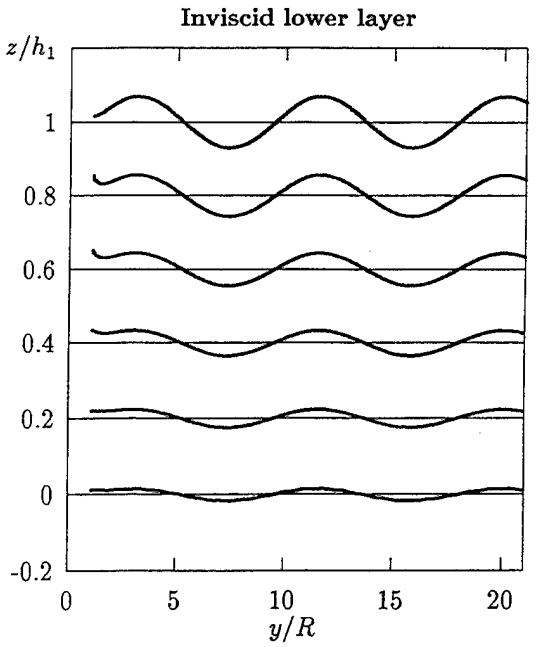


Fig. 11 Nondimensional vertical displacement of a fluid particle in the upper layer : R/h_1=0.9, h_2/h_1=0.4, τR=0.6

For instance, Fig.12 and Fig.13, display a strong dependence of the nondimensional added masses and damping coefficients

$$\overline{a}_{33} = 2a_{33}/\pi\rho_1 R^2;\ \overline{b}_{33} = 2b_{33}/\pi\rho_1\omega R^2;$$

on the density ratio and frequency of oscillation.

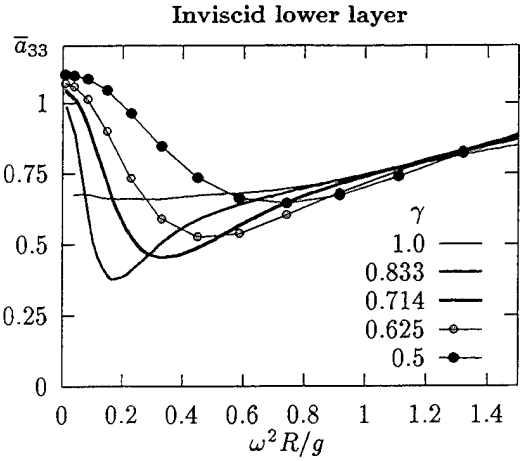


Fig. 12 Added mass coefficient for heave motion: R/h_1=0.9, h_2/h_1=0.4

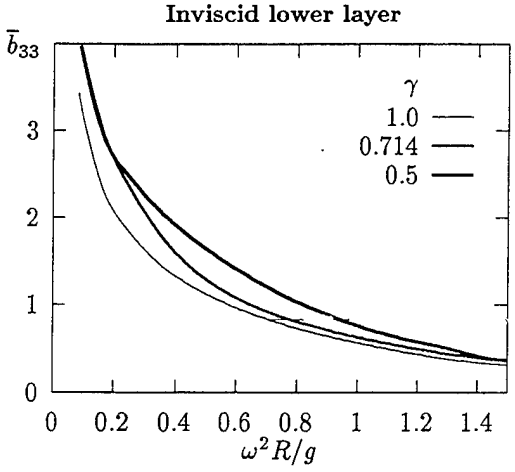


Fig. 13 Damping coefficient for heave motion: R/h_1=0.9, h_2/h_1=0.4

Comparing Fig.10 and Fig. 11 against Fig.12 we can see that the most appreciable decrease in the added masses occurs when the amplitude of the interfacial wave reaches a maximum.

Fig.14 and Fig.15 demonstrate that the heave added masses drastically depend on the depths ratio $r_h = h_2/h_1$, whereas the dependence of the heave damping coefficient is less pronounced, but nevertheless, quite recognizable.

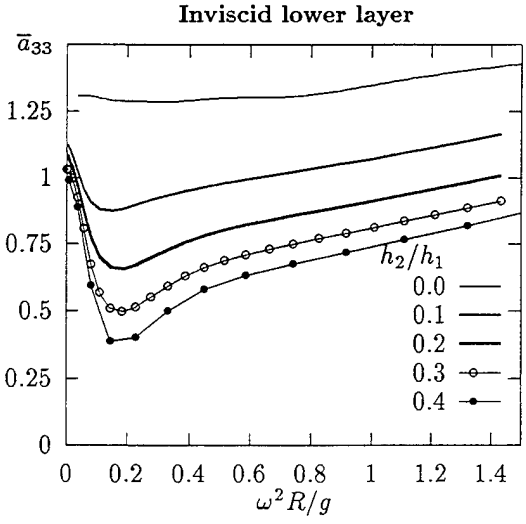


Fig. 14 Added mass coefficient for heave motion: R/h_1=0.9,γ=0.833

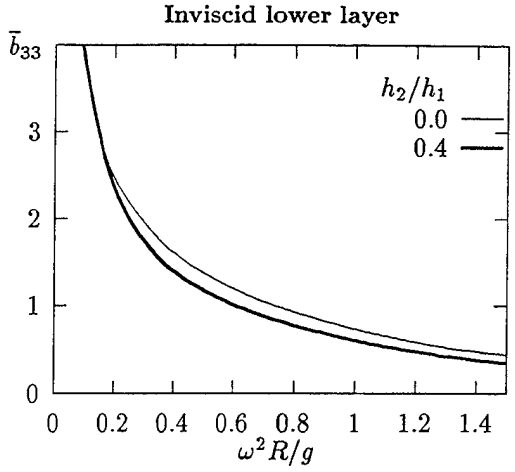


Fig. 15 Damping coefficient for heave motion: R/h_1=0.9,γ=0.833

It is also instructive to consider here the limiting cases where the two-layer model renders a one layer model, i.e:

1. $\nu \to \infty$;
2. $\gamma \to 0$;
3. $\gamma \to 1$ and $\nu \to +0$.

In cases 1 and 2 the interface may be replaced by a rigid lid and the depth of the single fluid layer is simply h_1. In case 3 the depth of the single layer is $h_1 + h_2$. For these conditions the present solution can be compared against the theoretical results of Yu and Ursell [27], and Sayer [29] (single layer models). Fig.16 and Fig.17 represent such a comparison for the added mass in heave and the corresponding wave amplitude ratio A_H (the ratio between the asymptotic wave amplitude at large distance from the body and the linear amplitude of the body oscillation).

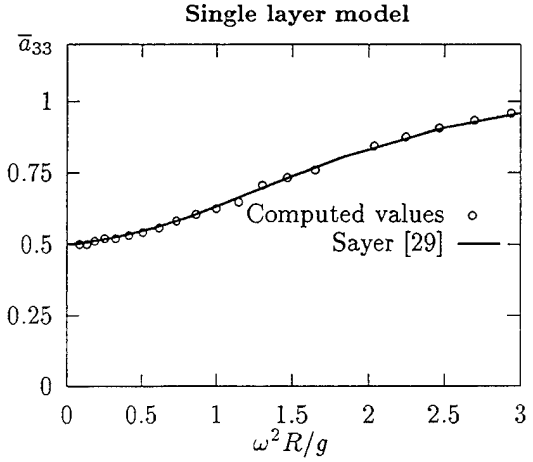


Fig. 16 Added mass coefficient: R/h_1=0.5

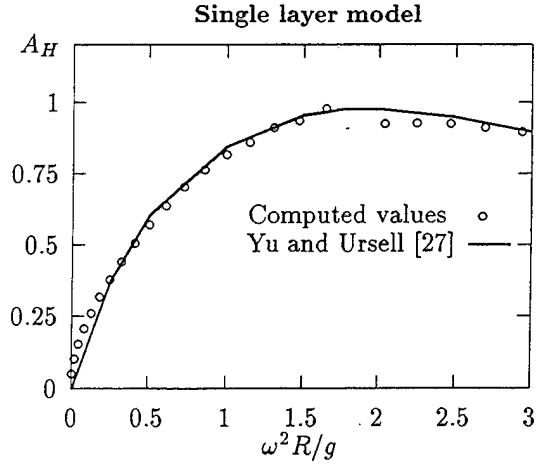


Fig. 17 Amplitude ratio: R/h_1=0.5

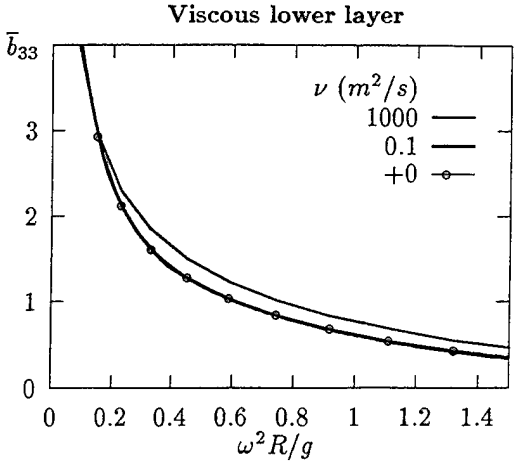


Fig. 19 Damping coefficient: γ=0.833, R/h_1=0.9, h_2/h_1=0.4

It can be clearly seen from these curves that except for a narrow range of irregular frequencies, the agreement is quite good.

Fig.18 and.Fig.19 display the dependence of the added mass and damping coefficient of a heaving cylinder on the viscosity of the lower layer. The evaluation of the corresponding Green function and its derivatives were done by invoking the integral representation (52).

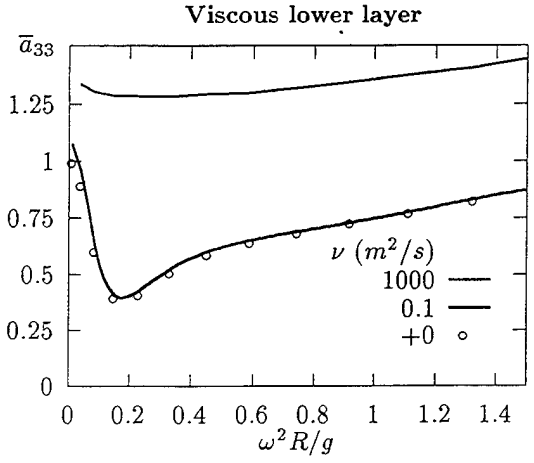


Fig. 18 Added mass coefficient: γ=0.833, R/h_1=0.9, h_2/h_1=0.4

Based on these figures one can conclude that even a relatively large viscosity ν=0.10 m^2/s has a negligible effect on the inertial coefficients.

2.5 Conclusions

The following brief conclusions may be drawn from the present theoretical investigation:

- The dead-water phenomenon is shown to exist for a body moving with a constant speed over a shallow mud layer as well as for a body undergoing periodic oscillations over a mud layer of finite depth.

- For a ship moving over a shallow layer of fluid mud with a relatively low speed $U \sim \sqrt{\epsilon \overline{h}}$, the induced wave resistance is mainly affected by the internal waves propagating on the "mud-water" interface. The maximum value of the wave resistance occurs at the vicinity of the critical densimetric Froude number $F_{R\overline{h}}$=1.

- For realistic values of the mud viscosity, i.e. for ν=10^{-1} to $10^{-3}m^2/s$, a considerable reduction in the wave resistance peak is attained.

- The added masses and damping coefficients of a heaving cylinder depend significantly on the frequency of oscillations ω, the density ratio ρ_1/ρ_2, the underkeel clearance and on the depth ratio $r_h = h_1/h_2$.

- The added masses and damping coefficients weakly depend on the mud viscosity within the range of interest $0 < \nu < 0.1$ m^2/s. Hence, for many practical purposes it is quite reasonable to evaluate the inertial coefficients by employing the model of two superposed inviscid fluid layers of finite depth.

Acknowledgements

This work was partially funded by the Israeli Ministry of Science and Arts (Research. Project No. 060541042; 060541022) and German-Israeli Foundation for R&D (Research Project I-200-168.10/94). The authors are indebted to both agencies for their continuous support.

The authors are grateful to Prof. H. Söding for attracting their attention to the mud flow problem as well as for discussing its various aspects. They are also pleased to acknowledge many helpful and interesting conversations with Prof. L. J. Doctors.

References

[1] Havelock, T.H. The Collected Papers of Sir Thomas Havelock on Hydrodynamics, (ed. by C. Wigley), Office of Naval Research, D.C., Washington, 1966.

[2] Kostyukov, A.A. The Theory of Ship Waves and Wave Resistance, Effective Communications Inc., Iowa City, Iowa, 1968.

[3] Newman, J.N. Marine Hydrodynamics, The MIT Press, Cambridge, Massachusetts, 1977.

[4] Sretenskii, L.N. The Theory of Wave Motion (Russian), Nauka, Moskow, 1977.

[5] Wehausen, J.V. and Laitone, E.V. "Surface Waves", Encyclopedia of Physics, Vol. **IX**, Springer-Verlag, Berlin, 1960, pp. 446–778.

[6] Kirsh, M. "Shallow Water and Channel Effects on Wave Resistance", J. Ship Research, **10**, 1966, pp. 164–181.

[7] Yeung, R.W. "Sinkage and Trim in First-Order Thin-Ship Theory", J. Ship Research, **16**, 1972, pp. 47–59.

[8] Tuck, E. "Shallow Water Flow Past Slender Bodies", J. Fluid Mechanics, **26**, 1966, pp.89–96.

[9] Lea, G.K. and Feldman, J.P. "Transcritical Flows Past a Slender Ship", Proc. 9-th Symp. on Naval Hydrodynamics, 1972, pp. 1527–1542.

[10] Mei, C.C. "Flow Around a Thin Body Moving in Shallow Water", J. Fluid Mechanics, **77**, 1976, pp. 737–751.

[11] Dalrymple, R. and Liu, P. "Waves Over Soft Muds: a Two-Layer Fluid Model", J. Physical Oceanography, **8**, 1978, pp. 1121–1129.

[12] Gade, G. "Effects of Nonrigid, Impermeable Bottom on Plane Surface Waves in Shallow Water", J. Marine Research, **16**, No.2, 1958, pp. 61–81.

[13] Hsiao, S.V. and Shemdin, O.H. "Interaction of Ocean Waves With a Soft Bottom", J. Physical Oceanography, **10**, 1980, pp. 605–610.

[14] MacPherson, H. "The Attenuation of Water Over a Non-Rigid Bed", J. Fluid Mechanics, **97**, 1980, pp. 721–742.

[15] Liu, L. and Mei, C.C. "Solitary Waves Over a Bingham-Plastic Seabed", Coastal Sediments 87, (Edited by N.C.Kraws),**1**, ASCE, 1987, pp. 325–347.

[16] Foda M.A., Hunt J.R. and Chou H.-T. "A Nonlinear Model For the Fluidization of Marine Mud by Waves", J. Geophysical Research, **98**, No. C4, 1993, pp. 7039-7047

[17] Sellmeijer, R. and Oortmerssen, G. van "The Effect of Mud on Tanker Manoeuvres", The Royal Institution of Naval Architects, 1983, pp. 105–120.

[18] Miloh T. and Tulin, M. P. "Dead Water Phenomena: A Non-Linear Theory of Wave Disturbance", Proc. of the 17th Symposium on Naval Hydrodynamics, Hague, 1989, pp. 127–148.

[19] Sabuncu, T. " The Theoretical Wave Resistance of a Ship Traveling Under Interfacial Wave Conditions", Norw. Ship. Model Exp. Tank, Trondheim, Publ. **63**, 1961.

[20] Tulin, M. P. and Miloh, T. "Ship Internal Waves in Shallow Thermocline: the Supersonic Case", Proc. of the 18th Symposium on Naval Hydrodynamics, Ann Arbor, Michigan, 1991, pp. 567–584.

[21] Miloh, T., Tulin, M.P. and Zilman, G. "Dead-Water Effects of a Ship Moving in Stratified Seas", ASME. J. Offshore Mechanics and Arctic Engineering, **115**, 1993, pp. 105–110.

[22] Uspenskii, P. "On the Wave Resistance of a Ship in the Presence of Internal Waves (Finite Depth Conditions)" (Russian), Akad. Nauk USSR Tr. Morskogo Gidrophizicheskogo Instituta, 1959, pp. 68–85.

[23] Criteria For the Depth of Dredged Navigation Channel. Marine Board, National Research Council, National Academy Press, Washington, D.C., 1983.

[24] Ursell, F. "Short Surface Waves Due to an Oscillating Immersed Body", Proc. Royal Society London, **A 220**, 1953, pp. 90–103.

[25] Ursell, F. "On the Virtual-Mass and Damping Coefficients for Long Waves in Water of Finite Depth", J. Fluid Mechanics, **76**, 1976, pp. 17–28.

[26] Haskind, M.D. The Hydrodynamic Theory of Ship Motion, (Russian), Nauka, Moskow, 1973.

[27] Yu, Y.S. and Ursell, F. "Surface Waves Generated by an Oscillating Circular Cylinder on Water of Finite Depth. Theory and Experiment", J. Fluid Mechanics, **11**, 1961, pp. 529–551.

[28] Kim, C.H. "Hydrodynamic Forces and Moments for Heaving, Swaying and Rolling Cylinders in Water of Finite Depth", J. Ship Research, **13**, 1978, pp. 137–54.

[29] Sayer, P." An Integral-Equation Method for Determine the Fluid Motion Due to a Cylinder Heaving on Water of Finite Depth", Proc. Royal Society London, **A 372**, 1980, pp. 93-110.

[30] Lewandowski, E.M. "Hydrodynamic Forces and Motion of a Cylinder Near a Vertical Wall", J. Ship Research, **36**, 1992, pp. 248–254.

[31] Yeung, R.W. and Vaidhyanathan, M. "Non-Linear Interaction of Water Waves With Submerged Obstacles", Int. J. Numerical Methods in Fluids, **14**, 1992, pp. 1111-1130.

[32] Yeung, R.W. and Ananthakrishnan, P. "Oscillation of a Floating Body in a Viscous Fluid", J. Engineering Mathematics, **26**, 1992, pp. 211-230.

[33] Yeung, R.W. and Wu, C.-f. "Viscosity Effects on the Radiation Hydrodynamics of Horizontal Cylinders", ASME. J. Offshore Mechanics and Arctic Engineering, **113**, 1991, pp. 334-343.

[34] Kochin, N.E. "On the Wave Resistance and Lift of Bodies Submerged in a Fluid", Sobranie Sochinenii (Russian), **2**, Akad. Nauk USSR, 1949, pp. 105–182.

[35] Lamb, H. Hydrodynamics, 6th edn., Cambridge University Press, 1932.

[36] Press, W.H., Flannery, B.P., Teukolsky, S.A. and Vetterling, W.T. Numerical Recipes, Cambridge University Press, 1989.

[37] John, F. "On the Motion of Floating Bodies II. Simple Harmonic Motions", Communications Pure Applied Mathematics **3**, 1950, pp. 45-101.

DISCUSSION

X. Chen
University of Stuttgart, Germany

S. Sharma
Mercator University, Germany

This is a very interesting paper with much practical relevance for inland and shallow water navigation since river bottoms are usually soft and muddy. We would like to comment on the reduction of wave resistance at near critical speeds due to viscosity of the bottom layer as found by the authors. A few year ago Thill (1991) and Miebach (1992) independently carried out wave pattern analysis of a Series 60 hullform in shallow water by the longitudinal and transverse cut method, respectively, in the Duisburg Towing Tank (VBD). Both found that the derived wave pattern resistance was very much smaller than the wave resistance estimated from a form-factor analysis of the measured total resistance. It was suspected that this could be related to the damping of wave orbital motion by friction on the tank bottom. Searching for a theorectical explanation, we derived 2-D and 3-D Green functions for a source in steady translation under a free surface over water of finite depth, including the effect of a linearized viscous boundary layer on the bottom, and calculated the wave resistance for certain configurations of a submerged source-sink pair. Two significant effects were found: (1) Wave damping in the wake of intensity increasing with decreasing speed and (2) Drastic wave resistance reduction near the cricial speed compared to the inviscid case. Both effects will cause the wave pattern analysis to underpredict the wave resistance in shallow water. The second effect agrees qualitatively with your results. But the problem treated by you is, of course, more general.

Thill, C. 1991 "Längschnittmethoden für die Analyse des Schiffswellensystems unter Berücksichtigung endlicher Wassertiefe," Diploma Thesis, RWTH Aachen.

Miebach, R. 1992 "Analyse des Wellenbildes eines Schiffes in flachem Wasser mit Hilfe der Querschnittsmethode," Diploma Thesis, RWTH Aachen.

Chen, X.-N. & Sharma, S. D. 1994a "Study of shallow water effects on ship wave resistance in 2-D case," Z. angew. Math. Mech. 74 (1994) 5, T431-T433.

Chen, X.-N. & Sharma, S. D. 1994b "Bottom viscous boundary layer effects on ship wave resistance in 2-D and 3-D cases," unpublished manuscript.

Nonlinear Theory of Asymmetric Motion of a Slender Ship in a Shallow Channel

X. Chen (University of Stuttgart, Germany),
S. Sharma (Mercator University, Germany)

ABSTRACT

A nonlinear theory, based on the technique of matched asymptotic expansions, is developed for the general problem of asymmetric motion of a ship moving in a shallow channel at sub-, trans- and supercritical speeds. Nonlinear shallow water wave theory is applied in the far-field; an improved slender body theory, in the near-field. The numerical task is reduced to the solution of a time-developing boundary-value problem of a modified Kadomtsev-Petviashvili equation. Numerical examples are worked out for a ship either in oblique motion along the channel centerline or in off-center motion without drift angle. The calculated longitudinal force, sinkage, trim, lateral force and yaw moment are presented systematically as functions of depth Froude number, wall separation and drift angle and compared with their measured values from towing tank model experiments; reasonable agreement is found. Several counter-intuitive new phenomena are observed. Calculated wave patterns, containing upstream solitons at near-critical speeds, are visualized.

NOMENCLATURE

Dimensional variables carry a superscript *, all others are nondimensional.

A^* typical wave amplitude
b_o^* beam at midship
$C(\hat{x},\tau)=C^*/r_o^*$ dynamic blockage coefficient of instantaneous submerged cross section
$C_O(\hat{x})$ static blockage coefficient of stillwater submerged cross section
$c=c^*/h^*$ under-keel clearance
$C_B=V_o^*/(l^* b_o^* d^*)$ block coefficient of hull
$C_P=V_o^*/(l^* S_o^*)$ longitudinal prismatic coefficient
C_r blockage coefficient for rectangular cross section
d^* draft of ship
$\boldsymbol{F}=(F_X,F_Y,F_Z)$ hydrodynamic force on the hull
$F=F^*/(\rho^* g^* C_p S_o^* l^*)$ nondimensional force
$F_{\hat{x}}$ longitudinal force
$F_{\hat{y}}$ lateral force
$H=H^*/h^*$ local water depth incl. wave elevation
h^* water depth in stillwater
$g^*=9.80665 m/s^2$ acceleration due to gravity
L^* typical wave length
l^* ship length (between perpendiculars)
$\mathbf{M}=(M_x,M_y,M_z)$ hydrodynamic moment on the hull
$M=M^*/(\rho^* g^* C_p S_o^* l^{*2})$ nondimensional moment
$M_{\hat{z}}$ yaw moment
$\mathbf{n}=(n_x,n_y,n_z)$ hull outward normal unit vector
$\mathbf{r}=(x,y,z)$ position vector
$r_o^*=\sqrt{S_o^*}$ near-field transverse reference length
$S(\hat{x})=S^*(\hat{x})/S_o^*$ static area of stillwater submerged cross section
$\hat{S}(\hat{x},\tau)$ dynamic area of instantaneous submerged cross section
S_o^* cross sectional area at midship
S_w wetted surface area of the hull in motion
S_w wetted surface area of the hull at rest
$\Delta S_w/S_{wo}$ wetted surface area increment
$s=s^*/l^*$ sinkage
$t=t^*\sqrt{\varepsilon g^* h^*}/h^*$ nondimensional time
$U=F_{nh}=U^*/\sqrt{g^* h^*}$ depth Froude number
U^* (dimensional) speed of ship
V_o^* displacement
$V\sqrt{\varepsilon}=\varphi_y$ cross flow velocity in y-direction

$\hat{V}\sqrt{\varepsilon} = \hat{V}^*/\varepsilon\sqrt{g^*h^*}$ cross flow velocity in $\hat{y}$-direction

w^* width of the channel

$Oxyz$ coordinate system aligned to motion direction

$O\hat{x}\hat{y}\hat{z}$ coordinate system obtained by rotating $Oxyz$ around z by drift angle α

α drift angle (angle of attack)

$\Delta\varphi = \varphi|_{y\to 0^+} - \varphi|_{y\to 0^-}$ potential jump across x axis

$\nabla^* = (\partial/\partial x^*, \partial/\partial y^*, \partial/\partial z^*)$ 3-D vector operator

$\varepsilon = A^*/h^*$ small parameter for wave nonlinearity

λw^* separation distance of the ship from the wall

$\mu = h^*/L^*$ small parameter for wave dispersion

ρ^* water density

θ trim angle, bow-up positive

$\Phi(x,y,z,t) = \Phi^*(x,y,z,t)/(h^*\sqrt{\varepsilon g^* h^*})$ disturbance velocity potential

$\Phi_o(x,y,t) = \Phi|_{z=0}$ bottom velocity potential

φ depth-averaged potential

$\tau = \varepsilon t$ slow time variable

$\zeta = \zeta^*/(\varepsilon h^*)$ elevation of free surface

INTRODUCTION

The trend of increasing ship size and speed makes restricted water hydrodynamics more important and difficult. The huge ship size makes the available water depth or restricted channel width relatively shallow and narrow, respectively. The high ship speed makes the free surface flow essentially nonlinear. In this paper we are concerned with the asymmetric problem of a slender ship moving uniformly in a straight rectangular shallow water channel parallel to the wall, either off-center or with a small drift angle, at subcritical, critical and supercritical speeds. This is originally a three-dimensional, nonlinear, unsteady problem, which we attempt to solve by the classical nonlinear shallow water wave theory upto a practical application stage.

It is well-known that shallow water wave equations are analogous to two-dimensional compressible flow equations, see Tuck (1978). The depth Froude number in hydrodynamics plays the same role as Mach number in aerodynamics, and the speed of shallow water waves is equivalent to the speed of sound. So a ship traveling in shallow water is somehow similar to a 2-D airfoil in compressible fluid. Tuck (1966) developed a linear technique of matched asymptotic expansions for a slender ship in shallow water, obtained zero wave resistance in the subcritical speed range and non-zero values at supercritical speeds, that is, exactly in agreement with the aerodynamic result. He also obtained good results for sinkage and trim in the off-critical range, which explain quite well the squat phenomenon in shallow water as described by, e.g., Graff, Kracht & Weinblum (1964). Of course, this linear model fails in the near-critical range. Some success in this gap was achieved by Lea & Feldman (1972) by use of an established transonic-flow numerical method for the transcritical motion of ships in shallow water. Later on, Mei (1976) extended this work to include dispersive effects in the near-critical range, but still for the time-independent steady-state problem.

Just this dispersive effect which exists in shallow water waves, but not in sound waves, brings about a particularly interesting nonlinear phenomenon, namely, that a ship in uniform motion in a shallow channel generates periodic solitary waves propagating upstream. Actually, it had been observed long ago in towing tank experiments, e.g., by Thews & Landweber (1935, 1936), Helm (1940), Kinoshita (1946), Graff (1962), Graff, Kracht & Weinblum (1964), etc. Recently revived interest and a theoretical understanding stem from the work by Wu &Wu (1982), who numerically solved one-dimensional Boussinesq equations to study a pressure patch moving on the free surface at a near-critical speed and found upstream solitons emitted periodically. Since then various investigations have been made, e.g., Huang, Sibul & Wehausen (1983), Ertekin, Webster & Wehausen (1984, 1986), Wu (1987) and so on. Here we restrict ourselves to the problem of a ship in shallow water.

Mei (1986), using matched asymptotic expansions, derived an inhomogeneous Korteweg & de Vries (KdV) equation for a slender ship moving at near-critical speed in shallow water and theoretically demonstrated solitons propagating upstream. Mei & Choi (1987) further developed this theory to calculate hydrodynamic forces on the ship, but only crude agreement with experiments was obtained because this theory cannot predict the two-dimensional waves around a real ship and in its wake. So Choi & Mei (1989) improved their theory by using a Kadomtsev & Petviashvili (KP) equation in the far field to take account of the 2-D effect. More numerical results were reported in Choi, Bai, Kim & Cho (1990) with another finite element method. Chen & Sharma (1992) pursued this method further and refined the slender body theory in the near-field by taking account of local wave elevation and longitudinal disturbance velocity. This amounts to including two non-negligible higher order effects: (1) interaction between waves generated at different cross-sections and (2) influence of longitudinal perturbation velocity on the linearized hull boundary condition. The KP equation in the far-field was solved numerically by an efficient finite difference method, namely, the fractional step algorithm with Crank-Nicolson-like schemes in each half step. Very good agreement with experiments was achieved in

wave resistance, sinkage, and trim for several ship models. Furthermore, Chen & Sharma (1994a) derived a KP equation from Boussinesq equations by keeping a higher nonlinearity in the lateral direction, making it valid for a wider speed range. It was shown that this modified KP equation has the same accuracy as Boussinesq and its linear stationary dispersion relation is even better than that of Boussinesq in the subcritical and transcritical ranges. More numerical results from this modified KP equation for a ship in a wider speed range are reported in Chen & Sharma (1994b) and compared with the model experiments of Graff et al. (1964) on the Taylor Standard Series as well as our own on a Series 60 hull.

Here we extend our theory and calculations to the asymmetric case of a ship moving parallel to the channel axis but either off-center or at a drift angle. This problem is probably of greater relevance to ship maneuvering than to propulsion. Most of the previous work on ship maneuvering and similar problems in restricted shallow water, e.g., Norrbin (1974), Beck (1977), Yeung & Hwang (1977), Yeung (1978), Hess (1978), Yeung & Tan (1980), Kleinau (1981), Kijima & Yasukawa (1984) and Davis (1986) ignored free-surface effects as unimportant. This was justified firstly because at sufficiently low speeds wave generation by the ship itself is not hydrodynamically significant; in other words, the Froude number is so small that the free surface may be replaced by an ideal rigid wall. Secondly, because the asymmetric flow around the ship hull with its 3-D geometry or configuration in a complex environment already made the problem quite difficult and some simplification was required. It can be shown by matched asymptotics that the asymmetric ship motion problem with a rigid free surface or linear/nonlinear shallow water waves, i.e., involving a cross flow through the clearance under the keel, is exactly or approximately equivalent to that of a porous two-dimensional airfoil moving in an incompressible or compressible linear/nonlinear fluid, respectively. If we consider such a motion at a high enough speed, the interaction of cross flow and the waves generated by the ship becomes significant and the whole flow becomes quite complicated. Asymmetry may even aggravate nonlinearity and instationarity, which are the two salient features in shallow water. We shall encounter certain phenomena that simply contradict our intuition.

The asymmetric flow around the ship is governed by a modified KP equation in the far-field asymptotically matched with an improved slender-body theory in the near-field. A suitable Kutta condition at the ship stern and continuity of velocity across the wake are imposed. The numerical task is then reduced to the solution of a time-developing boundary-value problem. Examples are worked out for either oblique ship motion at small drift angles along channel centerline or non-drifting off-center motion parallel to channel sidewall. Calculated longitudinal force, sinkage, trim, wetted surface area increment, lateral force and yaw moment are presented systematically as functions of depth Froude number, wall separation and drift angle, as well as compared with measurements in the towing tank.

GENERAL PROBLEM FORMULATION

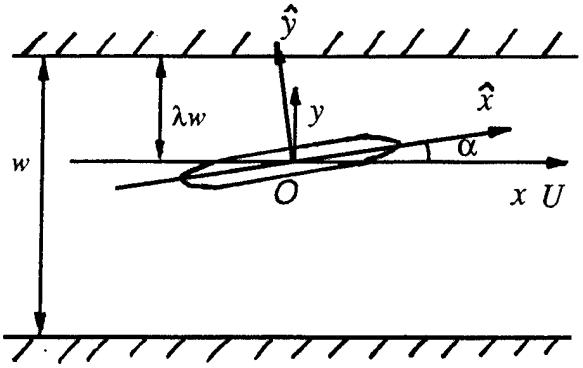


Fig. 1 Schematic of the problem.

We consider a slender ship, free to heave and pitch, moving at constant velocity parallel to the axis of a straight rectangular shallow water channel, not necessarily along the channel centerline, with or without a small drift angle. The flow is assumed to be incompressible and irrotational. Moreover, we limit ourselves to the long-term asymptotic flow without any time-dependent forcing effects, i.e., to the autonomous system, although finally we can easily see that this theory holds valid also for the radiation problem of a ship under slow-oscillation except in the rolling mode as well as for the diffraction problem of a ship in incident waves of sufficiently low encounter frequency. We start with dimensional variables marked by asterisks '*' and later change to unmarked nondimensional variables. A Cartesian coordinate system $Ox^*y^*z^*$ moving at the same speed as the ship is used with origin O located in the midship section, Ox^* along the direction of motion, plane Ox^*y^* on the quiet free surface, and z^* positive upward, see Nomenclature and Fig. 1. The flow is then exactly governed by the Laplace equation in the fluid domain,

$$\Phi^*_{x^*x^*} + \Phi^*_{y^*y^*} + \Phi^*_{z^*z^*} = 0, \quad -h^* < z^* < \zeta^*, \quad (1)$$

by the kinematic and dynamic conditions on the free surface,

$$\zeta^*_{t^*} - U^*\zeta^*_{x^*} + \Phi^*_{x^*}\zeta^*_{x^*} + \Phi^*_{y^*}\zeta^*_{y^*} = \Phi^*_{z^*}, \quad z^* = \zeta^*, \quad (2)$$

$$\Phi^*_{t^*} - U^*\Phi^*_{x^*} + \left|\nabla^*\Phi^*\right|^2/2 + g^* z^* = 0, \quad z^* = \zeta^*, \quad (3)$$

and by the boundary conditions on the ship hull,

$$F_{t^*} - U^* F_{x^*} + \nabla^* \Phi^* \bullet \nabla^* F = 0,$$

$$F(x^*, y^*, z^*, t^*) = 0, \quad (4)$$

on the horizontal channel bottom,

$$\Phi^*_{z^*} = 0, \qquad z^* = -h^*, \quad (5)$$

and on the vertical channel sidewalls,

$$\Phi^*_{y^*} = 0, \qquad y^* = -(1-\lambda)w^*, \ \lambda w^*. \quad (6)$$

It is assumed that the fluid is initially at rest, so the initial condition is

$$\nabla^* \Phi^* = 0, \quad \zeta^* = 0, \qquad t^* = 0, \quad (7)$$

and for finite time the radiation condition is

$$\nabla^* \Phi^* \to 0, \quad x^* \to \pm\infty. \quad (8)$$

But this radiation condition must be modified in the actual numerical computation, specially for the downstream boundary, because the computational domain must remain finite.

Moreover, in asymmetric motion the ship, particularly with a sharp stern in a real fluid, generates circulation around itself and experiences a lift force. Associated with it is a vortex wake shed behind the ship. The Kutta condition at the after end and continuity conditions across the wake are necessary. Because the ship can be seen as a very-small-aspect-ratio foil, it is in general insufficient for a 3-D flow to construct a Kutta condition only at the trailing edge. However, for the ship in shallow water and very small drift angle the entire free-vortex sheet can be assumed to be shed from the ship stern since vertical flow is hampered by the channel bottom and the vortices otherwise produced at the keel are forced along the length of the ship. Perhaps, the shallow water wave theory can only accept a 2-D Kutta condition at the stern. In the wake the detailed flow is complicated. In the unsteady case the longitudinal velocity of the outer potential flow may be discontinuous across the wake, while the transverse velocity and pressure are continuous, which can be exploited to determine the discontinuity of the potential across the wake line. But for the asymptotic steady or very slowly varying flow, the starting vortex produced initially runs downstream far away from the ship, so that the longitudinal velocity is also continuous; consequently, only a constant cross-jump of the potential exists along the entire wake line until infinity.

The pressure p^* is expressed by Bernoulli's equation,

$$p^* = -\rho^* (\Phi^*_{t^*} - U^* \Phi^*_{x^*} + \left|\nabla^* \Phi^*\right|^2 / 2 + g^* z^*). \quad (9)$$

The resulting forces and moments acting on the ship are found by pressure integration on the hull:

$$\mathbf{F}^* = -\int_{S_w} p^* \mathbf{n} dS^*, \quad \mathbf{M}^* = -\int_{S_w} p^* (\mathbf{r}^* \times \mathbf{n}) dS^*. \quad (10)$$

SCALE ANALYSIS AND MATCHED ASYMPTOTICS

We analyze the problem by the technique of matched asymptotic expansions. A key step in it is scale analysis, i.e., selection of small parameters and suitable scales for all variables. As the ship considered here is slender, a slenderness parameter is defined as

$$\delta = r_o^* / l^* << O(1), \quad r_o^* = \sqrt{S_o^*}. \quad (11)$$

Assuming the waves generated by the ship to be weakly nonlinear and long compared with water depth, we have

$$\varepsilon = A^*/h^*, \mu = h^*/L^*, O(\varepsilon) = O(\mu^2) << O(1). \quad (12)$$

We select here $\varepsilon=\mu^2$, which only means assigning the same order to dispersion and nonlinearity of waves, but not a quantitative restriction at all, because the theory can automatically adjust both effects; actually, it does not change the dimensional description of the shallow water wave theory at all.

Using the concept of matched asymptotics, we now divide the flow region into two parts, namely, near-field and far-field, which mean the fields near to and far from the ship, respectively. In the near-field the typical length scale for transverse directions y^* and z^* is r_o^* and for the longitudinal direction x^* it is l^*, while in the far-field the typical length scale for the horizontal directions x^* and y^* is L^* and for the vertical direction z^* it is h^*. Since $r_o^* << L^*$ the ship location is seen as a line-cut in the far-field. The time scale, which is the same in both fields and suitably of the order of the period of the waves, should be very long since we are seeking the long-term asymptotic state. Based on these scales, we can separately formulate the problems with multiple-scale expansions for each field and then match them with each other asymptotically in space. It is expected that the original three-dimensional problem can be recast into two two-dimensional problems in the horizontal plane and the vertical cross-section plane in the far-field and near-field, respectively.

NONLINEAR SHALLOW WATER WAVE THEORY IN THE FAR-FIELD

Based on the shallow water wave assumption, we can normalize the variables in the far-field as

$$\zeta = \frac{\zeta^*}{\varepsilon h^*}, \quad \Phi = \frac{\Phi^*}{\sqrt{\varepsilon} h^* \sqrt{g^* h^*}}, \quad (x, y) = \frac{\sqrt{\varepsilon}}{h^*}(x^*, y^*),$$

$$z = \frac{z^*}{h^*}, \quad t = \frac{\sqrt{\varepsilon} t^* \sqrt{g^* h^*}}{h^*}, \quad p = \frac{p^*}{\rho^* g^* h^*}. \quad (13)$$

By a Taylor expansion of disturbance velocity from

the bottom to the free surface, 3-D Laplace equation (1) and horizontal bottom condition (5) yield

$$\Phi = \Phi_o - \frac{\varepsilon}{2!}(z+1)^2\nabla^2\Phi_o + \frac{\varepsilon^2}{4!}(z+1)^4\nabla^2\nabla^2\Phi_o. \quad (14)$$

In terms of the depth-averaged potential,

$$\varphi = \frac{\int_{-1}^{\varepsilon\zeta}\Phi dz}{1+\varepsilon\zeta} = \Phi_o - \frac{\varepsilon}{3!}(1+\varepsilon\zeta)^2\nabla^2\Phi_o + O(\varepsilon^2), \quad (15)$$

or inversely

$$\Phi_o = \varphi + \frac{\varepsilon}{6}(1+\varepsilon\zeta)^2\nabla^2\varphi + O(\varepsilon^2), \quad (15')$$

and substituting expression (14) into the free surface kinematic and dynamic conditions (2) and (3), we obtain the Boussinesq equations,

$$\zeta_t - U\zeta_x + \nabla\bullet[(1+\varepsilon\zeta)\nabla\varphi] = 0, \quad (16)$$

$$\varphi_t - U\varphi_x + \frac{1}{2}\varepsilon|\nabla\varphi|^2 + \zeta = \frac{\varepsilon}{3}\nabla^2(\varphi_t - U\varphi_x), \quad (17)$$

and the expression for pressure in terms of wave elevation,

$$p = \varepsilon\zeta - z + \frac{\varepsilon}{2}[(1+\varepsilon\zeta)^2 - (1+z)^2]\nabla^2\zeta + O(\varepsilon^2), \quad (18)$$

where ∇^2 is 2-D Laplace operator. Substituting ζ from (17) into (16), considering the flow varies even more slowly, i.e., $\tau = \varepsilon t$, and neglecting higher-order terms than $O(\varepsilon)$, we get

$$2\varepsilon U\varphi_{x\tau} + (1-U^2)\varphi_{xx} + (1+\varepsilon U\varphi_x)\varphi_{yy} + \frac{\varepsilon U^2}{3}(\varphi_{xxxx} + \varphi_{xxyy}) + \frac{3\varepsilon U}{2}(\varphi_x^2)_x + 2\varepsilon U\varphi_{xy}\varphi_y = 0. \quad (19)$$

In fact, the above equation is precise to same order as Boussinesq equations (16) and (17). Discussion on stationary dispersion relation of its linearized form given by Chen & Sharma (1994a) shows that the term φ_{xxyy} will make the dispersion relation differ more from the exact one of linear finite depth theory than without it in the subcritical and transcritical speed ranges. Hence, it is believed that the equation without φ_{xxyy} will produce better results than that with it. So we choose the following equation as the governing equation in the far-field,

$$2\varepsilon U\varphi_{x\tau} + (1-U^2)\varphi_{xx} + (1+\varepsilon U\varphi_x)\varphi_{yy} + \frac{\varepsilon U^2}{3}\varphi_{xxxx} + \frac{3\varepsilon U}{2}(\varphi_x^2)_x + 2\varepsilon U\varphi_{xy}\varphi_y = 0, \quad (20)$$

which is still of KP-type, i.e., two-dimensional KdV-type. The channel sidewall boundary condition (6) becomes

$$\varphi_y = 0, \quad y = -(1-\lambda)\sqrt{\varepsilon}\,w^*/h^*,\ \lambda\sqrt{\varepsilon}\,w^*/h^*. \quad (21)$$

The elevation of free surface is expressed as

$$\zeta = U\varphi_x - \varepsilon\varphi_\tau - \frac{1}{2}\varepsilon|\nabla\varphi|^2 - \frac{\varepsilon U}{3}\nabla^2\varphi_x. \quad (22)$$

IMPROVED SLENDER BODY THEORY IN THE NEAR-FIELD

If the ship moves with a drift angle α, we must set up a new near-field coordinate system $O\hat{x}\hat{y}\hat{z}$, whose axis $O\hat{x}$ is in the ship centerplane, see Fig. 1. It is related with $Ox^*y^*z^*$ as

$$\hat{x}^* = x^*\cos\alpha + y^*\sin\alpha, \quad \hat{y}^* = y^*\cos\alpha - x^*\sin\alpha, \quad \hat{z}^* = z^*, \quad (23)$$

where the drift angle α may be of order $O(\delta)$. Upon introducing the nomalization in the near-field,

$$\hat{x} = \hat{x}^*/l^*, \hat{y} = \hat{y}^*/r_o^*, \hat{z} = \hat{z}^*/r_o^*, \hat{\zeta}(\hat{x},\hat{y},t) = \zeta^*/r_o^*,$$

$$\hat{\Phi}(\hat{x},\hat{y},\hat{z},t) = \Phi^*/(\sqrt{\varepsilon}h^*\sqrt{g^*h^*}), \quad (24)$$

we get approximately from (1-5),

$$\hat{\Phi}_{\hat{y}\hat{y}} + \hat{\Phi}_{\hat{z}\hat{z}} = -\delta^2\hat{\Phi}_{\hat{x}\hat{x}} = -\varepsilon\delta^2(l^*/h^*)^2\varphi_{xx}, \quad (25)$$

$$\hat{\Phi}_{\hat{z}} = O(\varepsilon\delta), \qquad \hat{z} = \hat{\zeta}, \quad (26)$$

$$F_{\hat{y}}\hat{\Phi}_{\hat{y}} + F_{\hat{z}}\hat{\Phi}_{\hat{z}} = \frac{S_o^*\cos\alpha}{\sqrt{\varepsilon l^*h^*}}F_{\hat{x}}(U - \varepsilon\varphi_x|_{y=0}), F = 0, \quad (27)$$

$$\hat{\Phi}_{\hat{z}} = 0, \qquad \hat{z} = -h^*/r_o^*. \quad (28)$$

In (25) and (27) we have used in advance the matching condition of longitudinal velocity. There is a formal solution for the linear inhomogeneous equation (25) with linear inhomogeneous boundary conditions (26-28),

$$\hat{\Phi} = \frac{S_o^*\cos\alpha}{\sqrt{\varepsilon l^*h^*}}F_{\hat{x}}(U - \varepsilon\varphi_x|_{y=0})\,\Psi_1(\hat{x},\hat{y},\hat{z}) - \varepsilon\delta^2(l^*/h^*)^2\,\Psi_2(\hat{x},\hat{y},\hat{z}) + \varepsilon\frac{r_o^*}{h^*}\hat{V}(\hat{x},\tau)\,\Psi_3(\hat{x},\hat{y},\hat{z}) + f_o(\hat{x},\tau), \quad (29)$$

where $\hat{V}(\hat{x},\tau)$ is the fluid velocity of cross-flow in $\hat{y}$-direction and f_o a constant solution, both of which will be determined by matching with the far-field solution, Ψ_1 and Ψ_2 are particular solutions, and Ψ_3 a homogeneous one, all of the Laplace equation, governed, respectively, by

$$\left.\begin{aligned}&\Psi_{1\hat{y}\hat{y}} + \Psi_{1\hat{z}\hat{z}} = 0,\\ &F_{\hat{y}}\Psi_{1\hat{y}} + F_{\hat{z}}\Psi_{1\hat{z}} = F_{\hat{x}}, \quad \text{on } F = 0,\\ &\Psi_{1\hat{z}} = 0, \text{ on } \hat{z} = \hat{\zeta} \text{ and } -h^*/r_o^*\end{aligned}\right\} \quad (30)$$

$$\left.\begin{aligned}&\Psi_{2\hat{y}\hat{y}} + \Psi_{2\hat{z}\hat{z}} = \varphi_{xx},\\ &F_{\hat{y}}\Psi_{2\hat{y}} + F_{\hat{z}}\Psi_{2\hat{z}} = 0, \quad \text{on } F = 0,\\ &\Psi_{2\hat{z}} = 0, \text{ on } \hat{z} = \hat{\zeta} \text{ and } -h^*/r_o^*\end{aligned}\right\} \quad (31)$$

$$\left.\begin{aligned}&\Psi_{3\hat{y}\hat{y}} + \Psi_{3\hat{z}\hat{z}} = 0,\\ &F_{\hat{y}}\Psi_{3\hat{y}} + F_{\hat{z}}\Psi_{3\hat{z}} = 0, \quad \text{on } F = 0,\\ &\Psi_{3\hat{z}} = 0, \text{ on } \hat{z} = \hat{\zeta} \text{ and } -h^*/r_o^*.\end{aligned}\right\} \quad (32)$$

We need not find their exact solutions if we can obtain their asymptotic nature in order to match the near-field solution with the far-field one. By applying the law of mass conservation to a transverse fluid element surrounded by the hull surface, free surface, channel bottom and two vertical control planes located far away from the ship, we have

$$\lim_{\hat{y}\to\pm\infty}\Big[\frac{S_o^*\cos\alpha}{\sqrt{\varepsilon}l^*h^*}F_{\hat{x}}(U-\varepsilon\varphi_x|_{y=0})\,\Psi_{1\hat{y}}(\hat{x},\hat{y},\hat{z}) - \varepsilon\delta^2(l^*/h^*)^2\,\Psi_{2\hat{y}}(\hat{x},\hat{y},\hat{z})\Big]$$

$$=\mp\frac{1}{2}\frac{r_o^{*3}\cos\alpha}{\sqrt{\varepsilon}l^*h^{*2}(1+\varepsilon\zeta_o)}\Big\{\frac{d}{d\hat{x}}\Big[\hat{S}(\hat{x},\tau)(U-\varepsilon u_o)\Big] +2\varepsilon\frac{h^*}{r_0^*}|\hat{y}|\frac{du_o}{d\hat{x}}\Big\}, \qquad (33)$$

where $u_o=\varphi_x|_{y=0}$ and $\zeta_o=\zeta|_{y=0}$. Further, for the homogeneous cross flow, Newman (1969) has given the asymptotic solution,

$$\lim_{\hat{y}\to\pm\infty}\Psi_3=\hat{y}\pm C(\hat{x},\tau), \qquad (34)$$

where $C(\hat{x},\tau)$ is called the blockage coefficient of a cross section of the hull. It can be generally calculated by a boundary element method or analytically for a few special cases, e.g., see Taylor (1973). Substituting (32) and (33) into (28) yields

$$\lim_{\hat{y}\to\pm\infty}\hat{\Phi}=-\frac{r_o^{*3}|\hat{y}|\cos\alpha}{2\sqrt{\varepsilon}l^*h^{*2}(1+\varepsilon\zeta_o)}\Big\{\frac{d}{d\hat{x}}\Big[\hat{S}(\hat{x},\tau)(U-\varepsilon u_o)\Big] +\varepsilon\frac{h^*}{r_0^*}|\hat{y}|\frac{du_o}{d\hat{x}}\Big\}+\varepsilon\frac{r_o^{*3}}{h^*}\hat{V}(\hat{x},\tau)\big[\hat{y}\pm C(\hat{x},\tau)\big]+f_o. \qquad (35)$$

Thus we get our near-field solution, which is an improvement over the classical one in the sense that it includes the effects of longitudinal disturbance velocity and of local wave elevation around the ship.

MATCHING CONDITIONS, KUTTA CONDITION AND CLOSURE OF THE PROBLEM OF KP EQUATION

The location of the ship is seen as a line-cut in the far-field view. We anticipate that the matching conditions will yield a boundary condition there for the KP equation (20).

According to the principle of matched asymptotics, i.e., the inner expansion of the far-field must be equal to the outer expansion of the near-field, we now establish the matching conditions, taking account of the slight rotation of $O\hat{x}\hat{y}\hat{z}$ from $Oxyz$ due to the drift angle,

$$\zeta|_{y\to0}=(r_o^*/\varepsilon h^*)\hat{\zeta}|_{\hat{y}\to\infty}, \qquad (36)$$

$$\cos\alpha\,\varphi_x|_{y\to0}=\frac{\sqrt{\varepsilon}l^*}{h^*}\hat{\Phi}_{\hat{x}}|_{\hat{y}\to\infty}, \qquad (37)$$

$$\frac{\partial\varphi}{\partial y}\Big|_{y=0^\pm}=\mp\frac{\sqrt{\varepsilon}}{2}\frac{S_o^*\cos^2\alpha}{\varepsilon^{3/2}l^*h^*(1+\varepsilon\zeta_o)}\times \frac{d}{d\hat{x}}\Big[\hat{S}(\hat{x},\tau)(U-\varepsilon u_o)\Big]+\sqrt{\varepsilon}V(\hat{x},\tau), \qquad (38)$$

$$\varphi|_{y\to0^+}-\varphi|_{y\to0^-}=2\varepsilon\frac{r_o^*}{h^*}\hat{V}(\hat{x},\tau)C(\hat{x},\tau), \qquad (39)$$

$$\varphi|_{y\to0^+}+\varphi|_{y\to0^-}=2f_o(\hat{x},\tau). \qquad (40)$$

We select

$$\varepsilon^{3/2}=\frac{S_o^*}{l^*h^*}, \qquad (41)$$

in order to normalize the coefficient of (38). V in (38) is the velocity in y-direction, which is related with $\hat{V}$ as,

$$V\cos\alpha+\varepsilon^{-3/2}(U-\varepsilon u_o)\sin\alpha=\hat{V}. \qquad (42)$$

So, substituting (42) and (39) into (38), we obtain the final boundary condition of the modified KP equation (20) at the ship location (the cut at y=0):

$$\frac{\partial\varphi}{\partial y}\Big|_{y=0^\pm}=\mp\frac{\sqrt{\varepsilon}}{2}\frac{\cos^2\alpha}{1+\varepsilon\zeta_o}\frac{d}{d\hat{x}}\Big[\hat{S}(\hat{x},\tau)(U-\varepsilon u_o)\Big] +\frac{\varphi|_{y\to0^+}-\varphi|_{y\to0^-}}{\cos\alpha\,2C(\hat{x},\tau)\varepsilon^2/\delta}-\frac{\tan\alpha}{\varepsilon}(U-\varepsilon u_o). \qquad (43)$$

In addition to the normal velocity matching condition serving as the boundary condition of the KP equation, the longitudinal velocity and wave elevation matching conditions (37) and (36), which have been used earlier in the formulation of the near-field, i.e., equations (25), (27) and (33), also play an important role by introducing the interaction of disturbance flow at different cross sections into the near-field solution. In fact, the final matching condition (43) includes such interaction effects.

The dynamic instantaneous submerged cross-sectional area $\hat{S}(\hat{x},\tau)$ should include the effects of running sinkage, trim and local wave elevation. If the ship sidewalls are nearly vertical and sinkage, trim and wave elevation are relatively small, the required cross-sectional area can be expressed approximately as

$$\hat{S}(\hat{x},\tau)=S(\hat{x})+\frac{b_o^*h^*}{S_o^*}b(\hat{x})\times\Big[\frac{l^*}{h^*}\big(s(\tau)-\hat{x}\theta(\tau)\big)+\varepsilon\zeta_o(\hat{x},\tau)\Big]. \qquad (44)$$

The instantaneous blockage coefficients should also include the above effects, thus requiring recalculation at every time step. Since individual runs of the applicable computer code, based on a 2-D boundary element method, at each step would be a time consuming task, we could tabulate in advance a series of values for different water levels and under-keel clearances for each cross-section and then simply interpolate for the current water level and

clearance at every time step while running the main program. If the under-keel clearance is not too large, yet another economy is possible. We only need to calculate the static blockage coefficients for the hull at rest, if we assume that the change with submergence is proportional to that for a corresponding rectangular cross section, for which analytic solutions of high order in small clearance are available, e.g., by Taylor (1973). Hence,

$$C(\hat{x},\tau) = C_o(\hat{x},\tau) \times C_r(H,c)/C_r(H_o,c_o), \qquad (45)$$

where

$$C_r(H,c) = \frac{b_o^* b(\hat{x})}{2r_o^*}(c^{-1}-1) + \frac{2h^*}{\pi r_o^*}H(1-\log 4c) + \frac{2h^*}{3\pi r_o^*}c^2 + \frac{281h^*}{90\pi r_o^*}c^4 + O(c^6), \qquad (46)$$

$$c = \left[h^* - d^* - l^*(s-\theta\hat{x})\right] \Big/ (h^* + \varepsilon\zeta_o h^*), \qquad (47)$$

$$H = 1 + \varepsilon\zeta_o, \qquad (48)$$

and $H_o = 1$, $c_o = 1 - d^*/h^*$. In the following numerical examples, we use the latter approach (45) for estimating the dynamic blockage coefficients since the clearances are not large in these cases.

Like a 3-D low aspect-ratio foil, the ship at drift angle or in other asymmetric flow will generate a circulation around itself, which produces a lift force. Hence, we must impose a suitable Kutta condition at the stern. Actually, we only need to capture the equivalent effect by imposing a Kutta condition for the far-field equation instead of bothering to examine the complicated stern flow in the near-field. It is the condition of equality of longitudinal velocity on both sides of the ship at the stern,

$$\Delta\varphi_x = \varphi_x\big|_{y=0^+} - \varphi_x\big|_{y=0^-} = 0, \quad \text{at the stern.} \qquad (49)$$

Since (39) holds originally for the 2-D case, it fails at the two ends of ship where 3-D effects are evident. At the bow, it is not too bad, because the jump $\Delta\varphi$ is automatically zero in the uniform inflow. But at the stern, since $\Delta\varphi \neq 0$ and $C \to 0$, equation (39) yields the unrealistic result $\hat{V} \to \infty$. So we must let V in (38) be determined by the Kutta condition rather than by (39) at the stern.

In essentially unsteady flow also the longitudinal velocities are discontinuous across the wake, i.e., on the negative x-axis behind the ship. The boundary condition there can be posed by the mass and momentum conservation law. In our asymptotic problem, however, the strong starting vortex generated by the initial acceleration from rest will have already wandered far away from the ship. It is, therefore, reasonable to assume a constant potential jump, across the entire length of the wake, of value identical to that at the stern without significant discontinuity of the longitudinal velocity. This implies that all velocity components are continuous in the wake region.

Now the initial-boundary value problem of the KP equation (20) is completely closed with zero initial condition, boundary conditions (43) on the ship centerplane, Kutta condition (49) at the ship stern, and normal condition (21) on the channel sidewall.

Here it is useful to establish connections with previous versions of the theory. By neglecting terms $\varphi_x\varphi_{yy}$ and $\varphi_{xy}\varphi_y$ and letting $U = 1 + \alpha\varepsilon$ in equation (20), it is reduced to a KP equation that was used by Choi & Mei (1989), as also by Chen & Sharma (1992) with slightly different coefficients. Further, neglecting higher orders in the matching condition, i.e., keeping only first order symmetric terms in equation (43), we get the classical linear result $\varphi_y\big|_{y\to 0^\pm} = \mp(1/2)\sqrt{\varepsilon}US_{\hat{x}}$ that was used by Choi & Mei (1989) for the symmetric case.

Our KP-type equation (20) with its boundary conditions is solved numerically by a finite difference method using an implicit fractional step algorithm, as explained in Chen & Sharma (1992).

HYDRODYNAMIC FORCES AND MOMENTS AS WELL AS TRIM AND SINKAGE

The pressure on the ship hull can be expressed approximately as

$$p = \varepsilon\zeta_o - z + O(\varepsilon^2). \qquad (50)$$

Hence, the wave resistance (negative longitudinal force) is given by

$$-F_{\hat{x}} = \frac{-F_{\hat{x}}^*}{\rho^* g^* C_p S_o^* l^*} = \frac{h^*}{l^* C_p}\int_{S_w} p\, n_{\hat{x}}\, \mathrm{d}S$$

$$= \frac{h^*}{l^* C_p}\left[-\int_{-1/2}^{1/2}\varepsilon\zeta_o\left\{\frac{\mathrm{d}}{\mathrm{d}\hat{x}}[S(\hat{x}) + \frac{b_o^* l^*}{S_o^*}b(\hat{x})(s-\hat{x}\theta)] + \frac{b_o^* h^*}{S_o^*}\varepsilon\zeta_o\frac{\mathrm{d}b}{\mathrm{d}\hat{x}}\right\}\mathrm{d}\hat{x} + \frac{\varepsilon^2 b_o^* h^*}{2S_o^*}\int_{-1/2}^{1/2}\zeta_o^2\frac{\mathrm{d}b}{\mathrm{d}\hat{x}}\mathrm{d}\hat{x}\right]. \qquad (51)$$

For a ship free to heave and pitch the sinkage s and trim θ are determined by equilibrium of forces in the vertical direction and of moments about the y-axis, respectively. Neglecting the inertial force and moment in view of very slow ship motion in these two degrees of freedom, we have two linear algebraic equations for the two unknowns s and θ,

$$\left.\begin{aligned}\int_{-1/2}^{1/2}[\zeta_o + \frac{l^*}{\varepsilon h^*}(s-\hat{x}\theta)]b(\hat{x})\,\mathrm{d}\hat{x} = 0,\\ \int_{-1/2}^{1/2}[\zeta_o + \frac{l^*}{\varepsilon h^*}(s-\hat{x}\theta)]b(\hat{x})\hat{x}\,\mathrm{d}\hat{x} = 0.\end{aligned}\right\} \qquad (52)$$

They are easy to solve.

For the lateral force and yaw moment, we cannot use the mean pressure expression (50). Instead, we apply a formula derived by Lighthill (1960) for a fish as slender body and also described in Newman (1977):

$$\frac{\partial F_{\hat{y}}^*}{\partial \hat{x}^*} = -\left(\frac{\partial}{\partial t^*} - \hat{U}^* \frac{\partial}{\partial \hat{x}^*}\right)\left[\hat{V}_b^*(\hat{x}^*, t^*) m_{\hat{y}\hat{y}}^*(\hat{x}^*)\right], \quad (53)$$

where $\hat{U}^*$ and $\hat{V}_b^*$ originally are $\hat{x}^*$ and $\hat{y}^*$ components of velocity of each section relative to the still fluid and $m_{\hat{y}\hat{y}}^*$ is the lateral added mass. For a two-dimensional body there is an exact relationship between the lateral added mass and the blockage coefficient (Newman 1969 (3.4) and Taylor 1973),

$$m_{\hat{y}\hat{y}}^* = -\rho^* S^* + 2\rho^* h^* C^*. \quad (54)$$

In our cases, the fluid pass around each cross section at velocity $\hat{V}^*$, so relatively $\hat{V}_b^* = -\hat{V}^*$ and $\hat{U}^* \approx U^*$. Further, the flow changes very slowly, so the time derivatives in equation (53) can be neglected. Thus it becomes

$$\frac{\partial F_{\hat{y}}^*}{\partial \hat{x}^*} = -\rho^* U^* \frac{\partial}{\partial \hat{x}^*}\left[\hat{V}^*(-S^* + 2h^* C^*)\right]. \quad (55)$$

Substituting the dimensional form of (39), i.e.,

$$2\hat{V}^* C^* = \Delta\varphi^* = \varphi^*\big|_{y^* \to 0^+} - \varphi^*\big|_{y^* \to 0^-}, \quad (56)$$

into (55) yields

$$\frac{\partial F_{\hat{y}}^*}{\partial \hat{x}^*} = -\rho^* U^* \frac{\partial}{\partial \hat{x}^*}\left[-\hat{V}^* S^* + h^* \Delta\varphi^*\right], \quad (57)$$

Integrating the above force density over the ship length, we have

$$F_{\hat{y}}^* = \int_{-l^*/2}^{l^*/2} \frac{\partial F_{\hat{y}}^*}{\partial \hat{x}^*} d\hat{x}^* = \rho^* U^* h^* \Delta\varphi^*\big|_{x^* = -l^*/2}, \quad (58)$$

$$M_{\hat{z}}^* = \int_{-l^*/2}^{l^*/2} \frac{\partial M_{\hat{z}}^*}{\partial \hat{x}^*} \hat{x}^* d\hat{x}^* = -F_{\hat{y}}^* l^*/2$$

$$+\rho^* U^* \int_{-l^*/2}^{l^*/2} (-\hat{V}^* S^* + h^* \Delta\varphi^*) d\hat{x}^*. \quad (59)$$

Finally, using the definitions introduced in the Nomenclature the nondimensional forms of equations (58) and (59) are found:

$$F_{\hat{y}} = \frac{F_{\hat{y}}^*}{\rho^* g^* C_p S_o^* l^*} = \frac{\sqrt{\varepsilon} U h^{*3}}{C_p S_o^* l^*} \Delta\varphi\big|_{\hat{x}=-1/2}, \quad (60)$$

$$M_{\hat{z}} = \frac{M_{\hat{z}}^*}{\rho^* g^* C_p S_o^* l^{*2}} = -F_{\hat{y}}/2 +$$

$$\int_{-1/2}^{1/2} \left(-\varepsilon^{3/2} U \frac{h^*}{C_p l^*} \hat{V} S + \sqrt{\varepsilon} U \frac{h^{*3}}{C_p S_o^* l^*} \Delta\varphi\right) d\hat{x}. \quad (61)$$

RESULTS AND DISCUSSION

The examples selected for calculation correspond exactly to the conditions of our recent model experiments in the Duisburg Shallow Water Towing Tank. A Series 60, block coefficient $C_B = 0.594$, hull of length $l^* = 4.689$ m, beam $b^* = 0.6252$ m and draft $d^* = 0.25$ m was towed in a channel of width $w^* = 9.81$m and water depth $h^* = 0.5$ m. So ε=0.16044 according to equation (41). The horizontal force, yaw moment, sinkage and trim were measured using appropriate guages. The experimental wave resistance was derived by subtracting from the total measured resistance an estimated viscous resistance being equal to the frictional resistance according to the ITTC 1957 correlation line times a form factor 1+k=1.175.

Blockage Coefficients

A computer code based on a 2-D boundary element method similar to Taylor (1973) was used to calculate static blockage coefficients of 41 cross-sections of the hull in stillwater. These results are presented in Fig. 2. The dynamic blockage coefficients at each time step were calculated by (45).

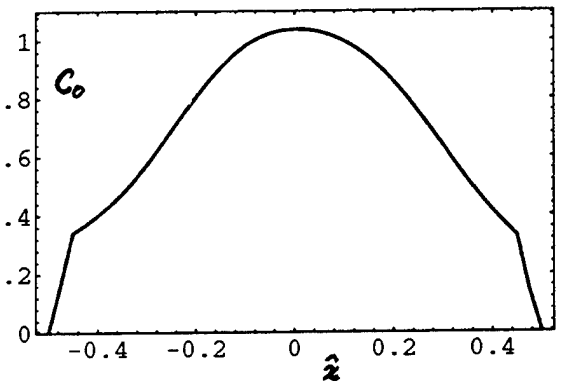


Fig. 2 Numerical blockage coefficient distribution for Series 60 (C_B=0.6) hull at h^*/d^*=2.

Off-Center Motion

This is the case of a ship moving without drift angle and parallel to the channel axis but off-center. In the ideal fluid regime, it is equivalent to one of two possible twin-hull configurations moving symmetrically in a channel of twice the width. The calculated longitudinal force, sinkage, trim, wetted surface area increment, lateral force and yaw moment as functions of depth Froude number are shown along with their measured values in Fig. 3 and 4 for two values of wall separation λ=0.1 and 0.2, respectively. Fig. 5 shows only their average

values as functions of λ at three speeds U=0.7, 1.0 and 1.3. We see that the calculated results match every trend of the experiments and show good quantitative agreement. The calculated wave patterns at these three speeds are visualized by density plots in Fig. 6; details around the ship, by contour plots in Fig. 7.

We observe the following three interesting new phenomena in calculations as well as measurements.

Suction and Repulsion by the Sidewall

It is well known, e.g., see Hess (1978) or Davis & Geer (1982), that a vertical sidewall exerts an attractive force on the ship, which increaces as the separation decreases, if the free surface is treated as a rigid plane. This is because the flow between the ship and the wall is faster than that on the open side, hence, the pressure is lower. Decreasing wall separation makes the flow faster and, therefore, the attractive force larger.

By contrast, we have found in our calculations and measurements that at transcritical and supercritical speeds in some off-center positions not too close to the wall, the ship experiences a repulsive lateral force (see Fig. 5 d). It is not difficult to understand if the waves generated by the ship are taken into account. Since the wave crests inside are higher than those outside, they will exert a repulsion. Thus we have two opposite effects competing with each other. At lower speeds the wave effect is weak and the original bank suction is dominant. But at higher speeds the wave effect prevails and the force becomes repulsive, provided the wall separation is not too small.

Wave Resistance Reduction

The wave resistance is not always the smallest in symmetric centerline motion. Sometimes at supercritical speeds, the wave resistance in off-center motion is significantly smaller than in the symmetric centerline case. The effect depends on where the shock-like bow-wave after reflection from the near wall hits the ship along its length. If it hits the afterbody, the positive pressure produced there tends to push the ship forward. But if the separation is sufficiently small, the reflected bow wave strikes the forebody creating an even higher wave elevation and associated wave resistance.

Instationarity

The asymmetric off-center motion aggravates the instationarity of the flow in the soliton-generating transcritical speed range. From Fig. 12 we can see that the variation of lateral force and yaw moment at U=1.2 is slow but terribly strong and the sign changes periodically. The same thing was observed in the experiment. So this speed range is dangerous for ship operation.

Oblique Motion

Now we turn to our other case of asymmetric motion, i.e., a ship moving with a small drift angle but along the cnterline of the channel. The longitudinal force, sinkage, trim, wetted surface area increment, lateral force and yaw moment as functions of depth Froude number are shown along with their measured values in Fig. 8 for α=4°. Fig. 9 shows only the average values as functions of drift angle α, at three speeds U=0.7, 1.0 and 1.3. We see that the calculated longitudinal force, sinkage and trim agree quantitatively with the measured values and that they are almost independent of drift angle in the calculation. However, the experiment shows some dependence on drift angle at transcritical and supercritical speeds.

The calculated lateral force and yaw moment agree well with measurements upto$U$=0.8. Beyond this point the measured lateral force increases abruptly to a large value while the yaw moment falls from a finite value to almost zero. But the calculated values show no such trends, they increase monotonically. The calculated lateral force and yaw moment is closely proportional to drift angle at all speeds, but the measured values behave so only upto U=0.8. The wave patterns at these three speeds are visualized by density plots in Fig. 10; details around the ship, by contour plots in Fig. 11. Fig. 13 shows the time history of the lateral force and yaw moment at four speeds.

The experimental phenomenon of the yaw moment jumping downward is believed to be due to flow separation. Beyond U=0.8 the waves generated become relatively steep which may cause the separation to occur earlier. Let us suppose the flow separation has occurred somewhere along the afterbody. Then there is a deadwater area behind the cross flow and the effective blockage coefficient there becomes large presumably. The lateral force there becomes correspondingly large. Consequently, the center of force moves from the forebody to midships. As a numerical experiment we can artificially multiply the blockage coefficient in equation (45) by a factor f_C given by

$$f_c = \begin{cases} 1, & \hat{x} > 0, \\ 1 - 2\hat{x}, & \hat{x} \le 0, \end{cases}$$

and redo the numerical calculations. It is found that the lateral force and yaw moment are really influenced by the factor as expected, i.e., they jump upward and downward, respectively.

ACKNOWLEDGEMENTS

One of the authors (X.-N. C.) was supported by a research project of the German Research Association (DFG). We thank Dr.-Ing. T. Jiang of Mercator University, Duisburg, and Dipl.-Ing. A. Gronarz of Duisburg Shallow Water Towing Tank for their help in conducting the model experiments.

REFERENCES

Beck, R.F. 1977 "Forces and Moments on a ship moving in a shallow channel," Journal of Ship Reserch, Vol. 21, pp. 107-119.

Chen, X.-N. and Sharma, S.D. 1992 "A slender ship moving at a near-critical speed in a shallow channel," Presented at 18th International Congress of Theoretical and Applied Mechanics, Haifa, Israel. Also accepted by Journal of Fluid Mechanics.

Chen, X.-N. and Sharma, S.D. 1994a "On the precision of shallow-water wave theory as applied to ship wavemaking," Annual Meetin of GAMM, Braunschweig, Germany.

Chen, X.-N. and Sharma, S.D. 1994b "A slender ship moves in a shallow channel," International Conference on Hydrodynamics, Wuxi, China.

Choi, H.-S., Bai, J.-W. and Cho, I.-H. 1990 "Nonlinear free surface waves due to a ship moving near the critical speed in a shallow water," Proceedings of 18th Symposium on Naval Hydrodynamics, Ann Arbor, pp.173-189.

Choi, H.S. and Mei, C.C. 1989 "Wave resistance and squat of a slender ship moving near the critical speed in restricted water," Proceedings of 5th International Conference on Numerical Ship Hydrodynamics, pp.439-454.

Dand, I.W. 1973 "The squat of full ships in shallow water," Transactions of Royal Institution of Naval Architects, Vol. 115, pp. 237-255.

Davis, A.M.J. 1986 "Hydrodynamic effects of fixed obstacles on ships in shallow water. Journal of Ship Reserch, Vol. 30, pp. 94-102.

Davis, A.M.J. and Geer, J.F. 1982 "The application of uniform-slender-body theory to the motion of two ships in shallow water," Journal of Fluid Mechanics, Vol. 114, pp.419-441.

Ertekin, R.C., Webster, W.C. and Wehausen, J.V. 1984 "Ship-generated solitons," Proceedings of 15th Symposium on Naval Hydrodynamics, Hamburg, pp.347-364.

Ertekin, R.C., Webster, W.C. and Wehausen, J.V. 1986 "Waves caused by a moving disturbance in a shallow channel of finite width," Journal of Fluid Mechanics, Vol. 169, pp. 275-292.

Fujino, M. 1968 "Experimental studies on ship maneuverability in restricted waters, Part 1," International Shipbuilding Progress, Vol. 15, pp. 279-301.

Fujino, M. 1970 "Experimental studies on ship maneuverability in restricted waters, Part 2," International Shipbuilding Progress, Vol. 17, pp. 45-65.

Graff, W. 1962 "Untersuchungen über die Ausbildung des Wellenwiderrstandes im Bereich der Stauwellengeshwindigkeit in flachem, seitlich beschränktem Fahrwasser," Schiffstechnik, Vol. 9, pp. 110-122.

Graff, W., Kracht, A. and Weinblum, G. 1964 "Some extensions of D.W. Taylor's standard series," Transations of Society of Naval Architects and Marine Engineers, Vol. 72, pp. 374-401.

Helm, K. 1940 "Effect of canal depth and width on ship resistance (in German)," Hydrodynamische Probleme des Schiffsantriebs, Teil 2, Ed. G. Kempf, Verlag Oldenbrurg, Munich and Berlin, pp.144-171.

Hess, F. 1978 "Bank suction cancelled by rudder deflection: a theoretical model," International Shipbuilding Progress, Vol. 25, pp. 7-13.

Huang, D.B., Sibul, O.J. and Wehausen, J.V. 1983 "Ships in very shallow water," Festkolloquium zur Emeritierung von Karl Wieghardt, Institut für Schiffbau der Universität Hamburg, Bericht Nr. 427, pp.29-49.

Kijima, K. and Tanaka, S. 1991 "Numerical study of cross flow drag by the vortex shedding model," Journal of Society of Naval Architects of Japan, Vol. 170, pp. 235-243.

Kijima, K. & Tanaka, S. 1992 "The cross flow drag acting on rectangular cross-sections with round edge," J. Soc. Nav. Arch. Japan, Vol. 172, pp.1-8.

Kijima, K. & Yasukawa, H. 1984 "Manoeuvrability of ships in narrow waterway," Journal of Society of Naval Architects of Japan, Vol. 156, pp. 25-37.

Kinoshita, M. 1946 On the restricted-water effect on ship resistance. Japan Society of Naval Architects, Vol.150, pp. 181-187.

Kleinau, D. 1981 "Hydrodynamische Masse und hydrodynamisches Maeeenträgheits-moment von Schiffen bei endlicher Wassertiefe," Schiffbauforschung,Vol. 20, pp. 247-256.

Lea, G.K., and Feldman, J.P. 1972 "Transcritical flow past slender ships," Proceedings of 9th Symposium on Naval Hydrodynamics, pp.1527-1542.

Lighthill, M.J. 1960 "Note on the swimming of slender fish," Journal of Fluid Mechanics, Vol. 9, pp. 305-317.

Matsumura, K. and Yoshida, Y. 1991 "Nonlinear lift characteristics of flat plate at incidence in shallow water," Journal of Society of Naval Architects of Japan, Vol. 170, pp. 245-252.

Maruo, H. 1989 "Evolution of the theory of slender ships," Schiffstechnik, Vol. 36, pp. 107-133.

Mei, C.C. 1976 "Flow around a thin body moving in shallow water," Journal of Fluid Mechanics, Vol. 77, pp. 737-752.

Mei, C.C. 1986 "Radiation of solitons by slender bodies advancing in a shallow channel," Journal of Fluid Mechanics, Vol. 162, pp. 53-67.

Mei, C.C. and Choi, H.S. 1987 "Forces on a slender ship advancing near the critical speed in a wide canal", Journal of Fluid Mechanics, Vol. 179, pp. 59-76.

Newman, J.N. 1969 "Lateral motion of a slender body between two parallel walls," Journal of Fluid Mechanics, Vol. 39, pp. 97-115.

Newman, J.N. 1977 Marine Hydrodynamics, Cambridge, Mass., M.I.T. Press.

Nowacki, H. 1960 "Über die Wechselseitigen Kraftwirkungen zwischen schiffsähnlichen Tauchkörpern," Schiff und Hafen, Jahrg. 12, 756-760.

Norrbin, N.H. 1974 "Bank effects on a ship moving through a short dredged channel," Proceedings of 10th Symposium on Naval Hydrodynamics, Washington, D.C., pp.71-88.

Ohmori, T. and Miyata, H. 1993 "Oblique tow simulation by a finite-volume method," Journal of Society of Naval Architects of Japan, Vol. 173, pp. 27-34.

Taylor, P.J. 1973 "The blockage coefficient for flow about an arbitrary body immersed in a channel," Journal of Ship Reserch, Vol. 17, pp. 97-105.

Thews, J.G. and Landweber, L. 1935 "The influence of shallow water on the resistance of a cruiser model," US Experimental Model Basin, Navy Yard, Washington, DC, Rep. no. 408

Thews, J.G. and Landweber, L. 1936 "A thirty-inch model of the SS Clariton in shallow water," US experimental Model Basin, Navy Yard, Washington, DC, Rep. no. 414.

Todd, F.H. 1953 "Some further experiments on single-screw merchant ship forms-Series 60," Transactions of the Society of Naval Architects and Marine Engineers, Vol. 61, pp. 519-589.

Tuck, E.O. 1966 "Shallow water flows past slender bodies," Journal of Fluid Mechanics, Vol. 26, pp. 81-95.

Tuck, E.O. 1978 "Hydrodynamic problems of ships in restricted waters," Annual Review of Fluid Mechanics, Vol. 10, pp. 33-46.

Tuck, E.O. and Taylor, P.J. 1970 "Shallow-water problems in ship hydrodynamics," Proceedings of 8th Symposium on Naval Hydrodynamics, Pasadena, pp. 627-659.

Wu, De-Ming and Wu, T.Y. 1982 "Three-dimensional nonlinear long waves due to moving surface pressure," Proceedings of 14th Symposium on Naval Hydrodynamics, Ann Arbor, Mich., pp.103-129.

Yeung, R.W. 1978 "On the interactions of slender ships in shallow water," Journal of Fluid Mechanics, Vol. 85, pp. 143-159.

Yeung, R.W. and Hwang W.-Y. 1977 "Nearfield hydrodynamic interactions of ships in shallow water," Journal of Hydronautics, Vol. 11, pp. 128-135.

Yeung, R.W. and Tan, W.T. 1980 "Hydrodynamic interactions of ships with fixed obstacles." Journal of Ship Reserch, Vol. 24, pp. 50-59.

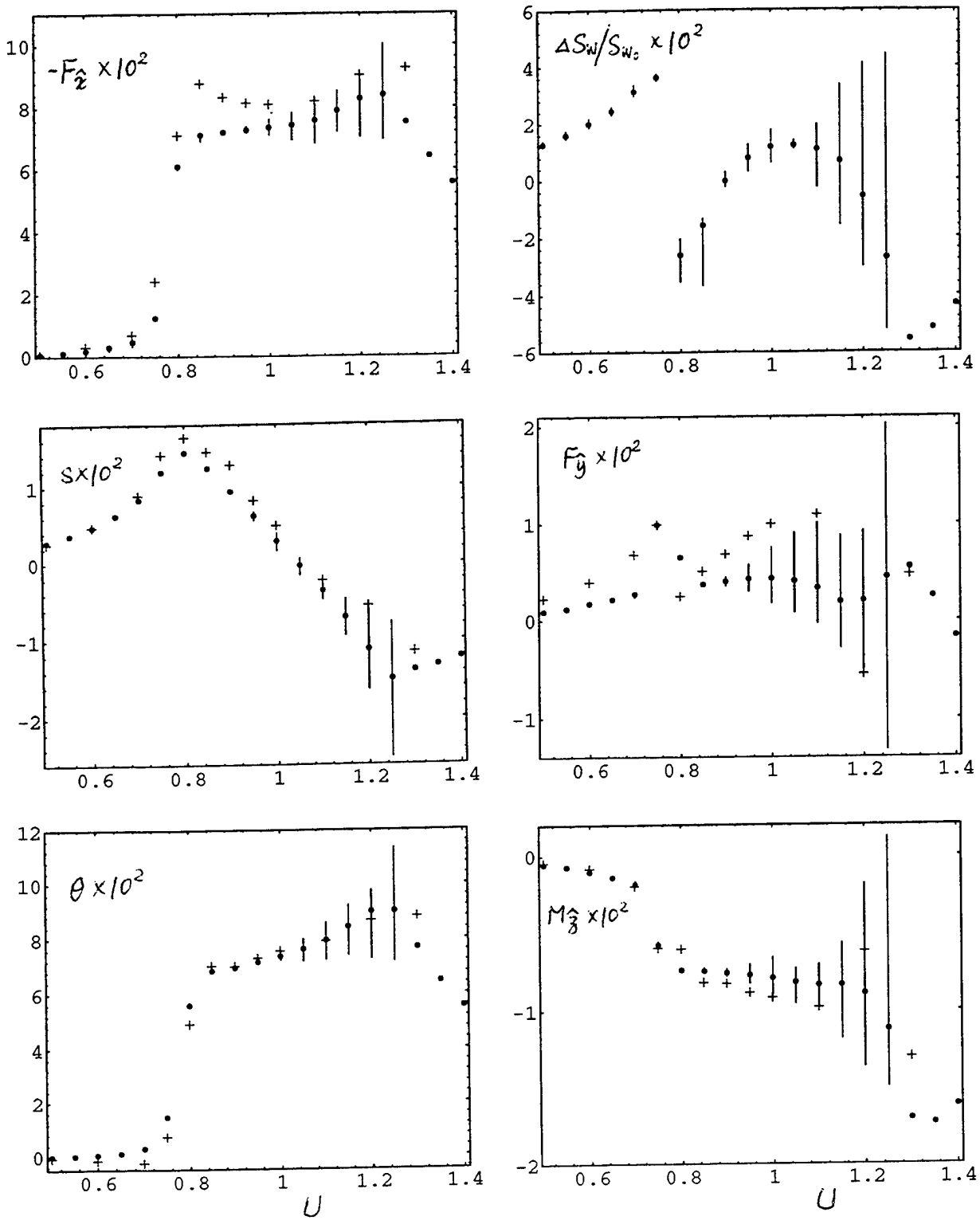


Fig.3 Calculated versus measured longitudinal force, sinkage, trim, wetted surface area increment, lateral force and yaw moment as functions of speed for Series 60 (C_B=0.6) model in off-center motion at h^*/d^*=2 and λ=0.1; dots denote the calculated average values, vertical bars represent the range of temporal variation from minimum to maximum in the calculations, and crosses mark measured mean values.

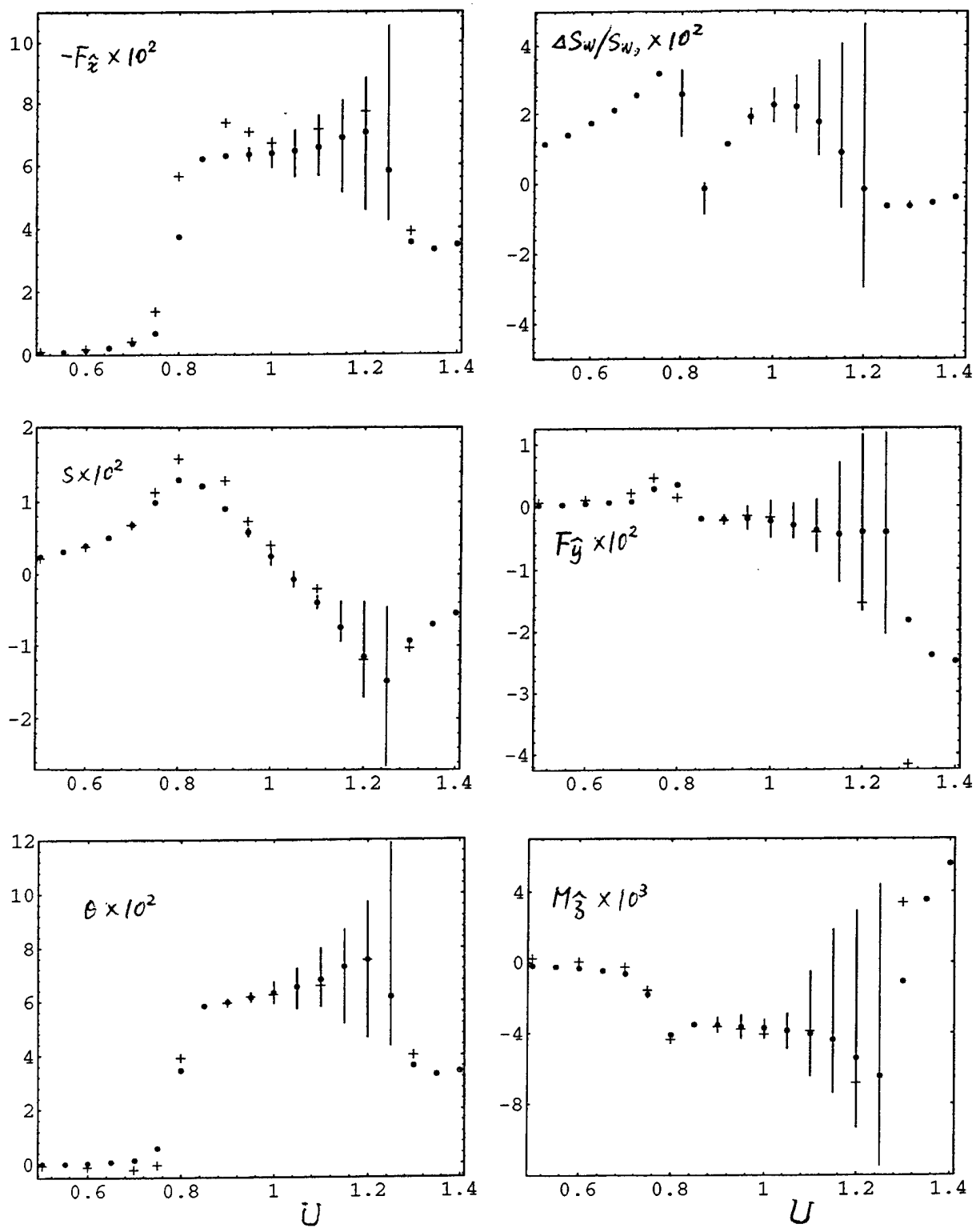


Fig. 4 Calculated versus measured longitudinal force, sinkage, trim, wetted surface area increment, lateral force and yaw moment as functions of speed for Series 60 (C_B=0.6) model in off-center motion at h^*/d^*=2 and λ=0.2; dots, vertical bars and crosses as in Fig.3.

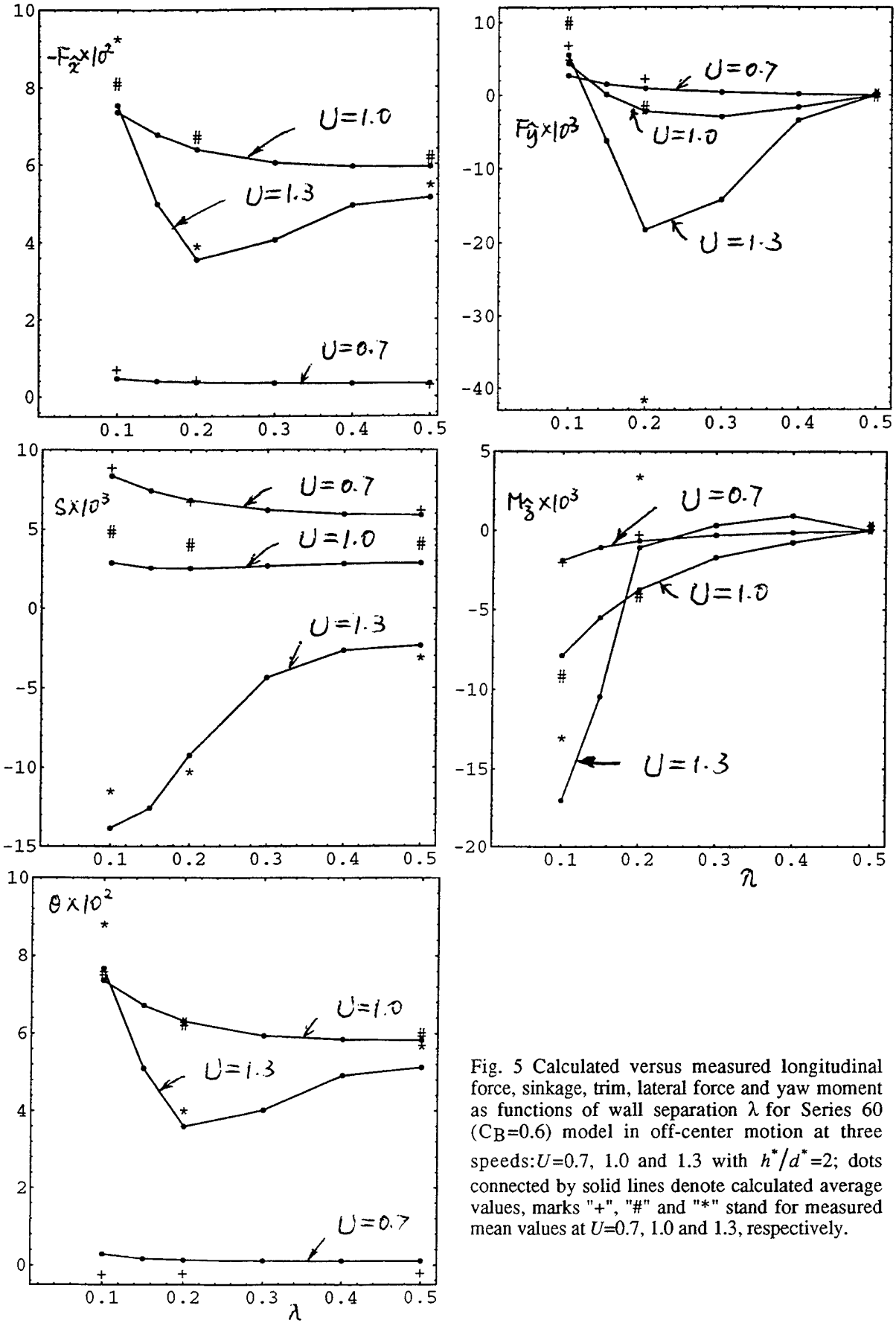


Fig. 5 Calculated versus measured longitudinal force, sinkage, trim, lateral force and yaw moment as functions of wall separation λ for Series 60 (C_B=0.6) model in off-center motion at three speeds: U=0.7, 1.0 and 1.3 with h^*/d^*=2; dots connected by solid lines denote calculated average values, marks "+", "#" and "*" stand for measured mean values at U=0.7, 1.0 and 1.3, respectively.

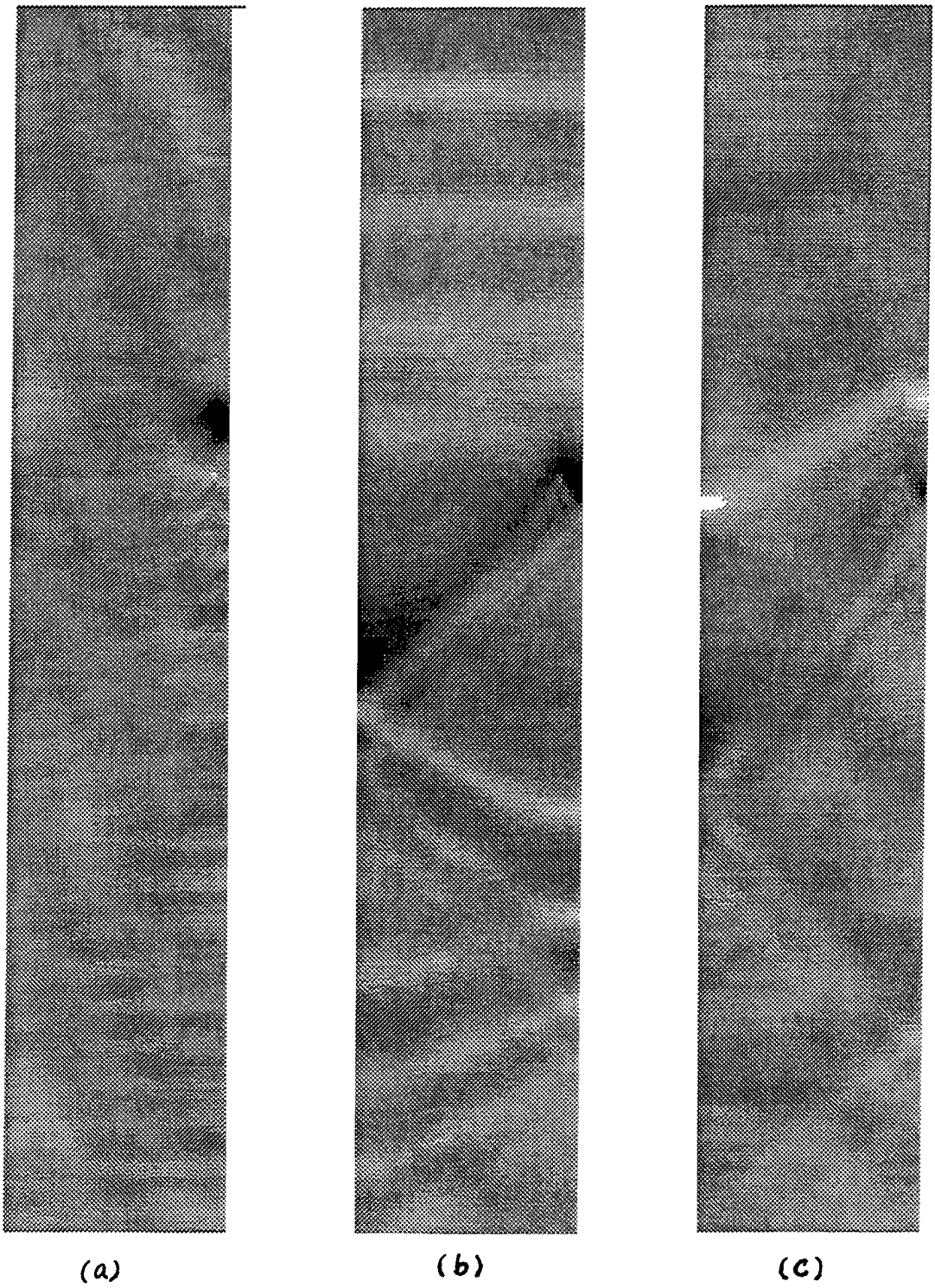
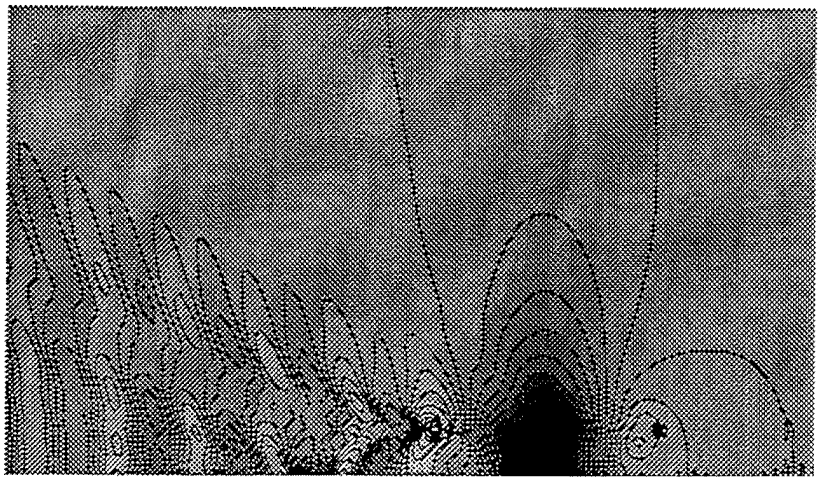
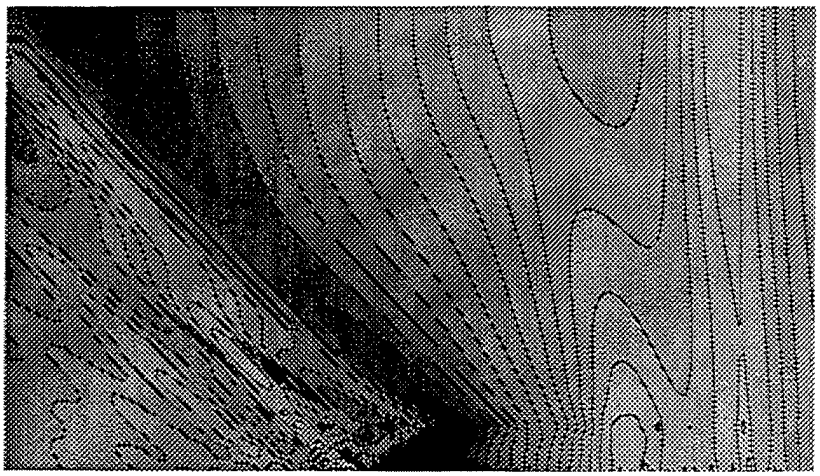


Fig. 6 Density plots of three typical calculated wave patterns of Series 60 (C_B=0.6) ship in off-center (λ=0.1) motion at subcritical, critical and supercritical speeds with h^*/d^*=2: (a) Kelvin-like wave pattern at U=0.7 and τ=8 with ζ in plot range (-1,1); (b) Havelock-like wave pattern and upstream solitons at U=1 and τ=16 with ζ in plot range (-2.5,2.5); (c) Mach -shock-wave-like pattern at U=1.3 and τ=8 with ζ in plot range (-3,3).

(a)



(b)



(c)

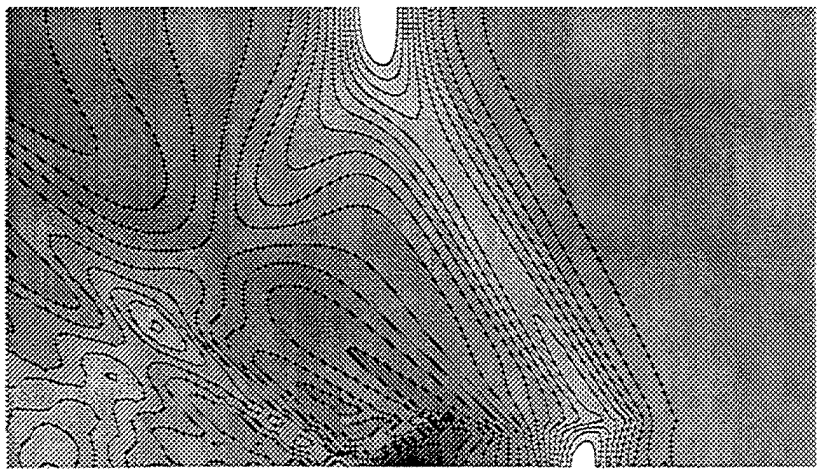


Fig. 7 Contour plots to visualize details near the ship in the three wave patterns of Fig. 6, where 10 contour lines are used to subdivide each plot range uniformly.

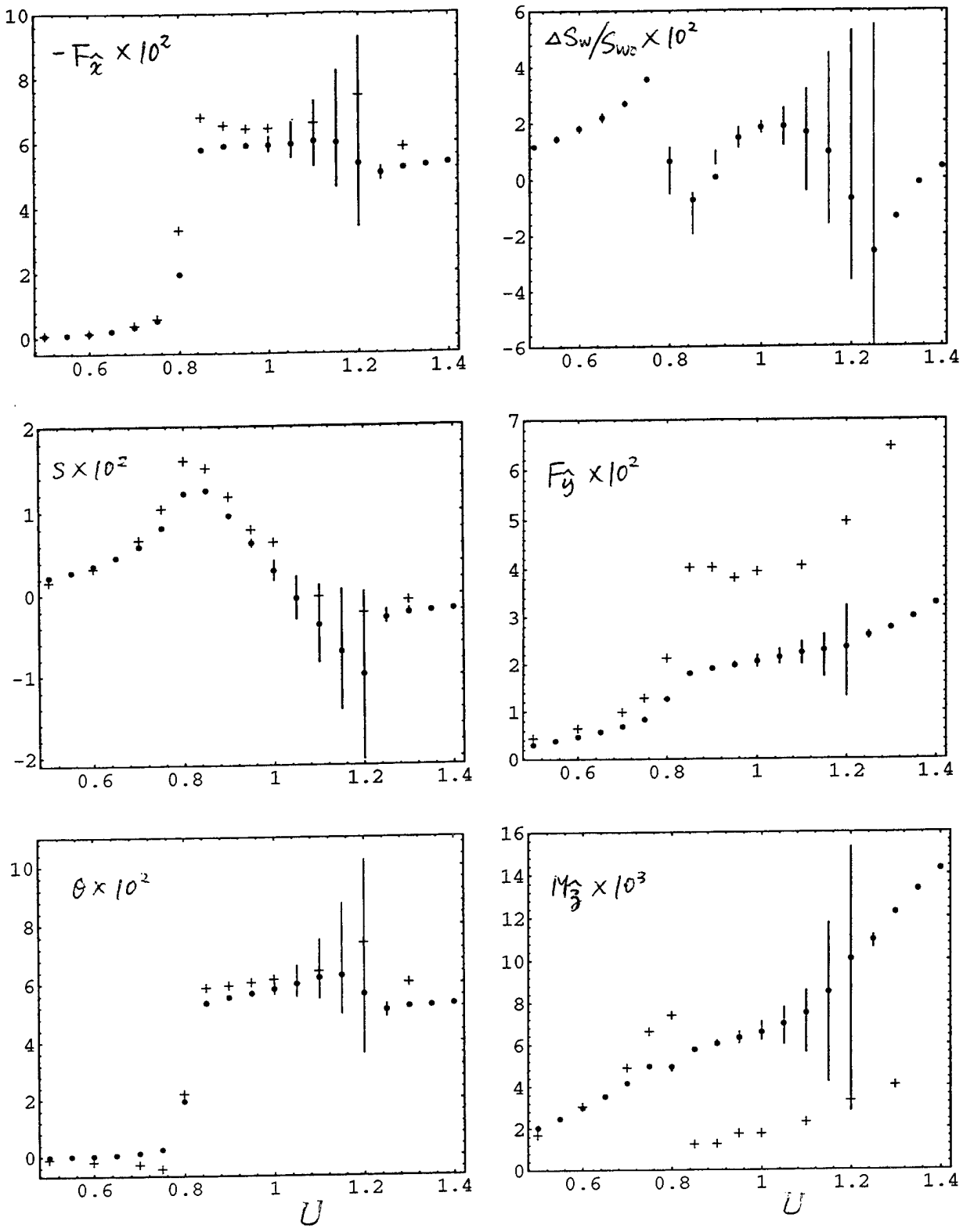


Fig. 8 Calculated versus measured longitudinal force, sinkage, trim, wetted surface area increment, lateral force and yaw moment as functions of speed for Series 60 (C_B=0.6) model in oblique motion along tank centerline at drift angle α=4° and h^*/d^*=2; dots, vertical bars and crosses as in Fig. 3.

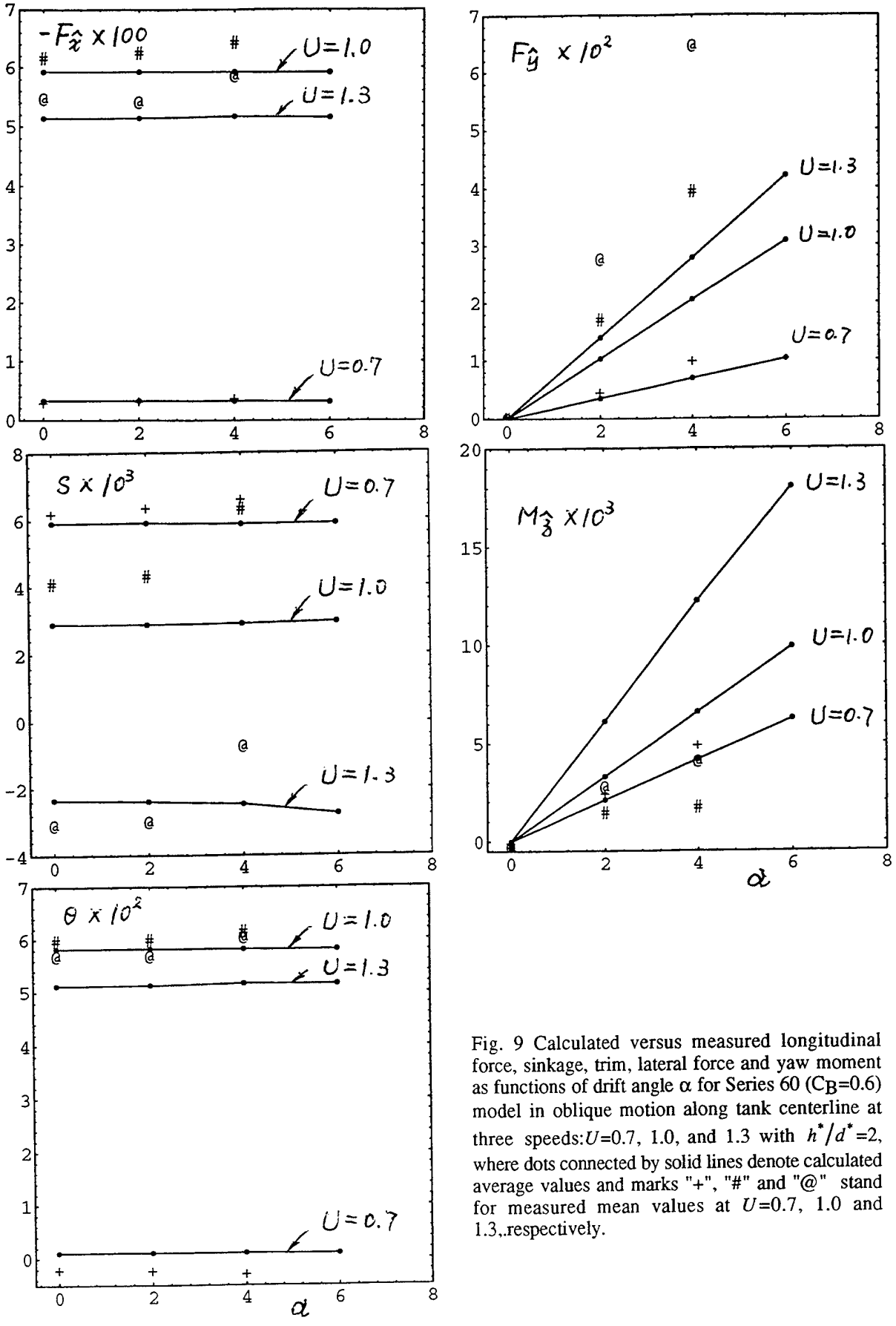


Fig. 9 Calculated versus measured longitudinal force, sinkage, trim, lateral force and yaw moment as functions of drift angle α for Series 60 (C_B=0.6) model in oblique motion along tank centerline at three speeds:U=0.7, 1.0, and 1.3 with h^*/d^*=2, where dots connected by solid lines denote calculated average values and marks "+", "#" and "@" stand for measured mean values at U=0.7, 1.0 and 1.3,.respectively.

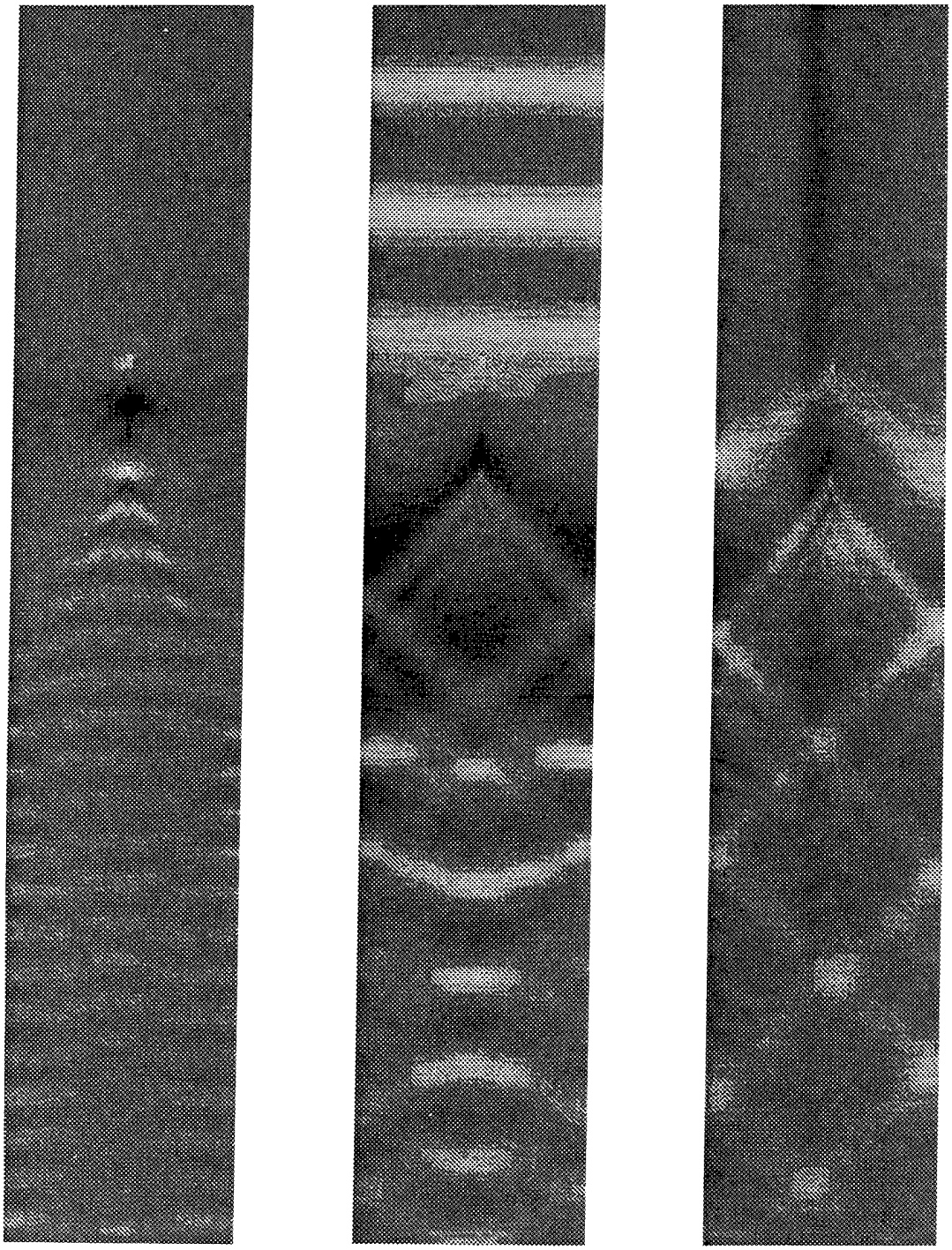
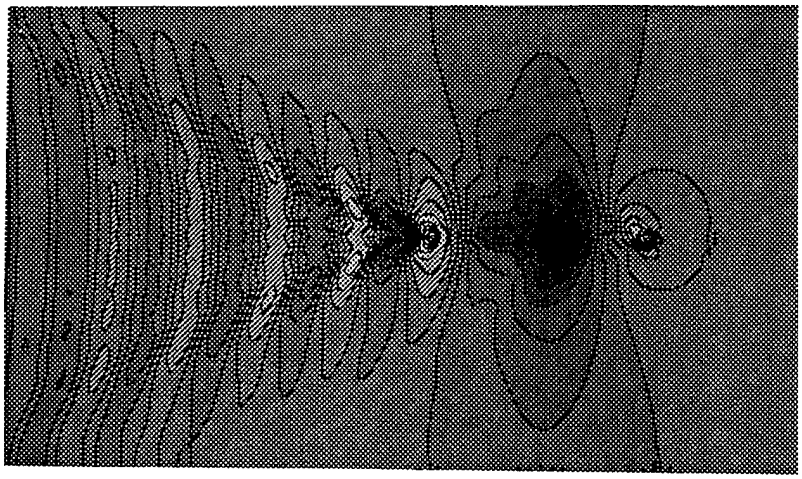
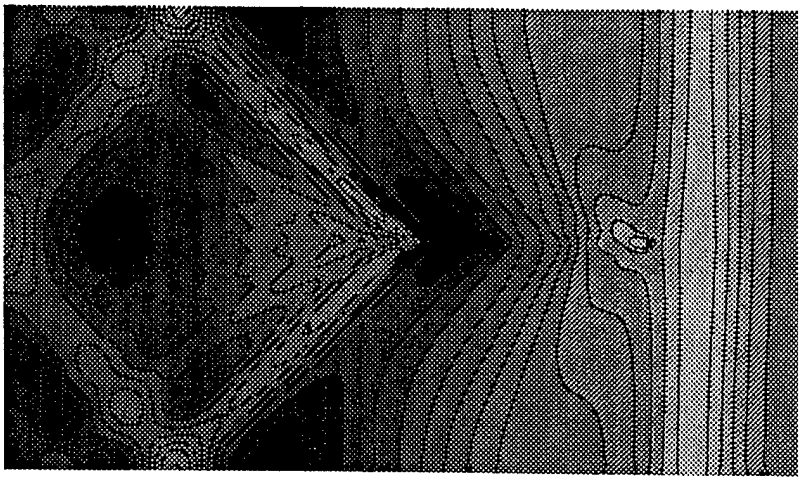


Fig. 10 Density plots of three typical calculated wave patterns of Series 60 (C_B=0.6) ship in oblique motion (α=-4°) along tank centerline at subcritical, critical and supercritical speeds with h^*/d^*=2: (a) Kelvin-like wave pattern at U=0.7 and τ=8 with ζ in plot range (-1,1); (b) Havelock-like wave pattern and upstream solitons at U=1 and τ=16 with ζ in plot range (-2.5,2.5); (c) Mach -shock-wave-like pattern at U=1.3 and τ=8 with ζ in plot range (-3,3).

(a)



(b)



(c)

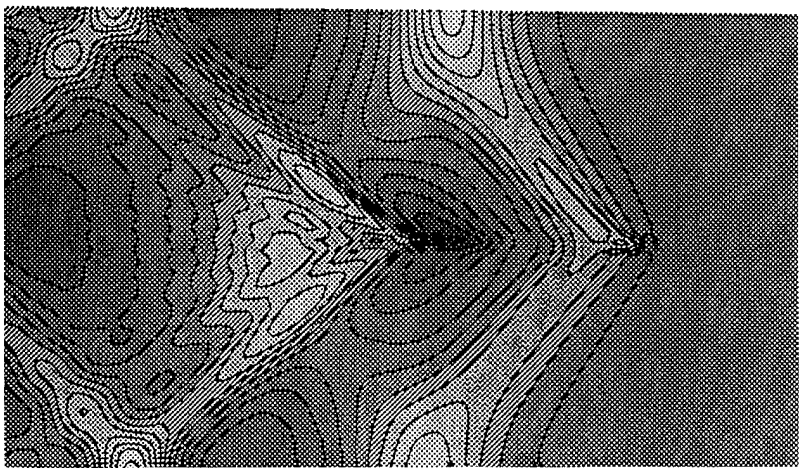
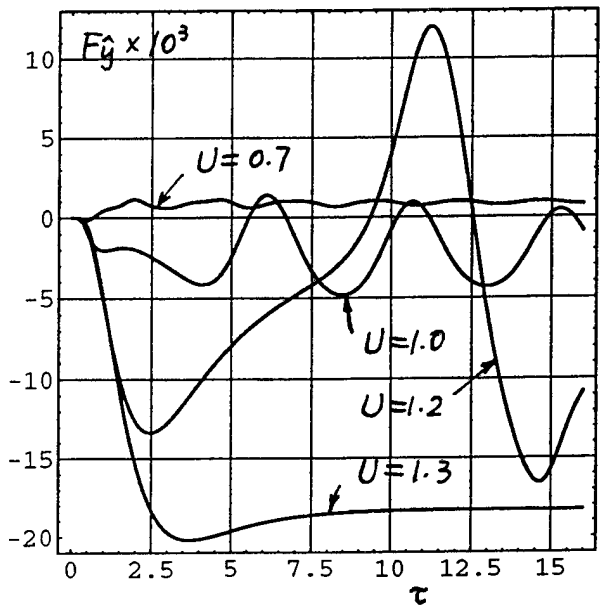
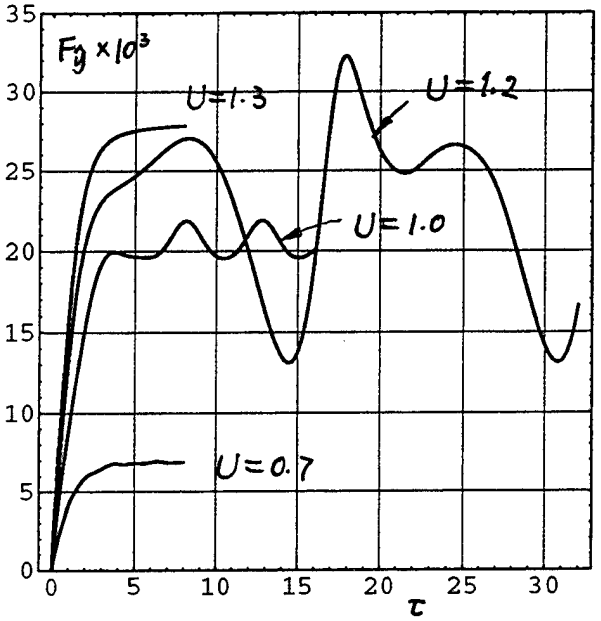
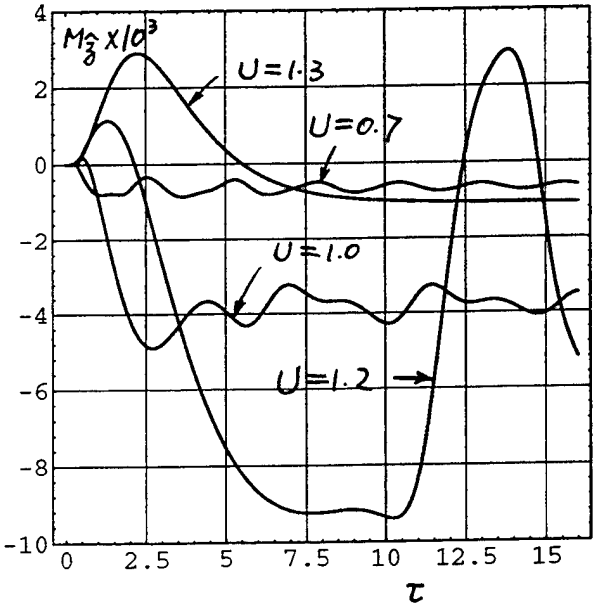


Fig. 11 Contour plots to visualize details near the ship in the three wave patterns of Fig. 10, where 10 contour lines are used to subdivide each plot range uniformly.







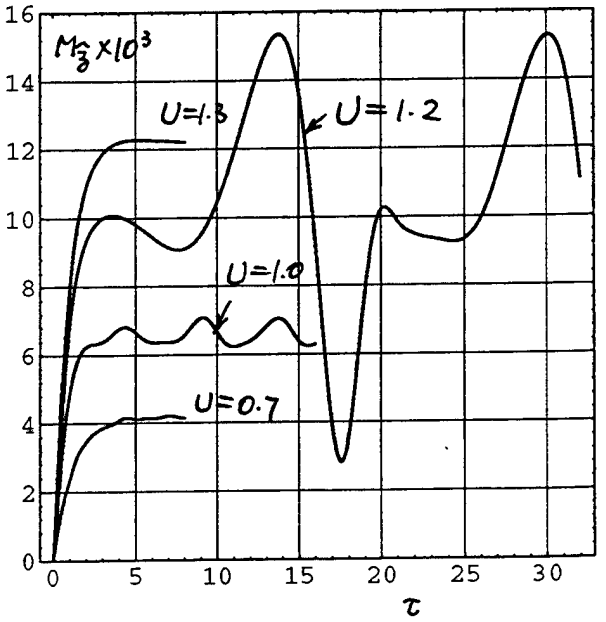


Fig. 12 Time history of lateral force and yaw moment in off-center case λ=0.2.

Fig. 13 Time history of lateral force and yaw moment in drift-angle motion α=4°.

DISCUSSION

J.L.H. Marchal
University of Liege, Belgium

I have one comment about the conclusion concerning the suction and repulsion of the ship by the sidewall. Important studies have been realized in my department between 1970 an 1974 about the movement of ship in shallow-water channel parallel to the axis but off-center. We have observed in our towing tank that the flow characteristics on one side of the ship are almost independent of those on the other side. So, you can observe for example a typical critical or supercritical flow between the channel bank and the ship; meanwhile on the other board the flow remains in the subcritical ranges. These different situations on each board of the ship induce transversal forces which can be repulsive or attractive depending on the distance between the ship and the bank, on the speed range and on the blockage coefficient. Repulsion by the sidewall is not mainly a question of wave crests effects. For more details, please read my paper presented at the PIANC Congress of Leningrad in 1977.

As maneuverability is concerned, it is mainly a problem of relative flow speeds on each board of the ship depending on the blockage coefficients.

AUTHORS' REPLY

Thank you for your very interesting observations. Since our mathematical model allows for different free-surface elevations and different longitudinal velocities on the two sides of the hull, we believe that the possibility of the flow being locally subcritical on one side and supercritical on the other is automatically included.

DISCUSSION

R. Beck
University of Michigan, USA

You seem to apply a Kutta condition at the stern for asymmetric blows. You also show the blockage coefficient going to zero at the stern. These two conditions are incompatible since a zero blockage coefficient implies there is no trailing edge. A sharp trailing edge is necessary to apply a Kutta condition. How do the authors apply both $C(x) = o$ and Kutta conditions at the stern?

AUTHORS' REPLY

You are absolutely right. We actually applied our Kutta condition a little ahead of the rear end of the waterline, i.e., at the physical location of the sharp vertical edge in the Series 60 hullform, where the blockage coefficient $C(x)$ is significantly nonzero. The rearmost panel in our model contributes to the longitudinal and vertical forces but not to the side force.

Linear and Nonlinear Calculations of the Free Surface Potential Flow Around Ships in Shallow Water

K. Kim, Y. Choi (Daewoo Shipbuilding and Heavy Machinery, Ltd., Korea), C. Jansson, (Chalmers University of Technology, Sweden), L. Larsson (Flowtech International AB, Sweden)

ABSTRACT

In the present paper, the shallow water effect on the free surface potential flow around ships is numerically investigated. The numerical methods developed are linear and nonlinear Rankine source panel methods. Rankine sources are distributed on the hull and part of the free surface and a symmetry condition is applied to simulate the bottom. The hull and the wavy free surface are discretized by parabolic, quadrilateral panels with a bi-linear distribution of sources.

An exact hull boundary condition is satisfied in both methods, but different free surface boundary conditions are used. The linear method is developed based on double model approximation and thus the free surface condition is linearized with respect to the flow with an undisturbed surface. In the nonlinear method the exact free surfece boundary conditions are approached in an iterative process, where in each iteration a condition, linearized about the previous solution, is satisfied on the previously calculated wavy surface. The process starts with the free surface as a rigid lid and stops when the change in wave height between two iterations is below a given value. There is no need to distribute sources on the bottom, which is considered the horizontal symmetry plane of the problem.

The methods have been applied for a number of test cases including the Wigley hull, the Series 60 C_B =0.60 hull and a twin hull for varying depth Froude numbers. Typical shallow water effects, such as the widening of the Kelvin angle and the sharp increase in wave resistance when approaching the critical Froude number are well predicted. In the paper detailed comparisons with recent measurements for the Series 60 C_B=0.6 hull and twin hull cases in the Duisburg and SSPA towing tank are made for the wave resistance, wave pattern, sinkage, trim and pressure distribution on the hull. Good agreement is demonstrated.

NOMENCLATURE

U_∞	Ship speed
V	Flow velocity with components (ϕ_x, ϕ_y, ϕ_z)
g	Acceleration of gravity
L	Length of ship
T	Draught of ship
H	Depth of water
F_n	Froude number
F_{nH}	Depth Froude number
α	Kelvin wave angle
C_B	Block coefficient
ϕ	Total velocity potential
Φ	Double model flow velocity potential
σ	Source strength
C_P	Pressure coefficient
h=z(x,y)	Wave elevation

INTRODUCTION

There is an appreciable change in potential flow when ship is passing from deep to shallow water. The first effect of the shallow water is the changes in resistance. The resistance of a ship is quite sensitive to the effects of shallow water. When a ship moves with a constant speed(U_∞) on the water surface, the resistance increases as the depth(H) of water decreases up to the critical depth and decreases again as H decreases

further. Often most of the change in resistance is due to the change in wave pattern. The wave pattern in deep water ($V << \sqrt{gH}$) consists of a double set of waves, the transverse and diverging waves as shown in Fig. 1, the wave pattern being contained between the straight lines making an angle α of 19 deg 28 min on each side of the line of motion of the point. As water depth decreases, the angle α increases and reaches 90 deg as V approaches $\sqrt{gH}$. When V exceeds $\sqrt{gH}$, α begins to decrease again. The wave pattern now consists only of diverging waves.

The effect upon resistance due to these changes in wave pattern in shallow water has attracted the interest of scientists for many years. Since Havelock[1] studied the effects of shallow water on the wave resistance and wave pattern for a point pressure impulse travelling over a free water surface in 1908, a number of different approximate methods have been proposed to investigate the hydrodynamic characteristics of ship in shallow water. Havelock[2], Schliching[3], Sretensky[4] proposed different approaches to obtain an appropriate formula for the ship resistance in shallow water. Kinoshita[5] extended Havelock's theory to satisfy the bottom boundary condition more exactly and Inui[6] further developed the theory to solve the channel problem. Kirsch[7] utilized linearized wave theory and Bai[8] used localized Finite Element Method to carry out calculations of wave making resistance for simplified hull form in various water depths and channel widths. Mueller[9] and Millward[10] carried out experiments and theoretical calculations based on linearized wave theory to investigate the effect of shallow water on the resistance of ship.

More recently the Rankine source panel method based on linear wave theory[11] has been applied to compute the wave resistance of ships in shallow water. Yasukawa[12] developed a first order panel method based on Dawson's approach for the linear free surface condition. The bottom boundary condition is satisfied exactly by covering part of the bottom surface with Rankine sources. Lee[13] improved the solution efficiency over Yasukawa's work by choosing the Green function to be the sum of the Rankine source and its image with respect to the bottom surface. Similary a symmetry condition is applied at the bottom surface in the present method to simulate the shallow water effect in a purely numerical way. The present linear method has been tested for a water jet catamaran to predict the effect of shallow water on wave pattern and wave resistance. Good agreement with the measurements made by SSPA is obtained.

An attempt to investigate the nonlinear free surface problem in shallow water was made by Ni[14] and Kim[15]. In the present paper, a further attempt to improve the accuracy has been made by taking account of the nonlinear effects in the free surface boundary condition. The solution of the wavy potential, which satisfies the exact boundary condition on the hull and the free surface, is obtained through iterations and in each iteration the free surface boundary condition is linearized, based on the small perturbation principle, about the previous solution. The iteration starts from the linear solution. In each iteration the hull and free surface panels are adjusted according to the new wavy surface and the sources are moved accordingly to simulate kinematic and dynamic boundary condition more exactly. Upon convergence - a converged solution is usually obtained after 6 to 10 iterations - the nonlinear terms go to zero and the solution is exact with respect to the boundary conditions. The method is a generalization of the potential flow module of the code SHIPFLOW[16], partly developed by the first author[17].

The present method has been applied to compute the hydrodynamic characteristics in shallow water for the Wigley hull and Series 60 hull with block coefficient 0.6. The importance of nonlinearity is discussed in some detail with relation to the effect of shallow water on wave pattern and wave resistance. Comparisons are made with experiment.

MATHEMATICAL FORMULATION

A ship, piercing the free surface, is assumed to be fixed in a uniform onset flow of velocity U_∞ and the flow is considered inviscid, irrotational and incompressible. Then the flow field around the ship may be described by a velocity potential ϕ, which is generated by a certain distribution of sources on a surface S and by the uniform onset flow in the X direction(see Fig. 2).

$$\phi(X,Y,Z) = \int \frac{\sigma(q)}{r(p,q)} dS + U_\infty X, \quad (1)$$

where $\sigma(q)$ is the source density on

the surface element dS and r(p,q) is the distance from the point q to the field point p(X,Y,Z) where the potential is being evaluated.

The potential ϕ given in Eq. (1) is governed by the Laplace equation

$$\nabla^2\phi = 0 \quad \text{in the fluid domain.} \qquad (2)$$

This is an elliptic partial differential equation which requires boundary conditions at all boundaries of the computational domain. These boundaries for the shallow water problem are the hull, the free water surface and sea bottom.

The hull boundary condition simply expresses the fact that the flow must be tangential to the hull surface, i. e. the normal component of the velocity must be zero:

$$\phi_n = 0 \qquad \text{on the hull.} \qquad (3)$$

In equation (3) and below the subscript n indicates differentiation in the normal direction. The same rule applies to the X, Y, Z directions.

At the free surface Z = h(X,Y) the flow must be tangential. Thus

$$\phi_{nfs} = 0, \qquad (\text{on } Z = h) \qquad (4)$$

where the subscript fs stands for the free surface. This surface is ,however, unknown to begin with. A second boundary condition is therefore required. This expresses the fact that the pressure is constant on the surface:

$$P = \text{constant.} \qquad (\text{on } Z = h) \qquad (5)$$

Taking the dot product of the normal vector to free surface and the velocity vector, Eq.(4) may be writtern as

$$D_1(\sigma,h) = \phi_x h_x + \phi_y h_y - \phi_z = 0, \quad (\text{on } Z = h) \qquad (6)$$

while (5) may be expressed using the Bernoulli equation as

$$D_2(\sigma,h) = gh + \frac{1}{2}(\nabla\phi \cdot \nabla\phi - U_\infty^2) = 0. \qquad (\text{on } Z = h) \qquad (7)$$

The kinematic boundary condition on the sea bottom is

$$\phi_n = 0 \quad \text{at the bottom surface.} \qquad (8)$$

In the infinite depth case, this equation is replaced by the condition that the disturbance due to body must vanish, i. e.

$$\nabla\phi = U_\infty \quad \text{as} \quad Z \to -\infty \qquad (9)$$

There is also a further condition to be required, i. e. waves uptream of the ship shall be prevented.

NUMERICAL METHOD

The exact problem defined by equations (1)-(9) is nonlinear, since the free surface boundary conditions (6) and (7) are nonlinear and should be exactly satisfied on the wavy surface Z = h(X,Y), which is unknown, and must be computed as a part of the solution. Thus, numerical methods, which have been applied to solve the problem, usually entail some kind of linearization procedure.

In the classical linearized wave theory, which has been the basis for the work in this area for the major part of the century, the free surface boundary condition is linearized about the undisturbed flow. All disturbances due to the ship must then be small, and the computed ships have to be very slender. This is not a good approximation for ships of normal fullness. A better approach based on double model linearized theory was proposed by Dawson[11]. In the double model linearized theory an exact boundary condition is satisfied on the hull and bottom surface, while on the free surface the boundary condition is linearized with respect to the double model solution. This solution can be found by specifying the free surface as a symmetry plane, i. e. to use a double model, made up of the underwater part plus its image in the undisturbed water surface.

For the deep water case, the double model linearized theory has been applied

frequently to predict the wave pattern and ship wave resistance. Successful predictions have been made for many practical applications, however, the accuracy for the shallow water case is relatively poor. The most significant inaccuracy can be found in the prediction of the wave patterns near the bow and stern region. The poor resolution may result partially from the fact that the waves in shallow water are very steep, so the double model approximation may not be valid. Another important fact is that the wave pattern near the bow and stern region is strongly influenced by the nonlinear terms and the linearized free surface condition can not simulate the exact boundary condition properely.

An attempt to improve the accuracy has been made in the present paper by taking the nonlinear effects into account in the free surface boundary condition. In contrast to the linear wave theory, in the present nonlinear method an exact boundary condition is satisfied both on the wetted hull surface and the wavy free surface. A single model with higher order panels both on the hull and free surface is used and the bottom surface is assumed to be a symmetry plane to simulate the shallow water effect as shown in Fig. 3. The influence of real hull panel as well as its image panel with respect to the bottom surface is taken into account on the computation of the velocity influence coefficient.

Introducing small perturbations($\delta\sigma$, δh) with respect to the known solutions(σ^0, h^0)

$$\sigma = \sigma^0 + \delta\sigma$$
$$h = h^0 + \delta h \qquad (10)$$

the nonlinear form of the free surface boundary conditions(6) and (7) can be linearized with respect to the known solution in a first order Tayor series expansion and the following relations may be derived from (6) and (7), see [17]

$$D_1(\sigma,h) = D_1(\sigma^0,h^0) + \frac{\partial}{\partial\sigma} D_1(\sigma,h^0)\sigma\delta + \frac{\partial}{\partial h} D_1(\sigma^0,h)\delta h$$
$$= \phi_x h_x^0 + \phi_y h_y^0 - \phi_z + \Phi_x\delta h_x + \Phi_y\delta h_y + (\Phi_{xz}h_x^0 + \Phi_{yz}h_y^0 - \Phi_{zz})\delta h = 0 \qquad (11)$$

$$D_2(\sigma,h) = D_2(\sigma^0,h^0) + \frac{\partial}{\partial\sigma} D_2(\sigma,h^0)\delta\sigma + \frac{\partial}{\partial h} D_2(\sigma^0,h)\delta h$$
$$= \left(1 + \frac{1}{g}(\Phi_x\Phi_{xz} + \Phi_y\Phi_{yz} + \Phi_z\Phi_{zz})\right)\delta h - \frac{1}{2g}(U_\infty^2 - \Phi_x^2 - \Phi_y^2 - \Phi_z^2 - 2(\Phi_x\delta\phi + \Phi_y\delta\phi_y + \Phi_z\delta\phi_z)) + h = 0 \qquad (12)$$

The partial increment of D1 and D2 should be found in such a way that a new velocity potential $\phi = \Phi^0 + \delta\phi$ induced by introducing small perturbations $\delta\sigma$ and δh should satisfy Eqs (6) and (7) on the new surface $h = h^0 + \delta h$. It is a fundamental assumption of the present method that the perturbations of source($\delta\sigma$) and wave elevation(δh) are small in certain senses. In a Taylor series, higher order terms in these quantities then become very small and can be neglected in each iteration . As pointed above these go to zero upon convergence.

Here the superscript, o, corresponds to the known solution. In the first iteration this may be either the double model solution or single model solution. Both possibilities have been tested and the difference in the results was not noticeable.

The nonlinear wave resistance theory goes further than the double model linearization. Rather than terminating the calculations after obtaining the linear solution, the process is repeated in an iterative scheme always linearizing about the previous solution, and applying the boundary condition on the wavy surface Z=h(X,Y) just obtained. The principle is explained in Fig. 4. The iteration starts from the linear solution. In each iteration the hull and the free surface panels are adjusted according to the new wavy surface and the sources are moved accordingly to simulate the boundary condition more exactly. In the new solution the kinematic and dynamic boundary conditions are satisfied simultaneously, i. e. the new source strength as well as the new wave elevation are obtained at the same time.

In the limit this procedure is exact, since the nonlinear terms neglected go to zero when the difference between two iteration goes to zero. Usually 6-10 iterations are required for convergence.

RESULTS

To investigate the shallow water effect on wave resistance and wave pattern around the hull, the method presented has been tested for the Wigley hull, the Series 60 C_B=0.6 hull and a 66 m water jet catamaran. The first two cases are computed using the nonlinear method while the linear method is used for the catamaran case. The free surface source panels are lifted one typical panel dimension above the free surface in the nonlinear computations since this has shown to improve the predicted wave length and to stabilize the iterative procedure. Higher order panels are used both on the hull and on the free surface. The free surface is in the first two cases covered by panels from three quarters a ship length upstream to one ship length downstream of the ship. The transverse extension of the free surface is 1.25 ship lengths. For the catamaran case the free surface is extended to one ship length upstream and to 0.9 ship lengths in the transverse direction. A numerical operator is used in the computation of the streamwise and transverse derivative of the free surface velocities. The streamwise derivatives are computed using a four point upstream operator and the transverse derivatives are computed using a central difference operator.

The numerical calculations were performed in the model free condition, i. e. the model can vary its vertical position and trim during the computation in the same way as the free-running model self-adjusts the position to achieve dynamic equilibrium during the experiment. Such a calculation has to be carried out iteratively. In each nonlinear iteration the sinking force and trimming moment are obtained from the computed pressure distribution on the hull. Thereafter the hull is repositioned in such a way that the force and moment are balanced. The wave resistance is obtained from higher order pressure integration over the hull surface.

The principal particulars of the Wigley hull and the Series 60 C_B=0.6 hull are summarized in Table 1, and the test conditions in the study of the shallow water effect on wave resistance for the Wigley hull and Series 60 C_B = 0.6 hull are listed in Table 2 and 3.

The Wigley Hull

The shallow water free surface flow around the Wigley hull moving with a constant ship speed of Fn=0.316 is computed for six different water depths, ranging from subcritical depth(H/T=6.4, 4.8, 3.2, 2.4 and 2.0) to supercritical depth(H/T=1.4) including critical depth(H/T=1.6). Numerical computations for nonlinear iteration are carried out first without any relaxation. The panel representation for the Wigley hull with 180 effective panels on the hull surface and 2640 square panels on the free surface is shown in Fig 5.

The convergence history of the computed wave profile is presented in Fig 6a for infinite water depth. The iteration procedure started from the linear wave and converged very quickly only after 3 to 4 iterations. The converged wave profile is plotted in Fig. 6b and compared with the measurements(dotted line) and linear wave profile(solid line). No great difference can be observed between the two computed wave profiles and both wave profiles give fairly good prediction. The nonlinear effect does not seem to be very significant when the water depth is very large(H/T = ∞). As water depth decreases to the critical depth, however, the difference becomes larger and the expected steeper bow and stern waves are generated as shown in Fig. 6c. This indicates that the second order nonlinear effect seems very significant for shallow water case although the hull is quite slender.

A similar trend can be observed for the convergence history of computed wave resistance as shown in Fig. 7. The iteration precedure converges after 8 to 12 iterations for all test cases. The converged wave resistance coefficient versus water depth Froude no. is presented in Fig 8. The wave resistance increases rapidly when the water depth approaches the critical depth. The wave resistance reaches its maximum not at the critical speed(F_{nH}=1.0) but at a slightly faster speed(F_{nH}=1.067).

Fig 9 shows the wave profile at the centerline and on the hull surface for different water depths. The amplitude and wave length become larger and longer as water depth decreases.

Wave patterns generated by the free running Wigley hull for five different water depths at Fn = 0.316 are presented in Fig 10. The predicted wave pattern in deep water is given in Fig 10a and compared with the measured one[18]. As can be seen in figure 10a, diverging waves radiating from the bow together with transverse waves following behind the stern of ship are well predicted and look very similar to the measured wave pattern given in Fig 10b. The predicted wave angle is 17 deg 20 min which is very similar to the measured one (approximatly 17.5 degree). This good agreement is partly due to the fact that the wave angle is measured in local fields where Kelvin wave is not fully developed. For values of H/T larger than about 2.4, a similar wave pattern can be observed in Fig 10c. As H/T decreases below this value the angle α increases and reaches its maximum as F_{nH} approaches 1.0(Fig 10e). At this critical condition, all the wave making effect is concentrated in a single crest at bow and very pronounced wave crests are created at stern.

The Series 60 C_B=0.6 Hull

Calculations were performed for the Series 60 C_B=0.6 hull at relative depths H/T=20.0, 3.2, 2.0, 1.5 and 1.2. The panel representation with 2980 effective panel elements are presented in Fig 11. The computations were carried out using an under relaxation of 0.5 on the source strength. Detailed comparisons with recent measurements in the BSHC[19] and Duisburg[21] towing tanks are made for the wave resistance, wave pattern, sinkage and pressure distribution on the hull.

Converged solutions were obtained for all test cases. The convergence history for nonlinear iterations and sinkage & trim iterations are presented in Figs 12 and 13. Usually 6 to 10 iterations for wave resistance calculation and 5 to 6 iterations for sinkage & trim calculation are required. A similar trend can be observed for the convergence history of the calculated wave profiles in Fig. 14 at different depth Froude numbers (a) Fn=0.350, H/T=3.2, (b) Fn=0.250, H/T=2.0 and (c) Fn=0.200, H/T=1.2 respectively.

The computed wave pattern for Fn=0.316 in deep water is shown in Fig. 15 and the wave profile is compared to the experimental results[22] at 4 longitudinal cuts in Figs 16a - d where the thick lines are experiments. The figures show a good correspondence between the computed and measured profiles except far downstream for the cuts close to the hull. The difference downstream of the hull is probably due to viscous effects in the wake of the hull.

The computed wave pattern resistance coefficients are compared with the linear calculations and measurements made by Lazarov & Angelov[19] in Fig. 17 at relative depths (a) H/T=20.0, (b) H/T=2.0 and (c) H/T=1.5 respectively. These measured values are obtained from the longitudinal cut wave analysis method for a 4.768 M model. The wave profile is measured in one longitudinal section parallel to the direction of motion at a distance Y/L=0.45 from the center plane. As can be seen from the figures, the present calculations show fairly good agreement with measurements and significant improvement over the linear method[19] is achived for all test cases. As expected the agreement between calculations and measurements is very good at H/T=20.0, but the disagreement increases with decreasing water depth. For water depth H/T=1.5, the computed resistance curve shows the same trend as the measurements, but the curve is shifted to higher velocities. A probable reason for this is that viscous effect, which is neglected in the present calculation, seems to be more important in shallow water than in deep water. But no clear-cut conclusion can be drawn.

In Figs. 18-22 detailed comparisons with measurements in the Duisburg towing tank are made for sinkage, wave patterns and pressure distribution around a free running model with a constant speed of Fn = 0.175 in shallow water, H/T = 3.2, 2.0 and 1.2.

The computed sinkage at the center of flotation are compared with the measurements made for two geosim models with different length(LWL) of 4.768 m(M1413) and 6.198 m(M1400) in Fig. 18. Most striking feature in the measurements is that there is a large difference between the sinkage of the two models. Very good correspondence between the computed and one of the measured values is obtained for H/T = 3.2 and 2.0, but for H/T = 1.2 the sinkage is a little bit underpredicted.

The computed wave pattern is shown in Fig. 19 and compared with the experimental results along the hull. Remarkable changes in the wave pattern can be observed in the measurements and

the typical shallow water effects of a widening of the Kelvin angle and of bow impounding - midship trough - stern impounding of wave profiles are fairly well predicted. The change of wave pattern is a consequence of the strong pressure changes around the hull caused by the restricted water depth. The pressure contour plot given in Fig. 20 explains the reason for the deep waves generated beside midship body in shallow water. The pressure gradient along the waterline is much steeper in H/T=1.2 than in H/T=2.0 as shown in Fig. 21. The deeper wave trough around the midship for H/T=1.2 is caused by the lower pressure developed there; the minimum Cp value being -0.414 compared to -0.215 for H/T=2.0. Another interesting point is that the equal pressure lines for H/T=1.2 are more vertical. This may imply that the flow tends to pass around the hull rather than below it. This is confirmed in the velocity vector plot given in Fig. 22.

Water Jet Catamaran

To investigate the ability to predict multihull cases and the effect of shallow water, linear calculations were carried out for a 66 m water jet catamaran, which had been tested in deep and shallow water in a speed range from 15 to 40 konts. In the shallow water case the depth was 10 m and the critical speed 19.3 knots, corresponding to a Froude number based on LWL of 0.41. For proprietry reasons no quantitative values can be given for this case.

Wave contours for 19.3 knots, deep and shallow water, are given in Figs 23 and 24. This Froude number is close to the critical one and there is a large difference between the wave patterns. In general, much steeper waves are generated in the shallow water case and the direction of the wave crests is close to 90 degrees, as expected.

The predicted wave resistance in deep water is computed with the measured residuary resistance based on ITTC-57 method in Fig 25. Fair agreement is noted. Since the lowest speed corresponds to a Froude number of only 0.32 the transom condition is probably violated there. Fair agreement is also noted between the measured and predicted trim angles, as can be seen in Fig. 26, and the same is true for the sinkage.

In Fig. 27 the change in wave resistance(residuary resistance) due to the shallow water is presented. As expected, there is a peak in resistance close to the critical speed. What is more unexpected is the drop in resistance for the higher speeds, compared to the deep water case. The magnitude of the change in wave resistance is well predicted except close to the peak where the effect of shallow water is underpredicted. The speed where the peak occurs is however well predicted. Also the trim change is well predicted, as appears from Fig. 28.

CONCLUSIONS

The shallow water effect on the free surface potential flow around ships is numerically investigated by linear and nonlinear Rankine source panel methods. Rankine sources are distributed on the hull and part of the free surface and a symmetry condition is applied to simulate the bottom. An exact hull boundary condition is satisfied in both methods, but different free surface boundary conditions are used. In the linear method the free surface condition is linearized with respect to double model flow while in the nonlinear method the exact free surfece boundary conditions are approached in an iterative process.

The present methods have been tested for the Wigley hull, the Series 60 C_B =0.6 hull and a water jet catamaran for varying depth Froude numbers. Detailed comparisons with recent measurements for the Series 60 and catamaran cases in the Duisburg and SSPA are made. Typical shallow water effects, such as the widening of the Kelvin angle and the sharp increase in wave resistance when approaching the critical Froude number are well predicted.

REFERENCES

1. Havelock, T. H., "The Propagation of Groups of Waves in Dispersive Media With Application to Waves on Water Produced by a Travelling Disturbance" Proceedings of the Royal Society, London, Vol 81, 1908

2. Havelock, T. H., "The Effect of Shallow Water on Wave Resistance", Proceedings of the Royal Society, A. Vol 100, pp499-505, 1922

3. Schlichting, O., "Ship Resistance in Water of Limited Depth-Resistance of Sea Going Vessels in Shallow Water" Jahrbuch der STG, Vol. 35, 1934

4. Sretensky, L. N., "A Theoretical Investigations of Wave Resistance',(in Russian), Joukovsky Central Institute for Aero-hydrodynamics Report 319, 1937

5. Kinoshita, M. & Inui, T., "Wave Making Resistance of a Submerged Spheroid, Ellipsoid and a Ship in a Shallow Sea", Journal of the Society of Naval Architects of Japan, Vol. 75, pp 119-135, 1953

6. Inui, T., "Wave-Making Resistance in Shallow Sea and in Restricted Water with Special Reference to its Discontinuities", Journal of the Society of Naval Architects of Japan, Vol. 76, pp1-10, 1954

7. Kirsch, M., "Shallow Water and Channel Effects on Wave Resistance", Journal of Ship Research, Vol. 10 No. 4, pp164-181, 1966

8. Bai, K. J., "A Localized Finite Element Method for Steady Three Dimensional Free Surface Flow Problems", 2nd International Conference on Numerical Ship Hydrodynamics, Berkeley, pp78-87, 1977

9. Mueller, M, "Analysis of the Potential Flow Field and of Ship Resistance in Water of Finite Depth", International Shipbuilding Progress, Vol. 32, No. 376, pp266-277, 1985

10. Millward, A., "The behaviour of High Speed Ship Forms When Operating in Water Restricted by a Solid Boundary" RINA, pp 189-204, 1985

11. Dawson, C. W., "A Practical Computer Method for Solving Ship-Wave Problems", Proceedings of the Second International Conference on Numerical Ship Hydrodynamics, 1977

12. Yasukawa, H., "Calculation of the Free Surface Flow around a Ship in Shallow Water by Rankine Source Method", Fifth ICNSH, pp451-461, 1989

13. Lee, S. J., "Computation of Wave Resistance in the Water of Finite Depth using a Panel Method", The Journal SNAK92, pp130-135, 1992

14. Ni, S. Y., "Higher Order Panel Method for Potential Flows with Linear or Nonlinear Free Surface Boundary Conditions", Ph D Thesis, Chalmers University of Technology, 1987

15. Kim, K. J. & Choi, Y. B., "A Numerical Calculation of Free Surface Potential Flow Field and of Ship Wave Resistance in Shallow Water by Fully Nonlinear Wave Theory", the 2nd Japan Korea Workshop, Osaka Japan, 1993

16. Larsson, L., Broberg, L., Kim, K. J. and Zhang, D. H., "A Method for Resistance and Flow Prediction in Ship Design", SNAME Annual Meeting, San Francisco, 1990

17. Kim, K. J., "Ship Flow Calculations and Resistance Minimization", Ph D Thesis, Chalmers University of Technology, 1989

18. Kasaka, Y., "On the Hydrodynamical Singulaities for Surface Ships with Special Reference to Line Integral", Ph D Thesis, Dept. of Naval Architecture, The Univ. of Tokyo, 1974

19. Lazarov, G & Angelov A, "A Study of Shallow Water Effect on Wave Resistance of Series 60 Models", 8th International Symp. Ship Hydromech. Wroclaw/Poland, 1989

20. Lewis, E. V.(Editor), "Principles of Naval Architecture", Published by SNAME, Vol II page 44, 1988

21. Report on Cooperative Experimental Program in Shallow Water, Resistance and Flow Commitee of 20th ITTC

22. Toda Y et al.,"Mean-Flow Measurements in the Boundary Layer and Wake Field of a Series 60 C_B=0.6 Ship Model for Froude Numbers 0.16 and 0.316, IIHR Reprt No. 352, August, 1991

Table 1 Main Parameters of the Wigley Hull and the Series 60 C_B=0.6 Hull

	Wigley Hull	Series 60 Hull
B/Lpp	0.100	0.1333
T/Lpp	0.0625	0.0625
B/T	16.0	2.50
C_B	0.444	0.600

Table 2 Test Codition in the Study of the Shallow Water Effect on Wave Resistance for the Wigley Hull(L/T=16, B/T=1.6)

	1	2	3	4	5	6	7
H/T	6.4	4.8	3.2	2.4	2.0	1.6	1.4
F_{nH}	0.45	0.50	0.58	0.71	0.89	1.00	1.07

Table 3 Test Condition in the Study of the Shallow Water Effect on Wave Resistance and Wave Pattern for the Series 60, C_B = 0.60 Hull

H/T	Ship Speed in Fn (F_{nH})
1.2	0.125(0.494), 0.150(0.593) 0.175(0.698), 0.200(0.791)
1.5	0.200(0.653), 0.210(0.686) 0.220(0.719), 0.230(0.751) 0.240(0.784)
2.0	0.150(0.459), 0.175(0.541) 0.200(0.613), 0.225(0.689) 0.240(0.735), 0.250(0.766)
3.2	0.200(0.484), 0.250(0.605) 0.300(0.726), 0.350(0.848)
20.0	0.150(0.134), 0.200(0.179) 0.250(0.223), 0.300(0.268)

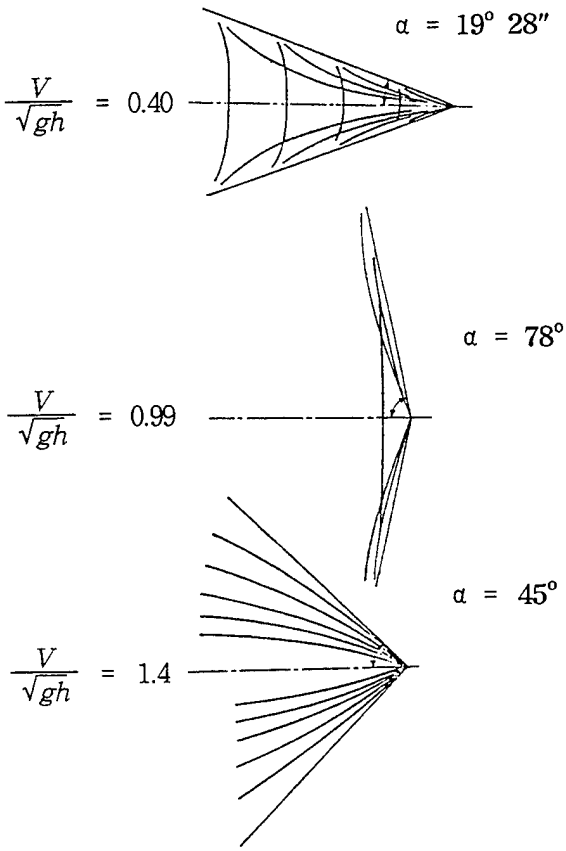


Fig.1 Effect of Shallow Water on Wave Pattern[20]

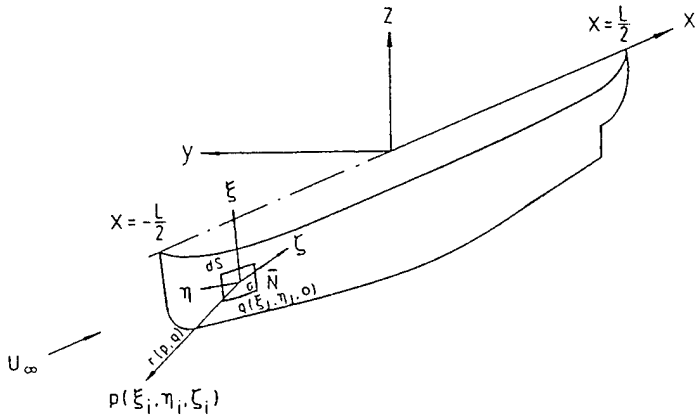


Fig.2 Coordinate System

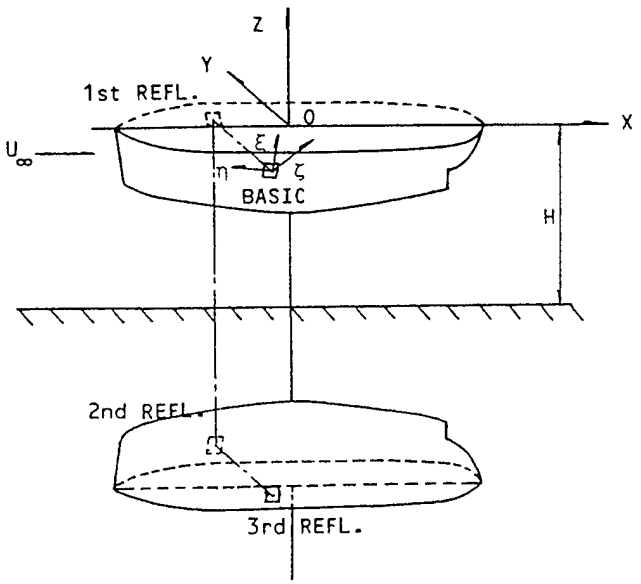


Fig. 3 Definition Sketch of Numerical treatment of Shallow Water Effect

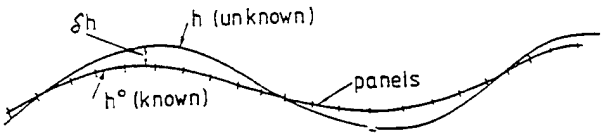


Fig. 4 Nonlinear Free Surface Iteration

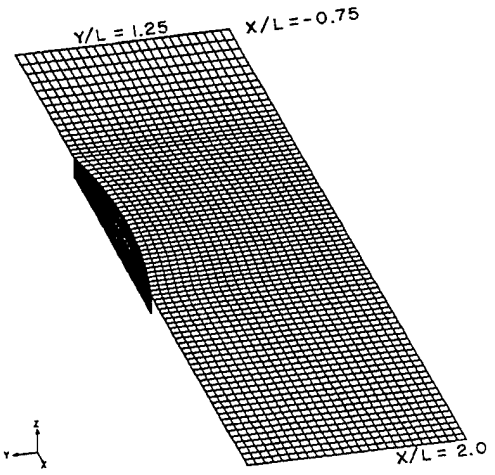


Fig. 5 Typical Panel Arrangement for the Wigley Hull

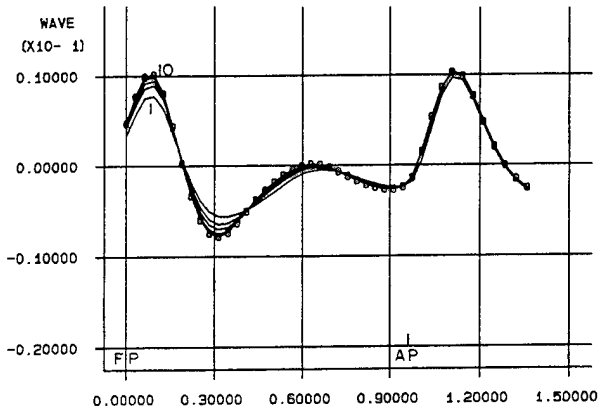


Fig. 6a Convergence History of the Computed Wave Profiles at Fn=0.316 for the Wigley Hull in Deep Water

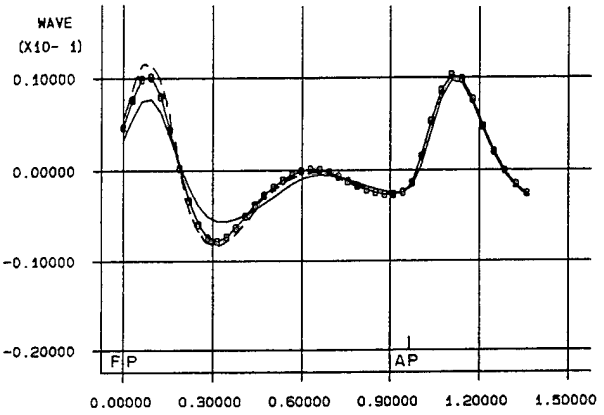


Fig. 6b Computed and Measured Wave Profiles at Fn=0.316 for the Wigley Hull in Deep Water.

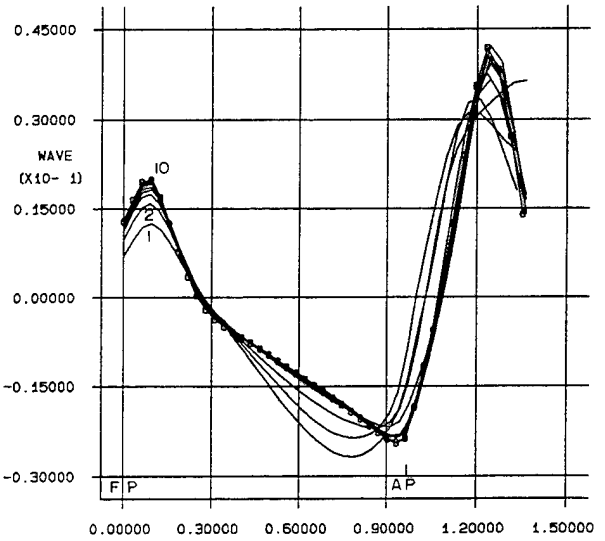


Fig. 6c Convergence History of the Computed Wave Profiles at Fn=0.316 for the Wigley Hull in Critical Depth of Water.

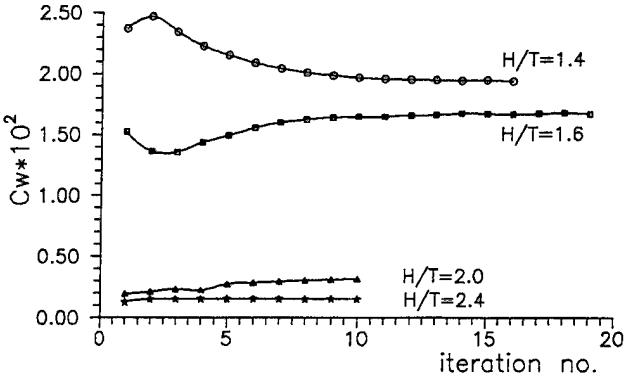


Fig. 7 Convergence History of the Computed Wave Resistance at Fn=0.316, the Wigley Hull

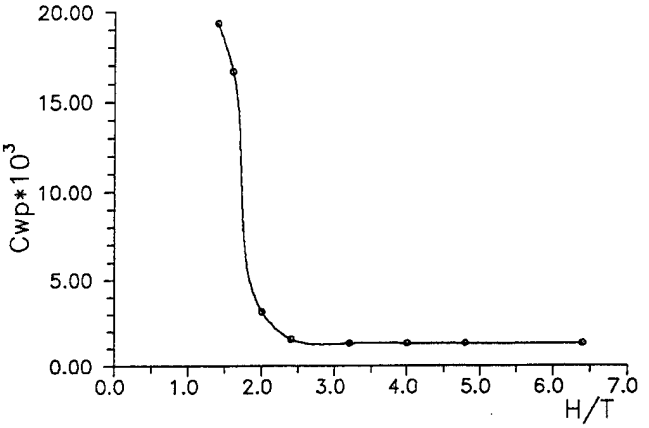


Fig. 8 Effect of Shallow Water on Wave Resistance for the Wigley Hull (Fn=0.316)

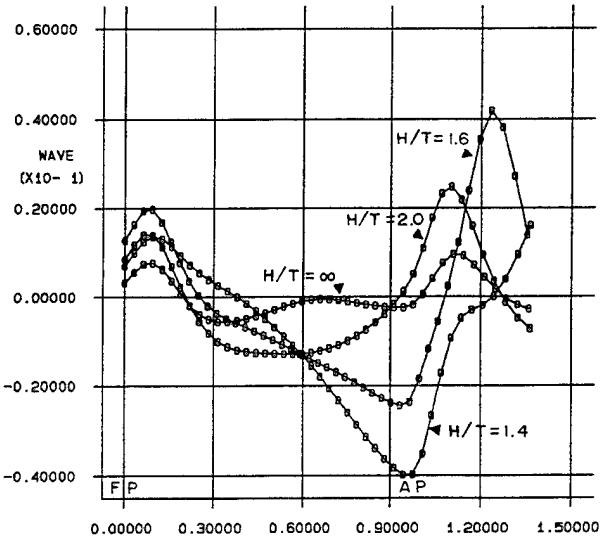
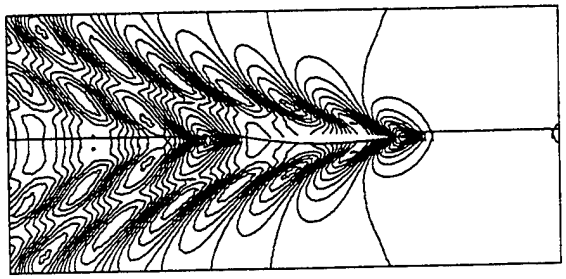
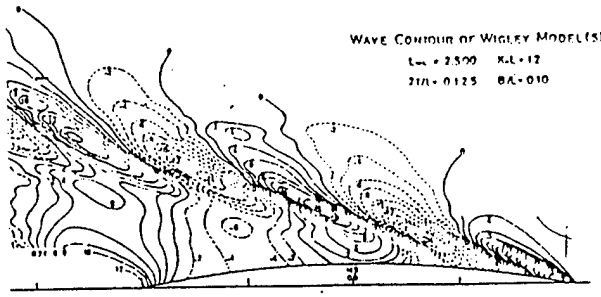


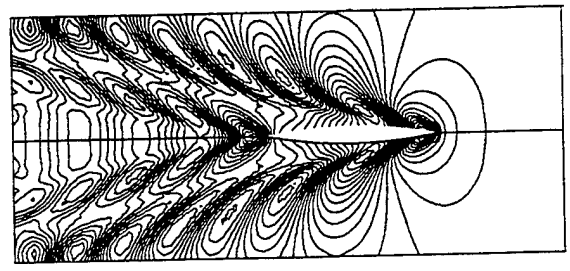
Fig. 9 Comparison of the Calculated Wave Profiles in Deep Water and Shallow Water for the Wigley Hull



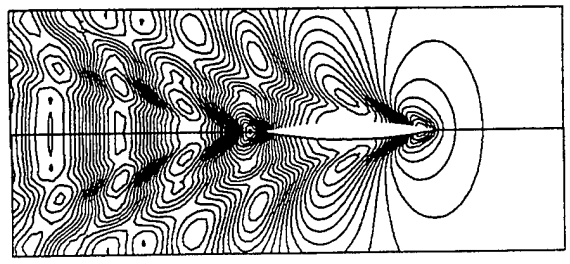
(a) Computed Wave Pattern in deep water



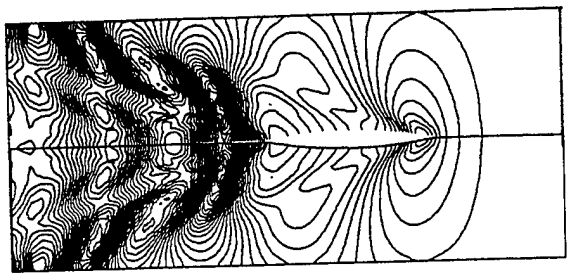
(b) Measured Wave Pattern in deep Water Experiment[18]



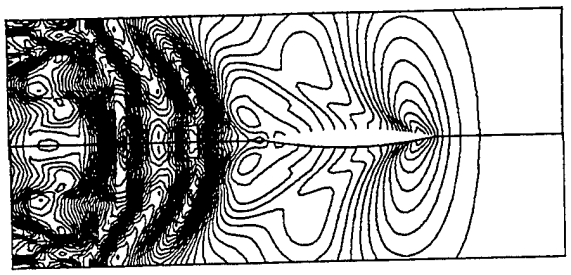
(c) Computed Wave Pattern at H/T=2.4



(d) Computed Wave Pattern at H/T = 2.0



(e) Computed Wave Pattern at H/T = 1.6



(f) Computed Wave Pattern at H/T = 1.4

Fig. 10 Wave Pattern Changes due to Decrease of Water Depth at Fn=0.316, the Wigley Hull

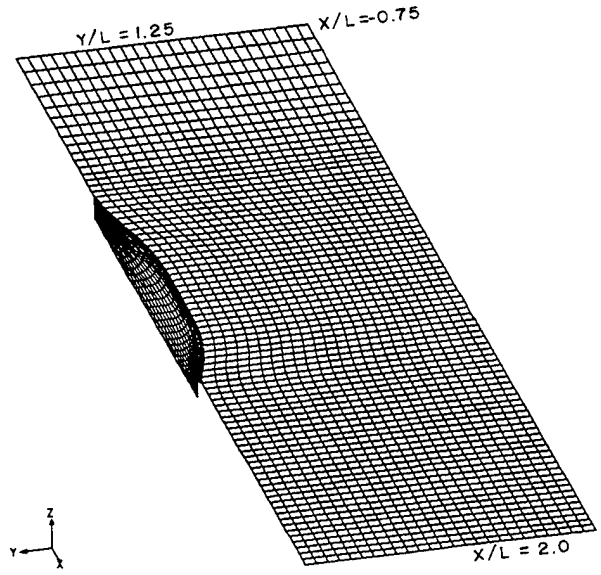
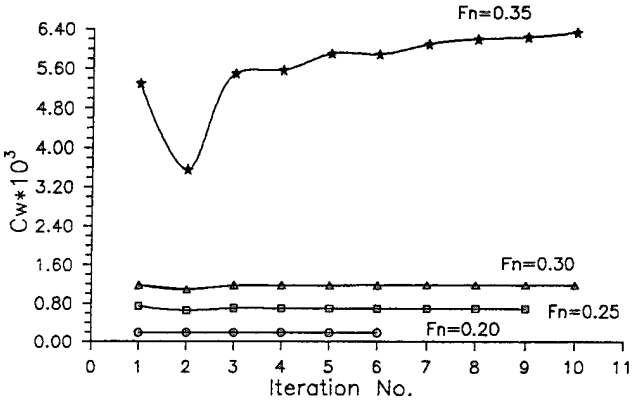
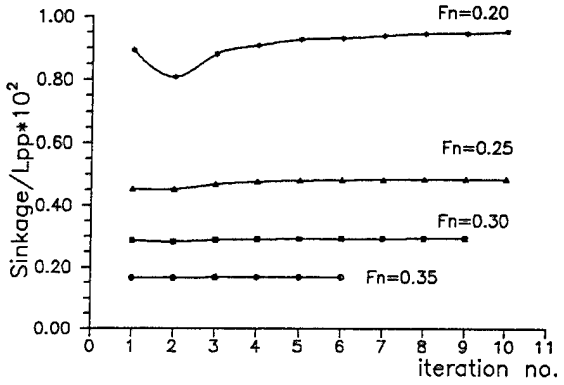


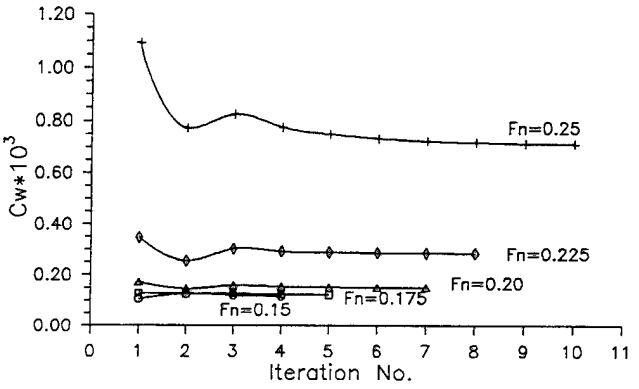
Fig. 11 Panel Arrangement for the Series 60, C_B=0.6 Hull



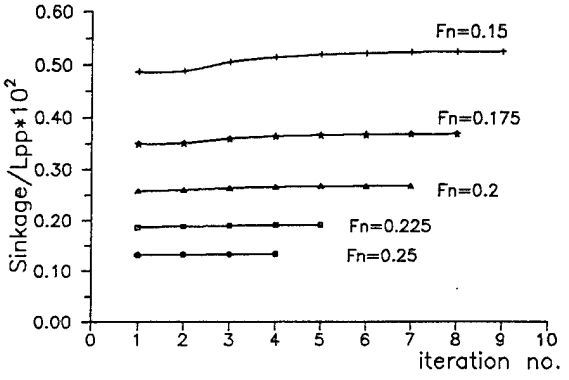
(a) H/T = 3.2



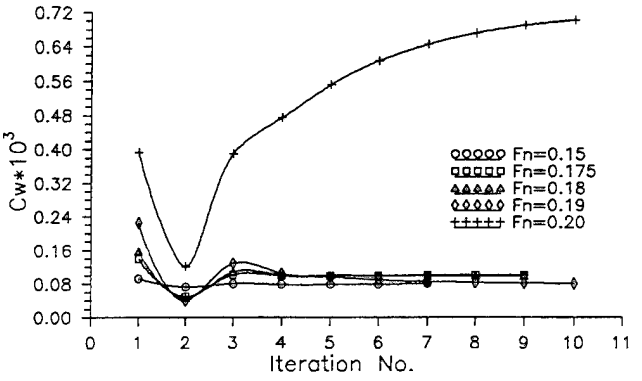
(a) H/T = 3.2



(b) H/T = 2.0

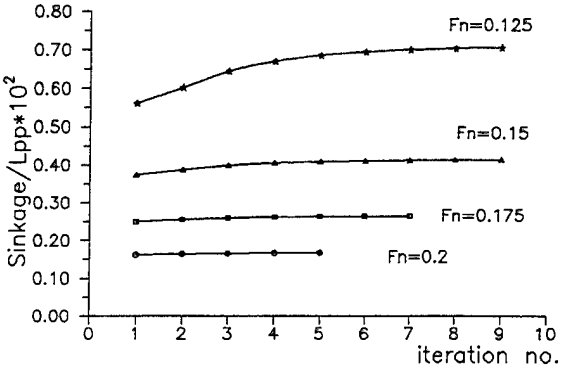


(b) H/T = 2.0



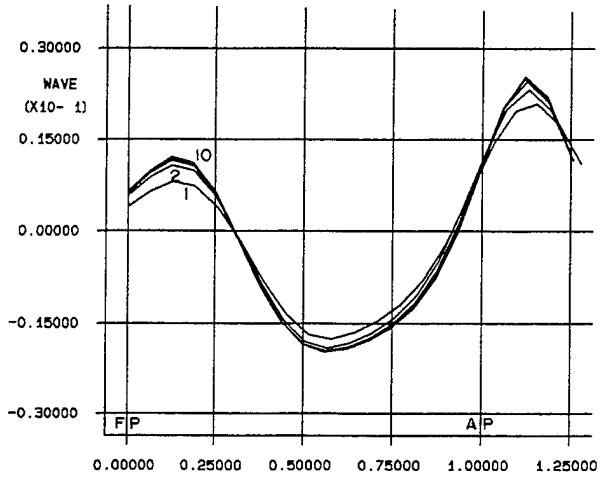
(c) H/T = 1.2

Fig.12 Convergence History of Wave Pattern Resistance for the Series 60, C_B=0.6 Hull

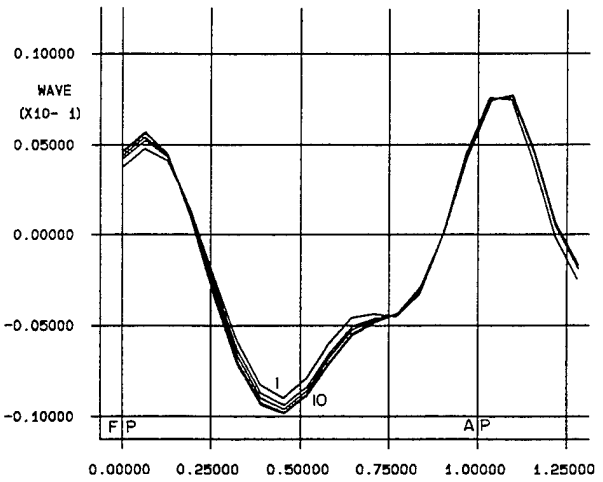


(c) H/T = 1.2

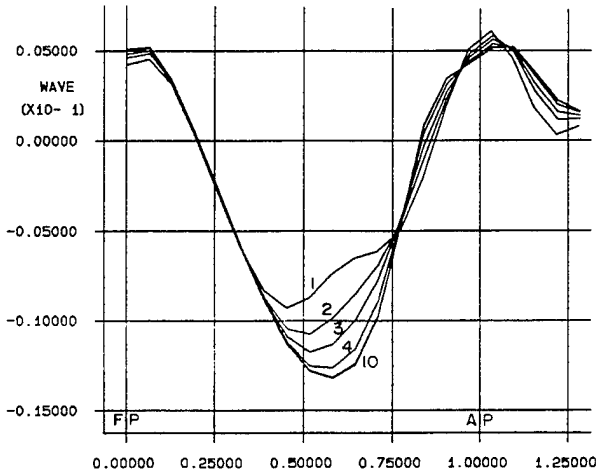
Fig. 13 Convergence History of Sinkage for the Series 60 C_B = 0.6 Hull



(a) H/T = 3.2



(b) H/T = 2.0



(c) H/T = 1.2

Fig. 14 Convergence History for Wave Profiles, the Series 60 C_B = 0.6 Hull

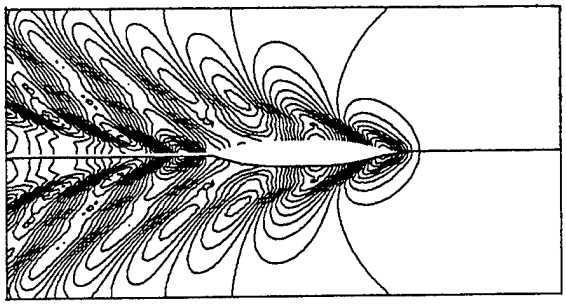
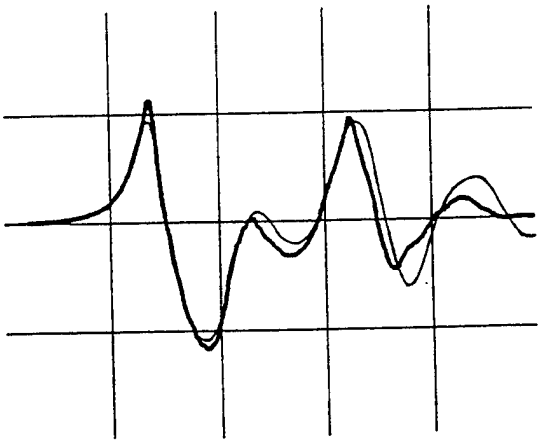
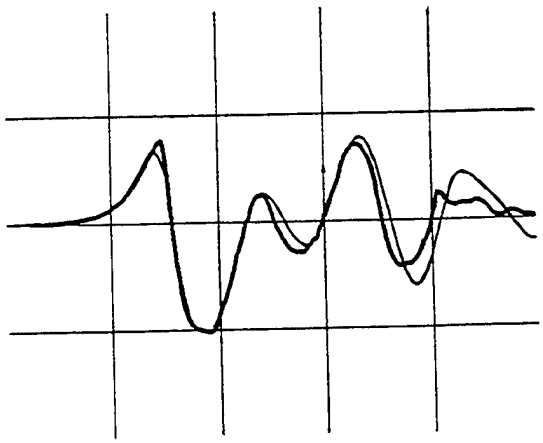


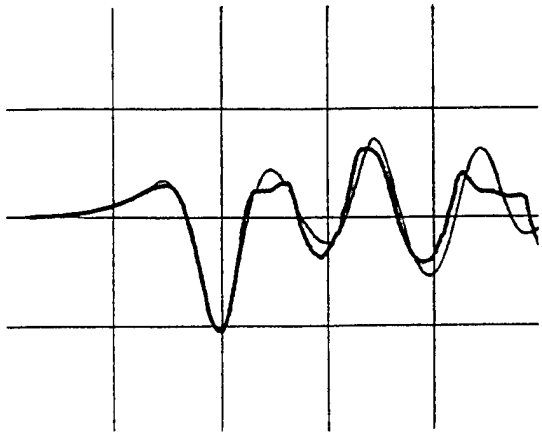
Fig. 15 Computed Wave Patterns at Fn=0.316 for Infinite Depth of Water



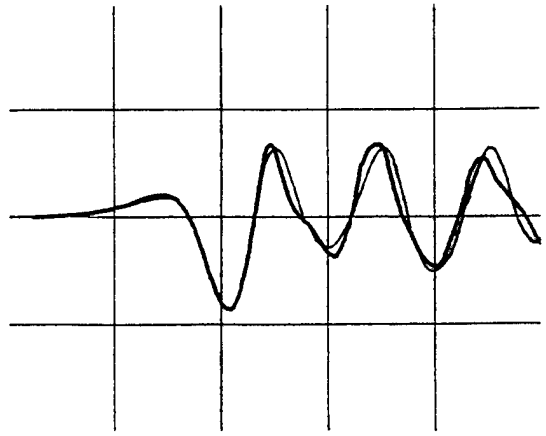
(a) y/L = 0.0755



(b) y/L = 0.1083

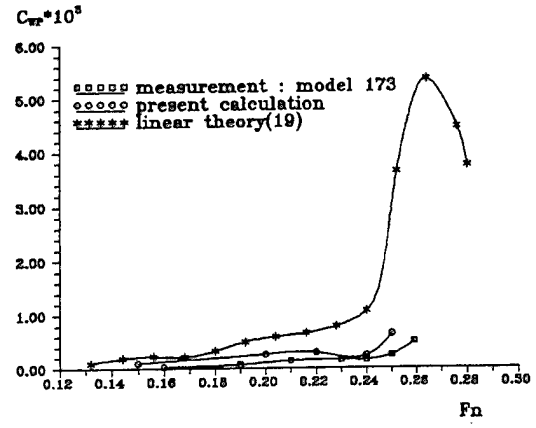


(c) y/L = 0.1739

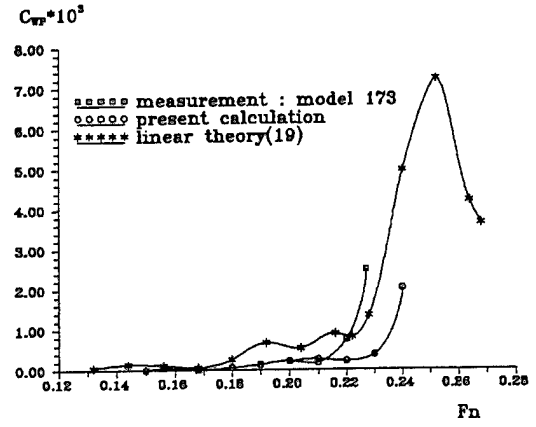


(d) y/L = 0.2067

Fig. 16 Comparison between Computed and Measured Wave Profiles at Fn=0.316 for the Series 60 C_B=0.6 Hull in Deep Water

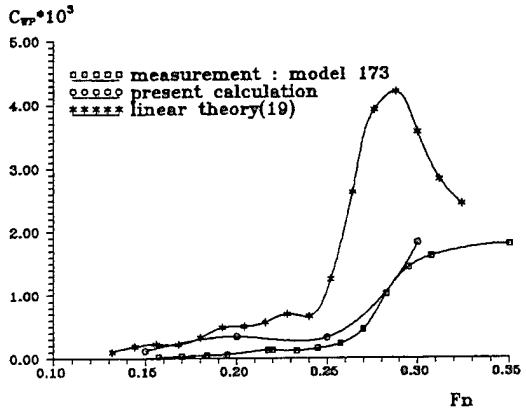


(b) H/T = 2.0

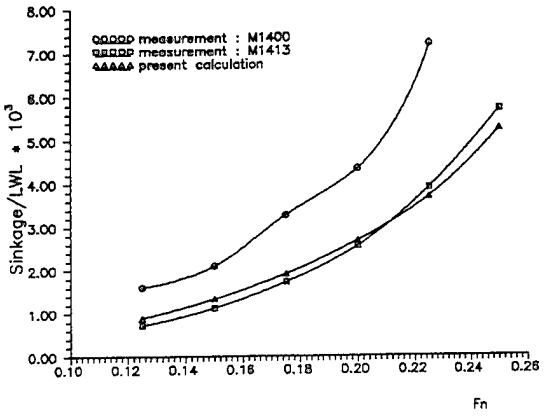


(c) H/T = 1.5

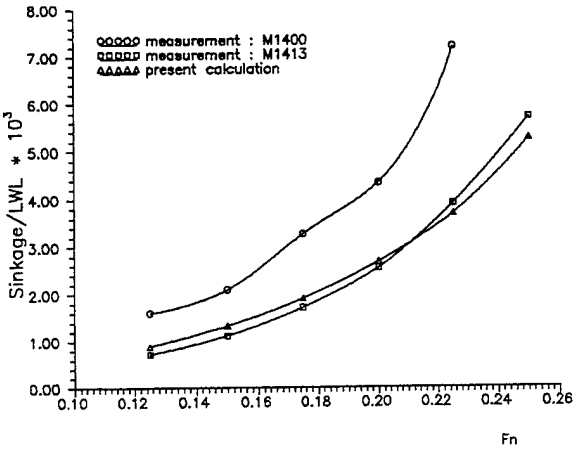
Fig. 17 Wave Pattern Resistance, the Series 60, C_B=0.6 Hull



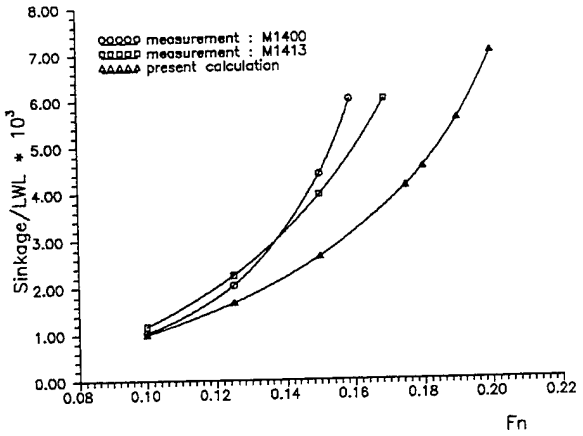
(a) H/T = 20.0



(a) H/T = 3.2

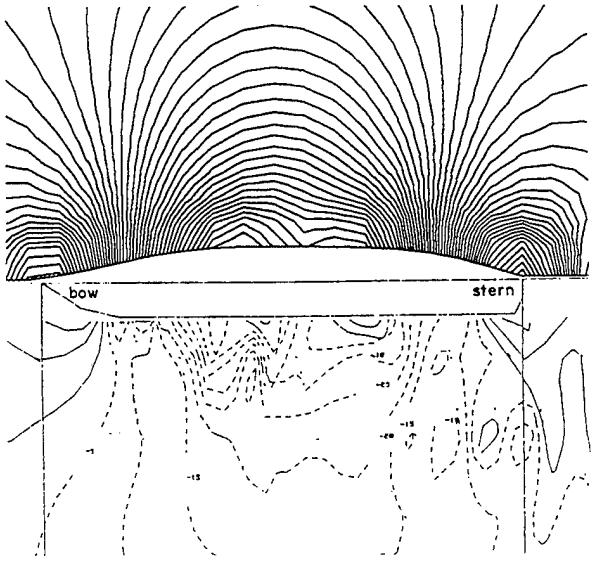


(b) H/T = 2.0

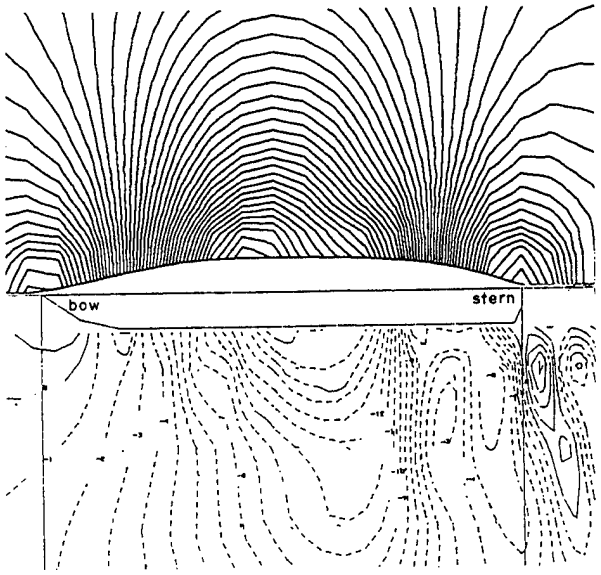


(c) H/T = 1.2

Fig. 18 Computed and Measured Sinkage for the Series 60 C_B=0.6 Hull

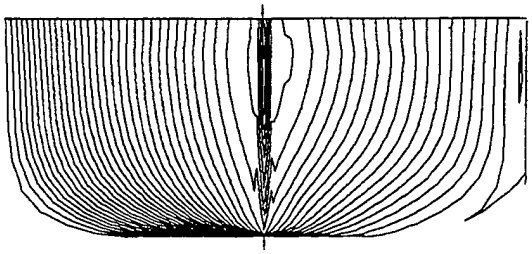


(a) H/T = 2.0

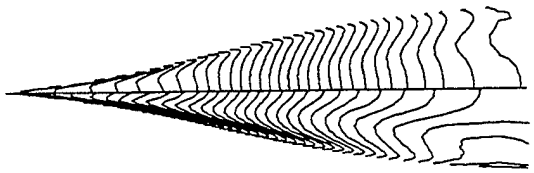


(b) H/T = 1.2

Fig. 19 Comparison between Computed Wave Patterns(top-half) and the Measurements(bottom-half) at Fn=0.175 for the Series 60 C_B=0.6 Hull



(a) front view
H/T=2.0(right), H/T=1.2(left)



(b) bottom view
H/T=2.0(bottom), H/T=1.2(top)

Fig. 20 Pressure contours at Fn=0.175 for the Series 60 C_B=0.6 Hull

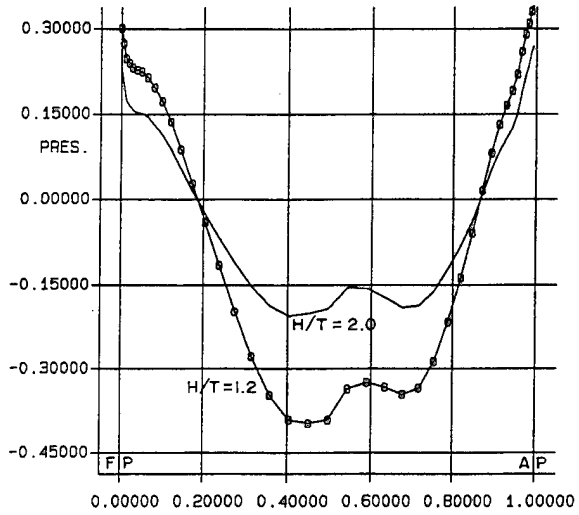
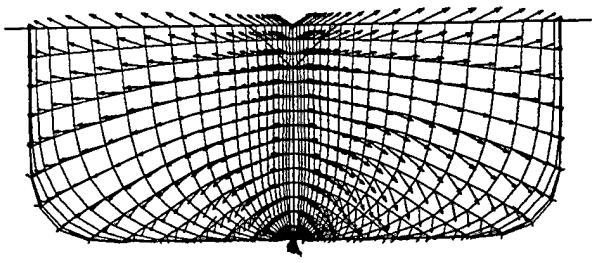


Fig. 21 Pressure Gradient along Design Load Waterline



H/T=1.2 H/T=2.0

Fig. 22 Velocity Vector Plot

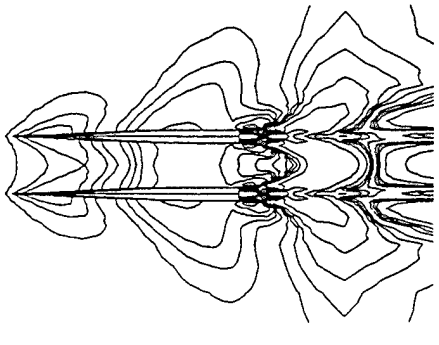


Fig. 23 Wave Pattern at 20 knots, Deep Water, Water Jet Catamaran

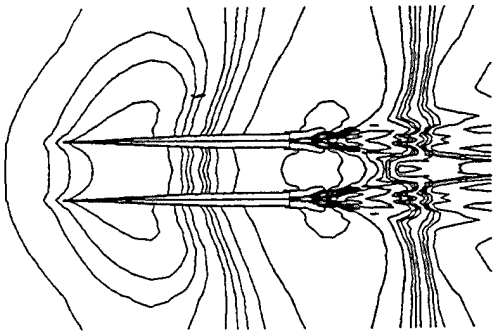


Fig. 24 Wave Pattern at 20 Knots, 10 m Water Depth.

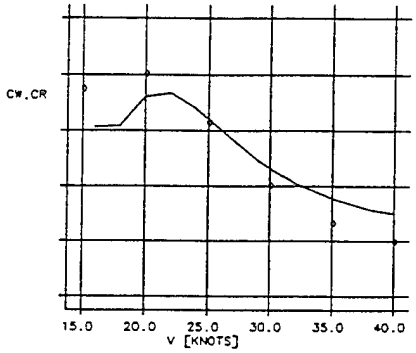


Fig. 25 Computed Wave Resistance in Deep Water. Symbols represent calculations.

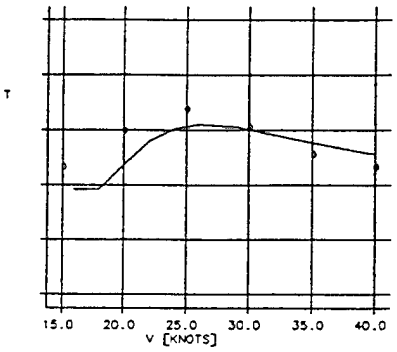


Fig. 26 Trim in Deep Water

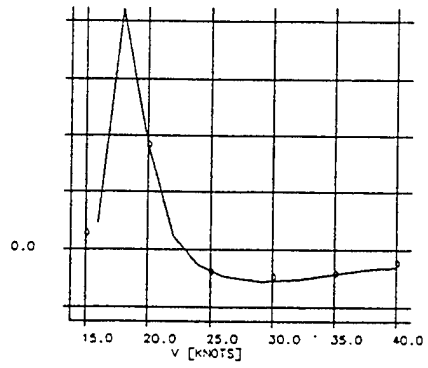


Fig. 27 Change in Wave Resistance at 10m Water Depth

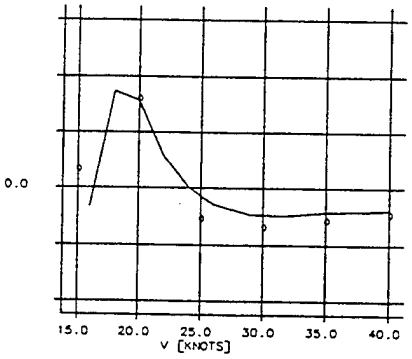


Fig. 28 Change in Trim at 10 m Water Depth

DISCUSSION

H. Choi
Seoul National University, Korea

When a ship moves near the critical speed in shallow water, it has long been observed experimentally and numerically that the wave field is hardly steady and there are wave components propagating upstream. I am curious to know how you obtained steady solutions and how you carried out wave pattern analysis.

Z. Zou
Universitat Hamburg, Germany

For ships traveling in shallow water and free to sink and trim, the hull may touch or nearly touch the bottom on some conditions so that the iteration will certainly break down or become difficult to converge. Did you encounter any problem in this respect in your computation?

K. Nakatake
Kyushu University, Japan

Several years ago, we tried to obtain the wave patterns shown in Fig. 1 using a Rankine source method for a point doublet. But we could not. Did you check your method for that case?

AUTHORS' REPLY

First of all, we would like to thank all discussants for their thoughtful remarks and comments.

We agree with Professor Choi's comment that a ship moving with a near critical speed generates a series of upstream advancing waves periodically and there also have been many reports on observations in nature of propagating upstream waves in a shallow water channel and towing tank. However, it is not quite certain yet that the forward running solitary waves are experimentally discernible when a ship is moving in a horizontally "unbounded" fluid domain. As far as the current authors know, only a few investigations have been made so far for the problem and it is still an open question whether it is a steady or an unsteady problem.

To better understand the related physical phenomena, this study was initiated, and thus the purpose of the present study is to investigate the generation of a nonlinear wave field by a ship moving with a near critical speed in a horizontally unbounded domain. In our preliminary study, we assumed that the flow is steady and consider only steady state solutions because it requires much less computation time. The present study demonstrates that converged solutions are always obtained through iterations for all test cases, and typical shallow water effects, such as the widening of the Kelvin angle and the sharp increase in wave resistance when approaching the critical speed, are well predicted. But this does not mean that the problem we are solving is necessarily steady. A more rigorous study should be pursued. It may be interesting to make an unsteady computation using the same code to see the importance of unsteadiness.

In reply to the questions raised by Dr. Zou: We have not encountered the difficulty mentioned by Dr. Zou, but we realize it could cause problems for smaller gaps between the hull and the sea bottom.

Professor Nakatake suggests that we check the method by computing the wave pattern for a point doublet. The point doublet could be an interesting test case, but it would call for some changes to the code, which can only handle physical bodies, so we have not yet tried it.

Observations of the Influence of Nuclei Content on the Inception and Form of Attached Cavitation

C. Li, S. Ceccio (University of Michigan, USA)

ABSTRACT

The inception and form of attached cavitation can be significantly effected by the presence of traveling bubbles. Traveling bubbles may induce transient regions of incipient attached cavitation. Furthermore, traveling bubbles may sweep away regions of developed attached cavitation. The number and size of traveling bubbles which will occur in a flow is strongly dependent on the freestream nuclei distribution. Consequently, bubble/attached cavity interactions provide a mechanism whereby the freestream nuclei distribution can significantly influence the inception and form of attached cavitation. Experiments were performed on a rectangular planform hydrofoil to investigate this phenomena. Individual cavitation nuclei were created in the flow via a focused laser beam to create individual traveling bubbles. These bubbles were observed as they interacted with the flow near the foil and as they interacted with developed attached cavitation present at the foil midcord. Tripping was used to stimulate turbulent transition in the boundary layer, and the interaction of the travelling bubbles differed for the smooth and tripped conditions. The differences in how the travelling bubbles interact with the boundary layer and the attached cavitation can be related to the state of the boundary layer.

NOMENCLATURE

c	hydrofoil cord length
P_O	freestream static pressure
P_V	water vapor pressure
q	dynamic head, $1/2\ \rho U_O^2$
$\mathbf{Re}_C$	Reynolds number based on hydrofoil cord, $U_O c/\nu$
$\mathbf{Re}_S$	Reynolds number based on streamwise distance from the hydrofoil leading edge, $U_O s/\nu$
s	streamwise distance from the hydrofoil leading edge
U_O	freestream velocity
α	hydrofoil attack angle
δ	laminar boundary layer thickness for a flat plate, $5\ s\ \mathbf{Re}_S^{-1/2}$
ν	water kinematic viscosity
ρ	water density
σ	cavitation number, $(P_O - P_V)/q$

INTRODUCTION

Cavitation researchers have long recognized the important influence the freestream nuclei content has on the overall cavitation process. Traveling bubble cavitation is directly related to the flux of nuclei into a low pressure region (Ceccio and Brennen (1991)), and the process of vortex cavitation inception is strongly influenced by

the freestream nuclei distribution (Maines and Arndt (1993)). The global cavitation patterns found on propellers and pumps can be greatly modified by changes in the nuclei spectrum (Kuiper (1979), Gindroz and Billet (1993)). In these studies, the inception and form of attached cavitation has also been influenced by changes in the nuclei spectrum. Kodoma, Tamiya, Take, and Kato (1979) demonstrated that attached cavitation on an axisymmetric headform could be transformed into a bubbly cloud given the presence of enough freestream nuclei, and Briancon-Marjollet, Franc, and Michel (1990) documented such interactions for flow over a hydrofoil. As the form of the attached cavitation changes, so too does the acoustic emission from the cavity (Shen, Gowing, and Ceccio (1994)). Furthermore, modification of the global cavitation pattern will effect the performance of cavitating devices (Arndt (1981)).

The inception and form of attached cavities are related to the underlying viscous flow near the cavitating surface. Inception of attached cavities may occur when a single critical nucleus is swept into a low pressure region near the flow surface. In another inception process, an unstable nucleus may be present on the mechanical flow boundary, and this nucleus will grow into an attached vapor cavity. This cavity will alter the surrounding flow, and, if the new flow permits, the cavity will be stable. Once a stable cavity is formed, no other nuclei are needed to preserve it. Consequently, changes in the freestream nuclei content are expected to have a weak influence on the inception and form of attached cavities.

However, the global pattern of attached cavitation is altered by changes in the freestream nuclei distribution. Briancon-Marjollet, Franc, and Michel (1990) have observed a mechanism which can explain this phenomenon: traveling cavitation bubbles will interact with attached cavities. These bubbles can create local attached cavities (Ceccio and Brennen (1991) and Kuhn de Chizelle, Ceccio, and Brennen (1994)) or may sweep away portions of otherwise stable cavities. In this study, we further explore the phenomenon of bubble/attached cavity interaction. In the present study, we explore the detailed interaction of travelling bubbles with the underlying viscous flow and developed attached cavitation.

EXPERIMENTAL SETUP

The experiments described below were consisted of several elements. A detailed description of the apparatus is provided in Tassin, Li, Ceccio and Bernal (1994). An abbreviated description is provided here of the blow down water tunnel, the test model, and the nucleus production apparatus.

Blow-down Cavitation Tunnel

The experiments were conducted in the University of Michigan Cavitation and Multiphase Flow Laboratory's Blow Down Water Tunnel (BDWT). The BDWT consists of two 400 gallon (1.51 m^3) tanks, a square contraction and test section, a diffuser, and connecting eight inch pipe. A series of control valves can connect either tank with a 600 gallon (2.27 m^3) vacuum receiver and/or an air pressure receiver charged to 100 psi. The upstream contraction has an area ratio of 4.4, and the test section is rectangular with dimensions 3 x 3 x 16.5 inches (7.62 x 7.62 x 41.9 cm). Operation of the tunnel follows the following steps. Water is moved into the upstream tank with the application of a small pressure difference across the two water free surfaces in both tanks. Approximately 400 gallons (1.15 m^3) of water is moved into the upper

tank, where the water is allowed to settle. Flow is induced in the test section by applying a positive pressure difference between the two tanks. The test section velocity is determined by this pressure difference, and the test section pressure is determined by the average absolute pressure above each free surface. A digital data acquisition system continually monitors the test section absolute pressure, the air pressure in the upstream and downstream tanks, and the water level in the downstream tank. The system can be run with either open or closed loop control, but most of the operation occurs with open loop control. A one component DANTEC 9055 Laser Doppler Velocimeter is used to monitor the freestream velocity. The BDWT can operate with a wide range of freestream velocity and pressure. The maximum test section velocity is 8.5 ft/s (approximately 25 m/s), and the maximum tunnel pressure is 100 psi (690 kPa), the minimum tunnel pressure is vacuum. Run times of approximately 10 to 20 seconds are possible with relatively constant test section velocity and pressure (within 5%).

Fresh water from the potable supply was used during the experiment. The water was filtered before transfer to the tunnel. The air content of the water was modified by applying a vacuum over the water free surface for a period of several hours. In this way, both the dissolved and free gas could be removed. The nuclei content of the water was controlled by controlling the time the water was permitted to settle between runs. All tests were conducted at room temperature (nominally 22 C).

Test Models

A rectangular planform hydrofoil was employed as a test models. The hydrofoil had a NACA 63_1A012 cross section with a cord of 3.26 inches (82.8 mm) and a span of 3 inches (76.2 mm). The hydrofoils were constructed out of brass, and the surfaces were highly polished. The foil mount permitted variation in attack angle from -7 to 7 degrees. Test section blockage at 0 degree angle of attack was 13% and at 7 degrees was 19%. The unmounted end of the hydrofoil was rounded to reduce the influence of side-wall cavitation on the visualization of the cavitating flow near the mid-span of the foil.

For some experiments, tripping was applied to the leading edge of the hydrofoils in order to stimulate transition to turbulence in the boundary layer of the flow over the suction side of the hydrofoil (Arakeri and Acosta (1973) and Huang (1984)). Care must be taken to prevent the roughness elements from cavitating themselves. A technique which proved successful was the application and of a thin strip of "Scotch" tape to the leading edge of the hydrofoil. The tape has a thickness of 0.002 inches (50 micrometers). No cavitation was observed near the tape strip.

Nucleus Production Apparatus

In order to examine the process of bubble/cavity interactions, it was desirable to control the occurrence of the traveling bubbles. All freestream nuclei could be effectively removed, as described above. A Nd-YAG laser was then used to create a single nucleus near the leading edge of the hydrofoil. The frequency doubled beam of the Nd-YAG laser (532 um) was focused to the desired point in the flow through a high energy optical port. The laser was pulsed once, creating either a single or several small nuclei. Usually, the largest nucleus will cavitate, creating a single traveling

bubble. The command which triggers the laser can then be used to trigger other data acquisition equipment. Still photographs were taken with a 35 mm Nikon MF camera, and high speed video images of up to 6000 frames per second were acquired with a Kodak Ektapro 1000 video tape recorder.

RESULTS

Presented below are observations made of the cavitating flow on the suction side of the test hydrofoil at 0 attack angle. It was observed that the phenomena described below were not sensitive to small variation in attack angle (α = +/- 4 degrees). The thickness of the foil reduced the effects of the leading edge radius on the flow (such as leading edge boundary layer separation). The freestream velocity for these tests was U_0=15 m/s, leading to a cord Reynolds number of $Re_C = 1.2x10^6$. Previous studies have shown that flows over similar foils are transitional with the boundary layer remaining laminar, and a laminar separation often will take place at or downstream of the point of maximum thickness (Franc and Michel (1985)). Leading edge roughness can stimulate turbulent transition of the boundary layer and was employed for that purpose in this study. The experiments conducted with the polished foil will be denoted as "smooth," and those with the tripping applied at the leading edge will be denoted as "tripped."

Inception of attached cavities without traveling bubbles

When the cavitation number is lower than the attached cavitation inception number, stable attached cavities may form on the suction side of the smooth hydrofoil. Stable cavities will occur when the active nuclei density of the freestream flow is small. By deaerating the water prior to the blow-down process, a low nuclei density can be achieved, and under these conditions, stable attached cavities will form near the midcord of the hydrofoil (Figure 1) In the streamwise direction, the surface of the attached cavity is a smooth steady laminar interface near the cavity detachment point. The interface then becomes wavy, and the further downstream regions are turbulent. In spanwise direction, the attached cavities form "finger-like" structures which are closely spaced together, but separated by what appears to be a thin flow of water.

The inception of attached cavities on the smooth foil was observed to occur in the following manner: once a small area of attached cavitation occurs on the hydrofoil surface, the cavity would spread rapidly spanwise to form a stable attached sheet. The inception process was observed to take approximately 50 - 60 milli-seconds. Meanwhile, as can be seen in Figure 2, the interfacial patterns, including streamwise laminar, wavy, and turbulent regions, and spanwise finger-structures are all established as the cavity grows. The first, incipient area of attached cavities formed via two different mechanisms. First, cavities began near the boundaries of the test section near the edges of the hydrofoils. Second, stable cavities formed from the incipient "tails" generated by the traveling bubbles, which will be discussed below. In this latter mechanism, traveling bubbles were observed to directly influence the inception of attached cavitation.

Figure 3 shows a series of video images of the attached cavity interface near the location of cavity separation. A time sequence is shown with time intervals of 1 millisecond, and the spanwise motion

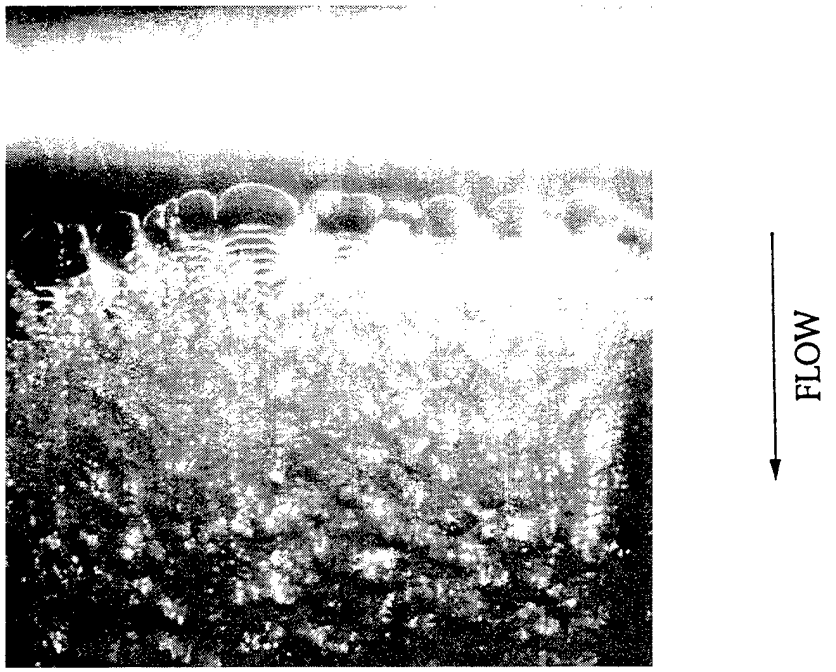


Figure 1- A stable attached cavity. The water of the BDWT was allowed to settle, allowing small bubbles to rise to the free surface. No travelling bubbles were observed during the run. U_0 = 15 m/s, σ = 0.28, α = 0^o. Image is scaled 1.60:1

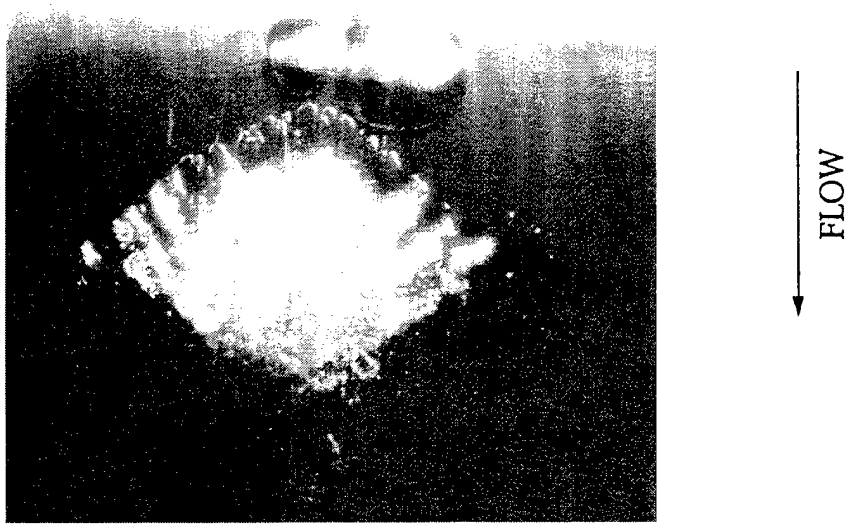


Figure 2- The inception of an attached cavity. This cavity was not created by the passage of a travelling bubble. U_0 = 14 m/s, σ = 0.40, α = 0^o. Image is scaled 1.60:1

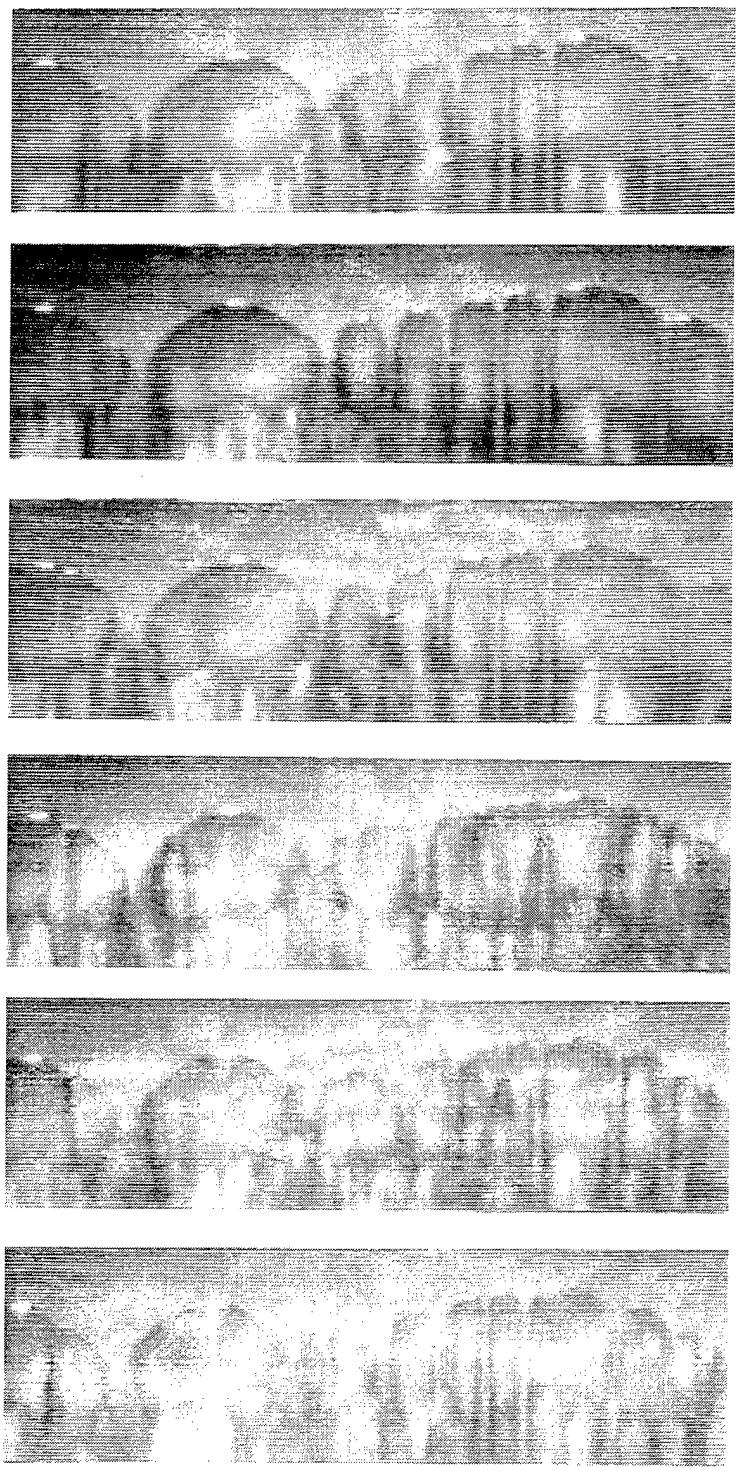


Figure 3- A time series of close-up images of the cavity interface near the point of cavity separation. The time between each image is 1 millisecond. Some of the cavity "fingers" move in the spanwise direction. U_O = 15 m/s, σ = 0.28, α = 0^o. Image is scaled 2.60:1

of the interfacial structures is evident.

Inception of attached cavitation did not occur on the tripped foil. This observation is consistent with those of Arakeri and Acosta (1973) and Huang (1984). In these studies, the effect of tripping was to eliminate the occurrence of attached cavitation on transitional axisymmetric bodies. By stimulating the transition to turbulence in the boundary layer, a laminar separation bubble which had occurred on the headform was eliminated, and attached cavitation was suppressed. A similar mechanism is most likely responsible for the suppression of attached cavitation on the hydrofoil observed in this study.

Bubble interactions with the attached cavity

It has been observed that high nuclei density in the freestream flow can suppress the formation of the stable attached cavities (Kodoma et al. (1979) and Briancon-Marjollet et al. (1990)). Instead, only traveling bubbles are observed to occur. To explore this phenomenon, we examined the interaction of a single bubble with a stable attached cavity. A pulsed laser was used to induce a single nucleus near the leading edge of the hydrofoil, slightly above the hydrofoil surface. Firing the pulsed laser creates an active nucleus which soon explodes into a traveling bubble. The bubble reaches a maximum volume before it reaches the leading edge of the stable sheet attached cavity further downstream. Photos, as well as the high speed videos, were taken to examine the details of the bubble/attached cavity interaction.

The interaction process occurred in the following steps. The bubble will approach the cavity leading edge and flow over the cavity, as shown in Figure 4. When the traveling bubble is above the leading edge of the attached cavity, the detachments and the laminar regions of the attached cavity are clearly seen through the bubble. Thus the bubble does not sweep the attached cavities by directly suppressing them. Instead, the suppression of the attached cavities occurs downstream of traveling bubble. Note, the attached cavities begin to disappear after the traveling bubble has passed. Two interesting phenomena were observed during this process. First, the suppressed region of the attached cavities looks like a "fork" pointing downstream, with approximately the same width of the bubble. The bubble does not sweep away the entire cavity it passes over. Secondly, the edges of the remaining attached cavities remains to be very sharp. The laminar region of the remaining cavity appears not to be influenced by the nearby suppressed cavity region. As the traveling bubble moves downstream, the sweeping action proceeds upstream of it. However, the cavity upstream of the bubble begins to reform by spreading spanwise, similar to the inception of the attached cavities. This closing process takes approximately 4-8 milli-seconds. Figure 5 presents a series of close-up images showing the sweeping process. Each image was taken in time steps of 333 microseconds. A travelling bubbles can be seen approaching the cavity interface on the let side of the image. The bubble passes over the cavity, the cavity is swept away, and the cavity re-closes. Figure 6 presents another view of the sweeping process.

A close-up side-view of the travelling bubble as is nears the attached cavity interface reveals several features of the flow. Figure 7 shows three images. The top image shows a travelling bubble wholly above the surface of the foil, and a thin film of liquid 1.0 mm in thickness separates the bubble from the surface of the hydrofoil. The

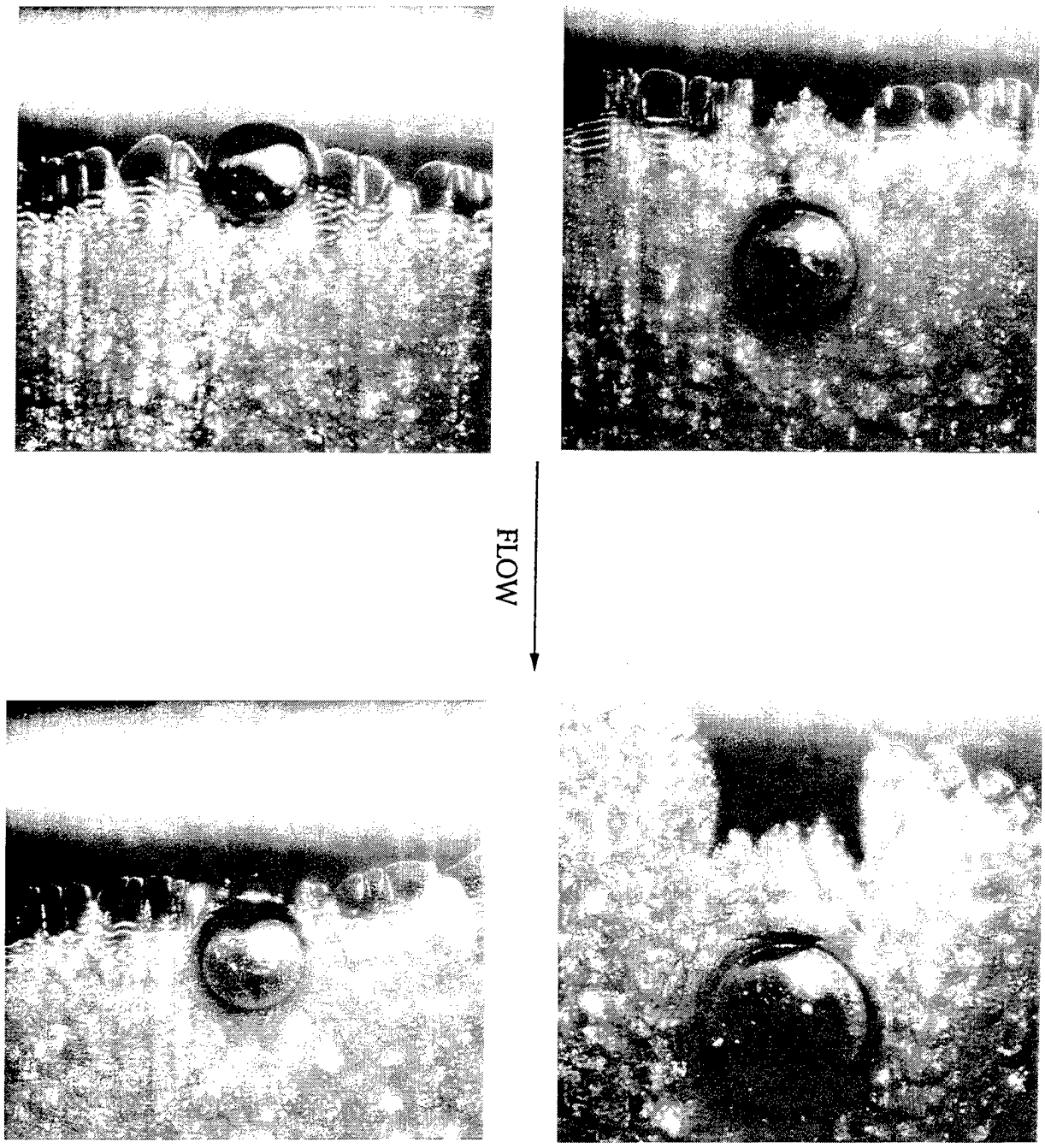


Figure 4- A series of images showing the sweeping process. A travelling bubble passes over the stable cavity. After it passes, a region of the attached cavity is swept away leaving a "fork" like region. U_O = 15 m/s, σ = 0.28, $\alpha = 0^o$ in the first three images, $\alpha = 6^o$ in the last image. Image is scaled 1.60:1

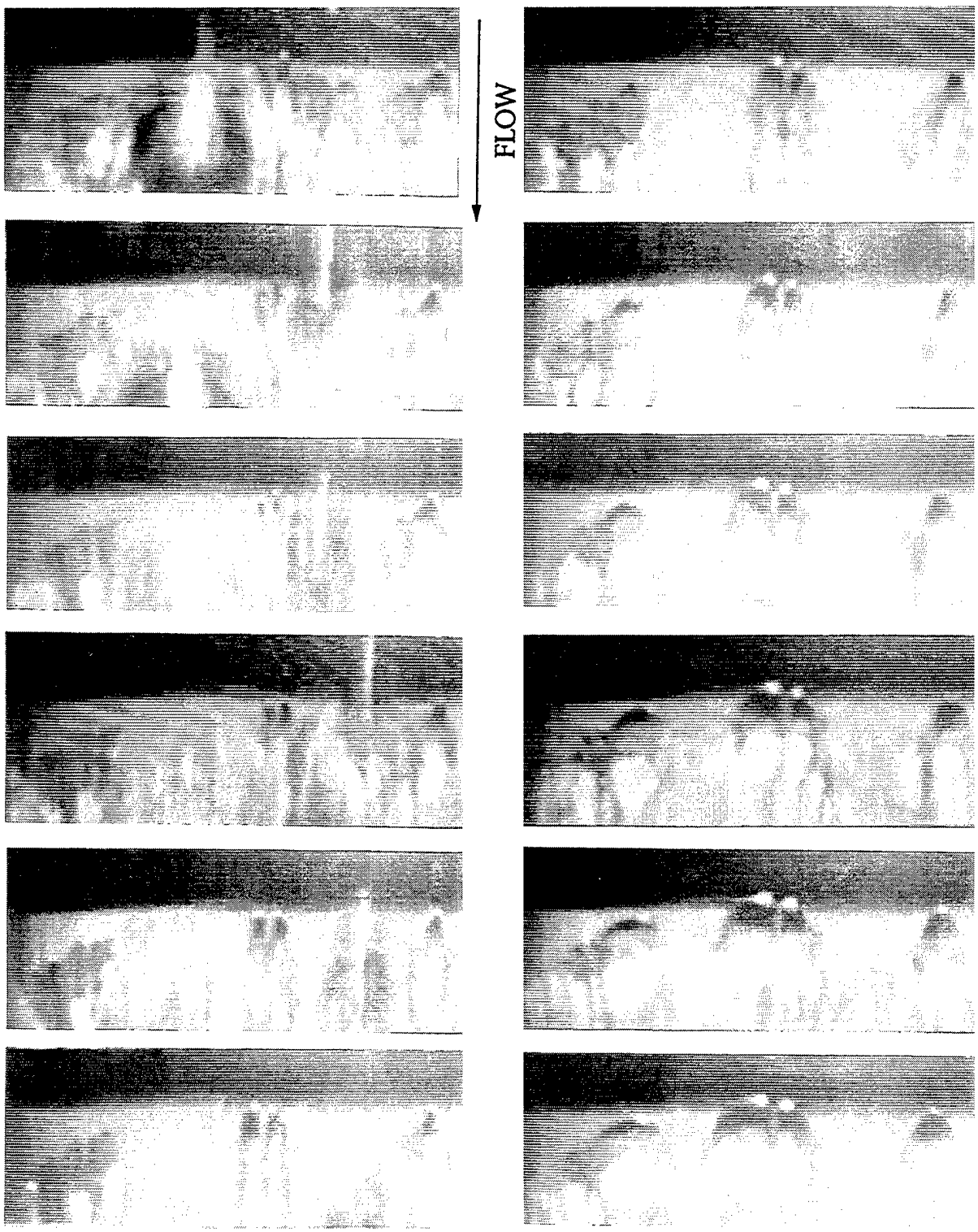


Figure 5- A time series of images showing the sweeping process. The time between each image is 333 microseconds. A travelling bubble is seen approaching the attached cavity and sweeping away a portion of the cavity. The cavity then re-closes. U_0 = 15 m/s, σ = 0.28, $\alpha = 0^o$. Image is scaled 1.15:1

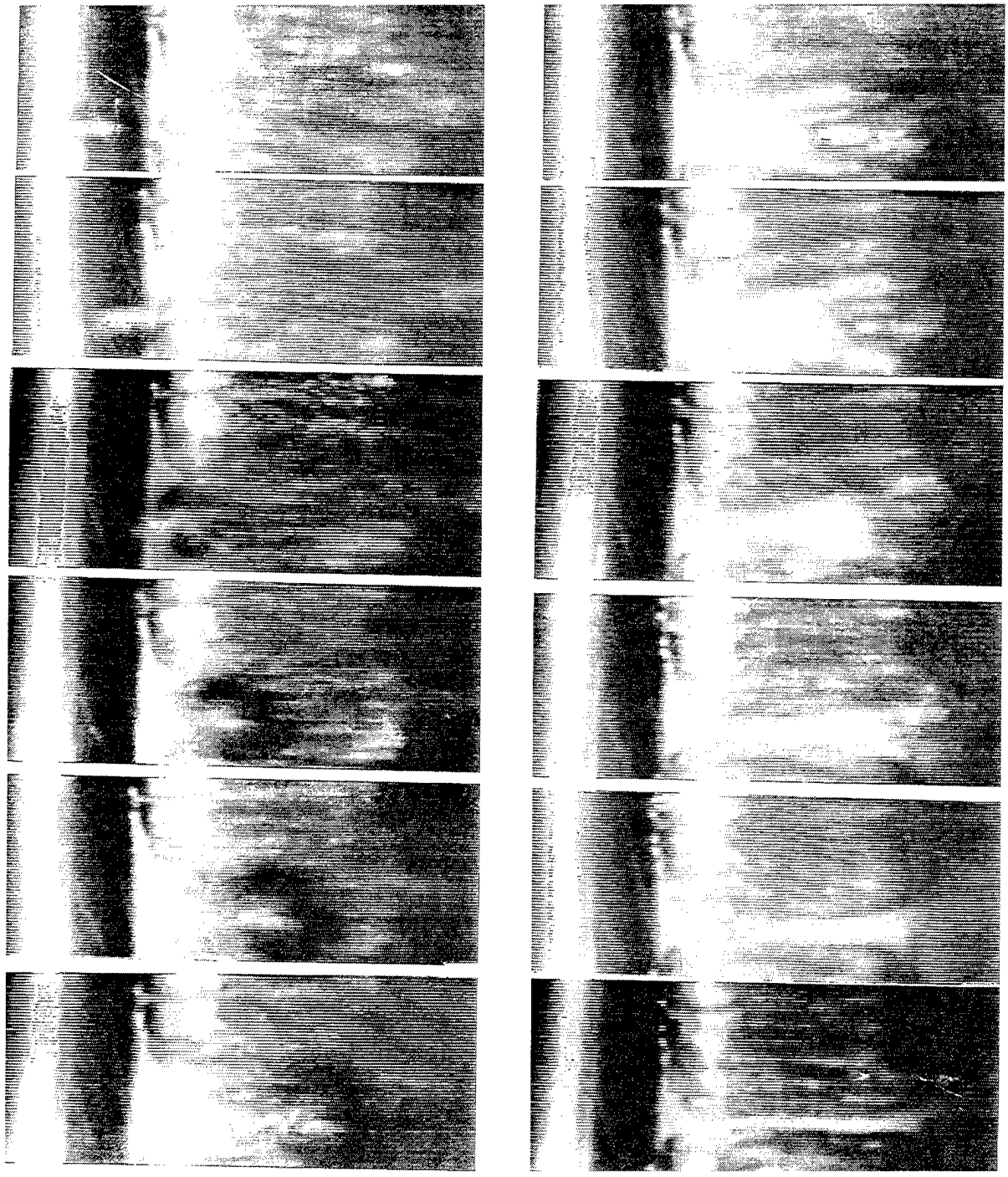


Figure 6- A time series of images showing the sweeping process. The time between each image is 333 microseconds. A travelling bubble is seen approaching the attached cavity and sweeping away a portion of the cavity. The cavity then recloses. U_O = 15 m/s, σ = 0.28, $\alpha = 0^o$. Image is scaled 1.50:1

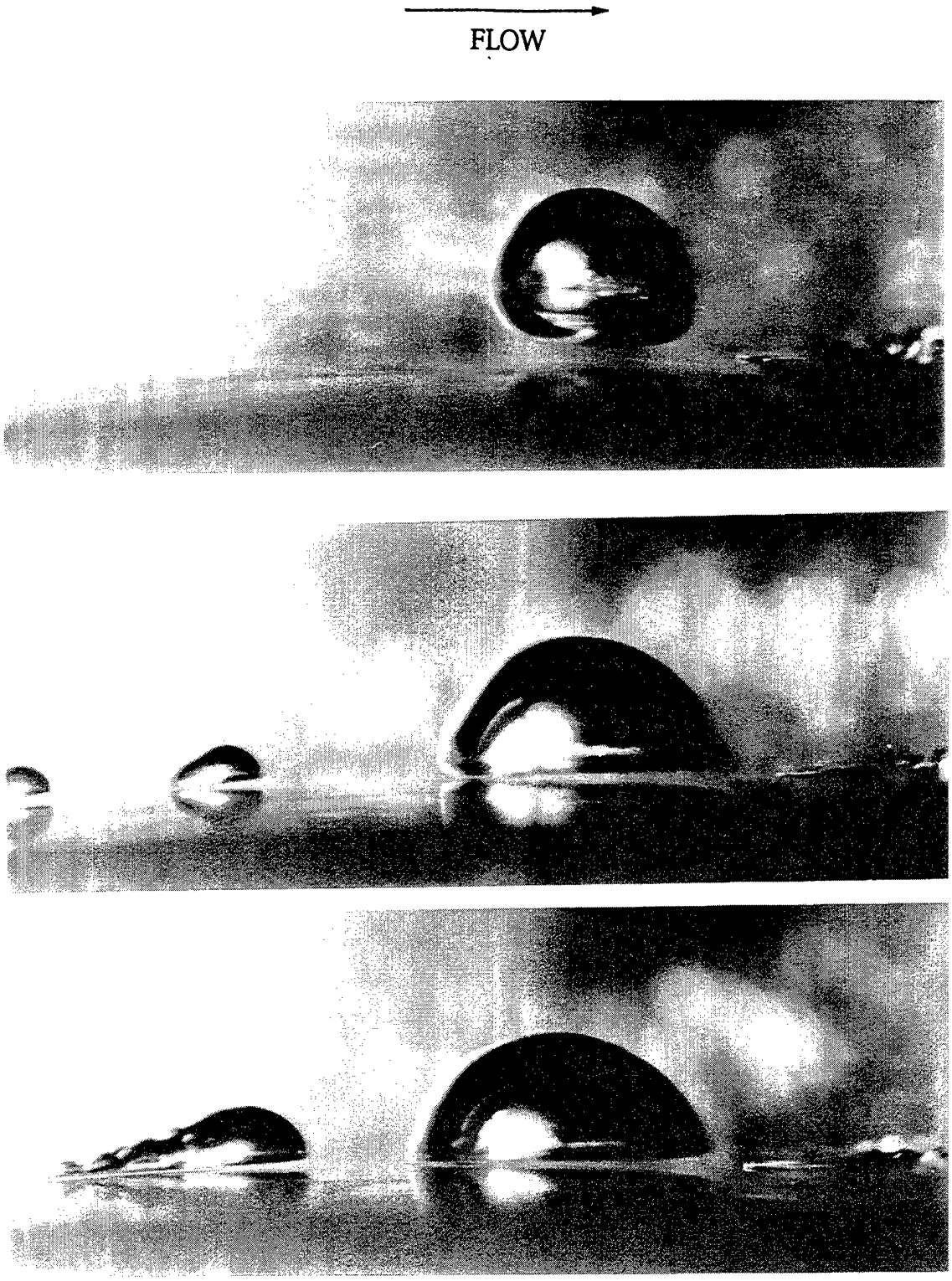


Figure 7- Three close-up images of travelling bubbles as they pass over the foil. The separation point of the attached cavity can be seen on the left. The top bubble is wholly above the hydrofoil surface, but the other bubbles are much closer to the surface. A small bubble begins to generate a "tail." U_O = 15 m/s, σ = 0.28, $\alpha = 0^o$. Image is scaled 5.60:1

leading edge of the attached cavity can be seen on the right of the image, and its thickness is approximately 350 micrometers. In this instance, the bubble may pass over the cavity interface, and it is possible that this bubble would not interact with the cavity. In the second and third image, the travelling bubble is much closer to the surface, and the film of fluid takes on a "wedge" shape. The trailing edge of the bubble seems to touch the foil surface; any fluid film in this region is less than 200 micrometers mm. As shown in these image, the bubble can initially travel over the attached cavity without directly interacting with it until the trailing edge of the bubble passes over the cavity.

The sweeping process will repeat itself as travelling bubbles continue to pass over the attached cavity. Indeed, if enough nuclei are present, the traveling bubbles will prevent the formation of a stable cavity. Instead, the surface of the foil will be covered only by traveling bubbles. Figure 8 shows the cavitation pattern on the hydrofoil under conditions of few and many freestream nuclei. For both cases, the freestream velocity and pressure are the same. With few nuclei present, a stable attached cavity forms. With many active nuclei in the freestream, traveling bubbles will form and sweep away the cavity.

Inception of bubble "tails"

The exploding and collapsing processes of the traveling bubbles can be easily observed when the cavitation number is slightly higher than the attached cavitation inception number. For both the smooth and the tripped cases, stable attached cavities did not develop, and only traveling bubbles occurred.

The active nuclei explode into traveling bubbles shortly after the leading edge of the hydrofoil, and these bubbles collapse near the foil trailing edge downstream. Both exploding and collapsing processes are extremely rapid, occurring within a fraction of a milli-second. For the smooth hydrofoil, bubbles grow close to the hydrofoil surface and they form semi-spherical "cap shapes" with the flat side against the hydrofoil surface. Many of these bubbles produce "tails," wedge shape, attached cavities on either spanwise edge of the bubble, as shown in Figure 9. The traveling bubbles then collapse downstream, while the "tails" attached cavities remain, as shown in Figure 10. If the cavitation number is higher than the attached cavitation inception number, these incipient attached cavities will soon disappear. This phenomena has been observed in previous studies (i.e. van der Meulin (1980) and Kuhn de Chizelle, Ceccio, and Brennen (1994)). Furthermore, not all travelling bubbles will generate tails, as seen in Figure 9. Figure 11 presents a time series of video images showing the passage of three travelling bubbles on the smooth headform. The first two travel along the headform surface and do not generate any tails. The fourth bubble does generate a tail which continues to grow after the bubble has passed downstream. Ultimately, the attached cavity will disappear. Figure 7 also shows the inception of a "tail" behind a small travelling bubble. In this case, the travelling bubble rides close to the hydrofoil surface. The appearance of travelling cavitation on the tripped hydrofoil differs from that described above. While some of the travelling bubbles pass without creating any tails, many more are seen to degenerate into local patches of attached cavitation. Figure 12 presents a time series of video images for this case, with each image taken after a time interval of 500 microseconds.

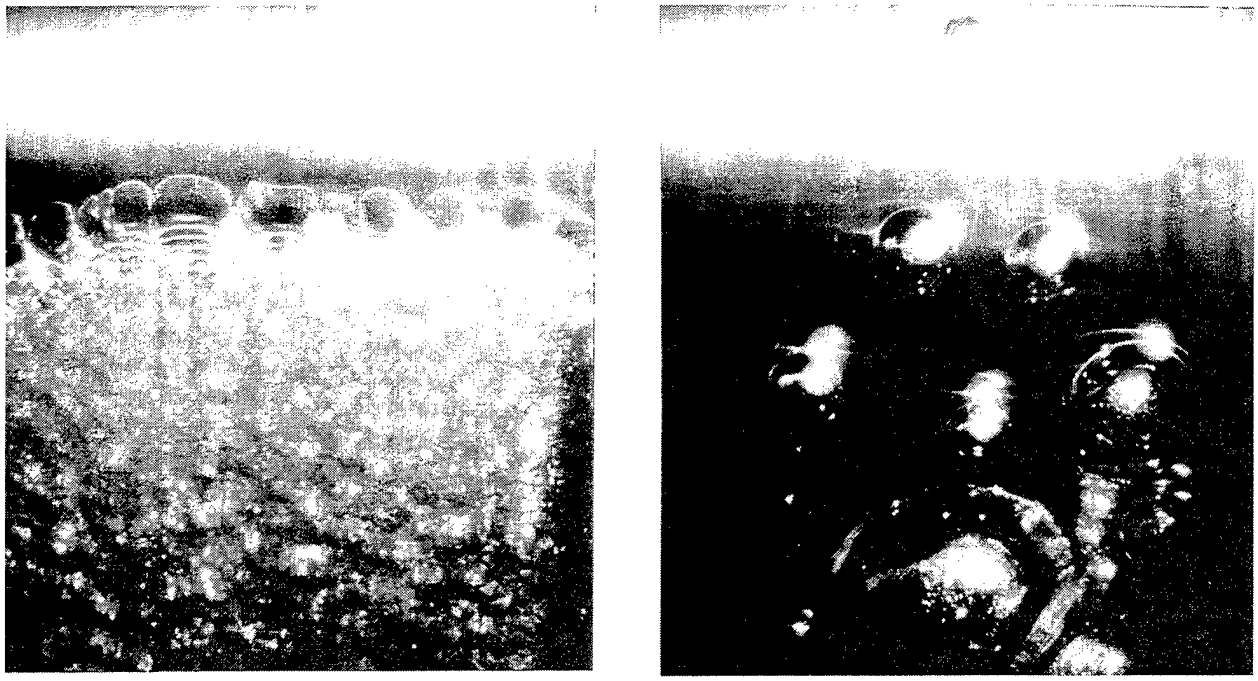


Figure 8- Cavitation as it occurs on the hydrofoil for the case of few and many nuclei present in the freestream. With the occurrence of travelling bubbles, the stable attached cavity is swept away and cannot reform. Uo = 15 m/s, σ = 0.28, α = 0^{o}. Image is scaled 1.60:1



Figure 9- A travelling bubble which has induced an upstream region of cavitation. Note the other bubble which has not generated a "tail." U_o = 14 m/s, σ = 0.40, α = 0^{o}. Image is scaled 1.60:1



Figure 10- The remnant of an induced attached cavity. The travelling bubble which created this "tail" has collapsed. Ultimately, this region of cavitation will be swept away. U_o = 14 m/s, σ = 0.40, α = 0^{o}. Image is scaled 1.60:1

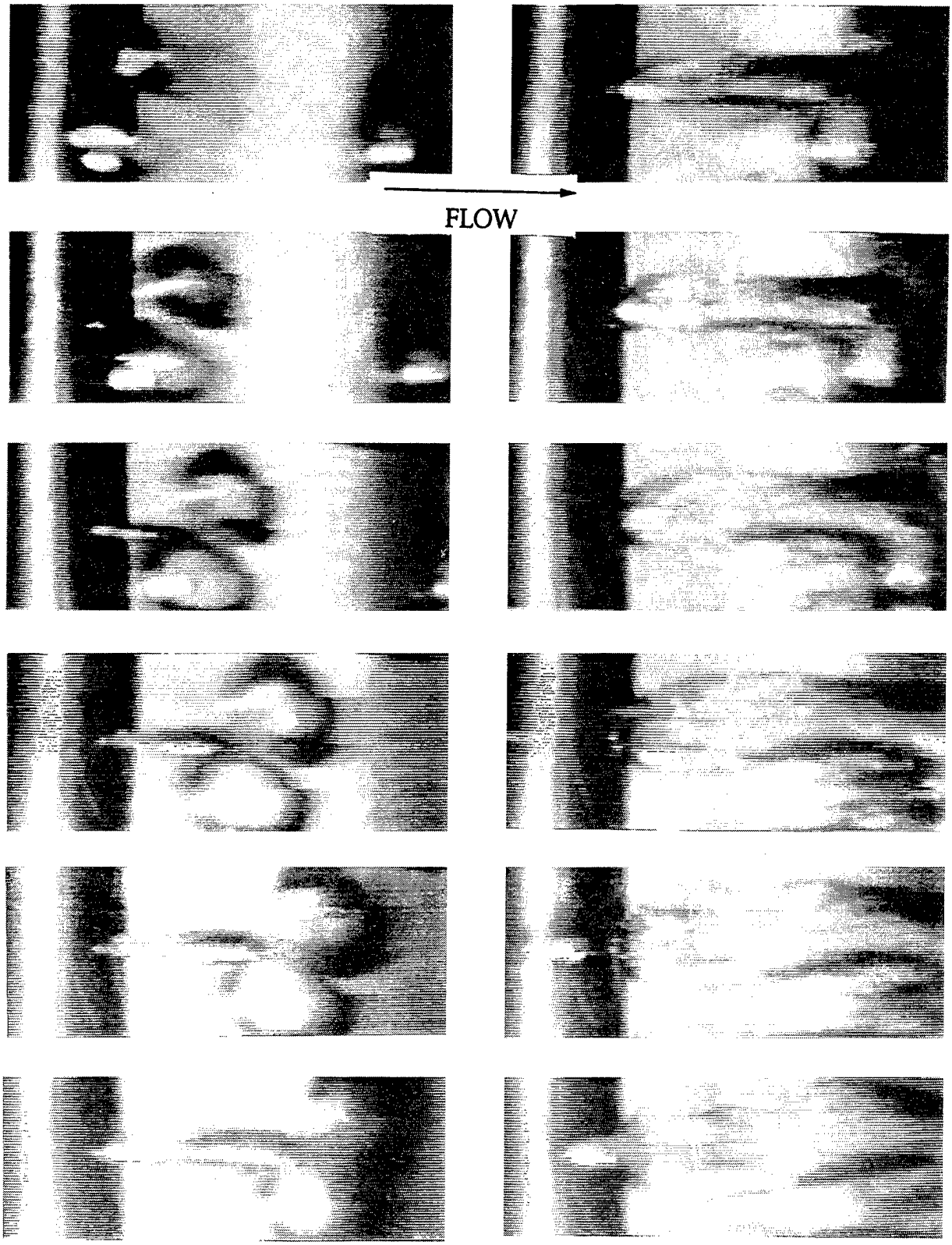


Figure 11- A time series of images showing the creation of a bubble "tail" by a travelling bubble. In this case, the hydrofoil is smooth. The time between each image is 333 microseconds. U_O = 15 m/s, σ = 0.28, $\alpha = 0^o$. Image is scaled 0.98:1

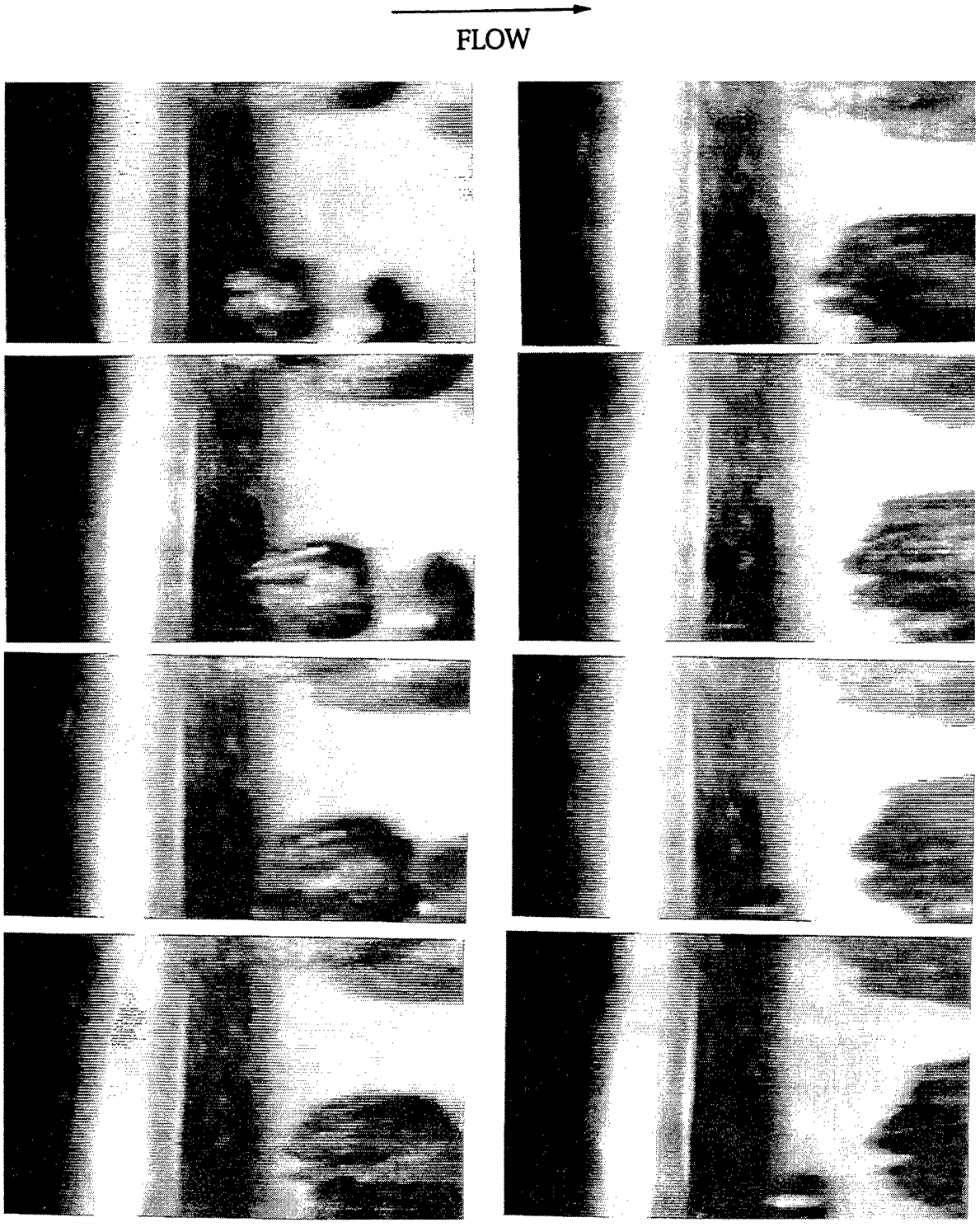


Figure 12- A time series of images showing the creation of a bubble "tail" by a travelling bubble. In this case, the boundary layer of the hydrofoil has been tripped. The time between each image is 333 microseconds. U_0 = 15 m/s, σ = 0.28, $\alpha = 0^o$. Image is scaled 1.15:1

CONCLUSIONS

The inception of attached cavitation near the midcord of the hydrofoil is most likely associated with separation of a laminar boundary layer in this region. This observation is supported by the fact that the midcord cavitation was suppressed by the application of a tripping strip near the leading edge of the foil. Consequently, it is reasonable to conclude that the boundary layer on the smooth foil is transitional, and the boundary layer on the tripped foil is turbulent. The differences in how the travelling bubbles interact with the boundary layer and the attached cavitation can be related to the state of the boundary layer.

Travelling bubbles were seen to interact with attached cavitation in the smooth foil. Several mechanisms for this interaction were proposed by Briancon-Marjollet, Franc, and Michel (1990), with emphasis given to the interaction of bubbles with the attached cavity through the local generation of turbulence in the region upstream of the passing bubble. This hypothesis was support by experimental observations disturbed dye streaks close to the foil surface upstream of some travelling bubbles. The idea that travelling bubbles stimulate local turbulent transition in the boundary layer is also consistent with the observations of the present study. Travelling bubbles which sweep away attached cavitation travel very close to the hydrofoil surface, as shown in Figure 7. The minimum thickness measured of the fluid film under the trailing edge of the bubble is approximately 200 micrometers. The thickness of a laminar boundary layer near the midcord of the foil is approximately given by δ, the thickness of a boundary layer formed over a plat plate. For the flow over the smooth foil, δ is approximately 250 micrometers. Thus, the trailing edges of the such travelling bubbles can certainly interact with and disturb the boundary layer, possibly by "squeezing" the thin film of fluid over which the bubble flows. The squeezing process may then cause local turbulent transition of the boundary layer. A transient turbulent region may then grow behind the bubble. It is this local turbulent region which will cause the local suppression of the attached cavitation. Travelling bubbles which flow above the hydrofoil surface, as shown in Figure 7, do not interact with the boundary layer and thus ride over the attached cavity and do not disturb it.

The creation of a local turbulent spot may also lead to the formation of a transient attached cavity behind the bubble. As shown in Figure 9, travelling bubbles induce local attached cavitation in regions of the foil upstream of the stable attached cavitation formation point. These cavities do not persist. It is known that the pressure fluctuations in a turbulent boundary layer can be on the order of 20% of the dynamic pressure, q (Huang and Peterson (1976)). Such pressure fluctuations may cause the inception of local attached cavitation if sub-critical surface nuclei are activated. Another inception mechanism would employ the travelling bubble as a macroscopic nucleus. Pressure fluctuations in the turbulent boundary layer may be strong enough to induce local regions of tension in the boundary layer. The nearby cavitation bubble can then "grow into" these regions of tension, creating an incipient cavity. The travelling bubble will continue to be convected by the flow. Ultimately, the cavity will be swept away, and the laminar boundary layer reforms. Unless another turbulent spot is induces, the flow will remain attached and laminar.

This mechanism is enhanced if the boundary layer is already

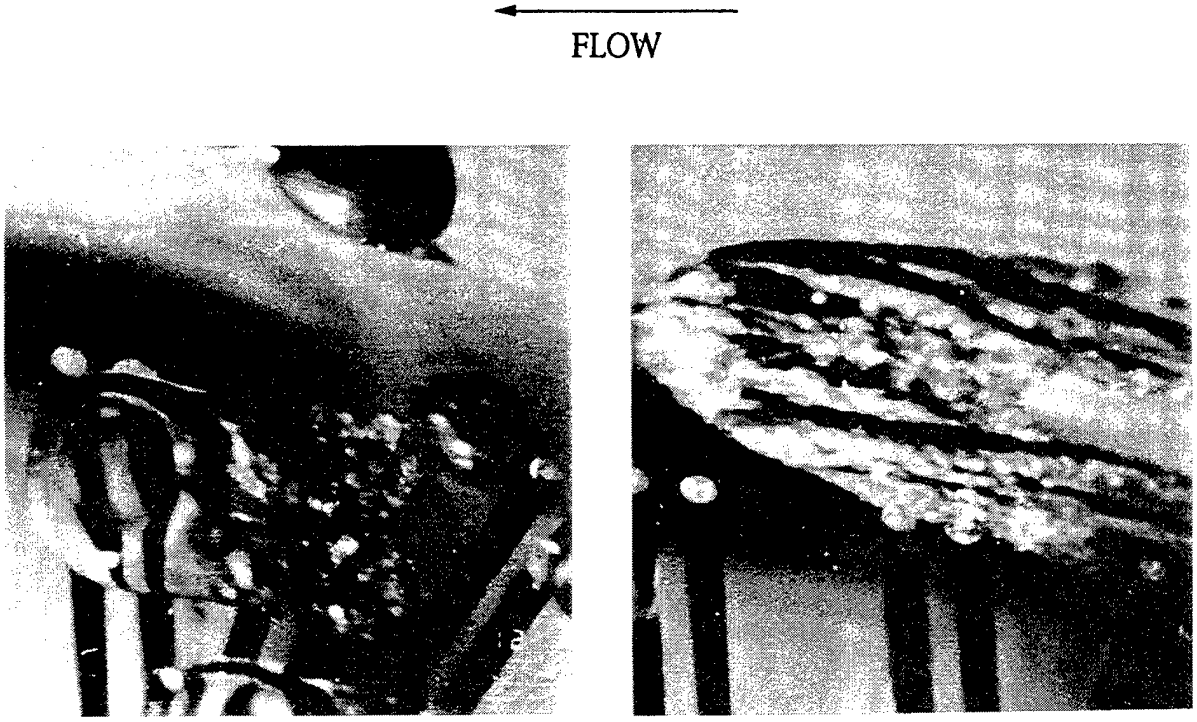


Figure 13- Cavitation events as they occur on a 25.4 cm diameter Schiebe body. U_O = 15 m/s, σ = 0.53. Image is scaled 2.91:1

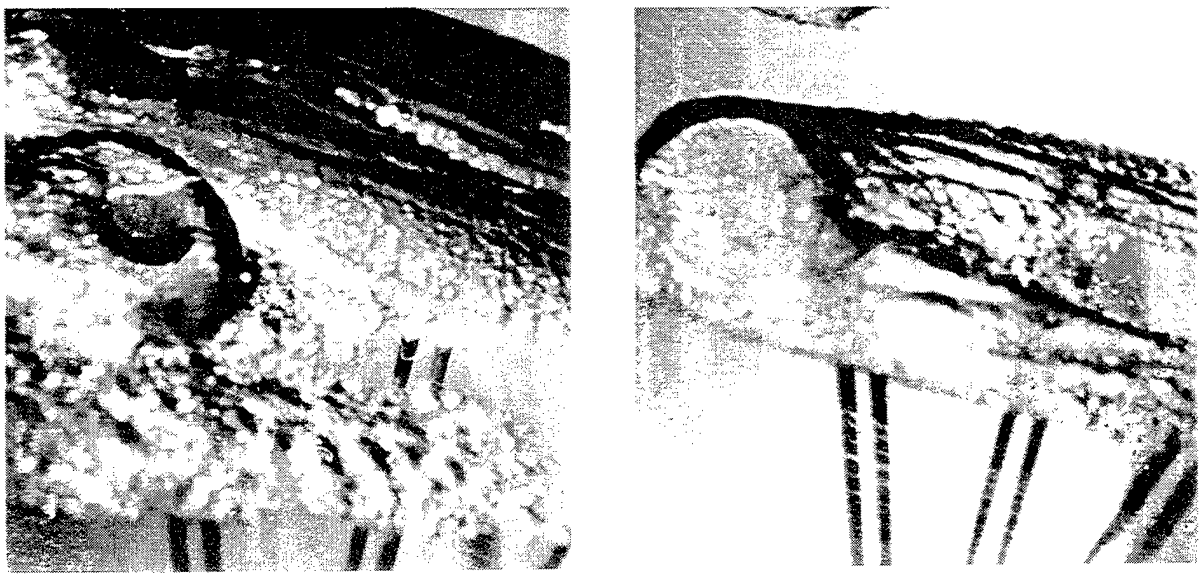


Figure 14- Cavitation events as they occur on a 50.8 cm diameter Schiebe body. U_O = 15 m/s, σ = 0.60. Image is scaled 1.38:1

turbulent. In the case of the tripped foil, the probability that a bubble will induce an incipient cavity in much higher. Experiments conducted with the tripped foil shown that travelling bubbles of almost any size will form local patches, as shown in Figure 12. These incipient attached cavities often engulf the original bubble which formed them. The cavities also do not persist indefinitely but are swept away.

These observations can be compared to those of Kuhn de Chizelle, Ceccio, and Brennen (1994). In this study, cavitation on three axisymmetric Schiebe headforms of diameter 2.54 cm, 25.4 cm, and 50.8 cm were examined. Examples of individual cavitation events which occurred on the 25.4 cm and 50.8 cm diameter bodies are shown in Figures 13 and 14. Travelling bubbles which occurred on the 2.54 cm diameter body almost never were accompanied by tails. Alternately, travelling bubbles on the 25.4 cm body frequently developed tails, and often degenerated into local patch cavitation, and travelling bubbles on the 50.8 inch diameter body almost always developed tails and frequently degenerated into local patch cavities. In the present study, cavitation event occurring on the tripped foil are similar to those which occurred on the two larger axisymmetric bodies. Bubble cavitation on the untripped hydrofoil was on average more similar to that of the small diameter axisymmetric body. Thus, the observed difference in the travelling cavitation events on the three headforms of the Kuhn de Chizelle, Ceccio, and Brennen (1994) study may be related to the state of the boundary layer in the cavitating region. Note also in Figure 14 that the attached cavity sweeping was also observed to occur on the larger headforms.

The inception of attached cavitation can be significantly influenced by the presence of traveling bubble cavitation. The formation of traveling bubbles, in turn, will depend strongly on freestream nuclei distribution. Consequently, the inception and formation of attached cavitation can be affected by the freestream nuclei distribution. The acoustic emission if individual cavitation bubbles is significantly reduced if the bubble strongly interacts with the boundary layer to form incipient attached cavitation (Kuhn de Chizelle, Ceccio, and Brennen (1994)). Thus, phenomena described here may lead to scale effects in the cavitation testing relating to both the type of cavitation present and the noise it produces. Furthermore, injection of air in and around regions of attached cavitation has been implemented in practical engineering designs to mitigate processes which lead to damage and noise. Bubble/attached cavity interactions like those observed here may occur as air is injected near attached cavities. We are continuing our study of this phenomenon to improve our understanding of the underlying physical mechanisms responsible for these interactions.

ACKNOWLEDGMENTS

The investigators would like to acknowledge the assistance of Po-Wen Yu and Ann Tassin during the performance of these experiments. This work was supported under ONR contract N00014-91-J-1063, and Dr. Edwin Rood was the contract monitor.

REFERENCES

Abbot, I. H. and von Doenhoff, A. E. 1958. Theory of Wing Sections. Dover p. 344.

Arakeri, V. H. and Acosta, A. J. 1973. "Viscous effects in the inception of cavitation on

axisymmetric bodies." Trans. A.S.M.E. I: J. Fluids Eng., Vol 199, pp. 155-176.

Arndt, R. E. A. 1981. "Cavitation in Fluid Machinery and Hydraulic Structures." Ann Rev. Fluid Mech., Vol. 13, pp. 273-328.

Briancon-Marjollet, L., Franc, J. P., and Michel, J. M. 1990. "Transient bubbles interacting with an attached cavity and the boundary layer." J. Fluid Mech., Vol. 218, pp. 355-376.

Ceccio, S. L. and Brennen, C. E. 1991. "Observations of the dynamics and acoustics of travelling bubble cavitation." J. Fluid Mech., Vol. 233, pp. 633-660.

Franc, J. P. and Michel, J. M. 1985. "Attached cavitation and the boundary layer: experimental investigation and numerical treatment." J. Fluid Mech., Vol. 154, pp 63-90.

Gindroz, B. and Billet, M. L. 1993. "Influence of the Nuclei on the Cavitation Inception for Different Types of Cavitation on Ship Propellers." Proc. A.S.M.E. Int. Symp. on Cavitation Inception, FED-Vol. 177, pp. 1-11.

Huang, T. T. 1984. "The effects of turbulence stimulators on cavitation inception of axisymmetric headforms." Proc. A.S.M.E. Int. Symp. on Cavitation Inception, FED-Vol. 16, pp. 89-101.

Huang, T. T. and Peterson, F. B. 1976. "Influence of viscous effects on model/full-scale cavitation scaling." J. Ship Research, Vol. 20, pp. 215-223.

Kodoma, Y., Tamiya, S., Take, N., and Kato, H. 1979. "The effect of Nuclei on the inception of bubbles and sheet cavitation on axisymmetric bodies." Proc. A.S.M.E. Int. Symp. on Cavitation Inception, pp. 75-86.

Kuhn de Chizelle, Y., Ceccio, S. L., and Brennen, C. E. 1994. "Observations, scaling, and modelling of travelling bubble cavitation." submitted for publication in the J. Fluid. Mech.

Kuiper, G. 1979. "Some experiments with distinguished types of cavitation on ship propellers." Proc. A.S.M.E. Int. Symp. on Cavitation Inception, pp. 171-206.

Maines, B. H. and Arndt, R. E. A. 1993. "Bubble dynamics of cavitation inception in a wing tip vortex." Proc. A.S.M.E. Cavitation and Multiphase Flow Forum, FED-Vol. 153, pp. 93-97.

Meulin, J. H. J., van der, 1980. "Boundary layer and cavitation studies of NACA 16-012 and NACA 4412 hydrofoils." Proc. 13th Symp. on Naval Hydrodynamics, Tokyo, pp. 195-217.

Shen, Y. T., Gowing, S., and Ceccio, S. 1994. "Salt Water Effects on Bubble and Sheet Cavitation." Proc. of 2nd Int. Symp. on Cavitation, Tokyo.

Tassin, A. L., Li, C. Y., Ceccio, S. L., and Bernal, L. P. 1994. "PIV measurements in cavitating flows." to be submitted to Experiments in Fluids

Nonlinear Analysis of Viscous Flow Around Cavitating Hydrofoils

S. Kinnas, S. Mishima, W. Brewer
(Massachusetts Institute of Technology, USA)

ABSTRACT

The flow around partially or super-cavitating hydrofoils is treated with a viscous/inviscid interactive method. The inviscid cavity flow model is based on a fully non-linear boundary element method, in which the boundary conditions are applied on the exact cavity surface. The viscous flow model is based on boundary layer theory applied on the compound foil, consisting of the union of the cavity and hydrofoil surface. The friction coefficient is forced to zero everywhere on the cavity. The cavity detachment point is determined from a criterion applied on the viscous flow on the hydrofoil upstream of the cavity. The effect of Reynolds number on the predicted cavity extent and volume for given cavitation number is studied when the angle of attack is kept fixed or when the lift coefficient is kept fixed. Finally, the *equivalent* cavitation number is proposed as a way of including the effects of viscosity in three-dimensions.

1 INTRODUCTION

A general potential-based boundary element method has been developed for the non-linear analysis of the inviscid cavitating flow around hydrofoils or propeller blades. The flow around partially or super-cavitating hydrofoils in two or three dimensions was addressed first. For given cavity extent (length) [11] or cavitation number[13, 6], the cavity shape, not known a priori, was determined in an iterative manner until the dynamic and the kinematic boundary conditions were both satisfied on the cavity boundary. The most important finding in [11, 13] was the fact that the iterative process for finding the cavity surface was converging *much* quicker than in previously developed velocity-based boundary element methods. In particular, it was found that even the cavity solution from the first iteration, in which the cavity panels were located on the hydrofoil surface underneath the cavity, was *very close* to the fully non-linear converged solution. The method was finally extended to include the analysis of time-varying cavitating flows around propeller blades [12], [5].

The boundary element method has been found to be a computationally efficient, robust and versatile tool for the inviscid analysis of cavitating flows around arbitrary geometries in two or three dimensions. Nevertheless, the method has the following shortcomings: (a) it only treats the inviscid flow around the foil and cavity, (b) it treats the cavity detachment point as an input parameter, and (c) it assumes the cavity to be followed by a zero (or given) thickness wake.

In the present paper, a method is presented to take into account all of the above. The method couples the existing inviscid flow solution to a boundary layer solution [4]. It was first applied for the analysis of the fully wetted flow around hydrofoils [4] as well as propeller blades [8]. Initially, the method was applied on partially cavitating hydrofoils [19] by making the "thin" cavity assumption. Now the method is extended to treat the flow around partially cavitating hydrofoils in *fully non-linear* theory, as well as the flow around super-cavitating hydrofoils. The method is applied on several hydrofoil geometries and the effect of Reynolds number on the cavity solution is investigated. Finally, a way of incorporating the effects of viscosity in three dimensions, via the *equivalent* cavitation number is proposed.

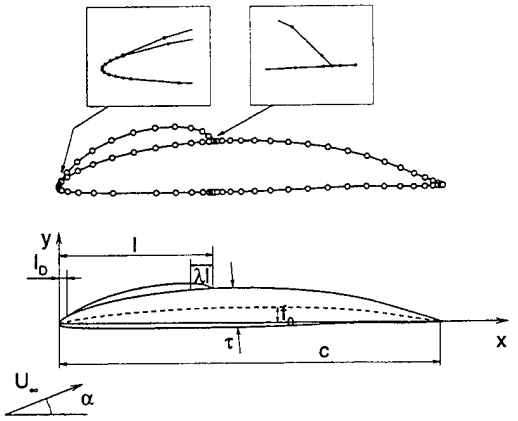


Figure 1: Partially cavitating hydrofoil in inviscid non-linear theory. Definition of main parameters. Panel arrangement on the cavity and foil is also shown for $N = 80$.

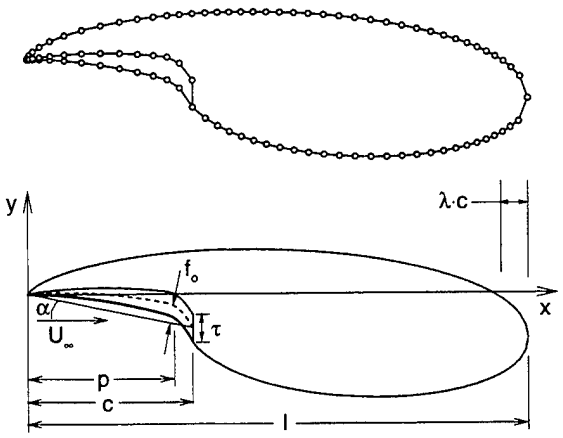


Figure 2: Super-cavitating hydrofoil in inviscid non-linear theory. Definition of main parameters. Panel arrangement on the cavity and foil shown for $N = 80$.

2 INVISCID CAVITY MODEL

Consider a partially or super-cavitating hydrofoil, shown in Figures 1 and 2, respectively, subject to an incoming flow $\boldsymbol{U}_\infty$ with an ambient pressure p_∞. The vapor pressure, corresponding to the temperature in the fluid, is equal to p_v, and the fluid density is equal to ρ. The main geometric parameters for the foil and cavity are defined in Figures 1 and 2. The cavitation number is defined as usual:

$$\sigma = \frac{p_\infty - p_v}{\frac{\rho}{2} U_\infty^2} \tag{1}$$

In inviscid flow, the velocity flow field $\boldsymbol{q}$ is defined in terms of the perturbation potential, ϕ:

$$\boldsymbol{q} = \boldsymbol{U}_\infty + \boldsymbol{\nabla}\phi \tag{2}$$

The perturbation potential, ϕ_P, at any point P in the flowfield, may be expressed in terms of its values on the cavity and foil surface, S, and on the trailing wake surface, W, by using Green's third identity [1]:

$$\epsilon\phi_P = \int_S \left[G\frac{\partial\phi}{\partial n} - \phi\frac{\partial G}{\partial n} \right] dS - \int_W \Delta\phi_W \frac{\partial G}{\partial n} dS \tag{3}$$

where $\epsilon = 1/2$ when $P \in S \cup W$ and $\epsilon = 1$ when $P \notin S \cup W$. G is the Green's function in unbounded flow, defined as the potential of a unit strength source in either two or three dimensions:

$$G_{2-D} = \frac{1}{2\pi} lnR \tag{4}$$

$$G_{3-D} = -\frac{1}{4\pi R} \tag{5}$$

where R is the distance between point P and the point of integration over S or W in equation (3). To determine ϕ on the foil and cavity surface we must invert the Fredholm integral equation of the second kind, resulting from applying equation (3) for $P \in S$. The following boundary conditions need to be applied:

- kinematic boundary condition on the non-cavitating (also called fully wetted) part of the foil:

$$\frac{\partial\phi}{\partial n} = -\boldsymbol{U}_\infty \cdot \boldsymbol{n} \tag{6}$$

  with $\boldsymbol{n}$ being the unit normal vector on the foil surface

- dynamic boundary condition on the cavity:

$$|\boldsymbol{q}_c| = U_\infty\sqrt{1+\sigma} \tag{7}$$

  where $\boldsymbol{q}_c$ is the fluid velocity vector on the cavity surface. In the case of two dimensions:

$$|\boldsymbol{q}_c| = \frac{\partial\phi}{\partial s} + \boldsymbol{U}_\infty \cdot \boldsymbol{s} = U_\infty\sqrt{1+\sigma} \tag{8}$$

  where $\boldsymbol{s}$ is the unit vector tangent to the cavity surface.

[1] Green's identity is identical to that for non-cavitating flows in which case S is the surface of the hydrofoil.

- pressure condition at cavity termination:

$$|\boldsymbol{q}_{tr}| = U_\infty \sqrt{1+\sigma}\,[1 - f(x)] \qquad (9)$$

  Where $\boldsymbol{q}_{tr}$ is the velocity vector over a transition region of length λ at the end of the cavity and f is an algebraic function of the chordwise distance x [13]. This corresponds to a pressure recovery cavity termination model [15]. In the case of super-cavitating flows we apply the "end parabola" model [5], which is a variation of the Riabouchinsky "end plate" model.

- closure condition at the end of the cavity.

- Kutta condition at the foil trailing edge.

In solving equation (3), the wetted foil and cavity surface are discretized into N ($N \times M$ in 3-D) linear (quadrilateral in 3-D) panels. Initially, a double cosine spacing was employed over the cavity and the fully wetted part of the foil [11]. A new panel arrangement, called the "blended" spacing (see Appendix A for details), is being used in this work. In addition to being more versatile, the present arrangement has been found to improve the rate of convergence of the cavity solution as well as that of the calculated forces.

Over each panel, the source strength (proportional to $\partial\phi/\partial n$) and the dipole strength (proportional to ϕ) are assumed to be constant. The potential jump in the wake, $\Delta\phi_W$, is taken to be equal to the difference of the potentials at the trailing edge panels on the same strip [16]. On each panel representing the fully wetted foil, the source strengths are known and given by equation (6) but the dipole strengths are unknown. On each panel representing the cavity, the dipole strengths are known and given by equations (7) or (9) but the source strengths are unknown. The unknown dipole or source strengths are determined by applying equation (3) on all panels and by inverting the resulting system of linear equations.

In applying the conditions mentioned previously, the surface of the cavity must be known. The procedure for determining the location of the cavity surface is given next:

In two-dimensions

The cavity surface is defined by the location of the cavity detachment point l_D, the location of the cavity end point l (also defined as the cavity length), and the cavity ordinates between these points. As already mentioned in the introduction, the location of the cavity detachment is assumed to be known in the inviscid cavity model. Thus the two-dimensional cavitating hydrofoil analysis can be formulated in terms of the following problems:

- For given l and l_D find the corresponding σ
- For given σ and l_D find l

In both these problems, described in detail in [11] and [13], the cavity shape is determined in an iterative manner. In brief, the cavity surface is updated until the kinematic boundary condition is satisfied on the cavity (in addition to the dynamic condition mentioned earlier):

$$\boldsymbol{q}_c \cdot \boldsymbol{n} = 0 \;; \quad \text{on the cavity} \qquad (10)$$

The first iteration for the cavity shape is taken to be:

- the foil surface under the cavity, for partially cavitating hydrofoils
- the cavity shape from linear theory, for super-cavitating hydrofoils

The iterative process has been found to converge quickly to the final cavity shape [11], [13]. In particular, even the first iteration has been found to produce a cavity shape which is remarkably close to the converged *fully non-linear* cavity shape.

In three-dimensions

The characteristics of the method in three-dimensions may be summarized as follows:

- It only carries the first iteration, thus utilizing the same panelling to that of fully wetted flows.
- It finds the cavity planform for *given* cavitation number and for given cavity detachment in an iterative manner, until the thickness of the cavity at its trailing edge is equal to zero everywhere along the span.
- It includes, in an iterative manner, the cross-flow terms in applying equation (7).
- It is able to handle arbitrary cavity planforms on a *fixed* grid. This became possible with the introduction of the *split panel technique* [13]. This technique enabled us to treat panels which were intersected by the trailing

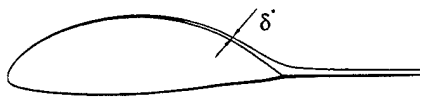


Figure 3: Non-cavitating hydrofoil with its boundary layer displacement thickness.

edge of the cavity as *one*, rather than two parts (i.e. the cavitating and the fully wetted part).

- It utilizes a *unified* formulation and numerical implementation for partial cavitation, supercavitation, as well as mixed partial/supercavitation [6].

3 VISCOUS FULLY-WETTED FLOW MODEL

3.1 Boundary Layer Equations

Consider a non-cavitating 2-D hydrofoil in uniform inflow $\boldsymbol{U}_\infty$, as shown in Figure 3. The viscous flow is assumed to be confined within a thin boundary layer on the foil and wake surface. The effect of viscosity on the inviscid flow is accounted via the "blowing sources", $\hat{\sigma}$, which are defined as:

$$\hat{\sigma} = \frac{d(U_e \delta^*)}{ds} \tag{11}$$

where U_e is the velocity at the "edge" of the boundary layer, δ^* is the displacement thickness and s is the arc-length along the foil or wake surface. For given U_e distribution, the boundary layer parameters are determined from the following equations [20], [17], [4]:

1. The momentum integral equation:

$$\frac{d\theta}{ds} + (2+H)\frac{\theta}{U_e}\frac{dU_e}{ds} = \frac{C_f}{2} \tag{12}$$

where θ is the momentum thickness, $H = \delta^*/\theta$ is the momentum shape factor, and C_f is the friction coefficient. In the wake of the foil the following condition is enforced:

$$C_f = 0 \ ; \quad \text{in the wake} \tag{13}$$

2. The kinetic energy integral equation:

$$\theta\frac{dH^*}{ds} + [2H^{**} + H^*(1-H)]\frac{\theta}{U_e}\frac{dU_e}{ds} = 2C_D - H^*\frac{C_f}{2} \tag{14}$$

3. A third equation which is different for laminar or turbulent flow:

   - for laminar flow:

$$\frac{d\tilde{n}}{ds} = \frac{d\tilde{n}}{dRe_\theta}\frac{dRe_\theta}{ds} \tag{15}$$

   where $\tilde{n}$ is the amplitude of the most amplified Tollmien-Schlichting wave.

   - for turbulent flow:

$$\frac{\delta}{C_\tau}\frac{dC_\tau}{ds} = 5.6\left[C_{\tau_{EQ}}^{1/2} - C_\tau^{1/2}\right] + 2\delta \times \left\{\frac{4}{3\delta^*}\left[\frac{C_f}{2} - \left(\frac{H_k - 1}{6.7H_k}\right)^2\right] - \frac{1}{U_e}\frac{dU_e}{ds}\right\} \tag{16}$$

   where C_τ is the maximum shear stress coefficient.

The variables H^*, H^{**}, C_D, $C_{\tau_{EQ}}$, H_k and Re_θ are defined in [4]. The necessary number of equations which interrelate these variables among themselves as well as with the unknowns are also given in [4].

In laminar flow, equations (12), (14) and (15) are solved with respect to the three unknowns: δ^*, θ and $\tilde{n}$. In turbulent flow, equations (12), (14) and (16) are solved with respect to the unknowns: δ^*, θ and C_τ. The transition from laminar to turbulent flow is defined when $\tilde{n}$ becomes equal to a specified critical value: $\tilde{n}_{crit}$. The option for specifying the transition point on either side of the hydrofoil is also available.

3.2 Viscous/Inviscid Flow Coupling

The presence of the blowing sources will modify Green's formula, equation (3), when applied on the foil surface, as follows [2]:

$$\frac{\phi^v}{2} = \int_S \left[G(-\boldsymbol{U}_\infty \cdot \boldsymbol{n})ds - \phi^v \frac{\partial G}{\partial n}\right] ds - \int_W \Delta\phi_W^v \frac{\partial G}{\partial n} ds + \int_{S\cup W} \hat{\sigma} G ds \tag{17}$$

[2] A discretized version of this equation was first given in [8].

where ϕ^v is the perturbation potential along the foil surface, modified due to viscous effects. Notice that the blowing sources are placed *on* the foil surface. ϕ^v satisfies the following (kinematic) boundary condition on the foil:

$$\frac{\partial \phi^v}{\partial n} = -\boldsymbol{U}_\infty \cdot \boldsymbol{n} + \hat{\sigma} \tag{18}$$

Equation (17) may be written in the following compact form:

$$\mathcal{A}\phi^v = \mathcal{B}\{-\boldsymbol{U}_\infty \cdot \boldsymbol{n}\} + \mathcal{C}\hat{\sigma} \tag{19}$$

where the linear operators $\mathcal{A}$, $\mathcal{B}$ and $\mathcal{C}$ are defined as:

$$\mathcal{A}\{f\} = \frac{f}{2} + \int_S f \frac{\partial G}{\partial n} ds + \int_W \Delta f_W \frac{\partial G}{\partial n} ds \tag{20}$$

$$\mathcal{B}\{f\} = \int_S f G ds \tag{21}$$

$$\mathcal{C}\{g\} = \int_{S \cup W} g G ds \tag{22}$$

with f being a continuous function of the arc-length along the foil surface and g being a continuous function of the arc-length along the foil and wake surface. Δf_W is equal to the jump in f at the foil trailing edge, between the pressure and suction side.

The perturbation potential ϕ^v may be found from inverting equation (19):

$$\phi^v = \mathcal{A}^{-1} \circ \mathcal{B}\{-\boldsymbol{U}_\infty \cdot \boldsymbol{n}\} + \mathcal{A}^{-1} \circ \mathcal{C}\{\hat{\sigma}\} \tag{23}$$

where $\mathcal{A}^{-1}$ is the inverse operator of $\mathcal{A}$. Equation (23) may also be written as:

$$\phi^v = \phi^{inv} + \mathcal{A}^{-1} \circ \mathcal{C}\{\hat{\sigma}\} \tag{24}$$

where ϕ^{inv} is the perturbation potential in inviscid flow, given from:

$$\phi^{inv} = \mathcal{A}^{-1} \circ \mathcal{B}\{-\boldsymbol{U}_\infty \cdot \boldsymbol{n}\} \tag{25}$$

The magnitude of the total velocity at the edge of the boundary layer, U_e, can then be determined from:

$$U_e = \boldsymbol{U}_\infty \cdot \boldsymbol{s} + \frac{\partial \phi^v}{\partial s} = U_e^{inv} + \mathcal{D}\{\hat{\sigma}\} \tag{26}$$

with $\boldsymbol{s}$ being the unit vector tangent to the foil or wake surface. U_e^{inv} is the magnitude of the total velocity on the foil or wake surface in *inviscid* flow:

$$U_e^{inv} = \boldsymbol{U}_\infty \cdot \boldsymbol{s} + \frac{\partial \phi^{inv}}{\partial s} \tag{27}$$

The operator $\mathcal{D}$ is defined as:

$$\mathcal{D} = \left[\frac{d}{ds}\right] \circ \mathcal{A}^{-1} \circ \mathcal{C} \tag{28}$$

Using equation (11), equation (26) may be written as:

$$U_e = U_e^{inv} + \mathcal{D}\left\{\frac{d(U_e \delta^*)}{ds}\right\} \tag{29}$$

or

$$U_e = U_e^{inv} + \mathcal{E}\{U_e \delta^*\} \tag{30}$$

with the operator $\mathcal{E}$ defined as:

$$\mathcal{E} = \mathcal{D} \circ \left[\frac{d}{ds}\right] \tag{31}$$

Equation (30) provides the actual mechanism for coupling the viscous with the inviscid solution. This equation must be solved together with the boundary layer equations (12), (14) and (15) or (16). The boundary layer equations are solved first, with $U_e = U_e^{inv}$, and the δ^* distribution on the foil and its wake is determined. Equation (30) is then solved with respect to U_e. The updated U_e is then used in solving the boundary layer equations once more. This process is repeated until convergence of the solution.

In solving the previously mentioned equations, the foil and its wake are discretized with N and N_W linear panels, respectively. The boundary layer variables δ^*, θ, C_τ (or $\tilde{n}$), and the edge velocity U_e are defined at the edges of each panel. Green's formula, equation (17), is discretized by assuming constant source and dipole distributions over each panel [9, 14]. The blowing source, $\hat{\sigma}$, on each panel is also assumed to be constant with its value given from [8]:

$$\hat{\sigma} = \frac{\Delta m}{\Delta s} \tag{32}$$

with m defined as the mass defect: $m = U_e \delta^*$. Δm is the difference between the m's at the edge of the panel and Δs is the arc-length of the foil between the edges of the panel.

The operators $\mathcal{A}$, $\mathcal{B}$ and $\mathcal{C}$ are discretized into the influence coefficient matrices with dimensions $N \times N$, $N \times N$ and $N \times N + N_W$, respectively [8]. The operator $[d/ds]$ is discretized into $[\Delta/\Delta s]$.



Figure 4: Partially cavitating hydrofoil with its boundary layer displacement thickness.

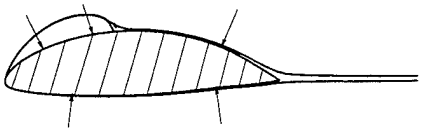


Figure 5: Hydrofoil and cavity surface on which inviscid and boundary layer flow equations are applied - "Thin" cavity approach.

4 VISCOUS CAVITY MODEL

4.1 Partially Cavitating Hydrofoil

Consider now a partially cavitating hydrofoil in viscous flow, as shown in Figure 4. The viscous flow in the vicinity of the cavity is assumed to be confined to a thin boundary layer. The-two phase flow in the vicinity of the cavity is ignored, and the fluid/vapor interface is treated as a constant pressure free-streamline. We present two approaches of formulating the viscous cavity model.

"Thin" cavity approach

In this case both the cavity and the boundary layer thickness are assumed to be "small". The panels representing the cavity are assumed to be located on the foil surface underneath the cavity, as shown in Figure 5. This is implemented in [19] by defining the cavity sources $\hat{\sigma}^c$ as follows:

$$\hat{\sigma}^c = \frac{d(U_e h)}{ds} \tag{33}$$

with h being the cavity thickness, defined normal to the foil surface. Notice the similarity of equation (33) with equation (11). The effects of cavity thickness are thus readily incorporated into equation (30) as follows:

$$U_e = U_e^{inv} + \mathcal{E}\{U_e\delta^* + U_e h\} \tag{34}$$

In other words, equation (34) makes no distinction between the cavity and the displacement thickness.

The dynamic boundary condition, equation (7), is implemented by requiring:

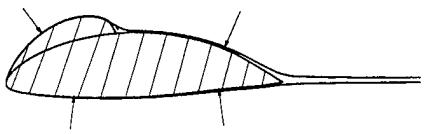


Figure 6: Hydrofoil and cavity surface on which inviscid and boundary layer flow equations are applied - Non-linear cavity approach.

$$U_e = U_\infty\sqrt{1+\sigma}\ ;\ \text{ on the cavity} \tag{35}$$

The boundary layer equations are now solved together with equations (34) and (35). It is assumed that *no* frictional forces can be sustained at the interface between the fluid and the vapor, i.e:

$$C_f = 0\ ;\ \text{ on the cavity} \tag{36}$$

A cavity termination model, similar to that described in Section 1, is applied. Cavity closure ($h = 0$) is imposed at the cavity trailing edge. An iterative algorithm (based on Newton-Raphson method) for solving the boundary layer and the cavity equations, is given in [19].

Non-linear cavity approach

In this case the cavity thickness is not assumed to be "small" compared to the foil thickness. The boundary layer displacement thickness though, is still assumed to be "small". The boundary conditions are now applied on the "non-linear" cavity and foil surface, shown in Figure 6. The "non-linear" cavity shape has resulted from the inviscid non-linear cavity theory, described in Section 2. The boundary layer equations now are integrated along the non-linear cavity and foil surface.

Equation (30) will now be modified to:

$$U_e^{NL} = U_e^{inv,NL} + \mathcal{E}^{NL}\{U_e^{NL}\delta^*\} \tag{37}$$

where the superscript NL corresponds to the "compound" foil, defined from the union of the original foil and the non-linear cavity surface. The velocity on the cavity will be given as:

$$U_e^{inv,NL} = U_\infty\sqrt{1+\sigma^{inv}} \tag{38}$$

where σ^{inv} is the cavitation number resulting from non-linear inviscid cavity theory, for given l_D and l.

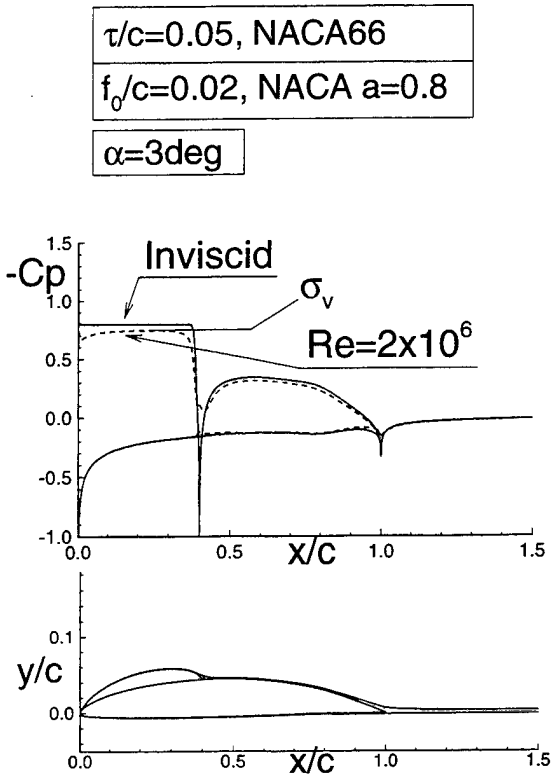


Figure 7: Pressure distribution on foil and cavity resulting from inviscid and viscous solution. The cavity resulting from inviscid *non-linear* model and the corresponding boundary layer displacement thickness are also shown. Definition of "viscous" cavitation number, σ_v.

Applying the boundary layer equations on the compound foil, with $C_f = 0$ on the cavity, will result in the displacement thickness and pressure[3] distributions, shown in Figure 7[4]. It may be seen on this figure that the assumption of "small" displacement thickness is still valid. Notice that the "viscous" $-C_p$ distribution on the cavity is lower than the inviscid (for which $-C_p = \sigma^{inv}$). Also notice that the viscous solution has perturbed "somewhat" the dynamic boundary condition, which requires the pressure distribution to be constant on the cavity. We define the cavitation number in the presence of viscosity (for l_D and l fixed) from:

$$\sigma^v = max[-C_p^v] \tag{39}$$

where C_p^v is the pressure coefficient in the presence of viscosity. This definition is also shown in Figure 7.

Even though the viscous pressure distribution shown in Figure 7 is "nearly" constant, it is still desired to "estimate" the error in cavitation number and cavity shape by ignoring the variation in pressure along the cavity. This is accomplished as follows:

If ϕ^{cor} is the "correct" perturbation potential which satisfies the "exact" dynamic boundary condition in viscous flow, equation (8), on the cavity, then :

$$\frac{\partial \phi^{cor}}{\partial s} + \boldsymbol{U}_\infty \cdot \boldsymbol{s}^{NL} = U_\infty \sqrt{1+\sigma^{cor}} \tag{40}$$

where the superscript "*cor*" corresponds to the "correct" solution, defined in the previous paragraph.

On the wetted foil, the following condition will be satisfied:

$$\frac{\partial \phi^{cor}}{\partial n} = -\boldsymbol{U}_\infty \cdot \boldsymbol{n} + \hat{\sigma}^{NL} \tag{41}$$

Equations (40) and (41) take the same form as equations (8) and (6) by adding the blowing source $\hat{\sigma}^{NL}$ to $-\boldsymbol{U}_\infty \cdot \boldsymbol{n}$. We thus treat the "correction" problem as a cavity problem (applied on the compound foil)[5] and determine ϕ^{cor} and σ^{cor}. The new value of $\partial\phi^{cor}/\partial n$ on the cavity is also determined. The cavity shape then needs to be corrected by h^{cor}, defined normal to the original cavity shape. If $\boldsymbol{n}^{cor}$ is the unit vector normal to the correct cavity shape, the following kinematic boundary condition must be satisfied:

$$[\boldsymbol{\nabla}\phi^{cor} + \boldsymbol{U}_\infty] \cdot \boldsymbol{n}^{cor} = \hat{\sigma}^{NL} \; ; \text{ on the cavity} \tag{42}$$

The normal vector, to first order in h^{cor}, will be given from [11]:

$$\boldsymbol{n}^{cor} = \boldsymbol{n}^{NL} - \frac{dh^{cor}}{ds}\boldsymbol{s}^{NL} \tag{43}$$

Combining equations (42) and (43) gives the following differential equation for h^{cor}:

$$U_\infty \sqrt{1+\sigma^{cor}}[1-f(x)]\frac{dh^{cor}}{ds} = \frac{\partial \phi^{cor}}{\partial n} + \boldsymbol{U}_\infty \cdot \boldsymbol{n}^{NL} - \hat{\sigma}^{NL} \tag{44}$$

[3] The pressure coefficient C_p is defined as: $C_p = 2(p - p_\infty)/(\rho U_\infty^2)$.

[4] The Reynolds number R_e is defined as: $R_e = \frac{U_\infty c}{\nu}$

[5] The effect of the blowing sources in the wake needs also to be included in the right-hand side of the resulting equations.

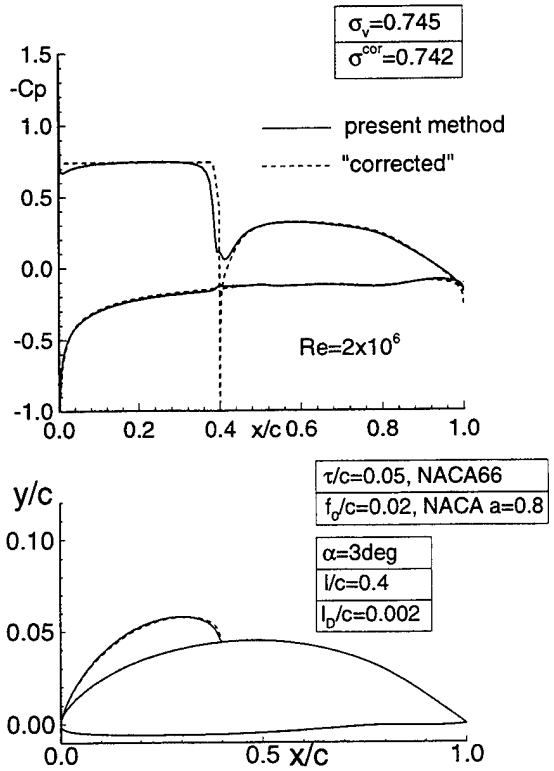


Figure 8: Non-linear cavity shape resulting from present method and "corrected" to satisfy the "exact" dynamic boundary condition. The corresponding pressure distributions are also shown.

Integrating equation (44) we find h^{cor} and the "correct" cavity shape given on Figure 8. The "correct" cavity pressure distribution is also given. Comparing the "correct" to the original cavity shape and cavitation number, we notice that the error is relatively small. This correction will be omitted from all subsequent results.

Cavity shapes, predicted by the present "non-linear" and the "thin" cavity formulation, for given cavitation number, are shown in Figures 9 and 10. As expected the results from the two methods are close to each other for cavities which are indeed thin when compared to the foil thickness. For cavities whose thickness is of the same order as the foil thickness, the "thin" cavity method overpredicts the cavity shape extent and size appreciably, as shown in Figure 10.

Cavity detachment

It is well known that the location of the cavity detachment point may affect (sometimes substantially) the predicted cavity extent and volume. Detaching the cavity at the leading edge of a round nose hydrofoil may often lead to non-

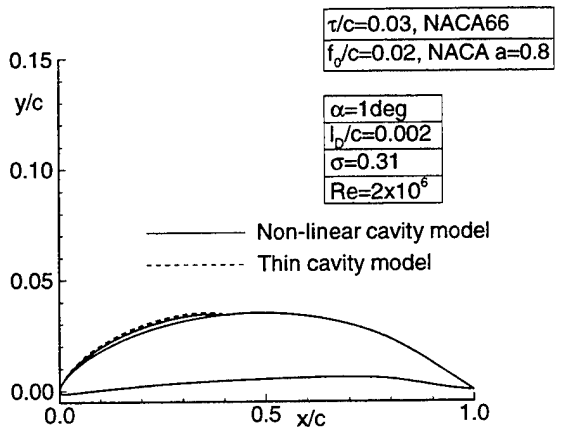


Figure 9: Cavity shapes predicted from thin and non-linear (present) cavity viscous models, for given cavitation number. Foil geometry and flow conditions produce a thin cavity in comparison to the foil thickness.

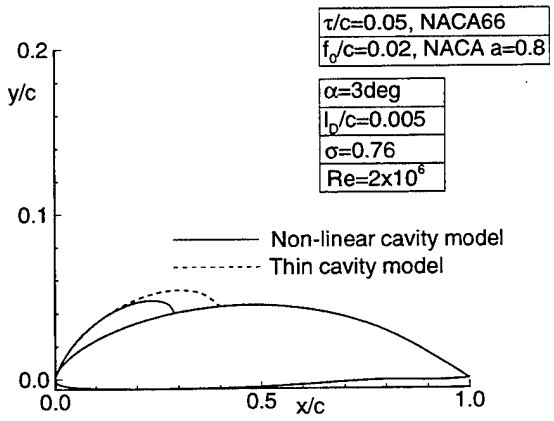


Figure 10: Cavity shapes predicted from thin and non-linear (present) cavity viscous models, for given cavitation number. Foil geometry and flow conditions produce a cavity with thickness which is comparable to the foil thickness.

physical solutions, i.e. cavities which intersect the foil. One such case is shown in Figure 11. The *smooth detachment* condition [6][18, 3] requires the slope and the curvature of the cavity at detachment to be equal to that of the foil. This condition ensures that the cavity does not intersect the foil at the leading edge and, at the same time, that the pressures on the wetted foil, upstream of the cavity, are *larger* than the cavity pressure. This condition is equivalent to requiring the slope of the pressure distribution with respect to the foil arc-length at the cavity leading edge to be equal to zero [2, 10]. Such a case is shown in Figure 12. The smooth detachment point (SDP) in this case was determined by applying the inviscid cavity model and by varying l_D until the resulting pressure distribution had a zero slope at the leading edge of the cavity. Detaching the cavity upstream of the SDP will produce a cavity which intersects the foil. Detaching the cavity downstream of the SDP will produce pressures upstream of the cavity which are smaller than cavity pressure. However, it is widely known that in reality the cavity detachment is well downstream of the SDP. In addition, pressures *smaller* than the cavity pressure have been measured on the wetted flow upstream of the cavity detachment. A semi-empirical cavity detachment criterion for cavitating headforms was introduced by Arakeri [1]. This criterion was later extended by Franc & Michel [7] in the case of cavitating hydrofoils. In brief, they found that for hydrofoils, the cavity detachment occurs immediately downstream of a laminar separation point (LSP). Laminar separation occurs when $H = \delta^*/\theta = 4$ [20]. We thus apply the present viscous method for different detachment points until the boundary layer calculation shows laminar separation just ahead of the cavity leading edge. The pressure distribution for cavity detachment at laminar separation is shown on Figure 13. Finally, the effect of the cavity detachment point on the solution is shown on Figures 14 and 15. The importance of having the "right" cavity detachment point on the cavity prediction is apparent from these figures.

Sensitivity of cavity model on λ, N

The numerics of the inviscid cavity model have been validated extensively in [11] and [13]. The numerics of the viscous fully wetted model have been validated in [8]. In this work, the sensitivity of the results from applying the present combined inviscid/viscous cavity flow model is

[6] Also called the Villat-Brillouin condition.

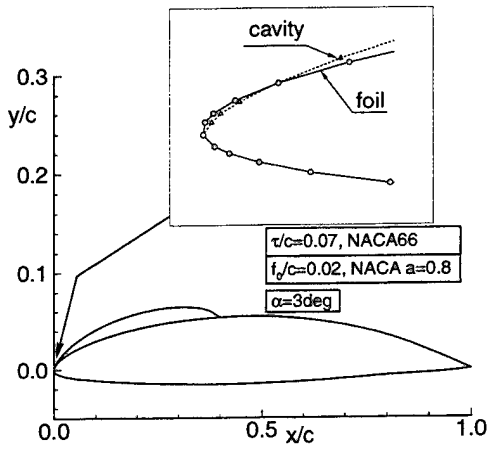


Figure 11: Cavity and foil surface at the leading edge. Cavity detachment at the LE.

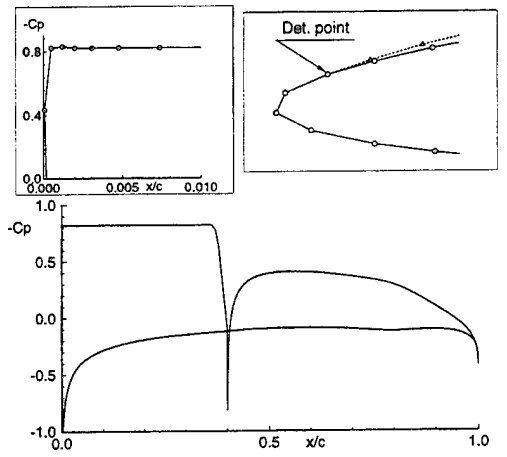


Figure 12: Pressure distribution on the foil and cavity. Smooth cavity detachment ($l_D = 0.0012$).

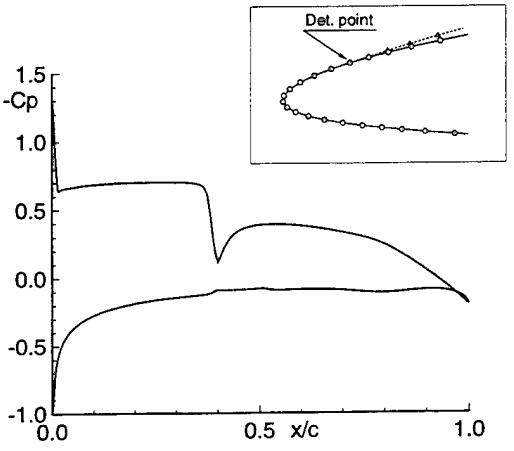


Figure 13: Pressure distribution on the foil and cavity. Cavity detachment set at laminar separation point ($l_D = 0.01$).

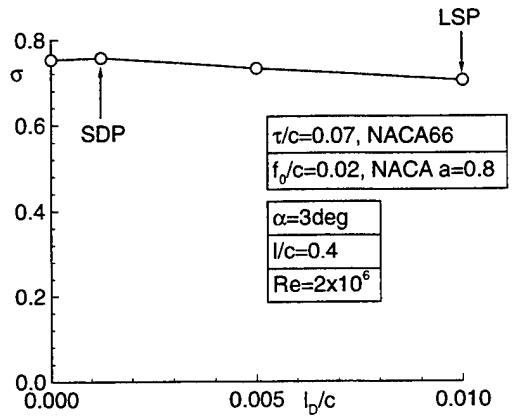


Figure 14: Effect of cavity detachment point on cavitation number.

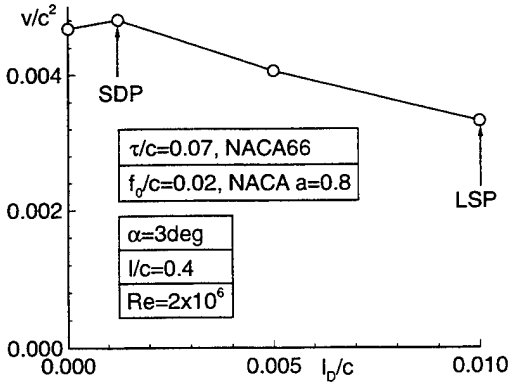


Figure 15: Effect of cavity detachment point on cavity volume.

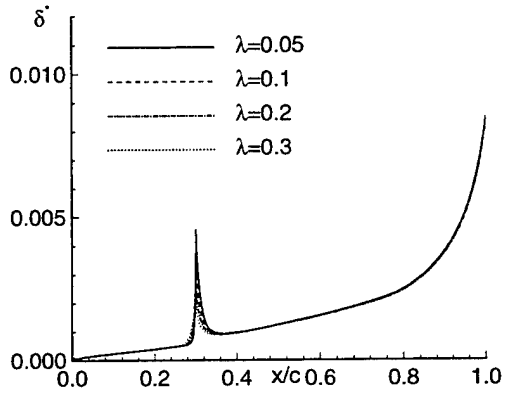


Figure 16: Effect of λ on boundary layer displacement thickness distribution.

studied. In Figure 16, the effect of the length of the cavity termination model λ on the predicted δ^* distribution on the suction side of the foil and cavity is shown. Notice that the predicted δ^* is practically the same everywhere on the cavity and foil, except in the vicinity of the cavity trailing edge. The effect of λ on the predicted solution is also shown on Table 1. It is again evident from this table that the results are practically independent of λ. This is a very fortunate characteristic of our method, since otherwise we would have to somehow determine λ from theory and/or experiment.

Finally, the convergence of the viscous cavity solution with number of panels N is given on Table 2.

Results

Results from applying the present method on partially cavitating hydrofoils are presented in this section. The hydrofoils consist of combinations of modified $NACA66$ thickness form and $NACA$ $a = 0.8$ camber form. The viscous calculations are performed for $Re = 2 \times 10^6$ and $Re = 2 \times 10^7$ which are representative Reynolds numbers for model and full-scale marine propeller applications, respectively. Figures 17 and 18 show the cavity length and volume versus cavity cavitation number, in inviscid and viscous flow. Notice that the cavity extent and size decrease substantially with decreasing Re. The cavity shapes for $\sigma = 1$ are shown in Figure 19. Notice the reduction in the lift coefficient, C_L, with decreasing Re. This reduction reflects the change in the pressure distribution, shown in Figure 7.

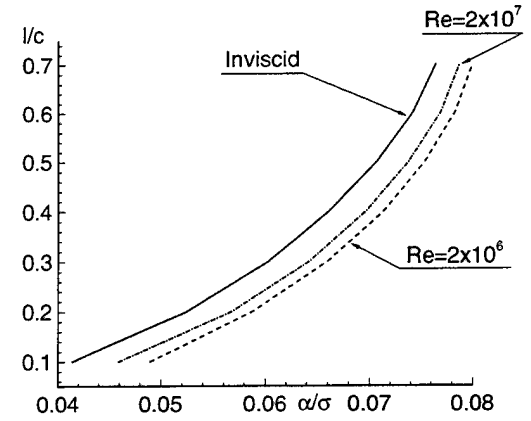


Figure 17: Cavity length versus cavitation number. Predicted by the inviscid and the present viscous method for two Reynolds numbers; $\tau/c = 0.04$, $f_o/c = 0.02$, $\alpha = 4°$.

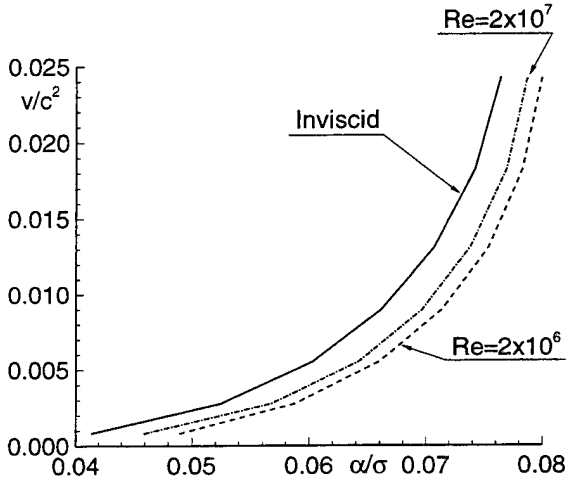


Figure 18: Cavity volume versus cavitation number. Predicted by the inviscid and the present viscous method for two Reynolds numbers; $\tau/c = 0.04$, $f_o/c = 0.02$, $\alpha = 4°$.

λ	σ	V/c²	C_L	C_D
0.05	0.754	0.00247	0.558	0.0119
0.1	0.755	0.00244	0.560	0.0119
0.2	0.758	0.00238	0.561	0.0118
0.3	0.761	0.00231	0.561	0.0118

Table 1: Effect of λ on viscous cavity solution: σ, V/c^2, C_L and C_D; $l/c = 0.3$, $NACA66(\tau/c = 0.07)$, $NACAa = 0.8(f/c = 0.02)$, $\alpha = 3°$, $Re = 2 \times 10^6$, $N = 200$

N	σ	V/c²	C_L	C_D
100	0.776	0.00250	0.566	0.0113
150	0.767	0.00245	0.564	0.0118
200	0.755	0.00244	0.560	0.0119

Table 2: Convergence of viscous cavity solution (σ, V/c^2, C_L and C_D) with number of panels. Partially cavitating hydrofoil; same foil geometry as in Table 1.

Another way of showing the effect of Re on cavity extent and size is by keeping the cavitation number as well as the lift coefficient constant. In this way, a direct comparison of the predicted cavity length and volume in inviscid or viscous flow for given flow conditions (σ) and design requirements (lift coefficient, C_L, or thrust coefficient in the case of propellers) can be made. In Figures 20, 21, 22 and, 23, contour plots of constant σ and C_L are drawn on the l/c vs. α and V/c^2 vs. α space. In this manner, someone can look at the crossings of the same values of σ and C_L for different Re.

The corresponding cavity lengths and volumes as well as the angle of attack (required to produce the same lift) can be found and compared for different Re. From these contour plots, it may be seen that the cavity volume and length *decrease* with decreasing Re for fixed σ and C_L. This is the reverse trend from that shown in Figures 17 and 18 where the cavity volume and length *increase* with decreasing Re for fixed σ and α. The predicted cavity shapes with fixed σ and C_L and for different Re are shown in Figure 24.

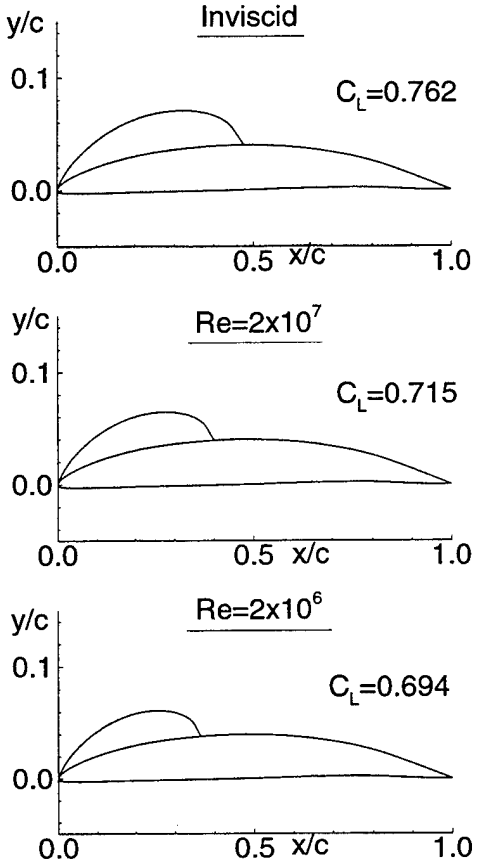


Figure 19: Cavity shapes predicted by the inviscid and the present viscous method for two Reynolds numbers. All hydrofoil sections are at $\alpha = 4^o$ and $\sigma = 1.0$. The corresponding lift coefficients are shown next to each foil; $\tau/c = 0.04$, $f_o/c = 0.02$.

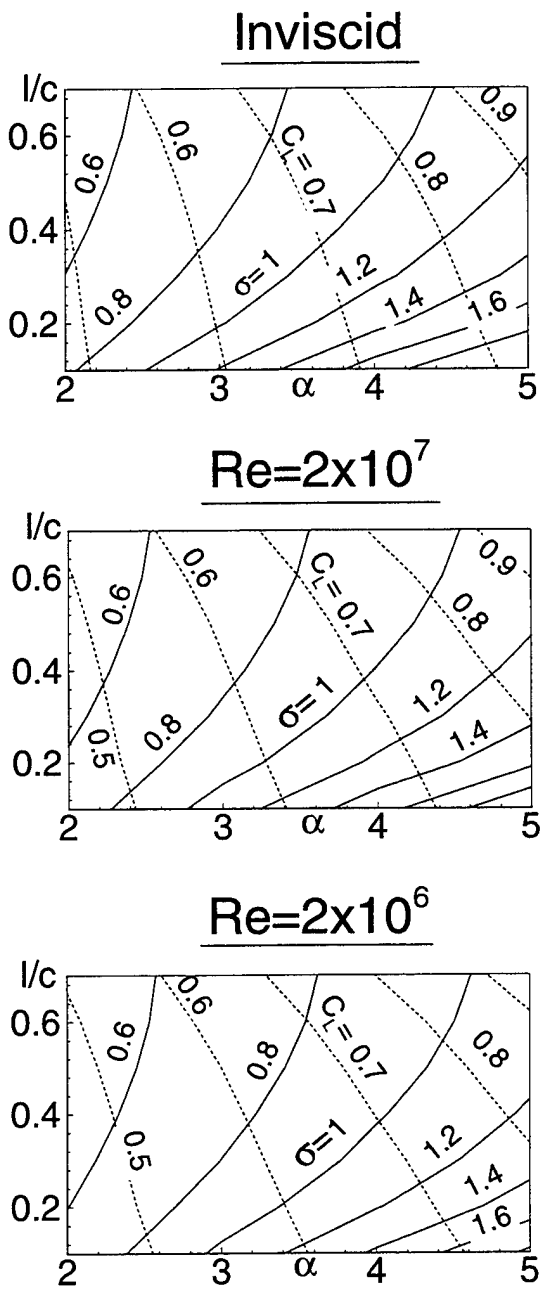


Figure 20: Contour plots of constant lift coefficient and cavitation number versus cavity length and angle of attack. Predicted by the present method for inviscid flow (top), $Re = 2 \times 10^7$ (middle) and $Re = 2 \times 10^6$ (bottom); $NACA66(\tau/c = 0.04)$, $NACA\ a = 0.8(f_o/c = 0.02)$.

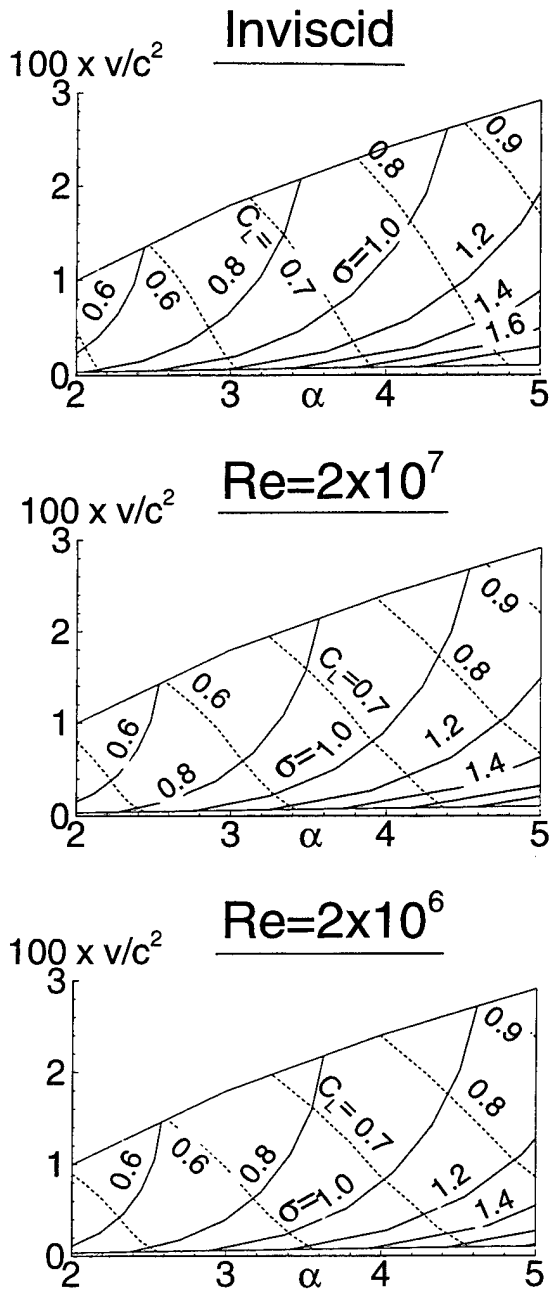


Figure 21: Contour plots of constant lift coefficient and cavitation number versus cavity volume and angle of attack. Predicted by the present method for inviscid flow (top), $Re = 2 \times 10^7$ (middle) and $Re = 2 \times 10^6$ (bottom); $NACA66(\tau/c = 0.04)$, $NACA\ a = 0.8(f_o/c = 0.02)$.

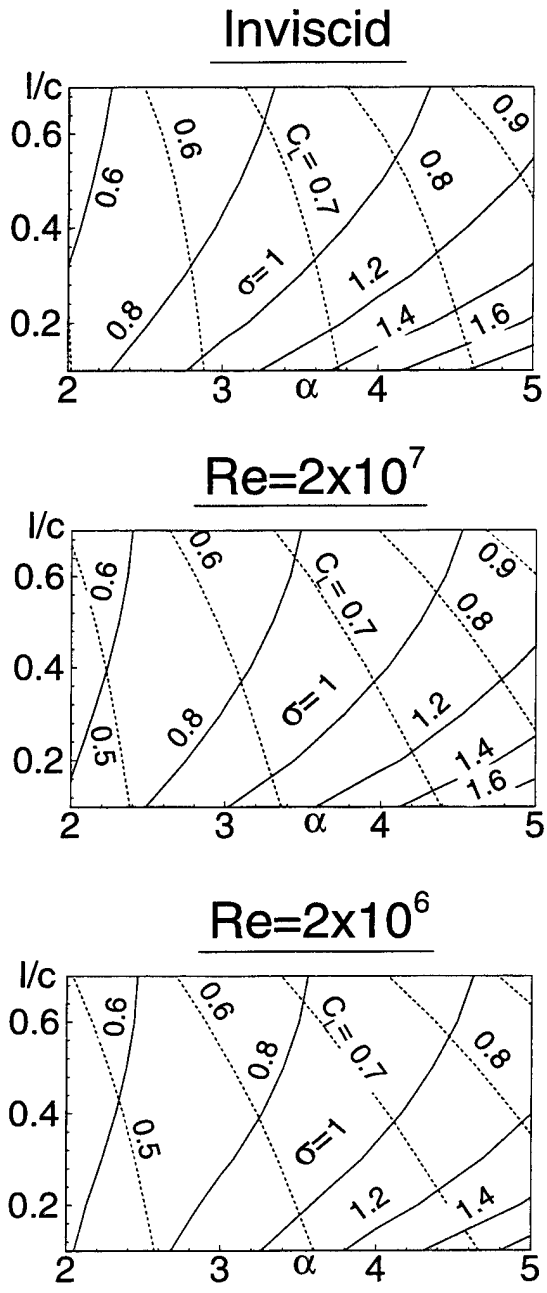


Figure 22: Contour plots of constant lift coefficient and cavitation number versus cavity length and angle of attack. Predicted by the present method for inviscid flow (top), $Re = 2 \times 10^7$ (middle) and $Re = 2 \times 10^6$ (bottom); $NACA66(\tau/c = 0.07)$, $NACA\ a = 0.8(f_o/c = 0.02)$.

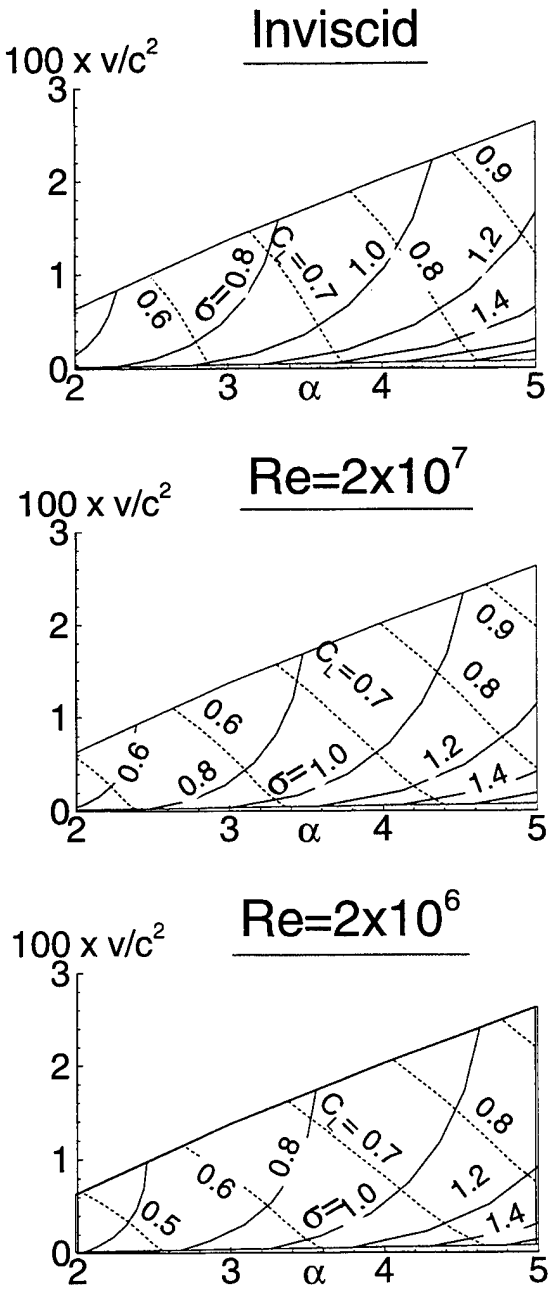


Figure 23: Contour plots of constant lift coefficient and cavitation number versus cavity volume and angle of attack. Predicted by the present method for inviscid flow (top), $Re = 2 \times 10^7$ (middle) and $Re = 2 \times 10^6$ (bottom); $NACA66(\tau/c = 0.07)$, $NACA\ a = 0.8(f_o/c = 0.02)$.

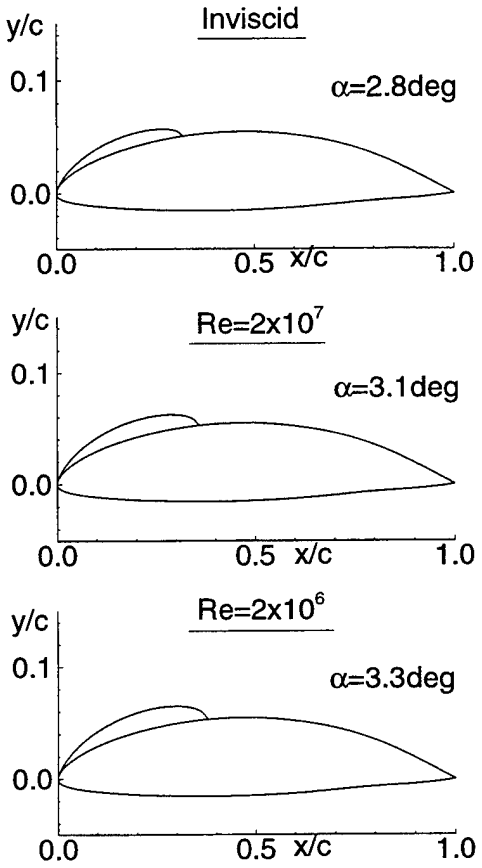


Figure 24: Cavity shapes predicted by the inviscid and the present viscous method for two Reynolds numbers. All hydrofoil sections are at $C_L = 0.6$ and $\sigma = 0.8$. The corresponding angles of attack are shown next to each foil. $NACA66(\tau/c = 0.07)$, $NACA\ a = 0.8(f_o/c = 0.02)$.

4.2 Super-Cavitating Hydrofoil

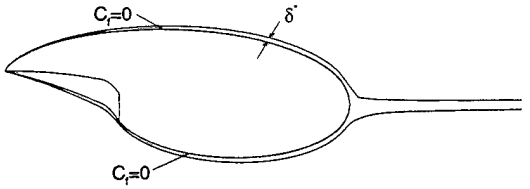


Figure 25: Super-cavitating hydrofoil with its boundary displacement thickness.

Consider a super-cavitating hydrofoil in viscous flow, as shown in Figure 25. In a similar manner, as in the case of partial cavitation, we first solve the inviscid cavity flow in non-linear theory [11]. We then apply the boundary layer equations on the compound foil, confined by the pressure side of the hydrofoil and the cavity boundary. A zero friction condition is applied everywhere on the cavity, as shown in Figure 25.

Results from applying this method are shown in Figure 26. The resulting boundary layer displacement thickness is shown at the top of the figure. The pressure distributions in inviscid and viscous flow are also shown. Notice that viscosity has a very small effect on the pressure distribution. The reader is reminded that this was not the case for partial cavitation, as may be seen in Figure 7. In other words, for super-cavitation, the cavitation number in viscous flow for given cavity length, l, is practically identical to that in inviscid flow. The friction coefficient, C_f, on the pressure side of the foil and cavity, is also shown at the bottom part of Figure 26.

The lift and drag on the hydrofoil are evaluated by integrating the pressure forces acting on all sides of the hydrofoil (the constant cavity pressure is applied on the cavitating sides of the hydrofoil) as well as the frictional forces acting on the wetted side of the hydrofoil. The convergence of the cavity solution and the predicted forces with number of panels is given on Table 3.

Finally the predicted σ, C_L, and C_D vs. l curves are shown in Figures 27 and 28, for a super-cavitating section at two angles of attack in inviscid flow and for two Reynolds numbers[7]. The super-cavitating section is a combination of a NACA 4digit camber form (with the maximum

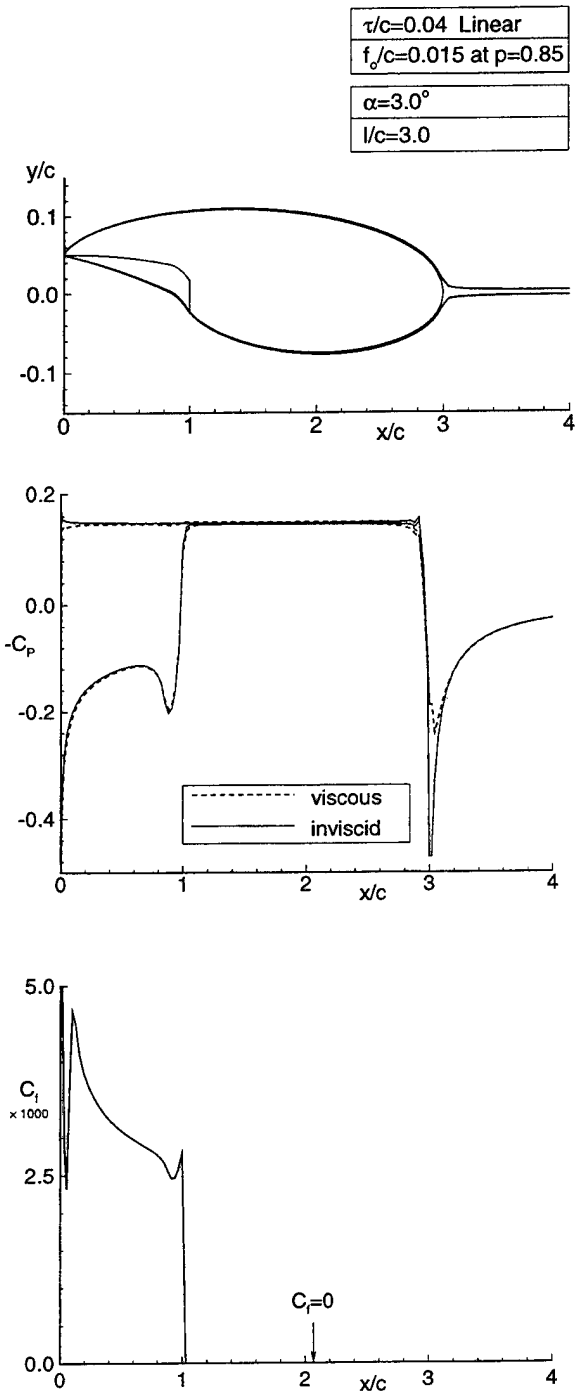


Figure 26: Super-cavitating hydrofoil in inviscid and viscous flow at $Re = 2 \times 10^7$. Cavity shape and boundary layer displacement thickness (top); pressure distributions (middle); and friction coefficient on the pressure side of the foil and cavity (bottom). All predicted by the present method.

[7]Based on l.

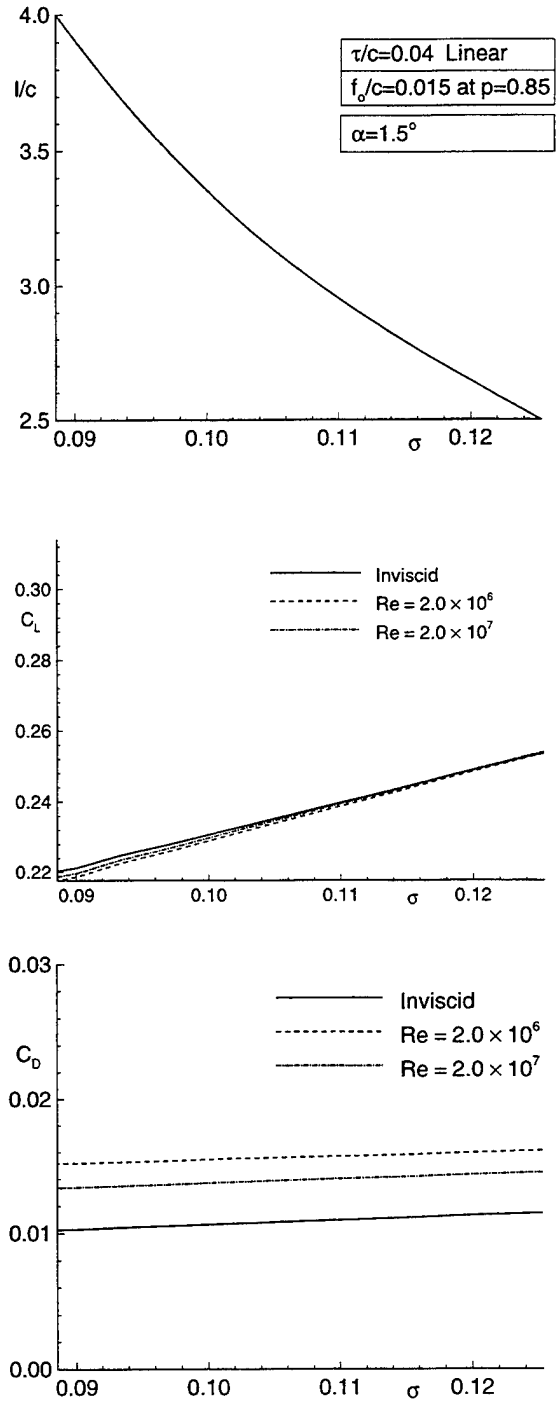


Figure 27: Cavity length, lift and drag coefficient versus cavitation number for a super-cavitating hydrofoil at $\alpha = 1.5°$, in inviscid and viscous flow; predicted by the present method.

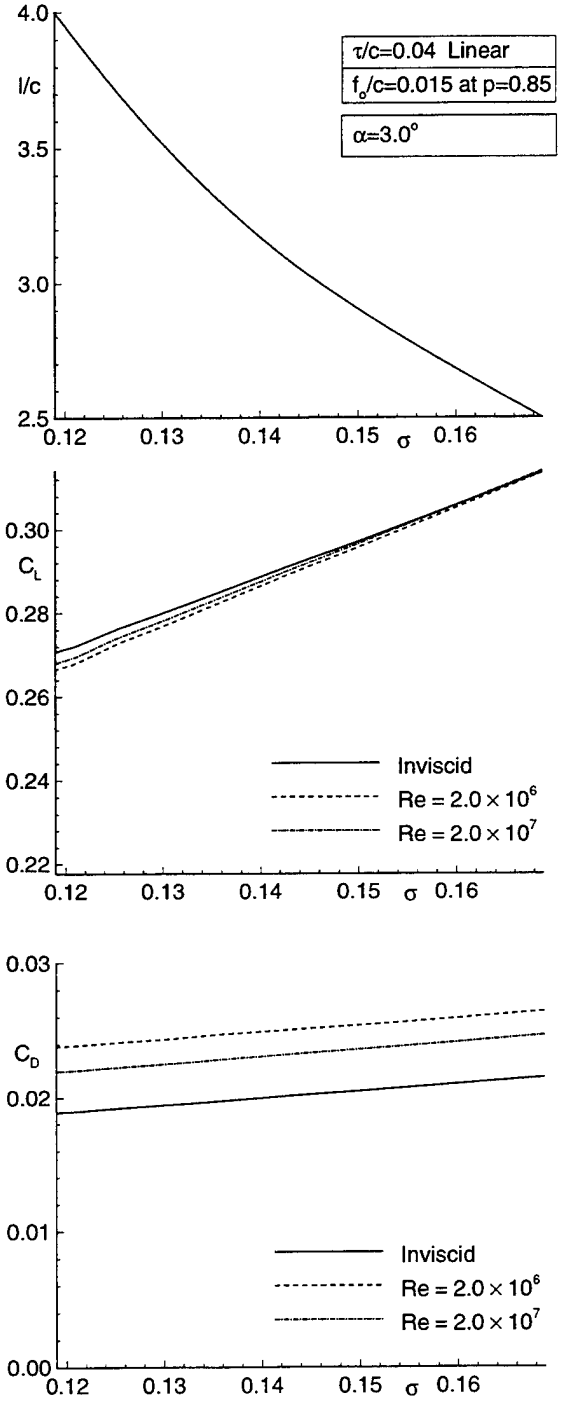


Figure 28: Cavity length, lift and drag coefficient versus cavitation number for a super-cavitating hydrofoil at $\alpha = 3°$, in inviscid and viscous flow; predicted by the present method.

N	σ	V/c^2	C_L	C_D
100	0.145	0.365	0.282	0.0219
160	0.146	0.364	0.287	0.0223
200	0.146	0.363	0.292	0.0231

Table 3: Convergence of viscous cavity solution (σ, V/c^2, C_L and C_D) with number of panels. Super-cavitating hydrofoil; $\tau/c = 0.045$, $f_o/c = 0.015$, $p = 0.85$, $\alpha = 3^o$.

camber f_o at $x = p$) and a linear thickness form. The effect of viscosity on lift coefficient is shown to be very small.

4.3 The "equivalent" σ

As already mentioned in Section 4.1, during the design of a hydrofoil or propeller the cavitation number and the lift (thrust) requirements must remain fixed. However, as was shown in Figures 20 to 23, inviscid theory would underpredict the extent and size of cavities. By using these figures, someone can find the "equivalent" σ in inviscid theory, which for the same lift coefficient would produce the same cavity volume (or length) as viscous theory for the given C_L and the original value of σ.

The equivalent σ, in the case of finite span hydrofoils or propellers, may be estimated by applying the 2-D theory on the local section geometry and lift coefficient at which the maximum extent of cavitation appears.

5 CONCLUSIONS

The viscous flow around cavitating hydrofoils was addressed by coupling an inviscid non-linear cavity model with a boundary layer solver. The cavity detachment point is set where laminar separation occurs just upstream of the cavity. In the case of partial cavitation, it was found that inviscid cavity theory: (a) overpredicts the cavity extent and volume for fixed cavitation number and angle of attack and, (b) underpredicts the cavity extent and volume for fixed cavitation number and lift coefficient. In the case of super-cavitation, the effect of viscosity on the predicted cavitation number for given cavity extent, was found to be negligible. The *equivalent* cavitation number was introduced as a way of including the effects of viscosity in the case of cavitating flows in three dimensions.

Future efforts will include: (a) *systematic* validation of the results of the present method with experiments and, (b) direct application of the method in three dimensions.

6 ACKNOWLEDGEMENTS

Support for this research was provided by the Applied Hydromechanics Research program administered by the Office of Naval Research and by an MIT/ Navy/ Industry Consortium on High Speed Propulsors with the following members: DTMB, OMC, Mercury, Volvo-Penta, IHI, Daewoo, El Pardo MB, HSVA, KaMeWa, Propellum, Rolla, Sulzer-Escher Wyss, Hyundai and Wartsila.

References

[1] H. Arakeri. Viscous effects on the position of cavitation separation from smooth bodies. *Journal of Fluid Mechanics*, vol 68(No. 4):pp 779–799, 1975.

[2] A.H. Armstrong. Abrupt and smooth separation in plane and axisymmetric flow. Technical Report No. 22/53, Mem. Arm. Res. Est., G.B., 1953.

[3] M. Brillouin. Les surfaces de glissement de Helmholtz et la resistance des fluides. *Ann. Chim. Phys.*, vol. 23:pp. 145–230, 1911.

[4] M. Drela. XFOIL: An analysis and design system for low Reynolds number airfoils. In *Lecture Notes in Engineering (Volume 54, Low Reynolds Number Aerodynamics)*, New York, 1989. Springer-Verlag.

[5] N. E. Fine. *Nonlinear Analysis of Cavitating Propellers in Nonuniform Flow.* PhD thesis, Department of Ocean Engineering, MIT, October, 1992.

[6] N.E. Fine and S.A. Kinnas. A boundary element method for the analysis of the flow around 3-d cavitating hydrofoils. *Journal of Ship Research*, 37:213–224, September 1993.

[7] J.P. Franc and J.M. Michel. Attached cavitation and the boundary layer: Experimental investigation and numerical treatment. *Journal of Fluid Mechanics*, vol. 154:pp 63–90, 1985.

[8] G.S. Hufford, M. Drela, and J.E. Kerwin. Viscous flow around marine propellers using boundary-layer strip theory. *Journal of Ship Research*, 38(1):pp. 52–62, March 1994.

[9] J.E. Kerwin, S.A. Kinnas, J-T Lee, and W-Z Shih. A surface panel method for the hydrodynamic analysis of ducted propellers. *Trans. SNAME*, 95, 1987.

[10] S.A. Kinnas and N.E. Fine. Analysis of the flow around supercavitating hydrofoils with midchord and face cavity detachment. *Journal of Ship Research*, 35(3):pp. 198–209, September 1991.

[11] S.A. Kinnas and N.E. Fine. Non-Linear Analysis of the Flow Around Partially or Super-Cavitating Hydrofoils by a Potential Based Panel Method. In *Boundary Integral Methods-Theory and Applications, Proceedings of the IABEM-90 Symposium, Rome, Italy, October 15-19, 1990*, pages 289–300, Heidelberg, 1991. Springer-Verlag.

[12] S.A. Kinnas and N.E. Fine. A nonlinear boundary element method for the analysis of unsteady propeller sheet cavitation. In *Proceedings of the Nineteenth Symposium on Naval Hydrodynamics*, Seoul, Korea, August 1992.

[13] S.A. Kinnas and N.E. Fine. A numerical nonlinear analysis of the flow around two- and three-dimensional partially cavitating hydrofoils. *Journal of Fluid Mechanics*, 254:151–181, September 1993.

[14] Jin-Tae Lee. *A Potential Based Panel Method for The Analysis of Marine Propellers in Steady Flow*. PhD thesis, M.I.T., Department of Ocean Engineering, August 1987.

[15] H. Lemonnier and A. Rowe. Another approach in modelling cavitating flows. *Journal of Fluid Mechanics*, vol 195, 1988.

[16] Luigi Morino and Ching-Chiang Kuo. Subsonic Potential Aerodynamic for Complex Configurations : A General Theory. *AIAA Journal*, vol 12(no 2):pp 191–197, February 1974.

[17] H. Schlichting. *Boundary-Layer Theory*. McGraw-Hill, Inc., 1979.

[18] H. Villat. Sur la validité des solutions de certain problem d' hydrodynamique. *J. de Math.*, vol 6(No. 10):pp 231–290, 1914.

[19] R.A. Villeneuve. Effects of viscosity on hydrofoil cavitation. Master's thesis, Massachusetts Institute of Technology, May 1993.

[20] F.M. White. *Viscous Fluid Flow*. McGraw-Hill, Inc., 1974.

A The Blended Spacing

When employing the inviscid cavity model, already described in Section 2, a panel arrangement is desired in which: (a) the number of panels at the foil and cavity leading edge is *independent* of the total number of panels; (b) the cavity detachment point and the cavity end are panel boundaries and (c) there is smooth transition of the panel size in the vicinity of the cavity start and end. Originally [11], two cosine spacings were used between the foil leading edge and the cavity end and between the cavity end and the foil trailing edge. This arrangement (called double cosine spacing) though, does not satisfy *all* of the desired requirements. In the process of introducing a new spacing the following problem must be addressed first:
Define a sequence of N intervals, Δx_i; $i = 1, ..., N$, between $x = a$ and $x = b > a$ which "blends nicely" to given intervals at the two ends (Δx_1 and Δx_N). To accomplish this we first make the following definitions:

$$\overline{\Delta x} = \frac{b-a}{N} \tag{45}$$

$$f(i;N) = \frac{\Delta x_i}{\overline{\Delta x}} \tag{46}$$

$$A = \frac{\Delta x_1}{\overline{\Delta x}} \tag{47}$$

$$B = \frac{\Delta x_N}{\overline{\Delta x}} \tag{48}$$

The progression $f(i;N)$ must then satisfy the conditions:

$$f(1;N) = A \tag{49}$$

$$f(N;N) = B \tag{50}$$

$$\Sigma_1^N f(i;N) = N \tag{51}$$

We define the following progressions, both of which automatically satisfy conditions (49) and (50):

$$f(i;N) = A\frac{N-i}{N-1} + B\frac{i-1}{N-1} + K_1\frac{(N-i)(i-1)}{(N-1)^2} \tag{52}$$

$$f(i;N) = A\left(\frac{N-i}{N-1}\right)^2 + B\left(\frac{i-1}{N-1}\right)^2 + K_2\frac{(N-i)^2(i-1)^2}{(N-1)^4} \tag{53}$$

The coefficients K_1 and K_2 are then determined from satisfying condition (51). It can be shown, after lengthy algebra, that:

$$K_1 = \frac{6(N-1)}{(N-2)}\left[1 - \frac{A+B}{2}\right], \tag{54}$$

and:

$$K_2 = \frac{30(N-1)^2}{(N^3-4N^2+6N-4)} \times \left[N-1-\frac{2N-1}{6}(A+B)\right] \tag{55}$$

We call the blended spacings defined from equations (52) and (53) linear and parabolic, respectively [8]. For both spacings there is a critical number of panels, beyond which the method results into $f(i;N) < 0$, i.e. negative intervals.

The blended grid, in the case of partial cavitation, is then defined as follows [9]:

- for $0 < x < l_D$: N_{LE} panels with half-cosine spacing.
- for $l_D < x < l$: N_C panels with parabolic blended spacing; the left end interval is set equal to the right end interval of the previous spacing, and the right end interval is set equal to Δx_{TE}^{C}.
- for $l < x < 1$: N_{FW} panels with parabolic blended spacing; the left end interval is equal to Δx_{TE}^{C} and the right end interval is equal to Δx_{TE}^{FW}.

Where $N_H = N/2$, $N_C = N_H \times l - N_{LE}$ and $N_{FW} = N_H - N_C - N_{LE}$ with N being the total number of panels. N_{LE} is defined from:

$$N_{LE} = N_R\left(\frac{l_D}{\rho_{LE}}\right)^{\frac{1}{2}} \tag{56}$$

[8] They become linear and quadratic functions of i for $K_1 = 0$ and $K_2 = 0$.

[9] The given number of panels refers to each side of the foil.

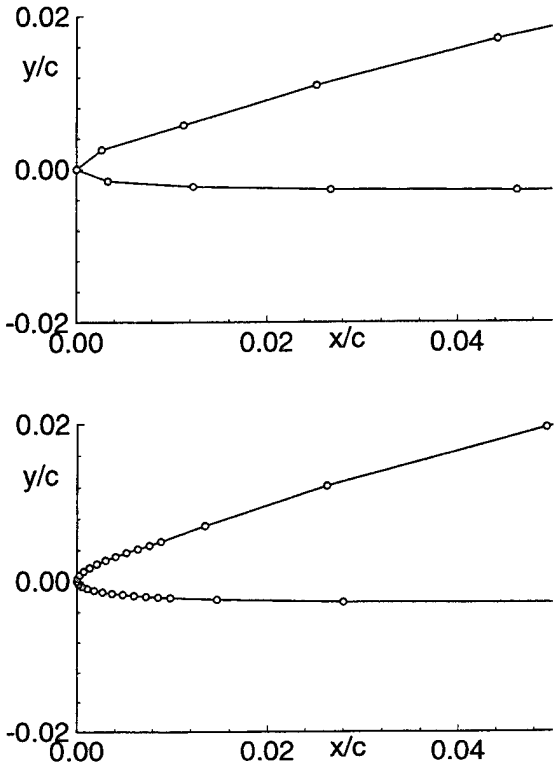
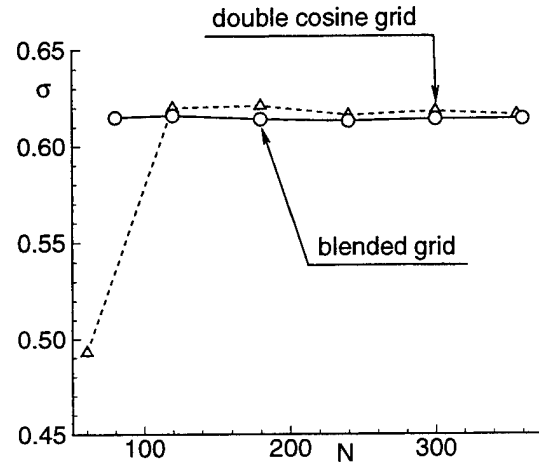


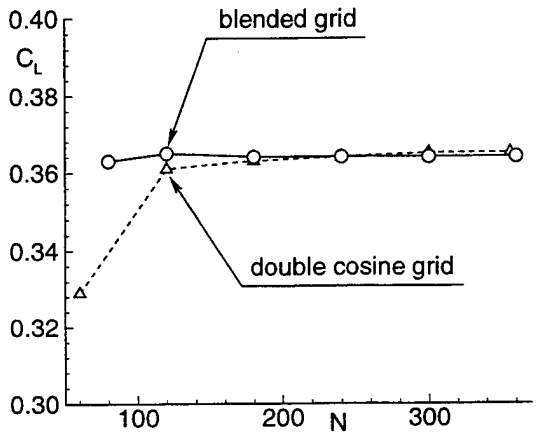
Figure 29: Arrangement of panels at the leading edge of a partially cavitating hydrofoil. Double cosine spacing (top) and blended spacing (bottom). The total number of panels is equal to 100 in both cases.

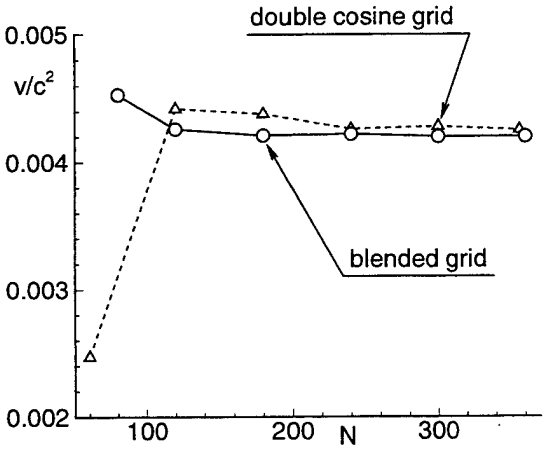
with N_R being a fixed number of panels for $0 < x < \rho_{LE}$ with ρ_{LE} being the leading edge radius. In our current spacing we have selected: $N_R = 3$ and $\Delta x_{TE}^{C} = \Delta x_{TE}^{FW} = 1/N_H$.

The panel arrangements in the vicinity of the leading edge, resulting from the original double cosine and the proposed blended spacing, are shown in Figure 29. Notice the finer resolution in the case of the blended spacing.

The convergence of the results with number of panels, from applying the inviscid cavity model on the two grids is shown in Figures 30 and 31. Notice that the cavity solution and the foil forces converge faster when the blended grid is employed. The improvement of the convergence by using the blended grid appears to be more pronounced in the calculation of drag, as expected, due to the higher panel resolution at the leading edge. The blended spacing has been found to improve the convergence of the presented viscous cavity model as well.







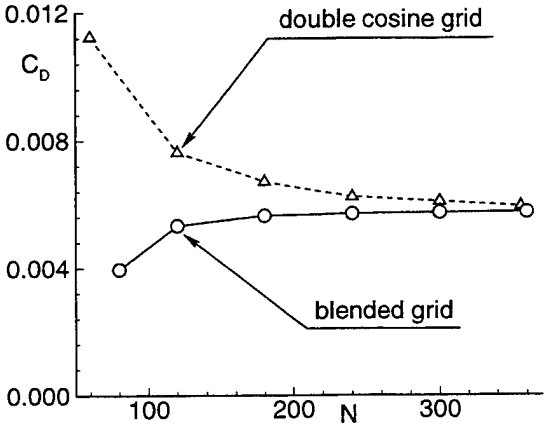


Figure 30: Convergence of the cavity solution predicted by the present method for two different panel arrangements; $\tau/c = 0.04$, $f_o/c = 0.02$, $\alpha = 3°$, $l/c = 0.35$, $l_D/c = 0.008$.

Figure 31: Convergence of the forces predicted by the present method for two different panel arrangements; same hydrofoil geometry as in the previous figure.

Artificial Variation Problems Method for Three-Dimensional Lifting Cavity Flows

A. Achkinadze, G. Fridman
(Marine Technical University of St. Petersburg, Russia)

ABSTRACT.

The artificial variation problem (AVP) method is discussed to analysis of nonlinear three–dimensional cavity flow problems based on variational approach together with mathematical programming methods. AVP method allows to substitute the differential or integral equation (system of equations) problem by the equivalent variation problem for the same unknown functions, which bring minimum value to the certain *artificial* functional. This *artificial* functional can be not connected with any physical characteristics of described object and minimisation of this functional can be not connected with optimisation process for these characteristics.

INTRODUCTION.

During last 125 years of theoretical and 99 years of experimental investigations of developed lifting cavity flows a lot of mathematical models and corresponding numerical methods for their realisation have been proposed . There are two directions of development of such mathematical models:

- the first one is connected with taking into account additional certain properties of the flow, such as gravitational, viscous, capillary, unsteady, three–dimensional effects *etc.*
- the second one provides more closely utilisation of modern numerical approaches, such as voracity and source lattice method, panel methods, mathematical programming methods *etc.*

The value of investigations in this fields depends on theoretical and engineering problems which could be covered by new approaches or valuable improvement of numerical algorithms. The artificial variation problems method proposed by authors in this paper belongs to the second group of methods which enable to treat and to successfully solve three–dimensional lifting cavity flow problems. In assumptions of "ideal" cavitation [1] (without effects of viscous and capillary) by using method we can construct effective algorithm to determine flow coefficient (lift, drag, *etc.*) and cavity volume and planform for both open and closed cavity closure models. Usually the detachment curve is founded from Brillouin–Villat condition or fixed previously. For example, such method is used in [2].

The problem under considerations was treated by lot of methods (see [3–9]). In all these papers it was emphasized that there are many difficulties (especially for non zero cavitation number) standing before when one constructs the process of successive approximations in order to determine cavity planform. The approach proposed by authors lets us overcome mentioned obstacles and beside this in the frame of linear theory and open cavity closure model gives an unique opportunity to solve the problems of optimal design of supercavitating profiles [10], wings of arbitrary planform [11,12] and blades of supercavitating propellers [13]. In these papers it was used the coincidence of minimized functionals of artificial and natural, "physical" variation problems. The method has some interesting perspective even for unsteady cavity flow problems [14].

From mathematical point of view artificial variation problem (AVP) method is approximate method for integral equations solution with unknown area of integrate. The traditional state-

ment of lifting cavity flow problem when all boundary conditions (dynamic and kinematics conditions on the cavity and wetted surface and detachment and cavity closure conditions) written as equations is replaced by "artificial variation" statement which formulated as a system of inequalities with artificial minimized functional. When this functional takes its minimum value which is equal to zero, solutions of traditional and variation problems coincide. The collocation and mathematical programming methods can be used for numerical realisation of proposed approach.

Author are understanding the term "mathematical programming" as a field of applied mathematics which is studying the algorithms for solutions of finite systems of linear or nonlinear equalities and inequalities (restrictions) under the condition that this solution brings minimum (or maximum) to the certain objective function. In contrast to classical calculus of variations and Lagrange multipliers method, proposed approach based on AVP method operates with both equalities and inequalities and at the same time determines an actual minimum (not only stationary point) even on the boundary of the region of integrate under consideration. These advantages enable to build the *artificial* minimize functional starting only from formal reasons that its minimum value lies on the boundary of the region and not from any energy or other physical reasons which need in the strong smooth of functions.

Mathematical programming problems are simplified in two cases:

– linear programming (optimization) with linear restrictions and objective funtional;

– quadratic programming (optimization) with linear restrictions and second order objective functional.

These variants will be cover in all examples in this paper.

First investigations which applied described AVP method [10,11,12] were executed in assumptions of the linear theory and open cavity closure model and therefore the linear programming was used. At the present paper AVP method was correctly extended and adopted to the both open and closed cavity closure models. Authors do not compare cavity closure models between themself (such research was carried out, for example, in [15]) because of AVP method is universal for the set of closure models.

We emphasise that the statement of the problem under consideration in this paper was formulated (see below) for more global assumptions then assumptions of the linear theory [16]. It was assumed only that the cavity thickness in comparison with the mean chord of the wing is small. As for other geometric flow parameters (including the thickness of the lifting surface and the incidence angle) they have a wide range of variations.

The AVP method for three–dimensional lifting cavity flow problems was numerically realizated in this paper by means of the panel method (note that recently the panel method successfully is used for the propeller problems [17,18]) and numerical lifting surface method. The cavitating wing thickness is modeling by source distribution on the base surface (that is exactly as for linear theory). But nevertheless even in this case AVP method is very effective and it gives numerical results which are in good agreement with experimental data. All these facts let us claim that AVP method is perspective and powerful method.

VARIATION AND TRADITIONAL STATEMENTS OF THE THREE–DIMENSIONAL LIFTING CAVITY FLOW PROBLEM.

Partially Cavitating Flows. Generalized Cavity Closure Model With "Reflector".

The problem to be considered in the present paper is the flow past a cavitating wing of finite (not small) thickness with given surface S. The surface S is smooth anywhere besides the preassigned curve l_B which is the trailing edge of the wing. At the same time curve l_B is the beginning of the surface S_W – the vortex wake surface which runs to the infinity after the wing. The surfaces of the cavities is S_{cav}. Symbol h denotes the cavity thickness measured in normal direction of S. Let us assume that the origin of the system of Cartesian coordinates (x, y, z) is placed on the l_B. The velocity vector $\vec{V}_\infty$ of the uniform stream is parallel with the X–axis. The problem under consideration is formulated for the three–dimensional irrotational (outside of surfaces S and S_W) flow of an ideal incompressible fluid without gravity. The function of the flow potential is

$$\Phi = \vec{V}_\infty x + \varphi \qquad (1)$$

where φ is the function of the perturbation velocity potential.

The traditional statement of the problem includes conditions for the desires harmonic function φ is as follows:

a) kinematics tangency condition on rigid wetted boundaries defined as $S \backslash S_{cav}$

b) dynamic (constant) pressure or $\nabla\varphi$ boundary conditions on the surfaces of all formed cavities S_{cav}.

c) conditions at infinity for velocity $\vec{V}_\infty$ and static pressure p_∞.

At the same time it is necessary to determine shapes of vortex wake surface S_W, cavity planforms S_{cav} and the height of the imaginary closure plate h_{cl} (for closed cavity closure models). The placement of this plate is unknown as well as the cavity surface. For given geometric parameters of the lifting surface S, the vapour pressure inside the cavity p_{cav} and the fluid density ρ the problem can be mathematically formalize as follows:

$$\frac{\partial^2\varphi}{\partial x^2} + \frac{\partial^2\varphi}{\partial y^2} + \frac{\partial^2\varphi}{\partial z^2} = 0 \quad \text{outside of } S \cup S_W \qquad (2)$$

$$\frac{\partial\varphi}{\partial n} = -\vec{V}_\infty \cdot \vec{n} \quad \text{on the } S \backslash S_{cav} \qquad (3a)$$

$$\frac{\partial\varphi}{\partial l} = -\vec{V}_\infty \cdot \vec{l} \quad \text{on the } H_{cl} \qquad (3b)$$

$$p^+ - p^- = 0 \quad \text{on the } S_W \qquad (4a)$$

$$\frac{\partial\varphi^+}{\partial n} - \frac{\partial\varphi^-}{\partial n} = 0 \quad \text{on the } S_W \qquad (4b)$$

$$|\nabla\varphi| < \infty \quad \text{on the } l_B \qquad (5)$$

$$\nabla\varphi \to 0 \quad \text{as } x \to -\infty \qquad (6)$$

$$p - p_{cav} = 0 \quad \text{on the } S_{cav} \qquad (7)$$

$$p - p_{cav} > 0 \quad \text{on the } S \backslash S^S_{cav} \qquad (8)$$

$$h \geq 0 \quad \text{on the } S_{cav} \qquad (9)$$

$$h = 0 \quad \text{on the } S \backslash S^S_{cav} \qquad (10)$$

where

S_{cav} and S^S_{cav} are the surface of all cavities on the wing and the projection of this surface onto the surface of the wing S respectively;

H_{cl} is the surface of the imaginary plate ("reflector") which closes the cavity volume, the height of this plate is equal to h_{cl};

"+" and "−" denote the limiting values of parameters on the upper and lower sides of the semi-infinite wake surface S_W which begins on the curve l_B, the trailing edge of the cavitating wing;

$\vec{n}$ and $\vec{l}$ are the local system of coordinates for any transverse wing section; at the same time l denotes the arc coordinate of a point on the surface of a mentioned wing section (see Figure 1).

Let us explain conditions (3a), (3b) and (8)–(10). All these conditions are the consequence of assumptions of the "ideal cavitation" and the accepted partially cavity closure model with closure plate H_{cl} which is normal to the wing surface S. On the surface H_{cl} the constant pressure condition is not fulfilled. Conditions (7), (8) and (9), (10) are the three–dimensional analogue of the first and second Brillouin conditions respectively for two–dimensional cavity flows [19,20].

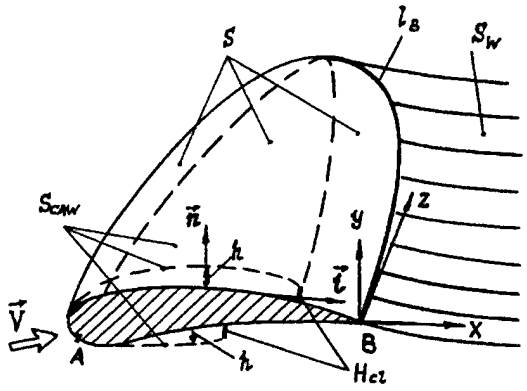


Figure 1: Flow pattern past a cavitating wing. Generalized cavity closure model with "reflector".

The cavity behaviour in the detachment and closure regions for three–dimensional flow is coincides in the main with behaviour for two–dimensional flow. This fact can be proved by using, in particularly, the method of Matched Asymptotic Expansions (MAE) [21,22]. The satisfaction of Brillouin conditions guarantees the smooth cavity detachment. The curve where cavity surface S_{cav} joins with closure plate H_{cl} (H_{cl} is perpendicular to the surface S) is the curve where the cavity curvature is equal to infinity. At the same time the curve where closure plate joins with the surface of the wing S is the line of stagnation points. The proposed three–dimensional model of partially cavita-

ting is three–dimensional analogue of the two–dimensional Riabouchinsky cavity closure model (model with "reflector", [20,23]). The AVP method does not set any restrictions on the number of cavities. For example, first cavity could replace on the suction side and the other one on the pressure side of the wing.

The variation approach to the statement of the boundary problem (2)–(10) under consideration consists of the generalization of boundary conditions on S_{cav} in order to exclude this surface from respective expressions. As a consequence we receive a set of appropriate solutions of new generalized variation problem. In order to select the solution of the initial problem the certain minimized artificial functional F is used.

Surfaces S and S_{cav} are replaced in conditions of the variation statement by new surface S_h. This surface is apart with distance $h(l,z)$ from the surface S. The value of $h(l,z)$ is measured in normal direction to the S and is positive as S_h lies outside of S. It should be mentioned that $h(l,z)$, strictly speaking, is not a cavity thickness. Assume that $\vec{n}_h$ denotes the outer normal to the surface S_h. All boundary conditions, both kinematics and dynamic, are fulfilled on the S_h, not on the unknown wetted part of the surface S and on the S_{cav}.

The variation statement of the boundary problem under consideration formulated in term of S_h is as follows:

$$\frac{\partial^2\varphi}{\partial x^2}+\frac{\partial^2\varphi}{\partial y^2}+\frac{\partial^2\varphi}{\partial z^2}=0 \quad \text{outside of } S_h \qquad (11)$$

$$\frac{\partial\varphi}{\partial n_h}=-\vec{V}_\infty\cdot\vec{n}_h \quad \text{on the } S_h \qquad (12a)$$

$$\frac{\partial\varphi}{\partial l}=-\vec{V}_\infty\cdot\vec{l} \quad \text{on the } H_{cl} \qquad (12b)$$

$$p^+-p^-=0 \quad \text{on the } S_W \qquad (13a)$$

$$\frac{\partial\varphi^+}{\partial n}-\frac{\partial\varphi^-}{\partial n}=0 \quad \text{on the } S_W \qquad (13b)$$

$$|\nabla\varphi|<\infty \quad \text{on the } l_B \qquad (14)$$

$$\nabla\varphi\to 0 \quad \text{as } x\to-\infty \qquad (15)$$

$$p-p_{cav}\geq 0 \quad \text{on the } S_h \qquad (16)$$

$$h\geq 0 \quad \text{on the } S_h \qquad (17)$$

$$h=0 \quad \text{on the } l_B \qquad (18)$$

$$F=\iint_{S_h}(p-p_{cav})\,h(l,z)\,ds\to\min \qquad (19)$$

where F is the artificial minimized functional.

Unknown quantities are the function of the perturbation velocity potential φ, surfaces S_W and S_h and function $h(l,z)$. The quantities p_∞, p_{cav}, $\vec{V}_\infty$ and wing surface S are given in advance.

It should be mentionned that the boundary problem (11)–(19) is not mixed in contrast to (2)–(10) problem.

Let us prove that traditional (2)–(10) and variation (11)–(19) problems are equivalent, i.e. their solutions, if they exist, are coincide.

First, the artificial minimized functional F has no negative values for any values of functions p and $h(l,z)$ which satisfy conditions (16) and (17).

$$F\geq 0 \qquad (20)$$

This is really true because of the functional F is the integral of the product of two non negative multipliers (left part of expressions (16) and (17) respectively). That is why we called F *artificial* functional. The property of having fixed sign of the functional F was reached by using of conditions–inequalities.

Second, from (20) and (19) we get that

$$\min F=0 \qquad (21)$$

Note that we assume that the solution of the variation problem (11)–(19) exists and the minimum value of the functional F can be reached. Below we shall prove that if the solution of the variation problem (11)–(19) does not exist then the traditional problem (2)–(10) has no solution too.

Third, from (21) we get that desired solution satisfies the following equality

$$F=\iint_{S_h}(p-p_{cav})\,h(l,z)\,ds=0 \qquad (22)$$

Therefore surface S_h includes only two subdomains S_1 and S_2 where following conditions fulfill:

$$p=p_{cav};\ h\geq 0 \text{ on the surface } S_1\subset S_h \qquad (23a)$$

$$p>p_{cav};\ h=0 \text{ on the surface } S_2\subset S_h \qquad (23b)$$

It is obvious that $S_1=S_{cav}$ and $S_2=S\backslash S_{cav}$. At the same time the condition (12a) includes the condition (3a), i.e. kinematics tangency condition on the surface $S\backslash S_{cav}$ because of on this part the surface S_h coincide with S due

to $h = 0$ as $p - p_{cav} > 0$. Thus all conditions of the traditional problems fulfilled when $F = 0$ and therefore varational problem (11)–(19) does not lose any solutions of the traditional problem (2)–(10).

At the same time the set of admissible solutions does not extend because of condition $F = 0$ leads only to subregions S_1 and S_2. Let us assume the contrary, namely that condition (10) is disturbed, i.e. $h > 0$ on the wetted part $S \backslash S^S_{cav}$ where $p - p_{cav} > 0$. Then in this region we obtain that $(p - p_{cav})\, h > 0$ and expression (22) can not reach the zero value. Therefore there is no solution which is correspond to the minimum value of functional (21). This is contradiction.

Below we formulate a set of explaining remarks to the aforementioned approach.

Remark 1. The condition (19) of the variation problem $F \rightarrow \min$ could be replaced by $F = 0$ and we obtain the system of equalities and inequalities. However going over a finite system from boundary problem by collocation method we should not strictly satisfy the condition $F = 0$ due to calculation errors. Therefore the desired solution could be lost. Minimized condition $F \rightarrow \min$ is more convenient in spite of the fact that it is necessary to solve the optimization problem.

Remark 2. The Euler integral shows the relation between pressure p and the function of the perturbation velocity potential φ [1]

$$\frac{p}{\rho} = \frac{p_\infty}{\rho} - \frac{(\nabla\varphi)^2}{2} - V_\infty \frac{\partial\varphi}{\partial x} \qquad (24)$$

where ρ is the fluid density.

Remark 3. Due to conditions (7) and (9) AVP method can take into consideration the subregions where cavity thickness is equal to zero. They are isobaric regions with $p = p_{cav}$; $h = 0$.

Remark 4. The proposed variation statement of the problem differs from classical variation principles. Namely, the set of restrictions includes inequalities and the minimum value of the objective function is situated on the boundary, not inside of the region. Therefore classical differential sufficient condition of decision problem could not applied.

Remark 5. Aforementioned approach was formulated in the assumptions of nonlinear theory in order to use the panel method (perturbation potential method). On each iteration's loop of successive approximations the simplified mathematical programming problem is solved. Simplification consists of assumption of small values of h. Then boundary conditions are projected from the surface S_h to the wing surface S. The normal closure plate H_{cl} degenerates into the curve l_{cl} on S where after linearization vorticity and source distributions have a square root singularity $1/\sqrt{|l - l_{cl}|}$. Thus for the small values of h_{cl} the surface S_h must be replaced by S in the statement of the problem (11)–(19). The condition (12b) modifies to $h = h_{cl} = 0$ on l_{cl} and corresponds to the closed cavity closure model.

Also other simplify assumptions could be used, for example, we should neglect the term of (24) $(\nabla\varphi)^2/2$ or should assume for vorticity distribution:

$$q \approx \frac{\partial h}{\partial l} \qquad (25)$$

Remark 6. The variation statement (11)–(19) could be extended for the regime of the supercavitating flow. To this end the condition (18) is excluded and a corresponding part of vortex wake surface S_W is added into the new surface S_h. Certainly, the shape of S_W must be approximately given on each iteration's loop of successive approximations process. Then the surface S_h must be arbitrarily extensive to include the desired three-dimensional cavity surface S_{cav}. The sufficiently choice of such surface S_h is always provided when $p_\infty > p_{cav}$ (cavitation number $\sigma > 0$).

Remark 7. The proposed three–dimensional extended closed cavity closure model with "reflector" leads to the additional problem connected with both partially and supercavitating regimes which could simultaneously realize on the wing. The displacement of the closure plate H_{cl} near and especially on the trailing edge of the cavitating wing l_B leads to unlikely jump of lift and drag coefficients and cavity surface. That is why in the next chapter authors propose an another cavity closure model with wake.

Partially Cavitating Flows. Generalized Cavity Closure Model With Wake.

The flow pattern acquires the form as shown on Figure 2. The boundary of the cavity has smooth curvature on both detachment and closure curves. The closure cavity curve joins with semi-infinite body of thickness $h = \text{const}$. Any section of this body forms the equidistant curve with surfaces S and S_W respectively. The

wake thickness at infinity is equal to h and the cavity closure condition for closed model does not fulfil. Thus the three–dimensional cavity closure model with equidistant partitions is used. Two–dimensional problem with analogous closure model was treated in [15,23,24].

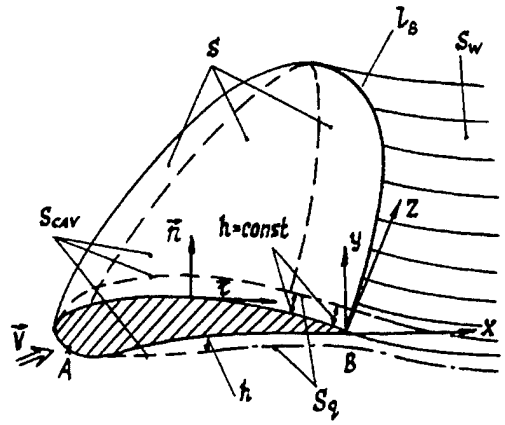


Figure 2: Flow pattern past a cavitating wing. Generalized cavity closure model with wake.

In order that state this problem it is necessary to take into consideration the additional semi-infinite wake region S_q which is situated after the cavity volume at the distance $h(l,z)$ from wing S and wake S_W surfaces. On the other hand we could exclude the closure plate H_{cl}. Thus the statement of the corresponding problem is as follows:

$$\Delta\varphi = 0 \quad \text{outside of } S \cup S_W \cup S_q \cup S_{cav} \tag{26}$$

$$\frac{\partial\varphi}{\partial n} = -\vec{V}_\infty \cdot \vec{n} \quad \text{on the } S\backslash(S_{cav} \cup S_q) \tag{27a}$$

$$\frac{\partial\varphi}{\partial n_h} = -\vec{V}_\infty \cdot \vec{n}_h \quad \text{on the } S_q \tag{27b}$$

$$p^+ - p^- = 0 \quad \text{on the } S_W \tag{28a}$$

$$\frac{\partial\varphi^+}{\partial n} - \frac{\partial\varphi^-}{\partial n} = 0 \quad \text{on the } S_W \tag{28b}$$

$$|\nabla\varphi| < \infty \quad \text{on the } l_B \tag{29}$$

$$\nabla\varphi \to 0 \quad \text{as } x \to -\infty \tag{30}$$

$$p - p_{cav} = 0 \quad \text{on the } S_{cav} \tag{31}$$

$$p - p_{cav} > 0 \quad \text{on the } (S \cup S_q)\backslash S_{cav} \tag{32}$$

$$\frac{\partial h}{\partial l} \geq 0 \quad \text{on the } S_{cav} \tag{33}$$

$$\frac{\partial h}{\partial l} = 0 \quad \text{on the } (S \cup S_q)\backslash S^S_{cav} \tag{34}$$

where S_q is equidistant surface to $S \cup S_W$.

The $\vec{n}_h$ denotes the outer normal to the surface S_h. The arc coordinate l for any wing section is counted from arbitrary point A outside of caviities (see figure 2) in the upstream direction independently from where the cavity is situated (on both pressure or suction side). The condition (33) indicates that the cavity thickness is monotone nondecreasing function. We shall accept that the curve where the cavity thickness reaches its largest value (for any wing section) is the cavity closure curve. The equidistant surface S_q begins from this curve.

It should be mentioned that in assumptions of this model there are no any disturbances of the curvature of the cavity boundary. Consequently the proposed model with wake could be extended and applied for both partially and supercavitating flow regimes which are simultaneously realize on the wing without any difficulties.

The analogous procedure of the passage to the variation statement of the problem was described in the previous section of the paper for the model with "reflector". It must be mentioned that the surface S_h in the expressions below is the surface which is lies at the distance $h(l,z)$ over the surfaces $S \cup S_W$.

The variation statement is as follows:

$$\frac{\partial^2\varphi}{\partial x^2} + \frac{\partial^2\varphi}{\partial y^2} + \frac{\partial^2\varphi}{\partial z^2} = 0 \quad \text{outside of } S_h \tag{35}$$

$$\frac{\partial\varphi}{\partial n_h} = -\vec{V}_\infty \cdot \vec{n}_h \quad \text{on the } S_h \tag{36}$$

$$p^+ - p^- = 0 \quad \text{on the } S_W \tag{37a}$$

$$\frac{\partial\varphi^+}{\partial n} - \frac{\partial\varphi^-}{\partial n} = 0 \quad \text{on the } S_W \tag{37b}$$

$$|\nabla\varphi| < \infty \quad \text{on the } l_B \tag{38}$$

$$\nabla\varphi \to 0 \quad \text{as } x \to -\infty \tag{39}$$

$$p - p_{cav} \geq 0 \quad \text{on the } S_h \tag{40}$$

$$\frac{\partial h}{\partial l} \geq 0 \quad \text{on the } S_h \tag{41}$$

on the point A for any wing section

$$h = 0 \tag{42}$$

$$F^* = \iint_{S_h} (p - p_{cav}) \frac{\partial h}{\partial l}\, ds \to \min \tag{43}$$

The function of the perturbation velocity potential φ, surfaces S_W and S_h are unknown quantities which bring minimum value to the artificial functional F^*. The quantities p_∞, p_{cav}, $\vec{V}_\infty$ and wing surface S are given in advance. It would be easy to see that minimized artificial functionals (19) and (43) for two three-dimensional cavity closure models differ one from other only in functions $h(l,z)$ and $\partial h/\partial l$ respectively.

The proof of the equivalence between traditional (26)–(34) and variation (35)–(43) statements of the problem is analogous to the proof for the model with "reflector". We would like to repeat only our argument on the contrary for this model. Let us take that the condition (34) was disturbed and $\partial h/\partial l > 0$ on the part of S_q or S where $p - p_{cav} > 0$. Then the integral in the part of (43) does not reach its minimum (zero) value and therefore such a solution is not appropriate.

All *remarks* which were made in the previous section of the paper remain after obvious corrections for the model with wake. It should be mentioned that after linearization there are no singularities of source distribution function at the end of the cavity and proposed approach could be applied for both partially and supercavitating flow regimes which are simultaneously realize on the wing.

In order that illustrate the advantages of AVP method let us solve the problem under consideration (closure model with wake) using assumptions of the linear theory.

NUMERICAL REALIZATION OF THE ARTIFICIAL VARIATION PROBLEM.

Linearization of the Artificial Variation Problem for the Closure Model With Wake.

At small magnitudes of the lifting flow parameters (such as incidence, wing and cavity thickness and curvature, *etc.*) the problem under consideration could be linearized ([12,16,25]). To this end the certain base surface S_{BS} lying on the (xz)–plane is accepted. This surface is bounded by the leading edge of the wing and by two parallel rays starting from wing's tips to the upstream directions. The kinematics tangency condition is projected onto the surface S_{BS} and the function $\partial\varphi/\partial n$ replaces by $\partial\varphi/\partial y$

The Euler integral (24) after linearization shows the relation between the pressure p and the function φ

$$\frac{p}{\rho} = \frac{p_\infty}{\rho} - V_\infty \frac{\partial\varphi}{\partial x} \tag{44}$$

The dynamic boundary condition could also be projected onto the surface S_{BS} which at the same time partially coincides with the wake surface S_W. After mentionned simplifications the linear artificial variation problem with closure model with wake is as follows:

$$\frac{\partial^2\varphi}{\partial x^2} + \frac{\partial^2\varphi}{\partial y^2} + \frac{\partial^2\varphi}{\partial z^2} = 0 \quad \text{outside of } S_{BS} \tag{45}$$

$$\frac{\partial\varphi^+}{\partial y} = V_\infty\left(\frac{\partial y^+}{\partial x} + \frac{\partial h^+}{\partial x}\right) \quad \text{on the } S_{BS} \tag{46a}$$

$$\frac{\partial\varphi^-}{\partial y} = V_\infty\left(\frac{\partial y^-}{\partial x} - \frac{\partial h^-}{\partial x}\right) \quad \text{on the } S_{BS} \tag{46b}$$

$$\frac{\partial\Gamma}{\partial z} = \frac{\partial\varphi^+}{\partial z} - \frac{\partial\varphi^-}{\partial z} \quad \text{on the } S_{BS}\cap S_W \tag{47a}$$

$$\Gamma(z) = \varphi^+ - \varphi^- \quad \text{on the } S_{BS}\cap S_W \tag{47b}$$

$$\nabla\varphi \to 0 \quad \text{as } x \to -\infty \tag{48}$$

$$\frac{\sigma}{2} - \frac{1}{V_\infty}\frac{\partial\varphi^\pm}{\partial x} \geq 0 \quad \text{on the } S_{BS} \tag{49}$$

$$\frac{\partial h^\pm}{\partial x} \geq 0 \quad \text{on the } S_{BS} \tag{50}$$

on the point A for any wing section;

$$h^\pm = 0 \tag{51}$$

$$F^{**} = \iint_{S^+_{BS}} \left(\frac{\sigma}{2} - \frac{1}{V_\infty}\frac{\partial\varphi^+}{\partial x}\right)\frac{\partial h^+}{\partial x}\,ds + \\ + \iint_{S^-_{BS}} \left(\frac{\sigma}{2} - \frac{1}{V_\infty}\frac{\partial\varphi^-}{\partial x}\right)\frac{\partial h^-}{\partial x}\,ds \to \min \tag{52}$$

$$\sigma > 0 \tag{53}$$

where S_{BS} is the two–sided surface; "+" and "−" denote the limiting values of functions on the upper and lower sides of the base surface S_{BS} and σ is cavitation number.

Vortex wake sheets lie on the surface $S_{BS}\cap S_W$ due to assumptions of the linear theory [1,17]. Function $\Gamma(z)$ denotes the value of circulation on any closed contour around the wing section with transverse coordinate z. This value does not depend on coordinates of the point of intersection of mentioned contour with the surface $S_{BS}\cap S_W$, i.e. free vortex sheet runs in upstream direction (direction of x-axis and $\vec{V}_\infty$). If the cavity appears only on the suction side ("+") of the lifting surface then the second term in the

expression (52) vanishes. Note that in this case the appropriate surface S_{BS}^{+} could be of finite area. It must cover the surface S_{cav}. Some additional aspects of this problem were formulated in [12,26].

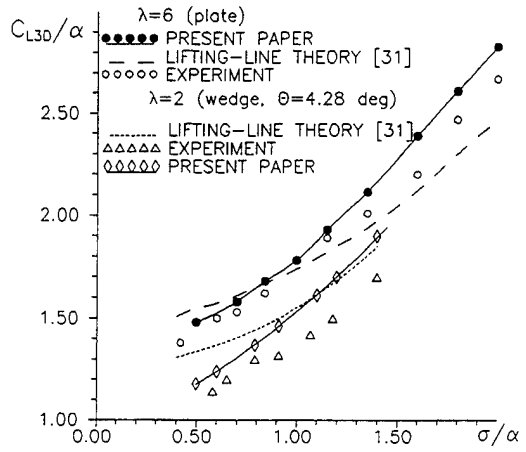


Figure 3: Lift coefficient of cavitating wing of rectangular planform without spoiler.

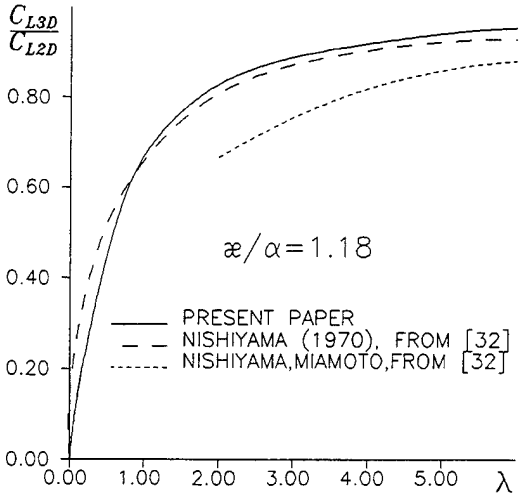


Figure 4: The correction factor C_{L3D}/C_{L2D} for a cavitating wing of rectangular planform.

The method of integral equations and collocation method were applied to solution of artificial variation problem (45)–(53). The vorticity $\gamma(x,z)$ and source $q(x,z)$ distribution are approximated by polygonal functions. Caring out the discretization we get the quadratic programming problem [27] with linear restrictions and second order objective functional. This functional could be linearized and then we obtain:

$$F_{lin}^{**} \cong \iint_{S_0^+} \left(\frac{\sigma}{2} q_{cav} - \frac{1}{V_\infty}\frac{\partial \varphi^-}{\partial y}\gamma + \right.$$

$$\left. + \frac{1}{V_\infty}\frac{\partial \varphi}{\partial x} q_0\right) ds \to \min \qquad (54)$$

where

S_0 denotes projection of wing surface onto the surface S_{BS};

symbol $\cong$ indicates that $F_{lin}^{**} \approx F^{**}$ due to neglected nonlinear term with vortex sheet induction $\partial\varphi^*/\partial y$

$$\iint_{S_0^+} \frac{1}{V_\infty}\frac{\partial \varphi^*}{\partial y}\gamma \, ds \, ;$$

ϕ^* is the perturbation potential of free vortex lying on the surface of $S_{BS} \cap S_W$;

q_{cav} denotes the source distribution which modeling the cavity;

q_0 denotes the source distribution which modeling the wing thickness;

γ denotes the vorticity distribution.

The linear programming problem with minimized functional (54) was treated by simplex method. The next section contains some numerical results for cavitating wing of arbitrary planform. It should be mentioned that proposed approach allows to use powerful additional methods to increase the precision of calculations in linear theory assumptions. For example, at this investigation authors used nonlinear edges and apex corrections for cases of sharp and rounded leading edge of a cavitating lifting surface and for trailing edge equipped with a spoiler of small a length ε and arbitrary inclination angle β [28]. This methodology of nonlinear local solutions in singularly perturbed three–dimensional lifting cavity flows was studied in papers [28,29,30] on the base of the method of matched asymptotic expansions (MAE), [21,22].

Numerical Results.

The cavitating wings of rectangular and elliptic planform are presented as examples of numerical calculations [28,29]. Figure 3 shows the three–dimensional lift coefficient C_L versus cavitation number σ for rectangular flat plate of

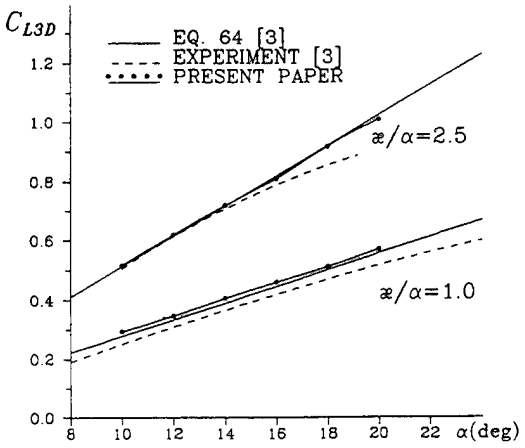


Figure 5: Lift coefficientof cavitating wing of elliptic planform, aspect ratio $\lambda = 3$

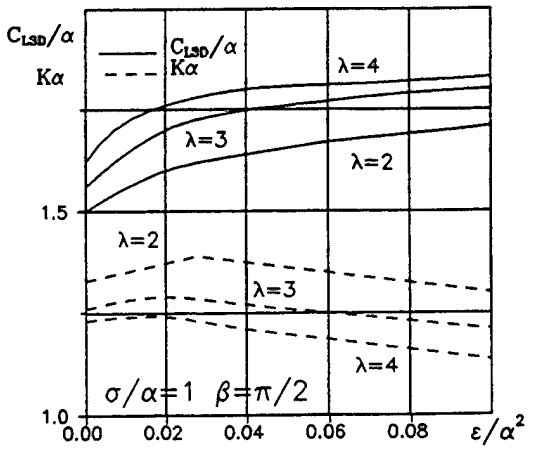


Figure 6: Lift coefficient and Lift/Drag ratio of a cavitating wing of rectangular planform with spoiler at the trailing edge.

aspect ratio $\lambda = 6$ and rectangular slender wedge of $\lambda = 2$ with angle of divergence $\Theta = 4.28°$. This numerical results are in good correspondence with the experimental data [8] and lifting line theory results [31].

The effect of the aspect ratio on the correction factor C_{L3D}/C_{L2D} is shown in Figure 4. In the same figure the correction factors obtained by the lifting–line theory by Nishiyama and by a lifting–surface theory by Nishiyama & Miamoto are shown for comparison, [32]

Figure 5 shows the results of [3] compared with present calculation for the surface of elliptic planform for aspect ratio $\lambda = 3$.

The curves for C_L and Lift/Drag ratio coefficient versus spoiler length are shown in Figure 6 for rectangular plate of finite span with spoiler at the trailing edge.

Singularities in the flow domain (on the leading edge and trailing edge equipped with a spoiler due to linearization of the problem) lead to the numerical results for lift and drag coefficients which are about 10–15% more than experimental data. Nonlinear edges corrections allow to reduce this difference to 3–5%.

CONCLUSION.

1. The AVP method is an effective instrument for solution of three–dimensional lifting cavity flow problem in assumptions of linear and (in a perspective) nonlinear theory.

2. Proposed approach could be applied to unsteady cavity problem and a problem with a number of cavities both on the pressure and suction side of lifting surface.

3. The approach advocated by the authors can be used for some other free surface lifting flow problems, for example three–dimensional planing flow problem, *etc.*

The authors are thankful to Professor Kirill Rozhdestvensky for his invaluable comments and discussions.

REFERENCE.

1. Milne–Thomson, L.M., "Theoretical Hydrodynamics", Macmillan & Co. Ltd.,St.Martin's Press, London, 1960.

2. Amromin, E.L., Vasiliev, A.V., Droblenkov, V.V., "On some approximations in theory of viscous capillarity cavity flows", Journal of Applied Mathematics and Theoretical Physics, No. 6, 1988, pp. 117–126, in Russian.

3. Leehey, P., Stellinger, T.S., "Force and Moment Measurements of Supercavitating Hydrofoils of Finite Span with Comparison to Theory", Transactions of ASME, series S, 1975, pp. 453–464.

4. Jiang, C.-W., Leehey, P., "Experimantal and Theoretical Investigation of Unsteady Supercavitating Hydrofoils of Finite Span",

Report No. 83481–4, MIT, Dept. of Ocean Engineering, 1971, 131 p.

5. Efremov, I.I., Roman, V.M., "Influence of a Free Surface and Walls on Characteristics of a Cavity Flow", Proceedings of the IUTAM Symosium, Nauka Publishing, Leningrad, USSR, 1971, pp. 165–173.

6. Widnall, S.E., "Unsteady Load on Supercavitating Hydrofoils of Finite Span", Journal of Ship Research, vol. 10, No. 2, 1966.

7. Tsen, L.F., Guilbaud, M., " A Theoretical and Experimental Study on the Planform of Superventilated Wings", Journal of Ship Research, vol. 18, No. 3, 1974.

8. Basin, M.A., Shadrin, V.P., "Wing Hydroaerodynamics in the vicinity of Boundaries", Sudostroenie Publishing, 1980, 304 p., in Russian.

9. Roman, V.M., "Calculation of the Supercavitating Wing Based on the Lifting Surface Theory", High Speed Hydrodynamics, Krasnojarsk, USSR, 1981, pp. 49–58, in Russian.

10. Achkinadze, A.S., "Linear Problem of Supercavitating Wing and Problem of Optimal Wing's Shape (Variational Approach)", Transactions of NTO named by A.N.Krylov, No. 217, 1974, pp. 139–164, in Russian.

11. Achkinadze, A.S., "Linear Programming Approach in the Supercavitating Fllow Problem", Transactions of NTO named by A.N.Krylov, No. 284, 1979, pp. 66–72, in Russian.

12. Achkinadze, A.S., "Application of Mathematical Pogramming Methods in the Linearized Theory of Cavity Flows", Proceedings of 12th SMSSH, BSHC, Varna, Bulgaria, vol. 2, 1983, pp. 32,1–32,19.

13. Achkinadze, A.S. Narvsky, A.S., "Supercavitating Propellers Design Education in Lifting Surface Theory and Method of Its Solution", Poceedings of 14th Conference of SMSSH, BSHC, Varna, Bulgaria, vol. 1, 1985, pp. 2,19–2,21.

14. Achkinadze, A.S., Samsonova, I.A., "Numerical Investigation of Unsteady Development of Axially Symmetric Cavity", Transactions of 3rd All-Union School on Hydrodynamics, Krasnojarsk, 1987, pp. 69–76, in Russian.

15. Rowe, A., Blottiaux, O. "Aspects of Modeling Partially Cavitating Flows", Journal of Ship Research, vol. 37, No. 1, 1993, pp. 34–38.

16. Tulin, M.P., Supercavitatinf Flows Small–Perturbation Theory", Journal of Ship Research, vol. 7, No. 3, 1964, pp. 37–43.

17. Lee, J.T., A Potential Based Panel Method for Analysis of Marine Propellers in Stteady Flow", MIT, Reports 87–13, Massachusetts, USA, 1987, 150 p.

18. Kinnas, S.A., Hsin, C.–Y., Keenan, D.P., "A Potential Based Panel Method for the Unsteady Flow Around Open and Ducted Propellers", Transactions of 18th Symposium on Naval Hydrodynamics, Michigan, 1990, pp. 1–18.

19. Birkhoff, G., Zarantonello, E.H., "Jets, Wakes and cavities", Academic Press, New York, 1957.

20. Gurevich, M.I., "Ideal Fluid Jet Theory", Nauka Publishing, Moscow, 1981, in Russian.

21. Van Dyke, M., "Perturbation Methods in Fluid Mechanics", Parabolic Press, Stanford, 1975, 271 pp.

22. Nayfeh, A.H., "Introduction to Perturbation Techniques", A Wiley–Interscience Publication, New York, 1981, 581 pp.

23. Yamaguchi H., Kato, H., "On Application of Non–Linear Cavity Flow Theory to Thick Foil Sections", Transactions of 2nd Conference on Cavitation, Edinburg, UK, 1983.

24. Bassanini, P., A Non–Linear Model for Fully and Partially Cavitating Flows", ZAMP, vol. 21, fasc. 5, 1970, pp. 754–767.

25. Tulin, M.P, Hsu, C.C., "New Applications of Cavity Flow Theory", Transactions of 13th Symposium on Naval Hydrodynamics, Tokio, Japan, 1980, pp. 107–131.

26. Fridman G.M., Goutkovich, R.G., "Cavitating Wing of Arbitrary Planform with Spoiler. Nonlinear Edges and Apex Corrections", Proceedigs of 24th Israel Conference on Mechanical Engineering, Haifa, Israel, 1992.

27. Hedly, G., "Nonlinear and Dynamic Programming", Academic Press, 1964.

28. Rozhdestvensky, K.V., Fridman, G.M., "Matched Asymptotics for Free Surface Lifting Flows with Spoilers", Mathematical Approaches in Hydrodynamics, Society for Industrial and Applied Mathematics. – Edited by T.Miloh, Philadelphia, 1991, chapter 36, pp. 499–517.

29. Fridman, G.M., Rozhdestvensky K.V., "Nonlinear Local Solutions in Singularly Perturbed Three–Dimensional Lifting Cavity Flows", Proc. of the II International Symp. on Cavitation, Tokyo, Japan, April 5–7, 1994, pp. 95–98.

30. Fridman, G.M., "Nonlinear Local Solutions in Singularly Perturbed Planing

Flows", Proceeding of 25th Israel Conference on Mechanical Engineering, Haifa, Israel, May 25–26, 1994.

31. Nishiyama, T., Ito, J., "Lifting–Line Approximation for Partially Cavitated Hydrofoils of Finite Span", Tohoku University, Technology Reports, vol. 44, No. 1, 1979, pp. 185–197.

32. Furuya, O., "Three–dimensional Theory on Supercavitating Hydrofoils Near a Free Surface", Journal of Fluid Mechanics, vol. 71, part 2, 1975, pp. 339–359.

Three-Dimensional Nonlinear Diffraction Around a Fixed Structure

A. DiMascio, M. Landrini, F. Lalli, U. Bulgarelli
(Istituto Nazionale per Studi ed Esperienze di Architettura Navale, Italy)

ABSTRACT

The computation of diffraction effects on a submerged obstacle in wavy flow is presented. The problem is analysed by means of both a linearized and a fully nonlinear mathematical model. The numerical solution is obtained by an integral representation of the perturbation velocity potential, coupled with an explicit time–marching algorithm that updates the wave elevation and the potential at the free surface.

The diffraction caused by a submerged cylinder and by a shoal was computed and the results were compared with the available experimental data.

NOMENCLATURE

$P \equiv (x, y, z)$	space vector position
t	time
$\mathbf{u}(P, t)$	velocity vector
$\Phi(P, t)$	velocity potential
D	flow domain
∂O	obstacle boundary
∂B	bottom
S	free surface
S_0	incident wave free surface
$\Upsilon(x, y, t)$	free surface elevation
$\phi(P, t)$	incident wave potential
$\tilde{\phi}(P, t)$	perturbation potential
$\eta(x, y, t)$	incident wave heigth
$\tilde{\eta}(x, y, t)$	perturbation wave heigth
g	acceleration of gravity
p	pressure
N	number of panels on the obstacle
M	number of point sources above the free surface
$G(P, P^*)$	Green function
$\sigma(P)$	source density at P
σ_j	constant source density on the j-th panel
∂O_j	j-th panel on the obstacle surface
$\partial \bar{O}_j$	mirror image of ∂O_j
P_k	location of the k-th point source above the free surface
$\bar{P}_k$	mirror image of P_k
Δt	time step
λ	wave length
k	wave number
T	wave period
H	$\Upsilon_{peak} - \Upsilon_{trough}$
h_m	minimum depth
h_M	maximum depth
U_∞	stream velocity
z_d	doublet immersion

INTRODUCTION

The computation of hydrodynamic loads on offshore structures has always received considerable attention by ocean engineers. A good estimation of the forces acting on bodies whose characteristic dimensions are much smaller than the length of the incident wave can be obtained by the classical Morison approch, where all the effects related to the disturbance caused by the structures on the wave field are neglected. Diffraction forces become important when the typical dimension of the body is comparable with the wave length. Analytical or asymptotical solutions have been given for the linearized radiation–diffraction problem in particular limiting cases, whereas various numerical techniques have been developed for arbitrary geometries. Nevertheless, the propagation of waves with large steepness can be properly described only when taking into account the nonlinear behaviour of the free surface; a numerical technique for handling such nonlinearities can be found in [1]. The need to include nonlinear terms when calculating the wave loading on marine structures is also well established, as there are many important phenomena that cannot be predicted by a linear theory. Namely, second order effects are responsible of non–zero mean forces [2] and play an important role in the stability analysis [3]. Nonlinear effects may also be important in the hydroelastic problem [4].

In the present work, the nonlinear diffraction of a Stokes wave train due to a fixed submerged obstacle is numerically studied. For computational purpouses, the velocity potential is split into the sum of an incident wave term and a perturbation potential. This splitting avoids the difficulties related to the generation of the incident wave train (by means of a numerical wakemaker) and simplifies the damping of the outgoing signals at the boundary of the truncated computational domain.

The numerical solution of the boundary value problem is based on an integral representation of the perturbation velocity potential, whereas a time–marching Eulerian algorithm is used to update the potential and the elevation of the free surface.

The analysis has been carried on for two test cases for which experimental data are available. In the first case [10] the interaction between an incident wave train and a submerged vertical cylinder is considered and the computed hydrodynamic forces are compared with the measured ones. Next, we have turned our attention to the wave pattern near a circular shoal subject to a Stokes wave; the numerically prediction is discussed in comparison with the experimental data reported in [11]. The computed wave profiles mirror the experimental ones in a satisfactory way in both tests.

MATHEMATICAL MODEL

The problem under investigation is the wavy flow of an inviscid fluid past a submerged obstacle. The flow being supposed incompressible and irrotational, the velocity vector $\mathbf{u}(P,t)$ can be expressed as the gradient of a potential $\Phi(P,t)$

$$\mathbf{u}(P,t) = \nabla\Phi(P,t) \tag{1}$$

where $P \equiv (x,y,z)$ is the space vector position and t is the time. The potential (harmonic in space) satisfies

$$\nabla^2\Phi = \frac{\partial^2\Phi}{\partial x^2} + \frac{\partial^2\Phi}{\partial y^2} + \frac{\partial^2\Phi}{\partial z^2} = 0 \quad \text{in} \quad D \tag{2}$$

D being the domain whose boundaries are the free surface of the water, the bottom of the sea and the surface of the obstacle (see fig.1).

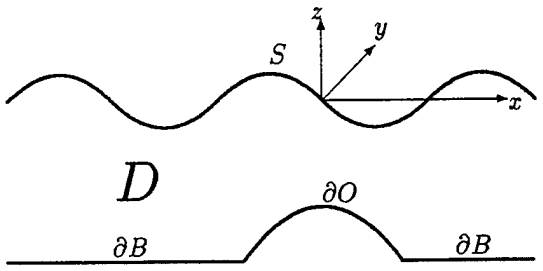


Figure 1: *Geometry of the problem*

The boundary conditions for this problem are:

1. zero normal flow onto the surface ∂O of the obstacle O and the bottom ∂B

$$\frac{\partial\Phi}{\partial n} = 0 \quad \text{on} \quad \partial O \cup \partial B \tag{3}$$

2. zero pressure at the free surface S, that, in terms of potential, reads

$$\frac{\partial \Phi}{\partial t} + \frac{1}{2}\nabla\Phi \cdot \nabla\Phi + g\Upsilon = 0 \qquad \text{on} \quad S \qquad (4)$$

$\Upsilon = \Upsilon(x, y, t)$ being the free surface height and g the acceleration of gravity;

3. the kinematic boundary condition for Υ

$$\frac{\partial \Upsilon}{\partial t} + \frac{\partial \Phi}{\partial x}\frac{\partial \Upsilon}{\partial x} + \frac{\partial \Phi}{\partial y}\frac{\partial \Upsilon}{\partial y} = \frac{\partial \Phi}{\partial z} \qquad \text{on} \quad S \quad (5)$$

Finally, the values of Φ and Υ must be assigned at $t = 0$

$$\Phi(P, 0) = \bar{\Phi}(P) \qquad \Upsilon(x, y, 0) = \bar{\Upsilon}(x, y) \qquad (6)$$

Nonlinear Formulation

For computational purpouses it is convenient to split the potential Φ into the sum of two functions:

$$\Phi = \phi + \tilde{\phi} \qquad (7)$$

where ϕ is an assigned potential and $\tilde{\phi}$ is the perturbation induced by the submerged obstacle. In the following ϕ is the potential of a permanent wave that satisfies, for any t,

$$\begin{aligned}
&\nabla^2\phi = 0 && \text{in} \quad D \\
&\frac{\partial \phi}{\partial n} = 0 && \text{on} \quad \partial B \\
&\frac{\partial \phi}{\partial t} + \frac{1}{2}\nabla\phi \cdot \nabla\phi + g\eta = 0 && \text{on} \quad S_0 \\
&\frac{\partial \eta}{\partial t} + \frac{\partial \phi}{\partial x}\frac{\partial \eta}{\partial x} + \frac{\partial \phi}{\partial y}\frac{\partial \eta}{\partial y} = \frac{\partial \phi}{\partial z} && \text{on} \quad S_0
\end{aligned} \qquad (8)$$

η being the elavation of the unperturbed free surface S_0 in absence of the obstacle; in all the simulations performed, a 2D Stokes wave was choosen as a particular solution of the problem (8). This wave may be computed with high accuracy by standard methods [5].

The perturbation $\tilde{\phi}$, on the bases of eqs.(2,7, 3,4,5,8), has to be harmonic in D

$$\nabla^2\tilde{\phi} = 0 \qquad \text{in} \quad D \qquad (9)$$

and must satisfy the boundary conditions

$$\frac{\partial \tilde{\phi}}{\partial n} = -\frac{\partial \phi}{\partial n} \qquad \text{on} \quad \partial O \cup \partial B \qquad (10)$$

$$\frac{\partial \tilde{\phi}}{\partial t} + \frac{1}{2}\nabla\tilde{\phi} \cdot \nabla\tilde{\phi} + \nabla\phi \cdot \nabla\tilde{\phi} + g\tilde{\eta} = -\frac{\partial \phi}{\partial t} - \frac{1}{2}\nabla\phi \cdot \nabla\phi - g\eta \qquad \text{on} \quad S \qquad (11)$$

$$\frac{\partial \tilde{\eta}}{\partial t} + \frac{\partial \Phi}{\partial x}\frac{\partial \tilde{\eta}}{\partial x} + \frac{\partial \Phi}{\partial y}\frac{\partial \tilde{\eta}}{\partial y} = \frac{\partial \Phi}{\partial z} - \frac{\partial \eta}{\partial t} - \frac{\partial \Phi}{\partial x}\frac{\partial \eta}{\partial x} - \frac{\partial \Phi}{\partial y}\frac{\partial \eta}{\partial y} \qquad \text{on} \quad S \quad (12)$$

where

$$\tilde{\eta}(x, y, t) = \Upsilon(x, y, t) - \eta(x, y, t) \qquad (13)$$

Finally, initial conditions have to be assigned for $\tilde{\phi}$ and $\tilde{\eta}$. In the computations performed, we have imposed

$$\tilde{\phi}(P, 0) = 0 \qquad \tilde{\eta}(x, y, 0) = 0 \qquad (14)$$

Although rather unrealistic (these initial conditions mimic a problem in which the obstacle suddenly appears at $t = 0$), conditions (14) were choosen because of theirs simplicity and for the lack of more detailed information about experiments.

The forces and moments acting on the obstacle are computed by integrating the pressure p on its surface. The pressure is given by the Bernoulli theorem

$$p = -\left(\frac{\partial \Phi}{\partial t} + \frac{1}{2}\nabla\Phi \cdot \nabla\Phi + gz\right) \qquad (15)$$

Linear Formulation

When the wave amplitude is small enough, the squares of the potential derivatives can be neglected, and the free surface boundary conditions can be enforced on the undisturbed water plane $z = 0$. These approximations lead to the following linear problem:

1. the incident wave potential ϕ is the solution of the problem

$$\begin{aligned} &\nabla^2\phi = 0 && \text{in} \quad D \\ &\frac{\partial\phi}{\partial t} + g\eta = 0 && \text{on} \quad z = 0 \\ &\frac{\partial\eta}{\partial t} = \frac{\partial\phi}{\partial z} && \text{on} \quad z = 0 \\ &\frac{\partial\phi}{\partial n} = 0 && \text{on} \quad \partial B \end{aligned} \tag{16}$$

2. the perturbation potential $\tilde{\phi}$ satisfies

$$\nabla^2\tilde{\phi} = 0 \quad \text{in} \quad D \tag{17}$$

$$\frac{\partial\tilde{\phi}}{\partial n} = -\frac{\partial\phi}{\partial n} \quad \text{on} \quad \partial B \cup \partial O \tag{18}$$

$$\frac{\partial\tilde{\phi}}{\partial t} + g\tilde{\eta} = 0 \quad \text{on} \quad z = 0 \tag{19}$$

$$\frac{\partial\tilde{\eta}}{\partial t} = \frac{\partial\tilde{\phi}}{\partial z} \quad \text{on} \quad z = 0 \tag{20}$$

The initial conditions remain the same as in the nonlinear problem.

The pressure is computed from the linear counterpart of the Bernoulli theorem

$$p = -\left(\frac{\partial\phi}{\partial t} + \frac{\partial\tilde{\phi}}{\partial t} + gz\right) \tag{21}$$

NUMERICAL MODEL

The solution $\tilde{\phi}$ of both the linear and the nonlinear problem formulated in the previous section can be expressed as

$$\tilde{\phi}(P) = \int_{\partial D} \sigma(P^*)G(P, P^*)dS^* \tag{22}$$

$G(P, P^*)$ being the Green function for the Laplacian in the 3D space, while σ is the simple layer potential strength on the fluid domain boundary.

In the numerical approximation, the surface of the obstacle ∂O is divided into N quadrilateral panels, on which the source distribution has been supposed piecewise constant [6]. On S, the integral (22) has been approximated by a distribution of M sources placed at a fixed distance above the free surface (i.e. the desingularized formulation suggested in [7] has been used). Finally, the presence of the bottom is taken into account by means of the method of images.

The abovementioned numerical representation of the perturbation potential can be summarized in the formula

$$\begin{aligned} &\tilde{\phi}(P) = \\ &\sum_{j=1}^{N} \sigma_j \left[\int_{\partial O_j} G(P, P^*)dS^* + \int_{\partial \bar{O}_j} G(P, P^*)dS^*\right] \\ &+ \sum_{k=1}^{M} \tilde{\sigma}_k \left[G(P, P_k) + G(P, \bar{P}_k)\right] \end{aligned} \tag{23}$$

where ∂O_j is the j-th panel on the surface of the obstacle, σ_j is the (constant) source density on it, $\partial\bar{O}_j$ is the mirror image of ∂O_j with respect to the bottom, P_k is the position of the k-th source above the free surface, $\tilde{\sigma}_j$ is the source strenght at P_k, and $\bar{P}_k$ is the image of P_k (see fig. 2).

Once the potential $\tilde{\phi}$ is expressed as in (23), a fourth order Runge–Kutta scheme is used to update the solution from t^n to $t^n + \Delta t = t^{n+1}$. Each intermediate stage of the Runge–Kutta algorithm is computed as follows:

- given the potential $\tilde{\phi}$ and its derivatives on $\partial O \cup S$ at the previous stage, the kinematic boundary condition (12) and the dynamic boundary condition (11) (or (20) and (19) in the linear case) are

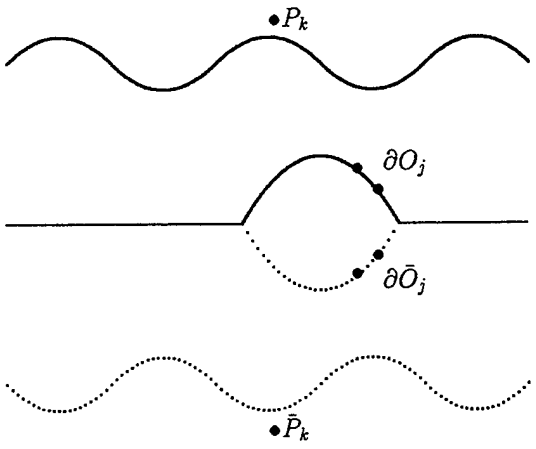


Figure 2: *Location of image source points and image panels*

used to update the free surface elevation and the potential on S;

- the new values of $\tilde{\phi}$ in the M collocation points on the free surface, and the Neumann boundary condition at the N collocation points on the body surface, expressed by means of (23), give rise to $N + M$ linear conditions relating the $N + M$ unknowns σ_j and $\bar{\sigma}_k$. The resulting linear system is solved by factorization of the coefficient matrix;

- the new values of σ_j and $\bar{\sigma}_k$ give the values of $\tilde{\phi}$ and its derivatives on $\partial O \cup S$ for the next Runge–Kutta stage.

The pressure on the obstacle is computed from (15) or (21). In these formulae, the gradient of $\tilde{\phi}$ on ∂B has already been computed, while the time derivative of the perturbation potential is still unknown. This term can be evaluated either by means of finite difference approximation or, with higher accuracy, by noticing [8] that $\partial\tilde{\phi}/\partial t$ is again an harmonic function that satisfies the boundary condition

$$\frac{\partial}{\partial n}\left(\frac{\partial \tilde{\phi}}{\partial t}\right) = -\frac{\partial}{\partial n}\left(\frac{\partial \phi}{\partial t}\right) \quad \text{on} \quad \partial B \qquad (24)$$

while its values on S are given by the kinematic boundary condition (12) or (20). This means that, if a discrete integral representation similar to (23) is used for $\partial\tilde{\phi}/\partial t$, one has to solve a linear system of equation in $N+M$ unknown whose coefficient matrix is the same of the linear system written for $\tilde{\phi}$ (which is already factorized and stored), while the right–hand side can be easily computed from the known values of ϕ and $\tilde{\phi}$.

NUMERICAL RESULTS

In this section, some numerical experiments are reported. In the first one the algorithm is checked by means of an available analitycal solution. In particular the evolution of the wave field due to a submerged doublet of intensity 0.0625 in a uniform stream (Froude number $U_\infty/\sqrt{gz_d} = 0.5656$ and submergence $z_d = 1$) is computed till the steady state is reached. The converged numerical solution is shown in figure 3 together with the analitical one [9]; such an exact solution is available for the linear problem and the numerical method was checked only for the corresponding linearized model. The computation is performed by using 2400 sources above the free surface (approximately 22 sources wavelength) while the time step was $0.025 z_d/U_\infty$. The steady contour lines of the wave height, obtained in about 1000 time steps, agree well with the exact solution.

Both the linear and the nonlinear model are then applied to the typical wave body interaction problem of a vertical submerged cylinder subject to an incident wave train; the measured forces acting on the body [10] are compared with the numerical predictions. In the computations shown in the following, the cylinder was placed in the middle of the computational free surface, 4 wavelengths long in the direction of wave propagation and 3.0 wavelengths wide in the transverse direction; due to the symmetry of the problem only half of the boundary domain is discretized with 420 panels on the body surface and 20×64 point sources above the free surface. The integration time step was $1/20$ of the incident wave period T. Figure 6 reports the nondimensional ratios of the loads on the cylinder to the wave amplitude as functions of the nondimensional wave number. The results refer to the linear simulation (solid lines) for three different ratios of the cylinder submergence over the depth of the water h_m/h_M, equal to 0.3, 0.2 and 0.1 respectively (see figure 4). In the same figure the broken lines show the forces acting on the cylinder subject to an oscillating flow proportional to $\exp(kz)\sin(kx - 2\pi t/T)$; in this approximation the velocity field satisfies the body boundary condition whereas at the free surface,

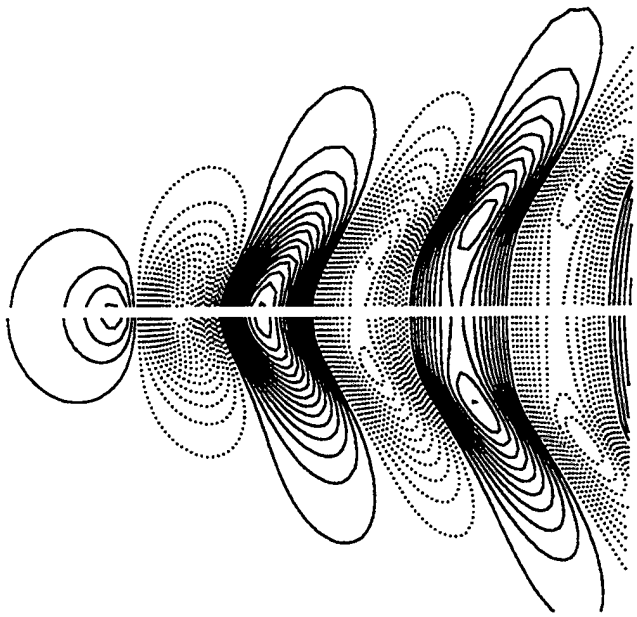


Figure 3: *Asymptotic numerical solution (top) vs. exact solution (bottom) for a doublet of intensity* 0.0625 *at a Froude number* $U_\infty/\sqrt{gz_d} = 0.5656$, $z_d = 1$ *being the submergence of the doublet. Wave elevation contours* $\Upsilon = -0.18, \ldots, 0.18(0.012)$. *Solid line: positive values; dots: negative values.*

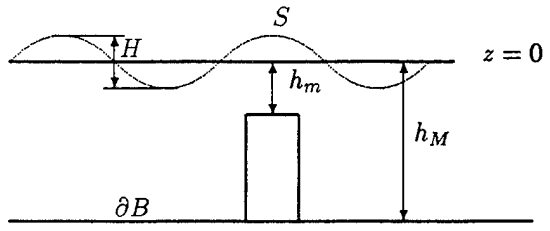


Figure 4: *Diffraction induced by a submerged cylinder: sketch of the problem*

neglecting the disturbance due to the body, no condition is enforced (infinite depth approximation). As expected, the difference between the two solutions is relevant only when h_m/h_M approaches zero, while for increasing values the results are closer and closer.

Though the numerical predictions agree well with the measures, the experimental data obtained at several wave amplitudes and fixed wavenumber exhibit a dependence of the forces on the height of the incidence train. However, as noticed in [10] "... no systematic trend has been identified in the scatter of variation with wave height, and it seems probable that this is a measure of the degree of experimental error". Such a hypothesys seems to be confirmed by the results shown in figure 7, where the nonlinear computation performed at the three different wave amplitudes for the case $h_m/h_M = 0.2$ substantially lies on the linear curve.

Of course, nonlinear effects are expected to dominate when the submergence decreases. In the experiments reported in [10] was observed that the main consequence of nonlinear interaction is a significant increase in wave steepness rather than a wave amplitude growth. Such a behaviour leads, for small submergence, to local wave breaking phenomena, that cannot be simulated with the Eulerian description of the free surface motion adopted in the present work.

More attention is focused on wave profiles rather than on forces in the last problem studied. The diffraction/refraction induced by a shoal of simple shape was analysed and the results were compared with data from a hydraulic model experiment [11]. A sketch of the experiment is shown in figure 9. The geometry of the

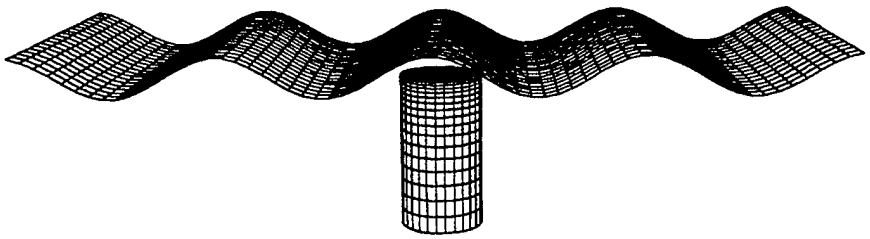


Figure 5: *Diffraction due to a submerged cylinder: sample grid.*

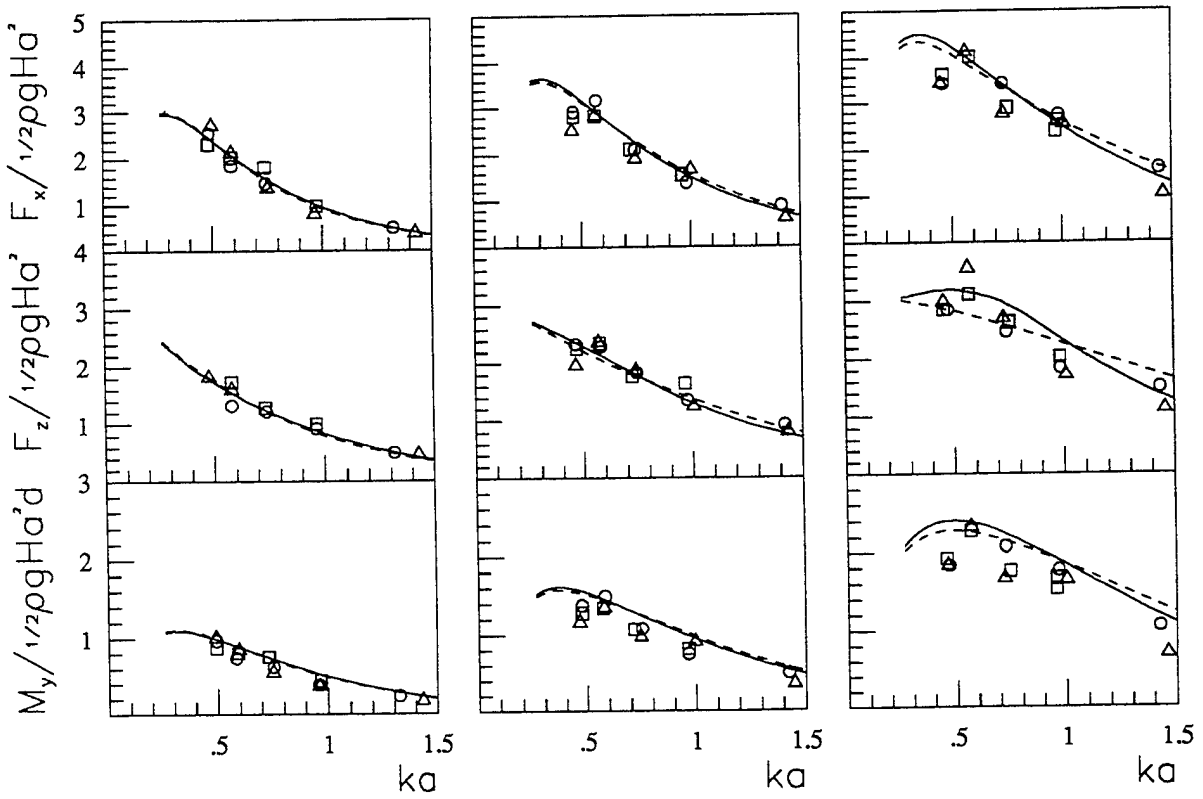


Figure 6: *Diffraction due to a submerged cylinder; linear computation. Left to right:* $h_m/h_M = 0.3, 0.2, 0.1$. *Top to bottom: nondimensional streamwise force, vertical force and capsizing moment on the cylinder vs. nondimensional wave number. Experimental data:* $H/a = 0.17(\triangle)$, $H/a = 0.22(\square)$, $H/a = 0.33(\circ)$. *Numerical results: solid line (with diffraction) and broken line (infinite depth approximation).* a*: cylinder radius,* H*: incident wave height,* k *wave number,* ρ*: density of the fluid,* g *acceleration of gravity.*

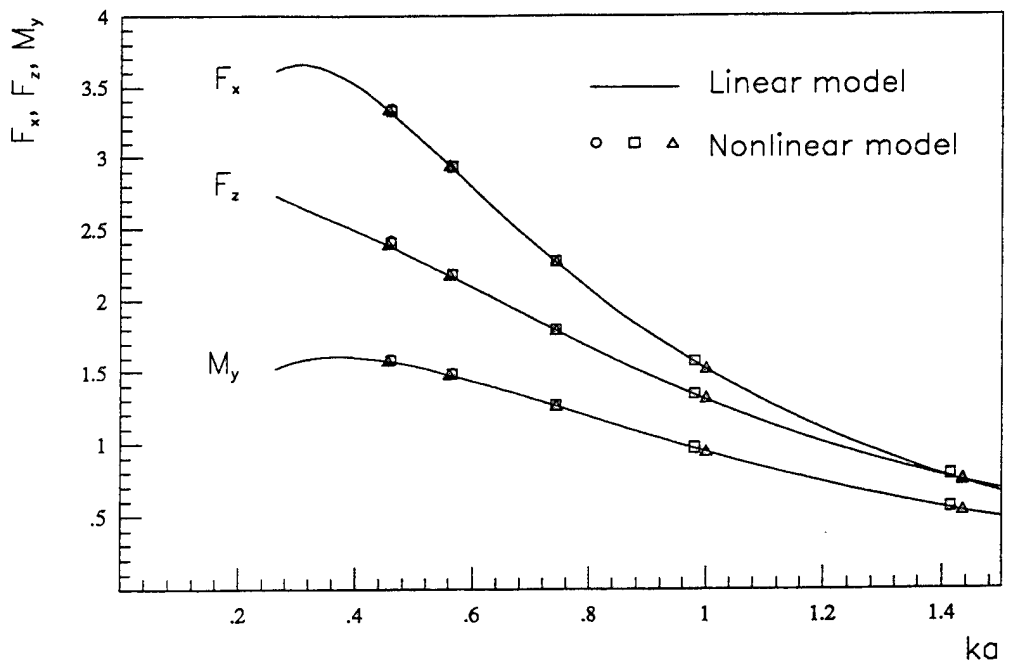


Figure 7: *Diffraction due to a submerged cylinder, nonlinear computation, case $h_m/h_M = 0.2$. Solid line: linear computation; symbols: nonlinear computation $H/a = 0.17(\triangle)$, $H/a = 0.22(\square)$, $H/a = 0.33(\circ)$.*

bottom is given by (see figure 8)

$$z = \begin{cases} (h_M - h_m)\left(\frac{x^2+y^2}{R^2}\right) + h_m & x^2 + y^2 < R^2 \\ h_M & x^2 + y^2 \geq R^2 \end{cases} \tag{25}$$

h_M, h_m being the maximum and minimum depth, respectively, and R is the radial extension of the shoal; in the experiment $R/\lambda = 2$, $h_M/\lambda = 0.375$ and $h_m/\lambda = 0.125$, where λ is the wave length.

In the computation, the shoal was discretized with 224 panels, and 32×64 sources were arranged above the free surface (6×11 wavelengths wide). The incident wave was chosen with a steepness $kH = 0.1$. The propagation of the disturbance due to the presence of the shoal can be observed in the figure 10 which reports the istantanueos contour levels of $\tilde{\eta}$. The wave pattern is more accurately analysed in the next figure 11, where the computed amplitude H is shown for both the linear and the nonlinear model. In the same figure the symbols show the maximum and minimum wave amplitude measured in the experiment at each station. In this case, near the shoal, the nonlinear model seems to give a better prediction of the wave height than the linear one (see figure 11 case $x/\lambda = 2.$). Far from the obstacle, as observed in the previous problem, both predictions lie within the range of experimental data.

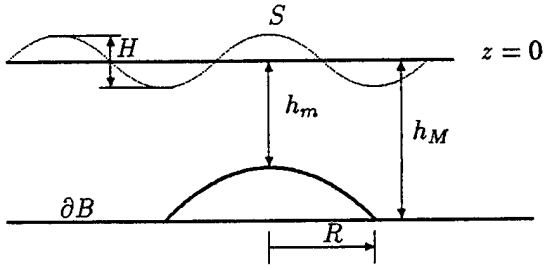


Figure 8: *Diffraction induced by a submerged cylinder: sketch of the problem*

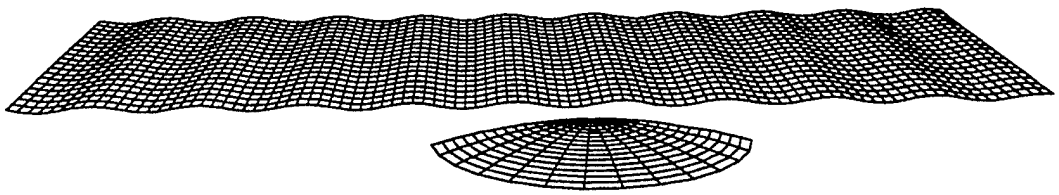


Figure 9: *Diffraction due to a shoal: sample grid.*

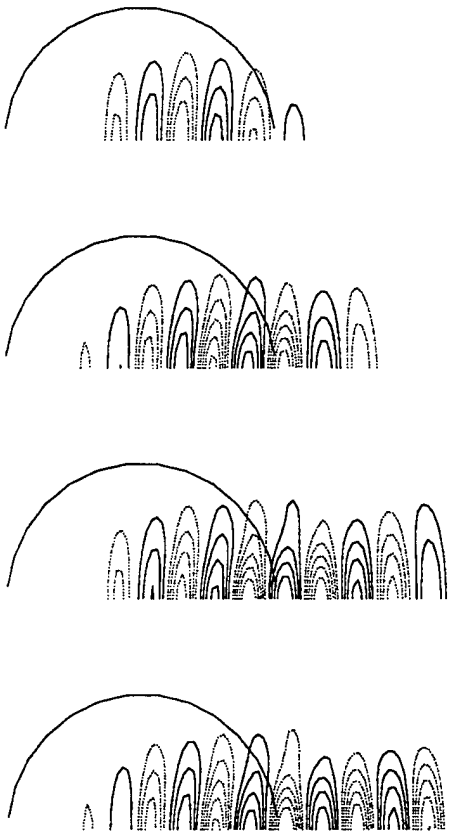


Figure 10: *Diffraction of waves due to a shoal; incident wave propagating from left to right. Nonlinear computation. Top to bottom: istantaneous perturbation wave heigth* $\bar{\eta} = \Upsilon - \eta$ *at* $t/T = 2.5, 5, 7.5, 10.$ T*: wave period. Levels* $-0.1, \ldots, 0.1(0.02)$

CONCLUDING REMARKS

Some preliminary results on the computation of wave diffraction have been discussed. Two sample experiments were considered in validating the model. In the analysis reported above both the forces acting on a submerged obstacle and the wave profiles were compared with the measured ones. It was found that the differences between the linear and the nonlinear model were of the same order of magnitude as the experimental uncertainties, at least in the range of parameters considered. The problem deserves a more detailed analysis in the case of steep incident waves or free surface piercing bodies.

ACKNOWLEDGEMENTS

The work was supported by the Italian Ministry of Merchant Marine in the frame of INSEAN research plan 1988-90.

REFERENCES

[1] Xu, H., Yue, D., "Computation of Fully Nonlinear Three–Dimensional Water Waves", Proc. 19^{th} Sym. Nav. Hydr. (1992).

[2] Grue, J., Palm, E., "The mean drift force and yaw moment on marine structure in waves and currents", J. Fluid Mech. 250 (1993).

[3] Takarada, N., Nakajima, T., Inoue, R., "A study on the capsizing mechanism of Semi–Submersible Platforms (1st Report)", J. Soc. Nav. Arch. Jap., 155 (1984).

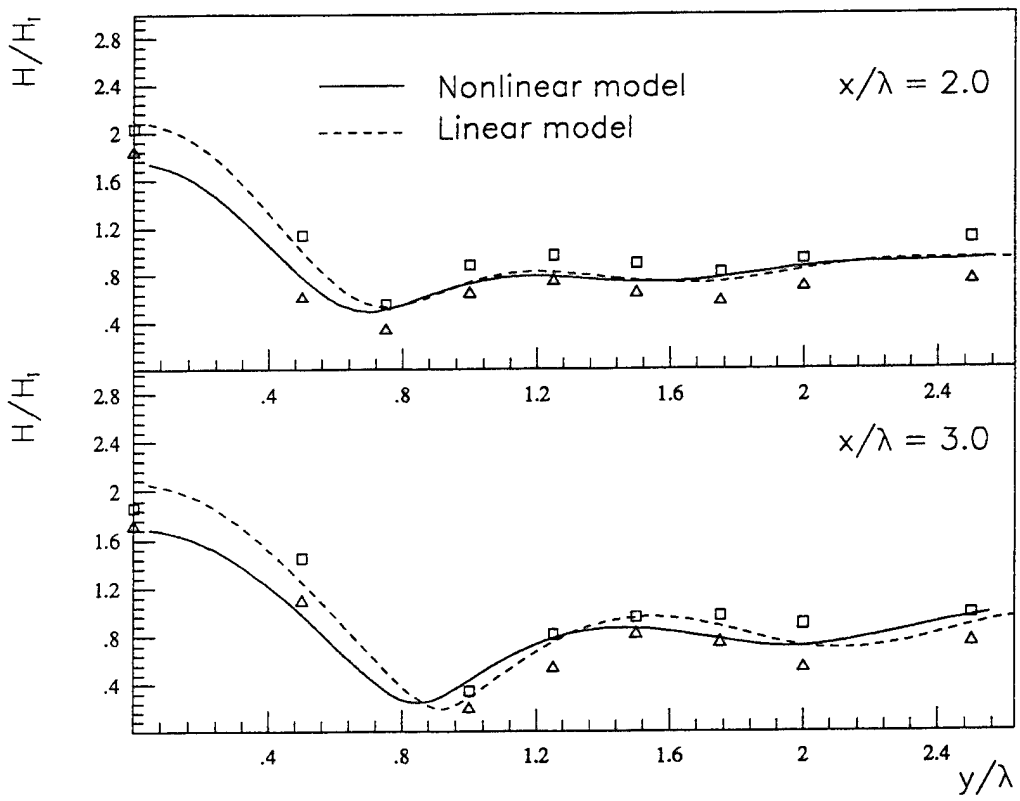


Figure 11: Diffraction due to a shoal. Mean wave amplitude for linear computation (broken line), nonlinear computation (solid line) and experiments (symbols); top to bottom: transerse cut at $x/\lambda = 2$ and at $x/\lambda = 3$. λ: wave length, H: wave amplitude, H_i: incident wave amplitude.

[4] Newman, J.N. "Deformable floating bodies", Abstracts of the 8th International Workshop on Water Waves and Floating Bodies, Canada (1993).

[5] Schwartz, L. W., "Computer Extension and Analytic Continuation of Stokes Expansion for Gravity Waves", J. Fluid Mech., 62, p.553–578 (1974).

[6] Hess, J.L., Smith, A., "Calculation of Potential Flows around Arbitrary Bodies", Prog. Aer. Sci., n.8, p. 1, (1966).

[7] Cao, Y., Schultz, W. W., Bech, R. F., "Three–dimensional Desingularized Boundary Integral Methods for Potential Problems", Int. J. Num. Meth. Fluids, vol.12, p.785–803 (1991)

[8] Cointe, R., "Nonlinear Simulation of Transient Free Surface Flows", Proc. 5^{th} Int. Conf. Num. Ship Hydr., p.239–250 (1989).

[9] Havelock, T.H., "The Wave Pattern of a Doublet in a Stream", Proc. Royal Society, London, Ser. A, Vol.121, p. 288 (1928).

[10] Hogben, N., Standing, R.G., "Experience in Computing Wave Loads on Large Bodies", Proc. of the 1975 Offshore Technology Conference, Houston,Texas, p. 413 (1975).

[11] Ito, Y., and Tanimoto, K. "A Method of Numerical Analysis of Wave Propagation. Application to Wave Diffraction and Refraction", Proc. Coast. Eng., p. 503–522 (1972).

Wave-Drift Forces on Ships in Cross-Flow Conditions

R. Huijsmans (Maritime Research Institute, The Netherlands),
L. Sierevogel (Delfth University of Technology, The Netherlands)

Abstract

In this paper the theory and applications will be discussed of a moored vessel oscillating in waves in the presence of a weak current. The theory is based on the extension of the small forward speed formulation of a translating oscillating source.The corresponding integral equations are derived for a sourcedistribution over the mean wetted surface of the vessel.The effect of the disturbance of the vessel to the stationary potential is covered by an integration of this effect over the free surface. The results of calculations based on this small forward speed expansion is validated against results of model test experiments. Also calculation on a restrained sphere were performed to correlate the results of our computations with those from Zhao et al [25] and Grue et al.[19] These model test experiments cover situations such as a vessel floating in waves and current from head-on to bow quatering conditions.The model tests were executed in the wave and current laboratory of MARIN. The results of model test show that a reasonable correlation is obtained for the current angles 180 and 135 degrees.

1 Introduction

Wave drift forces on moored floating bodies can be considerably influenced by the effect of steady current. Current speeds up to 2 m/s may lead to an increase of 100 % of the wave drift forces. The effect of the current also describes a part of the low frequency reaction force on the ship. Especially in the surge direction were by nature the damping of the ship is low we see a large contribution of this wave drift damping to the total damping of the mooring system. The description of the existance of this wave drift damping effect was discussed by Wichers et al [14]. In a later paper he also elucidated the physical understanding of this phenomena [24]. The description of this effect mathematically, has been studied nowadays by a number of authors (huijsmans [10] and Huysmans et al [11] and Hermans[7], Zhao and Faltinsen [25] ,Nossen Grue and Palm [19] Newman [18] Emmerhof et al [2]) Also the effect of shallow can be incorporated nowadays in nearly in same way the deep water theory was derived.(For details see Grue et al [4] We assume that potential theory can be applied and viscosity effects will be neglected.The floating body responds to monochromatic incoming waves from arbitrary direction while the current speed need not to be head on. The problem is solved to leading order in the wave amplitude and forward speed using boundary integral equations.The first order wave exciting forces are calculated both using haskind relations as well as from the solution of the diffraction problem with forward speed.

From the impulse balance consideration the expression of the wave drift forces are derived.Essentially this formulation was also developed by hermans [7] and Grue [3].From the forward speed dependency of the wave drift forces the wave drift damping coefficient can be calculated numerically.

Nowadays also time domain type of techniques based on rankine sources exist which solve the 3-d linearized hydrodynamic problem with forward speed.(see Prins et all[22]) Although they still require a large computational effort the progress made in this area is quite surprising. In section 2 the boundary value problem is presented and in section 3 the solution for the forward speed problem is formulated .In section 4 the wave drift forces are considered. In section 5 the results of model tests are discussed and presented together with results from computation.

2 The Boundary value problem

2.1 Mathematical formulation

To compute the hydrodynamic forces, we need an expression for the potential. In this chapter the velocity potential is split into a steady and a non-steady part. Also the integral equation (and the free surface condition) for the potential is derived. In the first section the velocity potential is presented and the non-steady part of this potential is described. The second section deals with the boundary condition on the free surface, the third section deals with the body boundary conditions. The last section gives the general equations for the steady potential.

2.2 The potential function

In this section the velocity potential is described and the time dependent part is split into a diffracted and radiated part.

The following restrictions apply:

- The fluid is an ideal fluid, there is no viscosity
- The fluid is incompressible and homogeneous
- The fluid has an irrotational motion
- There is a gravity force field g
- The depth h is supposed to be infinite

The fluid velocity $\underline{u}$ is expressed by the gradient of a velocity potential Φ.

$$\underline{u}(\underline{x},t) = \nabla\Phi(\underline{x},t) \tag{1}$$

Because the fluid is incompressible and homogeneous and the fluid density ρ is constant $\nabla \cdot \underline{u} = 0$.The potential function Φ satisfies Laplace's equation in the fluid domain.

$$\nabla^2\Phi = 0 \tag{2}$$

The total velocity potential function will be split into a steady and a non-steady part.

$$\Phi(\underline{x},t;U) = Ux + \overline{\phi}(\underline{x};U) + \tilde{\phi}(\underline{x},t;U) \tag{3}$$

In this equation U is the incoming imperturbed velocity field, obtained by considering a coordinated system fixed to a ship moving under a drift angle α.

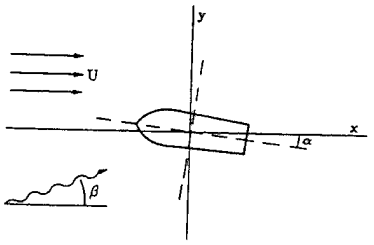


Figure 1: System of Axis

The time dependent part of the potential $\tilde{\phi}$ consist of an incoming diffracted potential $\tilde{\phi}_D$ and radiated wave potential $\tilde{\phi}_R$ time harmonic with frequency ω, where ω is the frequency in the coordinate system fixed to the ship or encounter frequency.
The radiation potential due to the motions of the body may be written:

$$\tilde{\phi}_R(\underline{x},t;U) = e^{-i\omega t}\sum_{j=1}^{6}\xi_j\phi_j(\underline{x};U) \tag{4}$$

where ξ_j is the amplitude of motion in the jth mode and ϕ_j is the corresponding potential.

The diffraction potential $\tilde{\phi}_D$ will be split into a diffracted wave potential ϕ_7 and an incident plane wave potential ϕ_0 due to the incoming waves. We will assume the incident waves are regular.

$$\tilde{\phi}_D(\underline{x},t;U) = e^{-i\omega t}\left(\phi_0(\underline{x};U) + \phi_7(\underline{x};U)\right) \tag{5}$$

$$\text{with} \quad \phi_0(\underline{x};U) = \frac{g\zeta_a}{\omega_0}e^{k_0[z+ix\cos\beta+iy\sin\beta]} \tag{6}$$

with ζ_a the amplitude of the incoming wave in direction β. The frequency and wave number, ω_0 respectively $k_0 = \frac{\omega_0^2}{g} = \frac{2\pi}{\lambda}$, are in the earth fixed coordinate system. The relation between the earth and ship fixed frequency ω_0 and ω is as follows:

$$\omega_0 = \omega - k_0 U\cos(\beta - \alpha) \tag{7}$$

2.3 The boundary condition on the free surface

The vertical elevation of any point on the free surface may be defined by a function $z = \zeta(x,y,t)$.

Newman[16, chapter 6] shows that the effects of the free surface must be expressed in terms of appropriate boundary conditions on this surface. In this section the free surface condition is derived.

The kinematic boundary condition can be derived most readily by requiring that the substantial derivative of the quantity $z-\zeta$ vanish on the free surface.

$$\frac{D(z-\zeta)}{Dt} = 0 \tag{8}$$

We have a dynamic and kinematic boundary condition on the free surface.

$$\left.\begin{array}{l} g\zeta + \Phi_t + \frac{1}{2}\nabla\Phi\cdot\nabla\Phi = \text{const.} \\ \Phi_z - \Phi_x\zeta_y - \Phi_y\zeta_y - \zeta_t = 0 \end{array}\right\} \text{ at } z = \zeta(x,y,t) \tag{9}$$

To expand the boundary condition from the free surface to the plane $z = 0$, we use Taylor series expansions of the potential and its derivatives. After insertion of the linearizations the free surface condition now becomes:

$$\begin{aligned} &\tilde{\phi}_{tt} + g\tilde{\phi}_z + 2U\tilde{\phi}_{xt} + 2\nabla\overline{\phi}\cdot\nabla\tilde{\phi}_t + \tilde{\phi}_t(\overline{\phi}_{xx}+\overline{\phi}_{yy}) \\ &+(U+\overline{\phi}_x)\cdot(U+\overline{\phi}_x)\tilde{\phi}_{xx} + +2(U+\overline{\phi}_x)\overline{\phi}_y\tilde{\phi}_{xy} + \\ &+\overline{\phi}_y\overline{\phi}_y\tilde{\phi}_{yy} + (2U\overline{\phi}_{xy} + \overline{\phi}_x\overline{\phi}_{xy} + \overline{\phi}_y\overline{\phi}_{yy})\tilde{\phi}_y + \\ &+(\overline{\phi}_x\overline{\phi}_{xx} + 2U\overline{\phi}_{xx} + \overline{\phi}_{xy}\overline{\phi}_y)\tilde{\phi}_x = \mathcal{O}(\tilde{\phi}^2) \end{aligned} \tag{10}$$

We assume $\tilde{\phi}(\underline{x},t;U)$ to be oscillatory (See section 2.2).

$$\begin{aligned} \tilde{\phi}(\underline{x},t;U) &= \tilde{\phi}_D + \tilde{\phi}_R = \\ &\left(\phi_0 + \phi_7 + \sum_{j=1}^{6}\phi_j\zeta_j\right)e^{-i\omega t} \\ &= \phi(\underline{x};U)e^{-i\omega t} \end{aligned} \tag{11}$$

The free surface condition is now written as:

$$-\omega^2\phi - 2i\omega U\phi_x + U^2\phi_{xx} + g\phi_z = D(U;\overline{\phi})\{\phi\} \text{ at } z = 0 \tag{12}$$

where $D(U;\overline{\phi})$ is a linear differential operator acting on ϕ as defined in equation (10).
We apply Green's theorem to a problem in D_i inside S and to the problem in D_e outside S where S is the ship's hull. The potential function inside S obeys condition (12) with $D = 0$, while the Green's function fulfills the homogeneous adjoint free surface condition.

$$-\omega^2 G + 2i\omega U G_\xi + U^2 G_{\xi\xi} + gG_\xi = 0 \tag{13}$$

The Green's function will be treated in the next section. In chapter 3.6 equations (12) and (13) will be used to derive a source and vortex distribution.

2.4 The body boundary conditions

In this section the body boundary conditions are derived. These body boundary conditions are used in the right hand side in the source strength and potential expressions in chapter 3.6.

The body boundary conditions for the unknown radiation and diffraction potential are (Newman[17]):

$$\frac{\partial\phi_j(\underline{x};U)}{\partial n} = \begin{cases} -i\omega n_j + Um_j & j = 1,\ldots,6 \\ -\frac{\partial\phi_0}{\partial n} & j = 7 \end{cases} \tag{14}$$

with

$$n_j = \begin{cases} \text{the normal vector } n & j = 1,2,3 \\ \text{the vector } x\times n & j = 4,5,6 \end{cases} \tag{15}$$

and

$$m_j = \begin{cases} m = -(n\cdot\nabla)(\nabla(\chi+x)) & j = 1,2,3 \\ m' = -(n\cdot\nabla)(x\times\nabla(\chi+x)) & j = 4,5,6 \end{cases} \tag{16}$$

with $\chi = \frac{\overline{\phi}}{U}$.

The normal derivatives of each radiation potential consists of a part that represents the normal velocity at the mean position of the body and a part that shows the change in the local steady field due to the motion of the body.
The m_j-terms are written in terms of the derivatives of the steady potential and the normal vector. The m_j-terms consist of second derivatives of the steady potential.

Computing these terms is a difficult problem because we divide the vessel into square panels with a constant source strength. In our numerical scheme we compute the second derivatives using carefull numerical differentiations.

2.5 The steady potential

This section gives the conditions of the steady potential, which are used by Hess and Smith[9].

The steady part of the velocity potential is given by $Ux + \overline{\phi}(\underline{x}; U)$, where Ux is the ambient uniform current and $\overline{\phi}(\underline{x}; U) = U\chi$ is the steady disturbance due to the body. The steady potential fulfills the body boundary condition.

$$\frac{\partial \chi(\underline{x})}{\partial n} = n_1 \text{ on } S \tag{17}$$

To compute the body boundary condition we need an expression for the derivatives of the steady potential.In principle one of the derivative can be circumvented if one uses stokes theorm and a Morino formulation for the velocity potential.However in our case we have estimated the derivative of the steady velocity by numerical differentiation.

3 Solution of the forward speed problem

3.1 The Green's function

To solve the free surface condition (equation (13)), we have to compute the Green's function. When we have a good expression for the Green's function we can compute the source and the potential distributions.
The first section of this chapter[1] gives the asymptotic expansion of the Green's function. In the second section the zero-order Green's function ψ_0 is treated. The third section gives a way to compute the first-order Green's function ψ_1: a transformation in the complex plane. The fourth section deals with the non-uniformity of the first-order Green's function.

3.2 The expansion of the Green's function

In this section we present an asymptotic expansion of the Green's function. The Green's function has the form:

$$G(\underline{x}, \underline{\xi}; U) = -\frac{1}{r} + \frac{1}{r_1} - \psi(\underline{x}, \underline{\xi}; U) \tag{18}$$

where $r = |\underline{x} - \underline{\xi}|$ and $r_1 = |\underline{x} - \underline{\xi}'|$.
$\underline{\xi}'$ is the image of $\underline{\xi}$ with respect to the free surface. This means with $\underline{\xi} = (\xi, \eta, \zeta)$, $r_1^2 = (x-\xi)^2 + (y-\eta)^2 + (z+\zeta)^2$.

[1] The subscripts $_0$ and $_1$ in this section are the terms of the asymptotic expansion and not the modes of motion as in the preceeding section

The Green's function has to be satisfied the conditions on by the velocity potential $\Phi(x, y, z, t)$:

1. $\nabla^2\Phi = 0, \quad z < 0, \quad (x, y, z) \neq (\xi, \eta, \zeta)$ (Laplace's equation)
2. $\Phi_{tt}(x, y, 0, t) + g\Phi_z(x, y, 0, t) = 0$ (linear free surface condition), with $x = \overline{x} - Ut$ and $m(t) = m\cos\omega t$
3. $\Phi(x, y, z, t) = \frac{\omega^2}{g}\frac{1}{r} + \psi_0(x, y, z, t)$, ϕ_0 harmonic everywhere in $z < 0$
4. $\lim_{z\to-\infty} \nabla\Phi = 0$ for all x, y, t (no flux on the sea-floor)
5. $\lim_{R\to\infty} \nabla\Phi = 0$ for all t, $R^2 = (x-\xi)^2 + (y-\eta)^2$
6. $\Phi(x, y, 0, 0) = \Phi_t(x, y, 0, 0) = 0$

The Green's function follows from the source function presented in Wehausen and Laitone[13]. In the case $\tau < \frac{1}{4}$, where $\tau = \frac{\omega U}{g}$, the function $\psi(\underline{x}, \underline{\xi}; U)$ is written as follows:

$$\psi(\underline{x}, \underline{\xi}; U) = \frac{2g}{\pi}\int_0^{\frac{\pi}{2}} d\theta \int_{L_1} dk\ F(\theta, k) + \frac{2g}{\pi}\int_{\frac{\pi}{2}}^{\pi} d\theta \int_{L_2} dk\ F(\theta, k) \tag{19}$$

where

$$F(\theta, k) = \frac{k \cdot e^{k[z+\zeta+i(x-\xi)\cos\theta]}\cos[k(y-\eta)\sin\theta]}{gk - (\omega + kU\cos\theta)^2} \tag{20}$$

These contours are chosen in such a way that when $R \to \infty$ then $\psi \to 0$, so the 'radiation' conditions are satisfied. The radiated waves are outgoing and the Kelvin pattern is behind the ship.
We only take $\tau < \frac{1}{4}$, because with that speed and wave frequency the vessel will not overtake the reflected waves. τ is a non-dimensional parameter defined as $\tau = \frac{\omega U}{g}$

The values k_i are the poles of $F(\theta, k)$.
A careful analysis of the asymptotic behaviour of $\psi(\underline{x}, \underline{\xi}; U)$ for small values of U leads to a regular and an irregular part.

$$\psi(\underline{x}, \underline{\xi}; U) = \psi_0(\underline{x}, \underline{\xi}) + \tau\psi_1(\underline{x}, \underline{\xi}) + \ldots + \tilde{\psi}_0(\underline{x}, \underline{\xi}) + \frac{U^2}{g}\tilde{\psi}_1(\underline{x}, \underline{\xi}) + \ldots \tag{21}$$

In Hermans and Huijsmans[8] it is shown that due to the highly oscillatory behaviour the influence

of $\tilde{\psi}$ may be neglected in our first-order correction for small values of τ.

The behaviour of k_1 and k_3 gives rise to a regular perturbation series with respect to τ. In contrast, k_2 and k_4 originates a highly oscillating contribution which gives rise to a non-uniform expansion. However, the position of the last two poles moves to infinity, therefore it can be treated separately. If $\tau \rightarrow 0$ the contours L_1 and L_2 become the same With $\kappa = \frac{\omega^2}{g}$ follows:

$$\psi_0(\underline{x},\underline{\xi}) = 2\int_L \frac{ke^{k(z+\zeta)}}{k-\kappa} J_0(kR)dk \qquad (22)$$

$$\psi_1(\underline{x},\underline{\xi}) = 4i\cos\theta' \int_L \frac{k^2 e^{k(z+\zeta)}}{(k-\kappa)^2} J_1(kR)\,dk \qquad (23)$$

where $\theta' = \arctan\frac{y-\eta}{x-\xi}$, or in an other way $R\cos\theta' = x-\xi$.

3.3 The zero-order Green's function ψ_0

In this section the zero-order Green's function of the asymptotic expansion is reiterated.

The equation (22) for ψ_0 can be split into the residue and the principal value integral

$$\begin{aligned}
&\psi_0(\underline{x},\underline{\xi}) = \pi i\left\{2ke^{k(z+\zeta)}J_0(kR)\right\}_{k=\kappa} + \\
&2\cdot PV\int_L \frac{ke^{k(z+\zeta)}}{k-\kappa}J_0(kR)dk = \\
&= 2\pi i\kappa e^{\kappa(z+\zeta)}J_0(\kappa R) + \\
&2\cdot PV\int_L \frac{ke^{k(z+\zeta)}}{k-\kappa}J_0(kR)dk \qquad (24)
\end{aligned}$$

The negative zero-order Green's function, without or with the Rankine singularity $-\frac{1}{r}$ is computed in the algorithm Fingreen, derived by Newman[15].

3.4 The first-order Green's function ψ_1

In this section the expressions to compute ψ_1 are given.

$$\begin{aligned}
\Re e\{\psi_1\} &= -4\pi\cos\theta' e^{\kappa(z+\zeta)}\kappa\left[(1+\kappa(z+\zeta))\,J_1(\kappa R)\right. \\
&+ \left.\kappa R J_0(\kappa R)\right] \\
\Im m\{\psi_1\} &= -4\pi\cos\theta' e^{\kappa(z+\zeta)}\kappa\left[(1+\kappa(z+\zeta))\,Y_1(\kappa R)\right. \\
&+ \left.\kappa R Y_0(\kappa R)\right] - \\
&-\frac{8}{\pi}\cos\theta'\int_0^\infty \frac{k^2K_1(kR)}{(\kappa^2-k^2)^2} \\
&\left[2\kappa k\cos k(z+\zeta) + (-k^2+\kappa^2)\sin k(z+\zeta)\right]dk \qquad (25)
\end{aligned}$$

A quick way to compute these Greens functions is derived by Huijsmans and Hermans [12] and by Grue [3]

3.5 The uniform expansion of the Green's function

The expression for ψ_1 makes clear that ψ_1 has a non-uniform behaviour for large R. This means that also $\psi = \psi_0 + \tau\psi_1$ behaves in a non-uniform way. In this section we are trying to write ψ as an uniform asymptotic expansion.
A large R means we handle with large vessels, the size of the vessel becomes large with respect to τ, $\tau R = \mathcal{O}(1)$.
If the size of the ship is order one with respect to τ it is sufficient to use the Green's function (equation (18)), with $\psi = \psi_0 + \tau\psi_1$, but to use equation (20) for ψ gives a non-uniform expression for large R. In our computational model we disregard the non uniform effect of ψ_1 with respect to R , we confine ourselves to the correction of ψ_1 in the region were R $\approx$ 0..It is however possible to reduce the effect of non uniform asymptotic expansion to larger value of R (see [11])

3.5.1 The far-field

We first compute the wave residue of equation (20) and secondly we apply the method of stationary phase.
As said at the end of section 3.2 k_2 and k_4 can be neglected, so L_1 and L_2 become the same, with one pole k_1. One is able to derive that, with the notation $x = \tilde{R}\cos\tilde{\theta}$ and $y = \tilde{R}\sin\tilde{\theta}$ ($\tilde{R}$ is the distance from the origin), follows:

$$\psi(\underline{x},\underline{\xi};U) = 2i\int_0^\pi g(\theta)\left[e^{i\kappa f_1(\theta)} + e^{i\kappa f_2(\theta)}\right]d\theta \qquad (26)$$

We now apply the method of stationary phase to the integrals with respect to θ [23].
After some algebra we see that equation (26) now becomes for all $\tilde{\theta}$:

$$\psi(\underline{x},\underline{\xi};U) \approx \sqrt{\frac{1}{\tilde{R}}}h(\underline{\xi},\theta)e^{k_1(\tilde{\theta})\left[z+i\tilde{R}\sqrt{1-4\tau^2\sin^2\tilde{\theta}}\right]} \qquad (27)$$

with the amplitude

$$h(\underline{\xi},\theta) = \sqrt{\frac{8\pi}{\kappa}} k_1(\tilde{\theta}) \cdot e^{+i\frac{\pi}{4}} \cdot$$
$$e^{k_1(\tilde{\theta})[\zeta + i\xi(-\cos\tilde{\theta} - 2\tau\sin^2\tilde{\theta}) + i\eta(-\sin\tilde{\theta} + 2\tau\cos\tilde{\theta}\,\sin\tilde{\theta})]} \tag{28}$$

with

$$k_1(\tilde{\theta}) = \kappa(1 + 2\tau\cos\tilde{\theta}) + \mathcal{O}(\tau^2) \tag{29}$$

In figure 2 the amplitudes of ψ and the far-field approximation of $\psi(= \mathrm{FF}\psi)$ are given.

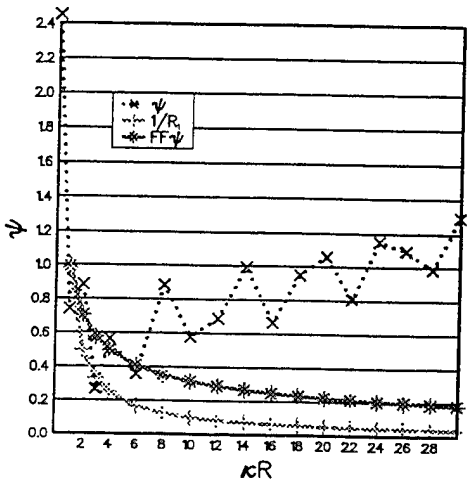


Figure 2: Amplitudes of ψ

3.6 Expansion of the potential

In this chapter the expansion of the potential is derived, using the integral formulation (the free surface condition, equation (12)) and the Green's function of chapter 3.
The first section treats the way Hermans and Huijsmans[8] derived the potential with the help of the source strength. The last section deals with the amplitude of the potential for the far-field.

3.7 The potential using the source strength

In this section the way Hermans and Huijsmans[8] derived the potential is treated. First the source strength is computed by using the free surface conditions. An expansion of source strength is derived. With the source strength we are able to compute an expansion of the potential.

Combining the formulation inside and outside the ship, equations (12) and (13), we may obtain a description of the potential function defined outside S by means of the source and vortex distribution. A derivation of this formulation is found in Brard[1].

$$\begin{aligned}
&-\iint_S \gamma(\underline{\xi})\frac{\partial}{\partial n}G(\underline{x},\underline{\xi})dS_\xi - \iint_S \sigma(\underline{\xi})G(\underline{x},\underline{\xi})dS_\xi \\
&-\frac{2i\omega U}{g}\int_{WL}\gamma(\underline{\xi})G(\underline{x},\underline{\xi})dS_\eta + \\
&+\frac{U^2}{g}\int_{WL}\Big[\gamma(\underline{\xi})\frac{\partial}{\partial\xi}G(\underline{x},\underline{\xi}) + \\
&-\left\{\alpha_t\gamma_t(\underline{\xi}) + \alpha_T\gamma_T(\underline{\xi})\right\}G(\underline{x},\underline{\xi})\Big]d\eta + \\
&+\frac{U^2}{g}\int_{WL}\alpha_n\sigma(\underline{\xi})G(\underline{x},\underline{\xi})d\eta + \\
&+\frac{i\omega}{g}\iint_{FS}G(\underline{x},\underline{\xi})D\{\phi\}dS_\xi = 4\pi\phi(\underline{x})
\end{aligned} \tag{30}$$

where $\alpha_t = \cos(0x,\underline{t})$, $\alpha_T = \cos(0x,\underline{T})$, $\alpha_n = \cos(0x,\underline{n})$
where n is the normal and t the tangent to the waterline and $T = t \times n$ the bi-normal.

It is clear that with the choice $\gamma(\underline{\xi})$ the integral along the waterline gives no contribution up to order U. The source distribution we obtain this way is not a proper distribution, because it expresses the function ϕ in a source distribution along the free surface with a strength proportional to derivatives of the same function ϕ. However, this formulation is linear in U and more over the integrand tends to zero rapidly for increasing distance R. So finally we arrive at the formulation:

$$\begin{aligned}
&-\iint_S \sigma(\underline{\xi})G(\underline{x},\underline{\xi})dS_\xi + \frac{U^2}{g}\int_{WL}\alpha_n\sigma(\underline{\xi})G(\underline{x},\underline{\xi})d\eta + \\
&+\frac{i\omega}{g}\iint_{FS}G(\underline{x},\underline{\xi})D\{\phi\}dS_\xi = 4\pi\phi(\underline{x})
\end{aligned} \tag{31}$$

Using the body boundary conditions, which are worked out in equation (14), at the mean position of the hull

$$\frac{\partial\phi(\underline{x})}{\partial n} = \nabla\phi\cdot\underline{n} = V(\underline{x}) \quad \text{at } \underline{x}\in S \tag{32}$$

and taking $\frac{\partial}{\partial n_x}$ of equation (31)

$$\begin{aligned}
&-2\pi\sigma(\underline{\xi}) - \iint_S \sigma(\underline{\xi})\frac{\partial G(\underline{x},\underline{\xi})}{\partial n_x}dS_\xi \\
&+\frac{U^2}{g}\int_{WL}\alpha_n\sigma(\underline{\xi})\frac{\partial G(\underline{x},\underline{\xi})}{\partial n_x}d\eta + \\
&+\frac{i\omega}{g}\iint_{FS}\frac{\partial}{\partial n_x}G(\underline{x},\underline{\xi})D\{\phi\}dS_\xi = 4\pi V(\underline{x}) \quad \text{at } \underline{x}\in S
\end{aligned} \tag{33}$$

The normal derivative $\frac{\partial}{\partial n_x}$ means the normal derivative in $\underline{x} = (x, y, z)$.
We consider small values of U, because $\tau = \frac{U\omega}{g} < \frac{1}{4}$. The source strength and potential function can be expanded as follows:

$$\sigma_j(\underline{\xi}, U) = \sigma_{j0}(\underline{\xi}) + \tau\sigma_{j1}(\underline{\xi}) + \mathcal{O}(\tau^2) \quad (34)$$

$$\phi_j(\underline{x}, U) = \phi_{j0}(\underline{x}) + \tau\phi_{j1}(\underline{x}) + \mathcal{O}(\tau^2) \quad (35)$$

$D\{\phi\}$ is the linear differential operator acting on ϕ as defined in equation (10). The quadratic terms in $\overline{\phi}$ are neglected. So $D\{\phi\}$ is $2\nabla\overline{\phi}\nabla\phi + \phi(\overline{\phi}_{xx} + \overline{\phi}_{yy})$. We now can write equation (33), at $\underline{x} \in S$, for $j = 1, \ldots, 7$:

$$-2\pi\sigma_{j0}(\underline{\xi}) - \int\int_S \sigma_{j0}(\underline{\xi})\frac{\partial G_0(\underline{x}, \underline{\xi})}{\partial n_x} dS_\xi = 4\pi V_{j0}(\underline{x}) \quad (36)$$

and

$$\begin{aligned} &-2\pi\sigma_{j1}(\underline{\xi}) - \int\int_S \sigma_{j1}(\underline{\xi})\frac{\partial G_0(\underline{x}, \underline{\xi})}{\partial n_x} dS_\xi \\ &= -\int\int_S \sigma_{j0}(\underline{\xi})\frac{\partial \psi_1(\underline{x}, \underline{\xi})}{\partial n_x} dS_\xi + \\ &+ i\int\int_{FS} \frac{\partial}{\partial n_x} G_0(\underline{x}, \underline{\xi})\,[2\nabla\chi\nabla\phi_{j0} + \\ &\phi_{j0}(\chi_{xx} + \chi_{yy})]\, dS_\xi + 4\pi V_{j1}(\underline{x}) \end{aligned} \quad (37)$$

where $G_0(\underline{x}, \underline{\xi}) = -\frac{1}{r} + \frac{1}{r_1} - \psi_0(\underline{x}, \underline{\xi})$, with ψ_0 is the zero speed pulsating wave sources, and $V_j(\underline{x}; U) = V_{j0}(\underline{x}) + \tau V_{j1}(\underline{x}) + \mathcal{O}(\tau^2)$ as in equation (14).

$$V_{j0}(\underline{x}) = \begin{cases} -i\omega n_j & j = 1, \ldots, 6 \\ -\frac{\partial\phi_0}{\partial n} & j = 7 \end{cases} \quad (38)$$

$$V_{j1}(\underline{x}) = \begin{cases} \frac{g}{\omega} m_j & j = 1, \ldots, 6 \\ 0 & j = 7 \end{cases} \quad (39)$$

The subscripts $_{j0}$ and $_{j1}$ mean respectively the zero- and first-order expansion in the jth mode of motion.
We have to take care that ω does not become too small, because then the factor $\frac{g}{\omega}$ becomes too large. A small ω makes the first-order term becomes much larger than the zero-order term. In that case we are trying to make an asymptotic expansion for small τ as well as small ω.

The potential function equation (35) now becomes:

$$\phi_{j0}(\underline{x}) = -\frac{1}{4\pi}\int\int_S \sigma_{j0}(\underline{\xi})G_0(\underline{x}, \underline{\xi})dS_\xi \quad (40)$$

$$\begin{aligned} \phi_{j1}(\underline{x}) &= \frac{1}{4\pi}\int\int_S \sigma_{j0}(\underline{\xi})\psi_1(\underline{x}, \underline{\xi})dS_\xi \\ &\quad -\frac{1}{4\pi}\int\int_S \sigma_{j1}(\underline{\xi})G_0(\underline{x}, \underline{\xi})dS_\xi \\ &\quad +\frac{i}{4\pi}\int\int_{FS} G_0(\underline{x}, \underline{\xi})\,[2\nabla\chi\nabla\phi_{j0} + \\ &\quad \phi_{j0}(\chi_{xx} + \chi_{yy})]\, dS_\xi \end{aligned} \quad (41)$$

So when we compute σ_{j0} and σ_{j1} with the equations (36) and (37), we can compute ϕ_{j0} and ϕ_{j1} with the equations (40) and (41).

The problem we get with this method is that we have to compute the second derivative of the steady potential in equation (37). In section 2.5 this problem is treated.

3.8 The amplitude distributions of the potentials

In this section the far-field potential is described. We define H_j the amplitude of this potential. We need this amplitude to compute the forces in chapter 3.9. The sum of the H_j's is used to compute the wave drift forces.

Far away from the body, we have a radiation condition stating that ϕ_j must have as outgoing waves:

$$\phi_j \approx \sqrt{\frac{1}{\tilde{R}}} H_j(\tilde{\theta}) e^{k_1(\tilde{\theta})\left[z + i\tilde{R}\sqrt{1 - 4\tau^2\sin^2\tilde{\theta}}\right]} \quad \text{for} j = 1, \ldots, 7 \quad (42)$$

The far-field approximations for the Green's functions are given in equation (27).

$$\psi(\underline{x}, \underline{\xi}; U) \approx \sqrt{\frac{1}{\tilde{R}}} h(\underline{\xi}, \theta) e^{k_1(\tilde{\theta})\left[z + i\tilde{R}\sqrt{1 - 4\tau^2\sin^2\tilde{\theta}}\right]}$$

with the amplitude

$$h(\underline{\xi}, \theta) = \sqrt{\frac{8\pi}{\kappa}} k_1(\theta)$$
$$e^{k_1(\tilde{\theta})[\zeta + i\xi(-\cos\tilde{\theta} - 2\tau\sin^2\tilde{\theta}) + i\eta(-\sin\tilde{\theta} + 2\tau\cos\tilde{\theta}\sin\tilde{\theta})] + i\frac{\pi}{4}}$$

with

$$k_1(\tilde{\theta}) = \kappa(1 + 2\tau\cos\tilde{\theta}) + \mathcal{O}(\tau^2) \quad (43)$$

The function H results from the asymptotic expansion of the far-field potentials in equation (31).

$$\begin{aligned} 4\pi\phi_j(\underline{x}) &= -\int\int_S \sigma(\underline{\xi})G(\underline{x}, \underline{\xi})dS_\xi + \\ &\quad +i\tau\int\int_{FS} G(\underline{x}, \underline{\xi})\,[2\nabla\chi\nabla\phi_j + \\ &\quad \phi_j(\chi_{xx} + \chi_{yy})]\, dS_\xi \end{aligned}$$

So the amplitude H of the potentials becomes

$$\begin{aligned} H_j(\theta) &= -\frac{1}{4\pi}\int\int_S \sigma_j(\underline{\xi})h(\xi,\theta)dS_\xi + \\ &+\frac{i\tau}{4\pi}\int\int_{FS} h(\xi,\theta)\left[2\nabla\chi\nabla\phi_j + \right. \\ &\left.\phi_j(\chi_{xx}+\chi_{yy})\right]dS_\xi \end{aligned} \quad (44)$$

with $h(\xi,\theta)$ as in equation (28).

We need the sum of the H_j's to compute the drift forces. We define:

$$H(\theta) = H_7 + i\omega\sum_{j=1}^{6} H^{(j)}\zeta_j \quad (45)$$

3.9 The wave forces

Once the velocity potential is known, we are able to compute the hydrodynamic forces using pressure integration.
In the first section we derive the added mass and the damping by computing the reaction forces. The second section gives the wave forces, computed by direct pressure integration and by the Haskind relation. We also compute the motion due to this forces. In the third section we compute the mean drift forces. The forces and motions are computed for a half-immersed sphere for verification with the results of Nossen et al [19].

3.10 The linearized wave exciting forces and the motions

In this section we compute the exciting forces by direct pressure integration (Hermans and Huijsmans[8]) and by the Haskind relation (Nossen et al.[20]). At the end we compute the motions due to this forces.

The exciting forces will be the forces due to the incident and the diffracted waves.

$$\begin{aligned} X_k &= F_{k0}(\underline{x}) + F_{k7}(\underline{x}) \quad (46) \\ &= -\int\int_S p_0(\underline{x})\cdot n_k dS - \int\int_S p_7(\underline{x})\cdot n_k dS \end{aligned}$$

The pressure due to the incident waves will be computed by integrating the incident wave potential ϕ_0 (equation (6)).
In Hermans and Huijsmans[8] a way to compute first order wave forces is described. The method is based on a direct pressure integration of the first order pressure.
As shown in the preceeding section the diffracted wave force leads to:

$$\begin{aligned} F_{k70} &= -i\rho\omega\int\int_S \phi_{70}\cdot n_k ds \\ F_{k71} &= -i\rho\omega\int\int_S \left[\phi_{71} - \frac{g}{\omega}\left(\frac{\partial\phi_{70}(\underline{x})}{\partial x}\right.\right. \\ &+ \left.\left.\nabla\chi(\underline{x})\cdot\nabla\phi_{70}(\underline{x},t)\right)\right]\cdot n_k ds \end{aligned} \quad (47)$$

In section 3.7 is shown that it is impossible to expand $V_7(\underline{x};\omega)$. So σ_{70} and ϕ_{70} depends of the speed U.

Nossen et al.[20] used Tuck's theorem to compute the first-order wave forces

$$\begin{aligned} X_k &= \rho\int\int_S \left[-i\omega\left(\phi_0+\phi_7\right)\right. \\ &+ \left. U\left(\nabla(\chi+x)\nabla(\phi_0+\phi_7)\right)\right]\cdot n_k dS = \\ &= \rho\int\int_S (\phi_0+\phi_7)[-i\omega n_k - Um_k]dS \\ &= \rho\int\int_S (\phi_0+\phi_7)\frac{\partial\phi_k^{(-\tau)}}{\partial n}dS \end{aligned} \quad (48)$$

with $k = 1,\ldots,6$ and $\phi^{(-\tau)}$ the reverse-flow potential.
Applying Green's theorem and the free surface conditions we can write:

$$\begin{aligned} X_k &= -\rho\int\int_{S_\infty}\left[\phi_0\frac{\partial\phi_k^{(-\tau)}}{\partial n} - \phi_k^{(-\tau)}\frac{\partial\phi_0}{\partial n}\right]dS \\ &+ 2i\tau\rho\int_{C_\infty}\phi_0\phi_k^{(-\tau)}dy \end{aligned} \quad (49)$$

Using the far-field approximations of $\phi^{(-\tau)}$ (equation (42)) with the reverse-flow, so τ becomes $-\tau$, and the incident waves potential (equation (6)) follows:

$$\begin{aligned} &X_k = -i\rho g\frac{\zeta_a}{\omega_0}\cdot \\ &\int_0^{2\pi}\left[\frac{k_1^{(-\tau)}\sqrt{1-4\tau^2\sin^2\theta} - k_0\cos(\theta-\beta)}{k_0+k_1^{(-\tau)}}\right. \cdot \\ &\left.+2\tau\cos\theta\right]\cdot\sqrt{R}\cdot H^{(-\tau)}(\theta)\cdot \\ &e^{i(k_0\cos(\theta-\beta)+k_1^{(-\tau)}\sqrt{1-4\tau^2\sin^2\theta})R}d\theta \end{aligned} \quad (50)$$

with $k_1^{(-\tau)}$ and $H^{(-\tau)}$ as in the equations (29) respectively (44) with the reverse-flow.
Using the method of stationary phase, the exciting forces can be computed the following way:

$$\begin{aligned} X_k &= \frac{\rho g\zeta_a}{\omega_0}\sqrt{\frac{2\pi}{k_0}}(1-\tau\cos\beta)\cdot \\ &H_k^{(-\tau)}(\beta+\pi+2\tau\sin\beta)\cdot e^{-\frac{i\pi}{4}} \end{aligned} \quad (51)$$

Or

$$X_k = \frac{\rho g \zeta_a}{\omega}\sqrt{\frac{2\pi}{k_0}}(1-2\tau\cos\beta)\cdot H_k^{(-\tau)}(\beta+\pi+2\tau\sin\beta)\cdot e^{-\frac{i\pi}{4}} \quad (52)$$

The following plots show the effect of speed on the first-order wave forces of a half-immersed sphere of radius a in head waves. In these examples the speed is $u = 0.4\ ms^{-1}$, so the Froude number $Fr = \frac{u}{\sqrt{ga}} = 0.04$ for u and $Fr = 0.08$ for $2u$. The results agree with Nossen[20].

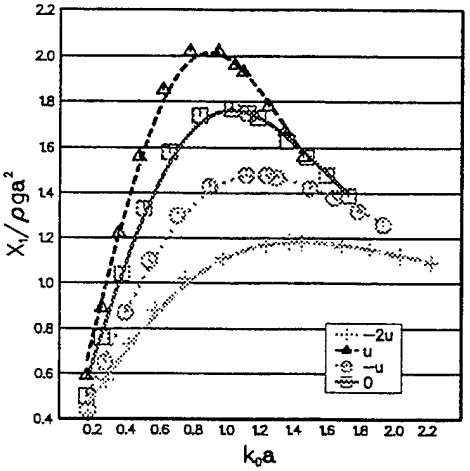


Figure 3: The surge exciting forces.

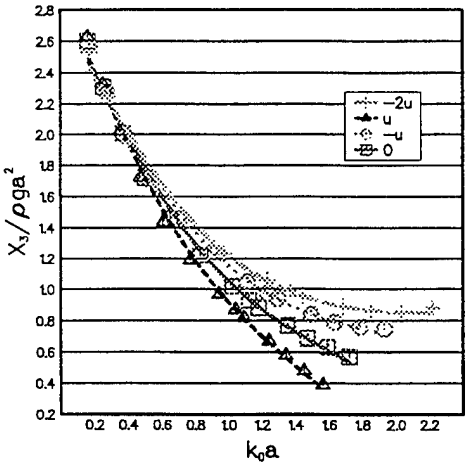


Figure 4: The heave exciting forces.

The motion due to the first-order wave forces will be computed:

$$(m+a(\omega))\ddot{x}(\omega)+b(\omega)\dot{x}(\omega)+cx(\omega) = X(\omega) \quad (53)$$

with m the mass of the body.

The following plots show the effect of speed on the motions of a half-immersed sphere of radius a in head waves .

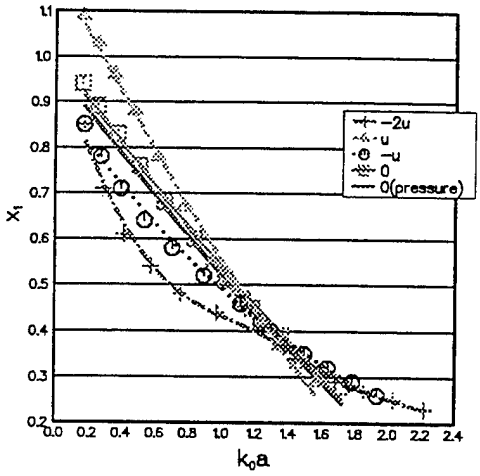


Figure 5: The surge motion.

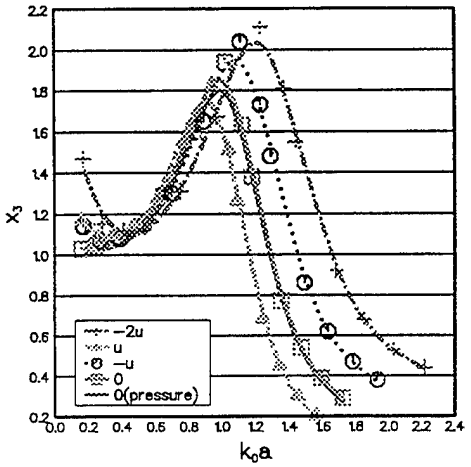


Figure 6: The heave motion.

3.11 The wave drift forces

In an earlier paper Huijsmans[10] used the expression of Pinkster[21] (pressure integration technique) to compute the wave drift forces , This expression contains derivatives of the velocity over the body surface which were cumbersome to compute. At this moment we are mainly interested in the constant component of the wave drift forces. In Hermans[6] (also by Grue [3]) a method is described that leads to results that are possibly more accurate numerically,since they do not require a numerical differentiation of the water velocity over the wetted surface of the body. The

mean drift force $\vec{F}$ is given by

$$\overline{F} = -\overline{\iint_{S\infty} (p\vec{n} + \rho\vec{v}\vec{v}\cdot\vec{n})dS} \qquad (54)$$

where the line above means time-average.

Grue and Palm[5] derived nearly the same expression for the drift forces as Hermans[6]. They not only use the Bernoulli equation, but also conservation of mass. $\overline{F}_x$ consists of two parts. The first one $F_x^{(1)}$, the sway force, behaves like $R^{-\frac{1}{2}}$, while the second term $F_x^{(2)}$, the wave drift force, behaves like R^{-1}.

$$F_x^{(1)} = \mathcal{A}\sqrt{\frac{2\pi}{\kappa}} \cdot \Re e\left\{H^*(\beta^*)e^{\frac{i\pi}{4}}\right\}\cos\beta + \mathcal{O}(\tau^2) \qquad (55)$$

$$F_x^{(2)} = -\frac{\rho}{4}\kappa\int_0^{2\pi} |H(\theta)|^2\left[\cos\theta - 2\tau\sin^2\theta\right]d\theta + \mathcal{O}(\tau^2) \qquad (56)$$

We also have two terms for $\overline{F}_y$.

$$F_y^{(1)} = \mathcal{A}\sqrt{\frac{2\pi}{\kappa}} \cdot \Re e\left\{H^*(\beta^*)e^{\frac{i\pi}{4}}\right\}\sin\beta + \mathcal{O}(\tau^2) \qquad (57)$$

$$F_y^{(2)} = -\frac{\rho}{4}\kappa\int_0^{2\pi} |H(\theta)|^2\left[\sin\theta + 2\tau\sin\theta\cos\theta\right]d\theta + \mathcal{O}(\tau^2) \qquad (58)$$

with

$$\begin{aligned} \mathcal{A} &= -\frac{\rho\omega^2}{2\omega_0}\zeta_a \\ H^* &= \text{the complex conjugate of } H \\ \beta^* &= \beta - 2\tau\sin\beta \end{aligned} \qquad (59)$$

The following plots show the effect of speed on the drift forces of a half-immersed sphere of radius a in head waves. In these examples the speed is $u = 0.4ms^{-1}$, so the Froude number $Fr = \frac{u}{\sqrt{ga}} = 0.04$ for u and $Fr = 0.08$ for $2u$.
Nossen[20] gives only the drift forces on the restrained sphere. The plot is the same as Nossen[20] has in his report.
We also give the drift forces on a free floating sphere. The effect of the stationary potential is small, but can not be neglected, so both figures are presented.

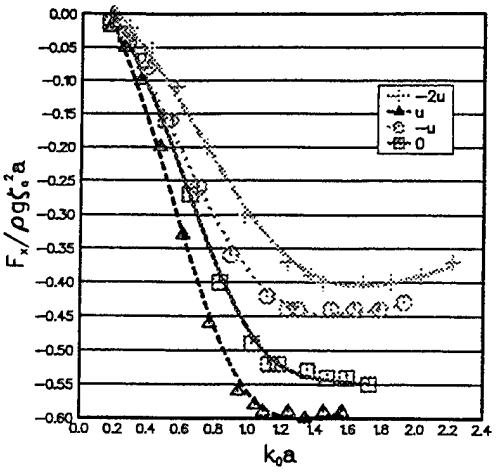


Figure 7: Drift forces on a restrained Sphere

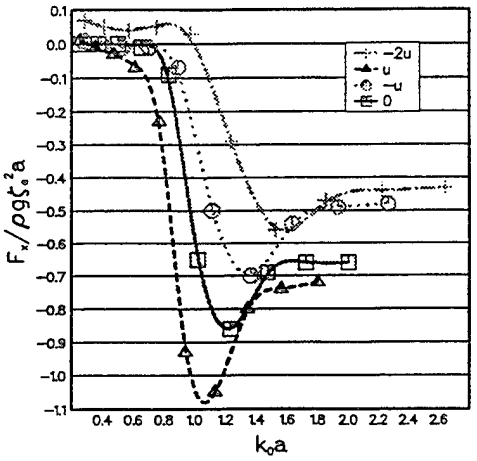


Figure 8: Free floating Spere without ϕ_s

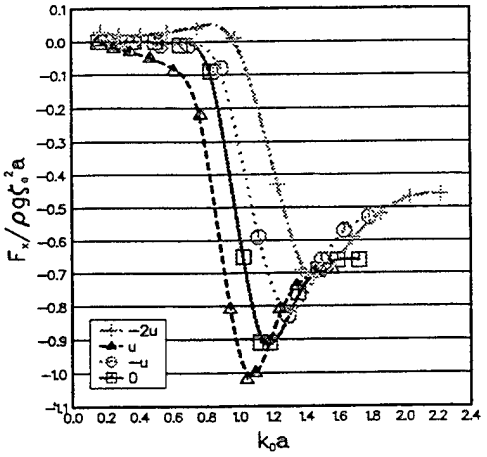


Figure 9: Free floating Spere with ϕ_s

4 Results of Model tests

In order to validate the results of our computations model test experiments. The tests comprised experiments in regular waves on a 200 kDWT tanker in both head on current and bow quatering current.The tanker was loaded at a 40 the fully loaded draft. Particulars of the 200 kDWT tanker is shown in next table.

Particulars of the set–up are shown below.

The spring in the mooring system were chosen such that no influence on the first order motion was to be expected. In the case the current was bow quatering only co-parallel waves were tested. In the head on current case the wave direction was 180 degrees (head on) and 210 degrees (bow quatering). The force signals as measured were evaluated with respect to their mean force. The current force as measured without the presence of the waves was used to correct the mean wave drift force . The resulting mean forces were tabulated as RAO for the wave drift forces. From the tests also the motions RAO's were obtained. Another way of establishing the wave drift damping coefficients is by doing an extinction test in a regular wave.This approach however is only practical for the head on current and wave situation.In the next graph the wave drift damping coefficients are displayed obtained from these extinction tests. From the definition of the wave drift damping coefficient it follows:

$$B_{x_{wd}} = -\frac{F_x^{U\neq 0} - F_x^{U=0}}{v}$$

Based on the theoretically obtained coefficients of the wave drift forces at zero speed and the experimentally determined coefficients of the wave drift damping we obtain an estimate for the wave driftforces at forward speed.

$$F_x^{U\neq 0} = F_x^{U=0} - B_{x_{wd}} * U$$

The resulting estimates are displayed in figure 12 together with the results from computations and measurements.

Designation	Symbol	Unit	Loading condition	
			40 % T	100 % T
Length between perpendiculars	LPP	m	310.00	310.00
Breadth	B	m	47.17	47.17
Depth	D	m	29.70	29.70
Draft even keel	T	m	7.56	18.90
Wetted area	S	m^2	13.90	22.80
Displacement volume	∇	m^3	88,956	234,994
Centre of buoyancy aft FPP (St. 20)	LCB	m	144.54	148.64
Centre of gravity above keel	KG	m	13.32	13.32
Transverse metacentric height	GM	m	13.94	5.78
Longitudinal radius of gyration in air	k_{yy}	m	82.15	77.47
Transverse radius of gyration in air	k_{xx}	m	15.30	14.77
Yaw radius of gyration in air	k_{zz}	m	83.90	79.30
Natural roll period in water	T_ϕ	s	10.1	14.4

Figure 10: Particulars of 200 kDWT tanker

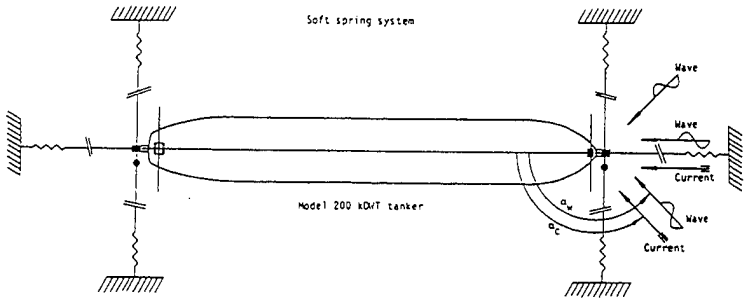


Figure 11: Set Up of Test

4.1 Comparison Theory–Experiments

From the model tests wave drift RAO function are obtained and plotted together with the results from computations in the following figures.

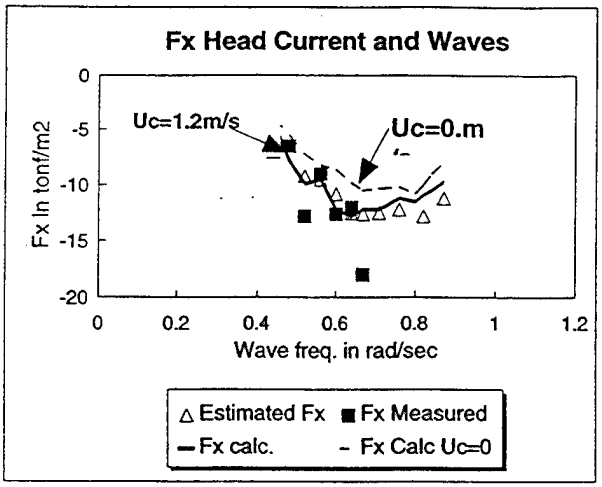


Figure 12: Head waves in 1.2 m/s head on current speed

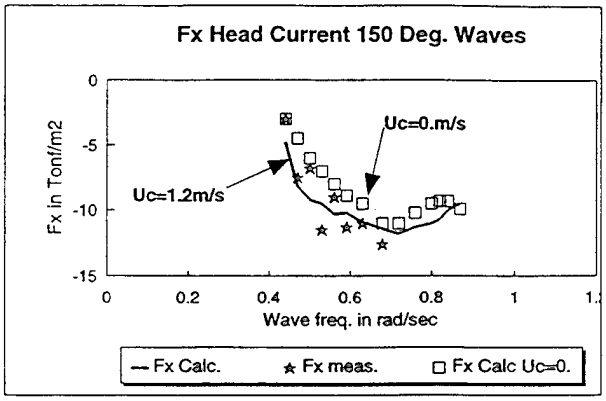


Figure 13: F_x Bow quatering waves in 1.2 m/s head on current speed

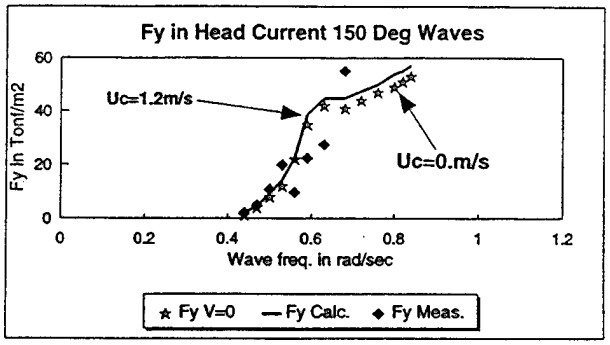


Figure 14: F_y Bow quatering waves in 1.2 m/s head on current speed

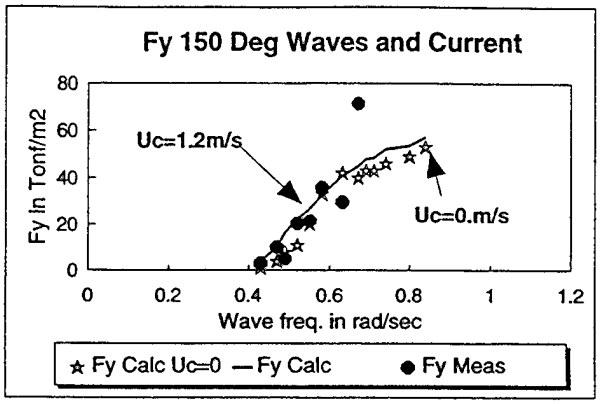


Figure 15: F_x Bow quatering waves in 1.2 m/s current speed co–parallel

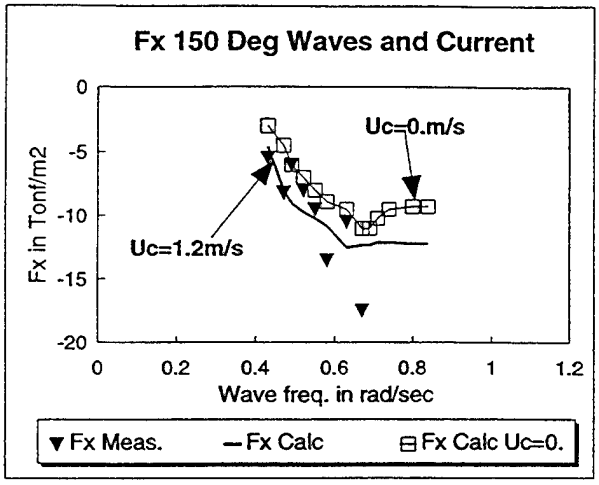


Figure 16: F_y Bow quatering waves in 1.2 m/s current speed co–parallel

5 Discussion

The purpose of this paper is to give an expression for the first- and second-order wave forces a floating body with moderate speed. In examining the results of computations and the results of model tests we observe that due to the limited water-depth shallow water effects influence the comparison of the wave drift force RAO's at the longer wave lengths.The computational model is essentially a deep water formulation whereas the the model tests were executed at a water level of 82.5 m . Also one sees an interesting phenomena that the surge wave drift forces are very sensitive to variations in current speed .Whereas the sway drift forces do not seem to be that sensitive for current speed variations under investigation. The estimated wave drift force for 1.2m/s head on wave and current case from the wave drift damping coefficients lie well within the accuracy bandwith of the measured wave drift forces.

The following items are worth to be reiterated:

- The first-order Green's function will be computed with the expression of derivatives of the zero-order Green's function. This reduces the CPU-time a lot with respect to the full forward speed formulations.
- The non-uniformity of the Green's function is solved as follows: We only use the asymptotic expansion at a finite distance from the source point. When $|\kappa R| > 1$ the second-order Green's function gets a non-uniform behaviour, but the far-field Green's function can be described by the zero-order Green's function ψ_0. So when $|\kappa R| > 1$ we can say that $\psi_1 \approx 0$.
- The expression of the drift forces seems to be acceptable. From the results of experiments and computations on the 200 kDWT tanker we observe a shift of the wave drift transfer function when the current angle changes from 180 degrees to 210 degrees. The shift corresponds to the $\omega_0 - \omega_e$ shift. However considering a linear transformation of the wave drift forces with speed, the level of the RAO of the wave drift force should also be shifted to 85 % of the 180 degrees current angle case.Since this not observed in both the results from experiments and computation one is lead to conclude that the lacking 15 % is due to the interaction of the current with the wave drift forces.

References

[1] R. Brard. The representation of a given ship form. *Journal of ship research*, Vol.16, 1972.

[2] O.J. Emmerhoff and P. Sclavounos. The slow drift motion of a array of cylinders. *journal of Fluid Mechanics*, 242, 1992.

[3] J. Grue. Drift forces and moments on ships advancing with small forward speed. *Ship Technology Research*, 1992.

[4] J. Grue and D. Biberg. Wave forces on marine structures with small speed in water of restricted depth. *Journal of Applied Ocean Research*, 15, 1993.

[5] J. Grue and E. Palm. Currents and wave forces on ships and marine structures. In *Dynamics of marine verhicles and structures in waves*, 1991.

[6] A.J. Hermans. *Second order wave forces and wave drift damping.* Report 91-34, Delft university of technology, 1991.

[7] A.J. Hermans. Second order wave forces and wave drift damping. *Ship Technology Research*, 38, 1991.

[8] A.J. Hermans and R.H.M. Huijsmans. The effect of moderate speed on the motion of floating bodies. *Schiffstechnik*, 1987.

[9] J.L. Hess and A.M.O. Smith. *Calculation of non-lifting potential flow about arbitrary three-dimensional bodies.* Report E.S.40622, Douglas Aircraft Co, Califonia, 1962.

[10] R.H.M. Huijsmans. Wave drift forces in current. In *16th Conf. on Naval Hydrodynamics*, 1986.

[11] R.H.M. Huijsmans and A.J. Hermans. The effect of the steady perturbation potential on the motion of a ship sailing in random seas. In *Fifth Int.Conf.on Numerical Ship Hydrodynamics*, 1989.

[12] R.H.M. Huysmans and A.J. Hermans. A fast algorithme for the calculation of 3– d ship-motions at moderate forward speed. In *Proceedings of Fourth Numerical Ship Hydrodynamic Conference*, 1985.

[13] Wehausen J. and Laitone E. *Surface Waves.* Volume 9 of *Handbuch der Physik*, SPRINGER VERLAG, 1960.

[14] Wichers J.E.W. and Van Sluys M.F. The influence of waves on low frequency hydrodynamic coefficients of moored vessels. In *Offshore Technology Conference*, 1979. 2625.

[15] J.N. Newman. The evaluation of the free surface green function. In *Fourth international conference on numerical ship hydrodynamics, Washington*, 1985.

[16] J.N. Newman. *Marine hydrodynamics.* The MIT press, 1977.

[17] J.N. Newman. The theory of ships motions. *Advances in applied mathematics*, Vol.18, 1978.

[18] J.N. Newman. Wave drift damping of floating bodies. *journal of Fluid Mechanics*, 1993.

[19] J Nossen, J. Grue, and E. Palm. On the solution of the radiation and diffraction problems for a floating body with a small forward speed. In *Fifth Int. Workshop on Water Waves and Floating Bodies*, 1989.

[20] J. Nossen, J. Grue, and E. Palm. Wave forces on three-dimensional floating bodies with small forward speed. *Journal of fluid mechanics*, Vol.227, 1991.

[21] J.A. Pinkster. *Low frequency second order wave exciting forces on floating structures.* Publication 650, Netherlands ship model basin, 1980.

[22] H. Prins and A.J. Hermans. Time domain calculations of the second order drift forces on a tanker in current and waves. In *Twentieth Symposium on naval hydrodynamics, Santa Barbara USA*, 1994.

[23] P. Stoker. *Water waves.* John Wiley, 1967.

[24] J.E.W. Wichers. *A simulation model for a single point moored tanker.* PhD thesis, Technical University Delft, 1988.

[25] R. Zhao and O. Faltinsen. Interaction between current waves and marine structures. In *Fifth Int.Conf.on Numerical Ship Hydrodynamics*, 1989.

Time-Domain Calculations of the Second-Order Drift Force on a Tanker in Current and Waves

H. Prins, A. Hermans
(Delft University of Technology, The Netherlands)

ABSTRACT

In this paper we solve the time-dependent linear equations which describe the interaction between a tanker and current and waves. The current is taken into account by means of the double-body potential. Our algorithm is based upon combining the time-dependent boundary conditions and the Laplace equation, and integrating the resulting equation in time. The algorithm is stable for every time-step and velocity of the ship. Results are presented for the hydrodynamic coefficients and drift forces. The hydrodynamic coefficients agree well with results found after transforming the equations into the frequency domain. Drift forces and moments have been calculated for both head and following waves.

NOMENCLATURE

Roman Symbols :

c	local phase velocity
D	deck of the hull
$\vec{F}_1$	first-order force
$\vec{F}_2$	second-order force
Fn	Froude number
g	gravitational acceleration
G	Green's function
H	hull surface
k	wave number
$\vec{M}_1$	first-order moment
$\vec{M}_2$	second-order moment
$\vec{n}$	normal vector, pointing out of the fluid domain
p	pressure
t	time
U	undisturbed horizontal velocity of the fluid
x, y, z	coordinate system fixed to the ship
$\vec{X}$	translational motion
z_b	z-coordinate of buoyancy point
z_g	z-coordinate of point of gravity

Greek Symbols :

$\vec{\alpha}$	displacement vector
β	angle of incidence of the waves
Δ	volume displacement
ζ	total wave height
ζ_a	wave height due to the incoming wave
ζ_r	relative wave height
ρ	density of the fluid
$\phi, \vec{\phi}$	unsteady potential
$\vec{\phi}_n$	normal derivative of the unsteady potential
ϕ_{inc}	potential due to the incoming wave
ϕ_m	potential due to the movement of the hull
ϕ_d	potential due to the diffracted wave
$\overline{\phi}$	steady potential
$\overline{\phi}_{db}$	double body potential
Φ	total potential
ω	frequency of encounter
ω_0	orbital frequency
$\vec{\Omega}$	rotational motion

INTRODUCTION

In the last decade numerous authors have attempted to solve the unsteady ship-motion problem. This problem is very important in predicting the behaviour of a ship in real sea-keeping, which includes the interaction between waves and velocity of the ship.

Most of the studies were done using the frequency domain rather than the physical time domain. Unfortunately, this restricts the theories to harmonic functions. This is not realistic, of course, for sea waves are not harmonic, especially not in the neighbourhood of a ship. Therefore we have studied the problem in the time domain. The major disadvantage, however, is the long computing time needed to solve the time-dependent problem. Fortunately this computing time decreases every year with the introduction of faster computers. So in the future this disadvantage will not be of importance any more. Therefore we have made a first step in the direction of solving the time-dependent ship-wave problem.

Recently, we studied both a two dimensional problem [6], and a three-dimensional problem [7]. The algorithm developed for these problems is both stable and accurate. In this algorithm the free-surface condition and the Laplace equation are integrated simultaneously in order to overcome instabilities at the free-surface. The results of both studies agreed very well with results found by Zhao [11], Pinkster [4] and Nossen [3]. Now this algorithm will be used studying the realistic three-dimensional problem of a commercial tanker.

The time-dependent three-dimensional problem has also been studied by Nakos [2]. However, we have severe objections against his way of integrating the free-surface, as stated in Prins [7]. Furthermore we will not only present hydrodynamic coefficients, but also drift forces acting on the object. For the case of non-zero forward speed the drift forces have not been shown in literature before.

In this paper, we will first describe the mathematical formulation of the problem. Then the algorithm is summarised and numerical results will be given. Finally a comparison will be made with literature and conclusions will be drawn.

MATHEMATICAL MODEL

The mathematical formulation given below is analogue to the one given in Prins [7], but now including rotational motion of the hull.

We consider a tanker floating in water of finite depth. A uniform current with velocity U is directed in the positive x-direction; regular incoming waves are traveling in the water-surface in a direction which makes an angle β with the positive x-direction, see Fig. 1. The coordinate system is chosen in such a way that the undisturbed free surface coincides with the plane $z = 0$ and the center of gravity of the hull is on the z-axis, with z pointing upwards. The hull is free to move in all directions and to rotate round the main axes.

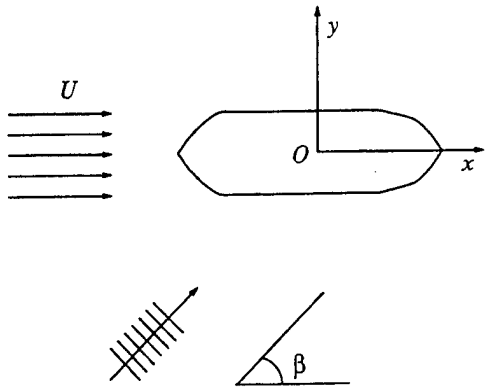


Figure 1: Aerial view of the geometry

We assume the fluid to be incompressible and we neglect the effect of viscosity. If we assume the flow to be irrotational, we can introduce a velocity potential Φ, which has to satisfy the Laplace equation

$$\vec{\nabla}^2\Phi = 0 \tag{1}$$

At the free surface we combine the well-known dynamic and kinematic boundary conditions to get

$$\frac{\partial^2\Phi}{\partial t^2} + 2\vec{\nabla}\Phi\cdot\vec{\nabla}\frac{\partial\Phi}{\partial t} + \frac{1}{2}\vec{\nabla}\Phi\cdot\vec{\nabla}\left(\vec{\nabla}\Phi\cdot\vec{\nabla}\Phi\right) + g\frac{\partial\Phi}{\partial z} = 0 \qquad \text{at} \quad z=\zeta \tag{2}$$

where the wave elevation ζ follows from

$$\zeta = -\frac{1}{g}\left\{\frac{1}{2}\left|\vec{\nabla}\Phi\right|^2 + \frac{\partial\Phi}{\partial t}\right\} \qquad \text{at} \quad z=\zeta$$

On the ship hull we have the condition that the normal velocity of the fluid should match the normal velocity of the ship:

$$\frac{\partial\Phi}{\partial n} = V_n \qquad \begin{matrix}\text{at instantaneous position}\\ \text{of ship hull}\end{matrix} \tag{3}$$

To ensure uniqueness of the solution we have to impose a radiation condition which will be specified later on.

The velocity potential that satisfies these equations, consists of a steady and an unsteady part; so we split it up as

$$\Phi(\vec{x},t) = \overline{\phi}(\vec{x}) + \phi(\vec{x},t)$$

Steady Potential

In order to calculate the unsteady potential we have to know the steady potential. Computation of the steady potential can be carried out by means of a Dawson approach, see for instance Raven [8]. But the major contribution to the second-order drift forces can be calculated by using the double-body potential instead of the complete steady potential. This approximation is valid only if the steady waves generated by the body are small compared to the incoming waves.

The double-body potential of a tanker is not known analytically and has to be calculated separately. This is done by using the solver for the time-dependent equations, but now with time independent boundary conditions. The double-body potential then follows from a matrix equation, which has to be solved only once. For more details about the solver, see the section Numerical Algorithm.

Unsteady Potential

The unsteady potential consists of all time-dependent parts of the total potential and is therefore composed of the incoming wave, the diffracted wave and the potential due to the movement of the ship. So we decompose the unsteady potential as

$$\phi(\vec{x},t) = \phi_{inc}(\vec{x},t) + \phi_d(\vec{x},t) + \phi_m(\vec{x},t) \quad (4)$$

If we linearize the free-surface condition (2) for $\phi(\vec{x},t)$ by assuming ϕ to be small compared to $\overline{\phi}$, which in its turn is small, we get

$$\frac{\partial^2\phi}{\partial t^2} + 2\vec{\nabla}\overline{\phi}\cdot\vec{\nabla}\frac{\partial\phi}{\partial t} + \left(\frac{\partial^2\overline{\phi}}{\partial x^2} + \frac{\partial^2\overline{\phi}}{\partial y^2}\right)\frac{\partial\phi}{\partial t} + g\frac{\partial\phi}{\partial z} = 0 \qquad \text{at} \quad z = 0 \quad (5)$$

In our study of a two-dimensional problem, we included the terms of $\mathcal{O}\left(U^2\right)$. Including them here, however, would cause us to calculate higher derivatives of ϕ at the free surface. This would require a very fine mesh which would increase the computation time considerably. Furthermore, they would give rise to a second-order time derivative of the normal derivative of ϕ, which causes some extra numerical difficulties, see also Nakos [2]. Therefore the terms of $\mathcal{O}\left(U^2\right)$ are left out for the moment. [1]

The linearized version of the body boundary condition (3) becomes

$$\frac{\partial\phi}{\partial n} = \frac{\partial\vec{\alpha}}{\partial t}\cdot\vec{n} - \vec{\alpha}\cdot\left(\vec{n}\cdot\vec{\nabla}\right)\vec{\nabla}\overline{\phi} + \vec{n}\cdot\left(\vec{\nabla}\overline{\phi}\cdot\vec{\nabla}\right)\vec{\alpha} \quad (6)$$

with $\vec{\alpha}$ the displacement vector of the ship, given by

$$\vec{\alpha} = \vec{X} + \vec{\Omega}\times\vec{x}$$

and $\vec{n}$ the normal pointing out of the fluid domain, see Timman [9].

Unlike the fluid domain our computational domain cannot be infinite, so we have to introduce artificial boundaries and proper boundary conditions. These conditions include the radiation condition. We choose this condition such that it absorbs the outgoing diffracted waves, but reflects on the outside the non-physical waves, introduced by the mathematical model. Generally, two waves travel forward and two travel backwards. So at each element of the boundary two waves have to be absorbed. This would lead to a second-order partial-differential equation as a boundary condition. However, the wave velocity of the second wave is low, so that it will not reach the boundary, reflect and disturb the calculation within the simulated time. Thus this slow-traveling wave is neglected in the radiation condition.

To derive such an absorbing radiation condition we used the Green's function satisfying the boundary condition at the free surface, for instance given by Wehausen and Laitone [10]. The asymptotic behaviour of this function for large r gives rise to the following condition:

$$\frac{1}{c(\gamma)}\frac{\partial\phi}{\partial t} + \frac{\partial\phi}{\partial r} = 0 \quad (7)$$

with

$$c(\gamma) = \frac{\omega}{k(\gamma)}$$

[1] In Prins [7] a different free-surface condition is given, due to typographical errors. However, the results presented there have been calculated using the above formula.

where $k(\gamma)$ is the local wavenumber. See Prins [7] for more details on the derivation of this condition. Unless the current velocity U is zero, condition (7) is different for every point on the boundary and it is based on the local wave velocity. The asymptotic analysis of the Green's function would give rise to an additional term $\frac{\phi}{2r}$. However, numerical experiments showed that this term was negligibly small.

At the bottom we have

$$\frac{\partial \phi}{\partial n} = 0$$

To be able to apply this condition close to the body, for instance in relatively shallow water, we mirrored the computational domain in the bottom and used the symmetry following from the above condition. This has the big advantage that the number of elements in the mesh does not vary with the depth of the fluid domain.

Movement Of The Ship

Because the tanker is free to move in all six possible directions, both the force and the moment are needed to calculate the linear movement of the hull. This first-order force is given by

$$\vec{F}_1 = \rho \int_H \left(\frac{\partial \phi}{\partial t} + \vec{\nabla}\phi \cdot \vec{\nabla}\overline{\phi} \right) \vec{n} ds$$

where ϕ is the potential due to the incoming and the diffracted wave, as the motion of the ship is yet unknown. For the moment we have

$$\vec{M}_1 = \rho \int_H \left(\frac{\partial \phi}{\partial t} + \vec{\nabla}\phi \cdot \vec{\nabla}\overline{\phi} \right) \vec{x} \times \vec{n} ds$$

If we do not consider incoming waves but forced oscillation of the ship, we can calculate the added mass and damping coefficients by fitting the force and moment to the acceleration and the velocity:

$$F_{1i} = -A_{ij} \frac{\partial^2 \vec{x}_j}{\partial t^2} - B_{ij} \frac{\partial \vec{x}_j}{\partial t}$$

This expression gives the force in direction i due to a motion in direction j. Note that there is no summation over the index j. For the moment an equivalent formula holds.

The movement of the ship can then be calculated by solving the following set of differential equations:

$$\boldsymbol{M} \frac{\partial^2 \vec{Y}}{\partial t^2} + \boldsymbol{A} \frac{\partial^2 \vec{Y}}{\partial t^2} + \boldsymbol{B} \frac{\partial \vec{Y}}{\partial t} + \boldsymbol{C} \vec{Y} = \mathcal{F}_{1i} \qquad i = 1, .., 6 \qquad (8)$$

with $Y^T = (X_1, X_2, X_3, \Omega_1, \Omega_2, \Omega_3)$. The mass matrix $\boldsymbol{M}$ is diagonal and consists of the mass and the relevant moments of inertia. $\mathcal{F}$ is the force or the moment, whatever is appropriate. The non-zero elements of C are

$$C_{33} = \rho g \int_D dA$$

$$C_{35} = C_{53} = -\rho g \int_D x dA$$

$$C_{44} = \rho g \left(z_b - z_g \right) V + \rho g \int_D y^2 dA$$

$$C_{55} = \rho g \left(z_b - z_g \right) V + \rho g \int_D x^2 dA$$

with D the deck of the hull.

Drift Force and Moment

Now that equation (8) enables us to calculate the movement of the ship, we can solve the equations for the total unsteady potential. Then the averaged second-order force and moment can be calculated by the formulas as derived in the appendix:

$$\left\langle \vec{F}_2 \right\rangle = \vec{\Omega} \times \left(M \frac{\partial^2 \vec{X}}{\partial t^2} \right) - \begin{pmatrix} 0 \\ 0 \\ \Omega_1 \Omega_3 C_{35} \end{pmatrix} - \int_H \rho \vec{\alpha} \cdot \vec{\nabla} \left(\frac{\partial \phi}{\partial t} + \vec{\nabla}\overline{\phi} \cdot \vec{\nabla}\phi \right) \vec{n} dA - \int_H \frac{1}{2} \rho \left| \vec{\nabla}\phi \right| \vec{n} dA + \int_{\mathrm{wl}} \frac{1}{2} \rho g \zeta_r^2 \vec{n} dl \qquad (9)$$

$$\left\langle \vec{M}_2 \right\rangle = \vec{\Omega} \times \left(\boldsymbol{I} \frac{\partial^2 \vec{\Omega}}{\partial t^2} \right) - \begin{pmatrix} -\Omega_2 \Omega_3 C_{44} \\ \Omega_1 \Omega_3 C_{55} \\ 0 \end{pmatrix} - \int_H \rho \vec{\alpha} \cdot \vec{\nabla} \left(\frac{\partial \phi}{\partial t} + \vec{\nabla}\overline{\phi} \cdot \vec{\nabla}\phi \right) (\vec{x} \times \vec{n}) \, dA - \int_H \frac{1}{2} \rho \left| \vec{\nabla}\phi \right| (\vec{x} \times \vec{n}) \, dA + \int_{\mathrm{wl}} \frac{1}{2} \rho g \zeta_r^2 \, (\vec{x} \times \vec{n}) \, dl \qquad (10)$$

Here ζ_r is the linearized relative wave-height, which can be calculated by using Bernoulli's equation and the displacement of the hull.

NUMERICAL ALGORITHM

To solve the problem described above, we use the same method as was used in Prins [6]. This method will be summarised below.

First we introduce the Green's function of the Laplacian in three dimensions:

$$G\left(\vec{x},\vec{\xi}\right) = -\frac{1}{4\pi}\frac{1}{|\vec{x}-\vec{\xi}|} \tag{11}$$

Then the problem can be reformulated into an integral equation with boundary conditions, using Green's second theorem. We discretize this integral equation by dividing the boundary into polygons, either quadrangles or triangles, and assuming the quantities to be constant on such an polygon. The collocation points are the centres of these polygons and the integral over such an element is calculated according to Fang [1] [2]. Thus we arrive at a set of linear equations which can be written as:

$$[A]\vec{\phi}(t) = [B]\vec{\phi}_n(t) \tag{12}$$

with $[A]$ and $[B]$ matrices built up by the Green's function and its derivative, and $\vec{\phi}_n$ a vector containing the normal derivatives of ϕ. Due to the bottom boundary condition the mirrored elements have exactly the same potentials as the elements themselves. Therefore the contribution of a mirrored element has been added to that of the corresponding element.

To obtain a stable algorithm we eliminate $\frac{\partial\vec{\phi}}{\partial n}$ by substituting the boundary conditions (5), (6) and (7) into (12), and integrate the resulting matrix equation in time. In this respect our algorithm differs from the one Nakos [2] uses: we do not integrate the free surface condition separately, but first substitute this condition into the discretized version of the Laplace equation and then integrate the resulting equation in time. This has been done in order to overcome instabilities which arise from the fact that the free-surface condition itself has eigenvalues with positive real part. This means that the integration of this condition is unstable for every time-stepping scheme, because the analytical solution is exponentially increasing. Combining the free-surface condition with the Laplace operator, these eigenvalues are transformed into eigenvalues with non-positive real part. The fact that Nakos still obtains sinusoidal waves is due to the numerical damping of his time-stepping scheme. This imposes restrictions on his time step and his mesh. Our algorithm, however, is stable for every time step and mesh.

The second-order time derivative has been discretized by a second-order difference and the first-order time derivative by its usual backwards second-order difference scheme. The spatial derivatives on both the hull and the free surface have been discretized by second-order difference schemes. Especially on the hull this has to be done very carefully. In our program the local curvature of the hull has been taken into account. This improves the accuracy of the derivatives considerably.

Thus discretising both time and space derivatives leads to the following overall matrix equation:

$$[A_1]\vec{\phi}_{i+1} = [A_2]\vec{\phi}_i + [A_3]\vec{\phi}_{i-1} + [A_4]\vec{\phi}_{i-2} + \vec{f}_{i+1} \tag{13}$$

with $\vec{f}$ a time-dependent vector, resulting from the body boundary condition. With the condition that the fluid is initially undisturbed, i.e. $\vec{\phi} = \mathbf{0}$ and $\frac{\partial\vec{\phi}}{\partial t} = \mathbf{0}$, this system can be solved.

RESULTS

The numerical algorithm presented in the previous section has been used to calculate the second-order drift forces and all other relevant quantities, such as added mass and damping coefficients and movements of the hull. We used a 200 kDWT tanker (particulars given in Table 1), sailing in relatively shallow water: the water depth is 1.2 times the draught. We calculated our results for three different speeds: $Fn = 0$, $Fn = .004$ and $Fn = .008$ (0, 0.5 and 1.0 knots).

The mesh on the hull consisted of 676 elements, see Fig 2. The free surface was discretized using the waterline shape of the hull, and was built up out of 20 non equi-distantial rings. Each ring was subdivided into 104 elements, the number of waterline elements on the hull. The artificial boundary was taken to be 2 wave lengths away from the hull.

[2] The paper by Fang contains some erroneous signs. These were corrected in our calculations.

The time integration was carried out over a time interval of 8 periods according to the frequency of encounter. On this interval 400 time steps were taken. The equations of motion were integrated using the implicit method of Crank-Nicholson.

Table 1: Particulars of 200 kDWT tanker

Designation	Unit	
Length	m	338.90
Breadth	m	47.31
Draught	m	18.90
Displacement Δ	m^3	233523.5
Centre of buoyancy below waterline	m	9.18
Centre of gravity below waterline	m	5.58
Moment of inertia roll	kg m^2	$5.77 * 10^7$
Moment of inertia pitch	kg m^2	$1.43 * 10^9$
Moment of inertia yaw	kg m^2	$1.49 * 10^9$

Our results were obtained by a direct pressure integration over the hull. To be able to differentiate the potential accurately, we have to keep in mind the existence of stagnation points, especially in cross-flow conditions. If we would neglect the existence of these points, we would have to approximate the gradient of the potential by using one-sided difference schemes. Using these points, however, increases the accuracy of our differentiation considerably. They can be taken into account by extrapolating the potential over the free surface and using this extrapolated point when discretising the derivatives on the hull.

As incoming potential we used

$$\phi_{inc} = \frac{g\zeta_a}{\omega} \cos(\omega t - kx) \frac{\cosh(k(z+h))}{\cosh(kh)}$$

with

$$-\omega^2 + 2kU\omega + g \tanh(kh) = 0$$

This potential does not satisfy the free-surface condition; this is corrected in the diffracted wave.

In Fig. 3 through Fig. 8 are given the added mass and damping coefficients in surge motion. These coefficients are fairly independent of the forward speed, except perhaps for A_{31} and B_{31}. Fig. 9 through Fig. 14 show the coefficients for heave motion. Only the coupling coefficients seem to depend on the speed. Comparison of Fig. 5 and Fig. 9 shows that the symmetry relation holds. However, for lower frequencies this relation seems to be violated in the case of the damping coefficients. From the weird behaviour of B_{13} we may conclude that this coefficients lacks accuracy in this frequency range. The same seems to be true for B_{53}. Note that the coupled forces and moments are much smaller than the force in the direction of the motion. Therefore it is very difficult to calculate these coefficients accurately. The coefficients in pitch motion are shown in Fig. 15 through Fig. 20. The symmetry relation is fulfilled very well, except for B_{35}, as mentioned before.

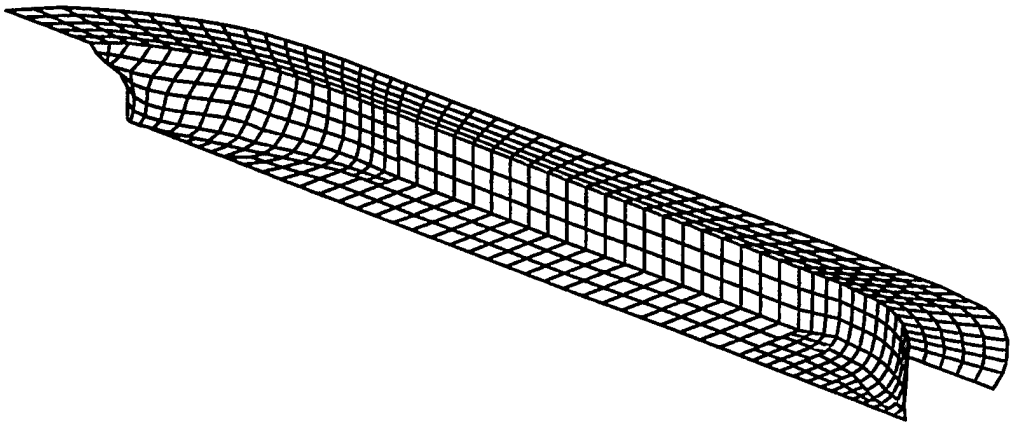


Figure 2: Panel-division on the hull and the first rings on the free surface

Fig. 21 shows the horizontal drift force in head waves for the three velocities: 0, 5 and 10 knots. With increasing speed, the maximal value of the drift force becomes considerably higher. This is mainly due to the blunt bow of the tanker. At middle frequencies the drift force seems to have some parts which are independent of the speeds. This may be due to the accuracy of the results. At higher frequencies, the curves seem to part, as was expected from asymptotical analysis. The zero-speed drift force agrees very well with the results shown by Pinkster [5]. Fig. 22 gives the vertical drift force. The forward speed has no influence on this drift force. This is probably due to the smooth shape of the bow in the z-direction. The same seems to hold for the pitch moment, shown in Fig. 23.

Finally, Fig. 24 through Fig. 26 show the drift forces and moment in following waves. For $Fn = .008$ the horizontal drift force seems to be unrealistic for low frequencies. The same can be observed from Fig 25. This is probably due to lack of accuracy at these low frequencies. Note that the vertical drift forces are approximately the same for head and following waves. Obviously the shape of the bow and stern resemble each other in the z-direction. This is not true for the x-direction, as can be seen from Fig. 21 and Fig. 24.

Our method also enables us to calculate drift forces and moments for other headings. However, problems arise for the roll motion caused by the inaccurate approximation of the roll damping coefficient. This is a well-known problem, which is a defect of potential theory, see Pinkster [5]. Therefore, results for these headings are not presented.

CONCLUSIONS

In this paper we tackled the time-dependent ship-wave problem. A numerical algorithm has been used which has been developed by Prins [6]. This algorithm is stable for every velocity and for every time step. We presented calculations for the added coefficients and drift forces for different values of the forward speed and different headings.

A disadvantage of our method lies in the fact that our absorbing boundary condition can only deal with harmonic waves. This forces us to calculate the interesting coefficients for several frequencies. This can be overcome by means of retardation functions, which will be a subject of research in the near future, or by using a frequency-independent condition.

ACKNOWLEDGMENT

The authors would like to thank the Maritime Research Institute Netherlands for kindly providing us with the mesh of the 200 kDWT tanker.

REFERENCES

[1] Fang, Z., "A new method for calculating the fundamental potential functions induced by a source/dipole polygon", Applied Mathematics and Mechanics, Vol.6, No. 7, July 1985, pp 675-680.

[2] Nakos, D.E., "Rankine panel methods for time-domain free surface flows", Proceedings of the Numerical Shiphydrodynamics Symposium, Iowa, 1993, pp 1129 - 1148.

[3] Nossen, J., Grue, J. and Palm, E., "Wave forces on three-dimensional floating bodies with small forward speed", Journal of Fluid Mechenics, **227**, 1991, pp 135-160.

[4] Pinkster, J.A., "Low frequency second order wave exciting forces on floating structures", PhD. thesis, 1980, Delft University of Technology, The Netherlands.

[5] Pinkster, J.A. and Huijsmans, R.H.M, "Wave Drift Forces in Shallow Water", Proceedings BOSS'92 London, 1992, pp. 1159-1183.

[6] Prins, H.J. and Hermans, A.J., "Time domain calculations of the second order drift force of a floating two dimensional object in current and waves", Journal of Ship Research, June 1994.

[7] Prins, H.J. and Hermans, A.J., "Time domain calculations of the second order drift force on a floating 3-D object in current and waves", Ship Technology Research, Vol. 41, No. 2, May 1994 and Vol. 41, No. 3.

[8] Raven, H.C., "A practical nonlinear method for calculating ship wavemaking and wave resistance", Proc. of the 19th Symposium on Naval Hydrodynamics, Seoul, South Korea, 1992.

[9] Timman, R. and Newman, J.N., "The coupled damping coefficients of a symmetric ship", Journal of Ship Research, Vol. 5, No. 4, 1962, pp 1-7.

[10] Wehausen, J.V. and Laitone, E.V., "Surface waves", Encyclopedia of Physics, Volume IX, Fluid Dynamics III, Springer-Verlag, Berlin, 1960

[11] Zhao, R. and Faltinsen, O.M., "Interaction between waves and current on a two-dimensional body in the free surface", Applied Ocean Research, Vol. 10, No. 87, 1988, pp 87-99.

APPENDIX

In this appendix we will sketch the derivation of the formulas for the drift force and moment.

The force acting on the hull is given by

$$\vec{F} = \int_H p\vec{n}dS$$

with H the instantaneous position of the wetted part of the hull. Because we do not know the actual position of the hull nor the shape of the wetted part, we split the integral into an integral over the averaged wetted surface at the averaged position and an integral over the oscillatory wetted surface at the averaged position (see Pinkster [4]). The integrand should then be expressed in a Taylor-series around the averaged position of the hull:

$$p_H = p_{H_0} + (\vec{X} + \vec{\Omega} \times \vec{x}) \cdot \vec{\nabla} p_{H_0} + \frac{1}{2}\left\{(\vec{X} + \vec{\Omega} \times \vec{x}) \cdot \vec{\nabla}\right\}^2 p_{H_0} + \ldots$$

and

$$\vec{n} = \vec{n}^{(0)} + \vec{\Omega} \times \vec{n}^{(0)}$$

Here we assumed that the motion of the hull is small.

Now we expand all quantities into a perturbation series:

$$\begin{aligned}
p_{H_0} &= p^{(0)} + \epsilon p^{(1)} + \epsilon^2 p^{(2)} + \mathcal{O}(\epsilon^3) \\
\vec{X} &= \epsilon\vec{X}^{(1)} + \epsilon^2\vec{X}^{(2)} + \mathcal{O}(\epsilon^3) \\
\vec{\alpha} &= \epsilon\vec{\alpha}^{(1)} + \epsilon^2\vec{\alpha}^{(2)} + \mathcal{O}(\epsilon^3) \\
\vec{x} &= \vec{x}^{(0)} + \epsilon\vec{\alpha}^{(1)} \times \vec{x}^{(0)} + \epsilon^2\vec{\alpha}^{(2)} \times \vec{x}^{(0)} \\
&\quad + \mathcal{O}(\epsilon^3) \\
\vec{n} &= \vec{n}^{(0)} + \epsilon\vec{\alpha}^{(1)} \times \vec{n}^{(0)} + \epsilon^2\vec{\alpha}^{(2)} \times \vec{n}^{(0)} \\
&\quad + \mathcal{O}(\epsilon^3)
\end{aligned}$$

Substituting these series and using Bernoulli's equation for the pressure on the hull, we find Archimedes' Law for the zeroth order of ϵ. The first order gives the exciting force and the restoring coefficients as used in (8). The second order in ϵ yields

$$\begin{aligned}
\left\langle \vec{F}_2 \right\rangle &= \vec{\Omega} \times \left(M\frac{\partial^2 \vec{X}}{\partial t^2} \right) - \begin{pmatrix} 0 \\ 0 \\ \Omega_1\Omega_3 C_{35} \end{pmatrix} \\
&\quad - \int_H \rho\vec{\alpha} \cdot \vec{\nabla}\left(\frac{\partial\phi}{\partial t} + \vec{\nabla}\overline{\phi} \cdot \vec{\nabla}\phi \right) \vec{n}dA \\
&\quad - \int_H \frac{1}{2}\rho \left|\vec{\nabla}\phi\right| \vec{n}dA + \int_{\text{wl}} \frac{1}{2}\rho g\zeta_r^2 \vec{n}dl \qquad (14)
\end{aligned}$$

where the last term is due to the oscillatory wetted surface. Here ζ_r is the relative wave height and is given by

$$\zeta_r = \zeta - X_3 - (\Omega_1 y - \Omega_2 x)$$

Note that the subscript of H_0 has been dropped for convenience.

Applying the same method to the drift moment we find for the zeroth order that the buoyancy point should be on the z-axis. The first order gives the excitation moments and the restoring coefficients. Finally, the second order gives rise to

$$\begin{aligned}
\left\langle \vec{M}_2 \right\rangle &= \vec{\Omega} \times \left(I\frac{\partial^2 \vec{\Omega}}{\partial t^2} \right) - \begin{pmatrix} -\Omega_2\Omega_3 C_{44} \\ \Omega_1\Omega_3 C_{55} \\ 0 \end{pmatrix} \\
&\quad - \int_H \rho\vec{\alpha} \cdot \vec{\nabla}\left(\frac{\partial\phi}{\partial t} + \vec{\nabla}\overline{\phi} \cdot \vec{\nabla}\phi \right) (\vec{x} \times \vec{n})\, dA \\
&\quad - \int_H \frac{1}{2}\rho \left|\vec{\nabla}\phi\right| (\vec{x} \times \vec{n})\, dA \\
&\quad + \int_{\text{wl}} \frac{1}{2}\rho g\zeta_r^2\, (\vec{x} \times \vec{n})\, dl \qquad (15)
\end{aligned}$$

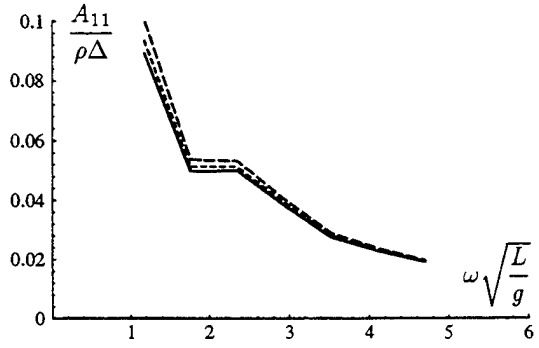


Figure 3: Added mass in surge for $Fn = 0$ (——), $Fn = .004$ (- - -) and $Fn = .008$ (– –)

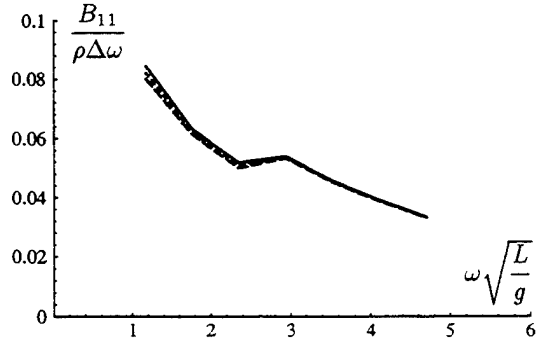


Figure 4: Added damping in surge for $Fn = 0$ (——), $Fn = .004$ (- - -) and $Fn = .008$ (– –)

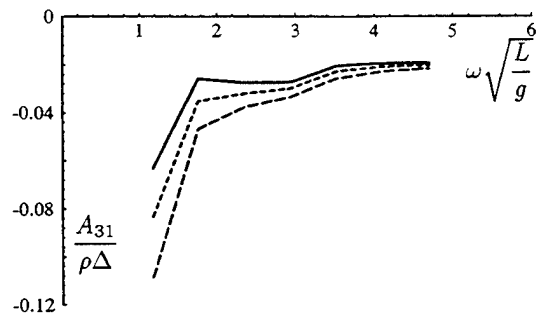


Figure 5: Coupled added mass in surge for $Fn = 0$ (——), $Fn = .004$ (- - -) and $Fn = .008$ (– –)

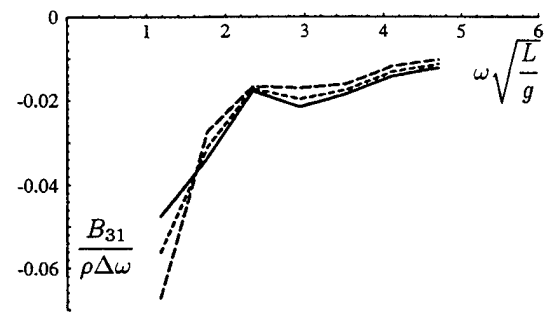


Figure 6: Coupled added damping in surge for $Fn = 0$ (——), $Fn = .004$ (- - -) and $Fn = .008$ (– –)

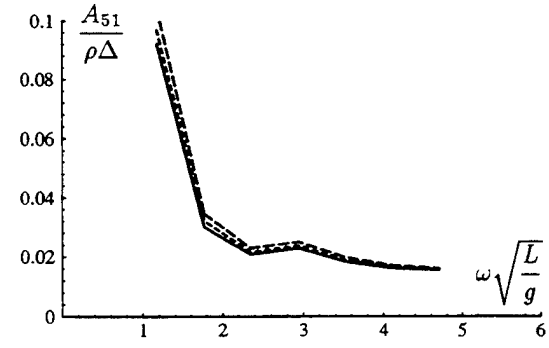


Figure 7: Coupled added mass in surge for $Fn = 0$ (——), $Fn = .004$ (- - -) and $Fn = .008$ (– –)

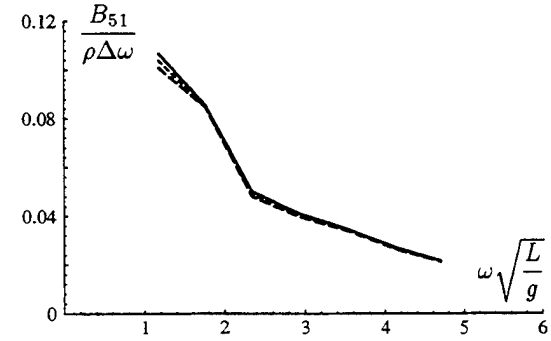


Figure 8: Coupled added damping in surge for $Fn = 0$ (——), $Fn = .004$ (- - -) and $Fn = .008$ (– –)

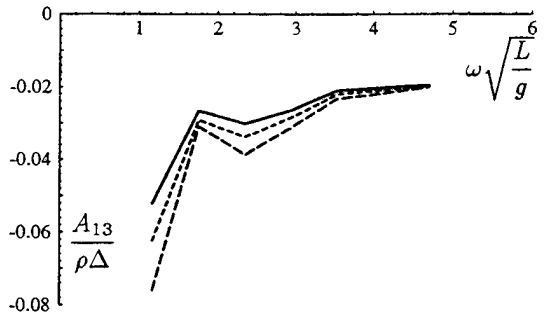


Figure 9: Coupled added mass in heave for $Fn = 0$ (——), $Fn = .004$ (- - -) and $Fn = .008$ (– –)

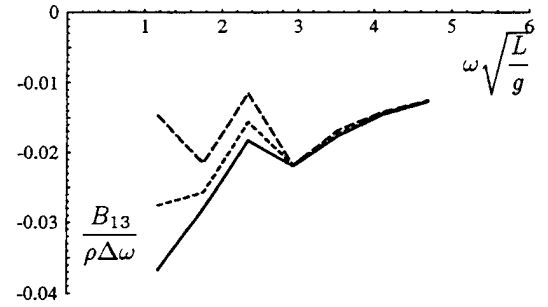


Figure 10: Coupled added damping in heave for $Fn = 0$ (——), $Fn = .004$ (- - -) and $Fn = .008$ (– –)

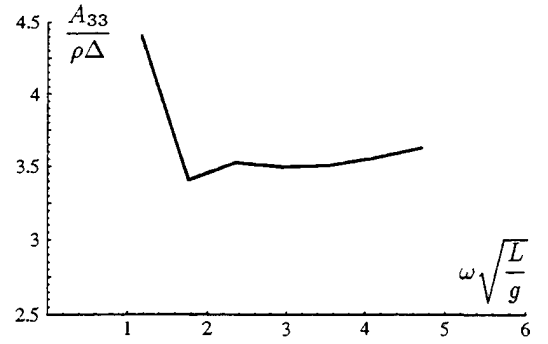


Figure 11: Added mass in heave for $Fn = 0$ (——), $Fn = .004$ (- - -) and $Fn = .008$ (– –)

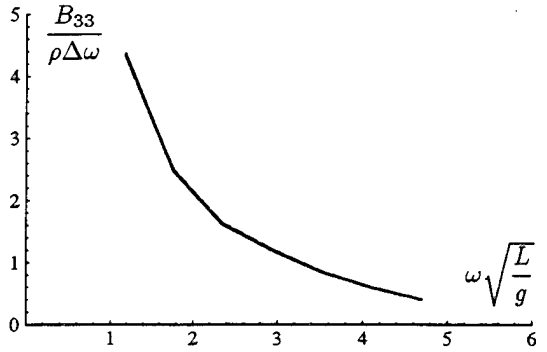


Figure 12: Added damping in heave for $Fn = 0$ (——), $Fn = .004$ (- - -) and $Fn = .008$ (– –)

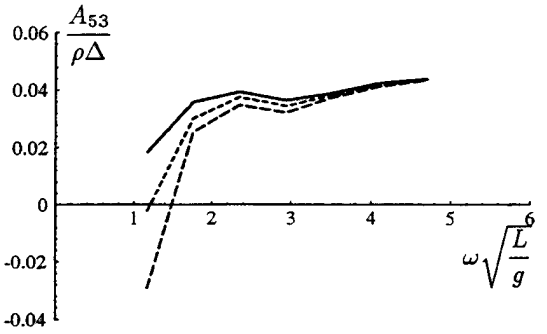


Figure 13: Coupled added mass in heave for $Fn = 0$ (——), $Fn = .004$ (- - -) and $Fn = .008$ (– –)

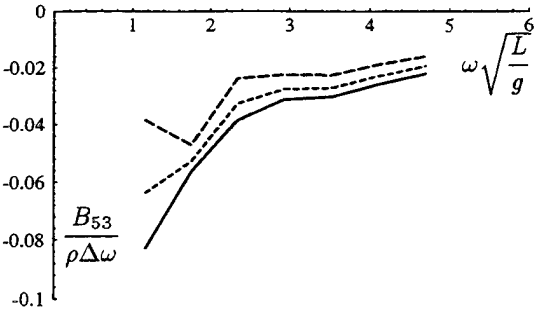


Figure 14: Coupled added damping in heave for $Fn = 0$ (——), $Fn = .004$ (- - -) and $Fn = .008$ (– –)

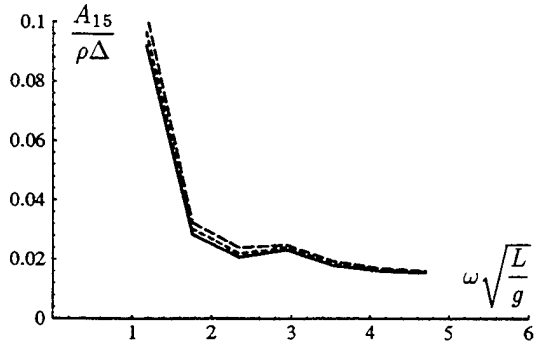


Figure 15: Coupled added mass in pitch for $Fn = 0$ (—), $Fn = .004$ (---) and $Fn = .008$ (– –)

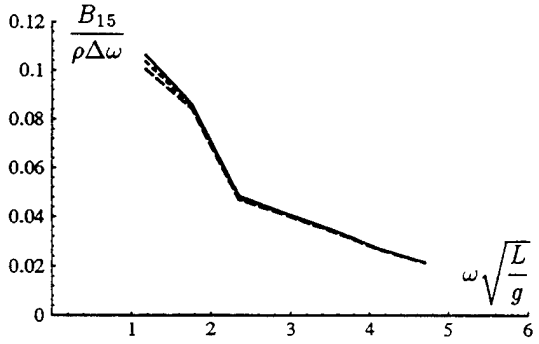


Figure 16: Coupled added damping in pitch for $Fn = 0$ (—), $Fn = .004$ (---) and $Fn = .008$ (– –)

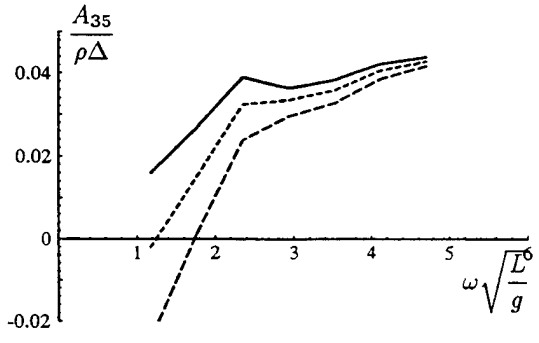


Figure 17: Coupled added mass in pitch for $Fn = 0$ (—), $Fn = .004$ (---) and $Fn = .008$ (– –)

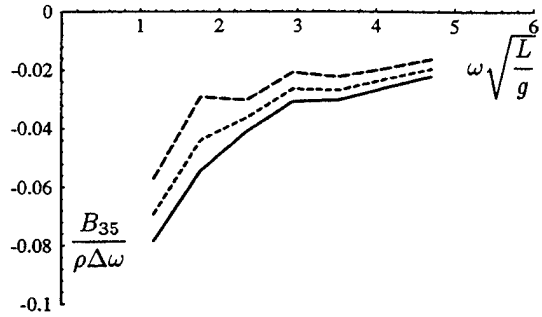


Figure 18: Coupled added damping in pitch for $Fn = 0$ (—), $Fn = .004$ (---) and $Fn = .008$ (– –)

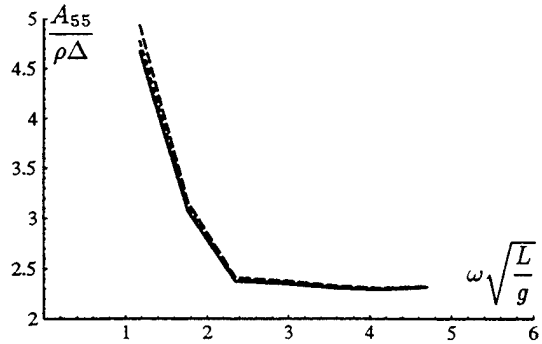


Figure 19: Added mass in pitch for $Fn = 0$ (—), $Fn = .004$ (---) and $Fn = .008$ (– –)

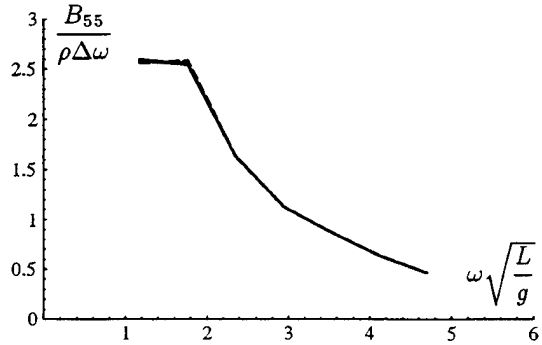


Figure 20: Added damping in pitch for $Fn = 0$ (—), $Fn = .004$ (---) and $Fn = .008$ (– –)

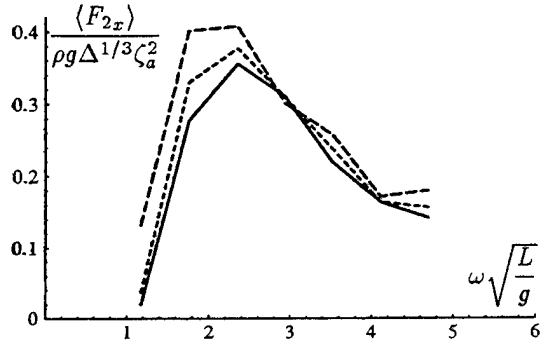


Figure 21: Horizontal drift force in head waves for $Fn = 0$ (——), $Fn = .004$ (- - -) and $Fn = .008$ (— —)

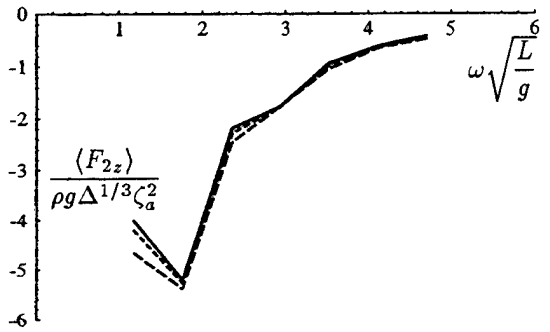


Figure 22: Vertical drift force in head waves for $Fn = 0$ (——), $Fn = .004$ (- - -) and $Fn = .008$ (— —)

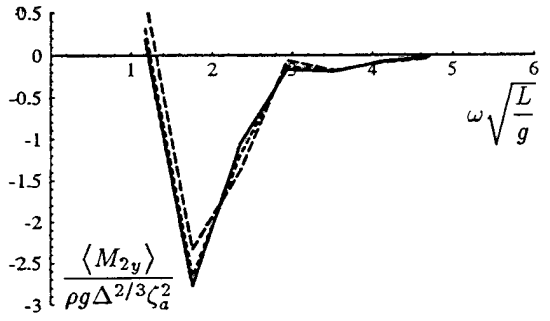


Figure 23: Pitch drift moment in head waves for $Fn = 0$ (——), $Fn = .004$ (- - -) and $Fn = .008$ (— —)

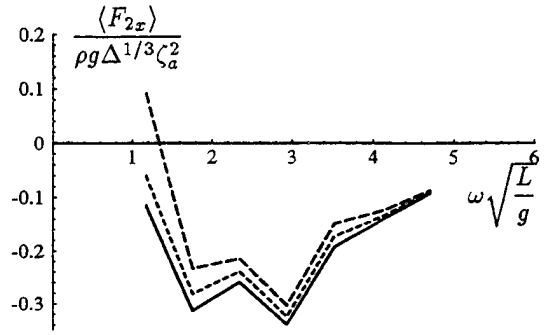


Figure 24: Horizontal drift force in following waves for $Fn = 0$ (——), $Fn = .004$ (- - -) and $Fn = .008$ (— —)

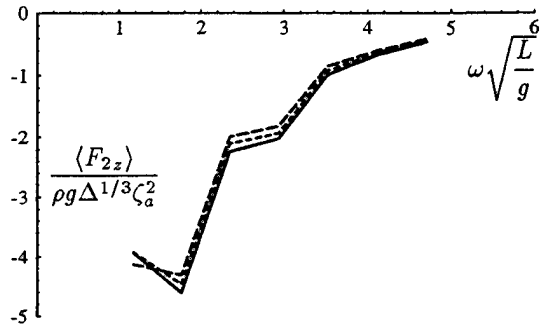


Figure 25: Vertical drift force in following waves for $Fn = 0$ (——), $Fn = .004$ (- - -) and $Fn = .008$ (— —)

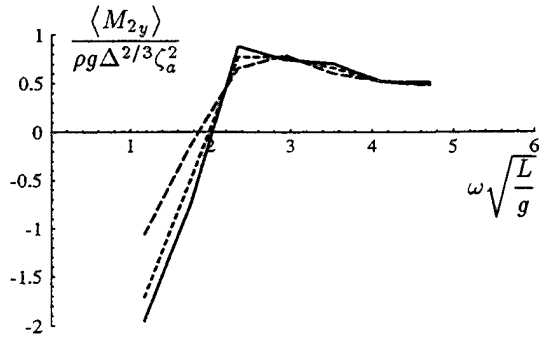


Figure 26: Pitch drift moment in following waves for $Fn = 0$ (——), $Fn = .004$ (- - -) and $Fn = .008$ (— —)

The Structure of Extreme Ocean Waves

O. Phillips (Johns Hopkins University, USA)

Abstract

This paper reviews recent work on the expected and measured profiles in space and time of extreme wave events in storm seas. It has been shown theoretically that asymptotically, in a Gaussian sea, the space-time profile of the sea surface near a high crest or a deep trough, normalized by the height or depth of the extremum approaches the space-time autocorrelation function of the sea surface as a whole. At a fixed spatial position (for example, at a tower or, approximately, at a moored buoy) the data reduces to a time series, and at a fixed instant (approximated by Scanning Radar Altimeter measurements) to a 'contour map' of the instantaneous sea surface. Various measurements made during the Surface Wave Dynamics Experiment (SWADE), from a North Sea tower and from an array of wave gages in the Mediterranean confirm special cases of the result. The space-time autocovariance, the Fourier transform of the wavenumber-frequency spectrum is of course not universal in form, so that extreme wave configurations differ among different storms and different current patterns which refract the waves. A number of examples are given to illustrate the range of extreme configurations found to date.

Notation

ζ = Surface displacement
x,t = Spatial location and time of occurrence of extremum
r,t = horizontal distance and time interval from extremum
$\sigma = \langle \zeta^2 \rangle$
ρ = space-time autocorrelation function of ζ
γ = numerical parameter, formally large.
$\langle\rangle$ = ensemble average

Introduction

Extreme or rogue waves are a hazard to those who venture upon the sea, whether in ships or on stationary platforms. According to a listing prepared by Penton Marine Salvaging Company of South Africa and kindly made available to me by Professor Marius Gerber of the University of Stellenbosch, during the decade 1982-91, there were 24 damaging events off the south-east coast of South Africa to oil tankers with a combined deadweight tonnage of over $5{\cdot}2 \times 10^6$ tonnes. A number of these involved bows stove in or carried away. In the design of marine platforms, a primary consideration is the height of extreme waves that can be expected within the lifetime of the structure. Time series of surface elevation are routinely taken on many of these platforms, though the directional distribution of the wave field is also important in determining the applied stress distribution on the structure. An upper limit in magnitude is probably given by the uni-directional limit.

These waves are frequently described by eyewitnesses as 'coming out of nowhere.' This of course does not imply that they spring up from an almost-calm sea—the extreme waves of interest are those in an already rough sea whose height may be two or more times the average wave height in the storm. The phrase 'coming our of nowhere' presumably means that the development of an extreme wave configuration is rapid and its lifetime short, possibly only a few wave periods. This suggests that they are formed by local transient phase coincidences in superimposed high energy packets of long waves. Abnormally high crests are usually described by eyewitnesses—they can be seen from afar—but abnormally deep troughs are probably more dangerous to shipping. The loss of forward buoyancy causes a ship to pitch bow-down as it drives forward into the far side of the trough, and not just the hull but the deck may be stove in.

Waves generated in a storm are refracted by currents and for appropriate coincidence of wave frequency and direction with current speed and direction, they can be focussed into a

relatively small area, with consequently higher local wave energy density and incidence of extreme events. Radiation stress interactions with currents can give further augmentation. The Agulhas current off eastern South Africa is notorious in the regard, as is the 'North Wall' of the Gulf Stream north of Cape Hatteras, where it leaves the coast. Extensive work has been done by Professor Gerber on ray tracing of waves from storms moving north-east against the Agulhas current, though little has been published in the technical literature; he shows that concentrations of energy density by a factor of 4 are by no means unusual.

In the sections following, the simple theoretical approximation connecting the mean configuration of the sea surface surrounding high crests or deep troughs to the space-time autocorrelation function of the field as a whole, will be discussed. Time series of surface displacements measured at a fixed point illustrate the simplest form of the result. It was indeed suspected to be true by Boccotti (1) as early as 1983 following a numerical analysis of sets of North Sea wave data. Apparently independently, Tromans et al. (2) proposed the same relation as a basis for design of off-shore structures, the so-called New Wave methodology. A sample of such measurements, using single and multiple point sensors will be described briefly and the two-dimensional Scanning Radar Altimeter measurements in a little more detail. These illustrate the range of extreme configurations found to date and their association with wave spectral characteristics.

Theoretical Results

The task of calculating the expected profile in space-time of the sea surface surrounding an extremum (high crest or deep trough) is straight-forward in principle but extraordinarily complicated in practice, involving multidimensional integrals and inversion of large algebraic matrices. The calculation is one of conditional probabilities: In a Gaussian wave field, what is the expected surface displacement at the point $\mathbf{x}+\mathbf{r}$ and time $t+\tau$ subject to the conditions that define a high crest (say) at $(\mathbf{x},t)$, namely $\zeta(\mathbf{x},t) > \gamma\sigma$ where γ is large, $\zeta(\mathbf{x},t) = 0$, $\ddot{\zeta} < 0$, $\zeta_x = \zeta_y = 0$, and $\zeta_{xx}\zeta_{yy} - (\zeta_{xy})^2 > 0$. Near the crest of a very high wave, there may be a multitude of gravity-capillary waves and so a cluster of local high maxima (and high minima) but these are irrelevant to our considerations and are in fact filtered out by most measurement techniques. It is consequently convenient to remove these from the calculation by local averaging or filtering, or the more formal narrow spectrum approximation used by Longuet-Higgins, (3).

The analyses of Boccotti (4) and Jonathan et al. (5) were concerned with the one-dimensional case of a simple time series, and they considered only the first two of the conditions above. Boccotti conjectured the extension to the full three-dimensional problem in $(\mathbf{x},t)$, again without regard to the last of these conditions. The ignoring of the second derivative conditions (which discriminate between local high maxima and minima) does seem to have a similar effect as a narrow spectrum approximation since clusters of microextrema near a single wave crest provide an ensemble of realizations of the rough surface for the averaging, rather than (in a narrow spectrum approximation) a single realization of the smoothed surface surrounding the high crest.

An even simpler approach, capable of providing directly a solution to the 3-D $(\mathbf{x},t)$ problem, is given by Phillips et al. (6). Rather than seeking the precise points where realizations of $\zeta(\mathbf{x},t)$ attain maxima, they consider those regions where, simply $\zeta \geq \gamma\sigma$ where (formally) γ is a number large compared with unity. For a given γ, at any instant those regions consist of isolated 'islands' each containing at least one maximum higher than $\gamma\sigma$, and as γ increases, the islands shrink, converging towards the maxima and then disappearing. Our interest is in large values of γ where the islands are rare, small and isolated, and the question is posed thus: Given that at $\mathbf{x},t$, say, $\zeta > \gamma\sigma$ where γ is large, what is the expected value of $\zeta(\mathbf{x}+\mathbf{r},t+\tau)$, the surface displacement at neighbouring points and instants, and what is the standard deviation about this expected value? Averages over clusters of point microextrema with $\zeta > \gamma\sigma$ are replaced by averages over the 'islands,' a kind of conditional local smoothing.

This, now, is a very simple calculation whose details are given by Phillips et al. (6). Briefly, if $\zeta_1 = \zeta(\mathbf{x},t)$ and $\zeta_2 = \zeta(\mathbf{x}+\mathbf{r}, t+\tau)$, the theorem of conditional probability, the distribution of ζ_2 given that $\zeta_1 \geq \gamma\sigma$ is

$$p(\zeta_2 | \zeta_1 \geq \gamma\sigma) = p(\zeta_2, \zeta_1 \geq \gamma\sigma)/p(\zeta_1 \geq \gamma\sigma) \quad \ldots\ldots \quad (1)$$

with the usual notation. If $p(\zeta_1, \zeta_2)$ is the two point probability density function,

$$p(\zeta_2, \zeta_1 \geq \gamma\sigma) = \int_{\sigma\gamma}^{\infty} p(\zeta_1 \zeta_2) d\zeta_1$$

and if the process is assumed to be Gaussian, the conditional probability is found from (1), from which the expected configuration of ζ_2 follows. It is found that

$$\zeta_2 = \gamma\sigma\rho(\mathbf{r},\tau)[f(\gamma)]^{-1} \qquad (2)$$

where

$$\rho(\mathbf{r},\tau) = \langle\zeta_1\zeta_2\rangle / \langle\zeta_1^2\rangle$$

is the autocorrelation function for the wave field as a whole and $f(\gamma)$ is an integral which asymptotes upwards to unity as γ increases. In particular, when $r=0$, $t=0$, the autocorrelation function $\rho(0,0) = 1$ and the average height of those waves higher than $\gamma\sigma$ is $\gamma\sigma[f(\gamma)]^{-1}$, a bit higher than $\gamma\sigma$. Consequently, (2) can be written as

$$\langle\zeta(x+r,t+\tau)\rangle = \langle\zeta x,t)\rangle_{\zeta>\gamma\sigma}\rho(r,t) \quad (3)$$

which gives the mean configuration surrounding high crests in terms of the autocorrelation function. The mean configuration of deep troughs is given by the same expression, with sign reversals.

The variance among realizations about the expected configuration can also be calculated. Near the extrema, where $\rho\equiv1$, the variance is $\gamma^{-2}\sigma^2$, which is small, so that there is relatively little variation in crest configuration from one extremum to another. Far from the crest, as $r\rightarrow\infty$, $\rho\rightarrow0$ and the variance approaches σ^2, that of the wave field as a whole. Phillips et al (6) give a formal calculation of the one-dimensional (time series) case under the narrow spectrum approximation which shows that, at least in this simplest case, the approximate results are accurate to relative order γ^2.

Except for the notion that surface waves generally interact weakly and consequently by the Central Limit Theorem, the probability distribution in a multicomponent sea should be close to Gaussian, these results contain no kinematics or dynamics. The free surface non-linearity leading to somewhat sharper crests and shallower troughs distorts the Gaussian towards a Gram-Charlier distribution, as demonstrated observationally by Kinsman (7) and theoretically by Longuet-Higgins (8). While equation (3) remains precisely accurate when $r=0$, $t=0$, one would expect the non-linearities to make the averaged configuration of high crests to be somewhat sharper than given by (3). We have, however, been unable to detect this effect in our comparisons. The fact that the results of the approximate theory are, in essence, purely statistical implies that they are applicable to other multi-dimensional Gaussian processes as well, but these will not be pursued here.

Measurements of Extreme Waves.

During the winter 1990-91, in the Surface Wave Dynamics Experiment (SWADE) many time series of wave surface displacements were obtained from National Data Center buoys under a

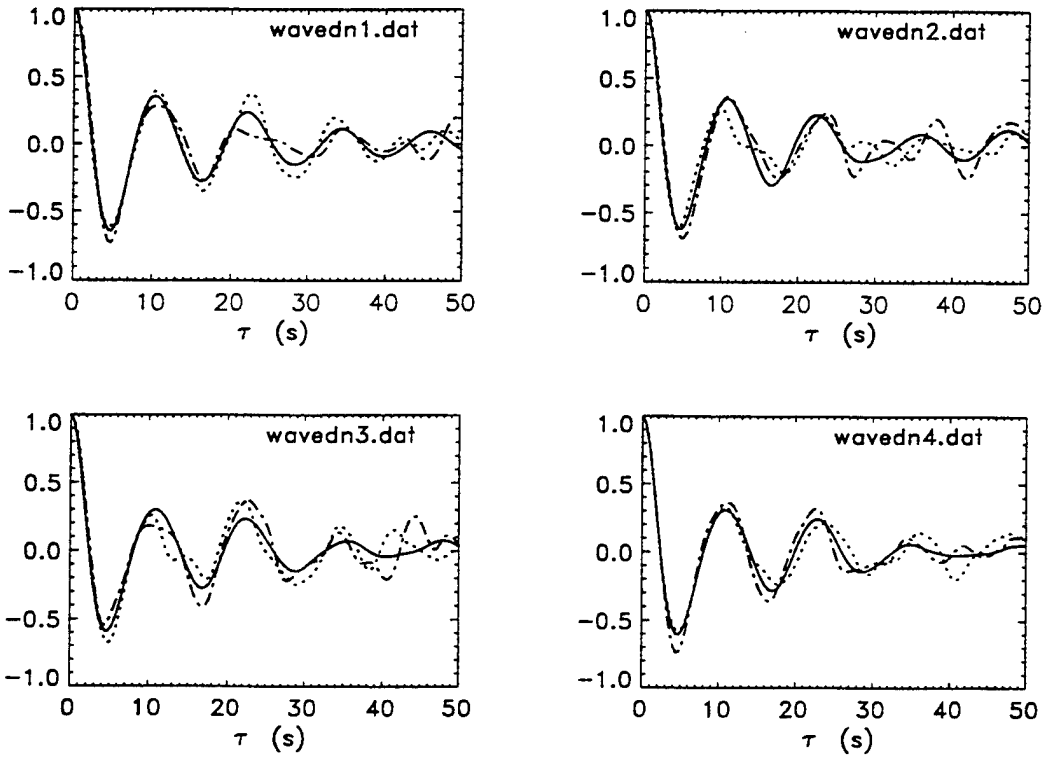


Figure 1. Temporal autocorrelation functions and average surface displacements before and after crests higher than 2·5σ. Data from SWADE.

variety of conditions. On 26 October 1990, an intense storm moved up the U.S mid-Atlantic coast and data obtained as time series illustrated the rather surprising accuracy of the result (3) in the special case $\mathbf{r}=0$ (Phillips et al.. 6). Figure 1 provides a representative example. It is derived from four sets of data, each ninety minutes long, chosen to represent reasonably steady wind and wave conditions during the storm. The continuous curves represent the temporal autocorrelation functions calculated from the entire data in each set, and the dotted and dot-dash curves represent mean surface displacements before and after the arrival of crests higher than $2{\cdot}5\sigma$, scaled according to equation (3). It is apparent that the three curves coincide very well for at least 1·5 wave periods on either side of the high crests, becoming more irregular beyond. Similar results have been obtained from offshore platforms by members of Shell Research Rijswijk, The Netherlands, as kindly communicated to me by Dr. Philip Jonathan, and have led to the adoption of the temporal autocorrelation function as a design wave for offshore platforms (the so-called New Wave methodology, Tromans et al., 2).

The response of ships to extreme wave events is dependent on the space-time history surrounding the extremum, and for this directional information on the wave field is crucial. During the intensive measurement periods of SWADE, many fine sequences of data were obtained by Dr. Edward J. Walsh of NASA Goddard and his colleagues that enable us (a) to calculate the spatial autocorrelation function, in effect at one instant, $\tau=0$, $\rho(\mathbf{r},0)$ over a swath of the sea surface; (b) to pick out the highest crests in the swath and average the sea surface heights at surrounding points relative to the crests and (c) test the usefulness of equation (3) as a predictor of spatial configurations of extreme events. These data were obtained by the Scanning Radar Altimeter (SRA) described by Parsons and Walsh (9) and are discussed by Phillips, Gu and Walsh (10). The SRA provides, in essence, a contour map of the sea surface along the swath, digitized at height increments of 10cm, the swath width being proportional to aircraft altitude. The portions of data analysed to date show considerable variations in extreme wave configurations under different storm conditions and configurations of currents, associated with differences in local wave directional spectra and autocorrelation functions. Two examples will be described briefly.

The first dataset was acquired at about 1730 LST on the afternoon of 4 March 1991 in the vicinity of 37.6°N, 73.3°W, about 150km offshore from Wallops Island, VA and close to NDBC meteorological buoy 44015 (Discus E). During the previous 3 days, the wind had been generally from the south over the mid-Atlantic seaboard, but for 7h prior to the measurement had been backing towards the west and dropping from 13-15m s^{-1} to 4-8m s^{-1}. The significant wave height at Discus E was 5·5 m at the overflight time.

Wave spectral characteristics at Discus E are shown in Figure 2. The directional frequency spectrum has a strong maximum at about 0.9Hz from 190°—a longcrested swell from the south—with higher frequencies tending towards the wind

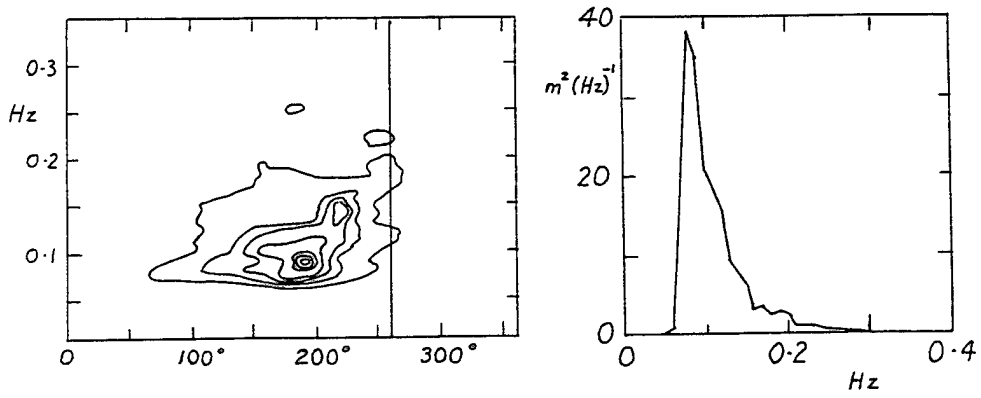


Figure 2. Directional-frequency and frequency spectra at buoy 44015, 1700 LST on 4 March. The directions are those from which waves propagate. Contours represent 0.01, 0.05, 0.1, 0.2, 0.6 and 0.8 of the peak.

direction, from 260°. The frequency spectrum is a simple textbook example—the wave field appears to be an uncomplicated, unidirectional, well-developed long fetch wave field.

The measured spatial autocorrelation function of surface displacement is shown in Figure 3. The configuration is long-crested

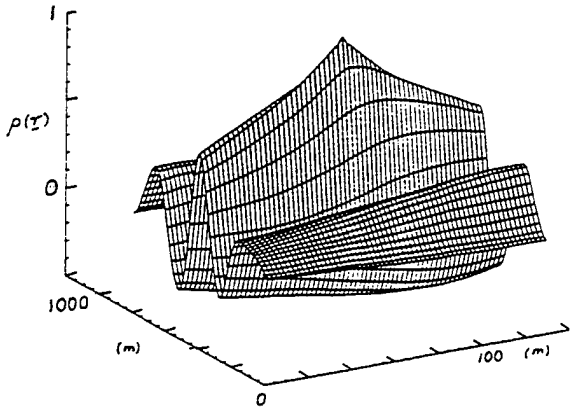


Figure 3. The spatial autocorrelation function for the entire SRA data swath, 4 March.

with a dominant wavelength of about 250m. The discontinuity in slope at r=0 can be interpreted as a consequence of the algebraic form of an equilibrium range spectral asymptote of k^{-4} or $k^{-3.5}$ in the wave-number spectrum for scales somewhat larger than the sampling intervals (2.1m across track and 14.2m along).

The data were then scanned to identify points at which $\zeta > \gamma\sigma$ for selected values of γ, and ensemble averages were constructed of the surface displacements at distances r from the high points identified. A couple of results are shown in Figure 4. Near the peak, the configurations are very similar (they overlay almost precisely) and the general form of the autocorrelation function of Figure 3 is apparent in the ensemble-averaged wave configurations of Figure 4. In the lower part of the Figure, γ=3, and there are fewer higher crests available to form the average, so that the noise level is higher especially in the skirts. The theory becomes more accurate as γ increases, but the statistics deteriorate!

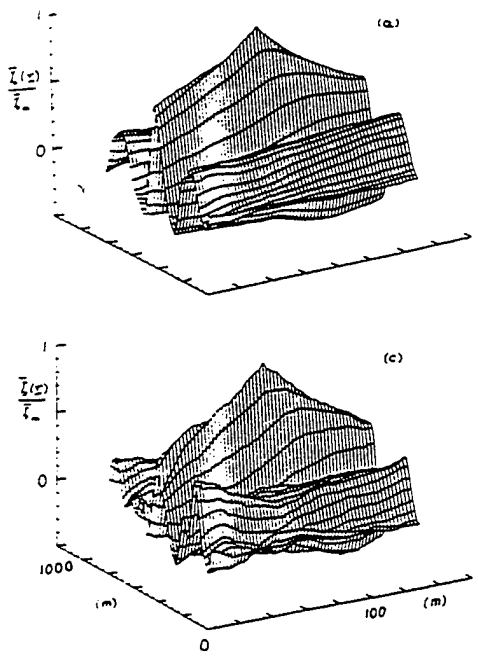


Figure 4. Mean surface configurations surrounding high crests in the swath of 4 March. (a) crests higher than 2σ, (c) crests higher than 3σ.

A contrasting situation was encountered the following day, on 5 March. Overnight, a cold air outbreak had occurred and by afternoon the local winds were from the north-west generating a fetch-limited wind sea superimposed on the still-dominant swell from the south. Dataset 5B was taken 400km offshore, near 36.3°N, 72.5°W, a little south and east of the Gulf Stream. Unfortunately there were no buoys in the vicinity but the directional frequency spectrum, calculated from the SRA swath is shown in Figure 5a. There is an inherent 180° ambiguity in these spectra but the meteorology clearly requires a low frequency swell generally from the south, together with higher frequency wind waves from N-NW. These 'real' spectral contributions are indicated by the unbroken lines of Figure 5a. A remarkable property of this spectrum is the wide directional spread (120° -240°) of the energetic 0.1Hz swells, not found at other locations, which is apparently a consequence of refraction of swells, incident at a glancing angle upon the Gulf Stream further to the south.

The autocorrelation function of the

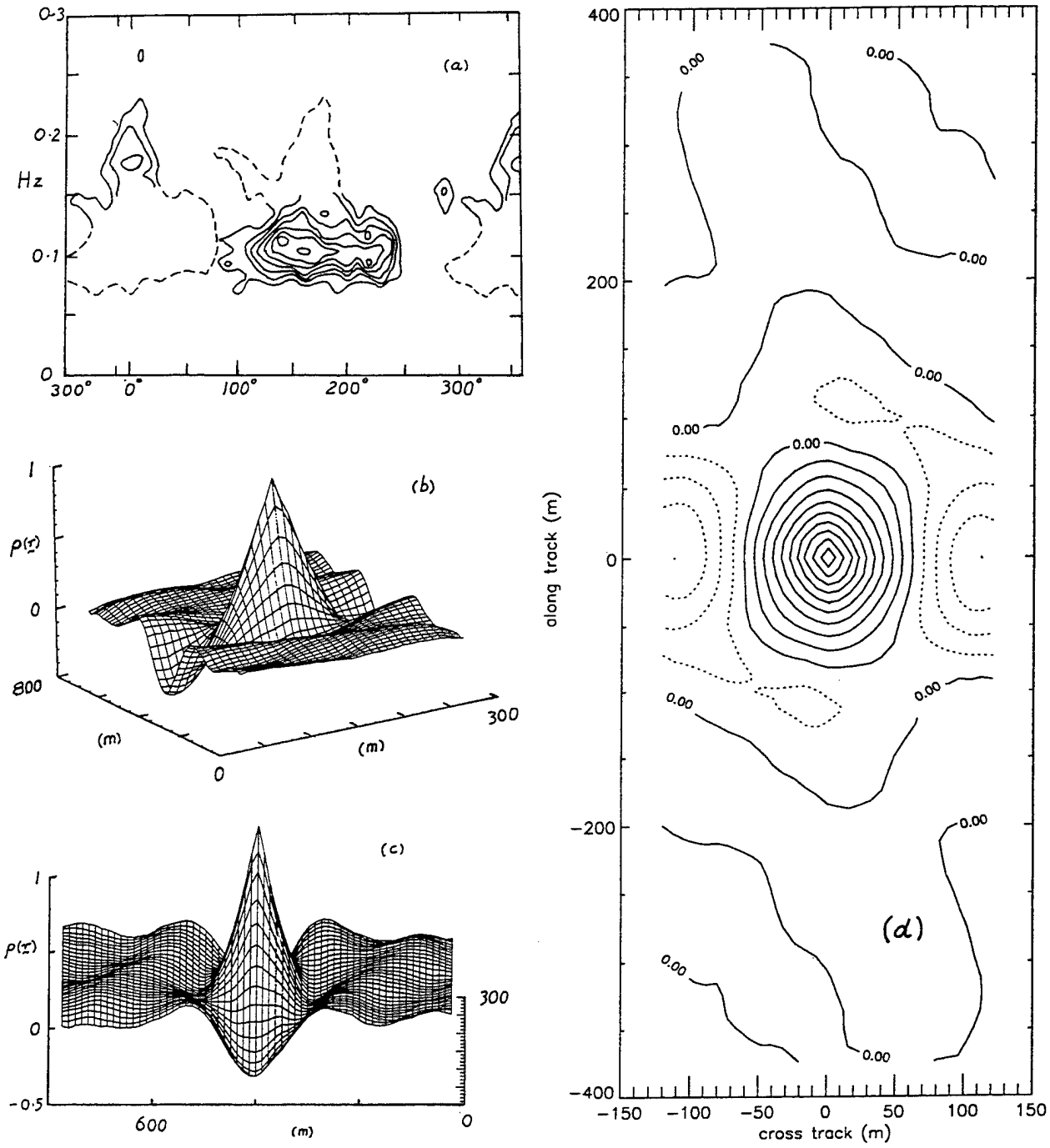


Figure 5. The autocorrelation function for dataset 5B, 5 March. (a) is the SRA directional frequency spectrum, (b) and (c) are two perspectives of the autocorrelation function and (d) a contour plot with equal scales along and across track.

wave field is shown in Figure 5 in various perspectives—it is evidently almost conical in form with outlying oscillations, long crested but of much smaller amplitude. If this almost conical form does represent the configuration of extreme crests, it presumably has the characteristics of a standing wave formed from wave groups travelling in almost opposite directions, in contrast with the progressive waves of Figure 4.

Figure 6 shows the mean configuration surrounding crests in the dataset 5B, and indeed it does mirror accurately the spatial autocorrelation function of Figure 5.

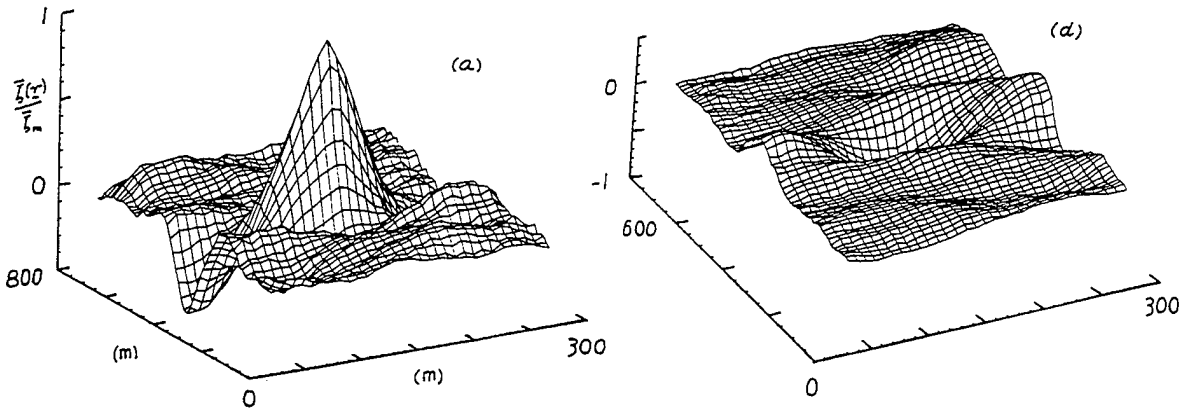


Figure 6. Mean surface configurations surrounding extrema in dataset 5B. (a) Crests higher than 2σ, (b) Troughs deeper than 2σ.

Figure 6b shows the mean surface configuration surrounding troughs deeper than 2σ. The minimum is out of sight but extends to -1 and presumably drops almost vertically as in a standing wave. To a helmsman in a rough sea, this may look like a black hole into which his boat may fall.

Towards a Design Wave Group

The most direct application of these results is the goal of defining an extreme wave group in space-time, or an ensemble of them, for ship design purposes—the question is then: What hull forms can best survive encounters with them? The problem for off-shore platforms is simpler since most of the information is contained in time series, and the variations in form of wave frequency spectra and autocorrelation functions are less than among wave-number spectra and spatial autocorrelation functions from different storm systems. Indeed, the 'New Wave' design methodology is being developed for immediate application to platform design, as mentioned earlier.

If the two-dimensional configuration of the surface is defined at the instant of extremum, and if one assumes that all wave components are travelling within an angular range of 180°, the prior and subsequent surface configurations can be found to a good approximation by integration in time. Boccotti (4) has used model spectra to illustrate this, but it would be clearly preferable to define the extreme events in terms of the spatial autocorrelation functions in storms of various types and locations with respect to major current systems. We are proceeding with this, to develop as many cases as are available for analysis.

Calculation of the time history involves taking the Fourier transform of the instantaneous extreme configuration, propagating the components at appropriate speeds and directions, followed by re-synthesis. One problem, exemplified in Figures 4 and 5, is that the swaths available do not define the shape or extent of the skirts of the wave shape in the transverse direction. From the purely mathematical point of view, there is nothing to be done about this—the cross-track spectral resolution is much worse than that along track. However, there are some physical conditions which provide integral constraints on the autocorrelation function, and so constrain its extrapolation beyond the measured swath. For example, the fact that the two-dimensional spectrum is zero at the origin (we are not interested in global-scale waves!) implies that the integral of $\rho(\mathbf{r})$ over the surface vanishes. If we can assume

that there is a maximum wavelength for measurable wind-generated storm waves, further constraints are possible, but these questions remain to be explored.

Acknowledgments

This research was supported by the US Office of Naval Research under contract N00014-90-J-1623. It is both timely and a pleasure to acknowledge with thanks the support of the Oceanography and Fluid Mechanics branches of ONR over a number of fruitful years.

References

1. Boccotti, Paolo, "Some new results on statistical properties of wind waves" Applied Ocean Research, Vol. 5, No. 3, 1983, pp. 134-140.

2. Tromans, P.S., Anaturak, A. and Hagemeijer, P., "A new model for the kinematics of large ocean waves—application as a design wave," Proceedings of the 1st Offshore and Polar Engineering Conference (ISOPE) Edinburgh. Vol 3, 1991, p. 64.

3. Longuet-Higgins, M.S. "Statistical properties of wave groups in a random sea state," Phil Trans. Roy. Soc. London, Vol. A312, 1984, pp. 219-250.

4. Boccotti, P. "On mechanics of irregular gravity waves," Atti d. Academia Nat. dei Lincci, Ser. 8, Vol. 19, 1989, pp. 111-170.

5. Jonathan, P., Taylor, P.H. and Tromans, P.S. "On the extremes of a linear random process: applications to ocean engineering." Unpublished manuscript.

6. Phillips, O.M., Gu, Daifang and Donelan, M. "Expected structure of extreme waves in a Gaussian sea. Part 1: Theory and SWADE buoy measurements," J. Phys. Oceanogr. Vol. 23, 1993, pp. 992-1000.

7. Kinsman, B., "Wind Waves; their generation and propagation on the ocean surface," 1965, Prentice-Hall, Inc., Englewood Cliffs, NJ.

8. Longuet-Higgins, M.S. "The effect of non-linearities on statistical distributions in the theory of sea waves. J. Fluid Mech., 17, 1963, pp. 459-480.

9. Parsons, C.L. and Walsh, E.J., "Off-nadir radar altimetry," IEEE Trans. Geosci. Remote Sens., Vol. 27, 1989, pp. 215-224.

10. Phillips, O.M., Gu, Daifang and Walsh, E.J., "On the expected structure of extreme waves in a Gaussian Sea, Part 2. SWADE Scanning Radar Altimeter results." J. Phys. Oceanogr., Vol. 23, 1993, pp. 2298-2309.

The Transition to Turbulence in a Spilling Breaker

J. Duncan, V. Philomin, H. Qiao
(University of Maryland, USA)

Abstract

The transition from laminar to turbulent flow in mechanically generated, gentle spilling breaking water waves is examined experimentally through surface profile measurements. It is found that as the wave steepens a bulge forms on the forward face of the wave near the crest and capillary waves form on the water surface ahead of the 'toe' of the bulge (see Fig. 1). This behavior is found to be in qualitative agreement with the theory of Longuet-Higgins [1]. The toe of the bulge then moves rapidly down the forward face of the wave and a train of large-amplitude waves with short wavelength grows rapidly on the surface of the bulge. These waves quickly break down into a random, rapidly evolving pattern indicating that the flow has become turbulent. The effect of the scale of the breaker on the breaking process described above is explored by using Froude-scaled wavemaker motions at average frequencies of 1.14, 1.26 and 1.42 Hz.

1 INTRODUCTION

Breaking waves in large, deep bodies of water are usually classified as spilling rather than plunging breakers. Depending on the history of the wind conditions and the fetch, a range of waves in the wind wave spectrum can break including the dominant wave as well as some of the shortest waves. These latter breaking events are frequently called microscale breakers [2]. When longer waves break, the time scale, which is probably some fraction of the wave period, is large and the surface evolution can be observed fairly well by a casual observer. As the breaker forms, the flow becomes turbulent in a small region around the crest. The mechanism that leads to this small turbulent region is not well understood though some investigators have hypothesized that it is initiated by a small curl at the crest[3]. After formation, the turbulent region seems to fall down the forward face of the wave gathering fluid as it travels. Air is usually entrained as long waves break and a whitecap is observed on the water surface.

When waves with lengths less than a meter or so break, the time scale is short and casual observations from a fixed reference frame do not reveal many details about the breaking process. It appears as though the wave crest suddenly becomes turbulent and the breaking process stops as quickly as it began. Because the kinetic energy of these short waves is relatively small, they usually do not entrain air bubbles and therefore the telltail white cap is not observed. A mechanism that leads to the formation of these short wavelength spilling breakers has been proposed by Longuet-Higgins and his co-authors [1, 4, 5]. This mechanism is initiated by an instability that causes a bulge to form on the forward face of the crest of a steep gravity wave (see schematic in Fig. 1). Capillary waves then form just below the 'toe' of the bulge where there is a sharp concave (upward) curvature. It is theorized that, in waves of short length, the vorticity shed by the viscous boundary layer of these capillary waves creates a vortical region in the crest of the gravity wave (Longuet-Higgins[6]). This vortical region then separates from the underlying flow and becomes turbulent.

In the present work, preliminary measurements from an experimental investigation of short-

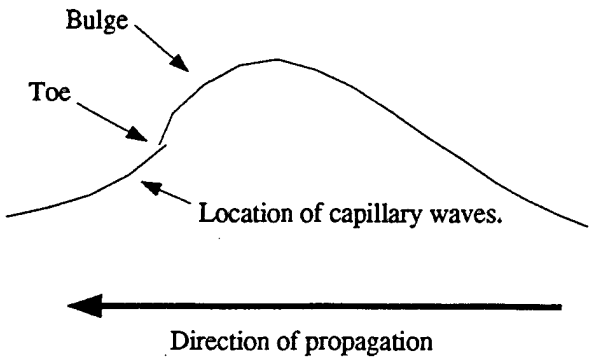


Figure 1: Schematic of the incipient breaking wave shape as proposed by Longuet-Higgins [1].

wavelength, gentle spilling breaking waves are presented. The measurements consist of wave profiles from high-speed movies (500 frames per second) taken in a reference frame moving with the wave crest. These movies reveal many features of the surface evolution that cannot be seen with the naked eye in a laboratory reference frame. Photographs from this investigation have been published in two recent articles, see references [7] and [8].

This paper is organized in four sections. In the following section (2), the experimental techniques are presented. The results are then presented and discussed in Section 3. Finally, in Section 4, the conclusions of the study are given.

2 EXPERIMENTAL TECHNIQUES

The experiments were performed in a tank that is 14.8 m long, 1.22 m wide and 1.0 m deep. The waves were generated mechanically by a vertically oscillating wedge that spans the width of the tank at one end. The side of the wedge closest to the end wall of the tank is vertical and the opposite side of the wedge is inclined at an angle of 30° from vertical. The wavemaker is driven by a ball-screw and linear-bearing mechanism that is in turn driven by a servo-motor. A computer-based feedback control system is used with a position sensor and a tachometer to provide precise control of the motion of the wedge. An instrument carriage that is driven by a towing wire and a separate servo-motor travels above the tank. The carriage rides on hydrostatic oil bearings rather than wheels; this produces a very low mechanical vibration level. The carriage is controlled by the same computer that controls the wavemaker. By trial and error, a set of carriage motion parameters was determined such that the carriage moved along the tank with the crest of the breaking wave.

The breaking waves were generated by a method similar to that described in Rapp and Melville [9]. In this method, a packet of waves with varying frequency is generated in a manner such that the packet converges as it travels along the tank. This convergence causes the amplitudes of the remaining waves in the packet to increase. Eventually, a breaking wave is formed if the initial wave amplitudes are large enough. Linear deep-water wave theory is used to compute a suitable motion for the wavemaker though the resulting wave motion is highly nonlinear when the packet converges. The wave packet consists of the sum of N sinusoidal components and the wavemaker motion to produce these waves is given by

$$z_w = w(t)A\sum_{i=1}^{N}\cos(x_b(\frac{\omega_i}{\bar{c}} - k_i) - \omega_i t). \quad (1)$$

where w is a window function which is described below, A is an adjustable constant, x_b is the horizontal position of the breaking event (by linear theory) measured from the back of the wedge, t is time, k_i and ω_i are, respectively, the wavenumber, and frequency of each of the $i = 1$ to N wave components, and $\bar{c}$ is the average of the group velocities $(0.5\omega_i/k_i)$ of the N components. The frequencies are equally spaced, $\omega_{i+1} = \omega_i + \Delta\omega$, where $\Delta\omega$ is a constant. The window function was chosen to give the wedge zero motion at times when the summation of components resulted in only a very small motion:

$$w(t) = 0.25(\tanh(\beta\bar{\omega}(t - t_1)) + 1) \quad (2)$$
$$(1 - \tanh(\beta\bar{\omega}(t - t_2))),$$

where β is a constant that determines the rise rate of the window function, chosen as 5.0, and $\bar{\omega}$ is the average of the N frequencies ω_i. The window function is nearly equal to 1.0 for most of the time between $t = t_1$ and $t = t_2$ and is zero at other times. The times t_1 and t_2 were chosen to allow the lowest and highest frequency components ($i = 1$ and $i = N$, respectively) to be generated and to travel to position x_b.

The wave profiles were measured from individual frames of a 16-mm movie taken at 500 frames

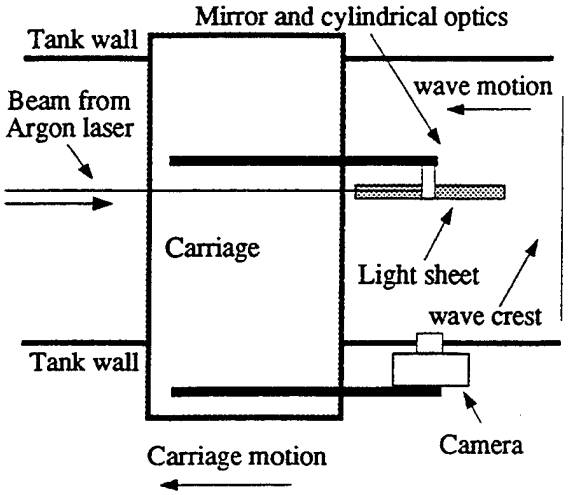


Figure 2: Schematic showing plan view of instrument carriage and optical system used to photograph the breaking waves.

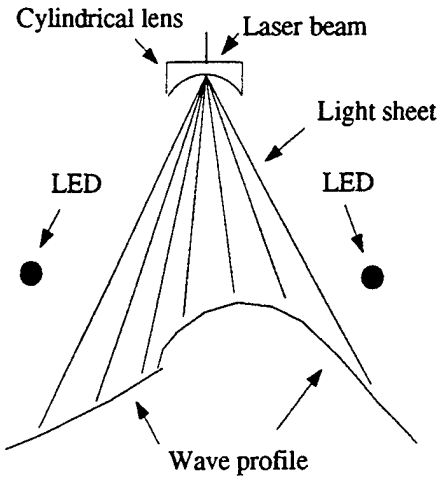


Figure 3: Schematic showing side view of wave with optical system used to create the light sheet. The water is mixed with fluorescent dye so that a glowing line is created along the centerline of the tank where the sheet enters the water.

per second in a reference frame nearly fixed with respect to the wave crest. The experimental setup is shown schematically in Figure 2. The camera is mounted on the carriage and views the wave from the side looking down from above the water surface with an angle of about 5° from the horizontal. A laser light sheet shines vertically down and is aligned with the centerline of the tank. Fluorescene dye is mixed with the water to a concentration of about 5 ppm. The dye in the light sheet glows and forms the light source for the pictures. The photographs clearly show the wave profile along the centerline of the tank where the light sheet enters the water. Two light-emitting diodes are attached to the carriage and positioned so that they appear in the upper left and right corners of the photographs. These dots are used to align successive images of the film. The dots are nearly horizontal and are 10.22 cm apart (see Figure 3).

The selected frames from the movie are digitized and stored for analysis. The profile of the wave is found by descending each column of pixels and finding the pixel where the light intensity increases above a preset threshold. The first bright pixel in each column below the images of the diodes is taken as the water surface. Using the centroids of the diodes and their know location above the mean water level, the wave profile is then reconstructed from the image data.

In the experiments described herein, breaking waves were generated from wedge motions with three different average frequencies ($\bar{f}$ = 1.14, 1.26, and 1.42 Hz, where $\bar{f} = \bar{\omega}/(2\pi)$). The water depth in the tank was the same in all cases (0.86 m); however, all other parameters of the generation process were Froude scaled. These Froude scaled parameters include the number of wave components, $N = 32$; the frequency increment, $\Delta\omega/\bar{\omega} = 0.0208$; the amplitude factor in the wedge motion, $A/\bar{\lambda} = 0.00124$ (where $\bar{\lambda} = 2\pi g/\bar{\omega}^2$ and g is gravitational acceleration); the time duration of the window function, $(t_2 - t_1)2.0\pi/\bar{\omega} = 8.00$; and the distance to the breaking event by linear theory, $X_b = 6.0\bar{\lambda}$. The mean position of the wedge was such that the vertical distance (h_w) between the lowest point of the wedge and the mean free surface was $0.397\bar{\lambda}$. The carriage speeds were 1.047, 0.978 and 0.927 m/sec for the $\bar{\omega} = 1.14$, 1.26, and 1.42 Hz waves, respectively.

In Froude scaling the wave generation process, the effects of surface tension and viscosity on the wave motion are not scaled. Surface tension effects scale according to the Weber number,

$$\frac{\Gamma}{\bar{\lambda}^3\bar{\omega}^2} \propto \Gamma\bar{\omega}^4, \qquad (3)$$

while viscous effects are scaled according to the

inverse of the Reynolds number.

$$\frac{\nu}{\lambda^2 \bar{\omega}} \propto \nu \bar{\omega}^3. \quad (4)$$

Thus, with the above mentioned frequencies the influence of surface tension will increase by a factor of 2.41 and the influence of viscosity will increase by a factor of 1.93 as the frequency increases. It should be pointed out that surface tension and viscosity not only effect the breaking process itself, but also the propagation of the waves from the wavemaker to the breaking point and to some extent the generation process.

The role of surfactants in this phenomenon is presently under investigation. During the experiments reported herein the surface of the tank was skimmed periodically but the surface tension was not measured. It is reasonable to assume that naturally occurring surfactants were present during the experiments. However, the phenomena described above were observed on numerous occasions. Since it is unlikely that the surfactant level was always the same, it is assumed that, though the details of the phenomena are probably affected by surfactants, the basic phenomenon occurs for a fairly wide range of surfactant levels. Recently, the surface tension in the tank has been measured with a Wilhelmy plate apparatus[10] about 30 minutes after skimming. The surface tension was in the range of 52 to 60 dynes/cm^2.

3 RESULTS AND DISCUSSION

Four photographs of the wave with $\bar{f} = 1.42$ Hz [8] are shown in Figures 4 to 7. These photographs were taken with a 35-mm camera at different times in the breaking process. They are from four separate realizations of breaking waves produced by the same wedge motion. In the first photograph, the bulge can be seen developing on the forward face of the wave. Wavy light rays can be seen in the foreground of the picture extending down from the water surface ahead of the toe of the bulge. These light rays originate from capillary waves on the water surface ahead of the toe in the following manner. As the light sheet enters the water at the centerline of the tank, the light sheet is focused or defocused by the curved water surface. Thus, under the crests of capillary waves, which have downward curvature, rays of high-intensity light illuminate the dye and the light from the dye is stronger than average in these rays. Under the troughs, which have an upward curvature, rays of low intensity light are found. If observed from under water, the bright and dark rays would be straight. However, the camera views the wave from above the water surface and so observes the light rays, which are from the capillary waves at the centerline of the tank, through the capillary waves on the water surface between the camera and the centerline of the tank. Thus, the light rays in the foreground of the photograph appear wavy rather than straight. The shape of the wave with the bulge and the capillary waves are in qualitative agreement with the theory of Longuet-Higgins [1]. The second photograph in the sequence, Figure 5, shows a similar wave shape but the bulge is much more pronounced and the toe of the bulge is much sharper. The first capillary wave ahead of the toe is now large enough in amplitude to be visible in the wave profile. Since the surface slopes and curvatures are much larger in this photograph, the underwater light rays form caustics and it is difficult to interpret the foreground of the photographs. In Figure 6 the toe of the bulge is further down the face of the wave and large ripples appear on the bulge. A short time later, Figure 7, the water surface has a random appearance, indicating that the flow has become turbulent.

Profiles taken from frames of the high-speed movies at various times during the breaking process for the three breaking waves with $\bar{f} = 1.14$, 1.26, and 1.42 Hz are presented in Figures 8, 9, and 10, respectively. The wave is moving from left to right relative to still water. Each profile is offset vertically by a fixed amount for clarity of presentation. The top profile is in the correct position relative to the undisturbed water level ($z = 0$). The sequence proceeds in time from the top profile to the bottom profile and the time intervals between the first and last profiles are given in the caption of each figure. The profiles were selected to show important features of the breaking events and so the time interval between profiles is not uniform. The vertical (z) and horizontal (x) scales in the photographs are nondimensionalized by λ_0, where $\lambda_0 = g/(2\pi \bar{f}^2)$. Thus, given the Froude-scaled manner in which the waves were generated (assuming that shallow water effects are not important), the wave shapes in the figures would be identical in the absence of viscous and surface tension effects. Each sequence starts with a smooth profile showing an asymmetric wave with a bulge on the forward face of the

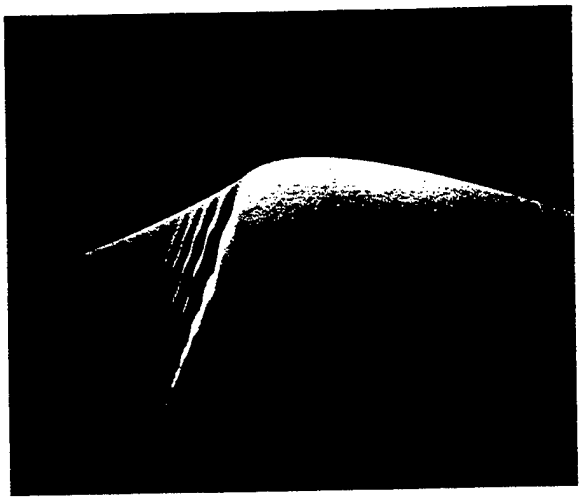


Figure 4: A photograph of a breaking wave $\bar{f} =$ 1.42 Hz. Initial formation of the bulge and capillary waves upstream of the toe of the bulge. The wave is moving from left to right relative to still water.

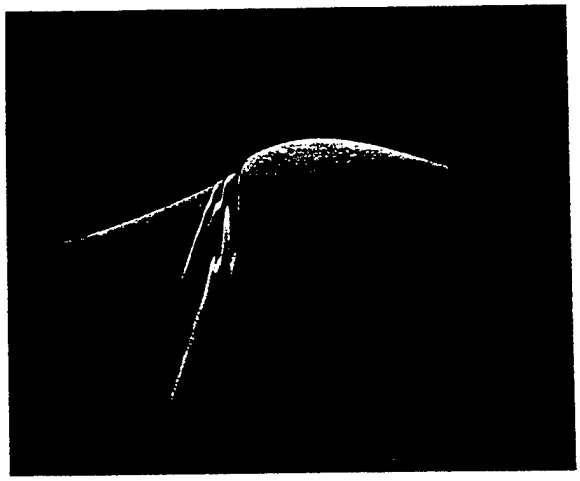


Figure 5: A photograph of a breaking wave $\bar{f} =$ 1.42 Hz. The bulge is well defined and the capillary wave just ahead of the toe is visible in the wave profile. The wave is moving from left to right relative to still water.



Figure 6: A photograph of a breaking wave $\bar{f} =$ 1.42 Hz. The toe of the bulge is further down the forward face of the wave and a train of ripples grows on the bulge. The wave is moving from left to right relative to still water.

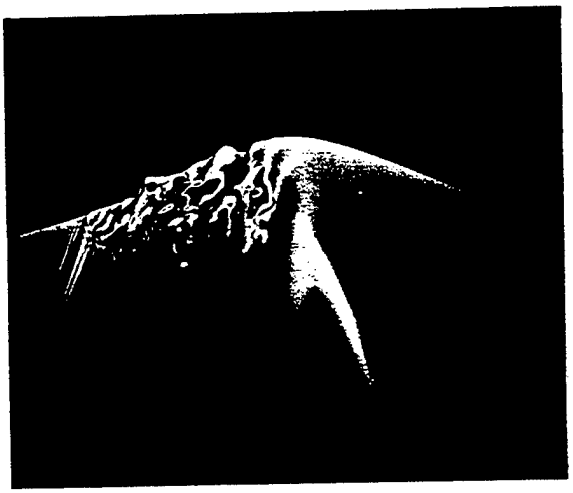


Figure 7: A photograph of a breaking wave $\bar{f} =$ 1.42 Hz. The surface has become disorganized indicating that the flow has become turbulent. The wave is moving from left to right relative to still water.

crest. The capillary waves are too small to be visible in the wave height profiles but are present in all three waves. Thus, at the point of incipient breaking, all three waves look qualitatively like the predictions of Longuet-Higgins [1]. After a short time, the bulge becomes more pronounced. As this happens, the toe of the bulge remains relatively stationary and becomes sharper. The toe-of the bulge is then seen to move rapidly down the forward face of the wave and as this happens ripples form over the surface of the bulge. The ripples are well defined in the next to the last profiles in Figures 8 and 9. They are still visible, but less well defined in Figure 10. In the final profile in each case, the water surface over the bulge has a random appearance in the movies and the

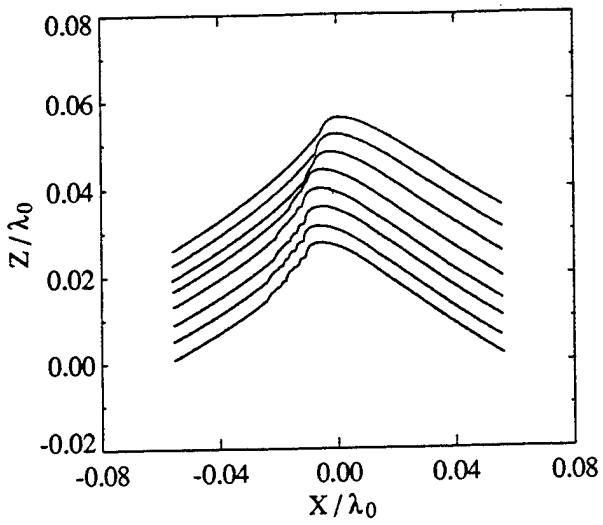


Figure 8: Profiles of the breaker with $\bar{f} = 1.14$ Hz. The top profile is in the correct position on the axes ($z = 0$ is the mean water level), but the lower profiles have been displaced vertically for clarity. Time increases from the top profile to the bottom profile. The time interval between the first and last profiles is 0.11 seconds.

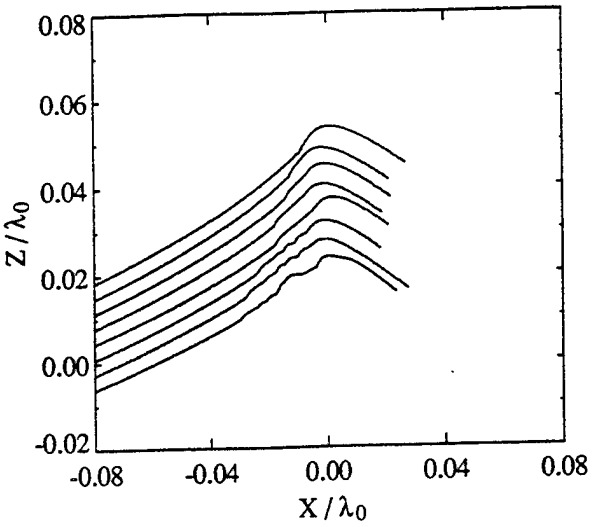


Figure 9: Profiles of the breaker with $\bar{f} = 1.26$ Hz. The top profile is in the correct position on the axes ($z = 0$ is the mean water level), but the lower profiles have been displaced vertically for clarity. Time increases from the top profile to the bottom profile. The time interval between the first and last profiles is 0.114 seconds.

flow is apparently turbulent. In examining several movies for each frequency, it was found that the ripples were present in every case but the extent to which they developed into a well defined wave train before the surface became random varied from realization to realization.

Several quantitative measurements were made from the image sequences in order to compare the three breaking waves. A schematic defining the measured quantities is given in Figure 11. The first measurement is the height of the crest versus time and is shown for all three waves in Figure 12. The origin of the time axis is the point in the movie where the toe of the bulge is first visible. This origin is somewhat imprecise so one should keep in mind when comparing one wave frequency to another that the curves can be shifted slightly in the horizontal direction. Note that in all three cases the height of the wave is relatively constant throughout the breaking process. The vertical axis of the figure is nondimensionalized by λ_0 so, if viscosity and surface tension were not factors in the wave generation, propagation and breaking process, one would expect the waves to have identical scaled heights. This is not the case; there is a monotonic increase in the scaled wave height

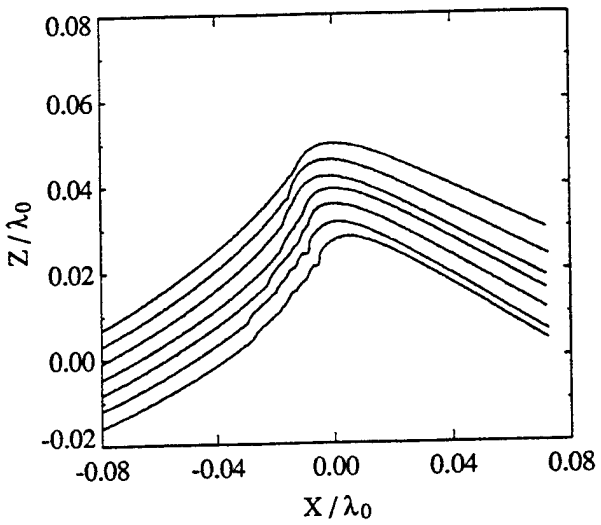


Figure 10: Profiles of the breaker with $\bar{f} = 1.42$ Hz. The top profile is in the correct position on the axes ($z = 0$ is the mean water level), but the lower profiles have been displaced vertically for clarity. Time increases from the top profile to the bottom profile. The time interval between the first and last profiles is 0.118 seconds

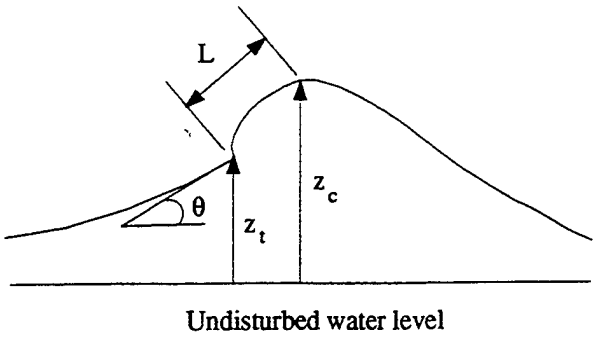


Figure 11: Schematic showing definitions of various quantities measured from the wave profiles.

as the frequency $\bar{f}$ decreases and the difference between the smallest and larges scaled height is about 5%. Note that from the first measurements to the last where the wave crest appears to be turbulent, the elapsed time is about $0.15T_0$. For the 1.42 Hz wave this is about 0.1 seconds. In a laboratory reference frame with the wave moving past the observer, the duration of 0.1 seconds is much too short for careful visual observation of the breaking behavior.

The second geometrical measurement that is of interest is the length from the crest of the wave to the toe of the bulge. Curves of this quantity divided by λ_0 are given in Figure 13 as a function of t/T_0. All three curves show a region of relatively constant length for early time (while the bulge is forming) followed by a region of increasing length as the toe moves down the wave face. The data for the 1.14 Hz and the 1.26 Hz waves are relatively similar, but the length from the crest to the toe is about 100% larger for the 1.42 Hz wave. Figure 14 is a plot of the vertical height from the crest to the toe of the bulge versus time and this plot shows very similar data to that in Figure 12.

The slope of the smooth water surface just ahead of the toe of the bulge is shown as a function of t/T_0 in Figure 15. In all three cases, the slope decreases with time. This is due to the fact that the toe is moving down the smooth wave face which has a slight upward curvature and remains relatively constant in shape during the short breaking process (see Figures 8, 9 and 10).

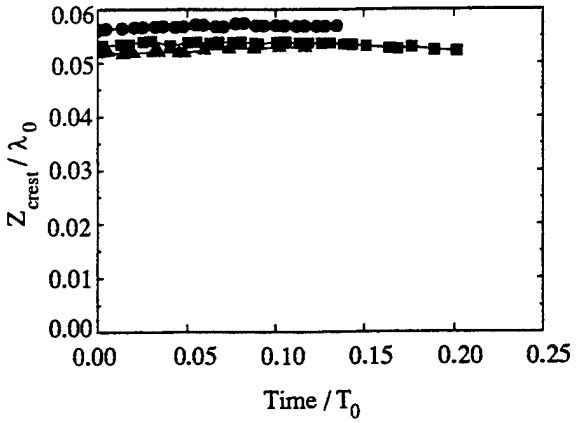


Figure 12: Height of breakers (Z_{crest}/λ_0) verses time (t/T_0): ● $\bar{\omega} = 7.16$ s^{-1}, ■ $\bar{\omega} = 7.92$ s^{-1}, ▲ $\bar{\omega} = 8.92$ s^{-1}.

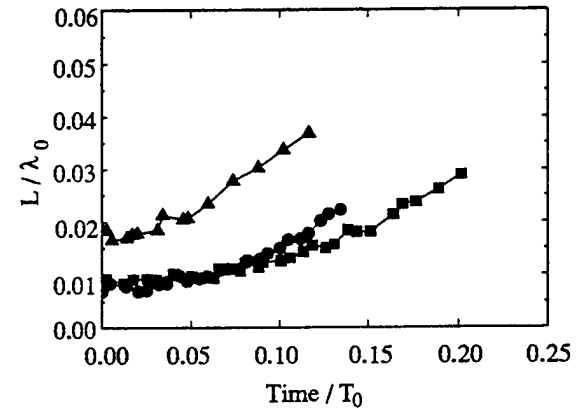


Figure 13: Distance from the crest of the wave to the toe of the bulge, (L/λ_0) verses time (t/T_0): ● $\bar{\omega} = 7.16$ s^{-1}, ■ $\bar{\omega} = 7.92$ s^{-1}, ▲ $\bar{\omega} = 8.92$ s^{-1}.

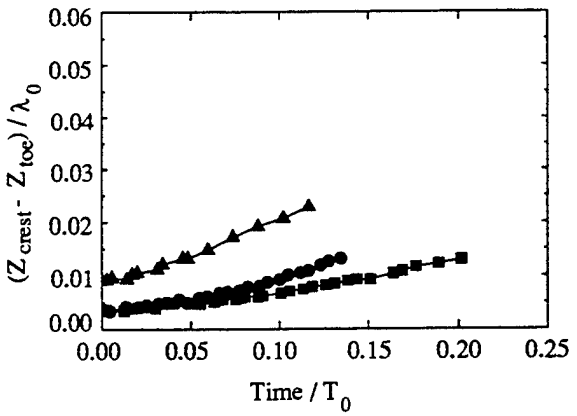


Figure 14: Height from the toe to the crest ($Z_{crest} - Z_{toe}/\lambda_0$) verses time ($t/T_0$): ● $\bar{\omega} = 7.16$ s^{-1}, ■ $\bar{\omega} = 7.92$ s^{-1}, ▲ $\bar{\omega} = 8.92$ s^{-1}.

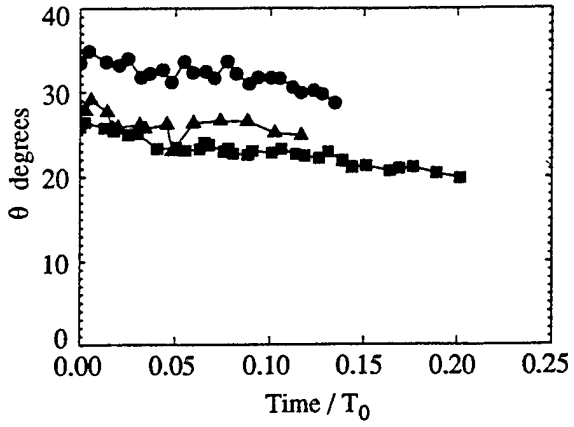


Figure 15: Slope of the smooth wave face ahead of the toe (θ) verses time (t/T_0): ● $\bar{\omega} = 7.16\ s^{-1}$, ■ $\bar{\omega} = 7.92\ s^{-1}$, ▲ $\bar{\omega} = 8.92\ s^{-1}$.

4 CONCLUSIONS

High-speed movies of gentle spilling breaking water waves with characteristic frequecies of 1.14, 1.26, and 1.42 Hz have revealed some new aspects of the mechanism by which these waves create turbulence. As the waves steepen, a bulge forms on the forward face in a manner predicted by Longuet-Higgins and his co-authors [1, 4, 5]. As the bulge forms the leading edge or toe of the bulge at first remains stationary, but then moves rapidly down the forward face of the wave. As it travels, ripples grow on the surface of the bulge and these ripples eventually break down into a random, quickly evolving shape, indicating that the underlying flow has become turbulent. It is theorized [7] that the ripples are a manifestation of unstable waves on a shear layer that is developed between the fluid in the bulge as it falls down the forward face of the wave and the underlying flow which is moving in the upslope direction. The three waves were generated in a Froude-scaled manner; however, it was found that the shapes of the breakers did not scale well with constant Froude number. In particular, it was found that the scaled length of the bulge ($L2\pi\bar{f}^2/g$) was about two times longer for the highest frequency wave when compared to the other two waves.

The authors gratefully acknowledge the support of the Office of Naval Research under contract N00014-90-J-1977.

References

[1] M. S. Longuet-Higgins, "The crest instability of steep gravity waves or How do short waves break?" Symposium on the Air-Sea Interface, Marseilles, France, June 24-30, (1993).

[2] M. L. Banner and D. H. Peregrine, "Wave breaking in deep water," *Ann. Rev. Fluid Mech.* Vol. 25, pp. 373, (1993).

[3] A. L. New, P. McIver and D. H. Peregrine, "Computations of overturning waves," *J. Fluid Mech.* Vol. 150, pp. 233, (1985).

[4] M. S. Longuet-Higgins and R. P. Cleaver, "Crest Instabilities of Gravity Waves. I. The inner solution.," *J. Fluid Mech.* Vol. 258 pp. 115, (1994).

[5] M. S. Longuet-Higgins, R. P. Cleaver, M. J. H. Fox "Crest Instabilities of Gravity Waves. II.," *J. Fluid Mech.* Vol. 259 pp. 333, (1994).

[6] M. S. Longuet-Higgins, "Capillary rollers and bores," *J. Fluid Mech.* Vol. 240, 659, (1992).

[7] J. H. Duncan, V. Philomin, M. Behres and J. Kimmel, "The Formation of Spilling Breaking Water Waves," *Physics of Fluids*, Vol. 6, No. 8, pp. 2558–2560, (1994).

[8] "Gallery of Fluid Motion," Special section in *Physics of Fluids*, Vol. 6, No. 9 (1994).

[9] R. Rapp and W. K. Melville, "Laboratory measurements of deep water breaking waves," *Phil. Trans. R. Soc. London Ser. A*, Vol. 331, pp. 735 (1990).

[10] C. A. Miller and P. Neogi, Interfacial Phenomena, Marcel Dekker, Inc., New York (1985).

DISCUSSION

K. Mori
Hiroshima University, Japan

In the conclusion of your presentation, you concluded that the fluid particle on the surface moves forward. How did you observe this forward moving? Although my experience is limited to the steady breaker, we observed the flow direction by making use of tufts to find no such forward flows.

AUTHORS' REPLY

In order to measure the flow field in our unsteady spilling breakers we are using particle image velocimetry techniques. These measurements are presently underway. As a preliminary qualitative method for obtaining the flow field, we used a high-speed movie camera to photograph the motion of particles in the flow. These movies, which were not shown in the presentation, indicate that in the reference frame moving with the wave crest the flow near the surface in the forward face of the crest moves forward and down the face of the wave during the transition from laminar to turbulent flow. We hope to present extensive measurements of this flow in the near future.

The Vortical Structure of a Near-Breaking Gravity-Capillary Wave

D. Dommermuth, R. Mui
(Science Applications International Corp., USA)

Abstract

A two-dimensional numerical simulation of a near-breaking 5cm gravity-capillary wave is performed. The free-surface boundary layer is resolved at the full-scale Reynolds, Froude, and Weber numbers. Seventeen million grid points are used to resolve the flow to within 1.2×10^{-3}cm. A robust numerical algorithm is developed to simulate flows with complex boundary-conditions and topologies including the effects of kinks. The numerical method is used to investigate the formation of parasitic capillary waves on the front face of a gravity-capillary wave. The parasitic capillary waves shed vorticity that induces surface currents that exceed fifteen percent of the phase velocity of the gravity-capillary wave when the steepness of the parasitic capillary waves is approximately 0.5 and the total wave steepness is 0.8. A mean surface current develops in the direction of the wave's propagation, and it is concentrated on the front face of the gravity-capillary wave. This current enhances mixing, and remnants of this surface current are probably present in post-breaking waves. Regions of high vorticity occur on the back sides of the troughs of the parasitic capillary waves. The vorticity separates from the free surface in regions where the wave-induced velocities are exceeded by the vorticity-induced velocities. The rate of energy dissipation of the gravity-capillary wave with parasitic capillaries riding on top is seventeen times greater than that of the gravity-capillary wave alone.

1 INTRODUCTION

The analyses of Longuet-Higgins, et al (1993 & 1994) show that the crest of a steep gravity wave is unstable. A toe forms on the forward face of the wave, just slightly forward of the crest. The formation of the toe may represent the initial stage of a spilling breaking wave. The high curvature near the toe is a source for the generation of parasitic capillary waves. The formation of parasitic capillary waves were first measured by Cox (1958). Longuet-Higgins (1963) has developed a theory that is based on the assumption that the parasitic capillary waves are steady in a frame of reference moving with the carrier wave. The numerical simulations of Dommermuth (1994b) show that the ripples actually undergo a nonlinear recurrence.

Okuda, et al (1977) and Ebuchi, et al (1987) observe that a strong vortical region forms in the crest of steep wind-generated waves in the neighborhood of the parasitic capillary waves. Based on a boundary-layer theory, Longuet-Higgins (1992) argues that the source of the vortical region, which he calls a vortical roller, is the parasitic capillary waves. Longuet-Higgins shows that the peak vorticity values occur slightly aft of a capillary wave's trough. A mean flux of vorticity is induced by capillary waves. Based on momentum arguments, he calculates that the resulting surface currents that would form beneath steep parasitic capillary waves can approach the phase speed of a gravity-capillary wave. The experiments of Duncan, et al (1994) confirm that as a gravity wave steep-

ens, a toe forms on the forward face near the crest. Capillary waves form ahead of the toe. On the bulge of fluid that forms behind the toe, Duncan, et al (1994) observe that large amplitude disturbances form. They conjecture that the disturbances are formed by an unstable interaction of the free surface with a shear layer beneath the bulge.

Based on an earlier investigation of vortex tubes interacting with a free surface (see Dommermuth, 1993), we make extensions to our theory that enable us to resolve the free-surface boundary layer beneath very steep gravity-capillary waves. We use this new capability to investigate the vortical structure of a 5cm near-breaking wave.

2 Mathematical Formulation

2.1 Field Equations

Let $\vec{u} = \vec{u}(x,z,t) = (u,w)$ represent the two-dimensional velocity field as a function of time. Applying Helmholtz's theorem gives:

$$\vec{u} = \nabla\phi + \vec{U}\,, \qquad (1)$$

where $\phi(x,z,t)$ is a velocity potential which describes the irrotational flow and $\vec{U}(x,z,t) = (U,W)$ is a solenoidal field which describes the vortical flow such that:

$$\nabla^2\phi = 0 \qquad (2)$$

$$\nabla\cdot\vec{U} = 0\,. \qquad (3)$$

Since ϕ satisfies Laplace's equation and the divergence of the rotational field $\vec{U}$ is chosen zero, the total velocity field $\vec{u}$ conserves mass. Note that $\vec{U}$ may contain a portion of the irrotational field depending on how the boundary conditions are defined.

Based on this Helmholtz decomposition of the velocity field, define the total pressure Π in terms of a rotational pressure P and an irrotational pressure as follows:

$$\Pi = P - \frac{\partial\phi}{\partial t} - \frac{1}{2}\nabla\phi\cdot\nabla\phi - \frac{1}{F_r^2}z\,. \qquad (4)$$

Here, the pressure terms are normalized by ρU_c^2 where U_c is the characteristic velocity and ρ is the density. $F_r^2 = U_c^2/gL_c$ is the Froude number and L_c is the characteristic length. The vertical coordinate z is positive upward, and the origin is located at the mean free surface. Substituting these decompositions (1 & 4) into the Navier-Stokes equations gives:

$$\frac{D\vec{U}}{Dt} + \left((\vec{U} - \vec{\mathcal{V}} + \nabla\phi)\cdot\nabla\right)\vec{U} + (\vec{U}\cdot\nabla)\nabla\phi = -\nabla P + \frac{1}{R_e}\nabla^2\vec{U}\,, \qquad (5)$$

where $D/Dt = \partial/\partial t + \vec{\mathcal{V}}\cdot\nabla$ is a substantial time derivative, $\vec{\mathcal{V}} = (\mathcal{X}_t, \mathcal{Z}_t)$ accounts for the motion of the interior flow due to the surface waves, $R_e = U_cL_c/\nu$ is the Reynolds number, and ν is the kinematic viscosity.

The field equations and the boundary conditions for the velocity field are used to deduce the rotational pressure in the fluid and the behavior of the rotational pressure near the boundaries. The divergence of the momentum equations (5) used in combination with the mass-conservation equations (2 & 3) are used to derive a Poisson equation for the rotational pressure. This equation expressed in indicial notation ($U_i = (U,W)$ & $V_i = (\mathcal{X}_t, \mathcal{Z}_t)$) is as follows:

$$\nabla^2 P = -\left(\frac{\partial U_j}{\partial x_i} - \frac{\partial V_j}{\partial x_i}\right)\frac{\partial U_i}{\partial x_j} - 2\frac{\partial U_j}{\partial x_i}\frac{\partial^2\phi}{\partial x_j\partial x_i}\,. \qquad (6)$$

Similarly, the momentum equations are also used to prescribe the normal derivative of the rotational pressure on the boundaries of the fluid. Thus, according to the divergence theorem, the rotational pressure is subject to the following solvability condition:

$$\int_S \frac{\partial P}{\partial n} = -\int_V ((\frac{\partial U_j}{\partial x_i} - \frac{\partial V_j}{\partial x_i})\frac{\partial U_i}{\partial x_j} + 2\frac{\partial U_j}{\partial x_i}\frac{\partial^2 \phi}{\partial x_j \partial x_i}) \ , \tag{7}$$

where V is a volume of fluid, S is the surface bounding the volume, and $\vec{n}$ is the unit outward-pointing normal on that surface.

2.2 Exact Free-Surface Boundary Conditions

Let the free-surface elevation be given by $z = \eta(x, y, t)$. Then the unit normal to the free surface is

$$\vec{n} = \frac{(-\eta_x, 1)}{\sqrt{\eta_x^2 + \eta_y^2 + 1}} \ . \tag{8}$$

The Helmholtz decomposition of the velocity field requires one additional boundary condition to be prescribed on the free surface. We impose that the rotational velocity is zero on the free surface:

$$\vec{\mathcal{U}} \cdot \vec{n} = 0 \ . \tag{9}$$

This constraint means that the evolution of the free-surface elevation is entirely prescribed in terms of the free-surface elevation itself and the velocity potential as follows:

$$\frac{\partial \eta}{\partial t} + \eta_x \phi_x - \phi_z = 0 \ , \tag{10}$$

where each term is evaluated on the free surface, $z = \eta$. If the normal derivative of the potential is chosen zero ($\phi_n = 0$) on all boundaries other than the free surface, then the mean free-surface elevation is conserved according to the above kinematic condition (10) and an application of Green's theorem.

In addition to the two kinematic conditions (9 & 10), also two stress conditions must be satisfied on the free surface. The normal stress condition is

$$\frac{d\phi}{dt} + \frac{1}{2}(\phi_x^2 - \phi_z^2) + \eta_x \phi_x \phi_z + \frac{1}{F_r^2}\eta - P$$
$$+\frac{2}{R_e}(n_z n_z (W_z + \phi_{zz}) + n_x n_z (W_x + U_z + 2\phi_{xz})$$
$$+n_x n_x (U_x + \phi_{xx})) = -P_a + \frac{1}{W_e}\frac{\eta_{xx}}{(1+\eta_x^2)^{3/2}} \ , \tag{11}$$

where $d/dt = \partial/\partial t + \eta_t \phi_z$ is a substantial time derivative, P_a is the atmospheric pressure, $W_e = \rho U_c^2 L_c / T$ is the Weber number, T is the surface tension, and (n_x, n_z) are the xz-components of the unit normal.

For a clean free surface, the tangential stress condition is

$$(U_z + W_x + 2\phi_{xz})(n_z n_z - n_x n_x)$$
$$+2(U_x - W_z + \phi_{xx} - \phi_{zz}) n_x n_z = 0. \tag{12}$$

2.3 Energy Conservation

The vector product of the total velocity and the momentum equations, integrated over the fluid volume, gives a formula for the conservation of energy. The transport theorem, in conjunction with the divergence theorem, may be used to simplify the resulting equation. Upon substitution of the exact free-surface boundary conditions, the following formula is derived:

$$\frac{d}{dt}\left(\int_V \frac{U_i U_i}{2} + \frac{1}{2}\int_{S_o} \eta_t \phi + \frac{1}{2F_r^2}\int_{S_o} \eta^2 \right.$$
$$\left. + \frac{1}{W_e}\int_{S_o} (\sqrt{1+\eta_x^2} - 1)\right) = -\int_{S_o} \eta_t P_a$$
$$-\frac{2}{R_e}\int_{S_f} n_i \frac{\partial \phi}{\partial x_j}\frac{\partial^2 \phi}{\partial x_i \partial x_j} - \frac{4}{R_e}\int_V \frac{\partial^2 \phi}{\partial x_i \partial x_j}\frac{\partial U_i}{\partial x_j}$$
$$-\frac{1}{R_e}\int_V (\frac{\partial U_i}{\partial x_j} + \frac{\partial U_j}{\partial x_i})\frac{\partial U_i}{\partial x_j} \ , \tag{13}$$

where S_f is the free surface and S_o is the projection of the free surface onto the xy-plane. The first term (dE_{uu}/dt) represents

the change in kinetic energy of the vortical portion of the flow integrated over the material volume of the fluid (V). The second and third terms ($dE_{\phi\phi}/dt$ & $dE_{\eta\eta}/dt$) represent the changes in the kinetic and potential energies of the waves. The fourth term (dE_s/dt) is the superficial energy due to surface extension. The first term on the right-hand side (dW_{pa}/dt) represents the power input by atmospheric forcing. The last few terms (dW_ν/dt) represent the power expended by viscous stresses. This term can be expressed as a function of the total velocity:

$$\frac{dW_\nu}{dt} = -\frac{1}{2R_e}\int_V (\frac{\partial u_i}{\partial x_j} + \frac{\partial u_j}{\partial x_i})^2 ,$$

which shows by virtue of the quadratic term that dW_ν/dt will result in a net decrease in energy. Note that the work due to stresses on all other boundaries other than the free surface is assumed to be zero.

3 NUMERICAL FORMULATION

The momentum equations (5), kinematic condition (10), and the normal stress condition (11) are integrated with respect to time using a third-order Runge-Kutta scheme. Each stage of the Runge-Kutta scheme is formulated to inhibit the accumulation of errors in the divergence of the rotational flow field. The rotational pressure is used to project the rotational velocity onto a solenoidal field (3 & 6) with zero normal velocity on the free surface (9). Laplace's equation for the potential (2) and Poisson's equation for the rotational pressure (6) are solved at each stage of the Runge-Kutta scheme, and a solvability condition is enforced for the rotational pressure. A multigrid solution scheme is used to solve the three-dimensional elliptic equations. Periodic boundary conditions are used on the sides of the domain and a free-slip boundary condition is used on the bottom. The numerical algorithm is implemented on a CM-5 parallel computer.

3.1 Gridding

Figure 1 illustrates the fully-staggered grid that is used in the numerical simulations. The solenoidal velocities (U, W) and the rotational pressure (P) are staggered relative to each other. The grid spacing is evenly spaced along the horizontal and vertical directions. As a reference point, the position of the grid points for the velocity potential are provided below:

$$\begin{aligned} x_{i,k} &= \Delta x\, i \\ z_{i,k} &= \eta_i - \Delta z(k-1) \ , \end{aligned} \qquad (14)$$

where $i = 1, IMAX$ and $k = 1, KMAX$ are the indices along respectively the $x-$ and $z-$axes. η_i is the free-surface elevation at $x = \Delta x\, i$. The grid spacings are $\Delta x = L/IMAX$ and $\Delta z = D/(KMAX - 1)$, where L is the length and D is the depth. Based on this mapping, the velocity of the grid points below the free surface is $\vec{V}_{i,k} = (0, \partial\eta_i/\partial t)$, which is independent of the depth.

3.2 The TAME algorithm

The numerical simulation of near-breaking waves at full scale is difficult because the wave steepness is order one, and the various length and time scales are disparate. The free-surface boundary layer is difficult to resolve because it is very thin relative to the wavelength and the wave amplitude. Numerical methods are also difficult to apply near the toe of a spilling breaker, where the kink in the geometry adversely affects the accuracy. The free-surface boundary conditions are difficult to impose even without kinks, especially the tangential-stress condition (12).

Based on earlier investigations of waves interacting with turbulence, we developed capabilities for simulating wave steepnesses up

to $\epsilon \approx 0.6$ (see Dommermuth, 1993, 1994a, & 1994b, Dommermuth & Novikov 1993, and Dommermuth, Novikov, & Mui 1994). The parametric mapping techniques that we used in those studies are difficult to apply to near-breaking waves. Parametric mappings are sensitive to grid irregularities such as kinks and to grid stretching, which is sometimes required to resolve boundary layers. For waves that are very steep, the elliptic equations associated with parametric mappings are difficult to solve because they lose diagonal dominance. The tangential free-surface stress condition is especially difficult to impose using a parametric mapping because the normal derivatives of two velocity components (three in 3-D) are required given only one boundary condition (two in 3-D). A desirable feature of parametric mappings is that finite-difference discretizations work well on parallel computers.

The numerical simulation of near-breaking waves required the development of a new numerical algorithm that we call Taylor's Accurate Method of Evaluation (TAME). TAME uses Taylor series expansions to evaluate functions and their derivatives directly in physical space. The TAME algorithm can have second- or higher-order accuracy, even on unstructured grids. The accuracy of the TAME algorithm is not sensitive to grid irregularities, grid stretching, or grid coarsening. TAME permits the evaluation of nonanalytic functions, and it can incorporate boundary conditions that are arbitrarily complex. Some examples of TAME's capabilities are illustrated in Figure 2. TAME can be used to calculate derivatives, to perform interpolation, extrapolation, and smoothing, to provide upwind biasing, and to enforce boundary conditions.

3.3 A TAME Laplacian

The stencil that is used to evaluate a TAME Laplacian is illustrated in Figure 3. The Laplacian operator is required in the Laplace equation for the velocity potential (2), the viscous diffusion terms (5), and the Poisson equation for the vortical pressure (6).

As an example of TAME's implementation, consider the Taylor-series expansion of the velocity potential:

$$\begin{aligned}\phi^{(i)} = \phi^{(0)} &+ \Delta x_i \phi_x^{(0)} + \Delta z_i \phi_z^{(0)} \\ &+ \frac{\Delta x_i{}^2}{2}\phi_{xx}^{(0)} + \Delta x_i \Delta z_i \phi_{xz}^{(0)} + \frac{\Delta z_i{}^2}{2}\phi_{zz}^{(0)} \\ &+ \frac{\Delta x_i{}^3}{6}\phi_{xxx}^{(0)} + \frac{\Delta x_i{}^2 \Delta z_i}{2}\phi_{xxz}^{(0)} \\ &+ \frac{\Delta x_i \Delta z_i{}^2}{2}\phi_{xzz}^{(0)} + \frac{\Delta z_i{}^3}{6}\phi_{zzz}^{(0)} \\ &+ \frac{\Delta x_i{}^4}{24}\phi_{xxxx}^{(0)} + \frac{\Delta x_i{}^3 \Delta z_i}{6}\phi_{xxxz}^{(0)} \\ &+ \frac{\Delta x_i{}^2 \Delta z_i{}^2}{4}\phi_{xxzz}^{(0)} + \frac{\Delta x_i \Delta z_i{}^3}{6}\phi_{xzzz}^{(0)} \\ &+ \frac{\Delta z_i{}^4}{24}\phi_{zzzz}^{(0)} \ , \end{aligned} \tag{15}$$

where $\phi^{(0)}$ is the value of ϕ at the Taylor-expansion point, $\phi^{(i)}$ are the values at neighboring points, and $\Delta x_i = x^{(i)} - x^{(0)}$ and $\Delta z_i = z^{(i)} - z^{(0)}$ are offsets in the horizontal and vertical directions, respectively.

On the nine-point stencil that is illustrated in Figure 3, second-order approximations to $\phi_x^{(0)}$, $\phi_z^{(0)}$, $\phi_{xx}^{(0)}$, $\phi_{xz}^{(0)}$, and $\phi_{zz}^{(0)}$ are obtained by selectively solving for terms in the Taylor-series expansion as illustrated in Figure 4. If the velocity potential, i.e. $\phi^{(i)}$, is known, then this procedure provides its derivatives, including the Laplacian, at all of the grid points. If, however, the solution to a boundary-value problem, is required, then the Laplace operator must be expressed in terms of the neighbors of $\phi^{(0)}$:

$$\phi_{xx}^{(0)} + \phi_{zz}^{(0)} = \sum_{i=1}^{8} c_i (\phi^{(i)} - \phi^{(0)}) \ , \tag{16}$$

where the coefficients, c_i, are derived by inverting the equations in Figure 4. This stencil for the interior points of the velocity potential is supplemented with other stencils

near the boundaries to impose either Dirichlet, Neumann, or mixed boundary conditions. The resulting boundary-value problem is amenable to iterative solution procedures because the the diagonal and the off-diagonal terms are multiplied by the same coefficients, which promotes diagonal dominance.

The TAME algorithm requires Gaussian elimination with partial pivoting to be performed at each grid point. This operation is performed in parallel on the CM-5 computer. An additional gain in efficiency could be realized by building a special computer chip to solve the TAME low-order systems-of-equations[1].

3.4 A TAME treatment of the free surface

The TAME algorithm has been developed primarily to treat the tangential-stress boundary condition on the free surface (see Equation 12). Figure 5 illustrates the stencil that is required to evaluate the viscous diffusion terms with the tangential-stress condition imposed. Ten samples of the $U-$velocity grid and eleven samples of the $W-$velocity grid are required for second-order accuracy on a curved free surface. (Note that $U^{(1)}$, which appears in the stress condition, is not on the $U-$velocity grid.) $U^{(2)}, U^{(3)}, \ldots, U^{(10)}$ and $W^{(1)}, W^{(2)}, \ldots, W^{(10)}$ are expanded about the locations of the points $U^{(0)}$ and $W^{(0)}$, respectively, as shown in Equation 15. The tangential-stress boundary condition is also expanded in a Taylor series about the same two points:

$$\begin{aligned}(U_z^{(0)} + \Delta x_1 U_{xz}^{(0)} + \Delta z_1 U_{zz}^{(0)} + \cdots + W_x^{(0)})(n_z^2 - n_x^2) \\ +2(U_x^{(0)} + \Delta x_1 U_{xx}^{(0)} + \Delta z_1 U_{xz}^{(0)} + \cdots - W_z^{(o)})n_x n_z \\ = -2\phi_{xz}^{(o)}(n_z^2 - n_x^2) - 2(\phi_{xx}^{(o)} - \phi_{zz}^{(o)})n_x n_z \ .\end{aligned}$$

The Taylor-series terms that are eliminated for both $U^{(0)}$ and $W^{(0)}$ include the $x-$, $z-$, $xx-$, $xz-$, $zz-$, $xxx-$, $xxz-$, $xzz-$, $zzz-$, and $xxzz-$derivatives. This leads to twenty independent equations for derivatives of $U^{(0)}$ and $W^{(0)}$ near the free surface. The diffusion terms are evaluated as $(U_{xx}^{(0)} + U_{zz}^{(0)})/R_e$ and $(W_{xx}^{(0)} + W_{zz}^{(0)})/R_e$, and they are then inserted into the Navier-Stokes equations (5). The points that are in the interior of the fluid are evaluated using the nine-point stencil that we have discussed in the previous section.

[1]Dr. Edwin P. Rood, private communication.

3.5 Numerical accuracy

The second-order accuracy of every TAME subroutine is tested by prescribing as input a quantity that has a known solution. The accuracy and the convergence rates of the elliptic solvers are also tested using known solutions. For a 4096×4097 grid, the elliptic solvers converge to machine accuracy using only sixteen iterations of V-cycle multigrid and ten iterations of a damped Jacobi smoother per V-cycle. Once the TAME tools have been validated, they are assembled to simulate free-surface waves. The final assembled code is tested using exact Stokes waves as initial conditions.

4 NUMERICAL RESULTS

4.1 The initial conditions

We consider the formation of parasitic capillary waves on the front face of a gravity-capillary wave. Let the characteristic length and velocity be denoted by $L_c = \lambda$ and $U_c = \sqrt{g\lambda}$, where λ is the length of the gravity-capillary wave and g is gravity. Then the Froude, Weber, and Reynolds numbers are $F_r = 1$, $W_e = \rho g \lambda^2/\sigma$, and $R_e = g^{1/2}\lambda^{3/2}/\nu$, where ρ is the fluid density, σ is the surface tension, and ν is the kinematic viscosity. For our numerical simulation of a $5cm$ wave, $F_r = 1$, $W_e = 331$, and $R_e = 35,000$. The two-dimensional numerical simulation is initialized using an exact solution for a gravity wave, and the parasitic capillaries are gener-

ated from rest due to a parametric resonance.

The initial steepness of the gravity wave is 0.2827, and the mean depth is equal to the length. We initially use an inviscid boundary-layer formulation (see Dommermuth, 1994b), and then we switch to full Navier-Stokes solutions after the parasitic capillary waves have reached their maximum steepness at time $t = 6.4$. A moderate resolution Navier-Stokes solution is used at first, and we then switch to a higher resolution Navier-Stokes solution at time $t = 6.6$ to establish convergence. The inviscid formulation enabled us to take larger time steps with a lower resolution than is possible with the fully-resolved Navier-Stokes formulation. We use 512×513 grid points for the inviscid simulation and 2048×2049 and 4096×4097 grid points for the viscous simulations. The time step of the inviscid simulation is $\Delta t = 4.0 \times 10^{-3}$, and the time steps of the viscous simulations are $\Delta t = 4.0 \times 10^{-4}$ and $\Delta t = 1.5 \times 10^{-4}$. Low-pass filtering of the free-surface elevation and the velocity potential permits larger time steps to be taken than is possible without low-pass filtering. The free-surface elevation and the velocity potential from the inviscid formulation are used as initial conditions for the Navier-Stokes formulation. The vortical portion of the flow develops from rest.

Based on a boundary-layer thickness $\delta^2 = 2/(R_e\sigma)$, where $\sigma^2 = 2\pi$ is the wave frequency, the resolutions of the boundary layer in the Navier-Stokes simulations are ten and twenty grid points. We are currently developing a capability that would permit even higher resolution of the free-surface boundary layer by using grid stretching. The present capability, with no grid stretching, is useful for investigating the effects of turbulence on the onset of wave breaking.

The calculation of sixteen hundred time steps of the inviscid boundary-layer formulation with 512×513 grid points required six hours on the 256-node partition on the CM-5 at the University of Minnesota Army High Performance Computing Research Center. The calculation of five hundred time steps of the Navier-Stokes formulation with 2048×2049 grid points required twenty-two hours on the 256-node CM-5 at the Naval Research Laboratory. Twenty time steps of the 4096×4097 simulation required ninety minutes on the NRL machine.

4.2 The vortical structure

Figure 6 illustrates the formation of ripples on a 5cm gravity-capillary wave. Parts (a) and (b) show the initial free-surface elevation and slope. Parts (c) and (d) show the the same quantities at time $t = 6.603$. The x-axis has been periodically extended to double the horizontal extent of the computational domain. The wave is propagating from right to left.

The initial wave steepness is approximately $\epsilon \approx 0.3$. When the parasitic capillary waves form, the steepness increases to $\epsilon \approx 0.8$. The formation of parasitic capillary waves leads to a significant increase in the rate of wave energy dissipation. Based on Equation 13, the rate of wave energy dissipation is

$$\frac{dE_w}{dt} = \frac{dE_{\phi\phi}}{dt} + \frac{dE_{\eta\eta}}{dt} + \frac{dE_s}{dt} ,$$

where E_w is the total wave energy, $E_{\phi\phi}$ is the wave kinetic energy, $E_{\eta\eta}$ is the wave potential energy, and E_s is the wave superficial energy.

According to the linearized theory of Lamb (1932),

$$\frac{dE_w}{dt} = -4\frac{k^2}{R_e}E_w(t=0) ,$$

where $k = 2\pi$ is the wavenumber of the gravity-capillary wave. Based on the present numerical results, dE_w/dt is seventeen times greater with parasitic capillary waves than without them. This result agrees with that of Longuet-Higgins (1962), who estimated an

order of magnitude increase for a 6cm carrier wave.

Figure 7 shows various quantities on the free surface at time $t = 6.603$ including: (a) the free-surface elevation, (b) the vorticity, (c) the tangential component of the solenoidal velocity field, (d) the tangential component of the potential velocity field, (e) the tangential component of the total velocity field, and (f) the normal component of the total velocity field. The normal component of the total velocity field is equal to the normal component of the potential velocity field because the normal component of the solenoidal velocity field is zero. The dashed horizontal curves are moving 401-point averages. The dashed vertical lines indicate the locations of the minima of the surface vorticity. The direction of the tangent ($\vec{t}$) is in the direction of wave propagation.

The extrema of the vorticity occur slightly aft of the wave troughs of the parasitic capillary waves, which agrees with the capillary-wave boundary-layer theory of Longuet-Higgins (1992). The extreme minima in vorticity occur behind the troughs because the wavy portion ($\nabla\phi$) of the flow sweeps the vorticity back and up against the troughs. Figure 7d shows that the wave-induced tangential velocities are positive in the troughs, in the opposite direction of wave propagation. Figure 7f shows that normal velocity is positive behind the troughs, i.e. upward on the right-hand sides of the troughs. These two components of velocity push the vorticity back and up against the troughs of the parasitic capillary waves.

At the wave crest, Longuet-Higgins had argued that the surface currents induced by the vortical roller are in the direction of wave propagation. In Figure 7c, our numerical simulations show that the surface currents induced by the vorticity are down the face of the wave. At the crest of the gravity-capillary wave (see Figure 7c for $0.55 \leq x \leq 0.65$), our numerical simulations show that the vorticity induces a very weak current that is in the opposite direction of wave propagation, which disagrees with Figure 12 in Longuet-Higgins' paper. Compared to the magnitude of the vorticity that occurs near the troughs of the parasitic capillary waves, the vorticity in the crest of the gravity-capillary wave is very weak, and its sign is the opposite of what Longuet-Higgins indicates in his Figure 12. We conjecture that a strong vortical roller with a sign that corresponds to the results of Longuet-Higgins and the wind-wave experiments of Ebuchi, et al (1987), could form under the action of wind, but without wind there is no strong vortical roller at the crest of a gravity-capillary wave.

The mean vorticity on the front face of the wave is negative as illustrated by the dashed curve in Figure 7b. The negative mean vorticity gives a mean tangential velocity that is down the face of the gravity-capillary wave. The mean surface current down the face is observed in Figure 7c. We conjecture that as the wave steepens and the vorticity becomes stronger, the tangential velocity that is induced by the vortical portion ($\vec{U} \cdot \vec{t}$) of the flow may cancel the tangential velocity that is induced by the wavy portion of the flow ($\nabla\phi \cdot \vec{t}$). We observe that $\vec{U} \cdot \vec{t}$ is ninety degrees out-of-phase with $\nabla\phi \cdot \vec{t}$. Although $\vec{U} \cdot \vec{t}$ oscillates, it is almost completely negative and has a mean negative value. $\nabla\phi \cdot \vec{t}$ oscillates positive and negative about the positive mean value that is induced by the gravity-capillary wave.

Figure 7c shows that the tangential velocity induced by the vortical portion of the flow is negative, in the direction of wave propagation. For very steep waves, $\vec{U} \cdot \vec{t}$ will be directly downward in the troughs of the parasitic capillary waves and $\nabla\phi \cdot \vec{t}$ will be upward. If the magnitude of $\vec{U} \cdot \vec{t}$ exceeds $\nabla\phi \cdot \vec{t}$, a vortex will be swept down into the fluid. Figure 7e shows that $\vec{U} \cdot \vec{t}$ reduces $\nabla\phi \cdot \vec{t}$ at the troughs and increases it at the crests of the parasitic capillary waves. Once the vortex is outside the boundary layer, the potential portion of the flow will sweep it back toward the crest

of the gravity-capillary wave.

The mean surface currents that are induced by vorticity are represented by the dashed lines in Figure 7c. Remnants of the surface currents are probably present even after the wave spills. Since $\vec{U} \cdot \vec{t}$ is down into the fluid when the parasitic capillary waves are very steep, it contributes to the transfer of energy, momentum, heat, and gases into the bulk of the fluid and the mixing of the upper few centimeters of the marine layer.

The enhanced mixing is evident in the experiments of Duncan, et al (1994). Their experiments show fluorescent dye being ejected below the parasitic capillary waves (see their Figure 3e). The number of eruptions of green dye correspond to the number of parasitic capillary waves. The shape of the outer envelop of the eruptions is similar to the envelop of the surface vorticity in our Figure 7b.

Duncan, et al (1994) conjectured that an instability occurs on a shear layer that is located between two layers of fluid. In a layer of fluid that is immediately below the parasitic capillary waves, the flow appears to be moving down the face in the experiments. This layer of fluid would correspond to $\vec{U} \cdot \vec{t}$ in our numerical simulations. In a slightly deeper layer, the flow is moving up the face of the wave. This deeper layer of fluid corresponds to $\nabla\phi \cdot \vec{t}$. We differ with Duncan, et al, however, in that we believe that the flow separates near the troughs of the parasitic capillary waves. This mechanism differs from the shear-layer instability of Duncan, et al. Figure 8 summarizes our results.

Figure 9 compares the free-surface vorticity as predicted by numerics to theory. The theory is based on Longuet-Higgins' (1992) analysis of capillary rollers and bores. For a steady progressive wave, the surface vorticity (ω^s) is proportional to the surface curvature (κ) and the tangential velocity (q):

$$\omega^s = -2\kappa q \ ,$$

where for our two-dimensional simulation:

$$\kappa = \frac{\eta_{xx}}{(1+\eta_x^2)^{3/2}}$$

$$q = (\frac{\partial\phi}{\partial x} + U + c_o)n_z - (\frac{\partial\phi}{\partial z} + W)n_x \ .$$

$c_o = \sqrt{\sigma/k}$ is the phase velocity, which we estimate using linear theory:

$$\sigma^2 = \frac{k^3}{W_e} + \frac{k}{F_r^2} \ .$$

σ is the wave frequency and $k = 2\pi$ is the wavenumber of the gravity-capillary wave.

In deriving the preceding equations, we have assumed that the gravity-capillary wave is steady. In fact, the envelop of the parasitic capillary waves undergoes a nonlinear recurrence as shown by Dommermuth (1994b). Despite this assumption and the linearized approximation for the phase velocity, the numerical predictions agree remarkably well with theory as shown in Figure 9. Note that the utility of Longuet-Higgins' theory is limited because the total tangential velocity must be known on the surface, not just the potential-flow velocity.

Figure 10 shows the structure of the vorticity that is below the first parasitic capillary wave. The $x-$ and $z-$axes have the same scale. The depth below the free surface is five boundary-layer thicknesses based on a boundary-layer thickness $\delta^2 = 2/(R_e\sigma)$. The vorticity is separating from the free surface where the total tangential velocity ($\vec{U}\cdot\vec{t} + \nabla\phi \cdot \vec{t}$) is changing sign. This is the point where the surface current starts to move down the face of the gravity-capillary wave.

5 CONCLUSIONS

Parasitic capillary waves form on the front face of steep gravity-capillary waves. Regions of high vorticity are located near the troughs of the parasitic capillary waves. The vorticity induces strong surface currents. For very

steep parasitic capillary waves ($\epsilon > 1$), the surface currents can become so strong that the flow separates and injects vorticity into the fluid below the troughs of the parasitic capillary waves. This injection of vorticity convects energy, momentum, heat, and air bubbles below the free surface. We speculate that the microbreaking event that is described in this paper models the small-scale details of much larger spilling breaking waves.

ACKNOWLEDGEMENTS

The development of our free-surface capability is financially supported by ONR under contract number N00014-93-C-0046 with Dr. Edwin P. Rood as program manager. This work is also supported in part by the Army Research Office contract number DAALO3-89-C0038 with the University of Minnesota Army High Performance Computing Research Center (AHPCRC) and the DoD Shared Resource Center at the AHPCRC. The numerical simulations have been performed on the CM-5 computers at Naval Research Laboratory and the AHPCRC.

REFERENCES

Cox, C.S. (1958) Measurements of slopes of high-frequency wind waves. *J. Marine Research*, **16**, 199-225.

Duncan, J.H., Philomin, V., Behres, M., & Kimmel, J. (1994) The formation of spilling breaking waves. *Phys. Fluids*, to appear.

Dommermuth, D.G. (1993) The laminar interactions of a pair of vortex tubes with a free surface. *J. Fluid Mech.*, **246**, 91-115.

Dommermuth, D.G. (1994a) The initialization of vortical free-surface flows. *J. Fluids Eng.*, **116**, 95-102.

Dommermuth, D.G. (1994b) Efficient simulation of short- and long-wave interactions with applications to capillary waves. *J. Fluids Eng.*, **116**, 77-82.

Dommermuth, D.G. & Novikov, E.A. (1993) Direct-numerical and large-eddy simulations of turbulent free-surface flows. In *Proc. of the 6th Inter. Conf. on Numer. Ship Hydro., Iowa City*, To appear.

Dommermuth, D.G., Novikov, E.A., & Mui, R.C.Y. (1994) The interaction of surface waves with turbulence. In *Proc. of the ASME Symp. on Free-Surface Turbulence, Lake Tahoe*, To appear.

Ebuchi, N., Kawamura, H., & Toba, Y. (1987). Fine structure of laboratory wind-wave surfaces studied using an optical method. *Boundary-Layer Met.*, **39**, 133-151.

Lamb, H. (1932) *Hydrodynamics*. Dover.

Longuet-Higgins, M.S. (1963) The generation of capillary waves by steep gravity waves. *J. Fluid Mech.*, **16**, 138-159.

Longuet-Higgins, M.S. (1992) Capillary rollers and bores. *J. Fluid Mech.*, **240**, 659-679.

Longuet-Higgins, M.S. & Cleaver, R.P. (1993) Crest instabilities of gravity waves. 1. The almost highest wave. *J. Fluid Mech.*, **258**, 115-130.

Longuet-Higgins, M.S., Cleaver, R.P., & Fox, M.J.H. (1994) Crest instabilities of gravity waves. 2. Matching and asymptotic analysis *J. Fluid Mech.*, **259**, 333-344.

Okuda, K., Kawai, S., & Toba, Y. (1977) Measurements of skin friction distribution along the surface of wind waves. *J. Oceanogr. Soc. Japan*, **33**, 190-198.

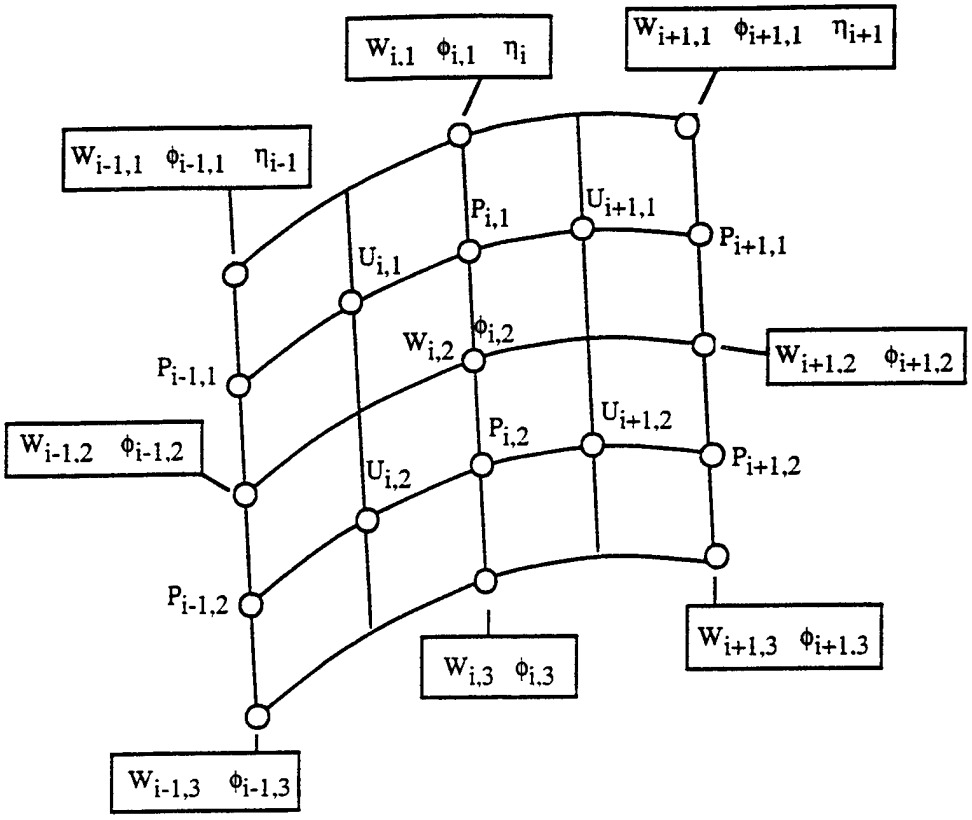
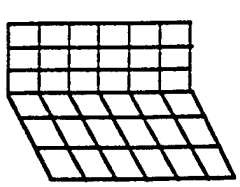
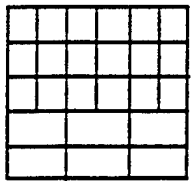


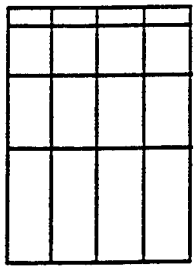
Figure 1: *The fully-staggered grid.*



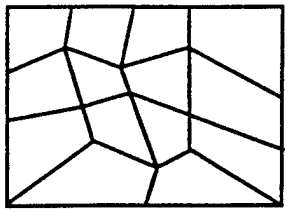
(a) Grid irregularities



(c) Grid coarsening



(b) Grid stretching



(d) Unstructured gridding

Figure 2: *TAME capabilities.*

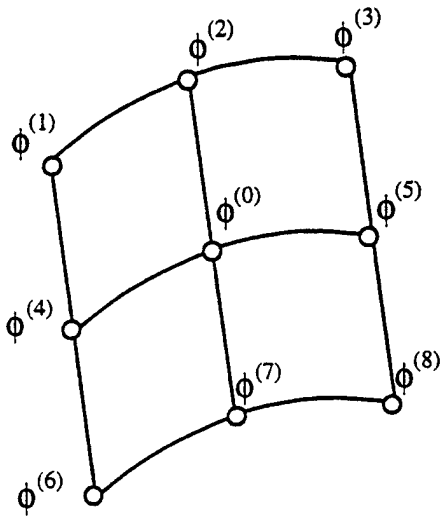


Figure 3: *Nine-point stencil for the evaluation of the Laplacian.*

$$
\begin{vmatrix}
\Delta x_1 & \Delta z_1 & \frac{\Delta x_1 \Delta x_1}{2} & \Delta x_1 \Delta z_1 & \frac{\Delta z_1 \Delta z_1}{2} & \frac{\Delta x_1^2 \Delta z_1}{2} & \frac{\Delta x_1 \Delta z_1^2}{2} & \frac{\Delta x_1^2 \Delta z_1^2}{4} \\
\Delta x_2 & \Delta z_2 & \frac{\Delta x_2 \Delta x_2}{2} & \Delta x_2 \Delta z_2 & \frac{\Delta z_2 \Delta z_2}{2} & \frac{\Delta x_2^2 \Delta z_2}{2} & \frac{\Delta x_2 \Delta z_2^2}{2} & \frac{\Delta x_2^2 \Delta z_2^2}{4} \\
\Delta x_3 & \Delta z_3 & \frac{\Delta x_3 \Delta x_3}{2} & \Delta x_3 \Delta z_3 & \frac{\Delta z_3 \Delta z_3}{2} & \frac{\Delta x_3^2 \Delta z_3}{2} & \frac{\Delta x_3 \Delta z_3^2}{2} & \frac{\Delta x_3^2 \Delta z_3^2}{4} \\
\Delta x_4 & \Delta z_4 & \frac{\Delta x_4 \Delta x_4}{2} & \Delta x_4 \Delta z_4 & \frac{\Delta z_4 \Delta z_4}{2} & \frac{\Delta x_4^2 \Delta z_4}{2} & \frac{\Delta x_4 \Delta z_4^2}{2} & \frac{\Delta x_4^2 \Delta z_4^2}{4} \\
\Delta x_5 & \Delta z_5 & \frac{\Delta x_5 \Delta x_5}{2} & \Delta x_5 \Delta z_5 & \frac{\Delta z_5 \Delta z_5}{2} & \frac{\Delta x_5^2 \Delta z_5}{2} & \frac{\Delta x_5 \Delta z_5^2}{2} & \frac{\Delta x_5^2 \Delta z_5^2}{4} \\
\Delta x_6 & \Delta z_6 & \frac{\Delta x_6 \Delta x_6}{2} & \Delta x_6 \Delta z_6 & \frac{\Delta z_6 \Delta z_6}{2} & \frac{\Delta x_6^2 \Delta z_6}{2} & \frac{\Delta x_6 \Delta z_6^2}{2} & \frac{\Delta x_6^2 \Delta z_6^2}{4} \\
\Delta x_7 & \Delta z_7 & \frac{\Delta x_7 \Delta x_7}{2} & \Delta x_7 \Delta z_7 & \frac{\Delta z_7 \Delta z_7}{2} & \frac{\Delta x_7^2 \Delta z_7}{2} & \frac{\Delta x_7 \Delta z_7^2}{2} & \frac{\Delta x_7^2 \Delta z_7^2}{4} \\
\Delta x_8 & \Delta z_8 & \frac{\Delta x_8 \Delta x_8}{2} & \Delta x_8 \Delta z_8 & \frac{\Delta z_8 \Delta z_8}{2} & \frac{\Delta x_8^2 \Delta z_8}{2} & \frac{\Delta x_8 \Delta z_8^2}{2} & \frac{\Delta x_8^2 \Delta z_8^2}{4}
\end{vmatrix}
\begin{vmatrix}
\frac{\partial \phi^{(0)}}{\partial x} \\
\frac{\partial \phi^{(0)}}{\partial z} \\
\frac{\partial^2 \phi^{(0)}}{\partial x^2} \\
\frac{\partial^2 \phi^{(0)}}{\partial x \partial z} \\
\frac{\partial^2 \phi^{(0)}}{\partial z^2} \\
\frac{\partial^3 \phi^{(0)}}{\partial x^2 \partial z} \\
\frac{\partial^3 \phi^{(0)}}{\partial x \partial z^2} \\
\frac{\partial^4 \phi^{(0)}}{\partial x^2 \partial z^2}
\end{vmatrix}
=
\begin{vmatrix}
\phi^{(1)} - \phi^{(0)} \\
\phi^{(2)} - \phi^{(0)} \\
\phi^{(3)} - \phi^{(0)} \\
\phi^{(4)} - \phi^{(0)} \\
\phi^{(5)} - \phi^{(0)} \\
\phi^{(6)} - \phi^{(0)} \\
\phi^{(7)} - \phi^{(0)} \\
\phi^{(8)} - \phi^{(0)}
\end{vmatrix}
$$

Figure 4: *System of equations for the evaluation of the Laplacian.*

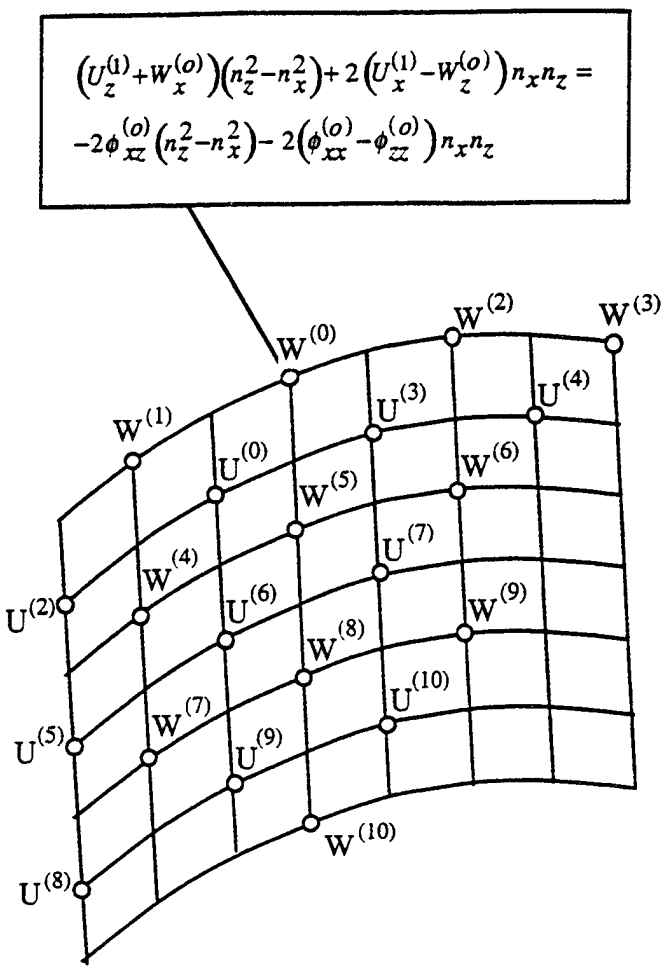


Figure 5: *Stencil for viscous diffusion terms with tangential-stress condition imposed.*

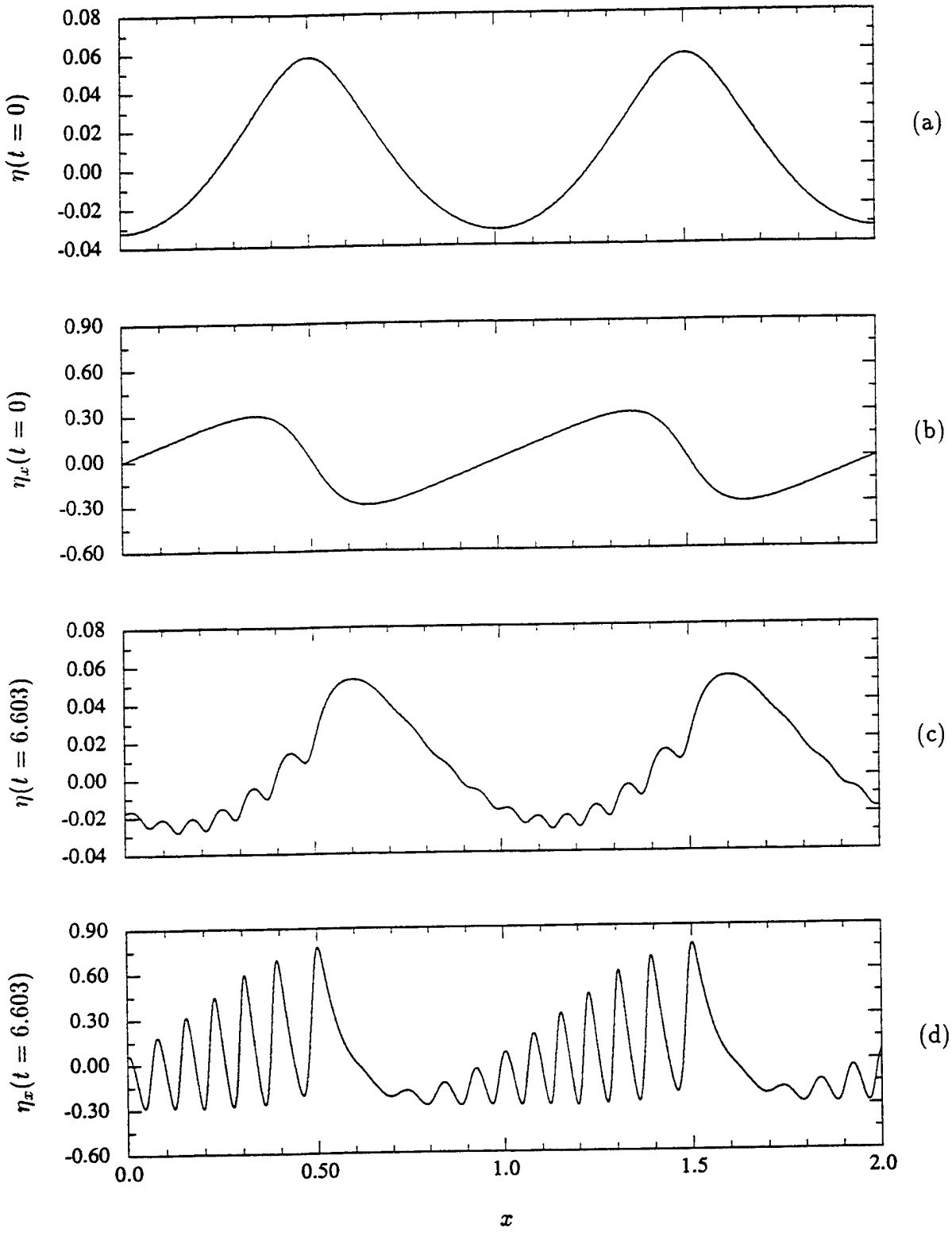


Figure 6: *Formation of ripples on a 5cm gravity-capillary wave.*

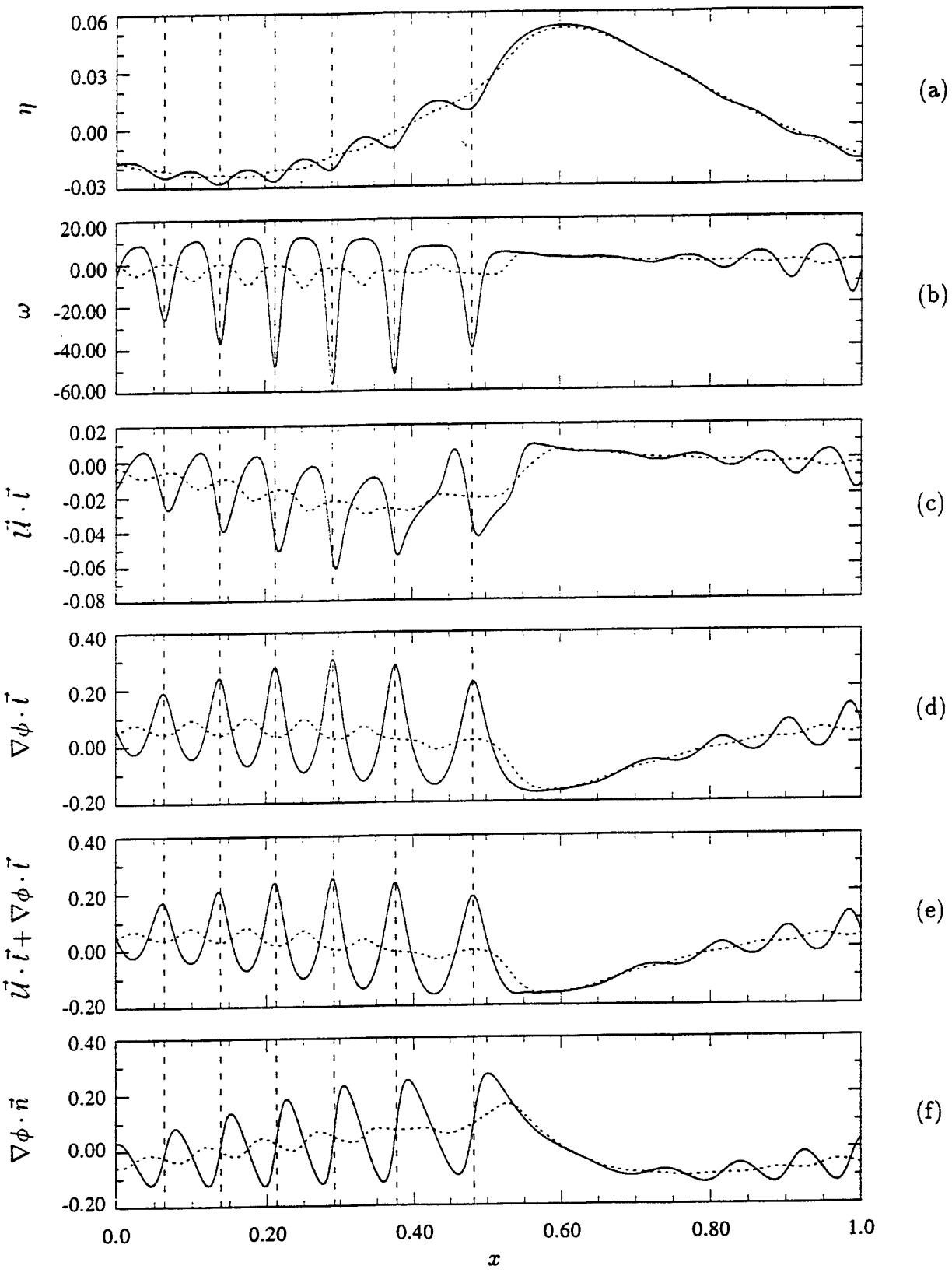


Figure 7: *Free-surface quantities.*

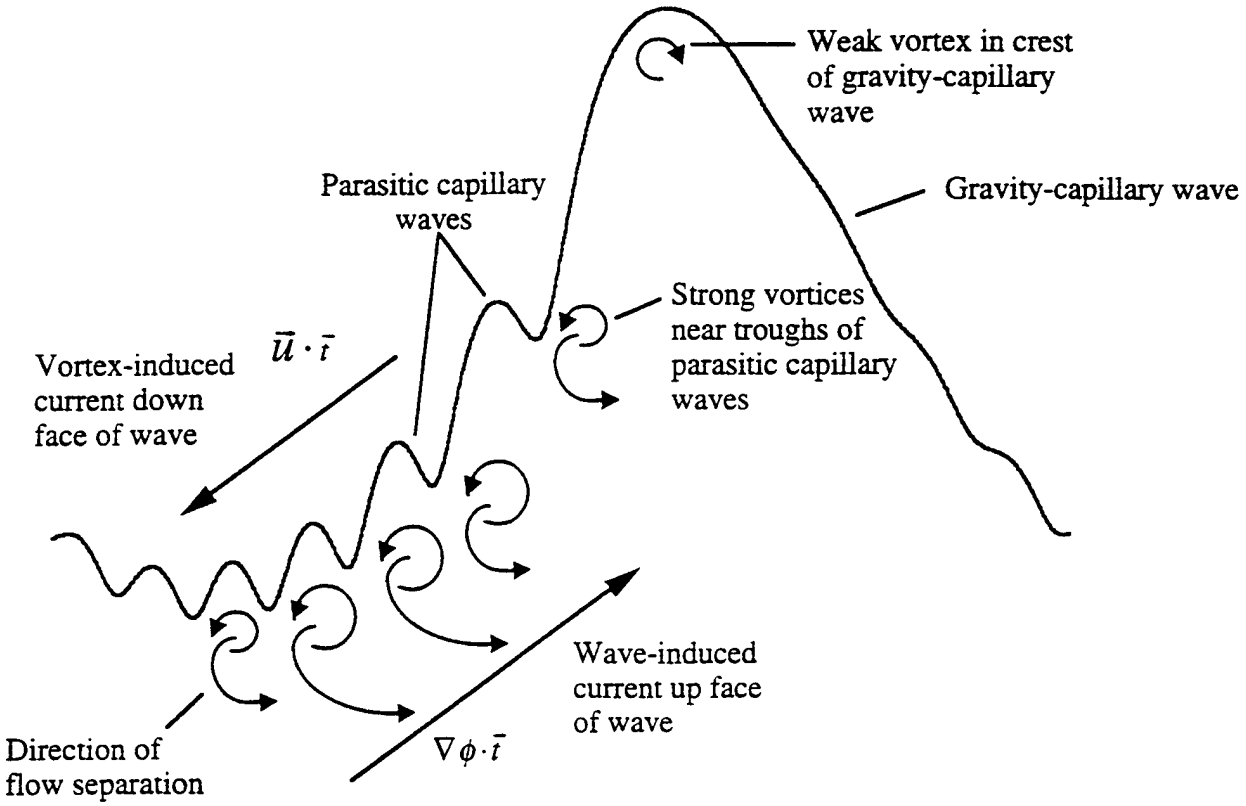


Figure 8: *The vortical structure and the velocity field of a near-breaking gravity-capillary wave with no wind effects.*

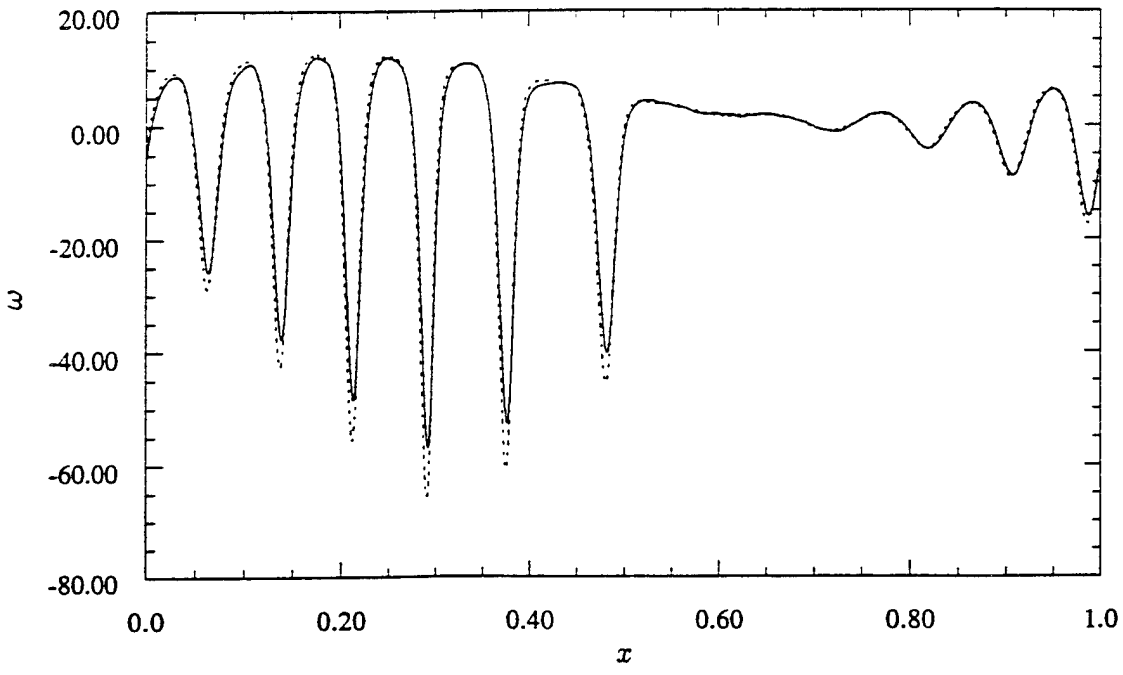


Figure 9: *Free-surface vorticity.* A comparison between numerics (———) and theory (- - - - -).

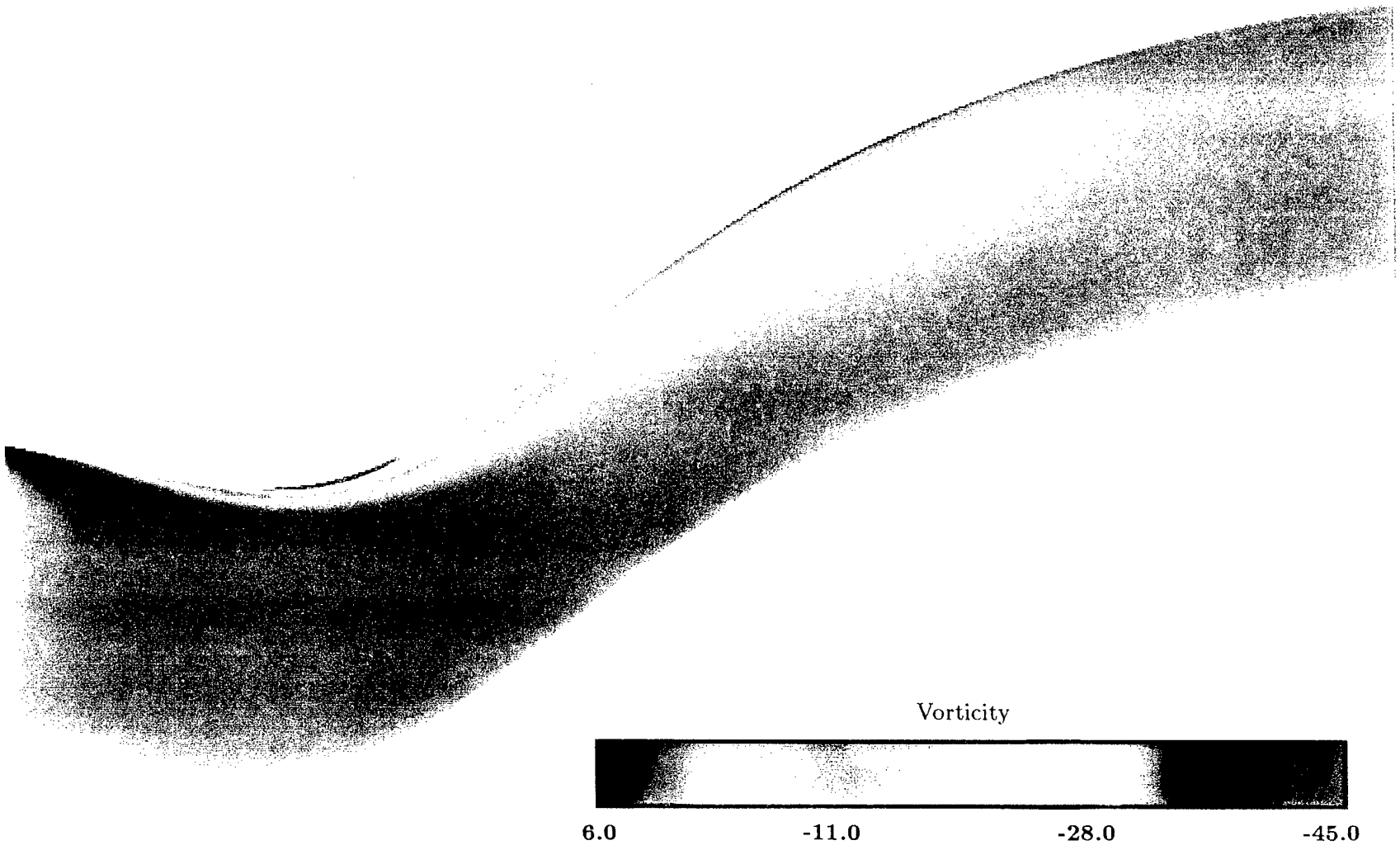


Figure 10: *Color contour plot of the vortical structure of a near-breaking gravity-capillary wave.*

DISCUSSION

P. Ananthakrishnan
Florida Atlantic University, USA

I would like to commend the authors for their fine efforts to solve the problem of spilling waves. This problem has become one of immense scientific interest, especially in view of the recent findings of Longuet-Higgins (e.g., *J. Fluid Mech.,* 1992) and experimental observations of Duncan et al. (*Phys. of Fluids*, 1994).

In the present work, the authors have used an "*inviscid* boundary-layer formulation" for the most part of the simulation (from $t = 0$ to $t = 6.4$, see Section 4.1). Full Navier-Stokes equations were considered only for a rather small duration of time (from $t = 6.4$ to $t \approx 6.6$) toward the end of the simulation after the capillary waves have reached their maximum steepness. I would like to know if there is any particular reason or basis for using such an *ad hoc* procedure in the simulation. Had your TAME algorithm for full Navier-Stokes equations been used right from the initial time $t = 0$, I wonder whether the corresponding results pertaining to the evolution of parasitic capillaries, free-surface vorticity, etc. would resemble those obtained in the present paper. Would the authors comment on this aspect of the simulation carried out in this work?

AUTHORS' REPLY

The formation of the capillary waves is primarily inviscid, so we do not expect the formation of the vortical layer to be sensitive to the initial conditions. We used the boundary-layer formation because it is an accurate and efficient method for generating capillary waves. The accuracy of the approximation is demonstrated by the prediction of the dissipation rate, which agreed with the exact formulation.

DISCUSSION

J. Duncan
University of Maryland, USA

The calculations in this paper are an important step toward the numerical simulation of breaking water waves which has in the past been treated as a potential flow and only calculated up to the point of incipient breaking. It seems to me that the authors' methods will enable the direct calculation of short-wave length spilling breakers through the breaking event and including the generation and evolution of the resulting turbulent flow field. I have a few comments on the present paper concerning mostly the qualitative comparisons made to my own experimental results. The comparisons are dangerous primarily because of the rather large difference in wave-length between the calcualtions ($\lambda = 5$ cm) and the experiments (about 77 cm). The capillary waves found in the experiments are located upstream of the toe of the bulge that forms on the forward face of the wave. These capillary waves had quite short wavelengths (about 2 mm). In the numerical calculations the capillary waves cover the entire forward face of the wave. I suspect that these differences in the capillary waves are due to the differences in the lengths of the waves under consideration. Do the authors concur with this suspicion? What is the likelihood that the authors will be able to do computations with wavelengths comparable to the experiments?

AUTHORS' REPLY

Yes, the differences in the wavelengths between your laboratory measurements and our numerical simulations affect the generation of the capillary waves. Using our present formulation, we can simulate longer wavelengths up to 10 cm. If we modify our formulation, we could perform a local analysis that may enable us to simulate much longer waves, up to a meter.

DISCUSSION

M. Longuet-Higgins
University of California at San Diego, USA

To obtain these results the authors have overcome great numerical difficulties. However, in comparing numerical calculations with previous laboratory experiments and with theory it is important to remember that the vorticity field is likely to depend critically on two parameters:

1. The slope parameter ak of the parasitic capillary waves. From the boundary-layer theory one expects that the mean vorticity will vary roughly as ak^2. In the experiments of Okuda et al. (1977) and Duncan et al. (1994) it appears that at the toe of the instability the surface slope is almost vertical, making ak of order 2. In the numerical calculations ak was only 0.8.

2. The Reynolds number, based on the radius of curvature r at the crest of the gravity-capillary wave (which determines the scale of the instability) and the phase-speed $U_c=(g\lambda)^{1/2}$. For gravity-waves, if the shape is held constant, the Reynolds number varies as $\lambda^{3/2}$. In the experiments of Okuda et al. (1977) λ was about 10 cm in those of Duncan et al. (1994) λ was of order 100 cm. In the present numerical calculations λ was only 5 cm. Therefore numerical calculations at larger wavelengths (or Reynolds number) are much to be desired. The theory of capillary rollers (Longuet-Higgins, 1992) assumed a large Reynolds number.

Of great interest are the longer capillary waves ("Type 2") which appear *above* the toe of the crest instability, in the experiments of Duncan et al. (1994). These quickly grow in amplitude and then collapse into turbulence. The idea that they are due to unstable shear waves on the shearing flow produced by vorticity shed from the parasitic ("Type 1") capillaries has been developed in a recent paper by Longuet-Higgins (Ref. 1). There it is shown that the linear rates of growth are in accord with a model for the instability of a shear flow having a free surface (Ref. 2). A simple model for the nonlinear stages of growth is also given in Ref. 1 and it is shown that the wavelength of the Type 2 instabilities is about four times that of the Type 1 instabilities. Further numerical experiments would help to validate these predictions.

Minor comment. On p. 9, bottom of column 1, the relation there given is exact, not approximate. In this sense it is hardly true to say (p. 9, column 2) that the utility of the theory is limited; rather it is the method of numerical computation.

Lastly, this reviewer would find it helpful if the authors could plot the velocity vectors, both in the computational frame of reference, and in a frame moving with approximately the mean speed of the separated flow. The latter would help one to visualize the eddying motion in the shear layer.

References

[1] Longuet-Higgins, M.S., "Shear instability in spilling breakers," *Proc. R. Soc. Lond.* A446 (8 Aug. 1994), pp. 399-409.

[2] Stern, M.E. and Adam, Y.A., "Capillary waves generated by a shear current in water," *Mem. Soc. R. Liège*, 6 (1974), pp. 179-185.

AUTHORS' REPLY

Our most recent research is focused on developing techniques for simulating steeper waves at higher Reynolds numbers. New results for a wave steepness of 1.25 and a wavelength of 5 cm do not differ significantly from the results reported in our paper. However, we plan to simulate waves that are near over-turning with wave steepnesses well above one. For these steeper waves, we expect the flow to separate beneath the parasitic capillary waves. In regard to simulating longer waves and higher Reynolds numbers, we plan to resolve the boundary layer of a near-breaking 10 cm gravity-capillary wave. Based on our normalization, this would correspond to a Reynolds number of Re = 99,000. The boundary-layer thickness is δ = 0.028 cm. To resolve this boundary layer, we will use grid stretching. The numerical simulation of higher Reynolds numbers is required to investigate how diffusion affects the shedding of vorticity beneath the parasitic capillary waves and the accumulation of vorticity in the crest of the gravity-capillary wave.

Based on the analyses of Professor Longuet-Higgins, the experiments of Professor Duncan including observations of his most recent videos, and our own numerical simulations, we suggest that there are at least two possible mechanisms that describe the onset of spilling when wind is not present. The initial stage of the first type of spilling breaking wave is characterized by the formation of a toe near the crest. Professor Longuet-Higgins' modeling of the toe

indicates that a shear instability may lead to rapid growth of long capillary waves behind the toe (see his reference in his discussion). Professor Longuet-Higgins provides supporting evidence based on laboratory experiments of Professor Duncan's group. As pointed out by Professor Longuet-Higgins in his discussion, this particular interpretation of the experiments requires further numerical investigation to prove that the capillary waves are generated by a shear instability as opposed to some other process, such as the generation of parasitic capillary waves. The numerical simulations will also quantify how capillarity, which is not modeled in Professor Longuet-Higgins' analysis, affects the initial formation of the toe (Longuet-Higgins et al., 1993 & 1994). We believe that a second type of spilling breaker bypasses the formation of a toe and proceeds directly to the formation of parasitic capillary waves. The parasitic capillary waves become so steep that the flow separates beneath them and vorticity is convected back toward the crest of the gravity-capillary wave. As the steepness of the parasitic capillary waves increases even further, bubbles of air are pinched off. Based on the most recent videos of Professor Duncan, this mechanism appears to be possible even at very long carrier wavelengths in excess of one meter. This second mechanism for the formation of a spilling breaker has not been investigated in the laboratory at the short wavelengths that we are simulating numerically.

Professor Longuet-Higgins' minor comment about his formula for the surface vorticity references a poorly worded section of our paper. We meant to convey that his theory is limited to steady flows and is as numerically intensive as our theory. Professor Longuet-Higgins' formula requires the total velocity field (irrotational and rotational) to predict the surface vorticity and, thus, requires the solution to the full Navier-Stokes equations. However, if the solution to the full Navier-Stokes equation is known, the surface vorticity can be predicted directly from the velocity field. Nevertheless, we used Professor Longuet-Higgins theory to confirm the accuracy of our numerical simulations. In addition, his theory is useful in providing estimates of surface vorticity when only the solution to the potential portion of the flow is known. We also note that certain types of laboratory measurements of steady flows may benefit from the application of Professor Longuet-Higgins' formula.

Figures 1 and 2 show the velocity fields that are induced by the potential and vortical portions of the flow, respectively. The wave is propagating from right to left. The tops of the figures correspond to the free surface, and the figures are four boundary-layer thicknesses deep. The frame of reference is moving with the wave in Figure 1 and it is fixed in Figure 2. The streamlines are parallel to the free surface in Figure 1 because the flow is nearly steady. In Figure 2, the streamlines are parallel to the free surface because the component of the vortical flow that is normal to the free surface is zero by construction.

In Figure 2, there are three strong vortices. The first vortex is located beneath the trough of the first parasitic capillary wave. The second vortex is behind the trough, and the third vortex is located beneath the crest of the gravity-capillary wave. For a longer wave than we have simulated, Professor Longuet-Higgins had predicted that vorticity diffused from beneath the parasitic capillary waves would lead to the formation of a vortical roller in the crest of gravity-capillary with a different sign than what is observed in Figure 2 (Longuet-Higgins, 1992). His predictions are based on laminar-flow analysis with no flow separation. We conjecture that wind stress or flow separation could lead to the formation of a vortical roller that would have the same sign as what is observed in laboratory studies of wind-wave generation, but in the absence of wind and if the flow has not separated, then the sign of the vorticity is as illustrated in Figure 2.

DISCUSSION

W. Schultz
University of Michigan, USA

This was a very nice paper. Some questions?

1. To what extent is the formation of the parasitic capillary waves affected by vorticity?

2. How important is the velocity decomposition to the success of your computations? And the choice of the extra boundary condition (9), is that critical?

3. (X_l, Z_l) must be nodel velocities, right?

4. Fig 6a and 6b don't seem to correspond.

5. AK = 1.25 or 2?

AUTHORS' REPLY

Thank you.

1. The initial formation of parasitic capillary waves is an inviscid process. The parasitic capillary waves form when their phase speed matches the local water-particle velocity of a sufficiently steep carrier-wave. For parasitic capillary waves that are very steep, the flow could separate beneath their troughs. The flow separation is a viscous phenomenon.

2. Any numerical errors that occur in the vortical portion of the flow do not adversely affect the wavy portion of the flow. As a result, our velocity decomposition enables us to calculate the wavy portion of flow with greater accuracy than is possible when no decomposition is used, especially when the free-surface boundary-layer is not resolved well.

3. Yes, (X_t, Z_t) are nodal velocities.

4. The slope of a steep wave is not a pure sinusoid. This explains why the slope plot in Figure 6a does not appear to match the elevation plot in Figure 6b.

5. Unsteady capillary waves can attain steepnesses that are well beyond Stokes limiting steepness for pure gravity waves ($ak \approx 0.44$).

DISCUSSION

R. Street
Stanford University, USA

Am I correct in summarizing that the advantage of massively parallel processor computers in handling the TAME algorithm is that you can disperse the Taylor calculations across a large number of processors and hence get all the independent evaluations at the grid points accomplished essentially simultaneously?

AUTHORS' REPLY

Yes, we distribute the TAME system-of-equations over all of the processors. On small parallel computers, the TAME scheme can be evaluated in parts. It is also possible to reduce the number of TAME operations by matching a TAME layer of grid points to a conventional finite-difference approximation. This technique, for example, could be used to impose complex boundary conditions on a curved boundary.

Wave Groups, Wave-Wake Interaction, and Wave Breaking: Results of Numerical Experiments

Y. Yao, P. Wang, M. Tulin
(University of California-Santa Barbara, USA)

ABSTRACT

A variety of wave breaking phenomena including the detailed morphology of breaking have been studied in numerical experiments carried out in a numerical wave tank, called LONGTANK, developed by the authors at the Ocean Engineering Laboratory at UCSB. Wave trains up to 100 waves in length may be calculated in the exact inviscid theory, and with high resolution. Experiments have been made on the modulational instability of almost monochromatic waves, on subsequent strong wave group formation, and on the deformation and breaking of waves in wave groups. Two types of breakers, differing mainly in scale, have been observed. Breaker shapes and splash have been studied in detail through to impact of the jet on the front face of the wave. Here, new experiments are reported on the interaction and breaking of the short waves near the crests of the longer waves. Magnifications in crest orbital velocities of weak short waves over 4 fold have been found on the crests of long waves of moderate steepness, leading to early breaking. A criterion for breaking is found to be satisfied in all experiments conducted to date: a wave will proceed to deform and break when and only when the crest orbital velocity associated with the wave's motion exceeds $d\omega/dk$, including corrections for steepness.

INTRODUCTION

As time passes, the importance of non-linear processes in ocean waves and in the free surface flow about ships becomes more and more apparent. Some major examples are: bow wave formation and breaking on wave resistance and wake vorticity generation; wave energy dissipation due to wind-wave breaking and its effect on spectral form and on energy downshifting; wave group formation and waveform deformation, and its effect on extreme wave heights and crest height at sea; the effect of wave steepening and breaking on remote sensing of the sea surface.

The possibility to study non-linear processes all the way through to breaking using inviscid computational methods, opens up the prospect of numerical experiments, which can be designed to explore wave phenomena far beyond the reach of analytical methods. In these numerical experiments, breaking and other strongly nonlinear wave processes can be studied in great detail and in a very controlled manner. We have been conducting such numerical experiments for over two years.

In a previous paper (Wang, *et al*, 1994), we have reported on earlier numerical simulations of the progress of unstable, deep water wave trains (a central wave and two resonant side bands), evolving toward strong group formation, deformation, and breaking. These simulations have been carried out using LONGTANK, a 2D fully non-linear numerical wave tank, based on a multi-subdomain modification of the Boundary Element Method. This multi-subdomain approach makes LONGTANK highly efficient, especially when simulating long time wave evolutions in space and allows for high resolution; a schematic of LONGTANK is shown as Figure 1. Figures 2-5 show the results of typical numerical experiments. Our computing approach also allows us to continue the calculation when the breaking jet touches the front face as if it doesn't see the water, Figure 6, or makes it possible to simulate the jet impact up to initiation of the water splash, Tulin *et al* (1994), Figure 7. These numerical experiments were designed to provide quantitative information on the mechanism of wave breaking and morphology of breaking waves. The success of the simulation is borne out by comparison of the results of tank experiments with numerical experiments, see Figure 4.

It has been typically observed, for sufficiently large initial wave steepness ($ak \geq 0.14$), that following wave group formation, strong deformation of the wave form occurs, the trough and crest both rise, there occurs a rapid increase in the

horizontal particle velocity at the wave crest, the front face steepens, cumulating in the formation of a jet; this breaking process coincides with the passage of a wave through the peak of the modulated wave group, as observed in the ocean, see Figures 1 & 2. A feature of the wave deformation is that the energy density in the front quadrant of the crest at the group peak becomes remarkably large compared to the density in the back quadrant of the same crest.

In this paper we discuss the morphology of breakers forming in wave groups, and the resulting dissipation and vorticity generation. In addition we report on the interaction between long and short waves, as simulated in LONGTANK, and particularly on the pronounced amplification of the short wave on the crest of the longer wave, and the subsequent breaking of the former.

An important result of the wave interaction simulation is to confirm the criterion for breaking which we had previously discovered in the case of breaking in wave groups. According to this criterion, waves will inevitably deform and proceed to breaking after and only after the orbital velocity at the crest of the wave reaches a value equal to $d\omega/dk$, including steepness corrections to the latter.

Finally, we review the implications of LONGTANK simulations for the prediction of extreme waves and extreme wave heights.

WAVE BREAKING in WAVE GROUPS

Breakers and Splash

An example of the formation of a breaker in a wave group is shown in Figure 2. The precise breaker shapes vary somewhat from case to case, depending on the exact conditions within the group. So far, two general types of breakers have been observed in LONGTANK simulations, Figure 3; one with a stronger fore-aft asymmetry, producing a larger breaker which reaches roughly halfway down the front face, and which we call "plunging"; the other with almost symmetrical front and back faces and a small jet (no surface tension is included) reaching less than a quarter of the distance down the front face, and which might be categorized as a "spilling" breaker. Both of these breakers are characterized by an initial jet formation when the particle velocity at the crest exceeds the phase speed, and by the growth of a thin jet which falls in a ballistic trajectory, as we have confirmed, Tulin *et al* (1994).

For the plunging breakers observed in LONGTANK, the duration from front face steepening to initial splash is about 14% of a wave period, compared to 10% for the spilling breaker.

The calculation of the motion much beyond splash requires further efforts, even without invoking the breakdown of the flow there to turbulence. However, it is possible to continue the calculation as if the jet does not see the free surface, see Figure 6. The case shown in here is about 8% of a wave period after initial jet impact, Figure 5 (b), and corresponds roughly to the condition that the initial splash has been overrun by the wave crest and is being ingested. In fact, we have not observed breakdown of the jet till 16% of a wave period after initial splash, which indicates that breaking can in principle continue well beyond the initiation of the splash, in agreement with experimental observations of both Bonmarin (1989, Figure 15) and Tallent *et al* (1990, Figures 3 & 5).

The initial stage of jet closure and splash can also be simulated, although the computing difficulty rises after impact and as a vortex sheet is created at the contact surface. A preliminary result is shown in Figure 7, and it is similar to the experimental observations of solitary plunging breakers in shallow water by Tallent *et al* (1990), Figure 8.

Dissipation and Vorticity Generation

Up to the stages calculated in Figures 6 and 7, the small jets already contain about 13% and 10% of the initial wave energy, and 16% and 12% of the horizontal momentum contained in a single wavelength of the initial wave. This demonstrates the significance of breaking as a source of conversion of wave energy and momentum into turbulence and surface drift. The excess of momentum loss over energy dissipation is clearly demonstrated, which will cause frequency downshifting, as we have shown analytically.

As the jet impacts, it encloses a cavity, and at this instant, a circulation Γ is created. To the extent that the air escapes or is broken down into smaller entrained bubbles, this circulation becomes converted into vorticity distributed within the breaker and its eventual residue in the water. The jet itself propagates downward after impact, creating an upward splash, eddies and turbulence, as indicated in Figure 8.

The vorticity created at cavity formation can be estimated from the present calculations. Figure 7 shows the tangential velocity along the boundary of the new cavity and at the common interface near the tip of the jet. The circulation, Γ, has been calculated in this case to yield a value of $0.038\lambda c_p$ (clock wise). To evaluate the influence of this generated vorticity on the following waves, we assume that the vorticity (Ω) corresponding to Γ, is uniformly distributed in the area S, under the wave crest and lying above the mean water level ($S = a\lambda/\pi$). Therefore $\Omega = \Gamma/S \approx 0.12\ c_p/a \approx [0.12/(ak)]\ \omega$, where ω is the wave frequency and k is the wave number. For linear deep water waves, with

amplitude a and wave frequency ω, the strain rate, $\partial u/\partial x$, at the wave crest is $(ak)\omega$. Therefore for a wave with a steepness $(ak) \approx 0.2$, the strain rate due to the breaker vorticity, Ω, is three times larger than that from the potential wave itself. As rough as this calculation is, it indicates the probable importance of the breaker vorticity in effecting the behavior of the following waves. Breaking wave experiments, Kolanai and Tulin (1993) support this suspicion.

An important effect of the breaker scar will be to generate weak currents in the water, such as are also generated due to the orbital velocity of longer waves. Therefore we have undertaken a numerical simulation of the interaction between short and long waves, leading to amplification, deformation and breaking of the shorter waves near the crest of the longer wave. Very strong non-linear effects occur for waves of small steepness, as small as ak=0.1.

BREAKING in a LONG-SHORT WAVE SYSTEM

Introduction

Asymptotic theory exists for the estimation of the behavior of a short wave passing through a moving current pattern (i.e. the longer wave), see Phillips (1977). This theory predicts that under certain circumstances the propagation of the short waves is blocked and their energy is greatly enhanced. This blockage condition was not realized in the systems we have studied, which are more pertinent to shorter wind waves riding on swell.

The above mentioned theory does show that the steepening of the short waves is essentially in phase with the elevation of the longer wave; this effect has also been measured experimentally, Phillips (1992). We have observed the same effect.

What we have discovered here, in addition, however, is that remarkable magnifications of the short wave crest orbital velocities can be generated (many fold in magnitude!) near the crests of relatively weak long waves. These seem to be associated with a deformation of the upper portion of the short wave, which very much "sharpens" the crest. Existing theory gives no hint of such effects. These large magnifications of crest orbital velocities lead to very early breaking of short waves. As a result, short waves may be suppressed by longer waves through which they ride, an effect which has been observed.

The Numerical Experiments

A series of LONGTANK simulations have been carried out to study wave breaking in a long-short wave system. A wave train of shorter wave length is first generated by a plunger wavemaker. When seven waves have propagated away down the tank, the wavemaker stops generating short waves. Immediately afterwards, the wavemaker decreases its frequency by half; therefore longer waves are generated which travel faster and eventually catch up with the short waves. The wavemaker stroke follows a cosine increase in the first periods of both short and long wave generation and a cosine decrease in the last period of short wave generation. In total, fourteen cases have been run in the LONGTANK, see Table 1.

Table 1 : Short-Long Wave Interaction Experiments Utilizing LONGTANK

Case	λ_S/H	λ_l/H	λ_l/λ_S	c_l/c_S	$(ak)_S$	$(ak)_l$	Break at
4.0	1.8				0.185		33.95 Ts
4.1	1.8	6	3.3	1.8	0.185	0.026	33.65 Ts
4.2						0.052	31.50 Ts
4.3						0.080	31.35 Ts
4.4						0.084	31.25 Ts
4.5						0.086	28.13 Ts
4.6						0.093	24.90 Ts
5.1	0.65	1.8	4	2	0.15	0.135	25.70 Ts
5.2					0.135		28.50 Ts
5.3					0.12		34.60 Ts
6.1	0.65	1.8	4	2	0.15	0.15	25.50 Ts
6.2					0.135		25.60 Ts
6.3					0.12		25.90 Ts
6.4*					0.1		-
7.4	0.65	1.8	4	2	0.1	0.165	32.60 Ts

* no breaking occurs as far as 40 Ts

It is normal for the leading wave in a propagating group to break prior to the other waves in the group and that happens here at 33.95 Ts for Case 4.0. The weakest long waves, Cases 4.1-4.4, propagate their way through the group from the rear, eventually reaching the front wave and causing it to break earlier, Figure 9 gives an example (Case 4.1). This effect flattens, and then for Case 4.5, the third short wave (from the back of the group) is caused to break.

Figure 10 shows an example of small short waves, $(ak)s = 0.1$, riding on long waves of medium steepness, $(ak)_l = 0.165$, Case 7.4. It is seen that near the crests of the long waves there are strong interactions between the long and short waves. These interactions sharpen the short waves and finally result in breaking.

It seems apparent in a long-short wave system that it is the short wave which breaks due to the mutual interaction. Therefore we have subtracted the long wave from the combined wave in order to see the interactive effect on the short wave and to compare the "reconstructed" short wave with its

original steepness and form. Figure 11 shows the reconstructed short wave in comparison with the original short wave, together with the pure long wave, Case 5.1. The short wave which is on the crest of the long wave has been pushed forward, its wavelength has decreased, its crest has been sharpened and the height substantially increased, it steepens, it deforms and breaks.

The strong interaction between these waves, usually begins when the long wave crest catches the short wave crest, as shown in Figure 12 (Case 4.3). The strength of the interaction depends on both the short wave and long wave steepnesses. Figure 12(a) shows that two short waves near the long wave crests are steepening and shortening simultaneously, but breaking does not occur during this stage because the horizontal particle velocity at the short wave crest is insufficient to meet the breaking criterion, as we discuss later. In Figure 12 (b), another steeper long wave crest catches the front wave in the short wavetrain, which is usually steeper than its following wave, and in this case breaking eventually occurs.

The Breaking Criterion

In our previous study of wave breaking in groups (Wang *et al*, 1994), we have found a criterion for the inception of wave breaking: deformation and breaking occur when and only when the horizontal particle velocity reaches the local group speed ($d\omega/dk$), where the dispersion relation has been used corrected to third order. When this criterion is reached, breaking will occur within a quarter of a wave period. This criterion has been strongly supported by these previous LONGTANK simulations both in deep and shallow water. We have also done a thorough data analysis of all the cases listed in Table 1, and the generalized criterion is again confirmed without any exceptions. Figure 13 shows all of the data from the LONGTANK simulations. Again, these clearly show that the horizontal particle velocity at the wave crest rather than the wave steepness determines whether breaking occurs or not. In cases of long-short wave interaction we have deduced the orbital velocities of the effected short wave by subtracting the original orbital velocities of the long wave from the total (i.e. reconstruction of the short wave). We have also used the local steepness of the effected short wave in calculating $d\omega/dk$.

The experiment of Phillips (1992) shows that the existence of the long wave will cause short wind waves to break near the crests of long waves just as observed here. In all the breaking cases in Table 1, wave breaking occurs at or a little bit off the long wave crest. We have mentioned that the short wave tends to be speeded up and thereby pushed forward on the top of the long wave crest. Therefore, when the long wave crest passes the short wave crest, there exists a relatively short time interval during which the short wave is effected strongly. During those interaction times, sooner or later, whenever the horizontal velocity of the effected short wave achieves the value of ($d\omega/dk$), then the short wave quickly breaks.

Examples are shown in Figure 14, where the horizontal particle velocities, u, are shown for several cases in Series 5 and 6. From left to right, the short wave is the same but the long wave steepness is increased; from top to bottom, the short wave steepness is decreased and the long wave remains the same. For Series 5, $(ak)_l$=0.135, the short wave with lower steepness takes a longer interaction time to break. For Series 6, $(ak)_l$ = 0.15, short waves of steepnesses from 0.15 to 0.12 break at almost the same time and at almost the same downtank distance, but there do exist small differences: in Case 6.1 the short wave breaks just before the long wave crest arrives; in Case 6.2 the short wave breaks almost on the long wave crest, taking a little longer interaction time; and in the Case 6.3 the short wave breaks immediately after the long wave crest has passed.

Notice the remarkable magnification of the horizontal particle velocity at its peak, earlier mentioned. It is this magnification which results in the sensitivity of short wave breaking to the longer waves. As an example, in the case of the weakest short wave, $(ak)_o$ = 0.1, its orbital velocity near the long wave crest has been magnified by a factor of 4 (for a crest which doesn't break) and 4.6 (just prior to deformation and breaking). These two waves are denoted as A and B, respectively, in Figures 15 (a) & (b)

EXTREME WAVE and CREST HEIGHT

Based on earlier calculations (Wang *et al*, 1994), we have made very favorable comparisons of the predicted breaking steepness in wave groups with tank experimental data of Su and Green (1986), but limited to relatively moderate initial wave steepness ($(ak)_o \geq 0.14$).

A major purpose in carrying out the long-short wave numerical experiments has been to see how weak current fields precipitate the breaking of waves of initially low steepness, and these experiments have been successful, as a wave of initial steepness 0.1 has been caused to break. The results of the numerical experiments reported here are shown in Figure 16 as Series 4-7. They further extend the verification of Su's curve, except at the lowest steepness; more experiments seem required.

These results are of interest for understanding the largest ocean waves, for they show that strong wave grouping or interactions with current or swell can increase wave height significantly, by as much as a factor of 2, see Figure 17 (a). The effect of the deformation of the wave during the breaking process is shown by the difference between the breaking and nonbreaking curves.

When waves deform in the process of breaking, the trough and crest both rise. As a results, the crest height becomes magnified between the time when deformation begins and when breaking actually occurs. This is a very significant effect as shown in Figure 17(b). The average ratio of crest height to wave height at breaking has been found to be 0.78 in LONGTANK experiments, in agreement with the tank data of Kjeldsen (1990) and Bonmarin (1989), confirming the numerical experiments. Therefore the maximum wave crest height can be as large as 1.5 or 1.6 times the initial wave height.

The range of steepnesses for which breaking ensues in LONGTANK numerical experiments is shown in Figure 15 by the cross-hatched area. It is compared to experiments conducted in a number of tanks. There is a considerable overlap in the LONGTANK and laboratory tank data. The higher steepnesses in the laboratory are waves which easily break according to our simulations and which we do not normally consider. The challenge for both the laboratory and LONGTANK is to produce breaking waves at the small steepness observed in the ocean by Holthuijsen and Herbers (1986) and which are considered typical of the ocean. The slope of their data is indicated by the dashed line, although their heights and periods are far off scale. The fact that both laboratory and LONGTANK data have not yet reached the low steepness of average ocean breaking waves, would seem to indicate that some additional mechanisms may be present in the ocean, which we have not yet considered. The rather startling effectiveness of wave interactions in promoting the breaking of shorter waves on the crests of longer waves does suggest possibilities, deserving further study.

CONCLUSIONS

Numerical experiments with LONGTANK demonstrate the feasibility of reproducing non-linear wave phenomena through to breaking with high resolution and in very good agreement with the limited laboratory data available.

These numerical experiments have revealed important quantitative information on the mechanism of breaking in wave groups and on the interaction between long and short waves. Certainly the most important discovery made in LONGTANK is that a seemingly precise criterion for the inception of breaking exists: a wave will proceed to deform and break when and only when the crest orbital velocity associated with the wave's motion exceeds $d\omega/dk$, including corrections for steepness. The deformation process is irreversible and involves a rise in both trough and crest and in front face steepening. The wave deformation process culminates in the formation of a small jet at the crest which extends, forming a thin jet which overflows in a ballistic trajectory, carrying wave energy and momentum with it. This jet impacts on the front surface of the wave creating a splash up, turbulences and foam. At the moment of jet impact, a substantial circulation is created around the newly formed cavity which eventually translates into vorticity and turbulence. Quantitative information on the inviscid stages of this process have been obtained in these numerical experiments including estimates of energy and momentum loss, and vorticity creation.

The mechanism of wave breaking in wave groups has been explored, and ocean observations on breaking near the peak of the wave group modulation have been confirmed. The transfer of wave energy into the front quadrant of the wave during passage up to the modulation peak, Tulin and Li (1992), has also been shown.

The passage of trains of long waves through trains of short waves has been shown to result in short wave steepening very near the crest of the longer waves and a remarkable increases in the crest orbital velocity associated with the short wave leading to early breaking.

The amplification of waves due to wave grouping and to wave-wave interaction has implications for wave loadings due to ocean waves. These experiments show that maximum wave heights can reach levels twice their normal values due to non-linear effects and that maximum crest amplitudes can reach values of 1.5 to 1.6 times the normal wave height. These maximum values are reached for breaking waves, although extreme non-breaking waves also show large and significant magnification.

ACKNOWLEDGEMENT

The authors are grateful for support from the Office of Naval Research, Ocean Technology Program, directed by Dr. Thomas Swean, and Lawrence Livermore National Laboratory, Ocean Imaging Project, directed by Dr. Richard Twogood.

REFERENCES

Bonmarin, P. and Ramamonjiarisoa, A. (1985), "Deformation to Breaking of Deep Water Gravity Waves," Experiments in Fluids, Vol. 3, pp 11-16

Bonmarin, P., (1989), "Geometric Properties of Deep-Water Breaking Waves," J. Fluid Mech., Vol. 209, pp 405-433

Holthuijsen, L.H. and Herbers, T.H.C., (1986), "Statistics of Breaking Waves Observed as Whitecaps in the Open Sea," J. Phys. Oceanography, Vol. 16, pp 290-297

Kjeldsen, S.P. (1990), "Breaking waves," Water Wave Kinematics (A. Torum and O.T. Gudmestad Ed.), pp. 453-473

Phillips, O.M.. (1977), The Dynamics of the Upper Ocean second edition, New York.

Phillips, O.M.. (1992), "Extreme Waves and Breaking Wavelets," Proc. 11th Australasian Fluid Mechanics Conf. Vol. 2, pp. 1081-1088

Su, M.Y. and Green, A.W. (1985), "Wave Breaking and Nonlinear Instability Coupling," The Ocean Surface (Y. Toba and H. Mitsuyas Ed.), pp. 31-38

Tallent, J.R., Yamashita, T. & Tsuchiya, Y. (1990), "Transformation Characteristics of Breaking Water Waves," Water Wave Kinematics (A. Torum and O.T. Gudmestad Ed.), pp. 509-523

Tulin, M.P. and Li, J.J., (1992), "On the Breaking of Energetic Waves", Intl. J. Offshore and Polar Engineering, vol. 2, No 1, pp. 46-53.

Tulin, M.P., Yao, Y. and Wang P., (1994), "The Simulation of the Deformation and Breaking of Ocean Waves in Wave Groups", Proc. 7th Intl. Conf. of Behavior of Offshore Structures (BOSS'94, (MIT)

Wang, P., Yao, Y. and Tulin, M.P. (1994), "Wave Group Evolution, Wave Deformation, and Breaking: Simulation Using LONGTANK, a Numerical Wave Tank," Intl. J. Offshore and Polar Engr. vol. 4, No 2.

Wang, P. (1993), "Numerical Research on (I) Ship Internal Waves, and (II) Breaking Waves," Ph.D Dissertation, (Univ. of California, Santa Barbara).

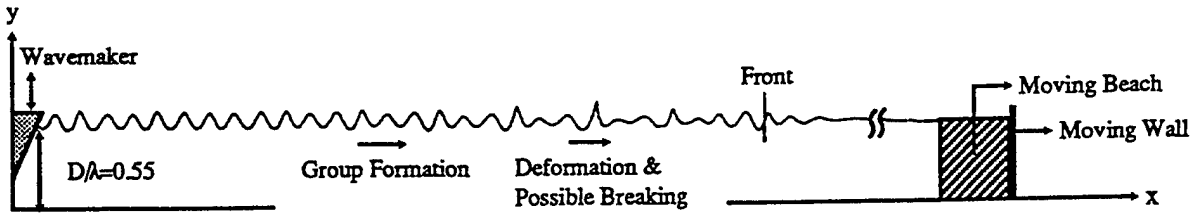


Figure 1 : Wave train generated by a wavemaker in a numerical wave tank - *LONGTANK* (schematic)

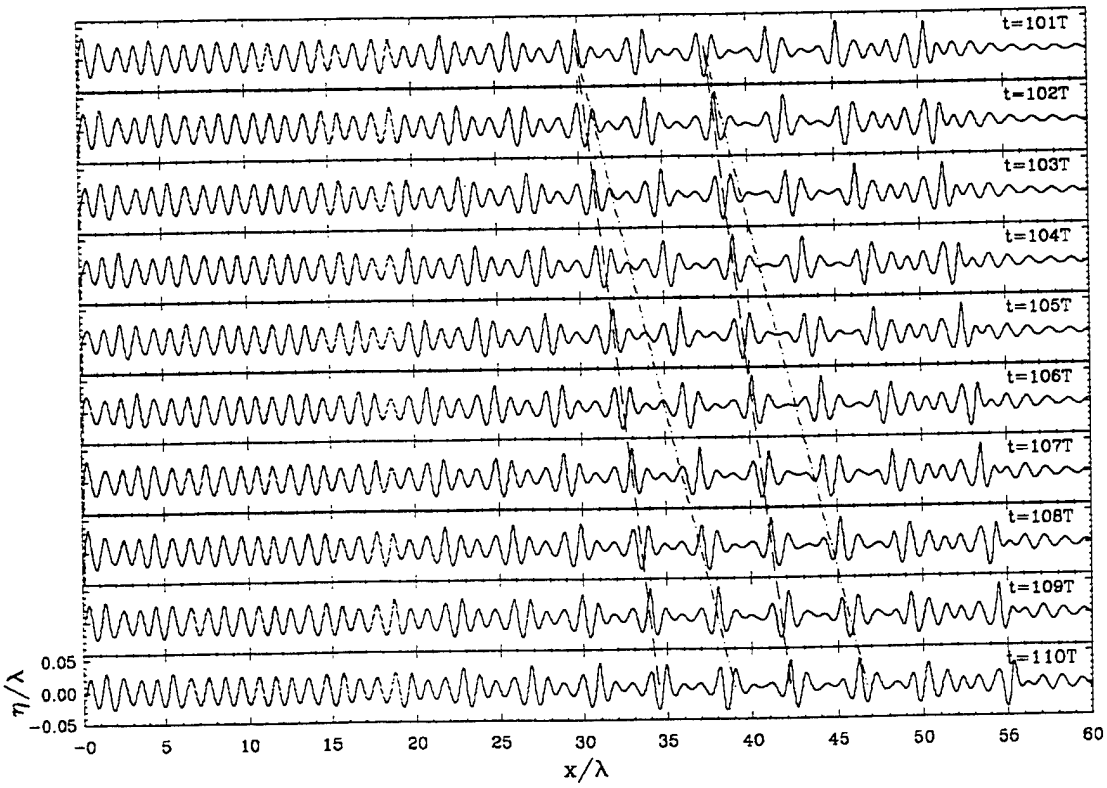


Figure 2 : *LONGTANK* simulations of modulational instability leading to strong grouping. The wavemaker is at the left.

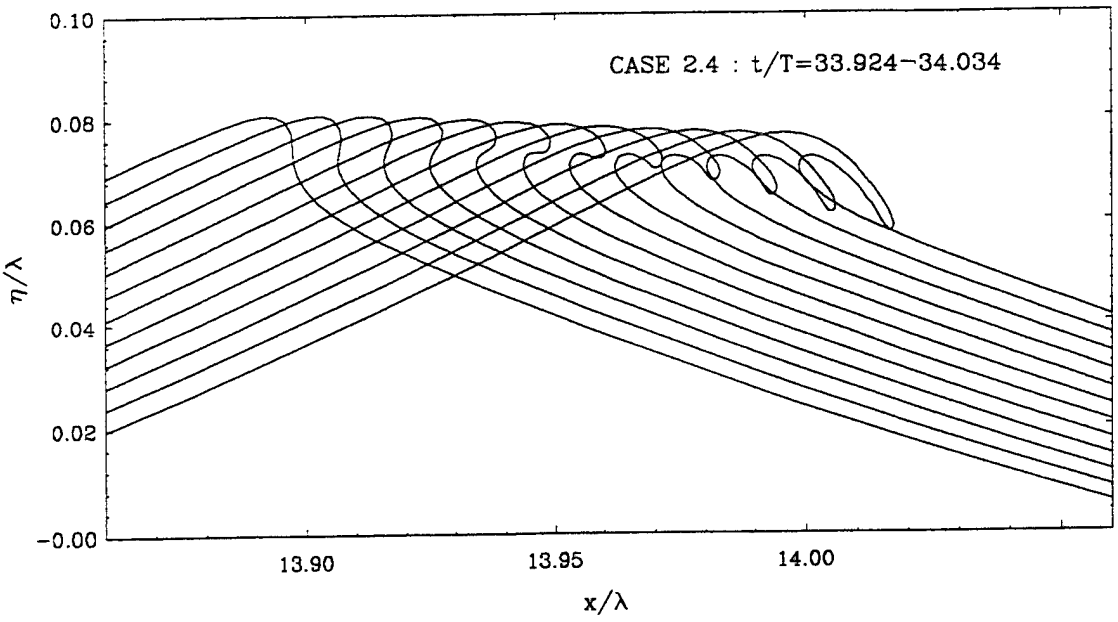


Figure 3 : Jet formation and a spilling breaker.

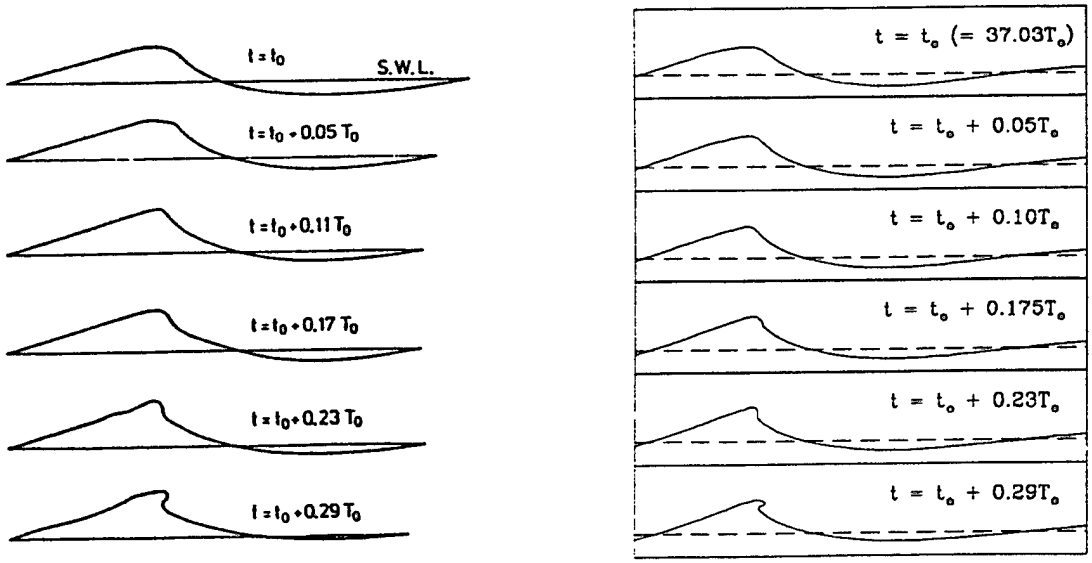


Figure 4 : Waveforms near breaking. On the left: from Bonmarin (1985), $(ak)_0 \approx 0.25$. On the right: from *LONGTANK* simulations, $(ak)_0 = 0.22$, Case 2.1a.

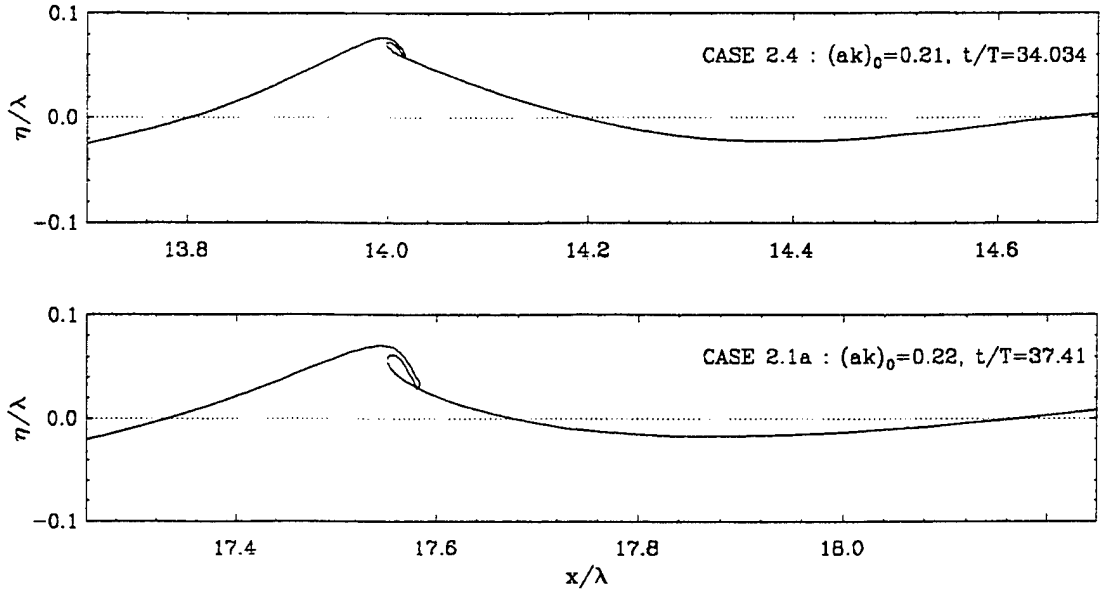


Figure 5 : Examples of two typical breaker types, "spilling" (upper) and "plunging" (lower).

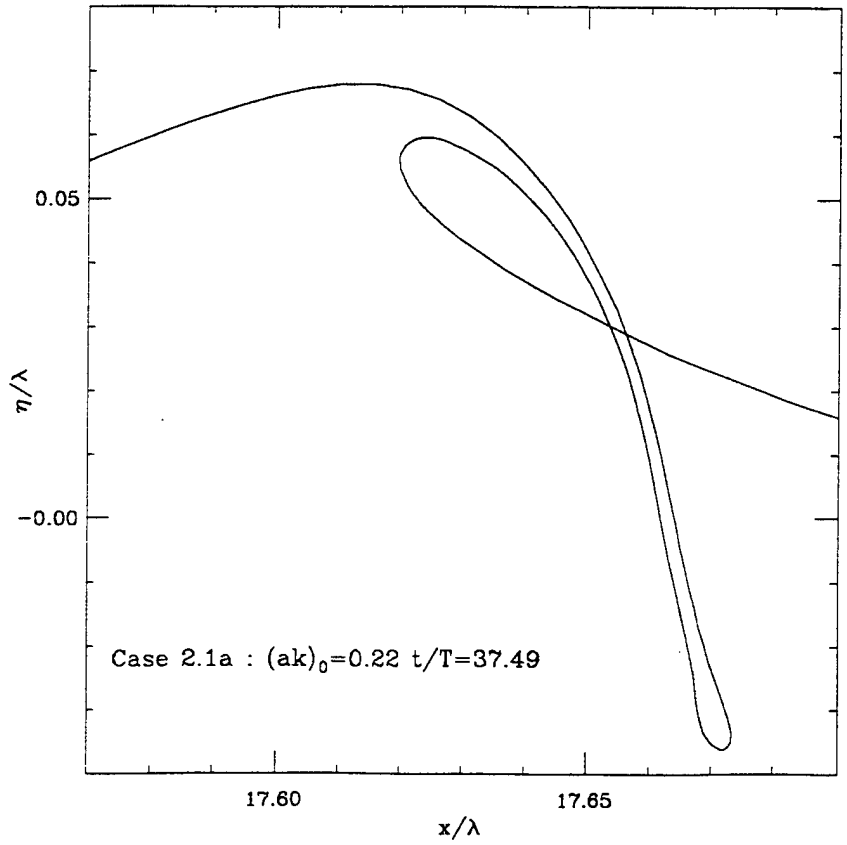


Figure 6 : Plunging breaker computed as if the breaker does not see the surface. This demonstrates the continuation of breaking after impact, as seen in photographs (Figure 8).

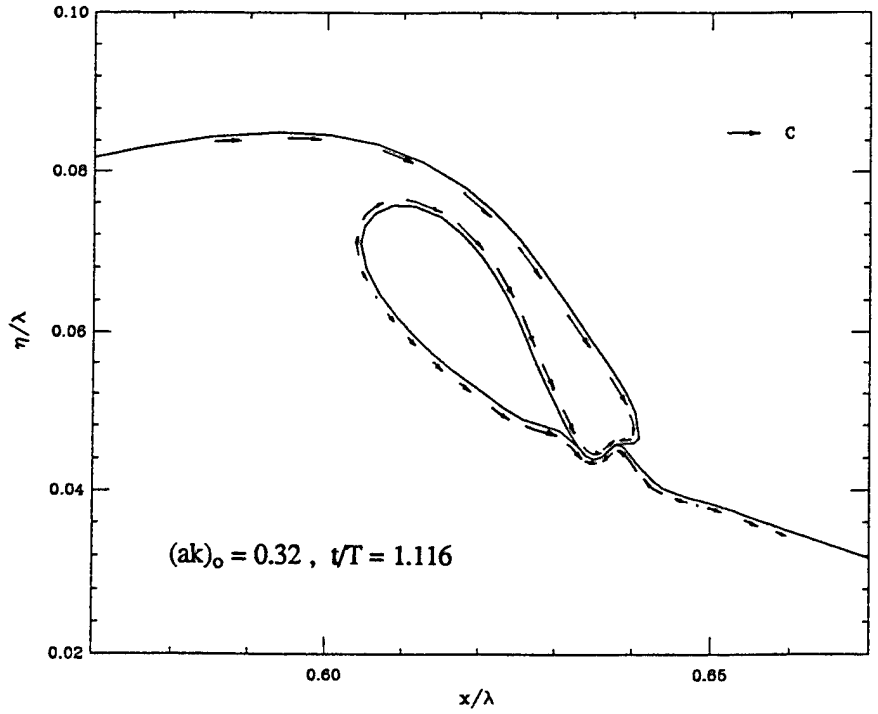


Figure 7 : Jet slightly after impact. A vortex sheet has formed at the contact surface and a large circulation has been created around the cavity.

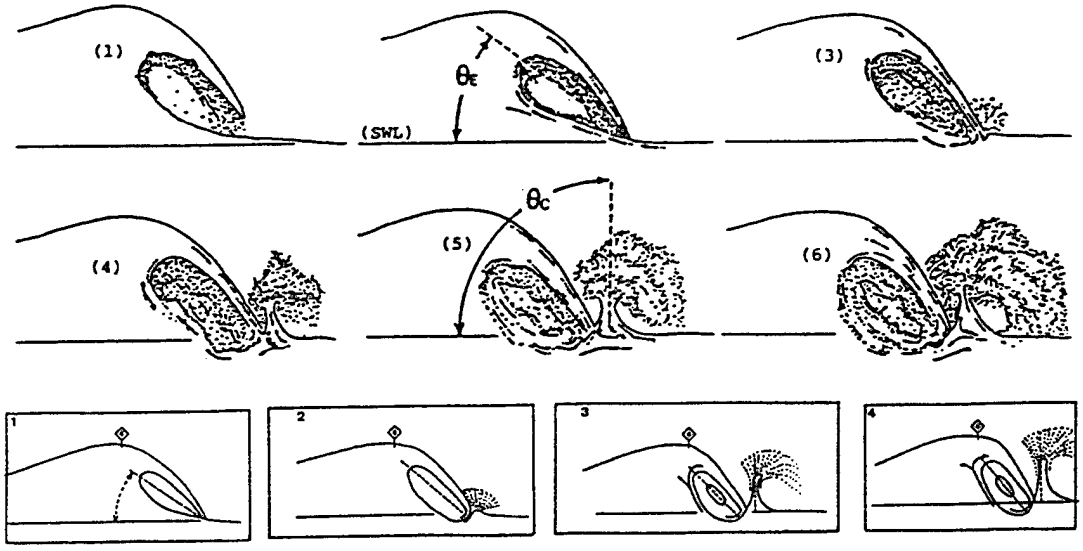


Figure 8 : Stages of breaking, after photographs by Tallert *et al* (1990). Compare lower box 2 with Figure 7.

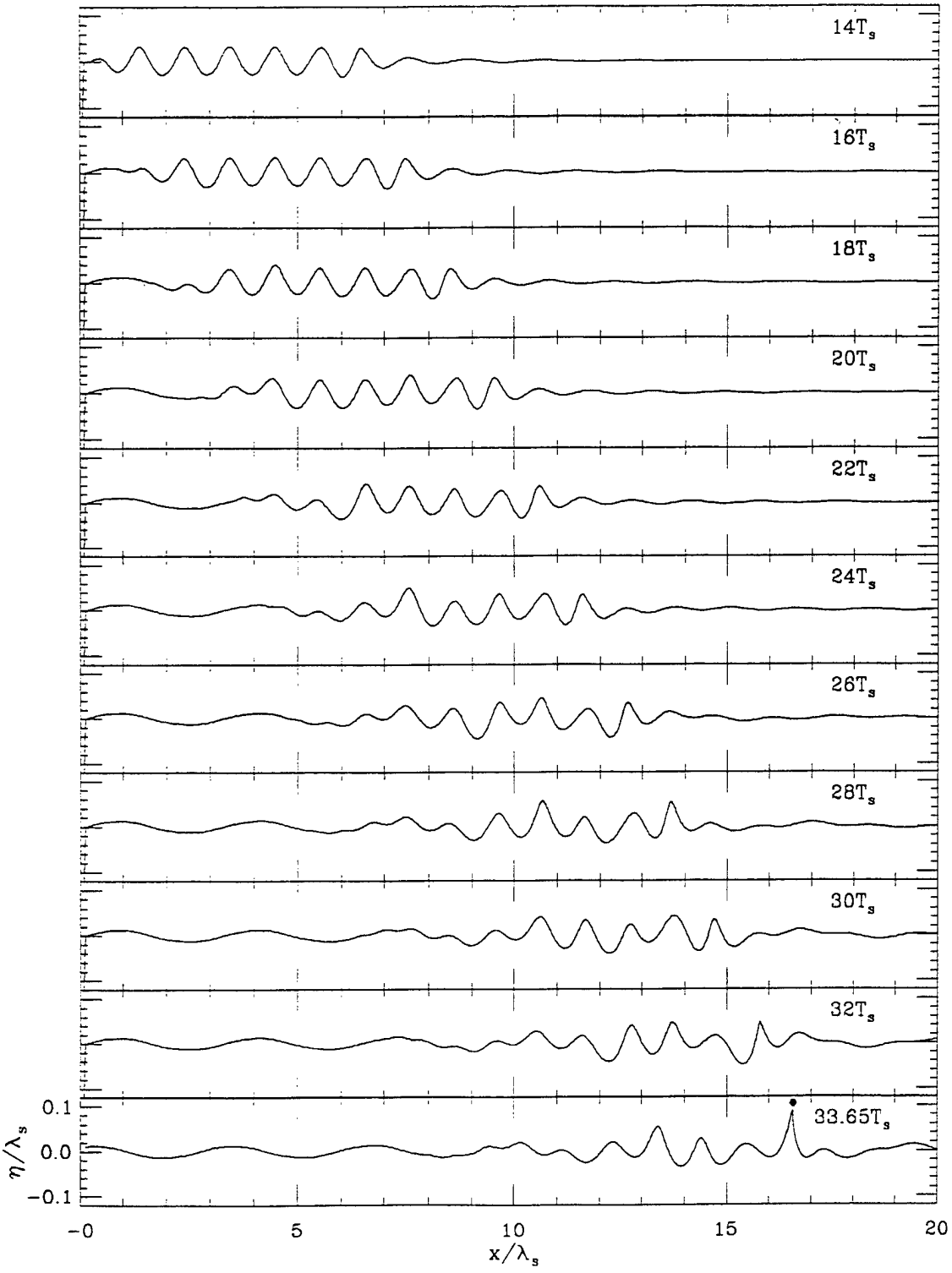


Figure 9 : A group of short waves is overcome from behind by a group of very long waves. Case 4.1: $c_l/c_s = 1.8$; $(ak)_l = 0.026$; $(ak)_s = 0.185$. Breaking is precipitated at the dot.

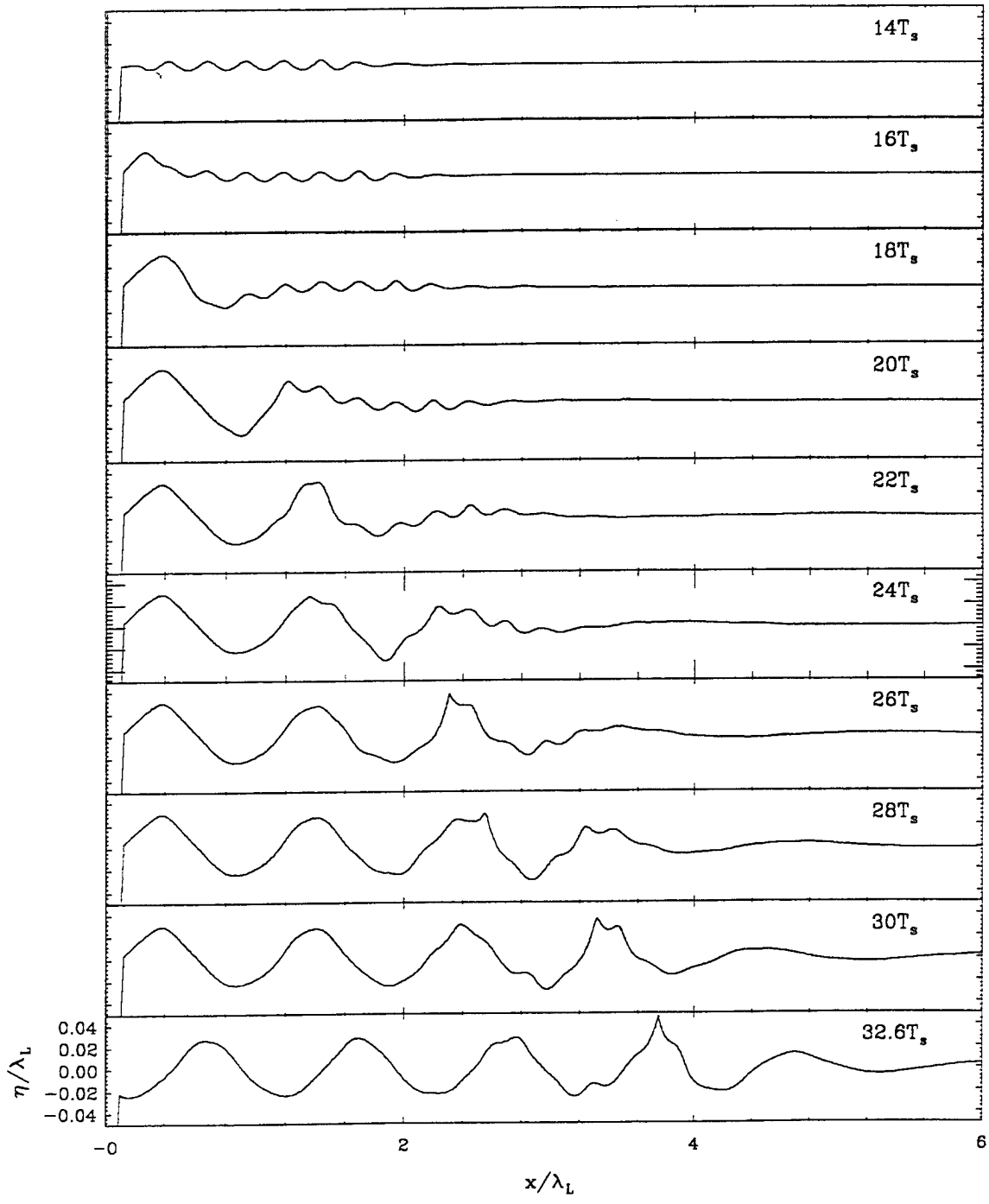


Figure 10 : Weak short waves breaking at the crest of a moderately steep longer wave.
Case 7.4 : $c_l/c_s = 2$; $(ak)_l = 0.165$; $(ak)_s = 0.10$.

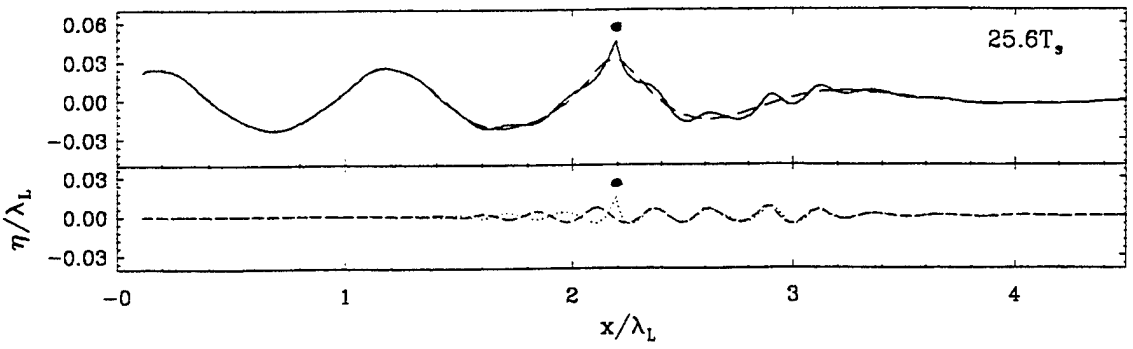


Figure 11 : Case 5.1 of short-long wave interaction. The reconstructed short wave (·····), shown below, is compared with the short wave train without interaction (- - -). The composite wave (——), shown above, is compared with the long wave without interaction (– – –). Note the speeding up and sharpening of the reconstructed short wave at the long wave crest.

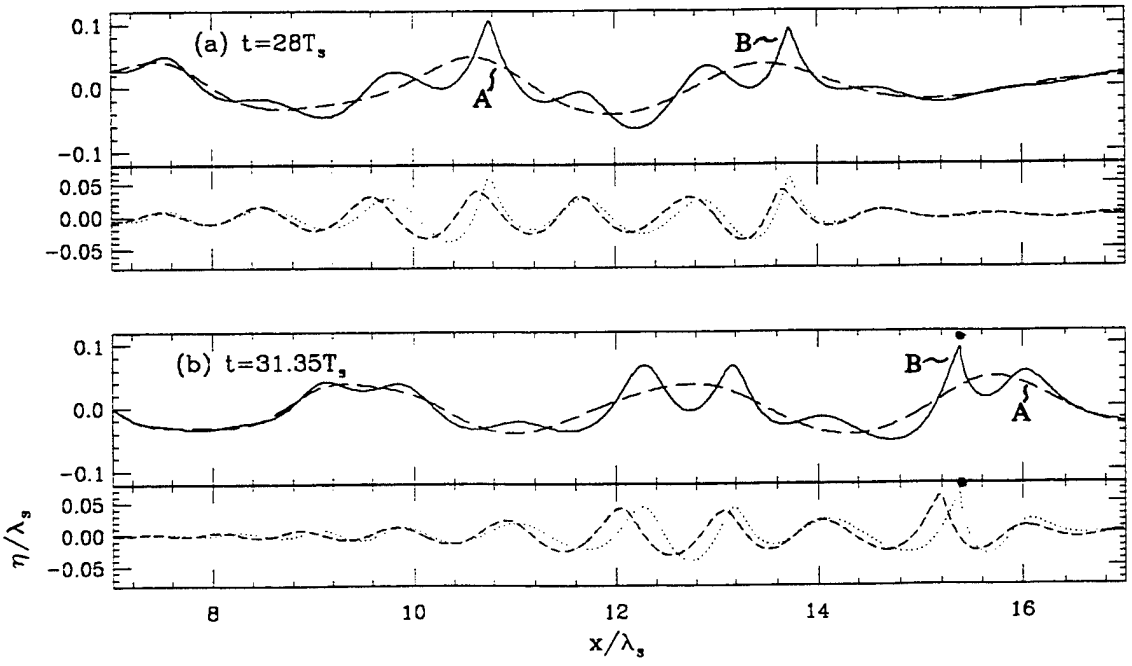


Figure 12 : Case 4.3 of short-long wave interaction. B breaks behind the crest of A. Notice again the sharpening of B. The reconstructed short wave (····), shown below, is compared with the short wave train without interaction (- -). The composite wave (—), shown above, is compared with the long wave without interaction (– –).

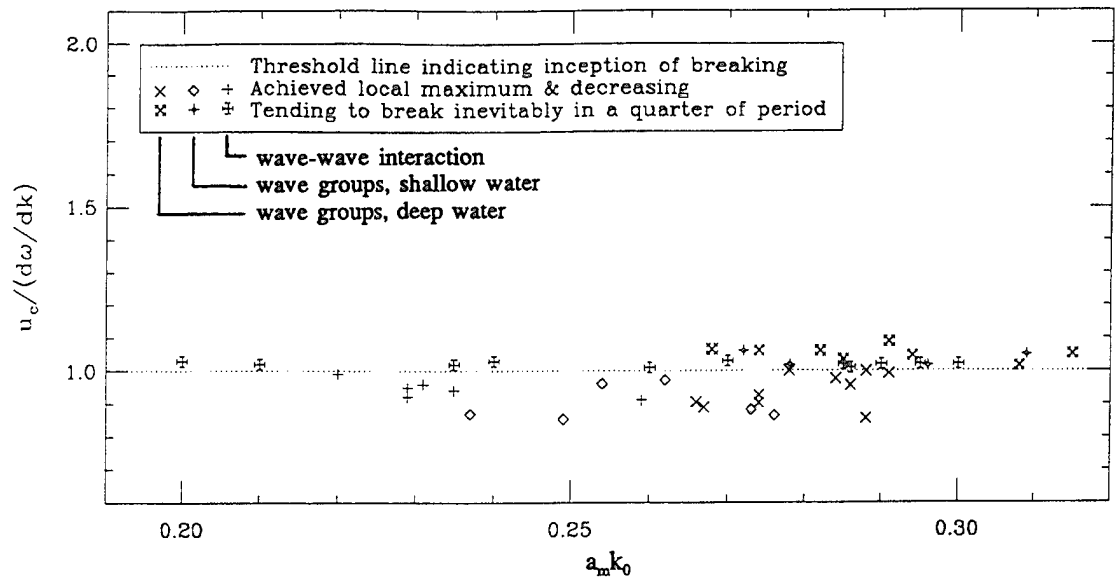


Figure 13: The ratio (crest particle velocity)/(wave group velocity), u_c/c_g, vs. $a_m k_0$. The horizontal line demarcates waves which did not proceed to breaking from those which did. The value of u_c is determined just prior to wave deformation and jet formation in the case of the breaking waves.

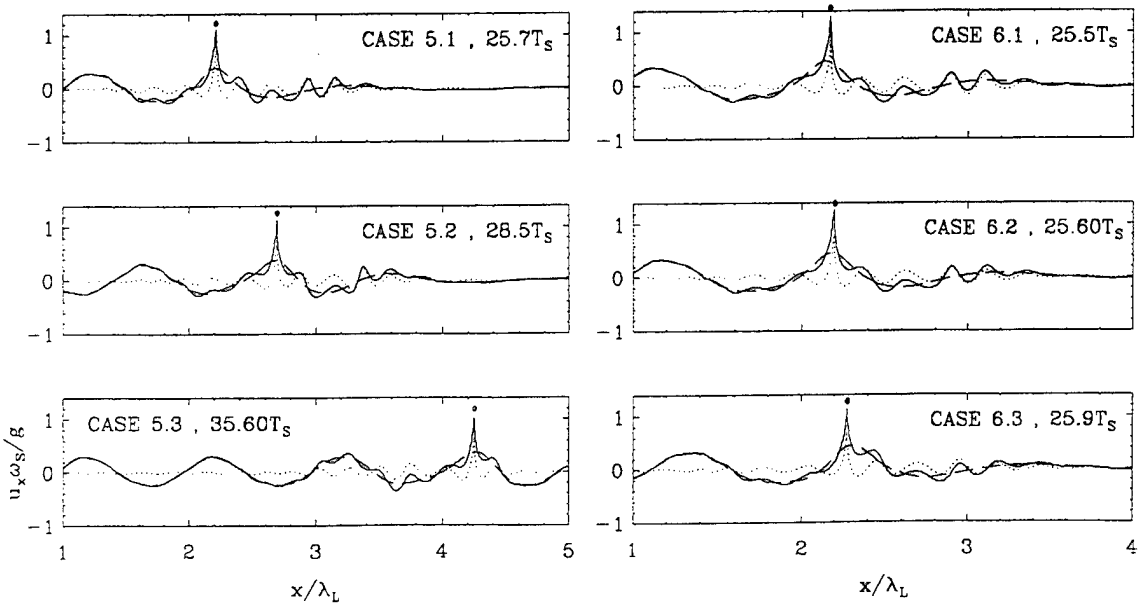


Figure 14 : In these cases, particle velocities are magnified strongly when the short wave reaches the vicinity of the long wave crest. This precipitates breaking; it is not the consequence of breaking. (···), the reconstructed short wave; (—), the composite wave; (– –) the long wave without interaction.

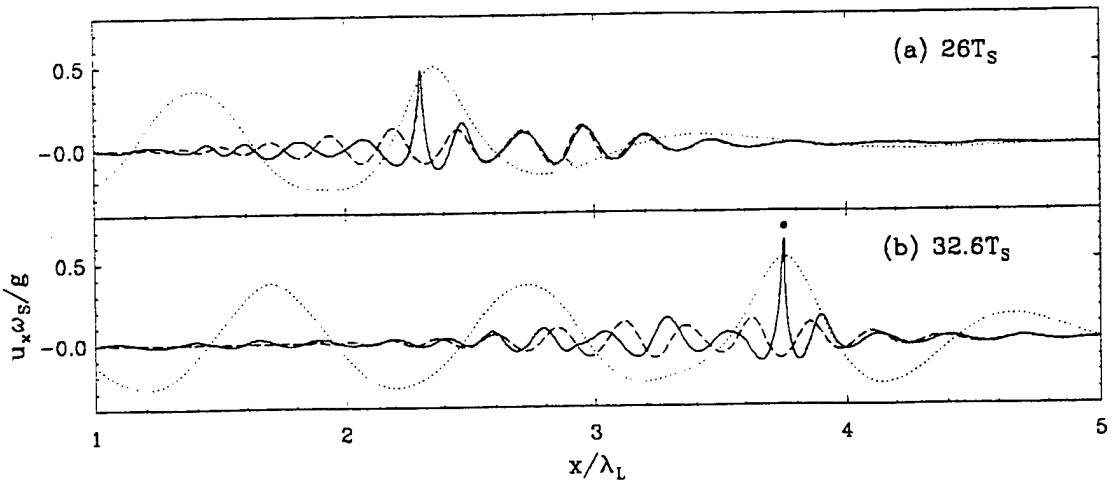


Figure 15 : Particle velocities for a reconstructed short wave of initial steepness, $(ak)_s = 0.1$. Note the remarkable magnification of the reconstructed orbital velocites, eventually precipitating breaking in (b). (—), the reconstructed short wave; (- -) the short wave train without interaction wave; (···) the long wave without interaction.

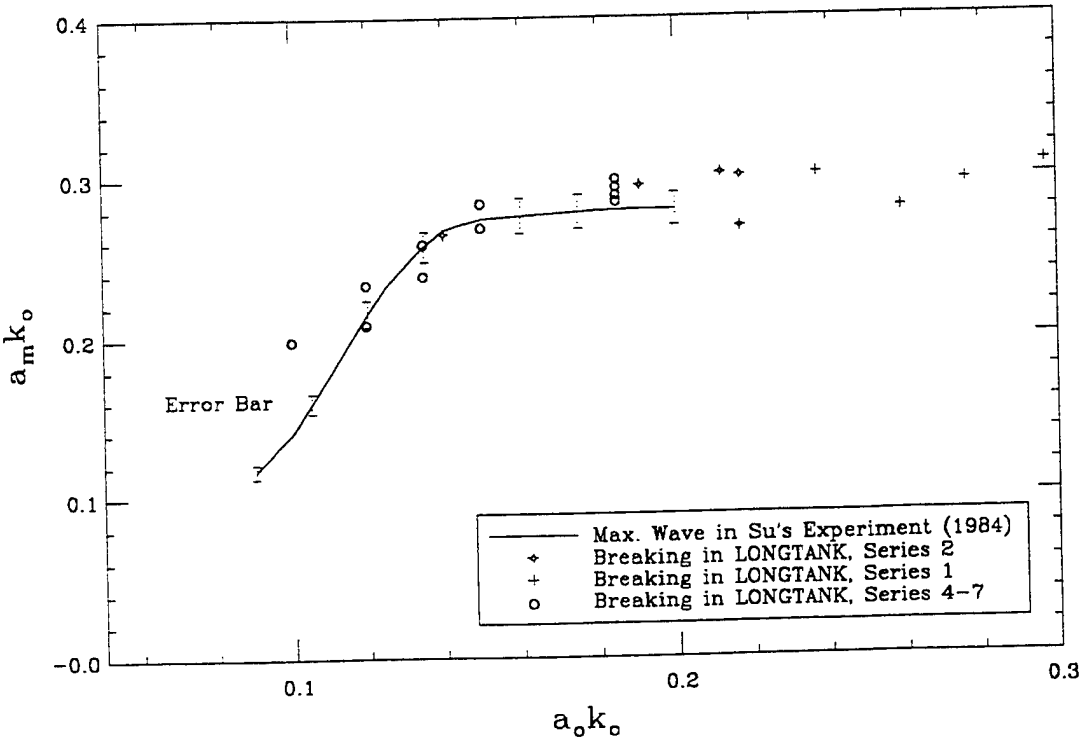


Figure 16 : Steepness at Breaking ($a_m k_0$) vs. initial steepness ($a_0 k_0$).

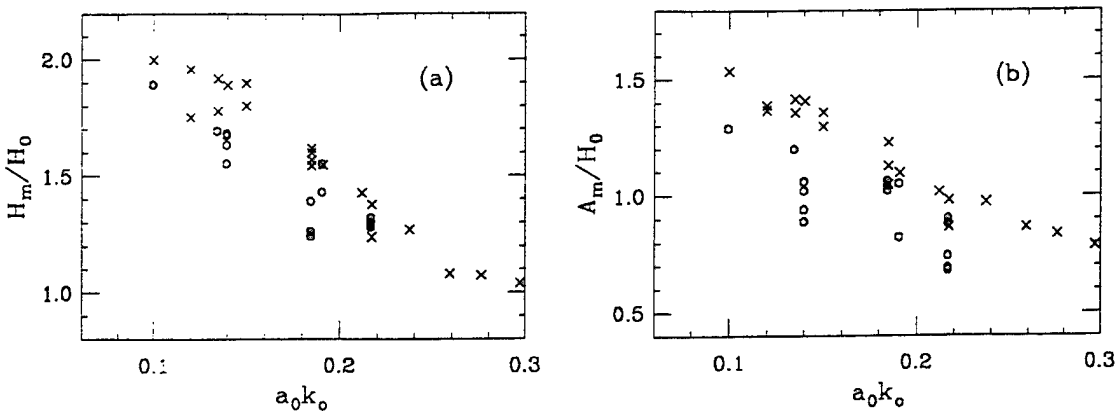


Figure 17 : Maximum wave heights, H_m, maximum wave crests, A_m, divided by initial wave height, H_0, vs. initial wave steepness. From *LONGTANK* experiments. (x) , breaking waves; (o), steep non-breaking waves.

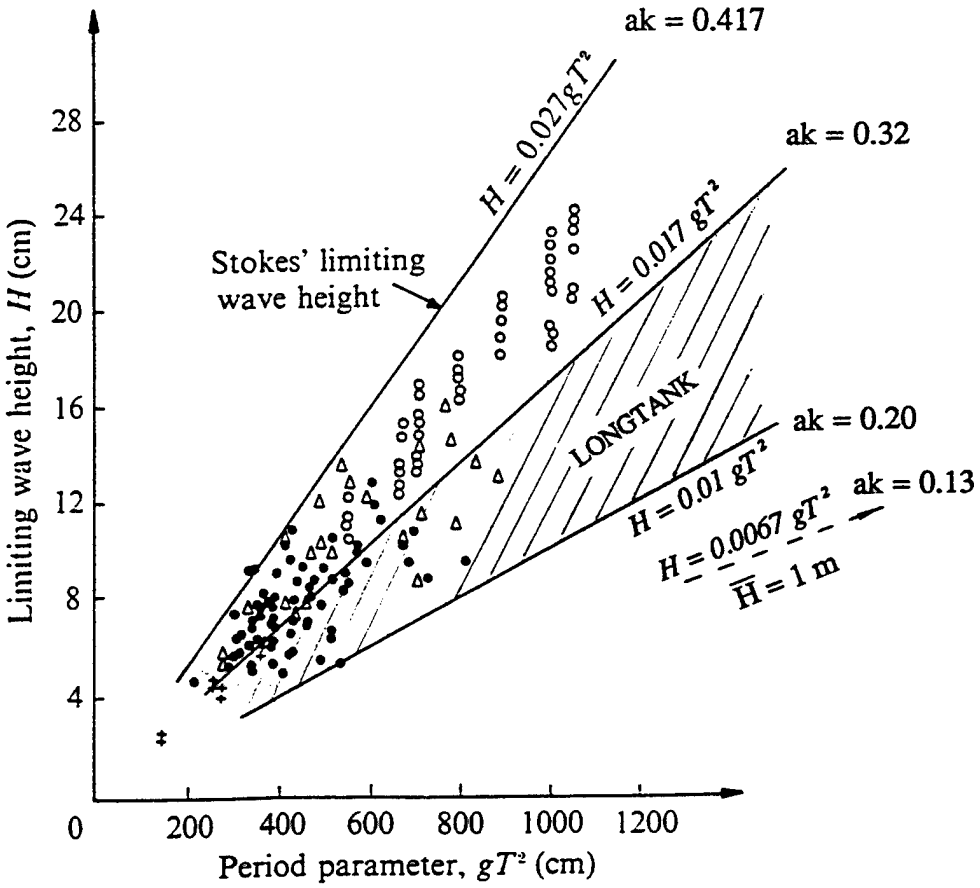


Figure 18 : Comparison of breaking wave height of LONGTANK experiments (shadowed region) with short tank experiments (+, Duncan,1981 ; Δ, Ochi and Tsai, 1983; o, Ramberg and Griffin, 1986; ●, Bonmarin,1989) and ocean data (- - - North Sea)

DISCUSSION

J. Duncan
University of Maryland, USA

The authors are to be congratulated for extending the state of the art in simulating breaking waves with boundary element flows and for increasing our understanding of the physics of breaking water waves. I am particularly intrigued by the result that the wave evolves to breaking within a quarter of the wave period if the horizontal particle velocity, u, exceeds dw/dk. From the data in Figure 13, it appears that $u = dw/dk$ is a reliable breaking criterion. I realize that this criterion has emerged from many numerical experiments rather than a theoretical analysis. But, I would like to know if the authors have any physical arguments to explain why the horizontal particle velocity is such a good predictor of incipient breaking and why the group velocity plays such an important role in this criterion.

AUTHORS' REPLY

We have by now made analytical considerations of the criteria utilizing exact equations, and we have made many numerical studies of the kinematical behavior of surface particles near breaking. The analytical studies show that the velocity history of particles on the surface just upstream of the wave peak near the envelope peak change their nature depending on the sign of $(u = dw/dk)$. The work will be published.

Kinematic and Dynamic Evolution of Deep Water Breaking Waves

O. Griffin, R. Peltzer, H. Wang (Naval Research Laboratory, USA),
W. Schultz (University of Michigan, USA)

Abstract

Spectral and piecewise-linear algorithms for two-dimensional potential flow were developed and used by Schultz, et al. (1994) to compare the onset of breaking for various means of energy input to the wave system. The computations show that certain wave-breaking criteria (potential energy or the more classical peak-to-peak wave height) are a function of the rate of energy input. Steep plunging waves occur when energy input rates are large. As the energy input rates become smaller there is a smooth transition to smaller spilling waves. The various energy input methods show similar breaking trends in the limit as the energy input rate becomes small—waves break when the potential energy becomes approximately 52 percent of the energy for the most energetic Stokes wave, with the formation of a singularity immediately before the crest. Experiments were performed in an NRL wave channel to exploit the dispersive properties of unsteady surface waves. The experiments have resulted in a highly resolved archive of breaking events ranging from wave steepening and incipient breaking, to spilling, and to plunging. The potential energy density, the crest front steepness, and other geometric properties of an incipient breaker vary only moderately about mean values for the range of these NRL experiments. These experiments provide some guidance to understanding the pivotal role played by wave breaking in the formation of radar 'sea spikes' on the ocean surface.

INTRODUCTION

The physical complexities of wave breaking in deep water are widely recognized, but still are not well understood after many years of study. Breaking waves are generally classified into two types: plunging, in which the forward face of the breaker overturns violently into the slope of the preceding wave; and spilling, in which the breaking and white-capping develop more gently from an instability near the wave crest. The fluid dynamics of deep water breaking, especially the outstanding theoretical issues and new measurement approaches, were assessed most recently by Longuet-Higgins (1988) and by Banner and Peregrine (1993). A related symposium evaluated the current state of knowledge for all aspects of wave breaking in order to stimulate further research in critical areas (Banner and Grimshaw, 1992).

Breaking waves are universally present over the ocean surface, and they play important roles in both the microwave and acoustic scattering processes at the surface (Kerman, 1988; Melville, et al., 1988). A thorough study of the physical processes associated with microwave backscattering from wind-generated waves up to the onset of breaking was performed recently by Ebuchi, et al. (1993). The observation of "sea spikes", or short duration events of increased scattering in the surface radar signature at low grazing angles of a few degrees, is attributed to the presence of steep and breaking waves (Wetzel, 1990; Trizna, et al., 1991). Similar scattering events at larger incidence angles away from grazing have been described by Jessup, et al. (1991a, 1991b). But there is some controversy and considerable discussion among specialists over the scattering mechanisms and conditions that produce the spike-like features. However, the steepness of the wave near the crest but prior to breaking is thought to play a leading role in the scattering process (Loewen and Melville, 1991).

Bright regions of enhanced surface scattering caused by breaking waves are highly observable in many visual and synthetic aperture radar (SAR) images of surface ship wakes which have been remotely sensed from air and space over the past fifteen years (Munk, et al., 1987; Reed, et al., 1990; Griffin, et al., 1992).

BACKGROUND

The fundamental experiments for studying two-dimensional wave breaking (apart from that induced by wind-wave interaction) fall into three main categories: (1) the focusing of essentially two-

dimensional waves in the lateral direction (Ramberg and Griffin 1987, Van Dorn and Pazan 1975); (2) the towing of a submerged object such as a hydrofoil to produce steady breakers (Duncan, 1981, 1983); and (3) the focusing of variable length waves from a modulated wavemaker or wave source to produce unsteady breakers (Dommermuth, et al., 1988; Duncan, et al., 1987; Rapp and Melville 1990; Peltzer, et al., 1993) or the overturning of an irregular wave train (Ochi and Tsai, 1983; Bonmarin, 1989) to produce unsteady breakers.

The most comprehensive laboratory study of unsteady deep-water breaking thus far is the work of Rapp and Melville (1990). The dispersive character of deep-water waves was used to focus a wave packet to generate a single unsteady breaking event at a controlled location in the wave channel. Losses of excess momentum and energy flux during breaking within a wave group ranged from 10 percent for spilling breakers to 25 percent for plunging breakers. Rapp and Melville found that the growth rate of the waves prior to breaking was an important factor in predicting breaking. This had been found previously by Van Dorn and Pazan (1975) and to a lesser extent by Ramberg, et al. (1985, 1987) in their convergent channel experiments.

Several of these experimental studies propose a wave-breaking criterion based on peak-to-peak (crest-to-trough) wave height. However, the validity of a standard or global criterion has been questioned (Melville and Rapp 1988), in part because peak-to-peak wave heights vary significantly during breaking and often decrease just before breaking. Clearly, no breaking criteria can be simple and precise. Schultz, et al. (1994) opt for a simple potential energy criterion in hopes that it can be more universally applied, although experimentally or computationally determined criteria are a function of many parameters. Extensive discussions of breaking criteria based on wave height are given in Ochi and Tsai (1983), Huang, et al. (1986), Xu, et al. (1986), Bonmarin (1989), and in Dawson, et al. (1991). Breaking criteria based on crest acceleration are discussed by Longuet-Higgins (1985) and Srokosz (1986). Experimental determination of the onset of breaking is difficult without detailed velocity measurements at the crest (Melville and Rapp, 1988; Van Dorn and Pazan, 1975), which are usually not available and are difficult to obtain.

Computational studies of breaking waves usually form the waves by applying a point pressure disturbance (Longuet-Higgins and Cokelet, 1976) or obtain breaking conditions simply from having sufficiently energetic initial conditions (Vinje and Brevig, 1981). While many algorithms have been developed that simulate breaking waves, Schultz, et al. (1994) were first to systematically study incipient breaking. For example, wave breaking caused by a modulated wavemaker has been verified computationally by Dommermuth, et al. (1988), but these computations were so expensive that only one experimental event was verified. In addition, previous computations tend to show plunging waves instead of the more commonly observed spilling breakers that regularly occur on the ocean surface.

Recently Schultz, et al. (1994) computationally examined the steepening and breaking of deep water waves generated by the experimental methods cited above. Only spatially periodic computations were used, so an ad hoc energy input term was deduced for the convergent wave channel. Although the periodic boundary conditions precluded studying the wavemaker problem, the effect of wave modulation was examined using a larger computational region (more than one primary wavelength) as in Dold and Peregrine (1986). The effect of beach reflections was modeled by putting a small standing wave component in the initial conditions. To crudely model waves produced by submerged hydrofoils a periodic array of simple submerged dipoles was used.

There are difficulties in interpreting the differences caused by the computational spatial periodicity as compared to temporal periodicity in many experiments. Also, experiments continue after breaking occurs, while the time-marching computations must stop at the first occurrence of breaking unless an ad hoc condition models the turbulence and air entrainment. Schultz, et al. show that accurate spectral computations break down sooner, indicating the possible formation of a singularity and evidence of the failure of potential theory before the wave crest approaches the forward face.

Recent measurements of the limiting wave height at breaking under various laboratory conditions are summarized in Table 1 and Fig. 1. Laboratory measurements of the limiting heights of regular deep water waves by Ochi and Tsai (1983), Ramberg and Griffin (1987), and Bonmarin (1989), have shown that the onset of breaking occurs at heights which are appreciably less than Stokes' theoretical limiting value. The present NRL experiments, as well as those of Bonmarin (1989), Rapp and Melville (1990), and Dawson, et al. (1991), show that the onset of breaking in unsteady wave groups or packets occurs at still lower *local* wave heights. The reduced wave heights at breaking from these experiments are represented in Table 1 by the corresponding values of the breaking coefficient or effective steepness σ' that are listed there. A mean value of $\sigma' = 0.019$ was obtained by Xu, et al. (1986) from their wave channel experiments, for their so-called dominant form of wind-induced incipient breaking.

RECENT COMPUTATIONAL ADVANCES

Although formal analytical techniques have been developed for small-amplitude gravity waves, the evolution of unsteady and steep waves must be solved numerically. The most efficient of the algorithms are based on boundary integral techniques. Even then, the algorithms can be time consuming. Hence, no thorough and complete parametric study has been performed on gravity waves. Usually, to reduce the computational effort, the problem domain is kept as small as possible by applying periodic boundary conditions. Schultz, et al. (1994) adopted this restriction also. Computations with many fundamental wavelengths inside the periodic domain have been made by Dold and Peregrine (1986), and the nonperiodic, fully nonlinear wavemaker problem has been computed by Dommermuth, et al. (1988). Casual observations of breaking waves show that they are not spatially periodic. Here we only present example results for the periodic problem, although by using a large spatial period the model can approximate results on an infinite domain.

The boundary integral numerical schemes for irrotational flow problems can be broken into three general approaches based on Green's functions (Longuet-Higgins and Cokelet, 1976; Vanden-Broeck, 1980), vortex dynamics (Baker, Meiron and Orszag, 1982), or the Cauchy integral theorem for complex potentials (Vinje and Brevig, 1981). The three techniques give equivalent results (McIver and Peregrine, 1981). Work by Dold and Peregrine (1984) has shown that algorithms based on the Cauchy integral theorem can be up to *50* times faster than Green's function algorithms and *10* times faster than those using vortex methods. Lin, et al. (1985) use the Cauchy formulation when solving two-dimensional problems and revert to the Green's function algorithm for axisymmetric problems. The efficiency of the complex algebra is significant.

A numerical wave channel simulation was developed recently by Wang, et al. (1993). Distances down the channel of 10^2 wavelengths were achieved based upon an efficient method of matrix diagonalization. The length of the computational domain permits the study of nonlinear sideband growth, wave deformation, and energy redistribution. The computed shapes of the waveforms at breaking are in good agreement with the photographs of Bonmarin and Ramamonjiarisoa (1985) and the wave profiles measured at breaking by Ramberg and Griffin (1987).

The present computations employ two algorithms based on the Cauchy integral theorem. The first is an improvement of a piecewise-linear algorithm of Vinje and Brevig (1981) as described in Schultz and Hong (1989). The second is a spectral technique similar to that proposed by Roberts (1983) and is described in Huh (1991). Both methods are discussed because the first method, although less accurate and more computationally intensive, is also more robust. Extensive comparisons are given by Schultz, et al. (1994).

In both methods, the physical domain is mapped to an approximate unit circle using a conformal transformation. This eliminates the periodic boundary conditions and sharp computational corners used by Vinje and Brevig (1981). All derivatives are taken in the conformed space—the piecewise-linear method uses three-point central differences while the spectral method takes derivatives in the spectral space of the conformed representation. The algebraic system that results from discretizing the integral equation is iteratively solved for both methods using a generalized minimum residual method (GMRES). Time marching fourth-order Runge-Kutta-Gill or predictor-corrector methods with an automatic adjustment of step size were both used, with the predictor-corrector method showing better computational efficiency, especially for the higher-accuracy computations. Schultz, et al. (1994) chose the LSODA package from Lawrence Livermore to march in time.

COMPUTATIONAL RESULTS

A first example based on the recent work of Schultz, et al. (1994) is to look briefly at gravity waves of permanent form, and suppress the Benjamin-Feir instability by applying periodic boundary conditions that do not allow subharmonic disturbances (Longuet-Higgins, 1978). The initial conditions for the time-marching code were obtained from the iterative method of Schwartz and Vanden-Broek (1979), applied in the absence of surface tension effects. The wave steepness $(y_{max} - y_{min})/2\pi$ was equal to 0.1 and 0.115, respectively for the two cases. These computed waves require special care in the choice of the error criteria for the time marching and the iterative solver because the amplitude is approaching the Stokes limit of $(y_{max} - y_{min})/2\pi \sim 0.14$.

The spectral computation conserved energy and mass to within one part in 10^9. Comparably the piecewise linear computation was within one part in 10^4 for the first wave and within one part in 10^3 for the steeper second wave. These waves do not exist experimentally because in reality they are subject to the Benjamin-Feir instability which is suppressed in the computed waves by the periodic boundary conditions.

Numerical simulations were performed for many values of the nondimensional amplitude a to determine the initial conditions that cause breaking or spilling. The amplitude a is really the steepness ak, scaled as in Schultz, et al., where k=1. It was

found that waves spill for a slightly larger than 0.27 but will progress indefinitely for a<0.26. Typical computations use N=60 or 80 for the number of nodes and Δt =0.1 or 0.05 for the time step. These results are somewhat sensitive to the initial conditions in that using a three-term Stokes wave height initial condition, such as

$$y = a \sin x + 1/2\, a^2 \sin 2x + 3/8\, a^3 \sin 3x, \qquad (1)$$

does not apply as large a perturbation to the steady form, and, hence the breaking is suppressed to slightly higher amplitudes.

Since the total energy is constant throughout an entire numerical simulation as well as an inviscid experiment (up to breaking), it would appear to be an ideal criterion to determine breaking. Unfortunately, without a carefully calibrated and instrumented wavemaker or the ability to measure the velocity everywhere in the flow field, the total energy cannot be measured. Instead, a steepness criterion *wave height/wavelength* has been used most commonly . Figure 2(a) shows that such a criterion varies widely in time for the two cases with initial conditions of a=0.27 and 0.28. The nonbreaking wave peak-to-peak height becomes higher than the value at a previous time for a wave that breaks. Hence, the height for a nonbreaking wave can exceed that of a wave that is breaking. The computations show that the wave breaks at less than the maximum peak-to-peak height. There is experimental evidence for this as well (Melville and Rapp, 1988).

However, the potential energy, although not constant in time, is approximately half the conserved total energy. Hence, it is much less variable than the peak-to-peak values and still can easily be determined from wave probe data. Figure 2(b) demonstrates that the computed RMS wave heights (or potential energies) for these same two initial conditions are more distinct. That is, the RMS height of the breaking wave with initial condition a=0.28 does not fall below the peaks of the nonbreaking wave with initial condition a=0.27, in contrast to the $(y_{max} - y_{min})$ data. This indicates that the potential energy may be a better criterion to determine whether an evolving wave will break. The computations also show that breaking does not occur at the peak of the potential energy. This can be anticipated since the increased fluid velocities near the crest increase the kinetic energy at the expense of the potential energy.

The potential energy at breaking is about 52 to 54 percent of the potential energy of the highest Stokes wave computed by Cokelet (1977). These percentages are approximately one percent higher when compared to the *limiting* Stokes wave, which has the 120 degree crest angle but is slightly less energetic.

The computational wave data are determined at the same instant of time for the results of Fig. 2(a), while experimental measurements using one wave probe are measured at one location over a temporal period. Figures 2(a) and 2(b) also compare spectral and piecewise-linear computations. The piecewise-linear computations proceed further before breaking down, but as these computations are refined, they approach the spectral computations and do not fail earlier when more stringent error requirements are applied. Additional discussion of these computations is given by Schultz, et al. (1994).

NRL EXPERIMENTS

Experiments were performed in an NRL wave channel to exploit the dispersive properties of unsteady surface waves in order to produce an extensive matrix of breaking events over an ensemble of controlled wave packet properties. These experiments were performed in the channel 30 m long, 1.2 m wide and 1 m deep, that is shown in Fig. 3. The channel as shown here is configured to perform not only the breaking wave experiments discussed here, but also wind field and surface radar backscatter measurements as well. Packets of waves were generated by a hydraulically-actuated paddle driven under computer control. The method of wave packet generation employed here represents a refinement of the chirp pulse generation technique for focusing the wave energy at a particular location in the channel.

Two examples of the wave generator inputs for the experiments are shown in Fig. 4. Only the amplitude and duration of the wave packet of twelve waves with a gaussian envelope were varied during the present experiments. The overall periods of the packet varied from 13 to 16 seconds, and the initial packet amplitudes from 0.09 to 0.25 m, in order to span a suitable range of breaking conditions. A typical arrangement of the wave gauges in the channel is sketched in Fig. 5(a). The experiments were performed to study the spatial and temporal evolution of kinematic properties such as wave asymmetry and front steepness, and dynamic properties such as potential energy or momentum flux.

The breaking conditions ranged from incipient breaking or gently spilling, to intermediate (white-capping), and to fully plunging (overturning). The temporal histories of the waves were measured using an array of seven conductivity gauges, and the waves' spatial evolution was recorded for eventual digital image processing using a high resolution (SVHS) video camera and recording system.

WAVE EVOLUTION

The evolution of a typical wave packet in the NRL wave channel is plotted in Fig. 5(b) for an initial condition which produces an incipient breaker. Each of the time histories plotted is the average of three independent realizations. The initial steepness (at gauge G1) of the wave which eventually breaks within the packet is $a_o k_o$=0.238. The local amplitude a_o at this wave gauge is taken as half the wave height H, a good approximation as shown in Fig. 5(b), and the wave number is $k_o=2\pi/l$, the local wavelength. The frequency factor FF34 refers to the packet (see Fig. 4) with the nominally largest period of the breaking wave of about 1.2 seconds. The evolution of the initially gaussian packet to a short, sharply peaked breaking wave train is evident as the downstream location of breaking (gauges G2, G6 at $k_o x$ =20.54) is reached. All of the events investigated in these experiments were limited to the first occurence of breaking in the packet, prior to any secondary breaking that was to follow.

The change in form of the steepest wave in the packet near breaking can be observed in the sequence of wave profiles shown in Fig. 6, again for the condition given by FF34. The profiles are individual frames that are 'grabbed' from the video recordings. The round wave still resembles the profile of a steep, symmetric Stokes wave. The increases in the steepness and asymmetry of the crest region which accompany the progression in severity of breaking are observable as the process evolves from a steep but non-breaking wave just before the incipient stage, to a spilling breaker, then to an intermediate level of breaking, and finally, to a fully plunging or overturning breaker. The onset of rippling and white water or bubbly flow at the crest appears at the incipient stage of breaking. Then a region of increasing agitation and flow complexity near the crest is formed as the breaking progresses through the intermediate stages toward full plunging or overturning. It is this progression which is discussed here in terms of the geometry or steepness and energy properties of the wave packet.

POTENTIAL ENERGY

The potential energy per unit of surface area v, averaged over the wavelength l is

$$v = \frac{1}{l}\left(\frac{\rho g}{2}\int_0^l \eta^2 dx\right) \qquad (2)$$

where ρ is the water density, g is the gravitational acceleration, η is the wave amplitude, and x is the direction of wave propagation. This equation can be expressed in the non- dimensional form

$$epl = \frac{2vk^2}{\rho g} = \frac{k^2}{N}\sum_{i=1}^{N}\eta_i^2 \qquad (3)$$

where the η_i are the N individual data points in the wave gauge record.

The spatial evolution of the potential energy per unit surface area, averaged over a wavelength (period), is plotted in Fig. 7(a) for the same wave/packet (FF=34). The potential energies span a range of initial conditions from steep, but non-breaking ($a_o k_o$= 0.224), to incipient breaking or spilling ($a_o k_o$=0.238), to intermediate ($a_o k_o$= 0.247), and to fully plunging ($a_o k_o$=0.248 and 0.255). The initial steepnesses for the packets FF37 and FF42 in Figs. 7(b) and 7(c) are somewhat greater. This variation is principally due to the range of the initial steepnesses $a_o k_o$ at gauge G1, which could be controlled only to a limited extent. This was because the first gauge G1 was at a fixed physical location relative to the wave generator, and gauges G2 to G7 were moved as the location of breaking changed for the different packets with different $a_o k_o$'s.

Two key features of the breaking event are present in these experiments. First, the potential energy at breaking increases as the progression in severity proceeds from spilling to fully plunging and overturning. And as the wave packet evolves along the channel, the spatial rate of change of the potential energy varies markedly with the severity of the breaking. The latter effect corresponds directly to the transformation of potential energy to kinetic energy and vice versa as the level of the breaking changes, and as the initial conditions of the wave packet are changed.

For the packet FF34, there is an overall decrease in potential energy *epl* as the packet travels from gauge G3 ($k_o x$=19.07) towards the onset of breaking at gauges G2, G6 ($k_o x$=20.54). This decrease in potential energy prior to breaking over approximately 0.5 m in along-channel distance accompanies a corresponding increase in kinetic energy while the total energy remains constant (except for small losses to boundary friction , etc.) in the finite-area wave channel. Rapp and Melville (1990) showed that such losses are minimal by comparison to the total energy of a similar packet. Much the same behavior is observed for the packet FF37.

However, the packet FF42 with the smallest breaking wave period (see Fig. 4) exhibits a different evolutionary history as shown in Fig. 7(c). The incipient breaking packet with $a_o k_o$=0.279 shows only a very small change in potential energy as $k_o x$

increases from 9.05 to 11.3 (gauge G3 to gauges G2,G6). The potential energies of the intermediate and lightly plunging packets with $a_o k_o$=0.294 and 0.298 initially remain nearly constant and only decrease over the short distance from $k_o x$=10.55 (gauge G5) to 11.3 (gauges G2,G6). The potential energy of the packet which evolves to a fully plunging event first increases up to $k_o x$=10.55, then decreases. Thus the evolutionary histories of the various breaking waves are dependent on the initial properties of the packet in terms of frequency content and initial amplitude or steepness.

Typical potential energies of the individual waves that break within the packet are *epl*=0.0319 (spilling) and *epl*=0.0469 (plunging) for FF34, and *epl*=0.0443 and 0.0709 respectively under the same nominal conditions for FF42. Only relative *(local/initial)* measurements of the evolution of the potential energy or momentum flux along the channel were made by Rapp and Melville (1985, 1990). To the extent that comparisons are possible their results are qualitatively similar to our measurements of *epl* that are shown here in Fig. 7.

Approximately 75 to 90 percent of the total potential energy is concentrated in the crest region at breaking, with the proportion of the crest potential energy becoming consistently smaller for plunging breakers than for spilling breakers. The potential energies of an evolving steep, unsteady wave train as computed by Schultz, et al. (1994) and measured in these NRL experiments are approximately half (52 to 54 percent) the potential energy of the highest symmetric Stokes wave, as computed by Cokelet (1977).

WAVE ASYMMETRY AND STEEPNESS

Several geometric properties which characterize the wave asymmetry and steepness have been identified by Kjeldsen and Myrhaug (1978), Bonmarin (1989), and Kjeldsen (1990) as giving important and unique evidence of the evolution of the breaking process. The degree of asymmetry of the crest is expressed by horizontal and vertical asymmetry factors suggested by Bonmarin and Kjeldsen, i.e. μ and λ, and the steepness is expressed at the front and rear of the wave crest, i.e. ε and δ as defined in Fig. 8. The crest front steepness ε, the ratio of the crest amplitude y_{max} to the distance F_1 from the crest to the previous zero level crossing, arguably is the most important of the four cited there.

The crest front steepnesses measured with the wave gauge array for the series FF34 and 42 are plotted in Fig. 9. The initial $a_o k_o$'s for each breaking wave/packet are the same as in Fig. 7. The smallest initial steepness corresponds to a steep but non-breaking wave packet. This is followed by an incipient or spilling breaker, an intermediate breaker, and two plunging breakers as before. The measured ε's in these experiments are in excellent agreement with the limited results of Bonmarin (1989) and Rapp and Melville (1990) for incipient spilling and plunging breakers. But the present experiments, as summarized in Fig. 9, give a more detailed history of the crest region evolution than any previous experiment. The maximum crest front steepnesses for a plunging breaker in Fig. 9 are ε=0.56 at FF34 and ε= 0.60 at FF42. For the NRL data set overall the largest plunging steepness is ε=0.62 for the wave packet denoted by FF37.

The vertical asymmetry $\lambda=F_2/F_1$ provides another measure of the deformation of the crest region as breaking is approached. The evolution of λ for the series FF34 and 42 is plotted in Fig. 10. Again the initial steepness conditions are as described above. All of the waves are essentially symmetric about the crest, or $\lambda \sim 1$, at the first wave gauge.For the non-breaking wave and the spilling (incipient) breaker the vertical asymmetry varies only moderately and decreases slightly as the location of breaking in the channel (gauges G2,G6) is approached. As the intermediate stage of breaking is approached, the wave profile about the crest becomes decidedly asymmetrical. When the plunging condition is reached the profile becomes still more asymmetric with the ratio F2/F1 approaching 2 just before breaking for the series FF34. The horizontal asymmetry μ, the ratio of the crest amplitude to the full wave height, changes only slightly as the breaking evolves from the incipient stage towards fully plunging ($0.72<\mu<0.80$) for these NRL experiments. Most of the increase in the wave steepness just prior to breaking results from the reduced length of the region forward of the crest, i.e. the crest front.

Much the same progression in asymmetry as the crest region increases in steepness can be observed from the video images in Fig. 6. Both the round and steep waves are quite symmetric about the crest, while the spilling breaker gives some evidence of the onset of asymmetry. As the plunging stage of breaking is reached, the vertical asymmetry from the images qualitatively matches well with the comparable wave gauge measurements. The results in Fig. 10 indicate that the geometry of the wave evolution towards breaking depends on the amplitude and frequency make-up of the wave packets as denoted by FF34 and 42. The other wave packet series show this same dependence as well.

For these NRL experiments the vertical asymmetry λ ranged from about 0.9 to 1.8. Longuet-Higgins and Cokelet (1978) computed a value λ =1.83 for a plunging breaker. From his wave packet experiments Kjeldsen (1990) found that $0.9 < \lambda < 2.2$,

while Bonmarin (1989) measured the range of $1.2<\lambda<2.1$.

ANALYSIS OF UNSTEADY BREAKING

For the analysis of a nonstationary localized phenomenon such as wave breaking, it is of interest to use techniques other than the traditional, global Fourier transform. This transform is most appropriate for signals which are periodic and stationary, but it is unsuitable for analyzing transient phenomena such as the unsteady evolution of a wave packet up to breaking. Instead, the Hilbert transform is used to obtain a detailed analysis of the time-varying amplitude and frequency behavior of the breaking wave (Long, 1994). While detailed geometric properties have been studied extensively as in this paper, analysis of the frequency content of the wave near breaking has received only limited attention.

The Hilbert transform y(t) is a convolution of the wave signal y(t) and the time windowing function $1/(\pi\ t)$ over the entire duration of the signal. It is written as

$$\tilde{y}(t) = \int_{-\infty}^{\infty} \frac{y(u)}{\pi(t-u)} du \qquad (4)$$

In conjunction with the original signal, the Hilbert transform is used to give the instantaneous envelope signal $A(t)$, the phase signal $\theta(t)$, and the frequency $f_0(t)$, as follows

$$A(t) = \left(y^2(t) + \tilde{y}^2(t)\right)^{1/2}$$

$$\theta(t) = \tan^{-1}\left(\tilde{y}(t)/y(t)\right) \qquad (5)$$

$$f_0(t) = \frac{1}{2\pi}\left(d\theta(t)/dt\right)$$

The Hilbert transforms of the measured wave data were obtained by using the MATLAB software package. Each of the time histories is an average of three independent realizations, and a total of seven wave packets were analyzed. These represent a subset of the ten cases considered for the FF34 and FF42 series in Fig. 9, omitting the intermediate wave in both series and the less severe plunging wave of FF34.

Figure 11 shows a time history of the wave elevation of these seven cases of 501 data points each corresponding to 2.5 sec on either side of the maximum elevation as measured at gauge G2 (where $t\text{-}t_{max}=0$). It should be emphasized that the Hilbert transforms were obtained for the entire measured time history which ranged from a minimum of 1,441 points to a maximum of 2,811 points. This figure clearly shows the differences in general amplitudes and periods between different waves in a given series and between the two series. The figure also generally confirms a wave period of approximately 1.16 sec for FF34 and 0.84 sec for FF42, as in Fig. 4.

A somewhat different and more concise view is obtained by plotting the instantaneous Hilbert amplitude $A(t)$ for the seven cases, as shown in Fig. 12. In addition to the differences between individual waves and series of waves, the figure clearly shows the asymmetry between the front and rear faces of the wave. The asymmetry is more pronounced for the steeper FF42 waves.

In order to provide a more precise view of the wave breaking process, the time variation of the instantaneous Hilbert frequencies f_0 is shown in Figs. 13, 14 and 15. Figure 13 shows f_0 for the seven cases in the narrow region $-0.3 < t\text{-}t_{max} < 0.3$. This more closely focuses on the breaking wave region. The most dramatic variation in frequency occurs in the region $-0.1< t\text{-}t_{max} < 0.1$, with a more gentle variation outside of this region. The maximum frequencies are approximately 1.35 and 1.5 Hz for the round waves, 1.75 Hz for both spilling waves, and 2.5, 3.4, 3.8 Hz for the three plunging waves. This figure also shows more clearly the difference between the two plunging waves for FF42.

Figure 14 shows a more global view of the evolution of the the breaking wave process. The figure shows the values of f_0 for gauges G3, G4, G5, and G2 in the interval $-0.5< t\text{-}t_{max} < 0.5$ for the plunging (omitting the least severe case for FF42), spilling, and round waves for FF34 and FF42. The figure shows that the evolution process is qualitatively similar for corresponding waves in both series. The frequency behavior is nearly constant with gauge location for the round waves, shows slight growth for the two spilling waves, and sharp growth for the two plunging waves, with the FF42 case showing the most severe growth. The trend is similar to the variation of crest front steepness with gauge location shown in Figs. 9(a) and (b).

It is also of interest to investigate the energy content of a segment of the wave around the breaking point as a function of frequency. Since the phenomenon is nonstationary, the shape of the function depends on the length of record which is chosen. Here, the length is chosen for the interval $-5.5 < t\text{-}t_{max} < 5.5$, which corresponds approximately to the interval of significant wave activity at gauge G2, as shown in Fig. 5. A Hilbert energy density spectrum $E_H(f0i)$ may be numerically constructed by summing the Hilbert energy $A^2\ dt/2$

contained in each frequency bin centered around f_{0i}, i=1,2,...,N_B-1,N_B, and dividing the result by the width of the frequency bin. The choice of N_B is governed by the conflicting requirements of choosing as large a value as possible to get a detailed definition of the shape of E_H and the opposing need to minimize the number of bins to obtain stable energy estimates.

Figure 15 shows E_H for N_B=14, with 12 of the bins equally spaced between 0.1 and 2.5 Hz, and the remaining two bins to account for $f_0 < 0.1$ and $f_0 >$ 2.5 Hz, respectively. Taking the typical number of samples in a bin, N_S, equal to 1,100/14=79, the normalized standard error of the energy estimate in a typical bin is approximately given by $\sigma=1/(N_S)^{1/2}$ =0.11. Within a given run series, E_H is highest for the plunging waves and lowest for the round waves at frequencies less than approximately 1.0 Hz. The round waves and steep waves have the highest energy at intermediate frequencies. Only the plunging waves have significant energy for frequencies greater than 1.8 Hz.

ADDITIONAL COMPARISONS

The potential energy *epl*, the crest front steepness ε , and the horizontal asymmetry μ measured at the incipient stage of breaking and beyond this condition are summarized in Figs. 16, 17 and 18, for several experimental runs which cover the range in Table 2. The incipient breaker properties are the first cases plotted for each run in these figures. Four wave packets which range from incipient to plunging are shown for Runs 34, 37, 39, 41 and 42. There is a distinct increase in the potential energy and crest front steepness as the breaking levels increase from incipient or spilling, to intermediate, and to plunging. The dependence on initial steepness is evident from the results in Figs. 16 and 17.

The horizontal asymmetry, the crest front steepness and the average potential energy density *of an incipent breaker* vary only moderately about their mean values (μ = 0.772, ε=0.299, *epl* =0.0346) for the nine wave packet series listed in Table 2. The present experiments are in good agreement with the recent numerical simulations of the same breaker properties μ, ε and *epl* by Schultz, et al. (1994), as well as the range of ε at incipient breaking from the experiments of Rapp and Melville (1990). Kjeldsen (1990) cites a value of μ=0.77 at the onset of breaking in a wave group from his laboratory experiments, again in good agreement with the present experiments. Bonmarin (1989) found that μ ranged from 0.69 to 0.77 for spilling vs. plunging breakers. For the NRL experiments shown in Fig. 18 the horizontal asymmetry ranged from μ = 0.72 to 0.80 depending on the severity of the breaking.

Table 3 gives the average of the crest front steepness ε, and the RMS of the average of the incipient breaking waves from Table 2. The RMS value proves to be a more reliable and consistent criterion than a steepness criterion for breaking inception (Schultz, et al., 1994) This is especially beneficial for the wave packet criterion because the RMS wave height can be predicted more directly and accurately than the wave steepness from simple group velocity considerations. These are not spatially periodic waves, and so a measure of breaking inception not based on wavelength is desirable – especially when the number of waves in a packet changes instantaneously as in this NRL example. The potential energy per unit surface area appears more consistent than the steepness in this regard, but the potential energy or its RMS value in this example uses the local wavenumber measured at the breaking location (from the results in Table 2) for nondimensional scaling.

CONCLUDING REMARKS

Recent computations by Schultz, et al. (1994) demonstrate that the potential energy of surface gravity waves is a better measure of the onset of breaking for steep nonlinear waves than either the wave height or wave slope. The computed wave height or steepness appears to have more erratic variations in time than the potential energy.

There is some experimental evidence that the square root of the potential energy (the RMS wave height) is better than the peak-to-peak wave height (or steepness) criteria in predicting an incipient breaking event. This is indicated by a smaller percentage variation of individual wave channel breaking events as compared to an average measure of the breaking .

The NRL experiments show that the initiation of unsteady breaking in a deep water wave group or packet depends on the initial packet conditions. Likewise, the evolution of the breaking wave's potential energy, and its crest steepness and asymmetry properties prior to breaking also are dependent on these conditions. But the potential energy density, the crest front steepness, and the horizontal asymmetry of an incipient spilling breaker vary only moderately about their mean values over the extent of these experiments. These properties of the wave thus may represent valid local indicators of the inception of breaking. The computed and measured potential energies at breaking here are approximately half that of the highest steady, symmetric Stokes (theoretical) wave.

These experiments demonstrate that the onset of breaking in a finite group or packet of waves consistently occurs at amplitudes (steepnesses) much lower than those measured for a train of regular

waves. Thus, global wave steepness criteria for the onset of breaking cannot be applied in general, and their use should be approached with some caution. This point also was noted by Xu, et al. (1986) from their study of laboratory wind-generated breaking, and by Rapp and Melville (1990) from their laboratory experiments with unsteady wave packets.

The onset of breaking depends on the energy input rate to the wave system, with the smallest values occurring when the *energy input rate* is small and spilling breakers are expected. A smooth transition to plunging breakers occurs (as conjectured by Longuet-Higgins and Cokelet, 1976) for higher waves that can be formed by a larger energy input rate. The dependence on the energy input rate further explains the scatter of breaking criteria derived from earlier experiments.

The Hilbert transform provides a promising alternative to the traditional global Fourier transform for the analysis of nonstationary local phenomena such as unsteady wave breaking. This method was applied to the results from the NRL wave channel experiments and gives a new perspective on the time varying evolution of a wave packet towards breaking. The instantaneous Hilbert amplitude clearly focuses on the asymmetry between the front and rear faces of the wave, and shows the pronounced asymmetry present in the steepest wave packets. The spatial evolution of the Hilbert frequency of the packet towards breaking in the wave channel shows nearly constant behavior for the steep but non-breaking waves, slight growth for spilling breakers, and a progression to sharp growth for fully plunging breakers. The trend is similar to the variation in crest front steepness obtained directly from the array of wave gauges. These initial results using the Hilbert transform approach agree well with the more traditional measurements of the wave properties near breaking that are employed in this study.

Kjeldsen (1990) proposed that the crest front steepness gives a unique geometrical measure of the wave evolution as breaking is approached, and the results of the present experiments bear this out. Indeed it may be the most important wave property from the standpoint of radar scattering. Loewen and Melville (1991) have proposed that a large portion of the radar backscatter from the wave precedes the onset of visible breaking. Then the geometric properties of the wave just prior to breaking dominate the scattering process. Wetzel (1990) also stresses the importance of some as yet undetermined properties of the local steepness geometry to the surface radar scattering. The present results tend to support these several propositions, but further work is warranted.

ACKNOWLEDGEMENTS

The experiments were performed and analyzed as part of a basic research program in free surface fluid dynamics supported by the Naval Research Laboratory. The work at The University of Michigan was supported by the Ocean Engineering Division of the Office of Naval Research, and the Program in Ship Hydrodynamics at The University of Michigan, funded by a University Research Initiative of ONR. The authors are grateful to Timothy Donato, Dr. Farid Askari and Dr. Lewis Wetzel of NRL for numerous helpful discussions on the radar scattering from breaking waves.

REFERENCES

Banner M.L., and Peregrine, D.H., "Wave Breaking in Deep Water," Ann. Rev. Fluid Mech., Vol. 25, 373-397, 1993.

Banner M.L., and Grimshaw, R.H.J. (eds.), *Breaking Waves*, Springer-Verlag: Berlin, 1992.

Bonmarin P., and Ramamonjiarisoa, A., "Deformation to breaking of deep water gravity waves," Exp. in Fluids, Vol. 3, 11-16, 1985.

Bonmarin, P., "Geometric properties of deep water breaking waves,"J. Fluid Mech., Vol. 209, 405-433, 1989.

Cokelet, E.D., "Steep gravity waves in water of arbitrary depth," Phil. Trans. Roy. Soc. Lond. A, Vol. 286, 183-230, 1977.

Dawson, T.H., Kriebel, D.L., and Wallendorf, L.A., "Breaking Waves in Deep Water Random Seas," *Proc. First Intl. Offshore and Polar Engrg. Conf.*, Vol. III, Edinburgh, 39-46, 1991.

Dold, J.W., and Peregrine, D.H., "Steep unsteady water waves: An efficient computational scheme," School of Mathematics, University of Bristol Internal Report AM-84-04, 1984 .

Dold, J.W., and Peregrine, D.H., "Water-wave modulation," School of Mathematics, University of Bristol Report AM-86-03, presented at the *20th Int. Conf. on Coastal Engrg.*, Taipei, 1986 .

Dommermuth, D.G., Yue, D.K., Lin, W.M., Rapp, R.J., Chan E.S., and Melville, W.K., "Deep-water plunging breakers: a comparison between potential theory and exper-iments," J. Fluid Mech., Vol. 189, 423-442, 1988.

Duncan, J.H., "An experimental investigation of breaking waves produced by a towed hydrofoil," Proc. R. Soc. Lond. A, Vol. 377, 331-348, 1981.

Duncan, J.H., "The breaking and non-breaking wave resistance of a two-dimensional hydrofoil," J. Fluid Mech., Vol. 126, 507-520, 1983 .

Duncan, J.H., Wallendorf , L.A., and Johnson, B., "An experimental investigation of the kinematics of breaking waves," Rept. EW-7-87, U.S. Naval Academy, 1987.

Ebuchi, N., Kawamura, H., and Toba, Y., "Physical Processes of Microwave Backscattering From Laboratory Wind Wave Surfaces," J. Geophys. Res. (Oceans), Vol. 98 (C8), 14,669-14,881, 1993.

Griffin, O.M., Peltzer, R.D., Reed, A.M., and Beck, R.F., "Remote Sensing of Surface Ship Wakes," Nav. Eng'rs. J., Vol. 104, 245-258, 1992.

Huh, J., "A Numerical Study of Capillary-Gravity Waves," Ph.D. thesis, University of Michigan, 1991.

Jessup, A.T., Melville, W.K., and Keller, W.C., "Breaking Waves Affecting Microwave Backscatter 1. Detection and Verification,"J. Geophys. Res. (Oceans), Vol. 96 (C11), 20,547-20,559, 1991.

Jessup, A.T., Melville, W.K., and Keller, W.C., "Breaking Waves Affecting Microwave Backscatter 2. Dependence on Wind and Wave Conditions," J. Geophys. Res. (Oceans), Vol. 96 (C11), 20,561-20,269, 1991.

Kerman, B.R. (ed.), *Sea Surface Sound, Natural Mechanisms of Surface Generated Noise in the Ocean*, Kluwer Academic: Dordrecht, 1988.

Kjeldsen, S.P., "Breaking Waves," in *Water Wave Kinematics*, A. Torum and O.T. Gudmestad (eds.), Kluwer Academic: Dordrecht, 453-473, 1990.

Kjeldsen, S.P., and Myrhaug, D., "Kinematics and dynamics of breaking waves—Main report," VHL Report, Trondheim, Norway, 1978.

M.R. Loewen and W.K. Melville, "Microwave and acoustic radiation from breaking waves," J. Fluid Mech., Vol. 224, 601-623, 1991.

Lin, W.-H., Newman, J.N., and Yue, D.K., "Non-linear forced motions of floating bodies," *Proc. 15th ONR Symp. on Naval Hydrodynamics*, National Academy Press: Washington, DC, 33-49, 1985.

Long, S.R., "The Hilbert Spectrum, A New Tool for Non-Steady Time Series Analysis," *Proc. Symp. on the Air-Sea Interface*, M. Donelan (ed.), Marseilles, June 1993, Kluwer Academic: Dordrecht, in press, 1994.

Longuet-Higgins, M.S., "The instabilities of gravity waves of finite amplitude in deep water: II. Sub-harmonics," Proc. R. Soc. Lond. A, Vol. 360, 489-505, 1978.

Longuet-Higgins, M.S., "Accelerations in steep gravity waves," J. Phys. Oceanog., Vol. 15, 1570-1579, 1985.

Longuet-Higgins, M.S., "Mechanisms of wave breaking in deep water," in *Sea Surface Sound*, B.R. Kerman (ed.), Kluwer Academic: Dordrecht, 1-30, 1988.

Longuet-Higgins, M.S. and E.D. Cokelet, "The deformation of steep gravity waves on water: I. A numerical method of computation," Proc. Royal Soc. Lond. A, Vol. 350, 1-26, 1976.

Longuet-Higgins, M.S. and E.D. Cokelet, "The deformation of steep gravity waves on water: II. Growth of normal mode instabilities," Proc. Royal Soc. Lond. A, Vol. 364, 1-28, 1978.

Melville, W.K., "The instability and breaking of deep-water waves," J. Fluid Mech., Vol. 115, 165-185, 1982.

Melville, W.K., and Rapp, R.J., "Momentum flux in breaking waves," Nature, Vol. 317, 514-516, 1985.

Melville, W.K., and Rapp, R.J., "The surface velocity field in steep and breaking waves," J. Fluid Mech., Vol. 189, 1-22, 1988.

Melville, W.K., Loewen, M.R., Felizardo, F.C., Jessup A.T., and Buckingham, M.J., "Acoustic and microwave signatures of breaking waves," Nature, Vol. 336, 54-59, 1988.

Munk, W.H., Scully-Power, P., and Zachariasen, F., "THE BAKERIAN LECTURE 1986 Ships from space," Proc. Roy. Soc. Lond. A, Vol. 412, 231-254, 1987.

New, A.L., McIver P., and Peregrine, D.H., "Computations of overturning waves," J. Fluid Mech., Vol. 150, 233-251, 1985.

Ochi, M.K., and Tsai, C.-H., "Prediction and occurrence of breaking waves in deep water," J. Phys. Oceanog., Vol. 12, 2008-2019, 1983.

Peltzer, R.D., Griffin, O.M., and Schultz, W.W., "Steepness and energy properties of deep water breaking wave packets," *Proc. Symp. on the Air-Sea Interface*, M. Donelan (ed.), Marseilles, June 1993, Kluwer Academic: Dordrecht, in press, 1994.

Peregrine, D.H., Cokelet, E.D., and McIver, P., "The fluid mechanics of waves approaching breaking," *Proc. Coastal Engineering Symp.*, ASCE, 512-528, 1980.

Ramberg, S.E., Barber, M.E., and Griffin, O.M., "Laboratory Studies of Steep and Breaking Deep Water Waves in a Convergent Channel," NRL Memorandum Report 5610, May 1985.

Ramberg, S.E., and Griffin, O.M., "Laboratory studies of steep and breaking deep water waves," Proc. ASCE, J. WPCO Eng., Vol. 113, 493-506, 1987.

Rapp, R.J., and Melville, W.K., "Laboratory measurements of deep-water breaking waves," Phil. Trans. Royal Soc. Lond. A, Vol. 331, 735-800, 1990.

Reed, A.M., Beck, R.F., Griffin O.M., and Peltzer, R.D., "Hydrodynamics of remotely sensed surface ship wakes," SNAME Trans., Vol. 98, 319-363, 1990.

Saad, Y., and Schultz, M.H., "GMRES: A generalized minimal residual algorithm for solving nonsymmetric linear systems," SIAM J. Sci. Stat. Comput, Vol. 7, 856-869, 1986.

Schultz, W.W., and Hong, S.-W., "Solution of potential problems using an overdetermined complex boundary integral method," J. Comput. Phys. , Vol. 84, 414-440, 1989 .

Schultz, W.W.,Huh, J., and Griffin, O.M., "Potential energy in steep and breaking waves," J. Fluid Mech., accepted for publication, 1994.

Srokosz, M.A., "On the probability of wave breaking in deep water," J. Phys. Oceanog., Vol. 16, 382-385, 1986 .

Su, M.-Y., Bergin, M., Marler, P., and Myrick, R., "Experiments on nonlinear instabilities and evolution of steep gravity-wave trains," J. Fluid Mech., Vol. 124, 45-72, 1982.

Trizna, D.B., Hansen, J.P., Hwang, P., and Wu, J., "Laboratory Studies of Radar Sea Spikes at Low Grazing Angles," J. Geophys. Res. (Oceans), Vol. 96 (C7),12,529-12,537, 1991.

Van Dorn, W.G., and Pazan, S.P., "Laboratory investigation of wave breaking. II: Deep water waves," Scripps Inst. Oceanog. Rep. 75-21, 1975 .

Vinje, T., and Brevig, P., "Numerical simulation of breaking waves," Adv. Water Resources, Vol. 4 , 77-82, 1981.

Wang, P., Yao, Y., and Tulin, M.P., "Wave Group Evolution, Wave Deformation and Breaking: Simuations Using *LONGTANK*, a Numerical Wave Tank," Proc. Third Int. Offshore and Polar Eng. Conf., Singapore, June 1993.

Wetzel, L.B., "Electromagnetic Scattering from the Sea at Low Grazing Angles," in *Surface Waves and Fluxes, Vol. II*, G.L. Geernaert and W.J. Plant (eds.), Kluwer Academic: Dordrecht, 109-171, 1990.

Xu, D., Hwang, P.A., and Wu, J., "Breaking of Wind-Generated Waves," J. Phys. Oceanog., Vol. 16, 2172-2178, 1988.

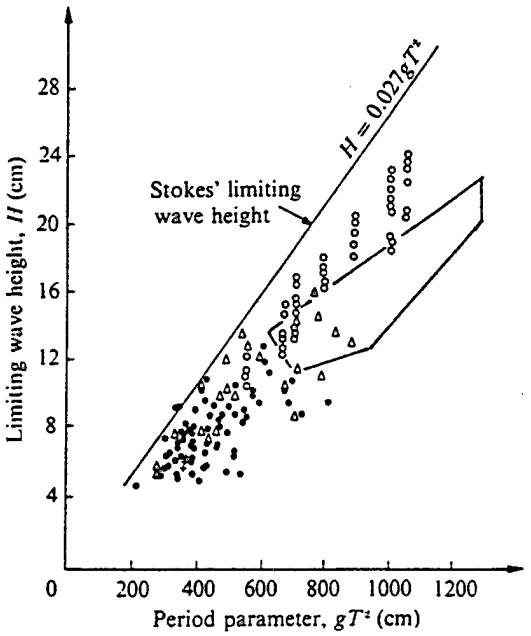


Fig. 1 Laboratory measurements of the limiting height H of deep water waves as a function of the period parameter gT^2. The legend for the experimental data in the figure is given in Table 1.

Table 1
Limiting Height of Deep Water Breaking Waves
Mean Values of the Breaking Coefficient $\sigma=H/gT^2$

Authors	Legend (Figure 1)	Breaker Type	
		Plunging	Spilling
Stokes (theoretical limit)		--	0.027
Ochi and Tsai (1983)	Δ	0.020	--
Ramberg and Griffin (1987)	O	--	0.021 (1)
Bonmarin (1989)	●	0.022 (2)	0.021 (4)
		0.020 (3)	0.020 (5)
Rapp and Melville (1990)	Enclosed	--	0.017-0.021 (4)
Present NRL experiments	Area	0.018-0.021 (2)	0.017-0.018 (4)

(1) Spilling and Lightly Plunging; (2) Typical Plunging; (3) Plunging;
(4) Typical Spilling; (5) Spilling; from Bonmarin (1989)

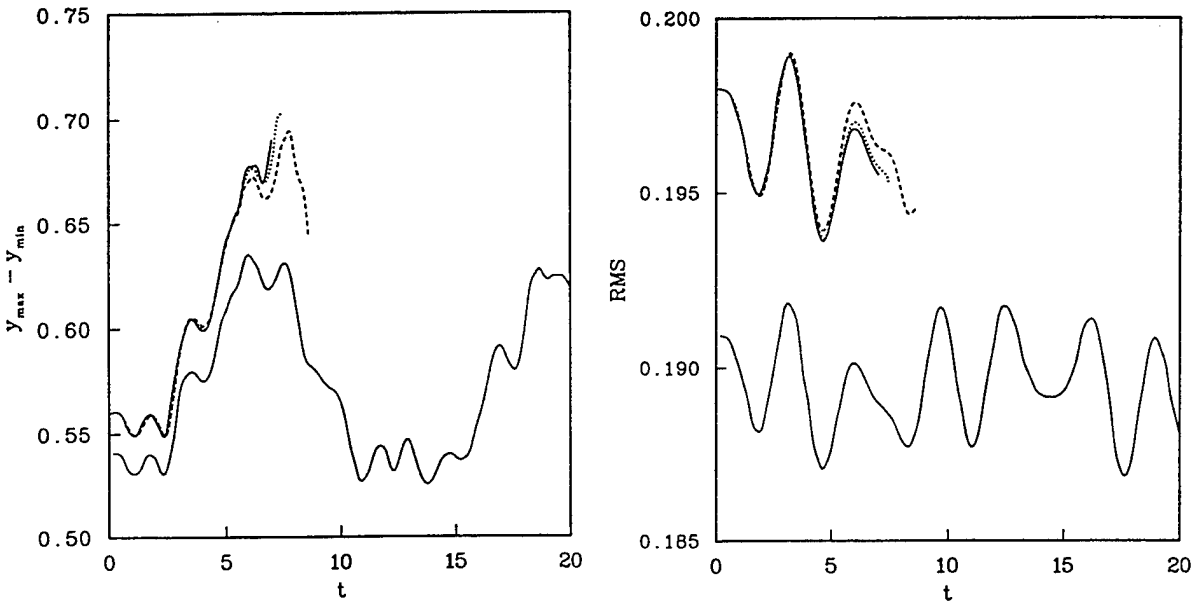


Fig. 2 (a) Peak-to-peak wave heights for a=0.27 and 0.28. Spectral, N=32,————; piecewise-linear, N=32,-- -- -- -- ; piecewise-linear, N=64, - - - - - - . (b) RMS wave amplitudes for the same two initial conditions.

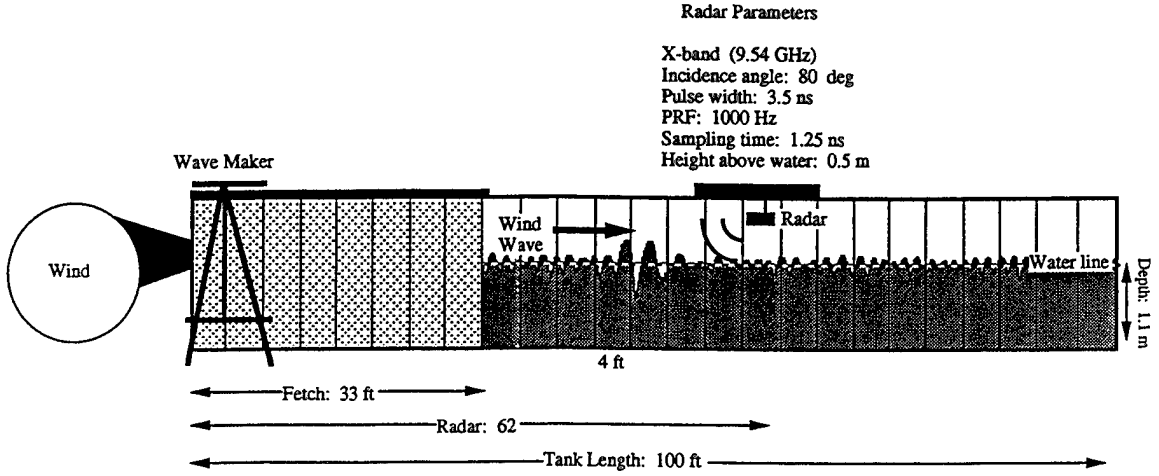


Fig. 3 Layout of the NRL deep water wave channel. The figure is a private communication (1994) from Dr. Farid Askari of NRL.

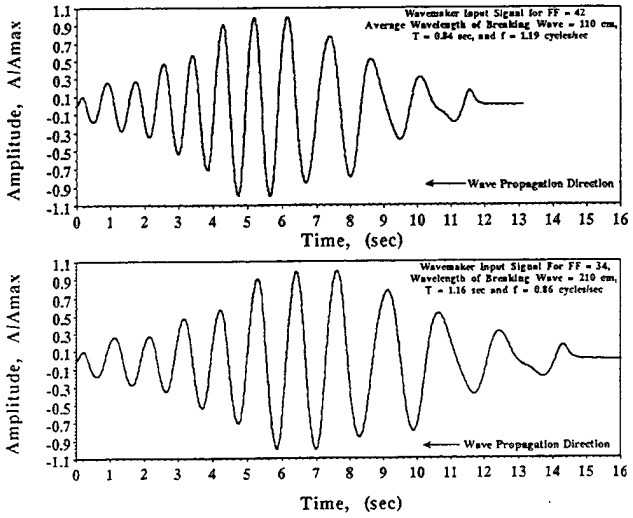


Fig. 4 Wave generator input signals for the gaussian wave packet employed in the NRL experiments. The two examples shown are for the packet conditions FF34 and 42.

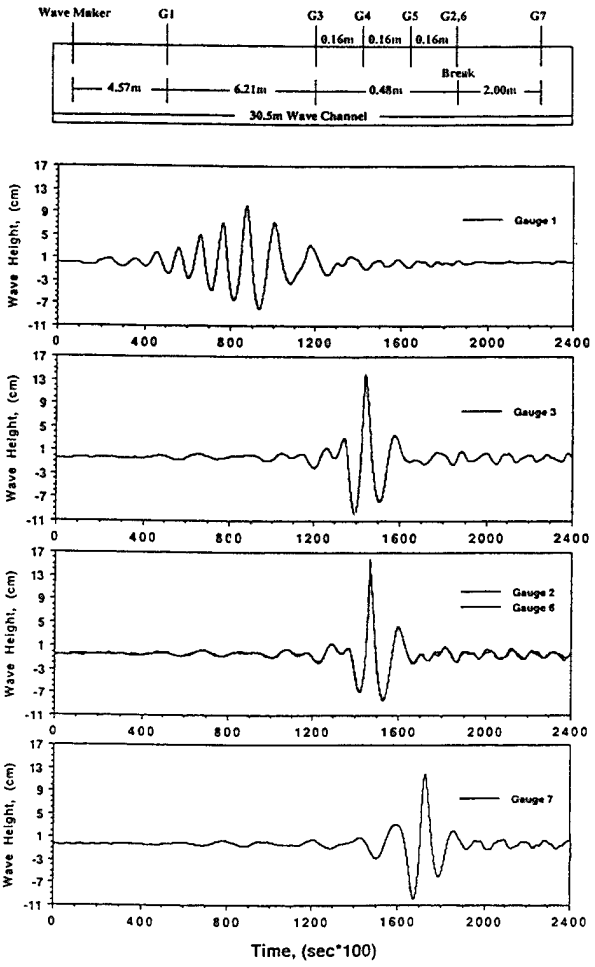


Fig. 5 (a) A line diagram of the relative locations of the wave gauges in the NRL wave channel. (b) Evolution of a wave packet measurement time history in the channel for initial wave paddle conditions which produce an incipient breaker. Frequency factor of the wave packet, FF34 (see Fig. 4 and Table 2).

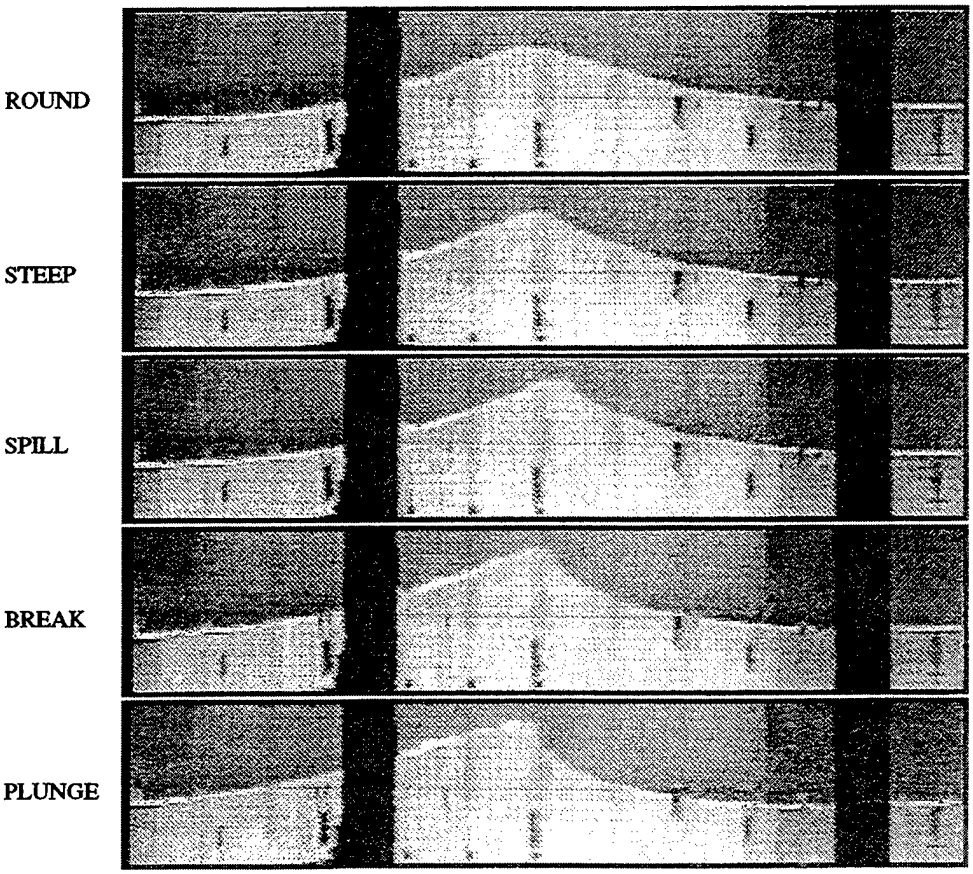
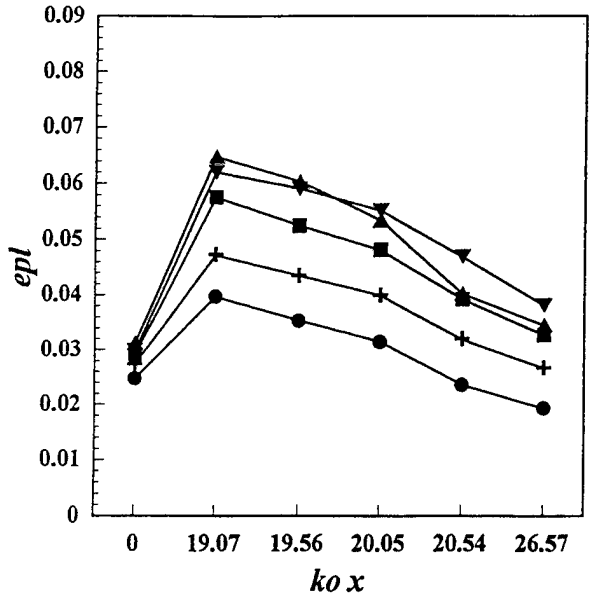
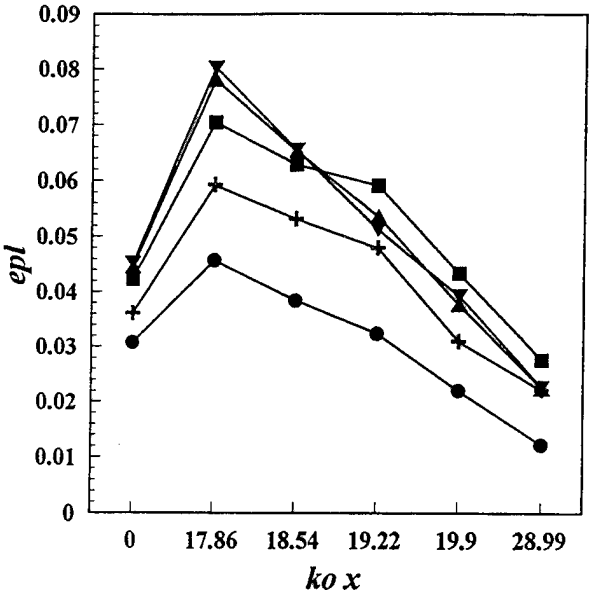


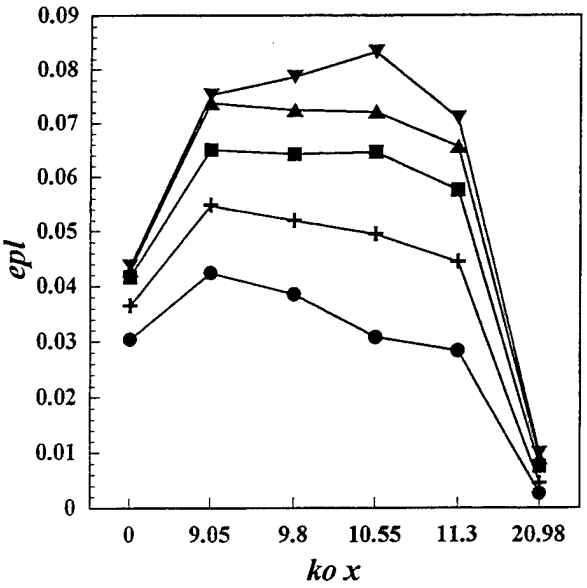
Fig. 6 Still video frames of a sequence of laboratory deep water wave profiles ranging in levels of steepness and breaking from round, to steep (near incipient), to spilling, to intermediate, and to plunging. Frequency of the wave packet, FF34.



(a) The frequency factor of the wave packet, FF34; and the wave breaking takes place at $k_o x$=20.54. Initial steepness, $a_o k_o$: ● 0.224, ✚ 0.238, ■ 0.247, ▲ 0.255, ▼0.248.

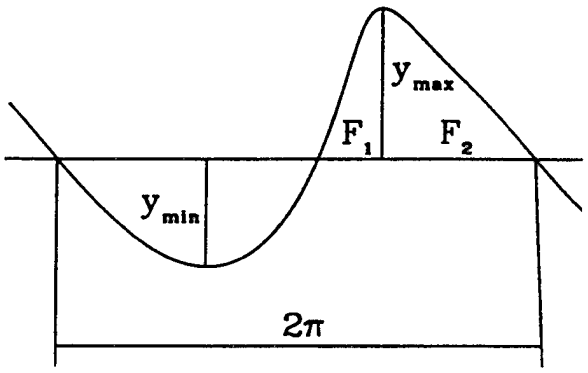


(b) Frequency factor, FF37, wave breaking at $k_o x$=19.90. Initial steepness, $a_o k_o$: ● 0.251, ✚ 0.273, ■ 0.294, ▲ 0.304, ▼ 0.306.



(c) Frequency factor, FF42; wave breaking at $k_o x$=11.30. Initial steepness, $a_o k_o$: ● 0.249, ✚ 0.279, ■ 0.294, ▲ 0.298, ▼ 0.302.

Fig. 7 Spatial evolution of the average potential energy per unit surface area, scaled by $2\ k^2$, with distance along the wave channel, scaled by the wavenumber k_o (at gauge G1).



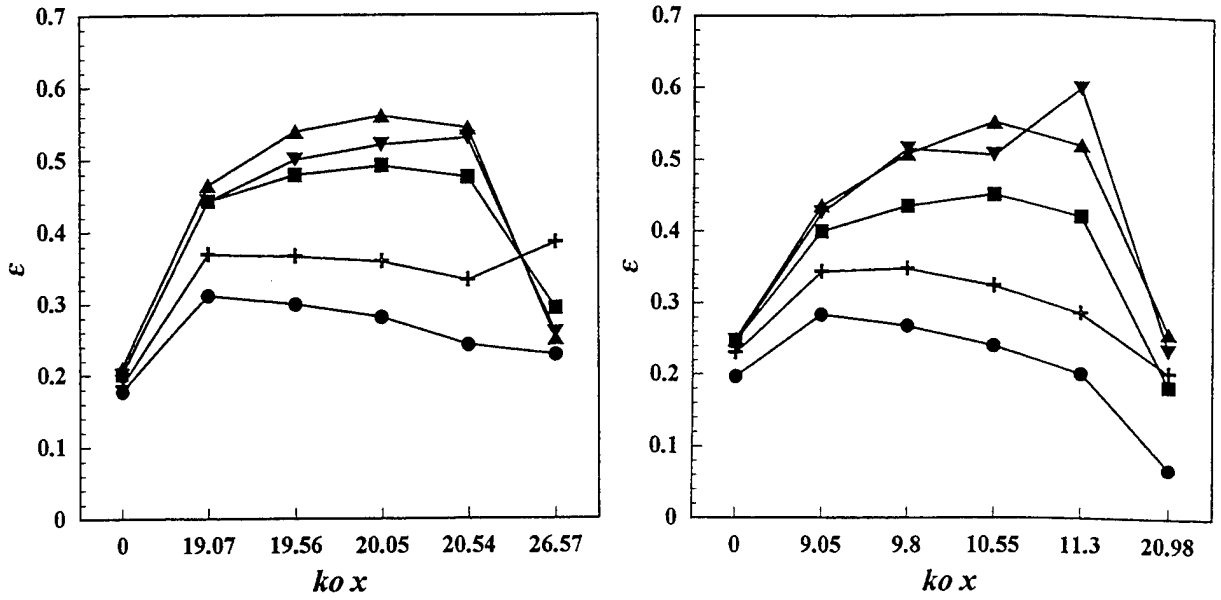
$$\mu = y_{max} / (y_{max} - y_{min})$$

$$\lambda = F_2 / F_1$$

$$\varepsilon = y_{max} / F_1$$

$$\delta = y_{max} / F_2$$

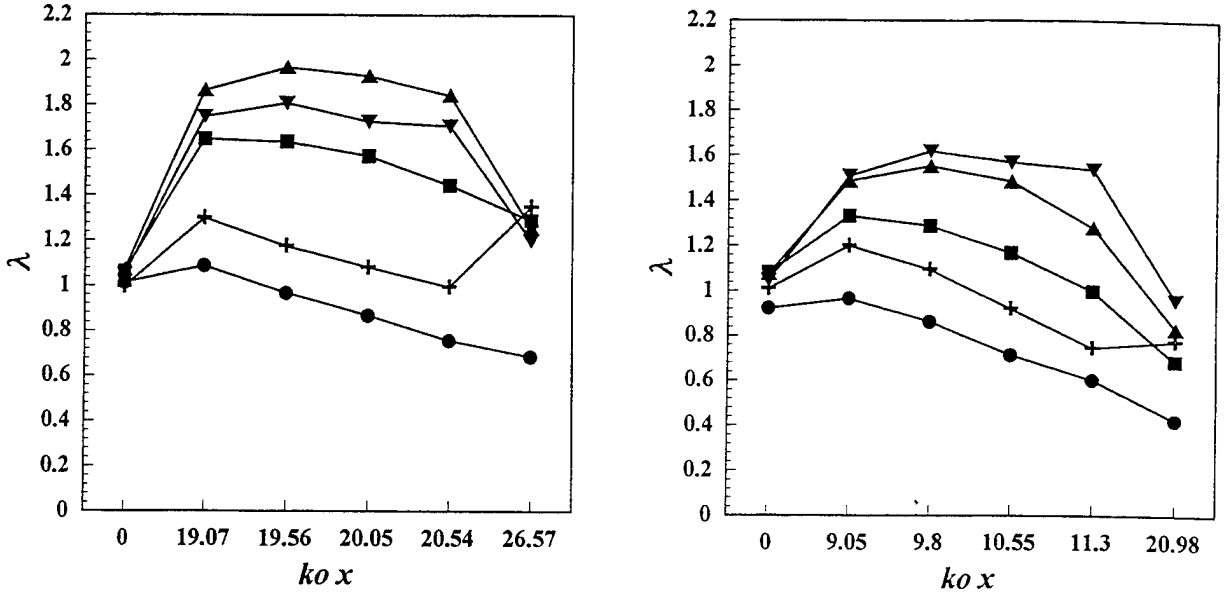
Fig. 8 Definition of the asymmetry and steepness properties of a steep, nonlinear wave. The wavelength is chosen equal to 2π for convenience in this sketch, in following the convention of Schultz, et al. (1994).



(a) Initial conditions as in Fig. 7(a).

(b) Initial conditions as in Fig. 7(c).

Fig. 9 Spatial evolution of the crest front steepness ε with distance along the wave channel.



(a) Initial conditions as in Fig. 7(a).

(b) Initial conditions as in Fig. 7(c).

Fig. 10 Spatial evolution of the vertical asymmetry λ with distance along the wave channel.

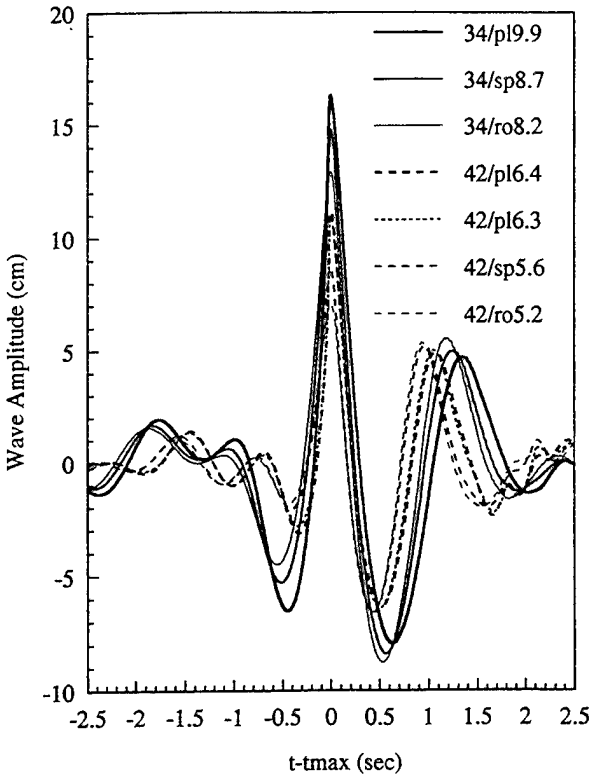


Fig. 11 The time history of the local wave elevation at gauge G2, the location of breaking.

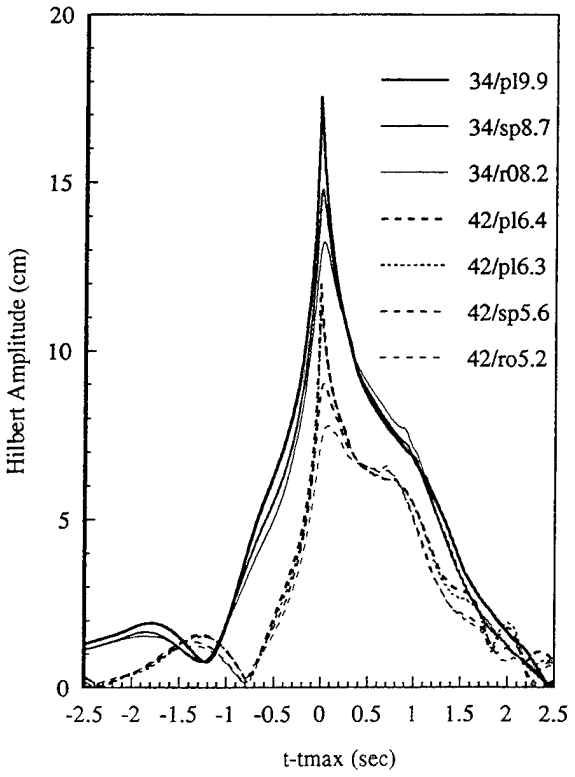


Fig. 12 The time history of the Hilbert amplitude at gauge G2.

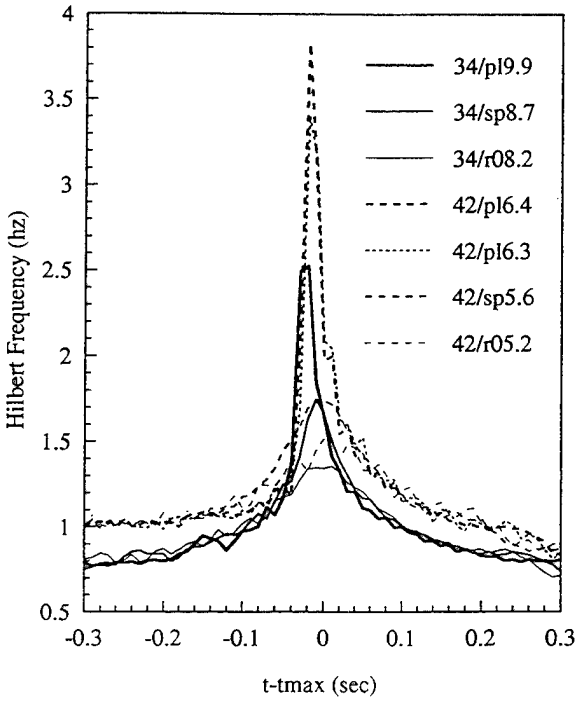


Fig. 13 The time history of the Hilbert frequency at gauge G2.

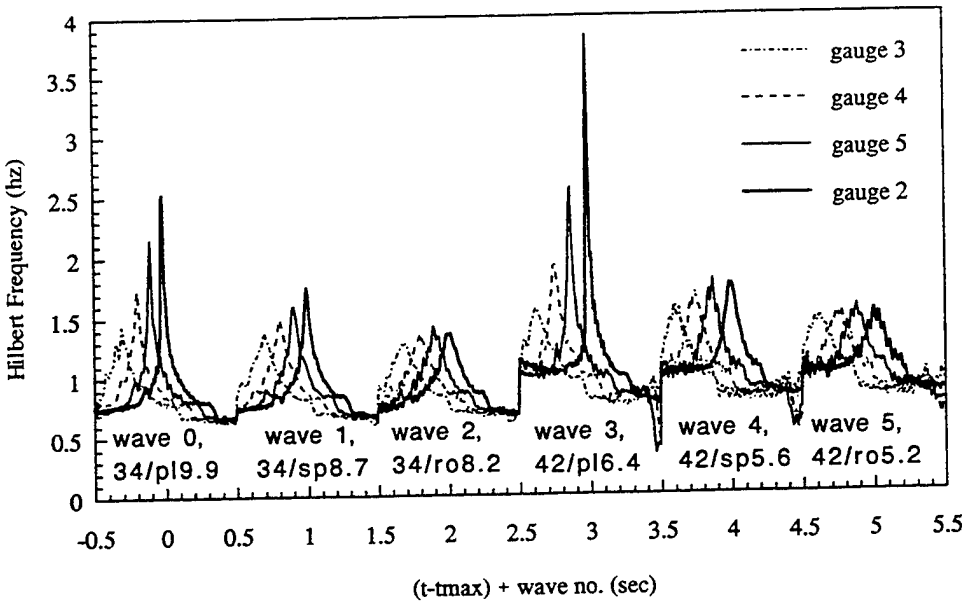


Fig. 14 The evolution of the Hilbert frequency at gauges G3, G4, G5 and G2. The gauge locations are given in Fig. 5(a).

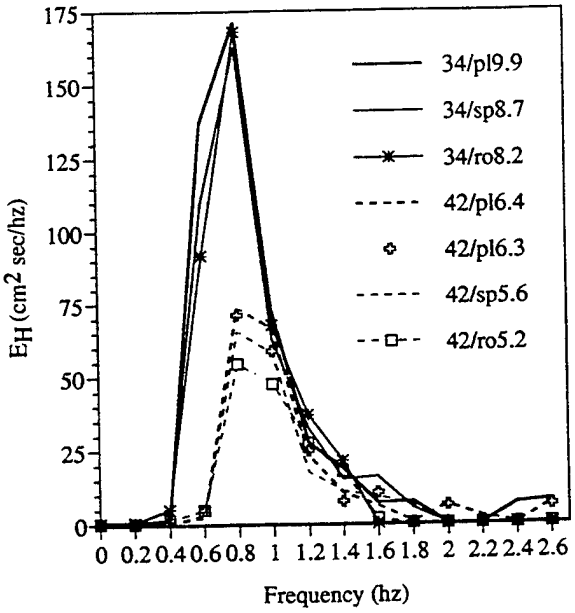


Fig. 15 The Hilbert energy density spectrum at gauge G2.

Table 2
Incipent Breaking of a Gaussian Wave Packet

FF	Initial Steepness $a_o k_o$	Horizontal Asymmetry μ	Crest Front Steepness ε	Potential Energy *epl*
34/8.7	0.238	0.736	0.333	0.0328
35/8.2	0.196	0.785	0.257	0.0287
36/7.7	0.230	0.766	0.362	0.0344
37/7.4	0.273	0.780	0.365	0.0309
38/6.8	0.231	0.752	0.293	0.0454
39/6.4	0.231	0.788	0.286	0.0296
40/6.2	0.237	0.786	0.260	0.0344
41/5.8	0.217	0.753	0.253	0.0322
42/5.6	0.279	0.802	0.282	0.0430
	Mean	0.772	0.299	0.0346
Expt[1]	0.23-0.26	--	0.28-0.35	--
Comp[2]	0.28	0.72	0.40	0.0382

1 From Rapp and Melville (1990), breaking wave packet (six measurements).
2 From Schultz, et al. (1994), initially steep, uniform wave train.

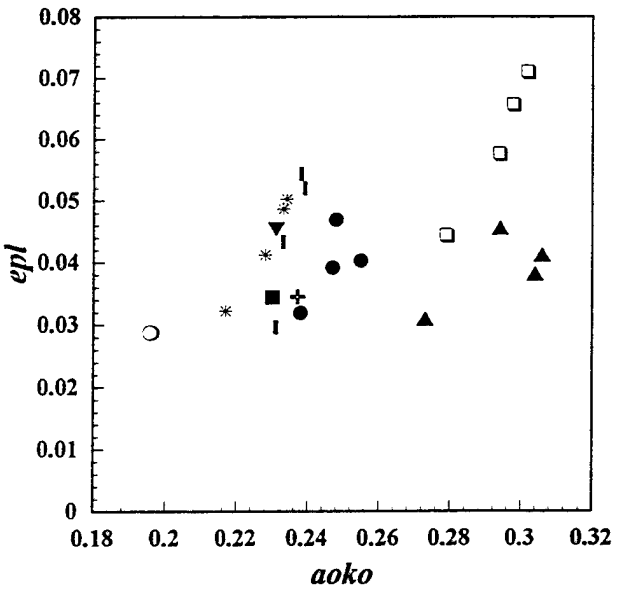


Fig. 16 The potential energy *epl* at breaking, measured during nine wave channel run series (see Table 2), as a function of the initial wave packet steepness. Legend for the data series: ● FF34, ○ FF35, ■ FF36, ▲ FF37, ▼ FF38, ❙ FF39, ✚ FF40, ✳ FF41, ❑ FF42.

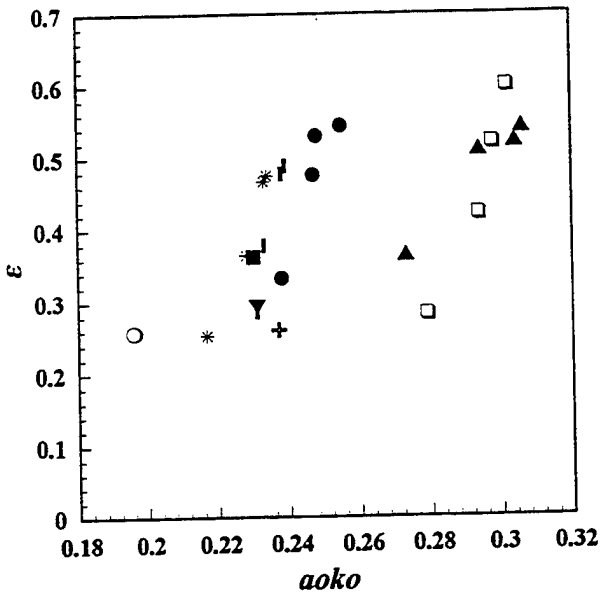


Fig. 17 The crest front steepness ε at breaking, measured during nine wave channel run series, as a function of the initial wave packet steepness. The legend for the data is the same as in Fig. 16.

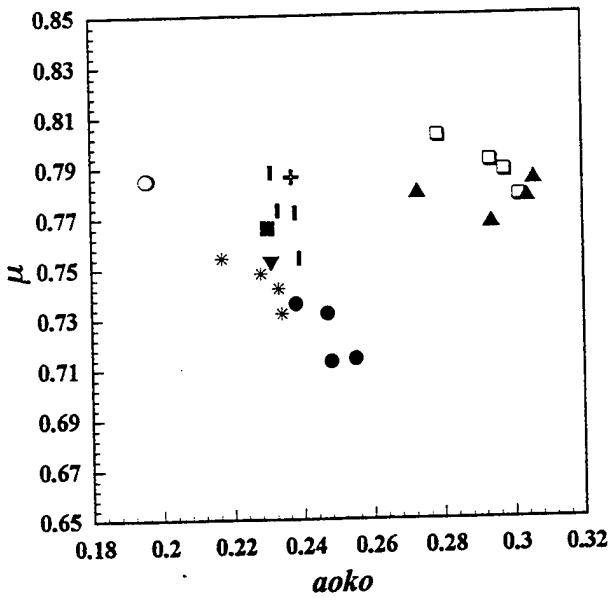


Fig. 18 The horizontal asymmetry μ at breaking, measured during nine wave channel run series, as a function of the initial wave packet steepness. The legend for the data is the same as in Fig. 16.

Table 3
Properties of Incipient Breaking Wave Packets

	ε	RMS
Experimental Mean	0.299	0.186
Experimental Standard Deviation (percent)	13.8	7.6
Prediction by Schultz, et al. (1994)	0.40	0.195
Prediction/Experiment Comparison (percent)	25	5

Physical Processes of the Local Air-Sea Interactions—Current Understanding and Outstanding Questions

Y. Toba (Tohoku University, Japan)

ABSTRACT

Overall similarity laws of wind waves as expressed by the 3/2-power law, and their possible applications to naval hydrodynamics are presented. For windsea generation area, the significant wave height can be given as a joint function of the wind speed and the significant wave period, and the steepness is also given as a function of the wave age. For sea areas where swells are present, these give the maximum values. Then as outstanding questions related, physical processes pertinent to the similarity laws, especially the friction velocity proportionality appearing in those expressions, are critically discussed from the point of view of experimental observations. Finally, also in relation to the similarity laws, a review is given on better parameterisations of breaking of wind waves, production of air bubbles and sea-water droplets by breaking waves.

INTRODUCTION

This paper is a kind of review with some new propositions. We do not intend to give a comprehensive review of the past works on physical processes at the air-sea interface, but focus, based on experimental observations, on local wind-windsea interaction processes at pure (swell free) windsea fields, in which overall similarity laws with the friction-velocity ($u*$) proportionality manifest themselves.

After a description of the overall similarity laws is given, their possible application to some aspects of the ocean wave statistics follows. Then a critical discussion is presented on outstanding questions with respect to elementary processes pertinent to this wind-windsea equilibrium. This overall situation with $u*$-proportionality does not seem to have been derived purely theoretically, and it is supposed that it is a result of strongly nonlinear self-adjustment processes of wind and windsea including wave breaking, with perturbations of waves, temporal local shear flows and turbulence with ordered motions, forming a continuum of the local air and water turbulent boundary layers.

In the last part are given recent studies in our group about parameterisations of breaking of wind waves, air-bubble entrainment in water, and sea-water droplet formation into the air.

OVERALL SIMILARITY LAWS OF WIND WAVES AND ITS POSSIBLE APPLICATION TO NAVAL HYDRODYNAMICS

Similarity Laws of Wind Waves – The 3/2-power Law

The wind waves have randomness spatially as well as temporarily. Nevertheless there are well-defined regularities statistically. Among them there are the 3/2-power law and the form of wind-wave energy spectra consistent with this law.

The 3/2-power law of wind waves as a macroscopic similarity law, which expresses the statistical state of windsea field in the generation area free of swells, is expressed by

$$H^* = BT^{*3/2},\ B = 0.062 \qquad (1)$$

where $H^* = gH_s/u*^2$, $T^* = gT_s/u*$, g is the acceleration of gravity, $u*$ the friction velocity of air, H_s the significant wave height, T_s the significant wave period, and B is an empirical constant (1). An alternative expression in a dimensional form is

$$H_s = B(gu*)^{1/2}T_s^{3/2} \qquad (2)$$

This form is interpreted as claiming that H_s and T_s cannot be independent of each other statistically, but there is a quasi-equilibrium state where H_s and T_s are strongly combined with each

other by the action of the wind which is represented by $u*$ (the concept of wind waves in quasi-equilibrium with the wind). Naturally the empirical constant B shows a fluctuation with the variation of the wind, within an order of +20% (2). Physical processes involved in this quasi-equilibrium between the wind and windsea with intrinsic fluctuation will be discussed in the next section.

The one-dimensional form of wind wave spectra in the high-frequency side, which is consistent with Eq. (1), and which is assumed to have a self-similarity form, is expressed by

$$\phi(\sigma) = \alpha_S g* u* \sigma^{-4}, \quad \sigma > \sigma_p \qquad (3)$$

where $\phi(\sigma)$ is the energy density, $g*$ the expanded acceleration of gravity to include the effect of surface tension, and σ is the peak angular frequency of wind waves (3, 4). In wind waves actually observed, we can see this form of spectra in some main part of the high frequency side called the equilibrium range. The value of the coefficient As seems to range between (6-12) x 10^{-2} (e.g., 4), and as will be discussed in the next section, fluctuates in response to the wind fluctuation.

Application to Naval Hydrodynamics – Wave Steepness, Joint Distribution of Wave Heights, Wave Periods and Winds

Equation (1) corresponds to a situation that, as a kind of equilibrium state of wind waves under the action of the wind, the steepness is statistically limited. This relation is expressed by

$$\frac{H_s k_s}{2\pi} = (2\pi)^{1/2} B \left(\frac{C_s}{u*}\right)^{-1/2} \left\{1 + 0.206 \left(\frac{C_s}{u*}\right)^{-1}\right\}^{2/3} \qquad (4)$$

where k_s is the significant wave-number and C_s is the phase speed of significant wave (5). The $C_s/u*$, the wave age of significant waves, in the second term appears as the consequence of an averaged local wind drift, of which the velocity is very large in the windward face of each individual waves and small or even of negative value on the lee side for small waves. Figure 1 shows Eq.(4) with some observation data. This relation can be used for conditions of growing windsea fields effectively free of swells.

The joint distribution of wave periods and amplitudes have been intensively studied (e.g., 6, 7). However, the 3/2-power law (1) claims that the distribution of wave heights should be better expressed by a combination of wave periods with $u*$, or the wind speed U_{10}, at least under growing windsea conditions, since Eq. (1) is conceptually expressed as

$$f(H_S, T_S, u*) = 0 \qquad (5)$$

In conditions where lower frequency swells superpose, this relation is to give the upper limit of H_S. If the wind suddenly becomes week, the data points come on a special region of the non-dimensional H^*–T^* diagram as expressed in Fig. 2, and Fig. 3 is a schematic explanation (cited from 8).

If we use the maximum wind speed values within, say, the past six hours, the upper limit of

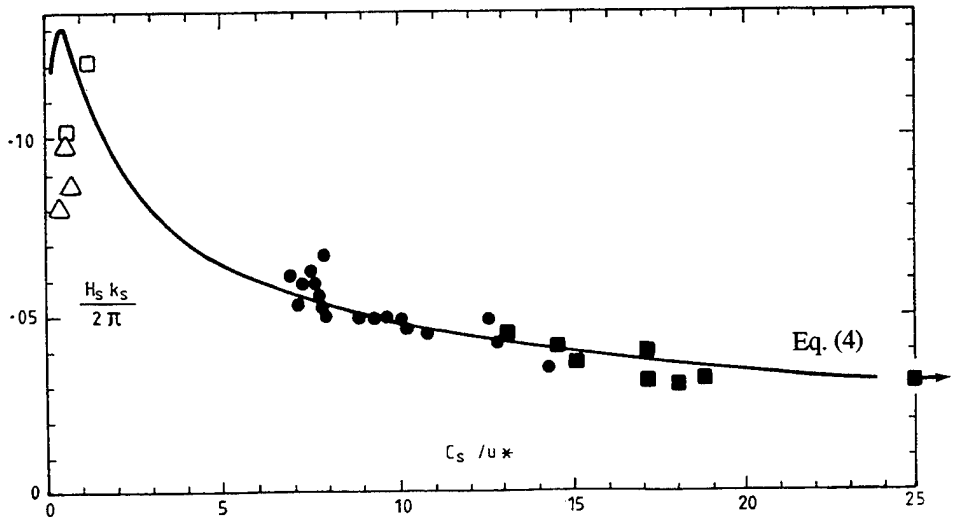


Fig. 1. Steepness of significant waves as a function of wave age. Closed symbols are from tower stations, and open from a laboratory. Cited from (5).

H_S will very well be given as a combined function of $u*$ and T_S. Figure 2 is thus considered as a better expression of combined probability density of H_S and T_S, incorporating $u*$.

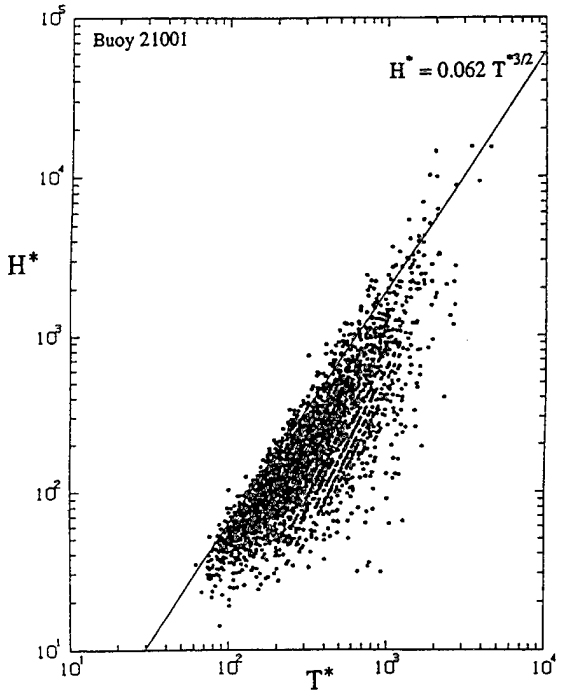


Fig. 2. The H^*–T^* diagram of data from an Ocean Data Buoy Station with Eq. (1). Cited from (8).

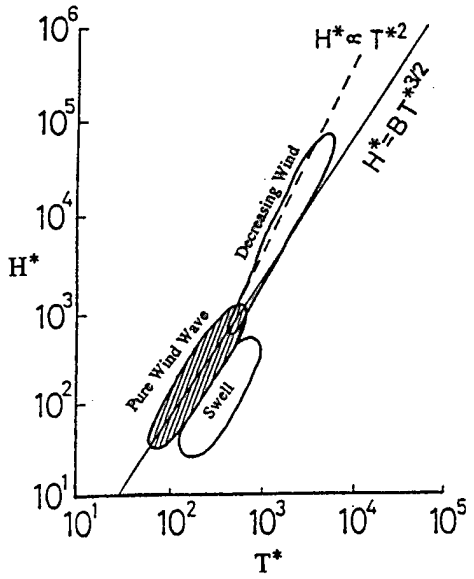


Fig. 3. Schematic picture of the scattering of data points on the H^*–T^* diagram (Fig. 2), according to three categories. Cited from (8).

OUTSTANDING QUESTIONS IN RELATION TO ELEMENTARY PROCESSES FOR THE WIND-WINDSEA EQUILIBRIUM

General Description of the Local Microphysical Processes

Microphysical processes at the air-water interface are characterized by the air-flow separation, reattachment of the high-shear layer of the air flow at the windward face of the waves causing a high tangential stress toward the crests, which in turn gives rise to the high vorticity region under the

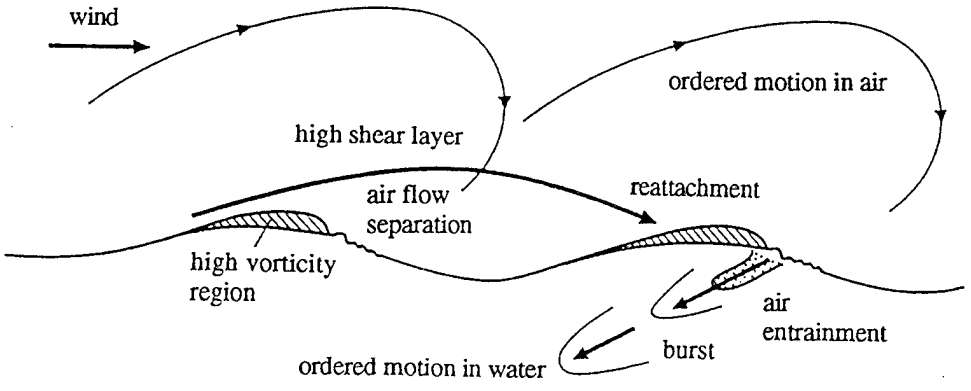


Fig. 4. A schematic picture of the microphysical processes at the air-water interface.

crest, and breaking of wind waves (e.g., 9, 10).

Wind waves are accompanied by ordered motions in water as well as in the air-flow above the wind waves (11, 12). Figure 4 summarize these microphysical processes at the air-water interface schematically.

Although this schematic picture is for young waves in a laboratory, the actual windsea field is of a continuous energy spectrum, which contains the high frequency part well expressed by this picture.

Energy Input and Dissipation by Wave Breaking

In the derivation of the $u*$-proportionality of Eq. (3), Phillips (4) invoked experimental observations by Plant (13) and Mitsuyasu and Honda (14), suggesting that the rate of spectral energy input from the wind S_w is proportional to $(u*/C)^2$. This expression also include $u*$ or the wave age. Mitsuyasu and Honda reported that this form was equally applicable to the case of water containing surfactant which made the wave surface smooth (14). In this case the effect of physical roughness of the water surface to the air flow is automatically included in the changed $u*$.

The aspects of the energy input from the air flow vary according to the wave situation. Mitsuyasu and Kusaba (15) reported by an experiment that the energy input to rough wave surfaces was 40-50 percent larger than the case of smooth wave surfaces, though the energy input for wave components was of the same order of magnitude. It seems to indicate that a larger value of energy entered to the rough surface causes much larger energy dissipation.

In fact, Hatori *et al.* (16), reported, by an experiment on the evolution of regular waves under the action of the wind, that the momentum retention rate, or the part of momentum which was retained as the momentum of regular wave component to the total momentum transferred from the wind to the water, reached about 50 percent. These values are much larger than the average value of the retention rate, which was reported to be at most 6 percent for very young wind waves (17). Hatori *et al.* (16) observed a few negative 50 percent values, and by visual observations they attributed these to dissipation due to wave breaking. A similar conclusion were also derived by independent experiments by Mitsuyasu (18) and Melville and Rapp (19).

In many theoretical works (e.g., 20, 21), energy input from the air to waves was estimated for air flows over component waves, though the air-flow separation and wave breaking are attributes of individual waves. In wave modeling studies (e.g., 22), the absolute values of energy dissipation was estimated as a residual between observed growth (not instantaneous, but steady) of waves and the sum of energy input and theoretical weakly nonlinear wave interactions. In these cases the absolute values of the three terms of source functions (input, wave interactions and dissipation) are assumed to be of the same order of magnitude with one another. However, the above-mentioned experimental observations suggest that the absolute values of the energy input and dissipation are much larger than usually assumed.

Also, as shown in Fig. 5, energy spectra for growing windsea follow very closely the form of Eq. (3), although the microscopic perturbations are conspicuous. In view of these, it is very plausible that all of the source function terms are much larger

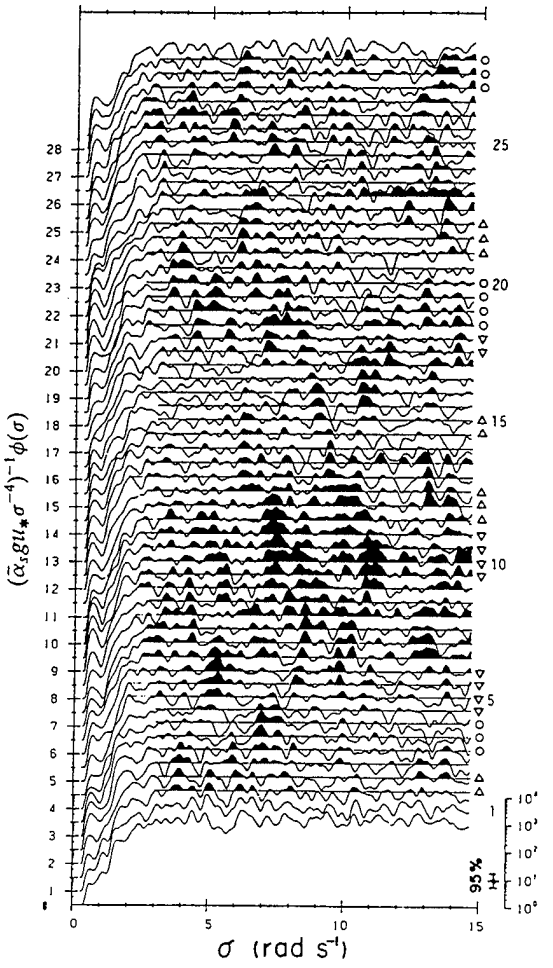


Fig. 5. An example of time series of wind-wave spectra obtained at an oceanographic tower station. The ordinate is the spectral density normalized by $\alpha_s g u* \sigma^{-4}$. The shaded ares represent local over-saturation. Cited from (34).

than usually assumed by wave modelers: much energy enters from the air to windsea, and much energy is being lost by wave breaking, and the wave interactions are much more effective by strongly non-linear processes. We will further consider this issue from a different point of view in the next section.

Origin of the $u*$-Proportionality

In Eq. (3) was given the windsea spectral form at the equilibrium range, which was consistent with Eq. (1). This also has the $u*$-proportionality. In the system of gravity wave interactions, Zakharov and Filonenko (23) showed that there is a wave spectral form proportional to σ^{-4}. However, it seems that there has been no purely theoretical derivation of the proportionality of the spectral level to $u*$.

The air and water boundary layers are coupled by approximate continuation of the vertical momentum flux which is represented by the air friction velocity $u*$, since the portion of the momentum retained as the wave momentum among the total momentum transferred from the air to the water is few percent (17). Thus $u*$ is the characteristic velocity for the coupled air and water boundary layers.

If we express turbulent velocities in the air and water boundary layers by u_a and u_w, route mean squares of these are proportional to $u*$ (24, 25, 26, 12). Wind waves are coupled with this $u*$, and the 3/2-power law Eq. (1) represents such a situation (27).

Equation (1) is also equivalent to the proportionality of the Stokes drift velocity u_0 of individual waves (with wave height H and period T) of windsea, to $u*$:

$$u_0 \ [= 2\pi^3 H^2/gT^3] = 2\pi^3 B^2 u* \qquad (6)$$

Combining the turbulent intensities of the air and water boundary layers, we have (12, 27),

$$u* \propto (\overline{u_a^2})^{1/2} \propto (\overline{u_w^2})^{1/2} \propto u*_w \propto u_0 \qquad (7)$$

Considering these observations, it is natural to suppose that the origin of the $u*$-proportionality is combined phenomena of the wave modulation, the action of the local stresses of the air flow over instantaneous individual-wave forms, and thus arisen very local shear flow at the individual wave surfaces. It is conjectured that the $u*$-proportionality is eventually performed by wave breaking either incipient or visible, related to these strongly nonlinear processes. This is the concept of breaking adjustment of wind waves (27).

Then, what determines the values of B in Eq. (1) or α_s in Eq. (3)? Or what does actually control the limit of wave steepness under the action of the wind? These questions are also issues to be solved.

To answer these questions, further elucidation of elementary processes which are relevant to the strongly nonlinear processes, including wind stress structure related to air flow separation, reattachment, the recirculation under the crest, wave modulation and wave breaking, in addition to purely water-wave processes such as capillary rollers, bores and crest instabilities as studied by Longuet-Higgins (28, 29). Close studies by experiment and theory on strongly nonlinear interactions including wave breaking, such as reported by Tulin and Li (30) will be an important direction.

If we approach these questions from microphysical aspects, we might immediately face a tall wall by virtue of complication of the phenomenon. And if we want to approach it from a more macroscopic aspects, we might have to retreat to the level of some integral constraint such as the continuity of momentum fluxes.

The approach from the integral constraint may still be important. For example, there are ordered motions in the turbulent boundary layers (e.g., 31, 11). However, in order to satisfy the constant flux of momentum, ordered motions themselves should perform a kind of self-adjustment so that the average velocity profile satisfies the logarithmic law.

Eqs. (1), (3), (4), (6) and (7) are all consistent with one another. However, which is the most fundamental for the quasi-equilibrium state between wind and windsea to be established? It is the outstanding question to be solved.

Perturbation in Wind-Windsea Equilibrium and C_D Variation

In relation to those questions, delicate fluctuation around these local equilibrium conditions occurs in processes for wind waves to adjust themselves to gustiness, as the fluctuation of α_s. At the same time, this delicate variation corresponds to a large fluctuation of the aerodynamic roughness parameter z_0 of the sea surface, which in turn corresponds to the variation of the drag coefficient C_D.

The same data with Fig. 5 can be used to discuss the detailed structure of wind stress variation (2, 32, 33). Figure 6 shows a time series obtained at the Shirahama Oceanographic Tower Station of Kyoto University (34). It is clearly seen that over- and under-saturation of the level of the equilibrium range of windsea occurs in relation to gustiness with

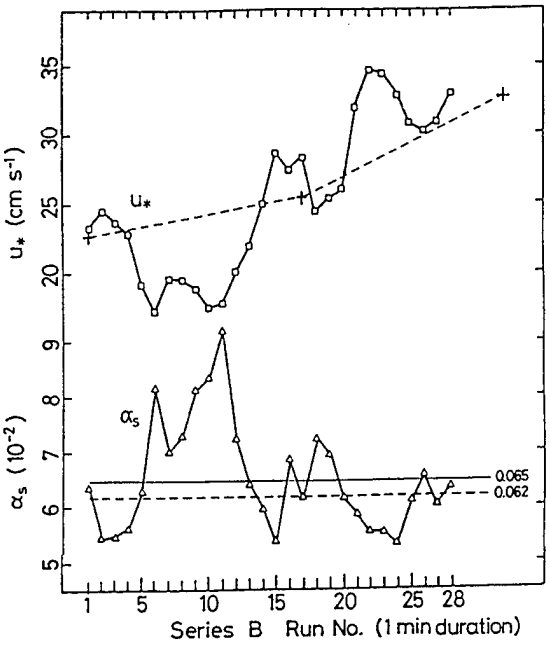


Fig. 6. An example showing that over- and under-saturation of the level of equilibrium rage of windsea occurs in relation to the short time scale $u*$-fluctuation. Cited from (34).

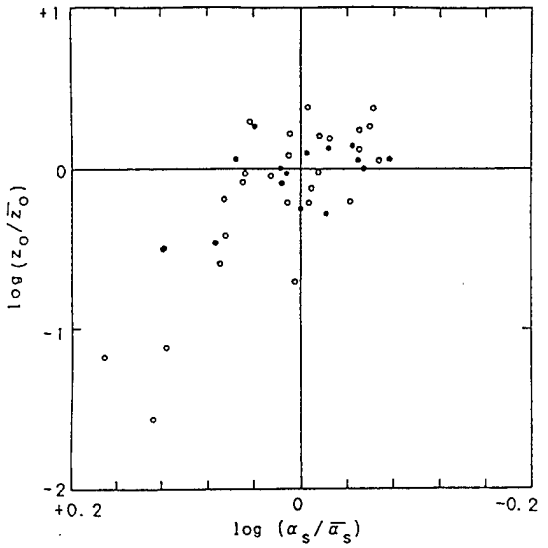


Fig. 7. Sea surface roughness parameter z_0 varies in concert with the over- and under-saturation. The original data are same with those of Fig. 6. Cited from (33).

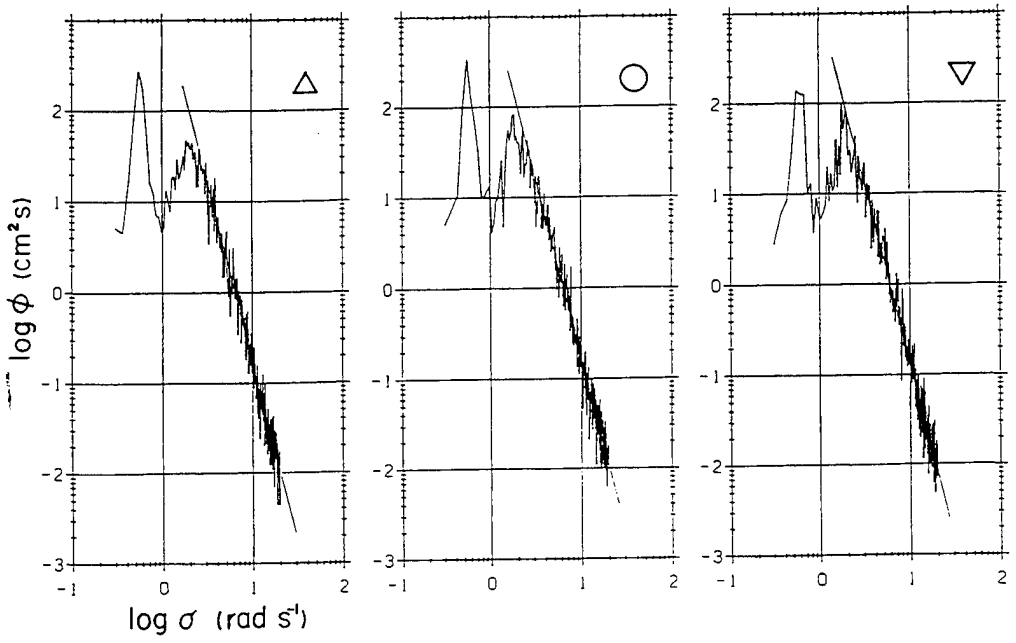


Fig. 8. Ensemble averages of ten of the raw spectra marked by triangles (increasing winds), circles (constant winds), and inverse triangles (decreasing winds), respectively, in Fig. 6. See that the shape of the spectral peak is more round in the increasing-wind case, and sharp in the decreasing-wind case. Cited from (34).

short-time scale $u*$ fluctuation. Figure 7 (33) shows that z_0 varies in concert with this over- and under-saturation.

As a physical interpretation, we can conjecture as follows. First there is a strong constraint for the water waves to satisfy, such as the spectral form proportional to σ^{-4}. As stated above, although there is a $u*$ -proportionality for a steady state, the level of wind-wave spectra cannot follow gustiness instantaneously, since the total energy of windsea field is already large. Thus, if the wind has increased, the energy level of windsea becomes under-saturation, and the energy near the spectral peak flows down to the higher frequency part (Fig. 8), and at the same time, the steepness of waves at the very high frequency part becomes larger to absorb energy from the air more effectively, and feed it to the equilibrium-range waves. This situation corresponds to increased values of z_0. If the wind becomes weak, the spectral level at the equilibrium range becomes over-saturation, the energy in the equilibrium range near the spectral peak goes up to the peak wave for the spectral peak to become steeper (Fig. 8), and at the very high frequency range capillary waves diminish and the water surface becomes more smooth, in order for the energy at the equilibrium range to go up to the very high frequency region and to go to dissipation. The latter effect makes z_0 of the drag coefficient small for this negative gust. This situation is illustrated in Fig. 9.

It is thus interpreted that the fluctuation of z_0, which is related to gustiness, is directly connected with the question of the origin of the $u*$-proportionality, possibly representing the mechanisms for the $u*$-proportionality to be kept more effectively.

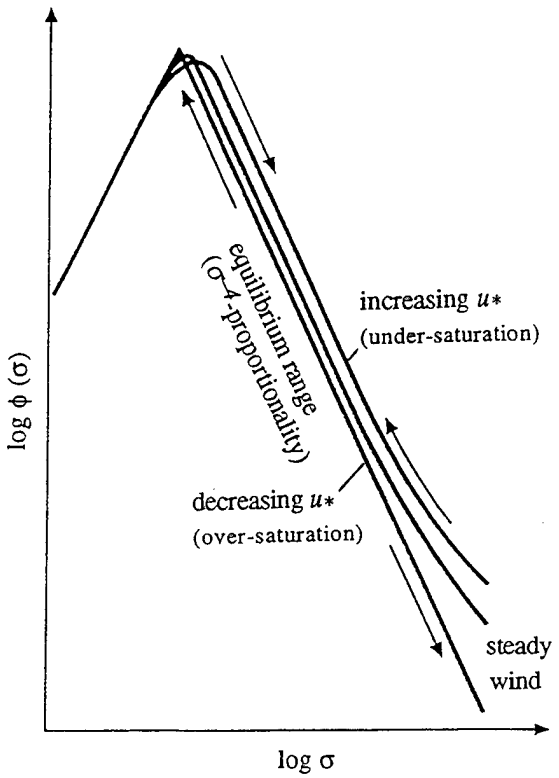


Fig. 9. A schematic picture of the response of windsea spectra to gustiness. Arrows indicate the direction of energy transfer.

PARAMETERISATION OF BREAKING WAVES, BUBBLE AND DROPLET FORMATION

Reynolds Number for Breaking Windsea

We may consider several forms of parameter which may represent the overall conditions for breaking of windsea. One of them is expressed by

$$R_B = u*L_s/\upsilon = u*^2/\upsilon\sigma_p \qquad (8)$$

where υ is the kinematic viscosity of the air, σ_p is the angular frequency of the peak of the windsea spectra (35). The parameter of Eq. (8) can be considered as a kind of Reynolds number, if we consider $L_s = 2\pi u*/\sigma_p$ as a length scale at the surface of waves, or the distance for a water particle moving with a speed of $u*$ within the significant wave period.

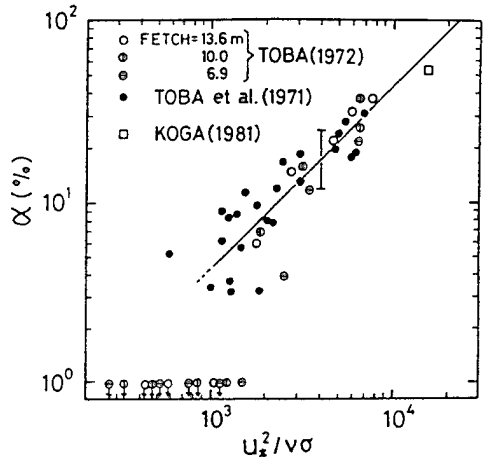


Fig. 10. Rate of breaking crests among individual waves traveling through a fixed point, A, plotted against R_B. The straight line is a 45 degree line. Cited from (35).

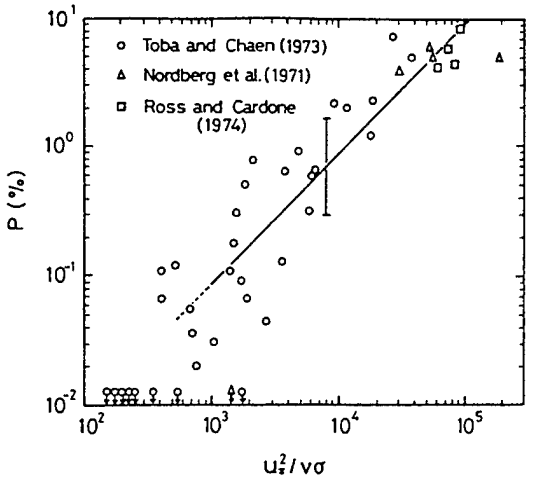


Fig. 11. Whitecap coverage as a function of R_B. The straight line is a 45 degree line. Cited from (35).

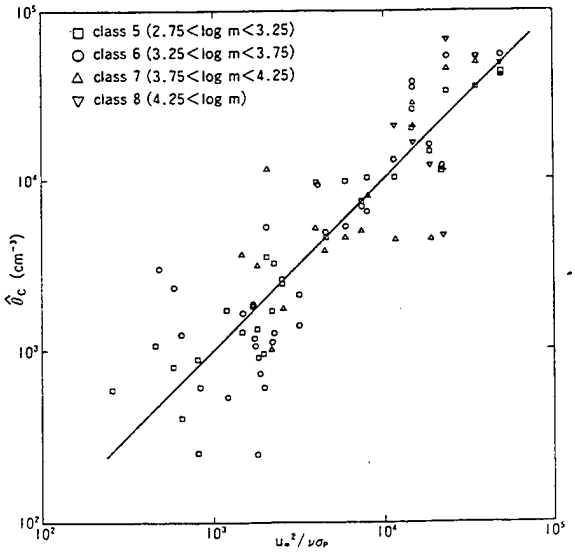


Fig. 12. A normalized concentration of sea water droplets plotted against R_B. The straight line is a 45 degree line. Cited from (36).

This number was proposed as a useful parameter representing overall conditions of the air-sea boundary processes. It can scale percentage α of individual wind-wave crests which are passing at a fixed point of the sea surface (say at the site of a wave gauge) with entraining air bubbles. Figure 10 shows that data in a wind-wave tank and from the sea collapse very well by this number. Figure 11 shows that this number can also scale well the percentage of whitecap coverage. Figure 12 (36) shows that the concentration of sea water droplets in the air boundary layer above the windsea can also be scaled well by this number.

In Eq. (8) σ_p is the measure representing the wind-wave conditions, and so in cases of sea conditions where dominant swells are present, we should use σ_p for the wind-wave part of the wave spectrum.

The value of α is one-dimensional wave breaking conditions by definition. However, if we assume similarity in two dimensional individual wave forms, it is easily understood that the α value is converted to the whitecap coverage value which is a two dimensional matter. Furthermore, looking at Fig. 12, it is at least expected that this number might also represent, to some extent, the three-dimensional conditions of breaking of windsea fields, though this issue has not been tested.

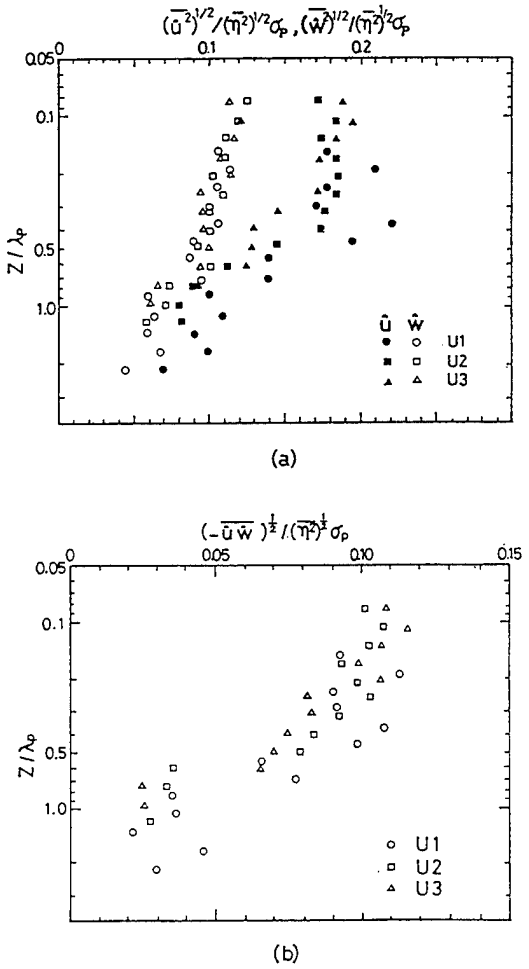


Fig. 13. Normalized vertical distribution of turbulent intensities (a) and Reynolds stress (b) under laboratory wind waves. Cited from (12).

A similar form of parameter as Eq. (8) is used to scale the average time between bursts in turbulent channel flows (37). In this case the boundary is a solid wall, and the phenomena are quite different. However, since wave breaking is a downward burst (10), the similarity seems interesting.

It may be worthwhile to note that a useful expression of the production rate of sea water droplets at the windsea surface, and the concentration of these droplets near the sea surface, are available (36).

Approximate Limit of the Depth of Bubble Entrainment

In Yoshikawa *et al.* (12), vertical distributions of turbulent intensities and Reynolds stress under laboratory wind waves were normalized by using σ_p, standard deviation of the surface displacement $\overline{\eta^2}$, and the wave length of the spectral peak wave λ_p, as shown in Fig. 13.

Considering that the steepness of wind waves is a function of the wave age as expressed by Eq. (4), if we normalize the ordinate of Fig. 13 by using H_s, or the significant wave height, instead of λ_p, then we reach a conclusion that a limit of the depth where downward burst reaches is about $5H_s$. This value is very well coincident with a flow visualization study of forced convection accompanying wind waves (Photo 2 of 38), and with the depth of bubble clouds measured by an acoustic technique by Thorpe (39).

ACKNOWLEDGMENTS

The author expresses many thanks to Professor Marshall P. Tulin who gave a chance for the author to present this paper at the Twentieth Symposium on Naval Hydrodynamics at Santa Barbara. He also acknowledge collaboration of members of the Physical Oceanography Group, Tohoku University, especially Dr. Naoto Ebuchi and Miss Shizue Goto in preparation of this paper.

REFERENCES

1. Toba, Y., "Local Balance in the Air-Sea Boundary Processes I. On the Growth Process of Wind Waves," Journal of the Oceanographical Society of Japan, Vol. 28, 1972, pp. 109-121.

2. Toba, Y., Iida, N., Kawamura, H., Ebuchi, N., and Jones, I.S.F., "The Wave Dependence of Sea-Surface Wind Stress," Journal of Physical Oceanography, Vol. 20, 1991, pp. 705-721.

3. Toba, Y., "Local Balance of the Air-Sea Boundary Processes III. On the Growth Process of Wind Waves," Journal of the Oceanographical Society of Japan, Vol. 29, 1973, pp. 209-220.

4. Phillips, O.M., "Spectral and Statistical Properties of the Equilibrium Range in Wind-Generated Gravity Waves," Journal of Fluid Mechanics, Vol. 156, 1985, PP. 505-531.

5. Bailey, R.J., Jones, I.S.F., and Toba, Y., "Sea-Surface Roughness Length Fluctuating in Concert with Wind and Waves," Journal of the Oceanographical Society of Japan, Vol. 47, 1991, pp. 63-79.

6. Goda, Y., "The Observed Joint Distribution of Periods and Heights of Sea Waves," Proceedings of the 16th International Conference on Coastal Engineering, Sydney, Australia, 1978, pp. 227-246.

7. Longuet-Higgins, M.S., "On the Joint Distribution of Wave Periods and Amplitudes in a Random Wave Field," Proceedings of the Royal Society of London, A, Vol. 389, 1983, pp. 241-258.

8. Ebuchi, N., Toba, Y., and Kawamura, H., "Statistical Study on the Local Equilibrium between Wind and Wind Waves by Using Data from Ocean Data Buoy Stations," Journal of Oceanography, Vol. 48, 1922, pp. 77-92.

9. Toba, Y., "Wind Waves and Turbulence," Recent Studies on Turbulent Phenomena, Tatsumi, T., Maruo, H. and Takami, H., eds., Association for Science Documents Information, Tokyo, 1985, pp. 277-296.

10. Ebuchi, N., Kawamura, H., and Toba, Y., "Bursting Phenomena in the Turbulent Boundary Layer Beneath the Laboratory Wind-Wave Surface," Natural Physical Sources of Underwater Sound, Kerman, B.R., ed., Kluwer Academic Publishers, The Netherlands, 1993, pp. 263-276.

11. Kawamura, H., and Toba, Y., "Ordered Motion in the Turbulent Boundary Layer over Wind Waves," Journal of Fluid Mechanics, Vol.197, 1988, pp. 105-138.

12. Yoshikawa, I., Kawamura, H., Okuda, K., and Toba, Y., "Turbulent Structure in Water Under Laboratory Wind Waves," Journal of the Oceanographical Society of Japan, Vol. 44, 1988, pp. 143-156.

13. Plant, W.J., "A Relationship Between Wind Stress and Wave Slope," Journal of Geophysical Research, Vol. 87, 1982, pp. 1961-1967.

14. Mitsuyasu, M., and Honda, T., "Wind-Induced Growth of Water Waves," Journal of Fluid Mechanics, Vol.123, 1982, pp. 425-442.

15. Mitsuyasu, M., and Kusaba, T., "On the Relation Between the Growth Rate of Water Waves and Wind Speed," Journal of the Oceanographical Society of Japan, Vol. 44, 1988, pp. 136-142.

16. Hatori, M., Tokuda, M., and Toba, Y., "Experimental Study on Strong Interaction Between Regular Waves and Wind Waves I," Journal of the Oceanographical Society of Japan, Vol. 37, 1981, pp. 111-119.

17. Toba, Y., "Stochastic Form of the Growth of Wind Waves in a Single-Parameter Representation with Physical Implications," Journal of Physical Oceanography, Vol. 8, 1978, pp. 494-507.

18. Mitsuyasu, H., "The Momentum Transfer from Wind to Waves," Journal of Geophysical Research, Vol. 90, No. C2, pp. 3343-3345.

19. Melville, W.K., and Rapp, R.J., "Momentum Flux in Breaking Waves," Nature, Vol. 317, 1985, pp. 514-576.

20. Janssen, P.A.E.M., "Quasi-Linear Theory of Wind-Wave Generation Applied to Wave Forecasting," Journal of Physical Oceanography, Vol. 21, No. 11, Nov. 1991, pp. 1631-1642.

21. Chalikov, D., and Makin, V. "Models of the Wave Boundary Layer," Boundary-Layer Meteorology, Vol. 56, pp.83-99.

22. The SWAMP Group, ed., Ocean Wave Modeling, Plenum Press, New York, 1985, pp.1-153.

23. Zakharov, V.E., and Filonenko, N.N., "Energy Spectrum for Stochastic Oscillations of the Surface of a Liquid," Dokaldy Akademii Nauk SSSR, Vol. 170, 1291-1295.

24. Jones, I.S.F., and Kenney, B.C., "The Scaling of Velocity Fluctuations in the Surface Mixed Layer," Journal of Geophysical Research, Vol. 82, 1977, pp. 1392-1396.

25. Jones, I.S.F. "Turbulence Below Wind Waves," The Ocean Surface, Toba, Y., and Mitsuyasu, M., eds., D. Reidel, Doldrecht, 1985, pp. 437-442.

26. Mitsuyasu, H., and Kusaba,T., "Wind Waves and Wind-Generated Turbulence in the Water," The Ocean Surface, Toba, Y., and Mitsuyasu, H., eds., D. Reidel, Doldrecht, 1985, pp. 389-394.

27. Toba, Y., "Similarity Laws of the Wind Wave and the Coupling Process of the Air and Water Turbulent Boundary Layers," Fluid Dynamics Research, Vol. 2, 1988, pp. 263-279.

28. Longuet-Higgins, M.S., "Capillary Rollers and Bores", Journal of Fluid Mechanics, Vol. 240, 1992, pp. 659-679.

29. Longuet-Higgins, M.S., and Cleaver, R.P., "Crest Instabilities of Gravity Waves Part 1. The Almost Highest Wave," Journal of Fluid Mechanics, Vol. 258, 1994, pp. 115-129.

30. Tulin, M.P., and Li, J.J., "A Mechanism for Wave Deformation and Breaking Intermediated by Resonant Side-Bands," Breaking Waves, Banner, M.L., and Grimshaw, R.H.J, eds., 1992, Springer-Verlag, Berlin Heidelberg, pp. 251-256.

31. Kline, S.J., Reynolds, W.C., Schraup, F.A., and Runstadler, P.W., "The Structures of Turbulent Boundary Layers," Journal of Fluid Mechanics, Vol. 30, 1967, pp. 741-773.

32. Toba, Y., and Ebuchi, N., "Sea-Surface Roughness Length Fluctuating in Concert with Wind and Waves," Journal of the Oceanographical Society of Japan, Vol. 47, 1991, pp. 63-79.

33. Toba, Y., Jones, I.S.F., Ebuchi, N., and Kawamura, H., "The Role of Gustiness in Determining the Aerodynamic Roughness of the Sea Surface." Proceedings of a Symposium on the Air-Sea Interface, Marseille, France, June 1993, In Press.

34. Toba, Y., Okada, K., and Jones, I.S.F., "The Response of Wind-Wave Spectra to Changing Winds. Part I: Increasing Winds," Journal of Physical Oceanography, Vol.18, 1988, pp. 1231-1240.

35. Toba, Y., and Koga, M., "A Parameter Describing Overall Conditions of Wave Breaking, Whitecapping, Sea-Spray Production and Wind Stress", Ocean Whitecaps and Their Roll in Air-Sea Exchange Processes, Monahan, E.C. and MacNiocaill, G., eds., Galway University Press, Galway, 1986, pp. 37-47.

36. Iida, N., Toba, Y., and Chaen, M., "A New Expression for the Production Rate of Sea Water Droplets on the Sea Surface," Journal of Oceanography, Vol. 48, 1992, pp. 439-460.

37. Luchik, T.S., and Tiederman, W.G., "Timescale and Structure of Ejections and Bursts in Turbulent Channel Flows," Journal of Fluid Mechanics, Vol. 174, 1987, pp. 529-552.

38. Toba, Y., Tokuda, M., Okuda, K., and Kawai, S., "Forced Convection Accompanying Wind Waves," Journal of the Oceanographical Society of Japan, Vol. 31, 1975, pp.192-198.

39. Thorpe, S.A., "Bubble Clouds and the Dynamics of the Upper Ocean," Quarterly Journal of the Royal Meteorological Society, Vol. 118, No. 503, Jan. 1992, pp. 1-22.

Attached Vortices in Free-Surface Turbulence

S. Kumar, R. Gupta, S. Banerjee
(University of California-Santa Barbara, USA)

ABSTRACT

The characteristics of coherent structures on the free surface of a channel flow are discussed. The term coherent is used to define organized motions on the free surface that persist in time. Experiments were conducted in a horizontal channel of cross-section 32 cm. x 10 cm and 450 cm long in the Reynolds number range of 1800 to 9000, where the Reynolds number was calculated based on the depth of flow and the free-surface velocity. The results so far indicate that the persistent structures on the free surface can be classified as upwellings, downdrafts and attached vortices. Upwellings and downdrafts are related to the bursts originating in the sheared region at the channel bottom and the vortices are generated at the edges of the upwellings. The population density and the persistence time of the various structures were measured for different flow conditions. The resulting data seems to favor mixed scaling for normalization Direct numerical simulations of the channel flow at a Reynolds number of about 2500 suggests that the high shear rate at the edges of the upwellings on the surface cause instabilities which grow into vortices. The most interesting structures from the viewpoint of free - surface turbulence, decaying far from the region in which it is generated, are the vortices. Direct numerical simulations indicate that they form a quasi-two-dimensional region near the free surface with interaction and pairing that lead to upcascading of energy at lower wave numbers.

NOMENCLATURE

d = flow depth
U = free surface speed
Re = Reynolds Number
t_p = weighted avg. persistence time
t_i = persistence time observed
N_i = number of vortices having persistence t_i.

INTRODUCTION

Hydrodynamics at a gas-liquid interface (free surface) is important in many engineering applications and in geophysics. The transfer of gases , for example, oxygen and carbon dioxide at the surfaces of water bodies is of obvious significance to environmental engineering related to oxidation ponds, reaeration of rivers etc. It is important to understand the nature of turbulence near the free surface to get a correct estimate of the mass and heat transfer across the interface. The mass transfer due to turbulence generated just below the free surface on the liquid side of the interface in a channel flow was discussed by [1]. Turbulence measurement close to the free surface has been carried out by [2], [3] and by [4] amongst others. This paper will be confined to the discussion of the macro characteristics of the organized structures at the free surface in a channel flow *viz.*, their size, population and persistence in time. A major motivation for this work is to understand what happens to turbulence near a free - surface. We are particularly interested in features that may arise from interactions with large subsurface structures, such as upwellings. The work has many possible implications. For example it may, amongst other applications, shed light on the origin of the large spiral structures seen in the oceans (size of the order of tens of kilometers) as observed in satellite photographs. These have also been termed 'modons' by geophysicists.

EXPERIMENTAL SETUP

Figure - 1 shows a sketch of the experimental setup. The arrangement consists of a horizontal channel 450 cm long with a cross section of 32 cm x 10 cm, and a controlled traverse

with a camera for taking time exposed photographs. The measurements were taken in the central 10 cm of the channel to minimize edge effects. The channel is made of steel plate 2 mm thick with a glass section of 50 cm for flow visualization from the sides. The flow characteristics in the channel are well documented in [5]. The results reported here are from processing the pictures taken of the free surface from the top. We are in the process of documenting the simultaneous visualization of the flow from the top and from the side, so as to get more information on the connection between the dynamics in the boundary layer close to the channel wall and the coherent structures seen at the free surface. Some work in this regard has been reported earlier by [4].

The free surface flow was visualized by sprinkling hollow glass microballoons on the surface and taking time exposed still photographs by a camera moving at a speed close to the speed of the free surface. The camera used was a Nikon 2000 with a 60 mm macrolens. This camera could take pictures at a maximum rate of 2.5 frames/ sec i.e., the minimum time interval between two consecutive pictures was 0.4 seconds. The direction of movement of the particles was determined by structuring the illuminating light. The field of view was illuminated by a constant light source (an ordinary light bulb of 50 watts) with a flashlight (Sunpack 383) triggering just before the camera shutter closed. The result was a streakline with a bright dot at its head. The camera shutter operation and the flashlight were synchronized by in-house -fabricated TTL electronic circuitry.

The light sources, camera and the control circuit were mounted on a belt driven traverse (Daedal 204000) which has a repeatability of 0.1 mm. The driving motor for the traverse was Compumotor S135 controlled by a Compumotor driver and 4 axis Compumotor indexer (AT6400) in an IBM PC.

The experiments were performed for different flow depths keeping the Reynolds number of the flow, based on flow depth and the free surface speed, approximately constant at 2800. The free surface speed was computed by placing a few styrofoam beads on the free surface and taking a time exposed picture (1/4 ~ 1/8 seconds) when these beads passed through the field of view of the stationary camera. The free surface velocity was computed from these streaklines.

The visualization was effected by sprinkling microballoons on the surface and following them at approximately the same speed as the free surface. Pictures were taken starting a distance of about 60 times the water depth, from the channel entrance, till about 1m before the end of the channel. This gave a clear distance of about 2 to 2.5m for taking pictures. The channel bottom was painted black to aid in visualizing the microballoons on the surface.

Figure 2 shows sample pictures of the free surface visualization with glass microballoons. The particle streaks in each frame correspond to a time of 0.4. The bright dot on the head of the streaks was placed 0.04 seconds before the end of the streak. The camera shutter was kept open for 0.4 seconds and the rewinding motor took another 0.4 seconds to advance the film. Hence, the time interval between two consecutive pictures was 0.4 seconds. These pictures also serve to illustrate the various kinds of coherent structures found on the free surface. Referring to Figure 2a, attached vortices are shown by closed streamlines and upwellings are seen as the relatively particle - free areas. The particles, as shown by the streaklines, flow into these areas from one side and flow out of these at the opposite side. These are the classical "splat - like" fluid packets (also called surface renewal structures [3]) which is formed due to the ejections in the boundary layer. These energetic ejections reach the free - surface, move with it for some time, and then move back into the bulk of the fluid flow. Also, to be noticed in the right hand bottom corner of Figure 2b is the region in the picture from where all streaklines are directed outward, giving it a source - like (star shaped) pattern. It would seem that these result from less energetic fluid packets from the boundary layer approaching the free surface. These ejections probably never reach the surface, but the volume of fluid displaced due to their approach towards the surface results in this net movement of fluid outward at the surface.

In the following sections, the population, size, growth, decay and persistence of these structures will be discussed with an emphasis on the features related to the attached vortices.

Experimental Conditions

The experiments described here were performed at a fixed Reynolds number, while the depth of flow and the rate of flow (i.e., the free surface velocity) were varied. The various parameters are listed in Table 1. The primary aim of this set of experiments was to see the effect of variation in depth on the characteristics of the persistent structures at the free surface. Other set of experiments with constant depth and variable free surface velocity is under way and the results should be available soon to understand the effect of surface speed on the coherent structures.

The Reynolds number of the flow was kept between 2600 to 2700. The reason for selecting this Reynolds number was to be in the range in which direct numerical simulations of channel flows have been carried out.

Table 1
Flow conditions

EXP. No.	d (cm)	U (cm/s)	Re
1	1.5	18.2	2722
2	1.9	14.1	2680
3	2.0	13.4	2680
4	2.4	11.0	2640
5	3.4	7.7	2620

Figures 3a to 3f show the characteristic flow field at the free surface for each of the flow conditions (Figure 3b is the flow visualization for the depth of 1.7 cm, although , this flow condition has not been analyzed quantitatively). A gradual change from a panorama combining many vortices and upwellings to a relatively quiet condition, with a noticeable increase in the size of the vortices, is observed going from a depth of flow of 1.5 cm to that of 3.4 cm.

Based on a large number of photographs taken for each case (nearly 100 for each flow condition), the following sections describe the properties of the various components of the flow field at the free surface.

Origin and Qualitative Behaviour of Attached Vortices

The origin of the upwellings (or the surface renewal eddies) lies in the boundary layer close to the channel wall ([3], [4]). Here we will concentrate on the origin of attached vortices. Figure 4 shows a series of photographs illustrating the role of upwellings in the inception of attached vortices and the subsequent development of these rotational structures. The sequence of photographs shows the parallel development of two pairs of anti - rotational vortices.

Figure 4a shows a small dark patch from which the microballoons are moving away. This is the upwelling formed due to the energetic bursts originating in the wall layer approaching the free surface and impinging on it. In the next two pictures the upwelling is more apparent at the free surface and an inception of rotational motion in opposite directions at the edge of the upwelling attached to the free surface may be seen. By the fourth picture frame the two anti rotational motions are seen to have developed into well formed pair of vortices rotating in opposite directions.

This sequence of events is typical in the generation of vortices. In general, an upwelling was observed to generate one or more pair(s) of counter - rotating vortices in the time it stays at the free surface.

The sequence of pictures in Figure 5 shows the annihilation of an attached vortex by a new upwelling. The well developed rotational motion seen in Figure 5a starts getting distorted by Figure 5c and is completely destroyed by 5e. In general, this was observed to be the main mechanism behind annihilation of vortices, especially for the flows of relatively lower depths. The other mechanisms observed were : interaction between two neighbouring vortices and, to a lesser extent, viscous dissipation of rotational motion. The last mechanism was found to be more important for higher depths of flow where the vortices have a long enough lifespan, as will be discussed later.

Figure 6.1 shows a pair of already formed counter - rotating vortices at the edge of an upwelling. The vortex rotating in the counter - clockwise direction is joined by another counterclockwise vortex, which can be seen well in Figure 6.4.. In the interval of the subsequent two pictures, the vortex rotating clocwise is seen to be absorbed due to its interaction with the neighbouring anti-clockwise vortex. This is again a very common phenomenon observed in visualizations. In some rare cases two vortices of opposite rotational motion were seen to merge to form a vortex of magnitude approximately equal to the difference in the magnitude of their vorticities. Merging of two vortices rotating in the same direction was observed frequently. In many instances, two vortices that have merged together, were seen to re-emerge as separate vortices at a later time. The reasons for this are not clear.

Quantitative Characteristics

Figure 7 shows a histogram of the number of vortices occurring in different size ranges. The plots are shown for different depths of flow. A comparison of these plots shows that the number of large vortices increases monotonically as the flow depth increases, however, the number of smaller vortices first increases until the flow depth of 1.9 cm and then decreases . The peak in the histogram shifts from within the range 0 - 200 (mm^2) to the range of 200 - 400 (mm^2) as the depth increases to 3.4 cm.

Figure 8 shows the average number of vortices and upwellings in the investigation area of size 16 cm x 10 cm. The average number was calculated from a set of runs, where each run consisted of following the flow and taking continuous photographs, which varied from 25 for the highest depth to about 10 for the lowest depth. 100 pictures in all were taken for each flow condition. The average number for each type of structure was first computed for each run and the final average value was then computed for the set of runs.

Figure 8a shows the average number of all vortices in the field of view (16 cm x 10 cm) as a function of the depth. Figure 8b shows the average number of upwellings for different depths. Both, the number of upwellings reaching the free surface, and the number of attached vortices observed, decrease as the depth increases. The data seems to suggest that the effect of flow depth can be divided into two regimes. At lower depths the number of structures reaching the free surface appear to decrease linearly as the depth increases, whereas the change is much more rapid as the depth is increased further. A direct correlation between the number of upwellings and the number of vortices suggests that the upwellings provide the main mechanism behind the generation of vortices.

Figures 8c and 8d show the average number of "new" vortices and average number of upwellings on the free surface. "New" means the structures that were generated during the span of time in which the photographs were taken i.e., all the structures that were seen to reach the surface or be generated after the measurement process started. The variation in the number of new upwellings with respect to depth shows the same trend as that for the total number of upwellings. However, the rate of decrease in the average number of new vortices at higher depths seems to be more rapid as compared to that of the average number of all vortices.

A monotonic decrease in the number of coherent structures on the free surface can be attributed to the fact that fewer of the bursts originating in the viscous sublayer reach the free surface as the depth of flow increases. The difference in the behaviour of the average number of all vortices as compared to that of new vortices can be explained as follows. The total number of vortices at any time on the free surface is a function of the number of new vortices generated and the duration for which these vortices survive (called the "persistence" time from now on). Hence, for low depths, although the number of vortices generated from an upwelling is higher, a large number of these newly generated vortices are short-lived because they appear to be annihilated by upwellings, giving a close correspondence between the equilibrium number (avg. number of vortices) and the number of new vortices. As the flow depth increases, the new vortices are more sheltered from the happenings in the boundary layer, resulting in a higher persistence time. As a results the equilibrium concentration of the vortices on the surface will decrease less rapidly as compared to the average number of new vortices generated.

Persistence

Figure 9 shows the histograms of the number of vortices in various intervals of duration of time given by a particular range. It can be seen that the fraction of vortices that have high persistence increases as the depth of flow increases. Based on these histograms a weighted average time of persistence is calculated for each case as follows

$$t_p = \Sigma t_i N_i / \Sigma N_i$$

Figure 9 shows the plot of weighted average persistence time for the attached vortices for various depths. Also, shown on the topmost plot of this figure is the average distance of persistence for each case, computed by multiplying the persistence time with the free surface speed. Figure 9(c) particularly shows the two regions of high rate of increase in persistence. It could be suggested from this graph that the life span of a newly generated vortex on the free surface increases faster than the decrease in the free surface speed (which decreases linearly with depth for constant Reynolds number) after a certain threshold depth of flow.

Direct Numerical Simulation

The direct numerical simulations have been performed using a pseudo spectral technique to clarify the behavior of turbulence near free surfaces in open channel flows. This method has been extensively used by many researchers to investigate the nature of turbulence in simple geometries (see for example [6]) and has become a standard method. The free surface is treated as a rigid slip wall, i.e. the liquid behaves as if it has very large surface tension. In the simulations considered here, the shear Reynolds number based on the depth of the channel, the friction velocity at the no-slip wall and the kinetic viscosity is 171. In the streamwise and spanwise direction, 32 and 64 Fourier modes are used respectively. In the wall-normal direction, 65 Chebyshev modes are used. The length, scaled by half depth of the channel, of the computational domain is $4\pi \times 2\pi \times 2$. This has been found (see [7]) to give sufficient resolution to capture all

essential features of the turbulent flow at this Reynolds number, which is about 2500 based on hydraulic diameter.

For fully developed channel flow, the three main types of structures observed in the experiments, i.e. upwelling, downdraft and attached vortices, are also realized in the direct numerical simulation. Figure 11 shows the streamlines on the free surface. The grey scale background indicates the surface-normal fluctuating velocity. The darker regions represent that the normal velocity is upwards which indicate upwellings, while the lighter regions are where the normal velocity is downwards which indicate downdrafts. It is seen that the streamlines converge in the regions of downdraft and diverge in the regions of upwelling. This is consistent with the experimental results observed in Figure 2.

Figure 12 shows the spatial structure of the attached vortices. The streamlines are on the free surface. The structures hanging beneath the vortices are the isosurfaces of the fluctuating static pressure of a low value which is used here as a scalar identifier of vortices. The region shown in the plot is a layer about 20 wall units below the free surface. One can see that the attached vortices are dominantly surface-normal.

The formation and evolution of attached vortices can be clearly observed by flow visualizations using the data base from direct numerical simulation. Figure 13 shows an instantaneous realization of a flow pattern on the free surface. A vortex is growing up at the edge of a upwelling, while another vortex formed early is being annihilated at the other side of upwelling. It is suggested that instablity of regions with high curvature at the edge of vortices induce the generation of vortices. The formation of the attached vortices can be further investigated by looking at the vortical structure beneath the free surface. Figure 14 shows isosurface of vorticities under an upwelling and vortices. In this figure, the structure of "dough nut" shape beneath the upwelling is the isosurface of the magnitude of the surface-parallel components of vorticity. The structures under the attached vortices are the isosurfaces of the surface-normal component of vorticity. It is suggested that the burst generated at the wall region carries fluid with high vorticity. As it reaching the free surface, it becomes an upwelling, and the surface-parallel vorticities have to reconnect with the surface to form attached vortices which carry surface-normal vorticity. This reconnection process is very similar to the cases studied in [8] where a pair of vortex tubes interact with a free surface and the normal connections of cross-axis vorticity with the free surface gives whirls.

The numerical simulations are also used to verify the conjecture that turbulence close to the free surface is essentially two-dimensional. This is done by changing the no-slip condition on the bottom wall to a free-slip condition. The turbulence generation mechanism is hence removed and turbulence undergoes a decaying process. The flow pattern in the surface region evolves into one with a number of surface-normal vortices which pair and merge. The back scattering of kinetic energy is observed. This shows that the energy is absorbed into isolated vortices which decay slowly. It is suggested that within region about 40 wall units below the free surface, the turbulence can be essentially considered as two-dimensional.

CONCLUSIONS

Through flow visualization of the free surface in a channel flow it is suggested that the interaction between the free surface and the ejections from the shear region near the channel bed provides the main mechanism behind the generation of attached vortices. It is also the main source of destruction of these vortices, other than viscous dissipation. The number of coherent structures at the free surface, and their persistence (both in time and the distance travelled) are directly related to the depth of flow at a fixed Reynolds number.

Direct numerical simulation of the channel flow at relatively low Reynolds number provides a good understanding of the process of vortex generation at the free surface and the nature of turbulence in the thin shear region beneath the free surface.

REFERENCES

1. Brutsaert, W., Jirka, G. H., ed., "Turbulence structure and turbulent diffusion near gas - liquid interfaces," Gas Transfer at Water Surfaces, 1st ed., D. Reidel Publishing Company, 1984, PP. 67 - 82.

2. Komori, S., Ueda, H., "Turbulence structure and transport mechanism at the free surface in an open channel flow," Int. Journal of Heat and Mass Transfer, Vol. 25, No. 4, 1982, pp. 513 - 521.

3. Komori, S., Murakami, Y., Ueda, H., "The relationship between surface - renewal and bursting motions in an open channel flow," Journal of Fluid Mechanics, Vol. 203, pp. 103 - 123.

4. Rashidi, M. and Banerjee, S., "Turbulence Structure in free-surface channel flows", Physics of Fluids, Vol. 31, No. 9, pp. 2491-2503.

5. Kaftori, D, "Structures in the turbulent boundary layer and its interaction with particles," Ph. D dissertation, June 1993, Univ. of California, Santa Barbara.

6. Kim, K., Moin, P. and Moser, R. "Turbulence statistics in a fully developed channel flow at low Reynolds number," J. Fluid Mechanics, Vol. 177, 1987, pp. 133-136.

7. Lam, K., and Banerjee, S. "On the condition of streak formation in a bounded turbulent flow," Phys. Fluids A , Vol. 72, 1992, pp.306-320.

8. Dommermuth, D. G., "The laminar ineteractions of a pair of vortex tubes with a free surface," J. Fluid Mechanics, Vol.246, 1993, pp. 91-115.

FIGURE CAPTIONS

Figure 1 : Sketch of the experimental setup.

Figure 2 : Coherent structures at the free surface in a channel flow, visualized by sprinkling hollow glass microballoons on the interface. (a) attached vortices and "splat_like" structures (upwellings). (b) source-like area from which all streaklines are moving away.

Figure 3 : Typical flow field at the free-surface for different flow conditions. (a) depth = 1.5 cm (b) depth = 1.7 cm (quantitative results for this case are not available now) (c) depth = 1.9 cm (d) depth = 2.0 cm (e) depth = 2.4 cm (f) depth = 3.4 cm. The Reynolds number for the flows were between 2600 - 2700.

Figure 4 : Inception and growth of a pair of counter-rotating vortices from the interaction of an upwelling with the free-surface. The consecutive frames are 0.4 secs. apart in time.

Figure 5 : Annihilation of an attached vortex by an upwelling impinging on the interface.

Figure 6 : Dissipation of two surface vortices due to mutual interaction.

Figure 7 : Histogram of the number of vortices in different ranges of size.

Figure 8 : (a) Average number of all vortices in the investigation area (16 cm x 10 cm) in one sequence of photographs. (b) Average number of all upwellings in the investigation area. (c) Average number of "new" vortices. (d) Average number of "new" upwellings.

Figure 9 : Histogram of the number of vortices in different ranges of life span.

Figure 10 : (a) Weighted mean of persistence time of the attached vortices for different depths of flow and constant Reynolds number. (b) Free surface speed for different depths. (c) Average distance of persistence of attached vortices at differents depths of flow.

Figure 11. Streamlines on the free surface. Bright regions indicate the downwards fluctuating normal velocity. Dark regions indicate the upwards fluctuating normal velocity.

Figure 12. The streamlines on the free surface and the isosurface of low static pressure in a layer about 20 wall units below the free surface. The low-pressure isosurface is used here as an indicator of the attached vortices.

Figure 13. A close-up view of a portion of streamlines on the free surface showing the formation and annihilation of vortices due to a upwelling reaching the free surface.

Figure 14. A three-dimensional view of the vortical structure beneath an upwelling. The structure with "doughnut" shape under the upwelling is the isosurface of the surface-parallel component of vorticity. The structures under the vortices are the isosurface of the surface-normal component of vorticity.

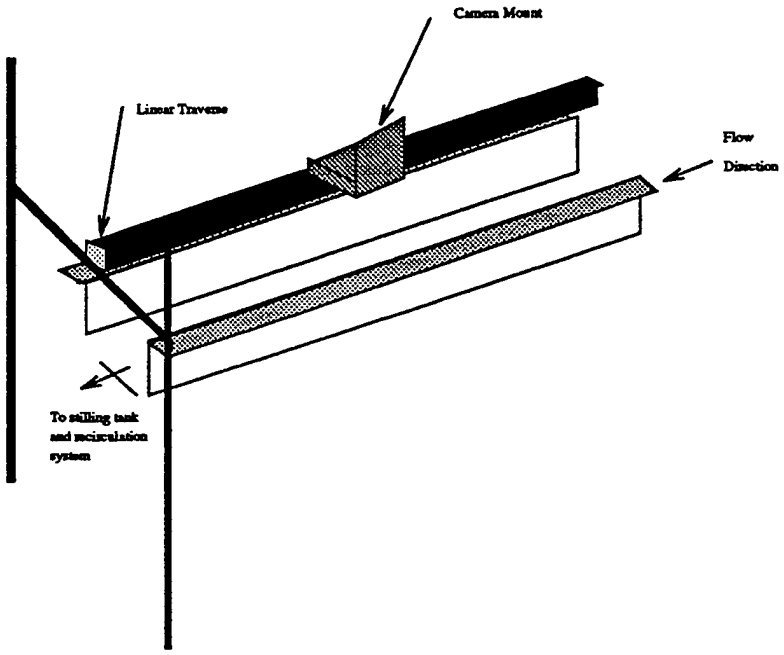


Figure 1 (a)

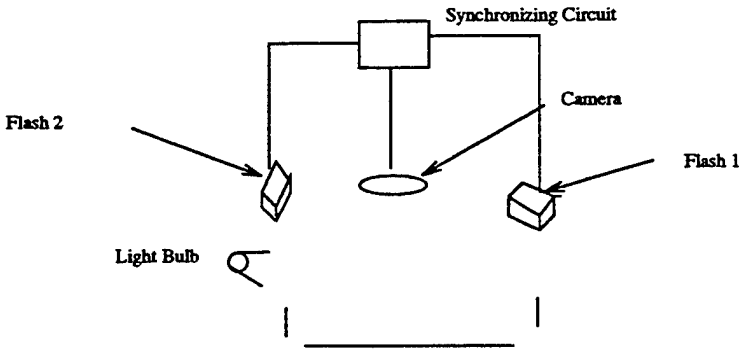
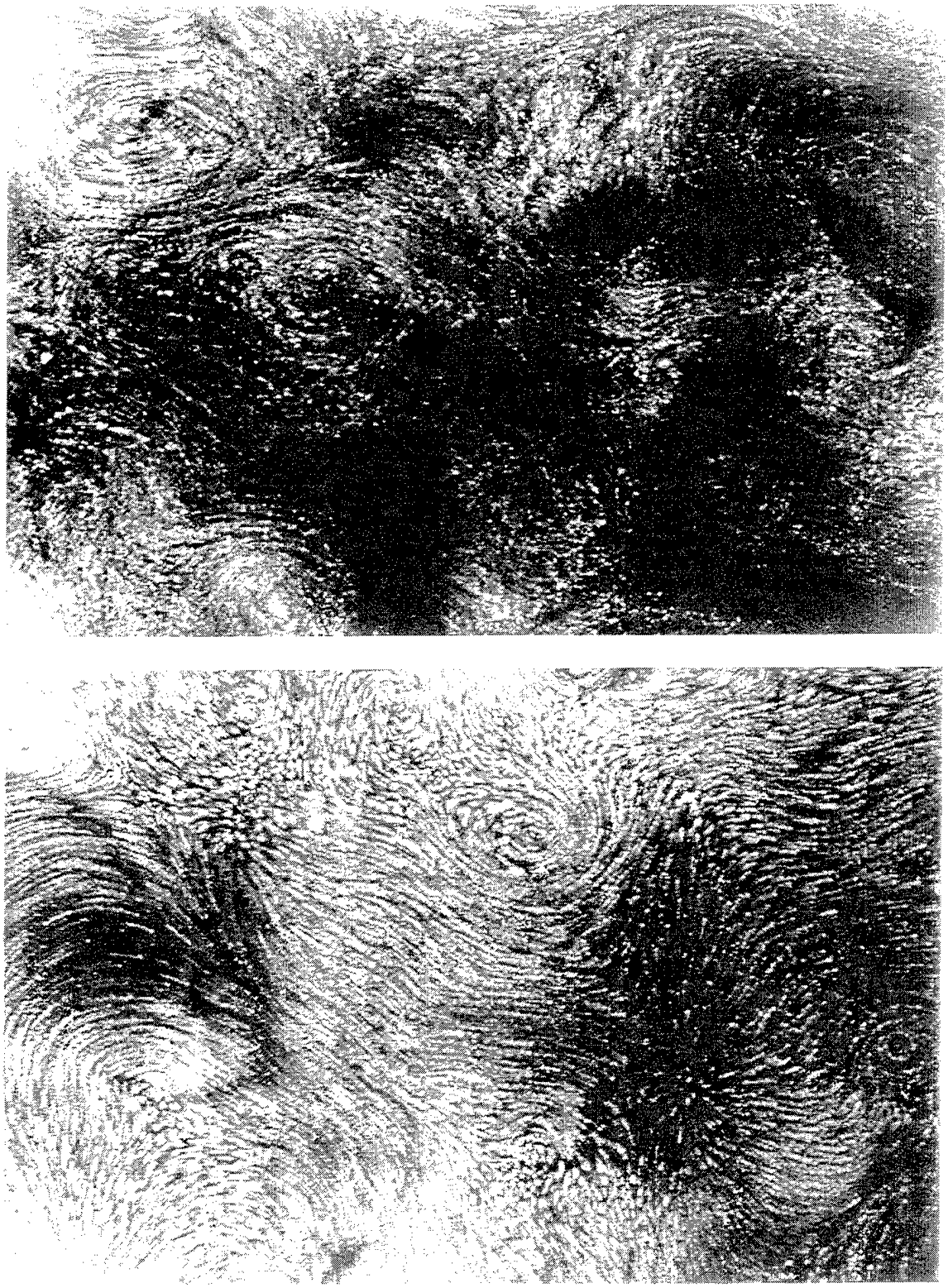
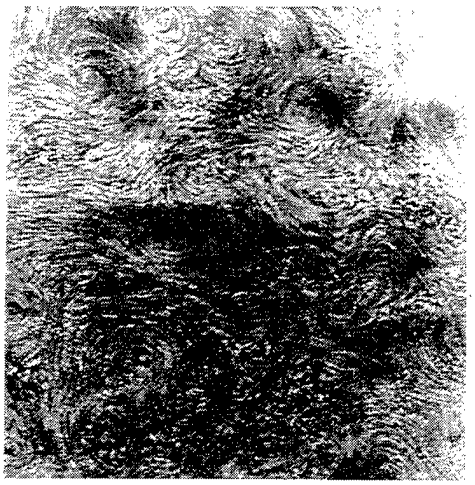


Figure 1 (b)

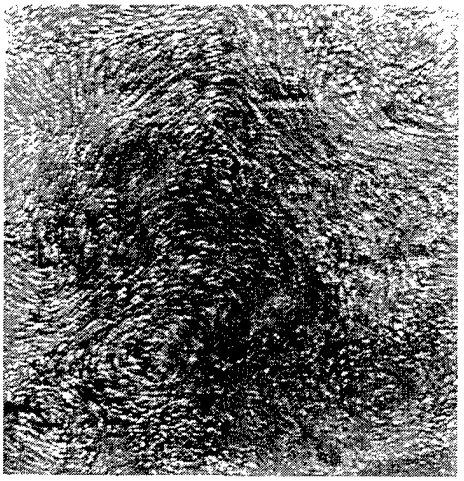


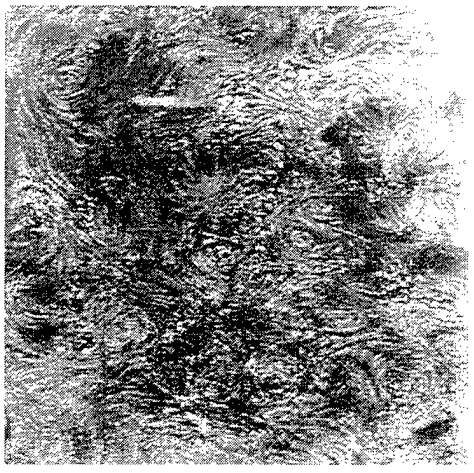
Top :Figure 2a
Bottom : Figure 2b







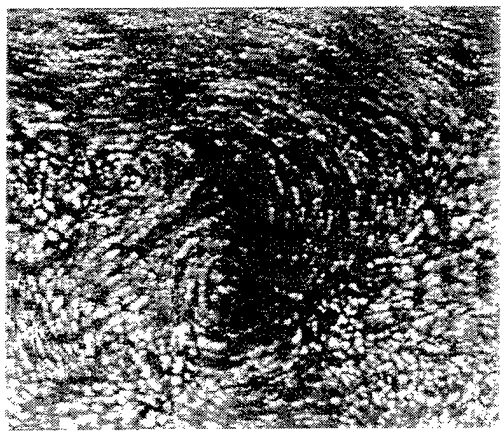


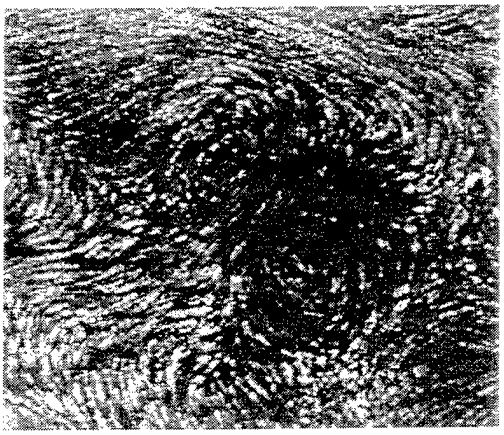


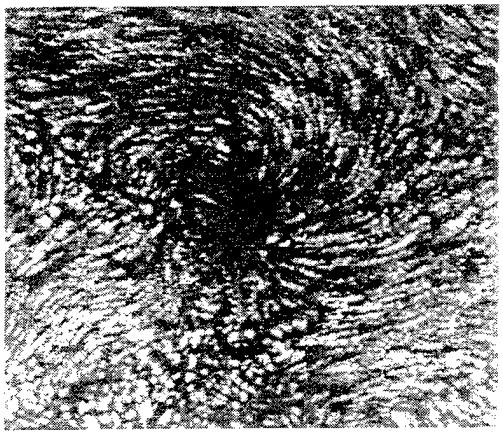


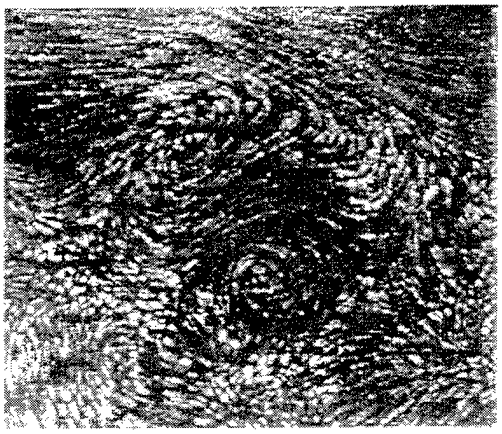
Bottom : Figure 3a
Top : Figure 3c

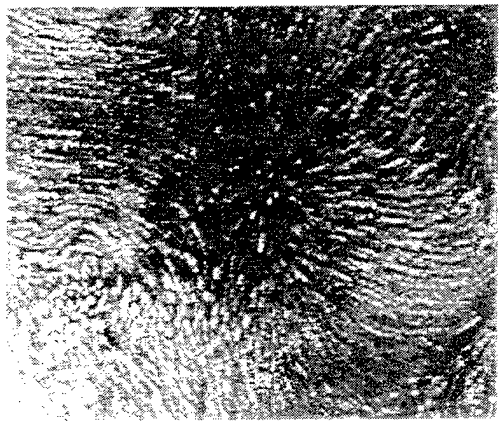
Bottom : Figure 3d
Top : Figure 3f

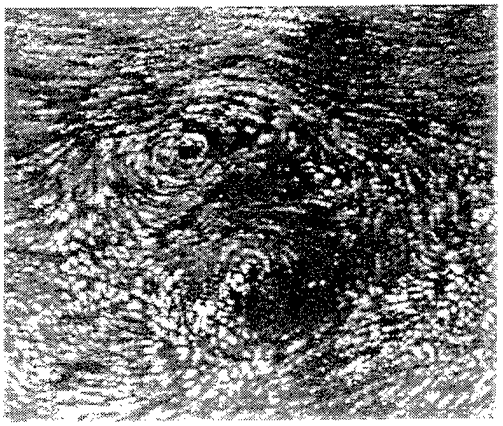










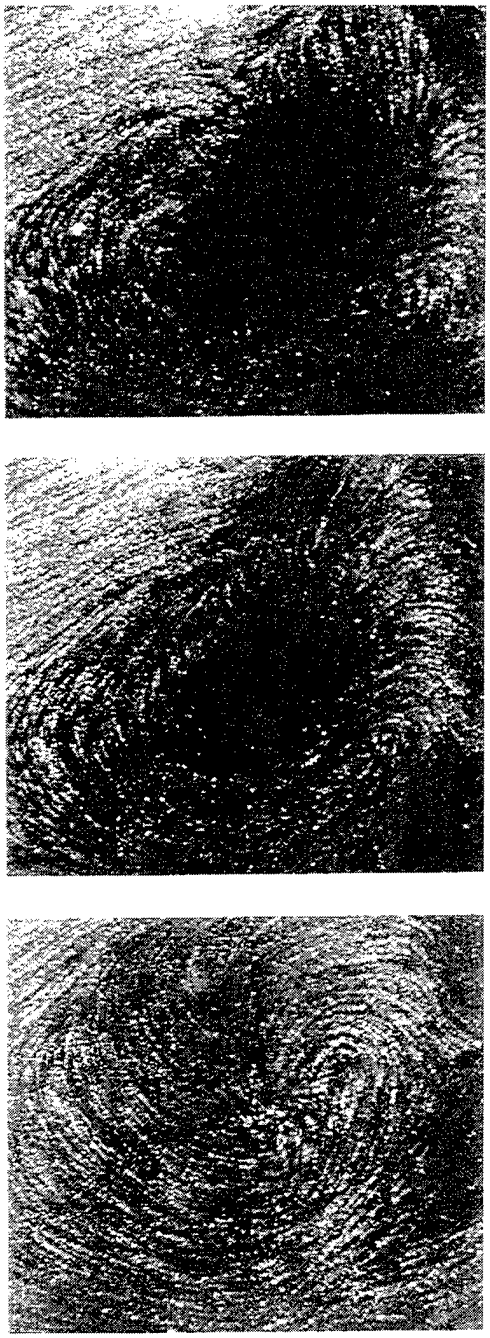


Bottom : Figure 4.1
Top : Figure 4.3

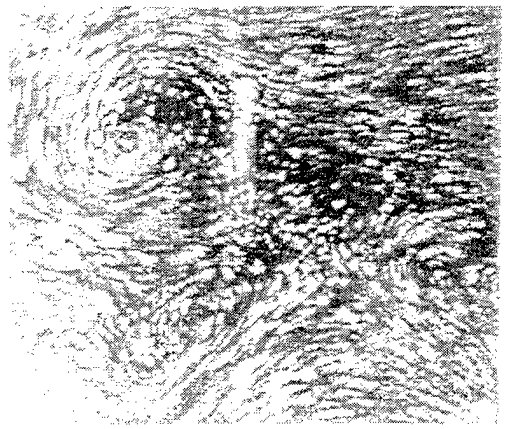
Bottom : Figure 4.4
Top : Figure 4.6

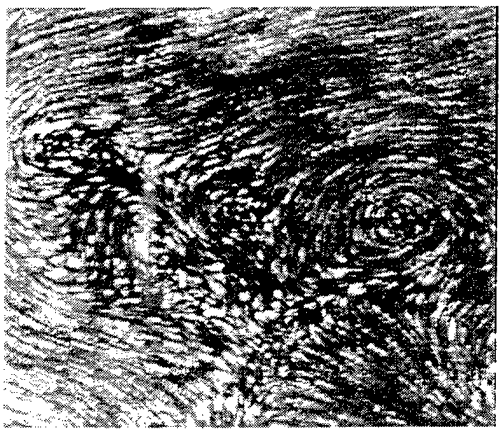


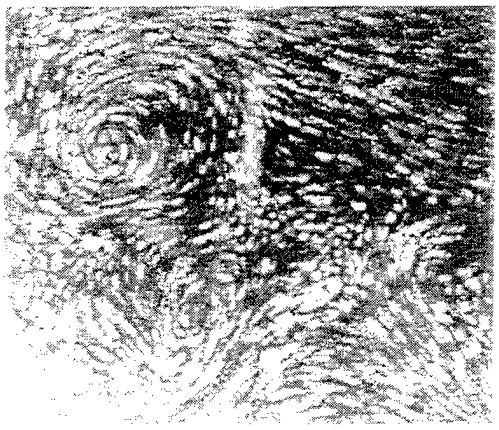
Bottom : Figure 5.1
Top : Figure 5.3

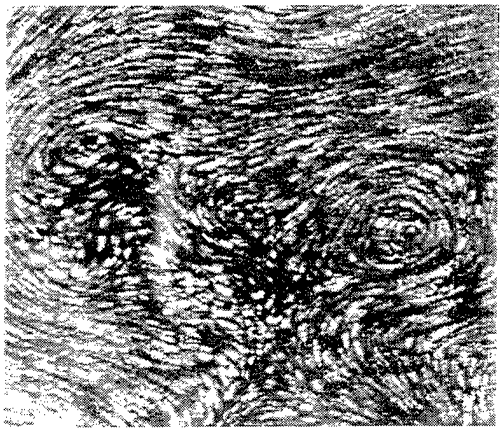


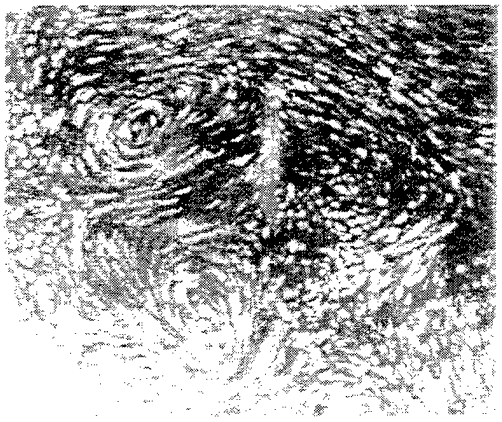
Bottom : Figure 5.4
Top : Figure 5.6

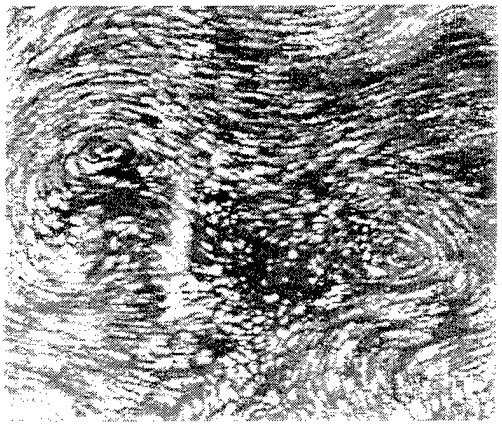












Bottom : Figure 6.1
Top : Figure 6.3

Bottom : Figure 6.4
Top : Figure 6.6

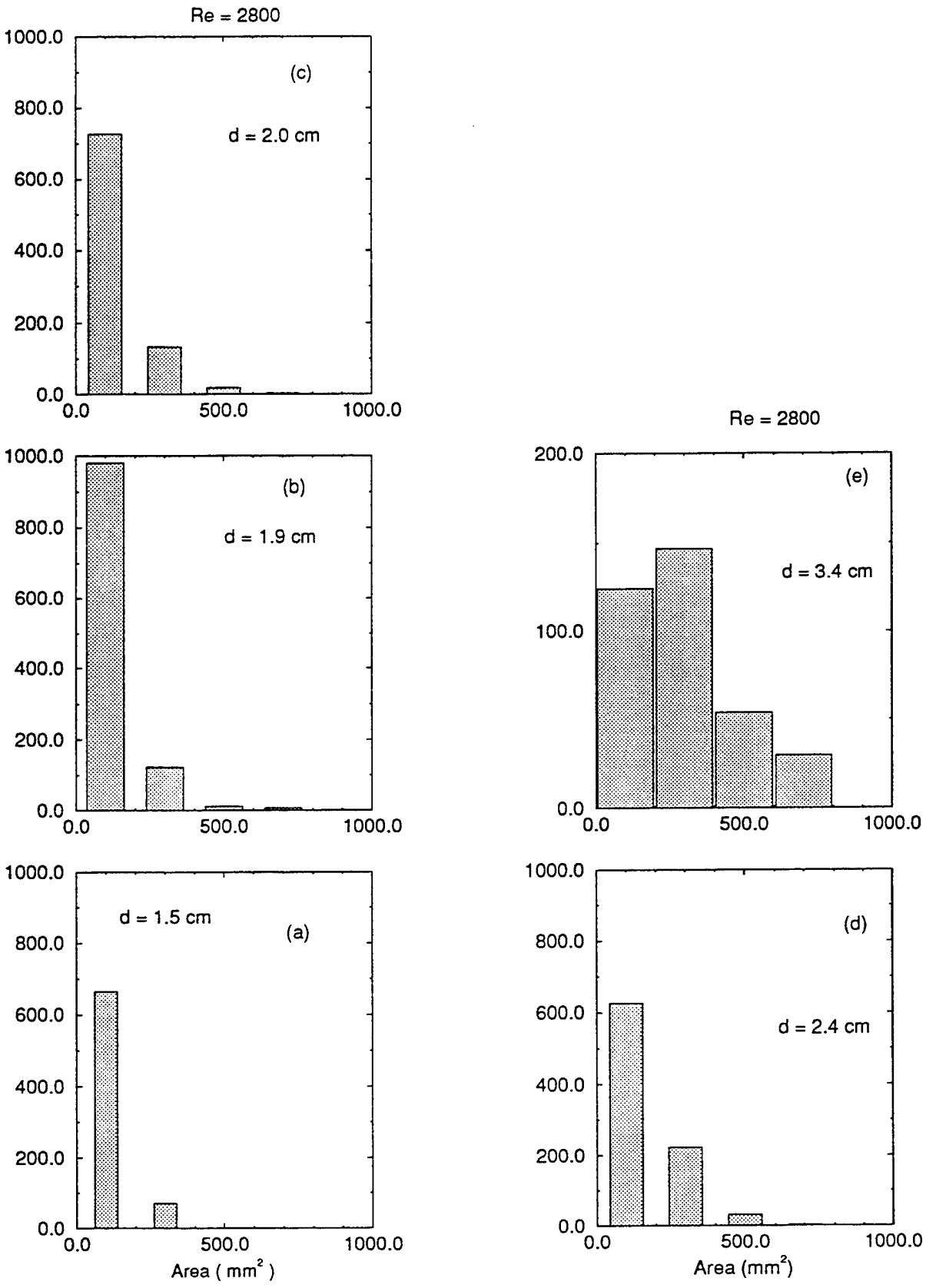
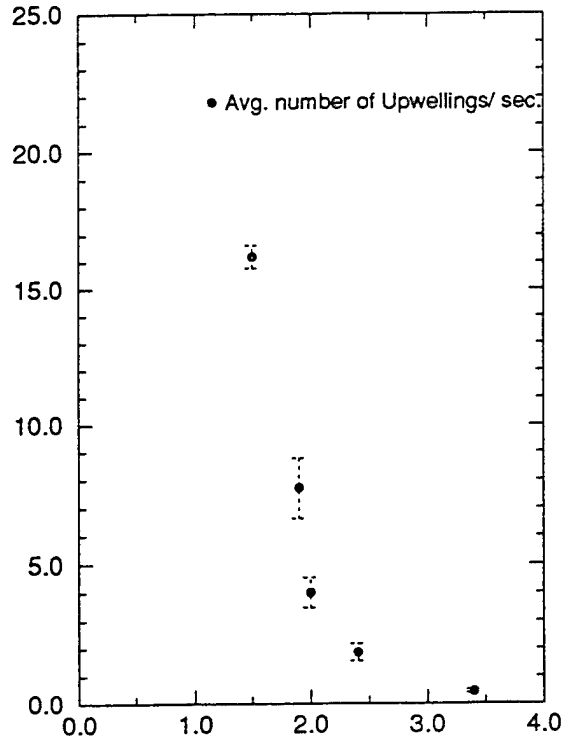
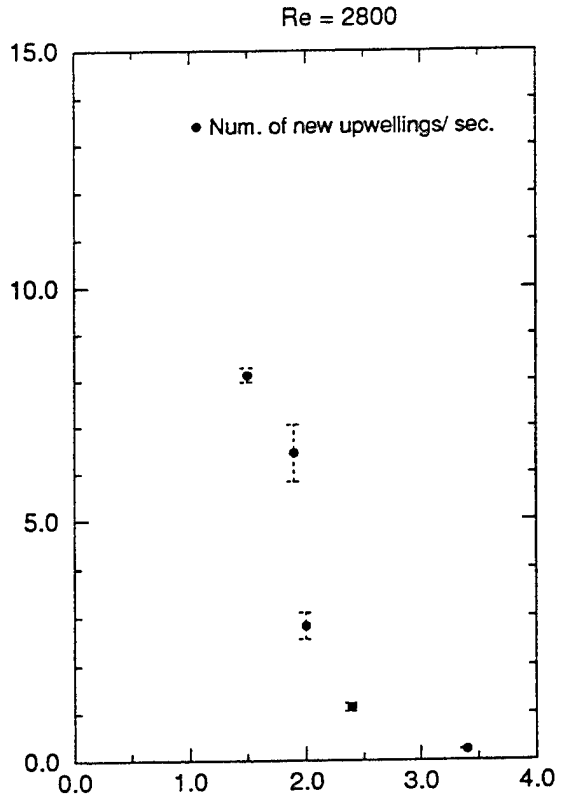

Re = 2800
(c)
d = 2.0 cm
1000.0
800.0
600.0
400.0
200.0
0.0
0.0
500.0
1000.0
(b)
d = 1.9 cm
(a)
d = 1.5 cm
Area (mm^2)
Re = 2800
(e)
d = 3.4 cm
100.0
(d)
d = 2.4 cm
Area (mm^2)

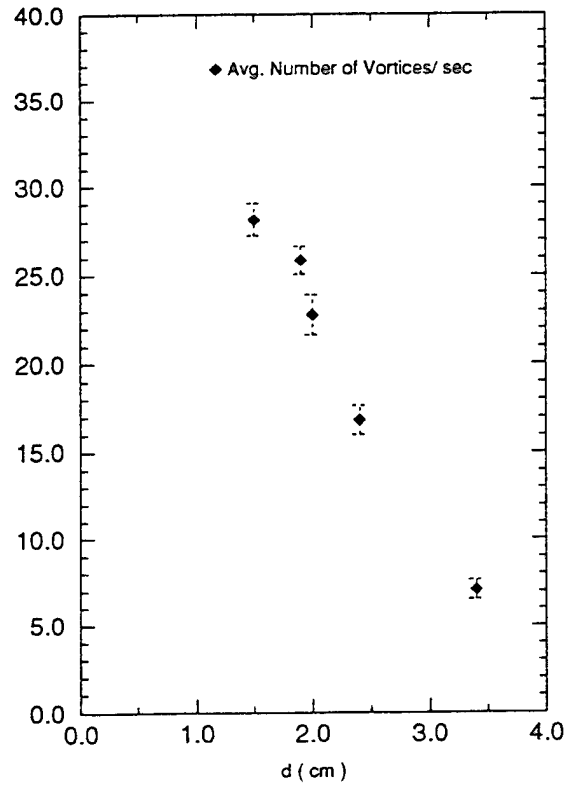
Figure 7

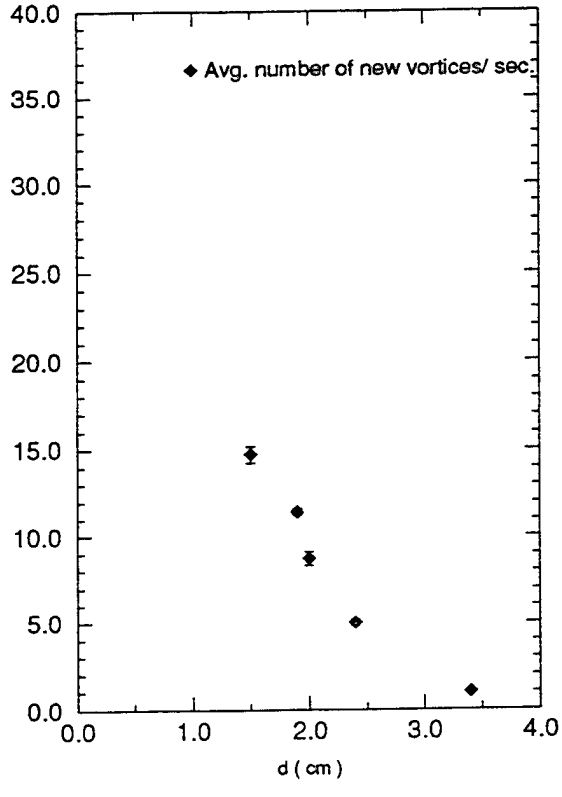


(b)



(d)





(c)

Figure 8 (a)

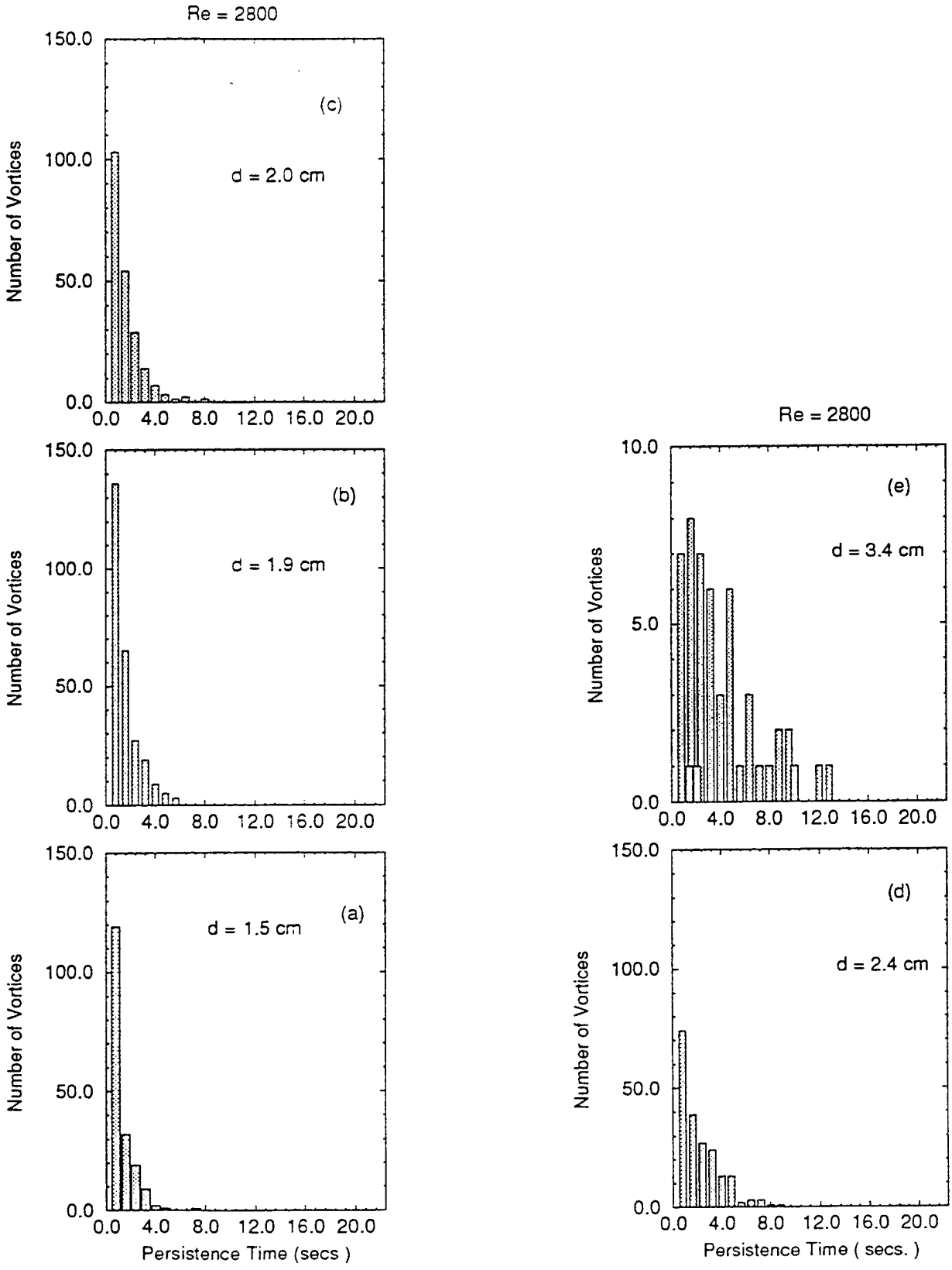

Re = 2800
(c)
d = 2.0 cm
(b)
d = 1.9 cm
(a)
d = 1.5 cm
Number of Vortices
150.0
100.0
50.0
0.0
0.0 4.0 8.0 12.0 16.0 20.0
Persistence Time (secs)
Re = 2800
(e)
d = 3.4 cm
(d)
d = 2.4 cm
10.0
5.0
Persistence Time (secs.)

Figure 9

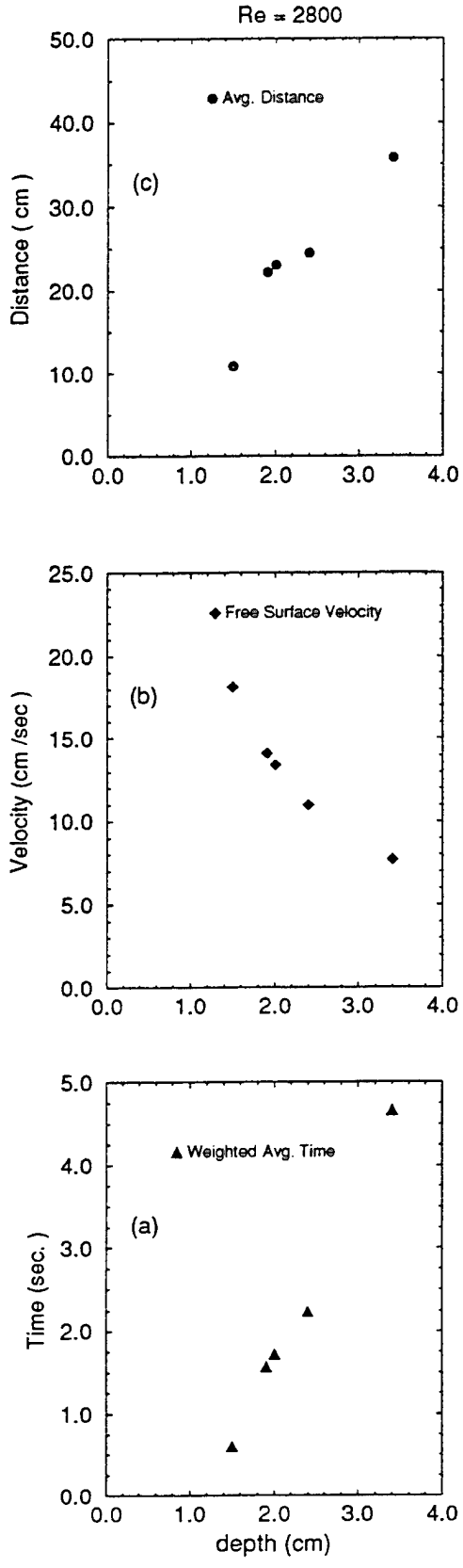

Re = 2800
Avg. Distance
(c)
Distance (cm)
50.0
40.0
30.0
20.0
10.0
0.0
0.0
1.0
2.0
3.0
4.0
Free Surface Velocity
(b)
Velocity (cm /sec)
25.0
20.0
15.0
10.0
5.0
0.0
Weighted Avg. Time
(a)
Time (sec.)
5.0
4.0
3.0
2.0
1.0
0.0
depth (cm)

Figure 10

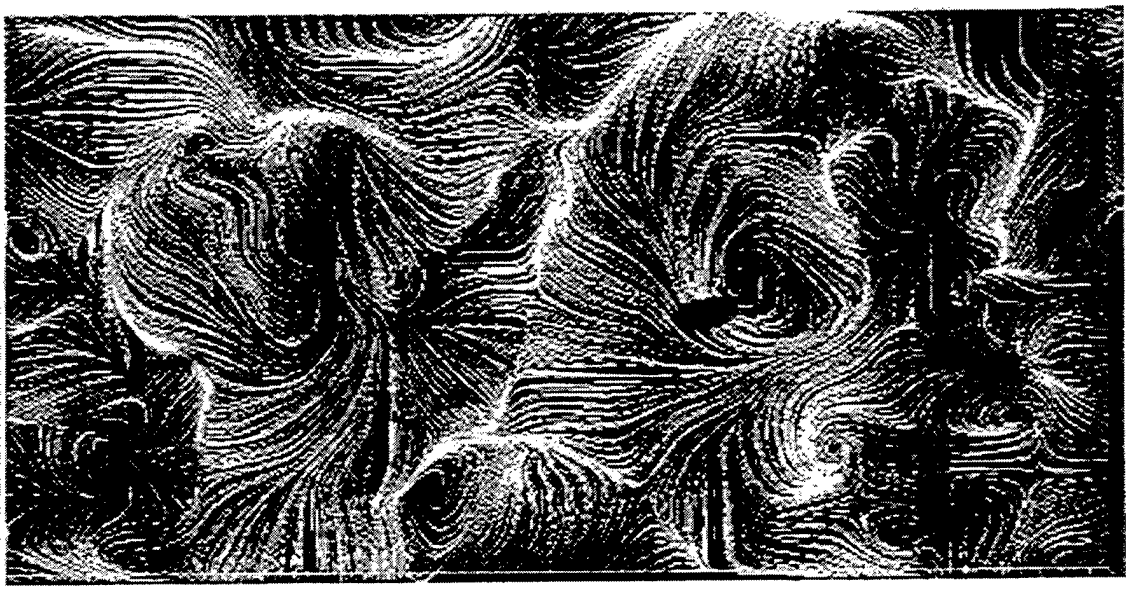


Figure 11

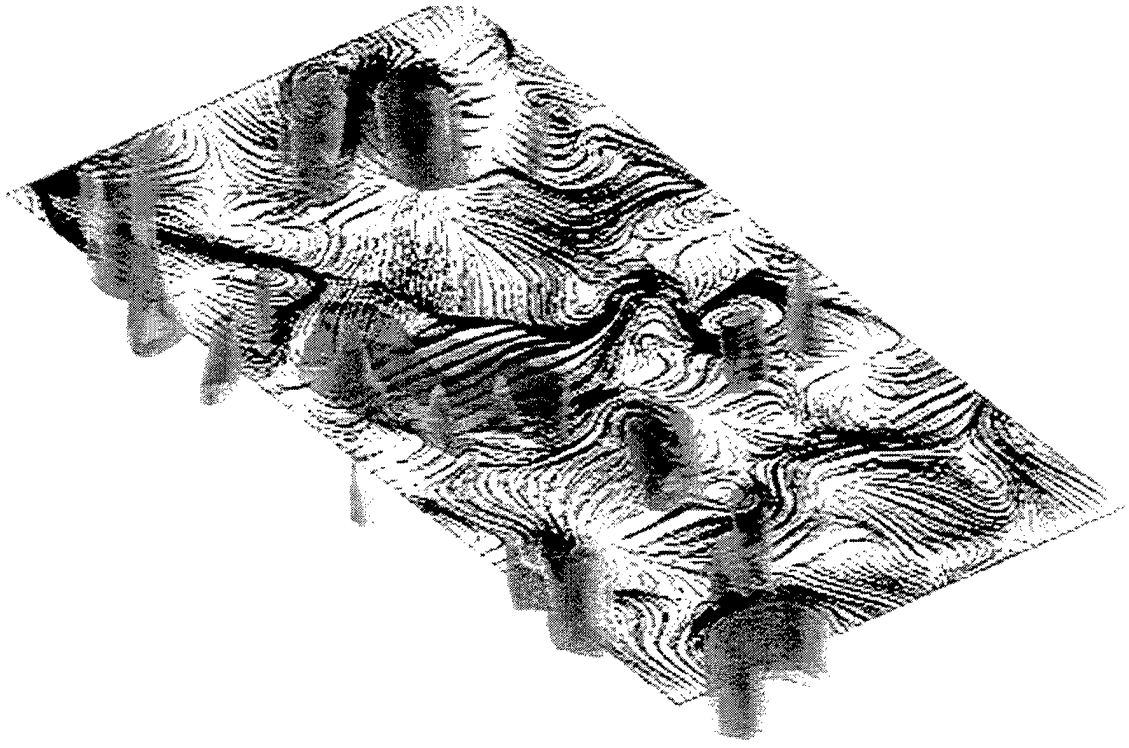


Figure 12

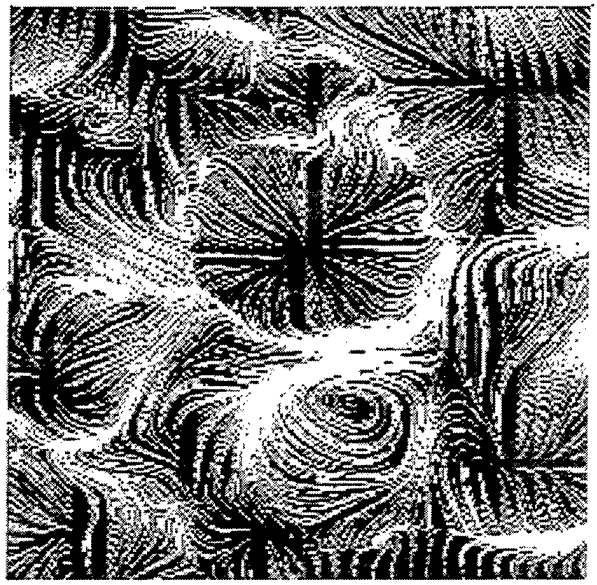


Figure 13

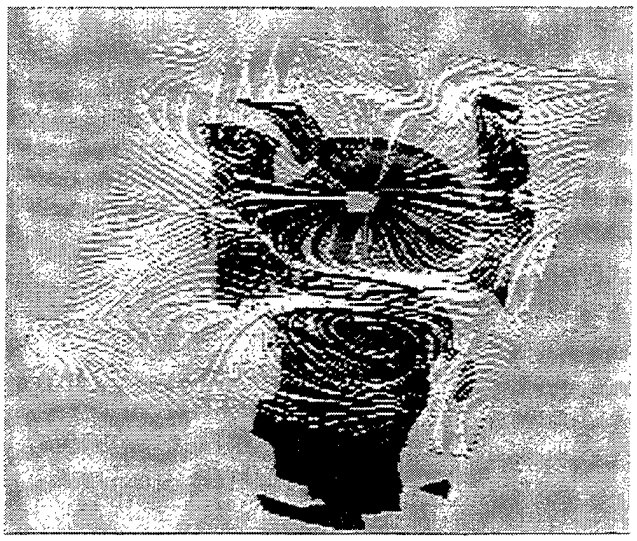


Figure 14

DISCUSSION

M. Graham
Imperial College, UK

It seems to me that this flow is essentially a stress-free surface damped turbulence, assuming, as I think would be the case, that vortical motion of the free surface is small so that the free surface boundary condition is effectively w=0. If so it would be interesting to compare the present and future results of these experiments with the theoretical and experimental results for homogeneous (grid generated) turbulence adjacent to shear free boundaries.

Dynamics of a Turbulent Jet Interacting with a Free Surface

N. Mangiavacchi, R. Gundlapalli, R. Akhavan
(University of Michigan, USA)

ABSTRACT

The structure and dynamics of turbulence in the presence of a free surface has been investigated by direct numerical simulations of a low Froude number, temporally growing, round turbulent jet which is issued below and parallel to a clean free surface. The free surface is found to affect the dynamics of turbulence within a 'surface layer' of thickness on the order of one lateral Taylor microscale (or 1/4 of the local vertical jet half-width). Within this layer, the vertical velocity fluctuations are inhibited and the turbulence kinetic energy is redistributed to the horizontal components. Analysis of energy and transfer spectra within the jet show the presence of a nearly two-dimensional turbulent state in the 'surface layer' characterized by a net reverse transfer of energy to the large scales and the presence of two distinct $k^{-5/3}$ and k^{-3} subranges in the energy spectra. Two classes of organized vortical structures could be identified within the 'surface layer' of the jet; (i) vortex tubes with axis parallel to the free surface oriented along the direction of the mean flow strain field and, (ii) vortex tubes with axis normal to the free-surface connected to the free-surface. The former are subject to three-dimensional dynamics and the usual cascade of energy to the small scales. The self-induced lateral motion of these vortices under the influence of their images leads to a large-scale secondary flow (the surface current), which is the origin of the significantly higher spreading rates of the jet in the lateral direction compared to its spreading rates in the normal direction. The second class of structures are connected to the free surface and form long-lasting isolated vortex tubes which grow with time and occasionally merge. The lack of strong vortex stretching in these structures in the vicinity of the free surface leads to their longevity and the establishment of a nearly two-dimensional turbulent state within the 'surface layer'.

NOMENCLATURE

k	wave number
ℓ	length scale of an eddy
H	depth of initial jet centerline below the free surface
R_o	initial half-radius of the jet
U_o	centerline velocity at t=0
$U_c(t)$	velocity at location of initial jet centerline at time t
g	acceleration due to gravity
$\vec{\omega}$	vorticity vector
$\vec{u}$	velocity vector
c	passive scalar concentration
ζ	mapped coordinate in Chebyshev domain
Λ	longitudinal integral scale
L_x	length of domain in axial direction
L_y	lateral distance from initial jet centerline to the point where velocity is $.5U_c(t)$
L_z	vertical distance from initial jet centerline to the point where velocity is $.5U_c(t)$
h	free surface elevation
λ_f	longitudinal Taylor microscale
λ_g	lateral Taylor microscale
$z_{1/2}$	jet half-width in vertical direction
$y_{1/2}$	jet half-width in lateral direction
$R_{1/2}$	jet half-radius
u', v', w'	velocity fluctuations in axial, transverse and vertical directions
T(k,z)	kinetic energy transfer spectra
T(k)	three-dimensional transfer spectrum
E(k)	kinetic energy spectrum

INTRODUCTION

Free surface turbulent flows occur in many areas of engineering ranging from industrial mixing processes to environmental flows to problems of naval hydrodynamics and oceanic sciences. Nevertheless, of the extensive literature devoted to turbulent flows surprisingly little concerns the dynamics of free surface turbulent flows.

There are two main ways in which the dynamics of turbulence near a free surface differs from that near a solid boundary;

(i) The free surface is free to move in the vertical direction. Therefore, when a turbulent eddy impinges on a free surface, part of its kinetic energy can be converted into the potential energy of surface waves. These waves, in turn, can travel downstream and affect the dynamics of turbulence in other parts of the flow. At high Froude numbers, this coupling between the energetics of turbulence and surface waves can be significant. At low Froude numbers, which is the focus of the present study, the wave amplitudes are sufficiently small for waves not to play an important role in the dynamics of turbulence. The free surface, in this case, acts as a barrier to vertical motion redistributing the vertical kinetic energy of turbulence into horizontal motion.

(ii) At the free surface, the no slip boundary condition on the tangential components of velocity encountered in wall flows is replaced by the requirement that the instantaneous shear stress must balance the surface gradients of the surface tension and the shear-stress on the air side of the free surface. For a clean surface with negligible wind velocities, this condition means that the mean and fluctuating components of the shear stress must vanish at the free surface.

When a turbulent velocity field approaches a free surface, its spectrum of eddies have to adjust to the above boundary conditions. These conditions were used by Hunt (1, 2) to develop a theory for the structure of turbulence in the vicinity of a free surface in the limit of negligible surface deformation. The turbulence away from the surface was assumed to be homogeneous and isotropic. The theory treats the turbulence structure within the surface-influenced-layer as a superposition of the original homogeneous turbulence plus an irrotational velocity field, driven by a source distribution at the surface, such that the vertical velocity fluctuations at the free surface vanish. The free surface is, therefore, assumed to have a purely kinematical effect represented by the formation of an image eddy whenever an eddy of scale ℓ appears within a distance ℓ of the free surface. The image eddy inhibits the movement of the original eddy towards the free surface and induces an additional tangential velocity at the surface such that the kinetic energy of turbulence is conserved. Aside from these kinematical effects, the dynamics of turbulence is assumed to proceed in the usual manner. In particular, the three-dimensional cascade of energy towards the small scales is assumed to be present near the free surface and the high wavenumber components of all three velocity components are assumed to conform to the universal $k^{-5/3}$ Kolmogorov spectrum.

The predictions of Hunt's (1, 2) theory were found to be in general qualitative agreement with experimental measurements of spectra and profiles of turbulence intensities in a free-surface grid-stirred tank by Brumley and Jirka (3). Nevertheless, these measurements reveal important dynamical effects which are not properly accounted for by the purely kinematical theory of Hunt. In particular, the experimental data show a higher concentration of turbulence energy at the low wavenumbers in the horizontal velocity components near the free surface than that predicted by Hunt's(1, 2) theory. Measurements also show the surface-induced anisotropy in the velocity fluctuations to extend to high wavenumbers, well into the inertial subrange, as the free surface is approached; in contrast to Hunt's theory which assumes no anisotropy at the high wavenumbers even near the free surface. Indeed, closer examination of the one-dimensional energy spectra in the experiments of Brumley and Jirka (3) shows the presence of two distinct subranges in the spectra of horizontal velocity components within the surface-influenced-layer; a $k^{-5/3}$ subrange at intermediate wavenumbers and a k^{-3} subrange at high wavenumbers. At large distances away from the free surface, the k^{-3} range disappears.

Similar trends can also be observed in the experimental measurements of Swean et al. (4) in turbulent planar free-surface jets. Close examination of the one-dimensional energy spectra of horizontal velocity components within the surface layer in these experiments also shows the presence of two distinct subranges; a $k^{-5/3}$ range at intermediate wavenumbers and a k^{-3} range at high wavenumbers. Furthermore, the data indi-

cate a trend for pile-up of energy in the horizontal velocity components near the surface as the jet moves downstream. The authors attribute this pile-up of energy to the presence of slowly dissipating, vertically oriented, coherent vortex tubes which connect normal to the free surface.

These connected vortex tubes, which have also been observed in a number of other experimental studies of free-surface flows (Madnia and Bernal(5), Sarpkaya and Suthon(6) , Gharib et al. (7), Dommermouth (8)), are indeed a major distinguishing feature of free surface turbulence from wall-bounded or free turbulent shear flows. At low Froude numbers, these vortices are not subject to significant stretching in the immediate vicinity of the free surface. Therefore, the cascade of energy to the small scales within such vortices is inhibited, leading to their longevity and the establishment of a nearly two-dimensional turbulent state in the immediate vicinity of the free surface. These vortex tubes, however, are not the only admissible class of vortical structures in the vicinity of a free surface. Another class might consist of vortex tubes which are oriented parallel to the free surface. In contrast to the former structures, these vortices are subject to strong vortex stretching and the usual cascade of energy to the small scales. Thus the overall dynamics of turbulence near the free surface is the result of a delicate balance between the dynamics of these two classes of structures.

The objective of the present study is to provide a better understanding of the dynamics of turbulence near a free surface, in particular with regards to the importance of two-dimensionality within the surface-influenced-layer and implications for the development of accurate subgrid-scale models for LES of free-surface turbulence. The studies are based on results from direct numerical simulations of a temporally growing submerged round jet which is issued parallel to a clean free surface. This flow exhibits many of the features of ship wakes and because of its inherent simplicity has served as a prototype flow in a number of experimental studies of free-surface turbulence (Madnia & Bernal(5), Anthony et al.(9) , Liepmann (10), Walker et al. (11)) in the recent years.

NUMERICAL METHODS

We investigate the evolution and dynamics of a temporally growing round jet which is issued parallel to a clean free surface at a depth

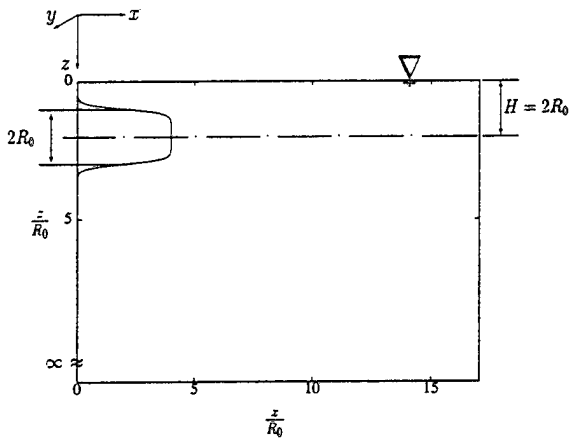


Fig. 1 Schematic of the jet and the coordinate system.

of one jet diameter below the surface ($H = 2R_o$). A schematic of the jet and of the coordinate system used in this study is shown in Figure 1.

The initial laminar jet had a Reynolds number, $Re_o = \frac{2R_oU_o}{\nu}$, of 4000 based on initial jet diameter and centerline velocity and a Froude number, $Fr = \frac{U_o}{\sqrt{gR_o}}$, of 0.25. This Froude number is small enough to allow the use of linearized free-surface boundary conditions in the simulations, thus resulting in significant savings in the required computational resources.

The evolution of the jet is tracked in a Cartesian coordinate system by solving the Navier-Stokes equations

$$\frac{\partial \vec{u}}{\partial t} = \vec{u} \times \vec{\omega} - \nabla \pi + \frac{1}{Re}\nabla^2 \vec{u} \qquad (1)$$

subject to the incompressibility constraint

$$\nabla \cdot \vec{u} = 0 \qquad (2)$$

where $\vec{\omega} = \nabla \times \vec{u}$ is the vorticity and $\pi = p + \frac{z}{Fr^2} + \frac{1}{2}|\vec{u}|^2$ is the dynamic pressure head. These equations were combined to obtain a second order equation for the normal component of vorticity and a fourth order equation for the normal component of velocity

$$\frac{\partial \omega_z}{\partial t} = \vec{k} \cdot \nabla \times (\vec{u} \times \vec{\omega}) + \nu \nabla^2 \vec{\omega}_z \qquad (3)$$

$$\frac{\partial \nabla^2 w}{\partial t} = -\vec{k} \cdot \nabla \times \nabla \times (\vec{u} \times \vec{\omega}) + \nu \nabla^4 w \qquad (4)$$

In addition, to provide direct comparisons with experimental flow visualization studies, a passive scalar with a Schmidt number of 0.7 was also imposed on the initial jet profile and its evolution was tracked by solving the scalar transport equation

$$\frac{\partial c}{\partial t} + \vec{u}.\nabla c = \frac{1}{Re.Sc}\nabla^2 c \qquad (5)$$

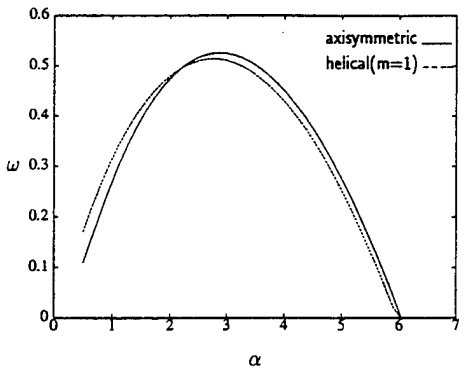


Fig. 2 Growth rates of axisymmetric and helical modes in the initial laminar profile as a function of the disturbance wavenumber.

The computations were performed using standard pseudospectral methods (Canuto et al. (12)) employing Fourier series in the streamwise (x) direction and mapped Chebyshev polynomials in the spanwise (y) and normal (z) directions. Two algebraic mappings

$$\frac{y}{R_o} = \frac{A\zeta}{(1-\zeta^4)^{1/4}} \tag{6}$$

and

$$\frac{z}{R_o} = \frac{B(1-\zeta)^{1/2}}{(1+\zeta)^{1/2}} \tag{7}$$

were used to map the $-\infty \leq y/R_o \leq \infty$ and $0 \leq z/R_o \leq \infty$ physical domain to the $-1 \leq \zeta \leq 1$ domain of Chebyshev polynomials. The scale factors $A = 5.0$ and $B = 9.6$ were chosen to produce a nearly uniform distribution of grid points in the central portion of the jet and a more concentrated distribution of grid points near the free surface.

Initial conditions for the runs were specified as a laminar jet with a blunt velocity profile (see Figure 1)

$$U/U_o = 0.5\{1 + \tanh[6.25(1 - r/R)]\} \tag{8}$$

on which a divergence-free, random noise disturbance field given by

$$\mathbf{u}'(\mathbf{x}) = \nabla \times (\mathbf{\Phi}(\mathbf{x}) \cdot I(r)) \tag{9}$$

was superimposed. Here $\mathbf{\Phi}$ is a three-dimensional isotropic random disturbance field (Rogallo (13)) whose spectral components were chosen to give $\mathbf{\Phi}$ an energy spectrum

$$E_\Phi(k) = \left(\frac{\Lambda}{1 + k^2\Lambda^2}\right) \tag{10}$$

The experimental data of Wygnanski and Fiedler (14) were used to specify the value of $\Lambda = 0.45R_o$ and the profile of $I(r) = \exp(-1.9r^2/R_o^2)$. The initial disturbance field had an energy of 10^{-4} relative to that of the mean flow. The passive scalar field was initialized with a profile identical to that of the mean flow (equation 8). No disturbances were imposed on the passive scalar.

Periodic boundary conditions were imposed in the homogeneous (x) direction. The assumed periodicity length was chosen to be $L_x/R_o = 16\pi/\alpha$, where $\alpha = 2.85$ corresponds to the wavenumber of the least stable (axisymmetric) eigenmode of the initial laminar profile. As shown in Figure 2, both axisymmetric and helical modes are nearly equally amplified at this wavenumber. The periodicity length of $16\pi/\alpha$ was chosen to accommodate not only the development of the fundamental mode, but also two successive subharmonics. Based on available experimental data on two-point longitudinal correlation lengths in round turbulent jets (Wygnanski and Fiedler, (14)) this domain is also large enough to ensure that the two-point statistics of the fully-developed turbulent jet are uncorrelated at a separation of one half the domain length in the streamwise direction. The flow was assumed to be quiescent ($\vec{u} = 0$) at large distances away from the jet ($y = \pm\infty$ and $z = \infty$), while at the free surface ($z = 0$) the linearized free-surface boundary conditions were imposed

$$\frac{\partial h}{\partial t} + u\frac{\partial h}{\partial x} + v\frac{\partial h}{\partial y} = w \tag{11}$$

$$\frac{\partial \omega_z}{\partial z} = 0 \tag{12}$$

$$\frac{\partial^2 w}{\partial z^2} = \frac{\partial^2 w}{\partial x^2} + \frac{\partial^2 w}{\partial y^2} \tag{13}$$

$$p + \frac{h}{Fr^2} = \frac{2}{Re}\frac{\partial w}{\partial z} \tag{14}$$

where h is the surface elevation.

Time advancement was carried out by a semi-implicit full-step time-stepping scheme (Orszag and Patera (15)), involving explicit evaluation of the convective terms using a second-order Adams-Bashforth scheme and implicit evaluation of the viscous terms using a Crank-Nicholson scheme. The fourth order equation for w was solved by decoupling it into two second order Poisson operators and imposing the boundary conditions (13) and (14) using an analytical Green's function approach (Domaradzki (16)). The second free-surface boundary condition for w was obtained from equation (14) by using the normal component of the Navier-Stokes equations

$$\frac{\partial^2 w}{\partial t \partial z} = -\frac{\partial}{\partial x}\vec{i}\cdot(\vec{u}\times\vec{\omega}) - \frac{\partial}{\partial y}\vec{j}\cdot(\vec{u}\times\vec{\omega}) + \frac{\partial^2 \pi}{\partial x^2} + \frac{\partial^2 \pi}{\partial y^2} + \nabla^2\frac{\partial w}{\partial z} \tag{15}$$

The resulting second-order Poisson operators were inverted using a collocation/diagonalization technique (Haidvogel and Zang (17), Haldenwang et al. (18)). Each Poisson solve requires $O(NX \cdot NY \cdot NZ^2 + NX \cdot NY^2 \cdot NZ)$ operations, roughly twice as many operations as in a Fourier/Fourier/Chebyshev code. These methods lend themselves to high efficiency parallel implementation on medium-grained distributed-memory parallel processors. The only operation that requires communication is the evaluation of the multi-dimensional FFT's, which can be computed using a transpose algorithm. The details of the parallel implementation is described in Mangiavacchi and Akhavan (19).

Simulations were carried out with a resolution of $128 \times 129 \times 129$ de-aliased modes in the streamwise, spanwise and normal directions on a partition of the SDSC 400-node Intel Paragon. The final fully-developed turbulent jet had a a turbulent Reynolds number of $Re_{\lambda_f} \approx 75$ based on longitudinal Taylor microscale ($Re_{\lambda_g} \approx 55$). The resulting grid spacing in the final turbulent jet was on the order of 3 Kolmogorov scales in the central portions of the jet.

RESULTS

Evolution of the Jet

The overall evolution of the free-surface jet with time is shown in Figure 3a. The growth of the jet is tracked by following the time histories of the jet half-widths $y_{1/2}(t)$ and $z_{1/2}(t)$ in the lateral and vertical directions, defined as the distance between the location of the maximum average streamwise velocity and the locations along horizontal and vertical planes where the average velocity has dropped to half the maximum value. Also shown in Figure 3a are the time histories of the maximum average streamwise jet velocity, $U_m(t)$, and the ratio of the jet Reynolds number, $Re_{z_{1/2}} = \frac{U_m z_{1/2}}{\nu}$, to the initial Reynolds number, $Re_o = \frac{R_o U_o}{\nu}$. These results should be compared with those shown in Figure 3b which show the evolution of a free jet with identical initial conditions evolving in an infinite medium without the influence of a free surface. The interval between $0 < tU_o/R_o < 15$ represents the growth and saturation of the initial disturbance fields in both jets. During this period, the sharp shear layers at the edges of the jet grow by viscous diffusion and the jet becomes less blunt. Nevertheless, since an invis-

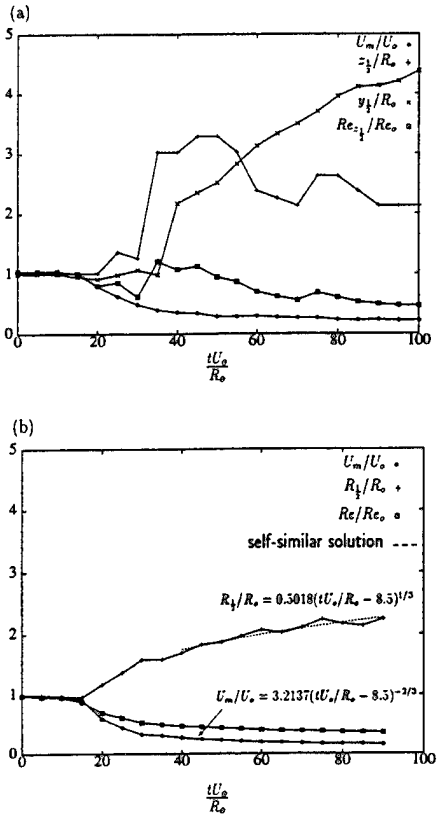


Fig. 3 (a) Evolution of the free surface jet half-widths in the transverse, $y_{1/2}(t)$, and vertical, $z_{1/2}(t)$ directions; the jet maximum average velocity, $U_m(t)$; and the jet Reynolds number, $Re_{z_{1/2}}(t) = U_m z_{1/2}/\nu$; (b) Evolution of the jet half-radius, $R_{1/2}(t)$; jet centerline velocity, $U_m(t)$; and jet Reynolds number, $Re_{R_{1/2}}(t) = U_m R_{1/2}/\nu$, in an equivalent free jet with identical initial conditions.

cid core continues to exist at the center of the jet, the jet half-width and the centerline velocity are not affected. The time $tU_o/R_o \sim 15$ signifies the start of the first vortex pairing in the jet, after which the jet experiences rapid transition to small-scale turbulence. By a time of $tU_o/R_o \sim 30$, the jet has become fully turbulent. In the case of the free-surface jet, this time also represents the start of the interaction of the jet with the free surface. As seen in Figure 3, the evolution of the free-surface jet is dramatically different from that of the free jet beyond this point. While the free jet gradually approaches a self-similar fully-developed turbulent state, the free-surface jet experiences a rapid rise in its vertical jet half-width upon first interaction with the free surface at $tU_o/R_o \sim 30$ which is accom-

panied by a simultaneous decline in the lateral jet half-width. These trends are reversed later on (beyond $tU_o/R_o \sim 60$) when the free-surface jet begins to approach a self-similar state. In the final fully-developed turbulent free-surface jet ($tU_o/R_o > 85$) the lateral jet half-width is nearly twice the half-width in the vertical direction. Similar trends have been observed in experimental studies of spatially-growing free-surface jets (Madnia and Bernal (5), Anthony and Willmarth (20)).

Figure 4(a,b) shows the evolution of the vorticity and passive-scalar fields in the free-surface jet. The initial structures formed from the saturation of the most linearly unstable modes are in the form of axisymmetric vortex rings. Subsequent evolution of these structures involves the instability of these vortex rings to azimuthal perturbations, the development of helical modes and pairings between various vortical structures. Traces of all these effects can be observed in the structure of the vorticity and passive scalar fields at $tU_o/R_o = 15$. In particular, the structure of the vorticity field (Figure 4a) shows the influence of an azimuthal mode with $m = \pm 5$, the development of asymmetry due to the presence of a helical mode with $m = 1$ and symmetric as well as asymmetric pairings between the various vortical structures. The azimuthal instabilities rapidly lead to the formation of braid streamwise vortex tubes, which are strengthened during the vortex pairings and result in rapid transition to small-scale turbulence. By $tU_o/R_o = 30$ the jet is already fully turbulent. The development of the jet beyond this time is strongly influenced by the presence of the free surface. Among other effects, the interaction with the free surface leads to significantly higher spreading rates of the jet in the lateral direction in a shallow layer near the free surface. This phenomenon, which has also been observed in a number of experimental studies of free-surface jets (Madnia and Bernal (5), Anthony et al. (9), Anthony and Willmarth (20)), is clearly evident in the structure of passive scalar and vorticity fields at $tU_o/R_o = 100$.

Turbulence Statistics

The time evolution of the mean turbulence statistics in the free-surface jet is shown in Figures 5 and 6. Profiles of the mean streamwise velocity, the turbulence intensities and the Reynolds shear stresses are presented along horizontal (Figure 5) and vertical (Figure 6) planes passing through the $(y_m = 0, z_m)$ location of the maximum mean streamwise velocity in the jet. Note that while the lateral location of the maximum mean streamwise velocity always remains in the center-plane (plane $y = 0$) of the original jet, the vertical $z = z_m$ location of this maximum begins to shift towards the free surface as the jet begins to interact with the free-surface beginning at $tU_o/R_o \sim 30$. The maximum velocity reaches the free surface at $tU_o/R_o \sim 40$ and remains there during the remainder of the evolution of the jet (Figure 5a).

At early times ($tU_o/R_o = 15$) the turbulence statistics in the free-surface jet are indistinguishable from that which would be obtained in a free jet. The asymmetry in the turbulence intensities observed at these early times in Figures 5b-d and 6b-d is due to the dominance of axisymmetric disturbances in the early stages of the evolution of the jet. The jet begins to interact with the free surface at $tU_o/R_o \sim 30$, shortly after experiencing transition to turbulence. The presence of the free surface inhibits the vertical velocity fluctuations ($\sqrt{\overline{w'^2}}$) within a thin 'surface layer' in the immediate vicinity of the free surface (see Figure 5d). Within this layer, the vertical turbulence kinetic energy is re-distributed to the kinetic energy of horizontal ($\sqrt{\overline{u'^2}}, \sqrt{\overline{v'^2}}$) motion and the turbulent fluctuations attain a strongly anisotropic character. The thickness of this 'surface layer' is estimated to be on the order of one lateral Taylor microscale (or 1/4 of the local vertical jet half-width in the present jet). The presence of the free surface also leads to significantly higher lateral spreading rates of the jet and lateral jet half-widths within the 'surface layer' compared to the spreading rates and jet half-widths in the vertical direction as seen in Figure 3.

The statistics shown in Figures 5 and 6 are in good qualitative agreement with experimental measurements in round and planar free-surface turbulent jets (Walker et al.(11)), Anthony and Willmarth (20). The trend for the point of maximum velocity to shift towards the free-surface is also seen in experimental data. The statistics during the initial evolution of the free surface-jet agree well with experimental data at downstream locations $\frac{x}{d} = 16, 32$. Experimental data at further downstream locations that correspond to later times in our simulation are not available for comparison.

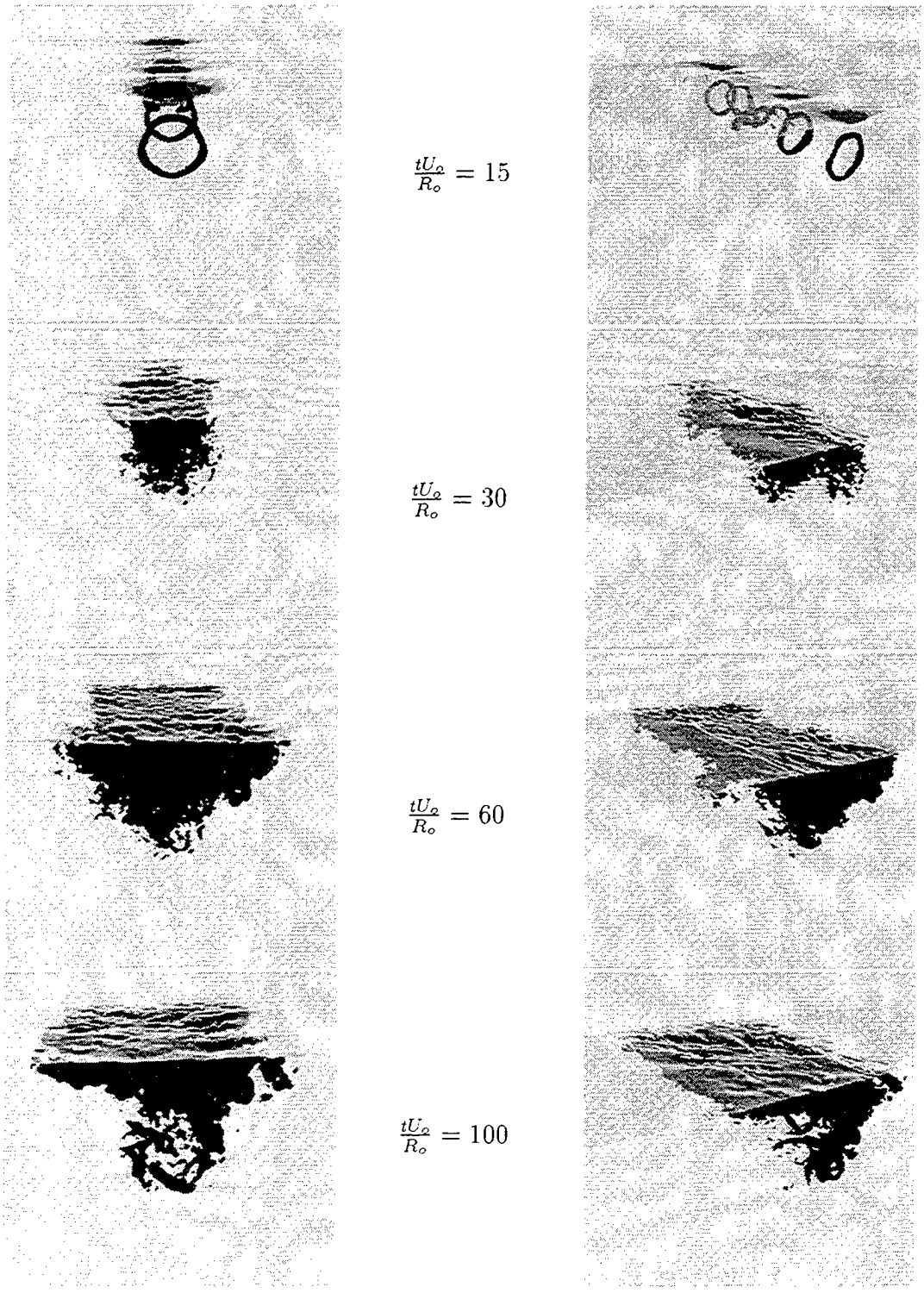


Fig. 4a Evolution of the vorticity field in the free-surface jet. The structures have been visualized by iso-surfaces of $\frac{|\omega|}{<|\omega|>} = 2.5$.

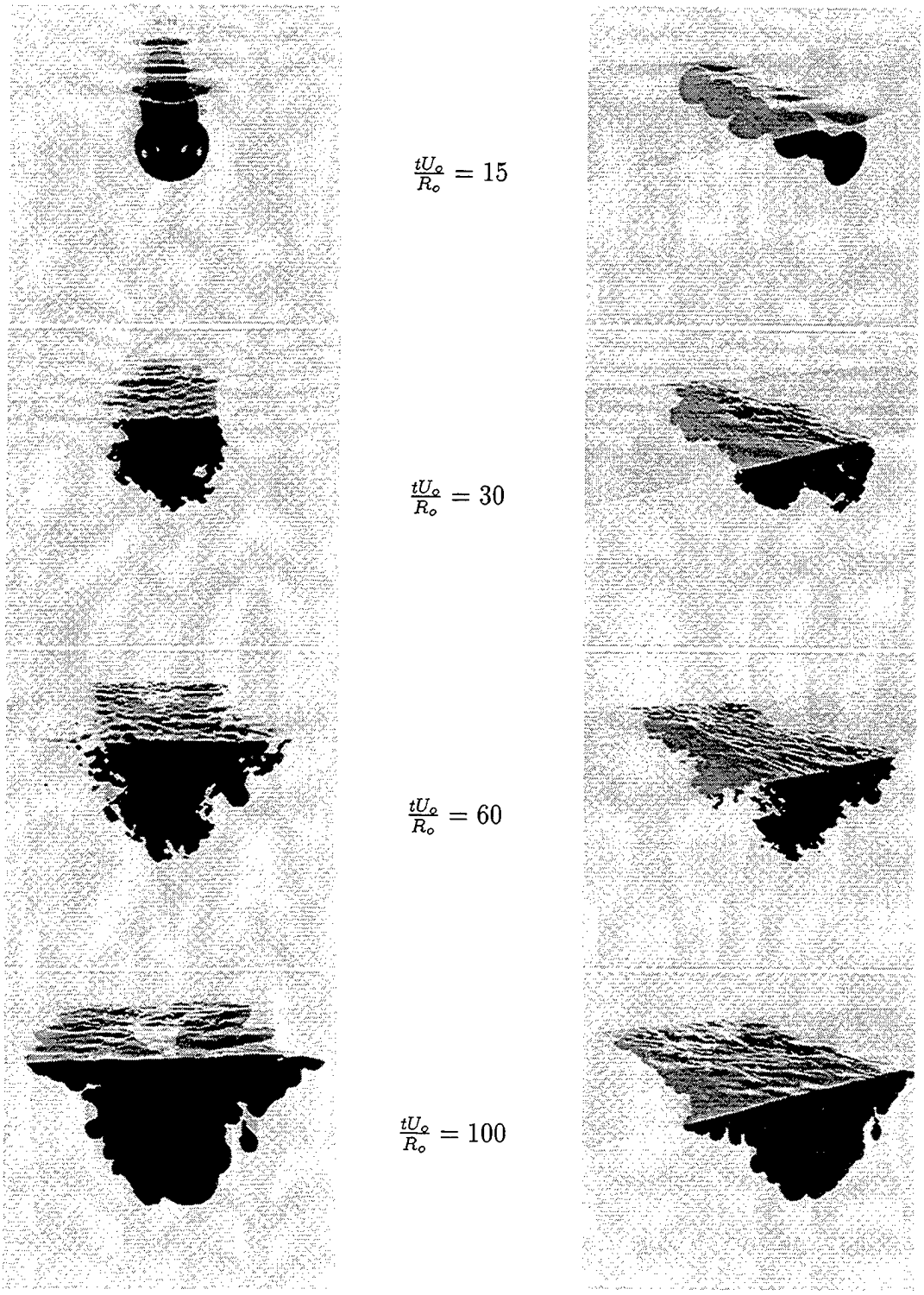


Fig. 4b Evolution of the passive scalar concentration field in the free-surface jet. The structures have been visualized by iso-surfaces of $\frac{c}{c_{max}} = 0.5$.

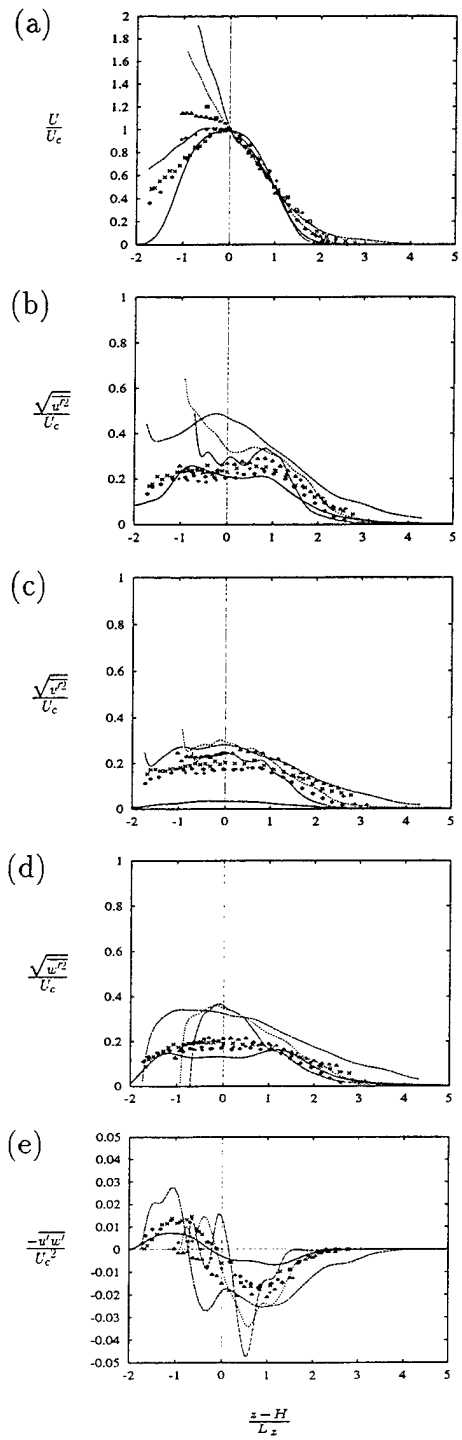


Fig 5. Profiles of (a) mean velocity, (b)-(d) turbulent intensities, and (e) the Reynolds shear stress in the plane $y = 0$. ——, $\frac{tU_o}{R_o} = 15$; – – –, 30; - - - -, 60; – · – · –, 100; experimental data of Anthony et al. (20); ◇, $\frac{x}{d} = 16$; +, 32; □, 64; Walker et al. (11); ×, $\frac{x}{d} = 16$; △, 32.

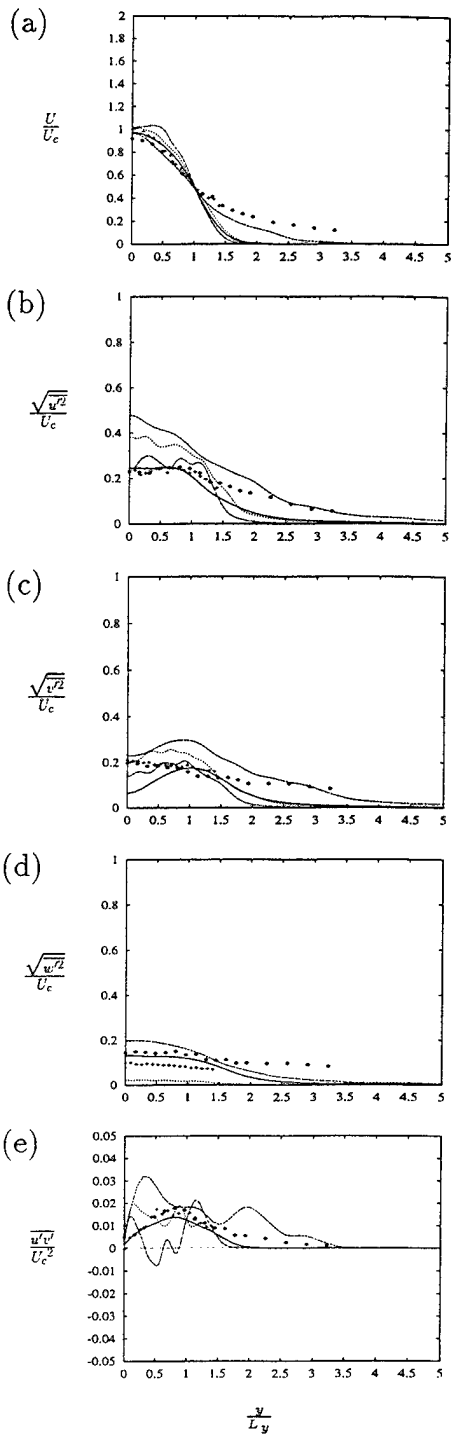


Fig 6. Profiles of (a) mean velocity, (b)-(d) turbulent intensities, and (e) the Reynolds shear stress in the plane $z = z_m$. ——, $\frac{tU_o}{R_o} = 15$; – – –, 30; - - - -, 60; – · – · –, 100; experimental data of Anthony et al. (20); ◇, $\frac{x}{d} = 32$; Walker et al. (11); +, $\frac{x}{d} = 32$.

Turbulence Spectra

The conversion of the vertical kinetic energy of turbulence into the kinetic energy of horizontal motion within the 'surface layer' of the jet leads to the establishment of a strongly anisotropic, nearly two-dimensional turbulent state within this layer. To gain a better understanding of the dynamics of turbulence within this layer, we next examine the spectra of kinetic energy and kinetic energy transfer in the jet.

Figure 7 shows the one-dimensional spectra of the turbulent velocity fluctuations in the jet at $tU_o/R_o = 100$ at various depths below the free surface. At large depths ($z/R_o \geq 2.0$) the turbulence is seen to have an isotropic character, manifested in Figure 7 by a collapse of the curves of one-dimensional spectra for the three components of velocity. As the free surface is approached, the low wavenumber components of the vertical velocity fluctuation is suppressed and the kinetic energy of these fluctuations is transferred into the horizontal (particularly streamwise) components of velocity. This anisotropy in the velocity fluctuations extends into progressively smaller scales, well into the inertial and dissipative ranges of turbulence, as the free surface is approached.

The behavior observed in Figure 7 is qualitatively consistent with that predicted by Hunt's (1, 2) theory, in which the free surface is assumed to affect a turbulent eddy of size ℓ only when the eddy is within a distance ℓ of the free surface. The primary effect of the free surface being the creation of an image eddy which suppresses the vertical velocity fluctuations at the surface and inhibits further movement of the original eddy towards the free surface. Thus the effect of the free surface is expected to be first felt at the lowest wavenumber components of the velocity and to then gradually extend to the high wavenumbers, consistent with the form of the spectra in the jet. Nevertheless, the results shown in Figure 7 also reveal important dynamical effects which are not properly accounted for in Hunt's (1, 2) theory. In particular, Hunt's theory assumes the high wavenumber components of all three components of velocity to be isotropic and to conform to the universal $k^{-5/3}$ Kolmogorov spectrum even at the free surface. In contrast, Figure 7 shows the anisotropy in the velocity fluctuations to extend to the smallest wavenumbers at the free surface. Furthermore, these results indicate the presence of two distinct subranges in the energy spectra; a $k^{-5/3}$ subrange at intermediate wavenumbers and a k^{-3} subrange at high wavenumbers. These two subranges are typical of 'two-dimensional' turbulence and suggest that the dynamics of turbulence in the 'surface layer' may indeed follow the governing laws of two-dimensional turbulence. Similar trends can also be observed in the experimental measurements of the energy spectra in planar free surface turbulent jets by Swean et al. (4) and in the free surface grid-stirred tank of Brumley and Jirka (3).

To investigate the two-dimensional character of turbulence within the 'surface layer' in further detail, we next examine the kinetic energy transfer spectra in the jet. Figure 8(a-e) shows the spectra of kinetic energy transfer $T(k,z)$ to a wavenumber $\mathbf{k} = (k_x, k_y)$ located on a horizontal plane at a depth z/R_o from the free surface. The transfer $T(k,z)$ is defined as

$$T(k,z) = -\sum_{k-\frac{1}{2}<|\mathbf{k}|\leq k+\frac{1}{2}} Real\{\hat{u'}^*_\alpha(k_x,k_y,z)\hat{N}_\alpha(k_x,k_y,z)\} \tag{16}$$

where $\hat{u'}^*_\alpha(k_x,k_y,z)$ is the complex conjugate of the planar Fourier transform of the component of the disturbance velocity in the plane z and $\hat{N}_\alpha(k_x,k_y,z)$ is the planar Fourier transform of the nonlinear terms in the Navier-Stokes equations arising from the turbulent fluctuations in the same plane. Note that $T(k,z)$ is different from the three-dimensional transfer spectrum, $T(k)$, defined as

$$T(k) = -\sum_{k-\frac{1}{2}<|\mathbf{k}|\leq k+\frac{1}{2}} Real\{\hat{u'}^*_\alpha(\mathbf{k})\hat{N}_\alpha(\mathbf{k})\} \tag{17}$$

which is commonly used in the study of three-dimensional turbulent flows. Indeed, $T(k,z)$ can be viewed as a projection of $T(k)$ onto a horizontal plane z. Figure 8f shows a comparison between the volume average of $T(k,z)$ in the jet and the volume average of the true three-dimensional transfer $T(k)$. The similarity between the two curves indicates that the dynamics of both quantities is similar.

The transfer spectra shown in Figure 8 demonstrate that on the average in the jet (Figure 8f) and at large depths from the free surface (Figures 8d, 8e) the dynamics of turbulence follows the rules of three-dimensional turbulence and is dominated by a net forward transfer of energy from the large scales of turbulent motion to the small scales. However, as the free surface is

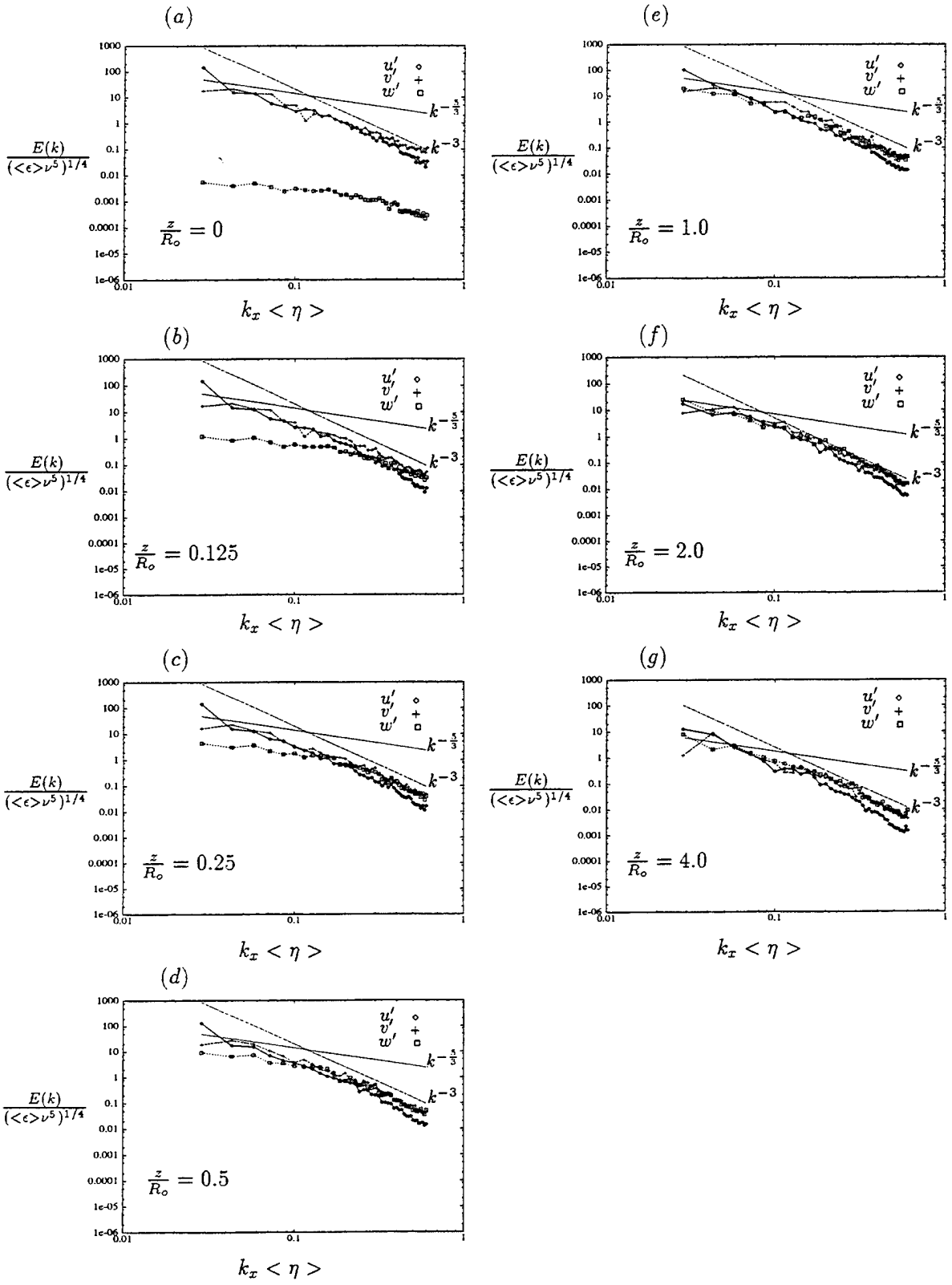


Fig. 7 One dimensional spectra of the turbulent velocity fluctuations at $\frac{tU_o}{R_o} = 100$ at various depths below the free surface.

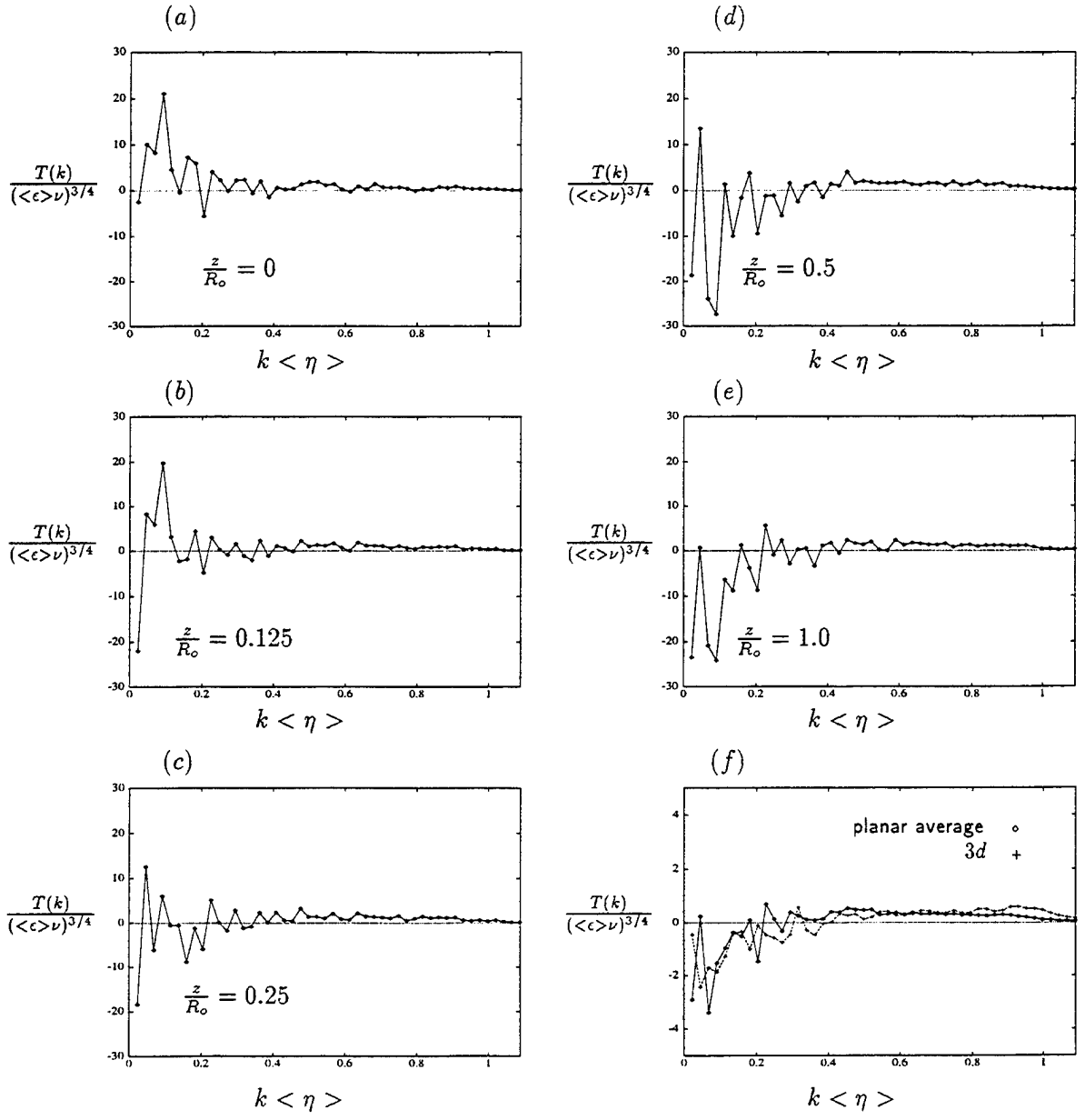


Fig. 8 (a-e) Kinetic energy transfer spectra in horizontal planes at various depths below the free surface at $\frac{tU_o}{R_o} = 100$, (f) comparison between the average planar transfer spectrum and the three-dimensional transfer spectrum in the jet at $\frac{tU_o}{R_o} = 100$.

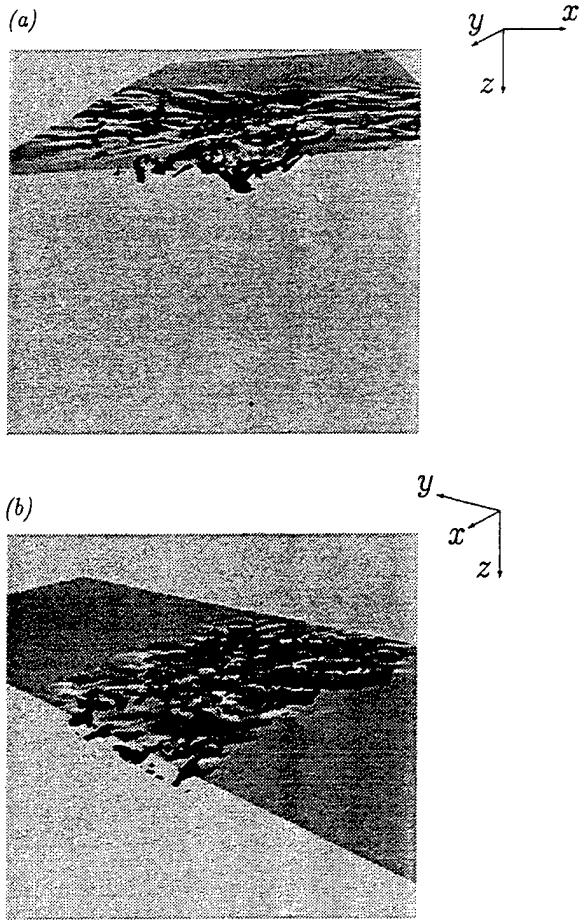


Fig. 9 Close-up view of the near-surface structures in the fully developed turbulent jet at $\frac{tU_o}{R_o} = 100$ showing (a) vortex tubes terminating normal to the surface leading to surface depressions, and (b) vortical structures parallel to the surface aligned with the direction of mean flow strain field.

approached (Figures 8a) the turbulence attains a two-dimensional character and its energetics is dominated by a net reverse transfer of energy to the large scales. Translated to an effective eddy viscosity, this means that the eddy viscosity has to be negative near the free surface. In the intermediate locations (Figure 8b, 8c), the overall dynamics of turbulence is determined by a delicate balance between the three-dimensional dynamics of the deep turbulence and the two-dimensional dynamics of turbulence in the immediate vicinity of the free surface.

This transition to 'two-dimensional' turbulence in the immediate vicinity of the free surface has to be accurately captured in any turbulence model used for the prediction of free surface turbulent flows. This makes the modeling of such flows substantially different from the well-studied examples of wall-bounded or free-shear flows.

Turbulence Structure

To investigate the origin of these phenomena, we next investigate the structure of turbulence in the vicinity of the free-surface. Figure 9 (a,b) shows the structure of the high intensity vorticity field in the free-surface jet at $tU_o/R_o = 100$. Two classes of organized vortical structures can be identified near the free-surface; (i) vortex tubes with axis parallel to the free surface oriented along the direction of the mean flow strain field and, (ii) vortex tubes with axis normal to the free surface connected to the surface.

The signature of both of these structures can be clearly seen in the top view of the free surface shown in Figure 10.

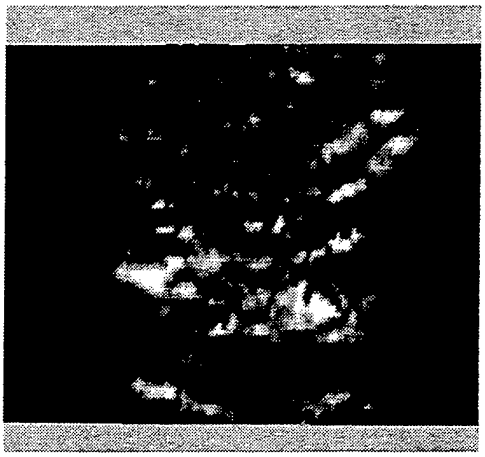


Fig. 10 Shadowgraph of the surface at $\frac{tU_o}{R_o} = 100$.

The parallel vortex tubes experience three-dimensional dynamics and the usual cascade of energy to the small scales. The self-induced lateral motion of these structures under the influence of their image leads to a large-scale mean secondary flow (see Figure 11) known as the surface current. This motion is the origin of the significantly higher lateral spreading rates of the jet compared to its spreading rates in the vertical direction. The downward motion induced by the image vortices prevents this class of struc-

tures from approaching the immediate vicinity of the free surface.

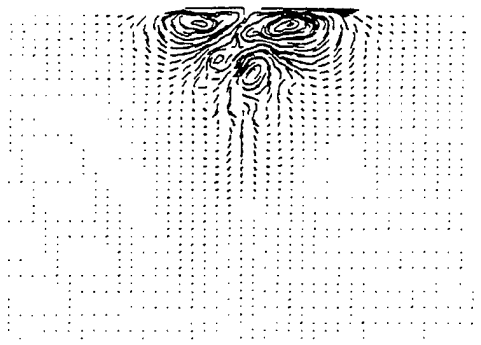


Fig. 11 The mean secondary flow established in the jet at $\frac{tU_o}{R_o} = 100$, visualized by mean particle trajectories.

The normal vortex tubes, on the other hand, connect to the free-surface and form long-lasting surface dimples on the free-surface (see Figure 10). The lack of strong vortex stretching in these structures in the immediate vicinity the free surface leads to their longevity and the establishment of a nearly two-dimensional turbulent state within the surface layer.

The overall dynamics of turbulence within the 'surface layer' is determined by a balance between the 'two-dimensional" dynamics of the connected vortical structures and the 'three-dimensional' dynamics of the parallel vortex tubes. Since the parallel structures can not approach the immediate vicinity of the free surface, the dynamics at the free surface is nearly two-dimensional. Further down, the connected vortex tubes bend and become parallel to the free surface (see Figure 9a) and the dynamics becomes fully 'three-dimensional'.

CONCLUSIONS

The dynamics of low Froude number, free surface turbulence has been investigated by direct numerical simulations of a temporally growing round turbulent jet which is issued below and parallel to a clean free surface. The statistics and structure of the jet is in good agreement with experimental measurements in free-surface jets. The presence of the free surface is found to affect the dynamics of turbulence within a 'surface layer' of thickness on the order of one lateral Taylor microscale. Within this layer, the turbulence has a two-dimensional character and is dominated by a net reverse transfer of energy to the large scales. These effects should be incorporated into any turbulence models intended for the prediction of free surface turbulent flows.

ACKNOWLEDGMENTS

This work was supported by Office of Naval Research under contract N00014-92-J-1750. The computations were performed on the San Diego Supercomputer Center Intel Paragon.

REFERENCES

1. Hunt, J.C.R., "Turbulence Structure in Thermal Convection and Shear Free Boundary Layers," Journal of Fluid Mechanics, Vol. 138, 1984, pp. 161-184.

2. Hunt, J.C.R., "Turbulence Structure and Turbulence Diffusion Near Gas-Liquid Interfaces," Gas Transfer at Water Surfaces (ed. W. Brutsaert & G. H. Jirka), 1984, pp. 67-82.

3. Brumley, B.H. and Jirka, G.H., "Near-Surface Turbulence in a Grid-Stirred Tank," Journal of Fluid Mechanics, Vol. 183, 1987, pp. 235-263.

4. Swean, T.F., Jr. Ramberg, and Miner, E.W., "Anisotropy in a Turbulent Jet Near a Free Surface," ASME Journal of Fluids Engineering, Vol. 113, 1991, pp. 430-438.

5. Madnia, K., and Bernal, L.P., "Interaction of a Turbulent Round Jet with a Free Surface," University of Michigan, Department of Aerospace Engineering, 1989, Technical Report No. 89-05.

6. Sarpkaya, T., and Suthon, P., "Interaction of a Vortex Couple with a Free Surface," Experiments in Fluids, Vol. 11, 1991, pp. 205-217.

7. Gharib, M., Weigand, A., and Novikov, E., "Interaction of Small Scale Turbulence with the Free Surface," Bulletin of American Physical Society, Vol. 37, 1992, pp. 1763.

8. Dommermouth, D.G., "The Laminar Interactions of a Pair of Vortex Tubes with a Free Surface," Journal of Fluid Mechanics, Vol. 246, 1993, pp. 91-116.

9. Anthony, D.G., Hirsa, A., and Willmarth, W.W., "On the Interaction of a Submerged Turbulent Jet with a Clean or Contaminated Free Surface," Physics of Fluids A, Vol. 3, 1991, pp. 245-247.

10. Liepmann, D., "The Near-Field Dynamics

and Entrainment Field of Submerged and Near-Surface Jets," Ph.D. Thesis, University of California, San Diego, 1990.
11. Walker, D.T., Chen, C.Y., and Willmarth, W.W., submitted to Journal of Fluid Mechanics, 1994.
12. Canuto, C., Hussaini, M.Y. , Quarteroni, A., and Zang T.A., "Spectral Methods in Fluid Mechanics," Springer-Verlag, 1987.
13. Rogallo, R.S., "Numerical Experiments in Homogeneous Turbulence," NASA Technical Memorandum 81315, 1981.
14. Wygnanski, I. and Fiedler, H., "Some Measurements in the Self-Preserving Jet," Journal of Fluid Mechanics, Vol. 38, 1969, pp. 577-612.
15. Orszag, S.A., and Patera, A.T., "Secondary Instability of Wall-Bounded Shear Flows," Journal of Fluid Mechanics, Vol. 128, 1983, pp. 347-385.
16. Domaradzki, A.J., "An Analytic Green's Functions Method in Pseudo-Spectral Navier-Stokes Solvers for Boundary Layer and Channel Flows," Journal of Computational Physics, Vol. 88, 1990, pp. 232-242.
17. Haidvogel, D.B., and Zang, T., "The Accurate Solution of the Poisson Equation by Expansion in Chebyshev Polynomials, " Journal of Computational Physics, Vol. 30, 1979, pp. 167-180.
18. Haldenwang, P., Labrosse, G., Abboudi, S., and Deville, M., "Chebyshev 3-D Spectral and 2-Pseudospectral Solvers for the Helmholtz Equation," Journal of Computational Physics, Vol. 55, 1984, pp. 115-128.
19. Mangiavacchi, N., and Akhavan, R., "Direct Numerical Simulations of Turbulent Shear Flows on Distributed Memory Architectures," Proceedings of the sixth SIAM Conference on Parallel Procedures in Scientific Computing, Vol. 1, 1993, pp. 61-64.
20. Anthony, D.G., and Willmarth, W.W., "Turbulence Measurements in a Round Jet Beneath a Free Surface," Journal of Fluid Mechanics, Vol. 243, 1992, pp. 699-720.

Direct Numerical Simulation of Free-Surface Wave Generated by Turbulent Shear Flow

M. Zhu, H. Miyata (University of Tokyo, Japan),
T. Hino (Ship Research Institute, Japan)

ABSTRACT

A preliminary analysis of free-surface wave generation by a turbulent shear-flow existing prior beneath the free-surface is carried out by means of direct numerical simulation. The initial state of simulation is inherited from the direct numerical simulation results of turbulent open-channel flow. The simulation is started by releasing the solid boundary into the free surface boundary. The nonlinear evolutions of free-surface waves as well as the flow structure beneath the free-surface are studied.

INTRODUCTION

A free-surface shear flow, is a typical phenomenon for wind-wave, ship wake and wave breaking, etc., and is significantly important in the fields of environmental science, remote sensing, ship hydrodynamics, chemical engineering and the other industrial production processing. The difficulties to treat this problem come from the existence of nonlinear free-surface, turbulent shear-flow and their interaction.

In principal, the free-surface shear-flow can be divided into two categories. One is due to the gas/liquid interaction such as the wind-wave generation problem. The other is due to the shear-flow or turbulent impinging from the liquid side such as the wakes of hydro-foil and ship, and the turbulent jet or plume beneath the free-surface. The present work is to study a three-dimensional mathematical model of turbulent shear-flow existing prior beneath the free-surface which lays in the latter category.

There are two simple models considered so far for this kind of model. One is the roll-up of a submerged vortex sheet close to the free-surface studied by Tryggvason (1988) and Yu & Tryggvason (1990). The other is a linear problem of two-dimensional shear-flow/surface interaction by Triantafyllou & Dimas (1989). In their extensive study, Dimas & Triantafyllou (1994) considered a shear-flow beneath the free-surface at infinite Reynolds number. They started their two-dimensional Euler computation with a shear-flow profile measured by Mattingly & Criminale (1972), superimposed a perturbation having the form of fastest growing linear instability model of the shear-flow (Triantafyllou & Dimas, 1989). However, the picture of flow structure they described is essentially two-dimensional, which is now widely known to be different from the three-dimensional case.

For the three-dimensional case, some important progresses have also been made in the field of gas/liquid interaction when the amplitude of free-surface wave is infinitely small. The phenomena beneath the free-surface are found somehow similar to those of wall turbulent boundary layer in terms of turbulent "streak" structure or "burst" mechanism (Komori, Murakami & Ueda, 1989; Lam & Banerjee, 1991). The free-surface is treated as a linear/free-slip boundary in the most of theoretical and numerical studies.

Komori, Nagaoka & Murakami (1993) mentioned that the transfer mechanism in the turbulent flow structure beneath the free-surface may be more similar to that of "Langmuir circulation". Langmuir circulation is the problem of wind-wave interaction

problem, well known for its vorticity structure parallel to the mean flow beneath the ocean surface and its formation of free-surface wave streaks associated with the longitudinal vorticity (Leibovich, 1977). This kind of organized vorticity structure is considered as the characteristics of three-dimensional structure beneath the sheared free-surface.

When the amplitude of free-surface wave is definite, both the nonlinear evolution of free-surface and the turbulent/surface-wave interaction are still unknown in many aspects. As pointed out by Sarpkaya (1993), it is difficult to find out a distinct turbulent structure in the vicinity of free-surface beneath since some basic features such as the wave modulation by turbulence are basically nonlinear and difficult for analysis. Therefore, it is undoubtedly useful to formulate a mathematical model and to implement a numerical experiment based on the time-dependent Navier-Stokes system subject to the complete, nonlinear free-surface conditions. This work is based on this kind of consideration.

This work investigates the nonlinear evolution of free-surface waves generated by the turbulent shear-flow. The initial state of simulation is fully developed turbulent shear-flow in an open-channel. A similar model has been studied by Leighton & McHugh (1993). They superimposed a linear surface-wave upon the turbulent open-channel flow. In this work, a different conception is considered. At the beginning of the simulation, the solid boundary of the turbulent open-channel flow is released into the free-surface, leaving a strong turbulent shear-flow beneath the free-surface. The physical phenomenon is similar to the wake of turbulent jet, of free-surface flow sheared by wind or a flat horizontal plate.

This paper consists of two parts. In the first part, a highly accurate, conservative and multi-grid finite-volume solution method is developed. The time-dependent Navier-Stokes equations in the Arbitrary-Lagrange-Euler (ALE) description are discretized into a fully conservative finite-volume formulation in the framework of a non-staggered, free-surface boundary-fitted coordinate system. A fifth-order upwind-biased flux-difference splitting scheme is facilitated for the nonlinear convection term. The solution procedure is based on the MAC algoritm. The Poisson equation is solved by means of a fast multigrid Gauss-Seidel/LU decomposition iteration method. This method is validated in the numerical analysis of a solitary wave propagation in a shallow channel by comparison with the previous studies.

In the second part, at first, a direct numerical simulation of turbulent flow in an open-channel is carried out. The simulated results are compared with the previous studies. Secondly, when the turbulent flow in an open-channel rearches a statistically stationary state, the solid boundary is released into the free-surface and the pressure gradient in the streamwise direction is turned off. The nonlinear evolutions of free-surface wave generated by the existing turbulent shear-flow as well as the flow structure beneath the free-surface are analyzed and discussed.

NUMERICAL METHOD

Formulation and Solution Method

The governing equations are formulated in so-called "partial transformation" in a framework of free-surface boundary-fitted coordinate system. The variables are collocated at the center of the cell in the computational domain. The continuity equation and the time-dependent Navier-Stokes equations in the Arbitrary-Lagrange-Euler (ALE) description for the incompressible flow are written as follows.

$$div\,(u) = 0, \tag{1}$$

$$\frac{\partial u}{\partial t} + div\,[(u - v)u] = -grad(P) + div\left[\frac{1}{R_e}\left(grad\,u + (grad\,u)^T\right)\right], \tag{2}$$

where u is the velocity and P is the dynamic pressure defined as follows.

$$P = \frac{p}{\varrho} + \frac{x^3}{F_n^2}, \tag{3}$$

p is the pressure, ϱ is the density of fluid, and x^3 is the vertical coordinate in direction with the free-surface elevation. The Reynolds number R_e and Froude number F_n are defined as follows.

$$R_e = \frac{U_0 H}{\nu}, \tag{4a}$$

$$F_n = \frac{U_0}{\sqrt{g H}}, \quad (4b)$$

where U_0 is the reference velocity and H is the depth of the physical region in this paper. g is the gravitational acceleration and ν is the molecular viscosity. v is the moving velocity of the free-surface boundary-fitted coordinate system and is defined implicitly in the following ALE inviscid flux formulation.

The ALE inviscid flux can be written in the following form.

$$F^j = \left(S^j \cdot u - \frac{dV^j}{dt}\right) q = \left(U^j - \frac{dV^j}{dt}\right) q, \quad (5)$$

where q is the arbitrary velocity component, U^j is the volume flux (mass flux) in j sweep, S^j is the surface vector of the cell in j sweep and F^j is the ALE inviscid flux for q in j sweep. The moving velocity v is represented by the time derivative of volume flux V^j which is defined by the movement of the surface vector S^j as shown in Fig.1. Therefore the relationship between the moving velocity and the time derivative of V^j is as follows (Rosenfeld & Kwak, 1991).

$$S^j \cdot v = \frac{dV^j}{dt}. \quad (6)$$

The convection term is spatially discretized by a fifth-order upwind-biased flux-difference splitting scheme based on the flux-difference splitting method by Sawada et al.(1987) as follows.

$$F^j_{i+\frac{1}{2}} = \frac{1}{2}\left(\tilde{U}^j_{i+\frac{1}{2}} - \left|\tilde{U}^j_{i+\frac{1}{2}}\right|\right) q_{i+\frac{1}{2}}^{+} + \frac{1}{2}\left(\tilde{U}^j_{i+\frac{1}{2}} + \left|\tilde{U}^j_{i+\frac{1}{2}}\right|\right) q_{i+\frac{1}{2}}^{-}, \quad (7)$$

where

$$\tilde{U}^j = U^j - \frac{dV^j}{dt}, \quad (8)$$

and $q_{i+\frac{1}{2}}^{+}$ and $q_{i+\frac{1}{2}}^{-}$ are defined as follows.

$$q_{i+\frac{1}{2}}^{-} = q_i + \Phi_1^{-}\,\delta q_{i-\frac{3}{2}} + \Phi_2^{-}\,\delta q_{i-\frac{1}{2}} + \Phi_3^{-}\,\delta q_{i+\frac{1}{2}} + \Phi_4^{-}\,\delta q_{i+\frac{3}{2}}, \quad (9a)$$

$$q_{i+\frac{1}{2}}^{+} = q_{i+1} - \Phi_4^{+}\,\delta q_{i-\frac{5}{2}} - \Phi_3^{+}\,\delta q_{i-\frac{3}{2}} - \Phi_2^{+}\,\delta q_{i-\frac{1}{2}} - \Phi_1^{+}\,\delta q_{i+\frac{1}{2}}, \quad (9b)$$

where

$$\delta q_{i+\frac{1}{2}} = q_{i+1} - q_i, \quad (10)$$

$$\Phi_1^{-} = \Phi_1^{+} = -\frac{2}{60}, \quad (11a)$$

$$\Phi_2^{-} = \Phi_2^{+} = \frac{11}{60}, \quad (11b)$$

$$\Phi_3^{-} = \Phi_3^{+} = \frac{24}{60}, \quad (11c)$$

$$\Phi_4^{-} = \Phi_4^{+} = -\frac{3}{60}. \quad (11d)$$

When the geometries of physical domain and flow are smooth, the above flux-difference splitting scheme is identical to the finite-difference scheme by Rai & Moin (1991).

The solution procedure is based on the fractional step method of the MAC algorithm. Time integration is implemented by a second-order Adames-Bashforth/Crank-Nicholson scheme. The mass flux U^j is defined at the cell surface of respective j sweep, contrasted with the velocity component defined at the center of computing cell. Therefore the continuity equation can be formulated in terms of the mass flux as follows.

$$\sum_j U^j = 0 \quad (12)$$

The mass flux is defined as follows.

$$U^j = S^j \cdot \left(\sum_k G_k(a)_k\right) - S^j \cdot \Delta t\, grad(P), \quad (13)$$

where a is defined at the center of computing cell as the summation of the convection term and the diffusion term in Navier-Stokes equation. G_k is the interpolation operator with respect to the position k. Therefore the first term means an interpolation of a from the cell center to the cell surface. A fourth-order interpolation is employed in the present study. Δt is the time interval. By inserting Eq.(13) into Eq.(12), the Poisson equation is defined as follows.

$$\Delta t \sum_j S^j \cdot grad(P) = \sum_j S^j \cdot \left(\sum_k G_k(a)_k\right). \quad (14)$$

The mass flux employed in the ALE inviscid flux of Eq.(5) is identical to that defined in Eq.(13). It is obvious that the divergence-free is inevitably important for raising the accuracy of high-order scheme in the convection term.

It is necessary to introduce a fast solution method for the pressure equation in a time-dependent Navier-Stokes simulation for turbulent flow since the pressure solution takes almost 80% CPU time of the computation in the MAC-type fractional step

method (Rosenfeld & Kwak, 1993). In this study, the Poisson equation is solved by a V-cycle multigrid technique applying to the Gauss-Seidel linear LU-decomposition iteration method. The basic multigrid method employed here is the so-called "correction scheme" for the linear Poisson equation, based on the method by Ghia et al.(1988). A V-cycle structure is used with two iterations at each multigrid stage. The test computation (not shown here) showed this method accelerated the computation at a speed of almost several hundred times.

Free-surface Condition

The nonlinear kinematic condition and dynamic condition at the exact wave elevation are applied at the free-surface in this study. In principle, the kinematic condition mantains the mass balance, while the dynamic condition corresponds to the momentum balance at the free-surface.

In the present study, the following kinematic condition in the Eulerian manner is used.

$$\frac{\partial \eta}{\partial t} = u^1 \frac{\partial \eta}{\partial x^1} + u^2 \frac{\partial \eta}{\partial x^2} - u^3 \quad , \qquad (15)$$

where the free-surface elevation η is in x^3 direction of a flow field $(u, r) = ((u^1, u^2, u^3), (x^1, x^2, x^3))$. The fourth-order centered finite-difference scheme is used for the spatial derivatives. The time integration is implemented in Euler-implicit manner by a predictor-corrector iterative method. The iteration is required to converge to machinery accuracy since the free-surface turbulent motions is studied in the present study. Usually less than 10 iterations are required for this procedure. A 5-point smoothing formula by Longuet-Higgins & Cokelet (1976) is introduced to prevent the free-surface configuration from the numerical spurious oscillation.

For simplicity, there is no surfacants acting at the free-surface in the present study. The dynamic condition employed in the present study is written in the following equation, which contains one along the normal direction of the deformed free-surface and two along the tangential directions.

$$-P\,\delta^{ij} n_i n_j + \frac{1}{R_e}\left(\frac{\partial u^i}{\partial x^j} + \frac{\partial u^j}{\partial x^i}\right) n_i n_j = -\frac{\varkappa}{W_b}\,\delta^{ij} n_i n_j \quad , \qquad (16)$$

where $\boldsymbol{n}=(n_i;\ i=1, 2, 3)$ is the normal vector of the deformed free-surface. $\varkappa$ is the surface curvature and W_b is the Weber number defined as follows.

$$W_b = \frac{\varrho U_0^2 H}{\sigma} \quad , \qquad (17)$$

where σ is the surface tension of fluid. The two tangential-free conditions are applied in the diffusion term of Navier-Stokes formulation and the normal condition is employed in the solution of Poisson equation.

Other Boundary Conditions

This work treats three cases of physical phenomena. They are 1) solitary wave propagation in shallow channel; 2) turbulent open-channel flow and 3) free-surface wave generation by turbulent shear-flow beneath the free-surface. The common conditions for these three-dimensional simulations are the periodic conditions in both the streamwise direction and the spanwise direction. The differences are boundary conditions in vertical direction.

In the case of solitary wave propagation, the upper boundary is the free-surface. The lower boundary is the solid boundary so that no-slip velocity condition and zero-pressure gradient condition are applied. In the case of turbulent open-channel flow, the upper boundary is the solid boundary. The lower is the symmetric boundary so that free-slip velocity condition and zero-pressure gradient condition are applied. In the case of free-surface wave generation by turbulent shear-flow, the upper is the free-surface. The lower is the symmetric boundary.

SOLITARY WAVE PROPAGATION IN SHALLOW CHANNEL

Condition of Simulation

A solitary wave travelling in a rectangular channel of uniform depth initially studied by Russell in 1837, is numerically analyzed in order to validate the numerical method presented in this paper,

subject to the nonlinear, complete free-surface conditions. Laiton's approximation of a solitary wave is employed in the present study (Laiton, 1960). The initial velocity and free surface elevation are defined as follows (Ramaswamy, 1990).

$$u^1 = A_0\, sech^2\, \Phi_0, \quad (18a)$$

$$u^2 = 0, \quad (18b)$$

$$u^3 = \sqrt{3\, A_0^3}\; x^3\, sech^2\, \Phi_0\, tanh\, \Phi_0, \quad (18c)$$

$$h = 1 + A_0\, sech^2\, \Phi_0, \quad (18d)$$

where

$$\Phi_0 = \frac{1}{2}\sqrt{3A_0}\,(x^1 - c\,t), \quad (19a)$$

$$c = \sqrt{1 + A_0}. \quad (19b)$$

All the variables are nondimensionalized by the depth H and the reference velocity $U_0 = \sqrt{g\,H}$. Therefore Froude number is at 1.0. For comparison with the previous study (Tang, Patel & Landweber, 1990), A_0 is set at 0.2, and the physical domain is 30 long, π wide and 1 deep. A 65 (streamwise) x 5 (spanwise) x 33 (vertical) grid is employed for the quais-three-dimensional computation domain. In the present study, three cases at Reynolds number 50, 500 and 50000 are computed.

Simulated Results

Fig. 2 shows the wave evolution of free-surface configuration at the different Reynolds number. Compared with almost the same study by Tang et al.(1990), the free-surface wave dampings due to the boundary layer at the bottom are quite well revealed except the small wavy profile at the leeward of the solitary wave. The reason of this is due to the periodic condition in the streamwise direction in the computation since the wavelength of solitary wave is basically infinite. An alternative study by Hino (1991) using a finite-volume method with the periodic condition also showed the same small wavy profile at the leeward. Tang et al.(1990) set both the upstream and downstream of the physical domain as the open boundary with zero-gradient condition. This effect of periodic condition for wave problem reminds that the cutoff of dominant wavelength by the periodic condition will raise some numerical spurious waves. Therefore, in the computation with periodic condition the Taylor Froude number F_λ should be no more than unit, i.e.,

$$F_\lambda = \frac{U_0}{\sqrt{g\lambda}} < 1.0, \quad (20)$$

where λ is the cut-off wavelength of periodic physical domain. This condition corresponds to that the wavelength of simulated wave should be shorter than the cut-off wavelength of periodic physical domain. This result will be useful for the computation of wave problem with periodic condition.

Fig.3 shows the comparisons of the computed attenuations of wave crest height with the theoretical approximation of Keulegan (1948) and Mei (1983). The wave crests at R_e= 50 and 50000 show less damping than those of Tang et al.(1990) but at Reynolds number 500 show more. It is thought that the viscous damping by the bottom boundary layer is not so large as shown by Tang et al.(1990) at R_e= 50000. Therefore the present study may show a better numerical result.

TURBULENT OPEN CHANNEL FLOW

Condition of Simulation

A number of direct simulations of the turbulent open channel flow have been carried out for the investigation of the turbulent structure both near the wall and beneath the flat free-surface (Lam & Benerjee, 1992; Handler at al., 1993). In the most studies in this field, the spectral method (Kim et al.,1987) is used. This is because the spectral method shows the most realistic spectra over wide range of Fourier space. However, it is difficult for the spectral method to apply to the turbulence with complex geometry. In contrast with the spectral method, the finite-difference method can not reveal the wide spectral property of flow due to the finite difference approximation but is feasible for the simulation of turbulence with complex geometry (Rai & Moin, 1991).

In the present study, a direct simulation of open-channel flow is carried out for two purposes. At first, a fully developed turbulence open-channel is required as the initial state for the free-surface wave generation by turbulent shear-flow beneath the free-surface. Secondly, at the same time,

a finite-volume solution method is then validated to answer the question that if the present method is capable for the simulation of turbulent flow with the dynamic free-surface.

Due to the limitations of the memory and CPU time on the computer, a rather coarse grid is facilitated here for the simulation. In the present study, a 33 (streamwise) x 33 (spanwise) x 65 (vertical) grid for a physical domain of ($2\pi \times \pi \times 1$)is introduced for the Reynolds number R_τ= 171, based on the channel depth H and the wall frictional velocity u_τ. This Reynolds number corresponds to the Reynolds number R_e defined in Eq.(4a) at 3100, where U_0 is the mean velocity at the center plane of the channel. The smallest grid used so far by spectral method for the open channel flow in the same dimension is that of Lam & Banerjee (1992), in which a 32x64x65 grid is used. For the finite-difference method for the simulation of a channel flow, the smallest one ever known is that of Rai & Moin (1991), in which a 64x64x65 grid is used (they called coarse grid case). Handler at al. (1993) used a 64x64x65 grid for a lower R_τ at 134 in their spectral simulation of a turbulent open channel flow.

A laminar velocity profile and 5% random disturbance of mean-flow are given as the initial state. The computation is implemented with a pressure gradient balancing the shear force at the wall.

Simulated Results

Fig. 4 and 5 show the time evolutions of total kinematic energy and enstrophy in the channel, respectively. The flow state becomes statistically stationary after dimensionless time T (tu_τ/H) = 30. Fig. 6 shows the total kinematic energy spectrum in the streamwise direction in the open channel, where k_1 is the wave number in x^1 direction. It indicates that the present finite-volume method is capable of revealing the spectral property of a turbulent flow.

Fig. 7 shows the velocity profile compared with the Spalding universal wall-law. There is small discrepancy between the computed velocity profile with the Nikuradze log-law, although the velocity gradient in the log-law region is good. Lam & Banerjee (1992) discussed in details about the velocity profile in the open channel. The velocity profile seems to have strong relationship with the rms velocity fluctuation profile. Fig. 8 shows the comparisons between the computed rms velocity fluctuations with the computational data of Lam & Banerjee (1992), the experimental data of Komori et al.(1982) and Rashidi & Banerjee (1988). The computed velocity fluctuations show the reasonable results near the interface plane ("free-surface") compared with the experimental data (Komori et al, 1982; Rashidi & Banerjee, 1988). However, near the wall region, there is a discrepancy betweent the present computation with that of Lam & Banerjee (1992). The vertical velocity fluctuation is underestimated in the present study while the streamwise counterpart is overestimated. The total turbulent kinematic energy is comparable with that of Lam & Banerjee (1992). This may be because that the grid points in the spanwise direction in the present study are too small to capture the whole turbulent flow structure near the wall. Fig.9 is the instantaneous streamwise velocity fluctuation near the wall at x^{3+}=1.5, showing the turbulent streaks structure near the solid wall. The averaged distance between the streaks is almost about 100 in viscous unit dimension, agreeing well with the other studies (Handler et al., 1993).

As a summary, although this simulation is carried out by a finite-volume method with a rather coarse grid, the basic features of turbulent open-channel flow are well revealed in terms of turbulent spectral property and turbulent intensity profile as well as the turbulent streaks structure near the wall. Therefore, it indicates that the present method is capable for the simulation of a turbulent flow.

FREE-SURFACE WAVE INDUCED BY TURBULENT SHEAR-FLOW

Condition of Simulation

A direct numerical simulation is carried out for the analysis of free-surface wave generation by a turbulent shear-flow existing prior beneath the free-surface. The initial state of simulation is inherited from

the direct numerical simulation results of turbulent open-channel flow described above. The simulation is started by releasing the solid boundary into the free surface boundary. The same dimensions of physical domain with the same grid points as the turbulent open-channel are employed.

For the numerical simulation of free-surface turbulent flow, there are two problems beside the numerical scheme. One is the resolution problem and the other is the size of physical domain problem. For a certain low Reynolds number, these two problems have been well discussed (Kim et al., 1987). However, for the free-surface turbulent flow involving the Froude number, these two problems are still open questions. It is unknown that in a direct simulation, how wide the region of wave number of the free-surface wave should be resolved at the certain Reynolds number and Froude number. Maybe this question is not meaningful since the phenomenon is not so simple as the turbulence in a channel. Under certain condition, the wave will break at any wave number, or will disperse by the capillary force or will dissipate by the viscous force. But as a practical problem, with a grid of certain resolution in a certain physical domain with periodic condition, neither the waves of very large wave number nor the waves of very small wave number can be resolved. That is, the wave number resolved satisfies the following relation.

$$1 < \frac{k}{F_\lambda^2} < \alpha N \qquad (21)$$

where F_λ is the Taylor Froude number, λ is the cut-off wavelength of periodic physical domain and N is the grid number. The left side means that no longer wave (small wave number) than the physical domain can be revealed really where the right hand side means no too short wave (large wave number) can be resolved because of the grid resolution limitation (α is the measure of the resolution for waves). In the present study, a numerical case of $\lambda = 2\pi$ and N=33, F_n= 0.7 (H=1) is tested. Therefore,

$$F_\lambda = \frac{1}{2}(\pi)^{-\frac{1}{2}} . \qquad (22)$$

In the turbulent channel flow, the largest scale of turbulence is considered to be sufficiently captured within the physical domain. However, for the free-surface turbulent flow, what is the largest wavelength generated by a certain turbulent flow is dependent on the Froude number. For a unit Froude number, $\lambda = 2\pi$ is considered as the smallest size for the wave generation by turbulence.

Simulated Results

Fig. 10 shows the prospect of the free-surface wave at T= 3.488 after releasing the solid boundary into the free-surface boundary. Fig.11 shows the contour plots of the free-surface wave induced by the turbulent shear-flow at T= 2.000 and 3.488. The free-surface seem to consist of the waves with a lot of wavelength. Compared with T= 2.000, the waves at T= 3.488 show more ordered formation.

A spectral analysis for the free-surface waves is carried out. Fig.12 is the directional wave spectrum : (a) x^1-direction and (b) x^2 - direction. There are distinct Fourier harmonicas over the unit wave number region. The spectra near the largest wave number show a little bit aliasing feature, especially in the x^1-directional spectrum. Therefore, the grid resolution may be not so sufficient for the free-surface wave at the Froude number considered here. The numerical verification is under investigation at this time.

Fig.13 shows the time evolution of the Fourier harmonicas in the wave spectrum : (a) x^1-direction and (b) x^2 - direction. Except the fourth harmonica, the lower-order harmonicas vary in time, indicating there are strong wave modulations associated with turbulence/surface wave interaction and wave/wave interaction.

Fig.14 shows the iso-surface contour of the instantaneous longitudinal velocity fluctuation beneath the free-surface. The red is the value at +0.05 and the blue is at -0.05. A distinct organized flow structure parallel to the mean flow direction appears beneath the free-surface wave. The wavelength of the structure in spanwise direction almost equals to the physical domain length in that direction. Therefore, it is necessary to further study the size of the physical domain in the spanwise direction to investigate the parallel flow structure beneath the free-surface.

CONCLUDING REMARKS

A highly accurate, conservative and multi-grid finite-volume solution method is developed and validated in the numerical analysis of a solitary wave propagation in a shallow channel and in the direct numerical simulation of an open-channel flow. That means the present numerical method is capable of simulating both the nonlinear free-surface waves and the turbulent flow.

A preliminary analysis of the free-surface wave generated by the turbulent shear-flow existing prior is carried out by means of direct numerical simulation. The simulation shows some interesting features of wave motion such as the wave modulation by turbulence/wave interaction and wave/wave interaction. The flow structure parallel to the streamwise direction beneath the free-surface is recognized. Several problems with respect to the direct numerical simulation of the free-surface turbulence phenomenon are raised and discussed. As the result, both the grid resolution for the waves at the corresponding Froude number and the physical domain of the simulation are required to be verified in the further investigation.

This work is sponsored by the Promotion Organization of Ship Research of JAPAN, 93REDAS No.10.

REFERENCES

Dimas, A. A., and Triantafyllou, G. S., "Nonlinear Interaction of Shear Flow with a Free Surface", Journal of Fluid Mechanics, Vol.260, 1994, pp.211-246.

Ghia, U., Ramamurti, R., and Ghia, K. N., "Solution of the Neumann Pressure Problem in General Orthogonal Coordinate Using the Multigrid Technique", AIAA Journal, Vol.26, No.5, 1988, pp.538-547.

Handler, R. A., Swean Jr.,T. F., Leighton, R. I., and Swearingen, J. D., "Length scales and the energy balance for turbulence near a free surface", AIAA Journal, Vol.31, No.11, Nov., 1993. pp.1998-2007.

Hino, T., unpublished, (1991).

Keulegan, G. H., J. Res. Nat. Bur. Standards, Vol.40, (1948).

Kim, J., Moin, P., and Moser, R., "Turbulence Statistics in Fully Developed Channel Flow at Low Reynolds Number", Journal of Fluid Mechanics, Vol.177, 1987, p.133.

Komori, S., Murakami, Y., and Ueda, H., "The Relationship Between Surface-Renewal and Bursting Motions in an Open Channel Flow", Journal of Fluid Mechanics, Vol.203, 1989, pp.103-123.

Komori, S., Nagaoka, R., and Murakami, Y., "Turbulent Structure and Mass Transfer Across a Sheared Air-Water Interface in Wind-Driven Turbulence", Journal of Fluid Mechanics, Vol.249, 1993, pp.161-183.

Laiton, E. V., "The Second Approximation to Cnoidal Solitary Wave", Journal of Fluid Mechanics, Vol.9, 1960, pp.430-.

Lam, K., and Banerjee, S., "On the Condition of Streak Formation in a Bounded Turbulent Flow", Physics of Fluids, A4(2), 1991, pp.306-320.

Leibovich, S., "On the Evolution of the System of Wind Drift Currents and Langmuir Circulations in the Ocean. Part 1. Theory and Averaged Current", Journal of Fluid Mechanics, Vol.70, part 4, 1977, pp.715-743.

Leighton, R. L., and McHugh, J., "The Interaction of Surface Waves with a Turbulent Flow", Abstracts of 1993 Free-Surface Turbulence Workshop, March, 1993, Caltech, Pasadena, CA.

Longuet-Higgins, M. S., and Cokelet, E. D., "The Deformation of Steep Surface Waves on Water", Proc. R. Soc. Lond., A. 350, 1976, pp.1-26.

Mattingly, G. E. and Criminale, W. O., "The Stability of an Incompressible Two-Dimensional Wake", Journal of Fluid Mechanics, Vol.51, 1972, pp.233-272.

Mei, C. C., The Applied Dynamics of Ocean Surface Waves, Wiley, New York, (1983), p.564.

Rai, M. M., and Moin, P., "Direct Simulations of Turbulent Flow Using Finite-Difference Schemes", Journal of Computational Physics, Vol.96, 1991, pp.15-53.

Ramaswamy, B., "Numerical Simulation of Unsteady Viscous Free Surface Flow", Journal of Computational Physics, Vol.90, 1990, pp.396-430.

Rashidi, M., and Banerjee, S., "Turbulence Structure in Free Surface Channel Flow", Physics of Fluids, Vol.31, 1988, p.2491.

Rosenfeld, M., and Kwak, D., "Multigrid Acceleration of a Fractional-Step Solver in Generalized Curvilinear Coordinate Systems", AIAA Journal, Vol.31, No.10, 1993, pp.1792-1800.

Rosenfeld, M., Kwak, D., and Vinokur, M., "A Fractional Step Solution Method for the Unsteady Incompressible Navier-Stokes Equations in Generalized Coordinate Systems", Journal of Computational Physics, Vol.94, 1991, pp.102-137.

Sarpkaya, T., "Turbulent Kinetic Energy in Vortex/Free-Surface Interaction", Abstracts of 1993 Free-Surface Turbulence Workshop, March, 1993, Caltech, Pasadena, CA.

Sawada, K. and Takanashi, S., "A Numerical Investigation and Wing/Nacelle Interferences of USB configuration", AIAA Paper 87-0455, 1987.

Tang, C. J., Patel, V. C., and Landweber, L., "Viscous Effects on Propagation and Reflection of Solitary Waves in Shallow Channels", Journal of Computational Physics, Vol.88, 1990, pp.86-113.

Triantafyllou, G. S., and Dimas, A. A., "Interaction of Two-Dimensional Separated Flows with a Free Surface at Low Froude Number", Physics of Fluids, A1, 1989, pp.1813-1821.

Tryggvason, G., "Deformation of a Free Surface as a Result of Vortical Flow", Physics of Fluids, Vol.31, 1988, pp.955-957.

Yu, D., and Tryggvason, G., "The Free-Surface Signature of Unsteady, Two-Dimensional Vortex Flow", Journal of Fluid Mechanics, Vol.218, 1990, pp.547-572.

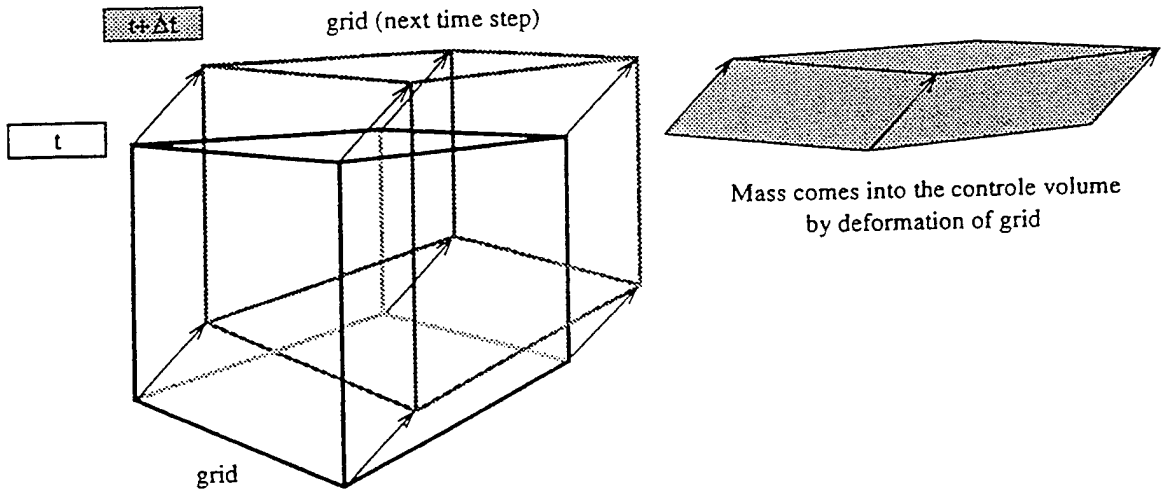


Fig. 1 Arbitrary-Lagrange-Euler volume flux change by the movement of surface vector

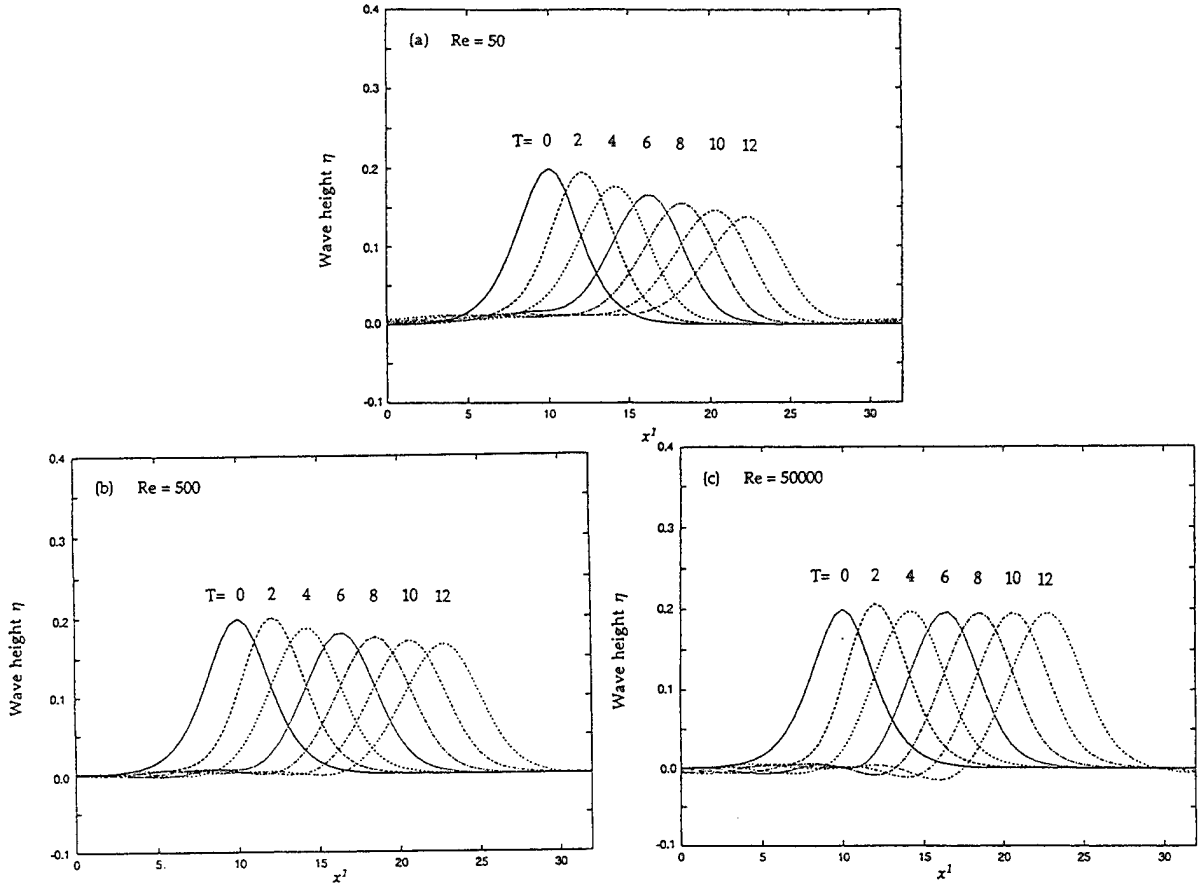


Fig. 2 Time evolution of wave profile at different Reynolds numbers

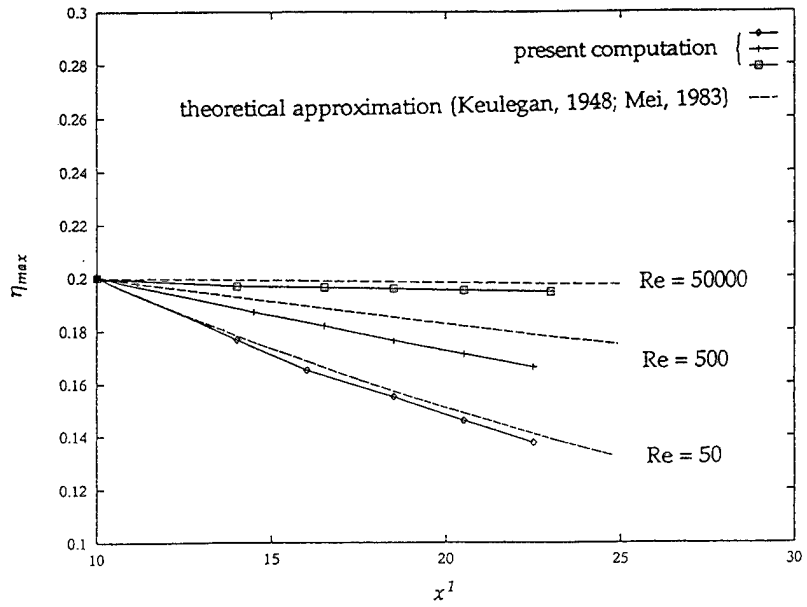


Fig. 3 Attenuation of wave crest height with distance

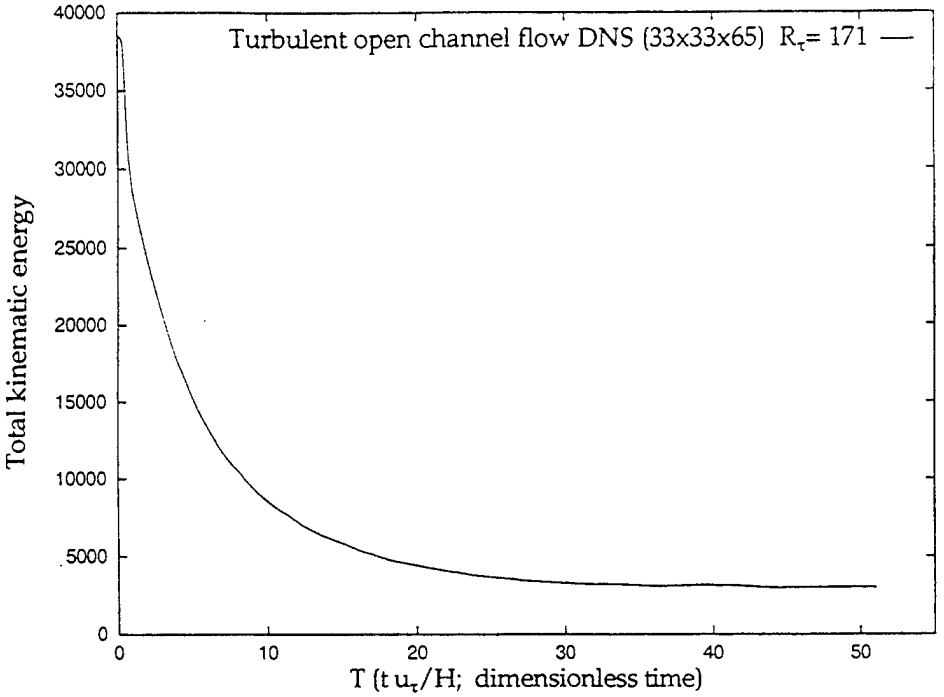


Fig. 4 Time evolution of total kinematic energy

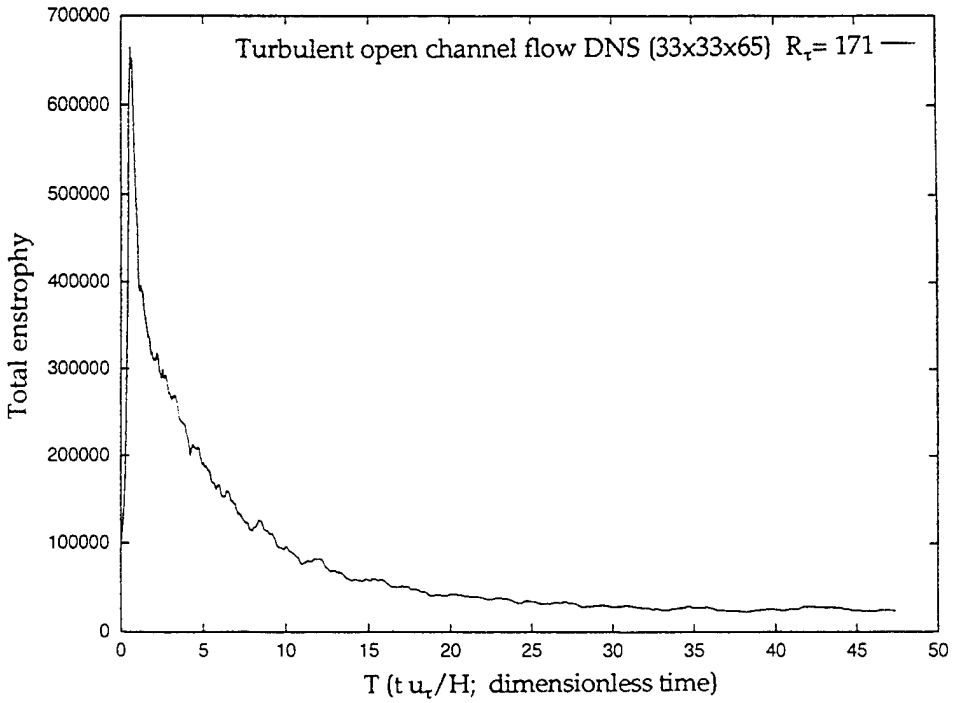


Fig. 5 Time evolution of total enstrophy

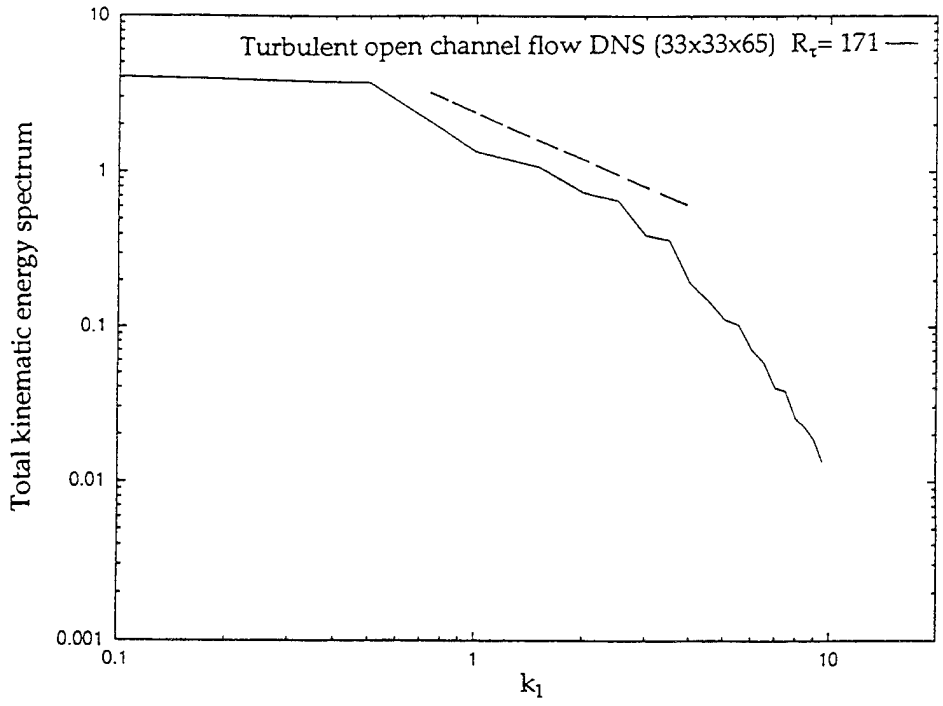


Fig. 6 Total kinematic energy spectrum

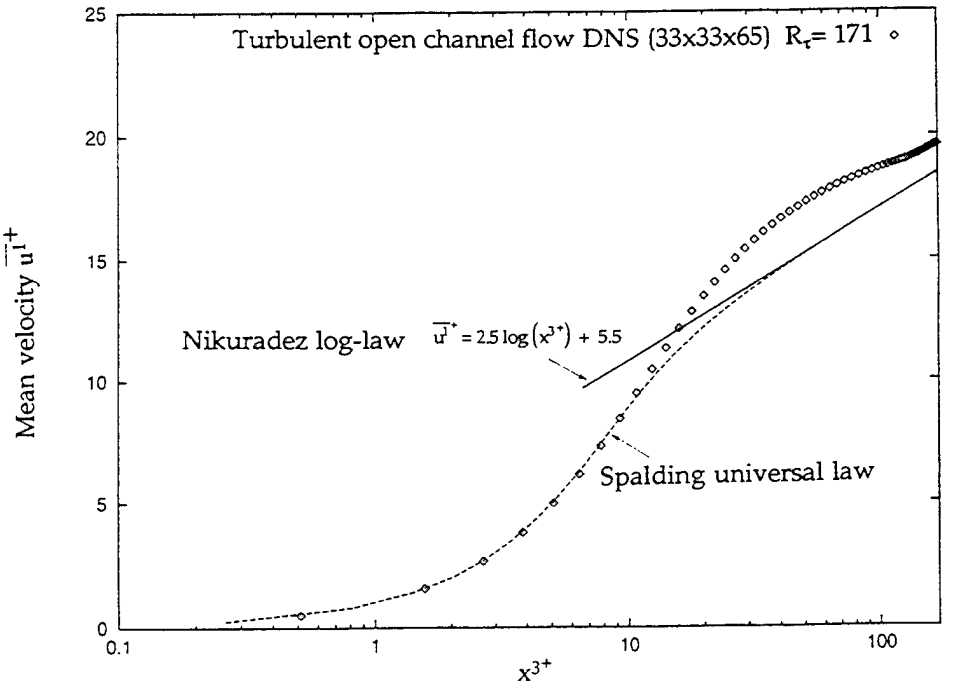


Fig. 7 Mean velocity profile

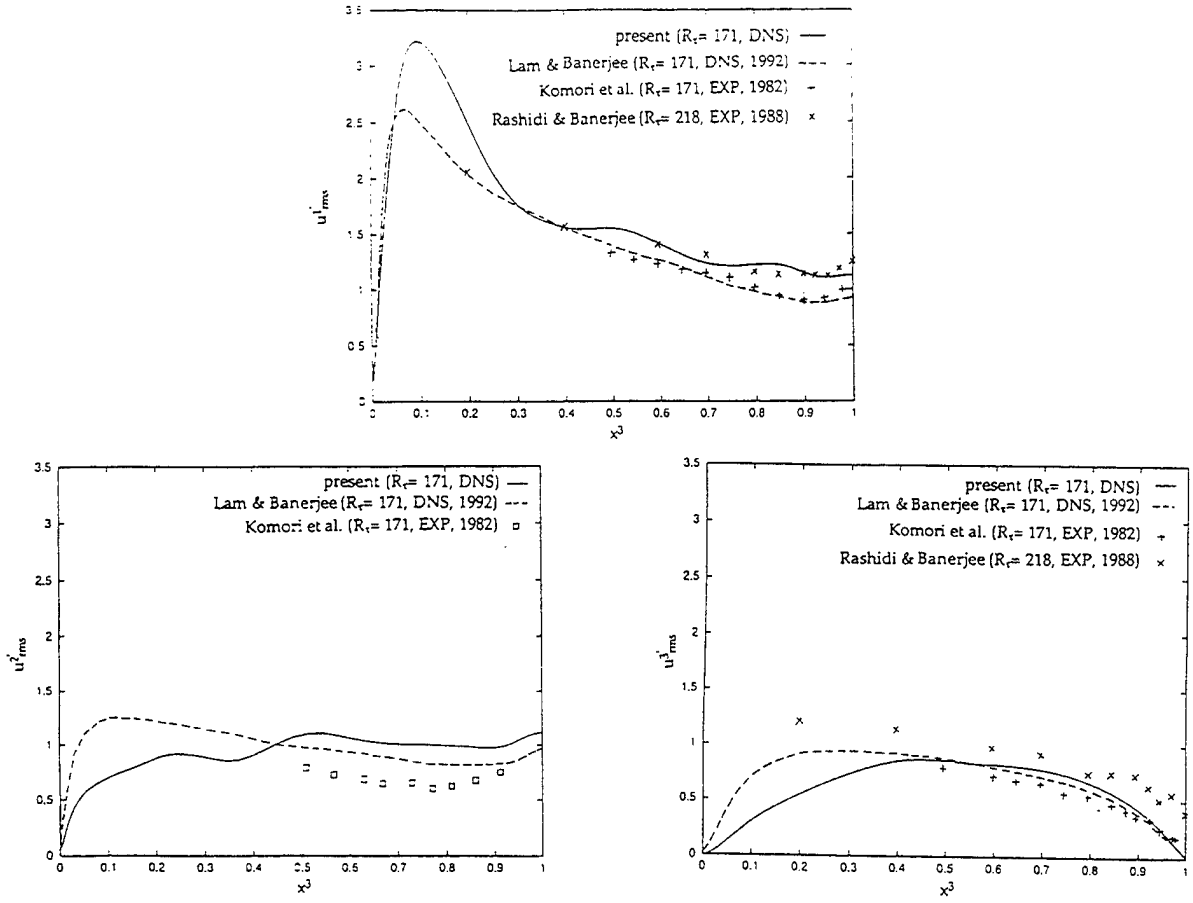


Fig. 8 Comparison between the computed rms velocity fluctuations with the open channel flow data of Lam & Banerjee (1992), the experimental data of Komori et al.(1982) and Rashidi & Banerjee (1988).

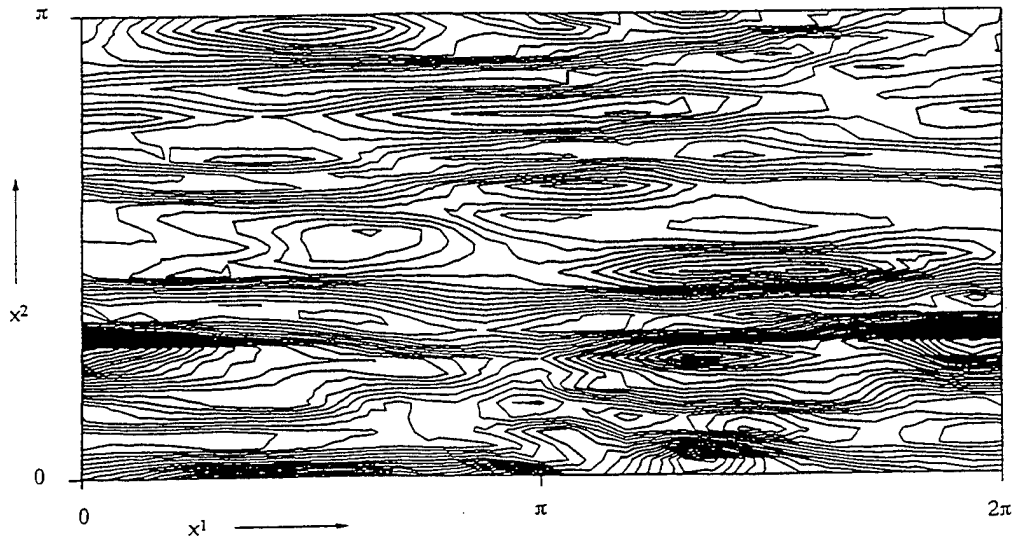


Fig. 9 Contour plot of the instantaneous longitudinal velocity fluctuation in an x^1-x^2 plane at x^{3+}= 1.5. interval= 0.2 u_τ

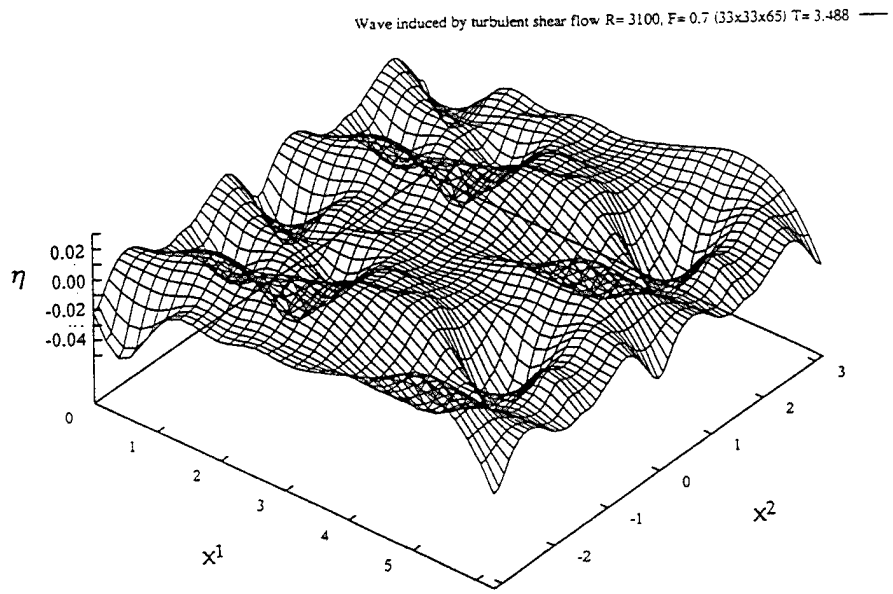


Fig.10 Prospect of free-surface wave induced by turbulent shear-flow (F_n= 0.7, T= 3.488) The length in the x^2-direction is twice the length of the computational domain

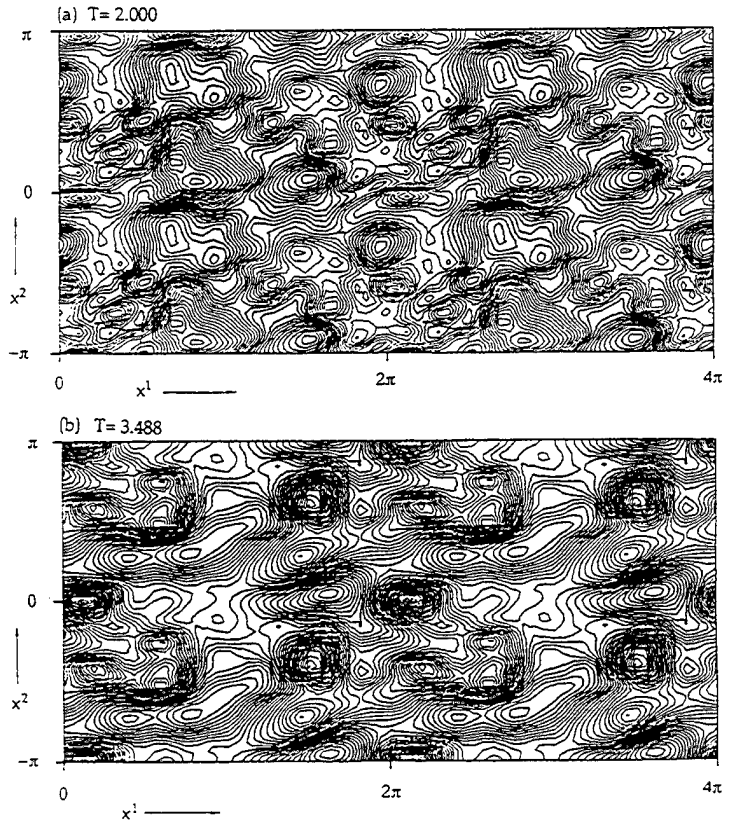
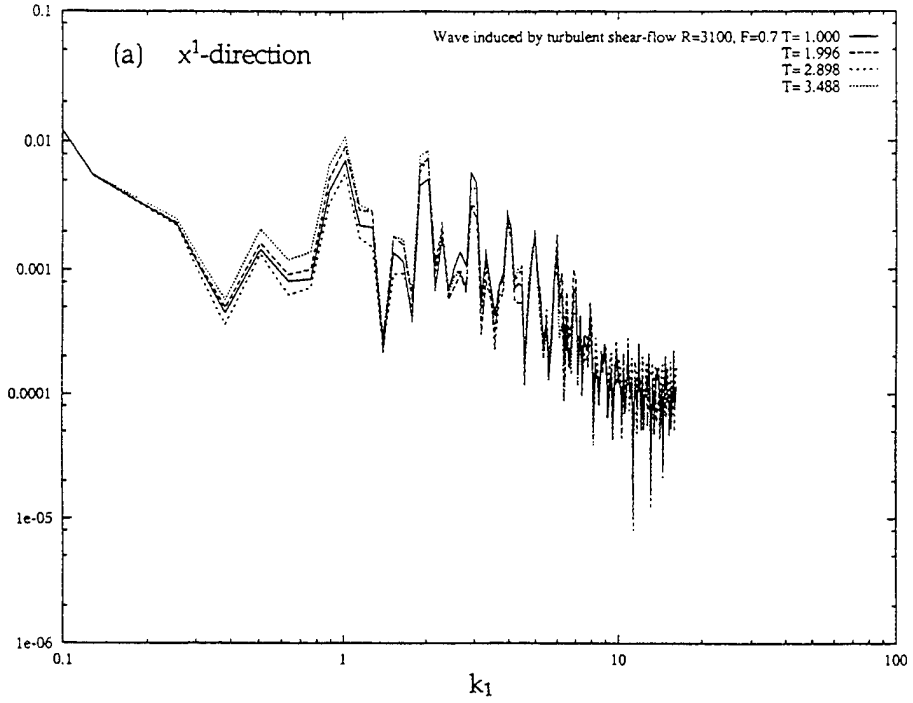


Fig.11 Contour plot of free-surface wave induced by turbulent shear-flow (F_n= 0.7) The length in both direction is twice the length of the computational domain interval= 0.002H.



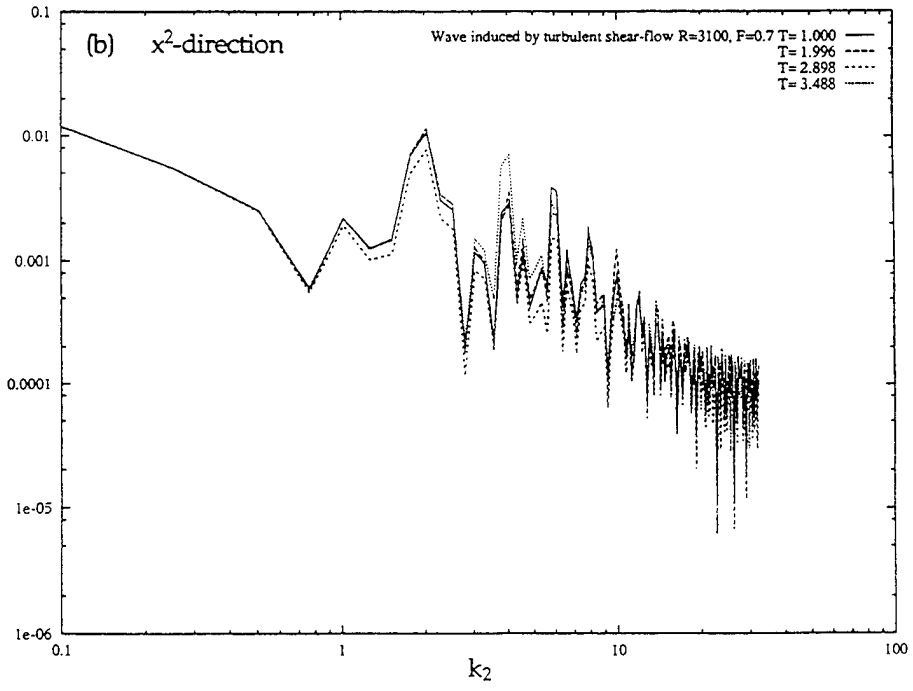
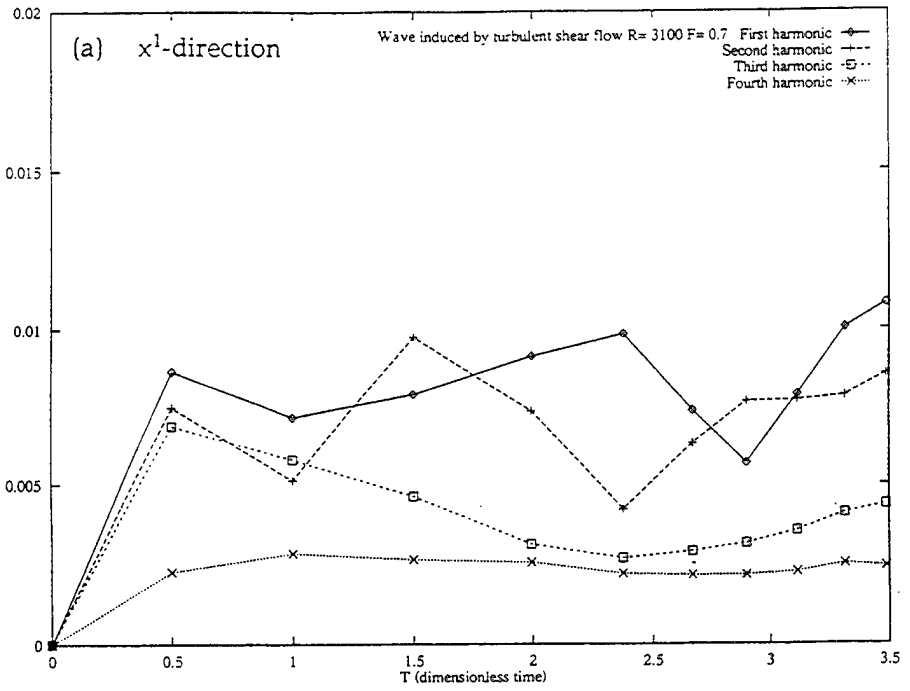


Fig.12 Wave spectrum (Fn = 0.7)



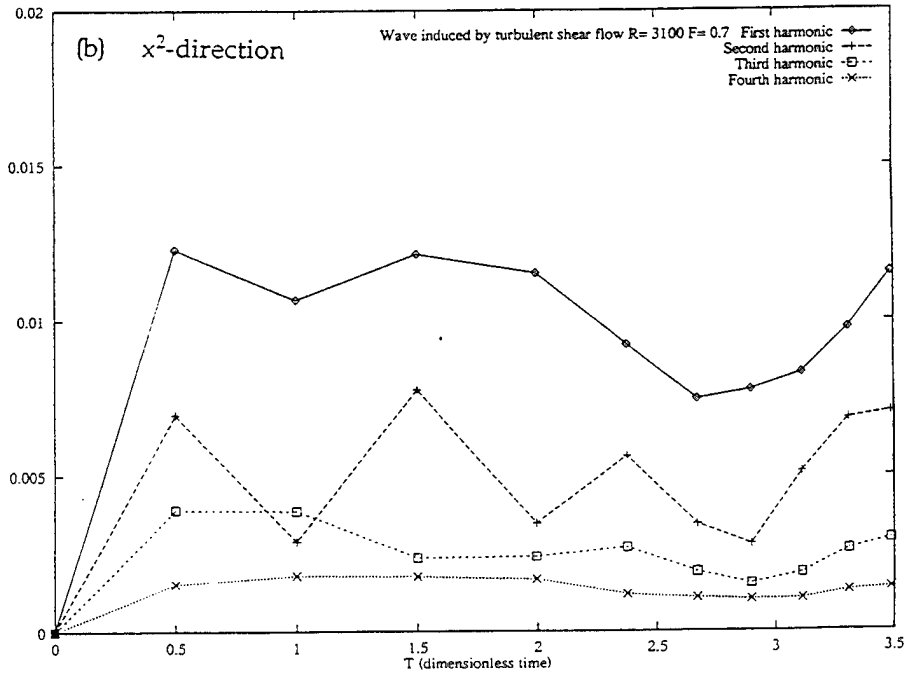


Fig.13 Evolution of wave spectrum harmonicas (Fn = 0.7)

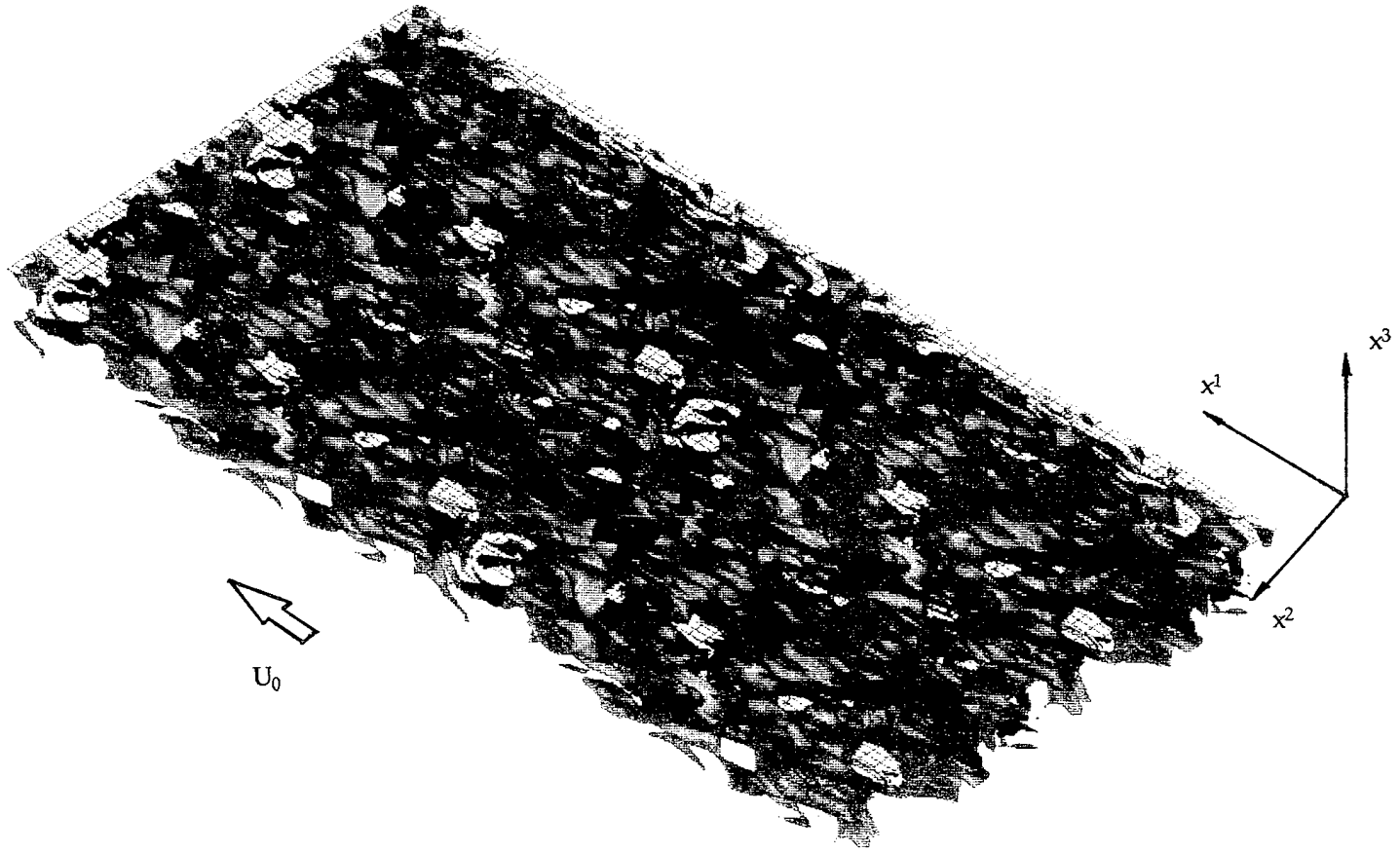


Fig. 14 Iso-surface contour of the instantaneous longitudinal velocity fluctuation beneath the free-surface (Fn= 0.7)
Red: +0.05; Blue: -0.05

Flow Structure Around a Surface-Piercing Blunt Body

E. Pogozelski, J. Katz (Johns Hopkins University, USA),
T. Huang (David Taylor Model Basin, USA)

ABSTRACT

The flow structure around a surface piercing, symmetric, two dimensional body is investigated in this paper. The focus is on phenomena around the bow that generate bubbly wakes. The experiments were performed in a towing tank and included velocity measurements using PIV and video photography above and below the surface. The development of a bow wave, that becomes larger and increasingly unstable with increasing Froude number, is demonstrated. When this wave breaks, a spilling breaker for the present case, it causes generation of some bubbles. However, the primary and distinctly different source of bubbles is located just downstream of the bow wave, at the point where the water level starts increasing again. The influx towards the model seems to impinge on the body, which causes splashing and generation of a bubbly wake. The process becomes evident at Froude numbers exceeding 0.15, and its severity increases with the Froude number. Velocity distributions and surface contours of water elevation demonstrate the mechanisms involved.

INTRODUCTION

Very little is known about the flow structure around surface piercing bodies, in spite of their significance to naval hydrodynamics. The primary reason is the complexity of this flow, which involves interaction of a free surface and the associated waves with a boundary layer, which is sometimes separated. Consequently, most existing numerical solutions of the flow around ships involve considerable simplifications. Classical models include assumptions of a slender body and inviscid flow, which were originated by Michell (1), developed by Tuck (2,3), and adopted for bow flows by Ogilvie (4). All are quite inaccurate near the bow region. More sophisticated quasi-analytical models, such as Dawson (5), still involve linearized free surface conditions that only satisfy the boundary conditions at the ship wall (see also a survey by Chapman (6)). Relatively recent attempts to implement complete Reynolds averaged Navier Stokes codes, such as Hino (7), provide promising results as far as gross flow phenomena (mean pressure distribution, etc.) are concerned, but suffer from typical problems associated with turbulence modeling, particularly near the free surface. There is also very limited experimental data on this flow, in part due to technical difficulties in performing measurements near the surface. Existing results, such as Fry and Kim (8), indicate that this three dimensional flow involves interaction of a boundary layer with non-linear bow waves and formation of large scale vortices. The presence of surface waves near the body can cause unsteady flow separation, resulting in an unsteady wake. Combined mean velocity and surface wave measurements were performed by Toda et al.(9) and Longo et al.(10).

As an added complexity, most bow flows cause generation of bubbly wakes, which together with the overall wake of the ship can be clearly identified over a large distance. Dominating contributors, as well as a means to control the formation of this bubbly wake, are not completely understood, and are the main subject of the research described in this paper. Our first objective is to identify primary mechanisms for generation of bubbles in the bow region. To simplify our problem we started with a surface piercing, two dimensional body and performed qualitative and quantitative observations of the flow and formation of bubbles in its bow region. As the results in this paper show, a bubbly wake is generated as the bow wave breaks (a spilling breaker in the present case). However, the primary source is located just downstream of the bow wave, where an influx of water towards the body impinges on it, causing

splashing and entrainment of bubbles. A description of the experimental setup and measurement techniques are provided in the next section. The chapters that follow contain experimental evidence for the mechanism of bubble generation, detailed description of the flow structure, and a discussion of the effect of Froud number on these phenomena.

EXPERIMENTAL SETUP

The experiments were performed in the 140 ft. towing tank located at the David Taylor Model Basin, CD/NSWC. This basin is 152 cm deep, 305 cm wide, and 4270 cm (140 feet) long. As shown in Figure 1, the test model is a two dimansional, .9144 meter (3 ft) chord, .305 meters (1 ft) wide, and 1.83 meters (6 ft) high (of which 90% was submerged), symmetric, sharp nosed foil. The nose and tail regions have different contours, in order to enable generation of two flow fields with the same body (by towing it backwards). Experiments were performed at zero incidence and at Froude numbers, Fr, based on body length, ranging between 0.051 and 0.51. The corresponding Reynolds numbers were 1.39×10^5 and 1.39×10^6, respectively. The experiments included velocity measurements using Particle Image Velocimetry (PIV), mapping of the surface contour (the approach will be described shortly), and video photography above and below the surface.

Details of the PIV setup and procedures, as well as the auto-correlation analysis technique used to compute the velocities, may be found in Dong et al. (11) and Fu et al. (12) . Briefly (see Figure 1), the light source was a 15 watt copper-vapor laser, whose beam was expanded to a 6 millimeter thick sheet. The flow was seeded with 50mm, neutrally buoyant, fluorescent particles, that were distributed in the water prior to each run. The vertical light sheet had to be oriented 25° from the cross plane so that the submerged camera would not be in the model's path. Pictures were recorded on Kodak T-Max P3200 B&W film, using a submerged 35 mm movie camera. Most images were recorded at a rate of 10 frames per second, beginning upstream of the nose and continuing downstream of the body into its wake. The laser was pulsed 3 times, with a 10 millisecond delay between consecutive pulses, while exposing a single frame.

The images were digitized with a Nikon LS3500 scanner at magnifications of 8 pixels/mm of flow (x/c =.21) and 16 pixels/mm of flow (x/c=.32, x/c=.62). During analysis, using the auto-correlation method, the typical window size was 64x64 pixels, and there was 50% ovelap between neighboring windows. Based on the particle density and typical dispalcement between traces, it is estimated that the relative error in velocity measurements is less than 3.5%. Most of the PIV data presented in this paper were recorded at Fr =0.153 ($Re=4.18 \times 10^5$). This conditions was selected since the phenomena of interest were clearly evident (as qualitative data at higher Fr confirm), but variations in surface elevation were small enough to allow clear view of the entire flow field.

The surface contour was measured using the intersection of the light sheet with the surface. The images were recorded with a submerged video camera, digitized and automatically analyzed. Qualitative observations below and above the surface were performed using a video camera.

RESULTS

A series of video images that illustrate the various phenomena involved are presented in Figure 2. The first three images (Figures 2a, 2b, 2c) are side views of the leading edge of the model, showing the increase in surface elevation with increasing Fr. The formation of capillary waves is also clearly evident. At Fr ≥ 0.35 these waves break, creating what appears to be a spilling breaker over the entire crest of the wave, as is demonstrated with a top view in Figure 2d. Images of the side of the model (Figures 2e, 2f, 2g) also show the bow waves generated upstream of the leading edge of the model. However, they also demonstrate that the primary and distinctly different source of bubbles is located further downstream, close to the point of maximum thickness on the model. Clear traces of this bubbly wake start appearing at Fr≥0.15, just downstream of the point of minimum water surface elevation near the body. As the Froude number is increased this wake becomes wider, but the starting point still remains downstream of the bow wave. For example, at Fr=0.25 (figure 2f), the crest of the bow still involves only capillary waves, and the bubbly wake appears close to the point of maximum thickness on the body. The picture is similar, but more severe at Fr=0.35 (Figure 2g). Video images recorded underwater (see a sample in Figure 7) confirmed the observations made above the surface. They also show that the origin of the wake is associated with an inrush of flow towards the surface, impingement and splashing. The phenomenon was similar, but increasingly more violent, with increasing Froude numbers.

We now focus on the flow at a mild state (Fr=0.15, free stream velocity of .457 m/sec). Figure 3 is a map of the surface contour. At this state, changes in the water elevation vary between

0.46" above the ambient level at the leading edge of the model to -0.75" at x/c=.30. The origin of the bubbles is located close to x/c=0.42, which is just downstream of the point of minimum water elevation.

Selected PIV data that illustrate the entire process are presented in Figures 4-6. The first vector map shows the cross flow (inclined at 25°) at x/c=0.21, where the decreasing water elevation and widening of the model cause an outward motion. At x/c=0.32, close to the point of maximum thickness of the body, there is hardly any cross flow, except for the corner of the water surface and the model (note that the vector map focuses on this corner at a larger scale). Here there is still some outward flow, but the vertical component of the velocity is reversed, as the surface elevation near the body starts increasing. Further downstream, at x/c=0.62, the trend is reversed as the body starts narrowing and the surface elevation keeps on increasing, causing the flow to turn towards the body. Note that the vertical component of the velocity is larger close to the corner of the body and the surface. Splashing and generation of bubbles is clearly associated with this upward motion. The connection is demonstrated in Figure 7 by a video image recorded by an underwater camera at a slightly higher velocity (Fr=.2). The image clearly shows the upward vertical motion of particles close to the corner, and the resulting splashing on the body surface. As shown in Figure 2d, at Fr=0.15 (the same as the PIV data), the inward rush already causes some bubbling. It also causes generation of a series of standing capillary waves, that extend from the model backward at an angle of about 25°.

CONCLUSIONS

Video photography and PIV data are used to demonstrate a mechanism of bubble generation near the surface of a symmetric, two dimensional, surface piercing body. The development of a bow wave, that becomes larger and increasingly unstable with increasing Froude number, is demonstrated. When this wave breaks at Fr=0.35, a spilling breaker in the present case, it causes generation of some bubbles. However, the primary and distinctly different source of bubbles is located just downstream of the bow wave, in the region where the water level starts increasing. The associated influx towards the model seems to impinge on the body, which results in splashing and generation of a bubbly wake. The process becomes evident at Froude numbers exceeding 0.15, and its severety increases with the Froude number. We are in the process of investigating this phenomenon further. Issues that will be addressed in future work include understanding of the flow involved, the effect of model shape (especially close to the point of influx towards the surface) and bluntness, viscous effects including separation (that does not occur near the point of bubbly wake generation), etc. We hope that PIV data in a horizontal plane will be instrumental in providing key answers.

ACKNOWLEDGMENTS:

This project is sponsored by the Office of Naval Research under grant number N00014-93-10204. The authors would like to thank Gary Roth and Manish Sinha for their help in preparing the manuscript.

REFERENCES:

1. Michell, J.H., "The Wave Resistance of a Ship," Phil. Mag., Vol. 45, No. 5, pp. 106-123.

2. Tuck, E.O., "A Systematic Asymptotic Expansion Procedure of Slender Ships," J. of Ship Research, Vol. 1, No. 8, pp. 15-23.

3. Tuck, E.O., "Shallow Water Flows Past Slender Bodies," J. of Fluid Mechanics, Vol. 26, pp. 81-95.

4. Ogilvie, T.F., "The Wave Generated by a Fine Ship Bow," Proceedings of the 9th Symposium on Naval Hydrodynamics, pp. 1483-1525.

5. Dawson, C.W., "A Practical Computer Method for Solving Ship Wave Problems," Proceedings, 2nd International Conference on Numerical Ship Hydrodynamics, U.C. Berkely, Sept. 19-21, pp. 30-38.

6. Chapman, R.B., "Survey of Numerical Solutions for Ship Free-Surface Problems," Proceedings, 3rd International Conference on Numerical Ship Hydrodynamics, Paris, France, June 16-19, pp. 5-16.

7. Hino, T., "Computation of a Free Surface Flow Around an Advancing Ship by the Navier-Stokes Equations," Proceedings of the 5th International Conference on Numerical Ship Hydrodynamics, Sept. 24-28, Hiroshima, Japan, pp. 103-116.

8. Fry, D.J., and Kim, Y.H., "Bow Flow of SurfaceShips," Proceedings of the 15th Symposium on Naval Hydrodynamics, Hamburg, Germany, pp. 319-346.

9. Toda, Y., Stern, F., and Longo, J., "Mean-Flow Measurements in the Boundary Layer and Wake and Wave Field of a Series 60 C_B =0.6 Ship Model - Part 1 : Froude Numbers 0.16 and 0.316," Journal of Ship research, , Vol. 36, No. 4, Dec., 1992, pp. 360-377.

10. Longo, J., Stern, F., and Toda, Y., "Mean-Flow Measurements in the Boundary Layer and Wake and Wave Field of a Series 60 C_B =0.6 Ship Model - Part 2 : Scale Effects on Near-Field Wave Patterns and Comparisons with Inviscid Theory," Journal of Ship research, , Vol. 37, No. 1, March, 1993, pp. 16-24.

11. Dong, R., Chu, S., and Katz, J., (1992), "Quantitative Visualization of The Flow Structure Within The Volute of a Centrifugal Pump, Part A : Technique," J. Fluids Engineering, Trans. of the ASME, Vol. 114, No. 3, 1992, pp. 390-395.

12. Fu, T. C., Shekarriz, A., Katz, J., and Huang, T. T., " Quantitative Visualization of Large Scale Wake Structures," Proceedings of the Nineteenth Symposium on Naval Hydrodynamics, August, 1992.

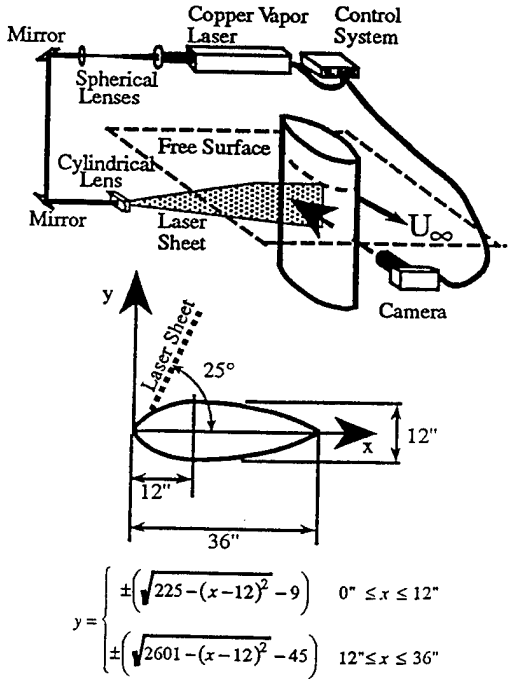
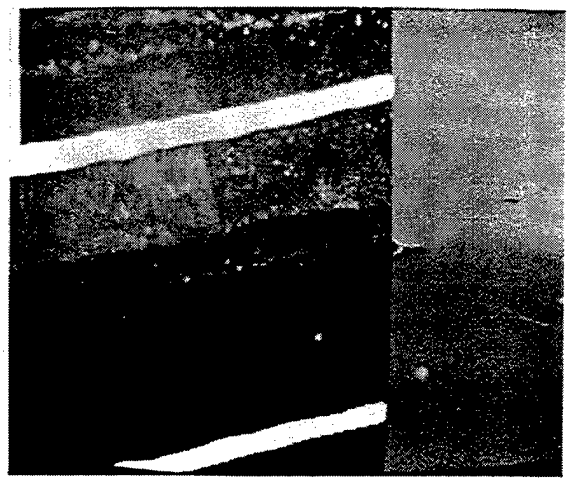
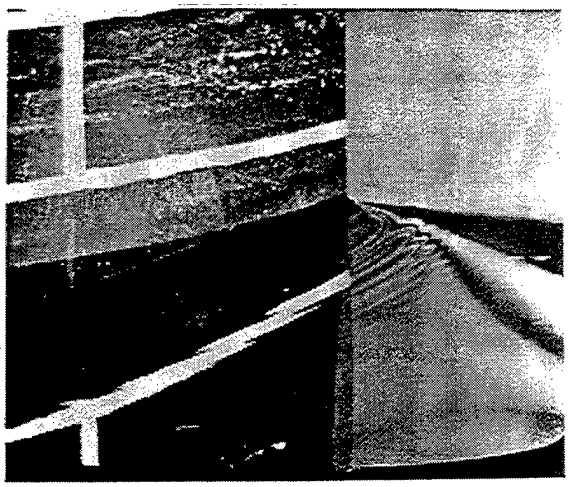


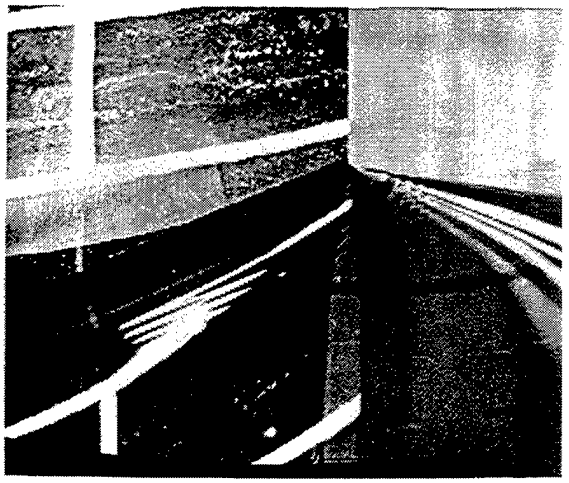
Figure 1: A schematic description of the experimental setup and model cross section.



a)

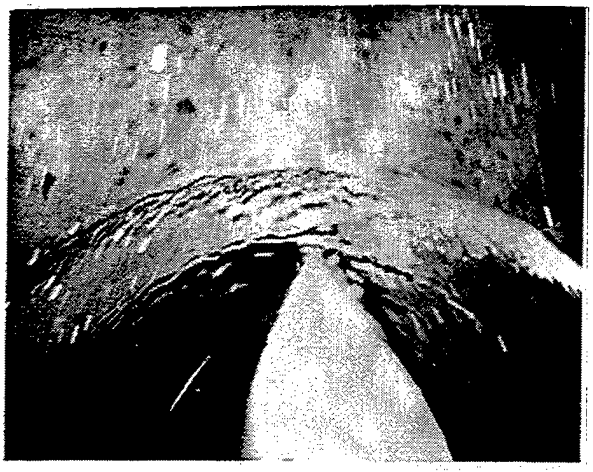


b)

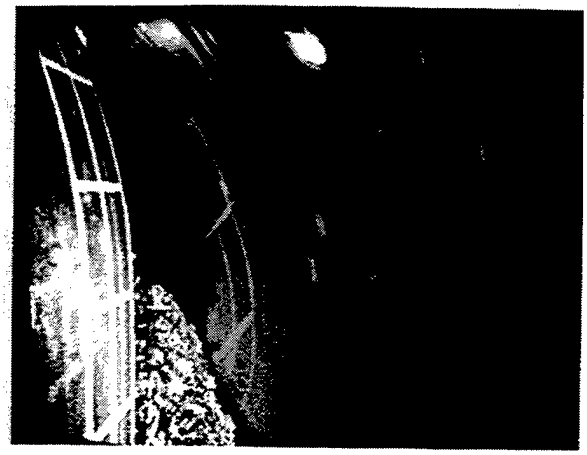


c)

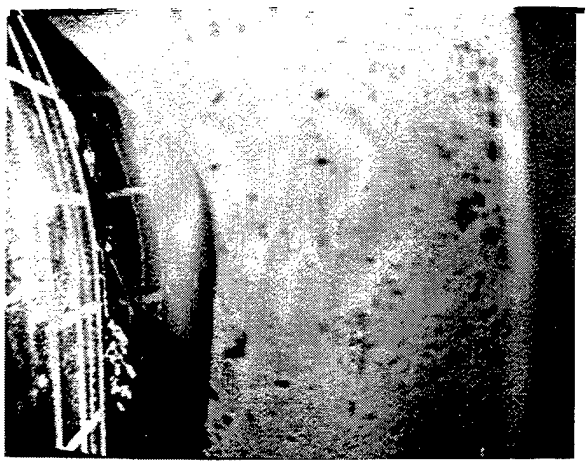
Figure 2a, b,c. Video images recorded above the surface. a,b, and c are side views of the leading edge, a) Fr=0.05; b) Fr=0.15; c) Fr=0.25.



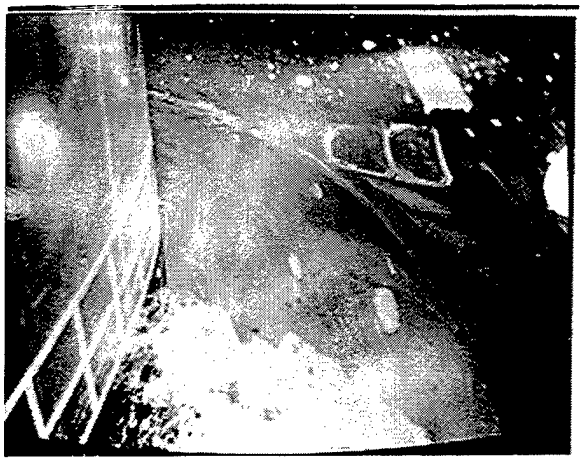
d)



f)



e)



g)

Figure 2d,e,f,g. Video images recorded above the surface. d) a top view of the bow region at Fr=3.5; e,f,g are views of the side of the model at e) Fr=0.15; f) Fr=0.25; g) Fr=0.35.

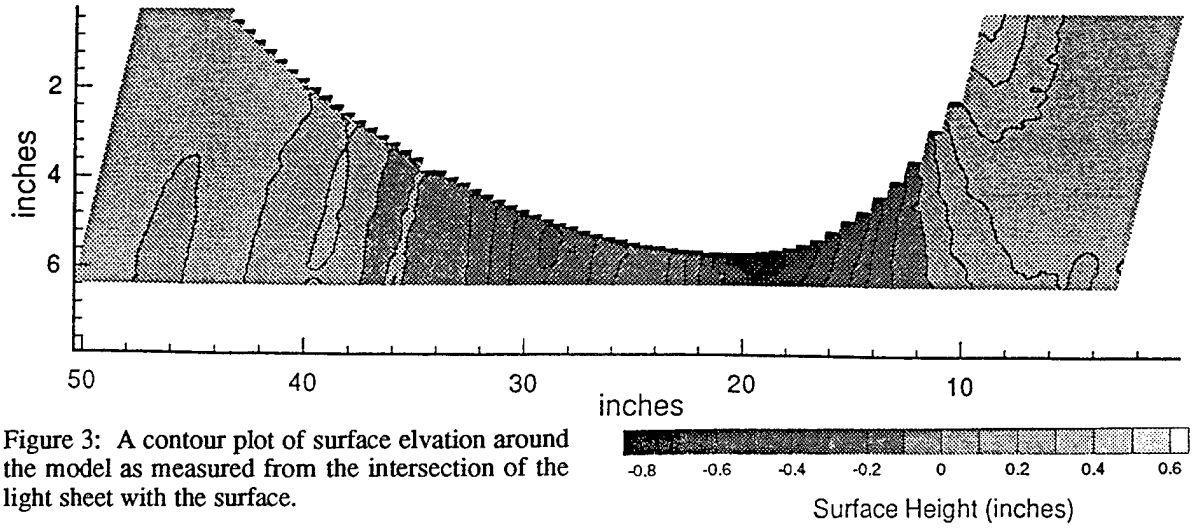


Figure 3: A contour plot of surface elvation around the model as measured from the intersection of the light sheet with the surface.

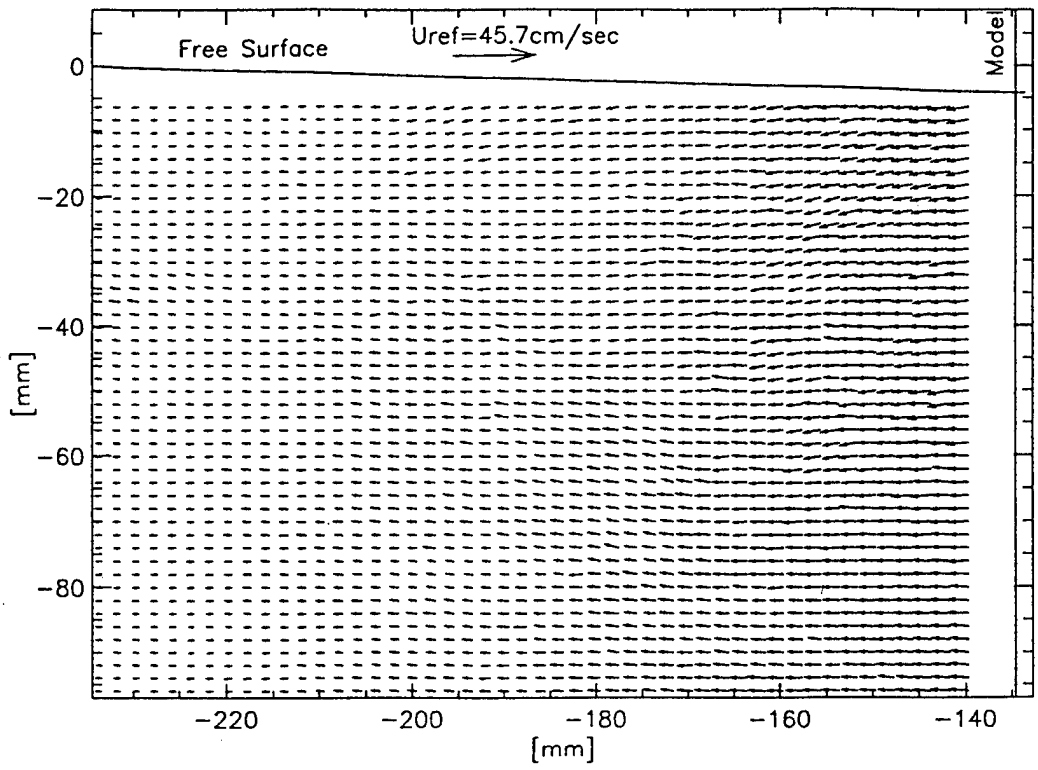


Figure 4: Velocity distribution at x/c=0.21 and Fr=0.15. The exact surface contour is also illustrated. The horizontal scale starts at the center of the model, and the verical scale starts at the undisturbed free surface.

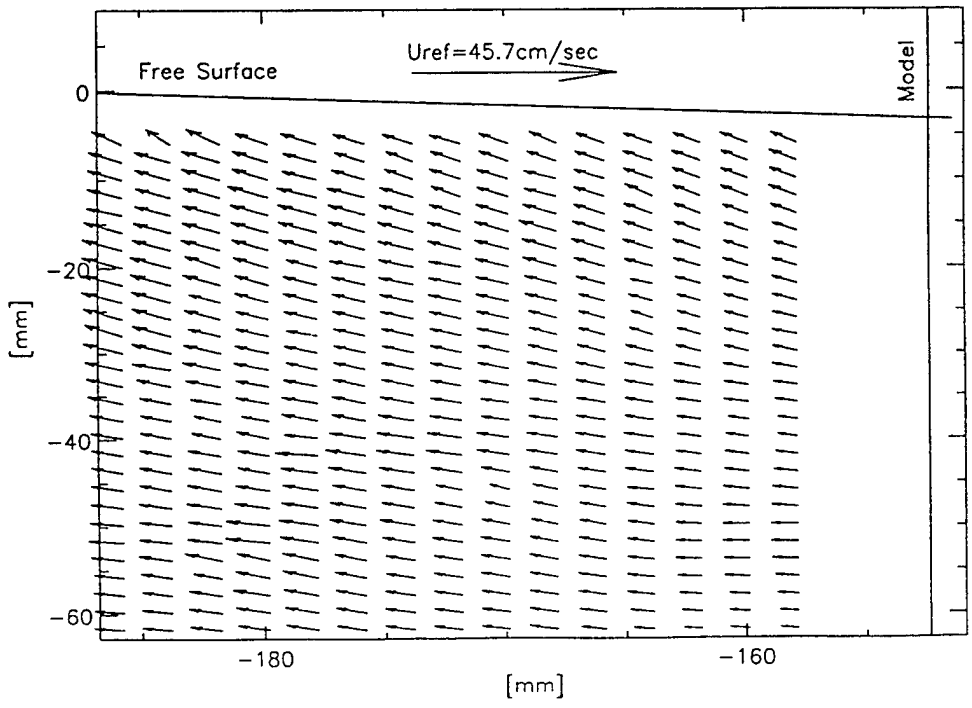


Figure 5: Velocity distribution at the corner of the model and the surface at x/c=0.32 and Fr=0.15. Note the high magnification. The exact surface contour is also illustrated. Coordinates are the same as figure 4.

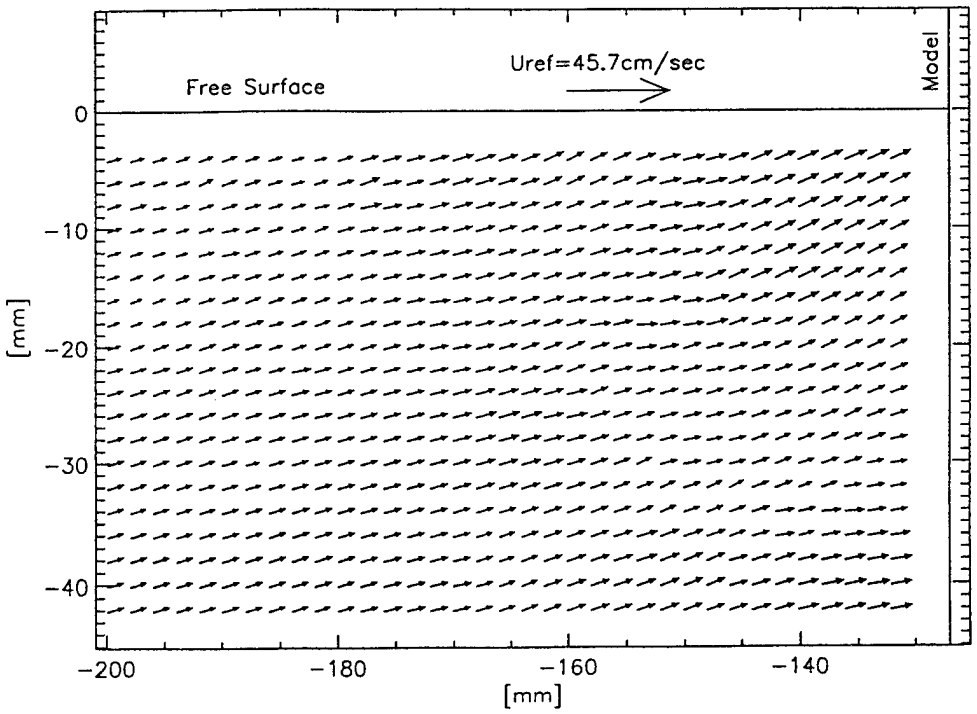


Figure 6: Velocity distribution at x/c=0.62 and Fr=0.15. Coordinates are the same as Figure 4.

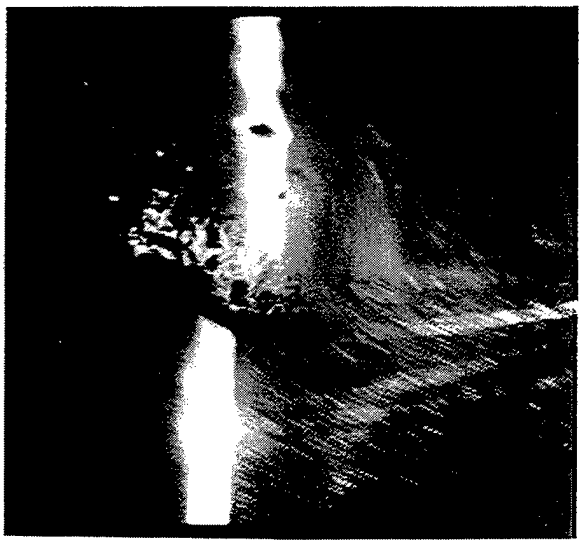


Figure 7: A video image at Fr=0.2 and x/c=0.44, showing the upward influx of water and resulting bubbly wake.

Numerical Prediction of the Effect of Forward Speed on Roll Damping

Y. Al-Hukail, P. Bearman, M. Downie (University of Newcastle upon Tyne, United Kingdom), J. Graham, Y. Zhao (Imperial College, United Kingdom)

ABSTRACT

Two vortex based methods are described for predicting roll damping of a floating hull in forward motion.

The first method uses the slender ship and low Froude number, rigid free surface approximations and leads to the prediction of the additional roll damping due to vortex shedding. This is assumed to emanate from the bilges, appendages or other specified lines along the hull and is represented by a concentrated vortex model. Results are presented for a representative deep displacement hull with rectangular cross-section, undergoing a range of combinations of roll and forward speed, including the extreme cases of roll at zero forward speed and forward speed alone without roll.

The second method matches a local vortex shedding model to an outer irrotational flow field given by a wave diffraction panel computation, extending earlier work without forward speed (1). The wave panel method is second order following (2) for small values of the parameter $\bar{U}\omega/g$ where $\bar{U}$ is the mean forward speed and ω is the roll frequency. Results for a rectangular floating barge hull and for a semi-submersible hull at the free surface are presented.

NOMENCLATURE

a Wave height, radius of spherical body (m)
A Roll response amplitude (radians)
b Hull beam
b_{ij} Damping force coefficient
B, B_V Roll damping coefficients, due to vortex shedding
C_D Drag coefficient
d Hull draught
F Froude number, $\bar{U} / (gL)^{\frac{1}{2}}$
F_V Force due to vortex shedding/m length
G, G^0, G^1 Greens function for a pulsating source (zero and first order)
g Gravitational acceleration
k Wave number
L Hull length
$\hat{M}$ Roll moment
(n_1,n_2,n_3) Outward normal (n_4 n_5 n_6 components of $\underline{x} \times \underline{n}$)
R_C Height of roll centre above mean free surface
S_B, S_F Body surface, free surface
t time,
D/Dt Convective derivative $\frac{\partial}{\partial t} + \bar{U}\frac{\partial}{\partial x_1}$.
T roll period ($2\pi/\omega$)
$\bar{U}$ Mean forward speed
V_e Velocity of edge in cross-flow plane
x_1, x_2 x_3 Coordinate axes fixed in the mean body position origin at the mean free surface (axial, transverse, upwards).
X_2,X_3 Coordinates of vortex in cross-flow plane
Γ Vortex circulation
η_i Amplitudes of body motion (i = 1 . . . 6)
Λ Period parameter $\bar{U}T / L$
ρ Water density
τ Expansion parameter $\bar{U}\omega / g$
Φ, ϕ, ϕ^0, ϕ^1 Velocity potential, disturbance potential, zero, first order components
ω Radian frequency

INTRODUCTION

Hydrodynamic damping arises on ship and other floating hulls due to potential flow effects, and in particular to wave radiation, separated flow (vortex shedding) effects and skin friction. At practical scales the effect of skin friction is usually small enough to be neglected in comparison with the first two sources of damping which exert pressure fields on the hull. In the case

of roll damping the wave radiation contribution may also be quite small and damping due to flow separation may be the major component. In many cases it is important to include both the wave field and the effects of vortex shedding. Hulls may also be specifically equipped with appendages such as bilge keels or fins in order to enhance the damping through vortex action.

Experimental work to measure and predict damping (3) has been carried out often with the aim of quantifying the damping due to different mechanisms or different components of the hull. Particular attention has been given to the effect of bilge radius and bilge keels (4, 5). Reference (6) shows, from experimental data, how the various components of the roll damping of a ship hull vary with forward speed (Froude number) and with roll frequency. The main component of the damping coefficient showing a continuous increase with Froude number is the 'lift' effect on the hull. This component grows linearly from zero at zero forward speed while eddy making components from for example bilge keels show negligible change with forward speed.

In the case of zero forward speed. the effects of eddy shedding have been incorporated in prediction methods both empirically and on the basis of a model of the vortex shedding (7, 8, 9). A computational method based on the work of (9) using an inviscid model of the separated flow field combined with a first order panel method for the wave field has been evaluated against experimental tests of rolling barge hulls and results are reported in (10) and (11). Early results showed good agreement for hulls with sharp right angle bilges or with bilge keels, but not for hulls with rounded bilges for which prediction of separation is more difficult. However use of a viscous model for the separated flow at a rounded bilge has significantly improved the agreement in that case even though the Reynolds number of the computation and experiment were not matched.

In order to incorporate the free surface wave field into computations of hydrodynamic damping in the presence of forward speed account must be taken of the change in the free surface boundary condition due to forward speed. For slender hulls travelling in the axial direction a change in the wave encounter frequency is sufficient. For non-slender flow fields the spatial variation of the quadratic velocity interaction over the free surface requires a special treatment, such as panelling, of the free surface near the body. Solutions of this problem for the slow drift wave field have been given in (2, 12, 13, 14).

The present paper presents two approaches to the computation of the viscous (eddy making) component of roll damping of a hull in steady motion. In the first case a slender hull in steady forward motion is assumed and the potential flow field of the hull is computed by the strip theory approach. The free surface is assumed to be rigid (technically a low Froude number assumption) and a concentrated vortex is assumed for the bilge vortices. Continuity of vorticity is maintained through the cross-flow strips. The vortex model, which is developed from a steady flow model for slender wings (15) is applicable to a ship in steady forward speed alone (without roll or other oscillations), for roll motion in the absence of forward speed or for a combination of both. A dimensionless period parameter Λ equal to forward speed x roll period / hull length is used to designate these cases.

The second approach extends to the forward speed case the earlier work (9, 1) which combined a local vortex solution with a panel method for the wave induced flow. In this case the method for slow drift motion (2) in which the wave potential is expanded in powers of a Froude number based on forward velocity and frequency $\left(\tau = \overline{U}\omega/g\right)$ is used for the computation of the wave field to which is added the above concentrated vortex model for the separated flow.

SEPARATED FLOW ON A SLENDER SHIP HULL

For the calculation of vortex shedding from a slender ship we make the following approximations:

(1) The free surface can be treated as a rigid 'lid'. This implies a low Froude number, particularly for the cross flow associated with the unsteady motion.
(2) b/L<<1 so that a strip theory approach can be used.
(3) The flow can be treated as inviscid with separation specified empirically. In the present case a ship hull having rectangular sections, as in Figure 1, is assumed. Vortex shedding in this case takes place from the sharp bilges.
(4) Infinite depth water.

With these assumptions the potential ϕ for the flow field in coordinates fixed in the hull satisfies

$$\Phi = \overline{U}\, x_1 + \phi(x_1; x_2, x_3) \qquad (1)$$

$$\frac{\partial^2\phi}{\partial x_2^2}+\frac{\partial^2\phi}{\partial x_3^2}=0 \qquad (2)$$

$$\frac{\partial\phi}{\partial x_3}=0 \quad \text{on } x_3=0 \text{ (free surface)} \qquad (3)$$

$$\frac{\partial\phi}{\partial n}\approx\frac{\partial\phi}{\partial x_2}n_2+\frac{\partial\phi}{\partial x_3}n_3 = -\bar{U}.n_1+ (R_c-x_3)\eta_4 n_2+x_2\eta_4 n_3$$
on the body surface (4)

$$\phi\to 0, \quad x_2, x_3\to\infty$$

ϕ here is the cross-flow potential induced partly by the interaction of the mean velocity $\bar{U}$ with the change of hull cross section in the direction of forward motion (x_1) and partly by the roll motion of the hull assumed to be about a roll centre at a height R_c above the mean free surface. Hence sway is incorporated into this definition of roll.

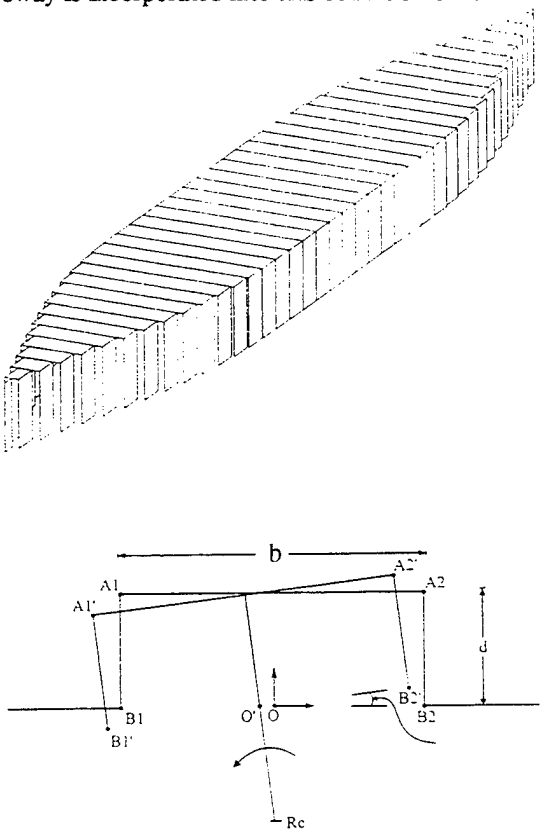


Fig. 1 Hull divided into strips and geometry of cross-section in roll (axes fixed in fluid)

These slender body equations allow a locally two-dimensional solution to be obtained for ϕ at each cross-section of the hull with ϕ only depending on x_1 through the boundary conditions.

It is now assumed that the flow separates from the sharp bilges of the hull under conditions for which a flow around and off the edge occurs. Under some conditions a flow onto a salient edge can occur and in that case shedding may be suppressed (see 16). Flow separation from bilges and sharp edges in slender and/or oscillatory flow tends to generate a vortex sheet which rolls up (Figure 2 showing here also previously shed vortices reflected in the free surface) and is shed as a concentrated cylinder of vorticity. The simplest model of this type of flow is that consisting of a single concentrated potential vortex filament representing the whole spiral proposed originally for a slender wing by Brown and Michael (15). The same model has been shown to apply to unsteady two dimensional flow (16) following the analogy between steady slender flow and unsteady two-dimensional flow in the cross-flow plane for

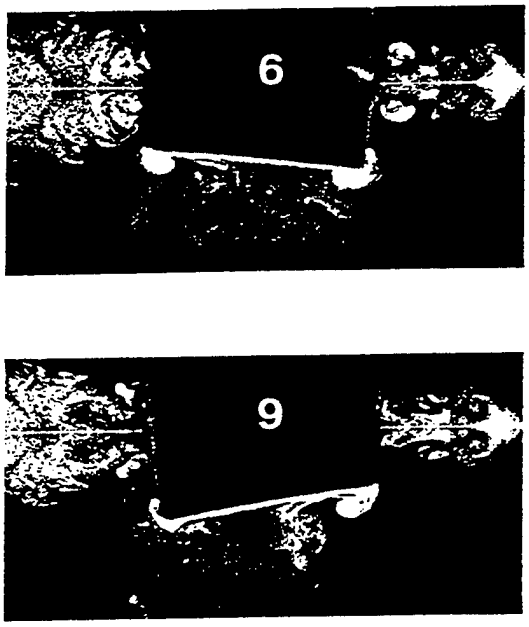


Fig. 2 Flow visualisation in the third cycle of roll motion from start up $\Lambda = 0$

which the derivative $\bar{U}\frac{\partial}{\partial x_1}$ is replaced by the time derivative $\frac{\partial}{\partial t}$. More sophisticated representations of vortex shedding use either an array of point or filament vortices to represent the sheets of vorticity, or higher order integrals along the sheets or full Navier-Stokes simulations. Comparisons show that for a right angled edge the

concentrated vortex model overestimates the vortex strength by about 10% compared to more accurate representations.

The complete model consists of the concentrated vortex filament together with a feeding sheet joining it to the edge from which it has been shed in order to preserve continuity of vorticity, since all the vorticity must originate at the body surface. The strength of the vortex and its position are then found by satisfying one scalar and one vector equation in each cross-flow plane. The first is the Kutta-Joukowski condition that the separation stream-surface leaves the body at an empirically determined separation line, in this case the sharp edge of the bilge. This is not an exact representation of a separating vortex sheet since it gives a full stagnation point in the cross-flow plane. The second is that the two components of force in the cross flow plane on the system of vortex and feeding sheet are respectively zero. This is a condensation of the requirement of zero pressure difference across the vortex sheet and is known as the Force condition.

In the general case of slender three-dimensional flow coupled with oscillations in roll in the cross-flow plane the convective derivative is $\frac{\partial}{\partial t} + \overline{U}\frac{\partial}{\partial x_1}$. In that case the shed vortex must satisfy (Kutta Joukowski)

$$n_3\frac{\partial\phi}{\partial x_2} - n_2\frac{\partial\phi}{\partial x_2} = \overline{U}\left(n_3\frac{\partial x_2}{\partial x_1} - n_2\frac{\partial x_3}{\partial x_1}\right) + (R_c - x_3)\eta_4 n_3 - x_2\eta_4 n_2 \qquad (5)$$

evaluated at the separation line ($x_{2e}(x_1)$, $x_{3e}(x_1)$, and (Force)

$$\left\{\begin{array}{l}\left(\frac{\partial}{\partial t} + \overline{U}\frac{\partial}{\partial x_1}\right)\left(\Gamma(X_2 - x_{2e})\right) = \Gamma\frac{\partial\phi}{\partial X_2} \\ \left(\frac{\partial}{\partial t} + \overline{U}\frac{\partial}{\partial x_1}\right)\left(\Gamma(X_3 - x_{3e})\right) = \Gamma\frac{\partial\phi}{\partial X_3}\end{array}\right\} \qquad (6)$$

$\Gamma(x_1,t)$ is the strength of the vortex located at $X_2(x_1,t)$, $X_3(x_1,t)$. The velocities on the right hand side of (6) are components of the finite part of the velocity field at the vortex location. Since the vortex is a potential vortex without a core there is also a singular component to the velocity at this location.

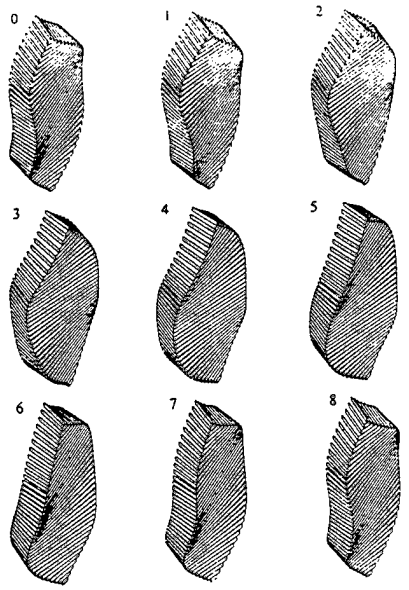


Fig.3 Equivalent twisted hulls for combined roll motion and forward speed.

The set of equations (1) - (5) are solved in the cross-flow plane (x_2, x_3) by transforming the flow region into a half-plane by means of a Schwartz-Christoffel transformation. The vortices appear as point vortices in the half-plane with corresponding images in order to satisfy the boundary conditions at the transformed hull and free surface. Equation (6) links the cross-flow planes through the evolution of vortices shed from the hull. This equation is solved by forward integration along the characteristics $(x_1 - \overline{U}t)$. The effect of the roll motion is then converted into equivalent twist distributions along the hull (Figure 3). The cross-flow geometry (hull and waterplane) changes at each phase of the roll cycle and strictly therefore a new transformation is required for each section at each step. In order to reduce the cost of this the boundary conditions are evaluated on the mean hull free-surface geometry assuming that the roll amplitude is small (Figure 4). The roll motion of the hull and the interaction of its changing cross-section with the forward speed are represented by source distributions on the boundary and some care is required to avoid shed vortices crossing the free surface.

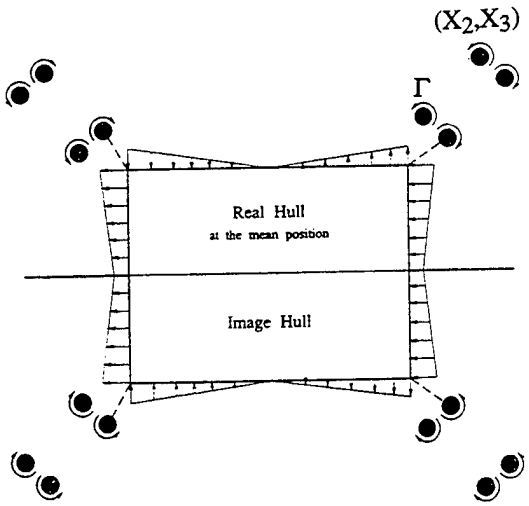


Fig.4 Schematic of rolling hull cross-section with boundary conditions approximated on mean hull position.

Since the simplified model used to represent the shed vortices does not represent the sheet in detail it is not capable of determining the moment at which a vortex sheet starts a new roll up. This process which leads to the formation of a new vortex structure and the shedding (severing from its edge) of the previously formed structure, occurs due to oscillatory motion of a shedding edge or equivalently if the geometry of the hull causes sufficient change of edge direction with respect to the forward motion direction. An example of the latter is the effect of hull broadening followed by hull taper. However the moment at which a new vortex forms is not simply determined and does not coincide with reversal of the relative incident cross flow at the edge because of induced velocity effects. Various criteria have been used to designate the moment of shedding in the present model. The simplest is when the rate of circulation growth $D\Gamma/Dt$ changes sign, i.e. when vorticity of opposite sign starts to be shed.

Oscillatory flows lead to pairs of vortices of opposite sign being shed which tend to convect away from the hull. There is some evidence that vortex pairing occurs when the vortices have nearly equal strength, the subsequent convected paths being then straight relative to the fluid. For this reason a shedding criteria used for most of the computations was based on equality of strength ($\Gamma_b = -\Gamma_a$, where Γ_b has been identified as forming a pair with Γ_a), rather than solely on $D\Gamma/Dt = 0$. Finite core size (desingularisation of the vortex velocity field) was also used to prevent excessive vortex convection velocities, particularly when close to a boundary. These are detailed in (17).

By removing the shedding criterion altogether a new vortex may be shed every integration step (or at pre-determined steps) and in this way a traditional multiple discrete vortex solution is computed. This approach was only carried out in some cases, because of the greater computational cost.

The pressure distribution and hence the hydrodynamic forces on the hull are calculated from Bernoulli's equation. In earlier work to compute the roll damping of a barge without forward motion (9) forces were calculated from the (classical) linearised form of Bernoulli's equation for small disturbances, proportional here to the roll amplitude. In the present case in order to investigate the accuracy of linearisation, both the linearised form and the full equation retaining the quadratic velocity terms were computed and the results compared.

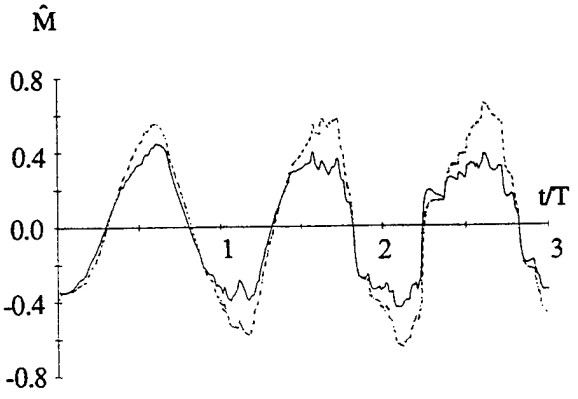


Fig.5 Time history of roll moment T = 6.67s, $\eta_4 = 0.2$rad, R_C = 0, b/d = 2.0, - - - linearised pressure eqn., ——— full pressure eqn.

RESULTS FOR A ROLLING HULL IN FORWARD MOTION

First of all tests were carried out for a rolling rectangular section barge without forward motion, $\Lambda = 0$, and the results compared with those of reference 9. Figure 5 shows a time history of the rolling moment due to vortex shedding computed from both the linearised and full pressure equations, for a moderate roll amplitude of 0.2 radians. Roll damping coefficients were evaluated from these time histories and averaged over three roll cycles. Tests using larger numbers of cycles showed that averaging over 3 gave accuracies to 10%. Typical results (Figure 6) show how the significance of the non-linear terms grows rapidly with amplitude of roll. From a number of these comparisons the contribution of the non-linear pressure component to the coefficient of roll damping is estimated to grow as $\left(\hat{\theta}_R\right)^{\frac{1}{2}}$, hence neglect of this term is only justified at very small amplitudes. Figure 7 shows the results for different roll centres compared with those of the earlier work (9). All the methods using the linearised pressure equation agree well whereas the non-linearised results show differences between the different methods of determining the time of the vortex shedding. The multi-vortex solution (Δ) is closest to that of (9) which also used a multi-vortex representation but in addition matched this 'universal' edge solution to the outer potential flow around the barge.

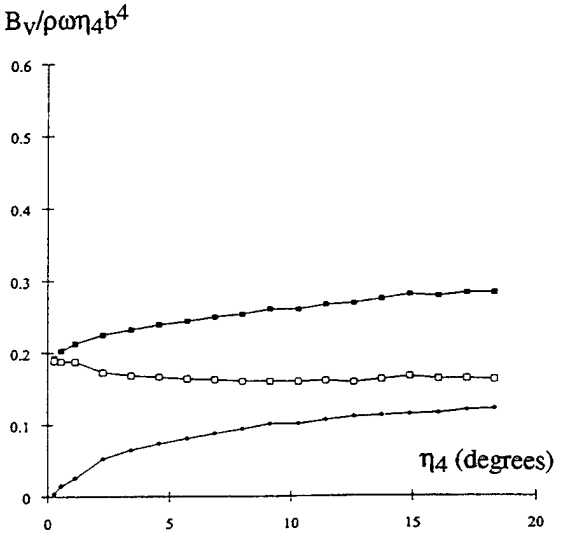


Fig.6 Variation of roll damping coefficient with roll amplitude. —□— linearised, —■— Full, —●— Difference, geometry as in Fig.5.

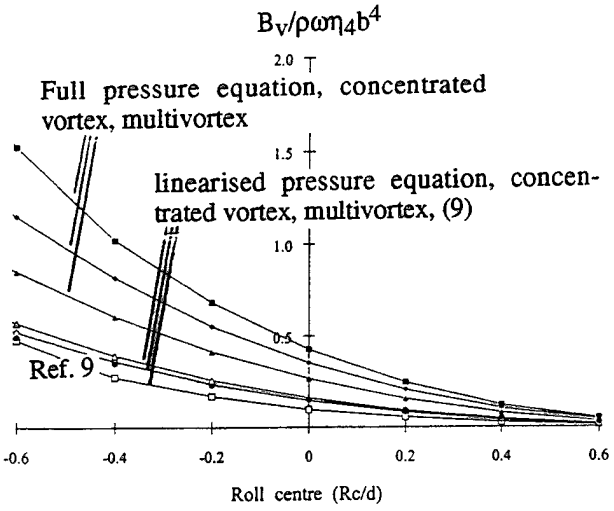


Fig.7 Variation of roll damping coefficient with roll centre —●— Ref. 9

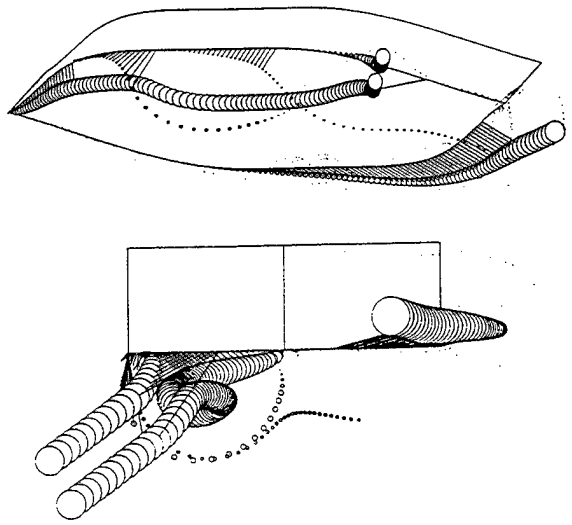


Fig.8 Hull in steady (5°) leeway. Vortex visualisation.

At the other extreme the method can be used to simulate flow about a ship hull in forward motion when the period of transverse motion has become infinite (i.e. $\Lambda = \infty$). An example of the vortex behaviour in such a case (a hull with steady leeway) is shown in Figure 8. This problem has previously been studied (18) using the same type of flow model and is relevant to

the interaction of hull vortices with propellers and rudder during ship manoeuvring.

The computational model has been developed to compute roll damping for general cases of forward speed (Λ = 0.5, 1.0 and 2.0). In the present case it has been applied to the deep draught block hull shown in Figure 1 and described in (18). An example of the vortex field for Λ =1 is shown in Figure 9. The pictures show a sequence at 60° intervals through the roll cycle and it can be seen that a combination of hull vortices as in steady leeway and vortex pairing as in roll without forward speed occurs.

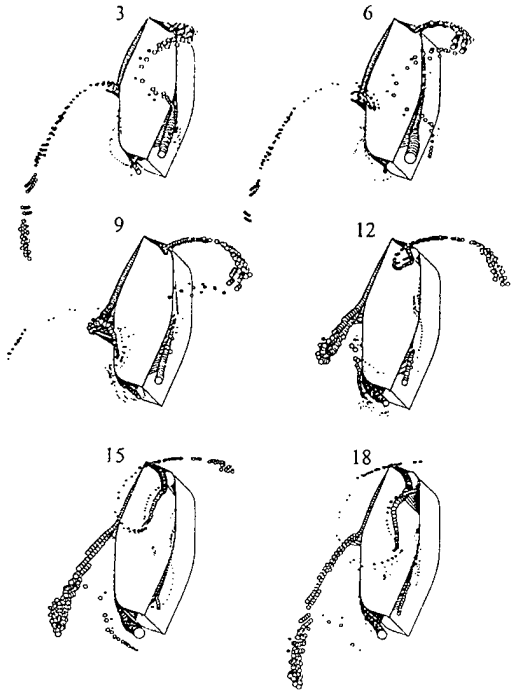


Fig.9 Rolling hull in forward motion Λ = 1.0, 60° intervals through cycle.

The distribution of hydrodynamic forces along the hull generally indicate a greater contribution to roll damping from the bow end than from the stern and very little from the midships of the naked hull. These may be integrated to give overall damping coefficients as shown in Figure 10 plotted against Froude number. In this figure the damping force is shown computed from the full pressure equation and from the linearised version Also shown are results from (4) for a different hull shape with rounded bilges for which the damping is lower. It is noticeable that both these results and those computed using the present linearised model for small roll amplitudes show very little increase in damping with Froude number. That this should be so when the forces induced by vortex shedding are computed linearly can be shown directly from the concentrated vortex model applied to a single shedding edge.

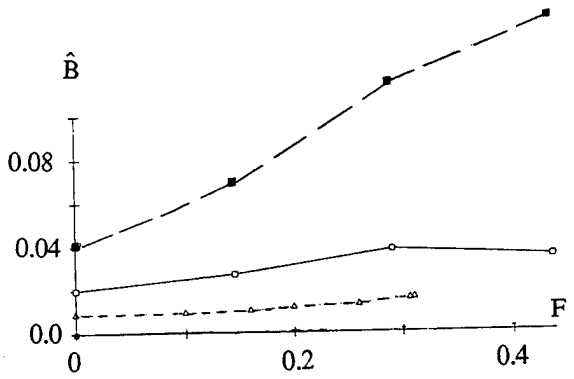


Fig.10 Variation of roll damping coefficient with forward speed. $\hat{\eta}_4 = 0.2$rad, R_C = 0, $\omega(b/2g)^{1/2} = 0.5$ ——— full eqn., —— linear, - - - - (4).

Generalising the result given in (16) to the case of a single right angled edge performing oscillatory motion about some roll axis parallel to the edge, with a steady axial velocity $\bar{U}$ superimposed, leads to a solution during the first part cycle for the vortex induced force on the edge:

$$F_v(x_1,t) = \rho K\left\{V_e^2 + \frac{1}{5}V_e^{-4/5}\frac{dV_e}{dt}\int_o^t V_e^{9/5}dt' - \frac{1}{5}V_e^{-4/5}\frac{dV_e}{dt}\int_o^s V_e^{9/5}dt'\right\} \quad (7)$$

where K is a constant, s = max(0, t-$x_1/\bar{U}$) and V_e is the velocity of the edge due to roll in the cross-flow plane. Only the last term depends on forward speed and can be shown to be small and negative, due to the reduction in the effectiveness of downstream portions of the edge by the vortex coming from the upstream portion of the edge.

The non-linear (velocity) contribution to the vortex damping appears to give an approximately linear increase in damping coefficient with Froude number. The same effect is seen in the 'lift' contribution from (6) and it is conjectured that this increase is associated with 'lift' on the hull

EFFECT OF SMALL FORWARD SPEED ON DAMPING INCLUDING WAVE-MAKING.

Computations have also been carried out to combine the effect of vortex shedding from the bilges of a hull with the effect of free surface waves and forward speed. In this case it is computationally expensive to carry out a complete time domain vortex shedding analysis for the whole hull for each incident wave or hull motion case. The more efficient approach described in (9) has therefore been adopted. A single vortex time history calculation is carried out for the representative edge geometry in the cross-sectional plane, in this case a right angle edge and the results of that are matched to an outer potential flow computation for the wave field of the body. Matching means that the inner flow field due to vortex shedding at the edge, calculated locally and scaled correctly, cancels the singularity in the outer potential flow at all edges deemed to be vortex shedding edges of the hull. This approach is described in detail in (9) and (1) and leads to the component of the vortex force at the fundamental frequency of the body motion or waves being added in the form of a coefficient to the force arising from the outer potential flow field. This method implies several assumptions which may be only partially justified:

(1) The amplitude of motion of the hull or waves is small and the important edges from which vortices are shed are long, so that the vortex formation and shedding process may be simulated on a strip theory basis in which the only important geometrical feature of the hull is the edge.

(2) The convection of vortices far from the edge and possible interactions with other parts of the hull or the free surface have negligible effect on the vortex force.

(3) The dominant component of the resulting vortex force is at the body or wave frequency.

Assumption (2) in particular can be questioned since the vortices undoubtedly do interact quite often with the free surface or other parts of the hull, as observed in (19) and also Figure 3.

In the present case the effect of forward speed is included in the analysis. This affects both the outer potential flow analysis for the wave field as well as the vortex shedding from the edges.

For the potential flow analysis the method of (2) has been followed in which the potential is expanded as a series

$$\Phi = \bar{U}x_1 + \phi^s + \phi^o + \tau\phi' + \ldots$$

in terms of the parameter $\tau = \bar{U}\omega/g = 2\pi F^2/\Lambda$ which is here assumed to be small. The steady flow field is given by a panel computation for the potential steady ϕ^S neglecting effects of the boundary layers or wake of the hull. ϕ^O contains all the components of the wave potential which are zero order in τ but first order in the motion amplitude. This satisfies the linearised free surface boundary condition and the only effect of forward speed is to change the frequency where incident waves are concerned to the wave encounter frequency. ϕ^O is computed by a standard panel method. ϕ^1 is the higher order component which results from the interaction between the steady flow field potential ϕ^S and ϕ^O. The potentials ϕ_0 and ϕ_1 satisfy the Green's function equations:

$$-2\pi\phi_j{}^o + \iint_{S_B} \phi_j{}^o \frac{\partial G^o}{\partial n} = \iint_{S_B} G^o n_j \, ds \qquad (8)$$

$$-2\pi\phi_j{}^1 + \iint_{S_B} \phi_j{}^1 \frac{\partial G^o}{\partial n} =$$
$$-2i \iint_{S_F} \phi_j{}^1 \left(\nabla_1 G^o . \nabla_1 \phi^s + \tfrac{1}{2} G^o . \nabla_1{}^2 \phi^s\right) ds$$
$$-\iint_{S_B} \phi_j{}^o \frac{\partial G^1}{\partial n} ds$$
$$+\iint_{S_B} \left(G^1 - \frac{g}{i\omega^2} \nabla G^o . \nabla \phi^s\right) n_j ds \qquad (9)$$

for each component ϕ_j of the potential. $G = G^O + \tau G' + \ldots$ is the expansion of the Green's function for a moving pulsating source, and ∇_1 is the gradient operator $\left(\frac{\partial}{\partial x_1}, \frac{\partial}{\partial x_2}, 0\right)$. S_B is the surface of the body and the free surface (S_F) integral requires panelling over part of S_F in the neighbourhood of the body.

A program to compute the potential flow field was written and tested against results published in (13) and (14). Good agreement was obtained provided sufficient attention was given to the number and distribution of the panels on the body

and the free surface. Figure 11 shows a comparison for the force components b_{13} and b_{31} on a half immersed sphere at F = 0.08.

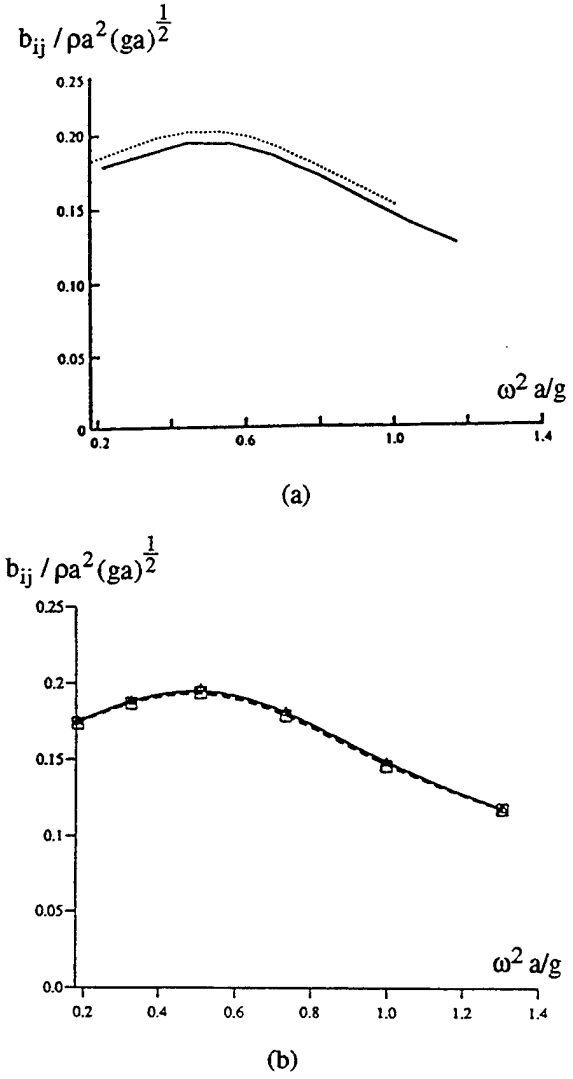


Fig.11 Force coefficients b_{13} and b_{31}, (a) from ref. 2, (b) present results

The effect of forward speed on the vortex shedding from the bilge edges was analysed using the result given earlier in equation (7) from which a factor was obtained for the change in vortex force due to roll motion as a function of forward speed, to be matched to the outer potential solution as before.

The combined analysis therefore generates terms of $0(\eta$ and $\eta\tau)$ for the potential part of the solution and $0(\eta^2)$ as shown by eqn.7 for the vortex part. Inclusion of the $0(\eta^2)$ vortex contribution when the $0(\eta^2)$ potential contribution is neglected appears inconsistent but is justified by the large size of the latter term for certain motions such as roll as was the case in the absence of forward speed.

The analysis has first been applied to a freely floating rectangular barge hull in beam waves shown for one side of the plane of symmetry in Figure 12. The barge was 82 m long by 27 m wide by 2.75 m draught. Two calculations were carried out with 184 and 544 panels respectively on the half body and 600 panels on the free surface. It was assumed that vortex shedding only occurred from the edges (bilges) parallel to the direction of forward motion. Figure 13 shows results for roll response in the absence of forward motion (184 body panels) and Figure 14 the two computations with forward motion. Roll response was computed by including the response equations and performing an iterated solution for each frequency as detailed in (1). In each case the solid line shows the result for wave damping alone and the dashed line includes the effect of vortex damping which is the dominant component for this motion and greatly reduces the roll response.

Comparison of the results show only a small effect of the number of body panels on the damping and as for the earlier ship hull computations very little effect of forward speed (admittedly itself small in this case).

Computations have also been carried out for a rectangular pontoon hull, typical of a semi-submersible, in forced sway motion at the free surface with and without small forward speed. The results of the computation for the sway drag coefficient are compared with the results of experimental tests described in (11). They are as follows:

F	$\omega/(g/)^{1/2}$	η^2/b	C_D computed	C_D measured
0	0.88	0.16	0.22	0.36
0	0.88	0.32	0.44	0.58
0.013	0.88	0.16	0.25	0.55
0.013	0.88	0.32	0.38	0.62

The above method being an extension of (9) computes the vortex force, which dominates in these cases, from the linearised pressure equation and as shown earlier this may account for the

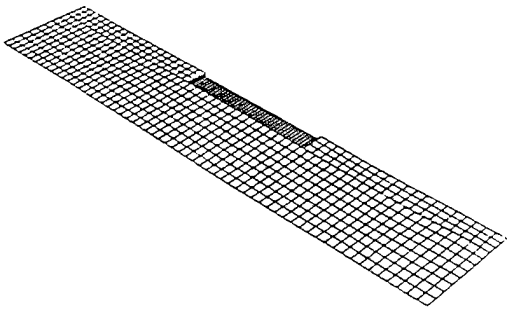


Fig.12 Panelling of barge hull and free surface (one side of plane of symmetry)

significant underprediction of the drag coefficients above for finite amplitudes. It is however also possible that with a method as above which uses piecewise constant potential over the panels, rather than sources or linear potential, that significant errors are introduced in the estimation of the strength of the singularity in velocity at the edge which drives the vortex shedding. This question is still under investigation.

CONCLUSIONS

Computations have been carried out to predict the effect of forward speed on roll damping of ship and other hulls including the effect of vortex shedding from the bilge edges. Two models have been used, one with a rigid lid approximation for the free surface and the other including wave effects up to $0(\eta\tau)$. The models demonstrate methods of incorporating vortex separation effects into hull response calculations without resorting to full three dimensional Navier Stokes computations. The results show that for edges parallel to the forward speed direction, typical of bilges and bilge keels there is very little increase in damping due to forward speed computed from the linearised pressure equation. If the quadratic velocity terms are included an approximately linear increase in damping coefficient with Froude number is found.

ACKNOWLEDGEMENT

This work was supported by the Behaviour of Fixed and Compliant Offshore Structures Managed Programme, which is promoted by the Marine Technology Directorate Ltd and sponsored by SERC, HSE, Amoco, BP, Elf, Statoil, ARE, Aker Engineering and Brown Root Marine.

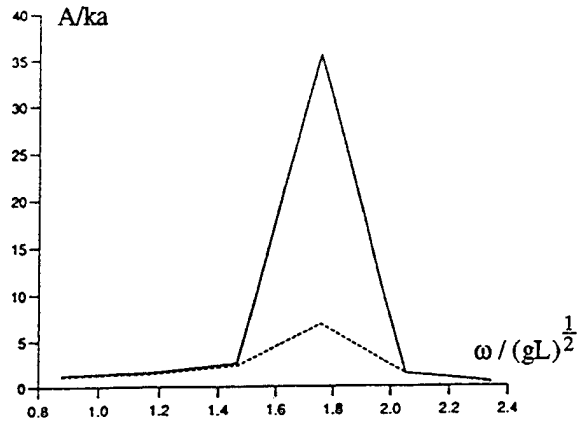
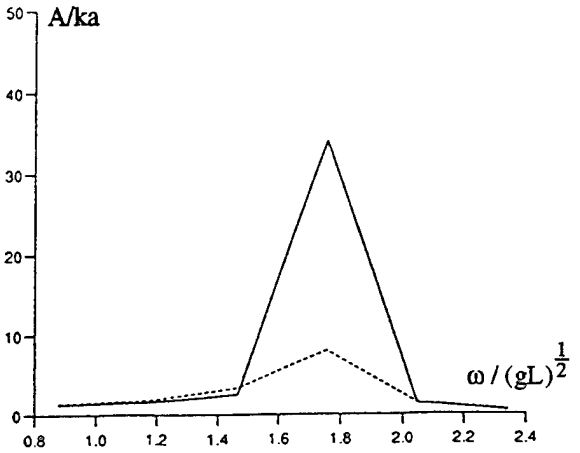


Fig.13 Roll response of barge at zero forward speed ($\Lambda = 0$) ——— potential flow only, - - - - - including vortex damping.



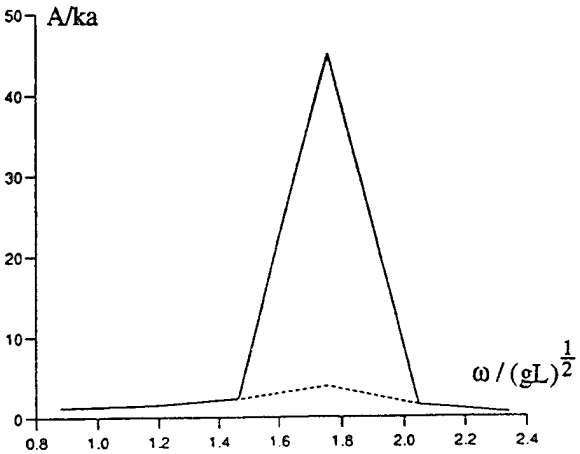


Fig.14 Roll response of barge with forward speed (1 m/s) —— potential flow only, - - - including vortex damping (a) 544 panels on 1/2 body, (b) 184 panels on 1/2 body, both with 600 panels on 1/2 free surface.

REFERENCES

1. Downie, M.J., Graham, J.M.R. and Zheng, X. 1991 Effect of viscous damping on the response of floating bodies. 18th Symp. Naval Hydrodynamics, p.59

2. Nossen, J., Grue, J. and Palm, E. 1991 Wave forces on three-dimensional floating bodies with small forward speed. J. Fluid Mech. **227**, p.135

3. Tanaka, N. 1961 On the eddy making resistance to the rolling of a ship hull. J. Soc. Nav. Arch. Japan, **109**, p.205

4. Ikeda, Y. Himeno, Y. and Tanaka, N. 1977 On the eddy making component of roll damping force on a naked hull. J. Soc. Nav. Arch. Japan, **142**, p.54

5. Ikeda, Y. Komatsu, K. Himeno, Y. and Tanaka, N. 1977 On the roll damping force of a ship. Effect of hull resistance pressure created by bilge keels. J. Kansai Soc. Nav. Arch. Japan, **165**, p.31.

6. Himeno, Y. 1981 Prediction of ship roll damping - state of the art. Dept. Nav. Arch. and Marine Engg. Univ. of Michigan, Rept. 239.

7. Brown, D.T., Eatock Taylor, R. and Patel, M.H. 1983 Barge motion in random seas - a comparison of theory and experiment. J. Fluid Mech. **129**, p.385

8. Robinson, R.W. and Stoddart, A.W. 1987 An engineering assessment of the role of non-linearities in transportation barge roll response. The Naval Architect July/Aug, p.65

9. Downie, M.J., Bearman, P.W. and Graham, J.M.R. 1988 Effect of vortex shedding on the coupled roll response of bodies in waves. J. Fluid Mech. **189**, p.243

10. Standing, R.G., Jackson, G.E. and Brook, A.K. 1992 Experimental and theoretical investigation into the roll damping of a systematic series of two-dimensional barge sections. Proc. Behaviour of Offshore Structures, 92, p. 1097, London

11. Downie, M.J., Graham, J.M.R., Zhao, Y.D. and Zhou, C.Y. 1994 Viscous damping of a submerged pontoon undergoing forced combined motions. Proc. 4th ISOPE Conf. Osaka, p.297.

12. Wu, G.X. and Eatock Taylor, R. 1990 The hydrodynamic force on an oscillating ship with low forward speed. J. Fluid Mech. **211**, p.333.

13. Zhao, R., Faltinsen, O.M., Krokstad, J.R. and Aanesland, V. 1988 Wave current interaction effects on large volume structures. Proc. Behaviour of Offshore Structures, **2**, p. 623, Trondheim

14. Zhao, R. and Faltinsen, O.M. 1989 Interaction between current, waves and marine structures. 5th Int. Conf. Num. Ship Hydrodynamics

15. Brown, C.E. and Michael, W.H. 1955 On slender delta wings with leading edge separation. NASA Tech. Note 3430.

16. Graham, J.M.R. 1977 Vortex shedding from sharp edges. Imperial College Aero Rept. 77-06, ISSN 0308 7247

17. Al-Hukail, Y.O. 1992 Roll damping due to vortex shedding from slender ship hulls in forward motion. PhD Thesis, University of London.

18. Bradbury, W.M.S. 1983 Large sailing ships - a fluid dynamic investigation. PhD. Thesis, University of London.

19. Braathen, A. 1987 Application of a vortex tracking method to the prediction of roll damping of a two-dimensional floating body. Dept Marine Tech. Norwegian. Inst. Tech Rept. UR-87-56.

DISCUSSION

S. Kinnas
Massachusetts Institute of Technology, USA

Could the authors comment on the validity of slender body theory, especially at the transition range of the geometry from "delta wing", like at the bow to "cylindrical body", like at midsection?

AUTHORS' REPLY

Slender body theory is quite satisfactory in the transition range between the bow and mid-hull sections, provided the transition is gradual. It is not, however, very satisfactory at the bow where rapid changes of geometry occur and this will introduce some error in this region.

The Influence of Vorticity upon Estimation of Manoeuvring Derivatives

G. Hearn, D. Clarke (University of Newcastle upon Tyne, United Kingdom), H. Chan, A. Incecik, K. Varyani (University of Glasgow, United Kingdom)

ABSTRACT

The main purpose of this research was to find an explanation for a disagreement between the measured longitudinal distribution of lateral forces and those predictions based upon slender body theory, for a manoeuvring ship. Considering a number of possible causes for the noted differences it was considered that the presence of trailing vortices at the stern was the most likely explanation. Two courses of action were undertaken. Firstly, it was demonstrated that the hull forms for which the lateral force prediction and the measurements differed, did in fact generate trailing vortices. The strength and position of these vortices was then measured. Secondly, a theoretical procedure was derived, which allowed the influence of the vortices to be included in the slender body predictions of the hull derivatives. It was found for the two hull forms considered, that the forces generated by the trailing vortices were of the correct magnitude to account for the previously noted discrepancy between the calculated and measured lateral forces.

INTRODUCTION

The provision of adequate manoeuvrability is of paramount importance for the safe navigation of a ship. Recently, the adoption of IMO Resolution A.751 (18) in November 1993 [1] has further increased the importance of manoeuvrability, since it requires that certain aspects of manoeuvrability are consciously addressed during the design of a ship. The requirements cover turning, yaw checking and stopping ability, giving criteria which must be satisfied.

The ability to estimate these required elements of ship manoeuvrability is dependent upon having an accurate mathematical model of the manoeuvring ship. This mathematical model is in turn totally dependent upon the manoeuvring coefficients or hydrodynamic derivatives contained within it. The problem of manoeuvring simulation is then reduced to one of being able to estimate or calculate the hydrodynamic derivatives with sufficient accuracy, and without resorting to captive model tests.

However, there is no complete theoretical method, which would allow the calculation of the hydrodynamic forces and moments acting on an arbitrary shaped body in a real fluid. In an ideal inviscid fluid, forces and moments generally act upon the body only in accelerated flow, with one exception, a moment due to sway velocity. This moment became known as the Munk Moment, due to his pioneering work on airship aerodynamics.

The success or failure of any calculation procedure for hydrodynamic derivatives is very much dependent upon the geometry of the body under investigation. With aircraft and missiles, the presence of wings and fins require the addition of circulation potentials, in order to satisfy the various trailing edge Kutta conditions. These additional potentials tend to dominate the flow and allow acceptable calculation of the forces and moments.

In the case of slender bodies, non-zero steady flow forces are achieved by considering that the body terminates with a blunt base, from which the flow separates. This separated flow forms a stream surface behind the body, with the same cross-section as the base. The forces and moments may be calculated from the nose of the slender body, up to the location of the

base. Successful results have been obtained for slender missiles with and without tail fins.

It was previously assumed by Clarke [2] that the slender-body strip method, developed by Bryson [3] for missiles, could be adapted to the case of a surface ship. The method requires a knowledge of the zero-frequency horizontal added mass coefficients at each two-dimensional cross-section along the length of the ship's hull. These added mass coefficients are readily determined from a knowledge of the ship's body sections by means of conformal mapping. Clarke [2] was able to integrate various functions of the added mass coefficients along the hull to obtain longitudinal distributions of the linear derivatives Y'_v, N'_v, Y'_r and N'_r.

To verify these calculations, Clarke [2] also obtained measurements of the longitudinal distribution of hydrodynamic force and moment, using a segmented model on a rotating arm. The data provided a direct comparison of the experimentally measured derivative distribution, with that calculated using the horizontal added mass distribution along the hull.

In general, the theoretical and the measured derivative distributions agreed very well, from the bow to a location about two-thirds of the length towards the stern. Aft of that location, the calculated and measured distributions progressively diverged. This discrepancy could have been due to several neglected phenomena, such as boundary layer growth, free surface effects, wave making, or a violation of the slender-body assumptions.

However, the most plausible explanation was that the effects of bilge vortices, which pass along the stern part of the ship, had been neglected. In order to test this hypothesis a combined theoretical and experimental study was undertaken.

Using the same hull forms as the previous segmented model experiments [2,4], new models were tested, and measurements of the vorticity in two transverse planes near the stern of each model were obtained. Flow visualisation using a miniature video camera and dye tracers clearly showed the starting points of the vortices and their rearward growth. Knowing the nature, strength and position of the vortices, it was then possible to evaluate the forces and moments which they would generate on the stern of the two hull forms.

The calculation of the vortex generated forces was accomplished by considering the impulse of a pair of counter rotating vortices, one on either side of the stern. The rate of change of the impulse with sway velocity, allowed an additional coefficient for each body section to be deduced, which was simply additive to the added mass coefficient arising from the slender-body theory. The previously mentioned expressions for the linear derivatives could then be easily modified to include vortex effects.

In this way the force and moment distributions along the two hull forms, which included vortex effects, were calculated. Comparison with the earlier segmented model results showed that the previous discrepancies in the stern region had been accounted for. The examples shown in the paper are for the sway force derivative Y'_v. Although it is felt that it has been shown that vortex effects must be included in any reliable derivative estimation procedure, the problem remains that in the general case the nature of the vortices is unknown. In this exercise the vortex strength and position have been determined experimentally, whereas in future a relatively simple means of estimating the vortex properties would be required. It has been shown that in some cases an accurate knowledge of the vortex positions is not necessary, whereas the vortex strength is very important. It is felt that this work has shown the necessity and importance of including vortex effects, without recourse to complicated CFD techniques, which may have obscured the simple relationships which have been derived here.

EARLIER TREATMENT OF SLENDER-BODY METHOD

In a previously developed method, Clarke [2] showed how the linear derivatives Y'_v, N'_v, Y'_r and N'_r could be determined using a slender-body strip method originally developed by Bryson [3] for similar studies with missiles. The method depended upon a knowledge of the zero-frequency horizontal added mass coefficients for the body sections of the hull form under consideration. These added mass coefficients C_H were defined as the ratio of the added mass of the particular

section to that of a circular section of the same draught. They were determined by a conformal mapping of the body section onto a circle in another complex plane.

This transformation could be expressed as an infinite Laurent Series

$$x = \sigma + \frac{a_1}{\sigma} + \frac{a_3}{\sigma^3} + \quad ..., \qquad (1)$$

if the body section is initially in the x-plane and the cirlce is in the σ-plane. It should be noted here that, the coordinate system has forced the definition of a complex number to be $x = y + iz$. The coefficients a_n define the transformation, and may be determined by considering equivalent Lewis sections, by Schwarz-Christoffel methods, or by numerical methods. The required added mass coefficient was shown by Summers [5] to depend only upon the residue at infinity, which is the coefficient a_1, so that

$$C_H = \frac{1}{T^2}(2(r^2 - a_1) - \frac{S}{\pi}) \quad , \qquad (2)$$

where T is the draught of the body section and S is twice the sectional area. The term r is the radius of the circle in the transformed σ-plane. By considering the forces generated on the hull in each cross-flow plane along the body, Clarke [2] was able to show that the linear derivatives were given by the following expressions

$$\begin{aligned}
Y'_v &= \pi\left(\frac{T}{L}\right)^2 \left[C_H\right]_S^B \\
N'_v &= \pi\left(\frac{T}{L}\right)^2 \left[C_H X'\right]_S^B - \int_S^B C_H dX' \\
Y'_r &= \pi\left(\frac{T}{L}\right)^2 \left[C_H X'\right]_S^B \\
N'_r &= \pi\left(\frac{T}{L}\right)^2 \left[C_H X'^2\right]_S^B - \int_S^B C_H X' dX' \quad ,
\end{aligned} \qquad (3)$$

where L is the hull length between perpendiculars and X' is the non-dimensional distance X/L of each body section from midships. The limits of integration being denoted by B and S, for the bow and stern sections respectively.

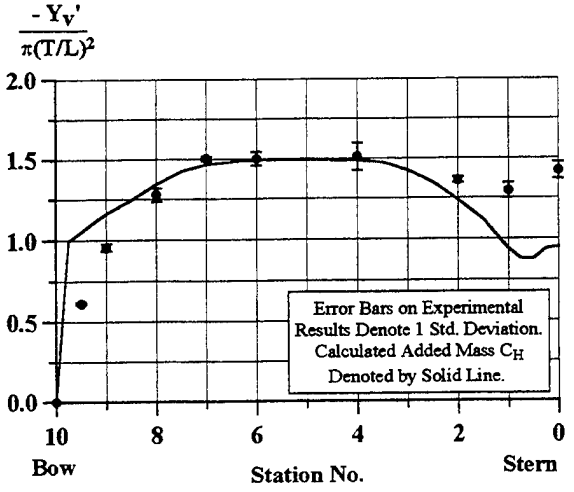


Figure 1. British Bombardier Segmented Model. Longitudinal Variation of Y_V' and C_H. Second Order Fit, Pure Sway Results Only.

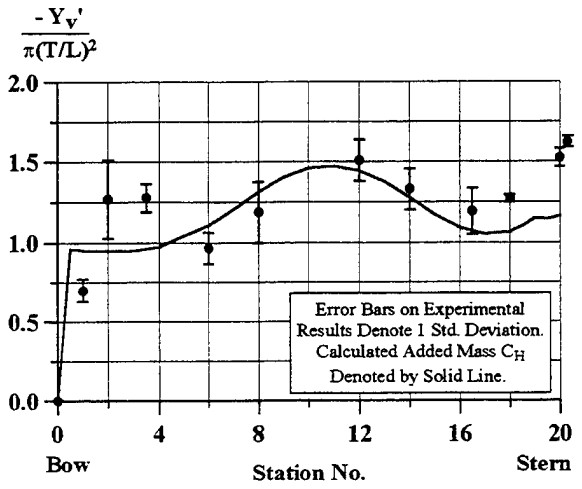


Figure 2. Mariner Segmented Model. Longitudinal Variation of Y_V' and C_H. Second Order Fit, Pure Sway Results Only.

In order to examine the validity of the expressions given in Equation (3), Clarke [2] and Burcher [4] carried out detailed tests on models of a tanker form, *British Bombardier*, and a *Mariner* form respectively. In these tests, carried out on a rotating arm, the models were laterally divided into nine and eleven segments respectively. The use of two sets of mounting rails allowed the forces generated on each segment to

be measured, for various values of drift angle and yaw rate. By analysis of these results it was possible to extract from the data, longitudinal distributions of the linear derivatives, from the bow, to the rear section of each segment in the models. These derivative distributions were then directly comparable to those calculated using Equation (3) for each model.

By returning to the original model tank records for the two segmented models [2,4], the data analysis has been repeated recently [6], and the fitting process revised to give error bounds on the derivative values. These revised data are shown in Figures 1 and 2 for the *British Bombardier* and *Mariner* hull forms respectively. A second-order fit was found to be statistically more appropriate, rather than the third-order fit, used originally by Clarke [2]. Also shown in Figures 1 and 2, are the derivative distributions calculated using Equation (3). Again, in this case the necessary added mass values have been recalculated, using a numerical conformal mapping scheme. This process involves the determination of the transformation coefficients, a_n in Equation (1), by a function minimisation process, which successively minimises the sum of squares of errors between the coordinates of the body section given by the current a_n values and those of the described section.

It can be seen in Figures 1 and 2, that for the distribution of the derivative Y'_v, the theoretical solid lines agree fairly well with the experimental segmented model results. However, there are some important differences at the stern of both models, in that the measured derivatives are significantly larger than those predicted from the slender-body theory. Clearly it is the value of the derivative Y'_v at the stern, which is the required value for use in any manoeuvring simulation studies. There are smaller differences in the bow regions, which are thought to be due to a break down in the 2-dimensional cross-flow assumptions of the slender body theory. In the case of the *Mariner* model however, the sinusoidal nature of the errors between the measured and calculated derivative distribution is thought to be due to surface elevation in the bow wave profile. It should be noted that the larger error bounds in the case of the *Mariner* are due to there being fewer experimental points in that case.

Returning to the differences at the stern of both models, the most plausible explanation was that the possible presence of trailing bilge vortices had been neglected by the slender-body theory. To test this hypothesis, a combined theoretical and experimental approach was devised.

The experimental model tests were carried out to establish the existence of trailing vortices on the two models. Then, having shown that they did exist, to measure their vorticity distribution in several cross-flow planes at the stern. This would also provide information on their location and starting point.

The theoretical approach taken here developed a method of calculating the forces generated on the stern sections of the models, using vortex impulse techniques. These forces are of course additional to those already present from the pure slender body calculation and the vortex induced forces should represent the differences between the measured and calculated derivative values at the stern of the models, as shown in Figures 1 and 2. However the theoretical vortex calculations would have to rely upon the experimental tests to provide the vortex strengths and locations. This two-pronged approach is described in the following sections.

EXTENSION OF STRIP THEORY TO INCLUDE VORTICES

In this section a method of accounting for the stern vortices will be described, which is consistent with the irrotational flow strip method developed by Clarke [2].

As a necessary precursor to this development, Hearn and Clarke [7] showed that the trailing vortices generated forces on the sterns were of the correct order of magnitude. However, they used the simple concept of a tail interference factor, as used in missile aerodynamics, where fins project from a circular section body. In the following, a more general approach is introduced using conformal mapping, where any arbitrary section may be considered.

As in the traditional strip method analysis, a body section is considered to be a double body mirrored in the undisturbed free surface. A schematic view of the ship and the coordinate system is shown in Figure 3a. It is assummed that any vortices which pass down the

body, having been shed upstream of the shaded (y,z) plane, will pass through the (y,z) plane, exterior to that two-dimensional cross-section, and will appear as two-dimensional vortices in that plane.

When the ship is moving forward with velocity U and with no sway or yaw, then pairs of shed vortices, together with their images above the water line and internal to the body cross section, will give rise to impulses in the (y,z) plane. However, the total impulse I will be identical to zero, as illustrated in Figure 3b for any single pair of symmetrically located port and starboard vortices.

If the ship is subjected to yaw and sway motion, the situation is quite different. As shown in Figure 3c, the vortices around the cross-section are all displaced from their original locations, and their total impulse is no longer identical to zero. A finite impulse I results, which is taken to be proportional to the total sway velocity V of the cross-section, and dependent on the distance X of the cross-section from the midship point, so that

$$I = \frac{\partial I(X)}{\partial V} \cdot V \quad , \tag{4}$$

where $V = v + rX$, with v being the sway velocity and r the yaw rate of the ship.

The time rate of change of the impulse will give rise to a sway force per unit length on the body, given by

$$\frac{dY}{dX} = \left(\frac{\partial}{\partial t} + \frac{dX}{dt}\frac{\partial}{\partial X}\right)\left(\frac{\partial I}{\partial V}(v+rX)\right) \quad , \tag{5}$$

using the generalised differential operator, due to the moving cross-flow plane, and noting that the impulse I is still a function of X.

Carrying out the differentiation implied in Equation (5), and non-dimensionalising in the conventional manner, gives

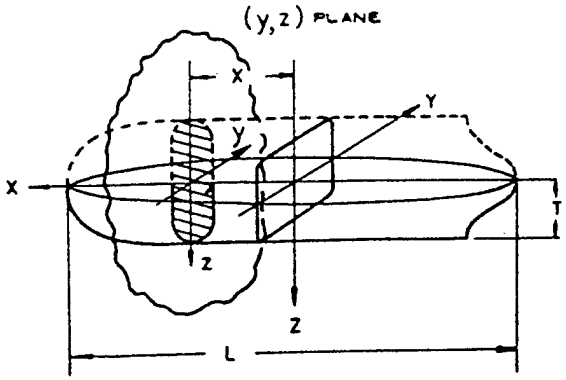
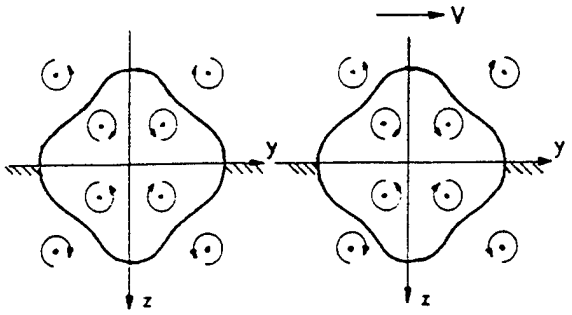


Figure 3a. Schematic View of Double Body.



(b) V = 0 , I = 0. (c) V ≠ 0 , I ≠ 0.

Figure 3b & c. Arrangement of Vortices in (y,z) Plane.

$$\begin{aligned}\frac{dY'}{dX'} = {} & 2\dot{v}'\frac{\partial I'}{\partial V'} + 2\dot{r}'X'\frac{\partial I'}{\partial V'} \\ & - 2v'\frac{\partial}{\partial X'}\left(\frac{\partial I'}{\partial V'}\right) \\ & - 2r'X'\frac{\partial}{\partial X'}\left(\frac{\partial I'}{\partial V'}\right) \\ & - 2r'\left(\frac{\partial I'}{\partial V'}\right) \quad .\end{aligned} \tag{6}$$

Now, defining a vortex influence coefficient I_H as

$$I_H = -\frac{1}{\pi(T/L)^2}\frac{\partial I'}{\partial V'} \quad , \tag{7}$$

we can integrate Equation (6) along the length of the hull to give the sway force, due to the vortices on the underwater part of the double body as,

$$\begin{aligned} Y' = &- \pi\left(\frac{T}{L}\right)^2 \int_S^B I_H dX' \cdot \dot{v}' \\ &- \pi\left(\frac{T}{L}\right)^2 \int_S^B I_H X' dX' \cdot \dot{r}' \\ &+ \pi\left(\frac{T}{L}\right)^2 \int_S^B \frac{\partial}{\partial X'}\left(I_H\right) dX' \cdot v' \\ &+ \pi\left(\frac{T}{L}\right)^2 \int_S^B \left(X' \frac{\partial}{\partial X'}(I_H) + I_H\right) dX' \cdot r' \end{aligned} \tag{8}$$

The moment acting on the hull due to the vortices is simply

$$N' = \int_S^B X' \frac{dY'}{dX'} dX' \quad . \tag{9}$$

The form of Equations (8) and (9) is identical to the form of the Equations developed by Clarke [2], for the hull in simple irrotational flow. In that case though, the added mass coefficient C_H appears, rather than the vortex influence coefficient I_H. However the forces and moments due to the irrotational flow without vortices, and those due to the presence of the vortices may be added together to give the total forces and moments. This amounts to using the term $(C_H + I_H)$, in Equations (8) and (9), rather than the term I_H. This fact may be deduced more rigourously by considering that the complex potentials of the flows in the two cross-flow planes may be added by superposition, one cross-flow plane giving rise to the added mass coefficient C_H and the other containing the vortices giving rise to the vortex influence coefficient I_H. Following Clarke [2], expressions for the linear velocity derivatives may be deduced from Equations (8) and (9) which incorporate the vortex effects as

$$\begin{aligned} Y'_v &= \pi\left(\frac{T}{L}\right)^2 \Big[C_H + I_H\Big]_S^B \\ N'_v &= \pi\left(\frac{T}{L}\right)^2 \Big[(C_H + I_H)X'\Big]_S^B \\ &\quad - \int_S^B (C_H + I_H) dX' \\ Y'_r &= \pi\left(\frac{T}{L}\right)^2 \Big[(C_H + I_H)X'\Big]_S^B \\ N'_r &= \pi\left(\frac{T}{L}\right)^2 \Big[(C_H + I_H)X'^2\Big]_S^B \\ &\quad - \int_S^B (C_H + I_H) X' dX' \quad . \end{aligned} \tag{10}$$

The above expressions in Equation (10) may be seen to be analogous to those of Equation (3), but now include the extra term I_H, the vortex influence coefficient. In the evaluation of the derivative expressions, the horizontal added mass coefficients C_H are determined by conformal mapping, and with a knowledge of the vortex strength and location, the vortex influence coefficient for each section may be determined from the same mapping function. Furthermore, any number of vortices or a distribution of vorticity may be treated in the same manner using superposition.

Returning to Equation (7) the vortex influence coefficient I_H may be modified to reflect the rate of change of impulse with lateral displacement y' of the two-dimensional cross-section as follows

$$I_H = -\frac{1}{\pi(T/L)^2} \frac{\partial I'}{\partial y'} \frac{\partial y'}{\partial V'} \quad , \tag{11}$$

where $\partial I'/\partial y'$ is the impulse position derivative and $\partial y'/\partial V'$ is the position sway derivative.

The impulse position derivative may be easily obtained for a semi-circular hull cross section, by considering a pair of counter-rotating vortices outside the section, together with their images at the reciprocal points inside the section and the mirror images above the water line.

It has been shown by Clarke and Hearn [6] that the impulse position derivative may be expressed as

$$\frac{\partial I'}{\partial y'} = \pi\left(\frac{T}{L}\right)^2\left[\frac{8\Gamma' r'\varsigma'\eta'}{\pi(\varsigma'^2+\eta'^2)^2}\right]\Re\Big(f'(x)\Big) \quad , \tag{12}$$

where the external vortices of strength Γ' are at points (ς', η') and $(-\varsigma', \eta')$ in the circle σ-plane, whose radius is r'. Since the transformation between the real ship section plane and the circle plane is defined as

$$\sigma = f(x) \quad ,$$

then the vortex locations in the real x-plane are (y', z') and $(-y', z')$, from the relationships

$$\varsigma' = \Re(f(x))$$
$$\eta' = \Im(f(x)) \quad ,$$

recalling that in this work, the coordinate system has forced the definition of a complex number to be $x = y + iz$.

By means of a transformation of the form given in Equation (1), the impulse position derivative defined in Equation (12) may be calculated for any hull section, for any vortex location and for unit vortex circulation.

Contours of equal impulse position derivative have been plotted in Figures 4 and 5 for body sections near the sterns of the *British Bombardier* and the *Mariner* respectively. Knowledge of the vortex locations in those cross-flow planes would allow the appropriate values of the impulse position derivative to be obtained from Figures 4 and 5. Similar figures may be drawn for any body section using the transformation appropriate to that section.

The position sway derivative may be deduced by assuming that the vortices shed from a longitudinal hull location X'_o move away from the hull, and at very small drift angles, it is proportional to the drift velocity. In particular, Clarke and Hearn [6] have shown that

$$\left(\frac{\partial y'}{\partial V'}\right)_{r'=0} = \frac{L}{T}X'\left(1 - \frac{X'_o}{X'}\right) \quad . \tag{13}$$

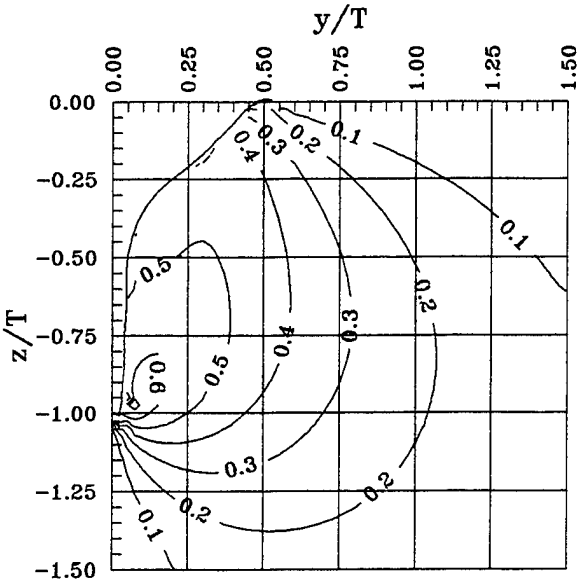


Figure 4. Contours of Normalised Impulse Position Derivative. $(\partial I'/\partial y')/[\pi(T/L)^2\ \Gamma']$ for British Bombardier. 14 Terms. Station 0.25. C_H = 0.940.

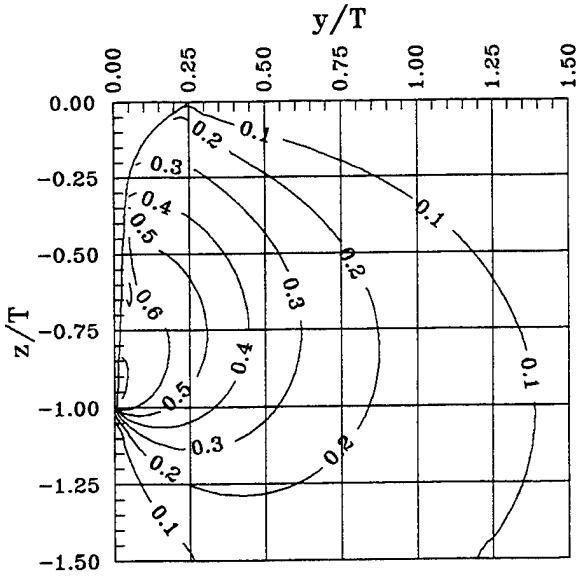


Figure 5. Contours of Normalised Impulse Position Derivative. $(\partial I'/\partial y')/[\pi(T/L)^2\ \Gamma']$ for Mariner. 13 Terms. Station 19.5. C_H = 0.983.

In the case of pure yaw motion, a similar argument may be used to show that

$$\left(\frac{\partial y'}{\partial V'}\right)_{v'=0} = \frac{L}{T}X'\left(\frac{1-\left(\frac{X'_o}{X'}\right)^2}{3-\left(\frac{X'_o}{X'}\right)^2}\right) \quad . \quad (14)$$

In order to investigate the differences between the measured and calculated Y'_v distributions shown in Figures 1 and 2, the vortex starting locations, strengths and positions must be found from experiment. This will allow the vortex influence coefficient I_H to be calculated for use in Equation (10), using Equations (11), (12) and (13). These experiments are described in the following section.

EXPERIMENTAL PROGRAMME

Here we present summary details of the models investigated, the apparatus used and the measurements undertaken. The *British Bombardier* and *Mariner* hull forms were selected for the experimental investigation, since extensive measured lateral force and yaw moment data were available from experiments carried out at Haslar [2,4]. In this programme a model length of 2.5m was selected to minimise the effect of tank blockage, corresponding to scale factors of 1/88.39 and 1/64.37 for the *British Bombardier* and *Mariner* hull forms respectively. The principal particulars of the ship models are given in Table 1. During the experiments the models were restrained in heave and pitch [8,9].

TABLE 1

PRINCIPAL PARTICULARS OF SHIP MODELS

	British Bombardier	*Mariner*
L	221 m	160.9 m
B	29.6 m	23.2 m
T_F	12.5 m	6.9 m
T_M	12.5 m	7.5 m
T_A	12.5 m	8.1 m
$\triangle$	67805 tonnes	17070 tonnes
x_{CG}	3.1 m	-3.8 m
U	15.62 kts	20.0 kts
λ	1/88.39	1/64.37
F_n	0.173	0.259

The total sway force and yaw moment acting on the models were measured by strain gauges attached to the two aluminium bars which connected the ship model to the towing carriage.

The pressure distribution over the wetted body surface of the *Mariner* model was measured at 380 locations, using diaphragm-type pressure gauges. A vortex meter having a 10mm diameter rotor with four unpitched blades was used to provide measurements of the vortex circulation Γ' at different stations along the hull. Views of the vortex patterns were taken by an underwater video camera. The vortices were traced by injecting a dye agent through convenient pressure tappings on the hull surface. In order to reduce diffusion of the dye tracer, the models were towed at a low speed and the flow rate of the dye was carefully controlled.

The sway force and yaw moment measurements confirmed the earlier measurements [2,4] and ensured that the models built at Glasgow University had the same hydrodynamic characteristics as those originally tested at Haslar. The results of sway force measurements for both models, together with the earlier measurements at Haslar, are shown in Figures 6 and 7. In the case of the *Mariner* model the lateral force values were cross checked by integrating the pressure measurements for drift angles of 2^o and 4^o [8,9].

The theory developed in the preceding section assumes that vortices of known strength and position exist. Confirmation of the existence of vortices being shed by the towed models of the *British Bombardier* and *Mariner* is thus an essential part of the justification of the presented theory. Initially this was investigated for zero or small drift angles. The distribution of vorticity was determined by direct vorticity measurements at 64 points on a predefined matrix either side of the model centre plane at selected sections. The vortex position measured at the two stations for the *British Bombardier* and *Mariner* models and the starting point of the stern vortices as observed from underwater visualisation [9] are shown in Figures 8 and 9 rexpectively. Also shown are the loci of vortices on the profile and waterplane views of the two hull forms. These positions were determined from flow visualisation, together with vortex measurements. These measurements confirm that stern vortices

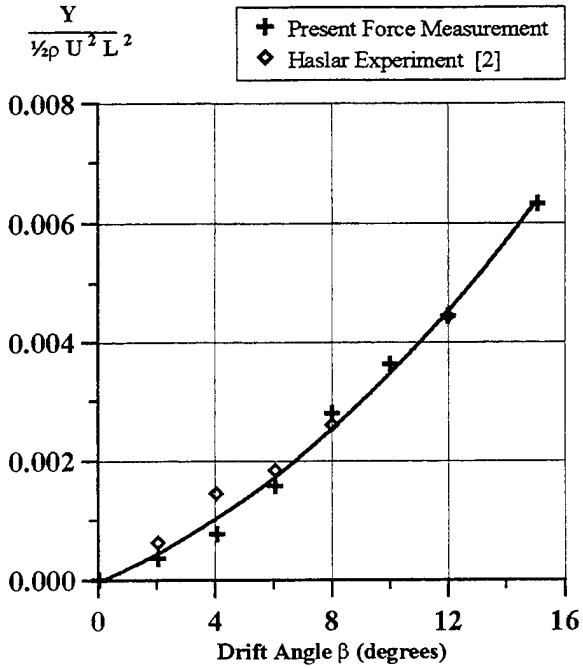


Figure 6. Variation of Lateral Force Coefficient on the British Bombardier with Drift Angle at Fn = 0.173.

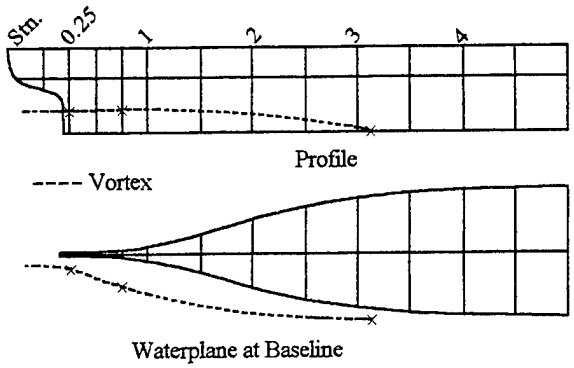


Figure 8. Location of Vortices for British Bombardier.

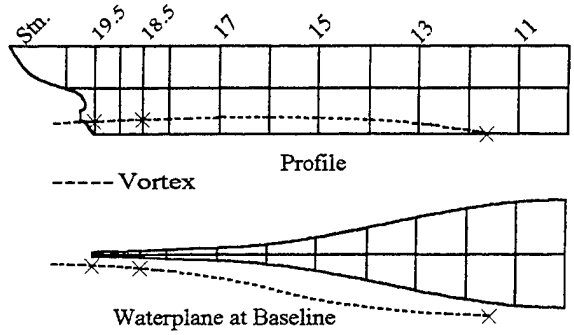


Figure 9. Location of Vortices for Mariner.

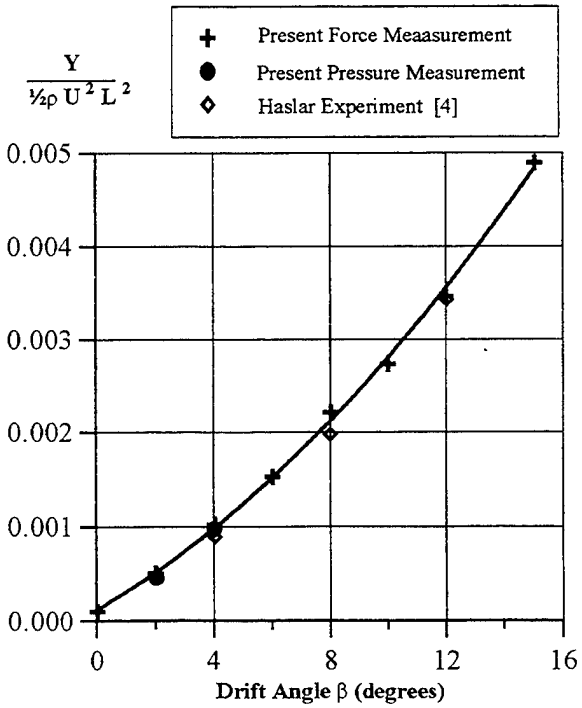


Figure 7. Variation of Lateral Force Coefficient on the Mariner with Drift Angle at Fn = 0.26.

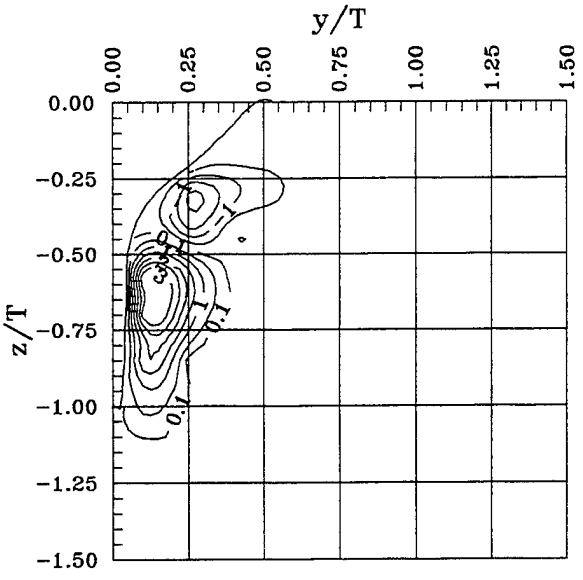


Figure 10. Contours of Measured Vorticity ($\zeta/10$) for British Bombardier. Station 0.25. Zero Drift Angle. Γ/UL = 0.0108. Contour Interval 0.5.

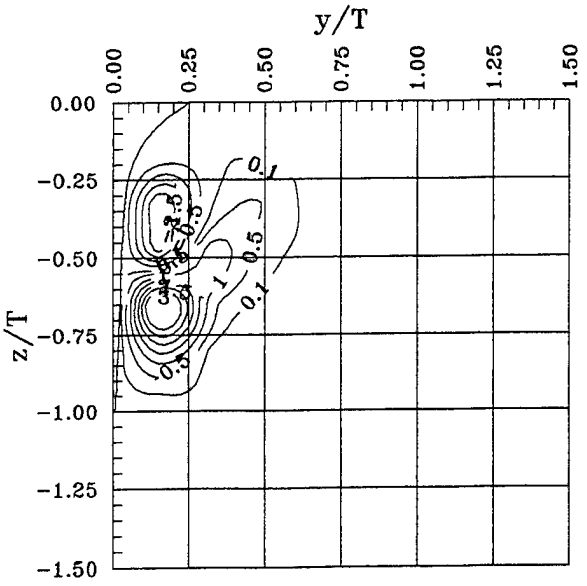


Figure 11. Contours of Measured Vorticity ($\zeta/10$) for Mariner. Station 19.5. Zero Drift Angle. Γ/UL = 0.00612. Contour Interval 0.5.

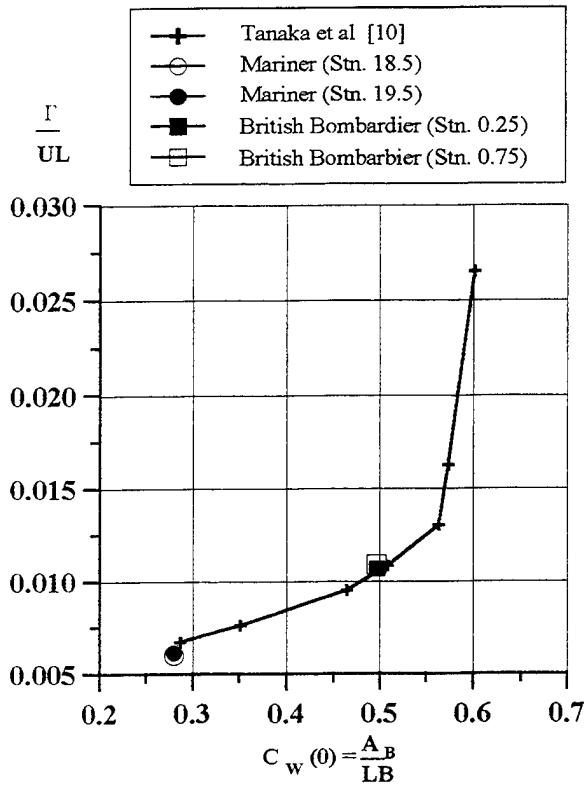


Figure 12. Comparison of Circulation Values.

exist around both the *British Bombardier* and *Mariner* models at zero drift angle. The circulation values Γ given in Figures 10 and 11 are obtained from the following equation.

$$\Gamma = \int\int_s \varsigma dA \qquad (15)$$

where:

ς = Vorticity (rad/s) = 2 x Ω x 2 π
Ω = Rotation frequency (Hz)
dA = Differential area element.

The integral given in Equation (15) was calculated using a Simpson's quadrature method. From an examination of the vortex contours given in Figures 10 and 11 it is suggested that the upper vortex core may shed from the bow region of the ship, whilst the lower core may shed from the stern region. The circulation values for zero drift angle are shown in Figure 12 to match well with those measured for different ship hull forms by Tanaka et. al. [10], who expressed the circulation values as a function of a non-dimensional area coefficient $C_w(0) = A_B/LB$, where A_B is the area of the flat of bottom. The measured pressure distributions were used to validate the global force and vortex measurements.

The experimental programme included vortex measurements and flow visualisation with small drift angles and currently the theory is being extended to incorporate the effects of vortices on longitudinal variation of lateral force and yaw moment. In parallel with this, further experiments and detailed analysis of vortex measurements are being carried out to investigate the distributions of bow and stern vortices.

CALCULATION OF VORTEX EFFECTS ON SWAY FORCE DERIVATIVE

The vorticity contours measured on the models of the *British Bombardier* and *Mariner* shown in Figures 10 and 11, and from Equation (15), it has also been shown that the total circulation Γ' is in good agreement with the experiments of Tanaka et. al. [10], as shown in Figure 12. One of the major objectives of this work was to calculate the vortex influence coefficient I_H, as given in Equation (11). Contours of the quantity

$$\frac{1}{\pi(T/L)^2\Gamma'}\frac{\partial I'}{\partial y'}$$

are shown in Figures 4 and 5, so that by selecting a value of the above parameter from the contour plots, at the coordinates appropriate to the vortex centroids shown in Figures 10 and 11, the impulse position derivative $\partial I'/\partial y'$ may be simply calculated. Since the vortex starting points are shown in Figures 8 and 9, then Equation (13) may be used to calculate a value of the position sway derivative $\partial y'/\partial V'$. From Equation (11) the vortex influence coefficient may be deduced at the two locations at the stern of the models where the vorticity was measured.

However, an alternative approach to the calculation of I_H, at the locations where the vorticity contours have been measured, may be carried out by considering that every element of vorticity represents a separate line vortex.

Writing Equation (15) as $\Gamma = \int\int \varsigma dydz$ and by normalising the coordinates by dividing by the draught T as shown in Figures 10 and 11, we can obtain an expression for the non-dimensionalised circulation $\Gamma' = \Gamma/UT$ which is

$$\Gamma' = \frac{10T}{U}\int\int\left(\frac{\varsigma}{10}\right)d\left(\frac{y}{T}\right)d\left(\frac{z}{T}\right) \quad , \qquad (16)$$

where the factor 10 has been inserted to give a convenient order of magnitude to the vorticity.

Then from Equation (11) we can write

$$I_H = -\frac{1}{\pi(T/L)^2\Gamma'}\frac{\partial I'}{\partial y'}\Gamma'\frac{\partial y'}{\partial V'} \quad , \qquad (17)$$

and on substituting Equation (16) into Equation (17) we get

$$I_H = -\frac{1}{\pi(T/L)^2\Gamma'}\frac{\partial I'}{\partial y'}\left[\frac{10T}{U}\int\int\left(\frac{\varsigma}{10}\right)d\left(\frac{y}{T}\right)d\left(\frac{z}{T}\right)\right]\frac{\partial y'}{\partial V'} \quad . \qquad (18)$$

Now Equation (18) reflects the procedure described above, where the impulse position derivative $\partial I'/\partial y'$ is taken at the centroids of the measured vorticty. However, if we wish to consider every element of vorticty as a separate line vortex, then it must be multiplied by its corresponding impulse position derivative at the same location, prior to evaluating the double integral.

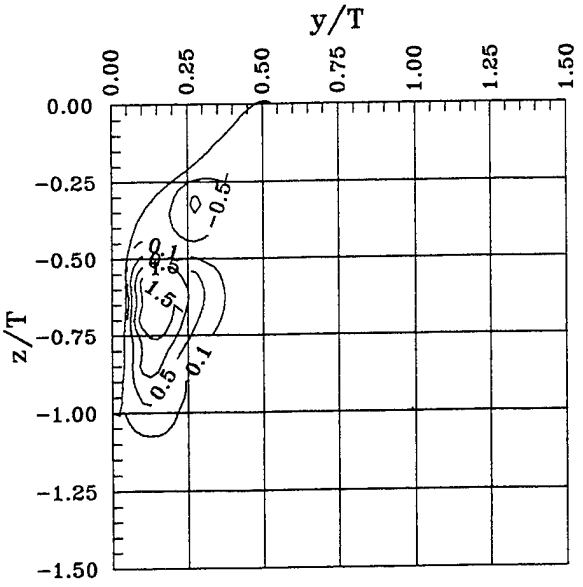


Figure 13. Contours of Normalised Impulse Position Derivative multiplied by Measured Vorticity. $[(\partial I'/\partial y')/(\pi(T/L)^2\ \Gamma')](\zeta/10)$ for British Bombardier. Station 0.25. Contour Interval 0.5.

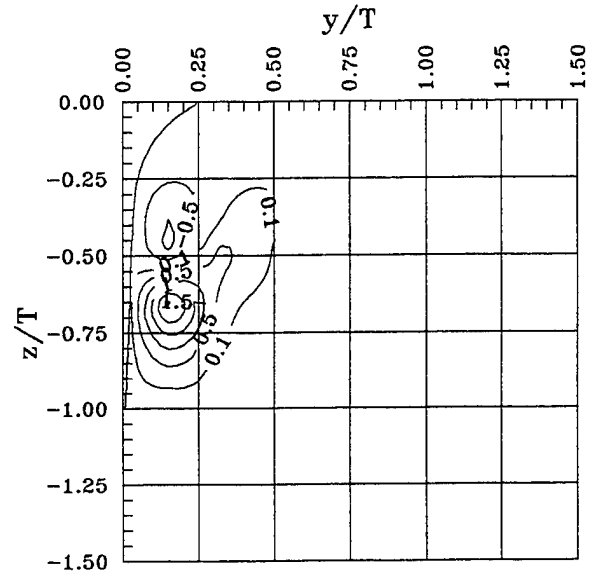


Figure 14. Contours of Normalised Impulse Position Derivative multiplied by Measured Vorticity. $[(\partial I'/\partial y')/(\pi(T/L)^2\ \Gamma')](\zeta/10)$ for Mariner. Station 19.5. Contour Interval 0.5.

Accordingly Equation (18) may be re-written as

$$I_H = -\frac{10T}{U}\left\{\int\int\left[\frac{1}{\pi(T/L)^2\Gamma'}\frac{\partial I'}{\partial y'}\right]\left[\frac{\varsigma}{10}\right]d\left(\frac{y}{T}\right)d\left(\frac{z}{T}\right)\right\}\frac{\partial y'}{\partial V'} \quad . \tag{19}$$

The integral inside the curly brackets was determined by taking the vorticity at every grid point in Figures 10 and 11, and multiplying it by the impulse position derivative at the corresponding grid point in Figures 4 and 5. The resulting values have then been plotted as contours in Figures 13 and 14, where the volume under the surface defined by the contours is equal to the term within the curly brackets in Equation (19).

A knowledge of the vortex starting point X'_o, from the experiments, allows the position sway derivative $\partial y'/\partial V'$ to be evaluated using Equation (13).

The procedure described above was carried out at two stations on both models, giving rise to a value of the vortex influence coefficient I_H at each of those stations. This coefficient I_H could then be summed with the added mass coefficient C_H at the same station, which according to Equation (10), gives rise to the value of the sway force velocity derivative Y'_v at the same location. The two values of the normalised derivative $-Y'_v/\pi(T/L)^2$ are shown for each model considered, in Figures 15 and 16, and denoted by a star symbol. The triangle symbols denote values of $(C_H + I_H)$ at intermediate points which have been deduced using the assumption that the vortex strength increases according to a square law, from the vortex starting location X'_o up to the value measured in the experiments at the forward measurement station. It can be seen in Figures 15 and 16, that the calculated derivative $Y'_v/\pi(T/L)^2$ agrees very well with those measured in the original segmented model tests [2,4].

In any general case, successful estimation of the sway force velocity derivative is dependent upon the ability to estimate the vortex position and strength. It should be noted in Figure 4 that there are areas of the cross-section plane where the value of the impulse position derivative is fairly constant. These locations happen to be where the vortices would probably occur in practice, suggesting that in some cases the vortex location does not need to be known

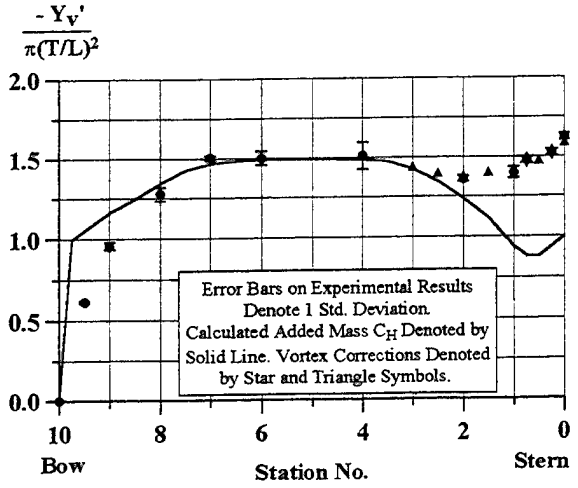


Figure 15. British Bombardier Segmented Model. Longitudinal Variation of Y_V' and C_H. Best "n th" Order Fit for Minimum Variance, Pure Sway Results Only.

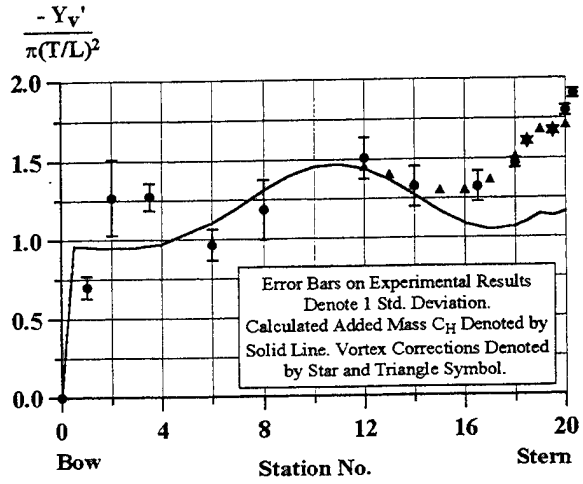


Figure 16. Mariner Segmented Model. Longitudinal Variation of Y_V' and C_H. Best "n th" Order Fit for Minimum Variance, Pure Sway Results Only.

with great accuracy. However it should be noted that the vortex influence coefficient as defined in Equation (17), for instance, is directly proportional to the circulation Γ'.

Since the type of model experiments described here cannot be repeated for every case under consideration, a simple means of estimating the vortex characteristics will need to be the subject of future studies.

CONCLUDING REMARKS

It has been shown by means of a combined theoretical and experimental study, that the discrepancies found in earlier studies [2], between experimentally measured derivative distributions and those due to calculation using a slender body strip method, were due to the neglect of the trailing vortices generated by the bilge corners of the hull forms. Experimental tests established the existence of the vortices and went on to measure their starting points, their strength and their locations as they passed down the hull.

The theoretical studies have extended the earlier slender-body strip method to include vortex effects, by considering the rate of change of the impulse of pairs of vortices, which could then be treated either discretely or as a distribution of vorticity. Combining the theoretical and experimental studies allowed the derivative estimates to be successfully corrected, so that they agreed very well with the measurements of the original segmented model tests.

Having demonstrated the importance of the trailing vortices, future work must be directed towards a simple means of estimating the nature of the vortices in order to allow other hull forms to be considered.

ACKNOWLEDGEMENTS

The funding of this work by the SERC through MTD Ltd. is gratefully acknowledged. The MOSES Steering Committee is thanked for their permission to publish the paper. The views expressed however are those of the Authors.

REFERENCES

1. International Maritime Organisation (IMO) Assembly Resolution A.751. (18), Adopted November 1993.

2. CLARKE, D., 'A Two-Dimensional Strip Method for Surface Ship Hull Derivatives: Comparison of Theory with Experiments on a Segmented Tanker Model', Journal of Mechanical Engineering Science, Vol. 14, No. 7, (Supplementary Issue), 1972, pp. 53-61.

3. BRYSON, A.E., 'Stability Derivatives for a Slender Missile with Application to a Wing-Body-Vertical-Tail Configuration', Journal of the Aeronautical Sciences, Vol. 20, No. 5, May 1953, pp. 297-308.

4. BURCHER, R.K., 'Captive Model Tests with a Segmented Mariner Hull-form'. Proceedings 13th ITTC, Berlin-Hamburg, 1972, pp. 107-120.

5. SUMMERS, R.G., 'On Determining the Additional Apparent Mass of a Wing-Body-Vertical-Tail Cross Section', Journal of Aeronautical Sciences, Vol. 20, No. 12, December 1953, p. 856.

6. HEARN, G.E. and CLARKE, D., 'Manoeuvring of Ships and Estimation Schemes (MOSES): The Influence of Vortices on the Calculation of Hull Derivatives', Proceedings of International Conference on Marine Simulation and Ship Manoeuvrability, MARSIM'93, St. John's, Newfoundland, Canada, Vol. 1, 26 September - 2 October 1993, 1, pp. 171-178.

7. CLARKE, D. and HEARN G.E., 'A Fundamental Investigation of the Hydrodynamics of a Manoeuvring Ship', MOSES Project Final Report, Department of Marine Technology, University of Newcastle upon Tyne, April 1994. (Currently Commercial in Confidence).

8. CHAN, H.S., VARYANI, K.S. and INCECIK, A., 'Experimental Investigation of the Hydrodynamics of a Ship Moving at a Drift Angle', University of Glasgow, Department of Naval Architecture and Ocean Engineering, Report NAOE 93-25, 1993.

9. VARYANI, K.S., INCECIK, A. and HANNAH, S.T., 'Experimental Investigation on the Hydrodynamic Forces and Vortices around a Cargo and Tanker Vessel for Linear Drift Angles', University of Glasgow, Department of Naval Architecture and Ocean Engineering, Report NAOE 94-16, March 1994.

10. TANAKA, H., KAWAKAMI, Y., UEDA, T., and TAKAHASHI, K., and YANAGIHARA, T.Y., 'Experimental Studies on Trailing Vortices of Ships', Proceedings of 2nd International Symposium PRADS 83, Tokyo and Seoul, 1983, pp. 295-302.

Turbulence in Trailing Vortex Pairs

W. Devenport, J. Zsoldos, C. Vogel
(Virginia Polytechnic Institute and State University, USA)

ABSTRACT

The turbulence structure associated with a pair of counter-rotating trailing vortices is examined through analysis of a large experimental database. The vortices were generated by two rectangular NACA 0012 half wings placed tip to tip, separated by 0.25 chordlengths (c). The database consists primarily of detailed 3-component hot-wire velocity records measured in planes 10 and 30 chordlengths (c) downstream of the wing leading edges for a chord Reynolds number of 260,000.

The data reveal much about the turbulence structure of the vortex cores, the surrounding spiral wakes, and their interaction. The wakes dominate turbulence structure outside the core regions. The drift of the vortex pair and the secondary flow they generate stretches and distorts the wakes, causes them to merge and separate again. While these events cause substantial changes in the organization and structure the wake-like character of the turbulence is never lost.

The interaction between the vortex cores, in addition to producing Crow instability, appears to be a crucial player in their decay. Specifically, the interaction seems to stimulate turbulence production in the vicinity of the otherwise laminar cores, accelerating their growth. This previously unobserved mechanism provides a possible physical explanation of the two-stages of vortex decay seen in the far wakes of lifting vehicles.

INTRODUCTION

Interactions of counter-rotating vortices generated by lifting surfaces are commonly seen in the far wakes of aircraft and marine vehicles. Perhaps the most well-known interaction is Crow[1] instability. Crow showed that a pair of infinite line vortices of opposite sign with finite cores are unstable to sinusoidal disturbances of specific wavelength along planes that lie at 45° to that joining the vortices. There have been numerous observations of full-scale aircraft wakes[2-4] and laboratory-scale flows[5-8] confirming Crow's theory. Crow instability is the primary mechanism causing the dissipation and break-up of a counter-rotating vortex pair. As the amplitude of Crow instability grows, it starts to become non-linear. Ultimately, at low background turbulence levels, the vortex cores link together and a series of ring vortices is formed. At higher turbulence levels, vortex bursting may diffuse the cores before linking can occur[4,7,8].

Crow instability and its consequences are of course only one part of the interaction between counter-rotating vortices. We would expect the straining field imposed by the vortices upon each other to substantially modify their mean flow and turbulence structure, especially when the ratio of core radius to vortex separation is significant. Quantitative velocity measurements on interacting trailing vortex pairs are rare, however, and there have been no studies in which the cross-sectional structure of such a flow has been examined in any significant detail. Surveys of the near-wakes of lifting wings[9-11] (where counter-rotating vortex interactions are insignificant) suggest that this structure may be fairly complex because of the wakes that surround and connect the vortex cores. Core axial and tangential velocity profiles have been measured in the far wakes of aircraft and wind-tunnel models by a number of authors[10,12-17]. These measurements were aimed at understanding the decay of the individual vortex cores, however, without reference to possible interactions between them. A relevant observation made in several of these studies,

is that the cores appear to undergo a two-stage decay. Over the first 30 to 100 spanlengths downstream of the generating wing the cores appear not to grow and their strength remains constant[18] - this is referred to as the plateau region. Decay then begins; core radius and peak tangential velocity varying as the square root of streamwise distance. No satisfactory physical explanations have been advanced to explain the onset of decay, but because of the large streamwise distance before decay begins, interaction between the tip vortices seems a possibility.

The measurement of trailing-vortices is not without its problems. Vortices tend to wander (i.e. their core location is a function of time) and be sensitive to probe interference. Wandering causes a fixed probe to greatly overestimate turbulence stresses in regions where there are significant mean velocity gradients. In severe cases it also substantially smooths mean velocity profiles. Baker et al.[19] conducted experiments on a trailing vortex generated by a rectangular wing in a water tunnel using laser Doppler velocimetry. They argued that vortex meandering decreased the maximum tangential velocities by 30% and increased the measured core radius by a factor of 2.2. Baker et al. attributed the wandering to freestream turbulence. Chigier and Corsiglia[20] and Corsiglia et al.[17] conducted triple hot-wire measurements on a trailing vortex in the NASA Ames 40x60 wind tunnel. They observed a spanwise meandering of about ± 2 chordlengths. As a result mean-velocity measurements made with a fixed hot-wire probe underestimated the peak tangential velocity by as much as 50%. Recently, Devenport at al.[11] have studied theoretically some effects of wandering on core velocity measurements. They derive simple expressions for the true core radius r_1 and peak tangential velocity $v_{\theta 1}$ in terms of values measured in the presence of wandering r_{1m} and $v_{\theta 1m}$; .

$$r_1 = r_{1m}\sqrt{1 - 2\alpha\sigma^2/r_{1m}^2}$$
$$v_{\theta 1} = v_{\theta 1m} r_{1m}/r_1 \qquad (1)$$

where α = 1.25643. They also develop a method for estimating the r.m.s. amplitude of wandering motions σ from single-point turbulence measurements. They show that, as long as the wandering is not too severe, its effects on mean-velocity field measurements can be reversed.

Probe interference problems in single-wing vortices have been reported by Orloff[21], Gasparek[22] and Mason and Marchman[23]. Orloff and Gasparek found that the trajectory of the vortex moved when a small diameter probe was inserted into the core. Mason and Marchman also found that a probe changed the vortex trajectory but only if it was pitched or yawed relative to the free stream direction. Stifle and Panton[24] examined the effects of passing a moving wire through the core of a single vortex produced by a delta wing. They found that disturbances introduced into the vortex core propagated both upstream and downstream with smaller disturbances produced by a slower moving wire.

The overall objective of the present investigation is to improve the understanding of turbulence in trailing vortex pairs and thus make them easier to predict. Detailed three-component velocity, turbulence and spectral measurements made in both co- and counter-rotating trailing vortex pairs have already been presented[25,26]. In this paper we analyze in more depth those measurements made in the counter-rotating vortex pair, making use of recent observations of an isolated trailing vortex generated under similar conditions. The new analysis reveals much about the turbulence structure of the vortex cores, the surrounding spiral wakes, and their interaction.

CONFIGURATION

The measurements were taken in the Virginia Tech Stability Wind Tunnel. Its test section (figure 1) has a square cross section 1.83m×1.83m and a length of 7.33m. Flow in the empty section is closely uniform with a turbulence intensity of less than .05% at 20m/s[27].

The vortex pair was generated using two identical half-wings mounted tip to tip. Both had a rectangular planform and NACA 0012 section with a chordlength c of 0.203m. Both were equipped with effective boundary-layer trips[26]. The wings, introduced from opposite walls of the test section, were mounted with their quarter chord lines collinear and perpendicular to the freestream. A tip separation of 0.25c was used and the angle of attack of both wings was fixed at 5°.

This configuration is a compromise between vortex age and Reynolds number. To obtain significant interaction between a counter-rotating vortex pair, they must be allowed to develop over a streamwise distance equal to many times the distance separating them. Given the length of most wind-tunnel test sections this means that, if the vortices are generated from opposing tips of the same wing, only a very small wing can be used and Reynolds

numbers will be correspondingly low. With two wings placed tip to tip, however, significant interaction can be generated without sacrificing Reynolds number.

RESULTS AND DISCUSSION

The cartesian coordinate system (x,y,z) (u,v,w) shown in figure 1 will be used in discussing results. Most results have been normalized on the wing chord c of 0.203m and the free-stream velocity U_{ref}. Measurements were made at a chord Reynolds number $Re_c = U_{ref}c/\nu$ of 260,000, corresponding to a free-stream velocity of about 20m/s.

Velocity and turbulence measurements were made using a miniature 4-sensor hot-wire probe calibrated directly for flow angle[25,26]. Hot-wires were used in preference to laser Doppler anemometry since the latter is not-well suited to the measurement of velocity spectra (essential if vortex wandering and turbulence are to be distinguished) and would be expected to encounter seeding problems in the core. However, with hot-wire anemometry it is essential to establish that there is no significant probe interference. This was done through a series of helium bubble flow visualizations, presented by Zsoldos and Devenport[25,26]. These clearly showed no influence of the probe on the core at the measurement point even with the probe moving through the core.

Measurements were made in two cross-sectional planes at x/c = 10 and 30. About 900 points were measured in each plane in nominally polar grids centered on the cores. At each point 614400 simultaneous samples of the three velocity components were recorded at a rate of 30 kHz (sufficient to calculate a detailed low-uncertainty spectrum) over a total sampling time of about 2 minutes. The detailed nature of the data set makes it suitable for many kinds of analysis. We present Reynolds averaged statistics, spectral results and high-pass filtered statistics, the latter providing a view of the turbulence structure in the core regions without the obscuring effects of wandering. Typical uncertainties in Reynolds averaged statistics are listed in table 1.

Measurements at x/c = 10

Figure 2a reveals the overall flow structure at x/c = 10 in terms of contours of axial normal stress $\overline{u^2}/U_{ref}^2$. Figure 3 shows flow structure in the core regions in terms of mean cross-flow velocity vectors, contours of mean axial velocity U/U_{ref}, mean streamwise vorticity $\omega_x c/U_{ref}$, axial normal stress $\overline{u^2}/U_{ref}^2$, cross-flow normal stress sum $(\overline{v^2}+\overline{w^2})/U_{ref}^2$ and turbulence kinetic energy production, normalized on U_{ref} and c. We plot the sum of the cross-flow normal stresses since it is invariant to rotation in the cross-flow plane.

Having drifted under their mutual induction, the vortices are centered at z/c=-0.66 at x/c=10. The cores have also moved apart from 0.25c at the wing tips to 0.45c here. This movement, also observed in helium-bubble flow visualizations[25] is a consequence of the Betz's conservation laws[30,31] governing the inviscid roll-up of each vortex. Specifically, the centroid of the vorticity distribution shed by each wing must remain fixed during the roll-up. Since the centroid is inboard of the tip the vortex cores are initially seen to move apart.

The circulating velocity fields produced by the vortices are clearly visible in the mean-velocity vectors (figure 3a). These combine to produce a strong upwash between the cores and a relatively weak downwash to either side. Carried with this flow are the wing wakes, seen most clearly in the turbulence-stress contours (figures 2a, 3d and e). These pass upward between the vortices, where they merge, and then roll into spirals around each core. Physically it seems that the spiral sections of wake must have passed between the vortices before merger began. These pictures therefore probably show the initial stages of merger, i.e. the beginnings of the viscous interaction between the vortices.

In addition to merger the wakes suffer lateral stretching, rates of shear strain and strong lateral curvature, all of which appear to have a significant influence on their turbulence structure. Lateral stretching is produced by the upward motion of the vortices and the acceleration of the flow between them. Rates of shear strain are imposed not only by the rotational velocity fields of the vortices but also by streamwise vorticity embedded within the wakes themselves. (Some of this vorticity is clearly visible in figure 3b). This vorticity, representing the un-rolled-up portions of the vortex sheets shed by each wing, should increase in strength as the vortex cores are approached. Rates of shear strain would tend to suppress large-scale turbulent structures and thus reduce turbulence levels in the wakes.

In the region immediately below the vortices (z/c>-0.4) the wakes are being stretched and consequently thinned by the upward motion of the vortex pair. The wake thickness, measured between the $\overline{u^2}/U_{ref}^2 = 5\text{x}10^{-5}$ contours, is about 0.2c here,

compared to 0.33c in the near two-dimensional (2D) portions of the wakes shed much further from the wing tips[26]. Stretching, of course, also influences the turbulence structure, increasing dissipation but also intensifying coherent turbulent structures aligned with the stretching direction. Turbulence normal stresses and velocity autospectra presented by Zsoldos and Devenport[26], in terms of the wake aligned velocity components u,v_n,v_s (figure 2a), show these effects. Approaching the vortices from below, peak levels of $\overline{v_s'^2}$ fall due to the increased dissipation, becoming a factor of 3 smaller than in the 2D portion of the wake. Peak levels of $\overline{u'^2}$ and $\overline{v_n'^2}$, being more closely associated with spanwise coherent structures, change little from their 2D values, however. At the same time velocity spectra show an intensification of the peak associated with the passage frequency of large scale wake structures, but a suppression of spectral levels at other frequencies.

Moving between the vortex cores the wakes merge and overall levels of $\overline{u'^2}/U_{ref}^2$ and $(\overline{v'^2}+\overline{w'^2})/U_{ref}^2$ increase by as much as a factor of two, creating local maxima. Stretching, which is at its greatest here, appears to be at least partly responsible for these effects. The strongest evidence for this is the tremendous anisotropy of the turbulence structure in this region. Figure 4 shows normal-stress profiles measured along a z-wise profile coincident with the plane of symmetry. Passing between the vortex centers $\overline{u'^2}$ and $\overline{v'^2}$, being associated with spanwise wake structures intensified by stretching, increase to maxima. By contrast $\overline{w'^2}$ is as low as 1/7th of $\overline{v'^2}$. The dominance of $\overline{v'^2}$ is also felt in the turbulence production in this zone (figure 3f). This is strongly positive below the line joining the vortex centers (z/c=-0.66) but is actually negative above. The reason is that $\overline{v'^2}\partial V/\partial y$, locally by far the largest contributor to production, reverses in sign with $\partial V/\partial y$ near z/c=-0.66. Velocity autospectra measured at the center of the merging region (z/c=-0.66, y/c=.02) are compared with corresponding spectra measured on the centerline of the 2D portion of the right-hand wake in figure 5. Consistent, with stretching, spectral levels are elevated in the vicinity of the peak associated with the passage of coherent spanwise structures, visible in the normal to wake component (figure 5b). It is rather surprising that the center frequency of this peak is only slightly higher (at fc/U_{ref}=4) in the merging region than in the 2D part of the wake. One would expect a frequency doubling in the merged region because of the presence of structures from both wakes.

Moving out of the merged region the wakes separate suffering strong lateral curvature in the process (see near z/c=-0.9, y/c=0.15 for the right-hand vortex) and a consequent suppression of turbulence levels. The wakes then straighten and turbulence levels once more increase reaching a second maximum (near z/c=-.7, y/c=0.37). Finally, turbulence levels fall as the wakes converge on the cores, presumably due to the increasing rates of shear strain and transverse curvature they experience. After coming out of the merging region, turbulence production recovers a more conventional wake-like form (figure 3f) and is concentrated in a crescent-shaped region that surrounds the wake centerlines.

The solid lines in figure 3b show both core edges defined as the locus of peak tangential velocity about each core center. The cores are both closely circular with radii of 0.044c. The velocity vectors (figure 3a) and a profile through the right-hand core (figure 6) shows that tangential velocities at the core edges vary substantially with circumferential location from 48% U_{ref} on the side closest to the plane of symmetry to 35% U_{ref} on the outer edge. This variation is partly a consequence of the fact that the cores lie at an angle of about 3° to the freestream direction and thus to the coordinate system in which these vectors have been resolved. (This is also why the point of zero cross flow velocity does not appear exactly at the core center.) The contours of $\omega_x c/U_{ref}$ (figure 3b), being less affected by this skewing, are approximately circular in the core regions and concentric with the core edges. A profile of axial mean velocity through the right-hand core center (figure 6) shows there to be a deficit, of maximum value 19%U_{ref}. The deficit is not symmetric, being considerably greater toward the inside edge of the core, partly because of the angle between the core and free stream. There is also a local peak in the profile close to the core center. Figure 3c shows this as an irregularity in the axial velocity contours on the right-hand side of the core. A similar peak appears at the mirror image location in the left-hand core. We have investigated the possibility that these peaks may be due to errors associated with the finite size of the hot-wire measurement volume (about 1mm) and high tangential velocity gradients. However, these errors seem too small and, furthermore, would be of opposite sign in the left and right-hand vortex cores. We are therefore in no

doubt that this feature is real. Such a peak could be a remnant of the axial velocity surplus that probably exists in the cores further upstream.

Within the core region the turbulence stress contours (figures 3d and e) show velocity fluctuations rising to a maximum. The large fluctuation levels at the core center are mostly a consequence of small amplitude wandering, also observed in helium-bubble flow visualizations[26]. If we assume that this is the only source of low-frequency fluctuations we can estimate, using the measured mean velocity gradient here and the method of Devenport et al.[11], an upper bound for the r.m.s. amplitude of the core motions. This turns out to be 3.7% of the core diameter. Given Devenport et al.'s correction formulae we would therefore expect the present measurements to over-estimate the true core size by only 0.7% and underestimate the peak tangential velocities around it by an equal amount. Likely errors in the measured turbulence stresses (estimated by multiplying the estimated amplitude of wandering motions by the local mean velocity gradients) are of course larger. Figures 2d and e show shaded regions within which wandering is estimated to have contributed more than 30% to the Reynolds stresses. (For comparison, 30% is approximately the contribution that inactive motion makes to the streamwise normal stress in an attached turbulent boundary layer.) For $\overline{u'^2}/U_{ref}^2$ this region only occupies a very small crescent shaped area towards the lower edge of the right-hand core. Even setting a much tighter tolerance of 10% only eliminates measurements made in the immediate vicinity of the cores. For $(\overline{v'^2}+\overline{w'^2})/U_{ref}^2$ the region is larger but still only extends about 1 core radius beyond its edge. Thus the vast majority of the turbulence-stress data outside the core regions can be considered free of substantial wandering effects. This is not to say that all the turbulence stresses here are generated by conventional turbulent processes. The elevated $\overline{u'^2}/U_{ref}^2$ levels around the core edge, for example, may well be due to core waves or distortions generated by the surrounding turbulence. Indeed this is indicated by the velocity spectra presented below.

Figure 7 shows autospectra of V and W velocity component fluctuations (plotted as $G_{vv}/U_{ref}c$ and $G_{ww}/U_{ref}c$ vs fc/U_{ref}, where f is frequency in Hertz) for various locations along the right half of the profile presented in figure 6. Locations are identified in terms of distance from the core center y_r/c, listed in the legend. Absolute locations are indicated by the dots marked on figure 3d.

The spectra at $y_r/c = 0.176$ and 0.126 show the character of velocity fluctuations in the curled up wing wake. These bear a qualitative resemblance to those measured in the 2D portion of this wake (figure 4), suggesting that the instantaneous turbulent structures here may not be that different, despite the strong distorting effects of the nearby vortex. The G_{vv} spectra show a peak presumably associated with the passage of large coherent structures in the vicinity of $fc/U_{ref} = 4$. Spectra of u-component fluctuations at these locations show an inertial subrange, indicating a well developed energy cascade.

Moving into the vortex core spectral levels at very low frequencies $fc/U_{ref} < 2$ rise dramatically as a consequence of the wandering. It seems probable that some of the wandering motions are associated with Crow[1] instability. A theoretical calculation of Crow instability requires an estimate of the core diameter where, in this context core refers to the region carrying the bulk of the streamwise vorticity. From figure 3b we choose this distance to be $0.15c$ (the diameter of the contour where the vorticity is 1/10th of its value at the core center) which, using Crow's results, implies a most unstable wavelength of $3.3c$ that would grow by a factor e (= 2.71828) over a streamwise distance of $10c$. A $3.3c$ wavelength implies a frequency fc/U_{ref} of 0.3. Spectral levels are strongly elevated around this frequency but the spectra do not show a distinct peak. This suggests that other sources of wandering may also be important at this stage.

While wandering dominates the low-frequency end of velocity spectra in the core, wave motion appears to be a factor at mid frequencies $2 < fc/U_{ref} < 20$. Here the diffuse hump in the G_{vv} spectra, attributed to the passage of large-scale structures in the wake, develops into two sharp peaks as the core is entered, at $fc/U_{ref} = 4.9$ and 8.2. These bear some resemblance to peaks seen at similar non-dimensional frequencies by Bandyopadhyay et al.[33], within the core of an isolated vortex, which they suspected were the result of axisymmetric and helical instabilities travelling along the core. The fact that there appears to be a connection between these peaks and the passage of large-scale structures in the surrounding wake may not be coincidence. Devenport et al.[11] have demonstrated that higher frequency velocity fluctuations in the core of an isolated trailing vortex tend to scale on the parameters of the wake that spirals around the vortex and not on those of the core. This behavior can be explained if the bulk of fluctuations in the core are

created by core motions and waves generated in response to the motion of large-scale structures of the surrounding wake.

At the high frequency end of the spectrum $fc/U_{ref} > 20$, where we would expect to see contributions from the smaller turbulent scales, spectral levels in both components fall by as much as an order of magnitude as the core is approached and entered. Bearing in mind the strong stabilizing effects of rotation, it is no surprise to see suppression of turbulence at the core center, However, it is a surprise to see it at the core edge (r/c = 0.04). The core edge is the region of maximum tangential rate of strain and therefore the place where we would expect the most production of turbulence from the rotational motion of the vortex. The absence of small scale turbulent fluctuations here suggests that such production may not take place or may be insignificant at this stage. Recent large eddy simulations by Ragab and Sreedhar[34] appear to show a complete absence of turbulence production in and around an isolated vortex core. Note that corresponding axial velocity spectra measured at the core center and edge show no inertial subrange or similar region, implying that the turbulent energy cascade is severely disrupted here.

The true turbulence structure in the core regions can be illustrated for a broader range of positions by plotting filtered statistics. In figure 8 we plot contours of $\overline{u'^2}/U_{ref}^2$ high pass filtered at frequencies of fc/U_{ref}=3 and 40, corresponding to length scales of 0.33c (7.3 core radii) and 0.025c (0.56 core radii) respectively. Filtering at fc/U_{ref}=3 (figure 8a) would be expected to eliminate most of the velocity fluctuations associated with wandering, but leave intact the bulk of fluctuations associated with coherent wake structures and core waves. The flow structure appears nearly identical to that shown by the conventional Reynolds averaged measurements (figure 8a) confirming that wandering is not an overwhelming contributor to the axial normal stress at this station. Filtering at fc/U_{ref}=40 (figures 8b, c and d) would be expected to eliminate all but the smaller turbulence scales. These contours show no maximum in the wake merging region between the cores. This is expected since the stretching of the wakes here should suppress smaller scale turbulence through increased dissipation. In the cores these contours show fairly constant but very low stress levels, perhaps indicating laminar flow. Outside the cores stress levels increase reaching local maxima that sit on diagonally opposite sides of the core about 1.25 core radii outside its edge. The cause of these maxima is not immediately clear. We will discuss them later along with the corresponding results for x/c=30.

Measurements at x/c = 30

Figure 2b shows the overall flow structure in terms of contours of axial normal stress $\overline{u'^2}/U_{ref}^2$. Figure 9 shows mean cross-flow velocity vectors, contours of mean axial velocity U/U_{ref}, mean streamwise vorticity $\omega_x c/U_{ref}$, axial normal stress $\overline{u'^2}/U_{ref}^2$, cross-flow normal stress $(\overline{v'^2}+\overline{w'^2})/U_{ref}^2$ and turbulence kinetic energy production in the vicinity of the cores, normalized on U_{ref} and c.

By x/c=30 the vortices are slightly further apart, their separation here being 0.52c. They have also drifted further under their mutual induction, to z/c=-1.73. The fact that the z-location of the vortex centers at x/c = 30 is less than three times that at x/c = 10 is an indication that the rate of drift decreases slightly. The mean velocity vectors, contours of streamwise vorticity and axial velocity (figures 9a, b and c) show a mean-flow structure very similar to that at x/c=10, though slightly diminished in intensity. The axial normal stress contours (figure 2b) still show the wing wakes which, having been further stretched by the upward drift of the cores, are only slightly thicker than at x/c=10. Turbulence stresses and velocity spectra measured in the portions of the wakes found below the core regions ($z/c > -1$) show the same features (increased anisotropy, an enhanced peak at the passage frequency of large structures) taken as symptomatic of lateral wake stretching at x/c=10. The merging region between the cores is less distinct than at x/c=10 but still apparently dominated by stretching. z-profiles of normal stresses along the plane of symmetry (figure 10) show, if anything, an even greater imbalance between $\overline{v'^2}$ and $\overline{w'^2}$. The large values of $\overline{v'^2}$ again lead to positive and negative regions of turbulence production below and above the line joining the vortex centers (figure 9f).

Apart from the merging region, the turbulence structure that envelopes the cores appears quite different than at x/c=10. Gone are the wake spirals, having been replaced by a more homogenous turbulence structure. Judging from the development of the flow implied by the velocity field measured at x/c=10, it seems that much of this turbulence should have originated in the wakes, having been brought through the merging region. The forcing together and then pulling apart of this wake fluid would have destroyed its large scale organization, producing the

structure seen here. Interestingly, velocity spectra in this region (see below) still appear wake-like, however, suggesting that the larger scale instantaneous flow structure may not be destroyed by this process.

The solid lines in figure 9b show both core edges. The cores are again closely circular with radii of 0.054c. A profile through the right-hand core (figure 11) shows peak tangential velocities varying from 34% U_{ref} on the side closest to the plane of symmetry to 25% U_{ref} on the outer edge. The contours of $\omega_x c/U_{ref}$ remain circular in the core regions and concentric with the core edges but peak vorticity levels are significantly less than at x/c = 10. A profile of axial mean velocity through the right-hand core center (figure 11) shows there to be a deficit, of maximum value 16%U_{ref}. The deficit is not only smaller but also more symmetric than at x/c = 10. In addition there is no evidence of local peaks in the axial velocity in either core.

The turbulence stress contours (figures 9d and e) again show velocity fluctuations rising to a maximum at the core center. Normal stress levels at the core center and measured mean-velocity gradients here suggest an upper bound for the amplitude of the core motions of 10.5% of the core diameter. Given Devenport et al.'s correction formulae we would therefore expect, as a worst-case scenario, the present measurements to over-estimate the true core radius by 5% and underestimate the peak tangential velocities around it by an equal amount. We therefore estimate, for example, a true core radius closer to 0.051c. Outside the core edge, mean-velocity errors rapidly become negligible. Figures 9d and e show shaded regions where it is estimated that wandering contributed more than 30% to the Reynolds stresses. For $\overline{u'^2}$ these regions still only cover the cores and their immediate surroundings. For $\overline{v'^2}+\overline{w'^2}$, however, these regions are much larger and we must rely more on spectra and filtered results to infer the turbulence structure.

Even after accounting for the possible effects of increased wandering it is clear that there is substantial decay of the cores between x/c=10 and 30. Core radius increases by about 16% and peak tangential velocities fall by about 22%. Significant decay over this distance is not observed in the equivalent isolated trailing vortex produced with one of the NACA 0012 half wings removed[11]. We therefore have strong circumstantial evidence that the interaction between the counter-rotating vortices stimulates a more rapid decay of their cores. Thus, it seems possible that the sudden onset of core decay in aircraft trailing vortices seen by previous authors is a consequence of interaction between the two tip vortices and not self induced.

We may gain insight into the turbulence structure in and around the cores from velocity autospectra. Figure 12 shows autospectra of V and W velocity component fluctuations for various locations along the right half of the profile presented in figure 11. Locations are indicated in the legend of figure 12 in terms of y distance from the core center y_r/c and are shown as dots in figure 9(d).

The spectra at y_r/c = 0.214 and 0.167 show the character of velocity fluctuations in the outer crescent of turbulent fluid surrounding the cores. Above fc/U_{ref}=1 these bear a remarkable resemblance to spectra measured in 2D portions of the wing wakes at x/c=30[26]. In particular, G_{vv} shows a peak at a frequency of 2.7 - close to the passage frequency of large-scale structures in the 2D regions. This peak frequency lower than that seen in the spiral wakes at x/c=10, but by an amount roughly consistent with the expected wake the development over the intervening streamwise length. These results suggest the seemingly unlikely conclusion that instantaneous turbulent structures surrounding the cores retain a strong memory of their origins, despite overwhelming curvature, strain and the merger process.

Below fc/U_{ref}=1 these spectra already show elevated levels due to wandering. Moving into the core these rise by more than two orders of magnitude. In contrast to x/c=10 the wandering motions here appear to a preferred frequency, since the G_{ww} spectrum develops a clear peak centered at fc/U_{ref} = 0.36. This is close to the frequency predicted for Crow instability of fc/U_{ref} = 0.3. (Note that using conditions at x/c=30 instead of those at x/c=10 in this prediction makes no significant difference to the results.) The direction of this dominant core motion is clearly shown by the double-peaked distributions of axial normal stress visible in both core regions (figure 9d). It is simple to show that these distributions are a consequence of oscillation of a near Gaussian axial velocity deficit along an axis coincident with a line joining the two peaks. These lines are seen to lie along ±45° planes consistent with Crow's prediction. Over the intervening distance between x/c=10 and 30 we would expect the amplitude of Crow instability to become magnified by a factor e^2, and thus associated spectral levels to increase by e^4 = 54.6. In fact the increase in G_{ww} at the core center is about ten fold. This explains why the spectra at x/c=10 show no distinct peak associated with this instability, it being

well buried in the surrounding spectrum.

In the middle frequency range $2 < fc/U_{ref} < 20$ the core center G_{vv} spectrum does show some evidence of core waves. However, only one peak is visible, centered at $fc/U_{ref} = 4.5$ - very close to the location of the lower-frequency peak seen at x/c=10. In addition this peak is spread over a significantly broader range of frequencies than at x/c=10.

At the high frequency end of the spectrum $fc/U_{ref} > 20$ spectral levels again fall as the core center is approached. However, the fall is much less than that seen at x/c=10. In addition, high frequency turbulent fluctuations at the core edge (r/c=0.051) are barely suppressed at all, in complete contrast to x/c=10. This change in relative spectral levels is not observed in the equivalent isolated vortex suggesting that some aspect of the interaction between the vortices is the cause.

The change in core structure implied by the above results is also apparent in the filtered statistics. In figure 13 we plot contours of $\overline{u^2}/U_{ref}^2$, high pass filtered at frequencies of fc/U_{ref}=3 and 40. Removing stress contributions from Crow instability and other wandering by filtering at fc/U_{ref}=3 (figure 13a), makes little difference to the turbulence structure (compare with figure 9d), except that it eliminates the double peaked core stress distributions. Filtering at fc/U_{ref}=40 (figures 13b, c and d) reveals the distributions of small-scale turbulence in and around the cores. Outside the core edges (figures 13 c and d) the turbulence structure is quite similar to that seen at $x/c = 10$. The two local maxima that sit on diagonally opposite sides of each the core are still visible, lying a little closer to the core edge than before. However, contrary to the expected decay, small scale turbulence levels outside the core are higher at $x/c=30$ and penetrate much deeper into the core, substantially changing its turbulence structure. Turbulence levels within the core vary much more than at $x/c=10$ and are considerably greater.

This change in core structure implies more turbulent mixing of core fluid and is thus consistent with the decay of core parameters observed above. It may also indicate that some production of turbulence from the rotational motion of the vortices has begun. If this is so we speculate that the two maxima seen outside of the edge of the cores are the centers of turbulence production, but confirming this will require further analysis of the data and, perhaps, new measurements. Such production could be stimulated by instability of the velocity fields surrounding each core brought on by the close proximity of the other vortex.

CONCLUSIONS

The turbulence structure associated with a pair of counter-rotating trailing vortices has been examined in detail through analysis of a large experimental database. The vortices were generated by two rectangular NACA 0012 half wings placed tip to tip, separated by 0.25 chordlengths (c). The database consists primarily of detailed 3-component hot-wire velocity records measured in planes 10 and 30 chordlengths (c) downstream of the wing leading edges for a chord Reynolds number of 260,000.

The vortices rise under their mutual induction drawing the two wing wakes upward between them. This motion stretches turbulence in the wakes, intensifying dominant spanwise turbulent structures within them while supressing smaller-scale turbulence. As a result the Reynolds stress tensor becomes strongly non-isotropic, dominated by velocity fluctuations in directions normal to the wakes and parallel to the free-stream. In between the vortices stretching becomes most intense. Its effects, combined with the rotational velocity fields of the vortices, result in some negative production of turbulence kinetic energy here.

As the wakes pass between the vortices they also come together. At x/c=10 this merging process has just begun. Turbulence levels in the merged region appear high, but this seems to be at least partly due to stretching. Velocity spectra here are wake-like. Above the merged region at x/c=10 the wakes separate again, each spiraling around its corresponding core. In the spiral, the wakes suffer strong lateral curvature and increasing rates of shear strain, both of which appear to influence turbulence levels. Despite these effects the spectral character of the turbulence remains similar to that of a two-dimensional wake.

At x/c=30 a similar merging region is seen between the vortices but the rest of the turbulence structure enveloping the cores appears quite different. Gone are the wake spirals, having been replaced by a more homogenous turbulence structure. Judging from the development of the flow implied by the velocity field measured at x/c=10, it seems that much of this turbulence should have originated in the wakes but, having been brought together in the merging region and then forced apart, it has lost its large scale organization. Further evidence of this comes in the form of velocity spectra in this region which are still very wake like.

The vortex cores themselves remain closely circular, increasing from a radius of 0.044c at x/c=10 to 0.051c at x/c=30. Peak tangential velocities vary

substantially around each core edge and reach a maximum at the point closest to the plane of symmetry. The average peak tangential velocity falls from 42% of the free-stream at x/c=10 to 30% at x/c=30. The rapid growth and decay of the cores with streamwise distance implied by these numbers is not seen in the core of an equivalent isolated trailing vortex. We therefore infer that some aspect of the interaction between the vortices stimulates the decay of their core.

Some vortex core wandering was observed, of r.m.s. amplitude 0.3%c and 1.1%c at x/c = 10 and 30, respectively (3.7% and 10.5% of the local core diameters). A substantial proportion of the motions at x/c=30 was due to Crow instability, with a frequency and direction very similar to that predicted by Crow's theory. Errors in mean-velocity measurements due to wandering were estimated and found to be small. Errors in turbulence stress measurements were found to be significant in and immediately surrounding the cores, especially at x/c=30. However, the turbulence structure here could still be deduced from velocity spectra and filtered statistics.

Velocity records were high pass filtered at two frequencies; fc/U_{ref}=3, eliminating fluctuations due to wandering but not those due to other inactive core motions (such as waves), and fc/U_{ref}=40, eliminating all but the smaller turbulence scales. Turbulence stress levels for fc/U_{ref}>3 show velocity fluctuations rising to a maximum inside the cores. Spectra show that much of this energy is associated with narrow peaks strongly reminiscent of those seen by Bandyopadhyay et al.[33] in isolated vortices. These may be produced by core waves stimulated by large turbulent structures in the surrounding wake fluid, since they occur at almost the same frequency.

Filtering at fc/U_{ref}>40 better reveals the turbulence structure in the core regions, which appears quite different at the two streamwise locations. At x/c=10 small-scale turbulence levels are very low and vary little within the cores, raising the possibility that the entire core flow may be laminar. At x/c=30 core turbulence levels are much greater, and vary more within the cores, suggesting more turbulent mixing. This increase in core activity, not observed in isolated vortices, is consistent with the relatively rapid decay of core parameters. It may indicate that some production of turbulence from the rotational motion of the vortices has begun. If this is so it seems likely that the centers of turbulence production lie about one core radius outside the core edges. Small scale turbulence levels show two local maxima here located on diagonally opposite sides of each core.

We conclude, therefore, that interaction between a pair of counter-rotating vortices appears to stimulate turbulent decay that is absent in an isolated vortex. This may explain why previous authors have observed two stages of trailing-vortex decay in the far wakes of aircraft and other lifting bodies.

ACKNOWLEDGEMENTS

The authors would like to thank Mike Rife and Gautam Sharma for their assistance in taking many of the above measurements. The financial support of ARPA, administered by Mr. Gary W. Jones and the Office of Naval Research, through ONR contracts N00014-90-J-1909 and N00014-91-J-1773 is also gratefully acknowledged.

REFERENCES

[1]Crow S C, 1970, "Stability theory for a pair of trailing vortices", AIAA Journal, vol 8, no. 12, pp. 2172-2179.

[2]Scorer R S and Davenport L J, 1970, "Contrails and aircraft downwash", Journal of Fluid Mechanics, vol. 43, part 3, pp. 451-464.

[3]Chevalier H, 1973, "Flight test studies of the formation and dissipation of trailing vortices", Journal of Aircraft, vol. 10, no. 1, pp. 14-18.

[4]Tombach I, 1973, "Observations of atmospheric effects on vortex wake behavior", Journal of Aircraft, vol. 10, no. 11, pp. 641-647.

[5]Eliason B G, Gartshore I S and Parkinson G V, 1975, "Wind tunnel investigation of Crow instability", Journal of Aircraft, vol. 12, no. 12, pp. 985-988.

[6]Sarpkaya T, 1983, "Trailing vortices in homogeneous and density-stratified media", Journal of Fluid Mechanics, vol. 136, pp. 85-109.

[7]Liu H-T, 1992, "Effects of ambient turbulence on the decay of a trailing vortex wake", Journal of Aircraft, vol. 29, no. 2, pp. 255-263.

[8]Sarpkaya T and Daly J J, 1987, "Effect of ambient turbulence on trailing vortices", Journal of Aircraft, vol. 26, no. 6, pp. 399-404.

[9]El-Ramly Z and Rainbird W J, 1977, "Flow survey of the vortex wake behind wings", Journal of Aircraft, vol. 14, no. 11, pp. 1102-1108.

[10]McCormick B W, Tangler J L and Sherrieb H E, 1968, "Structure of trailing vortices", Journal of Aircraft, vol. 5, no. 3.

[11]Devenport W J, Rife M C, Liapis S I and Miranda J, 1994, "Turbulent trailing vortices", AIAA 32nd Aerospace Sciences Meeting, Reno NV, Jan. 10-13, AIAA-94-0404.

[12]Ciffone D L and Orloff K L, 1974, "Axial flow measurements in trailing vortices", AIAA Journal, vol. 12, no. 8, pp. 1154-1155.

[13]Ciffone D L and Orloff K L, 1975, "Far-field wake-vortex characteristics of wings", Journal of Aircraft, vol. 12, no. 5, pp. 464-470.

[14]Ciffone D L and Orloff K L, 1976, "Application of laser velocimetry to aircraft wake vortex measurements", *Wake Vortex Minimization*, NASA SP409, pp. 157-192.

[15]Burnham D C, Sullivan T E and Wilk L S, 1976, "Measurement of wake vortex strength by means of acoustic back scattering", Journal of Aircraft, vol. 13, no. 11, pp. 889-894.

[16]Wilson D J, Zalay A D, Brashears M R, Craven C E, Shrider K R and Jordan A J, 1979, "Full-scale wake flow measurements with a mobile laser Doppler velocimeter", Journal of Aircraft, vol. 16, no. 3, pp. 155-161.

[17]Corsiglia V R, Schwind R G and Chigier N A, 1973, "Rapid scanning, three-dimensional hot-wire anemometer surveys of wing-tip vortices", Journal of Aircraft, vol. 10, no. 12, pp. 752-757.

[18]Iversen J D, 1976, "Correlation of turbulent trailing vortex decay data", Journal of Aircraft, vol. 13, no. 5, pp. 338-342.

[19]Baker G R, Barker S J, Bofah K K and Saffman P G, 1974, "Laser anemometer measurements of trailing vortices in water", Journal of Fluid Mechanics, vol. 65, pp. 325-336.

[20]Chigier N A and Corsiglia V R, 1972, "Wind tunnel studies of wing wake turbulence", Journal of Aircraft, vol. 9, pp. 820-825.

[21]Orloff K L, 1971, "Experimental investigation of upstream influence in a rotating flowfield", PhD thesis, University of California, Santa Barbara.

[22]Gasparek E, 1960, "Viscous decay of a vortex", MS thesis, Syracuse University, NY.

[23]Mason W H and Marchman J F, 1972, "Far-field structure of an aircraft trailing vortex, including effects of mass injection", NASA CR 62078.

[24]Stifle K E and Panton R L, "Experiments concerning the theories of vortex breakdown", AIAA 29th Aerospace Sciences Meeting, Reno, NV, Jan 6-9. Paper AIAA-91-0736.

[25]Zsoldos J S and Devenport W J, 1992, "An experimental investigation of interacting vortex pairs", 19th Symposium on Naval Hydrodynamics, Seoul, South Korea, August..

[26]Zsoldos J S and Devenport W J, 1992, "An experimental investigation of interacting vortex pairs", Report VPI-AOE-191, AOE Dept., VPI&SU, Blacksburg, VA. Avail. NTIS. Note that vortex wandering estimates made in this report are in error.

[27]Choi K and Simpson R L, 1987, "Some mean-velocity, turbulence, and unsteadiness characteristics of the VPI&SU Stability Wind Tunnel", Report VPI-AOE-161, VPI&SU, Blacksburg, VA.

[28]Bilanin A J, Teske M E, Donaldson C duP and Snedeker R S, "Viscous effects in aircraft trailing vortices", *Wake Vortex Minimization*, NASA SP409, pp. 61-128.

[29]Devenport W J, Sharma G and Glegg S A L, 1992, "Turbulence measurements in trailing vortices for BWI noise prediction", VPI-AOE-192, AOE Dept., VPI&SU, Blacksburg, VA.

[30]Betz D, 1933, "Behavior of vortex systems", NACA TM 713.

[31]Donaldson C duP and Bilanin A J, 1975, "Vortex wakes of conventional aircraft", AGARD AG-204.

[32]Devenport W J, Glegg S A L, Wittmer K and Rife M C, 1993, "Perpendicular blade vortex interaction and its implications for helicopter noise predictions", Final Technical Report to NASA Langley under grant NAG-1-1119. Available from AOE Dept., VPI&SU, Blacksburg VA.

[33]Bandyopadhyay P, Stead D and Ash R, 1991, "Organized nature of a turbulent trailing vortex", AIAA Journal, vol. 29, no. 10, pp. 1627-1633.

[34]Ragab S and Sreedhar M, 1994, "Large scale structures in a trailing vortex", 25th AIAA Fluid Dynamics Conference, Colorado Springs, CO, June 20-23, Paper 94-2316.

Quantity	Uncertainty[1]	Uncertainty[2]
U	0.015	0.015
V,W	0.025	0.025
$\overline{u'^2}$	3.1×10^{-6}	1.4×10^{-5}
$\overline{v'^2}$	9.5×10^{-6}	1.5×10^{-5}
$\overline{w'^2}$	9.9×10^{-6}	2.0×10^{-5}
$\overline{u'v'}$	4.3×10^{-6}	1.4×10^{-5}
$\overline{v'w'}$	4.5×10^{-6}	2.3×10^{-5}
$\overline{u'w'}$	2.9×10^{-6}	8.5×10^{-6}

Table 1. Uncertainties in velocity measurements calculated for 20:1 odds at typical locations in [1]wake and [2]core regions. All uncertainties are in terms of U_{ref} or U_{ref}^2 as appropriate.

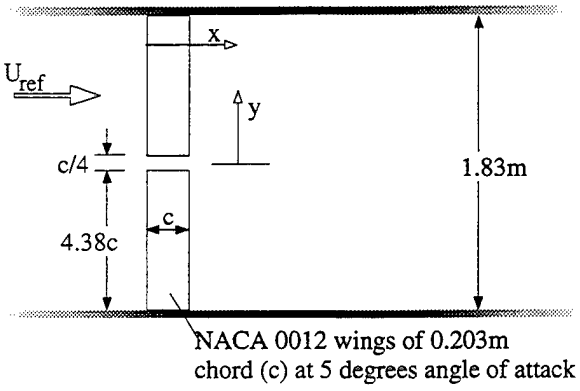


Figure 1. Schematic of the stability wind tunnel test-section showing the NACA 0012 half wings and the coordinate system. Coordinate z is measured out of the paper.

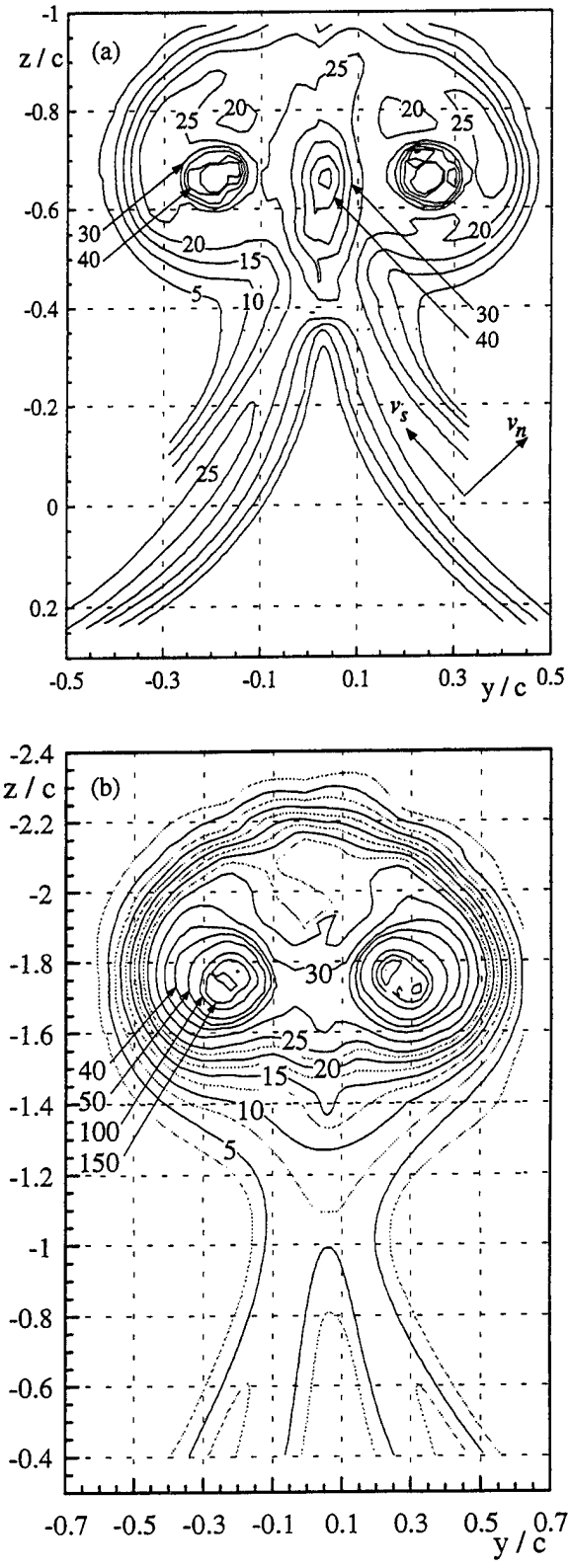


Figure 2. Contours of $\overline{u^2}/U_{ref}^2$ x 10^5 at (a) x/c=10 and (b) x/c=30. Note difference in distance scales.

(a) Mean cross-flow velocity vectors

(b) Contours of mean streamwise vorticity normalized on U_{ref} and c. Solid lines show core edge.

(c) Contours of mean axial velocity U/U_{ref}

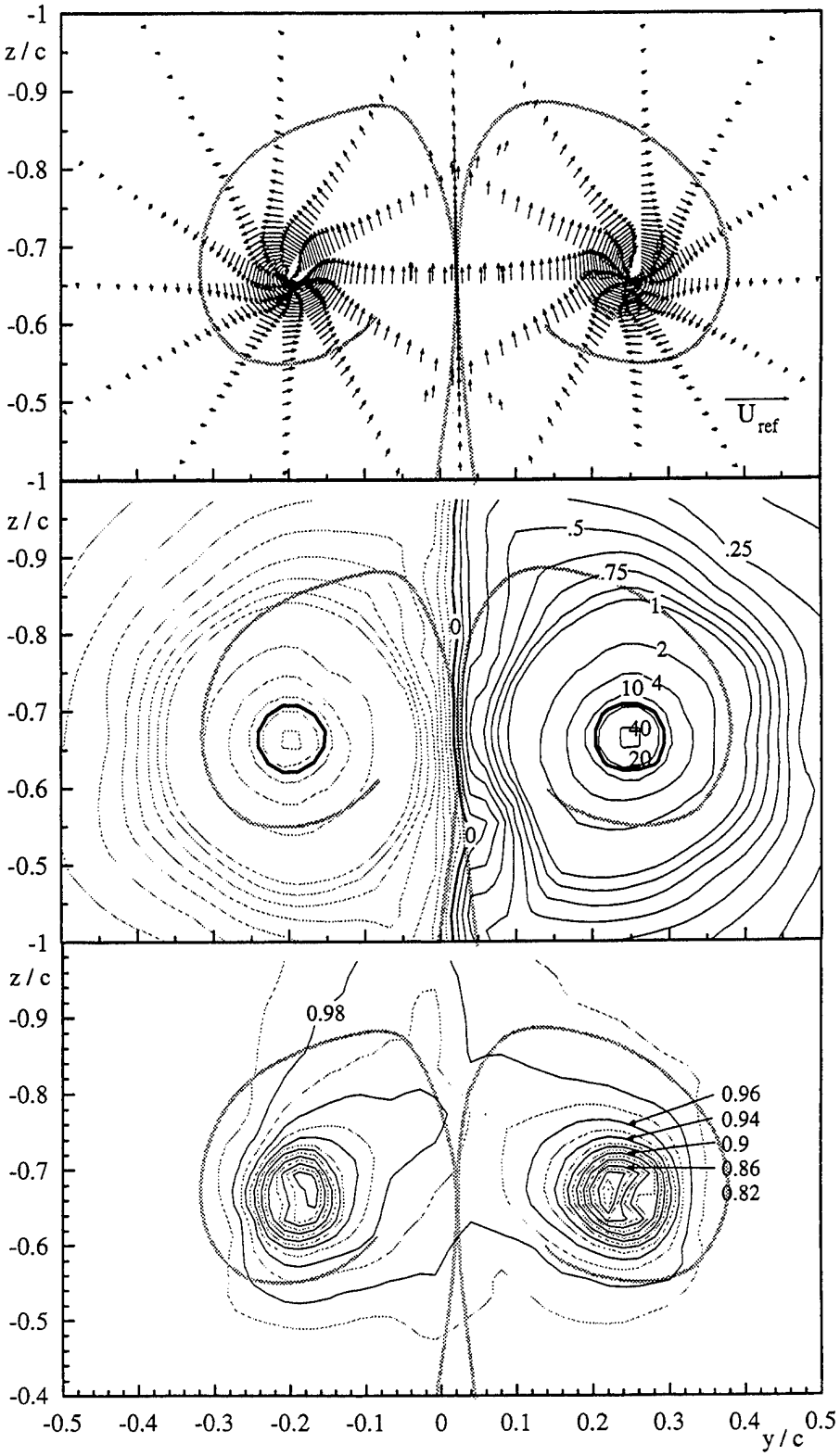


Figure 3. Reynolds-averaged velocity measurements at x/c = 10. Gray line shows wake centerlines defined by locus of peak axial normal stress.

(d) Contours of axial normal stress $\overline{u^2}/U_{ref}^2 \times 10^5$
Dots show locations of autospectra in figure 7

(e) Contours of the sum of cross-flow normal stresses $(\overline{v^2}+\overline{w^2})/U_{ref}^2 \times 10^5$

(f) Contours of turbulence knietic energy production normalized on c and U_{ref}
Grey lines - negative levels.
Black lines - positive levels.
Spacing between contour levels is 5×10^{-5}

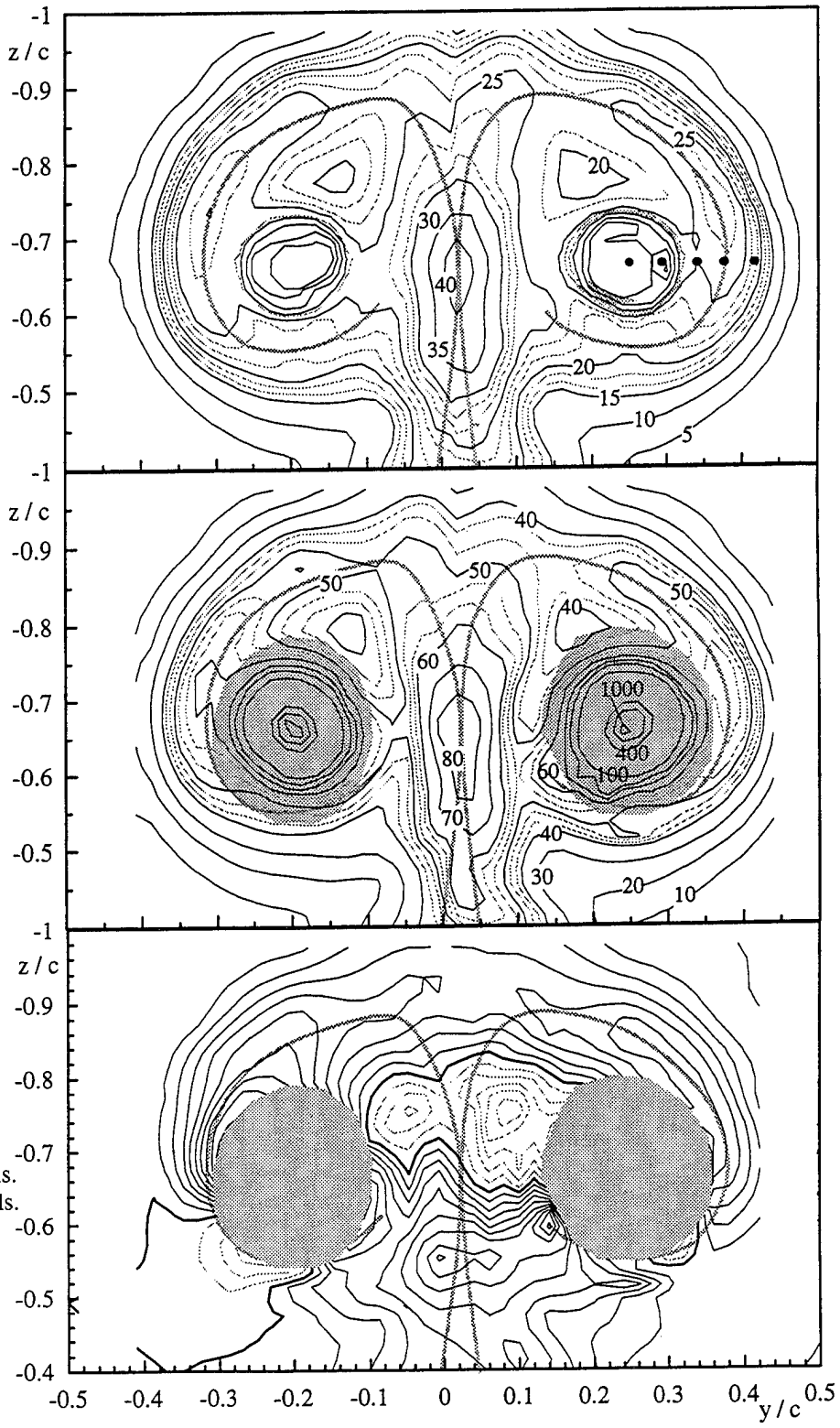


Figure 3. Reynolds-averaged velocity measurements at x/c = 10. Gray line shows wake centerlines defined by locus of peak axial normal stress. Shaded regions indicate where wandering has contributed more than 30% to the normal stress plotted.

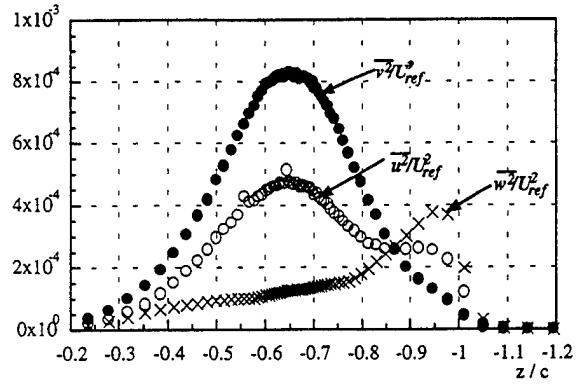


Figure 4. Normal stress profiles at y/c=0.023 along the plane of symmetry between the vortices at x/c=10.

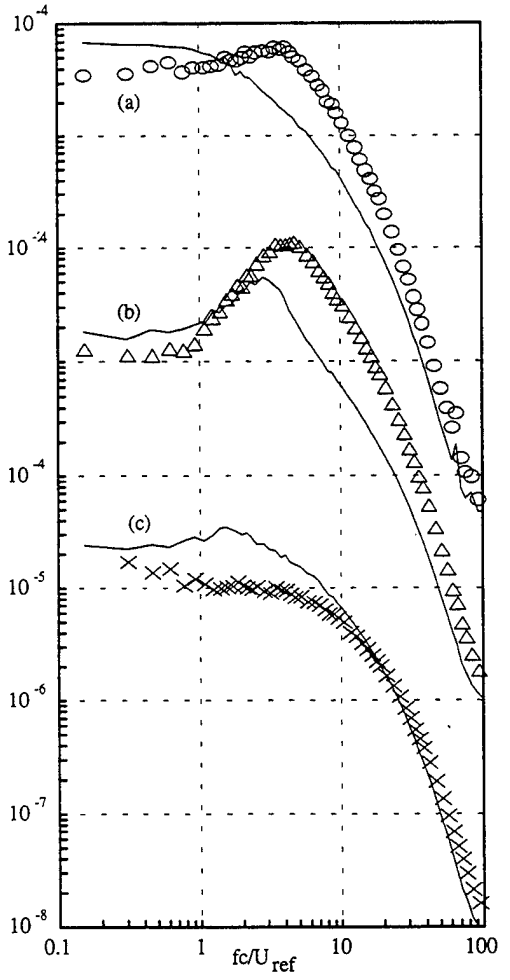


Figure 5. Autospectra of velocity fluctuations measured at the center of the merged region (symbols) compared with thos measured at the center of the 2D portion of the wake. (a) Axial component. (b) Normal-to-wake component and (c) Component parallel to wake centerline. Spectral levels normalized on U_{ref} and c.

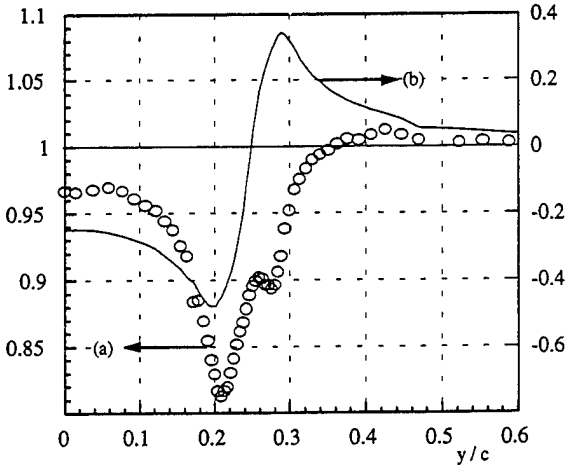


Figure 6. Mean velocity profiles through the right-hand core center at x/c=10. (a) Axial velocity. (b) Tangential velocity as seen in the W component.

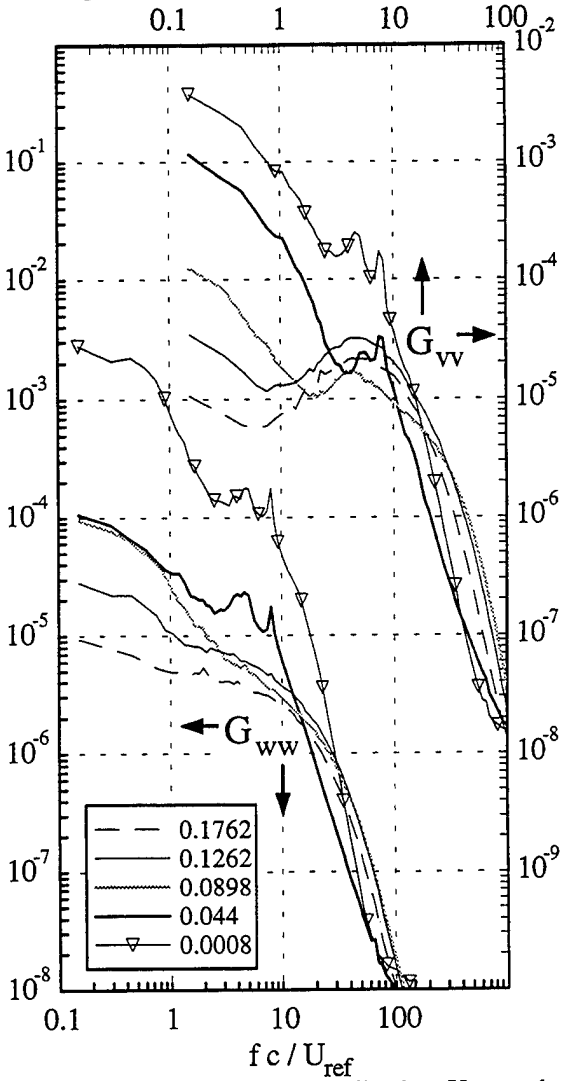


Figure 7. Velocity spectra normalized on U_{ref} and c at locations along the right-hahd half of the profile in figure 6. Legend shows y-locations relative to the core center at y/c=0.25. Absolute locations indicated by dots in figure 3d.

(a) Contours of axial normal stress $\overline{u^2}/U_{ref}^2 \times 10^5$ high-pass filtered at fc/U_{ref} =3.

(b) Contours of axial normal stress $\overline{u^2}/U_{ref}^2 \times 10^6$ high-pass filtered at fc/U_{ref} =40.

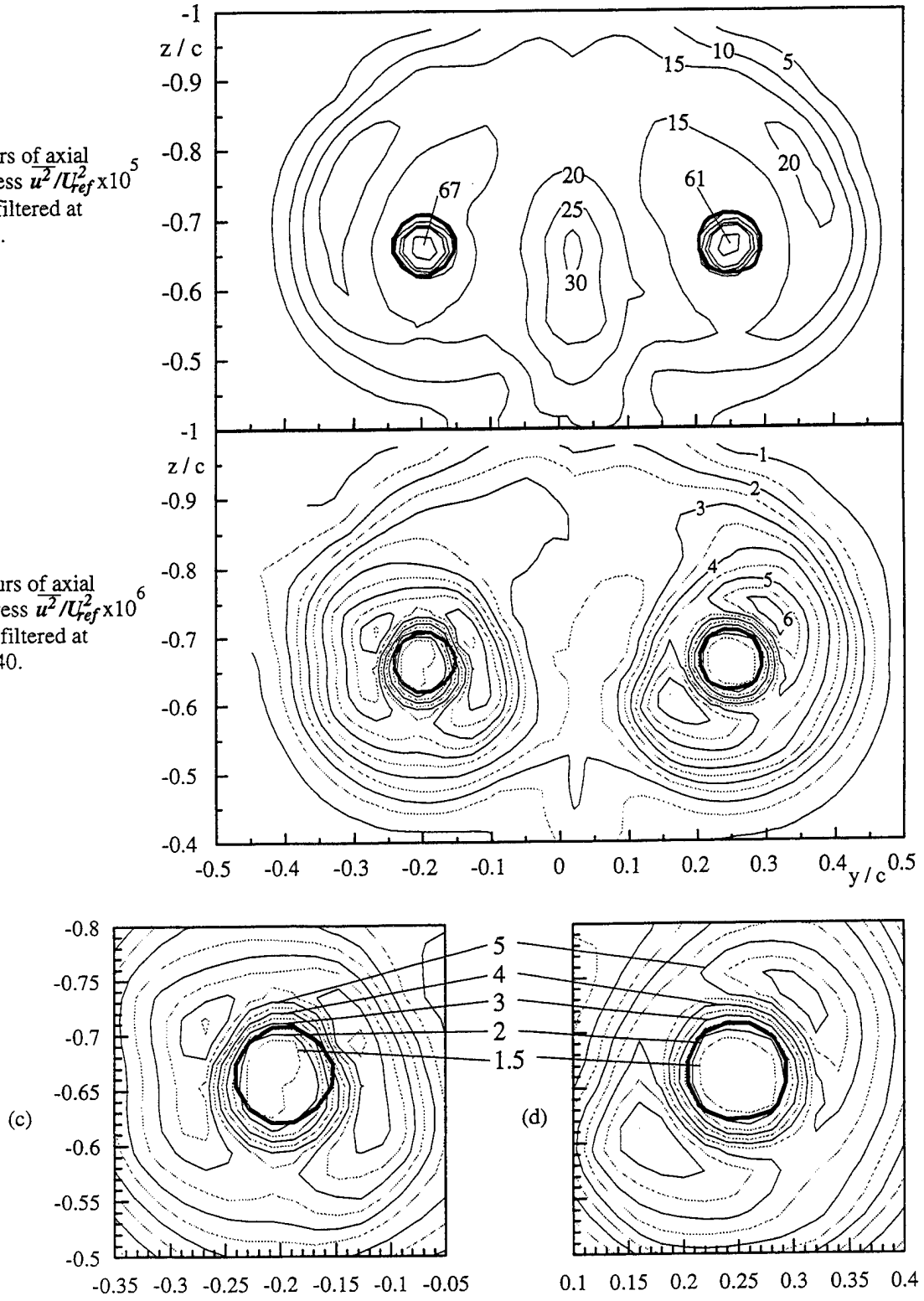


Figure 8. High-pass filtered turbulence normal stress distributions at x/c=10. Parts (c) and (d) show detailed views of the left and right-hand core regions for part (b).

(a) Mean cross-flow velocity vectors

(b) Contours of mean streamwise vorticity normalized on U_{ref} and c. Solid lines show core edge.

(c) Contours of mean axial velocity U/U_{ref}

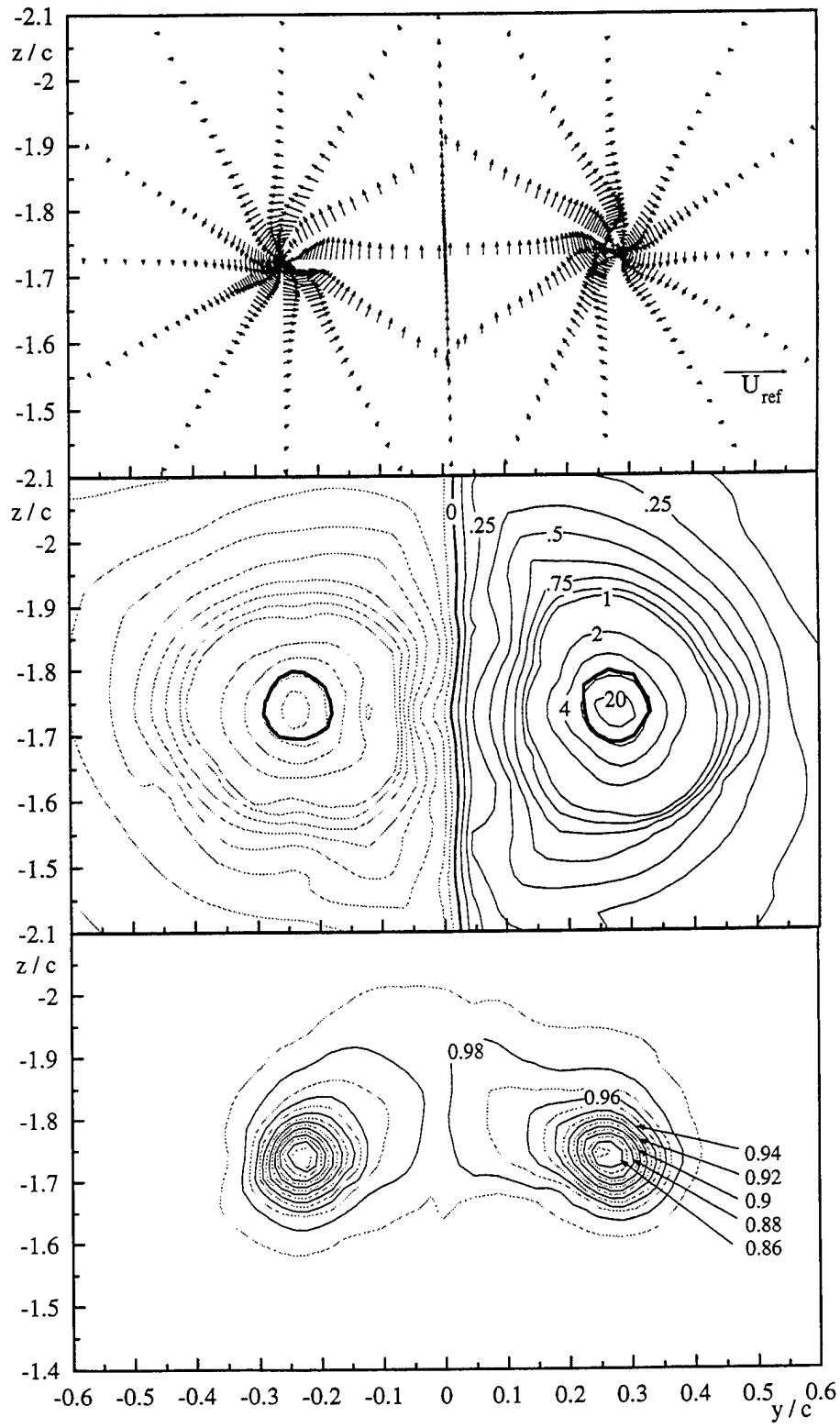


Figure 9. Reynolds-averaged velocity measurements at x/c = 30.

(d) Contours of axial normal stress $\overline{u^2}/U_{ref}^2 \times 10^5$ Dots show locations of autospectra in figure 12

(e) Contours of the sum of cross-flow normal stresses $(\overline{v^2}+\overline{w^2})/U_{ref}^2$ x 10^5

(f) Contours of turbulence knietic energy production normalized on c and U_{ref} Grey lines - negative levels. Black lines - positive levels. Spacing between contour levels is 5 x 10^{-5}

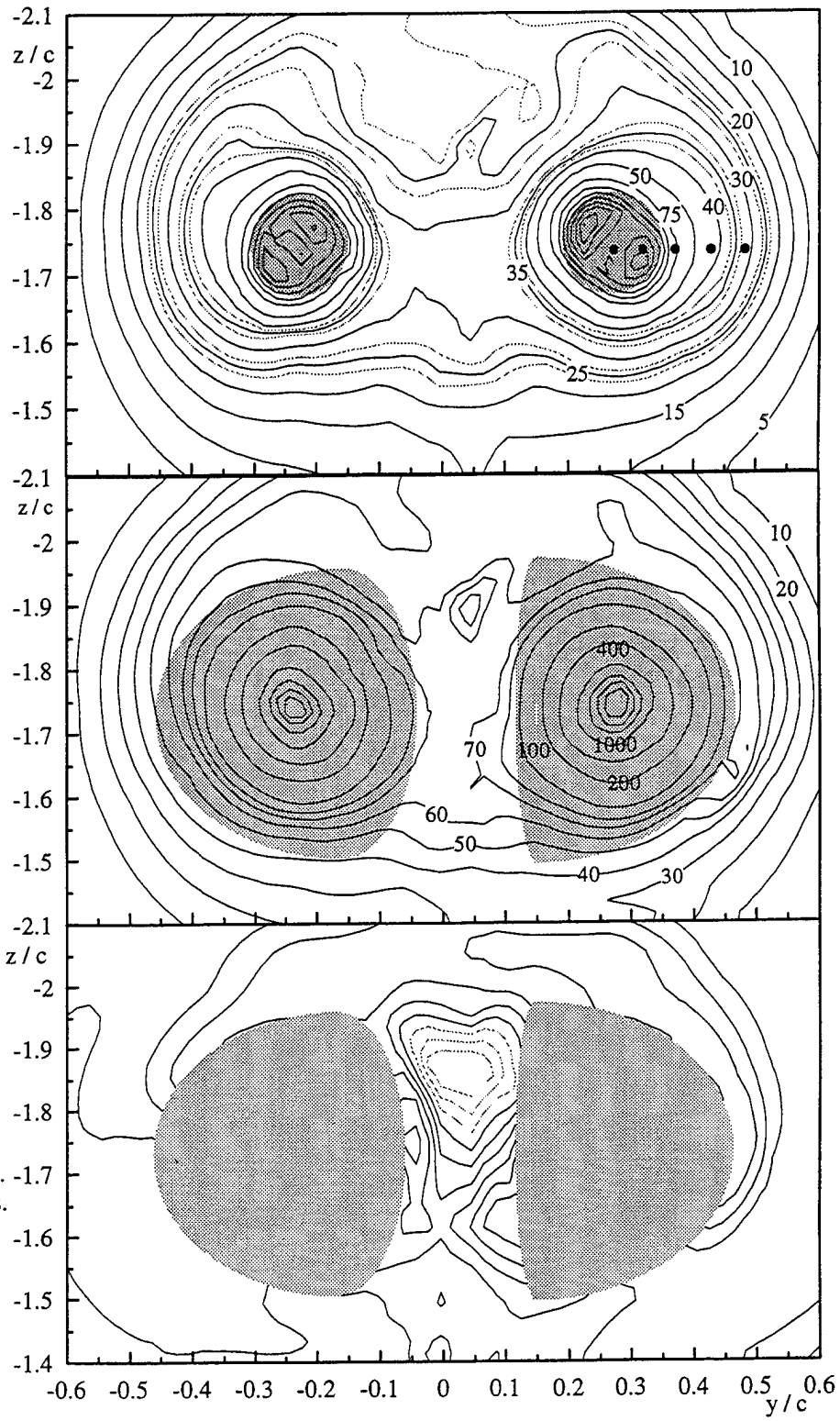


Figure 9. Reynolds-averaged velocity measurements at x/c = 30. Shaded regions indicate where wandering has contributed more than 30% to the normal stress plotted.

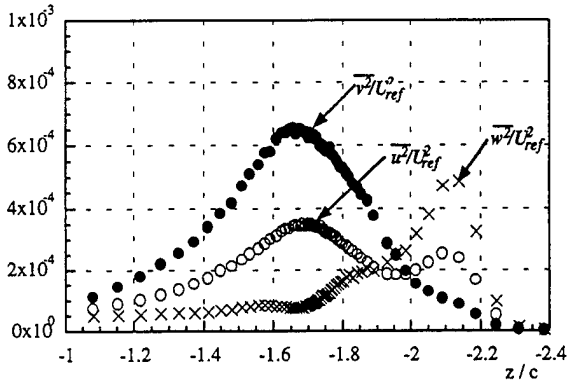


Figure 10. Normal stress profiles at y/c=0.02 along the plane of symmetry between the vortices at x/c=30.

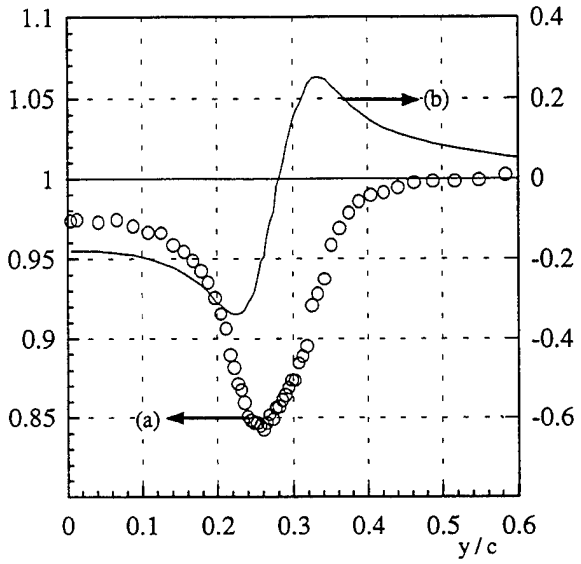


Figure 11. Mean velocity profiles through the right-hand core center at x/c=30. (a) Axial velocity. (b) Tangential velocity as seen in the W component.

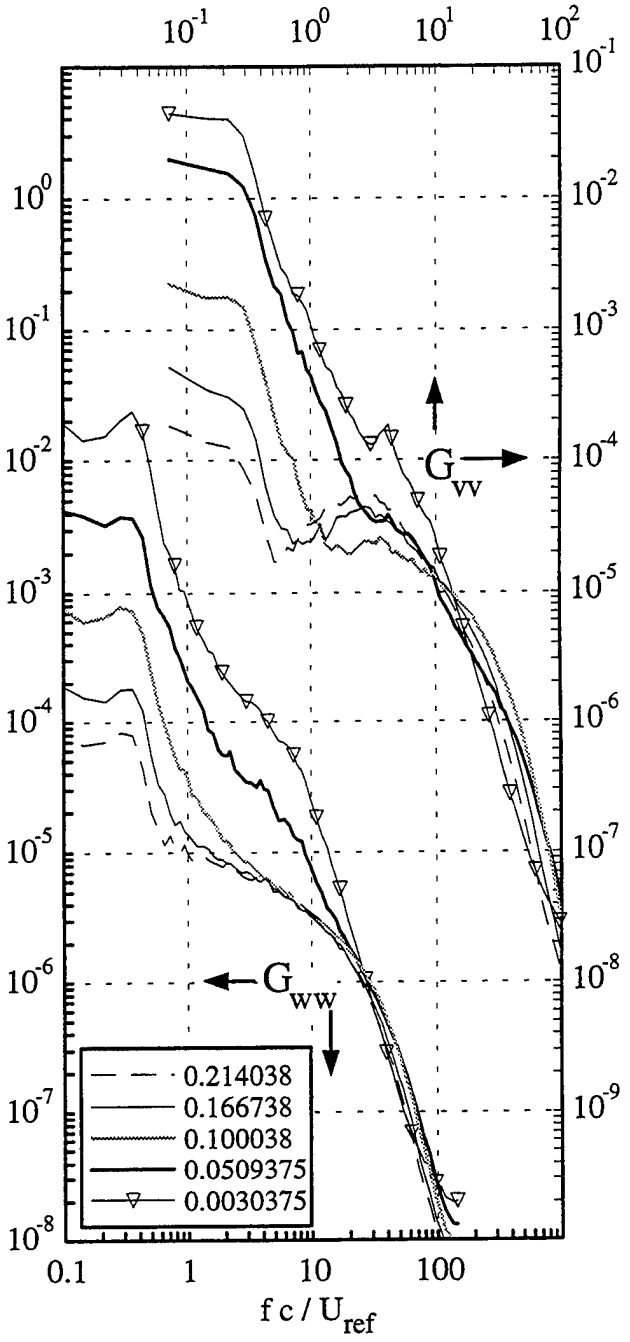


Figure 12. Velocity spectra normalized on U_{ref} and c at locations along the right-hand half of the profile in figure 11. Legend shows y-locations relative to the core center at y/c=0.25. Absolute locations indicated by dots in figure 9d.

(a) Contours of axial normal stress $\overline{u^2}/U_{ref}^2 \times 10^5$ high-pass filtered at fc/U_{ref} =3.

(b) Contours of axial normal stress $\overline{u^2}/U_{ref}^2 \times 10^6$ high-pass filtered at fc/U_{ref} =40.

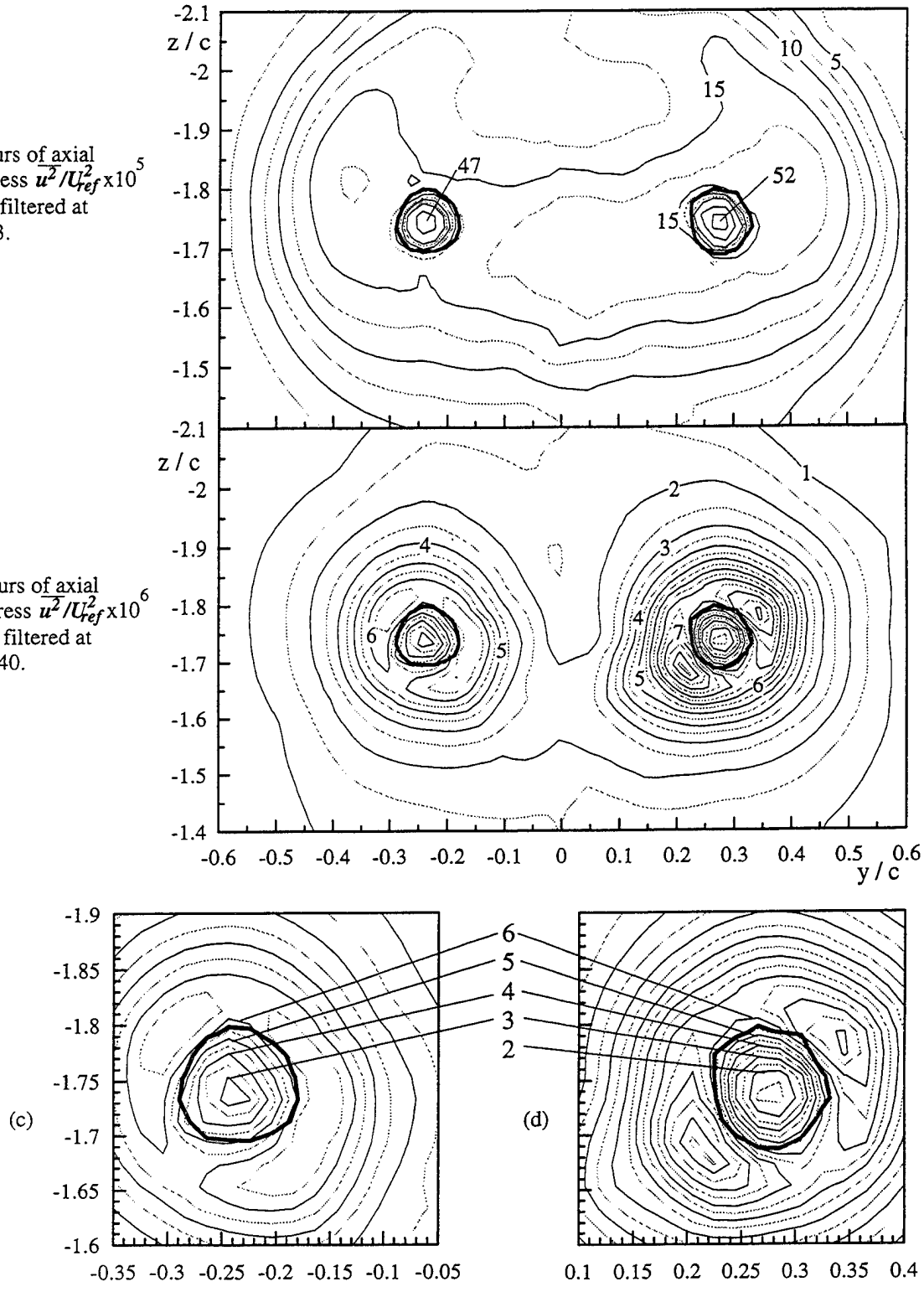


Figure 13. High-pass filtered turbulence normal stress distributions at x/c=30. Parts (c) and (d) show detailed views of the left and right-hand core regions for part (b).

DISCUSSION

M. Graham
Imperial College, UK

The direction in which the wing wakes feed into the vortex in your experiment is the reverse of the usual direction. Did you think that this may influence the results?

AUTHORS' REPLY

The trailing vortex pair was generated by two opposing wing tips. This configuration allowed substantial interaction between the vortices to be observed while maintaining a high Reynolds number. However, the price paid was that certain details of the turbulence structure of this flow are not the same as if the vortices had been generated by opposite tips of the same wing. Most notably, the vortex cores are not connected by a single, roughly horizontal, section of wing wake as they would be in this case.

The questions here would seem to be whether these differences might have affected the primary conclusion of the paper (that counter-rotating trailing vortices decay initially as laminar flows and then, as a consequence of mutual induction, undergo transition to turbulent decay). We believe not, since many previous studies of conventionally generated vortex pairs (see Iversen[1] and references therein) show that such vortices undergo a two-stage decay, entirely consistent with the present findings. Furthermore, we would expect the instability producing transition to be an inviscid one (specifically Widnall's[2] short-wave instability) operating on the mean-velocity field. Outside the immediate vicinity of the cores the wakes have little influence on the mean-velocity or vorticity fields (see figures 3a, b, and c of the paper for example). It therefore seems unlikely that their exact arrangement would have substantially affected the presence of the instability.

---

[1] Iversen, J.D., 1976, "Correlation of turbulent trailing vortex decay data," Journal of Aircraft, Vol. 13, no. 5, pp. 338-342.

[2] Widnall, S.E.; Bliss, D. B.; and Tsai, C., 1974, "The instability of short waves on a vortex ring," Journal of Fluid Mechanics, Vol. 66, part 1, pp. 35-47.

Hydroelastic Analysis of a Flexible Bag Structure

T. Ulstein, O. Faltinsen
(The Norwegian Institute of Technology, Norway)

ABSTRACT

A numerical and analytical study of the interaction between a flexible bag structure and the free water surface is presented. The flexible bag is the stern seal of a SES and behaves hydrodynamically as an unsteady two-dimensional planing surface at high Froude numbers. A solution of the water entry problem is found by combining the solution for an unsteady lifting surface in infinite fluid with an integral equation for the wetted length. The "dry" mode superposition approach for the flexible behavior of the bag is combined with extensive use of analytical expressions for the excitation and reaction forces. The curvature of the bag and the coupling between the elastic longitudinal and transverse oscillations are accounted for. Scaling of water entry of a flexible bag is discussed. The relative importance of main parameters of the bag influencing the cobblestone oscillations of a SES is presented.

1 INTRODUCTION

During the last decade an increasing interest for high speed marine vessels is observed. One concept is the surface effect ship (SES). The idea with a SES is to partly lift the vessel out of the water by trapping an air cushion between two catamaran hulls, a bow skirt and a stern seal (see Figure 1). A consequence is that the resistance of a typical SES is lower than the resistance of a similar sized catamaran in most sea states of practical interest.

A problem with the SES is high vertical accelerations in very small sea states. This phenomenon is often referred to as the cobblestone effect and is a resonance effect due to the compressibility of air in the air cushion. The cobblestone effect is excited because the water waves dynamically change the air cushion volume. This resonance phenomenon occurs at high frequencies relative to the resonance frequencies for the rigid body motions of displacement ships of similar length. The two lowest resonance frequencies in the air cushion of a 30-35 m long SES are approximately 2 Hz and 5 Hz. Due to the frequency of encounter effect there are waves with sufficient energy in small sea states that excite these resonance oscillations. The eigenfunction for the dynamic air cushion pressure is constant in space for the lowest eigenfrequency and represents acoustic resonances for the higher eigenfrequencies. The rigid

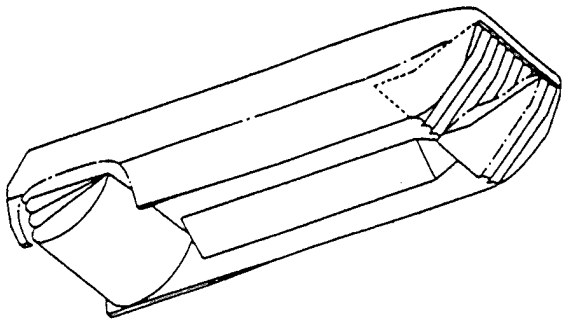


Figure 1: Sketch of a SES air cushion with a bow finger seal and a 3-loop flexible bag seal aft. Toyama, Ono and Nishihara [1].

ship motions in this frequency range are small, but the vertical acceleration level is high. The hydrodynamic damping due to the rigid ship motions is negligible in this frequency range. Important damping mechanisms are due to the air flow into the air cushion through the fans and the air leakage underneath the seals and through louvers that are part of a ride control system. Steen [2] found in his studies of the cobblestone effect, that the dynamics of the stern seal bag was important for the global acceleration level in low sea states. He considered the effect of a dynamically varying leakage area underneath the seal together with the deformation of the bag due to change in the air cushion pressure at the stern. The deformation of the bag was analyzed quasistatically. The dynamically varying leakage area and the deformation of the bag will have a similar effect on the air cushion as a moving piston at the end of a long tube. The acoustic waves in the air cushion were shown to be significantly effected by this mechanism. Steen neglected the hydroelastic interaction between the bag stern seal and the free water surface. By hydroelastic interaction we mean that the hydrodynamic loading is a function of the structural deformations resulting from the hydrodynamic loading. This interaction is focused on in this paper and is believed to effect the cobblestone oscillations.

The flexible bag behaves hydrodynamically as an unsteady planing surface at high Froude numbers. The authors are not aware of any analysis of the unsteady interaction between a flexible bag structure and the free water surface. However, Doctors [3] studied the two-dimensional steady planing of a flexible beam with bending stiffness. He used linearized potential theory to solve the hydrodynamic boundary value problem. The effect of gravity was included. Bessho and Komatsu [4] studied the two-dimensional unsteady planing problem based on a frequency domain solution of an airfoil. The analysis accounts for the effect of the wetted length change, but does not consider deformations of the planing surface.

The following analysis presents a numerical and analytical study of the unsteady interaction between a flexible bag structure and the free water surface. The flexibility is mainly due to axial stiffness in the bag structure. However, the effect of bending stiffness is also included. The hydrodynamic part of the problem has similarities with the linearized unsteady foil problem. An important difference is that the wetted length of the structure changes rapidly with time. The wetted length is found from a non-linear integral equation, by generalizing what Wagner [5] did in the case of slamming. A difference is that the forward speed of the bag is included.

The bag structure is pressurized with air, and it is deformed due to the hydrodynamic pressure distribution on the wetted surface of the bag and the compressibility of air in the bag. The unsteady deformation of the bag is found by a numerical time integration. High numerical accuracy is needed. This has been achieved by using the "dry" mode superposition approach for the flexible behavior of the bag in combination with extensive use of analytical expressions for the excitation and reaction forces. "Dry" mode superposition implies that the eigenvalue problem is solved without accounting for the hydrodynamic reaction forces and the pressure forces due to the compressibility of air in the bag. The finite radius of curvature of the bag and the coupling between the elastic longitudinal and transverse oscillations are found to be important.

Results for the volume change of the air cushion due to the bag motion, indicate that the interaction between the free water surface and the bag structure may be important for the excitation of the cobblestone oscillations. In order to draw any further conclusions, a more complete model of the coupling between the bag and the air cushion of the SES is necessary.

2 STRUCTURAL MODELLING OF THE BAG

The analysis of the bag structure will be simplified. A two-dimensional problem is solved in a cross-section of the bag structure in the longitudinal plane of the SES. The bag structure is modelled as a cable. The bag is not touching the water in the static case and the pressure force acting on the bag is an order of magnitude larger than the gravity force. The contributions from gravity will appear as restoring terms in the dy-

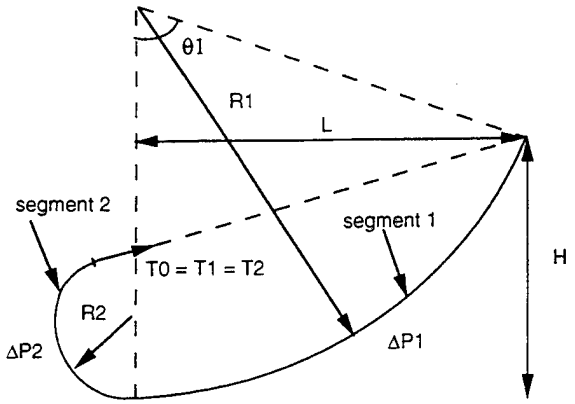


Figure 2: Static geometry of the 1-loop flexible bag seal. The bag consists of two circle segments with constant radii of curvature (R_1 and R_2). The tension in the two segments is constant and equal to T_0. ΔP_i = static pressure difference across segment i.

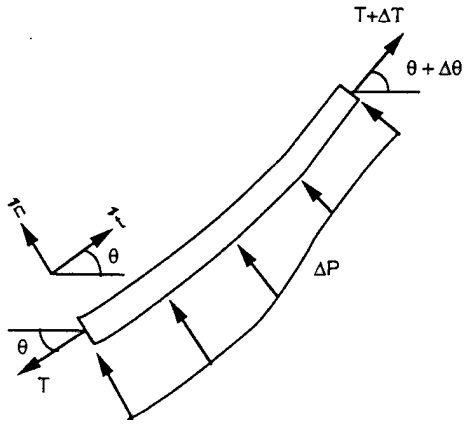


Figure 3: Infinitesimal element of a two- dimensional cable model of the bag. Tension and pressure forces are shown together with the definition of the coordinate system used in the dynamic analysis of the bag.

namic case and will be negligible compared to the tension terms. The effect of gravity is therefore neglected. This implies that the bag structure is modelled as a weightless but not massless cable.
The bag geometry is shown in Figure 2. The problem is simplified by assuming that the bag has only one loop. The bag geometry consists of two circle segments with different radii of curvature, because of different pressure differences over the two segments. Details about the solution of the static case can be found in Steen [2]. The length L, and the height H, are known geometric parameters. The unknowns are T_0, R_1, R_2 and θ_1, where T_0 is the constant tension in the cable. R_1 and R_2 are the radii of curvature for the two cable segments and θ_1 is the angle defined in Figure 2. It is assumed that the tangent to the loop is continuous and horizontal at the connecting point of the two cable segments.
To derive the equations of dynamic motions for a cable, force equilibrium of an infinitesimal element must be satisfied (see Figure 3). The orthogonal coordinate system that is used, is fixed to the static geometry, where the longitudinal coordinate is pointing in the tangential direction of the cable.
The equations of motions are derived by making a perturbation on the known static solution. All non-linear dynamic terms are neglected. Compatibility gives a relationship between tension and the motion in the transverse and the longitudinal directions. The radius of curvature is assumed constant and equal to R. This means that the equations of motions are set up separately for the two cable segments with different radii of curvature and then afterward linked together with the boundary conditions. The equations of motions can be written as (see Bliek [6]),

$$M_m \ddot{\eta}_n = T_0 \frac{\partial^2 \eta_n}{\partial s^2} + \frac{(T_0 + EA)}{R} \frac{\partial \eta_t}{\partial s} - \frac{EA}{R^2} \eta_n + \Delta P \qquad (1)$$

and

$$M_m \ddot{\eta}_t = EA \frac{\partial^2 \eta_t}{\partial s^2} - \frac{EA}{R} \frac{\partial \eta_n}{\partial s} \qquad (2)$$

where η_n and η_t are respectively the motions in the transverse and longitudinal directions. M_m is the structural mass per unit length of the cable. T_0 is the static tension in the cable, E the

elasticity modulus of the material and A the cross dimensional area of unit width. s is the longitudinal coordinate and ΔP is the dynamic pressure acting on the cable. ΔP includes the effect of internal and external pressure. Dot stands for time derivative.

We will show how the solution of equation (1) and (2) can be represented by a "dry" mode superposition approach. We will first focus on how the eigenvalues and the corresponding mode shapes are determined. The following solution of the general form is considered,

$$\begin{aligned} \eta_n(s,t) &= C_n e^{D_j s} e^{i\omega_j t} \\ \eta_t(s,t) &= C_t e^{D_j s} e^{i\omega_j t} \end{aligned} \quad (3)$$

where C_n and C_t are constants. D_j can be interpreted as the wave number that is yet unknown. i is the complex unit, t is the time variable and ω_j is the circular eigenfrequency. The solution defined by equation (3) is substituted into the governing equations defined by (1) and (2) with ΔP set equal to zero. This results in a set of two coupled linear equations with the constants C_n and C_t as the unknowns. In order to find a nontrivial solution of this equation system, the determinant must be equal to zero. The roots of the resulting equation give the relation between the eigenfrequencies and the wavenumbers, D_j, and is therefore interpreted as the dispersion relation of the cable.

Assuming that $\frac{T_0}{EA} \ll 1$, the four possible complex roots $D_j = \pm\hat{k}_j$ and $D_j = \pm\hat{\mu}_j$ can be written as,

$$\hat{k}_j^2 = \frac{-M_m\omega_j^2(1 + \frac{T_0}{EA} + K_j^1 + K_j^2)}{2T_0} \quad (4)$$

and

$$\hat{\mu}_j^2 = \frac{-M_m\omega_j^2(1 + \frac{T_0}{EA} + K_j^1 - K_j^2)}{2T_0}. \quad (5)$$

Here

$$\begin{aligned} K_j^1 &= \frac{T_0}{M_m\omega_j^2 R^2} \text{ and} \\ K_j^2 &= \sqrt{1 + 6K_j^1 + (K_j^1)^2} \\ &+ \frac{(K_j^1 - 1)}{\sqrt{1 + 6K_j^1 + (K_j^1)^2}} \frac{T_0}{EA} \\ &+ O((\frac{T_0}{EA})^2). \end{aligned}$$

Since R is finite, we cannot neglect K_j^1 for all values of ω_j. By studying equations (4) and (5), we see that $\hat{\mu}_j$ is real for low frequencies and imaginary for higher frequencies. The $\hat{k}_j$-value is always imaginary so that $\hat{k}_j = ik_j$ where k_j is real. The solution for the mode shapes can therefore be written as follows;

$\hat{\mu}_j$ is real ($\hat{\mu}_j = \mu_j$),

$$\begin{aligned} \phi_j^n(s) &= c_{j1}\cos k_j s + c_{j2}\sin k_j s \\ &+ c_{j3}\cosh \mu_j s + c_{j4}\sinh \mu_j s \\ \phi_j^t(s) &= c_{j5}\cos k_j s + c_{j6}\sin k_j s \\ &+ c_{j7}\cosh \mu_j s + c_{j8}\sinh \mu_j s \end{aligned} \quad (6)$$

and $\hat{\mu}_j$ is imaginary ($\hat{\mu}_j = i\mu_j$),

$$\begin{aligned} \phi_j^n(s) &= c_{j1}\cos k_j s + c_{j2}\sin k_j s \\ &+ c_{j3}\cos \mu_j s + c_{j4}\sin \mu_j s \\ \phi_j^t(s) &= c_{j5}\cos k_j s + c_{j6}\sin k_j s \\ &+ c_{j7}\cos \mu_j s + c_{j8}\sin \mu_j s. \end{aligned} \quad (7)$$

Here $\phi_j^n(s)$ and $\phi_j^t(s)$ are respectively the mode shapes in the transverse and longitudinal directions of vibration mode j. The relationships between the coefficients c_{j1}, c_{j2}, c_{j3}, c_{j4} and c_{j5}, c_{j6}, c_{j7}, c_{j8} are found by substituting the solutions in equation (6) or (7) into the governing equations (1) and (2) with $\Delta P = 0$. The terms proportional to either sine, cosine, hyperbolicsine or hyperboliccosine are collected and the resulting coefficients ahead of each of these terms are set equal to zero.

To find the eigenfrequencies and the four remaining coefficients, the boundary conditions have to be used. The geometry is defined in Figure 4. Two circle segments with different radii are coupled together at point A. Continuity of the deflections must be satisfied at this point. The tangent to the loop at this point must also be continuous.

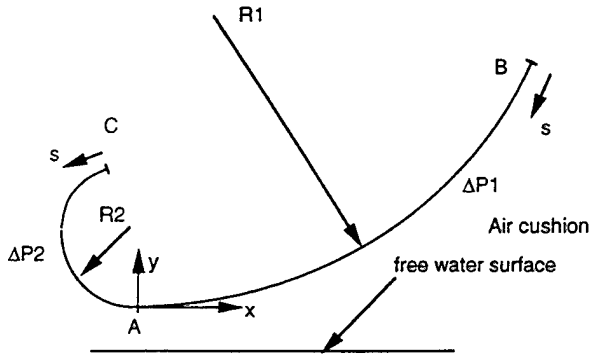


Figure 4: Static bag geometry with definition of the two different cable segments. The two different longitudinal coordinates used, are also shown for the two segments. The local xy-coordinate system is used in the hydrodynamic analysis. See Figure 2 for further explanations.

In addition the dynamic tension has to be continuous at the connecting point A of the two cable segments. The boundary conditions are written as follows,

$$\begin{aligned}
&\text{Point A:} \quad \phi^n_{j1} = \phi^n_{j2} \text{ and } \phi^t_{j1} = -\phi^t_{j2} \\
&\text{Point A:} \quad \frac{d\phi^n_{j1}}{ds} = -\frac{d\phi^n_{j2}}{ds} \\
&\text{Point A:} \quad \frac{d\phi^t_{j1}}{ds} - \frac{1}{R_1}\phi^n_{j1} = \frac{d\phi^t_{j2}}{ds} - \frac{1}{R_2}\phi^n_{j2} \\
&\text{Point B:} \quad \phi^n_{j1} = 0 \text{ and } \phi^t_{j1} = 0 \\
&\text{Point C:} \quad \phi^n_{j2} = 0 \text{ and } \phi^t_{j2} = 0. \qquad (8)
\end{aligned}$$

where the second subscript denotes cable segment 1 or 2. Another boundary condition were used by Ulstein and Faltinsen [7] at the connecting point A. Continuity in the tangent to the longitudinal deflections was used instead of continuity in the dynamic tension at the connecting point A. This former boundary condition leads to an unphysical discontinuity in the dynamic tension.
The solution described by equation (6) or (7) is now substituted into the boundary conditions defined in equation (8) for the points A, B and C. An equation system of eight equations with eight unknown coefficients is obtained (four unknowns respectively both for cable segment 1 and 2). The eigenfrequencies are found by setting the determinant of this equation system equal to zero. This is done in order to find nontrivial solutions for the unknown coefficients. When the eigenfrequencies are found, the unknown coefficients and the mode shapes can be determined. The coefficients are normalized so that the largest coefficient is 1.
The eigenfunctions represent a complete set of solutions. The motions in the transverse and longitudinal directions can therefore be written as,

$$\eta_n(s,t) = \sum_{i=1}^{\infty} a_i(t)\phi^n_i(s) \qquad (9)$$

and

$$\eta_t(s,t) = \sum_{i=1}^{\infty} a_i(t)\phi^t_i(s). \qquad (10)$$

Here $a_i(t)$ is the principal coordinate of vibration mode number i. Equation (9) and (10) are substituted into the governing equations (1) and (2). The two equations are multiplied with ϕ^n_j and ϕ^t_j, respectively and integrated over the length L, of the two cable segments. The resulting two set of coupled equations of motions are added as follows,

$$[M^n_{ji} + M^t_{ji}]\ddot{a}_i + [C^n_{ji} + C^t_{ji}]a_i = \int_0^L \Delta P \phi^n_j ds \qquad (11)$$

where

$$\begin{aligned}
M^n_{ji} &= M_m \int_0^L \phi^n_i \phi^n_j ds \\
C^n_{ji} &= -T_0 \int_0^L \frac{d^2\phi^n_i}{ds^2}\phi^n_j ds \\
&\quad -(T_0 + EA)\int_0^L \frac{1}{R}\frac{d\phi^t_i}{ds}\phi^n_j ds \\
&\quad +EA\int_0^L \frac{1}{R^2}\phi^n_i \phi^n_j ds \\
M^t_{ji} &= M_m \frac{(T_0 + EA)}{EA}\int_0^L \phi^t_i \phi^t_j ds
\end{aligned}$$

$$C^t_{ji} = -(T_0 + EA)\int_0^L \frac{d^2\phi^t_i}{ds^2}\phi^t_j ds + (T_0 + EA)\int_0^L \frac{1}{R}\frac{d\phi^n_i}{ds}\phi^t_j ds.$$

$M^n_{ji} + M^t_{ji}$ and $C^n_{ji} + C^t_{ji}$ are not generally zero for j $\neq$ i. The forcing term consisting of the generalized pressure (total modal force) on the right hand side in equation (11), can be decomposed into a term dealing with volume change of the bag-volume and a term dealing with the hydrodynamic impact pressure. Based on this decomposition the following can be written,

$$\begin{aligned}\int_0^L & \Delta P\phi^n_j ds \\ &= K_{bag}\sum_{i=1}^{\infty}\int_0^L\int_0^L a_i(t)\phi^n_i(\xi)d\xi\phi^n_j(s)ds \\ &\quad + \int_0^L p(s,\eta_n,t)\phi^n_j(s)ds \qquad (12)\end{aligned}$$

where K_{bag} is defined as $\Delta pressure = K_{bag} \cdot \Delta volume$. $\Delta volume$ is the dynamic volume change that causes a dynamic pressure change ($\Delta pressure$) due to the compressibility of the air in the bag. This implies that the bag volume is modelled as an enclosed volume. K_{bag} is set equal to zero in the presented calculations. This is partly based on results by Steen [2]. However, in order to study the effect of the dynamic bag pressure properly one needs to analyze the coupling between the bag pressure and the air cushion pressure.

A fourth order Runge Kutta method is used in the numerical time integration of the equation system defined in (11).

3 THE BAG AS AN UNSTEADY PLANING SURFACE

To study the dynamics of a given bag design, one must be able to analyze the hydrodynamic impact forces on the bag when it hits the free water surface. The following hydrodynamic analysis assumes a two-dimensional geometry in a longitudinal cut of the vessel, an incompressible medium and a high Froude number F_n, of the order of magnitude ten. Here $F_n = U/\sqrt{gl}$ where U is the forward speed of the SES. This velocity appears as a free stream velocity relative to the bag structure. l is a characteristic wetted length and g is the acceleration of gravity. The high Froude number implies that gravity can be neglected. The effect of gravity for the steady planing problem is discussed by Ogilvie [8] and Wagner [9].

We will analyze the behavior of a planing bag bouncing on the free water surface as a water entry problem, assuming a large forward speed of the SES relative to the relative vertical velocity between the bag structure and the water surface. The wetted length of the bag will vary strongly through the impact on the free water surface. The hydrodynamic loading will be much larger then the aerodynamic loading due to the relatively low pressure in the air cushion and inside the bag. This implies that the immersion of the bag will be low. The body boundary conditions can therefore be transferred to a straight horizontal line. This leads to a square root singularity in the hydrodynamic pressure at the spray root in the planing problem. The modal hydrodynamic forces defined by the last integral on the right hand side of equation (12), will not be effected by the detailed behavior of the flow at the spray.

We will assume that the vertical motions of the bag are negligible and consider the effect of the vertical fluid motions due to incident waves. A right-handed local xy-coordinate system that moves with the forward speed U of the vessel (see Figure 4) is used. The origin is fixed at the lowest point of the static bag configuration (point A in Figure 4). The x-axis is positive pointing toward the upstream direction of the undisturbed fluid flow and the y-axis is positive pointing upward. The undisturbed free stream velocity U is in the negative x-direction relative to this coordinate system. Since potential flow is assumed, the separation point must be determined a priori. Point A in Figure 4 is chosen. The body boundary conditions are transferred to a straight horizontal line that corresponds to the x-axis ($y = 0$) defined above (see Figure 4 and 5).

The initial condition is that $\phi = 0$ on $y = 0$ where

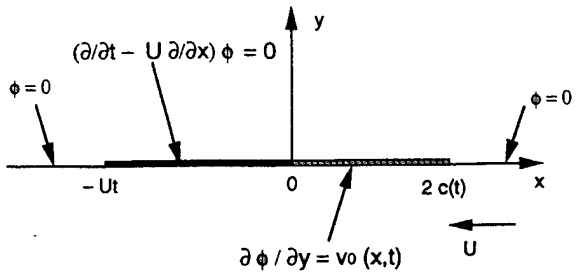


Figure 5: Hydrodynamic boundary value problem. ϕ = velocity potential. $2c(t)$ = wetted length of the bag. U = forward speed of the bag.

$\phi(x,y,t)$ is the velocity potential for the water flow caused by the bag. The linearized kinematic free surface boundary condition can be written as,

$$\frac{\partial \phi}{\partial y} = (\frac{\partial}{\partial t} - U\frac{\partial}{\partial x})\eta \qquad (13)$$

for $y = 0$, $x < 0$ and $x > 2c(t)$. Here $\eta(x,t)$ is the free surface deflection and $c(t)$ is an approximation of the half wetted length. By neglecting gravity and linearizing the dynamic free surface condition it follows that

$$(\frac{\partial}{\partial t} - U\frac{\partial}{\partial x})\phi = 0 \qquad (14)$$

for $y = 0$, $x < 0$ and $x > 2c(t)$. Equation (14) says that the velocity potential ϕ is unchanged when following a particle with the free stream velocity $-U$ on the free water surface ($y = 0$). We will divide the free water surface into different regions. In the regions $x > 2c(t)$ and $x < -Ut$ a fluid particle on the free surface will start on the free surface at $t = 0$ with the initial value $\phi = 0$. This means

$$\phi = 0 \quad \text{at} \quad x < -Ut\ ,\ x > 2c(t)\ ,\ y = 0. \qquad (15)$$

When $-Ut < x < 0$, we will use equation (14) i.e.,

$$(\frac{\partial}{\partial t} - U\frac{\partial}{\partial x})\phi = 0 \quad \text{at} \quad -Ut < x < 0\ ,\ y = 0. \qquad (16)$$

The body boundary condition can be written as,

$$\frac{\partial \phi}{\partial y} = v_0(x,t) \quad \text{at} \quad 0 < x < 2c(t),\ y = 0 \qquad (17)$$

where $v_0(x,t) = -V(t) + \frac{\partial \eta_{bag}(x,t)}{\partial t} - U\frac{\partial \eta_{bag}(x,t)}{\partial x}$. Here V(t) is the vertical velocity (positive in the positive y-direction) of the incident waves at $x = c(t)$ and $y = 0$. A characteristic wave length of the incident waves is assumed large relative to $2c(t)$. $\eta_{bag}(x,t)$ describes the unsteady geometry of the bag, that is the vertical distance between a point on the bag and a horizontal line defined by $y = 0$.

At the trailing edge (separation point) we will require that the flow leaves the wetted surface smoothly and that the hydrodynamic pressure

$$p = -\rho(\frac{\partial \phi}{\partial t} - U\frac{\partial \phi}{\partial x}), \qquad (18)$$

is continuous and equal to the atmospheric pressure $p = 0$ (Kutta condition). Here ρ is the mass density of water. The solution of this boundary value problem can be found from the linear solution of an unsteady foil in infinite fluid. In the latter solution a vortex sheet is shed into the wake downstream of the foil. The boundary condition in the wake is no pressure jump across the vortex sheet. This boundary condition can be written as,

$$-\rho(\frac{\partial \phi}{\partial t} - U\frac{\partial \phi}{\partial x})^+ + \rho(\frac{\partial \phi}{\partial t} - U\frac{\partial \phi}{\partial x})^- = 0 \qquad (19)$$

for $-Ut < x < 0$ and $y = 0$. Here the superscript $-$ denotes just below $y = 0$ and the superscript $+$ denotes just above $y = 0$. The boundary condition for $x < -Ut$, $x > 2c(t)$ and $y = 0$, is $\phi = 0$ in this problem. By using that

$$\frac{\partial \phi(x,0^+,t)}{\partial x} = -\frac{\partial \phi(x,0^-,t)}{\partial x}, \qquad (20)$$

at $-Ut < x < 0$ and $y = 0$, a relationship between ϕ^+ and ϕ^- can be obtained by integrating equation (20) in the x-direction and using that $\phi = 0$ for $x = -Ut$ and $y = 0$. We obtain

$$\phi(x,0^+,t) = -\phi(x,0^-,t) \qquad (21)$$

for $-Ut < x < 0$ and $y = 0$. If equation (21) is used in equation (19) we get,

$$(\frac{\partial}{\partial t} - U\frac{\partial}{\partial x})\phi^- = 0 \quad \text{at} \quad -Ut < x < 0\ ,\ y = 0. \tag{22}$$

This boundary condition is exactly the same as the boundary condition defined in equation (16). The unsteady foil problem satisfies the same Kutta condition as the planing surface problem. By using the same body boundary condition in the unsteady foil problem it has now been shown that the artificial unsteady foil problem satisfies the boundary conditions for the unsteady planing problem in the lower region below $y = 0$. The solution of the unsteady foil problem is therefore used. The solution of this hydrodynamic boundary value problem (HBVP) can be represented as a vortex distribution over the wetted body surface and the trailing vortex sheet (Newman [10]). When $0 < x < 2c(t)$, the vortex density is

$$\gamma(x,t) = \frac{2}{\pi[x(2c(t)-x)]^{1/2}} \times \left(PV \int_0^{2c(t)} \frac{[\xi(2c(t)-\xi)]^{1/2}}{\xi - x} v_0(\xi,t)d\xi + \frac{1}{2}\int_{-Ut}^{0} \frac{[\xi(\xi - 2c(t))]^{1/2}}{\xi - x}\gamma(\xi + Ut)d\xi \right). \tag{23}$$

Here PV means the principal value of the integral. The velocity $v_0(x,t)$ at the wetted surface in equation (23) can be written as,

$$v_0(x,t) = \hat{v}_0(t) + \hat{v}_1(t)\cos\theta \tag{24}$$

where $x - c(t) = c(t)\cos\theta$. $\hat{v}_0(t)$ and $\hat{v}_1(t)$ are defined as,

$$\hat{v}_0(t) = \frac{1}{\pi}\int_0^{\pi} v_0(\theta,t)d\theta \tag{25}$$

and

$$\hat{v}_1(t) = \frac{2}{\pi}\int_0^{\pi} v_0(\theta,t)\cos\theta d\theta. \tag{26}$$

The vortex density γ in the wake is found by using that the vorticity defined by equation (23) is finite at the trailing edge (Kutta condition). The following equation is obtained,

$$\int_{-Ut}^{0} \sqrt{\frac{\xi - 2c(t)}{\xi}}\gamma(\xi + Ut)d\xi = \pi c(t)(2\hat{v}_0(t) - \hat{v}_1(t)). \tag{27}$$

A time domain analysis is carried out, where the wetted length will vary from zero to a finite value. The separation point is fixed in space at the lowest point of the static bag configuration (point A in Figure 4).

To find the wetted length, an integral equation is set up, based on keeping track of particles on the free water surface that hit points on the upstream side of the bag at different time instants t. The particles are convected in the free stream direction with the free stream velocity U. The vertical displacement is found from integration in time of the vertical fluid velocity v, at $y = 0$. This vertical velocity v can be written as,

$$v(x,t) = -\frac{1}{2\pi}\int_{-Ut}^{2c(t)} \frac{\gamma(\xi,t)}{\xi - x}d\xi \tag{28}$$

where $x > 2c(t)$ and $y = 0$. The vortex distribution given by equation (23) is substituted into equation (28) between the integration limits 0 and $2c(t)$, and the order of integration is interchanged. The vortex distribution in the wake ($-Ut < x < 0$) is found by equation (27). The vertical displacement of the free water surface relative to the undisturbed free water surface, is denoted pile-up of water. The non-linear integral equation of the unknown wetted length (2 c(t)), can be formulated as,

$$0 = \eta_0 + \eta_{bag}(2c(t),t) - \int_0^t V(\tau)d\tau - \int_0^t v(x = 2c(t) + U(t-\tau),\tau)d\tau. \tag{29}$$

Here η_0 is the vertical distance between the lowest point of the bag (point A in Figure 4) and the free water surface at $t = 0$. Pile-up of water is represented by the last term on the right hand

side of equation (29). It is assumed that the bag is flexible, and has a shape described by $\eta_{bag}(x,t)$ in the impact region. We decompose the bag geometry as follows,

$$\eta_{bag}(x,t) = \bar{\eta}_{bag}(x) + \hat{\eta}_{bag}(x,t). \qquad (30)$$

Here $\bar{\eta}_{bag}(x)$ describes the static configuration of the bag and $\hat{\eta}_{bag}(x,t)$ is the transverse dynamic perturbation of the bag i.e., $\hat{\eta}_{bag}(x,t) = \eta_n(s,t)$. It follows from Figure 4, that $L_1 - s \approx x$ in the impact region. L_1 is the length of cable segment 1 and s is the tangential coordinate at segment 1. $v(x = 2c(t) + U(t-\tau), \tau)$ is the vertical velocity upstream the leading edge of the wetted surface given by equation (28). The right hand side of equation (29) is equal to the vertical distance between a point on the bag and a particle at the disturbed free water surface for $x = 2c(t)$. When the bag leaves the free water surface, a negative pile-up of water is possible for $x = 2c(t)$. The wetted surface will most probably be ventilated in this case, and the hydrodynamic forces will therefore be small. The hydrodynamic force is set equal to zero when a negative pile-up is encountered.
When the wetted length and the vorticity on the wetted surface are known, the modal hydrodynamic force can be found. The hydrodynamic pressure acting on the bag is found by using equation (18). The modal hydrodynamic force can be written as,

$$\begin{aligned}
&\int_0^L p(s,\eta_n,t)\phi_j^n(s)ds \\
&= -\rho \int_0^{2c(t)} \frac{\partial \phi(x,0^-,t)}{\partial t}\phi_j^n(s)dx \\
&\quad + \frac{1}{2}\rho U \int_0^{2c(t)} \gamma(x,t)\phi_j^n(s)dx \\
&= F_{exc,j}(t) - \sum_{i=1}^{\infty} C_{ji}a_i(t) \\
&\quad - \sum_{i=1}^{\infty} B_{ji}\dot{a}_i(t) - \sum_{i=1}^{\infty} A_{ji}\ddot{a}_i(t). \qquad (31)
\end{aligned}$$

The terms on the right hand side of equation (31) are obtained by collecting terms that explicitly depend on $a_i(t)$, $\dot{a}_i(t)$ and $\ddot{a}_i(t)$, respectively. The remaining terms are collected in $F_{exc,j}(t)$. $F_{exc,j}(t)$ and the coefficients A_{ji}, B_{ji} and C_{ji} are implicitly functions of the coefficients $a_i(t)$ through their dependence on $c(t)$ and $\frac{dc(t)}{dt}$. This decomposition is carried out in order to move as much as possible of the total modal hydrodynamic force over to the left hand side of equation (11). The terms proportional to $a_i(t)$, $\dot{a}_i(t)$ and $\ddot{a}_i(t)$ are moved over to the left hand side in the numerical time integration of equation (11). This improves the numerical stability and accuracy in the numerical time integration. Equation (31) indicates that there are interaction effects between all vibration modes. Since $F_{exc,j}(t)$, C_{ji}, B_{ji} and A_{ji} depend on $a_i(t)$, an iteration for the solution of $a_i(t)$ has to be carried out at each time step. Three iterations are mainly used in this analysis.
Equation (18) shows that the velocity potential is needed in the calculation of the modal force. The velocity potential on the wetted surface, can be written as

$$\phi(x,t) = -\frac{1}{2}\int_x^{2c(t)} \gamma(x,t)dx. \qquad (32)$$

This follows from the relationship between γ and $\partial\phi/\partial x$ and that the velocity potential goes to zero at the leading edge. The expression for the vortex distribution on the wetted surface given in equation (23) is substituted into equation (32), and the order of integration is interchanged. The resulting expression for the velocity potential is used in the first term of the hydrodynamic pressure defined by equation (18). The relationship between γ and $\partial\phi/\partial x$ is used together with equation (23) in the last term of equation (18).
It is assumed that the vortex strength in the wake can be approximated by piecewise constant segments of vorticity in the numerical approximations of equations (23) and (27). This requires that the time step is kept small relative to the time scale of the problem. The length of each segment is set equal to $U\Delta t$. Δt is the constant time step used in the numerical time integration during the impact. Analytical integration over each segment is performed. This integration is only important on the segments near the trailing edge of the bag (point A in Figure 4).

We will now show how the pile-up of water is calculated. We write

$$\int_0^t v(x(\tau),\tau)d\tau = \sum_{m=1}^{M_v} \int_{t_m}^{t_m+\Delta t} v(x(\tau),\tau)d\tau \quad (33)$$

where $t_m = (m-1)\Delta t$ and $t = M_v\Delta t$. The induced vertical velocity $v(x(\tau),\tau)$ defined by equation (28) has a square root singularity at the leading edge ($x = 2c(t)$). $v(x(\tau),\tau)$ is rewritten as

$$v(x(\tau),\tau) = \frac{\tilde{v}(x,\tau)}{\sqrt{x(x-2c)}} \quad (34)$$

so that the singular behavior can be properly integrated. In order to capture variations of $\tilde{v}(x,\tau)$ in time, the timestep Δt is divided into N sub-timesteps ($\Delta t = \sum_{n=1}^{N} \Delta t_n$). Since the strongest variation of $\tilde{v}(x,\tau)$ is near the leading edge, the sub-timesteps are decreased by using a cosine spacing. $\tilde{v}(x,\tau)$ is approximated over each sub-timesteps by a linear function in time defined by,

$$\tilde{v}(x,\tau) \approx A_n + B_n\tau. \quad (35)$$

This means that,

$$\int_{t_m}^{t_m+\Delta t} v(x(\tau),\tau)d\tau \approx \sum_{n=1}^{N} \int_{\Delta t_n} \frac{A_n + B_n\tau}{\sqrt{x(x-2c)}}d\tau. \quad (36)$$

The time dependence of the coordinate x and the half wetted length c over the timestep Δt in the integral defined in equation (36) is written as,

$$x = x_0 - U\tau \text{ and } c = c_0 + c_1\tau. \quad (37)$$

The integral on the right hand side of equation (36) can be integrated analytically. For $m = M_v$, N is chosen to be in the range from 10 to 15, in order to obtain a satisfactory accuracy. For $m < M_v$, N is set equal to 1. Far away from the wetted surface we can write

$$\int_{t_m}^{t_m+\Delta t} v(x(\tau),\tau)d\tau \approx \Delta t\left[\frac{\tilde{v}(x,\tau)}{\sqrt{x(x-2c)}}\right] \quad (38)$$

where x and c are evaluated at the midpoint of the timestep. Here far away means that $(x-c)/c$ is greater than 10. The discretized version of equation (29) is used to find the wetted length at each time step by an accelerated iteration procedure.

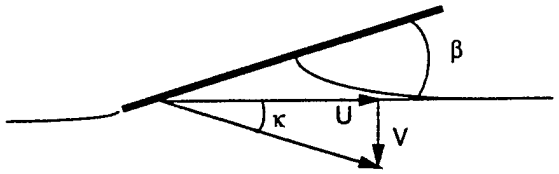


Figure 6: Rigid wedge that hits the free water surface with constant velocity (U, V). Sedov [11]

The numerical method has been verified by comparing with analytical results for lift on rigid foils in infinite fluid. Both the Wagner problem and a harmonically oscillating foil has been studied. The analytical solutions are based on linear theory and can be found in Newman [10]. The Wagner problem analyzes a flat plate of zero angle of attack, that suddenly is given a constant angle of attack.

Our numerical method has also been compared with the analytical solution by Sedov [11]. He studied a flat rigid wedge that enters the water with constant fall velocity (see Figure 6). The flow underneath the wedge at different time instants is dynamically similar. The vertical and horizontal components of the fall velocity are called V and U. The angle of attack β and the angle between the fall velocity and the horizontal velocity κ ($\approx V/U$) are assumed small. Results for the non-dimensional wetted length and lift force are presented in Figure 7. The results are only dependent on the ratio β/κ. The upper figure shows the ratio between the half wetted length with and without the pile-up of water. Neglection of pile-up of water is referred to as a Von Karman approach. The lower figure shows the non-dimensionalized lift force. $h = Vt$ is the immersion of the trailing edge relative to the undisturbed free water surface. We can barely see the difference between the numerical and the analytical solution.

As long as the time step Δt, is small relative to the duration t_{impact} of the impact, numerical tests

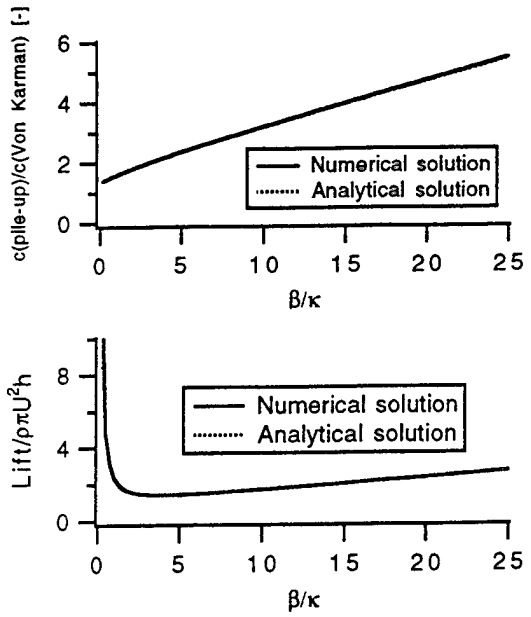


Figure 7: Results for non-dimensional half wetted length $c(t)$ and non-dimensional lift force for a rigid wedge that hits the free water surface with constant velocity. $h = Vt$ is the immersion of the trailing edge relative to the undisturbed free water surface. t = time and U = horizontal component of fall velocity. β and κ are defined in Figure 6.

have shown that our solution converges as Δt decreases. $\Delta t = \frac{t_{impact}}{100}$ has mainly been used in this study. Since $\Delta x = U\Delta t$, the length Δx of each vortex element is reduced when the timestep is reduced. The numerical solution for a rigid wedge mentioned above is not dependent on the time step. The reason is that the strengths of the vortices shed in the wake are not a function of time. The numerical approximation assuming piecewise constant segments of vorticity in the wake is therefore exact in this special case.

4 SCALING OF THE DYNAMIC IMPACT

The results from the numerical simulations are made non-dimensional in order to generalize the dynamics of a bag-structure hitting the free water surface. This is done by choosing a time scale, a length scale and a deformation scale characterizing the problem. These scales are used to non-dimensional the equations that defines the static equilibrium and the equations of motions. Non-dimensional parameters are then formed.

The length L of the bag is chosen as length scale (see Figure 2). The equations that define the static equilibrium, are made non-dimensional with respect to this length. The non-dimensional radius of curvature for circle segment 1 is then only dependent on the ratio H/L of the bag. The non-dimensional radius of curvature for circle segment 2 is dependent on both H/L and $\Delta P_1/\Delta P_2$. ΔP_1 and ΔP_2 are the static pressure differences across cable segment 1 and 2, respectively. Since the remaining parameters in the static problem can be expressed by ΔP_1, L, H/L and $\Delta P_1/\Delta P_2$, the static solution is only dependent on the non-dimensional parameters H/L and $\Delta P_1/\Delta P_2$.

The time and deformation scales are called T and N in the following derivation. Equations (1) and (2) can be made non-dimensional with the following result,

$$\ddot{\hat{\eta}}_n = \frac{T_0T^2}{L^2M_m}\frac{\partial^2\hat{\eta}_n}{\partial\hat{s}^2} + \frac{(T_0+EA)T^2}{L^2M_m}\frac{1}{\hat{R}}\frac{\partial\hat{\eta}_t}{\partial\hat{s}} - \frac{EAT^2}{L^2M_m}\frac{1}{\hat{R}^2}\hat{\eta}_n + \frac{\Delta PT^2}{M_mN} \tag{39}$$

and

$$\ddot{\hat{\eta}}_t = \frac{EAT^2}{L^2M_m}\frac{\partial^2\hat{\eta}_t}{\partial\hat{s}^2} - \frac{EAT^2}{L^2M_m}\frac{1}{\hat{R}}\frac{\partial\hat{\eta}_n}{\partial\hat{s}}. \tag{40}$$

Here $\hat{t} = t/T$, $\hat{s} = s/L$, $\hat{\eta}_n = \eta_n/N$, $\hat{\eta}_t = \eta_t/N$ and $\hat{R} = R/L$. Non-dimensional parameters are found from these two equations. Three of these non-dimensional parameters can be defined as,

$$\frac{T_0T^2}{L^2M_m},\ \frac{EAT^2}{L^2M_m} \text{ and } \frac{(T_0+EA)T^2}{L^2M_m}. \tag{41}$$

Since $T_0 + EA \approx EA$, the two last parameters are the same. The time scale T is chosen so that the first parameter is equal to one. This means that,

$$T = L\sqrt{\frac{M_m}{T_0}}. \tag{42}$$

This time scale is proportional to the natural periods of a string with length L, tension T_0 and structural mass per unit length M_m. The second parameter defined in equation (41) can be rewritten as EA/T_0 by using equation (42). We will now focus on the excitation term in equation

(39), that is $\Delta P T^2/M_m N$. Since the interaction between the dynamic bag deformation and the bag pressure is neglected ($K_{bag} = 0$), ΔP is equal to the hydrodynamic pressure p, acting on the wetted surface of the bag-structure. This hydrodynamic pressure can be written in the following form,

$$\begin{aligned} p &= -\rho\frac{\partial\phi}{\partial t} + \frac{1}{2}\rho U\gamma \\ &= -\rho\Big(\dot{V}_R c(t) f_1(\theta) + V_R \dot{c(t)} f_2(\theta) \\ &+ U\int d\hat{\xi} f_3(\theta,\hat{\xi})\gamma \\ &+ \frac{\dot{c(t)}L}{c(t)} f_2(\theta)\int d\hat{\xi} f_4(\theta,\hat{\xi})\gamma\Big) \\ &+ \rho U\Big(V_R f_5(\theta) \\ &+ \frac{L}{c(t)} f_6(\theta)\int d\hat{\xi} f_4(\theta,\hat{\xi})\gamma\Big). \end{aligned} \tag{43}$$

Here V_R is the relative normal velocity on the wetted surface of the bag. V_R is assumed to be constant in space in the following discussion. θ is defined as $x - c(t) = c(t)\cos\theta$ where $c(t)$ is half the wetted length, γ is the vorticity in the wake downstream the wetted surface of the bag and $\hat{\xi} = \xi/L$. The functions f_1, f_2, f_3, f_4, f_5 and f_6 are non-dimensional. The order of magnitude of the half wetted length can be written as,

$$c(t) = O\left(\sqrt{\frac{1}{2}R_1 V_R(t - t_{init})}\right) \tag{44}$$

where t_{init} is the initial impact time. This relation follows from the analysis of a rigid bag structure that hits the free water surface with a constant vertical velocity V_R and where pile-up of water is neglected.

The relative velocity is scaled as $\hat{V_R} = V_R T/N$. By using the Kutta condition in the unsteady planing problem (see equation (27), with $\hat{v}_0 = V_R$ and $\hat{v}_1 = 0$) it follows that

$$\int d\xi\sqrt{\frac{\xi - 2c(t)}{\xi}}\gamma = 2\pi c(t) V_R. \tag{45}$$

This means that γ is scaled as $\hat{\gamma} = \gamma T/N$. By multiplying the pressure given in equation (43) by $T^2/M_m N$, the following non-dimensional parameters follow,

$$\frac{\rho^2 R_1 N}{M_m^2}, \frac{\rho U T}{M_m} \text{ and } \frac{\rho L}{M_m}. \tag{46}$$

To sum up, the following six non-dimensional parameters have been found,

$$\begin{aligned} &\frac{H}{L}, \frac{\Delta P_1}{\Delta P_2}, \frac{EA}{T_0}, \\ &\frac{\rho^2 R_1 N}{M_m^2}, \frac{\rho U T}{M_m} \text{ and } \frac{\rho L}{M_m}. \end{aligned} \tag{47}$$

The characteristic deformation scale N will be related to the maximum immersion of the rigid bag. N can be expressed in terms of the vertical velocity V of the free water surface and the initial gap η_0 between the lowest point of the bag and the free surface at $t = 0$. We define

$$V(t) = V_a \sin\frac{2\pi}{T_p}t. \tag{48}$$

Only one oscillation period will be discussed. The rigid body immersion of the bag occurs in the time interval $t_{init} < t < T_p - t_{init}$ where $t_{init} = T_p \arccos(2\beta - 1)/2\pi$. The following relationship can be set up

$$\eta_0 = (1 - \beta)\frac{V_a T_p}{\pi} \tag{49}$$

where β is the ratio between the rigid body immersion of the bag and the double motion amplitude $V_a T_p/\pi$ of the free surface (see Figure 8). N is chosen as

$$N = \beta V_a T_p. \tag{50}$$

5 RESULTS AND DISCUSSION

Numerical results will be presented and discussed in this section. First the effects of including structural damping and bending stiffness will be focused on and justified. Next some results from verification of the hydroelastic model will be shown. This model is then used to compute the effect of varying the non-dimensional parameters obtained in the previous section.

The physical quantity focused on in this analysis is the dynamic volume pumping of the bag-structure due to the impact with the free water

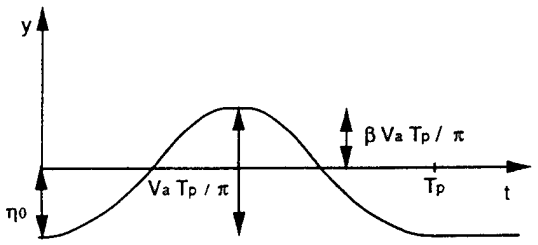


Figure 8: Definition of the motion of the free water surface.

surface. The dynamic volume pumping is defined as the time derivative of the integrated transverse deflection along cable segment 1 facing the air cushion (see Figure 4). The dynamic transverse motion of point A in Figure 4 is also of some interest in connection with the air leakage underneath the bag-structure. Earlier investigations by Steen [2] have shown that these quantities are important for the cobblestone effect on a SES.

The external input data used as a starting point for the non-dimensional parameter variation are presented in Table 1. Linear structural damping is introduced in the equations of motions defined in equation (11). The linear structural damping coefficient is set equal to $2\omega_i(M_{ii}^n + M_{ii}^t)\xi$ and included in the diagonal terms of the structural modal damping matrix. Here ω_i is the eigenfrequency for mode number i. M_{ii}^n and M_{ii}^t are defined in equation (11). ξ is the relative critical damping ratio. $\xi = 0.01$ is used in this analysis. Calculations with $\xi = 0.02$ showed small differences. The structural damping cause the high frequency motions resulting from very high modes to quickly damp out.

Large hydrodynamic forces occur on the wetted length of the bag during impact with the free water surface. The local restoring forces of the flexible bag are small relative to the hydrodynamic forces. This can be illustrated by Figure 9. The upper figure in Figure 9 shows a sudden increase in the wetted length during the first impact. The reason for this sudden increase may be explained by the lower figure. The deformation is mainly confined to the region of the wetted surface where

Description	Symbol	Value
Height of bag	H	1.40 m
Length of bag	L	2.00 m
Diff. pressure, segment 1	ΔP_1	750 N/m
Diff. pressure, segment 2	ΔP_2	5250 N/m
Rad. of curv. , segment 1	R_1	2.12 m
Rad. of curv., segment 2	R_2	0.30 m
Arc length, segment 1	L_1	2.60 m
Arc length, segment 2	L_2	0.84 m
Static tension	T_0	1596 N
Axial stiffness	EA	$0.6 \cdot 10^6$ N
Structural mass	M_m	4.3 kg/m
Vert. vel. amp.	V_a	2.35 m/s
Oscil. period	T_p	0.2 s
Rel. immersion	β	0.1
Forward speed of the SES	U	23.1 m/s

Table 1: An example of data used in the simulations of hydroelastic bag impact.

the hydrodynamic pressure is applied. Due to this local deformation and the fact that the free water surface is approaching the bag in the vertical direction, this sudden increase in the wetted length is explained. In the time interval ($0.0808 < t < 0.0823$) where the sudden increase in wetted length occurs, the hydrodynamic forces are small. This may be explained by equation (17), where $v_0(x,t) = -V(t) + \frac{\partial \eta_{bag}(x,t)}{\partial t} - U\frac{\partial \eta_{bag}(x,t)}{\partial x}$. The bag is accelerated and deformed in the impact region after the initial time of impact. This implies that the two last terms are cancelling the first one representing the vertical velocity of the free water surface.

The separation point of the flow (trailing edge) is fixed at $x = 0.0[m]$ in the numerical results presented in Figure 9. In reality the flow will probably detatch or separate from the bag ahead of this x value e.g. $x \approx 0.06[m]$ for time $t \approx 0.082[s]$. This "premature" detachment has been discussed by Tuck [12] in the case of a two-dimensional

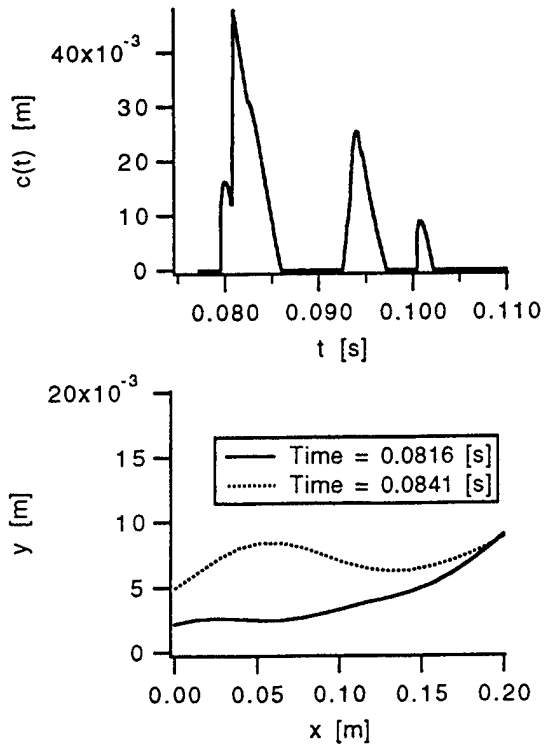


Figure 9: Upper Figure: half wetted length $c(t)$ as function of time t. Lower Figure: two snap shots of the deformed bag in the impact region during the first impact. Bending stiffness is $EI = 0[Nm^2]$. Input data is tabulated in Table 1. xy-coordinate system is defined in Figure 4.

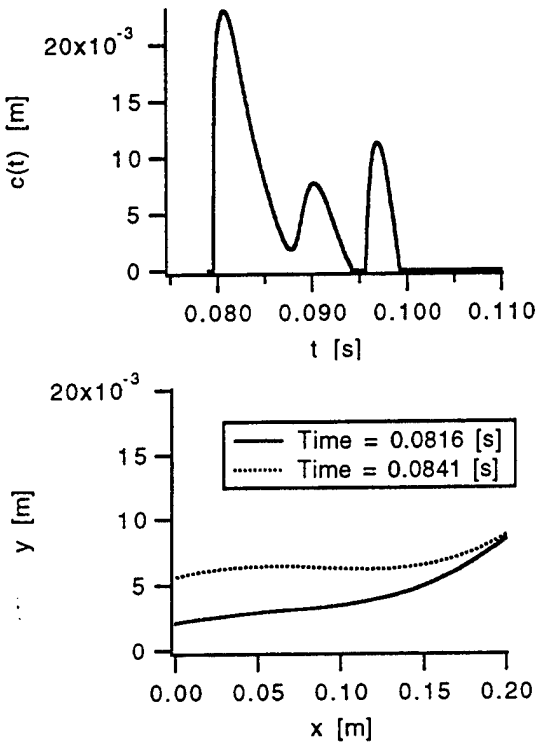


Figure 10: Upper Figure: half wetted length $c(t)$ as function of time t. Lower Figure: two snap shots of the deformed bag in the impact region during the first impact. Bending stiffness is $EI = 4.0[Nm^2]$. Input data is tabulated in Table 1. xy-coordinate system is defined in Figure 4.

steady planing surface. If a separation point ahead of $x = 0.0[m]$ e.g. $x \approx 0.06[m]$ for time $t \approx 0.082[s]$, were used, the hydrodynamic forces would not be small.

If bending stiffness is included, the results presented in Figure 9 will be different. An example with $EI = 4.0[Nm^2]$ is presented in Figure 10. The effect of bending stiffness is implemented by introducing the term $-EI\ \partial^4\eta_n/\partial s^4$ on the right hand side of equation (1). The non-dimensional parameter characterizing the effect of bending stiffness is EI/L^2T_0. The bending stiffness causes the local deformation due to the hydrodynamic load to be distributed over a larger length. This implies that "premature" detachment is less likely to occur.

Results showing the effect of bending stiffness are presented in Figure 11. The upper figure shows the half wetted length as a function of time. Energy spectra S(f) are shown as functions of frequency f ([Hz]) in the two lower figures . The energy spectrum can be expressed as,

$$S(f) = \frac{G(f)\tilde{G}(f)}{2\Delta f} \qquad (51)$$

where G(f) is a complex quantity resulting from the Fast Fourier Transform of the time signal g(t) of the studied variable over the time interval defined by $1/\Delta$ f. $\tilde{G}(f)$ denotes the complex conjugate of G(f). t is time ([s]) .

The middle and lower figures in Figure 11 show the energy spectra for the transverse motion of point A in Figure 4 and the volume pumping due to the bag motion. The energy spectra for the volume pumping and the transverse motion are less sensitive to the bending stiffness then the wetted length. This indicates that the hydrodynamic impulse (integrated hydrodynamic force in

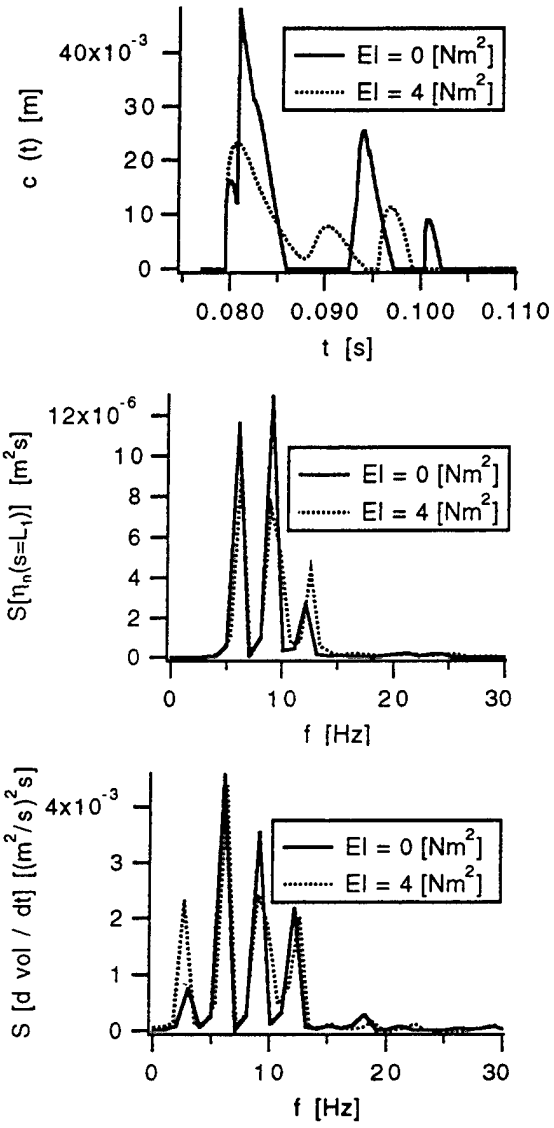


Figure 11: Upper Figure: half wetted length $c(t)$ as function of time t. Middle Figure: energy spectrum of transversal motion η_n of point A in Figure 4 as function of frequency f. Lower Figure: energy spectrum of volume pumping $dvol/dt$ as function of frequency f. Input data is tabulated in Table 1.

time) is more important for the volume pumping and the transverse motions of point A than the details in the wetted length and the hydrodynamic forces.

Hydroelastic deformation of the bag during the impact of the bag with the free water surface, may lead to physical phenomena that are not accounted for in the presented hydrodynamic model. One example is negative pile-up. Ventilation will probably occur in this case and a hydrodynamic model treating the water exit problem should be considered. This is more likely to occur when bending stiffness is neglected. Problems with convergence both with respect to the number of mode shapes and the time step was experienced when bending stiffness was not included. 70 mode shapes were used in the calculations with no bending stiffness, that are presented in Figure 11. Still, the results for volume pumping and transverse motion of point A were not completely converged. To avoid these problems, bending stiffness is included in the structural model. This increases the local restoring force. Based on the results presented in Figure 11 it is believed that the over all motion of the bag is not sensitive to the bending stiffness. From here on the bending stiffness is set equal to $EI = 4.0[Nm^2]$.

Results from a convergence study by the complete model together with a simplified hydroelastic load model are presented in Figure 12. The modal force (see equation (31)) is calculated as

$$\int_0^L p(s,\eta_n,t)\phi_j^n(s)ds \approx \phi_j^n(s = L_1 - c(t)) \int_0^{2c(t)} p(x,\eta_n,t)dx \quad (52)$$

in the simplified load model. Figure 12 shows that the results for the transverse motion of point A and the volume pumping have converged when thirty mode shapes are used in the calculations. Results for the simplified load model are also presented in this figure. The simplified load model predicts very well the transverse motion of point A and the volume pumping. One reason for this is that the maximum half wetted length is small

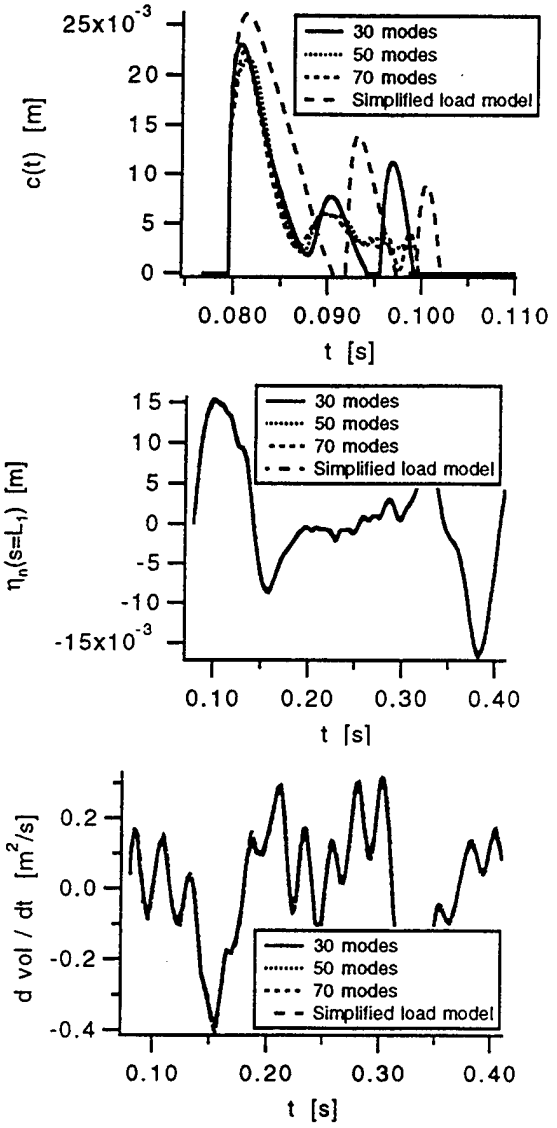


Figure 12: Upper Figure: half wetted length c(t) as function of time t. Middle Figure: transverse motion η_n of point A in Figure 4 as function of time t. Lower Figure: volume pumping $dvol/dt$ as function of time t. Input data is tabulated in Table 1.

compared to the wave length corresponding to mode shape number thirty (c_{max} / $\lambda_{30} \approx 0.1$). The difference between the wetted length $2c(t)$ for the complete and simplified load model is larger. Since the higher mode shapes are triggered differently in the simplified load model, the local deformation in the impact region and the wetted length are influenced.

It is interesting from a design point of view to know what external parameters that are important for the dynamic impact of a bag structure. The six non-dimensional parameters defined in equation (47) will be used in the following text to discuss the impact of the bag. One set of parameters has been used as starting point for the parameter variation, and is given in Table 1. It has been found that the volume pumping caused by the bag and the transverse motion of the lowest point of the bag are mainly dependent on three of the non-dimensional parameters. That is,

$$\frac{\Delta P_1}{\Delta P_2}, \frac{H}{L} \text{ and } \frac{\rho^2 R_1 N}{M_m^2}. \tag{53}$$

We will only focus on the two last non-dimensional parameters in the following discussion. The first non-dimensional parameter is assumed to be constant. That means that the ratio between the excess pressure in the air cushion and the excess pressure in the bag is constant. Results as a function of H/L for a constant value of $\rho^2 R_1 N/M_m^2$ equal to 5408 are presented in Figure 13. When considering the cobblestone effect, the frequency of interest is approximately 5 [Hz] for a 30-35 [m] long SES. This corresponds to the lowest natural frequency for the acoustic modes inside the air cushion. This is approximately equivalent to a non-dimensional frequency of 0.5. The lowest figure in Figure 13, shows that volume pumping at a non-dimensional frequency of 0.5 is small for H/L equal to 0.5 and 0.7. It is considerably larger for $H/L = 0.9$. Despite this there is large increase in volume pumping if the frequency is shifted up or downwards on the frequency axis. The middle figure shows that the non-dimensional transverse deformation at the lowest point of the bag (point A in Figure 4) can be large when $H/L = 0.5$. There are relatively large differences between the response for

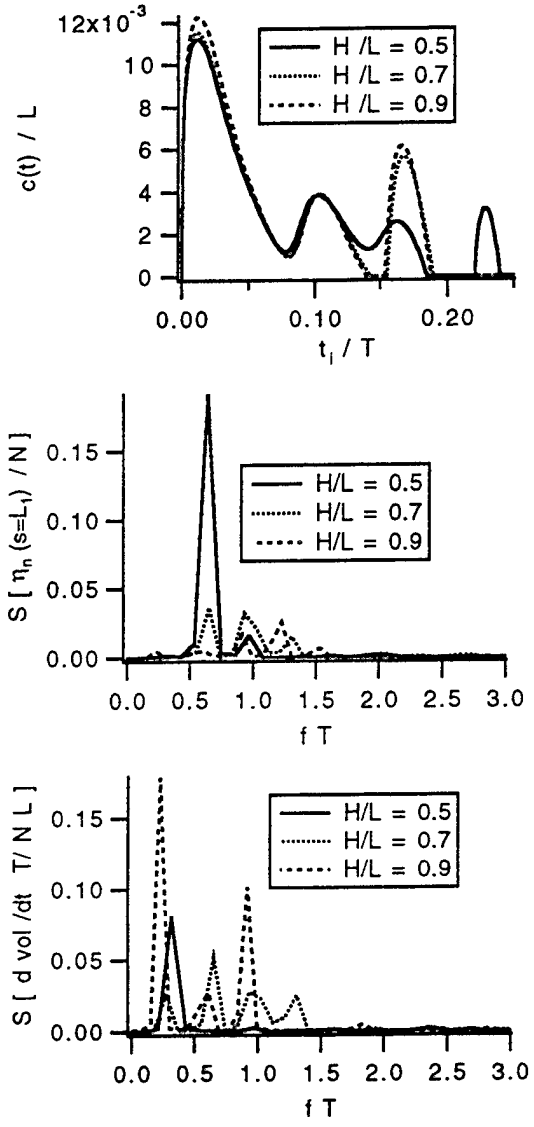


Figure 13: Results for non-dimensional wetted length $c(t)/L$, transverse motion spectrum $S[\eta_n/N]$ at point A in Figure 4 and volume pumping spectrum $S[dvol/dtT/NL]$ for different H/L ratios. The remaining non-dimensional parameters defined in equation (47) are kept constant. t_i/T is non-dimensional time and fT is non-dimensional frequency. $t_i = t - t_{init}$ where t_{init} is the time of initial impact. H and L are defined in Figure 2 and N is defined by equation (50). T is defined by equation (42).

different H/L-values. The non-dimensional frequency of oscillation for the vertical motion of the free water surface is approximately 0.5 for these calculations. The calculations indicate that this frequency of oscillation is less important than the natural frequencies of the bag. The peaks of the response shown in the two lower figures in Figure 13 correspond approximately to the natural frequencies of the bag-structure.

Results for the variation of β, that is variation of the non-dimensional parameter $\rho^2 R_1 N/M_m^2$, are shown in Figure 14. H/L is constant and equal to 0.7. When β is increased, it means that the rigid body immersion of the bag increases. The upper figure in Figure 14, shows that maximum wetted length is not significantly increased, while the duration of the impulse is increased. This is a result of the flexibility of the bag. This is also reflected in the two lower figures in Figure 14. The difference in non-dimensional response for the volume pumping and transverse deformation at point A in Figure 4 is small at least in the non-dimensional frequency region near 0.5. Based on the way the response is made non-dimensional, we may conclude that the response in volume pumping and transverse motion of the lowest point on the bag is approximately proportional to the deformation scale $N = \beta V_a T_p$, at least in the frequency region near 0.5. This indicates that the effect of volume pumping will increase with increasing β. There is relatively small response at a non-dimensional frequency of 0.5, but a small shift in frequency may result in a significant increase of the response (see two lower figures in Figure 14).

To get the order of magnitude of the volume pumping caused by the bag due to the impact with the free water surface, a typical volume pumping amplitude can be compared with the effect of a typical leakage area amplitude underneath the bag. The dynamically varying leakage area was found by Steen [2] to be important for the cobblestone effect. We obtain the following approximate value of the dynamic leakage amplitude by assuming that these two effects are of the same order of magnitude,

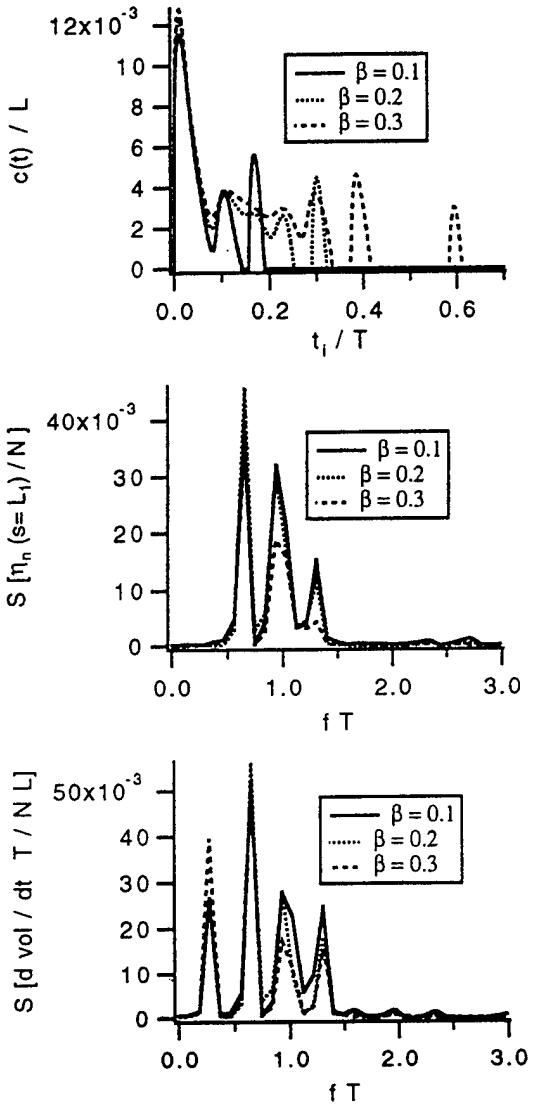


Figure 14: Results for non-dimensional wetted length $c(t)/L$, transverse motion spectrum $S[\eta_n/N]$ at point A in Figure 4 and volume pumping spectrum $S[dvol/dtT/NL]$ for different β values. This implies that $\rho^2 R_1 N/M_m^2$ is varied, while the remaining non-dimensional parameters defined in equation (47) are kept constant. t_i/T is non-dimensional time and fT is nondimensional frequency. $t_i = t - t_{init}$ where t_{init} is the time of initial impact. β is defined by equation (49) and M_m = structural mass per unit length of the cable. For further explanations see Figure 13.

$$\Delta h \approx (dvol/dt)/\sqrt{2p_c/\rho_{air}} \approx 1[cm]. \quad (54)$$

Here p_c is the excess pressure in the air cushion, ρ_{air} is the density of air and Δh is the dynamic leakage amplitude. This indicates that the effect of the volume pumping of the bag due to the impact with the free water surface, may be of the same importance for the cobblestone effect as the dynamic leakage variation. Since the presented analysis is a local analysis, one should be careful to conclude about the cobblestone effect. A more complete analysis where both the effect of more loops on the bag and the coupling to the air cushion pressure, is necessary.

6 CONCLUSIONS

A numerical and theoretical two-dimensional study of the interaction between the free water surface and the flexible bag stern seal of a SES is presented. The bag is pressurized with air, and is deformed due to the hydrodynamic pressure distribution on the wetted surface of the bag and the compressibility of air in the bag. High numerical accuracy is needed. This has been achieved by using the "dry" mode superposition approach for the flexible behavior of the bag. The coupling between the elastic longitudinal and transverse oscillations as well as the curvature are accounted for.

The hydrodynamic boundary value problem is solved as a water entry problem, assuming a large forward speed of the SES relative to the relative vertical velocity between the bag structure and the water surface. The flexible bag behaves hydrodynamically as an unsteady two-dimensional planing surface. A solution of this problem is found by combining the solution for an unsteady lifting surface in infinite fluid with an integral equation for the wetted length of the bag. The integral equation is a generalization of what Wagner [5] did for slamming. An important difference is the effect of the forward speed of the bag.

It is found that bending stiffness improves the robustness of the numerical solution of the wetted surface of the bag. Results indicate that the over all motion of the bag structure is not sensitive to bending stiffness.

Two parameters have been found to be of special importance for the volume pumping and the transverse motion of the lowest point of the bag (point A in Figure 4). That is the relative rigid body immersion of the bag and the ratio H/L where H is the height and L is the length of the bag defined in Figure 2. The volume pumping and the transverse motion of point A is approximately proportional to the rigid body immersion of the bag.

7 ACKNOWLEDGEMENTS

This work is part of a dr.ing. study of one of the authors (T. Ulstein) and has received financial support by The Research Council of Norway (NFR). The computer time is supported by the Norwegian Supercomputing Committee (TRU).

REFERENCES

1. Toyama, Y., Ono S. and Nishihara, S. "Seal System of a Large Surface Effect Ship," Intersociety High Performance Marine Vehicle Conference and Exhibit- HPMV'92, American Society of Naval Engineers, Washington D.C., 1992.

2. Steen, S. "Cobblestone Effect on SES," Dr.ing thesis, 1993, Norwegian Institute of Technology.

3. Doctors L.J., "Theory of Compliant Planing Surfaces," 2nd Int. Conf. on Numerical Ship Hydrodynamics, University of California, Berkeley, 1977.

4. Bessho M., Komatsu M. "Two-dimensional unsteady planing surface," JSR, Vol. 28 ,No. 1., 1984.

5. Wagner, H. "Über Stoß- und Gleitvorgänge an der Oberfläche von Flüßigkeiten," Zeitschrift für Angewandte Mathematik und Mechanik Vol.12 No. 4., 1932, pp. 193-215.

6. Bliek A. "Dynamic Analysis of Single Span Cables," PhD Thesis, 1984, Dept. of Ocean Engineering, MIT.

7. Ulstein T., Faltinsen O. "Hydroelastic behavior of the flexible bag stern seal of a SES," Hydroelasticity in Marine Technology, Trondheim, Norway, 1994.

8. Ogilvie, T.F. "Singular perturbation problems in ship hydrodynamics," Report no: 096, Dept. of Naval Architecture and Marine Engineering, The University of Michigan, 1970.

9. Wagner, H. "Planing of watercraft," Washington:NACA, Technical memorandum no.1139, 1948.

10. Newman, J.N. "Marine hydrodynamics," Cambridge:The MIT Press, 1977.

11. Sedov, L. "On the theory of unsteady planing and the motion of a wing with vortex separation," Washington:NACA, Technical memorandum no.942, 1940.

12. Tuck, E.O., "A review of the planing surface problem," International symposium on computer methods for partial differential equations, Lehigh University, Bethlehem, 1984.

DISCUSSION

W. Schultz
University of Michigan, USA

This is an interesting analysis. Are the pressures in the bag and cushion considered constant? It would seem that the aerodynamics of the leaking air would be required for an accurate accounting of the bag dynamics. Any comment?

L. Doctors
University of New South Wales, Australia

In Figure 5 (as it appeared in the presentation), the pressure in the cushion region is shown to be zero (or atmospheric) rather than the cushion pressure. Can you clarify why you can ignore the static cushion pressure in the dynamic problem? In my own work on the motions of air-cushion vehicles, I found that that steady state static depression of the free water surface had a profound influence on the dynamic behavior. This was principally due to the fact that linear superposition could not be applied to the problem of interaction between the skirt and the water surface.

AUTHORS' REPLY

The pressures in the air cushion and in the bag are considered constant in the presented analysis. Here only a local analysis has been considered. Due to the fact that the bag pressure is coupled to the global air cushion pressure at the bag, the bag pressure and the air cushion pressure have been considered constant for the sake of simplicity in the presented local analysis.

We are now working on a more complete analysis where the bag pressure is coupled to the air cushion pressure. In this case, the air cushion pressure and the bag pressure will no longer be constant. We agree with the discussion of Prof. Schultz that the aerodynamics of the leaking air will be required for an accurate accounting of the bag dynamics. This effect we also intend to include in the more complete analysis.

We reply to the discussion of Prof. Doctors as follows. Given the wetted length of the bag, the problem is linear. The hydrodynamic boundary value problem of the static depression of the free water surface underneath the air-cushion can therefore be solved separately from the hydrodynamic boundary value problem of the bag. In the problem of finding the wetted length of the bag there will be a coupling between these two problems due to the static deformation of the free water surface. Due to the high forward velocity of the SES the wave length that corresponds to the static deformation of the free water surface due to the static cushion pressure, is much larger than typical wetted lengths of the bag. This indicates that the coupling will be small.

Blunt-Body Penetration into a Slightly Compressible Liquid

A. Korobkin (Lavrentyev Institute of Hydrodynamics, Russia)

ABSTRACT

This paper is concerned with the unsteady plane liquid motion due to the penetration of a blunt undeformable body through its free surface. The liquid is assumed to be ideal and slightly compressible, both the effects of viscosity, surface tension and gravity are neglected. At the initial stage of the entry, when the compressibility of the liquid is of major importance, the flow is described within the framework of the acoustic approximation. The main feature of the problem is the existence of a contact line between the free surface and the entering body surface. The position of this line is unknown in advance and is to be determined together with the solution of the problem. Near the contact line, the flow of the liquid is nonlinear, approximately quasi-stationary and is described by the subsonic jet theory. Both mass and kinetic energy of the spray jet generated by the impact are under investigation. It is shown that at large time, a half of the energy is concentrated in the bulk of the flow and the another half does in the spray jets.

INTRODUCTION

The problem of interaction between a solid body and a liquid with a free surface attracts a widespread attention of both scientists and engineers. Interest in this field of hydrodynamics arose more than a half century ago in connection with the problem of the landing of flying boats. The processes of such kind are essentially unsteady and characterized by existence of a contact line between the free surface of the liquid and the solid-body surface. Detailed investigation of the processes can be applied to problems in ship hydrodynamics (slamming problems), ocean engineering (impact of sea waves on coastal structures and ocean platforms) and sea ballistics. Many advanced marine vehicles (catamaran, SES, SWATH) have their flat structures which are elevated above the water surface. While operating in waves, those structures can, however, contact the liquid and resulting high hydrodynamic loads can occur. The loads can lead to hull vibration, damage of the structure and loss of the ship speed.

The initial stage of the interaction, which immediately follows the instant of the first contact between the liquid and the body, is of particular interest. At this stage the topology of the flow, the hydrodynamic load, the body acceleration and some other values are significantly changed, that determines the further evolution of the impact process. In some cases (for example, for flat-bottom or blunt-body impact) these changes are of shock character and the liquid compressibility has to be taken into account. On the other hand, experimental studies indicate that the hydrodynamic loads reach their maximum values just after the impact and then vanish quite quickly. The analysis of the initial stage of the liquid-

solid interaction can give helpful estimates for the dynamic-strength investigations of the bottom plating behaviour and provides also initial data for further numerical calculations.

The first theories of liquid-solid impact (the penetration theories of von Karman [1] and Wagner [2], impact theory of Sedov [3]) were directed to a global description of the process. A lot of problems were solved on the basis of these theories. As was noted in a review of Korobkin & Pukhnachov [4], some global characteristics can be determined with good accuracy from quite simple knowledge of the interaction mechanism. But in some cases, more complete information about the impact is required. This is necessary not only for calculation of local characteristics but in some cases for theoretical understanding of the phenomenon on the whole.

The ideal incompressible liquid model is usually used under both numerical and analytical studies of the liquid-solid impact. Unfortunately, this model is not able to describe some important details of the blunt-body impact. For example, this model predicts infinite hydrodynamic pressures just after the impact moment and it cannot describe the formation of spray jets. The main reason why this model fails at the initial stage is connected with the fact that the velocity of a signal propagation in the model is infinite. This approximation is valid only if accelerations of liquid particles are not very large (this is not so for the impact of a plate floating on the liquid surface) and if the speed of the involving the liquid particles in motion, i.e. the speed of expansion of the wetted part of the entering body bottom, is much less than velocity of a signal propagation (sound velocity). Therefore, in the case of both flat-bottom and blunt-body impact we need to take into account the acoustic effects, i.e. the effects which are connected with the finite value of the sound velocity.

The sound velocity c_0 for water is approximately $c_0 = 1500 m/sec$. But the impact velocities in ship hydrodynamics are relatively small, they are of the order of some meters per second. That is why the Mach number $M = V/c_0$ where V is the impact velocity is very small. This means that the variation of the liquid density under the impact is small and the sound velocity which, in general, is dependent of the density can be taken approximately as constant. Moreover, the velocities of the liquid particles can be assumed of the order of V and are small compared with c_0.

In this case the equations of the motion of a compressible liquid can be simplified, that leads to the so called acoustic theory of the impact. In this theory the boundary conditions on the free surface and on the contact region can be taken on the undisturbed liquid level and can be linearized in the leading order as $M \to 0$. The physical reason for this is that the duration of the impact stage, when the liquid compressibility is of major importance, is very small and, hence, the deviation of the liquid boundary from its initial position can be neglected in comparison with the dimension of the contact spot.

In order to estimate the stage duration, we consider the case of a parabolic contour entry. Initially the liquid is at rest and occupies a lower half-plane ($y' < 0$) and the body touches its free surface ($y' = 0$) at a single point taken as the origin of the Cartesian coordinate system $x'Oy'$ (dimensional variables are denoted by a prime). At some instant of time, taken as initial ($t' = 0$), the body begins to penetrate the liquid vertically with a constant velocity V. External mass forces and surface tension are neglected. Then the entering contour position at the moment t' is

$$y' = \frac{x'^2}{2R} - Vt' \qquad (1)$$

where R is the radius of the curvature at the body top. The coordinate $x'_*(t)$ of the right-hand side point where the contour (1) intersects the undisturbed liquid level ($y' = 0$) is

$$x'_*(t) = \sqrt{2RVt'}.$$

Therefore, the speed of involving liquid particles in motion is equal to

$$\frac{dx'_*}{dt'} = \sqrt{\frac{RV}{2t'}}$$

which just after the impact moment ($t' = 0$) is much greater than the sound velocity c_0. Hence, the free surface remains undisturbed at the initial stage during which $dx'_*/dt' > c_0$. At this stage the intersection points $x' = \pm x'_*(t)$, $y' = 0$ move at a supersonic velocity, which is why the stage is referred to as the supersonic one. The duration of the supersonic stage T can be found from the equality $(dx'_*/dt')(T) = c_0$ which gives

$$T = \frac{R}{2V} M^2.$$

The dimension of the wetted part of the entering body at the end of this stage is equal to $2x'_*(T) = 2RM$.

To analyse the initial stage of the impact, where the liquid compressibility is the governing factor, let us change to dimensionless variables, which are designated by the above-mentioned terms without a prime. We take the half-width of the contact region at the end of the supersonic stage RM as the lengthscale and the impact velocity V as the velocity scale of liquid particles. The quantity RM/c_0, being $2T$, is taken as the timescale. Therefore, the liquid-particle displacements are $O(RM^2)$ as $M \to 0$, which allows us to use the acoustic theory and to put the boundary conditions on the undisturbed initial level of the liquid.

The entry of a parabolic shape is considered for simplicity only: all the results except as otherwise noted are also valid in the general case.

FORMULATION OF THE PROBLEM

In non-dimensional variables, which are designated by the above-mentioned terms without a prime, the liquid flow is described by the velocity potential $\phi(x, y, t)$, for which the boundary-value problem has the form

$$\phi_{tt} = \phi_{xx} + \phi_{yy} \ \ (y < 0),$$

$$\phi = 0 \ \ (y = 0, \ \ | \, x \, | > a(t)),$$

$$\phi_y = -1 \ \ (y = 0, \ \ | \, x \, | < a(t)), \qquad (2)$$

$$\phi = \phi_t = 0 \ \ (y < 0, \ \ t = 0),$$

$$\phi \to 0 \ \ (x^2 + y^2 \to \infty).$$

After scaling both the sound velocity and the impact velocity are equal to unity in the new variables. The interval $-a(t) < x < a(t)$ corresponds to the wetted part of the entering contour. The points $x = \pm a(t)$, $y = 0$ correspond to the contact points of the water surface with the surface of the rigid body. The function $a(t)$ is unknown in advance, method of its calculation was suggested by Korobkin [5]. The position of the entering contour is given by the equation $y = M(x^2/2 - t)$. At the supersonic stage, $0 < t < \frac{1}{2}$, we have $a(t) = (2t)^{\frac{1}{2}}$. After the escape of the shock wave generated under the impact onto the free surface, it was found that $a(t) = (3(5 + 8t)^{\frac{1}{2}} - 5)/4$ [5] when $\frac{1}{2} < t < \frac{11}{2}$ (the beginning of the subsonic stage).

The problem (2) was analysed for the supersonic stage [6] and for the subsonic stage [7] in detail. Main attention was paid to the pressure distribution over the contact region and to the geometry of the flow domain. It was shown that the acoustic approximation fails near the contact points, where the pressure and the velocities of the liquid particles are much greater than inside the main liquid domain. This fact indicates that near the contact points the liquid flow is nonlinear and the deformation of the free surface can be very large. This means that the inner solution near the contact points has to be constructed to describe fine structure of the flow. Asymptotic analysis of the original problem for $M \to 0$ shows that at the initial stage of the impact the flow region must be divided onto the following parts: 1) the main region where the free surface deformation is negligible small, and the wetted part of the entering contour can be approximately changed for a plate; 2) the root of the spray jet where the curvature of the free surface is large; 3) spray jet. It was shown that inside the jet root the flow is two-dimensional, nonlinear, and quasi-stationary in the leading order as $M \to 0$ [8]. In order to determine the flow characteristics in the jet root, the subsonic jet

theory can be used. The liquid particles are accelerated in the jet root region and then they are thrown out the region at the double velocity of the contact point and tangentially to the bottom. Further these particles are not affected by any forces due to the pressure inside the jet is near the atmospheric one. This means that the particles in the jet move inertially. Hence, all parameters of the spray jet are determined by the characteristics of the flow in the jet root region.

Let us assume that the body shape is given in the dimensionless variables by the function $f(x)$ where $f(0) = 0$, $f'(0) = 0$. Then the asymptotic behaviour of the free surface, $y = \eta(x,t)$, near the right-hand side contact point, $x = a(t)$, $y = 0$, can be written as

$$\eta(x,t) = f(a(t)) - t - A(t)\sqrt{x - a(t)} + \cdots \tag{3}$$

where the function $A(t)$ must be found together with $a(t)$. The inner solution in the jet root region allows us to find the jet thickness $\delta(t)$ as

$$\delta(t) = \frac{\pi}{16}\frac{A^2(t)}{\sqrt{1 - \dot{a}^2(t)}}. \tag{4}$$

Dot stands for the time derivative. It is of importance that just after the escape of the shock wave onto the free surface, $t \to T+0$, the jet thickness is small and increases then with time. Correspondingly, the mass of the liquid $2Q(t)$, which leaves the main volume at the instant t is equal to $2\dot{a}(t)\delta(t)$. The factor 2 is due to there is two jets in the plane case.

In the leading order as $M \to 0$, the vertical component of the liquid particle velocity can be neglected, compared to the horizontal one $U(x,t)$, and the jet characteristics are given in the parametrical form

$$x = 2\dot{a}(\tau)(t - \tau) + a(\tau),$$

$$U = 2\dot{a}(\tau),$$

$$h = \delta(\tau) \mid 1 - 2\frac{\ddot{a}(\tau)}{\dot{a}(\tau)}(t - \tau) \mid^{-1}, \tag{5}$$

$$S = -1 + 2\dot{a}(\tau)f'(a(\tau))(t-\tau) + f(a(\tau)) - \tau.$$

where τ is the non-dimensional parameter, $T < \tau < t$. Here $M^2 h(x,t)$ is the jet thickness, the equation $y = MS(x,t)$ describes the shape of the upper boundary of the jet. In the axisymmetrical case, the formulae (5) remain be valid except of the equation for the jet thickness. This equation now takes the form

$$h(x,t) = \delta(\tau) \mid 1 - 2\frac{\ddot{a}(\tau)}{\dot{a}(\tau)}(t - \tau) \mid^{-1} \tag{6}$$

$$\times \left[1 + 2\frac{\dot{a}(\tau)}{a(\tau)}(t - \tau)\right]^{-1}$$

where x is the radial coordinate. Analysis of the jet geometry was presented earlier [8]. In the present paper we are concerned with the integral characteristics of the spray jets generated under the liquid-solid impact. We shall determine the asymptotic behaviours of the jet energy and the jet mass as $t \to \infty$.

KINETIC ENERGY AND MASS OF THE SPRAY JET IN THE PLANE CASE

The kinetic energy of the jet K_j is given as

$$K_j = \frac{1}{2}\varrho_0 c_0^2 L^2 M^2$$

$$\times \int_{a(t)}^{x_*(t)} \int_0^{h(x,t)} [U^2(x,t) + O(M^2)]\, dy\, dx$$

where $x = x(t,\tau)$, $x_*(t) = x(t,T)$, L is a half of the contact region width at the end of the supersonic stage ($L = RM$ for a parabolic contour), ϱ_0 is the liquid density. In the leading order as $M \to 0$, we obtain

$$K_j = \frac{1}{2}\varrho_0 L^2 V^2 \int_{a(t)}^{x_*(t)} U^2(x,t)h(x,t)\, dx + \cdots$$

It is convenient to change the integration variable for τ and to take into account that

$$dx = x_\tau(t,\tau)\, d\tau.$$

Using (5), we get

$$hx_\tau = -\delta(\tau)\dot{a}(\tau),$$

$$K_j = 2\varrho_0 L^2 V^2 \left[\int_T^t \delta(\tau)\dot{a}^3(\tau)\, d\tau + O(M^2)\right].$$

The formula (4) makes it possible to obtain the expression for the jet energy, which does not contain any characteristics of the jet

$$K_j = \frac{\pi}{8}\varrho_0 L^2 V^2 \int_T^t \frac{A^2(\tau)\dot{a}^3(\tau)\,d\tau}{\sqrt{1-\dot{a}^2(\tau)}} + \cdots \tag{7}$$

The last integral is regular for finite times t and tends to infinity as $t \to \infty$. In order to prove this statement, we should notice that the solution of the problem (2) tends to the Wagner solution for the incompressible liquid model as $t \to \infty$. This means that the asymptotic behaviour of the liquid flow for large times does not depend on the process history and can be found using the incompressible liquid model only. Therefore, the pressure distribution over the contact region is given as

$$p(x,0,t) = \frac{a(t)\dot{a}(t)}{\sqrt{a^2(t)-x^2}} \tag{8}$$

$$(\mid x \mid < a(t)),$$

and the vertical velocity $v(x,0,t)$ of the free surface, $\mid x \mid > a(t)$, $y = 0$, as

$$v(x,0,t) = \frac{\mid x \mid}{\sqrt{x^2 - a^2(t)}} - 1 \tag{9}$$

when $t \to \infty$ [2].
The equation (9) allows us to find the asymptotics of the function $A(t)$ for large times

$$A(t) = \frac{\sqrt{2a(t)}}{\dot{a}(t)} + \cdots$$

For the blunt-body impact the velocity $\dot{a}(t)$ of the contact region expansion vanishes with time. Hence, the asymptotic behaviour of the integrand in (7) is

$$\frac{A^2(t)\dot{a}^3(t)}{\sqrt{1-\dot{a}^2(t)}} = 2a(t)\dot{a}(t) + \cdots \tag{10}$$

as $t \to \infty$. In the blunt-body case, we have that $a(t) = O(t^\alpha)$ as $t \to \infty$ where $0 < \alpha < 1$. Thus

$$a(t)\dot{a}(t) = O(t^{2\alpha-1})$$

and the integral in (7) tends to infinity as $t \to \infty$. This means that the asymptotic behaviour of the jet kinetic energy $K_j(t)$ as $t \to \infty$ is determined by the asymptotics of the integrand. Taking (10) into account, we obtain

$$K_j(t) = \frac{\pi}{8}\varrho_0 L^2 V^2 a^2(t) + \cdots \tag{11}$$

as $t \to \infty$.
The kinetic energy of the main bulk of the liquid $K_m(t)$ is defined in the dimensionless variables by the formula

$$K_m(t) = \frac{1}{2}\varrho_0 V^2 L^2 \int_{-\infty}^{0}\int_{-\infty}^{\infty} (\phi_x^2 + \phi_y^2)\,dx\,dy.$$

The velocity potential $\phi(x,y,t)$ is approximately harmonic function in the lower half-plane $y < 0$ for large times. Taking into account the Green's second indentity and the boundary conditions in (2), we find

$$K_m(t) = -\frac{1}{2}\varrho_0 V^2 L^2 \int_{-a(t)}^{a(t)} \phi(x,0,t)\,dx + \cdots$$

The potential distribution over the contact region is given by the incompressible liquid model as $t \to \infty$

$$\phi(x,0,t) = -\sqrt{a^2(t) - x^2} + \cdots$$

Therefore,

$$K_m(t) = \frac{\pi}{4}\varrho_0 V^2 L^2 a^2(t) + \cdots \tag{12}$$

On the other hand, the energy $E(t)$, which is necessary to apply to the entering body to compensate the hydrodynamic force $F(t)$ and to conserve a constant velocity of penetration V, is

$$E(t) = \varrho_0 V^2 L^2 \int_0^t F(t)\,dt$$

where

$$F(t) = \int_{-a(t)}^{a(t)} p(x,0,t)\,dx.$$

For large times

$$F(t) = \pi a(t)\dot{a}(t) + \cdots$$

that follows from (11). Therefore, we have got

$$E(t) = \frac{\pi}{2}\varrho_0 V^2 L^2 a^2(t) + \cdots \qquad (13)$$

asymptotically as $t \to \infty$.
The equations (11), (12), (13) give the final equality

$$E(t) = K_m(t) + 2K_j(t) + \cdots$$

which is asymptotically valid for large times. Thus, for an arbitrary blunt-body shape a half of the energy, lost by the entering body, is concentrated in the bulk of the flow and the another half does in the spray jets.
The jet mass $M_j(t)$ is defined as

$$M_j(t) = \varrho_0 M^2 L^2 \int_T^t Q(\tau)\, d\tau.$$

The asymptotic behaviour of $M_j(t)$ as $t \to \infty$ can be found in the same manner as it was done above and we get

$$M_j(t) = \frac{\pi}{8}\varrho_0 M^2 L^2 \int_T^t \frac{a(\tau)\, d\tau}{\dot{a}(\tau)} + \cdots$$

Let us assume that $a(t) = kt^\alpha$, $k > 0$, $0 < \alpha < 1$, then

$$M_j(t) = \frac{\pi}{16\alpha}\varrho_0 M^2 L^2 t^2 + \cdots,$$

$$K_j(t) = \frac{\pi}{8}k^2 \varrho_0 V^2 L^2 t^{2\alpha} + \cdots$$

as $t \to \infty$. The average velocity of the jet $V_{av}(t)$, which is defined by

$$K_j = \frac{1}{2} M_j V_{av}^2,$$

is equal approximately to

$$V_{av}(t) = \sqrt{2\alpha} k c_0 t^{-2(1-\alpha)}$$

for large times. It can be seen that $M_j(t)$ and $K_j(t)$ grow in time, but $V_{av}(t)$ vanishes. The integral characteristics of the spray jet are useful to estimate the damage caused by this jet impact onto ship structures.

KINETIC ENERGY AND MASS OF THE SPRAY SHEET IN THE AXISYMMETRICAL CASE

The kinetic energy of the spray sheet is given as

$$K_s(t) = \frac{1}{2}\varrho_0 c_0^2 L^3 M^2 \times$$

$$\int_0^{2\pi}\int_{a(t)}^{x_*(t)} \left(\int_0^{h(x,t)} U^2(x,t)\, dy \right) x\, dx\, d\theta + \cdots$$

as $M \to 0$. Here L is the radius of the contact region at the end of the supersonic stage, x is the radial coordinate, y is the vertical coordinate, θ is the angular coordinate, $x_*(t) = x(t,T)$, ϱ_0 is the liquid density. We obtain

$$K_s(t) = \pi \varrho_0 V^2 L^3 \int_{a(t)}^{x_*(t)} U^2(x,t) x\, dx + \cdots$$

Inserting (4)-(6) into the integral, one can write

$$K_s(t) = \frac{\pi^2}{4}\varrho_0 V^2 L^3$$

$$\times \int_T^t \frac{A^2(\tau) a(\tau) \dot{a}^3(\tau)\, d\tau}{\sqrt{1 - \dot{a}^2(\tau)}} + \cdots \qquad (14)$$

In contrast to the plane case, there is not any method to calculate the functions $a(t)$, $A(t)$ in the axisymmetrical case. But we can assume that for large times the flow of a slightly compressible liquid will be approximately the same as in the incompressible liquid model. Within the framework of the incompressible liquid model the axisymmetrical water-entry problem was solved by Schmieden [9]. His results allow us to find that

$$A(t) = \frac{2}{\pi}\frac{\sqrt{2a(t)}}{\dot{a}(t)} + \cdots,$$

$$\phi(x,0,t) = -\frac{2}{\pi}\sqrt{a^2 - x^2} + \cdots \qquad (15)$$

$$p(x,0,t) = \frac{2}{\pi}\frac{a\dot{a}}{\sqrt{a^2 - x^2}} + \cdots$$

$$(|\, x \,| < a(t)),$$

as $t \to \infty$. Inserting (15) into (14) and taking into account that the speed of the contact spot expansion $\dot{a}(t)$ vanishes in time, we get the asymptotics of $K_s(t)$ as $t \to \infty$

$$K_s(t) = \frac{2}{3}\varrho_0 V^2 L^3 a^3(t) + \cdots$$

The kinetic energy of the main bulk of the liquid $K_{am}(t)$ is defined in the dimensionless variables by

$$K_{am} = \pi \varrho_0 V^2 L^3 \int_{-\infty}^{0} dy \int_0^{\infty} (\phi_x^2 + \phi_y^2) x \, dx.$$

The last formula can be rewritten using the Green's second identity and the boundary condition on both the free surface $x > a(t)$, $y = 0$, and the contact spot, $0 < x < a(t)$, $y = 0$, for large times as

$$K_{am} = -\pi \varrho_0 V^2 L^3 \int_0^{a(t)} \phi(x, 0, t) x \, dx + \cdots$$

With the help of (15) we find

$$K_{am}(t) = \frac{2}{3}\varrho_0 V^2 L^3 a^3(t) + \cdots$$

We have found that asymptotically

$$K_{am}(t) \approx K_s(t)$$

as $t \to \infty$.
The body energy $E_a(t)$ lost under the penetration is calculated in the same manner as in the plane case and is equal to

$$E_a(t) = \frac{4}{3}\varrho_0 V^2 L^3 a^3(t) + \cdots$$

as $t \to \infty$. Therefore,

$$E_a(t) \approx K_{am}(t) + K_s(t)$$

for large times.
The liquid mass $M_s(t)$ leaving the main liquid volume with spray sheet is

$$M_s(t) = 2\pi \varrho_0 M^2 L^3 \int_T^t a(\tau) Q(\tau) \, d\tau.$$

Taking (4) into account, we find the exact formula

$$M_s(t) = \frac{\pi^2}{8}\varrho_0 M^2 L^3 \int_T^t \frac{A^2(\tau)\dot{a}(\tau)a(\tau)}{\sqrt{1 - \dot{a}^2}} \, d\tau.$$

When $a(t) = kt^\alpha$, $0 < \alpha < 1$, the asymptotics of $M_s(t)$ as $t \to \infty$ is given as

$$M_s(t) = \varrho_0 M^2 L^3 \frac{k t^{2+\alpha}}{\alpha(\alpha + 2)} + \cdots$$

In the case the curvature of the axisymmetrical body R is different from zero and infinity, we have $\alpha = \frac{1}{2}$, $k = 3^{\frac{1}{2}}$, $L = RM$, $t = t'V/(M^2 R)$, and the last formula gives

$$M_s(t) = \frac{3^{\frac{1}{2}} 4}{5}\varrho_0 R^3 \left(\frac{t'V}{R}\right)^{\frac{5}{2}} + \cdots$$

For example, if $V = 6m/sec$, $R = 5m$ then $M_s(0.01sec) = 13.6kg$ and $M_s(0.1sec) = 4320kg$. Correspondingly, in the plane case

$$M_j(t) = \frac{\pi}{8}\varrho_0 R^2 \left(\frac{t'V}{R}\right)^2 + \cdots$$

The last formulae can be derived also using the incompressible liquid model when $t'V/R \to 0$.

CONCLUSION

It was proved in the present paper that a half of the energy lost by the body under its penetration the water surface transfers to the kinetic energy of the spray jet generated under the impact. The another half of the body energy is concentrated in the bulk of the liquid. Those proportions have to be understood in an asymptotical sense as $t \to \infty$. This means, for example, that the energy taken away by the acoustic wave initiated under the water impact can also grow in time. But in any case this part of energy will be much less than the kinetic energy of the jet.
It is worth to notice that the fact that only a half of the entering body energy transfers to the kinetic energy of the main liquid flow was known many years ago [10]. But to calculate the kinetic energy of spray jets was quite difficult. In order to do this, it is necessary to describe the process of the jet formation. The process is dependent of the liquid compressibility.

That is why the calculation of the jet energy became possible only after the developing acoustic theory of the water impact.

REFERENCES

1. Von Karman, Th., "The Impact on Seaplane Floats during Landing," NACA Tech. Notes 321, 1929.
2. Wagner, H., "Uber Stoss- und Gleitvorgange an der Oberflache von Flussigkeiten," ZAMM, Vol. 12, 1932, pp. 193-215.
3. Sedov, L.I., "On Impact of a Solid Body Floating on Surface of Incompressible Liquid," Tr. Tsentr. Aerodin. Inst. 187, 1934.
4. Korobkin, A.A. and Pukhnachov, V.V., "Initial Stage of Water Impact," Ann. Rev. Fluid Mech., Vol. 20, 1988, pp. 159-185.
5. Korobkin, A.A., "Acoustic Approximation in the Problem of Penetration of a Blunt Contour into Ideal Fluid," Zh. Prikl. Mekh. Tekh. Fiz., Vol. 4, 1992, pp. 48-54.
6. Korobkin, A.A., "Blunt-Body Impact on a Compressible Liquid Surface," J. Fluid Mech., Vol. 244, 1992, pp. 437-453.
7. Korobkin, A.A., "Blunt-Body Impact on the Free Surface of a Compressible Liquid," J. Fluid Mech., Vol. 263, 1994, pp. 319-342.
8. Korobkin, A.A., "Formation of High-Speed Jets under a Liquid-Solid Impact," Lavrentyev Institute of Hydrodynamics, (unpublished).
9. Schmieden, C., "Der Aufschlag von Rotations-korpern auf eine Wasseroberflache," ZAMM, Vol. 33, 1953, pp. 147-151.
10. Fabula, A.G., "Ellipse-Fitting Approximation of Two-Dimensional Normal Symmetric Impact of Rigid Bodies in Water," Fifth Midwestern Conference on Fluid Mechanics, Univ. of Michigan, 1957, pp. 299-315.

Application of the Flux-Vector Splitting Method to Capture Shock Waves and Calculate Pressure in Ship Slamming

X. Wang, Z. Huang, C. Hsiung
(Technical University of Nova Scotia, Canada)

ABSTRACT

The Flux-Vector Splitting Method is applied to analyze the air flow between the ship bottom and the water surface during slamming. As the air is trapped between the ship bottom and the water surface, it is compressed and escapes from the bottom edges. As the bottom is close to the water surface, the velocity of the air flow at the edges approaches the local sonic speed and an air-water mixture is generated. This flow of air-water mixture is simplified as a free air jet. When the bottom touches the water surface, an air cushion is trapped. A mathematical model is established for this trapped air cushion, where the shock waves are numerically captured and the slamming pressure is calculated. For solving the nonlinear governing equations, a numerical scheme is derived based on the Flux-Vector Splitting method. Computed results of slamming pressure and captured shock waves are presented and discussed.

NOMENCLATURE

$[B]$ = Jacobian matrix of $\vec{F}$.
c_0 = velocity of sound in the undisturbed air.
c_a = velocity of sound in the air.
e = total energy per unit volume of gas.
$\vec{F}$ = flux vector of the air flow.
g = gravitational acceleration.
h = thickness of the air layer.
H = initial dropping height.
l = half breadth of the ship hull.
$m = \rho u$, mass flow rate.
M = mass of the ship hull per unit length.
M_a = Mach number of air.
p = pressure in the air flow.
p_0 = pressure of the undisturbed air.
$[T]$ = eigenvector matrix of $[B]$.
t = time variable.
$u(x,t)$ = horizontal velocity of air flow.
$V(t)$ = falling velocity of the ship hull.
γ = gas constant.
ϵ = internal energy per unit mass of gas.
$\zeta = \xi + i\eta$, complex variable.
$\bar{\zeta} = \bar{\xi} + i\bar{\eta}$, nondimensional complex variable.
η_w = elevation of the water surface.
λ_i = eigenvalues $i = 1, 2, 3$
ρ = density of air.
ρ_0 = density of undisturbed air.
ρ_w = density of water.

INTRODUCTION

Ship slamming is an important field of study in ship hydrodynamics. Both experimental and theoretical investigations have been conducted. Although the theoretical prediction of slamming has been improved significantly, the estimation of slamming load on a flat bottom is still mainly based on empirical formulae [1], [2], [3].

The existing theoretical approaches are mostly applicable to wedge-shaped bodies with large deadrise angles [4] [5]. For a ship section with a flat bottom, the theoretical modelling of slamming is complicated. There are two physical phenomena involved. One is the compressible air flow between the hull and the water surface; and the other is the mixture of air and water in the

region of the outboard extremities of the hull.

Experiments have been carried out both for flat bottoms and for wedges by dropping models from various heights onto a calm water surface [1] [6]. It has been observed that before the hull bottom touches the free surface, a compressible air layer(CAL) is developed between them and the air in the CAL escapes from two edges of the bottom. When the hull bottom touches the free surface, a trapped air cushion(TAC) is formed. The experiments verified that the maximum slamming pressure on the flat bottom is caused by the compressed air flow [1] [6]. The slamming pressure in the CAL was analyzed by using the method of characteristics, and the deformation of the water surface was taken into account [6] [8]. It has also been noticed that shock waves exist and travel from the edges to the center of the flat hull bottom with a local velocity of sound in the TAC [6]. In Verhagen's work [6], the mathematical model used in the TAC was different from that used in the CAL. He assumed that at the moment the TAC was formed, the downward velocity of the water surface under the hull bottom was only a function of time and was independent of the space-coordinate. In his method, the air flow was neglected in the horizontal direction and the pressure was thus space-independent. Furthermore, the shock waves could not be caught with this approach.

When the air escapes from the edge of the bottom, the air and water is mixed. This situation is complicated to describe with proper mathematical models. Both Johnson [9] and Verhagen assumed that the flow is like a uniform jet. A simplified model was introduced in [7]. The flow was considered as a free air jet (FAJ). The pressure in the jet was constant and equal to the atmospheric pressure.

The Flux-Vector Splitting Method [10] is applied in this paper to solve the nonlinear equations for slamming pressure on a flat ship bottom. This method is applicable to solve the governing equations for the cases of the CAL, TAC and FAJ. A numerical scheme is devised on the basis of this method. The characteristic method gives exact solutions if computation is carried out along the characteristic curves on which the Riemann invariants are constants. However, the numerical computation is complicated, since the characteristic meshes determined by the solution in the numerical calculation are not regular, so that when the CAL becomes very thin and the pressure increases rapidly some numerical errors are easily introduced. Although the finite difference schemes are convenient to use from the point of view of mesh design and numerical computation, the numerical scheme has to be designed based on the propagation of pressure waves in order to obtain a convergent result, especially in the case of the existance of discontinuities. The Flux-Vector Splitting Method has the advantages of both the characteristics and finite difference methods. The pressure and velocity are traced along the characteristic directions, the regular finite difference meshes can be simply devised, and the numerical solutions are stable and convergent.

A mathematical model is established for the air flow in the CAL and in the TAC. The similar finite difference scheme in the CAL is applied to capture the shock waves and to calculate the maximum slamming pressure in the TAC. Using this model, the shock waves travelling inside the TAC can be simulated. The pressure and velocity in the TAC are both time and space dependent. The velocity of air flow in the FAJ can also be calculated with the Flux-Vector Splitting method.

THE FLUX-VECTOR SPLITTING METHOD

Governing Equations

In order to simplify the slamming problem for a flat bottom ship, it is necessary to make the following assumptions:

1. A two-dimensional ship section with a flat bottom of $2l$ in width is falling downward at a velocity $V(t)$, as shown in Fig. 1. The flat bottom keeps parallel to the horizontal surface.
2. The Cartesian coordinate system is set up as shown in Fig. 1. The ship bottom is symmetrical about the center-line, which is the y axis, positive upwards. The x-axis is along the surface of the calm water toward the right, The origin is located at the intersection of the calm water surface and the center line of the flat bottom.

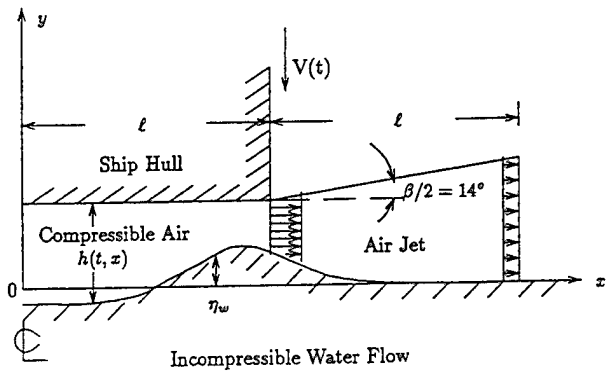


Figure 1: Air flow in CAL and FAJ

3. In the region of the mixing air and water, the flow of the mixture is assumed to be a free air jet with the following conditions:

$$\begin{aligned} &\text{for } x > l \\ &p = p_0 \\ &\rho = \rho_0 \\ &c_a = c_0 \end{aligned}$$

4. The thicknesses of the air layer between the water surface and the bottom is small, therefore it is reasonable to assume that $h/l << 1$, and that the air motion between the flat-bottom and the free-surface can be described as the one-dimensional, compressible, invicid and unsteady flow.

5. When $M_a = 0.3$, the rate of change of density $\partial\rho/\rho$ is approximately equal to 0.05. If $M_a > 0.3$, the air flow is considered to be compressible. Therefore the pressure can be expressed as

$$p = (\gamma - 1)(e - \frac{\rho u^2}{2}) \tag{1}$$

6. The viscous effect is neglected.

Based on above assumptions, the governing equations can be derived from the conservation laws of mass, momentum and energy:

$$\begin{cases} \frac{\partial(\rho h)}{\partial t} + \frac{\partial(\rho u h)}{\partial x} &= 0 \\ \frac{\partial u}{\partial t} + u\frac{\partial u}{\partial x} &= -\frac{1}{\rho}\frac{\partial p}{\partial x} \\ \frac{\partial e}{\partial t} + u\frac{\partial e}{\partial x} &= -\frac{1}{\rho}\frac{\partial(pu)}{\partial x} \end{cases} \tag{2}$$

where h is the thickness of the air flow.

Substituting the continuity equation into the momentum and energy equations, equation (2) becomes

$$\begin{cases} (\rho)_t + (\rho u)_x &= -\frac{\rho}{h}(h_t + uh_x) \\ (\rho u)_t + (\rho u^2 + p)_x &= -\frac{\rho u}{h}(h_t + uh_x) \\ e_t + [(e+p)u]_x &= -\frac{e}{h}(h_t + uh_x) \end{cases} \tag{3}$$

where e is the total energy per unit volume,

$$e = \rho\epsilon + \frac{\rho u^2}{2} \tag{4}$$

and ϵ is the internal energy per unit mass.

The one-dimensional system of conservation laws (3) can be expressed by

$$\vec{U}_t + \vec{F}_x = \vec{U} \cdot R \tag{5}$$

where $\vec{U}$ is a vector and $\vec{F}$ is the so-called "flux vector",

$$\vec{U} = \begin{bmatrix} \rho \\ m \\ e \end{bmatrix} \tag{6}$$

$$\vec{F}(U) = \begin{bmatrix} m \\ \frac{m^2}{\rho} + p \\ \frac{(e+p)m}{\rho} \end{bmatrix} \tag{7}$$

where $m = \rho u$, and

$$R = -\frac{1}{h}(h_t + uh_x) \tag{8}$$

Substituting (4) into (1), the flux vector $\vec{F}(U)$ can be rewritten as

$$\vec{F}(U) = \begin{bmatrix} m \\ (\gamma-1)e + \frac{(3-\gamma)m^2}{2\rho} \\ \frac{\gamma em}{\rho} - \frac{(\gamma-1)m^3}{2\rho^2} \end{bmatrix} \tag{9}$$

can be expressed as a homogeneous function of $\vec{U}$:

$$\vec{F} = [B]\vec{U} \tag{10}$$

where

$$[B] = \frac{\partial \vec{F}(U)}{\partial \vec{U}} \tag{11}$$

and

$$\frac{\partial \vec{F}(U)}{\partial \vec{U}} = \begin{bmatrix} 0 & 1 & 0 \\ \frac{(\gamma-3)u^2}{2} & (3-\gamma)u & \gamma-1 \\ (\gamma-1)u^3 - \frac{\gamma e u}{\rho} & \frac{\gamma e}{\rho} - \frac{3(\gamma-1)u^2}{2} & \gamma u \end{bmatrix}$$

is the Jacobian matrix.

The eigenvalues of $[B]$ are

$$\begin{cases} \lambda_1 = & u \\ \lambda_2 = & u + c_a \\ \lambda_3 = & u - c_a \end{cases} \tag{12}$$

Equation (3) can be expressed as:

$$\vec{U}_t + [B]\vec{U}_x = \vec{U} \cdot R \tag{13}$$

Flux-Vector Splitting

In the flux vector splitting method, the governing equations are expressed in terms of the flux vector $\vec{F}$. The flux vector is then split into two subvectors $\vec{F}_+$ and $\vec{F}_-$. $\vec{F}_+$ corresponds to the positive eigenvalue of the Jacobi matrix, and $\vec{F}_-$ is associated with the negative eigenvalue. According to the directions of pressure wave propagation, which can be determined by the eigenvalues, the backward finite difference is devised for $\vec{F}_+$ and the forward finite difference for $\vec{F}_-$.

If $[T]$ is the eigenvector matrix of $[B]$, and $[T]^{-1}$ is the inverse matrix of $[T]$, then

$$[T]^{-1}[B][T] = [\Lambda] = \begin{bmatrix} \lambda_1 & 0 & 0 \\ 0 & \lambda_2 & 0 \\ 0 & 0 & \lambda_3 \end{bmatrix} \tag{14}$$

$[T]$ and $[T]^{-1}$ can be derived as:

$$[T] = \begin{bmatrix} 1 & \alpha_0 & \alpha_0 \\ u & \alpha_0(u+c_a) & \alpha_0(u-c_a) \\ \frac{u^2}{2} & \alpha_0(\frac{u^2}{2} + uc_a + \frac{c_a^2}{\gamma-1}) & \alpha_0(\frac{u^2}{2} + uc_a - \frac{c_a^2}{\gamma-1}) \end{bmatrix}$$

$$[T]^{-1} = \begin{bmatrix} 1 - \frac{u^2}{2}\gamma_1 c_a^{-2} & \gamma_1 u c_a^{-2} & -\gamma_1 c_a^{-2} \\ \beta_0(\frac{\gamma_1}{2}u^2 - uc_a) & \beta_0[c_a - \gamma_1 u] & \beta_0\gamma_1 \\ \beta_0(\frac{\gamma_1}{2}u^2 + uc_a) & -\beta_0[c_a + \gamma_1 u] & \beta_0\gamma_1 \end{bmatrix}$$

where $\alpha_0 = \frac{\rho}{c_a\sqrt{2}}$, $\beta_0 = \frac{1}{\rho c_a\sqrt{2}}$ and $\gamma_1 = \gamma - 1$.

Based on the stability analysis [10], λ_l ($l = 1, 2, 3$) can be further split into λ_l^+ and λ_l^-. Then the backward and forward finite difference operators can be properly chosen according to the eigenvalues of λ_l^+ and λ_l^-, i.e.

$$\lambda_l = \lambda_l^+ + \lambda_l^- \qquad l = 1, 2, 3 \tag{15}$$

where λ_l^+ and λ_l^- are given as follows:

$$\lambda_l^+ = \frac{\lambda_l + |\lambda_l|}{2} \quad and \quad \lambda_l^- = \frac{\lambda_l - |\lambda_l|}{2} \tag{16}$$

From (15) and (16), $[\Lambda]$ can be split into two matrices:

$$[\Lambda] = [\Lambda^+] + [\Lambda^-] \tag{17}$$

where

$$[\Lambda^+] = \begin{bmatrix} \lambda_1^+ & 0 & 0 \\ 0 & \lambda_2^+ & 0 \\ 0 & 0 & \lambda_3^+ \end{bmatrix} \tag{18}$$

and

$$[\Lambda^-] = \begin{bmatrix} \lambda_1^- & 0 & 0 \\ 0 & \lambda_2^- & 0 \\ 0 & 0 & \lambda_3^- \end{bmatrix} \tag{19}$$

Since $[B] = [T][\Lambda][T]^{-1}$, we have

$$\begin{aligned} \vec{F} &= [T][\Lambda][T]^{-1}\vec{U} \\ &= [T][\Lambda^+][T]^{-1}\vec{U} + [T][\Lambda^-][T]^{-1}\vec{U} \end{aligned} \tag{20}$$

$\vec{F}$ is split into

$$\vec{F} = \vec{F}^+ + \vec{F}^- \tag{21}$$

where

$$\vec{F}^+ = [T][\Lambda^+][T]^{-1}\vec{U} \tag{22}$$

$$\vec{F}^- = [T][\Lambda^-][T]^{-1}\vec{U} \tag{23}$$

Substituting (21) into (5),

$$\vec{U}_t + \vec{F}_x^+ + \vec{F}_x^- = \vec{U} \cdot R \tag{24}$$

In order to obtain a stable solution numerically, $\vec{F}_x^+$ has to be approximated by the backward finite difference and $\vec{F}_x^-$ by the forward finite difference [10].

Second-Order Scheme

In order to develop a second-order finite difference scheme, the MacCormack approach [12] is employed in the numerical computation. The backward difference is used in the predictor step, and the foreward difference is used in the corrector step.

The predictor step is

$$\overline{U_j^{n+1}} = U_j^n - \Delta t \frac{\nabla F_j^n}{\Delta x} + R_h \tag{25}$$

where Δt and Δx are the lengths of time step and spatial step, respectively, and

$$R_h = -U_j^n(h_j^n - h_j^{n-1} + \Delta t u_j^n \frac{\nabla h_j^n}{\Delta x}) \tag{26}$$

where

$$\nabla F_j = F_j - F_{j-1} \tag{27}$$

and the corrector step is

$$U_j^{n+1} = \frac{1}{2}(\overline{U_j^{n+1}} + U_j^n) - \frac{1}{2}\Delta t \frac{\overline{\Delta F_j^{n+1}}}{\Delta x} + R_h \tag{28}$$

where

$$\Delta F_j = F_{j+1} - F_j \tag{29}$$

The flux term F can be splitted into F^+ and F^- which are assosiated with λ^+ and λ^-, respectively. If the λ is positive, we choose the backward operator, otherwise we choose forward operator. By splitting the flux term F, the finite difference equations become:

$$\overline{U_j^{n+1}} = U_j^n - \Delta t \frac{\nabla (F^+)_j^n}{\Delta x} - \Delta t \frac{\Delta (F^-)_j^n}{\Delta x} + R_h \tag{30}$$

$$U_j^{n+1} = \frac{1}{2}(\overline{U_j^{n+1}} + U_j^n) - \frac{1}{2}\Delta t \frac{\nabla (F^+)_j^n - \nabla^2 (F^+)_j^n}{\Delta x} - \frac{1}{2}\Delta t \frac{\Delta (F^-)_j^n - \Delta^2 (F^-)_j^n}{\Delta x} + R_h \tag{31}$$

where

$$\nabla^2 F_j = F_j - 2F_{j-1} + F_{j-2} \tag{32}$$

and

$$\Delta^2 F_j = F_{j+2} - 2F_{j+1} + F_j \tag{33}$$

The Flux-Vector Spliting method splits the flux term into components in order to effectively use the extrapolation procedures along the directions of the characteristic lines. The finite difference grids are used in numerical computations so that the approach can take advantages of the characteristic method and the finite difference method effectively.

The above finite difference schemes will be applied to solve the slamming problems regarding to the air flow in the CAL and the FAJ.

COMPRESSIBLE AIR LAYER

When the bottom is just starting to drop down, the Mach number, M_a, is very small. At this stage, the air flow between the ship bottom and the water surface is considered incompressible. The initial thickness and velocity of the compressible air flow can be obtained from the motion of the incompressible flow. In order to solve

the governing equations for the flow in the CAL, the flow in the FAJ, the elevation of water surface, and the interaction of water and air flow, the initial conditions and boundary conditions have to be defined.

Effect of the Free Air Jet

Two approaches can be used to calculate the pressure under the bottom. The first approach is to start computation from the center ($x = 0$) of the bottom to the edge ($x = l$); The other approach is from the center to the end of the air jet ($x = 2l$). In the first approach, there is a singularity of pressure at the edge of the plate, and we have to specify $u(t, l)$ by extrapolation as a boundary condition. However, using the second approach, we can obtain results in the CAL, and also efficiently calculate the distribution of velocity in the air jet.

The air flow at the bottom edge escapes with the maximum velocity under the bottom. The behavior of air flow at the bottom edge is quite similar to the compressed flow at the throat of a nozzle. Therefore we consider the flow as a free air jet.

The property of the free air jet has been studied by Birkhoff [14]. The jet, from Ref. [7], expands with an angle $\beta = 25^o$ to 30^o. The pressure in the FAJ is taken to be the atmospheric pressure. The distribution of velocity in the FAJ is determined in Ref. [7] as:

$$u(t,x) = \frac{h(t,l)u(t,l)}{h(t,l) + (x-l)tan(\beta/2)} \qquad (34)$$

We calculate the distribution of velocity with the Flux-Vector Splitting method, and the equation (34) is employed to provide the boundry condition of velotity at $x = 2l$.

Deformation of the Water Surface

During slamming, the pressure on the water surface will make a wave elevation which will also affect the air flow between the bottom and the water surface. The water surface elevation can be obtained according to Wehausen & Laitone [13] for the slamming problem in which the impact pressure lasts a very short time span:

$$\frac{\partial \eta_w}{\partial t}|_{y=0} = -\frac{1}{\pi \rho_w} \int_0^t \int_{-l}^{l} \frac{\frac{\partial p}{\partial \xi}}{x-\xi} d\xi d\tau \qquad (35)$$

where η_w is the elevation of water surface and ρ_w is the water density.

Interaction of Water-Surface and Air Flow

Since h, $\frac{\partial h}{\partial x}$ and $\frac{\partial p}{\partial x}$ affects the numerical results in computation, we have to consider the effect of the water surface to the compressed air layer, and vice versa.

The relation between the thickness of air layer h and the elevation of water surface is:

$$-\frac{\partial h(t,x)}{\partial t} = V(t) + \frac{\partial \eta_w(t,x)}{\partial t} \qquad (36)$$

The pressure in the compressed air layer under the bottom causes the water surface to deform, and $\frac{\partial p}{\partial x}$ directly affects the shape of water surface. A singularity exists at the bottom edge, thus $\frac{\partial p}{\partial x}$ must be set to zero in order to obtain a meaningful wave elevation.

Initial Conditions

When the hull is just starting to drop , the air flow is incompressible. The bottom dropping velocity V can be found from:

$$M \cdot dV/dt = M \cdot g - \int_{-l}^{l} (p - p_0) dx \qquad (37)$$

If we consider that the air is initially incompressible, the pressure distribution can be obtained [6] as follows:

$$p(t,x) - p_0 = \rho_0 \frac{l^2 - x^2}{h^2} \{ (\frac{dh}{dt})^2 - \frac{h}{2} \frac{d^2h}{dt^2} \} \qquad (38)$$

where the thickness of air layer $h(t) = h_0 - \int_0^t V(t)dt$. The sonic speed can be derived as:

$$\frac{c_a(0,x)}{c_0} = 1 + \frac{r-1}{2}\frac{l^2V_0^2}{h_0^2c_0^2}\cdot$$
$$(1-\frac{x^2}{l^2})\{1+\frac{1}{2}\frac{h_0}{V_0^2}(\frac{dV}{dt})_{t=0}\} \quad (39)$$

The initial distribution of velocity in the CAL can be expressed as:

$$\frac{u(0,x)}{c_0} = \frac{xV_0}{h_0c_0} \quad (40)$$

In computation, we start to compute the compressible air flow in the CAL as the Mach number $u(0,l)/c_0$ reaches 0.1.

Boundary Conditions

Since the air flow is symmetrical about the y axis, the boundary conditions at the center of the bottom, $x = 0$, are:

- $u(t,0) = 0,$
- $\frac{\partial\rho(t,0)}{\partial x} = 0$
- $\frac{\partial c_a(t,0)}{\partial x} = 0$

At the end of the jet, $x = 2l$

- $u(t,2l) = \frac{h(t,l)u(t,l)}{h(t,l)+(x-l)tan(\beta/2)}$
- $\rho(t,2l) = 1.29 \quad kg/m^3$
- $c_a(t,2l) = 330.0 \quad m/sec$

To avoid specifying $u(t,l)$ at the boundary $x = l$, the computation domain is set to be within $0 < x < 2l$. Then $u(t,2l)$ can be reasonally assigned at the end of the free air jet. The length of the air jet is taken as $l = 0.2\ m$.

SHOCK WAVES IN THE TAC

When the ship bottom just touches the water surface a trapped air cushion (TAC) is formed. In the TAC, the compressible air is trapped in between the water surface and the bottom where the shock waves may be formed. This phenomenon has been discussed by Verhagen [6]. He showed that the shock waves travel from the edges to the center of the bottom with the local sonic velocity. The experimental results also clearly showed that the maximum slamming pressure occurs in the traped air cushion. In this paper, we use numerical method to reveal this phenomenon.

A mathematical model is established for capturing shock waves in the TAC. At the instant when the air is trapped in between the dropping bottom and the water surface, the distribution of velocity can be assumed to be zero except at the edge where Therefore we can assume that the initial conditions for the air flow in the air cushion $(-l < x < l)$ are:

- $\rho(0,x) = \rho(t_1,x)$
- $c_a(0,x) = c_a(t_1,x)$
- $u(0,x) = 0$

where the t_1 is the time when the bottom touches the water surface.

The boundary conditions are:

- $\rho(t,\pm l) = \rho_0$
- $c_a(t,\pm l) = c_0$
- $u(t,\pm l) = \mp c_0$

where $\rho_0 = 1.29\ \ kg/m^3$ and $c_0 = 330\ \ m/sec.$

The thickness of the compressed air layer h is assumed to be constant. Therefore the effect of h can be neglected from (3).The governing equations for the compressed air flow in the trapped air cushion are:

$$\begin{cases} \frac{\partial\rho}{\partial t} + \frac{\partial(\rho u)}{\partial x} & = 0 \\ \frac{\partial(\rho u)}{\partial t} + \frac{\partial(\rho u^2+p)}{\partial x} & = 0 \\ \frac{\partial e}{\partial t} + \frac{\partial[(e+p)u]}{\partial x} & = 0 \end{cases} \quad (41)$$

The Flux-Vector form of the governing equation is

$$\vec{U}_t + \vec{F}_x = 0 \quad (42)$$

The second-order finite difference equations are as follows,

the predictor step:

$$\overline{U_j^{n+1}} = U_j^n - \Delta t \frac{\nabla (F^+)_j^n}{\Delta x} - \Delta t \frac{\Delta (F^-)_j^n}{\Delta x} \quad (43)$$

the corrector step:

$$U_j^{n+1} = \frac{1}{2}(\overline{U_j^{n+1}} + U_j^n) - \frac{1}{2}\Delta t \frac{\nabla (F^+)_j^n + \nabla^2 (F^+)_j^n}{\Delta x} - \frac{1}{2}\Delta t \frac{\Delta (F^-)_j^n + \Delta^2 (F^-)_j^n}{\Delta x} \quad (44)$$

The shock waves can be numerically captured based on this mathematical model, and the maximum slamming pressure can also be computed.

NUMERICAL RESULTS

A flat bottom ship section is adopted in computation, with $m/\rho_w l^2 = 0.5$ and $l = 0.2$ m. The numerical schemes have been developed for the flow computation in the CAL, FAJ, and TAC. $\frac{dt}{dx} = 0.4$ and the Courant number $(c_a + u)\frac{dt}{dx} = 0.95$ are chosen in all computations.

The initial normal atmospheric conditions are taken as follows:

- $g = 9.81 \quad m/sec.^2$
- $\rho_0 = 1.29 \quad kg/m^3$
- $\rho_w = 10^3 \quad kg/m^3$
- $p_0 = 10^5 \quad N/m^2$
- $c_a = 330.0 \quad m/sec.$
- $\gamma = 1.4$

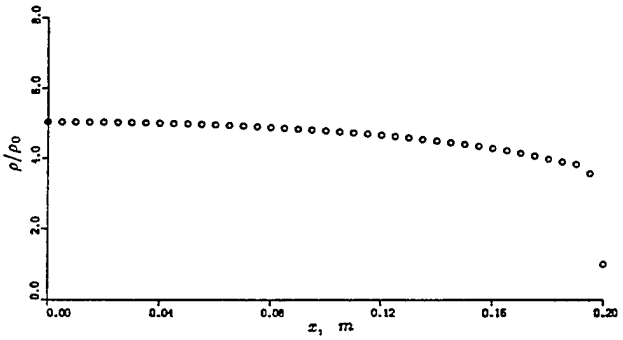


Figure 2: Distribution of density in CAL

At the instant when the bottom almost touches the water surface, the numerical results are obtained for the case of the dropping height $H = 0.4$ m. As shown in Fig. 2, the distribution of density in the CAL is decreased from the center to the edge of the bottom along the x-direction. The air is gradually compressed from the edge to the center.

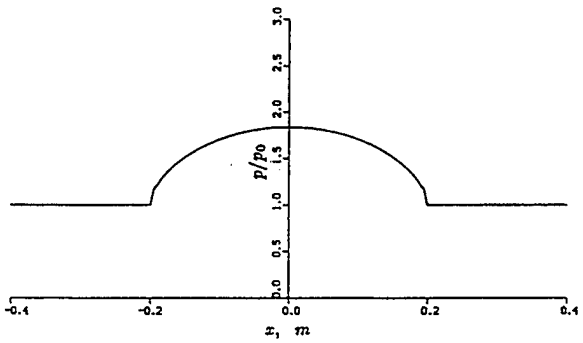


Figure 3: Distribution of pressure in CAL

In Fig. 3, the distribution of air pressure in the CAL is presented. The maximum pressure along x-axis is at the center of the bottom before the TAC is formed. In the FAJ, the pressure keeps as the constant atmospheric pressure. The pressure

is increased from the edge to the center of the bottom along the x-axis.

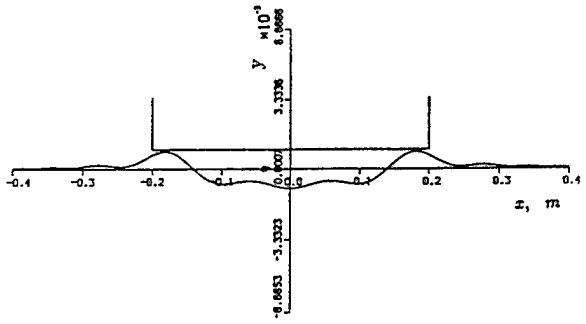


Figure 4: Water surface under a ship flat bottom

The water elevation caused by the air pressure is shown in Fig. 4. The locations of the wave crests are controlled by $\partial p/\partial x$. In the region of the air jet, the pressure is constant, therefore $\partial p/\partial x = 0$. If $\partial p/\partial x$ is not set to zero near the edge of the bottom in the region of the air jet, the wave crests may move into the region of the air jet.

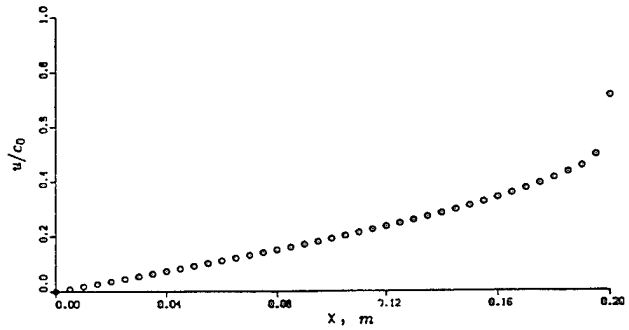


Figure 5: Distribution of velocity in CAL

The distribution of velocity in the CAL is shown in Fig. 5. The velocity of air flow is increased from $x = 0$ to $x = l$. At the edge of the bottom, the velocity of air flow increases with time. When the bottom is dropping close to the crests of the water wave, the velocity of air flow at the edges approaches to the sonic speed. The velocity of air flow increases very rapidly near the edge of the bottom.

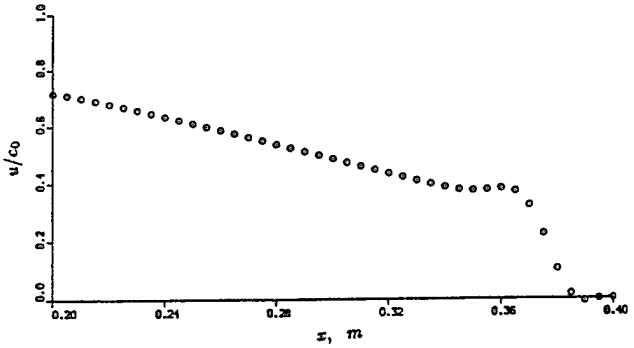


Figure 6: Distribution of velocity in FAJ

The distribution of velocity of air flow in the region of the free air jet is shown in Fig. 6. With such distribution of velocity, reasonable numerical solutions in the CAL can be obtained.

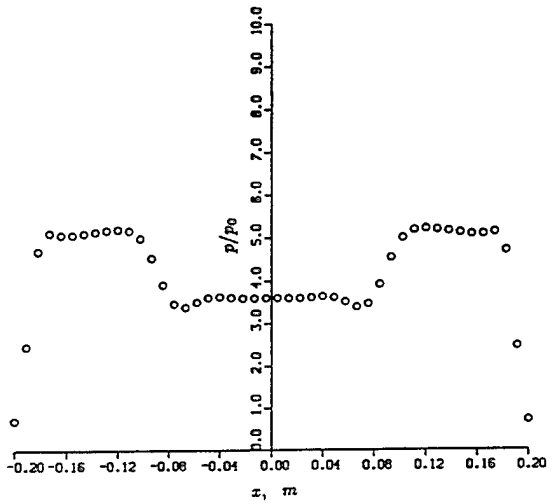


Figure 7: Captured shock waves in TAC

The distribution of pressure in the TAC is shown in Fig. 7. It is clearly demonstrated that a shock wave is formed in the TAC. The time history of the slamming pressure in the TAC is shown in Fig. 8. The shock wave travels from edges to the center of the bottom. It also shows the spatial distribution of the slamming pressure. The

local maximum pressure is built up as the shock wave passes there. The numerical results indicates that the maximum slamming pressure in TAC is almost a constant along the bottom. This property has been experimentally discovered by Verhagen [6].

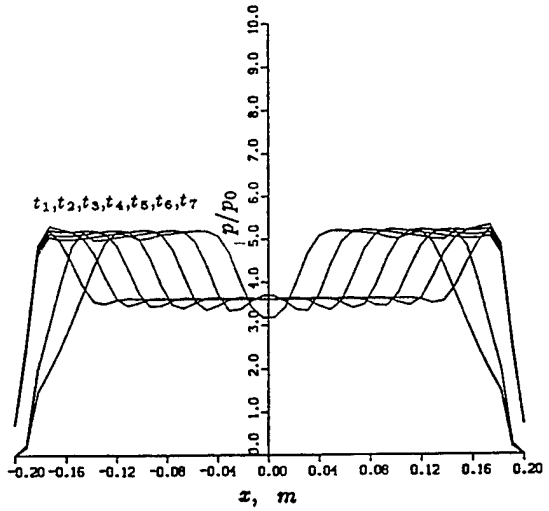


Figure 8: Travelling shock waves for $H = 0.4\ m$

The numerical results for the dropping heights $H = 0.2\ m$ and $0.04\ m$ are shown in Fig. 9 and 10. The slamming pressure in these two cases shows the same property as that for $H = 0.4$ in Fig. 8. The maximum pressure is proportional to the initial dropping height.

The maximum slamming pressure which we obtained from the computation and Verhagen's experimental results [6] are given in Table 1. It can be seen from Table 1 that the numerical results of maximum slamming pressure are quite agreeable with the experimental results.

H	Maximum Pressure p/p_0	
	Experimental [6]	Numerical
0.4 m	3.5—5.2	5
0.04 m	1.2—1.25	1.6

Table 1: Comparison of maximum slamming pressure

Fig. 11 shows the variation of the maximum slamming pressure versus the mass of the ship section. We find that the maximum slamming pressure is sensitive to the mass only when M is very small.

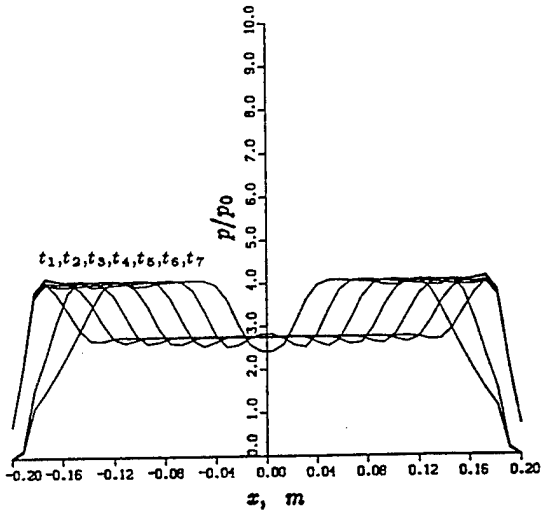


Figure 9: Travelling shock waves for $H = 0.2\ m$

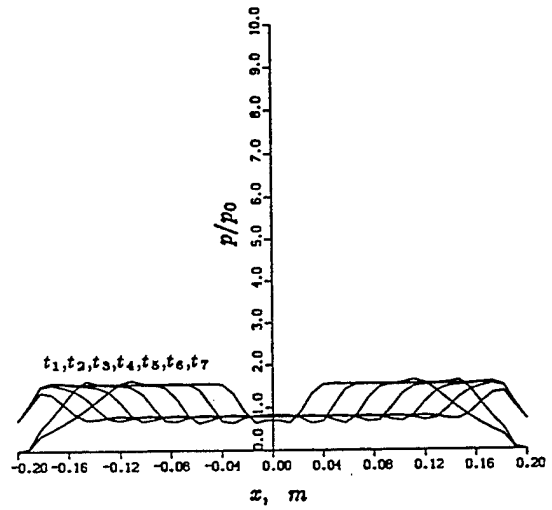


Figure 10: Travelling shock waves for $H = 0.04\ m$

CONCLUSIONS

The slamming impact of a ship with a flat bottom has been analyzed and investigated with the Flux-Vector Splitting Method. The mathematical models for the flow in the compressible air layer and trapped air cushion are illustrated. Numerical scheme based on the Flux-Vector Splitting method is derived. Using this

method, the slamming pressure has been computed and the shock waves have been numerically captured.

The velocity is increased from zero to the local sonic speed along the x-axis with time when the bottom approaches the crests of the water surface. The performance of the compressed air in the passage between the bottom and the water surface is similar to the compressible flow in a nozzle. The mixture of air and water at the bottom edge is simplified as a free air jet. The velocity of air in the jet decreases along the x-axis from the local sonic speed at the bottom edge and increases with time before the bottom touches the water surface. The pressure, density and sonic speed are taken as the atmospheric conditions in the FAJ.

Interaction between the air flow and the water surface in the CAL and FAJ has been considered. A water wave under the ship bottom is produced. The deformed wave surface responds to the pressure variation along the bottom of the ship hull.

Shock waves travelling from the edge to the center of the bottom have been computed. The maximum slamming pressure attains a constant value during the period when the shock waves are formed and travel to the center. It is important to calculate the maximum slamming pressures and to determine their locations for structural analysis. The maximum slamming pressures which we obtained from the dropping heights $H = 0.4\ \ m$, $H = 0.2\ \ m$ and $H = 0.04\ \ m$ are reasonable compared with the experimental results.

The Flux-Vector Splitting method has been shown to be a powerful tool to solve slamming problems. This method has the advantages of both the characteristic method and the finite difference method. Thus the effects caused by shock waves in the trapped air cushion on the ship structure can be effectively invastigated.

ACKNOWLEDGEMENT

This research work was supported by the Natural Sciences and Engineering Research Council of Canada, and the Defense Research Establishment Atlantic, Canada.

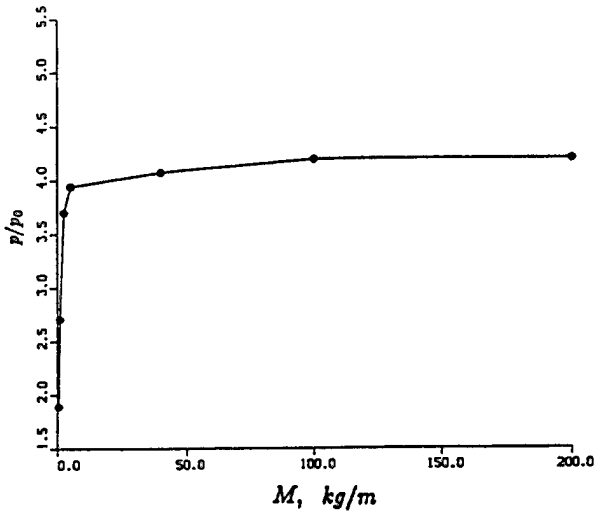


Figure 11: Effect of Falling Mass

References

[1] Chuang, S. L., "Experiments on Slamming of Wedge-Shaped Bodies", Journal of Ship Research, Vol. 11, No. 3, September 1967.

[2] Chuang, S. L., "Experiments On Flat Bottomed Slamming", Journal of Ship Research., Vol. 10, No. 1, Mar. 1966.

[3] Ochi, M. K. and Motter, L. E., "Prediction of Slamming Characteristics and Hull Reponses for Ship Design", Trans. SNAME, Vol. 81, 1973, pp. 144-176.

[4] Greenhow, Martin and Lin, Woei-Min, "Numerical Simulation of Nonlinear Free Surface Flows Generated by Wedge Entry and Wavemaker Motions", Proceeding of the Fourth International Conference on Numerical Ship Hydrodynamics, Washington, D. C., 1985

[5] Dobrovol'skaya, Z., "On Some Problems of Similarity Flow of Fluid with a Free Surface", Journal of Fluid Mech., Vol. 36, 1969

[6] Verhagen, J. H. G., "The Impact of a Flat Plate on a Water Surface", Journal of Ship Research, Vol. 11, No. 4, Dec. 1967.

[7] Koehler, Buford R., Kettleborough, Jr. and Kettleborough C. F., "Hydrodynamic Impact of a Falling Body upon a Viscous Incompressible Fluid", Journal of Ship Research, Vol. 21, Sept. 1977.

[8] Huang, Z. and Hsiung, C. C., "A Hydro-aero-Elastic Model for Slamming of a 2-D Ship Hull Section", The Sixth International Workshop on Water Waves and Floating Bodies, Woods Hole, Massachusetts, April 14-17, 1991.

[9] Johnson, R. S., "The Effect of Air Compressibility in a First Approximation to the Ship Slamming Problem", Journal of Ship Research, Vol. 12, No. 1, 1968.

[10] Steger, Joseph L. and Warming, R. F., "Flux Vector Splitting of the Inviscid Gas dynamic Equations with Application to Finite-Difference Methods", Journal of Computational Physics, Vol. 40 , 1981, pp. 263—293.

[11] Liepmann, H., W. and Roshko A., Elements of Gasdynamics, John Wiley and Sons, New York, 1957.

[12] MacCormack, W. and Baldwine, B. S., "A Numerical Method for Solving the Navier-Stokes Equations with Application to Shock Boundary Layer Interactions", AIAA Paper, 75—1, Pasadena, Calif., 1975.

[13] Wehausen, J. V. and Laitone E. V., "Surface Waves", Encyclopedia of Physics, Vol. 9, Springer-Verlag, Berlin, 1960.

[14] Birkhoff, G., and Zarantonello, "Jet Wakes and Cavities", Applied Mathematics and Mechanics, Vol. 2, 1957, pp. 298-313.

Interaction of Bubbles with Turbulent Flow: Particle Tracking and Flow Field Characterization

A. Kolaini, S. Sinha, V. Rajendran
(University of Mississippi, USA)

ABSTRACT

An experiment has been designed to investigate the dynamic behavior of bubbles injected into water jets. It has been observed that if bubbles remain in the center of the jet, they break into two or more smaller bubbles. If an adult bubble is injected into the high shear-induced regions of the jet, acoustic re-excitation occurs. 3-D stereoscopic particle tracking velocimetry (SPTV) and hot wire anemometry were implemented for measuring the flow parameters and resulting bubble response in a turbulent jet. A single bubble was injected into the field where two high-speed video cameras were capturing images of the response of the bubble. The Reynolds number of turbulence, based on the root-mean-square turbulent velocity, and the Taylor lateral microscale, was estimated to be approximately 1200. This leads to a Kolmogorov microscale of about 33 μm. The characterization of the dynamics of bubbles in a turbulent flow field depend on three factors: (1) the estimated integral and micro-length scales; (2) the corresponding Reynolds numbers; and (3) the critical Weber numbers for both bubble distortion and breakup. A critical Weber number was estimated to be 0.52 for an adult bubble re-excitation without breakup and 1.10 for bubble breakup.

1. INTRODUCTION

1.1 Background

Much work has been done in the past on the dynamics of a single air bubble in water subject to various forms of excitation. However, the mechanisms of excitation of a single bubble, or a bubble cloud, by a turbulent pressure field not yet fully understood. In general, the pressure spectrum of a turbulent flow is relatively broad, and there is the possibility that large changes in bubble volume and surface may arise from the small spectral intensity of the pressure at the natural resonance frequency of the bubble.

Some of the earliest studies of noise in the ocean were published in 1948 by Knudson et al. Since then, much progress has been made toward the understanding of ocean ambient noise. We now know that many sources contribute to ocean ambient noise. Some of these bubble-related mechanisms are splash or rain noise (Prosperetti et al., 1989), hail and snow (Crum et al., 1992), breaking waves (Medwin and Daniel, 1990; Loewen and Melville, 1994; Kolaini and Crum, 1994) and capillary waves (Longuet-Higgins, 1993; Kolaini et al., 1994). The noise from these sources is all bubble-related. How a bubble makes noise is a fundamental question that has important consequences in many fields, especially in oceanography.

In the ocean, bubbles can be distorted or deformed by turbulent flow fields created by dynamics of breaking waves and Langmuir circulation. An important scientific question is what role the shape oscillation of bubbles play in monopole acoustic radiations. The linear theory predicts that, the most efficient mechanism that a bubble has for the emission of sound into the far-field is through volume pulsations where the higher modes (surface modes) of oscillations are volume preserving and thus radiate inefficiently. Recently, however, Longuet-Higgins (1989) suggested that volume pulsations might derive energy from the nonlinear coupling of surface and volume modes. Longuet-Higgins (1991) and Ffowcs-Williams and Guo (1991) have debated what effect these surface oscillations have on the

volume pulsations. Longuet-Higgins (1989) predicted that the distortion modes could contribute to the far field sound radiation by producing a monopole radiation of sound at a second order of magnitude. Ffowcs-Williams and Guo used the method of multiple scales to examine the problem. They acknowledged that a transfer of energy from the surface mode to the volume mode occurs at the exact resonance, and that a periodic exchange will occur near resonance. However, they believe that the amount of energy exchanged is so small that no significant sound radiation occurs.

The issue has been much-debated in the acoustics community, because the overwhelming contribution to ambient noise in the ocean is due to bubbles. However, there is a fundamental disagreement about how a bubble produces sound. Therefore, a more complete understanding of the basic physics of sound generation by bubbles is of considerable importance. It is well known that turbulence is a weak radiator of sound. The radiation properties of turbulent flow in water have been shown to be greatly modified by the presence of a small distribution of air bubbles in the turbulence (Crighton and Ffowcs-Williams, 1969). This process may be relevant to underwater sound generation at low and high frequencies.

1.2 Significance of the present work

It has been recently shown that the injection of a single bubble into an axisymmetric fully developed turbulent flow resulted in fission and fusion of the bubble (Kolaini et al., 1992; Kolaini, 1994). The sound produced by bubbles encountering turbulent flow fields depends upon the Reynolds stresses and the mean velocity field. The knowledge of the flow field is of paramount importance for an understanding of sound production mechanisms in a turbulent flow. In this paper we discuss the turbulent flow field characterization of a submerged water jet containing bubbles.

1.3 An assessment of available experimental techniques

In order to study and understand the mechanisms which govern the exchange of energy between the liquid and bubbles, one has to be able to measure velocities in both phases simultaneously. This is an extremely challenging problem since intrusive hot-film probes cannot be used. Non-intrusive point-wise measurement techniques like laser-Doppler velocimeters will also fail to identify much of the interesting physics. Full-field quantitative imaging techniques like Particle Image Velocimetry (PIV), are probably the only methods which may work (Hassan, 1991). These methods rely on optically recording the positions of small tracer particles, along with the bubbles, over several time steps.

Although commercial packages for 2-D PIV are currently available, these cannot capture the essence of the 3-D turbulent structures which play a crucial role in bubble deformation. Therefore, a 3-D adaptation of this technique is needed. Two approaches have generally been used to attain this; namely, (1) holographic imaging, and (2) multi-view stereoscopic imaging. Holographic imaging enables storing 3-D information on one image, but suffers from a reduction in accuracy in depth perception, and the need for elaborate data reduction processes and equipment. Orthogonal stereoscopic imaging can in principle remove both shortcomings, but suffers from restrictions imposed by depth of field limitations of the imaging lenses. A method employing orthogonally acquired holograms, as implemented by Weinstein et al. (1985) does not suffer from depth of field limitations, and can provide very accurate estimates of particle positions. However, the complexity of data reduction effectively rules out this method for analyzing large number of data points over a large number of time steps. Therefore, the present study used the nonholographic stereoscopic technique, which will henceforth be referred to as Stereoscopic Particle Tracking Velocimetry (SPTV).

Although SPTV is simple in principle, and investigators have attempted to use it for different types of flows, an acceptable level of performance has yet to be reached. The main reason for this is that any practical implementation of SPTV ultimately reduces to a complex multi-variable optimization problem with many conflicting requirements. With this in mind, the present work focuses on comparing SPTV measurements with hot-film anemometer (HFA) data for turbulent flow in the liquid phase. The range of applicability of each method is discussed in view of unraveling the liquid-bubble interaction physics.

2.0 EXPERIMENTAL SET-UP

A simple experiment was set up that injected bubbles into an axisymmetric, turbulent jet. Fig. 1 shows the schematic of the experimental setup. It consists of two high-speed Kodak Ekta-Pro video cameras and a video digitizer, a three watt Lexel Argon Ion laser, a PC 486, 50 kHz for data and image processing, a

plenum chamber, water tank (62 cm x 62 cm x 3.3 m), a Cole-Palmer peristaltic pump, and a bubble generating mechanism. The plenum chamber contained an interchangable nozzle through which the jet was discharged to the tank. The Cole-Parmer pump was used to pump water at a controlled flow rate into a plenum chamber. The nozzles were replaceable type with diameters ranging from 3.2 mm to 12.4 mm. In this paper, we discuss jets produced by only the 3.2 mm diameter nozzle. SPTV as well as a 2-D TSI cross-wire hot film probe were used to characterize the flow field.

The SPTV technique utilized the high-speed video cameras. This technique enables quantitative, non-intrusive measurements of free turbulent structures containing a bubble. The tracer particles used in the experiment were made of polystyrene (S.G. 1.04) and were 100-200 μ in size. A laboratory syringe pump was used to seed the particles into the jet. The syringe was placed on top of the plenum vertically above the nozzle. The particle injection arrangement was found to impart minimal disturbances to the actual flow.

The Argon Ion laser along with a system of optical lenses and mirrors was used to illuminate the test section with a volume of approximately 1.5 cm (width), 3.0 cm (height), and 2.0 cm (depth). The cameras which consisted of 105 mm Nikon lenses were connected to the Ekta-Pro real time digitizer and the captured images were stored on large-capacity magnetic tapes. A real-time Digital Vision Image grabber was used to grab images and the digitized data were downloaded to a PC-486 microcomputer for further processing. The images were captured at the rate of 2000 frames per second.

3.0 EXPERIMENTAL PROCEDURES

3.1 System calibration

The optical axis of the cameras were set at an angle of 35° with respect to each other. There were focused in the middle of the test section. Spatial calibration of the cameras over the entire test volume was done using reference grid points whose spatial coordinates were known within 2.5 μm. This grid was placed inside the test volume for calibration, using an electronically controlled mechanical positioner capable of 65 μ/step in x, y, and z direction. Fig. 2 shows the photograph of the jet with velocity of 2.2 m/sec. A special colored dye was used to visualize this image. The reference points were photographed in three planes (by moving the grid across the width of the tank). The images were processed much the same way the particles would be processed. The 3-D positions of the reference points (x,y,z) were reconstructed by data reduction equations based on colinearity conditions from the corresponding image coordinates xi_p and yi_p in each camera. Since two cameras were used, four equations were employed for each reference point. These equations are,

$$xA_p = xA_{PP} - f_A \cdot \frac{a_{11}(Xp - X_{OA}) + a_{12A}(Y_P - Y_{OA}) + a_{13A}(Z_P - Z_{OA})}{a_{31A}(X_P - X_{OB}) + a_{32A}(Y_P - Y_{OA}) + a_{33A}(Z_P - Z_{OA})}, \quad (1)$$

$$yA_p = yA_{PP} - f_A \cdot \frac{a_{21A}(Xp - X_{OA}) + a_{22A}(Y_p - Y_{OA}) + a_{23A}(Z_p - Z_{OA})}{a_{31A}(X_p - X_{OB}) + a_{32A}(Y_p - Y_{OA}) + a_{33A}(Z_p - Z_{OA})}, \quad (2)$$

$$xB_p = xB_{PP} - f_A \cdot \frac{a_{11B}(Xp - X_{OB}) + a_{12B}(Y_p - Y_{OB}) + a_{13BA}(Z_p - Z_{OB})}{a_{31B}(X_p - X_{OB}) + a_{32B}(Y_p - Y_{OB}) + a_{33B}(Z_p - Z_{OB})}, \quad (3)$$

and

$$yB_p = yB_{PP} - f_B \cdot \frac{a_{21B}(Xp - X_{OB}) + a_{22B}(Y_P - Y_{OB}) + a_{23B}(Z_P - Z_{OB})}{a_{31B}(X_P - X_{OB}) + a_{32B}(Y_P - Y_{OB}) + a_{33B}(Z_P - Z_{OB})}, \quad (4)$$

where X_{Oi}, Y_{Oi}, Z_{Oi} are coordinates of the projective centers for two cameras. The coefficients a_{ij}, are the elements of 3x3 rotational transformation matrices needed to align the (x,y,z) world coordinates with respect to the two imaging axis. The f_i, is the principal distance, which is the distance between a camera projective center and its principal point. The xi_{PP}, yi_{PP} are coordinates of the principal point where i = A and B indicating camera A and B. The principal point of the camera is the image of lens center formed on the image plane of the camera.

There are nine unknowns for each camera. The unknowns are X_{Oi}, Y_{Oi}, Z_{Oi}, a_{ij}, f_i, xi_{pp}, yi_{pp}. These equations relate the point $P(x_p, y_p, z_p)$ in space to its image coordinates xi_P, yi_P. The first six of the 9 camera parameters are the camera's exterior parameters and the remaining are the interior parameters. These equations were solved simultaneously by employing a non-linear least squares method to get the 9 (converged) camera parameters. Using the camera parameters and the image coordinates, the spatial locations (x,y,z) of the reference points are reproduced. Comparison of these reproduced spatial coordinates with the known object point coordinates (which were measured earlier) revealed a lateral shift in the x,y and z coordinates. The bias errors were caused by multi-media refraction

as a result of viewing through air, water and the glass wall of the tank. These systematic (bias) errors are readily subtracted (Mangla, 1992; Sinha & Kuhlman, 1992) from the reproduced x,y,z coordinates. These procedures completed the calibration of the system. After the calibration, the RMS errors of the coordinates were measured to be 70, 170(depth), and 70 microns in x,y and z directions, respectively. The predicted positions of the particles were, however, significantly less accurate due to additional uncertainties in estimating the particle image coordinates.

3.2 Image and data processing

The determination of image coordinates of white particles on dark background is a trivial task (Fig. 3). After removing some of the non-uniformities of the background, the following steps were used to determine the image coordinates:

1. Particle image thresholding
2. Particle identification and validation.
3. Stereoscopic matching of the particle images in each time step.
4. Particle tracking over subsequent time steps.
5. Calculating the x ,y, z coordinates of particles using the camera parameters bias error correction.
6. Calculating instantaneous velocities.
7. Calculating fluctuating components in x, y, z directions.
8. Calculating Reynolds stress tensor components.

The gray level thresholding was done to enhance the particle images from the surrounding. Size threasholding was performed to facilitate identification and to differentiate particles from background noise. Centroids of the enhanced particle images were determined. The bias errors in the reference points calculated in the calibration stage were interpolated using a multiquadric interpolator on to the centriodal positions of these enhanced particle images. The interpolator parameters were optimized (Sinha & Kuhlman, 1992) during the calibration stage and positions of the same particle were determined in successive image frames. Knowing the initial and final positions of a particle and the elapsed time the instantaneous velocities were estimated,

$$U = \frac{x_f - x_i}{\Delta t},\ V = \frac{y_f - y_i}{\Delta t},\ \text{and}\ W = \frac{z_f - z_i}{\Delta t}.$$

The locations of these velocities were taken as the midpoint between the particle initial and final positions. The velocity vector at any instant is given by $\vec{V} = U\hat{i} + V\hat{j} + W\hat{k}$, where $\vec{V}(x,y,z,t) = \overline{V}(x,y,z,t) + V'(x,y,z,t)$ and

$$\overline{V} = \frac{1}{T}\int_0^T V\,dt = \frac{1}{n\Delta t}\sum_{i=1}^{n} \overline{V}_i \Delta t\,, \qquad (5)$$

where n is the number of time steps and V'(x,y,z,t) is the fluctuating velocity vector. After calculating the mean velocity by Eq. (5) the fluctuating components of velocities were obtained by

$V'(x,y,z,t) = V(x,y,z,t) - \overline{V}(\bar{x},\bar{y},\bar{z})$. Similarly the fluctuating velocity vector is $v' = u'\hat{i} + v'\hat{j} + w'\hat{k}$, and the Reynolds stress tensor component can be estimated by the expression,

$$\overline{u'v'} = \frac{1}{n}\sum_{i=1}^{n} u'_i(\bar{x}, \bar{y}, \bar{z}, i\Delta t)v'_i(\bar{x}, \bar{y}, \bar{z}, i\Delta t)\cdot$$

Similar expressions can be written for the other five components of the symmetric stress tensor, $\overline{u'^2}$, $\overline{u'w'}$, $\overline{v'^2}$, $\overline{v'w'}$, $\overline{w'^2}$.

3.3 Automatic Matching and Tracking of Particles

Due to recent advancements in imaging techniques data processing of images with numerous numbers of particle is possible. With the nozzle velocity at 2.2 m/s, the flow field was photographed at 2000 frames/sec using Kodak Ekta-Pro high-speed video cameras. Typical particle images containing a bubble of 1.1 mm radius are shown in four consecutive but not sequential frames in Fig. 3. The particle images in each frame were digitized, and processed to obtain estimates of the particle image centriods. Overlapping particle images, identified by their relatively larger sizes, were excluded to reduce errors. However, this also resulted in significant data dropout. This procedure was followed by matching (determining corresponding images of a particle in the other view at the same time step) and tracking (determining correspondence through the next and subsequent time steps). An algorithm was developed (Rajendran, 1993) to automatically match and track using geometrical search criteria. Non-unique matches were examined for tracks in the next step, failing which they were discarded. About 50 to 70 particle pairs were identified each time step. This resulted in about the same number of velocity vectors, obtained by dividing particle displacements by the time interval. Data for 100 frames (50 ms total) were processed.

4. RESULTS AND DISCUSSIONS

4.1 Bubble deformation

Prediction of the bubble deformation and breakup in a turbulent flow field is a formidable problem, primarily because of the inherent theoretical and experimental difficulties in treating turbulent two-phase flows.

The detailed quantitative characterization of bubble deformation due to interactions with high Reynolds number flow fields is an ongoing research. In this paper we discuss the effect of the overall velocity field on bubble deformation and subsequent acoustic emissions utilizing both the SPTV and HFA velocity field measurement techniques. The SPTV technique provides us with the nearly instantaneous spatial velocity field measurement, while the HFA technique can be useful in long-time temporal averaging of the fluctuating velocity components.

Before injecting bubbles into the turbulent flow field, the distribution of mean velocity, mean shear, turbulent intensities, and length scales of the water jet were measured at a distance of x/D ~ 10 by means of 2-D hot film anemometer. At 10 diameter from the nozzle, the flow is in a fully developed turbulent region. The mean horizontal velocity distribution in the jet is shown in Fig. 4. Görtler (1942) developed a theory for round submerged jets with velocity profile of (Schlichting, 1979)

$$\frac{\bar{U}}{U_{max}} = \left(1 + \frac{\xi^2}{4}\right)^{-2}, \qquad (6)$$

where $\xi = 15.2\,\frac{r}{x}$, and $U_{max} = 7.4\,(J/\rho)^{1/2}/x$. The term J is the jet momentum, ξ is the similarity variable, ρ is the density of the water, U_{max} is the maximum velocity at the center of the jet, and x is the distance from the nozzle exit. A comparison of the mean horizontal velocity measurements with Eq. (6) shows a very good agreement. The radial distribution of turbulent fluctuating velocities are shown in Fig. 5. The size of the mixing region is related to the integral length-scale L_x while the time-scale is related to the local mean shear $\frac{\partial U}{\partial r}$. The product of these two quantities is shear velocity. Since the rate of production of turbulent kinetic energies (TKE) is proportional to the mean shear, it seems likely that a relation exists between the turbulent intensity and the shear velocity. Therefore, the turbulent intensity can be expressed as,

$$\frac{u'}{U_{max}} \simeq \text{const.}\left(\frac{x}{D}\right)\left|\frac{\partial(U/U_{max})}{\partial(r/D)}\right|. \qquad (7)$$

The measured turbulent intensity is in good agreement with Eq. (7) providing the value of the constant in Eq. (7) to be about 0.035. The turbulent intensity has a maximum value at a region where shear stress is maximum and vice versa. At $r \simeq R$, the mean velocity is small and the local turbulent fluctuation of velocities is relatively large. This region of the flow field plays an important role in the adult bubble deformation and subsequent acoustic radiation.

The longitudinal and transverse rms turbulent intensities, u' and v', shown in Fig. 5 have the same general trend and order of magnitude. Therefore, it is reasonable to assume that the flow field under consideration is homogeneous and isotropic and that the eddies in question maybe in the inertial (-5/3 power) subrange. This assumption is unlikely to be valid in an overall sense though it may be reasonable locally or for the high wavenumber (small) eddies which are of primary interest. using these assumptions, the lateral Taylor microscale can be estimated to be (Hinze, 1975)

$$\lambda_g \cong \sqrt{2\,\overline{u'^2}\Big/\overline{\left(\frac{\partial u'}{\partial r}\right)^2}}. \qquad (8)$$

The value of λ_g measured at x/D ~ 10 and $r \cong R$ is about 0.23 cm. The Reynolds turbulence number $Re_{\lambda g} = \frac{\sqrt{\overline{u'^2}}\lambda_g}{\upsilon}$ based on the root-mean-square turbulent velocity and lateral microscale, λg, is equal to about 1200. The Kolmogorov microscale η is therefore given by

$$\eta = \lambda_g\,(15)^{-1/4}\,(Re_\lambda)^{-1/2}, \qquad (9)$$

and equal to 3.3×10^{-3} cm. The life time of the turbulent Kolmogorov eddies can be estimated to be around 71 μsec using $\tau_\eta = \eta/\sqrt{\overline{u'^2}}$. The life-time of the Taylor microscale, $\tau_{\lambda g} = \lambda_g/\sqrt{\overline{u'^2}}$ is estimated to be about 5.1 msec. Consider a bubble of a radius 1.1 mm with a resonance frequency *f* given by (Minnaert, 1933),

$$f = \frac{1}{2\pi R}\sqrt{\frac{3\gamma P_0}{\rho}}, \qquad (10)$$

where R is the radius of the bubble, P_0 is the atmospheric pressure, ρ is the water density, and γ is the ratio of the specific heats and equals to 1.4

for adiabatic processes. Therefore, the resonance frequency of this size bubble is 3.3 kHz and is very close to the measured value (3.18 kHz). The bubble oscillation period falls between eddies with a life-time ranging, $\tau_\eta < \tau < \tau_{\lambda g}$. This implies that the bubble will have enough time to respond to dynamic fluctuations. The eddies with length scales greater than the Kolmogorov scale and much smaller than the Taylor microscale may be responsible for bubble deformation and surface mode oscillations. These observations are consistent with Longuet-Higgins (1992) prediction that the shape oscillations of bubbles will necessarily be accompanied by the emission of a monopole component of radiated sound. The analysis of splitting of drops and bubbles due to the capillary and dynamic pressures were made by Kolmogorov (1949), and Hinze (1975). Kolmogorov concluded that the fate of a bubble depends on two nondimensional ratios, the Weber number defined as

$$We = \frac{\rho \overline{v^2}}{\sigma / 2R} \tag{11}$$

and ratio of length scales $\frac{2R}{\eta}$, where σ is surface tension in dyn/cm. For our case $2R >> \eta$, and for high Reynolds numbers the wave numbers of the energetic eddies and the dissipation range wave numbers are widely separated. Under these circumstances, Kolmogorov's universal equilibrium theory postulates an inertial subrange at the lower end of the equilibrium range where energy transfer through the spectrum is independent of viscosity and where

$$\overline{v^2} = 2.0\,(2\varepsilon R)^{2/3}\,, \tag{12}$$

where ε is the energy dissipation per unit mass and time. Under these conditions Eq. (11) will have a new form,

$$(We)_{critical} = 6.35\left(\frac{\rho}{\sigma}\,\varepsilon^{2/3}\,R^{5/3}\right). \tag{12}$$

Since the small-scale structure of turbulence at a large Reynolds number is always approximately isotropic (Fig. 5), therefore,

$$\varepsilon = 15\upsilon\,\frac{\overline{u'^2}}{\lambda_g^{\,2}}\,, \tag{13}$$

where λ_g is defined by Eq. (8). To obtain the lowest Weber umber at which bubble deformation and subsequent acoustic radiation will occur, we use the maximum Reynolds shear stress $\rho\overline{u'^2}$ in a region where the surface mode of the bubble may have coupled with volume pulsation as was suggested by Longuet-Higgins (1992). The resulting critical Weber number is about 0.52. The critical Weber number at which bubble breakup will occur is about 1.10 and is slightly smaller than values predicted by Sevik and Park (1973). It should be noted that these two Weber numbers, 0.51 and 1.10, were calculated based upon the values of the high shear-induced region and center of the jet, respectively.

4.2 Post-processing the SPTV data

In order to determine the details of the flow that can be practically unraveled by SPTV, experiments were conducted in a circular water jet at about 10 diameters downstream of a 3.2 mm diameter nozzle. Earlier acoustic measurements (Kolaini, 1994) showed that adult bubbles injected in this region acoustically can be re-excited without breakup.

Since the obtained velocity vectors were rather sparse, and unevenly distributed in space, a Multiquadric 3-D spatial interpolator (Sinha and Kuhlman, 1992) was initially used. However, this resulted in smoothing the velocity profiles unrealistically. Therefore a different approach was followed here which involved dividing the measurement volume into small regular control volumes. The velocity vectors over the entire 100 time steps were assigned to which ever control volume they fell in. The vectors within each control volume were then averaged, and the average value assigned to the center of the control volume. Deviations of the instantaneous velocities from the time-averaged means indicated the fluctuating components. The fluctuating components were therefore calculated for each control volume, every time step. If a control volume had more than one velocity vector at a given time step, the fluctuating components were averaged. On the other hand, several control volumes had no assigned velocity vectors over many time steps. These facts were taken into account for computing turbulent Reynolds stresses and scales. In order to simulate traversing the jet across a diameter with a hot-film probe, some of the control volumes were selected as concentric rings, centered about the jet axis. It is to be noted, however, that the results obtained this way depend heavily on the choice of control volumes.

Fig. 6 shows profiles of the mean U, V and W velocities normalized with respect to the maximum centerline velocity at this location. As expected, the cross-stream velocities are nearly zero, while the streamwise velocity approximates

the familiar Görtler profile (Eq. 6). Error propagation in the SPTV processes were accentuated in the estimates of the Reynolds stress components. Within limits of experimental uncertainties the three shear stresses were found to have the same order of magnitude as those measured with the HFA.

The principal advantage of SPTV over point-wise velocity measurement techniques is that it enables estimation of the vorticity field. Since the vorticity estimates are dependent on the spatial density of the data (Sinha and Kuhlman, 1992), data for all 100 frames were pooled. The resulting vorticity field therefore contained a range of vortices with time scales from 0.5 to 50 ms. Figs. 7a-c show contours of the streamwise vorticity component Ω_X, and the spanwise components Ω_Y and Ω_Z, respectively on the central vertical (X-Y) plane. Contour levels of 750, 500, 250 and 0 s^{-1} are shown. Positive and negative values indicate the sense of rotation. Vortical structures outside this range were found to be extremely small, for the total 50 msec period, and have therefore not been shown. As expected, the streamwise component is seen to be significantly weaker, while Ω_Y and Ω_Z values are comparable. Since errors in estimates of the Z-velocity (depth direction) were highest compared to the other two components, the Z-vorticity estimates are the most accurate.

The vortical structure depicted in Fig. 7c can be assumed to represent eddies of varying strengths and sizes which existed during the 50-ms period. If a bubble is present in the flow field, it will be acted upon by the vortices. Severe bubble deformation can occur if the bubble falls in the junction of two strong counter rotating vortices (i.e. a strong strain field). The average spacings of the centers of vortices, as estimated from the Ω_Z contour plots ranged between 3.2 mm to 7 mm (from -750 s^{-1} to 750 s^{-1}), depending upon the vorticity strength. These spacings indicate the approximate diameter of a bubble which may be deformed by a vortex of a given strength. It is interesting to note that the minimum spacing is at about 3.2 mm corresponding to a vortex strength of 500 s^{-1}. This is therefore the most densely spaced vortical structure within the spatial and temporal resolution of the SPTV measurements. This diameter compares extremely well with the lateral microscale. The time scale of these eddies is 2 ms, which is about one half the time scale associated with the lateral microscale. The eddies responsible for re-excitation of the bubble are however much smaller than those measured by the lateral microscale. However, the data density in the present SPTV measurements was insufficient to resolve these.

Photographs of deforming bubbles in the flow field (Kolaini et al. 1994) have indicated that bubbles usually undergo severe deformations without breakup prior to re-excitation. Not every bubble of a particular size displays this behavior. It is speculated at this point that the re-excitation or breakup of the bubble can be directly attributed to the presence of a vortical structure of the appropriate strength and size. However, this can only be verified by simultaneously imaging the bubbles with the particles with faster rate (i.e. 6000 f/s) which is currently under consideration.

5. CONCLUSIONS

Preliminary SPTV experiments and HFV measurements of a turbulent jet were performed. Both methods showed that at x/D ≈ 10, the mean velocity field closely approximates the fully developed Görtler profile. The turbulent stresses were found to be about the same in all directions, thereby confirming the isotropicity of the turbulence. It has been shown that an adult bubble injected into a fully developed turbulent field experiences a severe deformation. This deformation (since the damping is very small) leads to bubble fission and fusion. The scaling analyses using both HFA and SPTV show eddies responsible for these phenomena fall between Taylor the lateral and Kolmogorov microscales.

The adult bubble fission and fusion by turbulent pressure fluctuations depend upon a critical Weber number. In the case of an adult bubble fusion, the critical number estimated to be around 0.52 while it is 1.10 for a bubble fission. The estimated critical Weber number for bubble break-up is slightly lower than the value predicted by Sevik and Parker (1973).

Even though, we used both the HFA and the SPTV techniques to estimate eddies responsible for deformation of a bubble, we were unable to measure eddies with life times less than 2 ms using the SPTV technique. The eddies responsible for re-excitation of the bubble are much smaller than those measured by SPTV. The primary sources of error in the SPTV data were in identifying the image coordinates of particle centroids (Sinha et al. 1994), and in the implied interpolations due to data pooling. The experimental facility, and the data processing software are currently being modified to address these shortcomings. Additionally, efforts are currently underway to image the flow and the bubbles simultaneously with faster rates (6000 fps).

ACKNOWLEDGMENT

The authors would like to thank Bogdan Marinescu for assisting in data collection using HFA. This work was supported partially by the Office of Naval Research.

REFERENCES

1. Crighton, D.G. and Ffowcs-Williams, J.E. , "Sound generated by turbulent two-phase flows," Journal of Fluid Mechanics, Vol. 36, 1969, p. 585.

2. Crum, L.A., Roy, R.A., and Prosperetti, A., "The underwater sounds of precipitation," Naval Research Reviews, 1992, pp. 2-12.

3. Ffowcs-Williams, J.E., and Gue, Y.P., "On resonant nonlinear bubble oscillations," Journal of Fluid Mechanics, Vol. 224, 1991, pp. 507-529.

4. Görtler, H., "Berechnung von Aufgaber der freien Turbulenz auf Gund eines Neuen Naherungsansatzes," Z. Angew. Math. Mech., Vol. 22, 1942, pp. 244-254.

5. Hassan, Y.A., Canaan, R.E., Blanckard, T.K., and Seeley, C.H., Jr., "Simultaneous velocity measurements of both components of two phase flow using particle tracking velocimetry,' American Society of Mechanical Engineers Fluid Engineering Division-128, 1991, pp. 85-99.

6. Hinze, J.O., Turbulence, 2nd ed., McGraw-Hill, New York, 1975.

7. Knudsen, S.J., Alford, R.S., and Emling, J.W., "Underwater ambient noise," Journal of Marine Ressearch, Vol. 7, 1948, pp. 410-429.

8. Kolaini, A.R., Markewicz, K., and Rajendran, V.P., "Acoustic characterization of a bubble injected into a fully developed turbulent flow field," Journal of the Acoustical Society of America, Vol. 93 No. 4, Part.2, 1993.

9. Kolaini, A.R., Crum, L.A., and Roy, R.A., "Bubble production by capillary-gravity waves," Journal of the Acoustical Society of America, Vol. 95 No. 4, 1994, pp. 1913-1921.

10. Kolaini, A.R., and Crum, L.A., "Observations of underwater sound from laboratory breaking waves and the implications concerning ambient noise in the ocean," Journal of the Acoustical Society of America, in press.

11. Kolaini, A.R., "Nonlinear coupling between surface mode and volume mode pulsations of a bubble in the turbulent flow field," to be submitted to Journal of the Acoustical Society of America.

12. Kolmogorov, A.N., "On the disintegration of drops in a turbulent flow," DoKlady Akad. Nauk., SSSR, Vol. 66, 1949, p. 925.

13. Loewen, M.R., and Melville, W.K., "An experimental investigation of the collective oscillations of bubble plumes entrained by breaking waves," Journal of the Acoustical Society of America, Vol. 95 No. 3, 1994, pp. 1329-1343.

14. Longuet-Higgins, S.M., "Monopole emission of sound by asymmetric bubble oscillation" Parts I and II, Journal of Fluid Mechanics, Vol. 201, 1989, pp. 525-565.

15. Longuet-Higgins, S.M., "Bubble noise mechanisms - A review," Natural Physical Sources of Underwater Sound, Kluwer, Dordrecht, Netherlands, 1993.

16. Longuet-Higgins, S.M., "Resonance in nonlinear bubble oscillations," Journal of Fluid Mechanics, Vol. 224, 1991, pp. 531-549.

17. Longuet-Higgins, S.M., "Nonlinear damping of bubble oscillations by resonant interaction," Journal of the Acoustical Society of America, Vol. 91, 1992, pp. 1414-1422.

18. Medwin, H.,and Daniel, A.C., "Acoustical measurements of bubble prediction by spilling breakers," Journal of the Acoustical Society of America, Vol. 88, 1990, pp. 408-412.

19. Mangla, N.L, "On improving the accuracy of stereoscopic particle imaging technique towards estimating the three dimensional vorticity field," M.S. Thesis, University of Mississippi, 1992.

20. Minnaert, M., "On musical air-bubbles and the sounds of running water," Philisophical Magazine, Vol. 16, 1933, pp. 235-248.

21. Prosperetti, A., Pumphrey, H.C., and Crum, L.A., "The underwater noise of rain," Journal of Geophysical Research, Vol. 94, 1989, pp. 3255-3259.

22. Rajandran, V.R., "Development of stereoscopic particle tracking velocimetry for turbulent flow field diagnostics," M.S. Thesis, University of Mississippi, 1993.

23. Schlichting, H., Boundary Layer Theory, 7th ed., McGraw-Hill, 1979.

24. Sevik, M., and Park, S.H., "The splitting of drops and bubbles by turbulent fluid flow," Journal of Fluid Mechanics, Vol. 58, 1973, pp. 53-60.

25. Sinha, S.K., and Kuhlman, P.S., "Investigating the use of stereoscopic particle streak velocimetry for estimating the three-dimensional vorticity field," Experiments in Fluids, Vol. 12 No. 6, 1992, pp. 377-384.

26. Sinha, S.K., Mangla, N.L., and Tang, Z., "Application of interpolations in steroscopic particle tracking velocimetry," Journal of Scientific Modeling and Compuation, in press.

27. Weinstein, L.M., Beeker, G.B., and Lindemann, A.M., "High speed holocinematographic velocimeter for studying turbulent flow control physics," AIAA, paper 85-0526, 1985.

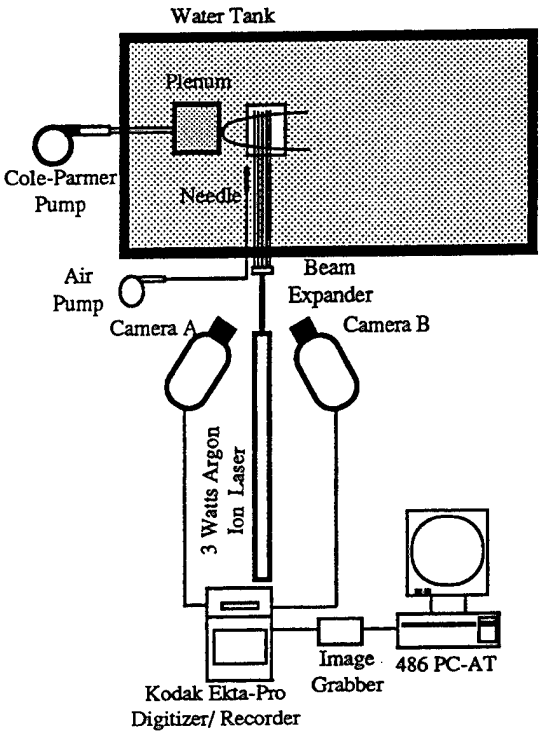


Fig. 1: Schematic drawing of the experimental set-up.

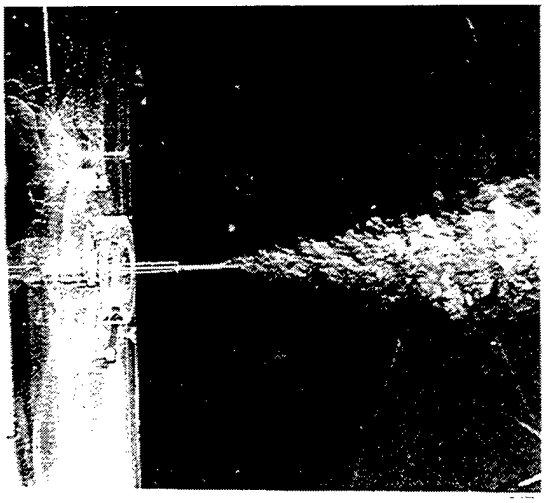


Fig. 2: Instantaneous photograph of the jet with velocity of 2.2 m/sec.

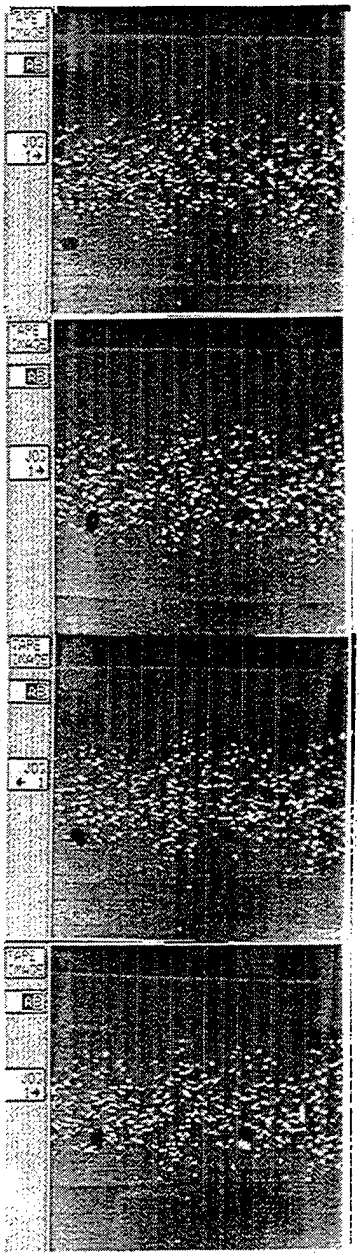


Fig. 3: Examples of the digitized stereoscopic high-speed images of a bubble with radius 1.1 mm injected into a fully developed turbulent jet with jet velocity of 2.2 m/sec. The imaging rate was 1000 frames/sec. These images are consecutive but sequential. Left half of each frame is the camera-A image, while the right half is the camera-B image. The bubble is seen as a large dark spot. The particles are white. The mean flow is from left to right.

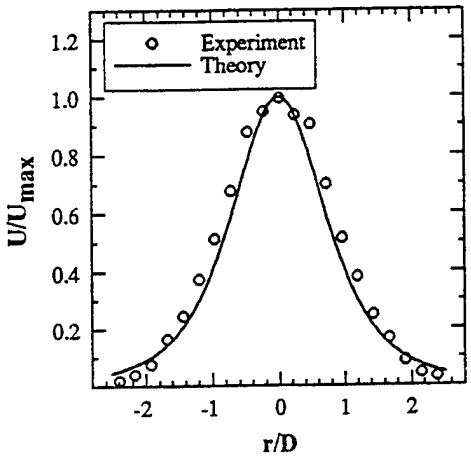


Fig. 4: Transverse distribution of the mean longitudinal component of the velocity at x/D ≈ 10 scaled with mean centerline velocity U_{max}.

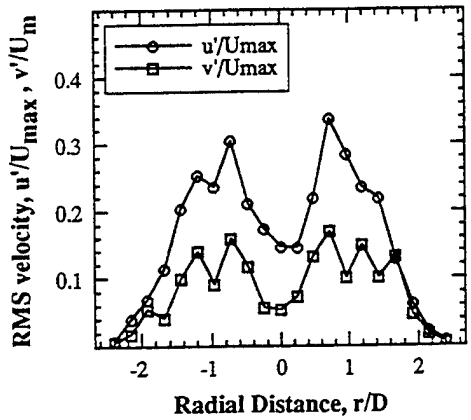


Fig. 5: The r.m.s. streamwise and transverse velocities fluctuations scaled with U_{max} as a function of r/D.

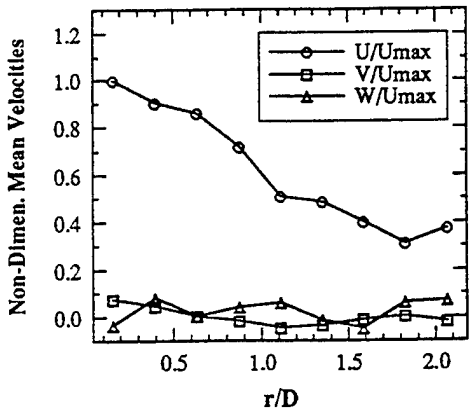


Fig. 6: The mean velocity components, U, V, and W as a function of r/D normalized with respect to U_{max} measured at x/D ≈ 10. The SPTV technique was used to measure these velocity distributions.

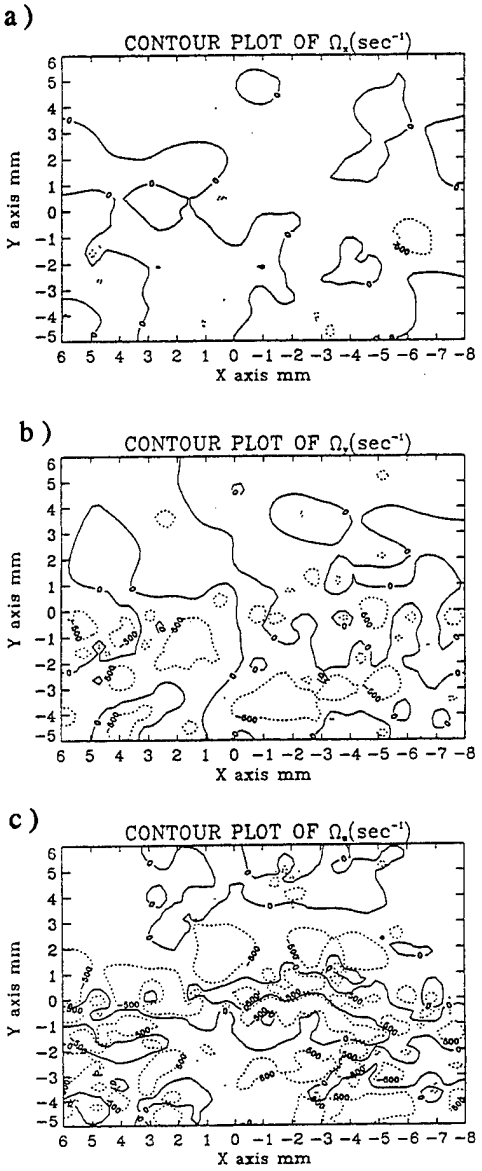


Fig. 7: Contour plots of vorticites measured at x/D ≈ 10 of a) X-direction, b) Y-direction, and c) Z-direction. Vorticites in levels +/- 705, 500, 250, and 0 s^{-1} are shown here.

DISCUSSION

H. Oguz
Johns Hopkins University, USA

This paper examines the interaction between a bubble and a turbulent flow experimentally. The significance of this process can be found in underwater acoustics, industrial gas-liquid reactors, aeration systems, etc. Here, the turbulent flow field is generated by a liquid jet emerging from an underwater nozzle and a single bubble is introduced by means of a hypodermic needle below the jet. The authors make a commendable effort to monitor the details of the bubble-flow field interaction. A novel idea introduced by this work is the simultaneous collection of optical and acoustical data. Since bubbles are strong acoustic scatters one would hope to establish a relationship between the flow field measured optically and the recorded acoustic signal.

This difficult experiment seems to have been carried out with great care. As for the theoretical analysis, the authors make use of the Kolmogorov's theory of turbulence. Bubble deformation and breakup can occur in the presence of a turbulent eddy of comparable size. The response of a bubble depends on the Weber number defined by

$$We = \frac{\rho v^2}{\sigma / 2R}$$

where R is the radius of the bubble, v^2 is the average value of the squares of the velocity differences, σ is the surface tension and ρ is the density. The description of the calculation of the critical Weber number $(We)_{crit}$ lacks certain details that may allow one to reconcile differences with other studies. According to Sevik and Park (1973) the critical Weber number for bubble breakup in a turbulent field is about 1.24. This value is nearly attained at high shear regions of the flow field where We is reported to be 1.10.

The connection between bubble shape oscillations and acoustic radiation is implied as if there exists a one-to-one correspondence between the two processes. In reality, pressure fluctuations caused by turbulent eddies may be more effective in causing acoustic excitation than shearing action that induces shape oscillations. In other words, it is entirely possible to register a strong acoustic pulse without observing any shape oscillations. Also, volume pulsations resulting from splitting bubbles are more likely to be caused by the jump in the equilibrium pressures after the breakup.

Finally, a recent work by Parthasarathy and Ahmed (1994) who examined the bubble breakup process in a vessel agitated by a turbine is worth mentioning. They also addressed the bubble breakup problem experimentally and employed similar ideas.

References

Parthasarathy, R. and Ahmed, N., "Bubble Size Distribution in a Gas Sparged Vessel Agitated by a Rushton Turbine," *Ind. Eng. Chem. Res.*, Vol. 1, 1994, pp. 703-711.

Sevik, M. and Park, S.H., "The Splitting of Drops and Bubbles by Turbulent Fluid Flow," *ASME J. Fluids Eng.*, Vol. 58, 1973, pp. 53-60.

Direct Simulations of Bubbly Flows

P.-W. Yu, A. Esmaaeli, S. Ceccio, G. Tryggvason
(University of Michigan, USA)

ABSTRACT

Direct numerical simulations of bubbles are presented. The full Navier-Stokes equations are solved by a finite difference/front tracking method that allows a fully deformable interface between the bubbles and the ambient fluid and the inclusion of surface tension forces. Two problems are discussed: The collapse of a three dimensional cavitation bubble in a shear flow near a wall and the rise of a two-dimensional buoyant bubble cloud. The computations for the cavitation bubbles suggest that a shear flow may prevent the formation of a reentrant jet during the late stages of the collapse. The bubble cloud simulations show that freely evolving bubbles generate considerable amount of small scale vorticity that leads to large velocity fluctuation and reduces the rise velocity of the bubbles.

NOMENCLATURE

α_i	void fraction
d_e	effective diameter of deformable bubbles
r_o	initial radius of cavitation bubbles
$\mathbf{u}$	velocity
u, v, w	components of the velocity vector
g	gravity acceleration
Δp	pressure difference
ρ	density
μ	viscosity
σ	surface tension
δ	three-dimensional delta function
ω	shear rate
$\langle uu \rangle$, $\langle vv \rangle$, $\langle uv \rangle$	Reynolds stresses
M	Morton number
Eo	Eotvos number
N	Galileo number
α, β, γ	Nondimensional numbers for cavitation
D	Deformation tensor
T	Stress Tensor

INTRODUCTION

The importance of bubbly flows to Naval systems can not be underestimated. While cavitation damage has been a prevailing concern in the past, current interest is strongly motivated by the acoustic properties of bubbles and bubbly flows. Advanced detection techniques pick up noise created by cavitation bubbles, and bubble clouds can distort a signal, leading to difficulties in detection as well as aiding in noise reduction and shielding. Bubble ejection into a boundary layer can lead to a substantial drag reduction, and bubbles can contribute to surface signatures detected by remote sensing techniques, both by creating short waves when encountering the surface, as well as by adding to the persistence of large scale wake motion, that, in turn, modifies small scale waves. In order to take advantage of the properties of bubbly flows, as well as to be able to control the formation and properties of such flows, an understanding, both on a macroscopic and microscopic level is essential.

While the generation of cavitation noise and cavitation erosion is basically a "one bubble" problem, detection and drag reduction involve the collective effect of a very large number of bubbles of a relatively small size. Consequently, the ultimate product of a research directed toward these applications is a macroscopic model, capable of predicting relatively low level information directly, based on only the statistical properties of the mixture. However, in order to derive either a large scale model from small scale information, or to close a system of averaged macroscopic conservation equation, it is necessary to have a thorough understanding of the microstructure of the flow. Bubbly flows often have large scale separation, so the prospects for a successful macroscopic model are reasonably good. However, the microstructure of bubbly lows is only simple when the mean bubble concentration is low, and when the bubbles can be considered to be moving in either completely

inviscid, or very viscous fluid. At intermediate Reynolds number the motion of a single bubble can be fairly complicated, and for higher bubble concentrations the bubbles will interact considerably.

Detailed measurement of bubble behavior is usually made difficult by the small spatial scales and the short time scales involved, and the use of computer simulations to complement experimental observations of bubble behavior is nearly as old as the application of computers to large scale fluid dynamic simulations. Generally, a number of simplifications, such as the assumption of inviscid or Stokes flow, have been made to render the problem tractable. Although these simplified models do can capture the significant physical processes of the flow involved, many of the fundamental problems of Naval interest require the solution of the full Navier-Stokes equations. We have recently developed a numerical method that appears to be suited for such simulations, and two application of the technique are discussed in this paper. First we discuss the collapse of a single cavitation bubble in a uniform shear; then we examine the collective behavior of a few buoyant bubbles.

One of the first use of computer simulations to aid in the understanding of bubble motion are the computation of a collapsing cavitation bubble by Plesset and Chapman's (1) and Mitchell and Hammitt (2). Both authors use a grid based finite difference method based on the MAC method of Harlow and Welch (3). Later authors have taken advantage of the fact that in some cases the liquid can be assumed to be inviscid and it is thus possible to reformulate the problem in terms of an integral equation over the bubble surface. See, for example, Blake and Gibson (4) and Chahine (5). Inviscid, boundary integral techniques have also been used to simulate the initial acceleration of buoyant bubbles (e.g., Baker and Moore, (6) and Yang, (7)). Since there is no drag, the bubbles deform continuously and the computations generally can only be carried out for a limited time. To compute the steady-state motion of bubbles, or the long time evolution of a bubble system it is necessary to include viscous effects. Ryskin and Leal (8) presented an extensive set of computations for the steady-state rise of a single axisymmetric bubble using a finite difference method and boundary fitted coordinates. By solving the full Navier-Stokes equations they investigated the effect of a finite Reynolds number for a wide range of parameters. This study still remains one of the most comprehensive numerical investigations of bubble motion. The computations clarified many open questions about bubble shapes and their wakes, but did not deal with unsteady aspects and interactions of bubbles with each other. Although other authors have repeated the single bubble computations of Leal and coworkers (see, e.g., Shopov *et al.*, (9)) the full unsteady motion and bubble/bubble interactions has not been dealt with in any detail by numerical simulations.

FORMULATION AND NUMERICAL APPROACH

The Navier-Stokes equations govern the fluid motion both inside and outside the bubbles and a single vector equation can be written for the whole flow field. In conservative form these are

$$\frac{\partial \rho \bar{u}}{\partial t} + \nabla \cdot \rho \bar{u}\bar{u} = -\nabla p + (\rho_o - \rho)\bar{g}$$

$$+ \nabla \cdot \mu\left(\nabla \bar{u} + \nabla \bar{u}^T\right) + \int \bar{F}_\sigma \delta\left(\bar{x} - \bar{x}_f\right) da.$$

Here, $\bar{u}$ is the velocity, p is the pressure, and ρ and μ are the discontinuous density and viscosity fields, respectively. $\bar{F}_\sigma$ is the surface tension force and g is the gravity acceleration. ρ_o is the average density and $\rho_o \bar{g}$ is a force to prevent uniform acceleration of the whole flow field in the direction of gravity when we use periodic boundary condition in that direction. Notice that the surface tension force has been added as a delta function, only affecting the equations where the interface is. The detailed form of $\bar{F}_\sigma$ will be discussed below. The above equations must be supplemented by additional conditions leading to an equation for the pressure. For both problems we assume that the ambient fluid is incompressible, so that

$$\nabla \cdot \bar{u} = 0$$

which, when combined with the momentum equations leads to a non-separable elliptic equation for the pressure. For the buoyant bubbles we take the fluid inside the bubbles to be incompressible also, but for cavitation bubbles we specify

$$p = p_v,$$

where p_v is the vapor pressure, inside the bubble, and specify pressure along one or more boundaries. We also have equations of state for the density and viscosity:

$$\frac{\partial \rho}{\partial t} + \bar{u} \cdot \nabla \rho = 0$$

$$\frac{\partial \mu}{\partial t} + \bar{u} \cdot \nabla \mu = 0.$$

These last two equations simply state that density and viscosity within each fluid remains constant.

The rise of a single buoyant bubble is governed by two nondimensional numbers, in addition to the ratios of the bubble density and viscosity to the ones of the outer fluid. The ratios of the material properties are usually small and have little influence on the motion. The remaining two numbers can be

selected in a number of ways. If we pick the density of the outer fluid, ρ, the effective diameter of the bubble, d_e, and the gravity acceleration, g, to make the other variables dimensionless we obtain:

$$N = \frac{\rho_o^2 d_e^3 g}{\mu^2}; \quad Eo = \frac{\rho_o g d_e^2}{\sigma}$$

The first number is sometimes called the Galileo or the Archimedes number (see ref. 10) and is a Reynolds number based on the velocity scale $\sqrt{gd_e}$. The second one is usually called the Eotvos number. The behavior of a single, clean, buoyant bubble is reasonably well understood. For low Eo, bubbles remain spherical and their terminal velocity is steady, usually expressed as a rise Reynolds number, is a function of N only. For low N, the bubbles remain spherical for all Eo, but at higher N the bubbles become ellipsoids as Eo increases, and eventually "spherical cap bubbles" at very high Eo. For moderate N, the ellipsoids have a steady state rise velocity, but at higher N, their motion is unsteady, following a zigzag or a helical path. At high N, the wake of spherical cap bubbles is usually turbulent. In the chemical engineering literature, N is usually replaced by the so-called Morton number, $M = g\mu_o^4/\rho_o\sigma^3 = \sqrt{Eo^3/N}$, which is a constant for a given fluid if the gravity acceleration is constant. For bubbly clouds where many bubbles rise together, the void fraction must also be specified and for more complex flow fields, such as a shear flow, additional parameters must be specified.

For cavitation bubbles in a shear flow, a different set of nondimensional numbers is more appropriate. The driving force is the difference between the vapor pressure inside the bubble and the ambient pressure, and in many cases the initial radius of the bubble and the density of the liquid are the main parameters. Using these to nondimensionalize other quantities, namely the shear rate, ω, the viscosity, μ, and surface tension, σ, we get:

$$\alpha = \omega r_o \sqrt{\frac{\rho}{\Delta p}}; \quad \beta = \frac{\mu}{r_o}\sqrt{\frac{1}{\rho \Delta p}}; \quad \gamma = \frac{\sigma}{r_o \Delta p}.$$

The same variables can also be used to generate a time scale, the Rayleigh time:

$$t_R = r_o \sqrt{\frac{\rho}{\Delta p}}.$$

The Rayleigh time is proportional to the collapse time of an unbounded, spherical vapor bubble. This time scale will be used to nondimensionalize time for the cavitation results. For initially spherical bubbles near a wall, we also need to specify how far the bubble center is from the wall, d. Thus we define

$$\delta^* = d / r_o.$$

To solve the Navier Stokes equations we use a fixed, regular, staggered grid and discretized the momentum equations using a conservative, second order centered difference scheme for the spatial variables and an explicit second order time integration method. The pressure equation, which is non-separable due to the difference in density between the drops and the ambient fluid, is solved by a Black and Red SOR scheme or a multigrid iteration. The novelty of the scheme concerns the way the boundary, or the front, between the drops and the ambient fluid is tracked. The front is represented by separate computational points that are moved by interpolating their velocity from the grid. These points are connected by triangular elements to form a front that is used to keep the density and viscosity stratification sharp and to calculate surface tension forces. At each time step information must be passed between the front and the stationary grid. This is done by a method similar to the one discussed by Unverdi and Tryggvason (11), that spreads the density jump to the grid points next to the front and generates a smooth density field that changes from one density to the other over two to three grid spaces. While this replaces the sharp interface by a slightly smoother grid interface, all numerical diffusion is eliminated since the grid-field is reconstructed at each step. The surface tension forces are computed from the geometry of the interface and distributed to the grid in the same manner as the density jump. Generally, curvature is very sensitive to minor irregularity in the interface shape, and it is difficult to achieve accuracy and robustness at the same time. However, by computing the surface tension forces directly by

$$\overline{F}_\sigma = \sigma \oint \bar{t} \times \bar{n} ds$$

where the integration is over the boundary of each element representing the front, we ensure that the net surface tension force is zero. This is important for long time simulations since even small errors can lead to a net force that moves the bubbles in an unphysical way.

As the bubbles move and deform, it is necessary to add and delete points at the front and to modify the connectivity of the points, to keep the front elements of approximately equal size and as "well shaped" as possible. This is described in Unverdi and Tryggvason (11).

The method and the code has been tested in various ways, such as by extensive grid refinement studies, comparison with other published work and analytical solutions for simple cases. It has also been used to investigate a number of other multifluid problems. Head-on collisions of drops have been computed by Nobari, Jan and Tryggvason (12), three-dimensional collisions by Nobari and Tryggvason (13); Unverdi

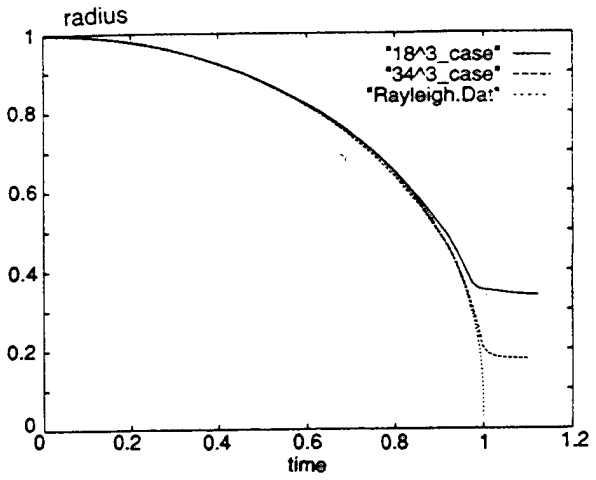


Figure 1. The collapse of a spherical bubble computed on a 16^3 and a 32^3 grid. The radius of the bubble is plotted versus time. Also plotted is the radius as predicted by the Rayleigh-Plesset equation.

and Tryggvason (14) simulated the collision of fully three dimensional bubbles; Ervin (15) investigated the lift of deformable bubbles rising in a shear flow (see also Esmaeeli, Ervin, and Tryggvason (16); Jan and Tryggvason (17) examined the effect of contaminants on the rise of buoyant bubbles and Nobari and Tryggvason (18) followed the coalescence of drops of different sizes. Nas and Tryggvason (19) presented simulation of thermal migration of many two dimensional bubbles.

RESULTS AND DISCUSSIONS.

Cavitating bubbles

To validate our implementation of the numerical method described in the previous section, and to assess how rapidly it converges under grid refinement, we have computed the collapse of a spherical vapor bubble and compared the results with the predictions of the Rayleigh-Plesset equation. The computations are done with the fully three-dimensional method, but in a relatively small computational domain. The pressure is prescribed on the boundary of the computational domain (whose side lengths are twice the initial diameter of the bubble) instead of at infinity as in the theory. This approximation, however, results in a relatively small error initially, when the pressure is nearly uniform. Indeed, the theory predicts that the difference between the pressure at infinity and at the boundary is less than 10% at 0.9 times the theoretical collapse time. Figure 1 shows the radius of the bubble for both a 16^3 and a 32^3 grid as well as the theoretical results. The results show that the evolution is well predicted during the early stages by both resolutions, but eventually the loss of resolution leads to a strong (and rather sudden) deviation from the analytical prediction. The resolution limit is reached when the radius of slightly less than 40% of the initial radius for the coarse grid and about 20% for the finer grid. This translates into about two and a half grid point across the bubble at the point when the results diverge. We have also examined the method by two-dimensional calculations, both for a bubble collapse as well as a "one-dimensional" collapse of a cavity at the end of a tube. In all cases do we find good accuracy for moderate resolutions.

Figure 2 shows the evolution for a bubble collapsing near a wall in a quiescent fluid. The bubble is shown at four times (not equispaced), and the view is from the side and above so the three dimensional aspects of the evolution are apparent. The computational domain is a cube whose bottom side is shown in the figure. The domain is resolved by 32^3 grid and the initial bubble diameter is 0.5 times the side length of the computational domain. The pressure is specified at the top of the computational domain, but both horizontal boundaries are periodic. Here, α=0, β=0.007, γ=0.288, and δ^* = 1.5. The bubble collapses in a way that is now well understood. After shrinking nearly spherically for a while, the "roof" of the bubble eventually "caves in" and a down ward moving jet forms that eventually pierces through the bubble. The volume of the bubble is plotted versus time in figure 3a where we have also plotted the results for a computation on a coarser and a finer grid as well. All the curves are in a reasonably good agreement initially, but at late times resolution effects appear. In figure 3b we plot the maximum velocity of the bubble surface which takes place at the tip of the downward moving jet, once it has formed. Initially, all computations are in a good agreement, but as the jet becomes thinner and the curvature at its tip higher, we eventually lose resolution and the jet is artificially slowed down. Even the finer two grids produce results that differ at large times. We note that the grid is uniform and that no attempt has been to refine around the jet. The results of Plesset and Chapman (1) are also plotted in figure 3b and those fall close to our medium resolution, suggesting that their jet was somewhat underresolved also.

In figure 4 we show the collapse of a bubble in a shear flow. Here, α=0.15, β=0.022, γ=0.288, and δ^*=1.5. The bubble is shown at time zero at the top, and then at three subsequent times, as in figure 2. This bubble also develops a jet, but now the shear deforms the bubble and moves the jet in the

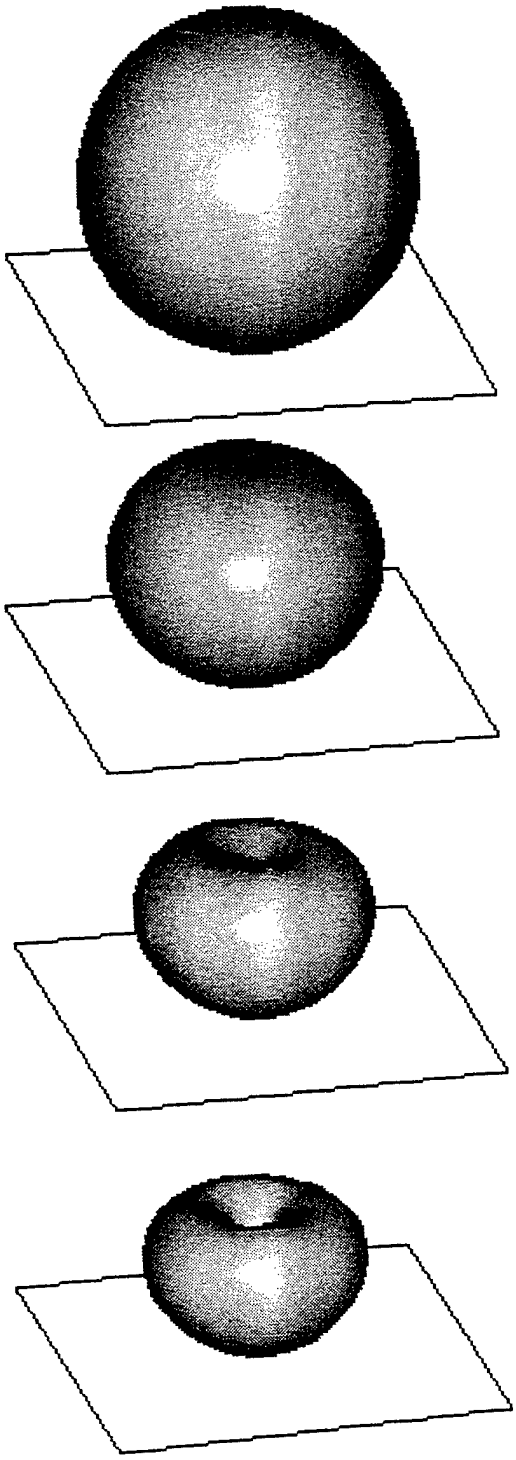


Figure 2. Computations of the collapse of a cavitation bubble near a wall. The computations are done in a cube computational box resolved by a 32^3 grid. The initial bubble diameter is 0.5 times the side length of the box. α=0, β=0.007, γ=0.288, and δ * = 1.5. The bubble is shown at times 0.0, 0.94, 1.1, and 1.16.

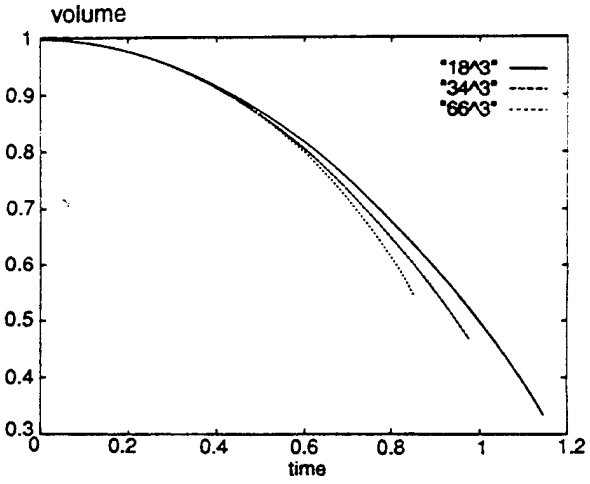


Figure 3a. The volume of the bubble in figure 2 versus time. Also plotted are the results from calculations on both a coarse 16^3 grid as well as a finer 64^3 grid.

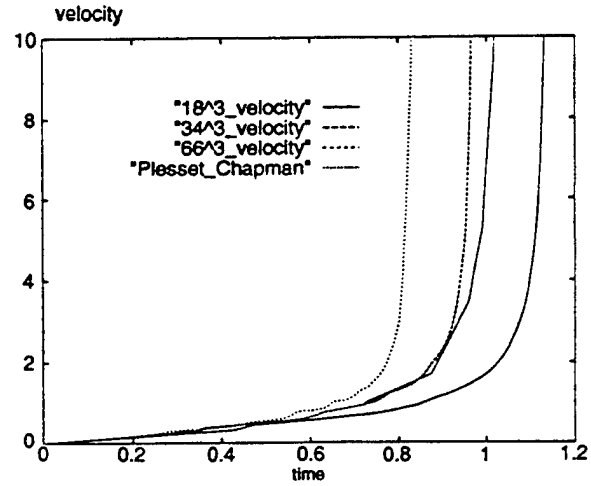


Figure 3b. The maximum downward velocity of the bubble surface for a non-sheared bubble as computed by three different resolutions.

downstream direction. How far downstream the jet moves during the collapse depends on the shear rate. We note that the jet is smaller here, as compared to the no-shear case, and we therefore run out of resolution earlier. As the shear is increased, the jet is displaced further back, and figure 5 shows the late time stage of three other calculations where the shear is larger than in figure 3. The jet is moved further backward than in figure 3, and in the bottom figure (highest shear) the jet has disappeared. The larger shear leads to an earlier appearance of underresolved scales and therefore to shorter time that we can reliably follow the evolution of the collapse. The results, nevertheless, show that the effect of shear is to change the bubble shape rather dramatically, and suggest that for strong shear no distinct jet will be

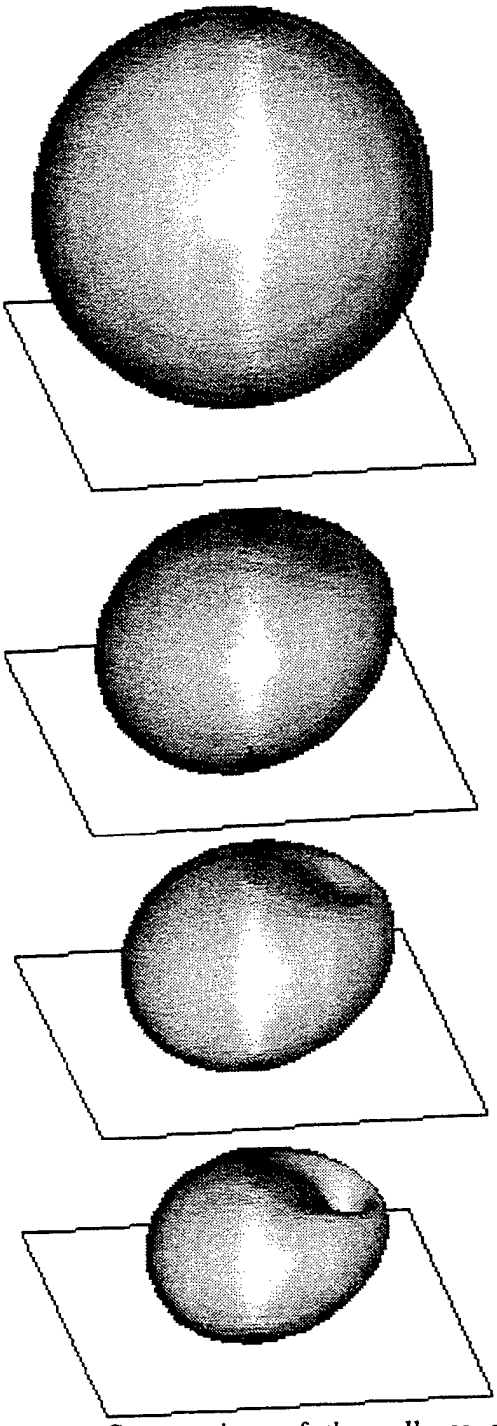


Figure 4. Computations of the collapse of a cavitation bubble in a shear flow near a wall. The bubble is shown at the initial time and three subsequent times. The computations are done in a cube computational box resolved by a 32 grid. The initial bubble diameter is 0.5 times the side length of the box. α=0.15, β=0.022, γ=0.288, and δ^*=1.5. The bubble is shown at times 0.0, 0.94, 1.1, and 1.16.

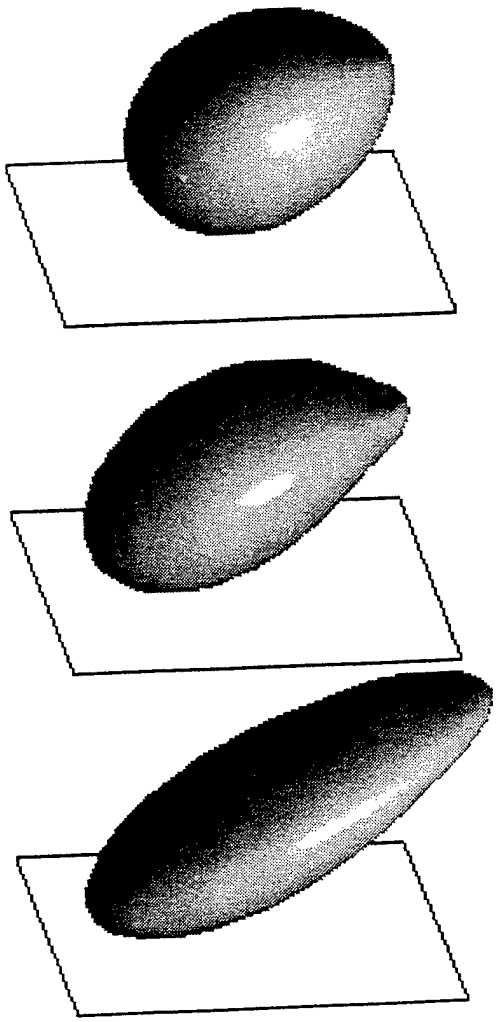


Figure 5. Late time in the collapse of three bubbles in a shear flow near a wall. The computations are done in a cube computational box resolved by a 32^3 grid. The initial bubble diameter is 0.5 times the side length of the box. The bubbles are all shown at t=1.04, and β=0.022 and γ=0.288 in all cases. α= 0.25, 0.5, and 1.0, respectively, from the top.

formed. Instead, the downstream side of the bubble will collapse first. For even stronger shear, the effect of shear and collapse combine to flatten the bubble into a slightly asymmetric "saucer" shape. To investigate the effect of shear on the rate of collapse, we plot, in figure 6 the volume of the bubbles for three different shear rates and compare it with the zero shear case. In spite of the considerable differences in shape, all computations give comparable results, except for the very strongest shear rates, showing that by the time the jet forms, the bubble has lost most of its initial volume.

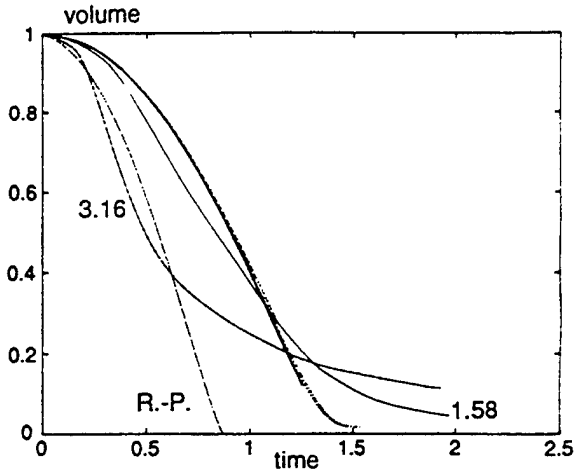


Figure 6. The volume of several bubbles as a function of time for different shear rate. The resolution is 32^3 all cases. For all runs, β=0.022 and γ=0.288. The nondimensional shear rate is α= 0.15, 0.25, 0.5, 1.0, 1.58, and 3.16. Also plotted are the results predicted by the Rayleigh-Plesset equation.

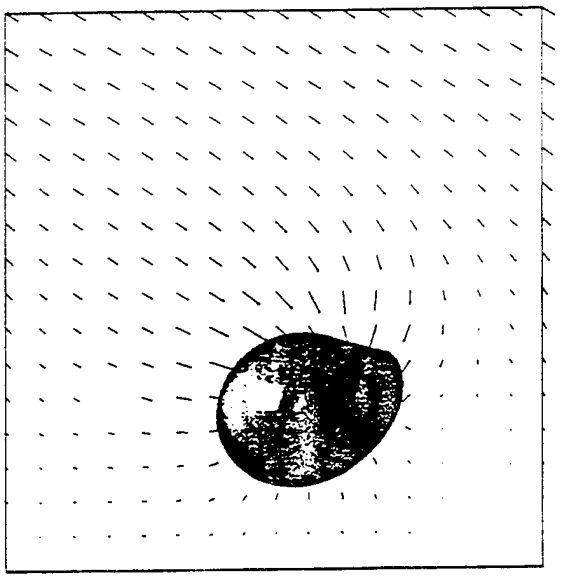


Figure 7. The velocity field in the center plane of a collapsing, sheared bubble. The conditions are those of the bubble shown in figure 4. t = 1.12.

We have yet to analyze the flow field for the three-dimensional calculations in detail (and are hindered in doing so because the relatively low resolution of the computations does not allow us to follow the evolution to very late times where the bubble has had any effects on the flow), but preliminary two-dimensional simulations suggest what to expect. For the no-shear case the collapse eventually results in two, counter rotating vortices but for the sheared bubble, only one vortex is visible at the final stage. The three-dimensional counterpart of the vortex pair for the bubble in quiescent fluid is a ring, but the three dimensional counter part of the single vortex for the sheared collapse must include trailing vortices extending downstream from the side of the bubbles. Indication of such trailing vortices are seen in the experimental photographs of Ceccio and Brennen (20). Figure 7 shows the velocity field in the centerplane of our computational box for the run in figure 2 for one instant in time. The velocity vector is plotted at every other grid point and shows clearly the asymmetry in the velocity field.

The above calculations were done for a linear velocity profile. The primary motivation for that is to simplify the problem as much as possible and add only one dimensionless number. This situation corresponds to a small bubble in a thick boundary layer, whereas in many experimental situations the opposite situation, where the bubble is relatively large compared to the boundary layer, is the case. For those problems the thickness of the boundary layer, and possibly its shape and rate of growth must also be accounted for in addition to the shear rate. We are currently examining problems with more complex boundary layer interactions as well as problems with time dependent external pressure.

Bubble clouds

Bubble clouds usually consists of a large number of bubbles, and it is the collective behavior of the bubbles in the cloud, rather than the motion of individual bubbles, that is of interest. Standard two-fluid models that are used in engineering prediction of such flows can be derived by averaging the Navier-Stokes equations over a small volume containing several bubbles (see Drew (21) for example). The averaged equations can take several different forms, one of which is:

$$\rho_i \frac{\partial \alpha_i < \bar{u}_i >}{\partial t} + \nabla \cdot \alpha_i < \bar{u}_i >< \bar{u}_i > +$$

$$\nabla \cdot \alpha_i < \bar{u}_i \bar{u}_i' >= -\nabla \alpha_i < p_i > +(\rho_o - \rho_i)\alpha_i \bar{g}$$

$$+\nabla \cdot 2\alpha_i \mu_i < D_i > -\frac{1}{V}\int T \cdot \bar{n} da$$

Here, D_i is the deformation tensor, T the stress tensor, and <> denotes a suitably averaged variable, which in our case is most conveniently taken to be volume averaging. V is the elementary volume over which the average is taken. If ϕ_i is defined to be 1 in phase i, and zero otherwise, then, for example, the average velocity is:

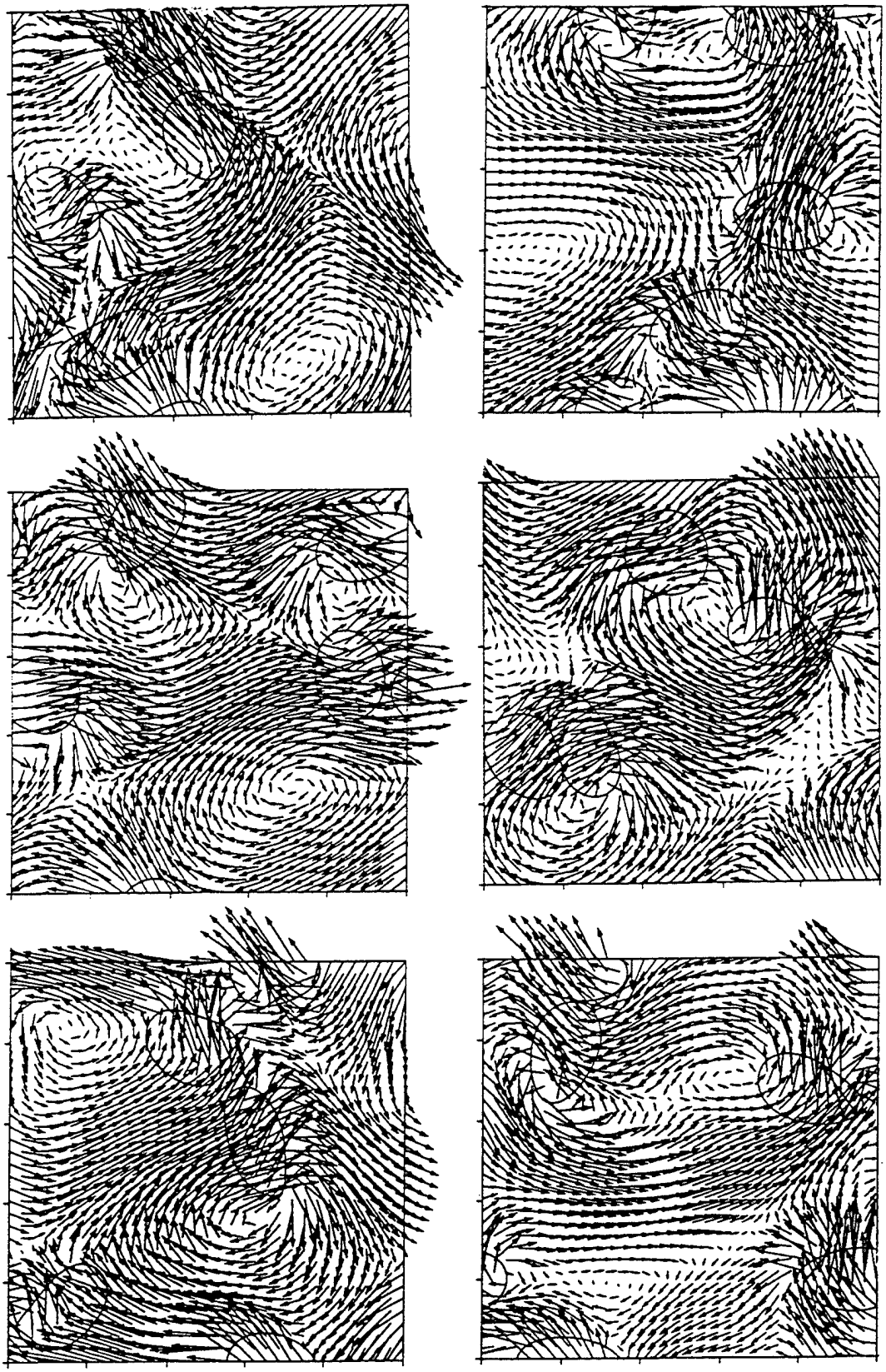


Figure 8. Six frames from a computation of the evolution of four bubbles in a periodic domain. Here, the void fraction is 0.126, density and viscosity ratios are 20, Eo=3, and N=1643. The bubbles and the velocity vectors are shown at t=25, 34, 44, 65,94 and 103, starting in the top left corner and reading down each column.

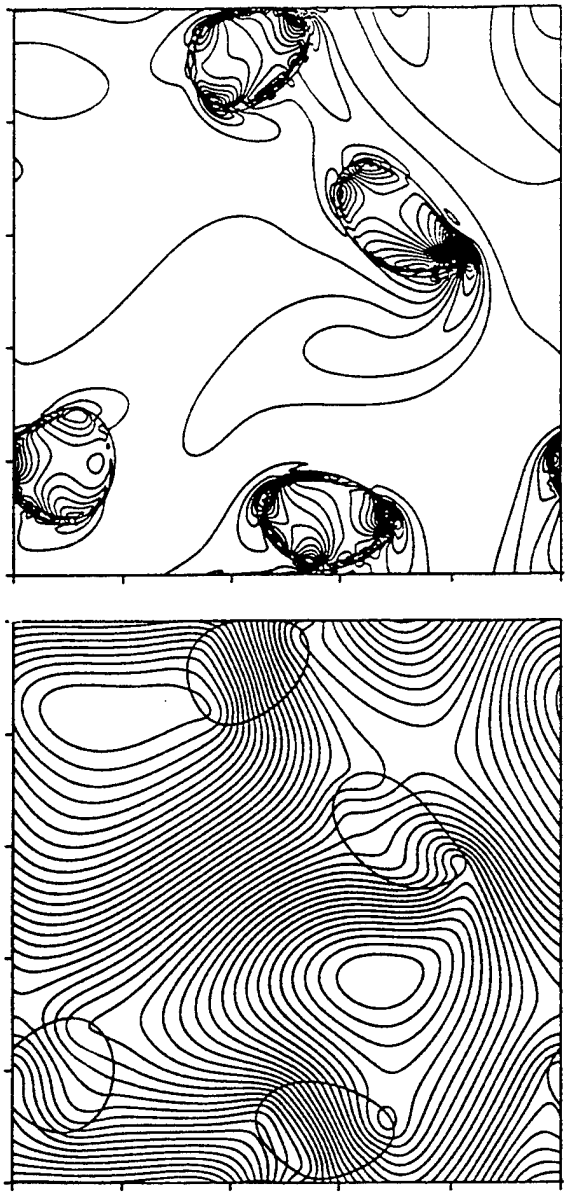


Figure 9. The vorticity (top frame) and the stream function (bottom frame) at t=22 for the run in figure 8.

$$< \bar{u}_i >= \frac{1}{\alpha_i V} \int_v \phi_i \bar{u} dv .$$

The volume fraction is defined as

$$\alpha_i = \frac{1}{V} \int_v \phi_i dv .$$

By averaging the incompressibility conditions, we find that alpha is governed by:

$$\frac{\partial \alpha_i}{\partial t} + \nabla \cdot < \bar{u} > \alpha_i = 0 .$$

The subscript i=1,2 denotes the different fluids and we have one set of equations for each fluid. This model is usually called the two-fluid model, as

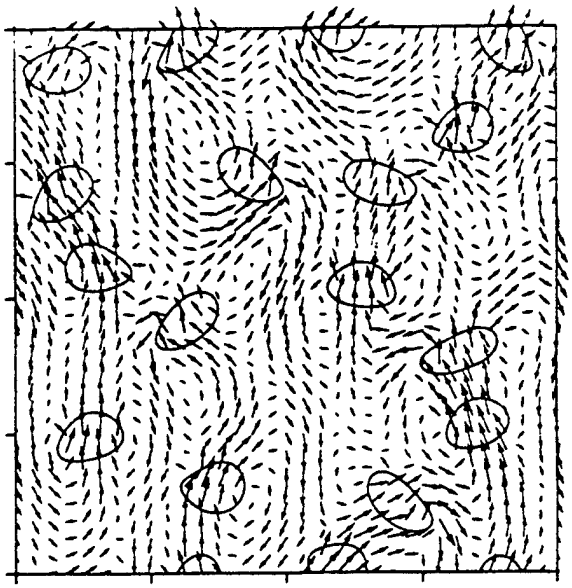


Figure 10. The shape of the bubbles and the velocity field for a simulation with 16 bubbles at time = 10. The grid used here is 386^2 and all parameters are the same as in figure 8

opposed to models that treat the fluids as one mixture. The momentum equation retain most aspects of the original Navier Stokes equations, with the addition of two new terms. These terms are generally unknown, and a closure relation must be postulated based on experimental data, simplified analysis or pure speculations, just as for the Reynolds equations for turbulent flow. For multifluid flow these terms are of two form. The first is due to velocity fluctuations, exactly analogous to the Reynolds stress term for turbulent flow, except that this term is usually non zero even at very low Reynolds numbers since the fluctuations are caused by the bubble motion (in addition to unsteady vorticity at higher Reynolds numbers). For this reason it is sometimes referred to as pseudo Reynolds stress, as opposed to true Reynolds stresses that are due to the fluid vorticity and can, of course, also be present in high Reynolds number bubbly flows. The second additional term is the averaged momentum exchange between the fluids or the average force that one fluid exerts on the other. This force can be further decomposed into several components, such as steady drag, added mass effect, lift, Basset force, etc. For homogeneous bubbly flow that is in a statistically steady state, this force is exactly balanced by the buoyancy force, and the average slip velocity is the only information needed to construct a drag coefficient for the mixture.

To help gain the insight needed to construct realistic closure models, we are in the process of conducting relatively large scale simulations of many bubble

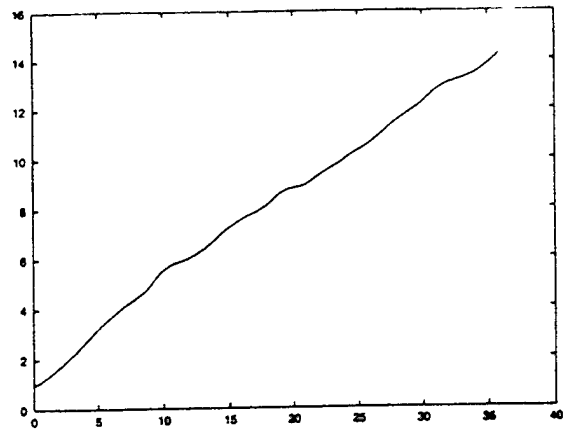


Figure 11. The vertical coordinate of the centroid of the bubbles in figure 8 versus time.

systems. In the computations presented here, we use a doubly periodic domain, so that the bubbles that exit the domain on one side, reappear on the other side. Such cell models have been proposed by several authors, see for example Brennen and Happel (22) for low Reynolds number flows and Wallis (23) for inviscid flows. Although there is no fundamental restriction to only one bubble per cell, most previous studies have had to make this assumption in order to make the problem tractable. Here, we do not have to do so.

We have conducted a number of two-dimensional simulations in doubly periodic domains with a relatively high void fraction where the bubbles interact strongly. Two-dimensions allow us to use considerably higher resolution than what is practical in three-dimensions thus allowing us to include many bubbles. Nevertheless, even in two-dimensions, resolution requirement increase rapidly with Reynolds number. Most of our early work has therefore been limited to very low Reynolds numbers where the resolution per bubble is modest. This has allowed us to do a number of runs for 16 to 32 bubbles where we have followed the evolution of the flow until the behavior has become completely independent of the initial conditions. We have also done a few three-dimensional computations with 2 to 4 bubbles to verify the trend seen in the two dimensional runs.

At higher Reynolds numbers we have so far been limited to a smaller number of bubbles and fewer runs. Figure 8 shows several frames from a calculation using only four bubbles. Here, $M=10^{-5}$ and Eo=3, so N=1643, and a single three-dimensional bubble in an unbounded domain would rise with a terminal Reynolds number of about 50. Both the bubble surface as well as the velocity vectors are show. The grid is 194^2 meshes, but the velocity is shown only at every 6th gridpoint. The bubbles are initially placed on a regular grid, but with strong perturbations. Initially, the bubbles rise vertically. For low Reynolds numbers the first instability is generally where the bubbles in each column catch up with each other. Here, this is not the case, and the bubble motion becomes irregular without such pairing taking place. The subsequent figures are sufficiently far apart that the flow field has changed greatly from one frame to the next one. All frames are characterized by very strong velocity fluctuations, both in the horizontal and the vertical direction. The velocity field contains both strong vortices as well as prominent internal stagnation points. Although the bubbles collide occasionally, and the fifth frame has been selected to show one such event, this is actually very rare. Indeed, a careful analysis of the results for this run showed only one other collisions. Considering the relatively long time computed, and the high void fraction, one must conclude that this is indeed a rare occurrence. For a slightly more informative view of the flow field, the vorticity and the stream function at time 22 is plotted in figure 9. This is a relatively early time, but the shed vorticity is clearly seen. We are in the process of computing the interaction of a larger number of bubbles for these parameters, and in figure 9 we show the early stage of a 16 bubble calculation on a 386^2 grid. The bubbles have deformed strongly and considerable interaction has already taken place. We have also computed the evolution of just a single bubble in a "unit cell" for these parameters, to provide a comparison with the four bubble run (see Esmaeeli, Ervin, and Tryggvason (16)). The bubble is predicted to wobble as it rises and to have an oscillatory rise velocity.

Figure 11 shows the centroid of the four bubbles in figure 8 as a fuction of time that originally occupy the period in which the computations are done. The units on the vertical axis are in terms of the "unit cell," in which the computational box is of dimension 2 by 2. During the time computed, the centroid has risen about 15 units, or, since the bubble diameter is 0.4, the bubbles have risen on the average about 37 bubble diameters. Although the curve is not completely straight due to fluctuations in the average rise velocity, it has a well defined average slope which gives a rise Reynolds number of about 21, except for the first 10 time units where the slope is steeper. During this initial time the bubbles are still rising vertically, without any significant vertical velocity fluctuations. We note that this is significantly lower than a single bubble in a periodic cell with the same void fraction would rise. Such a bubble has a rise Reynolds number of about 32, which is still lower than for a single three dimensional bubble in an unbounded domain. To show the fluctuations better, we plot in figure 12 the path of each bubble that started out in the period

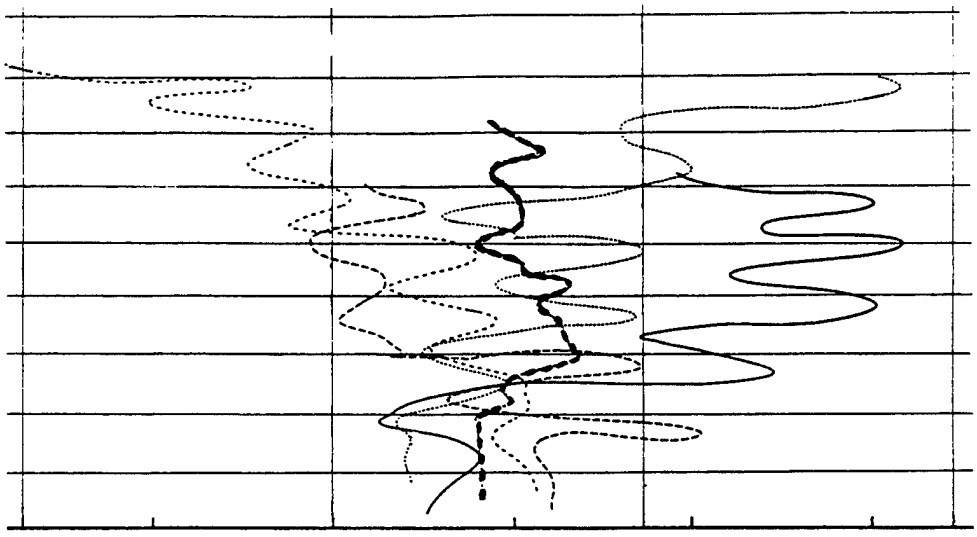


Figure 12. The path of the bubbles in the computations in figure 8. The boundaries of the periodic domain are denoted by thin horizontal and vertical lines. The thick line is the path of the centeroid. Notice that the vertical scale is greatly compressed as compared with the horizontal one.

that we simulate. The path of the centroid is also plotted (thick dashed line). While the centroid shows relatively little horizontal fluctuations (as one would expect, with larger number of bubbles the fluctuations are even less), the individual bubbles undergo large fluctuations and are dispersed both horizontally as well as vertically.

The velocity of the centroid of the bubbles in figure 8, as well as from a computation with 9 bubbles that has only been run for about half the time of the 4 bubble one, is plotted in figure 13. Notice that the vertical scale is greatly compressed as compared to the horizontal one. While the average velocities are relatively close, and both lines show relatively strong fluctuations, the fluctuations are larger for the run with the fewer bubbles. The fact that the mean velocities are close for both runs, suggest that freely evolving bubbles in a bubbly cloud at these Reynolds numbers rise slower than bubbles that are constrained to remain in a regular array (one bubble per unit cell). This contrast with our results for low Reynolds numbers, where clustering of bubbles generally lead to larger rise velocities for a freely evolving array. Here, we see less clustering and we suspect that the large velocity fluctuations in the liquid are responsible for this reduction. Figure 14 shows the vertical and horizontal Reynolds stresses for both the 4 and the 9 bubble run. Initially, the vertical velocity fluctuations, $\langle vv \rangle$, rise rapidly as the bubbles are accelerated upward, but as the horizontal fluctuations, $\langle uu \rangle$, increase, the vertical fluctuations decrease significantly although they remain large compared to the mean. During the second half of the run, where the evolution has approached a statistically steady state, the vertical and the horizontal fluctuations are of a comparable magnitude. Again, this contrast with lower Reynolds number results where the horizontal fluctuations are much smaller. In both plots the fluctuations are larger for the smaller number of bubbles, but the average values are comparable. The average of the cross term, $\langle uv \rangle$, should be zero and this is supported by our results.

CONCLUSIONS

Two examples of the use of direct numerical simulations to investigate the dynamics of bubbly flows are discussed. Although the results are somewhat preliminary, both examples demonstrated well the power of the approach.

The simulations of the cavitating bubble showed how shear can alter the collapse mode and in some cases eliminate the reentrant jet seen for stationary bubbles. These results were obtained on an uniform three-dimensional grid and generally we found that we ran out of resolution at the end of the computations. Three dimensional computations are generally very demanding on computer resources and it is important to use the available resolution in places where the solution is changing rapidly. We have implemented non-uniform grids for an axisymmetric version of our method and the addition of that capability to our three-dimensional code

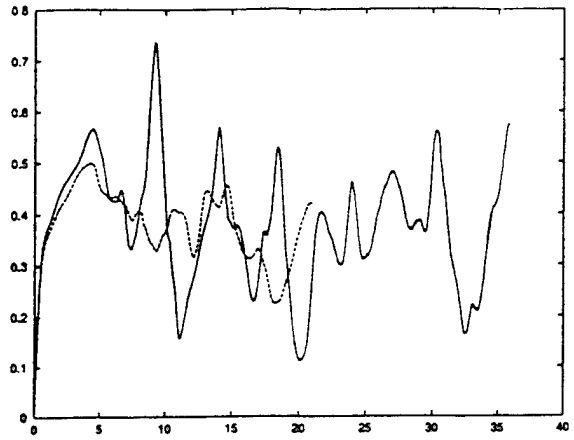


Figure 13. The average rise velocity of the bubbles versus time from both the 4 bubble run in figure 8 (solid line) and another run with 9 bubbles (dashed line)

should allow us to better resolve the late stages of the collapse.

The bubble cloud simulations suggest that for the parameter values simulated here there is considerable generation of unsteady vorticity by the bubble motion and that this vorticity induces large fluctuations on the bubble motion. Although long time simulations of many bubbles are necessary to obtain a reasonable statistical description of theflow, the results here show that such simulations can be done. The primary limitation is of course that these simulations are only two dimensional. We have done a number of fully three-dimensional simulations of two bubbles, and the possibility to do a many bubble three-dimensional simulation appears within reach. However, as with many new tools, considerable practice is need before the tool can be used effectively and the two-dimensional simulations provide us with the opportunity to explore what direct simulations can do for multiphase flow research, and therefore be in better position to take advance of three-dimensional results, which are likely to expensive and time consuming.

ACKNOWLEDGMENT

This work is supported by the Office of Naval Research under contracts N00014-91-J-1084 and N00014-91-J-1063 with Dr. E.P. Rood as technical monitor, and NSF grant CTS-913214. Some of the computations were done on the computers at the San Diego Supercomputer Center which is sponsored by the NSF.

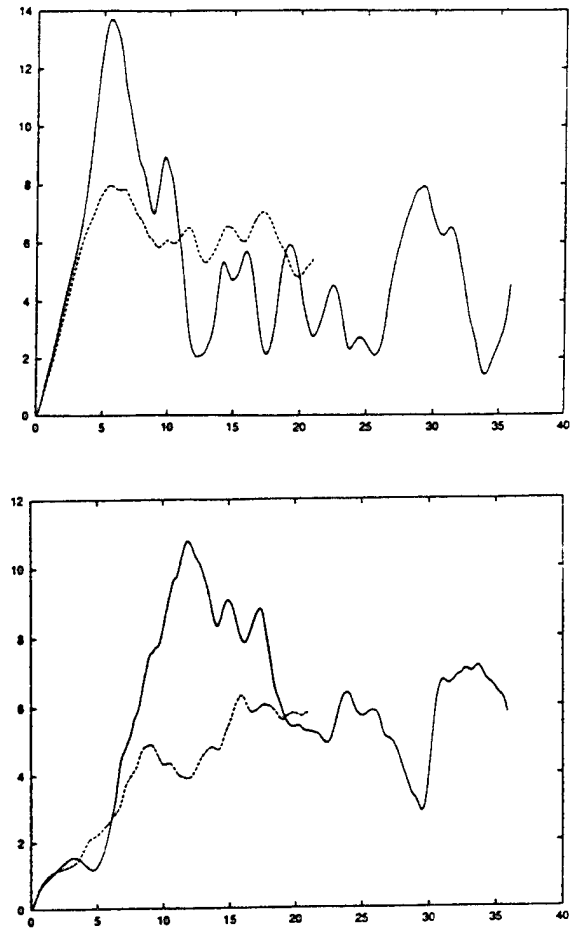


Figure 14. The Reynolds stresses for the 4 bubble run in figure 8 (solid line) and another run with 9 bubbles (dashed line). Top frame, vertical fluctuations $<vv>$. Bottom frame: horizontal fluctuations $<uu>$.

REFERENCES

1. Plesset, M.S. and Chapman, R.B.: 1971, Collapse of an initially spherical vapor cavity in the neighborhood of a liquid boundary, *J. Fluid Mech.* **47**, pp. 283-290

2. Mitchell, T. M. and Hammitt, F.G.: 1973, Asymmetric Caviataion Bubble Collapse, *J. Fluids. Eng.*, pp. 29-37.

3. Harlow, F. H. and Welch, J. E.: 1965, Numerical calculation of time-dependent viscous incompressible flow of fluid with free surfaces, *Phys. Fluids*, **8**, pp 2182-2189,

4. Blake, J.R. and Gibson, D.C.: 1987, Cavitation bubbles near boundaries, *Ann. Rev. Fluid Mech.* **19**, pp. 99-123

5. Chahine, G.L.: 1990. Numerical modeling of the dynamic behavior of bubbles in nonuniform flow field, *Numerical Methods For Multiphase Flows* **91**, pp. 57-64

6. Baker, G.R. and Moore, D.W.: 1989, The rise and distortion of a two-dimensional gas bubble in an inviscid liquid, *Phys. Fluids* **A1**, pp. 1451-1459

7. Yang, Ym.: 1992, The initial value problem of a rising bubble in a 2-dimensional vertical channel, *Phys. Fluids* **A**, pp. 913-920

8. Ryskin, G. and Leal, L.G.: 1984, Numerical solution of free-boundary problems in fluid mechanics. part 2. Buoyancy-driven motion of a gas bubble through a quiescent liquid, *J. Fluid Mech.* **148**, pp. 19-35

9. Shopov, P.J., Minev, P.D., Bazhekov, I.B. and Zapryanov, Z.D.: 1990, Interaction of a deformable bubble with a rigid wall at moderate Reynolds numbers, *J. Fluid Mech.* **219**, pp. 241-271

10. Clift, R., Grace, J. R., and Weber, M. E.: 1978, *Bubbles, Drops, and Particles* (Academic Press)

11. Unverdi, S.O. and Tryggvason, G.: 1992, A front-tracking method for viscous, incompressible, multi-fluid flows, *J. Comput Phys.* **100, No. 1**, pp. 25-37

12. Nobari, M. R., Jan Y.-J., and Tryggvason, G.: 1994, Head-on collisions of drops-a numercial investigation, submitted for publication

13. Nobari, M. R. and Tryggvason, G: 1994, Numerical simulations of drop collisions, *Proc. AIAA Meeting and Exhibit*, Reno NV

14. Unverdi, S.O. and Tryggvason, G.: 1992, Computations of multi-fluid flows, *Physica D* **60**, pp. 70-83

15. Ervin,E.: 1993, *Computations of bubbles and drops in a shear flow.* Ph.D. Thesis. The University of Michigan

16. Esmaeeli, A., Ervin, E. A., and Tryggvason, G.: 1994, Numerical simulations of rising bubbles, (Ed: J.R. Blake), *Proc. IUTAM Conference on Bubble Dynamics and Interfacial Phenomena*

17. Jan, Y.-J., and Tryggvason, G.: A computational study of contaminated bubbles. Submitted for publication.

18. Nobari, M. R. and Tryggvason, G: 1994, Head on collision of drops- a numercial investigation, submitted for publication

19. Nas, S. and Tryggvason, G.: 1993, Computational investigation of the thermal migration of bubbles and drops, *Proc. ASME Winter Annual Meeting*, FED-**175**, pp. 71-83.

20. Ceccio, S. L. and Brennen, C. E.: 1991, Observations of the dynamics snf acoustics of travelling bubble cavitation, *J. Fluid Mech.*, **233**, pp. 633-660.

21. Drew, D.A.: 1983, Mathematical modeling of two-phase flow, *Ann. Rev. Fluid Mech.* **15**, pp. 261-291

22. Brenner, H. and Happel, J.: 1965, *Low Reynolds number hydrodynamics* (Noordhoff International Publishing)

23. Wallis, G. B.: 1992, Macroscopic properties of a twp-phase potential dispersion compound of identical unit cells, *Int. J. Multiphase Flow*, **18, No. 6**, pp. 989-1017.

Experimental Study of a Bubbly, Turbulent, Free Shear Layer

P. Rightley, J. Lasheras
(University of California-San Diego, USA)

ABSTRACT

Bubble-turbulence interaction in a two dimensional free shear layer is analyzed experimentally, investigating the influence of the large coherent structures present in the mixing region. A homogeneous, polydispersed distribution of small gas bubbles is added to one side of a two stream horizontal water tunnel. The streams are allowed to mix at the trailing edge of a splitter plate. The bubbles, present in a low void fraction, have small Weber and Stokes numbers and remain spherical throughout the flow. Time and conditionally-averaged measurements of the carrier phase velocity field, bubble size volume pdf and concentration of the dispersed phase are made using optical techniques. It is shown that the initial evolution of the bubbly, free shear layer is characterized by large inhomogeneities in both the bubble size volume pdf and the void fraction.

NOMENCLATURE

a	bubble radius
D	bubble diameter
g	gravity vector
I	light intensity
I_0	light intensity w/o bubbles present
L	propagation length through test section
u	carrier phase velocity
V	bubble velocity
x	streamwise spatial coordinate
y	longitudinal spatial coordinate
z	spanwise spatial coordinate
$\overline{\alpha}$	z-averaged void fraction
ν	carrier phase kinematic viscosity
ρ_F	carrier phase density
ρ_P	dispersed phase density

INTRODUCTION

The characterization of particle-turbulence interactions is of fundamental importance to a wide variety of applications. More specifically, understanding bubble-fluid interaction in turbulent flows is a keystone in the development of models related to naval, chemical and nuclear reactor safety applications. Due to the highly complex nature of the interface between the phases, transfer laws for mass, momentum and energy are difficult to define, leading to the use of empirically based closure assumptions that may be difficult to justify. Although models based on such assumptions may be successful for specific applications, they often do not allow for a full understanding of the physical mechanisms involved. Thus, the complete experimental characterization of the evolution of the two phases in a prototypical, turbulent, bubbly flow is critical to the general formulation of bubbly flow models. Toward this goal, an experimental study is conducted of a bubbly, turbulent, free shear layer.

Studies of turbulent, two-dimensional, free shear flows over the past two decades have stressed the importance of large scale, spanwise, coherent, vortical structures in the evolution of the layer [1,2]. Such a flow is both well understood and possesses the prototypical characteristics of an anisotropic, non-homogeneous turbulent flow. The interaction of the bubbles with such an underlying flow (especially the large scale structures) forms the basis of this study.

A significant amount of theoretical and numerical work has been done regarding the dispersion of buoyant and heavy particles in free shear layers [3,4,5]. This work assumed no modification of the base flowfield due to the presence of the dispersed phase. One result of this one-way coupling work is that, depending on the bubble's Stokes number and on the ratios between the viscous relaxation and buoyancy times to the bubble entrainment time, the

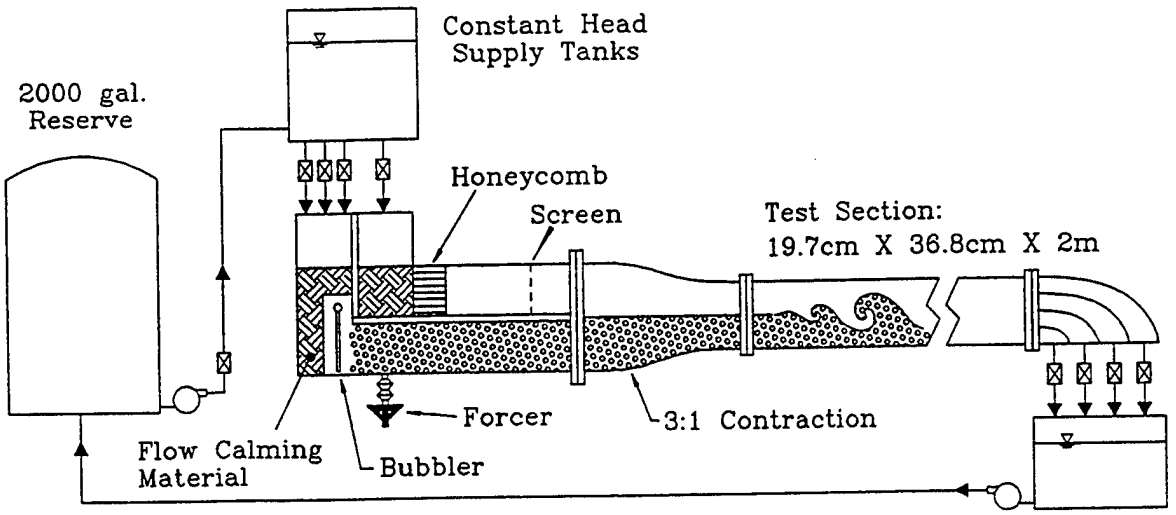


Figure 1: Experimental Facility

interaction between the bubbles and the large eddies may result in bubble accumulation near the center of the spanwise vortices [4,5]. Thus, the presence of the large scale structures will not only affect the dispersion of bubbles throughout the shear layer, but due to the possible creation of large local void fractions the underlying flowfield itself may be influenced. Detailed experimental work similar to that presented in this paper, regarding the one-way coupling of water droplets in air, has also been carried out [6,7].

It is well known that in free shear layers, after the three dimensional transition, the energy of the small scales increases appreciably at what is called the mixing transition [8]. Modification of the turbulent energy spectra of the small scales following this transition may also occur [9,10] through the dispersed phase interacting with the small scales of the flow. Previous research [9] has noted an effect of the dispersed phase on the slope of the turbulence spectrum at high wavenumbers, though the bubble size in that case was on the order of the Taylor microscale. A numerical study [10] has noted an effect of small, heavy particles present in a very low void fraction on the turbulence spectra.

In this study, care was taken to create flow conditions for which it is possible to determine the contributions of the various terms in the momentum equation of the bubbles and so that modern optical flow diagnostic techniques can be applied. For the flow conditions described in this paper, turbulence modification in the region of study is expected to be negligible. The results presented here form a preliminary part of a longer study still in progress. The intent of this project is to provide a detailed experimental investigation of the evolution of both the carrier and dispersed phases in a free shear layer.

EXPERIMENTAL FACILITY AND MEASUREMENTS

The experimental facility consists of the horizontally oriented, two-stream water channel depicted in Figure 1. Each of the streams is independently supplied and controllable. Care is taken to match the stream's temperatures so that index of refraction differences will not exist within the mixing region, since these would disrupt optical flow diagnostics. Free surfaces exist at the channel's supply points and along the test section. The water exiting the test section is pumped to holding tanks where the bubbles are allowed to settle out of the system before the water is recirculated. The forcing mechanism consists of a modified audio speaker and a bellows driven by a function generator. This arrangement provides a small pressure perturbation to the flow used to enhance the growth rate of the most unstable wavelength in the shear layer. Figure 2 describes the coordinate axes used in this paper.

The bubbles were injected into the lower, faster moving side well upstream of the test section, though they can be added to either side. The bubbles are created using the "novel" injection scheme depicted in Figure 3. Water, saturated with CO_2 at 90 psi by a water carbonator, is expanded as a jet through small holes drilled into a grid of brass tubes. The resulting negative pressure step that the

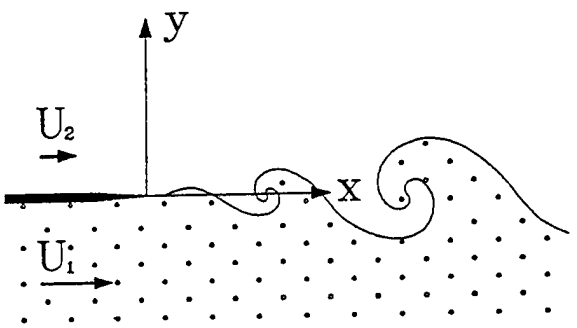


Figure 2: Coordinate Axes

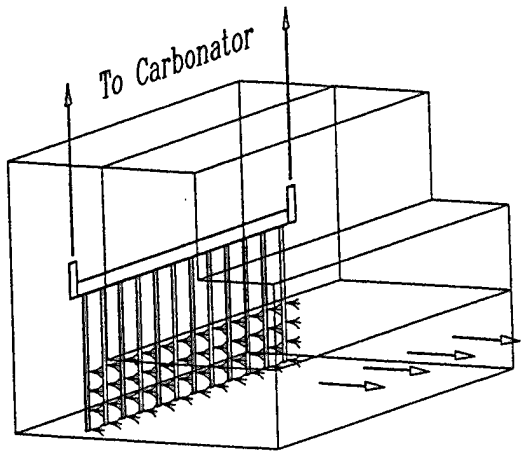


Figure 3: Bubble Generation

carbonated water experiences causes homogeneous nucleation to occur in the jet. Due to the rapid mixing with non-carbonated water, the bubble growth is limited, resulting in a small polydispersed bubble size distribution. Bubble production is not uniform in the vertical direction due to varying pressure steps along the small brass tubing, however, the mixing induced by the jets homogenizes the bubble sizes throughout the stream. Any bubbles produced that are too large rise rapidly and are removed by the free surface just downstream of the injection location. Accumulations of bubbles on the underside of the splitter plate in the slow moving flow prior to the contraction are removed by suction.

Characterization of the flow was made using several techniques, including flow visualization, laser attenuation, laser diffraction particle sizing and laser Doppler velocimetry (LDV). Both instantaneous and time averaged flow visualization was performed by creating a light sheet at the midplane of the experimental facility and observing the light scattered from either fluorescein dye (in the case without bubbles) or the dispersed phase itself. The Malvern 2600 HSD was used for particle sizing measurements. In this system, a laser beam propagates across the spanwise extent of the facility. The low angle scattering of the beam can be analyzed in the context of Franhaufer diffraction theory to provide the volume-size pdf of the dispersed phase within the laser beam. The nature of this system limits it to time and spanwise-averaged results.

The laser attenuation measurements also use a laser beam propagating in the spanwise direction. A photodiode measures the intensity of the laser beam after passing through the flowfield. For dilute systems of spherical particles, it can be shown from Mie theory [10] that the attenuation of the beam intensity across the test section, I/I_0, will be given by

$$-\ln(I/I_0) = 3L\overline{\alpha}\int_0^\infty \frac{\overline{p}df(D)}{D}dD \qquad (1)$$

Even though such attenuation measurements include the effects of both size and concentration, such measurements can be used to study the qualitative spatial and temporal evolution of the bubble void fraction [10]. Due to the quick response of the photodiode, instantaneous, time and conditionally-averaged measurements may be made with this device. It should be noted that the attenuation is averaged across the entire spanwise extent of the flow and therefore three dimensional effects can contribute to some homogenization of the data.

A Dantec LDV system was used with two burst spectrum analyzers to provide two components of velocity simultaneously (streamwise and longitudinal). The LDV was operated in 180° backscatter mode with the transmission and reception occurring through the side wall of the test section. Titanium dioxide particles were used to seed the flow. These measurements provide instantaneous, time and conditionally-averaged velocity values at a single point in the flow. The velocities presented in this paper were measured in the absence of the dispersed phase, however, the bubble generation grid was operated using tap water in order to duplicate

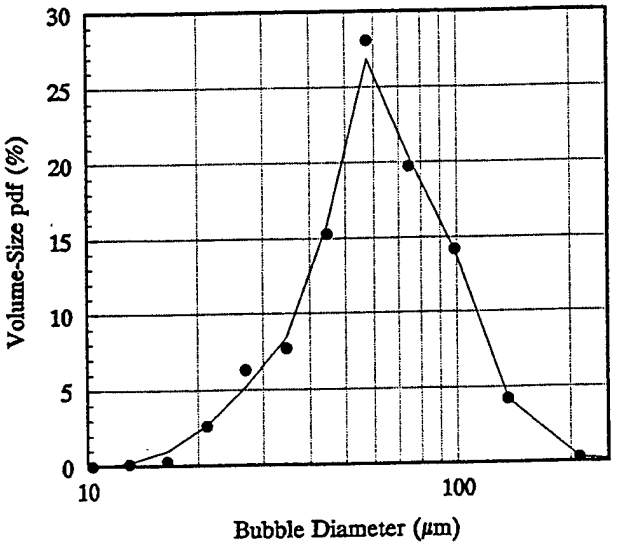


Figure 4: Initial Bubble Volume-Size pdf

the lower stream's initial conditions.

EXPERIMENTAL CONDITIONS

For the results presented here, the lower, bubble-laden stream was moving at 16.5 cm/s while the upper stream moved at 4.0 cm/s, with freestream rms values of 6% and 4%, respectively. This provided a velocity ratio of 4.1 and an average convective velocity of 10.25 cm/s. The Reynolds number based on integral momentum thickness grew from 183 at x = 2 cm to 546 at x = 12 cm the farthest downstream location studied here. The flow perturbation introduced by the forcing system was a single 2.0 Hz sinusoid. This, combined with the average convective velocity, gives a wavelength of the Kelvin-Helmholtz billows of approximately 5 cm.

The time-averaged bubble volume-size pdf in the freestream just below the tip of the splitter plate is shown in Figure 4. It can be seen to be nearly log-normal with a Sauter mean diameter of approximately 50 μm. A vertical traverse of the bubble-laden freestream below the tip of the splitter plate shows the bubble volume-size pdf and the concentration of bubbles rises slightly when moving vertically due to gravitational settling. Using Equation (1) with the volume-size pdf of Figure 4 and a time-averaged laser attenuation measurement at the same point give a freestream void fraction of approximately 2×10^{-5}. Though this is a small value for the void fraction, it should be noted that, even at this value, 50 percent of the laser beam propagating through the freestream was attenuated. Also, bubble-bubble interaction (agglomeration, etc.) can be ignored at this freestream void fraction except in regions of locally high void fraction as may exist near the cores of the spanwise vortical structures when there is sufficient shear.

The momentum equation for a small, spherical particle moving in a nonuniform fluid flow is given by [12]

$$\begin{aligned}\frac{4}{3}\pi a^3 \rho_P \frac{d\mathbf{V}}{dt} &= 6\pi a \nu \rho_F (\mathbf{u}-\mathbf{V}) \\ &+ \frac{4}{3}\pi a^3(\rho_P - \rho_F)\mathbf{g} \\ &+ \frac{4}{3}\pi a^3 \rho_F \frac{D\mathbf{u}}{Dt} \\ &+ 6a^2\rho_F \int_0^t \frac{\sqrt{\pi\nu}}{\sqrt{t-\tau}} \frac{d}{d\tau}(\mathbf{u}-\mathbf{V})\, d\tau \\ &+ \frac{1}{2}\frac{4}{3}\pi a^3 \rho_F \frac{d}{dt}(\mathbf{u}-\mathbf{V}) \qquad (2)\end{aligned}$$

The five terms on the right-hand side of (2) represent the forces acting on the particle which result from Stokes drag, buoyancy, the fluid acceleration, the Basset history, and the effect of the added mass. Equating the buoyancy and drag forces gives a method of computing the bubble terminal velocity in a still fluid. From Figure 3, we can estimate our bubble sizes as ranging from 20 μm to 200 μm in diameter, which gives approximate terminal rise velocities from 0.01 cm/s to 10 cm/s. Likewise, equating the fluid acceleration and drag terms in Equation (2) can give an estimate for the "entrainment velocity." Estimating the vorticity distribution in the core of large eddies in the free shear layer as a modified Rankine vortex [3] gives approximate entrainment velocities ranging from 0.001 cm/s to 1 cm/s toward the center of the vortex. The Stokes and Weber numbers for all bubbles were less than 0.01 and 0.05, respectively.

The small Weber numbers associated with the bubbles strongly suggests that they remain spherical throughout the flow, making them amenable to optical measurement techniques. The two streams present flat mean velocity profiles in the freestream with the bubbles being relatively homogeneously dispersed in the faster, bottom stream. Ratios of bubble rise velocities to the average convective velocity range approximately from 0.001 to 1.0 with the ratios for the entrainment velocity being an order of magnitude smaller.

RESULTS

From the instantaneous flow visualization presented in Figure 5 one can conclude that bubble



Figure 5: Instantaneous Bubble Dispersion Field

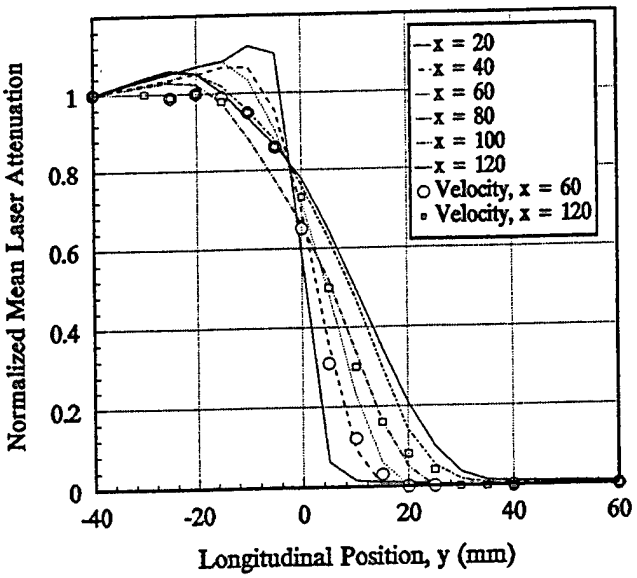


Figure 6: Normalized Mean Attenuation Profiles

dispersion in the initial, developing region of a free shear layer with small amplitude forcing exhibits a high degree of inhomogeneity and coherency in the concentration field. The flow is from left to right and lighting is from above, illuminating the central 5 cm of the span. The end of the splitter plate can be seen on the left hand side of the image which extends to a distance of 16 cm downstream (approximately 3 wavelengths). The bubble dispersion in the initial, developing region of the shear layer is seen to be dominated by groups of bubbles rising into the mixing region, separated by tongues of non-bubbly fluid. These structures are qualitatively very similar to those seen by Winant and Browand [2] for homogeneous fluids with fluorescein dye in the lower layer. Some homogenization of the apparent concentration field is observed to begin to occur in the farthest downstream quarter of Figure 5. The onset of this homogenization seems to coincide with an increase in the number of small scales seen in similar visualizations without the bubbles present.

Some global characteristics of the flow and dispersion fields are presented in Figures 6 and 7. The nonzero slope of the mean attenuation profiles in the freestream are attributable to gravitational settling. The shape of the velocity and attenuation profiles are somewhat dissimilar, though the attenuation profiles also include the effect of the change of the bubble volume-size pdf through the layer. Due to the nonzero slope of the mean attenuation profiles in the freestream, it is not straightforward to define integral thicknesses. Therefore, the longitudinal position where the profile reached 5 per-

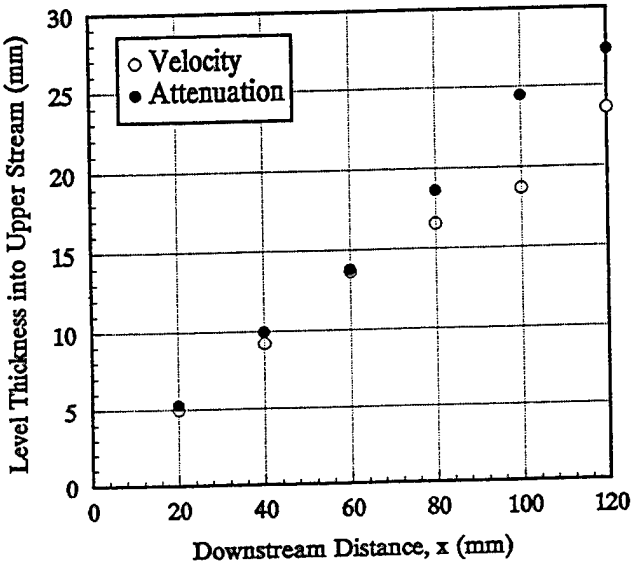


Figure 7: Growth Rate into Upper Stream

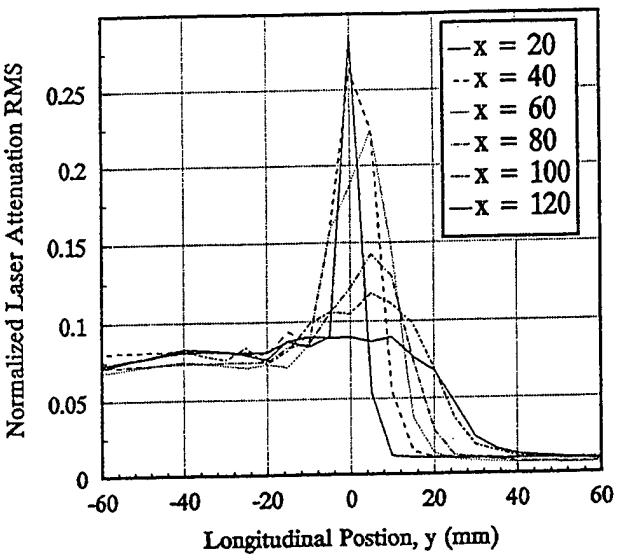


Figure 8: Normalized Attenuation RMS Profiles

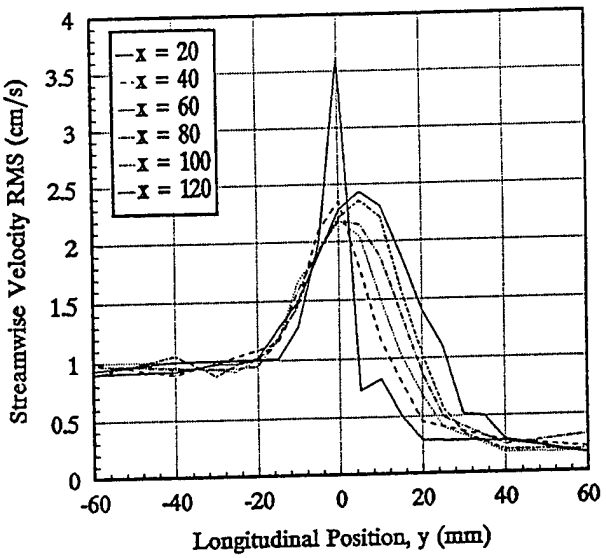


Figure 9: Velocity RMS Profiles

cent of the freestream (y = -40 mm) value was used as a measure of the growth rate of the mixing region. In this study, the concentration field tended to have a growth rate identical to that of the carrier phase for only approximately one wavelength downstream. Farther downstream than this, the momentum growth rate into the slower stream slows down as has been seen before (especially for forced free shear layers), while the attenuation field continues to grow nearly linearly.

The normalized rms laser attenuation provides insight into the spanwise-averaged evolution of the particle concentration field (Figure 8). These profiles have been normalized with the mean freestream laser attenuation values for each downstream location. The magnitude of the peak of the rms erodes monotonically with downstream distance, however, two distinct regions can be seen. The first region maintains relatively sharp peaks of high rms values which decrease only slightly downstream. The second region is revealed through a sudden decrease in the maximum rms value. The region maintaining high peak values of the rms is representative of a high degree of coherence in the concentration field, both streamwise and spanwise. The onset of the second region of lower rms peak values seems to begin somewhat before the transition to smaller scales in the base flow is observed. This region suggests a loss of coherence within the concentration field in either the streamwise or spanwise directions, or both. Indeed, this homogenization is sufficient at x = 120 mm to keep the peak rms value at nearly its freestream value. The preferential growth of the bubble dispersion layer into the slow speed stream (which is a characteristic of the homogeneous free shear layer) can be seen from the motion of the peak rms values into the upper layer.

It is interesting to compare the rms profiles for the velocity field without the bubbles present to those for the concentration field (Figure 9). With the exception of the first profile, the peak rms values for the velocity on the centerline of the test section remain essentially constant with downstream distance (within the range studied). This suggests little loss of streamwise coherence downstream which is in general agreement with the body of data [1,2] suggesting the importance of the large, persistent, coherent structures in the development of the free shear layer. It should be noted that a loss of spanwise coherence would not necessarily be noticed in these profiles, and so the comparison with the concentration profiles cannot be complete.

To examine the structure of the developing bubble dispersion region along with the carrier phase velocity field, conditional averages are presented in Figures 10 and 11. These phase-averaged measurements were obtained by recording the forcing function simultaneously with the laser attenuation signal. The attenuation signal was then discretized into bins based on the phase of the forcing function, resulting in an effective ensemble average over approximately 120 Kelvin-Helmholtz structures. Similar averaging was performed on the LDV data using a triggering output of the function generator after subtracting the average convective velocity. Each part of Figures 10 and 11 depicts one entire cycle of

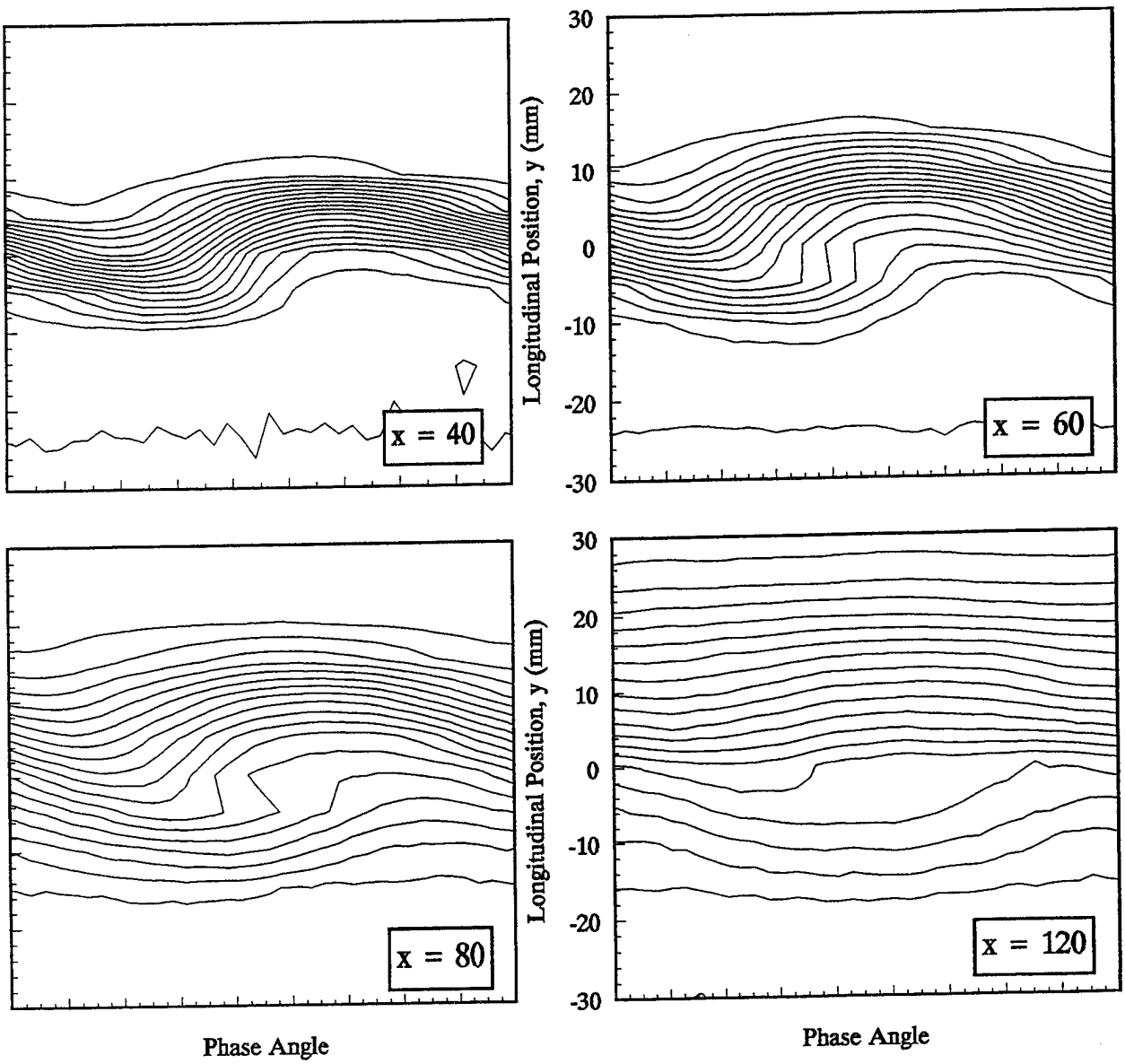


Figure 10: Phase-Averaged Laser Attenuation Surfaces

the forcing function at a given downstream location. The phases of the concentration and velocity fields for each downstream location are aligned. An important characteristic to note is the fact that the regions of bubbles rising into the upper layer do so near the cores of the spanwise vortical structures. This is qualitatively dissimilar to the behavior of heavy particles in such a regime [6,7] which rise in "streaks" through the braid region and over the cores, however, this dissimilarity is to be expected. Analytical works [3,4,5] point out that the term representing the fluid acceleration in equation (2) changes sign for buoyant particles and always points toward the core of vortical structures. Therefore, this entrainment velocity translates the bubbles entering the dispersion region toward the cores of the coherent structures. This same analytical work also describes the process by which bubbles escape the free shear layer, primarily through the regions near the free stagnation points. This provides one of the mechanisms for streamwise homogenization of the concentration field. This is manifested through the smearing of the phase-averaged attenuation field which can be seen occurring in Figure 10 as the flow progresses downstream. By x = 120 mm, the attenuation field maintains very little streamwise coherence, though the velocity field does not seem to experience this smearing to the same degree. It should be noted

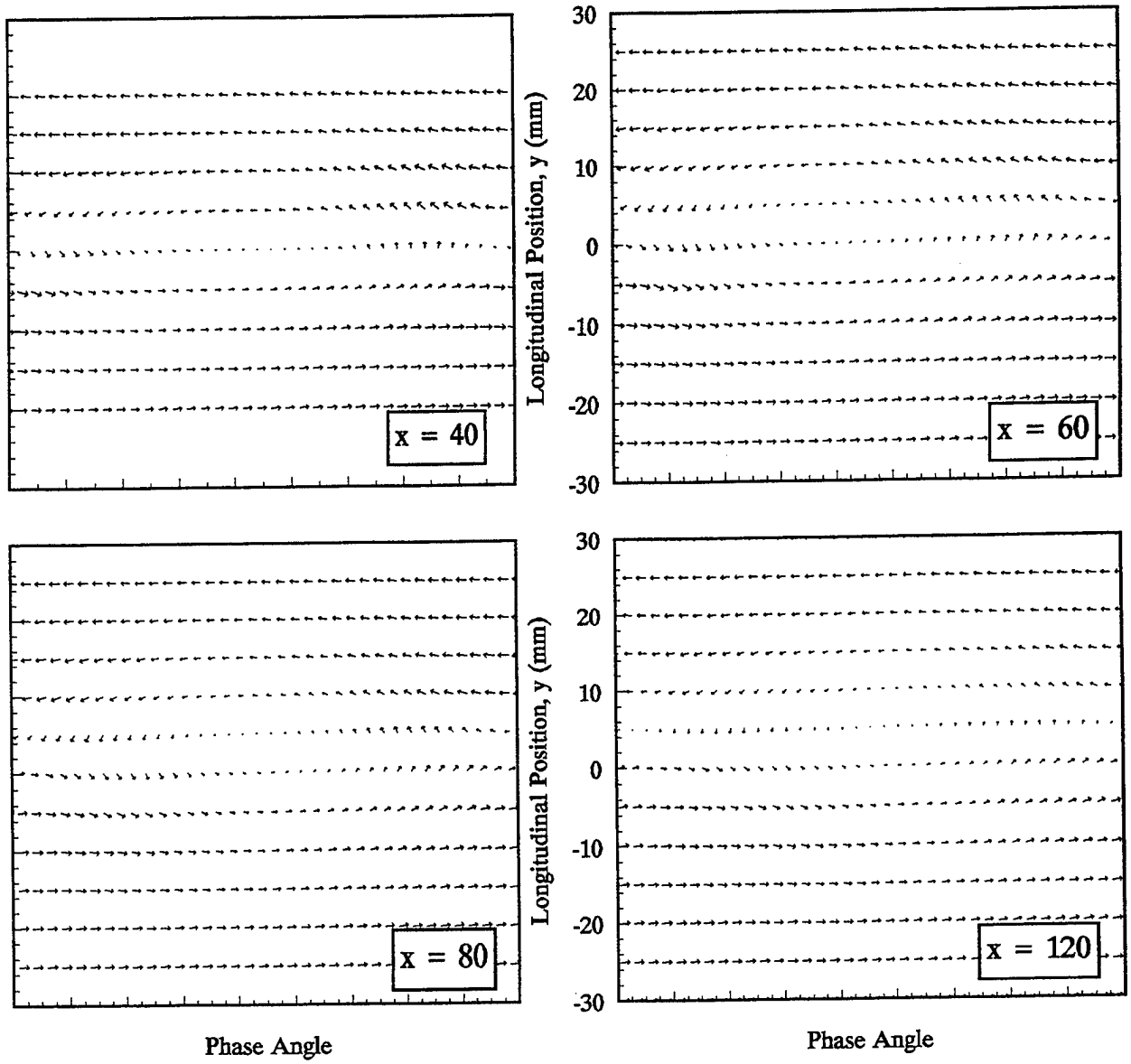


Figure 11: Phase-Averaged Velocity Fields

again that loss of spanwise coherence will also influence these comparisons, though this is not believed to be the predominant factor. These results are clearly consistent with the rms profiles presented earlier.

Time and spanwise averaged bubble volume-size pdf's for several downstream locations are presented in Figure 12. The flow conditions for this data are slightly different from those presented previously, though not significantly. It can be seen that, as the mixing region is traversed vertically at each downstream location, the pdf's tend to larger sizes. This is intuitively obvious due to the importance of gravity for these conditions. However, the pdf's do not show a simple transition from small to large sizes. Instead, they consistently become noticeably bimodal within the mixing region. The transition to larger sizes appears to occur as the growth of a larger mean, nearly log-normal pdf and the decay of the peak of the original freestream log-normal pdf. A single log-normal pdf with a high mean value would presumably exist just at the upper edge of the mixing layer, however, at such a vertical location, there were not enough bubbles to make a measurement. These bimodal pdf's result from the passage of the large scale structures within the mixing layer. If the core regions of these structures possess bubbles distributed similarly to the freestream

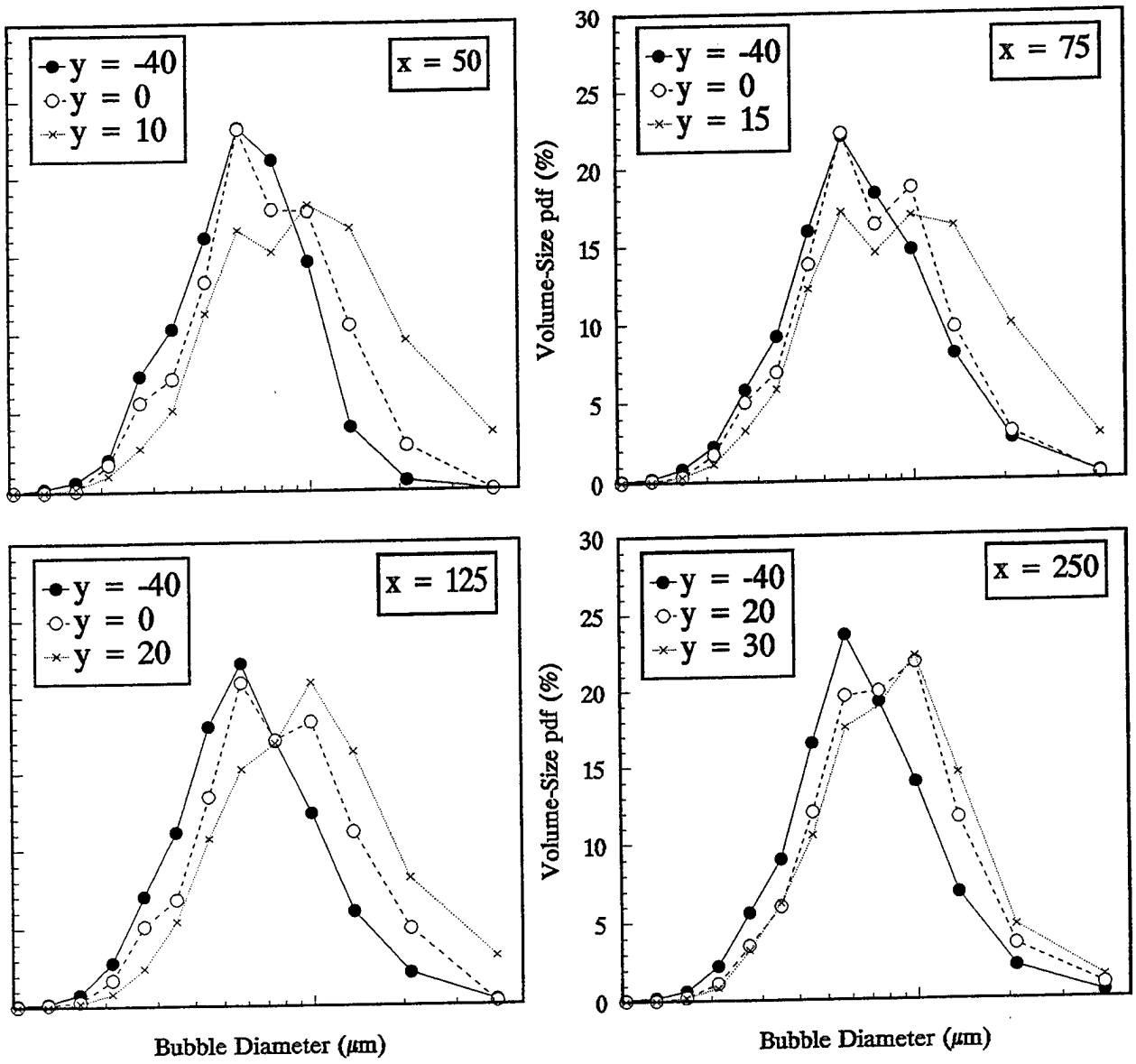


Figure 12: Time-Averaged Bubble Volume-Size pdf's

and the braid region is populated with larger bubbles escaping the layer through the braid regions between the cores, a time average would likely result in such a bimodal pdf. It is important to note the persistence of this feature. This bimodality can still be seen, albeit with a reduced depth of modulation, 5 wavelengths downstream, even though the coherence of the attenuation field was lost after only 2 wavelengths.

CONCLUSIONS

Qualitative experimental results have been presented characterizing the evolution of the dispersed phase in a bubbly free shear layer. The initial, developing region of the shear layer is seen to be characterized by inhomogeneities in both the bubble volume-size pdf's and the void fraction, which are associated with the large scale, coherent structures present in the mixing layer. Bubbles escaping through the shear layer at the regions near the free stagnation points associated with the large scale structures and three dimensionalization are seen to increase the homogenization of the void fraction as the flow evolves. However, the bimodal nature of the bubble volume-size pdf's remains apparent 5 wavelengths downstream. Further work is directed towards a more complete characterization of both

phases including the effect of a polydispersed distribution of small bubbles on the carrier phase itself.

The authors gratefully acknowledge the support of the ONR under contract # N00014-91-J-1252.

REFERENCES

1. BROWN, G. L. & ROSHKO, A., "On density effects and large structure in turbulent mixing layers," Journal of Fluid Mechanics, **64**, 1974, pp. 775-816.

2. WINANT, C. D. & BROWAND, F. K., "Vortex pairing: the mechanism of turbulent mixing-layer growth at moderate Reynolds number," Journal of Fluid Mechanics, **63**, 1974, pp. 237-255.

3. TIO, K-K, & LASHERAS, J. C., "The dynamics of a small spherical particle in steady, two-dimensional vortex flows," AIAA/SAE/ASME/ASEE 29th Joint Propulsion Conference, AIAA-93-1874, 1993.

4. TIO, K-K, LASHERAS, J. C., GAÑÁN-CALVO, A. M. & LIÑÁN, A., "The Dynamics of Bubbles in Periodic Vortex Flows," Applied Scientific Research, **51**, 1993, pp. 285-290.

5. RUETSCH, G. R. & MEIBURG, E., "On the motion of small spherical bubbles in two-dimensional vortical flows," Physics of Fluids A, **5**, 1993, pp. 2326-2341.

6. LÁZARO, B. J. & LASHERAS, J. C., "Particle dispersion in the developing free shear layer," Journal of Fluid Mechanics, **235**, 1992, pp. 143-221.

7. KIGER, K. T. & LASHERAS, J. C., "Experimental characterization of the influence of vortex pairing on particle dispersion and kinetic energy transfer in a two-phase, turbulent shear layer," Journal of Fluid Mechanics, in preparation.

8. BREIDENTHAL, R., "Structure in turbulent mixing layers and wakes using a chemical reaction," Journal of Fluid Mechanics, **109**, 1981, pp. 1-24.

9. LANCE, M. & BATAILLE, J., "Turbulence in the liquid phase of a uniform bubbly air-water flow," Journal of Fluid Mechanics, **222**, 1991, pp. 95-118.

10. ELGHOBASHI, S. & TRUESDELL, G. C., "On the two-way interaction between homogeneous turbulence and dispersed solid particles. I: Turbulence modification," Physics of Fluids A, **5**, 1993, pp. 1790-1801.

11. LÁZARO, B. J. , "Particle dispersion in turbulent free shear flows," Ph.D. dissertation, University of Southern California, 1989.

12. MAXEY, M. R. & RILEY, J. J., "Equation of motion for a small rigid sphere in a nonuniform flow," Physics of Fluids, **26**, 1983, pp. 883-889.

Effects of Regular Waves on the Body Submerged in a Stratified Fluid

E. Ermanyuk, I. Sturova
(Lavrentyev Institute of Hydrodynamics, Russia)

ABSTRACT

It is a common practice in marine hydrodynamics to assume that the density of fluid is constant in the entire domain. Indeed, the density of sea water does vary with the depth. When a body is moving in this stratified fluid, the variation of the density affects on the hydrodynamic loads. This is associated with the power required to generate the internal waves. In stratified fluid the incident waves may be both the surface and internal waves.

The present paper will describe the experimental measurements of hydrodynamic loads due to internal waves on a restrained sphere located either under the pycnocline or inside of it ; and the theoretical analysis of a 2-D linear problem on radiation and scattering of the surface and internal waves by a horizontal cylinder placed under a pycnocline. Contrary to the theoretical investigations, the force action on a 3-D as opposed to 2-D body is simpler to determine experimentally.

NOMENCLATURE

x	horizontal axis
y	vertical axis
t	time
ρ_1	density of upper layer
ρ_2	density of lower layer
$\epsilon = \frac{\rho_2 - \rho_1}{\rho_1}$	relative density variation
g	gravity acceleration
$\bar{g} = \frac{\epsilon g}{2+\epsilon}$	modified gravity acceleration
$\rho(y)$	fluid density distribution in undisturbed state
η_0	oncoming wave amplitude
ω	oncoming wave frequency
KC	Keulegan-Carpenter number
Re	Reynolds number
N	Brunt-Vaisala frequency
U	velocity of a body

INTRODUCTION

The dynamic interaction of floating bodies with stratified fluid was first recognized as the phenomenon of dead water. This phenomenon was studied by Ekman [1] in the series of classical experiments demonstrating the role of internal Froude number (see, also Nikitina [2]). In the case of the linearly stratified fluid the drag on the moving bodies has been experimentally studied by Mason [3], Lofquist and Purtell [4] for a sphere and by Castro and Snyder [5] for 2-D obstacles. It was shown that the flow over a body is generally affected by stratification, the drag depends on Reynolds and Froude numbers and cannot be easily decomposed in wave and viscous components using a simple (say, Froude's) hypothesis. The generation of internal waves by moving sources has been extensively studied, both theoretically and experimentally; for the review see Stepanyants et al. [6], Voisin [7]. Among the less known dynamic effects, it is pertinent to note the possibility of ricochet for a body moving at an angle to two-fluid interface that was experimentally shown by Chervyakov [8].

An extensive theoretical investigation of the wave resistance for floating and submerged bodies in the two-layer fluid has been performed at the St. Petersburg Marine Technical University

(former Leningrad Shipbuilding Institute) (see, for example, Vasilieva [9]).

The problem of the dynamic action of incident internal waves on free or restrained bodies has been less studied compared to the above-mentioned problems. The attention to this problem was drawn in the connection with extensive development of underwater vehicles, submersibles and offshore structures. Some practical examples concerning submerged bodies are described in [10]. C.O'D.Icelin [see 11] suggested the consideration of the *Thresher* accident in the context of internal waves. The action of internal waves on the moored drillship has been studied in the full-size experiments by Osborne et al. [12].

The goal of this paper is to give a more detailed description of the free/restrained body interaction with stratified sea. To do this, the complex approach is adopted. The typical environmental features of internal waves and definition of parameters is given in Section 2. The experimental part (Section 3) treats the internal waves loading on a fixed submerged sphere both in homogeneous fluid and in the mixed layer separating the fluids of different densities. It should be noted that the special case of a body placed in the mixed layer presents considerable difficulties for a correct theoretical analysis, being, however, of immediate practical interest as the most stable position for a free submerged body.

The theoretical analysis (Section 4) is carried out in the linear treatment assuming that the fluid is ideal and incompressible. The sharp and smooth pycnoclines are simulated by two-layer fluid with homogeneous layers and three-layer fluid, involving the linearly stratified upper and middle layers and the homogeneous lower layer, respectively. In a two-layer fluid, the upper layer can be both infinite and bounded by a rigid lid or free surface. In a three-layer fluid, the upper layer is bounded by a rigid lid. In all the cases concerned, a submerged body is fully located in the lower layer of infinite depth. The fluid motion in this layer is assumed to be potential.

2. CHARACTERISTICS OF INTERNAL WAVES. DEFINITION OF DIMENSIONLESS PARAMETERS

Internal waves are commonly observed everywhere in oceans (see, for example, Miropolskii [13]. The existence of internal waves is conditioned by the vertical density gradient due to temperature and/or salinity variation with depth. The total density difference across the ocean depth ranges up to 5 %. A typical density distribution is characterized by the presence of a quasi-homogeneous 20-100 m thick upper layer, followed by the sharp season thermocline with increasing density. Below the level of 50-200 m the density variation with depth becomes less pronounced. This is the main thermocline layer where the density gradually increases to the depth about 1 km. The lower ocean is practically homogeneous.

The amplitudes of internal waves in the main thermocline may reach 100 m with the corresponding wavelengths of tens kilometers. However, from the dynamic standpoint, the responses of underwater vehicles, submersibles and offshore structures are most pronounced under the action of short-period internal waves in the season thermocline.

Normally, the density variation $\varepsilon = \rho_2/\rho_1 - 1$ in the season thermocline is of order 0.01, where ρ_2 and ρ_1 are the densities of lower and upper fluid layers respectively. The characteristic period of internal waves in the season thermocline ranges from 5 to 60 min. This waves are moderately sized with the amplitudes about 5-30 m and wavelengths about 500-8000 m. Generally, long waves are nearly sinuous, whereas the short ones are strongly non-linear and propagate in groups of several waves.

The characteristic lengths of marine structures fall within the range between 10-200 m. Normally, these lengths are small as compared to wavelengths. Thus, a complete solution of the diffraction problem would be essential either for large gravity platforms and study of diffracted wave motion over uneven bottom with the aim of pre-

diction of local wave kinematics or in the case of pronounced modal behavior when the length of diffracted waves may be comparable with the length of a body.

The knowledge of local wave kinematics is required for the prediction of the loads exerted by internal waves on submerged bodies. For a small (compared to wavelength) body, the force action of the wave flow of stratified fluid is characterized by four local parameters, i.e. Keulegan-Carpenter number $KC = 2\pi\zeta_1/l$, Reynolds number $Re = \zeta_1\omega l/\nu$, dimensionless frequency $\bar{\omega} = \omega/N$ and orbital shape parameter $f = \zeta_2/\zeta_1$ where ω is the angular frequency of oncoming waves, ζ_1 and ζ_2 are the local amplitudes of horizontal and vertical motions of fluid particles, l is the charateristic length of a body, ν is kinematic viscosity, $N = \sqrt{-\frac{g}{\rho}\frac{d\rho}{dy}}$ is Brunt-Vaisala frequency, where $\rho(y)$ is the fluid density distribution in the undisturbed state with the y -axis pointed vertically upwards.

For the above-mentioned range of wave periods and characteristic lengths of a body, the values of parameters would run to $KC \sim 0.2 \div 80, Re \sim (1 \div 360) \cdot 10^6$. The value of the orbital shape parameter f is generally small as the length of internal waves is large compared to the thermocline depth. The dimensionless frequency varies from $\bar{\omega} \sim 0.1$ in the thermocline to $\bar{\omega} \sim 200$ for the upper ocean after storm.

3. EXPERIMENTS

The surface-wave loading on surface-piercing and submerged bodies is the subject of the extensive literature. The detailed review of the works treating the wave loading on vertical and horizontal cylinders is given, for example, in [14,15]. The wave loads on a submerged sphere have been studied in [16,17]. Four types of the loading have been observed depending on the orbital shape parameter f and the effects of flow separation controlled by KC and Re.

The present study of the force exerted by internal waves on a fixed sphere has been conducted with the aim of qualitative description and quantitative evaluation of different types of loading. The parameters of the problem were varied within the ranges: $Re = 10 \div 280, KC = 0.06 \div 0.95, f = 0.8 \div 1.0$.

Experimental setup

The experiments were performed in the test tank $(6 \times 0.2 \times 0.6m)$. The test tank was filled with two liquids of different density. The top layer consisted of water with density $\rho_1 = 0.999g/cm^3$ and bottom layer consisted of a solution of glycerin in water with density $\rho_2 = 1.010g/cm^3$. The diagram of the experimental installation is shown in Fig. 1.

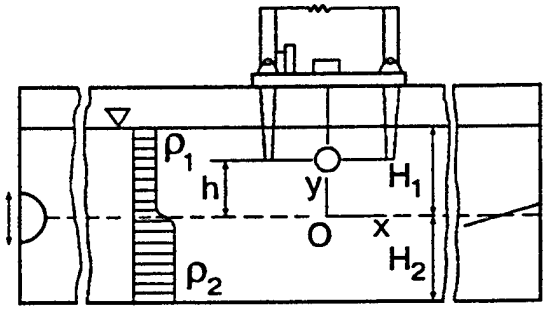


Fig. 1.

Internal waves were generated with the help of a half-cylinder undergoing heaving motion along the end wall of the test tank. The opposite end of the test tank was equipped with a wave breaker in the form of a plate sloping at an angle of 6° with respect to the horizontal plane. Two-component balances were used for the measurement of the forces acting on the sphere. The forces were transferred with the help of strings and streamlined arms to the flexible elements whose deformation was measured by inductive displacement sensors. The maximum load in the experiments did not exceed $9 \times 10^{-4}N$. The spring displacement of the sphere under the action of such a force did not exceed $4.5 \times 10^{-3}mm$. The diameter of the sphere $d = 4cm$. The minimum natural frequency of the balances with the model suspended on them in water was 2.7 Hz and maximum frequency of the loading in the experiments did not exceed 0.24 Hz. A fixed rectangular reference system Oxy (see Fig.1) is used. The origin of

the reference system is located beneath the center of the sphere. The $x$axis is horizontal, and in the unperturbed state of the liquid it coincides with the line of constant density $\rho_0 = (\rho_1 + \rho_2)/2$, taken as a conventional interface; the y -axis is directed vertically upwards. The Oxy plane coincides with the vertical symmetry plane of the test tank. Incident internal waves propagate in the positive x direction. In this reference system the density distribution with depth may be approximated by the relation

$$\rho(y) = \rho_0 - 0.5(\rho_2 - \rho_1)\tanh(y/\delta)$$

where δ is the parameter characterizing the thickness of the layer of variable density (pycnocline). In the experiments this parameter ranged from 0.42 to 0.58 cm. The parameters of the internal waves were recorded with the help of a resistive-type wavemeter. The wavemeter was placed at the longitudinal coordinate of the center of the sphere. This made it possible to evaluate the phase shifts between the oscillations of the wave profile and the forces acting on the sphere. The wave amplitudes and the forces were recorded before the arrival of the reflected waves, although the amplitude of these waves in the test section did not exceed 5 % of the amplitude of the incident waves. In the present problem it is most convenient to make comparisons to the linear theory of waves in ideal, unbounded, two-layer fluid. The sufficient condition for modeling of infinite depths is

$$\omega^2 H_{1,2}/\bar{g} > 3, \qquad (1)$$

where $\varepsilon = 0.011$, $H_1(H_2)$ is the depth of the top (bottom) layer, $\bar{g} = \varepsilon g/(2+\varepsilon)$. The minimum value of $H_{1,2}$ in the experiments was 0.25 m. Moreover, the parameter $d/H_{1,2}$ must be small. In the experiments this ratio did not exceed 0.16.

Results and discussion

The experiments were performed in two series. The wave loads due to internal waves acting on the sphere located in the homogeneous layer were studied in the first series. For this the sphere was placed far enough from the interface to meet the condition $h > (a+\eta_0+3\delta)$ where h is the distance from the center of thepsphere to the $x$axis, $a = d/2$ is the radius of the sphere, η_0 is the amplitude of internal waves. The frequency of waves and the distance h were varied. The results of this series of experiments are presented in Fig. 2.

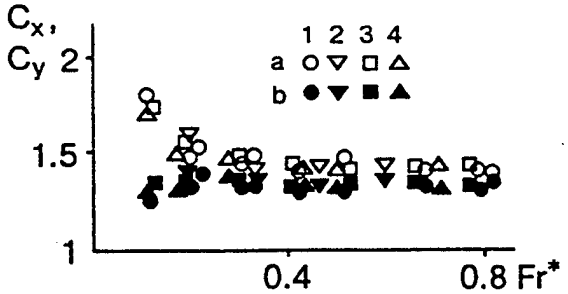


Fig. 2.

The values of the parameter $\mathrm{Fr}^* = \omega^2 a/\bar{g}$, which in such problems plays the role of internal Froude number, are plotted along the abscissa. The coefficients of the horizontal and vertical forces, defined as

$$C_x = F_{xa}/\rho_1 V\dot{u}_a, \quad C_y = F_{ya}/\rho_1 V\dot{w}_a \qquad (2)$$

are plotted along the ordinate. In Eq.(2) V is the volume of the sphere; $\dot{u}_a = \dot{w}_a = \eta_0\omega^2 \times \exp(-\omega^2 h/\bar{g})$ is the amplitude of the local accelerations of fluid particles at the depth corresponding to the center of the sphere evaluated from the linear theory of waves in ideal unbounded two-layer fluid, F_{xa} and F_{ya} are the amplitudes of the horizontal and vertical forces respectively. The sets of symbols a and b refer to the coefficients C_x and C_y, respectively; the variants 1–4 correspond to relative depths $h/d = 1.38$, 1.66, 1.81, 2.09.

The lower limit for the experimental values of Fr^* is conditioned by low efficiency of the wave-breaker for the long waves, whereas the upper limit is theoretically imposed by the maximum Brunt-Vaisala frequency (in our experiments this maximum falls within $3.1 \div 3.6 rad/s$). However, the viscous attenuation of short waves imposes the frequency limit about 50 % of this value.

The condition for the absence of any influence of the bottom and the free surface (1) holds for $Fr^* > 0.24$. It follows from Fig. 2 that C_x and C_y are virtually constant and close to 1.5, i.e. the value predicted by the theory of ideal liquid for a sphere in oscillatory flow (see [18] for consideration). The increase in C_x and decrease in C_y for small values of Fr^* are due to the approximation of kinematics of fluid particles used for normalization in Eq.(2). When evaluating the amplitudes of local accelerations according to the theory of two-layer fluid of finite depths H_1 and H_2 coefficients C_x and C_y were found to be constant in the entire range of experimental values of Fr^*.

The relation (2) with constant C_x and C_y presumes that the loads from a wave of unit amplitude have a maximum at $\omega_* = \sqrt{\bar{g}/h}$ for a prescribed depth of sphere. This relation was satisfied in the experiments with the accuracy 1%.

The phase shifts between the internal waves and oscillations of the vertical and horizontal forces show that the loads are mainly determined by the inertial component. The phase shift is $\psi_1 = 90° + \phi_1$ for the horizontal force and $\psi_2 = 180° + \phi_2$ for the vertical force. The phase lags due to viscosity $\phi_1 = 9° \mp 2°$ and $\phi_2 = 18° \mp 2°$ are small and virtually independent on frequency.

In such problems the forces are decomposed in inertial and drag components using the Morison equation. For the special case of a sphere this equation is

$$F_x = \frac{1}{8}C_{dx}\rho\pi d^2 u\sqrt{u^2+w^2} + \frac{1}{6}C_{mx}\rho\pi d^3\dot{u},$$

$$F_y = \frac{1}{8}C_{dy}\rho\pi d^2 w\sqrt{u^2+w^2} + \frac{1}{6}C_{my}\rho\pi d^3\dot{w} \quad (3)$$

where u and w are the horizontal and vertical components of the velocity of the fluid particles; $\dot{u}$ and $\dot{w}$ are the local accelerations; C_{dx} and C_{dy} are the coefficients of the drag forces; C_{mx} and C_{my} are the coefficients of the inertial forces.

Equations (3), together with information on the phase shifts, give the following relations

$$C_x\cos(\omega t-\phi_1) = \frac{3}{8\pi}C_{dx}KC\sin\omega t + C_{mx}\cos\omega t,$$

$$C_y\sin(\omega t-\phi_2) = -\frac{3}{8\pi}C_{dy}KC\cos\omega t + C_{my}\sin\omega t.$$

The experimental results for the sphere located in the homogeneous layer are represented well by the Morison equation with $C_{mx} = C_x\cos\phi_1$, $C_{my} = C_y\cos\phi_2$ and $C_{dx} = 8\pi C_x\sin\phi_1/3KC$, $C_{dy} = 8\pi C_y\sin\phi_2/3KC$ ($C_{mx} = 1.43, C_{my} = 1.26, C_{dx} = 1.7/KC, C_{dy} = 3.4/KC$). These values of the coefficients agree well with the results obtained for regular surface waves [16,17].

The forces acting on a sphere located in the pycnocline were studied in the second set of experiments. In this case the buoyancy force dominated over the inertial force so that the summary vertical force varied virtually in phase with the oscillations of the interface. For the moderate wave amplitudes ($\eta_0/a \sim 0.5$), the visual study showed that the sphere located in the middle of the pycnocline had minor effects on the shape of internal waves and on the density distribution. Thus, the vertical force may be expressed by the equation

$$F_y = F_b - \frac{1}{6}C_{my}\rho\pi d^3\dot{w}$$

where F_b is the buoyancy force determined as follows:

$$F_b = \pi\int_{-a}^{a}\rho(y-\eta_0\sin\omega t)(a^2-y^2)dy.$$

The experimental value of the coefficient $C_{my} = 1.04$. It implies very low value of the added mass coefficient $C_{ay} = C_{my} - 1 = 0.04$. The negative values of the added mass coefficient are reported in [19] for the free oscillating body piercing the interface of miscible liquids.

The horizontal force acting on the sphere located in the middle of the pycnocline ($h = 0$) oscillates at the double frequency compared to the frequency of oncoming waves. This is nonlinear effect of the second-order inertial loads due to variability of the volume immersed in the upper and lower layers of nearly equal densities. For the equal depths of upper and lower layers $H_1 = H_2 = H_0$ and moderate values of η_0/a, the second-order horizontal inertial load may be

written as follows:

$$F_x = \rho C'_{mx} \eta_0^2 \omega^2 S \coth kH_0 \sin 2\omega t$$

where C'_{mx} is the coefficient of the second-order inertial force, $S = \pi a^2$ is the cross-sectional area of the sphere . The experimental value $C'_{mx} = 1.2$.

If the center of the sphere is somewhat displaced from the middle of the pycnocline (i.e. $h \neq 0$), then the time-dependence of F_x and F_y is , generally, strongly non-linear. The corresponding trajectories (hodographs) of the tip of the summary force vector presented as Lissajous figures are shown in Fig. 3 for different locations of the sphere. The hodographs illustrate the relative importance of the first- and second-order wave effects. Here, the horizontal and vertical force components are presented in the non-dimensional form, the maximum scale of the buoyancy force $\varepsilon\rho g\pi d^3/6$ being used for normalization. Arrows indicate the sequence of time.

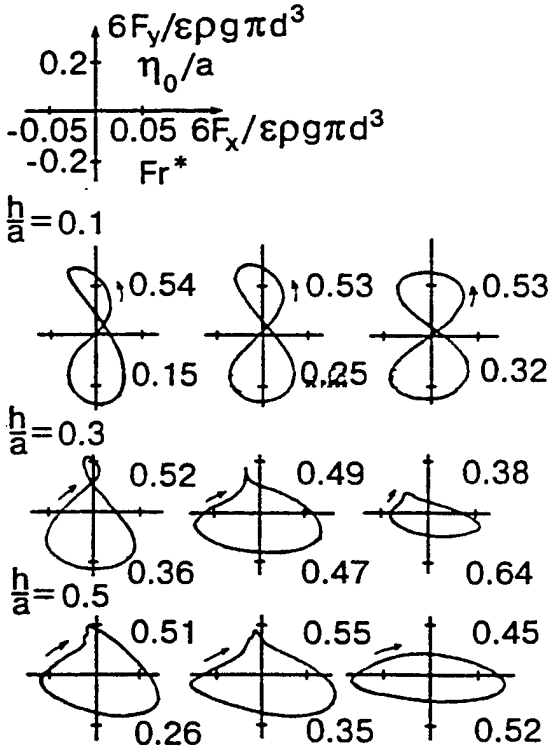


Fig. 3.

When increasing h, the disturbances of the local wave field due to the presence of the sphere became more pronounced. At intermediate $h \sim (0.3 \div 0.5)a$, the ring-shaped wave disturbance with the features of the second-mode (varicose) radial solitary wave is generated in pycnocline at the entry of the sphere in a wave crest. For $h \sim 0.5a$, the jet currents are observed as wave crests hit the lower part of the sphere. The jet currents are similar to those observed for slamming. The characteristic hodographs are presented in Fig 3. Noteworthy are new time scales introduced by 'internal' slamming. Upon the passage of the wave crest, the lower fluid flow down from the lower part of the sphere forming a 'stem' remaining in fluid up to the passage of the next wave crest. This 'stem' is easily observable because of high density gradients at its boundaries. The analogous structure is typical for the problem of a body emerging through liquid-liquid interface (see for example [20]).

Thus, depending on the location of a body relative to pycnocline, four characteristic types of the wave loading may be identified:

a) For a body located in a quasi-homogenious layer ($\bar{\omega} \gg 1$), the evaluation of the loading at first approximation may be obtained from the Morison equation. As it has been shown for a circular cylinder [21], for Re $> 10^5$ the inertia and drag force coefficients have a weak dependence on KC and Re gradually approaching some definite values. For the bodies of complicated geometry, the force coefficients may be obtained in experiments with the oscillatory flow in U-tube at high Re. The solution of the diffraction problem is required for the large bodies.

The order of magnitude of the loads due to internal waves can be inferred from the Table 1 presenting the estimate based on the Morison equation for the case of the horizontal cylinder (diameter 10 m , length 100 m) aligned parallel to the wave crests. The values of the force coefficients are $C_{mx} = C_{my} = 1.8, C_{dx} = C_{dy} = 0.6$ (see [21]). The wave kinematics is evaluated from the theory of ideal two-layer fluid with the upper layer of 150 m and the lower layer of infinite depth. The wave amplitude varies within the re-

alistic limits from 5 m for the waves with the period of 5 min to 30 m for the waves with the period exceeding 20 min. The force magnitudes are nondimensionalized using the weight of the body as the force scale.

Table 1.

wave period	5 – 20 min	20 – 60 min
important flow effects	inertial	viscous
wave length	500 – 2500 m	2500 – 8000 m
	force amplitude / body weight	
close to free surface		
horizontal force	$3 \cdot 10^{-4}$	10^{-3}
vertical force	negligible	negligible
close to pycnocline		
horizontal force	$4 \cdot 10^{-4}$	10^{-3}
vertical force	$3 \cdot 10^{-4}$	$6 \cdot 10^{-5}$

From the Table 1, one can see that the drag force generated by the surface currents due to long internal waves with the period 20 – 60 min are predominant for the body located near the free surface. At the typical mooring line characteristics (see [22]) the horizontal body offset under the action of these forces may be of order several meters. This estimate is consistent with the field experiments [12].

For the body located near the thermocline, the inertial loads due to internal waves with the periods 5 – 20 min may be also of interest.

b) As a body approaches the thermocline, the influence of the density gradient increases. The buoyancy force and the vertical component of the inertial force act in phase opposition. The idea of the existence of the depth where these forces may cancel each other has been proposed and experimentally verified by Razumeenko (personal communication). It should be noted that when the body is small, so that the local density distribution may be considered as linear, the above effect occurs at $\bar{\omega} = 1$, i.e. when the frequency of the incident waves is equal to the local Brunt-Vaisala frequency. It is pertinent to note the drastic reduction of the added mass coefficient at this frequency that was demonstrated in the calculations [23] for the ellipsoid oscillating in a linearly stratified fluid.

c) For the body located in the thermocline, the vertical load due to the variable buoyancy force dominates. The coefficient of the vertical inertial force may be markedly reduced. The effects of the modal behavior of internal waves and 'internal' slamming may be pronounced at certain range of parameters.

d) The special case of a body piercing the pycnocline is characterized by high-order horizontal load oscillating at the double frequency compared to the frequency of oncoming waves. This load is of second order with respect to the wave amplitude for inertial force and of third order for drag force.

From the standpoint of the body motions, it should be noted that the characteristic natural period of the horizontal motions of the moored structures is of order 1–2 min and the natural frequences of heave motion for small bodies in the stratified fluid has the order of local Brunt-Vaisala frequency (see [24] for consideration of the free oscillations of a sphere) In the case of short natural periods, it is worth noting new short time scales is introduced by 'internal' slamming and by high order loads of double frequency. In the case of the natural periods comparable to the periods of oncoming internal waves, resonant motions may occur. In this connection, the effects of encounter frequency for the underwater vehicles advancing in internal waves and motions of submerged elongated vertical bodies piercing the thermocline are of particular interest.

4. THEORETICAL ANALYSIS

The 2-D linear problem on radiation and scattering of the small-amplitude surface and internal waves by a horizontal cylinder moving at constant depth under a pycnocline is considered.

Previously the problem of a submerged body advancing in regular water waves has been considered only for surface waves in homogeneous fluid. The most efficient method of its solution for bodies of complicated shape in a 2-D and 3-D flows is recognized the coupled finite element

method (CFEM) [25, 26]. The velocity potential is represented by the finite element method in a narrow region surrounding a body and by the boundary integral equation in the outer region. This method may be also used in a stratified fluid if the density varies only on the depths above and below a submerged body.

The presentation of the below-mentioned theoretical results is given in more detail in Sturova's papers [27-31]. The case of the two-layer fluid under a lid involving a possible occurrence of the only free internal waves is most completely analyzed.

Let the fixed frame of reference be taken with the $\bar{x}$-axis directed along an equilibrium position of the interface, orthogonally with respect to a cylinder axis, and the y-axis pointed vertically upwards. In the undisturbed state, the upper layer with the thickness H and density ρ_1 occupies the domain $-\infty < \bar{x} < \infty$, $0 < y < H$, the lower one, with the density $\rho_2 = \rho_1(1+\varepsilon)$ $(\varepsilon > 0)$, occupies the domain $-\infty < \bar{x} < \infty$, $y < 0$. The fluid flow in each layer is irrotational.

In the fixed frame of reference the incident potential may be written as

$$\psi_0^{(s)} = \frac{i\omega_0}{k_0}\phi_0^{(s)} \exp[i(\omega_0 t \mp k_0 \bar{x})],$$

$$\phi_0^{(1)} = -\frac{\cosh k_0(y-H)}{\sinh k_0 H}, \quad \phi_0^{(2)} = e^{k_0 y},$$

where the incident wave frequency ω_0 depends on the wave number k_0 according to the dispersion relation,

$$\omega_0 = \Omega(k_0), \quad \Omega(k) = \sqrt{\varepsilon g k / B(k)},$$

$$B(k) = 1 + \varepsilon + \coth kH,$$

signs '+' and '-' correspond to waves travelling from right and from left, respectively, superscript s is equal to 1 for the upper layer and 2 for the lower one.

In the moving reference frame $x = \bar{x} - Ut$ the total potential can be written as

$$\Phi^{(s)}(x,y,t) = -Ux + U\bar{\Phi}^{(s)}(x,y) + \\ + \mathrm{Re}\sum_{j=0}^{4} \eta_j \Phi_j^{(s)}(x,y) e^{i\omega t},$$

where $\bar{\Phi}^{(s)}$ is the steady potential due to the unit forward speed; the components $\Phi_j^{(s)}$ $(j = 1,2,3)$ are the radiation potentials due to motions of the cylinder with unit amplitude in each of three degrees of freedom; η_j are the corresponding motion amplitudes; $\Phi_0^{(s)} = \phi_0^{(s)} \exp(\mp i k_0 x)$ and $\Phi_4^{(s)}$ are the potentials of the incident and diffracted waves, respectively; and $\eta_0 = \eta_4$ is the incoming wave amplitude. In the moving reference frame, the incident waves arrive with the encounter frequency $\omega = \omega_0 \mp k_0 U$.

Based on the assumptions of linear potential flow theory, we can write the following governing equations for the steady potential

$$\Delta\bar{\Phi}^{(1)} = 0 \quad (0 < y < H),$$
$$\Delta\bar{\Phi}^{(2)} = 0 \quad (y < 0) \qquad (4)$$

with boundary conditions

$$\partial\bar{\Phi}^{(1)}/\partial y = 0 \quad (y = H),$$
$$(1+\varepsilon)\frac{\partial^2\bar{\Phi}^{(2)}}{\partial x^2} - \frac{\partial^2\bar{\Phi}^{(1)}}{\partial x^2} + \frac{\varepsilon g}{U^2}\frac{\partial\bar{\Phi}^{(1)}}{\partial y} = 0,$$
$$\frac{\partial\bar{\Phi}^{(1)}}{\partial y} = \frac{\partial\bar{\Phi}^{(2)}}{\partial y} \quad (y = 0),$$
$$\frac{\partial\bar{\Phi}^{(2)}}{\partial y} \to 0 \ (y \to -\infty),$$
$$\frac{\partial\bar{\Phi}^{(s)}}{\partial x} \to 0 \ (x \to \infty), \left|\frac{\partial\bar{\Phi}^{(s)}}{\partial x}\right| < \infty \ (x \to -\infty).$$

The boundary condition for $\bar{\Phi}^{(2)}$ should be satisfied at a mean position of the body surface L: $\partial\bar{\Phi}^{(2)}/\partial n = n_x$ $(x, y \in L)$, where $\vec{n}$ is the inward normal of the cylinder surface and n_x is the component of $\vec{n}$ in the x-direction.

The radiation and diffraction components of the potential satisfy the equations, similar to (4), with boundary conditions

$$\partial\Phi_j^{(1)}/\partial y = 0 \quad (y = H), \qquad (5)$$
$$(1+\varepsilon)D\Phi_j^{(2)} - D\Phi_j^{(1)} + \varepsilon g \partial\Phi_j^{(1)}/\partial y = 0,$$
$$\partial\Phi_j^{(1)}/\partial y = \partial\Phi_j^{(2)}/\partial y \quad (y = 0), \qquad (6)$$
$$\partial\Phi_j^{(2)}/\partial y \to 0 \quad (y \to -\infty), \qquad (7)$$
$$\partial\Phi_j^{(2)}/\partial n = i\omega n_j - U m_j \ (j = 1,2,3),$$

$$\partial\Phi_4^{(2)}/\partial n = -\partial\Phi_0^{(2)}/\partial n \quad (x,y \in L),$$

where

$$D \equiv (U\partial/\partial x - i\omega)^2,\ (n_1,n_2) = (n_x,n_y),$$

$$n_3 = (y-y_0)n_x - (x-x_0)n_y,$$

$$(m_1,m_2,m_3) = \left\{ \frac{\partial^2\bar{\Phi}^{(2)}}{\partial n\partial x}, \frac{\partial^2\bar{\Phi}^{(2)}}{\partial n\partial y}, \right.$$

$$\left. \frac{\partial}{\partial n}\left[(y-y_0)\left(\frac{\partial\bar{\Phi}^{(2)}}{\partial x}-1\right) - (x-x_0)\frac{\partial\bar{\Phi}^{(2)}}{\partial y}\right]\right\},$$

x_0 and y_0 are the coordinates of a point with respect to which the body oscillates rotationally.

The radiation condition for $\Phi_j^{(s)}$ $(j=1,...,4)$ states that a wave travelling in the direction of the forward speed and with its group velocity larger than the forward speed is far in front of the body, and otherwise the waves propagate behind.

The moving body in waves is affected by the hydrodynamic force $\vec{F}$ and moment M determined by integrating the fluid pressure $p = -\rho_2(\partial\Phi^{(2)}/\partial t + |\nabla\Phi^{(2)}|^2/2)$ over the cylinder surface L

$$\vec{F} = \int_L p\vec{n}dl, \quad M = \int_L pn_3 dl. \qquad (8)$$

The representation $\vec{F} = (F_1,F_2)$, $M = F_3$ is commonly used and for the linearized problem Eq.(8) is substituted for the sum

$$F_j = F_{sj} + \mathrm{Re}(F_{nj} + F_{ej})e^{i\omega t}, \qquad (9)$$

where the first term is due to a steady speed of the body and equals

$$F_{sj} = \rho_2 U^2 \int_L (\partial\bar{\Phi}^{(2)}/\partial x - |\nabla\bar{\Phi}^{(2)}|^2/2)n_j dl.$$

The second term in (9) is the contribution from the unsteady potentials $\Phi_j^{(2)}$ $(j=1,2,3)$. Three components of the force and the moment are written in the matrix form

$$F_{nj} = \sum_{k=1}^{3} \eta_k \tau_{jk},$$

$$\tau_{jk} = -\rho_2 \int_L (i\omega\Phi_k^{(2)} + \vec{V}\nabla\Phi_k^{(2)})n_j dl,$$

where $\vec{V} = U\nabla(\bar{\Phi}^{(2)} - x)$ is the velocity vector of a steady flow in the lower layer relative to the moving reference frame. The radiation forces are represented in the form $\tau_{jk} = \omega^2\mu_{jk} - i\omega\lambda_{jk}$, where μ_{jk} and λ_{jk} are known as the added masses and damping coefficients, respectively.

The exciting forces are determined as follows

$$F_{ej} = -\rho_2\eta_0 \int_L [i\omega(\Phi_0^{(2)} + \Phi_4^{(2)}) +$$

$$\vec{V}\nabla(\Phi_0^{(2)} + \Phi_4^{(2)})]n_j dl.$$

To use the coupled finite element method it is necessary to determine the Green function $G^{(s)}(x,y,\xi,\eta)$, satisfying the equations

$$\Delta G^{(1)} = 0 \quad (0 < y < H),$$

$$\Delta G^{(2)} = 2\pi\delta(x-\xi, y-\eta) \quad (y<0)$$

and boundary conditions similar to (5)-(7). The solution of the problem for the Green function in the lower layer $G^{(2)}$ takes the form:

$$G^{(2)} = \ln(rr_1) + 2(1+\varepsilon)\mathrm{pv}\int_0^\infty \frac{B(k)}{kP(k)}e^{k(y+\eta)} \times$$

$$\times \left\{ \left[(U^2k^2-\omega^2)^2 - (U^2k^2+\omega^2)\Omega^2(k)\right]\cos k(x-\xi) + \right.$$

$$\left. +2i\omega kU\Omega^2(k)\sin k(x-\xi)\right\} dk +$$

$$+\pi\{\alpha_1 \exp[k_1(y+\eta-i(x-\xi))] -$$

$$-\alpha_2 \exp[k_2(y+\eta-i(x-\xi))] -$$

$$-\alpha_3 \exp[k_3(y+\eta+i(x-\xi))] +$$

$$+\alpha_4 \exp[k_4(y+\eta+i(x-\xi))]\},$$

where pv indicates the principal-value integration,

$$r^2 = (x-\xi)^2 + (y-\eta)^2,\ r_1^2 = (x-\xi)^2 + (y+\eta)^2,$$

$$P = \prod_{s=1}^{4} P_s,\ P_{1,2}(k) = Uk + \omega \mp \Omega(k),$$

$$P_{3,4}(k) = Uk - \omega \mp \Omega(k),$$

$$\alpha_s = \frac{i(1+\varepsilon)\Omega(k_s)B(k_s)}{2k_s[U - \gamma c_g(k_s)]}$$

$(\gamma = 1$ at $s = 1,2,3$ and $\gamma = -1$ at $s = 4)$,

$c_g(k_s) = d\Omega/dk\ |_{k=k_s}$ is the group velocity of the wave k_s. The equation $P_1(k) = 0$ has two

simple real solutions, k_1 and k_2, with $k_1 > k_2$, if only

$$U < U_c, \quad \omega < \omega_c, \tag{10}$$

where $U_c = \sqrt{\varepsilon g H}$ is the critical velocity for a steady problem in the two-layer fluid and $\omega_c = \Omega(k_c) - U k_c$ is defined post-solving the equation $c_g(k_c) = U$. Solutions k_1 and k_2 coincide, if $\omega = \omega_c$, and are absent, if conditions (10) are not met. There are no real solutions for equation $P_2(k) = 0$. In contrast, the equations $P_3(k) = 0$ and $P_4(k) = 0$ always possess unique real solutions, such as k_3 and k_4, respectively, with $k_3 > k_4$.

With $H \to \infty$, the k_s solutions are equal to

$$k_{1,2} = \frac{\bar{g}}{2U^2}(1 - 2\tau \pm \sqrt{1 - 4\tau}),$$

$$k_{3,4} = \frac{\bar{g}}{2U^2}(1 + 2\tau \pm \sqrt{1 + 4\tau}),$$

where $\tau = \omega U/\bar{g}$. In this case $\omega_c = \bar{g}/4U$. With $\varepsilon \to \infty$ one will obtain the known solution for a homogeneous fluid with a free surface [25].

The numerical calculations are performed for the elliptic cylinder

$$x^2/a^2 + (y + h)^2/b^2 = 1,$$

where a and b are the large and small half-axes of the ellipse, h is the depth of submergence of its center under the interface.

The steady loads (a wave resistance, a lift and a trim moment) has been studied extensively for the different types of the density stratification in [27]. The numerical calculations are compared with the approximate analytical solution based on the use of the Kochin function and suitable for a body deeply submerged under the interface.

For simplicity let us give the approximate solution for a wave resistance in the two-layer fluid under a lid :

$$F_x = -\frac{(1 + \varepsilon)\rho_2 \Omega(\lambda)}{2B(\lambda)[U - c_g(\lambda)]} K^2(\lambda).$$

Here λ is the root of an equation $\Omega(\lambda) = U\lambda$, which exists only at $U < U_c$ and K is the Kochin function for the elliptic cylinder

$$K(\lambda) = 2\pi U b \sqrt{\frac{a + b}{a - b}} J_1(\lambda\sqrt{a^2 - b^2}) e^{-\lambda h},$$

where J_1 is the Bessel function of the first order. For small values of the product $\lambda\sqrt{a^2 - b^2}$ the Kochin function may be presented $K(\lambda) \approx \pi U b \lambda (a + b) e^{-\lambda h}$. The wave resistance determined by this means is called the dipole solution.

The approximate solution for the wave resistance in two-layer fluid with a free surface presents a sum of surface and internal wave contributions.

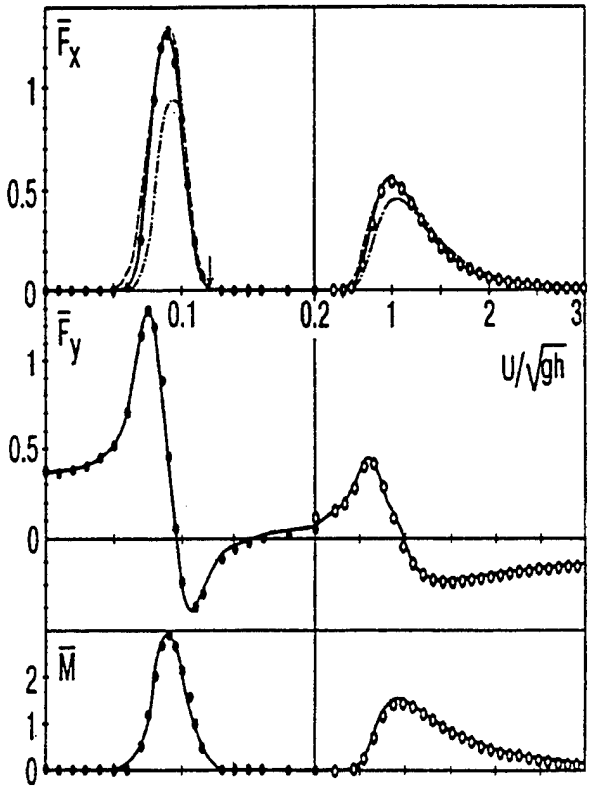


Fig. 4.

A steady loads for the elliptic cylinder in the two-layer fluid with a free surface determined by CFEM with the element number $m = 18$ are shown in Fig. 4 for $a = h = 2b$, $\varepsilon = 0.03$, $H = b$, $x_0 = 0$, $y_0 = -h$ (solid lines). The following designations are used

$$(\bar{F}_x, \bar{F}_y) = (-F_x, F_y)/\rho_2 U^2 b,$$

$$\bar{M} = -M/\rho_2 U^2 b^2.$$

The above values are compared with similar ones for the two-layer fluid under a lid (dark points) over the range of the Froude number $0 < \mathrm{Fr} = U/\sqrt{gh} < 0.2$ and for a homogeneous fluid ($\varepsilon =$

0) (light points) over the range $0.2 < \mathrm{Fr} < 3$. In Fig. 4 are shown the approximate solution (dot-and-dash line) for a wave resistance and dipole solution (dash line). With small values of the froude number, the internal waves are principally excited and their characteristics agree practically with those of the two-layer fluid under a lid. Then with increasing Fr the generation of the internal waves ceases and the only surface waves are excited. The critical velocity of the body for internal waves shown with an arrow is $U_c/\sqrt{gh} = 0.1224$.

In the three-layer model of a smooth pycnocline the fluid density distribution in the undisturbed state takes the form:

$$\rho(y) = \begin{cases} \rho_1 & (H_1 < y < H_1 + H_2), \\ \rho_1 \left[1 + \varepsilon \left(1 - \frac{y}{H_1}\right)\right] & (0 < y < H_1), \\ \rho_2 = \rho_1(1+\varepsilon) & (y < 0), \end{cases}$$

where H_1, H_2 are the depths of middle and upper layers, respectively. The fluid flow in the upper and lower layers is irrotational. The wave flow equation for the middle linearly stratified layer is used in the Boussinesq approximation.

The steady loads in the three-layer fluid are presented in Fig.5 at $\varepsilon = 0.03$, $H_1 = b$, $H_2 = 0.5b$, $a = 2b$, $h = 1.5b$. In Fig.5 are shown the results of CFEM (solid lines), the approximate solution for the wave resistance (dash-and-dot line) and dipole solution (dash line). The following critical velocities of generating appropriate modes of internal waves are depicted (arrows with numbers): $U/\sqrt{gh} = 0.1137$ ($n = 1$), $0.0336 (n = 2)$, 0.0186 ($n = 3$). For comparison with the two-layer fluid, the value $\bar{h} = h + H_1/2$ is entered, which defines the distance from the body centre to the pycnocline midline. Fig. 5 gives the only range of values $U/\sqrt{gh} \geq 0.013$ wherein there are yet no more than three internal modes. From the comparison of Figs. 4 and 5 it is obvious that the internal wave in the two-layer fluid and the first wave mode in the three-layer one have a similar hydrodynamic effect.

The solutions of radiation and diffraction problems at $U = 0$ are obtained for the two-layer fluid bounded both by a rigid lid and by a free surface [28,29]. In the diffraction problem, apart

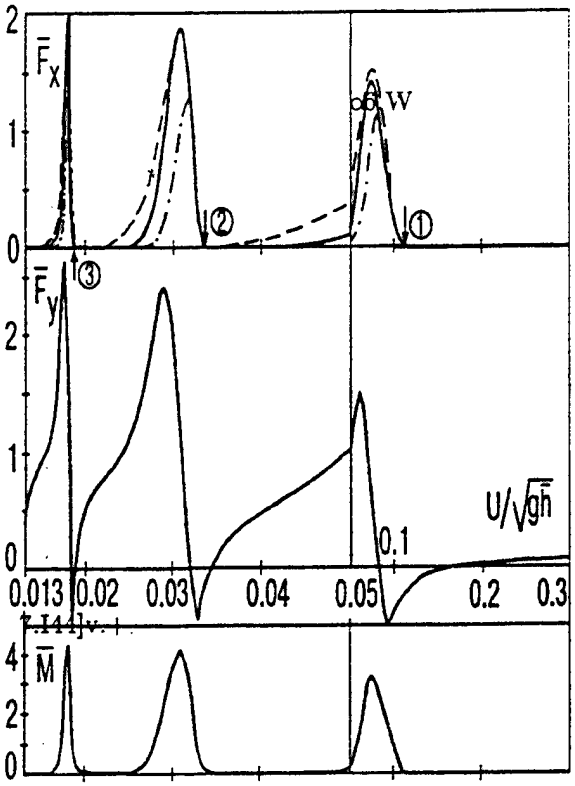


Fig. 5.

from exciting forces, also is determined the behavior of scattered waves in a far field. The reciprocity identities relating the solutions of radiation and diffraction problems are derived. The radiation load for the elliptic cylinder in the two-layer fluid with a free surface is demonstrated in Figs. 6,7.

The flow parameters coincide with those used in Fig.4. The coefficients μ_{ij} and λ_{ij} are compared with similar values for the two-layer fluid under a lid (dark points) and the homogeneous fluid (light points). For the damping coefficient λ_{ij}, the approximate solution obtained by the Kochin function is shown with dash-and-dot line and the dipole solution is denoted with dash line. The values μ^*_{jj} are equal to the added masses coefficients for the elliptical cylinder in the unbounded homogeneous fluid $(\mu^*_{11}, \mu^*_{22}, \mu^*_{33}) = \pi\rho_2[b^2, a^2, (a^2 - b^2)^2/8]$.

With small frequency of body oscillation, the internal waves are significantly excited and their

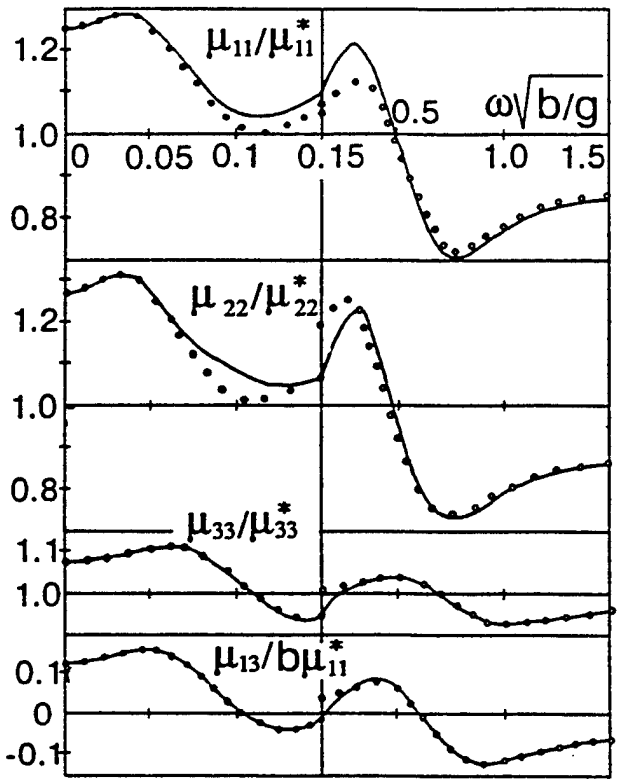


Fig. 6.

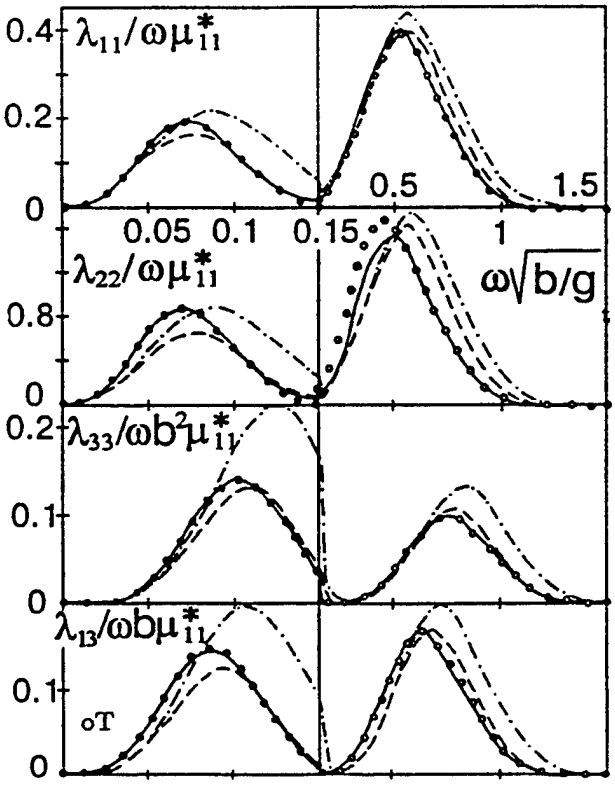


Fig. 7.

characteristics agree practically with those of the two-layer fluid under a lid. As the frequency increases, the generation of internal waves weakens and the surface waves whose characteristics are slightly affected by the density variation become dominant.

An interesting peculiarity of the diffraction problem for stratified fluid is that when the given mode wave incidents on a body it scatters not only into itself but also into all the other modes. This is one of the mechanisms of energy redistribution due to wave motions, in particular, that of the surface wave energy transfer to depth.

Based on the approximate solution for a deep submerged body, the influence of anomalous frequency dispersion of internal waves on the processes of scattering and generation is determined [30]. This internal waves are characterized by a nonmonotonic behavior of their group velocities. One example of this fluid is a three-layer one involving linearly stratified upper and middle layers and a homogeneous lower one. In this case the mode 'leap-frog' is observed when the excitement of higher modes is more intensive then of lower ones.

For radiation and diffraction problems with forward speed all the components of loads are correlated for the cylinder moving under the free surface in a homogeneous fluid and under the interface in the unbounded and the bounded by lid two-layer fluid [31]. Contrary to the case without forward speed the added mass and damping coefficients have no longer the symmetry properties and there are some motion regimes where the damping coefficients take negative values. Starting from the assumption of a deep submersion of a body, the amplitudes of radiation and diffraction waves in the far field as well as the diagonal damping coefficients and exciting forces are calculated. The numerical calculations of μ_{ij} and λ_{ij} are shown in Figs.8,9 for the elliptic cylinder located under the free surface in the homo-

geneous fluid (a), under the interface in the two-layer unbounded fluid (b) and in the two-layer fluid with a bounded upper layer (c) given the same parameters as in Fig.4 and $U/\sqrt{\bar{g}b} = 0.4$.

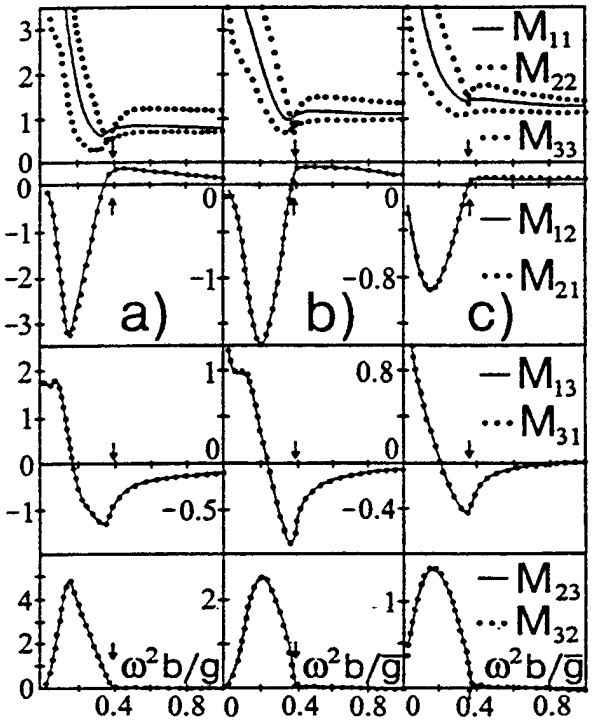


Fig. 8.

In Fig.9 are shown also the approximate values of λ_{jj} for the same three cases of the fluid density stratification. The following designations are used

$$M_{jj} = \mu_{jj}/\mu^*_{jj}, (M_{12}, M_{21}) = (\mu_{12}, -\mu_{21})/\mu^*_{11},$$

$$(M_{13}, M_{23}, M_{31}, M_{32}) = \frac{(\mu_{13}, \mu_{23}, \mu_{31}, -\mu_{32})}{b\mu^*_{11}},$$

$$\Lambda_{jj} = \pi b\omega\lambda_{jj}/\bar{g}\mu^*_{jj},$$

$$(\Lambda_{12}, \Lambda_{21}) = (\lambda_{12}, -\lambda_{21})\omega/\rho_2\bar{g}b,$$

$$(\Lambda_{13}, \Lambda_{23}, \Lambda_{31}, \Lambda_{32}) = (\lambda_{13}, \lambda_{23}, \lambda_{31}, -\lambda_{32})\omega/\rho_2\bar{g}b_2.$$

With forward speed the approximate solution is seen to provide a quite rough representation for damping coefficients, especially for λ_{33}. The values $\omega_c^2 b/\bar{g} = 0.3906$ (Figs. 8,9a,b) and 0.3642 (Figs. 8,9c) are indicated by arrows.

As may be seen from Figs.8,9 the relation of Timman-Newman for the given velocity of the body holds very well.

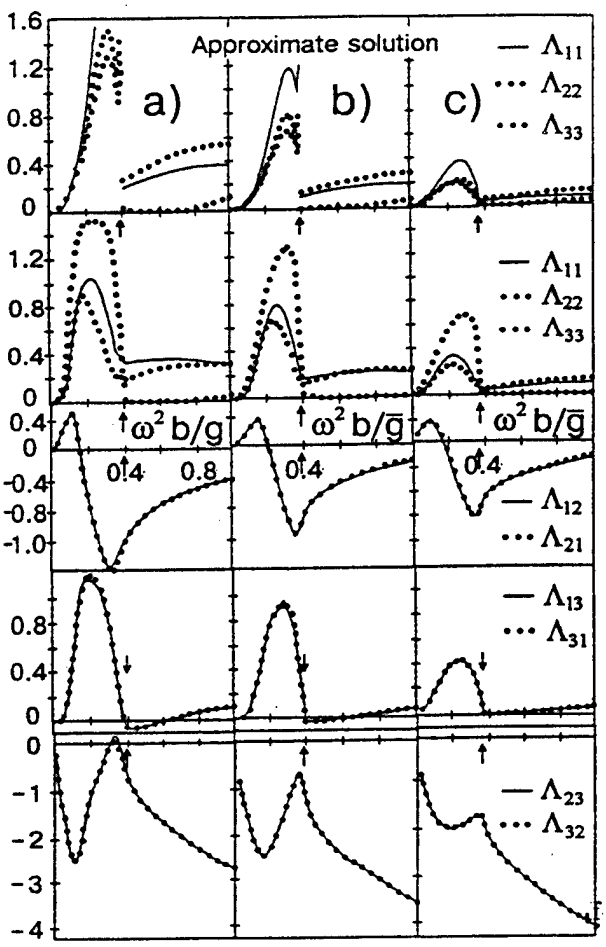


Fig. 9.

The numerical results for the exciting forces are presented in Fig.10 with the head incoming wave (Fig.10a) and with the following incoming wave (Fig.10b). The flow parameters coincide with those used in Figs.8,9. The curves 1–3 are shown for the cases of the homogeneous fluid, the two-layer unbounded fluid and the two-layer fluid with a bounded upper layer, respectively.

The values $k_0 b = 1.5626$ and $k_0 b = 1.8277$ (fig.5b) are indicated by arrows and conform to the critical frequencies ω_c in the cases of the unbounded and bounded upper layers, respectively.

CONCLUSIONS

The outlined results may be considered as one of the first attempts of experimental and theoretical investigation of the influence of oncoming internal waves on the hydrodynamic loads acting

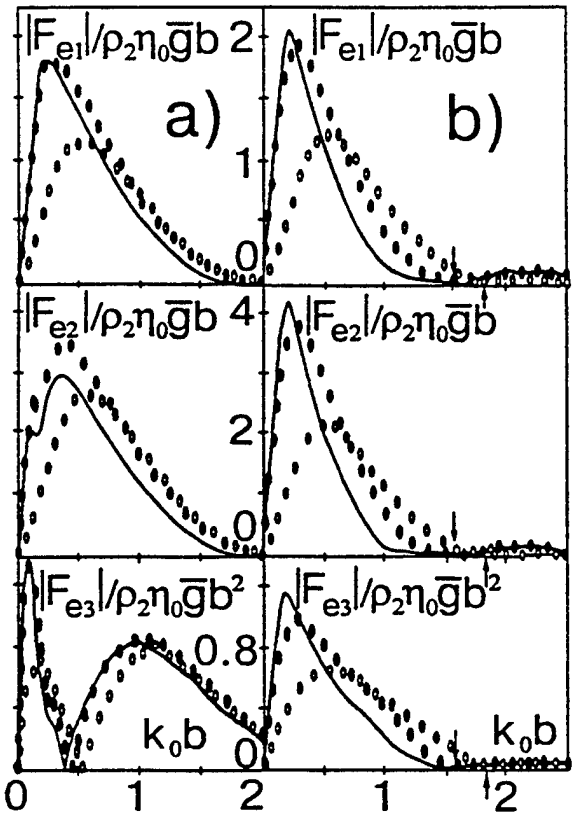


Fig. 10.

on a submerged body. It is shown that the fluid stratification is affected significantly the hydrodynamic loads on a submerged body over certain ranges of the forward speed and the incident wave frequencies.

For the body located in the homogeneous fluid layer, the internal wave loading is generally analogous to the case of the surface waves taking into account the modified gravity acceleration. The hydrodynamic forces acting on a body in pycnocline show a wide range of specific features. Consequently, the interaction of a body with the incident waves present the greater variety of types as compared to the case of homogeneous fluid.

ACKNOWLEDGEMENT

We want to thank Prof. V.I.Bukreev for valuable suggestions.

REFERENCES

1. Ekman, V.W., "On Dead Water," Scientific Results of the Norwegian North Polar Expedition 1893-1896, Vol. 5,No. 15, 1904, pp.1-150.

2. Nikitina, E.A., "Resistance of the Ships in 'Dead Water'," Izvestiya Akademii Nauk SSSR, Otdelenie Tekhnicheskich Nauk, Mekhanika i Mashinostroenie, No. 9, 1959, pp. 188-192 (in Russian).

3. Mason, P.J., "Forces on Spheres Moving HorIzontally in a Rotating Stratified Fluid,"Geophysical and Astrophysical Fluid Dynamics, Vol. 8, No. 2, 1977, pp. 137-154.

4. Lofquist, K.E.B., Petrel, L.P., "Drag on a Sphere Moving Horizontally Through a Stratified Liquid,"Journal of Fluid Mechanics, Vol. 148, 1984, pp.271-284.

5. Castro, I.P., Snyder, W.H., Baines, P.G., "Obstacle Drag in Stratified Flow," Proceedings of the Royal Society of London, Vol.A249, No. 1876, 1990, pp. 119-140.

6. Stepanyants, Yu.A., Sturova, I.V., Teodorovich, E.V., "The Linear Theory of the Generation of the Surface and Internal Waves," Itogi Nauki i Tekhniki. Mekhanika Zhidkosti i Gaza, Vol. 21, 1987, pp.92-179 (in Russian).

7. Voisin, B., "Rayonnement des Ondes Internes de Gravite. Application aux Corps en Mouvement," These de doctorat de l'Universite Paris 6, 1991.

8. Chervyakov, M.S., "The Model Investigations of the Motion of a Rigid Body in the Stratified Fluid," Research Submersibles and Underwater robots, P.P.Shirshov Institute of Oceanology of Academy of Sciences of the USSR, 1986, pp. 21-22 (in Russian).

9. Vasilieva, V.V., "The Internal Waves and the Wave Resistance of the Submerged Bodies," Trudy VHTO imeni akademika Krylova, Sudostroenie, Leningrad, 1990, pp. 140-153.

10. Piccard, J.,"Sun under Water," Mysl', Moscow, 1974 (in Russian).

11. Glinskii, N.T.,"Internal Waves in Seas and Oceans," Nauka, Moscow, 1973(in Russian).

12. Osborne, A.R., Burch, T.L., Scarlet, R.I., "The Influence of Internal Waves on Deep-Water Drilling," Journal of Petroleum Technology, No.

30, 1978, pp.1497-1504.

13. Miropolsky, Yu.Z., "Dynamics of Internal Gravity Waves in the Ocean," Gidrometeoizdat, Leningrad, 1981.

14. Moberg, G., "Wave Forces on a Vertical Slender Cylinder," Report Series A:16, 1988, Department of Hydraulics, Chalmers University of Technology, Goteborg, Sweden.

15. Chaplin, J.R.,"Wave Forces on a Horizontal Cylinder Beneath Waves," Journal of Fluid Mechanics, Vol.147, 1984, pp. 449-464.

16. Iwata,K., Mizutani, N., Kasai, S., "Irregular Wave Forces Acting on a Submerged Sphere," Coastal Engineering in Japan, Vol. 30, No. 1, 1987, pp. 117-130.

17. Iwata, K., Mizutani, N., "Wave Forces Acting on a Submerged Sphere Under Regular Progressive Wave," Proceedings of the Japan Society of Civil Engineers, No. 405, 1989, pp. 215-224.

18. Lighthill,J.," Fundamentals Concerning Wave Loading on Offshore Structures," Journal of Fluid Mechanics, Vol. 173, 1986, pp. 667-683.

19. Pylnev, Yu.V., Razumeenko, Yu. V.,"Investigation of Damped Oscillations for a Float of a Special Shape Deeply Imbedded into Homogeneous and Stratified Fluid," Izvestiya Akademii Nauk SSSR, Mekhanika Tverdogo Tela, No. 4, 1991, pp. 71-80 (in Russian).

20. Chopov, P.J., Minev, P.D., "The Unsteady Motion of a Bubble or a Drop Towards a Liquid-Liquid Interface," Journal of Fluid Mechanics, Vol. 235, 1992, pp. 123-143.

21. Sarpkaya, T., "Vortex Shedding and Resistance in Harmonic Flow about Smooth and Rough Cylinders at High Reynolds Numbers," NPS-59SL76021, Naval Postgraduate School, Monterey, California, 1976, pp.183.

22. Faltinsen, O.M., "Sea Loads on Ships and Offshore Structures," 1st ed., Cambridge University Press, Cambridge, 1990.

23. Lay, R.Y.S., Lee, C.M., "Added Mass of a Spheroid Oscillating in a Linearly Stratified Fluid," International Journal of Engineering Science, Vol. 19, No. 11, 1981, pp. 1411-1420.

24. Larsen, L.H., "Oscillation of a Neutrally Buoyant Sphere in a Stratified Fluid", Deep-Sea Research, Vol. 16, No. 6, 1969, pp.587-603.

25. Wu, G.X., Eatock Taylor, R.,"Hydrodynamic Forces on Submerged Oscillating Cylinders at Forward Speed,"Proceedings of the Royal Society of London, Vol. A414, No. 1846, 1987, pp.149-170.

26. Wu, G.X., Eatock Taylor, R., "The Numerical Solution of the Motions of a Ship Advancing in Waves," Fifth International Conference on Numerical Ship Hydrodynamics, Hiroshima, Japan, 1989, pp.386-394.

27. Sturova, I.V., "Effect of Internal Waves on the Hydrodynamical Characteristics of a Submerged Body," Izvestiya RAN, Fizika Atmosfery i Okeana, Vol. 29, No. 6, 1993, pp.732-738 (in Russian).

28. Sturova, I.V., "Two-Dimensional Submerged Body Without Forward Speed in Waves of Two-Layer Fluid," Izvestiya RAN, Mekhanika Zhidkosti i Gaza, No. 3, 1994, pp.144-155 (in Russian).

29. Sturova, I.V.," Scattering of Surface and Internal Waves on Submerged Body," Computational Technology, Novosibirsk, Vol.2, No. 4, 1993, pp.30-45 (in Russian).

30. Sturova, I.V., "Effect of Anomalous Dispersion Dependence on Scattering and Generation of Internal Waves," Prikladnaya Mekhanika i Tekhnicheskaya Fizika, No. 3, 1994, pp.47-53 (in Russian).

31. Sturova,I.V., "Two-Dimensional Submerged Body at Forward Speed in Waves of Two-Layer Fluid," Prikladnaya Mekhanika i Tekhnicheskaya Fizika (in Russian)(in press).

A Method for Simulation of Viscous, Nonlinear, Free-Surface Flows

B. Hodges, R. Street, Y. Zang
(Stanford University, USA)

ABSTRACT

Presented is a numerical method for simulating free-surface flows through solution of the time-dependent, incompressible, Navier-Stokes equations and the non-linear dynamic and kinematic boundary conditions. The numerical method uses boundary-fitted curvilinear coordinates with a finite-volume, time-splitting, approximate-factorization method formulated in primitive variables on a non-staggered grid. The pressure Poisson equation is solved using a multigrid technique. A new extension of domain decomposition methods is developed which involves splitting the free surface from the fluid volume for the iterative enforcement of the pressure equation and the dynamic boundary condition. A derivation in curvilinear coordinates of the Eulerian kinematic boundary condition is presented and is used for advancing the free surface in a Crank-Nicolson formulation. Development of the numerical method is presented for three dimensions; preliminary results are given from two-dimensional non-linear simulations of standing waves.

NOMENCLATURE

This paper uses tensor notation with the Einstein summation convention implied unless otherwise specifically noted.

- a wave amplitude
- B_i discrete operator for pressure gradient
- C_i discrete operator for convective terms
- d depth
- D_α : $\alpha = 1,2,3$; discrete operators for approximate-factorized diffusive terms
- D_I implicit discrete operator for diagonal diffusive terms
- D_E explicit discrete operator for off-diagonal diffusive terms
- e_{ij} rate of strain tensor
- F_{ij} flux tensor in Cartesian momentum equation
- F_i^q flux tensor in curvilinear momentum equation
- F function representing curvilinear space position of free surface
- g acceleration due to gravity
- g^{qr} contravariant metric tensor
- g_{qr} covariant metric tensor
- H free surface height measured in physical space
- $\mathcal{H}$ free surface height measured in curvilinear space
- I identity matrix
- J Jacobian
- k wave number
- L wave length
- L_1, L_2 discrete linear operators for dynamic boundary condition
- n_i normal unit vector
- p reduced dynamic pressure
- P pressure
- Q_i discrete operator for grid motion
- S_i source of discretized momentum equation
- S_1, S_2 discrete source terms for dynamic boundary condition

t time (at fixed location in physical space)

t_i tangent unit vector

T wave period

u_i Cartesian velocity

u_i^* intermediate Cartesian velocity

U^q contravariant velocity

U^{*q} intermediate contravariant velocity

U characteristic velocity of wave

x_i Cartesian (physical space) coordinates

$\dot{X}^q$ grid volume flux

Z free surface vertical coordinate in physical space

Greek Symbols

δ_{ij} Kronecker delta

Δt time step

Δs thickness of free surface

γ gradient of pressure variable (ϕ) at free surface

μ dynamic viscosity

ν kinematic viscosity

ϕ pressure variable

ρ density

ψ second derivative of pressure variable (ϕ) at free surface

τ time (at fixed location in computational space)

ξ^q curvilinear coordinates

ω wave frequency

Subscripts

i, j, k indices for Cartesian or covariant vectors

$S+$ quantity computed in air at free surface

$S-$ quantity computed in water at free surface

$S-1$ quantity computed at first cell center inside free surface

$S-2$ quantity computed at second cell center inside free surface

Superscripts

q, r, s, t indices for contravariant vectors

n, $n+1$ discrete time step

1 INTRODUCTION

Simulations of flows with free-surface effects have been of interest to the numerical community both for their real-world engineering applications and for the challenges which moving-boundary problems present. The physical phenomena that have been modelled using free-surface numerical techniques cover a wide range of areas, including water waves, viscous surface films, bubble dynamics, vortex/free-surface interactions, and geophysical flows. The numerical methods used have been as varied as the phenomena modelled, and include boundary integral methods, spectral methods, finite element methods and finite volume methods. To date, no single approach has been proven superior, and the complexities of free surface phenomena almost guarantee that there will never be one perfect method for all free-surface problems.

In this paper, we develop a technique that is suitable for addressing free-surface wave problems; where the primary characteristic of the flow is nonlinear viscous wave motions of a contiguous free surface. Numerical simulations of this type of free-surface flow face several fundamental problems, including the need for accurate free-surface advancement, enforcement of the non-linear dynamic boundary condition, and practical computation in three dimensions. Both finite element and finite volume methods have been used in the past to study free-surface wave motions [1]. We shall, however, limit our introductory discussion to finite volume methods, which appear to have more promise for future simulation of fully-turbulent flows.

The primary purpose of this paper is to present a numerical method for free-surface flow simulation that incorporates a new method for enforcing the non-linear dynamic boundary condition and uses a curvilinear coordinate derivation of the kinematic boundary condition to advance the free surface.

The new approach to the dynamic boundary condition is to computationally separate the free surface and the fluid volume, then link them through an iterative scheme. This strategy is borrowed from the method of domain decomposition, where solutions on adjacent do-

mains are iterated until the intergrid conditions converge. In our case, rather than enforcing a complicated dynamic boundary condition on the upper boundary of the fluid domain, a simple Dirichlet boundary condition is enforced and refined iteratively with separate computations of the dynamic boundary condition. This "surface decomposition" method may have its ultimate use in coupled simulations of air-water interfaces with decomposed domains consisting of the air volume, the free surface, and the water volume. In such an application, the free surface would be the communication channel for iteratively enforcing the boundary conditions on the two fluids.

The derivation of the Eulerian kinematic boundary condition in this paper is based upon a Taylor-series expansion in curvilinear space, and is similar to the derivation of the Eulerian kinematic boundary condition in physical space by Mei [2]. The curvilinear derivation is advantageous because it allows the simulation of free surfaces which do not remain single-valued in physical space.

Previous finite volume simulations of free-surface flows can roughly be grouped into two categories: 1) "fixed grid" simulations where the governing equations are discretized in physical space on a fixed Cartesian grid while the free-surface moves within the grid; and 2) "moving grid" simulations where a boundary-conforming grid that moves with the free surface is generated.

Most fixed-grid simulations trace their ancestry to the marker-and-cell (MAC) method of Harlow and Welch [3], which uses moving marker particles to track the position of the free surface on a fixed, Cartesian grid. Modified versions of this method are still useful [4] [5] [6]; however, the fundamental drawback of MAC simulations is that the boundary of the computational domain does not lie on the boundary of the fluid. The partially empty cells along the boundary make it difficult to conserve mass and accurately invoke the dynamic boundary condition.

An interesting and relatively new approach using a fixed grid is the "level set" interface technique [7] [8], which is suitable for simulating a coupled domain of two fluids with an immiscible interface. This technique does not explicitly track the position of the free-surface interface, but instead defines a smooth function for the distance from each fixed grid point to the free surface. The simulation solves for this level-set function along with the fluid flow equations. The position of the interface is computed by interpolation from level-set values at the fixed grid points. The level-set technique has an interesting ability to handle flows where the topology of the interface may be changing, such as with combining and dividing bubbles. The major drawback of this method appears to be in the handling of the dynamic boundary condition. As illustrated by Sussman *et al.* [7], the dynamic boundary condition cannot be directly discretized on the free surface in a level-set method because the surface is not given a discrete representation. Instead, the dynamic boundary condition is represented by a smoothed delta function which depends on prescribing a "thickness" of the interface that is greater than the spatial discretization. This requires the discretization be extremely fine, or an unrealistically thick interface be prescribed. We suspect this method may not prove practical for simulating the complicated dynamic boundary condition of a free-surface wave that includes transport of scalars on the surface and spatial variations in the surface-tension coefficient. However, an intriguing possibility worthy of future investigation is a method that combines a level-set solution in computational space (to capture bubble effects) with a boundary-fitted moving grid (to compute a discretized, free-surface wave). This combination might allow efficient computation of breaking waves with bubble effects and surfactant transports on the free surface.

Moving-grid simulations are generally designed with the boundary of the computational domain coincident with the physical domain. This provides a framework for enforcing the dynamic boundary condition directly on the boundary of the computational domain. Most moving-grid simulations generate a structured system of boundary-fitted curvilinear coordinates to map the Cartesian coordinates of points in physical space to a regular orthogonal grid in "computational space". This approach is discussed in greater detail in §2.1 of this paper. An unusual exception to this approach has been developed by Hino *et al.* [9] for steady-state simulations using an unstructured, moving grid that is discretized wholly in physical space.

Two different methods of curvilinear-coordinate grid generation have been used in finite-difference free-surface simulations. One approach [10] [11] [12] is to simplify the computation of grid motion by using what might be termed a "restricted" boundary-fitted grid. In this scheme, the free surface is typically repre-

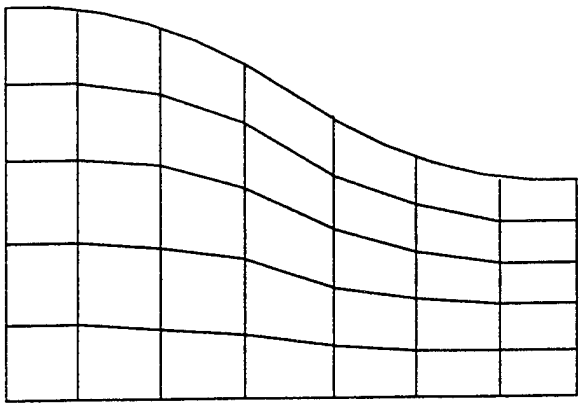


Figure 1: Restricted curvilinear coordinate grid

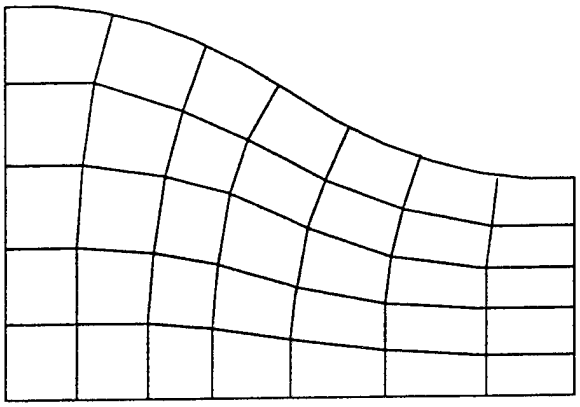


Figure 2: Generalized curvilinear coordinate grid

sented by a series of particles whose horizontal Cartesian coordinates (x, y) are fixed and whose vertical Cartesian coordinate (z) follows the free surface motion along fixed vertical grid lines, as shown in figure (1).

A second approach to moving-grid generation is to use "generalized" boundary-fitted curvilinear coordinates [13] [14]. This method generates smoothly curved grid lines in physical space and allows the grid to be tailored to the requirements of the fluid domain, as shown in figure (2). A generalized curvilinear grid is preferable to a restricted grid because of the ability of the former to handle large surface deformations with minimum grid skewness. This is discussed in greater depth in §2.2.

A number of different numerical techniques have been used to advance the free surface in the solution of viscous free-surface problems. Fully-implicit techniques have been developed for restricted curvilinear coordinates [10], for generalized curvilinear coordinates [14], and for unstructured grids [9] [15]. These techniques simultaneously solve a coupled set of equations consisting of the Navier-Stokes equations, the kinematic and dynamic boundary conditions, and one or more grid generation equations. The advantage of the fully-implicit technique is that the free-surface advance is coupled directly to the flow solution and the dynamic boundary condition, which is arguably more accurate than uncoupled methods. The disadvantage is that significant computational complexity is involved in the coupling of grid generation to the flow solution. To date, the only three-dimensional fully-implicit approach for the Navier-Stokes equations found in the literature is limited to steady-flow solutions [15].

A three-dimensional approach for unsteady flow which appears to effectively advance the free surface without a fully-implicit coupling is that of Dommermuth [11]. His method uses a third-order Runge-Kutta time integration of a kinematic boundary condition based on Helmholtz decomposition.

To avoid the problems associated with simultaneous solution of the flow and grid, many free-surface simulations use explicit free-surface advancement [6] [13] [12] [16] [17]. Explicit techniques generally suffer from the accumulation of error in the free-surface advance over long simulation times; however, the explicit Eulerian technique is a stable and effective method for conducting shorter simulations to investigate phenomena and develop numerical techniques.

Three different forms of the Eulerian kinematic boundary condition are found in the literature: 1) numerical enforcement of the physical space Eulerian kinematic boundary condition [9] [10] [11] [15]; 2) computation of a curvilinear transformation of the physical space Eulerian kinematic boundary condition [6] [13] [12] [14]; and 3) rotation of the Cartesian space frame to enforce the physical space Eulerian kinematic boundary condition in a more suitable orientation [17]. The first two methods are unusable for waves which do not remain single-valued in physical space. The third method, rotation of the coordinate system, does allow computation of a free-surface that is not single-valued in physical space; however, the surface must remain single-valued in the rotated Cartesian space frame, which eliminates the method from use with overturning waves. Most of the approaches to the kinematic boundary condition track the surface by the movement of particles that are required to

move vertically in physical space; this has some drawbacks in the accuracy of the free surface advance for steep waves (see §2.5).

There has been a wide range of numerical flow solvers used in free-surface simulations. As of this date, no method can be said to be superior and we shall not try to debate the pros and cons of the various approaches in this paper. However, in order to put our method in perspective, it is worthwhile to briefly mention some of the approaches that other authors have taken. Dommermuth [11] has implemented a three-dimensional technique that uses fourth- and sixth-order finite differences with a third-order Runge-Kutta scheme. This method is unique in that it uses Helmholtz decomposition to split the governing equations into irrotational and vortical flow parts, which provides the free-surface advance through an equation involving the solenoidal velocity potential rather than the Cartesian or curvilinear velocity. Park *et al.* [6], Hinatsu [12], and Miyata *et al.* [13] use time-splitting methods that are discretized on a staggered grid. Hino *et al.* [9] have developed an artificial-compressibility multigrid method that is suitable for steady-state solutions about ship hull forms. Ohring and Lugt's [14] fully-implicit method uses artificial compressibility to solve for unsteady flow in two dimensions. Wang and Leighton [16] have developed a spectral method that discretizes the Navier-Stokes equations in a vertical-velocity, vertical-vorticity formulation that is suitable for periodic boundary condition problems. An entirely different approach was taken by Zhan and Zhaoshun [18], who investigated the characteristics of a drift current with regular waves by decomposing the surface motion into phase-averaged and fluctuating parts.

The numerical approach in this paper is similar to those of Park *et al.* [6], Hinatsu [12], and Miyata *et al.* [13] in the use of finite-volume discretization of primitive variables with a time-splitting technique. Our numerical approach differs by: 1) advancing the free surface in a method that is not limited to single-valued waves; 2) applying a non-staggered grid to reduce storage requirements for metric terms; and, 3) utilizing a multigrid solver for solution of the pressure Poisson equation with iterative enforcement of the dynamic boundary condition. Our numerical method is an adaptation of the method developed by Zang [19] for fixed-boundary problems which has been shown to be second-order accurate in space and time as well as computationally efficient in three dimensions. The kinematic boundary condition enforcement is discretized by the "time-splitting implicit" method of Chan and Street [20].

This is an interim report on a project whose goal is the development of a three-dimensional, time-dependent, Navier-Stokes simulation of finite-amplitude progressive water waves over an imposed current with non-linear dynamic and kinematic boundary conditions. Presented in this paper are the three-dimensional mathematical and numerical foundation of the method and preliminary two-dimensional simulation results for standing waves in a rectangular basin.

The main body of this paper is divided into four sections, beginning with the mathematical formulation and discretization of the governing equations, §2, followed by a description of the numerical method, §3, a description of the surface decomposition method, §4, and a summary of results from numerical simulations, §5.

2 MATHEMATICAL FORMULATION AND DISCRETIZATION

2.1 Computational Domain and Coordinate Mapping

For moving-grid numerical simulations, "boundary-fitted curvilinear coordinates" are often used. This technique is not unique to moving-grid problems, but has been applied to fixed-grid, finite-difference methods with complicated boundary shapes. The boundary-fitted curvilinear coordinate method is based on the concepts of tensor analysis and coordinate transformation that can be found in textbooks such as Aris [21]. Numerical application of boundary-fitted curvilinear coordinates involves developing a coordinate system which matches the boundaries in physical space and maps to a regular orthogonal grid in computational space.

The distortions of the curvilinear coordinate system as viewed from physical space, figure (2), are measured as metric terms. The metric terms are created when the governing equations are transformed into a regular orthogonal grid in computational space. Using this technique, an irregular domain in physical space can be discretized with a structured (e.g. finite difference) numerical method on a regular grid in

computational space while maintaining the simulation boundary coincident with the physical boundary. The main disadvantages of this technique are that the governing equations are more complicated when transformed to computational space and the requirement to store metric terms can overwhelm computer memory. However, improvements in computer speed and memory storage have made the use of curvilinear coordinate transformations more practical, and they can be considered a standard technique for simulations with non-moving grids and irregular boundaries.

The extension of boundary-fitted curvilinear coordinate methods from fixed-boundary to moving-boundary problems is relatively straightforward and is described by Thompson *et al.* [22]. Numerical implementation, however, can be computationally costly because a new grid and new metric terms must be computed at each time step. Implementation of boundary-fitted curvilinear coordinates requires that transformation operators be used to transform the governing equations from physical space to computational space. The operators are derived from the chain rule for partial differential equations. For a moving grid these operators can be presented as [22]:

$$\frac{\partial}{\partial x_j} = \frac{\partial \xi^q}{\partial x_j}\frac{\partial}{\partial \xi^q} \tag{1}$$

$$\frac{\partial}{\partial t} = \frac{\partial}{\partial \tau} - \frac{\partial x_j}{\partial \tau}\frac{\partial \xi^q}{\partial x_j}\frac{\partial}{\partial \xi^q} \tag{2}$$

where x_j, with $j = 1,2,3$ are the physical space coordinates; ξ^q with $q = 1,2,3$ are the computational space coordinates; $\partial/\partial t$ is a time derivative taken at a fixed point in physical space; and $\partial/\partial\tau$ is a time derivative taken at a fixed point in computational space, and repeated subscript/superscript combinations imply summation.

2.2 Grid generation

Boundary-fitted curvilinear coordinate grids can be generated either using restricted or generalized methods as discussed in the introduction to this paper. Restricted boundary-fitted curvilinear coordinates are a useful simplification as long as the free surface deformations remain small. For steep waves, restricted coordinates provide a highly skewed grid: the grid parallelpipeds will be significantly distorted from the ideal rectangular shape. Such grid skewness is undesirable since it generally results in a decrease in accuracy [22]. The use of generalized boundary-fitted coordinates can avoid this problem by using a grid generation method that minimizes grid skewness.

Restricted curvilinear coordinate systems also suffer from a lack of boundary orthogonality. While it is not possible to generate a completely orthogonal grid for an arbitrarily-shaped, three-dimensional domain, it is possible to generate a grid that is orthogonal to the boundaries. There are distinct advantages in the implementation of numerical techniques with boundary orthogonality. As shown by Zang [23] for a fixed grid, a non-orthogonal boundary in a finite-volume method requires a pressure boundary condition as well as a velocity boundary condition for the Poisson pressure equation to prevent an inconsistent solution. The use of boundary orthogonality removes the requirement for the pressure boundary condition. Furthermore, in deriving a discrete form of the dynamic boundary condition, boundary orthogonality provides significant simplification by removing two of the three skew metric terms at the free-surface. That is, for a free surface $\xi^3 = 1$, boundary-orthogonality provides $g^{13} = g^{23} = 0$.

Generalized boundary-fitted curvilinear coordinates can be produced through algebraic methods (i.e. interpolation from the boundaries) or the solution of a set of partial differential equations (typically a Laplace or Poisson equation) [22]. Algebraic, generalized, grid-generation methods are an improvement over the restricted-coordinate technique since the grid developed can be boundary orthogonal and grid skewness can be reduced. Algebraic methods have low computational cost since they use direct solution rather than iteration techniques. However, algebraic methods do not necessarily produce the optimum grid with minimum skewness, thus they might be considered inferior to partial differential equation methods for generating curvilinear coordinates. A Poisson-solution method will generate a grid with minimum skewness in generalized coordinates, but has the disadvantage of requiring iterative smoothing to obtain a final grid. Depending on the shape of the domain, a Poisson grid-generation method can become the major driver of computational time for a free-surface simulation.

In order to have control over grid skewness, we have incorporated into our code sections from the EAGLE grid generation package developed at Mississippi State University [24]. This code uses an algebraic generation method

(transfinite interpolation) as an input to a Poisson smoother, while leaving the user control over the level of smoothing and the maximum number of iterations (which may be set to zero for purely algebraic computation of generalized curvilinear coordinates). The free-surface is represented by a cubic spline over which the ends of grid lines may freely move so as to obtain a smooth grid with boundary orthogonality.

2.3 Non-staggered grid

The governing equations are discretized using the non-staggered grid technique developed by Zang [19]. This method solves for the pressure and the three Cartesian components of velocity at the grid centers and the normal volume flux through grid face. The main advantage of this technique over a staggered-grid method is the savings of storage for the metric terms. Zang's non-staggered grid method requires the storage of one set of metrics, consisting of nine vector surface area components ($J^{-1}\partial\xi^q/\partial x_i$), six non-trivial mesh skewness components ($J^{-1}g^{qr}$), and the inverse Jacobian, or cell volume (J^{-1}) for each control volume. In contrast, a staggered-grid method may require up to seven sets of metric terms for each control volume [25] [26].

To adapt the non-staggered grid method for use in free-surface simulations, a full set of metric terms is defined on each cell face of the free surface. This allows the dynamic boundary condition to be discretized with greater accuracy without significantly impacting the overall data storage requirements.

2.4 Navier-Stokes equations

The time-dependent, constant-density, incompressible Navier-Stokes equations in physical space can be written as:

$$\frac{\partial u_i}{\partial t} + \frac{\partial F_{ij}}{\partial x_j} = 0 \qquad (3)$$

$$\frac{\partial u_j}{\partial x_j} = 0 \qquad (4)$$

where $u_i : i = 1,3$ are the Cartesian (physical space) components of velocity, and the Cartesian momentum flux tensor (F_{ij}) is:

$$F_{ij} = u_j u_i + p\delta_{ij} - \nu\frac{\partial u_i}{\partial x_j} \qquad (5)$$

where ν is the kinematic viscosity, δ_{ij} is the Kronecker delta, and the reduced dynamic pressure (p) is related to the density (ρ), total pressure (P) and the vertical Cartesian coordinate (x_3) by:

$$P = \rho(p - gx_3) \qquad (6)$$

In order to simulate a flow with a free surface in boundary-fitted curvilinear coordinates, equations (1) and (2) are used to transform the physical space Navier-Stokes equations into computational space. To complete the transformation, we must utilize the metric identity [22]:

$$\frac{\partial}{\partial\xi^q}\left(J^{-1}\frac{\partial\xi^q}{\partial x_i}\right) \equiv 0 \qquad (7)$$

and the conservation of space [27],

$$\frac{\partial}{\partial\tau}\left(J^{-1}\right) - \frac{\partial}{\partial\xi^q}\left(J^{-1}\frac{\partial\xi^q}{\partial x_j}\frac{\partial x_j}{\partial\tau}\right) = 0 \qquad (8)$$

By applying equations (1), (2), (7) and (8) to equations (3) and (4) it is possible to formulate the Navier-Stokes equations in time-dependent boundary-fitted curvilinear coordinates as,

$$\frac{\partial}{\partial\tau}\left(J^{-1}u_i\right) + \frac{\partial}{\partial\xi^q}\left(J^{-1}F_i^q\right) = 0 \qquad (9)$$

$$\frac{\partial}{\partial\xi^q}\left(J^{-1}U^q\right) = 0 \qquad (10)$$

where the curvilinear momentum flux tensor (F_i^q) is:

$$F_i^q = \left[U^q - \dot{X}^q\right]u_i + \frac{\partial\xi^q}{\partial x_i}p - \nu g^{qr}\frac{\partial u_i}{\partial\xi^r} \qquad (11)$$

and other curvilinear quantities are defined as:

$$J^{-1} = det\left|\frac{\partial x_i}{\partial\xi^s}\right| \qquad (12)$$

$$U^q = \frac{\partial\xi^q}{\partial x_j}u_j \qquad (13)$$

$$\dot{X}^q = \frac{\partial\xi^q}{\partial x_j}\frac{\partial x_j}{\partial\tau} \qquad (14)$$

$$g^{qr} = \frac{\partial\xi^q}{\partial x_j}\frac{\partial\xi^r}{\partial x_j} \qquad (15)$$

Following the method developed by Zang [19], to discretize the momentum equation we apply the explicit 2nd-order Adams-Bashforth method to the convective terms and the off-diagonal viscous terms, with the implicit Crank-Nicolson scheme for the diagonal viscous terms. The addition of the free surface to Zang's method

requires a grid flux term which accounts for the convective motion of the grid. An explicit Euler discretization in the velocity is used for the grid flux term with an average of the time (n) and $(n+1)$ metrics. The pressure is removed from the momentum equation by a predictor-corrector method and a new pressure variable (ϕ) is defined. A further simplification is made by using a second-order accurate approximate factorization on the left hand side of the discretized momentum equation. The resulting system can be presented as:

1. predictor step

$$(I - D_1^{n+1})(I - D_2^{n+1})(I - D_3^{n+1})(u_i^* - u_i^n) = S_i \quad (16)$$

2. pressure Poisson equation

$$\frac{\delta}{\delta\xi^q}\left(J^{-1}g^{qr}\frac{\delta\phi}{\delta\xi^r}\right)^{n+1} = \frac{1}{\Delta t}\frac{\delta}{\delta\xi^q}\left(J^{-1}U^{*q}\right) \quad (17)$$

3. corrector step

   (a) for the Cartesian velocity (on cell centers):

$$u_i^{n+1} = u_i^* + \left[\frac{\Delta t}{J^{-1}}B_i(\phi)\right]^{n+1} \quad (18)$$

   (b) for the normal component of contravariant velocity (on cell faces):

$$(U^q)^{n+1} = U^{*q} - \Delta t\left(g^{qr}\frac{\delta\phi}{\delta\xi^r}\right)^{n+1} \quad (19)$$

where the pressure variable (ϕ) is related to the reduced pressure (p) by:

$$B_i(p) = \left[J^{-1} - \frac{\Delta t}{2}D_I\right]\frac{B_i(\phi)}{J^{-1}} \quad (20)$$

the source term of the predictor, equation (16) is:

$$\begin{aligned} S_i = \frac{\Delta t}{(J^{-1})^{n+1}}\Bigg\{ & \frac{3}{2}\left(C_i^n + D_E^n[u_i^n]\right) \\ & - \frac{1}{2}\left(C_i^{n-1} + D_E^{n-1}[u_i^{n-1}]\right) \\ & + \frac{1}{2}\left(D_I^n[u_i^n] + D_I^{n+1}[u_i^n]\right) \\ & + Q_i + (J^n - J^{n+1})u_i^n\Bigg\} \end{aligned} \quad (21)$$

The use of time $(n+1)$ metric terms in the source of the predictor is allowed because our numerical method (see §3) solves for the time $(n+1)$ free surface position and the curvilinear grid prior to the solution of the predictor step.

Discrete operators from equations (16), (18), (20), and (21) are defined as:

$$D_\alpha(\,) = \frac{\Delta t}{2J^{-1}}\frac{\delta}{\delta\xi^\alpha}\left\{\nu J^{-1}g^{\alpha\alpha}\frac{\delta}{\delta\xi^\alpha}(\,)\right\} \quad (22)$$

where $\alpha = 1, 2, 3$ with no summation.

$$D_E(\,) = \frac{\delta}{\delta\xi^q}\left\{\nu J^{-1}g^{qr}\frac{\delta}{\delta\xi^r}(\,)\right\}_{q\neq r} \quad (23)$$

$$D_I(\,) = \frac{\delta}{\delta\xi^q}\left\{\nu J^{-1}g^{qr}\frac{\delta}{\delta\xi^r}(\,)\right\}_{q=r} \quad (24)$$

$$C_i = -\frac{\delta}{\delta\xi^q}\left\{J^{-1}U^q u_i\right\} \quad (25)$$

$$B_i(\,) = -\frac{\delta}{\delta\xi^q}\left\{J^{-1}\frac{\delta\xi^q}{\delta x_i}(\,)\right\} \quad (26)$$

$$Q_i = \frac{\delta}{\delta\xi^q}\left\{\left(J^{-1}\dot{X}^q\right)^{n+\frac{1}{2}}u_i^n\right\} \quad (27)$$

In the operator Q_i, we use equation (14) to define:

$$\left(J^{-1}\dot{X}^q\right)^{n+\frac{1}{2}} = \frac{1}{2\Delta t}\left\{J^{-1}\frac{\delta\xi^q}{\delta x_j}\bigg|^n + J^{-1}\frac{\delta\xi^q}{\delta x_j}\bigg|^{n+1}\right\}(x_j^{n+1} - x_j^n) \quad (28)$$

Note that in this method, the effect of the moving grid is carried in the grid velocity term (Q_i) which is the net contravariant flux of physical space through the sides of a control volume cell as viewed from computational space. The grid flux is a part of the source term for the computation of the intermediate (u^*) velocity, but does not explicitly appear in the pressure Poisson equation or the corrector steps. Therefore, the Poisson solver and corrector steps are only indirectly affected by the moving grid.

2.5 Kinematic boundary condition

The kinematic boundary condition is the Lagrangian condition that a particle on the surface must remain on the surface. It is possible to use the Lagrangian condition directly and advance the free surface by moving marker particles based upon their velocity at the free surface; however, this method has been shown to be unstable

in long simulations where the free-surface is advanced explicitly [20]. For fully-implicit solutions where the kinematic boundary condition is coupled in an implicit solution of the velocity, such instability should not occur with the Lagrangian boundary condition.

As an alternative to the Lagrangian approach, the kinematic boundary condition in physical space can be written in a physical space Eulerian form which can be obtained through a Taylor series expansion [2]:

$$\frac{\partial H}{\partial t} = u_3 - u_1\frac{\partial H}{\partial x} - u_2\frac{\partial H}{\partial y} \qquad (29)$$

where H is the height of the free surface measured from some horizontal baseline in physical space This form of the kinematic boundary condition is enforced on surface particles that are restricted to vertical motion in physical space, and is ideally suited to restricted curvilinear coordinate applications.

It has been demonstrated [12] that curvilinear coordinate transformations (equations (1) and (2)) can be applied to the physical space Eulerian kinematic boundary condition (equation (29)) for use in numerical simulations. The simulations that have used this approach [6] [12] have retained the underlying vertical motion restriction on surface particles, thereby making the methods unsuitable for waves which do not remain single-valued.

A more general approach that does not have a single-valuedness restriction in physical space requires deriving the Eulerian kinematic boundary condition directly in curvilinear coordinates. We have not seen this form of the kinematic boundary condition used by any previous authors and, therefore, present the derivation here even though it is, in some senses, a trivial extension of the textbook derivation of the physical space Eulerian kinematic boundary condition by Mei [2].

To directly obtain a curvilinear Eulerian kinematic boundary condition, we will consider a *fixed* curvilinear space (ξ^1, ξ^2, ξ^3) such that the free-surface is single valued in ξ^3. Note that we are not requiring the curvilinear coordinate system to be boundary-fitted or moving for this derivation. Define F as a scalar function for the free surface such that:

$$F(\boldsymbol{\xi}, t) = \xi^3 - \mathcal{H}(\xi^1, \xi^2, t) = 0 \qquad (30)$$

where $\boldsymbol{\xi}$ is a vector representing the curvilinear coordinates of a surface position at time t, and $\mathcal{H}$ is the height of the free surface measured from $\xi^3 = 0$ along a line of constant ξ^1 and ξ^2 in fixed curvilinear space. After some small time Δt, the free surface has moved, while the curvilinear coordinate system remains fixed. We require that Δt is small, so the free surface remains single valued in ξ^3. Therefore,

$$\begin{aligned} &F(\boldsymbol{\xi} + \mathbf{U}\Delta t, t + \Delta t) \\ &\quad = F(\boldsymbol{\xi}, t) + \left(\frac{\partial F}{\partial t} + \mathbf{U}\cdot\nabla F\right)\Delta t \\ &\qquad + O(\Delta t)^2 \end{aligned} \qquad (31)$$

where $\mathbf{U}$ is the contravariant vector velocity of a point on the surface. It follows that:

$$\frac{\partial F}{\partial t} + \mathbf{U}\cdot\nabla F = 0 \qquad (32)$$

Substitution of equation (30) provides the curvilinear kinematic boundary condition in *fixed* curvilinear coordinates as:

$$\frac{\partial \mathcal{H}}{\partial t} = U^3 - U^1\frac{\partial \mathcal{H}}{\partial \xi^1} - U^2\frac{\partial \mathcal{H}}{\partial \xi^2} \qquad (33)$$

To discretize the kinematic boundary condition, equation (33), we use a time-splitting implicit method that applies a Crank-Nicolson discretization for the surface position [20]:

$$\begin{aligned} &\mathcal{H}^{[n+1]} - \mathcal{H}^{[n]} = \\ &\Delta t\left\{U^{3^{[n]}} - \frac{U^{q^{[n]}}}{2}\left(\frac{\delta\mathcal{H}^{[n]}}{\delta\xi^q} + \frac{\delta\mathcal{H}^{[n+1]}}{\delta\xi^q}\right)\right\} \\ &\qquad + O(\Delta t)^2 \qquad : q = 1, 2 \end{aligned} \qquad (34)$$

Now, we require that the *fixed* curvilinear grid used in the above derivation be boundary-fitted to the time (n) free surface; that is, at the surface:

$$\mathcal{H}^{[n]} = \xi^{3^{[n]}}\Big|_{surface} = \text{constant} \qquad (35)$$

then the gradients of the time (n) free-surface height relative to the ξ^1 and ξ^2 curvilinear coordinates will disappear, since:

$$\frac{\delta\mathcal{H}^{[n]}}{\delta\xi^q} = \frac{\delta\xi^{3^{[n]}}}{\delta\xi^q} = 0 \qquad : q = 1, 2 \qquad (36)$$

An approximate-factorization of equation (34) using equation (36) provides our discrete kinematic boundary condition,

$$\left(I + \frac{\Delta t}{2} U^1 \frac{\partial}{\partial \xi^1}\right)\left(I + \frac{\Delta t}{2} U^2 \frac{\partial}{\partial \xi^2}\right)\left(\mathcal{H}^{n+1} - \mathcal{H}^n\right)$$

$$= \Delta t \left(U^3\right)^n + O\left(\Delta t\right)^2 \qquad (37)$$

Solution of equation (37) in three dimensions requires the inversion of two tridiagonal matrices to obtain $\mathcal{H}^{n+1}$. To obtain the time $(n+1)$ physical space position of a particle on the surface, we can use:

$$\Delta x_i = \frac{\partial x_i}{\partial \xi^3} \Delta \xi^3 \quad : \quad i = 1, 3 \qquad (38)$$

with equation (35) this can be written as:

$$x_i^{n+1} = x_i^n + \left(\mathcal{H}^{n+1} - \mathcal{H}^n\right)\left(\frac{\partial x_i}{\partial \xi^3}\right)^n \qquad (39)$$

Our method requires that at time (n) there is a fixed curvilinear grid that is boundary-fitted in the ξ^3 coordinate. To find the change in the ξ^3 coordinates of the free surface at some small time later with reference to the same fixed grid, we apply equation (37). Then equation (39) is used to obtain the physical space coordinates of the free surface. The new free surface can then be used to generate a new boundary-fitted grid. The advantage of this method over a curvilinear transformation of (29) is that equation (33) is enforced upon points which move along a line of constant ξ^1 and ξ^2 curvilinear coordinates rather than a line of constant x and y physical coordinates. As a result, the single-valuedness requirement in physical space is replaced by a single-valuedness requirement in curvilinear space, which is a less restrictive condition for a boundary-fitted coordinate system.

2.6 Dynamic boundary condition

The full equation for the dynamic boundary condition is quite complicated, and can be found in Scriven [28] and Aris [21]. If we neglect surface tension and its gradients, inertia of the surface, gradients of the dilational force, force due to total curvature and velocity, effects of varying normal velocity, normal forces due to dilation and shear, and the viscosity of the upper fluid, then we can write the dynamic boundary condition for an incompressible fluid in its classic form (similar to that in Batchelor [29]):

$$P_{S+} - P_{S-} = -2\mu e_{ij} n_i n_j \qquad (40)$$

$$e_{ij} t_i n_j = 0 \qquad (41)$$

where the subscripts $S+$ and $S-$ indicate the pressure on the upper and lower sides of the free surface, e_{ij} is the rate-of-strain tensor, and n_i and t_i are the unit normal and tangent vectors, respectively.

Equations (40) and (41) are a form of the dynamic boundary condition that does not provide for straightforward implementation in a boundary-fitted curvilinear coordinate numerical method; therefore, our approach will begin with the tensor form of the full equation from Scriven [28]. By applying the same simplifications used to get equations (40) and (41), along with the definition of the reduced pressure (equation (6)) and the requirement that the curvilinear coordinate system be boundary orthogonal, the dynamic boundary condition can be presented as:

$$\left(p_{S+} - p_{S-}\right) - g\left(Z_{S+} - Z_{S-}\right) = -2\nu U^3_{,3} \qquad (42)$$

$$U^1_{,3} = -g_{33}\left\{g^{11} U^3_{,1} + g^{12} U^3_{,2}\right\} \qquad (43)$$

$$U^2_{,3} = -g_{33}\left\{g^{22} U^3_{,2} + g^{12} U^3_{,1}\right\} \qquad (44)$$

where Z_{S+} and Z_{S-} are the vertical physical space coordinates on either side of the free surface along a curvilinear coordinate line that is normal to the free surface. Defining Δs as the thickness of the free surface, it follows that:

$$Z_{S+} - Z_{S-} \leq \Delta s \qquad (45)$$

In order to neglect the thickness of the free surface while maintaining second order accuracy in space, we require:

$$\Delta s \leq \left(\Delta x\right)^2 \qquad (46)$$

where Δx is the grid spacing (measured in physical space) at the free surface. Equations (45) and (46) allow equation (42) to be written as:

$$\left(p_{S+} - p_{S-}\right) = -2\nu U^3_{,3} + O\left(\Delta x\right)^2 \qquad (47)$$

Note that the differentiation in equations (43), (44), and (47) is covariant tensor differentiation and requires the application of Christoffel symbols for deriving a discrete implementation.

In order to get the reduced pressure (p) from equation (47) into terms of the pressure variable (ϕ), we multiply equation (20) by $\delta \xi^r / \delta x_i$, with a sum over $i = 1, 2, 3$; then use equations (7), (15), (24) and (26) to obtain:

$$J^{-1}g^{qr}\frac{\delta p}{\delta\xi^q} = J^{-1}g^{qr}\frac{\delta\phi}{\delta\xi^q}$$

$$-\frac{\Delta t}{2}\frac{\delta\xi^r}{\delta x_i}\frac{\delta}{\delta\xi^q}\left\{\nu J^{-1}g^{qs}\frac{\delta}{\delta\xi^s}\left(\frac{\delta\xi^t}{\delta x_i}\frac{\delta\phi}{\delta\xi^t}\right)\right\} \quad (48)$$

Let $r = 3$ and apply boundary orthgonality so that $g^{13} = g^{23} = 0$, then equation (48) can be reduced to:

$$\frac{\delta p}{\delta\xi^3} = \frac{\delta\phi}{\delta\xi^3} - O(\Delta t) \quad (49)$$

A discrete version of equation (49) across a free surface of thickness $(\xi^3_{S+} - \xi^3_{S-})$, in curvilinear space, can be written as

$$p_{S+} - p_{S-} = \phi_{S+} - \phi_{S-} - O(\Delta t)(\xi^3_{S+} - \xi^3_{S-}) \quad (50)$$

The relationship between physical and curvilinear coordinates, equation (38), provides:

$$Z_{S+} - Z_{S-} = \frac{\partial x_3}{\partial\xi^q}(\xi^q_{S+} - \xi^q_{S-}) \quad (51)$$

where Z_{S+} and Z_{S-} are the vertical physical space coordinates on either side of the free surface along a curvilinear coordinate line that is normal to the free surface. Our grid spacing (in physical space) is defined as Δx while the grid spacing in curvilinear space is 1, so we can write:

$$Z_{S+} - Z_{S-} = \Delta x(\xi^3_{S+} - \xi^3_{S-}) \quad (52)$$

Using equations (45) and (46), it follows that,

$$\Delta x \geq \xi^3_{S+} - \xi^3_{S-} \quad (53)$$

Because our numerical method uses an explicit discretization (Adams-Bashforth) for the convective terms, we are subject to the Courant-Friedrichs-Lewy condition:

$$\frac{u\Delta t}{\Delta x} < 1 \quad (54)$$

So, if we apply equations (53) and (54) to equation (50), the result is second-order accurate in space:

$$p_{S+} - p_{S-} = \phi_{S+} - \phi_{S-} - O(\Delta x)^2 \quad (55)$$

Applying equation (55) and some algebra and tensor manipulation, the dynamic boundary condition of equations (43), (44), and (47) can be reduced to a form that can be more readily implemented in a numerical method:

$$\frac{\partial U^3}{\partial\xi^3} = -\frac{1}{2\mu}(\phi_{S+} - \phi_{S-}) - \frac{1}{2}g^{33}\left(U^1\frac{\partial g_{33}}{\partial\xi^1} + U^2\frac{\partial g_{33}}{\partial\xi^2}\right) \quad (56)$$

$$\frac{\partial U^1}{\partial\xi^3} = -g_{33}\left\{g^{11}\frac{\partial U^3}{\partial\xi^1} + g^{12}\frac{\partial U^3}{\partial\xi^2}\right\} \quad (57)$$

$$\frac{\partial U^2}{\partial\xi^3} = -g_{33}\left\{g^{22}\frac{\partial U^3}{\partial\xi^2} + g^{12}\frac{\partial U^3}{\partial\xi^1}\right\} \quad (58)$$

3 NUMERICAL METHOD

We have expanded the non-staggered grid, approximate-factorization, time-splitting method of Zang [19] to handle moving grids and a free surface. Previous authors [22] [27] have noted that appropriate discretization of the Jacobian in a moving grid method is important in maintaining numerical accuracy. In our method, the Jacobian is updated using the conservation of space, equation (8). By applying the definition of the grid flux, $\dot{X}$, equation (14), with an explicit Euler discretization, the conservation of space can be written as:

$$(J^{-1})^{n+1} = (J^{-1})^n + \Delta t\frac{\delta}{\delta\xi^q}\left(J^{-1}\dot{X}^q\right)^{n+\frac{1}{2}} \quad (59)$$

Equation (59) requires that the change in the physical-space volume contained in a computational space cell must be computed by summing the fluxes of physical space through the faces of the computational space cell. This ensures that space is numerically conserved and prevents an inconsistency between the Jacobian computation and the convective grid flux term, equation (27). To demonstrate that our moving grid method is second-order accurate in both space and time, numerical simulations of a decaying vortex (without a free surface) have been conducted and are reported in §5.1.

The numerical method can be summarized as:

1. Use the kinematic boundary condition to advance the free surface from time (n) to time $(n+1)$.

2. Compute grid and metrics for time $(n+1)$ grid using algebraic or Poisson solution method.

3. Solve for u_i^* at center of cells.

4. Use quadratic interpolation (QUICK [30]) to obtain the normal component of U^* on each cell face.

5. Use surface decomposition to solve the Poisson pressure equation for the pressure variable ϕ, coupled with the dynamic boundary condition (which solves for the contravariant velocity U^q on the free surface and the pressure variable ϕ_{S-} at the free surface).

6. Compute time $(n+1)$ Cartesian velocity (u_i) at cell centers.

7. Compute time $(n+1)$ contravariant velocity components normal to cell surfaces, U^q.

8. Compute all three components of contravariant velocity U^q on free surface

The free surface advance (step 1) and the u^* computation (step 3) are straightforward numerical implementations of equations (37) and (16) using vectorized tridiagonal solvers. The grid generation (step 2) uses the EAGLE code discussed in §2.2. The surface decomposition solution of the Poisson pressure equation and the dynamic boundary condition (step 5) is the most interesting part of our method and is covered in-depth in §4. Applying the corrector equations (steps 6 and 7) provides the three components of Cartesian velocity at the cell centers in the fluid volume, and one contravariant flux at each cell edge by solving equations (18) and (19). In order to advance the free surface using the kinematic boundary condition in the next time step, it is necessary to compute all three contravariant velocity components on the free surface (step 8). This can be done by using the dynamic boundary condition, equations (56), (57), and (58), and the contravariant velocity normal to the free surface (computed in the surface decomposition).

4 SURFACE DECOMPOSITION

Inherently, the invoking of the dynamic boundary condition presents difficulties for a Poisson solver due to the complicated interrelation between the boundary pressure and velocity gradients that is found in equations (56), (57), and (58). It is possible to directly enforce the dynamic boundary condition in the relaxation of the Poisson pressure equation; however, this is likely to impact future utility of the code. The difficulties involved can be illustrated by considering that the dynamic boundary condition directly affects only the layer of control volumes adjacent to the surface; however, in a multigrid method, this influence is moved progressively further into the domain as the grid is coarsened. This presents challenges in the derivation and coding of the restriction and interpolation operators that are used for mesh coarsening and refinement. Our investigations lead us to believe that this will make it difficult to develop future refinements of the dynamic boundary condition with reasonable amounts of effort.

To get around this problem, we have adapted the domain decomposition methods of Zang [31] to split the solution of the dynamic boundary condition from the solution of the pressure Poisson equation. That is, we decompose our solution into a two-dimensional surface and a three-dimensional volume for the pressure solution step. In Zang's method (as originally developed), the pressure Poisson equation is relaxed iteratively through decomposed domains using one or two V-cycles of the multigrid solver on each domain. Pressure and velocity boundary conditions are exchanged only at the finest multigrid level. The result is a method that quickly converges to a consistent pressure field over decomposed domains. Our new adaptation manipulates the dynamic boundary condition into an equation for the pressure at the free-surface and an equation for the contravariant flux across the free-surface. Therefore, we can alternately sweep the free-surface and the volume in a manner similar to that presented by Zang [31]. Our information exchange at the free-surface provides the pressure Poisson equation with a Dirichlet contravariant-velocity boundary condition without requiring any changes in the restriction and prolongation operators. This method is more suitable for future expansions since the dynamic boundary condition can be changed by working only with the surface domain, without affecting the volume domain and the fluid-flow Poisson solver.

In addition to those already presented, two other types of equations are required to obtain our discrete implementation of the dynamic boundary condition. One is a discrete representation of the contravariant velocity on the free

surface based upon the gradient of the contravariant velocity at the free surface and below the free surface:

$$U^{*q}\Big|_S = U^{*q}\Big|_{S-1} + \frac{1}{4}\frac{\delta}{\delta\xi^3}U^{*q}\Big|_S + \frac{1}{4}\frac{\delta}{\delta\xi^3}U^{*q}\Big|_{S-1} \quad (60)$$

where subscript (S) indicates the discrete quantities are evaluated at the cell face on the free surface, and subscript $(S-1)$ indicates the quantities are evaluated at the cell center inside the free surface.

The second type of equation required for completeness is an interpolating method for computing the first and second derivatives of the pressure variable (ϕ) at the free surface from the pressures at and below the free surface. For a two-dimensional flow with a one-dimensional surface we have tested both linear and quadratic interpolating forms, which can be written in the general form:

$$\gamma \equiv \frac{\delta\phi}{\delta\xi^3}\Big|_S = \alpha_1\phi_{S-} + \alpha_2\phi_{S-1} + \alpha_3\phi_{S-2} \quad (61)$$

$$\psi \equiv \frac{\delta^2\phi}{(\delta\xi^3)^2}\Big|_S = \alpha_4\phi_{S-} + \alpha_5\phi_{S-1} + \alpha_6\phi_{S-2} \quad (62)$$

where quantities subscripted with S and $S-1$ are as noted above, while ϕ_{S-} indicates the pressure in the water at the free surface, and ϕ_{S-2} indicates the pressure at the center of the second cell center inside the free surface.

The derivation of the three-dimensional discretized equations to be enforced as the dynamic boundary condition in the two-dimensional surface domain is too long to present in this paper. The method requires that equations (56), (57), (58), (60), (61), and (62), be manipulated to express the dynamic boundary condition as two linear operators: one for the contravariant velocity component normal to the free surface,

$$L_1\left(U_S^3\right) = S_1\left(\phi_{S-}, \phi_{S-1}, U_{S-1}^*, \gamma, \psi\right) \quad (63)$$

and a second operator for the pressure in the water at the free surface,

$$L_2\left(\phi_{S-}\right) = S_2\left(\phi_{S+}, U_{S-1}^*, U_S^3, \gamma\right) \quad (64)$$

where ϕ_{S+} indicates the pressure in the air at the free surface.

For a three-dimensional flow with a two-dimensional free surface, the linear operators L_1 and L_2 take a discretized Poisson-like form and are solvable by multigrid methods. For the two-dimensional flows with one-dimensional surfaces that we have tested to date, the linear operators take on tridiagonal form and are solved by inversion. The coupled two-dimensional surface decomposition method can be summarized as:

1. Solve the free-surface pressure equation (64), for an estimated free-surface pressure (ϕ_{S-}), using the pressure gradient and contravariant velocity from the last iteration.
2. Solve the free surface contravariant velocity equation (63) for an estimated contravariant velocity $\left(U_S^3\right)$ at the surface.
3. Repeat steps 1 and 2.
4. Perform one multigrid V-cycle, relaxing equation (17) to obtain a pressure estimate in volume.
5. Compute the estimated free-surface pressure gradient, γ, and second derivative of pressure, ψ, from equations (61) and (62) respectively.
6. Repeat steps 1 through 5 until convergence.

We expect that the three-dimensional implementation of this method (currently under development) will involve two V-cycles of the free surface pressure and contravariant velocity multigrid equations for each V-cycle of the Poisson pressure equation. This method is likely to be more costly in computational time than a direct application of the dynamic boundary condition, but the overall computational costs should still be reasonable since they should be less than that for a three-dimensional, two-grid, domain decomposition case, such as Zang [31] has already shown to be feasible.

5 SIMULATION RESULTS

5.1 Decaying Vortex with a Moving Grid

The use of second-order accurate discretizations does not guarantee second-order accuracy in a numerical simulation [32]. This is especially true

with boundary-fitted curvilinear coordinates and moving grids. We have conducted several simulations of a decaying vortex to demonstrate that our Navier-Stokes solution method is second-order accurate in time and space with a moving grid, The decaying vortex is an analytical solution of the two-dimensional Navier-Stokes equations over the domain of $(0 \leq x_1, x_2 \leq \pi)$ that can be written as:

$$u_1 = -\cos(x_1)\sin(x_2)\,e^{-2t} \quad (65)$$

$$u_2 = \sin(x_1)\cos(x_2)\,e^{-2t} \quad (66)$$

$$p = -0.25\,[\cos 2x_1 + \cos 2x_2]\,e^{-4t} \quad (67)$$

Figure (3) provides simulation results showing the reduction of the RMS velocity error with the increase in grid points from 8x8, to 16x16, to 32x32. Three different error lines are shown: the first represents the results for a fixed grid; the second is for a grid that is fixed in shape, but translates through the decaying vortex domain; the third is for a grid that has boundaries which remain fixed, but whose interior grid lines are stretched with each time step. It can be seen that accuracy is approximately second-order in all these cases.

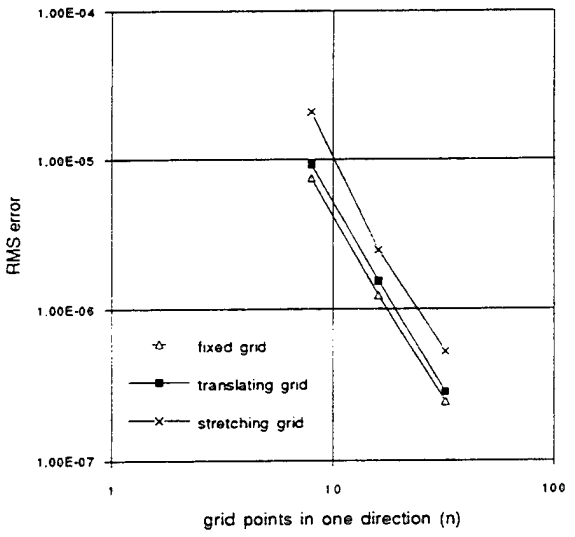


Figure 3: Decaying vortex accuracy

5.2 Standing Waves

To test the ability of our code to simulate a free surface, we performed simulations of standing waves in a two-dimensional rectangular basin. Free-slip boundary conditions were used for the sides and bottom of the 32 x 32 cell domain so that the simulations could be compared to nonlinear and linear standing wave theory. The grid points were distributed evenly in both directions. Using the wavelength $L = 1$ to non-dimensionalize the domain, the width is 0.5, and the depth d is 0.5. Simulations were run for small-amplitude waves with a non-dimensional wave height (or steepness) of 0.01 and for finite-amplitude waves with a non-dimensional wave height of 0.1. Using the wave amplitude a and the wave number k, these cases have ak values of 0.031 and 0.31, respectively. We conducted simulations at Reynolds numbers of 10, 100, and 1000 to illustrate capabilities of the simulation code with the relatively coarse grid. The Reynolds number is defined as:

$$Re = \frac{L\mathcal{U}}{\nu} \quad (68)$$

with ν as the kinematic viscosity, and $\mathcal{U}$ as the characteristic Cartesian velocity based upon the wave amplitude (a) and the wave frequency (ω):

$$\mathcal{U} = a\omega \quad (69)$$

From Lamb [33], the damping of a free wave due to viscosity as a function of time can be approximated from:

$$a(t) = a(0)e^{-2\nu k^2 t} \quad (70)$$

Note that this is based upon an energy dissipation argument for linear waves in deep-water, so we can only expect this to provide a rough guide to our expected damping.

From Wiegel [34] we can obtain predictions of wave period and shape for linear and nonlinear standing waves. Both linear and non-linear irrotational wave theory predict the wave period (T) for an inviscid wave as:

$$T = \sqrt{\frac{2\pi L}{g}\left(\tanh\frac{2\pi d}{L}\right)^{-1}} \quad (71)$$

For our simulation domain this provides a theoretical period of 1.1339 seconds.

According to linear theory for small amplitude waves, the wave shape should be a sinusoid, where the surface height (H) above the still water level is:

$$H(x,t) = a\sin(kx)\sin(\omega t) \quad (72)$$

where ω is the wave frequency $(2\pi/T)$. Nonlinear theory for finite amplitude standing waves predicts a wave shape given by:

case	ak	Re	initial wave shape	comparison of simulation and theory: period difference[1]	wave height difference[2]	linear wave shape difference[3]	nonlinear wave shape difference[3]
1a	0.031	10	linear	0.32 %	1.1 %	0.39 %	0.32 %
1b	0.031	10	non-linear	0.32 %	1.1 %	0.37 %	0.31 %
2a	0.031	100	linear	0.23 %	0.76 %	1.5 %	0.54 %
2b	0.031	100	non-linear	0.23 %	0.64 %	1.1 %	0.22 %
3a	0.31	10	linear	11 %	0.59 %	0.33 %	0.20 %
3b	0.31	10	non-linear	11 %	0.64 %	0.33 %	0.12 %
4a	0.31	100	linear	0.87 %	1.9 %	2.4 %	0.59 %
4b	0.31	100	non-linear	0.87 %	1.1 %	2.2 %	0.37 %
5a	0.31	1000	linear	0.32 %	6.4 %	1.2 %	0.53 %
5b	0.31	1000	non-linear	0.87 %	3.7 %	1.2 %	0.32 %

NOTES:

1. "period difference" is mean difference between the simulation wave period and theoretical period for the four oscillations simulated, and is expressed as a percentage of the theoretical period.
2. "wave height difference" is RMS difference between the simulation and theoretical wave height for crests at $x = 0$ from the first through fourth periods, and is expressed as a percentage of the wave height.
3. the "wave shape difference" is the RMS difference between the simulation wave shape and theory for one wave, expressed as a percentage of the wave height, and measured at the second wave period for case 3 and the fourth wave period for all other cases.

Table 1: Simulation Summary

$$H(x,t) = a\sin(kx)\sin(\omega t) - \frac{1}{2}ka^2\coth(kd)\cos(2kx)\left\{\sin^2(\omega t) - \frac{3\cos(2\omega t) + \tanh^2(kd)}{4\sinh^2(kd)}\right\} \quad (73)$$

Note that for a small amplitude standing wave, the wave shape predicted by linear and non-linear theory are practically indistiguishable.

We have run simulations using both the linear and non-linear free-surface shape as an inital condition in order to examine the ability of the method to move toward the correct free-surface shape. A summary of the simulation conditions and comparisons between simulation results and theory are presented in table (1). Note that the results show excellent agreement for both the nonlinear wave shape and viscous damping of the wave height. In all cases, the wave shape is closer to the theoretical nonlinear shape than to the linear shape. The wave shape difference was computed independently of the effects of viscous damping by using the simulated wave amplitude in equations (72) and (73) instead of the theoretical amplitude from equation (70). Similarly, an adjustment was made for the difference between the theoretical period and the simulation period by applying a small time shift to adjust the theoretical crest to the same time as the simulation crest. The simulations show an increase in the simulation wave period with increasing viscosity, which is a realistic physical result.

To provide a better picture of the simulation accuracy, we present two types of graphs which compare the results of typical simulations to linear and nonlinear theory. Figures (4), (6), (8), (10), and (12) show the height of the free surface at the wall $x = 0$ as a function of non-dimensional time (which is obtained using the theoretical period computed from equation (71)). The lines for linear and nonlinear theory are based on equations (72) and (73) with equation (70) used to compute the theoretical amplitude as a function of time. Figures (5), (7), (9), (11), (13), and (14) compare the wave shape for the simulation wave and theory.

Figures (4) and (5) present results for case 1b, showing that the simulation of a small amplitude standing wave at a low Reynolds number maintains the correct wave profile and is damped as predicted by theory. The results for case 1a (using a linear initial wave shape), are indistinguishable from the results from case 1b (using the non-linear initial wave shape). Figures (6) and (7) present results for the small amplitude standing wave at a Reynolds number of 100, case 2b. These graphs demonstrate that the simulation of viscous, small-amplitude wave still

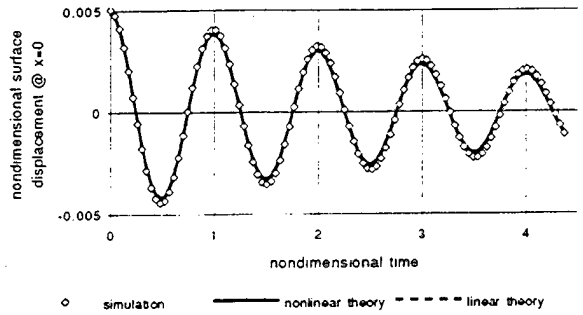


Figure 4: Free surface wall height, case 1b; $Re = 10$, $ak = 0.031$

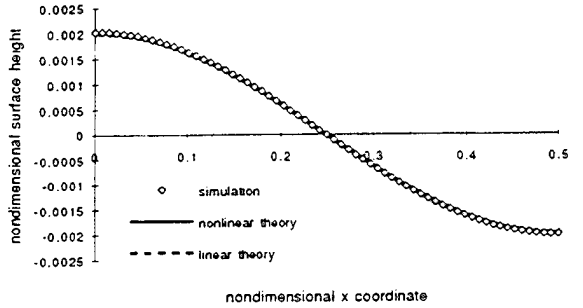


Figure 5: Free surface wave shape, case 1b; $Re = 10$, $ak = 0.031$

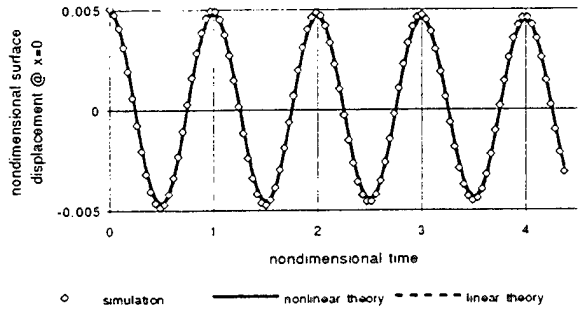


Figure 6: Free surface wall height, case 2b; $Re = 100$, $ak = 0.031$

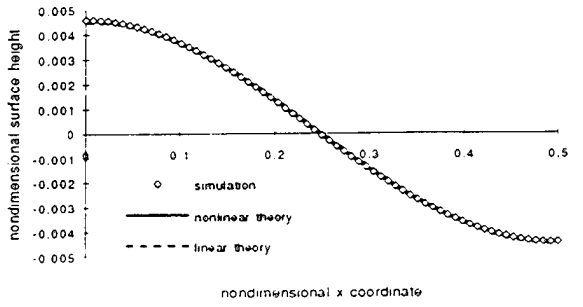


Figure 7: Free surface wave shape, case2b; $Re = 100$, $ak = 0.031$

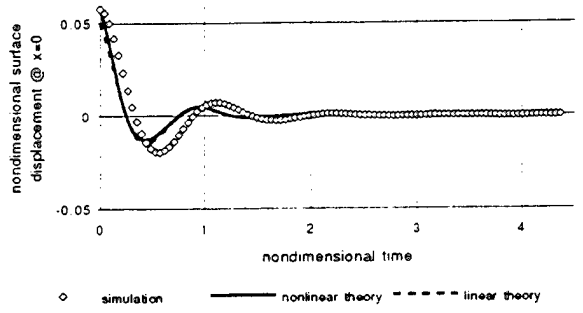


Figure 8: Free surface wall height, case 3b; $Re = 10$, $ak = 0.31$

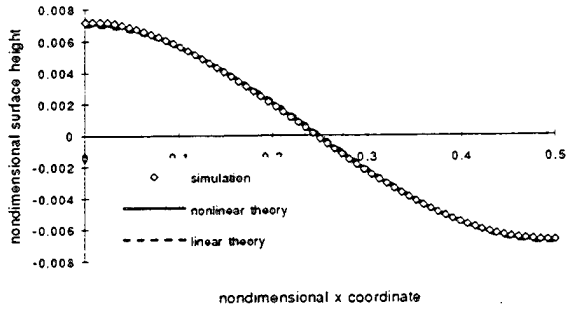


Figure 9: Free surface wave shape, case 3b; $Re = 10$, $ak = 0.31$

follows the linear and nonlinear theory both in wave shape and in period.

Figures (8) and (9) present results for the finite amplitude standing wave at $Re = 10$, case 3b. In this case, the wave is rapidly damped out. It can be seen that the period for the simulation is significantly greater than that for the theory. This result is not unreasonable, as one would expect that a highly viscous flow will oscillate at a slower period than that predicted by inviscid theory.

Figures (10) and (11) present results for the finite amplitude standing wave at $Re = 100$ with an initial nonlinear wave shape, case 4b. It can be seen that linear and non-linear theory are not coincident and the simulation wave shape follows nonlinear theory very closely.

Figures (12) and (13) present results for case 5b ($Re = 1000$) for an initially nonlinear wave shape. It can be seen that this case is at the limit of our ability to resolve the viscous effects with the coarse grid used in the simulation.

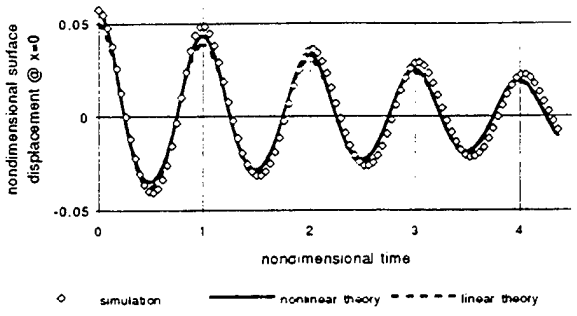


Figure 10: Free surface wall height, case 4b; $Re = 100$, $ak = 0.31$

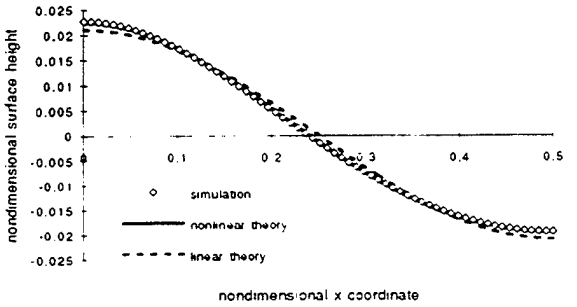


Figure 11: Free surface wave shape, case 4b; $Re = 100$, $ak = 0.31$

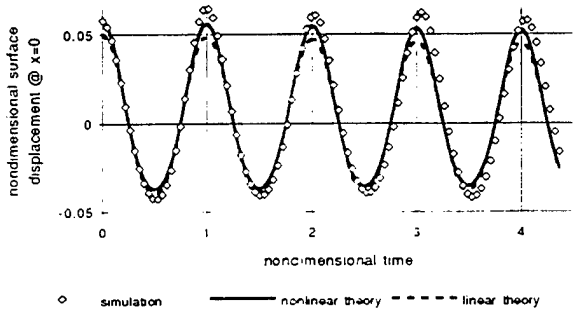


Figure 12: Free surface wall height, case 5b; $Re = 1000$, $ak = 0.31$

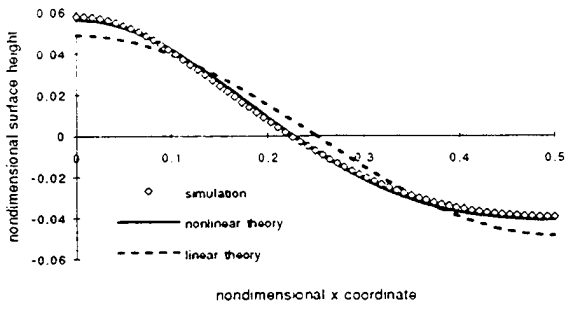


Figure 13: Free surface wave shape, case 5b; $Re = 1000$, $ak = 0.31$

To show that the simulation can evolve a nonlinear wave from an initially linear profile, figure (14) presents the wave shape for case 4a, which is similar to case 4b, (shown in figure (11)), except that the initial wave shape is a sinusoid from linear theory.

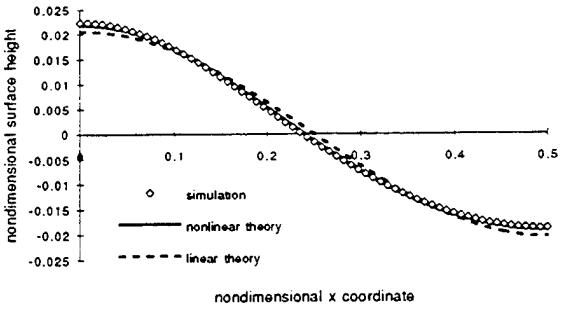


Figure 14: Free surface wave shape, case 4a; $Re = 100$, $ak = 0.31$

CONCLUSION

The numerical method presented has been shown to be second-order accurate in time and space with a moving grid, and has been shown to effectively simulate two-dimensional nonlinear waves. The method presented for deriving the kinematic boundary condition does not artificially restrict the free surface movement or limit wave shapes to single-valued functions in physical space. The surface decomposition method presented has been shown to be effective in the simulation of two-dimensional non-linear waves, and it is expected that future three-dimensional implementation will provide an effective method for invoking extremely complicated implementations of the dynamic boundary condition.

ACKNOWLEDGMENTS

The authors gratefully acknowledge the support of the Fluid Dynamic Program, Office of Naval Research under grant nos. N00014-91-J-1200 and N00014-94-J-0190.

References

[1] Floryan J.M., and Rasmussen, H., "Numerical methods for viscous flows with moving boundaries," *Appl. Mech. Rev.*, Vol. 42, 1989, pp. 323-340.

[2] Mei, C.C., *The Applied Dynamics of Ocean Surface Waves*, Wiley-Interscience, 1983.

[3] Harlow F.H., and Welch, J.E., "Numerical calculation of time-dependent viscous incompressible flow of fluid with a free surface," *Physics of Fluids*, Vol. 8, 1965, pp. 2182–2189.

[4] Hino, T. "Computation of viscous flows with free surface around an advancing ship," Presented at the second international colloquium on viscous fluid dynamics in ship and ocean technology, Osaka, Japan, September 1991.

[5] Thomas, T.G., and Leslie, D.C., "Development of a conservative 3-D free surface code," *J. Hydraulic Research*, Vol. 30, 1992, pp. 107–115.

[6] Park, J.-C., Zhu, M., and Miyata, H., "On the accuracy of numerical wave making techniques," *J. of The Society of Naval Architects of Japan*, Vol. 173, 1993, pp. 35–44.

[7] Sussman, M., Smereka, P., and Osher, S., "A level set approach for computing solutions to incompressible two-phase flow," Department of Mathematics, CAM Report 93-18, University of California, Los Angeles, June 1993.

[8] Zhu, J., and Sethian, J., "Projection methods coupled to level set interface techniques," *J. Comp. Physics*, Vol. 102, 1992, pp. 128–138.

[9] Hino, T., Martinelli, L., and Jameson, A., "A finite-volume method with unstructured grid for free surface flow simulations," Presented at the sixth international conference on numerical ship hydrodynamics, Ship Research Institute, Tokyo, Japan, August 1993.

[10] Loh, C.Y., and Rasmussen, H., "A numerical procedure for viscous free surface flows," *Appl. Numerical Mathematics*, Vol. 3, 1987, 479–495.

[11] Dommermuth, D.G., "The laminar interactions of a pair of vortex tubes with a free surface," *J. Fluid Mech.*, Vol. 246, 1993, 91–115.

[12] Hinatsu, M., "Numerical simulation of unsteady viscous nonlinear waves using moving grid system fitted on a free surface," *J. of Kansai Society of Naval Architects, Japan*, No. 217, 1992, pp. 1–12.

[13] Miyata, H., Zhu, M., and Watanabe, O., "Numerical study on a viscous flow with free-surface waves about a ship in steady straight course by a finite-volume method," *J. Ship Research*, Vol. 36, 1992, pp. 332–345.

[14] Ohring, S., and Lugt, H.J., "Two counter-rotating vortices approaching a free surface in a viscous fluid," Report 89/013, David Taylor Research Center, 1989.

[15] Farmer, J., Martinelli, L., and Jameson, A., "Multigrid solutions of the Euler and Navier-Stokes equations for a series 60 Cb = 0.6 ship hull for Froude numbers 0.160, 0.220 and 0.316 (program 1: Navier-Stokes formulation)," CFD Workshop Tokyo, Japan, March 1994.

[16] Wang, H.T., and Leighton, R.I., "Three-dimensional vortex interactions with a free surface," *Recent Advances and Applications in Computational Fluid Dynamics*, Vol. FED-103, ASME, 1990, pp. 213–222.

[17] Kassinos, A.C., and Prusa, J., "A numerical model for 3-D viscous sloshing in moving containers," *Recent Advances and Applications in Computational Fluid Dynamics*, Vol. FED-103, ASME, 1990, pp. 75–86.

[18] Zhan, C., and Zhaoshun, Z., "Numerical calculation of drift current in wind waves," *Acta Oceanologica Sinica*, Vol. 11, No. 2, 1992, pp. 179–188.

[19] Zang, Y., Street, R.L., and Koseff, J.R., "A non-staggered grid, fractional step method for time-dependent incompressible Navier-Stokes equations in general curvilinear coordinate systems," To appear in *J. Comput. Physics*, Aug. 1994.

[20] Chan, R.K.-C., and Street, R.L., "SUMMAC – A numerical model for water waves," Technical Report 135, Stanford University, Aug. 1970.

[21] Aris, R., *Vectors, Tensors, and the Basic Equations of Fluid Mechanics*, Dover, New York, 1962.

[22] Thompson, J.F., Warsi, Z.U.A., and Mastin, C.W., *Numerical Grid Generation*, Elsevier Science Publishing Co., New York, 1985.

[23] Zang, Y., *On the Development of Tools for the Simulation of Geophysical Flows.* PhD thesis, Stanford University, Dept. Mech. Eng., 1993.

[24] Thompson, J.F., "Current developments in grid generation for complex configurations," *Ocean Waves Mechanics, Computational Fluid Dynamics, and Mathematical Modelling*, Southampton, 1990, pp. 321–340.

[25] Perng, C.Y., *Adaptive-Multigrid Computations for Incompressible Flows, Including Geometry, Temperature, and Salinity Effects.* PhD thesis, Stanford University, Dept. Mech. Eng., 1990.

[26] Meakin, R.L., and Street, R.L., "Simulation of environmental flow problems in geometrically complex domains. Part I: A general coordinate transformation," *Computer Methods in Applied Mechanics and Engineering*, Vol. 68, 1988, pp. 151–175.

[27] Demirdžić, I., and Perić, M., "Space conservation law in finite volume calculations of fluid flow," *International J. for Numerical Methods in Fluids*, Vol. 8, 1988, pp. 1037–1050.

[28] Scriven, I.E., "Dynamics of a fluid interface," *Chemical Engineering Science*, Vol. 12, 1960, pp. 98–108.

[29] Batchelor, G.K., *Fluid Dynamics.* Cambridge University Press, 1967.

[30] Leonard, B.P., "A stable and accurate convective modelling procedure based on quadratic upstream interpolation," *Computer Methods in Applied Mechanics and Engineering*, Vol. 19, 1979, pp. 59–98.

[31] Zang, Y., Street, R.L., and Koseff, J.R., "A composite-multigrid method for solving unsteady incompressible Navier-Stokes equations in complex geometries," In *Numerical Methods in Laminar and Turbulent Flow*, Vol. VII, Pineridge Press, 1991, pp. 1485–1495.

[32] Kim, J., and Moin, P., "Application of a fractional-step method to incompressible Navier-Stokes equations," *J. Comp. Physics*, Vol. 59, 1985, pp. 308–323.

[33] Lamb, H., *Hydrodynamics.* Dover, 1945.

[34] Wiegel, R.L., *Oceanographical Engineering.* Prentice-Hall, Inc., 1964.

A Panel Method for Lifting Potential Flows Around Three-Dimensional Surface-Piercing Bodies

Z. Zou, H. Söding (Universität Hamburg, Germany)

ABSTRACT

A panel method using Rankine singularities for calculating steady three-dimensional lifting potential flows about surface-piercing bodies is presented. The disturbance potential is expressed by a source distribution on the body surface and free surface, and by a normal dipole distribution on the body centerplane and in the wake. The singularity strengths are determined so that the corresponding boundary conditions and the Kutta condition at the trailing edge are satisfied.

Numerical procedure is especially developed for a ship in steady motion at small drift angles. The flow around the ship is divided into a symmetric one due to the longitudinal motion of the ship and an antisymmetric one due to the lateral motion, which are determined in sequence. Numerical results are presented for three ship hulls: a Wigley hull, a Series 60 with $C_B = 0.60$ and a Mariner type hull.

NOMENCLATURE

$\vec{A}$	$= \nabla(\frac{1}{2}\nabla\Phi \cdot \nabla\Phi)$, approximation to the particle acceleration
B	Hull breadth, or Coefficient as defined in Equation (8)
C_N	$= N/\frac{1}{2}\rho V_s^2 SL$, yaw-moment coefficient
C_w	$= R_w/\frac{1}{2}\rho u^2 S$, wave-resistance coefficient
C_Y	$= Y/\frac{1}{2}\rho V_s^2 S$, lateral-force coefficient
$\vec{F}$	Force acting on the hull due to the pressure of the fluid
F_n	$= u/\sqrt{gL}$, Froude number
g	Gravitational acceleration
h	Water depth
L	Hull length
$\vec{M}$	Moment acting on the hull due to the pressure of the fluid
$\vec{n}$	$= (n_1, n_2, n_3)$, unit normal vector pointing into the hull
N	Yaw moment
N_v	$= \frac{\partial N}{\partial v}$, hydrodynamic coefficient
N'_v	$= N_v/\frac{1}{2}\rho L^3 u$, non-dimensional hydrodynamic coefficient
p	Pressure of the fluid
R_w	Wave resistance
S	Wetted hull surface area at rest
S_B	Wetted hull surface
T	Hull draught
u	Forward velocity of the ship
v	Sway velocity of the ship
$\vec{V}_s$	$= (u, v, 0)$, ship's speed
$\vec{W}$	$= \nabla\Phi - \vec{V}_s$, approximation to the relative velocity
x, y, z	Cartesian coordinates
Y	Lateral force
Y_v	$= \frac{\partial Y}{\partial v}$, hydrodynamic coefficient
Y'_v	$= Y_v/\frac{1}{2}\rho L^2 u$, non-dimensional hydrodynamic coefficient
β	Drift angle
ΔT	Dynamic sinkage
$\Delta\vartheta$	Dynamic trim
ζ	Negative free-surface elevation
Z	Approximation to ζ
ρ	Water density
σ	$= 2\Delta T/F_n^2 L$, non-dimensional sinkage
τ	$= 2\Delta\vartheta/F_n^2$, non-dimensional trim
ϕ	Disturbance velocity potential
Φ	Approximation to ϕ or ϕ_s
ϕ_s	Symmetric velocity potential due to the longitudinal motion of the ship
φ	Antisymmetric velocity potential due to the lateral motion of the ship

1. INTRODUCTION

About thirty years ago, three-dimensional panel method for flow computation began its development and design application as Hess and Smith (1) proposed the first three-dimensional surface-source method for calculating incompressible nonlifting potential flows about arbitrary configurations in an unbounded fluid. At the early development stage, efforts were made mainly by investigators in the field of aerodynamics for whom lift force is all-important, so that emphasis was put on the means of handling lift. A three-dimensional panel method for lifting potential flows was developed by Rubbert and Saaris (2) by adding dipole panels on the wing camberplane to the surface-source method of Hess and Smith. Alternatively, Hess (3) extended the method of Hess and Smith to lifting potential flows in an unbounded fluid by using dipole panels on the surface of the lifting portion of the configurations. Since then, numerous panel methods for computing lifting potential flows in an unbounded fluid have been successfully developed in the field of aerodynamics.

In contrast with the application in aeronautical engineering, three-dimensional panel methods were applied a little later to marine hydrodynamics problems involving surface ships, and main development efforts were directed towards nonlifting flows. A typical case is the wave resistance computation. Since the pioneering work of Dawson (4) who used Rankine source distribution on both the hull surface and the portion of the undisturbed free surface surrounding the hull, various three-dimensional Rankine source panel methods with different degree of complexity regarding the free-surface boundary condition, from linear to fully nonlinear, have been developed for solving the steady wave resistance problem. In recent years, there have also been a few efforts devoted to the unsteady ship motion problem by using three-dimensional Rankine panel methods. However, in almost all of the approaches, lifting effects remain unconsidered.

On the other hand, many problems in marine hydrodynamics are associated with lifting flow phenomena. A body with forward speed will experience hydrodynamic lift force and moment whenever the body or the flow is asymmetrical. For a symmetric body, e.g. a ship, such effects can be due to maneuvering and/or transverse motions in waves, or due to interaction with other bodies or rigid boundaries in the neighbourhood. Because of the complexity of the flow phenomena involved, lifting flows around surface-piercing bodies were calculated in the past mainly under assumptions concerning the body geometry and speed. Traditionally, thin-wing theory or slender-body theory are used and/or the free surface is replaced by a plane rigid wall. However, in order to understand better the hydrodynamic mechanisms involved, more rational numerical methods which can account for three-dimensional and free-surface effects should be applied.

Regarding the calculation of three-dimensional lifting potential flows around surface-piercing bodies, there are only few papers published. Xia and Larsson (5) developed a panel method for computing free-surface flows around yawed three-dimensional bodies by combining Dawson's method for nonlifting free-surface flows with the method of Hess for lifting flows in an unbounded fluid. Only keels of sailing yachts and foils were treated as lifting portion of the configurations. A similar method was proposed by Raven (6), but with vortices inside the lifting surface and with a Kutta condition in a form similar to the hull boundary condition.

Alternatively, Maniar et al. (7) developed a three-dimensional panel method using Kelvin singularities for calculating steady flow past a yawed surface-piercing plate, while Guilbaud et al. (8) reported an effort with Kelvin singularity panel method for calculating free-surface lifting flows including thickness effect.

A more practical panel method for free-surface lifting flows with marine application was proposed by Nakatake et al. (9). They considered steady motion of a yawed ship, utilized a Rankine source distribution on the hull surface and a part of the free surface and a distribution of Rankine type vortices on the centerplane of the ship, with the free vortices extending obliquely backwards into infinity. The nonlinear free-surface boundary condition and a pressure-equality Kutta-condition were satisfied iteratively. Numerical results were presented for a Wigley hull in deep water without sinkage and trim.

In the present paper, a three-dimensional panel method using Rankine singularities for computing free-surface lifting potential flows is described. This method is similar to that of Nakatake et al. and is especially developed for conventional ships in steady motion at small drift angles with free-surface effects. The hull is treated as a lifting body which pierces the free surface. In addition to the Rankine source distribution on the hull surface and a portion of the free surface surrounding the hull, a distribution of Rankine type normal dipoles on the centerplane

of the ship and in the wake is used to create circulation. Correspondingly, a Kutta condition is imposed along the trailing edge of the hull.

In the next section, the physical problem is first described mathematically, resulting in a boundary-value problem. Then the method of solution is explained in Section 3. In Section 4, numerical results are presented and discussed for three ships, a Wigley hull, a Series 60 hull with $C_B = 0.60$ and a Mariner type hull, and compared with other published numerical and experimental results where available.

2. MATHEMATICAL FORMULATION

A surface ship in steady oblique motion in deep water or in shallow water with constant depth is considered. The fluid is disturbed only by the ship.

We adopt a right-handed ship-fixed (except for the squat) Cartesian coordinate system o-xyz. The origin of the system is located at the intersection of the centerplane, the midship section and the undisturbed free surface, with x-axis pointing forward, z-axis vertically downward and y-axis to starboard. The ship's speed $\vec{V}_s$ is directed under an angle, the drift angle β, relative to the x-axis, see Figure 1. The ship is free to sink and trim.

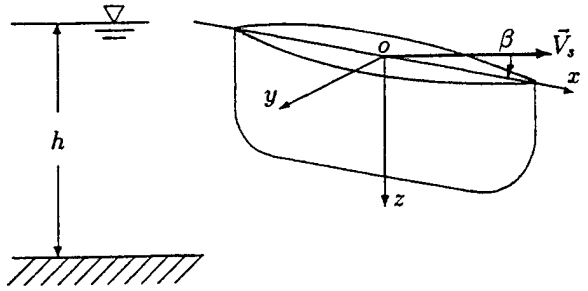


Figure 1. Coordinate system

It is assumed that the fluid is inviscid and incompressible. The absolute velocity of the fluid is represented by the gradient of a disturbance velocity potential $\phi(x, y, z)$ which satisfies Laplace's equation in the fluid domain and the following boundary conditions:

1) Kinematic boundary condition on the free surface $z = \zeta(x, y)$:

$$(\nabla\phi - \vec{V}_s) \cdot \nabla\zeta = \phi_z, \qquad (1)$$

where $\vec{V}_s = (u, v, 0)$, with u and v the forward and sway velocity of the ship, respectively; ζ is the negative free-surface elevation.

2) Dynamic boundary condition on the free surface $z = \zeta(x, y)$:

$$\zeta = \frac{1}{g}\left(-\vec{V}_s \cdot \nabla\phi + \frac{1}{2}\nabla\phi \cdot \nabla\phi\right), \qquad (2)$$

where g is the gravitational acceleration.

3) Kinematic boundary condition on the wetted ship surface S_B:

$$\nabla\phi \cdot \vec{n} = \vec{V}_s \cdot \vec{n}, \qquad (3)$$

where $\vec{n} = (n_1, n_2, n_3)$ is the unit normal vector pointing into the hull.

4) Kinematic boundary condition on the bottom $z = h$:

$$\phi_z = 0. \qquad (4)$$

5) Disturbance-decay condition at infinity:

$$\nabla\phi \to (0, 0, 0). \qquad (5)$$

Moreover, the velocity potential should satisfy a radiation condition which states that no waves appear ahead of the ship at a great distance, and a Kutta condition which requires the velocity at the trailing edge to be finite.

Eliminating the unknown free-surface elevation ζ from (1) and (2), we obtain a single boundary condition on the free surface:

$$(\nabla\phi - \vec{V}_s) \cdot \nabla\left(-\vec{V}_s \cdot \nabla\phi + \frac{1}{2}\nabla\phi \cdot \nabla\phi\right) = g\phi_z \quad \text{on } z = \zeta(x, y). \qquad (6)$$

The obtained boundary-value problem for the velocity potential is highly nonlinear, since the boundary conditions on the free surface are nonlinear and should be imposed on the boundary, the position of which is not known a priori. In order to solve this problem iteratively, the boundary conditions on the free surface are linearized about Z and Φ, the approximations to ζ and ϕ, respectively. Using Taylor series expansions and neglecting the higher-order terms, we obtain from (2) and (6):

$$\zeta - Z = \frac{\vec{W} \cdot \nabla\phi - \frac{1}{2}\nabla\Phi \cdot \nabla\Phi - gZ}{g - \vec{W} \cdot \nabla\Phi_z} \quad \text{on } z = Z(x, y), \qquad (7)$$

$$\begin{aligned} &\{2[\vec{A} - \nabla(\vec{V}_s \cdot \nabla\Phi)] + B\vec{W}\} \cdot \nabla\phi \\ &\quad + \vec{W} \cdot [(\vec{W} \cdot \nabla)\nabla\phi] - g\phi_z \\ &\quad = 2\nabla\Phi \cdot [\vec{A} - \nabla(\vec{V}_s \cdot \nabla\Phi)] \\ &\quad + B\left(\frac{1}{2}\nabla\Phi \cdot \nabla\Phi + gZ\right) \end{aligned} \quad \text{on } z = Z(x, y), \qquad (8)$$

where

$$\vec{W} = \nabla\Phi - \vec{V}_s,$$
$$\vec{A} = \nabla\left(\frac{1}{2}\nabla\Phi\cdot\nabla\Phi\right),$$
$$B = \frac{\left\{\vec{W}\cdot[\vec{A} - \nabla(\vec{V}_s\cdot\nabla\Phi)] - g\Phi_z\right\}_z}{g - \vec{W}\cdot\nabla\Phi_z}.$$

From the solution of this boundary-value problem we can calculate the force and moment acting on the hull:

$$\vec{F} = \iint_{S_B} p\,\vec{n}\,dS, \tag{9}$$
$$\vec{M} = \iint_{S_B} p\,(\vec{R}\times\vec{n})\,dS, \tag{10}$$

where $\vec{R} = (x, y, z)$ is the position vector, and p the pressure which is given by

$$p = \rho\left(\vec{V}_s\cdot\nabla\phi - \frac{1}{2}\nabla\phi\cdot\nabla\phi + gz\right), \tag{11}$$

where ρ is the density of the fluid.

3. METHOD OF SOLUTION

3.1 General

The boundary-value problem is solved by a panel method using Rankine singularities. The velocity potential is represented by a source distribution on the ship surface and a part of the free surface, and by a normal dipole distribution on the centerplane of the ship and downsteam of the trailing edge. The ship surface up to a horizontal plane above the undisturbed free surface is discretized into triangular or quadrilateral panels. On each of the panels, a source distribution with constant density is used. The portion of the free surface surrounding the ship is discretized into quadrilateral panels. The source distribution on the free surface is raised to a horizontal plane above the free surface and replaced by point sources as in Jensen et al. (10). Additionally, the semi-infinite dipole sheet is discretized and replaced by a system of discrete horseshoe vortices. The singularity strengths are determined so that the boundary conditions on the hull surface and free surface and the Kutta condition at the trailing edge are satisfied simultaneously. In case of shallow water, the method of images is used to satisfy the boundary condition on the bottom. In order to satisfy the radiation condition, the numerical technique of "staggered grid" suggested by Jensen et al. is used. Under the assumption of small drift angles, the point sources above the free surface are shifted backwards relative to the collocation points on the free surface only in the longitudinal direction.

3.2 Decomposition of the Flow

In comparison with the wave resistance problem, the flow around a yawed ship is not symmetric about the centerplane of the ship. To solve the resulting boundary-value problem by using a panel method, the boundary surface on both sides of the centerplane must be paneled and covered with singularities, so that the computational burden would be increased substantially. In order to avoid this, the flow is divided into a symmetric one due to the longitudinal motion and an antisymmetric one due to the lateral motion of the ship. Correspondingly, the velocity potential ϕ consists of a symmetric part ϕ_s and an antisymmetric part φ:

$$\phi = \phi_s + \varphi. \tag{12}$$

It is assumed that the drift angle is so small that $\varphi \ll \phi$ on the free surface. Hence the original boundary-value problem for ϕ can be linearized about the solution of the symmetric flow. This results in a boundary-value problem for ϕ_s and another one for φ, which can be determined in sequence.

Consequently, only one half of the boundary surface and flow field need to be considered, and the centerplane of the ship serves as an image plane. The source strengths on the image body and on the original body are equal in magnitude, and have same sign for the symmetric flow and opposite sign for the antisymmetric flow, respectively. On the other hand, the distribution of dipoles or vortices is only required for the antisymmetric flow, and, as explained in the following, will be put on the symmetry plane of the ship.

3.3 Solution for the Symmetric Flow

The boundary-value problem for the symmetric velocity potential is solved first. This problem corresponds to the wave resistance problem with

$$\vec{V}_s = (U, 0, 0), \tag{13}$$

where $U = u$ is the forward speed of the ship.

For this nonlifting flow problem, only a symmetric source distribution on the hull surface and free surface is required, while the source strengths are determined by satisfying boundary conditions at the collocation points on the hull surface and free surface. The dipole distribution and the corresponding Kutta condition are unnecessary here.

From (3), (8) and (13) we obtain

$$\nabla\phi_s \cdot \vec{n} = U\, n_1 \qquad \text{on } S_B, \tag{14}$$

$$\begin{aligned}&[2(\vec{A} - U\nabla\Phi_x) + B\vec{W}] \cdot \nabla\phi_s \\ &\quad + \vec{W} \cdot [(\vec{W} \cdot \nabla)\nabla\phi_s] - g\phi_{sz} \\ &\quad = 2\nabla\Phi \cdot (\vec{A} - U\nabla\Phi_x) \\ &\quad + B\left(\frac{1}{2}\nabla\Phi \cdot \nabla\Phi + gZ\right) \\ &\qquad\qquad \text{on } z = Z(x,y). \end{aligned} \tag{15}$$

Here Φ and Z are approximations to ϕ_s and ζ due to the longitudinal motion.

Correspondingly, we obtain from (7) and (13):

$$\zeta = Z + \frac{\vec{W} \cdot \nabla\phi_s - \frac{1}{2}\nabla\Phi \cdot \nabla\Phi - gZ}{g - \vec{W} \cdot \nabla\Phi_z} \qquad \text{on } z = Z(x,y). \tag{16}$$

This boundary-value problem is solved iteratively, starting from $Z = 0$ and $\Phi = 0$ (Neumann-Kelvin formulation). During each iteration step, the source strengths are determined from (14) and (15) at first. Then the free-surface elevation is calculated using (16); the wave resistance, the vertical force and trim moment are obtained by integration of the pressure over the wetted ship surface; and the sinkage and trim are determined from the dynamic equilibrium of the ship. This iterative procedure is continued until the nonlinear boundary condition on the free surface is satisfied.

3.4 Solution for the Antisymmetric Flow

After the problem for symmetric flow is solved, we obtain from (3), (8), (12), (14) and (15) a linear boundary-value problem for the antisymmetric velocity potential φ:

$$\nabla\varphi \cdot \vec{n} = v\, n_2 \qquad \text{on } S_B, \tag{17}$$

$$\begin{aligned}&\{2[\vec{A} - \nabla(\vec{V}_s \cdot \nabla\Phi)] + B\vec{W}\} \cdot \nabla\varphi \\ &\quad + \vec{W} \cdot [(\vec{W} \cdot \nabla)\nabla\varphi] - g\varphi_z = 0 \\ &\qquad\qquad \text{on } z = Z(x,y). \end{aligned} \tag{18}$$

Here Φ and Z are now the symmetric velocity potential and free-surface elevation due to the longitudinal motion of the ship, and $\vec{V}_s = (u, v, 0)$.

The antisymmetric flow is a lifting potential flow. To represent this flow, not only the antisymmetric source distribution on the hull surface and free surface, but also the dipole distribution on the centerplane of the ship and in the wake are required. Under the assumption that the drift angle is small, the dipole sheet downstream of the trailing edge is put on the symmetry plane of the ship. This simplification is necessary, because otherwise the decomposition of the flow into a symmetric part and an antisymmetric part would be disturbed.

Corresponding to the dipole distribution, a Kutta condition should be imposed along the trailing edge of the hull. In this paper, it is applied indirectly by requiring the pressure on the collocation points of the hull panels adjacent to the trailing edge on both sides to be equal. This pressure-equality Kutta condition is nonlinear and must be satisfied by an iterative procedure, see e.g. Hess (3) and Nakatake et al. (9). However, by dividing the velocity potential ϕ into a symmetric part Φ and an antisymmetric part φ, this condition can be linearized, Zou (11), in the form

$$\nabla\Phi \cdot \nabla\varphi - u\,\varphi_x = v\,\Phi_y. \tag{19}$$

(19) is linear about the antisymmetric velocity potential φ and is satisfied at the collocation points of the hull panels adjacent to the trailing edge of the hull on the considered (starboard) side. Supposing that there are N_K panels on the hull adjacent to the trailing edge, so there will be N_K linear equations obtained by satisfying (19). Consequently, the number of unknowns introduced by the dipole distribution should not exceed N_K. To ensure this, the semi-infinite dipole sheet on the symmetry plane of the ship is divided horizontally into strips according to the hull panels adjacent to the trailing edge. On each strip, the dipole strength is assumed to change linearly from zero at the leading edge to a nonzero value at the trailing edge. This dipole distribution is equivalent to a vorticity distribution, the vertical component of which is independent of the longitudinal coordinate, between the leading edge and trailing edge. For steady flows, the dipole strength on each strip on the free dipole sheet must be constant and equal to the dipole strength on the ship at the trailing edge in order to satisfy the pressure-continuity condition cross the dipole sheet. Correspondingly, the vertical component of the equivalent vorticity distribution downstream of the trailing edge is zero. In the numerical procedure, vorticity distribution instead of dipole distribution is used. This vorticity distribution is, after discretization, replaced by a system of horseshoe vortices. Figure 2 illustrates the distribution of horseshoe vortices on the k-th

strip, where the strip between the leading and trailing edge is discretized into N_X panels.

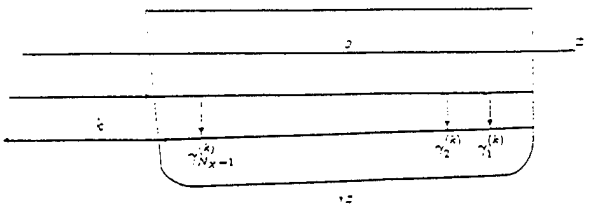


Figure 2. Horseshoe vortices on the k-th strip with $\gamma_1^{(k)} = \gamma_2^{(k)} = \cdots = \gamma_{N_X-1}^{(k)} = \gamma^{(k)}$

The boundary conditions (17), (18) and the Kutta condition (19) are used to determine the antisymmetric velocity potential φ. In contrast with the calculation of symmetric flow, the antisymmetric flow is calculated once only, thus the nonlinear effects of the antisymmetric potential on the free-surface conditions are neglected.

From the solutions for the symmetric and antisymmetric velocity potential we can calculate the total free surface elevation and the hydrodynamic lateral force and yaw moment acting on the ship.

From (7) follows

$$\zeta = Z + \frac{\vec{W}\cdot(\nabla\Phi + \nabla\varphi) - \frac{1}{2}\nabla\Phi\cdot\nabla\Phi - gZ}{g - \vec{W}\cdot\nabla\Phi_z} \quad \text{on } z = Z(x,y), \quad (20)$$

where Φ and Z are the velocity potential and the free-surface elevation due to the longitudinal motion, respectively.

In order to determine the free-surface elevation on the other side of the symmetry plane of the ship, the numerator in (20) is divided into a symmetric part $\Delta\zeta_N^{(s)}$ and an antisymmetric part $\Delta\zeta_N^{(a)}$, and correspondingly, the denominator into $\Delta\zeta_D^{(s)}$ and $\Delta\zeta_D^{(a)}$, with

$$\begin{aligned}
\Delta\zeta_N^{(s)} &= -u\Phi_x + \frac{1}{2}\nabla\Phi\cdot\nabla\Phi - gZ - v\varphi_y,\\
\Delta\zeta_N^{(a)} &= -v\Phi_y + \nabla\Phi\cdot\nabla\varphi - u\varphi_x,\\
\Delta\zeta_D^{(s)} &= g - \nabla\Phi\cdot\nabla\Phi_z + u\Phi_{xz},\\
\Delta\zeta_D^{(a)} &= v\Phi_{zy}.
\end{aligned}$$

The free-surface elevation on the other side of the symmetry plane of the ship is

$$\zeta = Z + \frac{\Delta\zeta_N^{(s)} - \Delta\zeta_N^{(a)}}{\Delta\zeta_D^{(s)} - \Delta\zeta_D^{(a)}}. \quad (21)$$

Similarly, the pressure in (11) is divided into a symmetric part $p^{(s)}$ and an antisymmetric part $p^{(a)}$, with

$$\begin{aligned}
p^{(s)} &= \rho\left(u\Phi_x - \frac{1}{2}\nabla\Phi\cdot\nabla\Phi + g\,z \right.\\
&\qquad \left. + v\varphi_y - \frac{1}{2}\nabla\varphi\cdot\nabla\varphi\right),\\
p^{(a)} &= \rho\,(v\Phi_y - \nabla\Phi\cdot\nabla\varphi + u\varphi_x).
\end{aligned}$$

The symmetric pressure induces only the wave resistance, the vertical force and trim moment, while the antisymmetric pressure causes only the lateral force, the yaw moment and roll moment. The lateral force Y and yaw moment N are obtained by pressure integration as

$$Y = \iint_{S_B} p^{(a)}\, n_2\, dS, \quad (22)$$

$$N = \iint_{S_B} p^{(a)}\,(x\,n_2 - y\,n_1)\, dS. \quad (23)$$

4. RESULTS AND DISCUSSION

The proposed method has been applied to three ship hulls, a Wigley model, a Series 60 with $C_B = 0.60$ and a Mariner class ship, at 0° and 5° drift angle in deep and shallow water. The free-surface elevation ζ, the wave resistance R_w, the dynamic sinkage ΔT and trim $\Delta\vartheta$ due to the forward speed, the lateral force Y and yaw moment N are calculated. In order to compare with measurements and other numerical results, the following non-dimensional coefficients are used:

$$\begin{aligned}
C_w &= \frac{R_w}{\frac{1}{2}\rho\,u^2\,S},\\
\sigma &= \frac{2\,\Delta T}{F_n^2\,L},\\
\tau &= \frac{2\,\Delta\vartheta}{F_n^2},\\
C_Y &= \frac{Y}{\frac{1}{2}\rho\,V_s^2\,S},\\
C_N &= \frac{N}{\frac{1}{2}\rho\,V_s^2\,S\,L},
\end{aligned}$$

where S is the wetted ship surface area at rest, L the ship length, F_n the Froude number, and $V_s = \sqrt{u^2+v^2}$.

Here numerical results are presented and discussed only for ships in deep water. Results in shallow water are given in Zou (12).

4.1 Wigley Hull

The underwater form of the hull at rest is given by

$$y = \frac{B}{2}\left(1 - \frac{4x^2}{L^2}\right)\left(1 - \frac{z^2}{T^2}\right),$$

where L, B and T are the length, breadth and draught of the hull, respectively. Above the waterline, sections are assumed vertical.

The panel distribution on the hull is shown in Figure 3. Correspondingly, Figure 4 shows the free-surface grid used in the calculation.

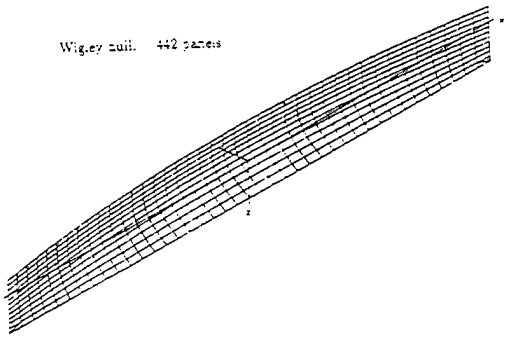


Figure 3. Panel distribution on Wigley hull

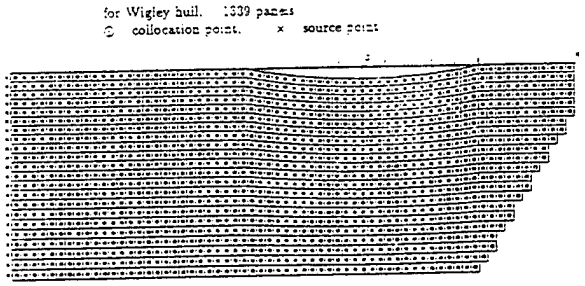


Figure 4. Free-surface grid for Wigley hull

In Figure 5, the wave-resistance coefficient at 0° drift angle is shown and compared with numerical results of Jensen (13) and measurements of Kajitani (14). Figure 6 illustrates the wave profile along the hull at $F_n = 0.27$ and $\beta = 0°$ in comparison with Jensen's result and the measurement of Shearer and Cross (15). The agreement is good.

Regarding oblique motion, there are only a few numerical results and experimental data by other authors available. In Figure 7 and Figure 8, the lateral-force and yaw-moment coefficients at 5° drift angle are shown together with numerical results of Nakatake et al. (9), Maruo and Song (16) and the experimental data of Kashiwagi (which are taken from Nakatake et al.). These figures illustrate that our results are relatively close to those of Nakatake et al., but ours oscillate over F_n more than those of Nakatake et al..

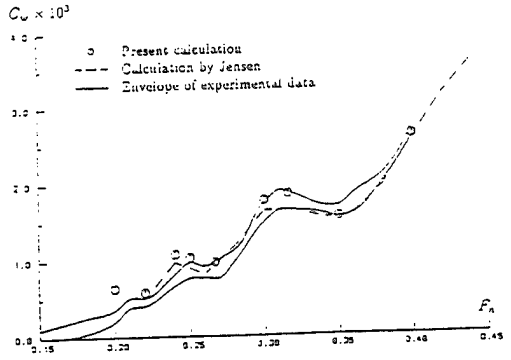


Figure 5. Wave-resistance coefficient of Wigley hull in deep water at $\beta = 0°$

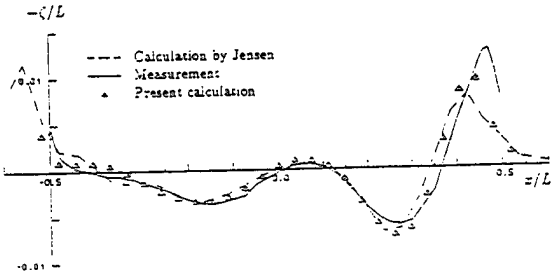


Figure 6. Wave profile along Wigley hull in deep water at $F_n = 0.27$ and $\beta = 0°$

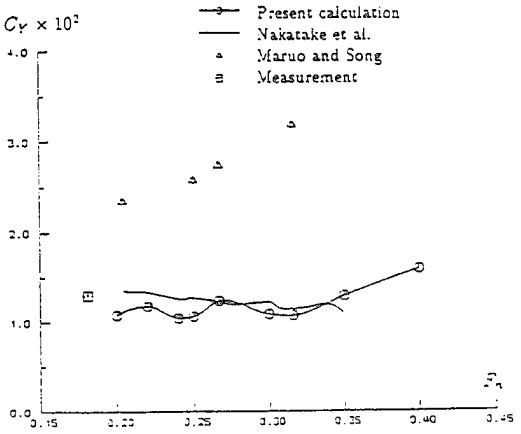


Figure 7. Lateral-force coefficient of Wigley hull in deep water at $\beta = 5°$

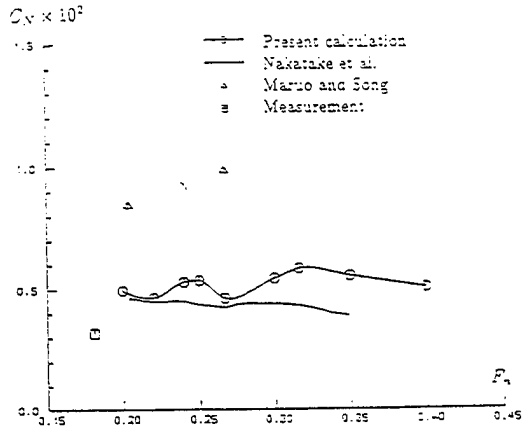


Figure 8. Yaw-moment coefficient of Wigley hull in deep water at $\beta = 5°$

Figure 9 illustrates the wave profiles along both sides of the hull at $F_n = 0.27$ and $\beta = 5°$.

Figure 10 and Figure 11 show the wave contours for the hull at $F_n = 0.25$, drift angle $\beta = 0°$ and 5°, respectively. In both cases the radiation condition is satisfied quite well.

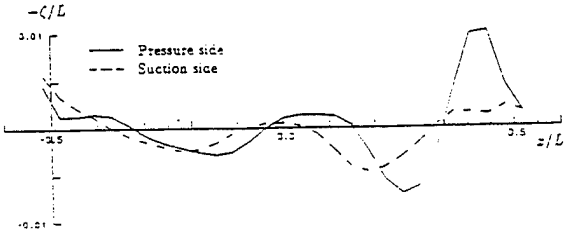


Figure 9. Calculated wave profiles along Wigley hull in deep water at $F_n = 0.27$ and $\beta = 5°$

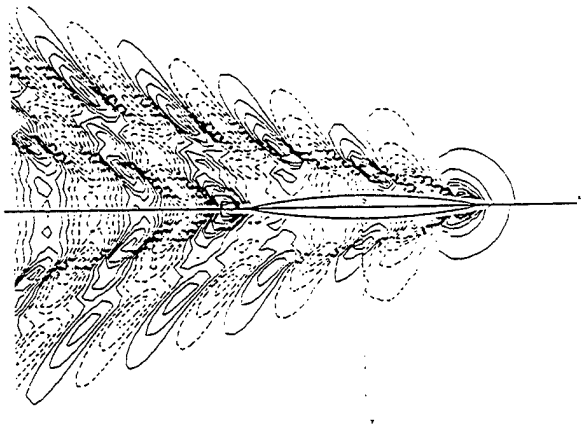


Figure 10. Calculated wave contours for Wigley hull in deep water at $F_n = 0.25$ and $\beta = 0°$ Lower half linear, upper half nonlinear result Distance between the contour lines: $0.8 \times 10^{-3}L$.

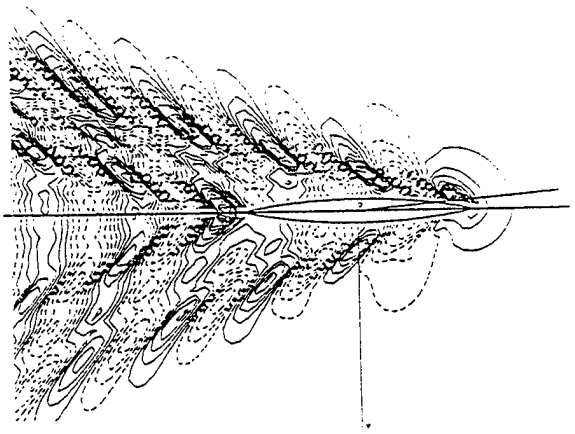


Figure 11. Calculated wave contours for Wigley hull in deep water at $F_n = 0.25$ and $\beta = 5°$ Distance between the contour lines: $0.7 \times 10^{-3}L$.

4.2 Series 60, $C_B = 0.60$

The lines and other data of the ship are given by Todd (17). Figure 12 shows the panel distribution on the hull, while Figure 13 illustrates a typical free-surface grid for this ship.

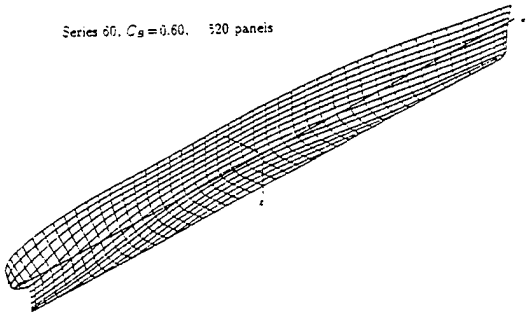


Figure 12. Panel distribution on Series 60 hull with $C_B = 0.60$

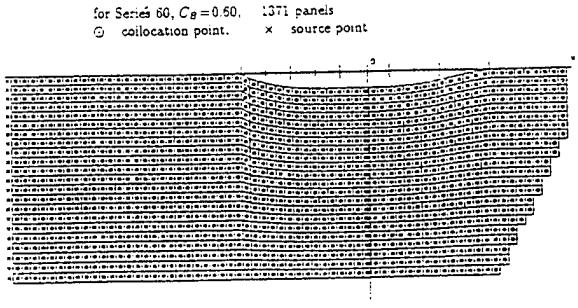


Figure 13. A typical free-surface grid for Series 60, $C_B = 0.60$

In Figure 14, the calculated wave-resistance coefficient is shown together with numerical results of Jensen and measurements of Ogiwara (18). It seems that the proposed method overestimated the wave resistance, especially at $F_n < 0.3$.

Figure 15 and Figure 16 show the lateral-force and yaw-moment coefficients at 5° drift angle respectively. Unfortunately, no experimental data or other comparable numerical results are available.

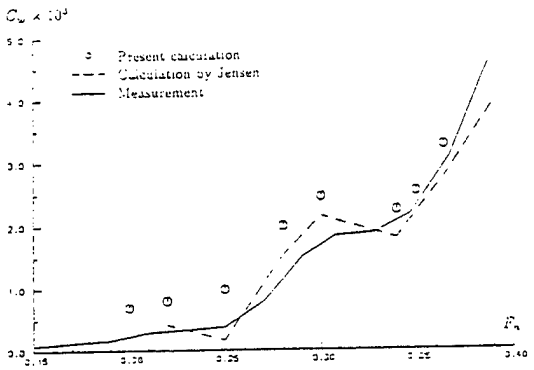


Figure 14. Wave-resistance coefficient of Series 60, $C_B = 0.60$ in deep water at $\beta = 0°$

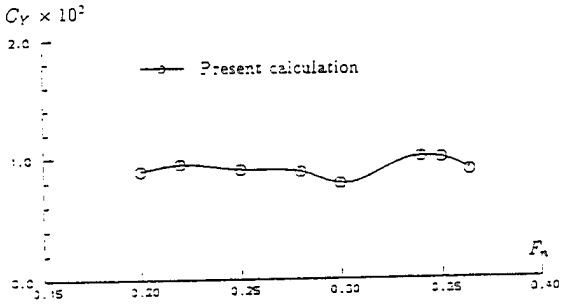


Figure 15. Calculated lateral-force coefficient of Series 60, $C_B = 0.60$ in deep water at $\beta = 5°$

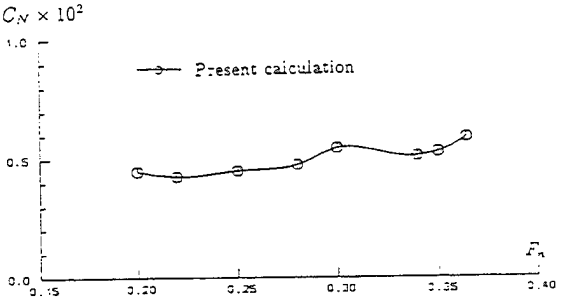


Figure 16. Calculated yaw-moment coefficient of Series 60, $C_B = 0.60$ in deep water at $\beta = 5°$

As examples, Figure 17 shows the calculated wave profile along the hull at $F_n = 0.25$ and $\beta = 0°$ in comparison with the measurement of Ogiwara, while Figure 18 and Figure 19 illustrate respectively the wave profiles and the wave contours for the hull at $F_n = 0.25$ and $\beta = 5°$.

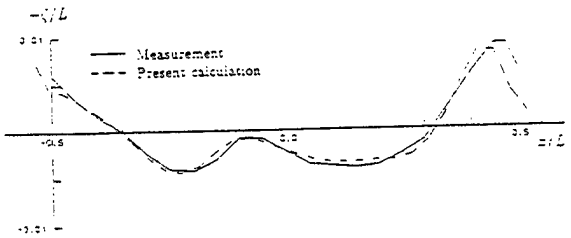


Figure 17. Wave profile along Series 60, $C_B = 0.60$ in deep water at $F_n = 0.25$ and $\beta = 0°$

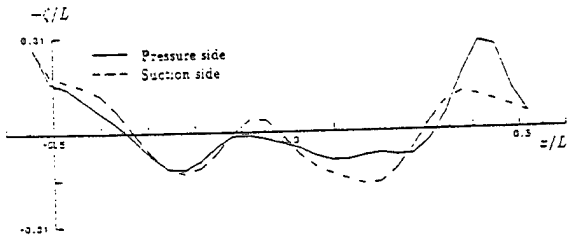


Figure 18. Calculated wave profiles along Series 60, $C_B = 0.60$ in deep water at $F_n = 0.25$ and $\beta = 5°$

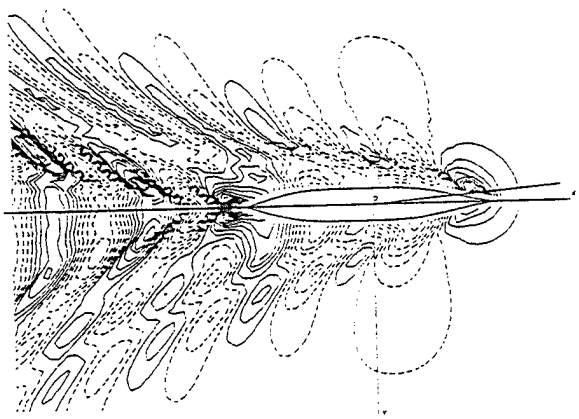


Figure 19. Calculated wave contours for Series 60, $C_B = 0.60$ in deep water at $F_n = 0.25$ and $\beta = 5°$
Distance between the contour lines: $0.9 \times 10^{-3} L$.

4.3 Mariner Ship

The Mariner ship is frequently used for investigating ship manoeuvrability. The lines and other ship data are given by Russo and Sullivan (19).

Figure 20 shows the panel distribution on the hull, while Figure 21 illustrates a typical free-surface grid for this ship.

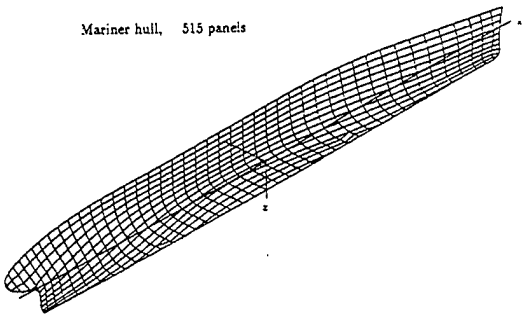


Figure 20. Panel distribution on Mariner hull

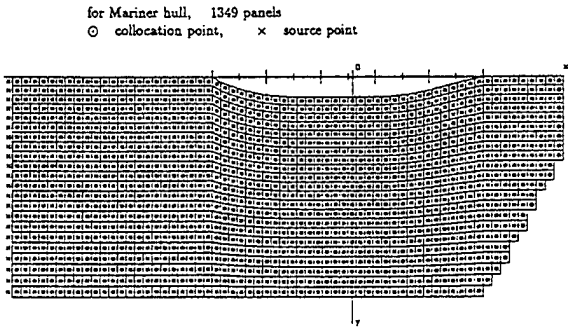


Figure 21. A typical free-surface grid for Mariner ship

The following non-dimensional hydrodynamic coefficients are used for comparison purpose:

$$Y'_v = \frac{Y_v}{\frac{1}{2}\rho L^2 u},$$

$$N'_v = \frac{N_v}{\frac{1}{2}\rho L^3 u}.$$

Under the assumption of small drift angles, the following linearization is used:

$$Y_v = \frac{\partial Y}{\partial v} = \frac{Y}{v} \approx \frac{-Y}{u\beta},$$

$$N_v = \frac{\partial N}{\partial v} = \frac{N}{v} \approx \frac{-N}{u\beta}.$$

Figure 22 and Figure 23 show the calculated lateral-force and yaw-moment coefficients at 5° drift angle in comparison with measurements of Fujino (20) and Wolff (21). The agreement of the calculated lateral force with the measurements is very good. On the other hand, the yaw moment calculated by our method is higher than measured. This difference is probably due to the effects of rudder and propeller, because the numerical results refer to the bare hull only, while the experiments were done with models having rudder and propeller.

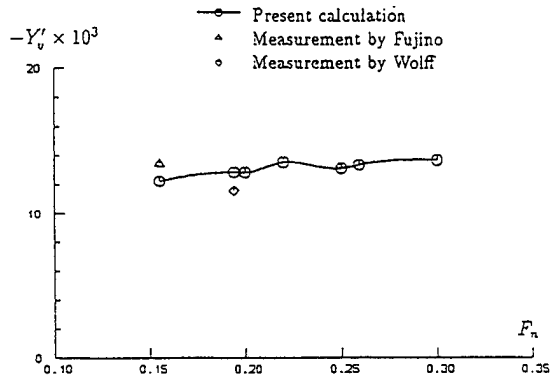


Figure 22. Lateral-force coefficient of Mariner hull in deep water at $\beta = 5°$

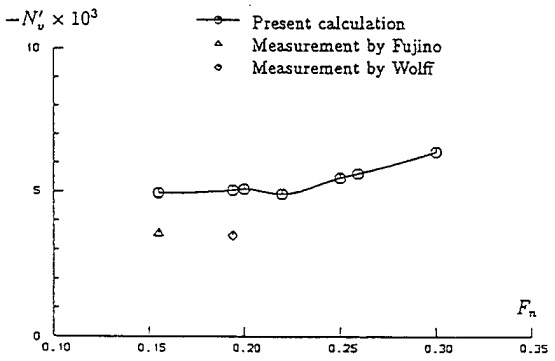


Figure 23. Yaw-moment coefficient of Mariner hull in deep water at $\beta = 5°$

In Figure 24, the wave profiles along both sides of the hull at $F_n = 0.22$ and $\beta = 5°$ are shown. Correspondingly, Figure 25 illustrates the wave contours for this case. It is seen that, although the radiation condition is well satisfied, the diverging waves at the pressure side of the hull have not been calculated properly. It seems that a finer panel grid on the free surface is required for this purpose.

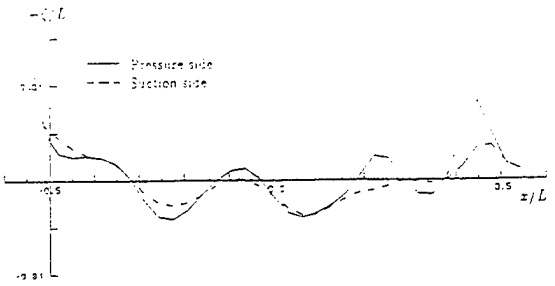


Figure 24. Calculated wave profiles along Mariner hull in deep water at $F_n = 0.22$ and $\beta = 5°$

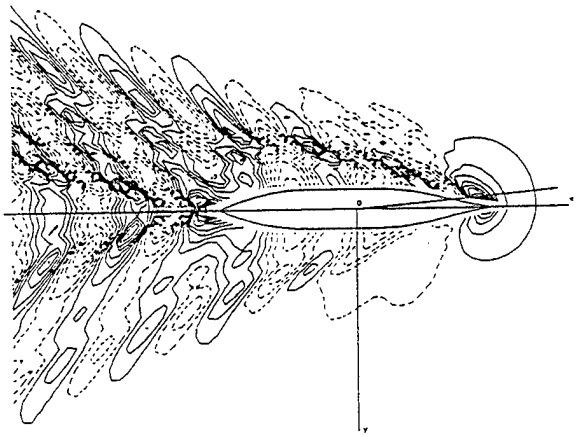


Figure 25. Calculated wave contours for Mariner hull in deep water at $F_n = 0.22$ and $\beta = 5°$ Distance between the contour lines: $0.8 \times 10^{-3} L$.

5. CONCLUDING REMARKS

A three-dimensional panel method using Rankine singularities for calculating free-surface lifting flows is developed and applied to ships in steady oblique motion. Computations for three ship hulls have shown the usefulness of the proposed method in calculating the flow and the hydrodynamic lateral force and yaw moment acting on practical ship forms.

The proposed method can be directly or by further extension applied to other steady lifting potential flows, such as to calculate the hydrodynamic interaction of catamaran hulls or between a vessel and its lifting appendages. It can also be extended to attack unsteady free-surface lifting flows concerned in the ship motion problem. An ongoing effort in this aspect is reported in Zou (22).

On the other hand, the proposed method has some disadvantages which restrict its application. At present this method is not applicable to bodies with immersed transom stern. Moreover, it will be inaccurate, if serious seperation along the length of the hull occurs. For these complicated cases, more effective and rational methods are required.

REFERENCES

1. Hess,J.L. and Smith, A.M.O., "Calculation of Nonlifting Potential Flow About Arbitrary Three-Dimensional Bodies", Journal of Ship Research, Vol.8, No.2, 1964, pp.22-44

2. Rubbert,P.E. and Saaris,G.R., "A General Three-Dimensional Potential-Flow Method Applied to V/STOL Aerodynamics", SAE Paper No.680304, presented at Air Transportation Meeting, New York, 1968

3. Hess,J.L., "Calculation of Potential Flow About Arbitrary Three-Dimensional Lifting Bodies", Douglas Aircraft Company, Report No. MDC J5679-01, 1972

4. Dawson,C.W., "A Practical Computer Method for Solving Ship-Wave Problems", Proceedings of the 2nd International Conference on Numerical Ship Hydrodynamics, Berkeley, USA, 1977, pp.30-38

5. Xia,F. and Larsson,L., "A Calculation Method for the Lifting Potential Flow Around Yawed, Surface-Piercing 3-D Bodies", Proceedings of the 16th Symposium on Naval Hydrodynamics, Berkeley, USA, 1986, pp.583-595

6. Raven,H.C., "Variations on a Theme by Dawson", Proceedings of the 17th Symposium on Naval Hydrodynamics, the Hague, Netherlands, 1988, pp.151-170

7. Maniar,H., Newman,J.N., and Xü,H., "Free-Surface Effects on a Yawed Surface-Piercing Plate", Proceedings of the 18th Symposium on Naval Hydrodynamics, Ann Arbor, USA, 1990, pp.273-282

8. Guilbaud,M., Coirier,J., and Ba,M., "Kelvin Singularity Approach to Compute Free-Surface Flows on Yawed and Heeled Bodies", Proceedings of the 7th International Workshop on Water Waves and Floating Bodies, Val de Reuil, France, 1992, pp.117-120

9. Nakatake,K., Ando,J., Komura,A., and Kataoka, K., "On the Flow Field and the Hydrodynamic Forces of an Obliquing Ship" (in Japanese), Transactions of West-Japan Society of Naval Architects, No.80, 1990, pp.1-12

10. Jensen,G., Bertram,V., and Söding,H.,

"Ship Wave-Resistance Computations", Proceedings of the 5th International Conference on Numerical Ship Hydrodynamics, Hiroshima, Japan, 1989, pp.593-605

11. Zou,Z.J., "Berechnung der Potentialströmung um einen schräg fahrenden Schiffsrumpf auf tiefem und flachem Wasser", Institut für Schiffbau der Universität Hamburg, Bericht Nr.541, 1994

12. Zou,Z.J., "Calculation of the Three-Dimensional Free-Surface Flow About a Yawed Ship in Shallow Water", Ship Technology Research, submitted for publication, 1994

13. Jensen,G., "Berechnung der stationären Potentialströmung um ein Schiff unter Berücksichtigung der nichtlinearen Randbedingung an der Wasseroberfläche", Institut für Schiffbau der Universität Hamburg, Bericht Nr.484, 1988

14. Kajitani,H., "A Wandering in Some Ship Resistance Components and Flow", Schiffstechnik, Band 34, Heft 3, 1987, pp.105-131

15. Shearer,J.R. and Cross,J.J., "The Experimental Determination of the Components of Ship Resistance for a Mathematical Model", Transactions of the Royal Institution of Naval Architects, Vol.107, 1965, pp.459-473

16. Maruo,H. and Song,W.S., "Numerical Appraisal of the New Slender Ship Formulation in Steady Motion", Proceedings of the 18th Symposium on Naval Hydrodynamics, Ann Arbor, USA, 1990, pp.239-257

17. Todd,F.H., "Series 60 - Methodical Experiments with Models of Single-Screw Merchant Ships", David Taylor Model Basin Report 1712, 1963

18. Ogiwara,S., "Tank Experiments and Numerical Works on Series 60 Model in IHI Ship Model Basin", Report to the Cooparative Experiment Program of 18th ITTC, Kobe, Japan, 1987

19. Russo,V.L. and Sullivan,E.K., "Design of the Mariner-Type Ship", Transactions of SNAME, Vol.61, 1953, pp.98-166

20. Fujino,M., "Experimental Studies on Ship Manoeuvrability in Restricted Waters, Part 1", International Shipbuilding Progress, Vol.15, No.168, 1968, pp.279-301

21. Wolff,K., "Ermittlung der Manövriereigenschaften fünf repräsentativer Schiffstypen mit Hilfe von CPMC-Modellversuchen", Institut für Schiffbau der Universität Hamburg, Bericht Nr.412, 1981

22. Zou,Z.J., "A 3D Panel Method for the Radiation Problem with Forward Speed", Proceedings of the 9th International Workshop on Water Waves and Floating Bodies, Kuji, Oita, Japan, 1994

Steady and Unsteady Ship Waves by a Higher-Order Boundary Element Method

S. Hong (Korea Research Institute of Ships & Ocean Engineering), H. Choi (Seoul National University, Korea)

Abstract

The steady and unsteady ship wave problems are studied numerically by using a higher-order boundary element method. Both the ship hull and the free surface are represented by 8-node iso-parametric elements. To realize the dispersion correctly and also to minimize the numerical damping of free surface waves, the velocity potential is assumed to vary bi-quadraticlly on each element. Kernel functions are evaluated by Gauss quadratures, but singular and quasi-singular integrals are evaluated with help of bi-cubic transformation(Cerreloza,1989), which turns out to be very accurate and efficient. Careful attentions are paid on the flow near the intersection between the ship hull and the free surface. At the same time various types of the radiation condition are examined to prevent wave reflection at numerical radiation boundaries. Among these, a parabolic-type partial differential operator is found promising so far. Numerical examples demonstrate the accuracy and the efficiency of the present method.

1. Introduction

Since Gadd(1976) and Dawson(1977) introduced the so-called Rankine source method to the wave resistance problem of ships, it has become one of major numerical tools in naval hydrodynamics due to the simplicity of its kernel function and its capability of treating various types of free surface conditions. However, this method invokes numerical dispersion and damping as like any other numerical methods. In addition, it bears some difficulties in implementing the radiation condition, which is due to the discretization of truncated free surface . Therefore the main stream of research on this method is directed to improvement of numerical dispersion and damping, and effective enforcement of the radiation condition.

Piers(1983), Jensen et al.(1986), Sclavounos and Nakos(1988), Nakos and Sclavounos(1990a) focused their researches on better treatment of the numerical dispersion and damping. Among these works, it is worthy to note that Sclavounos and Nakos(1988) used the bi-quadratic spline scheme to allow the variation of velocity potentials on free surface panels. They analyzed the stability of the scheme in Fourier space and found that it is free of numerical damping and it satisfies the dispersion relation for a wide range of wave frequencies. In this work, they also proposed a Kutta-like radiation condition at upstream. While Jensen(1987), Raven(1988) and Nakos(1990) contributed to the development of effective radiation conditions. Ni(1987), Kim and Lukas(1990) took nonlinear free surface conditions into account. Bertram(1990) and Nakos et al.(1990b) applied the Rankine source method to unsteady ship motion problems.

Recently higher-order boundary element methods(HOBEM) are getting popular because they provide more accurate solutions with smaller number of panels. To name a few, Matsui et al.(1987) and Liu et al.(1991,1992) applied HOBEM to unsteady wave problems of floating offshore structures and demonstrated its efficiency and accuracy. Boo(1993) extended it to the steady ship wave problem and also to the nonlinear wave simulation generated by a 2-D wavemaker.

In this paper we describe a new scheme which has been constructed by taking advantages of the bi-quadratic spline scheme and the higher-order boundary element method, we have taken the advantages selectively depending on computation domains. Boundary surfaces are represented by

8-node boundary elements to describe curved surfaces of a ship and its neighboring free surface more accurately. The variation of the velocity potential complies with the characteristics of the 8-node element on the body surface. But on the free surface it is assumed to follow that of the bi-quadratic spline scheme.

As numerical examples, steady and unsteady Neumann-Kelvin problems are considered. The wave resistance computed for a submerged spheroid is compared with the analytic result of Farell(1973). Comparisons are also made for Series 60(C_B = 0.6) with experiments and other numerical results. Hydrodynamic coefficients for a modified Wigley are calculated and compared with Nakos and Sclavounos(1990b). The agreement is in general quite satisfactory. Lastly, as the first step to deal with problems for low reduced frequencies, $\tau = \frac{U\omega}{g} < \frac{1}{4}$, a parabolic-type operator is tested as the upstream radiation condition. The idea is developed based on the observation of upward propagating waves, which largely depend on the so-called k_1 wave number(Hoff, 1990). The relevance of this operator has been confirmed in the case of unsteady Kelvin source potential.

2. Formulation of Boundary-value Problem

The fluid is assumed to be inviscid and incompressible, and the flow irrotational. The governing equation becomes the Laplace equation for the velocity potential.

$$\nabla^2\Phi(\vec{x},t) = 0, \quad \vec{x} \text{ in fluid domain } V \qquad (1)$$

A Cartesian coordinate system, $\vec{x} = (x, y, z)$, is taken which moves with ship's mean speed U. The positive x-axis points upstream and the positive z-axis directs against the gravity. The following boundary conditions are to be fulfilled on the surfaces which enclose the fluid domain(see Fig. 1).

• Body Boundary Condition

$$\frac{\partial\Phi(\vec{x},t)}{\partial n} = \vec{V}_B(\vec{x},t)\cdot\vec{n} \quad on\ S_B \qquad (2)$$

• Free Surface Condition

$$\Phi_{tt} + 2\nabla\Phi\cdot\nabla\frac{\partial\Phi}{\partial t} + \frac{1}{2}\nabla\Phi\cdot\nabla(\nabla\Phi\cdot\nabla\Phi) + g\Phi_z = 0 \quad on\ z=\zeta \qquad (3)$$

• Bottom Condition

$$\nabla\Phi \longrightarrow 0 \quad \text{as} \quad z \longrightarrow -\infty \qquad (4)$$

• Radiation Condition

The disturbed fluid motion should vanish at infinity.

The total potential $\Phi(\vec{x},t)$ may be decomposed into three parts; the basic flow $\bar{\phi}(\vec{x})$, the steady wave flow $\phi(\vec{x})$ and unsteady wave flow $\psi(\vec{x},t)$.

$$\Phi(\vec{x},t) = \bar{\phi}(\vec{x}) + \phi(\vec{x}) + \psi(\vec{x},t) \qquad (5)$$

In the case that the basic flow is chosen to be uniform stream, $\bar{\phi}(\vec{x}) = -Ux$, and the free surface condition is linearized, the well-known Neumann-Kelvin problem is deduced.

The linearized boundary conditions are as follows:

• Steady Case

$$U^2\phi_{xx} + g\phi_z = 0 \quad on\ z=0, \qquad (6)$$

$$\zeta(x,y,0) = \frac{U}{g}\phi_x, \qquad (7)$$

$$\frac{\partial\phi}{\partial n} = Un_1 \quad on\ S_B. \qquad (8)$$

• Unsteady Case

$$\left(\frac{\partial}{\partial t} - U\frac{\partial}{\partial x}\right)^2\psi + g\psi_z = 0 \quad on\ z=0, \qquad (9)$$

$$\zeta(x,y,0;t) = -\frac{1}{g}\left(\frac{\partial}{\partial t} - U\frac{\partial}{\partial x}\right)\psi, \qquad (10)$$

$$\frac{\partial\psi}{\partial n} = \sum_{j=1}^{6}\left(\frac{\partial\eta_j}{\partial t}n_j + \eta_j m_j\right) \quad on\ S_B, \qquad (11)$$

where

$$\vec{n} = (n_1, n_2, n_3)$$
$$(n_4, n_5, n_6) = \vec{x}\times\vec{n}.$$

It is to note that non-zero m-terms are $m_5 = Un_3$ and $m_6 = -Un_2$.

Based on the Neumann-Kelvin linearization, wave resistance and hydrodynamic forces are derived as below:

Wave Resistance R_w

$$R_w = \iint_{S_B} pn_1 ds, \qquad (12)$$

$$p = -\rho(\frac{1}{2}\nabla\phi\cdot\nabla\phi - U\phi_x). \qquad (13)$$

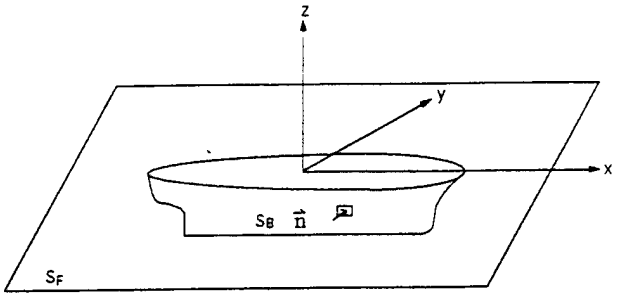


Figure 1: Coordinate system

Added Mass and Damping

$$a_{ij} = -\frac{\rho}{\omega^2}\Re\left\{\iint_{S_B}(-i\omega\tilde{\psi}_j - U\tilde{\psi}_{j_x})n_i ds\right\}, \quad (14)$$

$$b_{ij} = -\frac{\rho}{\omega}\Im\left\{\iint_{S_B}(-i\omega\tilde{\psi}_j - U\tilde{\psi}_{j_x})n_i ds\right\}. \quad (15)$$

Where $\Re$ and $\Im$ stand for the real and the imaginary part, respectively. The radiation potential is given by

$$\psi(\vec{x},t) = \Re\left\{e^{-i\omega t}\sum_{j=1}^{6}\eta_j\tilde{\psi}_j\right\}. \quad (16)$$

3. Application of HOBEM

In higher-order boundary element methods, surfaces are represented by a sum of curved elements, which are expressed in terms of bi-quadratic or bi-cubic iso-parametric shape functions. Physical quantities such as velocity potential and normal velocity are approximated with help of the same shape functions. Therefore boundary-value problems are solved more accurately by using a HOBEM.

In this paper, 8-node bi-quadratic elements are adopted to describe the geometry of the whole boundary surfaces(body surface and free surface). The velocity potential is to vary in accordance with the geometrical property. But the velocity potential on the free surface is determined by using the bi-quadratic spline scheme. The reason is that the bi-quadratic spline scheme has the same order of accuracy as the cubic-spline scheme as pointed out by Sclavounos and Nakos(1988). They also proved that the scheme is a robust and accurate algorithm. The basic idea of the present method is to utilize the proven advantages of HOBEM and the bi-quadratic spline scheme .

3.1 8-node Boundary Element

For 8-node boundary elements, coordinates and physical variables are approximated by a weighted sum of their values evaluated at nodes(Brebbia et al.,1989).

$$x_j = \sum_{k=1}^{8} N^k x^k,\ y_j = \sum_{k=1}^{8} N^k y^k,\ z_j = \sum_{k=1}^{8} N^k z^k \quad (17)$$

$$\Phi_j = \sum_{k=1}^{8} N^k \Phi^k, \quad \Phi_{j_n} = \sum_{k=1}^{8} N^k \Phi_n^k$$

Here the superscript k denotes the local node number and the subscript j the element number. The shape functions are defined by

$$\begin{aligned}
N^1(\xi_1,\xi_2) &= \tfrac{1}{4}(1+\xi_1)(1+\xi_2)(\xi_1+\xi_2-1)\\
N^2(\xi_1,\xi_2) &= \tfrac{1}{4}(1-\xi_1)(1+\xi_2)(-\xi_1+\xi_2-1)\\
N^3(\xi_1,\xi_2) &= \tfrac{1}{4}(1-\xi_1)(1-\xi_2)(-\xi_1-\xi_2-1)\\
N^4(\xi_1,\xi_2) &= \tfrac{1}{4}(1+\xi_1)(1-\xi_2)(\xi_1-\xi_2-1)\\
N^5(\xi_1,\xi_2) &= \tfrac{1}{2}(1-\xi_1^2)(1+\xi_2)\\
N^6(\xi_1,\xi_2) &= \tfrac{1}{2}(1-\xi_2^2)(1-\xi_1)\\
N^7(\xi_1,\xi_2) &= \tfrac{1}{2}(1-\xi_1^2)(1-\xi_2)\\
N^8(\xi_1,\xi_2) &= \tfrac{1}{2}(1-\xi_2^2)(1+\xi_1)
\end{aligned} \quad (18)$$

where (ξ_1,ξ_2) are the normalized coordinates of the mapped plane(see Fig. 2).

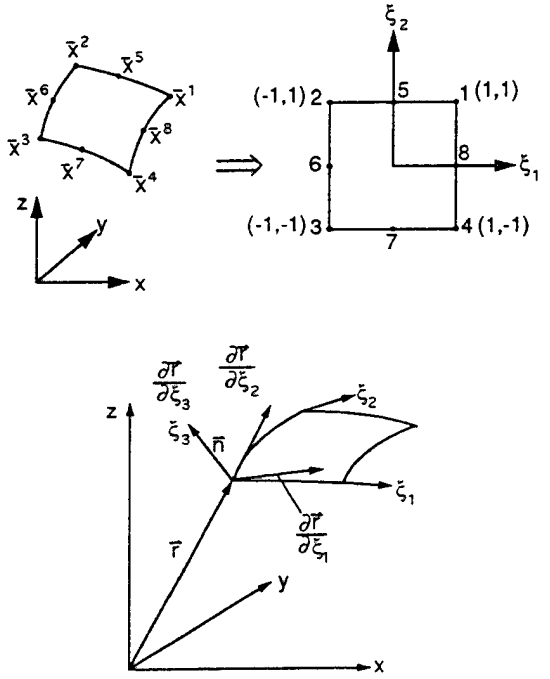


Figure 2: 8-node boundary element

Since the velocity potential is given in terms of the mapped coordinates, the velocity is calculated

by the following coordinate transformation.

$$\begin{pmatrix} \frac{\partial \Phi}{\partial x} \\ \frac{\partial \Phi}{\partial y} \\ \frac{\partial \Phi}{\partial z} \end{pmatrix} = J^{-1} \begin{pmatrix} \frac{\partial \Phi}{\partial \xi_1} \\ \frac{\partial \Phi}{\partial \xi_2} \\ \frac{\partial \Phi}{\partial \xi_3} \end{pmatrix} \tag{19}$$

where

$$J = \begin{pmatrix} \frac{\partial x}{\partial \xi_1} & \frac{\partial y}{\partial \xi_1} & \frac{\partial z}{\partial \xi_1} \\ \frac{\partial x}{\partial \xi_2} & \frac{\partial y}{\partial \xi_2} & \frac{\partial z}{\partial \xi_2} \\ \frac{\partial x}{\partial \xi_3} & \frac{\partial y}{\partial \xi_3} & \frac{\partial z}{\partial \xi_3} \end{pmatrix}$$

3.2 Bi-quadratic Spline Scheme with 8-node Element

In the Rankine source method, the free surface is to be discretized properly. It is well known that it invites some distortion of numerical dispersion as well as numerical damping. Therefore the choice of discretization of the free surface should be carefully made to minimize the distortion and the damping.

In our study, the bi-quadratic spline scheme is used for the velocity potential on the free surface. Its outstanding performance, i.e. free of numerical damping and excellent numerical dispersion is proved by a systematic stability analysis in Fourier space by Sclavounos and Nakos(1988). In order to treat the curved element near the waterline precisely, we normalize the bi-quadratic spline function on a mapped plane.

$$\begin{aligned} \tilde{b}_{ij}(\xi_1, \xi_2) &= b_i(\xi_1) b_j(\xi_2) \\ &= b_{ij}(\vec{x}) \end{aligned} \tag{20}$$

with $\vec{x} = \sum_{k=1}^{8} N^k \vec{x}^k$, where the orthogonality of the spline function has been utilized. The one-dimensional equal spaced quadratic spline function is written in a normalized form.

$$b(\xi) = \begin{cases} b_{j-1} = \frac{1}{8}(\xi_1 + 1)^2 \\ b_j \quad = \frac{1}{4}(-\xi_1^2 + 3) \quad -1 \le \xi_1 \le 1 \\ b_{j+1} = \frac{1}{8}(-\xi_1 + 1)^2 \end{cases} \tag{21}$$

Then the velocity potential on the free surface is given by the sum of basis function multiplied by its weight evaluated at the panel centroid.

$$\begin{aligned} \Phi(\vec{x}) &= \sum_{i=1}^{N_x} \sum_{j=1}^{N_y} \tilde{b}_{ij} \tilde{\varphi}_{ij} \\ &= \sum_{m=1}^{N_x \cdot N_y} B_m(\vec{x}) \varphi_m, \ (m = (i-1) \cdot N_x + j) \end{aligned} \tag{22}$$

The subscripts i and j represent the $i-th$ element in x-direction and the $j-th$ element in y-direction, respectively. N_x denotes the number of panels in x-direction on the free surface and N_y that in the y-direction. The derivatives of the velocity potential on the free surface take a similar form. The derivatives of the basis function can be obtained by the coordinate transformation.

$$\begin{pmatrix} \frac{\partial B}{\partial x} \\ \frac{\partial B}{\partial y} \end{pmatrix} = J_1^{-1} \begin{pmatrix} \frac{\partial B}{\partial \xi_1} \\ \frac{\partial B}{\partial \xi_2} \end{pmatrix} \tag{23}$$

$$\begin{pmatrix} \frac{\partial^2 B}{\partial x^2} \\ \frac{\partial^2 B}{\partial x \partial y} \\ \frac{\partial^2 B}{\partial y^2} \end{pmatrix} = J_2^{-1} \begin{pmatrix} \frac{\partial^2 B}{\partial \xi_1^2} \\ \frac{\partial^2 B}{\partial \xi_1 \partial \xi_2} \\ \frac{\partial^2 B}{\partial \xi_2^2} \end{pmatrix} \tag{24}$$

where

$$J_1 = \begin{pmatrix} \frac{\partial x}{\partial \xi_1} & \frac{\partial y}{\partial \xi_1} \\ \frac{\partial x}{\partial \xi_2} & \frac{\partial y}{\partial \xi_2} \end{pmatrix}$$

$$J_2 = \begin{pmatrix} \frac{\partial x}{\partial \xi_1}^2 & 2\frac{\partial x}{\partial \xi_1}\frac{\partial y}{\partial \xi_1} & \frac{\partial y}{\partial \xi_1}^2 \\ \frac{\partial x}{\partial \xi_1}\frac{\partial x}{\partial \xi_2} & \frac{\partial x}{\partial \xi_1}\frac{\partial y}{\partial \xi_2} + \frac{\partial x}{\partial \xi_2}\frac{\partial y}{\partial \xi_1} & \frac{\partial y}{\partial \xi_1}\frac{\partial y}{\partial \xi_2} \\ \frac{\partial x}{\partial \xi_2}^2 & 2\frac{\partial x}{\partial \xi_2}\frac{\partial y}{\partial \xi_2} & \frac{\partial y}{\partial \xi_2}^2 \end{pmatrix}$$

3.3 Application of HOBEM to Integral Equation

Taking the inner product of the velocity potential Φ with $\nabla^2 G$ and integrating over the fluid domain, we get the following integral equation. It is equivalent to Green's second identity.

$$\begin{aligned} \iiint_V \Phi \nabla^2 G dv &= -\Phi \\ &= \iint_S \Phi \frac{\partial G}{\partial n} ds - \iiint_V \nabla \Phi \nabla G dv \\ &= \iint_S \left[\Phi \frac{\partial G}{\partial n} - \frac{\partial \Phi}{\partial n} G \right] ds, \end{aligned} \tag{25}$$

where the normal vector $\vec{n}$ is defined as positive inward the body surface, $\vec{x}$ and $\vec{\xi}$ are the coordinates of field and source points.

The free surface and the body surface are discretized into N_{SF} and N_B curved elements, respectively. Then the collocation is made at the centroids of free surface panels. But the node points are taken as collocation points for the body surface. Finally we obtain the following algebraic equations.

$$\alpha_{ij}\phi_j = \beta_{ik}\frac{\partial \phi_k}{\partial n} \tag{26}$$

$$(i,j = 1, N_{SF}+N_D;\ k = N_{SF}-1..N_{SF}+N_D)$$

$$\left\{\begin{array}{rcl} \alpha_{ij} & = & C_i\delta_{ij} + A_{ik} + \tilde{A}_{ij} + \hat{A}_{ij} \\ A_{ik} & = & \sum_{m=1}^{n} \frac{1}{2\pi} PV \int\int_{\Delta S_{j,m}} N^{k(m)} \frac{\partial}{\partial n}(\frac{1}{r}) ds \\ \tilde{A}_{ij} & = & B_j(\vec{x}_i) + \sum_{m=1}^{N_{SF}} \frac{1}{2\pi} \int\int_{\Delta S_m} \left\{ \frac{U^2}{g} B_{j\xi\xi}(\vec{\xi}) \right. \\ & & \left. -i\frac{2U\omega}{g} B_{j\xi}(\vec{\xi}) - \frac{\omega^2}{g} B_j(\vec{\xi}) \right\} \frac{1}{r} ds \\ \hat{A}_{ij} & = & \sum_{m=1}^{N_{SF}} \frac{1}{2\pi} \int\int_{\Delta S_m} B_j(\vec{\xi}) \frac{\partial}{\partial n}(\frac{1}{r}) ds \\ \beta_{ik} & = & \sum_{m=N_{SF}+1}^{N_{SF}+N_B} \frac{1}{2\pi} \int\int_{\Delta S_m} N^{k(m)} \frac{1}{r} ds \end{array}\right. \tag{27}$$

where,

$$\phi_j = \left\{\begin{array}{l} \varphi_j \ (j = 1..N_{SF}) \\ \bar{\phi}_j \ \text{ or } \ \psi_j \ (j = N_{SF}+1..N_{SF}+N_D) \end{array}\right.$$

N_{SF} : number of elements on free surface
N_B : number of elements on body surface
N_D : number of nodes on body surface
n : number of elements including node k
$k(m)$: global node number at $m-th$ element
C_i : solid angle at $i-th$ node / 2π
δ_{ij} : Kronecker delta function
U : ship speed
g : gravitational acceleration
ω : circular frequency

3.4 End Conditions at Waterline

When the collocation is made at the node points of all panels, some conflicts arise at the waterline for surface-piercing bodies. It is the case for the conventional HOBEM. Boo(1993) circumvented this difficulty by introducing the so-called discontinuous elements. Such a difficulty does not occur in our case, because the collocation points of the free surface are not located at the waterline. Instead we need an imaginary free surface panel, which penetrates the body surface, as long as the spline scheme is used. In fact it was applied for the end conditions to determine the weight of imaginary free surface panels along the waterline. Two conditions are imposed for the imaginary panel as end conditions at the waterline.

$$\frac{\partial \Phi_B}{\partial n_B} = \frac{\partial \phi_F}{\partial n_B} \quad \text{at waterline} \tag{28}$$

$$\Phi_B = \Phi_F \quad \text{at waterline} \tag{29}$$

In the above equations, the subscripts B and F denote the body surface and the free surface, respectively. Eq.(28) makes the normal velocity on the free surface equal to that on the body surface along the waterline. While eq.(29) enforces the velocity potential on the body surface to be equal to that on the free surface along the waterline. Numerical results reveal that the second condition contributes to smooth the wave profile at the stem and stern, where the geometry is quite complicated.

3.5 Radiation Condition

As only a finite portion of the free surface is actually taken in computation, a proper radiation condition should be imposed at truncated free surface boundaries. Nakos(1990) proposed the Kutta-like radiation condition for the steady and unsteady flows.

$$\left(\frac{\partial}{\partial t} - U\frac{\partial}{\partial x}\right)\psi(\vec{x_0}, t) = \left(-i\omega - U\frac{\partial}{\partial x}\right)\psi(\vec{x_0}) = 0. \tag{30}$$

$$\left(\frac{\partial}{\partial t} - U\frac{\partial}{\partial x}\right)^2\psi(\vec{x_0}, t) = \left(-i\omega - U\frac{\partial}{\partial x}\right)^2\psi(\vec{x_0}) = 0. \tag{31}$$

This radiation condition is not relevant to apply for subcritical reduced frequencies, $\tau, \frac{1}{4}$, because it was assumed that there are no waves propagating upstream. For subcritical reduced frequencies, however, there exists a wave system propagating upstream. This wave system is known to be governed by k_1 wave(Hoff, 1990) and thus it can be approximated by a plane wave propagating upstream with this wave number.

$$\zeta \sim A_0 e^{i(k_1 x - \omega t)}, \tag{32}$$

$$\psi \sim B_0 e^{i(k_1 x - \omega t)}, \tag{33}$$

$$k_1 = \frac{\omega^2}{g}\left\{\frac{1-\sqrt{1-4\tau}}{2\tau}\right\}^2,$$

where A_0 and B_0 are complex amplitudes. Thus obtained velocity potential and wave elevation satisfy the following parabolic-type operator. Therefore we adopt it as a new radiation condition for subcritical reduced frequencies.

$$\begin{aligned}&\left(\frac{\partial}{\partial t}+C_1\frac{\partial}{\partial x}\right)\psi(\vec{x_0},t)\\&=\left(-i\omega+C_1\frac{\partial}{\partial x}\right)\psi(\vec{x_0})=0\end{aligned}\qquad(34)$$

$$\begin{aligned}&\left(\frac{\partial}{\partial t}+C_1\frac{\partial}{\partial x}\right)\zeta(x_0,t)\\&=\left(\frac{\partial}{\partial t}+C_1\frac{\partial}{\partial x}\right)\left(\frac{\partial}{\partial t}-U\frac{\partial}{\partial x}\right)\zeta\\&=\left(-i\omega+C_1\frac{\partial}{\partial x}\right)\left(-i\omega-U\frac{\partial}{\partial x}\right)\psi(\vec{x_0})=0\end{aligned}\qquad(35)$$

$$C_1=\frac{\omega}{k_1}$$

The performance of the proposed radiation condition has been investigated for the unsteady Kelvin source potential.

In addition to it, a radiation condition $\Phi_{yy}=0$ is imposed at the lateral truncation boundary under the assumption that the velocity changes negligibly small in that direction.

4. Numerical Results and Discussions

4.1 Wave Resistance of a Submerged Spheroid

To validate the present method, the wave resistance of a submerged spheroid is calculated. The calculation conditions are summarized as below:

free surface	:	$-1.5L<x<2.5L$
		$-1.6L<y<0.0L$
		$N_{SF}=45\times 16$
		$\Delta x=L/10,\ \alpha=\frac{\Delta x}{\Delta y}=1$
		$F_h=\frac{U}{\sqrt{g\Delta x}}=.95\sim 2.53$
body surface	:	$N_B=10\times 4,\ N_D=133$
Froude number	:	$F_N=0.3\sim 0.8.$

As shown in Fig. 3, the present result coincides quite well with the analytic result of Farell (1973) and also with the numerical result of Doctors & Beck(1987). Sclavounos and Nakos(1988) used 400 panels on the half body to obtain satisfactorily accurate result for the same model by Rankine source method. In our case we needed only 40 panels. This agreement with relatively small number of panels demonstrates the advantage of higher-order boundary element methods.

The convergence test is shown in Fig. 4, where the panel resolution on the free surface is kept constant as $F_h=2.53$ for $F_N=0.8$. The error is defined as the relative deviation from the Farell's analytic solution. Cosine spacing is taken in the longitudinal direction, while even spacing is taken in the circumferential direction. The increase of panels(N_L) from 5 to 20 in the longitudinal direction does not bring any decisive improvement in accuracy. But the increase in the circumferential direction(N_θ) from 2 to 8 enhances the accuracy. But as clearly indicated in the figure, the error can be hardly decreased for $N_B>40$. Based on these, we may conclude that accurate numerical results can be obtained for submerged bodies by a HOBEM, when the free surface wave resolution is $F_h>1$.

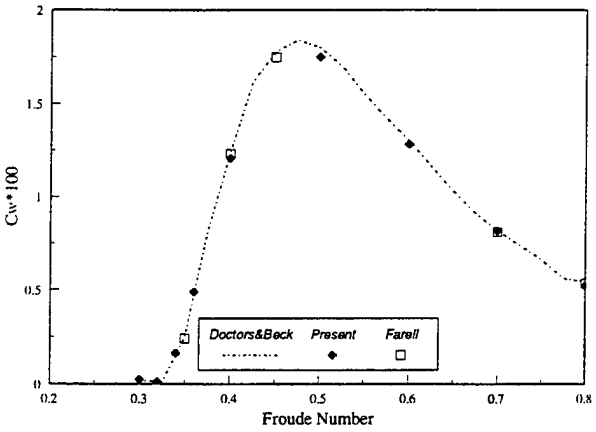


Figure 3: Wave resistance of a submerged spheroid($L/B=5,\ H/B=0.8$)

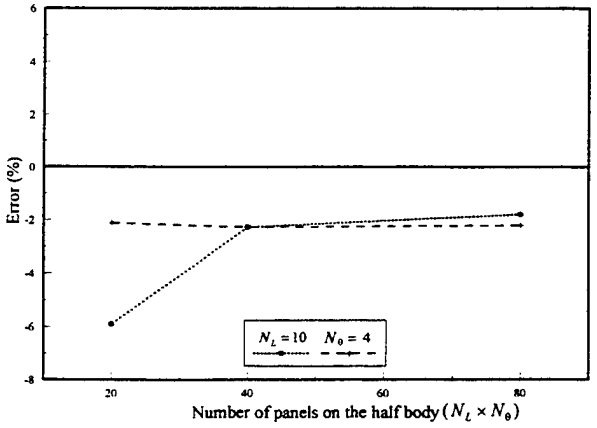


Figure 4: Convergence test of HOBEM

4.2 Wave Resistance of Series 60

Series 60($C_B = 0.6$) is chosen to examine the wave resistance of a real ship hull form. The calculation conditions are

free surface	:	$-1.0L < x < 1.5L$
		$-1.0L < y < 0.0L$
		$N_{SF} = 51 \times 15$
		$\Delta x = L/20,\ \alpha = \frac{\Delta x}{\Delta y} = 1.5$
		$F_h = \frac{U}{\sqrt{g\Delta x}} = .98 \sim 1.56$
body surface	:	$N_B = 20 \times 4,\ N_D = 289$
Froude number	:	$F_N = 0.22 \sim 0.35.$

A typical panel representation is illustrated in Fig. 5. Our results are compared with those of Kim and Lukas(1990) as well as experiments (ITTC,1984). Fig. 6 shows the wave resistance coefficients. The shadow region means the confidence interval of experimental results. Our result falls inside the shadow region and it is closer to the nonlinear result than the linear one of Kim and Lukas(1990). To clarify it, we have examined the wave field. Fig. 7 shows the numerical and experimental wave elevations along the waterline. It is to observe that the present result predicts lower bow waves and higher stern waves than the experimental data. As a result our wave resistance at this speed must be smaller as indicated in Fig. 6. We also examined the linear and nonlinear wave elevations given by Kim and Lukas(1990), but there is no such a clear indication in their result.

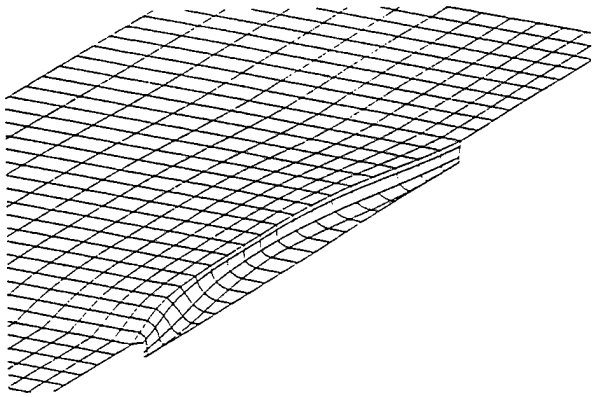


Figure 5: Panel representation of Series 60($C_B = 0.6$)

4.3 Flow near Waterline

To confirm if the waterline end condition is properly imposed, the wave elevation along the waterline is calculated based on the body surface panels as well as based on the free surface. The

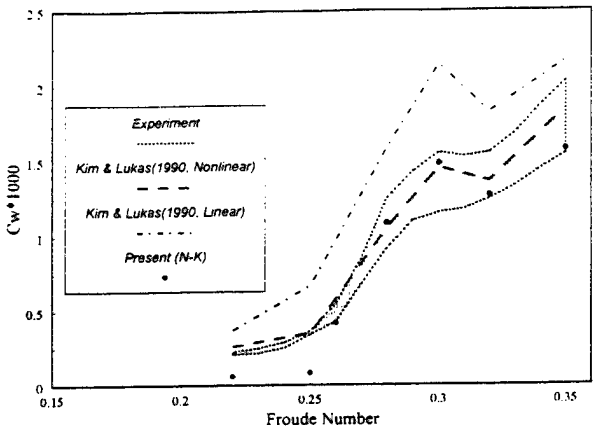


Figure 6: Wave resistance coefficients of Series 60($C_B = 0.6$)

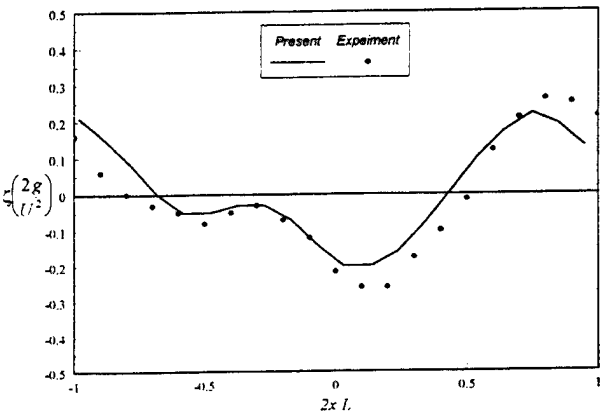


Figure 7: Wave elevation along the waterline(Series 60, $C_B = 0.6, F_N = 0.32$)

agreement between two results is quite satisfactory except small discrepancies at the stem and the stern. This discrepancy seems to be caused by different approximations of the velocity potential on each surfaces.

To look at the effects of the waterline end conditions, wave elevations are calculated by using different end conditions. In Fig. 8, the dotted line corresponds to the case when only eq.(28) is imposed and the solid line to the case when both conditions eq.(28) and eq.(29), are used. No significant differences are found except the stem and stern, where the solid line is smoother than the dotted line. In this sense, the additional condition given by eq.(29) seems to play a role of smoothing wave profile when the body geometry change abruptly.

It is well known that the computation are difficult as the free surface panels adjacent to the waterline becomes smaller. This problem is in-

herent to any numerical schemes. in which the free surface condition is linearized. To test the sensitivity for the change of panel size on the free surface near waterline in y-direction. calculations are made for various panel aspect ratios. $\alpha(\frac{\Delta x}{\Delta y}) = 1.0, 1.5, 2.0$ and 3.0. In these computations, Δx is kept constant as $L/20$. As shown in Fig. 9, the computed wave resistance varies significantly depending on the aspect ratio of the panel. In particular when the aspect ratio is as large as 3.0, the deviation becomes drastically large for high Froude numbers. The main source of this deviation comes from the radical change of stern waves for different panel aspect ratios as shown in Fig. 10. It is conjectured that the stern wave seems to be sensitive to the end condition, eq.(28), which acts as an additional forcing to the free surface panels. It is interesting to note that Nakos and Sclavounos(1994) obviously had a similar difficulty and introduced a low-pass filter for smoothing the basis flow. which acts as a forcing of the double-body free surface condition. In our study no additional filtering technique has been tried.

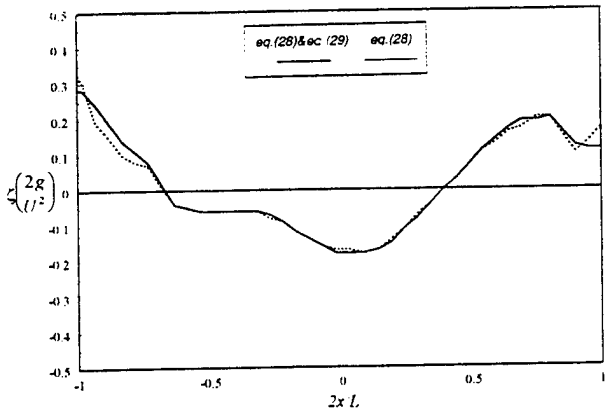


Figure 8: Wave elevation along the waterline for 2 different end conditions($F_N = 0.35$, Series 60, $C_B = 0.6$)

4.4 Unsteady Kelvin Source Potential for $\tau < \frac{1}{4}$

As a first step to develop an unsteady radiation condition, we extended the Rankine source method to subcritical reduced frequencies, $\tau < \frac{1}{4}$. Calculations are made for $\tau = 0.1, 0.2$, $K_0 = \frac{g}{U^2} = 1$ ($F_h = 2$, $\alpha = 1$). The submerged depth is $d = \frac{0.3}{K_0}$. Fig. 11 compares the velocity potentials computed by the present method with those

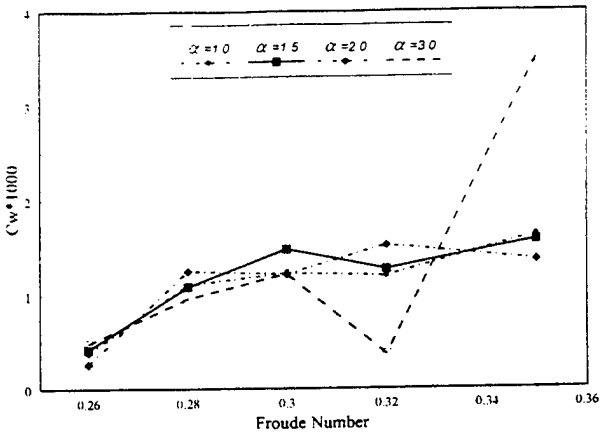


Figure 9: Variation of wave resistance for free surface panel aspect ratios(Series 60, $C_B = 0.6$)

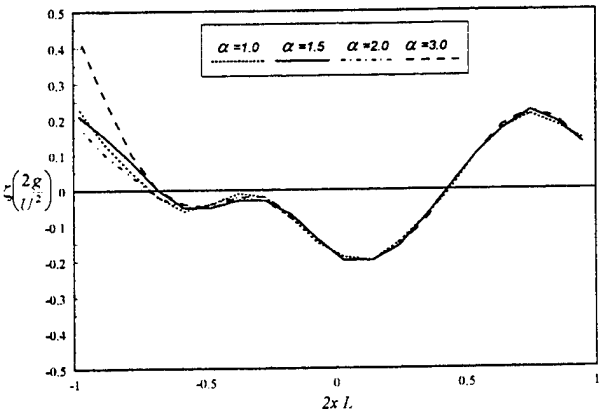


Figure 10: Variation of wave elevation for free surface panel aspect ratios($F_N = 0.32$, Series 60 $C_B = 0.6$)

by the Green function method. In each figure the lower half corresponds to the result by a Rankine source and the upper half to that by a unsteady Kelvin source. Two results are very similar except the upstream wave field. In reality, the upstream waves is very low in our result.

Fig. 12 shows the numerical results for two different radiation conditions with $\tau = 0.2$. Our result with a parabolic-type radiation condition is shown in Fig. 12a, and that with the Kutta-like condition of Nakos is given in Fig. 12b. In both figures the upper part is the result by using a unsteady Kelvin source while the lower one is that by a Rankine source. As clearly observed in the figure, the present result contains less distortion near the source and upstream. Therefore it may be concluded that the proposed radiation condition can be effectively applied for subcritical reduced frequencies.

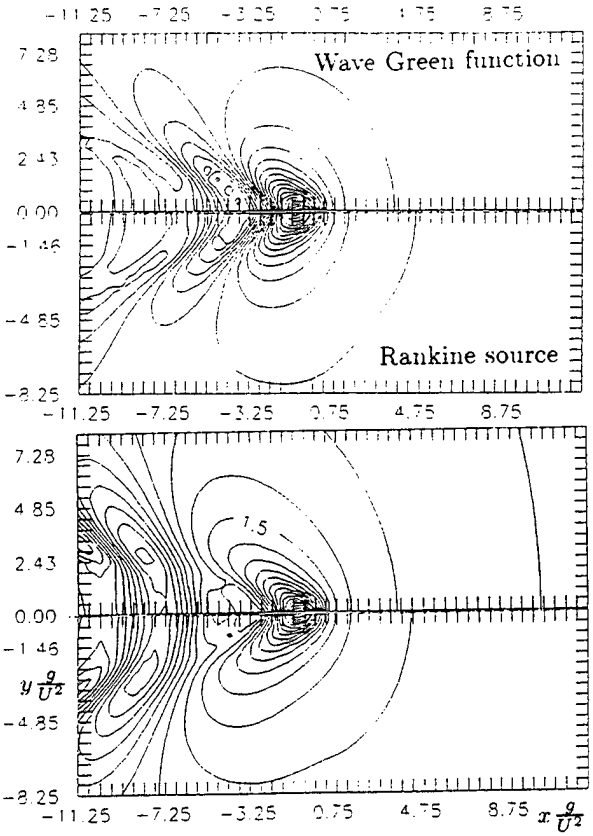


Figure 11: Wave contour of unsteady Klevin source potential for $\tau = 0.1$(upper) and $\tau = 0.2$(lower)

4.5 Hydrodynamic Coefficients of a Modified Wigley

A modified Wigley model is taken to investigate the hydrodynamic coefficients. The modified Wigley model is a variation of the standard parabolic Wigley model, which has a fuller mid-body(see Nakos,1990).

The calculation conditions are

free surface	:	$-0.8L < x < 1.2L$
		$-1.0L < y < 0.0L$
		$N_{SF} = 40 \times 20,\ 60 \times 30$
		$\Delta x = L/20,\ L/30$
		$\alpha = \frac{\Delta x}{\Delta y} = 1.0$
		$F_h = \frac{U}{\sqrt{g\Delta x}} = 1.34,\ 1.64$
body surface	:	$N_B = 20 \times 4,\ 30 \times 6$
		$N_D = 289,\ 613$
Froude number	:	$F_N = 0.3$
nond. frequency	:	$\omega_n = \omega\sqrt{\frac{L}{g}} = 2.5 \sim 5.0.$

The added mass and damping coefficients for heave and pitch are given in Fig. 13 $\sim$ Fig. 16.

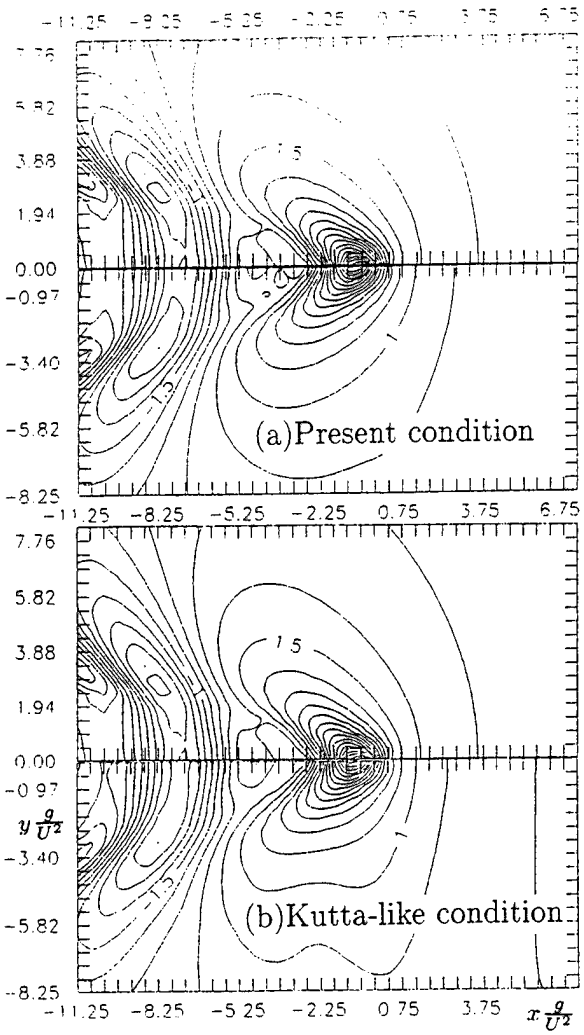


Figure 12: Wave contour of unsteady Klevin source potential for $\tau = 0.2$((a):present radiation condition, (b):Kutta-like radiation condition)

In these figures, the solid line corresponds to the double-body linearized model and dotted line to the linearized Neumann-Kelvin method, both given by Nakos. The present result shows in general good agreement with the linearized Neumann-Kelvin method, except the case of heave-pitch coupled dampings. It is found that differences between two discretizations of $N_B = 20 \times 4$ and $N_B = 30 \times 6$ are small, only the results of the finer case($N_B = 180$) are shown in figures. But there are clear differences in the result of Nakos and Sclavounos(1990b) for the model with same dicretizaions. It implies that a more accurate representation of body surface enhances the numerical convergence for a given resolution of the free surface panels. Fig. 17 shows the real part of the

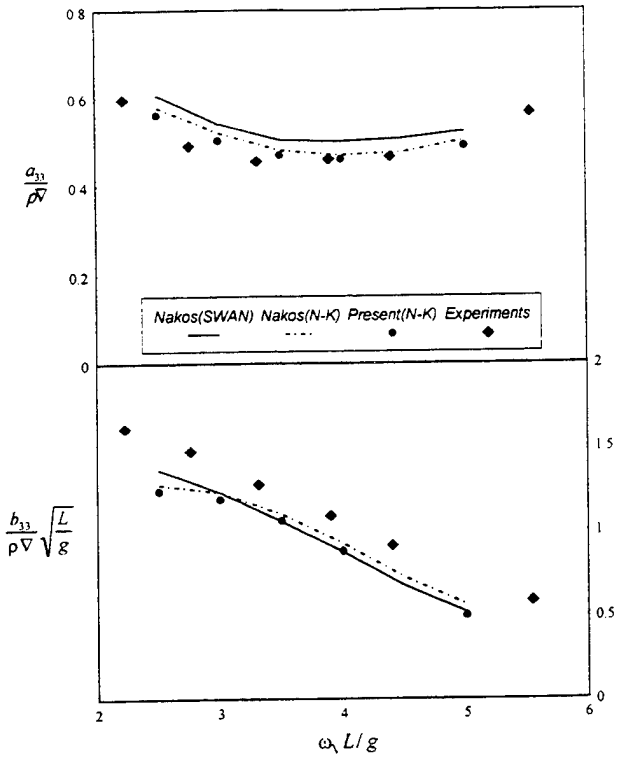


Figure 13: Heave added mass and damping coefficients of a Modified Wigley

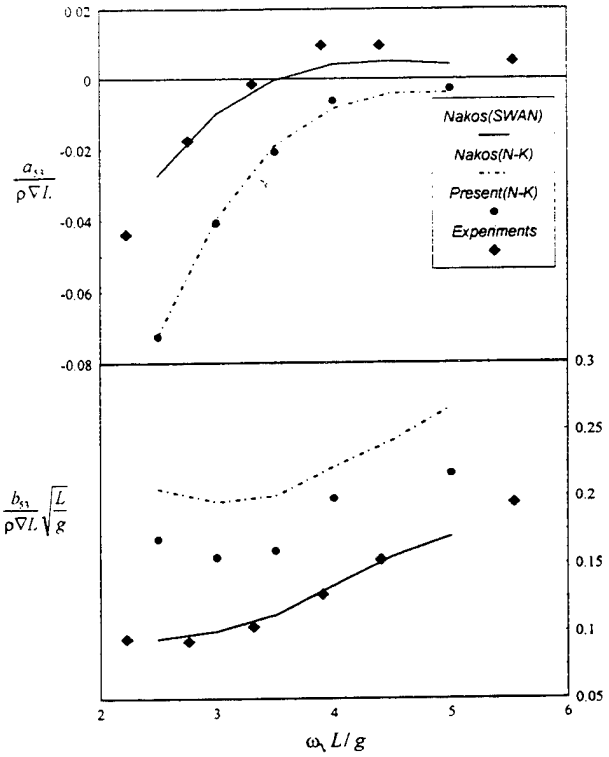


Figure 15: Coupled heave added mass and damping coefficients of a Modified Wigley

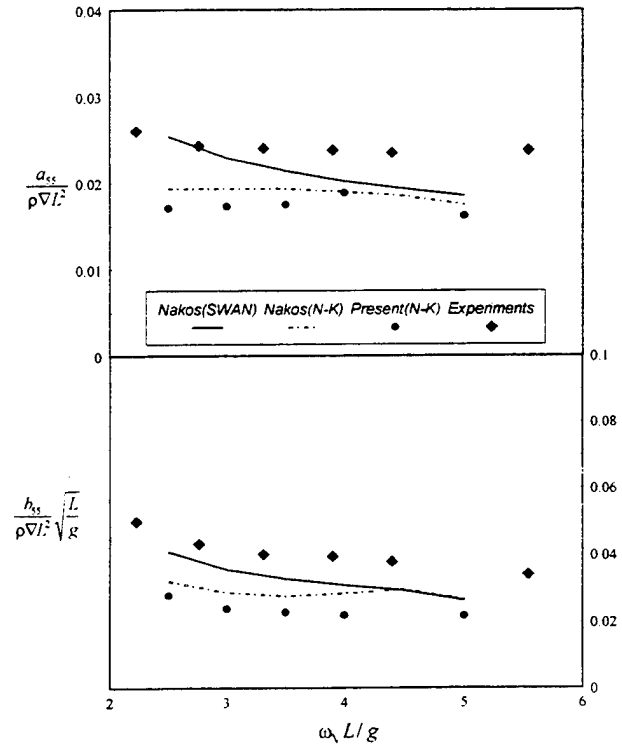


Figure 14: Pitch added mass and damping coefficients of a Modified Wigley

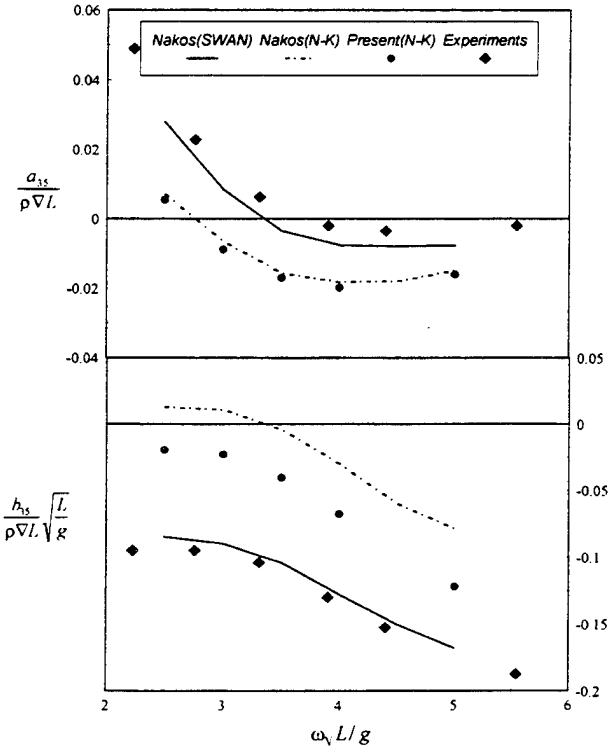


Figure 16: Coupled pitch added mass and damping coefficients of a Modified Wigley

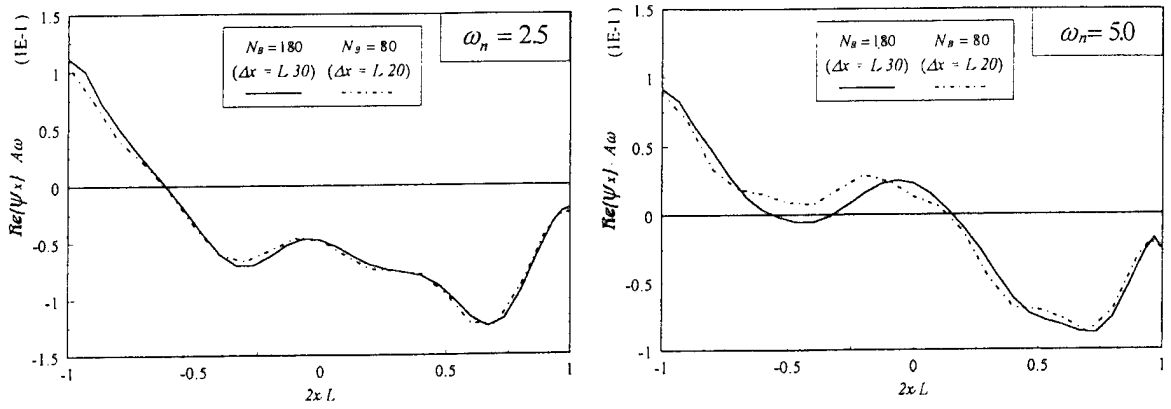


Figure 17: x-componet of unsteady velocities along the waterline due to heave

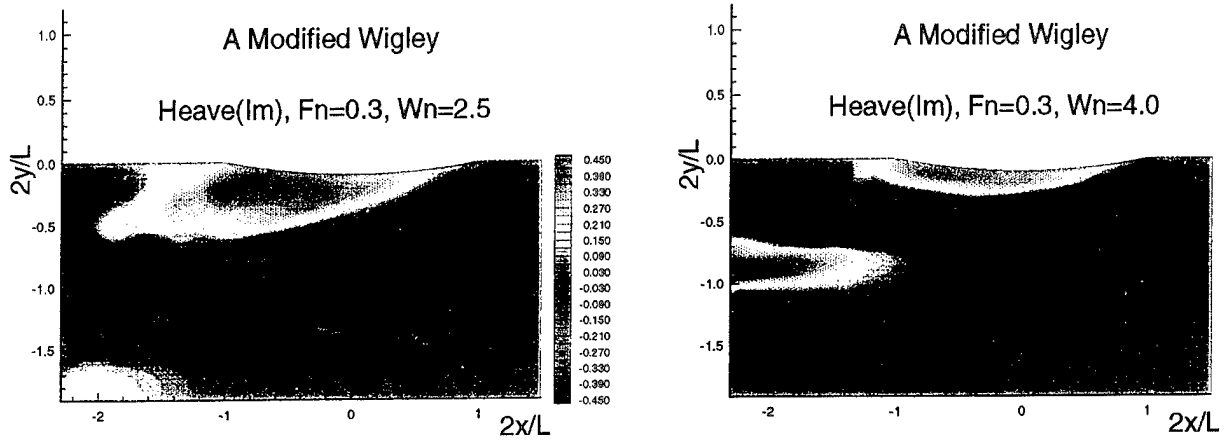


Figure 18: Unsteady wave patterns due to heave of a Modified Wigley

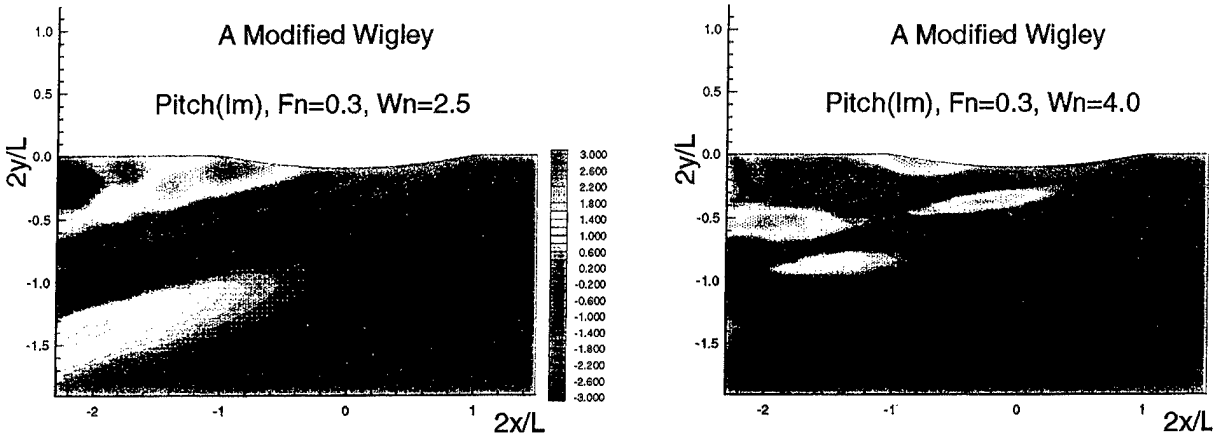


Figure 19: Unsteady wave patterns due to pitch of a Modified Wigley

x-component velocity along the waterline due to heave($\omega_n = 2.5, 5.0$). The solid line stands for the case of $N_B = 30 \times 6$ and the dotted line for the case of $N_B = 20 \times 4$, respectively. The velocity profiles are similar each other not only for low frequency($\omega_n = 2.5$) but also for high frequency($\omega_n = 5.0$). It supports that the present method is useful with a smaller number of panels.

The radiated wave patterns due to heave and pitch are shown in Fig. 18 and Fig. 19, respectively. The waves shown here seem to be almost two-dimensional. Namely the crest line of the waves becomes parallel to the x-axis as the frequency increases. In the case of heave, the motion is symmetric with respect to the midship. Therefore the generated waves propagate downstream with keeping the symmetry. But in the case of pitch, the generated waves consist of an anti-symmetric pair, i.e. elevation and depression as clearly observed in Fig. 19.

5. Conclusion

An effective numerical method has been developed for the steady and unsteady wave problems, which selectively utilizes the higher-order boundary element method and the bi-quadratic spline scheme. As shown in numerical examples, its capability of describing body surfaces more closely enhances the numerical accuracy and efficiency.

It is found that the wave elevation and resistance are sensitive to the aspect ratio of panels adjacent to the waterline. Further research is required for any conclusions.

A parabolic-type radiation condition is derived for unsteady free surface problems with $\tau < \frac{1}{4}$. Numerical results support its usefulness.

Extensions of the method to steady nonlinear problems and the ship motion problems are the topics of our next research.

Acknowledgement

This work was financially supported by the Ministry of Science and Technology(MOST) under contract number UCN293-1720.D. The authors would like to thank to Professors Bai, K.J and Rhee K.P. for their suggestions made during this work.

References

Bai, K.J. and McCarthy, J.H.(1979) , Proceedings of the Workshop on Ship Wave-Resistance Computations, DTNSRDC, Bethesda, Md. 20084, USA.

Bathe, K-J.(1982) , Finite Element Procedures in Engineering Analysis, Prentice-Hall, USA

Bertram, V.(1990) , "A Rankine Source Method for Forward-Speed Diffraction Problem", Ph.D. Thesis, University of Hamburg.

Boo, S.Y.(1993) , "Application of Higher Order Boundary Element Method to Steady Ship Wave Problem and Time Domain Simulation of Nonlinear Gravity Waves", Ph.D. dissertation, Texas A&M University.

Brebbia, C.A. and Domingez, J.(1989) , Boundary Elements An Introductory Course, Computational Mechanics Publications, Southampton.

Broenze, J. and Romate, J.E.(1992) , "Absorbing Boundary Conditions for Free Surface Wave Simulations with a Panel Method" , Journal of Computational Physics 99, pp146-158.

Cerreloza, M. and Alarcon, E.(1989) , "A Bi-cubic Transformation for the Numerical Evaluation of the Cauchy Principal Value Integrals in Boundary Elements", Intern. Journal for Numerical Methods in Eng., Vol.28, pp987-999.

Dawson, C.W.(1977) , "A Practical Computer Method for Solving Ship-Wave Problems", 2nd International Conference on Numerical Ship Hydrodynamics, Univ. of California, Berkely, USA.

Doctors, L.J. and Beck, R.F.(1987) , "Convergence Properties of the Neumann-Kelvin Problem for a Submerged Body", JSR, Vol. 31, No. 4

Farell, C.(1973) , "On the Wave Resistance of a Submerged Spheroid", JSR, Vol. 17

Gadd, G.E.(1976) , "A Method of Computing the Flow and Surface Wave Pattern Around Hull Forms", Trans. Royal Inst. Naval Arch., Vol. 113.

Hess, J.L. and Smith, A.M.O.(1962) , "Calculations of Non-Lifting Potential Flow about Arbitrary Three-Dimensional Bodies", Report E.S.40622, Douglas Aircraft Company, Inc., Long Beach, CA.

Hoff, J.R.(1990) , "Three-Dimensional Green Function of a Vessel with Forward Speed in Waves", Ph.D. Thesis, Institute for Marine Hydrodynamics, Trondheim, Norway.

Jensen, G., Mi, Z.-X. and Söding, H.(1986) , "Rankine Source Methods for Numerical Solutions of Steady Wave Resistance Problem", 16th Symposium on Naval Hydrodynamics, USA.

Jensen, G., Bertram, V. and Söding, H.(1989) , "Ship Wave Resistance Calculation", Proceedings of the 5th Inter. Conf. on Numerical Ship Hydrodynamics. Hiroshima, Japan.

Jensen, P.S.(1987) , "On the Numerical Radiation Condition in the Steady-state Ship Wave Problem", JSR, Vol. 31, No. 1, pp14-22.

Kang, C.G. et al.(1990) , "Wave Resistance by a Higher Order Panel Method", KRISO Report UCE468-1404.D, Korea.

Kim, Y.H. and Lucas, T.R.(1990) , "Nonlinear Ship Waves", Proc. of 18th Symposium on Naval Hydrodynamics. Ann Arbor, Michigan

Liu, Y.H., Kim, C.H. and Lu, X.S.(1991a) , "Comparison of Higher-Order Boundary Element and Constant Element Methods for Hydrodynamic Loadings". International Journal of Offshore and Polar Engineering 1, No.1, pp8-16.

Liu, Y.H., Kim, C.H. and Kim, M.H.(1991b) , "The Computation of Mean Drift Forces and Wave Run-Up by Higher Order Boundary Element Method", Proceedings of the 1st Intern. Offshore and Polar Engineering Conference, Edinburgh, UK, pp476-483.

Matsui, T., Kato, K. and Shirai, T.(1987) , "A Hybrid Integral Equation Method for Diffraction and Radiation of Water Waves by Three-Dimensional Bodies", Computational Mechanics, Vol.2, pp67-76.

Nakos, D.E.(1990) , "Ship Wave Patterns and Motions by a Three Dimensional Rankine Panel Method", Ph.D. Thesis, Massachusetts Institute of Technology, USA.

Nakos, D.E. and Sclavounos, P.D.(1990a) , "On Steady and Unsteady Wave Patterns", JFM, Vol.215, pp263-288.

Nakos, D.E. and Sclavounos, P.D.(1990b) , "Ship Motions by a Three-Dimensional Rankine Panel Method", 18th Symposium on Naval Hydrodynamics. USA.

Nakos, D.E. and Sclavounos, P.D.(1994) , "Kelvin Wakes and Wave Resistance of Cruiser- and Transom-Stern Ships". JSR. Vol. 38, No. 1, pp9-29.

Newman, J.N.(1978) , "Theory of Ship Motion". Advances in Applied Mechanics. Vol. 18.

Ni, S.Y.(1987) , "Higher Order Panel Methods for Potential Flows with Linear or Nonlinear Free Surface Boundary Conditions", Ph.D. dissertation, Division of Marine Hydrodynamics, Chalmers University of Technology, Goteborg, Sweden.

Noblesse, F. and McCarthy, J.H.(1983) , Proceeding of the Second DTNSRDC Workshop on Ship Wave-Resistance Computations, DTNSRDC, Bethesda, Md 20084, USA.

Ogilvie T.F. and Tuck, E.O.(1969) , "A Rational Strip Theory for Ship Motions, Part 1", Rep No. 613. Dept. Naval. Arch. Marine Eng., University of Michigan, Ann Arbor, USA.

Oskam, B.(1982) , "Stability Analysis of Panel Methods", NLR report AT-82-002U, The Netherlands.

Piers, W.J.(1983) , "Discretization Schemes for the Modelling of Free Water Surface Effects in First-order Panel Methods for Hydrodynamic Applications", NLR report TR-83-093L, The Netherlands.

Press, W.H. et al.(1986) , Numerical Recipes, The Art of Science Computing, Cambridge University Press.

Raven, H.C.(1988) , "Variation on a Theme by Dawson", 17th Symposium on Naval Hydrodynamics, The Hague, The Netherlands.

Sclavounos, P.D. and Nakos, D.E.(1988) , "Stability Analysis of Panel Methods for Free-Surface Flows with Forward Speed", 17th Symposium on Naval Hydrodynamics, The Hague, The Netherlands.

Schumaker, L.L.(1981) , Spline Functions: Baisc Theory, 1st ed.,Wiley, New York, pp118-142.

Wehausen, J.V.(1973) , "The Resistance of Ships", Advances in Applied Mechanics, Vol. 13.

A Review of Reynolds Stress Models for Turbulent Shear Flows

C. Speziale (Boston University, USA)

Abstract

A detailed review of recent developments in Reynolds stress modeling for incompressible turbulent shear flows is provided. The mathematical foundations of both two-equation models and full second-order closures are explored in depth. It is shown how these models can be systematically derived for two-dimensional mean turbulent flows that are close to equilibrium. A variety of examples are provided to demonstrate how well properly calibrated versions of these models perform for such flows. However, substantial problems remain for the description of more complex turbulent flows where there are large departures from equilibrium. Recent efforts to extend Reynolds stress models to non-equilibrium turbulent flows are discussed briefly along with the major modeling issues relevant to practical Naval Hydrodynamics applications.

1. Introduction

Turbulent shear flows are of central importance for a variety of Naval Hydrodynamics applications ranging from flow around submerged bodies to free surface flows. Most of these turbulent flows are at extremely high Reynolds numbers – and in complex geometrical flow configurations – where the application of direct or large-eddy simulations are all but impossible for the foreseeable future. Reynolds stress models are likely to remain the only technologically feasible approach for the solution of these problems for the next few decades to come, if not beyond (see Speziale [1]).

It is widely believed that Reynolds stress models are completely ad hoc, having no formal connection with solutions of the full Navier-Stokes equations for turbulent flows. While this belief is largely warranted for the older eddy viscosity models of turbulence, it constitutes a far too pessimistic assessment of the current generation of Reynolds stress closures. It will be shown how second-order closure models and two equation models with an anisotropic eddy viscosity can be systematically derived from the Navier-Stokes equations when one overriding assumption is made: the turbulence is locally homogeneous and in equilibrium. Moderate departures from equilibrium – where there are weak inhomogeneous effects – can then be accounted for in a relatively straightforward fashion.

A brief review of zero and one equation models based on the Boussinesq eddy viscosity hypothesis will first be given in order to provide a perspective on the earlier approaches to Reynolds stress modeling. However, it will then be argued that since turbulent flows contain length and time scales which can change dramatically from one flow configuration to the next, two-equation models constitute the minimum level of closure that is physically acceptable. Typically, modeled transport equations are solved for the turbulent kinetic energy and dissipation rate from which the turbulent length and time scales are built up; this obviates the need to specify these scales in an ad hoc fashion for different flows. While two-equation models represent the minimum acceptable level of closure, second-order closure models constitute the highest level of closure that is currently feasible from a practical computational standpoint. It will be shown how the former models follow from the latter in the equilibrium limit of homogeneous turbulence (see Speziale, Sarkar and Gatski [2] and Gatski and Speziale [3]). However, it will be demonstrated that the two-equation models which are formally consistent with second-order closures have an *anisotropic eddy viscosity with strain-dependent coefficients* – features that the most commonly used models do not possess.

For turbulent flows that are only weakly inhomogeneous, full Reynolds stress closures can then be constructed by the addition of turbulent diffusion terms that are formally derived via a gradient transport hypothesis. Properly calibrated versions of these mod-

els are found to yield a surprisingly good description of a wide range of two-dimensional mean turbulent flows that are near equilibrium. In particular, plane turbulent shear flows are accurately described with the stabilizing or destabilizing effect of a system rotation predicted in a manner that is quantitatively consistent with hydrodynamic stability theory. However, existing second-order closures are not currently capable of properly describing turbulent flows that are far from equilibrium and have major problems with wall-bounded turbulent flows. In regard to the latter point, it will be argued that we do not currently know how to properly integrate second-order closure models to a solid boundary with the no-slip condition applied. A variety of ad hoc wall damping functions are currently used that depend on the unit normal to (and/or the distance from) the wall – a feature that makes it virtually impossible to reliably apply these models in complex geometries. Consequently, in many applications of second-order closures to wall-bounded turbulence, the integration is carried out by matching to law of the wall boundary conditions, which do not formally apply to complex turbulent flows. The really disturbing feature here is that many of the commonly used second-order closures are not even capable of reproducing law of the wall results for an equilibrium turbulent boundary layer unless an ad hoc wall reflection term is added. This term typically depends inversely on the distance from the wall, further compromising the ability to apply these models in complex geometries. Entirely new approaches to the modeling of complex non-equilibrium and wall-bounded turbulent flows will be discussed briefly.

A variety of illustrative examples involving turbulent shear flows will be provided in order to amplify the central points discussed in this paper. In addition, a special effort will be made to address the crucial issues in turbulence modeling that are relevant to practical Naval Hydrodynamics applications.

2. Basic Equations of Turbulence

We will consider the incompressible turbulent flow of a viscous fluid under isothermal conditions. The velocity field v_i and kinematic pressure P are solutions of the Navier-Stokes and continuity equations given by

$$\frac{\partial v_i}{\partial t} + v_j \frac{\partial v_i}{\partial x_j} = -\frac{\partial P}{\partial x_i} + \nu \nabla^2 v_i \tag{1}$$

$$\frac{\partial v_i}{\partial x_i} = 0 \tag{2}$$

where ν is the kinematic viscosity and the Einstein summation convention applies to repeated indices. As in all traditional studies of turbulence modeling, the velocity and kinematic pressure are decomposed into mean and fluctuating parts as follows:

$$v_i = \overline{v}_i + u_i, \quad P = \overline{P} + p \tag{3}$$

where an overbar represents a Reynolds average. This Reynolds average can take a variety of forms for any flow variable ϕ:

Homogeneous Turbulence

$$\overline{\phi} = \lim_{V \to \infty} \frac{1}{V} \int_V \phi(\mathbf{x}, t) d^3x \tag{4}$$

$$\overline{\phi} = \overline{\phi}(t) \quad \text{(Spatial Average)}$$

Statistically Steady Turbulence

$$\overline{\phi} = \lim_{T \to \infty} \frac{1}{T} \int_0^T \phi(\mathbf{x}, t) dt \tag{5}$$

$$\overline{\phi} = \overline{\phi}(\mathbf{x}) \quad \text{(Time Average)}$$

General Turbulence

$$\overline{\phi} = \lim_{N \to \infty} \frac{1}{N} \sum_{\alpha=1}^{N} \phi^{(\alpha)}(\mathbf{x}, t) \tag{6}$$

$$\overline{\phi} = \overline{\phi}(\mathbf{x}, t) \quad \text{(Ensemble Average)}.$$

In (6), α represents a given realization of the turbulence.

The *Ergodic Hypothesis* is assumed to apply. In a homogeneous turbulence,

$$\overline{\phi}_{\text{ensemble}} = \overline{\phi}_{\text{spatial}} \tag{7}$$

whereas in a statistically steady turbulence,

$$\overline{\phi}_{\text{ensemble}} = \overline{\phi}_{\text{time}}. \tag{8}$$

For general turbulent flows that are neither statistically steady nor homogeneous, ensemble averages should be used (cf. Hinze [4] for a detailed discussion of these issues).

The Reynolds-averaged Navier-Stokes and continuity equations take the form (cf. Hinze [4])

$$\frac{\partial \overline{v}_i}{\partial t} + \overline{v}_j \frac{\partial \overline{v}_i}{\partial x_j} = -\frac{\partial \overline{P}}{\partial x_i} + \nu \nabla^2 \overline{v}_i - \frac{\partial \tau_{ij}}{\partial x_j} \tag{9}$$

$$\frac{\partial \overline{v}_i}{\partial x_i} = 0 \tag{10}$$

where

$$\tau_{ij} \equiv \overline{u_i u_j} \tag{11}$$

is the Reynolds stress tensor.

The Reynolds-averaged Navier-Stokes equation is not closed until a model is provided that ties the Reynolds stress tensor τ_{ij} to the global history of the mean velocity $\overline{v}_i$ in a physically consistent fashion. In mathematical terms, τ_{ij} is a functional of the global history of the mean velocity field, i.e.,

$$\tau_{ij}(\mathbf{x},t) = \mathcal{F}_{ij}[\overline{\mathbf{v}}(\mathbf{x}',t');\mathbf{x},t] \quad \mathbf{x}'\epsilon\mathcal{V},\ t'\epsilon(-\infty,t) \tag{12}$$

where $\mathcal{F}_{ij}[\,\cdot\,]$ denotes a functional over space and time, and $\mathcal{V}$ represents the fluid volume. In (12), it is understood that there is an implicit dependence on the initial and boundary conditions for u_i and, hence, on those for the entire hierarchy of moments constructed from the fluctuating velocity. For the construction of Reynolds stress closures, it is typically assumed that the initial and boundary conditions for any turbulence correlations beyond the Reynolds stress tensor and dissipation rate merely serve to set the level of the length and time scales (see Lumley [5] and Speziale [1]).

3. Zero and One Equation Models

The Reynolds stress tensor can be decomposed into isotropic and deviatoric parts as follows:

$$\tau_{ij} = \frac{2}{3}K\delta_{ij} + {}_D\tau_{ij} \tag{13}$$

where the deviatoric part ${}_D\tau_{ij}$ is a symmetric and traceless tensor. Virtually all of the commonly used Reynolds stress models in this class are based on the Boussinesq hypothesis where it is assumed that

$${}_D\tau_{ij} = -\nu_T\left(\frac{\partial\overline{v}_i}{\partial x_j} + \frac{\partial\overline{v}_j}{\partial x_i}\right) \tag{14}$$

given that ν_T is the eddy viscosity. For most incompressible turbulent flows, the isotropic part of the Reynolds stress tensor $\left(\frac{2}{3}K\right)$ is not needed for the determination of the mean velocity field since it can simply be absorbed into the mean pressure $\overline{P}$ in (9).

The eddy viscosity can be written as

$$\nu_T = \frac{\ell_0^2}{t_0} \tag{15}$$

where ℓ_0 is the turbulent length scale and t_0 is the turbulent time scale – quantities that can vary dramatically with space and time for a given turbulent flow. In *zero equation models*, both ℓ_0 and t_0 are specified algebraically by empirical means. The first successful zero equation model based on the Boussinesq eddy viscosity hypothesis was Prandtl's mixing length theory (see Prandtl [6]). In Prandtl's mixing length theory,

$$\nu_T = \ell_0^2\left|\frac{d\overline{u}}{dy}\right| \tag{16}$$

where $\ell_0 = \kappa y$ is the mixing length, κ is the von Kármán constant, and y is the normal distance from a solid boundary. This representation is only formally valid for thin turbulent shear flows – near a wall – where the mean velocity is of the simple unidirectional form $\overline{\mathbf{v}} = \overline{u}(y)\mathbf{i}$.

Several decades later, this simple mixing length model was generalized to multi-dimensional turbulent flows. Three alternative tensorially invariant forms have been proposed:

Smagorinsky [7] Model

$$\nu_T = \ell_0^2(2\overline{S}_{ij}\overline{S}_{ij})^{1/2} \tag{17}$$

Cebeci-Smith [8] Model

$$\nu_T = \ell_0^2\left(\frac{\partial\overline{v}_i}{\partial x_j}\frac{\partial\overline{v}_i}{\partial x_j}\right)^{1/2} \tag{18}$$

Baldwin-Lomax [9] Model

$$\nu_T = \ell_0^2(\overline{\omega}_i\overline{\omega}_i)^{1/2} \tag{19}$$

where $\overline{S}_{ij} = \frac{1}{2}(\partial\overline{v}_i/\partial x_j + \partial\overline{v}_j/\partial x_i)$ is the mean rate of strain tensor and $\overline{\omega} = \nabla\times\overline{\mathbf{v}}$ is the mean vorticity vector. The former model has been primarily used as a subgrid scale model for large-eddy simulations whereas the latter two models have been used for Reynolds-averaged Navier-Stokes computations in aerodynamics. Each of these models reduces to the simple mixing length formula (16) in the thin shear flow limit. However, they suffer from the same deficiency as the original mixing length model in their need for an ad hoc specification of the turbulent length scale ℓ_0 – a task that is all but impossible to do reliably in complex turbulent flows.

Beyond the length scale specification problem with zero equation models, there is another criticism that can be raised: it is not physically consistent to build up the turbulent velocity scale from the mean velocity gradients as done in (17) - (19). The proper measure of the turbulent velocity scale is the intensity of the turbulent fluctuations (i.e., we should take $v_0 = K^{1/2}$ where $v_0 \equiv \ell_0/t_0$). Hence, a more physically consistent representation for the eddy viscosity is given by

$$\nu_T = K^{1/2}\ell_0. \tag{20}$$

Prandtl [10] – who expanded on many of the earlier ideas of Kolmogorov [11] – developed a one-equation model based on (20) wherein a modeled transport equation for the turbulent kinetic energy was solved. Subsequent to this early work, a variety of researchers have proposed one-equation models along these lines for near-wall turbulent flows (cf. Norris and Reynolds [12] and Rodi, Mansour and Michelassi [13]).

One-equation models based on the solution of a modeled transport equation for the turbulent kinetic energy still suffer from one of the major deficiencies of mixing length models: they require the ad hoc specification of the turbulent length scale which is virtually impossible to do reliably in complex three-dimensional turbulent flows. Recently, one-equation models have been proposed based on the solution of a modeled transport equation for the eddy viscosity ν_T (see Baldwin and Barth [14] and Spalart and Allmaras [15]). These models do alleviate the problem of having to specify the turbulent length scale in the definition of the eddy viscosity (20). Nonetheless, an ad hoc specification of length scale must be made in the destruction term within the modeled transport equation for ν_T which depends empirically on the distance from the wall.

This leads us to one of the central points of this paper: the turbulent length and time scales (ℓ_0, t_0) are *not* universal; they depend strongly on the flow configuration under consideration. Consequently, *two-equation models* – wherein transport equations are solved for two independent quantities that are directly related to the turbulent length and time scales – represent the *minimum acceptable level of closure*. In the most common approach, the turbulent length and time scales are built up from the turbulent kinetic energy K and dissipation rate ε (i.e., $\ell_0 \propto K^{3/2}/\varepsilon$, $t_0 \propto K/\varepsilon$) with modeled transport equations solved for K and ε. These two-equation models should be formulated with a properly invariant *anisotropic eddy viscosity* that is nonlinear in the mean velocity gradients. The standard Boussinesq eddy viscosity hypothesis makes it impossible to properly describe turbulent flows with: (a) body force effects arising from a system rotation or from streamline curvature, and (b) flow structures generated by normal Reynolds stress anisotropies (e.g., secondary flows in non-circular ducts).

At this point, it would be useful to comment on the most sophisticated level of Reynolds stress closure that is now practical. Limitations in computer capacity, and issues of numerical stiffness, appear to make *second-order closure models* – wherein modeled transport equations are solved for the individual components of the Reynolds stress tensor along with a scale equation – *the highest level of closure* that is currently feasible for practical computations.

4. Turbulent Transport Equations

The transport equation for the fluctuating velocity u_i, which is obtained by subtracting (9) from (1), takes the form

$$\frac{\partial u_i}{\partial t} + \overline{v}_j \frac{\partial u_i}{\partial x_j} = -u_j \frac{\partial u_i}{\partial x_j} - u_j \frac{\partial \overline{v}_i}{\partial x_j} - \frac{\partial p}{\partial x_i} + \nu \nabla^2 u_i + \frac{\partial \tau_{ij}}{\partial x_j}. \tag{21}$$

This equation can be written in operator form as

$$\mathcal{N} u_i = 0. \tag{22}$$

The Reynolds stress transport equation is obtained by constructing the second moment

$$\overline{u_i \mathcal{N} u_j + u_j \mathcal{N} u_i} = 0. \tag{23}$$

Its full form is given by (cf. Hinze [4])

$$\frac{\partial \tau_{ij}}{\partial t} + \overline{v}_k \frac{\partial \tau_{ij}}{\partial x_k} = -\tau_{ik} \frac{\partial \overline{v}_j}{\partial x_k} - \tau_{jk} \frac{\partial \overline{v}_i}{\partial x_k} + \Phi_{ij} - \varepsilon_{ij} - \frac{\partial C_{ijk}}{\partial x_k} + \nu \nabla^2 \tau_{ij}. \tag{24}$$

In (24),

$$\Phi_{ij} \equiv \overline{p \left(\frac{\partial u_i}{\partial x_j} + \frac{\partial u_j}{\partial x_i} \right)} \tag{25}$$

$$\varepsilon_{ij} \equiv 2\nu \overline{\frac{\partial u_i}{\partial x_k} \frac{\partial u_j}{\partial x_k}} \tag{26}$$

$$C_{ijk} \equiv \overline{u_i u_j u_k} + \overline{p u_i} \delta_{jk} + \overline{p u_j} \delta_{ik} \tag{27}$$

are, respectively, the pressure-strain correlation, the dissipation rate tensor and the turbulent diffusion correlation.

The transport equation for the turbulent kinetic energy $K \equiv \frac{1}{2}\tau_{ii}$ is obtained by contracting (24):

$$\frac{\partial K}{\partial t} + \overline{v}_j \frac{\partial K}{\partial x_j} = \mathcal{P} - \varepsilon - \frac{\partial}{\partial x_j} \left(\frac{1}{2} \overline{u_i u_i u_j} + \overline{p u_j} \right) + \nu \nabla^2 K \tag{28}$$

where

$$\mathcal{P} \equiv -\tau_{ij} \frac{\partial \overline{v}_i}{\partial x_j} \tag{29}$$

$$\varepsilon \equiv \nu \overline{\frac{\partial u_i}{\partial x_j} \frac{\partial u_i}{\partial x_j}} \tag{30}$$

are, respectively, the turbulence production and the turbulent dissipation rate. By constructing the moment

$$2\nu \overline{\frac{\partial u_i}{\partial x_j} \frac{\partial}{\partial x_j} (\mathcal{N} u_i)} = 0, \tag{31}$$

a transport equation for the turbulent dissipation rate ε can be obtained. This equation takes the form [1]

$$\frac{\partial \varepsilon}{\partial t} + \overline{v}_i \frac{\partial \varepsilon}{\partial x_i} = \mathcal{P}_\varepsilon - \Phi_\varepsilon + \mathcal{D}_\varepsilon + \nu \nabla^2 \varepsilon \qquad (32)$$

where

$$\mathcal{P}_\varepsilon = -2\nu \overline{\frac{\partial u_k}{\partial x_i}\frac{\partial u_k}{\partial x_j}\frac{\partial \overline{v}_i}{\partial x_j}} - 2\nu \overline{\frac{\partial u_i}{\partial x_k}\frac{\partial u_j}{\partial x_k}\frac{\partial \overline{v}_i}{\partial x_j}}$$

$$-2\nu \overline{\frac{\partial u_k}{\partial x_i}\frac{\partial u_k}{\partial x_j}\frac{\partial u_i}{\partial x_j}} - 2\nu \overline{u_k \frac{\partial u_i}{\partial x_j}\frac{\partial^2 \overline{v}_i}{\partial x_j \partial x_k}} \qquad (33)$$

$$\Phi_\varepsilon = 2\nu^2 \overline{\frac{\partial^2 u_i}{\partial x_j \partial x_k}\frac{\partial^2 u_i}{\partial x_j \partial x_k}} \qquad (34)$$

$$\mathcal{D}_\varepsilon = -2\nu \frac{\partial}{\partial x_j}\left(\overline{\frac{\partial p}{\partial x_i}\frac{\partial u_j}{\partial x_i}}\right) - \nu \frac{\partial}{\partial x_j}\left(\overline{u_j \frac{\partial u_i}{\partial x_k}\frac{\partial u_i}{\partial x_k}}\right) \qquad (35)$$

are, respectively, the production, destruction and turbulent diffusion of dissipation.

Both two-equation models and second-order closure models are obtained by modeling the Reynolds stress transport equation (24) and the dissipation rate transport equation (32). *Second-order closures* are obtained by modeling the *full* Reynolds stress transport equation. *Two-equation models* are formally obtained by assuming that the turbulence is locally homogeneous and in equilibrium; the Reynolds stress anisotropies are then derived algebraically from (24) and a modeled version of (28) for the turbulent kinetic energy is solved.

5. Two-Equation Models

It will now be shown how two-equation models can be systematically derived from the Reynolds stress transport equation. As alluded to earlier, two-equation models – with an algebraic representation for the Reynolds stresses – are obtained by assuming that the turbulence is locally homogeneous and in equilibrium. Hence, we start with the Reynolds stress transport equation for homogeneous turbulence given by:

$$\dot{\tau}_{ij} = -\tau_{ik}\frac{\partial \overline{v}_j}{\partial x_k} - \tau_{jk}\frac{\partial \overline{v}_i}{\partial x_k} + \Phi_{ij} - \varepsilon_{ij}. \qquad (36)$$

Since, the fluctuating pressure p is a solution of the Poisson equation

$$\nabla^2 p = -\frac{\partial u_i}{\partial x_j}\frac{\partial u_j}{\partial x_i} - 2\frac{\partial \overline{v}_i}{\partial x_j}\frac{\partial u_j}{\partial x_i} \qquad (37)$$

it follows that the pressure-strain correlation can be written in the form

$$\Phi_{ij} = A_{ij} + M_{ijkl}\frac{\partial \overline{v}_k}{\partial x_l} \qquad (38)$$

In (38),

$$A_{ij} = \frac{1}{4\pi}\overline{\int_{-\infty}^{\infty}\!\!\int\!\!\int \frac{1}{|\mathbf{x}-\mathbf{x}^*|}\frac{\partial u_k^*}{\partial x_l^*}\frac{\partial u_l^*}{\partial x_k^*}\left(\frac{\partial u_i}{\partial x_j} + \frac{\partial u_j}{\partial x_i}\right) d^3x^*} \qquad (39)$$

$$M_{ijkl} = \frac{1}{2\pi}\overline{\int_{-\infty}^{\infty}\!\!\int\!\!\int \frac{1}{|\mathbf{x}-\mathbf{x}^*|}\frac{\partial u_l^*}{\partial x_k^*}\left(\frac{\partial u_i}{\partial x_j} + \frac{\partial u_j}{\partial x_i}\right) d^3x^*} \qquad (40)$$

are, respectively, the slow and rapid terms which are obtained by implementing the Green's function solution of (37) for an infinite flow domain.

In the developments to follow, extensive use will be made of the Reynolds stress and dissipation rate anisotropy tensors defined as

$$b_{ij} = \frac{\tau_{ij} - \frac{2}{3}K\delta_{ij}}{2K} \qquad (41)$$

$$d_{ij} = \frac{\varepsilon_{ij} - \frac{2}{3}\varepsilon\delta_{ij}}{2\varepsilon} \qquad (42)$$

respectively (see Lumley [16] and Reynolds [17]). Furthermore, use will be made of the transport equation for the turbulent kinetic energy which is exact for homogeneous turbulence:

$$\dot{K} = P - \varepsilon \qquad (43)$$

Eq. (43) is obtained by contracting (36). The direct substitution of (38) - (42) into (36) yields the Reynolds stress transport equation

$$\dot{b}_{ij} = -\frac{2}{3}\overline{S}_{ij} - \left(b_{ik}\frac{\partial \overline{v}_j}{\partial x_k} + b_{jk}\frac{\partial \overline{v}_i}{\partial x_k} - \frac{2}{3}b_{kl}\frac{\partial \overline{v}_k}{\partial x_l}\delta_{ij}\right)$$

$$+\frac{1}{2K}\left(\varepsilon \mathcal{A}_{ij} + K\mathcal{M}_{ijkl}\frac{\partial \overline{v}_k}{\partial x_l}\right) - \frac{\varepsilon}{K}d_{ij} \qquad (44)$$

given in terms of the anisotropy tensors alone. In (44), $\mathcal{A}_{ij} \equiv A_{ij}/\varepsilon$ and $\mathcal{M}_{ijkl} \equiv M_{ijkl}/K$ are the dimensionless slow and rapid pressure-strain terms.

The fundamental assumptions underlying two-equation models are that the turbulence is *locally* homogeneous and an equilibrium state is reached where

$$b_{ij}, d_{ij}, \mathcal{A}_{ij}, \mathcal{M}_{ijkl}, \frac{K}{\varepsilon}$$

attain constant values that are largely independent of the initial conditions. In general, A_{ij} and M_{ijkl} are functionals, in wavevector space $\mathbf{k}$, of the energy spectrum tensor $E_{ij}(\mathbf{k},t)$ where

$$\tau_{ij} = \int_{-\infty}^{\infty}\!\!\int\!\!\int E_{ij}(\mathbf{k},t)d^3k \qquad (45)$$

(cf. Reynolds [17]). This has prompted turbulence modelers to construct one-point models for $\mathcal{A}_{ij}$ and $\mathcal{M}_{ijkl}$ of the form (Lumley [16])

$$\mathcal{A}_{ij} = \mathcal{A}_{ij}(\mathbf{b}), \quad \mathcal{M}_{ijkl} = \mathcal{M}_{ijkl}(\mathbf{b}). \tag{46}$$

It should be said at the outset that models of the form (46) cannot be expected to apply to general homogeneous turbulent flows since nonlocal effects in wavevector space are neglected; it is well known that M_{ijkl} is of the form (cf. Reynolds [17])

$$M_{ijkl} \sim \int_{-\infty}^{\infty}\int\int \frac{k_i k_j}{k^2} E_{kl}(\mathbf{k},t)d^3k. \tag{47}$$

However, for homogeneous turbulent flows that are in equilibrium, there is evidence to suggest that $\mathcal{A}_{ij}, \mathcal{M}_{ijkl}$ and b_{ij} achieve constant values that are independent of the initial conditions as alluded to earlier (homogeneous shear flow represents a prime example; see Tavoularis and Corrsin [18]). Any constant tensor can be written as a finite expansion in three linearly independent vectors that are also constant. Since b_{ij} is a symmetric tensor, its eigenvectors are linearly independent; hence, (46) is expected to be formally valid for a homogeneous turbulence that achieves this type of structural equilibrium.

Speziale, Sarkar and Gatski [2] showed that for *two-dimensional* mean turbulent flows that are homogeneous and in equilibrium, the pressure-strain correlation reduces to the simple general form:

$$\begin{aligned}\Phi_{ij} &= \epsilon\mathcal{A}_{ij}(\mathbf{b}) + K\mathcal{M}_{ijkl}(\mathbf{b})\frac{\partial \overline{v}_k}{\partial x_l} \\ &= -C_1\epsilon b_{ij} + C_1^*\epsilon\left(b_{ik}b_{kj} - \frac{1}{3}b_{mn}b_{mn}\delta_{ij}\right) \\ &\quad + C_2K\overline{S}_{ij} + C_3K\left(b_{ik}\overline{S}_{jk} + b_{jk}\overline{S}_{ik}\right. \\ &\quad \left. - \frac{2}{3}b_{kl}\overline{S}_{kl}\delta_{ij}\right) + C_4K(b_{ik}\overline{\omega}_{jk} + b_{jk}\overline{\omega}_{ik})\end{aligned} \tag{48}$$

where

$$\overline{S}_{ij} = \frac{1}{2}\left(\frac{\partial \overline{v}_i}{\partial x_j} + \frac{\partial \overline{v}_j}{\partial x_i}\right) \tag{49}$$

$$\overline{\omega}_{ij} = \frac{1}{2}\left(\frac{\partial \overline{v}_i}{\partial x_j} - \frac{\partial \overline{v}_j}{\partial x_i}\right) \tag{50}$$

are, respectively, the mean rate of strain tensor and the mean vorticity tensor. In (48), $C_1 - C_4$ are constants that are not necessarily universal; in principal, their specific numerical values can vary from one flow to the next. However, it is encouraging to note that, consistent with its definition (47), the basis expansion (48) has a rapid part that is linear in τ_{ij} and, hence, linear in the energy spectrum tensor. It is only in the limit of two-dimensional mean turbulent flows that the general basis expansion for $(46)_2$ satisfies this linear consistency condition – a result of the fact that II, III and b_{33} achieve universal equilibrium values in the two-dimensional limit (Speziale, Sarkar and Gatski [2]). For uniformly strained turbulent flows near equilibrium, there is substantial evidence from physical and numerical experiments to suggest that the quadratic return term in (48) (with coefficient C_1^*) can be neglected without introducing an appreciable error. Then, the representation (48) becomes completely *linear* in the Reynolds stress tensor. This allows for the superposition of solutions and maintains consistency with the linearity of the rapid pressure-strain correlation in the energy spectrum tensor – a property that follows from its definition as stated above. In the opinion of the author, this constitutes the primary reason for the relative success that (46) has had in the description of two-dimensional mean turbulent flows that are near equilibrium. The applicability of (46) to non-equilibrium turbulent flows or to three-dimensional mean turbulent flows is highly debatable. In regard to the latter case, the general basis representation for $(46)_2$ is highly nonlinear in b_{ij} (see Lumley [16], Reynolds [17] and Speziale [1]) – and, therefore, nonlinear in the energy spectrum tensor – in violation of (47).

If we neglect the anisotropy of dissipation, then in the equilibrium limit where $\dot{b}_{ij} = 0$, Eq. (44) reduces to the following linear system of algebraic equations (see Gatski and Speziale [3]):

$$\begin{aligned}b_{ij}^* &= -\overline{S}_{ij}^* - b_{ik}^*\overline{S}_{jk}^* - b_{jk}^*\overline{S}_{ik}^* + \frac{2}{3}b_{kl}^*\overline{S}_{kl}^*\delta_{ij} \\ &\quad + b_{ik}^*\overline{W}_{kj}^* + b_{jk}^*\overline{W}_{ki}^*\end{aligned} \tag{51}$$

where

$$\overline{S}_{ij}^* = \frac{1}{2}g\frac{K}{\epsilon}(2 - C_3)\overline{S}_{ij} \tag{52}$$

$$\overline{W}_{ij}^* = \frac{1}{2}g\frac{K}{\epsilon}(2 - C_4)\overline{\omega}_{ij} \tag{53}$$

$$b_{ij}^* = \left(\frac{C_3 - 2}{C_2 - \frac{4}{3}}\right)b_{ij} \tag{54}$$

$$g = \left(\frac{C_1}{2} + \frac{\mathcal{P}}{\epsilon} - 1\right)^{-1}. \tag{55}$$

For turbulent flows in non-inertial frames of reference, Coriolis terms must be added to the right-hand-side of (44) along with a non-inertial correction to the pressure-strain correlation model (48). As shown by

Gatski and Speziale [3], these terms can be accounted for *exactly* by simply replacing (53) with the extended expression

$$\overline{W}^*_{ij} = \frac{1}{2} g \frac{K}{\varepsilon}(2 - C_4)\left[\overline{\omega}_{ij} + \left(\frac{C_4 - 4}{C_4 - 2}\right) e_{mji}\Omega_m\right] \tag{56}$$

where e_{mji} is the permutation tensor and Ω_m is the angular velocity of the reference frame (in an inertial frame of reference, where $\Omega_m = 0$, the expression (56) reduces to (53)).

Equation (51) constitutes a set of linear algebraic equations for the determination of b^*_{ij} in terms of $\overline{S}^*_{ij}$ and $\overline{W}^*_{ij}$; the solution to (51) is of the general mathematical form

$$\mathbf{b}^* = \mathbf{f}(\overline{\mathbf{S}}^*, \overline{\mathbf{W}}^*). \tag{57}$$

As first suggested by Pope [19], the general solution to the implicit algebraic stress equation (51) is of the form:

$$\mathbf{b}^* = \sum_{\lambda=1}^{10} G^{(\lambda)}\mathbf{T}^{(\lambda)} \tag{58}$$

where

$$\begin{aligned}
&\mathbf{T}^{(1)} = \overline{\mathbf{S}}^*, && \mathbf{T}^{(6)} = \overline{\mathbf{W}}^{*2}\overline{\mathbf{S}}^* + \overline{\mathbf{S}}^*\overline{\mathbf{W}}^{*2} - \tfrac{2}{3}\{\overline{\mathbf{S}}^*\overline{\mathbf{W}}^{*2}\}\mathbf{I}\\
&\mathbf{T}^{(2)} = \overline{\mathbf{S}}^*\overline{\mathbf{W}}^* - \overline{\mathbf{W}}^*\overline{\mathbf{S}}^*, && \mathbf{T}^{(7)} = \overline{\mathbf{W}}^*\overline{\mathbf{S}}^*\overline{\mathbf{W}}^{*2} - \overline{\mathbf{W}}^{*2}\overline{\mathbf{S}}^*\overline{\mathbf{W}}^*\\
&\mathbf{T}^{(3)} = \overline{\mathbf{S}}^{*2} - \tfrac{1}{3}\{\overline{\mathbf{S}}^{*2}\}\mathbf{I}, && \mathbf{T}^{(8)} = \overline{\mathbf{S}}^*\overline{\mathbf{W}}^*\overline{\mathbf{S}}^{*2} - \overline{\mathbf{S}}^{*2}\overline{\mathbf{W}}^*\overline{\mathbf{S}}^*\\
&\mathbf{T}^{(4)} = \overline{\mathbf{W}}^{*2} - \tfrac{1}{3}\{\overline{\mathbf{W}}^{*2}\}\mathbf{I}, && \mathbf{T}^{(9)} = \overline{\mathbf{W}}^{*2}\overline{\mathbf{S}}^{*2} + \overline{\mathbf{S}}^{*2}\overline{\mathbf{W}}^{*2} - \tfrac{2}{3}\{\overline{\mathbf{S}}^{*2}\overline{\mathbf{W}}^{*2}\}\mathbf{I}\\
&\mathbf{T}^{(5)} = \overline{\mathbf{W}}^*\overline{\mathbf{S}}^{*2} - \overline{\mathbf{S}}^{*2}\overline{\mathbf{W}}^*, && \mathbf{T}^{(10)} = \overline{\mathbf{W}}^*\overline{\mathbf{S}}^{*2}\overline{\mathbf{W}}^{*2} - \overline{\mathbf{W}}^{*2}\overline{\mathbf{S}}^{*2}\overline{\mathbf{W}}^*
\end{aligned} \tag{59}$$

are the integrity bases ($\{\cdot\}$ denotes the trace). Pope [19] only obtained the solution to (51) corresponding to the Launder, Reece and Rodi [20] model simplified to two-dimensional mean turbulent flows in an inertial frame – a case for which the calculations become much simpler since only the integrity bases $\mathbf{T}^{(1)} - \mathbf{T}^{(3)}$ are linearly independent. Gatski and Speziale [3] showed that the general solution (58) for three-dimensional turbulent flows is as follows:

$$\begin{aligned}
G^{(1)} &= -\tfrac{1}{2}(6 - 3\eta_1 - 21\eta_2 - 2\eta_3 + 30\eta_4)/D, & G^{(6)} &= -9/D\\
G^{(2)} &= -(3 + 3\eta_1 - 6\eta_2 + 2\eta_3 + 6\eta_4)/D, & G^{(7)} &= 9/D\\
G^{(3)} &= (6 - 3\eta_1 - 12\eta_2 - 2\eta_3 - 6\eta_4)/D, & G^{(8)} &= 9/D\\
G^{(4)} &= -3(3\eta_1 + 2\eta_3 + 6\eta_4)/D, & G^{(9)} &= 18/D\\
G^{(5)} &= -9/D, & G^{(10)} &= 0
\end{aligned} \tag{60}$$

$$D = 3 - \frac{7}{2}\eta_1 + \eta_1^2 - \frac{15}{2}\eta_2 - 8\eta_1\eta_2 + 3\eta_2^2 - \eta_3 + \frac{2}{3}\eta_1\eta_3 - 2\eta_2\eta_3 + 21\eta_4 + 24\eta_5 + 2\eta_1\eta_4 - 6\eta_2\eta_4 \tag{61}$$

$$\begin{aligned}
\eta_1 &= \{\overline{\mathbf{S}}^{*2}\},\ \eta_2 = \{\overline{\mathbf{W}}^{*2}\},\ \eta_3 = \{\overline{\mathbf{S}}^{*3}\},\\
\eta_4 &= \{\overline{\mathbf{S}}^*\overline{\mathbf{W}}^{*2}\},\ \eta_5 = \{\overline{\mathbf{S}}^{*2}\overline{\mathbf{W}}^{*2}\}.
\end{aligned} \tag{62}$$

While the results provided in (60) - (62) constitute the general solution of (51) for three-dimensional turbulent flows, questions can be raised about its overall usefulness. As alluded to earlier, (51) is based on the use of (48) which is only formally valid for *two-dimensional* mean turbulent flows that are near equilibrium. For two-dimensional mean turbulent flows, (60) - (62) simplifies substantially to the form

$$b^*_{ij} = -\frac{3}{3 - 2\eta^2 + 6\xi^2}\left[\overline{S}^*_{ij} + \overline{S}^*_{ik}\overline{W}^*_{kj} + \overline{S}^*_{jk}\overline{W}^*_{ki} - 2\left(\overline{S}^*_{ik}\overline{S}^*_{kj} - \frac{1}{3}\overline{S}^*_{kl}\overline{S}^*_{kl}\delta_{ij}\right)\right] \tag{63}$$

where

$$\eta \equiv (\overline{S}^*_{ij}\overline{S}^*_{ij})^{1/2}, \quad \xi = (\overline{W}^*_{ij}\overline{W}^*_{ij})^{1/2} \tag{64}$$

By making use of (52) - (55), we can write (63) in terms of the Reynolds stress tensor as follows:

$$\tau_{ij} = \frac{2}{3}K\delta_{ij} - \frac{3}{3 - 2\eta^2 + 6\xi^2}\left[\alpha_1\frac{K^2}{\varepsilon}\overline{S}_{ij} + \alpha_2\frac{K^3}{\varepsilon^2}(\overline{S}_{ik}\overline{W}_{kj} + \overline{S}_{jk}\overline{W}_{ki}) - \alpha_3\frac{K^3}{\varepsilon^2}\left(\overline{S}_{ik}\overline{S}_{kj} - \frac{1}{3}\overline{S}_{kl}\overline{S}_{kl}\delta_{ij}\right)\right] \tag{65}$$

where

$$\alpha_1 = g\left(\frac{4}{3} - C_2\right) \tag{66}$$

$$\alpha_2 = \frac{1}{2}g^2\left(\frac{4}{3} - C_2\right)(2 - C_4) \tag{67}$$

$$\alpha_3 = g^2 \left(\frac{4}{3} - C_2\right)(2 - C_3) \tag{68}$$

The coefficients α_1, α_2 and α_3 are *not* constants but rather are related to the coefficients $C_1 - C_4$ and g. In mathematical terms, they are "projections" of the fixed points of $\mathcal{A}_{ij}$ and $\mathcal{M}_{ijkl}$ onto the fixed points of b_{ij}, which can vary from one flow to the next. *However, for 2-D turbulent flows, $C_1 - C_4$ can be approximated by constants due to the linear dependence on b_{ij} which allows us to use superposition.*

Gatski and Speziale [3] evaluated $C_1 - C_4$ using the SSG second-order closure which will be discussed later; this model was calibrated largely based on the use of data for homogeneous shear flow (see Table 1).

Equilibrium Values	LRR Model	SSG Model	Data
$(b_{11})_\infty$	0.158	0.204	0.201
$(b_{22})_\infty$	-0.123	-0.148	-0.147
$(b_{12})_\infty$	-0.187	-0.156	-0.150
$(SK/\epsilon)_\infty$	5.32	5.98	6.08

Table 1. Comparison of the predictions of the Launder, Reece and Rodi (LRR) model and the Speziale, Sarkar and Gatski (SSG) model with the experimental data of Tavoularis and Corrsin [18] for homogeneous turbulent shear flow.

The constant values that are taken for $C_1 - C_4$ are given by (see Gatski and Speziale [3]):

$$C_1 = 6.80,\ C_2 = 0.36,\ C_3 = 1.25,\ C_4 = 0.40 \tag{69}$$

It should be noted at this point that if (63) is applied to turbulent flows that are far from equilibrium, singularities can arise through the vanishing of the denominator containing η and ξ (it is straightforward to show that this cannot happen in equilibrium turbulent flows). Hence, this model needs to be regularized before it is applied to complex turbulent flows that are not in equilibrium. This can be accomplished via a Padé type approximation whereby

$$\frac{3}{3 - 2\eta^2 + 6\xi^2} \approx \frac{3(1 + \eta^2)}{3 + \eta^2 + 6\xi^2\eta^2 + 6\xi^2} \tag{70}$$

(see Gatski and Speziale [3]). It is a simple matter to show that (70) constitutes an excellent approximation for turbulent flows that are near equilibrium and, unlike the original expression, is a bounded and non-negative function for *all* values of η and ξ.

The representation (63) constitutes an anisotropic eddy viscosity model of the general form

$$b_{ij} = a_{ijkl}\frac{\partial \overline{v}_k}{\partial x_l} \tag{71}$$

where the fourth rank tensor a_{ijkl} depends on the symmetric and antisymmetric parts of the mean velocity gradients. Quadratic models of this type have recently been obtained by Yoshizawa [21], Speziale [22] and Rubinstein and Barton [23] based on two-scale DIA, continuum mechanics and RNG based techniques, respectively (in regard to the latter, see Yakhot and Orszag [24]). Furthermore, it must be noted that while the traditional implicit algebraic stress models such as that due to Rodi [25] (which is of the general form (51)) have an explicit solution of the form (63), they are ill-behaved and can give rise to divergent solutions when applied to non-equilibrium turbulent flows. This explains why previous anisotropic corrections to eddy viscosity models have only had limited success:

(i) A quadratic expansion is not adequate; the coefficients should depend nonlinearly on rotational and irrotational strain rates.

(ii) Only the regularized explicit solution to algebraic stress models – which has just recently emerged – has the proper such dependence. Traditional algebraic stress models are ill-behaved and should not be applied to complex turbulent flows that are significantly out of equilibrium.

If we have a clear cut separation of scales where

$$\eta,\ \xi \ll 1$$

then (65) reduces to the eddy viscosity model

$$\tau_{ij} = \frac{2}{3}K\delta_{ij} - 2C_\mu\frac{K^2}{\varepsilon}\overline{S}_{ij} \tag{72}$$

which forms the basis for the standard $K - \varepsilon$ model of Launder and Spalding [26]. However, in basic turbulent shear flows, we do not have a separation of scales: η and ξ are of order one. Nonetheless, there are some circumstances where (65) yields results that are comparable to (72). For example, in the logarithmic region of an equilibrium turbulent boundary layer, the explicit algebraic stress model (65) yields

$$\tau_{xy} = -C_\mu\frac{K^2}{\varepsilon}\frac{d\overline{u}}{dy} \tag{73}$$

for the shear stress, where

$$C_\mu \approx 0.094 \tag{74}$$

given that $\partial\overline{v}_i/\partial x_j = d\overline{u}/dy\ \delta_{i1}\delta_{j2}$. This is virtually identical to the standard $K - \varepsilon$ model which, for this case, yields (73) with $C_\mu = 0.09$. Of course, for more complex turbulent flows the models are substantially

different; unlike the standard $K-\varepsilon$ model, the explicit algebraic stress model has a strain-dependent eddy viscosity and anisotropic eddy viscosity terms.

In order to achieve closure, a modeled transport equation for the turbulent dissipation rate ε is needed. For homogeneous turbulence, the exact transport equation (32) for the turbulent dissipation rate reduces to:

$$\dot{\varepsilon} = -\varepsilon_{ij}\frac{\partial \overline{v}_i}{\partial x_j} - \varepsilon_{ij}^{(c)}\frac{\partial \overline{v}_i}{\partial x_j} - 2\nu\overline{\frac{\partial u_k}{\partial x_i}\frac{\partial u_k}{\partial x_j}\frac{\partial u_i}{\partial x_j}} - 2\nu^2\overline{\frac{\partial^2 u_i}{\partial x_j \partial x_k}\frac{\partial^2 u_i}{\partial x_j \partial x_k}} \tag{75}$$

where ε_{ij} is the turbulent dissipation rate tensor defined in (26) and

$$\varepsilon_{ij}^{(c)} = 2\nu\overline{\frac{\partial u_k}{\partial x_i}\frac{\partial u_k}{\partial x_j}} \tag{76}$$

is the complementary dissipation rate tensor. If we introduce the anisotropy of dissipation tensors

$$d_{ij} = \frac{\varepsilon_{ij} - \frac{2}{3}\varepsilon\delta_{ij}}{2\varepsilon} \tag{77}$$

$$d_{ij}^{(c)} = \frac{\varepsilon_{ij}^{(c)} - \frac{2}{3}\varepsilon\delta_{ij}}{2\varepsilon} \tag{78}$$

(where $\varepsilon \equiv \frac{1}{2}\varepsilon_{ii} \equiv \frac{1}{2}\varepsilon_{ii}^{(c)}$), a simple closure can be developed for the production of dissipation terms in (75). Here, it is assumed that

$$d_{ij} = C_d\, b_{ij}, \quad d_{ij}^{(c)} = C_d^*\, b_{ij}, \tag{79}$$

which physically implies that the anisotropy of dissipation is proportional to the anisotropy of the Reynolds stresses due to the fact that the former follows from the latter as a result of the energy cascade from large to small scales. Results from Direct Numerical Simulations (DNS) of homogeneous shear flow (Rogers, Moin and Reynolds [27]) only provide justification for (79) as, at best, a low order approximation.

The third correlation on the right-hand-side of (75) can be written in the form

$$2\nu\overline{\frac{\partial u_k}{\partial x_i}\frac{\partial u_k}{\partial x_j}\frac{\partial u_i}{\partial x_j}} = -\frac{7}{3\sqrt{15}}S_K R_t^{1/2}\frac{\varepsilon^2}{K} \tag{80}$$

where

$$S_K = -\frac{6\sqrt{15}}{7}\frac{\overline{\frac{\partial u_k}{\partial x_i}\frac{\partial u_k}{\partial x_j}\frac{\partial u_i}{\partial x_j}}}{\left(\overline{\frac{\partial u_m}{\partial x_n}\frac{\partial u_m}{\partial x_n}}\right)^{3/2}} \tag{81}$$

is the generalized velocity derivative skewness and $R_t \equiv K^2/\nu\varepsilon$ is the turbulence Reynolds number. For isotropic turbulence, (81) reduces to the classical definition of the velocity derivative skewness which is given by $S_K = -\overline{(\partial u/\partial x)^3}/[\overline{(\partial u/\partial x)^2}]^{3/2}$ (here we define the skewness with the negative gauge). In spectral space, the destruction of dissipation term on the right-hand-side of (75) behaves as follows:

$$2\nu^2\overline{\frac{\partial^2 u_i}{\partial x_j \partial x_k}\frac{\partial^2 u_i}{\partial x_j \partial x_k}} \sim 2\nu^2\int_0^\infty k^4 E(k,t)dk \tag{82}$$

where $E(k,t)$ is the three-dimensional energy spectrum. Consequently, most of the contributions to this term occur at high wavenumbers where the energy spectrum scales with the Kolmogorov length scale, $l_k \equiv \nu^{3/4}/\varepsilon^{1/4}$. With this Kolmogorov scaling, it follows that

$$2\nu^2\overline{\frac{\partial^2 u_i}{\partial x_j \partial x_k}\frac{\partial^2 u_i}{\partial x_j \partial x_k}} = \frac{7}{3\sqrt{15}}G_K R_t^{1/2}\frac{\varepsilon^2}{K} + C_{\varepsilon 2}\frac{\varepsilon^2}{K} \tag{83}$$

(see Speziale and Bernard [28]). The direct substitution of (79), (80) and (83) into (75) yields the transport equation

$$\dot{\varepsilon} = -C_{\varepsilon 1}\frac{\varepsilon}{K}\tau_{ij}\frac{\partial \overline{v}_i}{\partial x_j} + \frac{7}{3\sqrt{15}}(S_K - G_K)R_t^{1/2}\frac{\varepsilon^2}{K} - C_{\varepsilon 2}\frac{\varepsilon^2}{K} \tag{84}$$

where $C_{\varepsilon 1} = C_d + C_d^*$ (in general homogeneous turbulence, $C_{\varepsilon 1}$, $C_{\varepsilon 2}$, S_K, and G_K can be functions of time). For equilibrium turbulent flows at high Reynolds numbers,

$$S_K = G_K \tag{85}$$

and $C_{\varepsilon 1}$ and $C_{\varepsilon 2}$ can be approximated as constants (when (85) is not valid, then ε changes on the Kolmogorov time scale – an extremely rapid change at high Reynolds numbers that constitutes a non-equilibrium flow situation). This leads us to the commonly used modeled dissipation rate equation for homogeneous turbulence:

$$\dot{\varepsilon} = -C_{\varepsilon 1}\frac{\varepsilon}{K}\tau_{ij}\frac{\partial \overline{v}_i}{\partial x_j} - C_{\varepsilon 2}\frac{\varepsilon^2}{K} \tag{86}$$

with $C_{\varepsilon 1}$ and $C_{\varepsilon 2}$ taken to be constants. Typically, $C_{\varepsilon 2}$ is determined from the decay of isotropic turbulence; for isotropic decay, (86) implies that (cf. Speziale [1])

$$K \sim t^{-\frac{1}{(C_{\varepsilon 2}-1)}}. \tag{87}$$

The most cited experimental data [29] indicates that the exponent of the decay law (87) has a mean value of approximately 1.2; this implies a value for $C_{\varepsilon 2} \approx$

1.83. In practice, a value of $C_{\varepsilon 2} = 1.90$ has been more commonly used starting with Launder, Reece and Rodi [20]. This typically has been used with a value of $C_{\varepsilon 1} = 1.44$ based on a calibration with a range of benchmark turbulent shear flows.

Recently, Speziale and Gatski [30] showed that when the effects of anisotropic dissipation are more rigorously accounted for, a variable $C_{\varepsilon 1}$ results that is of the form $C_{\varepsilon 1} = C_{\varepsilon 1}(\eta, \xi)$. This form is obtained by starting with a modeled transport equation for the full tensor dissipation ε_{ij}. An algebraic equation – analogous to that obtained from the ASM approximation for the Reynolds stress – is arrived at when the standard equilibrium hypothesis

$$\dot{d}_{ij} = 0$$

is invoked. For two-dimensional mean turbulent flows, it has the exact form:

$$\begin{aligned} d_{ij} &= -2C_{\mu\varepsilon}\left[\overline{S}^*_{ij} + \left(\frac{\frac{7}{11}\alpha_3 + \frac{1}{11}}{C_{\varepsilon 5} + \mathcal{P}/\varepsilon - 1}\right)\right. \\ &\quad \times(\overline{S}^*_{ik}\overline{\omega}^*_{jk} + \overline{S}^*_{jk}\overline{\omega}^*_{ik}) \\ &\quad + \left(\frac{\frac{30}{11}\alpha_3 - \frac{2}{11}}{C_{\varepsilon 5} + \mathcal{P}/\varepsilon - 1}\right)\left(\overline{S}^*_{ik}\overline{S}^*_{jk}\right. \\ &\quad \left.\left. - \frac{1}{3}\overline{S}^*_{mn}\overline{S}^*_{mn}\delta_{ij}\right)\right] \end{aligned} \tag{88}$$

where

$$\begin{aligned} C_{\mu\varepsilon} &= \frac{1}{15(C_{\varepsilon 5} + \mathcal{P}/\varepsilon - 1)}\left[1\right. \\ &\quad + 2\overline{\omega}^*_{ij}\overline{\omega}^*_{ij}\left(\frac{\frac{7}{11}\alpha_3 + \frac{1}{11}}{C_{\varepsilon 5} + \mathcal{P}/\varepsilon - 1}\right)^2 \\ &\quad \left. - \frac{2}{3}\left(\frac{\frac{15}{11}\alpha_3 - \frac{1}{11}}{C_{\varepsilon 5} + \mathcal{P}/\varepsilon - 1}\right)\overline{S}^*_{ij}\overline{S}^*_{ij}\right]^{-1} \end{aligned}$$

$$\overline{S}^*_{ij} = \overline{S}_{ij}\frac{K}{\varepsilon}, \quad \overline{\omega}^*_{ij} = \overline{\omega}_{ij}\frac{K}{\varepsilon}$$

and $C_{\varepsilon 5}$ and α_3 are constants (Speziale and Gatski [30]). The substitution of these algebraic equations into the contraction of the ε_{ij} transport equation yields the scalar dissipation rate equation (86) with

$$C_{\varepsilon 1} = 1 + \frac{2}{15C_\mu}\left[\frac{(1+\alpha)(C_{\varepsilon 5} + C_\mu\eta^2 - 1)}{(C_{\varepsilon 5} + C_\mu\eta^2 - 1)^2 + \beta_1^2\xi^2 - \frac{1}{3}\beta_2^2\eta^2}\right] \tag{89}$$

where

$$\eta = (2\overline{S}^*_{ij}\overline{S}^*_{ij})^{1/2}, \quad \xi = (2\overline{\omega}^*_{ij}\overline{\omega}^*_{ij})^{1/2}$$

$$\alpha = \frac{3}{4}\left(\frac{14}{11}\alpha_3 - \frac{16}{33}\right), \quad \beta_1 = \frac{7}{11}\alpha_3 + \frac{1}{11}$$

$$\beta_2 = \frac{15}{11}\alpha_3 - \frac{1}{11}, \quad C_{\varepsilon 5} \approx 5, \quad \alpha_3 \approx 0.6.$$

The constants α_3 and $C_{\varepsilon 5}$ were evaluated using DNS results for homogeneous shear flow (Rogers, Moin and Reynolds [27]).

For two-dimensional turbulent shear flows that are in equilibrium, (89) yields

$$C_{\varepsilon 1} \approx 1.4$$

which is remarkably close to the traditionally chosen constant value of $C_{\varepsilon 1} = 1.44$. It is interesting to note that an alternative variable $C_{\varepsilon 1}$ of the form $C_{\varepsilon 1} = C_{\varepsilon 1}(\eta)$ was recently proposed by Yakhot *et al.* [31] based on a heuristic Padé approximation. However, the model of Speziale and Gatski [30] depends on rotational as well as irrotational strain rates (η, ξ). It has long been recognized that the dissipation rate is dramatically altered by rotations. The results of Speziale and Gatski [30] clearly show that this effect can be rationally incorporated by accounting for anisotropic dissipation. To the best knowledge of the author, this model constitutes the first systematic introduction of rotational effects into the scalar dissipation rate equation. Previous attempts to account for this effect (see Raj [32]; Hanjalic and Launder [33]; and Bardina, Ferziger and Rogallo [34]) were largely *ad hoc*.

For *weakly* inhomogeneous turbulent flows that are near equilibrium, we can extend the K and ε transport equations by the addition of turbulent diffusion terms that are obtained by a formal expansion technique:

$$\frac{\partial K}{\partial t} + \overline{\mathbf{v}}\cdot\nabla K = \mathcal{P} - \varepsilon + \frac{\partial}{\partial x_i}\left(\frac{\nu_T}{\sigma_k}\frac{\partial K}{\partial x_i}\right) + \nu\nabla^2 K \tag{90}$$

$$\frac{\partial \varepsilon}{\partial t} + \overline{\mathbf{v}}\cdot\nabla\varepsilon = C_{\varepsilon 1}\frac{\varepsilon}{K}\mathcal{P} - C_{\varepsilon 2}\frac{\varepsilon^2}{K} + \frac{\partial}{\partial x_i}\left(\frac{\nu_T}{\sigma_\varepsilon}\frac{\partial \varepsilon}{\partial x_i}\right) + \nu\nabla^2\varepsilon \tag{91}$$

where σ_k and σ_ε are constants that typically assume the values of 1.0 and 1.3, respectively.

This model can be integrated directly to a solid boundary, where the no-slip condition is applied, without the need for *ad hoc* wall damping functions. It is only necessary to remove the singularity in the destruction of dissipation term

$$-C_{\varepsilon 2}\frac{\varepsilon^2}{K}$$

on the right-hand-side of (91). Durbin [35] argued that this expression should be replaced with the term

$$-C_{\varepsilon 2}\frac{\varepsilon}{T}$$

where T is the turbulent time scale. For high Reynolds number turbulence, $T = K/\varepsilon$; for low Reynolds number turbulence near a wall, the turbulent time scale is proportional to the Kolmogorov time scale, i.e., $T \propto \sqrt{\nu/\varepsilon}$. These considerations lead Durbin [35] to propose the expression

$$T = \max\left[\frac{K}{\varepsilon}, C_K\sqrt{\nu/\varepsilon}\right]$$

where C_K is a constant of order one. A damping function, however, can also be used. Namely, we can take the destruction term to be

$$-C_{\varepsilon 2} f_2 \frac{\varepsilon^2}{K}$$

where f_2 is a wall damping function which, for example, can be chosen to be of the form

$$f_2 = 1 - \exp(-R_y/10)$$

where $R_y \equiv K^{1/2}y/\nu$ is the turbulence Reynolds number based on the distance y from the wall. No wall damping is needed in the eddy viscosity; the strain-dependent terms in the eddy viscosity provide natural damping as the wall is approached (see Speziale and Abid [36]).

We will now consider several non-trivial applications of the two-equation model discussed herein which can be referred to as an explicit algebraic stress model (ASM) based on the SSG second-order closure. The first case that will be considered is homogeneous shear flow in a rotating frame (see Figure 1). In this flow, an initially isotropic turbulence (with turbulent kinetic energy K_0 and turbulent dissipation rate ε_0) is suddenly subjected to a uniform shear with constant shear rate S in a reference frame rotating steadily with angular velocity Ω. In Figures 2(a)-2(c), the time evolution of the turbulent kinetic energy predicted by this new two-equation model is compared with the large-eddy simulations (LES) of Bardina, Ferziger and Reynolds [37], as well as with the predictions of the standard $K-\varepsilon$ model and the full SSG second-order closure. From these results, it is clear that the new two-equation model yields the correct growth rate for pure shear flow ($\Omega/S = 0$) and properly responds to the stabilizing effect of the rotations $\Omega/S = 0.5$ and $\Omega/S = -0.5$. These results are remarkably close to those obtained from the full SSG second-order closure as shown in Figure 2. In contrast to these results, the standard $K-\varepsilon$ model overpredicts the growth rate of the turbulent kinetic energy in pure shear flow ($\Omega/S = 0$) and fails to predict the stabilizing effect of the rotations illustrated in Figures 2(b)-2(c). Since the standard $K-\varepsilon$ model makes use of the Boussinesq eddy viscosity hypothesis, it is oblivious to the application of a system rotation (i.e., it yields the *same* solution for all values of Ω/S). The new two-equation model predicts unstable flow only for the intermediate band of rotation rates $-0.09 \leq \Omega/S \leq 0.53$; this is generally consistent with linear stability theory that predicts unstable flow for $0 \leq \Omega/S \leq 0.5$.

In Figure 3, the prediction of this new two-equation model for the mean velocity profile in rotating channel flow is compared with the experimental data of Johnston, Halleen and Lezius [38] for a rotation number $Ro = 0.068$. It is clear from these results that the model correctly predicts that the mean velocity profile is *asymmetric* in line with the experimental data – an effect that arises from Coriolis forces. In contrast to these results, the standard $K-\varepsilon$ model incorrectly predicts a symmetric mean velocity profile identical to that obtained in an inertial frame (the standard $K-\varepsilon$ model is oblivious to rotations of the reference frame, as alluded to above). As demonstrated by Gatski and Speziale [3], the results obtained in Figure 3 with this new two-equation model are virtually as good as those obtained from a full second-order closure. This is due to the fact that a representation is used for the Reynolds stress tensor that is formally derived from a second-order closure (the SSG model) in the equilibrium limit. It is now clear that previous claims that two-equation models cannot systematically account for rotational effects were erroneous.

Two examples will now be presented that illustrate the enhanced predictions that are obtained for turbulent flows exhibiting effects arising from normal Reynolds stress differences. Here, we will show results obtained from the nonlinear $K-\varepsilon$ model of Speziale [22]. For turbulent shear flows that are predominantly unidirectional, with secondary flows or recirculation zones driven by small normal Reynolds stress differences, a quadratic approximation of the anisotropic eddy viscosity model discussed herein collapses to the nonlinear $K-\varepsilon$ model (see Gatski and Speziale [3]). In Figure 4, it is demonstrated that the nonlinear $K-\varepsilon$ model predicts an eight-vortex secondary flow, in a square duct, in line with experimental observations; on the other hand, the standard $K-\varepsilon$ model erroneously predicts that there is no secondary flow. In order to be able to predict secondary flows in non-circular ducts, the axial mean velocity $\overline{v}_z$ must give rise to a non-zero normal Reynolds stress difference $\tau_{yy} - \tau_{zz}$ (see Speziale and Ngo [39]). This requires an *anisotropic* eddy viscosity (any isotropic eddy viscosity, including that used in the standard $K-\varepsilon$ model, yields a vanishing normal Reynolds stress difference which makes it impossible to describe

these secondary flows).

In Figure 5, results obtained from the nonlinear $K-\varepsilon$ model are compared with the experimental data of Kim, Kline and Johnston [40] and Eaton and Johnston [41] for turbulent flow past a backward facing step. It is clear that these results are excellent: reattachment is predicted at $x/H \approx 7.0$ in close agreement with the experimental data. In contrast to these results, the standard $K-\varepsilon$ model predicts reattachment at $x/H \approx 6.25$ – an 11% underprediction. This error predominantly results from the inaccurate prediction of normal Reynolds stress anisotropies in the recirculation zone as discussed by Speziale and Ngo [39]. As alluded to above, the new two-equation model can be integrated directly to a solid boundary with no wall damping. In Figure 6, the skin friction coefficient obtained from this model – plotted as function of the Reynolds number based on the momentum thickness, R_θ – is compared with experimental data and with results obtained from the $K-\varepsilon$ model with wall damping. Clearly, the results are extremely good.

6. Second-Order Closure Models

These more complex closures are based on the full Reynolds stress transport equation with turbulent diffusion:

$$\frac{\partial \tau_{ij}}{\partial t} + \overline{v}_k \frac{\partial \tau_{ij}}{\partial x_k} = -\tau_{ik}\frac{\partial \overline{v}_j}{\partial x_k} - \tau_{jk}\frac{\partial \overline{v}_i}{\partial x_k} + \Phi_{ij} - {}_D\varepsilon_{ij} - \frac{2}{3}\varepsilon\delta_{ij} - \frac{\partial C_{ijk}}{\partial x_k} + \nu\nabla^2\tau_{ij} \qquad (92)$$

where ${}_D\varepsilon_{ij}$ is the deviatoric part of the dissipation rate tensor. Full second-order closure models are needed for turbulent flows with:

(i) Relaxation effects;

(ii) Nonlocal effects arising from turbulent diffusion that can give rise to counter-gradient transport.

In virtually all existing full second-order closures for inhomogeneous turbulent flows, Φ_{ij} and ${}_D\varepsilon_{ij}$ are modeled by their homogeneous forms. The pressure-strain correlation Φ_{ij} is modeled as

$$\Phi_{ij} = \varepsilon\mathcal{A}_{ij}(\mathrm{b}) + K\mathcal{M}_{ijkl}(\mathrm{b})\frac{\partial \overline{v}_k}{\partial x_l} \qquad (93)$$

as discussed earlier. In Section 5, the equilibrium limit of the Speziale, Sarkar and Gatski (SSG) model was provided. For turbulent flows where there are departures from equilibrium, the SSG model takes the form (see Speziale, Sarkar and Gatski [2])

$$\begin{aligned}\Phi_{ij} &= -(C_1\varepsilon + C_1^*\mathcal{P})b_{ij} + C_2\varepsilon\left(b_{ik}b_{kj} - \frac{1}{3}b_{kl}b_{kl}\delta_{ij}\right) + (C_3 - C_3^* II_b^{1/2})K\overline{S}_{ij} \\ &\quad + C_4K(b_{ik}\overline{S}_{jk} + b_{jk}\overline{S}_{ik} - \frac{2}{3}b_{kl}\overline{S}_{kl}\delta_{ij}) \\ &\quad + C_5K(b_{ik}\overline{W}_{jk} + b_{jk}\overline{W}_{ik})\end{aligned} \qquad (94)$$

where

$$C_1 = 3.4,\ C_1^* = 1.80,\ C_2 = 4.2,\ C_3 = \frac{4}{5}$$

$$C_3^* = 1.30,\ C_4 = 1.25,\ C_5 = 0.40,\ II_b = b_{ij}b_{ij}.$$

The Launder, Reece and Rodi [20] model is recovered as a special case of the SSG model if we set

$$C_1 = 3.0,\ C_1^* = 0,\ C_2 = 0,\ C_3 = \frac{4}{5},\ C_3^* = 0,$$

$$C_4 = 1.75,\ C_5 = 1.31.$$

In most applications, at high Reynolds numbers, the Kolmogorov assumption of local isotropy is typically invoked where

$${}_D\varepsilon_{ij} = 0$$

(then, $\varepsilon_{ij} = \frac{2}{3}\varepsilon\delta_{ij}$ and a modeled transport equation for the scalar dissipation rate ε is solved that is of the same general form as that discussed in Section 5). However, this assumption is debatable as discussed by Durbin and Speziale [42]. More generally, a representation of the form

$${}_D\varepsilon_{ij} = 2\varepsilon d_{ij}$$

can be used where the algebraic model (88) of Speziale and Gatski [30], discussed in Section 5, is implemented.

The only additional model that is needed for closure in high-Reynolds-number inhomogeneous turbulent flows is a model for the third-order diffusion correlation C_{ijk}. This is typically modeled using a gradient transport hypothesis:

$$C_{ijk} = \mathcal{D}_{ijklmn}\frac{\partial \tau_{lm}}{\partial x_n}. \qquad (95)$$

Some examples of commonly used models are as follows: *Launder, Reece and Rodi [20] Model*

$$C_{ijk} = -C_s\frac{K}{\varepsilon}\left(\tau_{im}\frac{\partial \tau_{jk}}{\partial x_m} + \tau_{jm}\frac{\partial \tau_{ik}}{\partial x_m} + \tau_{km}\frac{\partial \tau_{ij}}{\partial x_m}\right) \qquad (96)$$

Mellor and Herring [43] Model

$$C_{ijk} = -\frac{2}{3} C_s \frac{K^2}{\varepsilon} \left(\frac{\partial \tau_{jk}}{\partial x_i} + \frac{\partial \tau_{ik}}{\partial x_j} + \frac{\partial \tau_{ij}}{\partial x_k} \right) \qquad (97)$$

Daly and Harlow [44] Model

$$C_{ijk} = -2 C_s \frac{K}{\varepsilon} \tau_{kl} \frac{\partial \tau_{ij}}{\partial x_l} \qquad (98)$$

where $C_s \approx 0.11$ is a constant. When these models are used in a full second-order closure, countergradient transport effects can be described.

There is no question that, in principle, second-order closures account for more physics. This is quite apparent for turbulent flows exhibiting relaxation effects. The return to isotropy problem is a prime example where suddenly, at time $t = 0$, the mean strains in a homogeneous turbulence are shut off; the flow then gradually returns to isotropy (i.e., $b_{ij} \to 0$ as $t \to \infty$). In Figure 7, results for the Reynolds stress anisotropy tensor obtained from the Speziale, Sarkar and Gatski (SSG) and Launder, Reece and Rodi (LRR) models are compared with the experimental data of Choi and Lumley [45] for the return-to-isotropy from plane strain (here, $\tau = \varepsilon_0 t / K_0$). It is clear from these results that the models predict a gradual return to isotropy in line with the experimental data. In contrast to these results, all two-equation models – including the more sophisticated one based on an anisotropic eddy viscosity derived herein – erroneously predict that at $\tau = 0$, b_{ij} abruptly goes to zero. In addition, it is worth noting that while the SSG model was derived and calibrated based on near equilibrium two-dimensional mean turbulent flows, it performs remarkably well on certain three-dimensional, homogeneously strained turbulent flows. The predictions of the SSG and LRR models for the normal Reynolds stress anisotropies, compared in Figure 8 with the direct simulations of Lee and Reynolds [46] for the axisymmetric expansion, demonstrate this point (here, $t^* = \Gamma t$ where Γ is the strain rate).

While the previous results are encouraging, it must be noted that the *Achilles heel of second-order closures is wall-bounded turbulent flows*:

(i) Ad hoc wall reflection terms are needed in most pressure-strain models (that depend inversely on the distance y from the wall) in order to mask deficient predictions for the logarithmic region of a turbulent boundary layer;

(ii) Near-wall models must typically be introduced that depend on the unit normal to the wall – a feature that makes it virtually impossible to systematically integrate second-order closures in complex geometries (see So *et al.* [47]).

In regard to the first point, it is rather shocking as to what the level of error is in many existing second-order closures for the logarithmic region of an equilibrium turbulent boundary layer, when no ad hoc wall reflection terms are used. This can be seen in Table 2 where the predictions of the Launder, Reece and Rodi (LRR), Shih and Lumley (SL), Fu, Launder and Tselepidakis (FLT) and SSG models are compared with experimental data (Laufer [48]) for the log-layer of turbulent channel flow. Most of the models yield errors ranging from 30% to 100%. These models are then typically forced into agreement with the experimental data by the addition of ad hoc wall reflection terms that depend inversely on the distance from the wall – an alteration that compromises the ability to apply a model in complex geometries where the wall distance is not always uniquely defined. Only the SSG model yields acceptable results for the log-layer without a wall reflection term. This results from two factors: (a) a careful and accurate calibration of homogeneous shear flow (see Table 3) and (b) the use of a Rotta coefficient $\frac{1}{2} C_1$ that is not too far removed from one (see Abid and Speziale [49]). The significance of these results is demonstrated in Figure 9 where full Reynolds stress computations of turbulent channel flow are compared with the experimental data of Laufer [48]. It is clear that the same trends are exhibited in these results as with those shown in Table 2 which were obtained by a simplified log-layer analysis.

The near-wall problem largely arises from the use of homogeneous pressure-strain models of the form (93) that are only theoretically justified for near-equilibrium homogeneous turbulence. Recently, Durbin [35] developed an elliptic relaxation model that accounts for wall blocking – and introduces non-local effects in the vicinity of walls – eliminating the need for ad hoc wall damping functions. While this is a promising new approach, it does not alleviate the problems that the commonly used pressure-strain models have in non-equilibrium homogeneous turbulence (the Durbin [35] model collapses to the standard hierarchy of pressure-strain models given above in the limit of homogeneous turbulence). The failure of these models in non-equilibrium homogeneous turbulence can be illustrated by the example shown in Figure 10. This constitutes a rapidly distorted homogeneous shear flow that, initially, is far from equilibrium since $SK_0/\varepsilon_0 = 50$ (the equilibrium value of SK/ε is approximately 5). It is apparent from these

CHANNEL FLOW

Equilibrium Values	LRR Model	SL Model	FLT Model	SSG Model	Experimental Data
b_{11}	0.129	0.079	0.141	0.201	0.22
b_{12}	-0.178	-0.116	-0.162	-0.160	-0.16
b_{22}	-0.101	-0.082	-0.099	-0.127	-0.15
b_{33}	-0.028	0.003	-0.042	-0.074	-0.07
SK/ε	2.80	4.30	3.09	3.12	3.1

Table 2. Comparison of the model predictions for the equilibrium values in the log-layer ($\mathcal{P}/\varepsilon = 1$) with the experimental data of Laufer [48] for channel flow.

HOMOGENEOUS SHEAR FLOW

Equilibrium Values	LRR Model	SL Model	FLT Model	SSG Model	Experimental Data
b_{11}	0.152	0.120	0.196	0.218	0.21
b_{12}	-0.186	-0.121	-0.151	-0.164	-0.16
b_{22}	-0.119	-0.122	-0.136	-0.145	-0.14
b_{33}	-0.033	0.002	-0.060	-0.073	-0.07
SK/ε	4.83	7.44	5.95	5.50	5.0

Table 3. Comparison of the model predictions for the equilibrium values in homogeneous shear flow ($\mathcal{P}/\varepsilon = 1.8$) with the experimental data of Tavoularis and Karnik [50].

results that all of the models perform poorly relative to the DNS of Lee *et al.* [51]. Even the SSG model, which does extremely well for homogeneous shear flow that is not far from equilibrium, dramatically overpredicts the growth rate of the turbulent kinetic energy for this strongly non-equilibrium test case.

In the opinion of the author, it is a vacuous exercise to develop more complex models of the form (93) using non-equilibrium constraints such as *Material Frame-Indifference (MFI) in the two-dimensional limit* (Speziale [52, 53]) or *realizability* (Schumann [54] and Lumley [16]). While these constraints are a rigorous consequence of the Navier-Stokes equations, they typically deal with flow situations that are far from equilibrium (two-dimensional turbulence and one or two-component turbulence) where (93) would not be expected to apply in the first place. Ristorcelli, Lumley and Abid [55] – following the earlier work by Haworth and Pope [56] and Speziale [57, 58] – developed a pressure-strain model of the form (93) that satisfies MFI in the 2-D limit. Shih and Lumley [59] attempted to develop models of the form (93) that satisfy the strong form of realizability of Schumann [54]. Reynolds [17] has attempted to develop models of this form which are consistent with Rapid Distortion Theory (RDT). All of these models involve complicated expressions for M_{ijkl} that are *nonlinear* in b_{ij}. From its definition, M_{ijkl} is linear in the energy spectrum tensor $E_{kl}(\mathbf{k}, t)$ (see Eq. (47)). Since,

$$b_{ij} = \frac{\tau_{ij} - \frac{2}{3}K\delta_{ij}}{2K}$$

where τ_{ij} is given by (45), it follows that models for M_{ijkl} that are nonlinear in b_{ij} are also nonlinear in E_{ij}. This is a *fundamental inconsistency* that dooms these models to failure. It is clear that is impossible to describe a range of RDT flows – which are linear – with nonlinear models (the principle of superposition is violated). Furthermore, Shih and Lumley [59, 60] unnecessarily introduce higher degree nonlinearities and non-analyticity to satisfy realizability. In the process of doing so, they arrive at a model that is neither realizable nor capable of describing even basic turbulent flows (see Speziale, Abid and Durbin [61], Durbin and Speziale [62] and Speziale and Gatski [63]).

Entirely new non-equilibrium models are needed

for the pressure-strain correlation and the dissipation rate tensor. The former should contain nonlinear strain rate effects and the latter should account for the effects of anisotropic dissipation and non-equilibrium vortex stretching where $S_K \neq G_K$ in (84) (see Bernard and Speziale [64] and Speziale and Bernard [28]). Models of this type are currently under investigation for the Office of Naval Research *ARI on Nonequilibrium Turbulence.*

7. Conclusion

The following conclusions and recommendations for Naval Hydrodynamics applications can now be made:

(1) For turbulent flows with complex wall bounded or free surface geometries, two-equation models with an anisotropic eddy viscosity – that are integrated directly to a solid boundary with the no slip condition applied – should be used for the immediate future. A new generation of two-equation models, systematically derived from second-order closures, has emerged that is far superior to the commonly used $K - \epsilon$ model and competitive with existing full second-order closures.

(2) There is no question that full second-order closure models do, in principle, account for more turbulence physics than two-equation models. However, current versions of these models have major problems when integrated directly to a solid boundary with the no-slip condition applied. They also perform poorly in even simple turbulent flows that are far from equilibrium. Until these problems are overcome, their use should be limited to free turbulent shear flows that are diffusion dominated or to wall bounded turbulent shear flows which exhibit complex turbulence physics that does not preclude the use of simple law of the wall boundary conditions.

Research is currently underway, as part of the Office of Naval Research *ARI on Nonequilibrium Turbulence*, to extend these models to turbulent flows that are far from equilibrium and to resolve the near-wall problem. With the incorporation of improvements along these lines, we should start to see Reynolds stress models make a major impact on the computation of the turbulent flows of relevance to Naval Hydrodynamics applications.

Acknowledgements

A significant portion of this research was funded by the National Aeronautics and Space Administration under Contract NAS1-19480 while the author was in residence at ICASE. Funding provided by the Office of Naval Research under Grant N00014-94-1-0088 (ARI on Nonequilibrium Turbulence, Dr. L. P. Purtell, Program Officer) is also gratefully acknowledged.

References

1. Speziale, C. G., "Analytical methods for the development of Reynolds stress closures in turbulence," *Ann. Rev. Fluid Mech.*, Vol. 23, 1991, pp. 107-157.

2. Speziale, C. G., Sarkar, S. and Gatski, T. B., "Modeling the pressure-strain correlation of turbulence: An invariant dynamical systems approach," *J. Fluid Mech.*, Vol. 227, 1991, pp. 245-272.

3. Gatski, T. B. and Speziale, C. G., "On explicit algebraic stress models for complex turbulent flows," *J. Fluid Mech.*, Vol. 254, 1993, pp. 59-78.

4. Hinze, J. O., *Turbulence*, 2nd ed., McGraw-Hill, New York, 1975.

5. Lumley, J. L., "Toward a turbulent constitutive equation," *J. Fluid Mech.*, Vol. 41, 1970, pp. 413-434.

6. Prandtl, L., "Über die ausgebildete turbulenz," *ZAMM*, Vol. 5, 1925, pp. 136-139.

7. Smagorinsky, J., "General circulation experiments with the primitive equations," *Mon. Weather Review*, Vol. 91, 1963, pp. 99-165.

8. Cebeci, T. and Smith, A. M. O., *Analysis of Turbulent Boundary Layers*, Academic Press, New York, 1974.

9. Baldwin, B. S. and Lomax, H., "Thin-layer approximation and algebraic model for separated turbulent flows," *AIAA Paper No. 78-257*, 1978.

10. Prandtl, L., "Über ein neues formelsystem für die ausgebildete turbulenz," *Nachr. Akad. Wiss. Göttingen Math. Phys. Kl*, Vol. 6, 1945, pp. 6-19.

11. Kolmogorov, A. N., "The equations of turbulent motion in an incompressible fluid," *Isv. Acad. Sci. USSR, Phys.*, Vol. 6, 1942, pp. 56-58.

12. Norris, L. H. and Reynolds, W. C., "Turbulent channel flow with a moving wavy boundary," *Stanford University Technical Report FM-10*, 1975.

13. Rodi, W., Mansour, N. N. and Michelassi, V., "One-equation near-wall turbulence modeling with the aid of direct simulation data," *ASME J. Fluids Eng.*, Vol. 115, 1993, pp. 196-205.

14. Baldwin, B. S. and Barth, T. J., "A one-equation turbulence transport model for high Reynolds number wall-bounded flows," *NASA TM-102847*, 1990.

15. Spalart, P. R. and Allmaras, S. R., "A one-equation turbulence model for aerodynamic flows," *AIAA Paper No. 92-439*, 1992.

16. Lumley, J. L., "Computational modeling of turbulent flows," *Adv. Appl. Mech.*, Vol. 18, 1978, pp. 123-176.

17. Reynolds, W. C., "Fundamentals of turbulence for turbulence modeling and simulation," in *Lecture Notes for Von Kármán Institute, AGARD Lect. Ser. No.* 86, 1987, pp. 1-66, NATO, New York.

18. Tavoularis, S. and Corrsin, S., "Experiments in nearly homogeneous turbulent shear flow with a uniform mean temperature gradient. Part I," *J. Fluid Mech.*, Vol. 104, 1981, pp. 311-347.

19. Pope, S. B., "A more general effective viscosity hypothesis," *J. Fluid Mech.*, Vol. 72, 1975, pp. 331-340.

20. Launder, B. E., Reece, G. J. and Rodi, W., "Progress in the development of a Reynolds stress turbulence closure," *J. Fluid Mech.*, Vol. 68, 1975, pp. 537-566.

21. Yoshizawa, A., "Statistical analysis of the deviation of the Reynolds stress from its eddy viscosity representation," *Phys. Fluids*, Vol. 27, 1984, pp. 1377-1387.

22. Speziale, C. G., "On nonlinear $K-\ell$ and $K-\varepsilon$ models of turbulence," *J. Fluid Mech.*, Vol. 178, 1987, pp. 459-475.

23. Rubinstein, R. and Barton, J. M., "Nonlinear Reynolds stress models and the renormalization group," *Phys. Fluids A*, Vol. 2, 1990, pp. 1472-1476.

24. Yakhot, V. and Orszag, S. A., "Renormalization group analysis of turbulence I. Basic theory," *J. Sci. Comp.*, Vol. 1, 1986, pp. 3-51.

25. Rodi, W., "A new algebraic relation for calculating the Reynolds stresses," *ZAMM*, Vol 56, 1976, pp. T219-221.

26. Launder, B. E. and Spalding, D. B., "The numerical computation of turbulent flows," *Comput. Methods Appl. Mech. Eng.*, Vol. 3, 1974, pp. 269-289.

27. Rogers, M. M., Moin, P. and Reynolds, W. C., "The structure and modeling of the hydrodynamic and passive scalar fields in homogeneous turbulent shear flow," *Stanford University Technical Report No. TF-25*, 1986.

28. Speziale, C. G. and Bernard, P. S., "The energy decay in self-preserving isotropic turbulence revisited," *J. Fluid Mech.*, Vol. 241, 1992, pp. 645-667.

29. Comte-Bellot, G. and Corrsin, S., "Simple Eulerian time correlation of full- and narrow-band velocity signals in grid-generated isotropic turbulence," *J. Fluid Mech.*, Vol. 48, 1971, pp. 273-337.

30. Speziale, C. G. and Gatski, T. B., "Modeling anisotropies in the dissipation rate of turbulence," *Bull. Am. Phys. Soc.*, Vol. 37, 1992, p. 1799.

31. Yakhot, V., Orszag, S. A., Thangam, S., Gatski, T. B. and Speziale, C. G., "Development of turbulence models for shear flows by a double expansion technique," *Phys. Fluids A*, Vol. 4,1992, pp. 1510-1520.

32. Raj, R., "Form of the turbulence dissipation equation as applied to curved and rotating turbulent flows," *Phys. Fluids*, Vol. 18, 1975, pp. 1241-1244.

33. Hanjalic, K. and Launder, B. E., "Sensitizing the dissipation equation to irrotational strains," *ASME J. Fluids Eng.*, Vol. 102, 1980, pp. 34-40.

34. Bardina, J., Ferziger, J. H. and Rogallo, R. S., "Effect of rotation on isotropic turbulence: Computation and modeling," *J. Fluid Mech.*, Vol. 154, 1985, pp. 321-336.

35. Durbin, P. A., "A Reynolds stress model for near-wall turbulence," *J. Fluid Mech.*, Vol. 249, 1993, pp. 465-498.

36. Speziale, C. G. and Abid, R., "A new near-wall model for Reynolds stress turbulence closures with no wall damping," *Bull. Am. Phys. Soc.*, Vol. 39, 1994, p. 1911.

37. Bardina, J., Ferziger, J. H. and Reynolds, W. C., "Improved turbulence models based on large-eddy simulation of homogeneous, incompressible turbulent flows," *Stanford University Technical Report No. TF-19*, 1983.

38. Johnston, J. P., Halleen, R. M. and Lezius, D. K., "Effects of a spanwise rotation on the structure of two-dimensional fully-developed turbulent channel flow," *J. Fluid Mech.*, Vol. 56, 1972, pp. 533-557.

39. Speziale, C. G. and Ngo, T., "Numerical solution of turbulent flow past a backward facing step using a nonlinear $K - \epsilon$ model," *Int. J. Eng. Sci.*, Vol. 26, 1988, pp. 1099-1112.

40. Kim, J., Kline, S. J. and Johnston, J. P., "Investigation of a reattaching turbulent shear layer: Flow over a backward facing step," *ASME J. Fluids Eng.*, Vol. 102, 1980, pp. 302-308.

41. Eaton, J. K. and Johnston, J. P., "Turbulent flow reattachment: An experimental study of the flow and structure behind a backward facing step," *Stanford University Report No. MD-39*, 1980.

42. Durbin, P. A. and Speziale, C. G., "Local anisotropy in strained turbulence at high Reynolds numbers," *ASME J. Fluids Eng.*, Vol. 113, 1991, pp. 707-709.

43. Mellor, G. L. and Herring, H. J., "A survey of mean turbulent field closure models," *AIAA J.*, Vol. 11, 1973, pp. 590-599.

44. Daly, B. J. and Harlow, F. H., "Transport equations in turbulence," *Phys. Fluids*, Vol. 13, 1970, pp. 2634-2649.

45. Choi, K. S. and Lumley, J. L., "Return to isotropy of homogeneous turbulence revisited," in *Turbulence and Chaotic Phenomena in Fluids* (T. Tatsumi, ed.), pp. 267-272, North Holland, New York, 1984.

46. Lee, M. J. and Reynolds, W. C., "Numerical experiments on the structure of homogeneous turbulence," *Stanford University Technical Report No. TF-24*, 1985.

47. So, R. M. C., Lai, Y. G. and Hwang, B. C., "Second-order near-wall turbulence closures: A review," *AIAA J.*, Vol. 29, 1991, pp. 1819-1835.

48. Laufer, J., "Investigation of turbulent flow in a two-dimensional channel," *NACA TN 1053*, 1951.

49. Abid, R. and Speziale, C. G., "Predicting equilibrium states with Reynolds stress closures in channel flow and homogeneous shear flow," *Phys. Fluids A*, Vol. 5, 1993, pp. 1776-1782.

50. Tavoularis, S. and Karnik, U., "Further experiments on the evolution of turbulent stresses and scales in uniformly sheared turbulence," *J. Fluid Mech.*, Vol. 204, 1989, pp. 457-478.

51. Lee, M. J., Kim, J. and Moin, P., "Structure of turbulence at high shear rate," *J. Fluid Mech.*, Vol. 216, 1990, pp. 561-583.

52. Speziale, C. G., "Some interesting properties of two-dimensional turbulence," *Phys. Fluids*, Vol. 24, 1981, pp. 1425-1427.

53. Speziale, C. G., "Closure models for rotating two-dimensional turbulence," *Geophys. & Astrophys. Fluid Dyn.*, Vol. 23, 1983, pp. 69-84.

54. Schumann, U., "Realizability of Reynolds stress turbulence models," *Phys. Fluids*, Vol. 20, 1977, pp. 721-725.

55. Ristorcelli, J. R., Lumley, J. L. and Abid, R., "A rapid-pressure correlation representation consistent with the Taylor-Proudman theorem materially-frame-indifferent in the 2-D limit," *ICASE Report No. 94-1*, NASA Langley Research Center, 1994.

56. Haworth, D. C. and Pope, S. B., "A generalized Langevin model for turbulent flows," *Phys. Fluids*, Vol. 29, 1986, pp. 387-405.

57. Speziale, C. G., "Second-order closure models for rotating turbulent flows," *Q. Appl. Math.*, Vol. 45, 1987, pp. 721-723.

58. Speziale, C. G., "Turbulence modeling in non-inertial frames of reference," *Theoret. & Comput. Fluid Dyn.*, Vol. 1, 1989, pp. 3-19.

59. Shih, T. H. and Lumley, J. L., "Modeling of pressure correlation terms in Reynolds stress and scalar flux equations," *Cornell University Technical Report FDA-85-3*, 1985.

60. Shih, T. H. and Lumley, J. L., "Critical comparison of second-order closures with direct numerical simulations of homogeneous turbulence," *AIAA J.*, Vol. 31, 1993, pp. 663-670.

61. Speziale, C. G., Abid, R. and Durbin, P. A., "On the realizability of Reynolds stress turbulence closures," *J. Sci. Comp.*, Vol. 9, 1994, pp. 369-403.

62. Durbin, P. A. and Speziale, C. G., "Realizability of second-moment closure via stochastic analysis," *J. Fluid Mech.*, Vol. 280, 1994, pp. 395-407.

63. Speziale, C. G. and Gatski, T. B., "Assessment of second-order closure models in turbulent shear flows," *AIAA J.*, Vol. 32, 1994, pp. 2113-2115.

64. Bernard, P. S. and Speziale, C. G., "Bounded energy states in homogeneous turbulent shear flow – An alternative view," *ASME J. Fluids Eng.*, Vol. 114, 1992, pp. 29-39.

FIGURES

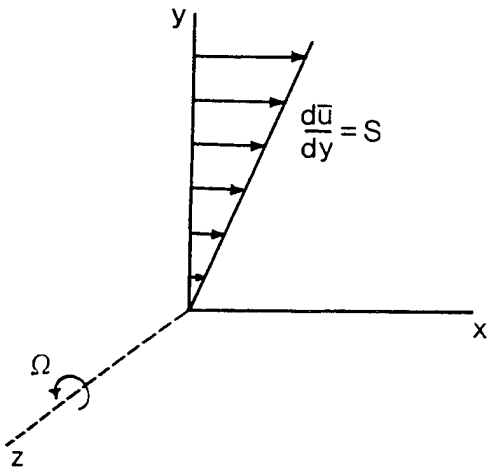


Figure 1. Schematic of homogeneous shear flow in a rotating frame.

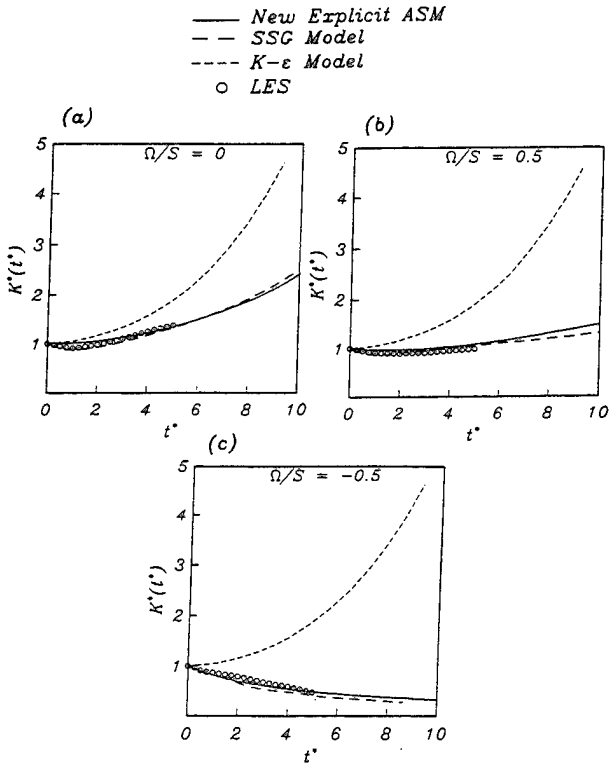


Figure 2. Time evolution of the turbulent kinetic energy in rotating homogeneous shear flow: Comparison of the model predictions with the large-eddy simulations of Bardina *et al.* [37]. (a) $\Omega/S = 0$, (b) $\Omega/S = 0.5$ and (c) $\Omega/S = -0.5$ (from Gatski and Speziale [3]).

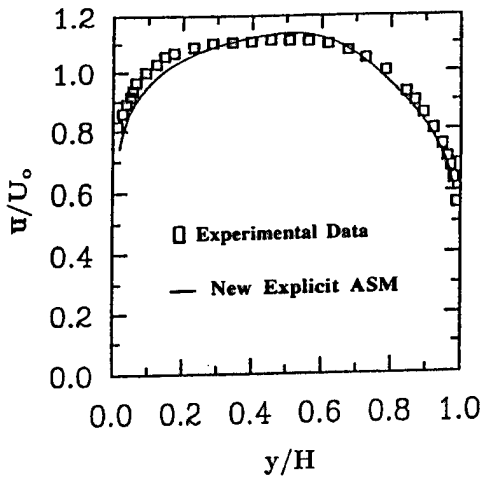


Figure 3. Comparison of the mean velocity profile in rotating channel flow predicted by the new explicit ASM of Gatski and Speziale [3] with the experimental data of Johnston, Halleen and Lezius [38].

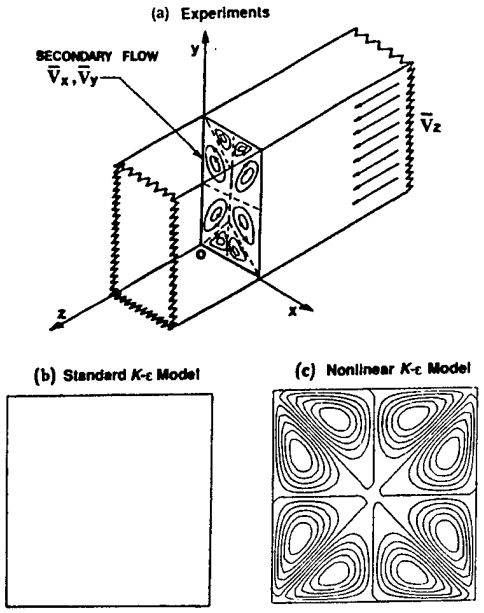


Figure 4. Turbulent secondary flow in a rectangular duct: (a) experiments, (b) standard $K-\varepsilon$ model, and (c) nonlinear $K-\varepsilon$ model of Speziale [22].

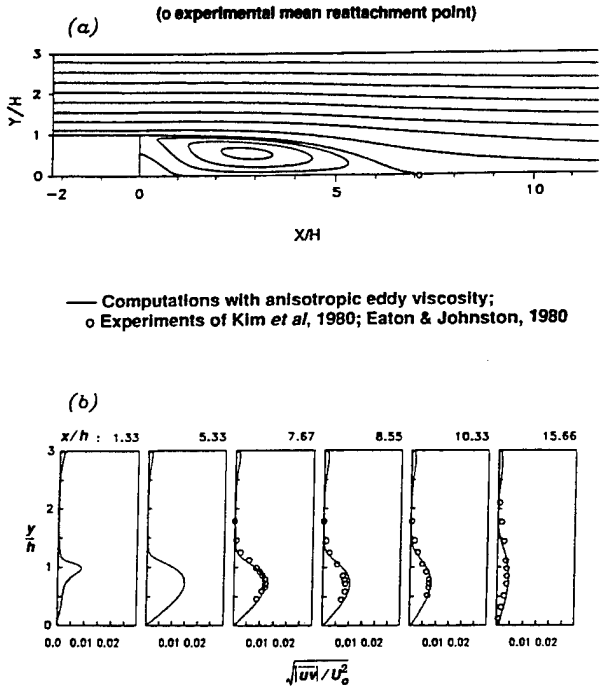


Figure 5. Turbulent flow past a backward facing step: comparison of the predictions of the nonlinear $K-\varepsilon$ model [22] with experiments. (a) Streamlines and (b) turbulent shear stress profiles.

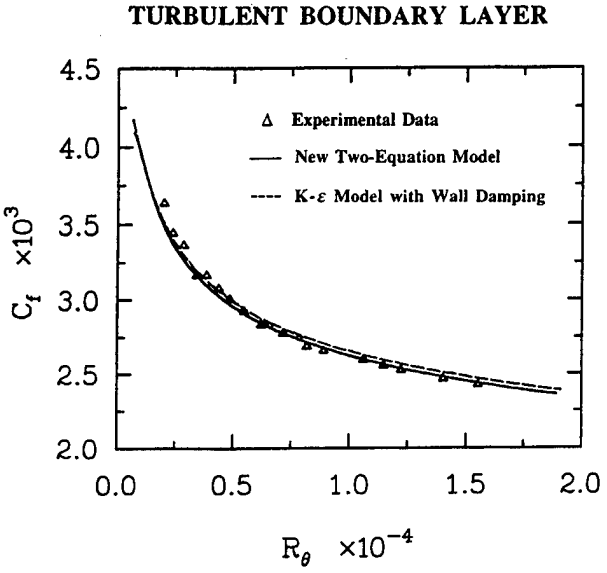


Figure 6. Comparison of the predictions of the explicit ASM of Gatski and Speziale [3] for skin friction with experimental data for the flat plate boundary layer (from Speziale and Abid [36]).

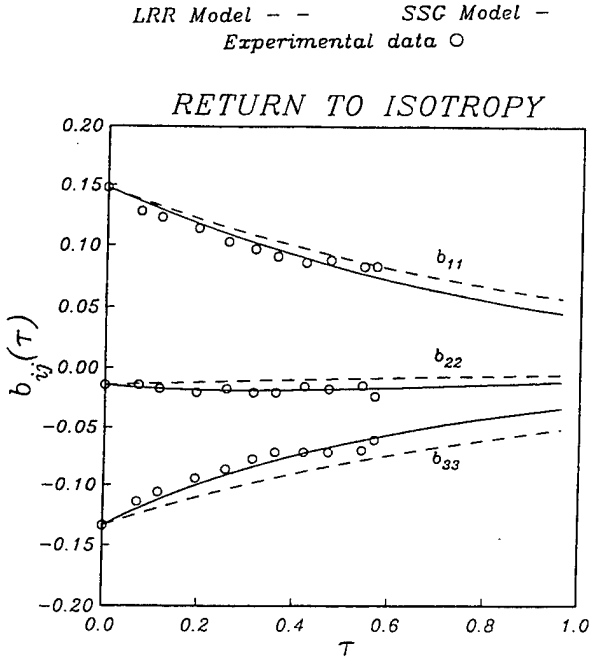


Figure 7. Time evolution of the anisotropy tensor in the return to isotropy problem. Comparison of the predictions of the LRR model and SSG model with the experiment of Choi and Lumley [45] (from Speziale, Sarkar and Gatski [2]).

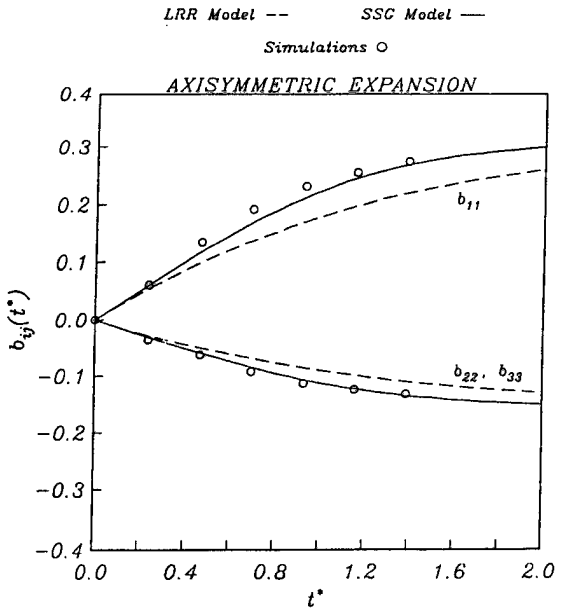


Figure 8. Time evolution of the anisotropy tensor in the axisymmetric expansion for $\epsilon_0/\Gamma K_0 = 2.45$. Comparison of the predictions of the LRR model and SSG model with the direct simulations of Lee and Reynolds [46].

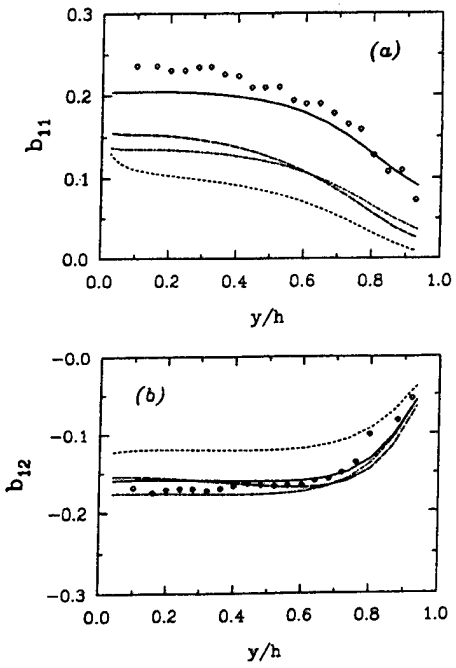


Figure 9. Comparison of full Reynolds stress calculations of channel flow with the experimental data ($\diamond$) of Laufer [48] for $Re = 61,600$. —— SSG model; - - - FLT model; - · - LRR model; and - - - SL model. (a) b_{11} component and (b) b_{12} component (from Abid and Speziale [49]).

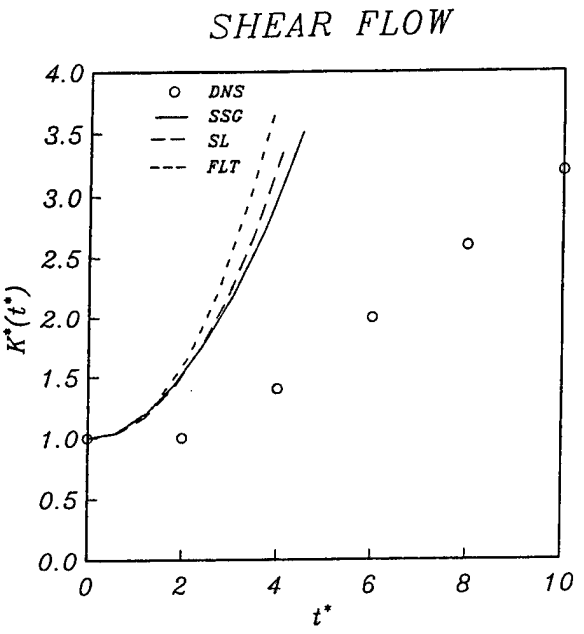


Figure 10. Comparison of the SSG, SL and FLT model predictions for the time evolution of the turbulent kinetic energy with the DNS results of Lee, Kim and Moin [51] for homogeneous shear flow ($SK_0/\epsilon_0 = 50$).

DISCUSSION

S. Banerjee
University of California at Santa Barbara, USA

I was struck by the similarity of your formulations for the anisotropic eddy viscosity with various viscoelastic models and in rheology. Rheologists, however, have tried to factor in structure, even at a molecular level (e.g. Sam Edwards & Dori a couple of decades ago) into their models. How is all the recent information about coherent structures impacting modelling of the Reynolds stresses?

AUTHOR'S REPLY

There is indeed a great similarity between Reynolds stress models with an anisotropic eddy viscosity and constitutive equations for viscoelastic fluids (the analogy between the mean turbulent flow of a Newtonian fluid and the laminar flow of a non-Newtonian fluid was first pointed out by Rivlin 1957 and then later expanded upon by Lumley 1970 and Speziale 1987). However, it is not as easy to factor structural information into Reynolds stress models as it is into viscoelastic models. In viscoelastic fluids, this is related to the material constitution of the fluid—which is flow independent—whereas in turbulence this constitutes a feature of the dynamics of the flow that can change from one configuration to the next. Nonetheless, a well constructed Reynolds stress model, that is valid for time-dependent flows, can, in principle, describe the qualitative features of coherent structures that arise from simple shear instabilities (the case of rotating shear flows discussed in my paper represents a prime example).

DISCUSSION

T. Huang
David Taylor Model Basin, USA

Charles, we appreciated your excellent presentation. I suggest that more comparisons on different turbulence models be made by local skin frictional and total skin frictional coefficients at a range of high Reynolds number. Prediction of drag coefficients is one of the most important applications of computational fluid dynamics. Therefore, we must also emphasize our research on turbulence models for application to drag prediction.

AUTHOR'S REPLY

I agree with you that it is crucial for a Reynolds stress model to yield accurate predictions for the skin friction. The new two equation model that I discussed in my presentation does precisely that for the turbulent flat plate boundary layer, without the need for ad hoc wall damping functions. I will add a plot of the skin friction as a function of the Reynolds number in the final draft of my paper (note: see Figure 6 of the paper which appears in this volume).

DISCUSSION

M. Tulin
University of California at Santa Barbara, USA

What progress has been made in the calculation of non-homogeneous flows (stratified, for example), which are so important in the ocean and atmosphere?

AUTHOR'S REPLY

Some preliminary but, nonetheless, significant contributions to the second-order closure modeling of stratified and buoyancy driven turbulent flows were made during the 1970s by Zeman, Lumley and others. However, progress has been slow since that time. In my opinion, serious questions can be raised about the appropriateness of using gradient transport models for the turbulent diffusion terms (these are used in virtually every existing second-order closure). Fundamentally, new representations for these terms are needed for the better description of the diffusion dominated turbulent flows that occur in the ocean and in the atmosphere—a difficult task that requires much more attention in the future.

Numerical Simulation of the Drift Motion of a Ship

E. Campana, P. Esposito, R. Penna (Istituto Nazionale per Studi ed Esperienze di Architettura Navale, Italy)

ABSTRACT

The computation of the steady free surface flow past a ship hull advancing with a drift angle is presented. Viscous effects are taken into account in the neighbourhood of solid walls and in the wake by the Reynolds averaged Navier–Stokes equations, whereas the assumption of irrotationality in the external flow allows a description by a potential model. Free surface boundary conditions have been implemented in a linearized form at the undisturbed waterplane. Suitable matching conditions are enforced at the interface between the viscous and the potential regions. Preliminary numerical and experimental results obtained for the Wigley hull, show the capability of the present approach to simulate the asymmetric flow structure.

NOMENCLATURE

$\mathcal{B}, \mathcal{B}'$	the wetted ship hull and its image
$\mathcal{D}$	fluid domain
$\mathcal{D}_p$	potential flow domain
$\mathcal{D}_v$	viscous flow domain
$Fr = \frac{U}{\sqrt{gL}}$	Froude number
g	acceleration of gravity
$\mathcal{H}(x, y)$	free surface elevation
J	jacobian
L	ship hull length
$\mathbf{l}$	unit vector tangent to the double model streamlines on $z = 0$
l	parameter defined along the double model streamlines on $z = 0$
$\mathbf{n}$	unit vector normal to Γ, oriented toward $\mathcal{D}_p$)
N_{NS}	number of iterations in the Navier–Stokes solver
$N = NS + NC$	number of boundary elements L_k used
NS	boundary elements arranged on $\mathcal{S}$
NC	boundary elements arranged on Γ
$P(x, y, z)$	field point
p	pressure
p_0	double model pressure
$Q \equiv (x_Q, y_Q, z_Q)$	source point
$\mathbf{q} \equiv (p, u, v, w)$	
$Re = \frac{UL}{\nu}$	Reynolds number
$\mathcal{S}$	free surface
$\mathcal{S}_p$	free surface $\in \mathcal{D}_p$
$\mathcal{S}_v$	free surface $\in \mathcal{D}_v$
$\mathbf{u} = (u, v, w)$	fluid velocity expressed in Cartesian components
$\mathbf{u}_0$	double model fluid velocity
U	free stream velocity
$\mathbf{V}_k$, $\mathbf{V}'_k$	influence matrices
$\mathcal{V}_n$	boundary condition for φ on Γ
$\tilde{\mathcal{V}}_n$	boundary condition for $\tilde{\varphi}$ on Γ
x, y, z	Cartesian coordinates in the body–fixed frame of reference
α	drift angle

β	pseudo–compressibility coefficient
Γ	interface between $\mathcal{D}_p$ and $\mathcal{D}_v$
Γ^*	secondary interface (overlapping)
ε_e	fourth order artificial dissipation coefficient
ε_i	second order artificial dissipation coefficient
ν	kinematic viscosity of water
ν_T	eddy viscosity coefficient
$\Phi = \varphi + \tilde{\varphi}$	velocity potential (defined in $\mathcal{D}_p$)
φ	potential of double model
$\tilde{\varphi}$	perturbation potential
σ	simple layer density for φ
$\tilde{\sigma}$	simple layer density for $\tilde{\varphi}$
$\underline{\underline{\tau}}$	stress tensor

INTRODUCTION

The prediction of the manoeuvrability of a ship requires information about the hydrodynamic forces and moments acting on the hull. These can be obtained experimentally with devices like Planar Motion Mechanism (PMM), steady state oblique tow tests or steady state rotating arm tests. From a numerical point of view it is possible to obtain the yaw coefficient by extrapolation of the lateral force for several small drift angles.

Some attempts of computing lateral forces have been made using both viscous and inviscid flow models ([1] - [5]).

In the inviscid ones, the ship may be treated as a thick wing of small aspect ratio, with sources distributed on the hull surface and a vortex distribution on the ship center plane [1], or with sorces and doublets distributed on the body and the wake surfaces [2], [3]. The wake surface is assumed to be parallel to the uniform flow and its position is fixed, being placed at the stern edge and at the keel line. These models gives satisfactory results once the separation line is known, as for the Wigley model. Unfortunately, this can be easily done only when the geometry is such to force the separation (i.e. sharp edges). Furthermore, to define the separation line in the case of 3D ship flows may not be an easy task. However, whether an approximate choice of the location of the separation line deeply influence the values of the hydrodynamical lateral force and the yaw moment is still to be investigated.

On the other hand, a fully viscous computation close to the hull allows a good prediction of generation and transport of vorticity in the boundary layer and in the wake. Thus an *a priori* estimation of the separation line is not required, nor a vortex sheet is needed to mimic the wake. Up to now, viscous appoaches in the computation of the flow around yawed ships, completely neglected the free surface effects [4], [5] (furthermore in [4] only the stern of the ship double model is considered). The difficoulty in considering these effects lies in the asymmetry of the flow, which implies that both port and starboard sides have to be discretized. If the complicate behaviour of the wave pattern has to be catched, this in turn implies an extremely large amount of grid points and, as a consequence, of CPU time.

To overcome these problems a viscous-inviscid formulation has been used here. Viscous effects have been considered only near the solid walls and in the wake, while the external flow field may be assumed to be inviscid.

The present method assumes a fixed decomposition of the fluid domain, with a matching surface, on which appropriate conditions are imposed, located *a priori*. A panel method is used for the solution of the potential free surface flow, whereas the Reynolds averaged Navier–Stokes (RANS) equations are discretized by a Finite Volume technique. The linearized model of Dawson [8] has been used in the external flow, where the double model flow is chosen as basis flow for the linearization of the free surface boundary conditions. In the internal region these conditions are linearized in the sense that they are imposed on the undisturbed water plane, while the nonlinear relation between pressure and velocity is retained. The choice of a linear potential model is dictated by the need of CPU time saving.

The matching conditions to be used with linearized free surface flows deserve a particular attention. In fact, the splitting of the external flow in a double model flow plus a perturbation term must be taken into account when forcing the matching conditions: the double model potential have to match the viscous double model flow, while the perturbation potential must be related to the difference between the free surface and the double model viscous flow. Therefore, a double model iterative computation is initially required to define the basis flow, then the free surface flow can be computed for each Froude number.

The present work can be seen as a sequel of [16, 17, 18], where the authors started the analysis of domain decomposition techniques for free surface flows. In

the previous work the global domain was divided into two non–overlapping zones; we have now analysed a domain decomposition with overlapping that seems to show better convergence properties in the iterative algorithm and a more regular transition of the solution from the inner to the outer domain at the matching boundaries.

MATHEMATICAL MODEL

In the following, we consider the steady flow past a ship hull $\mathcal{B}$ floating in an incompressible viscous fluid. The flow domain is bounded by the free surface $\mathcal{S}$, by the hull surface and extends to infinity. We assume a body-fixed reference frame with the x-axis aligned with the uniform flow and the z-axis positive upwards (fig. 1).

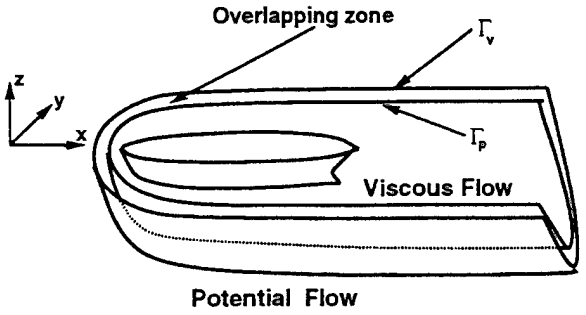


Figure 1: Computational sub–domains and overlapping zone

The fluid is assumed inviscid and the flow irrotational in the subdomain $\mathcal{D}_p$ of the flow domain $\mathcal{D}$ that lies outside the surface Γ_p , whereas viscosity effects are taken into account in the inner region $\mathcal{D}_v$ bounded by Γ_v and the hull surface (see fig. 1). The two subdomains intersect over the region between Γ_p and Γ_v.

The variables have been nondimensionalized by the ship length L and the free stream velocity U. Two parameters characterise the flow: the Froude number $Fr = U/(gL)^{\frac{1}{2}}$ and the Reynolds number $Re = UL\rho/\mu$, where ρ is the fluid density, g the acceleration of gravity and μ the dynamic viscosity.

The Outer Region

The fluid velocity $\mathbf{u} = (u, v, w)$ can be written as the gradient of a scalar function Φ:

$$\mathbf{u}(x, y, z) = \nabla\Phi(x, y, z) \qquad (1)$$

The potential Φ is harmonic in $\mathcal{D}_p$. The boundary condition to be enforced are:

- Neumann boundary conditions on Γ_p, i.e.

$$\frac{\partial\Phi}{\partial n} = \mathcal{W}_n \quad on\ \Gamma_p \qquad (2)$$

where $\mathcal{W}_n$ is the matching condition to be specified later on.

- At the free surface $\mathcal{S} : z = \mathcal{H}(x, y)$ the pressure must be equal to the atmospheric pressure and therefore constant. From the Bernoulli theorem we have the dynamic condition:

$$\mathcal{H}(x, y) = \frac{Fr^2}{2}\{1 - |\nabla\Phi[x, y, \mathcal{H}(x, y)]|^2\}$$

where surface tension has been neglected. The tangency of the flow to the unknown free surface gives the kinematic boundary condition

$$\frac{\partial\mathcal{H}}{\partial x}\frac{\partial\Phi}{\partial x} + \frac{\partial\mathcal{H}}{\partial y}\frac{\partial\Phi}{\partial y} = \frac{\partial\Phi}{\partial z}$$

For computational purposes, the potential Φ is split into the double model term φ and the perturbation term $\tilde{\varphi}$:

$$\Phi(x, y, z) = \varphi(x, y, z) + \tilde{\varphi}(x, y, z) \qquad (3)$$

The double model potential φ is used as basis flow for the linearization. It describes the flow past the body $\mathcal{B}$ and its image $\mathcal{B}'$, symmetric with respect to the (x, y)–plane (i.e. $\varphi_z(x, y, 0) \equiv 0$). The double model potential satisfies the matching condition

$$\frac{\partial\varphi}{\partial n} = \mathcal{V}_n \quad on\ \Gamma_p \qquad (4)$$

The perturbation term describes the departure of the flow from the double model solution. It satisfies

$$\frac{\partial\tilde{\varphi}}{\partial n} = \tilde{\mathcal{V}}_n \quad on\ \Gamma_p \qquad (5)$$

where $\tilde{\mathcal{V}}_n$ is such that

$$\frac{\partial\varphi}{\partial n} + \frac{\partial\tilde{\varphi}}{\partial n} = \frac{\partial\Phi}{\partial n} = \mathcal{V}_n + \tilde{\mathcal{V}}_n = \mathcal{W}_n \quad on\ \Gamma_p \qquad (6)$$

$\mathcal{V}_n$ will be specified with $\mathcal{W}_n$ in the "MATCHING CONDITIONS" section. Then, the free surface boundary conditions are linearized following Dawson [8]: the squares of the derivatives of $\tilde{\varphi}$ are neglected and the kinematic and dynamic boundary conditions are merged to yield the unified boundary condition

$$\varphi_l^2\tilde{\varphi}_{ll} + 2\varphi_l\varphi_{ll}\tilde{\varphi}_l + \frac{1}{Fr^2}\tilde{\varphi}_z = -\varphi_l^2\varphi_{ll} \qquad (7)$$

where all terms in φ are known from the double model solution, and l is the curvilinear abscissa defined along the double model streamlines on $z = 0$.

Finally, the asymptotic behavior of the wave potential $\tilde{\varphi}(x, y, z)$ at infinity must be specified. Waves should never propagate upstream; this gives the radiation condition:

$$\lim_{x \to -\infty} |\nabla \tilde{\varphi}(x, y, z)| = 0 \qquad (8)$$

for every fixed (y, z) in $\mathcal{D}_p$.

The Inner Region

The RANS equations describe the flow in the inner region $\mathcal{D}_v$. The velocity field is divergence free

$$\nabla \cdot \mathbf{u} = 0 \qquad \text{in } \mathcal{D}_v$$

and the momentum equation has to be satisfied

$$\mathbf{u} \cdot \nabla \mathbf{u} + \nabla P = \nabla \cdot \underline{\underline{\tau}} \qquad \text{in } \mathcal{D}_v$$

In the previous equation P is the 'total' pressure, i.e. the sum of the pressure term and the gravity term

$$\nabla P = \frac{\nabla p}{\rho} + \frac{\mathbf{k}}{Fr^2} = \nabla \left[\frac{p}{\rho} + \frac{z}{Fr^2} \right]$$

$\mathbf{k}$ being the unit vector aligned with the z-axis. $\underline{\underline{\tau}}$ is the stress tensor, including the turbulent stresses

$$\underline{\underline{\tau}} = \left(\frac{1}{Re} + \nu_T\right) \left[(\nabla \mathbf{u}) + (\nabla \mathbf{u})^T \right]$$

ν_T being the kinematic eddy viscosity. In the present work the Baldwin–Lomax turbulence model [11] has been used.

Apart from the surface Γ_v at which the potential and the viscous solutions are matched (this topic will be discussed later on), the boundary conditions to be imposed are the standard ones for Navier–Stokes computations. At the solid wall no slip conditions are enforced, i.e. velocity is set to zero at the boundary (no conditions are required for the pressure). On the free surface, the boundary conditions to be satisfied are the following:

- the kinematic boundary condition

$$u \frac{\partial \mathcal{H}}{\partial x} + v \frac{\partial \mathcal{H}}{\partial y} = w \qquad (9)$$

- the dynamic boundary condition (constant pressure on $\mathcal{S}_v$)

$$P = \frac{\mathcal{H}}{Fr^2} \qquad (10)$$

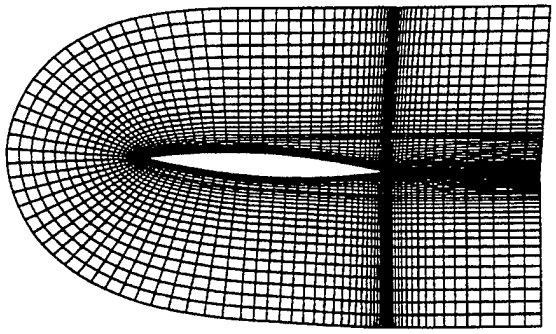


Figure 2: Viscous and inviscid free surface grids: $\alpha = 4°$

- zero tangential stresses

$$\tau_{xz} = 0 \qquad \tau_{yz} = 0 \qquad (11)$$

NUMERICAL MODEL

Since the study is extended to ships advancing in rectilinear motion with a drift angle, in the numerical solution of the mathematical model depicted before we cannot exploit the symmetry of the problem about the (x, z)-plane and therefore port and starboard sides are discretized. The topology of the computational grid is of C-type in the (ξ, η)-plane, as shown in fig. 2. C-periodicity conditions in the wake are imposed for the viscous flow.

Potential Solver

The solution of the mathematical model described in sec. 3.1 can be obtained by a panel method. The double model term φ can be represented by a simple layer potential distributed on Γ_p

$$\varphi(P) = \int_\Gamma \sigma(Q) \left[\frac{1}{|P - Q|} + \frac{1}{|P - Q'|} \right] dS_Q \qquad (12)$$

where $P = (x, y, z) \in \mathcal{D}_p$, $Q = (x_Q, y_Q, z_Q) \in \Gamma_p$, $Q' = (x_Q, y_Q, -z_Q)$.

If (12) is introduced in (4) we obtain the integral equation to be solved numerically. To this end, the boundary Γ_p of $\mathcal{D}_p$ is discretized into N_Γ plane quadrilateral elements L_k, , $k = 1, \ldots, N_\Gamma$ and the simple layer intensity $\sigma(Q)$ is assumed piecewise constant. The discrete form of the integral equation (4) for $\sigma(Q)$ reads

$$\sum_{\substack{k=N_S+1\\k\neq i}}^{N}\sigma_k\left\{\frac{\partial}{\partial n_P}\int_{L_k}\left[\mid P-Q\mid^{-1}+\mid P-Q'\mid^{-1}\right]dS_Q\right\}_{P=P_i}-2\pi\sigma_i=\mathcal{V}_n(P_i) \tag{13}$$

for $i = N_S+1, \ldots, N$. Equation (13) can be rewritten in the following form:

$$\sum_{\substack{k=N_S+1\\k\neq i}}^{N}\sigma_k[\mathbf{n}(P_i)\cdot(\mathbf{V}_k(P_i)+\mathbf{V'}_k(P_i))]-2\pi\sigma_i=\mathcal{V}_n(P_i) \tag{14}$$

where $\mathbf{V}_k \equiv (V_{k_x}, V_{k_y}, V_{k_z})$ and $\mathbf{V'}_k \equiv (V'_{k_x}, V'_{k_y}, V'_{k_z})$ are

$$\begin{aligned}\mathbf{V}_k(P) &= \int_{L_k}\frac{P-Q}{\mid P-Q\mid^3}dS_Q \\ \mathbf{V}'_k(P) &= \int_{L_k}\frac{P-Q^*}{\mid P-Q'\mid^3}dS_Q\end{aligned} \tag{15}$$

The resulting system of N_Γ linear equations in the N_Γ unknowns σ_k is solved with the LU factorization.

Similarly, the perturbation term $\tilde{\varphi}$ can be represented by a simple layer potential on Γ_p and the part $\mathcal{S}_p$ of the free surface included in the boundary of $\mathcal{D}_p$:

$$\tilde{\varphi}(P)=\int_{\Gamma_p\cup\mathcal{S}_p}\tilde{\sigma}(Q)\frac{1}{|P-Q|}dS_Q \tag{16}$$

where $Q = (x_Q, y_Q, z_Q) \in \Gamma_p \cup \mathcal{S}_p$. As for the double model problem, (16) is introduced in (5) and (7) to obtain the integral equations to be solved numerically. We discretize $\Gamma_p \cup \mathcal{S}_p$ into $N = N_S + N_\Gamma$ plane quadrilateral elements $L_k, k = 1, \ldots, N$. N_Γ denotes the number of panels located on Γ_p and N_S the number of those located on the average free surface $\mathcal{S}_p$. The discrete forms of equation (5) is

$$\sum_{\substack{k=1\\k\neq i}}^{N}\tilde{\sigma}_k[\mathbf{n}(P_i)\cdot\mathbf{V}_k(P_i)]-2\pi\tilde{\sigma}_i=\tilde{\mathcal{V}}_i(P_i)\quad(i=N_S+1,\ldots,N) \tag{17}$$

while, for equation (7)

$$\begin{aligned}&[\varphi_l(P_i)]^2\sum_{\substack{k=1\\k\neq i}}^{N}\tilde{\sigma}_k\mathbf{l}(P_i)\cdot\nabla[\mathbf{l}(P_i)\cdot\mathbf{V}_k(P_i)]+ \\ &2\varphi_l(P_i)\varphi_{ll}(P_i)]\sum_{\substack{k=1\\k\neq i}}^{N}\tilde{\sigma}_k\mathbf{l}(P_i)\cdot\mathbf{V}_k(P_i) \\ &+\frac{1}{Fr^2}[\sum_{\substack{k=1\\k\neq i}}^{N}\tilde{\sigma}_kV_{zk}(P_i)-2\pi\tilde{\sigma}_i]= \\ &-[\varphi_l(P_i)]^2\varphi_{ll}(P_i)\quad(i=1,\ldots,N_S)\end{aligned} \tag{18}$$

where $\mathbf{l}(P_i)$ is the unit vector tangent to the double model streamlines on $z = 0$, and

$$\varphi_l(P_i)=\left[\varphi_x^2(P_i)+\varphi_y^2(P_i)\right]^{\frac{1}{2}}$$

The derivatives of $\mathbf{V}_k(P)$ are approximated with second order upwind finite differences along the coordinate lines. The upwind bias on each coordinate direction is determined by the corresponding double model velocity component. The radiation condition (8) is enforced in the following discrete form:

$$\sum_{\substack{k=1\\k\neq j}}^{N_j}\tilde{\sigma}_kV_{zk}(P_j)-2\pi\tilde{\sigma}_j=0 \tag{19}$$

where $j = 1, \ldots, N_j$ is the index set corresponding to all panels whose control points $P_j \equiv (x_j, y_j, 0)$ are such that $x_j < x_r$, where $x = x_r$ is a plane that lies halfway the beginning of the potential domain and the bow of the ship. These equations replace the N_j equations (18) corresponding to the control points P_j.

The linear system (17),(18),(19) of N equations in the N unknows $\tilde{\varphi}_k$ is solved, as in the double model problem, by LU factorization.

The reader is referred to [9] for a rigorous and extensive discussion of the topics illustrated in this section.

Navier–Stokes Solver

A well established implicit scheme developed in [12] has been used for the numerical solution of the problem described in sec. 3.2.

A pseudo–transient formulation due to Chorin [10] is used to solve the steady state incompressible RANS equations. In this scheme the continuity equation is replaced by a transient counterpart

$$\frac{\partial p}{\partial t}+\beta\,\nabla\cdot\mathbf{u}=0 \tag{20}$$

where β is the pseudo–compressibility factor. The resulting system of conservation laws is

$$\frac{\partial\mathbf{q}}{\partial t}+\frac{\partial\mathbf{F}^1}{\partial x}+\frac{\partial\mathbf{F}^2}{\partial y}+\frac{\partial\mathbf{F}^3}{\partial z}=\frac{\partial\mathbf{q}}{\partial t}+\frac{\partial\mathbf{F}^i}{\partial x_i}=0 \tag{21}$$

where

$$\mathbf{q} = \begin{pmatrix} p \\ u \\ v \\ w \end{pmatrix} \qquad \mathbf{F}^1 = \begin{pmatrix} \beta u \\ u^2 + p - \tau_{xx} \\ uv - \tau_{yx} \\ uw - \tau_{zx} \end{pmatrix}$$

$$\mathbf{F}^2 = \begin{pmatrix} \beta v \\ vu - \tau_{xy} \\ v^2 + p - \tau_{yy} \\ vw - \tau_{zy} \end{pmatrix} \qquad \mathbf{F}^3 = \begin{pmatrix} \beta w \\ wu - \tau_{xz} \\ wv - \tau_{yz} \\ w^2 + p - \tau_{zz} \end{pmatrix}$$

If $(\xi, \eta, \zeta) \equiv (\xi_1, \xi_2, \xi_3)$ is a curvilinear coordinate system, and we set $(x, y, z) \equiv (x_1, x_2, x_3)$, equation (21) can be recast in the form

$$\frac{\partial \mathbf{q}}{\partial t} + \frac{1}{J}\frac{\partial}{\partial \xi_k}\left[J\xi_{k,i}\mathbf{F}^i\right] = 0 \tag{22}$$

where the summation convention on repeated indices is adopted from here on for sake of conciseness, J is the Jacobian and $(\cdot)_{,i} \equiv \dfrac{\partial(\cdot)}{\partial x_i}$.

A finite volume technique is used to discretize equation (22). The inner region $\mathcal{D}_v$ is divided in hexahedra V_{ijk}. The application of the Gauss theorem in the control volume V_{ijk} yields

$$\frac{\partial \mathbf{q}_{ijk}}{\partial t} + \mathbf{R}(\mathbf{q})_{ijk} = 0 \tag{23}$$

with

$$\mathbf{R}(\mathbf{q})_{ijk} = \frac{1}{V_{ijk}} \iint_{S_{ijk}} \mathcal{F} \cdot \mathbf{n}\, dS = 0$$

where S_{ijk} is the boundary of V_{ijk}, $\mathbf{n} = (n_x, n_y, n_z)$ is the outer normal to S_{ijk} and $\mathcal{F} = (\mathbf{F}^1, \mathbf{F}^2, \mathbf{F}^3)$. In the numerical approximation the values of $\mathcal{F}$ on the faces of the cell V_{ijk} are needed for the discretization of equation (23): a simple averaging of neighbouring points is used to obtain velocity and pressure, while the stress tensor is evaluated by centered differencing.

The time marching procedure follows Beam and Warming [13]

$$\frac{\mathbf{q}^{n+1} - \mathbf{q}^n}{\Delta t} = (1-\theta)\left.\frac{\partial \mathbf{q}}{\partial t}\right|^n + \theta \left.\frac{\partial \mathbf{q}}{\partial t}\right|^{n+1} = -(1-\theta)\,\mathbf{R}(\mathbf{q}^n) - \theta\,\mathbf{R}(\mathbf{q}^{n+1}) \tag{24}$$

where $0 \le \theta \le 1$. Using a Taylor expansion, equation (24) can be written in "delta" form

$$\left[\delta\mathbf{q} + \frac{\theta\Delta t}{J}\frac{\partial}{\partial \xi_l}\left(J\xi_{l,m}\mathbf{A}^m\delta\mathbf{q} + J\xi_{l,m}\mathbf{B}^{m,r}\frac{\partial \delta\mathbf{q}}{\partial \xi_r}\right)\right]^n = -\Delta t\mathbf{R}(\mathbf{q}^n) \tag{25}$$

where $\delta\mathbf{q}^n = \mathbf{q}^{n+1} - \mathbf{q}^n$, $\mathbf{A}^m$ and $\mathbf{B}^{m,r}$ are the jacobians of $\mathbf{F}^m$:

$$\mathbf{A}^m = \frac{\partial \mathbf{F}^m}{\partial \mathbf{q}} \qquad \mathbf{B}^{m,r} = \frac{\partial \mathbf{F}^m}{\partial \mathbf{q}_{\xi_r}}$$

A direct solution of the system of algebraic equations (25) would be too expensive, thus an approximate factorization technique is used to reduce it to the solution of three simpler problems, with block tridiagonal coefficient matrix:

$$\left[\mathbf{I} + \theta\Delta t\left(\mathcal{A}^1 + \mathcal{A}^2 + \mathcal{A}^3\right)\right]\delta\mathbf{q}^n \simeq \left(\mathbf{I} + \theta\Delta t\mathcal{A}^1\right)\left(\mathbf{I} + \theta\Delta t\mathcal{A}^2\right)\left(\mathbf{I} + \theta\Delta t\mathcal{A}^3\right)\delta\mathbf{q}^n \tag{26}$$

with accuracy $O(\Delta t)$. The operator $\mathcal{A}$ introduced in the factorization is defined as

$$\mathcal{A}^l = \frac{1}{J}\frac{\partial}{\partial \xi_l}\left(J\xi_{l,m}\mathbf{A}^m + J\xi_{l,m}\mathbf{B}^{m,l}\frac{\partial}{\partial \xi_l}\right)$$

with no summation on l. It can be noticed that all the second order mixed derivative in $\delta\mathbf{q}$ were discarded in the implicit part of the system to maintain the tridiagonal structure. This approximation, however, does not affect the steady state solution.

To ensure the numerical stability of the scheme, a fourth order artificial dissipation term is added to both sides of (26). Thus the flux at the interface $\xi_1|_{i+\frac{1}{2},j,k}$ is modified according to

$$\tilde{\mathcal{F}} \cdot \mathbf{n}|_{i+\frac{1}{2},j,k} = \mathcal{F} \cdot \mathbf{n}|_{i+\frac{1}{2},j,k} + \varepsilon_e\overline{V}(\mathbf{q}_{i+2,j,k} - 3\mathbf{q}_{i+1,j,k} + 3\mathbf{q}_{i,j,k} - \mathbf{q}_{i-1,j,k}) \tag{27}$$

ε_e being a parameter $O(1)$ and $\overline{V}$ the average volume of the two neighbouring cells. A second order term is added to each tridiagonal operator in the left-hand side

$$\tilde{\mathcal{A}}^l = \frac{1}{J}\frac{\partial}{\partial \xi_l}\left(J\xi_{l,m}\mathbf{A}^m + J\xi_{l,m}\mathbf{B}^{m,l}\frac{\partial}{\partial \xi_l} - \varepsilon_i\overline{V}\frac{\partial}{\partial \xi_l}\right)$$

where ε_i is again $O(1)$.

The final form of the system of equations is, then

$$\left(\mathbf{I} + \theta\Delta t\tilde{\mathcal{A}}^1\right)\left(\mathbf{I} + \theta\Delta t\tilde{\mathcal{A}}^2\right)\left(\mathbf{I} + \theta\Delta t\tilde{\mathcal{A}}^3\right)\delta\mathbf{q}^n = -\Delta t\tilde{\mathbf{R}}(\mathbf{q}^n) \tag{28}$$

where $\tilde{\mathbf{R}}(\mathbf{q}^n)$ includes the artificial dissipation terms.

It can be shown that the steady state solution is second order accurate and that the above scheme is unconditionally stable in the linear case if $\theta \ge 0.5$

and $\varepsilon_i \geq 2\varepsilon_e$. The reader is referred to [12] and [13] for a detailed discussion.

In the implementation of the numerical code, all the metric terms in the above relations were computed in a finite volume fashion, i.e. the Jacobian J_{ijk} was set equal to the volume cell V_{ijk} and the terms like $J\xi_i$ at the cell interfaces $\xi = const.$ are computed, for instance, as

$$\begin{aligned} J\xi_x|_{i+\frac{1}{2},j,k} &= n_x \Delta S_{i+\frac{1}{2},j,k} \\ J\xi_y|_{i+\frac{1}{2},j,k} &= n_y \Delta S_{i+\frac{1}{2},j,k} \\ J\xi_z|_{i+\frac{1}{2},j,k} &= n_z \Delta S_{i+\frac{1}{2},j,k} \end{aligned} \tag{29}$$

where (n_x, n_y, n_z) is the outer normal to the interface and $\Delta S_{i+\frac{1}{2},j,k}$ is the area of the interface between $V_{i,j,k}$ and $V_{i+1,j,k}$.
A speedup in the computation can be achieved if a local time step is used

$$\Delta t_{ijk} = C J_{ijk}^{\frac{1}{3}}$$

with C a stability parameter.
The boundary conditions are enforced as follows:

solid wall At the cell interface of the hull surface **u** is set to zero. The normal gradient of the velocity, needed for the computation of the stress at the boundary, is computed with a first order one–side difference, while the pressure is simply extrapolated from the cell center adjacent to the wall.

outflow The flow is supposed to be completely developed in this region and therefore both the pressure and the velocity vector are extrapolated (null gradient) from internal values.

free surface The wave elevation $\mathcal{H}$ is updated at each iteration by means of the unsteady kinematic boundary condition

$$\frac{\partial \mathcal{H}}{\partial t} + u\frac{\partial \mathcal{H}}{\partial x} + v\frac{\partial \mathcal{H}}{\partial y} = w \tag{30}$$

which is discretized with a finite difference scheme

$$\mathcal{H}_{ij}^{n+1} = \mathcal{H}_{ij}^{n} - \Delta t \left[\left(u\xi_x + v\xi_y\right)_{ij} \frac{\partial \mathcal{H}}{\partial \xi}_{ij} + \left(u\eta_x + v\eta_y\right)_{ij} \frac{\partial \mathcal{H}}{\partial \eta}_{ij} \right] \tag{31}$$

The spatial derivatives of $\mathcal{H}$ in (31) are computed with second order upwind differences.

Once $\mathcal{H}$ is known, the total pressure at the free surface is computed from (10). The velocity components are simply extrapolated from the values at the cell center below the waterplane. Condition (11) has not been used, because the dimension of the cells near the free surface does not allow the resolution of the boundary layer at the water–air interface, which is extremely thin, being $O(Fr/Re^{\frac{1}{2}})$.

Applications of this scheme to double model ship flow calculations can be found, for instance, in [14] or in [15].

MATCHING ALGORITHM

The numerical algorithm used to couple the inner and the outer solution is the most important step of the whole procedure. The choice of the exchanged variables and the location of the matching surface may deeply affect the convergence rate or even cause the failure of the algorithm. In the previous version of the method [16], a non-overlapping domain decomposition scheme was used. The values of the tangential component of the velocity and the pressure of the potential field at the matching surface were used as boundary conditions for the Navier–Stokes solver, while the normal component of the viscous solution was used as Neumann condition in the potential flow. With this kind of approach, the convergence was reached within round-off errors but the convergence rate was not very satisfactory and some relaxation factors had to be used when matching the solutions. Furthermore, non-smooth transition from the inner to the outer domain was observed.

In the present work, the algorithm has been changed: the flow domain is divided in two subdomains that overlap in a small region, as illustrated in fig. 1 and fig. 3. These subdomains are bounded by Γ_p and Γ_v, which are the boundaries of the potential and viscous zones, respectively. The thickness of the overlapping region is equal to half the height of the outermost cells in the inner grid (fig. 3).

In the iterative coupling procedure, the solution computed in the first domain is used to feed the solution in the other domain with the boundary conditions, that is, in terms of the total potential Φ:

- from the potential solver we get the velocity vector and the pressure at the grid point B on Γ_v (see fig. 3); these values are enforced as boundary conditions on the viscous flow

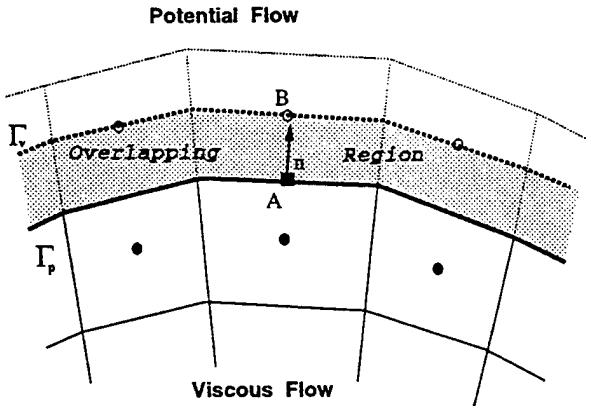


Figure 3: Location of the exchanged variables at the matching interfaces

$$\begin{aligned} \mathbf{u}|_{\Gamma_v} &= \nabla\Phi|_{\Gamma_v} \\ p|_{\Gamma_v} &= \tfrac{1}{2}(1 - \nabla\Phi\cdot\nabla\Phi)\big|_{\Gamma_v} \end{aligned} \tag{32}$$

- the normal component of the velocity at the control point A on Γ_p (see fig. 3) is computed from the viscous flow solution. This value is then used as a Neumann condition for the potential problem (see eq. 2)

$$\frac{\partial\Phi}{\partial n}|_{\Gamma_p} = \mathcal{W}_n = \mathbf{u}\cdot\mathbf{n}|_{\Gamma_p} \tag{33}$$

This new scheme improves the convergence rate, makes the relaxation factors useless and ensures a smooth transition across the matching surface.

A further comment regarding matching conditions is worth making. In fact, if condition (33) cannot give rise to any doubt (it is just a Neumann condition for the Laplace equation), the same cannot be said for (32). This condition is redundant for the incompressible Navier–Stokes equations, because only the velocity vector and not the pressure, or alternatively only the pressure and the tangential components of velocity, should be assigned on the boundary. On the other hand, the matching surface is placed where both viscous dissipation and vorticity are supposed to be negligible. Therefore, the value of the pressure on the outermost cell centres (that lie on Γ_p) is computed from the Bernoulli theorem.

As to the numerical implementation of matching conditions, we remind that for computational reason the potential flow field is expressed as the sum of a double model potential φ and a perturbation potential $\bar{\varphi}$. The multidomain solution has to be consistent with this decomposition, and therefore the solution must be obtained in two steps:

1. *Double Model Flow:* The solution is computed with the conditions

$$\begin{cases} w_0 = 0 \\ \dfrac{\partial u_0}{\partial z} = 0 \text{ on } \mathcal{S}_v \quad \text{and} \quad \dfrac{\partial\varphi}{\partial z} = 0 \text{ on } \mathcal{S}_p \\ \dfrac{\partial v_0}{\partial z} = 0 \end{cases} \tag{34}$$

on the waterplane $z = 0$, while the matching conditions on Γ_p and Γ_v are

$$\mathbf{u}_0\big|_{\Gamma_v} = \nabla\varphi\big|_{\Gamma_v} \tag{35}$$

$$p_0\Big|_{\Gamma_v} = \frac{1}{2}(1 - \nabla\varphi\cdot\nabla\varphi)\Big|_{\Gamma_v} \tag{36}$$

$$\frac{\partial\varphi}{\partial n}\Big|_{\Gamma_p} = \mathcal{V}_n = \mathbf{u}_0\cdot\mathbf{n}\Big|_{\Gamma_p} \tag{37}$$

where $\mathbf{u}_0$ and p_0 are the velocity vector and the pressure in the inner double model solution.

2. *Free Surface Flow:* Once the double model solution is obtained with the desired accuracy, the free surface flow can be computed. The matching conditions to be enforced are slightly more complex than in the previous step. In fact, the potential $\bar{\varphi}$ is a perturbation with respect to the double model flow and therefore it must be related to the difference between the free surface velocity field and the double model velocity field in the viscous domain. At the same time, the viscous solution, which is not split, must be related to the total potential. This yields the following matching conditions:

$$\mathbf{u}\Big|_{\Gamma_v} = \bar{\mathcal{V}}_n = \nabla(\varphi + \bar{\varphi})\Big|_{\Gamma_v} \tag{38}$$

$$p\Big|_{\Gamma_v} = \frac{1}{2}\left(1 - \nabla(\varphi+\bar{\varphi})\cdot\nabla(\varphi+\bar{\varphi})\right)\Big|_{\Gamma_v} \tag{39}$$

$$\frac{\partial\bar{\varphi}}{\partial n}\Big|_{\Gamma_p} = \mathbf{u}\cdot\mathbf{n}\Big|_{\Gamma_p} - \mathbf{u}_0\cdot\mathbf{n}\Big|_{\Gamma_p} \tag{40}$$

It is easy to verify that if (37) and (40) are summed, the global matching condition (33) is satisfied.

The standard application of a multidomain decomposition technique would require the iterative coupling of the converged flow fields, each computed for assigned boundary conditions on the matching surfaces, as done in [19].

The solution of the potential field for both the double model and the free surface problem is not very expensive to be computed, in that the problems are linear and therefore the coefficient matrix of the resulting system of equations can be computed and stored in factorized form at the beginning of the computation. In fact, the coupling procedure affects only the RHS of the system of equations in the unknown σ or $\tilde{\sigma}$, and therefore the solution can be calculated by back–substitution at each global step. We remark that in the potential free surface problem the coefficient matrix depends only on the double model solution that has already been computed at the previous stage, and therefore does not change while iterating, because the two problems have been solved separately, unlike that in [19].

On the contrary, the steady solution of the Navier–Stokes equations is extremely time consuming, because we have to deal with a system of coupled nonlinear equations, that must be solved iteratively. However, the convergence of the viscous solver to the steady state solution seems not to be required. In all the test cases we have performed, the Navier–Stokes solver was iterated for a fixed number N_{NS} of steps (typically $1 \leq N_{NS} \leq 100$) and the global algorithm never failed to converge. However, the number of sub–iterations affects the global convergence rate. Some properties of the algorithm have been investigated in [20]: in particular the dependence of the numerical solution on the grid size, on the position on the surface Γ_p (and consequently on the size of the viscous subdomain) and on the artificial viscosity parameter ε_e.

NUMERICAL RESULTS

With this approach, numerical results for the case of a ship advancing in a straight course, have been presented in [18],[20]. The major modifications we have introduced are associated with the boundary condition at the wake and with the size of the computational domain. With these changes the numerical simulation can predict the asymmetric structure of the flow observed experimentally. As a first application of the present method, the simulation of a Wigley hull advancing in a oblique course for a drift angle $\alpha = 4°$ at $Fr = 0.220$ and $Re = 4.5 \times 10^6$ has been carried

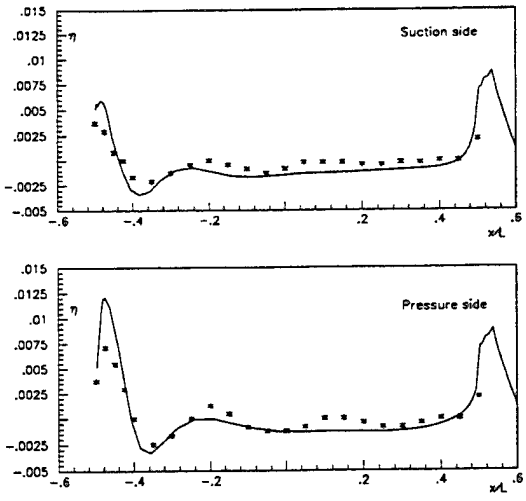


Figure 4: Wave profile near the hull; $Fr = 0.220$, $Re = 4.5 \times 10^6$, $\alpha = 4°$: suction (top) and pressure (bottom) sides. (———) numerical results, (* * *) experimental data [21].

out. For this computation we used $120 \times 15 \times 22$ cells in the inner viscous domain (streamwise, normal, and girthwise directions respectively), 120×17 panels on the free surface, and 120×22 panels on Γ_p.

The wave profile along the hull for the pressure and the suction sides is shown in fig. 4 in comparison with some experimental data obtained at INSEAN [21] (figs. 7.a, 7.c). Figs.7.b, 7.d show a 3D view of the hull and the computed free surface. The wave profile at the bow is dramatically modified with respect to the case $\alpha = 0$, since the different pressure values in that area, between port and starboard side, imply respectively an increase and a lowering of the wave height. The numerical results were able to catch the main features of the flow: the position of the first maxima of the wave profile and the shift of the first trough between the pressure and the suction side are well predicted. Another effect of the angle of incidence of the ship is the thickening of the boundary layer on the suction side (especially near the stern) and its thinning on the pressure side. This behaviour is well reproduced by the numerical result reported in fig. 5 where the contour map of the u component shows the asymmetry of the boundary layer and the wake. Finally, contour maps of the u component of the velocity (fig. 6) and of the crossflow velocity (fig. 8) at some transversal sections indicate the distorted wake pattern of the Wigley hull.

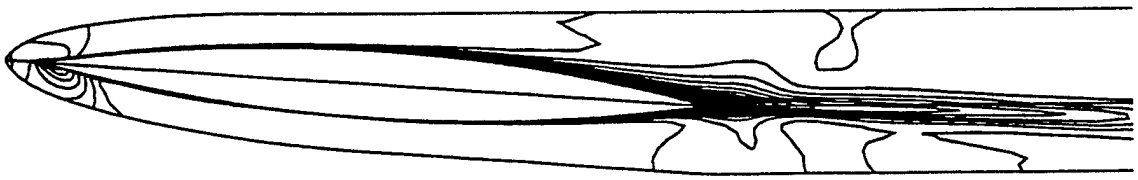


Figure 5: Contour map of u component of velocity on the $z = 0$ plane show the boundary layer and the wake in the inner viscous domain ($\alpha = 4°$)

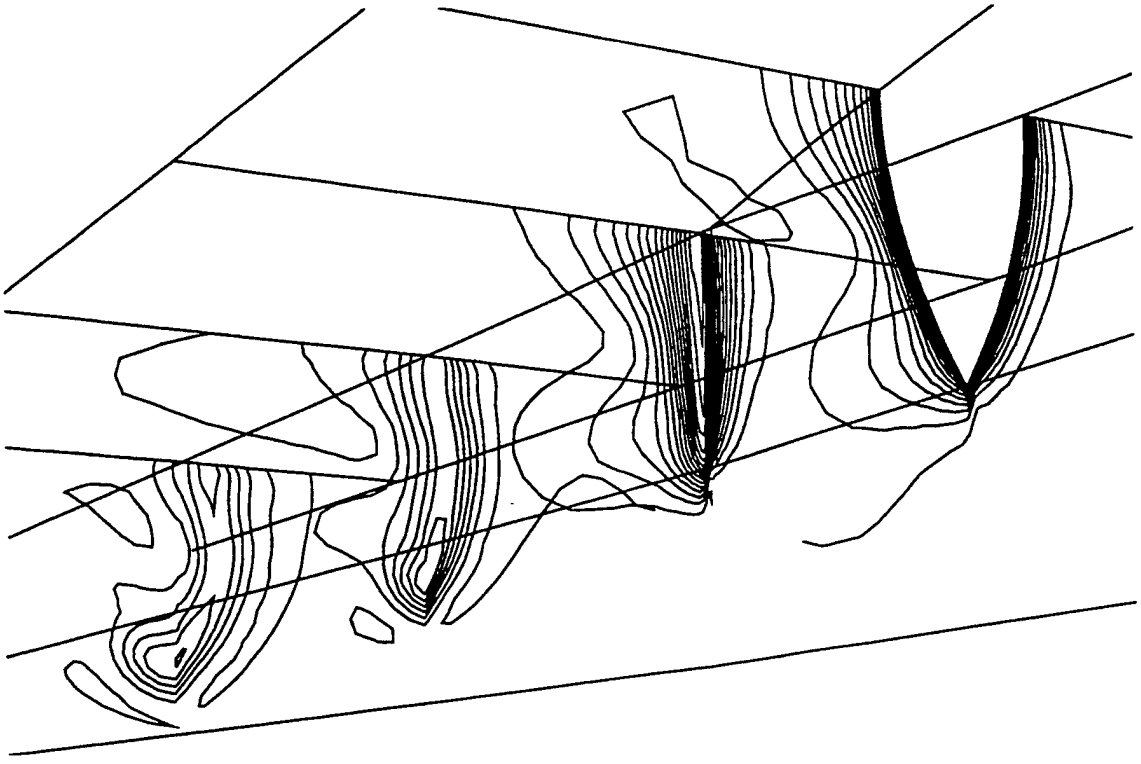


Figure 6: Contour map of u component of velocity in some transversal sections ($\alpha = 4°$)

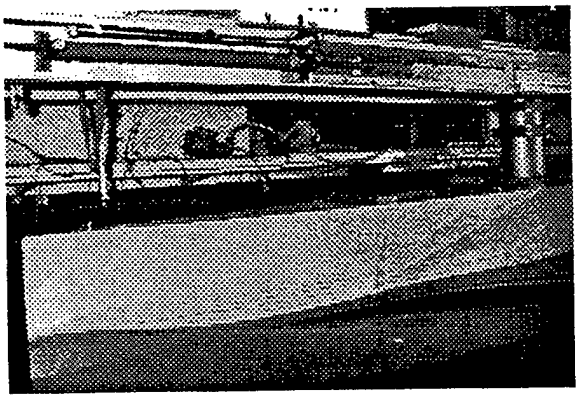


Figure 7.a: Wave profile near the hull: suction side [21].

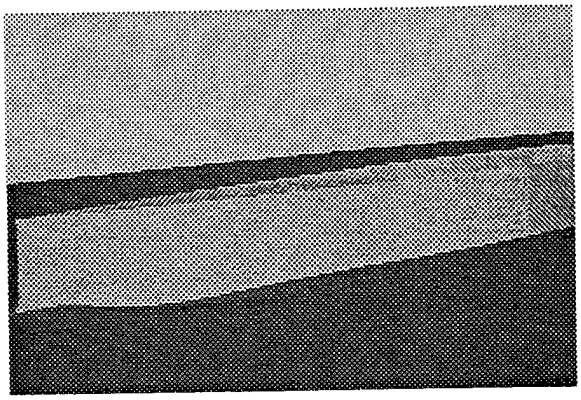


Figure 7.b: A perspective view of the suction side of the computed free surface flow past the Wigley hull.

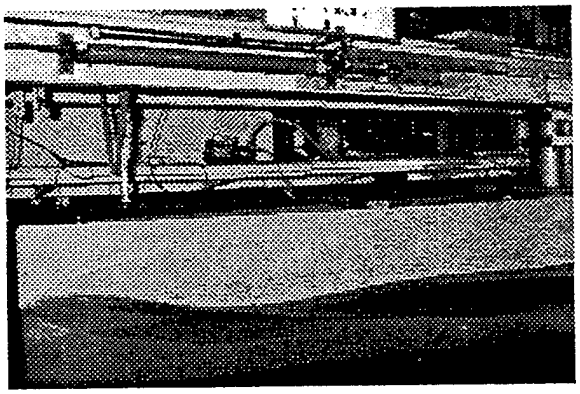


Figure 7.c: Wave profile near the hull: pressure side [21].

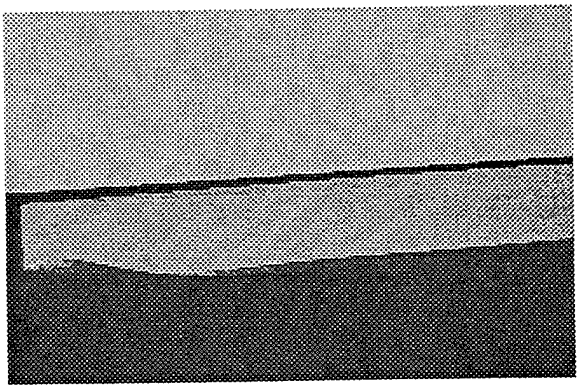
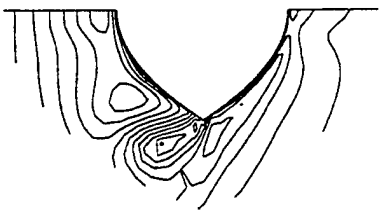
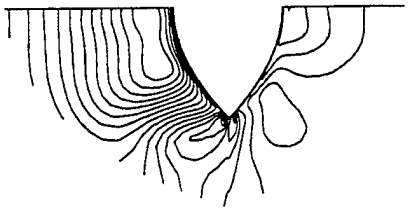


Figure 7.d: A perspective view of the pressure side of the computed free surface flow past the Wigley hull.

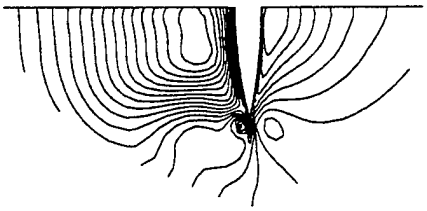
Figure 7: Experimental [21] and numerical wave pattern



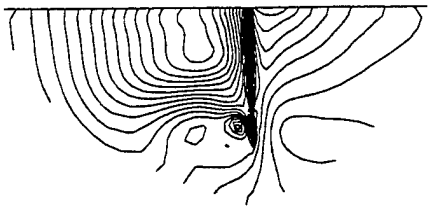
x = 0.593



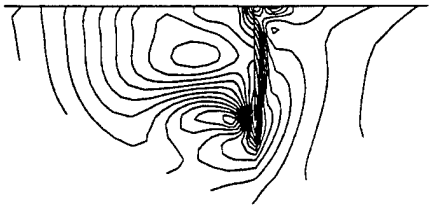
x = 0.811



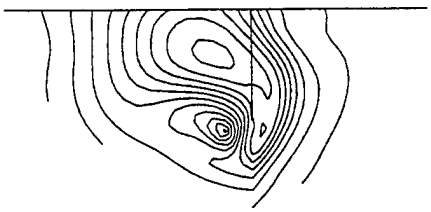
x = 0.962



x = 1.000



x = 1.053



x = 1.369

Figure 8: Crossflow velocity contour maps at different transversal sections (stations are given in the ship reference frame).

CONCLUDING REMARKS

The steady motion of ship advamcing with an angle of drift is solved numerical by a viscous–inviscid approach. The method take into account the free surface effects and may be considered as a first step in the simulation of this complex ship flow. The resolution of the numerical results can be further improved, but the method was capable in predicting some important feature of this flow.

ACKNOWLEDGEMENTS

The work was supported by the Italian Ministry of Merchant Marine in the frame of INSEAN research plan 1988-90.

REFERENCES

[1] K. Nakatake, A. Komura, J. Ando, K. Kataoka,"On the Flow Field and the Hydrodynamic Forces of an Obliquing Ship", Trans. of the West-Japan Soc. N. A., Vol.80, 1990, pp 1-12, (in japanese)

[2] Y. Tahara, "A Boundary Element Method for Calculating Free Surface Flows around a Yawed Ship", J. Kansai Soc.N.A., Vol. 218, 1992, pp.55-67

[3] Z.J. Zou, " A 3D Panel Method for Free Surface Flows around Ships of Small Angles of Yaw", 8th Inter. Workshop on Water Waves and Floating Bodies, St. John's, Newfoundland (Canada), May 1993

[4] V.C. Patel, S. Ju, J.M. Lew, "Viscous Flow Past a Ship in a Cross Current", Proc. 18th ONR Symposium on Naval Hydrodynamics, Ann Arbor, Michigan (USA), 1990.

[5] T. Ohmori, H. Miyata, "Oblique Tow Simulation by a Finite-Volume Method", J. Soc. Naval Arch. Japan, Vol. 173, 1993, pp.27-34

[6] M. Ikehata, Y. Tahara,"Influence of Boundary Layer and Wake on Free Surface Flow around a Ship Model", Nav. Arch. and Ocean Eng., Vol.26, p.71 (1988).

[7] Tahara, Y., Stern, F., "An Interactive Approach for Calculating Ship Boundary Layer and Wakes for Nonzero Froude Number", Proc. 18th ONR Symposium on Naval Hydrodynamics, Ann Arbor, Michigan, 1990.

[8] Dawson, C.W.,"A Practical Computer Method for Solving Ship-Wave Problems", 2nd Int. Conf. on Numerical Ship Hydro., Berkeley, 1977.

[9] Bassanini, P., Bulgarelli, U., Campana, E., Lalli, F., "The Wave Resistance Problem in a Boundary Integral Formulation", to be published on Surv. Math. Ind..

[10] A.J. Chorin, "A Numerical Method for Solving Incompressible Viscous Flow Problems", J. Comput. Phys., Vol.2, pp.12-26 (1967)

[11] Baldwin, B.S., Lomax, H. "Thin Layer Approximation and Algebraic Model for Separated Turbulent Flows", AIAA Paper 78-257, (1978)

[12] Kwak,D., Chang, J.L.C., Shanks, S.P., Chakravarthy, S.R., "A Three-Dimensional Incompressible Navier–Stokes Flow Solver Using Primitive Variables", AIAA J., Vol.24, pp.390-396 (1986)

[13] R.M. Beam, R.F. Warming, "An Approximate Factorization Scheme for the Compressible Navier–Stokes Equations", AIAA J., Vol.16, pp.393-402 (1978)

[14] Di Mascio, A., Esposito, P.G., "Numerical Simulation of Viscous Flows past Hull Forms", The Second Osaka Inter. Coll. on Viscous Fluid Dyn. in Ship and Ocean Tech., Sept. 27-30, 1991

[15] Kodama, Y., "Grid Generation and Flow Computation for Practical Ship Hull Forms and Propelleres Using the Geometrical Method and the IAF Scheme", Fifth International Conference on Numerical Ship Hydrodinamics, pp. 71-85, Hiroshima 1989

[16] Campana, E., Di Mascio, A., Esposito, P.G., Lalli, F., "Viscous–Inviscid Coupling in Ship Hydrodynamics", XI Australasian Fluid Mech. Conf., Hobart (Australia), 1992.

[17] Campana, E., Di Mascio, A., Esposito, P.G., Lalli, F., "A Multidomain Approach to Free Surface Viscous Flows", in Workshop on Water Waves and Floating Bodies, St John's, Newfoundland, Canada, (1993).

[18] Campana, E., Di Mascio, A., Esposito, P.G., Lalli, F., "Domain Decomposition in Free Surface Viscous Flows",in Proc. of the Sixth Int. Conf. on Numerical Ship Hydrodynamics, Iowa City, (1993).

[19] Chen, H.-C., Lin W.-M., Weems, K.M., "Interactive Zonal Approach for Ship Flows Including Viscous and Nonlinear Wave Effects" in Proc. of the Sixth Int. Conf. on Numerical Ship Hydrodynamics, Iowa City, USA (1993).

[20] Campana, E., Di Mascio, A., Esposito, P.G., Lalli, F., "Viscous–inviscid coupling in Free Surface Ship Flows", submitted to J. Comput. Phys.

[21] INSEAN Tech. Rep. N. 1/R.2224, 1994

DISCUSSION

K. Mori
Hiroshima University, Japan

In your viscous computation is the shearing stress condition on the free-surface described by (11) taken into account? If not, let me have your opinion about the neglect. This is because it is neglected in most computations.

AUTHORS' REPLY

The shear stress condition on the free surface is neglected. As it is stated in Sec. "Navier -Stokes," condition (11) has not been used in the computation because the grid has not enough resolution near the free surface. Regarding the effects of the simplified conditions on the free surface, we think that it does not affect the solution very much, since we are solving the linearized problem. Thus in this case the zero vertical gradient conditions on the velocity components, together with the dynamic condition (10), are compatible with the true boundary conditions.

Prediction of Incompressible Tip Vortex Flows

L. Eça, J. Falcão de Campos (Instituto Superior Técnico, Portugal),
M. Hoekstra (Maritime Research Institute, The Netherlands)

Abstract

A numerical method for the calculation of incompressible viscous flow at the tip of wings is applied to the calculation of the flow at the tip of a wing with elliptical planform. The predictions are compared with experimental results in the vortex formation region and in the near-wake. The numerical method is based on a finite-difference discretisation of the Reynolds-averaged Reduced Navier-Stokes equations for steady incompressible flow, supplemented with an algebraic eddy-viscosity turbulence model. The computed results show good agreement with the experimental data as far the vortex position and the general flow characteristics are concerned. However, the size of the vortex core is overestimated, which is attributed to inadequate turbulence modelling and locally insufficient grid resolution.

Nomenclature

$\vec{a}^i$	-	Contravariant base vectors.
c	-	Wing mean chord.
c_o	-	Wing root chord.
C_p	-	Pressure coefficient, $\left(C_p = \frac{p-p_\infty}{\frac{1}{2}\rho U_\infty^2}\right)$.
g^{ij}	-	Contravariant metric tensor.
$\sqrt{g}$	-	Jacobian of the coordinate transformation.
p	-	Pressure.
Re	-	Reynolds number, $\left(Re = \frac{U_\infty c}{\nu}\right)$.
U_∞	-	Free-stream velocity.
U^i	-	Cartesian velocity components.
V^i	-	Contravariant velocity components.
$\overline{V}^i$	-	Velocity dependent variables, $\left(\overline{V}^i = \sqrt{g_{ii}} V^i\right)$.
x, y, z	-	Cartesian coordinates.
ξ, η, ζ	-	Curvilinear coordinates.
μ	-	Fluid effective viscosity.
ν	-	Fluid kinematic viscosity.
ρ	-	Fluid mass density.
τ^{ij}	-	Stress tensor.

1 Introduction

The tip vortices generated by marine propellers are often associated with cavitation. Tip vortex cavitation is usually the first type of cavitation to appear and can be a major source of noise. Design optimization requires the capability of accurate prediction of a propeller's behaviour with regard to tip vortex cavitation, either by experiment or by computation.

It is well-known, however, that viscous effects play an important role in the inception of tip vortex cavitation. Scale effects influence therefore the results of experimental investigations on reduced-size propellers. The correction of experimental results for scale effects is still guided by the classical work of McCormick, [1]. More recent studies have been reported in e.g. [2], [3], [4] and [5], but a considerable uncertainty remains. Computational studies, on the other hand, are usually frustrated by the complexity of the problem. Nevertheless, the computational approach seems the most promising in improving our insight and prediction capability.

In incompressible flow, the first approaches to the calculation of tip vortex flows were reported by Govidan *et al.* in [6] and [7]. Govidan

et al. used the parabolised Reynolds-averaged Navier-Stokes equations to calculate tip vortex flows. In Govidan's approach, streamwise diffusion is neglected and the streamwise pressure gradient is obtained from inviscid flow calculations. The present approach, [8], also neglects streamwise diffusion, because tip vortex flows have a predominant flow direction, but the streamwise pressure gradient is obtained in the solution. This means that only a partial parabolisation is accomplished because the elliptic character of the equations is retained in the pressure field. This approach was proposed by Rubin, [9], for flows with a predominant flow direction. As shown by Rubin in [10], these equations contain all the important terms of the Navier-Stokes equations for high Reynolds number flows. Rubin's analysis also shows that the diffusion terms in the normal, η, momentum may also be neglected. In [11], Rubin *et al.* refer to these equations as the Reduced Navier-Stokes equations.

The present method was developed from the ship stern flows calculation method of Hoekstra and Raven, [12], [13], [14] and [15]. A zonal approach is adopted by decomposing the flow domain into an outer inviscid region and a viscous region. The outer inviscid flow is computed with a conventional source-based potential flow panel code. The viscous flow close to the tip is computed by a finite-difference approximation of the Reynolds-averaged Reduced Navier-Stokes, RNS, equations. An eddy viscosity algebraic turbulence model based on the formulation of Cebeci and Smith, [16], completes the mathematical model. The first numerical studies with the method were made for wings of rectangular planform, [17], to investigate the numerical implementation of the boundary conditions and the sensitivity of the solution to the location of the boundaries of the computation domain.

The predictions of the flow at the tip of a rectangular wing with a squared tip were compared with experimental results in [17] and [8]. The correlation between the vortex location of the predictions and of the experimental results is excellent for three different angles of attack, [8]. Also the calculated flowfield away from the vortex center is in excellent agreement with the experimental results. However, the vortex core size is over predicted in all the calculations, with a consequent underprediction of maximum transverse velocities.

The lack of discretization in the vortex core region and the turbulence model are likely to be responsible for the overprediction of the vortex core size. The insufficient grid resolution in the vortex core region may require the use of adaptative grids and the conception of a turbulence model suitable for tip vortex flows is a complex problem. At this stage of the development we have not yet addressed these problems. Our focus is to investigate the possibility of predicting, with the present method, the formation of the tip vortex on a wing with a more representative shape of a propeller blade. Therefore, the present paper presents : The latest version of the computational method in section 2. A brief description of the experimental programme undertaken to obtain data for comparison with the predictions in section 3. The results of the application of the method to the calculation of the flow at the tip of a wing with elliptical planform and its comparison with experimental results in section 4. The conclusions of this paper are summarized in section 5.

2 Computational Method

2.1 Mathematical Formulation

The Reynolds-averaged Navier-Stokes equations can be written in several different forms. The present choice of neglecting streamwise diffusion implies that the equations should be written in a roughly flow conforming coordinate system. The strong conservation form of the equations in general boundary-fitted curvilinear coordinate systems, see for example [18], expresses conservation of momentum in the coordinate directions of a cartesian coordinate system, (x, y, z), [19]. In general, the x, y, z directions of a cartesian coordinate system are not flow conforming and so the strong conservation form of the momentum equations may not be compatible with the physical approximations assumed in the momentum equations.

The contravariant form is for our purposes a more attractive way to write these equations. This form of the equations expresses conservation of mass and momentum along the ξ, η, ζ directions of a boundary-fitted curvilinear grid, which may also be a flow conforming coordinate system. This form of the equations is not a strong conservation form, [19], and so unphysical source terms may appear in the discretized equations, [20]. To minimize the effects of these source terms, the equations are written with the cartesian velocity components, U^i, as the dependent variables, [20].

For steady incompressible flow the equations of conservation of mass and momentum along the ξ, η, ζ directions can be written as :

$$\vec{a}^i \cdot \frac{\partial \vec{U}}{\partial \xi^i} = 0, \tag{1}$$

$$\rho \left(\vec{a}^j \cdot \vec{U} \right) \left(\vec{a}^i \cdot \frac{\partial \vec{U}}{\partial \xi^j} \right) + g^{ij} \frac{\partial p}{\partial \xi^j} - \left(\frac{\partial \tau^{ij}}{\partial \xi^j} \right)^\star = 0, \tag{2}$$

with

$$\tau^{ij} = \mu \left[g^{im} \left(\vec{a}^j \cdot \frac{\partial \vec{U}}{\partial \xi^m} \right) + g^{jm} \left(\vec{a}^i \cdot \frac{\partial \vec{U}}{\partial \xi^m} \right) \right], \tag{3}$$

and

$$\left(\frac{\partial \tau^{ij}}{\partial \xi^j} \right)^\star = g^{im} \left(\vec{a}^j \cdot \frac{\partial}{\partial \xi^j} \left(\mu \frac{\partial \vec{U}}{\partial \xi^m} \right) \right) + g^{jm} \left(\vec{a}^i \cdot \frac{\partial}{\partial \xi^j} \left(\mu \frac{\partial \vec{U}}{\partial \xi^m} \right) \right) + A, \tag{4}$$

$$A = \left(\vec{a}^i \cdot \frac{\partial \vec{a}^m}{\partial \xi^j} \right) \left(\vec{a}^j \cdot \mu \frac{\partial \vec{U}}{\partial \xi^m} \right) + \left(\vec{a}^j \cdot \frac{\partial \vec{a}^m}{\partial \xi^j} \right) \left(\vec{a}^i \cdot \mu \frac{\partial \vec{U}}{\partial \xi^m} \right). \tag{5}$$

The tensorial summation convention applies; $\vec{a}^i$ are the contravariant base vectors,

$$\vec{a}^i = \left(\frac{\partial \xi^i}{\partial x}, \frac{\partial \xi^i}{\partial y}, \frac{\partial \xi^i}{\partial z} \right);$$

p is the pressure, ρ the fluid mass density, μ the fluid effective viscosity[1], ξ is a streamwise coordinate, η a coordinate normal to the wall and ζ a transverse coordinate, $\sqrt{g}$ is the Jacobian of the transformation between the two systems and g^{ij} is the contravariant metric tensor. A partial parabolisation is obtained by neglecting the streamwise diffusion in the momentum equations, i. e. the terms with $j = 1$ in the viscous terms of equations (4). The elliptic character of the equations is retained in the pressure field.

As mentioned before, the use of equations thus simplified implies that a physical meaning is attached to the grid, since diffusion is neglected in the streamwise direction. This means that if the ξ, η, ζ system is roughly flow conforming, the use of contravariant velocity components as dependent variables is much more attractive than the use of cartesian components, because it enables the possibility of using the physical characteristics of the flow in the solution procedure.

Taking into account these considerations, the RNS equations written with the cartesian components, U^i, as the dependent variables are used to obtain the discretized equations, but the dependent variables used in the calculation are the contravariant velocity components. This means that the relations between cartesian components and contravariant components, V^i,

$$U^i = \frac{\partial x^i}{\partial \xi} V^1 + \frac{\partial x^i}{\partial \eta} V^2 + \frac{\partial x^i}{\partial \zeta} V^3, \tag{6}$$

are used to obtain the final form of the discretized equations after the discretization of the equations (1) and (2). With this procedure, we exploit the numerical advantages of discretizing the contravariant RNS equations with U^i as velocity dependent variables, and keep the flow-conforming contravariant velocity components as the dependent variables of the discretized equations.

At a grid singularity ,($\sqrt{g} = 0$), the metric relations of the coordinate transformation are not applicable. This means that the relations between cartesian and contravariant velocity components can not be applied at grid singularities. In the present approach, grid singularities are dealt with explicitly. The cartesian components at grid singularities are obtained by the arithmetic mean of the surrounding nodes in a previous iteration[2] and substituted in the discretized equations.

The present discretization procedure and the explicit treatment of the cartesian velocity components at grid singularities avoids all the restrictions imposed by grid singularities on the choice of the dependent variables. To obtain velocity dependent variables which are independent of the grid line spacing in the computational domain, the physical components of the contravariant velocity components, $\overline{V}^i$, are chosen as the velocity dependent variables. These are defined by

$$\overline{V}^i = V^i \sqrt{g_{ii}},$$

where

$$g_{ii} = \frac{\partial x}{\partial \xi_i}^2 + \frac{\partial y}{\partial \xi_i}^2 + \frac{\partial z}{\partial \xi_i}^2.$$

The flow solution is obtained by solving the continuity and momentum equations with the appropriate boundary conditions. The velocity component in the normal direction, V^2, is obtained by solving the continuity equation and the

[1] The fluid effective viscosity, μ, is obtained with an isotropic eddy-viscosity algebraic turbulence model, see section 2.1.2

[2] The solution procedure has to be iterative due to the non-linearity of the equations.

three momentum equations are used to obtain the remaining two components of the velocity and the pressure. The coupling of the equations is maintained in the solution process. The diffusion terms in the η momentum equation are dropped. As mentioned by Rubin *et al.* in [11], if the η coordinates are locally normal to ξ - at least near boundaries - all the diffusion terms in the momentum equation in the normal direction, η, may be dropped. This means that normal pressure variations, $\frac{\partial p}{\partial \eta}$, are essentially inviscid in origin and so the present set of equations represents an extension of interacting boundary layer theory.

2.1.1 Boundary Conditions

The flow around the tip of a wing has six boundaries. A schematic view of these boundaries in the physical and computational domain is given in figure 1. The six boundaries of the flow domain are denoted as follows : The inlet[3] $ABCD$ and the outlet $EFGH$. The external boundary $BFGC$, the wing surface and the inner[4] boundaries $ABFE$ and $CDHG$, which constitute the inlet and outlet of the cross-flow.

The inlet boundary is placed downstream of the stagnation region, because in the present method a downstream calculation procedure is used. The inlet boundary is not a natural boundary of the flow and so the choice between Dirichlet and Neumann boundary conditions is not clear, because in both cases some approximations will be required to specify the boundary conditions. From the implementation point of view, a straightforward option is to specify the three velocity components at the inlet boundary. However, it may be difficult to obtain a good estimate of the inlet velocity profiles and this may produce a non-smooth behaviour of the solution near the inlet boundary, [17]. Neumann boundary conditions proved to be more efficient in the earlier tests of the method, [17]. However, the method becomes more time consuming.

In the present approach the inlet velocity profiles are calculated solving equations (1) and (2) at the inlet station assuming that the streamwise gradients of velocity and pressure are equal to the ones obtained in a potential flow calculation, [21]. In the boundary layer region the velocity gradients are obtained from standard boundary layer profiles, [22]. At the boundaries of the inlet station the boundary conditions applied are equal to the ones described below. With these approximations the inlet velocity profiles may be obtained before starting the sweeping process.

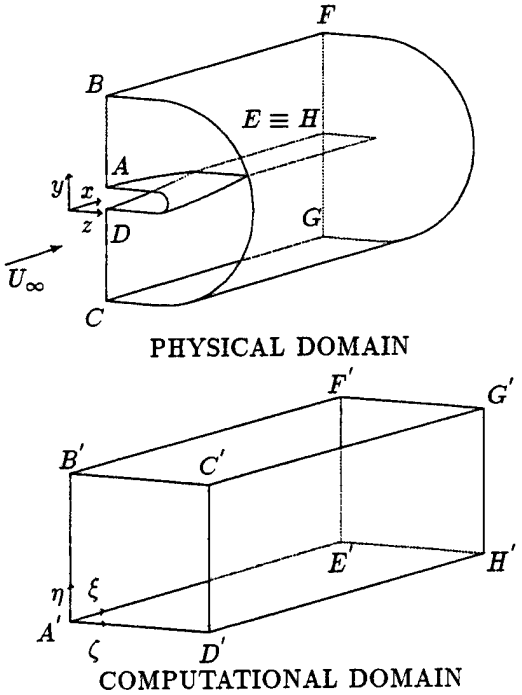


Figure 1: Illustration of the boundaries of the calculation of the flow at the tip of wings in the physical and computational domains.

At the outlet boundary a pressure boundary condition is required. In the present calculations the streamwise pressure gradient was set equal to zero, which proved to be an acceptable choice in the earlier tests of the method, [17].

The typical cross-sections of the wing and of the wake in the physical space and in the computational domain are illustrated in figure 2.

Boundary BC is the external boundary (surface $BFGC$ of figure 1), where the tangential components of the velocity and the pressure are prescribed by a potential flow calculation, [21]. Boundaries AB and DC are the inlet and outlet of the cross-flow (surfaces $ABFE$ & $CDHG$ of figure 1). To obtain a finer discretization of the tip vortex region, for a given number of grid nodes, the inner boundary is placed close to the tip. This means that at the inner boundary approximate boundary conditions will have to be used. In the present applications the cross-stream derivatives ($\frac{\partial}{\partial \zeta}$) of the cartesian velocity compo-

[3] In figure 1 the inlet boundary is a spanwise section of the wing.

[4] In figure 1 the inner boundary is a chordwise section of the wing.

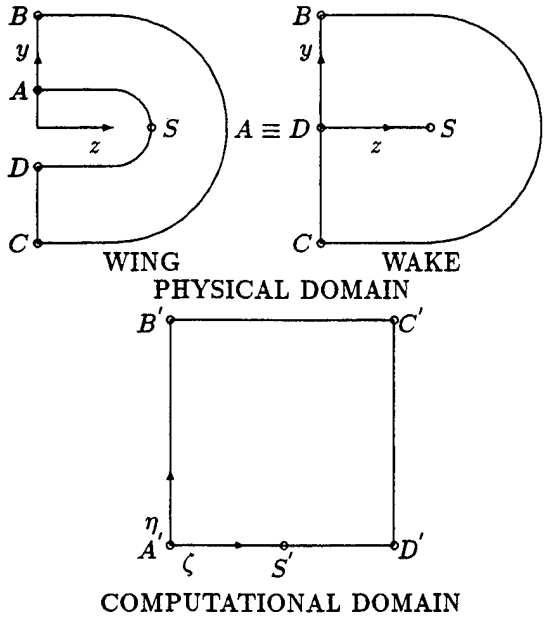


Figure 2: Illustration of the typical cross-section on the wing and wake and of the computational domain.

nents and of the pressure were set equal to zero.

Boundary AD has different properties in the cross-sections located on the wing and on the wake. On a cross-section of the wing it coincides with the wing surface, where the no-slip condition applies. The three velocity components are set equal to zero and the flow is calculated down to the wing, without wall functions. At the wake section, boundary AD is a fictitious boundary in the physical space. All the variables have to be calculated along this 'boundary', since the boundary nodes of the computational domain are field nodes in the physical space. At point S where the transformation is singular, $\sqrt{g} = 0$, the procedure mentioned above for grid singularities is applied.

2.1.2 Turbulence Model

There is a wide range of turbulence models available in the literature varying from the simple eddy-viscosity turbulence models, which can be algebraic or solve one or two transport equations, to the more complex second moment closures, which solve transport equations for each of the Reynolds stresses appearing in the momentum equations.

Although the turbulence model may play a sginificant role in the present predictions, as suggested by the results of Deng *et al.* in a ship case, [23], at this stage of the development we still use the simple algebraic isotropic eddy-viscosity model of Cebeci & Smith, [16]. This option is mainly justified by the lack of guarantee that the computer time penalty for the use of a more sophisticated model will improve the predictions, as shown by Deng *et al.* in [23]. The present implementation of the Cebeci & Smith turbulence model follows an approach similar to the one given by Cebeci *et al.* in [24]. A detailed description can be found in [8].

2.2 Numerical Solution

2.2.1 Discretized Equations

The continuity and contravariant momentum equations written for the cartesian velocity components, (1) and (2), are discretized in a single block regular grid by a finite-difference approximation. All the variables are defined on the grid nodes, (i, j, k)[5] since grid staggering is not used and Newton linearization is applied to the convective terms. The momentum equation in the ξ and ζ directions are discretized at the nodal points (i, j, k). The momentum equation in the normal direction, η, is discretized at $(i, j + \frac{1}{2}, k)$ and the continuity equation at $(i, j - \frac{1}{2}, k)$. The discretization schemes are identical to the ones used in the method for the calculation of ship stern flows [12] to [15]. A detailed description of their implementation can be found in [8]. With a careful discretization of the diffusion terms, [20], the present discretization technique only requires first derivatives of the grid coordinates.

2.2.2 Solution Procedure

The solution procedure is based on the one used in the code PARNASSOS, [12], [13], [14] and [15]. Here we will only describe the major features of the procedure. A more detailed description can be found in [8]. The solution is obtained iteratively by a space-marching process. Two iteration cycles can be distinguished : the local and the global iteration process.

The local iteration process refers to the solution of the flow at a streamwise station where all the grid nodes have the same main-stream coordinate, ξ. The solution is obtained simultaneously for all the variables with a Coupled Strongly Implicit Procedure (CSIP), [9]. Iteration is required

[5] The indices refer to the ξ, η and ζ direction, respectively.

by the non-linearity of the differential equations and by the incomplete factorization of the CSIP.

The discretized momentum equations at a streamwise station where all the grid nodes have the same main-stream coordinate, ξ, include the pressure field at the downstream station. This implies that in order to obtain the solution by a space-marching process in the main-stream direction, the pressure field at the downstream stations has to be taken from a previous sweep. The downstream marching process has to be repeated until the pressure field does not change between consecutive sweeps of the domain. This iterative procedure constitutes the global iteration process. To increase the convergence rate of this process each downstream sweep is followed by an upstream sweep to update the pressure field, [15]. The two sweeps form a predictor-corrector method for the pressure, which is constructed adding a quasi-time derivative of the pressure to the ξ momentum equation, [15]. Another improvement in the pressure field convergence can be obtained by using a multiple stepsize in the first sweeps to allow a rapid approach of the correct pressure level, [14]. This means that the grid is initially coarse in the main-stream direction and is subsequently refined in two or three stages.

3 Experiments

To verify the results of the calculations a set of experiments has been carried out at MARIN on a wing of elliptical planform. The experiments included detailed Laser-doppler velocity (LDV) measurements of the three velocity components on two planes along the wing chord and one plane in the wake.

The experiments were conducted in the Large Cavitation Tunnel (CT) of MARIN. The tunnel has a 4 m long test section with a 0.90 m × 0.90 m cross-section with rounded corners. The maximum velocity attainable in the test section is about 10 m/s.

The wing selected for the experiments has an elliptical planform with an aspect ratio of 4. The wing is without twist and has a NACA 0015 section. The wing has the following dimensions: half-span $s = 0.450m$, average chord $c = 0.225m$ and root chord $c_o = 0.2865m$. The wing is mounted vertically on the bottom of the tunnel in the mid-part of the test section, as shown in figure 3. The wing incidence can be varied from the outside with a resolution of 0.1 deg. The wing has been instrumented with pressure taps for measuring the pressure distribution in previous work and the wing zero lift incidence in the tunnel was determined by comparing the pressure on both sides of the wing at a spanwise location 0.85 and chordwise position 0.15 for the tunnel speeds of 4 and 8 m/s. The difference in zero lift incidence for these two speeds were insignificant.

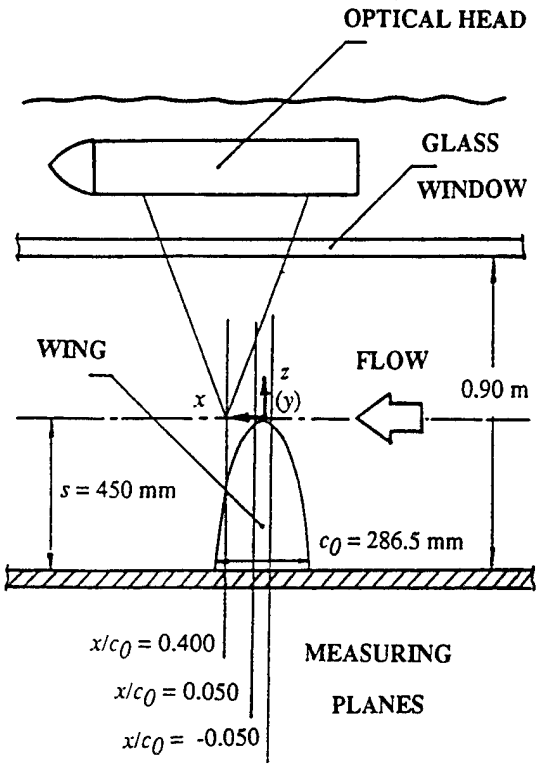


Figure 3: Schematic of wing and LDV arrangement in the test section of the Large Cavitation Tunnel.

For LDV measurements, the tunnel is fitted with a water basin mounted on the top of the test section, figure 3. All optical components of the LDV system are assembled in an optical head, which is traversed inside the basin filled with water by a y-z computer-controlled traversing system. The system allows the positioning of the LDV measuring volume inside a 0.12 m × 0.15 m window with a resolution of 0.1 mm. The optical access to the test section is made through a 31.5 mm thick glass window, which is now being used for measurements in cavitating conditions.

The MARIN LDV system is a two-colour backscatter system for simultaneous measurement of the three velocity components [25], [26]. The laser light is supplied by a 4 W Argon-ion laser and is transmitted to the optical compo-

nents of the system in the optical head by a monomode fiber. In the optical head the laser light is separated into five beams. The measuring volume defined by the intersection of the 5 beams has the approximate dimensions 0.4 mm × 0.4 mm × 1.3 mm. The three signals containing velocity information are analysed by three burst spectrum analysèrs (BSA) for extraction of the Doppler frequencies. To increase the data rate, the flow in the tunnel was seeded with particles of Iriodin 110 with an average size of 10 μm. The velocity data were collected during a measuring time of 10 s with a maximum number of velocity samples of 1000 on each channel. In a number of measuring points in the highly turbulent velocity region close to the vortex, the measuring time was increased to 30 s with a maximum number of samples of 3000.

In this set of experiments with the elliptical wing all the LDV measurements were made at the angle of attack $\alpha = 6$ deg and Reynolds number based on the root chord of 1.1×10^6. The measurements were made in three traverse planes, as shown in figure 3. The upstream measuring plane, $x = -14.3$ mm, $x/c_o = -0.05$ is very close to the inlet station of the viscous flow calculation in the tip region. In the intermediate plane, $x = 14.2$ mm, $x/c_o = 0.05$, the tip vortex has just formed and is still very close to the wing's surface. The last downstream plane, $x = 114.7$ mm, $x/c_o = 0.40$ is located in the wake. The stepsize used in the two planes on the wing is 1 mm and the stepsize used in the downstream plane in the wake is 1.5 mm.

4 Results and Discussion

Calculations were carried out for the wing of elliptical planform used in the experimental program described in section 3. The calculations were all performed on a DEC Station 3000 AXP.

In all the calculations, the global iteration process was stopped when the maximum pressure difference between consecutive sweeps, $(\Delta C_p)_{max}$, was less than 5.0×10^{-3}. The convergence criteria of the CSIP were differences between consecutive iterations of less than $1.0 \times 10^{-3} U_\infty$ in the physical components of the velocity and 2.0×10^{-4} in C_p. The calculations were performed for an angle of attack of 6 degrees and a Reynolds number of 1.1×10^6.

4.1 Grid Characteristics

The approximations assumed in the momentum equations imply that a flow conforming grid must be generated. For wings with rectangular planform, [17], this is a straightforward grid generation problem, but for a wing with elliptical planform the problem is more complex. The main difficulty is the location of the inlet boundary. The ξ lines must be roughly aligned with the main stream direction and the η lines should be normal to the wing surface. This means that at the tip the inlet boundary must be placed close to the tip. This location of the inlet boundary, at a small distance from the region of tip vortex formation, imposes an additional difficulty to the specification of the inlet boundary conditions. The influence of the location of the inlet boundary in the inlet boundary conditions is investigated in the following section.

Following the sensitivity studies reported in [17], the boundaries of the viscous flow region were placed at the following locations :

- The inner boundary, inlet and outlet of the cross-flow is placed at a distance of 40% of the root chord length inboard of the tip of the wing.
- The distance between the external boundary and the wing is 30% of the root chord length.
- The outlet boundary is 1.6 root chords downstream of the tip.
- In the region close to the inner boundary, the inlet boundary is located 10% of the local chord downstream of the leading edge. Close to the tip two different locations of the inlet boundary were tested :

  - $\frac{x}{c_o} = -0.06$, (denoted as GRID A)
  - $\frac{x}{c_o} = -0.11$, (denoted as GRID B).

In GRID A, the inlet boundary at the tip is only 1% of the root chord upstream of the plane $\frac{x}{c_o} = -0.05$ measured in the experimental program.

In both grids, the discretization of the viscous flow region was performed with a $145 \times 71 \times 61$ grid. The grid was generated with a 3-D elliptic grid generator, based on the approach of the Eagle code, [27]. The stretching of the grid lines in the normal direction is applied algebraicly and the distance of the first grid node to the wall is specified to guarantee a maximum distance of the first grid node to the wing surface of $y_n^+ = 2$, where $y_n^+ = \frac{u_\tau y_n}{\nu}$ and y_n is the distance to the wall. An illustration of the grid is given in figure

4. To obtain a clearer visualization of the grid the plots do not include all the grid lines.

The experimental measurements were performed on planes perpendicular to the undisturbed flow. The grid does not coincide with the measuring planes and so linear interpolation along the ξ lines was used to obtain the predicted velocity components at the measured planes.

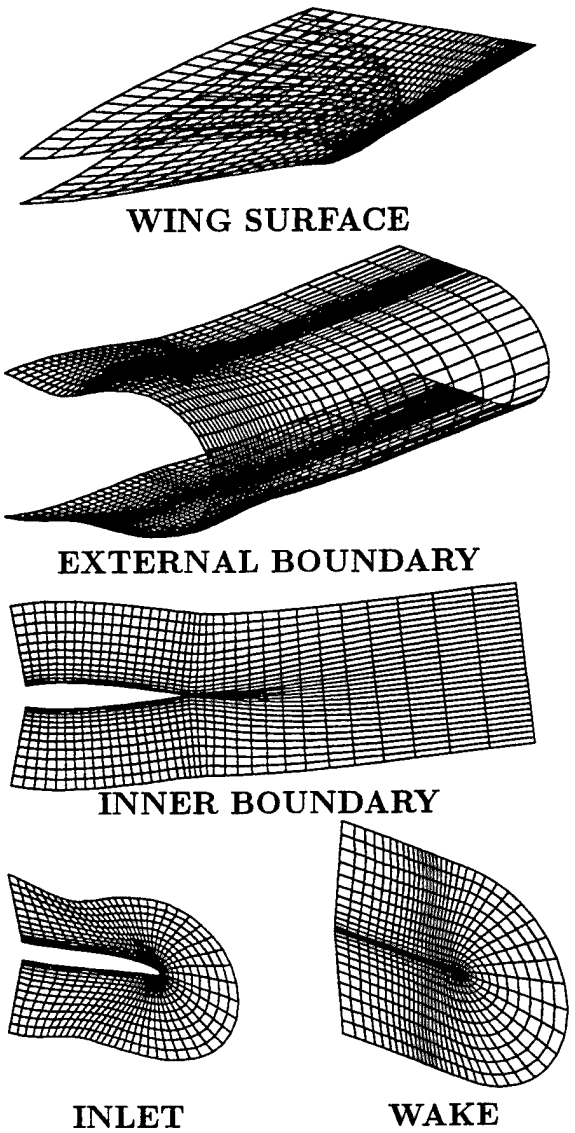


Figure 4: Illustration of the grid used in the calculation of the flow at the tip of an elliptical wing.

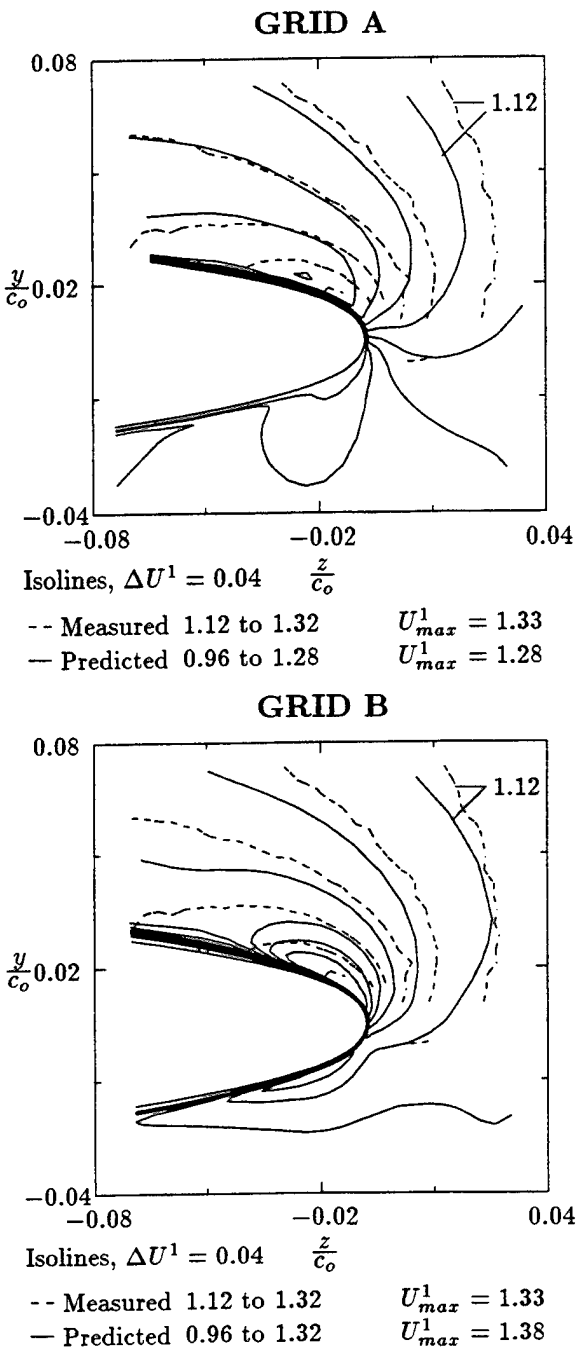


Figure 5: Comparison between predicted and experimental axial velocities at $\frac{x}{c_o} = -0.05$, for the flow at the tip of an elliptical wing with a Reynolds number of 1.1×10^6 and an angle of attack of 6 degrees.

4.2 Initial Condition

The quality of the inlet boundary conditions was evaluated comparing the predictions with the experimental measurements at $\frac{x}{c_o} = -0.05$. Figure 5 presents the comparison between predicted and experimental axial velocities. Figure 6 shows the potential flow solution and the viscous predic-

tions obtained in GRID A. In both viscous predictions the viscous effects seem to be overpredicted, resulting in a thicker boundary layer region. This overprediction of viscous effects is larger in GRID B where the inlet boundary was moved upstream. The predictions obtained in GRID A show a fair correlation with the experimental results, with the exception of the upper surface close to the tip, where the maximum axial velocity is clearly underpredicted.

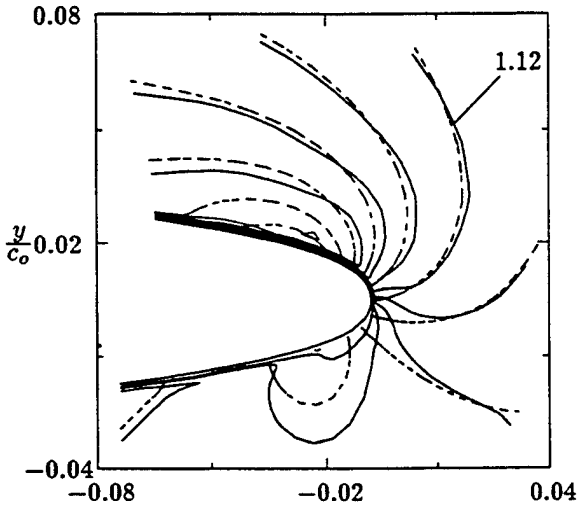


Figure 6: Comparison between the potential and viscous flow predictions of axial velocities at $\frac{x}{c_o} = -0.05$, for the flow at the tip of an elliptical wing with a Reynolds number of 1.1×10^6 and an angle of attack of 6 degrees.

The transverse velocity fields predicted by viscous flow solutions and potential flow solution are compared with the experimental measurements in figures 7, 8 and 9. A good agreement is obtained between the predictions obtained in GRID A and the experimental results. On the upper surface close to the tip, the magnitude of the predicted viscous flow transverse velocity components is lower than in the measurements. Neither from the predictions nor the measurements is any sign of vortex formation yet discernable. The results obtained in GRID B show a significant reduction of the magnitude of the transverse velocity components. These is a significant velocity component pointing downward to the wall on the upper surface, indicating a close approach to the vortex formation. The correlation between predictions and experimental results is clearly worse than the one obtained in GRID A.

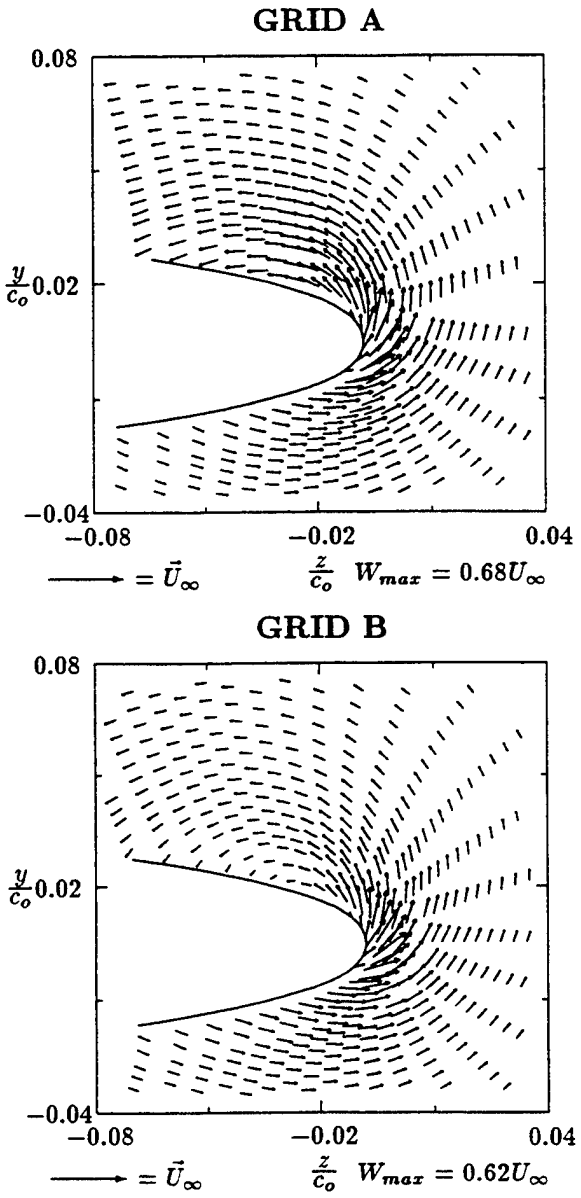


Figure 7: Predicted transverse velocity field at $\frac{x}{c_o} = -0.05$, for the flow at the tip of an elliptical wing with a Reynolds number of 1.1×10^6 and an angle of attack of 6 degrees.

These results show the importance of the inlet boundary conditions for this calculation. An unsuccessful attempt was made to perform the calculation using the potential flow solution[6], il-

[6] Including standard boundary layer profiles close to the

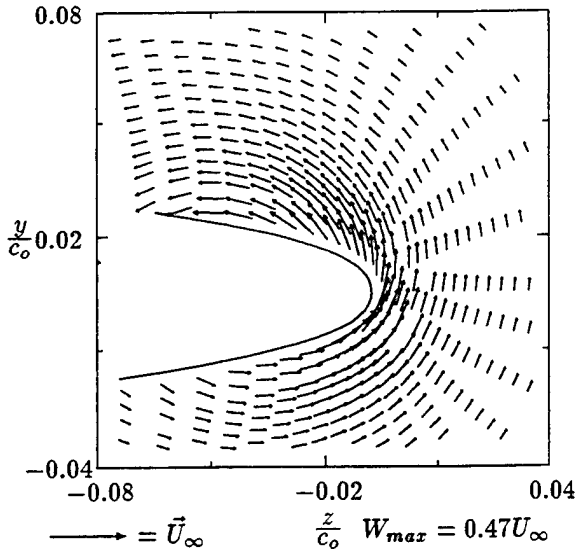


Figure 8: Potential flow prediction of the transverse velocity field at $\frac{x}{c_o} = -0.05$, for the flow at the tip of an elliptical wing with an angle of attack of 6 degrees.

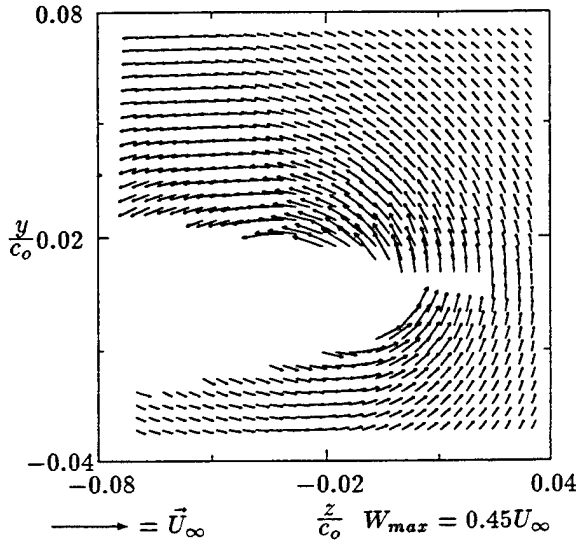


Figure 9: Measured transverse velocity field at $\frac{x}{c_o} = -0.05$, for the flow at the tip of an elliptical wing with a Reynolds number of 1.1×10^6 and an angle of attack of 6 degrees.

lustrated in figures 6 and 8, as the initial condition in GRID A. Large pressure oscillations were obtained close to the inlet station. It was not possible to obtain a converged solution in the finer grids[7] and a strong separation of the streamwise flow close to the inlet boundary was predicted already with the sweeps performed with the stepsize of 4. We note that for wings of rectangular planform the influence of small inaccuracies in the inlet boundary conditions was restricted to a small region close to the inlet boundary.

The comparison of the predictions with the measurements shows that the generation of the inlet boundary profiles and the calculation of the viscous region in the initial stations overpredict the viscous effects. We note that in the present approximation the flow is assumed to be fully turbulent and the approximations assumed are fairly simple for such a complex flow. Nevertheless, a fair correlation was obtained between the predictions obtained in GRID A and the experimental results. Due to the poor prediction of the inlet flow obtained in GRID B, the correlation between predictions and experimental results for the other two measured stations is clearly worse in GRID B. Therefore, in the following results we will restrict ourselves to the predictions obtained in GRID A.

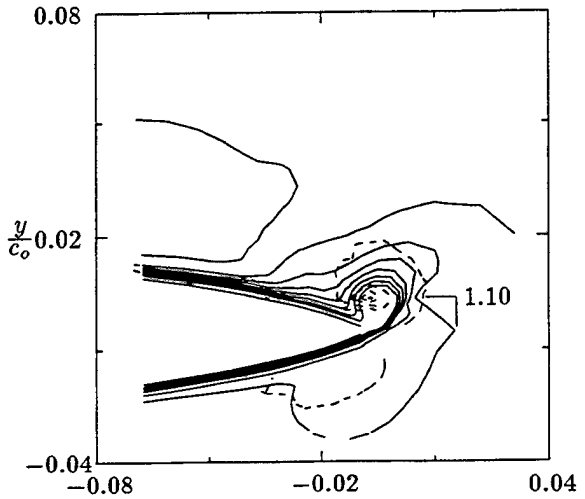


Figure 10: Comparison between predicted and experimental axial velocities at $\frac{x}{c_o} = 0.05$, for the flow at the tip of an elliptical wing with a Reynolds number of 1.1×10^6 and an angle of attack of 6 degrees.

wall.

[7] As mentioned before, the sweeping procedure uses a multiple stepsize in the initial sweeps.

4.3 Vortex Formation

The experimental program included also the stations at $\frac{x}{c_o} = 0.05$ and $\frac{x}{c_o} = 0.40$. At $\frac{x}{c_o} = 0.05$ the vortex as just been formed and the last station is in the wake. These two stations were selected to evaluate the predictions of the tip vortex formation with the present method.

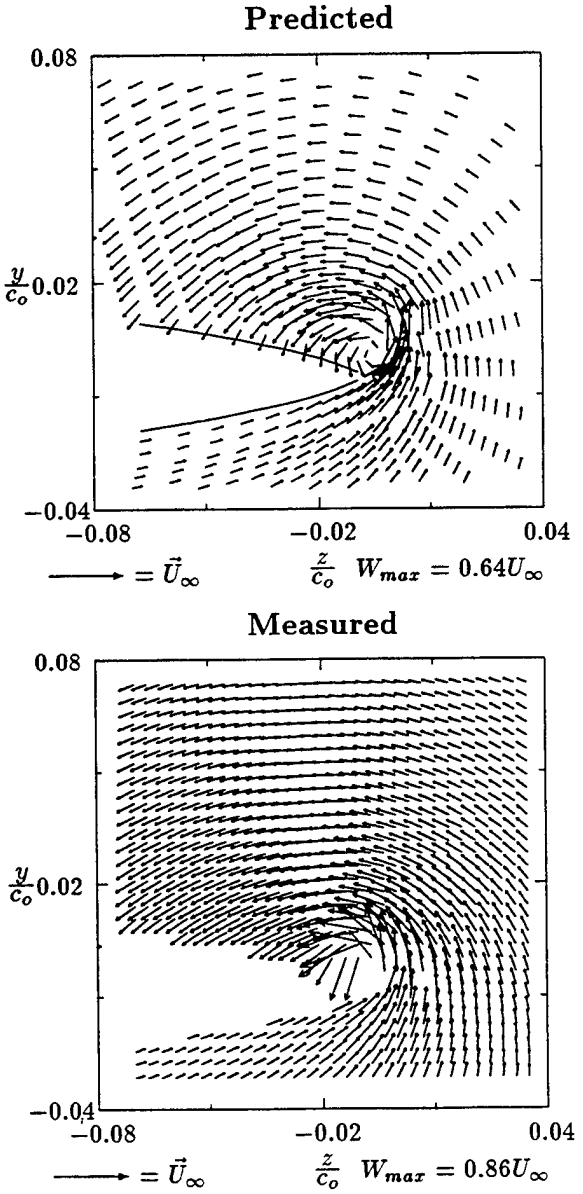


Figure 11: Comparison between predicted and experimental transverse velocity fields at $\frac{x}{c_o} = 0.05$, for the flow at the tip of an elliptical wing with a Reynolds number of 1.1×10^6 and an angle of attack of 6 degrees.

The comparison between predicted and experimental axial velocities at $\frac{x}{c_o} = 0.05$ is presented in figure 10. The predicted and measured transverse velocity fields at the same station are plotted in figure 11. A fair correlation is obtained for the axial velocity components, but the velocity reduction in the vortex core is overpredicted (0.75 predicted, 0.90 measured). The transverse velocity components are in good agreement with the experiments. The size of the vortex core seems to be overpredicted but the position of the vortex is well predicted. The maximum transverse velocity component is underpredicted (0.64 predicted compared with 0.86 measured). All these differences indicate that the vortex is excessively diffused in the predictions.

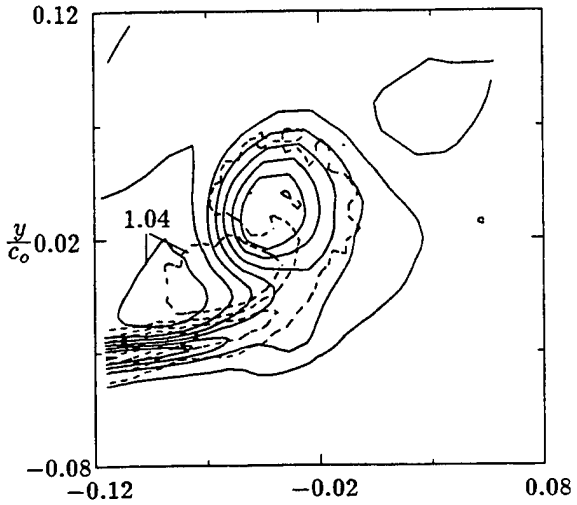


Figure 12: Comparison between predicted and experimental axial velocities at $\frac{x}{c_o} = 0.40$, for the flow at the tip of an elliptical wing with a Reynolds number of 1.1×10^6 and an angle of attack of 6 degrees.

Figure 12 includes the comparison between the predicted and the experimental axial velocity components at $\frac{x}{c_o} = 0.40$. The transverse velocity fields of predictions and measurements are compared in figure 13. The maximum and minimum values of the axial velocity components are in very good agreement. The isolines pattern of the predictions is similar to the experimental one but the velocity at the vortex core is again underpredicted. The predicted transverse velocity field shows the correct prediction of the locations of the tip vortex and of the vortical wake. The vor-

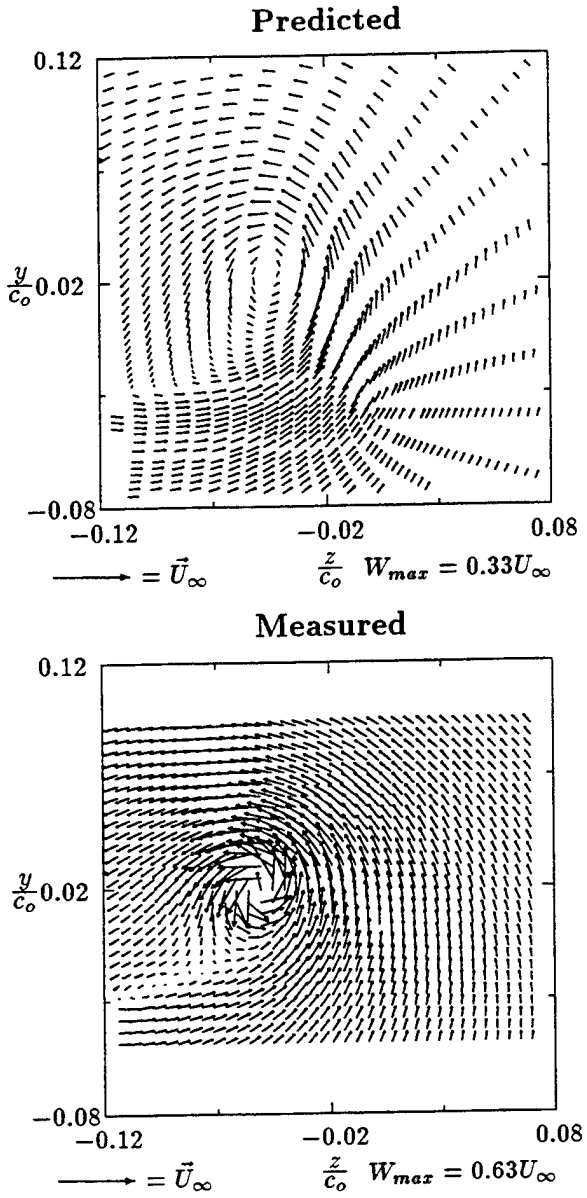


Figure 13: Comparison between predicted and experimental transverse velocity fields at $\frac{x}{c_o} = 0.40$, for the flow at the tip of an elliptical wing with a Reynolds number of 1.1×10^6 and an angle of attack of 6 degrees.

tex core size is clearly overpredicted. The comparison of the present grid spacing at the vortex core with the experimental results indicates that the present number of grid lines is too small to resolve the high gradients existing in this region.

Assuming that the vortex is axisymmetric, it is possible to estimate the vortex center from the locations where the transverse velocity components change sign in horizontal or vertical traverses. This approach was used by Falcão de Campos *et al.* in [28] to obtain the vortex center position of this flow in three different stations. Using the same approach, the predicted vortex center location was obtained as a function of $\frac{x}{c_o}$. The approximation of an axisymmetric vortex is poor close to the tip, which causes some oscillations in the $\frac{y}{c_o}$ location of the predictions. Figure 14 presents the comparison between the predicted vortex center location and experimental results of Falcão de Campos *et al.*, [28]. The differences between predictions and measurements are fairly small showing that although the vortex core is excessively diffused its location is correctly predicted.

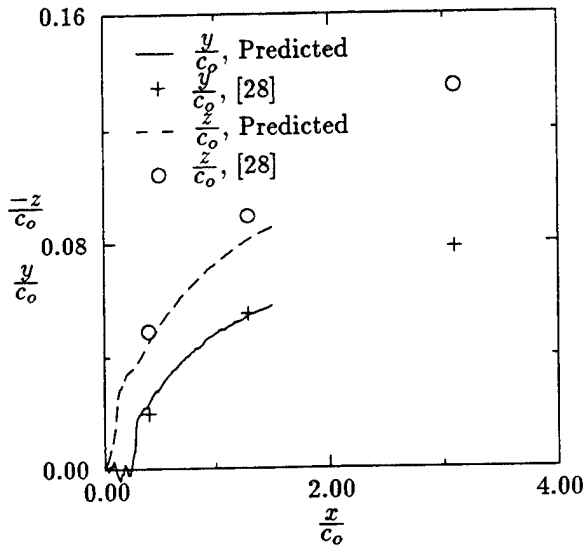


Figure 14: Comparison between the prediction of the location of the vortex center and experimental results

The isobars at the three measured stations are plotted in figure 15. The results show a suction peak at the wing surface more intense than the suction peak in the vortex core. However, the excessively diffused vortex, strongly affects the prediction of the pressure in the vortex core. The significant increase of pressure in the vortex core between the stations at $\frac{x}{c_o} = 0.05$ and $\frac{x}{c_o} = 0.40$ illustrates the effect of the vortex core size in the pressure.

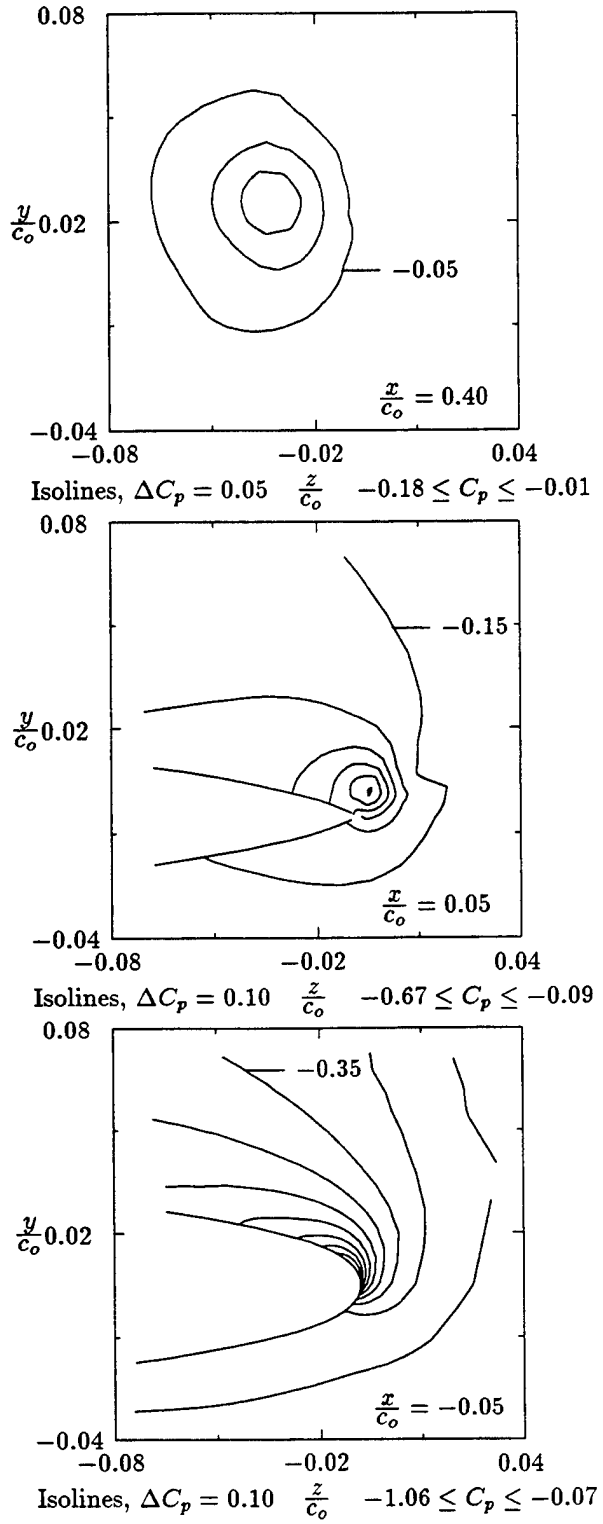


Figure 15: Predicted transverse pressure field at $\frac{x}{c_o} = -0.05$, $\frac{x}{c_o} = 0.05$ and $\frac{x}{c_o} = 0.40$, for the flow at the tip of an elliptical wing with a Reynolds number of 1.1×10^6 and an angle of attack of 6 degrees.

5 Conclusions

The prediction of the flow at the tip of a wing with elliptical planform with a numerical method based on the Reynolds-averaged Navier-Stokes equations has been investigated. LDV measurements of the three velocity components were made to validate the numerical results.

The approximations assumed in the momentum equations, where streamwise diffusion is neglected, imply some geometrical restrictions to the grid. In the present zonal approach, the inlet boundary at the tip must be placed very close to the tip of the wing. The comparison between predictions and measurements showed that the inlet boundary conditions are critical for a good prediction of the flow. The results show that the method overpredicts the viscous effects at the tip of the wing, which affects the prediction of the formation of the tip vortex. A better correlation with experimental results was obtained with the inlet boundary positioned slightly more downstream.

The method was capable of predicting most of the flow features of the vortex formation process on the wing. A good correlation with experimental results was obtained for the three velocity components in the tip region except in the vortex core. The method overpredicts the viscous core size and underpredicts the maximum transverse velocity in the vortex core, which precludes an accurate prediction of the core suction peak. This result was not unexpected and must be caused by the inadequate turbulence model and insufficient grid resolution near the vortex core. However, the prediction of the vortex center location is in good agreement with experimental results.

The comparison between the predictions and the experimental results presented in this paper suggests that the present numerical method is a promising approach to a better understanding of tip vortex flows.

References

[1] McCormick B.W. - *On Cavitation Produced by a Vortex Trailing from a Lifting Surface.* - Journal of Basic Engineering, Transactions of the ASME, September 1962, pp. 369-379.

[2] Arndt R.A.E., Higuchi H., Quadrelli C.J. - *Tip Vortex Cavitation.* - Cavitation and

Multiphase Flow Forum, ASME, New York, 1985.

[3] Higuchi H., Arakeri V.H., Arndt R.E.A. - *Further Studies on Tip Vortex Cavitation.* - Cavitation and Multiphase Flow Forum, ASME, New York, 1986.

[4] Arndt R.A.E., Higuchi H., Ikohagi T. - *Tip Vortex Cavitation.* - Proceedings of the International Symposium on Propeller and Cavitation, Wuxi, China, April 1986.

[5] Arakeri V.H., Higuchi H., Arndt R.E.A. - *Analysis of Recent Tip Vortex Cavitation Inception Data.* - Proceedings of the $21^{\underline{th}}$ American Towing Tank Conference, Washington, August 1986.

[6] Govidan T.R., Levy R., Shamroth S.J. - *Computation of The Tip Vortex Generation Process for Ship Propeller Blades* - 4^{th} International Conference on Ship Hydrodynamics, Washington D.C., 1985.

[7] Govidan T.R., Jong F.J., Levy R., Shamroth S.J. - *Validation of a Forward Marching Procedure to Compute The Tip Vortex Generation for Ship Propeller Blades* - 17^{th} Symposium on Naval Hydrodynamics, August-September 1988, The Hague, The Netherlands.

[8] Eça L. - *Numerical Solution of the Parabolised Navier-Stokes Equations for Incompressible Tip Vortex Flows* - PhD Thesis, Instituto Superior Técnico, Lisbon, March 1993.

[9] Rubin S.G. - *Incompressible Navier-Stokes and Parabolised Navier-Stokes Formulations and Computational Techniques.* - Computational Methods in Viscous Flows, Vol. 3 in the series Recent Advances in Numerical Methods in Fluids (ed. Habashi) Pineridge Press, 1984.

[10] Rubin S.G. - *Global Relaxation Procedure for a Reduced Form of the Navier-Stokes Equations.* - Proceedings of the $9^{\underline{th}}$ International Conference on Numerical Methods in Fluid Dynamics, Lecture Notes in Physics, Vol. 218, Springer-Verlag, 1985, pp. 62-71.

[11] Rubin S.G., Tannehill J.C. - *Parabolized/Reduced Navier-Stokes Computational Techniques.* - Annual Review of Fluid Mechanics, Vol. 24, 1992, pp. 117-144.

[12] Raven H.C., Hoekstra M. - *A Parabolised Navier-Stokes Solution Method for Ship Stern Flow Calculations.* - 2^{th} International Symposium on Ship Viscous Resistance, Goteborg Sweden, March 1985.

[13] Hoekstra M., Raven H.C. - *Application of a Parabolised Navier-Stokes Solution System to Ship Stern Flow Computation.* - Osaka International Colloquium on Ship Viscous Flow, Osaka Japan, October 1985.

[14] Hoekstra M., Raven H.C. - *Ship Boundary Layer and Wake Calculation with a Parabolised Navier-Stokes Solution System.* - 4^{th} International Conference on Numerical Ship Hydrodynamics", Washington D.C., 1985.

[15] Hoekstra M. -*Recent Developments in a Ship Stern Flow Prediction Code.* - 5^{th} International Conference on Numerical Ship Hydrodynamics, Hiroshima, September 1989.

[16] Cebeci T., Smith A.M.O. - *Analysis of Turbulent Boundary Layers.* - Academic Press, November 1984.

[17] Eça L., Falcão de Campos J.A.C., Hoekstra M. - *Computation of the Tip Vortex Flow on Three-Dimensional Foils with a Parabolised Navier-Stokes Solver.* - Sixth International Conference on Numerical Ship Hydrodynamics, IOWA, August 1993.

[18] Warsi Z.U.A. - *Conservation Form of the Navier-Stokes Equations in General Nonsteady Coordinates.* - AIAA Journal, Vol. 19, February 1981, pp 240-242.

[19] Hoekstra M. - *Some Fundamental Aspects of the Computation of Incompressible Flows.* - Second Osaka International Colloquium on Ship Viscous Flow, September 1991, Osaka Japan.

[20] Eça L.R.C., Hoekstra M. - *Discretization of the Parabolised Navier-Stokes Equations.* - First European Computational Fluid Dynamics Conference, Brussels, September 1992.

[21] Raven H.C. - *Berekening van de potentiaalstroming rond draagvlakken met het programma DAWSON*, (in Dutch)

"*Calculation of Potential Flow on Lifting Surfaces with the Program Dawson*, (Engl. Transl.) - MARIN Report Nº 50501-1-RD, May 1985.

[22] Hoekstra M. - *Generation of Initial Velocity Profiles for Boundary Layer Calculations.* - Marin Report Nº 50028-1-SR, March 1980.

[23] Deng G.B., Queutey P, Visonneau M. - *Navier-Stokes Computations of Ship Stern Flows : A Detailed Comparative Study of Turbulence Models and Discretization Schemes.* - Sixth International Conference on Numerical Ship Hydrodynamics, IOWA, August 1993.

[24] Cebeci T., Clark R.W., Chang K.C., Halsey N.D., Lee K. - *Airfoils with Separations and the Resulting Wakes.* - Journal of Fluid Mechanics, Vol. 163, 1986, pp. 323-347.

[25] Gottmer M.C., de Bruin W., van der Kooij J. - *Three Component Laser-Doppler Velocimetry. Technique and Application.* - MARIN Report Nº 50889-1-RM, November 1989.

[26] Gottmer M.C., Aalbers A.B., Falcão de Campos J.A.C., Nienhuis U. - *Recent Experience with 3-D LDV Measurements at MARIN.* - Developments in Marine Technology, Vol 10., *Hydrodynamics : Computations, Model Tests and Reality.*, van den Boom H.J.J. Editor, Elsevier 1992, pp 521-531.

[27] Thompson J.F. - *A General 3D Elliptic grid generation system on a composite block structure.* - Computer Methods and Applied Mechanics and Engineering, Vol. 64, 1987, pp. 377-411.

[28] Falcão de Campos J.A.C., George M.F., Mackay M. - *Velocity Measurements of the Tip Vortex Flow in the Near-Wake of Hydrofoils.* - 1993, Submitted for publication to the Journal of Fluids Engineering.

DISCUSSION

D. Fruman
ENSTA/GPI, France

This is more of a comment than a question. In my recent review paper on tip vortex cavitation , I have reported work conducted in France[1,2,3] to numerically simulate the tip vortex flow using two commercially available codes, namely FIDAP and STAR-CD. The conclusions reached are very much analogous to the ones of the paper under discussion: whatever the code, a good qualitative description of the vortex roll-up is achieved, but the vortex core size (outside of the tip) is overestimated and the maximum tangential velocity is underestimated. In view of this, it is our belief that, for achieving good qualitative agreement between the experimental and the numerical results, it is essentially necessary to improve the spatial definition. Experimentally, LDV allows to have measurements for steps as small as 30Tm in a radial direction. Numerically, the grid has to follow the vortex path and have radial mesh sizes of the order of 0.003 of the oil maximum chord or less. Moreover, refinements of the turbulence simulation will require to have a model adapted to a rotating flow situation.

[1] Fruman, D. H., Recent Progress on the Understanding and Prediction of Tip Vortex Cavitation, Proceedings of the Second International Symposium on Cavitation, H. Kato, editor, pp. 19-29, 1994.

[2] Dupont, P. And Cerrutti, P., Comparison between Tip Vortex Development Calculation and Measurements on an Elliptical Platform, Third European FIDAP Users Group Meeting, Heidelberg, Germany, 1991.

[3] Pauchet, A., Briancon-Marjollet, L, Gowing, S., Cerrutti, P. And Pichon, T., Effects of Foil Size and Shape on Tip Vortex Cavitation Occurrence, Proceedings of the Second International Symposium on Cavitation, H. Kato, editor, pp. 133-139, 1994.

DISCUSSION

T. Miloh
Tel-Aviv University, Israel

What is optimal choice of the matching surface?

AUTHORS' REPLY

The matching surface must be located in a region where viscous effects are supposed to be negligible. In this sense there is a dependence on the drift angle; nevertheless, drift angles of 20° may be reasonably tackled.

DISCUSSION

J.De Kat
MARIN, The Netherlands

To what extent does appropriate location of the matching boundary depend on the drift angle?

AUTHORS' REPLY

The dependence of the numerical solution on the position on the matching surface (and consequently on the size of the viscous subdomain) is reported in fig. 1, where the wave elevations on the hull and in the wake, obtained with two different positions of the matching surface, are shown. The solid line is the wave profile computed with the matching surface placed at 1/20 of the ship length aside from the hull. The broken line is the wave profile computed with a matching surface much closer to the ship (1/100). The two computations are in reasonable agreement, although in the second case the boundary of the viscous subdomain is very near to the region where viscous effects are important.

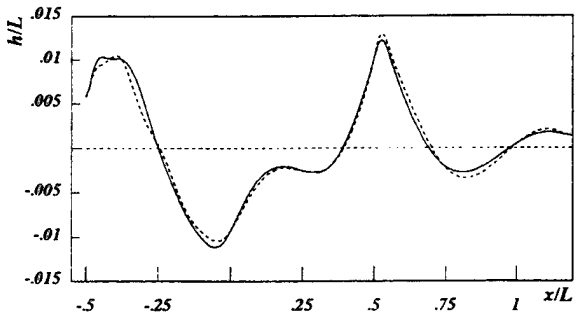


Figure 1: Wave profile on the hull: comparison between $\Gamma_p = L/20$ solution (solid line) and $\Gamma_p = L/100$ solution (dashed line) for the free surface flow past the S60 hull $Fr = 0.316$ $Re = 4 \times 10^6$ $\alpha = 0$.

Near-Field Flow Predictions for Ship Design

K. Weems, R. Korpus, W.-M. Lin, M. Fritts (Science Applications International Corp., USA), H.-C. Chen (Texas A&M University, USA)

ABSTRACT

This paper describes an ongoing effort to integrate state-of-the-art computational techniques – a Reynolds-Averaged Navier-Stokes (RANS) code with nonlinear free-surface capability, second-order closure turbulence modeling, and integrated propeller flow modeling – into a system for predicting near-field ship flows. The combination of these methods provides a new level of realism for modeling the flow field around a ship, including thick turbulent boundary layers, separated flow, vortex generation and evolution, free surface effects, and propeller/hull coupling. The bottlenecks caused by inadequate grid generation methods and a lack of code integration, which have prevented the use of these numerical methods for practical configurations in design time frames, have been substantially alleviated by the incorporation of zonal calculation techniques, advanced gridding tools, and a "chimera" gridding method that allows arbitrary grid block overlap.

To demonstrate the predictive capability of the method, flow calculation results are presented for a variety of configurations: the HSVA tanker, the appended "SUBOFF" submarine, a submarine body with propeller, and a Series 60 surface ship. The complex problem of using advanced flow analysis techniques in naval and commercial ship design is discussed as well. Finally, recommendations for the ongoing development, validation, and application of near-field ship flow prediction codes are presented.

INTRODUCTION

The naval and commercial ship design communities have long needed a predictive capability to address the complex interaction between a ship's boundary layer, the nonlinear free-surface, and the propulsor. In commercial ship design, the prediction of near-field flows is central to the problems of unsteady propeller loads, cavitation, and propeller-induced hull vibrations. The solution of these problems requires detailed knowledge of the turbulent stern flow (including thick and perhaps separated boundary layers), bilge vorticity, and propeller/hull interaction. In naval ship design, near field flow predictions are needed to develop designs with reduced acoustic and non-acoustic signatures, particularly through the prediction of propeller acoustic output and the far field wakes observed by synthetic aperture radar.

Unfortunately, the technology for making these predictions has not been available to the designer. Until quite recently, ship designs were developed using regression and empirical formulas alone. At best, the use of flow codes was restricted to potential flow calculations augmented by boundary layer predictions to approximate viscous effects. Propeller calculations were performed using empirically generated effective wakes, and the propeller's interaction with the hull was approximated with the "thrust deduction coefficient." The free surface could usually be predicted using linear approximations, but was generally neglected in any viscous flow calculations. While RANS flow solvers are now available to provide greater accuracy with detailed viscous flow predictions, their use has remained somewhat restricted by the lack of realistic turbulence modeling and the complications of grid generation. Design applications were further restricted the lack of integrated geometry modeling and grid generation makes design modifications, regridding, recalculation, and redesign very expensive exercises.

Techniques capable of providing the required flow detail for a wide range of hull forms

are beyond the complexity of these previously available design tools, particularly for large block coefficient, single screw, or extreme transom designs. The further development and validation of computational fluid dynamics codes, and their integration with geometry modeling and gridding tools are necessary steps in the effort to provide practical viscous flow prediction. The last five years have seen significant advances in these areas, and the new code systems now becoming available herald the arrival of a more efficient, validated viscous flow prediction capability for design. The bulk of this paper presents the unique capability of one of these code systems – one which combines geometry modeling, advanced gridding tools, and a RANS solver incorporating state-of-the-art Reynolds stress turbulence modeling, nonlinear free surface modeling, and embedded propeller modeling. Results from recent validation studies for surface ships and submarines are provided.

The paper also discuses plans for building this capability into a practical computational design tools. This development would not be conceivable without the progress in computational fluid dynamics as discussed above. Now that sufficient accuracy seems attainable, it is time to build an integrated design system with quantitative evaluation of error and the propagation of that error through system sensitivities into quantified estimates of design risk. The final sections of the paper discuss the requirements for a computational design system that addresses the use of computational fluid dynamics from the designers perspective.

Background

The idea of applying computational fluid dynamics – in particular, viscous flow codes – to the flow around a ship's hull is hardly a new one. In 1980, SSPA Maritime Consulting and the International Towing Tank Conference (ITTC) sponsored a Ship Boundary Layer Workshop in Göteborg, Sweden. The purpose of the workshop was to examine the state-of-the-art of numerical computations around ship hulls and to set the direction of ongoing research. As suggested by the title, the principle computation methods represented at the workshop were based on boundary layer theory. The primary conclusion of the workshop was that boundary layer theory was too limiting when applied to stern and wake flows.

In 1990, SSPA, Chalmers University of Technology (CTH), and the Iowa Institute of Hydraulic Research (IIHR) sponsored the Workshop on Ship Viscous Flow, which was also held at CTH in Sweden. Workshop participants, mostly using Navier-Stokes solvers, performed viscous flow calculations on the HSVA tanker configuration and a "Mystery" hull form variation. While most of the calculations predicted the development of the hull boundary layer with good accuracy, none properly predicted the development of the bilge vortex or its effect on the flow. The conclusion was that more sophisticated turbulence models and improved grid resolution would be required to capture this vortex.

At about the same time as the Workshop on Ship Viscous Flow, the Advanced Research Projects Agency (ARPA) conducted the SUBOFF program. In SUBOFF, RANS code developers and users from several American universities, government laboratories, and private companies were funded to perform blind calculations of the viscous flow around a submarine with various combinations of appendages. Simultaneously, wind and water tunnel experiments were carried out. The results of the competition were disappointing. While many of the calculations were able to capture the features of viscous submarine flow, few showed good quantitative agreement with the experimental results. The overall conclusion from the SUBOFF program was that while RANS codes were able to capture most of the features of viscous submarine flow, significant improvements were still required before they could be applied to practical submarine design problems. In particular, grid generation and turbulence modeling were singled out as weaknesses in the state-of-the-art.

In March of 1994, Japan's Ship Research Institute (SRI) hosted the CFD Workshop Tokyo 1994 to revisit the SSPA investigations using more up to date RANS and free surface codes. Viscous and inviscid calculations were requested for a Series 60 C_B=0.60 hull form at two speeds, Fr=0.160 and Fr=0.316. In general, the near-field flow features, including hull surface pressure, viscous boundary layer, and free surface elevations at the hull side, were well predicted by those Navier-Stokes calculations that included nonlinear free surface effects. In addition, both the skin friction and pressure components of resistance were fairly well predicted. However, it was noted that wave patterns away from the ship side were not accurately predicted. In addition to the Series 60 calculations, double body viscous flow calculations were repeated for the HSVA and

"Mystery" tanker hull forms in order to follow up on the 1990 SSPA workshop. The newer HSVA results showed that codes utilizing state-of-the-art anisotropic turbulence models (including the second-order closure described herein), can finally capture the bilge vorticity missed in Göteborg. It should be noted, however, that the more common isotropic models continued to exhibit the same problems shown in 1990. Calculations for the SRI Workshop made with the present capability are presented in References [1, 2] and discussed later in this paper.

Current Effort

The capability described in this paper is the result of an ongoing effort to create a viscous flow prediction system for naval architecture applications. The effort can be divided into two distinct topics: computation fluid dynamics (CFD) and computational design. In the CFD area, the effort has focused on developing the capabilities necessary for marine applications (such as free surface and propeller models) and on correcting deficiencies discovered during the workshops (such as turbulence modeling and grid generation). In the area of computational design, emphasis has been placed on the integration of these codes into a system suitable for design applications.

The effort is described as ongoing, since the development of advanced flow codes and especially computational design technology must continue hand in hand with their application to design problems. While CFD techniques are on the threshold of providing many realistic and practical calculations, reliable full scale ship computations remain a complex task. More importantly, computational design must be developed as a complete technology – with emphasis on accuracy only at the level needed by the designer, quantified error estimates propagated into risk assessments, evaluation of system sensitivities and integration with developing ship synthesis models.

NUMERICAL METHOD

This section describes the RANS-based numerical method that forms the core of our near-hull flow prediction capability. The computational system described herein consists of three main parts: the Finite-Analytic Navier-Stokes (FANS) code for computing viscous, turbulent flows; the non-linear zonal free-surface model for including free surface effects; and the propeller modeling system for incorporating propulsor effects. The sections that follow will discuss each of these capabilities in sufficient detail for a cursory understanding of the total system. It should be noted, however, that most of these methods have already been described in previous publications, and the reader will often be referred there for more detail.

Discretization of the Navier-Stokes Equations

In Cartesian coordinates (x_1, x_2, x_3, t), the incompressible, Reynolds-averaged Navier-Stokes equations are:

$$\frac{\partial U_i}{\partial x_i} = 0 \tag{1}$$

$$\frac{\partial U_i}{\partial t} + U_j \frac{\partial U_i}{\partial x_j} + \frac{\partial p}{\partial x_i} - \frac{1}{Re}\frac{\partial^2 U_i}{\partial x_j \partial x_j} + \frac{\partial(\overline{u_i u_j})}{\partial x_j} - F_i = 0 \tag{2}$$

where U_i, $(\overline{u_i u_j})$, and p represent Cartesian mean velocities, Reynolds stresses, and pressure, respectively, and repeated indices indicate summation. The term F_i is included for modeling of distributed force fields such as propulsors, and is assumed known. The Reynolds number, $Re = U_o L/\nu$, is based on the length and velocity scales, L and U_o, used to non-dimensionalize the equations.

The exact form of the Reynolds stresses depend on the turbulence model being used. FANS currently includes four different models: two of the k-ε type and two of the second moment closure type. If a k-ε model is used, Equations 2 are modified by first substituting the Boussinesq approximation

$$-(\overline{u_i u_j}) = \nu_t \left(\frac{\partial U_i}{\partial x_j} + \frac{\partial U_j}{\partial x_i} \right) - \frac{2}{3}\delta_{ij} k \tag{3}$$

where k is the turbulent kinetic energy, $\nu_t = 0.09k^2/\varepsilon$ is the eddy viscosity, and ε is its dissipation rate. For the second moment closure models, Equations 2 are solved with the Reynolds stresses inserted directly. The models themselves will be described in the next section.

For solutions involving real-world geometries, Equations 1 and 2 must first be transformed into body-fitted coordinates. The transformation used in FANS maps the Cartesian independent variables (x_1, x_2, x_3, t) into (generally non-orthogonal) body-fitted coordinates $(\xi^1, \xi^2, \xi^3, \tau)$,

but leaves the dependent unknowns in Cartesian space. The transformed momentum equations become:

$$\frac{\partial U_i}{\partial \tau} + \left(b_j^k U_j + \frac{1}{Re} g^{jm} \Gamma_{jm}^k \right) U_{i,k} + b_i^j p_{,j} - \frac{1}{Re} g^{jk} U_{i,jk} + b_j^k (\overline{u_i u_j})_{,k} - F_i = 0 \qquad (4)$$

where b_j^k refers to the inverse transformation tensor $\partial \xi^k / \partial x_j$, g^{jk} refers to the inverse of the fundamental metric tensor g_{ij}, and Γ_{jm}^k represents a Schwartz-Christoffel symbol of the second kind. Subscripts following commas denote covariant differentiations with respect to (ξ^1, ξ^2, ξ^3).

In FANS, transport equations like Equation 4 are discretized using the finite-analytic method [3]. This is accomplished by first rewriting each equation in the form of a general convection/diffusion problem, and then linearizing by assuming the coefficients constant over each computational cell. The resulting equations can be written in generic form using ϕ as a typical conserved quantity:

$$\frac{\partial \phi}{\partial \tau} + C_k \phi_{,k} - \frac{1}{Re} g^{kk} \phi_{,kk} = S \qquad (5)$$

where $C_k \triangleq b_j^k U_j + g^{jm} \Gamma_{jm}^k / Re$, and $S \triangleq -b_i^j p_{,j} - b_j^k (\overline{u_i u_j})_{,k} + F_i + g^{mk} \phi_{,mk} / Re$, $m \neq k$. Note that if a k-ε model is used, the Boussinesq approximation will cause some of the Reynolds stress terms in S to appear convective and/or diffusive. FANS moves such terms to the left-hand-side so as to maximize their implicit treatment.

The finite-analytic method solves Equations 5 analytically in each computational cell using separation of variables. Evaluation of the analytic solution at a grid point then provides a means to relate the unknowns to their nearest neighbors. Although almost any time or space stencil could be used, we have found the best compromise of resolution and efficiency is obtained with Euler implicit time differencing, a 9-point cross-flow plane stencil, and a 3-point streamwise stencil. This "lumping" of upstream and downstream influences into single points greatly simplifies the solver, and does not significantly effect convergence. The exact form of the solution, however, is still quite complicated and will not be repeated here. Additional details can be found in Reference [3].

The coupling between pressure and velocity is accomplished using the hybrid SIMPLER/PISO algorithm of Chen and Patel [4]. The method satisfies continuity of mass by requiring the contravariant velocities, $U^i \triangleq b_j^i U_j$, to have vanishing divergence at each time step, *i.e.* $U_{,i}^i = 0$. Pressure is introduced using the concept of pseudo-velocities, and when combined with the finite-analytic discretization gives the expected Poisson's equation for pressure. The approach differs from other SIMPLER methods in that it introduces contravariant pseudovelocities at staggered grid point locations while leaving pressure (and all other dependent variables) at the grid nodes. It is also unique from most PISO methods in that complete iteration of the pressure solver is performed at every time step, thereby ensuring local conservation of mass at every grid point.

Turbulence Models

The two k-ε turbulence models incorporated in FANS are based on the multi-layer approach of Chen and Patel [4, 5]. These models solve implicitly for the turbulent kinetic energy and its dissipation rate in the fully turbulent portion of the flow, but reduce to one-equation k-l models in the viscous sublayer. When transformed to body-fitted curvilinear coordinates, the fully turbulent portion of the model is:

$$\frac{\partial k}{\partial \tau} + U^i k_{,i} - b_j^i \left[\left(\frac{1}{Re} + \nu_t \right) b_j^m k_{,m} \right]_{,i} - P + \varepsilon = 0, \qquad (6)$$

$$\frac{\partial \varepsilon}{\partial \tau} + U^i \varepsilon_{,i} - b_j^i \left[\left(\frac{1}{Re} + \frac{\nu_t}{1.3} \right) b_j^m \varepsilon_{,m} \right]_{,i} - 1.44 \frac{\varepsilon}{k} P + 1.92 \frac{\varepsilon^2}{k} = 0 \qquad (7)$$

$$P \triangleq \frac{\nu_t}{2} \sum_{i=1}^{3} \sum_{j=1}^{3} \left(b_j^k U_{i,k} + b_i^k U_{j,k} \right)^2 \qquad (8)$$

In the near-wall regions, the two-layer model requires the rate of turbulent dissipation to be specified algebraically rather than computed from (7). The required relations, taken from Chen and Patel, are:

$$\varepsilon = \frac{k^{3/2}}{\ell_\varepsilon} \qquad (9)$$

where ℓ_ε is a dissipation length scale equal to $C_\ell y [1 - \exp(-R_y / A_\varepsilon)]$, y is the normal distance to the closest wall, and R_y is the wall Reynolds number $Re\sqrt{k}y$. The constants C_ℓ and A_ε are chosen to yield a smooth distribution of dissipation rate

between the two regions, and take the values $C_\ell = \kappa C_\mu^{-3/4}$, $\kappa = 0.418$, $C_\mu = 0.09, and\ A_\epsilon = 2C_\ell$.

Implementation of such a two-layer model requires a mechanism for switching between implicit and algebraic dissipation rates. The first k-ε option available in FANS (hereafter referred to as the "standard" two-layer model) handles this switching on a block by block basis – *i.e.* a block is assumed either entirely implicit or entirely algebraic. This approach has the disadvantage that an estimate of viscous sublayer thickness is needed before the grid can be blocked. To circumvent this deficiency, a block-independent two-layer version was developed. The modified model automatically switches dissipation calculations for each point in the grid, and will use the algebraic approach if the wall Reynolds number R_y is less than 250. Efficiency and vectorizability are maintained using a chimera-like data blanking algorithm to avoid breaking the solver loops each time a change in model is needed.

A second improvement has been added to the automated two-layer model to alleviate the accuracy problems of traditional k-ε models in adverse pressure gradients. Known as "sensitization to irrotational strains" [6], the idea is to modify the production of dissipation to better mimic the behavior of ε to pressure-induced strains. In FANS, this is accomplished by breaking the production term from Equation 7 into two pieces, one containing only solenoidal-like derivatives, and the other containing only irrotational ones [7]:

$$P_{sol} = \frac{\nu_t}{2} \sum_{i=1}^{3} \sum_{j=1}^{3} \left(b_j^k U_{i,k} + b_i^k U_{j,k} \right)^2 \; i \neq j \quad (10)$$

$$P_{irr} = \nu_t \left(b_i^k U_{i,k} \right)^2 \quad (11)$$

$$P = P_{sol} + \frac{C_{\varepsilon 3}}{1.44} P_{irr} \quad (12)$$

Validation studies have shown that $C_{\varepsilon 3}$ is better taken at Rodi's value of 2.4 [8] than Launder's original suggestion of 4.44.

The first Reynolds stress model available in FANS is the fully implicit second order closure of Speziale, *et al.* [9]. Hereafter referred to as SSG, this model solves six independent Cartesian Reynolds stress equations in body-fitted coordinates:

$$\frac{\partial(\overline{u_i u_j})}{\partial \tau} + U^m (\overline{u_i u_j})_{,m} = P_{ij} + D_{u\,ij} + D_{p\,ij} + D_{v\,ij} + \Phi_{ij} - \epsilon_{ij} \quad (13)$$

where

$$P_{ij} = -\left((\overline{u_i u_m}) b_m^k U_{j,k} + (\overline{u_j u_m}) b_m^k U_{i,k} \right) \quad (14)$$

and

$$D_{v\,ij} = \frac{g^{mn}}{Re} \left((\overline{u_i u_j})_{,mn} - \Gamma_{mn}^k (\overline{u_i u_j})_{,k} \right) \quad (15)$$

are the production and viscous diffusion, respectively. The four terms

$$D_{u\,ij} \triangleq -\partial \overline{u_i u_j u_m} / \partial x_m \quad (16)$$

$$D_{p\,ij} \triangleq -\partial \overline{u_i p'} / \partial x_j - \partial \overline{u_j p'} / \partial x_i \quad (17)$$

$$\Phi_{ij} \triangleq \overline{p' (\partial u_i / \partial x_j + \partial u_j / \partial x_i)} \quad (18)$$

$$\epsilon_{ij} \triangleq 2 (\overline{\partial u_i / \partial x_k \partial u_j / \partial x_k}) / Re \quad (19)$$

are the turbulent transport, pressure transport, pressure/strain, and dissipation, respectively, and must be modeled.

As with most Reynolds stress closures, SSG models the dissipation rate as $\epsilon_{ij} = 2\delta_{ij}\varepsilon/3$, and lumps turbulent transport $D_{u\,ij}$ and pressure transport $D_{p\,ij}$ into a single term [10]:

$$D_{u\,ij} + D_{p\,ij} = 0.22 b_m^k \left(\frac{k}{\varepsilon} (\overline{u_m u_n})\ b_n^p\ (\overline{u_i u_j})_{,p} \right)_{,k} \quad (20)$$

What sets the SSG model apart is its treatment of Φ_{ij}, the pressure-strain term. That part of the model is fairly complicated, however, and will not be reprinted here. Details of the fully turbulent portion can be found in Reference [9], and the near-wall modifications are given in References [11] and [12].

The final unknown in the Reynolds stress equations is the isotropic dissipation rate ε. FANS uses a scaler representation for this quantity that is similar to the one used in the second (*i.e.* automated) k-ε model described above. Two changes are required, however, before Equation 7 can be applied to a Reynolds stress model. First, the turbulent contribution to diffusion, $\nabla \cdot \nu_t \nabla \varepsilon$, must be replaced with a diffusion arising from Reynolds stresses rather then eddy viscosity. FANS uses the same Daly and Harlow model (Equation 20) applied to the Reynolds stress equation diffusion term. The second change required in Equation 7 is the removal of Launder's sensitization to irrotational strains.

The second Reynolds stress closure available in FANS is the explicit Algebraic Stress Model (ASM) of Gatski and Speziale [13]. Hereafter referred to as GS, this model can simu-

late many of the anisotropic turbulence phenomena normally requiring full Reynolds stress solutions, but without the six additional unknowns. Its availability adds greatly to the practicality of Navier-Stokes methods in that anisotropic flows can be computed for about half the cost of an implicit Reynolds stress solution (*i.e.* six unknowns instead of ten). GS uses the k and ε models directly from Equations 6 and 7 (including the automated two-layer switching), except that Launder's modifications have again been left out.

GS provides a significant improvement over previous ASMs. Because it was specifically developed for transformation invariance in non-inertial reference frames, it has proven more accurate then non-invariant models for flows with strong rotation (*e.g.* vorticity). Although validation is not yet complete, it is believed this advantage will alleviate many of the problems previous models exhibit with excessive dissipation of vorticity.

Multi-Block Grid Capability

FANS solves the governing equations for mean flow and turbulence on structured multiple block grids. Within each block, the grid is defined as an ordered set of points $(\xi_1, \xi_2, \xi_3) = (i, j, k)$, where $i, j, k = 1, 2, 3, \ldots$, but no corresponding structure is required between blocks. Each block is allowed to overlap its neighbors in any convenient manner so long as their union completely covers the domain, *i.e.* no point-to-point connectivity is required between blocks. FANS works on only one block at a time, and communication between blocks is performed by interpolation routines designed to be consistent with the discretization [7]. The technique is referred to as Arbitrary Block Overlapping (ABO) and is similar to chimera schemes except that no points are allowed outside the flow domain. Addition of this last capability would essentially only require a more diverse data structure.

The development of ABO has added greatly to the practicality of RANS solutions. Multi-block grids can now be developed without regard to the smoothness with which blocks fit together, and the fine resolution required near a body need not extend into the far field. Thus, grid generation is greatly simplified, and accurate solutions can be obtained with fewer points. The process is further streamlined through the addition of a preprocessing utility called PREFANS. PREFANS reads ABO grids and calculates all the required block connections and interpolation parameters automatically. The amount of input required from the user is actually *reduced* compared to conventional multi-block structured grids.

Two options are available in FANS for manipulating computer memory requirements: the required variables can either be stored in core, as is typical of most RANS codes, or they may be stored off-line using a disk-based Data Management System (DMS). The DMS version can require significantly less memory, and was designed to run on small machines. It works by locating solution data in files stored on physical (or solid-state) disk, and only reads into core what is needed for solving one block at a time.

One final grid generation related utility is available with FANS. Referred to as GRIDQUAL, this utility performs a point-by-point check on multi-block grids using a number of criteria known to effect solution accuracy. Both tabular and graphical output are given, and can be very helpful for identifying grid induced solution problems (either accuracy related or stability related) *before* a computation is attempted.

General Solution Procedure

Two versions of the FANS code have been developed: one using Cartesian independent variables in three dimensions and one using either cylindrical or Cartesian variables for two-dimensional flows. The solution procedure is the same for each, and consists of an outer iteration over time and an inner loop over the blocks of the grid. Within each block, the discretized equations are solved in a scalar implicit manner using an ADI technique in the cross-flow plane and iterative relaxation in the streamwise direction. The pressure solver is sub-iterated at each time step to allow conservation of both mass and momentum at every iteration. Once an updated solution is available within a block, its boundary data is transmitted to all matching faces through data management surface files.

Unlike RANS codes utilizing upwind discretizations, the finite-analytic method does not rely on CFL related stability criteria. Globally constant time-steps can therefore be employed without the limits usually imposed by very small grid cells. For large cases, convergence can be further improved by starting the solution with a coarsened mesh created by removing every other point. Such a solution can usually be obtained in about one eighth the time of a fine grid calculation, and provides an excellent starting point for the detailed computation. Because the required

coarsening and fine grid re-interpolation can be quite complicated for multi-block grids, utilities called COARSEN and REFINE are provided to automate the process.

The k-ε and GS versions of FANS require about 25×10^{-6} seconds of Cray C-90 CPU time per grid point pre iteration (including sub-iteration). Implicit SSG model applications require about twice that amount. FANS's total memory requirement is 71 words per grid point for a k-ε solution, and 89 words per grid point for a fully implicit SSG solution. The required total can be split between core memory and off-line storage by using different options in the data management system. The number of iterations required for a converged solution varies greatly depending on the application. Simple geometries started from coarse grid solutions can converge as quickly as a few hundred iterations, whereas complex separated flows can require many thousands. An interactive graphics utility called CONVERGE is provided for monitoring convergence statistics as the run progresses. CONVERGE plots time histories of Euclidean norms, maximum norms, and computed forces, and allows users to interpret convergence using their own judgement.

Unsteady Capability

While unsteady RANS applications have traditionally required prohibitively large human and computational resources, such application are finally becoming practical. Unlike RANS codes utilizing artificial compressibility, however, FANS is ready for this transition without modification. The pressure solver has been specifically developed for unsteady applications, and ensures that mass is conserved at every time step and every point in the grid. The recent addition of a chimera-grid capability and advanced Reynolds stress turbulence models make FANS an ideal code for examining complex unsteady flows.

Recent unsteady applications have focused primarily on acoustic problems. Thus far, FANS has been used to compute the unsteady pressure field behind automotive side-view mirrors, and is now being applied to compute Lighthill sources for acoustic transmission problems. While it must be understood that Reynolds averaged codes can not be expected to provide turbulent time scales, a number of commercial flow problems exist where the lower frequencies are important. As this work progresses, therefore, it is planned to provide FANS with post-processor utilities for calculating Lighthill sources and for solving wave transmission problems in practical acoustics applications.

Free Surface Model

Free surface effects are modeled using a hybrid zonal approach developed under ONR's Nonlinear Ship Motion Program [14, 15, 16]. In this zonal model. FANS is used in the near field to resolve the turbulent boundary layer, wake, and nonlinear waves, while potential flow methods are used to provide the ship-generated waves away from the hull.

For the inner domain calculation, a nonlinear free surface boundary condition has been implemented in the FANS code. As part of the FANS calculation, the free surface elevation at each free surface grid point is computed and the grid is stretched to match the computed elevation. An exact free surface boundary condition can then be imposed on the free surface grid face. The calculation is continued until the free surface elevations converge.

For steady ship flow problems, the inviscid flow calculations are made using the Ship Lift And Wave (SLAW) code [17]. The SLAW code is a Rankine source free surface potential flow method (a lá Dawson [18]) which incorporates a linearized free surface boundary condition, collocation point shift radiation condition, and a choice of nonlifting or lifting hull singularity models. SLAW was developed under SAIC's IR&D program as a ship resistance code and has been applied to a variety of ship forms ranging from sailing yachts to SWATHs.

The viscous-inviscid interaction is captured through a direct matching of the velocity and pressure fields in the overlapping region between the RANS and potential flow domains. Initially, the velocity distribution on the outer face of the RANS domain is computed by a full domain SLAW calculation. After the inner domain RANS calculation is completed, far-field SLAW calculations are made using the RANS velocities on an intermediate matching surface. A fully interacting solution is obtained by iterating between the RANS and SLAW calculations. Validation calculations show convergence within three iterations at higher Froude numbers. At lower Froude numbers, iteration is not usually required.

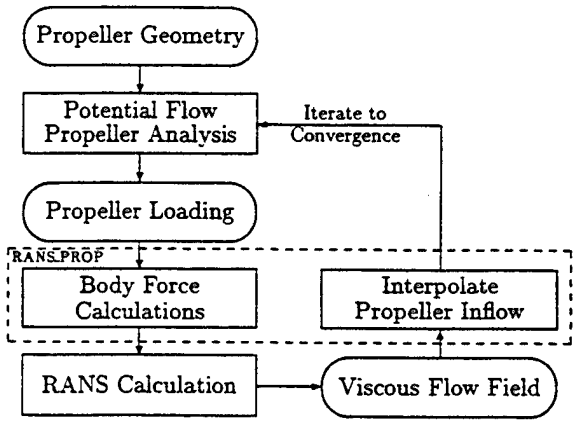


Figure 1: RANS/Propeller Analysis System

Propeller Model

In order to model the interaction between a ship's or submarine's viscous flow field and its propeller, a RANS/propulsor flow model has been developed under ARPA's Submarine Technology Program. The model was developed in two steps. First, a body force model was added to the FANS code so that the effects of a propulsor could be included in the viscous flow calculation [7]. Second, an interface was built between FANS and a number of potential flow propeller codes so that the propeller/wake coupling could be automated [19].

The body force approach was chosen since it provides a convenient method for modeling propellers as a three-dimensional force field distribution over a background computational grid. Thus, the effects of a propeller, including axial, radial, and swirl forces, can be included directly into the RANS calculation without the complication of resolving each propulsor element. The system was developed for both the propeller "design" problem – in which the desired propeller loading is known – and the "analysis" problem – in which the propeller geometry is known.

The propeller "design" problem is the easier of the two because the loading is specified *a priori* and is not dependent on the viscous flow field. First, a suitable body force distribution is created for the specified loading. Second, the RANS code is used to compute the viscous flow field including the propeller effects. Finally, the resulting inflow at the propeller is extracted, and a design program such as MIT's PBD-10 is used to compute the required blade shape.

In the propeller "analysis" problem, however, the viscous flow field will depend on the propeller loading and the propeller loading will depend on the viscous flow field, so an iterative approach has been implemented as shown in Figure 1. The approach uses a RANS code to compute the viscous flow field, and a potential flow propeller analysis code to compute propeller performance, including blade loading and the propeller-induced velocity field. The RANS_PROP interface was designed to automate this process while allowing quick interchange of the RANS and/or propeller model components. RANS_PROP has modules for interpolating the total propeller inflow from the RANS flow field, subtracting the propeller-induced component of inflow to get effective wake, preparing propeller analysis code input files, extracting blade loading from propeller analysis output files, and computing the appropriate RANS body force propeller distribution. By iterating between the RANS, RANS_PROP, and propeller analysis codes, the propeller/hull interaction can be computed.

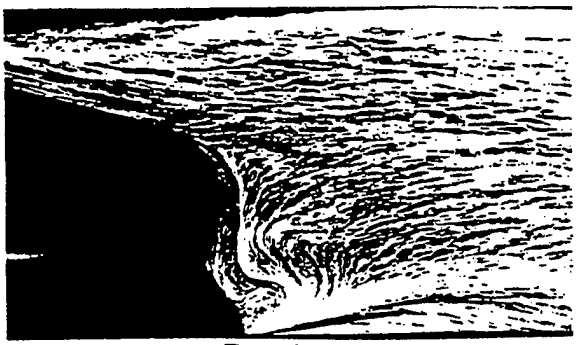
While RANS_PROP was originally configured to work with FANS and MIT's Propeller Steady Force (PSF-2) vortex lattice code, the code is designed so that other components can be substituted as needed. As long as the required analysis programs are available, propulsor configurations of almost any complexity can be modeled without affecting the complexity of the RANS calculation.

COMPUTATIONAL RESULTS

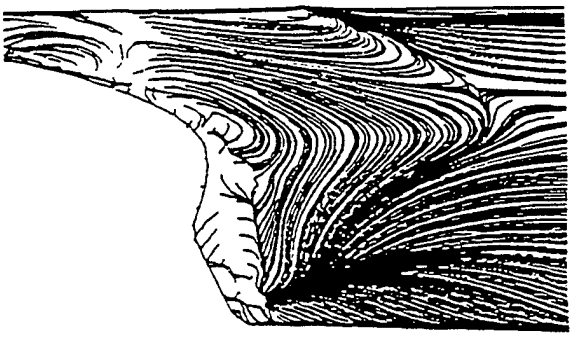
This section summarizes flow calculations for four configurations: the HSVA tanker, the appended "SUBOFF" submarine hull, a submarine-like body with propeller, and a Series 60 surface ship. The Series 60 calculations include both free surface and propeller effects.

HSVA Tanker

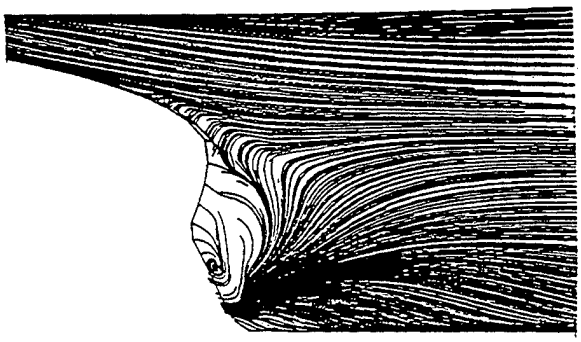
The first sample calculations presented are for the HSVA tanker studied as part of CFD Workshop Tokyo 1994. As noted previously, this hull form was selected for the workshop because the 1990 workshop calculations failed to predict the development of bilge vortices. To demonstrate the effect of turbulence modeling, FANS calculations were made with three different turbulence models on the same grid: the basic two-layer k-ε model, the automated two-layer k-ε model with Launder/Rodi corrections, and the SSG Reynolds stress closure model. The calculations were made



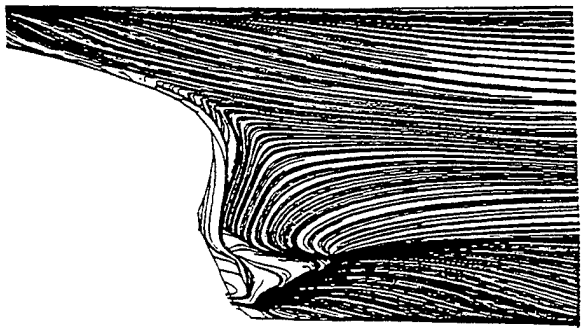
Experiment



Conventional K-ϵ model



Improved K-ϵ model

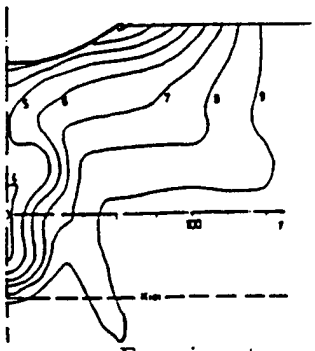


Reynolds Stress Closure Model

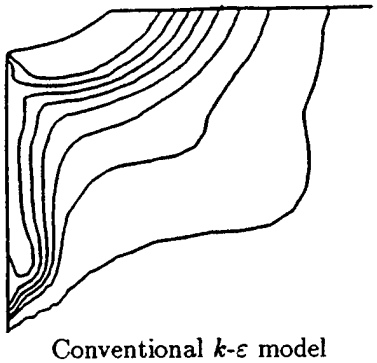
Figure 2: HSVA Surface Streamlines

at a Reynolds number of 5×10^6 on a grid with 370,000 points and free surface effects were neglected.

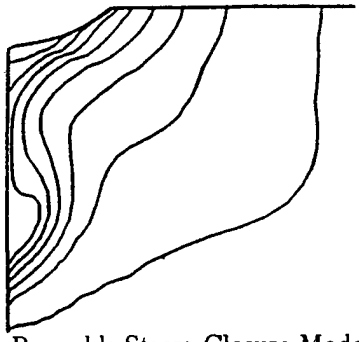
Figure 2 compares measured and computationed surface streamlines over the stern of the HSVA hull. The first computational result uses the basic two layer k-ε model and shows an excessively large separation region at the stern. The second result uses the modified k-ε model and shows that the separation region is predicted much more accurately. This is not surprising since the Launder/Rodi corrections were developed specifically to improve the behavior of turbulence dissipation in adverse pressure gradients. The surface streamline for the last calculation, which uses the SSG Reynolds stress closure model, shows very good, but not perfect, agreement.



Experiment



Conventional k-ε model



Reynolds Stress Closure Model

Figure 3: HSVA Axial Velocity Contours

Figure 3 compares experimental and computational axial velocity contours at the propeller plane ($x/L = 0.505$). The bilge vortex creates a "hook" in the contours that is clearly visible in

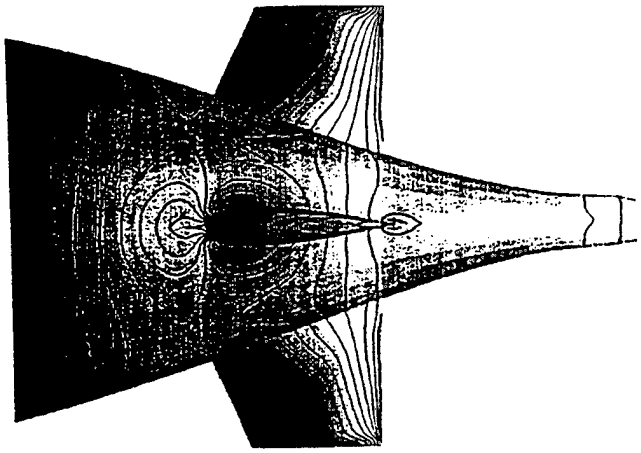


Figure 4: SUBOFF Surface Pressure Contours

the experimental data. The unmodified k-ε results miss this hook and show a significant separation area near the waterline. The SSG results show much better agreement, including the hook, though the strength of the bilge vortex seems to be underpredicted. This underprediction may be due to insufficient grid resolution of the bilge/keel of the ship. The need for advanced anisotropic turbulence models like SSG for complex 3-D flow field is clearly demonstrated.

Appended SUBOFF Body

This section describes a computation for the SUBOFF body with stern appendages. The configuration, which consists of only a hull and four identical stern appendages, was one of several configurations analyzed as part of ARPA's SUBOFF program, which was completed in 1990. The SUBOFF program, which included extensive wind and water tunnel experiments [20], evaluated the ability of existing CFD capabilities to compute the viscous flow around a submarine with various combinations of appendages. The present calculation was made using the SSG Reynolds stress model at a Reynolds number, based on hull length, is 1.2×10^7. Figure 4 shows the geometry and contours of computed surface pressure over the appendages and aft portion of the hull.

Figure 5 compares computed and measured contours of axial velocity at the propeller inflow plane ($x/L = 0.978$) just aft of the appendages. The thick body boundary layer and the effect of the stern appendages is clearly visible. The discrepancy between the computed and measured body boundary layer profiles, which shows up here as radially shifted contours, is mostly due

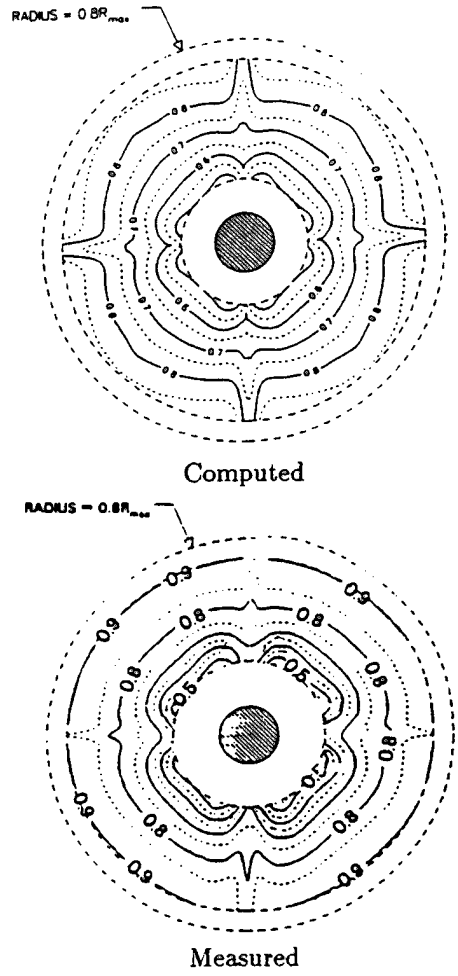


Figure 5: SUBOFF Axial Velocity Contours

to an overly coarse grid and is not seen in the fine grid calculations performed for other SUBOFF configurations. However, some of this discrepancy may be caused by tunnel blockage in the experiment. Comparison of surface pressure, for example, shows that the blockage has a significant effect on the forward third of the hull. Unfortunately, no fine grid study has been performed for the appended case.

Despite the coarse grid, the effect of the stern appendages is well predicted. Two major effects on the axial flow are discernible. First, the boundary layer on the appendage sides creates a momentum deficit, which is visible at the outer radii of the plot. Secondly, the appendage/hull junction creates a "horseshoe" vortex that interacts with the boundary layer. The effect appears as a pair of contra-rotating vortices, one on each side of the appendage root, and creates a region of *higher* axial velocity (thinner boundary layer) immediately behind the appendage by "pulling" high momentum fluid down toward the hull. This

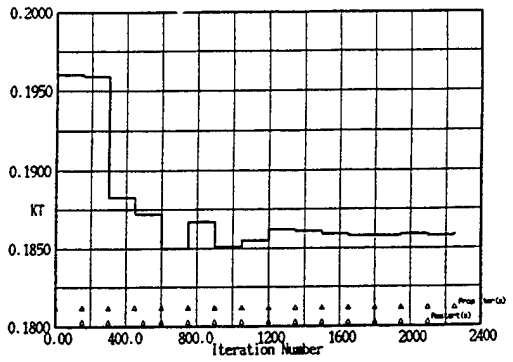


Figure 6: Propeller Thrust History for Submarine Body

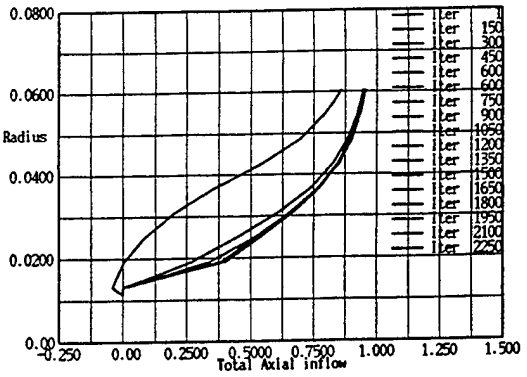


Figure 7: Axial Inflow History for Submarine Body

effect is most noticeable close to the hull surface since the junction vortices remain close to the surface. Both the calculations and the experiments show these features clearly. The appendages also create vorticity at their tips, but the effect of this vorticity is outside the propeller diameter and not visible in these plots. A more detailed analysis of this calculation and additional second-moment closure validation calculations are presented in Reference [21].

Submarine Body with Propeller

The RANS_PROP flow system was validated with calculations around an unappended submarine-like body with and without a propeller. This body was chose because validation quality experimental data was available. The Reynolds number based on hull length was 6×10^6. FANS calculations were performed with the modified k-ε two-layer turbulence model. The propelled case included a four bladed B-series propeller (B4.40 P/D=0.68) at an advance coefficient (J) of 0.47. MIT's PSF-2 code was used for the propeller analysis, and RANS_PROP handled the FANS/PSF iteration. In the experiment, the model was supported by an aft-mounted sting. The sting was also modeled in the calculation.

The FANS calculation for the hull with propeller was initialized using the converged FANS solution with the body force set to zero. 2,250 FANS iterations were then made, with RANS_PROP run after every 150 iterations to update the propeller performance.

The history of the computed propeller thrust coefficient (K_T) is shown in Figure 6. The final converged thrust and torque are $K_T = 0.1859$ and $K_Q = 0.0210$, and are within 3% of the reported experimental values.

The history of the axial component of the

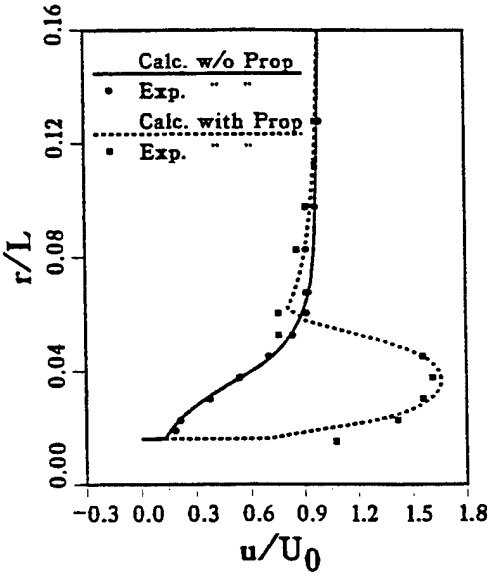


Figure 8: Comparison of Computed Axial Velocity with Experimental Measurements

interpolated total propeller inflow is shown in Figure 7. The initial total wake, which was interpolated from the no-propeller solution, shows a very thick boundary layer including a significant separation region at the root. As the propeller accelerates the flow, however, the separated region disappears and the inflow profile becomes more full. The reduction of the viscous deficit results in and increase of the effective inflow which causes the drop in K_T shown in Figure 6.

Figure 8 compares computed versus measured profiles of axial velocity at $x/L = 1.032$ (the propeller is located at $x/L = 1.015$). The comparison to the experimental data is extremely good for both the propelled and un-propelled cases.

Figures 9 and 10 show centerplane ($z = 0$) plots comparing the computed FANS flow field with and without the propeller. The views are close ups of the propeller region of the config-

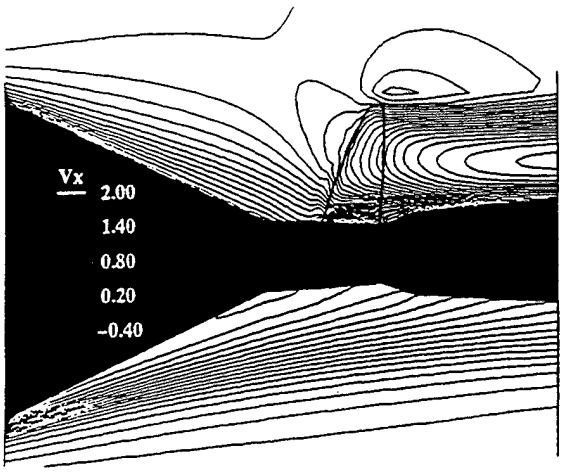


Figure 9: Computed Axial Velocity Contours for Submarine Body with and without Propeller

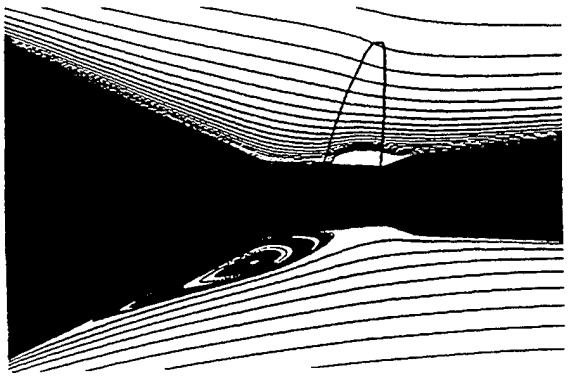


Figure 10: Computed Streamlines for Submarine Body with and without Propeller

uration with the flow coming from the left and the mounting sting on the right. In these plots, the top half of the plot shows the solution with the propeller while the bottom half is the no-propeller solution. The sweep of the propeller blade is shown as an outline in the top half of the figure. Figure 9 compares contours of constant axial velocity. The propeller-induced shear layers, the dramatic reduction of boundary layer thickness, and the elimination of separation are all clearly visible.

Figure 10 compares computed streamlines in the stern regions. The streamlines are computed at regular radial grid intervals, starting near the aft end of the hull slightly upstream of the propeller. For the sake of comparison, the tangential (swirl) velocity induced by the propeller has been suppressed by restricting the streamlines to $z = 0$ planes. The large hull separation region in the no-propeller case (bottom half of the plot) is clearly visible, as is the extent of the small separation region computed at the root of

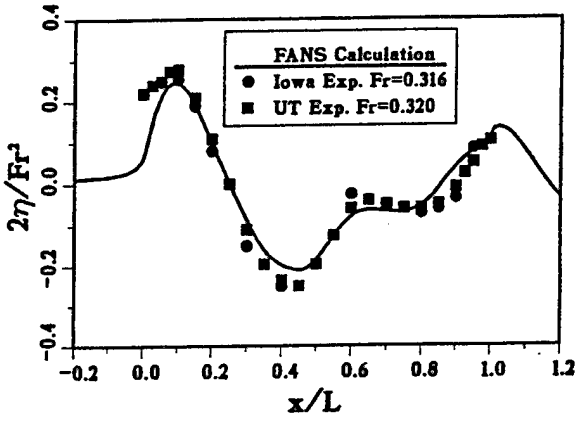


Figure 11: Waterline Elevation for Series 60, Fr=0.316

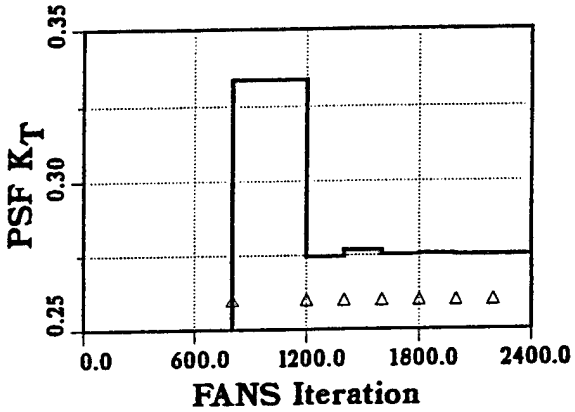


Figure 12: Propeller Thrust Convergence For Series 60

the operating propeller (top half of the plot). The streamlines for the calculation with the propeller also show the dramatic thinning of the boundary layer and the contraction of the flow through the propeller.

For additional results and a more thorough discussion of this validation case, see Reference [19].

Series 60 Surface Ship

Flow calculations have also been made for the Series 60, $C_B = 0.6$ hull form. Model tests for this geometry have been made at the University of Iowa that include the effects of the free surface [23] and propeller [24]. Calculations were made at the model scale Reynolds number of 4×10^6 for Froude number, Fr=0.0 (double body) and Fr=0.316. For each Froude number, calculations were made with and without the propeller.

For the unpropelled case, the Fr=0.316 calculations were presented at the CFD Work-

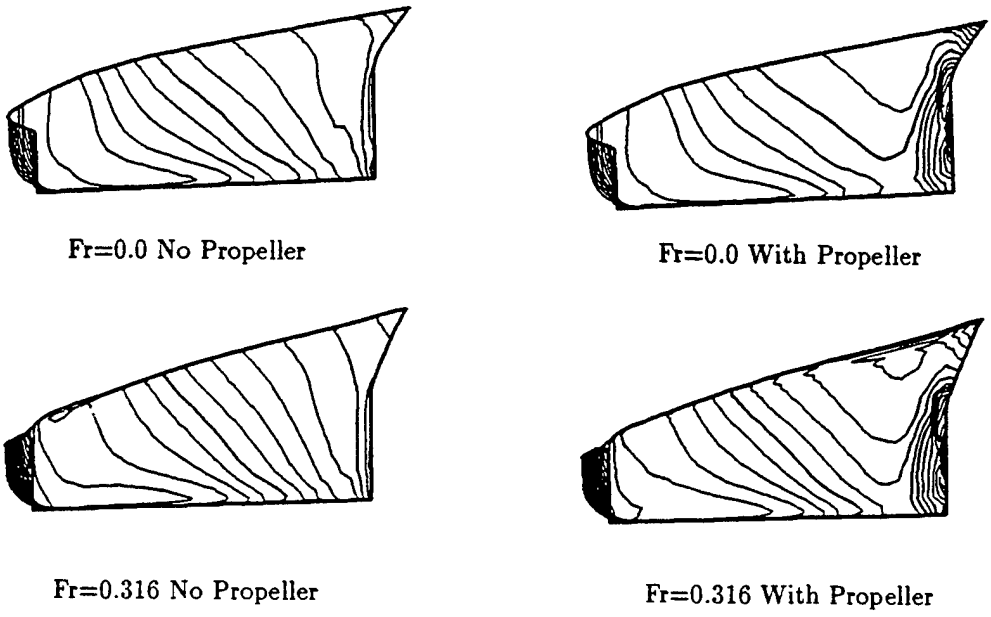
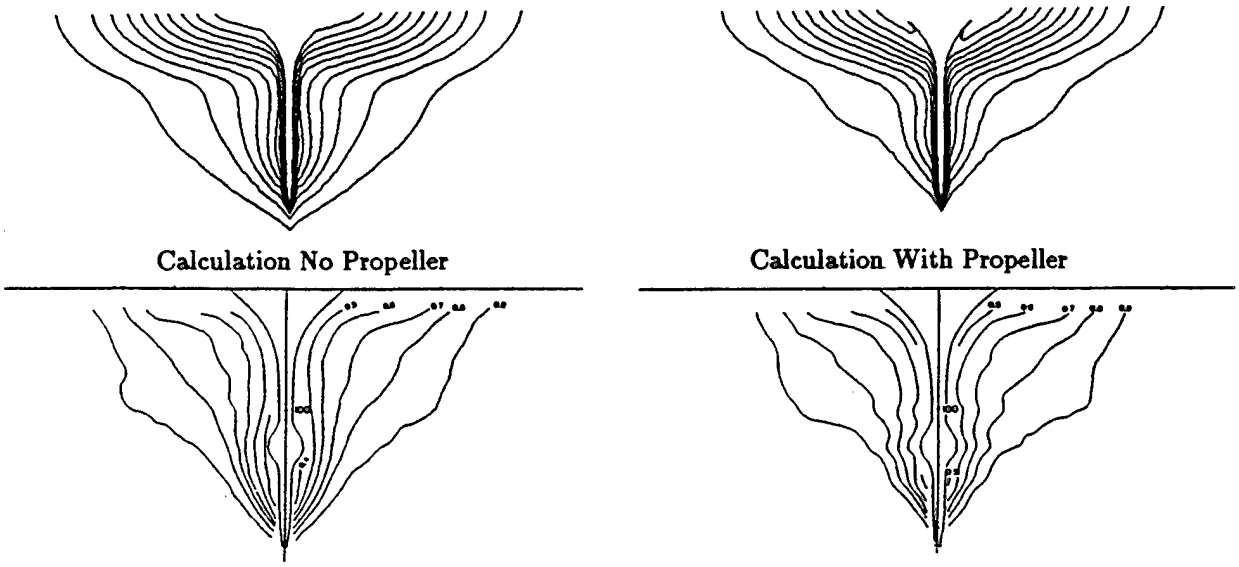


Figure 13: Series 60 Stern Pressure Contours

shop Tokyo 1994, and are discussed in detail in Reference [1]. This zonal calculation used FANS with a nonlinear free surface boundary condition in the near field and the SLAW linear free surface potential flow code in the far-field. In the near field, the grid is stretched to match the computed free surface elevation and an exact boundary condition is applied on this surface. Figure 11 shows the computed free surface elevation along the side of the ship. Comparison with the experimental data shows good agreement, but that the peaks and troughs are underpredicted and the shape of the shoulder wave is not quite right. This discrepancy is most likely due to grid resolution, since the free surface has been matched rather crudely by stretching the grid points vertically near the ship hull. A more sophisticated approach, which follows a spline representation of the complete ship hull, is under development to alleviate this problem. As with all the RANS results presented at the SRI workshop, the waves away from the ship side decay too rapidly and do not agree well with the experimental wave field. This decay is most likely a resolution problem since many grid points are required for each wave, and indicates that further work is required before accurate wave fields can be computed.

Propelled calculations were performed using MIT's PSF-2 vortex lattice propeller analysis code to model the five-bladed MAU propeller described in Reference [24]. The RANS_PROP code was used to interface the viscous flow calculation and the potential flow analysis. For both Froude numbers, the advance coefficient (J) of the propeller was 0.654 and the calculation was started from the unpropelled result. Figure 12 shows the propeller thrust convergence history for the Fr=0.0 calculation. When the propeller is first turned on (after 800 FANS iterations), the initial thrust coefficient (K_T) is quite high. As the propeller accelerates the flow and thins the boundary layer over the ship's stern, the effective inflow increases and K_T drops, converging in just a few iterations. The triangles on the plot mark the points at which the body forces were updated by interpolating propeller inflow from the RANS result and recomputing the propeller performance. The converged K_T is 0.275 and the torque coefficient (K_Q) is 0.0445. These are higher than the experimental values of $K_T = 0.234$ and $K_Q = 0.0411$, probably due to an overprediction of boundary layer thickness and the use of steady propeller analysis. For more detailed ship calculations, an unsteady propeller analysis code should be used to include the effects of the circumferentially varying inflow.



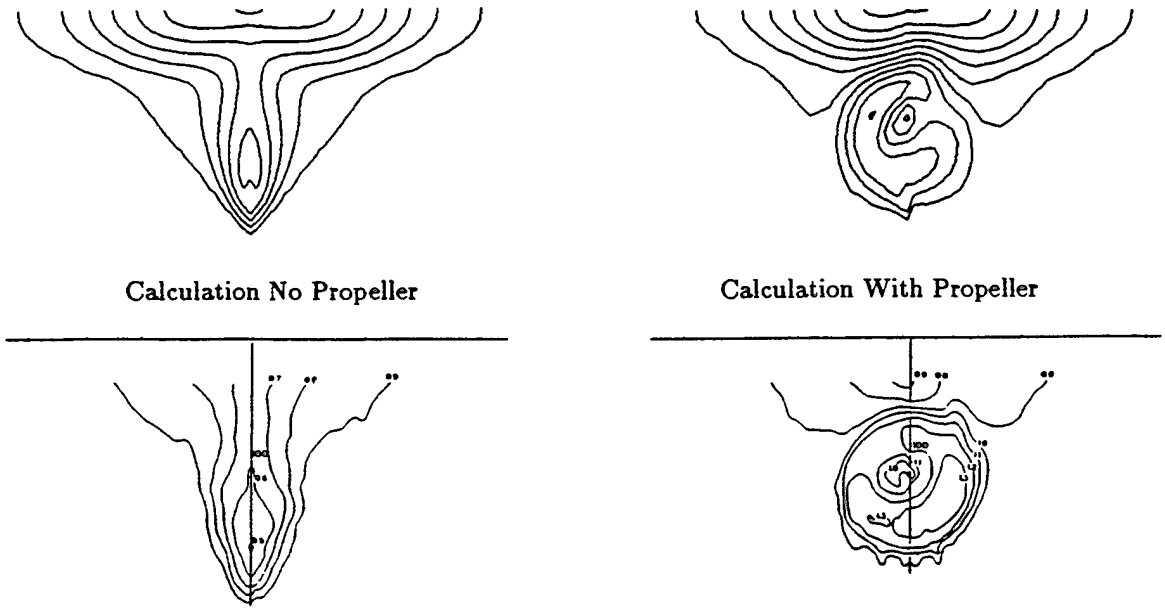
Calculation No Propeller

Calculation With Propeller

Experiment No Propeller

Experiment With Propeller

Figure 14: Series 60 Axial Velocity Contours - $x/L = 0.975$



Calculation No Propeller

Calculation With Propeller

Experiment No Propeller

Experiment With Propeller

Figure 15: Series 60 Axial Velocity Contours - $x/L = 1.05$

The Fr=0.316 with propeller calculations showed very similar behavior, with a final K_T of 0.2793 and K_Q of 0.0450. The free surface calculation had a slightly thicker boundary layer, which in turn caused slightly higher propeller thrust and torque. The effect of the propeller on the computed free surface elevation was minimal.

Figure 13 shows pressure contours over the stern for all four calculations. The contour increment is $\Delta C_P = 0.02$ with the $C_P = 0.0$ contour drawn in bold. The uneven waterline on the Fr=0.316 shows how the grid has been fitted to the computed free surface elevation. The plots with propeller show that the propeller effects the pressure over about the last 20% of the hull. These pressure distributions agree fairly well with the experimental values shown in [24], though the propeller effect is slightly exaggerated because of the overpredicted thrust.

Figures 14 and 15 compare computed and measured axial velocity contours at two planes. The $x/L = 0.975$ plane is just upstream of the propeller while the $x/L = 1.05$ plane is just downstream. Results are shown for Fr=0.0 with and without propeller. The Fr=0.316 results are similar but show a slightly thicker boundary layer and some variations at the free surface. The effect of the propeller at the upstream location is a subtle thinning of the viscous wake, while downstream the effect is more dramatic. While the thickness of wake is overpredicted by the calculations, the wake's shape and the effect of the propeller are quite good.

DESIGN APPLICATION ISSUES

The ultimate application of developed near-field flow predictive capability should be related to specific design problems. It should be noted that while RANS code systems like the present one are reaching a level of maturity where they can be applied to design problems by expert users, they are not yet *tools* in the traditional sense that can be applied as "black boxes". A collaborative effort between the designer and hydrodynamicist is required both to maximize the success of the calculations and to guide further development of the code system.

Multi-Level Code System

Two key requirements for the application of CFD to design are the integration of codes into complete flow analysis systems, and the use of multiple levels of sophistication as the analysis proceeds. Integration of the CFD code into a system including geometry modeling, grid generation, flow visualization, and performance evaluation is required so that the impact of design variation or configuration changes can be rapidly and efficiently evaluated. In particular, the generation of computational grids for realistic configurations has proved to be a major obstacle toward the practical application of RANS codes. The present system uses the Air Force's highly interactive GRIDGEN code [25], grid resplining, reblocking, and quality evaluation utilities developed at SAIC and FANS's arbitrary block overlap capability to speed up the creation of suitable grids.

The use of multiple analysis tools of varying levels of accuracy, ease-of-use, robustness, and cost, is important in building an comprehensive analysis system. With multiple tools available, trade offs between cost and accuracy can be made to ensure the appropriate level of analysis for the stage of the design process. In addition, lower level analyses can be used to enhance the accuracy of higher level analyses while mitigating the cost and risk. For example, inviscid potential flow calculations should be used with RANS analysis since the inviscid calculation can guide grid design, help verify convergence, and highlight the effects of viscosity. The multi-level analysis approach can also be applied within a single analysis code. RANS calculations for complicated ship configurations may be preceded by calculations on a coarse grid, simplified configurations (*e.g.* unappended body), simpler turbulence model, or neglected free surface effects.

SAIC's implementation of the multi-level approach is called the Interactive Design, Evaluation, and Analysis System (IDEAS) [26]. The development of this system was motivated by experience in the design of the 1987 America's Cup winner *Stars & Stripes*. While originally developed to build a design system based on potential flow seakeeping codes, it is admirably suited to RANS viscous flow applications.

On a larger scale, the multilevel approach is not restricted to CFD techniques. Empirical tools and procedures ranging from knowledge of existing ships, appendages, and propulsors to the ITTC friction line form an important first level of analysis that must be considered as part of the design system. Model tests must be included in this multilevel framework since they provide another level of design analysis. In addition, CFD can be used to support, plan, and analyze the

model test, while the model tests can be used to verify the CFD results.

Design Problems

The principle design applications of the current system relate to prediction of viscous stern flow, particularly the detailed viscous inflow to the propeller. Detailed knowledge of the propeller inflow is critical to the design and/or selection of propulsors that maximize efficiency while minimizing undesirable effects such as vibration and cavitation. By incorporating the nonlinear free surface and propeller models into the RANS computation, both the effects of the free surface on the propeller inflow and the effect of the propeller on the free surface are computed. Similarly, the propeller model allows the propeller's performance in the viscous wake to be evaluated, and the true *effective* wake to be computed.

Propeller inflow prediction is especially important for commercial ships with heavily loaded single propellers operating in the viscous stern flow. While viscous propeller inflow is not as important to most naval combatants (whose design usually allows the propellers to be positioned outside of the hull boundary layer), it will continue to be important in the development of transport and support ships such as the new generation of fast transports and auxiliaries.

Other stern flow applications include the prediction of the wake behind appendages, and the interaction of the rudder with the viscous flow field, free surface, and propeller. Appendage flow is of particular interest for submarine design. The sail and stern appendages have a very significant impact on propeller inflow because of the viscous wake deficit behind the appendages and the interaction of junction "horseshoe" vortices with the body boundary layer. Appendage and junction flows and their interaction with the free surface may also be important in the design of racing yachts.

Transom sterns may eventually be a key application for this system. While linear potential flow methods with simple transom models have been fairly successful in predicting the performance of conventional high speed transoms, they are unable to analyze off-design conditions (*e.g.* wet transom) and are too limited for modeling extreme transom stern designs. A coupled RANS/free surface capability provides a more fundamentally sound basis for analyzing the problem.

A potential application to naval ship design is the evaluation of the non-acoustic detection characteristics of candidate hull forms. Near-field RANS calculations can be applied to compute realistic starting conditions for parabolized Navier-Stokes (PNS) far-field wake calculations, which until now had to rely on approximate near-field models built up from empirical data.

While force prediction is not the focus of this paper, the calculation of resistance is a potentially important application of the near-field ship flow capability. With its free surface and propeller models, the current system can be used for computing almost all ship resistance components, including skin friction, form drag, wave resistance, appendage drag, and thrust deduction. Drag calculations made to date have been very encouraging: drag values for the HSVA and Series 60 ship forms, unappended submarine bodies, and 2-D foils have agreed well with experimental values. Since most of the resistance components can be adequately predicted using simpler empirical or computational methods, however, RANS is is probably unnecessary for force predictions of conventional designs.

FUTURE DEVELOPMENT

As mentioned earlier, the capability described in this paper is the result of an ongoing effort to create a viscous flow prediction system for naval architecture applications. The development efforts can be divided into two main areas: computation fluid dynamics and computational design. In the CFD area, numerical methods have progressed to the point where they are now ready to be applied to design problems. However, the ship flow prediction problem has not been completely solved. Continued development is required for the modeling of more complicated free surface flows, such as those around transom sterns, and for full scale ship calculations.

In the computational design area, interactive grid generation, multi-level analysis, chimera grids, and improved code robustness have all enhanced the ability to obtain viscous flow calculations for practical configurations. Many ship flow problems important to design have been identified that can be computed with current capabilities. However, the complexity of the problem is such that an expert hydrodynamicist is still required to guide the calculations, and the hydrodynamicist/designer collaboration is needed to develop procedures for incorporating CFD results into the ship design process. Furthermore, the complex issues of quantified accuracy, risk assessment, and

ship synthesis models have yet to be adequately addressed.

For now, RANS-based methods like the current one should be applied to design while research continues in CFD and computational design. Such studies, which must be carried out jointly by hydrodynamicists and designers, are necessary to create procedures for design analysis, for modifying the design process to incorporate and exploit advanced numerical results, and to set the focus for future research.

Also, CFD-based research and validation needs to focus on actual modern ship geometries including large C_B low speed tankers, high speed container ships with large overhanging sterns, and fast naval combatants. Older hull forms like Series 60 are no longer completely relevant to current ship design. However, they continue to be used because those are the configurations for which extensive experimental data is available. Therefore, the database of experimental ship flow and ship performance data should be expanded to include modern designs and, if possible, full scale data.

Accuracy and Risk

Despite efforts in code validation, error estimation for CFD remains unsatisfactory. For flow prediction to be useful for design, the possible error for any design parameters must be evaluated with respect to variations in the design variables. That is, the system sensitivities must be evaluated from a synthesis model for the design, and re-evaluated as the design progresses. Coupling the possible error in each design parameter with its corresponding sensitivities leads to a measure of the accuracy required in assessing the design's performance with respect to that parameter. Alternatively, propagation of the error through the system sensitivities provides a measure of the risk involved in relying on that particular method for evaluation. Detailed knowledge of accuracy requirements and the acceptable level of risk is the only rational method for determining whether an educated guess, a full RANS calculation, or something in between, is appropriate for the evaluation. Non-expert use of computational fluid codes for design will ultimately depend upon the availability of error estimates and system sensitivities.

Error estimation is generally very difficult. For the CFD codes discussed in this paper, the error estimates must include: error in modeling the geometry and in gridding, truncation error, convergence error, error introduced through theory and code approximations, error introduced in modeling (*e.g.* propeller and turbulence models), experimental error in validations, and scaling errors. It will not be easy to obtain reliable estimates of these individual errors. In some cases, new techniques are necessary, such as adaptive gridding driven by solution error.

In addition to estimates of the error introduced through computation, it is also necessary to quantify the error inherent in other design procedures, including regression techniques, empirical rules-of-thumb, experimental procedures, and scaling from model to full scale. A comprehensive approach to error estimation in ship design does not yet exist. In some areas error estimates are not even attempted. Unless a systematic approach is begun to record both the best available estimates of error and the rationale behind them, it will be very difficult to improve current practice.

As our knowledge improves, better estimates will replace these initial crude estimates. This iterative, systematic approach probably represents our best chance at preserving and improving current design knowledge and practice. In addition to providing a quantified measure of design risk, it will allow us to discern the gaps in our capability, and enable us to assign resources to fill those gaps.

Full Scale Effects

Perhaps the greatest benefit that CFD offers for ship design is the potential to predict flow fields at full scale Reynolds numbers. Few validated full scale ship or submarine calculations have been made. There are several reasons for this. First, grid resolution requirements at Reynolds numbers of 10^9 and above require multimillion point grids to adequately model realistic ship geometries. The extremely fine boundary layer spacings make the generation of such grids difficult and the convergence of CFD codes very slow. Secondly, the accuracy of available turbulence models at these Reynolds numbers has not been adequately demonstrated. Finally and perhaps most importantly, there is a critical lack of quality data for full scale validation, particularly for ships.

In 1990, limited FANS calculations were made for a submarine with sail at full scale Reynolds number with some success [27]. A qualitative analysis of the results showed that the hull boundary layer was reasonably well predicted, but the sail vorticity dissipated too rapidly down-

stream. Because of the lack of detailed full scale experimental data for the configuration, a quantitative validation was not possible. While subsequent improvements in grid generation, turbulence modeling, and computational capabilities would make full scale calculations more practical today, validation would still be very difficult.

CONCLUSIONS

A near-field ship flow numerical prediction capability is presented which combines a zonal RANS/nonlinear free-surface method, an interacting RANS/propeller flow model, and a new second-order closure turbulence model. The combination of these three methods has resulted in a state-of-the-art computational system for modeling ship flow fields including thick turbulent boundary layers, separation, vortices, free surface effects, and propeller/hull coupling. The capability incorporates zonal calculation techniques, advanced gridding tools, and chimera arbitrary block overlapping to allow detailed flow calculations for real configurations to be made in practical time frames. Calculations have been presented which demonstrate the system's ability to model both propeller/hull interaction and free surface effects as well as demonstrate the need for second-order closure turbulence modeling.

While numerical capabilities like the current one have not completely solved the ship flow problem, they have reached a level of maturity where they can and should be applied to ship design problems. Viscous flow design studies carried out jointly by hydrodynamicists and designers are needed to establish design procedures incorporating advanced flow calculations while driving continued research in areas like full scale turbulence modeling and computational risk assessment.

ACKNOWLEDGEMENTS

This ship flow calculations presented in this work have been supported by the Office of Naval Research (E. Rood). The development of the FANS code and near-field flow capability has been supported by the Office of Naval Research (E. Rood and J. Fein) and by the Advanced Research Project Agency's Submarine Technology Program (G. Jones).

Most of the computations for this paper were performed on the CRAY C90 and YMP of Cray Research Inc. at Eagen, Minnesota under the sponsorship of C. Hempel. Other calculations and computer code development were done on the CRAY YMP at the Texas A & M Supercomputer Center and on the Convex 220 and Convex 3840 at the ARPA-funded U.S. Navy Hydrodynamic/Hydroacoustic Technology Center at David Taylor Research Center. We are grateful to Cray Research Inc. and to ARPA for the use of these computing resources.

References

[1] Chen, H.C., Lin, W.M., and Weems, K., "Calculations of Viscous Nonlinear Free-Surface Flows Using an Interactive Zonal Approach," *Proceedings CFD Workshop Tokyo 1994*, Ship Research Institute, 1994, pp. 105-114.

[2] Chen, H.C., Lin, W.M., and Weems, K., "Second Moment RANS Calculation of Viscous Flow Around Ship Hulls," *Proceedings CFD Workshop Tokyo 1994*, Ship Research Institute, 1994, pp. 275-284.

[3] Chen, H.C., Patel, V.C., and Ju, S., "Solutions of Reynolds-Averaged Navier-Stokes Equations for Three-Dimensional Incompressible Flows," *Journal of Computational Physics*, Vol. 88, No. 2, pp. 305-336, 1990.

[4] Chen, H.C. and Patel, V.C., "The Flow Around Wing-Body Junctions," *Proc. 4th Symposium on Numerical and Physical Aspects of Aerodynamic Flows*, Long Beach, CA, 1989.

[5] Chen, H.C. and Patel, V.C., "Near-Wall Turbulence Models for Complex Flows Including Separation," *AIAA Journal*, Vol. 26, No. 4, pp. 641-648, 1988.

[6] Hanjalic, K. and Launder, B. E., "Sensitizing the Dissipation Equation to Irrotational Strains," *Journal of Fluids Engineering*, Vol. 102, No. 34, 1980.

[7] Korpus, R., "Body-Force Propulsor Models and Other Related Improvements to the FANS Code," SAIC-92/1132, 1992, Science Applications International Corporation, Annapolis, Maryland.

[8] Rodi, W. and Scheuerer, G., "Scrutinizing the k-ε Model Under Adverse Pressure Gradient Conditions," *Journal of Fluids Engineering*, Vol. 108, pp. 174-179, 1986.

[9] Speziale, C., Sakar, S., and Gatski, T., "Modeling the Pressure-Strain Correlation of Turbulence: An Invariant Dynamical Systems Approach," *Journal of Fluid Mechanics*, Vol. 227, pp. 245-272, 1991.

[10] Daly, B. and Harlow, F, "Transport Equa-

tions in Turbulence," *The Physics of Fluids*, Vol. 13, pp. 2634-2649, 1970.

[11] Chen, H.C., "Assessment of Reynolds Stress Closure Models for Appendage-Hull Junction Flows," Submitted to *Journal of Fluids Engineering*, 1994.

[12] Shima, N., "A Reynolds-Stress Model for Near-Wall and Low-Reynolds-Number Regions," *Transactions of the ASME*, Vol. 110, pp. 38-44, 1988.

[13] Gatski, T. and Speziale, "On Explicit Algebraic Stress Models for Complex Turbulent Flows," *Journal of Fluid Mechanics*, Vol. 254, pp. 59-78, 1993.

[14] Chen, H.C. and Lin, W.M., "Interactive RANS/LAMP Coupling Schemes and Their Applications to Ship Flows," SAIC-91/1021, 1991, Science Applications International Corporation, Annapolis, Maryland.

[15] Chen, H.C. and Lin, W.M., "Interactive RANS/LAMP Calculations of Ship Flows Including Viscous and Wake Effects," SAIC-92/1049, 1992, Science Applications International Corporation, Annapolis, Maryland.

[16] Chen, H.C., Lin, W.M., and Weems, K., "Interactive Zonal Approach for Ship Flows Including Viscous and Nonlinear Wave Effects," *Proceedings 6th International Conference on Numerical Ship Hydrodynamics*, Office of Naval Research, 1993.

[17] Letcher, J., Weems, K., Oliver, C., Shook, D., and Salvesen, N., "SLAW: Ship Lift and Wave, Theory, Implementation, and Numerical Results," SAIC-89/1196, 1989, Science Applications International Corporation, Annapolis, Maryland.

[18] Dawson, C., "A Practical Computer Method for Solving Ship-Wave Problems" *Proceedings 2nd International Conference on Numerical Ship Hydrodynamics*, University Extension Publishers, Berkeley, CA, 1977, pp 30-38.

[19] Weems, K. and Korpus, R., "A RANS Based Propeller/Hull Interaction Analysis System," SAIC-93/1068, 1993, Science Applications International Corporation, Annapolis, Maryland.

[20] Huang, T.T., Liu, H.L., Groves, N.C., Forlini, T.J., Blanton, J.N., and Gowing, S., "Measurements of Flows Over an Axisymmetric Body with Various Appendages (DARPA SUBOFF Experiments)," *19th Symposium on Naval Hydrodynamics*, Seoul, Korea, 1992.

[21] Chen, H.C., "Studies of Submarine Flows By a Second-Moment Closure," Submitted to *Journal of Fluids Engineering*, 1994.

[22] Yang, C.-I., Hartwich, P. M., and Sundaram, P., "A Navier-Stokes Solution of Hull-Ring Wing-Thruster Interaction," *Proceedings Office of Naval Research 18th Symposium on Naval Hydrodynamics*, Hiroshima, Japan, 1993.

[23] Toda, Y., Stern, F., and Longo, J., "Mean-Flow Measurements in the Boundary Layer and Wake and Wave Field of a Series 60 C_B = .6 Ship Model for Froude Numbers .16 and .316," IIHR Report 352, 1991, Iowa Institute of Hydraulic Research, The University of Iowa, Iowa City, Iowa.

[24] Toda, Y., Stern, F., Tanaka, I., and Patel, V., "Mean-Flow Measurements in the Boundary Layer and Wake of a Series 60 C_B = .6 Ship Model With and Without a Propeller," IIHR Report 326, 1998, Iowa Institute of Hydraulic Research, The University of Iowa, Iowa City, Iowa.

[25] Steinbrenner, J.P., Chawner, J.R., and Fouts, C.L., "The GRIDGEN 3D Multiple Block Grid Generation System," Vols. I & II, WRDC-TR-90-3022, 1990, Wright Patterson AFB, Ohio.

[26] Salvesen, N., "IDEAS: Interactive Design, Evaluation and Analysis System," Presented at International Symposium on CFD and CAD in Ship Design, Maritime Research Institute Netherlands, Wageningen, The Netherlands, 1990.

[27] Fritts, M., Comstock, E., Lin, W.-C., and Salvesen, N., "Hydro-Numeric Design: Performance Prediction and Impact on Ship Design," SNAME Annual Meeting, San Francisco, California, 1990.

Calculation of Boundary Layer Considering Free-Surface Effect Around Ship Hulls

Y. Wang, Q. Wang
(Dalian University of Technology, China)

ABSTRACT

For a unsteady incompressible fluid with nonlinear free surface condition and with infinite water depth the Navier-Stokes equations and the additional Poisson equation are applied to determine the viscous flow parameters around ship hulls and to calculate the viscous resistance. SSPA 720 model is used to examine this computation and the corresponding results show that both mathematic model and numerical method are qualitatively reasonable at low Reynolds number only.

INTRODUCTION

The one of cruxes to calculate viscous flow around ship hulls is considering free surface effect on boundary layer in which the symmetrical model assumption can not be made and a free surface boundary condition must be taken into account. In fact to determine viscous flow an interaction between inviscid and viscous flow should be considered and the flow parameters near body wall and the wave-making on free surface may be provided in this computation.

The Cartesian coordinates (x, y, z, t) in the physical domain are used and they can be transformed into the body-fittted coordinates (ξ, η, ζ, t) to define the corresponding computation domain which assures the easiness of the treatment of boundary conditions and the control of the grid spaceings. The Navier-Stokes equations with the continuity equation are still employed to be the governing equation system to describe viscous flow around ship hulls in which the Poisson equation is also adopted to determine the pressure term. As all simulation for the laminar flow at low Reynolds number in this computation no turbulence models are introduced in order to control the computer resources and to save the CPU time. The computation domain is defined by the nonlinear free surface condition, by the no-slip body boundary condition, and by the uniform flow conditions.

Velocity field is calculated by the finite-difference form of the Navier-Stokes equations in the time-marching procedure. At the steady step of simulating computation both velocity and pressure distribution can be determined in the flow field and at the free surface and the hull viscous resistance and the wave-

making form can be calculated. A ship model named 720 provided by SSPA is used to simulate viscous flow considering the effect of free surface around ship hulls.

MATHEMATICAL MODELS

Coordinate System

A Cartesian coordinates $x^i(x, y, z, t)$ are adopted in the physical domain in which x along inflow to the stern, y along the breadth outwards, and z along the draft upwards, and origin at the centre of design waterline plane. The body-fitted coordinates $\xi^i(\xi, \eta, \zeta, t)$ are transformed by the following formulae[3]

$$\begin{cases} x=\xi \\ y+iz=\sum_{n=1}^{N}\sum_{m=1}^{M} r^{3-2n}A_{mn}\xi^{m-1}exp[(3-2n)\theta] \\ 0\leqslant\theta\leqslant\pi \end{cases} \quad (1)$$

in which

$$\begin{cases} r=r(\xi,\eta)=1+L(\eta)G(\xi) \\ L(\eta)=\sum_{i=1}^{I} b_i\eta^{i-1} \\ G(\xi)=\sum_{j=1}^{J} c_j\xi^{j-1} \\ L(0)=0,\ r(\xi,0)=1.0 \end{cases} \quad (2)$$

The coefficient matrix A_{mn}, b_i, and c_j can be obtained from the mapping of body sections and the stretching functions of local and global stretching respectively.

Governing Equations

The governing equations, the continuity and the Navier-Stokes equations, can be written in the physical coordinates

$$\begin{cases} u^j_{x^j}=0 \\ u^i_t+u_ju^i_{x^j}=-P_{x^i}+\frac{1}{Re}u^i_{x^jx^j} \\ i=1,\ 2,\ 3\ ;\ j=1,\ 2,\ 3 \end{cases} \quad (3)$$

in which

$$\begin{cases} x^i=(x,\ y,\ z) \\ u^i=(u,\ v,\ w) \\ P_{x^i}=(P_x,\ P_y,\ P_z+\frac{1}{Fn^2}) \\ Re=U_0L/\nu \\ Fn=U_0/\sqrt{gL} \end{cases} \quad (4)$$

where U_0 is the uniform flow velocity, u^i are the velocity components, P is pressure, and L is the characteristic length of ship hull. All variables are nondimensionalized by L, U_0, L/U_0, and ρU_0^2 respectively. The subscripts in Eq.s(3) and Eq.s(4) mean the partial differential.

The continuity and the Navier-Stokes equations are transformed into the following form[1]

$$\begin{cases} \xi^j_{x^i}u^i_{\xi^j}=0 \\ u^i_t+U^ju^i_{\xi^j}=-\xi^j_{x^i}\Phi_{\xi^j}+\frac{1}{Re}(\nabla^2u^i) \\ i=1,\ 2,\ 3\ ;\ j=1,\ 2,\ 3 \end{cases} \quad (5)$$

in which the unscaled contravariant velocity components are

$$U^i=(U,\ V,\ W)=\xi^j_{x^i}u^j \quad (6)$$

the pressure excluding the hydrostatic component is

$$\Phi=P-\frac{z}{Fn^2} \quad (7)$$

and the viscous term can be expressed as follows

$$\nabla^2 u^i = (\xi^j_{x^k})^2 u^i_{\xi^j\xi^j} + 2(\xi^j_{x^k}\xi^{j+1}_{x^k}) u^i_{\xi^j\xi^{j+1}} + (\xi^j_{x^kx^k}) u^i_{\xi^j} \quad (8)$$

where $i=1,2,3$; $j=1,2,3$ ($j>3$ taking $j=1$); and $k=1,2,3$ respectively.

Pressure Distribution

The Poisson equation method[2] is applied to calculate the pressure term in Eq. s(3) based on the velocity components on the time step ahead. From the Navier-Stokes equations in the vector form the pressure gradient can be expressed into

$$\frac{\partial u}{\partial t} = \nabla P + (-u \cdot \nabla u + \nu \nabla^2 u) \quad (9)$$

Taking discrete form in the time domain for Eq. s(9) and taking divergence for it the Poisson equation to determine pressure term can be written as

$$\nabla^2 P = \nabla \cdot Q^n / \Delta t \quad (10)$$

where $Q^n = \Delta t(-u \cdot \nabla u + \nu \nabla^2 u)^n + u^n$. It is transformed into the body-fitted coordinates from Eq. s(5) as follows

$$\nabla^2 \Phi = -\{\xi^j_{x^i}[U^k u^i_{\xi^k} - \frac{1}{Re}(\nabla^2 u^i)]_{\xi^j}\} - D_t \quad (11)$$

with $i=1,2,3$; $j=1,2,3$; and $k=1,2,3$ respectively. In the above equation D_t is the numerical error from the continuity equation in Eq. s(5).

Metrical Quantities

All of the metrical quantities in Eq. s (5)~(11) are deduced from the grid geometric parameters as

$$\begin{cases} \xi^j_{x^i} = (x^{j+1}_{\xi} x^{j+2}_{\xi} - x^{j+2}_{\xi} x^{j+1}_{\xi})/J \\ i=1,2,3 \ ; \ j=1,2,3 \\ i,j>3 \text{ taking } i,j=i,j-3 \end{cases} \quad (12)$$

and

$$\begin{cases} \xi^i_{x^jx^j} = (\xi^i_{x^j})_{\xi}\xi_{x^j} + (\xi^i_{x^j})_{\eta}\eta_{x^j} + (\xi^i_{x^j})_{\zeta}\zeta_{x^j} \\ i=1,2,3 \ ; \ j=1,2,3 \end{cases} \quad (13)$$

where

$$\begin{cases} J = (x_{\xi^i} y_{\xi^{i+1}} z_{\xi^{i+2}}) - (x_{\xi^{i+2}} y_{\xi^{i+1}} z_{\xi^i}) \\ i=1,2,3 \ ; \ j=1,2,3 \\ i>3, \text{ taking } i=i-3 \end{cases} \quad (14)$$

BOUNDARY AND INITIAL CONDITIONS

Free Surface Conditions

Two conditions for defined free surface are adopted in this simulation. The hydrostatic condition means that pressure on the free surface is equal to the atmospheric pressure, P_0, i.e.

$$P = P_0 \quad \text{on} \quad \zeta = 0 \quad (15)$$

The kinematic condition describes that the vertical velocity component for fluid particles on the free surface is identity with the vertical derivative of the free surface form and is written as

$$\begin{cases} h_t + U h_{\xi} + V h_{\eta} - (1 - r\cos\theta) W = 0 \\ h = r\sin(\theta) \end{cases} \quad (16)$$

Eq. (16) can be transformed into the finite-difference form with the same manner as the Navier-Stokes equations (5). All of velocity components on the free surface may be extrapolated equally from the velocity at the lower grid points.

Other Boundary Conditions

The no-slip condition is limited on the body wall boundary, for velocity

$$u=v=w=0 \tag{17}$$

and for pressure term

$$\frac{\partial P}{\partial n}=\frac{\partial P}{\partial \xi}cos(\hat{n}\xi)+\frac{\partial P}{\partial \eta}cos(\hat{n}\eta)+\frac{\partial P}{\partial \zeta}cos(\hat{n}\zeta) \tag{18}$$

The uniform flow and the hydrostatic pressure are given on the inflow boundary as

$$\begin{cases} u=1.0 \\ v=w=\Phi=0 \\ h=0 \end{cases} \tag{19}$$

and on the wake flow boundary as

$$\frac{\partial u}{\partial \xi}=\frac{\partial v}{\partial \xi}=\frac{\partial w}{\partial \xi}=\frac{\partial P}{\partial \xi}=\frac{\partial h}{\partial \xi}=0 \tag{20}$$

as well as on the both flank boundaries as

$$\frac{\partial u}{\partial \eta}=\frac{\partial v}{\partial \eta}=\frac{\partial w}{\partial \eta}=\frac{\partial P}{\partial \eta}=\frac{\partial h}{\partial \eta}=0 \tag{21}$$

On the other boundary pressure, velocity and wave height can be extrapolated equally from the inside.

Initial Conditions

The initial condition is a still state where velocity for fluid particle and wave height at free surface are zero and pressure equals to hydrostatics, i. e.

$$\begin{cases} u=v=w=h=0 \\ P=P_0 \end{cases} \tag{22}$$

NUMERICAL COMPUTATION

A SSPA Model No. 720 is used to simulate viscous flow considering free surface effect around its hull with 7. 067 in length-beam ratio, 2. 398 in beam-draft ratio and 0. 675 of block coefficient. The computation domain is defined as

$$-0.7\leqslant x\leqslant 1.0\ ,\ 0\leqslant y\leqslant 0.5\ ,\ -0.5\leqslant z\leqslant 0$$

The F. P. of the model is located at $x=-0.5$, $y=0$ and the A. P. at $x=0.5$, $y=0$. The still water level is $z=0.0$. The minimum spaceings of the grid measured in the computation coordinates are 0. 02, 0. 02 and 0. 03 in ξ, η and ζ directions respectively. The numbers of the grid points are $80\times 25\times 15$. The time increment Δt is 0. 0005. The computation are carried out under the conditions of $Re=10^4$ which is limited to be low and laminar flow only and of $Fn=0.25$ which can reach in the 5000-th time step near almost steady motion.

At the steady state the distribution of pressure on hull surface along each water line and of velocity component in the direction of normal to hull surface for each section from F. P. to A. P. can be obtained and the contour map of calculated wave configuration for given Froude number at free surface can be also provided in which the viscous flow around ship hull considering free surface effect has been simulated from this computation.

In order to investigate the effect of free surface on viscous flow around ship hulls both the global and local resistance coefficients for the friction and the viscous-pressure resistance are calculated and the comparative analysis between different computation methods provided by Nagamatsu and Wang is carried out in Tab. 1—

3. The friction and the visous-pressure resistance coefficients in Tab. 1 and Tab. 2 are calculated based on the following relations

$$C_F=\frac{L^2}{2S}\int_{-1}^{1}C'_F dx \qquad (23)$$

$$C_{VP}=\frac{L^2}{2S}\int_{-1}^{1}C'_{VP} dx \qquad (24)$$

where L is ship length and S is wetted surface, with corresponding Reynolds number $Re=10^7$. The local resistance coefficients of C'_F and C'_{VP} in Tab. 3 are the value on the section station which No. 20 at F. P. and No. 1 at A. P. respectively.

Friction Resistance Coefficient

Tab. 1

Computation from	$C_F\times10^3$
present result	3. 400
thin layer theory[4]	2. 960
higher order theory[4]	2. 958
Nagamatsu[5]	3. 040
1957 ITTC line	3. 0

Viscous-Pressure Resistance Coefficient

Tab. 2

Computation from	$C_{VP}\times10^3$
presentt result	1. 34
higher order theory[4]	1. 29
Nagamatsu[5]	1. 31

Distribution of Viscous Resistance Coefficients with Station

Tab. 3

Station No.	$C'_F\times10^3$		$C'_{VP}\times10^3$	
	[4]	present results	[4]	present results
18	0. 501	0. 478	−0. 107	−0. 091
16	0. 643	0. 526	−0. 143	−0. 127
14	0. 679	0. 587	−0. 129	−0. 009
12	0. 642	0. 633	−0. 071	0
10	0. 571	0. 607	0	0
8	0. 570	0. 614	0	0. 135
6	0. 557	0. 605	0. 1	0. 273
4	0. 495	0. 572	0. 5	—

CONCLUDING REMARKS

A numerical simulation for a viscous flow around ship hull with a free surface from the finite-difference solutions of the Navier-Stokes equations is developed and an exploratory calculation for SSPA Model 720 is carried out and some essential results are presented in this paper. It should be pointed out that the mathematic models to describe the viscous flow with a free surface are reasonable and the numerical procedure to make solution of the Navier-Stokes equations is advisable. In fact the project of viscous-inviscid interaction or interaction between boundary layer and free surface around ship hulls is an important and a complex interested research in marine hydrodynamics and such as the simulation of the higher Reynolds number flow, the introduction of the turbulent models, and the treatment of the wake flow and the stern waves are the most pressing subjects at present. Thus, this present result is an essential and a begining investigation in this research field.

REFERENCES

1. Hino, T., "Numerical Simulation of a Viscous Flow with a Free Surface around a Ship Model", Journal of The Society of Naval Architects of Japan, Vol. 161, 1987, pp. 1—9.

2. Chan, K.C., Street, R.L., "A Computer Study of Finite-Amplitude Water Waves", Journal of Computational Physics, Vol. 6, 1970, pp. 68—94.

3. Wang, Y.Y., "Auto-Generation Method of Numerical Grid for Surface and Field around Ship Hulls", Journal of Dalian University of Technology, Vol. 30, No. 3, May 1990, pp. 318—323.

4. Wan, D.C., "The Calculation of Viscous Resistance for Ship Hulls", Dec. 1989, Dalian University of Technology, Dalian, China.

5. Nagamatsu, T., "Calculation of Viscous Pressure Resistance of Ships based on a Higher-Order Boundary Layer Theory", Journal of The Society of Naval Architects of Japan, Vol. 147, 1980, pp. 134—141.

DISCUSSION

L. Larsson
Chalmers University of Technology, Sweden

This is an interesting progress report on a method which could be quite powerful when a turbulence model has been incorporated. I have two questions:

1. At the ONR Symposium in 1984, Dr. Broberg and myself presented a boundary layer method using the same conformal mapping grid generator as the authors. Later we had to abandon this when solving the Navier-Stokes equations, since it was very difficult to generate a smooth transition of the grid into the wake. Have the authors had any problems of this kind? How is the matrix determined in the wakes?

2. It is stated that the computation for the SSPA Model 720 is carried out at $R_n = 10^4$, i.e. in the laminar flow regime. But the comparison with others seems to be at $R_n = 10^7$. How is that possible?

AUTHORS' REPLY

Thank you for your comments. The authors will reply to your two questions.

The body-fitted coordinates as Eq. (1) are applied in which the coordinate system is composed with grid of hull surface and outside field. To achieve the transform from Cartesian coordinates x^i to body-fitted coordinates ξ^i the following essentials should be paid attention to:

The mapping of body section. In order to increase the fitting accuracy for body lines, especially for after-body sections, Lewis section is used to be initial values and then cubic spline function is also employed to be firstly approximate values. The final result can be obtained from the trial-and-error computation.

The local stretching function. The velocity profile of u in boundary layer is used to be sample when determining the coefficients b_i.

The global stretching function. To ensure covering all regions considering both viscous and wave-making effects, the development of boundary layer along hull length direction for plate boundary layer and Kelvin wave system is referenced to be sample when determining the coefficients c_j.

To be a comparative analysis some computations about C_F, C_{vp} and their distribution along hull stations are listed in Tables 1-3 respectively. All final values in these tables are the corresponding condition of $R_e=10^7$ which is extrapolated from respective computation condition based on the plate friction law provided by 1957 ITTC line.

Three-Dimensional Flow Around a Surface-Piercing Body

R. Yeung, X. Yu
(University of California-Berkeley, USA)

ABSTRACT

A pseudo-spectral formulation for solving unsteady, three-dimensional motion of an inviscid or viscous fluid with a free surface is presented. The formulation is implemented in cylindrical coordinates to study flows about a vertical surface-piercing structure. In these coordinates, a highly effective and accurate method is developed for treating the Poisson equation. Numerical solutions of three-dimensional inviscid wave motion in an annular domain are validated against analytical solutions. The high accuracy and efficiency of the method are pointed out. By an appropriate choice of the location of an outer boundary, the annular domain can be made laterally unbounded. A three-dimensional Cauchy-Poisson wave evolution problem in the annular domain is solved to illustrate the applicability of the method to complex wave problems. The procedure for extending this three-dimensional solver to obtain solutions of the Navier Stokes equations is detailed. The formulation is based on a projection method for treating the momentum equations and pressure Poisson equation. Validation is made against an analytical solution of Stokes's second problem in cylindrical coordinates. Several studies for viscous flow in an "annular cavity" are presented so as to compare the effects of a wall or free-slip "free surface". Finally, with the full free-surface conditions, results for a viscous Cauchy-Poisson wave problem are presented. The success of these investigations establishes the capability of the present methodology for examining the "mixed-boundary shear flow" near a surface-piercing structure, in which the complex interaction of vorticity, free surface, and possibly surface tension is yet to be clearly understood.

Nomenclature

$\mathcal{B}$	=	bottom of the fluid domain (at $z = -d$)
$\mathcal{F}$	=	free surface (at $z = 0$)
F_r	=	Froude number
g	=	gravitational acceleration
$K.E.$	=	kinetic energy in the fluid domain
L, M, N	=	number of grids in the r, θ and z directions
$\mathbf{n}$	=	(n_x, n_y, n_z) unit normal to fluid
p	=	total pressure in the fluid
P	=	dynamic pressure in the fluid
$P.E.$	=	potential energy in the fluid domain
$\mathcal{Q}_r$, $\mathcal{Q}_\theta$, $\mathcal{Q}_z$	=	difference operators in r, θ and z directions
(r, θ, z)	=	cylindrical coordinates in physical space
r_i, r_o	=	inner and outer radii of the fluid domain
(R, Φ, Z)	=	normalized cylindrical coordinates
Re	=	Reynolds number
$\mathcal{S}$	=	body surface (at $r = r_i$)
t	=	time
$T.E.$	=	total energy in the fluid domain
$\tilde{U}$	=	characteristic velocity
u, v, w	=	velocity component in r, θ and z directions
(u^*, v^*, w^*)	=	auxiliary velocity vector
(u^{**}, v^{**}, w^{**})	=	auxiliary velocity vector
$(\hat{u}, \hat{v}, \hat{w})$	=	auxiliary velocity vector
(U, V, W)	=	prescribed velocity vector on moving boundary
Δt	=	time increment
η	=	free-surface elevation
ρ	=	density of fluid
Σ	=	outer boundary (at $r = r_o$)
ϕ	=	velocity potential
Ω	=	fluid domain

1 INTRODUCTION

In recent times, there has been considerable advances in the development of predictive models for computing flows about ship hulls (see e.g. [1] - [5]), which include consideration of the effects of viscosity. Important progress has also taken place in the development of boundary element methods ([6] and [7]). The aim of these works is to ultimately replace traditional tank experiments by CFD codes which will be used interactively by designers of ships or other marine structures to develop more economical and more efficient designs.

As evidenced in [8], many of these existing techniques rely on the assumption that the mean flow about the hull is steady, while there are increasing experimental and numerical evidence that the vorticity structures near a free surface behave in an unsteady manner ([9], [10]). These observations apply even at typical scales used in a model-testing tank. The behavior of the fluid motion in the region near the hull and the free surface has been most intriguing and is yet to be understood. Because it is a region which involves the confluence of two types of boundary conditions, the free surface and the non-slip body, it has recently been named the "mixed-boundary shear flow" region. This region would generate flow features that are distinctly different from each of the two types of boundary surfaces if present only by itself.

Perhaps one of the more well-known physical features which comes from such a region is the generation and intensification of the so-called necklace vortices from the bow area of a ship ([11]). In their recent work based on an elaborate fully nonlinear free surface and viscous-flow model, Yeung and Ananthakrishnan [12] found that a clean free surface was unable to generate a very strong cross-stream vortex. This disagrees somewhat with Baba's [13] stipulation that the bow–free-surface juncture bears the same vorticity intensification phenomenon of the "wing-fuselage" juncture of Hawthorne [14]. However, Yeung and Ananthakrishnan's results are for the case of two-dimensional flows, its immediate implications to three-dimensions are still not obvious. Although the extension of their technique to three-dimensional problems is straightforward, the demand on computational resources and grid resolution is stringent. Another issue closely related to the mixed-boundary shear flow is the well known difficulty of having a convergent solution of the waterline integrals in inviscid-fluid wave-resistance computations of ship hulls. This issue is addressed from a different viewpoint in another paper of this session ([15]).

In order to investigate the flow structure in this mixed-boundary shear region, it is necessary to develop an accurate and efficient three-dimensional method that is less vulnerable to grid density as many standard finite-difference solvers are. Further, it is worthwhile to define a canonical problem, for which analytical validation of the accuracy of the method can be carried out, presumably at least for certain simple limiting boundary conditions.

To meet the first goal, a pseudo-spectral formulation is adopted. During the past two decades, spectral methods and their pseudo counterparts have been extensively studied and applied to the numerical solution of many fluid dynamics problems ([16]-[20]). Their efficiency and accuracy are outstanding. Such properties will be well demonstrated in this paper. Spectral methods are somewhat restrictive in their abilities to handle general geometries; however, this is not an insurmountable restriction.

To meet the second objective, the canonical problem chosen is a vertical surface-piercing cylinder enclosed by another vertical cylindrical surface, upon the latter a variety of far-field conditions may be applied. The fluid domain is bounded on top by a free surface and by a solid bottom boundary. In its simplest form, the canonical problem would be to examine the three-dimensional inviscid or viscous flow bounded in an annular domain of finite height. Cylindrical shapes may be viewed as non-ship like, but they are of great practical significance in many marine-related applications. Further, in terms of quantitative descriptions of separated flows, such shapes offer a more stringent test than most streamlined or thin-body shapes. Finally, with a minor increase in mathematical complexity, spheroidal hulls can be considered as natural generalizations of the double cylinder configuration. Much ground work has been done to enable the successful development of this new and powerful solution method [21]. Intermediate progress of some of these exciting developments and capabilities are reported here.

In Section 2 of the paper, the basic development of the spectral method for the case of an inviscid fluid is introduced and detailed. For inviscid-fluid motion, the boundary-integral formulation remains the most popular approach. Under this category, there are two basic approaches, one is

based on the availability of a time-dependent free-surface Green function, whose numerical evaluation is non-trivial ([22] and [23]). The other is based on the so-called Rankine-source formulation, in which case the free-space source is distributed on the free-surface ([24] and [25]). This latter approach normally leads to a larger number of unknowns and requires the use of an approximate open-boundary condition. As an illustration of our pseudo-spectral method development, we first demonstrate the accuracy and efficiency of a Poisson solver in cylindrical coordinates. Solutions for two test problems corresponding to wave motion in the annular (or cylindrical) domains are examined. In particular, the Cauchy-Poisson problem for this geometry is solved and presented (Sec. 2.4). This sloshing problem is of practical interest in its own right.

Section 3 provides the formulation and numerical details of how the viscous-flow problem is tackled as a non-trivial extension. This methodology follows the projection method that had been successfully developed by Yeung and Ananthakrishnan ([12] and [26]). Central to the present procedure is the availability of a fast Poisson solver, developed in Sec. 2.2 in anticipation of its role in the solution of the Navier Stokes equations. Viscous-flow solutions are presented in Section 4 for three types of test problems: a) A rotating cylinder undergoing periodic motion, which corresponds to Stokes's second problem [27] for a cylindrical body; b) An annular fluid cavity driven by a continuously sliding wall; and c) A cylinder oscillating vertically in an annular cavity trapped on top by a free-slip or solid wall. Finally, the Cauchy-Poisson problem in Sec. 2.4 is re-solved for the case of a viscous flow. It is evident from the success of these computations that a detailed knowledge of the vortical structures in the mixed-boundary shear region of a surface-piercing body can be obtained in the very near future.

2 WAVE-BODY INTERACTION IN AN INVISCID FLUID

2.1 Mathematical Formulation

In this section the theoretical background for solving transient three-dimensional free-surface flows of an inviscid fluid is briefly reviewed. For simplicity, a cylindrical coordinate system is used throughout to validate a number of ideas, although extensions to other shapes are possible on the same framework. Consider a fixed cylindrical co-

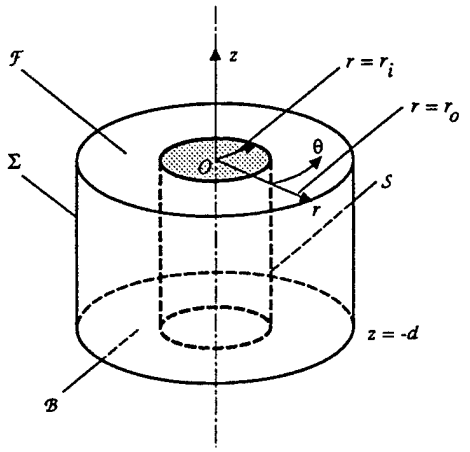


Figure 1: Notation and coordinate system.

ordinate system (r, θ, z) chosen so that the $z-$axis points vertically upwards and the undisturbed free-surface is at $z = 0$ (see Fig. 1). The fluid region Ω is enclosed by the cylindrical body boundary $\mathcal{S}$ located at $r = r_i$, free-surface $\mathcal{F}$ at $z = 0$, far-field boundary Σ at $r = r_o$, and a bottom $\mathcal{B}$ located at $z = -d$.

Under the assumptions that the flow is irrotational and the fluid incompressible, it can be established that there exists a velocity potential of the flow ϕ, which satisfies the Laplace equation,

$$\nabla^2 \phi = 0 \tag{1}$$

in the domain Ω, with the following boundary conditions:

On $\mathcal{F}$, a Dirichlet condition for ϕ can be obtained by a advancing the potential in the time using the linearized dynamic condition:

$$\frac{\partial \phi}{\partial t} = -g\eta, \tag{2}$$

where g is the gravitational acceleration, and $\eta(r, \theta, t)$ is the free-surface elevation. The latter satisfies the following linearized kinematic condition:

$$\frac{\partial \eta}{\partial t} = \frac{\partial \phi}{\partial z} \quad . \tag{3}$$

On $\mathcal{S}$, which may be considered to have a prescribed velocity $\mathbf{V}$, the appropriate normal derivative for ϕ is

$$\phi_n = \mathbf{V} \cdot \mathbf{n}, \tag{4}$$

where $\mathbf{n}$ is a normal on the body surface pointing outwards of Ω. On $\mathcal{B}$, the following no-flux condition is applicable:

$$\phi_z = 0. \tag{5}$$

On the far-field boundary Σ, we may impose

$$\phi = 0 \tag{6}$$

as an approximation to an open boundary if Σ is taken to be sufficiently large, or

$$\phi_n = 0 \tag{7}$$

if it is a solid vertical boundary.

To complete the problem, initial conditions for ϕ itself and its time derivative on $\mathcal{F}$ should be specified.

2.2 Pseudo-Spectral Method of Solution

2.2.1 *A Poisson-equation solver*

It is well known that the Poisson equation has many important application in fluid mechanics. Here we will develop a pseudo-spectral formulation to solve this equation, using some ideas similar to Tan [28]. For the present problem in cylindrical coordinates, we will exploit Chebyshev polynomials in the vertical direction and Fourier modes in the circumferential direction. The resulting ordinary differential equations for the radial direction are solved by a spectral collocation method [16] with a diagonalization technique. The method developed can treat both homogeneous and inhomogeneous boundary conditions of the Dirichlet, Neumann, or mixed type, which encompasses the classes of boundary conditions encountered in many fluid-mechanics application.

For the right-handed cylindrical coordinate system (r, θ, z) shown in Fig. 1, the independent variables are defined in the following ranges:

$$\begin{array}{ccccc} r_i & \leq & r & \leq & r_o \\ 0 & \leq & \theta & \leq & 2\pi \\ -d & \leq & z & \leq & 0 \end{array} \tag{8}$$

where r_i and r_o are the radii of the inner and outer cylindrical boundaries respectively. It is convenient to map the above domain into a normalized computational domain (R, Φ, Z) such that

$$\begin{array}{ccccc} -1 & \leq & R & \leq & 1 \\ -1 & \leq & \Phi & \leq & 1 \\ -1 & \leq & Z & \leq & 1 \end{array} \tag{9}$$

by using the following relations:

$$\begin{array}{rcl} r & = & \zeta R + \xi \\ \theta & = & (1+\Phi)\pi \\ z & = & \kappa(-1+Z) \end{array} \tag{10}$$

where $\zeta = \frac{1}{2}(r_o - r_i)$, $\xi = \frac{1}{2}(r_o + r_i)$, and $\kappa = d/2$ are scale and translational factors.

In (R, Φ, Z), the Poisson equation $\nabla^2 U = S(R, \Phi, Z)$, as a generalization of (1), can be written as:

$$\left[\mathcal{L} + \frac{1}{(\zeta R + \xi)^2 \pi^2}\frac{\partial^2}{\partial \Phi^2} + \frac{\partial^2}{\kappa^2 \partial Z^2}\right] U(R, \Phi, Z) = S(R, \Phi, Z), \tag{11}$$

where

$$\mathcal{L} \equiv \frac{1}{\zeta^2}\frac{\partial^2}{\partial R^2} + \frac{1}{\zeta(\zeta R + \xi)}\frac{\partial}{\partial R}. \tag{12}$$

Here we use U to designate the more general case of an unknown function where the Poisson instead of the Laplace equation is satisfied. Clearly, for inviscid-fluid applications defined in Sec. 2.1, one would simply take $S = 0$.

The boundary conditions in Eqns. (2), (3), (5), (6) or (7) can be treated as special cases of the following generalized form:

$$\alpha_\pm U(\Phi, Z) + \beta_\pm \frac{\partial U(\Phi, Z)}{\partial R} = F_\pm(\Phi, Z), \quad \text{at} \quad R = \pm 1 \tag{13}$$

$$A_\pm U(R, \Phi) + B_\pm \frac{\partial U(R, \Phi)}{\partial Z} = H_\pm(R, \Phi), \quad \text{at} \quad Z = \pm 1 \tag{14}$$

with all $\alpha_\pm$, $\beta_\pm$, $A_\pm$, and $B_\pm$ considered given constants.

In our spectral approach to the solution of Eqn. (11), the functions U, S, $F_\pm$, and $H_\pm$ are approximated by truncated Chebyshev-Fourier series of the form:

$$\left\{ \begin{array}{c} U(R, \Phi, Z) \\ S(R, \Phi, Z) \\ F_\pm(\Phi, Z) \end{array} \right\} = \sum_{m=-\frac{M}{2}}^{\frac{M}{2}-1} \sum_{n=0}^{N} \left\{ \begin{array}{c} U_{mn}(R) \\ S_{mn}(R) \\ f_{\pm mn} \end{array} \right\} e^{im\pi\Phi} T_n(Z), \tag{15}$$

and

$$H_\pm(R, \Phi) = \sum_{m=-\frac{M}{2}}^{\frac{M}{2}-1} h_{\pm mn}(R) e^{im\pi\Phi} \tag{16}$$

where the Chebyshev polynomials $T_n(Z)$ are given by $\cos[n \cos^{-1} Z]$. Note that by assumption, we consider S_{mn}, $f_{\pm mn}$, and $h_{\pm mn}$ as given, while

the sequence U_{mn} are unknown functions to be solved for.

By introducing a Chebyshev-Tau representation [16] to incorporate the boundary conditions (14) at $Z = \pm 1$, and by applying the recurrence relations for the derivatives of Chebyshev polynomials, we can rewrite:

$$\frac{\partial^2 U}{\partial Z^2} = \sum_{m=-\frac{M}{2}}^{\frac{M}{2}-1} \sum_{n=1}^{N-1} U_{mn}^{(0,2)}(R) e^{im\pi\Phi} T_n(Z), \quad (17)$$

where

$$U_{mn}^{(0,2)}(R) = \sum_{q=0}^{N-2} \gamma_{nq} U_{mq}(R) + D_{mn}(R). \quad (18)$$

Expressions for γ_{nq} and $D_{mn}(R)$ can be derived after some effort and form the crux of the present numerical development. The lengthy expressions for γ_{nq} and $D_{mn}(R)$ in terms of known quantities, are omitted here for clarity of exposition. Substitution of the above results (Eqns. 17 and 18) into the Poisson equation (11) yields:

$$\left[\mathcal{L} - \frac{m^2}{(\zeta R + \xi)^2}\right] U_{mn}(R) + \frac{1}{\kappa^2} \sum_{q=0}^{N-2} \gamma_{nq} U_{mq}(R) = S_{mn}(R) - \frac{1}{\kappa^2} D_{mn}(R) \equiv \sigma_{mn}(R) \quad (19)$$

for $m = -\frac{M}{2}$ to $\frac{M}{2} - 1$, and $n = 1$ to $N - 1$.

To avoid solving Eqn. (19) with full coupling between m with n, we first proceed to diagonalize a matrix Γ with elements γ_{nq}. Γ is of dimension $N - 1$. Thus we assume

$$\epsilon^{-1} \Gamma \epsilon = \Lambda, \quad (20)$$

where Λ is a *diagonal* matrix of dimension $N - 1$ with diagonal elements λ_n, $n = 1, .., N-1$, as the eigenvalues. ϵ is the associate eigenvector *matrix*, and ϵ^{-1} its inverse. Next, if we consider the matrices $\mathbf{U}$ and $\mathbf{\Sigma}$ to be defined by elements U_{mn} and σ_{mn}, we may define correspondingly a matrix $\hat{\mathbf{U}}$ with elements $\hat{U}_{mn}$ and $\hat{\mathbf{\Sigma}}$ with elements $\hat{\sigma}_{mn}$ by the following relations:

$$\begin{aligned} \mathbf{U} &= \hat{\mathbf{U}} \epsilon^T, \\ \mathbf{\Sigma} &= \hat{\mathbf{\Sigma}} \epsilon^T, \end{aligned} \quad (21)$$

where the superscript T denotes transpose.

Thus by Eqns. (20) and (21), Eqn. (19) reduces to:

$$\left[\mathcal{L} - \frac{m^2}{(\zeta R + \xi)^2}\right] \hat{U}_{mn}(R) + \frac{1}{\kappa^2} \lambda_n \hat{U}_{mn}(R) = \hat{\sigma}_{mn}(R) \quad (22)$$

for $m = -\frac{M}{2}$ to $\frac{M}{2} - 1$, and $n = 1$ to $N - 1$. The significance of Eqn. (22), in comparison to Eqn. (19), is that the system of ordinary differential equations in (22) is uncoupled in m and n. Had we not made this transformation, we would have to face with the insurmountable task of solving $m \times n$ coupled differential equations.

To solve the system of ODE's defined by Eqn. (22), we were successful in employing either a fourth-order differencing scheme or a Chebyshev collocation method [16], the latter option, constituting a consistent full spectral form, yields the highest accuracy.

2.2.2 *Treatment of the free-surface conditions*

As pointed out earlier, the potential ϕ and wave elevation η on the free surface $\mathcal{F}$ are obtained by integrating Eqns. (2) and (3) respectively. Implicit difference schemes are used here because of their excellent stability properties [30]. To implement such schemes, the following iterative procedure is employed

$$\eta_{(p+1)}^{k+1} = \eta^k + \frac{\Delta t}{2} (\phi_{z\,(p)}^{k+1} + \phi_z^k) \quad (23)$$

$$\phi_{(p+1)}^{k+1} = \phi^k - g \frac{\Delta t}{2} (\eta_{(p)}^{k+1} + \eta^k). \quad (24)$$

Here the superscript k denotes an index of the time step and p denotes the index of iterations within a given time step. The iteration process is halted after the *pth* iteration when

$$|\phi_{z\,(p)}^{k+1} - \phi_{z\,(p-1)}^{k+1}| \leq \varepsilon, \quad (25)$$

where ε is a prescribed tolerance value. An absolute accuracy of $\varepsilon = 10^{-10}$ was used for all cases of results presented.

2.3 Analytical Validations

Before proceeding to some general and more complex problems, it is essential to establish the accuracy and convergence characteristics of the procedure presented in Sec. 2.1 and 2.2. For this purpose, we test the procedure against two analytical solutions that can be worked out relatively easily.

In the first case, we wish to verify that the Poisson solver for Eqn. (11) to (14) can treat any arbitrary function of S. Here we assume an analytical form of $U(r, \theta, z)$ defined below (in Eqn. 26), and evaluate $S(r, \theta, z)$ corresponding to Eqn. (11) accordingly. The boundary conditions (13) and (14) can be imposed by taking

the left-hand side as given and the right-hand side computed. Then the numerical algorithm for the solution of U is applied with S, F, and H as given. The numerical solution can then be compared with the exact solution for different types of boundary conditions.

For this test, we take $U(r, \theta, z)$ as

$$U(r,\theta,z) = \left[\cos\left\{\frac{\pi}{2\zeta}(r-\xi)-\frac{\pi}{2}\right\}+\sin\left\{\frac{\pi}{2}2\zeta(r-\xi)-\frac{\pi}{2}\right\}\right] \times \left[\cos\left\{\pi(\frac{\theta}{2\pi}-1)\right\}+\sin\left\{\pi(\frac{\theta}{2\pi}-1)\right\}\right] \times \left[\cos\left\{\frac{\pi}{2}(Z-1)\right\}+\sin\left\{\frac{\pi}{2}(Z-1)\right\}\right] \tag{26}$$

with $r_i = 1$, $r_o = 10$. The boundary conditions considered are taken to be one of the following four types:

$$\begin{aligned} &\text{(a) Dirichlet Conditions:} && \alpha_\pm = A_\pm = 1, \\ &&& \beta_\pm = B_\pm = 0; \\ &\text{(b) Neumann Conditions:} && \alpha_\pm = A_\pm = 0, \\ &&& \beta_\pm = B_\pm = 1; \\ &\text{(c) Mixed Conditions:} && \alpha_\pm = A_\pm = 1, \\ &&& \beta_\pm = B_\pm = 1; \\ &\text{(d) Dirichlet on } R = \pm 1 && \alpha_\pm = B_\pm = 1, \\ &\text{and Neumann on } Z = \pm 1: && \beta_\pm = A_\pm = 0. \end{aligned} \tag{27}$$

Once the solution for U has been obtained, its pointwise error can be computed over the entire domain Ω. In Table 1 the maximum pointwise error Er of the numerical solution in Ω, relative to the exact analytical solution, is shown for a range of grid resolution. In these and later computations, the grid resolution is measured by the number of radial grids, L, and the number of spectral terms in the circumferential direction, M, and the number of spectral terms in the vertical direction, N. Table 1 shows that the value of the error Er decreases exponentially as the grid number N increases for each of the above four types of boundary conditions. The timings shown in Table 1 are based on an IBM 320H workstation. It is clear from these results accuracy of the level of machine precision of 13 digits can be achieved for $O(10,000)$ grid points, and at the order of few seconds.

To demonstrate the flexibility of the procedure, as well as to test the accuracy of our algorithm in the handling of wave-related problems, we solve, as the second test case, an axisymmetric Cauchy-Poisson wave problem [29]. Problems of this type usually consist of specifying an initial elevation

Table 1: Maximum pointwise errors vs. grid resolution for various boundary conditions

Type of boundary conditions	Resolutions $L \times M \times N$	Maximum pointwise error Er	CPU time (sec)
Dirichlet on all boundaries	5 x 16 x 16	5.53E-04	0.39
	10 x 16 x 16	2.51E-09	1.15
	20 x 16 x 16	3.54E-13	4.17
	30 x 16 x 16	3.21E-13	9.38
Neumann on all boundaries	5 x 16 x 16	1.35E-02	0.39
	10 x 16 x 16	1.99E-07	1.15
	20 x 16 x 16	7.62E-13	4.15
	30 x 16 x 16	7.76E-13	9.37
Mixed on all boundaries	5 x 16 x 16	4.56E-02	0.38
	10 x 16 x 16	1.64E-07	1.15
	20 x 16 x 16	9.89E-13	4.18
	30 x 16 x 16	9.90E-13	9.39
Dirichlet on $R = \pm 1$, Neumann on $Z = \pm 1$	5 x 16 x 16	1.04E-03	0.40
	10 x 16 x 16	2.96E-09	1.15
	20 x 16 x 16	6.26E-13	4.18
	30 x 16 x 16	6.24E-13	9.25

or velocity of the surface wave, and one is required to predict the wave evolution at subsequent time. The governing equations are given in Sec. 2.1, with the initial conditions to be specified. Here we assume the initial conditions to be of an *axi-symmetric* wave form that occurs between two concentric impermeable vertical cylinders located at $r = r_i$ ($\mathcal{S}$), and at $r = r_o$ (Σ):

$$\frac{\partial \phi}{\partial t} = \exp\left\{-[r-(r_i+r_o)/2]^2\right\} \equiv f(r), \quad \text{at } t = 0 \tag{28}$$

$$\phi = 0, \quad \text{at } t = 0 \tag{29}$$

An analytical solution of the above problem can be derived by the use of Laplace transform and separation of variables. The details are omitted here. The final result for the wave elevation is

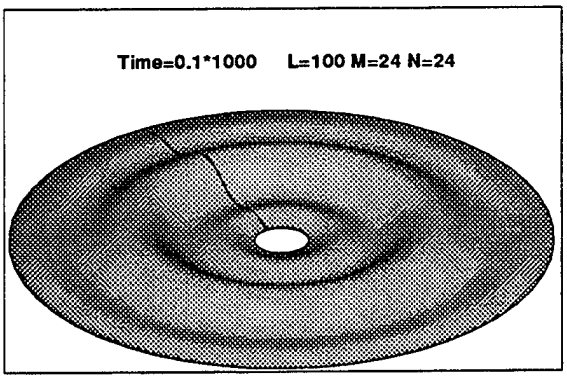
$$\eta(r,t) = g_0 + \sum_{n=1}^{\infty} g_n \left[J_0(k_n r) - \frac{J_1(k_n r_i)}{N_1(k_n r_i)} N_0(k_n r)\right] \cos \omega_n t \tag{30}$$

where J_ν and N_ν are the Bessel functions of the first and the second kind, and of order ν. k_n is the nth zero of the following equation for k

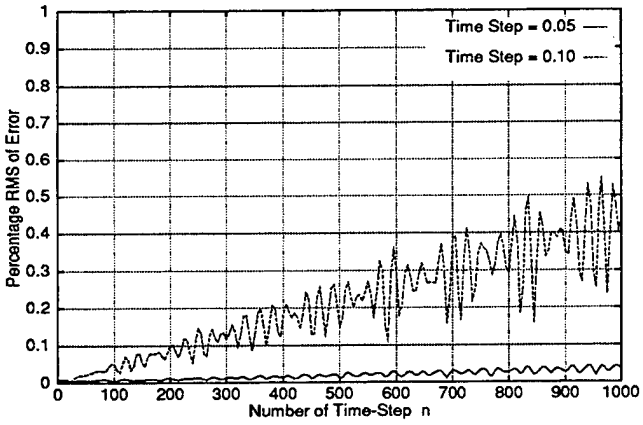
$$J_1(kr_i)N_1(kr_o) - J_1(kr_o)N_1(kr_i) = 0. \tag{31}$$

The "natural" frequencies ω_n satisfy a finite-depth "dispersion relation":

$$\omega_n^2 = g k_n \tanh k_n d. \tag{32}$$



(a)



(b)

Figure 2: Free-surface elevation at $t(g/r_i)^{1/2} = 100.0$ (left) and the root mean square of errors of free-surface elevation as a function of time steps (right) in an axisymmetric Cauchy-Poisson wave problem.

The coefficients g_n in Eqn. (30) are given analytically in terms of $f(r)$:

$$g_0 = \frac{\int_{r_i}^{r_o} rf(r)dr}{\int_{r_i}^{r_o} rdr},$$

$$g_m = \frac{\int_{r_i}^{r_o} rf(r)\left[J_0(k_m r) - \frac{J_1(k_m r_i)}{N_1(k_m r_i)}N_0(k_m r)\right]dr}{\int_{r_i}^{r_o} r\left[J_0(k_m r) - \frac{J_1(k_m r_i)}{N_1(k_m r_i)}N_0(k_m r)\right]^2 dr}, \quad \text{for } m = 1, 2, 3.... \tag{33}$$

The numerical solution of this problem was obtained using the spectral method detailed in Sec. 2.2. The results of the computed wave elevation $\eta_c(r,t)$ were compared with the corresponding analytical solution $\eta_a(r,t)$ given by Eqn. (30). Excellent agreement was found at every value of

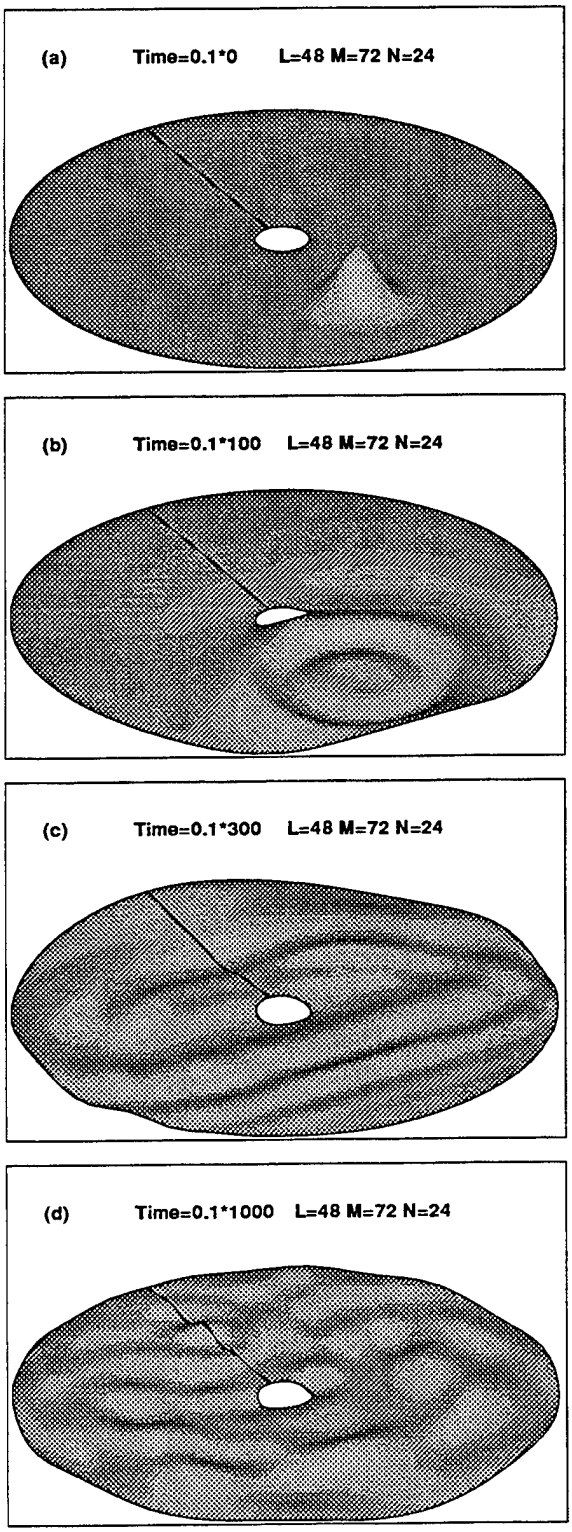


Figure 3: Instantaneous free-surface elevation plots for the Cauchy-Poisson wave problem, L, M, N representing resolution in the radial, circumferential, and vertical directions.

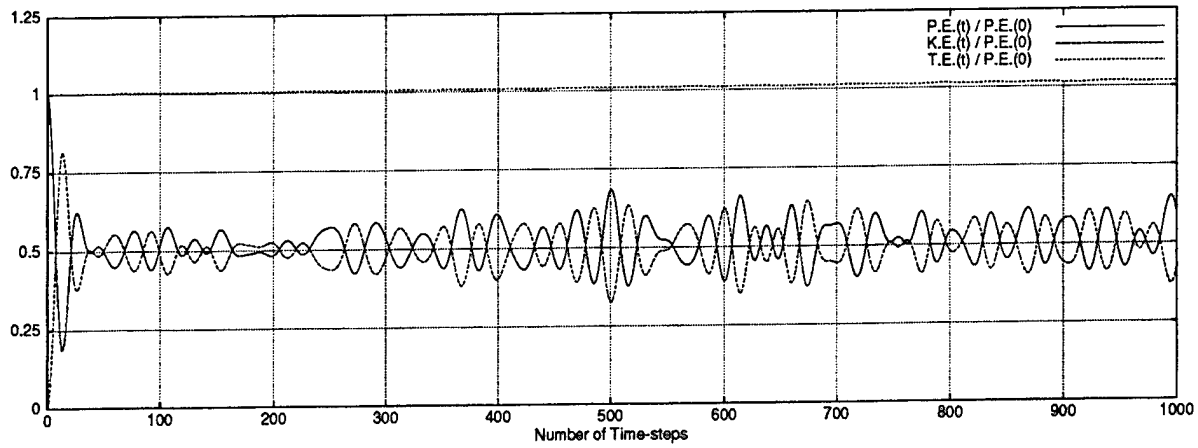


Figure 4: Energy balance in the Cauchy-Poisson wave problem of Fig. 3

t. Fig. 2a shows the free-surface elevation for one such simulation at non-dimensional time $t\sqrt{g/r_i} = 100$. The RMS error in free-surface elevation as a function of time is defined as

$$E_{RMS}(t) = \sqrt{\frac{\int_S \{[\eta_c(r,t) - \eta_a(r,t)]/\eta_0\}^2 \, dS}{S}} \tag{34}$$

where η_o is the elevation for the initial free-surface pulse, and S the planform area of the free surface. A plot of $E_{RMS}(t)$ versus the time-step index n is given in Fig. 2b. For $L = 100$, $M = 24$ and $N = 24$, the error was found to be bounded by 0.5% when a non-dimensional time step $\Delta t\sqrt{g/r_i}$ of 0.1 was used, but reduced drastically to a mere 0.05% if the time step was halved. These results lend credence to the potential and effectiveness of the method.

2.4 Wave Sloshing in an Annular Domain

A non-axisymmetric version of the Cauchy-Poisson wave problem solved in Sec. 2.3 is treated in this section. This has full three-dimensional features. Consider a non-axisymmetric initial wave elevation located between two cylindrical walls. This initial wave form is taken, for mathematical convenience, to be the following:

$$\eta(r,\theta,t=0) = \exp\left\{-[r\cos\theta - (r_i + r_o)/2]^2 - [r\sin\theta]^2\right\}. \tag{35}$$

Its shape is depicted in Figs. 3a. Because of the reflections of waves from the outer wall and their interference with the inner cylinder, the free surface evolves in a complicated manner. The results are shown in Figs. 3b to 3d. The outward-moving "ring waves" of the pulse (Fig. 3b) first hit the outer cylinder and rebound, interestingly, almost as a plane wave system (Fig. 3c). The inward-moving ring waves diffract around the inner cylinder and eventually bounce off the far side of the outer cylinder to interact with the "plane waves" which somewhat encircle around the inner cylinder to reach the far side. When all these waves meet at the far end, they evolve into waves of much shorter lengths, moving at much lower spatial velocities. All these flow features are well captured by a radial grid dimension of merely 48 points.

It is important to validate the accuracy of the solution. As a measure of the accuracy of this type of computation, we will demonstrate that the flow retains the same total energy as the initial wave pulse. We define the following energy quantities following Yeung [30]: the total energy ($T.E.$) in the fluid domain as the sum of its kinetic and potential parts

$$\begin{aligned} T.E.(t) &= K.E.(t) + P.E.(t) \\ &= \int_{\mathcal{S}\cup\mathcal{F}\cup\Sigma\cup\mathcal{B}} \frac{1}{2}\rho\phi\phi_n dS + \int_{\mathcal{F}} \frac{1}{2} g\eta^2 dS \end{aligned} \tag{36}$$

where the contributions to the first integral from $\mathcal{S}$, Σ and $\mathcal{B}$ vanish because $\phi_n = 0$. Clearly, in the absence of any energy source, $T.E.$ must stay constant. Fig. 4 shows that the error in the total energy is no more than 2% of the initial potential energy of the wave form $P.E.(t = 0)$ even after a thousand steps of simulation. Interestingly, by the principle of equal energy distribution, one observes that $P.E.$ and $K.E.$ each hovers around and converges to the value of 0.5. This confirms that the wave motion would never vanish completely, which is to be expected in the absence of viscosity.

3 WAVE-BODY INTERACTION IN A VISCOUS FLUID

The formulation of the free-surface problem in a viscous fluid is similar to that given in [12]. The Navier-Stokes equations are complemented by dynamic free-surface boundary conditions representing the stress continuity relations. The stress conditions are linearized here for simplicity. Approximate conditions are used for the closure of the open boundary.

These equations are presently solved in cylindrical coordinates using a fractional-step method, which is based on the so-called projection method, proposed by Chorin [31] and others. In this method, an intermediate auxiliary velocity field is first evaluated using the momentum equations without the pressure term. An ADI scheme is used here for this purpose. The pressure field satisfies a Poisson equation, which, in the present work, is handled efficiently and accurately by the pseudo-spectral formulation described in Sec. 2.2. A pressure correction step concludes the procedure.

3.1 Governing Equations

If we take $\tilde{U}$ as a characteristic velocity, r_i or d as a characteristic length, the Navier-Stokes equations for incompressible viscous flow in cylindrical coordinates (see Fig. 1) can be written as:

$$\frac{\partial u}{\partial t} + u\frac{\partial u}{\partial r} + \frac{v}{r}\frac{\partial u}{\partial \theta} + w\frac{\partial u}{\partial z} - \frac{v^2}{r} = \frac{1}{Re}\left[\nabla^2 u - \frac{u}{r^2} - \frac{2}{r^2}\frac{\partial v}{\partial \theta}\right] - \frac{\partial P}{\partial r},$$

$$\frac{\partial v}{\partial t} + u\frac{\partial v}{\partial r} + \frac{v}{r}\frac{\partial v}{\partial \theta} + w\frac{\partial v}{\partial z} - \frac{uv}{r} = \frac{1}{Re}\left[\nabla^2 v - \frac{v}{r^2} - \frac{2}{r^2}\frac{\partial u}{\partial \theta}\right] - \frac{1}{r}\frac{\partial P}{\partial \theta},$$

$$\frac{\partial w}{\partial t} + u\frac{\partial w}{\partial r} + \frac{v}{r}\frac{\partial w}{\partial \theta} + w\frac{\partial w}{\partial z} = \frac{1}{Re}\left[\nabla^2 w\right] - \frac{\partial P}{\partial z}, \qquad (37)$$

where $\nabla^2 = \frac{\partial^2}{\partial r^2} + \frac{1}{r}\frac{\partial}{\partial r} + \frac{1}{r^2}\frac{\partial^2}{\partial \theta^2} + \frac{\partial^2}{\partial z^2}$ is the Laplacian operator in cylindrical coordinates. Eqn. (37) is complemented by the continuity equation:

$$\frac{1}{r}\frac{\partial (ru)}{\partial r} + \frac{1}{r}\frac{\partial v}{\partial \theta} + \frac{\partial w}{\partial z} = 0. \qquad (38)$$

Here, Re is an appropriately defined Reynolds number, say $\tilde{U} r_i/\nu$ or $\tilde{U} d/\nu$. The quantity P represents the non-dimensional dynamic pressure, which is related to the total pressure p by

$$P = p + \frac{z}{F_r^2}, \qquad (39)$$

where F_r is a Froude number.

Next, the boundary conditions that govern the viscous-wave problem are defined:

On the body $\mathcal{S}$, the following no-slip conditions are used:

$$u = U(t), \quad v = V(t), \quad w = W(t), \qquad (40)$$

where $U(t)$, $V(t)$ and $W(t)$ are prescribed instantaneous velocities on the body.

On the free surface $\mathcal{F}$, the boundary conditions can be linearized from the exact kinematic and stress-continuity relations (see e.g. [32]). The linearized dynamic boundary conditions are:

$$\begin{aligned} \frac{\partial u}{\partial z} + \frac{\partial w}{\partial r} &= 0, \\ -P + \frac{\eta}{F_r^2} + \frac{2}{Re}\frac{\partial w}{\partial z} &= 0, \quad \text{at } z = 0 \\ \frac{\partial v}{\partial z} + \frac{1}{r}\frac{\partial w}{\partial \theta} &= 0. \end{aligned} \qquad (41)$$

They provide the appropriate conditions for velocities and pressure. The kinematic condition is:

$$\frac{\partial \eta}{\partial t} = w, \qquad \text{at } z = 0 \qquad (42)$$

which determines the free-surface elevation η in a manner similar to Eqn. (3). Note the boundary conditions in Eqns. (41) to (42) are satisfied on the mean free-surface $z = 0$, in order to be consistent with the linearization procedure.

It is worthwhile to point out that the free-surface boundary conditions in Eqns. (41) and (42) can be somewhat simplified if one considers the Froude number to be sufficiently low so that $Fr^2/Re \ll 1$ or $\tilde{U} \ll {r_i}^2 g/\nu$. This assumption yields the so called "free-slip boundary condition":

$$\frac{\partial u}{\partial z} = 0, \quad \frac{\partial v}{\partial z} = 0, \quad w = 0 \qquad \text{at } z = 0. \qquad (43)$$

Physically, this represents a flow symmetry of the velocity field about $z = 0$, with no shear stress and no wave elevation. In the viscous-flow solutions presented in this paper, we will restrict ourselves to flows governed by Eqn. (43) only.

To complete the problem description, we may impose the following far-field boundary condition on Σ,

$$u = 0, \quad v = 0, \quad w = 0, \quad \text{and} \quad P = 0, \qquad (44)$$

This approximation is asymptotically correct for a boundary sufficiently far away. We also note in passing that the use of RANS and the incorporation of turbulent models is possible within the present solution framework.

3.2 Numerical Procedure

Numerical solution for Eqns. (37) and (38) are obtained at each time step $t = k\Delta t$, for a given time increment Δt. Consider difference schemes of Eqns. (37) and (38):

$$\frac{1}{\Delta t}(\mathbf{u}^{k+1} - \mathbf{u}^k) = \mathcal{Q}\left[-(\mathbf{u}\cdot\nabla)\mathbf{u} + \frac{1}{Re}\tilde{\nabla}^2\mathbf{u}\right] - \nabla P^{k+1}, \tag{45}$$

$$\nabla\cdot\mathbf{u}^{k+1} = 0, \tag{46}$$

where $\mathcal{Q}$ is a suitable difference operator (to be defined in the next section), and $\tilde{\nabla}^2$ is the operator in brackets of Eqn. (37).

The numerical algorithm for solving Eqns. (45) and (46) is given as follows. We first introduce an auxiliary velocity field $\hat{\mathbf{u}}$, satisfying

$$\frac{1}{\Delta t}(\hat{\mathbf{u}} - \mathbf{u}^k) = \mathcal{Q}\left[-(\mathbf{u}\cdot\nabla)\mathbf{u} + \frac{1}{Re}\tilde{\nabla}^2\mathbf{u}\right], \tag{47}$$

and we subtract Eqn. (47) from Eqn. (45) to obtain

$$\frac{1}{\Delta t}(\mathbf{u}^{k+1} - \hat{\mathbf{u}}) = -\nabla P^{k+1}. \tag{48}$$

Though Eqn. (47) is not of a momentum conservation form, it can be easily seen that Eqn. (47) and Eqn. (48) are numerical consistent with Eqn. (45) if one eliminates the auxiliary velocity $\hat{\mathbf{u}}$. If we apply divergence operator onto Eqn. (48), we get a discretized Poisson equation for P^{k+1}:

$$\nabla^2 P^{k+1} = \frac{1}{\Delta t}\nabla\cdot\hat{\mathbf{u}}, \tag{49}$$

where ∇^2 is a Laplacian difference operator. Note that Eqn. (46) has been used to derive Eqn. (49).

After the P^{k+1} has been calculated from Eqn. (49), it is substituted into Eqn. (48) to obtain $\mathbf{u}^{k+1}$. This formulation is a variation of Chorin's method [31], and was implemented by Yeung and Ananthakrishnan [12].

3.2.1 *Calculation of Auxiliary Velocities* $\mathbf{u}^*$, $\mathbf{u}^{**}$ *and* $\hat{\mathbf{u}}$

The difference operator $\mathcal{Q}$ in Eqn. (46) will be explained in some detail. A similar treatment was used by Goda [33]. To calculate an auxiliary velocity $\hat{\mathbf{u}}$, the following difference schemes are introduced into Eqn. (47):
For $\hat{u}$:

$$\begin{aligned}
\frac{1}{\Delta t}(u^* - u^k) &= -u^k u_r^* + \frac{1}{Re}[u_{rr}^* + \frac{1}{r}u_r^* - \frac{u^*}{r^2}] \\
&\equiv \mathcal{Q}_r u^*, \\
\frac{1}{\Delta t}(u^{**} - u^*) &= -\frac{v^*}{r}u_\theta^{**} + \frac{{v^k}^2}{r} + \frac{1}{Re}[\frac{1}{r^2}u_{\theta\theta}^{**} - \frac{2}{r^2}v_\theta^k] \\
&\equiv \mathcal{Q}_\theta u^{**} + A_1^k, \\
\frac{1}{\Delta t}(\hat{u} - u^{**}) &= -w^{**}\hat{u}_z + \frac{1}{Re}[\hat{u}_{zz}] \\
&\equiv \mathcal{Q}_z\hat{u};
\end{aligned} \tag{50}$$

For $\hat{v}$:

$$\begin{aligned}
\frac{1}{\Delta t}(v^* - v^k) &= -u^k v_r^* + \frac{1}{Re}[v_{rr}^* + \frac{1}{r}v_r^* - \frac{v^*}{r^2}] \\
&\equiv \mathcal{Q}_r v^*, \\
\frac{1}{\Delta t}(v^{**} - v^*) &= -\frac{v^*}{r}v_\theta^{**} - \frac{u^k v^k}{r} + \frac{1}{Re}[\frac{1}{r^2}v_{\theta\theta}^{**} + \frac{2}{r^2}u_\theta^k] \\
&\equiv \mathcal{Q}_\theta v^{**} + A_2^k, \\
\frac{1}{\Delta t}(\hat{v} - v^{**}) &= -w^{**}\hat{v}_z + \frac{1}{Re}[\hat{v}_{zz}] \\
&\equiv \mathcal{Q}_z\hat{v};
\end{aligned} \tag{51}$$

For $\hat{w}$:

$$\begin{aligned}
\frac{1}{\Delta t}(w^* - w^k) &= -u^k w_r^* + \frac{1}{Re}[w_{rr}^* + \frac{1}{r}w_r^*] \\
&\equiv \mathcal{Q}_r w^*, \\
\frac{1}{\Delta t}(w^{**} - w^*) &= -\frac{v^*}{r}w_\theta^{**} + \frac{1}{Re}[\frac{1}{r^2}w_{\theta\theta}^{**}] \\
&\equiv \mathcal{Q}_\theta w^{**}, \\
\frac{1}{\Delta t}(\hat{w} - w^{**}) &= -w^{**}\hat{w}_z + \frac{1}{Re}[\hat{w}_{zz}] \\
&\equiv \mathcal{Q}_z\hat{w};
\end{aligned} \tag{52}$$

where $\mathbf{u}^*$, $\mathbf{u}^{**}$ are auxiliary velocities, newly introduced for simplifying the computations. However, these variables do not require extra storage, because $\mathbf{u}^*$ and $\mathbf{u}^{**}$ can share the same storage with $\hat{\mathbf{u}}$. $\mathcal{Q}_r$, $\mathcal{Q}_\theta$ and $\mathcal{Q}_z$ are difference operator in the r, θ and z directions. A_1^k are A_2^k are known

functions defined as:

$$A_1^k = \frac{{v^k}^2}{r} - \frac{2}{Rer^2} v_\theta^k,$$
$$A_2^k = -\frac{u^k v^k}{r} + \frac{2}{Rer^2} u_\theta^k. \tag{53}$$

The scheme in Eqns. (50) - (52) is a variation of the ADI method [34]. Consistency of the above procedure can be easily shown. If we take Eqn. (50) for example, it can be rewritten as:

$$\begin{aligned} u^* &= (1-\Delta t \mathcal{Q}_r)^{-1} u^k, \\ u^{**} &= (1-\Delta t \mathcal{Q}_\theta)^{-1}[u^* + \Delta t A_1^k], \\ \hat{u} &= (1-\Delta t \mathcal{Q}_z)^{-1} u^{**}. \end{aligned} \tag{54}$$

Elimination of the intermediate velocities u^* and u^{**} yields the following:

$$\begin{aligned} \hat{u} &= (1-\Delta t \mathcal{Q}_r)^{-1}(1-\Delta t \mathcal{Q}_\theta)^{-1} \\ &\quad [(1-\Delta t \mathcal{Q}_z)^{-1} u^k + \Delta t A_1^k] \\ &= (1+\Delta t \mathcal{Q}_r + \Delta t \mathcal{Q} + \Delta t \mathcal{Q}_z) u^k \\ &\quad + \Delta t A_1^k + O(\Delta t^2) \end{aligned} \tag{55}$$

This shows that the present procedure is an approximation of Eqn. (47).

Note that Eqns. (50) - (52) are of implicit forms for each intermediate velocity $\mathbf{u}^*$, $\mathbf{u}^{**}$ and $\hat{\mathbf{u}}$. Thus, by von Neumann's linear stability theory [34], each of these schemes is unconditionally stable, assuming that the each coefficient of nonlinear terms is a local constant. Although each of Eqns. (50) - (52) is independently stable, the total stability condition of Eqns. (50) - (52) and Eqn. (48) is not strictly established.

The above Eqns. (50)-(52) can be further rewritten and regrouped into the following three sets of ordinary differential equations (ODE's):

For $\mathbf{u}^*$:

$$\begin{aligned} &u_{rr}^* + (\frac{1}{r} - Reu^k) u_r^* + (-\frac{1}{r^2} - \frac{Re}{\Delta t}) u^* = -\frac{Re}{\Delta t} u^k, \\ &v_{rr}^* + (\frac{1}{r} - Reu^k) v_r^* + (-\frac{1}{r^2} - \frac{Re}{\Delta t}) v^* = -\frac{Re}{\Delta t} v^k, \\ &w_{rr}^* + (\frac{1}{r} - Reu^k) w_r^* - \frac{Re}{\Delta t} w^* = -\frac{Re}{\Delta t} w^k; \end{aligned} \tag{56}$$

For $\mathbf{u}^{**}$:

$$\begin{aligned} &u_{\theta\theta}^{**} - Rerv^* u_\theta^{**} - \frac{Rer}{\Delta t} u^{**} = -\frac{Rer^2}{\Delta t} u^* - Rer^2 A_1^k, \\ &v_{\theta\theta}^{**} - Rerv^* v_\theta^{**} - \frac{Rer}{\Delta t} v^{**} = -\frac{Rer^2}{\Delta t} v^* - Rer^2 A_2^k, \\ &w_{\theta\theta}^{**} - Rerv^* w_\theta^{**} - \frac{Rer}{\Delta t} w^{**} = -\frac{Rer^2}{\Delta t} w^*; \end{aligned} \tag{57}$$

For $\hat{\mathbf{u}}$:

$$\begin{aligned} &\hat{u}_{zz} - Rew^{**} \hat{u}_z - \frac{Re}{\Delta t} \hat{u} = -\frac{Re}{\Delta t} u^{**}, \\ &\hat{v}_{zz} - Rew^{**} \hat{v}_z - \frac{Re}{\Delta t} \hat{v} = -\frac{Re}{\Delta t} v^{**}, \\ &\hat{w}_{zz} - Rew^{**} \hat{w}_z - \frac{Re}{\Delta t} \hat{w} = -\frac{Re}{\Delta t} w^{**}. \end{aligned} \tag{58}$$

The ODE's (56) and (58) are solved by a Chebyshev spectral collocation method, and Eqn. (57) is solved by a Fourier spectral collocation method, subject to the boundary conditions given below.

3.2.2 *Implementation of Boundary Conditions*

As an example of the treatment of $\hat{u}$ in Eqn. (50), the boundary conditions for u^*, u^{**} and $\hat{u}$ are formally written as

$$\begin{aligned} u^* &= u^{k+1} - \Delta t(\mathcal{Q}_\theta u^{k+1} + A_1^{k+1} + \\ &\quad \mathcal{Q}_z u^{k+1} - \mathcal{G}_r P^{k+1}), \\ u^{**} &= u^{k+1} - \Delta t(\mathcal{Q}_z u^{k+1} - \mathcal{G}_r P^{k+1}), \\ \hat{u} &= u^{k+1} - \Delta t(-\mathcal{G}_r P^{k+1}), \end{aligned} \tag{59}$$

where $\mathcal{G}_r$ denotes the gradient difference operator in r direction. Eqn. (59) above is derived by subtracting Eqn. (50) from the actual numerical momentum equation for u^{k+1}. In the actual computations, we use an explicit version for the pressure term in Eqn. (59), i.e., the P^k is used in place of P^{k+1}. Particularly, the first equation in Eqn. (59) is used as the boundary condition for the first ODE in Eqn. (56), and the third equation in Eqn. (59) for the first ODE in Eqn. (58). Since no boundary conditions are needed for the solution of the second ODE in Eqn. (57) because of the periodic assumption implied in the circumferential direction θ, the second equation in Eqn. (59) can be discarded. The boundary conditions in Eqn. (59) can thus be rewritten as:

$$\begin{aligned} u^* = &\quad u^{k+1} - \Delta t(\mathcal{Q}_\theta u^{k+1} + A_1^{k+1} + \\ &\quad \mathcal{Q}_z u^{k+1} - \mathcal{G}_r P^k) \quad \text{at } r = r_i \text{ or } r_o, \\ \hat{u} = &\quad u^{k+1} - \Delta t(-\mathcal{G}_r P^k) \\ &\quad \text{at } z = -d \text{ or } 0. \end{aligned} \tag{60}$$

The boundary conditions for v and w can be derived similarly and are given by:

$$\begin{aligned} v^* = &\quad v^{k+1} - \Delta t(\mathcal{Q}_\theta v^{k+1} + A_2^{k+1} + \\ &\quad \mathcal{Q}_z v^{k+1} - \mathcal{G}_\theta P^k) \quad \text{at } r = r_i \text{ or } r_o, \\ \hat{v} = &\quad v^{k+1} - \Delta t(-\mathcal{G}_\theta P^k) \\ &\quad \text{at } z = -d \text{ or } 0, \end{aligned} \tag{61}$$

and

$$\begin{aligned} w^* = \quad & w^{k+1} - \Delta t(\mathcal{Q}_\theta w^{k+1} + \\ & \mathcal{Q}_z w^{k+1} - \mathcal{G}_z P^k) \quad \text{at } r = r_i \text{ or } r_o, \\ \hat{w} = \quad & w^{k+1} - \Delta t(-\mathcal{G}_z P^k) \\ & \text{at } z = -d \text{ or } 0, \end{aligned} \tag{62}$$

where $\mathcal{G}_\theta$ and $\mathcal{G}_z$, similarly, denote gradient difference operators in the θ and z directions.

For the particular problems at hand, the boundary conditions in Eqns. (60) to (62) can be further simplified by using their physical boundary conditions, which, in normal and tangential coordinates, fall into one of the following forms: (a) The no-slip wall condition

$$u_n = u_{\tau_1} = u_{\tau_2} = 0, \tag{63}$$

or (b) The free-slip boundary condition

$$u_n = 0, \qquad \frac{\partial u_{\tau_1}}{\partial n} = \frac{\partial u_{\tau_2}}{\partial n} = 0, \tag{64}$$

where u_n, u_{τ_1} and u_{τ_2} denote the velocity components along the normal (n) and two tangential (τ_1 and τ_2) directions of the boundary surface, respectively.

For numerical implementation of the above two boundary conditions, we set the normal component of the auxiliary velocity $\hat{\mathbf{u}}$ to be the same as the actual velocity $\mathbf{u}^{k+1}$:

$$\hat{u}_n = {u_n}^{k+1} \tag{65}$$

Then Eqn. (65) together with Eqn. (48) implies the following homogeneous Neumann condition for P^{k+1} on these boundaries:

$$\frac{\partial P^{k+1}}{\partial n} = 0. \tag{66}$$

Thus, the boundary conditions for auxiliary velocity $\hat{\mathbf{u}}$ in the second equations of Eqn. (60) to (62) can be reduced to:

$$\begin{aligned} \hat{u} &= -\Delta t(-\mathcal{G}_r P^k) \\ \hat{v} &= -\Delta t(-\mathcal{G}_\theta P^k) \\ \hat{w} &= 0 \qquad \text{for } z = -d \text{ or } 0 \end{aligned} \tag{67}$$

for the case of no-slip wall, and

$$\begin{aligned} \frac{\partial \hat{u}}{\partial z} &= -\Delta t(-\mathcal{G}_r \frac{\partial P^{k+1}}{\partial z}) = 0 \\ \frac{\partial \hat{v}}{\partial z} &= -\Delta t(-\mathcal{G}_\theta \frac{\partial P^{k+1}}{\partial z}) = 0 \\ \hat{w} &= 0 \qquad \text{for } z = -d \text{ or } 0 \end{aligned} \tag{68}$$

for the case of free-slip wall. We note in passing that Eqn. (63) and (64) have been used to derive the above expressions.

3.2.3 *Solution of the Pressure Equation*

In cylindrical coordinates, Eqn. (49) can be rewritten more explicitly as:

$$\nabla^2 P = \frac{1}{\Delta t}\left[\frac{1}{r}\frac{\partial (r\hat{u})}{\partial r} + \frac{1}{r}\frac{\partial \hat{v}}{\partial \theta} + \frac{\partial \hat{w}}{\partial z}\right]. \tag{69}$$

This falls precisely into a form that was discussed in Sec. 2.2, subject to the appropriate boundary conditions. The treatment of this pressure Poisson equation follows directly from spectral method described earlier.

4 RESULTS AND DISCUSSIONS OF VISCOUS FLOWS

4.1 A Test Case

In order to validate our solution method, especially its ability to handle large-time simulations, we solve as a three-dimensional test problem that corresponds to a cylindrical version of the Stokes's second problem for a viscous flow over an oscillating wall.

Consider a solid cylinder of radius r_i spinning about its axis with angular frequency ω in an initially still and unbounded viscous fluid. If we choose to non-dimensionalize the flow parameters by r_i and ω, the non-dimensional circumferential velocity at the cylinder surface is specified as

$$v(1,t) = \begin{cases} 0 & \text{when } t < 0 \\ \sin(t) & \text{when } t \geq 0. \end{cases} \tag{70}$$

The circumferential momentum equation governing such a flow can be written as:

$$\frac{\partial v}{\partial t} = \frac{1}{Re}\left(\frac{\partial^2 v}{\partial r^2} + \frac{1}{r}\frac{\partial v}{\partial r} - \frac{v}{r^2}\right), \tag{71}$$

where the Reynolds number Re is defined as $\omega r_i^2/\nu$. A steady-state solution of the above equation is of the form

$$v(r,t) = Im[f(r)e^{it}]. \tag{72}$$

It is not difficult to derive that

$$f(r) = \frac{K_1(\frac{1+i}{2}\sqrt{Re}r)}{K_1(\frac{1+i}{2}\sqrt{Re})}, \tag{73}$$

where K_1 denotes the first order modified Bessel function of the second kind.

To test our code, we choose to solve this problem as a fully three-dimensional problem. Specifically, free-slip boundary conditions (64) are used

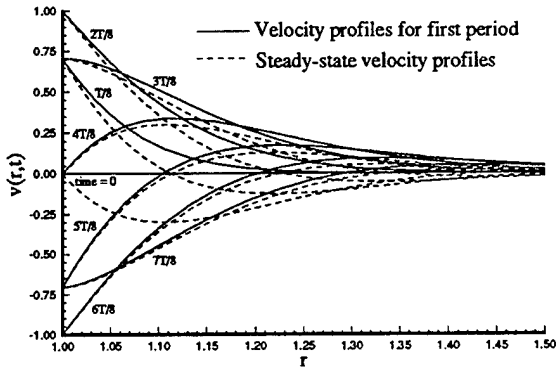


Figure 5: Velocity profiles in the first period of motion and in steady-state.

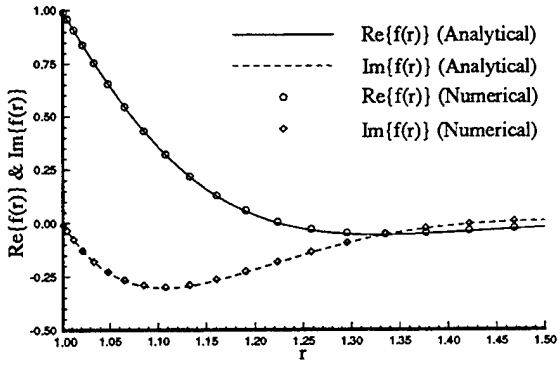


Figure 6: Real and imaginary parts of $f(r)$ in Eqn. (72).

on top $\mathcal{F}$, the bottom $\mathcal{B}$ and the far-field Σ boundaries. Here the far-field boundary Σ is taken to be a distance of 10. Grid resolution of $L = 48$, $M = 16$ and $N = 24$, and Reynolds number $Re = 100$ is chosen for this study. Fig. 5 shows a sample of the velocity profiles $v(r,t)$ at eight instants of time during the first period of oscillation and the corresponding steady-state profile at the 7th cycle. Numerical results show that the transients are only significant during the first couple of cycles of oscillation. To show the accuracy of our numerical solution, we further plot in Fig. 6 a comparison of the real and imaginary parts of function $f(r)$ (Eqn. 72) with the numerical values. Excellent agreement is observed.

4.2 Flows in a Cylindrical Cavity

In this section, we proceed to solve a series of cylindrical cavity flow problems, in which the fluid is entirely enclosed by solid boundaries, and the

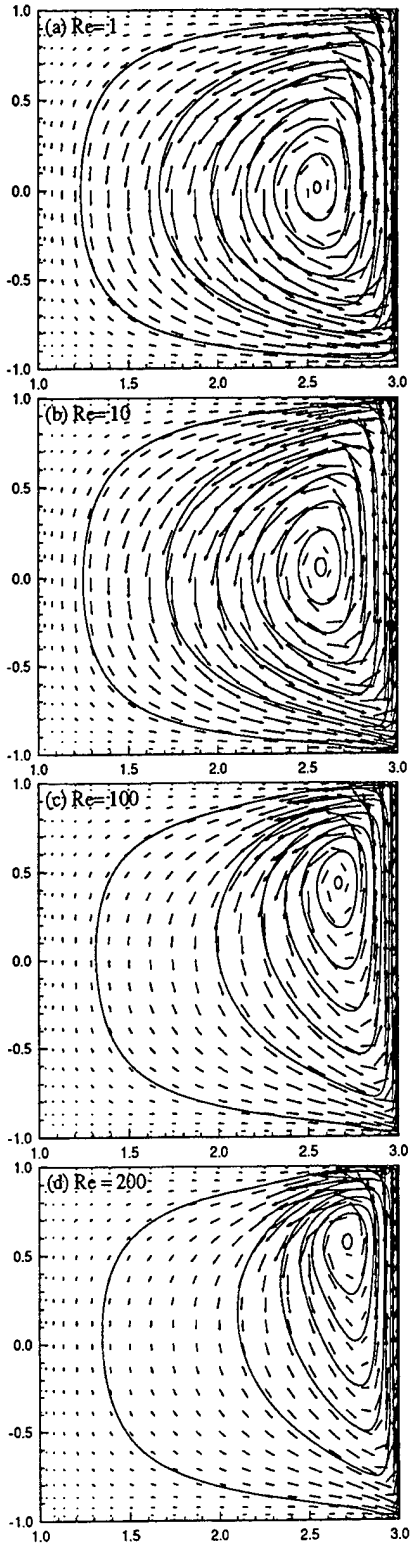


Figure 7: Steady-state streamlines in a cylindrical cavity for different Reynolds numbers (driven by outer cylinder): (a) $Re = 1$, $t = 2.0$; (b) $Re = 10$, $t = 2.0$; (c) $Re = 100$, $t = 3.0$; (d) $Re = 200$, $t = 3.0$.

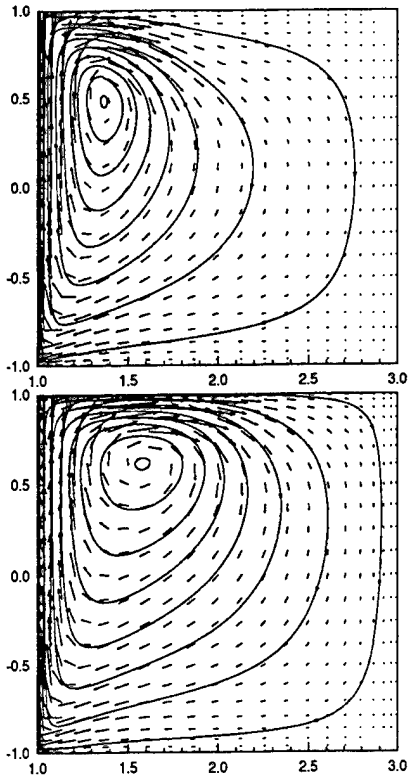


Figure 8: Steady-state flow in a cylindrical cavity, driven by inner cylinder: (top) wall at all boundaries; (bottom) free-slip wall on top.

flow is driven by an impulsively-started sliding motion of one of the boundaries. The two-dimensional version of this problem is well known (see e.g. [35]). It has often served as a testing ground for competing numerical methods, the objective of the competition being to prove that one's favorite method reveals accurately more realistic details of the flow than other methods with comparable computation efforts. There is little literature for the (three-dimensional) cylindrical cavity case, however.

Imagine a three-dimensional flow enclosed in a cylindrical region (see Fig. 1) where boundaries $\mathcal{F}$, $\mathcal{B}$ and $\mathcal{S}$ are stationary walls, while the remaining boundary Σ slides upwards with a constant speed W starting at $t = 0$. To solve this problem, we first non-dimensionalize the flow parameters by the following natural choice of primary variables: the height of domain d and wall velocity W. The Reynolds number Re is defined by Wd/ν. No-slip boundary conditions (63) are applied at all these boundaries.

The possibility of a steady-state solution in this problem is investigated. The three-dimensional code was run for t as large as 4.0, using a time step $\Delta t = 0.01$, for a grid resolution of $L \times M \times N = 24 \times 16 \times 24$ until less than 0.01 percentage change in the velocity field was noted. It was found that steady-state solution is approached as early as $t = 3.0$ for the case of $Re = 200$, and a somewhat larger value for higher Reynolds numbers. To accentuate the vortical patterns, only results for up to a value of $Re = 200$ are shown here. At higher Reynolds numbers, only a very thin vortical structure exists near Σ.

In Fig. 7, we show the velocity-vector plots for four different Reynolds numbers on a plane of constant circumferential angle θ. Also plotted are the streamline patterns. Since the cavity is driven axisymmetrically (which is not a restriction in our method), the solution is axisymmetric. It is of interest to observe that at Reynolds number smaller than 10 (see Fig. 7(a),(b)), the core of the characteristic ring vortex is located at the mid-height of the cavity ($z = -d/2$). Considerable "symmetry" of the streamline patterns about the mid-height plane is observed. As the Reynolds number increases, the core of the primary vortex is driven towards the top wall and towards the sliding surface.

As mentioned earlier, the free-slip boundary condition corresponds to a special limit of the free-surface boundary condition. It is of interest to note that a steady-state configuration is also reached when the top surface $\mathcal{F}$ is replaced by a free-slip wall (defined by Eqn. 43). Fig. 8 contrasts the steady-state flow patterns of the no-slip $\mathcal{F}$ with that of the a free-slip $\mathcal{F}$. In this run, the inner cylinder $\mathcal{S}$ is given the steady vertical velocity while the outer cylinder has a no-slip wall condition. From this figure, we notice a larger vortical structure in the free-slip case. This is consistent with the expectation that a free-slip wall is less restrictive to horizontal flow motion than a no-slip wall, thus allowing vortex to grow more freely.

4.3 An Oscillating Cavity with Free-Slip Boundary Condition

In this section, we study the time-evolution of the cylindrical cavity flow driven by an oscillatory inner wall in the presence of either a free-slip $\mathcal{F}$ or a no-slip $\mathcal{F}$. This flow, with minor modifications in the boundary conditions on some of the boundary surfaces, can mimic the vorticity structures generated by a hull surface of a ship in heaving motion.

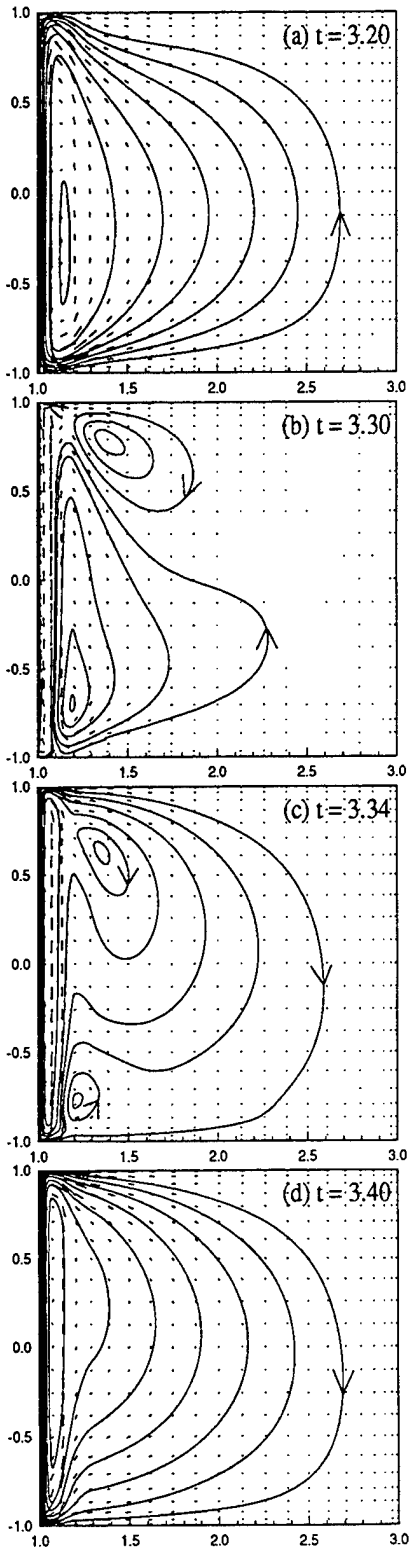


Figure 9: Cylindrical cavity flow driven by an oscillatory wall, free-slip wall on top: (a) $t = 4T$; (b) $t = 4\frac{5}{40}T$; (c) $t = 4\frac{7}{40}T$; (d) $t = 4\frac{10}{40}T$, where T is the period of oscillation.

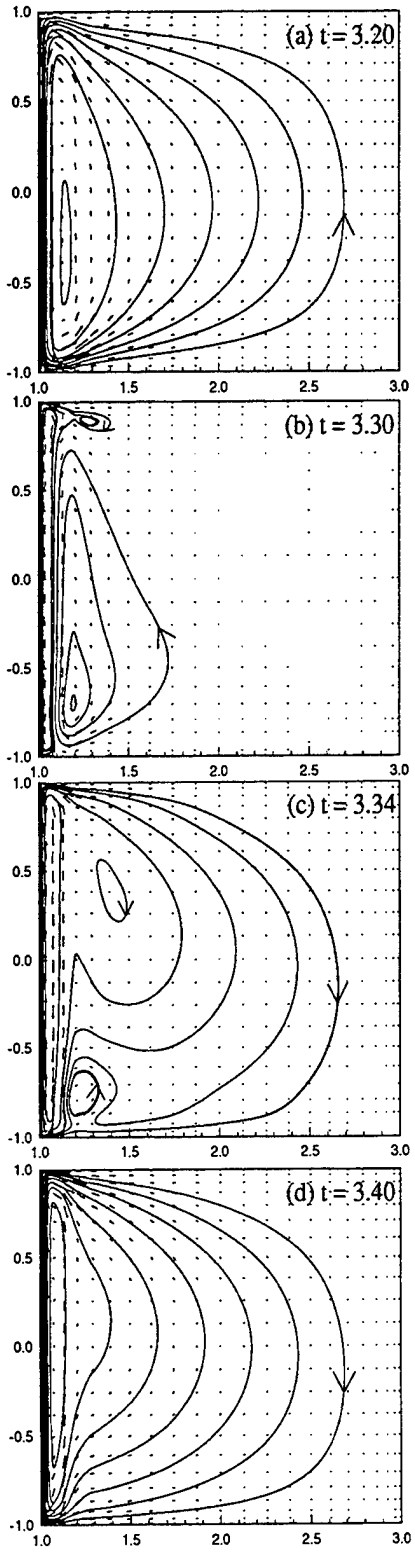


Figure 10: Cylindrical cavity flow driven by an oscillatory wall, no-slip walls on all boundaries: (a) $t = 4T$; (b) $t = 4\frac{5}{40}T$; (c) $t = 4\frac{7}{40}T$; (d) $t = 4\frac{10}{40}T$, where T is the period of oscillation.

Consider again the flow configuration in Fig. 1, where the bottom boundary $\mathcal{B}$ and outer cylinder Σ are stationary walls, and upper boundary $\mathcal{F}$ is assumed to be a free-slip wall. The flow is driven by the motion of a no-slip inner cylinder $\mathcal{S}$, which oscillates periodically along the $z-$axis with prescribed velocity

$$W(t) = \begin{cases} 0 & \text{when } t < 0 \\ W_0 \sin(\omega t) & \text{when } t \geq 0 \end{cases}, \quad (74)$$

where W_0 is the amplitude of the vertical velocity, and ω the angular frequency of oscillation.

Nondimensionalization is carried out in the same manner as Sec. 4.2. For convenience, the distance between the inner and outer cylinders is chosen to be the same as the height of domain d. The Reynolds number, defined in this case by $W_0 d/\nu$, is set to 100. The non-dimensional period of oscillation T is defined by $2\pi W_0/\omega d$, and is taken to be 0.8.

Numerical results are obtained by a mesh size of $L \times M \times N = 24 \times 16 \times 24$, and time steps $\Delta t = 0.01$ and 0.02 have been used to check convergence, which is excellent. Because of the nonlinear nature of the Navier-Stokes equations, a periodic solution is not expected. However, the flow is found to display an "almost" periodic behavior with a "steady streaming" effect [27].

Fig. 9 shows the velocity vectors and pathlines corresponding to four instants of time $t = 4T$, $4\frac{5}{40}T$, $4\frac{7}{40}T$, and $4\frac{10}{40}T$ during the first quarter cycle of the fifth period of oscillation. It is interesting to study the vortex evolution in this case. In Fig. 9b, the inner cylinder has just reversed its direction of motion and is in the process of picking up some velocity. A thin shear layer is formed next to the cylinder while a small clockwise (ring) vortex is generated under the top surface, but above the counter-clockwise vortex, a residue of the earlier quarter cycle of motion (Fig. 9a). This clockwise vortex later becomes dominant in the flow region while the counter-clockwise vortex shrinks to the lower corner (Fig. 9c). In Fig. 9d, the clockwise ring vortex has replaced the counter-clockwise vortex of Fig. 9a, and becomes the only visible vortex. The flow pattern in the second quarter of oscillation varies relatively slowly, while the pattern for the last two quarters represents a change of flow direction relative to the first two quarters.

To study the effects of a free-slip wall, we replace the free-slip wall at upper boundary $\mathcal{F}$ by a no-slip wall. For comparison purposes, the results for this case are shown in Fig. 10 in the same sequence as Fig. 9. The difference of these two flows appears to be less distinct when compared with the steady-state cases shown in Fig. 8, in which the inner cylinder $\mathcal{S}$ is moving continuously upwards, instead, oscillating.

4.4 Wave Sloshing of a Viscous Fluid in an Annular Domain

In this last results section, we present some preliminary results of a viscous flow with free surface. The Cauchy-Poisson wave problem solved in Sec. 2.4 is studied here for a *viscous* fluid. In order to understand the comparative effects of viscosity, the results of viscous flow are compared with their inviscid counterparts.

We first non-dimensionalize the flow parameters by the following primary variables: the radius of inner cylinder r_i, and gravitational acceleration g. The Reynolds number Re is defined by $\sqrt{g r_i} r_i/\nu$, and Froude number F_r is equal to unity. Linearized free-surface boundary conditions (41) are applied on free surface $\mathcal{F}$, while no-slip boundary conditions (63) are chosen on the inner cylinder $\mathcal{S}$, the outer cylinder Σ, and the bottom $\mathcal{B}$. The initial wave form is taken to be

$$\eta(r, \theta, t = 0) = A \exp\left\{-2.651\left[(r\cos\theta - 2.318)^2 + (r\sin\theta)^2\right]\right\}, \quad (75)$$

where A is the initial wave elevation at the center of the hump, which is located at $r = 2.318$. This corresponds to a hump located closer to the cylinder than in Eqn. 35, thus generating a higher velocity as the pulse "impacts" on cylinder.

Numerical results for both viscous and inviscid flows are obtained by a mesh size of $L \times M \times N = 64 \times 64 \times 32$ and a time step $\Delta t = 0.05$. The Reynolds number Re is set as $10,000$ for the case of viscous flow. A is taken to be 0.1 in these computations. In order to capture the major wave-body interaction, the two three-dimensional codes were run for t as large as 12.50. Before viscosity effect plays a major role, the flow features of viscous and inviscid flows are expected to be similar during the early stage of simulation. This is evident from Fig. 11, in which the free-surface elevations at $r = 1$ (body-free-surface intersection) and $r = 2.318$ (center of initial hump) are plotted as functions of time. Furthermore, Fig. 11 shows that the waves are damped out sooner in a viscous fluid than in an inviscid fluid. This can also be observed from the perspective view of the overall field plotted in Fig. 12.

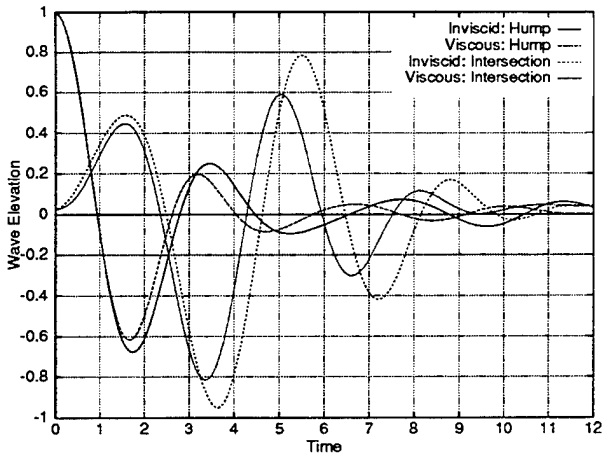


Figure 11: Time histroy of wave elevation at $r = 1$ and $r = 2.318$, for the plane $\theta = 0$. The results for the case of $r = 1$ have been enlarged by a factor of 20 for clarity.

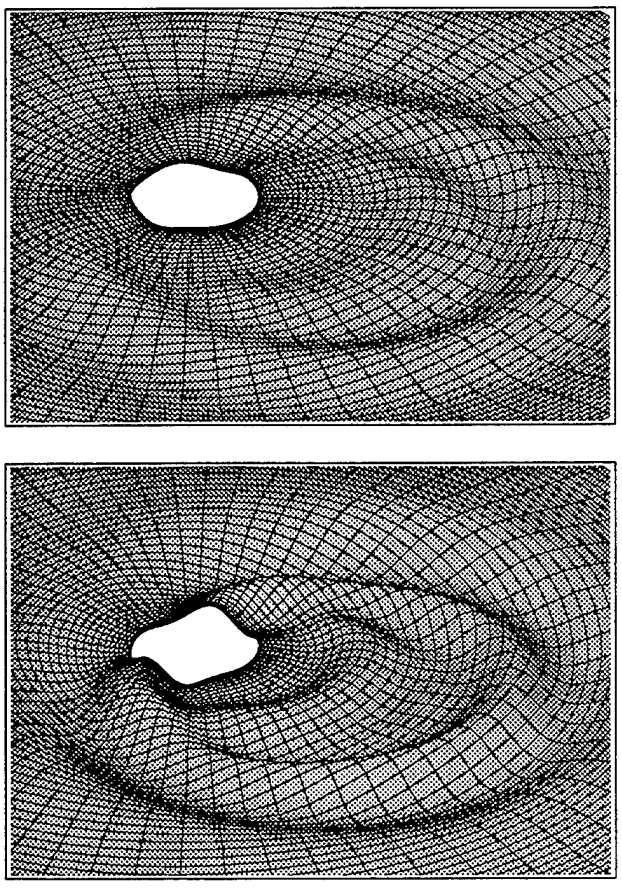


Figure 12: Free-surface elevations for the cases of viscous flow (top) and inviscid flow (bottom) at $t = 12.00$. The elevations have been enlarged for clarity.

For a close look at the viscous-flow results, we include a vorticity plot and a surface-contour plot in Figs. 13 and 14. In Fig. 13, the velocity vectors are overlaid onto a vorticity contour plot in the vertical plane of symmetry under the prescribed wave form for $t = 12.00$. Two vortices of opposite signs can be clearly seen near the intersection of the body and the free surface. A boundary layer immediately above the bottom is also observed.

Fig. 14 shows the free-surface elevation contours at the same instant of time. Also plotted are the velocity vectors on the free surface. It is of interest to note that the vorticity component *normal* to the free surface is vanishingly small (not shown) except near the body. This suggests vortex structures generated by the surface motion are primarily parallel to the water surface. These and other data of an extensive nature will offer valuable insights for understanding vortical free-surface flows near a body.

5 CONCLUSIONS

In this paper, a very effective pseudo-spectral method has been described and demonstrated for studying the motion of an inviscid or viscous fluid in a cylindrical domain. High resolution, low computational requirements, and the ability to handle a wide class of boundary conditions are the salient features of this method. The method has been applied to predict the evolution of waves within the confine of two concentric cylinders. Excellent accuracy and convergence characteristics were observed. As a new development, the method was applied to obtain solutions of the Navier Stokes equations in the same type of domain, but subject to no-slip or free-slip wall conditions. The formulation for this viscous-flow problem is similar to the fractional step projection algorithm of [26]. Solutions for several vortical flows in an annular domain driven by steadily moving or periodically oscillating walls were examined in detail. Finally, with the full free-surface conditions, results for a *viscous* Cauchy-Poisson wave problem are obtained. These preliminary results suggest some intricate vortex structures that need to be further studied. The present method is capable of capturing such flow details in the mixed-boundary shear region. It is worthy to mention that the inclusion of strongly convective effects associated with forward motion can be incorporated. With additional analysis, it is also possible to include the consideration of boundary shapes such as elliptical struts or ellipsoidal hulls.

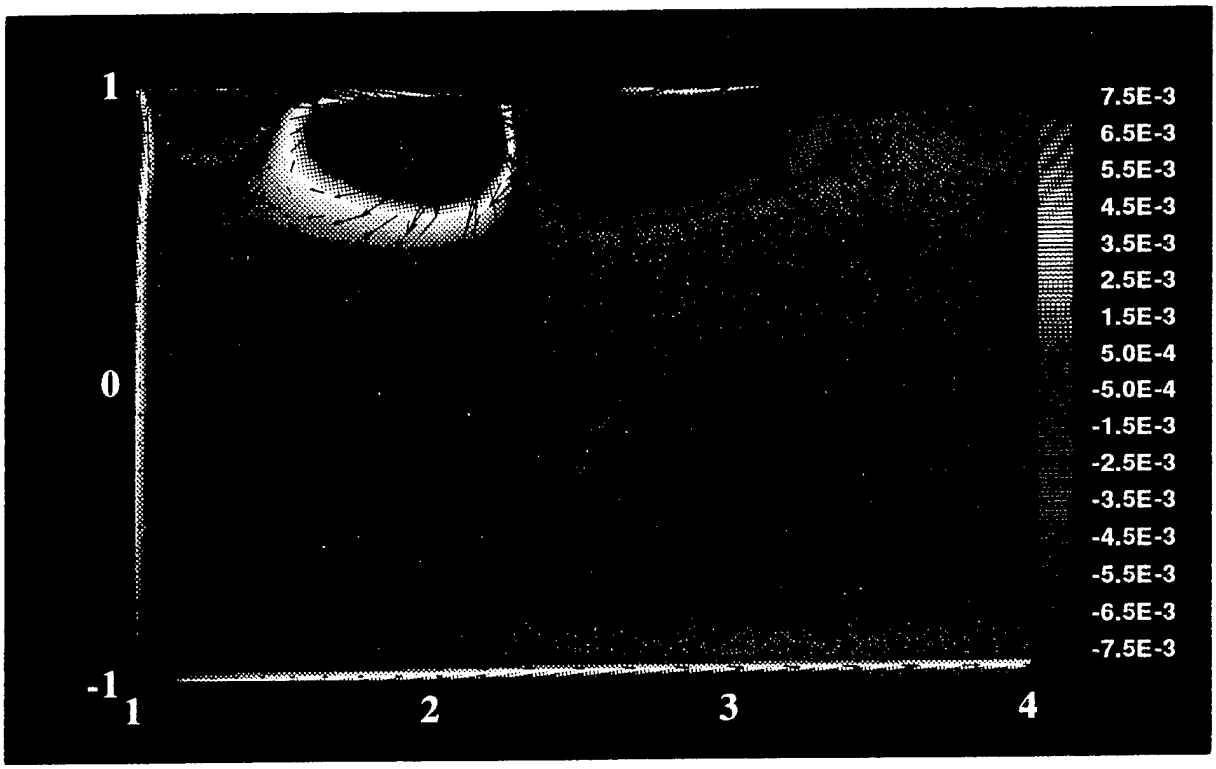


Figure 13: Velocity vectors and vorticity contours in the plane $\theta = 0$ at $t = 12.00$.

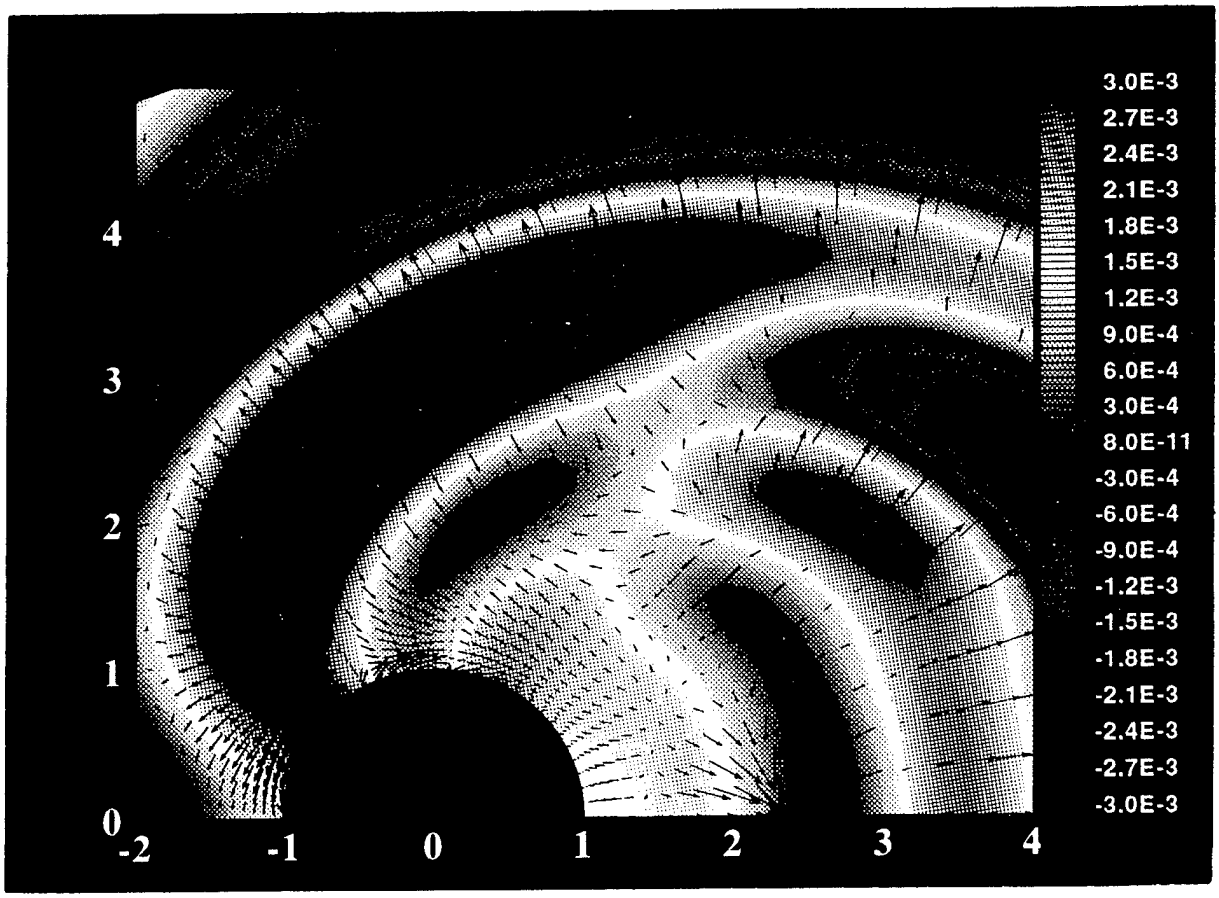


Figure 14: Elevation contours and velocity vectors on the free-surface at $t = 12.00$.

ACKNOWLEDGEMENTS

Research reported here has been supported by the Office of Naval Research under grant N00014-91-J1155, as well as a general grant from the Shell Foundation. The authors would like to express their gratitude to these sponsors. Acknowledgement is also made to Dr. P. Ananthakrishnan who had participated in many useful discussions.

References

[1] Miyata, H., Toru, S. and Baba, N., "Difference Solution of a Viscous Flow with Free-Surface Wave about an Advanced Ship," *Journal of Computational Physics*, Vol. 72, 1987, pp. 393-421.

[2] Tahara, Y., Stern, F. and Rosen, B., "An Interactive Approach for Calculating Ship Boundary Layers and Wakes for Nonzero Froude Number," *Journal of Computational Physics*, Vol. 98, 1992, pp. 33-35.

[3] Farmer, J., Mattinelli, L. and Jameson, A., "Fast Multigrid Method for Solving the Nonlinear Ship Wave Problem with a Free Surface," *Proceedings of the 6th. International Conference on Numerical Ship Hydrodynamics,* Iowa city, IA., 1993, pp. 4-1–4-17.

[4] Hino, T., "Computation of Free Surface Flow Around an Advancing Ship by the Navier-Stokes Equations," *Proceedings of the 6th International Conference on Numerical Ship Hydrodynamics,* Hiroshima, Japan, 1989, pp. 103-117.

[5] Chen, H. C., Lin, W. M. and Weems, K. M., "Second-Moment RANS Calculations of Viscous Flow Around Ship Hulls", *CFD Workshop Tokyo 1994,* Tokyo, Japan, 1994.

[6] Nakos, D. E., Nestegard, A., Ulstein, T. and Sclavounos, P. D., "Seakeeping Analysis of Surface Effect Ships," *Proceedings of the 1st International Conference on Fast Sea Transportation,* Trondheim, Norway, 1992, pp. 413-428.

[7] Raven, H. C., "A Practical Nonlinear Method for Calculating Ship Wavemaking and Wave Resistance," *Proceedings of the 19th Symposium on Naval Hydrodynamics,* Seoul, South Korea, 1992.

[8] Paulling, J. R., *Proceedings of the 20th International Towing Tank Conference,* Berkeley, CA., Vol. I, 1993, pp. 17-68.

[9] Grega, L. M., Wei, T., Leighton, R. and Neves, J., "Examination of Secondary Flows Along a Vertical Wall/Free-Surface Corner," *1994 ONR Workshop on Free-Surface Turbulence Flows,* Pasadena, CA., 1994.

[10] Leighton, R., "The Rate of Strain in Turbulent Channel Flow," *1994 ONR Workshop on Free-Surface Turbulence Flows,* Pasadena, CA., 1994.

[11] Baba, E., "Wave Breaking Resistance of Ships," *International Seminar on Ship Wave Resistance,* Tokyo, Japan, 1976.

[12] Yeung, R. W. and Ananthakrishnan, P., "Vortical Flows with and without a Surface-Piercing Body," *Proceedings of the 19th Symposium on Naval Hydrodynamics,* Seoul, South Korea, 1992.

[13] Baba, E., "Some Free Surface Phenomena Around Ships to be Challenged by Numerical Analysis," *Proceedings of the 3rd International Conference on Numerical Ship Hydrodynamics,* Paris, France, 1981, pp. 9-23.

[14] Hawthorne, W. R., "The Secondary Flow about Struts and Airfoils," *Journal of the Aeronautical Sciences,* Vol. 21, 1954, pp. 588-608.

[15] Sclavounos, P. D., "The Interaction of Viscous Flow with a Free Surface near a Solid Boundary," *20th Symposium on Naval Hydrodynamics,* Santa Barbara, CA., 1994.

[16] Gottlieb, D. and Orszag, S. A., "Numerical Analysis of Spectral Methods: Theory, and Application," *SIAM,* Philadelphia, PA., 1977.

[17] Hussaini, M. and Zang, T., "Spectral Methods in Fluid Dynamics," *Annual Review of Fluid Mechanics*, Vol. 19, 1987, pp. 339-367.

[18] Korczak, K. Z. and Patera, A. T., "An Isoparametric Spectral Element Method for Solution of the Navier-Stokes Equations in Complex Geometry," *Journal of Computational Physics*, Vol. 62, 1986, pp. 361-382.

[19] Tan, C. S., "A Multi-domain Spectral Computation of Three-Dimensional Laminar Horseshoe Vortex Flow Using Incompressible Navier-Stokes Equations," *Journal of Computational Physics*, Vol. 85, 1989, pp. 130-158.

[20] Yeung, R. W., "A Hybrid Integral-Equation Method for Time-Harmonic Free-Surface Flow," *Proceedings of the 1st International Conference on Numerical Ship Hydrodynamics,* Bethesda, MD., 1975, pp. 581-607.

[21] Yeung, R. W., Yu, X. and Ananthakrishnan, P., "Interaction of Transient Waves with a Circular Surface-Piercing Body," Report No. NAOE 93-1, Department of Naval Architecture and Offshore Engineering, University of California at Berkeley, August 1993.

[22] Wehausen, J. V., "Initial value problem for the motion in an undulating sea of a body with fixed equilibrium position," *Journal of Engineering Mathematics*, Vol. 1, 1967, pp. 1-19.

[23] Korsmeyer, F. T., Lee, C. H., Newman, J. N. and Sclavounos, P. D., "The analysis of wave effects on tension-leg platforms," *Proceedings of Offshore Mechanics and Arctic Engineering Conference*, Houston, TX., Vol. 2, 1988, pp. 1-14.

[24] Bai, K. J. and Yeung, R. W., "Numerical solution to free-surface flow problems," *Proceedings of the 10th Symposium on Naval Hydrodynamics*, Cambridge, MA., 1974, pp. 609-647.

[25] Nakos, D. E. and Sclavounos, P. D., "Ship motions by a three-dimensional ranking panel method," *Proceedings of the 18th Symposium on Naval Hydrodynamics*, Ann Arbor, MI., 1990, pp. 21-40.

[26] Yeung, R. W. and Ananthakrishnan, P., "Oscillation of a Floating Body in a Viscous Fluid," *Journal of Engineering Mathematics*, Vol. 26, 1992, pp. 211-230.

[27] Schlichting, H., *Boundary-Layer Theory*, 6th ed., McGraw-Hill, New York, 1968.

[28] Tan, C. S., "Accurate Solution of Three-Dimensional Poisson Equation in Cylindrical Coordinate by Expansion in Chebyshev Polynomials," *Journal Computational Physics*, Vol. 59, 1985, pp. 81-95.

[29] Lamb, H., *Hydrodynamics*, 6th ed., Dover Publication Inc., New York, 1932.

[30] Yeung, R. W., "Numerical Methods in Free Surface Flows," *Annual Review of Fluid Mechanics*, Vol. 14, 1982, pp. 395-442.

[31] Chorin, A. J., "Numerical Solution of Incompressible Flow Problems," *Studies on Numerical Analysis*, Vol. 2, 1968, pp. 64-71.

[32] Wehausen, J. V. and Laitone, E. V., "Surface Waves," *Handbuch der Physik*, Vol. 9, Springer, Berlin, 1960.

[33] Goda, K., "A Multistep Technique with Implicit Difference Schemes for Calculating Two- or Three-Dimensional Cavity Flows", *Journal of Computational Physics*, Vol. 30, 1979, pp. 76-95.

[34] Sod, G. A., *Numerical Methods in Fluid Dynamics*, Cambridge Univ. Press, Cambridge, England, 1985.

[35] Sherman, F. S., *Viscous Flow*, McGraw-Hill, New York, 1990.

DISCUSSION

K. Mori
Hiroshima University, Japan

Although the use of cylindrical coordinate for a flow around a vertical cylinder is geometrically convenient, it may not be a good choice for the free surface flow. This is because the grid size in circumferential direction becomes larger as the radius increases. Needless to say, the grid size must be small enough compared with the wave length. Even though the number of grids is large enough, the size can not be controlled when the cylindrical coordinates are used. Eventually, the wave may not properly propagate or develop in the far region apart from the cylinder (large radius).

AUTHORS' REPLY

It is true that in cylindrical coordinates the grid size in circumferential direction increases as the radius, and will affect the accuracy for implementing free-surface conditions. However, for the hydrodynamic problems being studied, our interest is mainly focused on the region near the inner cylinder, where relatively few grid points will yield high resolution even in the circumferential direction. Our numerical results also show that free-surface flow can be simulated accurately with a reasonable number of grid points in cylindrical coordinates. Our excellent energy check is a proof (see Fig. 4).

Finally, the spectral-based Poisson solver and momentum-equation solvers developed by us are found to be relatively insensitive to grid spacings in the physical space, thus assuring high accuracy even with a rather coarse grid. Further, since this numerical method is very efficient, an increase in grid points does not cause much penalty.

DISCUSSION

M. Zhu
University of Tokyo, Japan

At first, you show a very efficient and accurate method which is promising for treating free-surface viscous flow problem. Could you show how you treat with body-free surface intersection where there is singularity in the computation? I believe that you use a linear-free surface condition in your work. Is your treatment of the intersection feasible for the nonlinear wave flow problem?

AUTHORS' REPLY

The singularity is avoided by assuming, for the free surface cells, a constant pressure through the boundary layer. In the nonlinear case the physical phenomena involved (sprays, breaking waves, . . .) are too complex to be taken into account in a ship flow simulation. In that sense we believe that a similar hypothesis could be used in the solution of the nonlinear problem.

DISCUSSION

E. Novikov
University of California at San Diego, USA

The most interesting part of these calculations is vorticity generation by an oscillatory wall (Figure 9), which can be observed experimentally. In order to mimic the vorticity structures generated by a hull surface of a ship in heaving motion, apart from geometrical factors, the fully nonlinear boundary conditions on the free surface should be imposed (instead of free-slip wall on top), because in reality the Froude number is not small. The Reynolds number should also be increased for several orders of magnitude or a subgrid-scale modelling of turbulence should be incorporated.

On the Intersection Flow Near a Fine Ship Bow

P. Sclavounos
(Massachusetts Institute of Technology, USA)

ABSTRACT

A fundamental study is undertaken of the flow near the bow of a ship advancing with constant forward speed. The objective is the derivation of a model which will enhance our understanding of this intersection flow and will allow its eventual integration into computational tools for the rational and accurate prediction of the flow around ship hulls.

The relevant length scales governing domains of the flow in the vicinity of the ship bow are identified along with the appropriate set of equations and boundary conditions viscous or ideal. A simple model is proposed for the treatment of the formation of spray around a thin bow with vertical boundary and finite draft. The sensitivity of this flow upon the bow slope at the stem is investigated and a model is proposed for the prediction of the spray strength.

1. INTRODUCTION

Significant progress has been achieved over the past decade towards the prediction of three-dimensional flow features around the hull of ships advancing in calm water and in waves. With the free surface modelled as a plane of symmetry, computational methods based on the solution of the three-dimensional Navier-Stokes equations have reached the state where they can reproduce detailed features of the viscous ship wake when equipped with advanced turbulence models. Several studies are in progress aiming to extend these methods in the presence of a free surface as witnessed in the recent Tokyo Workshop on Near Field Ship Hydrodynamics [1]. Important issues to address in the presence of a free boundary are the proper treatment of the intersection flow along the ship waterline, particularly near the ship bow, and the development of proper turbulence models in the vicinity of a free surface.

In the absence of viscous effects, computational methods aiming to model steady and unsteady free surface flows past ships have also enjoyed significant progress. The majority of ideal flow methods are based on the distribution of Rankine singularities over the ship hull and the mean or actual position of the free surface and have been capable to predict with promising accuracy three-dimensional features of the steady flow not affected appreciably by viscous or nonlinear effects ([2],[3]). In the unsteady problem, such methods have been successful in predicting the seakeeping properties of realistic ship forms in waves of moderate steepness ([4],[5]). While strong free-surface nonlinearities have been treated with success in model two and three-dimensional problems ([6],[7]), they have not yet be integrated into realistic ship flows in calm water and in steep ambient waves.

A common hurdle facing both classes of methods is the proper modelling of the intersection flow along the ship waterline, particularly where significant free surface nonlinearity coexists with viscous effects. For a vertical flat plate in an ambient regular wave various flow regimes which arise in this intersection flow have been identified and discussed in [8]. One of the principal conclusions of this study is the need to better understand the flow in the vicinity of the free-surface boundary intersection where nonlinear free-surface, viscous and surface-tension effects are potentially of comparable importance.

The present paper undertakes this task for the intersection flow which arises around a fine ship

bow with finite but small thickness, advancing with steady forward velocity. A semi-infinite fine bow with vertical wall sided boundary, finite draft and wedge or cusp-like entrance angles is considered. In Section 2, the exact problem statement is carried out and the relevant flow length scales are identified. Section 3, reviews two-dimensional ideal flow approximations for bow flows and draws upon the insights gained from such models. In Section 4 a three-dimensional model for the treatment of the flow around thin bows is developed and a methodology is proposed for the prediction of the spray strength for wedge and cusp-like waterline entrance angles. Section 5, discusses the coupling of ideal, viscous and surface tension effects and outlines directions of future research.

2. PROBLEM STATEMENT

Figure 1a illustrates the plan view of a fine ship bow and a Cartesian coordinate system (x,y,z) with the x-axis pointing upstream and the z-axis upwards, with the $z=0$ plane coinciding with the calm water surface. Denote by $y=b(x)$ the half-beam distribution of the bow on the $z=0$ plane, such that $b(0)=0$. The precise form of the function $b(x)$ will be discussed in a later section, while the assumption is made that the derivative $b'(x)$ is a sufficiently small quantity. A uniform inflow with velocity U far upstream is incident upon the bow shown in Figure 1 which is allowed to be of infinite extent in the negative x-direction.

A characteristic length-scale is introduced by assuming that the bow is wall-sided with uniform draft T, as illustrated in Figure 1b. Denote by g the acceleration of gravity and by ν the water kinematic viscosity. It follows that only one geometrical length scale is available, T, along with two dynamic length-scales, $\delta_I = U^2/g$ and $\delta_\nu = \nu/U$. Laminar flow will be assumed throughout the present study.

The flow around this model geometry is governed by the following equations and boundary conditions:

a) The Navier Stokes equations apply in the fluid domain.

b) A zero-velocity condition must be enforced on the bow boundary.

c) The kinematic free surface condition states that a fluid particle on the free surface cannot find its way into the fluid domain.

d) The dynamic free surface condition states that the normal and tangential stresses on the free surface must vanish, on the assumption that the air density is negligible relative to that of the water.

e) Far upstream the free surface elevation and its slope must vanish.

The set of equations a-e are highly nonlinear even for laminar flow and their solutions even for the idealized geometry considered in the present study is not yet possible. Progress towards their treatment has been achieved by identifying domains of the flow where either viscous or ideal flow effects may dominate or where the free surface conditions accept a linear treatment.

Figure 2 illustrates a cross section of the flow past the bow shown in Figure 1. A number of flow domains are identified and their respective physics are discussed below.

Domain 1:

At a sufficiently large distance from the body boundary and the free surface, the effects of viscosity are unimportant and the flow is governed by the Laplace equation. More precisely, the vorticity shed by the bow boundary cannot penetrate Domain 1.

Domain 2:

At a sufficiently large distance from the body boundary and over a small distance from the actual position of the free surface a thin free surface boundary layer develops. This layer develops because of the incompatibility of the irrotationality condition in Domain 1 with the condition of vanishing shear stresses on the actual position of the free surface. A comprehensive discussion of the equations governing this layer may be found in [9]. The thickness of this layer turns out to be small and its impact upon the flow in the remainder of the flow domains is negligible.

Domain 3:

Near the body boundary and at a sufficiently large distance from the free surface, a classical boundary layer develops which may be treated either via the direct solution of the Navier Stokes equation or by introducing boundary layer-approximations. It is

however important to point out that its properties are driven by the pressure gradient induced by the exterior potential flow. Often, this pressure gradient may be approximated by that of a double body flow, an assumption which is undoubtedly convenient but questionable near the ship bow or further downstream at high Froude numbers.

Domain 4:

In the vicinity of the intersection of the bow boundary with the free surface the body boundary layer is strongly influenced by the free surface conditions which may or may not be possible to state in linearized form. The viscous flow of Domain 3 which is removed from the free surface may be assumed to be driven by the pressure gradient induced by a linearized potential flow. This is however not possible to justify in principle in Domain 4 where the free surface flow may be nonlinear.

Domain 5:

In Domain 5 spray may develop and the local flow may be affected by a combination of viscous, surface tension and strongly nonlinear free surface effects. This flow region is evidently the most difficult to study numerically or analytically. Yet, it is the complexity of the flow in Domain 5 which is the primary motivation of the present study and the selection of the simplified bow shape under consideration.

Of all the domains illustrated in Figure 2, the length scales of Domains 2 and 3 follow from classical boundary layer theory over a solid boundary and a free surface. The length scale of Domain 5 is by no means obvious at the present stage. It will be the principal subject of the next section which reviews several studies of the two dimensional free-surface flow caused by an impulsively started wavemaker.

3. BOW FLOWS AND TWO-DIMENSIONAL WAVEMAKER PROBLEM

The natural approach to the solution of the flow equations in Domains 1-5 is to start with the ideal flow in Domain 1 where several linear and nonlinear solutions have been obtained in the literature in two and three-dimensions. The flow solution in Domain 1 then defines the pressure gradient driving the viscous flow in Domains 3-5, but more importantly determines the limiting behavior of these flows at sufficiently large distances from the body boundary.

Several aspects of the flow in Domain 1 and insight into the strong free surface nonlinearity of the flow in Domain 5 may be revealed by approximating the flow along the transverse cut of the bow flow shown in Figure 1 as that caused by a vertical paddle of draft T pushed impulsively against a free surface.

Ignoring for the moment the free surface boundary layer in Domain 2, the nonlinear ideal flow equations in Domain 1 are stated next. By virtue of irrotationality, the flow velocity in Domain 1 may be stated as the gradient of the velocity potential

$$\Phi(x,y,z)=-Ux+\phi \tag{1}$$

where ϕ denotes the disturbance potential which along with the total potential satisfies the three dimensional Laplace equation

$$\nabla^2\Phi=\nabla^2\phi=0 \tag{2}$$

in the fluid domain. Denoting by $\zeta(x,y)$ the unknown position of the free surface, the nonlinear kinematic condition takes the form

$$-U\frac{\partial\zeta}{\partial x}+\frac{\partial\phi}{\partial y}\frac{\partial\zeta}{\partial y}+\frac{\partial\phi}{\partial x}\frac{\partial\zeta}{\partial x}=\frac{\partial\phi}{\partial z}, \quad z=\zeta(x,y) \tag{3}$$

The dynamic condition may be stated as follows

$$-U\frac{\partial\phi}{\partial x}+g\zeta+\frac{1}{2}\nabla\phi\cdot\nabla\phi=0, \quad z=\zeta(x,y) \tag{4}$$

On the bow boundary the a condition of zero normal flux yields

$$\frac{\partial\phi}{\partial n}=-Un_1=-U\frac{db}{dx} \tag{5}$$

With respect to a Cartesian coordinate system fixed in space, the convective derivatives in the streamwise direction which involve a linear product with the velocity U, may be replaced with time derivatives, according to the Galilean transformation

$$-U\frac{\partial}{\partial x}=\frac{d}{dt} \qquad (6)$$

It follows that the three dimensional equations may be cast in the alternative form

$$\frac{d\zeta}{dt}+\frac{\partial\phi}{\partial y}\frac{\partial\zeta}{\partial y}+\frac{\partial\phi}{\partial x}\frac{\partial\zeta}{\partial x}=\frac{\partial\phi}{\partial z}, \quad z=\zeta(x,y) \qquad (7)$$

$$\frac{d\phi}{dt}+g\zeta+\frac{1}{2}\nabla\phi\cdot\nabla\phi=0, \quad z=\zeta(x,y) \qquad (8)$$

$$\frac{\partial\phi}{\partial n}=\frac{db}{dt} \qquad (9)$$

which along with the three-dimensional Laplace equation complete the statement of the ideal flow equations with respect to a frame fixed in space.

The transition from equations (7)-(9) to a two-dimensional set is accomplished by assuming that convective derivatives in the x-direction are small compared to y- and z-derivatives in the Laplace equation and free surface conditions by virtue of the bow slenderness. A discussion of the validity of this approximation will be postponed until the next section.

The elegant consequence of this slenderness assumption is that equations (7)-(9) reduce to the nonlinear equations governing the time-domain motion of a wavemaker with horizontal displacement b(t), a function of time. The time dependence of b(t) may be inferred by the bow shape with respect to the body fixed frame and the relationship

$$b(t)=b[x(t)], \quad x(t)=-Ut \qquad (10)$$

Two kinds of wall-sided bows of finite draft T will be considered.

THE WEDGE

The waterline shape of a wedge is simply a straight line which is here assumed to form a small angle α with the y=0 plane. Therefore the definition of b(x) and b(t) with respect to the body and space fixed frames follows from (10) in the form

$$b(x)=-x\tan\alpha=Ut\tan\alpha \qquad (11)$$

It follows that the normal velocity on the wedge is constant and approximately equal to $U\alpha$. With respect to the space fixed frame it is zero for $t<0$ and equal to $U\alpha$ for $t>0$. This is thus the case of an **impulsive velocity** for the two-dimensional wavemaker.

THE CUSP

The waterline of a cusp is a parabola which vanishes at x=0. Again b(x) and b(t) are defined as follows

$$b(x)=\frac{1}{2}\beta x^2=\frac{1}{2}\beta U^2t^2 \qquad (12)$$

where β is a small parameter with dimensions of inverse length. Here the normal velocity on the cusp grows linearly with x and with respect to the space fixed frame linearly in time from a zero value at t=0. This is the case of a **ramp velocity** for the wavemaker.

The wavemaker velocity is hereafter defined as $U_i(t)$ where, i=1 corresponds to the impulsive and i=2 to the ramp velocity profiles. Evidently, U(t) = 0 for $t<0$ while for $t>0$

$$U_1(t)=\alpha U \quad U_2(t)=\beta U^2t \qquad (13)$$

The evolution of the free surface of the two dimensional impulsive wavemaker problem has been the subject of many linear and nonlinear studies. Several aspects of the problem have been resolved while certain others await treatment.

A comprehensive analysis of this problem was carried out in [10]. In that study earlier results were reproduced a new insight into the nature of the evolution of the free surface was gained. The principal conclusions of this and subsequent studies are summarized below. They will motivate their extension to the three dimensional problem in Section 5.

It is appropriate at this stage to introduce the

following non-dimensional definitions of the two spatial coordinates

$$\eta = \frac{y}{gt^2}, \quad w = \frac{z}{gt^2} \tag{14}$$

For a sufficiently small wavemaker velocity U(t), the free surface initial value problem (7)-(9) may be linearized. Two domains of the linear solution deserve particular attention with respect to their relevance to the exact nonlinear problem. They are discussed below:

Outer Solution: $\eta \to \infty$

The solution of the linear free surface problem may be carried out with standard methods. For large values of η, the free surface elevation and vertical velocity on $z=0$ assume the asymptotic expansions:

$$\zeta_1 = \frac{\alpha U}{\pi} t \ln(1+\frac{T^2}{y^2}), \quad \zeta_2 = \frac{\beta U^2}{2\pi} t^2 \ln(1+\frac{T^2}{y^2}) \tag{15}$$

for the impulsive and ramp velocity profiles respectively. The corresponding vertical velocities on the $z=0$ plane take the form

$$w_1 = \frac{\alpha U}{\pi} \ln(1+\frac{T^2}{y^2}), \quad w_2 = \frac{\beta U^2}{2\pi} t \ln(1+\frac{T^2}{y^2}) \tag{16}$$

The most common interpretation of the outer solution of the impulsive wavemaker problem is to assume that (y,z) are fixed and allow $t \to 0$. Alternatively, (y,z) may be allowed to approach infinity for finite time.

Yet, it is the first interpretation which is the most interesting of the two. The small-time asymptotic expansions (15)-(16) where originally derived in [11] via a formal ascending series expansion in time and were shown to follow from the solution of a linear pressure release free surface problem where the leading order velocity potential vanishes on the $z=0$ plane. The same result was recovered by the large η expansion of the linear solution derived in [10]. Yet more important is the finding that this asymptotic expansion is in very good agreement with **fully nonlinear** computations of the impulsive wavemaker problem carried out in [12].

It may therefore be concluded that the outer expansions (15)-(16) are the leading-order representations for large η of the nonlinear impulsive wavemaker problem. This property will exploited in three dimensions in Section 4 where the corresponding expansions will be derived for the three-dimensional bow.

Inner Solution: $\eta \leq O(1)$

Over distances from the wavemaker comparable to or smaller than the characteristic length scale gt^2 the flow may be fully nonlinear and a jet may develop. Moreover, the flow may be locally affected by surface tension and viscous effects. Our understanding of this flow regime is to date incomplete.

The behavior of the **linear solution** in this inner domain was studied systematically in [10]. This analysis revealed that the free surface elevation develops a highly-oscillatory behavior with increasing wavenumber in the limit as $\eta \to 0$, superimposed upon a slowly varying trend. The amplitude of this perhaps unphysical rapid oscillation was found to decrease as the power law governing the displacement of the wavemaker for small times was allowed to increase. Including surface tension effects, the study of the same linear problem was undertaken in [13]. Surface tension suppressed the high-wavenumber wiggles in the inner domain, and was found not to affect significantly the solution in the outer domain. The findings of these two studies suggest that the linear solution may be an accurate model of the flow in the inner domain if the power law governing the translation of the wavemaker is sufficiently large. It was suggested in [10] that a quadratic law, or a ramp velocity, is sufficient to justify linear theory, therefore implying the lack of a jet-like flow at the wavemaker.

It was shown in [13] and [14] that the consistent formulation of the free surface flow in the inner domain consists of a fully nonlinear set of equations. Promise towards their solution, subject to the well established validity of (15)-(16), was demonstrated

by the use of Lagrangian formulation in [14]. This approach deserves further attention and will the subject of future research since it appears to be closely related to the modelling of the spray root generated by three-dimensional bows.

A study of the linearized flow around a wedge-like bow based on the slender-body approximations introduced in the present study was carried out in [15]. Bow wave profile predictions were compared with experimental measurements for two wedge-like bows, one with a small and the second with a larger entrance angle. The agreement was generally found to be satisfactory, yet the need to include the complete three-dimensional effects was evident. As a first step in that direction, the derivation of the three-dimensional outer solution for two bow shapes is carried out in the next section, extending the corresponding outer expansions derived in [10] and [11] for the two-dimensional wavemaker problem.

4. OUTER SOLUTION FOR 3D BOW FLOW

The studies of the impulsive two-dimensional wavemaker problem discussed in the previous section, offer valuable guidance towards the treatment of the three-dimensional flow past a fine ship bow. In the present section, the corresponding outer solution will be derived for the wedge and cusp bows, extending the outer expansions (15)-(16) for the impulsive wavemaker problem.

The *outer domain* is here defined as the region where the transverse non-dimensional length scales

$$\eta=\frac{yU^2}{gx^2}, \quad w=\frac{zU^2}{gx^2} \tag{17}$$

are large. The equivalence of (17) and (14) follows upon substitution of (10) in (14). It follows from (17) that the outer solution may be obtained as the leading-order high-Froude number approximation of the exact equations (3)-(4) governing the flow in Domain 1 [see Figure 2]. In the ensuing analysis the third non-dimensional coordinate xg/U^2 is assumed to be of order one.

The leading order high Froude number approximation of the dynamic free surface condition (4) subject to the radiation condition of vanishing wave elevation upstream, is merely the pressure release condition

$$\phi=0, \quad z=0 \tag{18}$$

The corresponding kinematic condition is

$$\frac{\partial\zeta}{\partial x}=-\frac{1}{U}\frac{\partial\phi}{\partial z}, \quad z=0 \tag{19}$$

Moreover, the disturbance potential is subject to the three dimensional Laplace equation in the fluid domain and the boundary condition (5) on the wavemaker.

The solution of (18)-(19) will therefore provide the leading order outer solution for the three-dimensional bow flow in Domain 1, which is expected to be valid in the linear as well as the nonlinear regime, as in two dimensions.

For fine ship bows the body boundary condition (5) may be transferred to the centerplane y=0, leading to a boundary value problem which accepts a closed-form solution in terms of a distribution of singularities on the bow centerplane, here allowed to extend to negative infinity. The solution is carried out using the theory of Fourier transforms. Let

$$\tilde{\phi}(y,z;k)=\int_{-\infty}^{\infty} dx\, e^{ikx}\, \phi(x;y,z) \tag{20}$$

$$\phi(x;y,z)=\frac{1}{2\pi}\int_{-\infty}^{\infty} dk\, e^{-ikx}\, \tilde{\phi}(y,z;k) \tag{21}$$

The Fourier transform of the leading order disturbance potential satisfies the modified Helmholtz equation in the fluid domain

$$\frac{\partial^2\tilde{\phi}}{\partial y^2}+\frac{\partial\tilde{\phi}}{\partial z^2}-k^2\tilde{\phi}=0 \tag{22}$$

and the same homogenous free-surface condition

$$\tilde{\phi}=0, \quad z=0 \tag{23}$$

Denoting for now V(x) the normal velocity to be enforced on the bow centerplane, it follows that

$$\frac{\partial\tilde{\phi}}{\partial y}=\tilde{V}(k), \quad y=0 \tag{24}$$

The set of equations (22)-(24) define a two-dimensional boundary-value problem symmetric about the y=0 plane which depends parametrically upon the Fourier wavenumber k. Its solution may be written as a distribution of sources over the bow centerplane. Recalling that the unit strength point source singularity which satisfies the modified Helmholtz equation is

$$G(r;k)=-\frac{1}{2\pi}K_0(|k|r) \tag{25}$$

where $K_0(z)$ is the modified Bessel function of order zero, it follows that

$$\tilde{\phi}(y,z;k)=-\frac{1}{\pi}\tilde{V}(k)\int_{-T}^{0}d\zeta\ [K_0(|k|r)-K_0(|k|r')] \tag{26}$$

where

$$r^2=y^2+(z-\zeta)^2, \quad (r')^2=y^2+(z+\zeta)^2 \tag{27}$$

The solution for the disturbance potential in the physical space then follows upon inversion of the Fourier transform (26) by substitution in (21).

In analogy to the two dimensional problem, the quantity which is more revealing that the disturbance potential itself, is the vertical velocity of the flow on the z=0 plane. Upon differentiation of (26) with respect to the z-coordinate, it follows that

$$\left(\frac{\partial\tilde{\phi}}{\partial z}\right)_{z=0}=\frac{2}{\pi}\tilde{V}(k)[K_0(|k|y)-K_0(|k|(y^2+T^2)^{1/2})] \tag{28}$$

and upon inversion in physical space the general solution follows in the form

$$(\phi_z)_{z=0}=\frac{1}{\pi^2}\int_{-\infty}^{\infty}dk\ e^{-ikx}\ \tilde{V}(k)$$
$$[K_0(|k|y)-K_0(|k|(y^2+T^2)^{1/2})] \tag{29}$$

The Fourier transform of the body normal velocity will next be determined for semi-infinite wedge and cusp bows using the theory of generalized functions developed in [16].

WEDGE BOW

The normal velocity of a wedge-like bow jumps from zero for positive x to a constant value equal to αU for negative values of x. It follows that its Fourier transform is related to that of the Heaviside step function, or

$$\tilde{V}(k)=\alpha U[\pi\delta(k)+\frac{i}{k}] \tag{30}$$

Upon substitution of (30) in the general solution (29) and inversion of the Fourier integral using the theory of generalized functions, the vertical velocity on the z=0 plane may be obtained explicitly in the form

$$(\phi_z)_{z=0}=\frac{U\alpha}{\pi}(sgnx-1)\ln(1+\frac{T^2}{y^2})$$
$$-\frac{U\alpha}{2\pi}sgnx\left[\ln\frac{x+(x^2+y^2)^{1/2}}{x+(x^2+y^2+T^2)^{1/2}}\right] \tag{31}$$

Expression (31) generalizes the small-time outer expansion of the wavemaker problem for a three-dimensional fine bow. The leading order term may be recognized as the two dimensional result which vanishes identically for positive x, or upstream of the bow. The second term in the right hand side is a three-dimensional effect.

It is of considerable interest to derive from (31) the small-x expansion of the vertical velocity near the bow stem. It follows that on y=0 and x>0 that

$$(\phi_z)_{z=0}\sim-\frac{U\alpha}{2\pi}\ln\left(\frac{2x}{T}\right) \tag{32}$$

indicating that the vertical velocity suggested by the

outer solution around a fine wedge bow is seen to develop a logarithmic singularity upstream of the bow. Weather this singularity will be decided by the solution of the inner flow equations which will almost certainly will end up being fully nonlinear.

For $x<0$ and in the limit as $y\to 0$, it follows form (31) that

$$(\phi_z)_{z=0}\sim -\frac{U\alpha}{\pi}\ln\left(\frac{y}{T}\right)+\frac{U\alpha}{2\pi}\ln\left(\frac{2x}{T}\right) \qquad (33)$$

It is seen from (33) that the logarithmic behavior found in the two-dimensional solution persists, but is corrected by a logarithmic singularity with respect to the x-coordinate of opposite sign to that obtained for positive values of the x-coordinate.

CUSP BOW

The Fourier transform of the normal velocity around cusp bow follows along similar lines in the form

$$\tilde{V}(k)=-\beta U^2[-\pi i\delta'(k)-\frac{1}{k^2}] \qquad (34)$$

Upon substitution in the general solution (29) and inversion using the theory of generalized functions, it follows that

$$(\phi_z)_{CUSP}=-xU\beta(\phi_z)_{WEDGE} -U^2\beta\frac{y}{2\pi}\left[\left(\frac{x^2}{y^2}+1\right)^{1/2}-\left(\frac{x^2}{y^2+T^2}+1\right)^{1/2}\right] \qquad (35)$$

The leading term in the right-hand side is merely a product of the solution for the wedge-like bow derived above, with α replaced by β, multiplied by x. The second term is regular in the limit as $x,y\to 0$.

The asymptotic behavior of this outer solution for the cusp bow as $(x,y)\to 0$ may be seen to follow from the corresponding behavior for the wedge bow multiplied by the x-coordinate. It takes the form

$$(\phi_z)_{CUSP}\sim -x\beta(\phi_z)_{WEDGE}-U\beta\frac{R}{2\pi T}, \quad R^2=x^2+y^2 \qquad (36)$$

As expected, the outer solution suggests that the asymptotic behavior of the vertical velocity near the stem of the cusp bow is more regular than that of the wedge bow.

5. SUMMARY AND FUTURE RESEARCH

Drawing upon the insight gained by two-dimensional studies of the impulsive wavemaker problem, a three-dimensional solution has been derived for the outer flow around a thin wedge and cusp bow with wall sided uniform boundary and finite draft. As in two dimensions, this solution is expected to be valid in the nonlinear regime and serves as the outer limit of the inner flow which may be governed by a fully nonlinear set of equations. As in two dimensions the solution of the inner flow is still lacking. Its treatment holds the key to the prediction of the strength of the spray root which is seen to develop in many bow shapes.

In Section 2, a number of domains were identified and the relative importance of viscous and ideal flow effects were discussed. The three-dimensional solution of the ideal flow equations in Domain 1, carried out in the preceding section, sets the stage for the formulation and solution of the flow equations in Domains 4 and 5 where nonlinear, viscous and surface tension effects are expected to be important. The flow in these domains will be driven by the velocity and pressure distributions derived in Section 4. Moreover, the singularity structure of the outer solution for the wedge and cusp like bows offer strong suggestions on the expected importance of nonlinear effects in Domains 4 and 5. It appears certain that the inner solution for the wedge like bow will be fully nonlinear. For the cusp bow, however, it appears likely that the significance of nonlinear free surface effects is reduced.

The importance of viscous effects on the evolution of the flow in Domains 4 and 5 and their impact upon the nonlinear evolution of the free surface is at best poorly understood. The flow solution in Domain 1, carried out in Section 4, suggests that the pressure gradient driving the inner flow has a well defined singular structure along the waterline. Classical boundary-layer theory is based on the assumption that the pressure gradient of the potential flow region is varying gently. In future research a rational formulation of the flow equations in Domains 4 and 5 carried out including viscous and fully nonlinear free surface effects. The matching of this formulation to the outer solution in Domain 1

will be sought and solutions will be attempted aiming to predict the generation and strength of the spray root.

6. ACKNOWLEDGMENTS

This study has been supported by the Office of Naval Research under grant N00014-94-1-0078, monitored by Dr. Edwin Rood.

7. REFERENCES

1. Workshop on Near Field Ship Hydrodynamics. (1994) Proceedings, Ship Research Institute, Tokyo, Japan.

2. Raven, H. (1992). "A practical nonlinear method for calculating ship wavemaking and wave resistance". *Proceedings*, 19th Symposium on Naval Hydrodynamcis, Seoul, Korea.

3. Nakos, D. E. and Sclavounos (1994). "Kelvin Wakes and Wave Resistance of Cruiser- and Transom Stern Ships". *J. Ship Research,* Vol. 38, No. 1, pp. 9-29.

4. Maskew, B., Tidd, D. M. and Fraser, J.S. (1994). "Prediction of Nonlinear Hydrodynamic Chracteristics of Complex Vessels Using a Numerical Time Domain Approach". *Proceedings*, 6th Int. Conf. Numerical Ship Hydrodyn., Iowa City, Iowa.

5. Sclavounos, P. D., Nakos, D. E. and Huang, Y-F. (1993) "Seakeeping and Wave Induced Loads on Ships With Flare by a Rankine Panel Method". *Proceedings*, 6th Int. Conf. Numerical Ship Hydrodyn., Iowa City, Iowa.

6. Zhao, R. and Faltinsen, O. (1993). "Water Entry of Two-Dimensional Bodies", *J. Fluid Mech.*, Vol. 246, pp. 593-612.

7. Dommermuth, D. G. and Yue, D.K.P. (1988). "The Nonlinear Three-Dimensional Waves Generated by a Moving Surface Disturbance". *Proceedings*, 17th Symposium on Naval Hydrodynamics, The Hague, The Netherlands.

8. Choi, J. E. and Stern, F. (1993). "Solid-Fluid Juncture Boundary Layer and Wake With Waves". *Proceedings*, 6th Int. Conf. Numerical Ship Hydrodyn., Iowa City, Iowa.

9. Mei, C. C. (1983). *The Applied Dynamics of Ocean Surface Waves.* John Wiley & Sons.

10. Roberts, J. (1987). "Transient Free-Surface Flows generated by a Moving Vertical Plate". *Q. J. Mech. Appl. Math.,* Vol. 40, Pt. 1.

11. Peregrine, D. H. (1972). "Flow Due to a Vertical Plate Moving in a Channel". Unpublished note.

12. Lin, W. M., Newman J. N. and Yue, D.K.P. (1984). "Nonlinear Forced Motions of Floating Bodies", Proceedings, 15th Symposium on Naval Hydrodynamics, Hamburg, Germany.

13. Joo, S. W., Schultz, W. W. and Messiter, A. F. (1989). "Uniformly Valid Solutions to the Initial Value Wavemaker Problem", Technical Report No. 89-01, The University of Michigan, Ann Arbor.

14. Cointe, R. (1991). "Free-Surface Flows Close to a Surface-Piercing Body". In *Mathematical Approaches in Hydrodynamics*, SIAM.

15. Ogilvie, T. F. (1972). "The Wave Generated by a Fine Ship Bow". Report No. 127, The University of Michigan, Ann Arbor.

16. Lighthill, M. J. (1958). *Fourier Analysis and Generalized Functions.* Cambridge University Press.

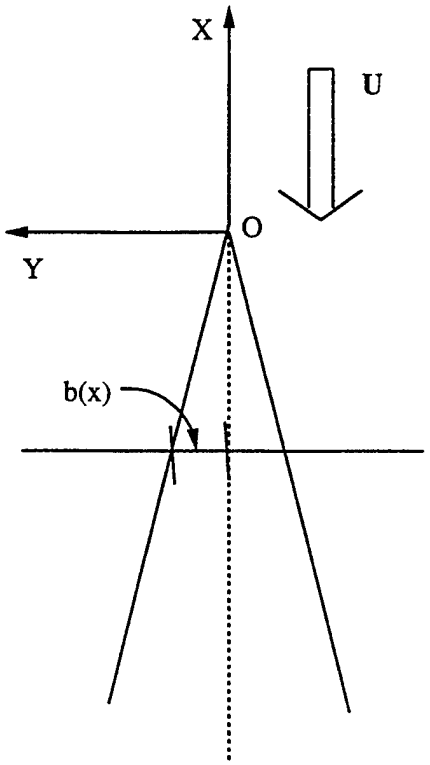


Figure 1a

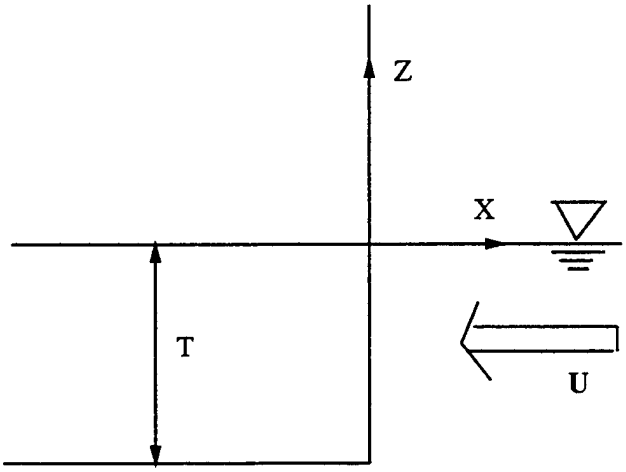
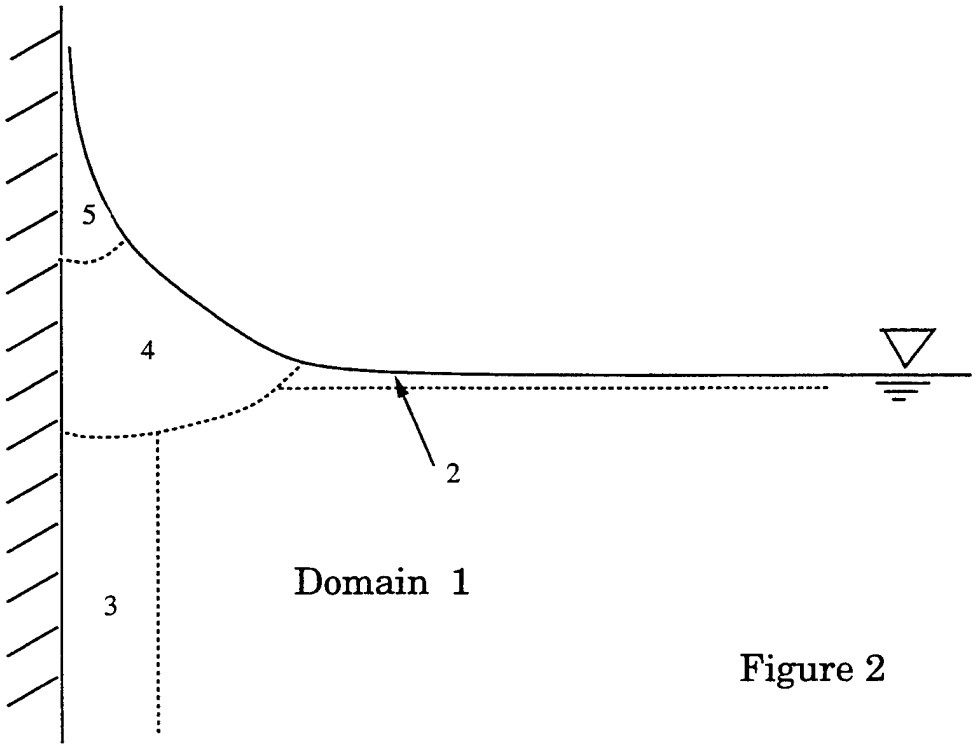


Figure 1b



Domain 1

Figure 2

DISCUSSION

R. Beck
University of Michigan, USA

1. Would your conclusions about the log singular behavior at the bow change if you used a finite width (i.e. body exact) wedge?

2. Would the conclusion change if the wedge was not sharp, but had a round harding edge?

DISCUSSION

M. Tulin
University of California at Santa Barbara, USA

The solution near the bow does not contain gravity as a parameter. Does that mean that in your solution there is a higher speed limit? If so, then I think that logarithmic singularity is associated with your treatment of the wedge as a thin ship in the Michell sense. If you dealt with the thickness of the wedge, then I think that the singularity would likely become algebraic (x^{β}). If so, Bob Beck has a good point in his question a moment ago.

AUTHORS' REPLY

Both Professors Beck and Tulin inquire about the vicinity of the bow, if the wedge angle were to be finite. While a conclusive answer would require an analysis similar to that carried out in the paper, I would be tempted to agree with both discussors that the logarithmic behavior of the normal velocity for the thin wedge will probably change to an algebraic power or possibly to the product of an algebraic and a logarithmic power. In response to Professor Beck's question if the asymptotic behavior would change if the wedge was round as opposed to being sharp, I doubt it would over distances from the bow stem a few times its radius of curvature.

DISCUSSION

A. Reed
David Taylor Model Basin, USA

Thank you for an interesting presentation. It is refreshing to see a problem in the midst of its solution—and to get some insight into the approach to the solution—as opposed to the solution to the problem. I found it interesting to see that you obtained a finite wave elevation at or just ahead of the bow (A logarithmic singularity is "finite"). I have two related questions. (1) How does your outer solution for the wedge relate to Francis Ogilvie's (1972) solution? (2) How does your solution relate to Maruo's slender body bow flow solutions/theory as presented in his Weinblum lecture or several years ago?

I look forward to watching your progress as you incorporate a viscous flow near field into your solution.

AUTHOR'S REPLY

We do indeed obtain a finite wave elevation at the bow. This result follows from the kinematic free surface condition (19) upon substitution of the asymptotic expression (31) for the vertical velocity and integration with respect to the x-coordinate. It is, however, important to bear in mind that this finite wave elevation is the result of an asymptotic analysis which is not valid in the immediate vicinity of the bow stem where the relevant flow equations are fully nonlinear and where surface tension effects may be important.

Along the same lines, the experiments you and Professor Ogilvie did carry out at the University of Michigan for wedge like bows do clearly suggest that the wave elevation is indeed finite and roughly half of that predicted by the present analysis!

We did not carry out a comprehensive comparison with the slender body approximations of Ogilvie and Maruo primarily because their approximations are based on the two-dimensional Laplace equation and the three-dimensional free surface condition. I would therefore not expect that their solutions will be able to reproduce the proper asymptotic behavior of the free surface elevation upstream of the bow. However, both these asymptotic theories are capable of predicting correctly the transverse asymptotic behavior of the free surface elevation downstream of the bow stem corresponding to the first term in equation (31).

Concerning the future directions of this research, we are currently in the process of generating a fully nonlinear solution of the free surface flow around a wedge with finite angle, including finite Froude number effects, which will be used to drive the viscous flow in the vicinity of the waterline.

DISCUSSION

L. Doctors
University of New South Wales, Australia

I remember Prof. Ogilvie's initial work on the flow near a fine bow in 1972 so it is very pleasing to see further development of this interesting work. At the beginning of your presentation you noted the importance of setting up a theory in which the bow has a finite draft.

Could you please expand on this point. In particular, do your formulas behave well when the draft is allowed to approach infinity?

AUTHOR'S REPLY

We decided to carry out this analysis for a wedge with finite draft for two reasons. A finite draft introduces a length scale which is otherwise absent in a high-speed asymptotic analysis of the free surface flow around a wedge of infinite draft. Furthermore, the infinite draft result is possible to obtain in the limit. The second reason is practical. One of the objectives of this study is the prediction of spray generation around the bow of realistic ships; therefore in such a context the assumption of infinite draft could lead to misleading predictions.

Concerning the behavior of our asymptotic analysis in the limit of infinite draft, and correcting my hasty response at the Symposium that the wave elevation tends to infinity, it is possible to see from equation (31) that a finite expression is obtained in the limit $T \to \infty$. Simply, the logarithmic singularity which arises from the leading term in (31) cancels a similar singularity which arises at the last term.

Numerical Simulation of a Wave-Viscous Flow about a Ship Including Propeller Effects

O. Watanabe, A. Masuko, Y. Shiorose
(Isikawajima-Harima Heavy Industries Co., Ltd., Japan)

ABSTRACT

A finite volume method for viscous flow around a ship with free surface is developed. The Reynolds-averaged Navier-Stokes equations are solved with SIMPLE algorithm. The $k-\varepsilon$ turbulence model with wall function is adopted. The curvilinear grid system is fitted both to the hull surface and to the free surface. Wave height is determined by solving the steady equation of kinematic free surface condition iteratively. Computational results are presented for Series-60 model at several speeds. Computed wave profiles on the hull surface agree well with experimental data and computed frictional resistance almost coincides with Schoenherr friction line. Computed pressure resistance is slightly high and wave contour is somewhat attenuated and diverged. Influence of the propeller action, influence of the grid spacing on the wave-viscous flow and possibility of the composite grid method in the wave-viscous flow calculation are discussed.

NOMENCLATURE

B =ship breadth
C_D, C_1, C_2 =constants for $k-\varepsilon$ model
C_f =local skin friction coefficient
C_T =thrust loading coefficient
d =ship draft
Fn =Froude number
g =gravitational acceleration
J =Jacobian
P =pressure
P_0 =atmospheric pressure
k =turbulent kinetic energy
n =calculation step number
P_k =production rate of turbulent kinetic energy
ΔP =amount of pressure jump
Rn =Reynolds number
$S_\Phi, S_\Phi^*, S_U, S_P$ =source terms in finite difference equation
S =wetted surface area of a ship
U =uniform flow velocity
u, v, w =velocity components
u_1, u_2, u_3 =the same as above
u^* =frictional velocity
x, y, z =Cartesian coordinates
x_1, x_2, x_3 =the same as above
Γ_Φ =diffusion coefficient in finite difference equations
ε =dissipation rate of turbulent kinetic energy
η_p =minimum grid spacing on the ship surface
μ =molecular viscosity
μ_e =effective viscosity
μ_t =turbulent viscosity
ξ, η, ζ =body fitted coordinates
ξ_1, ξ_2, ξ_3 =the same as above
Φ =dependent variable in finite difference equations
ρ =fluid density
$\sigma_k, \sigma_\varepsilon$ =Effective Schmidt numbers for k and ε

INTRODUCTION

The problem of wave-viscous flow interaction and the problem of hull-propeller-rudder interaction are the traditional problems in ship hydrodynamics.

The first theoretical treatment of this problem was carried out by Okabe and Jinnaka (1). They proposed the idea that the effect of viscosity on the ship wave is a displacement effect of boundary layer. Since then a lot of theoretical studies were devoted to this problem. However it cannot be said that the whole aspects of the interaction between wave and viscous flow is explained by the theoretical approach.

Recently CFD technique has progressed in ship hydrodynamics and the problem of wave-

viscous flow interaction has been tackled by the numerical method. The first work in this field was done by Miyata et al. (2). They solved the Navier-Stokes equations of rotational form with MAC type algorithm. General curvilinear coordinate system was fitted to the hull surface and free surface. The wave height was derived by solving discretized kinematic free surface condition. Almost the all methods developed after that followed this treatment of free surface (3),(4),(5) except (6).

Last March, CFD WORKSHOP TOKYO was held in Japan and ten papers were presented about the wave-viscous flow calculation around Series-60. Conclusion made by Mori et al.(7) pointed out the following aspects. The agreements with measured data were rather good concerning the wave profile on the hull surface and the resistance. However the agreements of wave patterns were poor and improvement of the results of wave patterns was the subject by means of the examination of grid spacing, free surface condition and so on. The most important aspect was that the flow had two independent parameters, namely the Reynolds number and the Froude number, and more attention should be paid to the wave length.

Along the same consideration with this last comment, Lungu et al.(8) attempted the composite grid approach in the calculation of two-dimensional wave-viscous flow around a submerged hydrofoil.

Concerning the hull-propeller-rudder interaction, Nakatake et al.(9) calculated by using Rankine-Source method. The hull, the propeller, the rudder and the free-surface are represented by the singurality distributions, and the viscous effect is taken into account roughly. In CFD field, Stern et al.(10) dealt with interactions between the hull and the propeller. Their finite analytic method for the Reynolds-averaged Navier-Stokes equation was coupled with a vortex lattice type propeller performance program giving propeller force. The propeller was modeled by body force which was given by the calculated propeller force. The viscous flow around Series-60 was calculated with propeller effects, however, the free-surface effect was not included.

The authors have been developing a method to calculate a viscous flow about a ship (11),(12),(13). It is based on a finite volume method and uses the $k-\varepsilon$ turbulence model with the wall function. The curvilinear grid system is fitted to the hull surface. In the present study, algorithm of the calculation of free-surface is added to the previous method by the moving boundary fitted grid system according to the wave deformation. The propeller effects are calculated by using a pressure jump model which substitutes the pressure difference equivalent to the thrust force at the propeller plane.

This method is applied to a flow about the Series-60 ship model with and without propeller, and availability of the method is investigated with comparison between measured and simulated results. Further, the effects of grid spacing are examined and the composite grid method which puts the free-surface grid system on the grid around a hull is tried.

WAVE-VISCOUS FLOW

Basic Equations

The governing time-averaged equations for steady three dimensional viscous flow including free surface in the Cartesian coordinate, $x_i=(x,y,z)$, are written in:

$$\frac{\partial}{\partial x_j}(\rho u_j)=0 \tag{1}$$

$$\frac{\partial}{\partial x_j}(\rho u_i u_j)=-\frac{\partial H}{\partial x_i}+\frac{\partial}{\partial x_j}\left[\mu_e\left(\frac{\partial u_i}{\partial x_j}+\frac{\partial u_j}{\partial x_i}\right)\right] \tag{2}$$

$$H=P+\rho g x_3 \tag{3}$$

where $u_i=(u,v,w)$ is velocity component, ρ is the fluid density, P is the pressure and g is the gravitational acceleration. μ_e is the effective turbulent viscosity as follows:

$$\mu_e=\mu+\mu_t=\mu+\frac{C_D\rho k^2}{\varepsilon} \tag{4}$$

where μ is the molecular viscosity, μ_t is the turbulent viscosity andC_D is the constant. k is the turbulent kinetic energy and ε is the dissipation rate of k. In the $k-\varepsilon$ turbulence model, k and ε are governed by the following equations:

$$\frac{\partial}{\partial x_j}(\rho u_j k)=\frac{\partial}{\partial x_j}\frac{\mu_e}{\sigma_k}+P_k-\rho\varepsilon \tag{5}$$

$$\frac{\partial}{\partial x_j}(\rho u_j \varepsilon)=\frac{\partial}{\partial x_j}\frac{\mu_e}{\sigma_\varepsilon}\frac{\partial \varepsilon}{\partial x_j}+C_1 P_k\frac{\varepsilon}{k}-C_2\rho\frac{\varepsilon^2}{k} \tag{6}$$

where P_k is the production rate of k and given by:

$$P_k=\mu_t\frac{\partial u_i}{\partial x_j}\left(\frac{\partial u_i}{\partial x_j}+\frac{\partial u_j}{\partial x_i}\right) \tag{7}$$

σ_k and σ_ε are effective Schimidt numbers for k and ε, and C_1 and C_2 are constants. The following standard values of these constants are used.

$$C_D = 0.09, C_1 = 1.44, C_2 = 1.92$$
$$\sigma_k = 1.0, \sigma_\varepsilon = 1.3 \tag{8}$$

Equations (1)(2)(5)(6) are represented in the following general form:

$$\frac{\partial}{\partial x_j}(\rho u_j \Phi) = \left(\Gamma_\Phi \frac{\partial \Phi}{\partial x_j}\right) + S_\Phi \tag{9}$$

where $\Phi = (1, u_i, k, \varepsilon)$ is a general dependent variable, Γ_Φ is a diffusion coefficient and S_Φ is a source term.

When a general curvilinear coordinate system $(\xi_1, \xi_2, \xi_3) = (\xi, \eta, \zeta)$ is introduced, in order to use a body fitted grid system, Eq.(9) is transformed to the following equation:

$$\frac{\partial}{J\partial \xi_j}(\rho G_j \Phi) = \frac{\partial}{J\partial \xi_j}\left(\Gamma_\Phi \frac{A_{ij}\partial \Phi}{J\partial \xi_j}\right) + S_\Phi^* \tag{10}$$

where $J = \partial(x, y, z) / \partial(\xi, \eta, \zeta)$ is the Jacobian of transformation, S_Φ^* is the modified source term including cross terms. A_{ij} is the metric coefficient for transformation and G_i is contravariant velocity component. When $a_{ij} = J(\partial \xi_i / \partial x_j)$ is defined, A_{ij} and G_i are written as follows:

$$A_{ij} = a_{ik} a_{jk} \tag{11}$$
$$G_i = a_{ij} u_j \tag{12}$$

Production term P_k in general curvilinear coordinate system is given by:

$$P_k = \mu_t \frac{a_{ji}\partial u_i}{J\partial \xi_j}\left(\frac{a_{ji}\partial u_i}{J\partial \xi_j} + \frac{a_{ij}\partial u_j}{J\partial \xi_i}\right) \tag{13}$$

Finite Difference Equation

The governing equations are discretized by the finite volume method. Variables u_i and H are set at staggered location to avoid spurious error. Integrating Eq.(10) over a control volume, the following finite difference equations are obtained.

$$\begin{aligned}
&\left[\rho G_1 \Phi \Delta\xi_2 \Delta\xi_3\right]_w^e + \left[\rho G_2 \Phi \Delta\xi_1 \Delta\xi_3\right]_s^n \\
&+\left[\rho G_3 \Phi \Delta\xi_1 \Delta\xi_2\right]_b^t \\
&= \left[\Gamma_\Phi \frac{A_{11}\partial\Phi}{J\partial\xi_1}\Delta\xi_2\Delta\xi_3\right]_w^e + \left[\Gamma_\Phi \frac{A_{22}\partial\Phi}{J\partial\xi_2}\Delta\xi_1\Delta\xi_3\right]_s^n \\
&+\left[\Gamma_\Phi \frac{A_{33}\partial\Phi}{J\partial\xi_3}\Delta\xi_1\Delta\xi_2\right]_b^t + S_\Phi^* J\Delta\xi_1\Delta\xi_2\Delta\xi_3
\end{aligned} \tag{14}$$

where $\Delta\xi_i$ is a side length of control volume and e, w, n, s, t and b are the integral limits. Adopting the Hybrid scheme to Eq.(14), the following algebraic equation is obtained.

$$\begin{aligned}
&A_P \Phi_P = A_E \Phi_E + A_W \Phi_W + A_N \Phi_N \\
&+ A_S \Phi_S + A_T \Phi_T + A_B \Phi_B + S_U
\end{aligned} \tag{15}$$

where

$$\begin{aligned}
A_E &= \left[0, D_{1e} - 0.5C_{1e}, -C_{1e}\right] \\
A_W &= \left[0, D_{1w} + 0.5C_{1w}, C_{1w}\right] \\
A_N &= \left[0, D_{2n} - 0.5C_{2n}, -C_{2n}\right] \\
A_S &= \left[0, D_{2s} + 0.5C_{2s}, C_{2s}\right] \\
A_T &= \left[0, D_{3t} - 0.5C_{3t}, -C_{3t}\right] \\
A_B &= \left[0, D_{3b} + 0.5C_{3b}, C_{3b}\right] \\
A_P &= A_E + A_W + A_N + A_S + A_T + A_B - S_P
\end{aligned} \tag{16}$$

and

$$\begin{aligned}
D_1 &= \Gamma_\Phi \frac{A_{11}\Delta\xi_2\Delta\xi_3}{J\Delta\xi_1}, C_1 = \rho G_1 \Delta\xi_2 \Delta\xi_3 \\
D_2 &= \Gamma_\Phi \frac{A_{22}\Delta\xi_1\Delta\xi_3}{J\Delta\xi_2}, C_2 = \rho G_2 \Delta\xi_1 \Delta\xi_3 \\
D_3 &= \Gamma_\Phi \frac{A_{33}\Delta\xi_1\Delta\xi_2}{J\Delta\xi_3}, C_3 = \rho G_3 \Delta\xi_1 \Delta\xi_2
\end{aligned} \tag{17}$$

where D_i is the coefficient of diffusion term and C_i is the coefficient of convection term. A sign $[\ ,\ ,\ ]$ means the maximum value in $[\ ]$. S_u and S_p are given by the following equation.

$$S_U + S_P \Phi_P = J S_\Phi^* \Delta\xi_1 \Delta\xi_2 \Delta\xi_3 \tag{18}$$

The velocity and pressure fields are solved by SIMPLE procedure. In order to solve Eq.(15) by using vector processor, the checker board method with SUR is adopted.

Free Surface Condition

Let the location of the free surface be $\zeta = \zeta(x, y)$, the free surface conditions are written as follows, omitting viscous stress and the surface tension on the free surface:

$$P = P_0 \tag{19}$$

$$F \equiv w - u\frac{\partial \zeta}{\partial x} - v\frac{\partial \zeta}{\partial y} = 0 \tag{20}$$

Here, P_0 is the atmospheric pressure and assumed zero in this study. Eq.(19) is the dynamic condition and eq.(20) is the kinematic condition.

In order to decide the location of the free surface, the kinematic condition Eq.(20) is solved iteratively. The new location at the (n+1)th step is

$$\zeta^{n+1} = \zeta^n + \alpha \cdot F^n \tag{21}$$

Here, α is the operator and this adjusts free surface movement of each calculation step so to be less than the minimum grid spacing near the free surface.

Other Boundary Conditions

In this study, H-O type grid topology is adopted and the computational domain is half under the assumption that the flow is symmetric to the center-plane. So there are six boundaries, that is, inflow, outflow, free surface, hull surface, outer boundary and center-plane.

At the inflow and outer boundary, the uniform flow velocity is imposed and the pressure is set to zero. k and ε are set at small positive value. All values are kept constant throughout the computation.

At the outflow boundary, all variables are set using zero-normal gradient condition.

On the center-plane boundary, symmetric conditions are imposed, namely, the normal velocity to the boundary plane is set to zero and the zero-normal-gradient is used for the other variables.

On the hull surface, no slip condition is given. The zero-normal-gradient for the pressure is imposed and the other flow variables are set to zero. The standard wall function is used since the $k-\varepsilon$ model cannot be adopted in the viscous sub-layer and transition layer near the hull surface.

Computational Grid

The computational grid is fitted both to the hull surface and to the free surface. In order to use the wall function, the nearest grid points to the hull surface should be within the log-law region. The minimum grid spacing η_p near the hull surface is set to 7×10^{-4}. This value satisfy the following equation at $Rn = 4.0\times10^6$.

$$\Delta Y^+ = \frac{\eta_p \rho u^*}{\mu} = \frac{\eta_p \rho U\sqrt{C_f/2}}{\mu} = 100 \tag{22}$$

Here, u^* is the frictional velocity and C_f is the local skin friction coefficient.

In order to deal with the free surface flow, the initial grid is prepared for the region from under still water level to somewhat above it. Then, in 0-th step level, the computational grid is generated using the initial grid, up to still water level. After that, in n-th step level, in order to fit wave height given by eq.(21), the new location of the grid is rearranged using initial grid and the calculated wave height as shown in Fig.1.

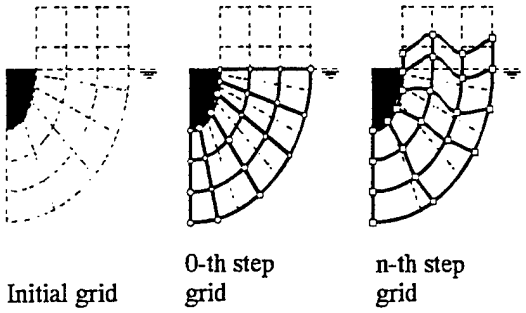


Fig.1 Schematic of grid rearrangement by movement of free surface

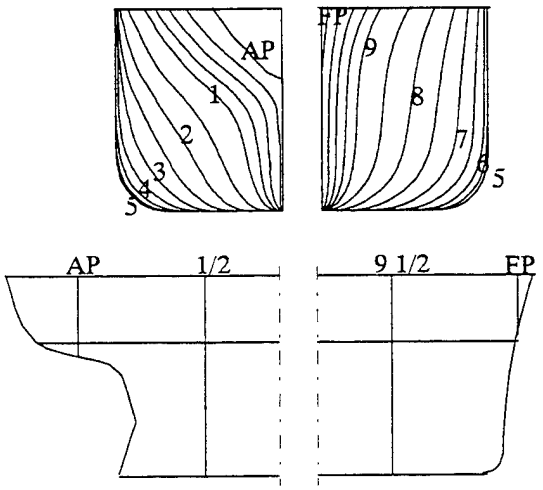


Fig.2 Configuration of Series-60 model

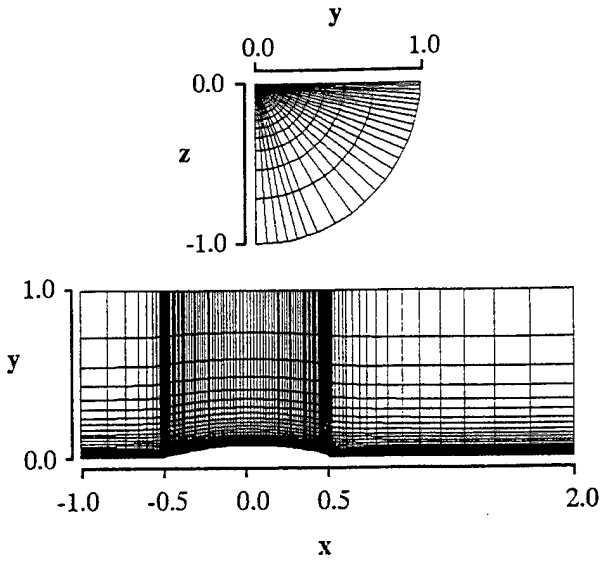


Fig.3 Computational domain and grid configuration

Calculation of Wave-viscous Flow

The calculation is carried out for the wave-viscous flow about a Series-60 model. The body configuration of the model is shown in Fig.2. The parameters L/B, B/d and C_B are 7.5, 2.5 and 0.6, respectively. Here, L, B, d and C_B are length, breadth, draft and block coefficient of the ship. All flow variables are made dimensionless with respect to ship length and uniform velocity U. The computations are carried out for the starboard only, since the flow about a ship in steady straight course is assumed to be symmetric. All computations are made for the model fixed condition. The origin of the coordinate system is set at the center of the ship. The inflow, outflow and outer boundaries are located at -1.0, 1.5 and 1.0, respectively. Therefore the location of the fore end and the after end of the ship are -0.5 and 0.5. Number of total grid points is 78000, 100 in longitudinal direction, 26 in girth wise direction and 30 in transverse direction. Minimum spacing on the hull surface and on the free surface are set to 7×10^{-4} and 1×10^{-3}, respectively. The grid system is shown in Fig.3. The movement of grid points on the free surface is set under 1×10^{-4} at each calculation step. Calculations are carried out under the following four conditions.

$$Fn = 0.16,\ Rn = 2.0\times10^{6}$$

$$Fn = 0.20,\ Rn = 2.5\times10^{6}$$

$$Fn = 0.25,\ Rn = 3.1\times10^{6}$$

$$Fn = 0.32,\ Rn = 4.0\times10^{6}$$

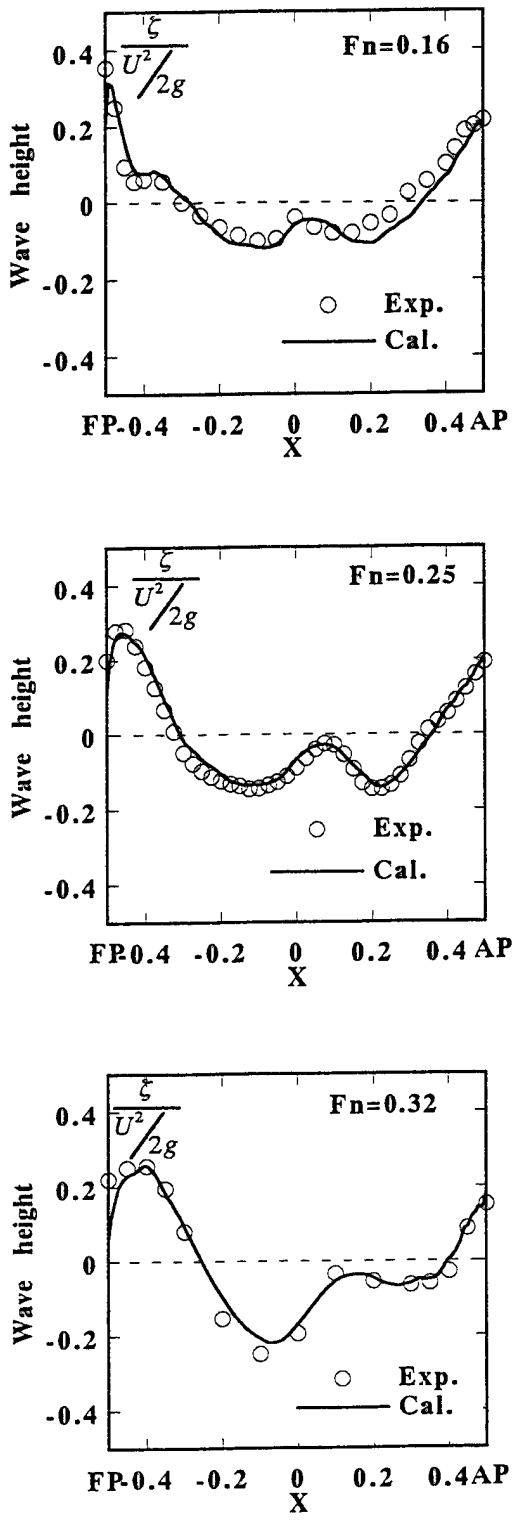


Fig.4 Wave profile on the hull surface

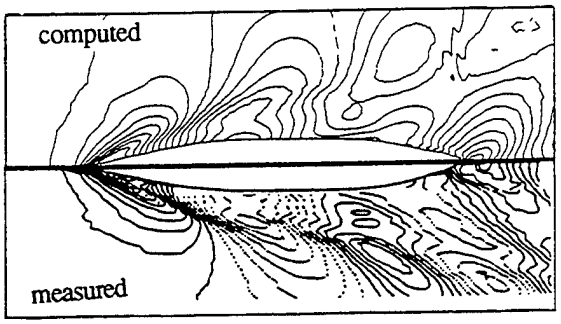


Fig.5 Comparison of wave contour at Fn=0.32

Here, Fn and Rn are the Froude number and the Reynolds number based on the ship length L, respectively. These combination of Fn and Rn are equivalent to the 4m model scale condition. The computation is continued up to 1000 calculation steps for each case. The calculations are executed by FACOM VP-2100 and the CPU time is about 90 minutes for each case.

The wave profile on the hull surface is compared with the measured results in Fig.4. The agreement seems to be well except the case of $Fn = 0.16$. Especially, the wave height at ship stern which is influence by the boundary layer shows satisfactory agreement. In both cases of $Fn = 0.25$ and $Fn = 0.32$, the computed wave height around the shoulder of the ship is a little higher than the measured one.

The comparison of wave contours are shown in Fig.5. In the computation, two crests and two troughs of bow wave and one trough and one crest of fore shoulder wave are observed. However, first trough of bow wave is attenuated and the second crest of bow wave diverges large. The angle between center-line and wave system is rather large compared with measured data.

The convergence histories of the resistance coefficients are shown in Fig.6. Each resistance coefficient is nondimensionalized by $1/2\rho U^2 S$, where S is the wetted surface area of the ship. The frictional resistance coefficient almost converges around 200 steps, however , convergence of the pressure resistance coefficient is slow. In the case of low Froude number, the significant oscillation appears on the pressure resistance coefficient. The amplitude of the oscillation tends to become small with Fn, and the period tends to become long.

The resistance coefficients curves is shown in Fig.7. The solid line is the total resistance, and the dotted line is the Schoenherr friction line. Because the pressure resistance somewhat oscillates shown as Fig.6, the average of last some periods is plotted. The computed frictional resistance coefficients well agree with the Schoenherr line, however, the computed pressure resistance is a little higher than the measured data.

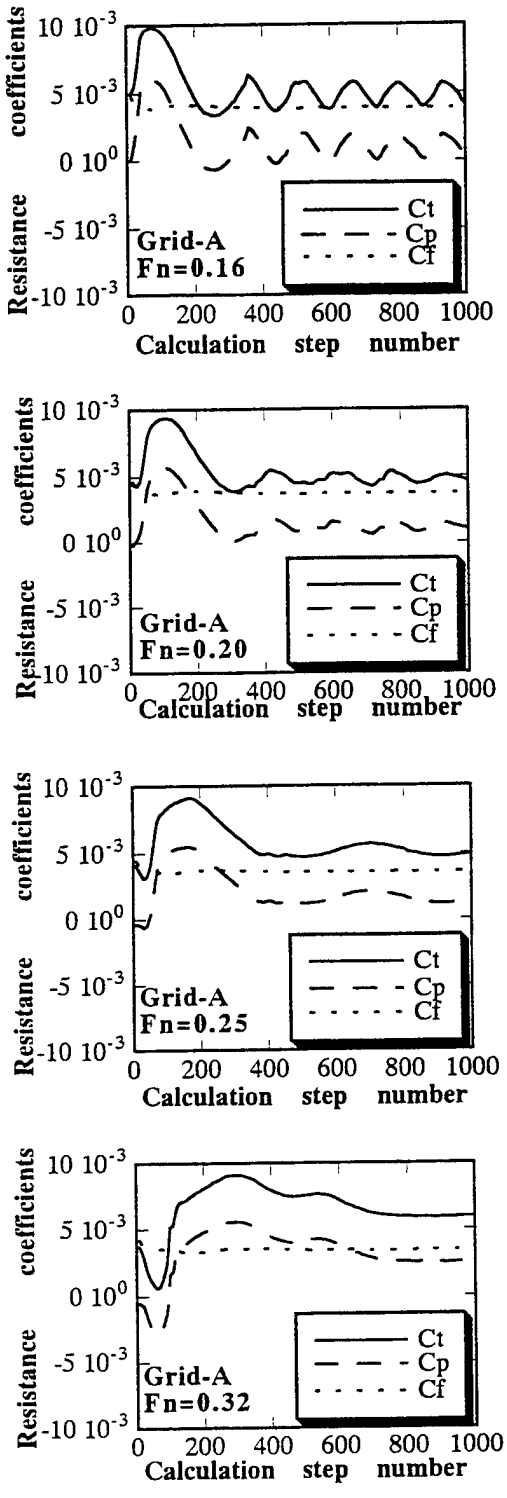


Fig.6 Convergence history of resistance coefficients

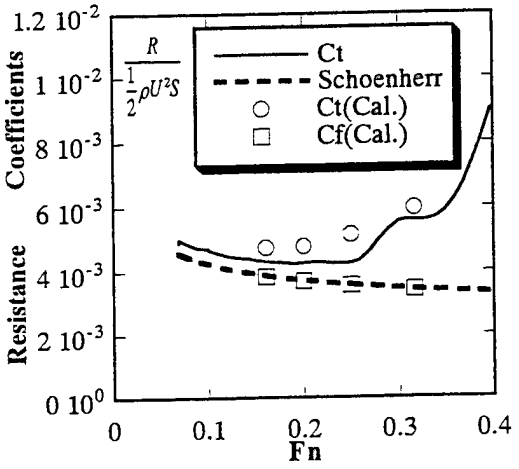


Fig.7 Resistance coefficients

Wave viscous flow including propeller effect

Effect of a propeller suction on the wave-viscous flow is carried out. In this calculation, the effect of the propeller is modeled by the pressure jump. This model is rather simple and cannot deal with rotating flow behind the propeller, however, it is applicable to examine the propeller effect on the upstream of the propeller.

In the pressure jump model, the amount of pressure jump ΔP is calculated from the measured thrust. Then it is added to the pressure gradient terms of the finite difference equation at the propeller section. In Cartesian coordinates, it is written as follows (see Fig.8) :

$$u_p : \frac{\partial P}{\partial x} = \frac{\left(P_p - \frac{\Delta P}{2}\right) - P_W}{\Delta x} \qquad (23)$$

$$u_e : \frac{\partial P}{\partial x} = \frac{P_E - \left(P_p + \frac{\Delta P}{2}\right)}{\Delta x} \qquad (24)$$

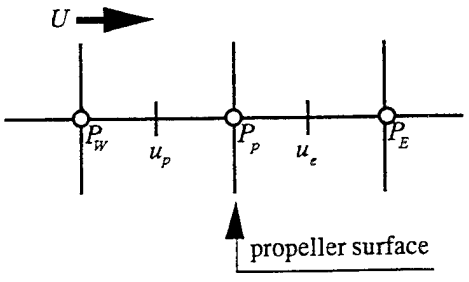


Fig. 8 Schematic of pressure jump

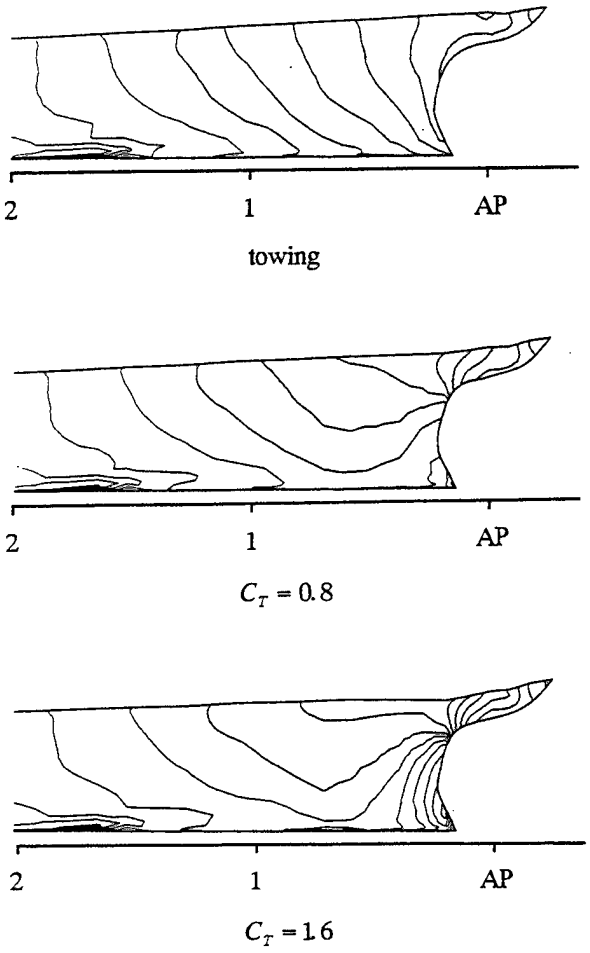


Fig.9 The effect of propellr on pressure distribution near the ship stern

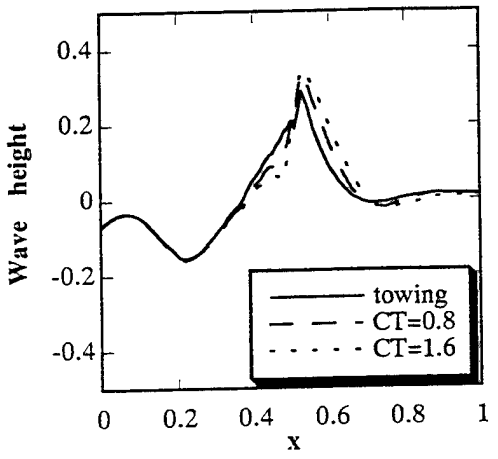


Fig.10 The effect of propeller on the ship-side wave profiles

Above manipulation is done at the points inside the propeller disk.

Calculations are carried out for the Series-60 model at the Reynolds number of 3.1×10^6 and the Froude number of 0.25. The diameter of the propeller disk is 0.037 and the propeller located at 0.488 downstream of midship and 0.021 above the keel line. The calculation is carried out for 200 steps starting from the previous result of calculation without propeller. Thrust loading conditions are C_T=0.8 and 1.6, C_T is a thrust loading coefficient and C_T=0.8 is the self-propulsion point of the 4m model.

Fig.9 shows the comparison of the pressure contour on the hull surface of stern with and without propeller. Reduction of the pressure due to propeller suction is observed upstream of the propeller near the keel. This area spreads with the thrust loading coefficient. The interval of the pressure near the free-surface becomes narrow with the thrust loading coefficient.

The wave profiles on the hull surface of stern with and without propeller are shown in Fig.10. It seems that the influence of the propeller on the wave profile is limited for the range of 0.3<x<0.5. The wave height is reduced for this range and the phase of stern wave moves toward the rear side slightly due to the action of the propeller.

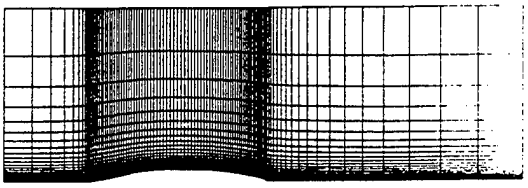
Table-1 Propulsion coefficients

	towing	$C_T=0.8$	$C_T=1.6$
$C_t\times10^3$	5.166	5.992	6.694
$C_f\times10^3$	3.565	3.602	3.630
$C_p\times10^3$	1.602	2.390	3.064
$1-t$		0.845	0.857

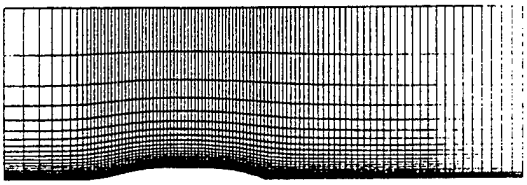
Table-1 shows the computed total resistance coefficient, frictional resistance coefficient, pressure resistance coefficient and thrust deduction factor. Thrust deduction factor is derived from the following equation :

$$1-t_{cal}=\frac{R_{towing}-(R_{self}-T_{given})}{T_{given}} \quad (25)$$

Here, T_{given} is the given thrust, R_{towing} is the computational total resistance of without propeller and R_{self} is the computational total resistance of with propeller. Main part of the change of resistance due to propeller action is the change of the pressure resistance, however, the frictional resistance also changes slightly. The thrust deduction factor is not so changed due to thrust loading coefficient but slightly increase with it.

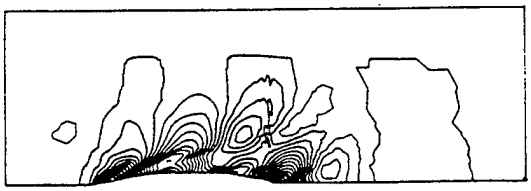


Grid-A 100×30×26

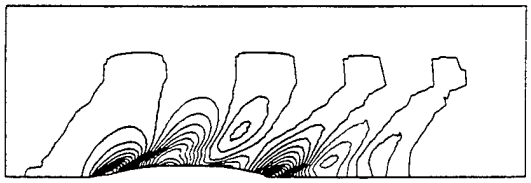


Grid-B 100×30×26

Fig.11 Comparison of computational grid



Grid-A



Grid-B

Fig.12 Comparison of wave contour at Fn=0.32

SOME EXAMINATIONS FOR THE WAVE-VISCOUS FLOW CALCULATION

Oscillation of resistance coefficient

In the previous chapter, we pointed out the problem of the oscillation of resistance coefficient in convergence history.

In Fig.5, some disturbances are found on the contour curves at the stern section and propagation of wave seems to be interrupted there. This seems to be due to the abrupt change of longitudinal grid spacing (see Fig.3). Oscillation of resistance may relate to this phenomenon.

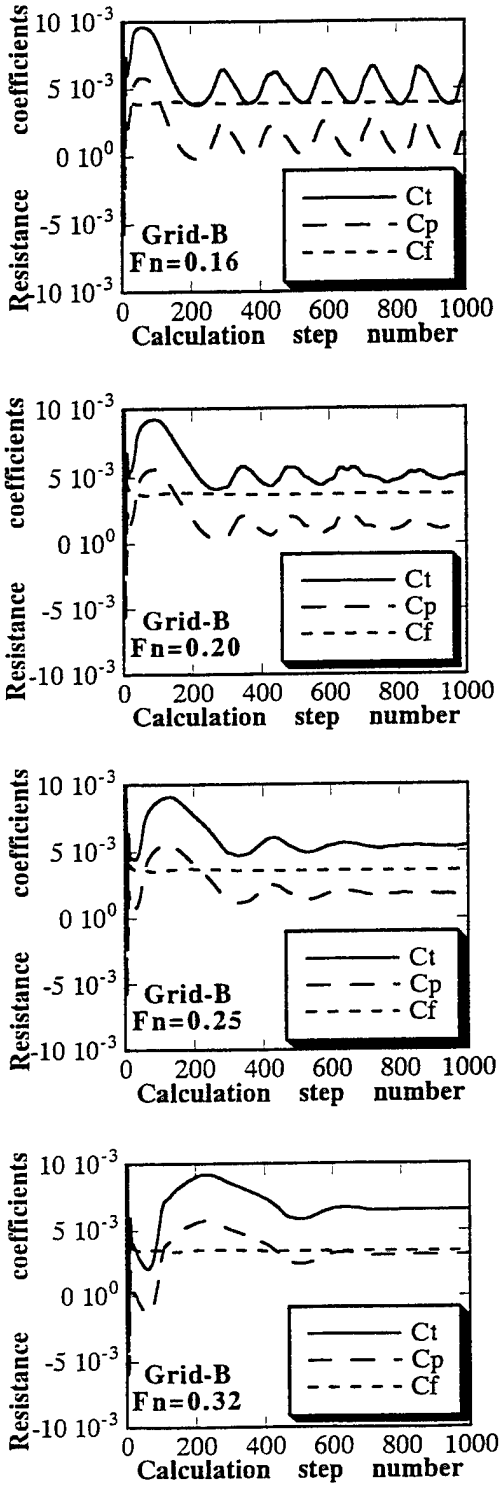
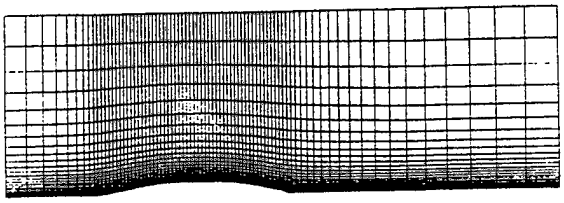
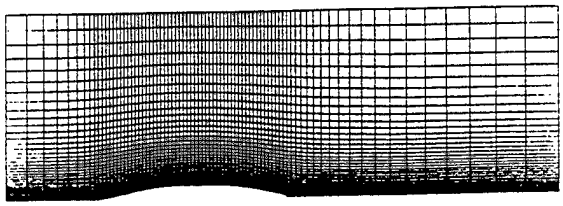


Fig.13 Time history of resistance coefficients

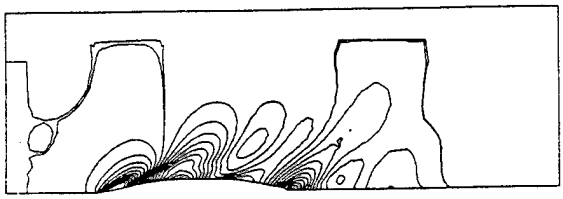


Grid-C 80×30×26

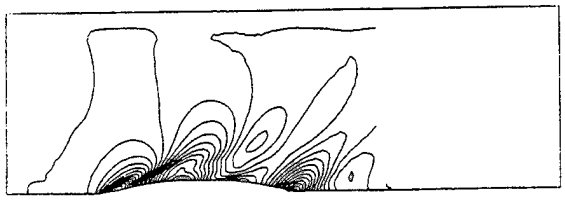


Grid-D 80×50×26

Fig.14 Computational grids for examination of transverse grid spacing



Grid-C



Grid-D

Fig.15 Comparison of wave contour (Change of transverse grid spacing) at Fn=0.32

In order to examine this, variation of grid spacing in longitudinal direction is changed as shown in Fig.11. In Grid-B, the number of grid point is kept as Grid-A and the variation of grid spacing is made more smooth.

Fig.12 shows the comparison of wave contour between Grid-A and Grid-B at Fn=0.32. In the result of Grid-B, there are no disturbances on the contour curves and wave propagates smoothly beyond the stern section. In Fig13., the oscillation of resistance coefficient is suppressed and resistance converges around 1000 step in the cases

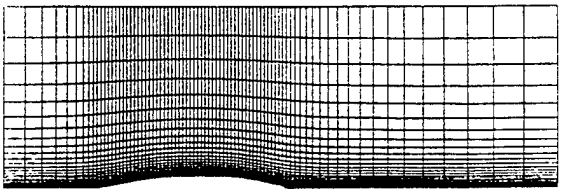
of Fn=0.25 and Fn=0.32. The result of Fn=0.20 is also toward convergence. However in the case of Fn=0.16, the oscillation still remains.

From the above results, it is found that one reason of the resistance oscillation is the smoothness of the grid spacing. However the reason is not clear about the oscillation in the case of Fn=0.16. The variation of longitudinal grid spacing might be still large to the short wave length at Fn=0.16.

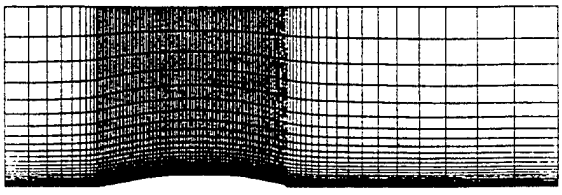
Examination of grid spacing

The calculated wave contour in Fig.5 is attenuated and somewhat divergent compared with measured one. Computational grids we use for the wave-viscous calculation are basically the same grid as for the viscous flow calculation. Grid spacing in transverse direction is small near the hull surface in order to capture boundary layer and wake, however, it gradually increases toward the outer boundary. The above problem may be due to the large grid spacing in transverse direction which cannot capture the diverging wave component.

In the wave calculation, grid spacing must be chosen to capture the wave configuration well. According to Mori et al.(7), the recommended grid size is less than $\lambda/30$ or $\lambda/20$ at most from the study of two-dimensional calculation., where λ is a wave length. This means that $\Delta x = 0.021$ in the case of Fn=0.32. On the hull surface, $\Delta x = 0.0125$ in Grid-A and $\Delta x = 0.020$ in Grid-B. Therefore this criteria is satisfied in the longitudinal direction in both grids.

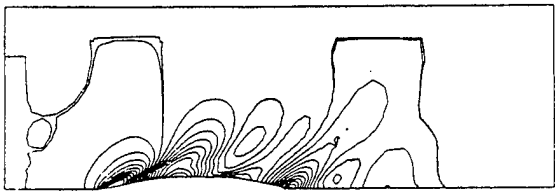


Grid-C $80 \times 30 \times 26$ (50 on the hull surface)

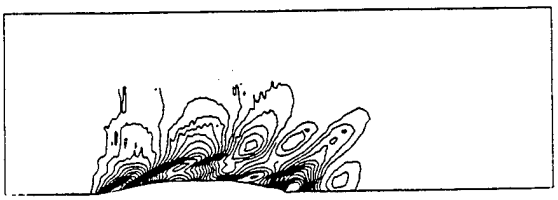


Grid-E $131 \times 30 \times 26$ (100 on the hull surface)

Fig.16 Computational grids for examination of longitudinal grid spacing



Grid-C



Grid-E

Fig.17 Comparison of wave contour (Change of longitudinal grid spacing) at Fn=0.32

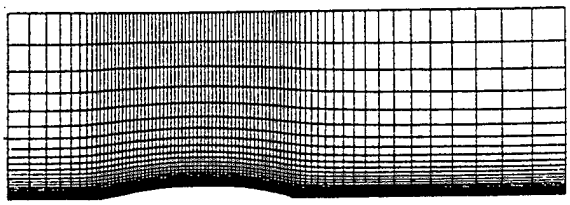
However this criteria is available only to the transverse wave component of propagation angle=0°. According to the linear ship wave theory, elementary waves of ship have their propagation angle from 0° to 90° and their wave lengths from 0 to $2\pi Fn^2$. From these considerations, Mori et al. mentioned about the importance of the grid spacing in transverse direction.

In order to examine the effect of transverse grid spacing, calculation using the grids in Fig.14 is carried out. In Fig.14, longitudinal grid spacing and minimum grid spacing in transverse direction are same in both grids and the number of grid point in transverse direction is increased from 30 of Grid-C to 50 of Grid-D. Fig.15 shows the comparison of wave contour between Grid-C and Grid-D at Fn=0.32. Although small difference is found, drastic improvement cannot be obtained by Grid-D.

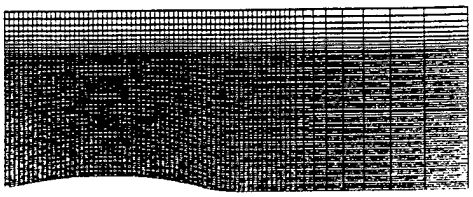
The grids in Fig.16 are for the examination of longitudinal grid spacing especially on the hull surface. Δx in Grid-C is 0.020 and Δx in Grid-E is 0.010. The minimum grid spacing and the number of grid point in transverse direction are same in both grids. Fig.17 shows the comparison of wave contour between Grid-C and Grid-E at Fn=0.32. In the result of Grid-E, some disturbances which seems to be due to abrupt change of variation of longitudinal grid spacing are observed on the contour lines. However the first trough of bow wave appears clearly and the angle between center-line and wave system becomes small. Clearly the result is improved.

From the above two results, following consideration can be made. In spite of the above

mention by Mori, grid spacing in transverse direction does not influence so much on the result compared with longitudinal grid spacing in the presence case. Longitudinal grid spacing is considered to be sufficiently enough to resolve transverse wave in any case. Therefore the cause of improved result in Grid-G is not the matter of simulation of wave propagation but the matter of simulation of wave source namely pressure distribution on the hull surface. It is considered that the wave contour does not change drastically due to grid spacing unless the wave source does not change as shown in Fig.15.



Grid-C $80 \times 30 \times 26$ (Hull grid)



Grid-F $71 \times 71 \times 21$ (Wave grid)

Fig.18 Two grid systems for the composite grid approach

Composite grid approach

As pointed out by Mori et al.(7), wave-viscous flow has two parameters that describe the phenomenon, namely the Reynolds number and the Froude number. In our calculation method, the same grid spacing can be used for wide range of the Reynolds number, from the model scale to the ship scale, because the standard wall function is adopted on the hull surface (13). However the grid spacing and computational domain may have to be changed considerably in the wave calculation, because the wave length varies with Fn^2. Considering the above fact, it is convenient in the wave-viscous flow calculation to prepare the two grid systems namely the viscous flow calculation grid (hull grid) and the wave calculation grid (wave grid) and to treat them interactively. This approach is one kind of the composite grid method.

In the composite grid method, the physical domain is subdivided into some sub-regions and the grids are generated for each sub-region. Communication among the grids is carried out by interpolation of the dependent variables at grid boundaries. This method is usually employed for computation of flow around a complex geometry. One of the famous method of composite grid approach is the Chimera method developed by NASA (14). One of the author employed this approach to calculate viscous three-dimensional flow passing through waterjet inlet (15). Lungu et al.(8) employed the composite grid method for the calculation of two-dimensional wave-viscous flow around a submerged hydrofoil.

Adopting the composite grid method to the wave-viscous flow around a hull is considered to have the following merits :

1) In the wave grid, grid can be generated and mesh on the free surface can be arranged independently from the hull geometry. Therefore the grid generation and the examination of the effect of grid spacing become easy.

2) For the change of the ship speed, only the wave grid must be changed. The resistance of the hull can be evaluated with the same hull grid for different ship speed.

Fig.18 shows one example of the two grid systems for our composite grid approach. Grid-C is the hull grid and Grid-F is the wave grid. Fig.19 shows how to overlay these two grids. In the case of Fig.19, Grid-F is set to join with j=10 line of Grid-C around a hull.

At the present time, full composite grid approach for our wave-viscous flow calculation is not yet completed and only the calculation in the wave grid using the information from the hull grid is carried out. The process is as follows:

1) Initial wave grid is generated using the wave height information of the hull grid.

2) Flow information (velocity, pressure, k and ε) is interpolated from the result of the hull grid at the planes of the inlet and the side toward a hull of the wave grid. Tri-linear interpolation of the following form is employed :

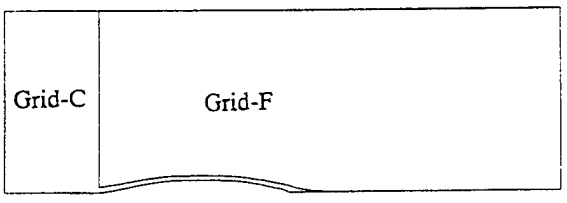
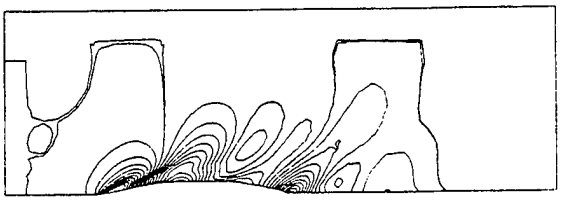
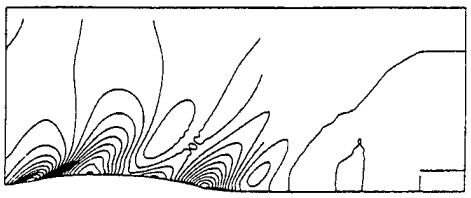


Fig.19 How to overlay the two grid systems in composite grid approach

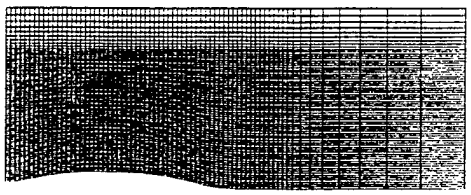


Grid-C

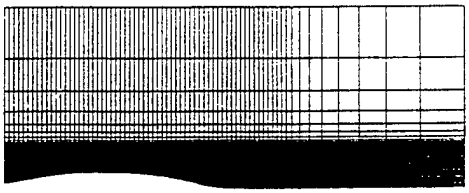


Grid-F

Fig.20 Comparison of wave contour between the hull grid and the wave grid at Fn=0.32



Grid-F $71 \times 71 \times 21$



Grid-G $71 \times 71 \times 21$

Fig.21 Comparison of wave grid

$$\phi = a_1 + a_2\xi + a_3\eta + a_4\zeta + a_5\xi\eta + a_6\xi\zeta + a_7\eta\zeta + a_8\xi\eta\zeta \qquad (26)$$

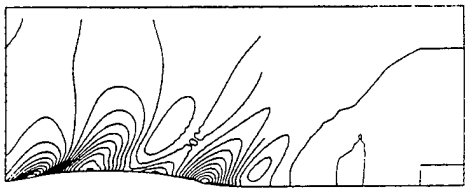
where $0 \le \xi, \eta, \zeta \le 1$ are the coordinates of the point to be interpolated and the a1-a8 depend upon the function values at the points forming the interpolation cell.

3) Flow calculation is carried out in the wave grid under the interpolated boundary values.

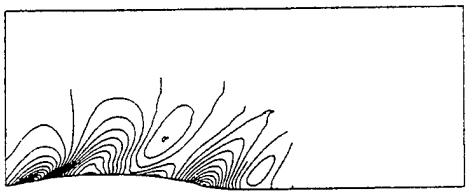
Fig.20 shows the comparison of wave contour between Grid-C and Grid-F. Boundary values of Grid-F are fixed to the interpolated results from Grid-C. Although some differences are exist, almost the same result with Grid-C is obtained in the calculation of Grid-F.

In order to see the difference due to transverse grid spacing, we carried out the calculation using Grid-G in Fig.21. Δy in Grid-G is about one third of Grid-F. Fig.22 shows the comparison of wave contour between Grid-F and Grid-G. In spite of the considerable difference of grid spacing, the result of Grid-G is almost same with grid-F. This is same with the result in Fig.15 and it seems to support the consideration that the wave contour does not change drastically due to the grid spacing unless the wave source does not change.

Further examination using the wave grid and development of the full composite grid method are the present subject for us.



Grid-F



Grid-G

Fig.22 Comparison of wave contour

CONCLUDING REMARKS

The conclusions of this paper are as follows:

(1) A finite volume method is developed for the viscous flow including free surface around a ship.
(2) The computation about a Series-60 model is carried out. The computational results of the wave profile on the hull surface and frictional resistance show good agreement with experimental ones. However, computed pressure resistance does not converged in low Fn case, and the calculated wave contour is attenuated and slightly divergent.
(3) The calculations of wave-viscous flow under propeller operating condition are carried out using the pressure jump model. Influence of the propeller action on the wave around the ship stern is represented.

(4) The effect of variation of longitudinal grid spacing is examined. When smooth grid spacing is used in longitudinal direction, the oscillation of the pressure resistance is suppressed except for low *Fn* case.
(5) The effects of transverse and longitudinal grid spacing are examined. In the present study, grid finess in transverse direction does not improve the result and longitudinal grid spacing improves the result cconsiderably
(6) A composite grid approach is tried for wave-viscous flow around a ship. Although the complete treatment of composite grid has not yet achieved, the difference due to grid spacing on the free surface is investigated by using this approach.

ACKNOWLEDGEMENTS

The authors are deeply indebted to Dr. S. Mizoguchi, Dr. T. Tsutsumi and Dr. S. Ishida of Ishikawajima-Harima Heavy Industries Co.,Ltd. for their supports and advises. Thanks are also given to the staffs of IHI towing tank for their helps.

REFERENCES

1. Okabe,J. and Jinnaka,T. : " On the Waves of Ships ", Report of the Research Institute for Fluid Engineering, Vol.7, 1950
2. Miyata,H., Sato,T. and Baba,N. : " Difference Solution of a Viscous Flow with Free-Surface Wave about an Advancing Ship ", Journal of Computational Physics, Vol.72, 1987, pp.393-421
3. Miyata,H., Zhu,M. and Watanabe,O. : " Numerical Study on a Viscous Flow with Free Surface Waves About a Ship in Steady Straight Course by a Finite-Volume Method ", Journal of Ship Research, Vol.36 No.4, 1992, pp.332-345
4. Farmer,J., Martinelli,L. and Jameson,A. : " A Fast Multigrid Method for Solving the Nonlinear Ship Wave Problem with a Free Surface ", 6th International Conference on Numerical Ship Hydrodynamics, Iowa, 1993
5. Liu,H. and Kodama,Y. : " Computation of Waves Generated by a Ship Using a NS Solver with Grobal Conservation ", Journal of the Society of Naval Archtects of Japan, Vol.173, 1993, pp.1-8
6. Hino,T. : " Computation of Free Surface Flow Around an Advancing Ship by the Navier-Stokes Equations ", 5th International Conference on Numerical Ship Hydrodynamics, Hiroshima, 1989, pp.103-117
7. Mori,K-H. and Hinatsu,M. : " Review of Program 1 -- Viscous Flow around Series 60 with Free-Surface ", Proceedings of CFD WORKSHOP TOKYO 1994, Vol.2, Tokyo, 1994, pp.79-93
8. Lungu,A. and Mori,K-H. : " Applications of Composite Grid Method for Free-Surface Flow Computations by Finite Difference Method ", Journal of the Society of Naval Architects of Japan, Vol.175, 1994, pp.1-10
9. Nakatake,K., Ando,J. and Kataoka,K. : " Free Surface Effect on Hull-Propeller-Rudder Interactions ", 17th Symposium on Naval Hydrodynamics, the Hague, 1988, pp.445-459
10. Stern,F., Kim,H.T., Zhang,D.H., Toda,Y., Kerwin,J. and Jessup,S. : " Computation of Viscous Flow Around Propeller-Body Configurations: Series 60 C_B=0.6 Ship Model ", submitted to Journal of Ship Research
11. Masuko,A., Shirose,Y. and Ishida,S. : " Numerical Simulation of the Viscous Flow Around Ships Including Bilge Vortices ", 17th Symposium on Naval Hydrodynamics, the Hague, 1988, pp.299-314
12. Masuko,A. and Ogiwara,S. : " Numerical Simulation of Viscous Flow around Practical Hull Form ", 5th International Conference on Numerical Ship Hydrodynamics, Hiroshima, 1989, pp.211-224
13. Shirose,Y. and Masuko,A. : " Numerical Simulation of Viscous Flow around a Full Scale VLCC and Its Geosim Models ", 2nd Osaka International Colloquium on Viscous Fluid Dynamics in Ship and Ocean Technology, Osaka, 1991, pp.271-290
14. Benek,J.A., Buning,P.G. and Steger,J.L. : " A 3-d Chimera Grid Embedding Technique ", AAA 7th Computational Fluid Dynamics Conference, Cincinnati, Oh, 1985, pp.322-331
15. Masuko,A. : " An Application of Grid Embedding Technique for Viscous Flow calculation in a Field of Ship Hydrodynamics (1st Report Numerical Simulation of Viscous Flow Passing Through Waterjet Inlets)", Journal of The Society of Naval Architects of Japan, Vol.174, 1993, pp.1-11(in Japanese)

Comparison of Calculated and Measured Loads on a Flared Body Oscillating in a Free Surface

B. Maskew (Analytical Methods, Inc., USA),
M.-L. Wang, A. Troesch (University of Michigan, USA)

ABSTRACT

Experimental and numerical results are presented for the hydrodynamic loads experienced by a cusped body which is oscillating vertically with forced harmonic motion in a free surface. Results are presented for a range of frequencies and a range of amplitudes of oscillation. The numerical calculations used a three-dimensional time domain panel method formulated for large amplitude motions and non-linear treatment of the free surface. The comparative study, which is still ongoing, indicates good agreement between the calculated and measured loads. The effects of tank wall boundaries may cause some discrepancies.

NOMENCLATURE

A	Amplitude of oscillation
Cp	Pressure coefficient $(p - p_{REF})/(1/2\ \rho V_{REF}^2)$
D	Diameter of top of body
dS	Element of surface
f	Frequency of oscillation
F_{dy}	Dynamic force
F_{hy}	Total hydrodynamic force = $F_{dy} + F_{st}$
F_{in}	Inertial force
F_{lc}	Force measured by load cell
Fr	Froude number, $V_{REF}/\sqrt{gL}$
F_{st}	Hydrostatic force
g	Acceleration due to gravity
L	Characteristic length (body diameter)
L_{REF}	Reference length, L/2
NB	Number of panels on the body
NS	Number of panels on free surface
NPAN	Total number of active panels
$\vec{n}$	Unit normal to the surface pointing into the fluid domain
p	Pressure
p_{REF}	Ambient atmospheric pressure
$\vec{r}$	Position vector in normalized space
s	Surface distance (normalized)
t	Time
$\vec{v}$	Normalized perturbation velocity, $\vec{v}/V_{REF} = -\nabla\phi$
$\vec{V}$	Perturbation velocity, $-\nabla\Phi$
V_{REF}	Reference speed (peak plunging speed of body)
x,y,z	Normalized Cartesian coordinates, $x = X/L_{REF}$, etc.
X,Y,Z	Cartesian coordinates, dimensional
μ	Doublet density, $\phi/4\pi$
σ	Source density, $-(\partial\phi/\partial n)/4\pi$
τ	Normalized time, $t \cdot V_{REF}/L_{REF}$
ρ	Water density
ϕ	Normalized velocity potential, $\Phi/L_{REF}/V_{REF}$
Φ	Velocity potential (units of length^2/time)

INTRODUCTION

Increasing demands for understanding the complexity of nonlinear free-surface flows, such as bottom and bow flare slamming and green water on deck, necessitate the experimental investigation on large-amplitude motion of an idealized axisymmetric flared body. Of particular interest are the nonlinear hydrodynamic phenomena of the flare-slamming and deck-wetness flows during large-amplitude oscillations. Among the many slamming experiments performed in attempting to investigate the forced vertical oscillations of different models are early slamming researches of a segmented ship model, a rectangular cylinder, wedges with different dead rise angles, and so forth. The experimental program described here is primarily designed to generate sets of quality experimental data, e.g., time-history

acquisitions, for comparison with time-domain numerical codes, as well as video recordings to provide qualitative information for breaking wave profiles and contact line dynamics.

The experimental tests were performed at the University of Michigan Marine Hydrodynamics Laboratory (MHL) to measure the time histories of the prescribed motions, the wave elevations and the resultant forces. The MHL's vertical motion mechanism (VMM) is used to conduct such large-amplitude oscillation experiments. The axisymmetric flared body was forced to oscillate sinusoidally with different frequencies and amplitudes so that different wave profiles, such as steep waves, local wave-breaking, spray sheets, and so on, could be observed. In this experiment, the measured data included time histories of the prescribed displacement, the resultant force, and the wave elevation at several locations away from the body. Video recordings were also taken in each run for qualitative photographs.

The problem of *predicting* the hydrodynamic impact loads has been under investigation for some time, starting with the classical formulation by Von Karman (1) and Wagner (2). There have been a number of approaches to the problem (see for example, the review by Troesch and Kang (3)), but the majority are for two-dimensional conditions, e.g., the wedge impact work of Greenhow (4), among others. There are a number of examples where two-dimensional methods are applied in a strip theory approach to ship slamming problems, e.g., Oliver (5), but, as pointed out in (3), this can be misleading in strongly three-dimensional situations such as at a ship's bow. The relatively few attempts at a three-dimensional method for impact loads, e.g., Miloh (6) or for simplified free surface conditions, e.g., Troesch and Kang (7), are really for axisymmetric conditions.

Earlier work by Troesch and Kang (3, 7) and Kang (8) applied a three-dimensional panel method to calculate the impact loads on the same flared body as is used in the present investigation. Numerical prediction of bottom impact loads for the body dropping freely into the water compared well with experimental measurements, but the flare impact load was overpredicted by the theory. The numerical calculations involved not only the prediction of the impact forces, but also the time integration of the equations of motion driven by these forces. Because of this, possible inaccuracies in the force prediction—due to such things as the simplified equipotential free surface boundary condition or the model discretization—could not be identified with certainty. The present tests are intended to isolate the impact force aspect by using a forced harmonic motion rather than a free fall. Thus the problem of predicting the impact force accurately can be investigated separately without the added uncertainty of solving the equations of motion as the falling body experiences these forces.

The new experimental measurements are compared with numerical calculations carried out using the USAERO/FSP computer code (Maskew (9, 10). This is a time-domain panel code whose basis differs from that used in the earlier calculations of Troesch & Kang (7) mainly in that the free surface treatment is fully non-linear. The code is being evaluated for non-linear seakeeping calculations for which an additional module is coupled to integrate the equations of motions (Maskew, Tidd and Fraser, 11). In principle, the code can treat large amplitude motions in steep waves and so the present comparisons are needed to help validate the prediction of impact forces.

One consideration of the numerical analysis is the proper treatment of the far field or truncation boundaries. If the numerical towing tank is to model the physical towing tank, then for zero speed or low speed calculations, tank wall reflection becomes an important issue. See, for example, the discussion by Cohen and Troesch (12) where the added mass and damping coefficients of an oscillating sphere between two vertical walls showed a large dependence on frequency of oscillation and wall separation. Those results showed that there were frequencies at which interaction was significant and frequencies at which the sphere appeared to oscillate in an effectively unbounded tank. While the sphere calculations were based upon a linear free surface condition, similar reflection effects will be present in fully nonlinear calculations as well. Consistent with that earlier work, the numerical and experimental comparisons for the flared body given in this paper display varying degrees of tank wall-body interaction.

EXPERIMENTS

In order to conduct the vertical forced oscillation tests on the idealized flared body, the VMM dynamometer, wave probes, and video recorder were set up in MHL's towing tank to record time histories of vertical motions, load cell forces, wave elevations and video information, respectively. The description of the experimental setup is shown in the schematic illustration of Fig. 1.

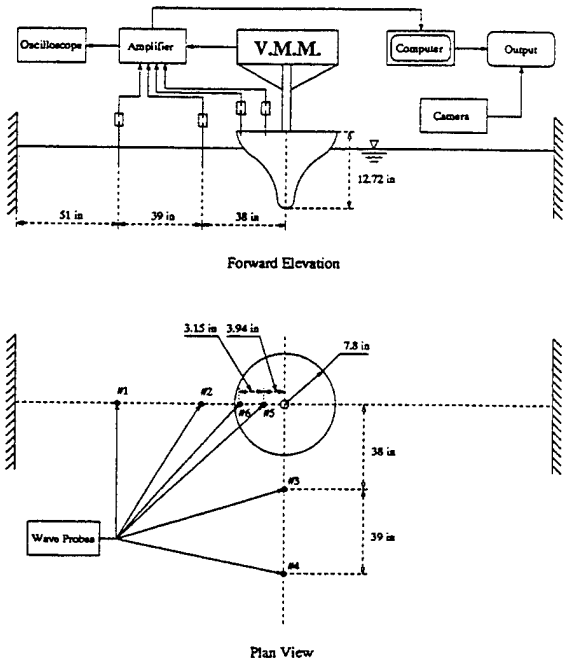


Fig. 1. Schematic Setup of the Experiment.

The VMM dynamometer was originally designed to determine the unsteady vertical forces acting on planing hulls (see Ashcroft, Troesch & Sullivan, 13). The dynamometer was designed to uncouple all forces and moments so that only pure vertical force and associated moments are measured. Two of the four load cells, which were originally configured to measure vertical forces and roll moments, were used in this test. The sum of two load cells gives the net vertical force while the difference of the two load cells was used to estimate the error of the experiment due to unbalanced mechanical vibration. The prescribed motions were sinusoidal oscillations with a starting ramp function. Four wave probes were installed to measure the wave elevation at different positions away from the body. In addition two wave probes were fixed on the deck of the body for the study of green water on deck. Finally, the video camera was set up to record wave profiles and observe the behavior of the free-surface intersection lines. As mentioned previously in the introduction, two types of large-amplitude oscillation experiments were conducted to investigate the slamming and deck wetness of the flared body oscillating in a free surface. Here these two cases are referred to as "deck dry condition" and "green water on deck", respectively. A range of oscillation frequencies and amplitudes were covered; details are shown in Table 1. The VMM is capable

Run Tests	Frequency (Hz)	Amplitude (in)	FFT Range ($sec.$)	Freeboard (in)
Deck Dry Condition				
06	0.907	0.976	10.0 - 36.471	3.0
07	0.598	0.903	10.0 - 36.787	3.0
08	0.895	1.873	10.0 - 36.832	3.0
09	0.598	2.056	10.0 - 36.783	3.0
10	1.220	1.087	10.0 - 36.259	3.0
11	0.719	0.908	12.0 - 34.271	3.0
12	1.221	1.357	10.0 - 36.216	3.0
13	0.720	1.997	10.0 - 37.795	3.0
14	1.213	1.471	10.0 - 36.389	3.0
15	0.718	1.393	20.0 - 36.723	3.0
16	0.599	1.623	10.0 - 36.743	3.0
17	0.909	1.503	10.0 - 32.011	3.0
Green Water on Deck				
18	0.908	1.732	10.0 - 36.453	0.0
19	1.221	1.435	10.0 - 36.216	0.0
20	0.720	1.908	10.0 - 37.811	0.0
21	0.598	1.632	10.0 - 36.765	0.0
22	1.223	0.848	10.0 - 36.173	0.0
23	0.905	1.110	10.0 - 36.538	0.0
24	0.719	0.825	10.0 - 37.834	0.0
25	0.598	1.257	10.0 - 36.778	0.0
26	1.222	1.455	10.0 - 36.195	0.0
28	0.719	2.189	10.0 - 37.819	0.0
29	0.597	2.372	10.0 - 36.801	0.0
30	0.905	1.858	10.0 - 36.515	0.0

Table 1. Test Matrix for the Experiments.

of driving a stroke of ± 4 *in* at a rate of ± 3 *in* per second. Therefore, the frequency and amplitude shown in Table 1 were selected to demonstrate the dominance of hydrostatic forces in the low-frequency oscillation, steep wave profiles in the moderate frequency oscillation, and the local breaking waves and spray sheets in the high-frequency oscillation. However, for the green water on deck cases, the general parameters were carefully selected to prevent the spray sheets from damaging the wave-probes or hitting the upper supporting structure.

Table 1 shows twenty-four tests with run numbers from 06 to 30. The missing run numbers were bad runs which have been discarded here. The time histories of the prescribed vertical displacement, Load Cells 1 and 2, the sum and difference of the load cells, four wave probes in the deck dry conditions and six wave probes in the green water on deck conditions have been recorded with individual run times equal to 40 seconds. Three thousand samples were taken in each run, i.e., the sampling internal Δt = 0.013333 seconds. Before the analog signals were digitized, they were passed through a multiple filter bank with a cut-off

frequency of 25 *Hz*. In Table 1, the freeboard values were also selected in each run so that different drafts were used to produce desirable wave profiles. The other information shown in Table 1 is provided for the later Fast Fourier Transform (FFT) analysis of the experimental results. These details are given in the Appendix. The "FFT Range" denotes the time segments of each run that was Fourier analyzed. Table 2 gives the offsets of the flared body whose isometric view is shown in Fig. 2. The flared body used in the experiments was a wooden and aluminum structure with thin yellow waterproof coating and black measuring marks. The total weight of the flared body plus the upper supporting structure is 22.8 *lbs*. The photograph in Fig. 3 shows the oscillating object, the wave profiles, and part of the upper supporting structure.

Formulation of Motion Equations

An inertial Cartesian coordinate system *OXYZ* with its origin on the still water surface and its *Z*-axis pointing upwards is shown in Fig. 2. It is assumed that the body strictly undergoes forced vertical motions under the action of load cells, hydrodynamic action and gravitational force, where the upward acting forces are defined as positive. The equations of motion can be set up by equating the above forces to the inertial force associated with acceleration of the body mass m. Here the motion equations representing the body moving in a vertical direction are presented for deck dry condition and green water on deck, respectively.

Radius R (*in*)	Height Z (*in*)	Radius R (*in*)	Height Z (*in*)
0.0000	0.0000	2.9023	5.9070
0.3849	0.0285	3.1071	6.3008
0.7550	0.1186	3.3434	6.6946
1.0961	0.2950	3.5836	7.0884
1.3951	0.5141	3.8632	7.4822
1.6404	0.7969	4.1546	7.8760
1.8228	1.1505	4.4854	8.2698
1.9350	1.4614	4.8733	8.6636
1.9729	1.5752	5.2691	9.0574
2.0084	1.9690	5.7219	9.4512
2.0360	2.3628	6.1866	9.8450
2.0576	2.7566	6.6119	10.2389
2.0970	3.1504	6.9309	10.6327
2.1659	3.5442	7.2223	11.0265
2.2447	3.9380	7.4784	11.4202
2.3392	4.3318	7.6752	11.8141
2.4534	4.7256	7.7854	12.4692
2.5973	5.1194	7.7933	12.7251
2.7290	5.5132		

Table 2. Offset Table of the Flared Body.

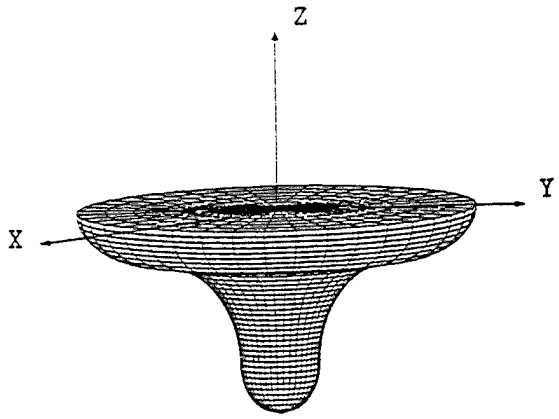


Fig. 2. Coordinate System and Body Geometry.

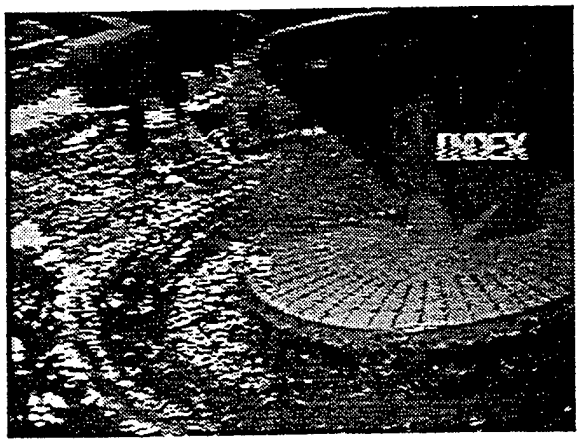


Fig. 3. Photograph of the Oscillating Body and It's Support Structure.

Deck Dry Condition

For the deck dry condition, the equations of motion can be expressed as

$$F_{lc}(t) + F_{hy}(t) - mg = m\ddot{Z} \qquad (1)$$

where F_{lc} (t) represents the load cell measurement by the VMM; F_{hy} (t) denotes the total hydrody-

namic force which, for potential flow, is given by Bernoulli's equations as follows

$$F_{hy}(t) = \int_{S(t)} \rho\left(-\Phi_t - \frac{1}{2}\nabla\Phi\cdot\nabla\Phi - gZ\right)n_3 dS \qquad (2)$$

The hydrodynamic force can be separated into dynamic and static terms, $F_{dy}(t)$ and $F_{st}(t)$, respectively, defined by

$$F_{dy}(t) = \int_{S(t)} \rho\left(-\Phi_t - \frac{1}{2}\nabla\Phi\cdot\nabla\Phi\right)n_3 dS \qquad (3)$$

and

$$F_{st}(t) = \int_{S_{(t)}} \rho(-gZ)n_3 ds \qquad (4)$$

with $S(t) = S_0(t) + \Delta S_\zeta$. The transient wetted body surface S(t) consists of the mean surface $S_0(t)$ below the Z = 0 plane which varies with the oscillation of the body and the difference ΔS_ζ between the transient wetted surface and the mean surface, which is due to the elevation; Φ is the velocity potential; mg is the gravitational force, and $\ddot{Z}$ is the vertical acceleration of the oscillating body.

Green Water on Deck

Two different approaches can be used to deal with the case of green water on deck. One is to treat the green water as added mass which is called the control volume integration method. Eq. (1) can be rewritten as

$$F_{ic}(t) + F_{hy}(t) - mg = M\ddot{Z} + \dot{M}\dot{Z} \qquad (5)$$

where *M* is the total mass consisting of the mass of the body and the added mass of the green water on deck; the dot indicates the differentiation with respect to time. The right-hand side of the above equation represents the time rate-of-change of the momentum of the body including the added mass contributed by the green water on deck. Another approach is the total surface integration which treats the action of the green water on deck as an external force. Its equation of motion has the same form as Eq. 1.

We adopt Eq. 1 to decompose the components of the total forces. In the experimental results presented later, the hydrostatic forces are computed with respect to S_0 (t).

NUMERICAL METHOD

Mathematical Model

The mathematical model is formulated for the treatment of large amplitude, rigid body motions in a free surface. An inertial Cartesian coordinate system, OXYZ, is used with its origin on the still water and its Z-axis pointing upwards, as shown earlier in Fig. 2. The description below is a specialization of the more general basis of the USAERO/FSP method presented in Maskew (10).

For the present problem, the effects of viscosity and surface tension are neglected. The perturbation velocity of the ideal fluid is described using the *negative* gradient of the velocity potential,

$$\vec{V} = -\nabla\Phi \qquad (6)$$

It is convenient to non-dimensionalize the problem with respect to certain reference quantities. Velocities are non-dimensionalized by a reference speed, V_{REF}, which will be the peak plunging speed of the body in this case. The geometry is non-dimensionalized by a reference length, L_{REF}, which is normally chosen as *half* the characteristic length of the problem, L. (The latter is used together with V_{REF} in the evaluation of Froude Number and Reynolds Number.)

In non-dimensionalized space, therefore, the perturbation velocity is $\vec{v} = \vec{V}/V_{REF} = -\nabla\phi$.

The potential is

$$\phi = \Phi/(L_{REF}\, V_{REF})$$

and time becomes

$$\tau = t\, V_{REF}/L_{REF}$$

The boundary value problem is formulated based on Green's Theorem with surface source and doublet distributions over the free surface and wetted part of the body surface:

$$\iint_{S-P}\left\{\mu\vec{n}\cdot\nabla\left(\frac{1}{r}\right) + \frac{\sigma}{r}\right\}dS - 2\pi\mu_p = 0 \qquad (7)$$

where r is the length of the vector from a surface element, dS, to the general point P on the surface. S-P signifies that the point P is excluded from the surface integral, the limiting process for the singular point when $r \to 0$ yields the local contribution, $2\pi\mu_p$ in Eq. 7. The local doublet value, μ, is defined as

$$\mu = \phi/4\pi \tag{8}$$

and the local source value, σ, is defined as

$$\sigma = \vec{n} \cdot \vec{v}/4\pi \tag{9}$$

For finite time, the disturbance due to the body motion vanishes at infinity, hence the surface integral in Eq. 7 may be performed over local surfaces only. Thus, with care, the free surface may be truncated at a distance which will accommodate the disturbance wave propagation within the time-scale of the simulation.

The pressure distribution throughout the flow field is provided by the unsteady Bernoulli equation which is written here in non-dimensional coefficient form:

$$C_P = -v^2 - z/F_r^2 + 2\,\partial\phi/\partial\tau \tag{10}$$

ρ is the water density and z is the height of a point measured positive upwards from the still free surface. F_r represents the Froude number which is defined as $V_{REF}/\sqrt{gL}$, g being the gravitational constant.

Eq. 10 gives the pressure coefficient for a stationary point; a point that is *moving* through the inertial system at a velocity, $\vec{V}_S$, experiences a pressure coefficient of

$$C_P = V_S^2 - V_R^2 - z/F_r^2 + 2\,d\phi/d\tau \tag{11}$$

where $d\phi/d\tau$ is the *total* derivative of φ experienced by the moving point. $\vec{V}_R$ is the fluid velocity *relative* to the point, i.e.,

$$\vec{V}_R = \vec{v} - \vec{V}_S \tag{12}$$

The normal component of the fluid relative to the body surface must be zero, i.e., $\vec{n} \cdot \vec{V}_R = 0$, hence, from Eq. 12, $\vec{n} \cdot \vec{v} = \vec{n} \cdot \vec{V}_S$. Thus, from Eq. 9, the source term for the body surface can be written:-

$$\sigma = \vec{n} \cdot \vec{V}_S/4\pi \tag{13}$$

With the body source distribution known, the solution of Eq. 7 provides the doublet distribution on the body.

On the free surface, the initial boundary conditions are that the potential, φ, and its normal derivative are zero and that the pressure is uniform. It is convenient to use the ambient static pressure as the reference pressure, in which case Cp = 0 on the free surface, and this is assumed to be transferred directly to the fluid, i.e., surface tension is neglected at this time. Using Eq. 11 for a surface point moving with the fluid, the total derivative of φ with respect to normalized time can be written

$$\frac{d\phi}{d\tau} = \left(z/F_r^2 - v^2\right)/2 \tag{14}$$

(since $V_S = v$ and $V_R = 0$ here)

Integrating Eq. 14 for φ and using Eq. 8, the free surface doublet distribution can be written

$$\mu(\tau) = \frac{1}{8\pi}\int_0^\tau \left(z/F_r^2 - v^2\right)d\tau \tag{15}$$

Thus, with Eq. 7 applied to the free surface, the doublet distribution is known and the solution provides the source term. This is opposite to the situation found for the body surface and so for the body in free surface, Eq. 7, becomes a mixed boundary value problem. The source solution on the free surface provides the *normal* component of the perturbation velocity, v_N. The *tangential* component of the perturbation velocity, v_T, is obtained from the surface *gradient* of the doublet, i.e.,

$$\begin{aligned} v_N &= 4\pi\sigma \\ \vec{v}_T &= -4\pi\nabla\mu \end{aligned} \tag{16}$$

The kinematic condition on the free surface can then be satisfied by moving the particle with the local flow for a small time step, i.e.,

$$\delta\vec{r} = \vec{v}\delta\tau$$

Hence, the location of a free surface particle can be obtained by integration with respect to time

$$r(\tau) = \int_0^\tau \vec{v}\,d\tau \tag{17}$$

Numerical Procedure

The solution of the boundary value problem in Eq. 7 is achieved using a quadrilateral panel discretization of the body and free surface. Assuming a *uniform* doublet and source distribution over each panel, the surface integrals in Eq. 7 can be performed in closed form for a panel acting at a point in the center of another panel. Thus, a set of simultaneous linear equations can be formed:

$$\sum_{K=1}^{NB} \mu_K C_{JK} + \sum_{K=NB+1}^{NPAN} \sigma_K B_{JK} + E_J = 0; \; J=1, \; NPAN \tag{18}$$

where $C_{JJ} = -2\pi$

$$E_J = \sum_{K=1}^{NB} \sigma_K B_{JK} + \sum_{K=NB+1}^{NPAN} \mu_K C_{JK}$$

NB, NS are the number of panels on the body and free surface, respectively, and NPAN = NB + NS.

μ_K, σ_K are the doublet and source densities on panel K, respectively. C_{JK}, B_{JK} are the influence coefficients, respectively, for the uniform doublet and source on panel K acting at the central point of panel J. (C_{JK}, B_{JK} are given in Maskew (14)).

In the numerical procedure, the body oscillatory motion over several cycles is discretized into a number of small time steps. At each step, the solution of the boundary value problem in Eq. 18, together with Eqs. 15 and 13, provide the instantaneous doublet and source distributions over the body and free surface. This allows the perturbation velocities to be evaluated.

$$\vec{v} = v_N \vec{n} + \vec{v}_T \tag{19}$$

The normal component is evaluated from the source value, $v_N = 4\pi\sigma$, and the tangential component, $\vec{v}_T$, is obtained from the surface gradient of the doublet, $\vec{v}_T = -4\pi\nabla\mu$. To evaluate the resultant tangential velocity vector, the doublet gradient is evaluated in two directions over each panel. A second-order differencing scheme is used over three panels in each direction.

With the perturbation velocity known, the panel pressures on the wetted part of the body surface can be evaluated using Eq. 11. The $d\phi/d\tau$ term is evaluated using second-order backward differencing based on the current and two previous solutions. This evaluation is complicated by the fact that the panel geometry changes at each time step in an automatic repanelling procedure (see below). Thus, for the evaluation of $d\phi/d\tau$, the *true* motion of the panel center must be used; this differs from the body motion, especially near the free surface.

The vertical hydrodynamic force coefficient acting on the body is obtained by integrating $-C_p n_z$ over the *wetted* part of the body surface. The intersection of the free surface with the body is computed at each time step within USAERO/FSP. The body and the free surface are then automatically repanelled to the instantaneous waterline using interpolation. This ensures a "clean" panelling relationship across the body/free surface intersection. The "dry" panels identified in this procedure are temporarily deactivated and removed from the system of equations in Eq. 18.

The free surface deformation is evaluated from Eq. 17 using a forward Euler scheme. A similar scheme is used in Eq. 15 to evaluate the new free surface doublet (i.e., potential) distribution for the next step.

Sensitivity Studies

A number of computer runs were made to test the sensitivity of the calculation with respect to panel density and time step size. For these tests, a pseudo axisymmetric condition was set up; a segment of the body geometry and free surface were constructed with a 10° wedge angle (Fig. 4), and the code was instructed to perform an azimuthal sum of 36 identical strength panels for each influence coefficient. This model allowed a wide range of panel densities and time step densities to be explored without requiring a large amount of computer time. Fig. 4 shows the body at two points in a cycle to illustrate the repanelling effect. A very low panel density is shown for clarity.

The conditions of experimental Run 12 were used as a basis for these runs; i.e., high frequency, f = 1.22 Hz, and a moderate amplitude, A = 1.5 *in* (3.81 *cm*). The radius for the "edge" of the free surface was set at 24 body diameters; this should allow ample time before a disturbance wave returns from the outer boundary. Each case was run for four cycles for a total time of 3.28 seconds.

The effect of body panel density on the integrated dynamic force history is shown in Fig. 5(a). The number of panels along the strip was varied from 20 to 100, while the time step size and the number of free surface panels were .01 seconds and 240, respectively (i.e., free surface panel size is

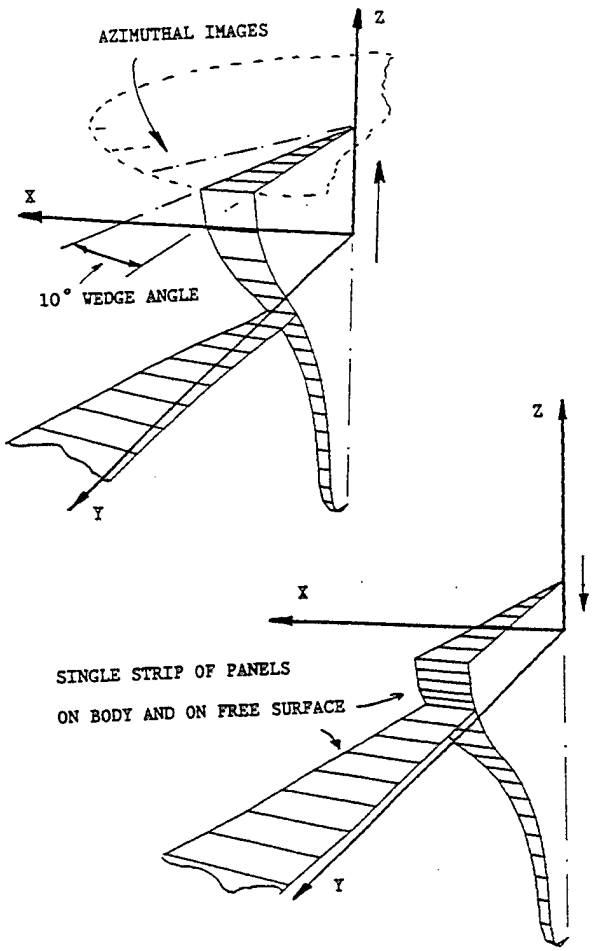


Fig. 4. Model Arrangement for Numerical Sensitivity Studies.

0.1 D). The main effect expected from the body panel density is with respect to the evaluation of surface gradients for the perturbation velocity and to the pressure integration for force. In fact, the integrated dynamic force history shows negligible effect in this range of panel density (the hydrostatic force had even less variation). Also, the calculations indicate a very rapid convergence to "steady state" following the impulsive start. The history of wetted area, Fig. 5(b), is also insensitive to panel density in this range. Panel densities lower than this would not be considered practical for this geometry because of the extensive repanelling required over the curve of the flare during the large amplitude motions (see Fig. 4).

Fig. 5(c) shows the history of wave height at the experimental station, W3 (38 *in* (96.5 *cm*) or 2.99 D from the body center). Except for a small difference in the first cycle, the wave height is es-

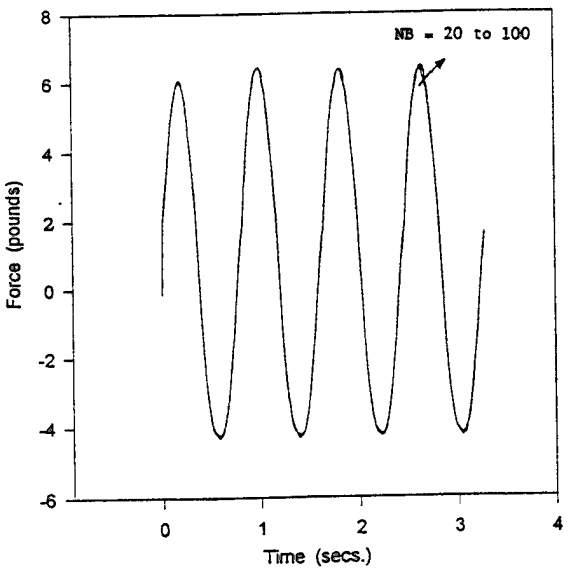


Fig. 5(a). Effect of Body Panel Density on Total Hydrodynamic Force

sentially converged with respect to body panel density. The figure also indicates that the wave height at this station would be essentially converged with respect to *time* in another cycle.

The effect of free surface panel density was examined using panel numbers NS = 120 to 960; the normalized panel size ranged from .2 D to .025 D. It would be expected that the detailed resolution of the free surface waves would be most affected by this parameter; NS = 120, for example, would not

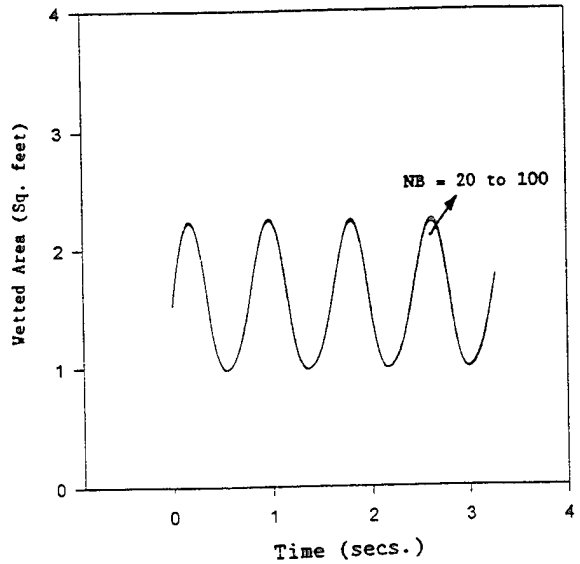


Fig. 5(b). Effect of Body Panel Density on Body Wetted Area.

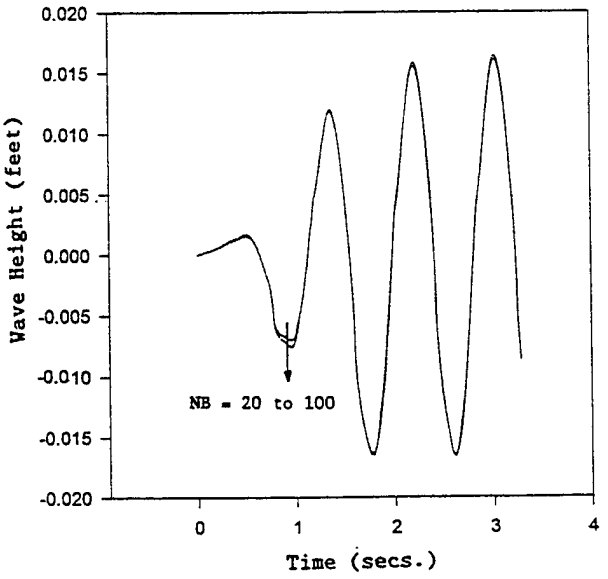


Fig. 5(c). Effect of Body Panel Density on Wave Height at Station W3.

be expected to capture much of the detail of the surface waves, but it would be useful to determine to what extent the integrated body load suffers because of this. Potentially, the low density case offers a significant saving in computational effort in a fully 3-D problem such as hull bow flare slam if the impact load is predicted with reasonable accuracy. Initial calculations with NB = 40 and δt = .01 showed a reasonable convergence of the body force (Fig. 6(a)), but a less satisfactory characteristic for the wave height (Fig. 6(b)). The implied number of panels required for a fully three-dimensional case would be impractical. The values plotted in Fig. 6(b) are the peak and trough for the fourth cycle. Earlier calculations had suggested a possible interdependency between free surface panel size and time step size, possibly arising from the simple Euler time integration scheme adopted, coupled with the physical movement of the free surface points in the Euler-Langrangian treatment; i.e., the movement of a panel corner in one time step should be significantly smaller than the local panel size. Preliminary results indicated that δt should vary as the square of panel size. Accordingly, the sensitivity study of the free surface panel density and the sensitivity to time step size were combined, the time step size varying from .015 to .004 over the present range of NS. This significantly improved the convergence of the wave height as shown in Fig. 6(b). The peak value of the integrated hydrodynamic load improved slightly over that for constant δ = .01.

One of the objectives of the present (ongoing) project is to determine to which extent the details of the jet/spray formation need to be modeled in order to obtain accurate predictions of the impact loads. A number of studies using two-dimensional methods have indicated that extremely high panel densities are needed to resolve the jet formation (15, 16); this would not be practical for treating a fully three-dimensional problem. If modeling the jet is necessary for accurate load predictions, then treatment in the three-dimensional case would clearly require a special local model of the jet (possibly semi-empirical) driven by computed local velocity conditions. One important parameter required for such a model would be the velocity of

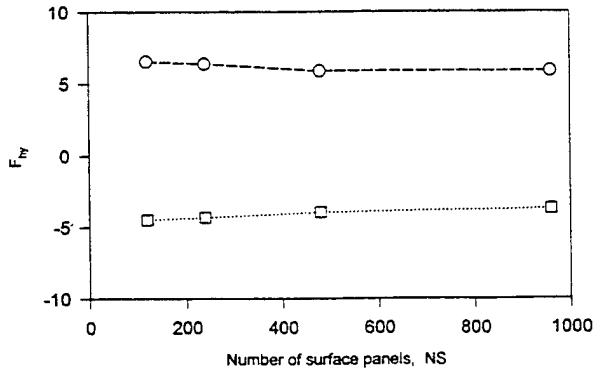


Fig. 6(a). Effect of Free Surface Panel Density on Maximum and Minimum Values of Hydrodynamic Force; f = 1.22 *Hz*, A = 1.5 *in* (3.81 *cm*)

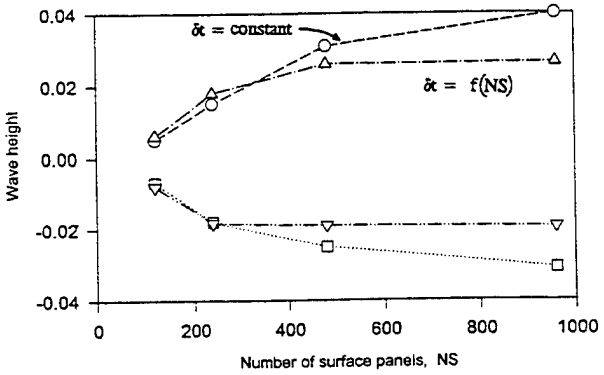


Fig. 6(b). Effect of Free Surface Panel Density on Maximum and Minimum Values of Wave Elevation at Station W3; *f* = 1.22 *Hz*, A = 1.5 *in* (3.81 *cm*)

the free surface adjacent to the body. The present sensitivity study, therefore, examined the convergence of the predicted vertical velocity component of the first free surface panel next to the body as the free surface panel density was varied. Fig. 7 shows a satisfactory convergence characteristic. The panel density on the body itself had little effect on this over the broad range considered here.

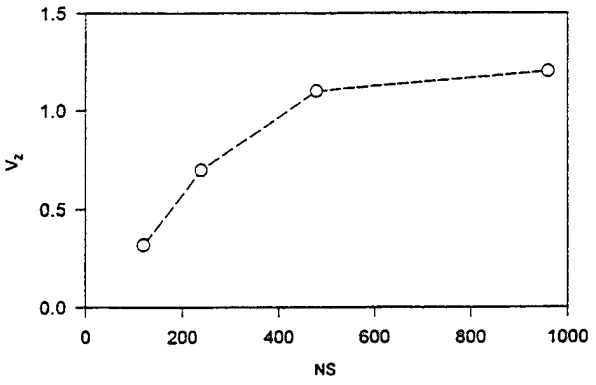


Fig. 7. Effect of Free Surface Panel Density on the Predicted V_Z Component Adjacent to the Body Side.

RESULTS AND ANALYSIS

Based upon Eq. 1, we know that the load cell measurement F_{lc} can be viewed as the combination of the dynamic term of the hydrodynamic force F_{dy}, the hydrostatic force F_{st}, the inertial force F_{in}, and the gravitational force. Here the gravitational force was measured to be 22.8 *lbs* (101.5 *N*) and the hydrostatic force can be readily obtained by Eq. 4. The inertial force can be obtained from the prescribed displacement measured in the experiment by differentiating twice.

In order to obtain accurate inertial forces, three different methods were evaluated for the calculation of the vertical acceleration of the oscillating body, as described below:

1) Assume the prescribed displacement is given by perfect sinusoidal oscillation, then the vertical acceleration can be calculated by

$$\ddot{Z}(t) = -\omega^2 Z(t)$$

2) Based upon the prescribed displacement measured in the experiment, a finite difference scheme is directly applied to calculate the vertical acceleration.

3) The FFT F^+ - F^- (i.e., the Fourier transform and the inverse Fourier transform, respectively) can be employed to calculate the vertical acceleration, as follows:

$$\ddot{Z} = F^-\{-\omega^2 F^+ [Z(t)]\}$$

The first two methods suffer from inaccuracies due to the noise induced by the mechanical vibration of the VMM. The third method can easily be used to filter the unwanted noise and yield accurate results by zeroing the FFT above frequencies of $w_c = \alpha w_o$ where w_c is the cutoff frequency, w_o is the fundamental frequency of the sinusoidal oscillation, and α is the cutoff frequency coefficient.

Selected experimental values for the first seven Fourier coefficients of the force and displacement time histories are given in the Appendix. Both the deck dry and green water on deck conditions are presented. The inertia force was calculated assuming a value of $\alpha = 6$. The coefficients are given in magnitude and argument form so that the time history, x(t) accurate through the sixth harmonic, is expressed as:

$$x(t) = \sum_{j=0}^{j=6} R_j \cos(\omega_j t - \phi_j)$$

where R_j and ϕ_j are the magnitude and phase of the jth harmonic, respectively. The table entries are nondimensionalized as follows: radian frequency $\omega(j)$ by $\sqrt{g/L}$ where L is the flared body diameter equal to 15.59 *in* (39.6 *cm*), the displacement amplitude A(j) by L, and the various force components by pgL^3.

Numerical calculations were completed for comparison with selected experimental cases. The computer program, USAERO/FSP assumed an axisymmetric domain with a boundary located at 24 body diameters as used in the sensitivity studies. The panel model used NB = 40 and NS = 480 with time step size δt = .01 *sec*. Time histories for these are shown in Figs. 8 and 9. A frequency sweep is shown in Fig. 8 where the inertial, load cell, and hydrodynamic forces (see Eqns. 3 and 4) for Cases 12, 15, 16, and 17 are given. The amplitude of oscillation for these four cases was approximately 1.5 *in* (3.81 *cm*) or A(1)/L = -0.096. Similar to Fig. 8, an amplitude sweep is shown in Fig. 9 where the numerical values are compared with Cases 11, 13, and 15. The frequency for these three cases was

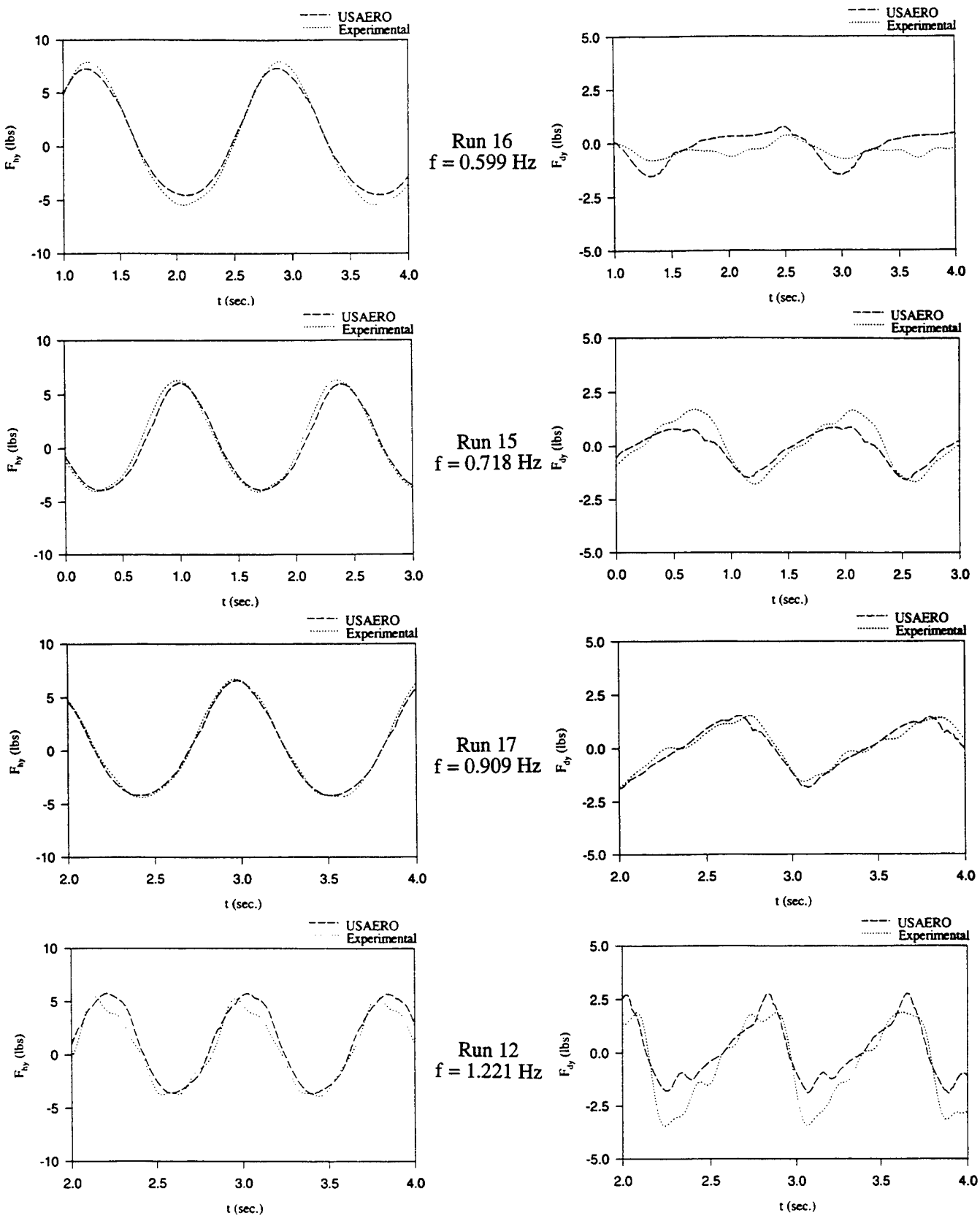


Fig. 8. Comparison of Calculated and Experimental Hydrodynamic Force Histories; Total Hydrodynamic Forces (left column) and Dynamic Forces (right column). Effect of Frequency of Oscillation; A ≡ 1.5 in (3.81 cm).

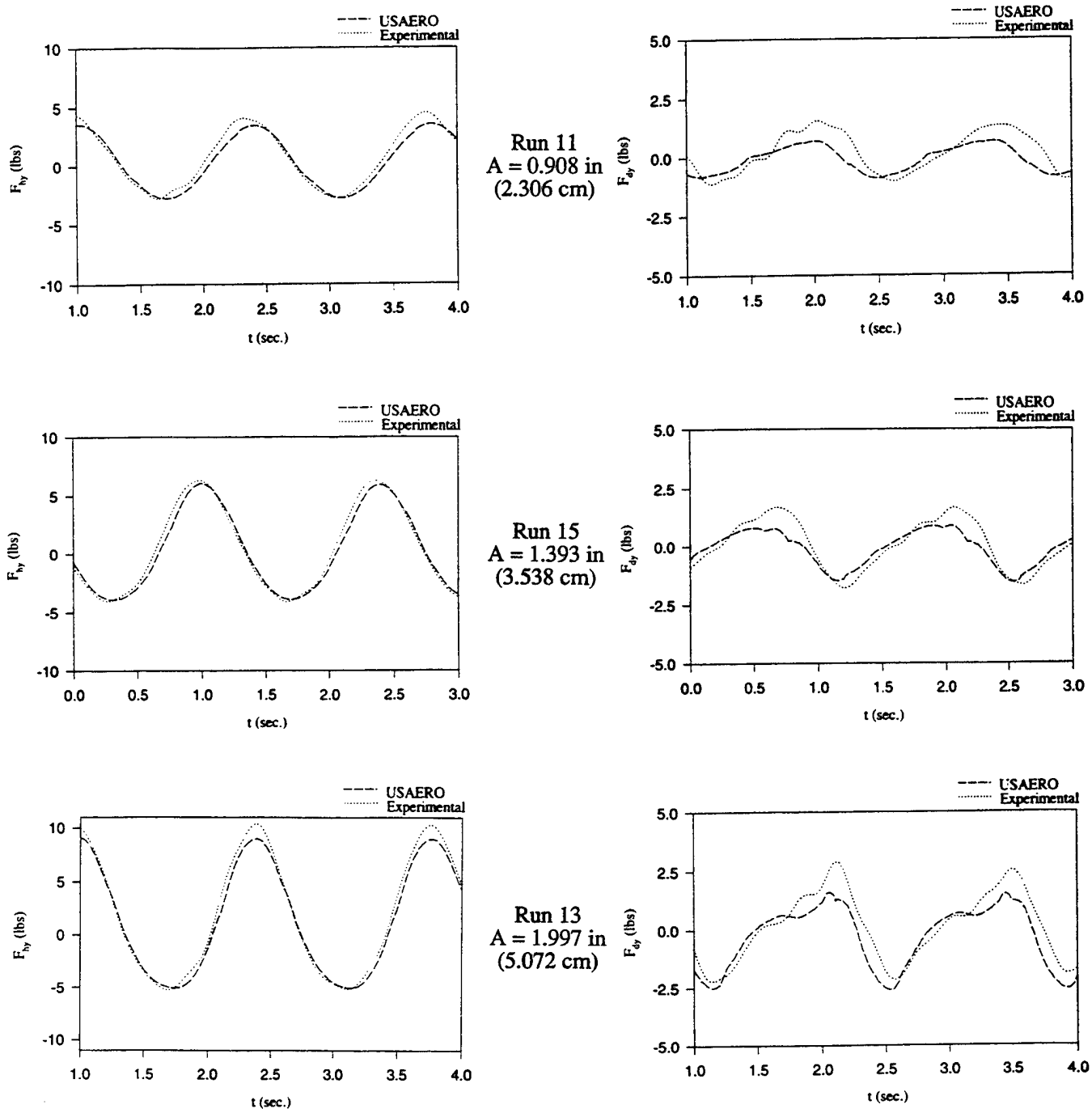
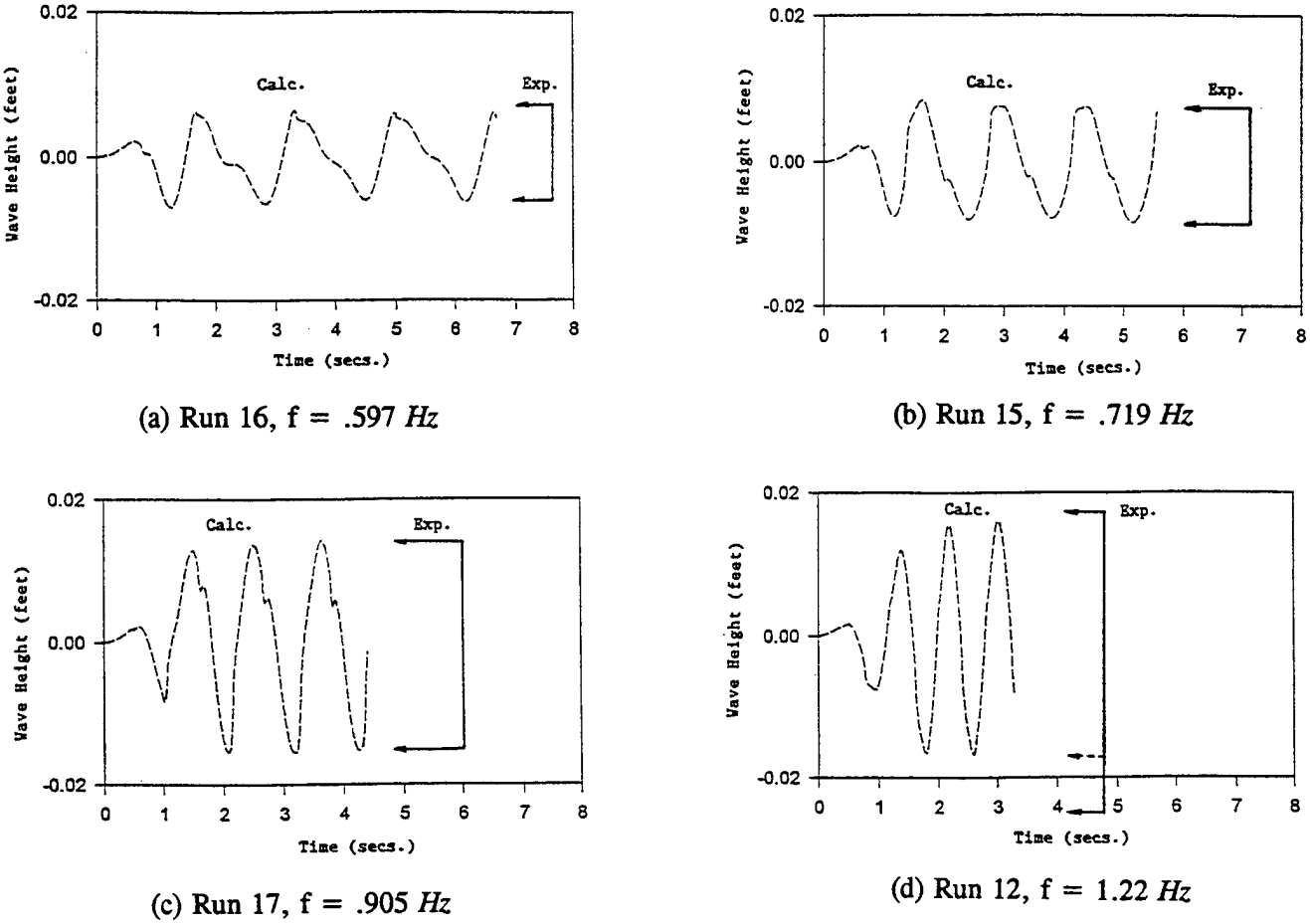


Fig. 9. Comparison of Calculated and Experimental Hydrodynamic Force Histories; Total Hydrodynamic Forces (left column) and Dynamic Forces (right column). Effect of Amplitude of Oscillation; f ≡ 0.719 Hz.



(a) Run 16, f = .597 *Hz*

(b) Run 15, f = .719 *Hz*

(c) Run 17, f = .905 *Hz*

(d) Run 12, f = 1.22 *Hz*

Fig. 10. Effect of Oscillation Frequency on Wave Elevation History at Station W3; A = 1.5 *in* (3.81 *cm*).

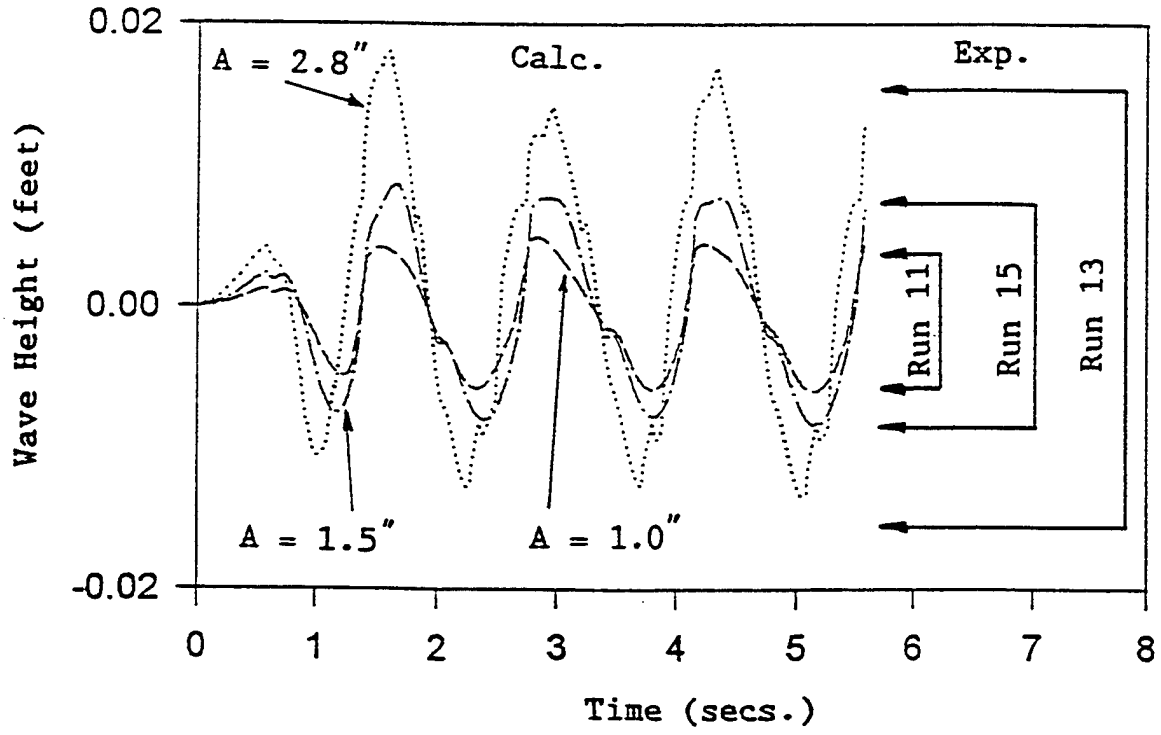


Fig. 11. Effect of Oscillation Amplitude on Wave Elevation History at Station W3; f = .719 *Hz*.

f = 0.719 *Hz*. For the force time histories shown in Figs. 8 and 9, the inertial loads were estimated based upon a value of α = 6. The approximation of dropping the higher harmonics in the vertical acceleration and therefore the inertia force, has a visible effect only at the highest frequency. Figs. 10 and 11 show comparisons between calculated and experimental wave elevations at wave probe W3. The same runs as shown in Figs. 8 and 9 are used.

Depending upon the frequency, numerical calculation and experiment show varying degrees of correlation. In general, the forces show significant nonlinearities. The hydrostatic force time histories, based upon S(t) for USAERO/FSP and $S_o(t)$ for experiment, are essentially equal indicating that the change in wetted surface, i.e, ΔS_ξ has little effect on the hydrostatic component for this particular body shape at these oscillation frequencies.

The numerical and experimentally inferred forces due to the dynamic terms in the pressure equation, i.e., Eq. 3, compare reasonably well in magnitude and phase for the low frequency cases, Runs 15, 16, and 17. For the higher frequency case, Run 12, there is a relatively larger difference between calculation and experiment. The increased difference may be due to tank wall interference. The frequency of oscillation for Case 16, the lower frequency, corresponds to the third transverse slosh mode of the towing tank, while Case 12, the highest frequency, is approximately midway between the twelfth and thirteenth modes. Cohen and Troesch (12) have shown that at frequencies where the tank slosh modes are excited, significant increases (greater than factors of two) can be experienced in added mass and damping coefficients. Conversely, at oscillation frequencies between tank sloshing and natural frequencies, it is possible to measure forces that are quite similar to those obtained in unbounded domains. See Fig. 12 where the added mass and damping coefficients for a sphere and fifteen images spaced 22 radii apart are given. The curves of the coefficients for a single sphere in unbounded water trace approximately a mean line through the values shown in Fig. 12. In an attempt to understand the effect of the tank walls, further numerical studies with boundaries formed by walls are currently being conducted. The experiments demonstrate the truncation boundaries

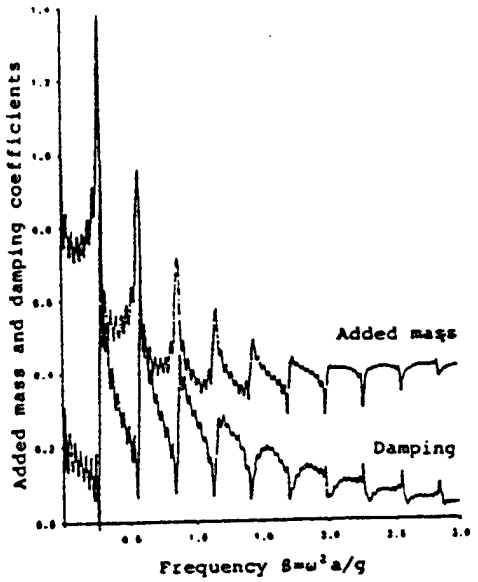


Fig. 12. Heave added mass and damping coefficients for a sphere and 15 images, spaced 22 radii apart (Cohen and Troesch (12).

in the numerical analysis, particularly those near the body, can have a significant influence on the hydrodynamic forces.

The wave elevations shown in Figs. 10 and 11 are for the first few cycles of motion, before the return of the reflected waves become significant. The averages of the first few experimentally measured wave peaks (maximum) and troughs (minimum) are also indicated. Here the correlation between theory and experiment is generally good over the frequency range. For high frequency case, Fig. 10(d), the measured troughs over the first few cycles are somewhat lower than the calculated values, however, about 16 seconds later the experimental values settle to a new steady value (shown dotted) that is very close to the predicted value. Even though station W3 is on the centerline, tank wall reflections will certainly be influencing the conditions by this later time.

The computations exhibit higher frequency waves being generated by the large motion. Fig. 13 shows a station cut through the body and free surface shortly after a wave has propagated from the body. The higher frequency wave system is superimposed on the main wave and is particularly evident in the

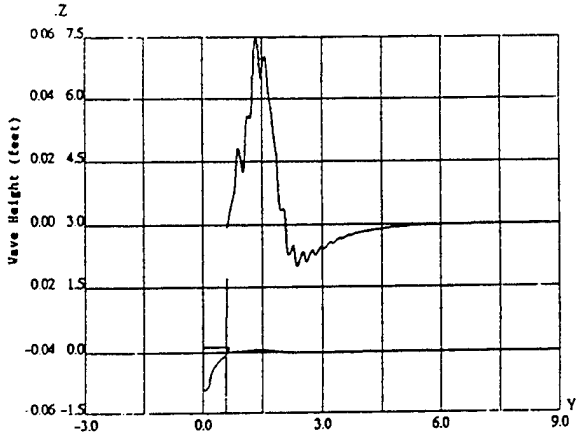


Fig. 13. High Frequency Waves in the Predicted Wave Elevation. CASE 12, $f = 1.22$ *Hz*, A = 1.5 *in* (3.81 *cm*)

region just preceding the wave. Later in the cycle, this high frequency feature is attenuated. Qualitatively, the appearance of the shorter waves was also observed by the experimental time histories and video recordings.

The cases discussed above are for the deck dry condition. Similar time histories were recorded for the green water on deck conditions, but are not presented here due to page limitations. The experimental force coefficients for both conditions are given in the Appendix. The primary difference between the two conditions is that the mean of the hydrodynamic force, i.e., the mean of Eq. 2, is positive for the deck dry condition and negative for the green water on deck condition. The nonlinear hydrostatic force, Eq. 4, acting as a stiffening spring, produces a net positive offset. This is the dominant component of the mean shift for the deck dry condition. Conversely, the increased mass associated with the green water on deck case offsets the hydrostatic component, the net result being a negative mean offset.

SUMMARY AND CONCLUSIONS

Numerical and experimental results are presented for forced, large amplitude oscillations of a flared body in a free surface. Critical issues that are being addressed in the on-going study include contact line behavior, jet development, sharp bow flare and green water on deck. The present results show varying degrees of correlation, depending upon the frequency of oscillation, the main discrepancy being at high frequency where the experimental dynamic pressure terms appear to be higher than predictable. This may be due to tank wall interference, and so further numerical studies will be conducted with the tank wall and tank bottom included in the model.

The numerical code used in the present study is a developing, general purpose hydrodynamic method which provides a rational technology for evaluating a naval vessel's nonlinear hydrodynamics. To be effective, such a computational tool needs to be evaluated in design situation. In particular, as is evident in the present study, careful treatment of truncation boundaries is required if extended numerical simulations are to be conducted.

ACKNOWLEDGEMENTS

The results presented here are from studies supported by the Office of Naval Research. The experiments were carried out under Contract DOD-G-N00014-90-J-1818 and the numerical calculations were supported under Contract N00014-90-C-0047.

REFERENCES

1. von Karmen, T., "The Impact on Seaplane Floats During Landing," NACA TN 321, 1929.

2. Wagner, H., "Landing of Seaplanes," NACA TN 622, 1931.

3. Troesch, A.W. and C.G. Kang, "Hydrodynamic Impact Loads on Three-dimensional bodies," 16th Symposium on Naval Hydrodynamics, U.C. Berkeley, CA, 1986.

4. Greenhow, M., "Wedge Entry Into Initially Calm Water," Applied Ocean Res., Vol. 9, No. 4, 1987.

5. Oliver, J.C., "Advanced Method for Ship Motion and Wave-Load Predictions," Ship Structure Committee Project, SR 1277, Giannotti and Assoc., Annapolis, Maryland, 1983.

6. Miloh, T., "Wave Slam on a Sphere Penetrating a Free Surface," Journal of Engineering Math., Vol. 14, No. 3, pp. 221-240, 1981.

7. Troesch, A.W. and C.G. Kang, "Evaluation of Impact Loads Associated with Flare Slamming," SNAME Spring Meeting/ STAR Symposium, Pittsburgh, PA, 1988.

8. Kang, C.G., "Bow Flare Slamming and Nonlinear Free Surface-Body Interaction in the Time Domain," Ph.D. Thesis, Dept. of NAME, Univ. of Michigan, 1988.

9. Maskew, B., "Prediction of Nonlinear Wave/Hull Interactions on Complex Vessels," 19th Symposium on Naval Hydrodynamics, Seoul, Korea, 1992.

10. Maskew, B., "USAERO/FSP, A Time-Domain Approach to Complex Free-Surface Problems," presented at the Symposium on High-Speed Marine Vehicles, Naples, Italy, February 1991.

11. Maskew, B., Tidd, D.M., and Fraser, J.M., "Prediction of Non-Linear Hydrodynamic Characteristics of Complex Vessels Using a Numerical Time-Domain Approach," presented at the Sixth International Conference on Numerical Ship Hydrodynamics, Iowa City, Iowa, August 2-5, 1993.

12. Cohen, S.B. and Troesch, A.W., "The Interaction of a Floating Body with Vertical Walls," Int. Shipbuilding Progra., 35 No. 401, pp 25-79, 1988.

13. Ashcroft, F.H., A.W. Troesch and P. Sullivan, "Design, Construction, and Initial Testing of a Vertical Motion Mechanism," Proc. 22nd ATTC, St. John's, NF, Aug. 8-11, 1989, pp. 204-210.

14. Maskew, B., "Program VSAERO Theory Document," *NASA CR-4023*, 1987.

15. Vorus, W.S., "An Extended Slender Body Model for Planing Hull Hydrodynamics," SNAME Great Lakes and Great Rivers Section, Cleveland, Jan. 23, 1992.

16. Zhas, R. and Faltinsen, O., "Water Entry of Two-Dimensional Bodies," *Journal of Fluid Mechanics*, 1993.

APPENDIX

Figs. A1 and A2 show photographs of wave profiles for Run 12 (dry deck condition) and Run 19 (green water on deck). Figs. A3(a) to (d) qualitatively demonstrate the wave progress and green water progress on deck during one period. Through careful observation of these figures, we can see that among the large steep or even breaking waves, there are short waves located in front of the wavefront. These small waves had been originally thought to be primarily capillary waves generated by surface tension. However, the numerical results also show similar waves induced by the high-frequency oscillations.

Finally, the non-dimensional Fourier coefficients for selected experimental results are tabulated for Runs 10 through 17, dry deck conditions, and for Runs 18, 19, 21, 22, 26 green water on deck conditions.

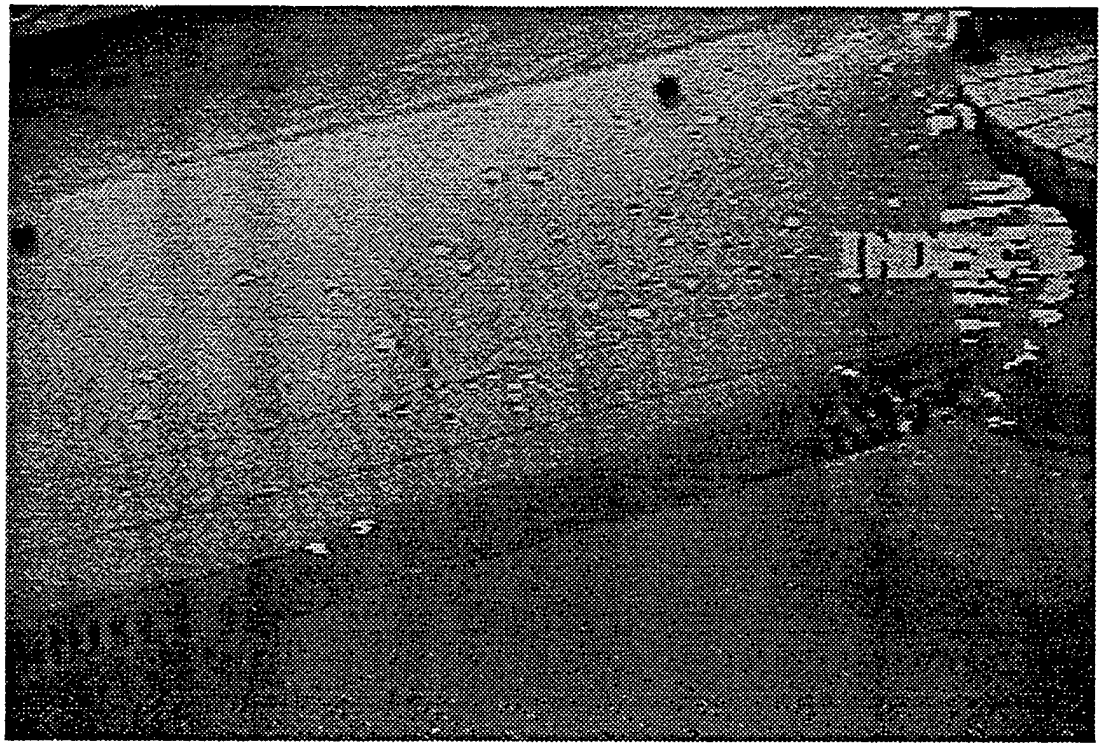
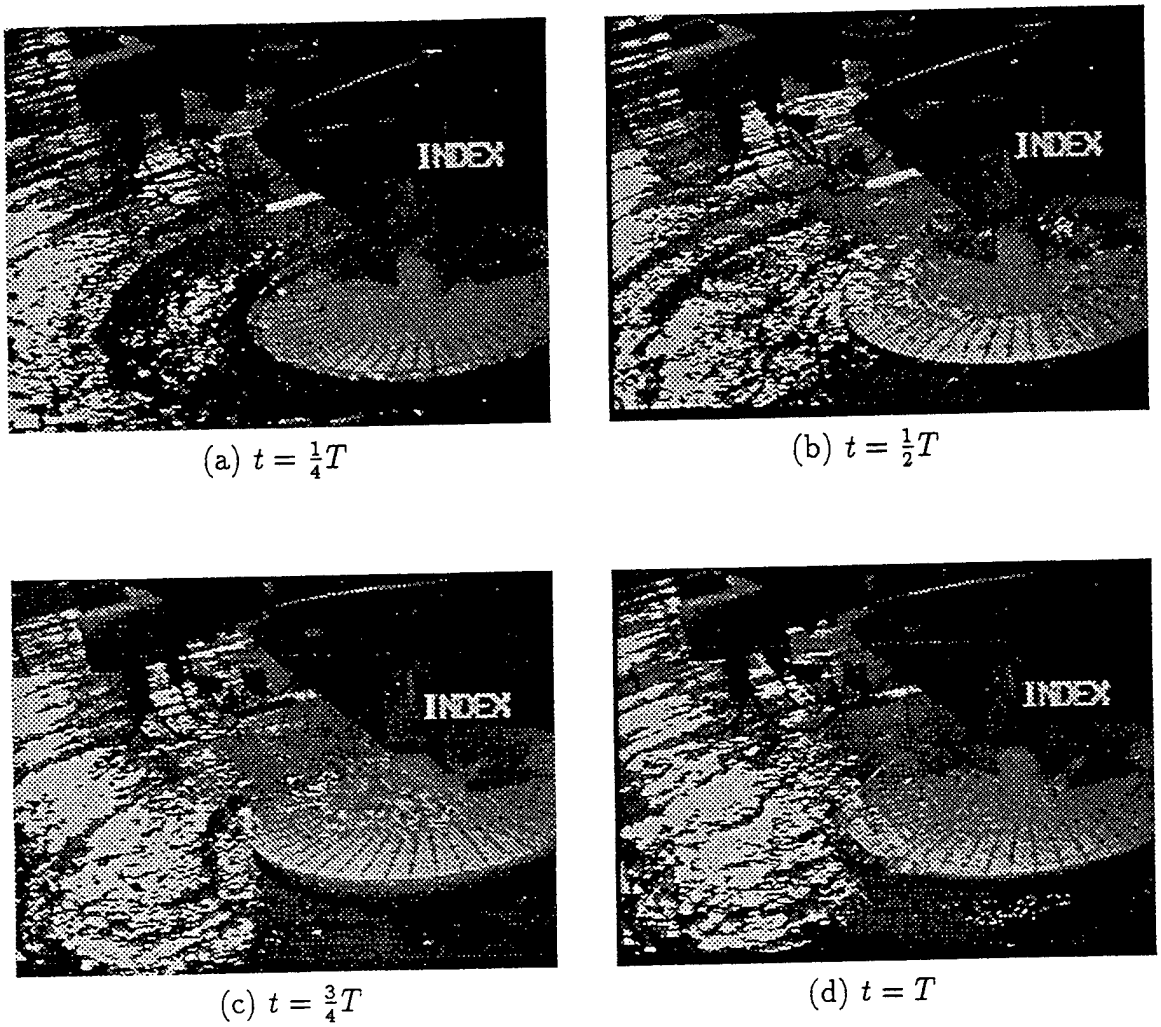


Fig. A1. Run 12, Wave Profiles.



Fig. A2. Run 19, Wave Profiles.



(a) $t = \frac{1}{4}T$ (b) $t = \frac{1}{2}T$

(c) $t = \frac{3}{4}T$ (d) $t = T$

Fig. A3. Run 19, Progress of Green Water on Deck During One Period.

Table A.1: Run 10, Nondimensional Fourier Coefficients: Gain and Phase

j	$\omega(j)$	$A(j)$	$\phi_A(j)$	$F_{h_y}(j)$	$\phi_{h_y}(j)$
0	.00000E+00	.91666E-02	.31416E+01	.77915E-02	.00000E+00
1	.15397E+01	.69752E-01	.21671E+01	.23898E-01	-.14971E+01
2	.30795E+01	.42090E-03	.11070E+01	.85197E-03	.31085E+01
3	.46192E+01	.31306E-03	.26143E+01	.23504E-03	.69417E+00
4	.61589E+01	.31580E-04	.17427E+01	.52671E-04	.28138E+00
5	.76987E+01	.13785E-03	.84475E+00	.36377E-03	-.10968E+01
6	.92384E+01	.16248E-03	-.29547E+01	.83963E-03	-.25679E+01
j	$\omega(j)$	$F_{d_y}(j)$	$\phi_{d_y}(j)$	$F_{st}(j)$	$\phi_{st}(j)$
0	.00000E+00	.31386E-02	.31416E+01	.10930E-01	.00000E+00
1	.15397E+01	.17755E-01	.29035E+01	.33863E-01	-.97460E+00
2	.30795E+01	.31509E-02	.14503E+01	.33351E-02	-.19486E+01
3	.46192E+01	.23673E-03	.13016E+01	.14111E-03	-.58434E+00
4	.61589E+01	.10909E-03	.15676E+01	.10700E-03	-.10819E+01
5	.76987E+01	.35391E-03	-.94782E+00	.54296E-04	-.24109E+01
6	.92384E+01	.90414E-03	-.25902E+01	.67385E-04	.26940E+00

Table A.2: Run 11, Nondimensional Fourier Coefficients: Gain and Phase

j	$\omega(j)$	$A(j)$	$\phi_A(j)$	$F_{h_y}(j)$	$\phi_{h_y}(j)$
0	.00000E+00	.10304E-01	.31416E+01	.76423E-02	.00000E+00
1	.90724E+00	.58213E-01	.11278E+01	.24745E-01	-.22138E+01
2	.18145E+01	.18129E-03	-.95503E+00	.17395E-02	.17806E+01
3	.27217E+01	.10808E-03	-.95553E+00	.55727E-03	-.14373E+01
4	.36290E+01	.70129E-04	-.19434E+01	.15614E-03	-.13595E+01
5	.45362E+01	.50248E-04	.94480E+00	.37745E-03	.98725E+00
6	.54435E+01	.13997E-04	.22071E+01	.16215E-03	.16128E+01
j	$\omega(j)$	$F_{d_y}(j)$	$\phi_{d_y}(j)$	$F_{st}(j)$	$\phi_{st}(j)$
0	.00000E+00	.19098E-02	.31416E+01	.95521E-02	.00000E+00
1	.90724E+00	.63955E-02	.20041E+01	.28345E-01	-.20139E+01
2	.18145E+01	.11278E-02	-.10133E+00	.23450E-02	.22562E+01
3	.27217E+01	.60367E-03	-.13806E+01	.56875E-04	.23499E+01
4	.36290E+01	.21943E-03	-.15632E+01	.73633E-04	.11351E+01
5	.45362E+01	.40203E-03	.99926E+00	.25015E-04	-.19602E+01
6	.54435E+01	.16373E-03	.15845E+01	.48764E-05	-.27843E+01

Table A.3: Run 12, Nondimensional Fourier Coefficients: Gain and Phase

j	$\omega(j)$	$A(j)$	$\phi_A(j)$	$F_{h_y}(j)$	$\phi_{h_y}(j)$
0	.00000E+00	.65297E-03	.00000E+00	.48637E-02	.00000E+00
1	.15413E+01	.87014E-01	-.23633E+01	.32052E-01	.26080E+00
2	.30826E+01	.16010E-02	-.39073E+00	.17701E-02	.31388E+00
3	.46239E+01	.31375E-02	-.90532E+00	.27284E-02	-.72586E+00
4	.61652E+01	.22577E-03	-.13888E+01	.18519E-02	-.96717E+00
5	.77065E+01	.49204E-03	-.21570E+01	.14634E-02	-.17734E+01
6	.92478E+01	.16394E-03	.64077E+00	.56197E-03	.42225E+00
j	$\omega(j)$	$F_{d_y}(j)$	$\phi_{d_y}(j)$	$F_{st}(j)$	$\phi_{st}(j)$
0	.00000E+00	.46875E-02	.31416E+01	.95512E-02	.00000E+00
1	.15413E+01	.20852E-01	-.14877E+01	.41213E-01	.78208E+00
2	.30826E+01	.53546E-02	-.11314E+01	.54251E-02	.16806E+01
3	.46239E+01	.42924E-02	-.75864E+00	.15680E-02	.23259E+01
4	.61652E+01	.20811E-02	-.93722E+00	.23662E-03	.24409E+01
5	.77065E+01	.16857E-02	-.18001E+01	.22624E-03	.11680E+01
6	.92478E+01	.60672E-03	.35160E+00	.60865E-04	.27833E+01

Table A.4: Run 13, Nondimensional Fourier Coefficients: Gain and Phase

j	$\omega(j)$	$A(j)$	$\phi_A(j)$	$F_{h_y}(j)$	$\phi_{h_y}(j)$
0	.00000E+00	.10626E-01	.31416E+01	.21768E-01	.00000E+00
1	.90877E+00	.12812E+00	.29189E+01	.54880E-01	-.39467E+00
2	.18175E+01	.61804E-03	.28338E+01	.75391E-02	-.10228E+01
3	.27263E+01	.18054E-03	-.17615E+01	.37520E-03	-.30452E+01
4	.36351E+01	.13004E-03	-.55017E+00	.17087E-03	.98205E+00
5	.45438E+01	.98900E-04	.19755E+01	.32811E-03	-.23604E+01
6	.54526E+01	.11562E-03	.19735E+01	.24007E-03	.26083E+01
j	$\omega(j)$	$F_{d_y}(j)$	$\phi_{d_y}(j)$	$F_{st}(j)$	$\phi_{st}(j)$
0	.00000E+00	.34968E-02	.31416E+01	.25264E-01	.00000E+00
1	.90877E+00	.12590E-01	-.25210E+01	.62442E-01	-.22252E+00
2	.18175E+01	.55488E-02	-.27343E+01	.99678E-02	-.43906E+00
3	.27263E+01	.46000E-03	-.29674E+01	.90753E-04	.50165E+00
4	.36351E+01	.35279E-03	-.41350E+00	.36420E-03	.22479E+01
5	.45438E+01	.30762E-03	-.25546E+01	.64915E-04	-.12064E+01
6	.54526E+01	.34706E-03	.23633E+01	.12814E-03	-.12498E+01

Table A.5: Run 14, Nondimensional Fourier Coefficients: Gain and Phase

j	$\omega(j)$	$A(j)$	$\phi_A(j)$	$F_{h_y}(j)$	$\phi_{h_y}(j)$
0	.00000E+00	.16463E-01	.00000E+00	.44495E-04	.00000E+00
1	.15320E+01	.94363E-01	.20400E+01	.29805E-01	-.15946E+01
2	.30639E+01	.18781E-02	.25118E+01	.26601E-02	.27302E+01
3	.45959E+01	.75681E-02	-.17991E+00	.65289E-02	.97101E-01
4	.61278E+01	.43646E-03	.97797E+00	.23291E-02	-.15914E+01
5	.76598E+01	.15599E-02	-.25662E+01	.45387E-02	-.26087E+01
6	.91917E+01	.14302E-03	.31245E+01	.28182E-02	.23368E+01
j	$\omega(j)$	$F_{d_y}(j)$	$\phi_{d_y}(j)$	$F_{st}(j)$	$\phi_{st}(j)$
0	.00000E+00	.37505E-02	.31416E+01	.37950E-02	.00000E+00
1	.15320E+01	.21935E-01	.27509E+01	.42878E-01	-.10968E+01
2	.30639E+01	.67334E-02	.14746E+01	.64273E-02	-.20714E+01
3	.45959E+01	.10026E-01	.23978E-01	.35468E-02	.30307E+01
4	.61278E+01	.30256E-02	-.14763E+01	.76051E-03	.20249E+01
5	.76598E+01	.52362E-02	-.25943E+01	.70103E-03	.64033E+00
6	.91917E+01	.30699E-02	.23676E+01	.26754E-03	-.44329E+00

Table A.6: Run 15, Nondimensional Fourier Coefficients: Gain and Phase

j	$\omega(j)$	$A(j)$	$\phi_A(j)$	$F_{h_y}(j)$	$\phi_{h_y}(j)$
0	.00000E+00	.11037E-01	.31416E+01	.10346E-01	.00000E+00
1	.90616E+00	.89360E-01	.13074E+01	.38122E-01	-.20220E+01
2	.18123E+01	.43880E-03	-.51646E+00	.39064E-02	.20378E+01
3	.27185E+01	.19795E-03	.62927E-02	.50830E-03	-.15227E+01
4	.36246E+01	.58617E-04	.14536E+01	.13948E-03	.61767E+00
5	.45308E+01	.14902E-03	.43583E+00	.32146E-03	.91975E+00
6	.54370E+01	.30375E-04	-.24332E+01	.12227E-03	.28396E+01
j	$\omega(j)$	$F_{d_y}(j)$	$\phi_{d_y}(j)$	$F_{st}(j)$	$\phi_{st}(j)$
0	.00000E+00	.53088E-02	.31416E+01	.15654E-01	.00000E+00
1	.90616E+00	.93870E-02	.21682E+01	.43571E-01	-.18341E+01
2	.18123E+01	.29023E-02	.30658E+00	.52254E-02	.26181E+01
3	.27185E+01	.53340E-03	-.13838E+01	.76474E-04	.29256E+01
4	.36246E+01	.15954E-03	-.11434E-01	.94462E-04	.20773E+01
5	.45308E+01	.40015E-03	.79308E+00	.90849E-04	-.28119E+01
6	.54370E+01	.12751E-03	-.30177E+01	.53037E-04	.13850E+01

Table A.7: Run 16, Nondimensional Fourier Coefficients: Gain and Phase

j	$\omega(j)$	$A(j)$	$\phi_A(j)$	$F_{h_y}(j)$	$\phi_{h_y}(j)$
0	.00000E+00	.22607E-02	.00000E+00	.88742E-02	.00000E+00
1	.75604E+00	.10411E+00	-.27156E+01	.48745E-01	.34424E+00
2	.15121E+01	.70231E-03	-.25807E+01	.47351E-02	.55184E+00
3	.22681E+01	.12037E-03	-.52584E+00	.31237E-03	-.59290E+00
4	.30241E+01	.44843E-05	-.27033E+01	.49845E-04	.16858E+01
5	.37802E+01	.81083E-04	-.12459E+01	.33098E-03	.44885E+00
6	.45362E+01	.14812E-03	-.11204E+01	.15532E-03	-.20466E+01
j	$\omega(j)$	$F_{d_y}(j)$	$\phi_{d_y}(j)$	$F_{st}(j)$	$\phi_{st}(j)$
0	.00000E+00	.38206E-02	.31416E+01	.12695E-01	.00000E+00
1	.75604E+00	.39962E-02	-.12895E+01	.49158E-01	.42546E+00
2	.15121E+01	.27713E-02	-.17937E+01	.69614E-02	.84031E+00
3	.22681E+01	.40850E-03	-.92612E+00	.15257E-03	.14817E+01
4	.30241E+01	.21163E-03	.16553E+01	.16182E-03	-.14957E+01
5	.37802E+01	.32383E-03	.28420E+00	.54315E-04	.18058E+01
6	.45362E+01	.22839E-03	-.16010E+01	.11076E-03	.21895E+01

Table A.8: Run 17, Nondimensional Fourier Coefficients: Gain and Phase

j	$\omega(j)$	$A(j)$	$\phi_A(j)$	$F_{h_y}(j)$	$\phi_{h_y}(j)$
0	.00000E+00	.49489E-02	.31416E+01	.10808E-01	.00000E+00
1	.11478E+01	.96389E-01	.13636E+01	.41470E-01	-.20153E+01
2	.22956E+01	.50265E-03	-.29630E+00	.37110E-02	.20498E+01
3	.34434E+01	.26520E-03	.53561E+00	.39161E-03	-.11079E+01
4	.45912E+01	.56076E-04	-.39698E+00	.21924E-03	-.37017E+00
5	.57390E+01	.10928E-03	.25326E+01	.61786E-03	.23763E+01
6	.68868E+01	.10968E-03	-.12383E+01	.39037E-03	.48135E+00
j	$\omega(j)$	$F_{d_y}(j)$	$\phi_{d_y}(j)$	$F_{st}(j)$	$\phi_{st}(j)$
0	.00000E+00	.34911E-02	.31416E+01	.14300E-01	.00000E+00
1	.11478E+01	.11451E-01	.23837E+01	.46299E-01	-.17778E+01
2	.22956E+01	.38928E-02	.23890E+00	.59829E-02	.27339E+01
3	.34434E+01	.42007E-03	-.91992E+00	.81262E-04	-.29408E+01
4	.45912E+01	.40559E-03	-.61871E+00	.20048E-03	.22505E+01
5	.57390E+01	.66371E-03	.23719E+01	.45945E-04	-.82950E+00
6	.68868E+01	.39892E-03	.31984E+00	.64238E-04	.21044E+01

Table A.9: Run 18, Nondimensional Fourier Coefficients: Gain and Phase

j	$\omega(j)$	$A(j)$	$\phi_A(j)$	$F_{h_y}(j)$	$\phi_{h_y}(j)$
0	.00000E+00	.15497E-01	.00000E+00	.18527E-01	.00000E+00
1	.11466E+01	.11107E+00	.16450E+01	.64308E-01	-.21427E+01
2	.22933E+01	.18573E-02	.17124E+01	.37259E-02	.19535E+01
3	.34399E+01	.15830E-02	-.13920E+01	.96256E-02	-.55111E+00
4	.45866E+01	.53035E-03	.23465E+01	.37977E-02	-.80220E+00
5	.57332E+01	.62626E-03	-.11109E+01	.28605E-02	-.71019E+00
6	.68799E+01	.28269E-05	-.23278E+01	.11207E-02	-.31062E+01
j	$\omega(j)$	$F_{d_y}(j)$	$\phi_{d_y}(j)$	$F_{st}(j)$	$\phi_{st}(j)$
0	.00000E+00	.77864E-01	.00000E+00	.59337E-01	.31416E+01
1	.11466E+01	.38526E-01	-.29161E+01	.45543E-01	-.15105E+01
2	.22933E+01	.18851E-01	.30596E+01	.17501E-01	.10950E+00
3	.34399E+01	.85752E-02	-.45949E+00	.13401E-02	-.11765E+01
4	.45866E+01	.37093E-02	-.17927E+01	.35687E-02	.25154E+00
5	.57332E+01	.24266E-02	-.70062E+00	.43471E-03	-.76368E+00
6	.68799E+01	.22147E-02	-.28896E+01	.11458E-02	.46376E+00

Table A.10: Run 19, Nondimensional Fourier Coefficients: Gain and Phase

j	$\omega(j)$	$A(j)$	$\phi_A(j)$	$F_{h_y}(j)$	$\phi_{h_y}(j)$
0	.00000E+00	.98626E-02	.00000E+00	.43162E-01	.31416E+01
1	.15413E+01	.92012E-01	-.19787E+01	.45632E-01	.57147E+00
2	.30826E+01	.21002E-02	.11066E+01	.46910E-02	-.83565E-01
3	.46239E+01	.62513E-02	.30871E+00	.13555E-01	.47439E+00
4	.61652E+01	.26365E-03	.29368E+01	.20892E-02	.28394E+01
5	.77065E+01	.65859E-03	.23433E+01	.60303E-02	.24249E+01
6	.92478E+01	.33399E-03	-.22978E+01	.32771E-02	.24022E+01
j	$\omega(j)$	$F_{d_y}(j)$	$\phi_{d_y}(j)$	$F_{st}(j)$	$\phi_{st}(j)$
0	.00000E+00	.46338E-02	.00000E+00	.47796E-01	.31416E+01
1	.15413E+01	.24848E-01	-.39696E+00	.37614E-01	.11471E+01
2	.30826E+01	.13573E-01	.20343E+01	.16507E-01	-.86216E+00
3	.46239E+01	.14897E-01	.42869E+00	.14915E-02	-.31410E+01
4	.61652E+01	.30831E-02	.23051E+01	.16683E-02	-.15280E+01
5	.77065E+01	.64857E-02	.24366E+01	.46125E-03	-.55087E+00
6	.92478E+01	.32083E-02	.21572E+01	.79538E-03	-.25187E+01

Table A.11: Run 21, Nondimensional Fourier Coefficients: Gain and Phase

j	$\omega(j)$	$A(j)$	$\phi_A(j)$	$F_{h_y}(j)$	$\phi_{h_y}(j)$
0	.00000E+00	.54245E-02	.31416E+01	.69884E-01	.31416E+01
1	.75528E+00	.10465E+00	-.67230E+00	.56732E-01	.18302E+01
2	.15106E+01	.40534E-03	-.22521E+01	.13323E-01	-.31410E+01
3	.22659E+01	.24738E-03	-.37246E+00	.32185E-02	-.24544E-01
4	.30211E+01	.20734E-03	-.15729E+00	.21840E-02	-.20495E+01
5	.37764E+01	.13235E-03	-.95699E+00	.33326E-02	.21538E+01
6	.45317E+01	.65777E-04	-.14876E+01	.27224E-02	.18476E+00
j	$\omega(j)$	$F_{d_y}(j)$	$\phi_{d_y}(j)$	$F_{st}(j)$	$\phi_{st}(j)$
0	.00000E+00	.20925E-01	.31416E+01	.48960E-01	.31416E+01
1	.75528E+00	.34418E-01	.11000E+01	.38647E-01	.24663E+01
2	.15106E+01	.18939E-01	-.21058E+01	.16693E-01	.17923E+01
3	.22659E+01	.32400E-02	-.55387E-01	.10189E-03	.17436E+01
4	.30211E+01	.23761E-02	-.19418E+00	.36509E-02	-.27242E+01
5	.37764E+01	.29918E-02	.20778E+01	.41671E-03	.27297E+01
6	.45317E+01	.23828E-02	.71389E+00	.13746E-02	-.88071E+00

Table A.12: Run 22, Nondimensional Fourier Coefficients: Gain and Phase

j	$\omega(j)$	$A(j)$	$\phi_A(j)$	$F_{h_y}(j)$	$\phi_{h_y}(j)$
0	.00000E+00	.65468E-02	.31416E+01	.34316E-01	.31416E+01
1	.15444E+01	.54402E-01	.43332E+00	.26147E-01	.30400E+01
2	.30889E+01	.22047E-03	.22759E+00	.12911E-02	-.17250E+01
3	.46333E+01	.87392E-04	.22433E+01	.69507E-03	.21515E+01
4	.61778E+01	.74737E-04	-.12963E+01	.27472E-03	.20944E+01
5	.77222E+01	.11435E-03	.22934E+01	.82594E-04	.26658E+01
6	.92667E+01	.10210E-03	-.16871E+01	.27884E-02	.55135E+00
j	$\omega(j)$	$F_{d_y}(j)$	$\phi_{d_y}(j)$	$F_{st}(j)$	$\phi_{st}(j)$
0	.00000E+00	.97429E-02	.31416E+01	.24573E-01	.31416E+01
1	.15444E+01	.13605E-01	.22178E+01	.19611E-01	-.27099E+01
2	.30889E+01	.78464E-02	.77579E+00	.89148E-02	-.22791E+01
3	.46333E+01	.11229E-02	.17715E+01	.54255E-03	-.18653E+01
4	.61778E+01	.14419E-02	-.14880E+01	.16944E-02	.17228E+01
5	.77222E+01	.25521E-03	-.12775E+01	.31823E-03	.20517E+01
6	.92667E+01	.25143E-02	.77732E+00	.65700E-03	-.47891E+00

Table A.13: Run 26, Nondimensional Fourier Coefficients: Gain and Phase

j	$\omega(j)$	$A(j)$	$\phi_A(j)$	$F_{h_y}(j)$	$\phi_{h_y}(j)$
0	.00000E+00	.22042E-01	.00000E+00	.56993E-01	.31416E+01
1	.15429E+01	.93334E-01	-.27806E+01	.46324E-01	-.21152E+00
2	.30857E+01	.23754E-02	-.42320E+00	.37485E-02	-.18316E+01
3	.46286E+01	.74645E-02	-.20661E+01	.16370E-01	-.19127E+01
4	.61715E+01	.48807E-03	.35321E+00	.24425E-02	-.44493E+00
5	.77144E+01	.13507E-02	-.15452E+01	.10974E-01	-.14123E+01
6	.92572E+01	.67506E-04	-.21451E+01	.27132E-02	.57440E-01
j	$\omega(j)$	$F_{d_y}(j)$	$\phi_{d_y}(j)$	$F_{st}(j)$	$\phi_{st}(j)$
0	.00000E+00	.39978E-02	.31416E+01	.52995E-01	.31416E+01
1	.15429E+01	.24557E-01	-.12879E+01	.40859E-01	.34597E+00
2	.30857E+01	.13771E-01	.51215E+00	.16607E-01	-.24672E+01
3	.46286E+01	.17187E-01	-.19505E+01	.10343E-02	.54919E+00
4	.61715E+01	.30666E-02	-.74023E+00	.10188E-02	.16291E+01
5	.77144E+01	.12266E-01	-.14083E+01	.12924E-02	.17669E+01
6	.92572E+01	.24593E-02	.36056E+00	.82028E-03	-.10509E+01

DISCUSSION

H. Choi
Seoul National University, Korea

I am very curious that the measured time history contains a lot of noise. In the case of forced oscillations, we normally do not have that much noise. Would you please explain where the noise came from?

AUTHORS' REPLY

The unwanted noise mainly came from the mechanical vibration of the VMM dynamometer and the towing tank carriage. Before the analog signals were digitized at a sampling frequency of 75 Hz, they were passed through a multiple filter bank with a cutoff frequency of 25.6. The FFT analysis is used to filter the noise numerically by zeroing the FFT above a certain frequency, say the sixth harmonic frequency.

DISCUSSION

M. Tulin
University of California at Santa Barbara, USA

You have explained that your method does not have sufficient resolution to calculate accurately the water rise near the hull. In connection with Jim White's question about calculating water over the deck, it should be mentioned that in Session M1, Professor Mario showed 2D+T calculations of bow impact in waves with water rise and thick jet formation; the resolution was very high. Water was followed to substantial height over the deck.

AUTHORS' REPLY

My remark concerning the panel density was in connection with resolving the thin jet formed during body impact, not the calculation of the water rise near the hull. Judging from the good agreement shown here between the calculated and measured loads and also free surface elevation, the general level of water rise to the base of the jet is represented very well by the calculation. I wanted to emphasize that the calculation shown here is from a fully *three-dimensional* nonlinear method and that the panel density used is consistent with *practical* treatment—with regard to currently available computer resources—of complete ships in waves. The very high panel densities used by Professor Mario and others in the pursuit of the details of jet formation in 2-D are not *currently* practical for complex three-dimensional situations; however, such work in 2-D should provide important insight into numerical modeling of jet effects in 3-D impact problems and should show to what extent the jet details need to be represented when computing slamming loads.

Computation of Viscous Marine Propulsor Blade and Wake Flow

F. Stern, D. Zhang, B. Chen, H. Kim (University of Iowa, USA),
S. Jessup (David Taylor Model Basin, USA)

ABSTRACT

Viscous-flow results are presented for the realistic SR7 turboprop and marine-propulsor P4119 and P4842 geometries, including both design and off-design conditions. For the design condition, overall close agreement with the data is shown for the performance, pressure and surface-streamline distributions, circumferential-average velocity profiles, phase-averaged flow, boundary-layer and wake development, and tip and hub/root vortices, including the significant effects of geometry. However, some differences are evident, which indicate lack of detailed resolution, e.g., certain aspects of the tip and hub/root vortices and boundary-layer and wake development. For the off-design condition, the results are similar and consistent with expectation, but with increased effects of lack of detailed resolution. The extensive results enable explication of the nature of the complex three-dimensional viscous propulsor blade and wake flow. Concluding remarks are provided, including comparison with inviscid-flow and related methods, prognosis for improvements, and future work.

NOMENCLATURE

c	chord length
C_D	section drag coefficient
C_p	pressure coefficient ($=2p/\rho VR^2$)
C_P	power coefficient ($=2\pi K_Q$)
D	propeller diameter
J	advance coefficient ($=U_o/nD$)
K_Q	thrust coefficient ($=T/\rho n^2D^4$)
K_T	torque coefficient ($=Q/\rho n^2D^5$)
Ma	Mach number
n	propeller revolutions per second ($=\omega/2\pi$)
p	pressure
Q	torque
R	propeller radius
Re	Reynolds number ($=U_oD/\nu$)
s	distance along chord or pitch helix
S_i,etc.	solution-domain boundaries
T	thrust
U_o	freestream velocity
U_τ	wall-shear velocity
VB	streamwise pitchline velocity in noninertial coordinates ($=W\cos\phi+U\sin\phi$)
ΔVB	wake velocity deficit ($=VB-VB_{min}$)
VN	normal pitchline velocity in noninertial coordinates ($=W\sin\phi-U\cos\phi$)
VR	resultant section inflow $[=U_o^2+(\omega r)^2]^{1/2}$
V	mean-velocity components in inertial or noninertial cylindrical coordinates ($=U,V,W$)
x,r,θ	cylindrical coordinates
y,y^+	normal distances
Δy	wake half width
β	blade angle
δ^*	displacement thickness
θ	momentum thickness
ν	fluid kinematic viscosity
ν_t	eddy viscosity
ξ,η,ζ	nonorthogonal curvilinear coordinates
ρ	fluid density
ϕ	pitch angle
ω_x	axial vorticity
Ω	propeller angular velocity ($=\omega,0,0$)

INTRODUCTION

Marine propulsors are unique in comparison to related applications (e.g., turbomachinery, turboprops, and rotors) in that they operate in the thick hull boundary layer and/or appendage wakes such that complex

naturally (hull flow) and forced (propulsor flow) unsteady interactions occur. In practice, inviscid-flow methods are used that rely on specified effective inflows, the latter of which, until the recent computational fluid dynamics (cfd) interactive approach of [1] was ill-defined. Although successful in providing a rational mechanics framework for calculating the effective inflow, the interactive approach is unable to predict the viscous propulsor blade and wake flow, which motivated the precursory cfd method of [2] that was demonstrated for an idealized propulsor-shaft configuration with infinite-pitch rectangular blades. The present work concerns further developments for realistic SR7 turboprop and marine-propulsor P4119 and P4842 geometries. Also of relevance is the concurrent work for unsteady-flow calculations [3,4].

The work for related applications is impressive, especially with regard to developments for complex configurations, but primarily involves cfd methods for compressible flow [5]. Modifications of these methods for incompressible flow are possible [6,7], but not trivial and problematical for unsteady-flow calculations, such that the present work is a justifiable alternative.

In the following, the computational method and experimental data are described and the computational conditions, grids, and uncertainty are given. Then, the results are discussed for the SR7, P4119, and P4842 for the design and in the former and latter cases off-design conditions. Lastly, some concluding remarks are made, including comparison with inviscid-flow and related methods, prognosis for improvements, and future work.

COMPUTATIONAL METHOD

The unsteady Reynolds-averaged Navier-Stokes (RaNS) and continuity equations with the Baldwin-Lomax turbulence model are solved for the mean-velocity components $V=(U,V,W)$, pressure p, and eddy viscosity ν_t. The transport equations for V are written in noninertial cylindrical coordinates (x,r,θ) rotating with constant angular velocity $\Omega=(\omega,0,0)$ in the physical domain and partially transformed into numerically-generated, boundary-fitted, nonorthogonal, curvilinear coordinates (ξ,η,ζ). Variables are nondimensionalized using the freestream velocity U_0 (=1), propeller diameter D (=1), and density ρ. The transformed equations are solved using a regular grid, finite-analytic discretization, a PISO-type velocity-pressure coupling algorithm, and the method of lines. Although the present solutions are for steady flow, the equations are solved in unsteady form with time serving as a convergence parameter. For laminar flow, $\nu_t=0$ and V and p are interpreted as instantaneous values.

The physical and computational domains are shown in figure 1. The boundary conditions are specified as follows: on the inlet plane S_i, uniform inflow with zero pressure gradient, i.e., $(U,V,W,p_\xi)=(1,0,\omega r,0)$; on the exit plane S_e, which is located in the far wake, axial diffusion is negligible and a zero-gradient condition is used for pressure, i.e., $(V_{\xi\xi},p_{\xi\xi})=0$; on the outer boundary S_o, uniform flow with zero pressure gradient, i.e., $(U,W,p_\eta)=(1,\omega r,0)$ and V is obtained from the continuity equation; on the shaft and blade surfaces S_s, S_{bs}, and S_{bp}, no-slip condition, i.e., $(U,V)=0$ and $W=0$ and ωr for rotating and nonrotating parts, respectively; on the periodic boundary planes S_{ps} and S_{pp}, periodic boundary conditions, i.e., $V/p(\xi,\eta,\zeta)=V/p(\xi,\eta,\zeta+\zeta_p)$ where ζ_p corresponds to the blade-to-blade interval; and on the symmetry axis L_s, symmetry conditions $(V,W)=0$ and $\partial(U,p)/\partial\eta=0$.

The grid was obtained using a modified version of PMESH [8], which employs algebraic methods with transfinite interpolation. H-grids were used with clustering near the shaft and blade surfaces and leading-, trailing-edge, and tip regions.

EXPERIMENTAL DATA

Initially, calculations were made for the SR7; since, PMESH was developed specifically for such geometries and its relatively high pitch (i.e., blade angle) was hoped to be easier to handle. Wind tunnel and flight data are available. In particular: surface-pressure data for a large-scale single-rotation configuration over a range of Mach numbers (Ma) and blade angles [9]; and laser-doppler velocimeter (ldv) data [10] and flow visualization studies [11] for counter-rotation configurations. Comparisons are made with tests 5-8 of [9]. As discussed later, Ma effects and uncertainty in blade angles for the data complicates the comparisons. Also, qualitative comparisons are made with [10,11]. Subsequently, calculations were made for P4119 and P4842 for which, without doubt, the most extensive marine-propulsor data is available, including flow-visualization studies and detailed boundary-layer and wake and tip, hub, and juncture vortex ldv data [12-15]. Calculations and comparisons are made with the complete set

of data. Also, although no data is available, off-design condition calculations were made for P4842. Reviews of other related data are provided by [9-14]. Also of relevance is the recently acquired multiple-blade-row data [16], which was the test case for [6]; however, detailed viscous-flow data is lacking.

COMPUTATIONAL CONDITIONS, GRIDS, AND UNCERTAINTY

The experimental and cfd conditions and propulsor geometries and cfd evaluation and data comparison locations are summarized in table 1 and figure 2. In general, the cfd conditions correspond to those of the data; however, there are some differences, especially for the SR7. For the SR7: the cfd Ma = 0, whereas Ma = .2 and .5 for the data; the Reynolds number ($Re=U_0D/\nu$) values for laminar (10^4) and turbulent (10^6) flow are less than that for the data (10^7), which is for natural transition; and there are differences in the blade-angle β values for which there was large uncertainty for the data, i.e., in addition to the indicated setting-angle ranges, the deformation angles were significant and undocumented. For P4119 and P4842: the cfd is for laminar and turbulent and, in the former case, laminar/turbulent with fixed transition locations based on the data, whereas the data is for both natural and leading-edge roughness transition.

A partial view of the P4842 grid is shown in figure 3 and is similar to those for the SR7 and P4119. The inlet, exit, and outer boundaries for P4119 and P4842 are located at x=(-3,4) and (-3,8), respectively, and r=2. The first grid points off the body surface are located in the range y^+ ($=ReU_\tau y_n$)<6 (P4119) and 10-20 (P4842). The grid distributions are 105x46x52=251160 (P4119) and 115x51x46 =269790 (P4842). The P4119 and P4842 grids are relatively fine and coarse, respectively, with regard to resolution of the blade boundary layer due to the differences in y^+ values for the first grid points off the body surface. The values of the time increment and underrelaxation factors for velocity and pressure are: .01; .5; and .1. The CRAY C90 time and central memory were about 25 min per 1000 global iterations and 25 mw. The convergence criterion was that the residual for all variables be about 10^{-4}, which was satisfied in about 500-1000 global iterations for the laminar solutions and an additional 500 global iterations for the turbulent solutions.

The following discussions are based on the complete results, which, as indicated in figure 2, are extensive; however, for brevity, only representative results are shown. Additional results are available upon request from the authors. The focus concerns the cfd and comparisons to the design-condition data with the terminology implied unless necessary for clarity. Lack of comparisons indicates lack of data.

SR7

The performance is also shown in table 1. The J and β trends are similar to the data; however, quantitative comparison is precluded due to the large uncertainty in β for the data. The turbulent vs. laminar solutions display smaller C_P values.

Typical surface-pressure distribution results for Test 7 are shown in figure 4, which are also indicative of the trends for Tests 5, 6, and 8. For design loading (i.e., for Tests 5 and 8 and at the inner radii for Tests 6 and 7 where the loading is relatively constant over the chord), satisfactory agreement is observed, whereas for off-design loading (i.e., at the outer radii for Tests 6 and 7 where large leading-edge and tip-region suction peaks are observed due to the influence of leading-edge and tip vortices), the agreement is less satisfactory due to the lack of resolution of the suction peaks. The $\beta=63.5^o$ particle traces (figure 5) display the nature of the predicted three-dimensional boundary layer with vortical/separation regions, including leading-edge and tip vortex and trailing-edge root separation, which is similar with the observed flow pattern; however, the surface-streamline patterns lack the details of the data with regard to the detachment/attachment lines. The overall and near-wake flow patterns are similar with expectation and data, respectively (e.g., evolution of blade boundary layers and wakes, tip vortex formation and trajectory, hub effects, etc.).

In summary, the design-loading results appear to be satisfactory, whereas the off-design results are not due to the lack of resolution of the leading-edge and tip vortex; however, geometric differences and uncertainty and lack of Ma effects (increased suction peaks and shock waves) and data precludes a definitive evaluation.

P4119 AND P4842

The predicted performance for the design (and off-design) condition is within 5-10% of the data, which is considered satisfactory in view of the present grid resolution and turbulence model, which is, in general, the case throughout the following discussions (see Concluding Remarks for discussion of prognosis for improvements)

and the differences between the present hub geometry and that used for the open-water tests and the fact that the data represents the difference between the measured propeller and hub-only loads.

Consistent with the performance predictions, figure 6a shows close agreement for the P4119 design-condition surface-pressure distributions, except at the inner radii near the trailing edge, which is likely because the data is based on velocity measurements at the boundary-layer edge and the Bernoulli equation and viscous effects are substantial in this region (i.e., trailing-edge root separation). The P4842 design-condition and inviscid-calculation results at mid-span show close agreement, whereas near the tip the differences are significant, which, here again, is likely due to viscous effects. For the off-design condition, suction and pressure peaks are indicated near the leading edge. The pressure contours (figure 6b) display the overall distributions and significant effects of geometry, i.e., differences between the P4119 and P4842 loading (larger loading per blade for P4842 than P4119, except near the hub and tip), pitch and skew distributions (P4119 has nearly constant pitch and zero skew, whereas P4842 has extreme variations of pitch and skew), number of blades (P4119 has 3 blades, whereas P4842 has 5 blades), hub geometry, etc.

The P4119 design-condition surface streamlines show remarkably close agreement: demarcation of regions of laminar/turbulent flow by increased/reduced radial-velocity magnitude; similarity between natural and leading-edge roughness transition and laminar/turbulent and turbulent flows, respectively; and trailing-edge root separation. Figure 7a shows the P4842 design-condition turbulent flow surface streamlines. The laminar patterns are similar. The patterns are complex in comparison to those for P4119, especially on the suction side, indicating profound geometry effects: leading-edge and tip vortices, large regions of significant spanwise flow, and trailing-edge root separation. For the off-design condition, the spanwise flow and regions of trailing-edge root separation and leading-edge and tip vortices are increased. There is a direct correspondence between the vortical/separation and low pressure regions (cf. figures 6b and 7). Figure 7b shows the design-condition data, which, although similar in many respects to figure 7a, indicates less spanwise flow.

Figure 8 shows wall-shear stress contours, which are consistent with expectation in indicating the fixed transition locations and boundary-layer thickening and vortical/separation regions.

Figure 9 shows the circumferential-average velocity profiles. Close agreement is observed for many aspects, including upstream (extent, axial acceleration, hub-induced outward radial flow, and preswirl flow) and downstream (very significant axial acceleration, radial contraction, and swirl flow) influences. However, the upstream and far downstream radial flow is under predicted and the inner/outer swirl flow is under/over predicted. Figure 10 shows the radial circulation distribution deduced from the swirl profile with differences consistent with the differences in the swirl profiles. Note the increased tip loading for P4119 vs. P4842. The off-design results shown in figures 9 and 10 display the increased loading effects and are consistent with expectation.

Figures 11-13 show the phase-averaged flow for P4119 for upstream, mid-chord, and downstream planes, respectively, including both noninertial and inertial coordinates and velocity components (VB,V,VN) and (U,V,W), respectively. For the upstream plane: the pitchline- and axial-velocity contours display leading-edge stagnation effects, which are largest at the closest proximity to the blade (i.e., at the root) and the blade-to-blade axial acceleration, which is largest at a position approximately midway between the blades and r/R=.7; the cross-plane vectors and particle traces indicate inward/outward radial flow in the stagnation region for the inner (r/R<.5) and outer (r/R>.5) radii, respectively, whereas in the blade-to-blade region the flow is primarily tangential towards the position of maximum axial acceleration (inertial) and clockwise, including a hub/root vortex close to the pressure side (noninertial); the pressure contours correlate with the axial-velocity contours, but with reverse trend in magnitude; and the detailed circumferential velocity profiles are in close agreement. Note that the far-upstream plane primarily displayed the influences of the rotating shaft with minimal influence of the propeller.

For the mid-chord plane: the pitchline- and axial-velocity contours display the low-velocity blade and hub boundary layers and tip-vortex region and the blade-to-blade axial acceleration with relatively larger values on the suction vs. the pressure side; the cross-plane vectors and particle traces (noninertial and inertial) indicate outward radial flow for both the pressure and suction boundary layers, except in the latter case, near the tip due to the effects of the tip vortex and the nature of the clockwise (i.e., pressure- to suction-side flow) passage and

tip vortices; the pressure contours display the blade loading and correlation with the axial-velocity contours and cross-plane vectors; and the pitchline- and axial-vorticity contours display relatively large values confined to the blade and hub boundary layers and tip-vortex region.

For the downstream plane: the pitchline- and axial-velocity contours display the low-velocity blade wake, hub boundary layer, and tip-vortex region and the blade-to-blade axial acceleration albeit with reduced magnitudes; the cross-plane vectors and particle traces (noninertial and inertial) indicate complex sheared flow within the blade wake (i.e., upward flow on the suction side and downward/upward flow on the pressure side for the inner (r/R<.7) and outer (r/R>.7) radii, respectively, whereas in the blade-to-blade region the flow is primarily tangential from the pressure to the suction side and the nature of the clockwise evolving tip vortex and hub/root vortex close to the suction side; the pressure contours indicate relatively lower/higher pressure within the hub boundary layer and tip vortex and blade wake, respectively; the pitchline- and axial-vorticity contours are similar to the mid-chord plane, but with increased extent and reduced magnitude; and the detailed circumferential profiles indicate over/under prediction of the wake width/deficit and lack of detailed resolution of the tip and hub/root vortices. Note that the trends for the far-downstream plane are similar to those just described, but with physical and considerable numerical dissipation such that due to the latter a reduction is shown in the resolution of the flow and agreement with the data.

The trends for P4842 are similar and consistent (figure 14); however, certain differences are apparent due to the significant effects of geometry: reduced influence at the upstream and downstream planes, except near r/R=.6 and .8, respectively, due to the differences in blade proximity; increased hub effects, including outward radial flow; and increasingly distorted flow patterns with downstream distance (stagnation flow, blade-to-blade flow, boundary layers and wakes, and tip and hub/root vortices), which roughly follow the blade skew/pitch distributions, apparently resulting in increased mixing. The off-design results are similar, but more exaggerated, which is the case, in general, such that they will not be further discussed.

Figures 15-18 show the boundary-layer development for P4119 for r/R=(.7,.9,.95,.975), respectively. Pressure-gradient and three-dimensional effects (i.e., overall outward radial flow and tip-vortex effects) are evident. The trends for both laminar and laminar/turbulent flow are similar, but with increased boundary-layer thickness for the latter case. On the suction side, the displacement thickness initially reduces (0<x/c<.6) and then rapidly increases (.6<x/c<1). The thickness increases towards the outer radii. On the pressure side, the displacement thickness gradually increases from the leading to trailing edge, except for r/R=(.9,.95,.975) where there is a small reduction near the trailing edge The thickness reduces towards the outer radii. The chordwise trends are consistent with the pitchline-pressure gradients and further exhibited by the pitchline-velocity profiles. Similarly, the radial trends are consistent with the radial-pressure gradients and further exhibited by the radial-velocity profiles. On the suction side: near the leading edge, the profiles are S-type with large outward values near the blade, whereas from mid-chord to the trailing edge the profiles become inward with increasing magnitude towards the outer part of the boundary layer and trailing edge, especially for r/R=(.9,.95). On the pressure side, the profiles display large outward values, especially near the blade, with increasing magnitude towards the trailing edge and outer radii. In general, the data shows similar trends; however, some differences are evident: differences in edge values, which is surprising in view of the close C_p agreement; reduced displacement thickness near the trailing edge for the outer radii on suction side; and complex pitchline-velocity profiles for r/R=.975 with large velocity deficits near the trailing edge.

Figure 19 shows the wake development for P4119 for r/R=(.7,.9). The nature of the wake recovery is displayed, including significant three-dimensional effects (recall earlier discussion of the cross-plane vectors within the blade wake at the downstream plane). Figure 20 shows the wake deficit, half width, and momentum thickness parameters, which, interestingly, follow two-dimensional correlations. Also shown is the radial distribution of the section drag coefficient, which also follows two-dimensional correlations for the outer radii, but not the inner radii due to the effects of the trailing-edge root separation and, additionally, indicates smaller/larger values for the inner/outer radii than inferred from the momentum thickness. The agreement with the data is similar as described earlier for the phase-averaged flow for the downstream and far-downstream planes.

Note that the trends for the inner radii (e.g., r/R=.3) show differences due to the effects of the trailing-edge root separation and passage and hub/root vortices: rapid increase of displacement thickness on the suction side near the trailing edge; large outward radial velocities on both sides near the blade surface with

increasing magnitude towards the trailing edge and inward radial velocities across the boundary layer on the pressure side with increasing magnitude towards the trailing edge; and large wake deficits and half widths and sheared radial velocities.

The trends for P4842 (figures 20-21) display significant differences: complex boundary-layer flow with increased three-dimensionality and rapid wake recovery, which is consistent with the surface streamlines and phase-averaged flow, respectively. In particular: on both sides, the displacement thickness is nearly constant along the chord, except near the trailing edge where it rapidly increases; on the suction side, the displacement thickness increases from r/R=.5 to .7, which corresponds to the region of significant spanwise flow, and then reduces from r/R=.7 to .9, whereas on the pressure side, the displacement thickness is large at r/R=.5, which corresponds to the region of trailing-edge root separation, and then reduces towards the outer radii r/R=.7 and .9; the radial-velocity profiles display large values and inward/outward variations along the chord; and initially larger ($s/\theta<150$) and subsequently ($s/\theta>150$) smaller deficits, overall significantly (i.e., order of magnitude) larger half widths, and smaller momentum thickness, except near the tip region.

Lastly, the details of the tip-vortex development and evolution are considered (figure 22). The tip-region velocity profiles for P4119 display the earlier referenced lack of detailed resolution of the tip vortex, i.e., the vortex is not fully resolved and diffused over a broader area. The vectors display the roll-up process, which initiates at about x/R=0 with subsequent intensification and inward radial and outward tangential migration off the blade surface. The parameters indicate the level of the maximum vorticity and circulation, core size, contraction, and angular and pitch trajectory. The trends are in agreement; however, the maximum values and contraction are under predicted, whereas the core size is over predicted.

Here again, the trends for P4842 display significant differences: the intensity of the roll-up process is reduced and elliptically shaped; large reductions in maximum values, radial core size, and contraction; and differences in angular and increased pitch trajectory.

CONCLUDING REMARKS

Viscous-flow results have been presented for the realistic SR7 turboprop and marine-propulsor P4119 and P4842 geometries, including both design and off-design conditions. For the design condition, overall close agreement with the data is shown for the performance, pressure and surface-streamline distributions, circumferential-average velocity profiles, phase-averaged flow, boundary-layer and wake development, and tip and hub/root vortices, including the significant effects of geometry. However, some differences are evident, which indicate lack of detailed resolution, e.g., certain aspects of the tip and hub/root vortices and boundary-layer and wake development. For the off-design condition, the results are similar and consistent with expectation, but, with increased effects of lack of detailed resolution. The extensive results enable explication of the nature of the complex three-dimensional viscous propulsor blade and wake flow.

The work has successfully demonstrated the ability of cfd in simulating marine-propulsor flow, including not only the usual inviscid-flow quantities (i.e., performance, pressure distributions, and circumferential and phase-averaged flow), but, additionally, the viscous blade and wake flow (i.e., boundary layers and wakes and tip, hub/root, and passage vortices). The accuracy is at least as good as the inviscid methods, especially in view of the present grid resolution and turbulence model, without the necessity of their ad hoc parameters (i.e., empirical viscous corrections) and superior to the earlier mentioned related work with regard to detailed resolution of the viscous flow. Furthermore, applications to design, including development of tip-vortex reduction schemes and minimization of blade wake interactions with downstream appendages etc. and extensions for off-design conditions, backing and crashback, and propulsor-body interactions are surely possible, including unsteady-flow calculations, without, in the case of propulsor-body interactions, requiring the specification of the fictitious effective wake.

Of course, improvements are expected through the incorporation of more advanced grid techniques (e.g., overlaid grids), turbulence modeling (e.g., Reynolds-stress models), and higher-order discretization procedures; however, these are the pacesetting issues of cfd such that it is recommended that such improvements be carried out in conjunction with extensions for unsteady-flow calculations, especially in view of the unique requirements for such simulations (e.g., unsteady turbulence models). As already pointed out, concurrent work on this topic is already underway, including a companion paper at this conference [4].

Lastly, more detailed boundary-layer data, including leading-edge and hub/root regions

and radial velocities, and turbulence data is imperative for further validation.

ACKNOWLEDGMENTS

This research was sponsored initially by ONR/DARPA SUBTECH Program Contract N00014-89-J-1342 under the administration of Dr. E. Rood and Mr. G. Jones and completed by ONR Grant N00014-92-J-1118 under the administration of Mr. Jim Fein. Computer funds were provided by the NASA Numerical Aerodynamic Simulation Program and by ONR NAVOCEANO Primary Oceanographic Prediction System.

REFERENCES

1. Stern, F., Kim, H.T., Zhang, D.H., Toda, Y., Kerwin, J., and Jessup, S., "Computation of Viscous Flow around Propeller-Body Configurations: Series 60 C_B = .6 Ship Model," J. Ship Research, Vol. 38, No. 2, June 1994, pp. 136-156.

2. Kim, H.T. and Stern, F., "Viscous Flow around a Propeller-Shaft Configuration with Infinite-Pitch Rectangular Blades," J. Propulsion Vol. 6, No. 4, 1990, pp. 434-444.

3. Paterson, E. G., "Computation of Natural and Forced Unsteady Viscous Flow with Application to Marine Propulsors," Ph.D. Thesis, Department of Mechanical Engineering, The University of Iowa, Iowa City, Iowa, May 1994; also, in part, Paterson, E. and Stern, F., "Computation of Unsteady Viscous Flow with Application to the MIT Flapping-Foil Experiment," Proceedings 6th International Conference on Numerical Ship Hydrodynamics, Iowa City, Iowa, August 1993.

4. Chen, B. Stern, F., and Kim, W.J., "Computation of Unsteady Viscous Marine Propulsor Blade and Wake Flow," Proc. 20th ONR Symposium on Naval Hydrodynamics, Santa Barbara, CA, August 1994.

5. Hall, E.J. and Delany, R.A., "Investigation of Advanced Counterroatation Blade Configuration Concepts for High Speed Turboprop Systems," NASA Contracter Report 187126, January 1993.

6. Dreyer, J.J. and Zierke, W.C., "Solution of the Average-Passage Equations for the Incompressible Flow Through Multiple-Blade-Row Turbomachinery," Applied Research Laboratory, Technical Report No. TR 94-05, February 1994.

7. Uto, S., "Computation of Incompressible Viscous Flow around a Marine Propeller," J. SNAJ, May 1993.

8. Warsi, S.A., "User's Guide to PMESH-A Grid-Generation Program for Single-Rotation and Counterrotation Advanced Turboprops," NASA Contractor Report 185156, December 1989.

9. Bushnell, P., "Measurement of the Steady Surface Pressure Distribution on a Single Rotation Large Scale Advanced Prop-Fan Blade at Mach Numbers from 0.03-0.78," NASA Contractor Report 182124, July 1988.

10. Podboy, G.G. and Krupar, M.J., "Laser Velocimeter Measurements of the Flowfield Generated by an Advanced Counter-Rotating Propeller," AIAA Paper 89-0434, January 1989.

11. Vaczy, C.M. and McCormick, D.C., "A Study of Leading Edge Vortex and Tip Vortex on Propfan Blades," ASME J. Turbomachinery, Vol. 109, No. 3, July 1987, pp. 325-331.

12. Jessup, S.D., "Local Propeller Blade Flows in Uniform and Sheared Onset Flows Using LDV Techniques", Proc. 15th ONR Symposium on Naval Hydrodynamics, Hamburg, Germany. 1984.

13. Jessup, S.D., "An Experimental Investigation of Viscous Aspects of Propeller Blade Flow," Ph.D. Thesis, The Catholic University of America, 1989.

14. Jessup, S.D., "Propeller Blade Flow Measurements Using LDV," ASME Fluids Engineering Division Summer Meeting, Lake Tahoe, Nevada, June 1994.

15. Jessup, S.D., private communications.

16. Zierke, W.C., Straka, W.A., and Taylor, P.D., "The High Reynolds Number Flow Through an Axial-Flow Pump," Applied Research Laboratory, Technical Report No. TR 93-12, November 1993.

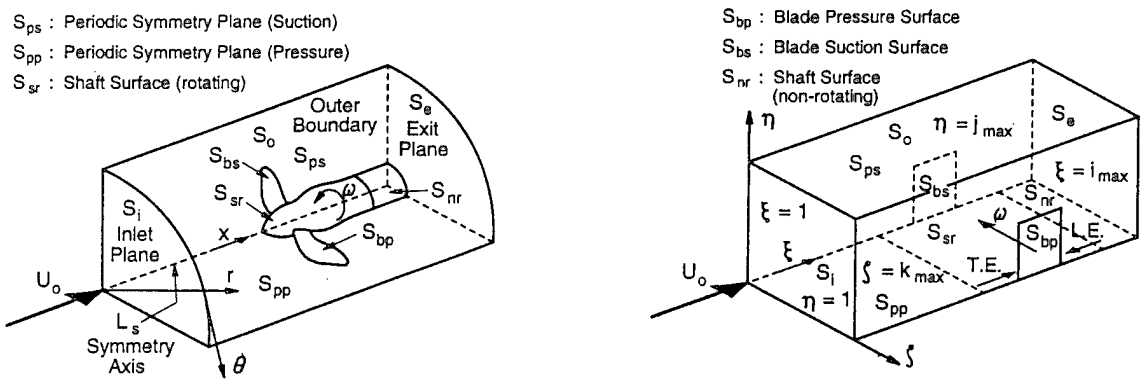
Table 1. Experimental and computational conditions and performance

SR7

	Test	Ma	Re	J	β	Cp	% error	Conditions
Exp.	5	.2	$1.3x10^7$	.88	26.6±1	.1±.002		Cutback
	6	.2	$1.3x10^7$	.883	31.3±.9	.25±.001		Take off
	7	.5	$3.2x10^7$	3.083	58.5±1	.642±.009		Ma,J=const.
	8	.5	$3.2x10^7$	3.067	55.1±.8	.361±.005		$\beta\downarrow \Rightarrow Cp\downarrow$
Calculation	5	0	10^4 10^6	.8926 .8926	26.5 26.5	.144 .100	44 0	
	6	0	10^4	.8951	31.5	.1889	24	
	7	0	10^4 10^6 10^6	3.105 3.105 3.101	59.5 59.5 63.5	.5469 .5228 .8157	15 19 21	
	8	0	10^4 10^6	3.091 3.091	56.0 56.0	.3402 .2596	6 28	

P4119 and P4842

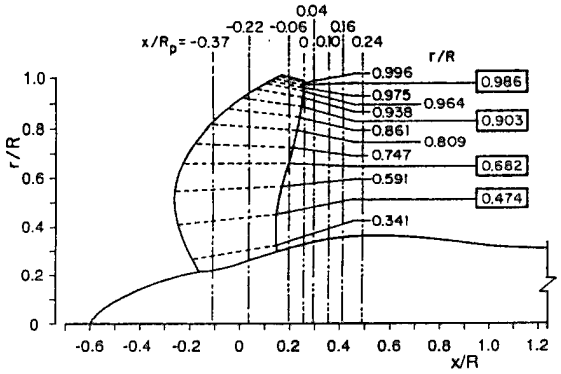
			Re	J	K_T	K_Q	η_0
P4119	design	Open water test	$7.67x10^5$	.833	.146	.0280	.692
		LDV data					
		Cal. laminar % error			.157 7.53	.0284 1.43	.733 5.92
		Cal. lam./turb. % error			.153 4.79	.0282 .71	.720 4.05
P4842	design	Open water test	$6.07x10^5$	.886	.310	.072	.62
		LDV data	$1.29x10^6$				
		Cal. laminar % error			.299 3.55	.0636 11.6	.662 6.77
		Cal. lam./turb. % error			.297 4.19	.0639 11.3	.656 5.81
	off design	Open water test	$6.07x10^5$	.7974	.350	.0779	.586
		Cal. laminar % error	$1.29x10^6$		.349 .29	.0723 7.19	.612 4.44
		Cal. lam./turb. % error			.342 2.29	.0712 8.60	.610 4.10



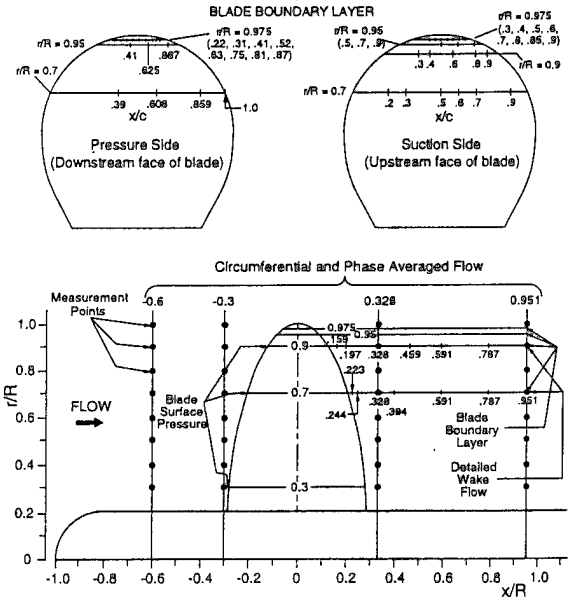
(a) physical domain

(b) computational domain

Figure 1. Definition sketch.

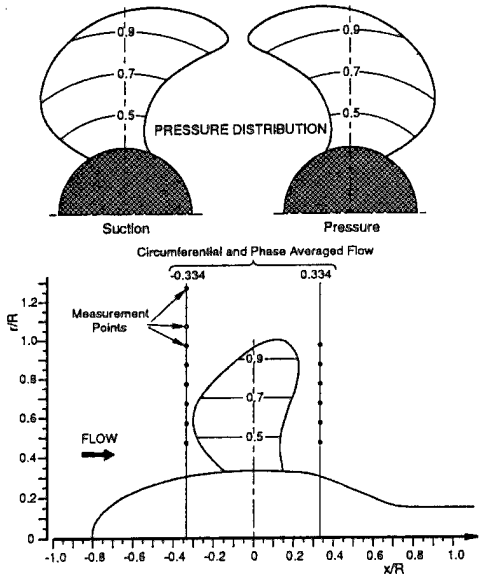


(a) SR7



(b) P4119

Figure 2. Propulsor geometries and summary of cfd evalution and data locations.



(c) P4842

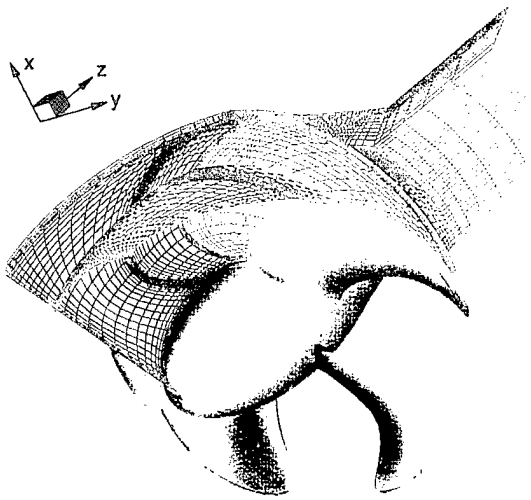


Figure 3. Computational grid: P4842.

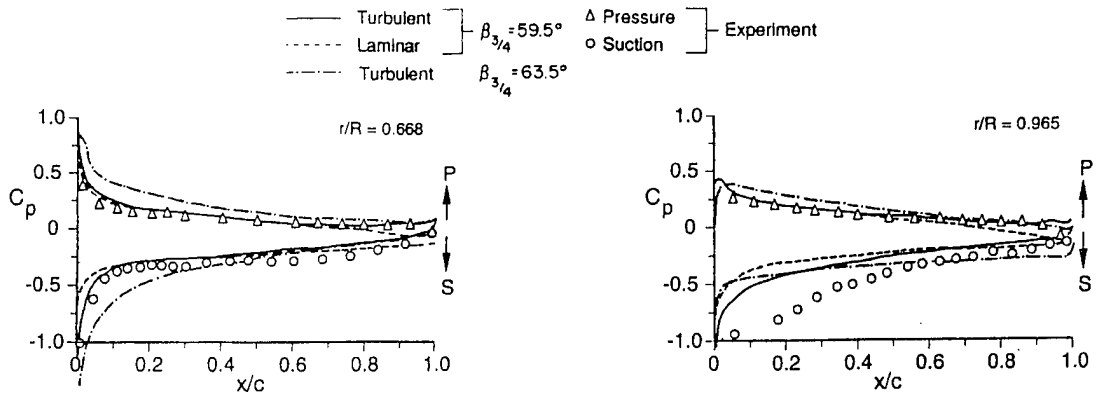


Figure 4. Surface-pressure distributions: SR7, Test 7.

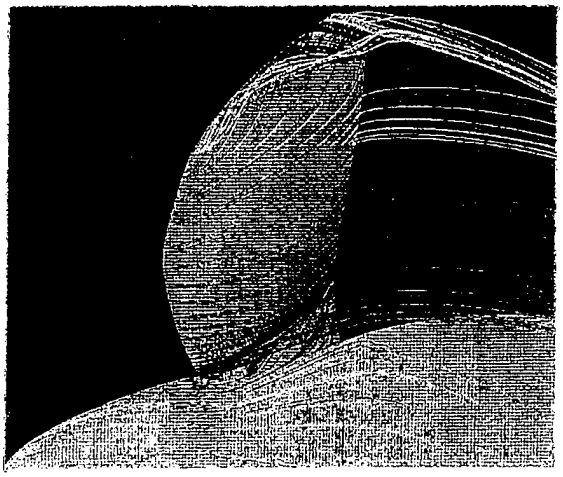
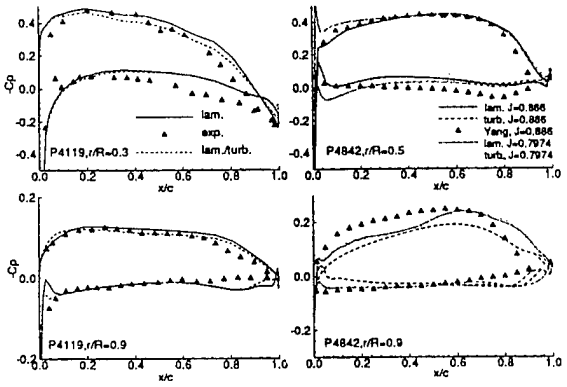
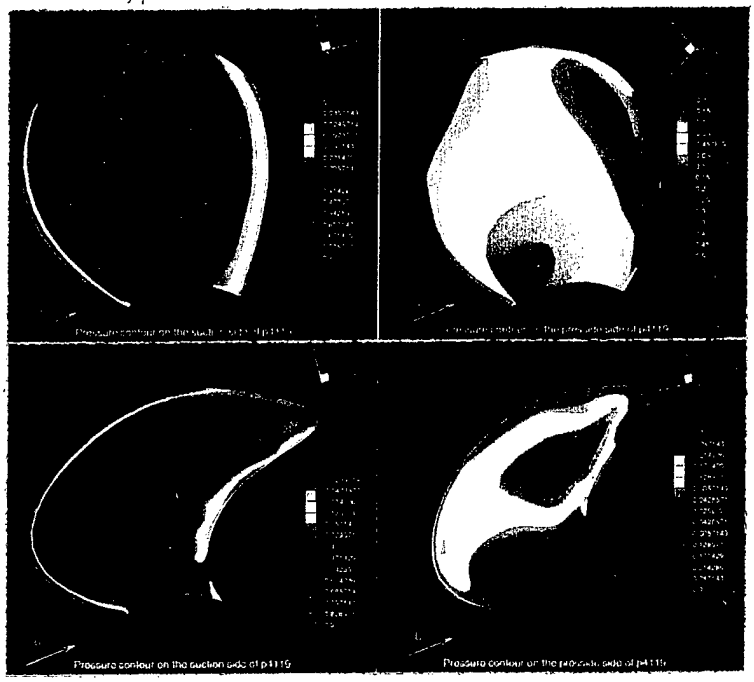


Figure 5. Particle traces: SR7, Test 7, turbulent flow, β = 63.5°.

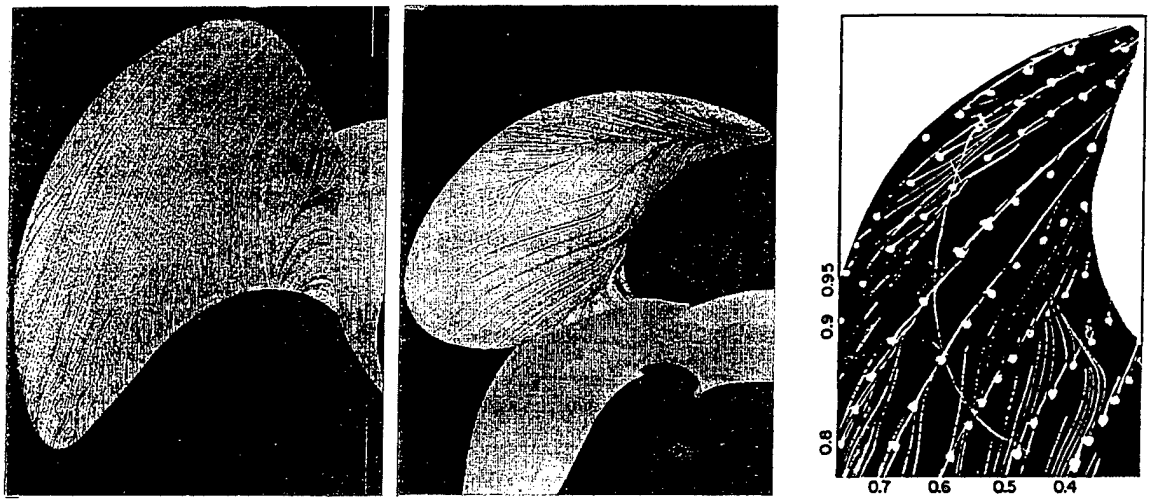


(a) profiles



(b) contours

Figure 6. Surface-pressure distributions: P4119, P4842.



(a) cfd, turbulent flow (b) data

Figure 7. Surface-streamlines: P4842.

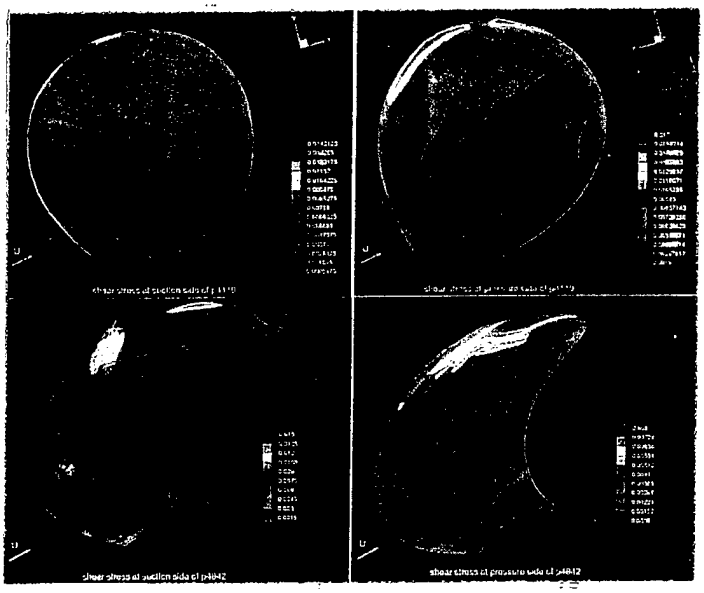


Figure 8. Wall-shear stress contours: P4119, P4842.

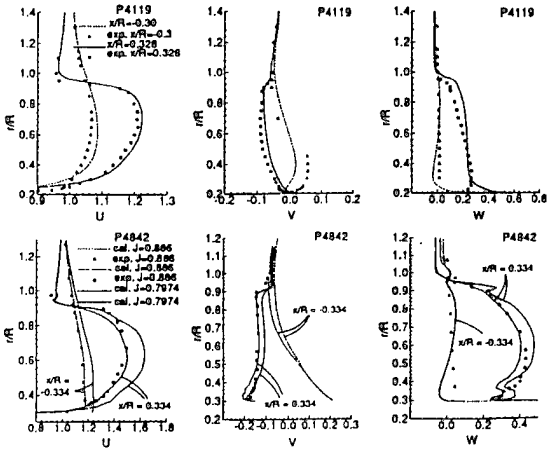


Figure 9. Circumferential-average velocity profiles: P4119, P4842.

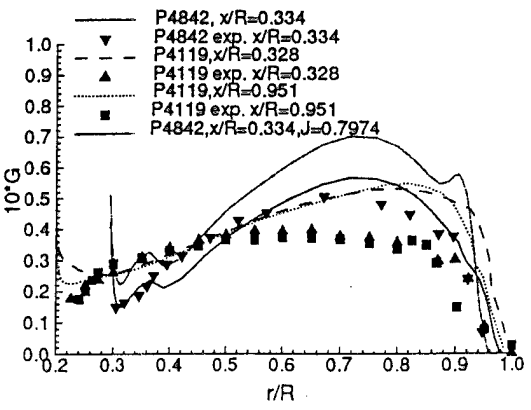
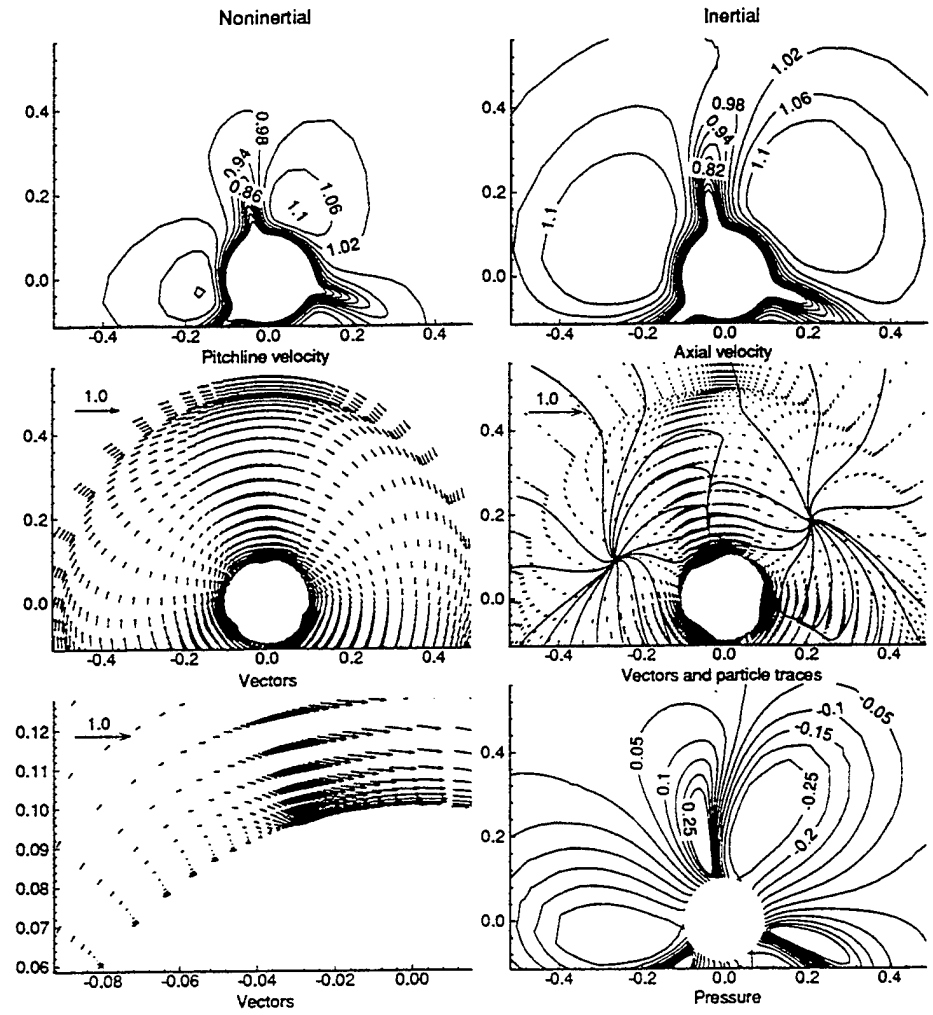
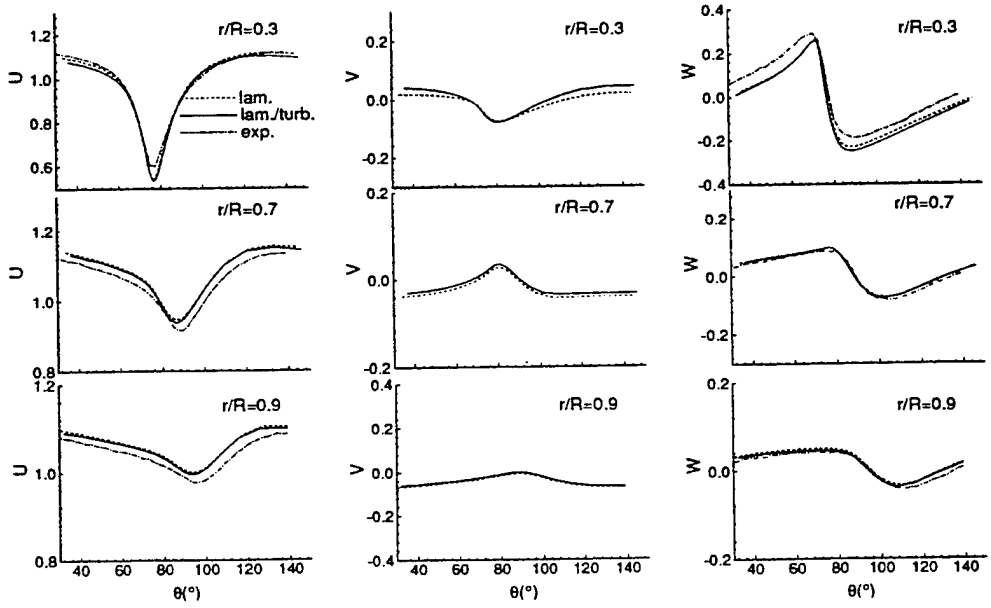


Figure 10. Circulation profiles.



(a) contours and vectors



(b) velocity profiles

Figure 11. Phase-averaged flow: P4119, x/R = -0.3.

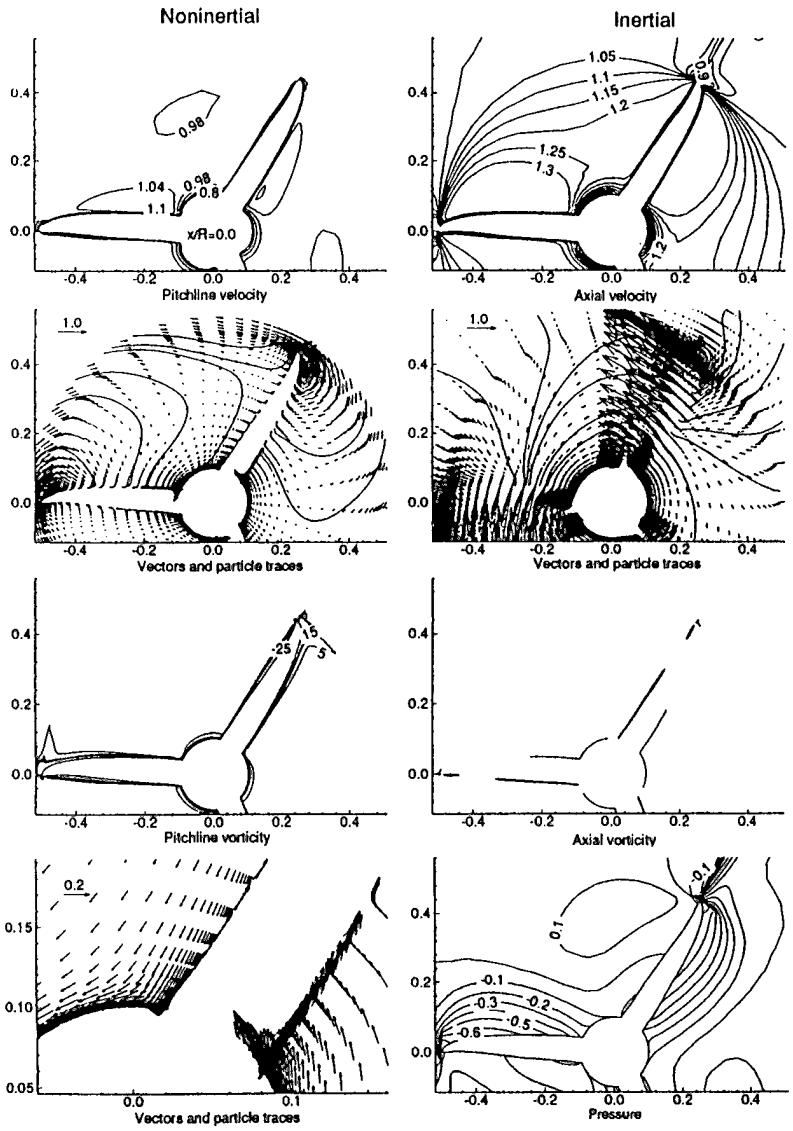
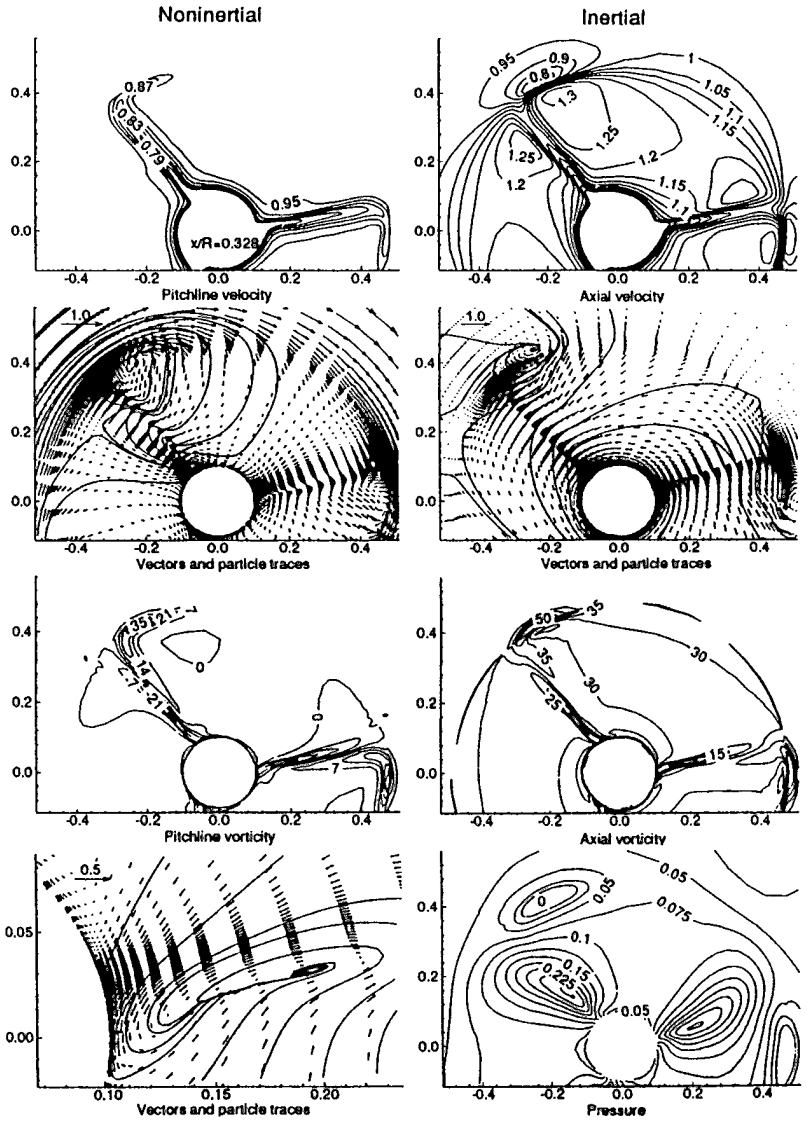
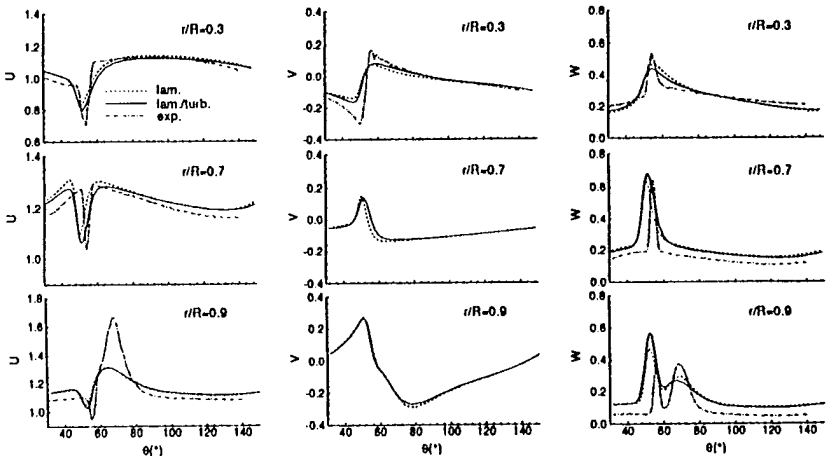


Figure 12. Phase-averaged flow: P4119, x/R = 0, contours and vectors.



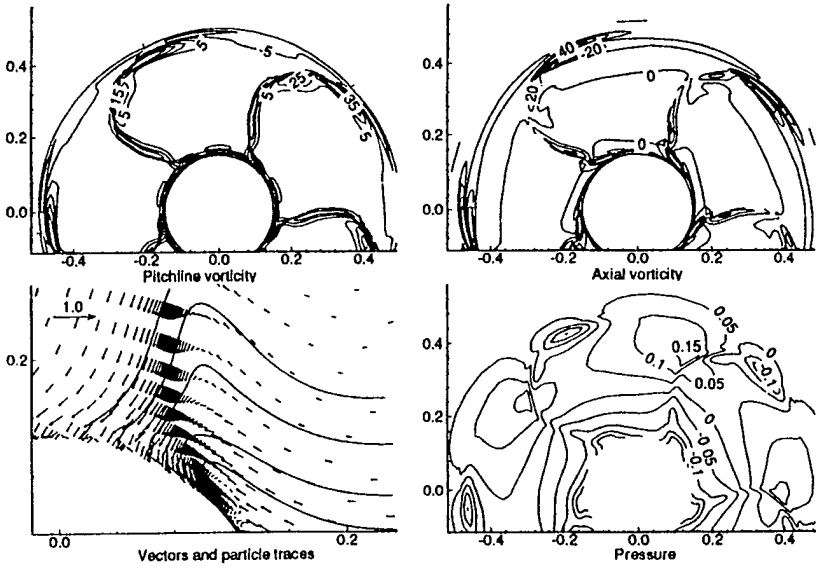
(a) contours and vectors

Figure 13. Phase-averaged flow: P4119, x/R = 0.328.

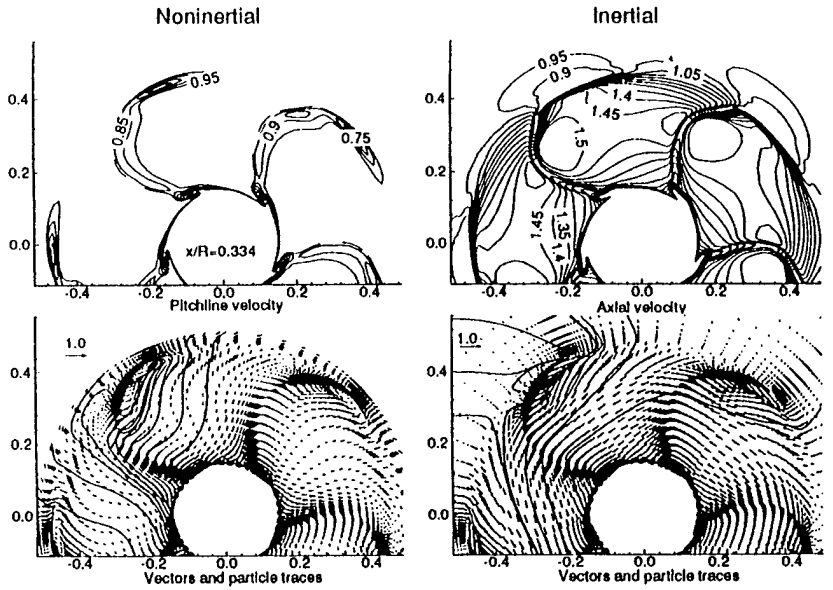


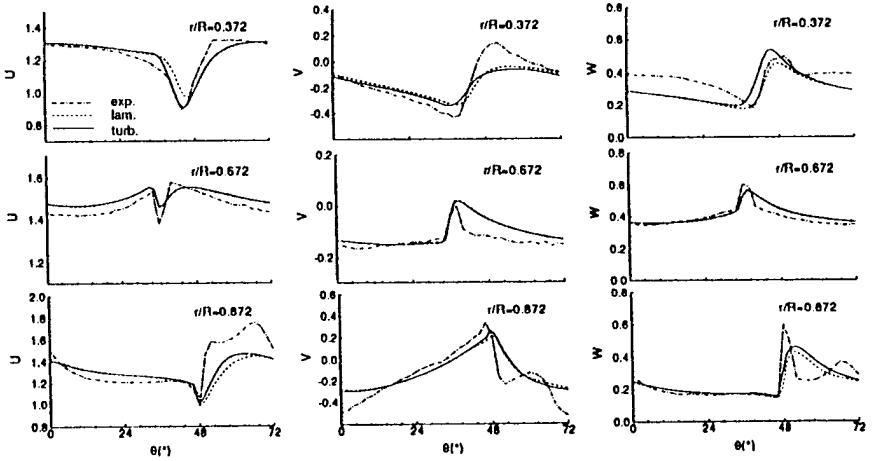
(b) velocity profiles

Figure 13. Concluded.



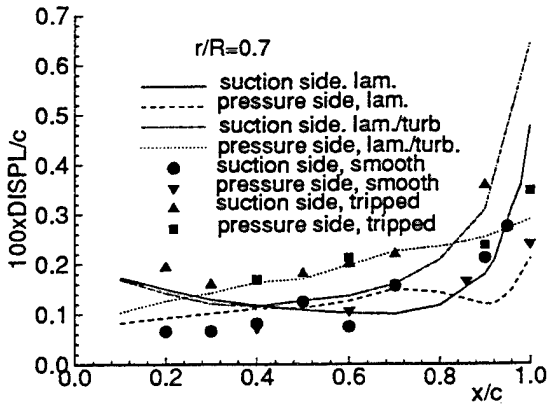
(a) contours and vectors



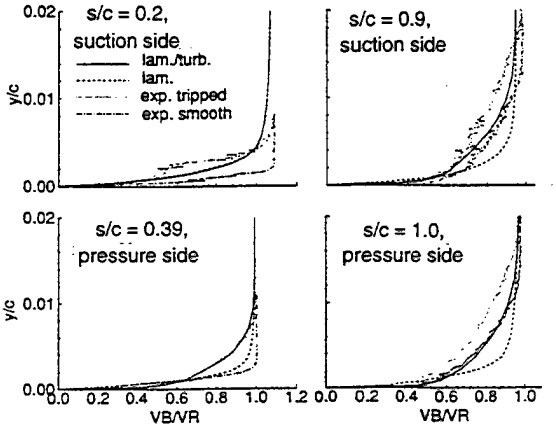


(b) velocity profiles

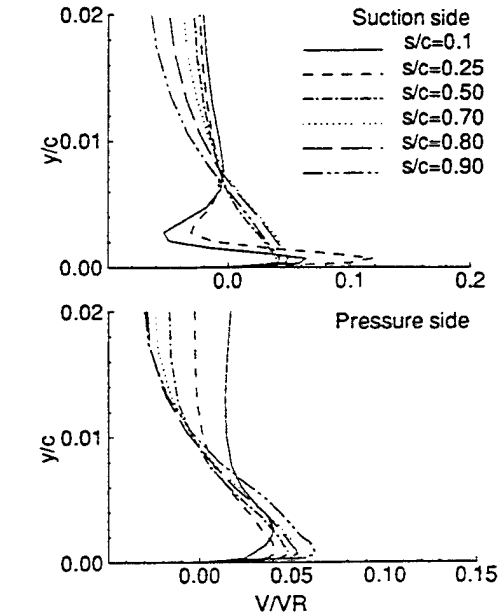
Figure 14. Phase-averaged flow: P4842, x/R = 0.334.



(a) displacement thickness

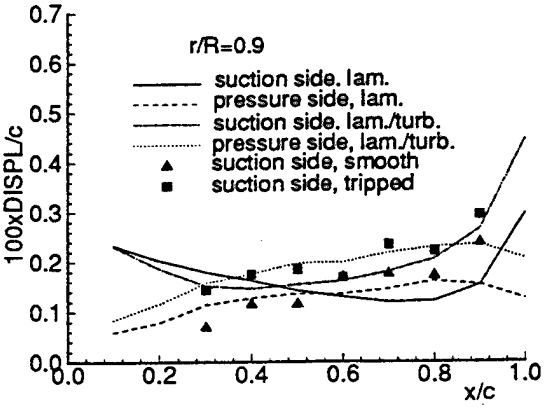


(b) pitchline-velocity profiles

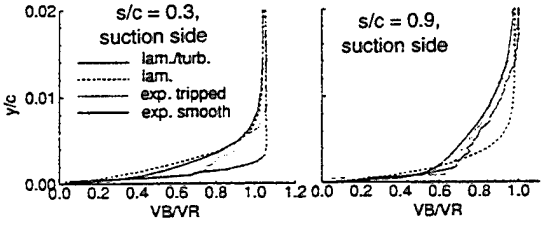


(c) radial-velocity profiles

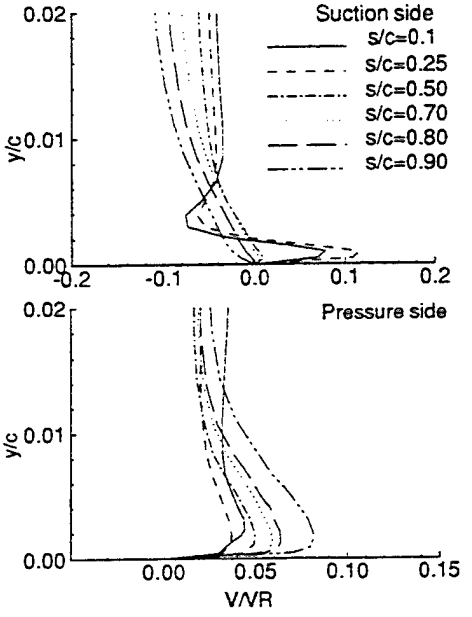
Figure 15. Boundary-layer flow: P4119, r/R = 0.7.



(a) displacement thickness

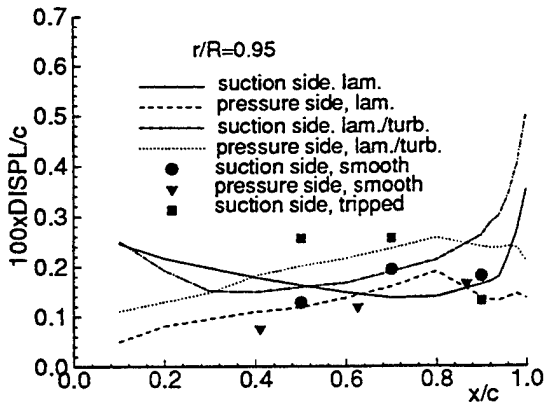


(b) pitchline-velocity profiles

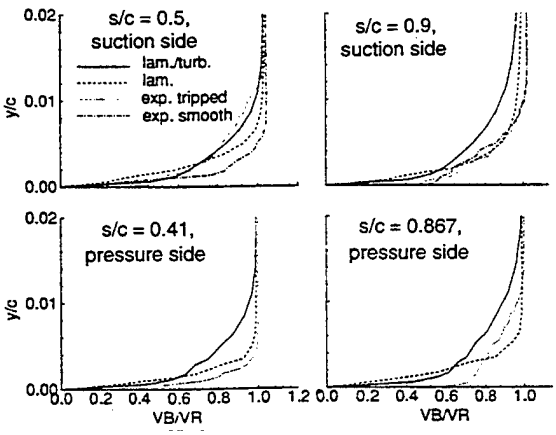


(c) radial-velocity profiles

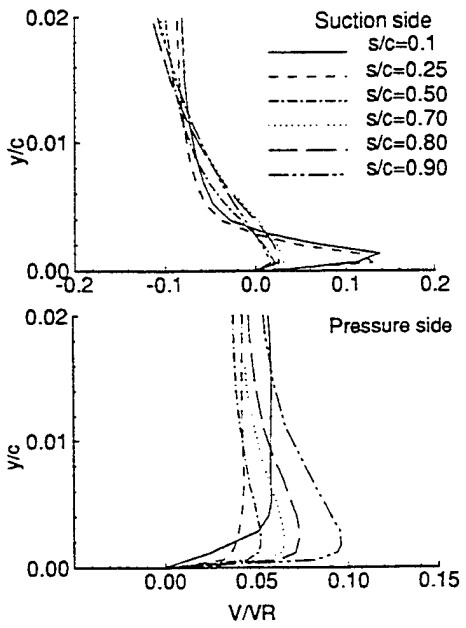
Figure 16. Boundary-layer flow: P4119, r/R = 0.9.



(a) displacement thickness

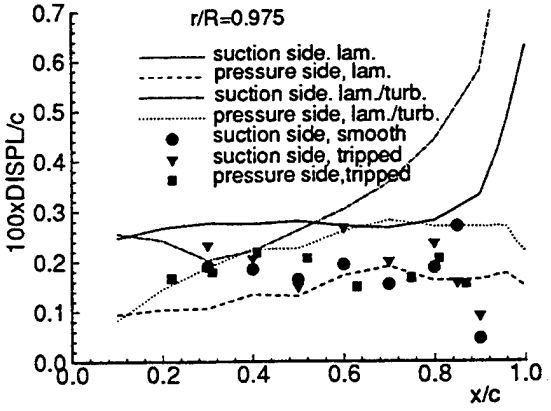


(b) pitchline-velocity profiles

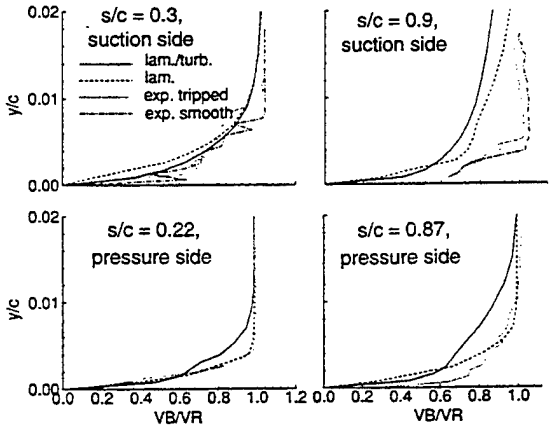


(c) radial-velocity profiles

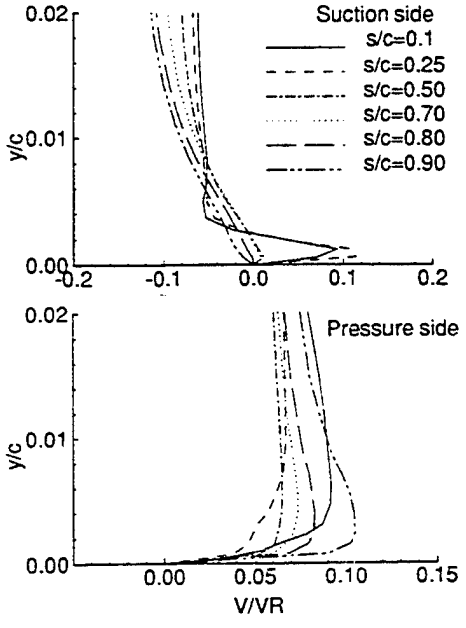
Figure 17. Boundary-layer flow: P4119, r/R = 0.95.



(a) displacement thickness

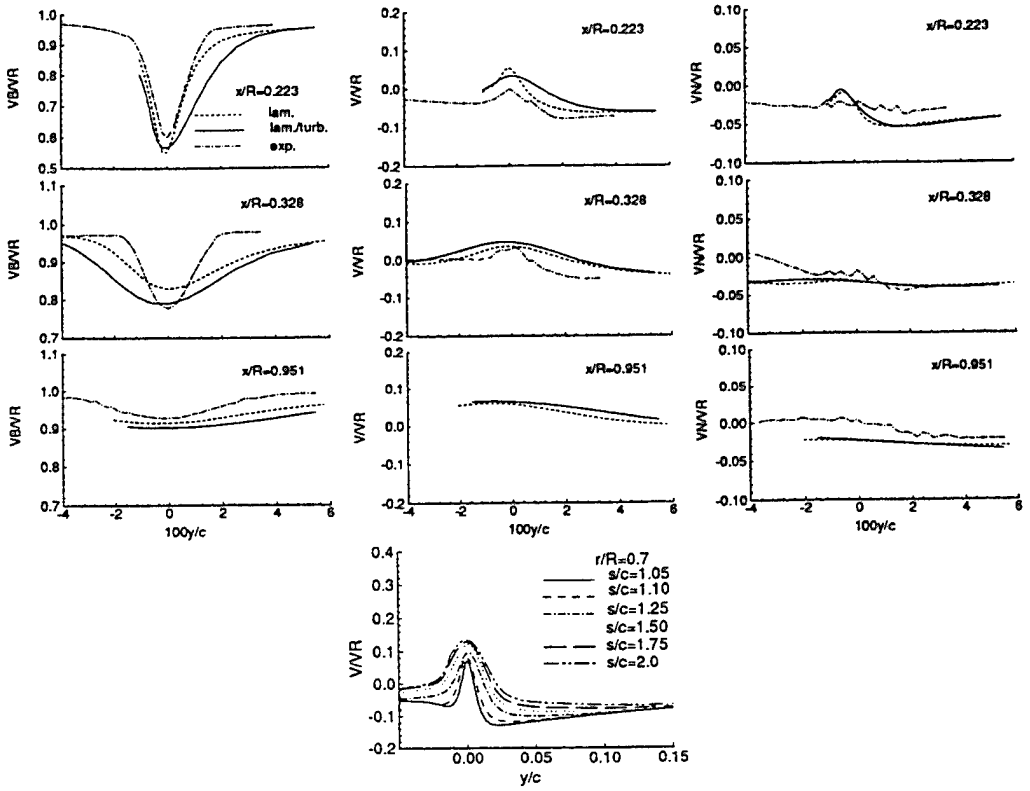


(b) pitchline-velocity profiles

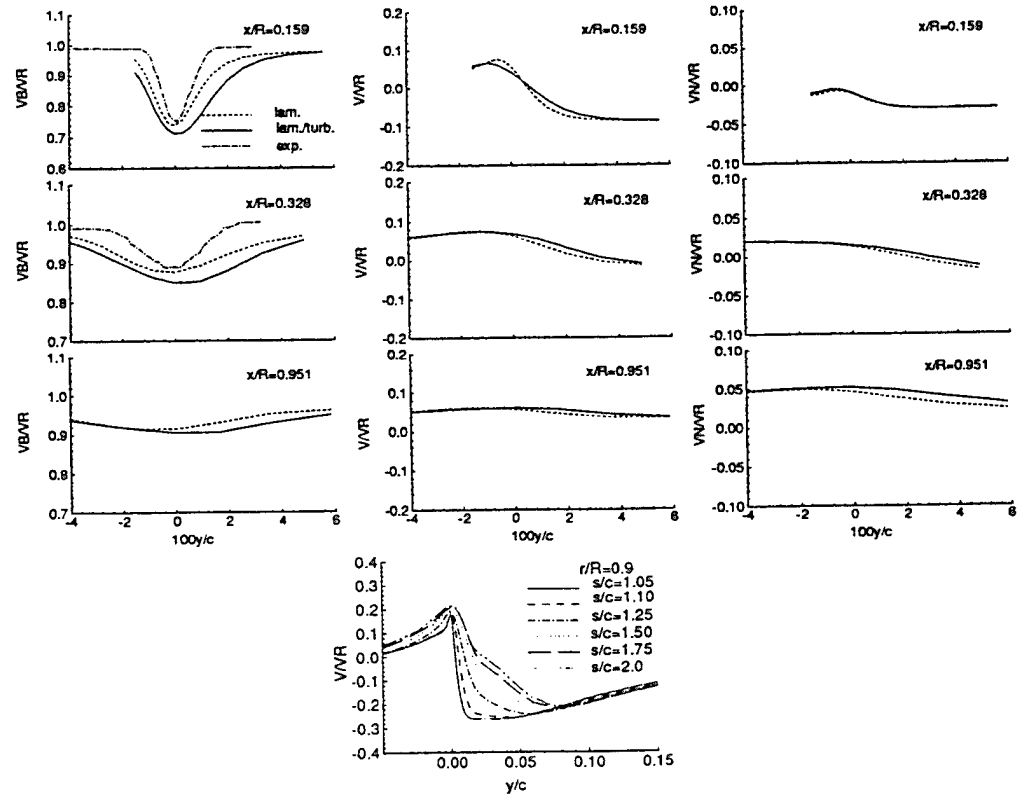


(c) radial-velocity profiles

Figure 18. Boundary-layer flow: P4119, r/R = 0.975.

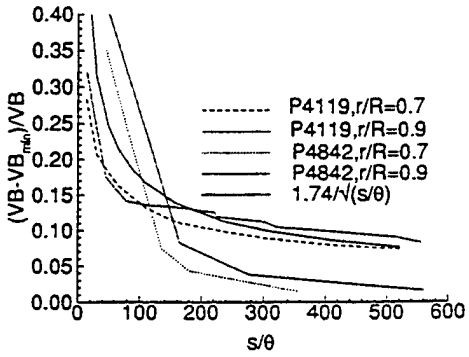


(a) r/R = 0.7

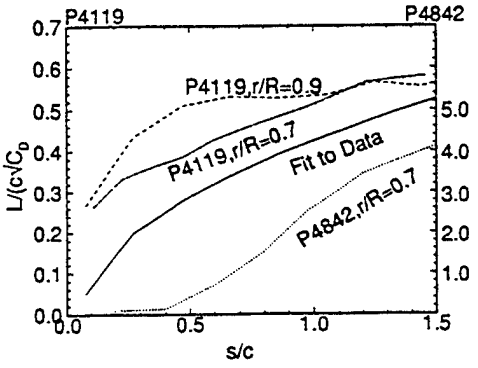


(b) r/R = 0.9

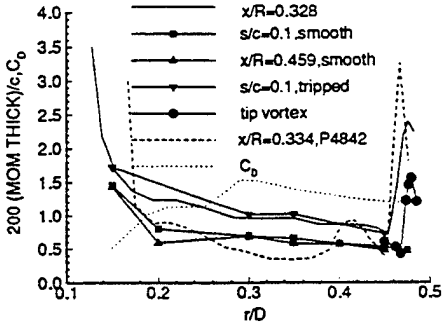
Figure 19. Wake flow: P4119.



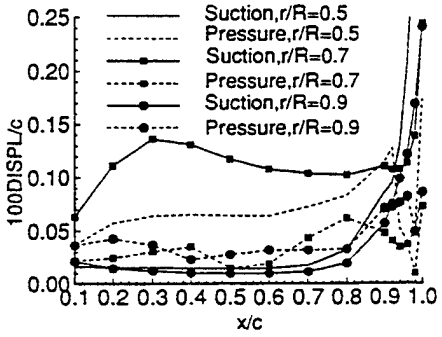
(a) deficit



(b) half width

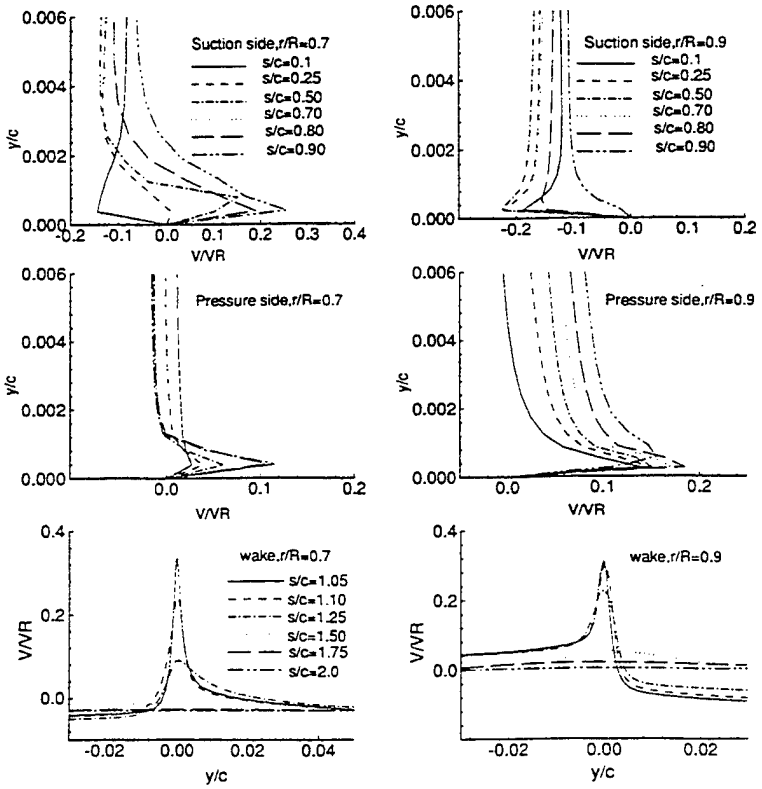


(c) momentum thickness and section drag coefficient



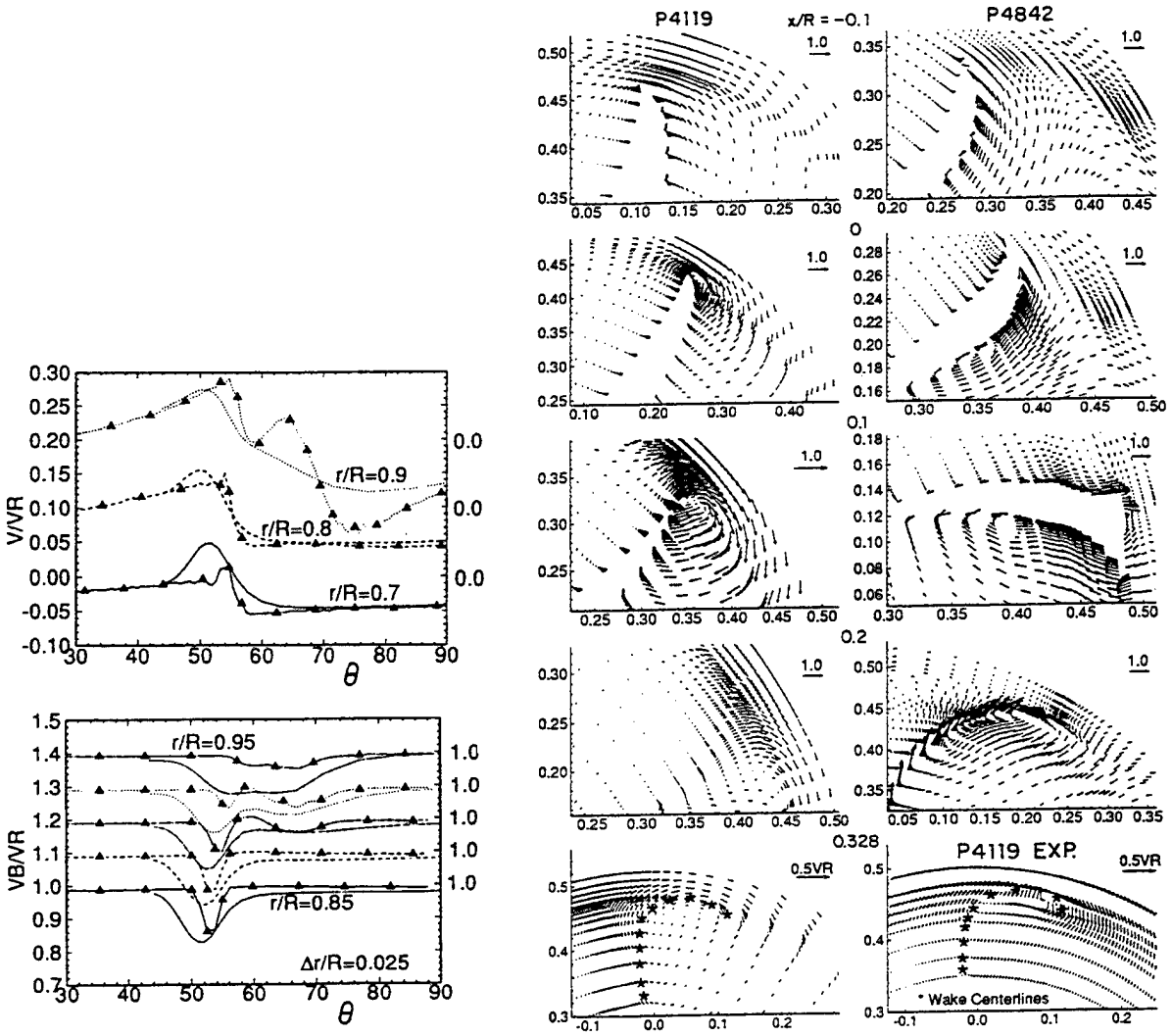
(a) displacement thickness

Figure 20. Wake parameters: P4119, P4842.



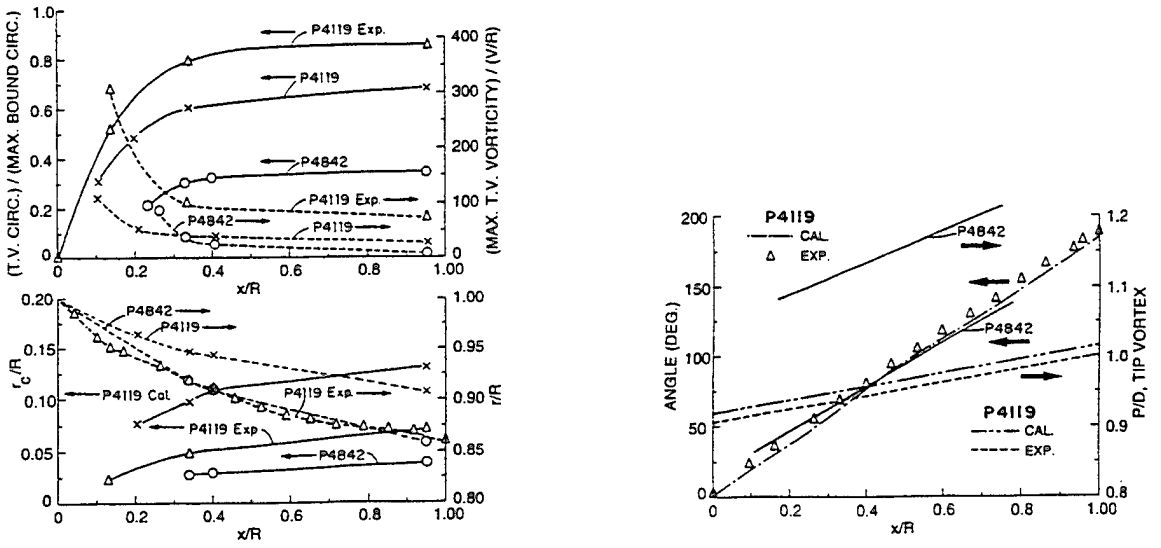
(b) radial-velocity profiles

Figure 21. Boundary-layer and wake flow: P4842.



(a) P4119 velocity profiles

(b) vectors (noninertial)



(c) parameters

Figure 22. Tip-vortex flow: P4119, P4842.

DISCUSSION

W. Day
David Taylor Model Basin, USA

The authors are to be thanked for providing such a large piece of valuable data on detailed flow and performance of propeller.

Could the authors comment on the following:

(1) In table 1 the torque coefficient is predicted very well for P4119 but is significantly underpredicted for propeller 4842. Is there any indication or explanation available in the flow calculation for this difference, and what do the authors consider to be the cause?

(2) In figure 7, a very nice detail is shown of the surface flow pattern on propeller 4842, indicating large radial flow patterns. Is this data for model scale Reynolds numbers and, if so, what would the authors expect the flow to show at much high Reynolds number, e.g. at ship scale?

S. Dong
China Ship Scientific Research Center, China

It is a nice paper to validate CFD results with experimental measurements. Two questions:

(1) As I know your experimental circulation distribution is determined by the LDV velocity measurements in the wake. Because of the contraction of the free vortex, especially near the tip, the corresponding radial position on the blade should be of some difference from the radial position in the wake where circulation is determined. How do you treat this difference?

(2) Pressure distribution determined by LDV velocity measurement and Bernoulli equations, how do you consider the viscous effect in using Bernoulli equation? Have you ever tried to validate this method with direct pressure measurements, even for simple form bodies?

Y. Lee
David Taylor Model Basin, USA

(1) For propeller 4119, figures 19 and 20b show the width of the predicted wake shear layer is much wider than the measured shear layer. This phenomena do not seem to exist for the boundary layer as shown in figures 15 and 16. Could the authors provide any explanation?

(2) The displacement thicknesses on pressure side in figures 15a and 16a behaves strangely at T.E. In figure 15a, why did the lam and lam/turb generate different trends? In figure 15a, why did it drop towards T.E.

AUTHORS' REPLY

We thank the discussants for their time and consideration of our work. Many of the issues raised are related to grid dependence and turbulence modeling. Grid-dependence tests for complex geometries such as marine propellers are a difficult task involving the investigation of many parameters. Recent results are provided in table 2 for P4119 in which the leading edge clustering was investigated with other parameters fixed, e.g., grid number and near-wall spacing y^+. Also, the CFD is for turbulent flow vs. the laminar/turbulent with fixed transition flow results presented in the paper. The tests indicate the following: (1) the accuracy improves from about 10% to 2-3% error for K_T and K_Q for coarse to fine leading-edge clustering factor; (2) increased axial grid from 100-110 (30-40 over the blade region) with fixed leading-edge clustering factor has a minimal influence; and (3) the grid for the results presented in the paper corresponds to a medium leading-edge clustering factor and the influence of laminar/turbulent with fixed transition is about 4% error for K_T and K_Q.

In response to Mr. Day, the grid dependence tests indicate that grid quality has a large influence on the results. High-quality grids such as the fine-grid results shown in table 2 for P4119 are more difficult to obtain for propellers with large skew and rake, i.e., the grid for the results presented in the paper for P4842 has large y^+ values and medium leading-edge clustering factor such that the results correspond to the accuracy of the coarse-grid results for P4119. We hesitate to conjecture as to the influence of high Re, but are currently making such calculations and hope to be able to answer this question in the future.

In response to Prof. Dong, both the experimental and CFD radial circulation distributions shown in figure 10 were deduced from the x/R=.334 swirl profiles neglecting the slipstream contraction, which has a

small influence, i.e., shifts the profile inward by about 3% r/R. Note that, as shown in figure 23, grid quality has a large influence on both the predicted swirl profile and radial circulation distribution. Validation of the pressure distribution determined by the Idv velocity measurement and Bernoulli equation by comparison with direct pressure measurements has not been done; however, surely such a procedure is limited to regions of weak viscous/inviscid interaction, as shown, e.g., in the present results.

In response to Dr. Lee, grid quality and turbulence modeling are expected to have a large influence on the results in the boundary-layer and wake regions. Currently we are investigating the influences of grid optimization for this region and turbulence model modifications for pressure gradient and wake blending (e.g., [3]) and hope to be able to answer this question in the future. We believe that the displacement-thickness trends shown in figures 15a and 16a are physically realistic and display the three-dimensional nature of the flow, i.e., combined effects of axial and radial pressure gradients.

Table 2. Grid dependence tests

No.	case	grid space	Fa.	K_T	%ow	%wt	$10K_Q$	%ow	%wt
1	paper	105x51x61	.05	.147	.7	4.5	.293	4.6	1.0
2	coarse	100x45x50	.20	.137	6.2	11.0	.255	8.9	12.0
3	medium	100x45x50	.05	.147	.7	4.5	.276	1.4	4.8
4	medium	110x45x50	.05	.147	.7	4.5	.276	1.4	4.8
5	fine	100x45x50	.02	.149	2.1	3.2	.283	1.1	2.4

Fa.: leading-edge clustering factor.
%ow: % error open-water test.
%wt: % error water-tunnel test.

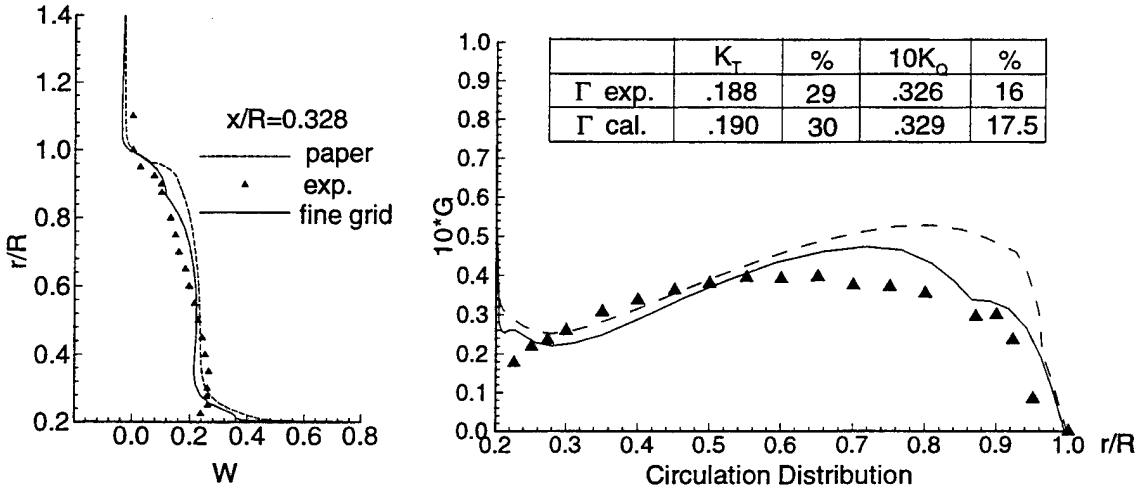


Figure 23. Influence of grid quality on predicted swirl profiles and radial circulation distributions

Three-Dimensional Navier-Stokes Solutions for a One-Stage Axial-Flow Pump

Y.T. Lee (David Taylor Model Basin, USA),
C. Hah, J. Loellbach (NASA Lewis Research Center, USA)

ABSTRACT

This paper is presented in two parts. First, steady-state analyses of the incompressible flow past a single-stage inlet guide vane (IGV)/rotor propulsion pump are presented and compared to experimental data. A steady multiple-blade-row approach is used to calculate the flowfields of the IGV and the rotor. The Reynolds-Averaged Navier Stokes (RANS) equations are solved along with the standard two-equation k-ε turbulence model. Numerical results for both mean flow and acoustic properties are compared with measurements in the wake of each blade row. Second, the same pump configuration is modified only at the rotor tip with a generic elliptical ring. Comparisons of flow features based on the computational results are presented.

NOMENCLATURE

C_1,C_2,C_3,C_4,C_μ	constants used in turbulence closure models
C_n	Fourier coefficients
C_p	pressure coefficient, normalized by rotor tip speed
c	chord length
f	function defined in Eq. (6)
IGV	inlet guide vane
k	turbulent kinetic energy
l	characteristic length
PS	pressure side
p	static pressure
r	radial
SS	suction side
t	tangential
U_i	mean velocity components
u_i	fluctuating velocity components
u_*	shear velocity
x_i (x,y,z)	cartesian coordinates
ε	turbulence dissipation rate
ν_{eff}	effective kinematic viscosity
ρ	density
$\sigma_k, \sigma_\varepsilon$	constants used in turbulence closure models
Ω_i	angular velocity of rotor

INTRODUCTION

For rotating machinery operating in incompressible flows, flow separation, cavitation and vortex formation and transportation are the dominant factors in determining the performance of the turbomachinery. Although "exact" simulation of the complex flow inside turbomachinery is not yet possible, computational methods for solving the RANS equations (1,2,3) are the state-of-the-art techniques for examining these flows numerically.

Recently, RANS solutions for incompressible flows in turbomachinery have emerged from more mature computational technologies for compressible flows. Stanier (4), for instance, extended Dawes' (5) viscous approach for marine open-water propeller calculations. And NASA Marshall Space Flight Center (MSFC) formed a consortium (6,7) to investigate the liquid fuel characteristics in rocket engines. Both pressure-based methods (1,8) and pseudocompressibility methods (2) have been used for pump inducer calculations.

This paper presents an incompressible flow solution for a single-stage IGV/rotor axial-flow pump and compares results with measurements of detailed wake structures after each blade row. The present numerical procedure uses a pressure-based approach. The turbulence closure is the standard k-ε model with a low-Reynolds-number modification near the wall. Based on this calculation method, an investigation was made to examine the difference in

flow features between two rotors with and without blade tip modification.

PUMP GEOMETRIES AND EXPERIMENTAL DATA

The baseline pump, shown in Fig. 1, was tested in the water. The pump consists of a 13-blade IGV and a 7-blade backward swept rotor. The IGV blades are lightly loaded and have a constant spanwise chord of 0.1743 m (0.572 ft). The rotor blades have a NACA 0016 Type II thickness distribution with the NACA 66 (modified) a=0.8 camberline. The rotor trailing edge is modified to prevent it from singing and has a special thick trailing-edge section and a flow recirculating region in its near wake. The blade rows of the IGV and the rotor are separated at the tip by nearly 130% of the IGV chord. Although the IGV wake exists and was measured, the large spacing between the IGV and the rotor minimizes the effect of the IGV wake on the rotor tip flow and its wake.

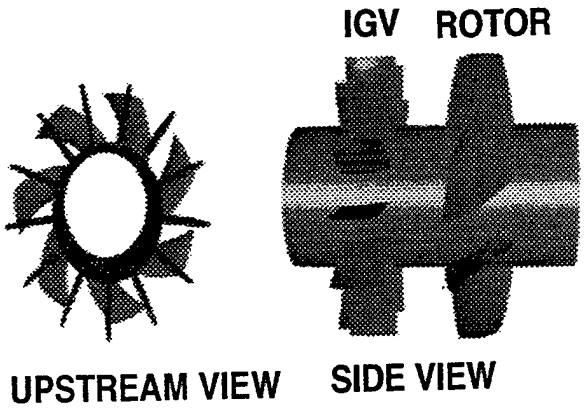


Figure 1 Configuration of the single-stage IGV-rotor pump

The present axial-flow pump tested in the HIREP facility (11) has a constant hub diameter of 0.5334 m (21 in.) and a constant casing diameter of 1.067 m (42 in). The pump operates at an inlet velocity of 10.67 m/s (35 fps) and an inlet pressure of 3.037 kg/cm^2 (43.2 psia). The rotor rotates at 260 rpm with a flow coefficient of 1.36 and a tip speed of 14.51 m/s (47.6 fps). The tested Reynolds number based on the chord of the IGV blade is 2.3 x 10^6.

The measured quantities include blade surface pressures, total pressures, inlet and wake velocities and turbulence quantities. The axisymmetric pump inlet velocities were surveyed using a five-hole probe at 37% IGV chord upstream of the IGV leading edge.

Five-hole probe surveys were also performed at 49.7% chord downstream of the IGV. These surveys provide three-component time-averaged velocities at eleven radial locations and cover 360 degrees circumference with 0.373° angular resolution. LDV velocity surveys were conducted at four axial stations located at 43.5% IGV chord upstream of the rotor tip leading edge and at 7.3%, 32.6% and 49% IGV chord downstream of the rotor tip trailing edge. The data include axial and tangential mean velocities and root-mean-square values of the turbulent fluctuating velocities. LDV surveys were also performed axially at r/r_{tip}= .881 (or 76.2% span) and from 45% IGV chord upstream of the rotor tip leading edge to 49% downstream of the rotor tip trailing edge. These surveys map the range of the rotor influence upstream of the rotor and the continuous wake formation downstream of the rotor. The details of the measurement matrix and measuring techniques are given in Zierke et al. (10).

The modified pump considered in the present numerical study has the same IGV and rotor blade geometries as the baseline pump. The hub and casing configurations are also the same as the baseline pump. The only difference between two pumps is at the rotor tip, as shown in Fig. 2. For the baseline rotor, the tip clearance is 0.4 % of the blade span. The modified rotor has a tip clearance of 3 % of the blade span. In addition, a generic ring is attached to the blade tip of the modified rotor. The mid-section of the ring has a length equal to the chord length of the blade tip profile and a constant thickness equal to the size of the tip clearance. An elliptic profile is used at the leading and trailing edges of the ring.

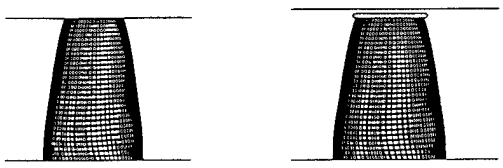


Figure 2 Baseline and modified rotors

PREDICTION METHOD

The steady incompressible RANS equations are solved for the flow past the current pump, i.e.

$$\frac{\partial U_i}{\partial x_i} = 0 \qquad (1)$$

$$\frac{\partial}{\partial x_j}(U_i U_j) + 2\varepsilon_{ijk}\Omega_j U_k = -\frac{1}{\rho}\frac{\partial p}{\partial x_i} + \frac{\partial}{\partial x_j}[\nu_{eff}(\frac{\partial U_i}{\partial x_j} + \frac{\partial U_j}{\partial x_i} - \frac{2}{3}\frac{\partial U_k}{\partial x_k}\delta_{ij}) - \overline{u_i u_j}] \qquad (2)$$

where U_i and u_i are mean and fluctuating velocities, Ω_i is the angular velocity, and $\nu_{eff} = \nu_{lam} + \nu_{tur}$. The turbulence model used to close the equations is the k-ε two-equation model. This model is modified to include the low Reynolds number effects (11) for the laminar sublayer region. The following additional equations are solved for the turbulent shear stresses,

$$U_i\frac{\partial k}{\partial x_i} = \frac{\partial}{\partial x_i}(\frac{\nu_{eff}}{\sigma_k}\frac{\partial k}{\partial x_i}) - \overline{u_i u_j}U_{ij} - \varepsilon - \frac{2\nu_{lam}k}{\ell^2} \qquad (3)$$

$$U_i\frac{\partial \varepsilon}{\partial x_i} = \frac{\partial}{\partial x_i}(\frac{\nu_{eff}}{\sigma_\varepsilon}\frac{\partial \varepsilon}{\partial x_i}) - C_1\frac{\varepsilon}{k}\overline{u_i u_j}U_{ij} - \frac{\varepsilon}{k}[C_2 f\varepsilon + \frac{2\nu_{lam}k e^{-C_4 u_* \ell/\nu_{lam}}}{\ell^2}] \qquad (4)$$

where

$$\nu_{eff} = \nu_{lam} + \frac{C_\mu k^2}{\rho\,\varepsilon}[1 - e^{-C_3 u_* \ell/\nu_{lam}}] \qquad (5)$$

and

$$f = 1 - \frac{0.4}{1.8}e^{-(\kappa^2/6\nu_{lam}\varepsilon)^2} \qquad (6)$$

The constants used in these equations are:

$$C_\mu = 0.09,\ C_1 = 1.35,\ C_2 = 1.8,\ \sigma_k = 1.0$$
$$\sigma_\varepsilon = 1.3,\ C_3 = 0.00115,\ C_4 = 0.5 \qquad (7)$$

These governing equations are solved with a pressure-based implicit relaxation method using a fully conservative control volume approach (12) for isolated rotor configurations. A third-order accurate interpolation scheme is used for the discretization of the convection terms and central differencing is used for the diffusion terms

In this study, the numerical procedure is expanded to handle a stage configuration. As the spacing between the IGV and the rotor is relatively large, a mixing plane is established approximately centered between the two blade rows. The computational grid of the pump stage is shown in Fig. 3. With the current steady-state multiple-blade-row calculations, the flowfields of the IGV and the rotor are computed iteratively.

For the IGV, the radial distribution of the static pressure at the exit of the computational domain is obtained from the rotor flowfield. At this plane, all of the other flow variables are extrapolated from the IGV interior solution.

For the rotor, radial distributions of all the flow variables at the inlet of the computational domain are obtained from the IGV solution. At this mixing plane, a classical mixing analysis is performed at each radial location to obtain circumferentially uniform values of velocity. The mixing analysis (13) is necessary to obtain a steady inlet condition for the rotor flowfield. The overall mass flowrate across the stage is determined by the specified velocity components at the inlet of the IGV. This calculation can also be performed by running two separate isolated blade row solutions. However, some human intervention during the solution process can be eliminated with the current procedure.

RESULTS AND DISCUSSION

Validation on Baseline Pump

The current prediction method was applied to the baseline axial-flow pump described previously. The pump was operating at the design flowrate of 430.42 m^3/min (15,200 ft^3/min).

The computational grid, as shown in Fig. 3 for the blade surface grid, was generated to give an orthogonal grid near the blade surfaces, particularly near the blade leading and trailing edges. Two different grid densities were used for the present calculations. The coarser grid is 102x39x29 (axial, blade-to-blade, spanwise) for the IGV and 102x39x35 for the rotor. The corresponding finer grids are 122x49x45 and 122x69x50. There are 6 (coarser grid) and 10 (finer grid) grid nodes used to

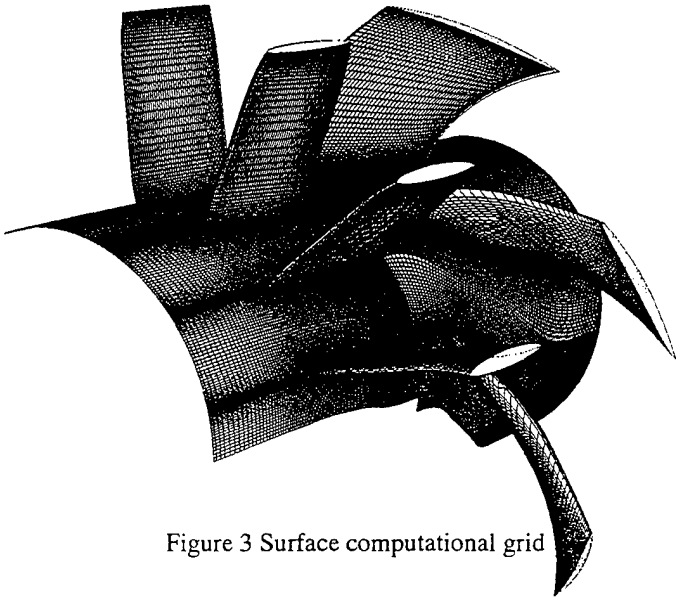


Figure 3 Surface computational grid

describe the tip-clearance region. Inside the tip gap, the grid is closed in the blade-to-blade direction and the periodicity condition is applied. Only minor variations are observed between the solutions obtained with the coarser and the finer grids (14).

Figure 4 shows the inlet conditions for each blade row as compared with the measured profiles. The experimental inlet axial-velocity profile for the IGV is located 37% chord upstream of the IGV blade. However, the computational inlet, located at 107% chord upstream, is prescribed by a boundary-layer profile. The comparison shown in Fig. 4a indicates that the measured boundary layer thicknesses at both the hub and casing walls are slightly thinner than the predicted ones. The rotor inlet was defined using the mixing analysis mentioned previously. Both the axial and the tangential velocities are compared in Fig. 4b at 43.5% IGV chord upstream of the rotor tip leading edge. Although the tangential component is slightly overpredicted, the comparison implies that the flowfield out of the IGV is correctly simulated by the present steady mixing analysis.

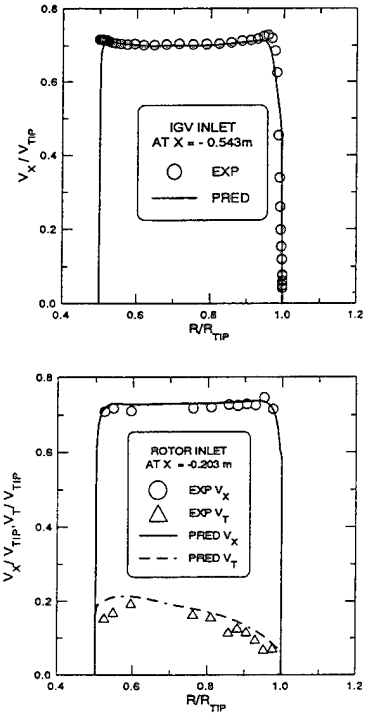


Figure 4 Comparisons of inlet conditions at IGV and rotor inlets

Figures 5 provide comparisons of the blade surface pressure on each blade row at the midspan location. The loading on the IGV blade is about half of that on the rotor blade. The loading decreases along the span towards the tip for both blades (14). This also suggests the three-dimensionality of the flowfield. Nevertheless, the blade surface pressure is well predicted.

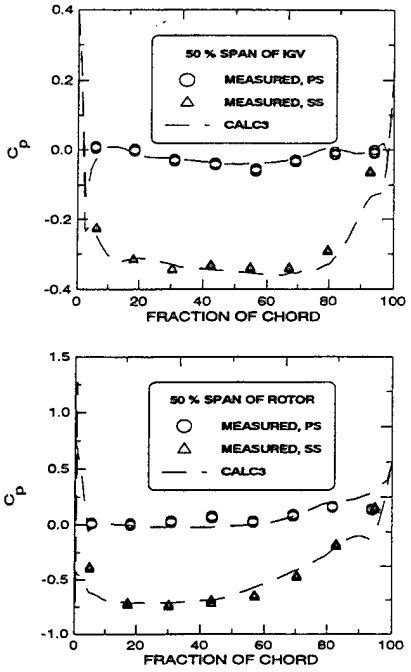


Figure 5 Pressure predictions on IGV and rotor blade surface

Secondary-flow patterns after each blade row were presented in (14). The present viscous solution slightly underestimates the size of the casing vortex along the radial direction in the IGV wake. However, it predicts much more accurately for the location of the casing vortex when compared with the invisicid solution. The rotor wake flow is quite different from the IGV wake. Since the radial velocity in the rotor wake was not measured, Fig. 6 shows the comparisons of the measured and predicted contours of the axial velocity at 49% IGV chord downstream of the rotor tip trailing edge. The radial expansion of the tip-clearance vortex is overpredicted as seen in the contour plots in Fig. 6. In addition, a very strong vortex due to the flow separation on the blade suction side occurs near the hub. This separation induced vortex is damped out quicker in the measurement than the prediction.

Detailed quantitative velocity comparisons in the IGV wake were given in (14). The predictions generally agree well with the measurements. Figure 7 compares predicted and measured velocity components for the rotor wake at three radii. The comparing axial location is shown in Fig. 7a. The axial-velocity comparison in the rotor wake agrees well with the measurements except at $r/r_{tip} = 0.905$,

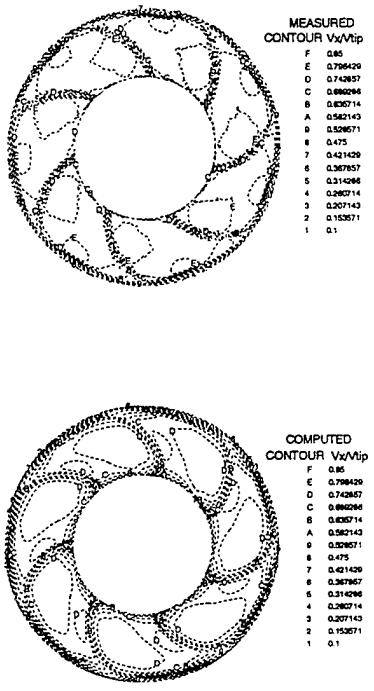


Figure 6 Axial velocity contours in the rotor wake for baseline pump

here the effect of the casing vortex dominates in the experiment. The underpredicted maximum velocity occurs closer to the blade suction side, shown also in Fig. 6, instead at the mid-pitch as in the experimental data. This mid-pitch activity from the measurement is associated with the larger swirling effect of the tip-clearance vortex. The relative tangential velocity in the rotor wake was generally overpredicted slightly.

Figures 8 shows the harmonic components of the measured and predicted rotor wake velocities shown in Fig. 7b. Similar comparisons in the IGV wake were presented in (14). The measured velocities were taken to cover 360° of the wake at each radius. Since these data reflect the variation between blade passages, significant noise exists in the experimental harmonic components. A simple filtering process was therefore used to eliminate those high harmonic components whose magnitude are less than or equal to the noise levels. The scale for the abscissas in Fig. 8 uses multiples of 7, reflecting the numbers of blades for the rotor. The agreement between the measurements and the predictions is good up to the 4th harmonics of the rotor blade passing frequency. The general agreement between the prediction and

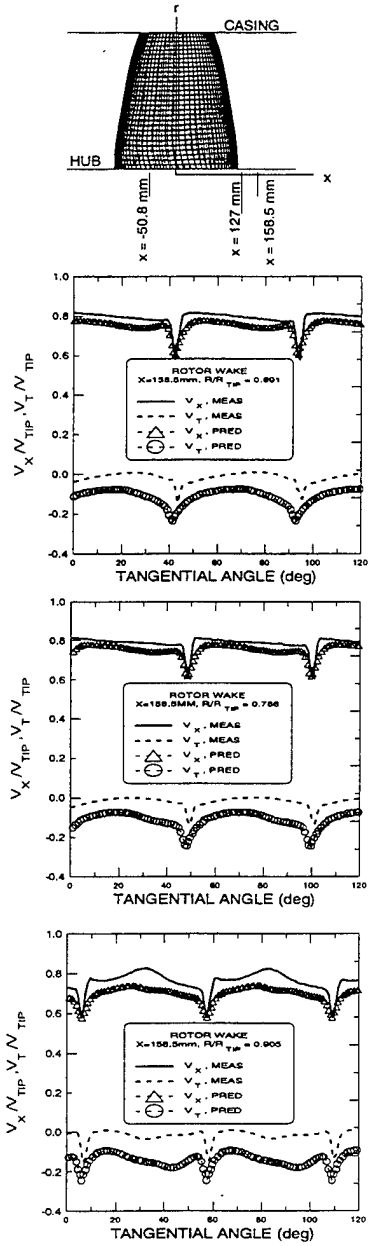


Figure 7 Wake velocity comparisons for the baseline rotor

the measurement indicates that the present solution method can provide useful acoustic predictions for this type of problem.

Flow Features for the Modified Rotor

The predicted pressure distributions on the blade surfaces for two rotors are shown in Fig. 9. The measured blade surface pressures for the baseline

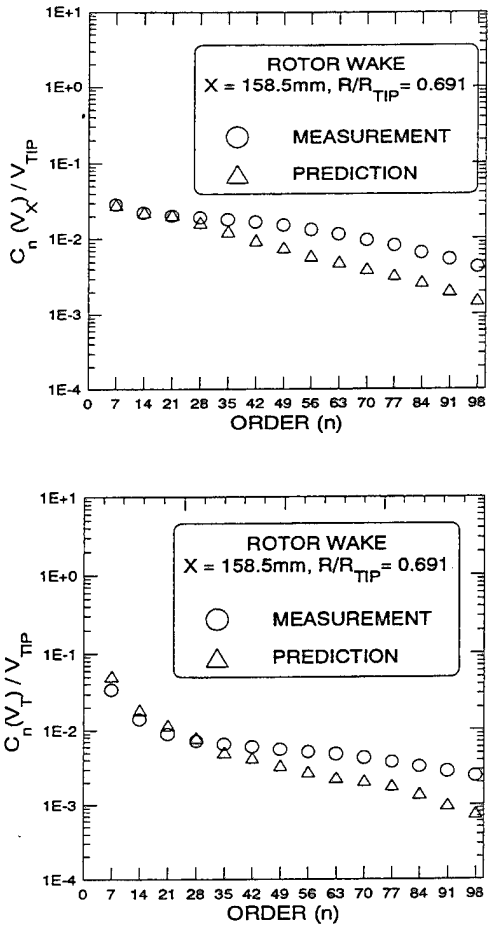


Figure 8 Harmonic components of the baseline rotor wake velocities shown in Fig. 7b

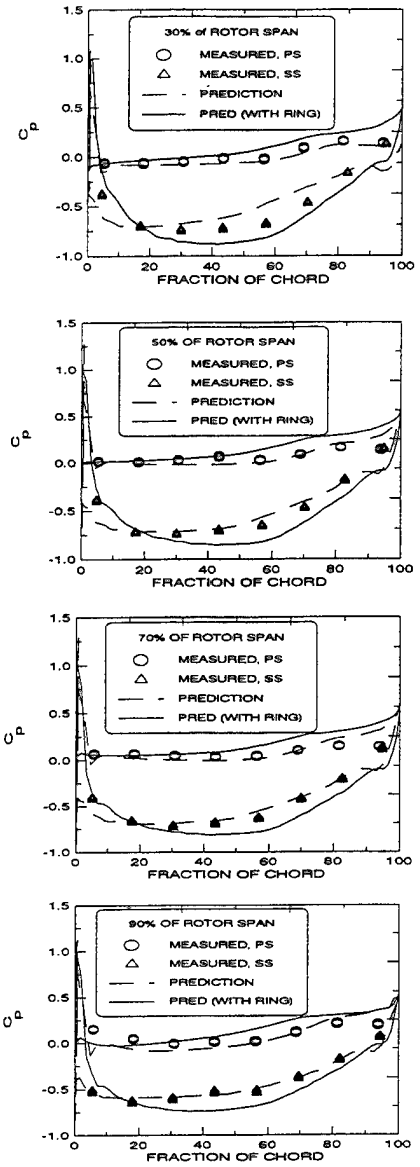


Figure 9 Blade pressure distributions of the baseline and modified rotors

rotor are also shown as the symbols. The comparisons indicate that the modified rotor sustains a larger total net loading compared to the baseline rotor. In addition, the leading edge loading for the modified rotor is also reduced.

Particle traces of the secondary flows and contours plots of the axial-component velocities for both rotors are shown in Figs. 10 and 11 at two axial cross sections, shown in Fig. 7a in relation to the rotor coordinates. The secondary flows were obtained by subtracting mean circumferential velocities from the total cross-flow velocity at each grid point. From the developments of these secondary flow patterns shown in Figs. 10a and 11a, the shroud vortex for the modified rotor is much weaker than that for the baseline rotor. Because of the reduction of the shroud vortex for the modified rotor, its hub vortex initially (i.e. at negative x-values) develops faster than the baseline rotor's hub vortex. Eventually the hub vortices from both rotors grow large enough to totally push the shroud vortex out to the casing wall. In comparing the contour plots of the axial-component velocities shown in Figs. 10b and 11b, the high velocity gradient occurs near the suction side of the baseline rotor. However, it distributes relatively uniform between the ring and the casing for the modified rotor. The secondary flow moves the low-momentum fluid near the pressure side to mix with high-momentum fluid near the suction side. This mixing balances the momentum distribution in the blade passage. The tip ring of the modified rotor slows down this mixing process initially. When the mixing reaches the hub, the difference in the contours between the two rotor flowfields becomes very small.

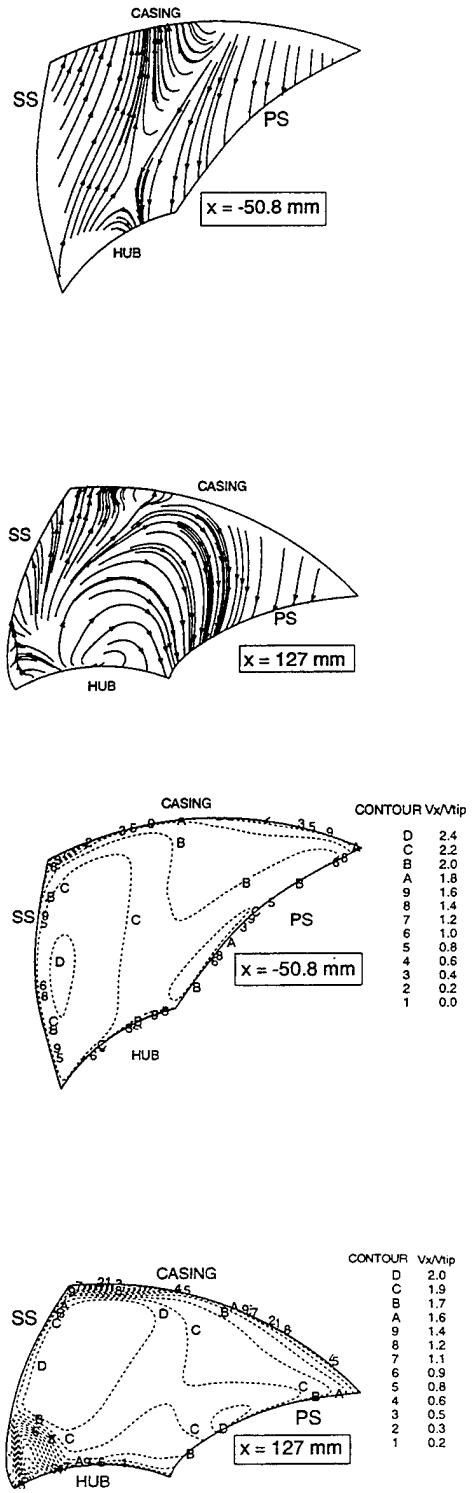


Figure 10 Secondary flows and axial velocity contours for baseline rotor wake

CONCLUSIONS

Steady-state RANS solutions for the incompressible flow past a single-stage inlet guide vane (IGV)/rotor axial-flow pump are presented. The prediction method uses a pressure-based scheme and a standard k-ε model with low-Reynolds-number approach near the wall for the turbulence closure. The steady multiple-blade-row calculation which uses a simple mixing plane works well for the present two-blade-row calculations. The solution compares well with the experiment in terms of IGV and rotor loadings and IGV wake structures which include qualitative wake vortex patterns and quantitative velocity comparisons. Although the vorticity characteristics of the IGV wake are primarily inviscid in nature, the present viscous solution predicts more localized root and casing vortices, in agreement with the measurement, than those obtained from the inviscid solution. For the rotor wake, the axial velocity was predicted accurately except near to the tip. However, detailed assessment of the effects of the tip-clearance vortex and turbulence modeling require further in-depth study.

The comparisons in flow features between the baseline rotor and the modified rotor, which has an elliptical ring section at the blade tip, indicate that the tip ring reduces the formation of the tip vortex and strengthens the root vortex initially in the blade passage. During the initial stage of the formation of the secondary flow, the tip ring also reduces the strength of the secondary flow for mixing low momentum fluid on the pressure side with the high momentum fluid on the suction side. When the fully developed stage is reached, the mixing process becomes similar between two rotors due to the limitation of the mixing area.

ACKNOWLEDGMENTS

This work was supported by the Applied Hydrodynamics Research Program (AHR) and the 6.2 Block Program for Hydrodynamics and Hydroacoustics of Internal Flow, sponsored by the Office of Naval Research and administrated at David Taylor Model Basin. Computer resources were provided by Numerical Aerodynamic Simulation (NAS) facility at NASA Ames Research Center.

REFERENCES

1. Chen, Y.S., "Compressible and Incompressible Flow Computations with a Pressure Based Method," AIAA Paper No. 89-0286, 1989.

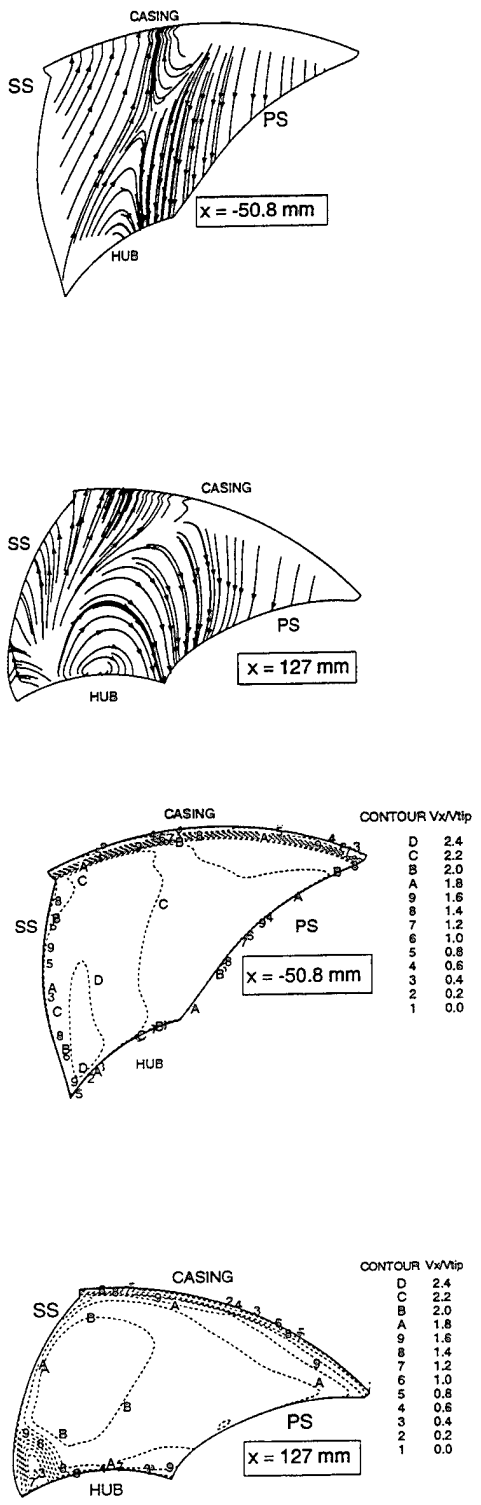


Figure 11 Secondary flows and axial velocity contours for modified rotor wake

2. Kiris, C., Chang, L., Kwak, D. and Rogers, S., "Incompressible Navier-Stokes Computations of Rotating Flows," AIAA Paper 93-0678, 1993.

3. Walker, P.J. and Dawes, W.N., " The Extension and Application of Three-Dimensional Time-Marching Analysis to Incompressible Turbomachinery Flows," *Journal of Turbomachinery*, Vol. 112, pp. 385-390, 1990.

4. Stanier, M.J., " Design and Evaluation of New Propeller Blade Section," Inter. Sym. on Propulsors and Cavitation, Hamburg, June 22-25, 1992.

5. Dawes, W.N., " Development of a 3D Navier-Stokes Solver for application to all Types of Turbomachinery," ASME Paper No. 88-GT-70, 1988.

6. Garcia, R., Jacson, E.D., and Schutzenhofer, L.A., "A Summary of the Activities of the NASA/MSFC Pump Stage Technology Team," Proceedings of the Fourth International Symposium on Transport Phenomena and Dynamics of Rotating Machinery, Honolulu, Hawaii, 1992.

7. Garcia, R., McConnaughey, P., and Eastland, A., "Activities of MSFC Pump Stage Technology Team," AIAA Paper No. 92-3232, 1992.

8. Chen, W.C., Pruger, G., Chen, D., and Eastland, A., "On the Use of a Three-Dimensional Navier-Stokes Solver for Rocket Pump Impeller Design," AIAA Paper No. 92-3223, 1992.

9. Farrell, K.J., McBride, M.W., and Billet, M.L., "High Reynolds Number Pump Facility for Cavitation Research," The Pennsylvania State University/ARL Technical Report No. TR 87-011, 1987.

10. Zierke, W.C., Straka, W.A. and Taylor, P.D., "High Reynolds Number Flow through an Axial-Flow Pump," The Pennsylvania State University/ARL Technical Report No. 93-12, 1993.

11. Chien, K.Y., "Predictions of Channel and Boundary-Layer Flows with a Low-Reynolds-Number Turbulence Model," *AIAA Journal*, Vol. 20, No. 1, pp. 33-38, 1982.

12. Hah, C., "Calculation of Three-Dimensional Viscous Flows in Turbomachinery With an Implicit Relaxation Method," *AIAA Journal of Propulsion and Power*, Vol. 3, No. 5, pp. 415-422, 1987.

13. Dring, R.P. and Spear, D.A., "The Effects of Wake Mixing on Compressor Aerodynamics," ASME paper 90-GT-132, 1990.

14. Lee, Y.T., Hah, C. and Loellbach, J., "Flow Analyses in a Single-Stage Propulsion Pump," ASME Paper No. 94-GT-139, 1994.

DISCUSSION

S. Jessup
David Taylor Model Basin, USA

I would like the explanation of why the predicted and measured tangential velocity downstream of the rotor shown in figure 7 are so different. There appears to be a relatively constant difference that is equivalent to the rotor inlet swirl implying a confusion net versus the relative V_t/V distribution. Also, the usefulness of viscous should be in the prediction of the blade wake flow. It appears that your method predicts rotor blade wakes that are much wider than measurements. Can you comment on this?

J. Kerwin
Massachusetts Institute of Technology, USA

The analysis of the flow around multi-component ducted propulsors is a challenging task for designers, and efforts to develop and validate better analytical tools are most welcome. The authors should be commended for providing extremely useful information to the propulsor community in their present paper.

While their computed results compare well in many respects with the measurements of Zierke, et al., a close inspection reveals some discrepancies which I hope the authors can clarify.

The first question is concerned with the circumferential mean tangential velocity behind each component, which is directly proportional to circulation and lift. In figure 4, the computed tangential velocity downstream of the IGV is about 9% higher than the measured value, which is not unreasonable (although designers might think this to be a large discrepancy). However, Figure 7 indicates that the measured tangential velocity downstream of the rotor is essentially zero, while the calculated value has a circumferential mean value of roughly V /V 0.15. The authors state that *the relative tangential velocity in the rotor wake was generally overpredicted slightly.* However, the tangential velocity corresponding to the design value of the circulation in the mid-span region is approximately V / 0.19, which is of the same order of magnitude as the discrepancy between the Navier-Stokes prediction and the experiment. Have I misinterpreted Figure 7, or is there possibly a problem in communicating tangential velocities in the mixing plane between the two components?

Since the rotor thrust and torque values were measured in the experiment, it would be useful to compare these values with those predicted from the Navier-Stokes code. Has such a comparison been made? This would not only be useful in assessing the usefulness of the Navier-Stokes code for actual design and analysis, but might shed some light on the apparent discrepancy in tangential velocities.

The authors also indicate that *only minor variations are observed between the solutions obtained with the coarser and finer grids.* It would be particularly helpful if these differences could be quantified in terms of the predicted thrust and torque values.

The authors show chordwise pressure distributions on the IGV and rotor in Figures 5 and 9. While the agreement with experiment is reasonable over most of the chord, it is notable that the experiments indicate essentially no load at the measurement point closest to the trailing edge, while the Navier-Stokes calculation predicts substantial load in this region. This discrepancy is similar to that found in the MIT *flapping foil* project[1] in which a large two-dimensional foil with an anti-singing trailing edge was the object of extensive testing and computation. Could the authors comment on the abilities of current Navier-Stokes codes in providing quantitative predictions of viscous behavior at the trailing edge?

AUTHORS' REPLY

Professor Kerwin and Dr. Jessup raised a valid point about the predicted tangential velocity in the rotor wake. The authors had overlooked this discrepancy when preparing the manuscript. This discrepancy between the measured and the predicted data was reexamined afterwards. We found that the original computed data was processed incorrectly and this error was corrected in the final paper.

The original purpose of this paper was to demonstrate the capability to predict the propeller wake for acoustic evaluation. It was not intended yet to be used as a propeller design tool. The thrust and torque were

[1]Lurie, E.H., *Unsteady Response of a Two-Dimensional Hydrofoil Subject to High Reduced Frequency Gust Loading,* Master's thesis, MIT Department of Ocean Engineering, MIT, May 1993

therefore not predicted. One can, however, get a rough estimate of the predicted thrust and torque based on the blade surface pressure predictions. For the blade surface pressure predictions, the coarse and fine grids generate indistinguishable results as shown in Fig. 5.

For the rotor trailing edge flow, as indicated by Professor Kerwin, the present rotor trailing edge shape closely resembles the trailing edge shape used in the MIT flapping foil project. The turbulence modeling is an important issue in predicting this flow correctly. The standard k-ε model has difficulty in simulating the present trailing edge flow. A simple modification of the turbulence length scale used at the inlet provides better agreement with the flow visualization as discussed in (14).

Dr. Jessup commented about the viscous wake thickness prediction. This is why the predicted data was drawn using symbols in Fig. 7 to indicate the number of points to construct the wake. This should be the same problem for the experimental data. In our solutions, we have 5 to 7 points to define the blade wake along the tangential direction.

An Integrated Method for Computing the Internal and External Viscous Flow Field Around the Ducted Propulsor Behind an Axisymmetric Body

L. Zhou, F. Zhao (China Ship Scientific Research Center, China)

ABSTRACT

This paper presents an effective method for computing the internal and external viscous flow field around the ducted propulsor behind an axisymmetric body by using a new Navier-Stokes equations solver with primitive variable continuity equation formulation. In the present numerical method, the calculation equation for pressure with well-defined coefficient, which form is similar to the artificial compressibility method, is developed. A semi-staggered grid system is adopted. Not only the advantage of staggered grid system can be retrained but the boundary conditions on the inner and outer surface of the duct can be also carried out easily. By using a special grid system and the programming technique for implementing the jump boundary condition on the duct surfaces, the internal and external viscous flow field around the ducted propulsor behind the axisymmetric body may be calculated integrally in an unified numbered grid system. Some configurations are calculated and compared with experimental date and numerical results of other methods. Illustrative calculations are also presented for a stern of axisymmetric body with the backstep fitted a duct to illustrate the capability of the present method. Beside that, the effect of axial distribution of body force is considered and discussed in order to extend the application range of the present method.

INTRODUCTION

It has been known in marine propulsion technology that the use of ducted propeller has often been an attractive alternative for ship and underwater vehicle propulsion as well. With a duct that accelerates the flow, the propulsive efficiency can be increased. With a duct that decelerates the flow, the inception of cavitation on the propeller can be delayed. In order to take advantage of the ducted propeller to obtain the desirable benefit, a clear understanding of the role it plays is important. The reliable numerical simulation of the flow field around the ducted propeller is a useful tool to gain understanding. Various potential theories have been used to model ducted propulsors in uniform flow with varying degrees of success. For a submerged vehicle, the propulsor is operating within the thick boundary layer developed near the stern. The potential methods cannot take into account the interaction between the ducted propulsor and the strong vorticity field inside the boundary layer. Thus, it is necessary to use Navier-Stokes equations solver for analyzing the viscous flow field around the ducted propulsor/stern. When a ducted propulsor operates in the non uniform wake of ship, the resulting flow field is that due to the hull, duct and propeller combination body. For this flow field, the exact treatment is to incorporate the actual propeller into a viscous flow calculation method and no-slip boundary condition must be satisfied on surfaces of the hull, duct and rotating blades of the propeller. However, it is still a very difficult problem today to solve the flow field of a hull, duct and propeller combination body by using such an exact method. The popular research work is that the body force field which presents the effect of propeller is incorporated into the Navier-Stokes equations. Beside that, another difficult problem raised due to the duct which divides the flow field into the internal and external flow field. In existed methods for computing the viscous flow field around the ducted propeller behind an axisymmetric body, the streamline-iteration method adopted by Schmiechen and Zhou [1] must know the flow rate entered the duct beforehand, and the multiblock iteration

method employed by Yang et al [2] and Dai et al [3] will increase CPU time.

In the present paper an effective method for computing the internal and external viscous flow field around the ducted propulsor behind an axisymmetric body is developed. In numerical method, the time-dependence Reynolds Average Navier-Stokes equation with primitive variable formulation is solved, k-ε two equation turbulence model is employed and the effect of the propeller inside the duct is modeled by a body force. There are three features in our numerical method. Firstly, by using the point relaxation method the continuity equation is transformed the calculation formula for the pressure, which has a formal resemblance to the formula of artificial compressibility method, but its coefficient is well-defined and depends on the geometric parameters of grid and the velocities in the neighborhood of the calculating points. Thus, the pressure adjustment is adapted to the neibouring flow field. The drawback of slow convergence for the pressure and residuum of the continuity equation in using the original artificial compressibility method, which is due to the inconsistency of artificial velocity of pressure wave propagation with the real physics, is overcome. Secondly, a semi-staggered grid system is developed, i.e. u, w, k, and ε are defined at the node of grid and v and p are defined on the usual staggered grid system. Therefore, not only the advantage of staggered grid system can be retrained but the boundary conditions on the inner and outer wall of the duct can be also easily carried out. Finally, by using a special grid system and the programming technique for implementing the jump boundary condition on the transformed duct wall, the internal and external viscous flow field around the ducted propulsor behind the axisymmetric body may be calculated integrally in an unified numbered grid system. Thus, two block iteration calculation between internal and external flow field inside and outside duct may be avoided and the computing time is saved. Three difference configurations are calculated and compare with experimental data and the numerical results of other methods. These are, 1.axisymmetric body with a duct, 2. axisymmetric body with a duct and an operating propeller, 3. accelerate ducted propeller. Illustrative calculation is also presented for a stern of axisymmetric body with the backstep fitted a duct to illustrate the capability of the present method, which can calculate a very full afterbody even with backstep. Beside that, the effect of axial distribution of body force is considered and discussed in order to extend the application range of the present method.

GOVERNING EQUATIONS AND BOUNDARY CONDITION

The nondimensional equations of axisymmetric viscous incompressible flow are written in cylindrical polar coordinates (x,r,θ) in the physical domain as follows:

$$\frac{\partial U}{\partial x}+\frac{1}{r}\frac{\partial}{\partial r}(rV)=0 \tag{1}$$

$$\frac{\partial U}{\partial t}+U\frac{\partial U}{\partial x}+V\frac{\partial U}{\partial r}+\frac{\partial}{\partial x}(p+\overline{uu})+\frac{\partial}{\partial r}(\overline{uv})+\frac{\overline{uv}}{r}-\frac{1}{Re}\nabla^2U=fb_x \tag{2}$$

$$\frac{\partial V}{\partial t}+U\frac{\partial V}{\partial x}+V\frac{\partial V}{\partial r}-\frac{W}{r}+\frac{\partial}{\partial x}(\overline{uv})+\frac{\partial}{\partial r}(p+\overline{vv})+\frac{\overline{vv}}{r}-\frac{\overline{ww}}{r}-\frac{1}{Re}(\nabla^2V+\frac{V}{r^2})=0 \tag{3}$$

$$\frac{\partial W}{\partial t}+U\frac{\partial W}{\partial x}+V\frac{\partial W}{\partial r}+\frac{WV}{r}+\frac{\partial}{\partial x}(\overline{uw})+\frac{\partial}{\partial r}\overline{vw}+2\frac{\overline{vw}}{r}-\frac{1}{Re}(\nabla^2W-\frac{W}{r^2})=fb_\theta \tag{4}$$

$$\frac{\partial k}{\partial t}+U\frac{\partial k}{\partial x}+V\frac{\partial k}{\partial r}=\frac{\partial}{\partial x}(\frac{1}{R_{eff}}\frac{\partial k}{\partial x})+\frac{1}{r}\frac{\partial}{\partial r}(\frac{1}{R_{eff}}r\frac{\partial k}{\partial r})+G-\varepsilon \tag{5}$$

$$\frac{\partial \varepsilon}{\partial t}+U\frac{\partial \varepsilon}{\partial x}+V\frac{\partial \varepsilon}{\partial r}=\frac{\partial}{\partial x}(\frac{1}{R_{eff}}\frac{\partial \varepsilon}{\partial x})+\frac{1}{r}\frac{\partial}{\partial r}(\frac{1}{R_{eff}}r\frac{\partial \varepsilon}{\partial r})+G_\varepsilon\frac{\varepsilon}{k}-C_{\varepsilon 2}\frac{\varepsilon^2}{k} \tag{6}$$

In above six equations U,V, and W is the mean velocity components in the (x,r,θ) coordinates system; p is the nondimensional pressure; $Re=\frac{U_\infty L}{\nu}$ is the Reynolds number defined in terms of characteristic velocity U_∞ , characteristic length L and molecular kinematic viscous ν ; k and ε are turbulent kinetic energy and its dissipation rate respectively; the barred quantities $\overline{uu}$, $\overline{uv}$ etc. are the Reynolds stresses normalized by U_∞^2 ; $\nu_t=\frac{C_\mu k^2}{\varepsilon}$ is

the eddy viscosity; R_{eff} is the effective Reynolds number

$$R_{eff} = \frac{1}{R_e} + \frac{\nu_t}{\sigma_\phi} \tag{7}$$

where $\phi = k$ for the k-equation (5) and $\phi = \varepsilon$ for the ε-equation (6); G is the turbulence generation term.

$$G = \nu_t \left\{ 2\left[\left(\frac{\partial U}{\partial x}\right)^2 + \left(\frac{\partial V}{\partial r}\right)^2 + \left(\frac{V}{r}\right)^2 \right] + \left(\frac{\partial U}{\partial r} + \frac{\partial V}{\partial x}\right)^2 + \left(\frac{\partial W}{\partial x}\right)^2 + \left(\frac{\partial W}{\partial r} - \frac{W}{r}\right)^2 \right\} \tag{8}$$

In the two-equation k-ε turbulence model each Reynolds stress is related to the corresponding mean rate of strain by the isotropic eddy viscosity ν_t as follows:

$$\begin{cases} -\overline{uv} = \nu_t \left(\dfrac{\partial U}{\partial r} + \dfrac{\partial V}{\partial x}\right) \\ -\overline{uw} = \nu_t \dfrac{\partial W}{\partial x} \\ -\overline{vw} = \nu_t \left(\dfrac{\partial W}{\partial r} - \dfrac{W}{r}\right) \\ -\overline{uu} = \nu_t \left(2\dfrac{\partial U}{\partial x}\right) - \dfrac{2}{3}k \\ -\overline{vv} = \nu_t \left(2\dfrac{\partial V}{\partial r}\right) - \dfrac{2}{3}k \\ -\overline{ww} = \nu_t \left(2\dfrac{V}{r}\right) - \dfrac{2}{3}k \end{cases} \tag{9}$$

The model constants are:

$$C_\mu = 0.09,\ C_{\varepsilon 1} = 1.44,\ C_{\varepsilon 2} = 1.92,\ \sigma_k = 1.0,\ \sigma_\varepsilon = 1.3$$

The above equations (1) - (9) form a set of closed solving equations. For the axisymmetrical internal and external flow as shown in the figure 1., the boundary conditions are as follows:

Inlet: V = W = 0, $k = 0.00375U_\infty^2$, $\varepsilon = k^{1.5}/2$, U is determined according to the boundary layer thickness of flat plate and 1/7 rule;

Exit: $\dfrac{\partial U}{\partial x} = \dfrac{\partial V}{\partial x} = \dfrac{\partial W}{\partial x} = \dfrac{\partial k}{\partial x} = \dfrac{\partial \varepsilon}{\partial x} = 0$

Solid surface: U = V = W = 0, $\partial k/\partial n = 0$, ε is determined by the wall function.

Outer boundary: U = 1, V = W = 0, $\dfrac{\partial k}{\partial n} = \dfrac{\partial \varepsilon}{\partial n} = 0$

Wake centerline: W = V = 0, $\dfrac{\partial U}{\partial n} = \dfrac{\partial k}{\partial n} = \dfrac{\partial \varepsilon}{\partial n} = 0$

H-TYPE BOUNDARY FITTED GRID SYSTEM AND SEMI-STAGGERED GRID

The current method of elliptic boundary fitted grid generation [4] has been rather ripe, but the relations between the choice of the grid type and the practical physical problem are lesser considered. In the present method H-type grid is selected. It has the advantages that the form of the grid, boundary and relatively location in the calculation domain are coincident with those in the physical domain. This is specially suitable to the present internal and external flow problem. However, it is difficult to generate the good quantitative grid for H-type grid by using single block method. Therefore, the multiblock grid generation method [5] is used. The sketch of multiblock grid region is shown in Fig.1. For this multiblock grid, by using the programming technique for implementing the jump boundary condition on the both side of transformed duct surface and for properly taking boundary data in calculating the inner points near the both side of duct surface, the flow field of multiblock H-type grid which corresponds to the internal and external flow field around the duct can be solved in single block grid system. Thus, multiblock iteration between internal and external flow field inside and outside duct may be avoided and the CPU time is saved.

To overcome the difficulty of implementing boundary conditions in the staggered grid system, and at the same time to keep the advantages of the staggered grid, the equations are discretized in the semi-staggered grid system, i.e. U, W ,k, and ε are defined at the normal grid nodes, V and p are defined at the original staggered grid nodes, as shown in Fig.2. Thus the original advantage of the staggered grid can be retrained. The solving pressure is related to the neighbouring nodes and the pressure oscillation can be efficiently controlled. The boundary conditions on the inner and outer wall of the duct can be also easily carried out. Discreted difference equations are written on the grid of U,V,W,p,k and ε, respectively.

DIFFERENCE DISCRETIZATION AND THE PRESSURE SOLVING EQUATION IN CONTINUITY FORMULATION

Firstly,the governing equations (1) - (9) are transformed into the boundary fitted grid systems. The discretization methods and forms for the five equations are the same. The up-wind discretization scheme is used in the convection terms in order to

keep the stability. For an example, the U equation is written as:

$$\frac{U^{n+1} - U^{n-1}}{2\Delta t} + AuU^{n+1} + BuP^{n+1} = 0 \qquad (10)$$

where the superscripts n+1 and n-1 represent the value at n+1 and n-1 time step, respectively, Δt is the time step, Au and Bu are coefficient matries after discretization.

We calculate the middle time layer value to obtain:

$$\frac{U^{*} - U^{n-1}}{2\Delta t} + AuU^{*} + BuP^{n} = 0 \qquad (11)$$

where U^{*} represents value of U^{n+1} at the middle time layer. By using point relaxation method for the equation (11), we have

$$U^{*(k+1)} = U^{*(k)} + \omega\left[\frac{1}{2\Delta t} I + A_u^0\right]^{-1} \cdot \left[-A_u^- U^{*(k+1)} - A_u^0 U^{*(k)} - A_u^+ U^{*(k)} - BuP^n - \frac{1}{2\Delta t}(U^{*(k)} - U^{n-1})\right]$$
$$= U^{*(k)} + \omega\left[\frac{1}{2\Delta t} I + A_u^0\right]^{-1} \cdot rmu \qquad (12)$$

where $U^{*(k)}$ represents the k times iteration value of n+1 step at the middle layer; ω is the relaxation factor;

rmu is the difference remainder of the U momentum equation,

$$rmu = -A_u^- U^{*(k+1)} - A_u^0 U^{*(k)} - A_u^+ U^{*(k)} - BuP^n - \frac{1}{2\Delta t}(U^{*(k)} - U^{n-1}) \qquad (13)$$

A_u^- and A_u^+ are the lower-triangular matrix and the upper-triangular matrix of Au respectively, A_u^0 is the diagonal matrix of Au, I is unit diagonal matrix.

The discretization method and form of the V equation is similar to the above U equation, and the continuity equation is discretized as :

$$CuU^{n+1} + CvV^{n+1} = 0 \qquad (14)$$

where Cu and Cv are the coefficient matrices.

The pressure equation is derived as follows by substituting U^{n+1} and V^{n+1} into the discretized form of the continuity equation (14)

$$\omega\left\{\left[\frac{1}{2\Delta t} I + A_u^0\right]^{-1} \cdot CuBu + \left[\frac{1}{2\Delta t} I + A_v^0\right]^{-1} \cdot CvBv\right\} P^{n+1}$$
$$= Cu\left\{U^{n+1(k)} + \omega\left[\frac{1}{2\Delta t} I + A_u^0\right]^{-1} \cdot \left[-A_u^- U^{n+1(k+1)} - A_u^0 U^{n+1(k)} - A_u^+ U^{n+1(k)} - \frac{1}{2\Delta t}(U^{n+1(k)} - U^{n-1})\right]\right\}$$
$$+ Cv\left\{V^{n+1(k)} + \omega\left[\frac{1}{2\Delta t} I + A_v^0\right]^{-1} \cdot \left[-A_v^- V^{n+1(k+1)} - A_v^0 V^{n+1(k)} - A_v^+ V^{n+1(k)} - \frac{1}{2\Delta t}(V^{n+1(k)} - V^{n-1})\right]\right\} \qquad (15)$$

Let us denote D as the coefficient matrix:

$$D = \omega\left\{\left[\frac{1}{2\Delta t} I + A_u^0\right]^{-1} Cu \cdot Bu + \left[\frac{1}{2\Delta t} I + A_v^0\right]^{-1} Cv \cdot Bv\right\} \qquad (16)$$

The equation (14) can be solved by point relaxation method. The initial value is assumed to be p^n and U^{*},and V^{*} calculated by p^n. The equation (15) is written as the following simple form

$$P^{n+1} = p^n - \frac{r_p}{D_p} \nabla \cdot \vec{V}^{*} \qquad (17)$$

where D_p are the diagonal elements of the matrix D; r_p is the pressure relaxation factor for the pressure.

The form of equation (16) is similar to the artificial compressibility method[6] and relaxation coefficient r_p is easily chosen. Because D_p has defined value, which is related to geometric parameters of the grid and the velocities at the neighbouring grid nodes, thus, the pressure adjustment is adapted to the neighbouring flow field. The drawback of slow convergence for the pressure and residuum of the continuity equation in using original artificial compressibility method, which is due to the inconsistency of artificial velocity of pressure wave propagation with the real physics, is overcome. Comparing SIMPLE method, the solution of a Possion equation can be avoid and the CPU time can be decreased.

The coefficients of above discretization have been strictly derived under the semi-staggered grid system in the references [7].

REPRESENTATION OF THE PROPELLER

As mentioned in the introduction, the popular research work on the hull-propeller interaction is the body force field presention of the propeller. In this method, the effect of the propeller is accounted for by the addition of body force terms in the source functions of Navier-Stokes equations. The essential parameters that defined the propeller effects are the thrust coefficient C_T, the torque coefficient C_Q , the advance coefficient J and the radial circulation distribution G(r). The same parameters are used to define the body force for the propeller model. The axial and circumferential body force per unit volume are obtained from the following equations:

$$fb_x = C_T R_p^2 G(r)/4\Delta x \int_{Rh}^{Rp} G(r)rdr ,$$
$$fb_\theta = C_Q R_p^3 G(r)/2r\Delta x \int_{Rh}^{Rp} G(r)rdr \qquad (18)$$

where R_h and R_p are the radii of propellor hub and blade tip respectively, and Δx is the thickness. Owing to the fact that, the blade circulation distribution depends upon the inflow at the propeller plane which in turn is influenced by the blade circulation. This mutual dependence implies that the body force fb_x and fb_θ which are functions of G(r) should be obtained by an iterative procedure. To complete this procedure, any propeller program can be used for this purpose.

If the discreted radial distributions for thrust and torque, $T(r_j)$ and $Q(r_j)$ j = 1,··· n, are known , From the formula

$$T = 2\pi\rho L^2 U_\infty^2 \Delta x \int_{Rh}^{Rp} fb_x(r)rdr$$
$$Q = 2\pi\rho L^3 U_\infty^2 \Delta x \int_{Rh}^{Rp} fb_\theta(r)r^2 dr \qquad (19)$$

The body force field can be obtained as follows

$$fb_x(r_j^*) = \frac{T(r_j)}{2\pi\Delta x\rho L^2 U_\infty^2 r_j^*(r_{j+1} - r_j)}$$
$$fb_\theta(r_j^*) = \frac{\theta(r_j)}{2\pi\Delta x\rho L^3 U_\infty^2 r_j^{*2}(r_{j+1} - r_j)} \qquad (20)$$

where $r_j^* = 0.5(r_j + r_{j+1})$. Of course, to determine $T(r_j)$ and $Q(r_j)$ also needs an iterative procedure.

The iterative procedure is follow as:

(1) The flow field around the stern of and axisymmetric body only with a duct is calculated, and the inflow of the propeller may be obtained.

(2) The propeller performance calculation is carried out under the calculated inflow condition. The dimensionless circulation distribution G(r) or the thrust and torque distributions T(r) and Q(r) may be calculated and consequently the body force distributions $fb_x(r)$ and $fb_\theta(r)$ may be obtained.

(3) The flow field around the stern of an axisymmetric body with a duct and the body force field is calculated, and by substracting the propeller induced velocity from the calculated total velocity and the new inflow of the propeller may be obtained.

(4) Repeat calculations of step (2) to step (3) until the convergence is reached.

NUMERICAL EXAMPLES

The four configurations that were calculated are 1. flow over the body with a duct, 2. flow over the body with a duct and an operating propeller, 3. flow over an accelerative ducted propeller and 4. flow over a stern of axisymmetric body with the backstep fitted a duct with rotor and stator. The calculated results are compared with available experimental data and the numerical results of other methods.

case 1. Flow over the Body with a Duct

This numerical example is taken from [2]. Figure 3 shows the calculated velocity vectors in the stern region by the present method. Figure 4 shows the results from both computation of Yang's method and experiment[2].

case 2. Flow over the Body with a Duct and an Operating propeller

This numerical example is also taken from [2]. In this case the circulation G(r) and consequently the body force was assumed to be given. Figure 5 shows the calculated velocity vectors in the stern region by the present method. Figure 6 shows the results from both computation of Yang's method and experiment[2]. Comparing the above figures it can be seen that the essential flow phenomena such as separation, acceleration and contraction can be realistically predicted by the present method.

case 3. Flow over the Accelerative Ducted Propeller

This numerical example is the ducted propeller combined duct BD18 with propeller 6510. It was tested[9] and calculated by full-panel method[10] at CSSRC. In this example the viscous flow approach to the computation of hull-propeller interaction is carried out and the panel method developed by Xing[10] is used in computing propeller. Figure 7 shows the calculated velocity vector field around the duct. Figure 8 shows the calculated velocity profiles at the various axial locations for the flow over the duct without propeller and the comparison with the calculated results of the panel method[10]. Figure 9 and Figure 10 show the convergence procedure of the interactive iteration in computing the radial distributions of thrust and torque respectively. Table 1 shows the convergence procedure of the interactive iteration in computing the propeller performance characteristics and the comparison with the experiment and the calculated result of the full panel method. The agreement is satisfactory.

Table 1

performance / iteration number	K_T	$10K_Q$
1	0.2137	0.340
2	0.1353	0.235
3	0.1570	0.265
4	0.1498	0.255
5	0.1522	0.259
experiment[9]	0.1612	0.286
full panel method[10]	0.159	0.297

case 4. Flow over a Backstep Stern Fitted Duct with Rotor and Stator

This case is an illustrative calculation to illustrate the capability of the present method. The configuration is a stern of axisymmetric body with the backstep fitted a duct with rotor and stator. Figure 11 shows the calculated flow field around this configuration. The calculations are also carried out for two forms of axial distribution of body force shown in Figure 12. Figure 13 shows the calculated velocity profiles for these two forms of axial distribution of body force. From the above figures it can be seen that the essential phenomena such as separation, vorticity, deceleration and contraction can be realistically predicted and the influence of the axial distribution form of body force can be responded.

CONCLUSION

A numerical method based on the H-type boundary fitted grid system, semi-staggered grid discretization and the new calculation equation for pressure was developed. Numerical results indicate that this numerical method is effective and is specially suitable to solve the internal and external flow field problem. In order to extend the availability of the present method the effects of the appendage and strut should be incorporated in the further research work.

ACKNOWLEDGMENT

The authors would like to express their thank to Ms.W.P.Xing for her help is carrying out the hull-propeller interaction calculation.

REFERENCES

[1] Schmiechen M. and Zhou L. D., " An Advanced Method for Design of Optimal Ducted Propeller behind Bodies of Revolution", Proc. of SNAME Spring Meeting, Pittsburgh, 1988.

[2] Yang, C.I., Hartwich, P. and Sundaram, P., "A Navier-Stokes Solution of Hull-Ring Wing-Thruster Interaction", 18th ONR Symposium on Naval Hydrodynamics,1990

[3] Dai, M.H., Gorski, J.J. and Haussling, H.J., "Computation of an Integrated Ducted Propulsor/Stern Performance in Axisymmetric Flow.", Proc. of Propellers/Shafting '91 Symposium, Virginia, Sep. 17-18, 1991

[4] Thompson,J.F., "Numerical Grid Generation", Morth Holland, N.Y.,1982

[5] Zhao, F. and L.D.Zhou, "A Coupled Generation Method for the General Three-Dimensional Multi-Block Grid", to be presented at Journal of Hydrodynamics.

[6] Chorin, A. J., " A Numerical Method for Solving Incompressible Viscous Flow Problems", Journal of Computational Physics, Vol.2 (1967), pp12-26

[7] Zhao, F. and L.D.Zhou, "The Flow Field Calculation around the Pump Jet", CSSRC Report,1993

[8] Stern, F., Kim, H.T., Patel, V.C. and Chen, H.C., "A Viscous Flow Approach to the Computation of Propeller-Hull Interaction", Journal of Ship Research, Vol. 32, No. 4, Dec. pp246-262, 1988

[9] Ye, Y. P., China Ship Scientific Research Center, Private Communication, April, 1994

[10] Xing, W. P., " Iteration Calculation in Panel Method for Performance Prediction of Multi-Body Flow.", CSSRC Report 1993

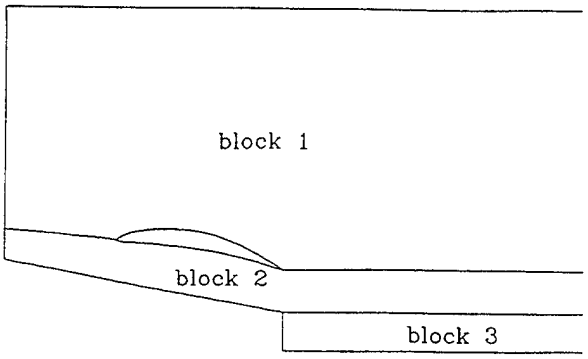


Fig. 1 Multi-Block Grid Region

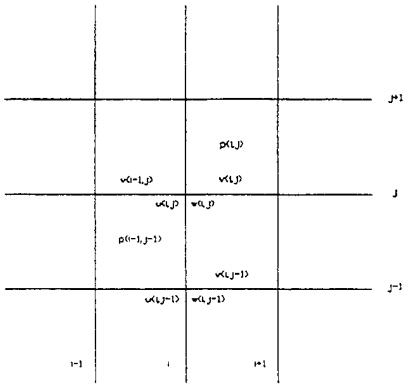


Fig. 2 Semi-Staggered Grid System

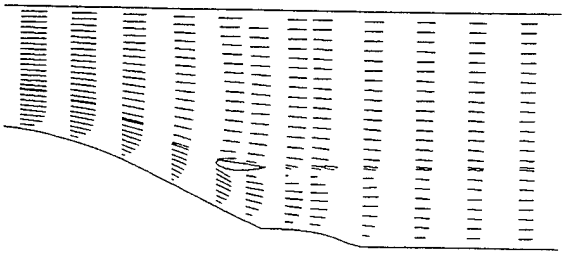


Fig. 3 Calculated Flow Field for Case 1

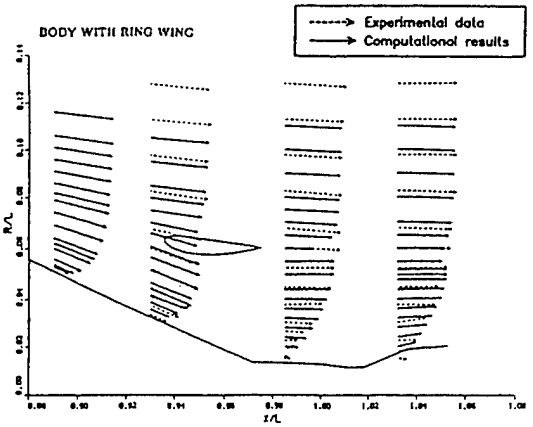


Fig. 4 Velocity Vectors in Stern Region for Case 1
(Experiment and Yang's Method)

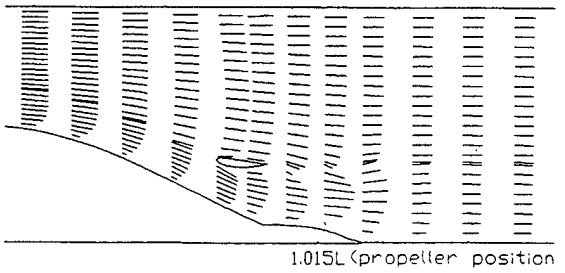


Fig. 5 Calculated Flow Field for Case 2

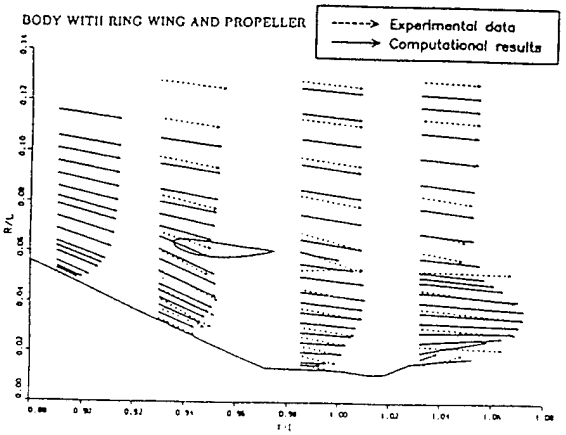


Fig. 6 Velocity Vectors in Stern Region for Case2
(Experiment and Yang's Method)

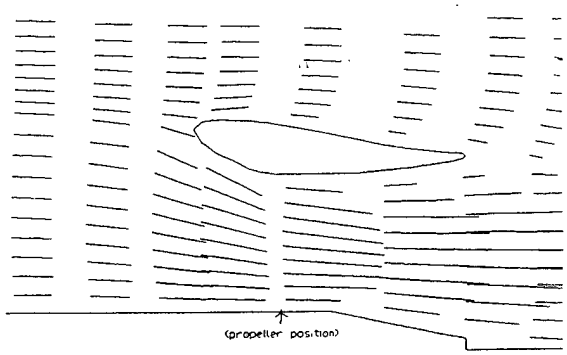


Fig. 7 Calculated Flow Field for Case 3

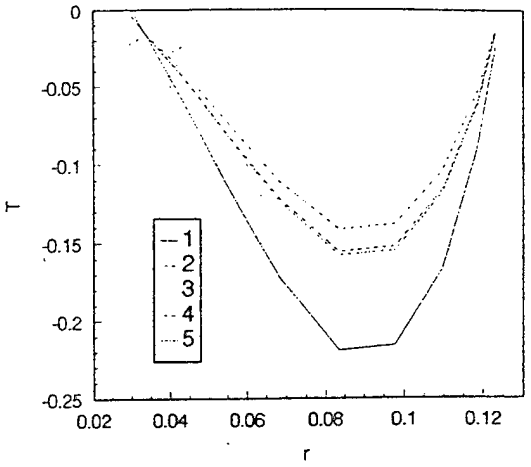


Fig. 9 Thrust Distribution for Propeller 6510 in Duct BD18

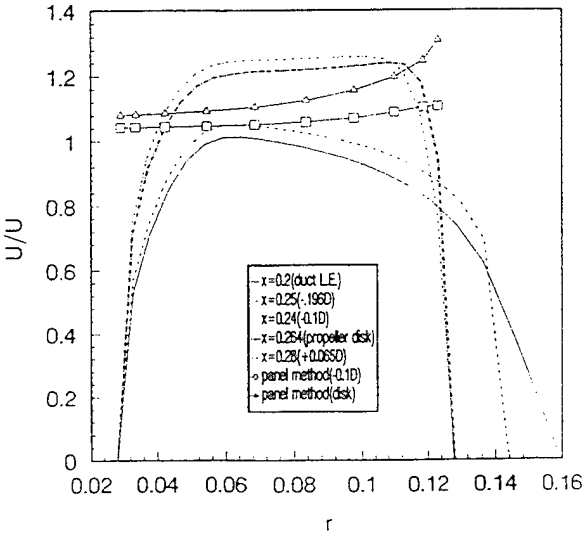


Fig. 8 Normal Wake of Duct BD18

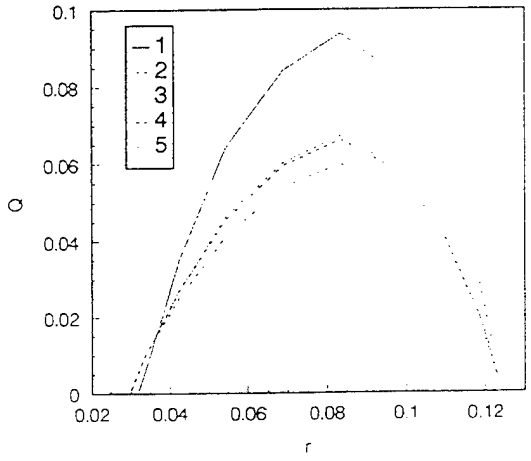


Fig. 10 Torque Distribution for Propeller 6510 in Duct BD18

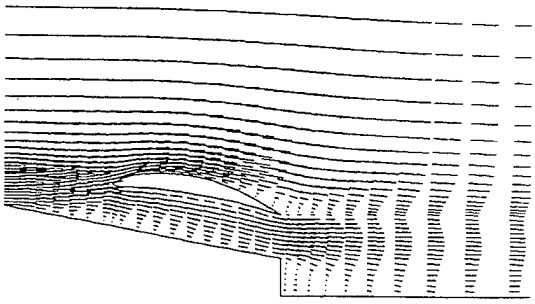


Fig 11. Calculated Flow Field For the Axisymmetric Body with a Backstep Stern Fitted a Duct

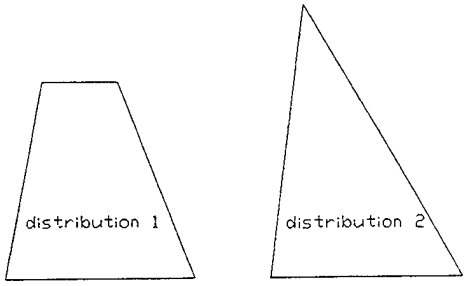


Fig. 12 Two Kind Axial Distribution Forms of Body Force Field

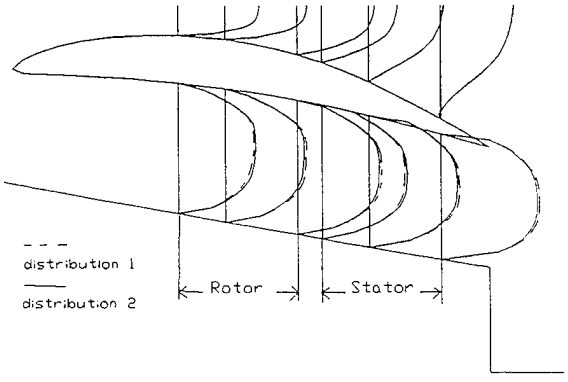


Fig. 13 Calculated Velocity Profiles for Two Axial Distribution Forms of Body Force Field

DISCUSSION

M. Schmiechen
Berlin Model Basin, Germany

Our colleagues at CSSRC are to be congratulated on the progress they have made in computing the flow field around ducted propulsors behind bodies of revolution since our joint project. We at VWS, the Berlin Model Basin, have continued our line of research as well. The basic idea of this systems engineering approach is to design for effective thrust rather than actual thrust. This is achieved by treating propulsors consistently as pumps and in the first place determining the design conditions for the actuators, i.e., the pump stages, for optimum propulsive performance (Schmiechen, 1993, 1994).

The advantage of this design for the effective thrust is, that from the beginning only optimum conditions are considered and that all interactions between hulls and propulsor components are implicitly accounted for without approximation at any load condition. The effective thrust equals the effective resistance, which does not necessarily equal the towing resistance for innovative hull integrated propulsor configurations. The actual thrust at the pump stage is not designed for as in all other methods, but is obtained at the end of the design as a by-product as usual in pump design. As the thrust at the duct, which roughly equals the suction at the hull, the actual thrust at the pump stage is irrelevant as far as the propulsive performance is concerned.

Along these lines ducted propellers for a body of revolution have been designed, manufactured and tested. The blade design on the basis of profile data from axial flow conditions was inadequate and will in future be replaced by CFD methods for pump stages developed at many places. Validation of design and computational procedures for these wake adapted configurations by model and full scale tests require of course adequate innovative test and analysis procedures based on local measurements or propulsion tests alone as proposed and successfully developed by the present discusser several years ago. (Schmiechen, 1991).

Additional references:

Schmiechen, M.: Entwurf und Bewertung von Düsenpropellern als Pumpen.
Presented at the STF Spechtag at Berlin/Potsdam on September 03./04. 1993. Trans. STG 87(1993).

Schmiechen, M.: Design and Evaluation of Ducted Propellers as Pumps.
To be presented at the International Shipbuilding Conference on the occasion of the Centennial of the Krylov Shipbuilding Research Institute at St. Petersburg on October 08./12. 1994.

Schmiechen, M.: 2nd INTERACTION Berlin '91. 2nd International Workshop on the rational theory of hull propeller interaction and its applications. VWS, the Berlin Model Basin, June 13./14. 1991. Proceedings. Mitteilungen der Versuchsanstalt für Wasserbau and Schiffbau, Heft 56, 1991.

Computation of Unsteady Viscous Marine Propulsor Blade and Wake Flow

B. Chen, F. Stern, W. Kim
(University of Iowa, USA)

ABSTRACT

Unsteady viscous-flow results are presented for the realistic marine-propulsor P4119 and P4132 geometries with idealized temporally and spatially oscillating axial inflows. The results are encouraging in demonstrating the feasibility of such large-scale computations and initial physical understanding of the complex unsteady three-dimensional flow. Fourier-series analysis is performed enabling discussion of amplitude and phase variations, which include large overshoots and lags/leads that, in general, correlate with the instantaneous angle of attack and, for the case of the spatial inflow, traveling-wave nature of the flow and agreement with the limited available data. However, clearly considerably more work needs to be done with regard to further development of the computational method and explication of the flow physics in order to reach the ultimate goal of complete configurations and propulsor-body interactions. Lastly, some concluding remarks are provided, including comparison with inviscid-flow methods, prognosis for improvements, and future work.

NOMENCLATURE

c	chord length
C_{ln}	nth-harmonic section lift coefficient
C_p	pressure coefficient ($=2p/\rho VR^2$)
ΔC_p	pressure difference
D	propeller diameter
f,f_n	Fourier-series variable and nth-harmonic amplitude, respectively
J	advance coefficient ($=U_o/nD$)
K_Q	thrust coefficient ($=T/\rho n^2D^4$)
K_T	torque coefficient ($=Q/\rho n^2D^5$)
L	wake half width
n	(1) propeller revolutions per second ($=\omega/2\pi$) (2) Fourier-series harmonic [=0 (steady) and >0 (unsteady)]
p	pressure
Q	torque
R	propeller radius
Re	Reynolds number ($=U_oD/\nu$)
s	distance along chord or pitch helix
S_i,etc.	solution-domain boundaries
T	thrust
U_i,U_n	total and nth-harmonic amplitude axial inflow, respectively
U_{mean}	0th-harmonic circumferential-average axial velocity
U_o	freestream velocity
U_τ	wall-shear velocity
VB	streamwise pitchline velocity in noninertial coordinates ($=W\cos\phi+U\sin\phi$)
ΔVB	wake-velocity deficit
VN	normal pitchline velocity in noninertial coordinates ($=W\sin\phi-U\cos\phi$)
VR	resultant section inflow $[=U_o^2+(\omega r)^2]^{1/2}$
V	Reynolds-averaged velocity components in inertial or noninertial cylindrical coordinates (=U,V,W)
x,r,θ	cylindrical coordinates
y,y^+	normal distances
α,α_n	total and nth-harmonic amplitude angle of attack, respectively
γ,γ_n	phase and Fourier-series nth-harmonic phase, respectively
δ^*	displacement thickness
θ	momentum thickness
ν	fluid kinematic viscosity
ν_t	eddy viscosity
ξ	frequency parameter ($=\omega U_o/D$)
ξ,η,ζ	nonorthogonal curvilinear coordinates
ρ	fluid density

ϕ pitch angle
Ω propeller angular velocity (=ω,0,0)

INTRODUCTION

In a companion paper at this symposium [1], computational fluid dynamics (cfd) steady-flow results for the realistic SR7 turboprop and marine-propulsor P4119 and P4842 geometries are presented, which showed overall good agreement with the data and enable explication of the nature of the complex three-dimensional viscous blade and wake flow. The present paper represents part of concurrent work for unsteady-flow calculations, which is the ultimate goal, including complete configurations and propulsor-body interactions.

The initial effort [2] was for two-dimensional flow and addressed three issues of particular importance in extending cfd for this goal: (1) forced unsteady flow (i.e., resolution of blade boundary layers and wakes with traveling-wave external flows, including comparisons with the Massachusetts Institute of Technology flapping-foil experiment, a parametric study of the effects of frequency, waveform, and foil geometry, and detailed analysis); (2) interaction of natural and forced unsteady flows (i.e., harmonic forcing of the naturally unsteady wake of a flat plate at incidence using an oscillating body-force field and trailing-edge flap); and (3) overlaid grids for resolution of fixed (hull) and moving (propulsor) boundary problems. The results are encouraging in showing close agreement with the data and successful application of overlaid grids and important in documenting the complex physics for such flows (i.e., boundary layers and wakes with analogy to Stokes layers and two-layer structure, upstream/downstream traveling pressure waves induced by viscous-inviscid interaction, and wake receptivity with lock-in, quasi-periodic, chaotic, and non lock-in states) and need for cfd.

The present effort involves extensions of [1,2] for unsteady three-dimensional viscous flow for realistic marine-propulsor geometries P4119 and P4132. Two initial test cases were selected, which, although idealized in maintaining blade-to-blade periodicity, are representative of the practical situation while reducing the scale of the computations, i.e., temporally and spatially oscillating axial inflows, which, hereafter, are simply referred to as temporal and spatial inflows. Some limited data is available for the latter case [3]. Although not as developed as [1,2], the work shows promise of cfd for the present application.

In the following, the computational method is described and the computational conditions, grids, and uncertainty are given. Then, the results are discussed for the temporal and spatial inflows, including comparisons with the data for the latter case. Also, steady-flow results are discussed for P4132, including comparison to the solution of [1] for both P4132 and P4119 and the mean values for the spatial inflow. Lastly, some concluding remarks are provided, including comparison with inviscid-flow methods, prognosis for improvements, and future work.

COMPUTATIONAL METHOD

[1,2] are based on extensions of [4] for realistic marine-propulsor geometries and time-accurate two-dimensional unsteady-flow calculations, respectively. Although, in principle, [1] could be directly extended for unsteady-flow calculations along the lines of [2], the scale of the computations for three-dimensional flow made such an approach prohibitive with regard to computational efficiency; therefore, further developments were required. In particular, the Piso- was replaced by a MAC-type velocity-pressure coupling algorithm along with additional vectorization. These modifications led to about a 20% increase in computational efficiency. The following provides an overview.

The unsteady Reynolds-averaged Navier-Stokes (RaNS) and continuity equations with the Baldwin-Lomax turbulence model are solved for the Reynolds-averaged velocity components $V=(U,V,W)$, pressure p, and eddy viscosity ν_t. The transport equations for V are written in noninertial cylindrical coordinates (x,r,θ) rotating with constant angular velocity $\Omega=(\omega,0,0)$ in the physical domain and partially transformed into numerically-generated, boundary-fitted, non-orthogonal, curvilinear coordinates (ξ,η,ζ). Variables are nondimensionalized using the freestream velocity U_0 (=1), propeller diameter D (=1), and density ρ. The transformed equations are solved using a regular grid, finite-analytic discretization, a, as already mentioned and to be described next, MAC-type velocity-pressure coupling algorithm, and the method of lines. Sub iterations for both pressure and velocity are used sequentially to obtain time-accurate solutions. For laminar flow, $\nu_t=0$ and V and p are interpreted as instantaneous values.

With a given initial condition (or solution at time t), the pressure at time $t+\Delta t$ is determined by solving a Poisson equation based on projected divergence-free velocity components.

The velocity at t+Δt is written in terms of the velocity at t using an explicit backward time derivative

$$(U_i)^{n+1}=(U_i)^n+\Delta t[(H_i)^n-\frac{1}{J}b_i^k\frac{\partial}{\partial\xi^k}p^{n+1}] \quad (1)$$

where $(H_i)^n$ contains convection, diffusion, and source terms, i.e.

$$(H_i)^n=\frac{1}{R_{eff}C_p}[\sum_{nb=1}^{8}C_{nb}(U_i)_{nb}+C_p(C_U(U_i)_U+$$

$$C_D(U_i)_D)-\{1+C_p(C_U+C_D)\}(U_i)_p-C_p(S_{U_i})_p]^n \quad (2)$$

and J is the Jacobian, b_i^k is the metric tensor, and C_{nb}, C_p, etc. are the finite-analytic coefficients. The continuity equation at t+Δt is given by

$$\frac{1}{J}\frac{\partial}{\partial\xi^m}[b_k^m(U_k)^{n+1}]=0 \quad (3)$$

Substituting (3) into (1) yields the desired Poisson equation

$$\frac{\partial}{\partial\xi^j}[\Delta tJg^{jk}\frac{\partial}{\partial\xi^k}p^{n+1}]=\frac{\partial}{\partial\xi^k}[b_k^m(U_k+\Delta tH_k)^n] \quad (4)$$

High-frequency oscillations associated with the use of a regular grid are avoided through the addition of artificial 4th-order dissipation implicitly by averaging coefficients and velocities at the staggered nodes. Figure 1 provides a flow chart of the computational method.

The physical and computational domains are shown in figure 2. The boundary conditions are specified as follows: on the inlet plane S_i, $V=(U_i,0,\omega r)$ and $p=0$ (temporal inflow) or $p_\xi=0$ (spatial inflow); on the exit plane S_e, which is located in the far wake, axial diffusion is negligible $V_{\xi\xi}=0$ and p is extrapolated (temporal inflow) or a zero-gradient condition is used $p_\xi=0$ (spatial inflow); on the outer boundary S_o, $(U,W)=(U_i,\omega r)$, V is obtained from the continuity equation, and p is obtained from the Euler equation (temporal inflow) or $p_\eta=0$ (spatial inflow); on the shaft and blade surfaces S_s, S_{bs}, and S_{bp}, no-slip condition, i.e., $(U,V)=0$ and $W=0$ and ωr for rotating and nonrotating parts, respectively; on the periodic boundary planes S_{ps} and S_{pp}, periodic boundary conditions, i.e., $V/p(\xi,\eta,\zeta)=V/p(\xi,\eta,\zeta+\zeta_p)$ where ζ_p corresponds to the blade-to-blade interval; and on the symmetry axis L_s, symmetry conditions $(V,W)=0$ and $\partial(U,p)/\partial\eta=0$.

The grid was obtained using a modified version of PMESH [5], which employs algebraic methods with transfinite interpolation. H-grids were used with clustering near the shaft and blade surfaces and leading-, trailing-edge, and tip regions.

COMPUTATIONAL CONDITIONS, GRIDS, AND UNCERTAINTY

The temporal and spatial inflow calculations are for P4119 and P4132, respectively, which corresponds to [1,3]. The propulsor geometries and cfd evaluation and data comparison locations (spatial inflow) are shown in figure 3. The cfd is for laminar and turbulent flow, whereas the data (spatial inflow) is for natural transition. In all cases, the Reynolds number ($Re=U_oD/\nu$) is 7.67×10^5. In general, only the turbulent-flow results are presented and discussed.

A partial view of the P4132 grid is shown in figure 4. The P4119 grid is similar to that used in [1]. The primary difference between the P4132 and P4119 grids is that in the former case a more uniform distribution is used in the blade-to-blade region in order to resolve the spatial variations, which, unfortunately, somewhat reduces the resolution of the boundary-layer and wake region [i.e., a reduction from 10-14 (P4119) to 5-6 (P4132) grid points in the boundary-layer and wake region]. The inlet, exit, and outer boundaries for P4119 and P4132 are located at x=(-3,4) and (-1.5,4), respectively, and r=2. The first grid points off the body surface are located in the range y^+ ($=Re U_\tau y$)<6-7. The grid distributions are 100x45x50=225000 (P4119) and 100x45x62=279000 (P4132). The P4119 and P4132 grids are relatively fine and coarse, respectively, with regard to resolution of the steady blade boundary layer and wake due to the differences in number of grids points in this region. The resolution requirements for the unsteady blade boundary layer and wake have yet to be determined; however, based on [2], both present grids are relatively coarse for this purpose. Note that single job run time restrictions and current overall supercomputer resources precluded the use of finer grids.

The values of the time increment and underrelaxation factors for velocity and pressure are: .0052 (temporal inflow) and .0011 (spatial

inflow); .5; and .1. The time increments correspond to 160 (temporal inflow) and 120 (spatial inflow) per period T. The CRAY C90 time and central memory were about 4 hr per period and 32 mw. The time-accuracy sub iteration convergence criterion was that the residual for all variables be about 10^{-4} with a minimum of 100 and 25 sub iterations for pressure and velocity, respectively.

The format of the discussions follows [1], i.e., performance, pressure and surface-streamline distributions, circumferential-averaged velocity profiles, phase-averaged flow, boundary-layer and wake development, and tip and hub/root vortices with the focus on the modification of these flow features due to the temporal and spatial inflows. Storage restrictions precluded complete analysis of the solutions over an entire period, although this problem hopefully will be remedied for future work. The analysis includes performance time histories, other flow features at t/T=(.25,.5,.75,1), and performance, pressure distribution, and boundary-layer and wake profile Fourier-series analysis

$$f(x,r,\theta)=f_o(x,r,\theta)+\sum_{n=1}^{2} f_n(x,r,\theta)\sin[n\xi t+\gamma_n(x,r,\theta)]$$

$$f_n(x,r,\theta)=(a_n^2+b_n^2)^{1/2}$$

$$\gamma_n(x,r,\theta)=\tan^{-1}(a_n/b_n) \qquad (5)$$

$$a_n=\frac{2}{T}\int_0^T f(x,r,\theta)\cos(n\xi t)dt$$

$$b_n=\frac{2}{T}\int_0^T f(x,r,\theta)\sin(n\xi t)dt$$

where γ_n is with respect to U_i (temporal inflow) or blade mid chord at top dead center (spatial inflow) and f represents any of the relevant variables. Also, comparisons are made with the Theodorsen and Sears/Horlock solutions for the temporal and spatial inflows, respectively, although, in the former case, the analogy is indirect due to the differences in far-field pressure and pressure gradient.

The following discussions are based on the complete results, which as indicated in figure 2, are extensive; however, for brevity, only representative results are shown. Additional results are available upon request from the authors.

TEMPORAL INFLOW

For the temporal inflow:

$$U_i=U_o+U_1\sin\xi t \qquad (6)$$

$$-\partial p/\partial x=U_1\xi\sin(\xi t+\pi/2) \qquad (7)$$

$$\alpha=\alpha_o+\alpha_1\sin(\xi t+\gamma_1) \qquad (8)$$

where U_1 (=.05) is the 1st-harmonic velocity amplitude, $\xi=\omega U_o/D$ (=7.54) is the frequency parameter, $\alpha_1=U_1\cos^2\phi/\xi r$ is the 1st-harmonic angle-of-attack amplitude for small U_1 (i.e., $U_1<<U_o$ or ωr), and $\gamma_1=\pi$. For r/R=(.5,.7,.9), $\alpha_1=(1.04^o,.89^o,.75^o)$ [or $\alpha_1=(\alpha_{max}-\alpha_{min})/2=(1.15^o,.95^o,.8^o)$] and the reduced frequency $k=\omega c/2VR=(.776,.62,.385)$. This corresponds to a relatively small-amplitude low-frequency oscillation with, as will be shown next, extreme response amplitudes, i.e., greater than the quasisteady values. Note that in the far field the pressure increases linearly with x due to the form of (7). Figure 5 shows $(U_i-U_o)/U_1$ and $(\alpha-\alpha_o)/\alpha_1$ vs. t and is useful for interpretation of the phase response.

The performance is shown in figure 6. A periodic solution is obtained within about 3 periods. The mean values $(K_T,K_Q)=(.138,.0248)$ indicate about a 10% difference from the steady solution of [1] due to changes both in the computational method and grid. Discussion of differences between the present and steady solution of [1] and between the mean values and the steady solution is deferred for P4132 and the spatial inflow. The 1st-harmonic amplitudes $(K_{T1},K_{Q1})=(.039,.0079)$ are 56 and 204%, respectively, larger than the quasisteady values, which is unexpected; since, such values are usually considered an upper bound. The phases indicate about 10^o lag and 30^o lead, respectively, relative to α. Note that due to geometric effects tip loading primarily contributes to K_T, whereas the full span loading contributes to K_Q such that the phase of the latter is consistent with the Theodorsen solution and the former is not due to viscous effects, as shown next in consideration of the surface-pressure distribution.

Figures 7a-c show ΔC_p(r/R=.7), ΔC_{p1}, and γ_1 profiles. ΔC_p oscillates about the mean value in correlation with α. ΔC_{p1} amplitude decreases with increasing radii, which is consistent with the corresponding decreasing α_1 values. At the outer radii, the amplitude is constant over the chord, whereas at the inner

radii, peaks are displayed near the leading and trailing edges. At the outer radii, the phase is nearly zero relative to α, except near the leading edge where relatively small leads are indicated. At the inner radii, large phase leads are indicated increasing from r/R=.7 to .5 and from the leading to the trailing edge. The section lift coefficient 1st-harmonic amplitude and phase for r/R=(.5,.7,.9) values are C_{l1}=(.072,.06,.045) and γ_1=(70°,23°,5°). The ΔC_p contours (figure 7d) display the overall distributions. The trends indicate similarity with the Theodorsen solution, especially for the mid radii: decreasing ΔC_{p1} amplitudes with increasing radii, which is consistent both with the present corresponding decreasing α_1 and increasing k values; constant ΔC_{p1} amplitude over the chord except for leading- and trailing-edge peaks; and corresponding section lift coefficient 1st-harmonic amplitude and phase values C_{l1}=(.061,.039,.021) and γ_1=(29°, 20°,5°). However, differences are also evident due to viscous trailing-edge root separation and tip vortex effects

The surface-pressure pitchline gradient 1st-harmonic amplitude on both sides is fairly flat, except for large leading- and trailing-edge peaks. On the pressure side, the phase for 0<s/c<.5 is about the average of α and $-p_x$ (i.e., 135°), and for .5<s/c<1, the outer radii follow α and the inner radii $-p_x$, whereas on the suction side, the phase is complex, but seems to correlate more with $-p_x$ than α.

The surface streamlines and wall-shear stress contours indicate oscillations about the mean patterns with decreased/increased trailing-edge root separation and tip-vortex effects on the suction and pressure sides for t/T=.25/.75 and .5/1, respectively. The former and latter are approximately in phase and lead α, respectively.

Figure 8 shows the circumferential-average velocity profiles. For the upstream plane, (U,V) follow U_i, but in and out of phase, respectively (i.e., the maximum/minimum for U corresponds to U_i and vice versa for V), and W is relatively unaffected, except near the root and tip. For the downstream plane, all three components correlate with α, but with phase differences: U indicates a lag, which also correlates with K_{T1}; and (V,W) are approximately in phase (i.e., large loading corresponds to increased radial and tangential velocities, which is consistent with the off-design calculations of [1]), except for W near the root and tip where a lag is indicated, which also correlates with U and K_{T1}. Other than the upstream plane W, the amplitudes are extreme, which corresponds to propeller-induced velocity and pressure overshoots and further explains the upstream/downstream V response. Figure 9 shows the radial circulation distribution deduced from the swirl profiles, which correlates with α similarly as W and, additionally, indicates extreme tip loading for t/T=1.

Figures 10-11 show the phase-averaged flow for the upstream and downstream planes for inertial and noninertial coordinates, respectively. The mean patterns and profiles are nearly the same as [1], although some detailed differences are evident. In general, the flow for the upstream and downstream planes correlates with U_i and α, respectively, in a similar manner as described earlier for the circumferential-average velocity profiles.

For the upstream plane: the axial-velocity contours display leading-edge stagnation effects, which oscillate about the mean with increased/decreased effects that correlate with α (i.e., minimum/maximum effects for t/T= .25/.75); the cross-plane vectors and particle traces indicate maximum inward/outward radial flow for .25/.75; and the detailed circumferential profiles show distortions in the stagnation region and (V,W) differences for the pressure vs. suction sides.

For the downstream plane: the pitchline -velocity contours display oscillations of the blade wake with maximum (t/T=1) and minimum (t/T=.5) widths corresponding to the loading; the cross-plane vectors and particle traces indicate minimum/maximum tip and hub/root vortices for t/T=.5/1, which also correlates with the loading; and the detailed circumferential velocity profiles show similar trends as the upstream plane, but with increased variations.

Figure 12 shows the boundary-layer development for r/R=.7. On the suction side, the shape of the displacement-thickness curves vs. t/T are similar to the mean curve, but with thinning/thickening which correlates with α, except for t/T=.75 where the shape is different due to the relatively larger values near the leading edge. On the pressure side, the displacement-thickness variations with t/T are relatively small. The detailed trends are exhibited by the pitchline- and radial-velocity 1st-harmonic amplitude and phase profiles. For the pitchline profiles: on the pressure side, for the inner radii the response is minimal, whereas for the outer radii large overshoots and phase leads are exhibited with decreasing magnitude for increasing s/c and r/R; and on the suction side, very large overshoots are exhibited with decreasing and increasing magnitude for increasing s/c and r/R, respectively, and phase lags/leads for the inner/outer radii. For both sides, the phase is

approximately consistent with that for the surface-pressure pitchline gradient. For the radial profiles: on the pressure side, overshoots are exhibited with no discernible s/c trends and increasing magnitude and decreasing phase lags for the outer radii; and on the suction side, the trends are similar, except increased and more complex amplitude profiles and phase leads.

Figure 13 shows the wake development for r/R=.7. The profiles are complex with large amplitude and phase variations. Figure 16 shows the wake deficit and half-width parameters, which lag and are approximately in phase with α, respectively.

The perturbation vectors and particle traces for r/R=.7 (figure 14) display the overall nature of the boundary-layer and wake flow: effects of U_i maximum/minimum and =0 for .25/.75 and .5,1, respectively; secondary separation zones on the suction side near the leading/trailing edge for .5/1; and large perturbations in the wake.

Lastly, the details of the tip vortex development and evolution are considered (figure 15). The vectors and particle traces and parameters display the overall and detailed trends, respectively: the maximum vorticity and contraction and the circulation and core size are 90° out of phase and lag and lead α, respectively. The former correlates with the radial circulation distribution and K_T.

P4132 STEADY FLOW

Before discussing the results for the spatial inflow, it is useful to discuss the steady-flow solution for P4132, including a comparison to the solution of [1] for both P4132 and P4119 and the mean values for the spatial inflow. The propellers are similar in that they have the same blade number, hub-diameter ratio, and thickness distribution and mean line. The difference is that the chord length of P4132 is half of P4119 with increased maximum thickness and camber distributions. However, both have nearly the same design-condition performance: J=.833; K_T=0.154; and K_Q=.027 (P4132) vs. .029 (P4119).

The performance is shown in table 1. The agreement with the data is relatively poor in comparison to the steady solution of [1] due, as already noted, to changes both in the computational method (i.e., velocity-pressure coupling algorithm) and grid. The reasons are uncertain, but indicate the need for continued improvements in the former. The mean values and steady solution differ by about 3-4%. The differences for the detailed flow between the steady solution and both the steady solution of [1] and the mean values are relatively small (except in the boundary layer); therefore, the following discussion focuses on the differences between the detailed flow for P4132 vs. P4119. The mean values for P4132 are provided in figures 19-23, 25-26, and 28. In general, the differences are consistent with expectation due to the increased thickness and camber for P4132.

Table 1 Performance: P4132

	K_T	$10K_Q$
Exp.	.155	.273
Steady [1]	.145	.255
%diff. vs exp.	6.5	6.6
Steady	.133	.234
%diff. vs exp.	14.2	14.3
Mean	.127	.225
%diff. vs exp.	17.0	17.6

At the outer radii, the surface-pressure distributions are similar in shape, but P4132 has larger pressure difference and pitchline gradient. At the inner radii, additionally the shapes differ due to the increased trailing-edge root separation for P4132. The surface streamlines for P4132 indicate increased trailing-edge root separation and spanwise flow, i.e., outward radial flow near the trailing edge for the full/half span on the suction/pressure sides. The circumferential-average velocity profiles and phased-average flow are nearly the same for the same relative axial positions from the blade leading and trailing edges. Some relatively small differences are evident primarily due to the effects of the increased trailing-edge separation for P4132: increased upstream outward radial flow near the hub; thicker hub boundary layer; and thicker blade boundary layers and wakes. The boundary-layer and wake development shows large differences for P4132 due to the earlier mentioned increased surface-pressure difference and pitchline gradient and trailing-edge root separation and outward radial flow: increased boundary-layer thickness, especially on the suction side near the trailing edge; and wider wakes and faster recovery, especially for the inner radii. Lastly, the tip-vortex development and evolution are also similar, although P4132 indicates a faster reduction in the maximum vorticity and reduced contraction.

SPATIAL INFLOW

For the spatial inflow in the inertial frame:

$$U_i=U_0+U_6\sin(6\theta+\gamma_6) \qquad (9)$$

where U_0 is the mean velocity (i.e., 0th-harmonic) and U_6 and γ_6 are the 6th-harmonic velocity amplitude and phase, respectively, all of which were specified based on the data. For r/R=(.3,.5,.7,.9), U_0=(1.001,.97,1.018,1.007), U_6=(.0051,.08,.1375,.1891), and γ_6=(-73°,-82°,-74°,-69°). Note that: other harmonics were in the data, but not specified due to the present use of periodic blade-to-blade boundary conditions; U_i was modified (i.e., reduced) based on the experimentally determined decay factors between the screen (x/R=-.432) and propeller (x/R=0) planes for the without-propeller condition (about 12% for r/R=.7) since computationally such decay is negligible; and the nature of the screen wake is such that the amplitude of U_6 is substantially reduced for the inner radii. In the noninertial frame:

$$U_i=U_0+U_6\sin(\xi t+\gamma_6) \quad (10)$$

$$\alpha=\alpha_o+\alpha_6\sin(\xi t+\gamma_6) \quad (11)$$

where $\xi=6\omega U_o/D$ (=45.2), γ_6=(-107°,-98°,-106°,-111°), $\alpha_6=(\alpha_{max}-\alpha_{min})/2$=(.16°,1.9°, 2.5°,2.7°), γ_6=(93°,82°,74°,69°), and $k=6\omega c/2VR$=(2.73, 2.34,1.85, 1.15). Figures 16 and 17 show U_i(r/R=.7) vs. θ and $(U_i-U_0)/U_6$ and $(\alpha-\alpha_o)/\alpha_6$ vs. t, including, in the former case, curves for all the harmonics and only the 6th-harmonic both with and without the decay factor.

The performance is shown in figure 18. Here again, a periodic solution is obtained within about 3 periods. In spite of the earlier discussed discrepancy for the steady solution, the 6th-harmonic amplitudes $(K_{T6}/K_T, K_{Q6}/K_Q)$=(.22,.17) are within 10% of the data and, furthermore, indicate (20,15)% reductions from the quasisteady values, which is consistent with expectation. Both phases are 120°, which is within 1% of the data and indicates about a 45° lead relative to α.

Figures 19a-c show ΔC_p(r/R=.7), ΔC_{p6}, and γ_6 profiles. ΔC_p oscillates about the mean value in correlation with α. ΔC_{p6} amplitude increases with increasing radii, which is consistent both with the corresponding decreasing k and increasing α_6 values. At the outer radii, there is a large leading-edge peak and then the amplitude decreases towards the trailing edge, whereas at the inner radii, the amplitude is constant over the chord. The phase is nearly constant and indicates a lead relative to α (decreasing from about 60° to 30° from the outer to the inner radii), except near the trailing edge where the values for the inner and outer radii reduce and the mid radii increase. The section lift coefficient 6th-harmonic amplitude and phase for r/R=(.3,.7,.9) values are C_{l6}=(.026,.06,.06) and γ_6=(140°,126°,95°). The C_p contours (figure 19d) display the overall distributions. The trends indicate similarity with the Sears/Horlock solution, especially for the mid radii: leading-edge peak and then decreasing towards the trailing edge ΔC_{p6} amplitudes; nearly constant ΔC_{p6} phase; and corresponding section lift coefficient 6th-harmonic amplitude and phase values C_{l6}=(.005,.07,.1) and γ_6=(191°,136°,93°). However, differences are also evident due to viscous trailing-edge root separation and tip vortex effects.

The surface-pressure pitchline gradient 6th-harmonic amplitude on both sides is fairly flat, except for large leading-edge and small trailing-edge peaks. On the pressure side, for the outer radii the phase values are similar to those for ΔC_{p6} (i.e., lead α by about 30°-60°), whereas for the inner radii, the phase is about -90° for 0<s/c<.6 and 90° for .6<s/c<1. On the suction side, the phase shows large variations about an average value of about -90°.

The wall-shear stress contours show oscillations about the mean patterns with decreasing amplitude with radii (i.e., the inner radii are relatively unaffected), which is consistent with U_6. On the pressure side, the minimum/maximum values occur for t/T=.5/1, and on the suction side, vice versa. On both sides, the oscillations correlate with α. The largest effects are near the leading edge and tip for the former and latter, respectively. The surface streamlines are relatively unaffected.

Figure 20 shows the circumferential-average velocity profiles. For the upstream plane, (U,W) are relatively unaffected, whereas V displays oscillations about the mean such that the outer and inner parts of the profile are 90° out of phase, i.e., maximum inward/outward flow for t/T=1/.5 and vice versa for the outer and inner parts, respectively. For the downstream plane, U is relatively unaffected and (V,W) display oscillations about the mean: the outer part of the V and the W profile correlate with α, but with a $\xi x/U_{mean}$=177° phase shift due to the traveling-wave nature of the flow; and the inner part of the V profile leads α by about 45°. The radial circulation distribution (figure 21) is similar and consistent with the W profile.

Figures 22-23 show the phase-averaged flow for the upstream and downstream planes for inertial and noninertial coordinates, respectively.

For the upstream plane: the axial-velocity contours display leading-edge stagnation effects, which oscillate about the mean with increased/decreased effects that correlate with α at the leading edge (i.e., minimum/maximum effects for t/T=.25/.75) and the traveling-wave nature of the flow is apparent in the circumferential variations; the cross-plane vectors and particle traces indicate inward/outward movement of the position of maximum axial acceleration with the minimum/maximum positions corresponding to t/T= .5/1, which is consistent with the circumferential-average flow; and the detailed circumferential velocity profiles show the traveling-wave nature of the U component, including reduced amplitude for the inner radii and distortion within the stagnation region, the inward/outward oscillations of the V component, especially for the blade-to-blade region, and the circumferential oscillations of the W component, especially in the stagnation region.

For the downstream plane: the pitchline -velocity contours display oscillations of the blade wake with maximum (t/T=.5) and minimum (t/T=1) widths corresponding to the loading and, here again, the traveling-wave nature of the flow is apparent in the circumferential variations; the cross-plane vectors and particle traces indicate maximum/minimum tip and hub/root vortices for t/T=.5/1, which also correlates with the loading; and the detailed circumferential velocity profiles show similar trends as the upstream plane, but with increased variations.

Lastly, for the phased-averaged flow, figure 24 shows the variation of U/U_0 vs. $\theta-\theta_w$ (where $\theta=\xi t$ and θ_w are in the noninertial and inertial frames, respectively) for x/R=0 and r/R=(.5,.7,.9), including data for the mid radii. The trends (i.e., minimum value in the blade-to-blade region and large/small peaks on the suction/pressure sides) and magnitude are accurately and under predicted (by about 5%), respectively.

Figure 25 shows the boundary-layer development for r/R=.7. On the suction side, the shape of the displacement-thickness curves vs. t/T are similar to the mean curve, but with thickening/thinning which follow the loading. On the pressure side, the displacement-thickness variations with t/T are small. Significant three-dimensional effects are apparent, especially for increasing s/c and r/R. The detailed trends are exhibited by the pitchline- and radial-velocity 6th-harmonic amplitude and phase profiles. For the pitchline profiles: on both sides, overshoots are exhibited with decreasing and increasing magnitude for increasing s/c and r/R and phase lags/leads, which are, in general, consistent with the surface-pressure pitchline gradient. Two-layer structures are evident, but not clearly resolved. For the radial profiles: the mean profiles display the nature of the increased three-dimensional flow for P4132 vs. P4119; and on both sides, overshoots are exhibited with no discernible s/c trends and increasing magnitude for the outer radii and phase lags/leads for inner/outer radii.

Figure 26 shows the wake development for r/R=.7. The profiles are complex with large amplitude and phase variations. Also, the half-width parameter oscillations correlate both with α and the traveling-wave nature of the flow. However, here again, it is apparent the the level of resolution is reduced in comparison to the P4119 results as, e.g., exhibited by the deficit parameter.

The perturbation vectors and particle traces for r/R=.7 (figure 27) display the overall nature of the boundary-layer and wake flow. The patterns are similar to those shown in [2], but with reduced resolution as already noted.

Lastly, the details of the tip vortex development and evolution are considered (figure 28). The vectors and particle traces and parameters display the overall and detailed trends, respectively: the oscillations correlate both with α (i.e., maximum tip vortex for t/T=1) and the traveling-wave nature of the flow (i.e., wave lengths corresponding to $2\pi U_{mean}/\xi$=.167). The radial contraction and core size are relatively unaffected.

CONCLUDING REMARKS

Unsteady viscous-flow results have been presented for the realistic marine-propulsor P4119 and P4132 geometries with idealized temporally and spatially oscillating axial inflows. The results are encouraging in demonstrating the feasibility of such large-scale computations and initial physical understanding of the complex unsteady three-dimensional flow. Fourier-series analysis is performed enabling discussion of amplitude and phase variations, which include large overshoots and lags/leads that, in general, correlate with the instantaneous angle of attack and, for the case of the spatial inflow, traveling-wave nature of the flow and agreement with the limited available data. However, clearly considerably more work needs to be done with regard to further development of the computational method and explication of the flow physics in order to reach the ultimate goal of complete configurations and propulsor-body interactions.

Included in [3] were comparisons with inviscid methods from which it was concluded that the overall accuracy (i.e., over a range of screen-wake harmonics) for unsteady thrust and torque amplitude and phase was about 20-25%, although for certain harmonics the accuracy was improved (e.g., for the present case the accuracy was comparable to that shown here). Also, the results were dependent on prescription of the propeller wake model for which there is considerable uncertainty. Thus, the present work further supports the conclusion in [1] regarding the merit of viscous vs. inviscid methods for the present problem.

Future work involves further developments of the computational method in conjunction with applications both for unsteady marine-propulsor blade and wake flow and propulsor-body interactions and detailed analysis for explication of the flow physics. With regard to the former, critical issues involve: spatial and time accuracy; efficient and accurate velocity-pressure coupling algorithms; optimization for large-scale computations; refined and advanced grid-generation techniques, including overlaid grids for propusor-body interaction applications; and development and implementation of advanced turbulence models. These, of course, are all pacesetting issues for cfd and thus will require long-term effort. With regard to the latter, applications include: parametric study for the spatial inflow, i.e., additional calculations for the 3rd-, 9th-, and 12th-harmonic cases; inclined shafts; crashback and backing; and complete configurations.

Lastly, it is critical that more data be acquired both for idealized geometries in support of the development of appropriated turbulence models and for realistic propulsor and propusor-body configurations for validation.

ACKNOWLEDGMENTS

This research was sponsored by ONR under Grants N00014-92-J-1118 and N00014-91-J-1203 under the administration of Mr. Jim Fein and Dr. Ed Rood. Computer funds were provided by the NASA Numerical Aerodynamic Simulation Program and by ONR NAVOCEANO Primary Oceanographic Prediction System. Also, Dr. S.D. Jessup, David Taylor Model Basin, is gratefully acknowledged for his significant contributions to this work both in providing the data and in discussion of the results.

REFERENCES

1. Stern, F., Zhang, D.H., Chen, B., Kim, H.T., and Jessup, S.D., "Computation of Viscous Marine Propulsor Blade and Wake Flow," Proc. 20th ONR Symposium on Naval Hydrodynamics, Santa Barbara, CA, August 1994.

2. Paterson, E. G., "Computation of Natural and Forced Unsteady Viscous Flow with Application to Marine Propulsors," Ph.D. Thesis, Department of Mechanical Engineering, The University of Iowa, Iowa City, Iowa, May 1994; also, in part, Paterson, E. and Stern, F., "Computation of Unsteady Viscous Flow with Application to the MIT Flapping-Foil Experiment," Proceedings 6th International Conference on Numerical Ship Hydrodynamics, Iowa City, Iowa, August 1993.

3. Jessup, S.D., "Measurement of Multiple Blade Rate Unsteady Propeller Forces," David Taylor Research Center, Ship Hydromechanics Department Research and Development Report, DTRC-90/015 May 1990.

4. Kim, H.T. and Stern, F., "Viscous Flow around a Propeller-Shaft Configuration with Infinite-Pitch Rectangular Blades," J. Propulsion Vol. 6, No. 4, 1990, pp. 434-444.

5. Warsi, S.A., "User's Guide to PMESH-A Grid-Generation Program for Single-Rotation and Counterrotation Advanced Turboprops," NASA Contractor Report 185156, December 1989.

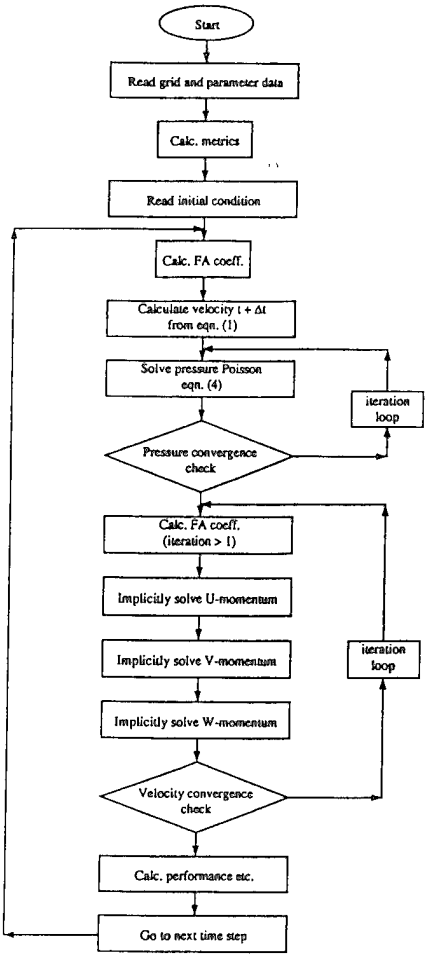
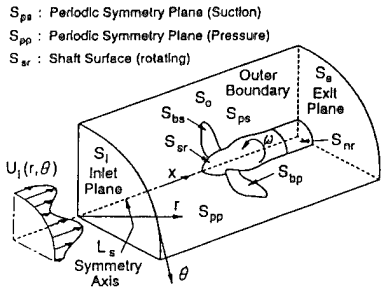
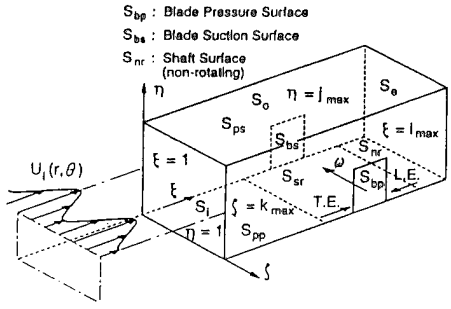


Figure 1. Computational method flow chart.

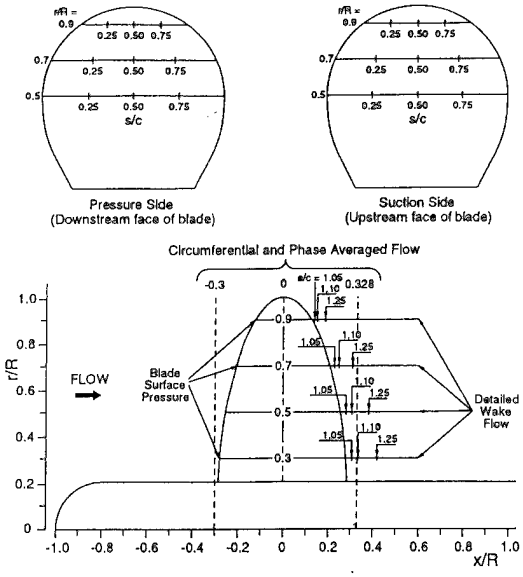


(a) physical domain

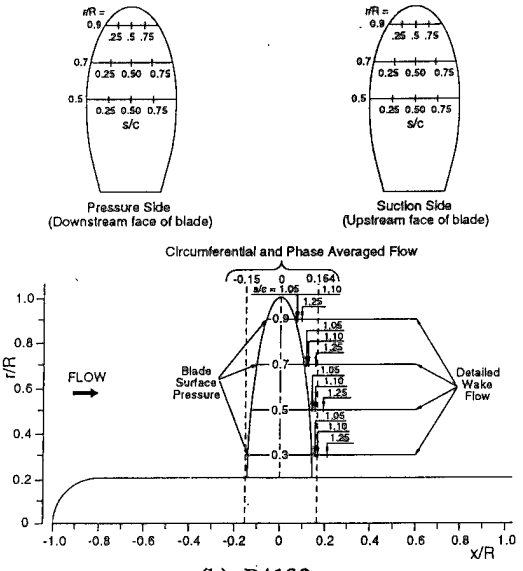


(b) computational domain

Figure 2. Definition sketch.



(a) P4119



(b) P4132

Figure 3. Propulsor geometries and summary of cfd evaluation and data locations.

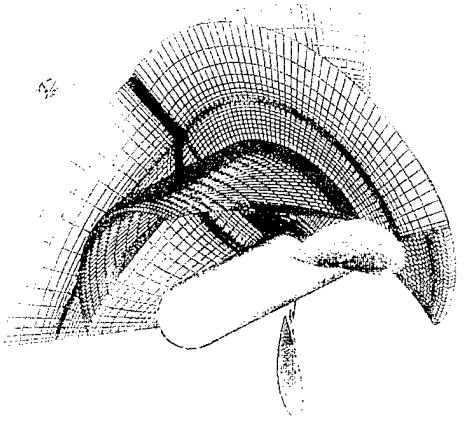


Figure 4. Computational grid: P4132.

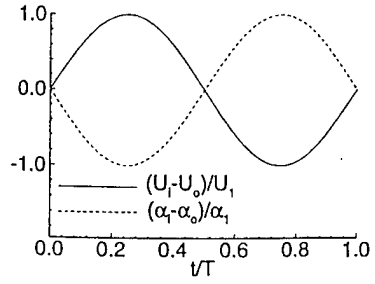


Figure 5. Temporal inflow 1st harmonic velocity and angle-of-attack amplitude.

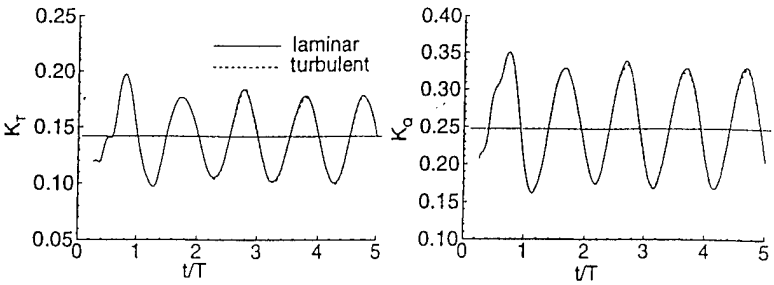
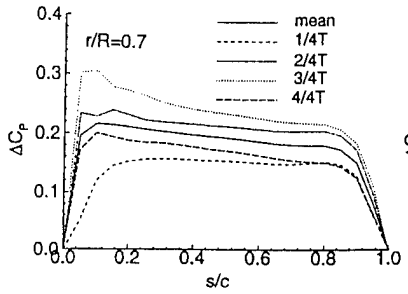
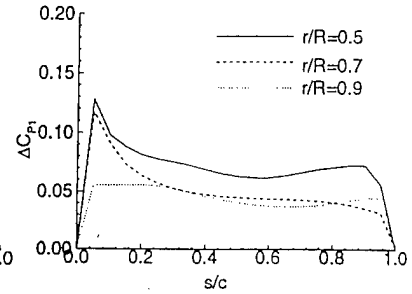


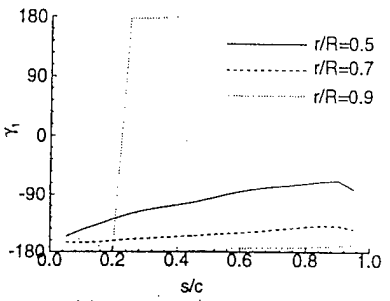
Figure 6. Performance time histories: P4119.



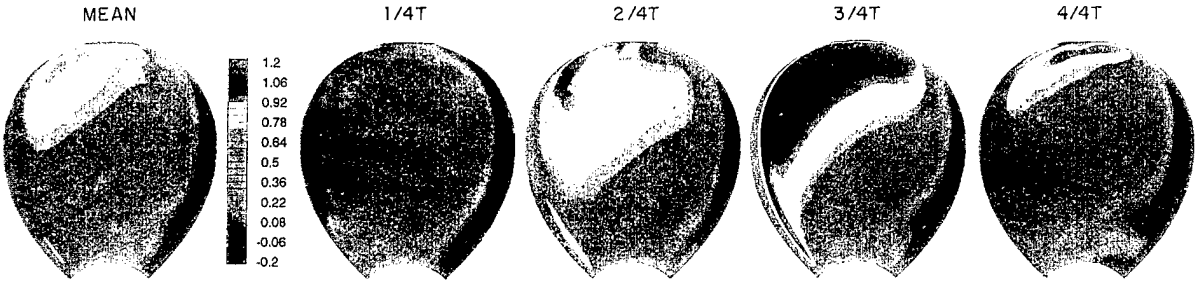
(a) pressure difference



(b) pressure-difference 1st-harmonic amplitude



(c) pressure-difference 1st-harmonic phase



(d) pressure-difference contours

Figure 7. Surface-pressure distributions: P4119.

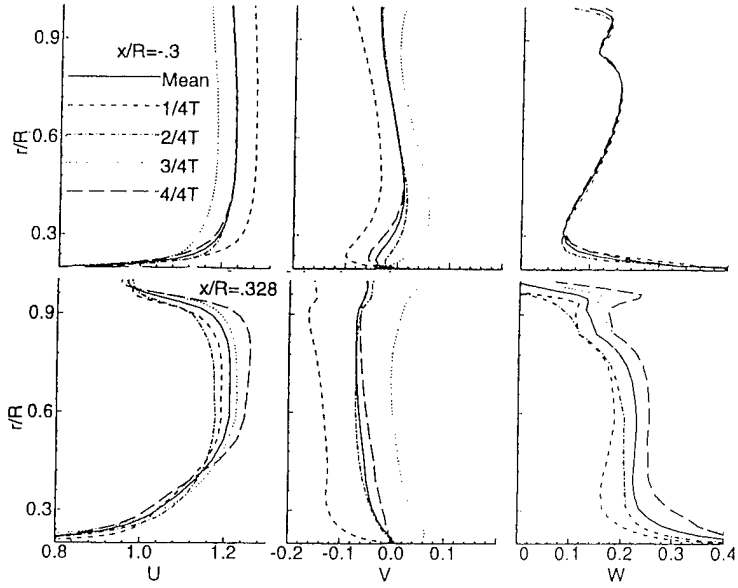


Figure 8. Circumferential-average velocity profiles: P4119.

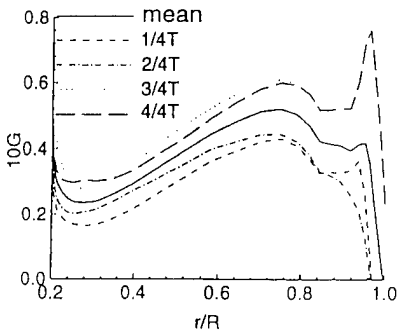
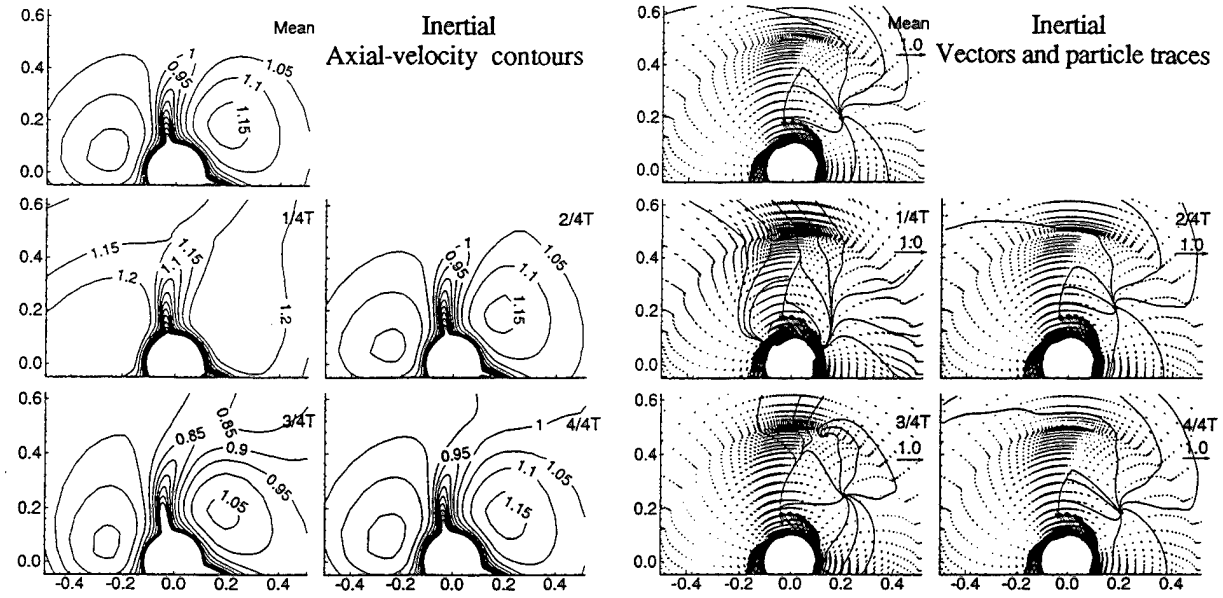
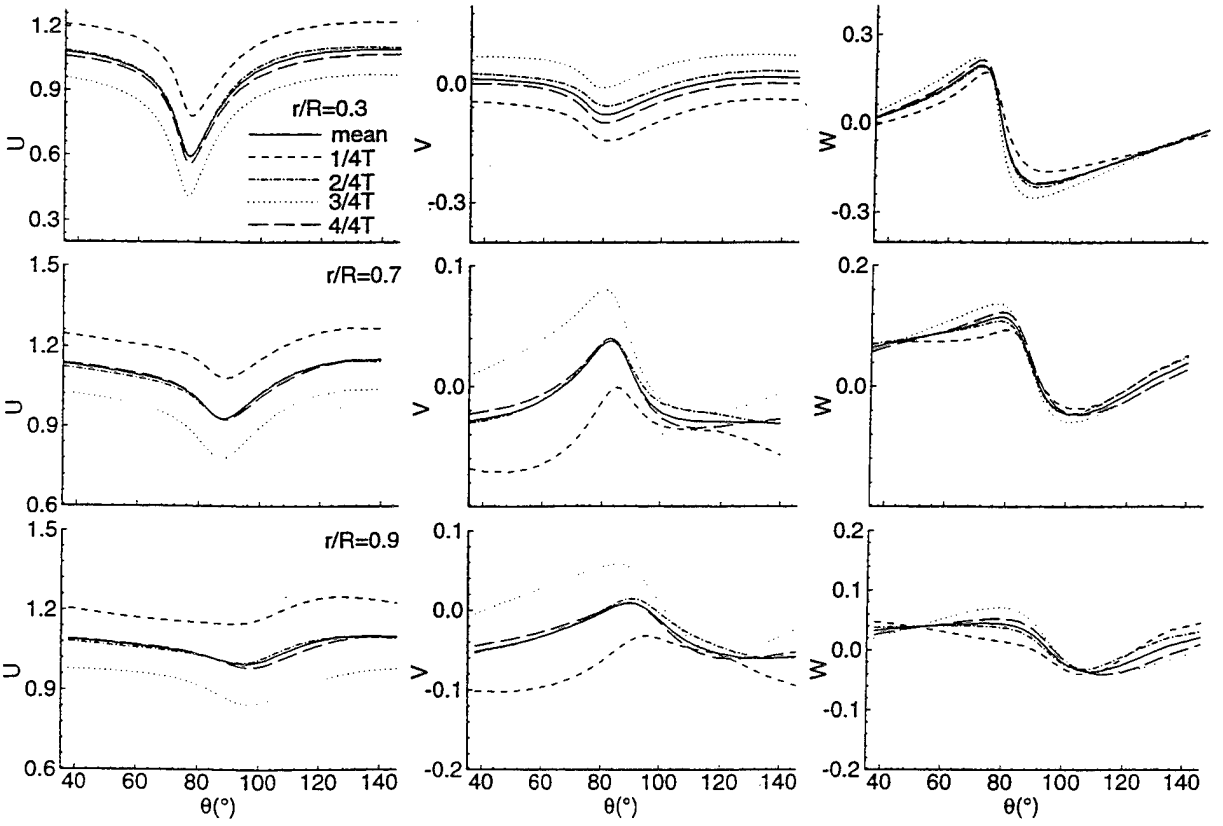


Figure 9. Circulation profiles: P4119, x/R=0.328.

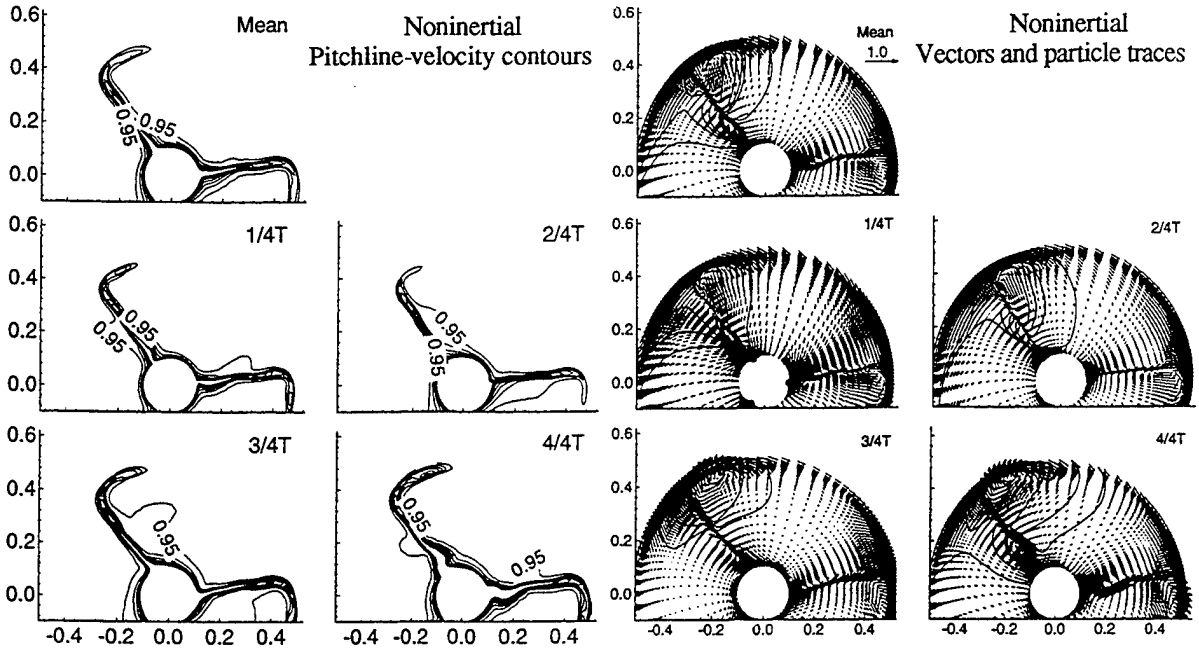


(a) contours and vectors

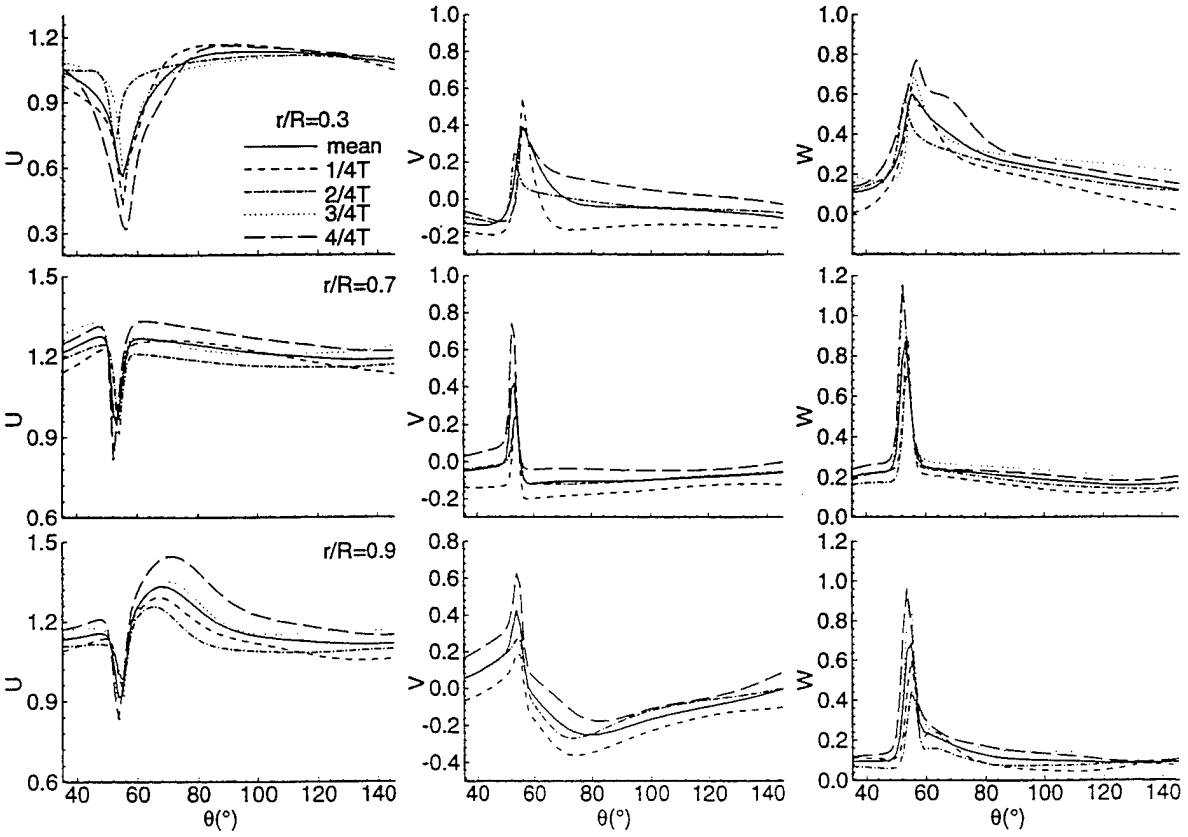


(b) velocity profiles

Figure 10. Phase-averaged flow: P4119, x/R=-0.3.

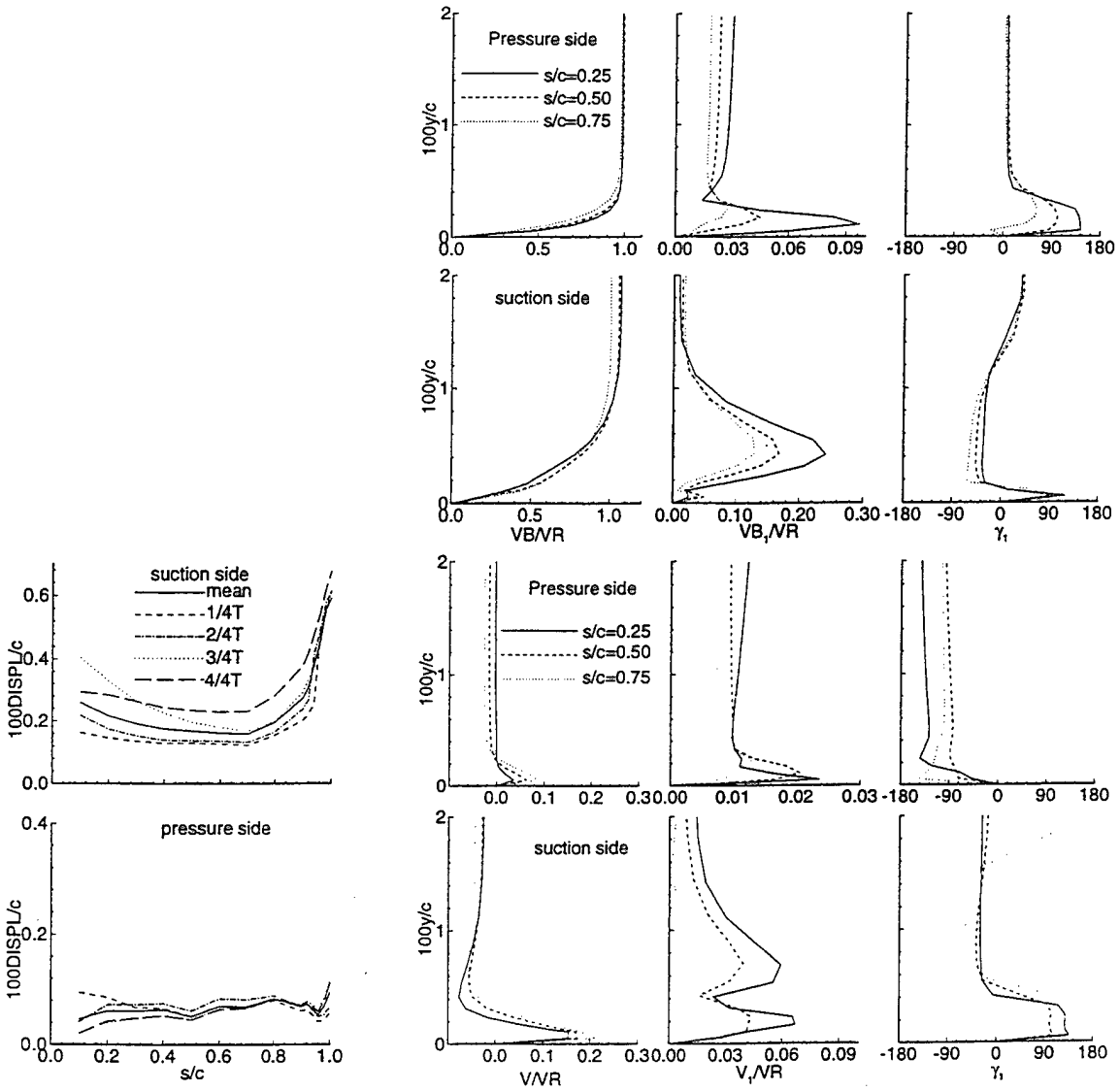


(a) contours and vectors



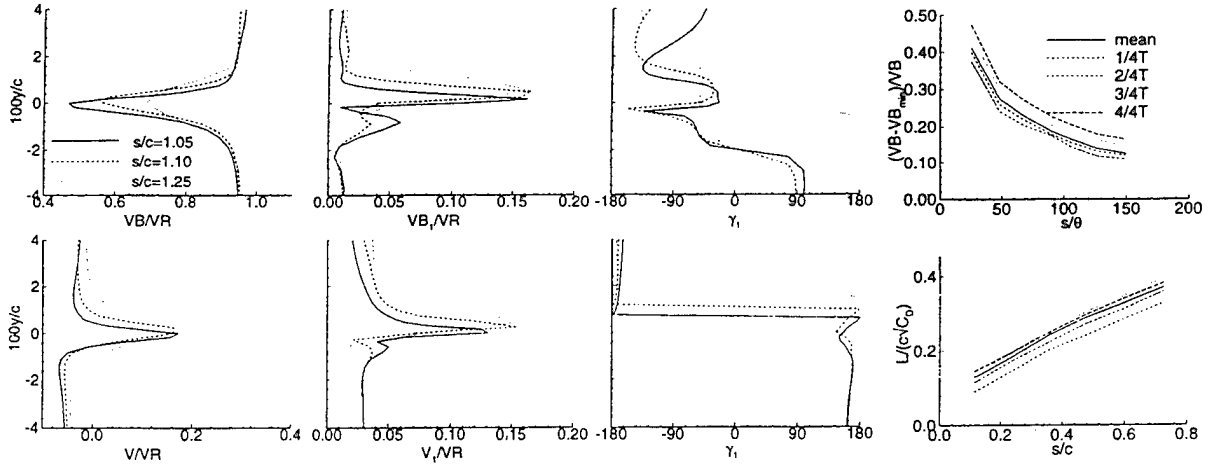
(b) velocity profiles

Figure 11. Phase-averaged flow: P4119, x/R = 0.328.



(a) displacement thickness (b) pitchline- and radial-velocity profiles

Figure 12. Boundary-layer flow: P4119, r/R=0.7.



(a) pitchline- and radial-velocity profiles (b) deficit and half-width parameters

Figure 13. Wake flow: P4119, r/R=0.7.

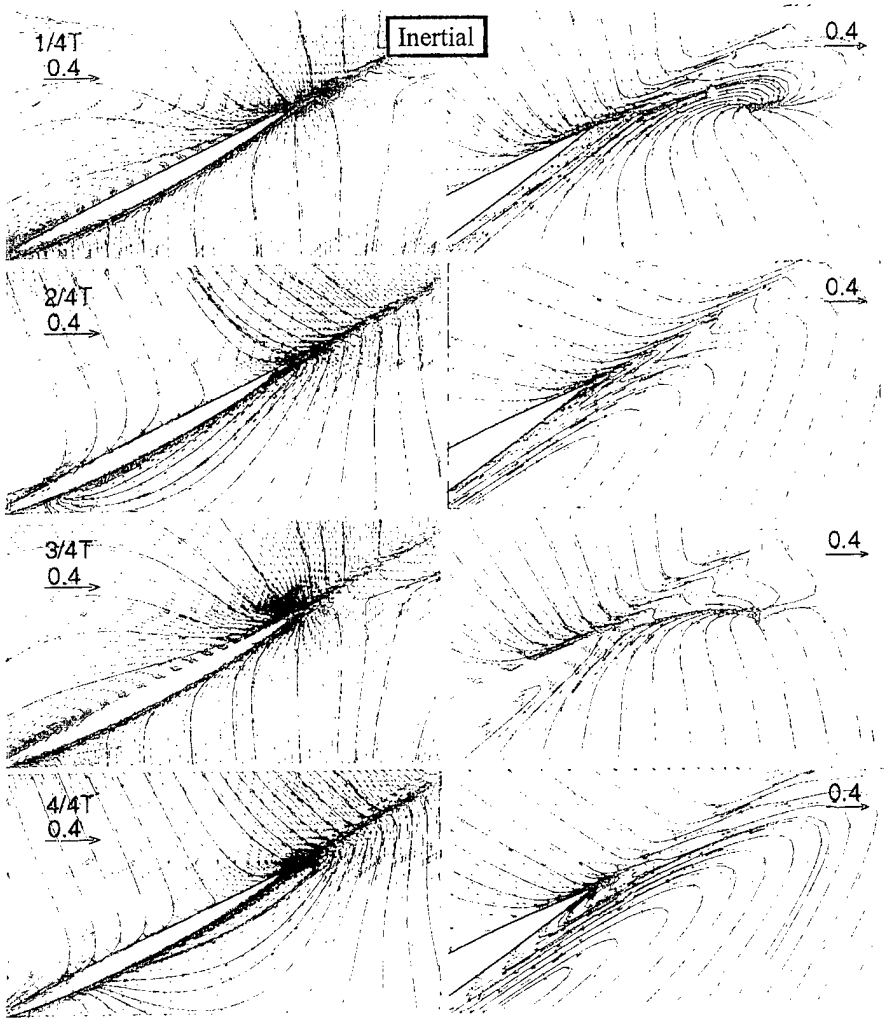
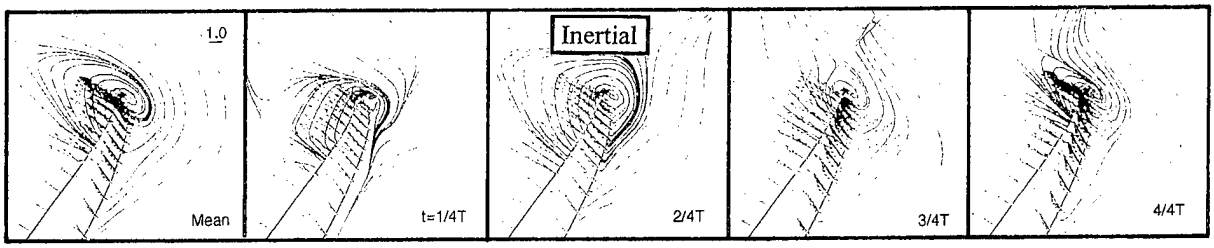
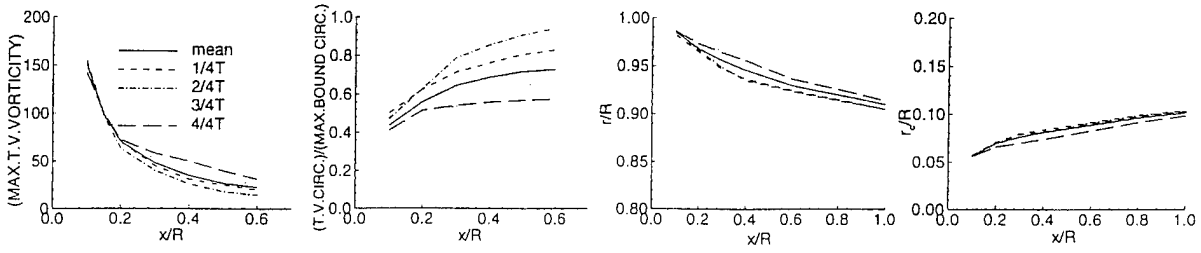


Figure 14. Perturbation vectors and particle traces: P4119, r/R=0.7.



(a) vectors and particle traces: x/R=0



(b) parameters

Figure 15. Tip-vortex flow: P4119.

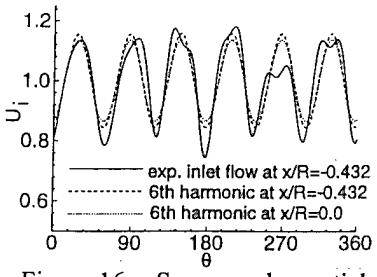


Figure 16. Screen wake spatial inflow at x/R=0.7.

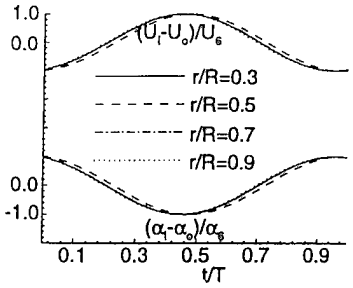


Figure 17. Spatial inflow 6th-harmonic velocity and angle-of-attack amplitude.

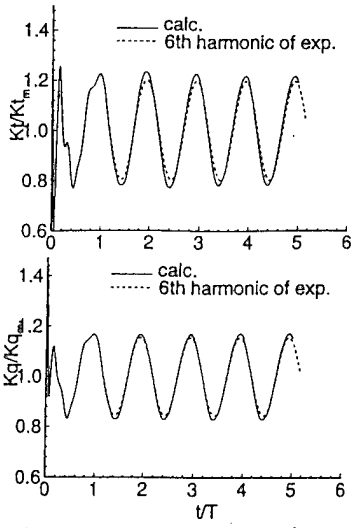
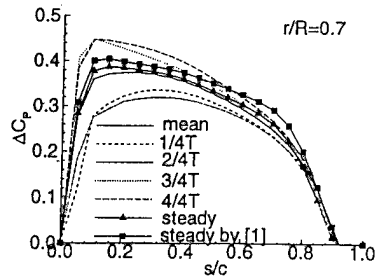
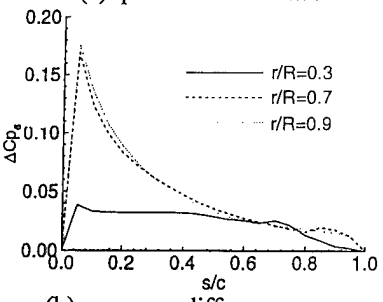


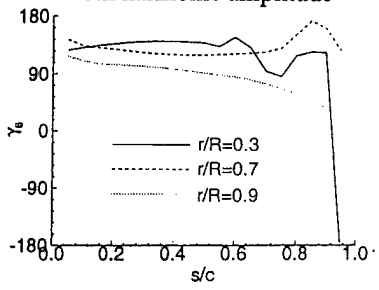
Figure 18. Performance time histories: P4132.



(a) pressure difference

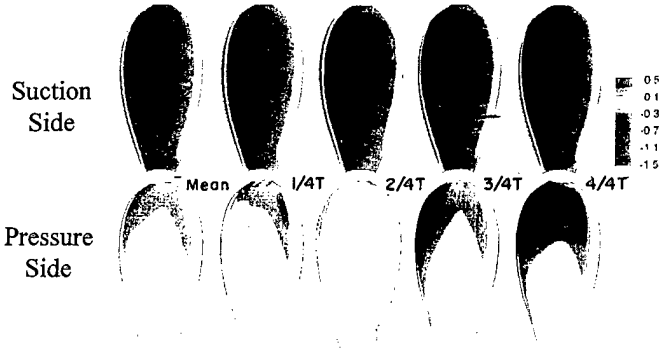


(b) pressure difference 6th-harmonic amplitude



(c) pressure difference 6th-harmonic phase

Figure 19. Surface-pressure distributions: P4132.



(d) pressure contours

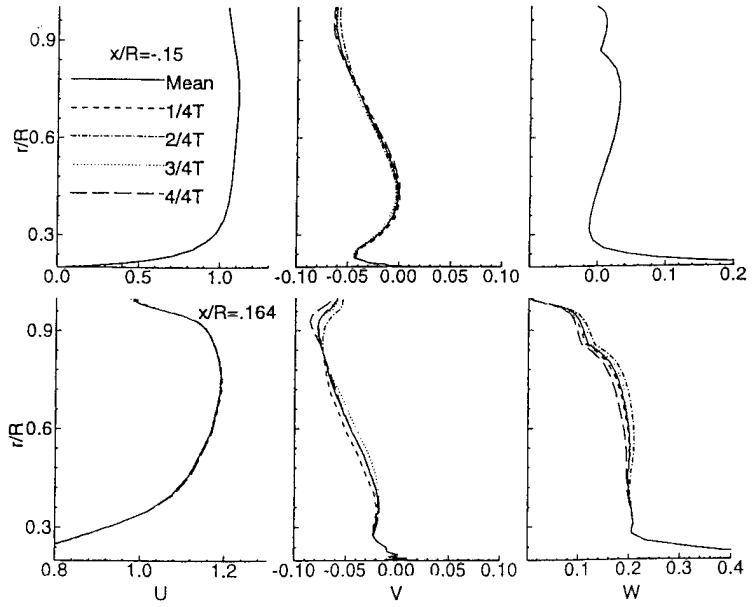


Figure 20. Circumferential-average velocity profiles: P4132.

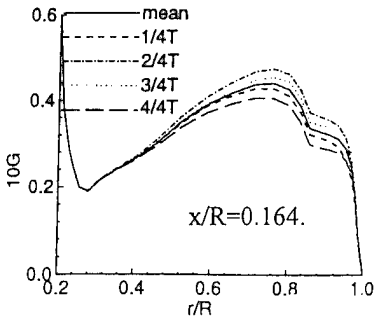
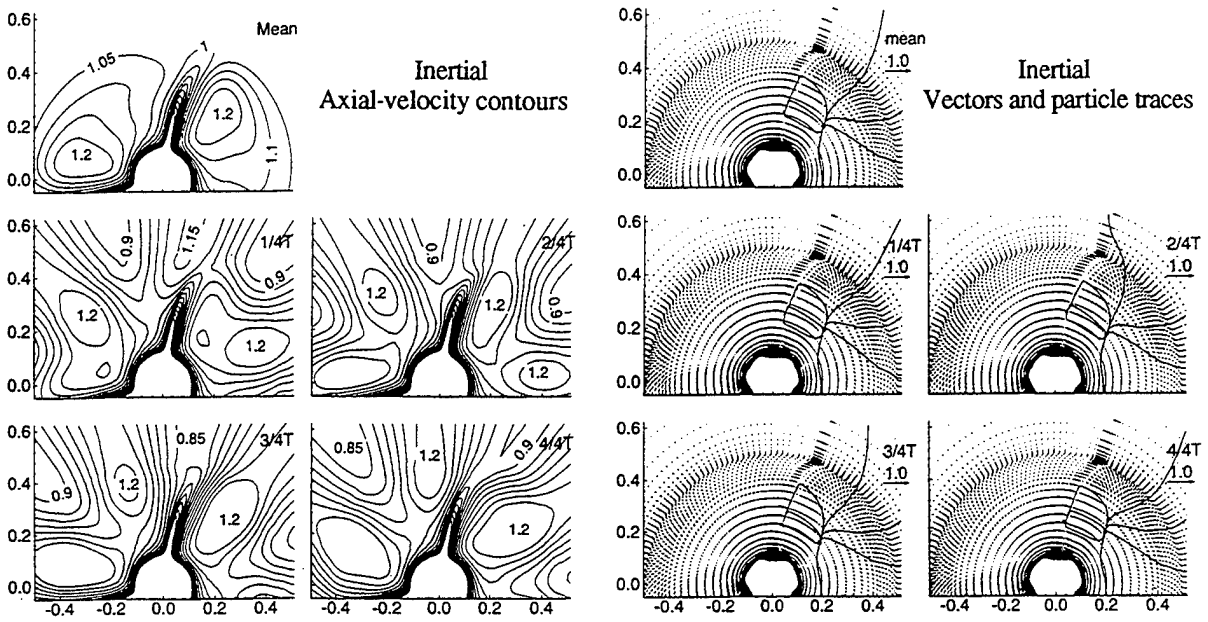
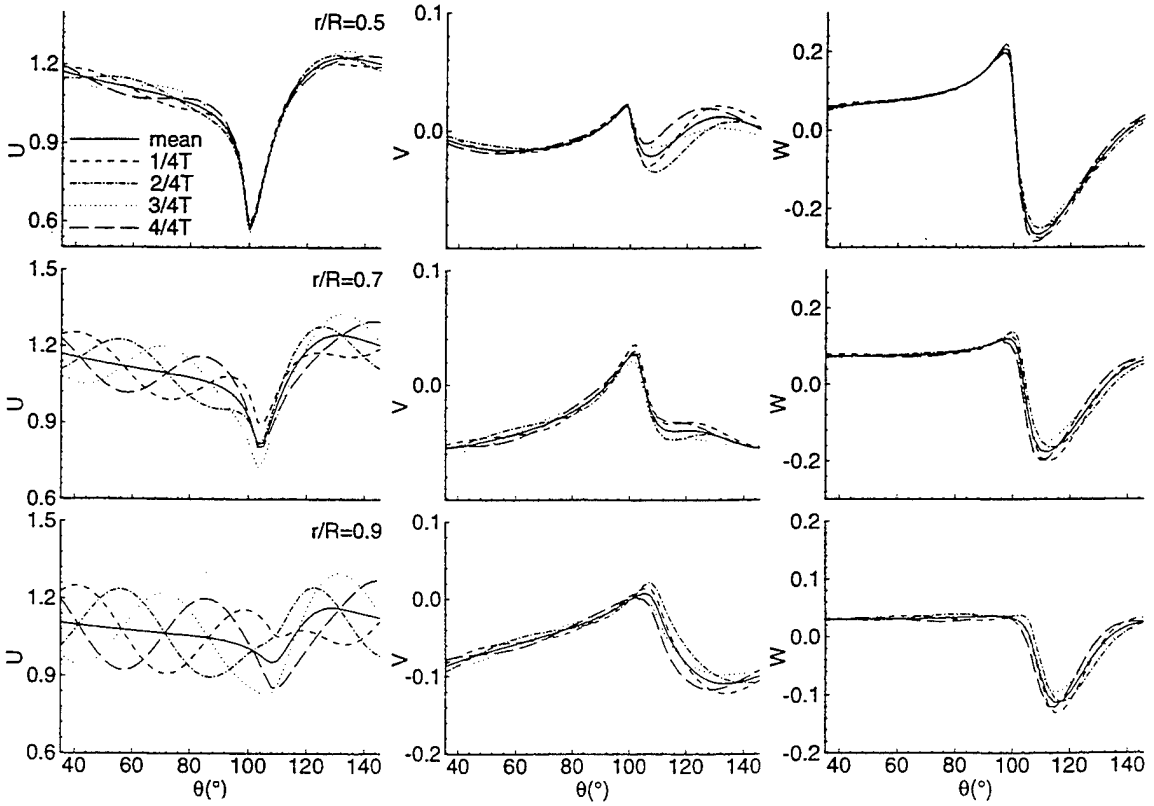


Figure 21. Circulation profiles: P4132.

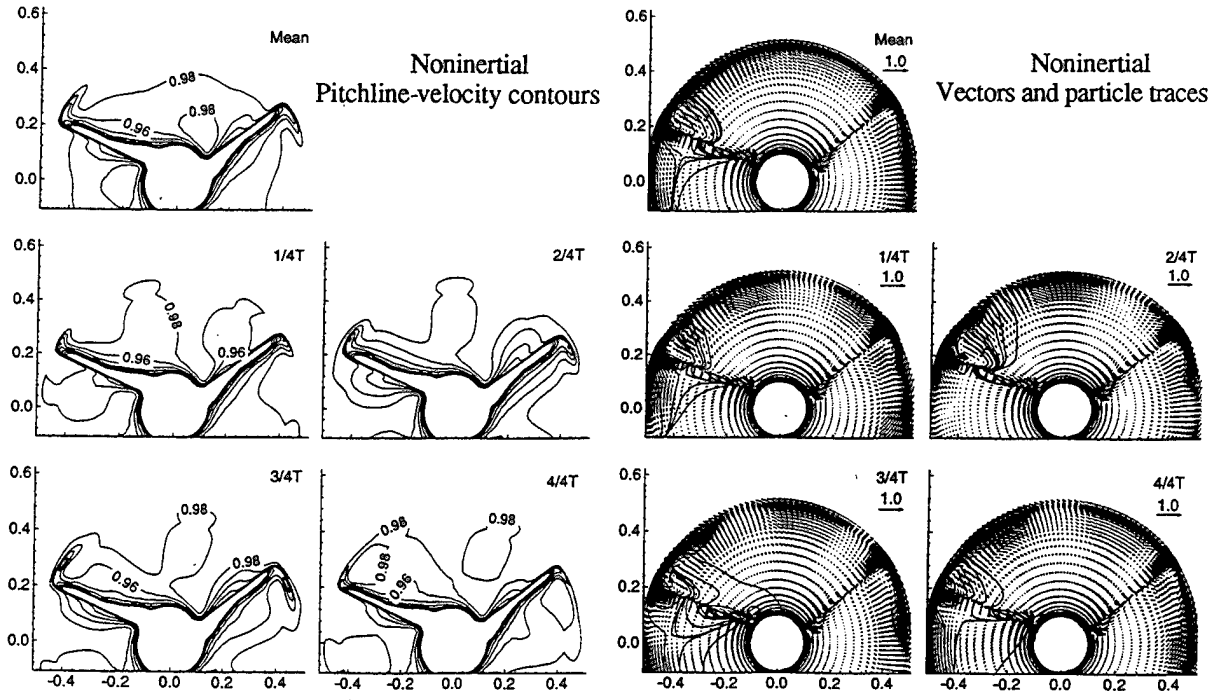


(a) contours and vectors

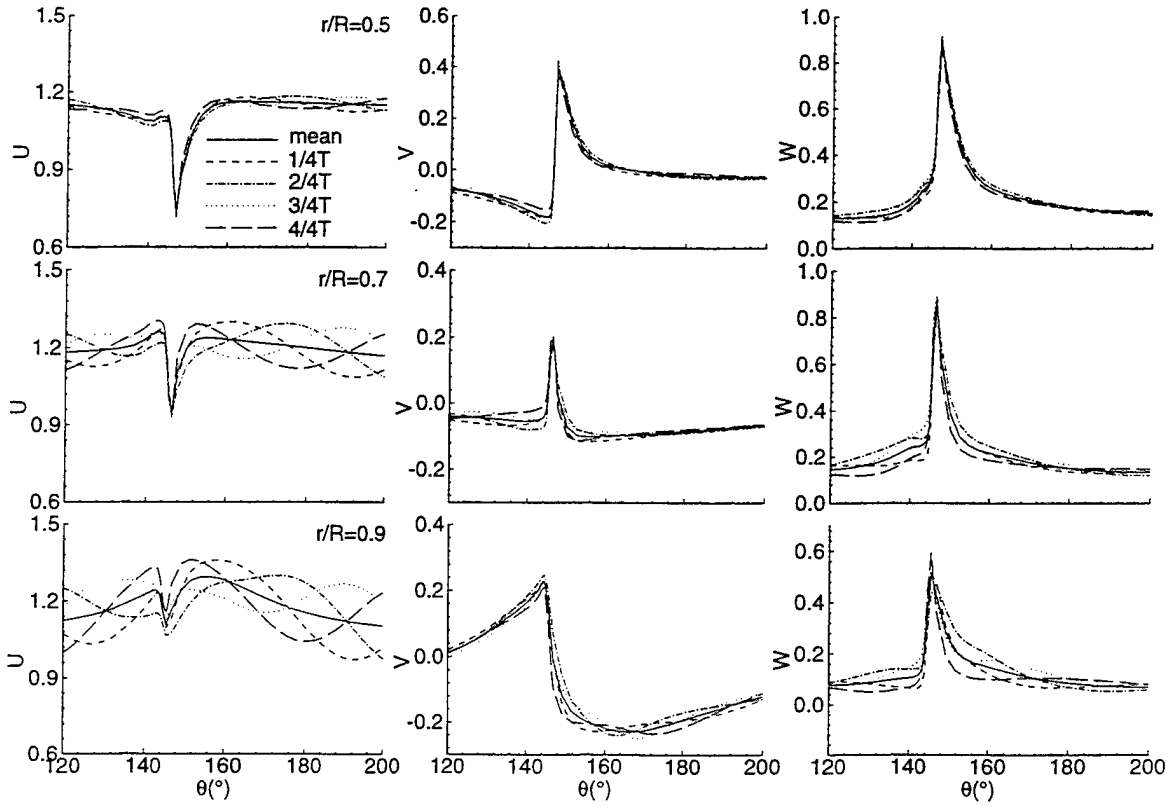


(b) velocity profiles

Figure 22. Phase-averaged flow: P4132, x/R=-0.15.

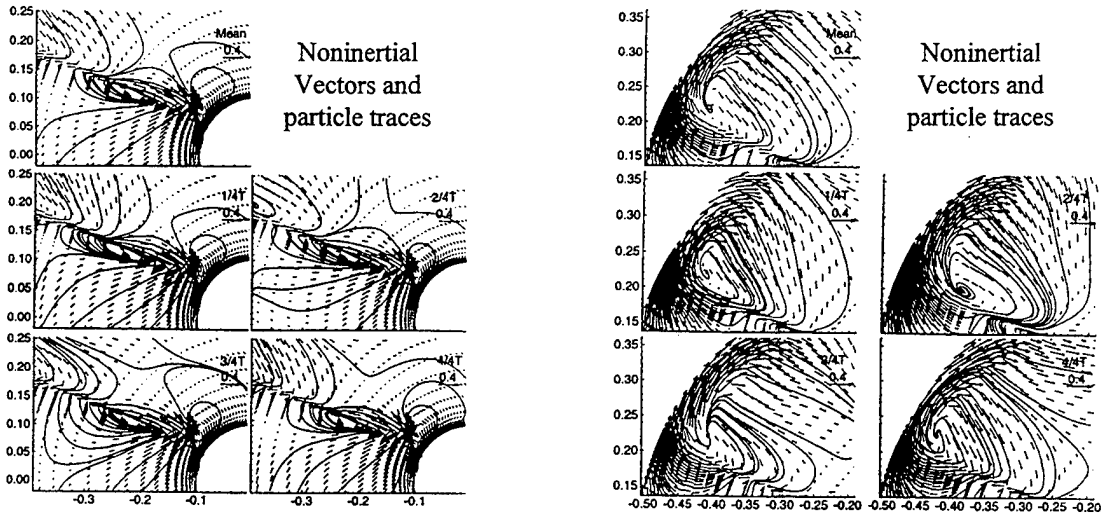


(a) contours and vectors



(b) velocity profiles

Figure 23. Phase-averaged flow: P4132, x/R=0.164.



(c) enlarged view

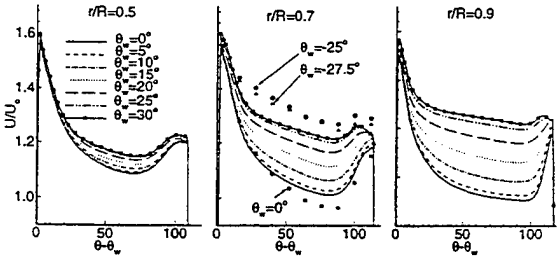
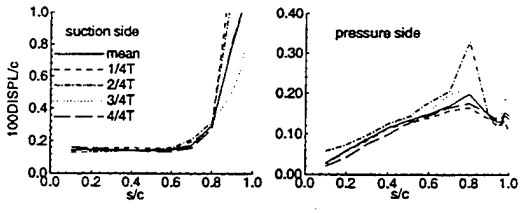
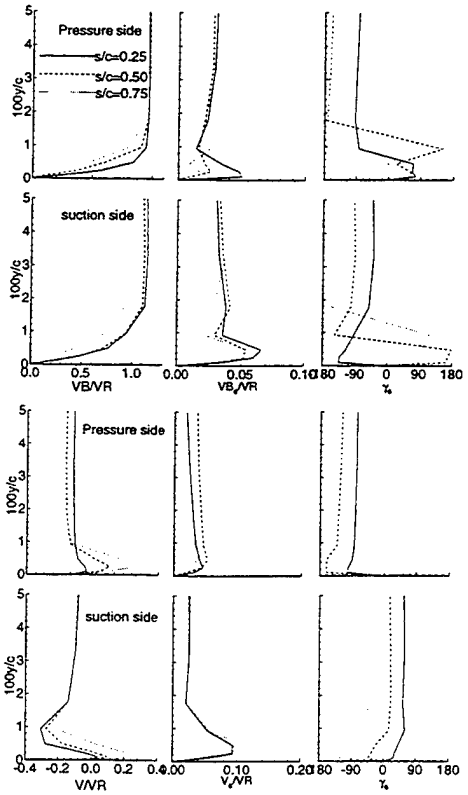


Figure 24. Phase-averaged flow: P4132, x/R=0, velocity profiles.

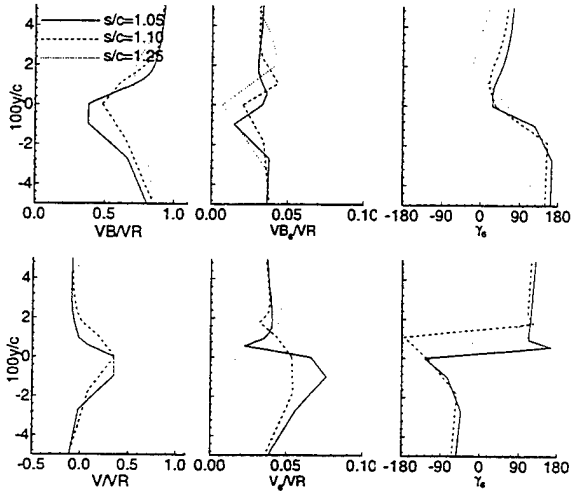


(a) displacement thickness

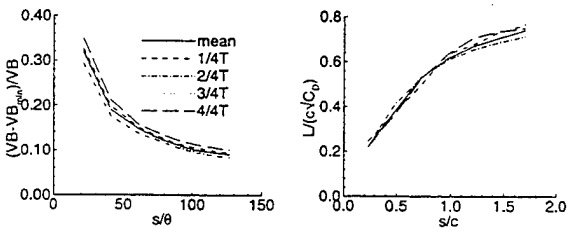


(b) pitchline- and radial-velocity profiles

Figure 25. Boundary-layer flow: P4132, r/R=0.7.

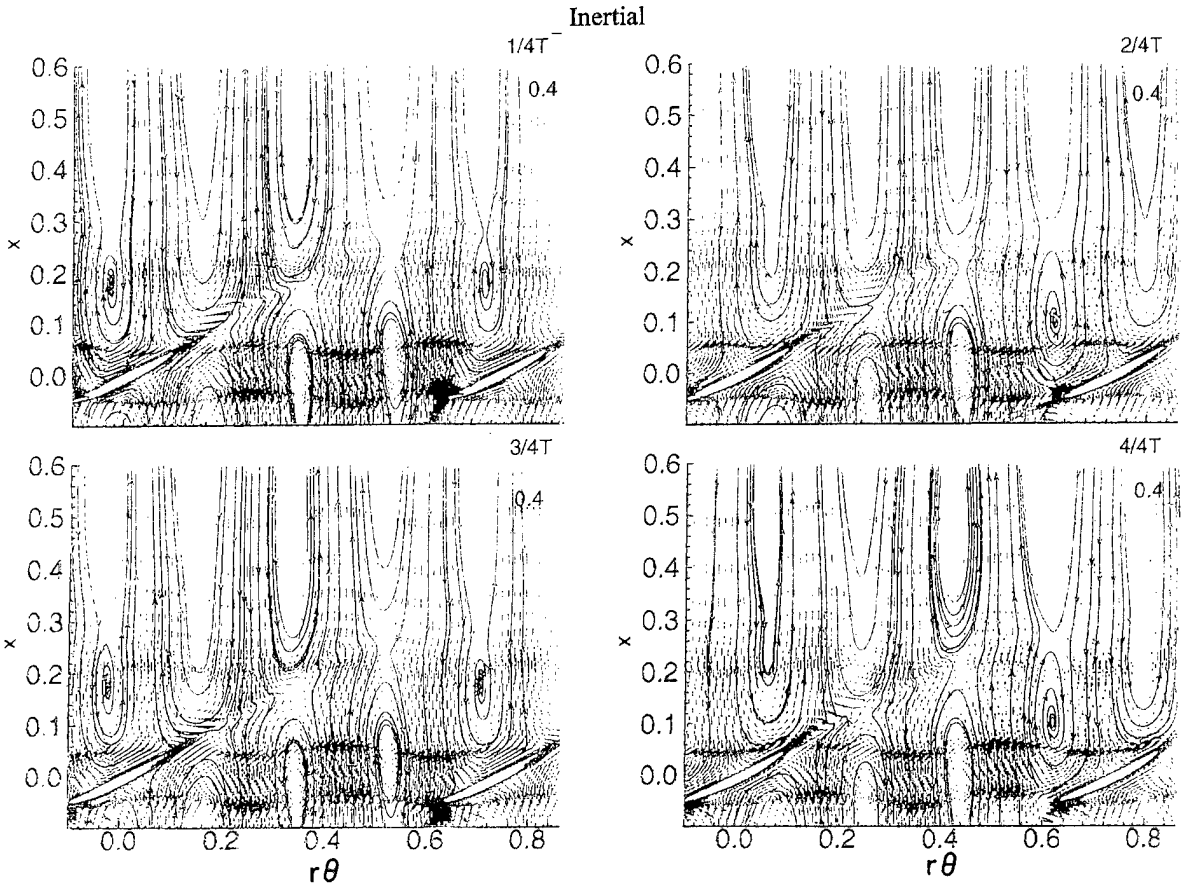


(a) pitchline- and radial-velocity profiles

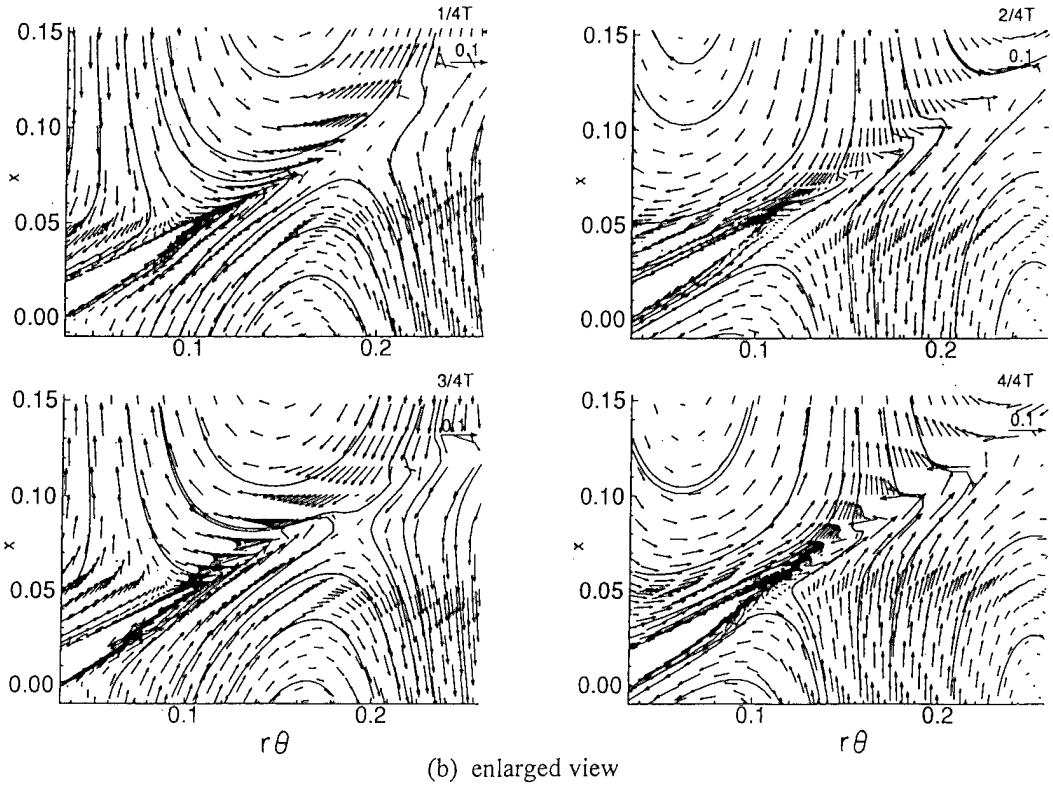


(b) deficit and half-width parameters

Figure 26. Wake flow: P4132, r/R=0.7.

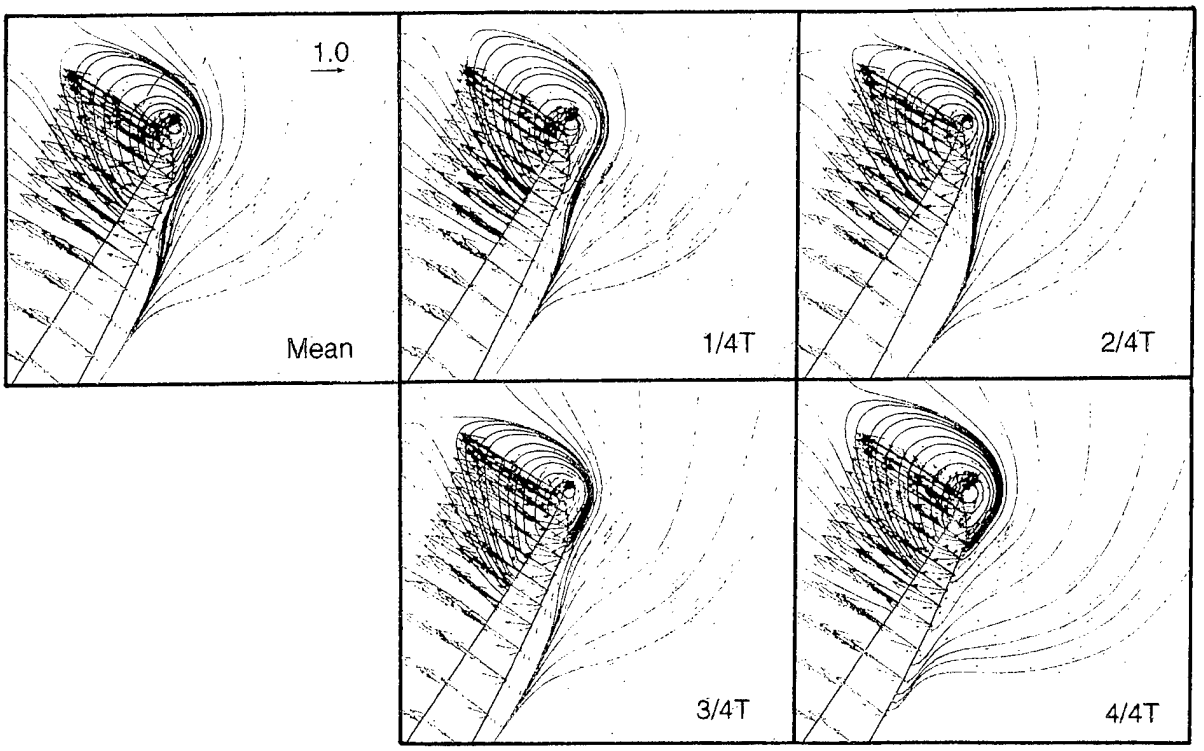


(a) blade-to-blade view

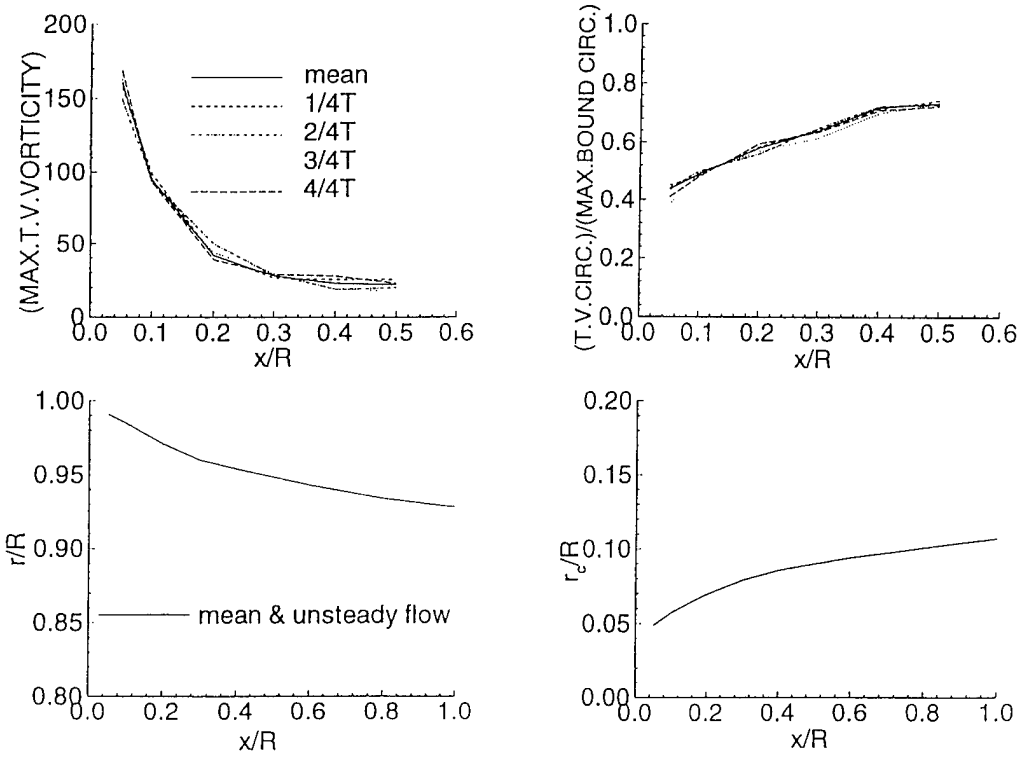


(b) enlarged view

Figure 27. Perturbation vectors and particle traces: P4132, r/R=0.7.



(a) vectors and particle traces: x/R=0



(b) parameters

Figure 28. Tip-vortex flow: P4132.

DISCUSSION

Y. Lee
David Taylor Model Basin, USA

I have a comment about propeller unsteady flow simulation for ship applications. In this paper, to vary the propeller flow temporally, or spatially is fine to study. This study, as similar to ffx experiment, does not include any vortex/blade interaction as happened in many ship applications.

J. Matusiak
Helsinki University of Technology, Finland

Do you take interaction of the blades into account? I understand that you model a single blade only (refer to figure 4).

Do you consider including cavitation in your method? If so what kind of cavitation do you expect to be able to evaluate?

AUTHORS' REPLY

We thank the discussants for their time and consideration of our work. In response to Dr. Lee, we agree that the temporally and spatially oscillating axial inflows are idealizations of the practical application of propeller-hull interaction, as was the ffx experiment; however, we believe that in both cases the results are important and provide insight with regard to practical applications. Currently, we are extending our work for practical applications. In response to Prof. Matusiak, the results include the effects of blade interaction, although the assumption is made that the flow is periodic for blade-to-blade intervals. We hope some day to be able to include cavitation in our method.

Lastly, we take this opportunity to clarify an issue raised in the paper, i.e., the differences between the steady solution and that of [1], as shown in table 1. Upon further examination it was found that the results for the steady solution of [1] were not fully converged. Table 2 provides the fully converged results and indicates agreement between the two steady solutions, as one would hope for. The explanation for the differences between the two steady solutions and the mean values are as yet unknown. Note that the grid quality for these results corresponds to that for the coarse grid of the grid dependency tests done for P4119 (see discussion for [1]).

Table 2. Performance: P4132 (steady [1] results corrected)

No.	case	grid space	Fa.	K_T	%wt	$10K_Q$	%wt
1	Piso	100x45x61	.20	.133	14.2	.243	11.0
2	Mac			.133	14.2	.234	14.3
3	Mean			.127	17.0	.225	17.6

Fa.: leading-edge clustering factor.
%wt: % error water-tunnel test.

Twentieth Symposium on

NAVAL HYDRODYNAMICS

Appendix—List of Participants

AUSTRALIA

Doctors, Lawrence J.
University of New South Wales

AUSTRIA

Strasser, Gerhard
Vienna Model Basin

BELGIUM

Marchal, J.L.J.
University of Liege

CANADA

Hsiung, Chi-Chao
Technical University of Nova Scotia

Huang, Zhenjia J.
Technical University of Nova Scotia

CHINA

Cui, Shen Hong
China Ship Scientific Research Center

Dong, Shi-Tang
China Ship Scientific Research Center

Wang, Yanying
Dalian University of Technology

Zhou, Lian-Di
China Ship Scientific Research Center

Zou, Zaojian
Wuhan University of Water Transportation

DENMARK

Baatrup, Jan
Technical University of Denmark

Jensen, Peter
Danish Maritime Institute

FINLAND

Matusiak, Jerzy
Helsinki Technical University

FRANCE

Collin, Jerome
MoD-DGA/DRET

Dern, Jean-Claude
Bassin d'Essais des Carenes

Fruman, Daniel H.
ENSTA/GPI

GERMANY

Chen, Xue-Nong
University of Stuttgart

Sharma, Som D.
Mercator University

Zou, Zaojian
Universitat Hamburg

ISRAEL

Miloh, Touvia
Tel-Aviv University

Zilman, Gregory
Tel-Aviv University

ITALY

Bailo, G. Maria
Italian Navy Ship Design Committee

Bulgarelli, Ulderico P.
Istituto Nazionale per Studi ed Esperienze di Architettura Navale

Campana, Emilio F.
Istituto Nazionale per Studi ed Esperienze di Architettura Navale

Lalli, Francesco
Istituto Nazionale per Studi ed Esperienze di Architettura Navale

JAPAN

Ikehata, Mitsuhisa
Yokohama National University

Maruo, Hajime
Yokohama National University

Mori, Kazu-Hiro
Hiroshima University

Nakatake, Kuniharu
Kyushu University

Song, Wusheng
Yokohama National University

Suzuki, Toshio
Osaka University

Toba, Yoshiaki
Tohoku University

Yamasaki, Hisashi
Yokohama Natinal University

Zhu, Ming
University of Tokyo

KOREA

Bai, Kwang-June
Seoul National University

Choi, Hang S.
Seoul National University

Hong, Sa-Young
Korea Research Institute of Ships & Ocean Engineering

Hwang, Jong Heul
Seoul National University

Kim, Keun Jae
Daewoo Shipbuilding and Heavy Machinery, Ltd.

Oh, Ilgeun
Samsung Heavy Industries Co., Ltd.

THE NETHERLANDS

De Kat, Jan
Maritime Research Institute

Huijsmans, Rene
Maritime Research Institute

Kuiper, G.
Maritime Research Institute

Oosterveld, Marinus
Maritime Research Institute

Prins, Henk
Delft University of Technology

van Daalen, Edwin
Twente University of Technology

van Oortmerssen, Gerard
Centrum Voor Wiskunde en Informatica

NORWAY

Faltinsen, Odd
Norwegian Institute of Technology

Loland, Geir
Marintek A/S

Ulstein, Tore
Norwegian Institute of Technology

PORTUGAL

Eça, Luis
Instituto Superior Técnico

SPAIN

Alaez, Jose A.
Canal de Experiencias Hidrodinamicas

SWEDEN

Allenstrom, Bjorn
SSPA Maritime Consulting AB

Broberg, Leif
Flowtech International AB

Carlson, Jan-Eric
Kamewa AB

Larsson, Lars
Flowtech International AB

UNITED KINGDOM

Ellis, Martin
British Defence Staff

Graham, J. Michael
Imperial College of Science, Technology & Medicine

Hearn, Grant
University of Newcastle-Upon-Tyne

Tan, Mingyi
University of Southampton

Thomas, Joseph
Vickers Shipbuilding & Engineering

Varyani, Kamlesh
University of Glasgow

Westlake, Paul
University of Southampton

Wu, G.X.
University College, London

UNITED STATES

Akhavan, Rayhaneh
University of Michigan

Arndt, Roger
University of Minnesota

Bannerjee, Sanjoy
University of California at Santa Barbara

Beck, Robert F.
University of Michigan

Brennen, Christopher E.
California Institute of Technology

Chahine, Georges L.
Dynaflow, Inc.

Chen, Bin
University of Iowa

Chung, Jin
Colorado School of Mines

Daouf, Nabil
Rockwell International

Day, Jr., William G.
David Taylor Model Basin

Devenport, William J.
Virginia Polytechnic Institute and State University

Dommermuth, Douglas G.
Science Applications International Corp.

Duncan, James H.
University of Maryland

Etter, Robert
David Taylor Model Basin

Fein, James A.
Office of Naval Research

Furey, Deborah
David Taylor Model Basin

Gupta, Rohit
University of California at Santa Barbara

Hart, Douglas
Massachusetts Institute of Technology

Hodges, Ben R.
Stanford University

Huang, Thomas T.
David Taylor Model Basin

Jagannathan, Sridhar
The Glosten Associates Inc.

Jessup, Stuart
David Taylor Model Basin

Kinnas, Spyros A.
Massachusetts Institute of Technology

Knowlton, Brian
University of California at Santa Barbara

Kolaini, Ali-Reza
University of Mississippi

Korpus, Richard
Science Applications International Corp.

Korsmeyer, F. Thomas
Massachusetts Institute of Technology

Kumar, Sanjeev
University of California at Santa Barbara

Lahey, Patrick
California Institute of Technology

Leal, L. Gary
University of California at Santa Barbara

Lee, Yu-Tai
David Taylor Model Basin

Lin, Cheng-Wen
David Taylor Model Basin

Lin, Woei-Min
Science Applications International Corp.

Maskew, Brian
Analytical Methods, Inc.

McCreight, Kathryn
David Taylor Model Basin

McDougald, Neil
University of California at Santa Barbara

Morgan, William B.
David Taylor Model Basin

Newman, J. Nicholas
Massachusetts Institute of Technology

Oshri, Ofer
University of California at Santa Barbara

Pan, Yu
University of California at Santa Barbara

Perez-Rojaas, Luis
Johns Hopkins University

Phillips, Owen M.
Johns Hopkins University

Powers, Edward
University of Texas at Austin

Purtell, L. Patrick
Office of Naval Research

Reed, Arthur M.
David Taylor Model Basin

Reisman, Garrett
California Institute of Technology

Rightley, Paul
University of California at San Diego

Rood, Edwin P.
Office of Naval Research

Salvesen, Nils
Science Applications International Corp.

Sclavounos, Paul
Massachusetts Institute of Technology

Sinha, Sumon
University of Mississippi

Speziale, Charles
Boston University

Stern, Frederick
University of Iowa

Street, Robert
Stanford University

Tulin, Marshall P.
University of California at Santa Barbara

Wang, Minglun
University of Michigan

Wang, Pei
University of California at Santa Barbara

Wehausen, John V.
University of California at Berkeley

White, James
U.S. Coast Guard Research & Development Center

Yao, Yitao
University of California at Santa Barbara

PLEASE CHECK THE APPROPRIATE BLOCK BELOW:

-AQ # AQ97-12-6355

☒ 1 copies are being forwarded. Indicate whether Statement A, B, C, D, E, F, or X applies.

☒ DISTRIBUTION STATEMENT A: Per Dixie Gordon
APPROVED FOR PUBLIC RELEASE: DISTRIBUTION IS UNLIMITED

☐ DISTRIBUTION STATEMENT B:
DISTRIBUTION AUTHORIZED TO U.S. GOVERNMENT AGENCIES ONLY; (Indicate Reason and Date). OTHER REQUESTS FOR THIS DOCUMENT SHALL BE REFERRED TO (Indicate Controlling DoD Office).

☐ DISTRIBUTION STATEMENT C:
DISTRIBUTION AUTHORIZED TO U.S. GOVERNMENT AGENCIES AND THEIR CONTRACTORS; (Indicate Reason and Date). OTHER REQUESTS FOR THIS DOCUMENT SHALL BE REFERRED TO (Indicate Controlling DoD Office).

☐ DISTRIBUTION STATEMENT D:
DISTRIBUTION AUTHORIZED TO DoD AND U.S. DoD CONTRACTORS ONLY; (Indicate Reason and Date). OTHER REQUESTS SHALL BE REFERRED TO (Indicate Controlling DoD Office).

☐ DISTRIBUTION STATEMENT E:
DISTRIBUTION AUTHORIZED TO DoD COMPONENTS ONLY; (Indicate Reason and Date). OTHER REQUESTS SHALL BE REFERRED TO (Indicate Controlling DoD Office).

☐ DISTRIBUTION STATEMENT F:
FURTHER DISSEMINATION ONLY AS DIRECTED BY (Indicate Controlling DoD Office and Date) or HIGHER DoD AUTHORITY.

☐ DISTRIBUTION STATEMENT X:
DISTRIBUTION AUTHORIZED TO U.S. GOVERNMENT AGENCIES AND PRIVATE INDIVIDUALS OR ENTERPRISES ELIGIBLE TO OBTAIN EXPORT-CONTROLLED TECHNICAL DATA IN ACCORDANCE WITH DoD DIRECTIVE 5230.25, WITHHOLDING OF UNCLASSIFIED TECHNICAL DATA FROM PUBLIC DISCLOSURE, 6 Nov 1984 (Indicate date of determination). CONTROLLING DoD OFFICE IS (Indicate Controlling DoD Office).

☐ This document was previously forwarded to DTIC on _____ (date) and the AD number is _____.

☐ In accordance with provisions of DoD instructions, the document requested is not supplied because:

☐ It will be published at a later date. (Enter approximate date, if known).

☐ Other. (Give Reason)

DoD Directive 5230.24, "Distribution Statements on Technical Documents," 18 Mar 87, contains seven distribution statements, as described briefly above. Technical Documents must be assigned distribution statements. 20th Symposium

Pat Mawby per
Dixie Gordon
Authorized Signature/Date

DIXIE GORDON
Print or Type Name

202-334-3523
Telephone Number

19970924 051